

In-One Kim
Editor

Radiology Illustrated

Pediatric Radiology

Radiology Illustrated

For further volumes:
<http://www.springer.com/series/11755>

In-One Kim
Editor

Radiology Illustrated: Pediatric Radiology

 Springer

Editor

In-One Kim, M.D.
Department of Radiology
Seoul National University Hospital
Seoul National University College of Medicine
Seoul
Republic of South Korea

ISBN 978-3-642-35572-1 ISBN 978-3-642-35573-8 (eBook)
DOI 10.1007/978-3-642-35573-8
Springer Heidelberg New York Dordrecht London

Library of Congress Control Number: 2014935879

© Springer-Verlag Berlin Heidelberg 2014

This work is subject to copyright. All rights are reserved by the Publisher, whether the whole or part of the material is concerned, specifically the rights of translation, reprinting, reuse of illustrations, recitation, broadcasting, reproduction on microfilms or in any other physical way, and transmission or information storage and retrieval, electronic adaptation, computer software, or by similar or dissimilar methodology now known or hereafter developed. Exempted from this legal reservation are brief excerpts in connection with reviews or scholarly analysis or material supplied specifically for the purpose of being entered and executed on a computer system, for exclusive use by the purchaser of the work. Duplication of this publication or parts thereof is permitted only under the provisions of the Copyright Law of the Publisher's location, in its current version, and permission for use must always be obtained from Springer. Permissions for use may be obtained through RightsLink at the Copyright Clearance Center. Violations are liable to prosecution under the respective Copyright Law.

The use of general descriptive names, registered names, trademarks, service marks, etc. in this publication does not imply, even in the absence of a specific statement, that such names are exempt from the relevant protective laws and regulations and therefore free for general use.

While the advice and information in this book are believed to be true and accurate at the date of publication, neither the authors nor the editors nor the publisher can accept any legal responsibility for any errors or omissions that may be made. The publisher makes no warranty, express or implied, with respect to the material contained herein.

Printed on acid-free paper

Springer is part of Springer Science+Business Media (www.springer.com)

Preface

Interpreting the radiological images of pediatric patients reminds us of a saying ‘A child is not merely a small adult’. In order to deal with pediatric diseases, the approaches of adult radiology in principle and daily practice need to be modified. The scope of pediatric radiology has now become wide and complex comparable with the adult medicine. We have tried to cover most of the topics and varieties of diseases in the pediatric radiology field, which was not an easy task.

Radiology Illustrated: Pediatric Radiology is designed to provide a practical overview of pediatric imaging diagnosis covering both common and uncommon disease states with rather typical illustrations. This book consists of concise keynote texts and case-based atlas of images with comprehensive reviews organized by the anatomic organs from the brain to the musculoskeletal system.

This book is directed to provide the most suitable reference in daily practice and study for radiology residents, fellows or students and informative help or teaching aides for general radiologists dealing with the care of children. It also serves as a practical guide of radiological approaches with a variety of imaging in pediatric disorders for pediatricians or pediatric physicians in various medical and surgical subspecialties.

I am very fortunate to have the opportunity of being part of this exciting work by virtue of the publisher, Springer, with capable colleagues in pediatric radiology, mostly the members of the Korean Society of Pediatric Radiology. I deeply appreciate the support of my colleagues who kindly gave their time and effort in writing the chapters. I dedicate the book to my teachers, parents and relatives, and most importantly to children with diseases. The production of this book was greatly inspired by the need to treat children who had to live through the pain of their sickness.

Seoul, Korea

In-One Kim, M.D.

Contents

Part I Neuroradiology: Brain/Spine

1	Congenital Anomalies of the Brain and Spinal Cord	3
	In-One Kim	
2	Metabolic Diseases of the Brain	45
	In-One Kim	
3	Infection and Inflammatory Diseases of the Central Nervous System	75
	In-One Kim	
4	Neoplasms of the Brain and Spine	105
	Ji Hye Kim	
5	Brain and Spine Injury and Cerebral Vascular Disorders	155
	Ji Hye Kim	
6	Neurosonography	209
	Young Seok Lee	

Part II Neuroradiology: Head and Neck

7	Congenital Malformations of the Head and Neck	257
	Hee Jung Lee	
8	Infectious and Traumatic Diseases	293
	Hye-Kyung Yoon	
9	Neoplasms of the Head and Neck	323
	Hee Jung Lee	

Part III Chest

10	CT Findings of Congenital Lung Malformations	363
	Hyun Woo Goo	
11	Neonatal Chest Imaging	381
	Young Hun Choi and In-One Kim	
12	Pediatric Airway Disorders	411
	Evan J. Zucker, Kushaljit S. Sodhi, Ricardo Restrepo, and Edward Y. Lee	
13	Infections	433
	Bernard F. Laya	
14	Tumors of the Pediatric Chest	473
	Gye Yeon Lim	

15 Pediatric Diffuse Lung Disease	507
Evan J. Zucker and Edward Y. Lee	
Part IV Cardiovascular System	
16 Pediatric Cardiac Imaging I: CT and MR Techniques	525
Whal Lee and Eun-Ah Park	
17 CT and MRI Findings of Cardiac Defects in Congenital Heart Disease	553
Hyun Woo Goo	
18 Congenital Thoracic Vascular Anomalies and Associated Airway Diseases . . .	573
Yang Min Kim	
Part V Abdomen	
19 Congenital and Neonatal Gastrointestinal Diseases	603
Sun Wha Lee	
20 Non-neonatal Gastrointestinal Diseases	629
So-Young Yoo	
21 Inflammation, Infection, and Neoplasms in the Abdomen	665
Jung-Eun Cheon	
22 Liver, Biliary Tract, Pancreas, and Spleen	683
Mi-Jung Lee and Myung-Joon Kim	
Part VI Genitourinary System	
23 Congenital Anomalies of the Upper Urinary Tract	723
Mi-Jung Lee	
24 Cystic Renal Disease and Neoplasms	759
Tae Il Han	
25 Urinary Tract Infection	793
Myung-Joon Kim	
26 Bladder and Urethra Disease	803
Su-Mi Shin	
27 Pediatric Uterus, Ovary, and Testis Diseases	835
Yong-Woo Kim	
Part VII Musculoskeletal System	
28 Genetic Skeletal Disorders	887
Jung-Eun Cheon	
29 Soft Tissue Diseases	913
Choon-Sik Yoon and Sungjun Kim	
30 Pediatric Skeletal Trauma	951
Tae Yeon Jeon and So-Young Yoo	
31 Infection and Inflammation of the Musculoskeletal System	969
Hee Kyung Kim	

32	Pediatric Bone Tumors	1007
	Hye-Kyung Yoon	
33	Pediatric Hip Disorders	1039
	Jung-Eun Cheon	
34	Miscellaneous Musculoskeletal Disease	1063
	Hong Eo	
	Index	1085

Part I

Neuroradiology: Brain/Spine

Congenital Anomalies of the Brain and Spinal Cord

1

In-One Kim

Contents

1.1	Introduction	4
1.2	Normal Development	4
1.2.1	Neurulation (Dorsal Induction)	4
1.2.2	Vesicle and Flexure Formation (Ventral Induction)	4
1.2.3	Neuronal Formation	4
1.2.4	Neuronal Migration	4
1.2.5	Myelination	4
1.3	Spectrum of Congenital Anomalies of the Brain	5
1.3.1	Cephalocele	5
1.3.2	Chiari II Malformation	5
1.3.3	Holoprosencephaly	5
1.3.4	Septo-optic Dysplasia	5
1.3.5	Lissencephaly	5
1.3.6	Polymicrogyria	6
1.3.7	Schizencephaly	6
1.3.8	Heterotopia	6
1.3.9	Dysgenesis of the Corpus Callosum	6
1.3.10	Dandy-Walker Complex	6
1.3.11	Joubert Syndrome	7
1.4	Phakomatosis	7
1.4.1	Neurofibromatosis Type 1 (Von Recklinghausen's Disease)	7
1.4.2	Tuberous Sclerosis (Bourneville's Disease)	7
1.4.3	Sturge-Weber Syndrome (Encephalotrigeminal Angiomatosis)	7
1.4.4	Neurofibromatosis Type 2	8
1.4.5	Von Hippel-Lindau Disease	8
1.4.6	Incontinentia Pigmenti	8
1.4.7	Neurocutaneous Melanosis	8
1.4.8	Ataxia-Telangiectasia	8
1.5	Congenital Anomaly of the Spinal Cord	9
1.5.1	Normal Development of Spinal Cord	9
1.5.2	Spectrum of Spinal Cord Anomalies	9
1.6	Illustrations: Congenital Anomaly of the Brain and Spinal Cord	11
1.6.1	Neurulation (Dorsal Induction)	11
1.6.2	Vesicle and Flexure Formation (Ventral Induction)	12
	References	43

I.-O. Kim, M.D.
Department of Radiology, Seoul National University Hospital,
Seoul National University College of Medicine,
101 Daehak-ro, Chongno-gu, Seoul 110-744, Korea
e-mail: kimio@snu.ac.kr

1.1 Introduction

Congenital anomalies of the brain and spinal cord cause considerable morbidity and mortality of infants and children. To recognize and distinguish anomalies from other types and causes of central nervous system disorders, the role of imaging becomes essential. Imaging is the key for the diagnosis of congenital anomalies, and imaging can be a guide to providing optimum management and genetic counseling. Knowledge of embryonic development of the central nervous system is important for understanding the anomalies of the brain and spinal cord. The classification of the anomalies according to the developmental process seems to be very useful for understanding individual diseases.

1.2 Normal Development

1.2.1 Neurulation (Dorsal Induction)

Neurulation is a process that forms a neural tube, which is a basic structure that forms the brain and spinal cord (Fig. 1.1). It is the first step in the formation of the central nervous system and begins about the second week of gestation. On the dorsal aspect of the embryonic disc, the notochord induces embryonic ectoderm and this thickens to form a neural plate. The neuroectoderm invaginates along its central axis to form the neural groove with neural folds on either side. The edge of the neural folds bends medially to contact and close in order to form the neural tube. Each end of the neural tube is called an anterior and posterior neuropore, and the closure of the neural tube begins at approximately the proximal two-thirds region and proceeds towards both ends at about the fourth week of gestation. The proximal two thirds of the neural tube will form the brain; the distal one third will become the spinal cord. The next phase of dorsal induction involves canalization and retrogressive differentiation, which leads to the formation of the caudal part of the neural tube. Brain anomalies resulting from neurulation defects include encephalocele and Chiari malformations. Dorsal induction is critical in the development of spinal cord development, and the early phase defect causes spinal dysraphisms such as myelomeningocele and lipomyelomeningocele; the later phase defect causes sacral agenesis, caudal regression, and tethered cord.

1.2.2 Vesicle and Flexure Formation (Ventral Induction)

The neural tube forms the brain vesicles and flexures between the 5th and 10th week of gestation (Fig. 1.2). Three vesicles are formed by expansion and constriction of

the neural tube – the forebrain (prosencephalon), midbrain (mesencephalon), and hindbrain (rhombencephalon). By subsequent constriction and bending of the vesicles, the prosencephalon forms the telencephalon (future hemispheres, putamen, caudate) and diencephalon (thalamus, hypothalamus, globus pallidus); the rhombencephalon forms the metencephalon (pons, cerebellum) and myelencephalon (medulla). These processes are also called ventral induction. The defect in the ventral induction results in the spectrum of holoprosencephaly. The Dandy-Walker malformation is regarded as the representative cerebellar dysgenesis resulting from the disturbance of vesicle formation.

1.2.3 Neuronal Formation

Neuronal cells of the embryonic cortex are formed from the germinal matrix and migrate to the surface. The germinal matrix, which lines the lateral and the third ventricles, forms at about 7 weeks' gestation and involutes between 28 and 30 weeks. Formation and maturation of normal neuronal cells is a complex process that involves neuronal proliferation, differentiation, and histogenesis. The defect in neuronal formation results in brain anomalies such as micrencephaly, megalencephaly, and neurocutaneous syndrome (Adachi et al. 2011).

1.2.4 Neuronal Migration

From the eighth week of gestation, neuronal cells migrate peripherally from the germinal matrix to the mantle zone of the hemisphere. Neuronal cells will migrate along the radial glial fibers, which guide the neuronal cell to a designated place in the cortical mantle. The neurons migrate in an “inside-out” sequence, except for the outer layer: those that will form the deepest cortical layer migrate first, followed by layers 5, 4, 3, and, finally, layer 2. This migration continues until 26 weeks' gestation, when the cortex of six layers is formed. Anomalies caused by the neuronal migration defect include lissencephaly, schizencephaly, polymicrogyria, and heterotopias (Barkovich et al. 1992).

1.2.5 Myelination

Myelination is the process of axonal ensheathment with myelin, which is essential for the functional maturation of a nerve fiber. Myelination begins at 6 months' gestation and continues until adulthood. The extent of myelination becomes similar with adults at 2 years of age. Congenital disturbances of myelination are mostly caused by metabolic disorders, which result in dysmyelinating diseases (Barkovich 2012).

1.3 Spectrum of Congenital Anomalies of the Brain

1.3.1 Cephalocele

Cephalocele is a herniation of the intracranial contents through a skull defect (Fig. 1.3). Meningocele refers to the herniation of the leptomeninges and CSF; encephalocele contains brain tissue. Encephaloceles are usually categorized according to the location where the skull defect presents. Occipital or parietal cephaloceles are usually associated with neurulation defect. The prognosis depends on the location, size, and content of the lesion or associated brain anomalies. Occipital cephaloceles usually contain dysplastic and gliotic brain tissue. It may be associated with Chiari II malformation or cerebellar dysplasia. Parietal cephaloceles arise between the lambda and bregma and are commonly associated with midline anomalies such as callosal agenesis or holoprosencephaly (Naidich et al. 1992). Frontoethmoidal cephalocele is more common in oriental populations and frequently associated with midline anomalies. Frontoethmoidal cephaloceles typically show erosion of the crista galli and they are not associated with neural tube defects.

1.3.2 Chiari II Malformation

Chiari II malformation is typically associated with myelomeningocele, which is representative of the neural tube defect (Fig. 1.4). The unified theory explains that the incomplete vesicle formation due to a CSF leak from the neural tube defect results in inadequate expansion of the rhombencephalon and subsequent incomplete development of the posterior fossa. The cerebellum is contained within the abnormally small posterior fossa and squeezed upward and downward. Upward herniation of the cerebellum results in a large tentorial incisura and cerebellar towering, and downward herniation results in the displacement of medulla, fourth ventricle, and cerebellum below the foramen magnum. Cerebellar vermis and cerebellar hemispheres often herniate into the spinal canal and cervicomedullary kink causes crowding of the craniocervical region. Aqueductal stenosis can also occur and hydrocephalus is present in up to 90 % of patients with myelomeningocele. The fourth ventricle is inferiorly displaced and elongated, and the lateral ventricles are frequently colpocephalic (McLone and Naidich 1992). These findings are well demonstrated on MR imaging. Other findings include tectal beaking, interdigitation of the gyri, prominent massa intermedia, stenogyria, and heterotopias. Chiari II malformation is a complex mesodermal anomaly that frequently accompanies callosal dysgenesis, dysplastic dura, and skull anomalies such as lacunar skull.

1.3.3 Holoprosencephaly

Holoprosencephaly is caused by incomplete division of the prosencephalon into telencephalon and diencephalons. Hemispheric and lobar cleavage becomes incomplete. Holoprosencephaly is classified into three types: alobar, semilobar, and lobar types. Alobar holoprosencephaly is the most severe form; it is characterized by a small pancake-shaped cerebrum without interhemispheric fissure, fused thalami, and a large holoventricle (primitive central monoventricle). A large dorsal cyst is usually connected to the holoventricle. A facial deformity is typically severe with a midline defect and hypotelorism, and cyclopia can be present in the most severe case. Babies born with holoprosencephaly is usually associated with major congenital anomalies and usually die soon after birth. Semilobar holoprosencephaly is associated with moderate clinical severity. The posterior portions of the cerebral hemispheres are partially developed and a falx cerebri and interhemispheric fissure are incomplete. The occipital horn of the lateral ventricle is normally formed and temporal horn is rudimentary, but frontal horn or septum pellucidum is usually absent (Fig. 1.5). The corpus callosum is absent, but white matter mass mimicking splenium can be seen. Basal ganglia are completely or partially fused. Facial anomalies are either absent or mild. Lobar holoprosencephaly is the least severe form and the brain looks almost normal except for the hypoplastic frontal horn and interhemispheric connection of the gyrus in the frontal region instead of corpus callosum (Barkovich 2012).

1.3.4 Septo-optic Dysplasia

Septo-optic dysplasia is regarded as being very mild on the spectrum of lobar holoprosencephaly characterized by absent septum pellucidum, hypoplastic optic nerves and chiasm, and hypothalamic pituitary dysfunction (Fig. 1.6). Frontal horn shows a flat anterior border that is typically square-shaped, and septum pellucidum is absent. Schizencephaly is frequently present (Barkovich et al. 1989).

1.3.5 Lissencephaly

Lissencephaly (agyria-pachygyria) is the most severe form of the neuronal migration anomalies; it shows smooth brain with shallow Sylvian fissure and almost no surface sulcation. Lissencephaly is composed of a four-layered cortex (molecular-outer cellular-cell sparse-inner cellular layer) instead of normal six-layer (Fig. 1.7). Cell sparse layer seems to be the result of laminar necrosis, which disturbs normal migration. Abnormally arrested neuronal cells during migration manifest as thickened cortex. MRI shows vertically shallow Sylvian fissure with figure of 8 appearance

and smooth thickened cortex with diminished white matter. A T2-weighted image frequently reveals a thin band of high-signal intensity below the surface of the brain that represents a laminar necrosis layer. In severe cases, hypoplasia of the corpus callosum and brainstem can be associated. Clinically, the patient shows microcephaly and severe mental retardation and refractory seizures. Systemic anomalies involving the eyes, ears, kidneys, and heart are common (Guerrini and Martini 2006).

1.3.6 Polymicrogyria

Polymicrogyria is also known as nonlissencephalic cortical dysplasia, which is usually indistinguishable from pachygyria without histologic examination (Barkovich and Kjos 1992a) (Fig. 1.8). Gross appearance varies from diffusely thickened irregular bumpy gyral patterns to focal areas of thickened flat cortex. MR frequently shows abnormal corticomedullary junction of the gyri or incomplete peripheral branching of the subcortical white matter with cortical thickening and prominent subarachnoid space over the polymicrogyria. Polymicrogyria is frequently associated with anomalous sulcus. Anomalous venous drainage due to persistent fetal vasculature is also common in the area of polymicrogyria, which can be mistaken as vascular malformation. Clinical manifestations are usually seizures, depending on the size and the location of the lesions (Tassi et al. 2002).

1.3.7 Schizencephaly

Schizencephaly is a cleft that extends from the lateral ventricle to the surface of the brain, which is lined with abnormal gray matter, usually in the form of polymicrogyria (Fig. 1.6). The cleft is most commonly located near the precentral or postcentral gyri and can be unilateral or bilateral. When the cleft is open, it is called open-lip type, and called closed-lip type when the cleft wall is opposed. In the case of the closed-lip type, a slight outpouching of the ventricle where the cleft meets gives the clue to the diagnosis. The septum pellucidum and optic nerve hypoplasia are frequently absent. Patients with schizencephaly can have seizures, mental retardation, or motor abnormalities, depending on the location (Barkovich and Kjos 1992b).

1.3.8 Heterotopia

Heterotopia refers to collections of nerve cells in abnormal locations resulting from the interruption of normal migration (Fig. 1.9). Premature transformation of radial glial fibers into astrocytes might be a possible explanation. Heterotopias can

be isolated or can be associated with other structural abnormalities. Clinical symptoms depend on the severity and associated anomalies. Usually patients have seizure disorders. Heterotopias can be nodular or band-like, focal, or diffuse. Heterotopias are isointense, with gray matter in all imaging sequences. The subependymal and periventricular regions are the most common locations. The band heterotopia appears as a layer of gray matter central to the cortex separated by a layer of normal white matter, the so-called double cortex. Pachygyria is frequently associated with band heterotopia (Barkovich et al. 1989, Guerrini and Martini 2006).

1.3.9 Dysgenesis of the Corpus Callosum

The corpus callosum forms from anterior to posterior between the eighth and 18th gestational week (Fig. 1.10). Callosal dysgenesis can be partial or complete, depending on the time of the intrauterine insult. In complete agenesis, the entire corpus callosum and cingulate sulcus are absent. White matter axons do not cross the corpus callosum; instead, they course longitudinally to form the bundle of Probst that indents the superomedial aspects of the lateral ventricles. The medial hemispheric gyri and sulci appear to have a radial arrangement around the high-positioned third ventricle. The lateral ventricles appear parallel and widely separated, and the trigones and occipital horns are dilated due to the lack of callosal support, a condition known as colpocephaly. The roof of the third ventricle may be absent or distended, and connected with a large interhemispheric cyst (Georgy et al. 1993). With partial dysgenesis, the rostrum and splenium are absent or hypoplastic, and the genu and body are variable in size. Interhemispheric lipoma can be associated with callosal dysgenesis, which is thought to be a malformation caused by the abnormal development of embryonic mesenchymal tissue. Callosal dysgenesis can be asymptomatic, but associated anomalies, such as heterotopia, encephalocele, Dandy-Walker malformation, polymicrogyria, or hydrocephalus can cause seizures, mental retardation, or hypothalamic dysfunction (Hetts et al. 2006).

1.3.10 Dandy-Walker Complex

The main feature of the Dandy-Walker complex is an enlarged posterior fossa with a hypoplastic or absent cerebellar vermis and cystic dilatation of the fourth ventricle (Fig. 1.11). The etiological mechanism is uncertain, but developmental abnormality of the fourth ventricle and cerebellar hemisphere is the probable explanation (Parisi and Dobyns 2003). On imaging, the posterior fossa is markedly enlarged and the tentorium and torcular herophili are positioned abnormally high. The cerebellar vermis is

hypoplastic and rotates over the posterior fossa cyst. The cerebellar hemispheres are variably hypoplastic and displaced anterolaterally. The floor of the fourth ventricle is present, but the cystic dilated ventricle balloons posteriorly. The brainstem may be hypoplastic or compressed. Associated anomalies include hydrocephalus, agenesis of corpus callosum, occipital encephalocele, heterotopia, and polymicrogyria. A Dandy-Walker variant is a condition when there is a mild degree of vermian hypoplasia and fourth ventricular cyst but the size of the posterior fossa is normal (Altman et al. 1992).

1.3.11 Joubert Syndrome

Joubert Syndrome is characterized by a dysgenetic vermis and small inferior and superior cerebellar peduncle (Fig. 1.12). The patients present with episodic tachypnea or apnea, abnormal eyeball movements, ataxia, and mental retardation. The deformity of the fourth ventricle is characteristic on axial MR imaging, with a batwing appearance. Associated anomalies are callosal dysgenesis, congenital retinal dystrophy, and oculomotor abnormalities. Cystic renal disease, such as juvenile nephronophthisis, can be associated with causing chronic renal failure (Kendall et al. 1990).

1.4 Phakomatosis

1.4.1 Neurofibromatosis Type 1 (Von Recklinghausen's Disease)

Peripheral neurofibromatosis (NF-1) is an autosomal dominant disorder and genetic defect located on the chromosome 17 (Smirniotopoulos and Murphy 1992). Characteristic features are café-au-lait spots, cutaneous neurofibromata, optic pathway glioma, pilocytic astrocytoma, kyphoscoliosis, vascular abnormality, and macrocrania. MR shows high-signal intensity lesions on T2-weighted images that involve the globus pallidus, posterior thalamus, cerebellar white matter, and the brainstem in over 80 % of the patients with NF-1. The lesions do not show mass effect or enhancement (Zimmermann et al. 1992). These are regarded as myelination abnormalities, as the genetic locus of NF-1 produces neurofibromin that is related to myelin precursor production in oligodendrocytes. Optic pathway gliomas can occur, and they are usually pilocytic astrocytomas. These tumors are solid enhancing astrocytomas and distort the optic pathway from the orbit to the optic radiation (Fig. 1.13). Non-optic gliomas can occur in NF-1. Plexiform neurofibromas are found in about one-third of patients with NF-1. They are multiple, tortuous,

cord-like, infiltrative masses that arise along the axis of a major nerve. The common location of plexiform neurofibroma is the ophthalmic division of the trigeminal nerve that is frequently associated with sphenoid wing defect and pulsating exophthalmos (Mentzel et al. 2005).

1.4.2 Tuberous Sclerosis (Bourneville's Disease)

Tuberous sclerosis is an autosomal dominant disorder associated with hamartomatous lesions in multiple organs (Fig. 1.14). The classic clinical triads are adenoma sebaceum, seizures, and mental retardation. Brain abnormalities are cortical tubers, benign white matter lesions, subependymal nodules, and subependymal giant cell astrocytomas. Cortical tubers are the most characteristic lesions that show signal abnormality and gyral expansion. Usually the cortical tuber shows low signal on T1- and high signal on T2-weighted images, but cortical tubers tend to be high on T1 and low signal on T2-weighted images in neonates and young infants. The white matter lesions are linear- or wedge-shaped abnormal signal lesions, which are believed to represent disorganized dysplastic white matter. Subependymal nodules are located near the caudate nucleus along the striothalamic groove of the lateral ventricle. The nodules show the same signal with the white matter and calcify with time. Subependymal giant cell astrocytomas locate at or near the foramen of Monro, causing obstructive hydrocephalus. The astrocytomas enhance strongly and they can grow with time (Braffman et al. 1992). Retinal hamartomas and cerebral vascular stenosis can be associated. Extracranial lesions are found in cutaneous tissue, kidneys (renal cyst, angiomyolipoma), heart (rhabdomyoma), lung (lymphangioma), and the vascular system (aneurysms, stenosis) (Seidenwurm and Barkovich 1992).

1.4.3 Sturge-Weber Syndrome (Encephalotrigeminal Angiomatosis)

Sturge-Weber Syndrome is characterized by a port-wine nevus in trigeminal distribution, leptomeningeal angiomatosis, seizures, hemiplegia, and glaucoma (Fig. 1.15). The etiology is believed to be faulty development of cortical venous drainage resulting in venous congestion with hypoxia of the affected cortex. Progressive atrophy and dystrophic calcification occur in the gyri underlying the angioma. On MR, enhancement of pial angioma and angiomatous enhancement of the choroid plexus are seen. Prominent medullary and subependymal veins can also be seen. The white matter of the involved gyri shows prominent hypointensity on T2-weighted images, which is thought to be related to

hemoglobin product deposits or changes with chronic ischemia. Gyrar calcifications take time to develop and are rare before age 2 (Benedikt et al. 1993).

1.4.4 Neurofibromatosis Type 2

NF-2 is a distinct form of the disease that is different both clinically and radiologically. It is much less common than NF-1 and is more common in young adults than in children. NF-2 has been identified with defects of chromosome 22 and the transmission mode is autosomal dominant inheritance (Fig. 1.16). Neoplasms of NF-2 are associated with tumors of coverings such as Schwann cells and meninges. The vestibulocochlear nerve is the one most frequently involved in NF-2 and bilateral acoustic schwannomas are the hallmark of NF-2. Acoustic tumors typically arise from the vestibular nerve and displace or engulf the cochlear and facial nerves. Multiple cranial nerve schwannomas should be suspected for the diagnosis of NF-2. Intracranial meningiomas are also common in NF-2 and they are often multiple. Multiple intraspinal, intradural, extramedullary masses are common and they are either schwannomas or meningiomas. Multiple masses along the spinal nerve roots can also be present in NF-2; they are usually schwannomas. Ependymomas, as intramedullary tumors, are also common in NF-2 (Nunes and MacCollin 2003).

1.4.5 Von Hippel-Lindau Disease

Von Hippel-Lindau Disease is an autosomal dominant disorder with a variable penetrance (Fig. 1.17). Principal manifestations include retinal angioma, cerebellar and spinal cord hemangioblastomas, and multi-organ neoplasm of the abdominal viscera. The diagnosis can be made with more than one hemangioblastoma of the CNS or one CNS hemangioblastoma plus visceral involvement. Visceral lesions include renal cell carcinoma, pheochromocytoma, and cyst of the kidney, liver, pancreas, or epididymis. Retinal angioma (hemangioblastoma) occurs in more than half of the patients and may be multiple and bilateral. Cerebellar hemangioblastomas occur in more than half of the patients and may be multiple. Less commonly involved sites are the brainstem or spinal cord, particularly the cervical or thoracic cord. Supratentorial hemangioblastomas are very rare. Neurological abnormalities include increased pressure, cerebellar dysfunction, hemorrhage, or myelopathy. The peak incidence for hemangioblastoma is in the fourth or fifth decade of life. Cerebellar hemangioblastoma frequently occurs as a cystic mass with a small, non-calcified vascular mural nodule. In contrast, the spinal cord tumors are predominantly solid or partially cystic. On MR imaging, the mural nodule or solid tumor shows strong homogenous

enhancement, and flow voids of the feeding artery and draining vein of the tumor can be identified. Cerebral angiography shows characteristic intense vascular nodules in the early arterial phase, with a dense, prolonged vascular staining (Slater et al. 2003).

1.4.6 Incontinentia Pigmenti

Incontinentia pigmenti is an uncommon X-linked disorder with characteristic skin lesions, dental and skeletal dysplasia, ocular abnormalities, and non-progressive CNS involvement (Fig. 1.18). The erythematous skin lesions appear early in infancy and become verrucous and hyperpigmented. Seizures, quadriplegia, ataxia, and mental retardation are frequent. Neuroimaging abnormalities include ischemic brain lesions involving the cortex and underlying white matter in watershed zones. Periventricular white matter can be involved, resulting in a feature suggesting periventricular leukomalacia. Ocular globes may show findings of persistent hyperplastic primary vitreous (Hennel et al. 2003).

1.4.7 Neurocutaneous Melanosis

Neurocutaneous melanosis is a syndrome composed of giant congenital melanocytic nevi on the head and neck or dorsal spine area (Fig. 1.19). Clinical manifestations include seizures, increased intracranial pressure, and chronic meningitis. CNS symptoms typically develop at less than 2 years of age. Symptomatic neurocutaneous melanosis has a poor prognosis, and the patients have an increased risk of cutaneous and CNS melanoma. Pathologically abnormal meningeal pigmentation and thickening due to melanocytic proliferation can be seen at the meninges and the brain, especially involving the cerebellum, brainstem, and basal ganglia. MR shows foci of T1 shortening due to the presence of melanin most commonly in the anterior temporal lobe, cerebellar nuclei, cerebellar white matter, and brainstem. Hydrocephalus, Dandy-Walker malformation, and arachnoid cyst can be present (Bittencourt et al. 2000).

1.4.8 Ataxia-Telangiectasia

Ataxia-telangiectasia is an autosomal recessive disorder that consists of oculocutaneous telangiectasia and cerebellar ataxia (Fig. 1.20). The patients also have severe immune deficiencies and a predisposition to malignant tumors. The gene abnormality is located on chromosome 11, which results in the derangement of detection of DNA damage or cellular repair. Ataxia and mucocutaneous telangiectasia

appear in early childhood, and recurrent bacterial and viral sinopulmonary infections occur, leading to pulmonary insufficiency. Malignant tumors, such as lymphomas and leukemia, develop in more than 10 % of younger patients, whereas epithelial malignancies can occur in adults.

Major radiologic abnormalities are cerebellar cortical atrophy that are more marked in the vermis showing prominent cerebellar folia and a dilated fourth ventricle. Hemorrhage can occur from the rupture of parenchymal telangiectasia. Cerebellar atrophy and progressive neurological deterioration should raise the question of ataxia-telangiectasia (Neyn 1999).

1.5 Congenital Anomaly of the Spinal Cord

1.5.1 Normal Development of Spinal Cord

1.5.1.1 Neurulation

Localized proliferation of the embryonic plate induced by the notochord forming neural groove and neural fold. Disjunction of the neural fold from the overlying ectoderm results in the formation of the neural tube. Closure of the neural tube in cranial and caudal direction completes the neurulation process.

Spinal dysraphism usually comes from the incomplete closure of the neural tube.

The neural tube induces development of mesenchymal structures such as vertebrae, neural arches, and paraspinal muscles.

1.5.1.2 Canalization and Retrogressive Differentiation

Caudal neural cells proliferate and coalesce to form caudal cell masses and differentiate retrogressively to form the conus medullaris, terminal ventricle, and filum terminale. Failure to regress results in tethered cord, tight filum terminale syndrome, and caudal spinal anomaly (Dias 2007).

1.5.2 Spectrum of Spinal Cord Anomalies

Open Spinal Dysraphism (Rufener et al. 2010)

Myelomeningocele/myelocele

Closed Spinal Dysraphism Lipomyelomeningocele/
lipomyelocele

Meningocele

Myelocystocele

Dorsal dermal sinus

Other Spinal Cord Anomalies Neurenteric cyst

Diastematomyelia

Intraspinous lipoma/lipoma of filum terminale

Caudal regression syndrome

1.5.2.1 Myelomeningocele

Myelomeningocele results from the defective closure of the neural tube due to complete non-disjunction of the neuroectoderm from the cutaneous ectoderm remaining as neural placode. The neural placode is exposed in the open air due to the accompanying skin defect. The exposed neural plate causes leakage of cerebrospinal fluid and associated high risk of infection obviates emergent surgical repair. CSF leakage supposedly causes Chiari malformation due to underdevelopment of posterior fossa (Fig. 1.21). Mesodermal maldevelopment causes abnormal development of bone, cartilage, and ligament, such as lacunar skull or dysplastic falx (McLone and Knepper 1989). Surgical treatment is for closure of the skin defect and untethering of the spinal cord, and retethering by scar is common. Imaging of the untreated myelomeningocele is not indicated due to the risk of infection.

1.5.2.2 Lipomyelomeningocele

Premature disjunction of an incomplete neural tube results in lipomatous differentiation of the overlying mesenchymal tissue. Clinical manifestation is usually lumbosacral back mass and intact skin covering with a lumpy mass composed of fatty tissue and accompanying meningocele. Lipomatous tissue connecting the posterior surface of dysraphic cord and subcutaneous fatty tissue causes tethering of the spinal cord. Intraspinous lipoma causes distortion of the cord and nerve roots and tethers the spinal cord (Fig. 1.22). Tethering of the cord can be associated with syringohydromyelia. Surgical treatment is for untethering of the cord and repairing the dural sac.

1.5.2.3 Meningocele

A meningocele is the herniation of the CSF-containing meningeal sac through a dorsal spinal defect into subcutaneous tissue with intact overlying skin (Fig. 1.23). The embryonic origin of the meningocele is unknown, and they are most common in the lumbosacral region (80 %). Meningocele does not contain spinal cord or neural tissue (Naidich et al. 1984).

1.5.2.4 Myelocystocele

Herniation of hydromyelic spinal cord or terminal ventricle through posterior spinal defects results in a skin-covered back mass containing a cyst (Fig. 1.24). Myelocystocele can be associated with meningocele or lipoma. Caudal regression syndrome or cloacal anomaly can be accompanied by a myelocystocele.

1.5.2.5 Dorsal Dermal Sinus

Incomplete disjunction of the neural tube from the cutaneous ectoderm results in the connection of the spinal cord and skin with the dermal sinus. The sinus, epithelial-lined tract, extends the cephalad and frequently terminates at the dural sac or the spinal cord and is associated with dermoid or

epidermoid-causing cord tethering (Fig. 1.25). Dermal sinus can deliver infection into the central nervous system and the most common clinical manifestation is CNS infection. Skin dimple, hairy nevus, or hyperpigmented patch is a frequent skin manifestation, predominantly in the lumbosacral region (Pang et al. 2010). A sacrococcygeal dimple can be a manifestation of a simple deep sacral dimple or pilonidal cyst.

1.5.2.6 Neurenteric Cyst

Neurenteric cyst results from an abnormal connection between dorsal ectoderm and gut, such as dorsal enteric fistula in the most severe form (Fig. 1.26). The cyst contains gastrointestinal epithelial lining and locates intraspinal or prevertebral space most commonly in the cervicothoracic level. Regional vertebral cleft is frequently associated.

1.5.2.7 Diastematomyelia

A persistent connection between the gut and dorsal ectoderm develops into the splitting of the notochord (Fig. 1.27). Split notochord causes sagittal clefting of the spinal cord with localized duplication of it. The two cords can be separated by a bony spur in about 50 % of the cases, but also by a fibrous band or just CSF. Two hemicords fuse distally to form a distal spinal cord. A bony bridge separating the hemicords

causes cord tethering. Cutaneous stigmata, such as hairy patch, nevi, and lipomas are common. Orthopedic abnormalities, such as scoliosis or neurologic symptoms due to cord tethering are common. The lumbar level is the most common site (usually between T9–S1) (Sinha et al. 2006).

1.5.2.8 Lipoma of Filum Terminale

Fatty change of the filum terminale is a frequent manifestation of filar thickening. A thickened filum terminale can cause cord tethering (Fig. 1.28). The tethered cord may terminate in a lipoma. A thickness of the filum over 2 mm should be suspected as an abnormal filum terminale that can cause tethering of the cord.

The normal level of the conus medullaris is about L2-L3 (L1-L2 in adults). Anything below the level of L3 should be suspected as abnormal (Hendrick et al. 1983).

1.5.2.9 Caudal Regression Syndrome

Caudal regression can be associated with an imperforate anus, malformed genitalia, renal anomaly, and sirenomelia (Fig. 1.29). Regression can range from coccyx to sacral or lumbosacral vertebral agenesis. Deformity of the distal end of the cord, such as blunt ending or posterior slanting instead of well-formed conus, is a characteristic imaging feature (Niegelstein et al. 1994).

1.6 Illustrations: Congenital Anomaly of the Brain and Spinal Cord

1.6.1 Neurulation (Dorsal Induction)

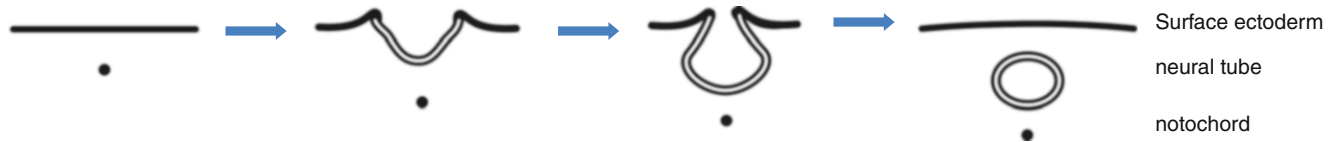


Fig. 1.1 Neurulation (dorsal induction). Simplified schematic drawing of the neurulation shows neural tube formation from the surface ectoderm induced by notochord. Proliferation of the neural ectoderm produces neural groove and fold and finally the tube and separated from surface ectoderm

1.6.2 Vesicle and Flexure Formation (Ventral Induction)

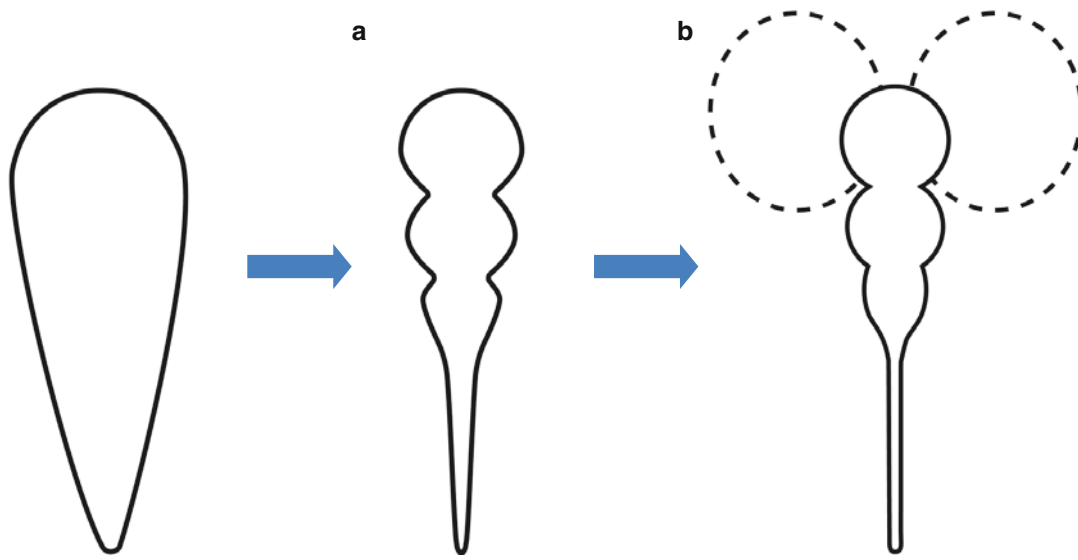


Fig. 1.2 Vesicle and flexure formation (ventral induction). Simplified schema shows expansion and constriction of neural tube forms prosencephalon, mesencephalon, and rhombencephalon (**a**). Telencephalons form from the prosencephalon (**b**)

1.6.2.1 Congenital Anomaly of the Brain

1.6.2.1.1 Encephaloceles

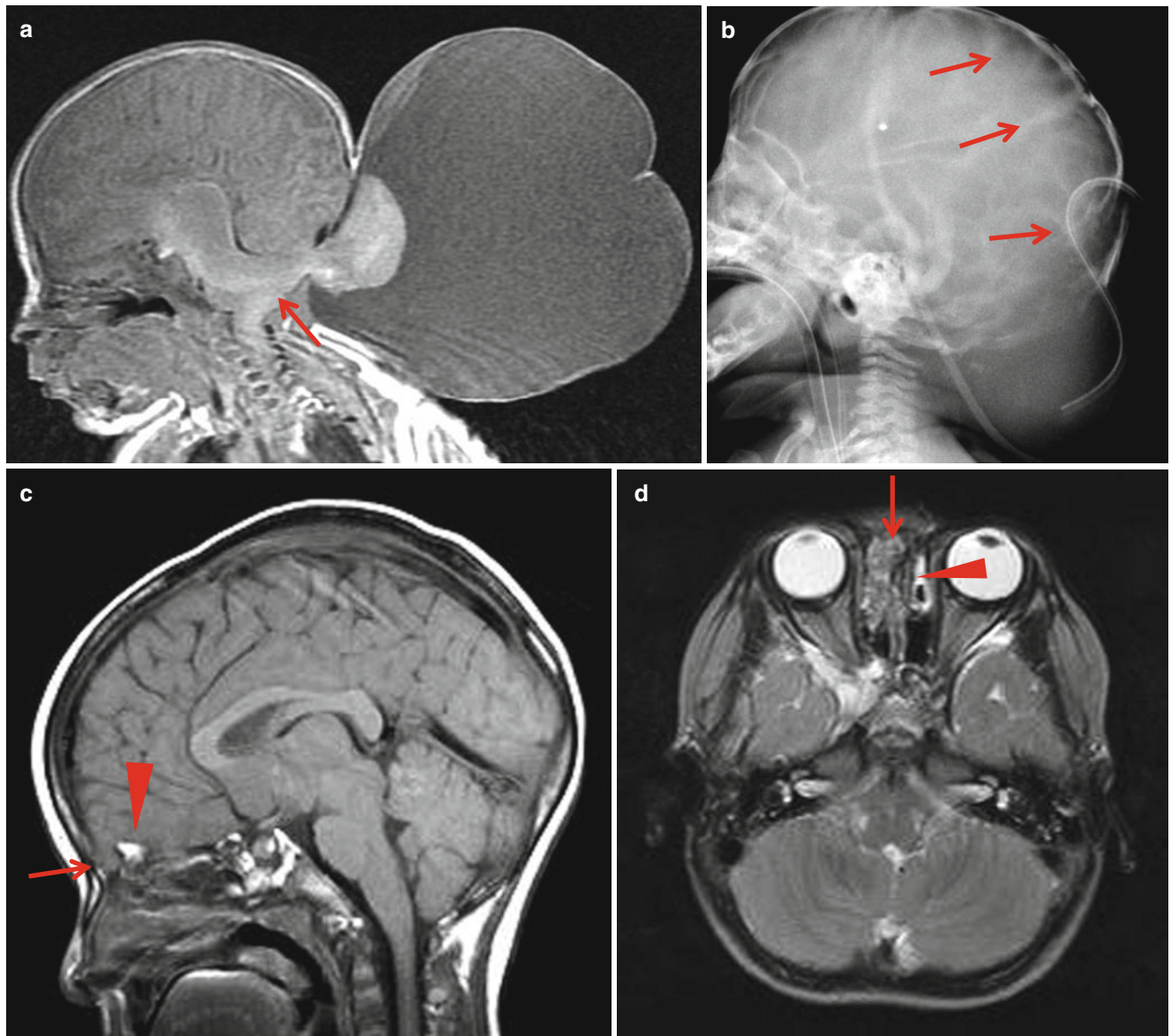


Fig. 1.3 Encephaloceles. (a) Large occipital encephalocele shows herniation of the cerebellum (arrow) and CSF through the occipital defect. Chiari malformation is accompanied. (b) Postoperative plain

skull radiograph shows lacunar skull (arrows). (c, d) Frontoethmoidal encephalocele shows herniation of the brain parenchyma (arrows) through the foramen cecum anterior to the crista galli (arrowheads)

1.6.2.1.2 Chiari Malformation in Myelomeningocele

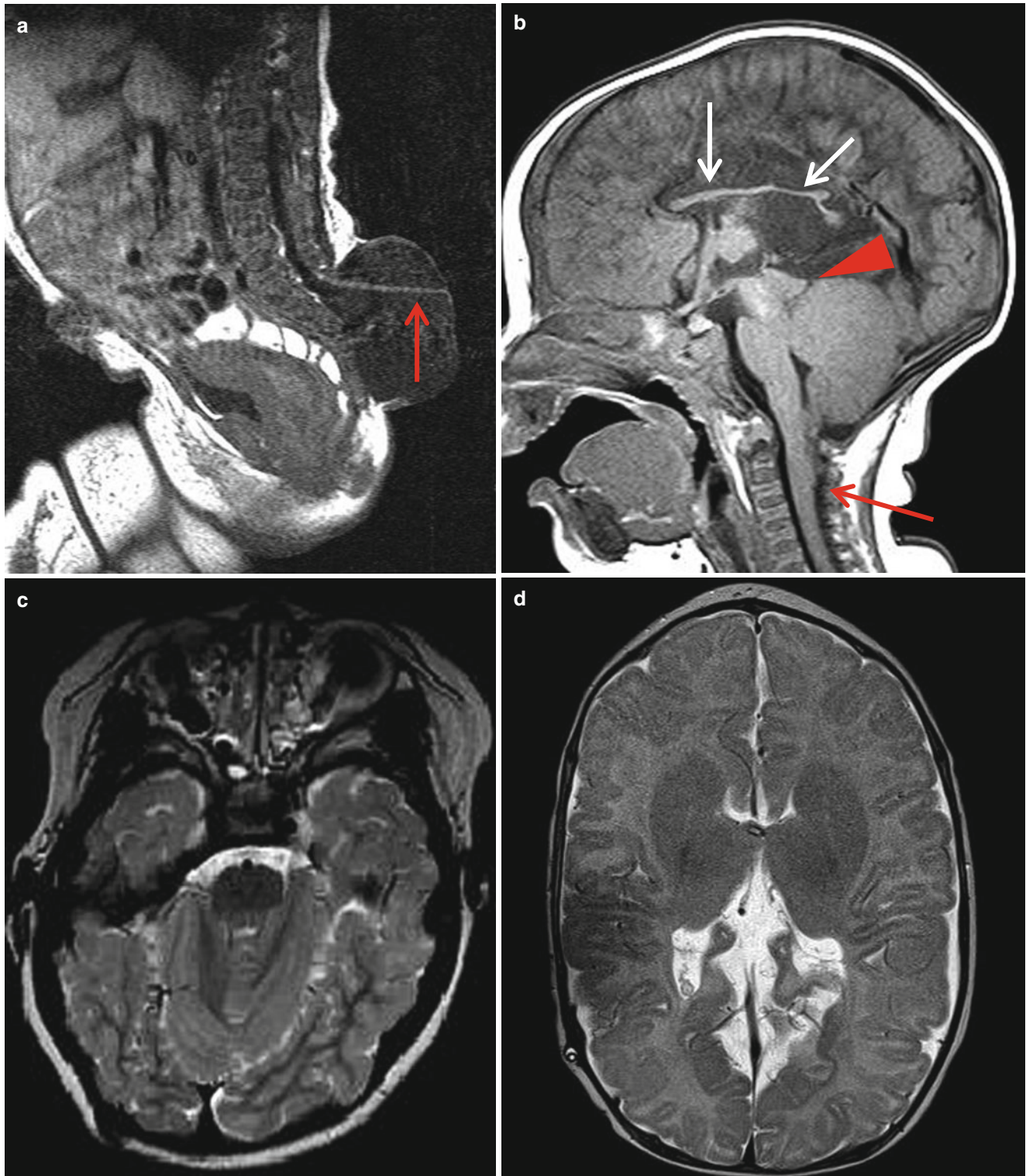


Fig. 1.4 Chiari malformation in myelomeningocele. (a) Herniated distal cord (*arrow*) is continuous with the neural placode in the outer surface of the meningocele. Overlying skin defect is also present. (b) Sagittal image shows downward herniation of the medulla and cerebellar vermis. The fourth ventricle is narrow and elongated and extends down into the foramen magnum. The cervicomedullary

kink is present at the C2 to C3 level. The tectum shows posterior beaking. Dysplastic corpus callosum shows scalloped thinning due to longstanding hydrocephalus (*white arrows*). (c) Axial T2-weighted image shows obliteration of the CSF space in the posterior fossa and squeezed appearance of the cerebellum. (d) Axial T2-weighted image shows dysplastic corpus callosum and falx

1.6.2.1.3 Holoprosencephaly, Semilobar Type

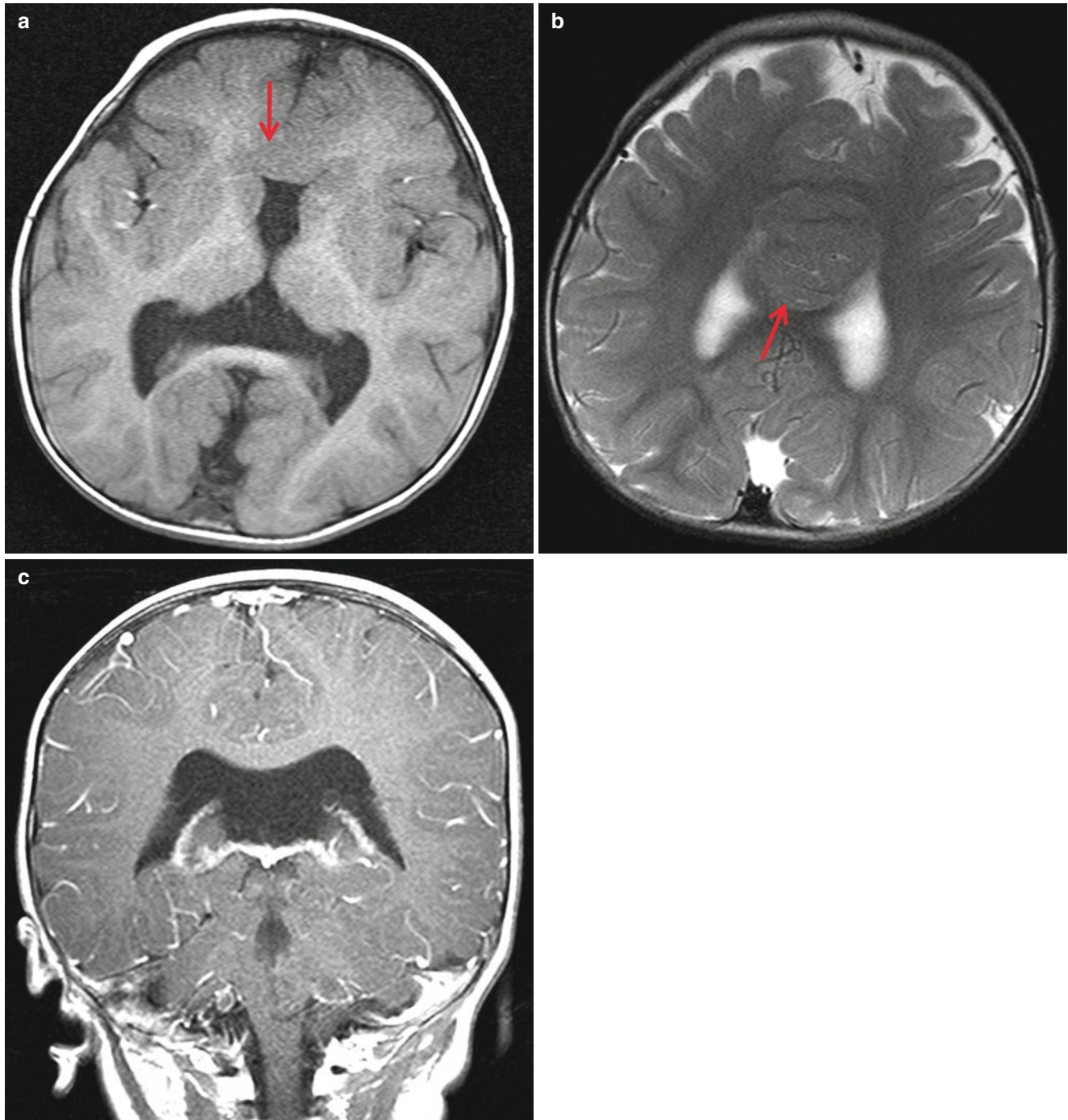


Fig. 1.5 Semilobar holoprosencephaly. (a) Frontal horn is hypoplastic and septum pellucidum is absent. Occipital horn is well formed. Hemispheric connection (arrow) is seen anterior to the frontal horn

instead of corpus callosum. (b) Interhemispheric gyral connection is evident over the lateral ventricles (arrow). (c) Coronal image shows fusion of the lateral ventricles in the posterior portion

1.6.2.1.4 Schizencephaly

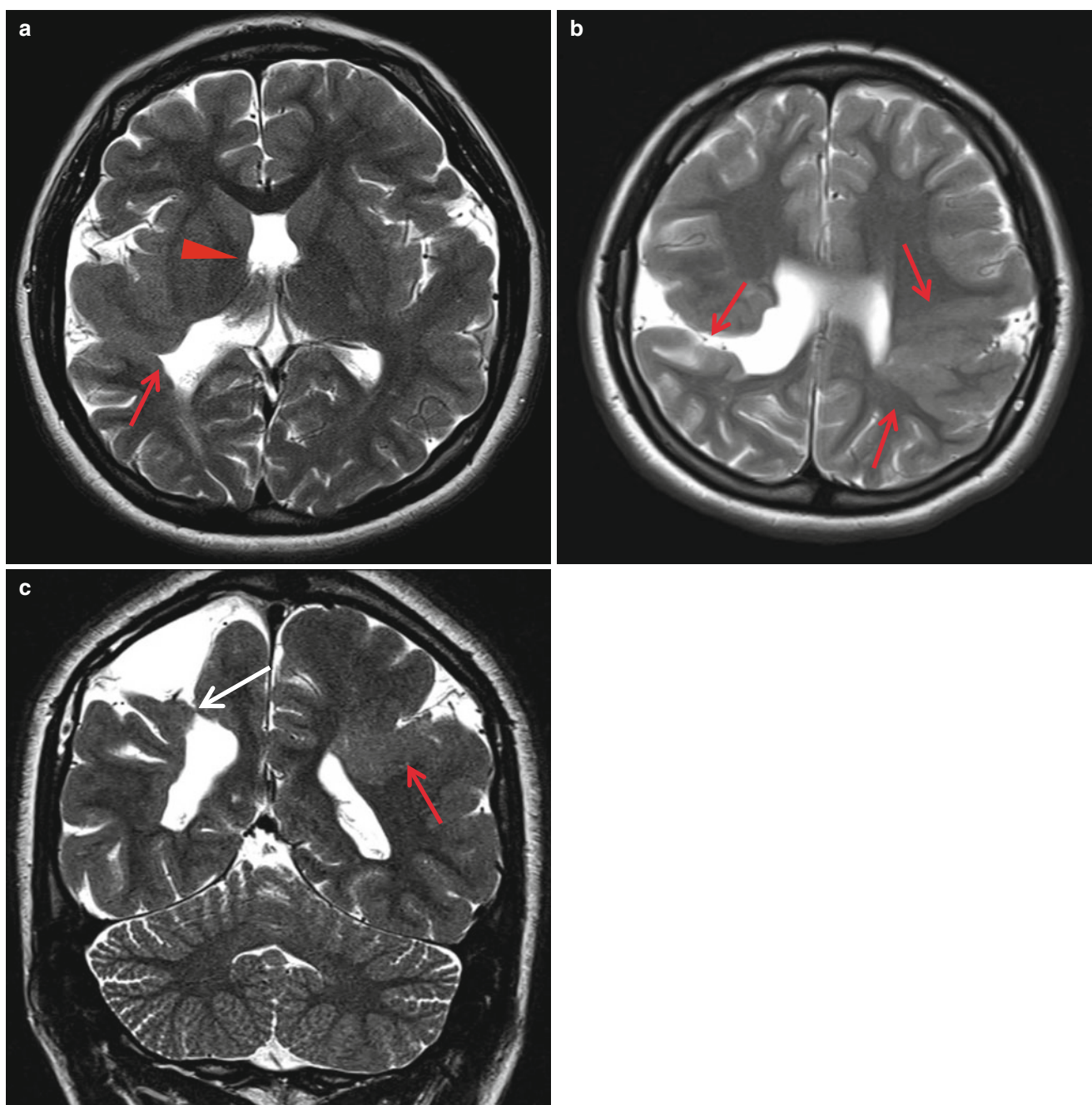


Fig. 1.6 Schizencephaly. (a) Thickened layer of gray matter extends from the cortex to the ventricular surface in the temporo-occipital region. Focal outpouching of the ventricle shows the opening of the cleft into the ventricle (arrow). Septum pellucidum is absent (arrowhead).

(b, c) Open-lip schizencephaly (white arrow) shows CSF filling the cleft along the cortex and ventricle. Closed-lip schizencephaly (arrows) shows opposed cleft by the polymicrogyria

1.6.2.1.5 Lissencephaly

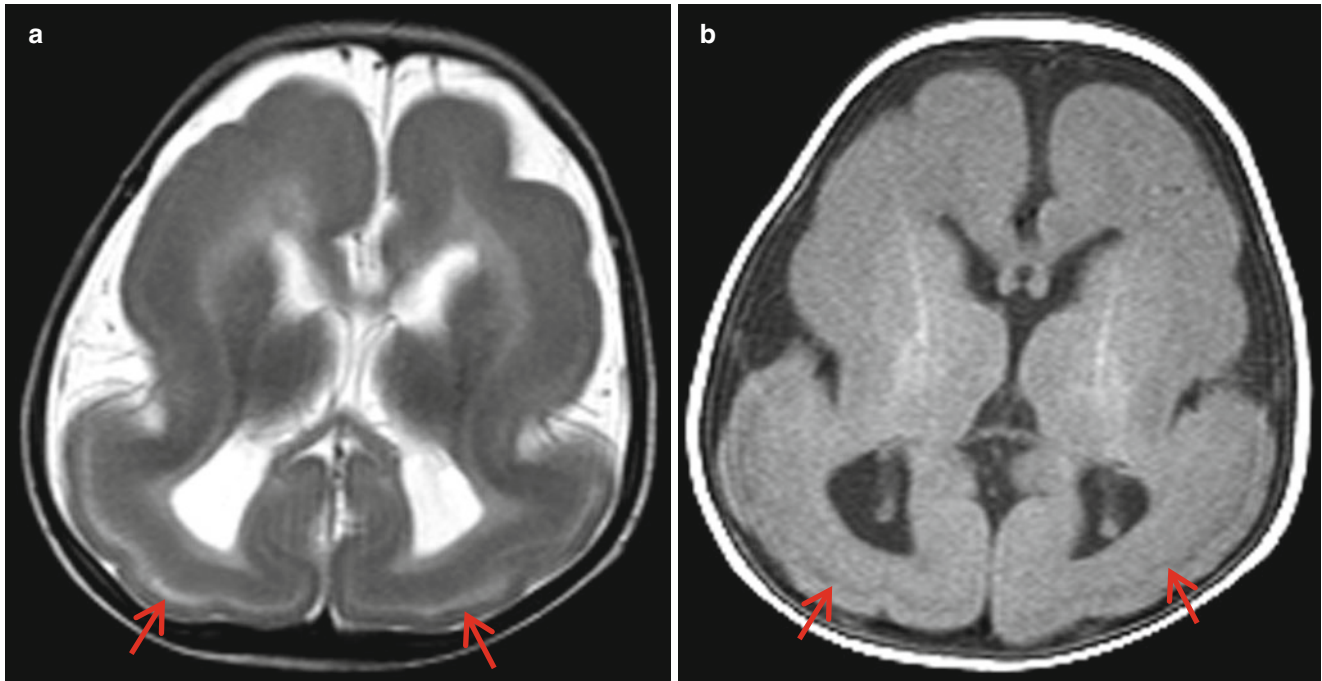


Fig. 1.7 Lissencephaly. (a) Axial T2-weighted image shows nearly smooth brain with shallow Sylvian fissure. The cortex is abnormally thick and outer linear band of high signal intensity (*arrows*) represents

layer of laminar necrosis. (b) T1-weighted image shows low signal intensity of the laminar necrosis layer

1.6.2.1.6 Polymicrogyria

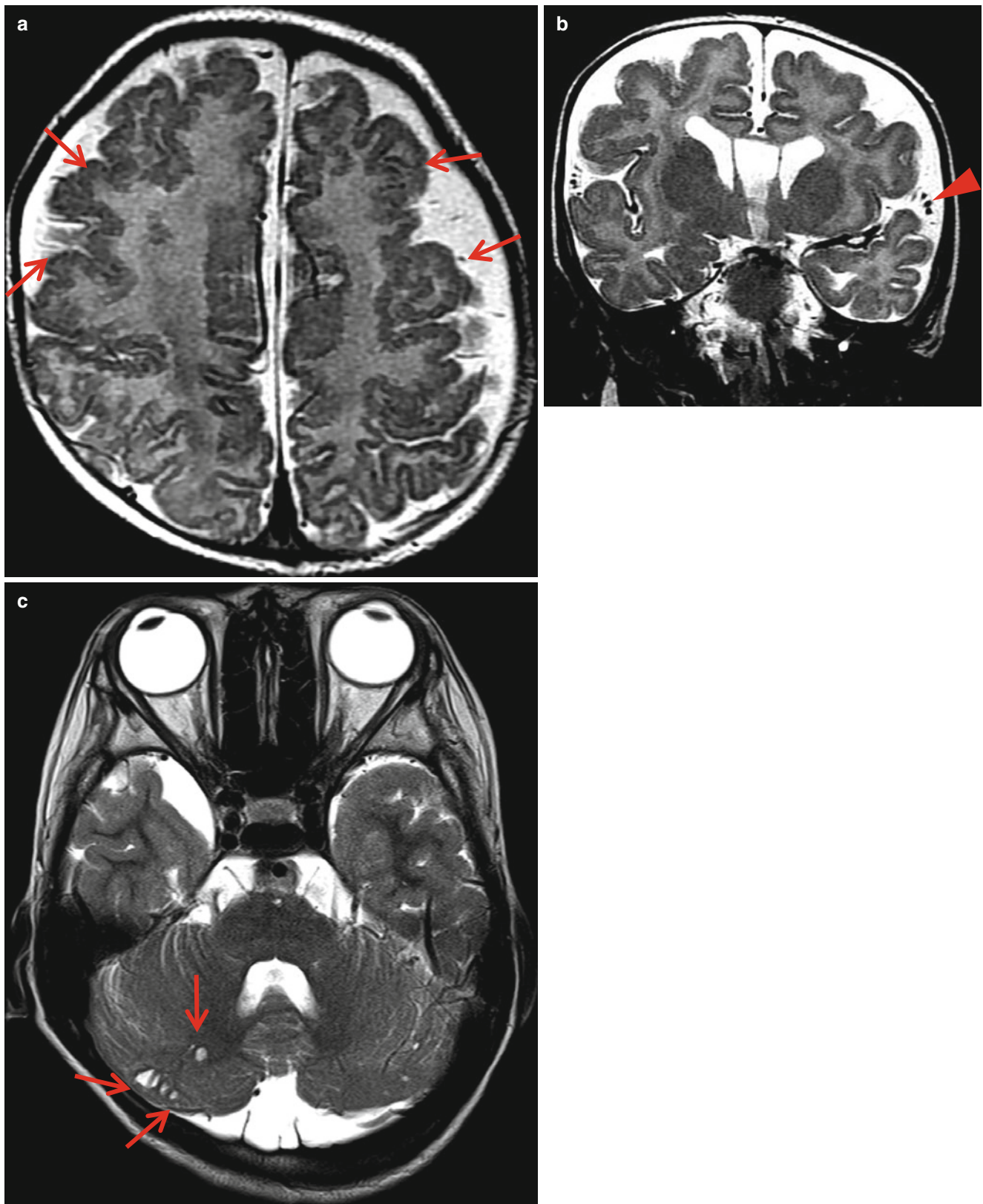


Fig. 1.8 Polymicrogyria. (a, b) T2-weighted image shows diffusely thickened irregular bumpy gyri (*arrows*) of both frontoparietal lobes with prominent overlying subarachnoid space. Sulcal abnormalities and

prominent venous structures (*arrowhead*) are also present. (c) Cystic lesions along the surface of the cerebellum (*arrows*) suggest engulfed subarachnoid spaces due to cerebellar migration abnormalities

1.6.2.1.7 Heterotopia

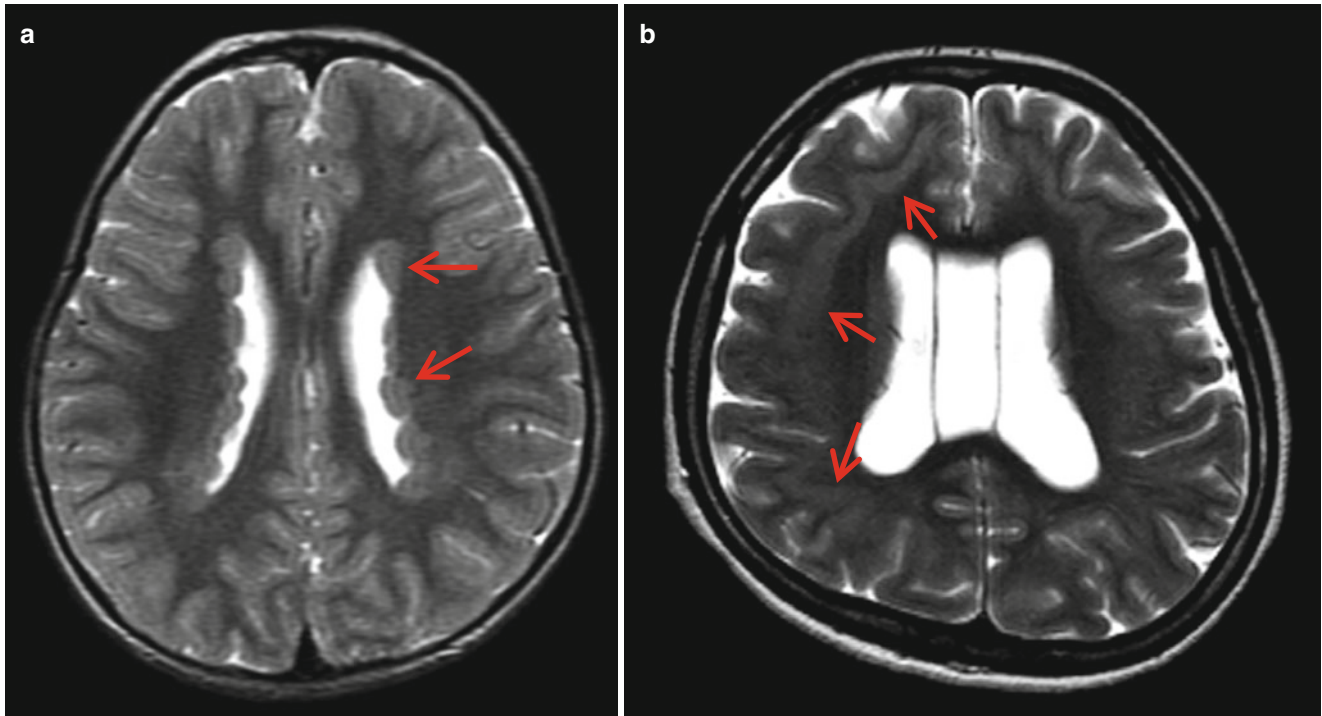


Fig. 1.9 Heterotopia. (a) Subependymal heterotopias show diffuse nodules of gray matter (*arrows*) along the both lateral ventricles. (b) Continuous layer of white matter (*arrows*) separates gray matter showing double cortex. The outer cortex shows smooth surface, suggesting pachygyria

1.6.2.1.8 Agenesis of the Corpus Callosum with Lipoma

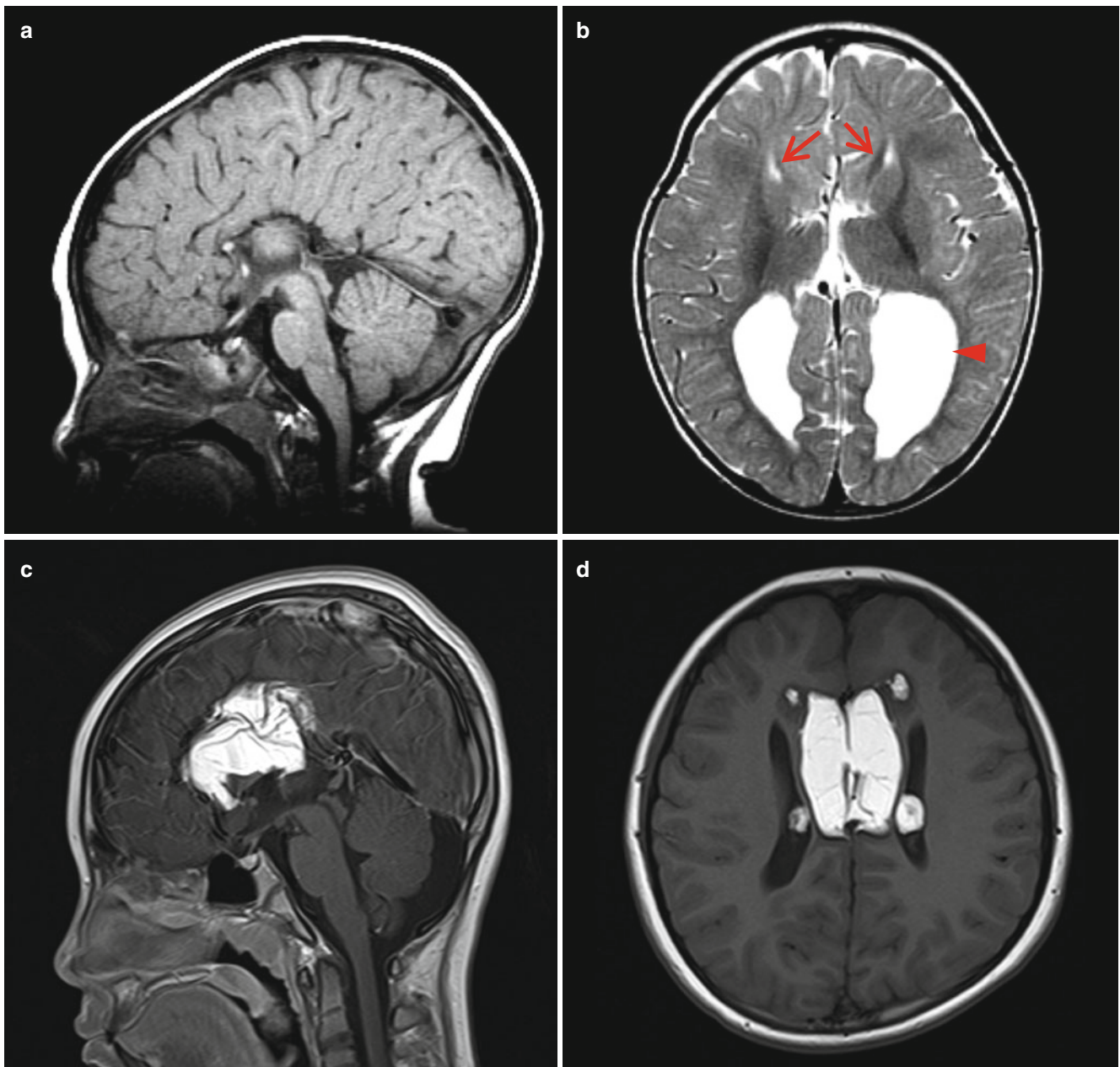


Fig. 1.10 Agenesis of the corpus callosum with lipoma. (a) Midsagittal image shows absent corpus callosum and the medial aspect of the cerebral sulci converge to the elevated third ventricle in radial arrangement. (b) Axial image shows parallel arrangement of the lateral ventricles and dilated occipital horns (*arrowhead*), so-called colpocephaly. Probst

bundles are seen as curvilinear white matter (*arrows*) indenting the medial aspect of the lateral ventricles. (c, d) T1-weighted image shows lipomas in the interhemispheric region with sulcal and ventricular extension. Corpus callosum is absent

1.6.2.1.9 Dandy-Walker Malformation

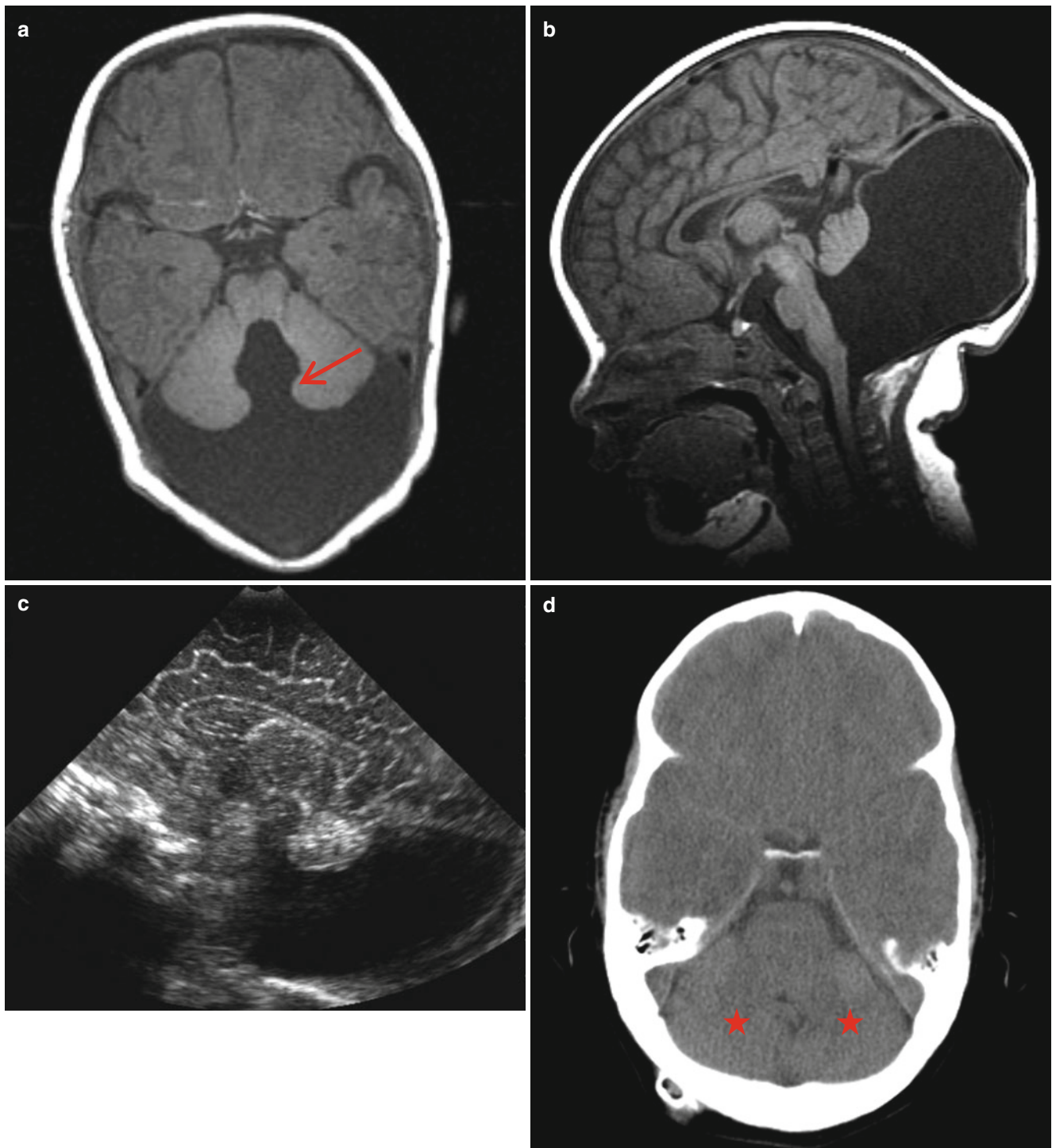


Fig. 1.11 Dandy-Walker malformation. (a) Axial image shows wide communication (*arrow*) of the fourth ventricle and the cyst displacing the hypoplastic cerebellum anteriorly. (b) Sagittal image shows large cyst occupying the inferior vermian region and elevating the tentorium

and venous sinus upwardly. Cerebellar vermis is superiorly displaced. (c) Sagittal image of brain US reveals the large cyst-displacing vermis. (d) Follow-up CT after 2 years of cystoperitoneal shunt shows regrowth of the cerebellar hemispheres (*arrows*)

1.6.2.1.10 Joubert Syndrome

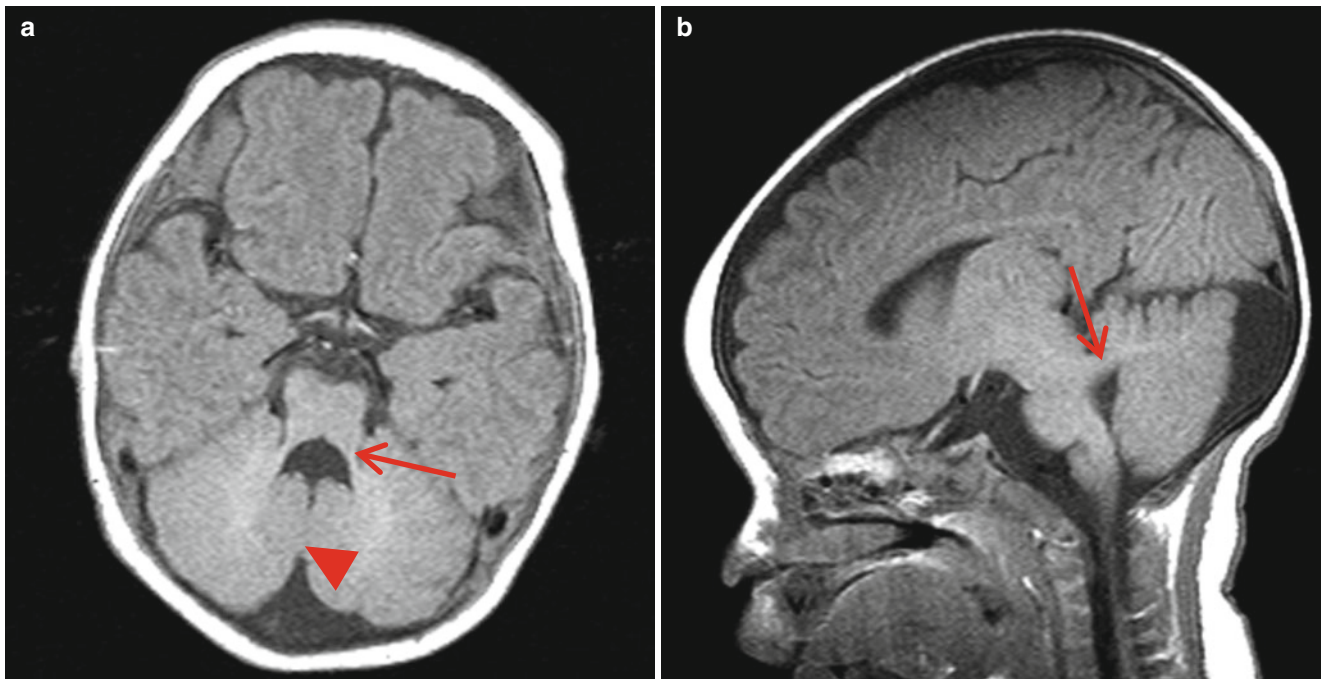


Fig. 1.12 Joubert syndrome. (a) Axial image shows batwing appearance of the fourth ventricle due to hypoplastic cerebellar peduncle (*arrow*) and cerebellar tonsillar opposition (*arrowhead*) instead of

inferior vermis. (b) Sagittal image shows horizontal orientation of the superior cerebellar peduncle (*arrow*) with deformed fourth ventricle

1.6.2.2 Phakomatosis

1.6.2.2.1 Neurofibromatosis Type 1

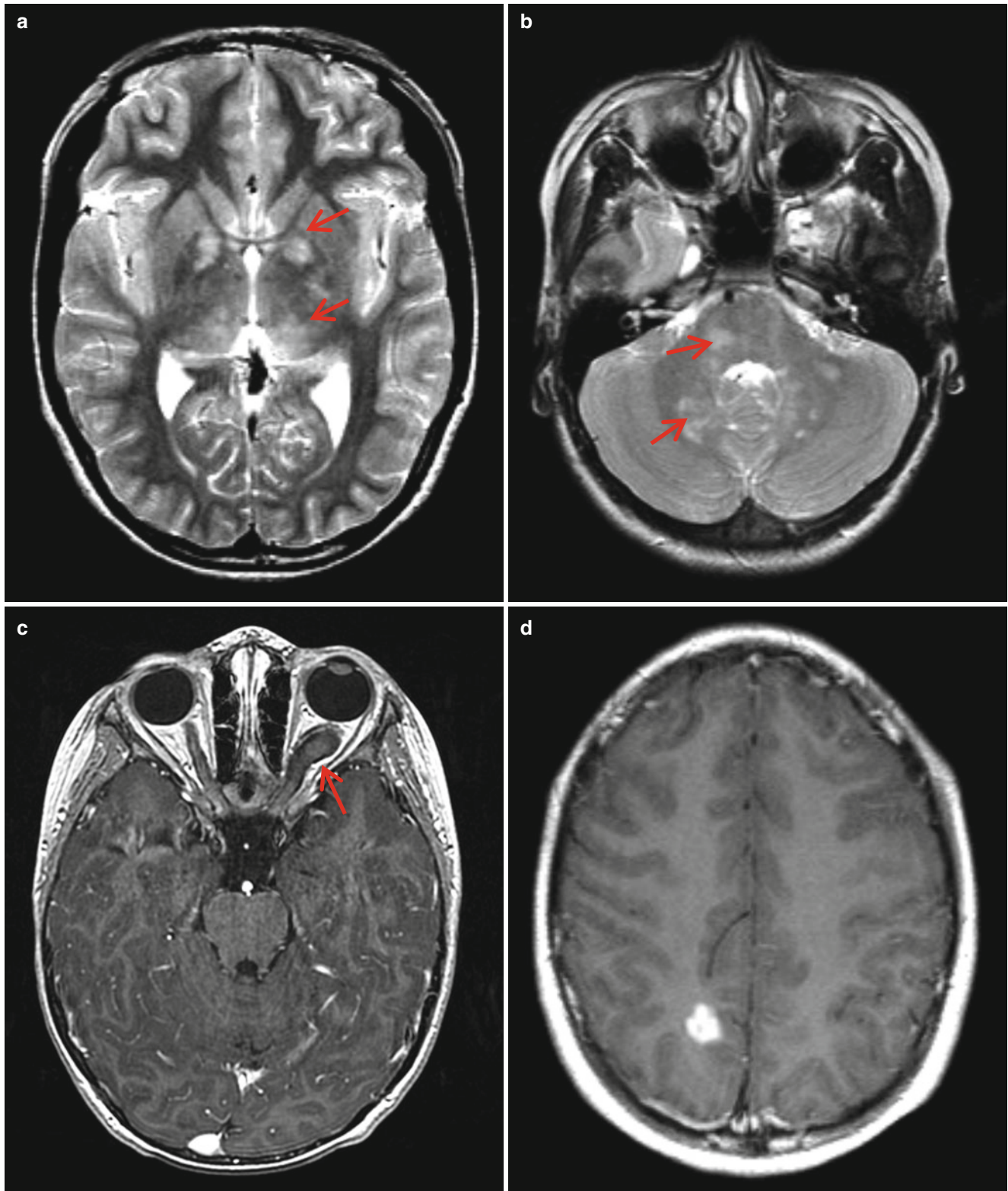


Fig. 1.13 Neurofibromatosis type 1. (a, b) Axial T2-weighted images show multiple nodular high signal intensity lesions (*arrows*) in the globus pallidus, posterior thalami, pons, and cerebellar white matter.

(c) Postcontrast image shows diffuse thickening of the left optic nerve with mild enhancement and dural ectasia (*arrow*). (d) Pilocytic astrocytoma reveals as a discrete enhancing nodule in the right parietal region

1.6.2.2.2 Tuberous Sclerosis

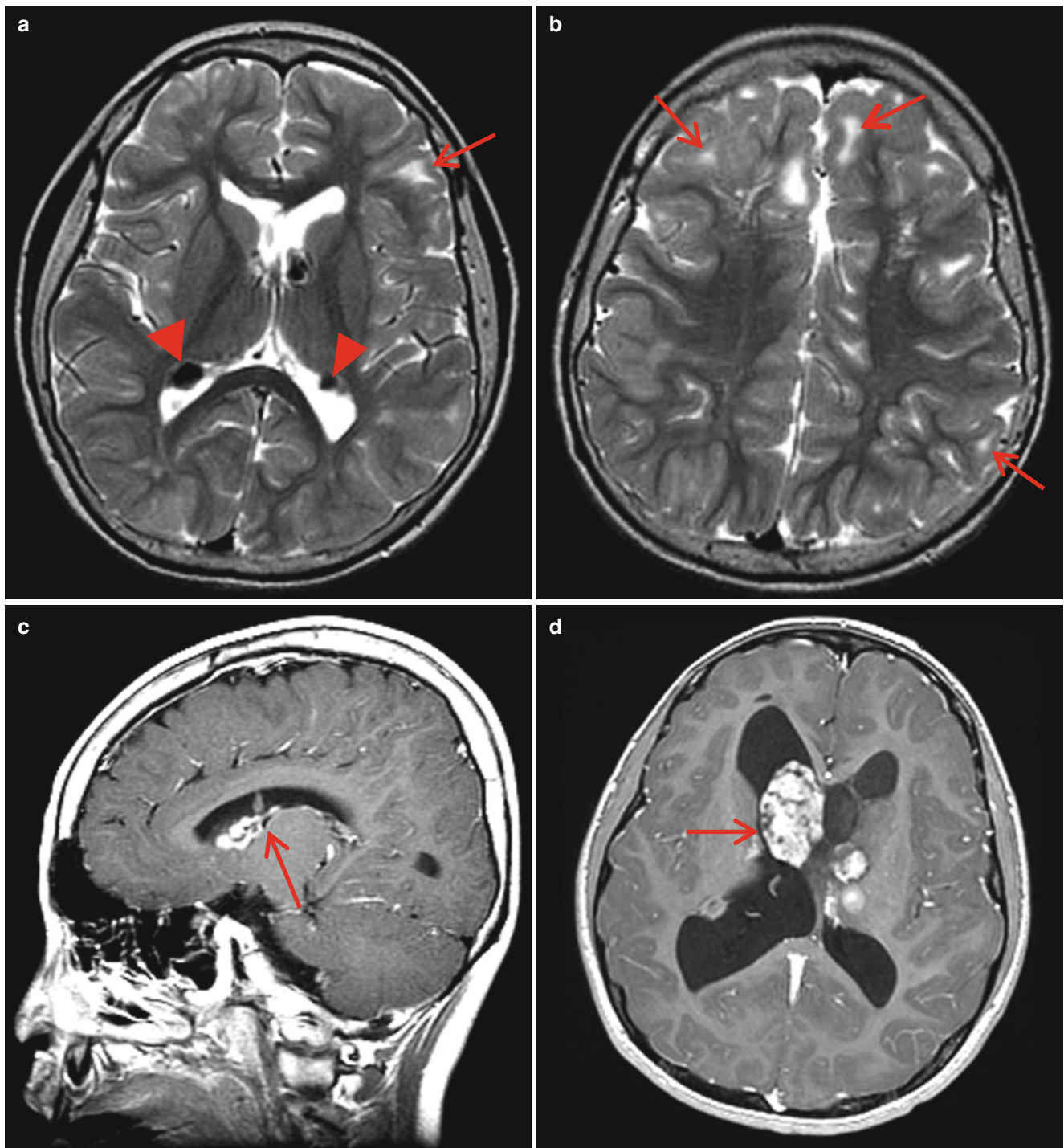


Fig. 1.14 Tuberous sclerosis. (a, b) T2-weighted image shows multiple subependymal tubers (*arrowheads*) along the wall of the lateral ventricles. The low signal intensities are due to calcifications. Cortical tubers (*arrows*) show multiple subcortical high signal intensity lesions with gyral expansion (*arrow*). (c) Postcontrast sagittal image shows

strong homogenous enhancement of the subependymal tubers over the caudate nucleus. The tuber shows vertical orientation (*arrow*). (d) The large enhancing mass lesion obstructing the foramen of Monro, suggesting subependymal giant cell astrocytoma (*arrow*)

1.6.2.2.3 Sturge-Weber Syndrome

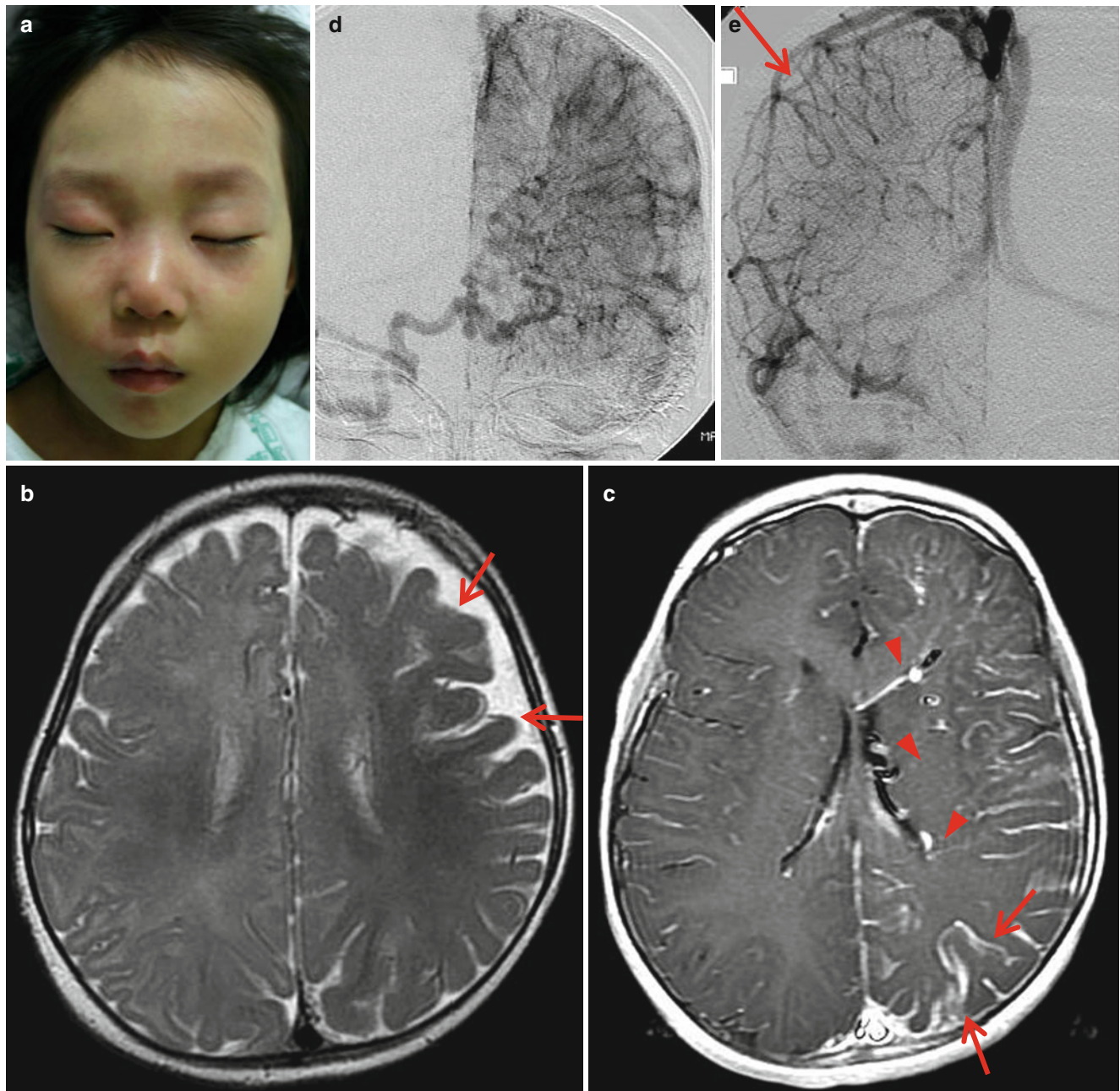


Fig. 1.15 Sturge-Weber syndrome. (a) Facial port-wine nevi located over the orbital and nasal region. (b) T2-weighted image shows atrophic gyri over the left hemisphere and exaggerated low signal intensities of the left hemispheric gyri (arrows). (c) Postcontrast image shows diffuse enhancement of the leptomeningeal angiomatosis in the left

cerebral hemisphere (arrows) and prominent deep and ependymal veins (arrowheads). (d) Venous phase of the right vertebral angiography shows indistinct superficial cortical veins and prominent deep veins. (e) Normal superficial veins (arrow) are well demonstrated in the right cerebellum

1.6.2.2.4 Neurofibromatosis Type 2

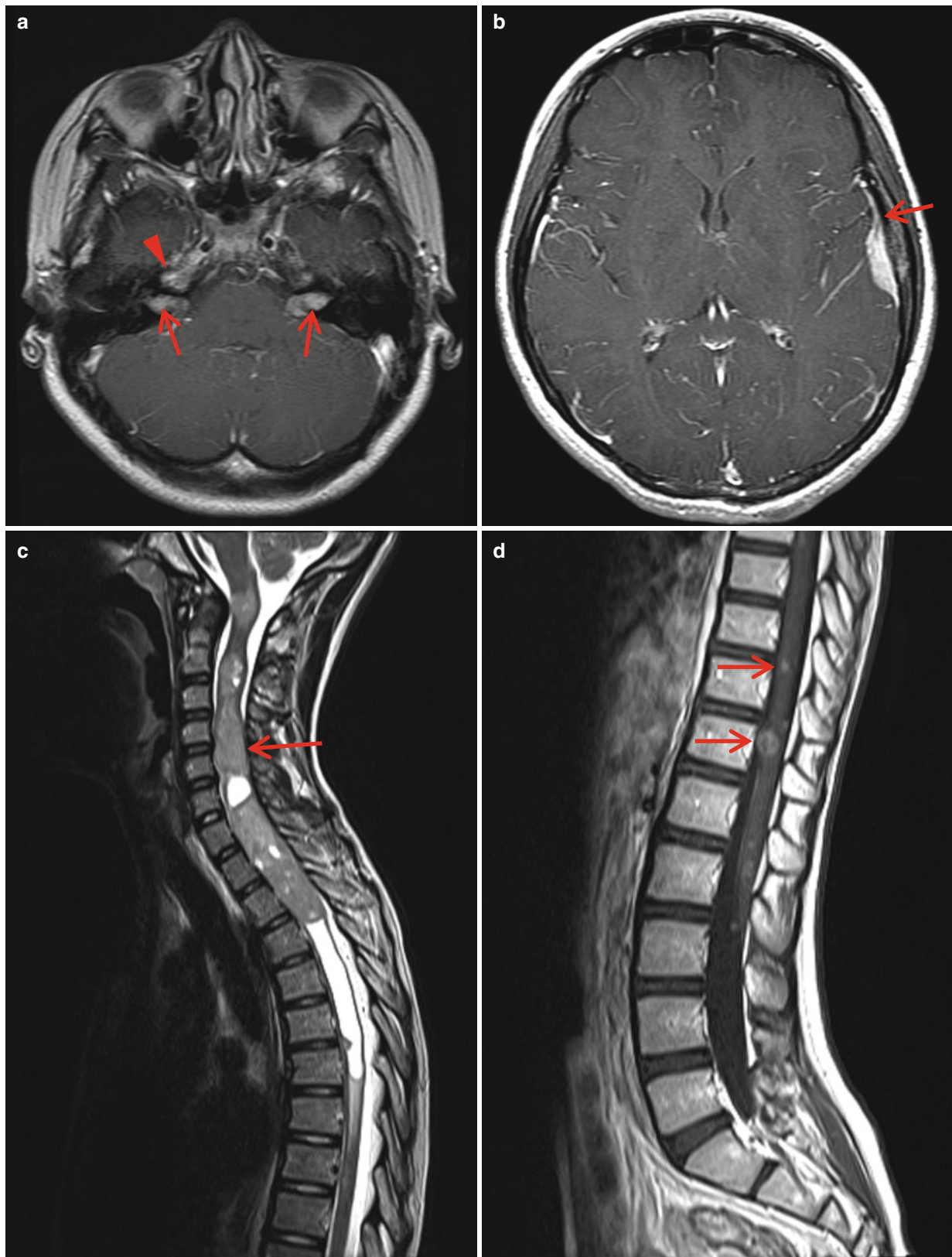


Fig. 1.16 Neurofibromatosis type 2. (a) Postcontrast T1 axial image shows bilateral acoustic neuromas (*arrows*) and enhancing nodules (arrowhead) within the right cavernous sinus. (b) Left temporal meningioma shows as a plaque-like enhancing mass with dural tail sign

(*arrow*). (c) Ependymoma along the cervicothoracic cord (*arrow*) shows diffuse medullary expansion with cystic components. (d) Multiple enhancing nodules (*arrows*) represent nerve root schwannomas

1.6.2.2.5 von Hippel-Lindau Disease

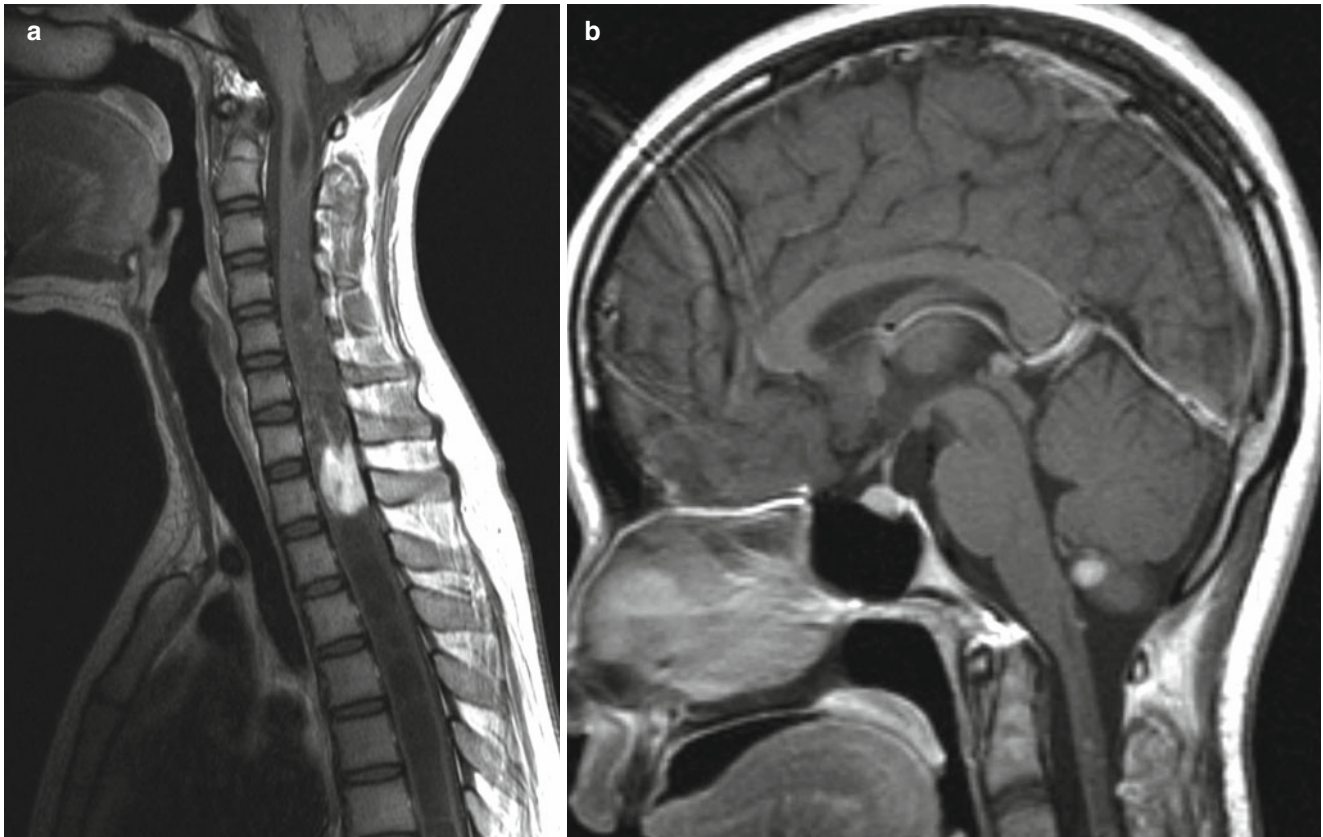


Fig. 1.17 von Hippel-Lindau disease with recurrent hemangioblastomas. **(a)** Postcontrast sagittal image of the spine shows a homogenous strong enhancing mass with cyst-like low signal of the distal spinal cord. Heterogeneous low-signal intensities of the spinal cord are seen

proximal to the enhancing mass. **(b)** Follow-up image after the removal of the spinal cord hemangioblastoma reveals a round enhancing nodule in the cerebellar tonsil and tiny nodules in the cervical cord region

1.6.2.2.6 Incontinentia Pigmenti

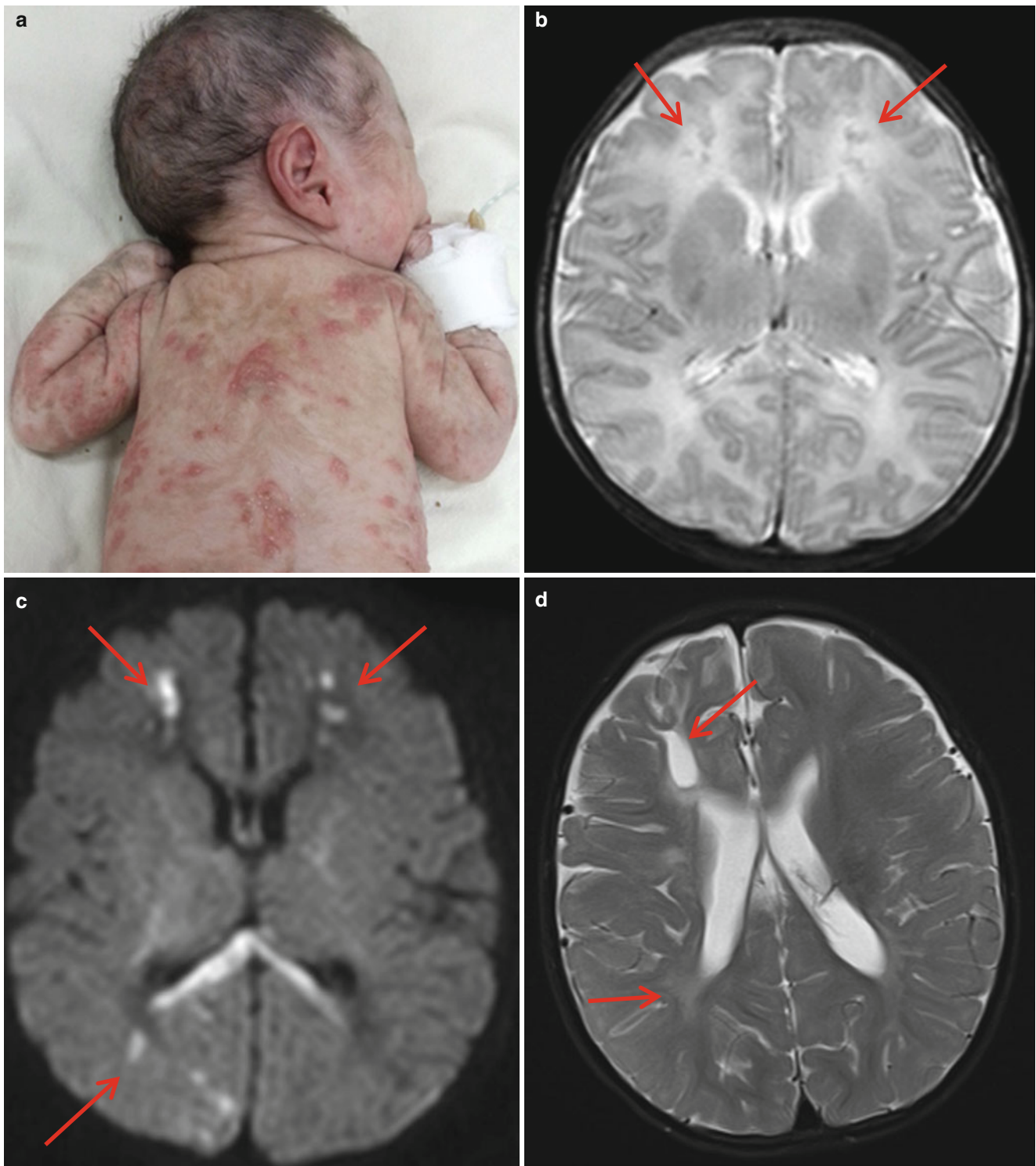


Fig. 1.18 Incontinentia pigmenti. (a) Newborn infant shows generalized skin desquamation and blister formations. (b) T2-weighted image shows multiple nodular low signal lesions (*arrows*). (c) Diffusion

image shows restricted diffusion of the nodular lesions (*arrows*). (d) T2-weighted image of another patient shows multifocal old ischemic lesions (*arrows*) in the subcortical and deep white matter areas

1.6.2.2.7 Neurocutaneous Melanosis

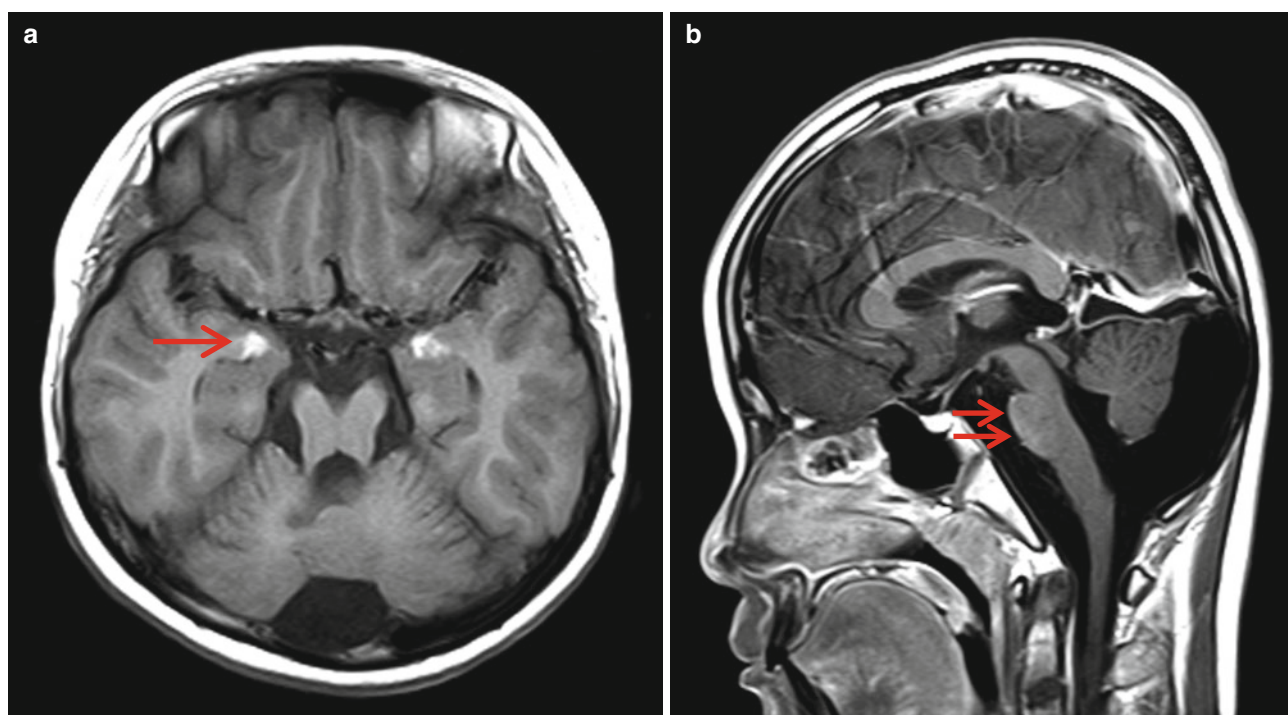


Fig. 1.19 Neurocutaneous melanosis. **(a)** T1 images show bilateral symmetric focal high-signal intensity in the anteromedial temporal lobes (*arrows*) and cerebellar folia. **(b)** Pons shows diffuse

high-signal intensity (*arrows*) and the retrocerebellar fluid collection suggests a Dandy-Walker variant

1.6.2.2.8 Ataxia-Telangiectasia

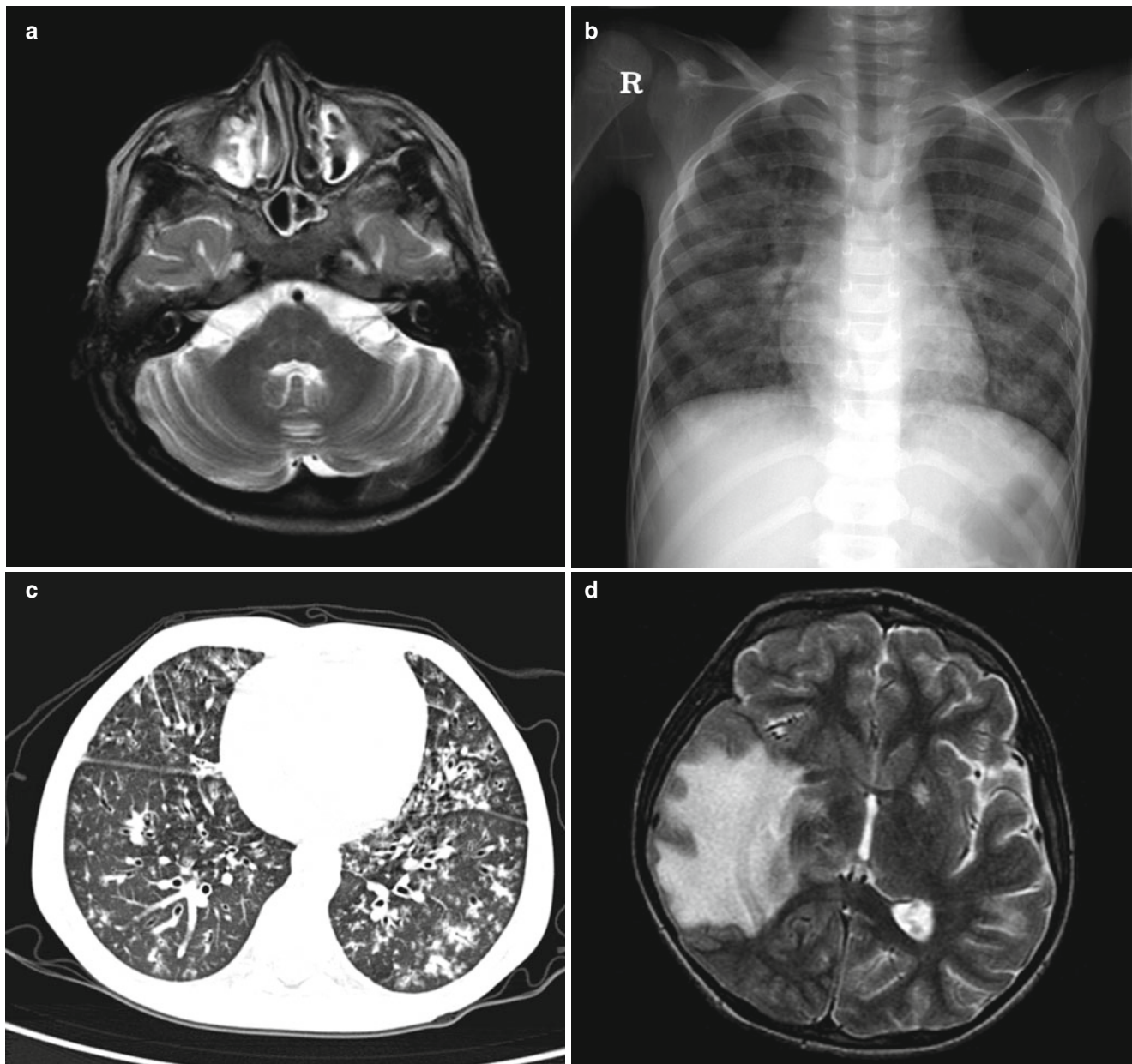


Fig. 1.20 Ataxia-telangiectasia with recurrent respiratory infection. **(a)** T2 axial image shows prominent folia in the entire cerebellum. **(b)** Plain chest radiography shows diffuse nodular infiltrations in both lungs. **(c)** High-resolution CT of the lung shows disseminated

bronchopneumonic infiltrations. **(d)** T2 axial image shows expansive high signal intensity lesion involving the right temporal lobe. The lesion was proved to be T-cell lymphoma

1.6.2.3 Congenital Anomaly of the Spinal Cord

1.6.2.3.1 Myelomeningocele

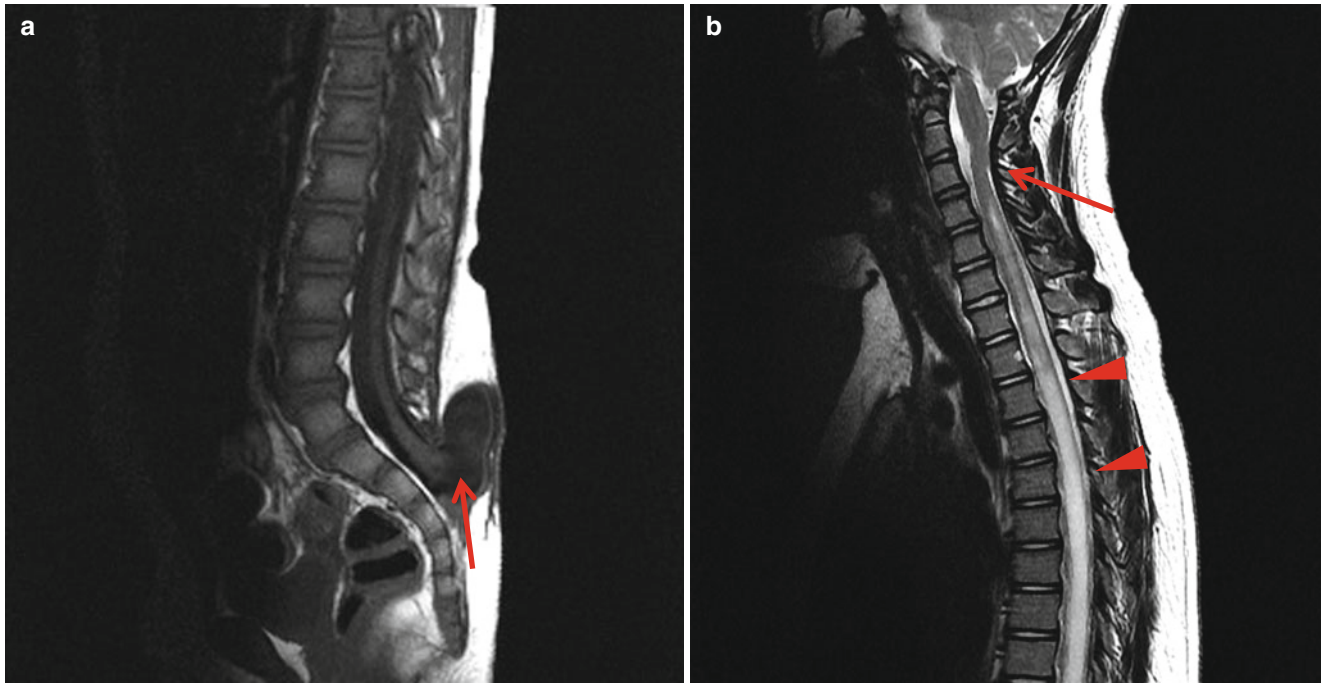


Fig. 1.21 Myelomeningocele. (a) T1-weighted image shows herniation of the distal cord connected with neural placode (*arrow*). (b) T2-weighted image shows Chiari malformation with cervicomedullary kink (*arrow*) and distal syringomyelia (*arrowheads*)

1.6.2.3.2 Lipomyelomeningocele

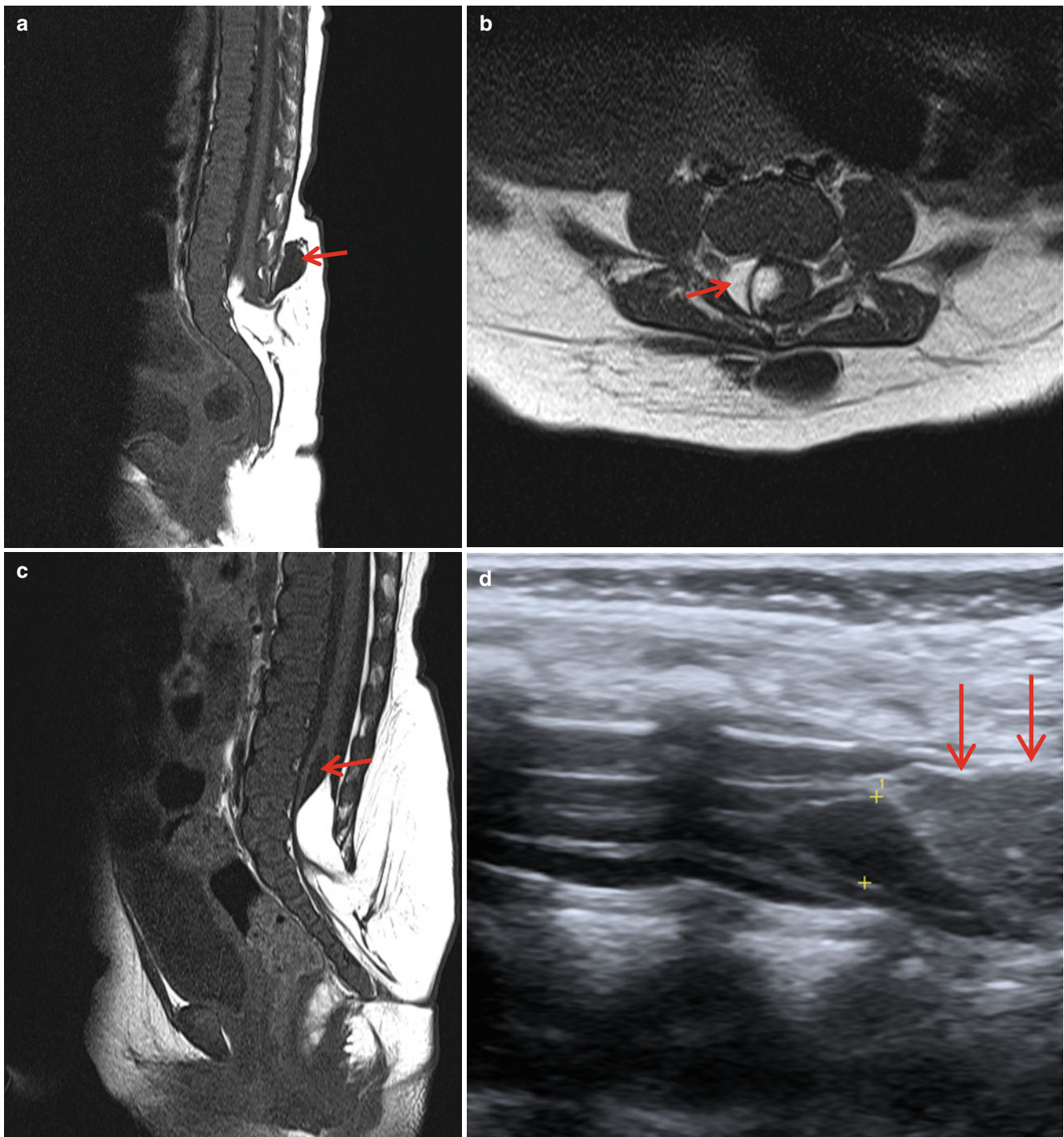


Fig. 1.22 Lipomyelomeningocele. (a) Low-lying spinal cord attached with lipoma connected with subcutaneous fatty tissue. Accompanied meningocele (*arrow*) is seen within the subcutaneous fatty mass. (b) Axial image shows lipoma displacing the cord to the right side.

(c) MR of lipomyelocoele shows hydromyelia (*arrow*) in the distal cord attached with lipoma. (d) Spinal US clearly demonstrates hydromyelia and lipoma (*arrows*)

1.6.2.3.3 Cervical Meningocele

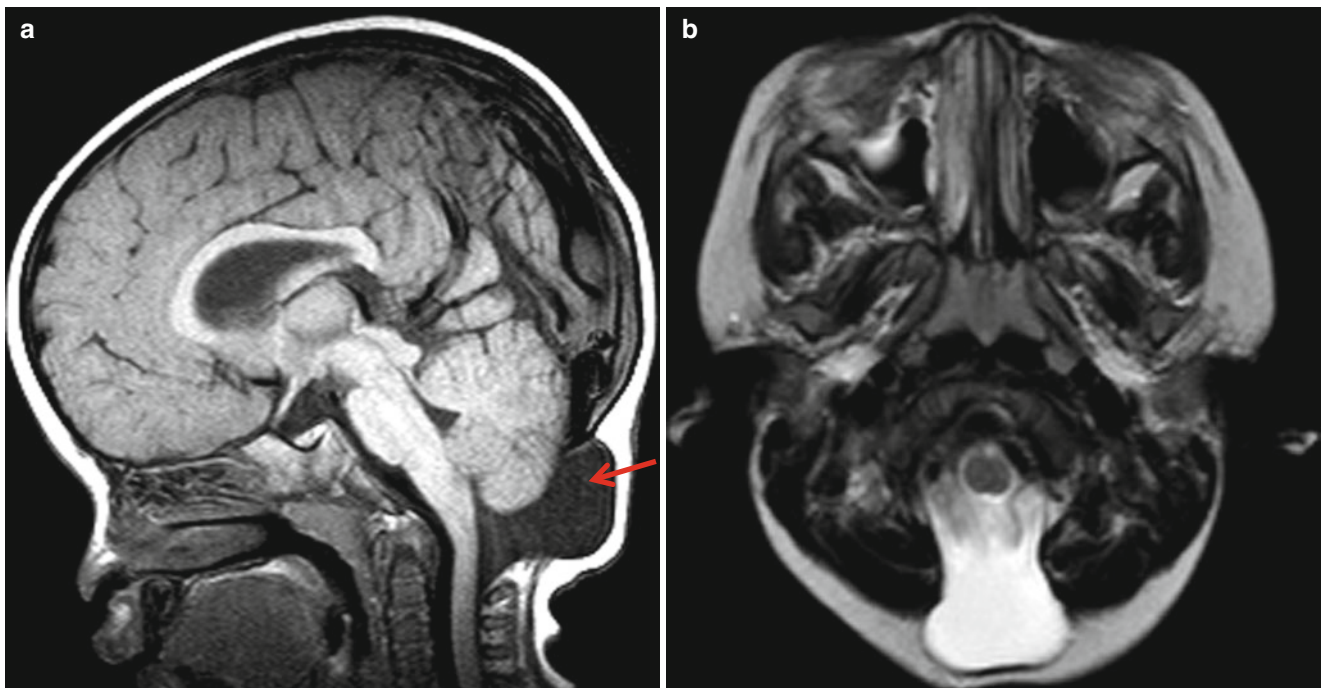


Fig. 1.23 Cervical meningocele. (a, b) CSF-containing meningeal sac (*arrow*) herniates through the posterior cervical spinal defect

1.6.2.3.4 Myelocystocele

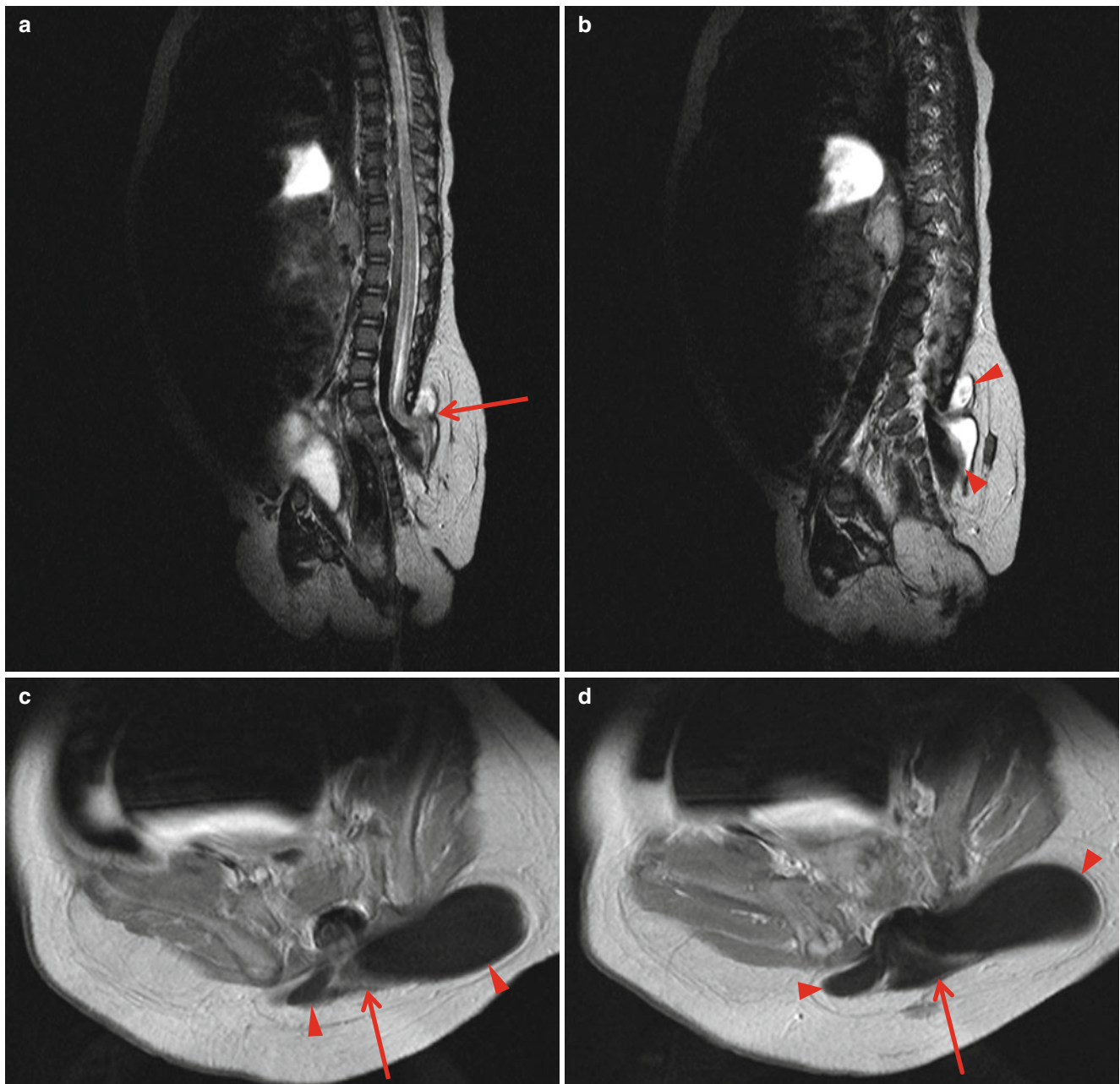


Fig. 1.24 Myelocystocele. (a, b) Sagittal images show herniation of the distal cord (*arrow*) and accompanied meningocele (*arrowheads*). Hydromyelia of the lower spinal cord is seen. (c, d) Axial image shows herniation of the hydromyelic cord (*arrow*) and accompanied menin-

gocele (*arrowheads*). (e, f) Another case with myelocystocele shows cystocele (*arrow*) and accompanied meningocele containing nerve roots (*arrowheads*). Herniation of the distal cord (*white arrows*) are well demonstrated with spinal US

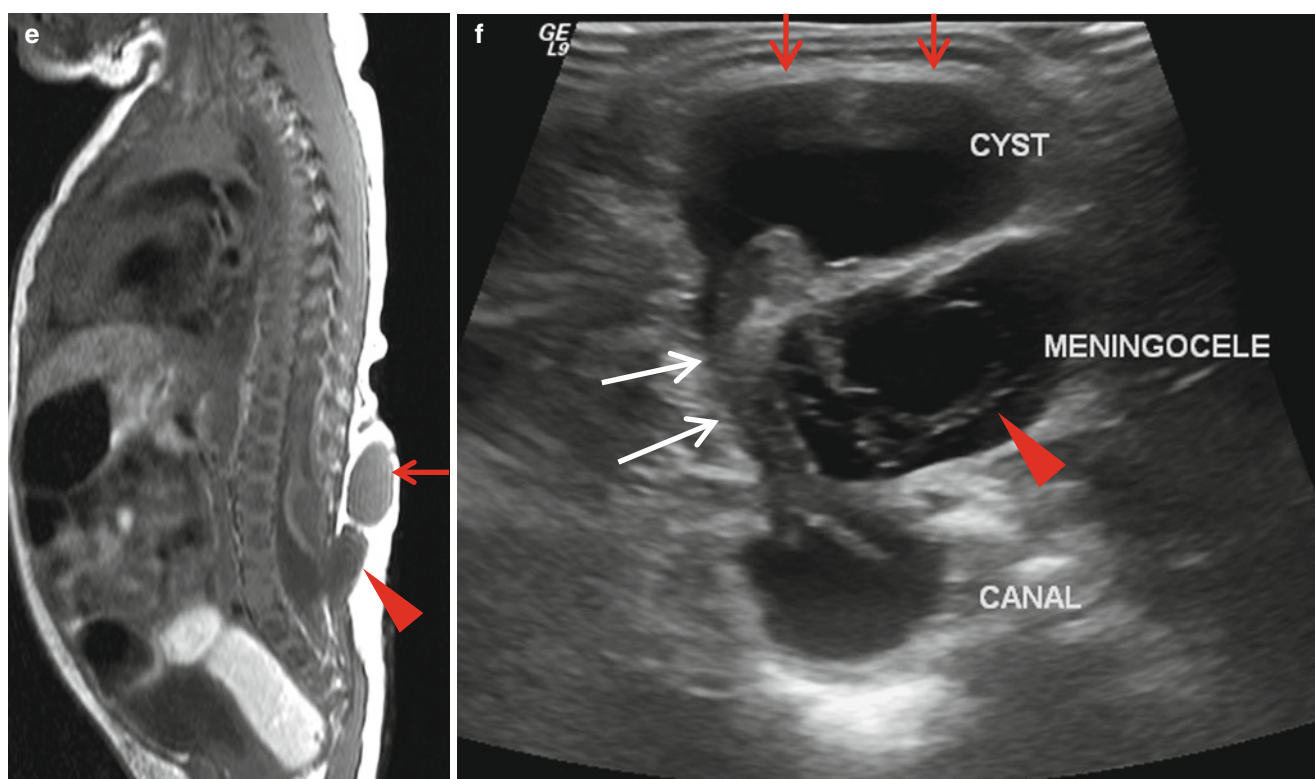


Fig. 1.24 (continued)

1.6.2.3.5 Dorsal Dermal Sinus with Intraspinal Infection

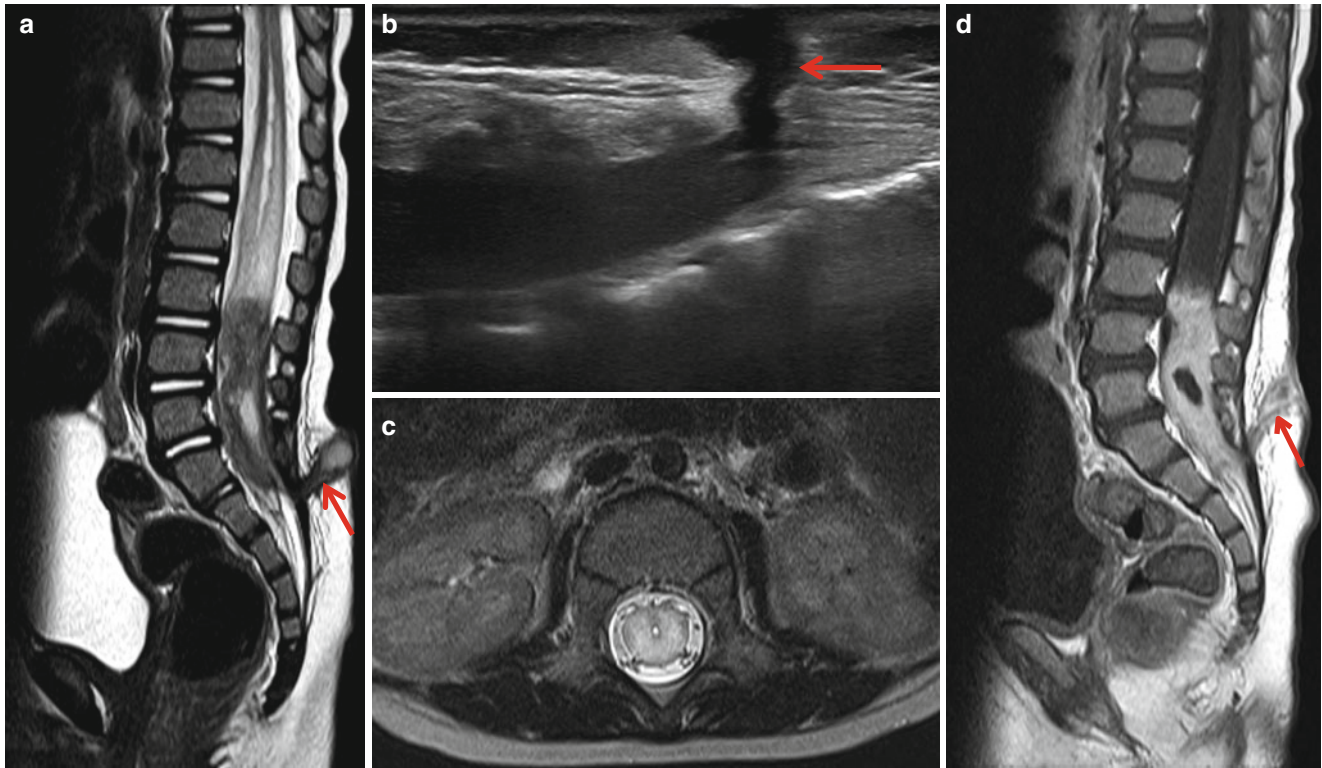


Fig. 1.25 Dorsal dermal sinus with intraspinal infection. (a) Dermal sinus tract (*arrow*) is connected with edematous low-lying spinal cord. Distal spinal cord shows heterogenous low signal intensity. (b) Spinal US demonstrates dorsal dermal sinus tract (*arrow*) connected with distal spinal cord. (c) Axial T2-weighted image shows diffuse swelling

of the cord. (d) Postcontrast image shows strong enhancement of the distal spinal cord and the sinus tract suggesting complicated infection. (e, f) Limited dorsal myeloschisis resembles dorsal dermal sinus. The sinus tract (*arrowheads*) tethering the cord revealed as fibrous tract instead of squamous epithelium

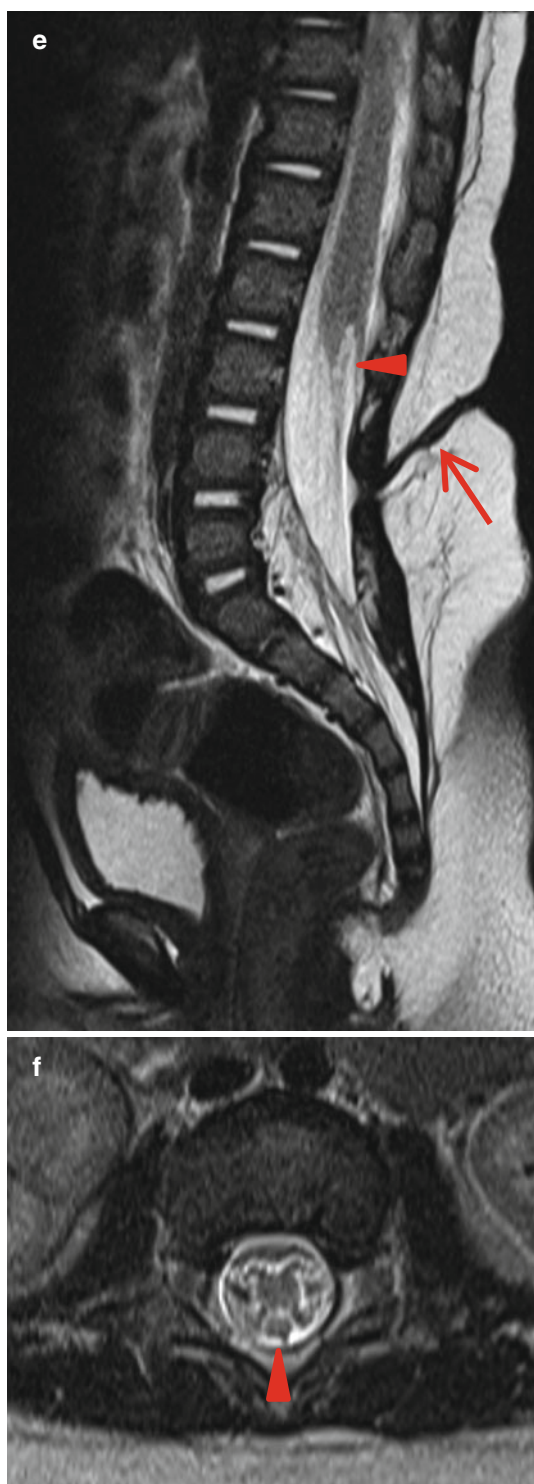


Fig. 1.25 (continued)

1.6.2.3.6 Neurenteric Cyst

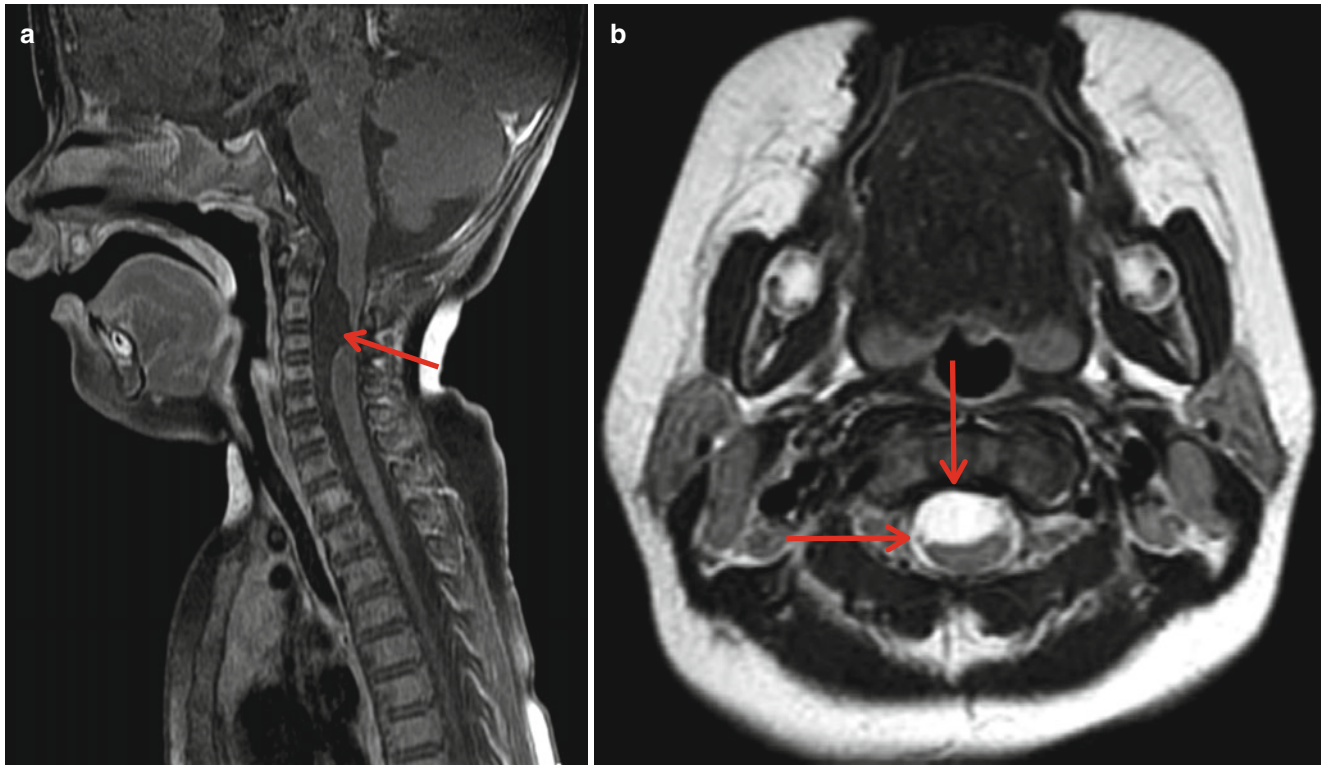


Fig. 1.26 Neurenteric cyst. (a, b) Intraspinal cystic mass (*arrows*) causes ventral indentation of the cervical cord. Vertebral anomaly was not present in this case

1.6.2.3.7 Diastematomyelia

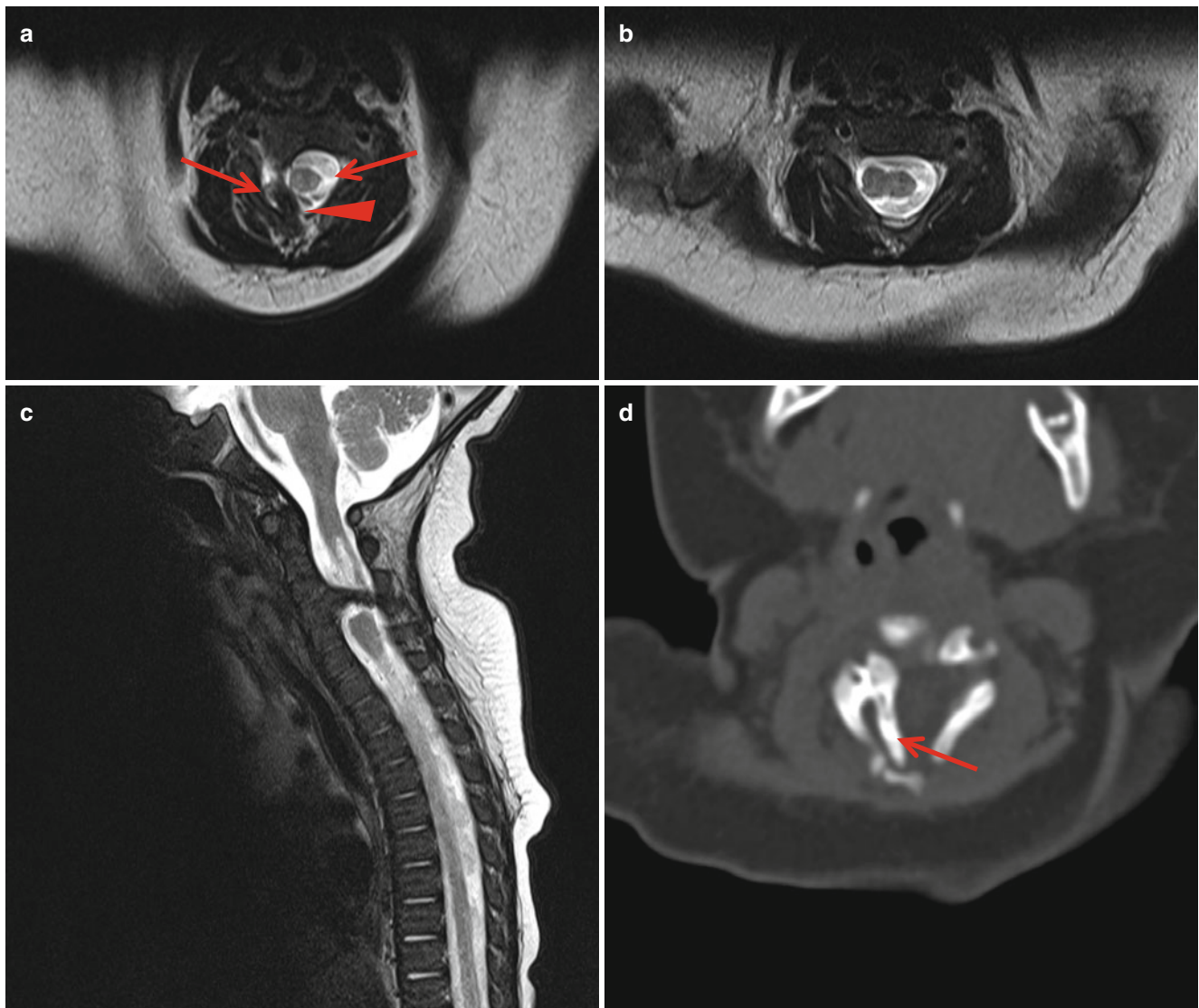


Fig. 1.27 Diastematomyelia. (a) T2-weighted axial image shows two hemicords (*arrows*) are split by bony bridge (*arrowhead*). (b) Two hemicords are reunited distal to the bony bridge. (c) Sagittal image

shows bony bridge traversing the spinal canal. (d) Bony bridge (*arrow*) is well demonstrated in CT

1.6.2.3.8 Lipoma of the Filum Terminale

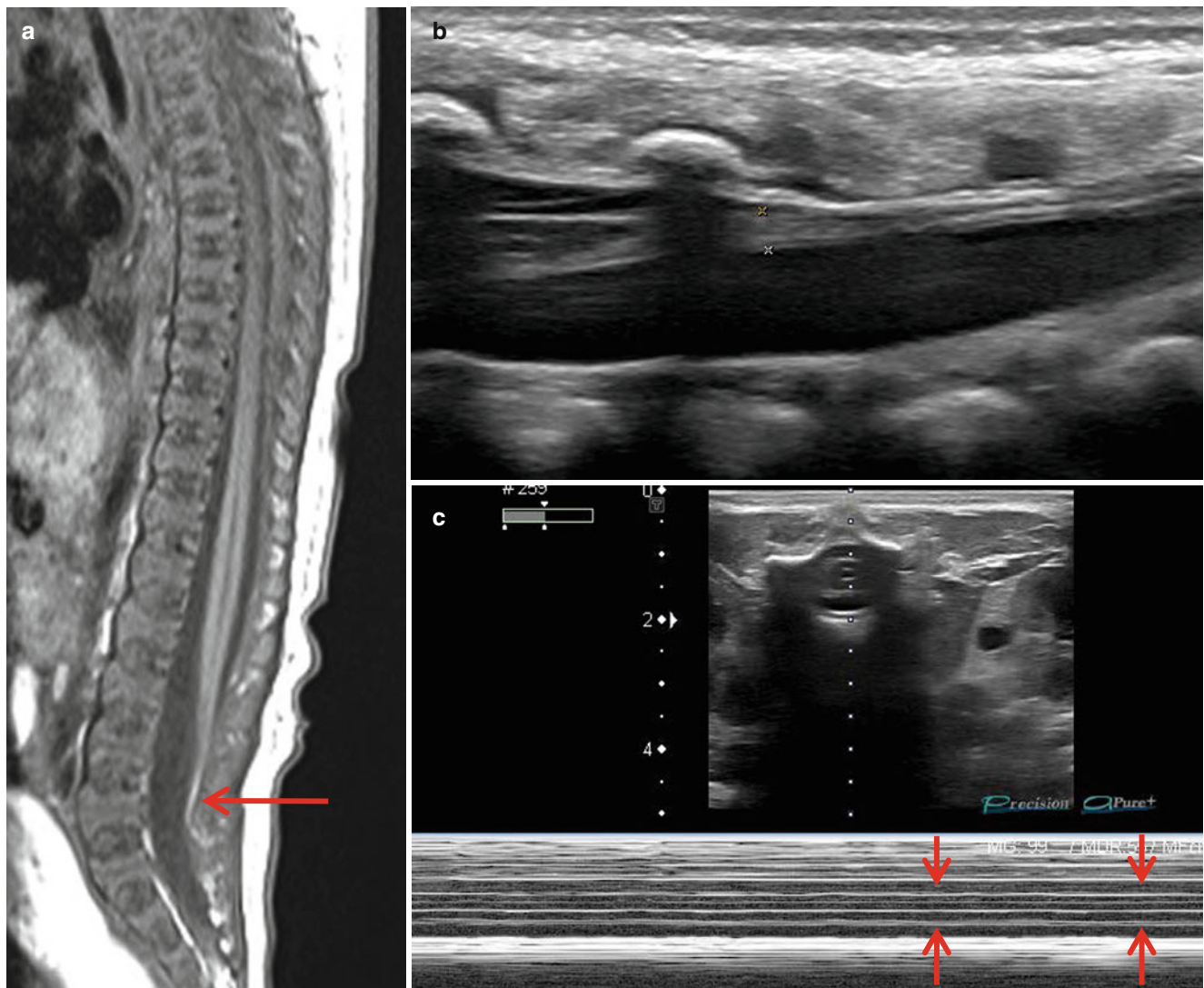


Fig. 1.28 Lipoma of the filum terminale. (a) Low-lying spinal cord with mild hydromyelia is tethered by a filar lipoma (*arrow*). (b) US of the distal spinal cord shows thickened echogenic filum terminale. (c) M-mode US shows decreased pulsatility (*arrows*) of the hydromyelic

spinal cord. (d) Fatty change of the filum terminale is tightly tethering the cord. (e) Postoperative change of the untethered filum terminale shows coiling appearance (*arrow*)

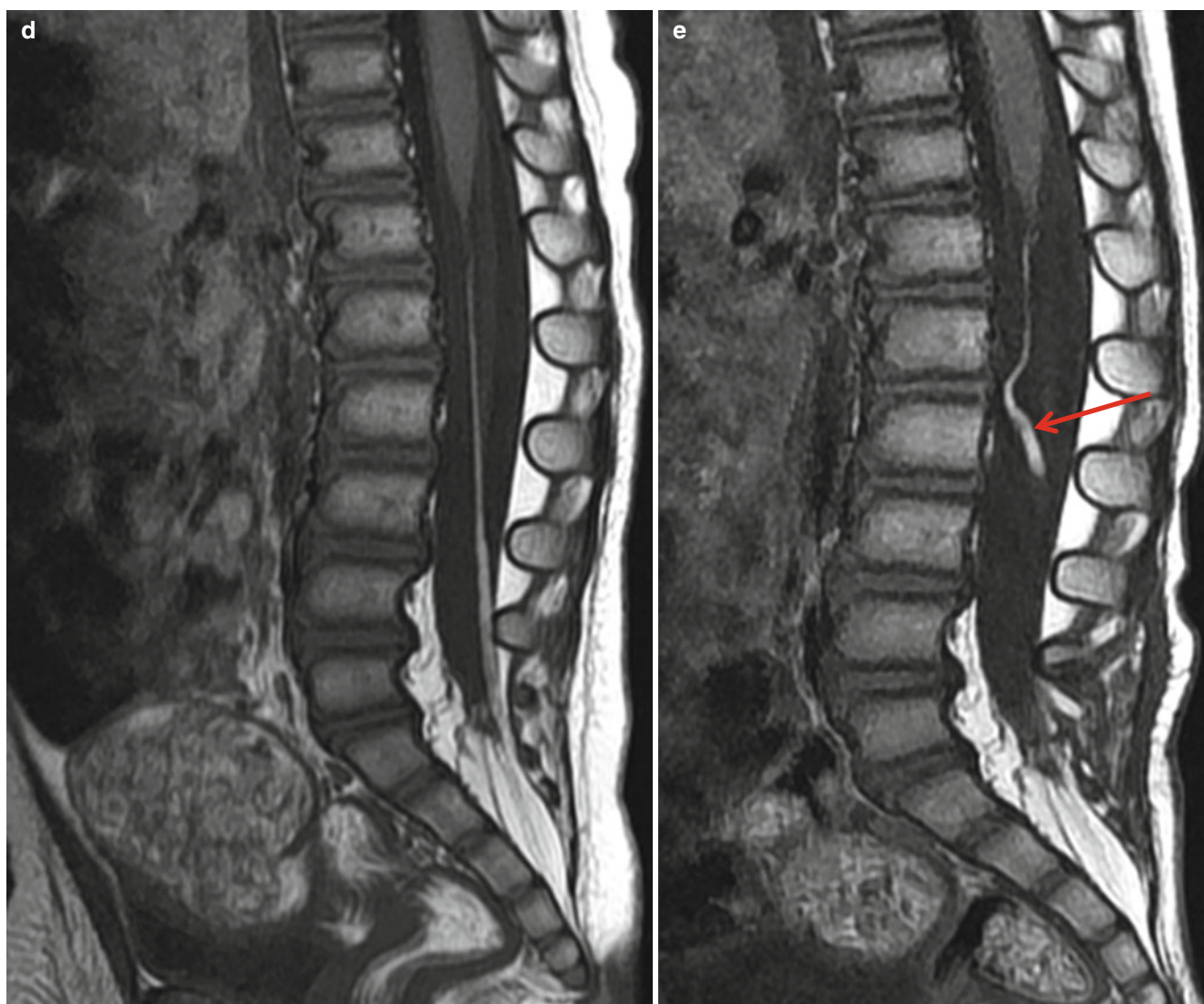


Fig. 1.28 (continued)

1.6.2.3.9 Caudal Regression Syndrome

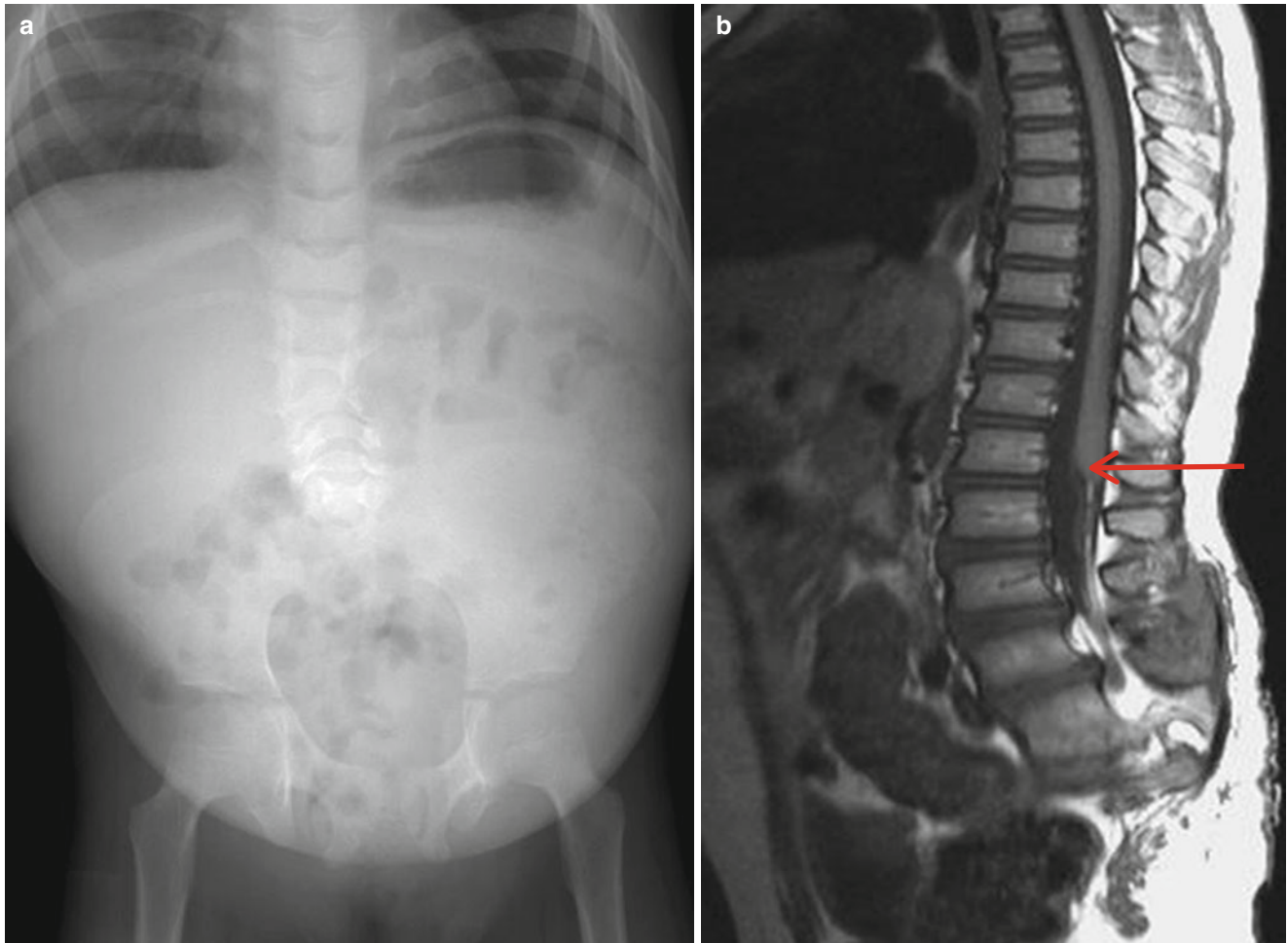


Fig. 1.29 Caudal regression syndrome. **(a)** Plain radiography shows close opposition of the ilium due to sacral agenesis. **(b)** Mid-sagittal image shows slanting (*arrow*) of the conus posteroinferiorly instead of normal cone shape and fatty filum. Sacrum and posterior neural arch of the distal lumbar spines are not formed

References

- Adachi Y, Poduri A, Kawaguchi A, et al. Congenital microcephaly with a simplified gyral pattern: associated findings and their significance. *AJNR Am J Neuroradiol*. 2011;32:1123–9.
- Altman NR, Naidich TP, Braffman BH. Posterior fossa malformation. *AJNR Am J Neuroradiol*. 1992;13:691–724.
- Barkovich AJ. Congenital malformations of the brain and skull, the phakomatosis. In: *Pediatric neuroimaging*. 5th ed. Philadelphia: Lippincott Williams & Wilkins; 2012a. p. 367–636.
- Barkovich AJ. Congenital anomalies of the spine. In: *Pediatric neuroimaging*. 5th ed. Philadelphia: Lippincott Williams & Wilkins; 2012b. p. 857–922.
- Barkovich AJ, Kjos BO. Nonlissencephalic cortical dysplasias: correlation of imaging findings with clinical deficits. *ANJR Am J Neuroradiol*. 1992a;13:95–103.
- Barkovich AJ, Kjos BO. Schizencephaly: correlation of clinical findings with MR characteristics. *AJNR Am J Neuroradiol*. 1992b;13:85–94.
- Barkovich AJ, Fram EK, Norman D. Septo-optic dysplasia: MR imaging. *Radiology*. 1989a;171:189–92.
- Barkovich AJ, Jackson Jr DE, Boyer RS. Band heterotopias: a newly recognized neuronal migration anomaly. *Radiol*. 1989b;171:455–8.
- Barkovich AJ, Gressens P, Evrard P. Formation, maturation, and disorders of brain neocortex. *AJNR Am J Neuroradiol*. 1992;13:423–46.
- Benedikt RA, Brown DC, Ghaed VN, et al. Sturge-Weber syndrome: cranial MR imaging with Gd-DTPA. *AJNR Am J Neuroradiol*. 1993;14:409–15.
- Bittencourt F, Marghoob A, Kopf A, Koenig K, Bart R. Large congenital melanocytic nevi and the risk for development of malignant melanoma and neurocutaneous melanocytosis. *Pediatrics*. 2000;206:736–41.
- Braffman BH, Bilaniuk LT, Naidich TP, et al. MR imaging of tuberous sclerosis: pathogenesis of this phakomatosis. Use of gadopentetate dimeglumine, and literature review. *Radiology*. 1992;183:227–38.
- Dias MS. Normal and abnormal development of the spine. *Neurosurg Clin N Am*. 2007;18:415–29.
- Georgy BA, Hesselink JR, Jernigan TL. MR imaging of the corpus callosum. *AJR Am J Roentgenol*. 1993;160:949–55.
- Guerrini R, Martini C. Genetic malformations of cortical development. *Exp Brain Res*. 2006;173:322–33.
- Hendrick EB, Hoffman HJ, Humphreys RP. The tethered spinal cord. *Clin Neurosurg*. 1983;30:457–63.
- Hennel SJ, Fkert PG, Volpe JJ, Inder TE. Insights into the pathogenesis of cerebral lesions in incontinentia pigmenti. *Pediatr Neurol*. 2003;29:148–50.
- Hetts SW, Sherr EH, Chao S, Gobuty S, Barkovich AJ. Anomalies of the corpus callosum: an MR analysis of the phenotypic spectrum of associated malformations. *AJR Am J Roentgenol*. 2006;187:1343–8.
- Kendall B, Kingsley D, Lambert SR, et al. Joubert syndrome: a clinico-radiological study. *Neuroradiol*. 1990;31:502–6.
- McLone DG, Knepper PA. The cause of Chiari II malformation: a unified theory. *Pediatr Neurosci*. 1989;15:1–12.
- McLone DG, Naidich TP. Developmental morphology for the subarachnoid space, brain vasculature, and contiguous structures, and the cause of the Chiari II malformation. *AJNR Am J Neuroradiol*. 1992;13:463–82.
- Mentzel H-J, Seidel J, Fitzek C, et al. Pediatric brain MRI in neurofibromatosis type 1. *Eur Radiol*. 2005;15:814–22.
- Naidich TP, Fernbach SK, McLone DG, Shlonik A. John Caffey Award. Sonography of the caudal spine and back: congenital anomalies in children. *AJNR Am J Neuroradiol*. 1984;5:221–34.
- Naidich TP, Altman NR, Braffman BH, et al. Cephaloceles and related malformations. *AJNR Am J Neuroradiol*. 1992;13:655–90.
- Neyn SM. Ataxia-telangiectasia, cancer, and pathobiology of the ATM gene. *Clin Genet*. 1999;55:289–304.
- Nievelstein RAJ, Valk J, Smit LME, Vermeij-Keers C. MR of the caudal regression syndrome: embryologic implications. *AJNR Am J Neuroradiol*. 1994;15:1021–209.
- Nunes F, MacCollin M. Neurofibromatosis 2 in the pediatric population. *J Child Neurol*. 2003;18:718–24.
- Pang D, Zovickian J, Oviedo A, Moes GS. Limited dorsal myeloschisis: a distinctive clinicopathological entity. *Neurosurgery*. 2010;67:1555–80.
- Parisi MA, Dobyns WB. Human malformations of the midbrain and hindbrain: review and proposed classification scheme. *Mol Genet Metab*. 2003;80:36–53.
- Rufener SL, Ibrahim M, Raybaud CA, Parmar H. Congenital spine and spinal cord malformations – pictorial review. *AJR Am J Roentgenol*. 2010;194:S26–37.
- Seidenwurm DJ, Barkovich AJ. Understanding tuberous sclerosis. *Radiology*. 1992;183:23–4.
- Sinha S, argarwal D, Mahapatra AK. Split cord malformations: an experience of 203 cases. *Childs Nerv Syst*. 2006;22:3–7.
- Slater A, Moore N, Huson S. The natural history of cerebellar hemangioblastomas in von Hippel-Lindau disease. *AJNR Am J Neuroradiol*. 2003;24:1570–4.
- Smirniotopoulos JG, Murphy FM. The phakomatoses. *AJNR Am J Neuroradiol*. 1992;13:725–46.
- Tassi L, Colombo N, Garbelli R, et al. Focal cortical dysplasia: neuropathological subtypes, EEG, neuroimaging and surgical outcome. *Brain*. 2002;125:1719–32.
- Zimmerman RA, Yachnis AT, Rorke CB, et al. Pathology of findings of cerebral high signal intensity in two patients with type 1 neurofibromatosis. *Radiology*. 1992;185(Suppl):123.

In-One Kim

Contents

2.1	Introduction	46
2.2	Pathophysiology	46
2.3	Imaging	46
2.4	Spectrum of Metabolic Brain Diseases	47
2.4.1	Lysosomal Disorders	47
2.4.2	Peroxisomal Disorders	47
2.4.3	Mitochondrial Disorders	48
2.4.4	Amino Acid Metabolic Disorders	48
2.4.5	Other Uncategorized Disorders	49
2.5	Illustrations: Metabolic Disease of the Brain	51
2.5.1	Schematic Drawing of Oligodendrocytes Extending Myelin Sheath over the Axons	51
2.5.2	MR Imaging of Normal Progression of Myelination	52
2.5.3	Delayed Myelination in Niemann-Pick Disease	55
2.5.4	Metachromatic Leukodystrophy	56
2.5.5	Krabbe Disease	57
2.5.6	Mucopolysaccharidoses	59
2.5.7	XR Adrenoleukodystrophy	60
2.5.8	Leigh Disease	61
2.5.9	MELAS	62
2.5.10	Glutaric Aciduria Type 1	63
2.5.11	Nonketotic Hyperglycinemia	64
2.5.12	Citrullinemia	65
2.5.13	Isovaleric Academia	66
2.5.14	Homocystinuria	67
2.5.15	Pelizaeus-Merzbacher Disease	68
2.5.16	Alexander Disease	69
2.5.17	Canavan Disease	70
2.5.18	Megalencephalic Leukoencephalopathy with Subcortical Cyst	71
2.5.19	Menkes Disease	72
2.5.20	Wilson's Disease	73
	References	74

I.-O. Kim, M.D.
 Department of Radiology, Seoul National University Hospital,
 Seoul National University College of Medicine,
 101 Daehak-ro, Chongno-gu, Seoul 110-744, Korea
 e-mail: kimio@snu.ac.kr

2.1 Introduction

Metabolic brain diseases can affect gray or white matter, but they frequently cause white matter disorders (also known as leukodystrophy), which result from the dysfunction of single or multiple enzymes. The term “leukodystrophy” refers to a group of genetically transmitted diseases in which abnormal metabolism of myelin constituents leads to progressive demyelination. Common concepts are demyelination and inborn error of metabolism. Chromosomal abnormalities are disclosed more in various metabolic diseases, and treatment modalities are becoming more optimistic; these include enzyme replacement, stem cell transplantation, or gene therapy.

Leukodystrophies comprise those disorders in which myelin is not formed properly, or myelin formation is delayed or arrested, or the maintenance of already formed myelin is disturbed. Damage to the myelin is mostly represented by the loss of myelin, i.e., demyelination. Myelin sheaths facilitate nerve conduction, so myelination means functional maturation of the nervous system. Demyelination results in delayed nerve conduction velocity, which means functional loss of nerve fibers.

A myelin sheath is a part of the cytoplasmic process of the oligodendrocyte, and the metabolism of oligodendrocytes is essential for the production and maintenance of normal myelin (Fig. 2.1). The metabolism of an oligodendrocyte will be disturbed by the organelles with the defective enzymes. The diseases can be categorized according to the defect of the organelles or amino acid metabolism, and the most frequently involved organelles are the lysosome, peroxisome, and mitochondria (Kendall 1992).

White matter diseases that result from lysosomal enzyme defects include metachromatic leukodystrophy, Krabbe disease, and storage diseases such as lipidoses or mucopolysaccharidoses. Peroxisomal enzyme defects cause classic adrenoleukodystrophy, Refsum disease, and Zellweger Cerebrohepatorenal syndrome. Mitochondrial disorders include Leigh disease, Kearns-Sayre disease, and the mitochondrial encephalomyelopathies such as mitochondrial encephalopathy, lactic acidosis, and stroke-like episodes (Cheon et al. 2002).

Although definite imaging diagnosis is difficult in many of the cases, the recognition of specific metabolic disorders can afford effective therapy and allow for genetic counseling and prevention of future cases. MR imaging can visualize the extent of tissue damage and narrows the spectrum of differential diagnosis to reach early diagnosis and treatment. MR imaging and MR diffusion or spectroscopy are expected to allow monitoring of the disease progression and treatment response and better understanding of the disorders (Knaap and Valk 2005; Kendall 1993).

2.2 Pathophysiology

In metabolic diseases, the normal metabolic pathways are blocked, resulting in the accumulation of abnormal biochemical products or insufficiency of normal products that are essential for the metabolism of tissues and organs. In the nervous system, the production of abnormal molecules or buildup of abnormal metabolites can result in the formation of abnormal myelin or toxic damage to the brain. Metabolic disorders can be divided into three pathophysiological considerations:

1. Defects in the synthesis or catabolism of molecules with pertinent symptoms. These include lysosomal disorders, peroxisomal disorders, and disorders of intracellular transport and processing.
2. Defects of energy production or end-organ failure of energy utilization, such as the brain, muscle, or liver. These include mitochondrial respiratory chain disorders, congenital lactic acidemias, and fatty acid oxidation defects.
3. Acute or progressive accumulation of toxic compounds related to food intake. These include disorders of amino acid metabolism, organic acidemias, congenital urea cycle defects, and sugar intolerances (galactosemia) (Patay 2005).

2.3 Imaging

Diagnosis of white matter disease is frequently difficult because of nonspecific clinical features or nonspecific imaging characteristics and diversity of biochemical abnormalities. So far, magnetic resonance (MR) imaging is the most sensitive diagnostic modality for evaluating white matter abnormality. Normal myelination progresses in an orderly fashion, and MR signal intensity of the pediatric brain changes continuously during the first 24 months of life. In the unmyelinated brain, the white matter is hypointense to the gray matter on T1-weighted images and hyperintense on T2-weighted images due to high water content. The signal intensity of the myelinated white matter becomes hyperintense on T1-weighted images due to the high lipid content of myelin, and hypointense on T2-weighted images (Fig. 2.2) (Barkovich et al. 1988). Demyelinated lesions show hyperintensity on T2-weighted images and hypointensity on T1-weighted images (Fig. 2.3). Although MR imaging is the most sensitive imaging tool, imaging strategies are necessary to take into account the selective vulnerability and pattern recognition of various diseases. Imaging features suggestive of leukodystrophies are myelination abnormality, symmetry or bilaterality, atrophy, and the progressive nature of the diseases. The presence of brainstem and

cerebellar involvement, contrast enhancement, spinal cord involvement, or associated malformation can be helpful for the differential diagnosis (Schiffmann and van der Knaap 2009). Diffusion image or MR spectroscopy can provide additional information (Barkovich 2000).

2.4 Spectrum of Metabolic Brain Diseases

2.4.1 Lysosomal Disorders

The lysosome is a storage organelle containing hydrolytic enzymes that has important functions in the phagocytosis of metabolic degradation products. Lysosomal dysfunction is usually caused by a single enzyme deficiency required for the metabolism of lipids, glycoproteins, or so-called mucopolysaccharides. Lysosomal enzymatic deficiencies lead to an abnormal accumulation of excess products destined for breakdown and recycling, which cause cellular dysfunction of oligodendrocytes, resulting in disintegration of the myelin sheath (Walkley 2009). Lysosomal disorders are storage diseases such as metachromatic leukodystrophy, Krabbe disease, lipidosis, or mucopolysaccharidosis.

2.4.1.1 Metachromatic Leukodystrophy

Metachromatic leukodystrophy is an autosomal recessive disorder, and the basic defect is decreased enzymatic activity of lysosomal enzyme (arylsulfatase A) or activator protein (saposin B). The enzyme is necessary for the normal metabolism of sulfatides, which are important constituents of the myelin sheath. Infantile, juvenile, and adult forms are recognized according to the clinical onset of disease. The infantile form is the most common, and progressive neurological dysfunction leads to muscular hypotonia, cerebral palsy, polyneuropathy, mental retardation and blindness within several years. Diagnosis can be made by measuring the activity of arylsulfatase in the leukocyte or in the urine.

MR imaging shows an initial patch white matter lesions, but later on there are diffuse bilateral symmetric hyperintense T2 signal intensity of the deep white matters. The peripheral subcortical white matters are spared until late in the disease, and tissue loss or brain atrophy is not a common feature until the later stages of the disease. Contrast enhancement is absent in the demyelinated white matter (Kim et al. 1997). Ultrasonography can show a thickened gallbladder wall due to the accumulation of the sulfatides (Kim et al. 1996a) (Fig. 2.4).

2.4.1.2 Krabbe Disease (Globoid Cell Leukodystrophy)

Krabbe disease arises from a deficiency of galactocerebroside β -galactosidase leading to the accumulation of cerebroside and demyelination. Chromosome 14 abnormality has

been described. Clinical onset typically occurs between 3 and 5 months of age. Progressive neurological deterioration begins with irritability and hypertonicity and rapidly evolves into a vegetative state. Death usually occurs by age 2–3.

MR imaging shows a hyperintense signal on T2-weighted imaging involving diffuse periventricular deep white matter. Rapid disease progression is common with diffuse brain atrophy in contrast to the metachromatic leukodystrophy (Fig. 2.5). Contrast enhancement can be present at the peripheral portion of the involved white matters. Calcification can be present in the basal ganglia (Cheon et al. 2002).

2.4.1.3 Mucopolysaccharidoses (MPS)

MPS are mostly autosomal recessive disorders characterized by enzyme deficiency with an inability to break down glycosaminoglycan (GAG), resulting in the accumulation of a toxic intracellular substrate. Clinical manifestations are variable skeletal and extraskelatal abnormalities that include dwarfism, lumbar kyphosis, macrocephaly, general osteoporosis, sensorineural deafness, aortic regurgitation, and hepatosplenomegaly. Currently, MPSs are classified into seven well-defined syndromes.

A typical MR finding of the brain is dilated perivascular spaces due to GAG accumulation, which gives rise to a cribriform appearance in the periventricular WM, corpus callosum, and basal ganglia on T1- and T2-weighted images. Macrocephaly or communicating hydrocephaly can be seen (Fig. 2.6). MPS patients may have cervical myelopathy owing to spinal canal stenosis or atlantoaxial subluxation (Rasalkar et al. 2011).

2.4.2 Peroxisomal Disorders

Peroxisomes are oxidative organelles that are present in all tissues, and especially abundant in the liver and kidney. They contain enzymes for the simple respiratory pathway: oxidase and catalase (peroxidase). Important functions of the peroxisome include β -oxidation of very long-chain fatty acid and biosynthesis of bile acids and plasminogens that are important in myelin production. There are two types of peroxisomal disorders: single peroxisomal enzyme deficiencies and peroxisomal biogenesis defects (PBDs). The most severe and important PBD is the Zellweger spectrum, and the most frequent peroxisomal disorder is X-linked adrenoleukodystrophy (XALD).

2.4.2.1 X-Adrenoleukodystrophy (ALD)

X-linked adrenoleukodystrophy is caused by the mutation of a gene on Xq28, causing an ALD protein defect leading to the accumulation of very long-chain fatty acids (VLCFA) in glial cells including oligodendrocytes.

The abnormal accumulation of VLCFA destabilizes myelin and results in progressive leukodystrophy. The classic form is an X-linked recessive disorder with clinical onset in the first decade of life. Adrenal insufficiency begins early in childhood. Neurological manifestations can begin with behavioral changes and progress to loss of vision, neurocognitive dysfunction, spasticity, and progressive motor and sensory deficits, and can lead to death within 5–8 years.

MR imaging shows typical symmetrical involvement of parieto-occipital deep white matter extending dorsoventrally. The descending tract involvement along the neuronal tract is also a typical feature (Barkovich et al. 1997). In a small percentage of the patients, frontal white matter involvement can be seen initially. Abnormal enhancement of the central zone of the involved white matter showing 3-zonal appearance of the white matter lesions is a characteristic finding (Fig. 2.7) (Kim et al. 1994).

2.4.2.2 Zellweger Syndrome

Zellweger syndrome is an autosomal recessive disease with hepatic dysfunction, severe hypotonia, and facial dysmorphism. Death usually occurs during the first year of life. MR imaging shows diffuse white matter abnormality and migration abnormality.

2.4.3 Mitochondrial Disorders

Mitochondria are the organelles that supply energy to cells in the form of ATP through the process of respiratory oxidation. Mitochondrial disorder is a group of diseases caused by dysfunctional mitochondria caused by mutations – acquired or inherited – in mitochondrial DNA (mtDNA) or in nuclear genes that code for mitochondrial components. Various enzyme deficiencies involve Krebs cycle and respiratory oxidation leading to insufficient energy supply and accumulation of lactate and pyruvate (Valanne et al. 1998). MR spectroscopy is useful, showing an abnormal high peak of lactate that supports the diagnosis of mitochondrial diseases (Detre et al. 1991). Organs of high energy demand such as brain, heart, and muscles especially extraocular muscles can cause clinical symptoms.

2.4.3.1 Leigh Disease (Subacute Necrotizing Encephalomyelopathy)

Leigh disease can be caused by mutations in mitochondrial DNA or by deficiencies of an enzyme called pyruvate dehydrogenase. Clinical signs include generalized weakness, lack of muscle tone, seizures, episodes of lactic acidosis, ophthalmoplegia, and progressive spasticity. Symptoms of Leigh disease usually progress rapidly. Abnormally high signals on

T2-weighted images in the basal ganglia, periaqueductal gray matter, and brainstem are characteristic (Fig. 2.8) (Hegde et al. 2011).

2.4.3.2 Mitochondrial Encephalopathy, Lactic Acidosis, and Stroke-Like Episodes (MELAS)

MELAS shows acute stroke-like lesions involving supra- and infratentorial structures. These lesions frequently do not follow the vascular territory, and multiple episodes of infarction-like lesions with migrating natures are common. The medial aspect of the occipital lobe is a rather frequent location of the lesions. Basal ganglia abnormalities are commonly present (Fig. 2.9). Cerebral angiography shows no evidence of vascular occlusion, and the stroke-like episode is probably caused by energy failure of the end organ. On diffusion MRI, the lesions frequently show normal diffusion or restricted diffusion only in a small portion of the lesion (Kim et al. 1996b).

2.4.4 Amino Acid Metabolic Disorders

Amino acids are metabolized in order to provide energy or to make other needed compounds. Amino acid metabolic disorders are a group of inherited defects of the degradation of amino acids causing metabolic block resulting in acute or progressive accumulation of toxic compounds. These include disorders of amino acid metabolism (phenylketonuria, homocystinuria, maple syrup urine disease, glutaric acidemia type 1 (Fig. 2.10) (Brismar and Ozand 1995), nonketotic hyperglycinemia (Fig. 2.11)), urea cycle defects (Takanashi et al. 2003) (Fig. 2.12), and organic acidemias. Organic acidemia (aciduria) is a particular metabolic disorder dealing with branched-chain amino acids including isoleucine, leucine, and valine. The four main types of organic acidemias are methylmalonic acidemia, propionic acidemia, isovaleric acidemia (Fig. 2.13), and maple syrup urine disease. Abnormal metabolites can cause selective vulnerability; for example, a high concentration of ammonia causes neuronal cell swelling, or elevated homocysteine causes venous and arterial thrombosis and infarcts (Fig. 2.14). Most amino acid disorders present with a severe encephalopathy in the neonatal period. Neurological damage and developmental delay are common factors in diagnosis, with associated symptoms ranging from poor feeding to slow growth, lethargy, vomiting, dehydration, seizure, malnutrition, hypoglycemia, hypotonia, metabolic acidosis, hyperammonemia, and, if left untreated, death (Thomas et al. 2010). Spongy myelinopathy involving the central myelin is common in amino acid disorders.

2.4.5 Other Uncategorized Disorders

2.4.5.1 Pelizaeus-Merzbacher Disease (PMD)

PMD is a rare X-linked recessive disorder with a prototype of a dysmyelinating leukodystrophy that is caused by a mutation in the proteolipid protein 1 (*PLP1*) gene on the long arm of the X chromosome in band Xq22 (Fig. 2.15). This mutation results in the abnormal expression or production of PLP. PLP1 is a myelin protein, so the disease affects the growth of the myelin sheath. PMD is a unique disease showing generalized myelin paucity on MR imaging. There are two forms: the classic form, showing a chronic protracted course, and the connatal form, showing either autosomal or X-linked recessive inheritance with early progression. Affected patients frequently show nystagmoid eye movements, spastic quadriplegia, intentional tremor, head tilting, ataxia, and developmental delays.

In classical PMD, MRI shows generalized absent myelination, but frank white matter destruction or early brain atrophy is not present. White matter tracts show generalized high-signal intensities on T2-weighted image and fluid-attenuated inversion recovery (FLAIR) image, including subcortical U-fibers and internal capsules (Takanashi et al. 1999).

2.4.5.2 Alexander Disease (AD)

AD is a rare, nonfamilial disorder caused by the mutation of glial fibrillary acidic protein (GFAP) gene (Fig. 2.16). It is characterized by progressive demyelination of the central nervous system and the accumulation of Rosenthal fibers within astrocytes. Affected patients typically present with megalencephaly and frontal preponderance of white matter abnormalities. Various clinical subtypes have been recognized: infantile, juvenile, and adult type. Most of the reported cases have been of the infantile variant, with early onset of macrocephaly and rapid neurological deterioration leading to early death. A neonatal variant is even more rapidly fatal. A less frequently reported subtype is the juvenile variant, in which macrocephaly is a less consistent feature and disease progression is less rapid. The pathological hallmark of the disease is the presence of Rosenthal fibers throughout the CNS that are abnormal intracytoplasmic proteinaceous inclusions in the astrocyte. A brain biopsy, which is an invasive procedure, is a diagnostic necessity, especially in cases of slow progression. MR imaging is quite sensitive and specific in diagnosing Alexander Disease. Megalencephaly and extensive cerebral white matter changes with frontal predominance are characteristic features. Periventricular rims with high signals on T1-weighted, and low signals on T2-weighted images and signal abnormalities of basal ganglia and thalami and brainstem, are frequent abnormalities.

The abnormal enhancement of caudate nuclei, anterior columns of the fornices, and periventricular areas are characteristic findings that help making the diagnosis (van der Knaap et al. 2001).

2.4.5.3 Canavan Disease (CD)

CD is a metabolic abnormality of N-acetyl aspartic acid (NAA) that is the second most concentrated amino acid in the brain and acts as a neuronal marker and osmolyte (Fig. 2.17). It is an autosomal dominant disease with a deficiency in aspartoacylase resulting in abnormal accumulation of NAA. The patients show characteristic macrocrania, seizures, progressive neurological deterioration, and psychomotor retardation. The clinical onset is within the first year of life. Extensive myelin edema, spongy degeneration, and cavitations of the white matters are seen pathologically. Involvement of subcortical U-fiber in the early course and progression in centripetal directions is a characteristic MR imaging feature. Later the entire white matters are involved and the globus pallidus and thalamus can be involved, but the putamen is frequently spared. MR spectroscopy shows an abnormally high peak of the NAA spectrum (Cheon et al. 2002).

2.4.5.4 Megalencephalic Leukoencephalopathy with Subcortical Cysts (MLC)

MLC is an autosomal recessive disorder due to mutations in the *MLC1* gene (Fig. 2.18). Macrocephaly is a characteristic feature, and it usually develops within the first year of life, but can be present at birth. The main presenting features after macrocephaly are slowly progressing spasticity and ataxia. Early psychomotor development is normal and the clinical course is relatively mild. Brain MRI findings were more serious than that of the clinical picture and consisted of characteristic diffuse supratentorial white matter high-signal intensity on T2-weighted images and low-signal intensity on T1-weighted images. Characteristic features are developing subcortical cysts of temporal, parietal, and frontal regions associated with generalized swelling of the abnormal white matter (van der Knaap et al. 1995).

2.4.5.5 Menkes Disease

Menkes Disease is a rare X-linked recessive disorder, characterized by neurodevelopmental delay in early infancy, failure to thrive, and seizures (Fig. 2.19). A defect of transmembrane P-type ATPase causes defective intestinal absorption of copper, leading to copper deficiency. Decreased activity of multiple copper-dependent enzymes causes hair and skin abnormalities and impaired blood vessel integrity resulting in vascular insufficiencies. Brain MRI shows progressive and extensive neuronal loss including gray and

white matter degeneration. Angiography shows tortuosity, kinking, and irregular luminal diameters of intracranial and extracranial vessels causing chronic ischemias. Advanced cases show diffuse brain atrophy with subdural hemorrhages (Rennert et al. 2009).

2.4.5.6 Wilson's Disease

Wilson's Disease is an autosomal recessive disorder with copper metabolic defect resulting in an abnormal accumulation of copper in various tissues, particularly in the liver and the brain (Fig. 2.20). The accumulation of copper is postulated to involve the aberrant intrahepatic processing of ceruloplasmin. The neurological symptoms associated with

Wilson's disease are assumed to be secondary to the accumulation of copper in the brain, causing destruction of the nerve cells.^{2,3} The most common MR finding in the neurological form of Wilson's disease is high-signal intensities involving the globus and putamen on T2-weighted image, but high-signal intensity on T1-weighted images can be seen in the globus pallidus, putamen, and mesencephalon in association with hepatic dysfunction. Bilateral high-signal intensity with central dark signal intensity lesions in the putamen or caudate nuclei is a characteristic feature with advanced neurological symptoms in Wilson's disease. Progressive brain atrophy is usually associated with it (Kim et al. 2006).

2.5 Illustrations: Metabolic Disease of the Brain

2.5.1 Schematic Drawing of Oligodendrocytes Extending Myelin Sheath over the Axons

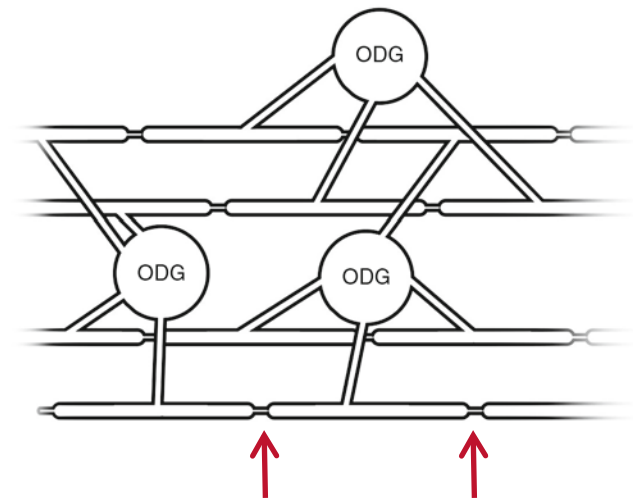


Fig. 2.1 Schematic drawing of oligodendrocytes (ODG) extending myelin sheath over the axons. The area devoid of myelin sheath is called as node of Ranvier (*arrows*), and the nerve impulse propagates from node to node, which is an important function of the myelin sheath for facilitating nerve conduction

2.5.2 MR Imaging of Normal Progression of Myelination

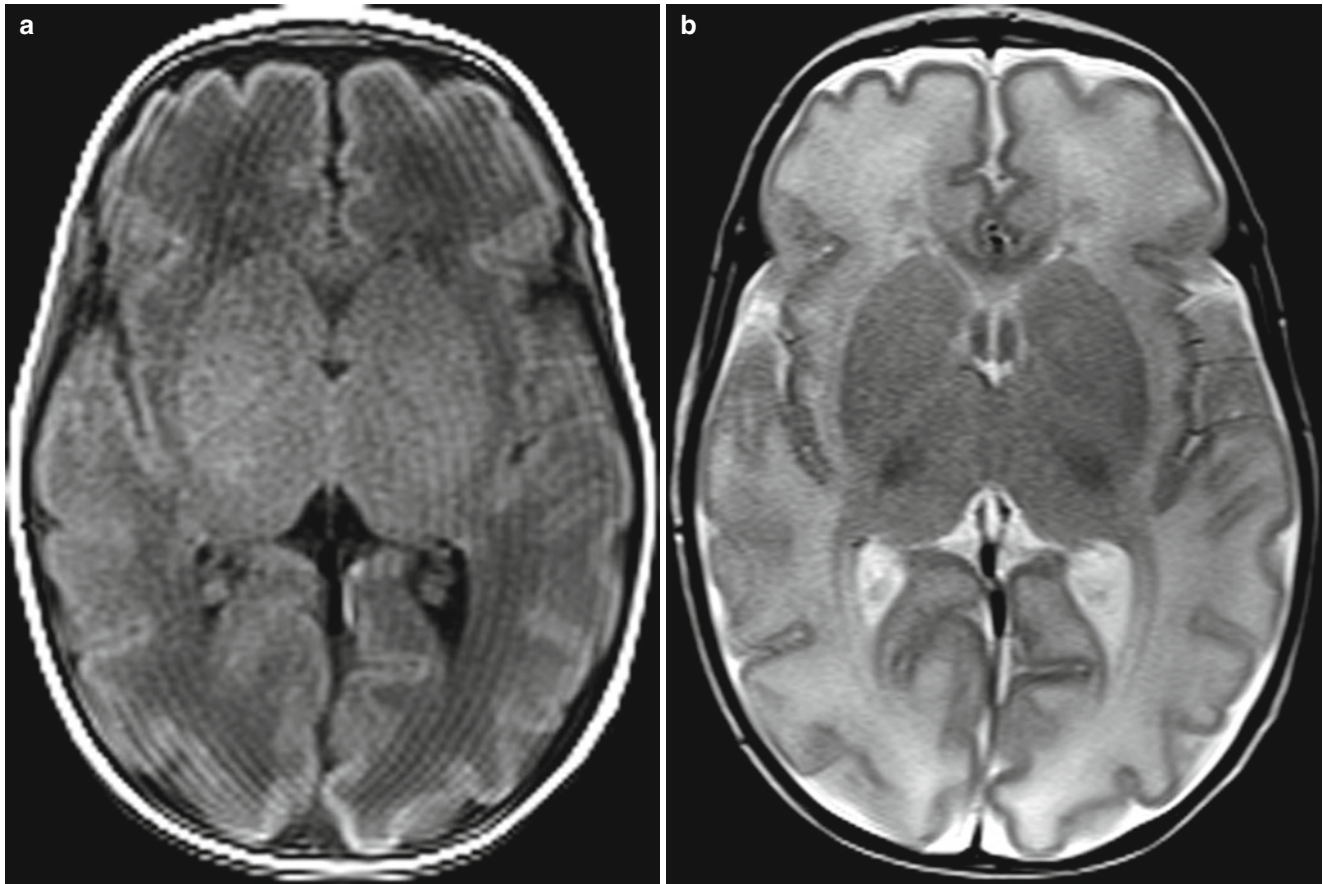


Fig. 2.2 MR imaging of normal progression of myelination. **(a, b)** MRI at 35 weeks of gestation. **(a)** T1-weighted image at 35 gestational weeks shows low-signal intensity of the white matters, including the internal capsules. Cerebral cortex shows high-signal intensity. The ventrolateral aspect of the thalamus and dorsolateral aspect of the lentiform nucleus show high-signal intensities. **(b)** T2-weighted image shows high-signal intensity of the white matters including the internal capsule. The ventrolateral thalamus shows myelinated low-signal intensity. **(c, d)** MRI at 1 month of age. **(c)** T1-weighted image shows myelinated white matter high-signal intensity in the posterior limb of internal capsules. **(d)** T2-weighted image shows low-signal intensity of the ventrolateral thalamus and the posterior limb of internal capsules.

(e) T1-weighted image at the age of 5 months shows high signal intensity of the anterior and posterior limbs of the internal capsule and the genu and splenium of the corpus callosum. Occipital white matter shows high-signal intensity in the deep and subcortical regions. **(f)** T2-weighted image at the age of 7 months shows myelinated low-signal intensities of the entire internal capsule, splenium, and genu of the corpus callosum. Subcortical and deep white matters show high-signal intensity. **(g)** T1-weighted image at the age of 1 year shows high-signal intensity of the entire white matters. **(h)** T2-weighted image at the age of 2 years shows low-signal intensity of the entire white matter as an adult pattern

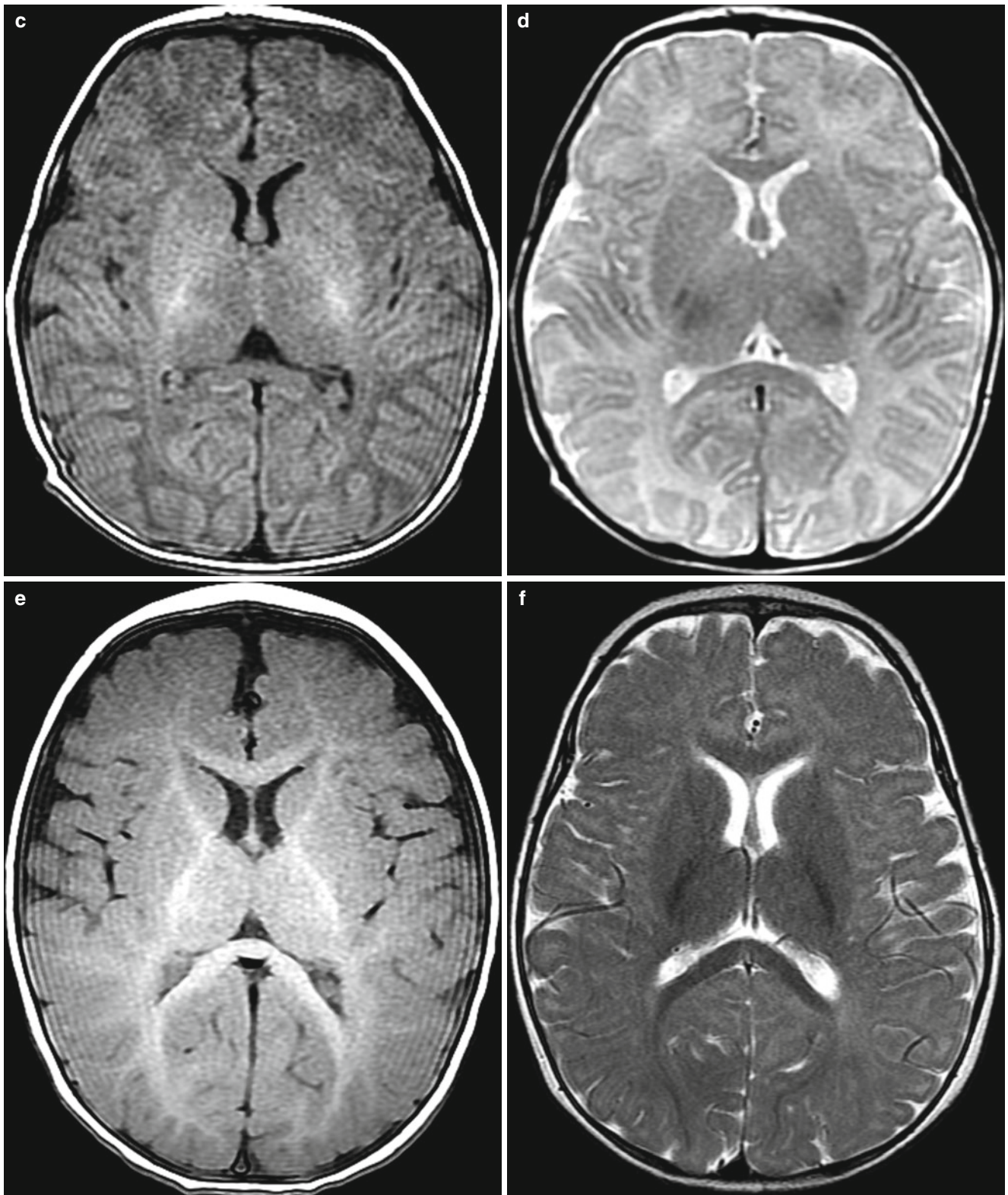


Fig. 2.2 (continued)

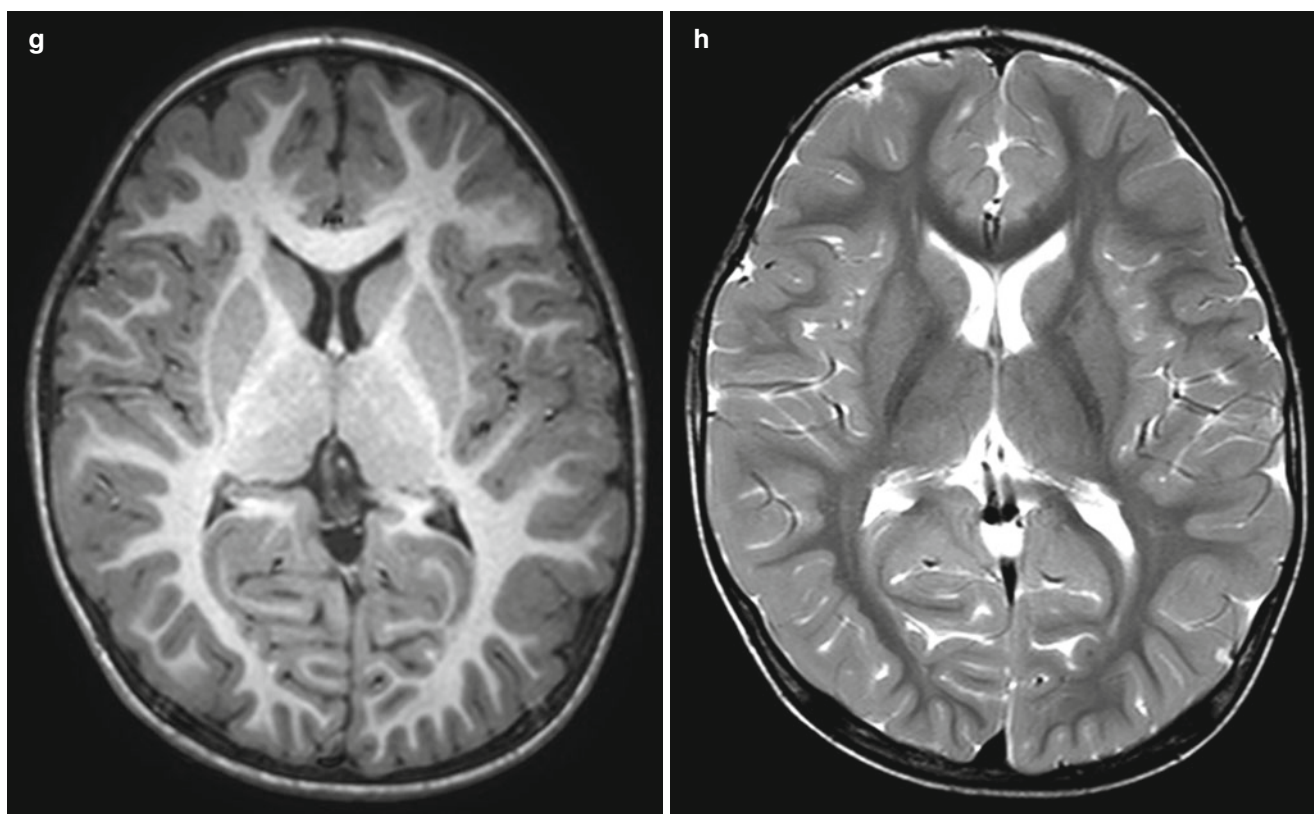


Fig. 2.2 (continued)

2.5.3 Delayed Myelination in Niemann-Pick Disease

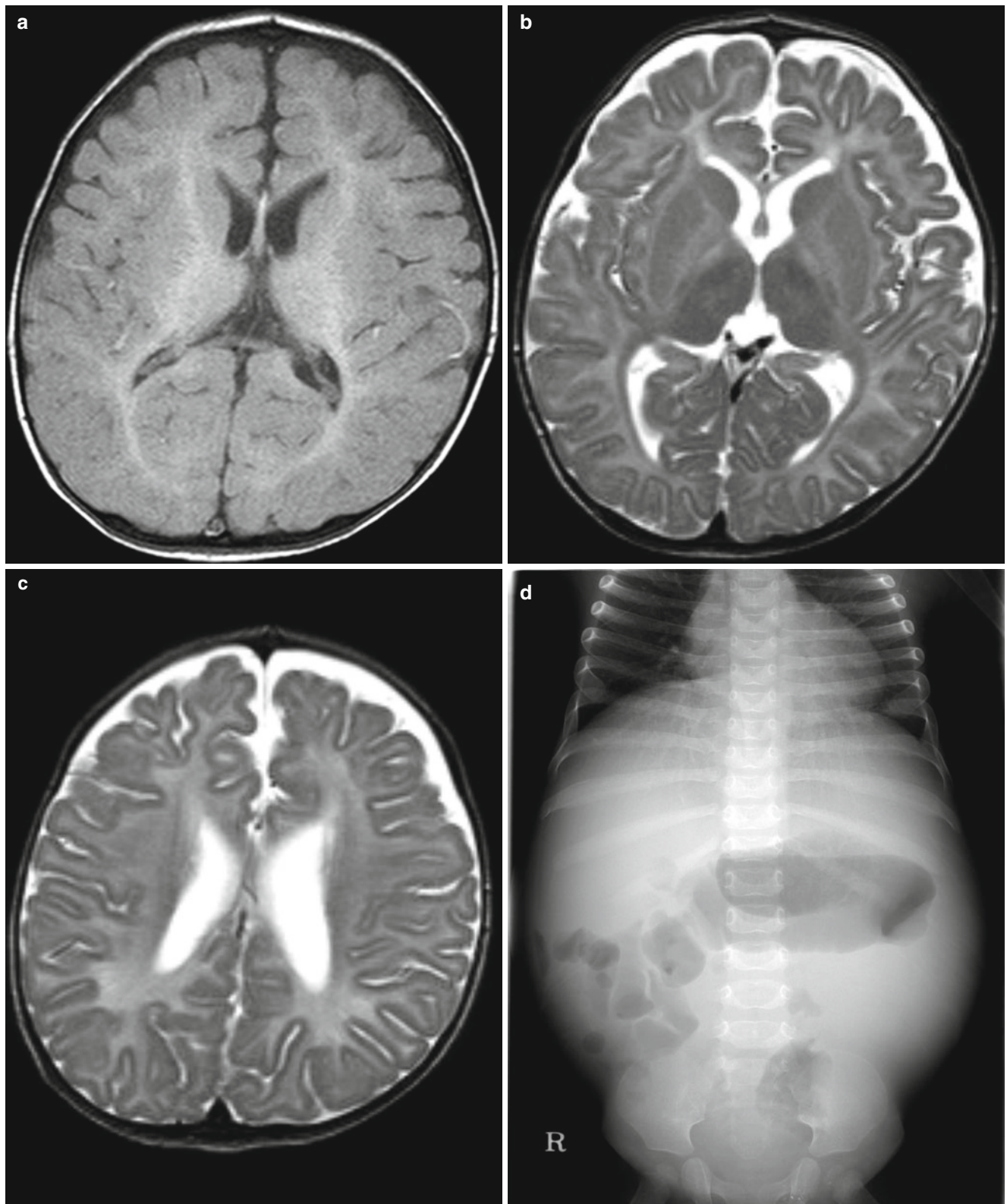


Fig. 2.3 Delayed myelination in Niemann-Pick disease at the age of 15 months. (a) T1-weighted image shows high- signal intensity of the internal capsules. (b, c) T2-weighted images show low-signal intensity of the posterior limb of the internal capsule and optic radiations. The

deep white matters are entirely unmyelinated. The myelination pattern is markedly delayed. (d) Plain radiography shows hepatosplenomegaly and the ribs show broadening and coarse trabeculation

2.5.4 Metachromatic Leukodystrophy

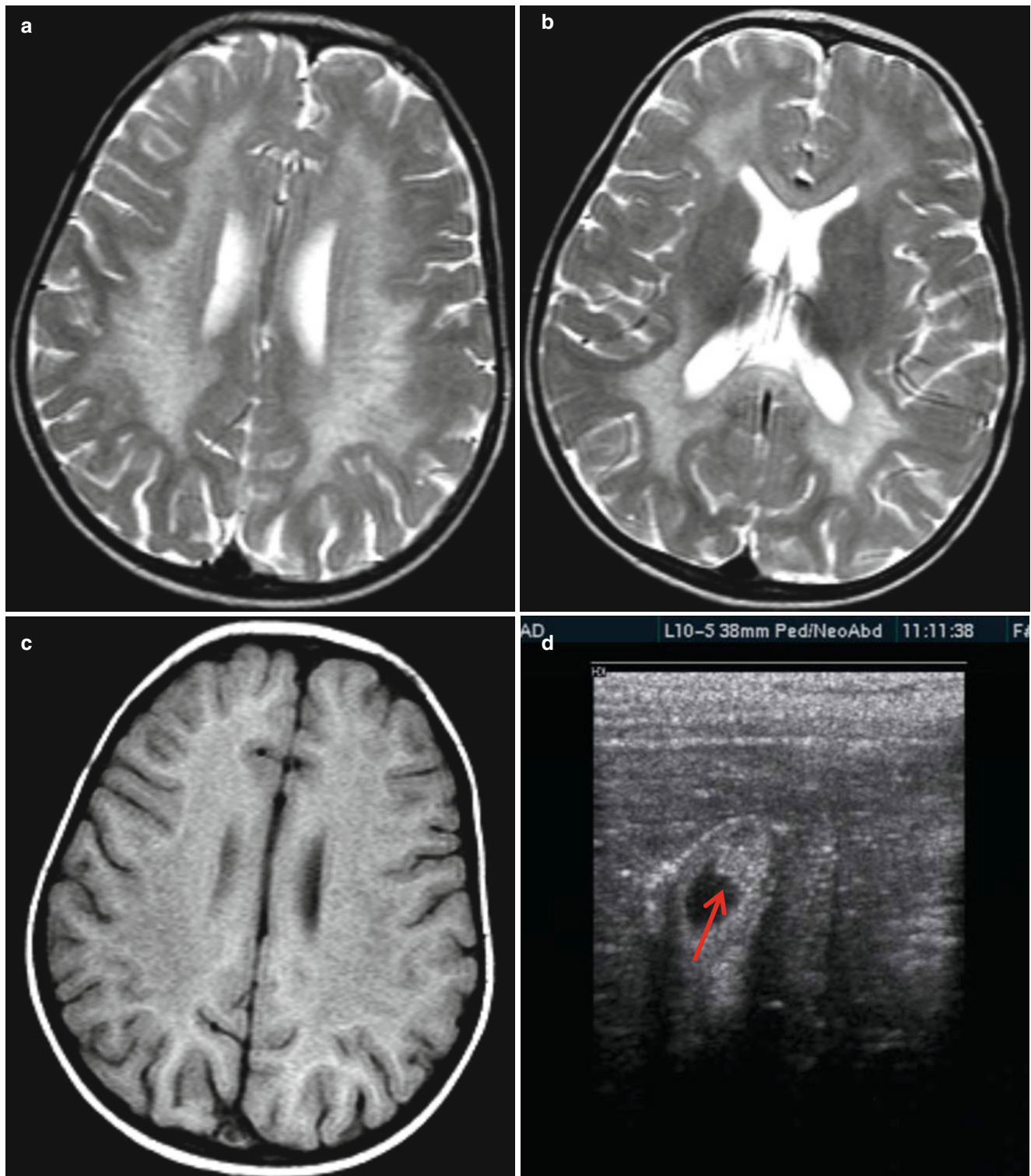


Fig. 2.4 Metachromatic leukodystrophy in a 2-year-old girl. (a, b) T2-weighted image shows bilateral symmetric, confluent high signals of the deep and periventricular white matter extending to the corpus callosum. Fine linear low signals within the high signals perpendicular

to the ventricles are seen due to spared axons seen with a leopard appearances. (c) The deep white matter shows diffuse low signals more prominent in the parietal region. (d) US of gallbladder shows thickening of the inner wall (arrow)

2.5.5 Krabbe Disease

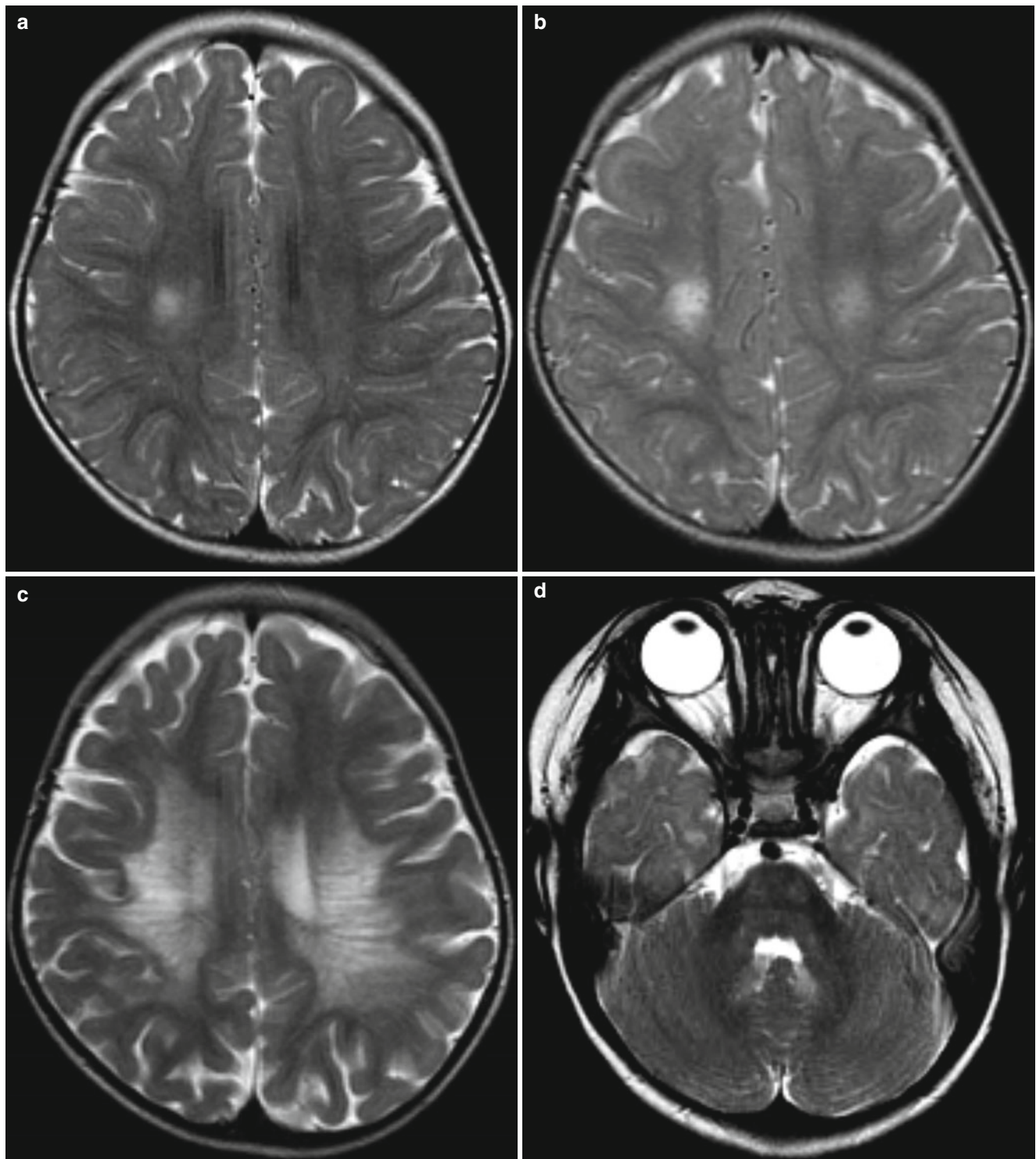


Fig. 2.5 Krabbe disease in an infant with irritability and spasticity (**a–d**). (**a**) T2-weighted image shows focal high signals in the right centrum semiovale. (**b**) Four-month follow-up image shows slight progression of the lesion and newly developed left white matter lesion. (**c**) Further follow-up after 1 year shows progression of the confluent

lesions in both deep white matters. (**d**) Signal abnormalities are also present in the pontine tracts and cerebellar white matters. (**e, f**) A 16-month-old girl with Krabbe disease shows advanced brain atrophy with symmetrical abnormalities of cerebral and cerebellar deep white matters. Subdural fluid collections are also present

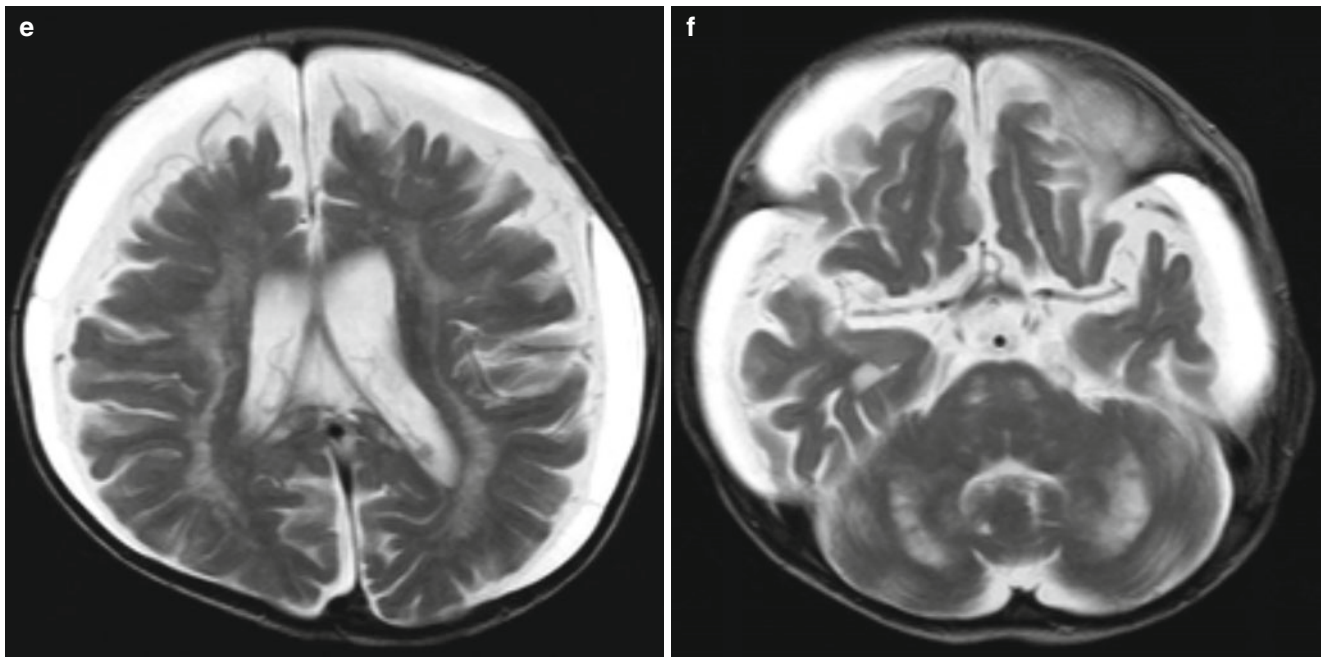


Fig. 2.5 (continued)

2.5.6 Mucopolysaccharidoses

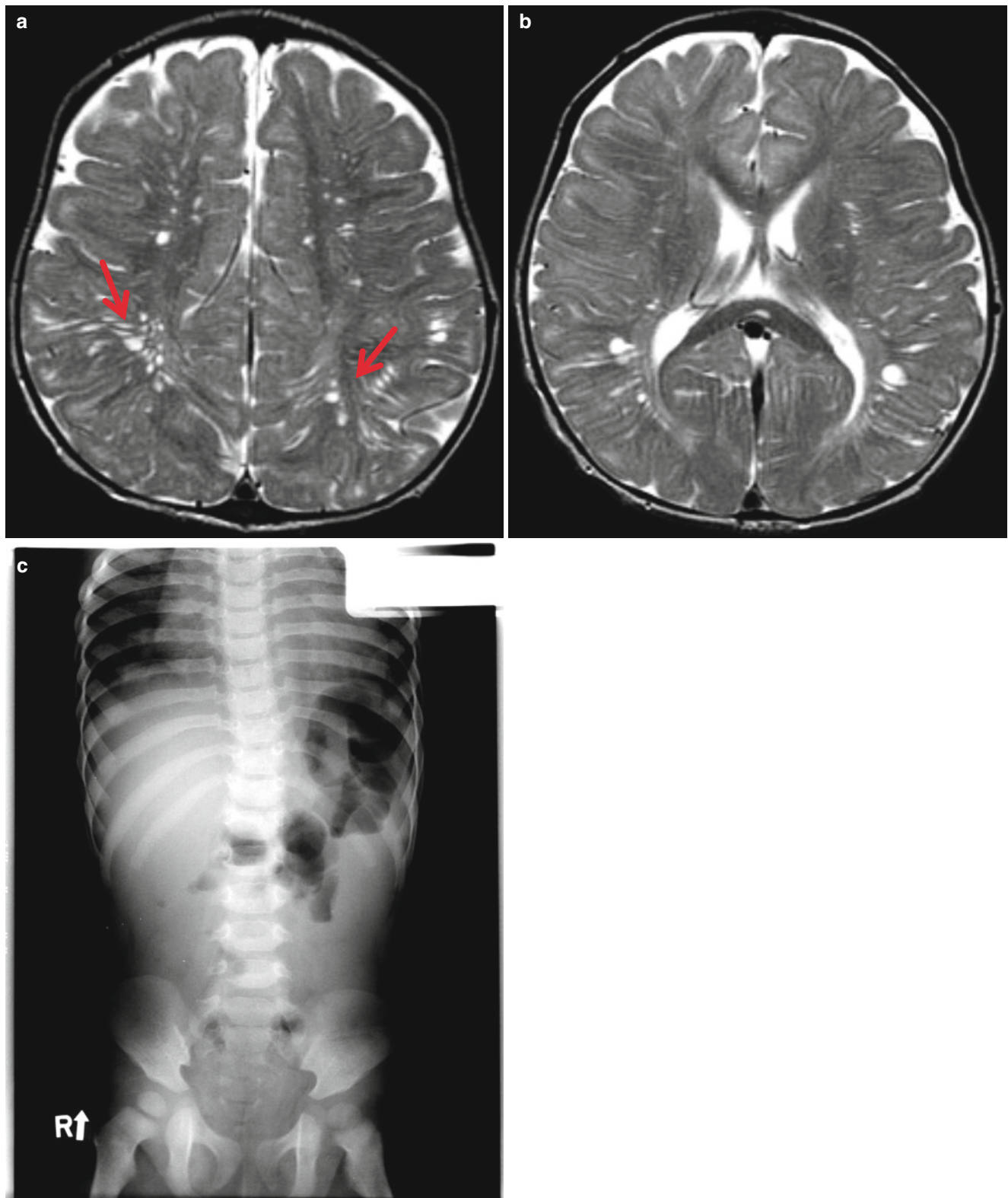


Fig. 2.6 A 2-year-old boy with mucopolysaccharidoses. (a, b) Prominent perivascular spaces are seen as streaky, radiating high signals within the deep and subcortical white matters (*arrows*) and the

corpus callosum. (c) Plain radiography shows medial constriction of the ribs with a canoe pedal appearance

2.5.7 XR Adrenoleukodystrophy

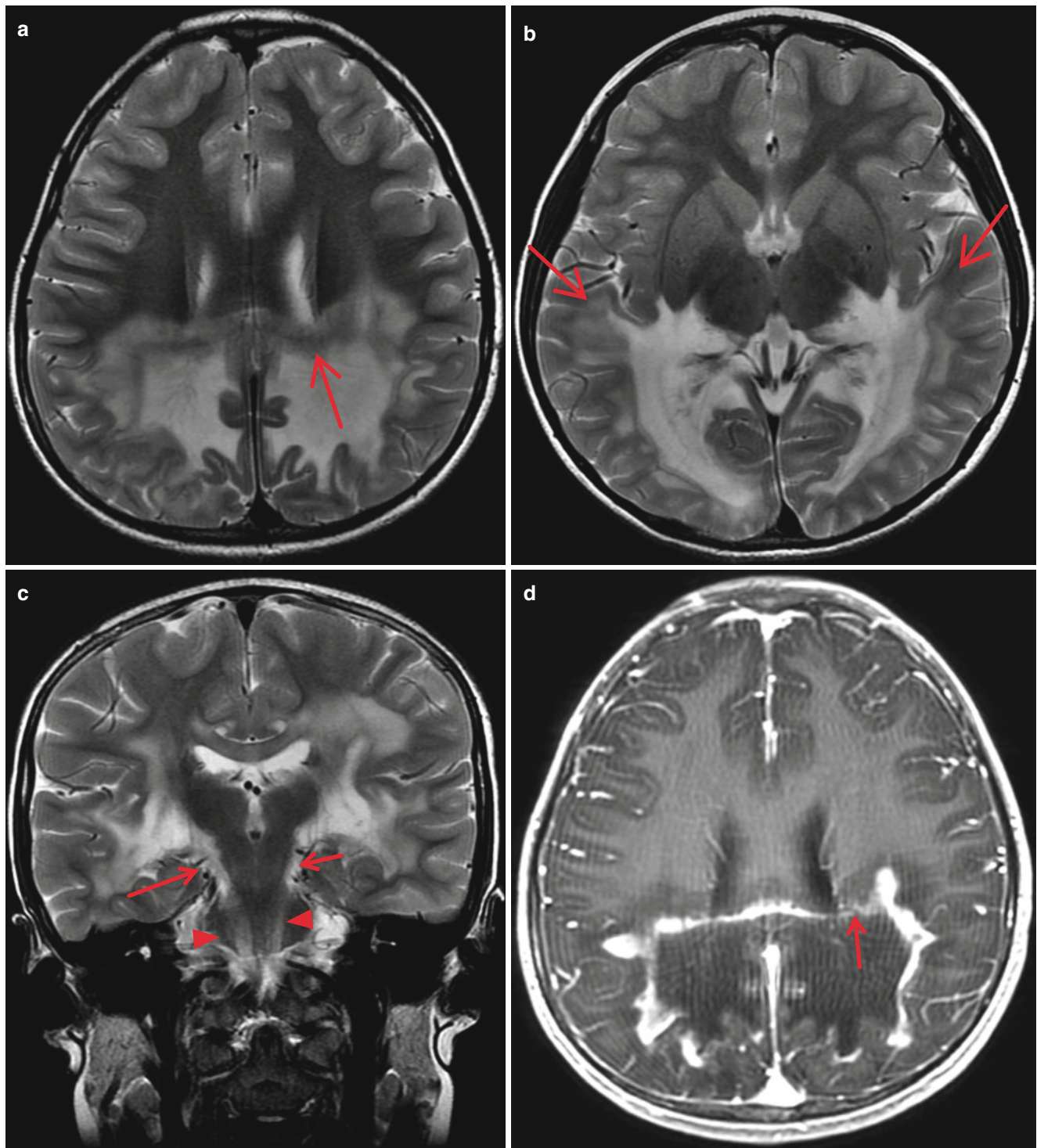


Fig. 2.7 XR adrenoleukodystrophy in an 8-year-old boy. (a) Demyelinated white matters are seen as bilateral confluent high-signal intensities in the parietal periventricular area extending anteriorly. The involved white matter shows three zonal layers with a central lower signal intensity layer (arrow) that shows strong enhancement (arrow) on postcontrast image, suggesting active inflammatory zone (d). (b)

Bilateral confluent demyelinating lesions involving the posterior periventricular and deep white matter extend anterolaterally to the acoustic radiations (arrows). (c) Coronal image showing demyelination extends inferiorly through the lateral lemniscus (arrows) and the descending tracts (arrowheads)

2.5.8 Leigh Disease

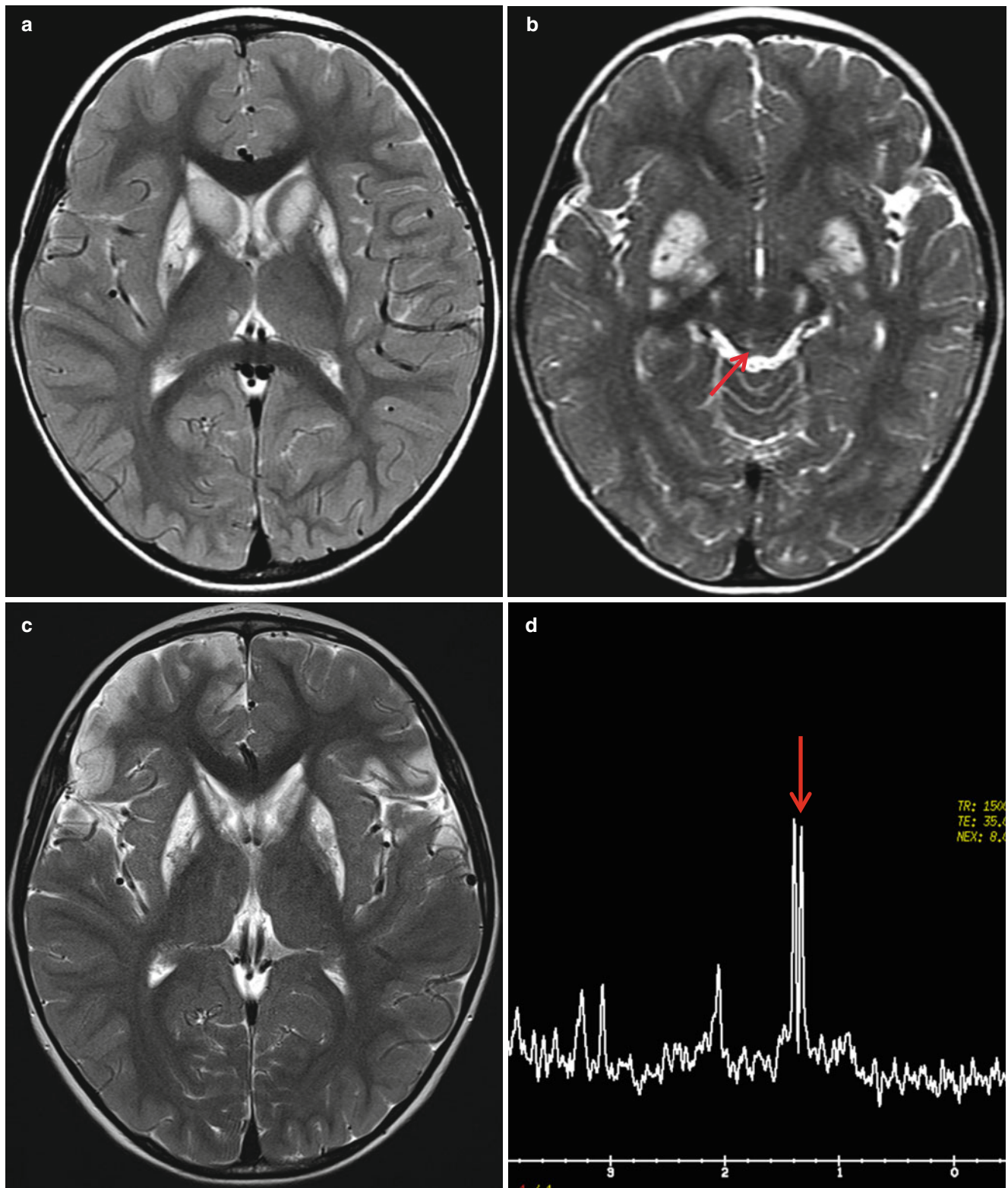


Fig. 2.8 Leigh disease in a 2-year-old boy with gait disturbance. (a, b) T2-weighted images show high-signal intensity of the basal ganglia, midbrain, and periaqueductal gray matter (*arrow*). (c) Follow-up image

after 2 years shows multifocal old infarct-like lesions in the frontal and temporal lobes. (d) MR spectroscopy shows high lactate peak (*arrow*). Mitochondrial DNA mutation was confirmed

2.5.9 MELAS

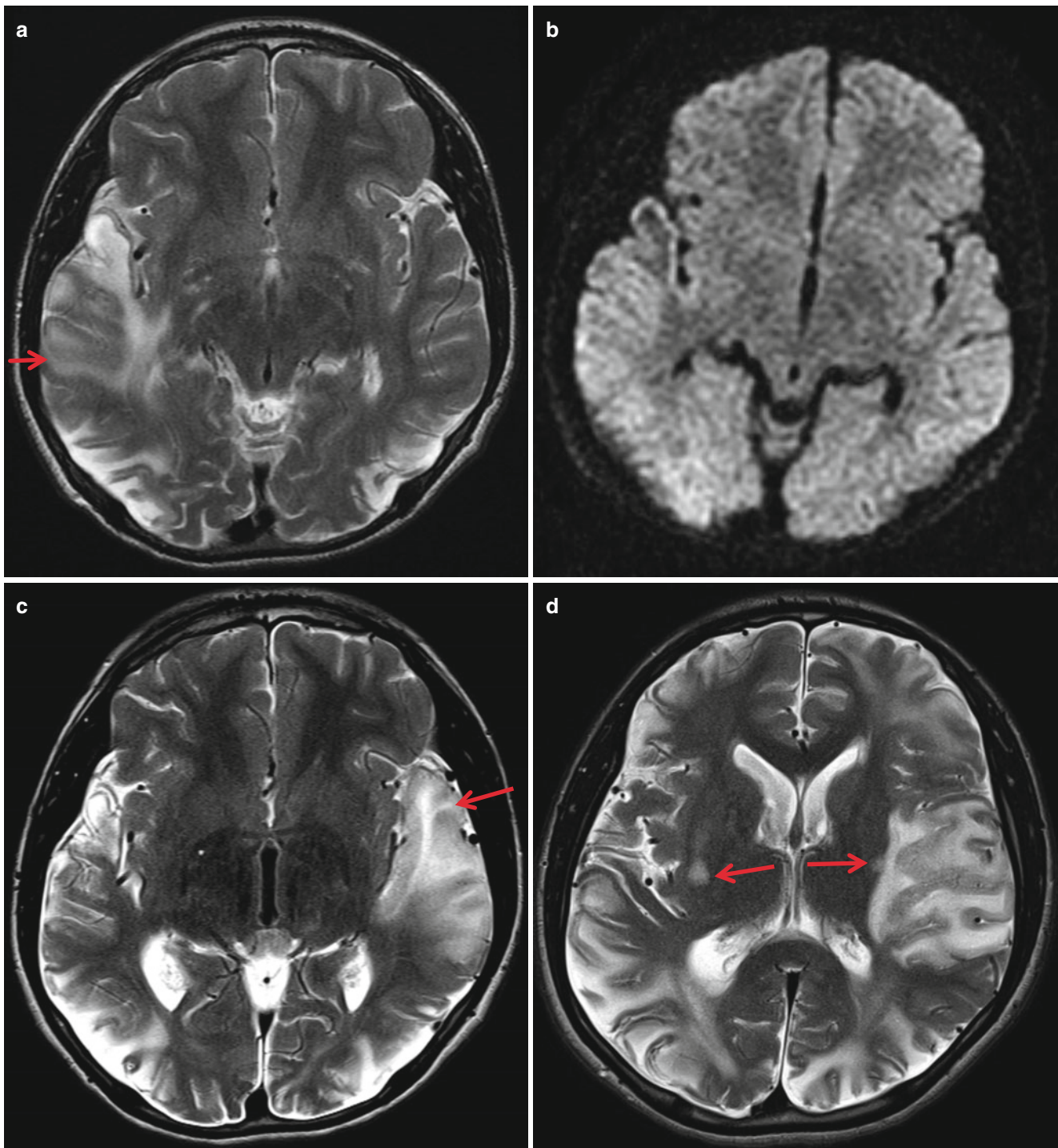


Fig. 2.9 MELAS in an infant with multiple episodes of sudden visual disturbance and stroke. **(a)** T2-weighted image shows acute swelling in the right temporal lobe (*arrow*) and old cortical atrophy in both occipital lobes. **(b)** Diffusion image shows no remarkable diffusion abnormality in the right temporal lobe lesion. **(c)** Newly developed acute swelling

in the left temporal lobe (*arrow*). The lesion showed restricted diffusion (not shown). **(d)** Another episode of acute swelling in the left high temporal and frontal lobe. New lesions are also seen in the basal ganglia (*arrows*)

2.5.10 Glutaric Aciduria Type 1

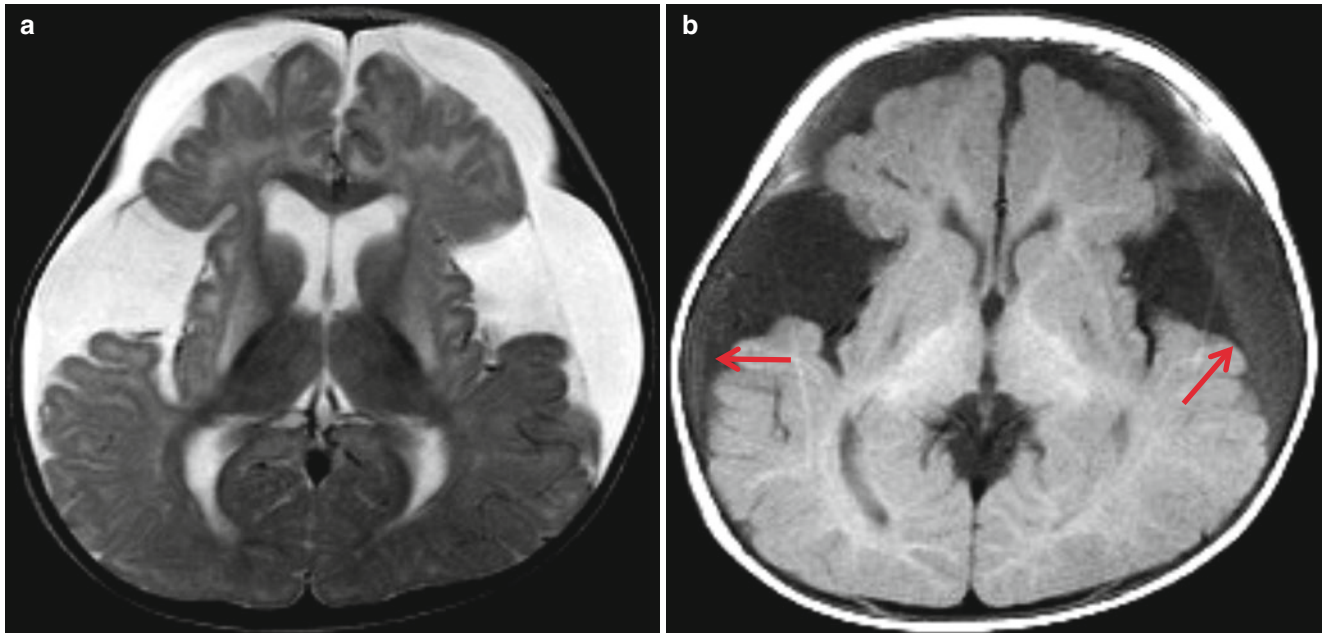


Fig. 2.10 Glutaric aciduria type 1 in a 9-month-old girl with macrocrania and developmental delay. **(a)** T2-weighted image shows a wide open Sylvian fissure and subarachnoid and subdural fluid collection in the frontotemporal region. Lenticular nucleus shows high-signal inten-

sity in both sides. **(b)** T1-weighted image also shows a wide Sylvian fissure with subdural fluid collections (*arrows*) and delayed myelination

2.5.11 Nonketotic Hyperglycinemia

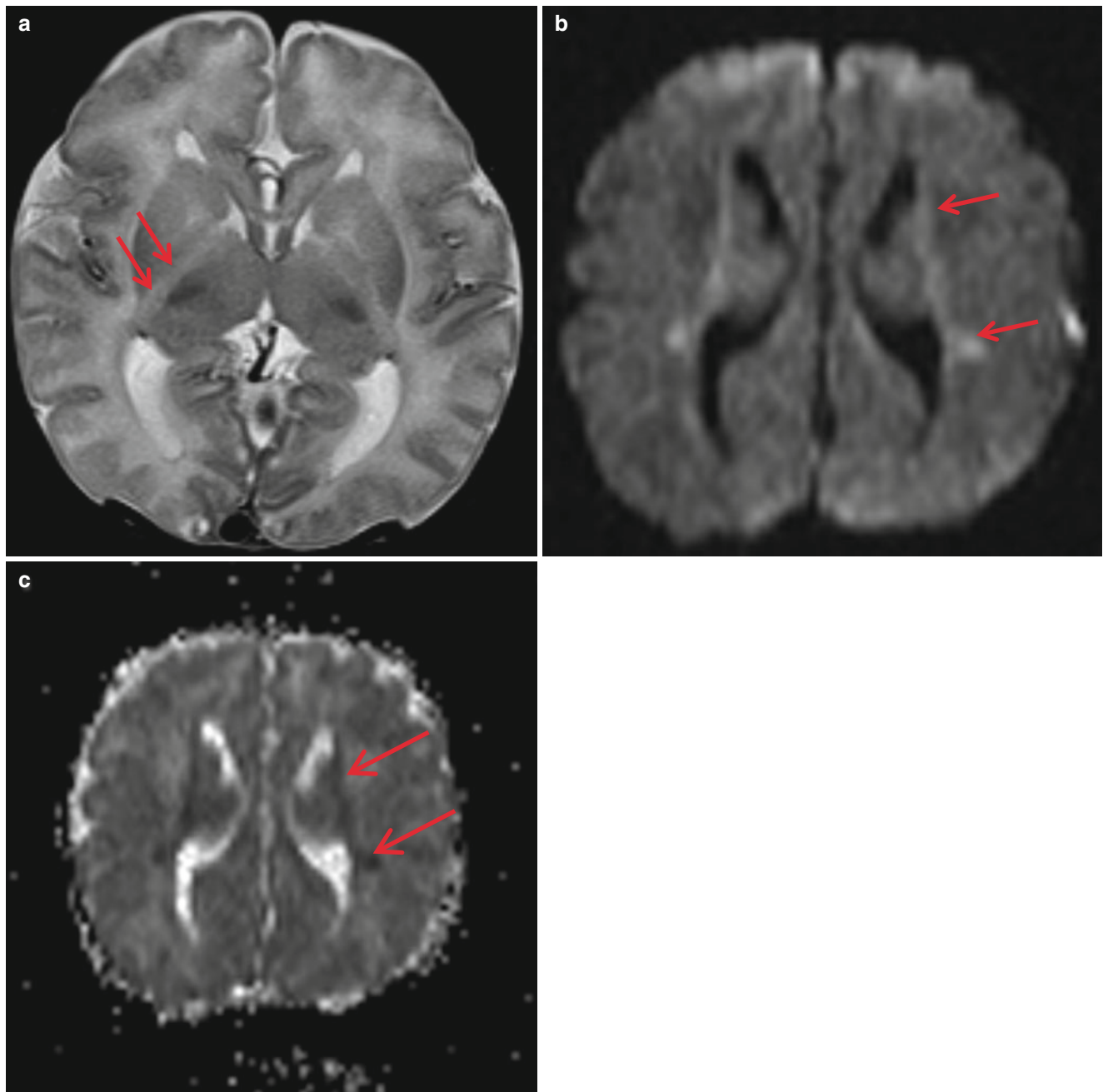


Fig. 2.11 Nonketotic hyperglycinemia with seizure. (a) T2-weighted image of a 5-day-old boy showed dysplastic corpus callosum and the high-signal intensity of the posterior limb of the internal capsule

(arrows). (b, c) Diffusion and ADC map shows diffusion abnormalities of the deep white matters (arrows)

2.5.12 Citrullinemia

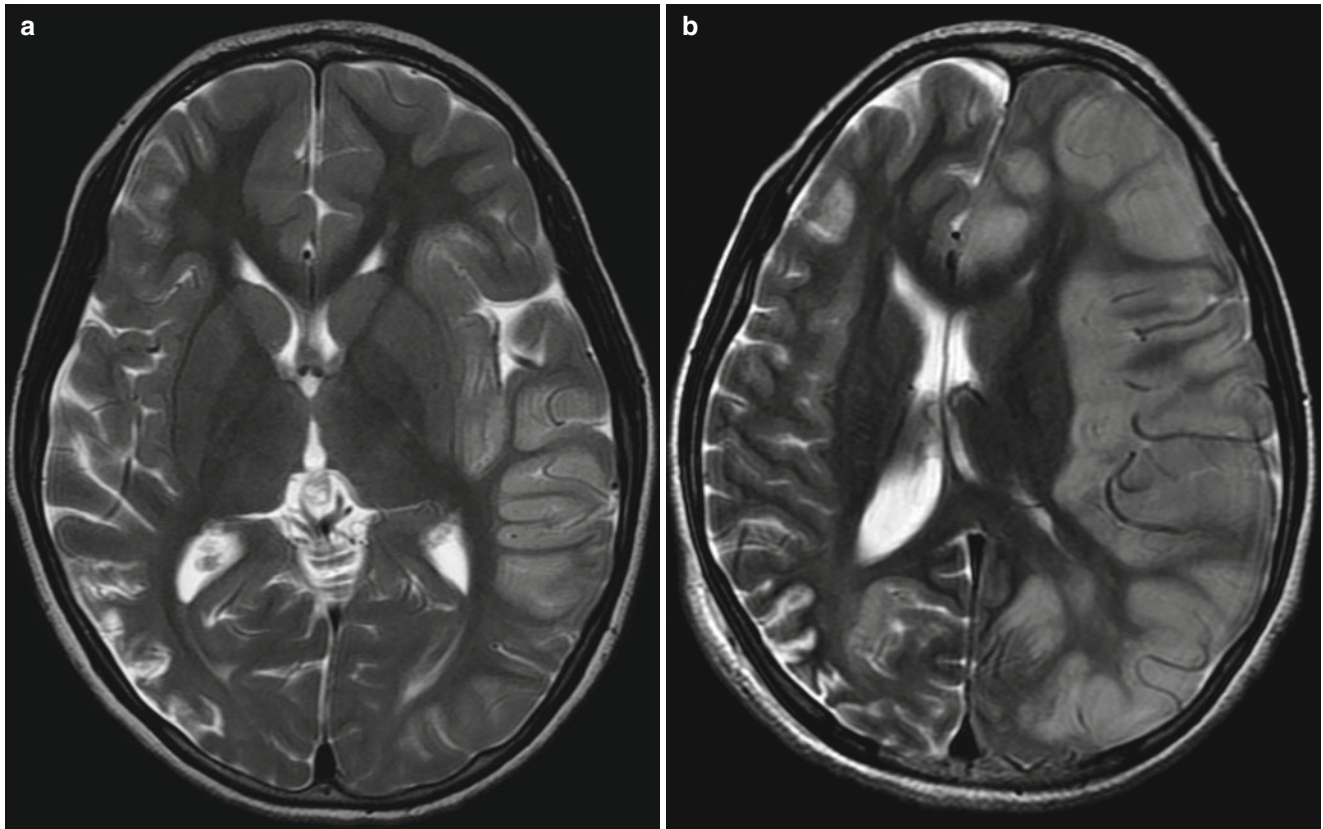


Fig. 2.12 Citrullinemia in a 16-year-old boy with drowsiness, fever, and stroke-like symptoms. **(a)** T2-weighted image shows gyral swellings involving the left insula and temporo-occipital cortex. Serum ammonia level was elevated. **(b)** Follow-up image after 5 days shows

progression of the cortical swelling extending to the whole left hemisphere and the right temporal and occipital lobes. The genetic defect of ornithine transcarbamylase deficiency was confirmed

2.5.13 Isovaleric Acidemia

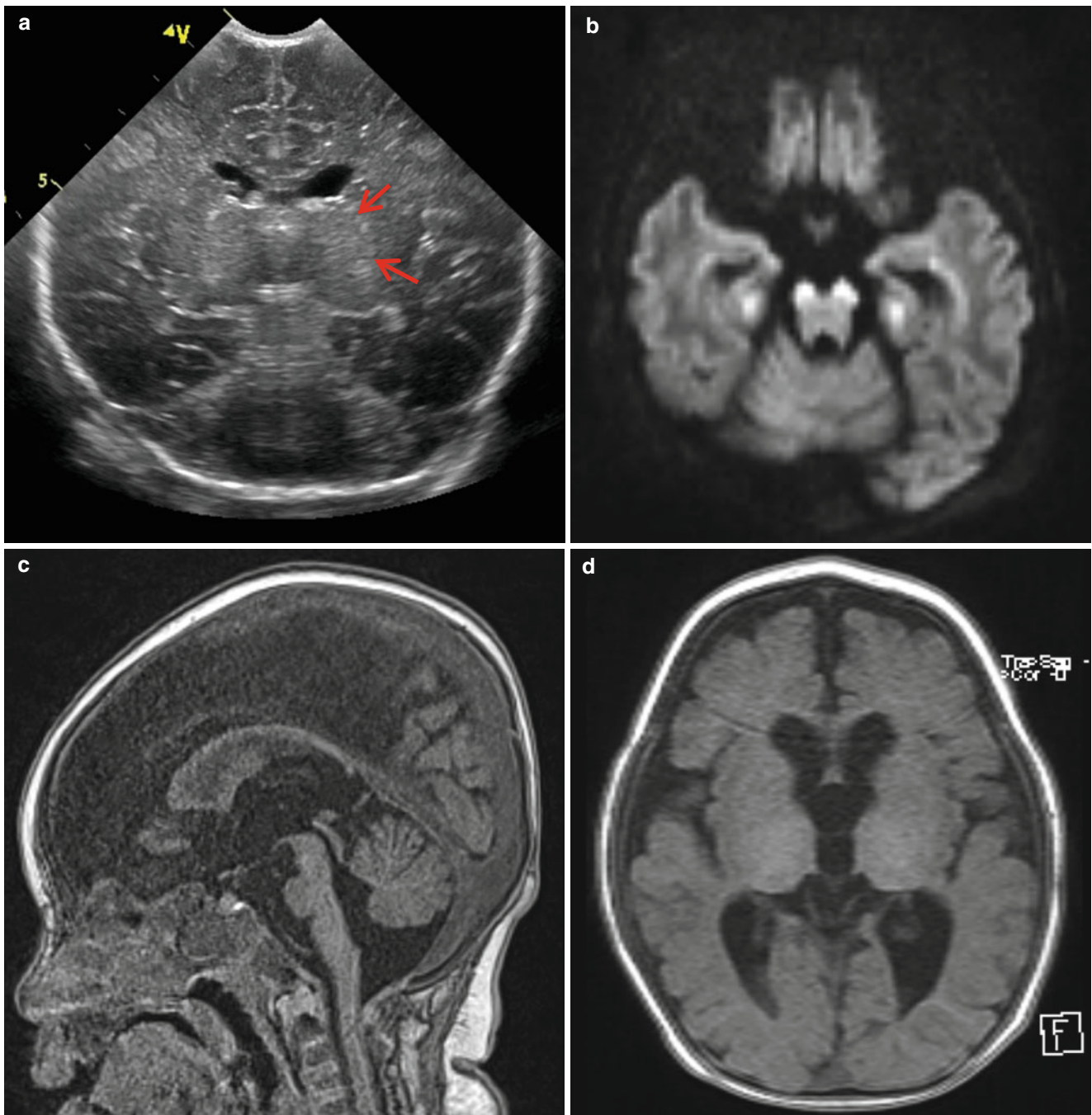


Fig. 2.13 Isovaleric acidemia in a term infant with weakness, seizure, and foul-smelling urine. (a) US of the brain shows subtle echogenic swelling of both the basal ganglia (*arrows*) and thalami and deep cortex of the frontal lobes. (b) Diffusion-weighted image at the age of 1 month shows bilateral symmetric diffusion restriction involving the midbrain

and temporal lobe and the deep white matters (not shown). (c, d) T1-weighted images after 6-month follow-up show thinning of mid-brain, pons, and the corpus callosum, and mottled high signals in the thalami. Moderate brain atrophy is seen

2.5.14 Homocystinuria

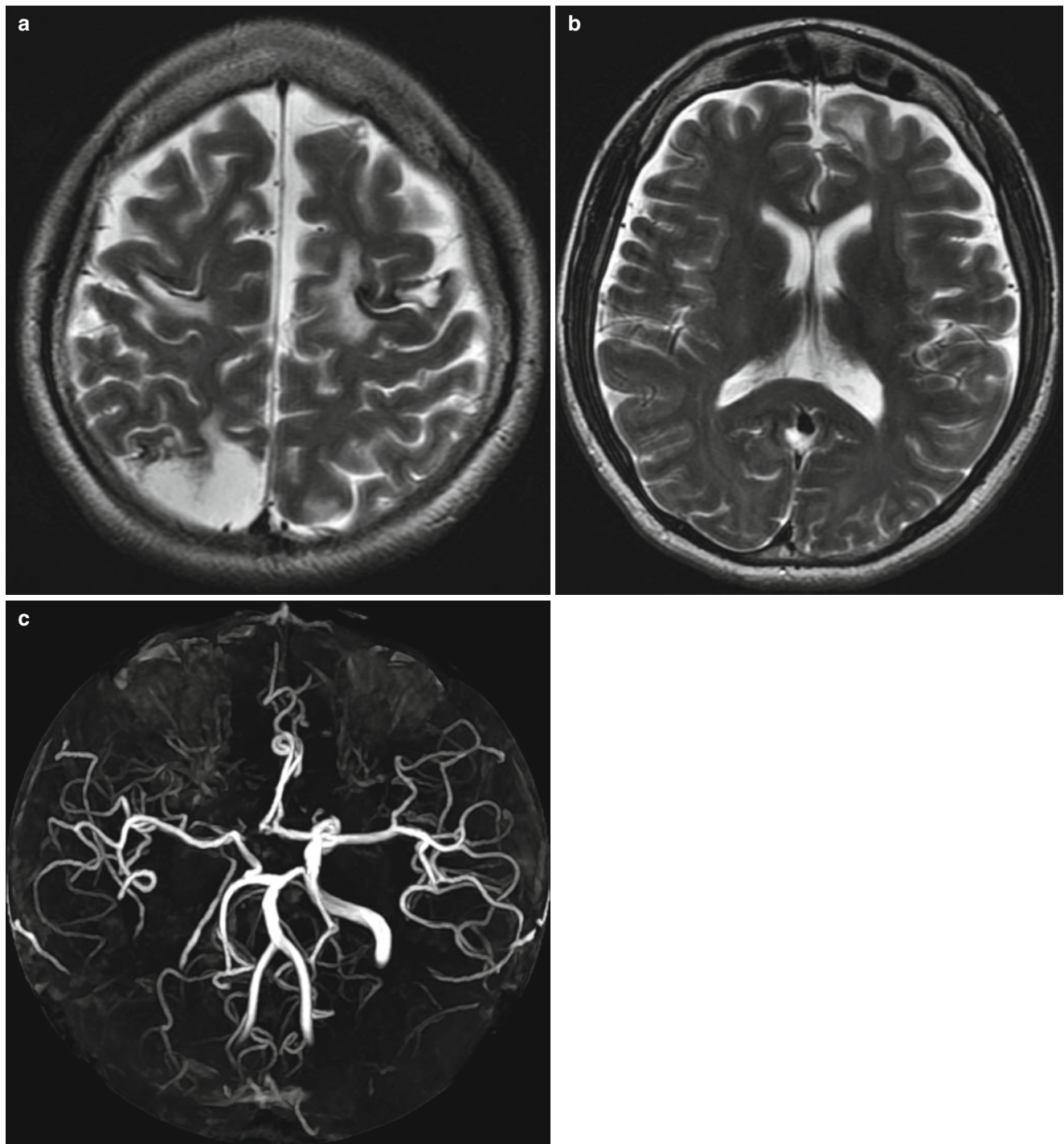


Fig. 2.14 Homocystinuria in a 24-year-old female patient with seizures and stroke. (a, b) T2-weighted image shows multifocal encephalomalacia with focal hemosiderin deposits suggesting old hemorrhagic

infarctions. (c) MR angiography shows intact major vasculatures in the brain and hypoplastic right A1 segment

2.5.15 Pelizaeus-Merzbacher Disease

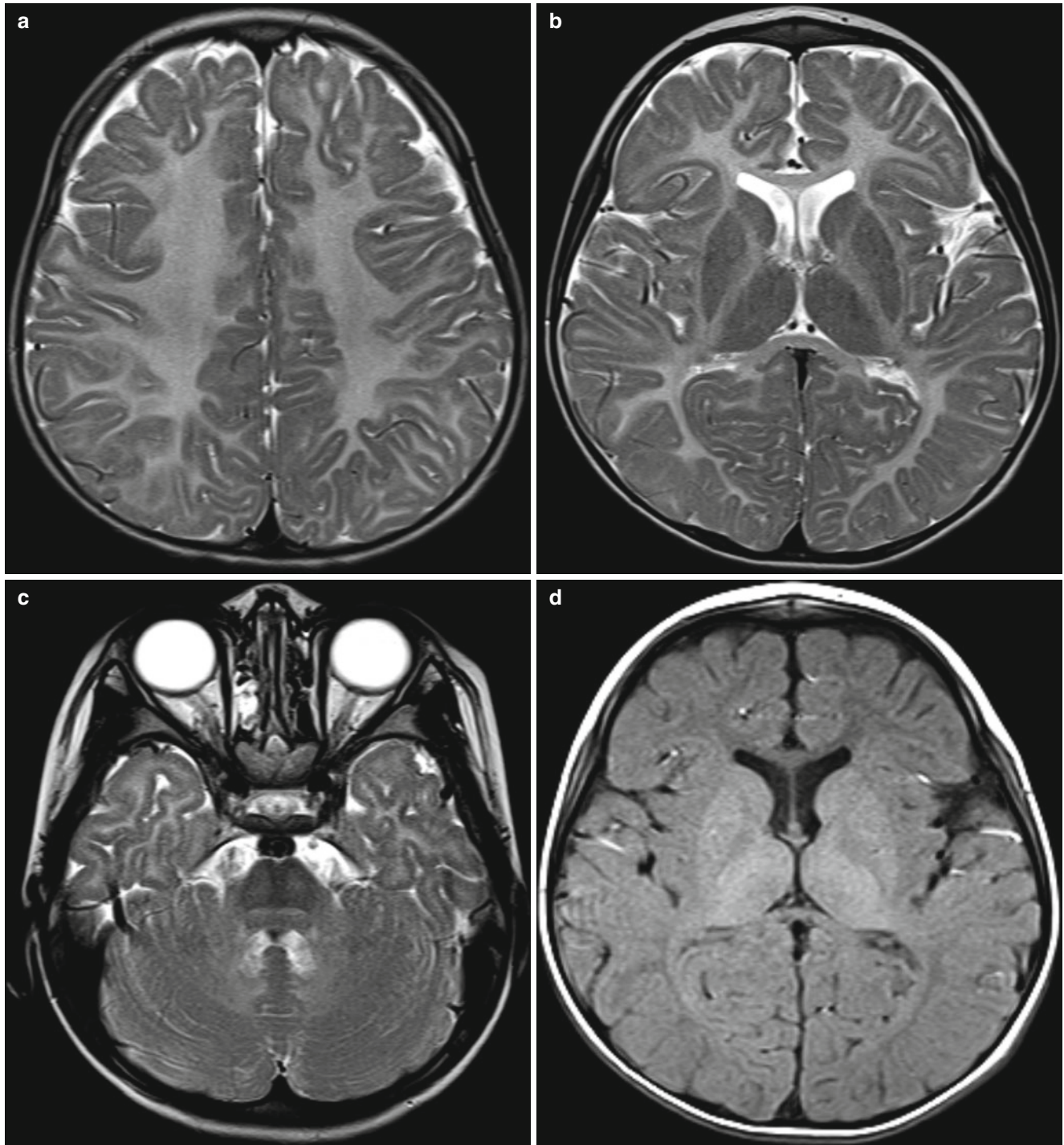


Fig. 2.15 Pelizaeus-Merzbacher disease in a 5-year-old boy. (a–c) T2-weighted images show high-signal intensity of the entire white matters, including internal capsule and cerebellar deep white matters.

There is no focal parenchymal destructive change or atrophy. (d) The entire white matters show low-signal intensity on T1-weighted image

2.5.16 Alexander Disease

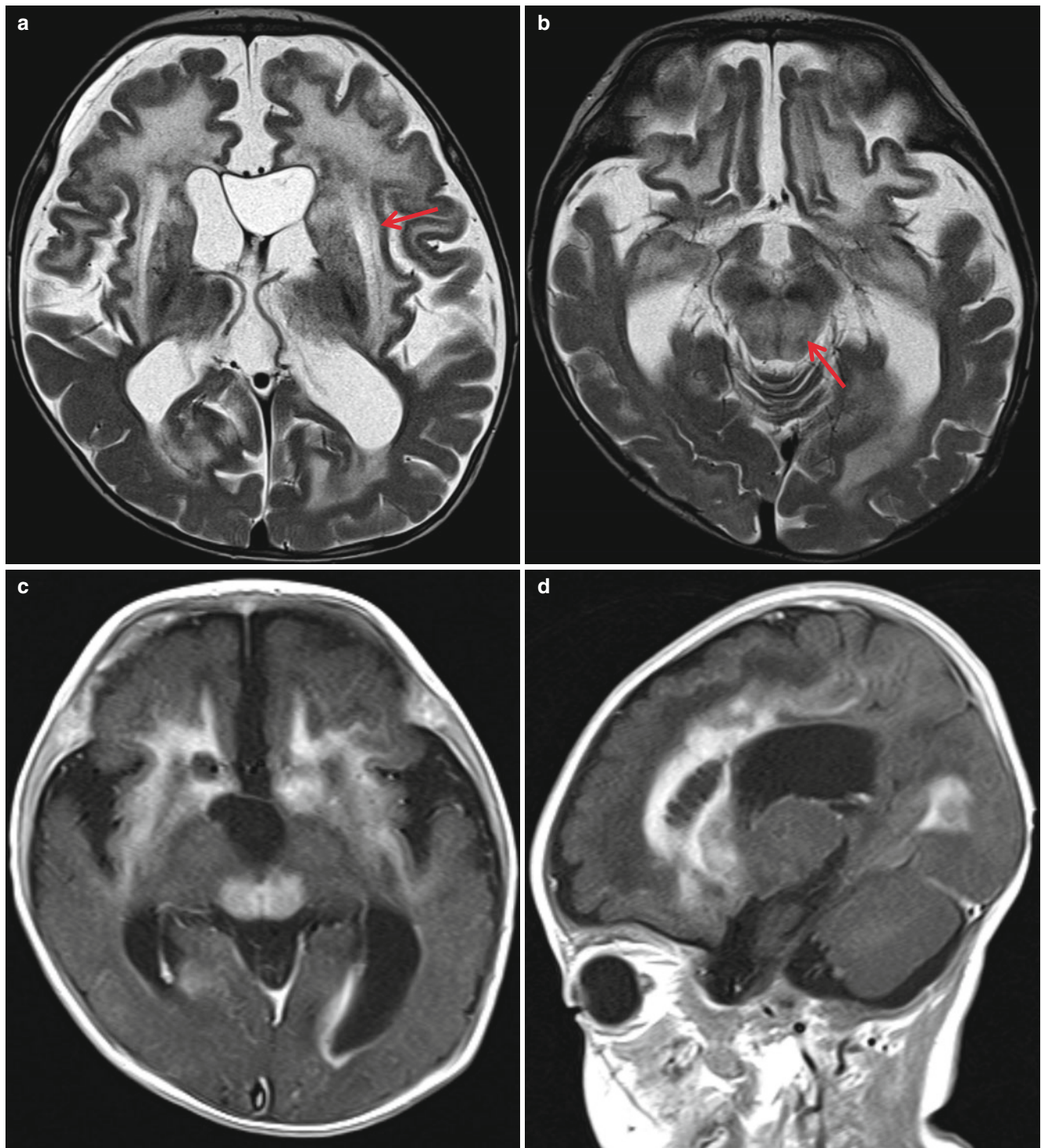


Fig. 2.16 Alexander disease in an 8-month-old boy with seizures and hydrocephalus. **(a)** T2-weighted image shows high-signal intensities of the frontal subcortical and deep white matters extending to the external and extreme capsules (*arrow*) posteriorly. Basal ganglia and thalamus were involved. The lateral ventricles are moderately dilated and ante-

rior subarachnoid spaces are slightly widened. **(b)** The image at the aqueduct level shows acute swelling of the tectum (*arrow*). **(c, d)** Postcontrast images show homogenous moderate enhancement of the periventricular regions and tectum

2.5.17 Canavan Disease

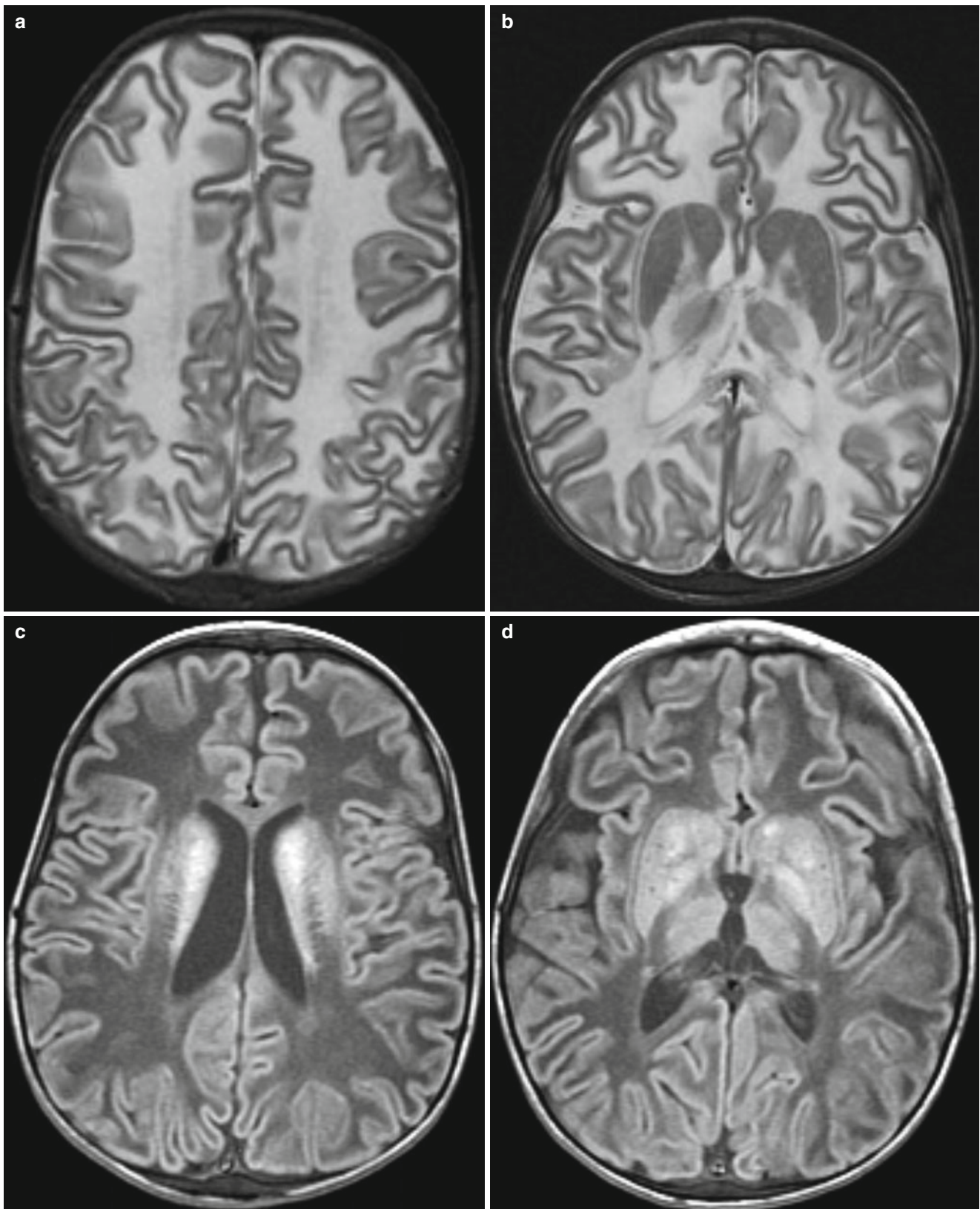


Fig. 2.17 Canavan disease in a 3-year-old girl with macrocrania and seizures. (a, b) T2-weighted images show high-signal intensity of the entire white matters. Globus pallidus and thalamus are involved and the

putamen is spared. The subcortical white matters are slightly increased in volume. (c, d) T1-weighted images show generalized low-signal intensity of the white matters

2.5.18 Megalencephalic Leukoencephalopathy with Subcortical Cyst

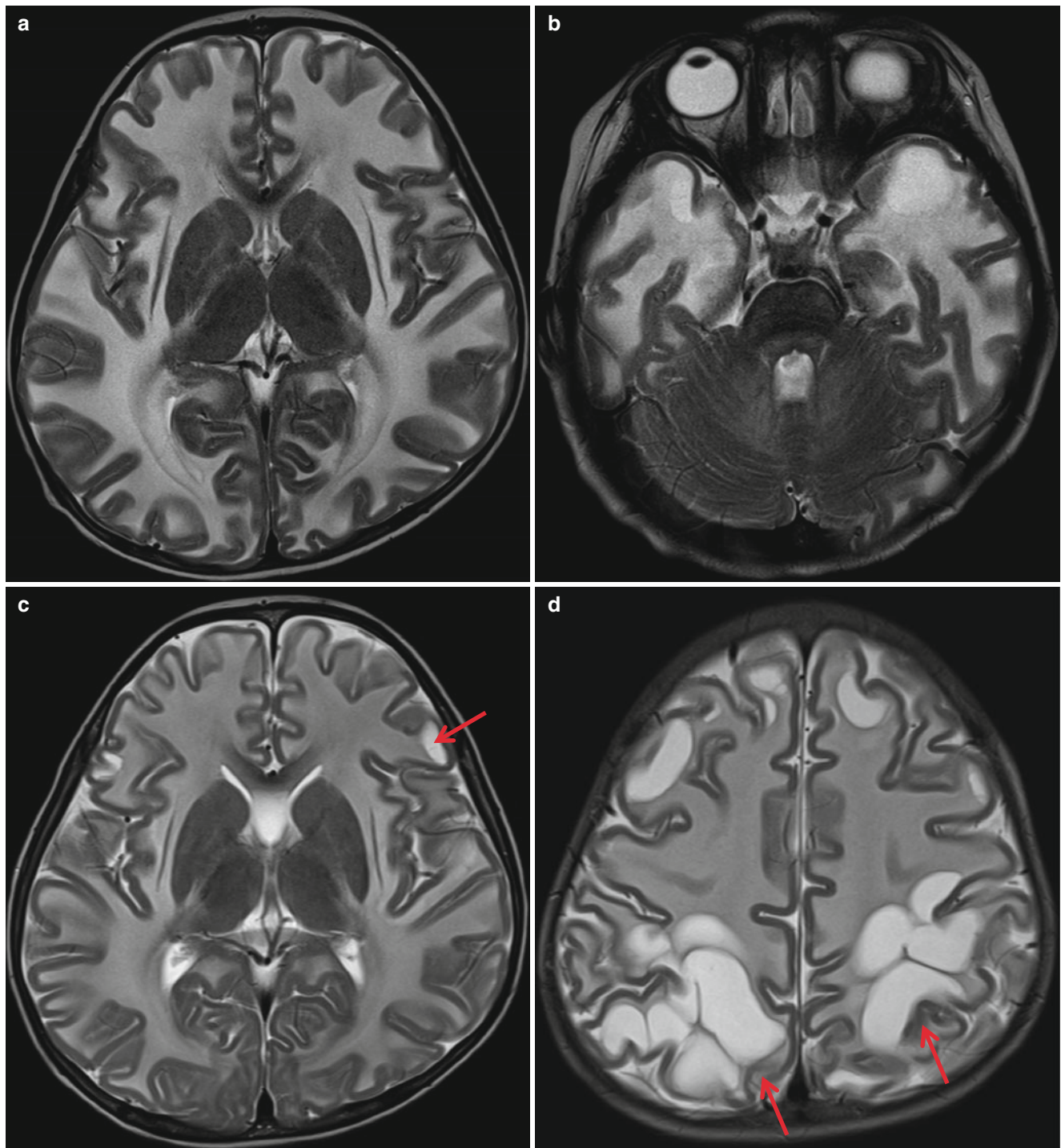


Fig. 2.18 Megalencephalic leukoencephalopathy with subcortical cyst in a 13-month-old girl with macrocephaly, developmental delay, and seizures. (a, b) T2-weighted images show extensive demyelination of the entire white matters including the internal capsule. The white matter

volume is slightly increased. Bilateral subcortical cyst. (c, d) One-year follow-up images show progression of the subcortical cyst formation (arrows)

2.5.19 Menkes Disease

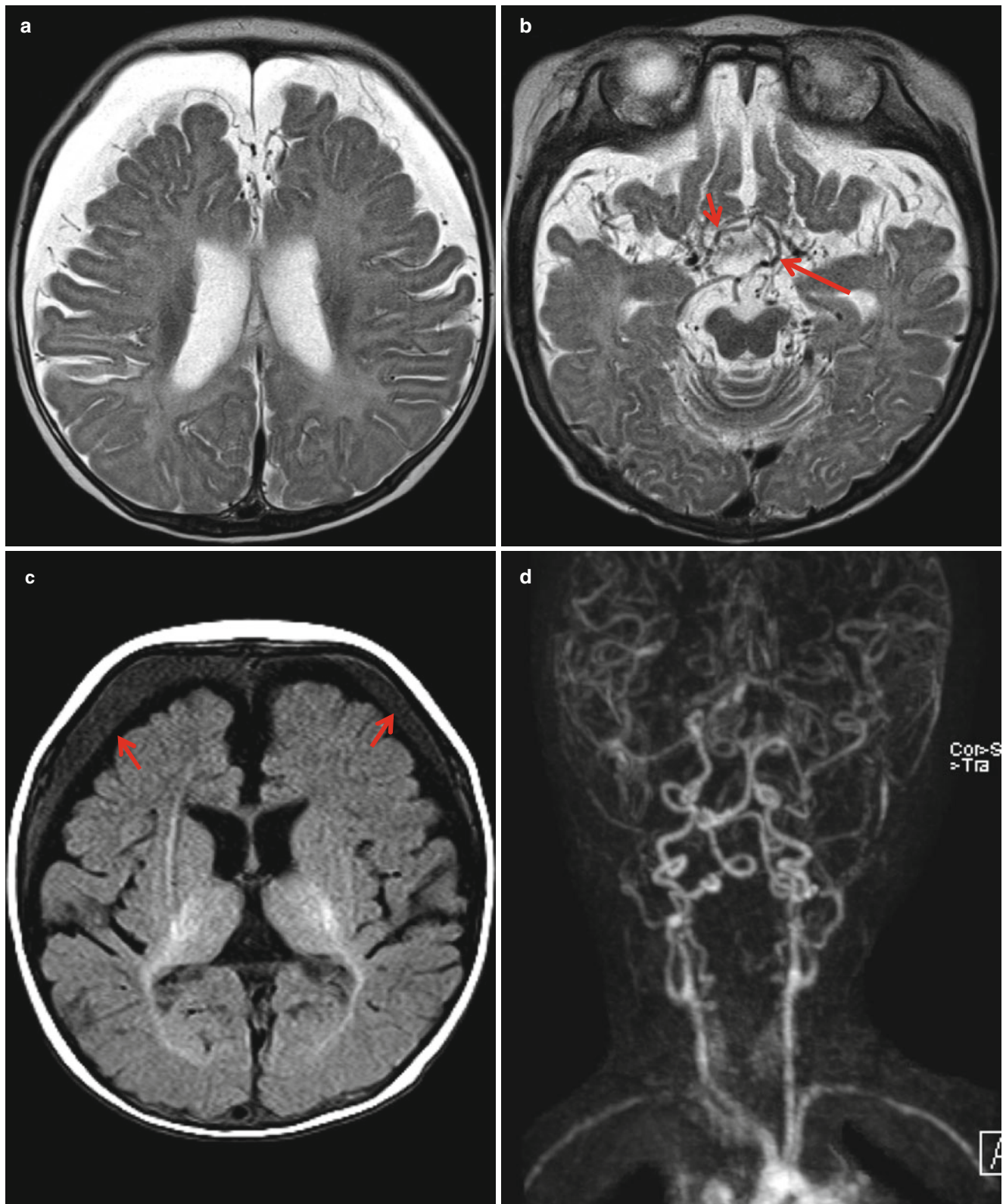


Fig. 2.19 Menkes disease in a 5-month-old boy with seizures and developmental delay. (a) T2-weighted image shows diffuse brain atrophy and the extra-axial fluid collections along the frontal region. (b) The basal image reveals marked tortuosity of the major intracranial vessels (arrows). (c) T1-weighted image shows bilateral subdural fluid col-

lection (arrows) presumed to be hemorrhage. Diffuse brain atrophy and delayed myelination are also present. (d) MR angiography shows extensive tortuosity and luminal irregularities of the intracranial and extracranial arteries

2.5.20 Wilson's Disease

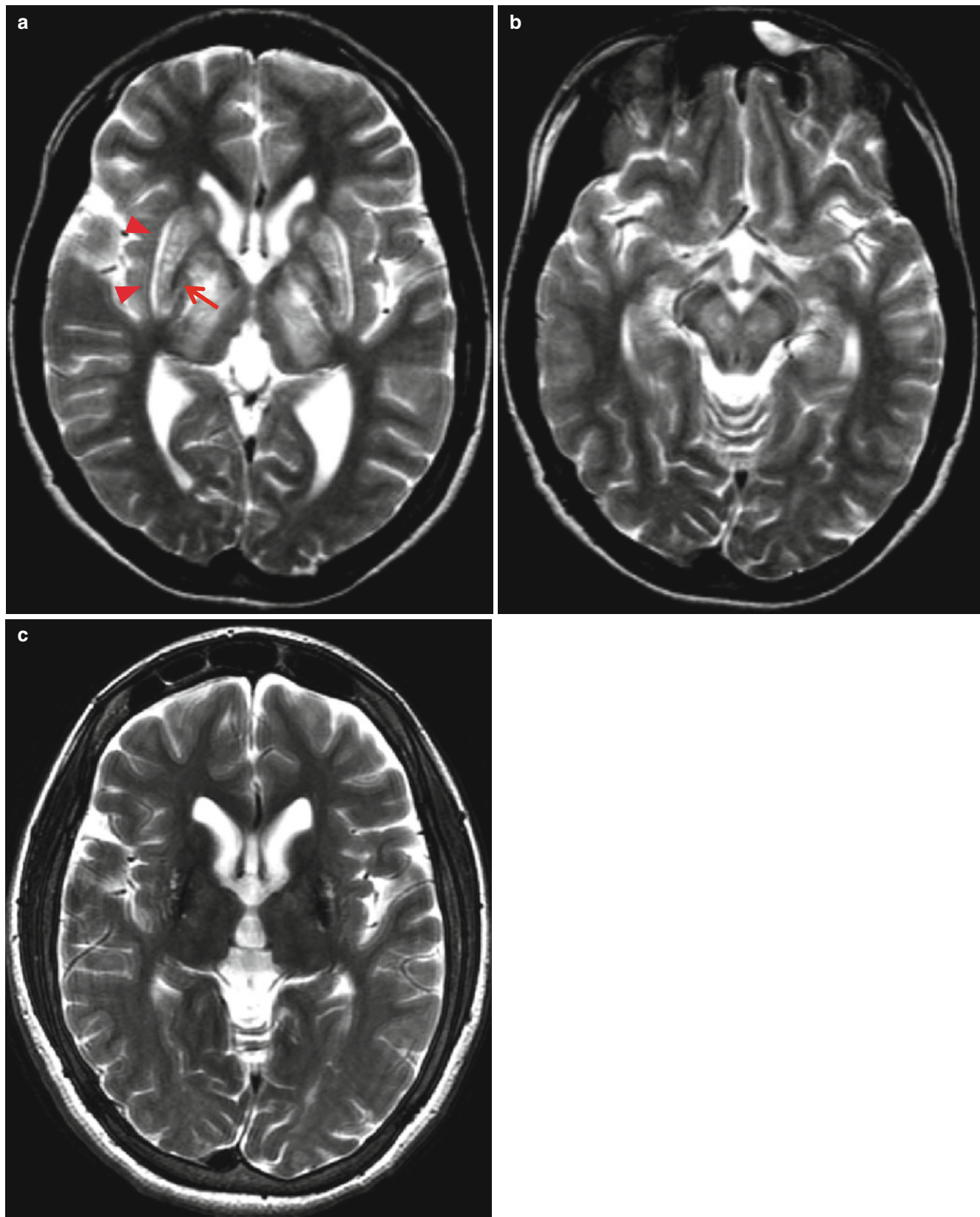


Fig. 2.20 Wilson's disease in a 14-year-old girl with seizures and dysarthria. (a, b) T2-weighted images show high-signal intensities involving the basal ganglia, thalamus, and the midbrain. Exaggerated linear high signals are seen in the outer margin of the putamen (*arrowheads*)

and low signals in the medial aspect of the putamen (*arrow*). (c) In a follow-up image after treatment with Trienten for 10 years, the previously noted high-signal intensities are almost resolved and low-signal intensities are still visible

References

- Barkovich AJ. Concepts of myelin and myelination in neuroradiology. *AJNR Am J Neuroradiol.* 2000;21:1099–109.
- Barkovich AJ, Kjos BO, Jackson DE, Norman D. Normal maturation of the neonatal and infant brain: MR imaging at 1.5T. *Radiology.* 1988;166:173–80.
- Barkovich AJ, Ferriero DM, Bass N, Boyer R. Involvement of the pontomedullary corticospinal tracts: a useful finding in the diagnosis of X-linked adrenoleukodystrophy. *AJNR Am J Neuroradiol.* 1997;18:95–100.
- Brismar J, Ozand PT. CT and MRI of the brain in glutaric acidemia type 1: a review of 59 published cases and report of 5 new patients. *AJNR Am J Neuroradiol.* 1995;16:675–83.
- Cheon JE, Kim IO, Hwang YS, et al. Leukodystrophy in children: a pictorial review of MR imaging features. *Radiographics.* 2002;22:461–76.
- Detre JA, Wang ZY, Bogdan AR, et al. Regional variation in brain lactate in Leigh syndrome by localized 1H magnetic resonance spectroscopy. *Ann Neurol.* 1991;29:218–21.
- Hegde AN, Mohan S, Lath N, Lim CCT. Differential diagnosis for bilateral abnormalities of the basal ganglia and thalamus. *RadioGraphics.* 2011;31:5–31.
- Kendall BE. Disorders of lysosomes, peroxisomes, and mitochondria. *AJNR Am J Neuroradiol.* 1992;13:621–53.
- Kendall BE. Inborn errors and demyelination: MRI and the diagnosis of white matter disease. *J Inherit Metab Dis.* 1993;16:771–86.
- Kim TK, Kim I-O, Kim WS, Yeon KM. MR imaging of childhood adrenoleukodystrophy. *J Korean Radiol Soc.* 1994;31:171–6.
- Kim TS, Kim I-O, Kim WS, Choi YS, Yeon KM, Hwang YS. Involvement of the gallbladder in childhood metachromatic leukodystrophy: ultrasonographic findings. *J Ultrasound Med.* 1996a;15:821–5.
- Kim I-O, Kim JH, Kim WS, Hwang YS, Yeon KM, Han MC. Mitochondrial myopathy-encephalopathy-lactic acidosis-and-strokelike episodes (MELAS) syndrome: CT and MR findings in seven children. *AJR Am J Roentgenol.* 1996b;166:641–5.
- Kim TS, Kim I-O, Kim WS, et al. MR of childhood metachromatic leukodystrophy. *AJNR Am J Neuroradiol.* 1997;18:733–8.
- Kim TJ, Kim I-O, Kim WS, et al. MR imaging of the brain in Wilson disease of childhood: findings before and after treatment with clinical correlation. *AJNR Am J Neuroradiol.* 2006;27:1373–8.
- Patay Z. Metabolic disorders. In: Carthy H, Brunelle F, Stringer DA, Kao SCS, editors. *Imaging children.* 2nd ed. London: Elsevier; 2005.
- Rasalkar DD, Chu WCW, Hui J, Chu C-M, Paunipagar BK, Li C-K. Pictorial review of mucopolysaccharidosis with emphasis on MRI features of brain and spine. *Br J Radiol.* 2011;84:469–77.
- Rennert J, Doelken R, Doelken M, Doerfler A. Menkes disease: MRI appearance of a rare neurodegenerative disorder. *J Pediatr Neurol.* 2009;7:317–20.
- Schiffmann R, van der Knaap MS. An MRI-based approach to the diagnosis of white matter disorders. *Neurology.* 2009;72:750–9.
- Takanashi J, Sugita K, Tanabe Y, et al. MR-revealed myelination in the cerebral corticospinal tract as a marker for Pelizaeus-Merzbacher's disease with proteolipid protein gene duplication. *AJNR Am J Neuroradiol.* 1999;20:1822–8.
- Takanashi J, Barkovich AJ, Cheng SF, Kostiner D, Baker JC, Packman S. Brain MR imaging in acute hyperammonemic encephalopathy arising from late-onset ornithine transcarbamylase deficiency. *AJNR Am J Neuroradiol.* 2003;24:390–3.
- Thomas B, Dossary NA, Widjaja E. MRI of childhood epilepsy due to inborn errors of metabolism. *AJR Am J Roentgenol.* 2010;194:W367–74.
- Valanne L, Ketonen L, Majander A, Suomalainen A, Pihko H. Neuroradiologic findings in children with mitochondrial disorders. *AJNR Am J Neuroradiol.* 1998;19:369–77.
- van der Knaap MS, Barth PG, Stroink H, et al. Leukoencephalopathy with swelling and a discrepantly mild clinical course in eight children. *Ann Neurol.* 1995;37:324–34.
- van der Knaap MS, Valk J. *Magnetic resonance of myelination and myelin disorders.* 3rd ed. Berlin: Springer; 2005.
- van der Knaap MS, Naidu S, Breiter SN, et al. Alexander disease: diagnosis with MR Imaging. *AJNR Am J Neuroradiol.* 2001;22:541–52.
- Walkley SU. Pathogenic cascades in lysosomal disease – why so complex? *J Inherit Metab Dis.* 2009;32:181–9.

In-One Kim

Contents

3.1	Introduction	76
3.2	Imaging	76
3.3	Spectrum of CNS Infection/Inflammation	76
3.3.1	Congenital Infections	76
3.3.2	Meningitis	77
3.3.3	Fungal Infection	77
3.3.4	Encephalitis	77
3.3.5	Infection-Associated Conditions	78
3.3.6	Inflammatory Conditions	79
3.4	Illustrations: Infection and Inflammatory Diseases of the Central Nervous System	80
3.4.1	Congenital CMV	80
3.4.2	Congenital Toxoplasmosis	81
3.4.3	Hemophilus Meningitis	82
3.4.4	Streptococcal Meningitis	83
3.4.5	Tuberculous Infection	84
3.4.6	Candidiasis	86
3.4.7	Herpes Simplex Encephalitis	87
3.4.8	Varicella Encephalitis	88
3.4.9	Enterovirus Infection	90
3.4.10	Subacute Sclerosing Panencephalitis	92
3.4.11	Brain Abscess	93
3.4.12	Acute Disseminated Encephalomyelitis	94
3.4.13	Acute Necrotizing Encephalopathy	96
3.4.14	Rasmussen Encephalitis	97
3.4.15	Multiple Sclerosis	98
3.4.16	Neuromyelitis Optica	100
3.4.17	Transverse Myelitis	101
3.4.18	Guillain-Barré Syndrome	102
	References	103

I.-O. Kim, M.D.
Seoul National University Hospital,
Seoul National University College of Medicine,
101 Daehak-ro, Chongno-gu, Seoul 110-744, Korea
e-mail: kimio@snu.ac.kr

3.1 Introduction

CNS infection in the pediatric age group causes significant morbidity and mortality as well as devastating effects on the rapidly developing brain. The inflammatory effect depends on the maturational status of the developing brain, timing of infection, or amount of pathogens. The routes of infections are diverse, including the vascular route, direct extension, or retrograde nerve axonal spread. The timing of infections is very important in the developing brain, resulting in malformations or destructive lesions. Neuroimaging plays important and growing roles in the diagnosis and therapeutic management of pediatric CNS infections. Etiologic diagnoses by imaging are usually limited, but certain imaging features can make specific diagnoses, such as herpetic or enteroviral infections. Computed tomography (CT) is still an important imaging modality in CNS infection, but MRI is the most valuable diagnostic tool, as in other CNS disorders. Ultrasonography (US) is an excellent imaging tool and easily available, especially for neonates and infants.

Inflammatory disorders involving the brain or spinal cord are also diverse and frequently difficult to differentiate from infectious or other inflammatory disorders. Clinical features are very important for making the diagnosis, but diagnostic imaging, especially the MRI, is frequently a crucial guide for diagnosis and treatment.

3.2 Imaging

Imaging in pediatric CNS infection is usually not for microbiological diagnosis, but more for detecting complications related to inflammatory reactions or monitoring the disease. US is often the initial imaging modality in neonates or infants; it is a useful screening procedure for the detection of complications such as hydrocephalus, calcification, infarction, cerebritis, abscess formation, or ventricular septations. CT is a useful modality in the evaluation of the brain abnormalities, particularly for the detection of calcifications or the evaluation of hydrocephalus. In infants, white matter abnormalities are difficult to detect with CT, and CT also has a disadvantage of ionizing radiation in the developing brain. MRI is an imaging modality of choice because of the excellent soft tissue contrast and the lack of radiation. MRI is useful in the evaluation of demyelination or gliosis, and it is more sensitive for the subtle changes of encephalitis or demyelination. Migration abnormalities in congenital infection or vascular abnormalities, such as venous thrombosis, can be more easily detected by MRI. Diffusion imaging is helpful in diagnosing infarction complicated by meningitis and differentiating abscesses from necrotic tumors.

3.3 Spectrum of CNS Infection/Inflammation

3.3.1 Congenital Infections

The route of infection is generally transplacental transmission, but ascending infection or direct contact during birth can be engaged. The extent and nature of damage on the developing nervous system depends on the limited ability to respond to an inflammatory injury. The timing of the injury is more important than its nature. Early injury during the first two trimesters causes congenital malformation, and later injuries cause destructive lesions.

3.3.1.1 Cytomegalovirus (CMV)

CMV is the most common cause of congenital viral infection of the CNS, usually by the transplacental route. Most common clinical features of symptomatic CMV infections are related to a disturbance of the reticuloendothelial system, such as hepatosplenomegaly or thrombocytopenia. Chorioretinitis, sensorineural hearing loss, and seizures are also present. The infection causes a multifocal necrotizing inflammatory process of the germinal matrix zone. The pathologic features can be different according to the timing of the infection. Periventricular calcification can be seen at a very early stage of involvement and migration abnormalities such as schizencephaly and polymicrogyria can occur later. Late gestational infection causes encephaloclastic lesions of porencephaly and hydranencephaly. CMV has an affinity for rapidly growing cells of germinal matrix, and the primary vascular dissemination results in ischemia. The imaging findings can be microcephaly with diminished white matter, anterior temporal lobe cyst, astrogliosis, calcification, delayed myelination, cortical malformation, and cerebellar hypoplasia. US can show lenticulostriate vasculopathy, intraventricular septations, and periventricular necrosis (Fig. 3.1) (de Vries et al. 2004; Fink et al. 2010).

3.3.1.2 Toxoplasmosis

Toxoplasmosis is the second most common (after CMV) congenital infection by *Toxoplasma gondii* (0.1–1/1,000 live births) through transplacental passage of the parasite, usually in the third trimester. Clinical features are similar to those of CMV, but macrocrania and chorioretinitis are more common. Toxoplasmosis reveals overall mortality of 11–14 %, and the survivors tend to have mental retardation, seizures, and spasticity. Pathologic lesions consist of multifocal granulomatous meningoencephalitis with necrosis and cortical destruction resulting in atrophy and microcephaly. Diffuse inflammatory infiltration of meninges and ependyma causes hydrocephalus. Calcifications are also common in basal ganglia, periventricular and subcortical white matter, or the cortex (Fig. 3.2). Early gestational infection can cause severe

neurologic abnormalities such as microcephaly, hydrocephalus, quadri- or diplegia, seizures, mental retardation, or blindness, but maldevelopment is not a typical feature (Knoblauch et al. 2003).

3.3.2 Meningitis

3.3.2.1 Neonatal Meningitis

Neonatal meningitis is the most common and serious intracranial bacterial infection during the neonatal period. The most common causative agents are enterobacteria, *E. coli*, and group B streptococcus. Premature male infants are more commonly affected. Usual clinical manifestations are sepsis, seizures, and increased intracranial pressure (ICP). Arachnoiditis, ventriculitis, vasculitis, or cerebritis occurs and abscesses, cerebral edema, or infarctions can be complicated. Chronic changes, such as hydrocephalus, encephalomalacia, or subdural effusion, can occur. US may be the initial imaging modality that shows increased echogenicity of sulci, gyri, focal parenchyma, or ventricular walls. Hydrocephalus, subdural effusion or empyema, or ventricular septations can be detected (Yikilmaz and Taylor 2008). CT shows similar findings, but parenchymal edema can be missed due to the unmyelinated white matter of the immature neonatal brain. MRI can give more information such as acute infarction or empyema. Diffusion MRI is very useful for diagnosing associated parenchymal infarction or subdural empyema (Fig. 3.3) (Polin and Harris 2001).

3.3.2.2 Acute Bacterial Meningitis in Infants and Children

Acute bacterial meningitis is the most frequent cause of acquired developmental delay. The most common organism is *Hemophilus influenza*, followed by meningococcus, pneumococcus, *Neisseria*, and streptococcus. They cause similar symptoms and signs of IICP, focal neurological deficit, fever, headache, nuchal rigidity, seizures, or cranial nerve palsy. Patients often have an associated otitis media or pharyngitis. The route of infections are usually hematogenous through leptomeningeal vessels or choroid plexus. Imaging findings are usually normal or nonspecific in noncomplicated meningitis. Imaging is usually for the monitoring of complications such as hydrocephalus, venous thrombosis, infarction, effusion or empyema, cerebritis, abscess, or ventriculitis (Fig. 3.4) (Vinchon et al. 2006). Infarctions can be due to venous thrombosis or arteritis. Diffusion MRI reveals diffusion restriction in infarction or empyema (Kim 2010).

3.3.2.3 Tuberculous Meningitis

Tuberculous meningitis occurs predominantly in infants and young children with miliary tuberculosis. Hematogenous dissemination plants small tuberculomas in the cortex, spinal

cord, meninges, or choroid plexus (Fig. 3.5). Nodules rupture into the subarachnoid space, resulting in meningitis. Proliferative, inflammatory meningeal exudates cause vasculitis of arteries traversing the exudates and disturbance of CSF circulation or absorption. Communicating or obstructive hydrocephalus are the most frequent imaging findings. Exudates are seen as an abnormal density of the basal cistern and abnormal enhancement of the cistern with or without enhancing tuberculomas on CT or MRI. Vasculitis is commonly involved in the medial lenticulostriate or thalamoperforating vessels, causing infarction in the caudate nucleus, hypothalami, and medial thalami (Fig. 3.6). Cortical infarctions are less common. Tuberculomas can calcify or cause surrounding vasogenic edema (Be et al. 2009).

3.3.3 Fungal Infection

3.3.3.1 Candidiasis

Candida infections cause sepsis and secondary meningitis in infants. *Candida* meningitis can be complicated in immunocompromised infants and usually progresses to abscess formation. Diffuse cerebritis and widespread microabscesses can occur in patients with prolonged antibiotic therapy. *Candida* can also cause vasculitis, resulting in infarction and hemorrhage (Fig. 3.7). In the case of immunocompromised patients, the abscesses often do not show sharply demarcated enhancing abscess capsules.

3.3.3.2 Cryptococcosis

Cryptococcosis is one of the most common fungi to involve the CNS. CNS infection occurs both in immunocompromised and immunocompetent hosts. Symptoms usually reflect cryptococcal meningitis. Images are similar with tuberculous meningitis showing basal cisternal exudates, hydrocephalus, infarction from vasculitis, and pseudocysts in the basal ganglial region involving the perivascular spaces. Parenchymal mass lesions with ring enhancement can be present in rare cases (Popovich et al. 1990).

3.3.4 Encephalitis

3.3.4.1 Viral Encephalitis

3.3.4.1.1 Herpes Encephalitis

HSV-I infection is more common in older infants and children. The HSV-I virus is spread by saliva or respiratory contact and transported along the sensory fibers to the Gasserian ganglion or olfactory nerve and extends to the anterior and middle cranial fossa. Pathology shows necrotizing meningo-encephalitis with hemorrhage. MRI shows parenchymal edema, hemorrhage more localized to the temporal area, and frontal lobe with predilection to the limbic system. The

lentiform nucleus is frequently spared. The lesions show diffusion restriction in the acute stage and progress rapidly to parenchymal tissue loss, hemorrhage, and calcification (Fig. 3.8). HSV-II infection is more common in neonates and causes disseminated CNS disease. MRI shows patches and widespread parenchymal abnormality with diffusion restriction, predominantly white matter (Fig. 3.8), and rapidly progresses to diffuse parenchymal destructive change and encephalomalacia (Baskin and Hedlund 2007).

3.3.4.1.2 Varicella Zoster Encephalitis

Varicella zoster infection causes chickenpox in children under 10 years of age. CNS complications of varicella infection affect less than 1 % of children with chicken pox and include acute cerebellar ataxia (varicella cerebellitis), multifocal leukoencephalopathy with multifocal parenchymal ischemic lesions (Fig. 3.9), and vasculitis causing VZV-associated stroke that frequently involve the basal ganglia (Fig. 3.10) (Ueno et al. 2002; Losurdo et al. 2006).

3.3.4.1.3 Enterovirus Infection

Enteroviral (poliovirus, coxsackievirus, echovirus, and a subtype of enterovirus) infection can occur by contact with infected feces or oropharyngeal secretion. Infection causes aseptic meningitis, spinal/bulbar poliomyelitis, encephalitis, and arteriopathy. Enterovirus-71 causes hand-foot-and-mouth disease (HFMD). Rhombencephalitis can occur, involving the dorsal medulla (Fig. 3.11) and pons, cerebellar dentate nucleus, midbrain, thalami, or basal ganglia (Fig. 3.12) (Ho et al. 1999). HFMD can also cause acute flaccid paralysis due to myelitis, more frequently involving the anterior horn cells of the spinal cord (Fig. 3.13) (Chong et al. 2003).

3.3.4.1.4 Subacute Sclerosing Panencephalitis (SSPE)

SSPE is a slowly progressing but usually fatal disease probably caused by reactivation of the measles virus. Clinical features are the insidious onset of behavioral change, mental retardation progressing to myoclonus, seizures, dementia, and quadriplegia. Pathology shows multifocal cortical or subcortical gliosis, demyelination, perivascular inflammatory infiltrates, and intranuclear inclusion bodies. MRI is the imaging of choice, but the MR findings can be nonspecific. MR abnormalities are most commonly bilateral gliotic lesions involving temporal and parietal white matter that extend to the corpus callosum and brainstem, and progressive brain atrophy (Fig. 3.14) (Gutierrez et al. 2010).

3.3.4.2 Bacterial Cerebritis/Abscess

Bacterial infection occurs from hematogenous spread, contiguous infection from the sino-nasal cavity, a penetrating wound, or cardiopulmonary malfunction. Major clinical presentations are fever, headache, increased intracranial

pressure or acute fulminant bacterial meningitis in neonates, and focal neurological deficit in children with brain abscess. Brain abscess evolves sequentially from early cerebritis to late cerebritis, early capsule formation, and late capsule formation over 1 or 2 weeks. Imaging shows edematous parenchyma and ring enhancement from the late cerebritis phase. The medial wall of the enhancing ring is usually thinner (Enzmann et al. 1983). In the newborn and the infant, encapsulated abscess frequently locates in the periventricular area that easily ruptures into the ventricle. They are frequently caused by *Citrobacter* or *Proteus mirabilis*. In older children, the frequent locations are the subcortical region or basal ganglia. Diffusion imaging shows restricted diffusion of the abscess content, which is very useful for differentiating abscesses from necrotic tumors. MR spectroscopy shows increased alanine and acetate in addition to the lactate peak (Fig. 3.15) (Cartes-Zumelzu et al. 2004).

3.3.5 Infection-Associated Conditions

3.3.5.1 Acute Disseminated Encephalomyelitis (ADEM)

ADEM is an immune-mediated demyelinating disease frequently occurring after infection or vaccination. Children and young adults are most commonly affected, and diagnosis is usually made by exclusion. Clinically, the onset is usually abrupt, 4–21 days after a viral illness or vaccination. Patients show widespread CNS dysfunction with multiple neurological abnormalities. The clinical course is usually monophasic, in contrast to the polyphasic course of multiple sclerosis. MRI shows increased signal intensity lesions in the white matter on T2 image involving the cerebrum, basal ganglia, thalamus, cerebellum, and brainstem. The periventricular white matters are frequently spared (Fig. 3.16). The involved white matters show variable enhancement. The bilateral optic nerve and spinal cord can be involved. Spinal cord lesions show confluent intramedullary signal abnormality (Fig. 3.17) (Dale et al. 2000; Yiu et al. 2009). Acute hemorrhagic encephalopathy is a hemorrhagic variant having a more fulminant course and poor outcome (Fig. 3.18) (Mizuguchi 1997).

3.3.5.2 Reye Syndrome

Reye syndrome is a severe encephalopathy with fatty degeneration of the liver and kidney, usually after acute viral illness. Acute symptoms of fever, vomiting, convulsion, and coma progress rapidly and mortality ranges up to 30–40 %. Patients show hepatomegaly and hepatic failure (elevated enzymes and ammonia). Toxic agents, such as salicylates, aflatoxin, and insecticides, have been associated. CT or MRI shows diffuse cerebral edema with or without basal ganglia and thalamic involvement and accentuated gray and white

matter differentiation. The disease is potentially reversible if properly managed in its early phase (Singh et al. 2011).

3.3.5.3 Rasmussen Encephalitis

Rasmussen encephalitis is a rare cause of seizures, progressive hemiplegia, and psychomotor deterioration. A probable etiology of viral or autoimmune origin is suggested. The common pattern is partial motor seizures in a previously healthy child, ultimately developing fixed hemiplegia. Initially the imaging is normal and the involved hemisphere shows progressive atrophy with T2 prolongation of the cortex, subcortical white matter, and basal ganglia. Atrophy usually involves the frontal and temporal lobes (Fig. 3.19) (Bien et al. 2005).

3.3.6 Inflammatory Conditions

3.3.6.1 Multiple Sclerosis (MS)

MS is a chronic inflammatory demyelinating disease of the brain and spinal cord (Fig. 3.20). The causes of MS are most likely some combination of immunologic, genetic, environmental, and infectious factors. The symptoms can be quite varied, and they include sensory changes, muscle weakness, difficulty in moving or ataxia, speech disturbances, visual problems, or cognitive or emotional disturbances. The course of MS is highly varied and unpredictable. In most patients, the disease is characterized initially by episodes of reversible neurological deficits that are often followed by progressive neurological deterioration. The disease is diagnosed on the basis of clinical findings and supporting evidence from MRI of the brain and examination of the cerebrospinal fluid for oligoclonal bands. Diagnosis can be made from multiple episodes of CNS demyelination separated in time and space. MRI is the most sensitive imaging tool, and the findings are time and space dissemination of multifocal white matter lesions on MRI at least 1 month after the previous clinical episode or previous MRI (Fig. 3.21). The white matter lesions are more prevalent in the periventricular region, but can also be in the juxtacortical or infratentorial regions (Dale et al. 2000).

3.3.6.2 Neuromyelitis Optica (NMO)

NMO is an idiopathic inflammatory demyelinating disorder predominantly affecting the optic nerves and spinal cord. NMO more frequently has a relapsing course and results from immune reaction to aquaporin-4, which is the dominant water channel in the central nervous system, located in foot processes of the astrocytes. Diagnostic criteria include optic neuritis and acute myelitis (Fig. 3.22). Longitudinally extensive spinal cord lesions in patients frequently involve the upper- to mid-thoracic cord with a predominant central gray matter pattern. Contiguous spinal cord MRI lesions frequently extend over 3 or more vertebral segments. The detection of NMO-IgG (binds to aquaporin-4) is highly specific for diagnosis. Demyelinating lesions in the brain can be present in periventricular white matter, the hypothalamus, brainstem, or cerebellum (Nandhagopal et al. 2010).

3.3.6.3 Acute Transverse Myelitis (ATM)

ATM is an inflammatory myelitis causing axonal demyelination. This demyelination arises idiopathically following infections or vaccinations or is associated with multiple sclerosis. Immune-mediated inflammation, such as exposure to a viral antigen, is a suggested mechanism. The lesions are inflammatory and typically involve the spinal cord on both sides (Fig. 3.23). With acute transverse myelitis, the onset is sudden and progresses rapidly within hours and days. Symptoms include weakness and numbness of the limbs as well as motor, sensory, and sphincter deficits, depending on the level and the extent of the spinal cord involved (Jacob and Weinshenker 2008).

3.3.6.4 Guillain-Barré Syndrome (GBS)

GBS is an acute immune-mediated polyneuropathy manifesting acute progressive motor weakness frequently manifesting as ascending type of paralysis. The patients usually recover within a few months. The diagnosis is based on clinical signs and elevated protein levels of CSF. Enhancement of the nerve roots, more frequently the ventral nerves, on MRI is a highly specific finding (Fig. 3.24). The absence of spinal cord edema or enhancement excludes transverse myelitis (Mulkey et al. 2010).

3.4 Illustrations: Infection and Inflammatory Diseases of the Central Nervous System

3.4.1 Congenital CMV

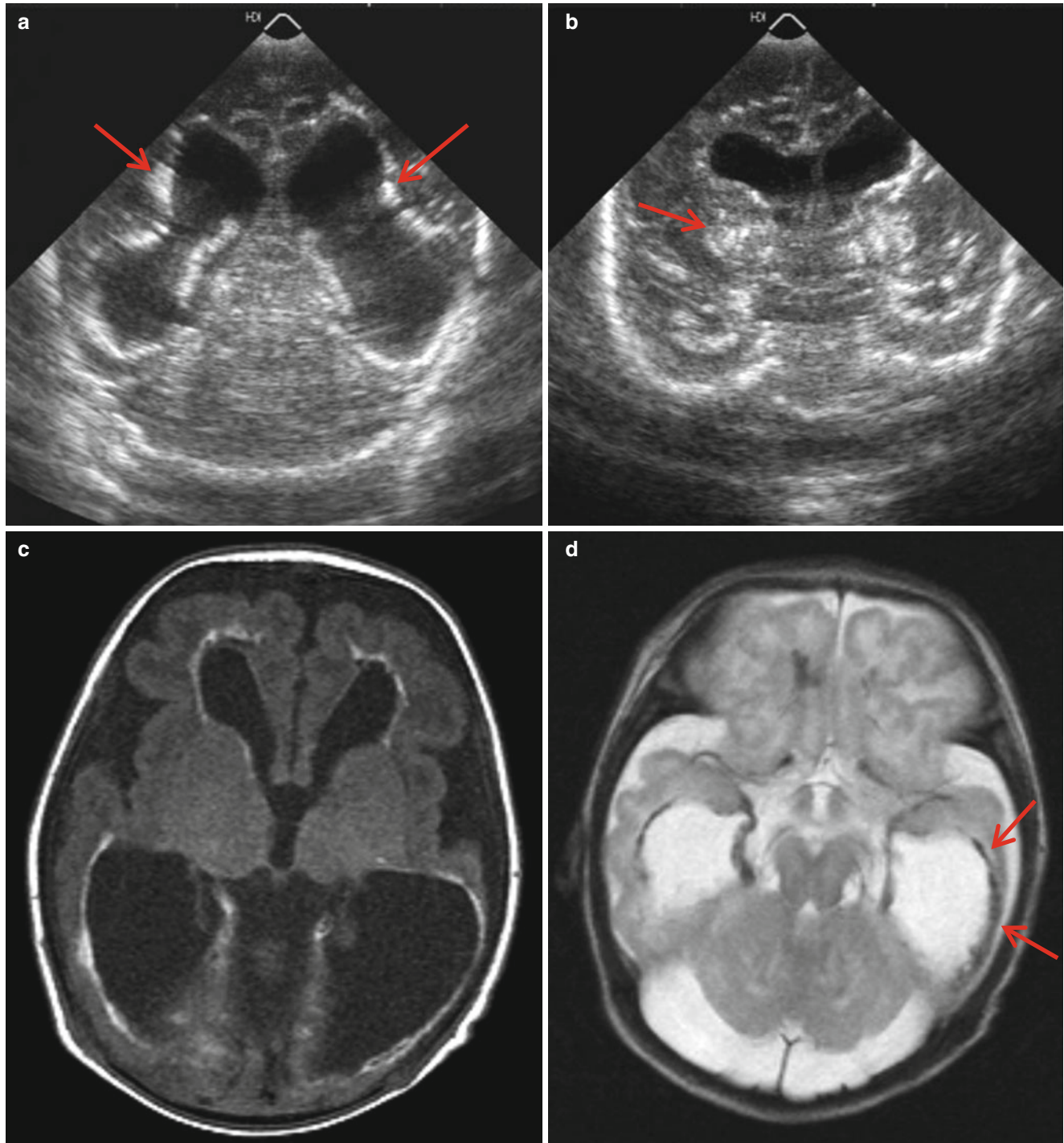


Fig. 3.1 Congenital CMV infection in a neonate with anemia, sensorineural hearing loss, and seizures. **(a)** US of brain shows dilation of both lateral ventricles with abnormal echogenic lining of the ventricular walls (*arrows*) suggesting calcifications. **(b)** Multiple linear echogenicities in both thalami (*arrow*) are seen as lenticulostriate vasculopathies. **(c)** T1-weighted image shows dilated ventricles with

high-signal intensities along the ventricular walls. Wide subarachnoid spaces suggest diffuse brain atrophy. **(d)** T2-weighted image shows low signal intensities lining the lateral ventricles (*arrows*) suggesting the ventricular wall calcifications. Widening of the retrocerebellar subarachnoid space is seen

3.4.2 Congenital Toxoplasmosis

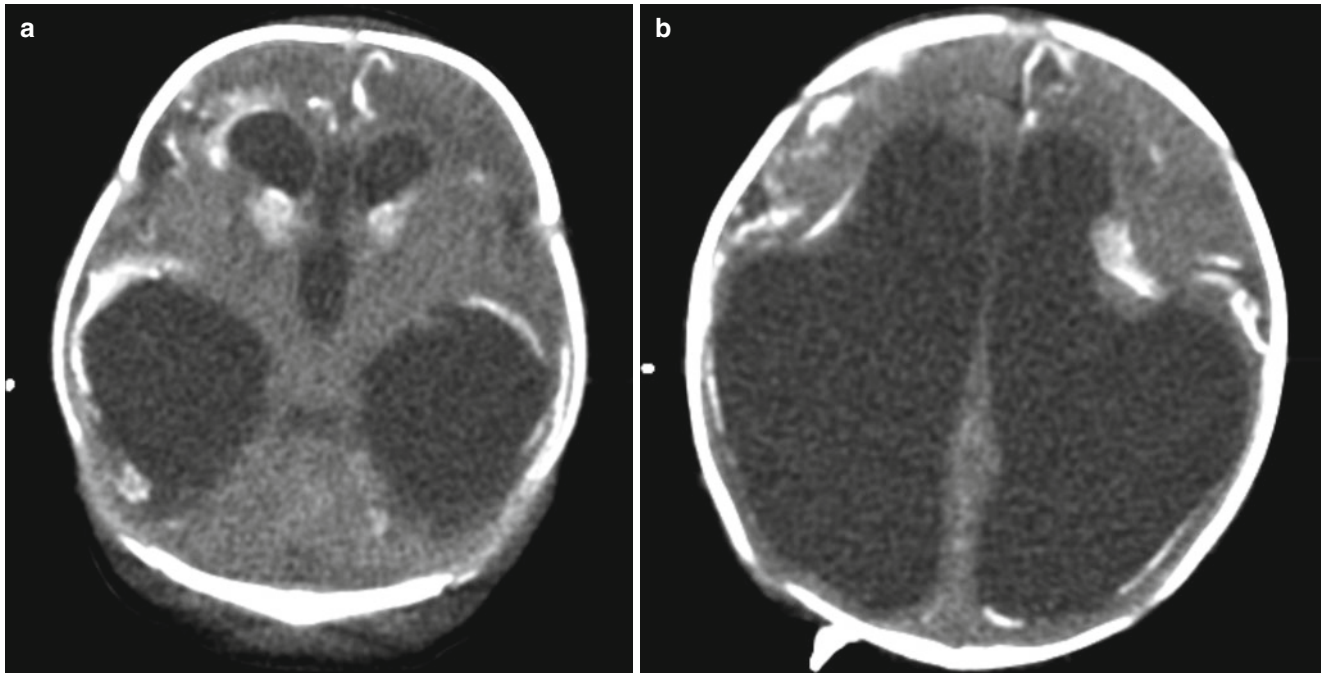


Fig. 3.2 A neonate with congenital toxoplasmosis. (a) CT shows markedly dilated lateral and third ventricles with ventricular wall calcifications. (b) Severe cortical thinning with multiple parenchymal and deep nuclear calcifications along with the ventricular wall calcifications

3.4.3 Hemophilus Meningitis

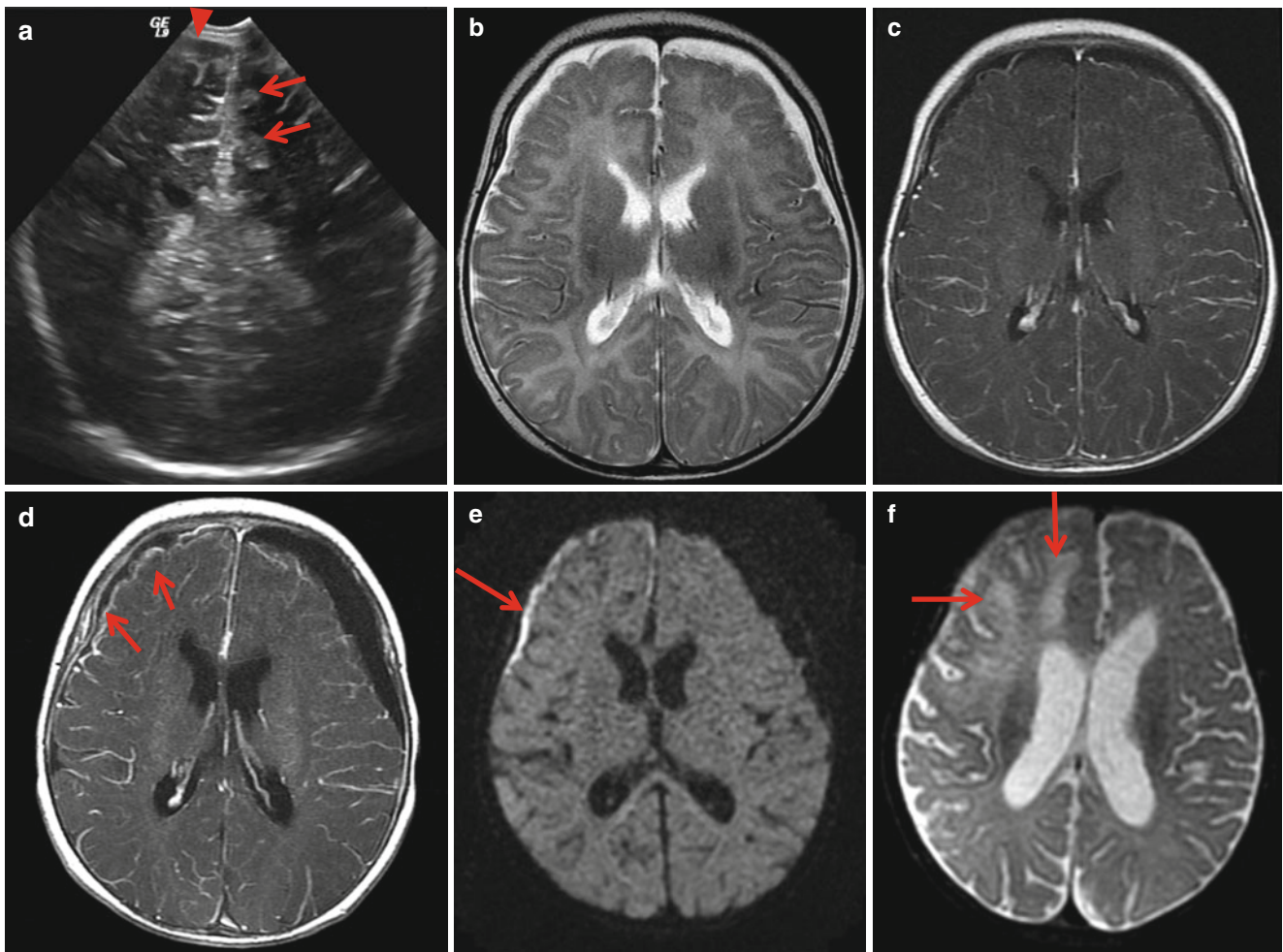


Fig. 3.3 A 3-month-old infant with hemophilus meningitis. (a) US shows increased echogenicities of the cerebral sulci (*arrows*) and extra-axial fluid collection in the frontal region (*arrowhead*). (b) T2-weighted image shows extra-axial fluid collections along both frontal region. (c) Postcontrast image shows no remarkable meningeal enhancement. (d) Follow-up image after 1 week shows progression of hydrocephalus and

extra-axial fluid collections. Meningeal enhancement is more prominent along the right-side fluid collection (*arrows*). (e) Diffusion image suggests complicated fluid collection in the right frontal region (*arrow*), such as subdural empyema. (f) Another week's follow-up shows parenchymal edema in the right frontotemporal lobe (*arrows*), suspecting complicated infarction and progression of ventriculomegaly

3.4.4 Streptococcal Meningitis

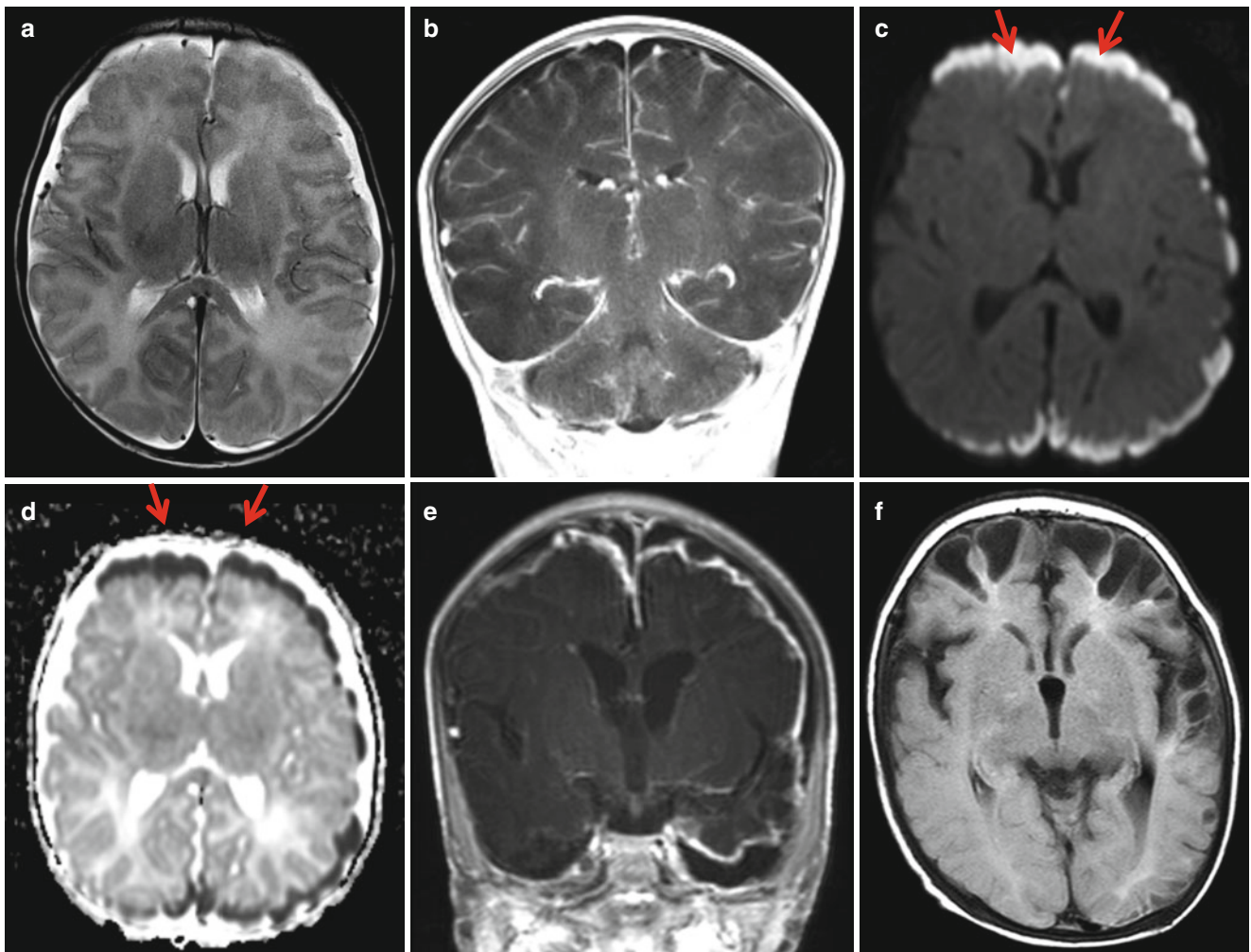


Fig. 3.4 A neonate with streptococcal meningitis. (a) T2-weighted image shows small amount of extra-axial fluid collections along the frontotemporal region. (b) Postcontrast MR image shows subtle meningeal enhancement over the convexity. (c) Diffusion and (d) ADC images show restricted diffusion of the extra-axial fluid (*arrows*), sus-

pecting a complication of subdural empyema. (e) Two-week follow-up image shows strong enhancement of the meninges under the fluid collections. Ventricles are moderately dilated. (f) 2-month follow-up study shows multifocal cystic encephalomalacia along the frontotemporal cortex due to gyral infarctions complicated by bacterial meningitis

3.4.5 Tuberculous Infection

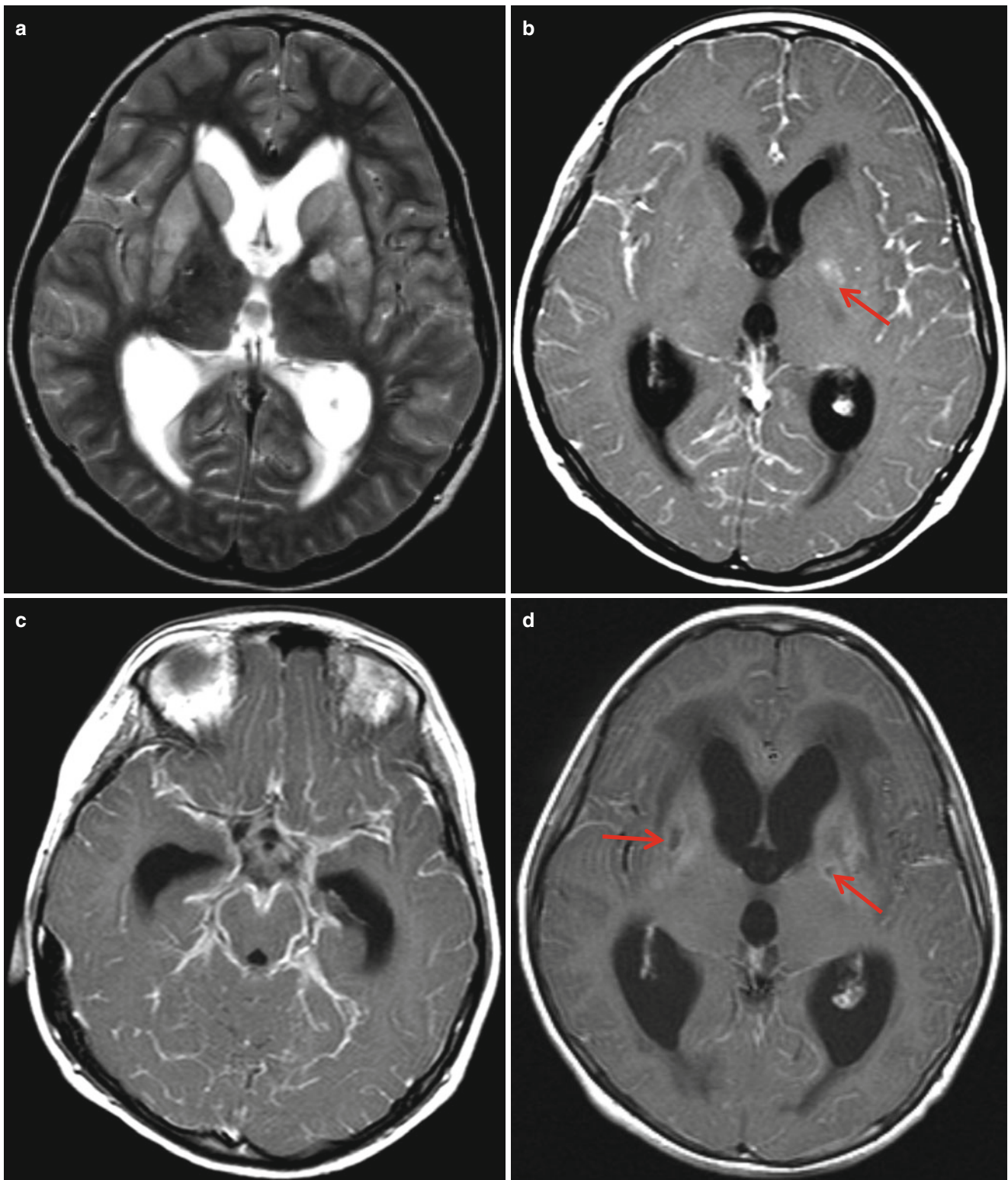


Fig. 3.5 Tuberculous meningitis in an 11-month-old boy. (a) T2-weighted image shows moderate hydrocephalus with bilateral basal ganglia edema. (b) Postcontrast image shows diffuse leptomeningeal enhancement and focal nodular enhancements in the left globus pallidus (arrow). (c) The meningeal enhancements are more extensive in the

basal cistern than the cortical surface. (d) T1-weighted image after 1 month shows progression of hydrocephalus and periventricular edema. Focal low signals of both lentiform nucleus (arrows) suspecting focal encephalomalacia

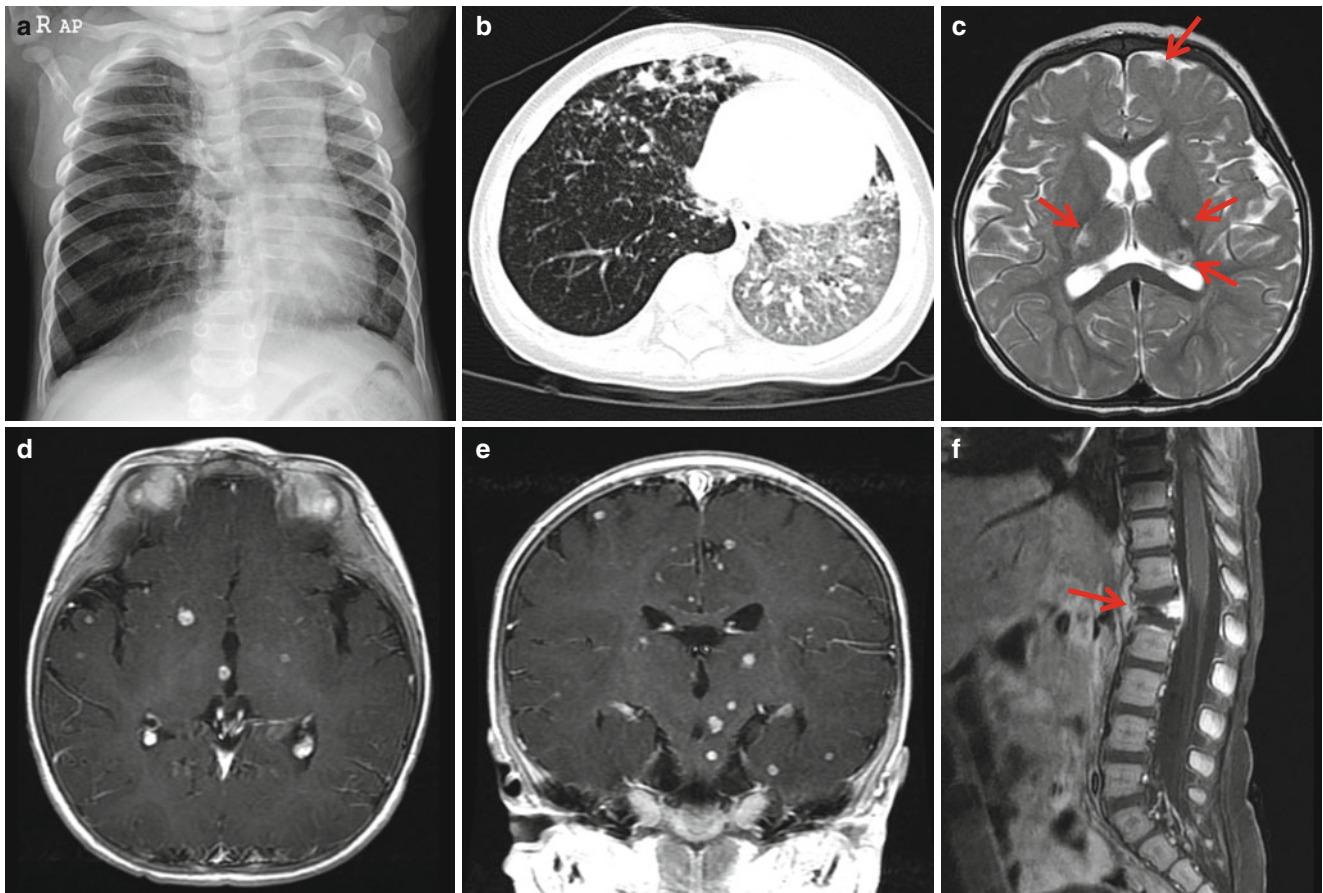


Fig. 3.6 Disseminated tuberculomas are in the brain and spine of a 9-month-old boy. **(a)** Plain chest radiograph shows decreased left lung volume with subtle fine nodules in the left lung. Right lung shows hyperaeration and focal atelectasis in the suprahilar area. **(b)** Miliary nodules and bronchopneumonic infiltrations are well demonstrated with CT. The left lung is hyperaerated. **(c)** T2-weighted image shows

multiple nodules in the deep nuclei. Right posterior thalamic lesion shows a nodule with central low signal. **(d, e)** Multiple ring-enhancing nodules are disseminated in the cerebrum, brainstem, and cerebellum (not shown). **(f)** Tuberculous spondylitis shows collapse of the L1 body and pre- and post-vertebral enhancing lesion (*arrow*)

3.4.6 Candidiasis

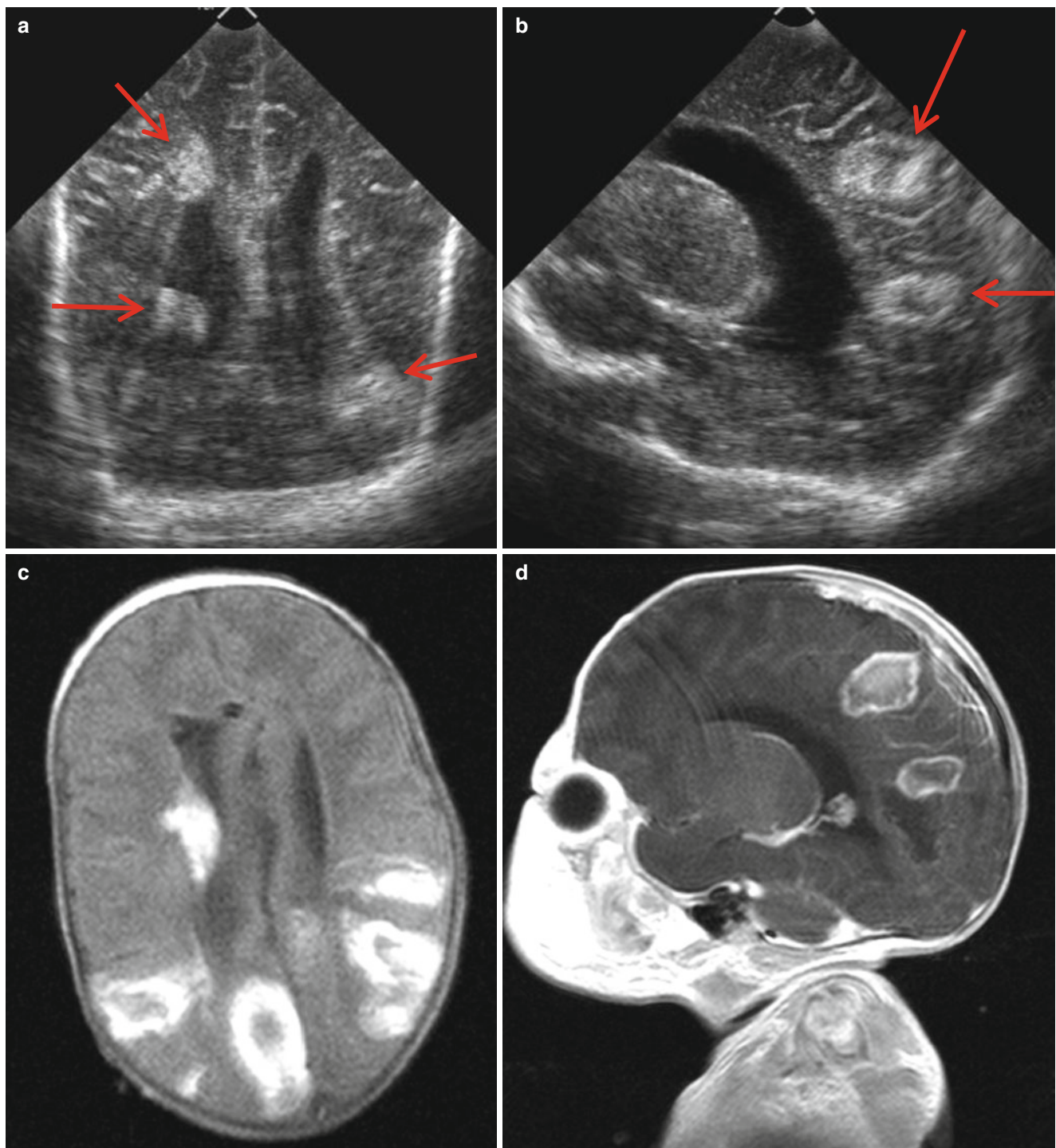


Fig. 3.7 A 6-week-old baby with myelomeningocele. (a, b) US shows hydrocephalus and multiple cavitary echogenic mass lesions in the cortical and periventricular area proven to be candidiasis (arrows). (c)

T1-weighted image shows multiple hemorrhagic lesions suggesting hemorrhagic infarction. (d) Postcontrast image suggests abscess formation due to septic embolism

3.4.7 Herpes Simplex Encephalitis

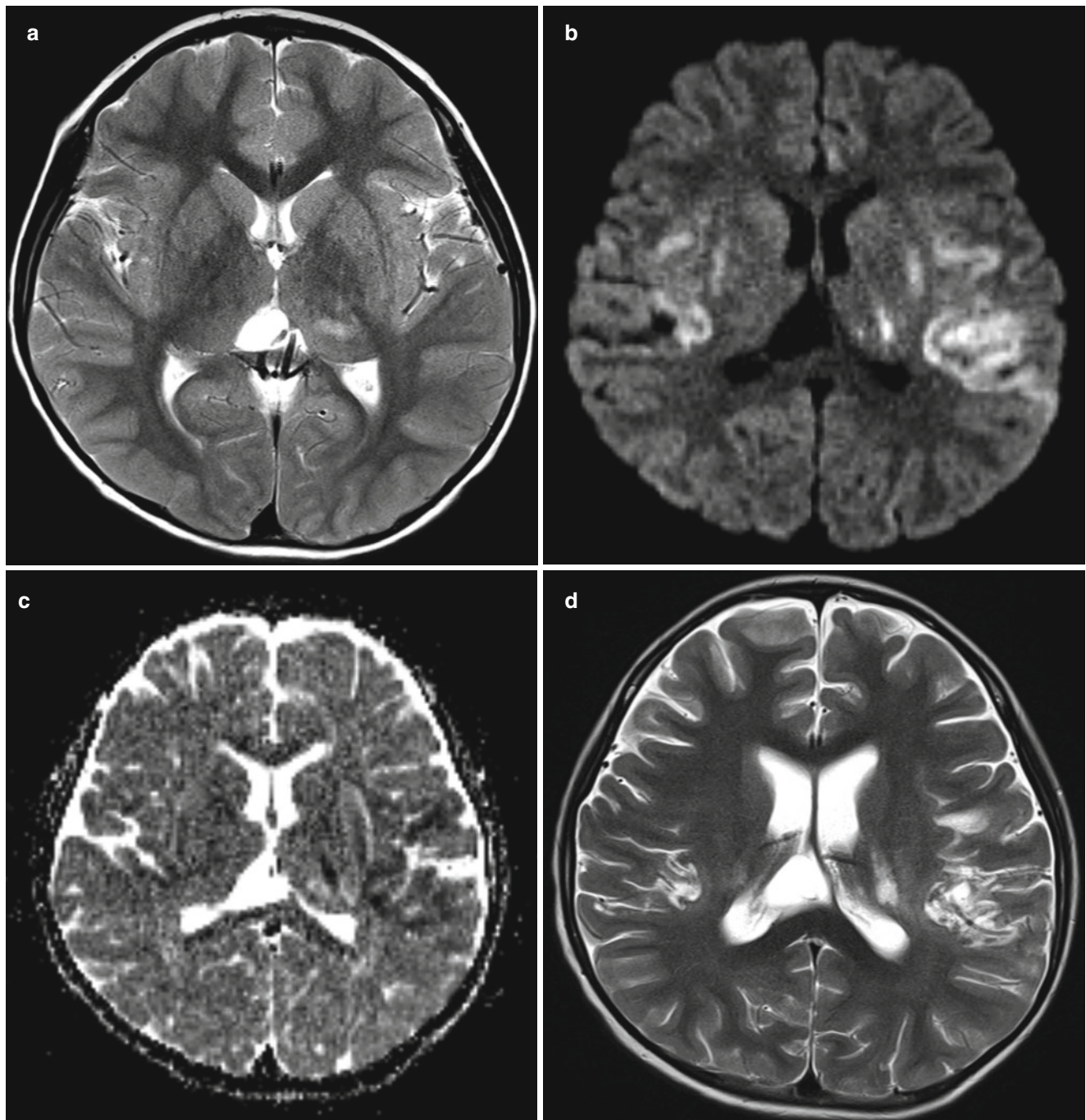


Fig. 3.8 A 5-year-old boy with herpes simplex encephalitis. (a) T2-weighted image shows subtle swelling of the temporal lobe and thalamus and posterior cingulate gyrus, predominantly in the left side. (b) Diffusion and ADC (c) images after 3 days show restricted diffusion

in both temporal and left thalamus. (d) Two-week follow-up image reveals rapid parenchymal loss of the involved area with mild brain atrophy

3.4.8 Varicella Encephalitis

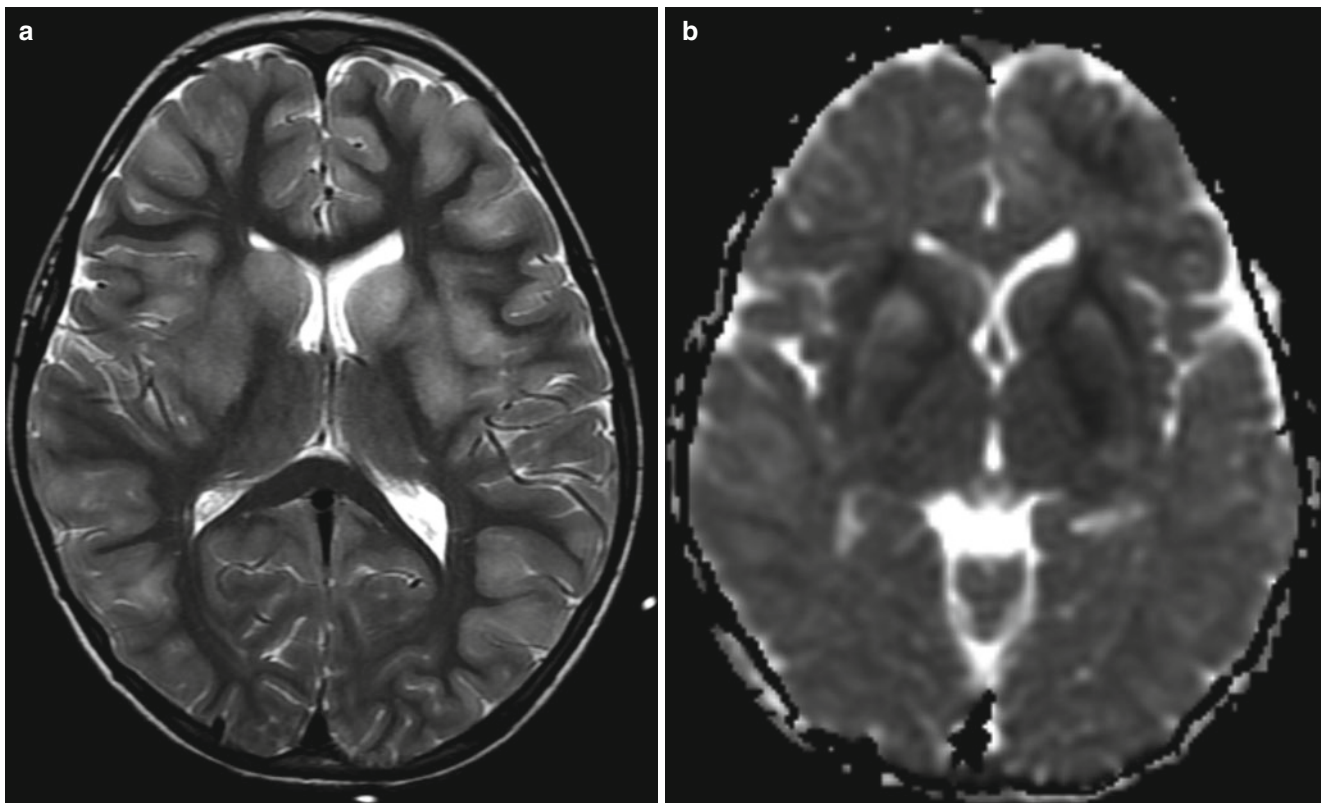


Fig. 3.9 Varicella encephalitis. (a) T2-weighted image shows disseminated lesions in the cortex and the basal ganglia. (b) Diffusion image shows restricted diffusion of the lesions

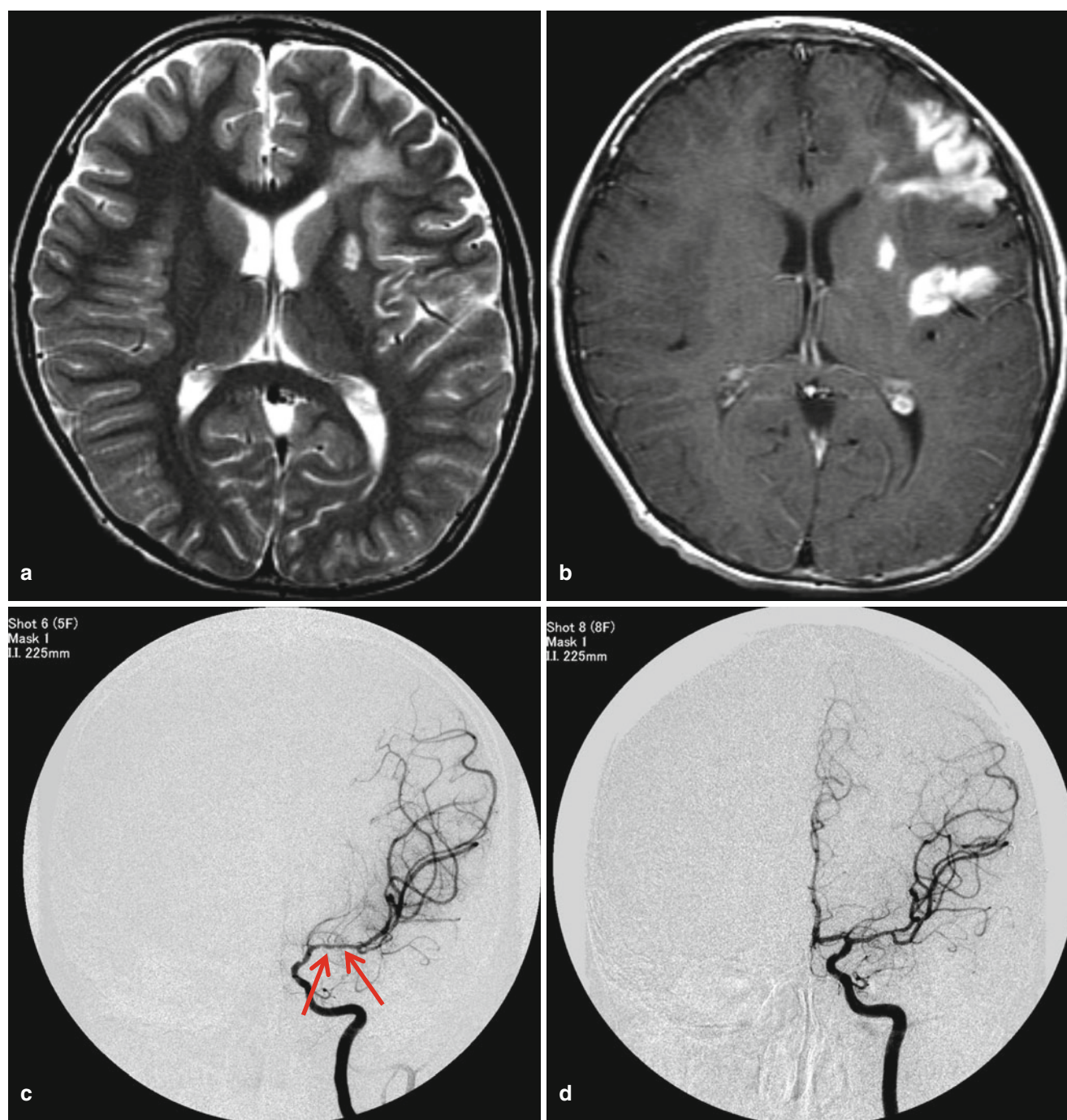


Fig. 3.10 An 8-month-old boy with right-side weakness suspecting post-viral angiitis. **(a)** T2-weighted image shows high signals in the left frontotemporal lobe and putamen. **(b)** Gyriform enhancement of the frontotemporal lesion and putamen suggests infarction. **(c)** Left distal

internal carotid artery (ICA) and proximal middle cerebral artery (MCA) show mild irregular narrowing (*arrow*). **(d)** Three-year follow-up arteriography shows improved irregularities with residual mild narrowing of the MCA

3.4.9 Enterovirus Infection

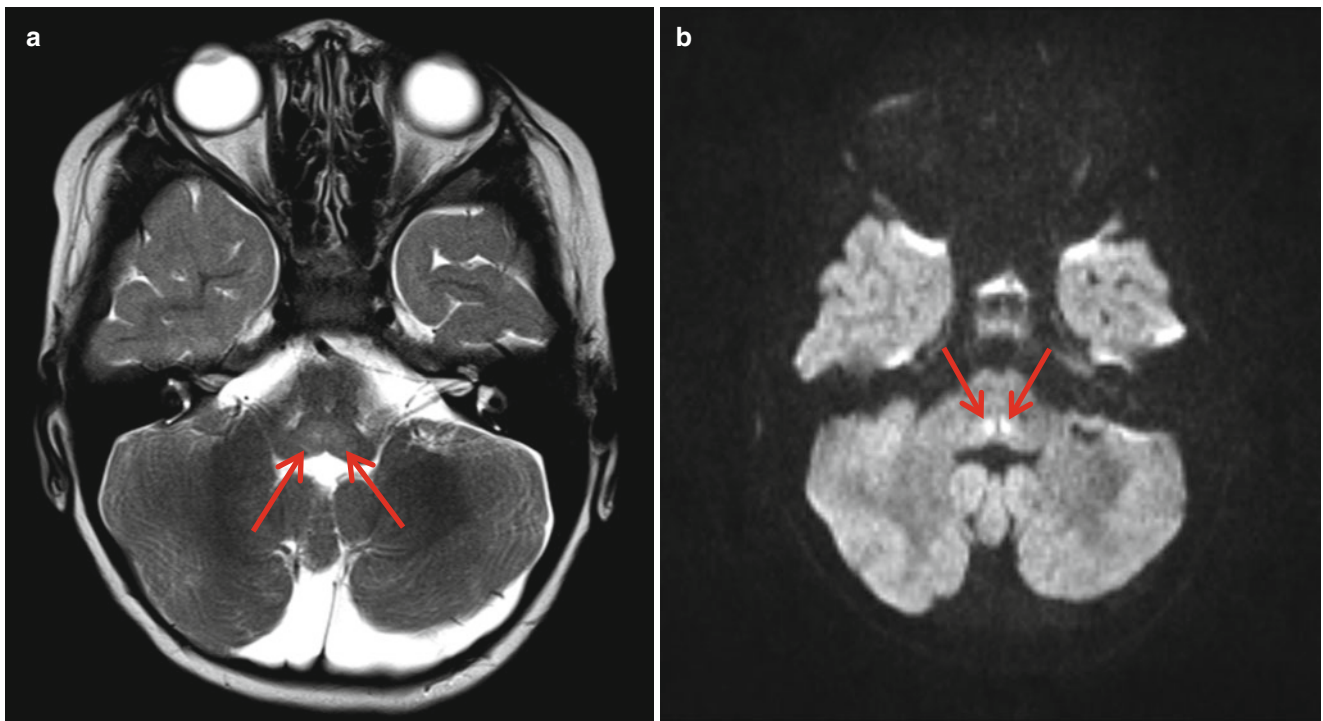


Fig. 3.11 A 3-year-old boy with fever and hand tremor 5 days after hand foot and mouth disease (HFMD). (a) T2-weight image shows subtle high signal in medulla (*arrows*). (b) Diffusion image reveals white matter tract lesions (*arrows*) in the dorsal medulla

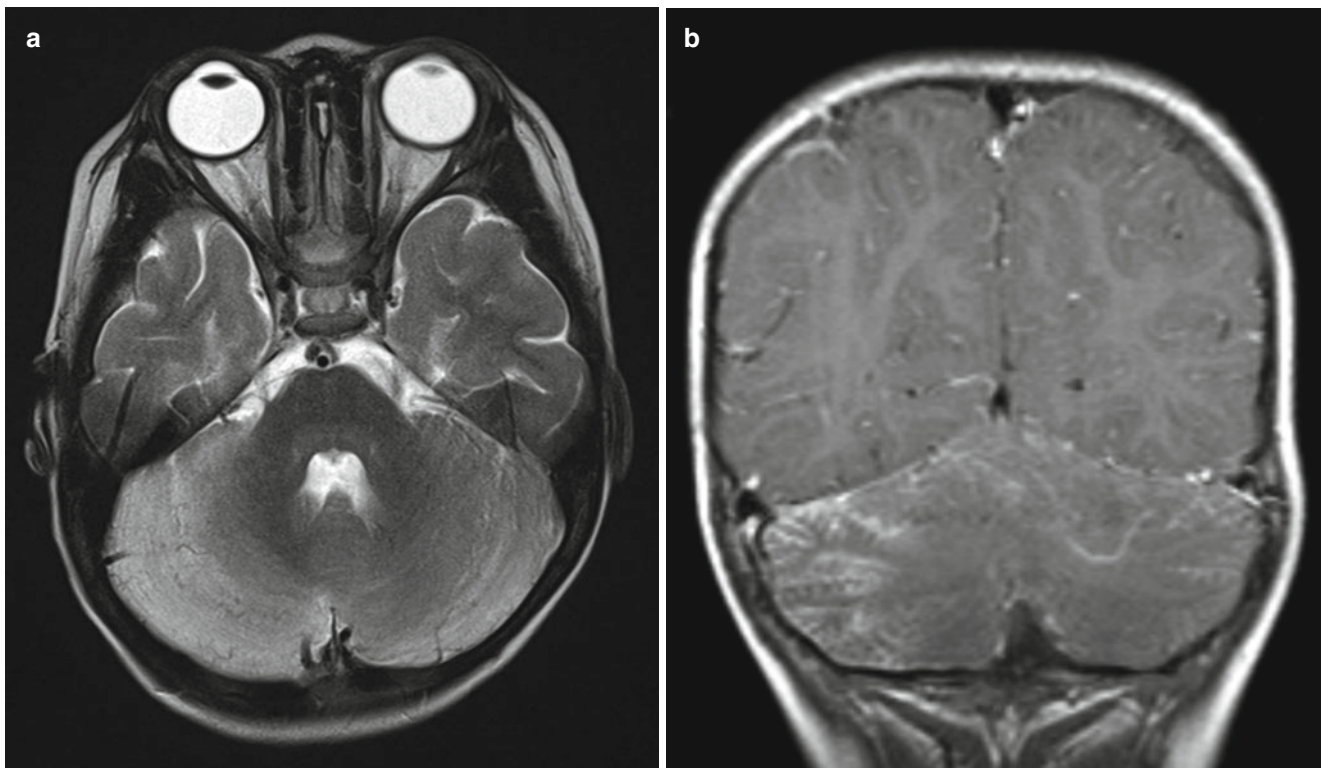


Fig. 3.12 Rhombencephalitis after HFMD due to enterovirus. (a) T2-weighted image shows diffuse cerebellar high-intensity signals predominantly in the right hemisphere. (b) Postcontrast image shows diffuse cerebellar hemispheric enhancement along the folia

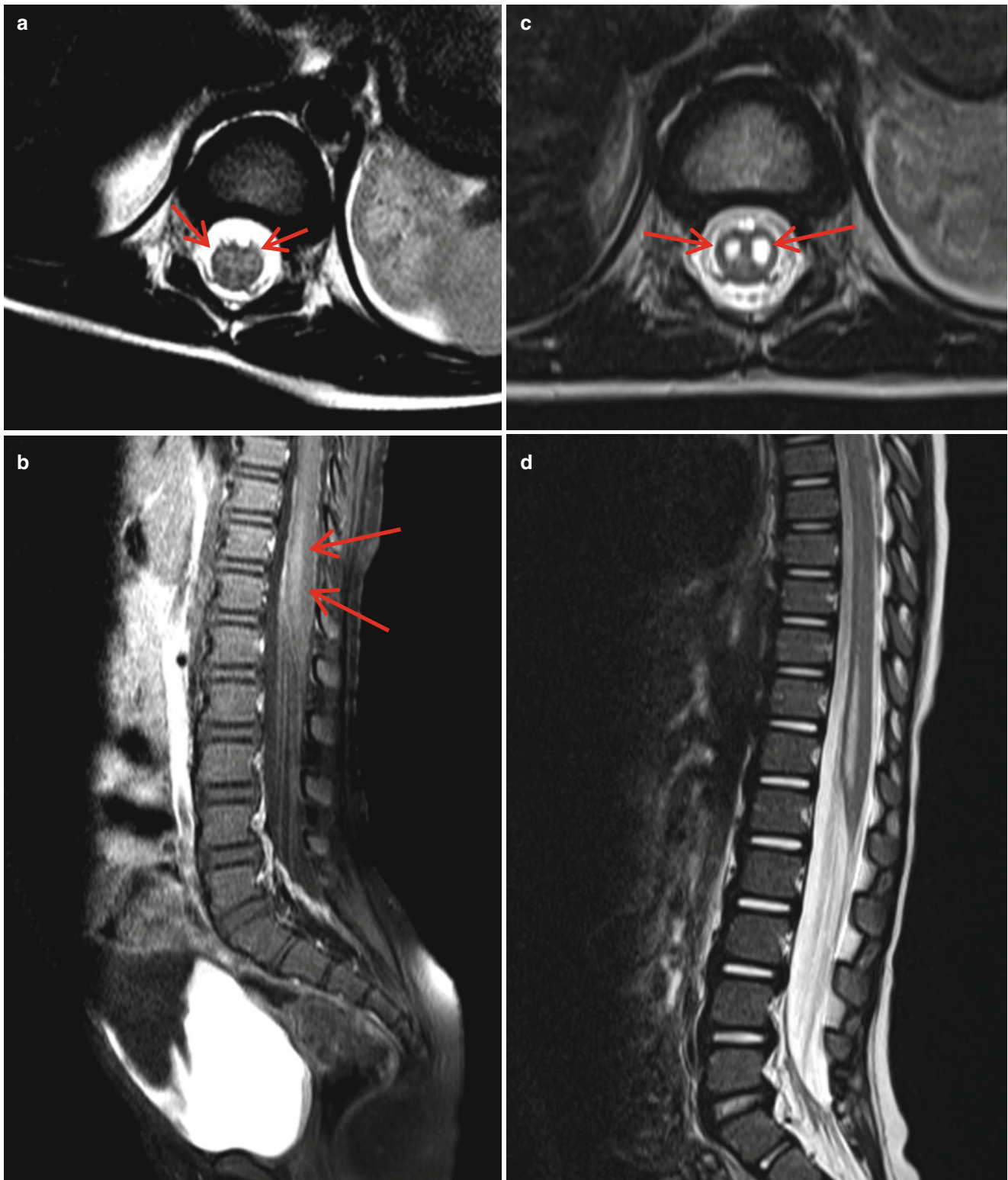


Fig. 3.13 Anterior horn cell involvement in transverse myelitis due to enterovirus. (a) T2-weighted image of the lumbar spine shows subtle increased signals (*arrows*) in the anterior aspect of the spinal cord. (b) Postcontrast image shows well-defined homogenous enhancement

(*arrows*) of the anterior portion of the distal spinal cord. (c, d) Follow-up images after 1 week show well-demarcated high-signal-intensity lesions (*arrows*) involving the anterior horn cells on T2-weighted images

3.4.10 Subacute Sclerosing Panencephalitis

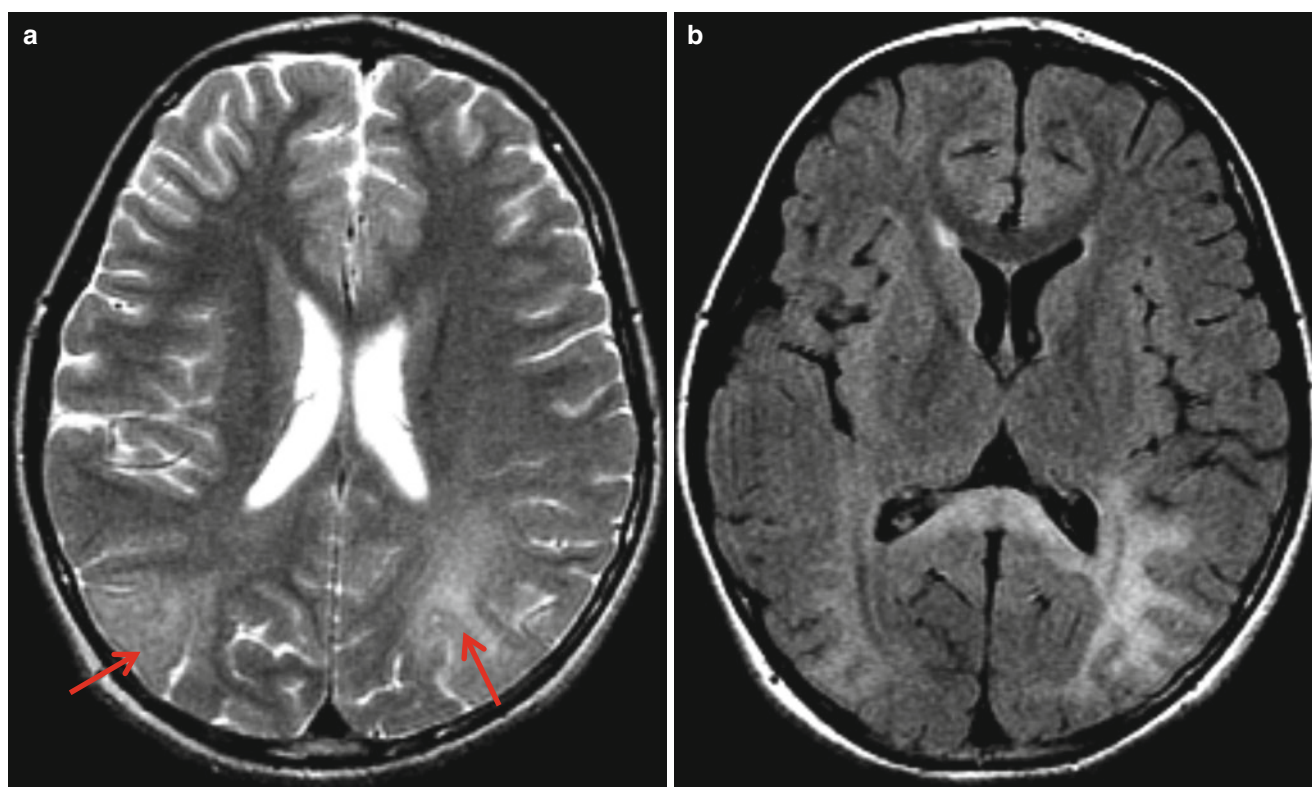


Fig. 3.14 SSPE in a 10-year-old girl with cortical blindness, myoclonic seizures, and psychotic behavior. **(a)** T2-weighted image shows bilateral parieto-occipital high-signal-intensity lesions involving sub-

cortical and deep white matter (*arrows*). **(b)** FLAIR image shows white matter lesion extending to the corpus callosum

3.4.11 Brain Abscess

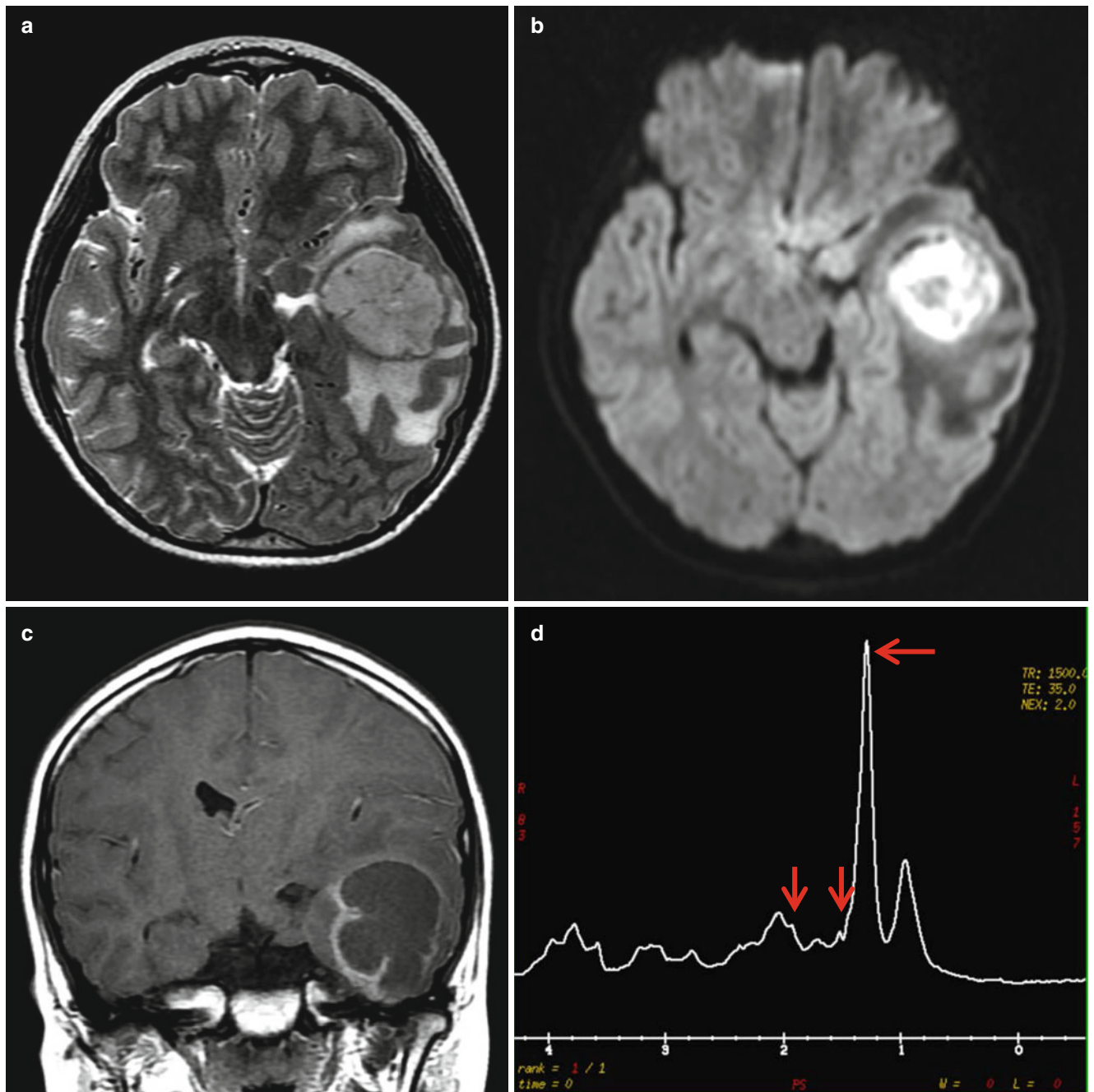


Fig. 3.15 Brain abscess in an 11-year-old boy with fever and headache. (a) T2-weighted image shows high-signal-intensity lesion with a surrounding low signal rim in the temporal lobe. (b) Diffusion image shows restricted diffusion of the content. (c) Postcontrast image shows

well-demarcated smooth enhancing rim. (d) MR spectroscopy reveals high lactate peak (1.33 ppm) of lesional content (arrowhead). Typical neuronal markers are not evident; instead, alanine (1.47 ppm) (red arrow) and acetate peaks (1.92 ppm) (white arrow) are present

3.4.12 Acute Disseminated Encephalomyelitis

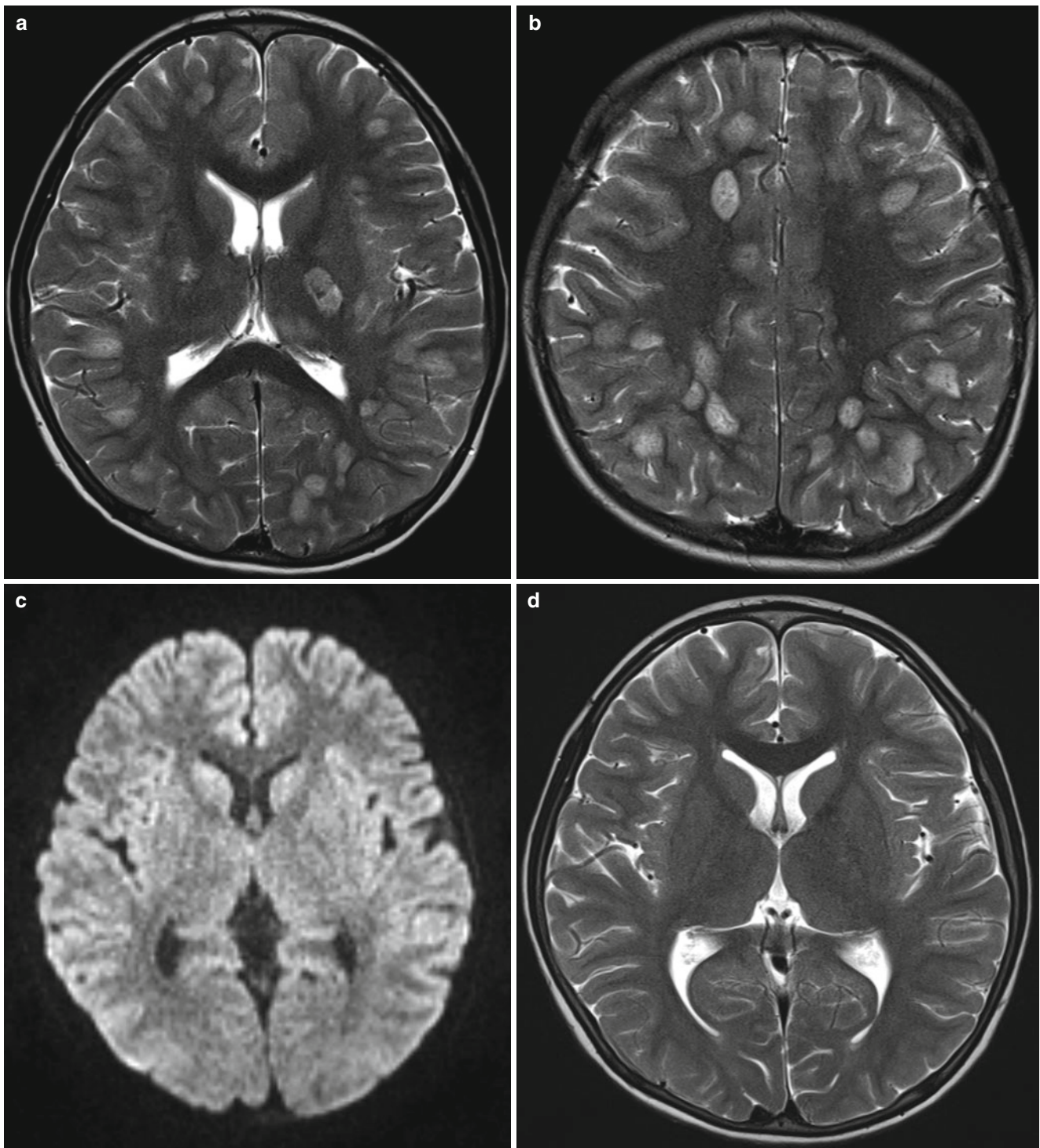


Fig. 3.16 Acute disseminated encephalomyelitis in a 5-year-old boy. (a, b) T2-weighted image shows disseminated ovoid high-signal-intensity lesions involving the subcortical and deep white matter, thalamus,

and internal capsule. (c) Diffusion image shows no evidence of diffusion abnormality of the lesions. (d) 3-month follow-up image shows complete resolution of the lesions

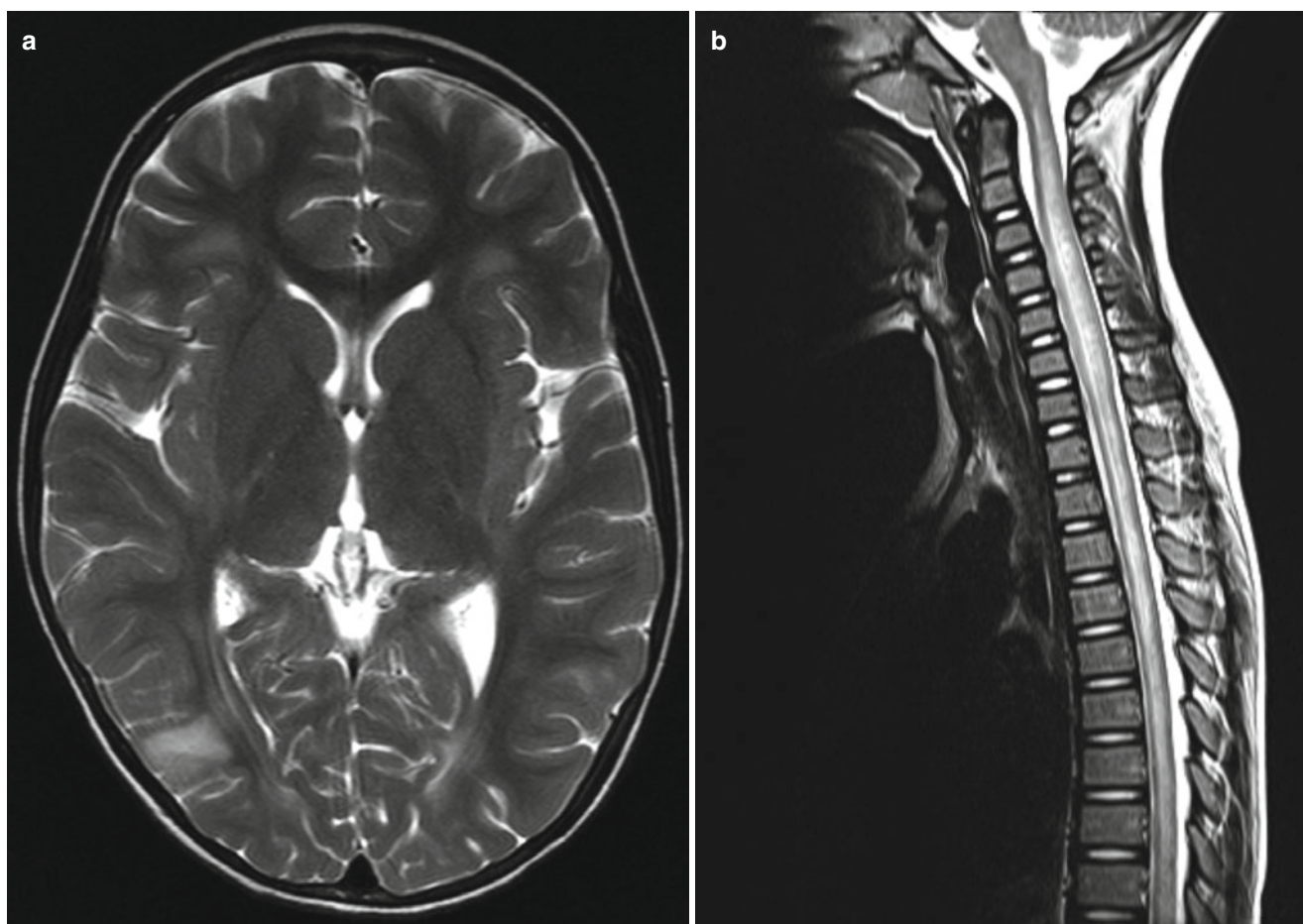


Fig. 3.17 ADEM in a 6-year-old girl with paraplegia and urinary difficulties. (a) T2-weighted image shows multiple patch subcortical and deep white matter lesions. (b) T2-weighted image of the spine shows

confluent spinal cord lesion involving the entire length of the cord. The patient completely recovered after steroid treatment

3.4.13 Acute Necrotizing Encephalopathy

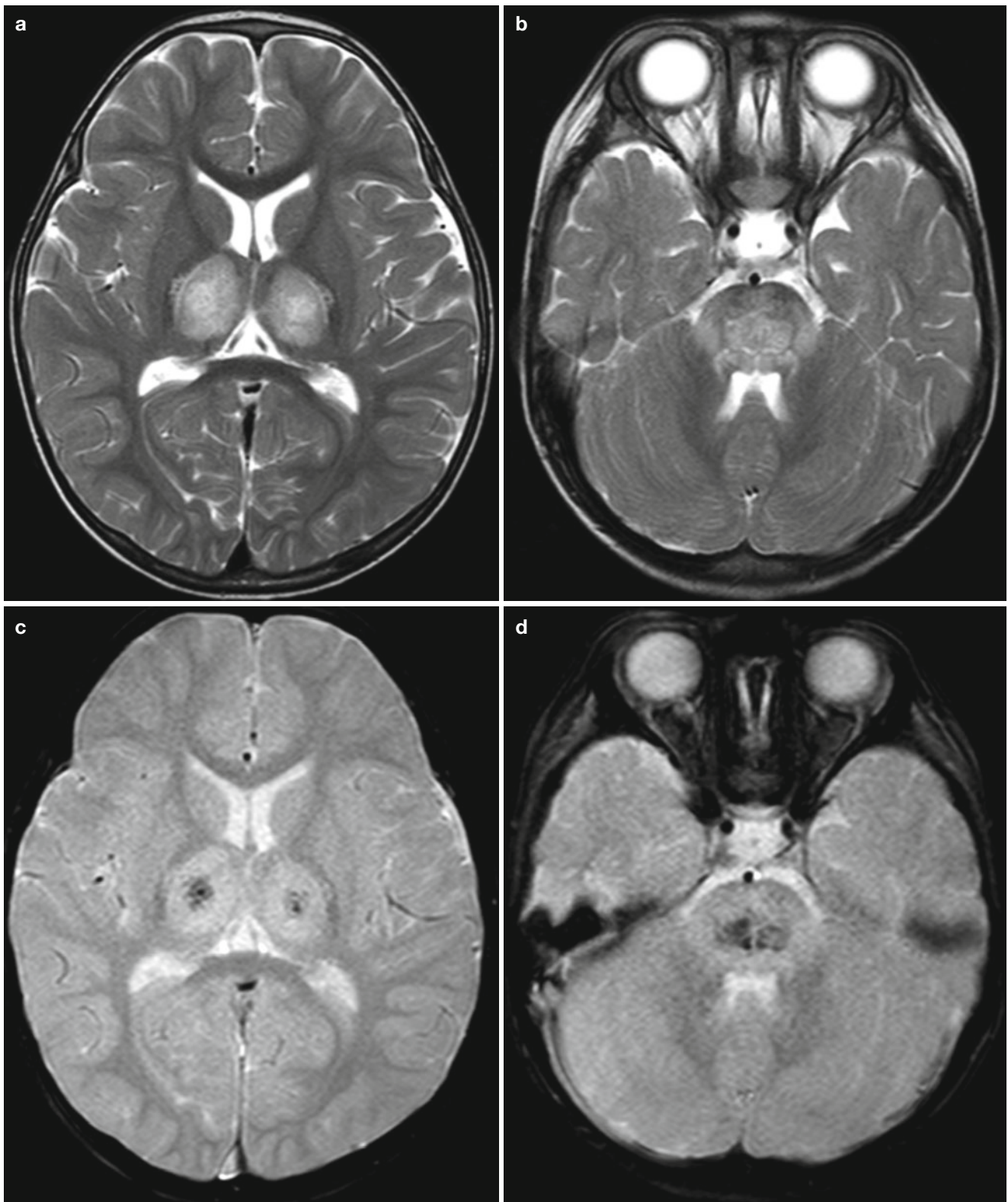


Fig. 3.18 Acute necrotizing encephalopathy in a 2-year-old boy with drowsiness and seizures after upper respiratory infection. (a, b) T2-weighted images show bilateral symmetric swelling and edema of

the thalamus and pons, especially in the tegmental region. (c, d) Gradient echo images show hemorrhagic component in the central portion of the lesions. The patient improved after steroid therapy

3.4.14 Rasmussen Encephalitis

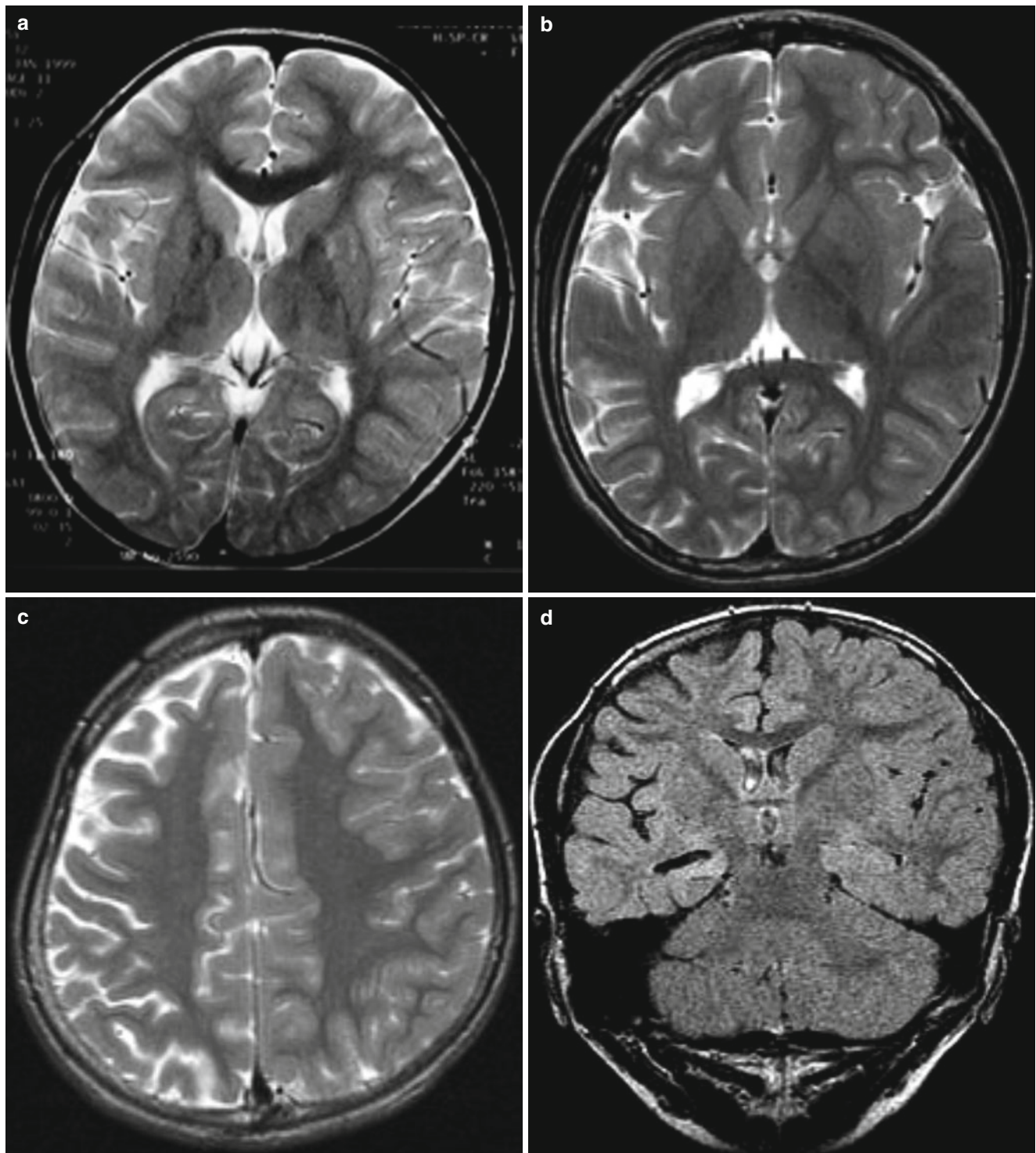


Fig. 3.19 Rasmussen encephalitis in a 7-year-old boy. (a) Initial MR image shows no remarkable abnormalities in the brain. (b, c) 2-year follow-up image shows unilateral right hemispheric atrophy without

definite signal abnormalities in the brain parenchyma. (d) Coronal FLAIR image also shows unilateral right hemispheric atrophy without definite focal parenchymal signal abnormality

3.4.15 Multiple Sclerosis

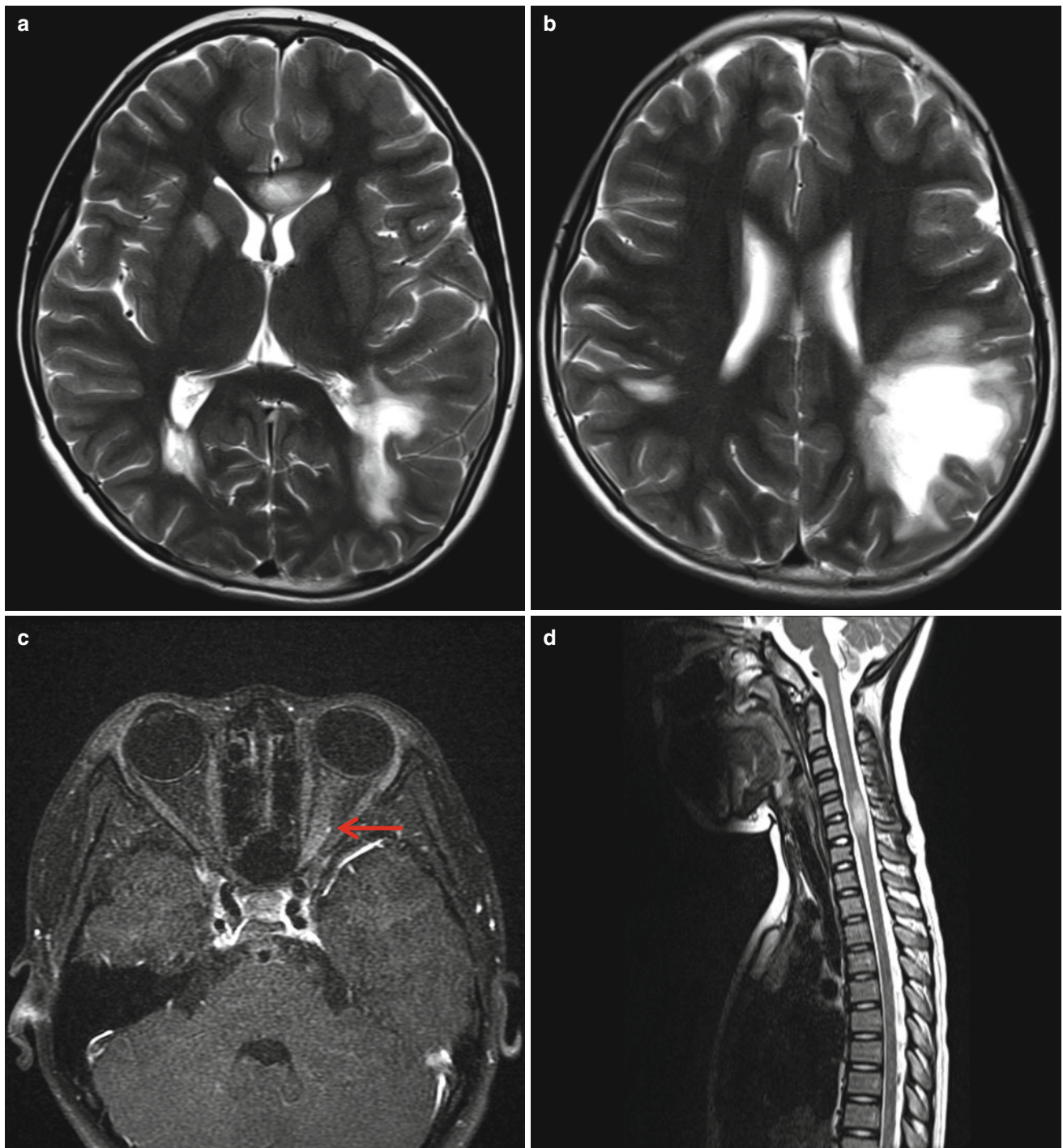


Fig. 3.20 Multiple sclerosis in a 9-year-old-girl with optic nerve and spinal cord involvement. **(a)** T2-weighted image shows multifocal white matter lesions including the corpus callosum and right internal capsule. **(b)** Periventricular and deep white matters are also involved.

(c) Left optic nerve involvement reveals swelling and enhancement (*arrow*). **(d)** Spinal cord lesion extends about two vertebral columns. The patient was negative for NMO-Ig

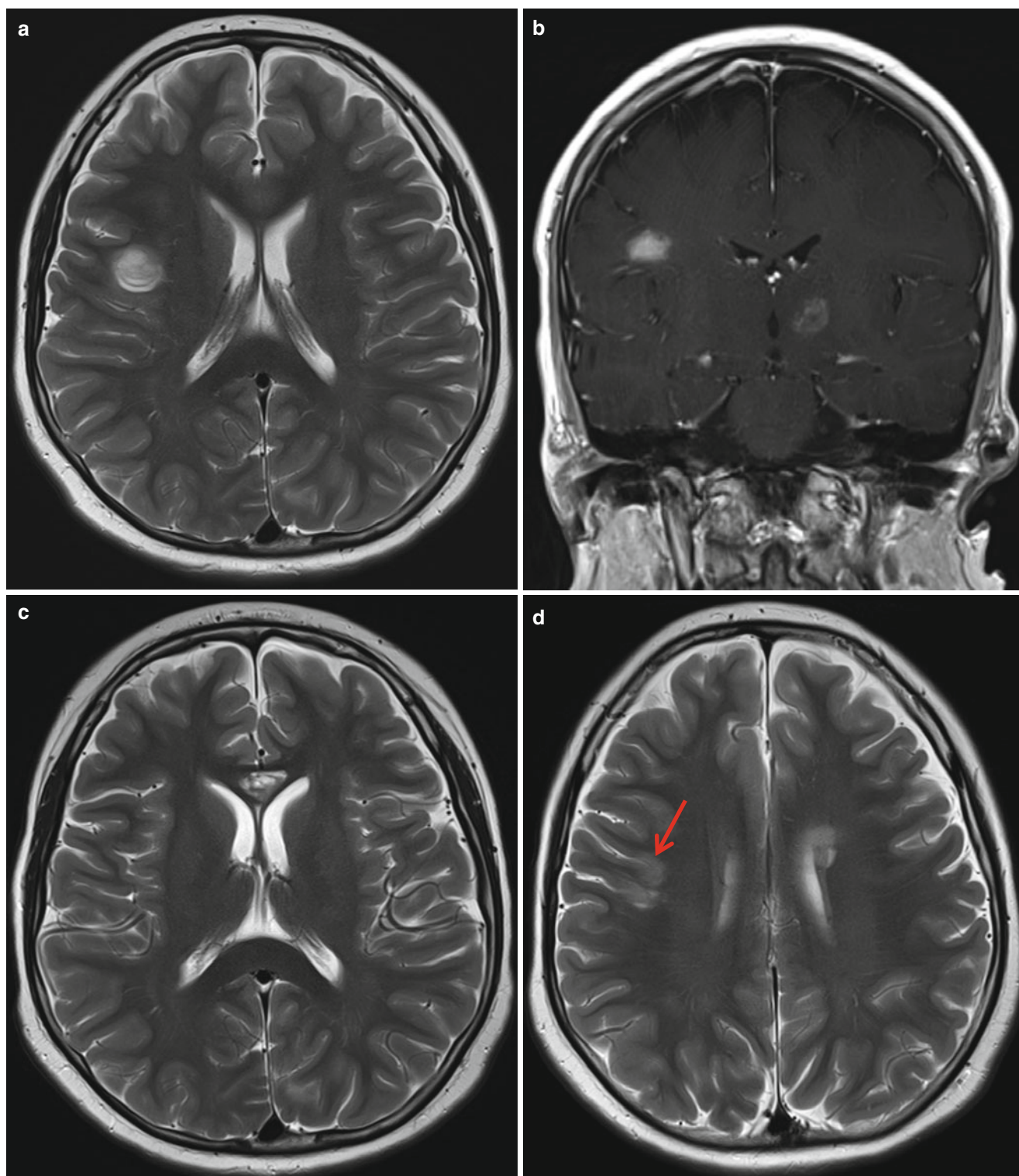


Fig. 3.21 Relapsing lesions in an 11-year-old boy with MS. (a) Initial MR shows focal lesion in the right frontal deep white matter. (b) Postcontrast image shows multiple enhancing nodular lesions including

left basal ganglia. (c, d) Three-month follow-up images reveal decreased right frontal lesion (*arrow*) and multiple new lesions in the corpus callosum and periventricular and subcortical white matters

3.4.16 Neuromyelitis Optica

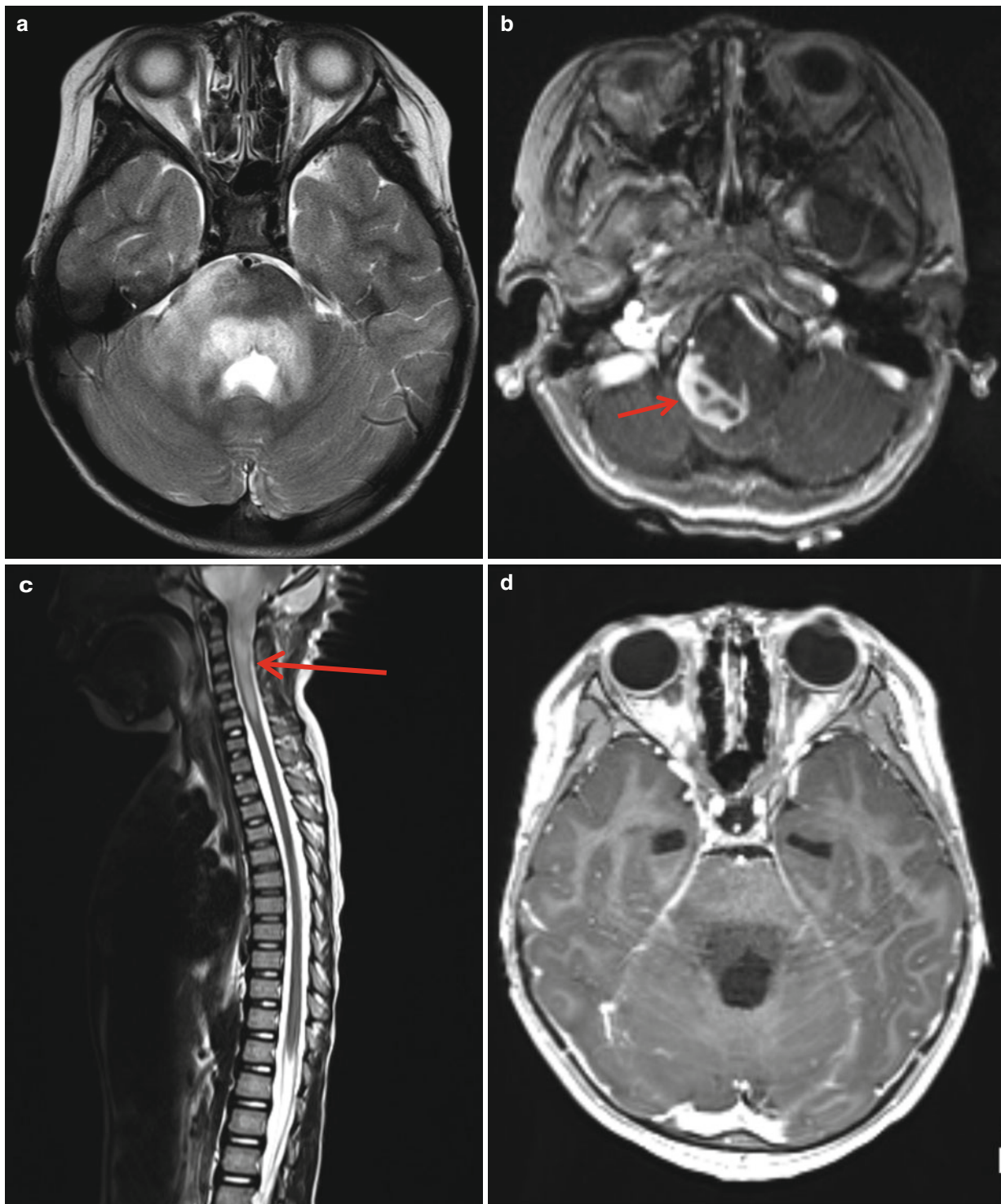


Fig. 3.22 Neuromyelitis optica in a 5-year-old boy with left arm weakness and optic neuritis. (a) T2-weighted image shows right pontocerebellar extensive lesion suspecting tumorous condition. (b) Postcontrast image shows well-demarcated strong enhancement

of posterolateral medulla (*arrow*). (c) T2-weighted image reveals confluent cervical cord lesion contiguously extending from the brainstem lesion (*arrow*). (d) Postcontrast image shows bilateral optic nerve enhancement

3.4.17 Transverse Myelitis

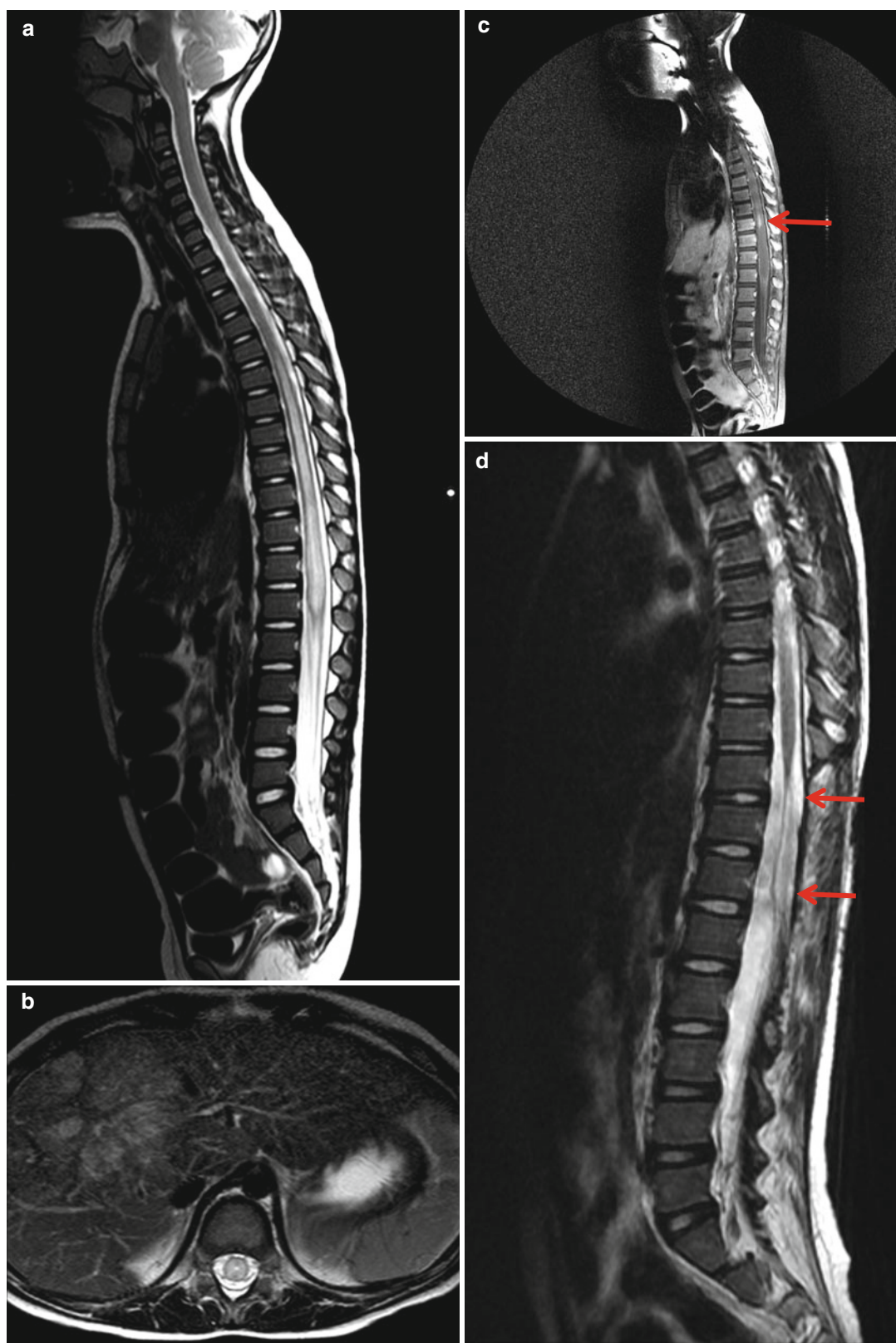


Fig. 3.23 Transverse myelitis in a 4-year-old girl with acute paraplegia and urinary incontinence after URI. (a) T2-weighted image shows diffuse confluent high-signal-intensity lesion in the thoracolumbar spine level. (b) Axial T2-weighted image shows generalized cord involve-

ment. (c) Postcontrast image shows focal enhancement dominantly in the ventral portion (*arrow*). (d) Follow-up image shows marked atrophy of the involved segment (*arrows*) of the cord

3.4.18 Guillain-Barré Syndrome

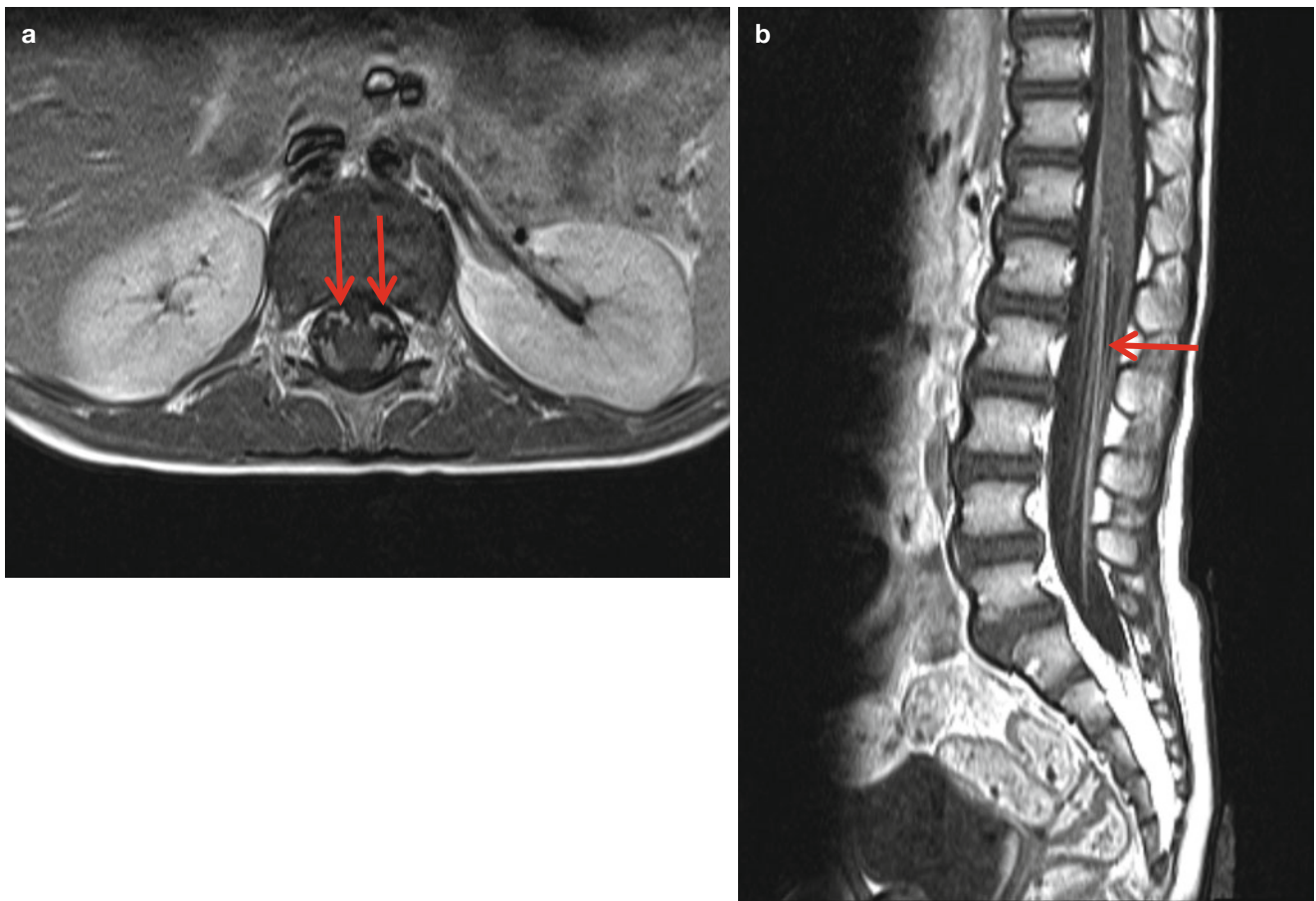


Fig. 3.24 Guillain-Barré syndrome in an infant. (a, b) Postcontrast images show enhancement of the nerve roots (*arrows*). Spinal cord reveals normal signal and no enhancement

References

- Baskin HJ, Hedlund G. Neuroimaging of herpes virus infections in children. *Pediatr Radiol*. 2007;37:949–63.
- Be NA, Kim KS, Bishai WR, Jain SK. Pathogenesis of central nervous system tuberculosis. *Curr Mol Med*. 2009;9:94–9.
- Bien CG, Granata T, Antozzi C, et al. Pathogenesis, diagnosis and treatment of Rasmussen encephalitis. A European consensus statement. *Brain*. 2005;128:454–71.
- Cartes-Zumelzu FW, Stavrou I, Castillo M, et al. Diffusion-weighted imaging in the assessment of brain abscess therapy. *AJNR Am J Neuroradiol*. 2004;25:1310–7.
- Chong CY, Chan KP, et al. Hand, foot and mouth disease in Singapore: a comparison of fatal and non-fatal cases. *Acta Paediatr*. 2003;92:1163–9.
- Dale R, de Sousa C, Chong WK, et al. Acute disseminated encephalomyelitis, multiphasic disseminated encephalomyelitis and multiple sclerosis in children. *Brain*. 2000;123:2407–22.
- de Vries LS, Gunardi H, Barth PG, Bok LA, Verboon-Macielek MA, Groenendaal F. The spectrum of cranial ultrasound and magnetic resonance imaging abnormalities in congenital cytomegalovirus infection. *Neuropediatrics*. 2004;35:113–9.
- Enzmann DR, Britt RH, Placone R. Staging of human brain abscess by computed tomography. *Radiology*. 1983;146:703–8.
- Fink KR, Thapa MM, Ishak GE, Pruthi S. Neuroimaging of pediatric central nervous system cytomegalovirus infection. *Radiographics*. 2010;30:1779–96.
- Gutierrez J, Issacson RS, Koppel BS. Subacute sclerosing panencephalitis: an update. *Dev Med Child Neurol*. 2010;52:901–7.
- Ho M, Chen ER, Hsu KH, et al. An epidemic of enterovirus 71 infection in Taiwan. *N Eng J Med*. 1999;341:929–35.
- Jacob A, Weinshenker BG. An approach to the diagnosis of acute transverse myelitis. *Semin Neurol*. 2008;28:105–20.
- Kim KS. Acute bacterial meningitis in infants and children. *Lancet Infect Dis*. 2010;10:32–42.
- Knoblauch H, Tennstedt C, Brueck W, et al. Two brothers with findings resembling congenital intrauterine infection-like syndrome (pseudo-TORCH syndrome). *Am J Med Genet*. 2003;120:261–5.
- Losurdo G, Giacchino R, Castagnola E, et al. Cerebrovascular disease and varicella in children. *Brain Dev*. 2006;28:366–70.
- Mizuguchi M. Acute necrotizing encephalopathy of childhood: a novel form of acute encephalopathy prevalent in Japan and Taiwan. *Brain Dev*. 1997;19:81–92.
- Mulkey SB, Glasier CM, Ei-Nabbout B, et al. Nerve root enhancement on spinal MRI in pediatric Guillain-Barré syndrome. *Pediatr Neurol*. 2010;43:263–9.
- Nandhagopal R, Al-Asmi A, Gujjar AR. Neuromyelitis optica: an overview. *Postgrad Med J*. 2010;86:153–9.
- Polin RA, Harris MC. Neonatal bacterial meningitis. *Semin Neonatol*. 2001;6:157–1762.
- Popovich MJ, Arthur RH, Helmer E. CT of intracranial cryptococcosis. *AJNR Am J Neuroradiol*. 1990;11:139–42.
- Singh P, Goraya JS, Gupta K, Saggar K, Ahluwalia A. Magnetic resonance imaging findings in Reye syndrome: case report and review of the literature. *J Child Neurol*. 2011;26:1009–14.
- Ueno M, Oka A, Koeda T, Okamoto R, Takeshita K. Unilateral occlusion of the middle cerebral artery after varicella-zoster virus infection. *Brain Dev*. 2002;24:106–10.
- Vinchon M, Joriot S, Jissendi-Tchofo P, Dhellemmes P. Postmeningitis subdural fluid collection in infants: changing pattern and indications for surgery. *J Neurosurg*. 2006;104:383–7.
- Yikilmaz A, Taylor GA. Sonographic findings in bacterial meningitis in neonates and young infants. *Pediatr Radiol*. 2008;38:129–37.
- Yiu EM, Kornberg AJ, Ryan MM, Coleman LT, Mackay MT. Acute transverse myelitis and acute disseminated encephalomyelitis in childhood: spectrum or separate entity? *J Child Neurol*. 2009;24:287–96.

Ji Hye Kim

Contents

4.1	Neoplasms of the Brain	106
4.1.1	Introduction.....	106
4.1.2	Pathophysiology	106
4.1.3	Imaging	106
4.2	Neoplasms of the Spine	112
4.2.1	Introduction.....	112
4.2.2	Intramedullary Tumors	112
4.2.3	Extramedullary Tumors	113
4.3	Illustrations: Neoplasms of the Brain and Spine	114
4.3.1	Neoplasms of the Brain	114
4.3.2	Neoplasms of the Spine	143
4.3.3	Miscellaneous	152
	References	154

J.H. Kim, M.D.
Department of Radiology, Samsung Medical Center,
Sungkyunkwan University School of Medicine,
50 Ilwon-Dong, Kangnam-Ku, Seoul 135-710, Korea
e-mail: jhkate@skku.edu

4.1 Neoplasms of the Brain

4.1.1 Introduction

Brain tumors are the most common solid tumors in children, and the second most common group of malignancies following leukemia. Pediatric brain tumors comprise 15–20 % of all brain tumors. The type of tumor, incidence, common location, and the outcome are different according to the age. Clinical presentations reflect increased intracranial pressure and local neurological impairment. The tumor may also be found incidentally. Overall, 5-year survival is known to be up to 70 %, but the outcomes are diverse depending on the tumor type and stage. Because treatment options such as irradiation and chemotherapy are limited in young children, extent of the surgical resection of the tumor is the most important for prognosis. Unfortunately, many adult survivors of childhood CNS malignancies can have treatment-related long-term sequela and increased risk of early death (Armstrong et al. 2009; Barkovich 2012).

4.1.2 Pathophysiology

In contrast to the adult onset tumors, which are mostly gliomas, pediatric brain tumors display many heterogeneous pathological types, and primitive lesions are common. Supratentorial tumors are more common in children younger than 2 years old, and neuroepithelial tumors are the most common tumor type, whereas in children greater than 2 years of age, posterior fossa tumors are more frequently encountered than supratentorial tumors, and they are comprised of medulloblastomas, ependymomas, cerebellar astrocytomas, and brain stem gliomas. These lesions can also occur in the supratentorial regions, and more diverse types of tumors including astrocytomas, neuroepithelial tumors, and germ cell tumors are encountered in the supratentorial region. After 12 years, tumors occur with equal frequency in both locations. Extraaxial tumors and metastatic tumors are less common in children (Panigrahy and Bluml 2009; Barkovich 2012).

4.1.3 Imaging

Compact cellularity, hemorrhage, and calcifications are reliably assessed as high attenuation on a precontrast CT scan. However, artifact from the bone may compromise the evaluation of the posterior fossa (Panigrahy and Bluml 2009).

MR imaging is more widely used in the diagnosis and follow-up of pediatric brain tumors, providing excellent anatomical detail with multiplanar imaging. 3D-gradient echo sequences are used as a navigation tool for surgical approach,

and functional MR imaging provides localization of motor and sensory cortex as well as the dominant language area of the brain (Fig. 4.39). Other advanced MR imaging also provide functional information, including cellularity, hemodynamics, and metabolism of the tumor. The lower ADC values obtained from diffusion-weighted imaging (DWI) means relative reduction of extracellular space in compact tumor cellularity, which is closely related with the grade or type of the tumors. ADC values are highest in pilocytic astrocytomas and lowest in the medulloblastomas among the posterior fossa tumors (Figs. 4.1 and 4.3) (Rumboldt et al. 2006). Diffusion tensor imaging (DTI) is used to evaluate the integrity of white matter tracts neighboring the tumor (Fig. 4.39c) (Cha 2006).

Perfusion MR imaging is also used to demonstrating tumor angiogenesis and capillary permeability. The maximal tumor rCBV tends to increase in high-grade fibrillary astrocytomas. However, tumor grading by using perfusion MR imaging is not always reliable. Both pilocytic astrocytomas and glioblastoma multiforme often demonstrate increased rCBV due to vascular hyperplasia. Moreover, oligodendrogliomas may have high rCBV, regardless of grade, and both ependymomas and choroid plexus tumors generally demonstrate markedly elevated rCBV and poor return to baseline owing to lack of blood–brain barrier (BBB), resulting in unreliable rCBV measurements (Rossi et al. 2010). Perfusion MRI can also distinguish radionecrosis from the recurred tumor. Radionecrosis generally exhibits decreased perfusion, while the tumor usually shows iso- or hyperperfusion (Fig. 4.40) (Cha 2006; Bobek-Billewicz et al. 2010). However, perfusion MRI is challenging in infants and young children because of the difficult venous access, decreased injection rates, and frequent motion artifacts. Perfusion MRI using arterial spin labeling, a technique which does not require bolus injection of contrast, may replace the conventional perfusion technique in young children (Barkovich 2012).

Proton MR spectroscopy demonstrates increased choline, decreased NAA, and stable creatinine in most of the tumors (Fig. 4.1e), and several characteristic metabolic patterns of specific tumors were described. It can also be used in differentiation of active tumor from treatment-related necrosis (Rossi et al. 2010). However, there is considerable overlap in the metabolite ratios of individual tumors (Bobek-Billewicz et al. 2010). Both perfusion MR imaging and MR spectroscopy are used in only limited cases of the pediatric patients, usually to distinguish treatment-related changes from recurred tumor, rather than to make a histological diagnosis (Cha 2006; Panigrahy and Bluml 2009).

4.1.3.1 Infratentorial Tumors

The four major pediatric posterior fossa brain tumors are medulloblastoma, pilocytic astrocytoma, ependymoma, and brain stem gliomas. In addition, atypical teratoid/rhabdoid

tumors (ATRT) and pilomyxoid astrocytomas were recently recognized. Several other less common tumors may also develop. Extraaxial neoplasms are less commonly encountered in pediatric patients than in adults, and they may arise from the cranial nerves, choroid plexus, skull base, and meninges (Naidich et al. 2013).

Clinical presentations are usually related with increased intracranial pressure, cranial nerve palsy, and cerebellar symptoms. Hydrocephalus in infants before closure of the cranial sutures may cause enlarged head, and cerebellar ataxia may be difficult to identify in infants and toddlers (Barkovich 2012).

4.1.3.1.1 Medulloblastomas

Medulloblastoma is a neuroectodermal tumor of the cerebellum, categorized as primitive small round cell tumors with multipotential differentiation. It is the most common malignant (WHO grade 4) pediatric brain tumor, accounting for about one-third of the posterior fossa tumors. Affected children are typically under 5 years of age, though an atypical type tends to be encountered in older ages (Fig. 4.4). Males are more commonly affected, and genetic defects have been identified. Basal cell nevus syndrome (Gorlin syndrome) is known to be associated with increased development of medulloblastoma, which is associated with multiple jaw cysts and dural calcification. Symptom onset is generally relatively recent, suggesting rapidly growing tumor, presenting with obstructive hydrocephalus (Barkovich 2012; Naidich et al. 2013).

Medulloblastomas most commonly arise from the roof of the fourth ventricle, the inferior medullary velum, whereas the ependymomas arise from the floor of the fourth ventricle. Solid portions of the medulloblastoma exhibit hyperdensity on precontrast CT, hypointense tumor relative to the other posterior fossa tumors on T2-weighted images, and restricted diffusion, reflecting increased cellularity (Fig. 4.3). Calcification and cystic portions may be seen up to 20 %, and the solid portions are enhanced variably after contrast administration (Figs. 4.3–4.5). Medulloblastomas have a tendency of subarachnoid spread, and MR imaging including whole brain and spine should be evaluated to establish the extent of the tumor (Figs. 4.5 and 4.6). Because of limited diagnostic sensitivity, both CSF cytology and spinal MRI should be used to diagnose leptomeningeal tumor (Fouladi et al. 1999). MR accuracy for leptomeningeal metastases increases with higher doses of contrast and volumetric acquisition of gradient echo imaging (Barkovich 2012).

4.1.3.1.2 Atypical Teratoid/Rhabdoid Tumors

Atypical teratoid/rhabdoid tumors (ATRT) were formerly diagnosed as medulloblastomas. Although ATRTs are classified as the same WHO grade 4 embryonal tumors as medulloblastomas, they present younger age group (2–4 years) and

do not respond to the standard treatment for medulloblastomas. Imaging appearances are similar to those of medulloblastomas with more tendency of off-midline location and aggressive behavior (Lee et al. 2009a).

4.1.3.1.3 Ependymomas

Ependymomas are relatively well-differentiated (WHO grade 2) tumors arising from ependymal cells lining the ventricle, accounting for about 15 % of the posterior fossa tumors. They arise most frequently in the fourth ventricle and less commonly in the cerebral hemispheres or spinal cord. Boys are slightly more commonly affected than girls, and usually encountered between 1 and 5 years of age. Anaplastic features can be seen in minor cases (Barkovich 2012).

Ependymomas typically demonstrate heterogeneous mass arising from the floor of the fourth ventricle extending through the foramen Luschka or foramen Magendie (Fig. 4.7). Although some of the medulloblastomas can also extend through the ventricular exit foramina, they show more bulbous extension. Ependymomas often insinuate around and encase neurovascular bundles, causing cranial neuropathy and complete resection difficult (Fig. 4.7d). Ependymomas can have diverse T2 intensities depending on the histological subtype. The solid portions are slightly hyperintense compared to the medulloblastoma on T2-weighted images with heterogeneity and variable contrast enhancement. Calcification, hemorrhage, and necrosis are common. Leptomeningeal spread at the time of presentation is less common than in medulloblastomas. CSF seeding is more common in anaplastic histologic type, infratentorial location, and in younger children (Barkovich 2012; Naidich et al. 2013).

4.1.3.1.4 Astrocytoma

Astrocytomas are the most common pediatric brain tumors, and the cerebellum is the most common site of childhood astrocytomas. The peak incidence is from birth to 9 years of age and can be encountered throughout the childhood. The majority of the cerebellar astrocytomas are juvenile pilocytic astrocytomas (JPA, WHO grade 1). JPAs are also encountered in the brain stem, hypothalamic/optic pathways, cerebral hemispheres, and spinal cord. JPAs are usually indolent lesions, and prognosis depends on the extent of resection. Patient outcome is excellent with reported 26-year survival rate up to about 90 %. Anaplastic astrocytomas are more common, and glioblastomas are rare in the pediatric age (Naidich et al. 2013).

The classic cerebellar JPAs tend to be cystic, cyst with a mural nodule (Fig. 4.2), or solid lesions (Fig. 4.1). The solid portions are usually hypodense on noncontrast CT and bright on T2-weighted images, suggesting less compact cellularity (Figs. 4.1 and 4.2). Calcification is present in 10–20 %, and hemorrhage is not common. JPAs usually demonstrate strong

contrast enhancement and increased perfusion. Low-grade gliomas other than JPA are generally poorly defined nonenhancing lesions on CT and MRI (Barkovich 2012; Naidich et al. 2013).

4.1.3.1.5 Brain Stem Tumors

Brain stem tumors account up to 25 % of the posterior fossa tumors in children, and are most common between 3 and 9 years of age with equal distribution in boys and girls. Clinical presentations and prognosis depend on their location in the brain stem. Tumors involving the midbrain tectum usually cause aqueductal obstruction; infiltrative pontine tumors may cause pyramidal tract sign, ataxia, and nystagmus; and medullary tumors are associated with lower cranial nerve palsy and apnea (Barkovich 2012).

The most common brain stem tumor is diffuse infiltrative glioma involving the pons. Pontine gliomas have the worst prognosis of all pediatric tumors because of inoperability and resistance to irradiation or chemotherapies. Pontine gliomas are usually fibrillary astrocytomas being hypodense on CT, hypointense on T1-weighted images, and hyperintense on T2-weighted images. They are not usually enhanced on postcontrast images. The tumor expands the pons, and the basilar artery may be partially engulfed (Fig. 4.8). Tumor extension into the cerebellar peduncle, prepontine cistern, or along the cranial nerves may be seen, and hydrocephalus is not common.

Other brain stem tumors tend to have a better prognosis, and most of them are low-grade astrocytomas or JPA. Tectal gliomas are extremely benign, and endoscopic third ventriculostomy alone is enough for the treatment in most cases (Fig. 4.9). Midbrain tumors other than tectum are mostly focal mass, and diffuse tumors are less commonly seen. The medullary tumors tend to have an exophytic growth pattern and tend to be JPAs (Fig. 4.10). Brain stem tumors detected in patients with neurofibromatosis type 1 (NF1) are most commonly focal tumors in the medulla, exhibiting very slow growth pattern (Barkovich 2012; Naidich et al. 2013).

4.1.3.1.6 Extraparenchymal Tumors

Bilateral acoustic schwannomas are typically found in patients with neurofibromatosis type 2 (NF2). Evaluation of other schwannomas or meningiomas is necessary. Schwannomas are hypodense or isodense on precontrast CT, causing enlargement of the bony canal and adjacent CSF space. On MRI, schwannomas have prolonged T1 and T2 relaxation times, associated with central necrosis and hemorrhage. Solid portions of the tumor are well enhanced after contrast administration (Fig. 4.11) (Barkovich 2012).

Dermoid and epidermoid tumors are more commonly found in the posterior fossa than in the supratentorial region. They arise from congenital rests of remained tissue as a result of incomplete disjunction of the neuroectoderm from the

cutaneous ectoderm at the time of neural tube closure. Epidermoid is frequently seen in the CPA, pineal region, suprasellar region, and middle cranial fossa, whereas dermoid is usually seen in the spinal canal, posterior fossa, and subfrontal area. Dermoid can be associated with dermal sinus tract, and calvarial defect can be seen on CT (Fig. 4.12c). Clinical presentation is associated with obstructive hydrocephalus, infection, or chemical meningitis due to leakage of the content. Epidermoid may show similar appearance with the arachnoid cyst. However, mildly heterogeneous internal content and restricted diffusivity on MRI suggest epidermoid. Dermoids contain fat component similar to lipoma. However, dermoids are less lobulated and displace nerves and vessels, while lipomas encase neurovascular structures. Both epidermoid and dermoid tumors are not enhanced unless infection is complicated (Fig. 4.12b) (Barkovich 2012).

4.1.3.2 Cerebral Hemispheric Tumors

Major childhood brain tumors in the cerebral hemispheres are astrocytomas, neuronal and mixed tumors, and embryonal tumors. Several astrocytoma subtypes (fibrillary astrocytomas, JPA, anaplastic astrocytomas, and glioblastoma multiforme), primitive neuroectodermal tumor (PNET), ependymoma, and ATRTs may be found either supratentorially or infratentorially. On the other hand, gangliogliomas, dysembryoplastic neuroepithelial tumors (DNET), pleomorphic xanthoastrocytomas, and subependymal giant cell astrocytomas tend to present only supratentorially. Germ cell tumors typically involve the pineal and suprasellar regions as well as in the basal ganglia, which can be associated with ipsilateral cerebral atrophy (Wallerian degeneration).

4.1.3.2.1 Astrocytomas

Astrocytomas are the most common pediatric tumors affecting all pediatric age groups with the peak age at 5–9 years. Astrocytomas comprise a wide range of neoplasms with different morphological features, growth potential, distribution, progression pattern, and clinical course. Most astrocytomas are low-grade (WHO grade 2–3) tumors that predominantly arise in the cerebellum, hypothalamic/optic pathway, and the midbrain and medulla. The high-grade (WHO grade 3–4) tumors are generally found in the cerebral hemispheres or pons (Barkovich 2012).

Like cerebellar astrocytomas, hemispheric astrocytomas are solid or mixed solid and cystic with variable composition. The solid portions of the astrocytoma tend to be variable attenuation and have prolonged T1 and T2 relaxation values. JPA exhibit high intensity on T2-weighted images and strong enhancement without edema (Fig. 4.13). Other low-grade astrocytomas are not well enhanced with mild or no peritumoral edema. In contrast, high-grade astrocytomas tend to show areas of necrosis, hemorrhage, more extensive surrounding edema, and restricted diffusion (Fig. 4.14) (Naidich et al. 2013).

Surgical resection alone is sufficient for most of the low-grade astrocytomas, while the prognosis of high-grade astrocytomas remains poor in spite of the addition of radiotherapy and chemotherapy.

4.1.3.2.2 Subependymal Giant Cell Astrocytoma

Subependymal giant cell astrocytomas (SEGA) develop in 5–15 % of patients with tuberous sclerosis. SEGAs arise from the ependymal hamartomas of the lateral ventricle, near the foramen Monro, causing hydrocephalus. The tumors are well-margined subependymal mass with enhancement. In addition, findings of tuberous sclerosis including multiple subependymal nodules and cortical/subcortical tubers are found in the brain (Fig. 4.15). Rarely the tumors can undergo malignant degeneration (Barkovich 2012).

4.1.3.2.3 Astroblastoma

Astroblastomas are uncommon neuroepithelial tumors of uncertain origin. These occur predominantly in the cerebral hemisphere of children and young adults (mean age of 14 years). Histological grade varies greatly, and clinical presentations include headache, vomiting, and seizures. Imaging appearance is similar to other glial neoplasms: well-demarcated solid and cystic mass in the cerebral hemisphere. Complete excision without radiotherapy is sufficient in low-grade variants (Salvati et al. 2009).

4.1.3.2.4 Oligodendrogliomas

Oligodendrogliomas are rare in children with reported incidence of 1 % of pediatric brain tumors. Boys are more commonly affected than girls. Generally, oligodendrogliomas are slowly growing tumors, commonly involving frontal and temporal lobes. Calcification and adjacent calvarial erosion may be seen on CT. MR imaging features of oligodendrogliomas are cortical involvement with frontal lobe predominance, intratumoral cysts and calcification causing susceptibility changes, and high rCBV. The tumors have prolongation of T1 and T2 relaxation, and enhancement is variable. Dense calcification and lack of enhancement are associated with better survival. Anaplastic oligodendrogliomas show rim enhancement and necrosis, similar to the findings of PNET or high-grade astrocytomas. rCBV is elevated in both low-grade and high-grade oligodendrogliomas in perfusion imaging. Increase in choline and presence of lactate and lipid are seen in high-grade tumors on MR spectroscopy (Barkovich 2012).

4.1.3.2.5 Gangliomas and Gangliocytomas

Gangliomas and gangliocytomas are uncommon neuronal and mixed neuronal glial tumors, usually found in older children or young adults. The affected patients have long-standing seizure or hypothalamic dysfunction according to the location of the tumor. The temporal lobes are most commonly

involved, followed by parietal, frontal, and occipital lobes; third ventricle; and hypothalamus. The tumor is usually a small well-defined mass, typically in the cerebral cortex, containing cysts without mass effect or edema (Fig. 4.16). The calcification is seen in 35 % of the patients. Cortical tumor may be accompanied by remodeling of the calvarium. The solid mass becomes hyperintense on T2-weighted images and variably enhanced. Astrocytomas, oligodendrogliomas, and dysembryoplastic neuroepithelial tumors (DNET) may show similar appearance (Barkovich 2012).

4.1.3.2.6 Dysembryoplastic Neuroepithelial Tumors

DNET is a benign cortical tumor of children or young adults presenting with partial complex seizure. They occur most commonly in the temporal lobe (60 %), followed by frontal lobe (30 %). DNETs are usually solid, but may have cystic components and adjacent focal cortical dysplasia (FCD type 3b) (Fig. 4.17). The solid masses are low attenuated on CT, and they exhibit hypointense T1 and hyperintense T2 signals on MR images. Calcification is seen in 30 % of the patients. Similar to the gangliomas and gangliocytomas, cortical DNET may erode the inner table of the skull. The tumors may extend into the subcortical area, and enhancement is variable (Naidich et al. 2013).

4.1.3.2.7 Supratentorial Ependymoma

Approximately one-third of ependymomas are supratentorial. Supratentorial ependymomas have a tendency to occur in older children, more often extraventricular in location, and less leptomeningeal tumor seeding than infratentorial ependymomas. The tumors are, however, often located near the ventricular margins and may extend into the ventricular system. Supratentorial ependymomas are well-demarcated heterogeneous masses that are isodense or hyperdense on noncontrast CT and isointense to gray matter on MR images, frequently containing cystic areas or calcifications with variable enhancement (Fig. 4.18). Differential diagnosis of hemispheric ependymomas includes teratoma, PNET, and ATRT (Barkovich 2012).

4.1.3.2.8 Primitive Neuroectodermal Tumors (PNET)

PNETs are undifferentiated highly cellular tumors, histologically similar to medulloblastoma, ATRT, pineoblastomas, and peripheral neuroblastomas. PNETs comprise less than 5 % of the pediatric supratentorial tumors, usually seen in young children less than 5 years of age. The affected patients present with seizure, focal neurologic deficit, or signs of increased intracranial pressure.

PNETs are typically seen as large cerebral white matter mass frequently containing necrosis and calcification. The mass is hyperdense on noncontrast CT and isointense to gray matter on T2-weighted images and DWI reveals restricted diffusion, suggesting compact cellularity. Hemorrhage may

be seen, and enhancement is variable (Fig. 4.19). Tumor cells have a tendency to disseminate along the CSF space (Barkovich 2012).

4.1.3.2.9 Atypical Teratoid/Rhabdoid Tumor

ATRT is a rare WHO grade 4 embryonal tumor diagnosed as medulloblastoma or PNET in the past. The vast majority of cases occur in young children less than 2 years of age. The posterior fossa, cerebral hemisphere, pineal region, septum pellucidum, and hypothalamus are the frequent tumor locations.

Pathologically, ATRTs are indistinguishable from a medulloblastoma/PNET except for the characteristic rhabdoid cells found in a small fraction of the tumor. ATRTs may be associated with rhabdoid tumors of the kidney.

ATRTs are typically seen as large heterogeneous masses with necrosis, cyst, and hemorrhage. The masses are often isodense to gray matter on CT, and calcification is common. On MR images, the solid portions are isointense and have reduced diffusion, suggesting compact cellularity. After contrast administration, ATRTs are usually heterogeneously enhanced (Fig. 4.20). Leptomeningeal dissemination of the tumor is seen in 20 % of the cases (Lee et al. 2009).

4.1.3.2.10 Germ Cell Tumors

Germ cell tumors are presumed to be neoplastic transformation of embryonic germ cells. There are germinomatous and nongerminomatous tumors, and the latter includes teratomas, choriocarcinoma, yolk sac tumor, and mixed germ cell tumors. Although germ cell tumors arise mainly in the mid-line locations including the pineal gland and the suprasellar and hypothalamic regions (Fig. 4.26), they can also arise in the basal ganglia and thalami (Fig. 4.21). Presenting symptoms are visual disturbance, progressive hemiparesis, seizure, precocious puberty, or diabetes insipidus (Lee et al. 2009). Boys more than girls in the second decade of life are commonly affected by germ cell tumors, but young children may also be involved. Germ cell tumors are curable tumors being sensitive to radiation therapy and chemotherapy. However, malignant types are more common in younger children, who are more vulnerable to radiation therapy. Human chorionic gonadotropin (hCG) and alpha-fetoprotein (aFP) are tumor markers of choriocarcinomas and yolk sac tumors, respectively (Barkovich 2012).

Germinomas usually appear with slightly high density on noncontrast CT, isointensity to gray matter on T1- and T2-weighted images, and reduced diffusivity on ADC map. Demarcation may be clear in the mass abutting the cistern or ventricle, but the interface with the brain parenchyma may be somewhat unclear. Germ cell tumors often show marked enhancement, and small cysts and calcifications may be present. Small basal ganglia germinomas show no mass effect or enhancement initially. Slightly high signal intensity on FLAIR or T2-weighted images and ipsilateral hemiatrophy

of the cerebrum in patients with progressive hemiparesis are quite suggestive findings of the basal ganglia germinomas. Methionine PET scan is helpful in the demonstration of small tumor, which is unclear in MRI or CT (Fig. 4.21) (Lee et al. 2009b). Tumor involvement of the pyramidal tract can result in long-standing hemiparesis and hemiatrophy of the cerebral peduncle. Later, mass effect, enhancement, or cysts may develop. Some heterogeneity may be seen in large tumors containing necrosis.

Teratomas appear as well-demarcated masses containing multiple cysts, calcifications, and fat. At least some part of the tumor may be well enhanced. Differentiation of malignant subtypes is not always possible on imaging, but the yolk sac tumors tend to have irregular appearance, and hemorrhage and elevated serum level of hCG are noted in choriocarcinoma. Immature or malignant subtypes or mixed germ cell tumors have more aggressive appearance with peritumoral edema than germinomas or teratomas (Naidich et al. 2013).

4.1.3.3 Sellar and Juxtasellar Tumors

The major pediatric suprasellar tumors are optic pathway/hypothalamic glioma, craniopharyngioma, and germ cell tumors.

4.1.3.3.1 Hypothalamic/Optic Astrocytomas

Hypothalamic/optic astrocytomas typically present in children of 2–4 years of age with visual disturbance. Endocrine dysfunction, hydrocephalus, and diencephalic syndrome (emaciation, pallor, and hyperactivity before the age of 3 years) may also be associated. About 20–50 % of the patients with optic pathway gliomas are associated with NF1. Orbital portion of the optic nerve is more frequently involved than the chiasmatic portion in patients with NF1. Hypothalamic/optic astrocytomas are seen as solid and cystic masses with T1 and T2 prolongation and strong enhancement (Deopujari et al. 2011; Barkovich 2012). Tumor extension into the posterior optic pathway to lateral geniculate body may be seen as high T2 signal intensity (Fig. 4.22).

Some of the hypothalamic/optic astrocytomas are more aggressive (WHO grade2) and have a tendency of leptomeningeal dissemination affecting younger children (Fig. 4.23). These astrocytomas are recently described as pilomyxoid astrocytoma (PMA) exhibiting slightly different histological features (lack of Rosenthal fibers, monomorphic features, and myxoid background) from the pilocytic astrocytomas. In addition to the suprasellar region, PMAs are also seen in the cerebellum or cerebral hemispheres in minor cases (Lee et al. 2011).

4.1.3.3.2 Craniopharyngioma

Craniopharyngiomas are presumed to arise from the remnants of the craniopharyngeal duct, accounting for half of the pediatric suprasellar tumors. The tumors develop anywhere

from the floor of the third ventricle to the pituitary gland. Peak incidence is between 10 and 14 years of age. Clinical presentations include headache, visual field defect, and pituitary/hypothalamic dysfunction. Craniopharyngiomas can be distinguished from the optic pathway gliomas by the cystic component (90 %) and presence of calcification (Fig. 4.24). The cystic portions may have T1 hyperintensity due to high protein content, and the solid portions may be heterogeneously enhanced. Large craniopharyngiomas may extend into the middle, anterior, or posterior cranial fossa, and the sellar may be enlarged with tumor extension (Deopujari et al. 2011).

4.1.3.3.3 Germinoma

About 35 % of the germ cell tumors are seen in the suprasellar area, equally affecting male and female patients, and both suprasellar and pineal germinomas are seen in 5–10 % of cases. Germ cell tumors can be differentiated from optic/hypothalamic gliomas by the characteristic iso- or hypointense T2 appearance, suggesting compact cellularity. When the mass is confined to the infundibulum and diabetes insipidus is present, Langerhans cell histiocytosis, germ cell tumors, lymphocytic hypophysitis, and other inflammatory conditions should be considered (Deopujari et al. 2011).

4.1.3.3.4 Hypothalamic Hamartoma

Hypothalamic hamartomas are heterotopic malformed neuronal tissue in the tuber cinereum. Boys are more frequently affected than girls, presenting precocious puberty, gelastic epilepsy, and neurodevelopmental delay. The tumors are well-defined isointensity masses projecting from the floor of the third ventricle. Large hamartomas may be slightly hyperintense on T2-weighted images due to the glial component. Contrast enhancement is not seen (Fig. 4.25) (Deopujari et al. 2011).

4.1.3.4 Pineal Region Tumors

The most common pediatric pineal tumors are germ cell tumors followed by pineal parenchymal tumors. Other pediatric tumors in the pineal region include astrocytomas and gangliogliomas. Epidermoids can also form pineal cystic lesions.

All of these tumors can cause obstructive hydrocephalus due to the compression to the aqueduct. Parinaud sign, diplopia, and precocious puberty may exist.

4.1.3.4.1 Germ Cell Tumors

About half of the germ cell tumors are in the pineal region, and 65 % of them are germinomas. They are hyperdense on noncontrast CT and hypointense on T2-weighted images due to hypercellularity and may be calcified. Diffusion of the solid portions is more restricted than normal parenchyma. Germinomas are well enhanced after contrast administration, and leptomeningeal tumor seeding may be seen (Fig. 4.26).

Teratomas are seen exclusively in males, and the peak incidence is in the first decade. There are mature and immature teratomas. They appear as well-margined heterogeneous masses containing solid portions, cysts, fat, and calcification. Ill-defined margin and peritumoral edema may be seen in immature or malignant teratomas. Malignant germ cell tumors include embryonal carcinoma, endodermal sinus tumor (yolk sac tumor), and choriocarcinoma (Barkovich 2012).

4.1.3.4.2 Pineal Parenchymal Tumors

Pineal parenchymal tumors are rare, and reports on their neuroimaging features are limited. Pineoblastomas are more common in pediatric age, and they are primitive small round cell tumors, classified as PNETs. Pineoblastomas are highly malignant tumors with a tendency of local invasion and CSF dissemination. They can be seen in patients with retinoblastoma.

Typical calcifications of pineoblastomas are “exploded” pattern of preexisting pineal calcification, whereas germinomas may displace calcified gland on CT scan. On MR images, differentiation between germ cell tumors and pineal parenchymal tumors is difficult. Pineoblastoma may extend to fill the quadrigeminal to supracerebellar cistern and invade cerebellar vermis.

Pineocytomas are very rare and tend to be smaller and less invasive (Barkovich 2012).

4.1.3.5 Other Pediatric Brain Tumors

4.1.3.5.1 Choroid Plexus Tumors

Choroid plexus papillomas and carcinomas in children are most commonly found in the atrium of the lateral ventricles, whereas the fourth ventricle is the most common site in adults. They are most frequently found in children of age before 5 years presenting with hydrocephalus. Both males and females are equally affected by this carcinoma. Choroid plexus papillomas appear as lobulated masses with calcification and hemorrhage (Fig. 4.27). The surface of the mass has papillary appearance, and homogeneous enhancement is noted after contrast administration. Carcinomas can be characterized by large irregular contoured masses, invasion of the parenchyma, and surrounding edema. Choroid plexus tumors can spread throughout the CSF space (Barkovich 2012).

MR spectroscopy of the choroid tumors shows only choline peak on long TE, which is more prominent in the carcinomas. In papilloma, myo-inositol is seen on short TE, which is absent in the carcinomas. Perfusion imaging shows increased rCBV in the tumor due to lack of BBB (Rossi et al. 2010).

4.1.3.5.2 Meningiomas

Pediatric meningiomas are very uncommon. Both male and female are equally affected, often seen in association with NF2 or following radiation therapy. Pediatric meningiomas

are more histologically aggressive, more cystic, and more frequently intraventricular and infratentorially located than in adult patients.

Meningiomas are large masses attached to the dura, choroid plexus, or ectopic dural rest in the Sylvian fissure (Fig. 4.28) (Chiocca et al. 1994). They are well-defined iso- to high-intensity masses on T2-weighted images and uniformly enhanced after contrast injection. Cysts, hemorrhage, or calcification may be seen. Perfusion imaging shows hypervascularity and persistent relaxivity due to the absence of BBB, and MRS shows elevated alanine (doublet at 1.47 ppm), choline, and glutamate/glutamine, and decreased NAA, creatinine, and myo-inositol. Angiography demonstrates tumor stain supplies by meningeal vessels, although parasitic supply from the cerebral vessels may be seen (Barkovich 2012).

4.1.3.5.3 Congenital Brain Tumors

Congenital tumors, defined as those presenting within 60 days of birth, account for 18 % of the infantile brain tumors and less than 2 % of overall childhood brain tumors. Supratentorial lesions are more common than infratentorial lesions. The clinical presentations are usually signs of increased intracranial pressure due to hydrocephalus or the large mass itself, including enlarged head, vomiting, lethargy, and separated sutures. Unexpected tumor bleeding may occur, and focal neurologic signs are not common. The prognosis is generally poor, because the congenital tumors are often large at the presentation, commonly malignant, and chemotherapy and radiotherapy are limited in this young age (Nejat et al. 2008; Parmar et al. 2011; Barkovich 2012).

The most common congenital brain tumor is the teratoma, which is usually found in the midline regions and seen as large, heterogeneous cystic/solid masses containing calcification and fatty tissue (Fig. 4.29). The other common tumor types are the embryonic tumors (PNET, ATRT), astrocytomas, ependymomas, and choroid plexus tumors. After 2 months of life, the neuroepithelial tumors are more common than teratoma (Parmar et al. 2011).

4.2 Neoplasms of the Spine

4.2.1 Introduction

Pediatric spine tumors encompass diverse pathologic lesions that differ based on the location and the age of the children. Pediatric patients can be affected by diverse primary and metastatic tumors, making the differential diagnosis and treatment options complex. In this chapter, the features of common pediatric spinal tumors are discussed, based on the location: intramedullary tumors, intradural–extramedullary tumors, and extradural tumors.

4.2.2 Intramedullary Tumors

Pediatric intramedullary spinal tumors are often slowly growing benign masses. Patients usually present with symptoms at or below the level of the spinal cord tumor. The most common signs and symptoms in young children are pain, weakness, and frequent falling. In older children, sensory changes, progressive scoliosis, and gait difficulties may develop. Bowel and bladder dysfunction are seen in more progressed disease (Barkovich 2012).

Involved spinal cord is enlarged retaining its normal location in contrast to the extramedullary mass, which may compress or displace the cord. Spinal cord tumors should be differentiated from demyelination seen in patients with acute disseminated encephalomyelopathy (ADEM) or multiple sclerosis (MS). Round or ovoid shape, significant enlargement of the cord, and presence of cysts favor tumors, while the presence of other demyelinating lesions in the brain highly suggests ADEM or MS. Follow-up imaging should be obtained in uncertain cases (Barkovich 2012).

4.2.2.1 Astrocytoma

The most common pediatric intramedullary tumors are astrocytomas (60 %), followed by ependymomas (30 %). Although spinal astrocytomas are generally lower-grade tumors than astrocytomas in the brain, malignant astrocytomas and glioblastomas are relatively more common in children than in adults.

Astrocytomas typically involve the long segment of the cord that causes diffuse cord expansion (Fig. 4.30). The thoracic cord is most commonly (67 %) involved followed by the cervical cord (49 %). Involvement of the entire spinal cord is more common in children than in adults. Because astrocytomas arise from cord parenchyma, they can be eccentrically located within the spinal cord, while the central location is the case for ependymomas. Astrocytomas usually have poorly defined margins, making surgical excision incomplete. Peritumoral edema, intratumoral cysts, and peritumoral cysts may be seen (Barkovich 2012).

In addition, these slow-growing tumors are associated with bony remodeling including posterior scalloping of the vertebrae, thinning of the pedicle or laminae, and scoliosis. Hemorrhage is less common than in ependymomas. Extensive leptomeningeal spread suggests high-grade tumors (Huisman 2009).

4.2.2.2 Ependymoma

Most pediatric spinal ependymomas are WHO grade 2 lesions. Myxopapillary ependymoma (WHO grade 1) that occurs exclusively within the conus or cauda equina is less common (8–12 %) in children than in adults (50 %). Prognosis in pediatric spinal ependymoma depends on tumor grade, completeness of resection, and presence of

dissemination at diagnosis (Merchant et al. 2000). Spinal ependymomas generally demonstrate heterogeneous high T2 and low T1 signal intensities. Contrast enhancement is more intense than that of astrocytomas. Ependymomas have a tendency to be located centrally on axial images, and often have sharper margin than that of astrocytomas. Intratumoral and polar cysts are more prominent than in astrocytomas. Characteristic hemosiderin staining especially at the superior and inferior margins is seen in about 20 % of cases. CSF dissemination at the time of diagnosis is more common with higher-grade tumors (Fig. 4.31) (Huisman 2009; Barkovich 2012).

Other intramedullary tumors in children are ganglioglioma, germinomas, PNET, ATRT, and oligodendrogliomas. Rarely CSF seeding of the brain tumor into the central canal may cause intramedullary mass (Fig. 4.6).

4.2.3 Extramedullary Tumors

Extramedullary tumors comprise about two-thirds of the pediatric spinal tumors. They are either intradural or extradural in origin, and extradural tumors are more common than intradural–extramedullary tumors. Clinical presentations are similar to intramedullary tumors and include weakness and pain.

4.2.3.1 Intradural–Extramedullary Tumors

4.2.3.1.1 CSF Dissemination of Tumors

CSF dissemination of tumors may occur in the spinal canal forming intradural–extramedullary (IDEM) tumors. Leptomeningeal tumor spread can be seen in pediatric brain tumors such as medulloblastoma (Fig. 4.5), ependymoma, germ cell tumors, anaplastic glioma, pineoblastoma, pilomyxoid astrocytoma, and choroid plexus tumors (Huisman 2009).

Postcontrast MR imaging best demonstrates tumor seeding as enhancing nodules coating the cord surface, cauda equine, and the thecal sac (Fig. 4.5). Veins on the midline surface of the cord should not be considered as tumor seeding. Artifact from postoperative hemorrhage or contrast leak may mimic CSF tumor seeding on MR scan obtained after suboccipital craniectomy, which can be avoided by preoperative MRI or delayed MR scan obtained at least 2 weeks after operation. Lumbosacral region is most commonly affected. The sensitivity of MR detection of subarachnoid tumor is

enhanced with increased dose of contrast and 3D acquisition with multiplanar reconstruction (Barkovich 2012).

4.2.3.1.2 Neurogenic Tumors

Other IDEM tumors include schwannoma (NF2, Fig. 4.32) or neurofibromas (NF1) associated with neurofibromatosis. These tumors may extend through widened neural foramen. They exhibit hyperintensity on T2-weighted images, and neurofibromas typically have central low intensity (target sign) due to collagen deposition. Enhancement after contrast injection is variable (Fig. 4.33) (Barkovich 2012).

4.2.3.1.3 Meningiomas

Meningiomas are another form of IDEM tumors, although extremely uncommon in children. They are smoothly marginated masses with homogeneous enhancement after contrast administration (Barkovich 2012).

4.2.3.1.4 Cysts

Developmental cysts including dermoid/epidermoid or neuroenteric cyst may be seen as IDEM mass in children. Neuroenteric cyst (Fig. 4.34) is one of the foregut duplication cysts. Neuroenteric cysts are usually extramedullary (80 %) and ventral in location associated with vertebral abnormalities. They are most commonly encountered in the thoracic region (42 %) (Barkovich 2012).

4.2.3.2 Extradural Tumors

Extradural tumors are usually epidural invasion of the extraspinal tumors such as neuroblastoma, ganglioblastoma, ganglioneuroma, leukemia, lymphoma, PNET (Fig. 4.35), and soft-tissue sarcoma. Paraspinal neurogenic tumors frequently enter the spinal canal through the neural foramen, forming a dumbbell-shaped mass. Epidural mass formation of leukemic cells (usually acute myelogenous leukemia) is called granulocytic sarcoma or chloroma. These epidural masses are isointense to neural tissue and homogeneously enhanced (Fig. 4.36). Similar appearance may be seen in PNET, but usually more heterogeneous containing cysts or necrosis. Abnormal bone marrow signal intensity may be seen in patients with leukemia or lymphoma due to tumor infiltration or marrow conversion (Barkovich 2012).

Finally, there are several rare tumors involving the vertebral column. They are Langerhans cell histiocytosis (Fig. 4.37), aneurysmal bone cyst (Fig. 4.38), giant cell tumor, Ewing sarcoma, osteogenic sarcoma, and osteoblastoma.

4.3 Illustrations: Neoplasms of the Brain and Spine

4.3.1 Neoplasms of the Brain

4.3.1.1 Infratentorial Tumors

4.3.1.1.1 Astrocytoma

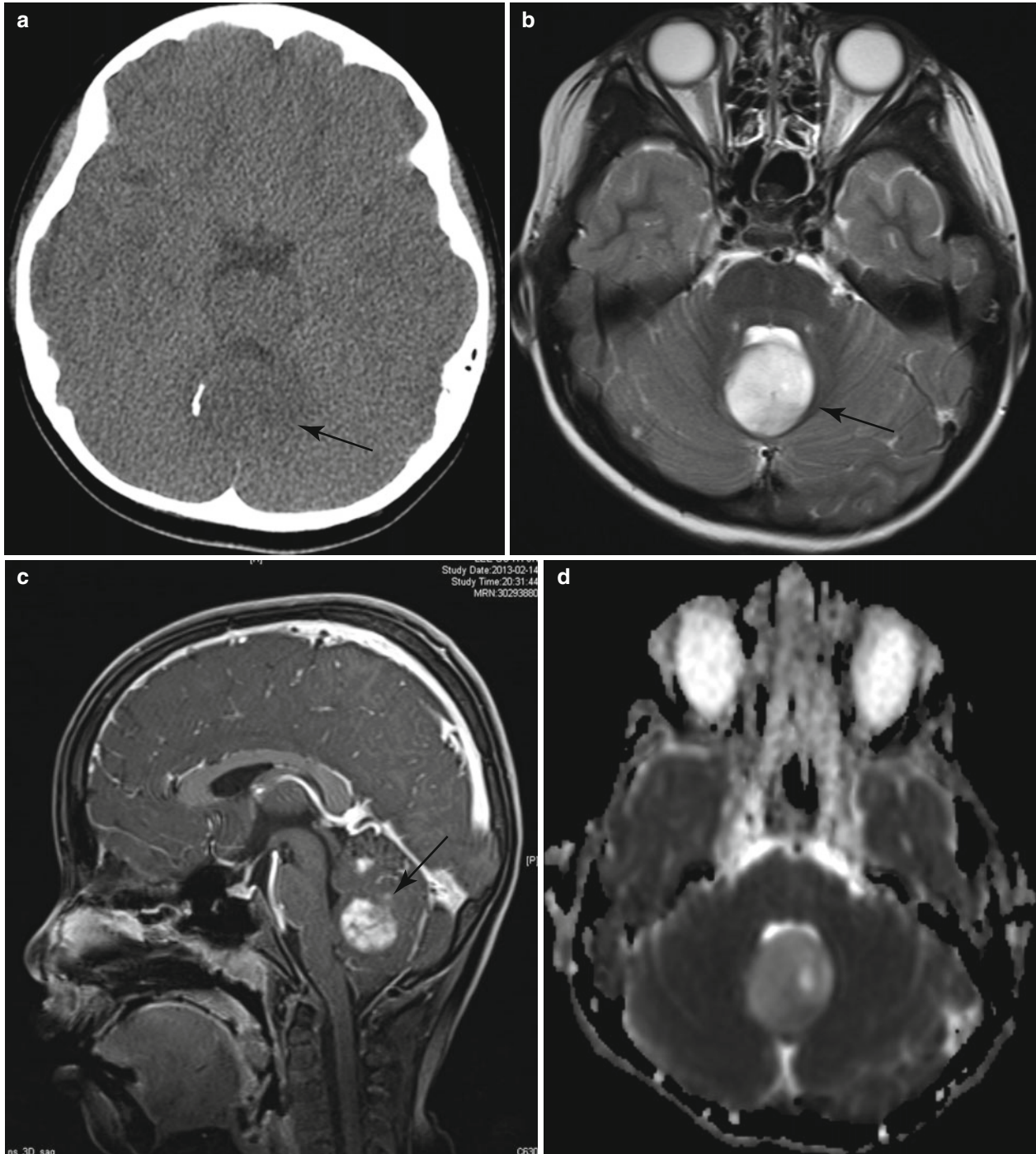


Fig. 4.1 Cerebellar pilocytic astrocytoma in a 7-year-old girl. (a) CT scan shows hypoattenuated mass (*arrow*) with calcification in the midline cerebellum. (b) The mass becomes bright on T2-weighted image, suggesting less compact cellularity. (c) Postcontrast image reveals strong enhancement of the mass. (d) Increased diffusion compared to

the normal cerebellar parenchyma is seen on ADC map. (e) Perfusion image (rCBV map) reveals slightly increased perfusion of the cerebellar mass (*arrow*) compared to the cerebellar hemisphere. (f) Choline/creatinine map obtained from multivoxel proton MRS in 2D array demonstrates increased choline in the tumor

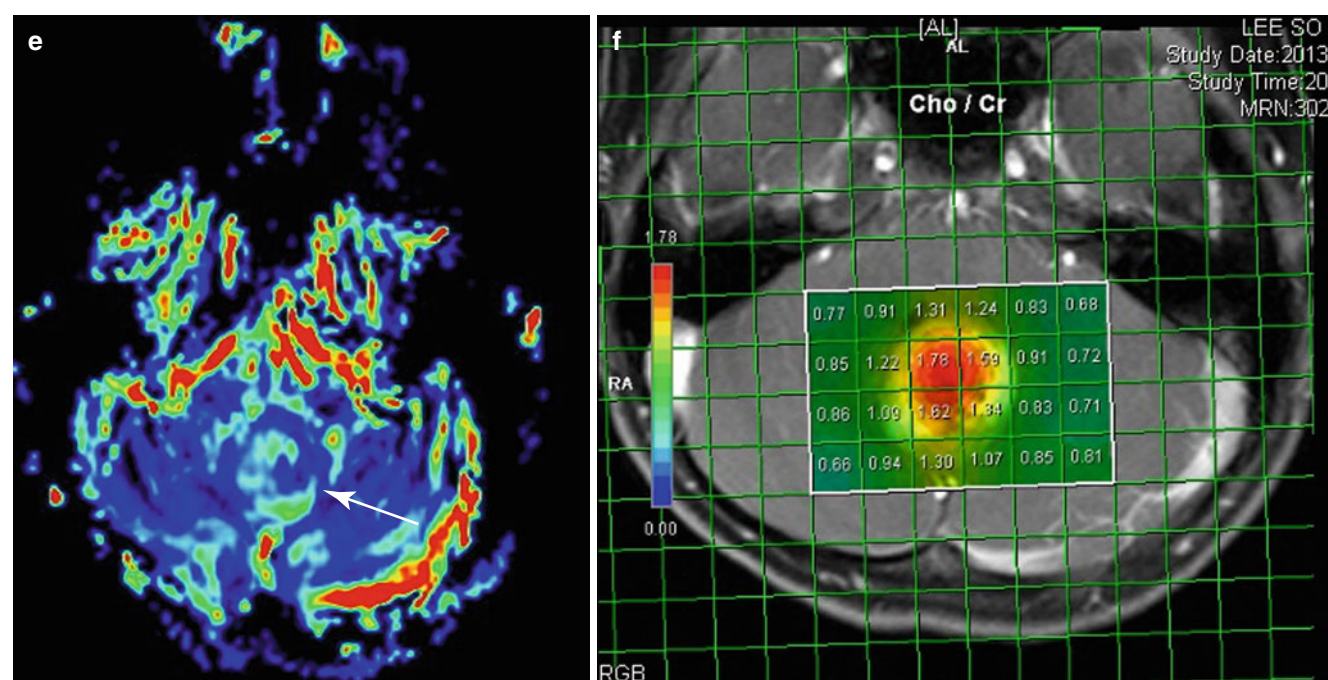


Fig. 4.1 (continued)

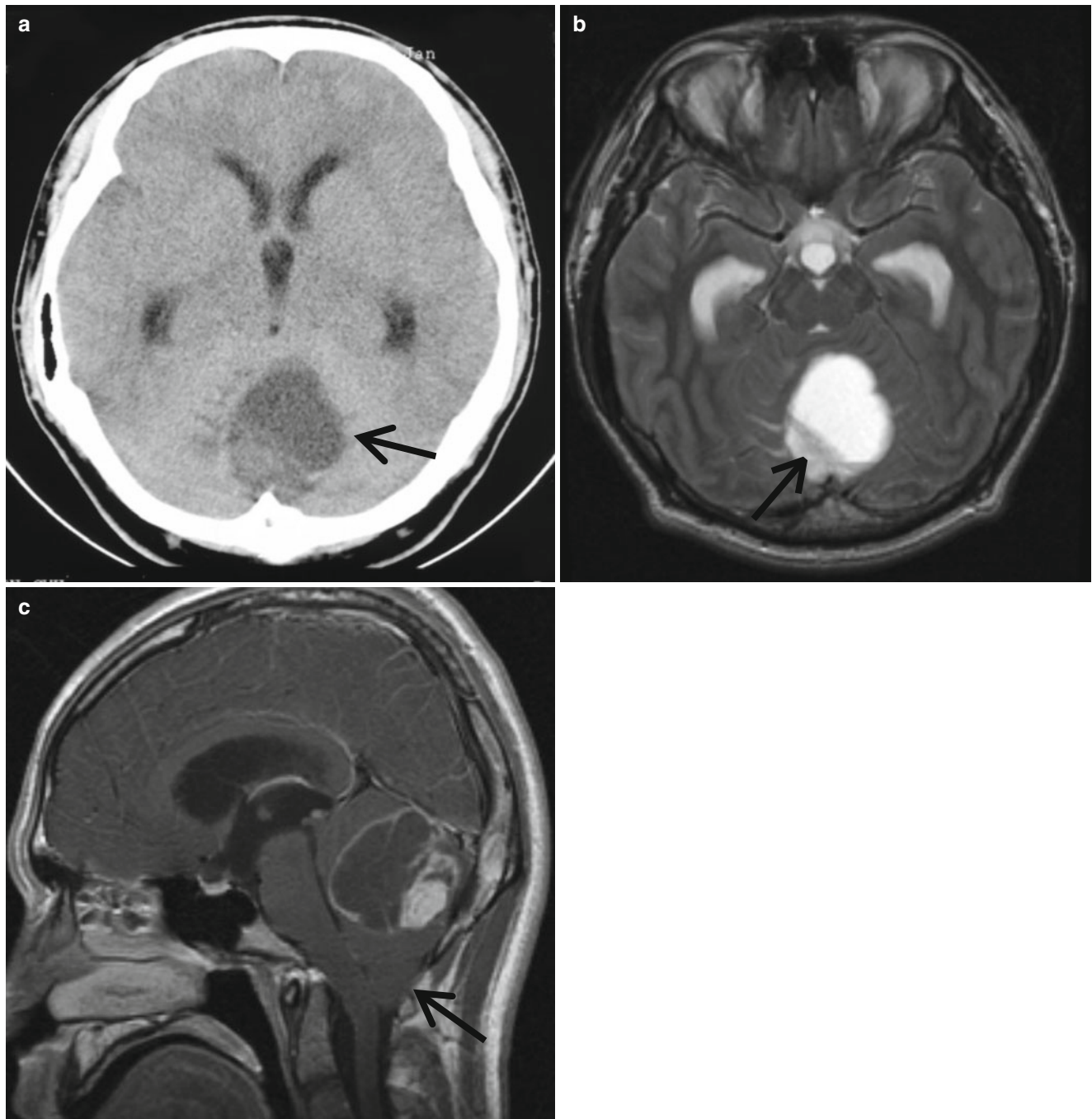


Fig. 4.2 Cystic cerebellar JPA in an 18-year-old boy. (a) CT scan shows cystic mass with solid portion (*arrow*), which appears low attenuated compared to the normal parenchyma. (b) Solid portion exhibits high intensity on T2-weighted image (*arrow*). (c) Postcontrast sagittal

image reveals strong enhancement of the solid portion and cystic wall. The fourth ventricle is compressed, and the cerebellar tonsil (*arrow*) is downward-displaced

4.3.1.1.2 Medulloblastomas

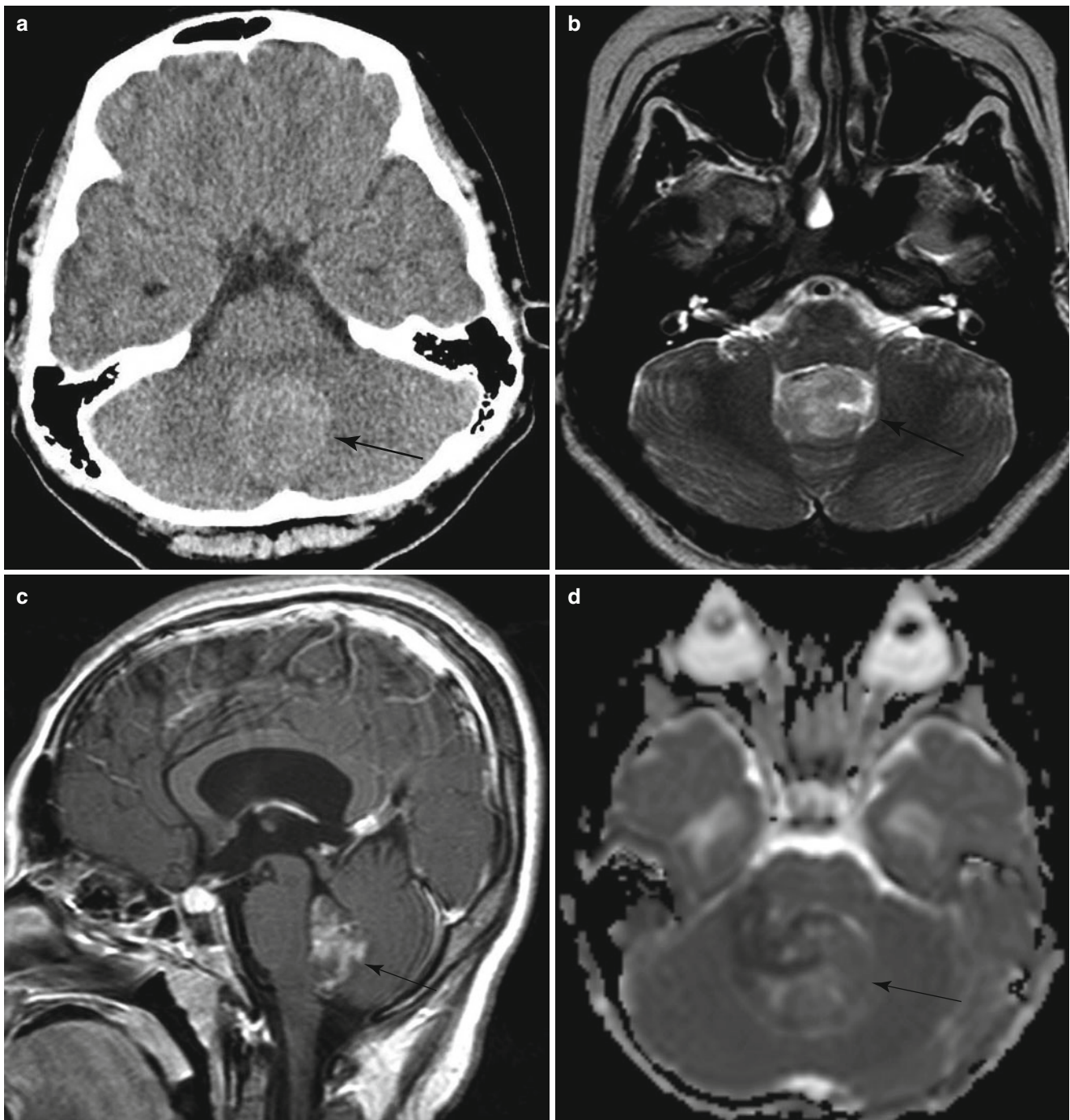


Fig. 4.3 Medulloblastoma in an 11-year-old girl. (a) Noncontrast CT shows hyperdense midline cerebellar mass (arrow). (b) The mass (arrow) shows slight hyperintensity compared to the gray matter on T2-weighted image. (c) Postcontrast sagittal image reveals the mass

arising from the roof of the fourth ventricle filling the ventricular lumen (arrow). (d) ADC map demonstrates isointensity to the normal parenchyma (arrow) and more restricted diffusion compared to the JPA in (Fig. 4.1d)

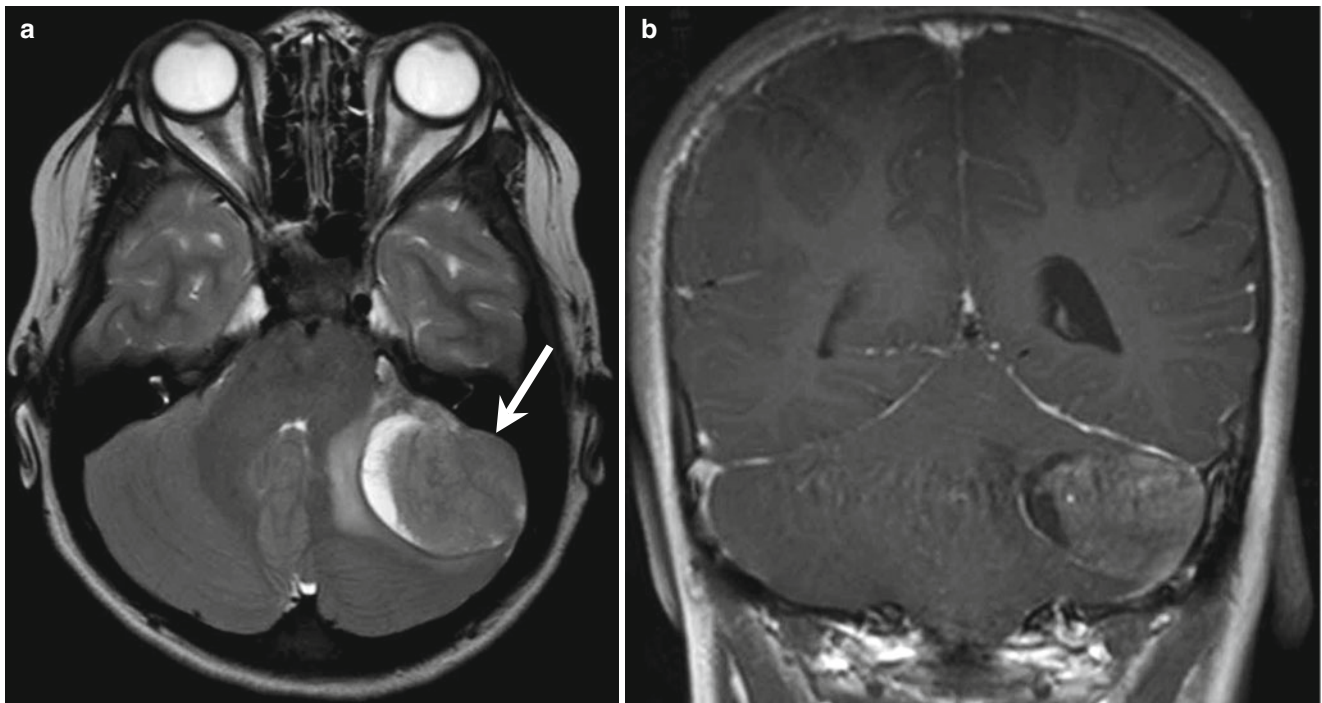


Fig. 4.4 Atypical medulloblastoma in a 16-year-old girl. **(a)** T2-weighted axial image shows well-defined iso-signal intensity mass (*arrow*) with peripheral cystic portion and surrounding edema in

the left cerebellar hemisphere. **(b)** Postcontrast coronal image reveals homogeneous enhancement of the solid portion and cyst wall



Fig. 4.5 Medulloblastoma with disseminated tumors in the CSF space. (a) Postcontrast axial image of the brain shows enhancing cerebellar tumor and enhancing lesions (*arrows*) in both cerebellopontine angles (CPA) and thick sulcal enhancement of both temporal lobes as well as enhancing folia suggesting disseminated tumor. (b) Postcontrast sagittal

image of the spine demonstrates extensive enhancing lesions along the spinal cord invading the parenchyma and along the cauda equina. (c) T2-weighted image shows enlarged cord with abnormal intensity and isointensity mass (*arrow*) in the thecal sac

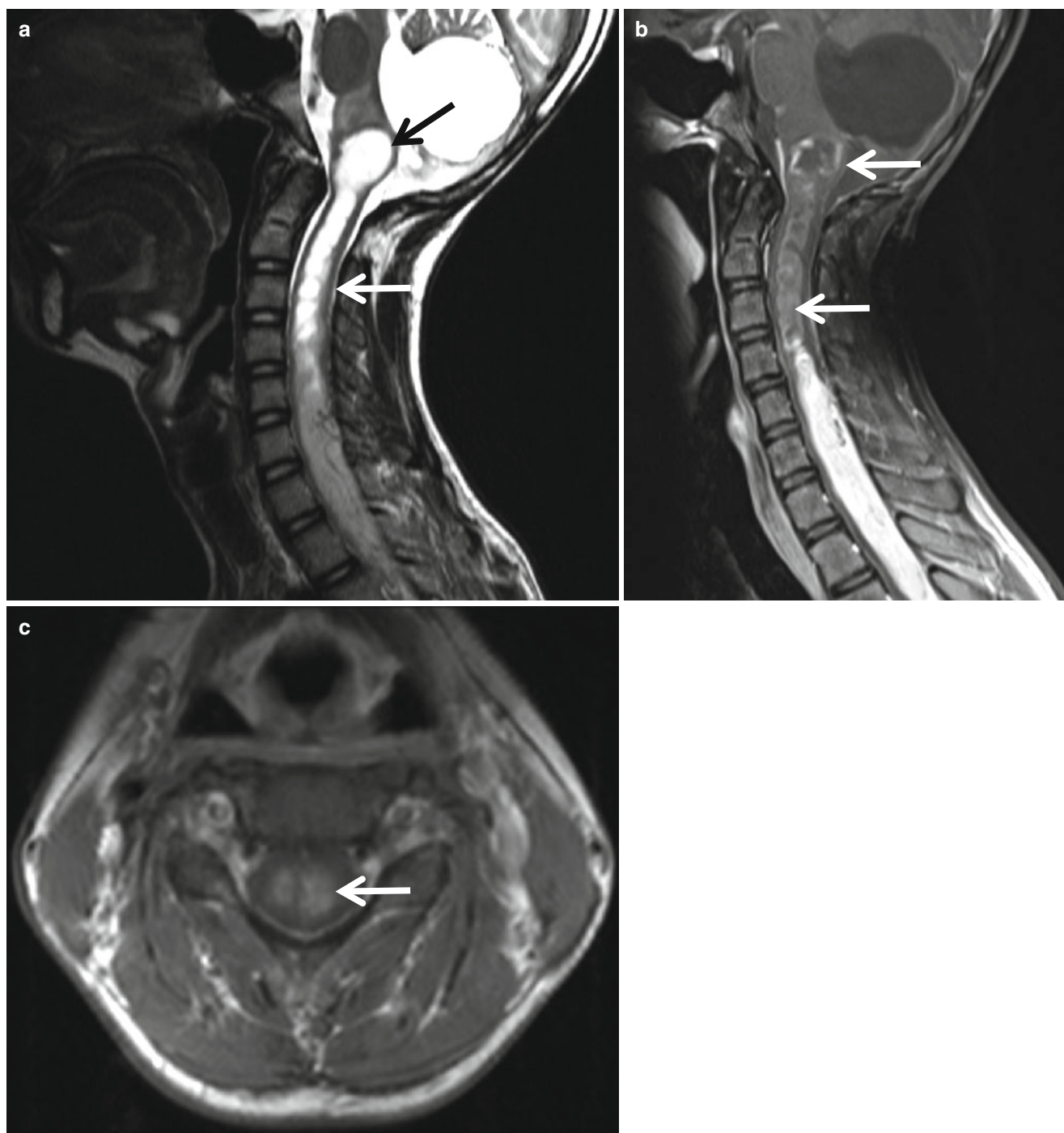


Fig. 4.6 Intramedullary lesion caused by central canal seeding of the medulloblastoma. (a) T2-weighted sagittal image shows hydrosyrinx of the upper cervical cord (*white arrows*), extending upward to the medulla (*arrow*) surrounded by edema, and extensive intramedullary masses. Prior surgical defect is seen in the cerebellum. (b) Lining of the cystic

lesion in the medulla and hydrosyrinx (*arrow*), lower solid portions, and distal cord surface are enhanced on a postcontrast sagittal image, suggesting tumor seeding. (c) Enhancing lesion (*arrow*) is seen at the central portion of the cord on a postcontrast axial image, suggesting tumor seeding through the central canal

4.3.1.1.3 Ependymomas

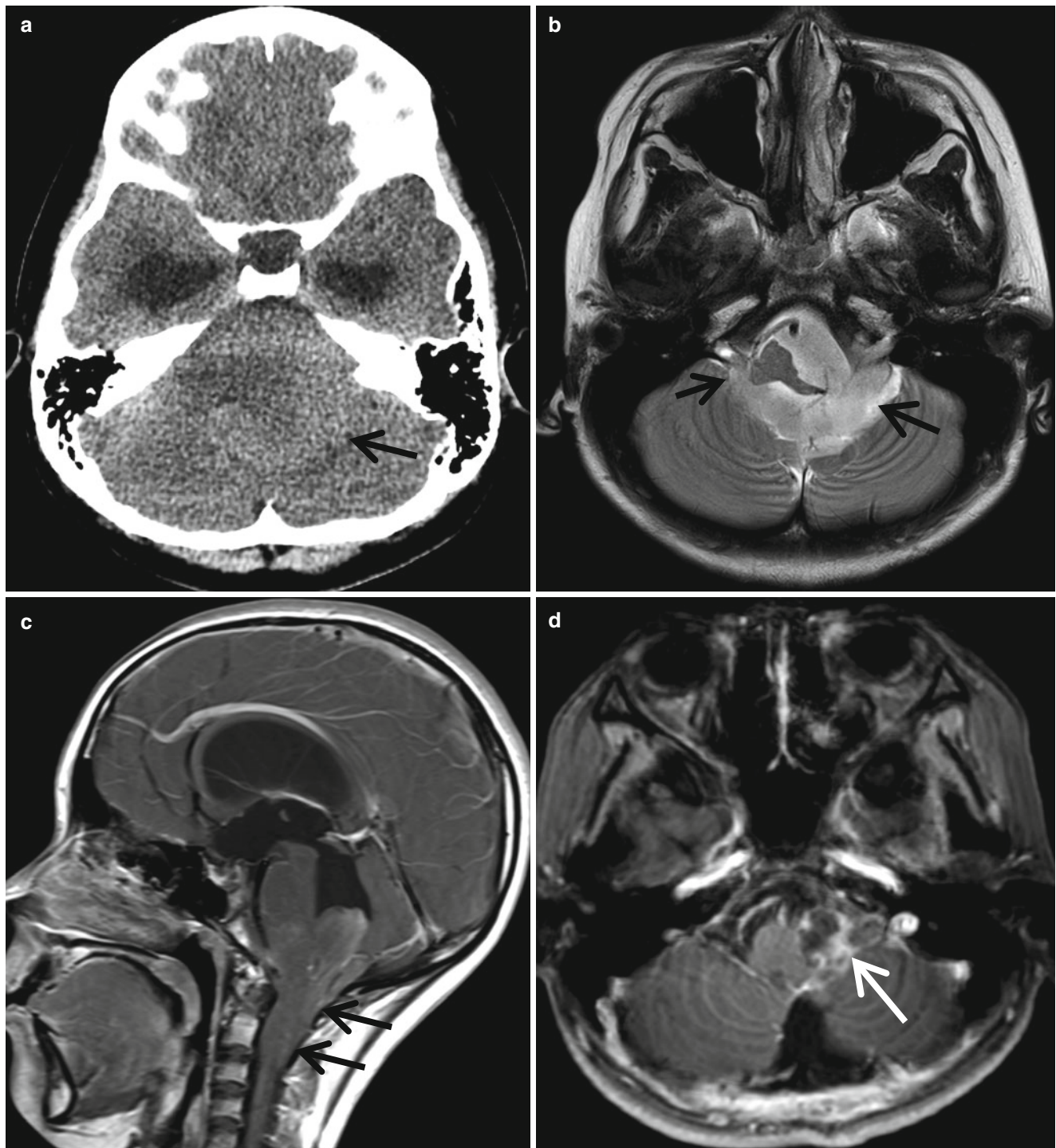


Fig. 4.7 Ependymoma in a 12-year-old girl. (a) CT scan shows isodensity mass in the cerebellum and distended temporal horns, suggesting obstructive hydrocephalus. (b) The mass is occupying the fourth ventricle extending through both the foramen of Luschka (arrow) into the CPA areas. Indentation and displacement of medulla are seen, and

the basilar artery is encased. (c) Tongue-like extension of the mass (arrows) is seen through the foramen of Magendie onto the posterior aspect of the upper cervical cord on a postcontrast sagittal image. (d) Postoperative follow-up MR image reveals residual tumor (arrow) in the left CPA

4.3.1.1.4 Brain Stem Tumors

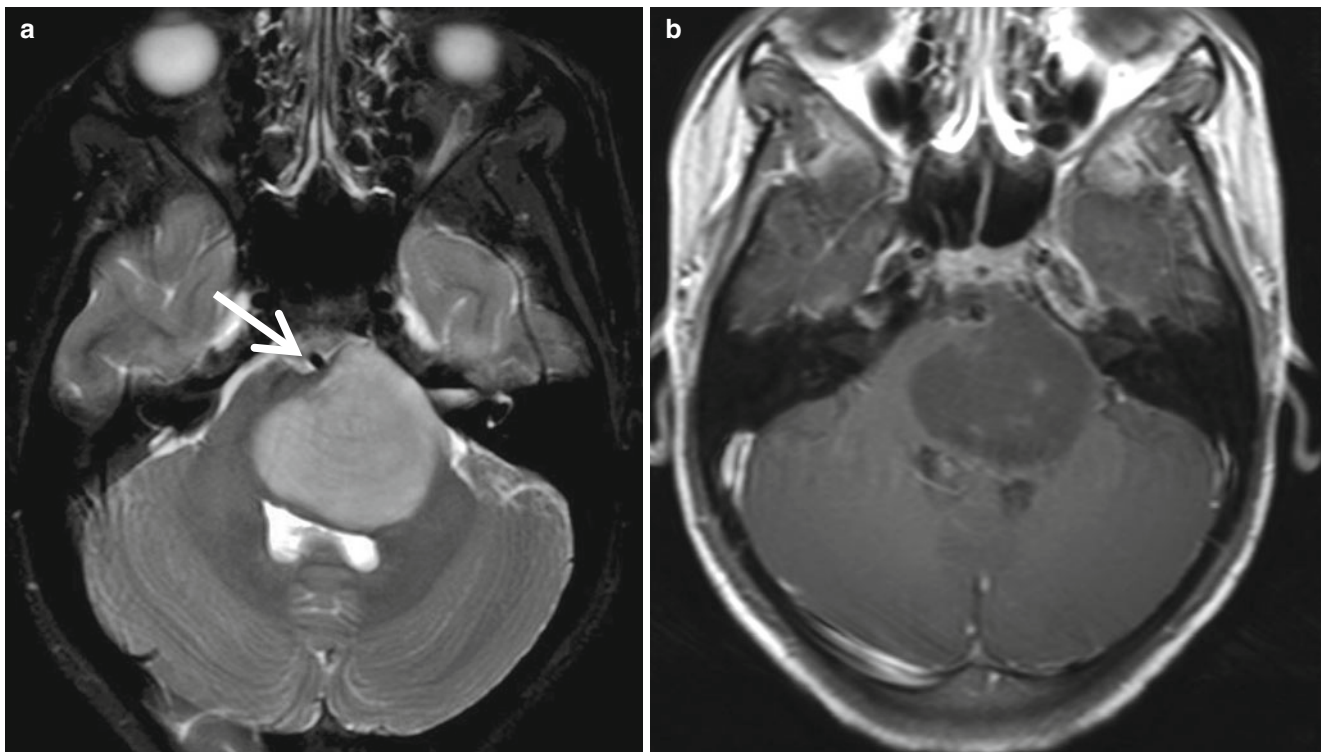


Fig. 4.8 Diffuse pontine glioma. (a) Large pontine mass is seen as high intensity expanding the pons on T2-weighted image. The basilar artery (arrow) is partially engulfed. (b) The mass is not well enhanced on postcontrast image

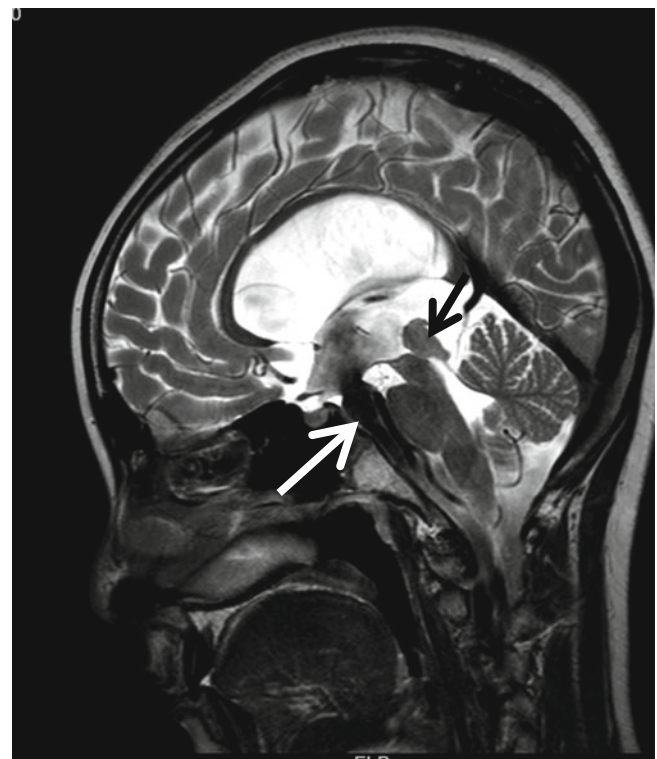


Fig. 4.9 Tectal glioma causing hydrocephalus in a 10-year-old boy who underwent endoscopic third ventriculostomy. T2-weighted sagittal image shows enlarged midbrain tectum (black arrow) causing aqueductal obstruction. Prominent flow artifact is noted (white arrow), suggesting patent defect at the floor of the third ventricle

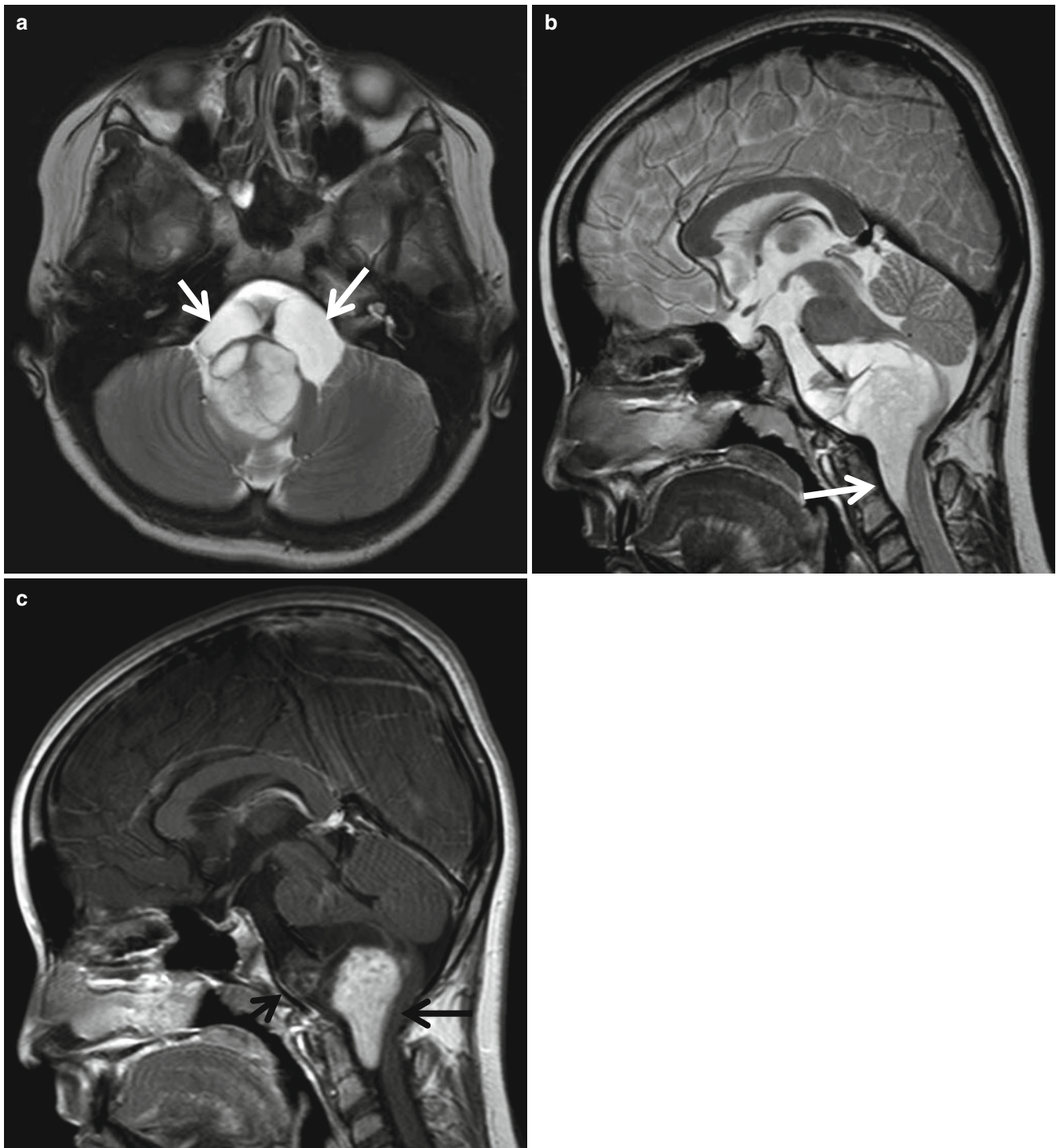


Fig. 4.10 Exophytic JPA involving the medulla in a 15-year-old boy. (a) T2-weighted axial image shows a well-defined solid and cystic mass arising from the medulla. The solid portion is very bright, and cystic portions (arrows) are encasing the basilar artery. (b) The mass is pro-

truded inferiorly anterior to the cervical cord (arrow) and superiorly compressing the pons on T2-weighted sagittal image. (c) The solid portions (arrows) are well enhanced on a postcontrast sagittal image

4.3.1.1.5 Extraparenchymal Tumors

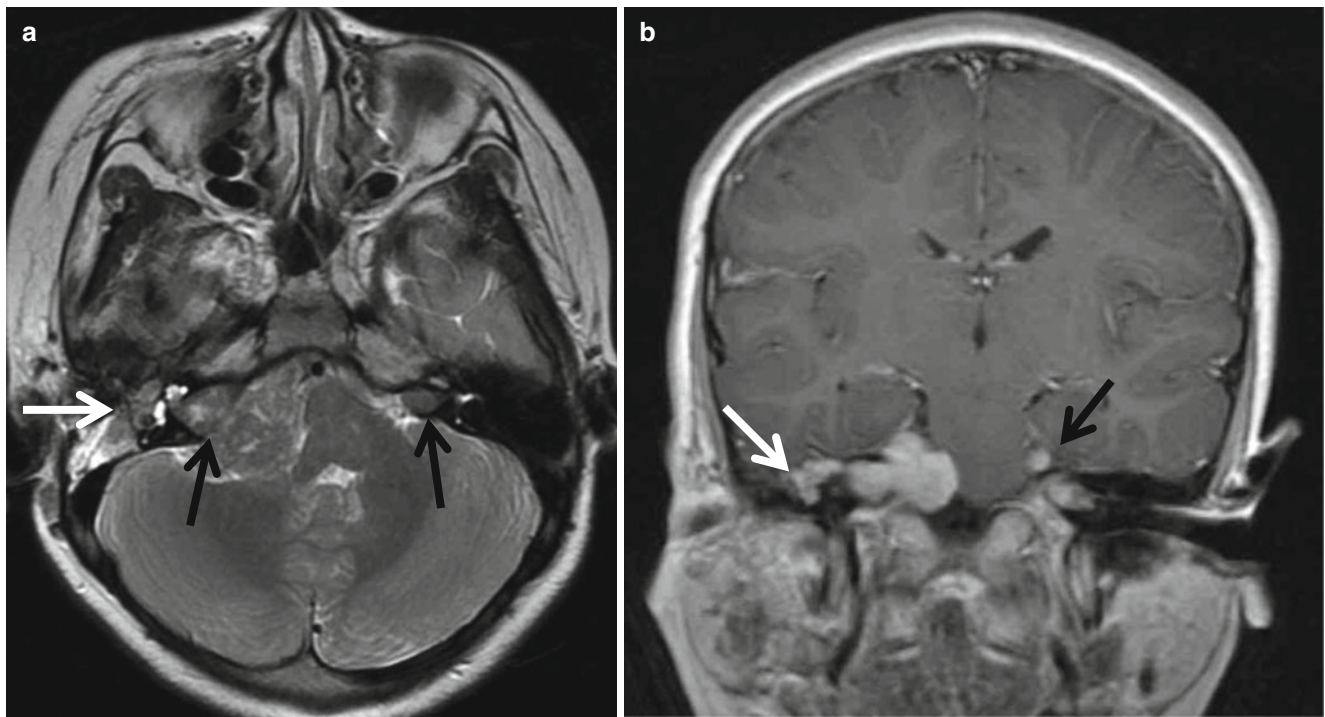


Fig. 4.11 Multiple cranial nerve tumors in patient with type 2 neurofibromatosis. **(a)** T2-weighted coronal image shows bilateral internal auditory canal masses (*black arrows*) of isointensity compared to the brain. The right one is extending to the CPA area compressing

the pons. Another mass is seen at the right facial nerve location (*white arrow*). **(b)** Postcontrast coronal image reveals multiple enhancing tumors involving bilateral acoustic nerves, right facial nerves (*white arrow*), and left trigeminal nerve (*black arrow*)

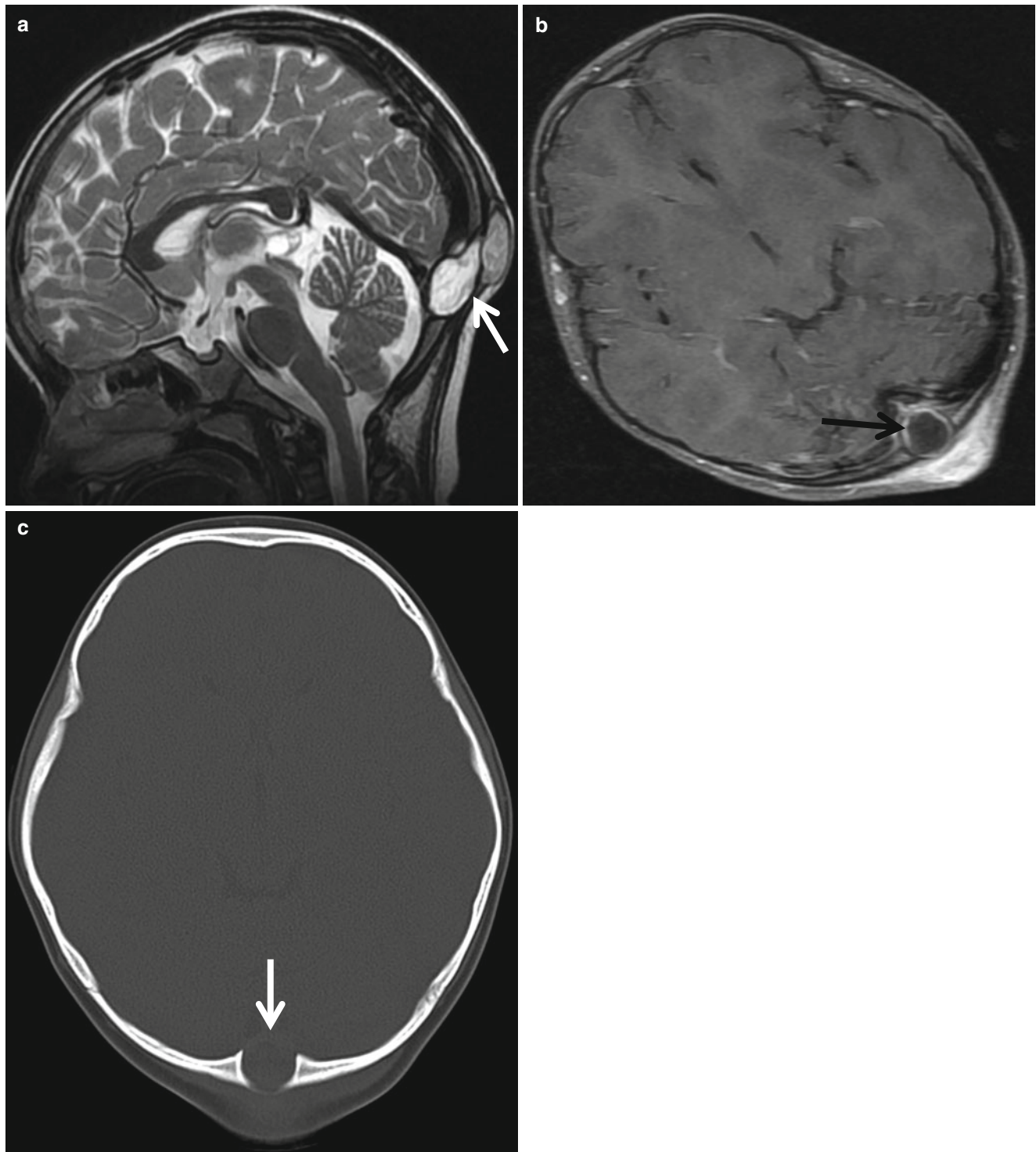


Fig. 4.12 Infected dermoid cyst. (a) T2-weighted sagittal image shows midline posterior cysts (*arrow*) involving both soft tissue in the scalp and occipital skull. (b) The cystic wall is enhanced (*arrow*), and more

patch enhancement is seen at the adjacent scalp suggesting infection on a postcontrast axial image. (c) CT scan demonstrates well-defined bony defect (*arrow*) at the occipital bone

4.3.1.2 Cerebral Hemispheric Tumors

4.3.1.2.1 Astrocytomas

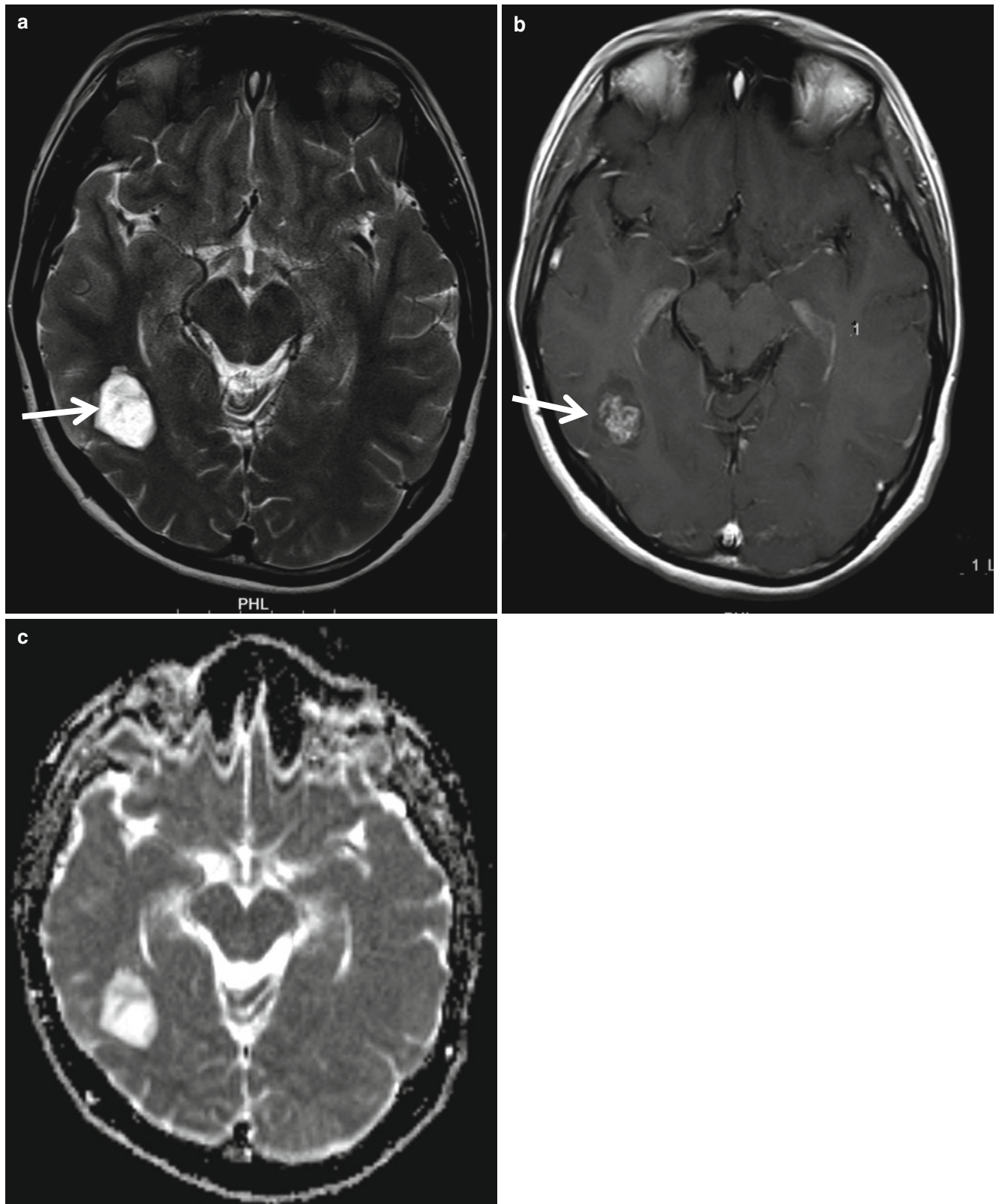


Fig. 4.13 Small hemispheric JPA in a 14-year-old boy. (a) T2-weighted axial image shows well-defined high-intensity mass (*arrow*) in the right temporo-occipital lobe. (b) The mass is heterogeneously enhanced after contrast administration. (c) Increased ADC is seen on water diffusion map

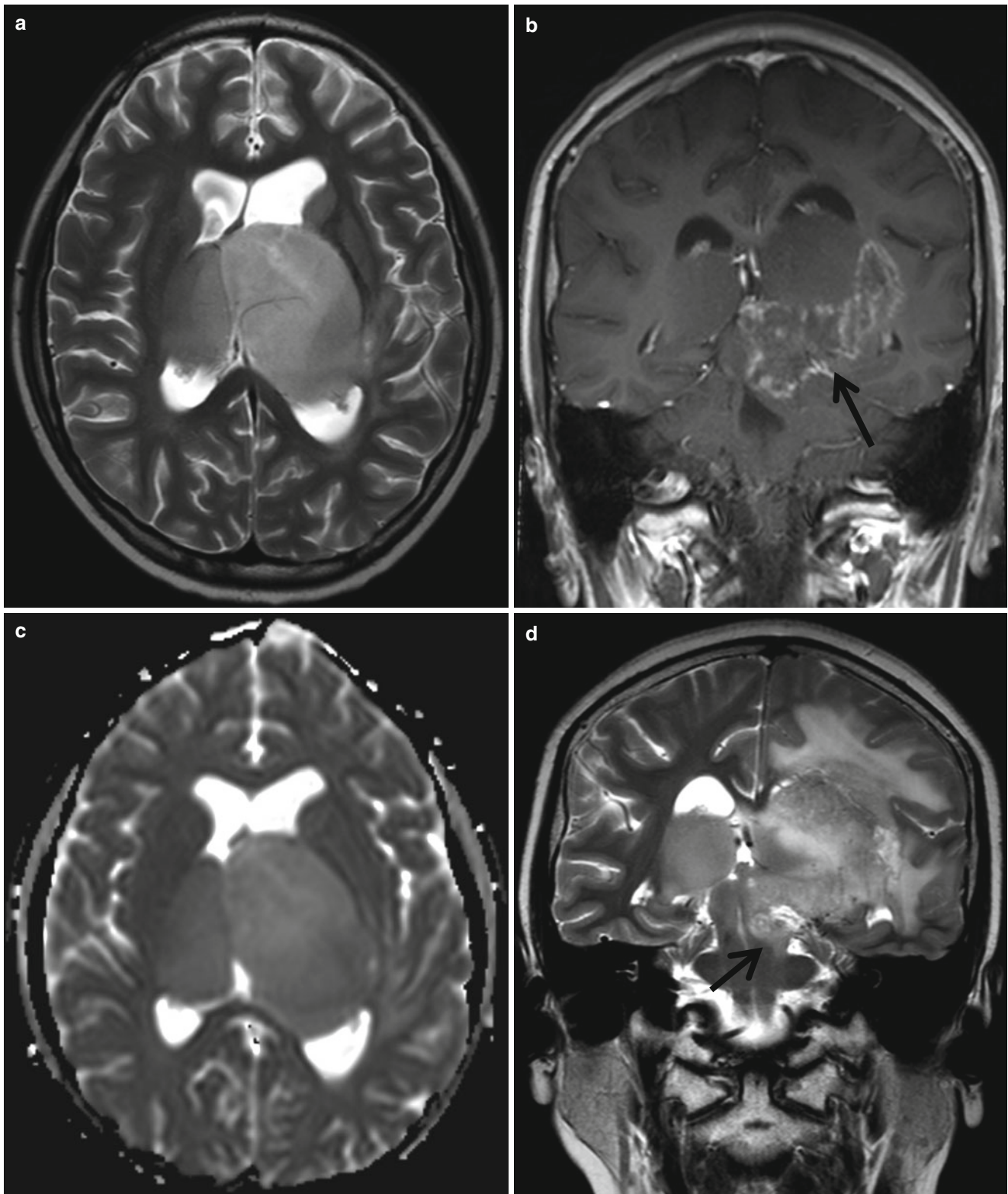


Fig. 4.14 Anaplastic astrocytoma involving bilateral thalami. (a) Bilateral thalamic mass causing enlarged thalami are seen on T2-weighted image. (b) Focal heterogeneous enhancement (arrow) is noted on postcontrast coronal image. (c) The mass exhibits iso-signal

intensity of ADC map. (d) Coronal T2-weighted image obtained 7 months later reveals progressed tumor extension into the brain stem (arrow) and extensive peritumoral edema

4.3.1.2.2 Subependymal Giant Cell Astrocytoma

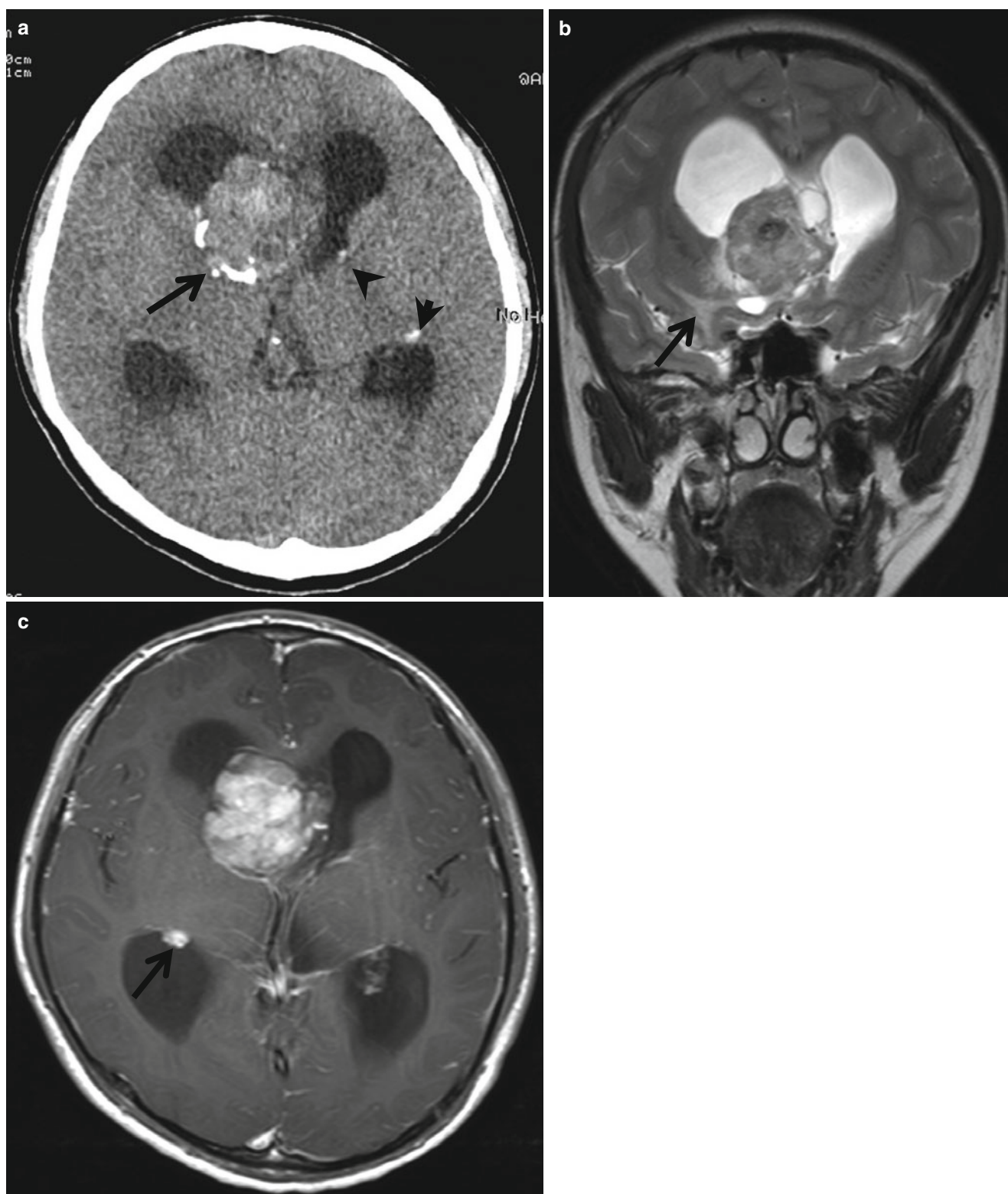


Fig. 4.15 Giant cell astrocytoma in a patient with tuberous sclerosis. (a) Precontrast CT scan shows lobulating mass with calcification (arrow) at the right foramen of Monro resulting in ventricular distension. Multiple subependymal calcified nodules are noted (arrowheads), suggesting tuberous sclerosis. (b) The mass shows slightly high intensity, containing dark spots associated with mild peritumoral edema on a

T2-weighted coronal image. Focal subcortical high-intensity lesion of adjacent right temporal lobe (arrow) is considered to be a subcortical tuber. (c) Postcontrast axial image shows heterogeneous tumor enhancement. Another small high-intensity subependymal nodule is seen in the right temporal horn (arrow)

4.3.1.2.3 Gangliomas and Gangliocytomas

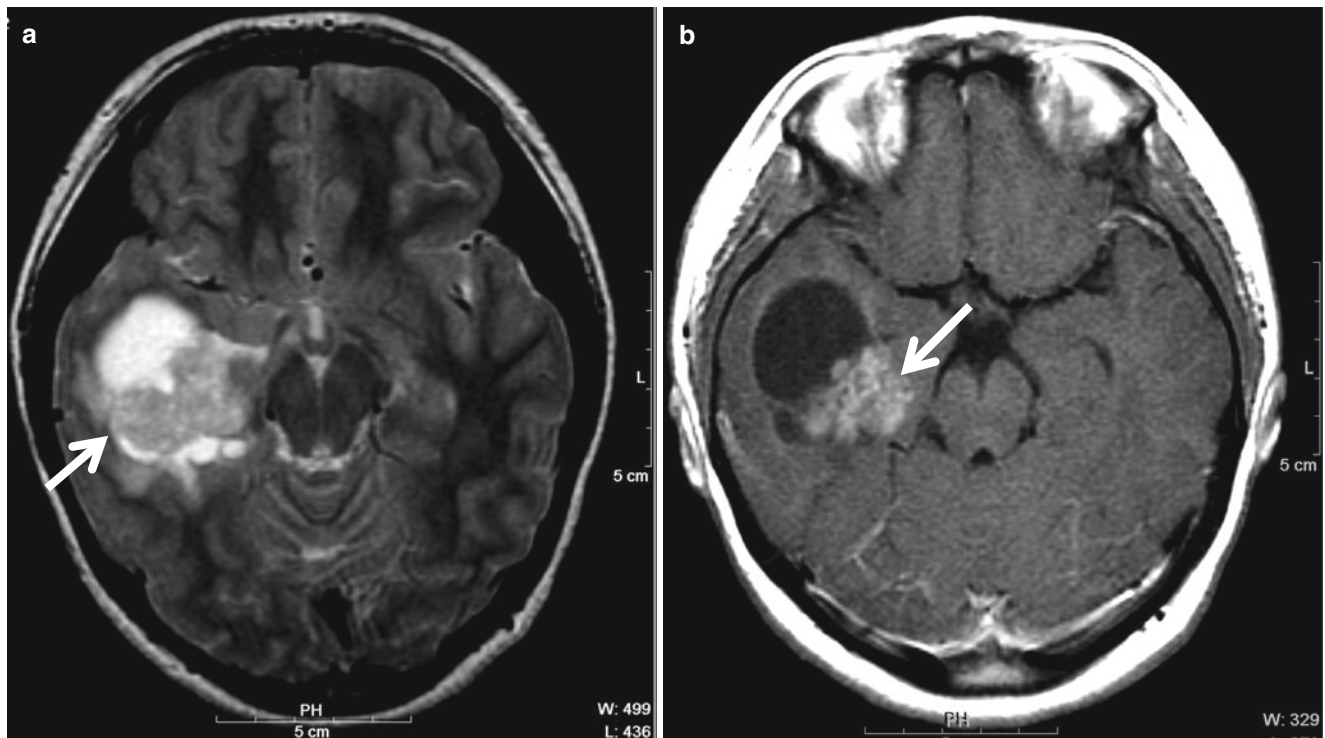


Fig. 4.16 Ganglioglioma in a 13-year-old girl. **(a)** T2-weighted image shows solid and cystic mass in the right temporal lobe (*arrow*). **(b)** The solid portion is heterogeneously enhanced (*arrow*), surrounded by mild edema on a postcontrast image

4.3.1.2.4 Dysembryoplastic Neuroepithelial Tumors

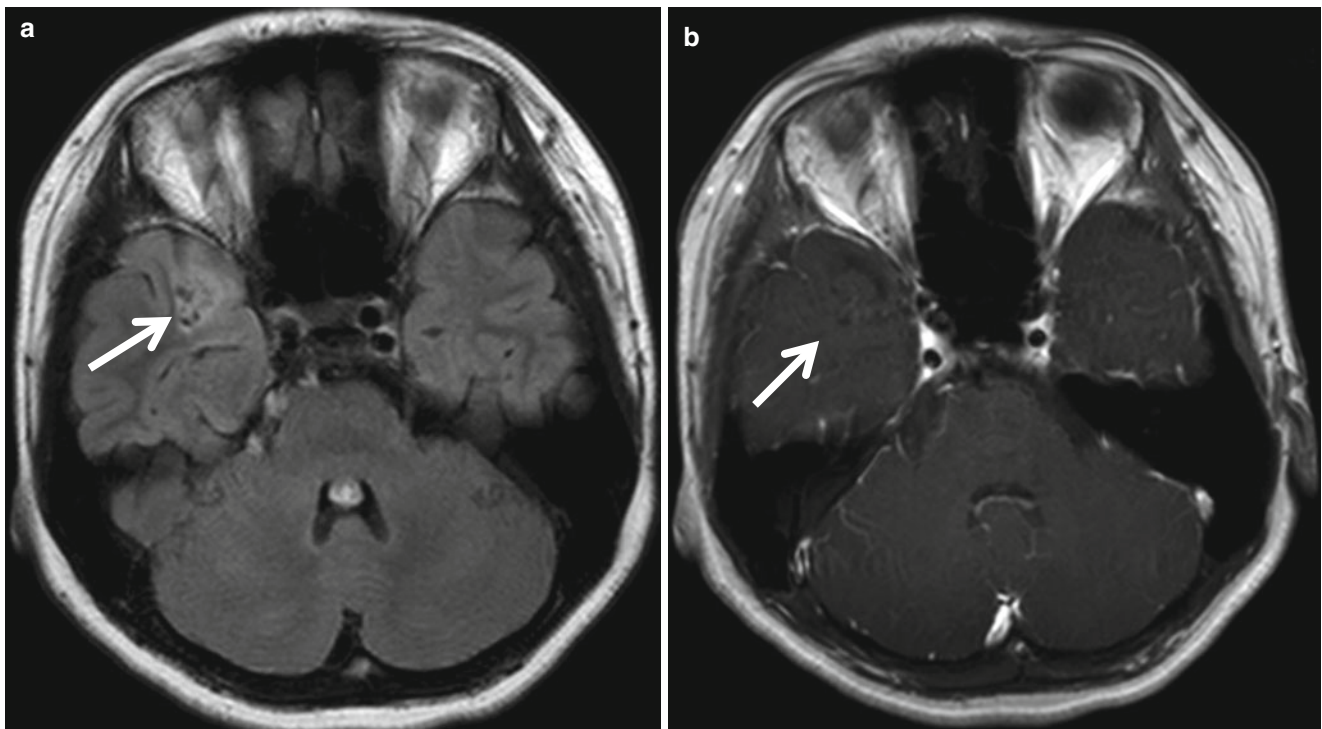


Fig. 4.17 Dysembryoplastic neuroepithelial tumor (DNET) associated with adjacent focal cortical dysplasia in a 14-year-old girl. **(a)** FLAIR image shows localized high-intensity lesion containing multiple tiny

cysts (*arrow*) in the right temporal lobe. Subtle hyperintensity is also noted at the adjacent cortex. **(b)** The lesion (*arrow*) is not enhanced on a postcontrast axial image

4.3.1.2.5 Supratentorial Ependymoma

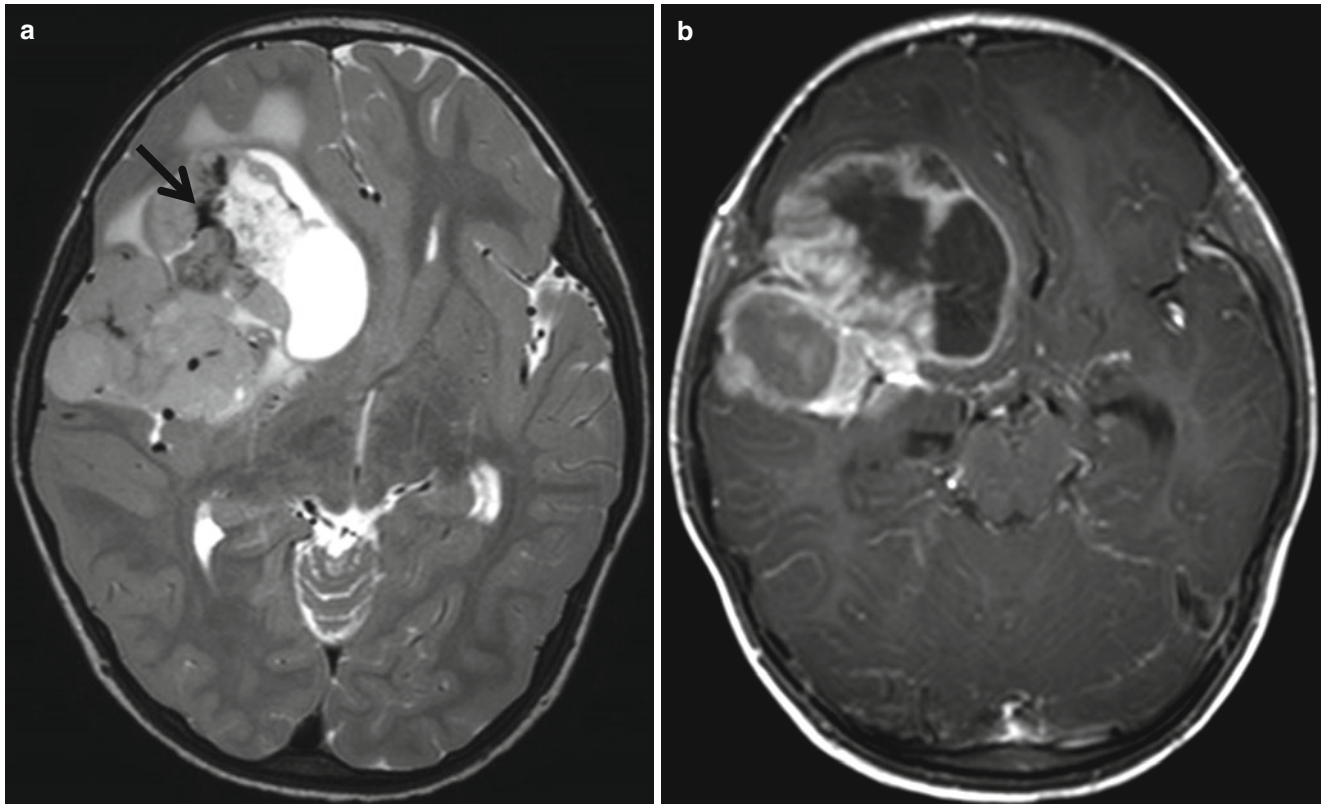


Fig. 4.18 Supratentorial ependymoma in a 3-year-old boy. **(a)** T2-weighted image shows solid and cystic mass in the right fronto-temporal lobe. The mass contains dark intensity (*arrow*), suggesting

calcification, and surrounded by mild edema. **(b)** The solid portion and cystic wall are enhanced on a postcontrast image

4.3.1.2.6 Primitive Neuroectodermal Tumors (PNET)

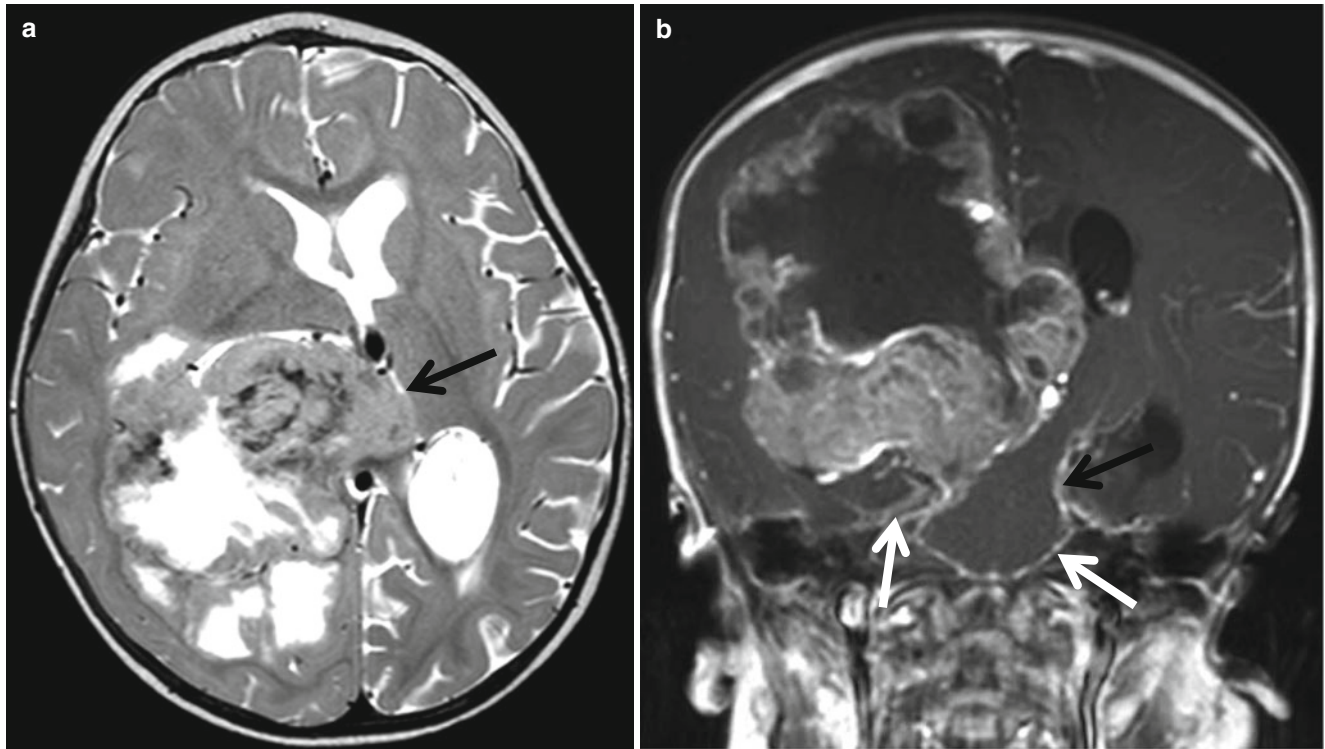


Fig. 4.19 Primitive neuroectodermal tumor (PNET) in a 1-year-old boy. (a) T2-weighted image shows large mass (*arrow*) containing necrosis and calcification in the right occipital lobe and thalamus. The solid portions are isointense to gray matter. (b) Postcontrast coronal

image reveals enhancement of the peripheral solid portion of the tumor. Intense enhancement of surface of the brain (*arrows*) suggests tumor seeding

4.3.1.2.7 Atypical Teratoid/Rhabdoid Tumor

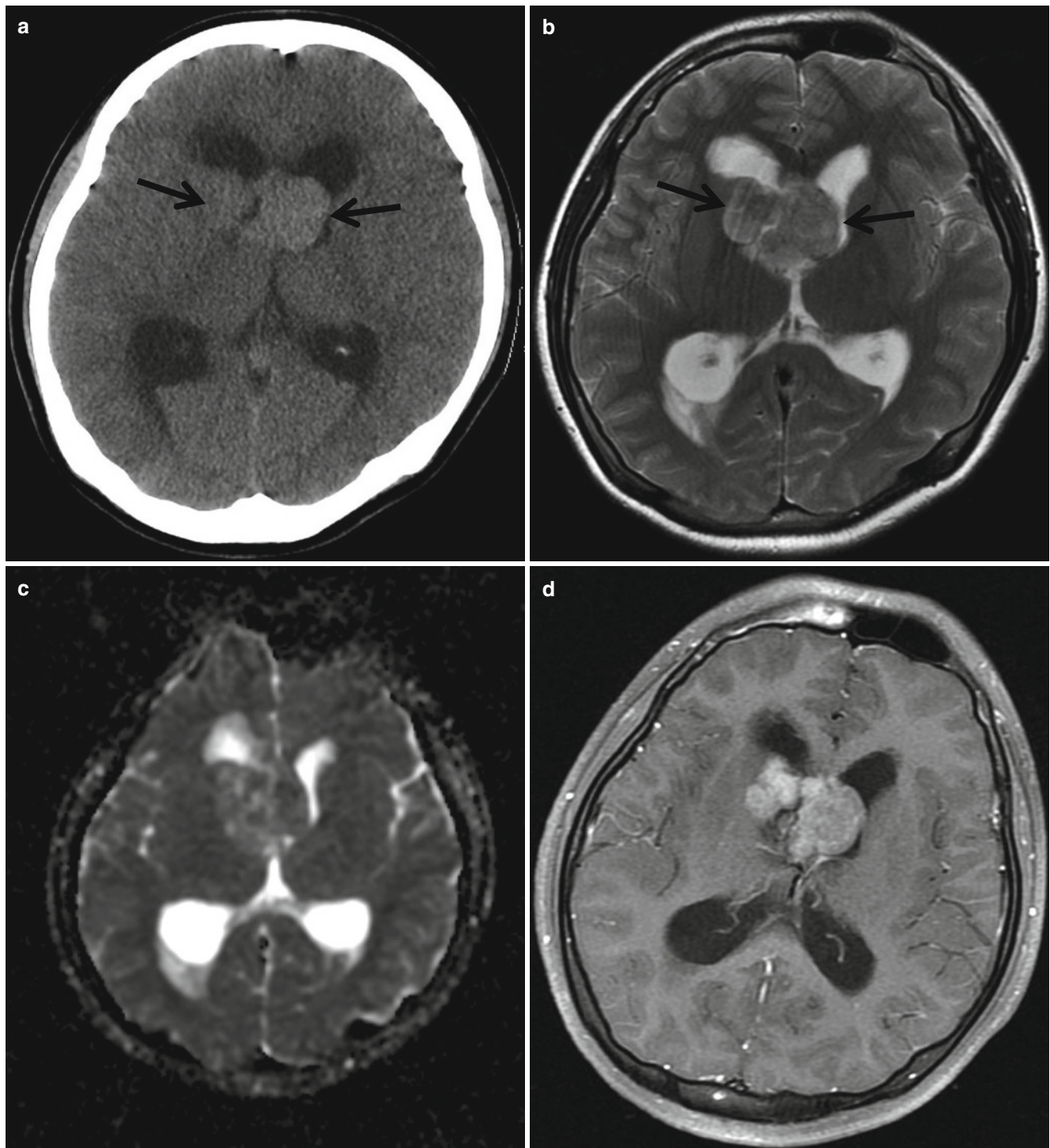


Fig. 4.20 Atypical teratoid/rhabdoid tumor (ATRT) in a 14-year-old boy. (a) CT scan shows lobulating high-density mass (*arrows*) at the foramen Monro causing hydrocephalus. (b) The mass (*arrows*) is

isointense on T2-weighted image. (c) The mass is isointense on ADC map, suggesting compact cellularity. (d) Postcontrast image reveals homogeneous enhancement of the tumor

4.3.1.2.8 Germ Cell Tumors

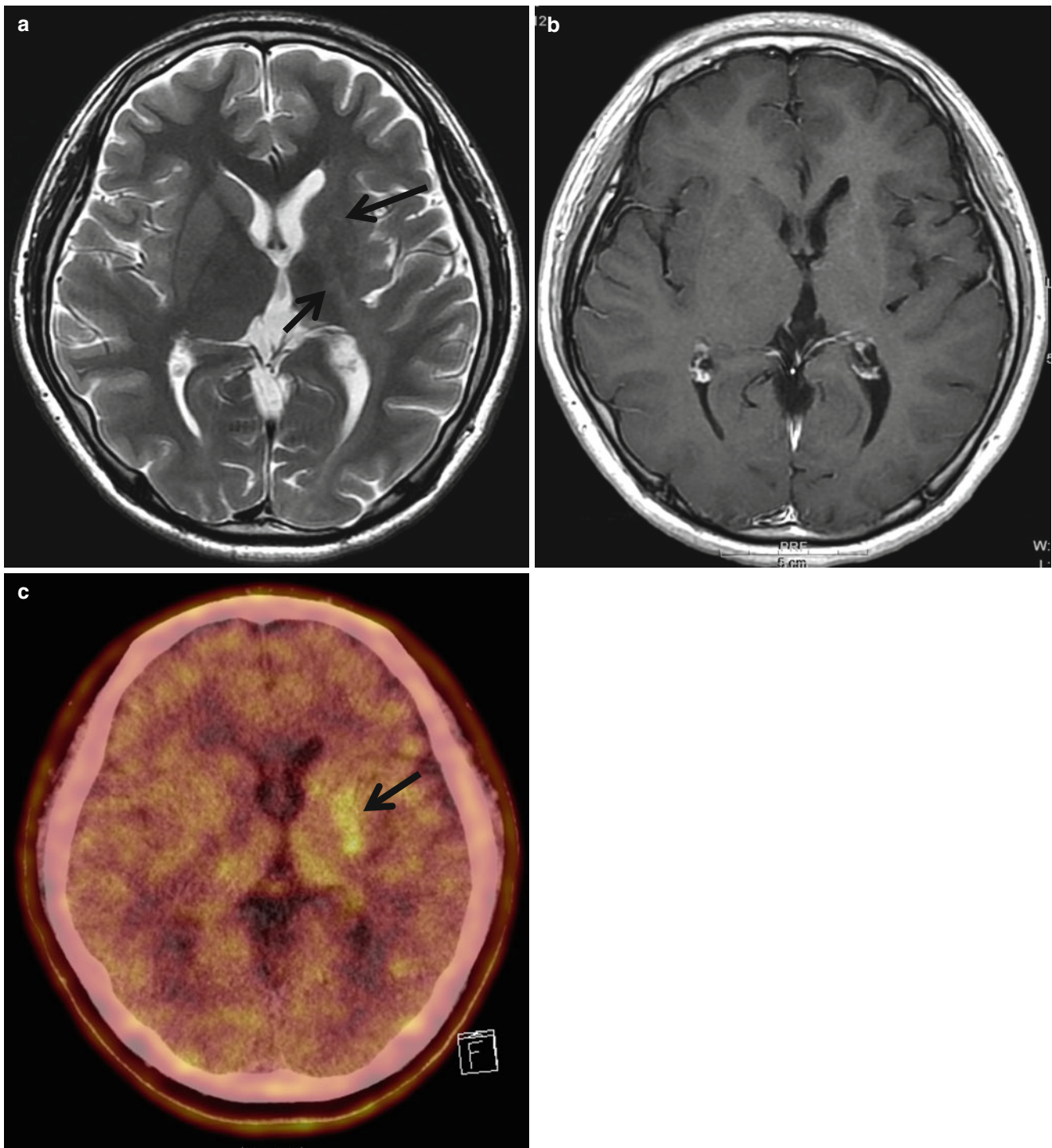


Fig. 4.21 Basal ganglia germinoma in a 14-year-old girl. (a) T2-weighted image shows subtle high-intensity lesion involving left internal capsule and basal ganglia (*arrow*), associated with ipsilateral atrophy of the basal ganglia and thalamus. (b) Postcontrast image

demonstrates no enhancing lesion. (c) Methionine PET scan reveals increased uptake of isotope at the left basal ganglia (*arrow*), suggesting active tumor involvement

4.3.1.3 Sellar and Juxtasellar Tumors

4.3.1.3.1 Hypothalamic/Optic Astrocytomas

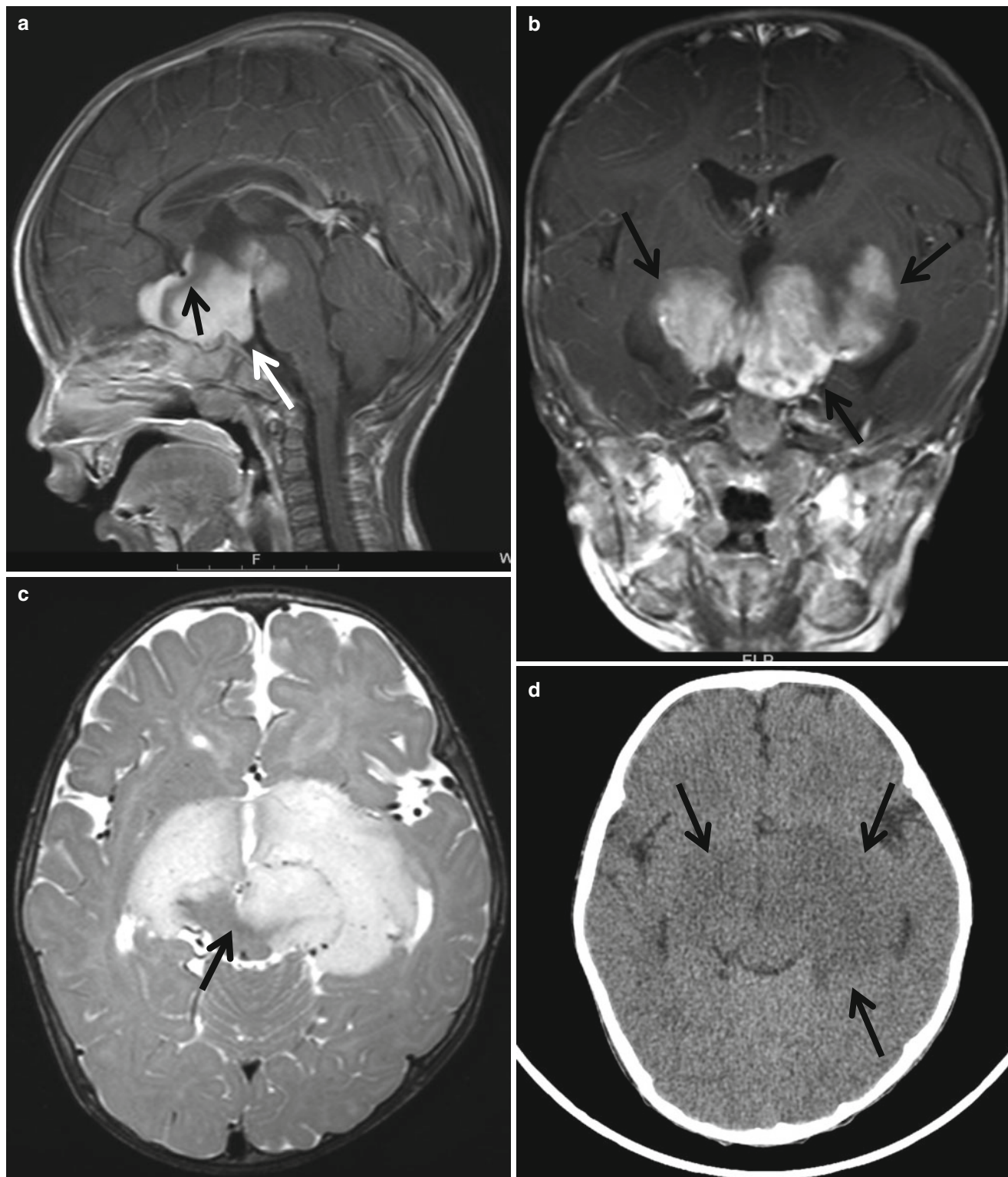


Fig. 4.22 Hypothalamic/optic glioma in a 7-month-old girl. (a) Postcontrast sagittal image shows a large enhancing mass involving suprasellar area extending to the preoptic cistern (*arrows*), third ventricle, and midbrain. Characteristic indentation by the anterior cerebral artery (*black arrow*) is noted. (b) Postcontrast coronal image reveals

chiasmatic hypothalamic mass extending to the bilateral thalami along the optic pathways. (c) The mass is bright on T2-weighted image extending to the optic radiations and to the brain stem (*arrow*). (d) Precontrast CT shows hypodense mass (*arrows*) compared to the normal parenchyma

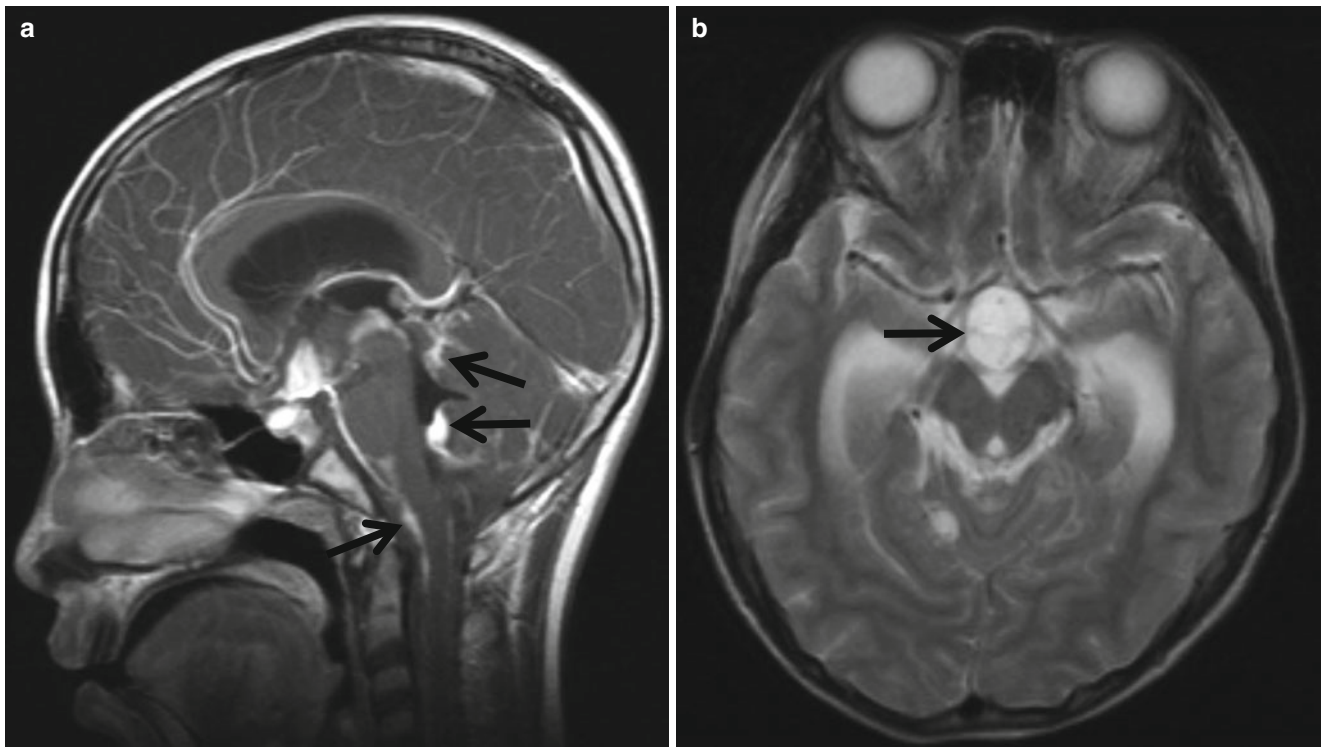


Fig. 4.23 Pilomyxoid astrocytoma with leptomeningeal dissemination. **(a)** Postcontrast sagittal image shows suprasellar enhancing mass and thick enhancement at the surface of the brain stem, cervical cord,

and cerebellum (*arrows*), suggesting tumor seeding along the CSF space. **(b)** The suprasellar mass is bright on T2-weighted image

4.3.1.3.2 Craniopharyngioma

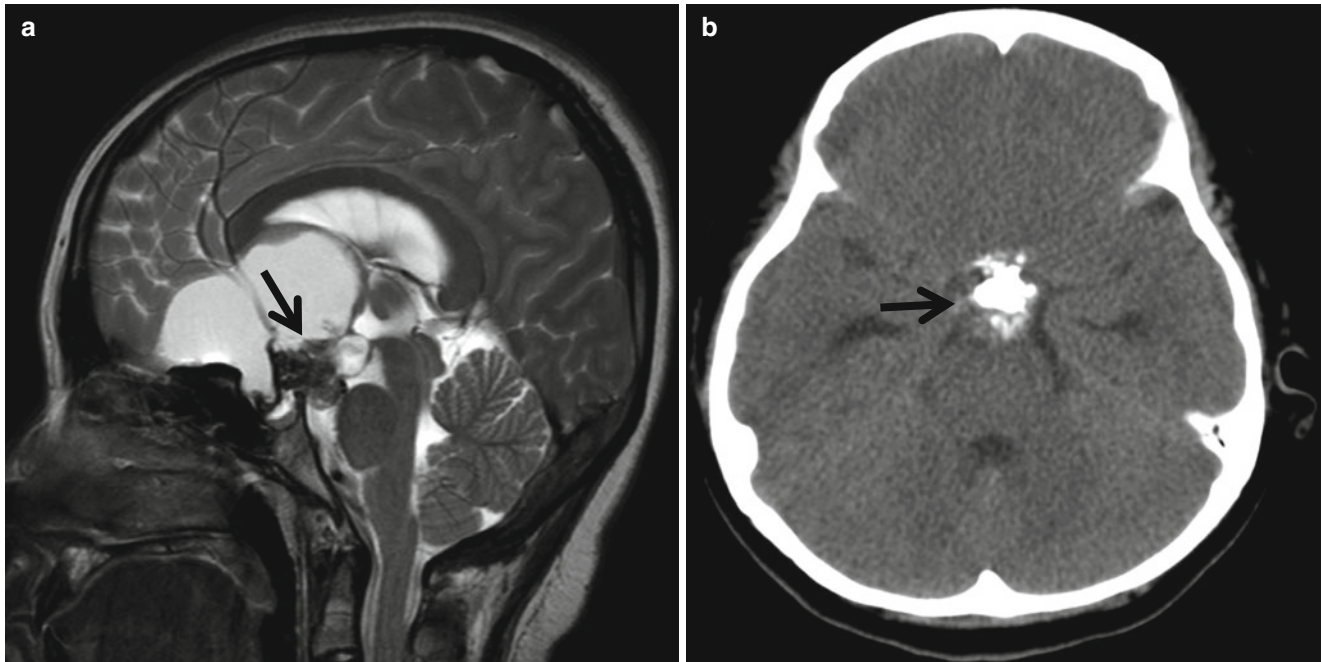


Fig. 4.24 Craniopharyngioma in a 15-year-old girl. (a) T2-weighted sagittal image shows large cystic and solid mass at the suprasellar area. Small solid portion is containing dark intensity (*arrow*), suggesting

hemorrhage or calcification. (b) CT scan demonstrates dense calcification of the mass (*arrow*)

4.3.1.3.3 Hypothalamic Hamartoma

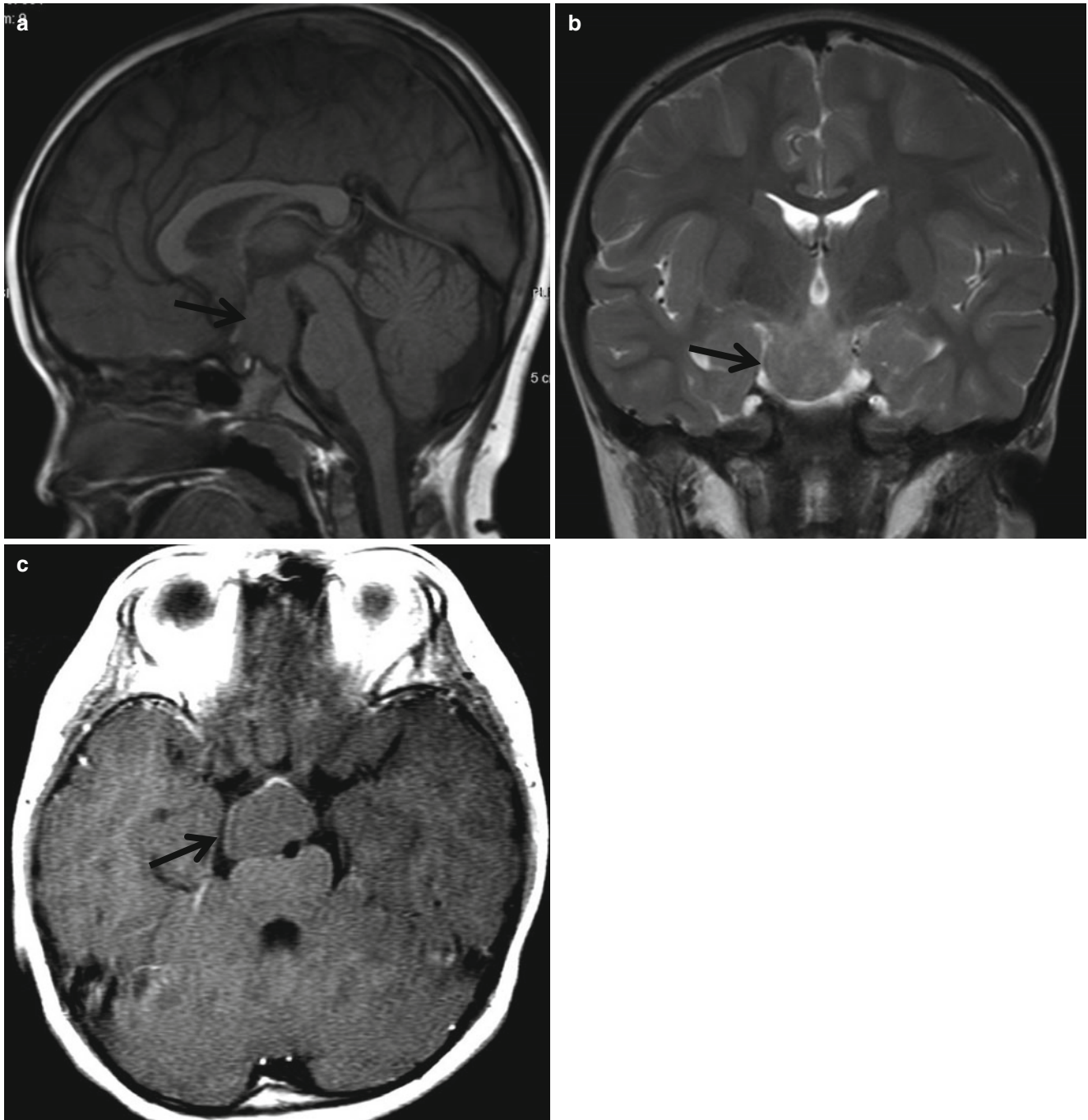


Fig. 4.25 Hypothalamic hamartoma. (a) Sagittal T1-weighted image shows isointensity mass (*arrow*) attached at the tuber cinereum of hypothalamus. (b) The lesion (*arrow*) is slightly high intensity on T2-weighted image. (c) Enhancement is not seen on a postcontrast image (*arrow*)

4.3.1.4 Pineal Region Tumors

4.3.1.4.1 Germ Cell Tumors

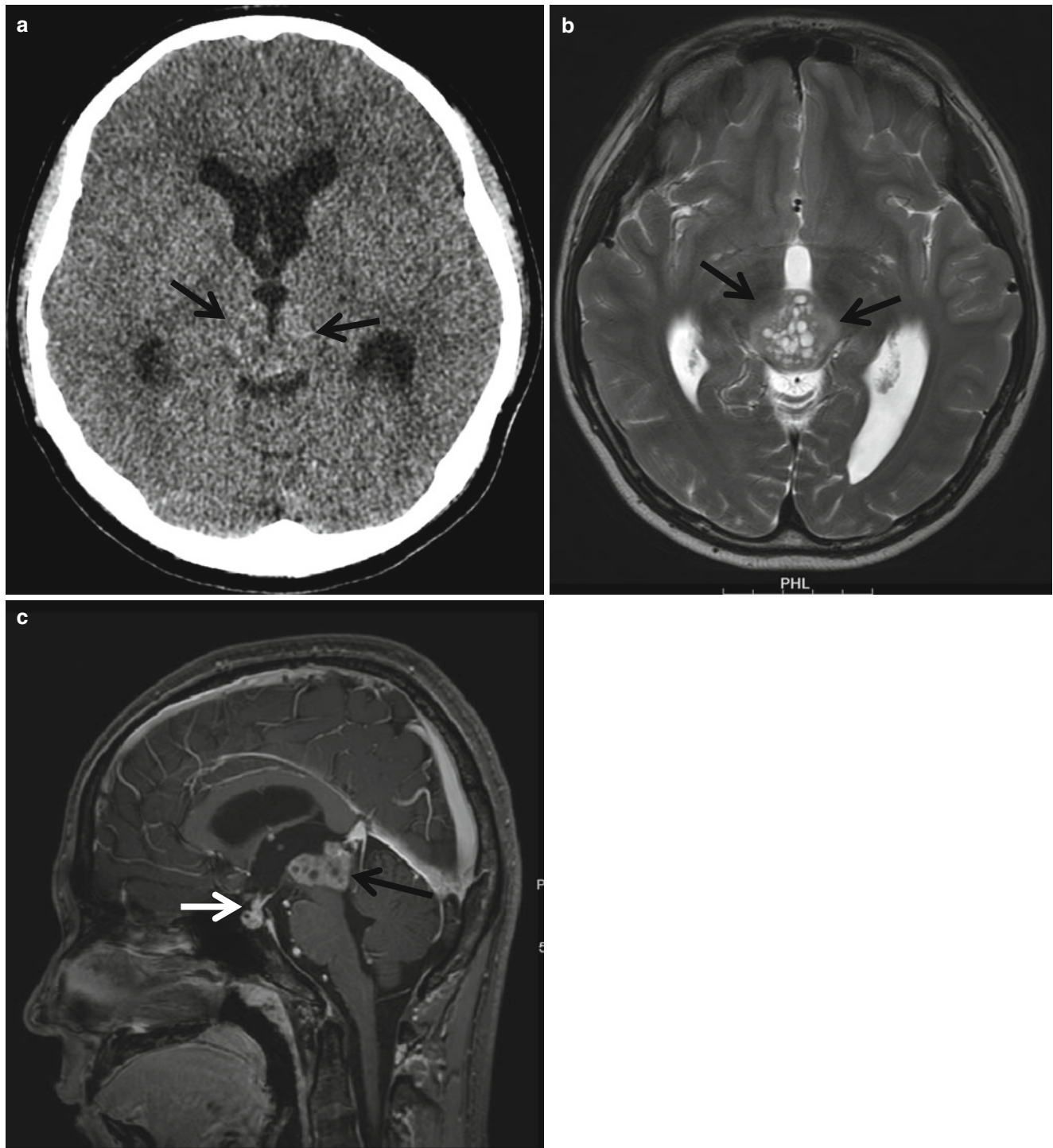


Fig. 4.26 Pineal and suprasellar germinoma in a 16-year-old boy. (a) CT scan shows isodense mass (*arrows*) at the pineal area. (b) T2-weighted image shows isointensity pineal mass (*arrow*)

containing small cysts. (c) Postcontrast sagittal image demonstrates enhancing mass in the pineal area (*black arrow*) and infundibulum extending to the sella (*white arrow*)

4.3.1.5 Other Pediatric Brain Tumors

4.3.1.5.1 Choroid Plexus Tumors

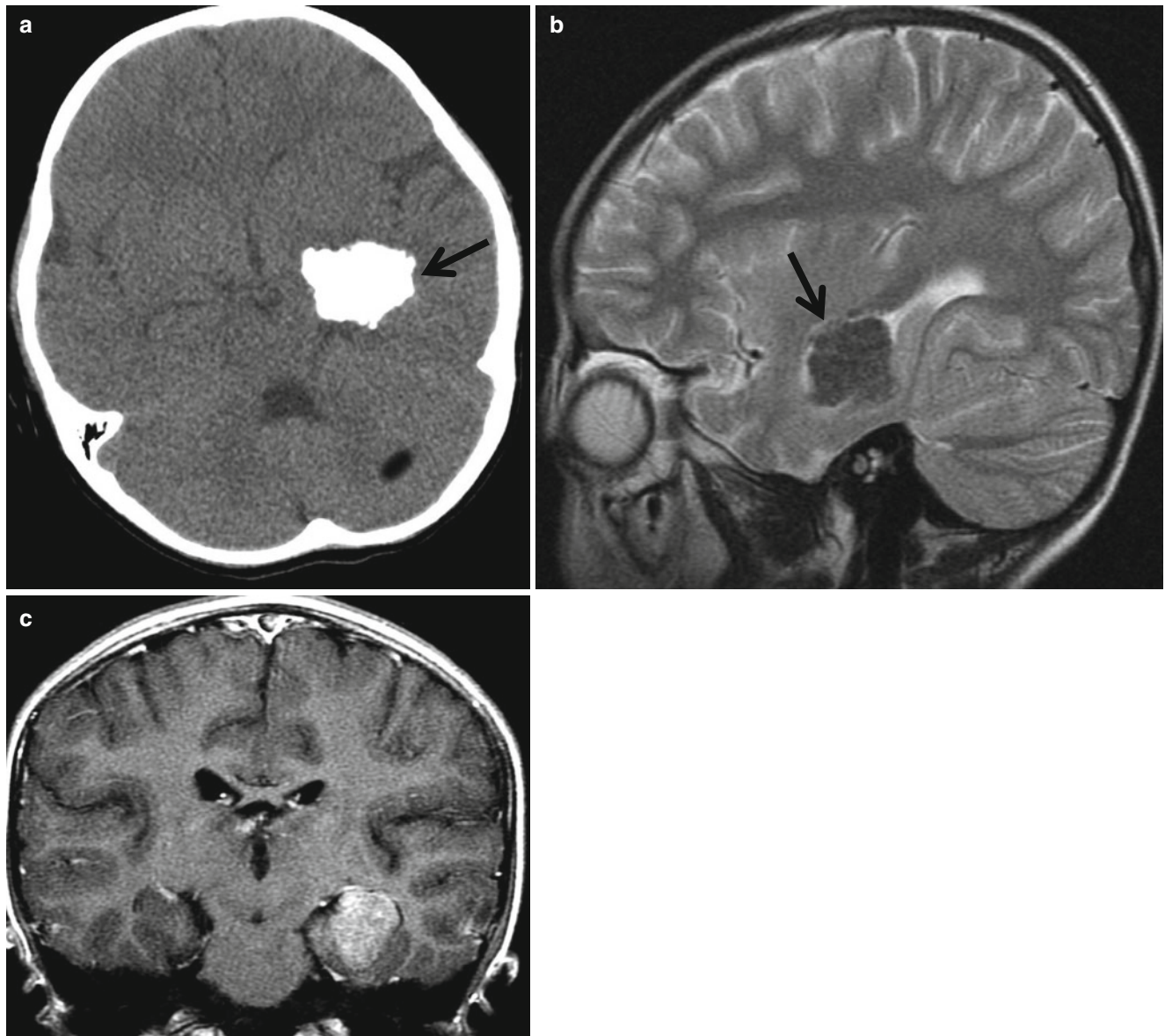


Fig. 4.27 Choroid plexus papilloma in a 6-year-old boy. (a) Precontrast CT shows densely calcified mass (*arrow*) in the left temporal lobe. (b) Sagittal T2-weighted image reveals hypointense mass within the temporal horn. (c) The mass is enhanced on a postcontrast image

4.3.1.5.2 Meningiomas

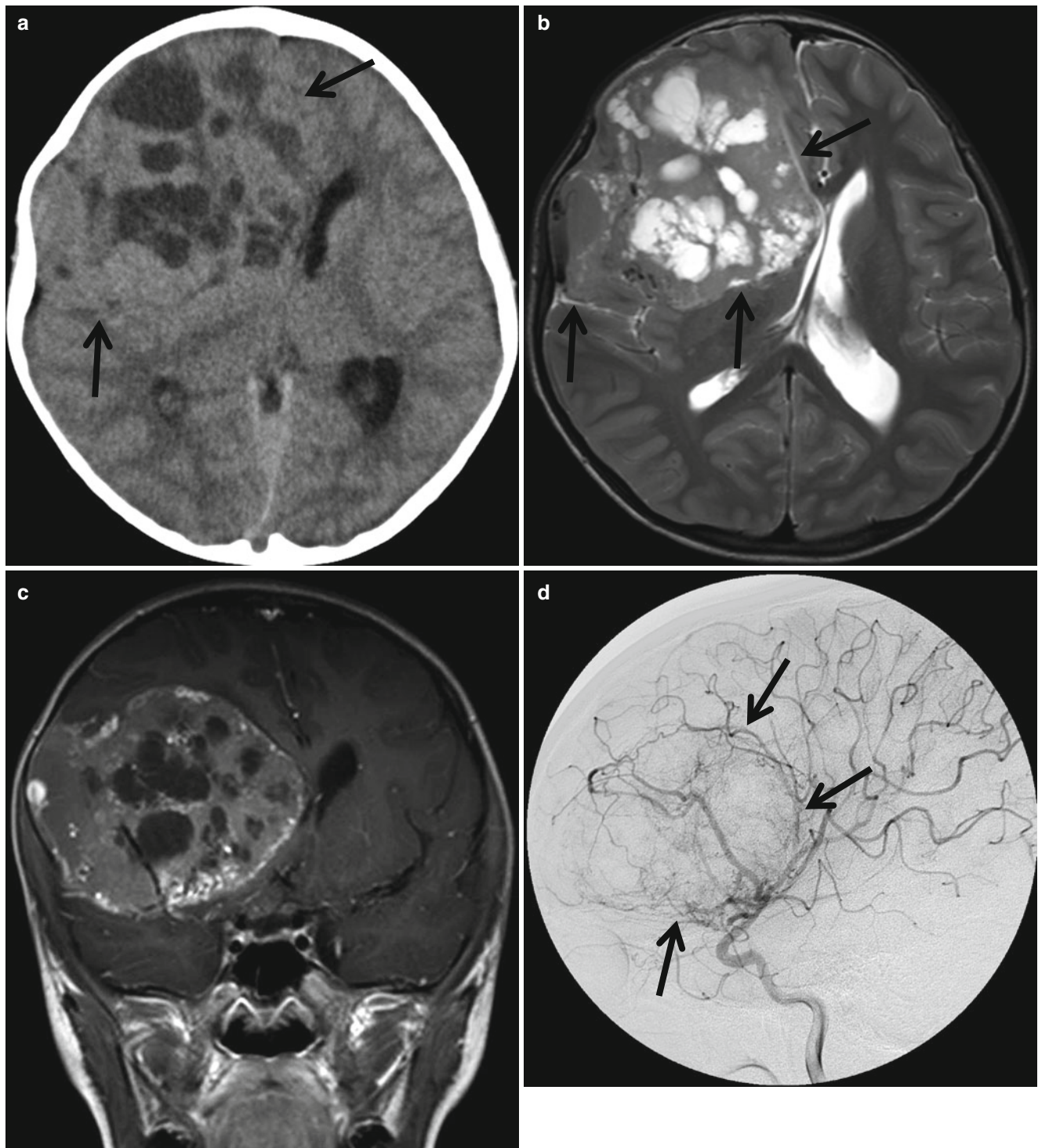


Fig. 4.28 Meningioma in a 17-year-old girl. (a) Precontrast CT shows a large isodense solid mass with cystic portions (arrows) in the right frontal lobe exerting mass effect. (b) The solid portion of the mass (arrows) exhibits isointensity to the gray matter on T2-weighted image. Demarcation of the mass is clear and thin CSF cleavage lines are seen

(arrows). The mass is assumed to arise from the ectopic dural rest in the Sylvian fissure. (c) The solid portions are well enhanced on a postcontrast image. (d) Angiography demonstrates tumor stain (arrows) supplied from the right internal cerebral artery mimicking intraparenchymal tumor. There was no tumor stain from the external carotid arteriography

4.3.1.5.3 Congenital Brain Tumors

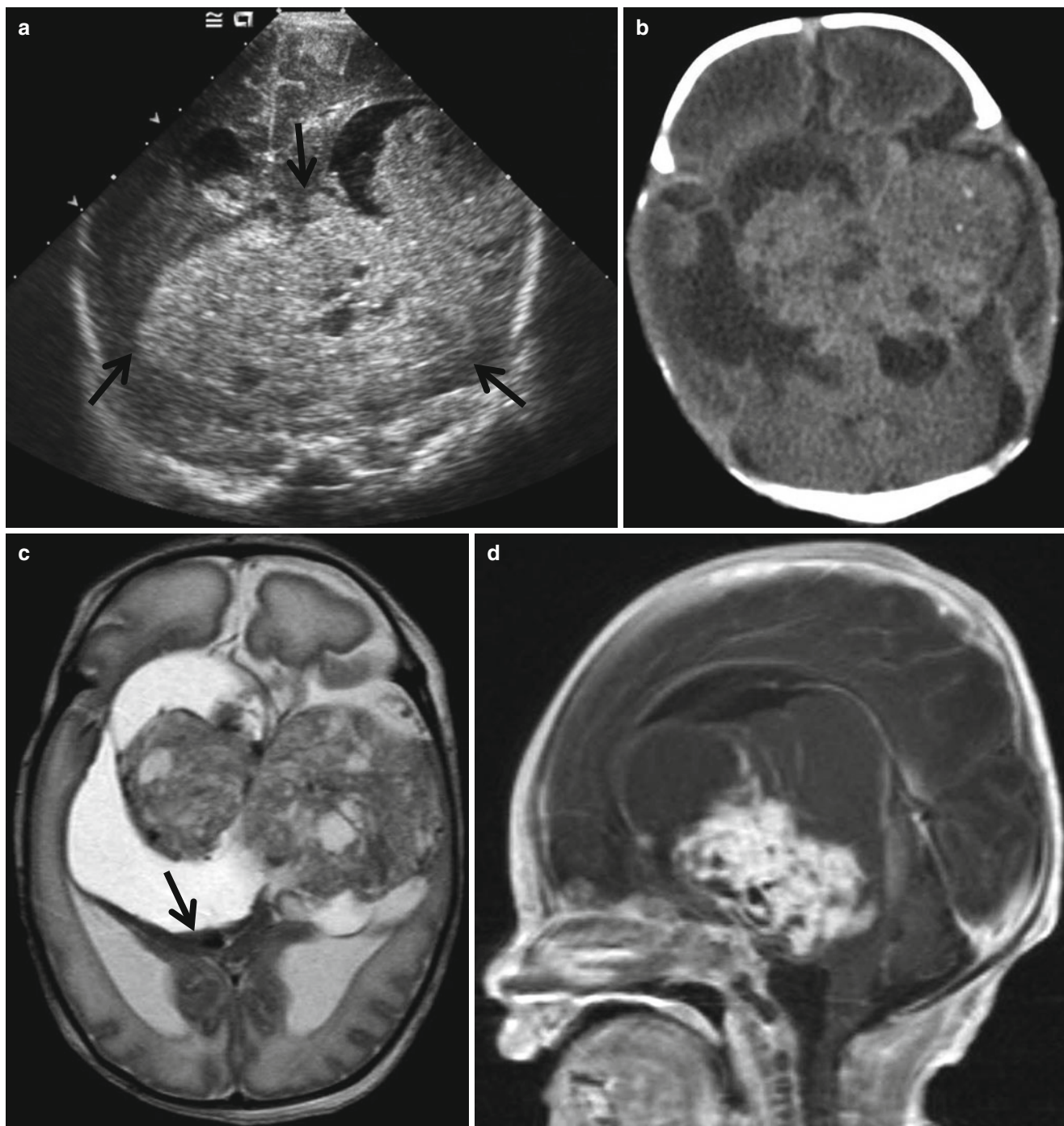


Fig. 4.29 Congenital immature teratoma in a neonate. (a) Brain sonography shows huge echogenic mass (arrows) with ventriculomegaly. (b) CT scan reveals a large solid and cystic mass with tiny calcifications occupying the central portion of the brain. (c) The solid portion is heterogeneously isointense on T2-weighted image containing signal

void suggesting hypervascular mass. Small amount of fluid level of dark signal intensity in the cyst (arrow) is suggesting hemorrhage. (d) Postcontrast sagittal image demonstrates strong enhancement of the solid portion

4.3.2 Neoplasms of the Spine

4.3.2.1 Intramedullary Tumors

4.3.2.1.1 Astrocytoma

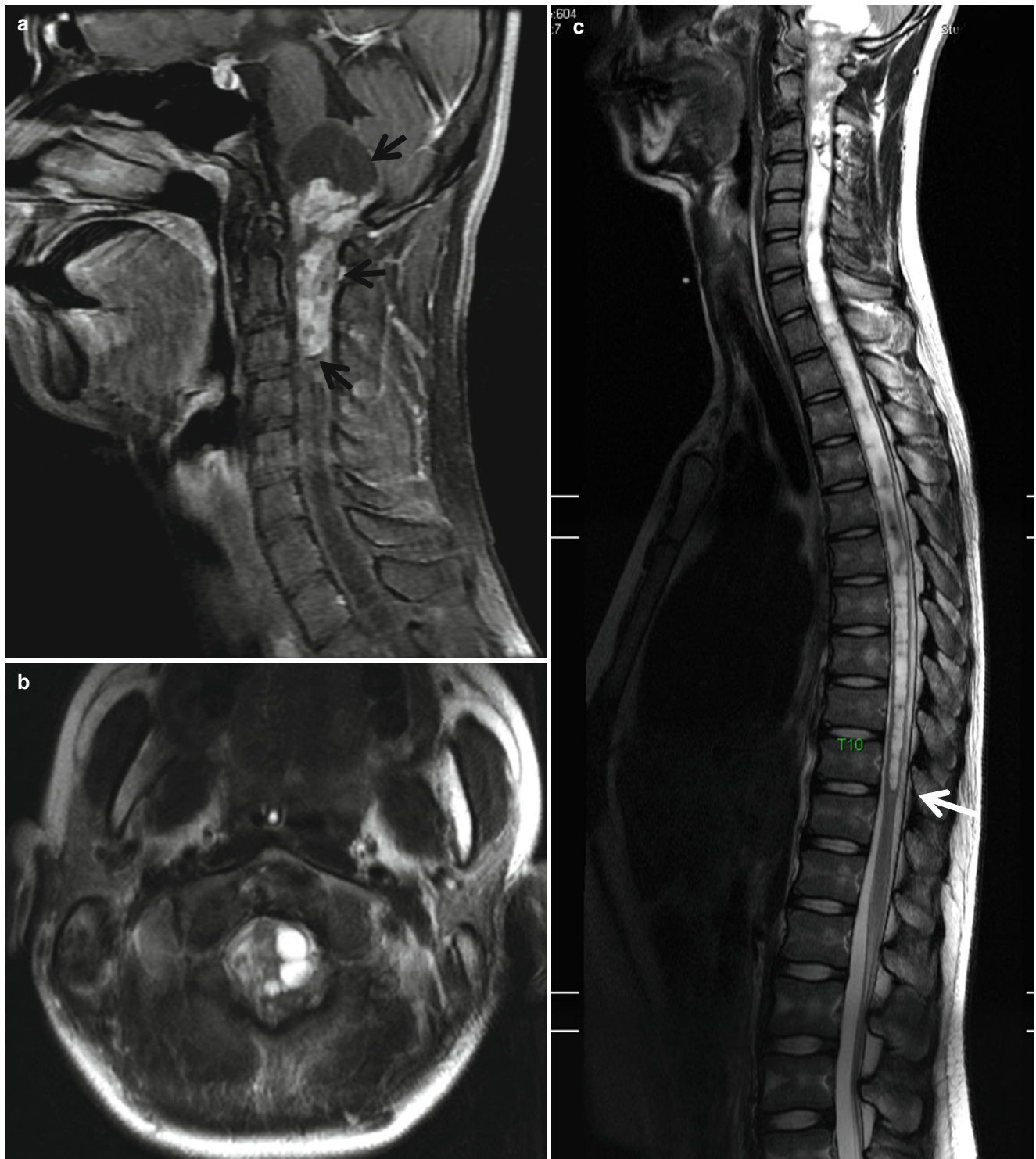


Fig. 4.30 Pilocytic astrocytoma of the cervical spinal cord and brain stem. (a) Postcontrast sagittal image shows solid and cystic mass (arrow) involving the cervical spinal cord and brain stem. (b) The mass

markedly expands the cervical cord containing eccentric cyst on T2-weighted axial image. (c) Whole spine sagittal image reveals extensive hydrosyrinx down to the level of the lower thoracic cord (arrow)

4.3.2.1.2 Ependymoma

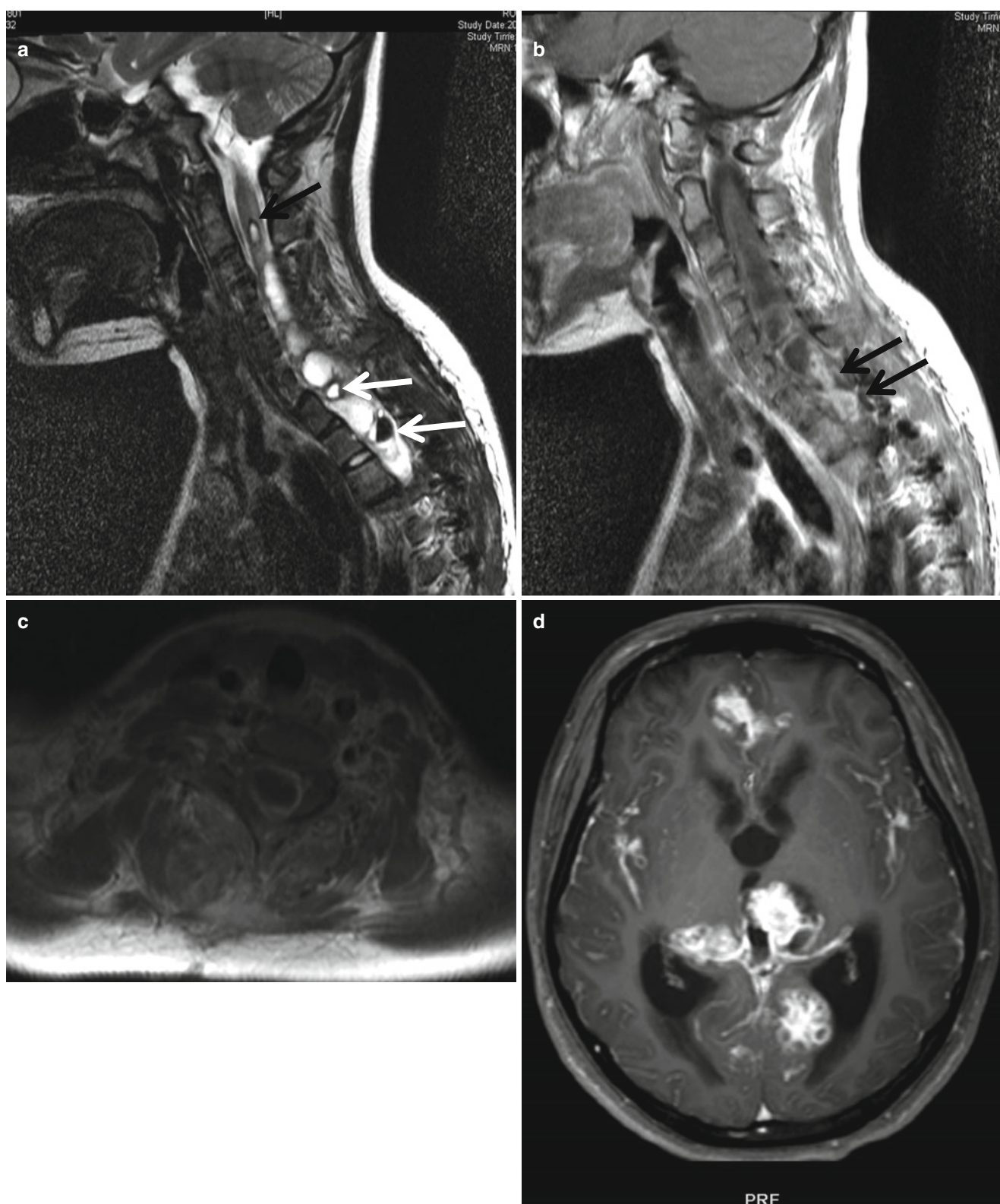


Fig. 4.31 Anaplastic ependymoma with CSF dissemination. (a) T2-weighted sagittal image demonstrates multicystic mass involving long segmental cervicothoracic cord. Lower spinal cavity is not visualized due to scoliotic curvature of the spinal column. Dark uppermost cystic wall (arrow) as well as multiple fluid levels within the cysts

(white arrows) suggest hemorrhage. (b) Intense contrast enhancement (arrows) is seen at the solid portions on postcontrast sagittal image. (c) Postcontrast axial image demonstrates cystic wall enhancement. (d) Postcontrast axial image of the brain reveals extensive tumor dissemination in the subarachnoid space

4.3.2.2 Intradural Extramedullary Tumors

4.3.2.2.1 Neurogenic Tumors

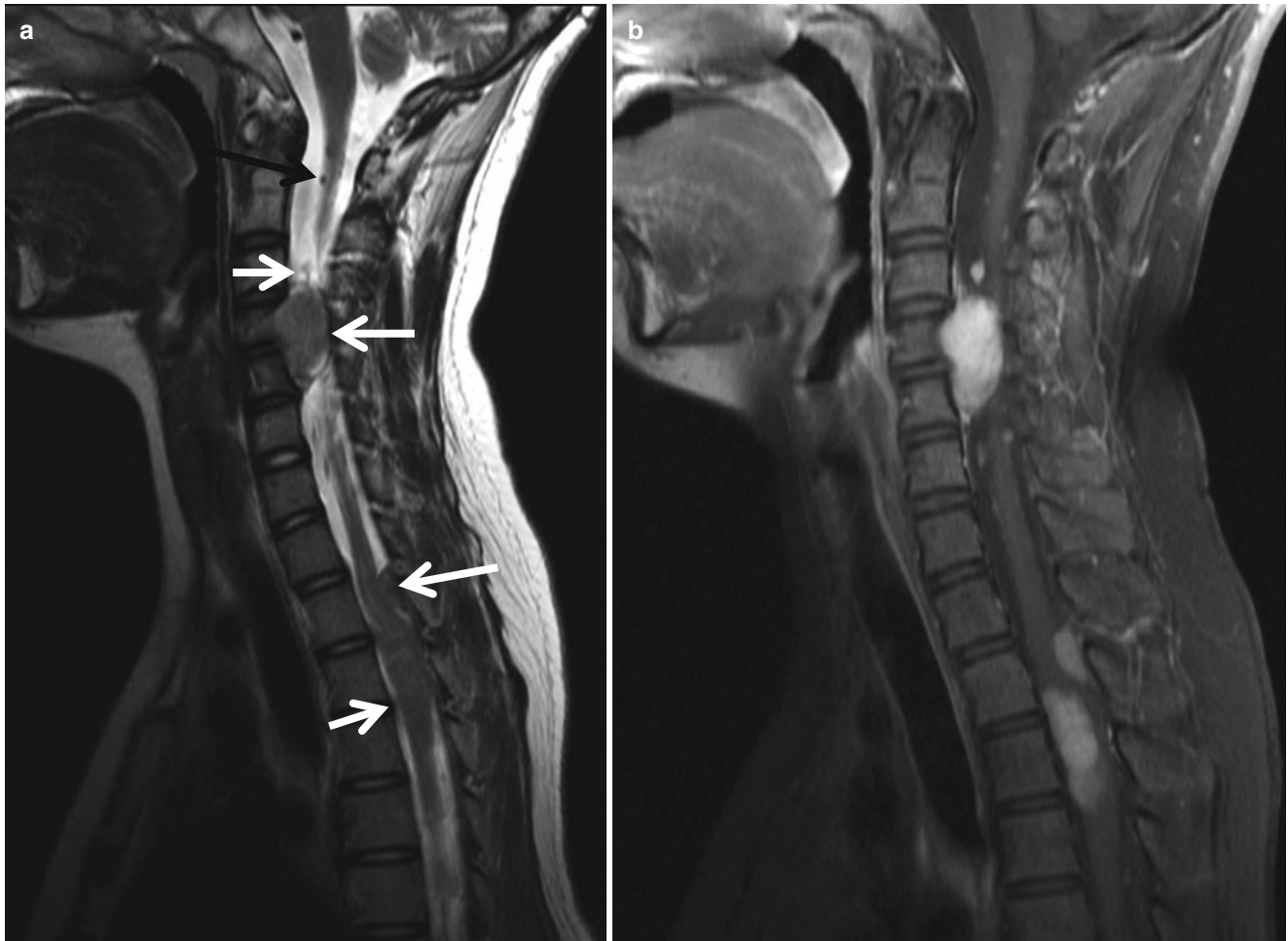


Fig. 4.32 Multiple schwannomas in a patient with type 2 neurofibromatosis. **(a)** T2-weighted sagittal image shows multiple IDEM masses of isointensity (*arrows*). The masses are scalloping the posterior surface

of the vertebra, and the spinal cord is displaced or compressed. **(b)** Postcontrast image reveals strong enhancement of the masses

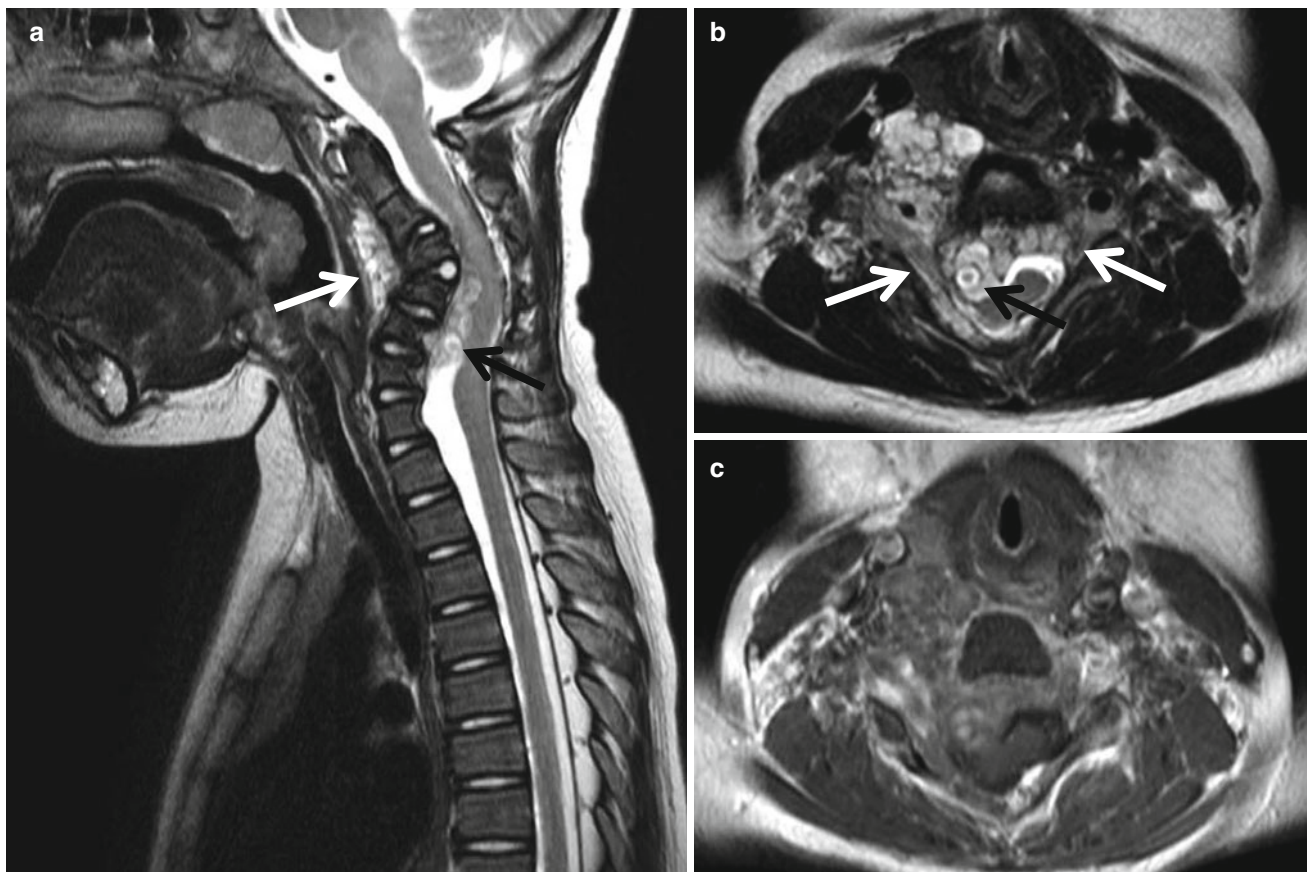


Fig. 4.33 Plexiform neurofibromas in a patient with type 1 neurofibromatosis. (a) T2-weighted sagittal image shows heterogeneous mass (*black arrow*) anterior to the cord with widening of the distal CSF space suggesting IDEM in location. In addition, adjacent kyphotic cervical spine and prevertebral mass (*white arrow*) were noted. Increased intensity of the compressed cord is suggesting myelopathy, and the medulla

is also involved by NF2. (b) T2-weighted axial image demonstrates both intra- and extradural lesions extending through the right neural foramina (*white arrows*). Central low intensity (*black arrow*) is a characteristic finding of neurofibroma. (c) The mass is heterogeneously enhanced on a postcontrast image

4.3.2.2.2 Neurenteric Cyst

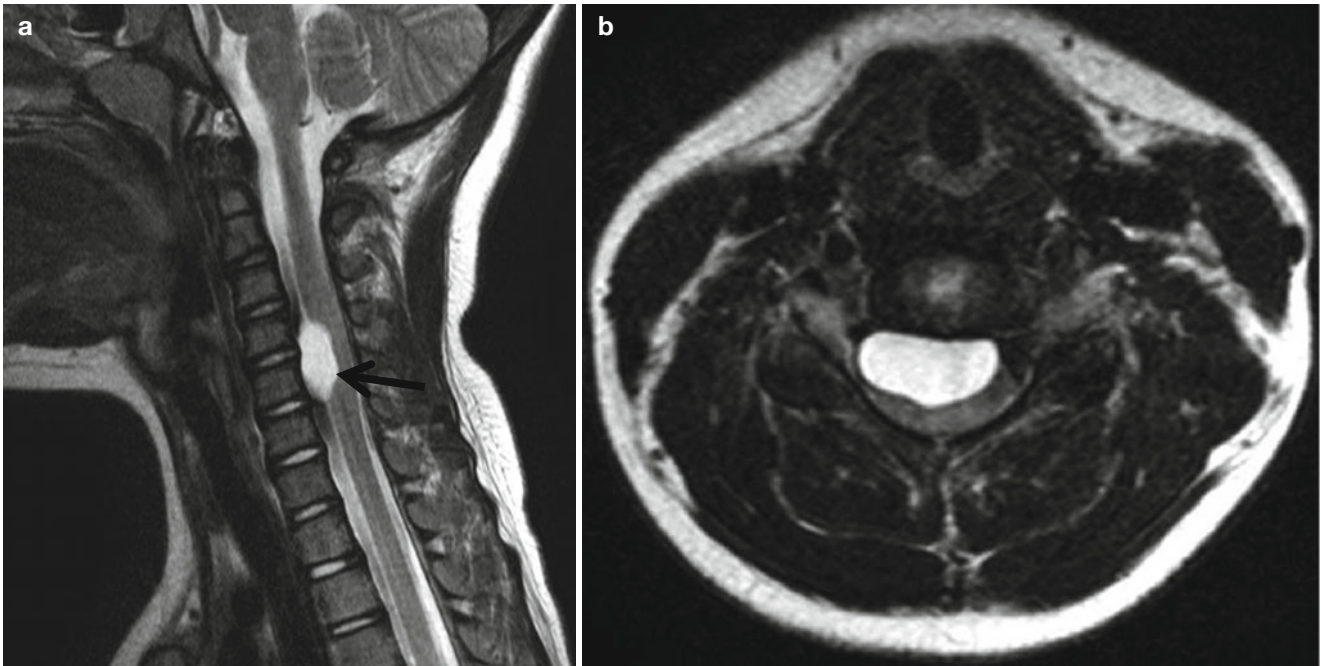


Fig. 4.34 Neurenteric cyst in a 3-year-old girl. (a) T2-weighted sagittal image demonstrates ovoid-shaped cyst (*arrow*), anteriorly located in the cervical spinal canal. (b) Axial image shows compressed cord by the mass

4.3.2.3 Extradural Tumors

4.3.2.3.1 Primitive Neuroectodermal Tumors (PNET)

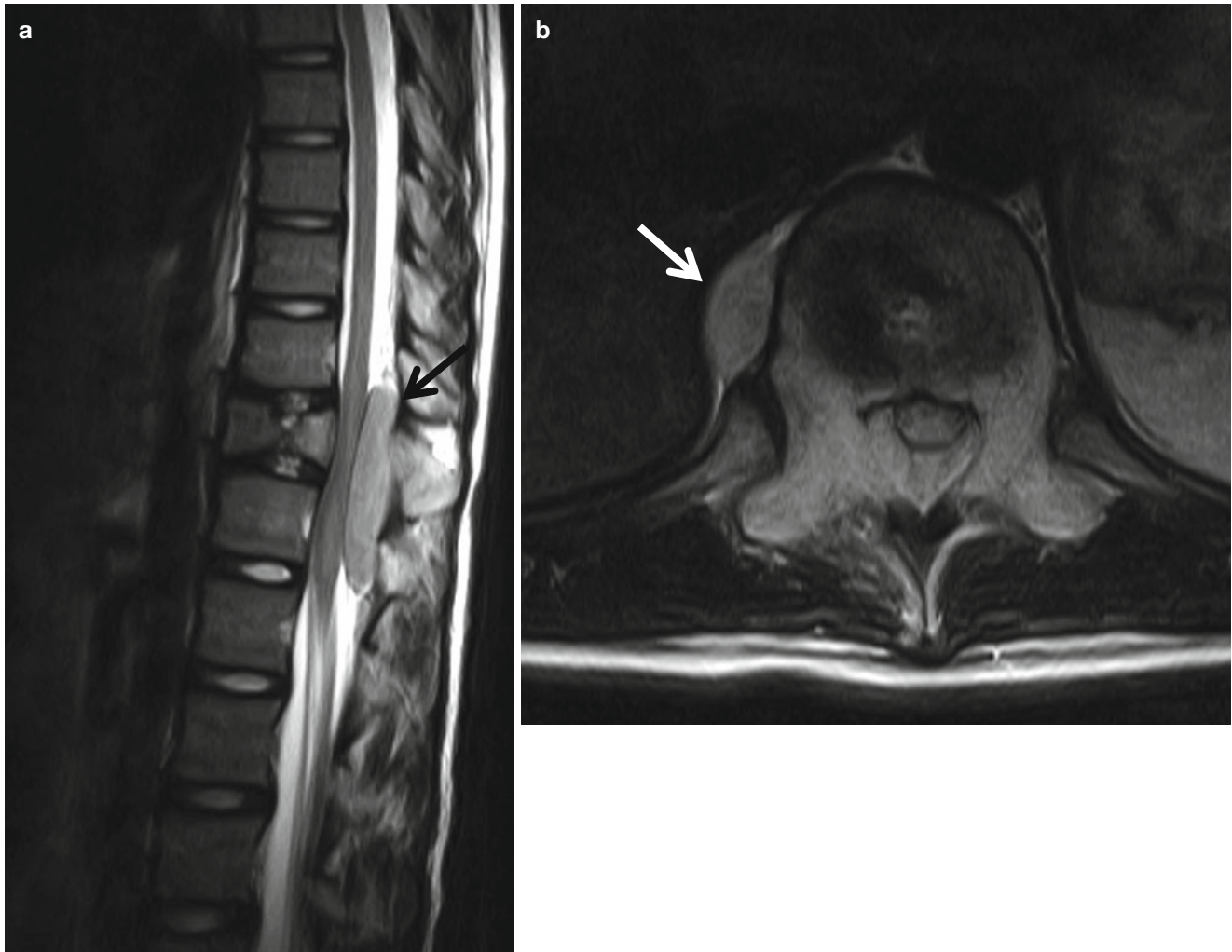


Fig. 4.35 PNET involving the spine forming epidural mass. (a) T2-weighted sagittal image demonstrates isointensity mass (*arrow*) posterior to the thoracic cord. T11 body is compressed, and posterior element is also involved. (b) Axial image at the level of T11 shows

tumor involvement of the body, pedicles, and spinous process forming epidural mass that is encasing dural sac. There is a small paraspinal mass (*arrow*)

4.3.2.3.2 Granulocytic Sarcoma

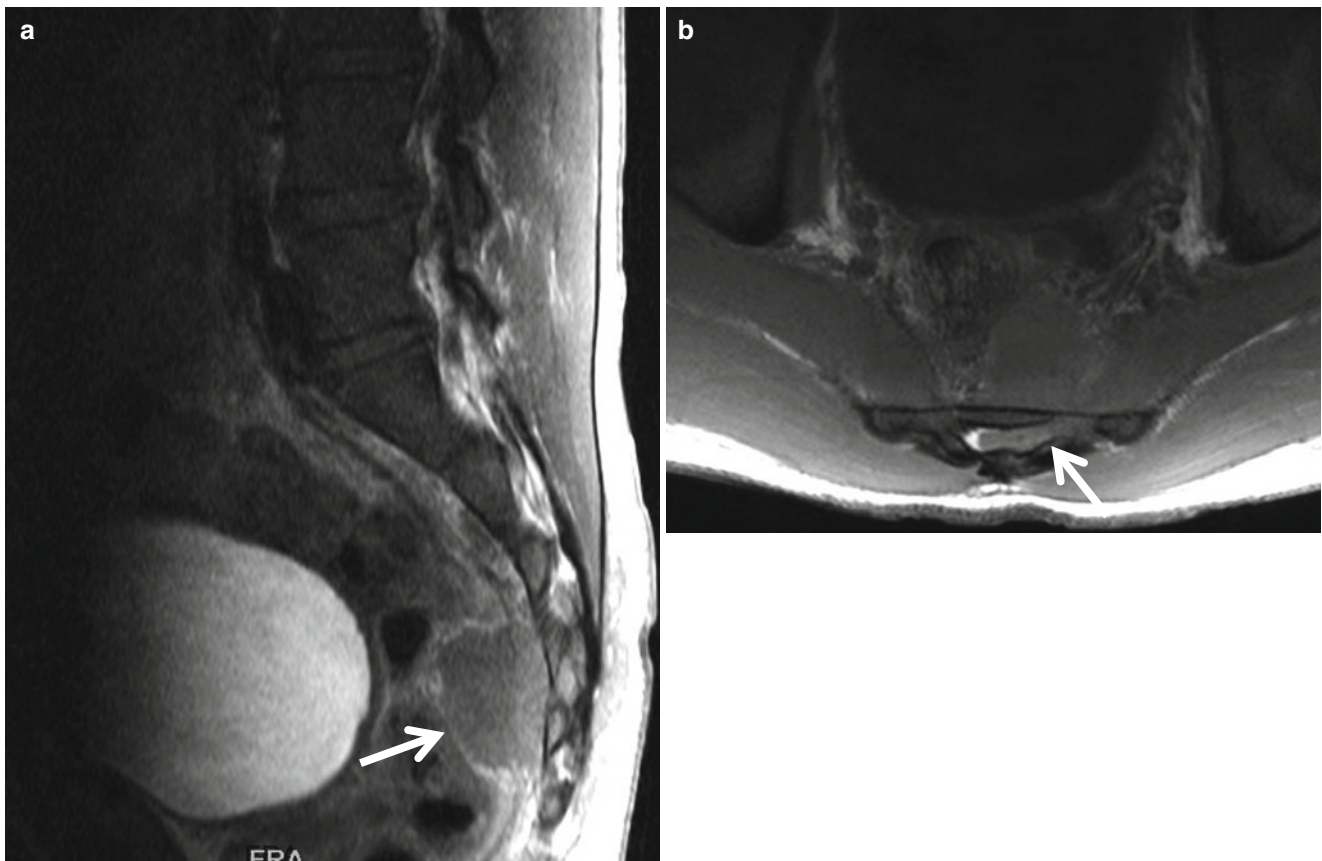


Fig. 4.36 Granulocytic sarcoma in a patient with acute myelocytic leukemia. **(a)** T2-weighted sagittal image shows well-defined presacral mass (*arrow*) exhibiting isointensity. **(b)** Presacral mass is enhanced

similar to the muscles extending through neural foramen into the spinal canal (*arrow*) on a postcontrast axial image

4.3.2.3.3 Langerhans Cell Histiocytosis

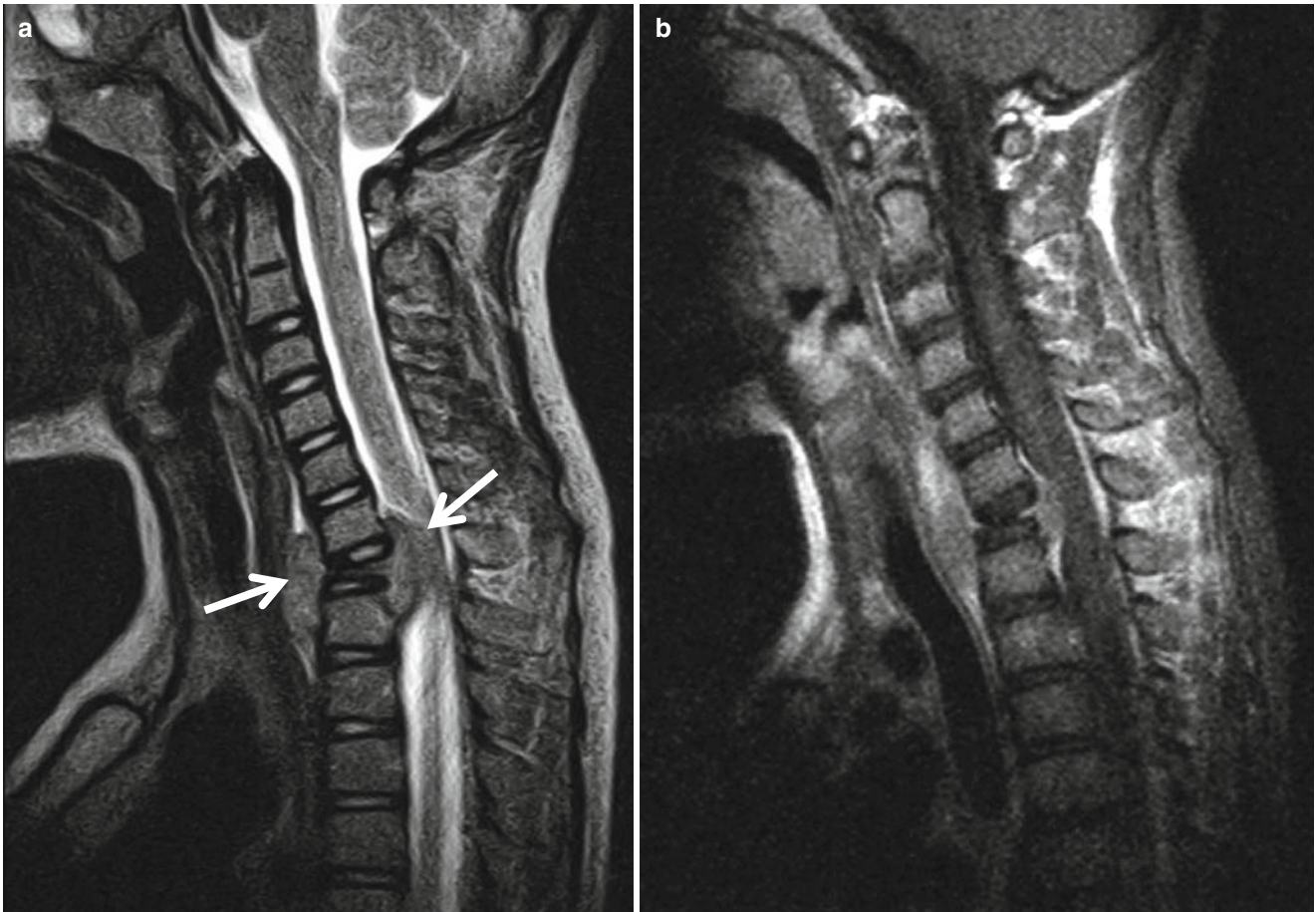


Fig. 4.37 Langerhans cell histiocytosis forming epidural mass. (a) T2-weighted sagittal image shows flat C7 vertebra associated with epidural and prevertebral masses (*arrows*) of iso-signal intensity. (b) The soft tissue masses are enhanced on a postcontrast image

4.3.2.3.4 Aneurysmal Bone Cyst

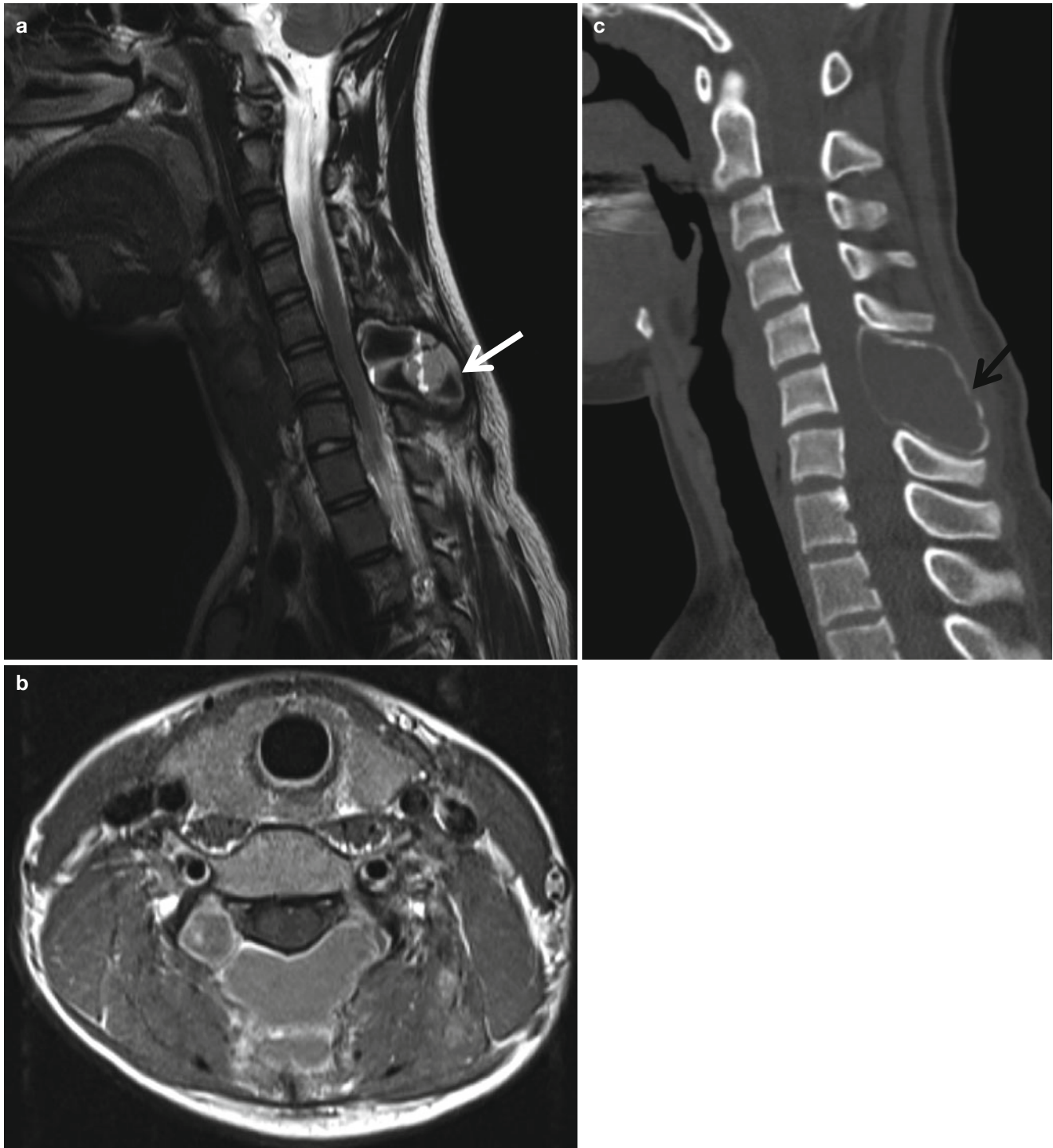


Fig. 4.38 Aneurysmal bone cyst involving spine. **(a)** T2-weighted sagittal image shows expansile cystic mass in the posterior neural arch of C6 (*arrow*). The lesion is multiseptated and contains fluid levels of

variable signal intensity suggesting hemorrhage. **(b)** Postcontrast axial image reveals expanded posterior arch with wall enhancement. **(c)** Sagittal reformatted CT scan reveals expansile bone cyst (*arrow*)

4.3.3 Miscellaneous

4.3.3.1 Functional MRI and Tractogram

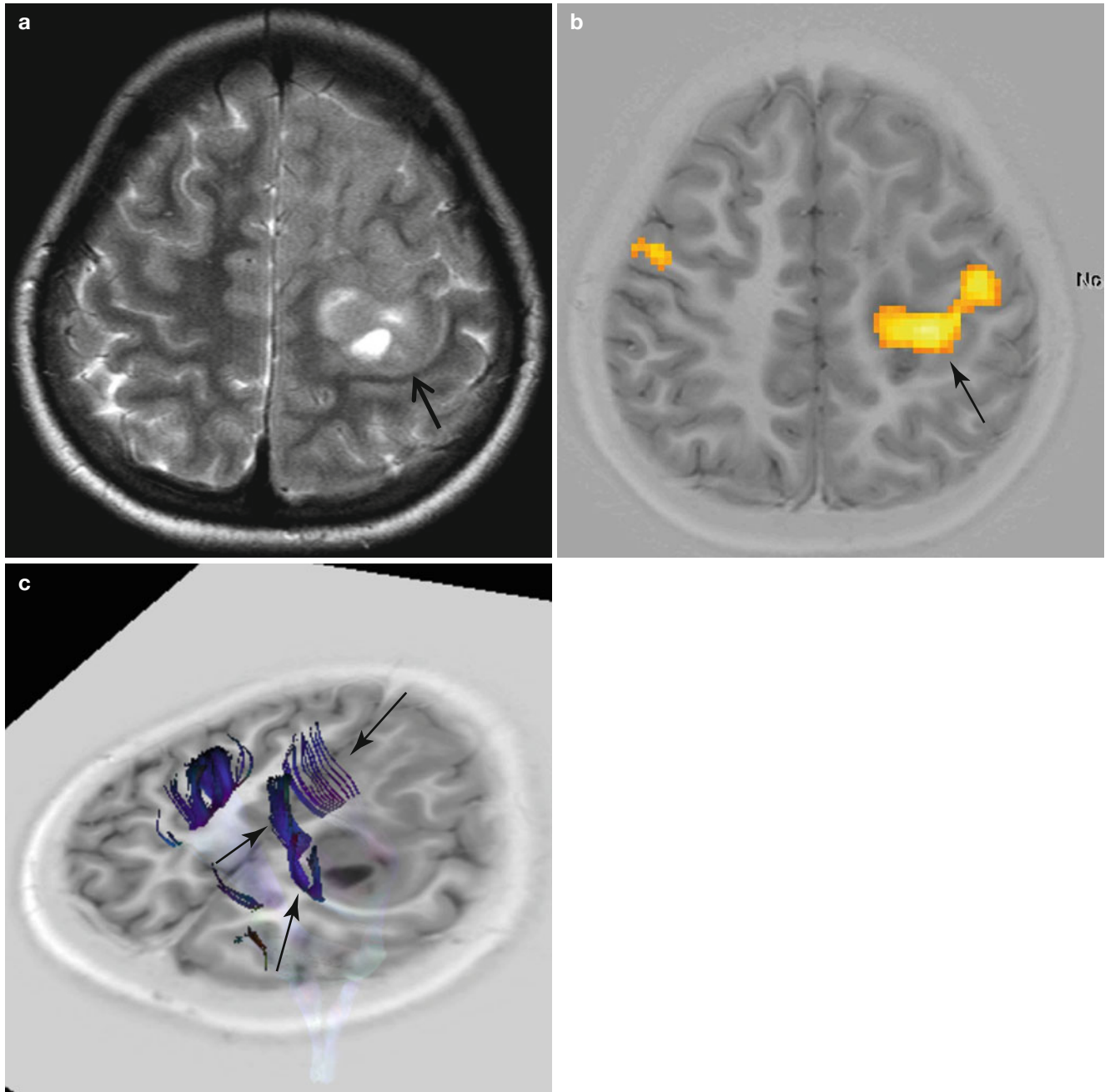


Fig. 4.39 Functional MRI and tractogram of malignant glioneuronal tumor in a 15-year-old girl. (a) T2-weighted image shows ill-defined iso-signal intensity mass (*arrow*) with mild edema in the left frontal lobe raising suspicion of motor and sensory cortex involvement.

(b) Functional MRI obtained with right-hand motion reveals that activated cortex is involved by the tumor (*arrow*). (c) Fiber tractogram demonstrates displaced and attenuated left corticospinal tract (*arrows*) by the tumor

4.3.3.2 Radionecrosis and Recurred Tumor

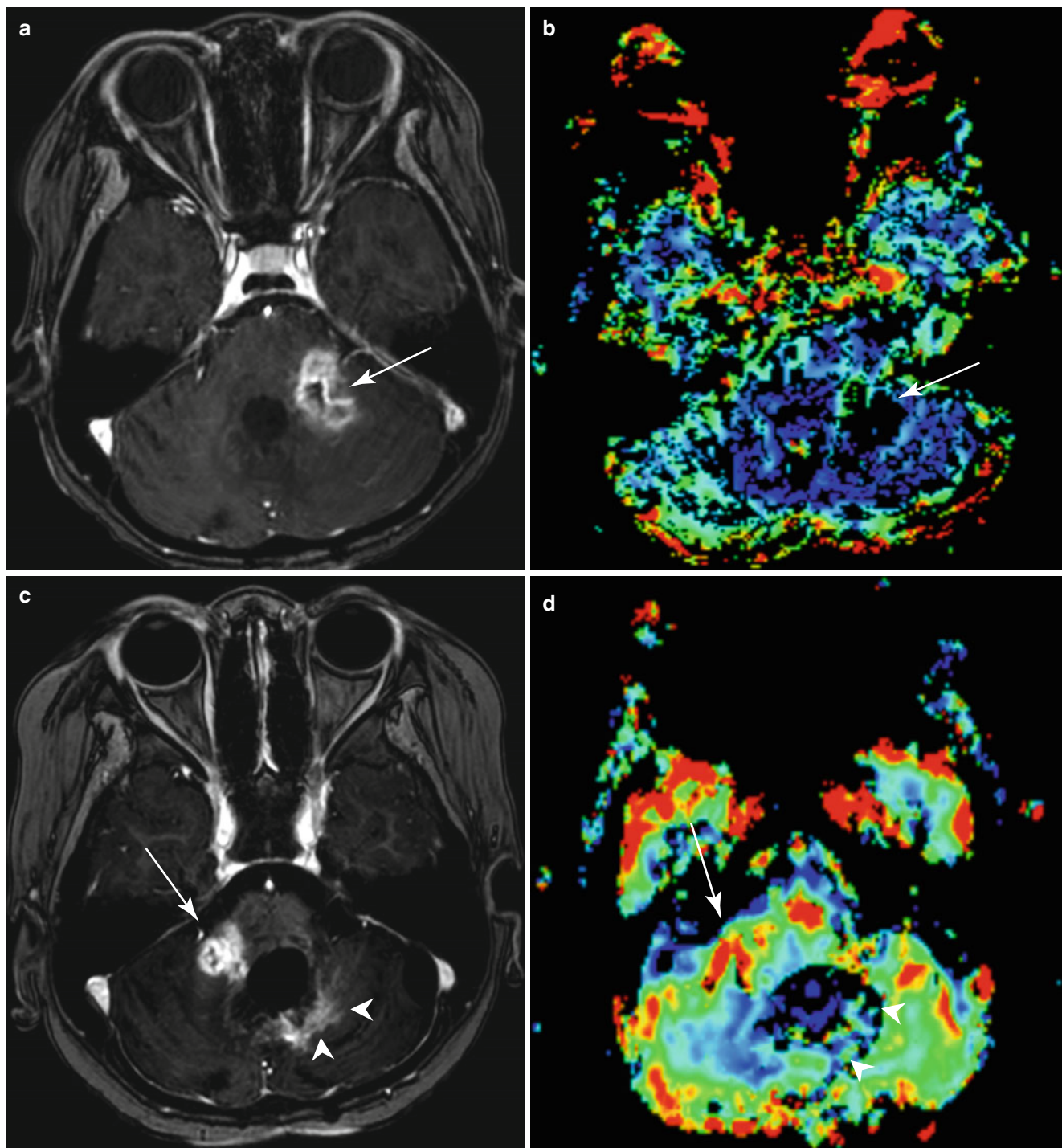


Fig. 4.40 Radionecrosis and recurred tumor in a 16-year-old girl with medulloblastoma treated by surgical excision, chemotherapy, and radiation therapy. (a) Postcontrast axial image of routine follow-up MRI shows newly appeared enhancing lesion (*arrow*) at the left cerebellar peduncle. (b) rCBV map obtained from perfusion imaging reveals decreased perfusion of the mass (*arrow*), suggesting radionecrosis rather than recurred tumor. (c) Postcontrast image obtained 6 months later without further treatment shows disappeared enhancing lesion of

the left cerebellar peduncle associated with atrophy. However, other enhancing lesions involving the right cerebellar peduncle (*arrow*) and posterior resection margin (*arrow heads*) are seen. (d) rCBV map demonstrates increased perfusion at the right cerebellar peduncle (*arrow*) suggesting possibility of the recurred tumor, although decreased perfusion is seen at the left posterior resection margin suggesting radionecrosis (*arrowheads*)

References

- Armstrong GT, Liu Q, Yasui Y, et al. Long-term outcomes among adult survivors of childhood central nervous system malignancies in the Childhood Cancer Survivor Study. *J Natl Cancer Inst*. 2009;101:946–58.
- Barkovich AJ. *Pediatric neuroimaging*. Philadelphia: Lippincott, Williams, and Wilkins; 2012.
- Bobek-Billewicz B, Stasik-Pres G, Majchrzak H, et al. Differentiation between brain tumor recurrence and radiation injury using perfusion, diffusion-weighted imaging and MR spectroscopy. *Folia Neuropathol*. 2010;48:81–92.
- Cha S. Update on brain tumor imaging: from anatomy to physiology. *AJNR Am J Neuroradiol*. 2006;27:475–87.
- Chiocca EA, Boviatsis EJ, Westmark RM, et al. Deep Sylvian fissure meningioma without dural attachment in an adult: case report. *Neurosurgery*. 1994;35:944–6. Discussion 946.
- Deopujari CE, Kumar A, Karmarkar VS, et al. Pediatric suprasellar lesions. *J Pediatr Neurosci*. 2011;6:S46–55.
- Fouladi M, Gajjar A, Boyett JM, et al. Comparison of CSF cytology and spinal magnetic resonance imaging in the detection of leptomeningeal disease in pediatric medulloblastoma or primitive neuroectodermal tumor. *J Clin Oncol*. 1999;17:3234–7.
- Huisman TA. Pediatric tumors of the spine. *Cancer Imaging*. 2009;9(Spec No A):S45–8.
- Lee IH, Kim JH, Suh YL, et al. Imaging characteristics of pilomyxoid astrocytomas in comparison with pilocytic astrocytomas. *Eur J Radiol*. 2011;79:311–6.
- Lee IH, Yoo SY, Kim JH, et al. Atypical teratoid/rhabdoid tumors of the central nervous system: imaging and clinical findings in 16 children. *Clin Radiol*. 2009a;64:256–64.
- Lee J, Lee BL, Yoo KH, et al. Atypical basal ganglia germinoma presenting as cerebral hemiatrophy: diagnosis and follow-up with 11C-methionine positron emission tomography. *Childs Nerv Syst*. 2009b;25:29–37.
- Merchant TE, Kiehna EN, Thompson SJ, et al. Pediatric low-grade and ependymal spinal cord tumors. *Pediatr Neurosurg*. 2000;32:30–6.
- Naidich TP, Castillo M, Cha S, et al. *Imaging of the brain*. Philadelphia: Elsevier Saunders; 2013.
- Nejat F, Kazmi SS, Ardakani SB. Congenital brain tumors in a series of seven patients. *Pediatr Neurosurg*. 2008;44:1–8.
- Panigrahy A, Bluml S. Neuroimaging of pediatric brain tumors: from basic to advanced magnetic resonance imaging (MRI). *J Child Neurol*. 2009;24:1343–65.
- Parmar HA, Pruthi S, Ibrahim M, et al. Imaging of congenital brain tumors. *Semin Ultrasound CT MR*. 2011;32:578–89.
- Rossi A, Gandolfo C, Morana G, et al. New MR sequences (diffusion, perfusion, spectroscopy) in brain tumours. *Pediatr Radiol*. 2010;40:999–1009.
- Rumboldt Z, Camacho DL, Lake D, et al. Apparent diffusion coefficients for differentiation of cerebellar tumors in children. *AJNR Am J Neuroradiol*. 2006;27:1362–9.
- Salvati M, D'Elia A, Brogna C, et al. Cerebral astroblastoma: analysis of six cases and critical review of treatment options. *J Neurooncol*. 2009;93:369–78.

Ji Hye Kim

Contents

5.1	Hypoxic–Ischemic Brain Injury	156
5.1.1	Introduction	156
5.1.2	Pathophysiology	156
5.1.3	Imaging	156
5.1.4	Patterns of Brain Injury in HIE	156
5.1.5	Injury in Preterm Infants	157
5.1.6	HIE in Term Infants.....	158
5.1.7	Clinical Significance and Treatment of HIE	158
5.1.8	Childhood Stroke	159
5.2	CNS Trauma in Infants and Childhood	159
5.2.1	Introduction	159
5.2.2	Birth Trauma	159
5.2.3	Postnatal Trauma in Infants and Young Children	160
5.2.4	Nonaccidental Injury	161
5.3	Cerebral Vascular Disorders in Children	161
5.3.1	Introduction	161
5.3.2	Arteriovenous Malformation.....	161
5.3.3	Vein of Galen Malformation	162
5.3.4	Cavernous Malformation.....	162
5.3.5	Developmental Venous Anomalies	162
5.3.6	Dural Arteriovenous Fistula	163
5.3.7	Moyamoya Syndrome	163
5.4	Illustrations: Brain and Spine Injury and Cerebral Vascular Disorders	164
5.4.1	Hypoxic Ischemic Brain Injury.....	164
5.4.2	CNS Trauma in Infants and Childhood.....	187
5.4.3	Cerebral Vascular Disorders in Children.....	199
	References	207

J.H. Kim, M.D.
Department of Radiology, Samsung Medical Center,
Sungkyunkwan University School of Medicine,
50 Ilwon-Dong, Kangnam-Ku, Seoul 135-710, Korea
e-mail: jhkate@skku.edu

5.1 Hypoxic–Ischemic Brain Injury

5.1.1 Introduction

Neonatal brain is vulnerable to hypoxic–ischemic injury, which is closely related with neurodevelopmental outcome in the future. Although the exact pathophysiology is not fully understood, asphyxia is the main event of diffuse hypoxic–ischemic encephalopathy (HIE), while focal stroke may be associated with arterial or venous infarct. The pattern of the injury and prognosis depend on the severity and duration of hypoperfusion and the degree of brain maturation. Although the clinical outcome is different, presentations of diffuse HIE and focal stroke during the neonatal period are often similar. Moreover, identification and characterization of the brain injury are important for prompt management. Therefore, neuroimaging has a significant role in the diagnostic workup for the treatment and prediction of prognosis of the babies. In this section, pathophysiology, imaging approach, and diverse patterns of HIE in both preterm- and term-born neonates will be discussed.

5.1.2 Pathophysiology

Asphyxia, defined as impaired exchange of oxygen and carbon dioxide, results in hypoxia, hypercarbia, and acidosis. Hypoxia and hypercarbia cause loss of cerebral autoregulation, resulting in pressure-passive blood flow that can lead to cerebral hypoperfusion in the setting of systemic hypotension. Premature babies are more vulnerable because cerebral autoregulation is not fully developed and more fluctuated systemic perfusion due to immature lung, incomplete closure of the patent ductus arteriosus, or sepsis. The resulting decreased cerebral blood flow, combined with hypoxia, triggers a cascade of biochemical reactions such as acidosis, release of excitotoxic neurotransmitters and inflammatory mediators, free radical formation, calcium accumulation, and lipid peroxidation. This process is called apoptosis or programmed cell death, eventually leading to neuronal cell death. The neonatal brain is quite resistant to hypoxia unless cerebral blood flow is compromised, because glucose or other energy substrates prevent brain damage. Thus, cerebral hypoperfusion is the primary cause of HIE that may result from either prenatal (placental abruption, impaired maternal oxygenation, or disrupted umbilical circulation) or postnatal events (circulatory arrest or severe pulmonary diseases). In addition to perinatal asphyxia, obstetric factors, metabolic disorders, and infection are postulated as other implicated factors. Reperfusion of the weak capillaries in the germinal matrix of the premature infants can cause hemorrhage (Chao et al. 2006).

During very early hypoxic–ischemic event, MR spectroscopy reveals depletion of nucleotide triphosphate (ATP) and increased lactate, and DWI reveals restricted diffusion, and they are normalized within 24 h, and then become abnormal again with deteriorated intracellular metabolism resulting in structural damage. This is an interesting concept of “secondary energy failure” (Badve et al. 2012; Barkovich 2012).

5.1.3 Imaging

Sonography (US) is a general screening tool for critically ill neonates at the bedside. Advantages of US include lack of radiation, portable scan, and relatively low cost. Moreover, Doppler examination offers information concerning vascular perfusion and intracranial pressure (increased RI in intracranial hemorrhage, cerebral edema, and hydrocephalus) or impaired cerebral autoregulation (Fig. 5.13), which is associated with patient outcome (Heinz and Provenzale 2009). However, US is operator-dependent, less sensitive to early or small parenchymal lesions, and limited to evaluate the cerebral convexity and posterior fossa. Moreover, parenchymal lesions identified by US are often nonspecific.

CT has a limited role in the evaluation of neonatal brain because of the poor contrast resolution owing to high water content of the brain and the disadvantage of radiation exposure. However, advanced CT technology enables a rapid screening for intracranial hemorrhage or fracture without sedation.

MR imaging is the best modality for the evaluation of the brain parenchyma with its excellent soft tissue contrast and multiplanar images. Although conventional MR imaging is less sensitive within the first few days after the ischemic event, diffusion-weighted imaging (DWI) can detect cytotoxic edema between 24 h and 6 days of the event. MR spectroscopy reveals elevated lactate and diminished NAA concentrations, which is more sensitive than DWI within the first 24 h after birth (Barkovich et al. 2001). Unfortunately, MR imaging has limitations, including the need for sedation and transport to outside of NICU (Chao et al. 2006; Barkovich 2012).

5.1.4 Patterns of Brain Injury in HIE

The patterns of brain injury depend on the degree of brain maturation and the severity and duration of the hypoperfusion event. The configuration of the vascular supply and metabolic state of the neonatal brain is determined by the brain maturation. Although there are some overlapping features, four patterns of brain injury are seen. In prolonged,

partial hypoxia or hypoperfusion, cerebral blood flow is redistributed to the metabolically active structures such as the basal ganglia, brain stem, and cerebellum. Therefore, vulnerable regions of the brain are the intervascular border zones. In the premature brain, periventricular white matter is the watershed area, because the entire cerebral white matter and cortex are supplied from the ventriculopetal arteries from the surface of the brain. Therefore, hypoxic–ischemic injury results in periventricular leukomalacia (PVL, Figs. 5.1 and 5.2). As the brain matures, vessels extend from the lateral ventricles into the brain, and the intervascular boundary zone moves to the parasagittal areas (Figs. 5.11 and 5.12) (Chao et al. 2006).

In severe hypoperfusion or total hypoxia, the deep gray matter and myelinated white matter are predominantly involved, because receptors for excitotoxic neurotransmitters are abundant in these metabolically active areas, and hence more vulnerable to the oxidative stress. The thalami and the brain stem are most frequently involved in the immature brain (Fig. 5.5), whereas the lateral thalami, basal ganglia, brain stem, hippocampi, and sensorimotor cortex are selectively involved in term infants (Figs. 5.13, 5.14, and 5.15). These areas correspond to the advanced myelination, increased perfusion, and increased glucose uptake on MR images and SPECT. The extent of injury increases with prolonged duration of the ischemic event (Chao et al. 2006; Barkovich 2012).

5.1.5 Injury in Preterm Infants

5.1.5.1 White Matter Injury

Ischemic injury to the late oligodendrocyte progenitors and subplate neuron of the premature babies results in selective vulnerability of the white matter. Typical pattern of injury with mild-to-moderate hypoperfusion in the premature brain is PVL, although the other part of the brain is also involved. In addition to the birth asphyxia, infection, metabolic disorders, congenital heart disease, and hydrocephalus may also cause periventricular white matter lesion (Barkovich 2012).

Initial US of the brain shows hyperechogenic periventricular white matter, and subsequent anechoic cavitation develops 2–6 weeks after injury (Fig. 5.1). In contrast to the normal periventricular halo, abnormal periventricular echogenicity is similar to choroid plexus or heterogeneous. However, the sensitivity and specificity of US diagnosis of PVL before the appearance of the cavitory lesions are not so high. MR images depict T1 hyperintense or hypointense areas and areas of T2 hyperintensity, evolving to multicystic lesions (Fig. 5.2a–c). End-stage PVL results in passively enlarged ventricles with irregular margins, periventricular white matter volume loss with increased T2 or FLAIR signal, thinning of the corpus callosum, and delayed myelination (Fig. 5.2d–f). Normal

areas of slow myelination at the peritrigonal white matter (terminal zones) may mimic abnormal signal intensity of late PVL. Normal terminal zones are separated from the ventricular wall by the intervening myelinated white matter without volume loss, while PVL lesions are abutting the ventricular wall (Barkovich 2012).

With advanced neonatal care and early MR imaging, PVL is becoming less common, and noncavitary injury is more commonly discovered and seen as small foci of hyperintense on T1-weighted images and hypointense on T2-weighted images (Fig. 5.3). These punctate white matter lesions show diffusion restriction and reduced FA. US significantly underestimates these noncavitary white matter lesions. In addition, diffuse white matter signal change called DEHSI (diffuse excessive high signal intensity) is described on MR imaging at term equivalent (Fig. 5.4). Although DEHSI was initially believed as white matter injury, there are many controversies on whether this represents white matter injury and worse outcome or not (Jeon et al. 2012). T2-hyperintense “caps” of the white matter adjacent to the frontal horns and “arrows” in the peritrigonal white matter are considered normal findings rather than DEHSI in neonates (Fig. 5.16) (Kidokoro et al. 2011).

5.1.5.2 Profound Injury

Severe hypotension or circulatory arrest in premature infants leads to injury of deep gray matter and brain stem (Fig. 5.5). White matter injury and germinal matrix hemorrhage (GMH) may also be seen simultaneously. US obtained 2–3 days after birth may reveal echogenic lesions in the basal ganglia and thalami (Fig. 5.5). Early MR imaging shows restricted diffusion in the dorsal brain stem and thalami in the first 2 days after injury. T1-hyperintensity and T2-hypointensity lesions involving thalami, posterior lentiform nuclei, and brain stem may appear subsequently. In the chronic phase, volume loss, astrogliosis, and calcification may be seen (Chao et al. 2006; Heinz and Provenzale 2009; Barkovich 2012).

5.1.5.3 Germinal Matrix and Intraventricular Hemorrhage

GMH is a reperfusion injury after hypoperfusion, and 90 % of these injuries have their onset within 4 days. GMH typically develops at the posterior aspect of the caudate head called ganglionic eminence (Fig. 5.6) and at the external granular layer of the cerebellum. Although GMH is readily detected by US, cerebellar hemorrhage is underestimated and increasingly detected in the preterm infants undergoing MRI (Fig. 5.7). GMH has been divided into four grades according to the extent. Grade 1 refers to GMH only (Fig. 5.6), grade 2 – hemorrhage extending to the ventricle (IVH) without distension (Fig. 5.8), grade 3 – IVH with ventriculomegaly (Fig. 5.9), and grade 4 – periventricular

hemorrhagic infarct (PVHI, Fig. 5.10). With the increase in the grade, the mortality rate and possibility of poor neurodevelopmental outcome increase (Barkovich 2012).

GMH is seen as an echogenic bulging at the caudothalamic groove on US and evolves to cystic lesion (Fig. 5.6). MR imaging is less sensitive than US in the detection of GMH (Fig. 5.6), and seen as dark signal intensity on T2-weighted images and iso- to hyperintensity on T1-weighted images (Fig. 5.8). IVH results in echogenic clot in the ventricle on US, which is sometimes difficult to differentiate from the echogenic choroid plexus. Doppler study may be helpful to demonstrate the vascularity of the choroid plexus. As liquefaction progresses, echogenic clot becomes sonolucent, and echogenicity of the ventricular endyma may increase. Ventricular enlargement may develop from the distension by large hematoma or obstruction of the CSF circulation by the clot (Fig. 5.9) or passive enlargement due to adjacent tissue loss. IVH is more sensitively diagnosed on MRI than US as dark signal intensity along the ventricular wall and clot within the lumen on T2-weighted and gradient echo images (Fig. 5.8). Subacute hemorrhage is hyperintense on T1-weighted images. PVHI is known to be venous infarct and distributes according to the occluded veins. Acute PVHIs are seen as heterogeneous bright echogenic lesions on US and T2 dark signal intensity on MR images (Fig. 5.10). Eventually, the lesion undergoes liquefaction and becomes cystic on images (Chao et al. 2006; Heinz and Provenzale 2009; Barkovich 2012).

5.1.6 HIE in Term Infants

Watershed injury caused by mild-to-moderate hypotension involves the cortex and the subcortical white matter between the major cerebral arteries in term infants (Figs. 5.11 and 5.12). This type of injury involving parasagittal areas often extends into the parieto-occipital areas or the precentral and postcentral gyri of the brain, if severe. Restricted diffusion is seen on DWI as early as within a day of injury (Fig. 5.11). Subsequent hyperintense T2 and hypointense T1 changes are seen, which are difficult to evaluate with US, because those areas are in close proximity to the calvaria (Heinz and Provenzale 2009). Later follow-up MR images reveal cortical thinning, cystic encephalomalacia, gliosis, and ex vacuo enlargement of the adjacent ventricle. Abnormal signal intensity suggesting gliosis becomes apparent as the white matter myelination appears. In addition, mushroom-shaped shrunken gyrus called ulegyria may be seen because of greater perfusion to the gyral apex than at the depth of the sulci (Fig. 5.12) (Barkovich 2012).

In profound asphyxia, the basal ganglia, posterior limb of the internal capsule, thalamus, brain stem, and sensorimotor

cortex are involved. The involved structures become hyper-echogenic on US 2–3 days after injury (Figs. 5.13 and 5.14) (Heinz and Provenzale 2009). Within a day of injury, restricted diffusion on DWI is seen, while conventional T1- and T2-weighted images become abnormal by day 3 of injury. T1-weighted images reveal hyperintense basal ganglia and thalami, which generally persist for 2–4 months (Fig. 5.15). This finding should be cautiously interpreted, because subtle increased signal intensity of the basal ganglia and normal myelinated ventrolateral nucleus of the thalami can also be seen in normal infants (Fig. 5.17) (Barkovich 2012). The T1 hyperintensity in profound hypoxic insult is more diffuse. Loss of hyperintensity of the posterior limb of the internal capsule on T1-weighted images, especially in conjunction with absent normal dark signal intensity on T2-weighted images, is an important evidence of hypoxic injury in a neonate with more than 37 weeks of gestational age (Figs. 5.14 and 5.15) (Heinz and Provenzale 2009; Barkovich 2012). More recently, relatively brighter signal in the posterolateral putamen compared with the posterior limb of the internal capsule has been found to be a sensitive discriminator of hypoxic–ischemic injury (Heinz and Provenzale 2009; Rutherford et al. 2010).

5.1.7 Clinical Significance and Treatment of HIE

Clinically, neonates with HIE may have low Apgar scores at delivery and metabolic acidosis. Apnea, seizures, and abnormal electroencephalograph (EEG) may be seen on the first day of life.

Although term infants with mild encephalopathy generally recover without deficit, 20 % of affected infants die in the neonatal period, and another 25 % develop significant neurologic sequelae. The overall prognosis is worse in preterm infants. Although the survival rates of very low birth weight infants increase, survivors are at high risk for neurodevelopmental disabilities, including cerebral palsy with spastic diplegia and cortical blindness. Even premature infants with normal neurological outcome have high incidence of cognitive impairment at the school age. The poor outcome is related with the severity of encephalopathy, the presence of cortical and basal ganglia injury on MR images, and severe EEG abnormalities.

Supportive management includes adequate ventilator care, prevention of hypotension, maintenance of normal level of blood glucose, fluid, and nutrition, and control of seizures and brain edema. Recent trials include therapeutic hypothermia, calcium channel blockers, magnesium, nitric oxide inhibitors, and other neuroprotective agents. Because there is only short early therapeutic window (2–6 h) for

effective interventions to reduce the severity of brain injury, early diagnosis of hypoxic–ischemic insult is important (Chao et al. 2006; Barkovich 2012).

5.1.8 Childhood Stroke

5.1.8.1 Arterial Infarct

About half of the pediatric strokes occur before 1 year of life. Clinical presentation depends on the affected area of the brain and age at the stroke. Younger patients have less significant deficit. Ischemic perinatal stroke is defined as focal arterial or venous infarct developed between 20 weeks of fetal life through the 28 days after birth. Symptoms and signs of the neonatal stroke are quite subtle. Half of the pediatric strokes are idiopathic, and many strokes are associated with coagulopathy, preeclampsia, chorioamnionitis, twin-to-twin transfusion, metabolic disorders, trauma, congenital heart disease, vasculopathy including moyamoya disease, and hematologic disease (Barkovich 2012).

US can detect neonatal infarct as hyperechogenic area initially (Figs. 5.18 and 5.19) and cystic evolution over 2–4 weeks. Hemorrhagic infarct is markedly hyperechogenic. CT is not commonly used because of the ionizing radiation and decreased conspicuity due to low attenuation of unmyelinated brain. In addition, evaluation of the venous thrombosis is limited due to high attenuation of the blood in neonates and infants. MRI with MR angiography is the study of choice for evaluation of the stroke. In neonates, acute edematous cortex is isointense to the adjacent white matter on spine echo sequences, which is called “missing cortex” sign (Fig. 5.18) (Barkovich 2012). FLAIR image is not sensitive for the identification of the neonatal infarct. Involved cortex exhibits T1, T2 shortening in subacute stage due to petechial hemorrhage, release of myelin lipid, or astroglial reaction (Fig. 5.18). Basal ganglia infarct may be missed on US or CT unless specific attention is paid (Fig. 5.19). Imaging appearances of focal infarct in older children are similar to adult infarcts. DWIs are most sensitive acute infarcts within 6 days of insult, and MR angiography demonstrates vascular lesion. Perfusion imaging is seldom used in infants and young children because of the difficult bolus injection of the contrast agent (Badve et al. 2012; Barkovich 2012).

5.1.8.2 Venous Infarct

Unexplained hemorrhagic infarct in children should raise suspicion for venous sinus thrombosis. Thrombosis of the superior sagittal sinus is associated with parasagittal hemorrhage (Fig. 5.20), and transverse sinus thrombosis may cause hematoma in the temporal lobe. Risk factors include coagulopathy, perinatal complication, middle ear infection, trauma, and connective tissue disease. The role of intravascular

thrombolysis is not well established in children, and venous sinus often resolves spontaneously (Barkovich 2012).

Venous sinus thrombus can be visualized on Doppler US in neonates as absence or alteration of the sinus flow. MR imaging shows parenchymal lesions composed of edema and hemorrhage, and acute thrombus as hypointense expanded sinus on gradient echo and subacute thrombus as hyperintense on T1-weighted images. MR venography with contrast shows absent flow at the involved sinus (Fig. 5.20). CT venography can demonstrate thrombosed sinus most precisely, although parenchymal lesions are more subtle than MR imaging (Badve et al. 2012; Barkovich 2012).

5.2 CNS Trauma in Infants and Childhood

5.2.1 Introduction

Pediatric trauma is unique in the immaturity of the CNS and surrounding skull and spinal column. Clinical significance of the intracranial hemorrhage may be different from the adult patients, and the state of myelination of axons within the white matter influences the tissue response upon injury. Moreover, because of increased elasticity of the soft tissues, lesser muscular development, relatively greater head size, lack of ossification, and more horizontal facet orientation, the pediatric spine is less stable than the adult spine. Therefore, spinal cord injury is more common in infants than in adults, and may even occur without any evidence of skeletal injury.

In this section, the unique aspects of pediatric trauma in birth injury, postnatal trauma, and nonaccidental injury will be discussed.

5.2.2 Birth Trauma

The process of birth is a blend of mechanical forces including contractions, compression, torques, and traction. When these forces are complicated with other factors, it may lead to hemorrhage, edema, tissue disruption, or fracture in the neonate. Use of obstetric instrumentation, large infants, breech delivery, and excessive traction during delivery may increase the risk of birth trauma (King and Boothroyd 1998).

Cephalhematoma is subperiosteal collection of blood, and its extent is limited by the suture lines. Cephalhematoma appears as a crescent-shaped lesion adjacent to the outer table of the skull, and skull fracture is associated in 5–20 % of cases (Fig. 5.21). Eventually, cephalhematoma resolves within several weeks or occasionally remains calcified (Fig. 5.22) (King and Boothroyd 1998). Caput succedaneum is subcutaneous hemorrhage and edema with poorly defined margins crossing the suture lines. It results from the pressure of the presenting part against the dilating cervix. Subgaleal

hemorrhage refers to hemorrhage below the aponeurosis, covering the scalp beneath the occipitofrontalis muscle, sometimes extending into the subcutaneous tissue of the neck. Depressed skull fracture may occur with the use of forceps in delivery (Fig. 5.23).

SDH is the most common intracranial hemorrhage during delivery and caused by laceration of subdural veins. MR imaging increased detection of SDH; many of them have little clinical significance unless accompanied by parenchymal injury, obstruction of CSF flow, or compression of the brain stem. Posterior fossa SDH is caused by tentorial laceration and occipital osteodiaschisis, resulting in massive bleeding from the ruptured vein of Galen, straight sinus, or transverse sinus, while laceration of falx and superficial cerebral veins leads to supratentorial SDH (King and Boothroyd 1998; Barkovich 2012). US, CT, and MR images demonstrate evolving hematoma according to the time spectrum (Fig. 5.24).

Epidural hemorrhage (EDH) is a very rare complication of birth trauma (Fig. 5.25). While EDH in adult is caused by laceration of the middle meningeal artery associated with a fracture crossing the groove at the inside of the skull, which needs prompt surgical evacuation, in the neonates and infants, EDH mostly results from laceration of the epidural vein that is less rapid and less dangerous (Barkovich 2012).

Spinal cord injury during delivery is rarely diagnosed and results from excessive traction or rotation. The lower cervical and upper thoracic region is frequently involved in breech delivery, and the upper and mid-cervical region is more involved in vertex delivery. EDH or SDH, intramedullary hemorrhage, cord edema, laceration, or transection of the cord may be observed. Occasionally, dural tear and, rarely, vertebral fractures or dislocations may be seen. The cervical cord or brain stem injury may lead to neonatal death with respiratory failure. The survivors may have weakness and hypotonia, and the true etiology may not be recognized or mistaken for neuromuscular disorder or hypoxic-ischemic encephalopathy (Vialle et al. 2007; Barkovich 2012).

MR imaging demonstrates cord injury, extramedullary hemorrhage, and surrounding soft tissue injury. T2-weighted images demonstrate cord edema as increased signal intensity and intramedullary hemorrhage as dark signal intensity. Extent of cord swelling and presence of medullary hemorrhage are associated with poor prognosis (Vialle et al. 2007).

5.2.3 Postnatal Trauma in Infants and Young Children

5.2.3.1 Head Trauma

Most of the pediatric head injuries are resulted from motor vehicle accidents, falls, sports activities, and child abuse. Skull fracture in infants heals within 6 months, while in

adults, healing requires several years. Leptomeningeal cyst or growing fracture is more common in young children less than 3 years old. Leptomeningeal cyst is formed by dural tear and interposed dura at the fracture site inhibiting the fracture healing, leading to gradually herniated meninges and brain tissue due to CSF pulsation (Fig. 5.30) (Barkovich 2012).

SDH is most common in infants and unexplained SDH should raise suspicion of nonaccidental injury in infants (Demaerel et al. 2002). Imaging reveals crescent-shaped fluid over the convexity crossing the sutures (Figs. 5.30, 5.31, and 5.32). If the SDH is isodense, careful observation of the mass effect is important. Outer margin of chronic SDH may be contrast-enhanced, as fibrovascular granulation tissue formation develops (Barkovich 2012). The signal intensity of the SDH evolves according to the stage of hemoglobin on MR images.

EDH is not common in young children, and clinical presentation is less urgent, because EDH usually originates from the tear of the dural vein rather than the middle meningeal artery, unlike in older children and adolescents. Moreover, suture separation can accommodate the mass effect of the hematoma (Barkovich 2012; Schunk and Schutzman 2012). Imaging appearances are identical to those seen in adults; lentiform hematoma between the skull and brain parenchyma may be associated with adjacent skull fracture (Fig. 5.25). Contusion or contrecoup injury of the brain may be seen.

CT scan demonstrates fracture, hemorrhage, pneumocephalus, mass effect, and herniation in acute setting. When the patient becomes stable, MR imaging reveals detailed information concerning shearing injury, small amount of SDH, or brain stem injury. T2-gradient echo images or susceptibility-weighted images are sensitive for the detection of hemorrhage.

Diffuse brain swelling after acute trauma or asphyxia is commonly seen resulting from the combination of edema and vasodilation due to loss of cerebral vascular autoregulation (Fig. 5.26) (Barkovich 2012). On CT and MRI, loss of gray and white matter differentiation, obliterated ventricles and cisternal spaces, and transtentorial or subfalcine herniation may occur. In addition, cerebral contusion and shearing injury may be seen (Fig. 5.27). Shearing injury is more common in infants, because unmyelinated white matter is less rigid and subarachnoid space is more prominent. If consciousness level of the patients is compromised, brain stem injury should be evaluated with MR imaging (Barkovich 2012).

5.2.3.2 Spinal Injury in Young Children

As described earlier, infants and young children have propensity of cord injury due to immaturity of the spinal column (Fig. 5.28). Spinal cord injury may occur without radiologic abnormality (SCIWORA). In young children less than 8

years, upper cervical injuries including fatal atlanto-occipital and atlanto-axial dislocation are common. Fracture usually occurs at the synchondrosis between the dens and the body of C2, which is best demonstrated by coronal and sagittal reformation of CT scan. However, edema and hemorrhage of the spinal cord and brain stem should be evaluated by MRI (Fig. 5.29). Fixed rotatory C1–C2 subluxation is usually seen in children less than 13 years of age. Diagnosis should be made with dynamic CT scans obtained with neutral position, and 45° to the right-turned position and 45° to the left-turned position. If there is rotatory fixation, no significant motion of C1 on C2 is seen in one direction. Fracture involving thoracolumbar spine is uncommon, but mostly occurs at T12–L2 level. Soft tissue injury involving ligament, cartilage, and growth plate is commonly seen (Barkovich 2012).

5.2.4 Nonaccidental Injury

Nonaccidental injury (child abuse) is much more common than accidental injury in infants less than 2 years of age. Head trauma is the most common cause of death or permanent neurological deficit in nonaccidental injury (Barkovich 2012). Brain imaging plays an important role in diagnosis of nonaccidental injury for prompt intervention and child protection. CT, MRI, and plain skull radiography are the standard imaging modalities.

Direct trauma or vigorous shaking may lead to skull fracture, SDH, SAH, and contusion of the brain (Figs. 5.31 and 5.32). Damage of the brain stem and upper cervical cord should be evaluated, because they may cause fatal outcome and be easily overlooked (Barkovich 2012).

Clinically, victims present with irritability, seizures, lethargy, reduced consciousness, or apnea, and the history of trauma is often vague or inconsistent. The presence of retinal hemorrhages and other evidence of physical abuse, such as unexplained bruising or fractures, should raise suspicion for the diagnosis (Fig. 5.30). Outcome is generally poor with high incidence of death and cognitive and neurologic deficits (Barkovich 2012).

Skull fracture may be seen on radiography and CT, and manifested as multiple, bilateral, widely separated (Fig. 5.30), or stellate in shape (Rajaram et al. 2011). Because fracture parallel to the scan plane can be missed on CT scan, scout view should be carefully evaluated. SDH is the most common intracranial finding of child abuse, and unexplained SDH in infants and young children should raise suspicion for child abuse (Rajaram et al. 2011). SDH is well visualized both on CT and MR images. Multistaged SDH (multiloculated or fluid–fluid level in acute phase) is particularly suggestive (Fig. 5.32). However, bilateral SDH may also be seen in patients with Menke's kinky hair disease (Fig. 5.33) and glutaric aciduria type 1 (Barkovich 2012). Common parenchymal injury includes contusion involving anterior

temporal and frontal lobes and infarct-like cortical and subcortical lesions (Figs. 5.31 and 5.32). DWI sensitively demonstrates acute lesion (Fig. 5.31b), and gradient echo or susceptibility image is useful for demonstration of the hemorrhage (Rajaram et al. 2011). Spinal injury may be seen in abused children, and cervical spine is especially vulnerable for shaking injury.

5.3 Cerebral Vascular Disorders in Children

5.3.1 Introduction

Cerebral vascular disorders are not common in pediatric patients. However, it is the main cause of nontraumatic intracranial hemorrhage after neonatal period. Cerebral vascular malformations are classified as arteriovenous malformations (AVMs), developmental venous anomalies, cavernous malformations, and capillary telangiectasia. There are several vasculopathies causing steno-occlusive lesions of the cerebral vessels resulting in childhood stroke.

5.3.2 Arteriovenous Malformation

AVMs are abnormal compact collections of abnormal thin-walled vessels connecting arteries and veins, resulting in arteriovenous (AV) shunting without true capillary bed. The transition between artery and vein can take place via tangle of abnormal vessels (nidus) or can be direct without any intervening network (brain or pial AV fistula). Although AVMs are a congenital abnormality, they often increase in size of the nidus with progressive dilation of feeding arteries and draining veins over time, presenting with intracranial hemorrhage or seizures later in life. Edema of the surrounding brain caused by venous hypertension can be seen evolving to astrogliosis or atrophy. Rapid flow of the arteries may cause aneurysm formation, and venous aneurysm can develop proximal to the stenosis (Geibprasert et al. 2010; Barkovich 2012).

Acute hemorrhage is seen as high attenuation on noncontrast CT (Fig. 5.34a). The nidus and enlarged vessels may be seen as blood density and become more apparent following contrast administration. Although CT angiography (CTA) demonstrates detailed images of AVMs, CTA has radiation exposure. MRI is an excellent screening tool in demonstration of the flow voids on T2-weighted images generated by fast flow, hemorrhage, and adjacent edema (Fig. 5.34). Although both CTA and MRA can demonstrate vascular configuration, catheter angiography must be performed to evaluate detailed angioarchitectures, including feeding arteries, draining veins, aneurysm, or venous stenosis (Fig. 5.34d).

Pial AVFs are seen as dilated high-flow feeders, most commonly at the level of the circle of Willis, associated with dilated venous pouch on the surface of the brain (Fig. 5.35). They are more commonly encountered in neonates and young children, and are frequently associated with hereditary hemorrhagic telangiectasia. Treatment options are microsurgical resection, endovascular occlusion, and radiosurgery (Geibprasert et al. 2010).

5.3.3 Vein of Galen Malformation

Vein of Galen malformations are a rare malformation due to an AV fistula of the median prosencephalic vein (MPV) (a precursor of the vein of Galen) and intracranial arteries. Straight sinus occlusion and persistent falcine sinus can be associated, and the vein of Galen becomes aneurysmal. These malformations can be antenatally diagnosed, and there is an increased male predilection (Geibprasert et al. 2010).

There are two types of malformations. Choroidal type is characterized by arteriovenous connection via plethoras of vessels of the prosencephalic vein resulting in great amount of fistula. They are usually diagnosed in the neonatal period, associated with high-output cardiac failure and cranial bruit. Mural type is composed of a few larger fistula associated with hydrocephalus due to venous hypertension or aqueduct stenosis in infants or older children (Fig. 5.36). Choroidal type is much more common than the mural type (Geibprasert et al. 2010).

Prenatal US reveals dilated MPV in the midline posteriorly, and cardiomegaly or hydrops fetalis may be seen. CTA in neonates with high-output cardiac failure is technically difficult due to the small volumes of contrast and very rapid passage of contrast in the circulation. The varix appears as a large mass, displacing the third ventricle with various signal intensities according to the presence and stage of the thrombus. Dilated feeders and venous drainage are also seen as flow voids on T2-weighted images. Surrounding parenchymal edema, hemorrhage, calcification, or atrophy may be seen. MRA would better delineate vascular anatomy. However, angiography remains the gold standard in full evaluation of the feeding vessels, dilated vein of Galen, and venous drainage (Fig. 5.36) (Barkovich 2012).

Both venous and arterial embolizations can be performed depending on the number of feeders. Ideally, embolization is delayed until 6 months of age for choroidal-type malformations, and more longer for mural types, to allow the cavernous sinus to mature. If cardiac failure is refractory in spite of aggressive medical management, embolization can be performed earlier. Shunting for the hydrocephalus may increase the risk of cerebral ischemia and intraventricular hemorrhage. Because the prognosis is determined by the

presence of cardiac failure, choroidal types presenting in the neonatal period are poor. Prior to endovascular intervention, morbidity and mortality is very high (Geibprasert et al. 2010; Barkovich 2012).

5.3.4 Cavernous Malformation

Cavernous malformations or cavernomas are collections of dilated capillary bed containing blood in various stages of oxidation. They represent the most common pediatric vascular lesion in the brain. These angiographically occult vascular malformations are often presented by the sudden onset of cerebral hemorrhage with acute focal neurologic deficits.

Cavernous malformations appear as slightly high attenuated lesion without edema on noncontrast CT and as well-demarcated round or lobulated mass of heterogeneous signal intensity surrounded by dark signal intensity on MR images (Fig. 5.37). They are enhanced mildly after contrast administration and should be differentiated with tumors. The pediatric cavernomas have higher rates of hemorrhage and larger dimensions than in adult patients, and often demonstrate atypical radiological findings (Fig. 5.38). Furthermore, other coexistent vascular malformations are common in children (Fig. 5.37) (Mottolese et al. 2001). Multiple lesions and an earlier presentation are seen in the familial form and association with radiotherapy for brain tumors.

Surgical excision after careful anatomical and functional evaluation is performed for symptomatic or rapidly growing lesions. There is limited role for radiosurgery in the management of pediatric cavernomas.

5.3.5 Developmental Venous Anomalies

Developmental venous anomalies (DVAs) or venous malformations are radially oriented dilated medullary or cortical veins draining into single dilated vein without AV shunt. DVAs are usually asymptomatic, but they can cause symptoms of venous ischemia or infarct if the outflow of the venous drain is stenotic or thrombosed. DVAs are believed to be formed as compensatory pathways recruiting dilated pre-existing transmedullary veins by occlusion or maldevelopment of the superficial or deep veins during embryonic period (Geibprasert et al. 2010).

DVAs can be identified as linear or curvilinear enhancing structures and dilated medullary veins (caput medusa) on CT and MR imaging (Fig. 5.39). DVAs only rarely cause bleeding; if DVA is discovered with cerebral hemorrhage, coexisting cavernous malformation should be sought (Fig. 5.37) (Geibprasert et al. 2010; Barkovich 2012).

5.3.6 Dural Arteriovenous Fistula

Dural AVFs are abnormal connections between the branches of the external carotid artery and small venules within the dura. Congenital dural AVFs tend to have large connection and increased flow causing presentations similar to those of the vein of Galen malformation and distended scalp veins (Geibprasert et al. 2010). CT and MR imaging findings include dilated cortical veins without nidus. The white matter lesions of low attenuation on CT or hyperintense T2 signal on MR imaging indicate venous congestion or infarction, which may be associated with hemorrhage. Chronic venous congestion may lead to curvilinear subcortical calcifications. Early venous filling, the connection with external carotid artery branches, and shunt location are demonstrated by angiography. Endovascular treatment can reduce the shunt flow, which may be combined with surgical therapy (Barkovich 2012).

5.3.7 Moyamoya Syndrome

Moyamoya disease is a progressive steno-occlusive disease of unknown etiology, which typically involves the supraclinoid

internal carotid arteries. The term *moyamoya syndrome* is used in cases in which the underlying disease (Down syndrome, neurofibromatosis, sickle-cell disease, or some other vasculopathy) can be identified. Extensive basal collaterals (usually lenticulostriate or thalamoperforator arteries) develop to compensate for the progressive stenosis, which have been described as moyamoya (Japanese for puff-of-smoke appearance) vessels on angiography. Most of the pediatric patients present with transient ischemic attack or stroke, whereas intracranial hemorrhage from the rupture of the collateral vessels is more common in adults (Barkovich 2012).

On CT and MR imaging, multiple infarcts of various stages distributing the intervascular boundary zones are seen. MR imaging can better delineate acute infarct with DWI, presence of bilateral supraclinoid internal carotid artery stenosis, and collateral formation. Angiography is performed for preoperative evaluation (Fig. 5.40). Perfusion MR imaging may be helpful for preoperative evaluation of area of relative ischemia and assessment of changed perfusion after revascularization surgery (Geibprasert et al. 2010).

Surgical treatment uses the external carotid artery (ECA) to indirectly place the tissue supplied from ECA in contact with the brain to make ingrowth of collaterals to the brain or directly anastomose to a cortical artery.

5.4 Illustrations: Brain and Spine Injury and Cerebral Vascular Disorders

5.4.1 Hypoxic Ischemic Brain Injury

5.4.1.1 Hypoxic Ischemic Brain Injury in Preterms; Periventricular Leukomalacia

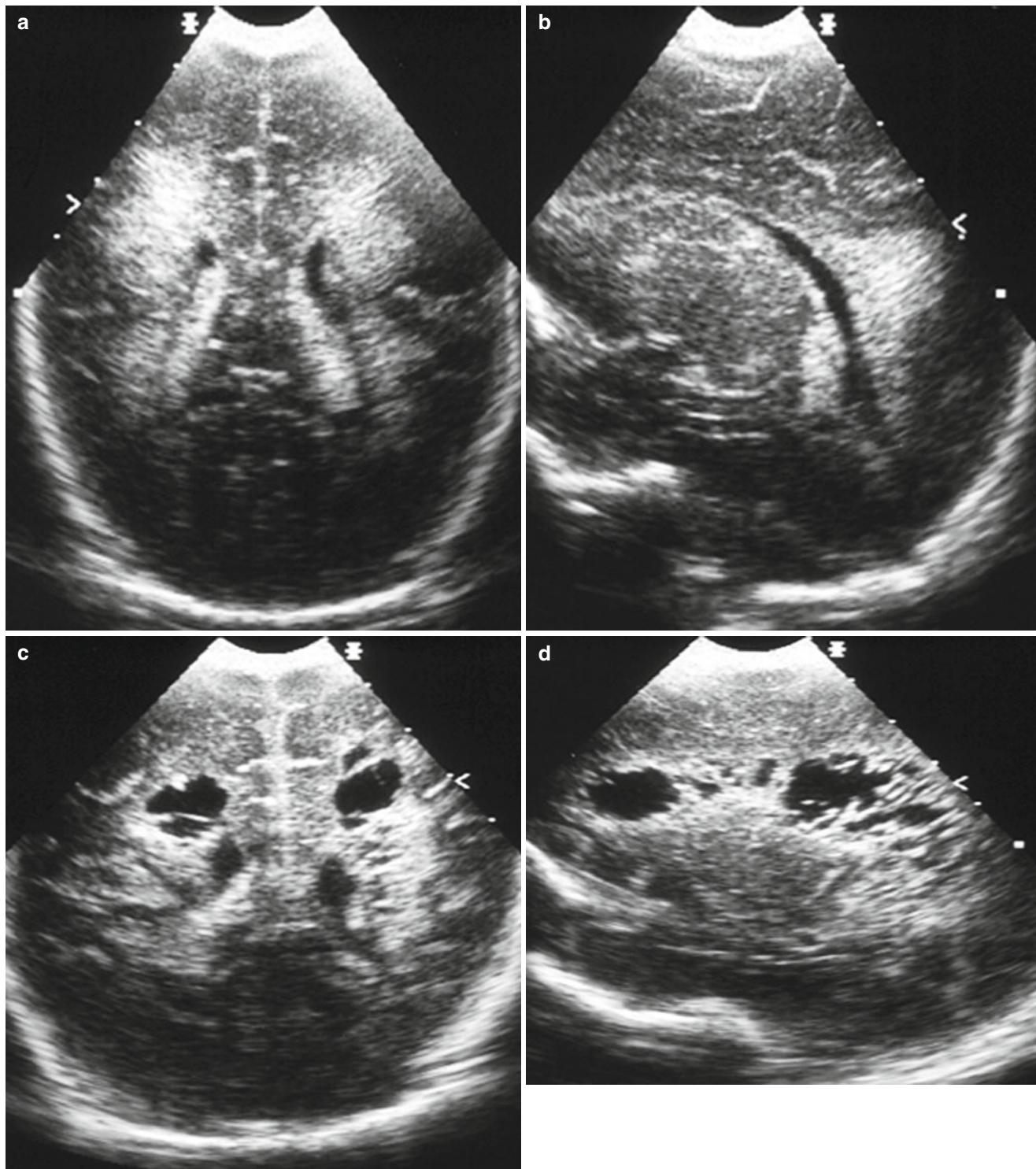


Fig. 5.1 Evolving periventricular leukomalacia (PVL) on US in pre-term neonate. (a, b) Initial coronal (a) and sagittal (b) US images obtained at 3 days of life show abnormally increased echogenicity of

the periventricular white matter. (c, d) Follow-up US images obtained 3 weeks later reveal multiseptated cystic encephalomalacia of the echogenic periventricular white matter

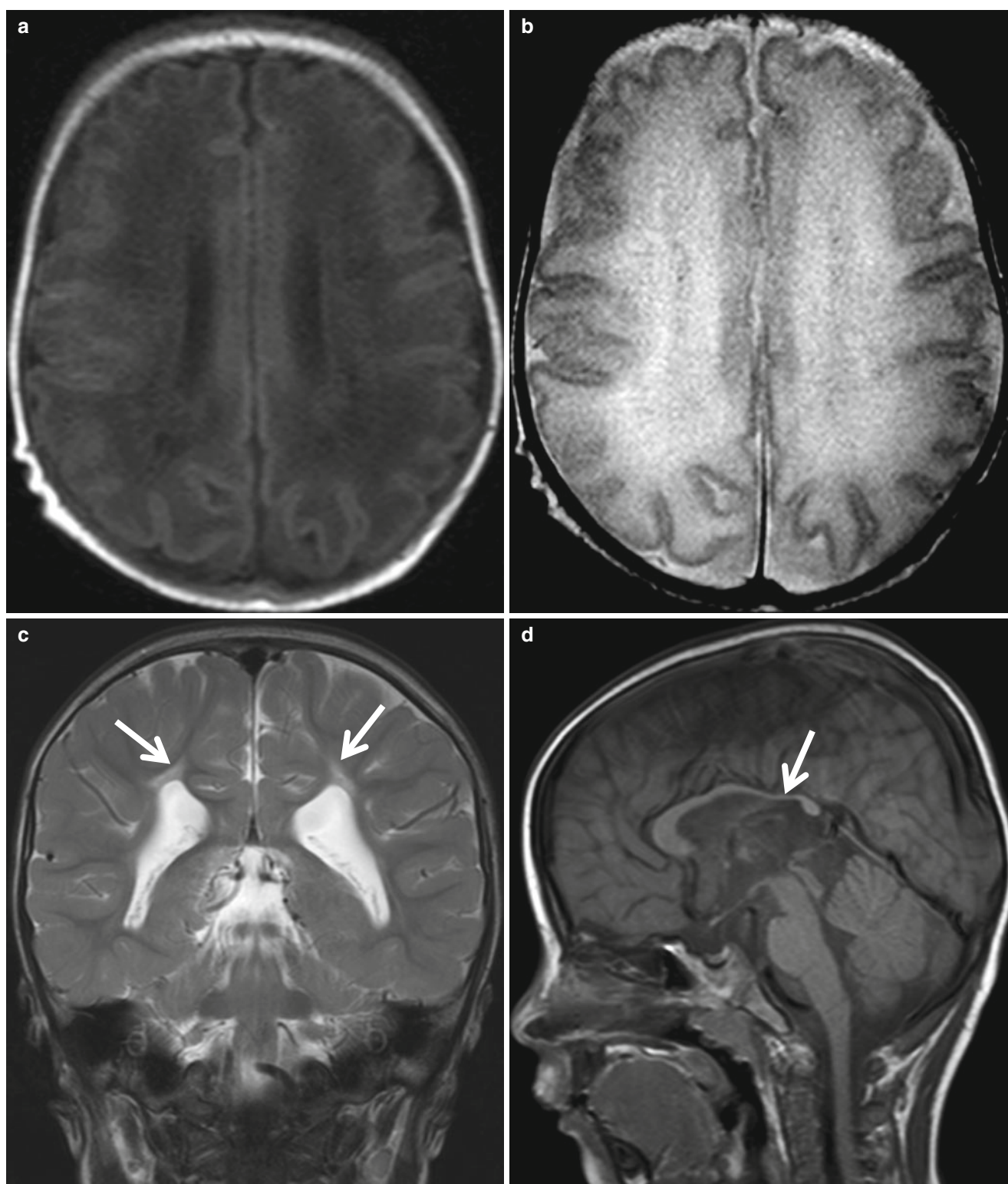


Fig. 5.2 Evolving PVL on MR imaging in preterm neonate. The deep white matter is hypointense on T1-weighted image (a) and hyperintense on T2-weighted image (b) obtained 2 weeks after the birth. Follow-up T2-weighted coronal image obtained 2 years later (c) shows passive enlargement of the lateral ventricles with undulated margins

and periventricular hyperintensity (arrows) abutting the ventricular ependyma. Sagittal T1-weighted image (d) demonstrates decreased volume of the posterior body and splenium of the corpus callosum (arrow)

5.4.1.2 Hypoxic Ischemic Brain Injury in Preterms; Noncavitary White Matter Injury

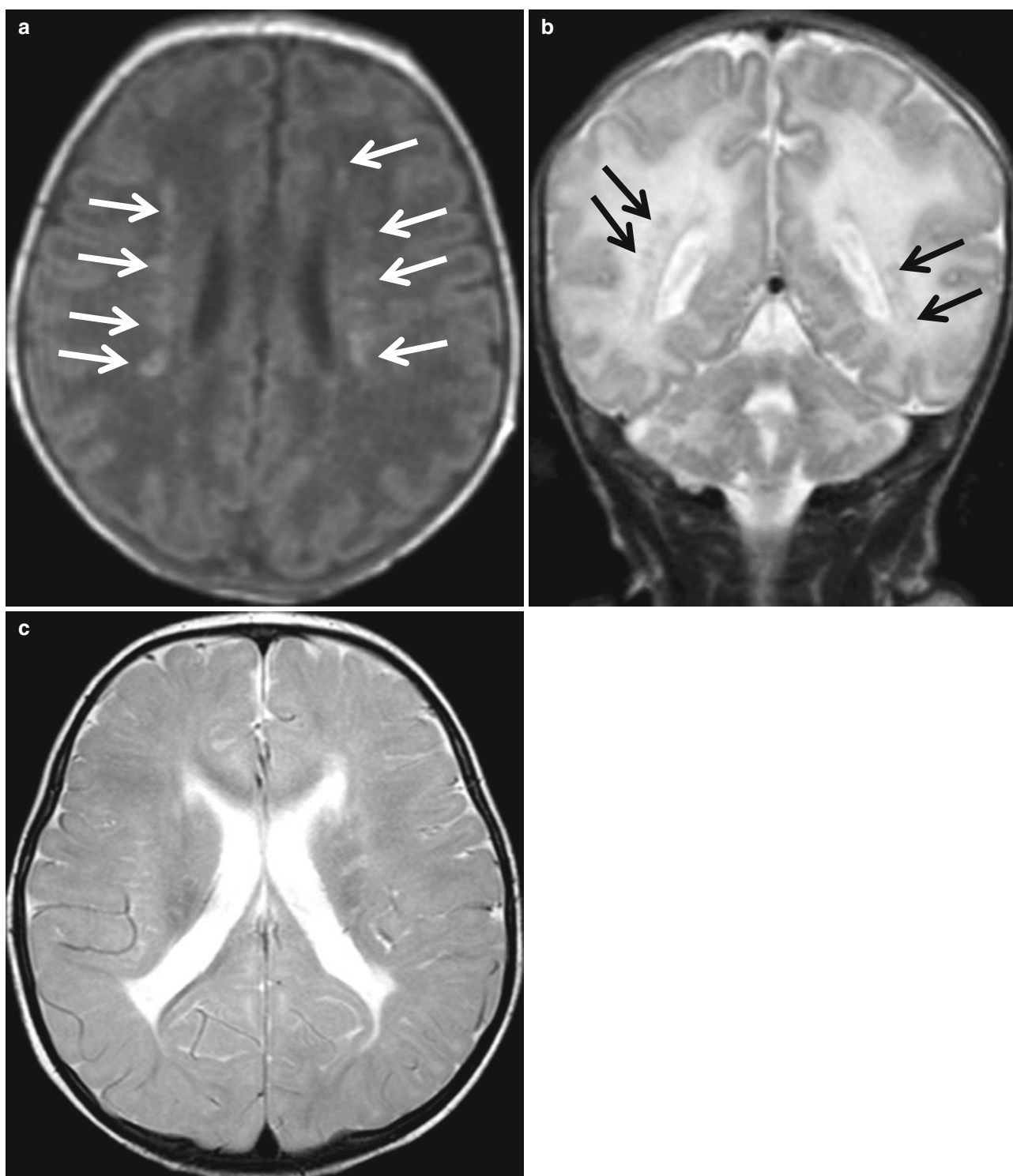


Fig. 5.3 Noncavitary white matter lesions in preterm neonate. There are multiple punctate white matter lesions (*arrows*) becoming hyperintense on T1-weighted image (**a**) and hypointense on T2-weighted

image (**b**). (**c**) Follow-up T2-weighted image obtained 2 months later shows enlarged ventricles and thin area of T2 hyperintensity along the ventricular surface, representing periventricular leukomalacia

5.4.1.3 Hypoxic Ischemic Brain Injury in Preterms; DEHSI (Diffuse Excessive High Signal Intensity)

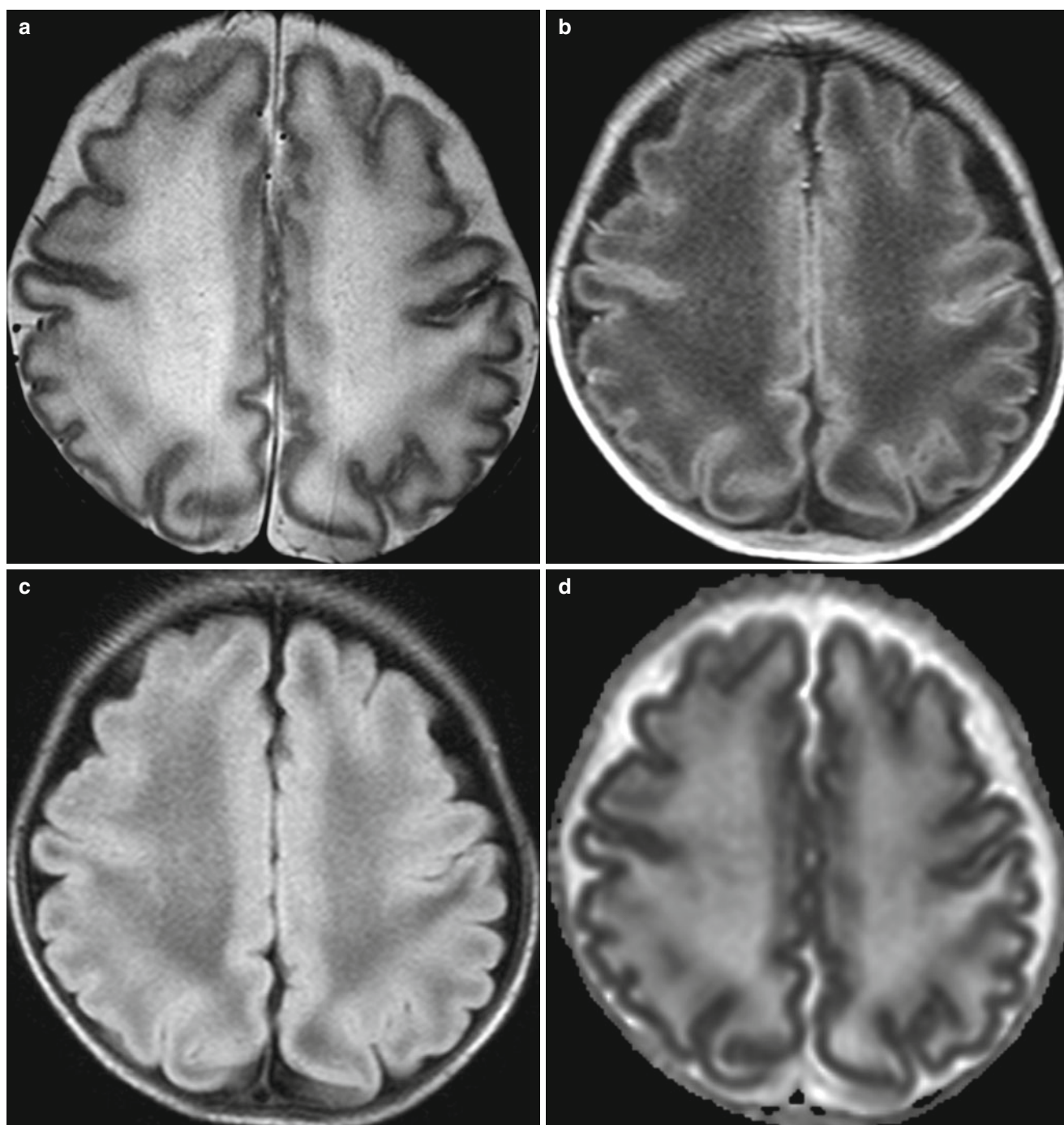


Fig. 5.4 Diffuse excessive high signal intensity (DEHSI) in preterm baby at corrected gestational age of 36 weeks. (a) T2-weighted axial image shows excessive higher signal intensity of the centrum semiovale

compared with unmyelinated subcortical white matter. DEHSI lesions exhibit low signal intensity on T1-weighted image (b) and FLAIR image (c) and increased diffusion on ADC map (d)

5.4.1.4 Hypoxic Ischemic Brain Injury in Preterms; Profound Injury

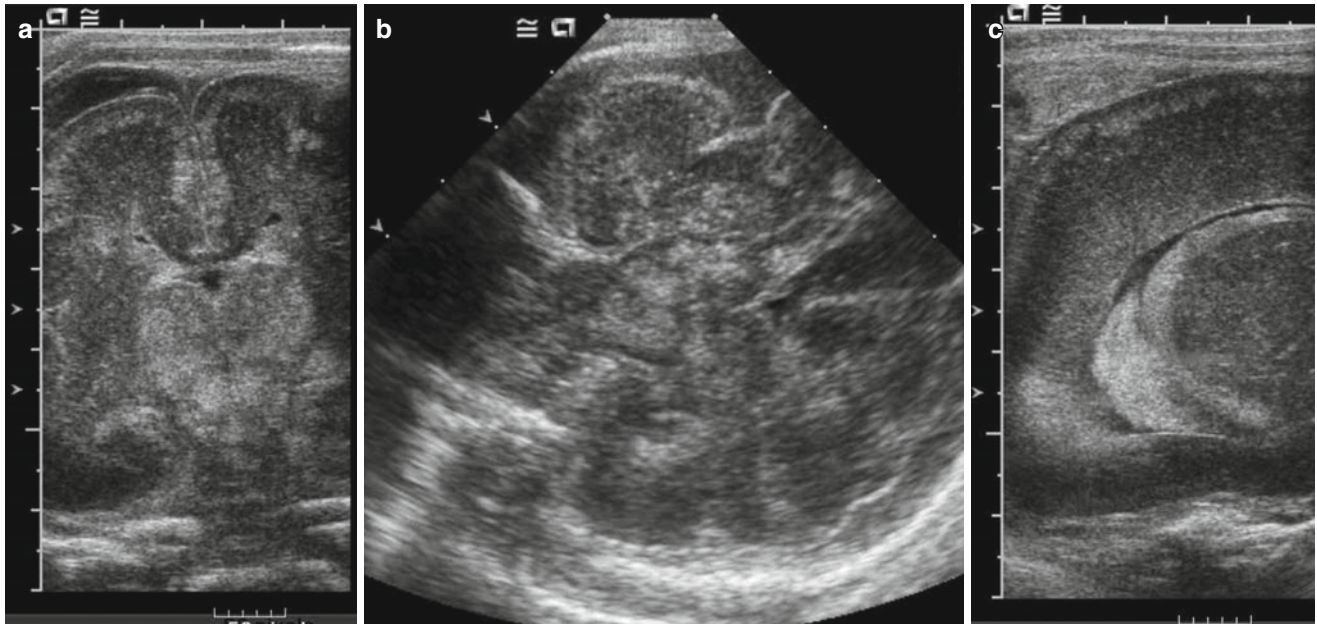


Fig. 5.5 Asphyxiated extremely preterm neonate with 25 weeks of gestational period. Coronal (**a**) and axial (**b**) images of the brain US show abnormally echogenic thalami and brain stem. (**c**) Subcortical layers and germinal layers along the ependyma on the thalamus are also echogenic on a sagittal scan

5.4.1.5 Germinal Matrix Hemorrhage and Intraventricular Hemorrhage

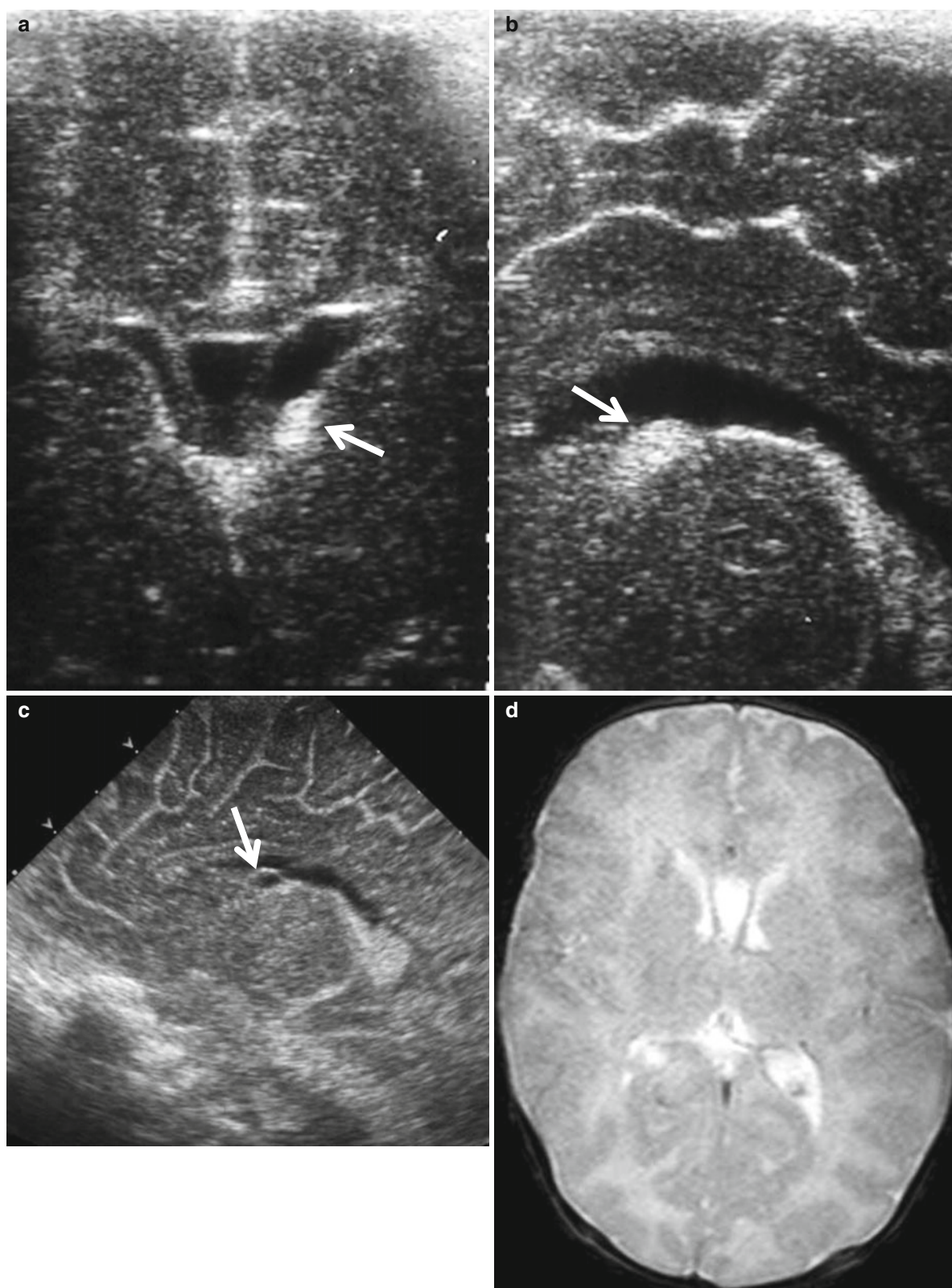


Fig. 5.6 Germinal matrix hemorrhage on US and MR images. (a, b) US obtained at 4 days of life reveals focal echogenic bulging (*arrow*) at the left caudothalamic groove (ganglionic eminence). (c) Cystic change

is evident on follow-up US (*arrow*), which is not well visualized on T2-weighted MR image (d) obtained on the same day

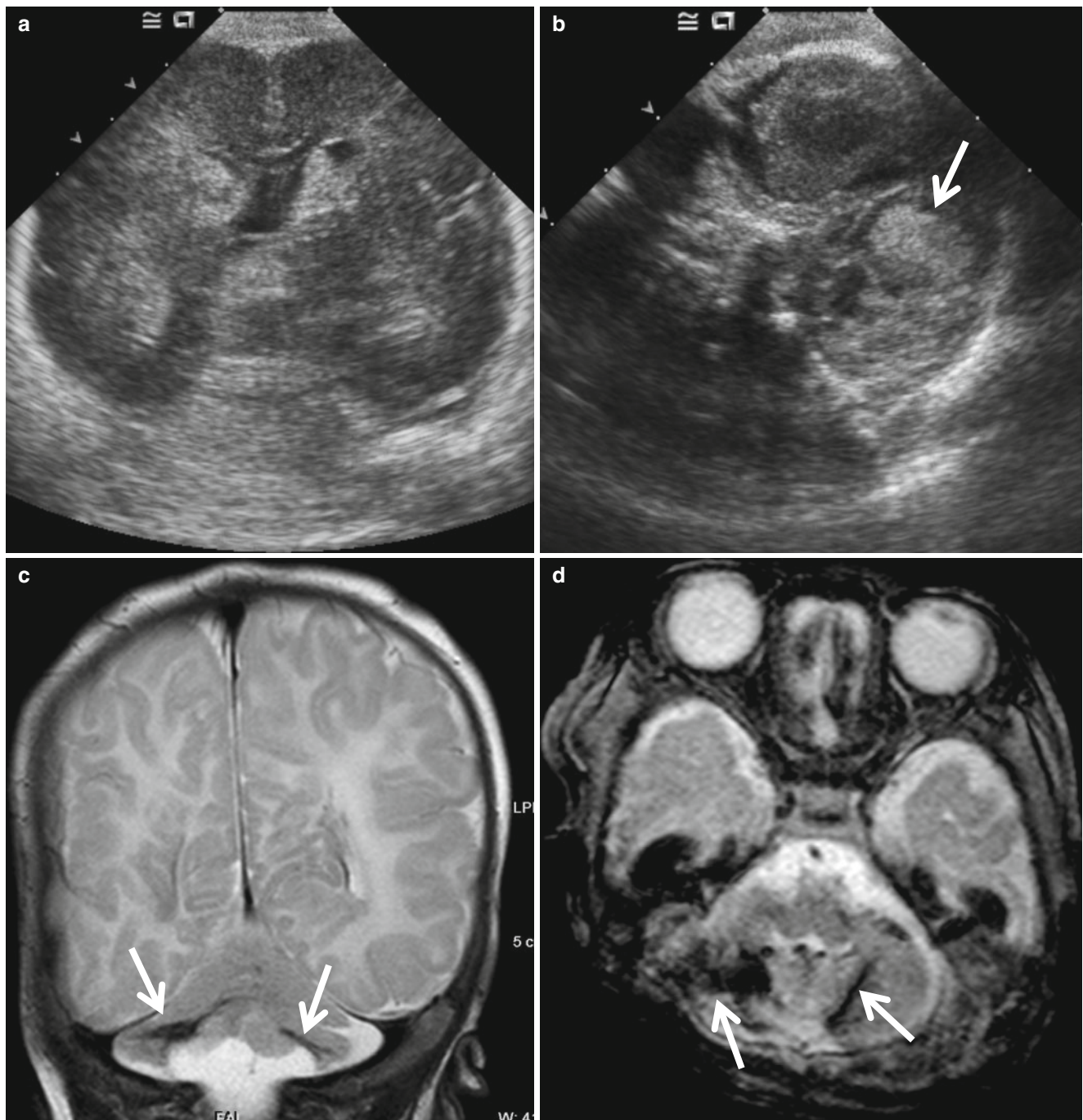


Fig. 5.7 Cerebellar hemorrhage in a neonate with GMH-IVH. (a) Coronal US image shows echogenic hemorrhage in the ventricles. However, cerebellar lesion is not evident because normal cerebellum is echogenic. (b) Echogenic hemorrhage (*arrow*) in the cerebellum is bet-

ter demonstrated on axial image obtained from the mastoid fontanel. (c) Bilateral cerebellar hemorrhage (*arrow*) with tissue loss is apparent on T2-weighted coronal image. (d) Gradient echo axial image demonstrate hemorrhage sensitively as dark signal intensity (*arrows*)

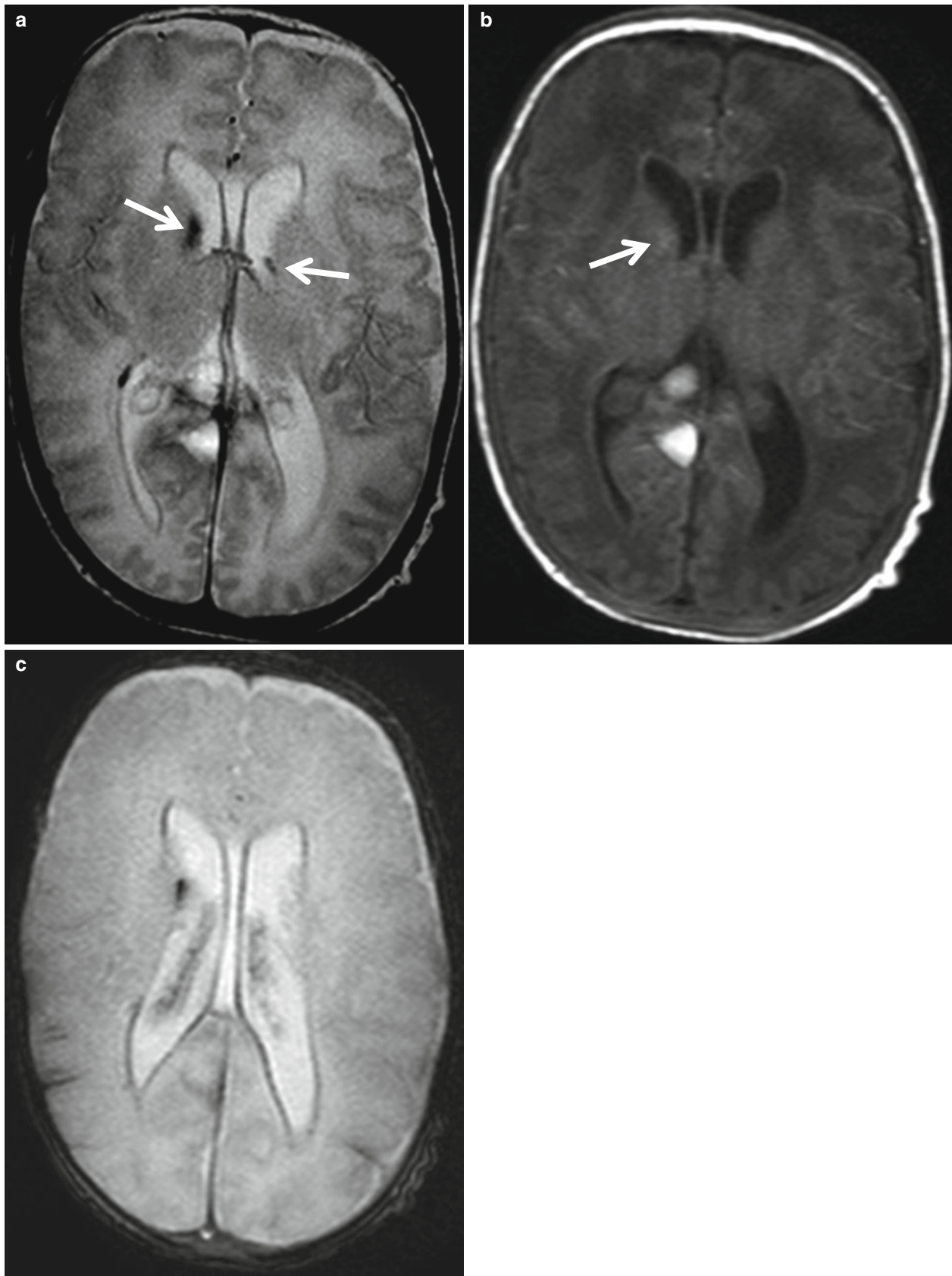


Fig. 5.8 GMH-IVH in MR images. (a) GMH is seen as dark signal intensity on T2-weighted image. Dark signal intensity along the ventricular margin suggests hemorrhage. (b) On T1-weighted image, GMH

is slightly hyperintense (*arrow*). (c) Gradient echo image more sensitively reveals hemorrhage as dark signal intensity

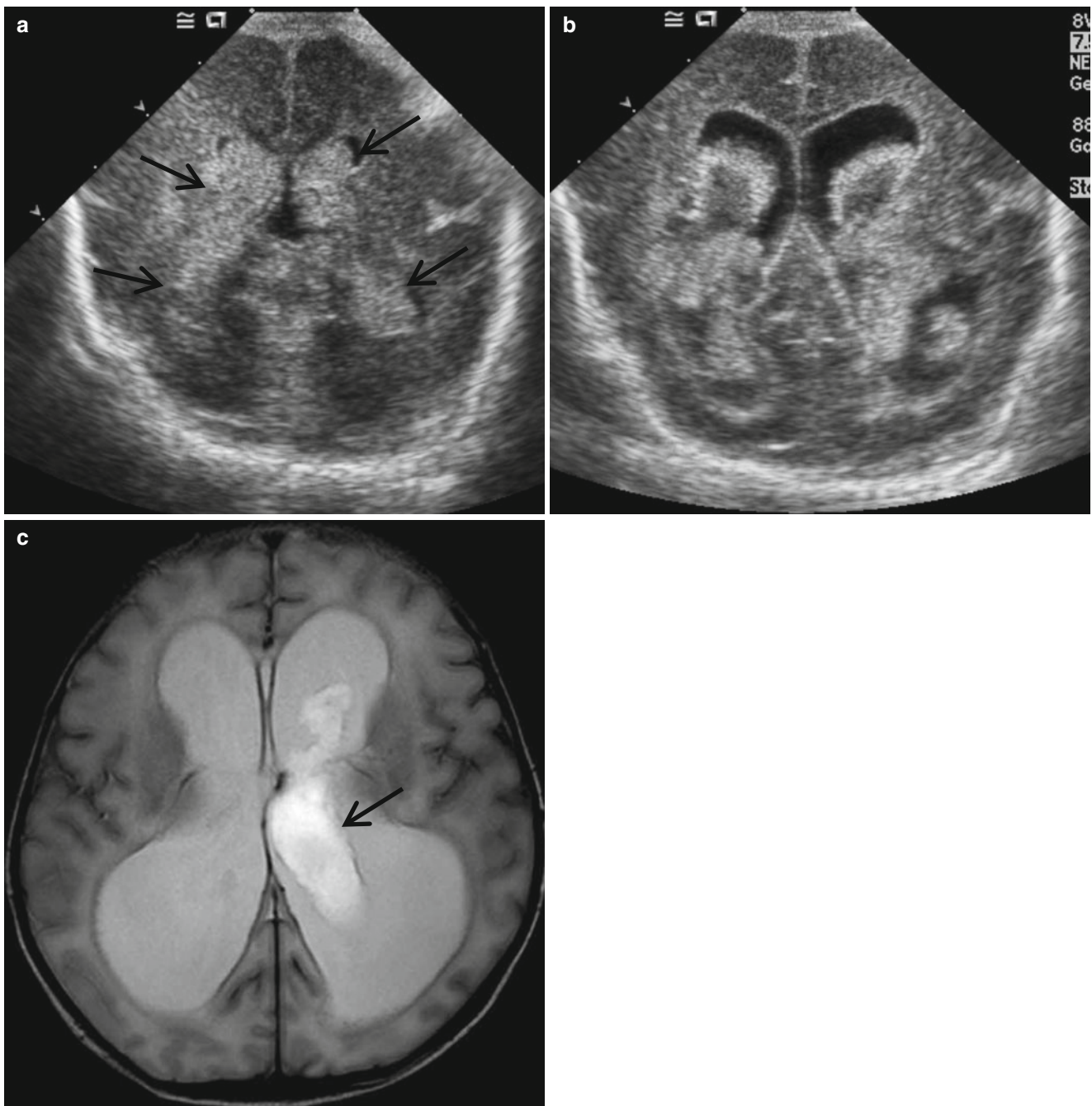


Fig. 5.9 Grade 3 IVH. (a) Coronal sonogram shows bilateral large echogenic hemorrhage casting the ventricles. The ventricles are slightly distended. (b) Follow-up US obtained 1 week later reveals further enlarged ventricles and central hypoechoic area within the hematoma

suggesting liquefaction. (c) Axial T2-weighted image shows progression of the ventricular distension and residual intraventricular clot (*arrow*) as high signal intensity

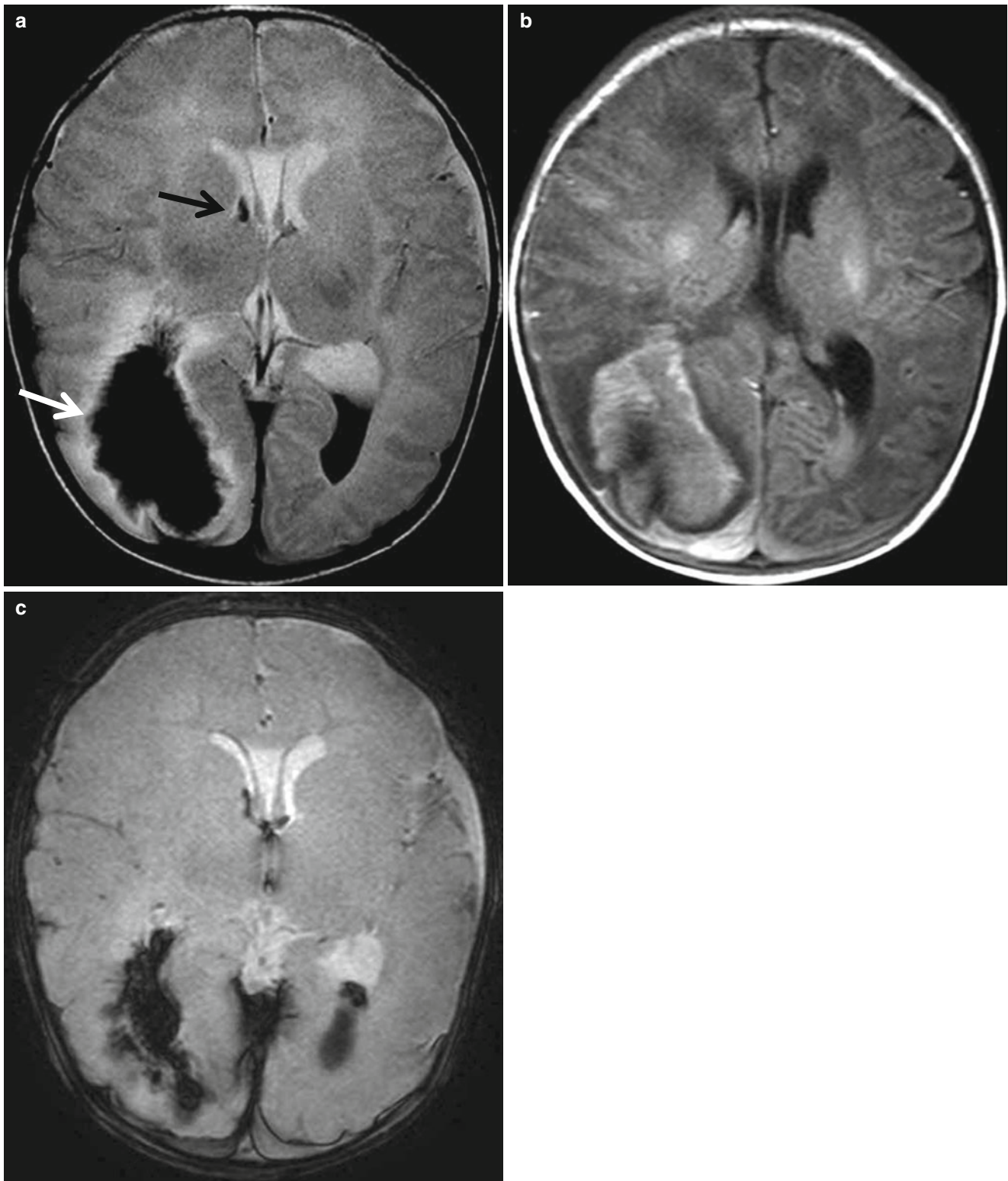


Fig. 5.10 Periventricular hemorrhagic infarct (PVHI). (a) T2-weighted image shows hypointense hemorrhage extending from the ventricle into the adjacent periventricular white matter (*white arrow*). The white matter surrounding the hemorrhage is hyperintense, and multiple streaky dark signal intensity lesions are extending from the white matter

hemorrhage, suggesting medullary veins. There are GMH (*black arrow*) and IVH seen as dark signal intensity fluid level. (b) Hemorrhagic lesions are seen as high signal intensity on T1-weighted image, suggesting subacute hemorrhage. (c) Gradient echo image shows hemorrhage as dark signal intensity

5.4.1.6 Hypoxic Ischemic Brain Injury in Terms; Watershed Injury

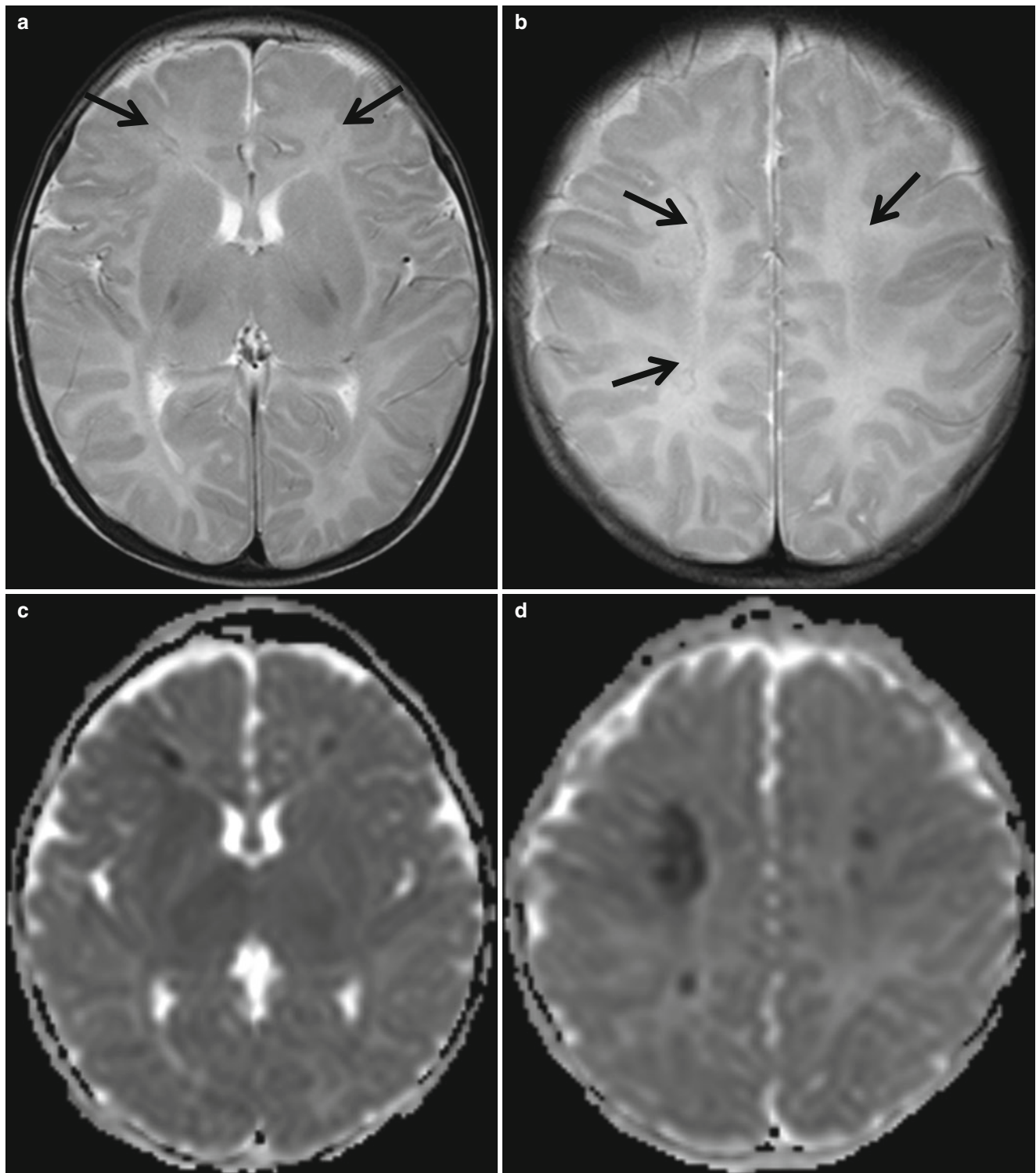


Fig. 5.11 Acute parasagittal injury in term neonate with complex heart disease. (a, b) T2-weighted axial images show subtle hypointense lesions at bilateral parasagittal areas (arrows). (c, d) ADC maps dem-

onstrate corresponding diffusion restriction suggesting acute cytotoxic edema or hemorrhage

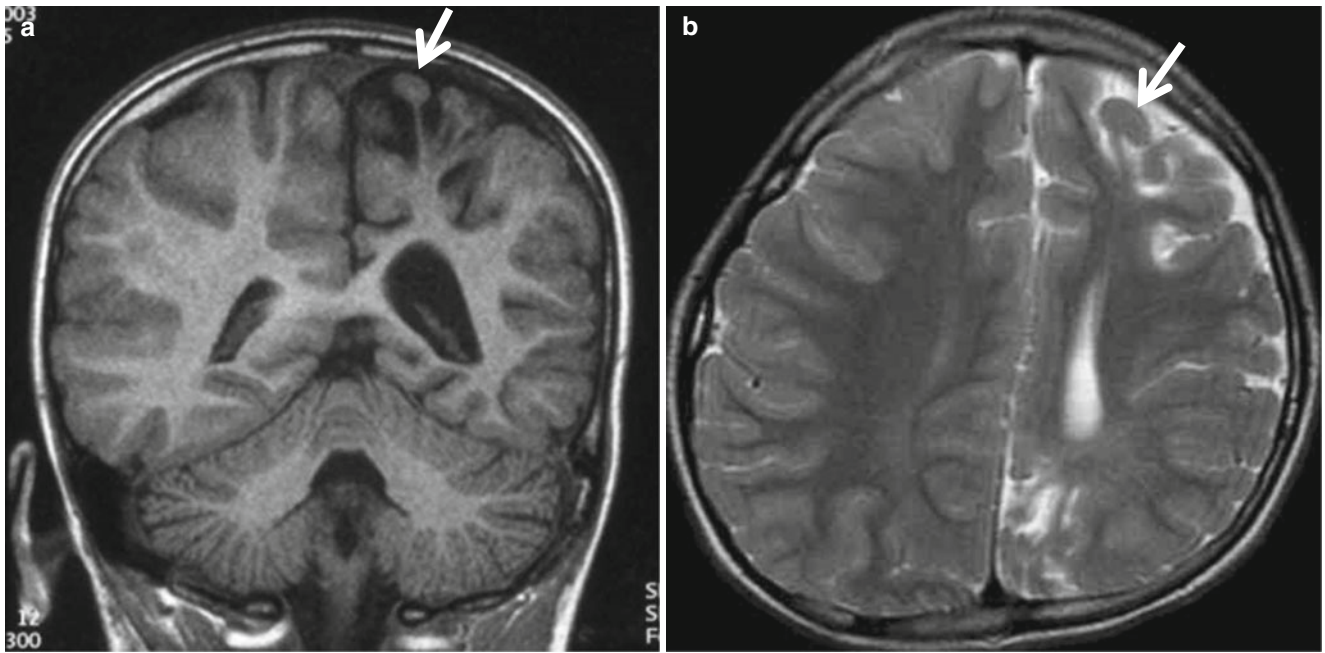


Fig. 5.12 Ulegyria in chronic watershed injury. T1-weighted coronal (a) and T2-weighted axial (b) images show more tissue loss at the depth of sulci than the superficial portion of the cortex resulting in mushroom-shaped gyri (*arrow*)

5.4.1.7 Hypoxic Ischemic Brain Injury in Terms; Profound Injury

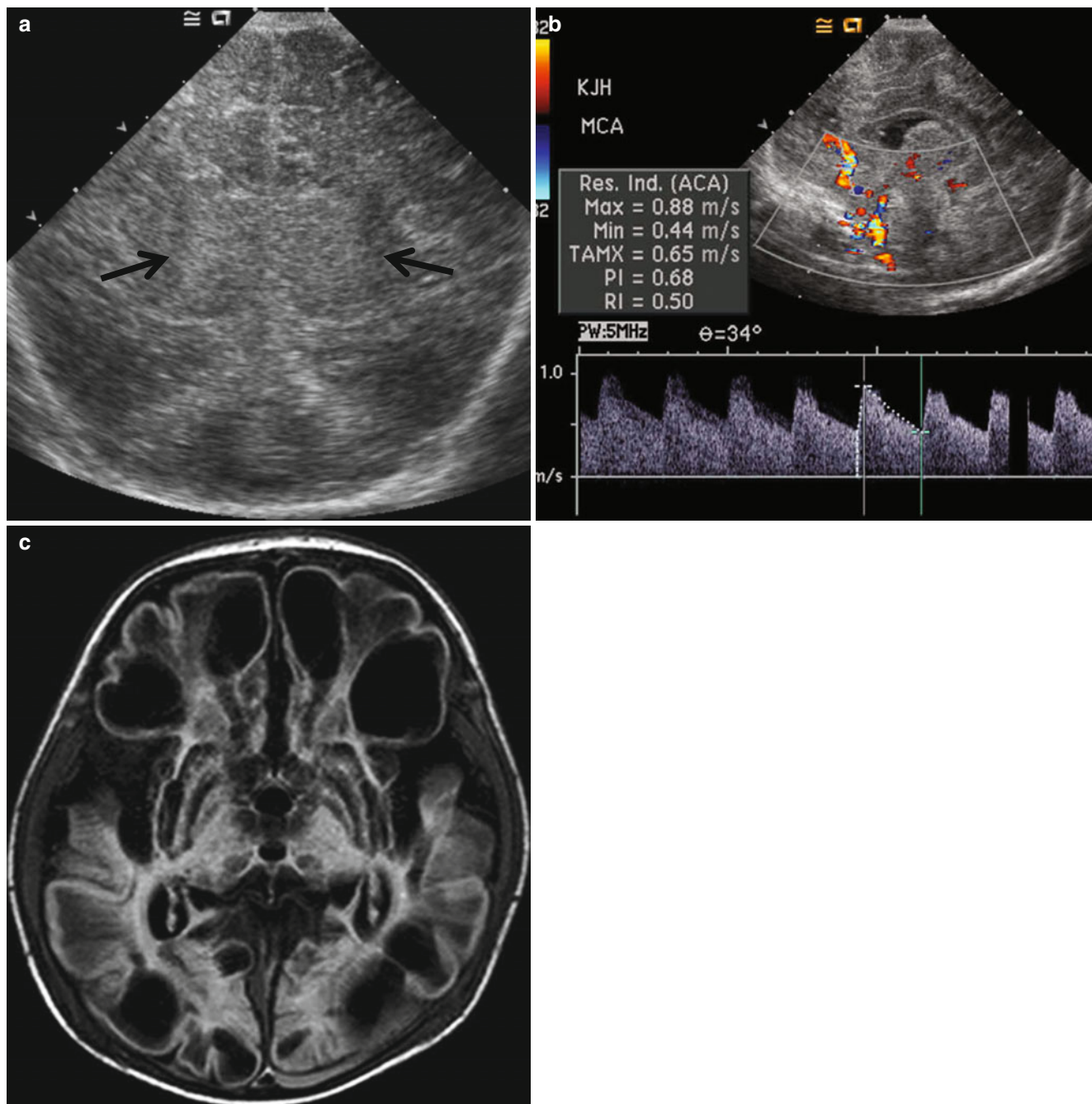


Fig. 5.13 Term neonate with birth asphyxia and meconium aspiration. (a) US shows diffuse swelling of the brain and increased echogenicity of the deep gray matter (arrows). (b) Doppler US demonstrates decreased RI (0.5) of the anterior cerebral artery in spite of the edema-

tous brain, suggesting impaired cerebral vascular autoregulation and decreased vascular resistance and increased end-diastolic flow. (c) Follow-up FLAIR image reveals extensive encephalomalacia of the brain and bilateral subdural hemorrhage

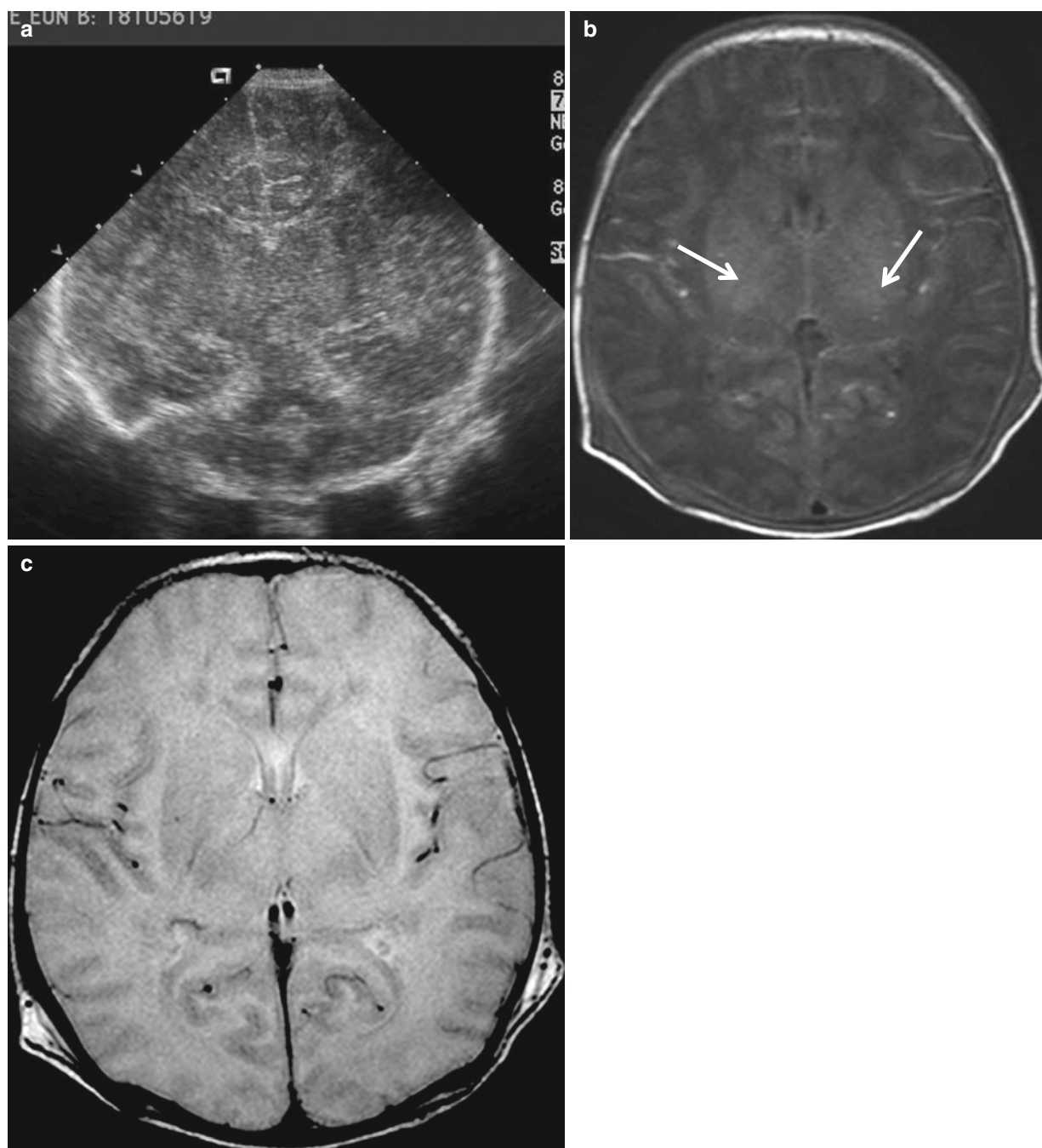


Fig. 5.14 Term neonate with meconium aspiration. (a) Sonography shows diffusely edematous brain and subtle echogenic thalami. (b, c) Normal posterior internal capsule myelin is absent on fast inversion recovery T1- and T2-weighted images (arrow), referred to as “absent

posterior limb sign.” (d) Serial ADC maps demonstrate diffusion restriction in the centrum semiovale, posterior internal capsule (arrow) and lateral thalami, midbrain, and dorsal pons (white arrow). (e) T2-weighted image obtained 10 months later shows extensive encephalomalacia

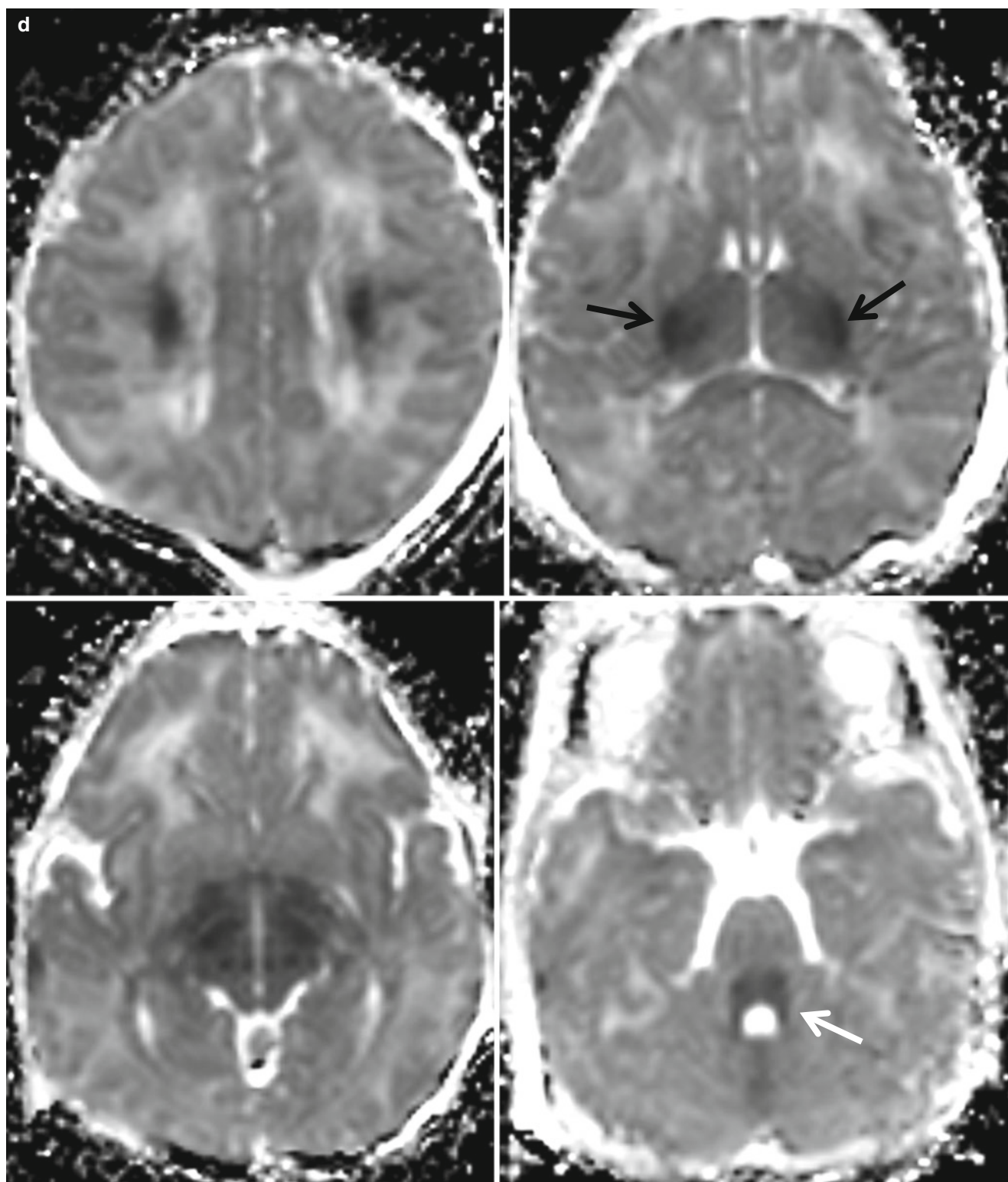


Fig. 5.14 (continued)

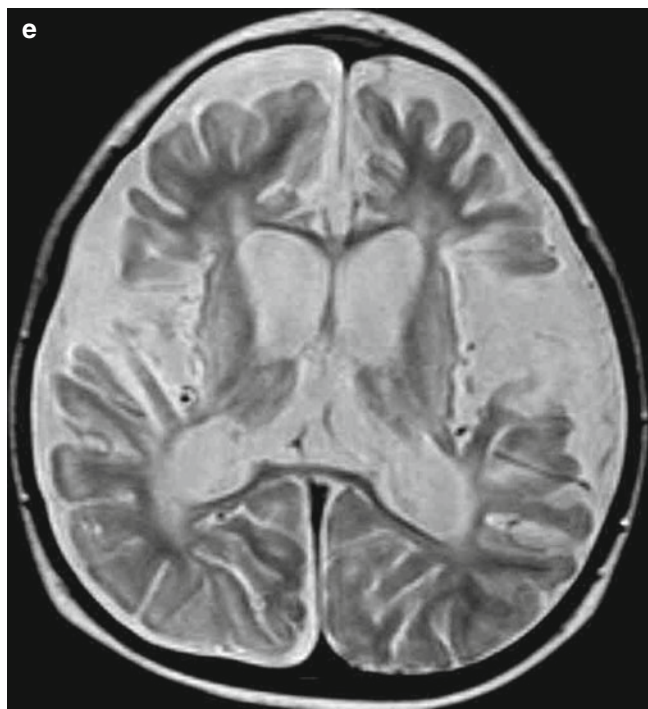


Fig. 5.14 (continued)

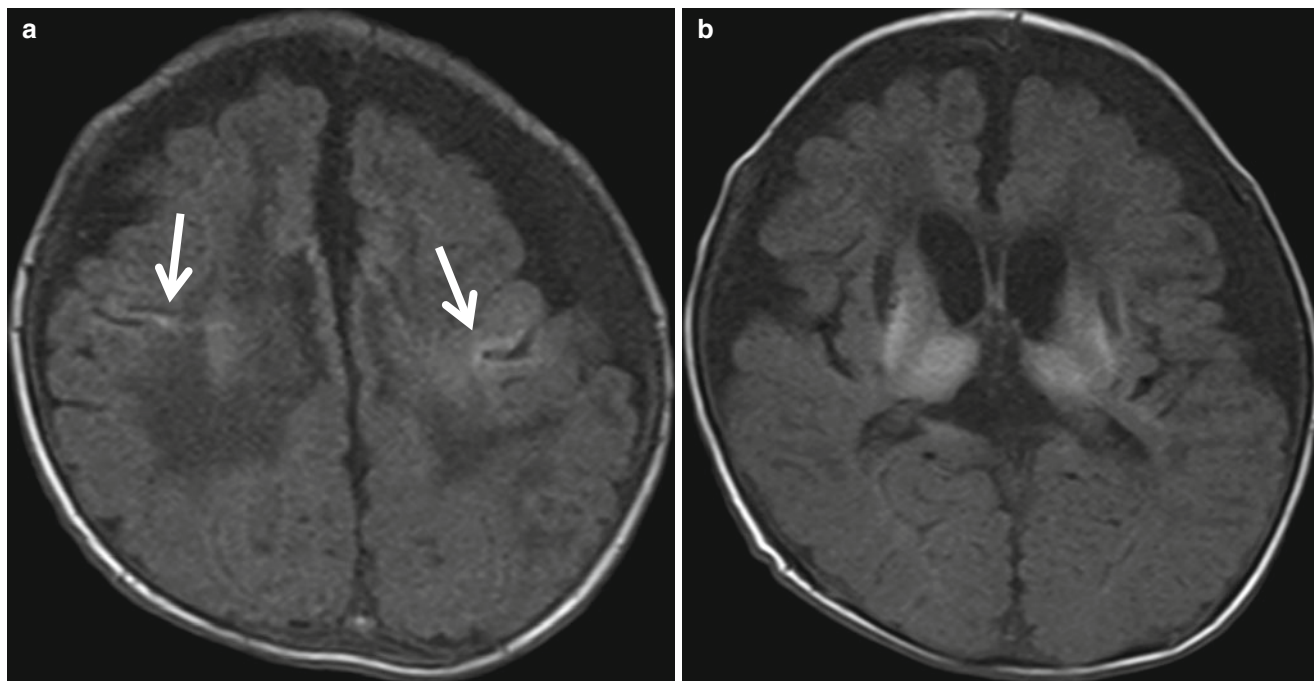


Fig. 5.15 Neonate born after 37 weeks of gestational period and placenta abruption. (a–c) Serial T1-weighted images demonstrate hyperintense lesions in the sensorimotor cortex (*arrows in a*), lateral thalami, basal ganglia, hippocampi (*arrows in c*), and brain stem, associated with volume loss. (d) Markedly decreased signal intensity in thalami

and excessive high intensity in the white matter are noted on T2-weighted image. (e) Follow-up T2-weighted image obtained at 2 years of age reveals diminished volume of the basal ganglia and thalami, enlarged ventricles, and disturbed myelination of the deep white matter (*arrow*)

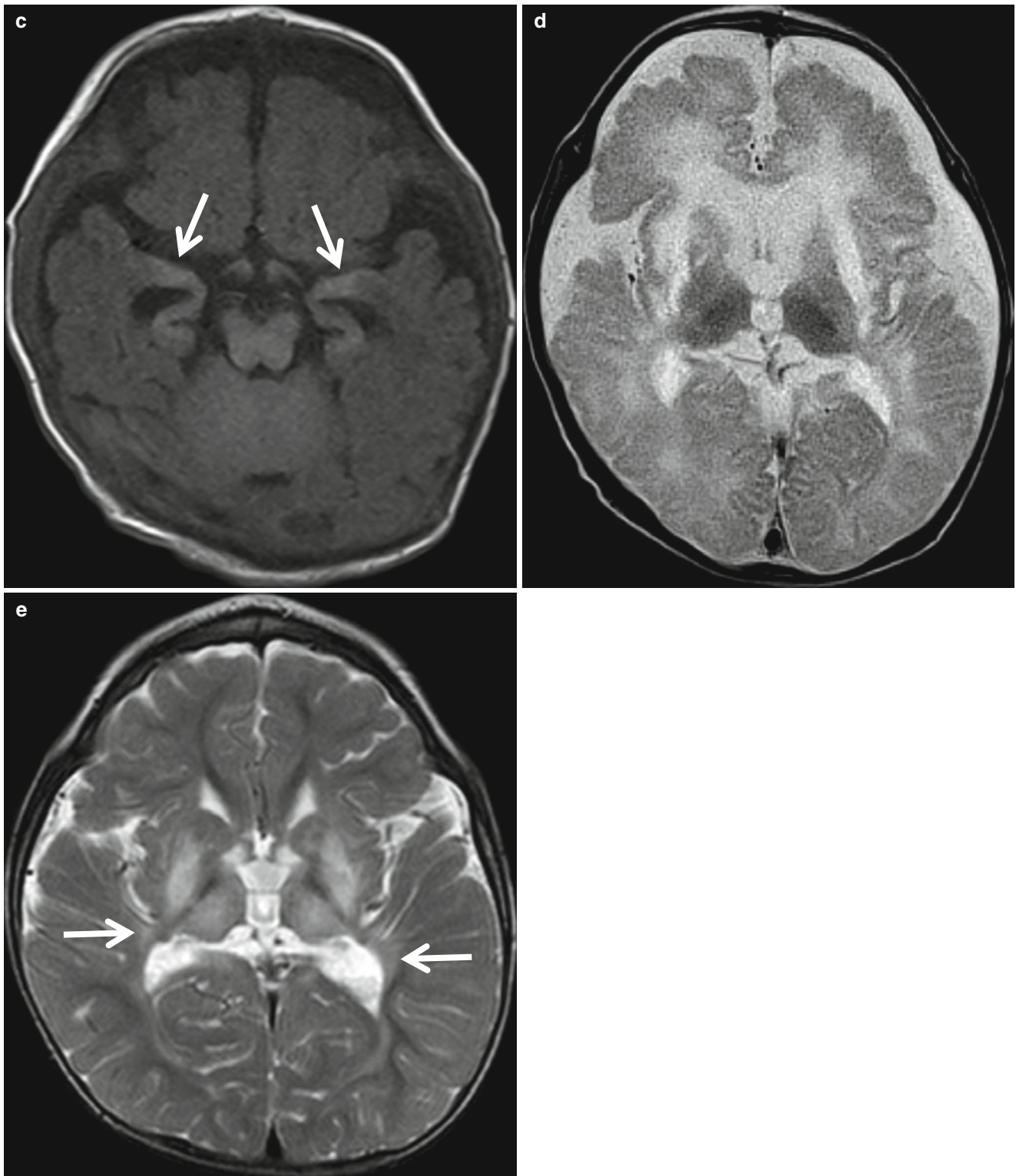


Fig. 5.15 (continued)

5.4.1.8 Hypoxic Ischemic Brain Injury; Normal Variant

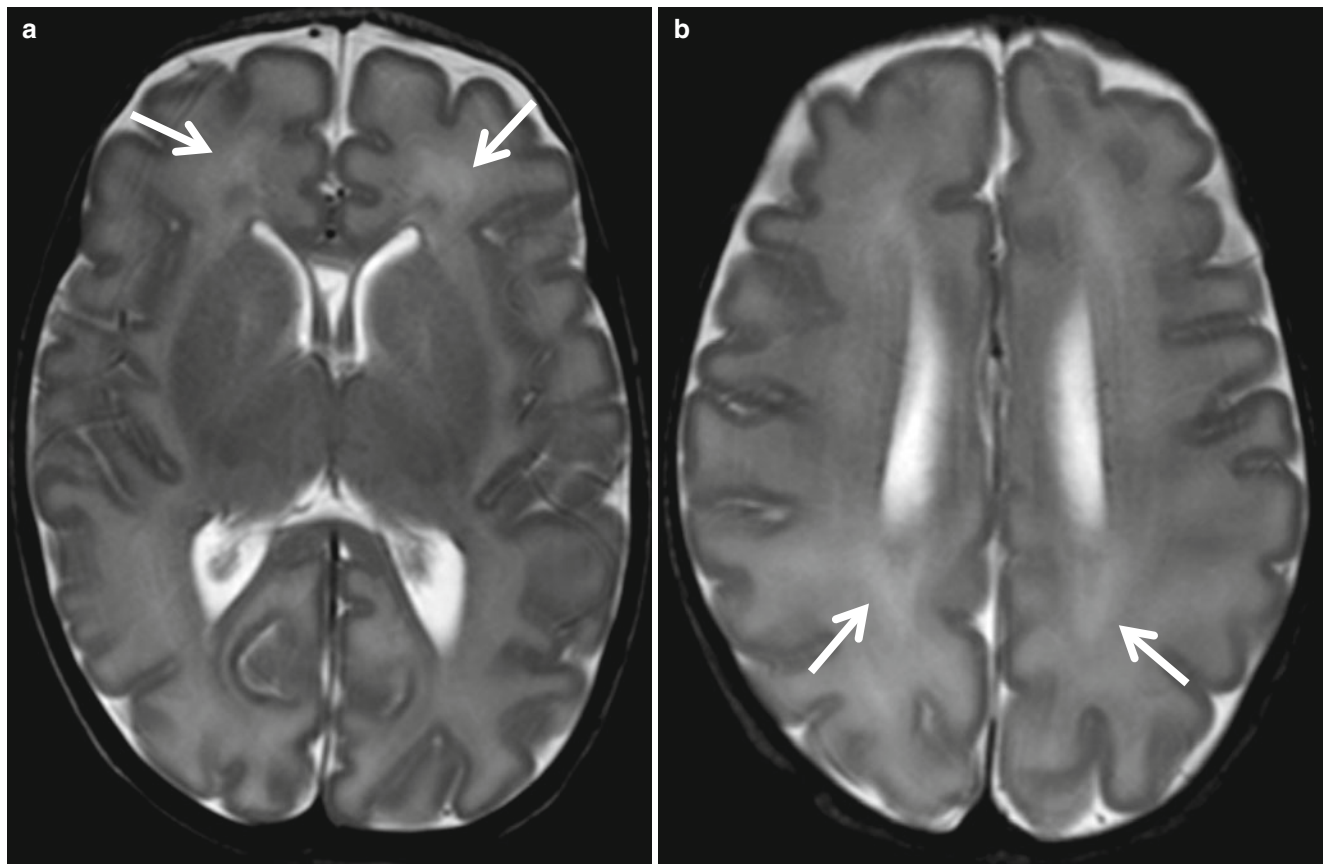


Fig. 5.16 Normal periventricular white matter in preterm baby at corrected gestational age of 35 weeks. (a) On T2-weighted image, developing white matter is seen as high signal intensity areas (*arrows*)

adjacent to the hypointense germinal layer. (b) This takes the form of arrowheads posteriorly (*arrows*)

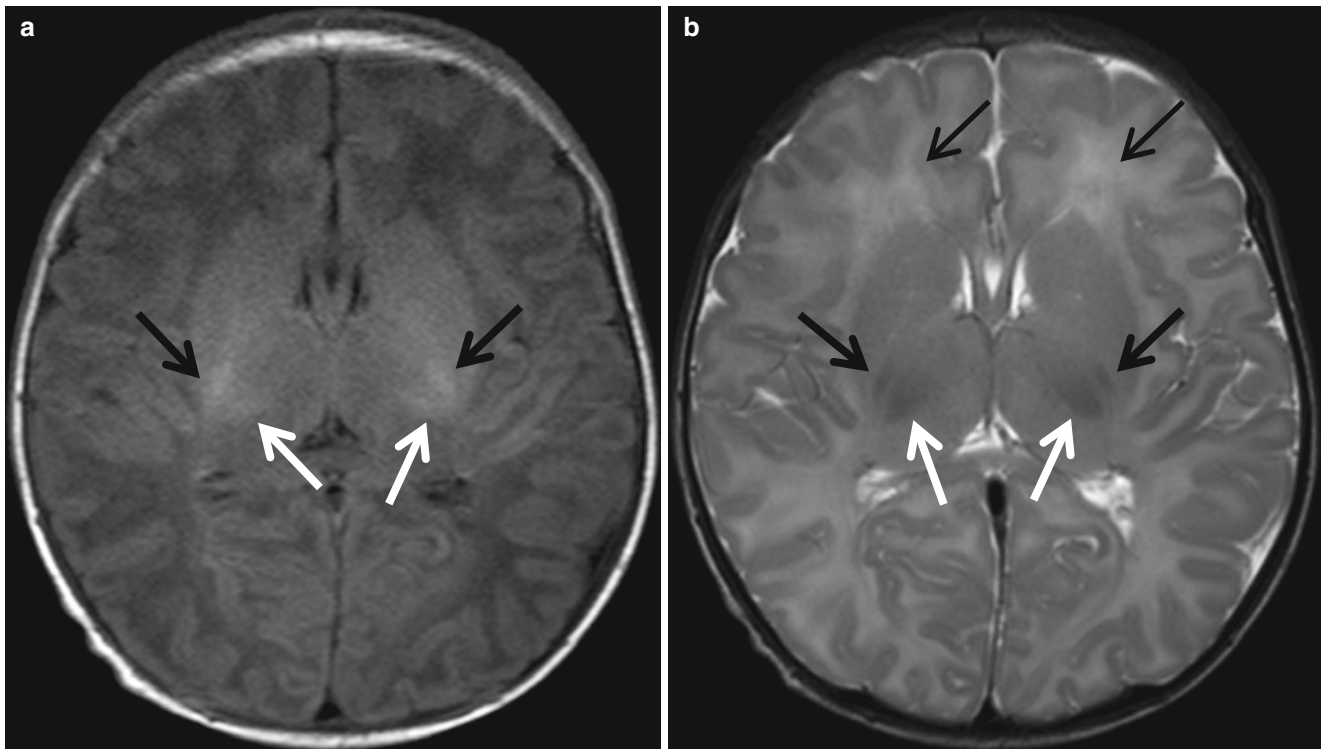


Fig. 5.17 MR images in a normal 4-day-old full-term neonate. **(a, b)** Axial T1-weighted image shows normally increased signal intensity of posterior limb of internal capsule (*arrows*) and ventrolateral nucleus of the thalami relative to basal ganglia and thalamus (*white arrows*). **(b)** The

posterior limb of the internal capsule (*arrows*) and ventrolateral nucleus of the thalami (*white arrows*) are hypointense on T2-weighted image. Anterior cap (*arrow*) is faintly visualized anterior to the frontal horn

5.4.1.9 Arterial Infarct

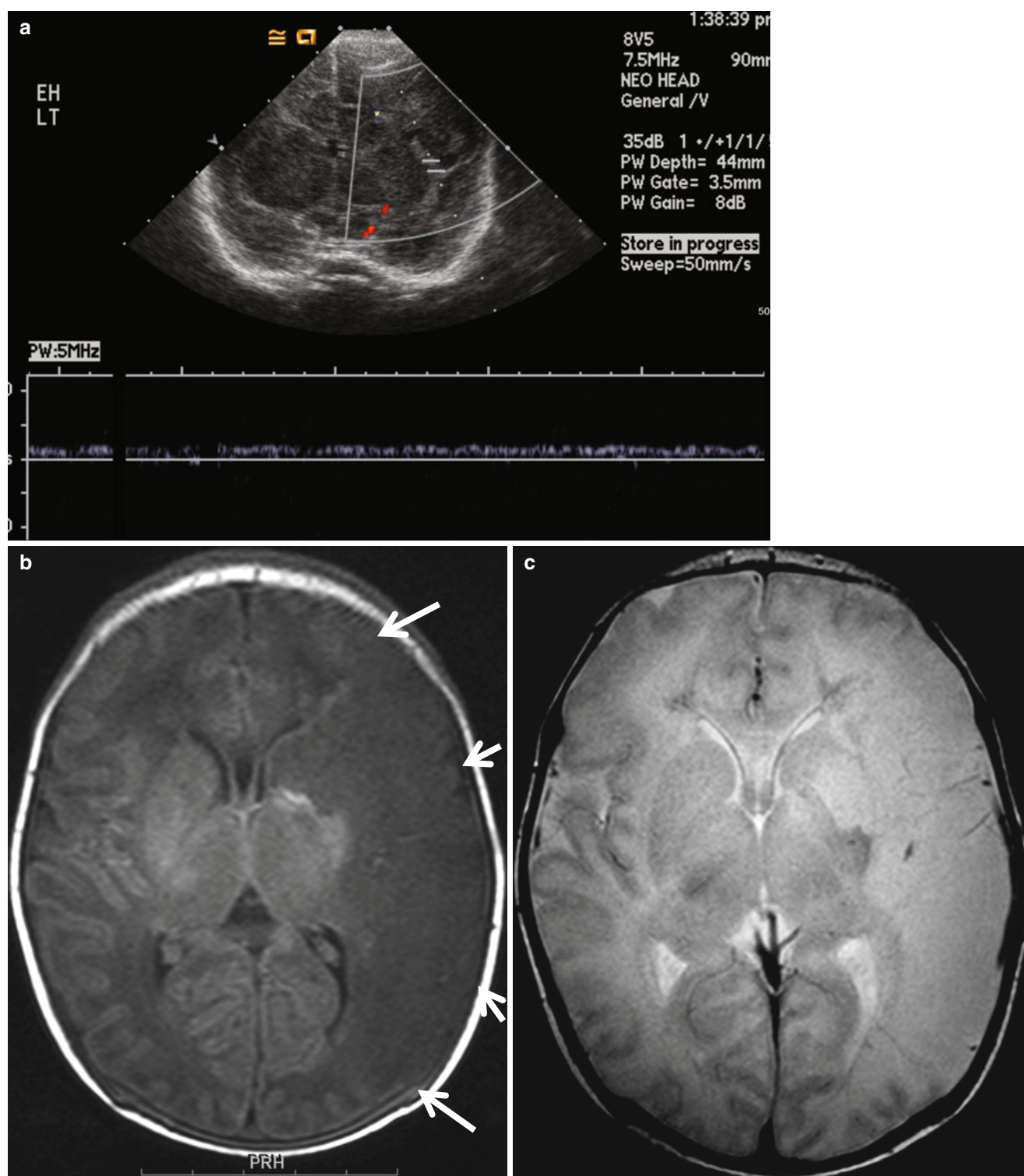


Fig. 5.18 Acute middle cerebral artery infarct in a neonate. (a) Very subtle increased echogenicity of the parenchyma is suspected, and left MCA flow is not visualized on Doppler US. (b) T1-weighted images show entire left MCA cortex and basal ganglia are hyperintense than the remaining gray matter and isointense with underlying white matter,

thus referred to as “missing cortex sign.” (c) T2-weighted images also show missing cortex as hyperintense compared with the remaining cortex at the left MCA area. (d) ADC map demonstrates reduced diffusion in the involved areas. (e) TOF MR arteriogram shows localized lack of flow-related enhancement at the left MCA (arrow)

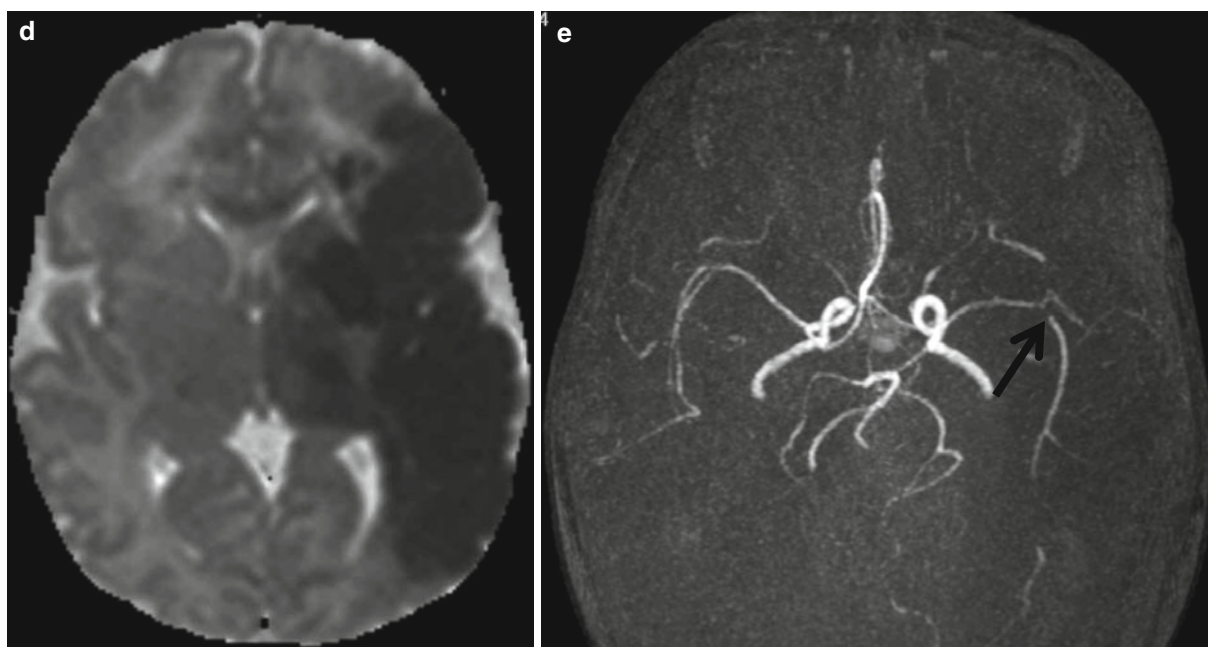


Fig. 5.18 (continued)

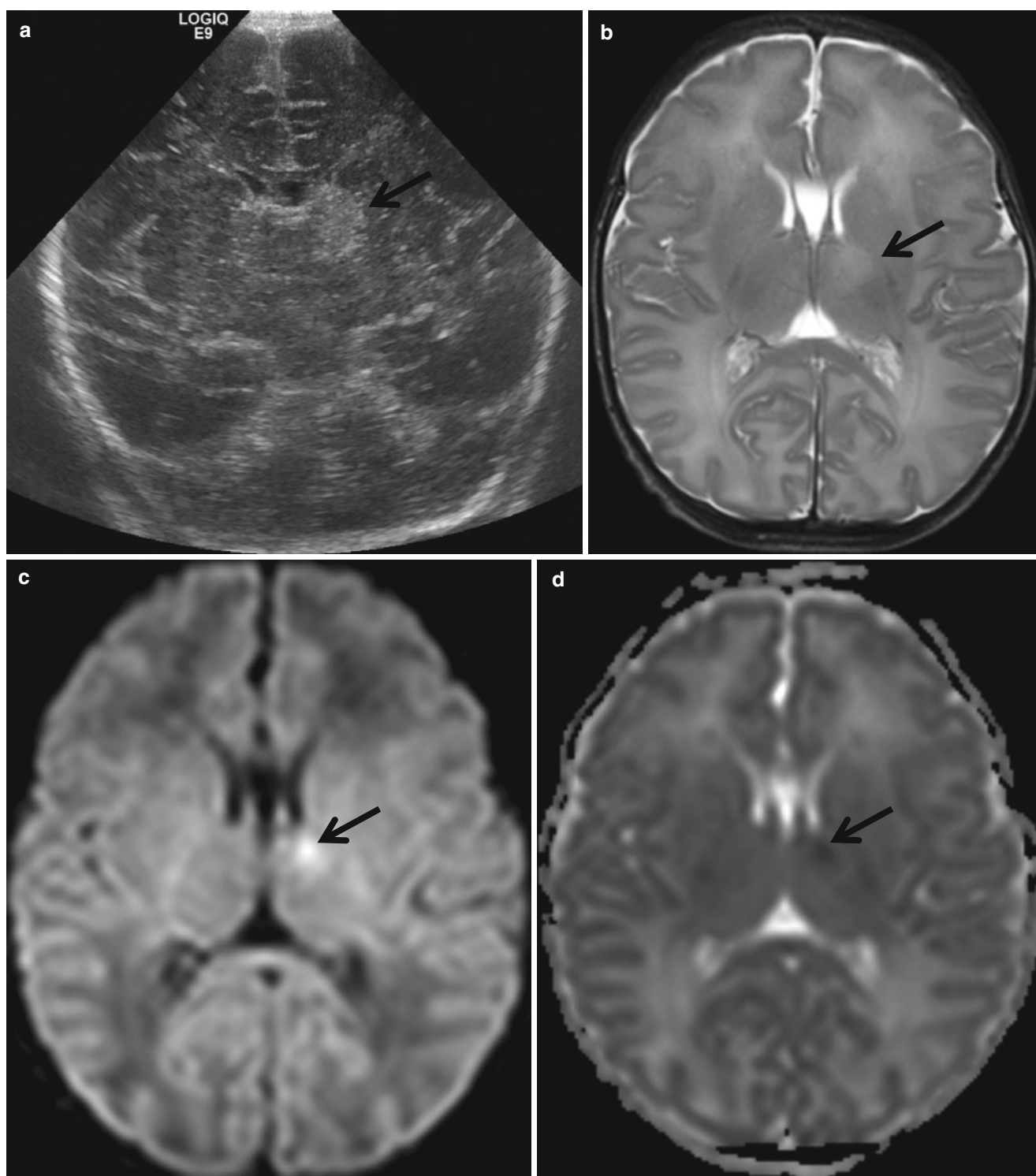


Fig. 5.19 Focal thalamic infarct in a neonate. (a) Coronal sonogram shows small echogenic area at the left thalamus (arrow). (b) T2-weighted image obtained the same day shows subtle high signal

intensity at the left thalamus (arrow). (c) Left thalamic lesion (arrow) is hyperintense on diffusion-weighted image. (d) Focal area of restricted diffusion (arrow) is seen at the left thalamus on ADC map

5.4.1.10 Venous Infarct

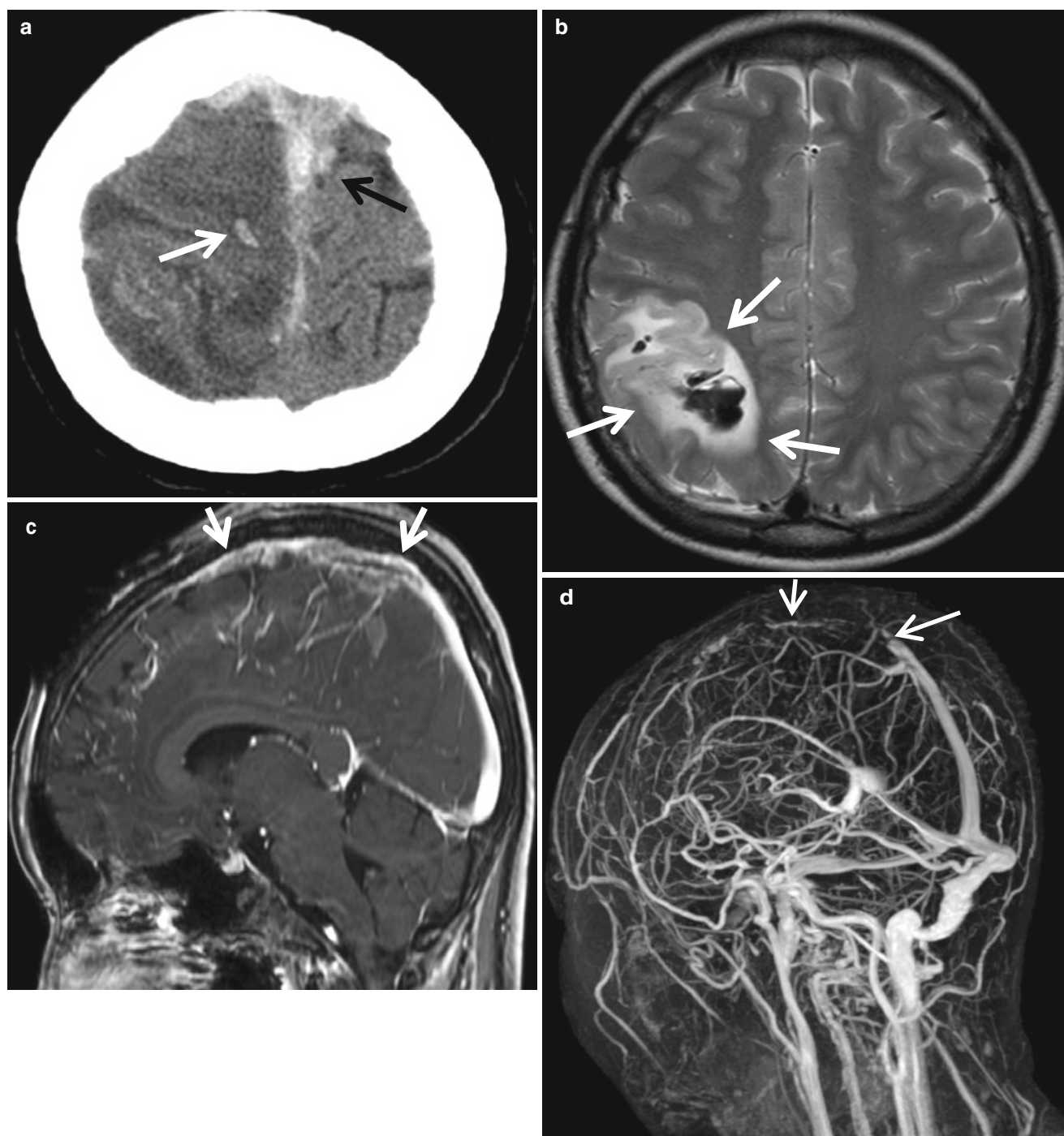


Fig. 5.20 Venous infarct, secondary to the superior sagittal sinus thrombosis. (a) Precontrast CT shows hyperdense superior sagittal sinus (black arrow) and adjacent parenchymal edema with hemorrhage (white arrow). (b) T2-weighted image shows large mass-like lesion containing hemorrhage and edema (arrows). (c) Postcontrast sagittal

T1-weighted image reveals isointense filling defects within the enhanced sinus (arrows). (d) MR venogram obtained after contrast administration demonstrates absent flow-related enhancement at the superior sagittal sinus (arrows)

5.4.2 CNS Trauma in Infants and Childhood

5.4.2.1 Birth Trauma

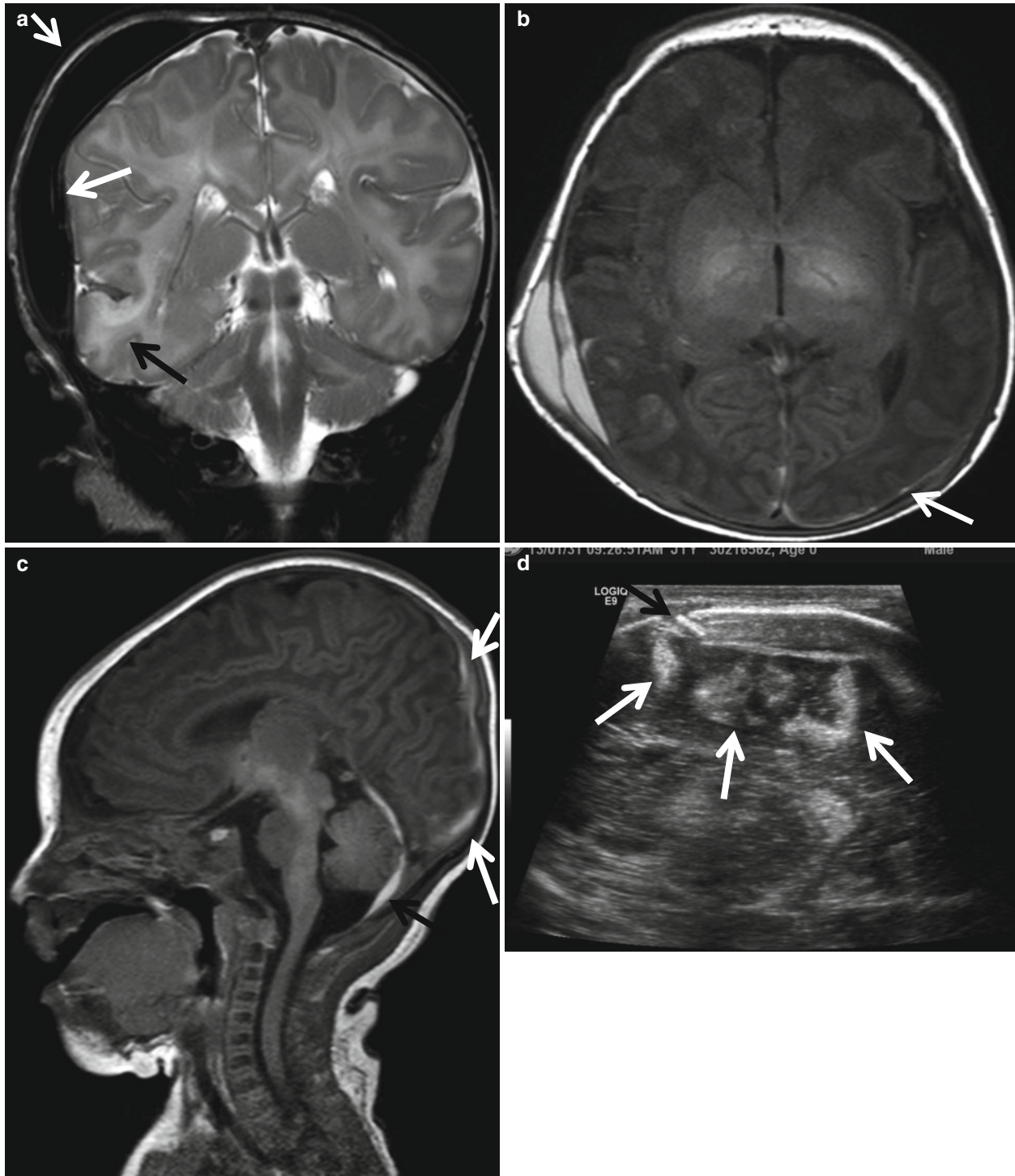


Fig. 5.21 Birth trauma. (a) T2-weighted coronal image shows right temporo-occipital cephalhematoma as dark signal intensity (*white arrows*). Note the depressed contour of the skull suggesting fracture. There is contusion at the adjacent occipital lobe (*black arrow*). (b) The cephalhematoma is hyperintense on T1-weighted axial image suggesting subacute lesion. Multifocal SDH is also noted at the inside of the cephalhematoma as well as along the left occipital lobe (*arrow*). There

are scattered high signal intensity lesions at the right temporo-occipital lobe, suggesting hemorrhagic contusion. (c) T1-weighted sagittal image reveals small amount of SDH in both the posterior fossa (*black arrow*) and supratentorial area (*white arrows*). (d) Transaxial sonogram shows displaced fracture fragment (*arrow*) and SDH. Echogenic parenchyma lesions (*white arrows*) are seen, suggesting hemorrhagic contusion

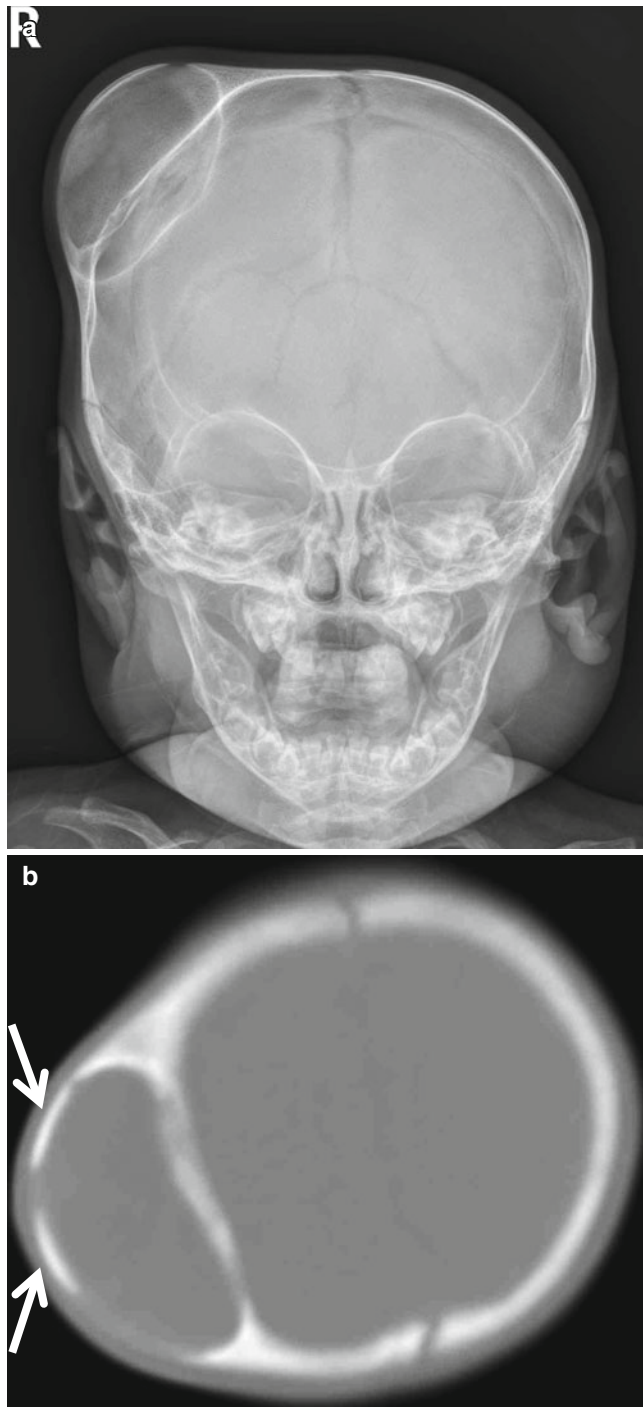


Fig. 5.22 Calcified cephalhematoma. (a) Skull radiography shows calcified bulging mass adjacent to the right parietal bone. (b) CT shows outer periosteal layer of the cephalhematoma has calcified (arrows)

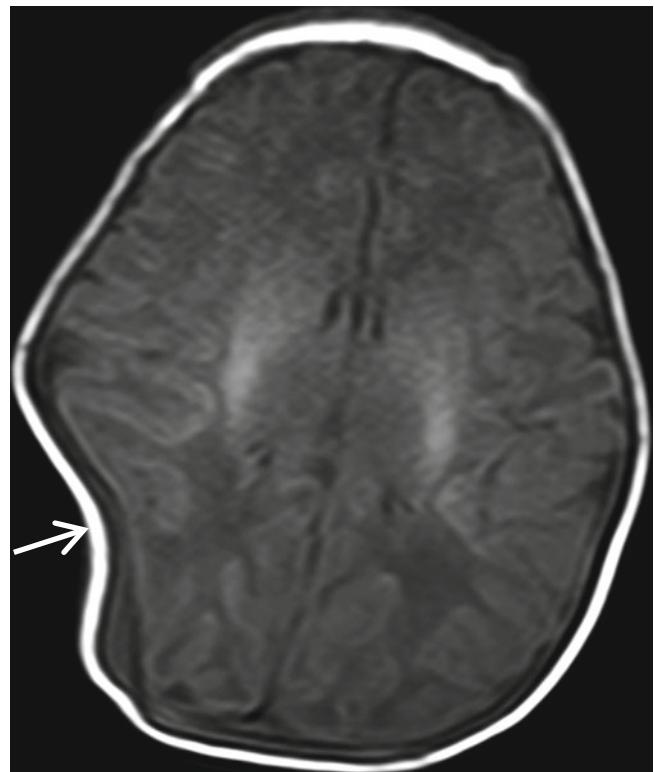


Fig. 5.23 Depressed skull fracture after forceps delivery. T1-weighted axial image shows depressed outer contour of the right temporo-occipital bone (arrow)

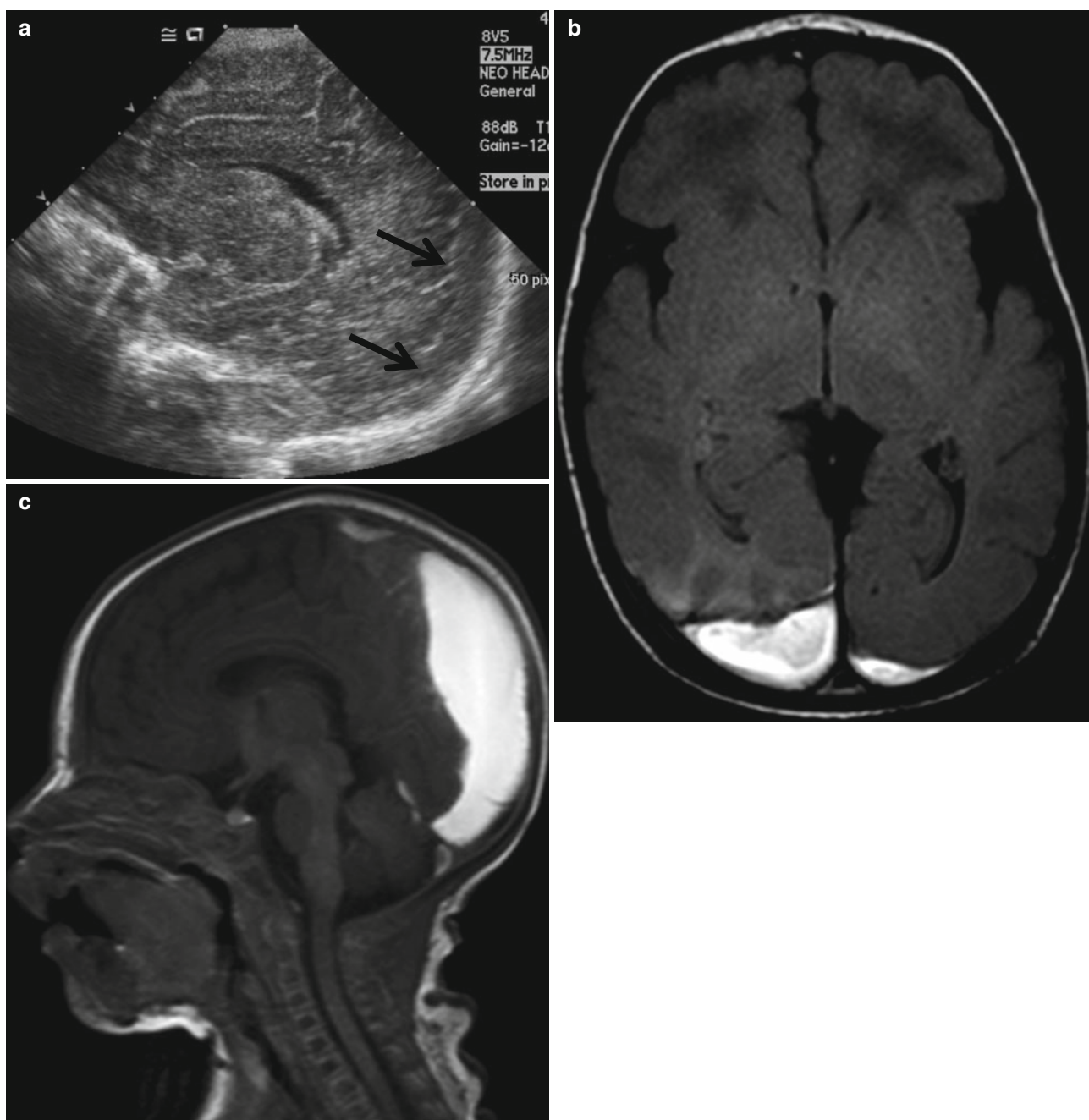


Fig. 5.24 Large amount of SDH. (a) Parasagittal sonogram shows isoechogenic extraaxial collection (*arrows*). (b, c) FLAIR axial and T1-weighted sagittal images demonstrate bilateral hyperintense SDH



Fig. 5.25 EDH in a neonate on the second day of life. Noncontrast CT shows hyperdense lentiform hematoma compressing the brain, adjacent to the fracture site (*arrow*). Large amount of cephalhematoma is also seen

5.4.2.2 Postnatal Trauma; Head Trauma



Fig. 5.26 Skull fracture with brain edema in a boy with a traffic accident. Precontrast CT shows fractured skull (*white arrow*) and tiny intracranial air (*black arrow*). Right lateral ventricle is collapsed, and subtle loss of gray–white differentiation of the right cerebral hemisphere is seen suggesting mild brain edema

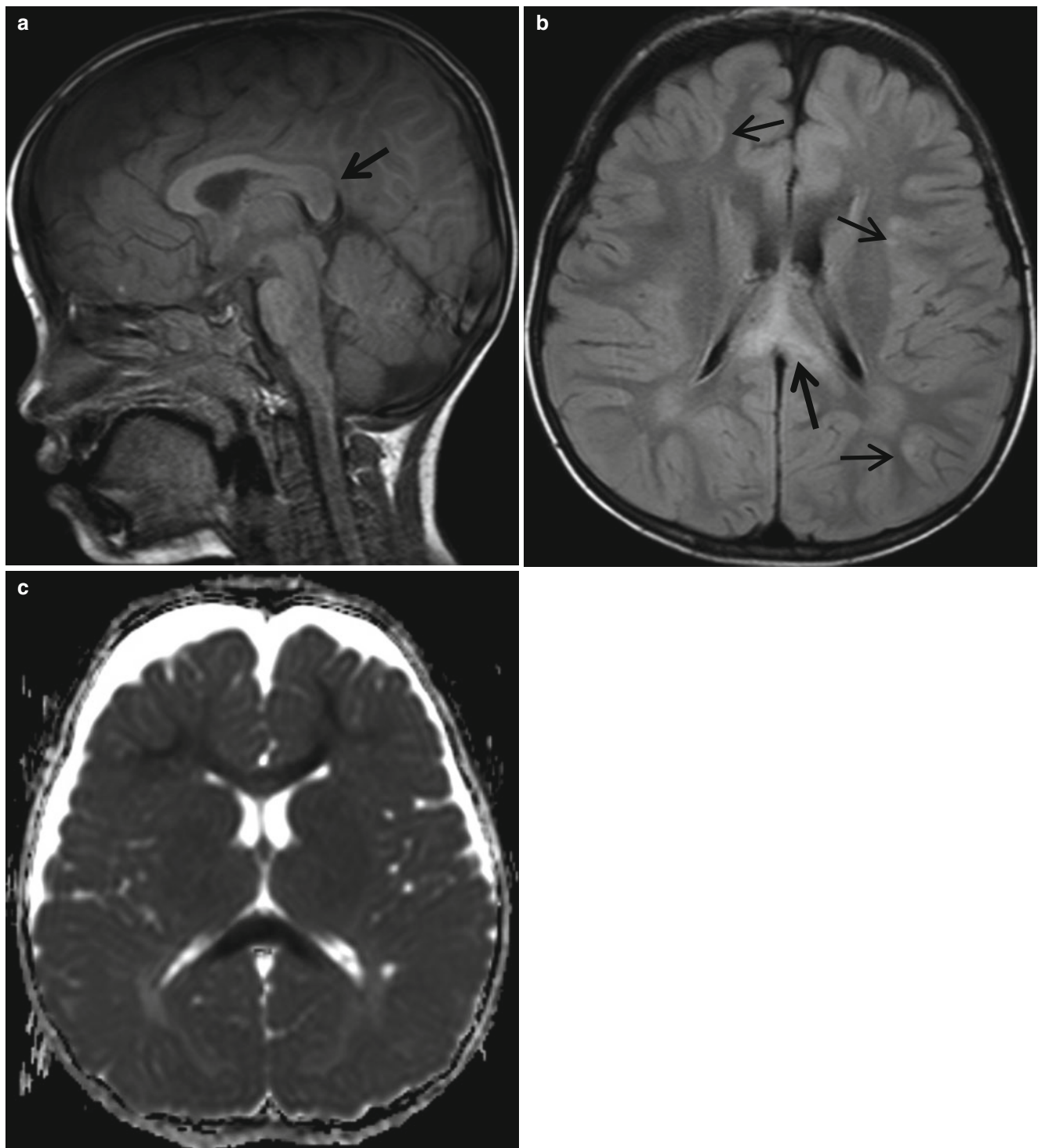


Fig. 5.27 Axonal injury. (a) T1-weighted sagittal image shows hypointense lesion at the splenium (*arrow*). (b) FLAIR image shows multiple high-intensity lesions at the splenium of the corpus callosum

(*large arrow*) and subcortical white matter (*small arrows*). (c) ADC map reveals diffusion restriction of the corpus callosum and peripheral white matter in both frontal lobes

5.4.2.3 Postnatal Trauma; Spinal Injury

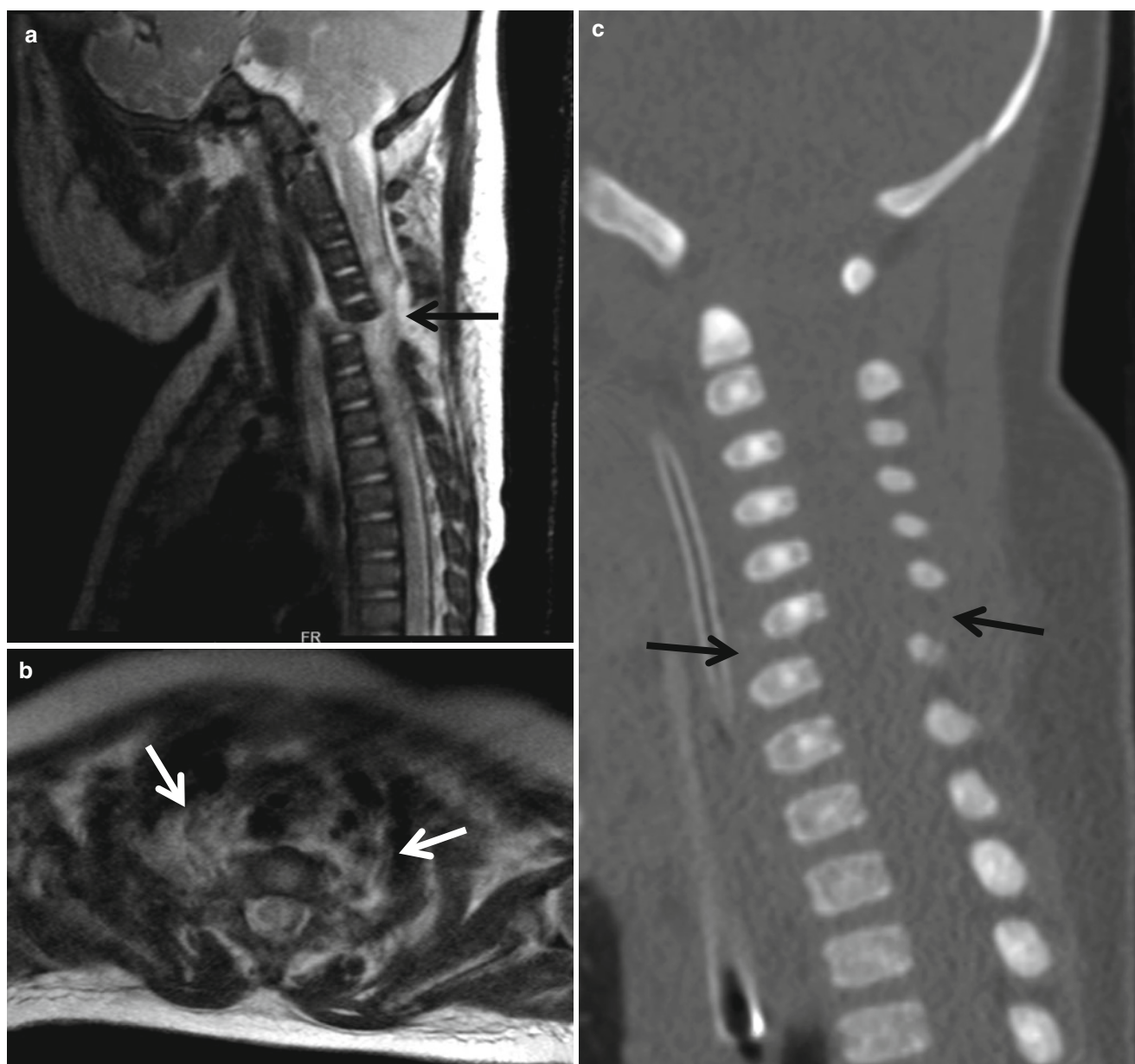


Fig. 5.28 Spinal injury in a neonate with traffic accident. (a) T2-weighted sagittal image shows fracture dislocation of the C6–7 level with prevertebral edema. The cervical cord is compressed by the displaced fragment anteriorly and epidural hemorrhage posteriorly (arrow). (b) T2-weighted axial image shows increased signal intensity

of the cord suggesting cord injury. Hyperintense edema and hemorrhage are also noted at the prevertebral space and mediastinum (arrows). (c) Sagittal reformation CT demonstrates disrupted bony alignment of the fractured cervical spine (arrows)

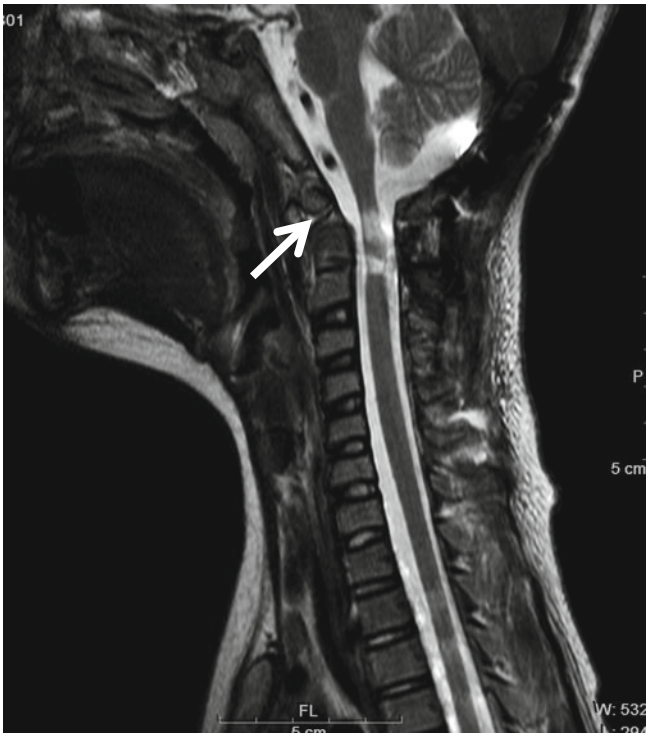


Fig. 5.29 Upper cervical injury in a 13-year-old boy. T2-weighted sagittal image shows fracture at the synchondrosis (*arrow*) between the dens and C2 body. Upper cervical cord at the same level is hyperintense and atrophic

5.4.2.4 Nonaccidental Injury

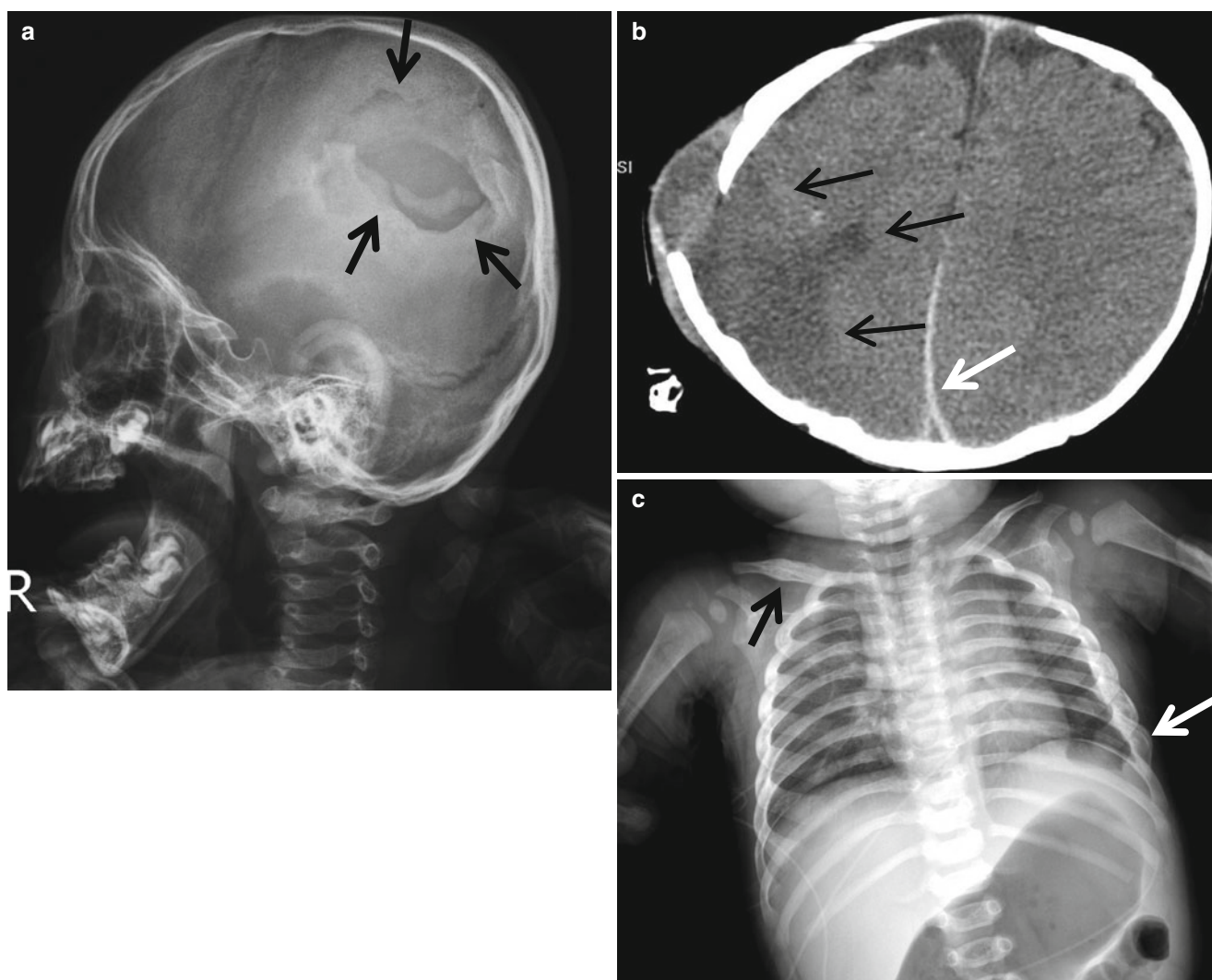


Fig. 5.30 Leptomeningeal cyst in nonaccidental injury. (a) Plain radiogram shows a well-defined lucent area (*arrows*) at the prior fracture site. (b) CT scan shows herniation of the CSF space through the dural defect causing increased defect. Previously noted encephalomalacia is filled

with isoattenuated fluid (*arrows*) suggesting hemorrhage. Recent SDH is seen along the falx (*white arrow*). (c) Chest radiography reveals old fracture deformity at the right clavicle (*black arrow*) and left seventh rib (*white arrow*)

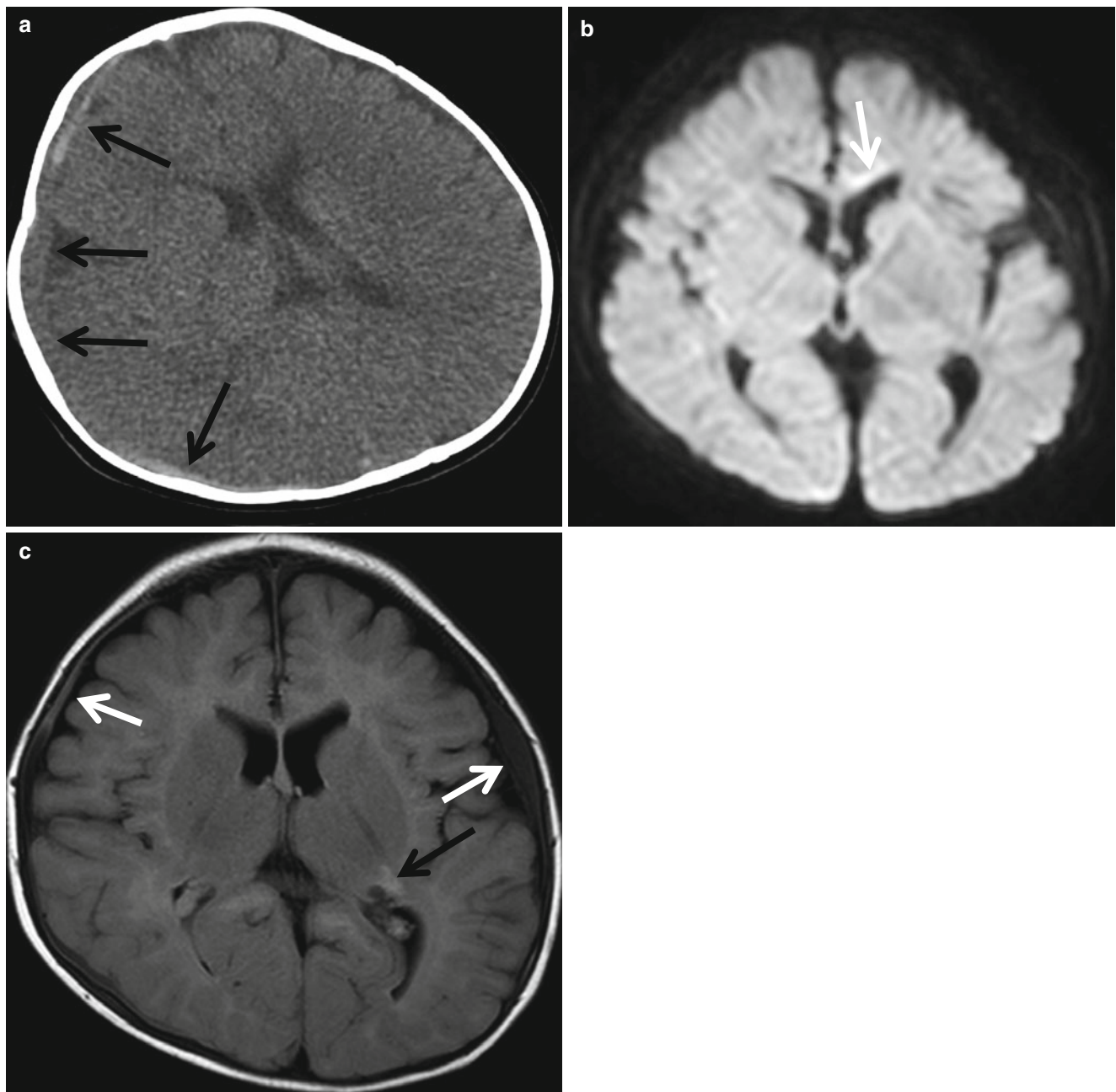


Fig. 5.31 Multistage SDH and parenchymal injury in nonaccidental injury. (a) Precontrast CT shows small amount of SDH of mixed iso- and high attenuation (*arrows*). (b) Diffusion-weighted image obtained 1 month later shows slightly hyperintense lesion in the left frontal lobe

(*arrow*). (c) The left frontal lesion is not seen on a FLAIR image, while there is an old parenchymal lesion with small encephalomalacia and gliosis (*black arrow*). Bilateral SDH (*white arrows*) of different signal intensities is also noted

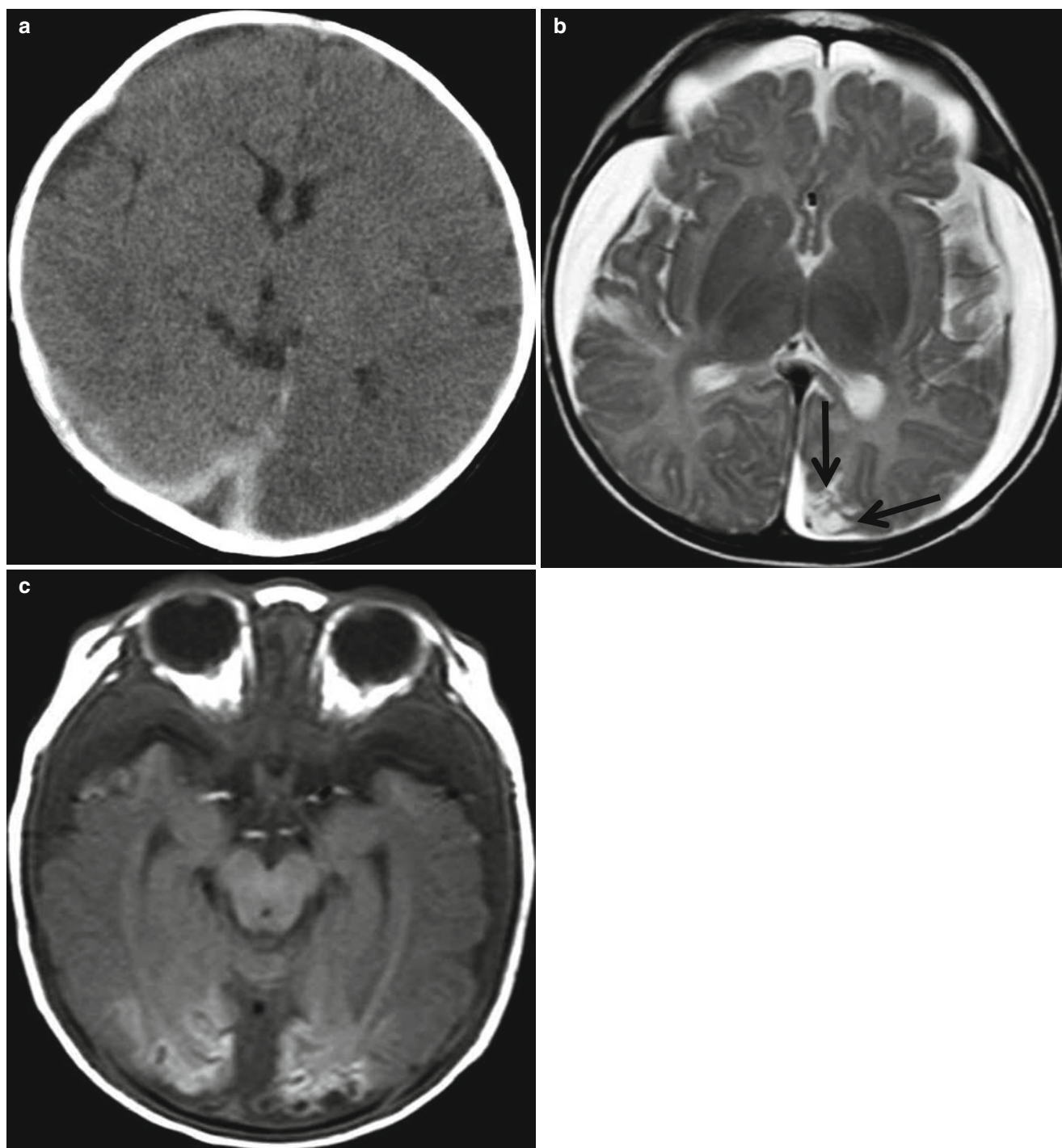


Fig. 5.32 Child abuse in a 1-month-old infant. (a) CT scan shows hyperdense SDH and subtle low attenuation of the left occipital lobe. (b) T2-weighted image obtained 1 month later reveals focal encephalomalacia

(arrows) in the left occipital lobe and large amount of bilateral SDH. (c) T1-weighted image at the higher level shows bilateral hyperintense occipital lesions, suggesting petechial hemorrhage

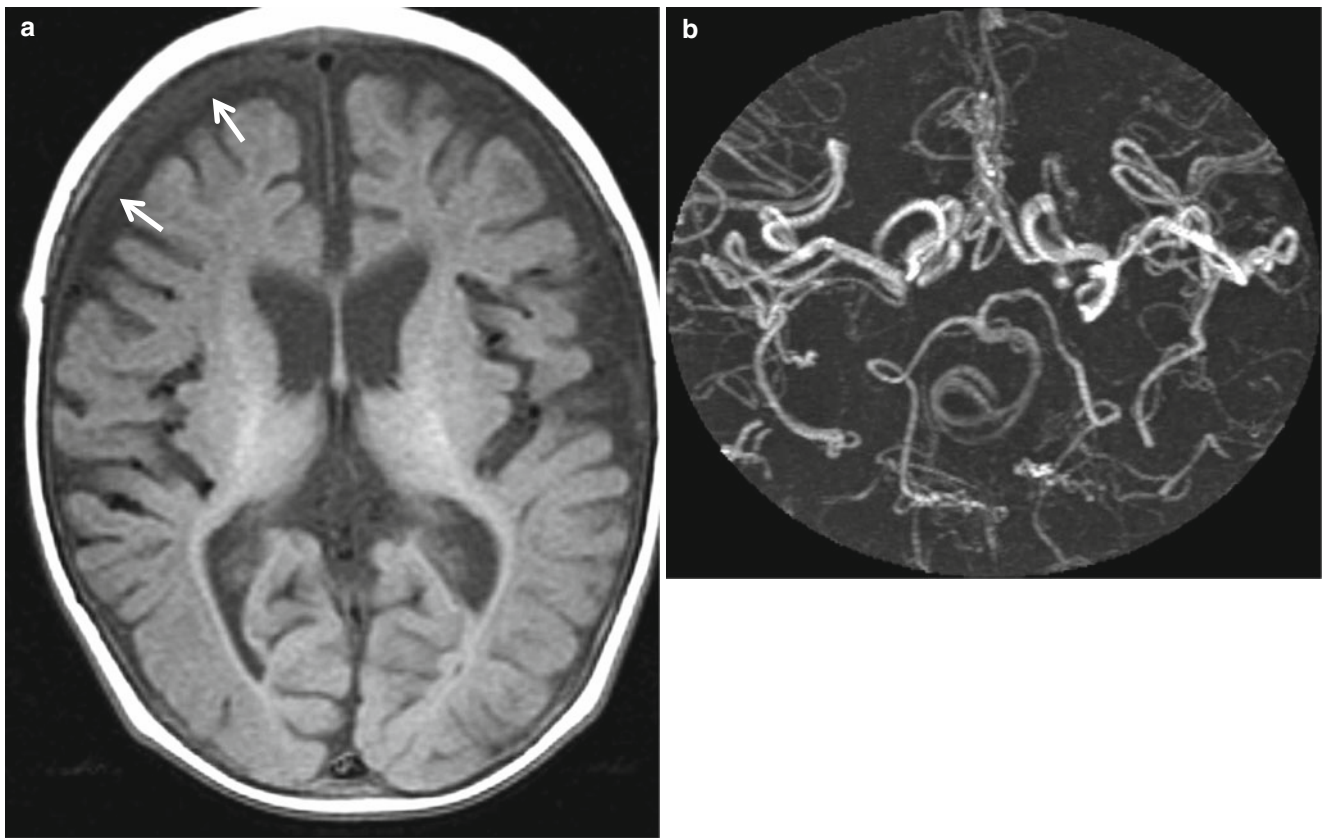


Fig. 5.33 Bilateral SDH in an infant with Menke's kinky hair disease. **(a)** T1-weighted image shows right SDH (*arrows*). In addition, the brain appears mildly atrophic, and prominent signal void vessels are seen. **(b)** MR angiography shows tortuous cerebral vessels

5.4.3 Cerebral Vascular Disorders in Children

5.4.3.1 Arteriovenous Malformation

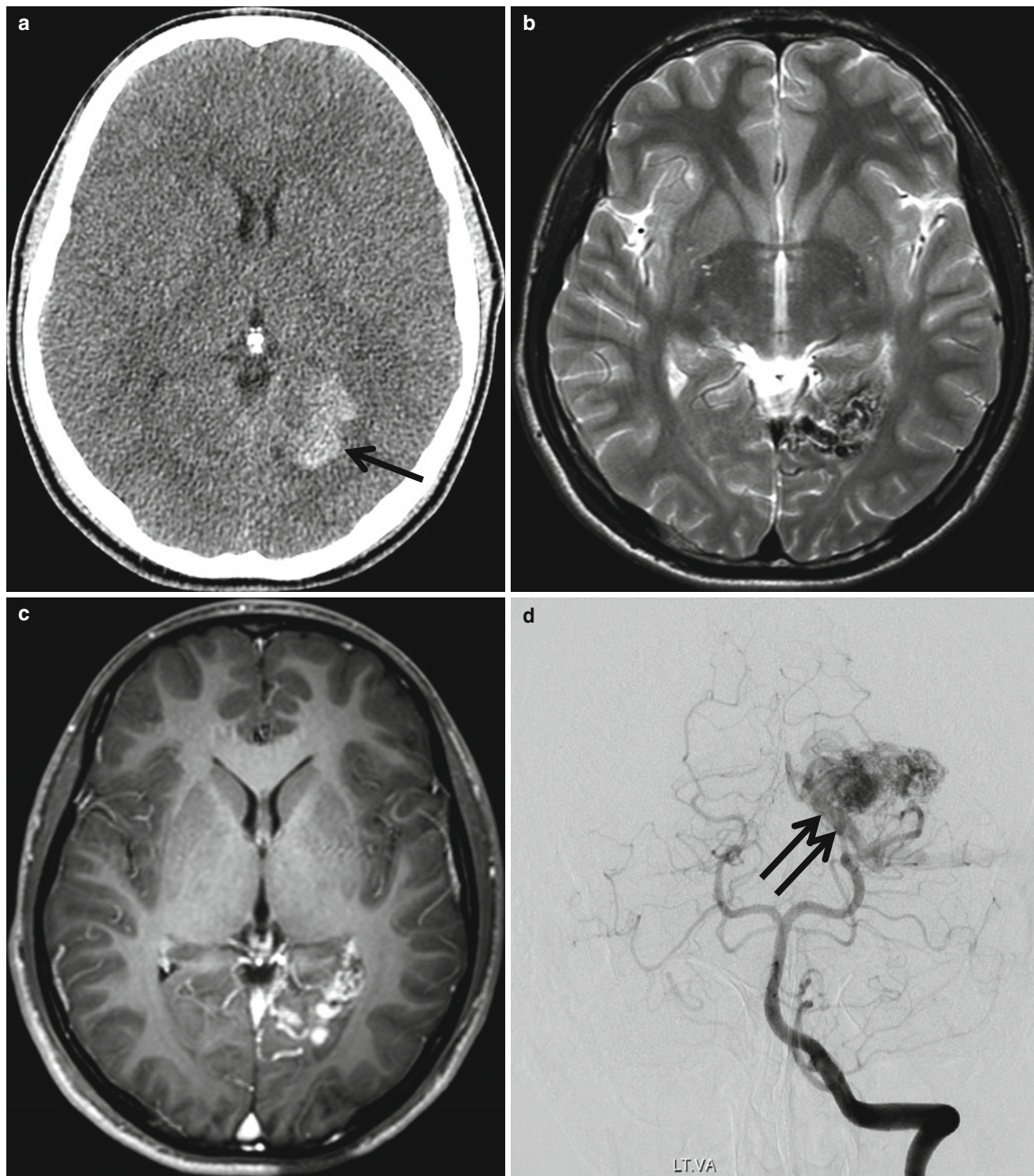


Fig. 5.34 ICH associated with AVM. (a) CT scan shows hyperdense hemorrhage (*arrow*) in the left occipital lobe. (b) T2-weighted image shows signal void entangled vessels at the same area. (c) Dilated

vascular enhancement is seen on postcontrast T1-weighted image. (d) AP image of vertebral arteriography demonstrates AVM fed by left posterior temporal artery. Early venous drain is also seen (*arrows*)

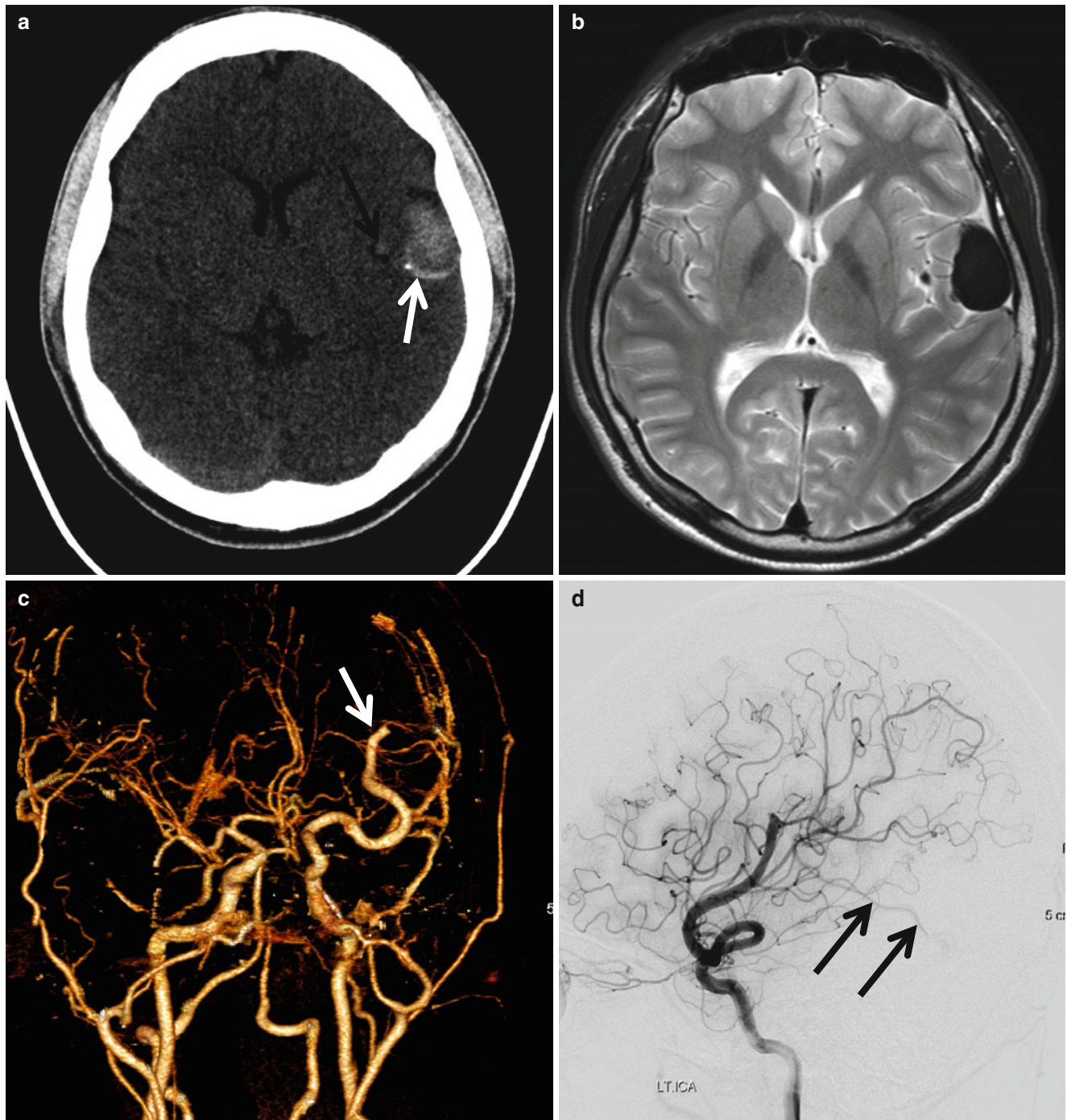


Fig. 5.35 Pial AV fistula in 2-year-old boy. (a) Precontrast CT shows hyperdense mass (dilated venous pouch, *white arrow*) in the left temporal region with tiny marginal calcification. A dilated vessel (*black arrow*) of same density is seen at the medial aspect of the mass. (b) T2-weighted image reveals dark signal intensity of the dilated venous pouch. (c) Oblique AP view of the CT angiography shows abruptly

dilated left MCA branch without significant tangled vessels (*nidus*). (d) Lateral view of the left internal carotid arteriography also shows abruptly dilated left MCA branch without nidus and early venous drain (*black arrow*). The venous pouch is not visualized, suggesting thrombosis

5.4.3.2 Vein of Galen Malformation

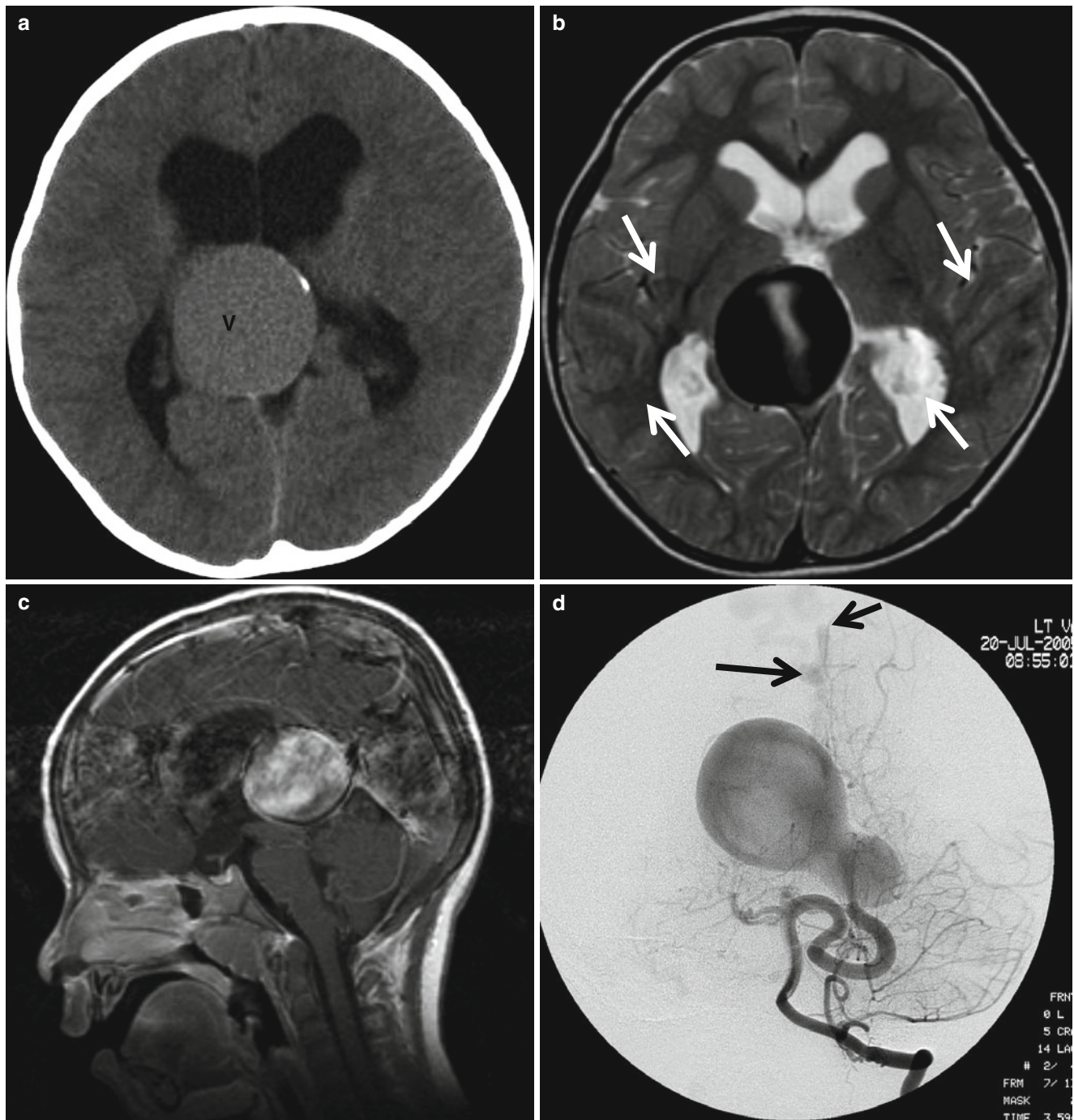


Fig. 5.36 Vein of Galen malformation in a 3-year-old boy. (a) Precontrast CT scan shows large central venous lesion (V) with ventricular enlargement. (b) T2-weighted image demonstrates dark signal intensity of the vein with phase misregistration artifact (*arrows*) due to the vascular flow. (c) Postcontrast sagittal T1-weighted image demonstrates markedly dilated central vein (vein of Galen) and more prominent phase misregistration artifact. Aqueductal compression caused

hydrocephalus. (d) AP projection of the left vertebral arteriography at the arterial phase shows large connection (mural type) between the left superior cerebellar artery and dilated median prosencephalic vein of Markovskii (vein of Galen) draining into persistent falcine sinus (*arrows*). (e) Lateral projection of the left vertebral arteriography after coil embolization reveals contrast, filling the vein of Galen drained into the falcine sinus (*arrows*). The straight sinus is absent

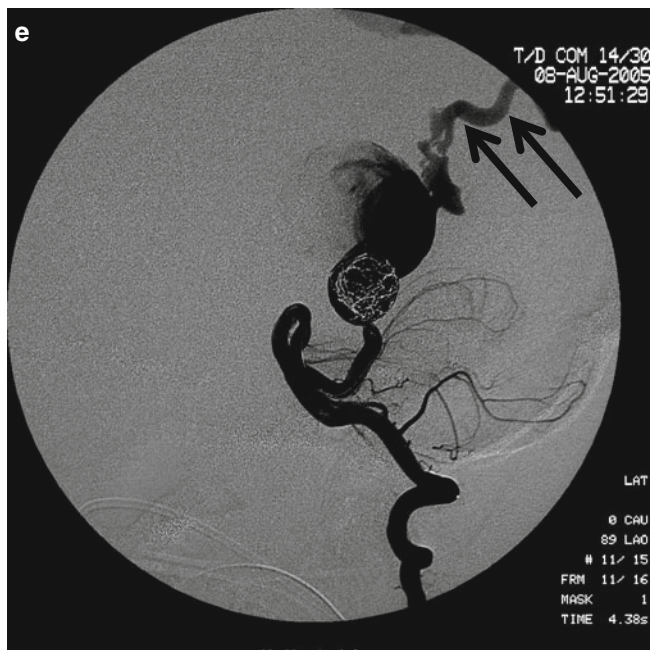


Fig. 5.36 (continued)

5.4.3.3 Cavernous Malformation

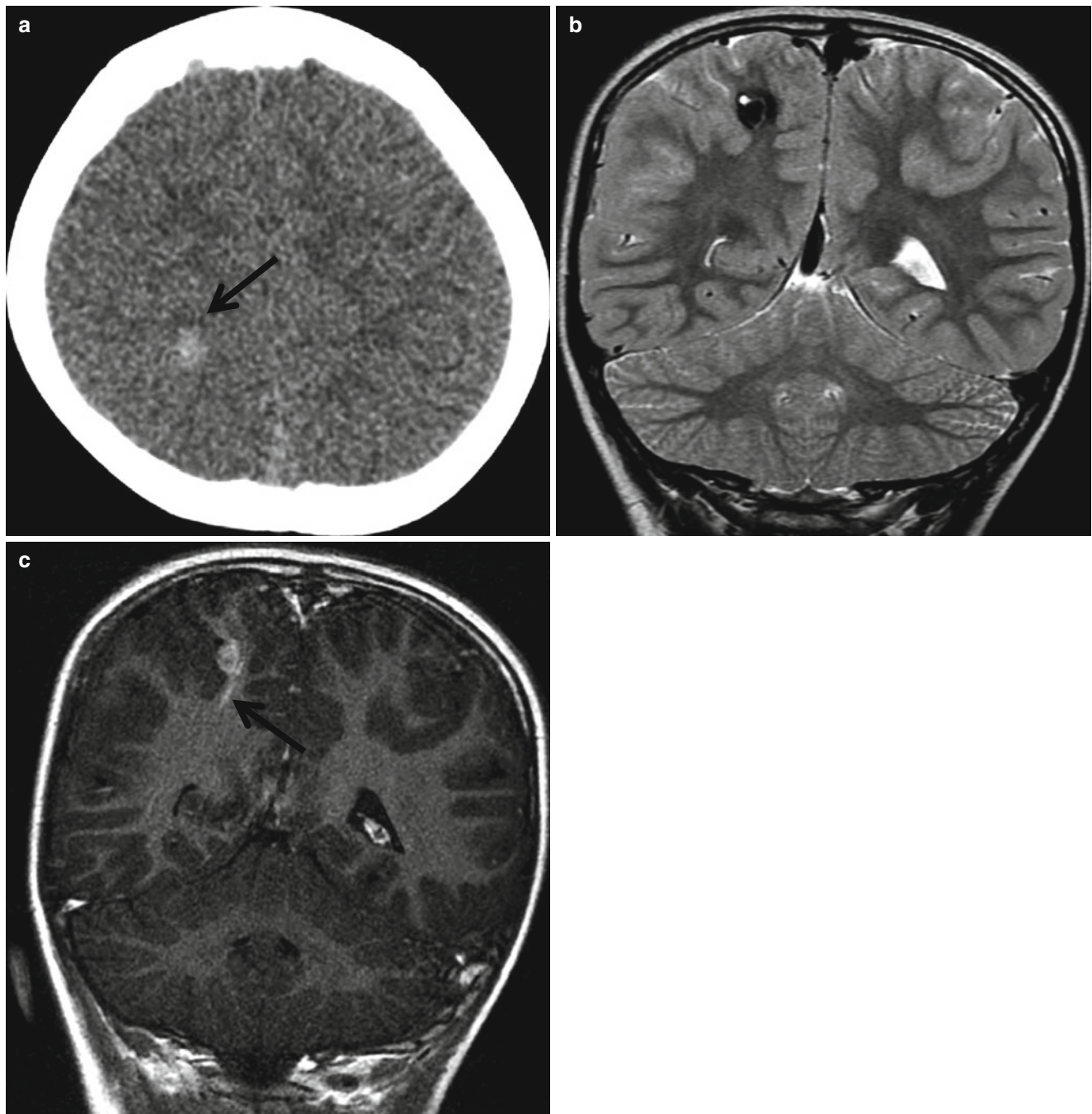


Fig. 5.37 Cavernous malformation associated with venous malformation. (a) Precontrast CT scan shows a small hyperdense lesion (*arrow*) in the right parietal lobe. (b) The mass is hypointense with central hyperintense area and rim on T2-weighted image. (c) Postcontrast

coronal T1-weighted image reveals enhancement of the cavernoma and adjacent linear venous enhancement (*arrow*), suggesting venous malformation

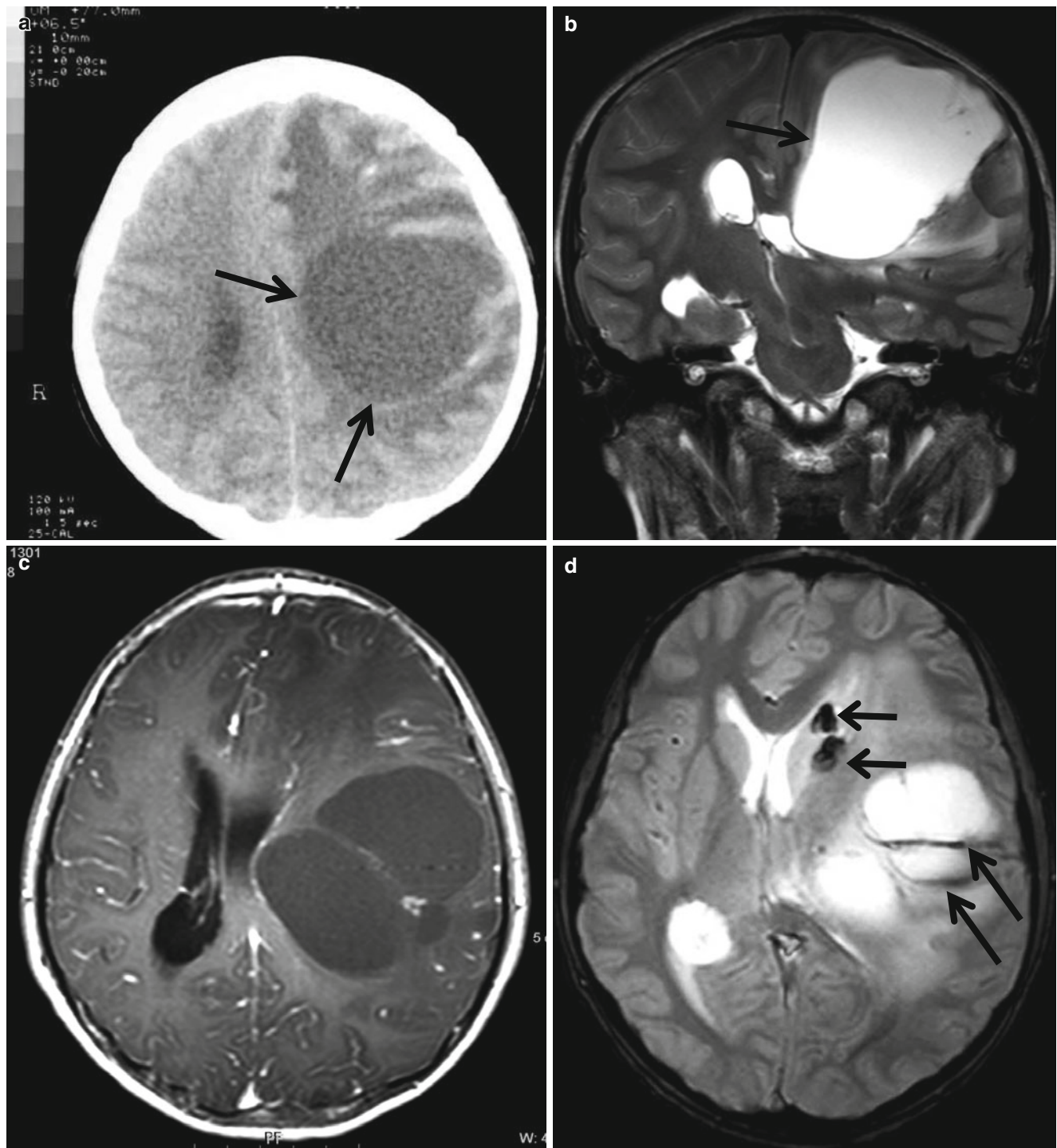


Fig. 5.38 Giant cavernous malformation mimicking brain tumor. (a) Precontrast CT scan shows large cystic mass with massive surrounding edema. (b) T2-weighted coronal image shows large cystic mass (arrow) with edema and mass effect. (c) The mass is not well enhanced on a

postcontrast T1-weighted image. (d) Gradient echo image reveals fluid level with dependent dark area (large arrows) in the cystic mass and other hemorrhagic spots (small arrows)

5.4.3.4 Developmental Venous Anomalies

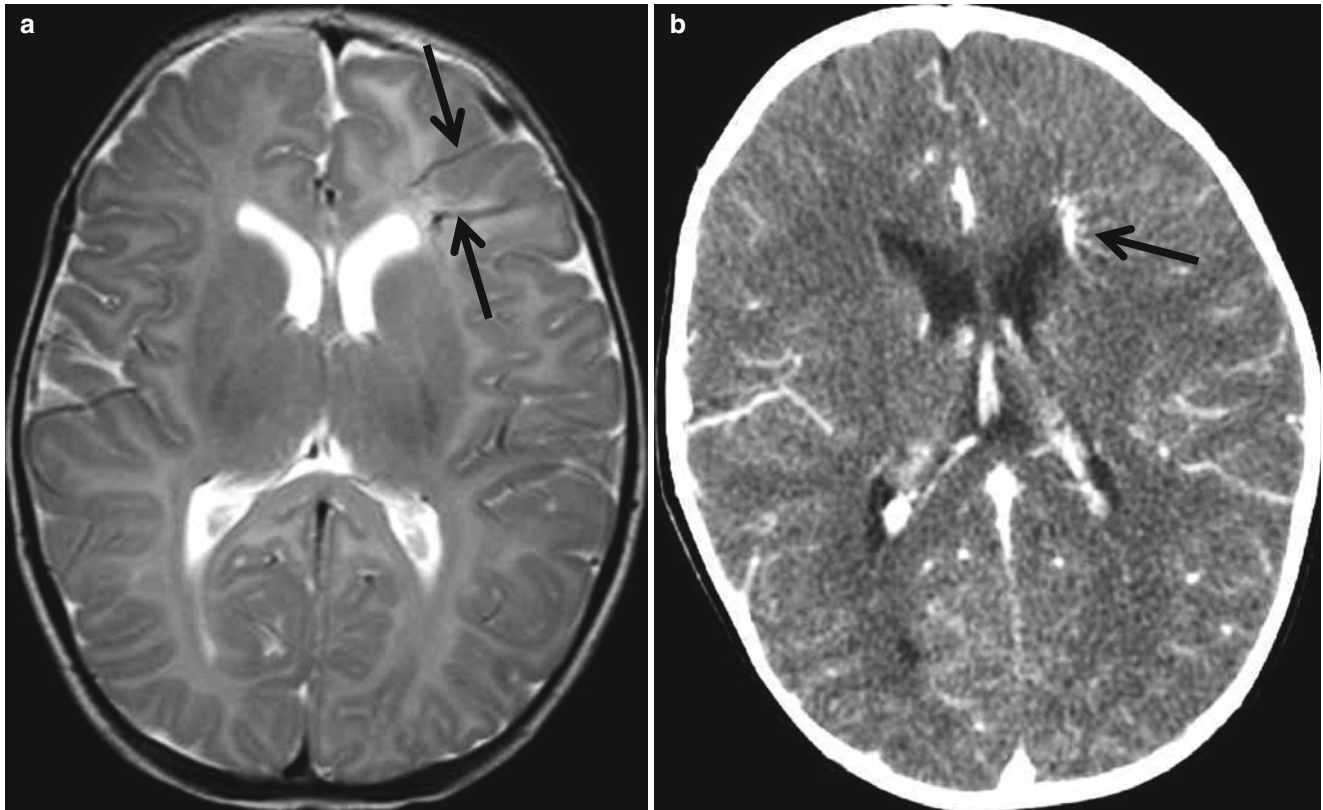


Fig. 5.39 Developmental venous anomaly. (a) T2-weighted image shows localized hyperintense parenchymal lesion in the left frontal lobe and multiple vessels (*arrows*). (b) Postcontrast CT demonstrates enhancing tuft of radially arranged vessels (*arrow*)

5.4.3.5 Moyamoya Syndrome

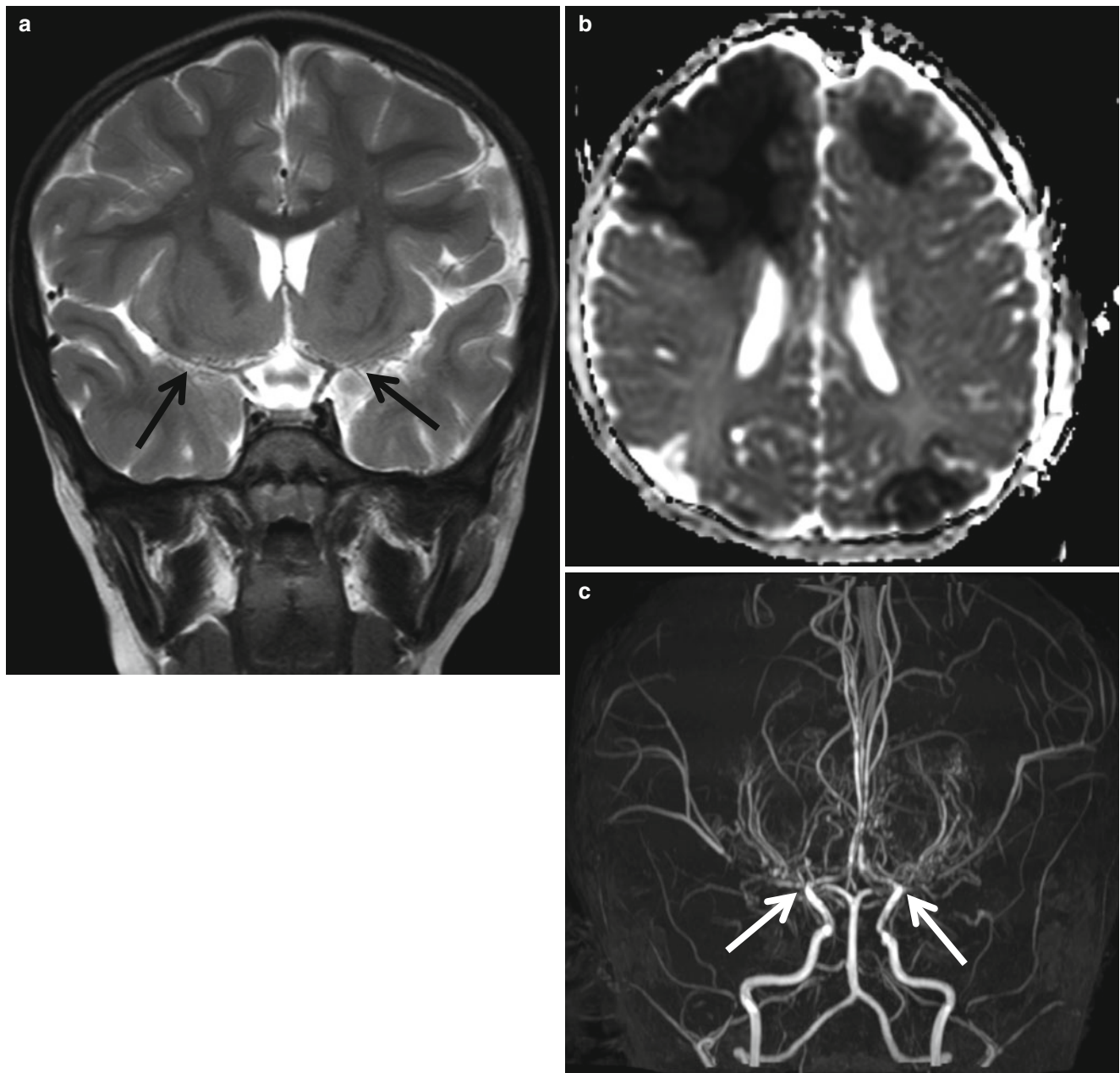


Fig. 5.40 Acute watershed area infarct in moyamoya disease. (a) T2-weighted coronal image obtained on the second day of stroke shows attenuated bilateral MCA (*arrows*). (b) ADC map reveals acute

cytotoxic edema. (c) MR angiogram shows steno-occlusive lesions at both the supraclinoid ICA (*arrows*) and numerous collateral formations. The posterior circulation is also involved

References

- Badve CA, Khanna PC, Ishak GE. Neonatal ischemic brain injury: what every radiologist needs to know. *Pediatr Radiol*. 2012;42:606–19.
- Barkovich AJ. *Pediatric neuroimaging*. Philadelphia: Lippincott, Williams and Wilkins; 2012.
- Barkovich AJ, Westmark KD, Bedi HS, et al. Proton spectroscopy and diffusion imaging on the first day of life after perinatal asphyxia: preliminary report. *AJNR Am J Neuroradiol*. 2001;22:1786–94.
- Chao CP, Zaleski CG, Patton AC. Neonatal hypoxic-ischemic encephalopathy: multimodality imaging findings. *Radiographics*. 2006;26 Suppl 1:S159–72.
- Demaerel P, Casteels I, Wilms G. Cranial imaging in child abuse. *Eur Radiol*. 2002;12:849–57.
- Geibprasert S, Pongpech S, Jiarakongmun P, et al. Radiologic assessment of brain arteriovenous malformations: what clinicians need to know. *Radiographics*. 2010;30:483–501.
- Heinz ER, Provenzale JM. Imaging findings in neonatal hypoxia: a practical review. *AJR Am J Roentgenol*. 2009;192:41–7.
- Jeon TY, Kim JH, Yoo SY, et al. Neurodevelopmental outcomes in preterm infants: comparison of infants with and without diffuse excessive high signal intensity on MR images at near-term-equivalent age. *Radiology*. 2012;263:518–26.
- Kidokoro H, Anderson PJ, Doyle LW, et al. High signal intensity on T2-weighted MR imaging at term-equivalent age in preterm infants does not predict 2-year neurodevelopmental outcomes. *AJNR Am J Neuroradiol*. 2011;32:2005–10.
- King SJ, Boothroyd AE. Cranial trauma following birth in term infants. *Br J Radiol*. 1998;71:233–8.
- Mottolese C, Hermier M, Stan H, et al. Central nervous system cavernomas in the pediatric age group. *Neurosurg Rev*. 2001;24:55–71.
- Rajaram S, Batty R, Rittey CD, et al. Neuroimaging in non-accidental head injury in children: an important element of assessment. *Postgrad Med J*. 2011;87:355–61.
- Rutherford M, Biarge MM, Allsop J, et al. MRI of perinatal brain injury. *Pediatr Radiol*. 2010;40:819–33.
- Schunk JE, Schutzman SA. Pediatric head injury. *Pediatr Rev*. 2012;33:398–410.
- Vialle R, Pietin-Vialle C, Ilharreborde B, et al. Spinal cord injuries at birth: a multicenter review of nine cases. *J Matern Fetal Neonatal Med*. 2007;20:435–40.

Young Seok Lee

Contents

6.1	Introduction.....	210
6.2	Spectrum of Normal and Abnormal Neurosonography.....	210
6.2.1	Cranial Sonography	210
6.2.2	Spinal Sonography.....	217
6.3	Illustrations: Neurosonography.....	218
6.3.1	Cranial Sonography	218
6.3.2	Spinal Sonography.....	250
	References	253

Y.S. Lee, M.D.
Department of Radiology, College of Medicine,
Dankook University, 119 Dandae-ro, Dongnam-Gu,
Cheonan, Chungnam 330-714, South Korea
e-mail: yslee@dkuh.co.kr

6.1 Introduction

Sonography, developed in the late 1970s, has been an essential diagnostic tool of neonatal brain and spinal diseases. Neurosonography has many advantages in diagnostic application for neonates. Sonographic techniques have been dramatically improved in resolution as well as combination with color Doppler for hemodynamic studies (Lowe and Bailey 2011a). In addition, sonography uses non-ionizing radiation and is easily portable for use on neonates, especially in neonatal intensive care units (NICUs) (Barr 1999). When cranial sonography is performed, neonatal anterior, posterior, and mastoid fontanelles are good for sonic windows. Sedation is not needed during sonography. Even if neonates move their heads, sonographic images can be achieved for accurate radiologic diagnoses. These advantages make sonography a primary imaging modality for the diagnosis of neonatal brain diseases (Lee et al. 1986). In this chapter, the clinical usage of neonatal cranial sonography will be emphasized and discussed. The scanning techniques, normal anatomy, normal variants and pitfalls of cranial sonography, and the sonographic findings of common pathologic conditions will be illustrated. In addition, spinal sonography as a screening procedure in infants will be reviewed.

6.2 Spectrum of Normal and Abnormal Neurosonography

6.2.1 Cranial Sonography

6.2.1.1 Scanning Techniques

The anterior, posterior, and mastoid fontanelles, are good sonic windows for sonography of neonatal brain diseases. The anterior fontanelle before closure at 4–26 months of age (mean age: 14 months) is the most common window of cranial sonography. Its average size is 2.1 cm and the size is big enough for the examination of most neonatal brain diseases. Sonography through the posterior fontanelle is useful in evaluating lesions of the medulla oblongata and cervical spine, which are adjacent to the posterior fossa and the foramen magnum. This method is available before age 2 months, due to the size of the posterior fontanelle, which is going to close after 2 months of age and ranges from 0.5 to 0.7 cm. Sonography through the mastoid fontanelle is valuable in evaluating the cortex and the extracerebral space along the cerebral convexity. For cranial sonography, a 5–8 MHz multi-focused real-time sector transducer is widely used, while a 5–15 MHz high-frequency linear transducer is practical for

structures adjacent to the fontanelles. The low-frequency transducer has a deeper penetration area and is helpful on neonates with small-sized fontanelles and during the closing fontanelle period. Color Doppler is useful for assessing blood flow patterns, velocity, and resistive index. Starting with cranial sonography, the operator can check the location and size of the anterior fontanelle. Air gaps between the anterior fontanelle and the transducer should be removed by applying ultrasound gel to the examining area for optimal diagnostic images. The neonate is usually in a supine position, and the transducer is placed on the fontanelle with gentle pressure. When Doppler study is performed, the operator should be careful with the transducer pressure, which can influence the Doppler result (Taylor 1992). The examiner can scan the neonatal brain from the anterior to the posterior areas with the transducer placed on the center of the anterior fontanelle in the coronal direction. The lesions on any side of the cranial hemispheres can be easily detected on the coronal view due to the anatomical symmetry of both cerebral hemispheres. After checking the landmark structures, scanning can be continued from the anterior to posterior direction. The transducer can be placed on the fontanelle in the sagittal direction afterwards. Both oblique sagittal images can be taken in the lateral direction after obtaining the mid-sagittal plane images. The sagittal plane parallel to the longitudinal axis of the lateral ventricle is very useful in evaluating the caudothalamic groove and the whole lateral ventricle. Sonography through the posterior and mastoid fontanelles can be a supplementary choice to acquire more information in the obscure areas, such as the posterior fossa, extracerebral spaces, and outer fields of the sector transducer through the anterior fontanelle (Fig. 6.1).

6.2.1.2 Anatomy

For accuracy and consistency of cranial sonography, it is necessary to make standard images through the anterior, posterior, and mastoid fontanelles. The anatomic landmarks are high echogenic structures of the sulci, fissures, cisterns, tentorium, ventricular walls, choroid plexus, periventricular echogenic halo, vermis, anterior pons, and corpus callosal margin.

It is recommended that cranial sonography contains basic reference planes on coronal scan (Standard Guidelines 2003). The recommended planes through the anterior fontanelle are in this order: the forepart of frontal horn, frontal horn of the lateral ventricle, the foramen of Monro, the body of the lateral ventricle and the third ventricle, the quadrigeminal cistern, and trigone of the lateral ventricle (Fig. 6.2). The sagittal planes are the midline image (including the entire corpus callosum, the third and fourth ventricles, brain stem, cerebel-

lar vermis, and cisterna magna), caudothalamic groove, the entire lateral ventricle, peritrigonal white matter, periventricular white matter, and the Sylvian fissure (Ko and Lee 2009) (Figs. 6.3 and 6.4).

The planes through the posterior fontanelle on coronal scan are the easily visible parts of white matter of the frontal lobe, frontal horn of the lateral ventricle, body of the lateral ventricle and third ventricle, splenium of the corpus callosum, the trigone of the lateral ventricle, the occipital horn of the lateral ventricle, the posterior cerebellar hemisphere, and the occipital lobe (Fig. 6.5). The sagittal planes are the midline image, the third and fourth ventricles, caudothalamic groove, lentiform nucleus and choroid plexus, and the centrum semiovale (Oh et al. 2010) (Fig. 6.6).

The planes through the mastoid fontanelle are the body of caudate nucleus and lentiform nucleus, head of the caudate nucleus and thalamus, third ventricle and midbrain, and cerebellar vermis and midbrain on oblique axial scans, and the periventricular white matter, basal ganglia, thalamus, and tentorium on oblique coronal scans (Kim and Lee 2011) (Fig. 6.7).

6.2.1.3 Normal Variants and Pitfalls

Sonographers can encounter various variants and pitfalls during cranial sonography (Enriquez et al. 2003; Lowe and Bailey 2011). They include echogenic pseudolesions, prominent calcar avis, periventricular echogenic halos in brain parenchyma, colpocephaly, various patterns of choroid plexus within the ventricle, and mechanical artifacts (Lee and Kim 1998).

Echogenic pseudolesions are artifacts that can occur when ultrasound beams reflect perpendicularly off the cerebral sulci and gyri, multiple parallel fibers in the thalamus, or posterior sonic enhancement through the dilated occipital horn of the lateral ventricle. These pseudolesions should be differentiated from cerebral hemorrhages or infarcts. Echogenic pseudolesions are the focal lesions mainly appearing near the surface of the cerebral cortex or in the thalamus without distortion of normal structures, and they disappear in multidirectional scannings (Siegel 2011). In contrast, hemorrhages or infarcts can be differentiated by distortions of the normal structures and persistent visualization (Fig. 6.8).

The calcar avis begins to develop in the 16th gestational week and forms the calcarine fissure. After being elongated and flexed during the 8th–10th gestational month, this calcarine fissure forms a white matter mound by compression of the medial side of the occipital horn of the lateral ventricle (DiPietro et al. 1985). On parasagittal ultrasound scans, the calcar avis can appear as an intraventricular mass-like lesion and be confused with an intraventricular hemorrhage.

A prominent calcar avis can be differentiated by detection of the calcarine fissure and its connection having the same echogenicity with the cerebral white matter (Fig. 6.9).

The periventricular echogenic halo appears in 97 % of premature infants born before the 32th gestational week. Radiating fibers of white matter and vascular plexus between the cerebral cortex and ventricular wall increase the ultrasonic interfaces and generate high echogenicity. The shorter the gestational period, the more prominent the periventricular echogenic halo. It should be differentiated from periventricular leukomalacia and hematoma (Grant et al. 1983). The echogenicity of the periventricular echogenic halo is the highest in a trigonal area of lateral ventricles and gradually decreases toward the frontal, occipital, and temporal lobes, and it is homogeneous, being mainly lower than that of the choroid plexus. But periventricular leukomalacia is characterized to a large extent by that of inhomogeneous periventricular echogenic lesions with distinct lobulated margins, cystic changes on follow-up examination, and the echogenicity of the periventricular leukomalacia being similar to or higher than that of the ipsilateral choroid plexus (Lee et al. 1993) (Fig. 6.10).

The choroid plexus in the lateral ventricle is usually thin at the temporal horn of the lateral ventricle and is smoothly thickened in the trigone, forming the glomus, and then it gradually thins anteriorly. Thus, if the thickened choroid plexus is noted in areas other than the glomus, hematoma or other pathology should be considered. However, various sonographic patterns of the choroid plexus reveal superior notching, central bulging, and inferior notching of the glomus in 34.3 % of normal newborn infants on sagittal view, and focal bulging and double patterns in 27 % on coronal view (Lee and Kim 1999) (Fig. 6.11).

6.2.1.4 Intracranial Hemorrhage

6.2.1.4.1 Germinal Matrix Hemorrhage (GMH)

The subependymal germinal matrix, as a source of cerebral neuroblast during the 10th–20th week of gestation and glioblasts or astrocytes during late pregnancy, faces the lateral ventricle on the ventrolateral side and almost disappears during the 32nd–34th week of gestation. This matrix consists of many fragile endothelial cells as a single layer. It can be easily damaged and bleed because there is a lot of blood flow and a lack of connective tissue support (Ghazi-Birry et al. 1997). Between the 28th and 32nd gestational week, the germinal matrix is the most prominent in the caudothalamic groove and the most common bleeding site of premature babies under 32 weeks. The subependymal germinal matrix hemorrhage is found in more than 90 % of the cases of premature babies 6 days after birth (Lee et al. 1987). However, it can be

seen on US prenatally or right after birth, and there may also be prenatal GMH. If hemorrhage occurs at the remaining germinal matrix along the subependymal layer of the lateral ventricle, sonographic imaging shows an echogenic lesion in the same area. The most common site of germinal matrix hemorrhage is a caudothalamic groove as a part of the ganglionic eminence. The most common sonographic finding of germinal matrix hemorrhage is an echogenic lesion between the floor of the frontal horn and the head of the caudate nucleus on coronal images and a caudothalamic groove on sagittal images. In some cases, an extended part of the echogenic choroid plexus between the foramen of Monro and the third ventricle can seem similar to the GMH. Therefore, the GMH should be diagnosed by detection in both the coronal and sagittal scans. The grading system suggested by Papile and colleagues (1983) is commonly used in the evaluation of the severity of GMH. Treatment and prognosis depend on this grading: Grade 1 is GMH confined to the subependymal germinal matrix (Fig. 6.12), Grade 2 is GMH and IVH without ventricular dilatation (Fig. 6.13), Grade 3 is GMH and IVH with ventricular dilatation (Fig. 6.14), and Grade 4 is GMH and IVH with intraparenchymal hemorrhage (Fig. 6.15). Sonographic diagnosis for intraventricular hemorrhage includes the echogenic materials anterior to the foramen of Monro, the extension of the choroidal echo complex into the occipital horn, the lumpiness of the intraventricular surface of the choroid plexus, and loss of its superoanterior tapering (Fig. 6.17). Beyond the confines of subependymal germinal matrix, the extended hemorrhage into the brain parenchyma shows intraparenchymal echogenic lesions. Grades 1 and 2 of the germinal matrix hemorrhage usually contain cystic changes and complete absorption on follow-up sonography within a few weeks. However, Grades 3 and 4 can progress to hydrocephalus, periventricular infarction, or secondary porencephaly. The early stages of periventricular hemorrhagic or nonhemorrhagic infarction may also have echogenic lesions, and identifying the interconnection between a germinal matrix hemorrhage and intraparenchymal hemorrhage is a critical finding.

Volpe has suggested a separate grading system for periventricular echo density corresponding to Grade 4 of intraparenchymal hemorrhages because of its difficulty in distinguishing them among other hemorrhages, as well as nonhemorrhagic and hemorrhagic infarctions on sonography (Volpe 2008). The grading of severity of GMH/IVH by ultrasound scan is as follows: Grade 1 is GMH with no or minimal IVH (<10 % of ventricular area on parasagittal view), Grade 2 is IVH (10–50 % of ventricular area on parasagittal view), and Grade 3 is IVH (>50 % of ventricular area, usually distending into the lateral ventricle). In addition, separate notations include periventricular echodensity (location and extent).

6.2.1.4.2 Intracranial Hemorrhage, Except for Germinal Matrix Hemorrhage

Intracranial hemorrhage, except for germinal matrix hemorrhage, can occur relatively uncommonly in the NICU by many causes of birth trauma, ischemia, blood dyscrasias, secondary coagulopathy, vascular malformation, and unstable blood pressure. Because of the different echogenicities according to the stage of hemorrhage, hemorrhages usually appear as echogenic lesions in acute or subacute stages on ultrasound scans, especially strongly echogenic patterns in blood clots or cystic patterns in a resolving stage. However, hemorrhages can occasionally not be differentiated from focal infarcts and other echogenic masses on sonography. Acute parenchymal hemorrhages appear as well-circumscribed echogenic masses in the cerebral or cerebellar hemispheres with mass effects and without blood flow, which is easily detected on an ultrasound scan (Fig. 6.16). Parenchymal hemorrhage can be resolved slowly as complete absorption or porencephalic change. Subdural hemorrhage is a more frequent event in the full-term infant than the premature infant. Under the weak point on both peripheral sides on the sector ultrasound scan through the anterior fontanelle, the sonographer should scrutinize peripherally in order to detect subdural hemorrhages, which appear as crescent echoic fluid collected along the convexity, tentorium, or the interhemispheric fissure, and which contain an ipsilateral mass effect. It is also helpful to detect subdural hemorrhages along the cerebral convexity on examination through the mastoid fontanelle or the temporal thin bone and along the tentorium through the posterior fontanelle (Fig. 6.18). Subarachnoid hemorrhages can be primary or secondary; secondary ones occur more commonly in premature infants, extending from intraventricular hemorrhages, parenchymal hemorrhages, and subdural hemorrhages. Even though it is relatively insensitive, the detection of subarachnoid hemorrhages on sonography can appear as leptomeningeal thickenings and echogenic fluid collections in the fissures, the sulci, or cisterns, and echoic masses formed in the posterior fossa by extraventricular extensions of intraventricular hemorrhages (Fig. 6.19). Color Doppler sonography is useful in differentiating between subdural and subarachnoid fluid and hemorrhages; these images show elongated cortical veins crossing the wide subarachnoid space, so-called “cortical vein” signs in subarachnoid fluid and the embedded cortical veins within the echogenic pia-arachnoid in the subdural fluid that have an absence of blood flow (Chen et al. 1996). Epidural hemorrhages are rare and are usually due to birth trauma. The sonographic findings of acute epidural hemorrhages are a lentiform echogenic fluid between the cerebral cortex and the skull and a surrounding mass effect (Fig. 6.20). Choroid plexus hemorrhages are more common in the full-term infant

than in the premature. Before a diagnosis of choroid plexus hemorrhage is made, it is very important to understand the various sonographic patterns of a normal choroid plexus as previously mentioned in the normal variation. Sonographic findings of the choroid plexus hemorrhage are a loss of anterior tapering of the choroid plexus, nodular or lobulated margins, heterogeneous echogenicities, absence of blood flow on color Doppler, and the resolving pattern on the follow-up study.

6.2.1.5 Hypoxic-Ischemic Encephalopathy

During the prenatal and postnatal periods and at birth, there are several pathophysiological causes that result in hypoxic-ischemic encephalopathy; these are placenta malfunction, congenital and acquired infections, toxic material exposure, maternal systemic illness spreading through the placenta, genetic disease, and perinatal asphyxia. Hypoxic-ischemic encephalopathy is the most common cause of mortality and morbidity in neonates less than 6 weeks old. The features of brain injuries are variable on the several steps of brain development. In early gestation, congenital malformations are the result of abnormalities during organogenesis. Abnormal histogenesis, proliferation, and migration can induce cortical developmental defects in middle gestational age and various brain injury features according to the vascular maturity in the end stage of gestation. On vascular development, the surface vessels adjacent to the cerebral cortex are more mature than the vessels in the deep brain before 34 gestational weeks, and the deep vessels are vulnerable to hypoxic-ischemia. They are fully developed from 34 to 36 gestational weeks, and the deep and superficial vessels can receive similar degrees of injury under these circumstances. It can be explained pathophysiologically for the periventricular leukomalacia of the premature baby and the destruction of three layers – the cortex, subcortical white matter, and deep gray matter – on the full-term baby under hypoxic-ischemic encephalopathy (Volpe 1989). The sonographic findings of hypoxic-ischemic encephalopathy also match according to the embryologic gestational age, and the findings are distinguishable between pre-term and full-term babies.

6.2.1.5.1 The Sonographic Features of Hypoxic-Ischemic Encephalopathy in the Premature Neonate

Periventricular leukomalacia, germinal matrix hemorrhage, and hemorrhagic venous infarctions are the most common disorders of brain injuries of premature babies (Carson et al. 1990). The periventricular white matter is the most vulnerable area under hypoxic-ischemia due to the developing vessels that are feeding them. The relatively more-developed

vessels and copious anastomotic vessels that maintain cortical blood flow on the cerebral cortex can somewhat protect it from hypoxic-ischemic encephalopathy. The most commonly affected areas for periventricular leukomalacia are the lateral ventricular trigones, the foramen of Monro, and centrum semiovale (Chao et al. 2006). The incidence rate of the disorder is 10–40 % of premature babies with low birth weight and it can cause spastic diplegia as a serious neurologic sequela on 6.5–10 % of the premature babies that survive (Lee et al. 2002).

Cranial sonography is the modality of choice for initial evaluation of periventricular leukomalacia, which may be difficult to distinguish from periventricular echogenic halos as a normal developing finding in the early stages. However, periventricular leukomalacia usually shows more extensive and heterogeneous echoes, more discrete margins, and persistent patterns on multidirectional scans than normal periventricular echogenic halos (Fig. 6.21). Normal periventricular halos are reduced on the posterior and mastoid fontanelle scans, which can be made by ultrasound anisotropic effects due to the connecting structures, such as axons and vessels to the periphery from the ventricles. The normal halo is also more homogeneous than the echo of leukomalacia and has an ill-defined border. The normal periventricular halo is usually more hypoechoic than the choroid plexus echogenicity. These are good points to distinguish from periventricular leukomalacia. Focal and diffuse petechial hemorrhages appearing as multiple punctuate hyperechoic lesions on sonography of the periventricular white matter are accompanied in 25 % of periventricular leukomalacias (Fig. 6.22). After 2–3 weeks, multiseptated small cysts appear and fuse with each other and are absorbed according to the length of time in periventricular leukomalacia (Lee and Yoo 2003). Sonographic detection of cystic necrosis in the periventricular white matter is the diagnostic clue for periventricular leukomalacia (Figs. 6.21 and 6.22). Central atrophy and secondary ventricular enlargement can be detected by the reduced periventricular white matter on the long-term sonographic observation of periventricular leukomalacia. In the case of local damaged ventricular membrane, ventricular diverticulum can be developed, which is connected with the ventricles. De Vries has devised the grading system for periventricular leukomalacia that depends on characteristics of periventricular white matter (De Vries et al. 1992). Cases with periventricularly increased echogenicity of 7 days or more are categorized as Grade I. Cases combined with hyperechogenicity and focal cystic change are classified as Grade II. Diffuse cystic change along the periventricular area is a criterion for Grade III. MR images are essential in evaluating the crucial features and the late sequela of periventricular leukomalacia (Yang et al. 1993).

6.2.1.5.2 The Sonographic Features of Hypoxic-Ischemic Encephalopathy in the Full-Term Neonate

Hypoxic or ischemic brain injury on the full-term baby is different from that of the pre-term baby. When hypoxic-ischemic encephalopathy is severe on the full-term baby, it can involve both the cerebral cortex – both white matter and the border zones located in interspaces of the anterior, middle, and posterior cerebral arteries. The border zone is located at the parasagittal area of cerebral cortex and subcortical white matter (Chao et al. 2006). Hypoxic-ischemic injuries have categorized two causes as incomplete and complete asphyxia. Cerebral superficial cortex and border zone white matter are mainly involved in incomplete asphyxia. In complete asphyxia, the thalamus, mesencephalon, hippocampus, and corticospinal pathway are commonly affected.

1. Diffuse Hypoxic-Ischemic Encephalopathy

Diffuse hypoxic-ischemic encephalopathy mainly occurs in the full-term neonate and affects the cerebral and cerebellar cortex, white matter, thalamus, brain stem, and others. The sonographic feature of acute diffuse hypoxic-ischemic encephalopathy is a diffusely increased echogenicity of the cerebral cortex and white matter. The sonographic features of brain edema, such as the loss of cerebral gyral-sulcal interfaces, insufficient arterial pulse, and compressed ventricles, appear on the first to fifth day after hypoxic brain injury, especially on coronal view. A US Doppler study may be useful in evaluating the prognosis of diffuse hypoxic-ischemic encephalopathy. The cerebral edema resulting in hypoxia shows three different groups of blood flow (Deeg et al. 1990). Group 1 reveals the normal blood flow velocity and normal resistive index (RI) with the best prognosis and normal development. The increased velocity in diastolic, peak end-systolic, and end-diastolic flow, as well as decreased RI, is shown in Group 2, and psychomotor and mental retardation are induced (Fig. 6.23). In comparison, Group 3 includes decreased flow in diastolic, peak end-systolic, and end-diastolic flow velocity with increased RI that is noted with the worst prognosis and causes severe brain injury and death. Some authors report a very high RI (100–190 %) due to reverse diastolic flow in severe brain injury. The late sonographic findings of diffuse hypoxic-ischemic encephalopathy vary, depending on the severity of the cases, from mild volume loss of the brain parenchyma to diffuse cystic encephalomalacia (Fig. 6.23). MRI is the modality of choice to assess the residual lesions. Diffuse hypoxic-ischemic encephalopathy finally develops with diffuse brain atrophy appearing as decreased volume of the parenchyma, ventriculomegaly, and extra-axial fluid accumulation.

2. Focal or Multifocal Hypoxic-ischemic Encephalopathy

Cerebral or cerebellar infarction can occur rarely on the term neonate with vascular occlusion. The middle cerebral artery is the most common site of infarction. Sonographic findings of acute infarction are increased echogenicities in the vascular territory and a surrounding mass effect (Fig. 6.25). The lesions are liquefied and become porencephaly on follow-up studies.

Parasagittal injury simultaneously involved in the cerebral gray and white matters commonly occurs in the parasagittal border zone between the frontal and occipital lobes. The sonographic diagnosis of parasagittal injury is more difficult than the diagnosis with CT or MRI. However, sonography can appear initially as a focal increased echogenicity in the parasagittal zone and subsequently as cystic change, focal atrophy, ipsilateral ventriculomegaly, and calcification (Fig. 6.27).

Selective hypoxic injury is a relatively rare disease among the hypoxic-ischemic encephalopathies that involve the basal ganglia and thalamus in the full-term neonate. Pathologically, the loss of neurons, gliosis, and hypermyelination are characteristics of calcifications that may accompany the vessel wall and the necrotic basal ganglia. The basal ganglia and thalamic infarctions appear as localized, broad hyperechogenicity of the basal ganglia and thalamus as well as decreased arterial pulsations (Fig. 6.26).

6.2.1.6 Infectious Disease

Clinically, early diagnosis and management of prenatal and postnatal infections are very important for lowering morbidity and mortality in infants. Meningitis is the most common neonatal intracranial infection by *Enterobacter* species. *Escherichia coli* and group B *Streptococcus* type 3 are also common causes. Most cases show insignificant clinical symptoms of meningitis during the first month. Even though radiological diagnosis is insensitive, radiological imaging plays an important role in the evaluation of structural changes and its complication by infectious disease (Fig. 6.28). Cranial sonography in the intracranial infection of the neonate is useful in assessing the degree and type of hydrocephalus and detecting other related abnormalities such as cerebral infarction, encephalitis, brain abscess, calcifications, lenticulostriate vasculopathy, ependymal and leptomeningeal thickening, and echogenic debris in the ventricles and the extracerebral spaces that include subdural empyema (Frank 1986) (Figs. 6.29, 6.30 and 6.31). Color Doppler enables access to additional information of increased or decreased vascular flow and vascular occlusion in the intracranial infection. The linear high-resolution transducer prefers to verify leptomeningeal thickening or hyperechoic sulci, echogenic pus in the subarachnoid and subdural spaces below the fontanelle.

These findings are very important for making a sonographic diagnosis of meningitis (Fig. 6.28). Intracranial congenital infections on cranial sonography do not usually reveal the specific findings according to the infected organisms, including TORCH.

6.2.1.7 Congenital Malformations

Congenital brain malformations can occur in the primary defects during the three embryological stages. The initial stage is cytogenesis, which is from molecules to cells, and the second is histogenesis, from cell to tissue. The last stage is organogenesis, which is from tissue to organ. The other cause of congenital brain malformation is the cerebral destructive change in neonatal cerebral ischemia, inflammation, and others. Among the stages, abnormality on the first stage, which can be observed microscopically, is beyond the sonographic diagnosis, but the abnormality on histogenesis and organogenesis and the destructive change can be diagnosed with sonography (Babcock 1986).

Sonography is usually good as a screening tool in most malformations. However, CT and MR are essential for figuring out the accurate extent and characteristics of the malformation. This chapter reviews sonographic findings of congenital malformation according to disorders of histogenesis, closure of the neural tube, diverticulation, neuronal proliferation, migration, sulcation, and destruction.

Disorders of histogenesis include vascular malformations and neurocutaneous syndrome. A vein of Galen malformation is a rare macroscopic anomaly that appears at the center of the brain and is easily visible on sonography. Sonographic findings are a well-circumscribed anechoic mass behind the third ventricle, the connection with dilated straight sinus and torcular herophili, and arterial pulsation on color Doppler, which can be distinguished from arachnoid cysts (Fig. 6.32). Other vascular malformations, such as arteriovenous malformations, venous malformations, cavernous malformations, and capillary telangiectasia, can be detected if the lesion is enough large and distributed in a central portion; otherwise, it cannot be easily diagnosed. Therefore, for an accurate diagnosis and assessment of characteristics, CT and MRI are necessary.

Most neurocutaneous syndromes in neonates are difficult to detect for the lesions on cranial sonography unless the lesions are huge or central. For instance, intracranial manifestations of tuberous sclerosis are subependymal nodules, tubers, white matter lesions, parenchymal cysts, vascular lesions, and giant cell astrocytoma. Among them, sonography can usually find subependymal nodules and calcifications along lateral ventricular walls, giant cell astrocytoma at the foramen of Monro, and parenchymal cysts, but cannot easily find other lesions within the brain parenchyma (Fig. 6.33).

Disorders of closure of the neural tube include dysraphic disorders, Chiari malformation, Dandy-Walker complex, and callosal dysgenesis. Most dysraphic disorders, such as anencephaly, encephalocele, meningocele, and myelomeningocele, are diagnosed upon physical examination. Sonography is usually used to detect accompanying findings in brain parenchyma, ventricles, meninges, or other lesions.

Chiari malformations are related with variable degrees to cerebellar dysplasia, spinal dysraphism, and meningocele or myelomeningocele. It has three types; among them, the Chiari malformation type 2 is the most common and can be discovered in infancy by sonography. Sonographic findings of type 2 are a cerebellum downward herniation, detected especially in the upper cervical canal on sagittal view, and nonvisualization of the sonolucent cistern magna. The inferior herniation can be easily seen on a suboccipital scan just inferior to the first cervical arch. The fourth ventricle cannot be seen or has a slit-like appearance. Other findings are prominent massa intermedia and colpocephaly, which results in obstruction by stretching or narrowing of the aqueduct by a downward cerebellar herniation. On coronal view, a “batwing” appearance can be seen due to the anterior and inferior pointing of the anterior horn of the lateral ventricle.

The Dandy-Walker complex is further classified as a Dandy-Walker malformation and a Dandy-Walker variant. The former is characterized by markedly enlarged posterior fossa, a balloon-like dilated fourth ventricle, inferior vermian agenesis, and hypoplastic cerebellar hemisphere. The latter manifests a less severe form, with its slightly enlarged posterior fossa, normal appearance of the fourth ventricle, retrocerebellar cyst, and partial vermian agenesis. Sonographic findings of the Dandy-Walker complex are large fluid-filled posterior fossa cysts by a markedly enlarged fourth ventricle, poor visualized vermis, small cerebellar hemispheres, and superior elevation of the tentorium, which are easily seen on midsagittal images, similarly with the CT and MRI.

The corpus callosum is a midline interhemispheric commissure that plays a role in the separation of learning and memory in both hemispheres. In callosal agenesis, interhemispheric commissural fibers make thick bundles of fiber (Probst bundles) on the superior medial side of each ventricle due to failure to cross. Callosal agenesis can develop in isolation or can be accompanied by midline lipoma, interhemispheric cysts, Dandy-Walker malformations, Chiari II malformations, polymicrogyria, gray matter heterotopias, and porencephaly. Sonographic findings are nonvisualization of the corpus callosum, wide separation and medial indentation of both lateral ventricles due to thickened Probst bundles, and colpocephaly. Other findings are elongation and upward dorsal displacement of the third ventricle and nonvisualization of normally seen gyri or sulci, which coexist with

the corpus callosum or cingulate sulcus, whereas medial parietal and occipital cerebral gyri or sulci gather toward the third ventricle on sagittal images (Fig. 6.34). About 30 % of the complete type shows interhemispheric cysts on sonography, which adheres to one side of the falx and which sometimes has connections with the lateral ventricle (Fig. 6.35). Lipoma in the interhemispheric fissure often shows a highly echogenic midline mass on sonography. Most of the partial callosal absence appears at the posterior part. However, anterior parts of callosal dysgenesis sometimes accompany cephalic herniations of the third ventricle and cause difficulties in sonographic diagnosis.

Disorders of diverticulation include holoprosencephaly, septo-optic dysplasia, and absence of septum pellucidum. Holoprosencephaly is a congenital anomaly as a result of division failure from prosencephalon to telencephalon between the 4th and 8th weeks of gestation; it has three types. The alobar type is the most severe and is characterized by midline defects such as cyclopia, hypotelorism, cleft palate, and micrognathia. The representative features on sonography are as follows: single, midline monoventricle; fused echogenic thalami; a holosphere connecting white matter and gray matter across the midline; posteriosuperior connection of a monoventricle resulting in the formation of a large dorsal sac or cyst; indistinct frontal horn, body, and occipital horn of lateral ventricle; and the absence of the third ventricle, falx, and interhemispheric fissure. However, the cerebellum and brain stem have relatively normal appearances. Sonographic findings of the semilobar type are a single ventricular body, fused thalami, separate rudimentary occipital and temporal horns, and a partially developed interhemispheric fissure, especially the posterior. The fourth ventricle, brain stem, and cerebellum usually have normal appearances (Fig. 6.36). The lobar type has no facial defect, fused frontal horns of lateral ventricles, and absent or incomplete septum pellucidum. Sonography of the lobar type appears as a square-shaped ventricle with a flat roof and angular corners, but with a normal separation of the occipital horns. It also shows a shallow anterior interhemispheric fissure and a normal appearance of mostly posterior interhemispheric fissure, thalami, and posterior horn of the lateral ventricle.

Septo-optic dysplasia (de Morsier syndrome) is clinically characterized by hypopituitarism, hypotelorism, and blindness due to optic nerve hypoplasia. Sonographic findings of septo-optic dysplasia are a partially or totally invisible septum pellucidum, squared or flattened frontal horns, enlarged recess of the third ventricle, and normal interhemispheric fissure (Fig. 6.37). Septo-optic dysplasia can be commonly accompanied by a closed type of schizencephaly. It is necessary to evaluate optic nerve hypoplasia with ophthalmoscopy and MRI to overcome the limitation of sonography.

Partial or entire defects of septum pellucidum may appear in isolated types or septo-optic dysplasia, holoprosencephaly, Chiari II malformations, schizencephaly, and hydranencephaly. Isolated types of septum pellucidum defect have no shallow anterior interhemispheric fissures and no optic tract abnormalities that can be differentiated from lobar holoprosencephaly and septo-optic dysplasia, respectively.

Hemimegalencephaly is characterized by partially or entirely hamartomatous overgrowth of a cerebral hemisphere resulting in defects of neuronal proliferation, cell migration, and organization. Sonographic findings of hemimegalencephaly are an enlarged cerebral hemisphere, dilated ipsilateral lateral ventricle, and decreased or absent of sulci. When hemimegalencephaly accompanies band heterotopias, cranial sonography characteristically shows a four-layered pattern of hypoechoic cortex, thick band-like hyperechoic subcortical white matter, inner hypoechoic heterotopia, and hyperechoic unmyelinated periventricular white matter (Fig. 6.38).

Disorders of migration and sulcation include lissencephaly, schizencephaly, heterotopic gray matter, and polymicrogyria. Schizencephaly is a migrational disorder characterized by irregular and full-thickness cleft from the subependymal layer of the ventricle to the surface of the cerebral cortex. There are two types: one is the open-lip type and the other the closed-lip type. In the closed-lip type, sonographic images will reveal a linear echogenic cleft due to a loss of CSF space within the apposed gray matters, focal tenting of the underlying ventricular wall, and widening of the ipsilateral cortical sulci (Fig. 6.40). On sonography, open-lip schizencephaly shows the fluid-filled cleft from the ventricular wall to the cortex, instead of a linear cleft of the closed-lip type (Fig. 6.39). Schizencephaly has occasionally been associated with an absent septum pellucidum and callosal dysgenesis. In closed-lip schizencephaly, it is more difficult to detect the cleft on sonography than for the open-lip type, and MRI is necessary for suspected closed-lip-type schizencephaly.

Hydranencephaly is a kind of destructive disorder that may arise from the occlusion of bilateral internal carotid arteries during fetal development. Cerebral hemispheres are replaced by CSF containing a thin-walled sac with nearly no brain mantle or sub-adjacent white matter. Sonographic findings are nearly invisible cerebral hemispheres, large fluid-filled supratentorial cavities, normal thalami, normal cerebellar hemisphere, and intact falx cerebri (Fig. 6.41). Differential diagnosis of hydranencephaly and severe hydrocephalus is very important because hydrocephalus can respond well to CSF shunting, and normal intelligence may be kept by early management. However, normal intellectual development cannot be expected in hydranencephaly. On sonography, severe hydrocephalus shows parenchymal bands along

the ventricular wall and echogenic choroid plexus within the ventricle, but hydranencephaly appears as a nearly invisible parenchyma with no demonstration of the choroid plexus (McGahan et al. 1988) (Fig. 6.42).

6.2.2 Spinal Sonography

With high resolution and the advancement of technology, spinal sonography has become an important tool in evaluating spinal dysraphism and other spine-related disorders in the infant. Because sonography can be performed through unossified posterior elements of the spine as an acoustic window, it is very useful to perform the scan before 3–6 months of age, starting with ossification of the posterior elements (Coley and Siegel 2011). Sonographic techniques recommend the use of a high-frequency linear transducer (5–17 MHz) with a greater spatial resolution, a wide field of view, a midline approach on the prone position in younger infants, and an off- midline in older

infants. As a routine examination, spinal sonography should confirm the level of the conus medullaris, pulsation of the spinal cord, the nerve roots, and the lowest end of the dural sac. Sonographic images occasionally reveal anatomic variants such as ventriculus terminalis (transient dilatation of the central canal) (Fig. 6.44) and a filar cyst (an oval hypoechoic structure at proximal filum terminale) (Fig. 6.43). The conus medullaris should not be located below L2–3. The conus end below this level and absent or decreased pulsation of the spinal cord and nerve roots are strong evidences of a tethered cord. In cases of spinal lesions, an additional evaluation of the location, such as extradural, intradural extramedullary, or intradural intramedullary; the connection between skin and dural sac; and the contents of the mass, such as CSF, calcification, and neural and fat components, are needed after verification of whether the lesion is covered by skin or not (Fig. 6.45). Non-skin-covered lesions, such as myelocele or myelomeningocele, have a limitation of sonographic application due to the risk of trauma or infection.

6.3 Illustrations: Neurosonography

6.3.1 Cranial Sonography

6.3.1.1 Scanning Technique

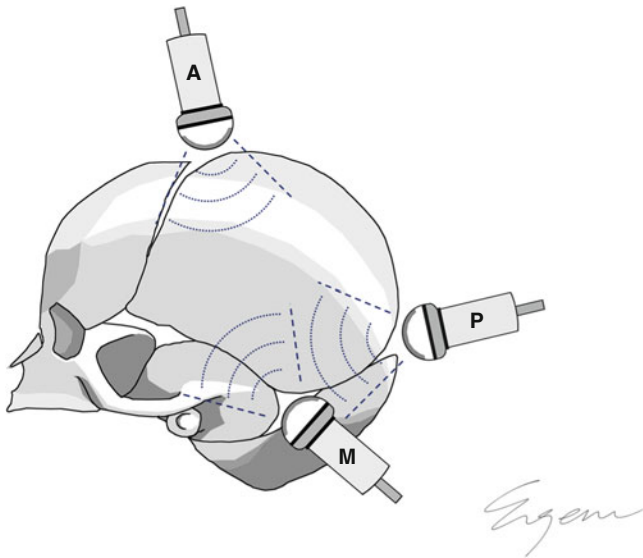


Fig. 6.1 Diagram of the lateral skull for the common sites of cranial sonography through anterior (A), posterior (P), and mastoid (M) fontanelles

6.3.1.2 Normal Anatomy

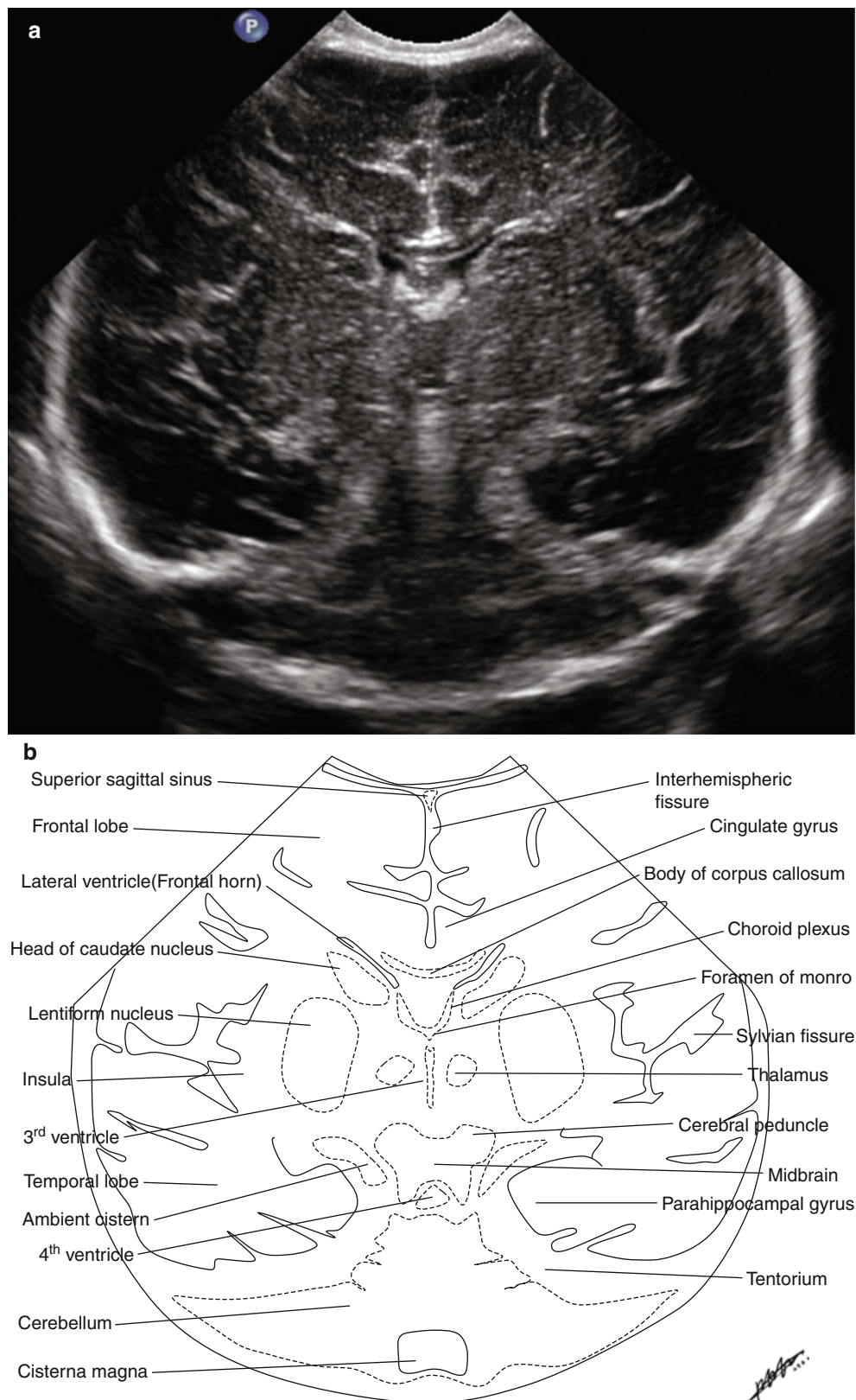


Fig. 6.2 (a and b) Coronal sonographic image (a) and schematic illustration (b) at the level of foramen of Monro through the anterior fontanelle

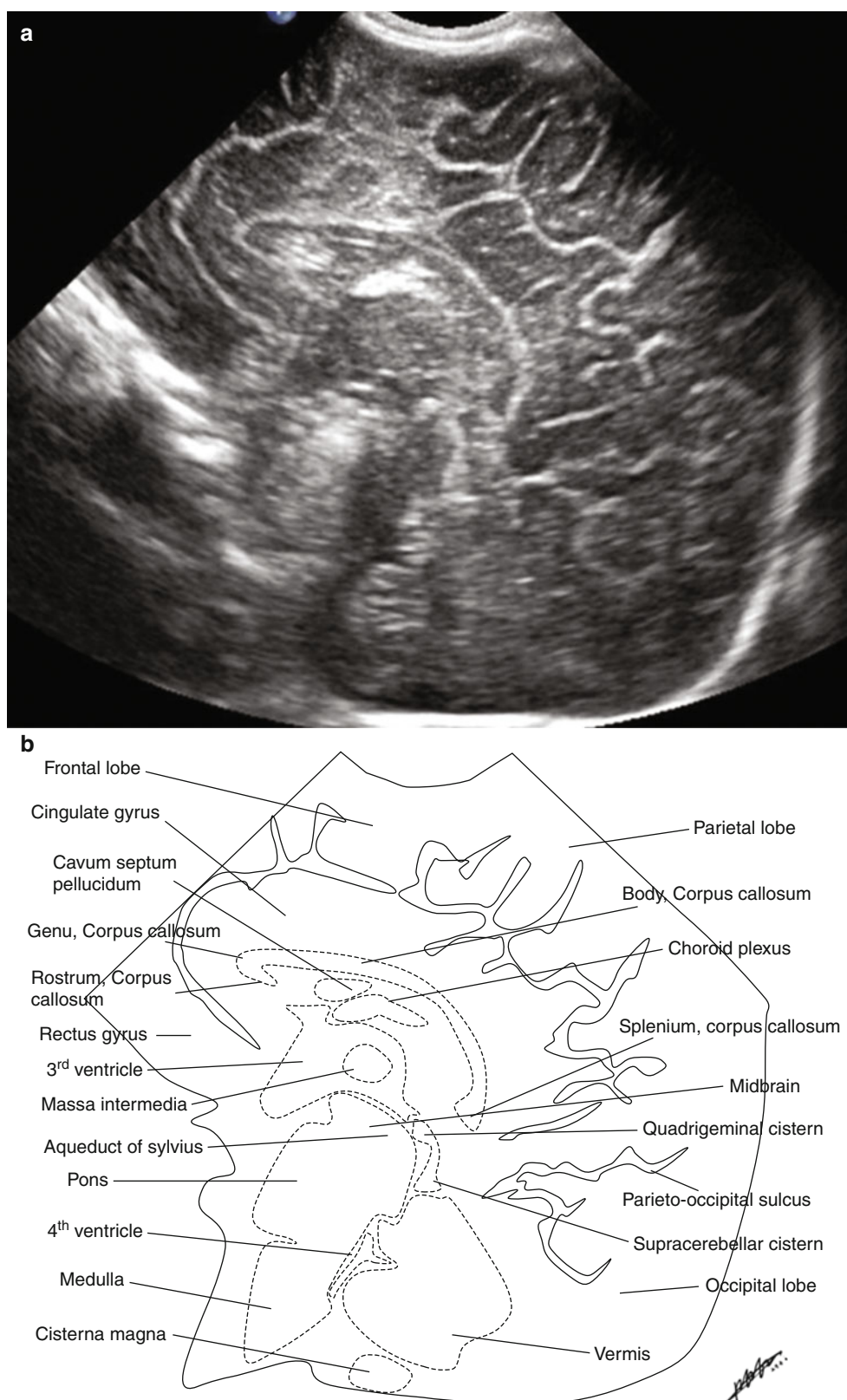


Fig. 6.3 (a and b) Midsagittal sonographic image (a) and schematic illustration (b) through the anterior fontanelle representing the whole corpus callosum, the third and fourth ventricles, brain stem, cerebellar vermis, and cistern magna

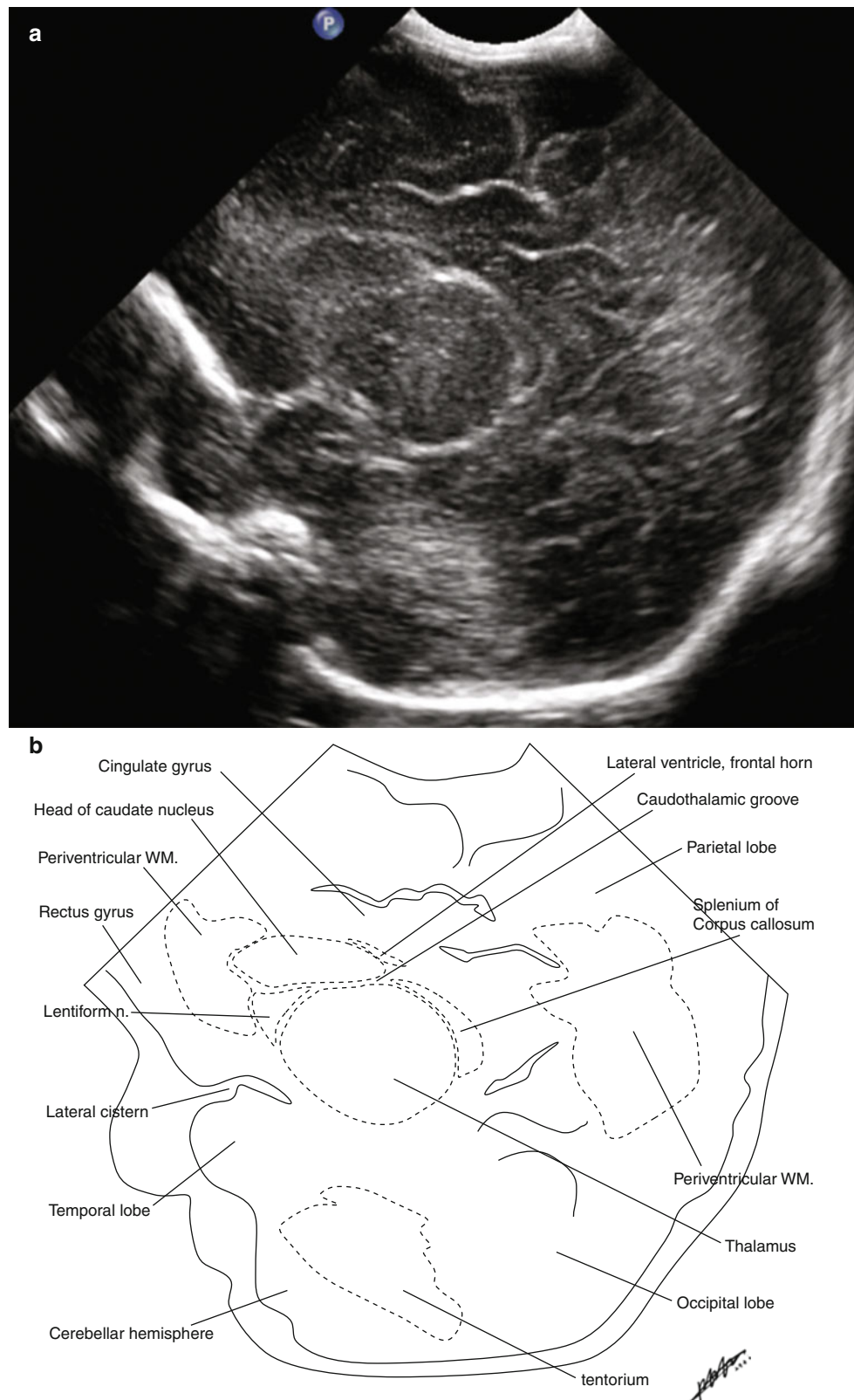


Fig. 6.4 (a and b) Right parasagittal sonographic image (a) and schematic illustration (b) at the level of the caudothalamic groove through the anterior fontanelle

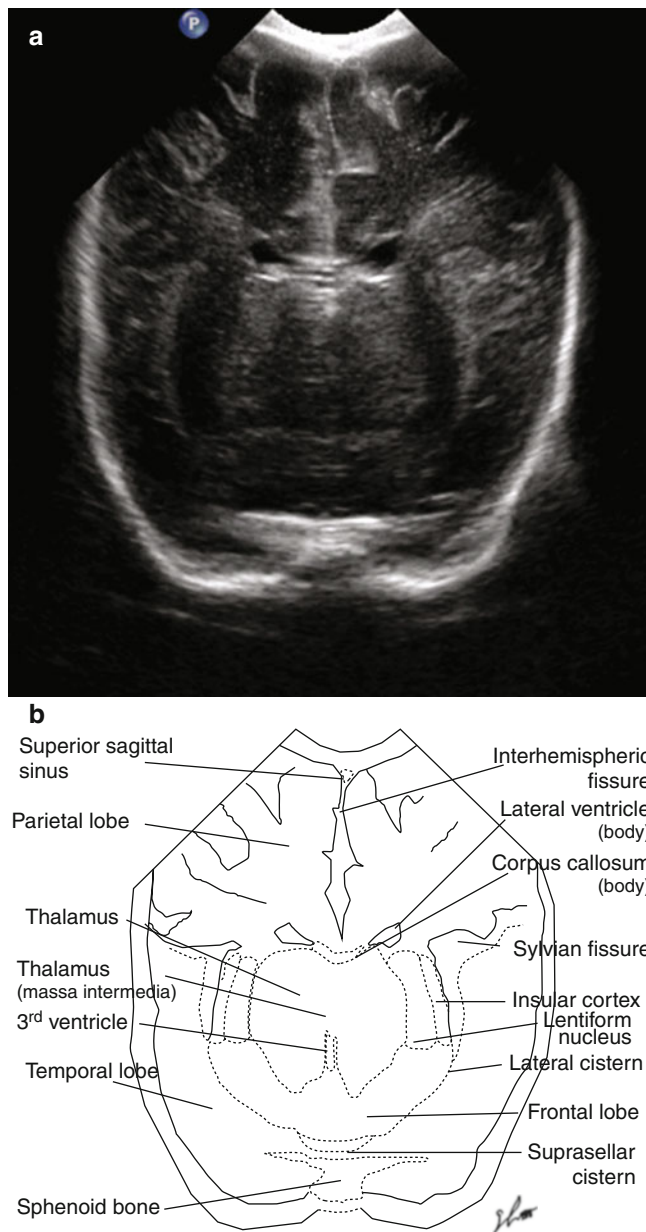


Fig. 6.5 (a and b) Coronal sonographic image (a) and schematic illustration (b) at the level of the bodies of the lateral and third ventricles through the posterior fontanelle

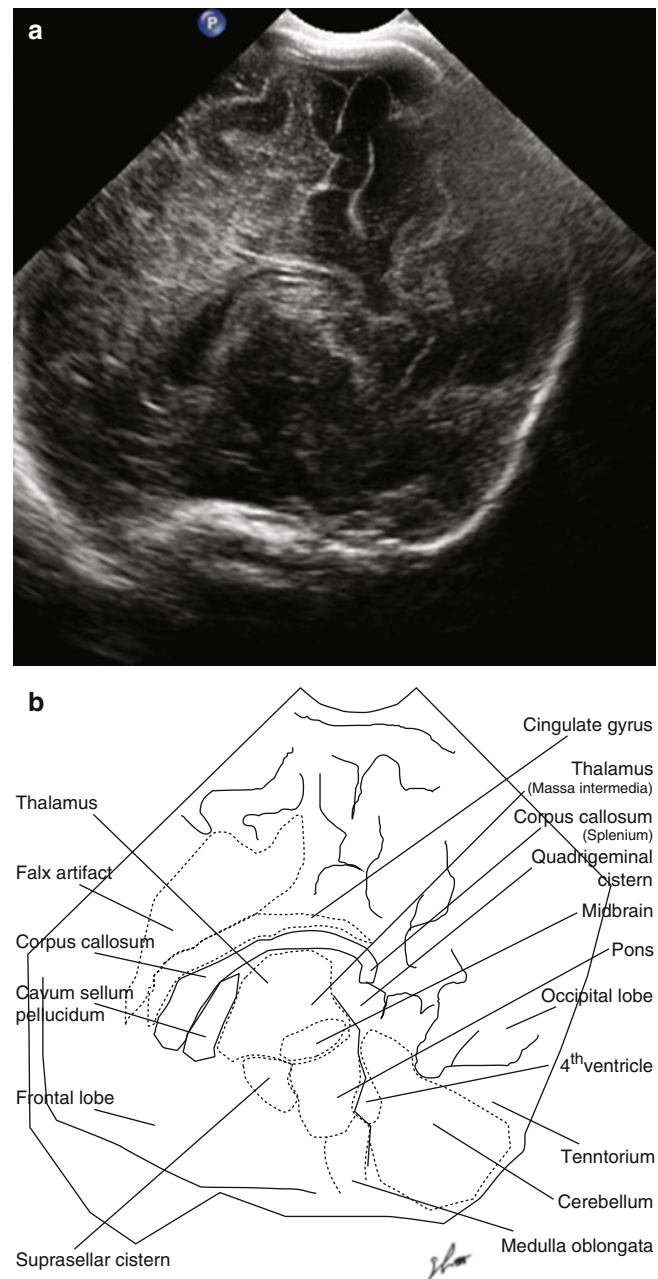


Fig. 6.6 (a and b) Midsagittal sonographic image (a) and schematic illustration (b) at the level of the corpus callosum and the third and fourth lateral ventricles through the posterior fontanelle

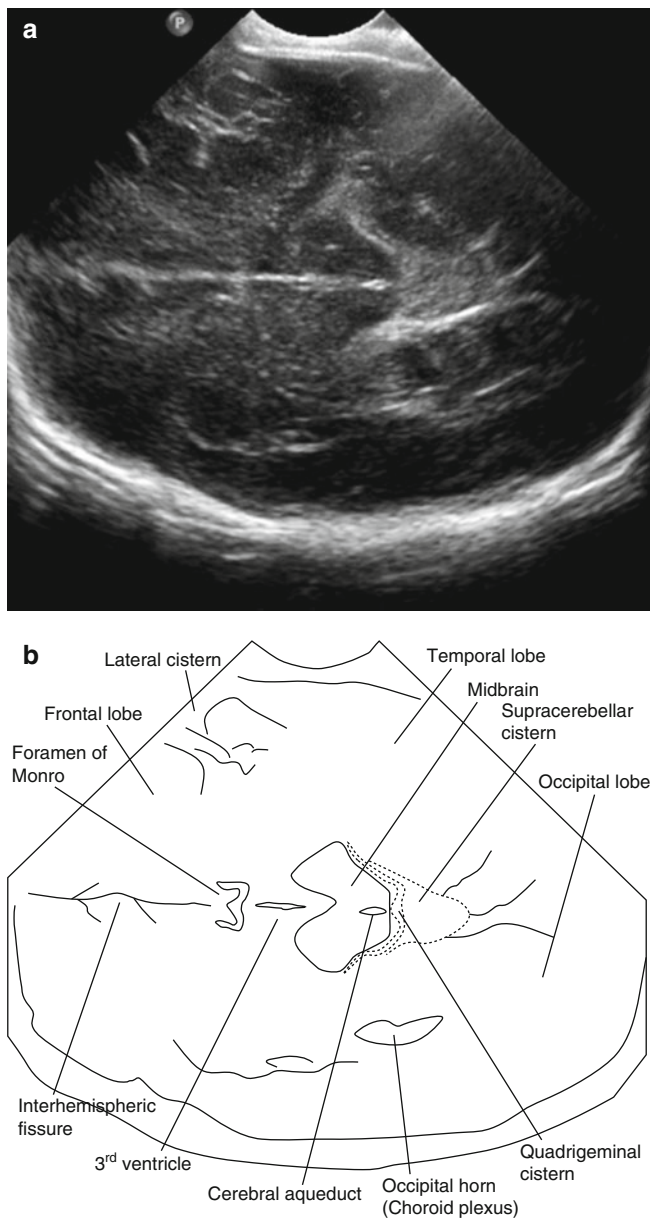


Fig. 6.7 (a and b) Oblique axial sonographic image (a) and schematic illustration (b) at the level of the third ventricle and midbrain through the mastoid fontanelle

6.3.1.3 Normal Variants and Pitfalls

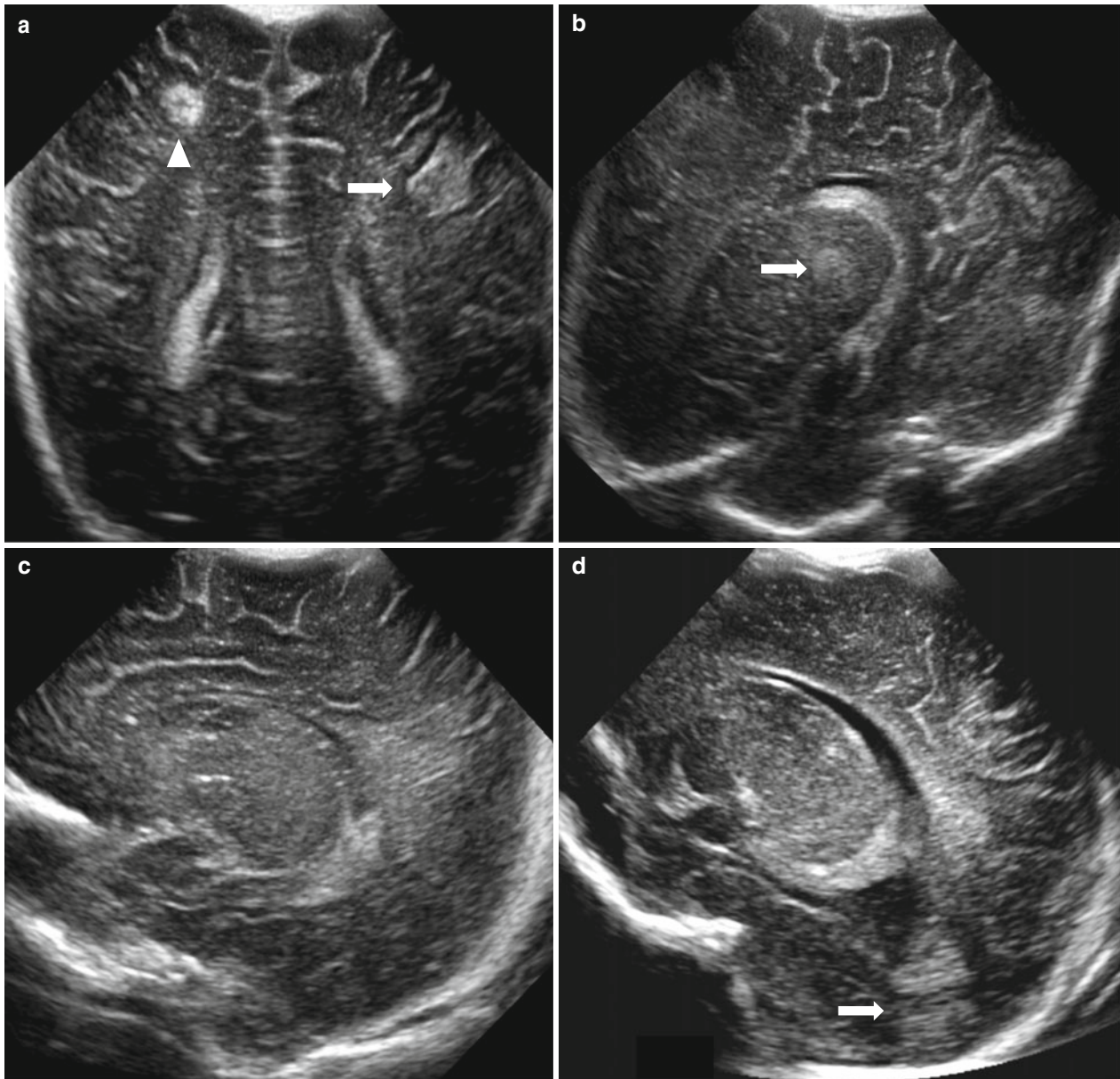


Fig. 6.8 Echogenic pseudolesion. (a) Posterior coronal scan through the anterior fontanelle in 1-day-old male neonate shows a triangular echogenic pseudolesion (*arrow*) in the left frontotemporal junction attached to adjacent sulci and a discrete, round echogenic lesion (*arrowhead*) in right frontal white matter apart from sulci confirmed as focal hemorrhagic infarct. (b) Left parasagittal scan through the posterior fontanelle in a 5-day-old male neonate shows a round echogenic

density in the left thalamus (*arrow*), so-called thalamic pseudolesion. (c) On left parasagittal scan through the anterior fontanelle, thalamic pseudolesion disappeared. (d and e) Left parasagittal scan through the anterior fontanelle in a 2-day-old male neonate (d) shows a focal echogenic pseudolesion (*arrow*) posterior to dilated occipital horn of left lateral ventricle, and on left parasagittal scan through the posterior fontanelle (e), it disappeared

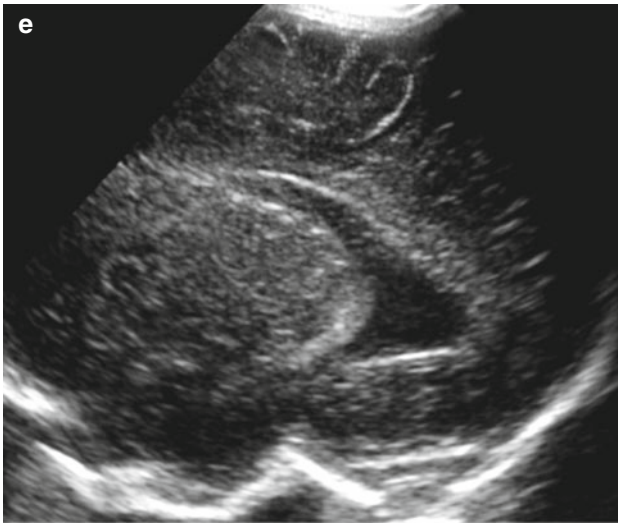


Fig. 6.8 (continued)

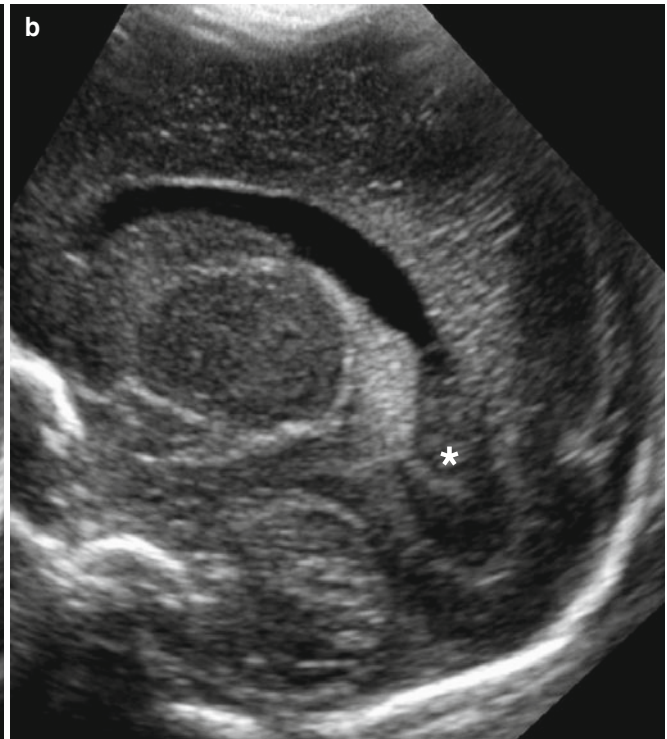


Fig. 6.9 Calcar avis in a 3-day-old female neonate. **(a)** Coronal image shows white matter mound (*) by compression of medial side of lateral ventricle. **(b)** Left parasagittal image shows intraventricular

hyperechoic mass (*) in the occipital horn of the lateral ventricle mimicking intraventricular hematoma

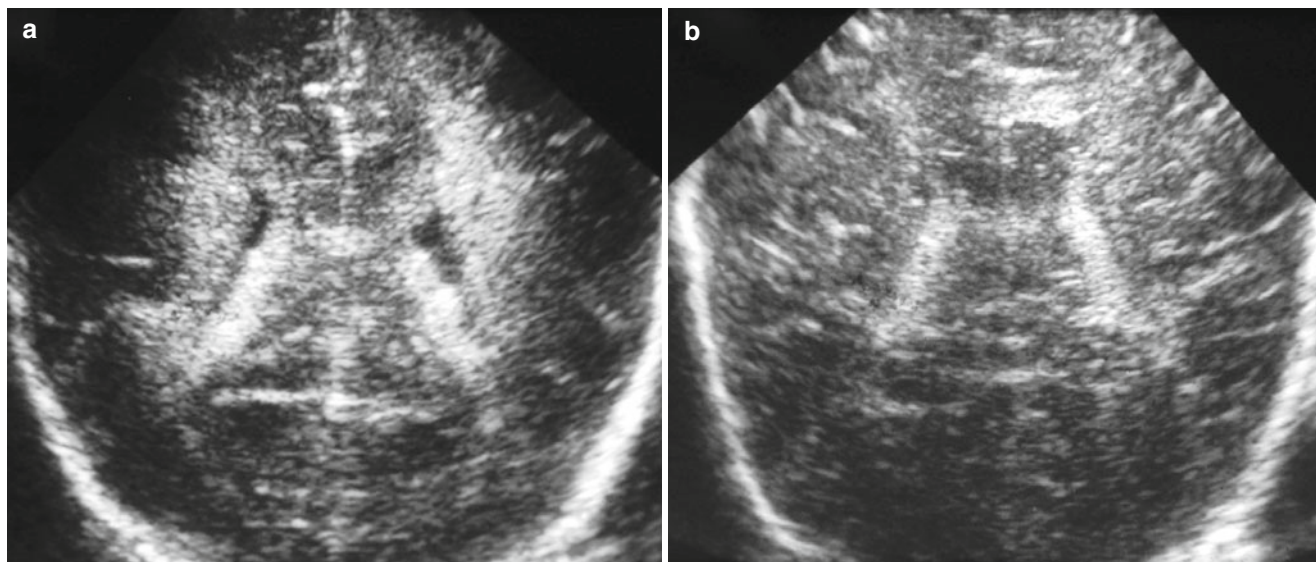


Fig. 6.10 Sequential changes of periventricular echogenic halo. (a) Coronal image of premature male infant at 30 weeks gestational age shows symmetrical, homogeneous, and high echogenic halos in

both periventricular white matters. (b) Coronal image at 41 weeks of the corrected age shows near disappearance of both periventricular echogenic halos

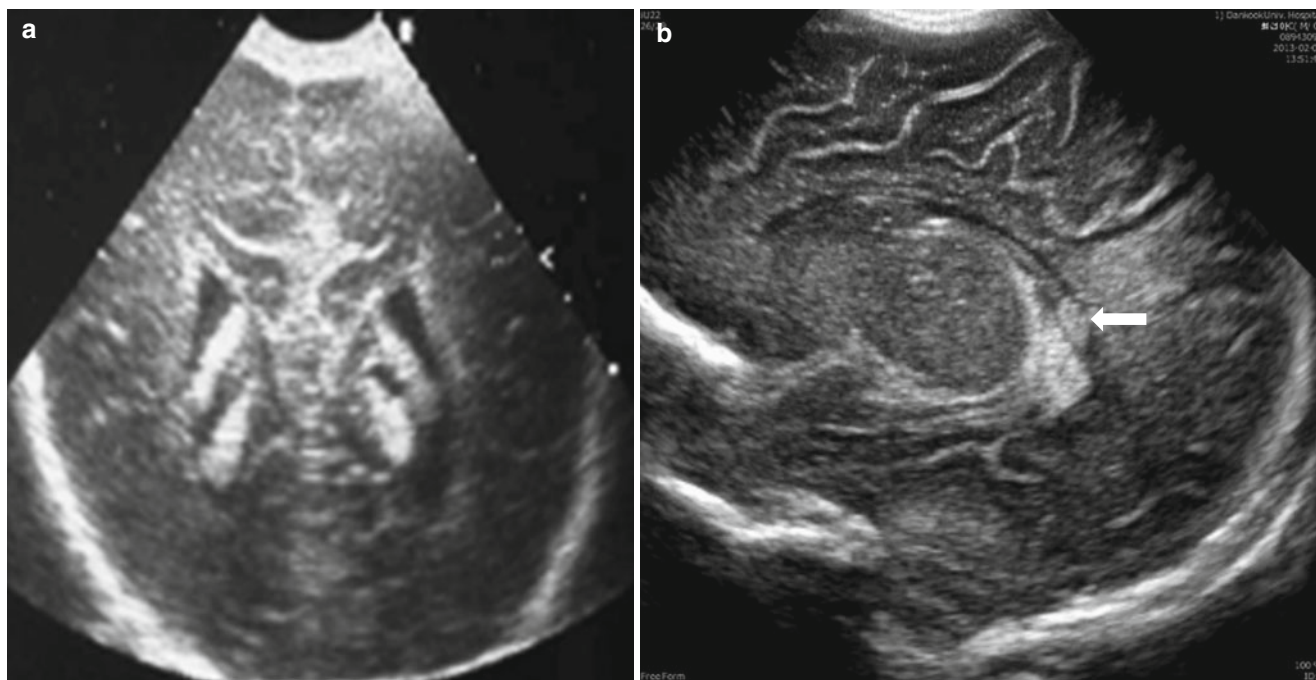


Fig. 6.11 Various patterns of normal choroid plexus. (a) Posterior coronal scan shows double patterns of choroid plexus in both lateral ventricles. (b) Parasagittal scan shows a nodular density (*arrow*) of the glomus

6.3.1.4 Germinal Matrix Hemorrhage

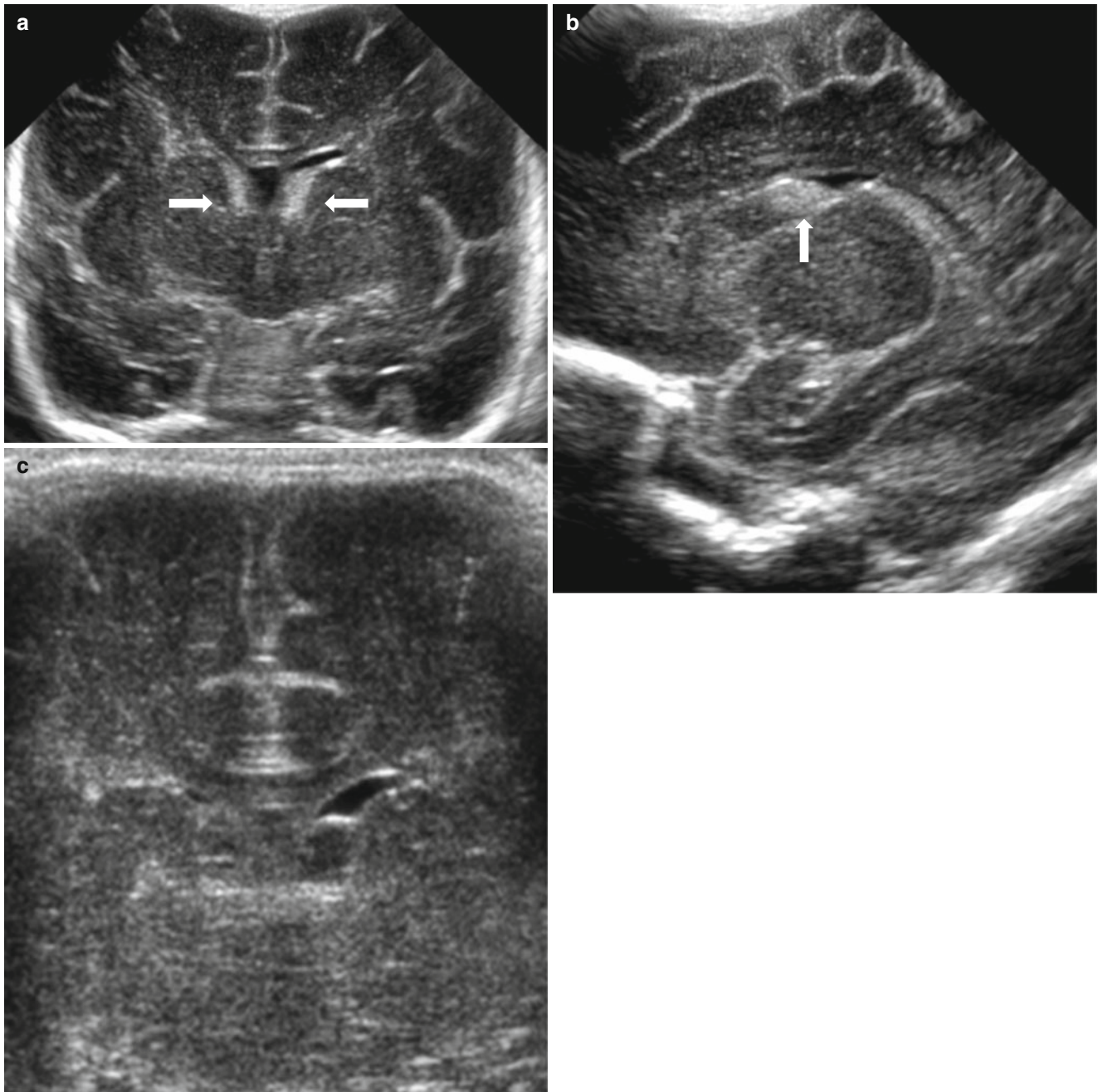


Fig. 6.12 Germinal matrix hemorrhage (GMH), Grade 1 in a 3-day-old female premature infant with 28 weeks gestational age. **(a and b)** Coronal **(a)** and right parasagittal **(b)** scans show ovoid-shaped-echogenic

lesions in both caudothalamic grooves (*arrows*). **(c)** Follow-up coronal scan, 3 weeks later, shows cystic changes in both caudothalamic grooves

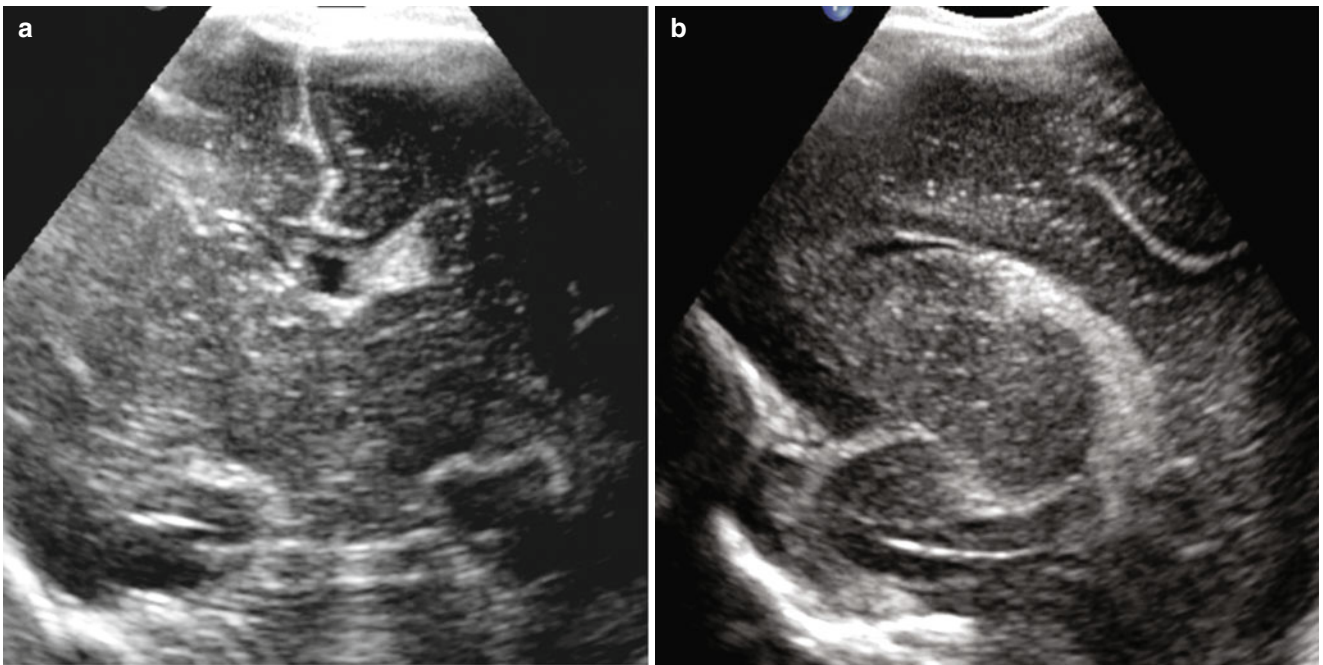


Fig. 6.13 GMH/IVH, Grade 2 in a 2-day-old female premature infant at 29 weeks gestational age. (**a** and **b**) Coronal (**a**) and left parasagittal (**b**) scans show echogenic materials in left caudothalamic groove extending into left lateral ventricle and no ventricular dilatation

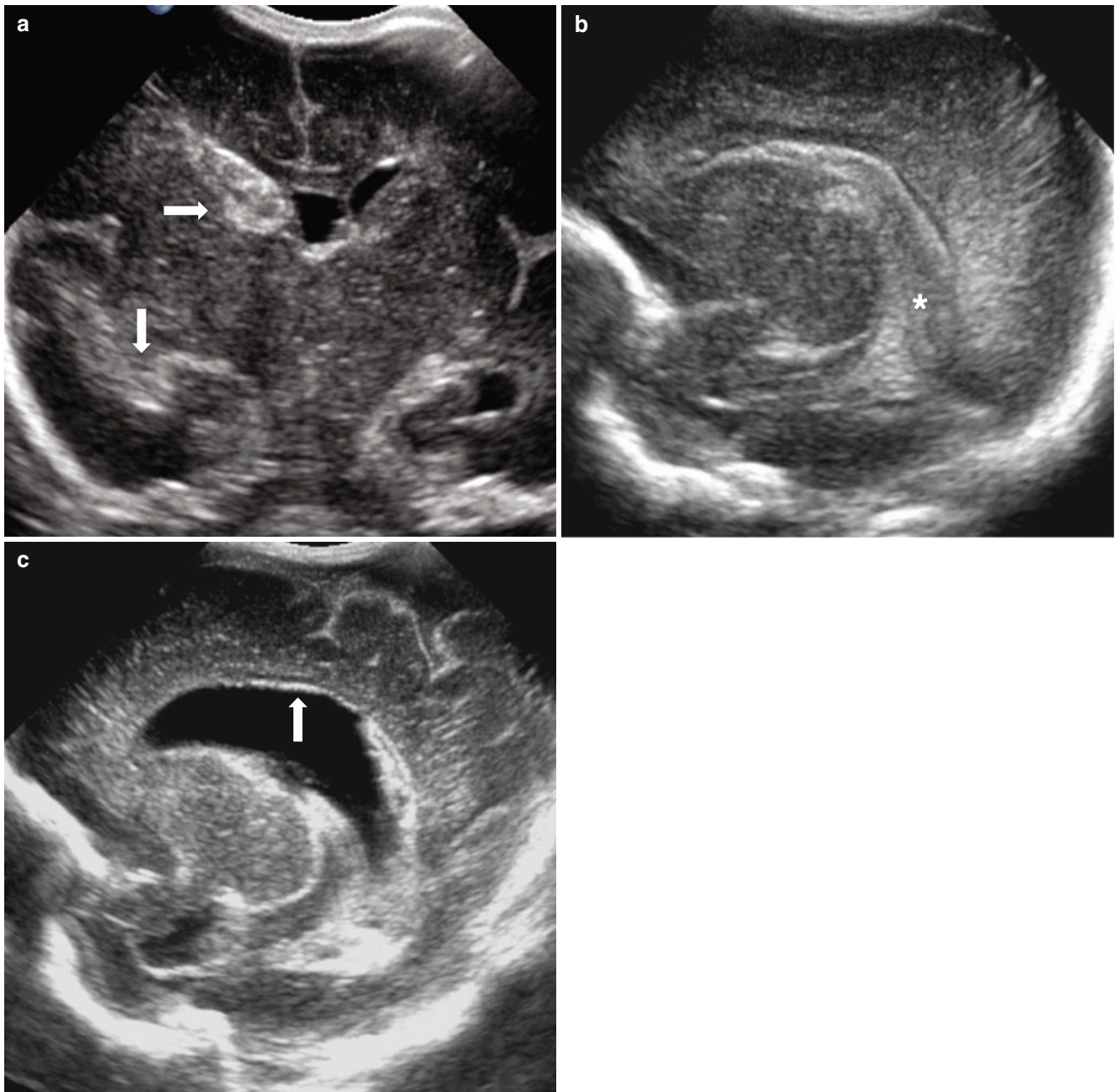


Fig. 6.14 GMH/IVH, Grade 3 in a 7-day-old female premature infant at 28 weeks gestational age. (a) Coronal scan shows large echogenic materials in right caudothalamic groove and temporal horn of right lateral ventricle (*arrows*) with dilatation of both lateral ventricles. (b) Right parasagittal scan shows echogenic materials in right caudothalamic groove extending into right lateral ventricle forming a

cast of ventricular configuration(*). (c) Right parasagittal scan, 4 weeks later, shows progressive dilatation of right lateral ventricle, heterogeneous echogenic materials in right lateral ventricle suggesting residual blood clots, and increased ependymal lining echoes (*arrow*) along ventricular walls due to secondary ventriculitis

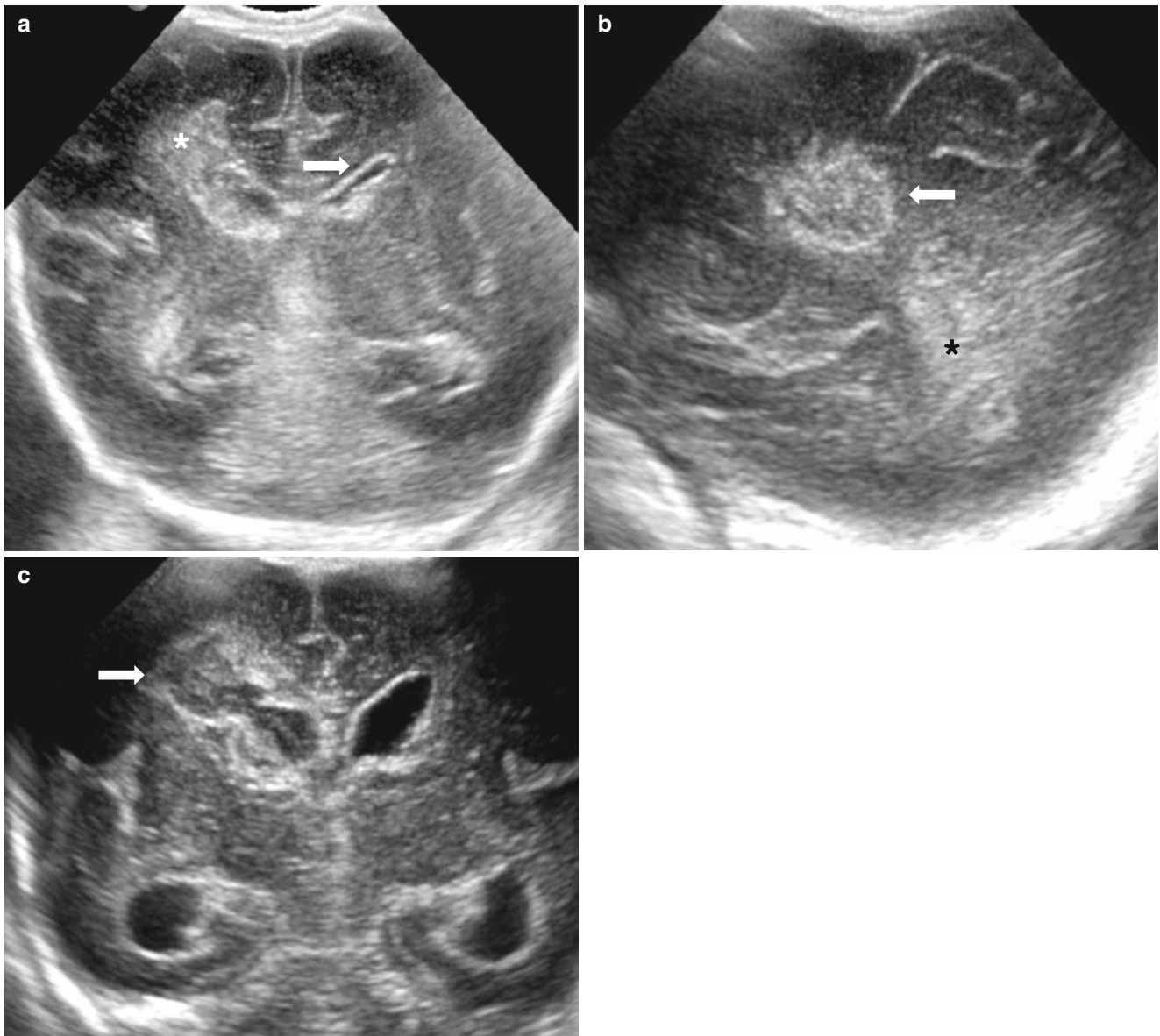


Fig. 6.15 GMH/IVH, Grade 4 in 1-day-old premature infant at 29 weeks gestational age. (a) Coronal scan shows echogenic materials in right caudothalamic groove extending into right frontal white matter (*) and in left caudothalamic groove and both temporal horns of lateral ventricles with increased ependymal lining echoes (arrow). (b) Right

parasagittal scan shows echogenic lesions in right frontal white matter as parenchymal hemorrhage (arrow) and in right lateral ventricle (*). (c) Coronal scan, 2 weeks later, shows cystic changes of right germinal matrix and parenchymal hemorrhage (arrow) and hydrocephalus

6.3.1.5 Intracranial Hemorrhage Except for GMH

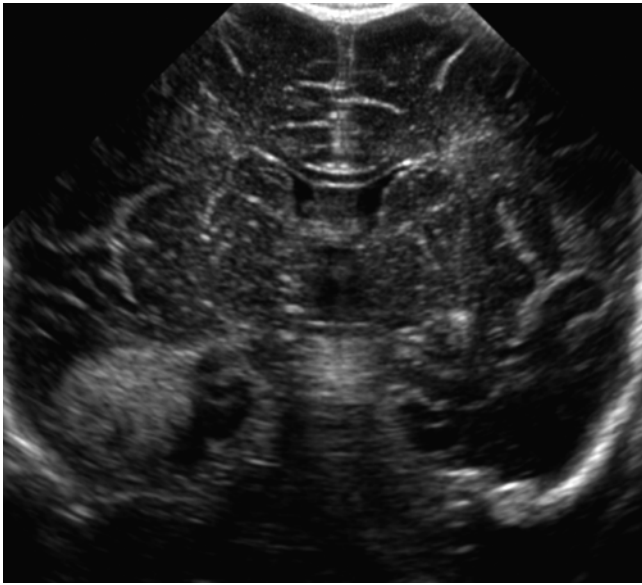


Fig. 6.16 Intracerebral hemorrhage in a 4-day-old female infant at 39 weeks gestational age. Coronal scan shows a round, discrete echogenic mass in right temporal lobe

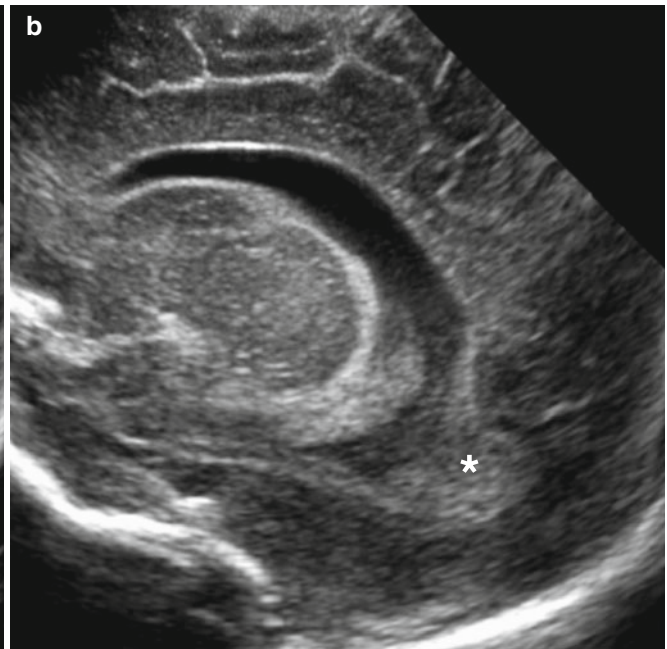
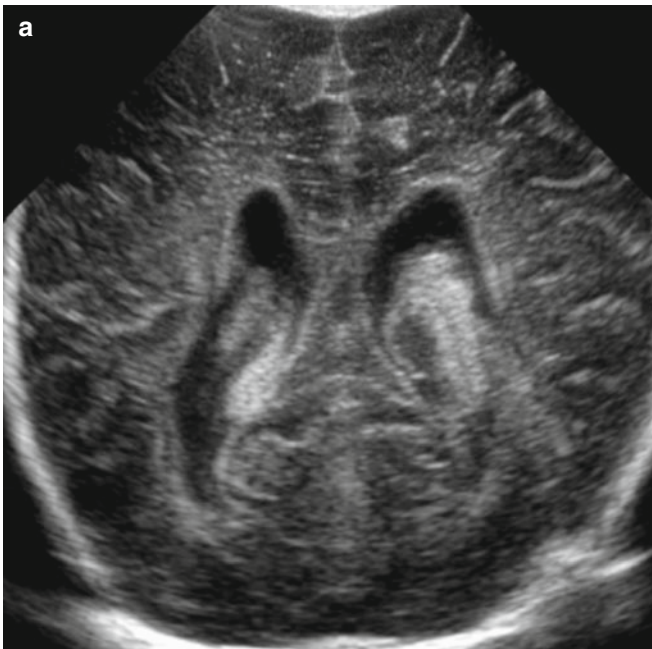


Fig. 6.17 Intraventricular hemorrhage in a 6-day-old infant with 36 weeks gestational age. **(a)** Posterior coronal scan shows heterogeneous echogenic lesions in both lateral ventricles with ventriculomegaly and increased ependymal echoes that cannot differentiate from normal

choroid plexus. **(b)** Right parasagittal scan shows echogenic materials (*) in posterior part of right lateral ventricle extending into the occipital horn representing as intraventricular hematoma

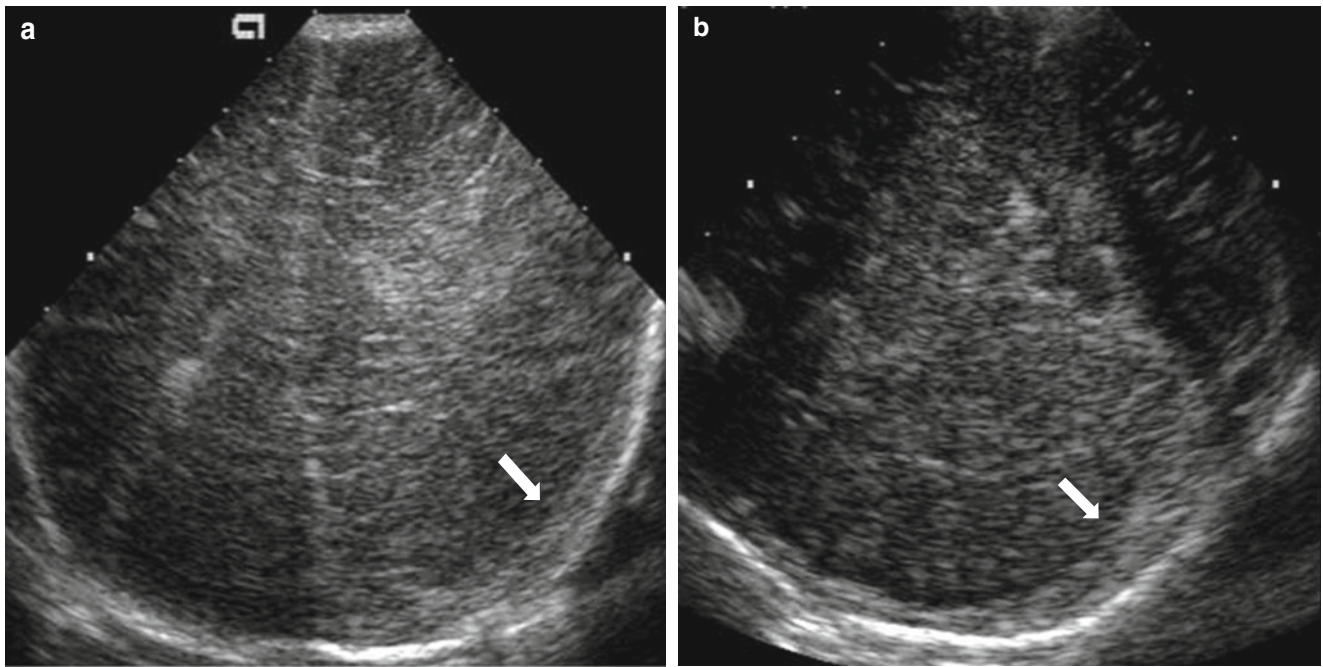


Fig. 6.18 Subdural hemorrhage and cerebral infarction in a neonate with hemophilia. **(a)** Coronal scan shows a crescent echogenic lesion along left cranial convexity (*arrow*) with increased echogenicities of the

underlying parenchyma and ipsilateral mass effect. **(b)** Axial scan through right mastoid fontanel also shows a crescent, echogenic lesion along left cranial convexity (*arrow*)

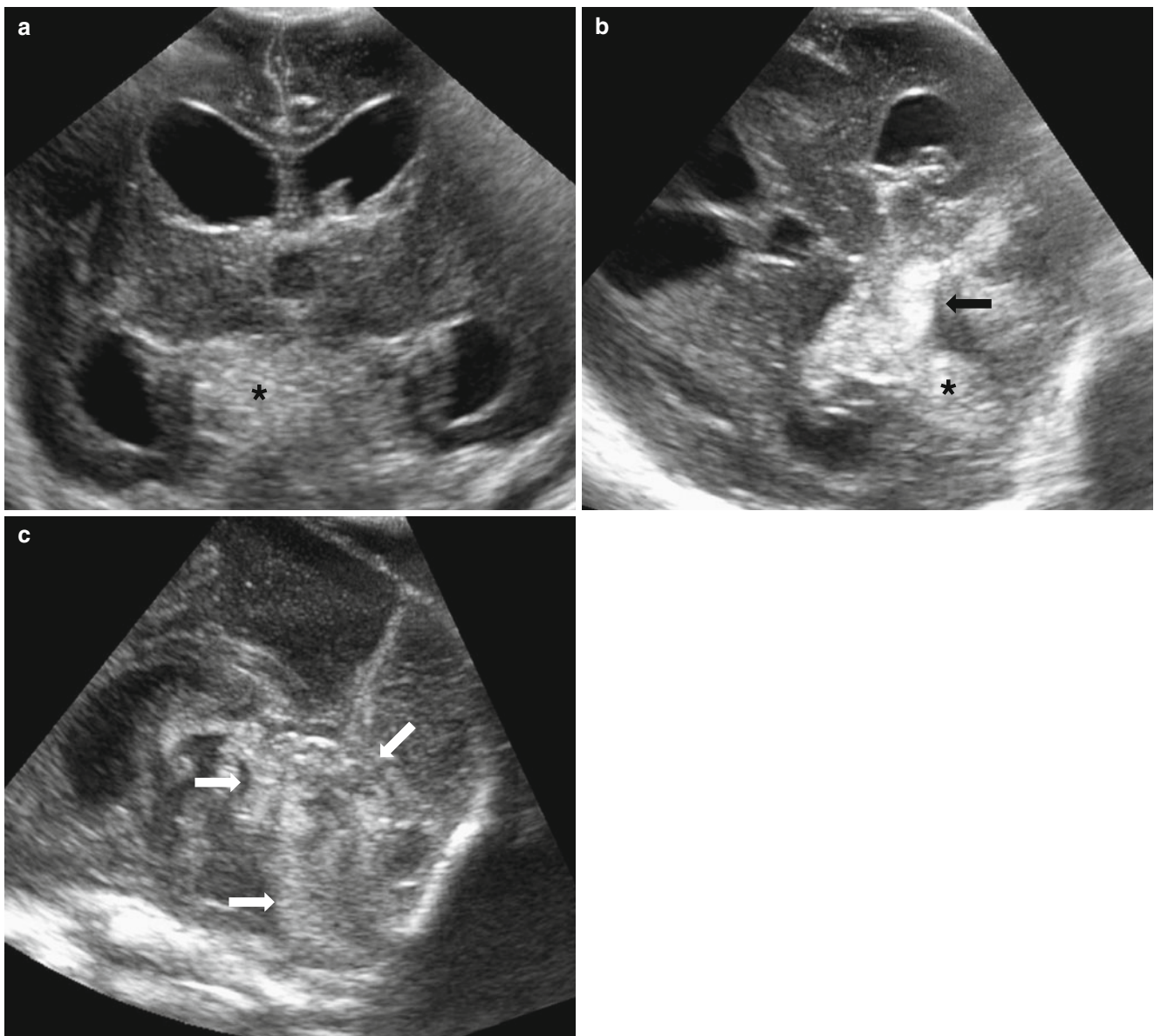


Fig. 6.19 Intraventricular and secondary subarachnoid hemorrhages in a 10-day-old premature male infant. (a) Coronal scan through the anterior fontanelle show various echogenic materials in the lateral, third and fourth ventricles, and posterior fossa (*) with intraventricular obstructive hydrocephalus. (b) Axial scan through the left temporal fontanelle demonstrates large extent of echogenic materials in the lateral and

fourth ventricles (*arrow*) as IVH and in posterior fossa (*) as secondary subarachnoid hemorrhage flowing out from IVH. (c) Midsagittal scan through the posterior fontanelle shows heterogeneous echogenic lesions in the third and fourth ventricles, cisterna magna, and superior cerebellar cisterns (*arrows*) as the combined pattern of intraventricular and secondary subarachnoid hemorrhages

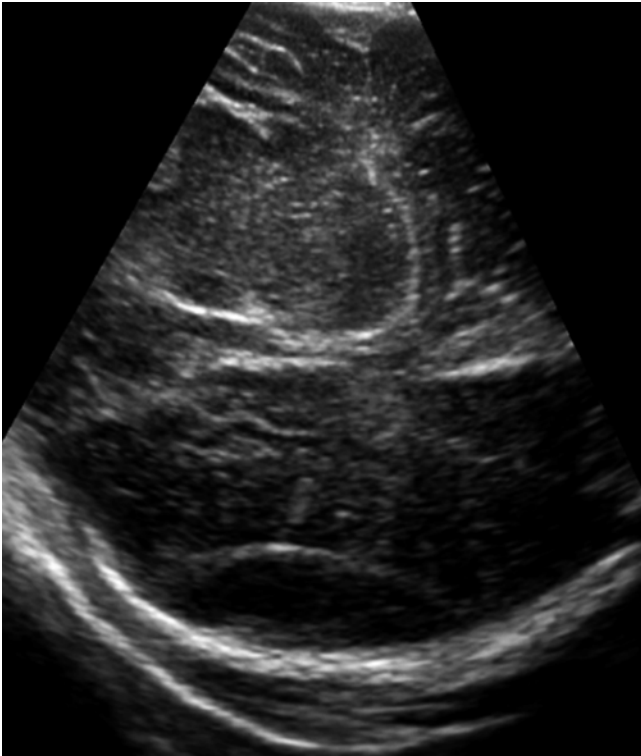


Fig. 6.20 Epidural hemorrhage in 1-day-old male term neonate with vacuum-induced vaginal delivery. Axial scan through the left mastoid fontanelle shows a lentiform, hypoechoic lesion along right parietal convexity with some echogenic debris and ipsilateral mass effect

6.3.1.6 Hypoxic-Ischemic Encephalopathy

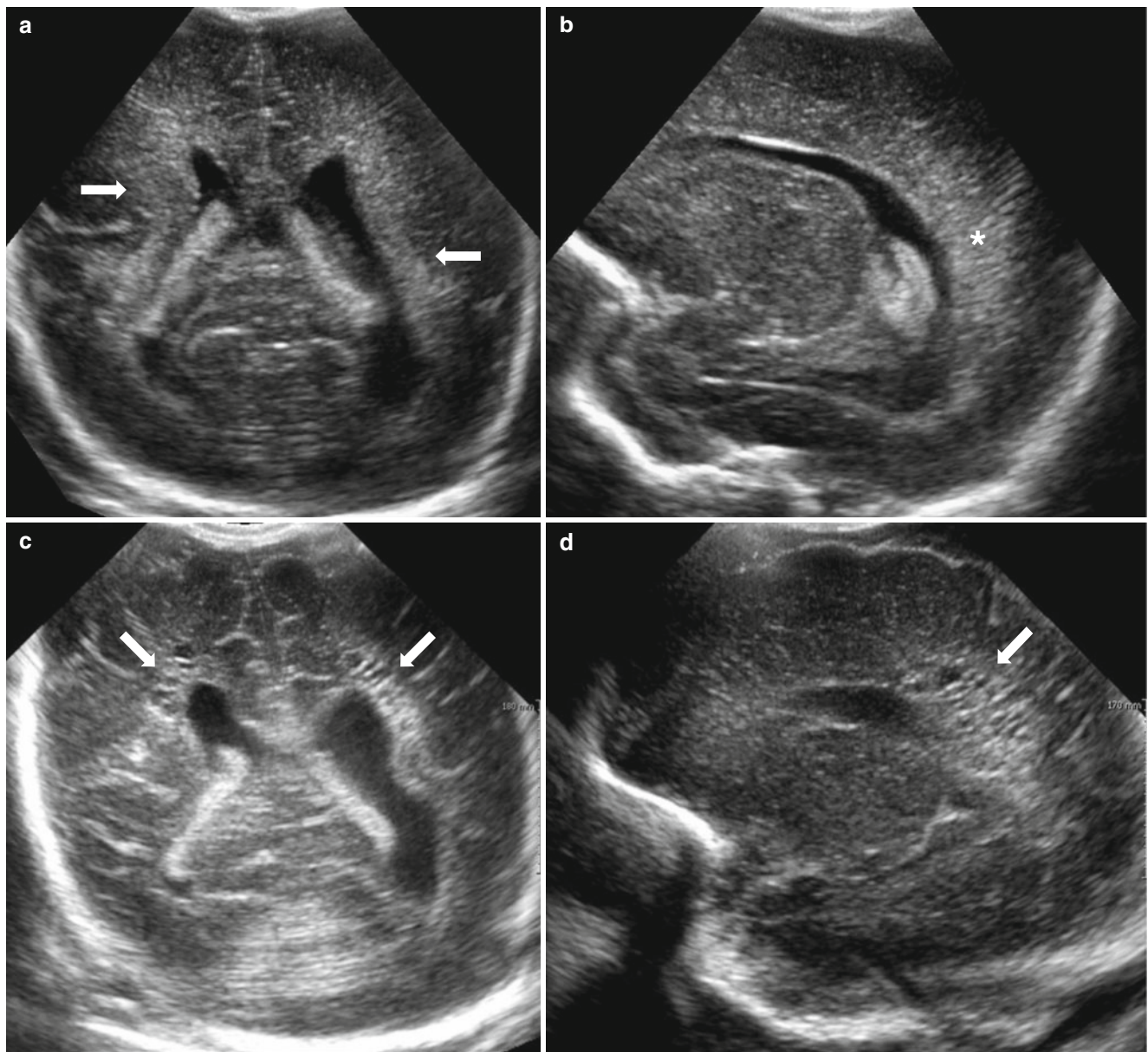


Fig. 6.21 Periventricular leukomalacia in a 3-day-old male premature neonate with 28 weeks gestational age. (a) Coronal scan shows discrete, extensive, and homogeneous echogenicities (*arrows*) in both periventricular white matters as well as the echogenicities of the corresponding choroid plexus. (b) Right parasagittal scan shows also

discrete echogenicities (*) in right peritrigonal white matter. (c and d) Follow-up coronal (c) and parasagittal (d) scans on 38 days later show multiseptate cystic lesions (*arrows*) in both periventricular white matters, especially peritrigonal areas that are confirmatory findings of periventricular leukomalacia

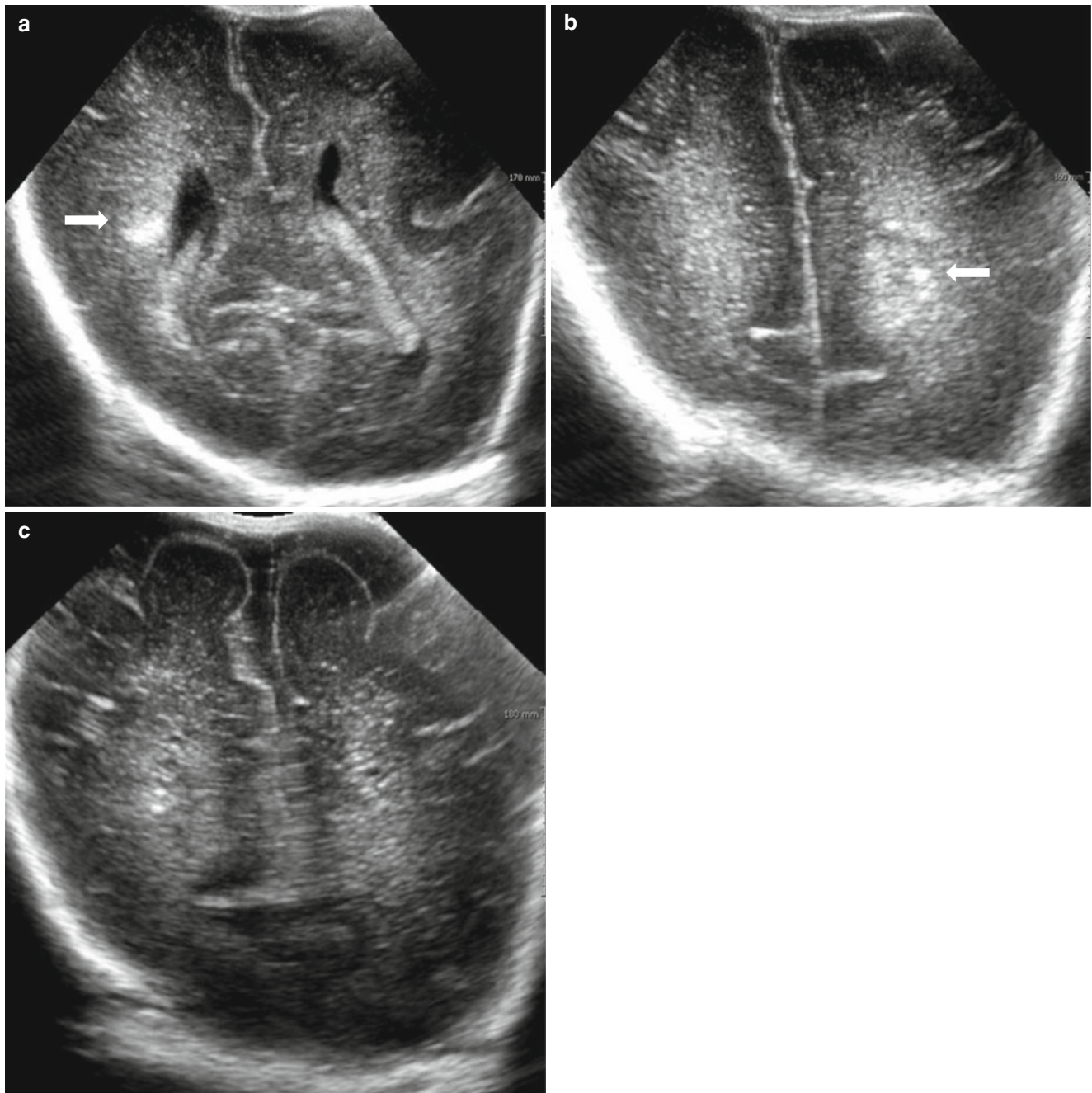


Fig. 6.22 Periventricular leukomalacia in the premature neonate in 1-day-old female premature infant at 28 weeks gestational age. (a and b) Coronal scans (a, b) show multifocal, heterogeneous echogenic lesions in both periventricular white matters including

more increased echogenic spot (*arrows*) than the ipsilateral choroidal echogenicity. (c) Follow-up coronal scan shows multiple cystic changes in both periventricular white matters

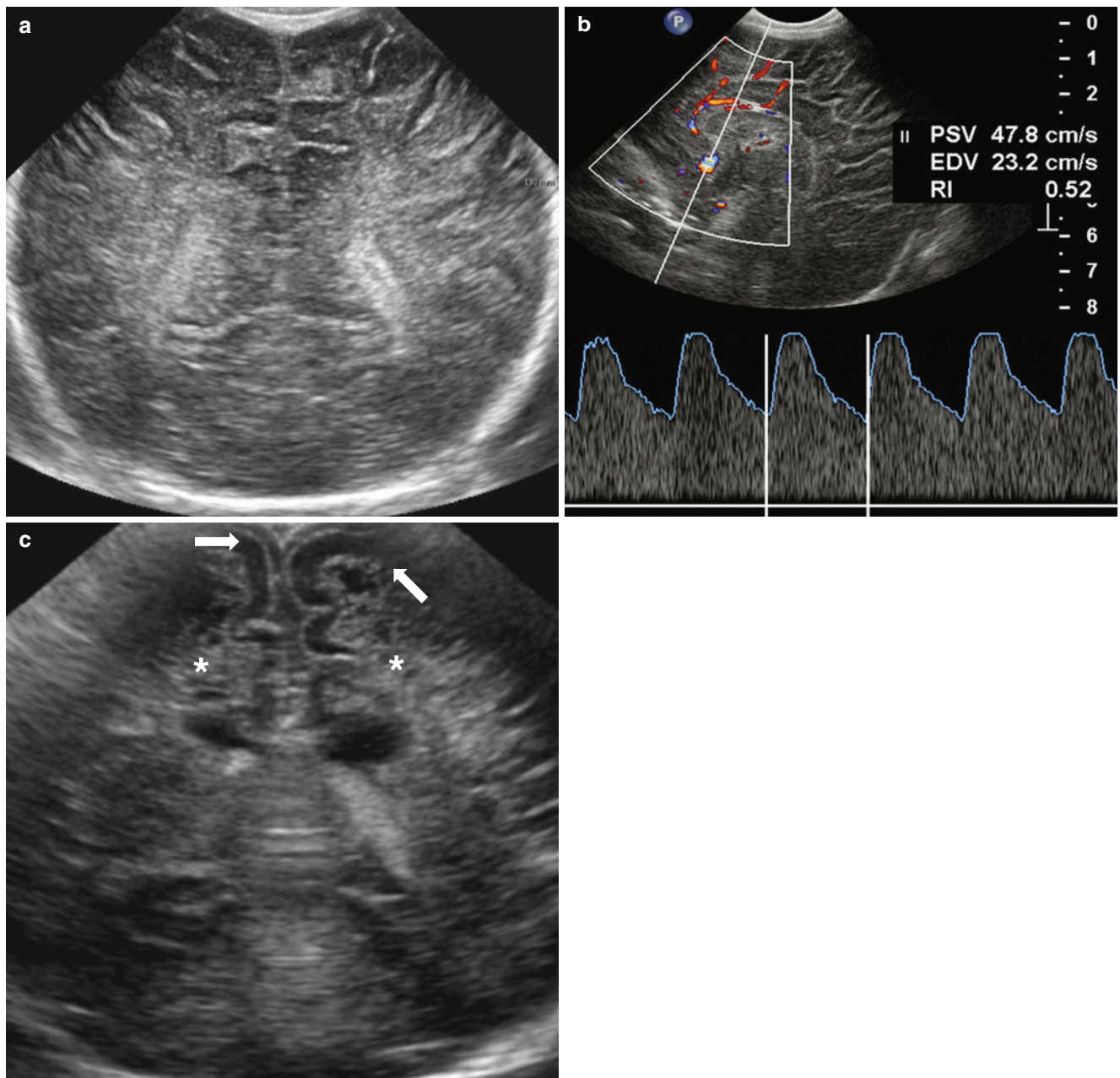


Fig. 6.23 Diffuse hypoxic-ischemic encephalopathy in the term neonate at 39+4 weeks gestational age. **(a)** Coronal scan shows diffuse, heterogeneous echogenicities of brain parenchyma with obliteration of ventricles and cortical sulci. **(b)** Color Doppler image on anterior cerebral artery shows decreased resistive index (0.52). **(c)** Follow-up

coronal scan 35 days later shows multiple cystic changes (*) in both frontal cortex and subcortical white matters with diffuse brain atrophy, secondary ventriculomegaly, and widening of extracerebral CSF spaces (*arrows*) suggesting cystic encephalomalacia

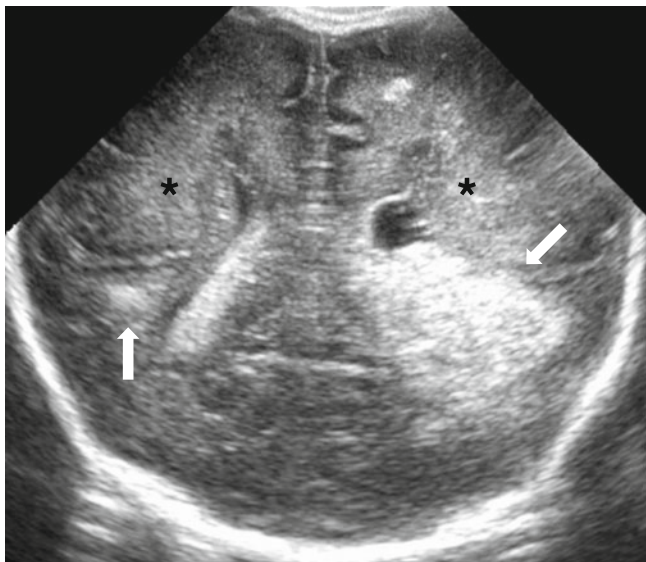


Fig. 6.24 Diffuse hypoxic-ischemic encephalopathy associated with IVH and periventricular hemorrhagic infarctions in the term neonate. Coronal scan shows diffusely increased echogenicities (*) of brain parenchyma suggesting diffuse hypoxic-ischemic encephalopathy. In addition, here is associated with densely echogenic lesions in left lateral ventricle extending into surrounding periventricular white matter and both sides of other periventricular white matters suggesting IVH and multiple periventricular hemorrhagic infarctions (*arrows*)

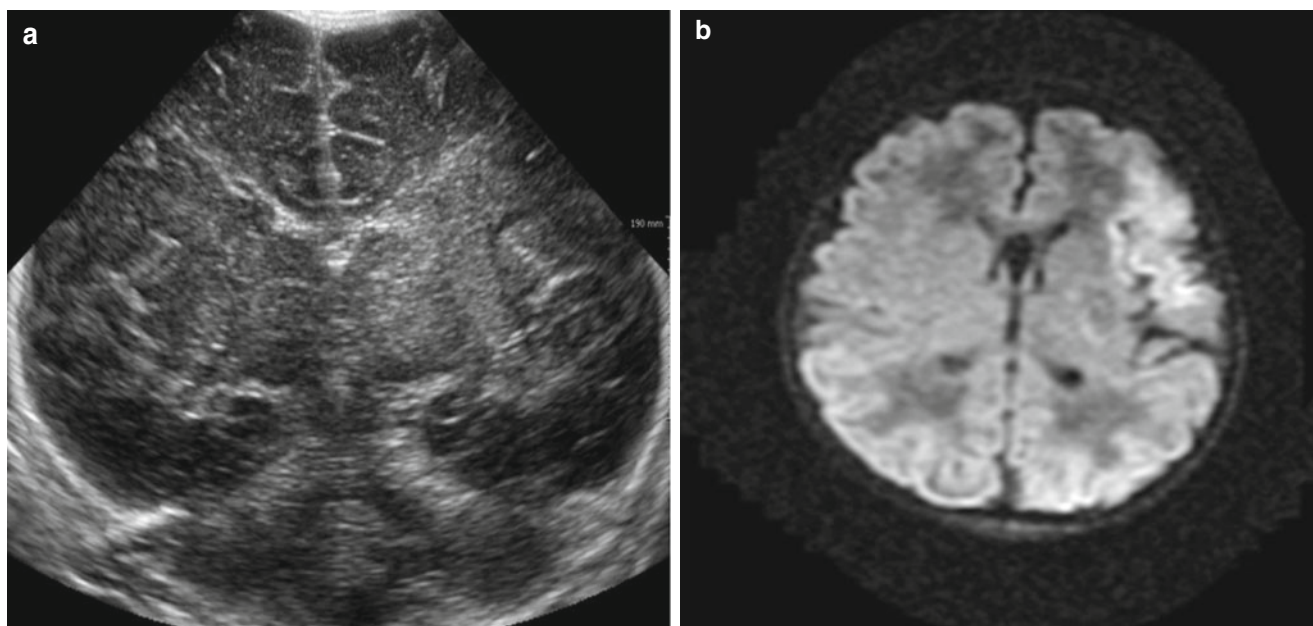


Fig. 6.25 Left middle cerebral infarction in a 2-day-old male infant at 39+1 weeks gestational age. (a) Coronal scan shows asymmetrical, increased echogenicities of left MCA territory. (b) On diffusion-weighted MR image, left MCA infarction can be confirmed

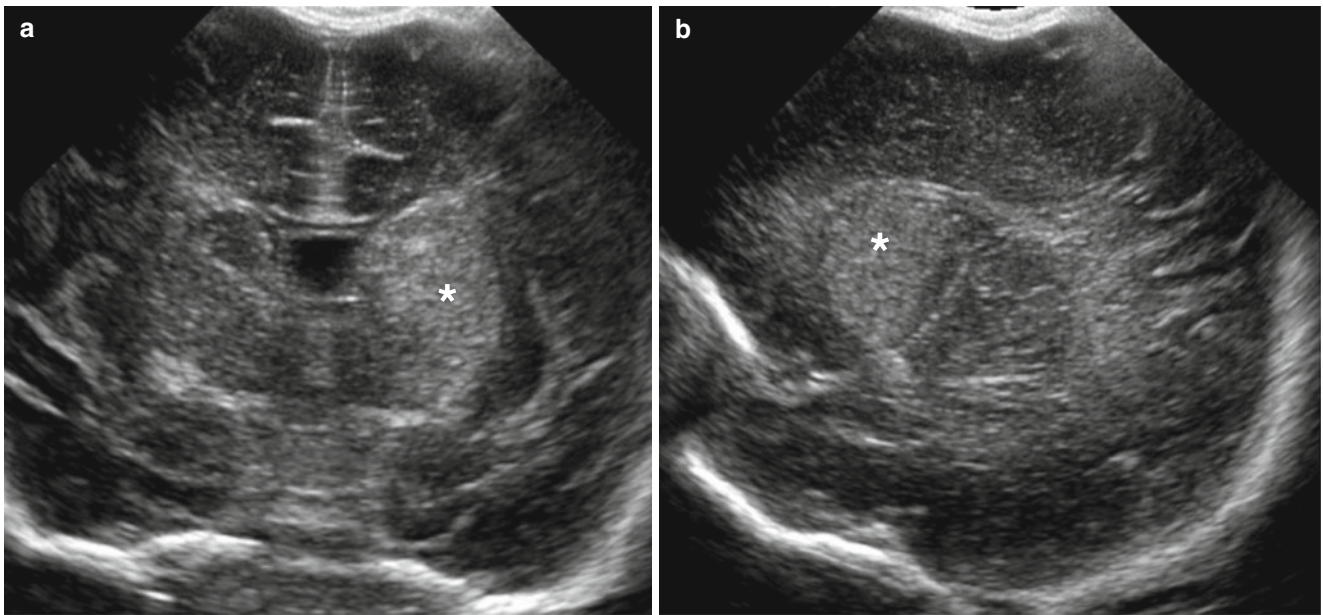


Fig. 6.26 Selective hypoxic-ischemic encephalopathy in a 3-day-old female infant at 36+6 weeks gestational age. (a and b) Coronal and left parasagittal scans show focal, homogeneous echogenic lesions in left basal ganglia (*)

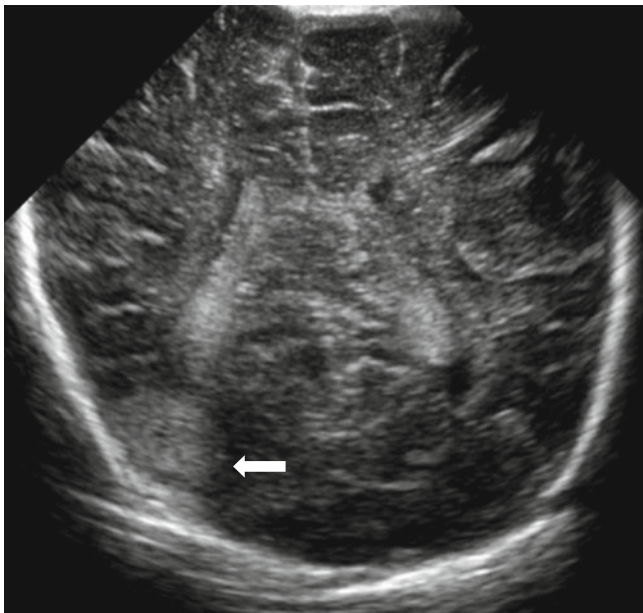


Fig. 6.27 Border zone infarction in junction of right middle and posterior cerebral arteries in a 1-day-old female infant at 37+4 weeks gestational age. Coronal scan shows focal echogenic lesions in junctional area of right MCA and PCA territories (*arrow*)

6.3.1.7 Infectious Diseases

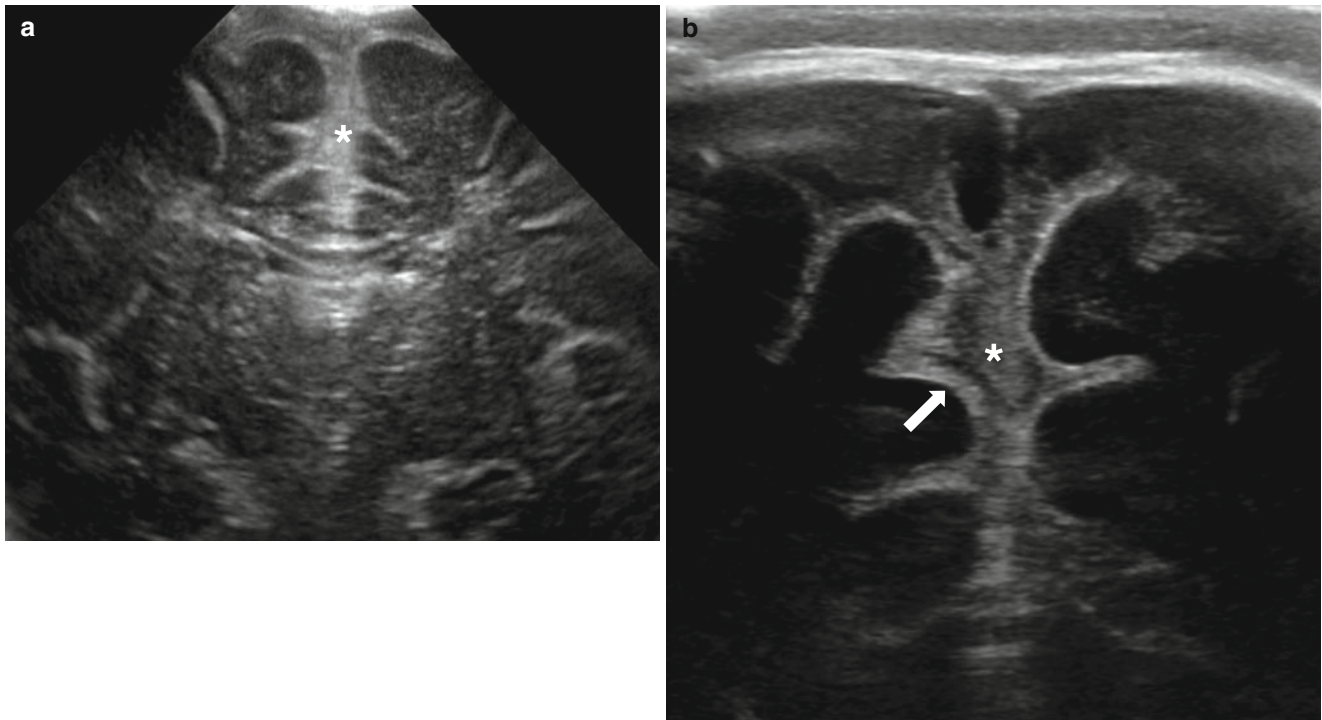


Fig. 6.28 Group B streptococcal meningitis in a 3-day-old female infant at 36 weeks gestational age. (a) Coronal scan shows echogenic materials (*) in anterior interhemispheric fissure with widening.

(b) Anterior coronal scan with 5–12 MHz linear transducer shows more distinct echogenic materials (*) in anterior interhemispheric fissures with leptomeningeal thickening (arrow) compatible with meningitis

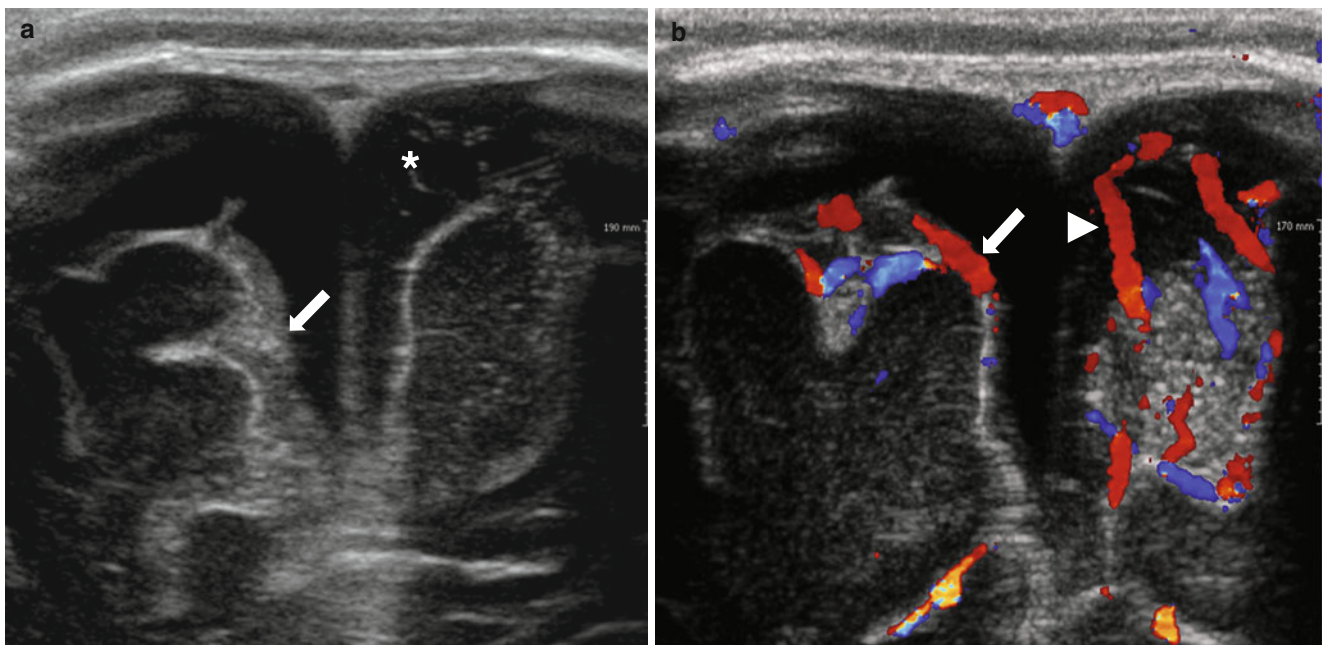


Fig. 6.29 Meningitis with subdural fluid collection infected by respiratory syncytial virus subgroup A in a 2-day-old female infant at 29+2 weeks gestational age. (a) Coronal scan with 12–5 MHz linear transducer shows echogenic materials (arrow) in subarachnoid space along right interhemispheric fissure with fluid collection in right subdural space and widening of left subarachnoid space (*) with

internal linear echoes. (b) Color Doppler scan shows the embedded cortical veins (arrow) within the pia-arachnoid in right echogenic subdural fluid and the elongated cortical veins (arrowhead) crossing the left wide subarachnoid fluid, so-called "cortical vein" sign. These findings can be differentiated between subdural and subarachnoid fluid and hemorrhage

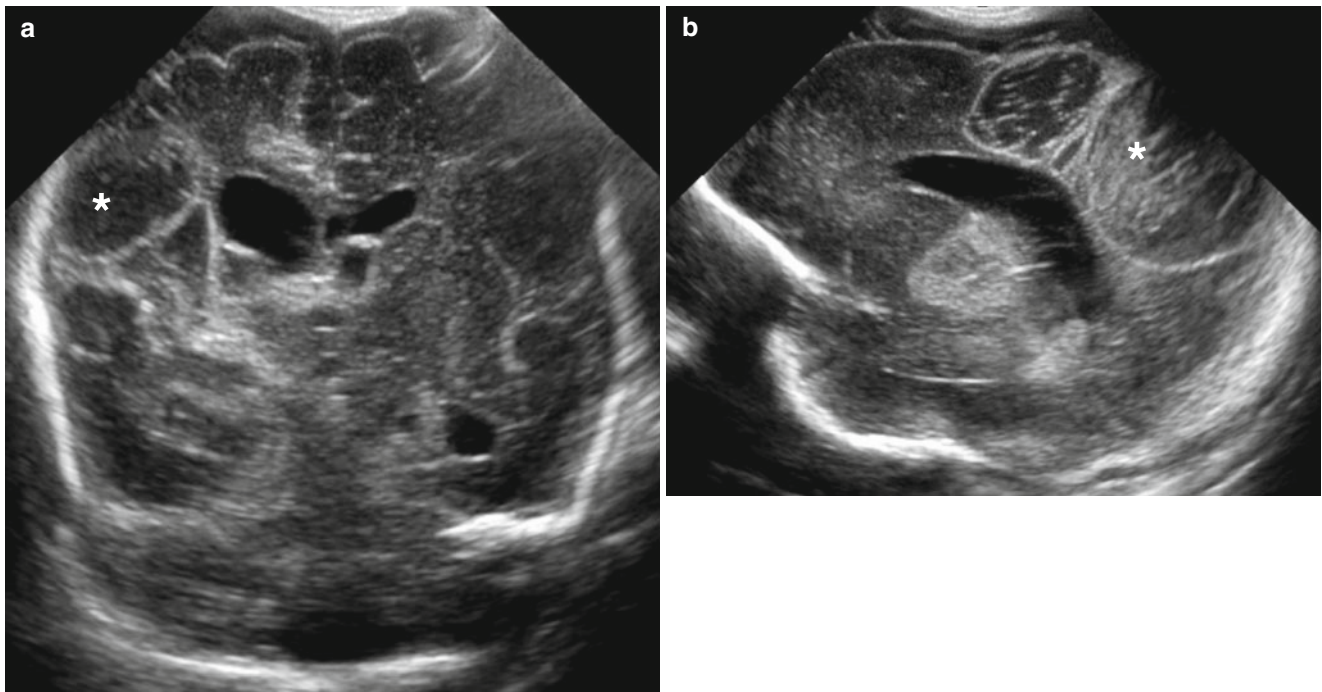


Fig. 6.30 Herpes encephalitis in a 3-day-old male infant at 25+3 weeks gestational age. (a and b) Coronal (a) and right parasagittal (b) scans show extensive gliosis (*) of right temporoparietal lobes with distortion

of underlying normal structures, heterogeneous echogenic lesions in right basal ganglia and thalamus, dilatation of lateral ventricles, and small subependymal cyst in left caudothalamic groove

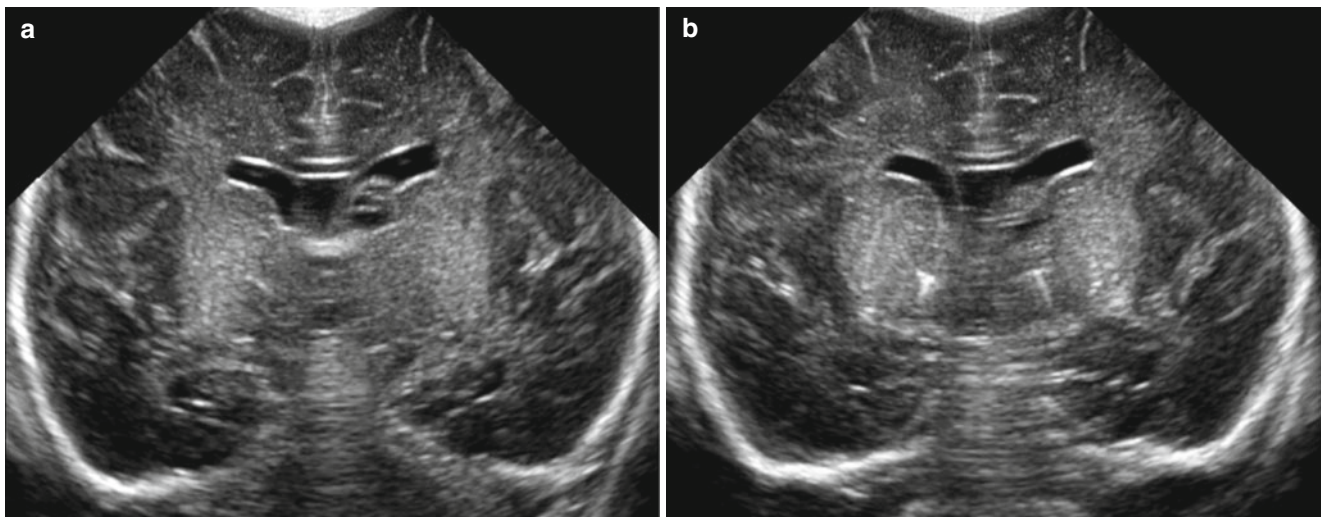


Fig. 6.31 Cytomegaloviral encephalitis in a 2-day-old male infant at 39+2 weeks gestational age. (a and b) Coronal scans (a, b) show homogeneously increased echogenicities in both basal ganglia, thalami

and frontal white matters, and multiple dense echogenic spots in both basal ganglia and thalami with small mixed echogenic cyst in left caudothalamic groove

6.3.1.8 Congenital Malformations

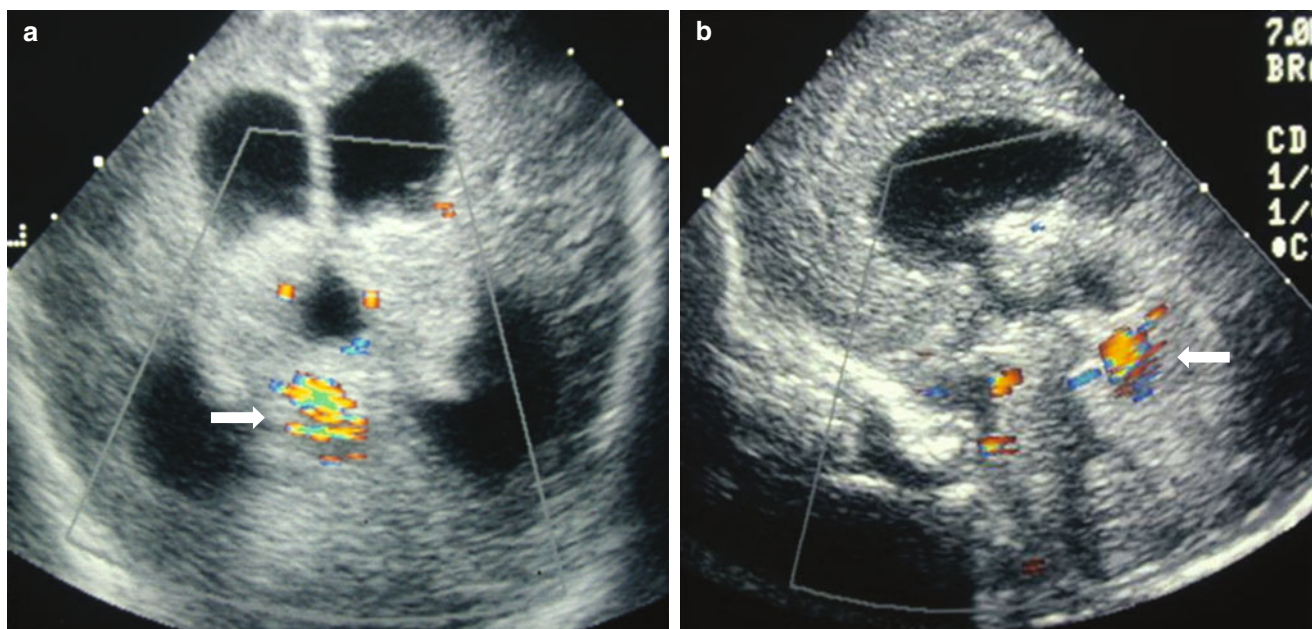


Fig. 6.32 Vein of Galen malformation. (a and b) Color Doppler coronal (a) and midsagittal (b) scans show obstructive hydrocephaly around the aqueduct of Sylvius and the dilated vein of Galen (arrows)

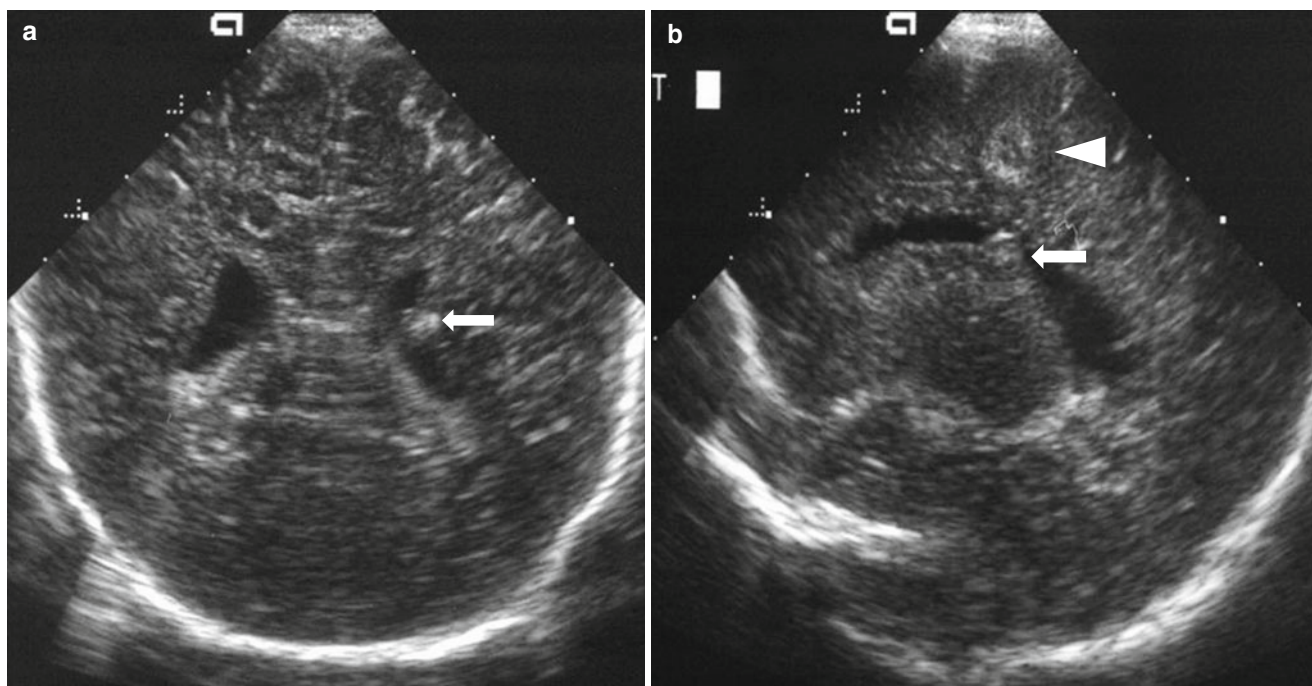


Fig. 6.33 Tuberosclerosis. (a and b) Coronal (a) and right parasagittal (b) scans shows subependymal echogenic nodules along both lateral ventricular walls (arrows) and an echogenic nodule (arrowhead) suggesting a tuber

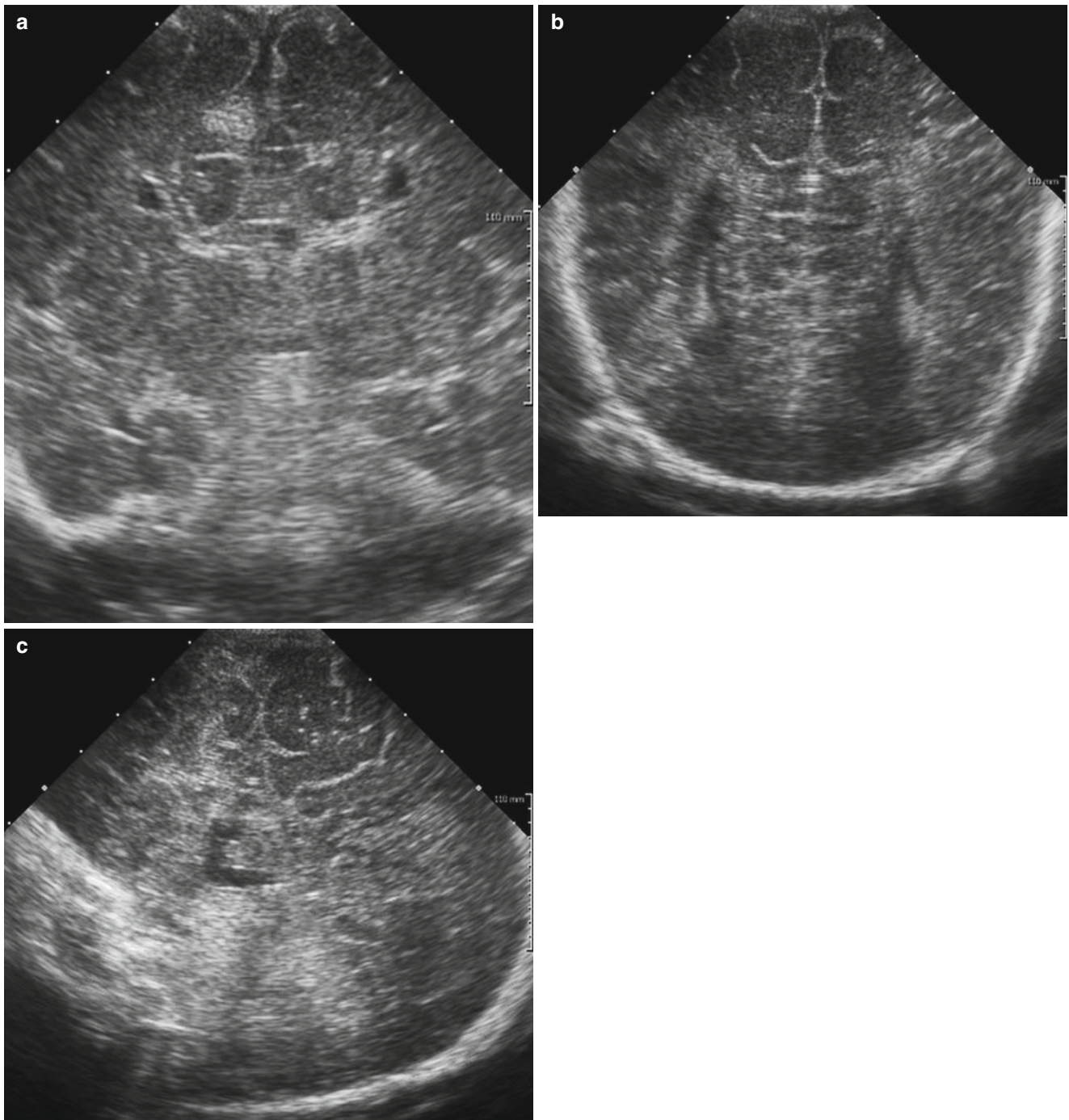


Fig. 6.34 Agenesis of corpus callosum in a 12-day-old male term infant. (a) Coronal scan shows absence of normal callosal echo, nonvisualization of normal gyri or sulci in areas of corpus callosum or cingulate sulcus, and wide separation of both frontal horns of lateral ventricles. (b) Posterior coronal scan shows parallel appearance of bodies of both

lateral ventricles with medial indentation, due to bundles of Probst and colpocephalic appearance of both lateral ventricles. (c) There are nonvisualization of central corpus callosal echoes, high position of third ventricle, and prominent massa intermedia on midsagittal scan

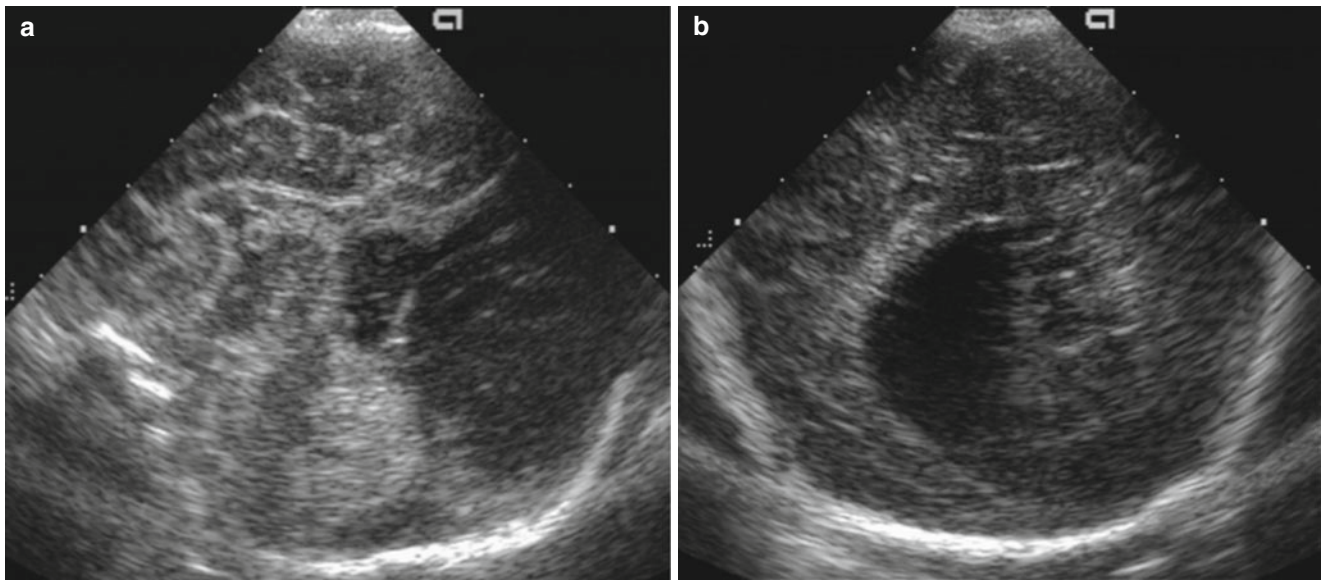


Fig. 6.35 Partial agenesis of corpus callosum with interhemispheric cyst in a 1-day-old female infant at 38+1 weeks gestational age. **(a)** Midsagittal scan shows partial absence of posterior part of

corpus callosum with large cystic lesion in posterior site of the brain. **(b)** Posterior coronal scan shows right parafalcine cyst with surrounding mass effect

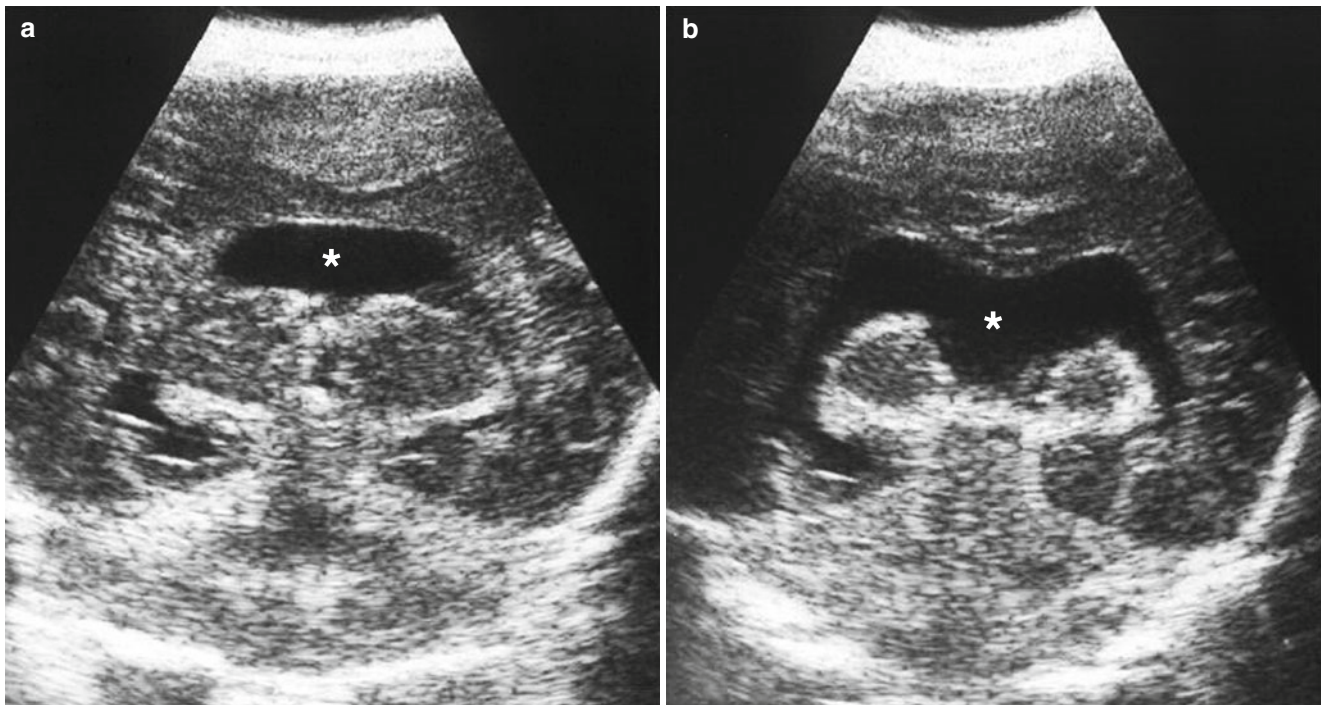


Fig. 6.36 Holoprosencephaly, semilobar types. **(a and b)** Anterior **(a)** and mid- **(b)** coronal scans show single ventricular body (*), partially fused thalami, separate rudimentary occipital and temporal

horns of both lateral ventricles, and normal appearances of the fourth ventricle, brain stem, and cerebellum as semilobar type

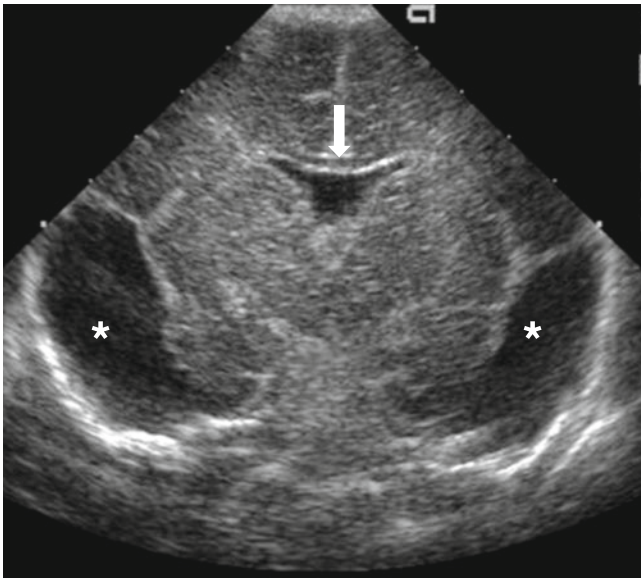


Fig. 6.37 Septo-optic dysplasia with cerebral hypoplasia. Coronal scan shows the fused, squared frontal horns (*arrow*) of both lateral ventricles with inferior beakings, no septum pellucidum and loss of both temporal lobes below Sylvian fissures replaced by cerebrospinal fluid (*)

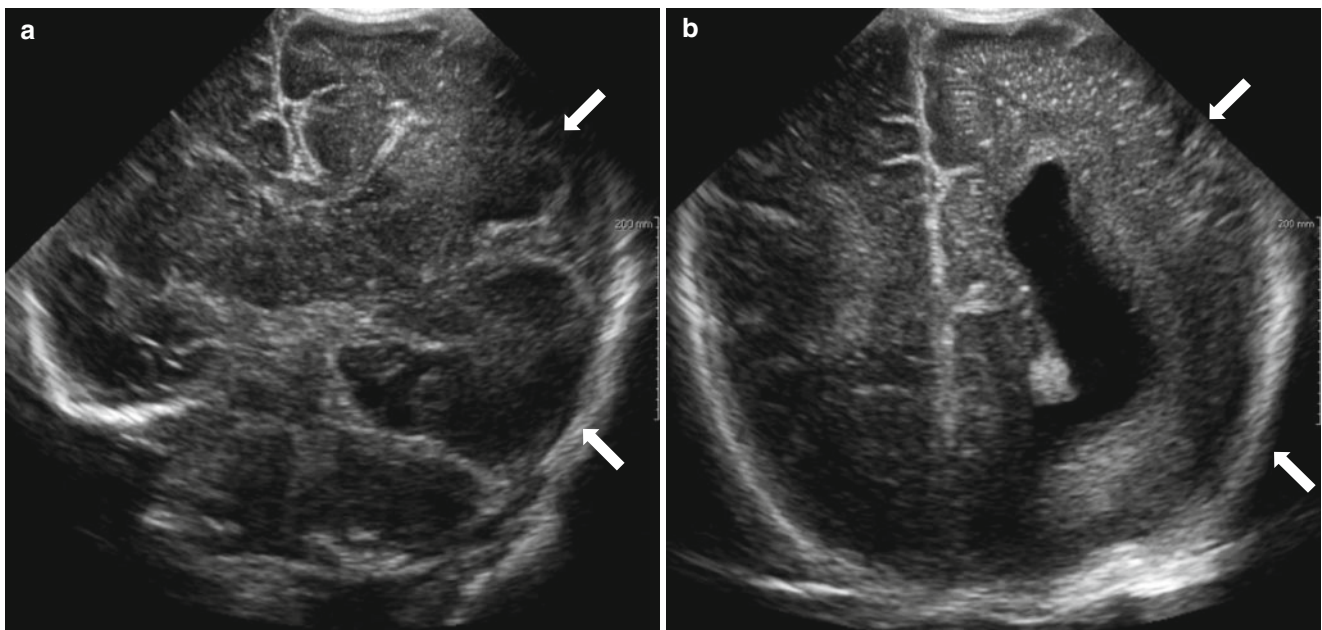


Fig. 6.38 Hemimegalencephaly in a 1-day-old female infant. (a and b) Mid- (a) and posterior (b) coronal scans show left enlarged cerebral hemisphere (*arrows*), the dilated lateral ventricle, and decreased sulci of left cerebral hemisphere. Additionally, on posterior coronal image (b), there are characteristically a four-layered pattern of hypoechoic

cortex, thick band-like hyperechoic subcortical white matter, inner hypoechoic heterotopia, and hyperechoic unmyelinated periventricular white matter in left cerebral hemisphere that mean the associated band heterotopia confirmed on MRI (not shown)

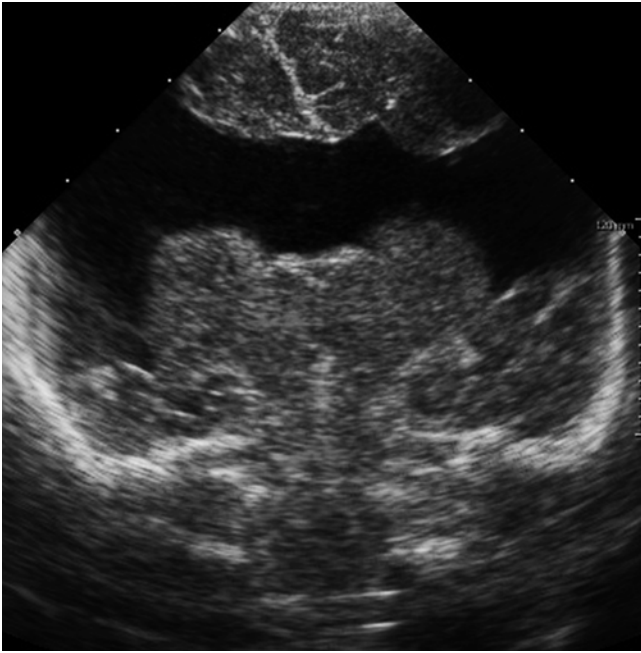


Fig. 6.39 Open-lip type of schizencephaly in a 1-day-old female infant at 37+2 weeks gestational age. Anterior coronal scan shows the large fluid-filled cleft in both frontoparietotemporal lobes from ventricular wall to the cortex and absence of septum pellucidum

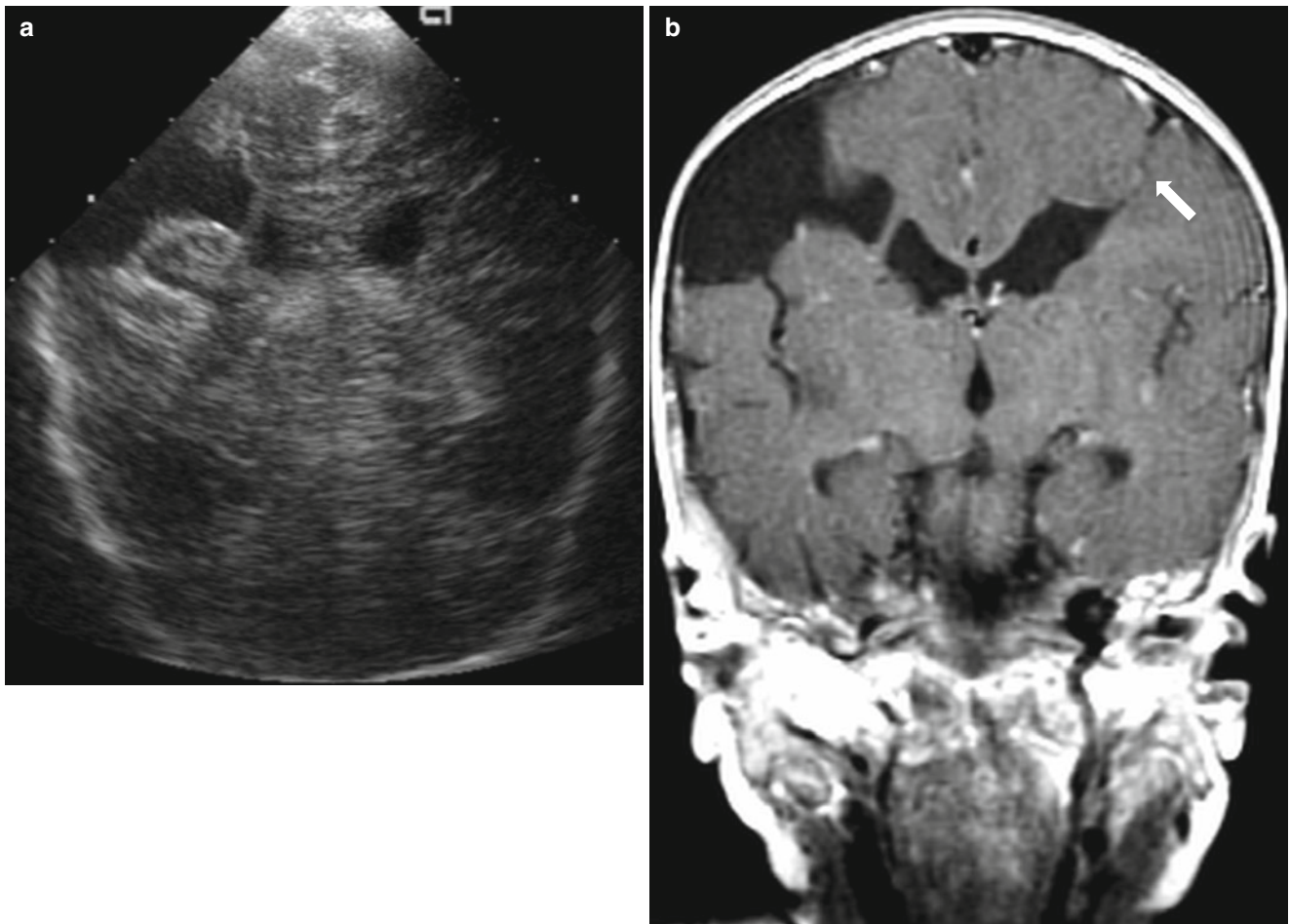


Fig. 6.40 Combined open- and closed-lip schizencephaly in a 6-month-old male infant. (a) Coronal scan shows large fluid-filled cleft in right frontal lobe but no cleft in left cerebral hemisphere.

(b) Coronal-enhanced T1-weighted MR image shows right open-lip and left closed-lip schizencephaly (*arrow*). Sonography is difficult to detect closed-lip schizencephaly, as this case

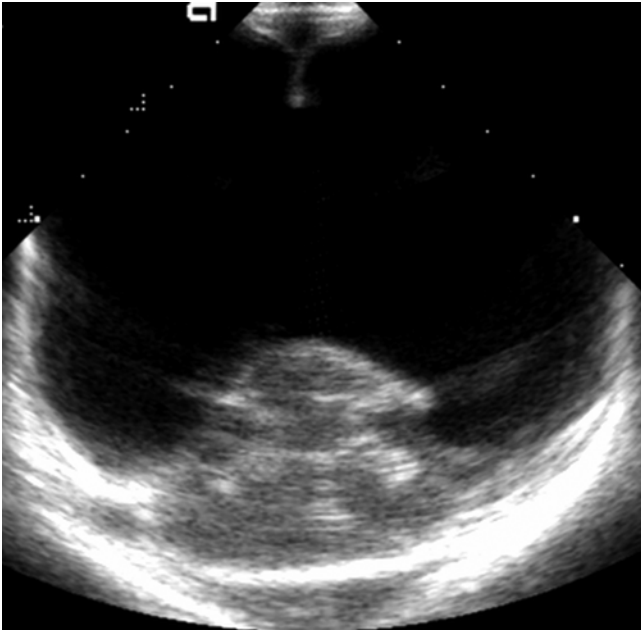


Fig. 6.41 Hydranencephaly in a 1-day-old female infant at 33+2 weeks gestational age. Coronal scan shows nearly no visible cerebral hemispheres, large fluid-filled supratentorial cavity, visible thalami and cerebellar hemisphere, and visible falx cerebri

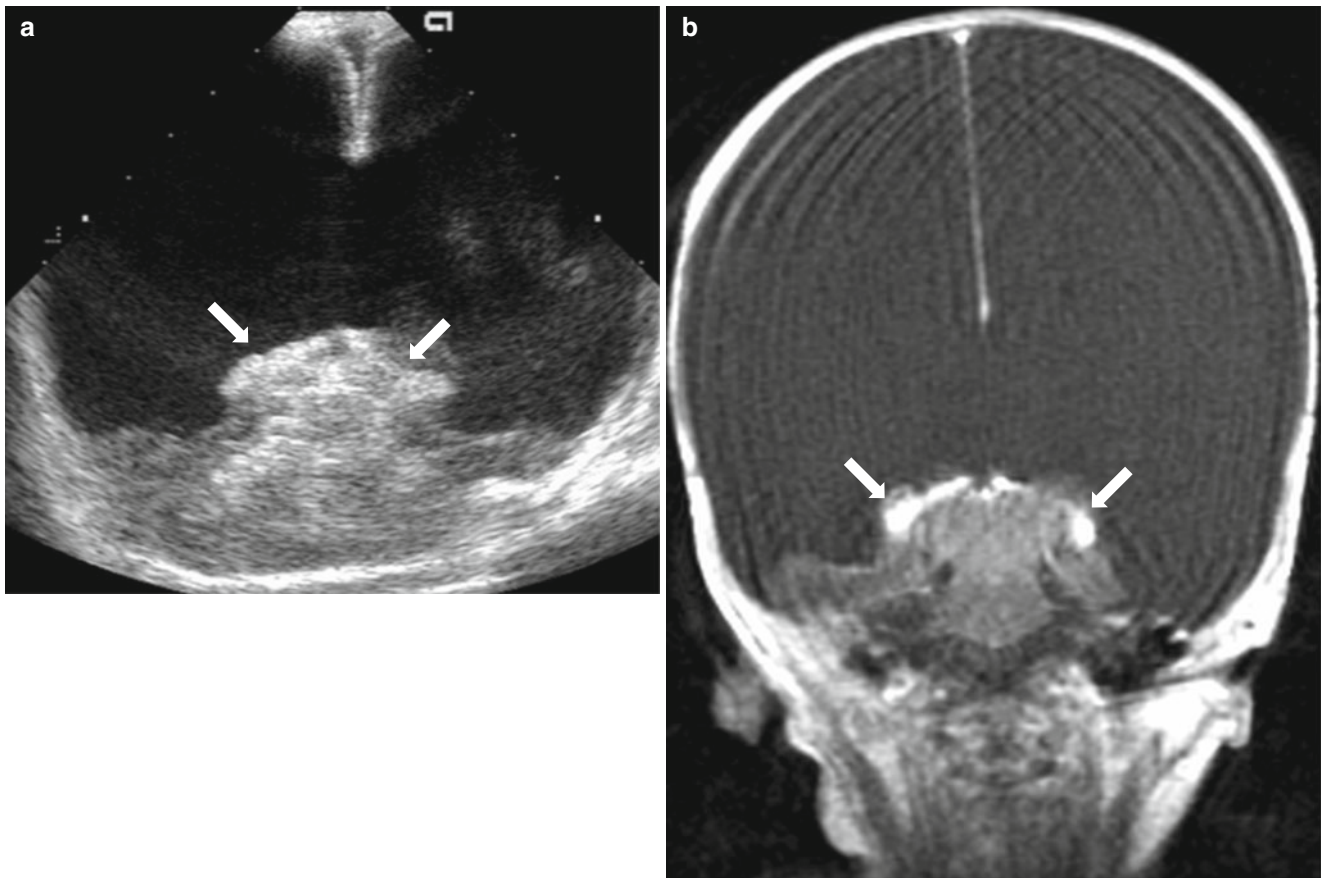


Fig. 6.42 Severe congenital hydrocephalus in a 1-day-old female infant at 39+3 weeks gestational age. **(a)** Anterior coronal scan through the anterior fontanelle shows severe dilatation of both lateral ventricles containing choroid plexus (*arrows*) that is differentiated from

hydranencephaly. **(b)** On enhanced coronal T1-weighted MR image, bilateral choroid plexus (*arrows*) in markedly dilated ventricles is enhanced

6.3.2 Spinal Sonography

6.3.2.1 Normal Anatomy and Variants

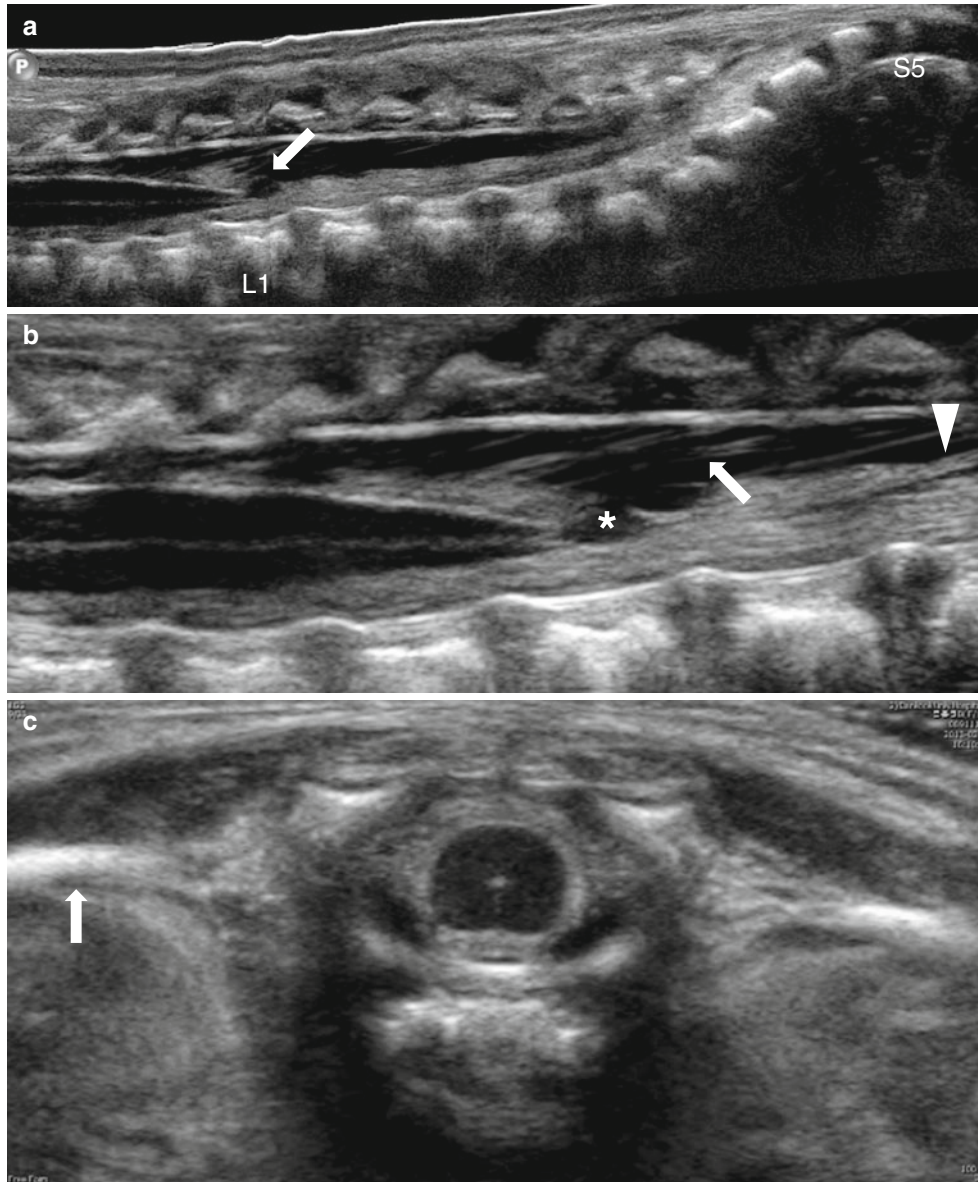


Fig. 6.43 Normal anatomy and a filar cyst in a 1-day-old male infant at 38+5 weeks gestational age. (a) Longitudinal panoramic view scan shows the level of conus medullaris at L1, the lowest portion of dural sac at S1 which can be counted upwardly from the last ossification center of S5. A small filar cyst (arrow) as anatomic variant is also noted just inferior to the conus. (b) Midsagittal scan with 5–15 MHz linear transducer well demonstrates the spinal cord, central canal, conus medullaris, a filar cyst (*), filum terminale (arrowhead), and nerve roots

(arrows). (c) Axial scan at level of the 12th rib (arrow) shows the spinal cord, central canal, and surrounding nerve roots. Detection of the 12th rib is useful to know the level of the conus medullaris. (d and e) Axial scans at the levels of the conus medullaris (d) and the cauda equina (e) show tip of conus medullaris (arrow), normal echogenic structures such as nerve roots (*), and filum terminale (arrowhead) forming the cauda equina

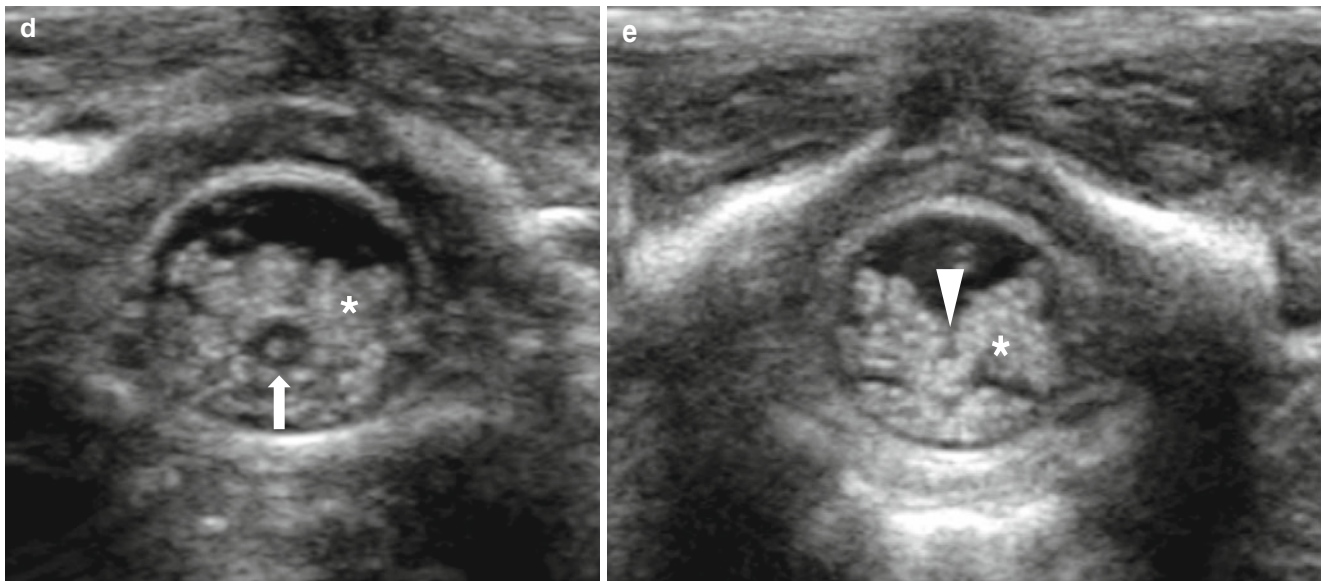


Fig. 6.43 (continued)

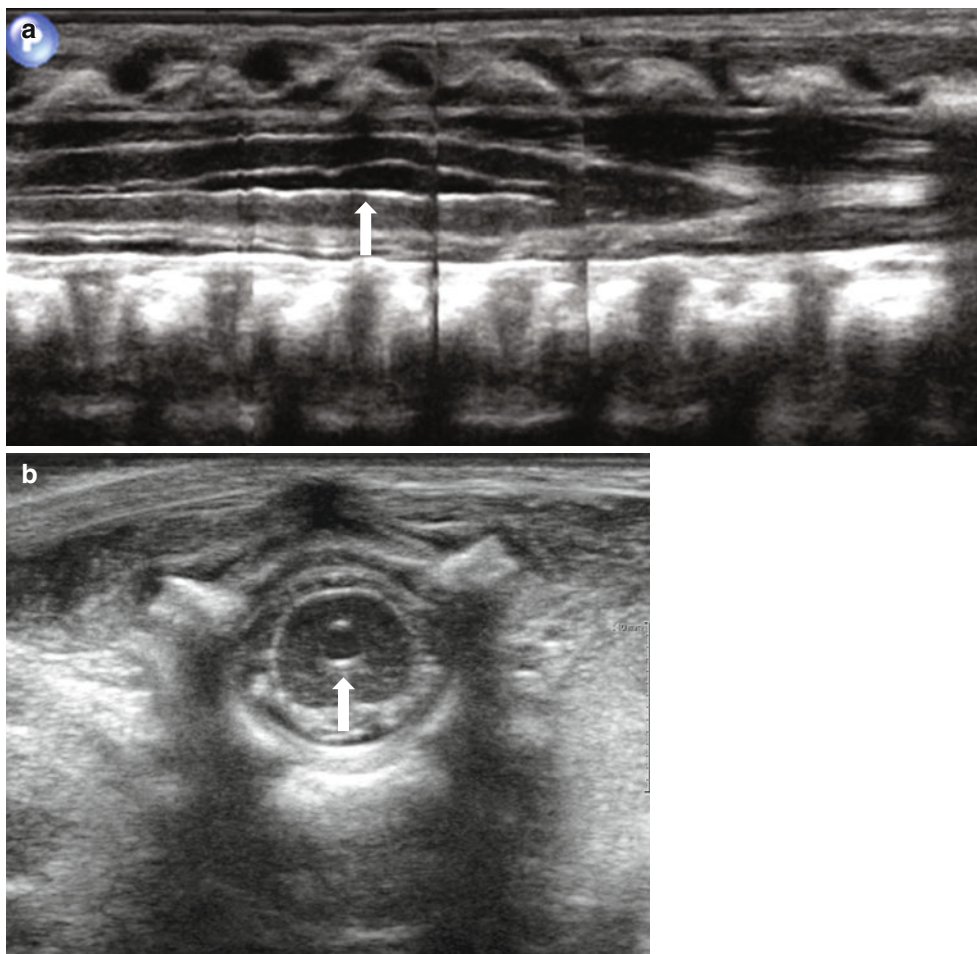


Fig. 6.44 Ventricular terminalis in a 2-day-old female infant at 30+5 weeks gestational age. (a and b) Longitudinal panoramic (a) and axial (b) scans show mild dilatation (arrow) of central canal in the distal spinal cord above the conus medullaris

6.3.2.2 Spinal Dysraphism

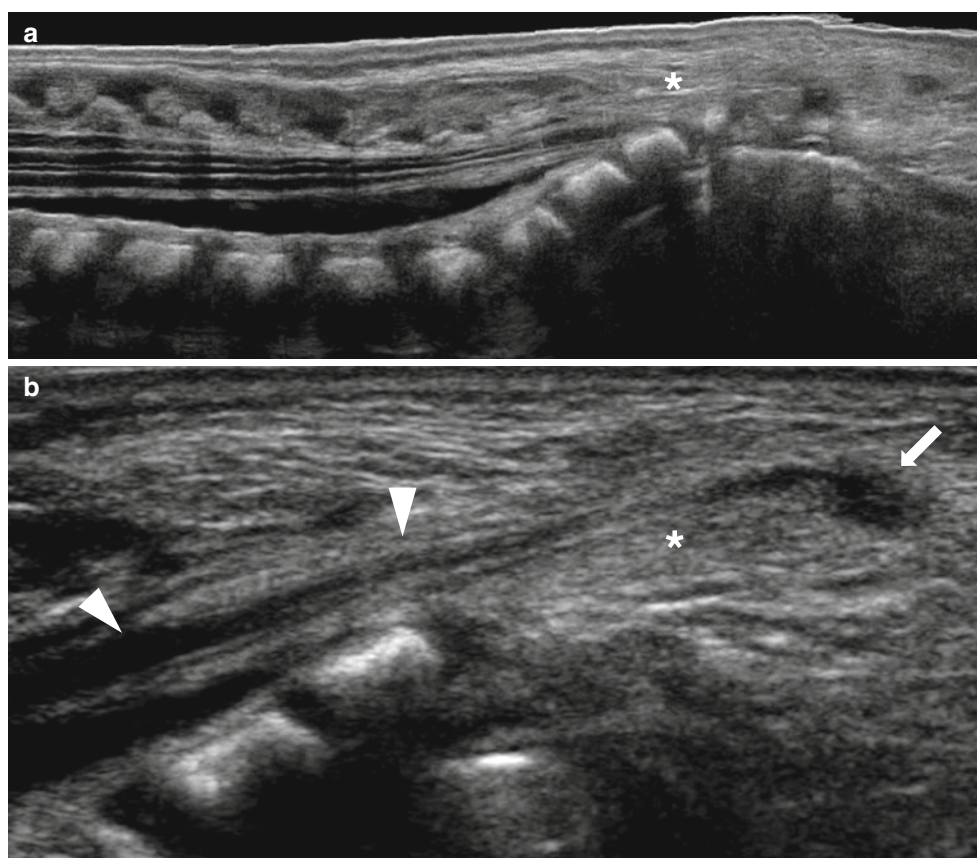


Fig. 6.45 Lipomyelomeningocele with tethered cord in a 10-day-old male infant. **(a)** Longitudinal panoramic view scan shows the spinal cord extending into the coccyx as lower lying of spinal cord associated with mild dilatation of central canal. Additionally, there are other surrounding echogenic materials (*) as intraspinal and extraspinal

lipoma. **(b)** Sagittal scan at the coccygeal area shows a tadpole-shaped cystic lesion as a meningocele (*arrow*), lower lying cord (*arrowheads*), and surrounding echogenic materials as lipoma (*)

References

- Babcock DS. Sonography of congenital malformations of the brain. *Neuroradiology*. 1986;28:428–39.
- Barr LL. Neonatal cranial ultrasound. *Radiol Clin North Am*. 1999;37:1139–45.
- Carson SC, Hertzberg BS, Bowie JD, et al. Value of sonography in the diagnosis of intracranial hemorrhage and periventricular leukomalacia: a postmortem study of 35 cases. *Am J Neuroradiol*. 1990;11:677.
- Chao CP, Zaleski CG, Patton AC. Neonatal hypoxic-ischemic encephalopathy: multimodality imaging findings. *Radiographics*. 2006. doi:10.1148/rq.26si065504.
- Chen C, Chou T, Zimmerman RA, et al. Pericerebral fluid collection: differentiation of enlarged subarachnoid spaces from subdural collections with color Doppler US. *Radiology*. 1996;201:389–92.
- Coley BD, Siegel MJ. Spinal ultrasonography. In: Siegel MJ, editor. *Pediatric sonography*. 4th ed. Philadelphia: Lippincott Williams & Wilkins; 2011.
- De Vries LS, Eken P, Dubowitz LMS. The spectrum of leukomalacia using cranial ultrasound. *Behav Brain Res*. 1992;49:1–6.
- Deeg KH, Rupprecht T, Zeilinger G. Doppler sonographic classification of brain edema in infants. *Pediatr Radiol*. 1990;20:509–14.
- DiPietro MA, Brody BA, Teele RL. The calcar avis: demonstration with cranial US. *Radiology*. 1985;156:363–4.
- Enriquez G, Correa F, Lucaya J, et al. Potential pitfalls in cranial sonography. *Pediatr Radiol*. 2003. doi:10.1007/s00247-002-0836-y.
- Frank JL. Sonography of intracranial infection in infants and children. *Neuroradiology*. 1986;28:440–51.
- Ghazi-Birry HS, Brown WR, Moody DM, et al. Human germinal matrix: venous origin of hemorrhage and vascular characteristics. *Am J Neuroradiol*. 1997;18:219–29.
- Grant EG, Schellinger D, Richardson JD, et al. Echogenic periventricular halo: normal sonographic finding or neonatal cerebral hemorrhage? *Am J Roentgenol*. 1983;140:793–6.
- Kim BM, Lee YS. Anatomic illustrations of cranial ultrasound images obtained through the mastoid fontanelle in neonates. *J Korean Soc Med Ultrasound*. 2011;30:201–8.
- Ko HG, Lee YS. Anatomic illustrations of cranial ultrasound images in the neonate: objective analysis of the oblique sonographic scans using MRI and a reconstruction program. *J Korean Soc Med Ultrasound*. 2009;28:117–25.
- Lee YS, Kim JH. Normal variations and pitfalls in neonatal neurosonography. *J Korean Soc Med Ultrasound*. 1998;17:241–8.
- Lee YS, Kim JH. The choroid plexus in normal full-term neonates: a study of morphological variety on sonography. *J Korean Radiol Soc*. 1999;40:795–800.
- Lee YS, Yoo DS. Cystic periventricular leukomalacia in the neonate: analysis of sequential sonographic findings and neurologic outcomes. *J Korean Radiol Soc*. 2003;49:5–62.
- Lee YS, Lee SS, Lee SI, et al. Neurosonography of cranial lesions in infants. *J Korean Radiol Soc*. 1986;22:185–94.
- Lee YS, Yu YJ, Lee SS, et al. Sonographic evaluation of GMH/IVH in infants with birth weight of less than 1,500 gm. *J Korean Radiol Soc*. 1987;23:722–9.
- Lee YS, Kim KI, Yang JH, et al. Analysis and its significance of periventricular echogenic halo at precystic stage of periventricular leukomalacia (PVL) in the preterm infant. *J Korean Soc Med Ultrasound*. 1993;12:94–9.
- Lee DK, Kwon BS, Lee YS, et al. Risk factors for cystic periventricular leukomalacia and neurologic outcomes according to cranial ultrasonography in preterm infants. *J Korean Soc Neonatol*. 2002;9:90–8.
- Lowe LH, Bailey Z. State-of-the-art cranial sonography: part 1, modern techniques and image interpretation. *Am J Roentgenol*. 2011a. doi:10.2214/AJR.10.6160.
- Lowe LH, Bailey Z. State-of-the-art cranial sonography: part 2, pitfalls and variants. *Am J Roentgenol*. 2011b. doi:10.2214/AJR.10.6203.
- McGahan JP, Ellis W, Lindford KK, et al. Congenital cerebrospinal fluid-containing intracranial abnormalities: a sonographic classification. *J Clin Ultrasound*. 1988;16:531–44.
- Oh SY, Lee YS, Yoo DS, et al. Anatomic illustrations of cranial ultrasound images through the posterior fontanelle in neonates: objective analysis of oblique sonographic scans using MRI and a reconstruction program. *J Korean Soc Med Ultrasound*. 2010;29:171–9.
- Papile LA, Munsick-Bruno G, Schaefer A. Relationship of cerebral intraventricular hemorrhage and early childhood neurologic handicaps. *J Pediatr*. 1983;103:273–7.
- Siegel MJ. Brain. In: Siegel MJ, editor. *Pediatric sonography*. 4th ed. Philadelphia: Lippincott Williams & Wilkins; 2011.
- Standard guidelines for ultrasound. Korean Society of Ultrasound in Medicine; 2003. pp. 60–5.
- Taylor GA. Effect of scanning pressure on intracranial hemodynamics during transcranial duplex US. *Radiology*. 1992;185:763–6.
- Volpe JJ. Current concepts of brain injury in the premature infant. *Am J Roentgenol*. 1989;153:243.
- Volpe JJ. Intracranial hemorrhage: germinal matrix-intraventricular hemorrhage of the premature infant. In: Volpe JJ, editor. *Neurology of the newborn*. 5th ed. Philadelphia: W. B. Saunders; 2008.
- Yang JH, Lee YS, Park HJ, et al. PVL in preterm infants: correlation of MR & US. *J Korean Radiol Soc*. 1993;29:1300–5.

Part II

Neuroradiology: Head and Neck

Hee Jung Lee

Contents

7.1	Introduction	258
7.2	Pathophysiology	258
7.3	Imaging	258
7.4	Spectrum of Congenital Head and Neck Malformations	258
7.4.1	Nasolacrimal Duct Cyst	258
7.4.2	Choanal Atresia	259
7.4.3	Pyriform Aperture Stenosis	259
7.4.4	Dermoid Cyst and Epidermoid Cyst	259
7.4.5	Thyroglossal Ductal Remnants	259
7.4.6	Branchial Apparatus Anomalies	260
7.4.7	Thymic Anomalies	260
7.4.8	Hypopharyngeal Cysts	260
7.4.9	Foregut Duplication Cysts	261
7.4.10	Vascular Malformations	261
7.5	Illustrations: Congenital Malformations of the Head and Neck	262
7.5.1	Nasolacrimal Duct Cyst	262
7.5.2	Choanal Atresia	263
7.5.3	Pyriform Aperture Stenosis	264
7.5.4	Dermoid and Epidermoid Cysts	265
7.5.5	Thyroglossal Duct Remnants	267
7.5.6	Branchial Apparatus Anomalies	270
7.5.7	Thymic Anomalies	279
7.5.8	Hypopharyngeal Cysts	282
7.5.9	Foregut Duplication Cysts	286
7.5.10	Vascular Malformations	288
	References	291

H.J. Lee, M.D., M.P.H.
Department of Radiology, Dongsan Medical Center,
Keimyung University School of Medicine,
56 Dalsung Ro, Daegu, 700-712, Korea
e-mail: hjlee@dsmc.or.kr

7.1 Introduction

Facial anomaly comprises anomalies of the nasolacrimal apparatus (nasolacrimal duct cyst), nasal cavity (choanal atresia, pyriform aperture stenosis), and nasofrontal region (dermoid cyst) (Lowe et al. 2000). Choanal atresia is rare, but it is the most common cause of congenital nasal obstruction. Congenital malformations of the neck can be classified as follows: embryonic remnants of thyroglossal duct (thyroglossal duct cyst, ectopic thyroid gland) or branchial apparatus (branchial sinus, branchial cyst, branchial fistula), thymopharyngeal duct anomalies, hypopharyngeal cysts (epiglottic cyst, vallecular cyst, laryngocele), foregut duplication cysts (enteric duplication cyst, bronchogenic cyst), and vascular malformations (lymphatic, venous) (Koeller et al. 1999; Sadler 2012; Som et al. 2003). Thyroglossal duct cyst is the most common congenital neck mass, while lymphatic malformation is the most common vascular malformation found in children. The anomalies arising from branchial apparatus show variable imaging and clinical features based on cyst, sinus, or fistula formation. The second branchial cleft cyst is the most common branchial apparatus anomaly. Most of the congenital neck masses are cystic in nature. However, ectopic thyroid gland and cervical thymus manifest as a mass mimicking a solid neoplasm of the neck. This chapter illustrates image findings of common congenital malformations of the head and neck in children by focusing on differential diagnosis.

7.2 Pathophysiology

Knowledge of the embryologic features and anatomy of the head and neck is essential for the evaluation of head and neck malformation. In addition, location and imaging findings of a lesion, clinical characteristics including the patient's age, and the presence of associated abnormality in the other sites of the body are helpful in differential diagnosis of congenital anomalies. The most common symptomatic clinical presentation is a sign of upper airway obstruction, especially for neonates and young infants.

Dermoid and epidermoid cysts are developmental cysts, typically located at the sites of embryologic fusion or the midline. Anomalies of thyroglossal ductal remnant occur at any site from the base of the tongue to the thyroid gland. Therefore, an anterior midline or paramedian cystic mass is typically a dermoid or thyroglossal duct cyst. Defect in branchial apparatus results in a wide spectrum of anomalies, which include fistulas, sinuses, cysts, and ectopic glands. Branchial cleft cyst is the most common branchial anomaly and can occur anywhere from the external auditory canal to the supraclavicular regions. Branchial cleft cysts and thymopharyngeal duct cysts are more laterally located and have characteristic positions in relation to the neck muscles and

vessels. Lymphatic malformations are most commonly located in the posterior triangle of the neck and manifest as multiloculated cystic masses, which grow by insinuating around adjacent structures.

7.3 Imaging

The goal of imaging for head and neck malformation should be focused on arriving at an accurate diagnosis with minimizing radiation exposure, particularly for the thyroid glands of children. Plain radiography is usually indicated for the initial evaluation of children with acute respiratory symptoms, which can be caused by a mass in the hypopharynx or neck. Lateral views are more useful for evaluation of the airway. Ultrasonography (US) often allows accurate diagnosis of cystic neck lesions, beyond simply by distinguishing cystic from solid lesions. For example, a cystic lesion with "oil on water" or "lipid-fluid" level on US is suggestive of a dermoid cyst. Color Doppler also helps to detect abnormal vascularity associated with infectious lesions, solid components of tumors in cystic lesions, and vascular malformations. Computed tomography (CT) and magnetic resonance (MR) imaging are best suited for the evaluation of neck masses located within the deep neck spaces. The presence of intralesional calcification or bony structure can be better evaluated with CT than with MR. In addition, shorter CT scan duration has important advantages over MR in the emergency clinical setting. MR is the imaging modality of choice to evaluate head and neck masses with suspected intracranial extension. Fluoroscopy-guided barium swallowing esophagogram and sinogram are also indicated for the detection of sinus or fistular tract that are sometimes associated with branchial apparatus anomalies. Radioisotope scintigraphy is valuable for the evaluation of suspected thyroid gland abnormalities.

7.4 Spectrum of Congenital Head and Neck Malformations

7.4.1 Nasolacrimal Duct Cyst

Nasolacrimal duct cyst is caused by failure of canalization in the nasolacrimal duct. The lesion produces a lacrimal sac mucocele, and it manifests as a mass in the inferomedial canthus in neonates. CT and MR images depict a thin-walled cystic mass that extends from the inferomedial canthus to the nasal cavity, along with the course of the nasolacrimal duct (Fig. 7.1). Bilateral high-grade obstruction can lead to occlusion of the nasal aperture. The differential diagnosis includes dermoid or epidermoid cyst and naso-orbital cephalocele. Dermoid cyst is more frequently located in the superolateral wall of the orbit and rare in neonates.

Naso-orbital cephalocele shows a bony defect in the anterior skull and orbital wall (Lowe et al. 2000; Morón et al. 2004).

7.4.2 Choanal Atresia

Choanal atresia is caused by incomplete canalization of the choanae, and it results in obstruction or narrowing of the posterior nasal cavity. Choanal atresia is rare. However, it is the main cause of congenital nasal obstruction due to an anatomic obstruction in infants. Choanal atresia is classified as osseous, membranous, or osseomembranous, and partially osseous atresia is in about 90 % of cases. CT is the imaging modality of choice. Imaging features include narrowing of the posterior choanae to a width of less than 0.34 cm in children under 2 years old, inward bowing of the posterior maxilla, fusion or thickening of the posterior and inferior parts of the vomer, and the presence of a bone or soft tissue septum crossing the posterior choanae (Fig. 7.2). Many anomalies are associated with choanal atresia, with CHARGE syndrome (coloboma, heart malformation, choanal atresia growth and/or mental retardation, genital anomalies, ear anomalies) being the major developmental association (Lowe et al. 2000; Morón et al. 2004).

7.4.3 Pyriform Aperture Stenosis

Pyriform aperture stenosis is caused by premature fusion and overgrowth of the medial nasal processes, resulting in narrowing of the anterior nasal opening. CT scan depicts inward bowing and thickening of the nasal process of the maxilla and narrowing of the pyriform aperture less than 8 mm in width compared to a normal aperture, which is not less than 11 mm (Fig. 7.3). Many anomalies are also associated with pyriform aperture stenosis, including holoprosencephaly, facial hemangiomas, pituitary dysfunction, and central megaincisor (Lowe et al. 2000; Morón et al. 2004).

7.4.4 Dermoid Cyst and Epidermoid Cyst

Dermoid and epidermoid cysts are ectodermal inclusion cysts lined by squamous epithelium. They are developmental cysts, and unlike teratomas, they are not neoplasms. Epidermoid cyst is lined solely by squamous epithelium with internal keratin pearl, while dermoid cyst contains variable skin appendages of sebaceous glands, hair follicles, and sweat glands (Smirniotopoulos and Chiechi 1995). *Dermoid cyst* is typically located at the sites of embryologic fusion in frontozygomatic (orbital), sphenofrontal (nasal), sphenosquamosal (ear), and other calvarial sutures. Nasal dermoid cyst may be associated with a sinus tract that extends in the prenasal space to the foramen cecum through the anterior skull base.

MR imaging is useful for tracing the tract into the cranium (Lowe et al. 2000; Morón et al. 2004). Orbital dermoid cyst is most commonly found in the upper outer quadrant or lacrimal fossa in more than 80 % of cases (Fig. 7.4). The floor of the mouth is the most common cervical location (Som et al. 2003) (Fig. 7.5). On US, dermoid cyst is a unilocular, cystic, or fatty mass in typical locations with or without pressure erosion (fossa formation) of the underlying bony cortex. They may show lipid material floating like supernatant “oil on water” over the heavier proteinaceous debris or “lipid–fluid” levels. Coalescence of fat into small nodules within the fluid matrix gives rise to the pathognomonic “sack of marbles” appearance on image findings. Epidermoid cyst is presumed to arise later in embryologic development than dermoid cyst, and it is typically lateral in location. Epidermoid cyst tends to be a unilocular and homogeneous cystic lesion. Unlike dermoid cyst, epidermoid cyst does not usually have the low attenuation values of fat. Occasionally, peripheral calcification and enhancement are present in epidermoid cyst (Fig. 7.6).

7.4.5 Thyroglossal Duct Remnants

Thyroglossal duct forms a bridge between the base of the tongue and the thyroid gland, and the anomalies can be found at any level along its tract. Anomalies of thyroglossal duct remnants result from incomplete development (agenesis and hypoplasia), obliteration (thyroglossal duct remnant), or descent (ectopia) of the thyroglossal duct.

Thyroglossal duct cyst (TGDC) is the most common congenital neck lesion (70 %) in pediatric population. It is located most commonly at infrahyoid (65 %), followed by suprahyoid (20 %), and at the level of the hyoid bone (15 %). Uncomplicated TGDC typically represents as a hypoechoic nodule or cyst with a thin wall either in the midline of the anterior neck close to the hyoid bone (suprahyoid or hyoid) or paramedian (infrahyoid) within the strap muscles (Figs. 7.7, 7.8, and 7.9). CT demonstrates a well-circumscribed cyst with thin enhancing wall (Figs. 7.8 and 7.9). Internal content of the cyst can be variable depending on the presence of inflammation, hemorrhage, associated ectopic thyroid tissue, or malignancy. Enhancing solid nodule within the cyst may represent ectopic thyroid tissue, and calcifications within the solid nodule suggest an evolving papillary thyroid carcinoma (Som et al. 2003). The differential diagnosis of a midline neck mass includes dermoid cyst and lymph node. Unlike TGDC, there is no intimate relation with the hyoid bone, and these lesions typically are located superficial to the strap muscles.

Ectopic thyroid gland most commonly occurs as a lingual thyroid with variable sizes and contours. CT demonstrates typical high attenuation (>100 H.U) of thyroïdal tissue by iodine content on preenhanced scan. The presence of a normal

functioning thyroid gland must be documented preoperatively by using US or radioisotope study (Koeller et al. 1999; Morón et al. 2004; Sadler 2012) (Figs. 7.10).

7.4.6 Branchial Apparatus Anomalies

Branchial apparatus anomalies are composed of a heterogeneous group of congenital malformations that arise from incomplete obliteration of pharyngeal clefts and pouches during embryogenesis (Sadler 2012; Som et al. 2003).

Each branchial apparatus has its arch separated by pouches on the internal endodermal side and by clefts on the external ectodermal side of the embryo. Branchial pouches are the Eustachian tube for the first arch, tonsillar fossa for the second arch, and pyriform sinus for the third and fourth arches. The first branchial apparatus has a persistent ectodermal cleft as the external auditory canal (EAC). The second, third, and fourth branchial clefts become enclosed in a common ectodermal-lined cavity called the cervical sinus of His, which appears along the anterior border of the sternocleidomastoid (SCM) muscle at the middle and lower third of the neck junction. The tissue between the endodermal pouch and the ectodermal cleft is mesoderm, and the mesoderm contains a dominant artery, nerve, cartilage, bone, and muscles. The endoderm of each pharyngeal pouch also gives rise to endocrine parenchyma of the parotid gland for the first arch, surface epithelium of the palatine tonsil for the second arch, and thymus and parathyroid glands for the third and fourth arches, respectively. Defect in branchial apparatus development results in fistulas, cysts, sinus tracts, ectopic glands, and cartilaginous remnants (Benson et al. 1992; Sadler 2012; Som et al. 2003).

A branchial cleft cyst is the most common branchial abnormality, which can occur anywhere from the EAC to the supraclavicular area. The cyst may contain internal air pockets in the presence of associated internal sinus or fistula tract.

The first branchial cleft cyst manifests as a cystic mass around the pinna and EAC (type I) or extending from the EAC to the angle of mandible (type II). A cyst may enlarge to present below the angle of the mandible or within or around the parotid gland (Fig. 7.11). The first branchial sinus tract may be present at the junction of the bone and the cartilage portion of the EAC.

The second branchial cleft cyst accounts for 80–90 % of branchial apparatus anomalies and manifests as a cyst typically located in the posterolateral to the submandibular gland, lateral to the carotid space, and anterior to the SCM muscle (Fig. 7.12). The second branchial sinus manifests as a tiny skin pit on the anterior border of the SCM muscle at the junction site of the middle and lower third of the neck, and the fistula tract may extend to the tonsillar fossa (Fig. 7.13).

The third branchial cleft cyst is located in the upper posterior cervical space or lower anterior neck (Fig. 7.14). *The fourth*

branchial cleft cyst may be located anterior to the aortic arch on the left or anterior to the subclavian artery on the right (Figs. 7.15 and 7.16). The third and fourth branchial sinus or fistula may manifest as recurrent thyroiditis. Esophagogram or sinogram may reveal a sinus or a fistula tract between the pyriform sinus and the skin pit in the lower anterior neck or adjacent to the anterior left thyroid lobe (Benson et al. 1992; Koeller et al. 1999; Som et al. 2003) (Fig. 7.17).

7.4.7 Thymic Anomalies

Thymic primordia arise from the third and fourth pharyngeal pouches. Spectrum of anomalies may occur anywhere along the thymopharyngeal duct into the mediastinum, resulting in failure of descent (cervical thymus), sequestration (ectopic thymus), or failure to obliterate (thymic cyst) (Sadler 2012). The majority of these anomalies are seen on the left side of the neck.

Cervical thymus is usually located lateral to the carotid sheath and anterior to the SCM muscle. US demonstrates a solid, homogeneous, and hypoechoic mass anterior to the SCM muscle and extending inferiorly from the angle of the mandible. Color Doppler image shows minimal vascular flow within the mass. MR demonstrates a well-circumscribed homogeneous mass with slight hypointensity on T1-weighted image, mild hyperintensity on T2-weighted image, and minimal enhancement after contrast enhancement. The mass does not invade or compress adjacent structures (Nasser and Eftekhari 2010) (Fig. 7.18). *Ectopic thymus* may be seen occasionally in the thyroid gland (Gimm et al. 1997) (Fig. 7.20). *Thymic cyst* is rare in children and located at the anterior cervical triangle on the left side, along the anterior margin of the SCM muscle extending or without extending into the anterior mediastinum. The cyst is unilobular or multilobular and may contain clear or complicated fluid (Cigliano et al. 2007).

7.4.8 Hypopharyngeal Cysts

A variety of terms have been used for cysts arising from the tongue base and hypopharynx based on their sites of origin, such as an epiglottic cyst, vallecular cyst (Figs. 7.22 and 7.23), or laryngeal cyst. Laryngocele is an air- or fluid-filled outpouching of the laryngeal saccule that communicates with the laryngeal ventricle (Fig. 7.24). Two pathogeneses have been proposed on their developmental origin, which are retention cysts as obstruction of mucus glands and embryological malformation arising from the fourth to sixth branchial arches. Most of the affected infants are presented with inspiratory stridor or symptoms of upper airway obstruction. US demonstrates a unilocular, thin-walled cyst

in the hypopharynx. MR is the diagnostic modality of choice for evaluation of the exact location. The signal intensity of the cysts is usually high on T2-weighted image and variable on T1-weighted image, depending on whether the cysts are filled with fluid, proteinaceous debris, or air (Chung et al. 2004; Suzuki et al. 2011).

7.4.9 Foregut Duplication Cysts

The primitive foregut gives rise to the oropharynx, the lower respiratory system, and the esophagus. Therefore, the foregut duplication cysts include enteric duplication cyst and bronchogenic cyst based on their epithelial lining (Sadler 2012). Most foregut cysts manifest during the first year of life, and the affected infants present with respiratory distress due to airway obstruction. The most common site of foregut duplication cysts in the head and neck is the oral cavity (Kieran et al. 2010) (Fig. 7.25). They can also occur along the course of the trachea and esophagus, and usually do not communicate with the trachea or esophagus (Fig. 7.26). US is very useful in demonstrating superficial cysts. The typical US appearance of enteric duplication cysts is that of a thick-walled cyst with or without a “double wall” sign, which consisted of an inner echogenic mucosal and outer hypoechogenic muscle layers, as in enteric duplication cysts arising from the other gastrointestinal tract. MR is preferred for the evaluation of its relationship with the trachea or esophagus. The differential diagnosis includes variable cysts according to their locations, such as dermoid cyst or TDGC in the tongue base and hypopharyngeal or branchial cleft cyst in the lateral neck.

7.4.10 Vascular Malformations

Vascular malformations are classified as arteriovenous, capillary, venous (cavernous hemangiomas), lymphatic (lymphangiomas or cystic hygromas), or combined, based

on their lining endothelium. Vascular malformations, unlike hemangiomas, do not show neoplastic endothelial proliferation (Mulliken and Glowacki 1982).

Lymphatic malformation develops from lymphatic sacs that fail to communicate with the remaining lymphatic system. The lesion is the most common vascular malformation among young children. Lymphatic malformation is commonly located in the posterior triangle of the neck, lower portion of the face, and axilla in the first 2 years of life. MR is the best modality to demonstrate the extent of the lesion. Macrocystic lymphatic malformation (cystic hygroma) has characteristic imaging features including multiseptated cystic mass that grows by insinuating around adjacent structures (Figs. 7.27 and 7.29). Depending upon the presence of internal hemorrhage, there may be fluid–fluid levels and variable signal intensity of the cysts on MR (Fig. 7.28). Lack of wall thickening or enhancement and absence of phleboliths differentiate lymphatic from venous malformations (Koeller et al. 1999; Morón et al. 2004; Som et al. 2003).

Venous malformation manifests in both children and adults, grows proportionate to the child, and does not regress spontaneously. Venous malformation frequently affects the oral cavity, skeletal muscles of the head and neck involving the masseter, pterygoid, trapezius, and SCM muscles. Imaging findings are variable according to their endothelial vessels. US can suggest the diagnosis of a venous malformation by demonstrating a multilocular mass with fluid-filled spaces or fluid–debris levels. Doppler US may not be able to demonstrate flow in the lesion, since venous malformation is a low-flow lesion. The characteristic imaging feature of venous malformation is the presence of phleboliths as laminated calcific densities on CT. The enhancement is initially heterogeneous, becoming more homogeneous on delayed images. MR imaging demonstrates a hyperintense mass of venous lakes on T2-weighted images, with occasional septation and variable enhancement (Fig. 7.30). Phleboliths appear as a focal signal void on both T1- and T2-weighted images (Baker et al. 1993; Som et al. 2003).

7.5 Illustrations: Congenital Malformations of the Head and Neck

7.5.1 Nasolacrimal Duct Cyst

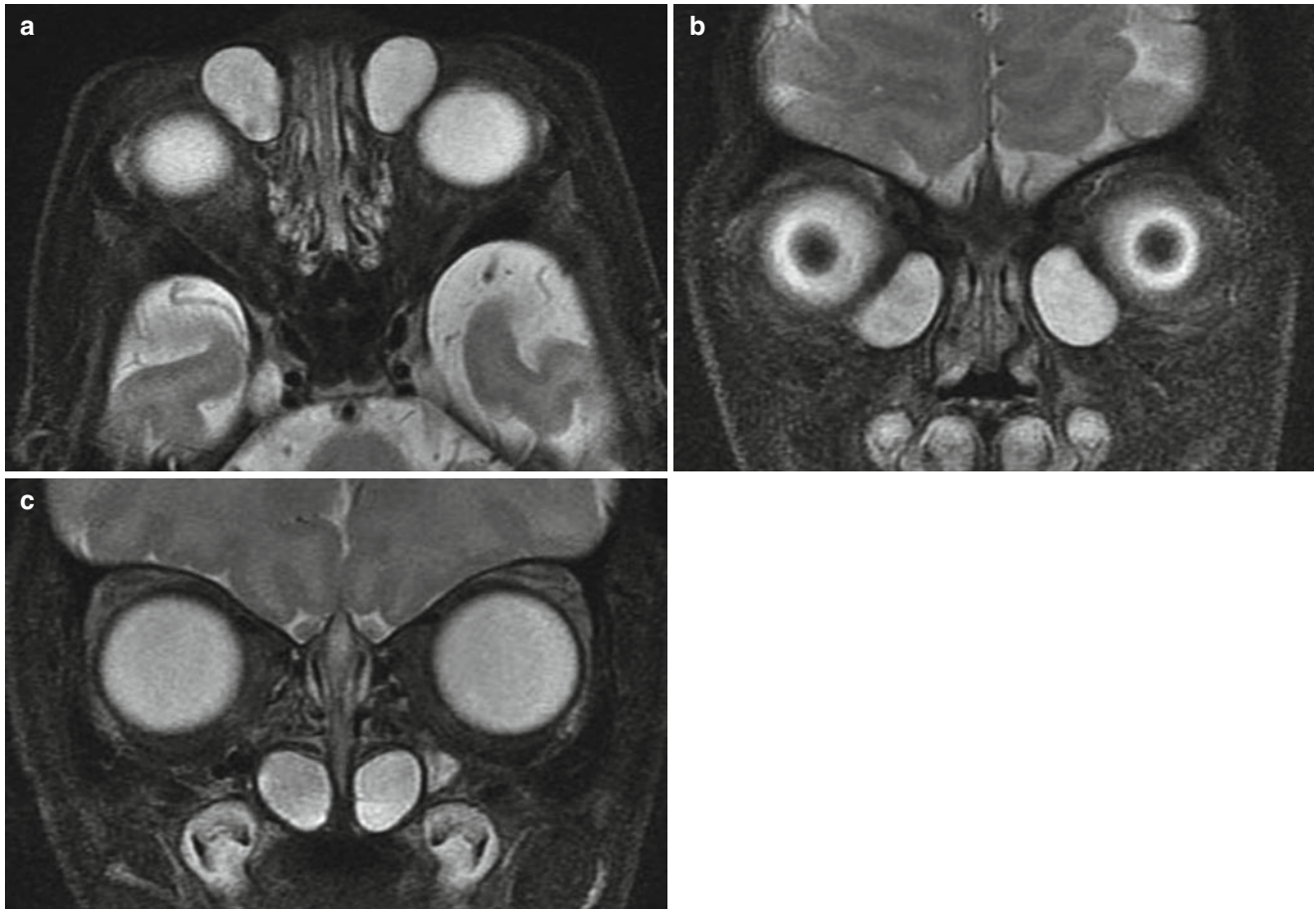


Fig. 7.1 Nasolacrimal duct cysts in a 15-day-old girl. (a) Axial T2-weighted image shows cystic masses in the medial canthus of both the orbits. (b, c) Coronal T2-weighted images show the cystic masses extending from the medial canthus into the nasal cavities along the nasolacrimal ducts

7.5.2 Choanal Atresia



Fig. 7.2 Choanal atresia in a neonate. Axial CT scan with a bone window shows narrowing of both choanae, thickening of the posterior and inferior parts of the vomer, and the presence of an air–fluid level in the left nasal cavity due to choanal obstruction. He also had bilateral external auditory canal atresia

7.5.3 Pyriform Aperture Stenosis

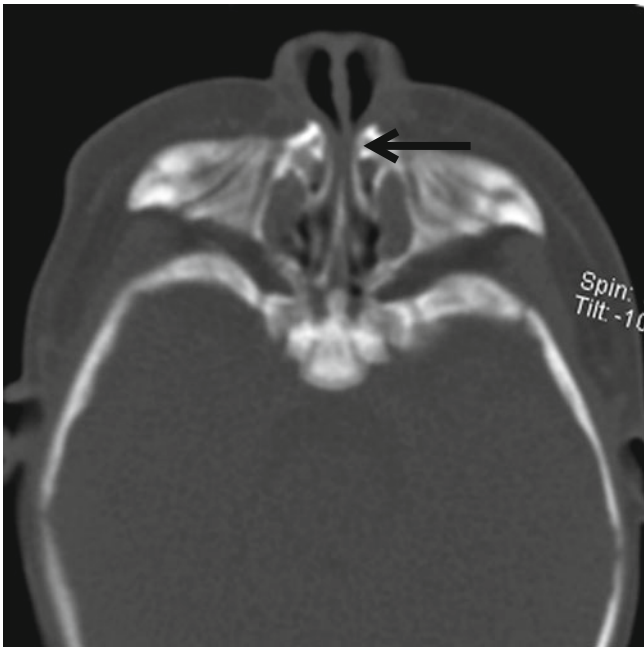


Fig. 7.3 Pyriform aperture stenosis in a 1-month-old infant. Axial CT scan shows inward bowing of the nasal process of the maxilla and narrowing of the anterior nasal cavity (*arrow*)

7.5.4 Dermoid and Epidermoid Cysts

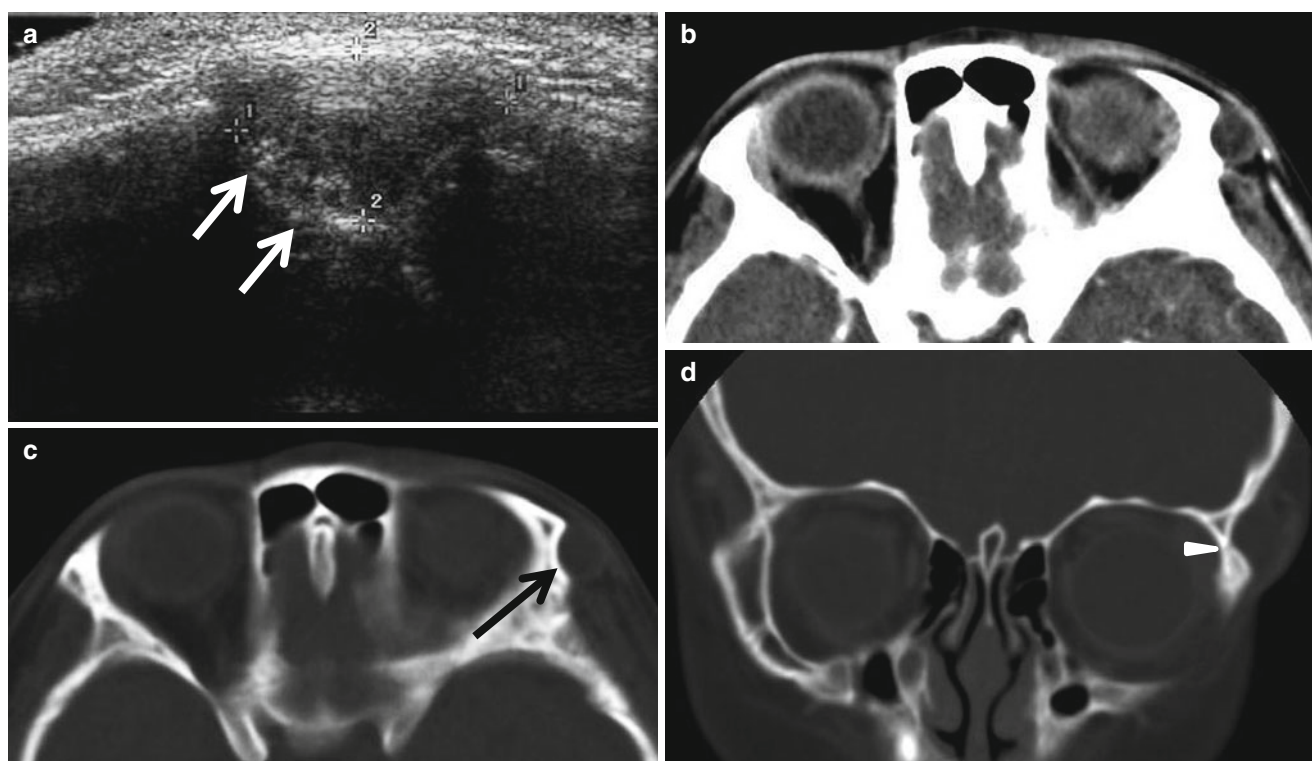


Fig. 7.4 Orbital dermoid cyst in a 5-year-old girl. (a) US shows an oval-shaped nodule with internal echogenic foci in the superolateral wall of the orbit. The underlying bony cortex of the orbital rim produces the appearance of a fossa (arrows). (b) Contrast-enhanced axial CT

scan shows a round fatty mass in the superolateral aspect of the left orbit. (c, d) Axial and coronal CT scans of bone window show osseous scalloping that produces the appearance of a fossa (arrow) with a sclerotic margin near the zygomaticofrontal suture (arrowhead)

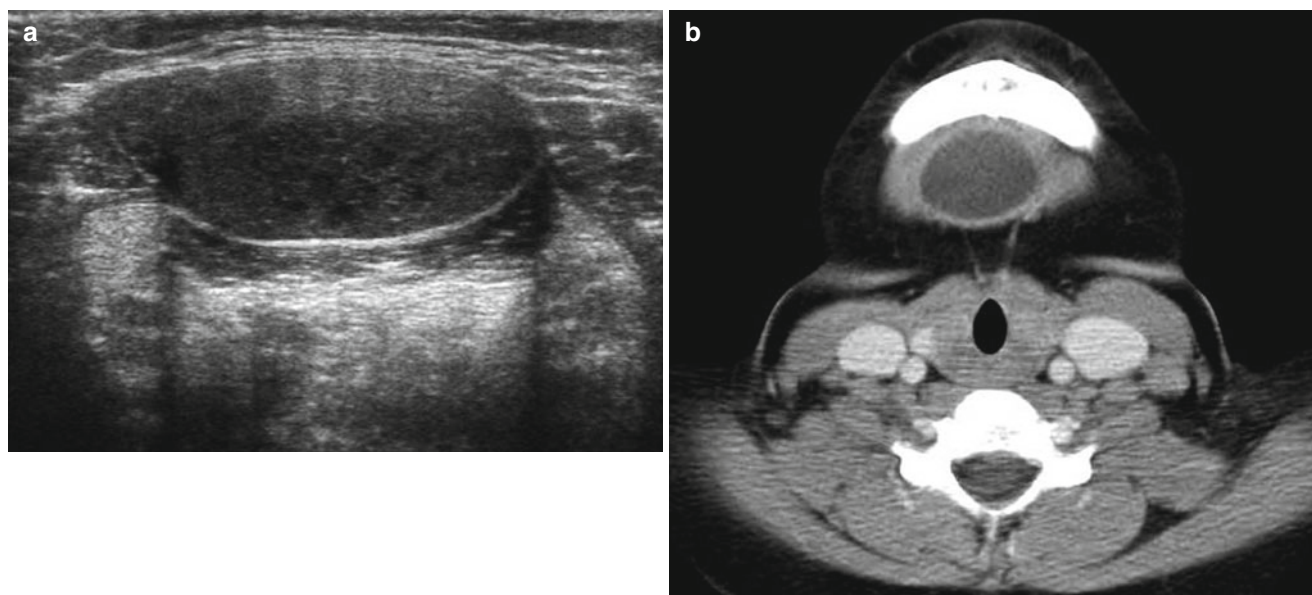


Fig. 7.5 Submental dermoid cyst in a 10-year-old boy. (a) US shows a hypoechoic cystic mass with internal echogenic lobules and foci. (b) Contrast-enhanced axial CT scan shows a round cystic mass in the

midline tongue base. The differential diagnosis includes thyroglossal duct cyst, dermoid cyst, cystic teratoma, and enteric duplication cyst

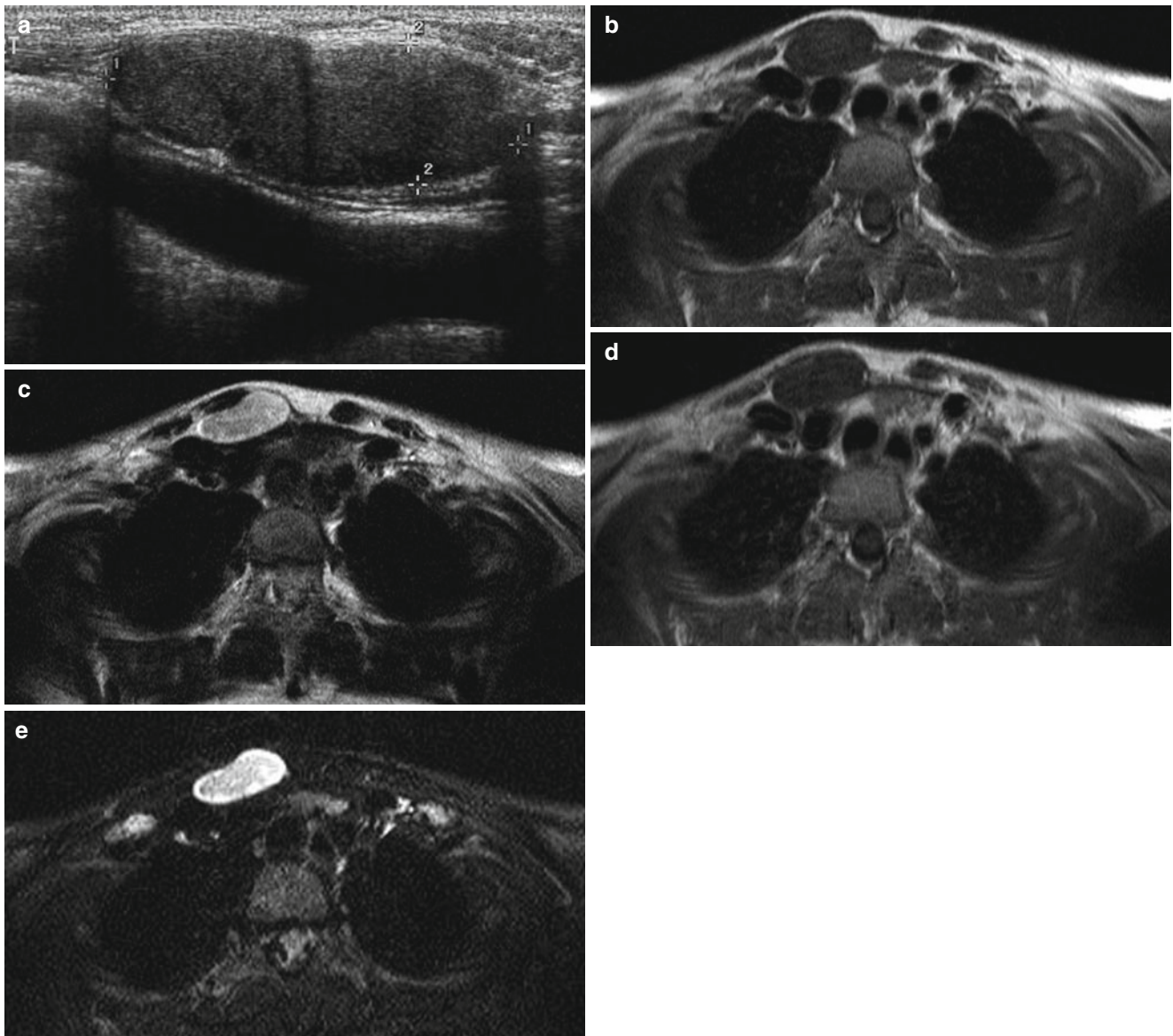


Fig. 7.6 Epidermoid cyst in a 10-year-old girl. (a) US shows a bilobed hypoechoic lesion in the region of the right sternoclavicular junction. Note the internal echogenic foci. (b–d) The mass appears as isosignal intensity on T1-weighted image (b) and slightly high signal intensity on

T2-weighted image (c) and demonstrates no contrast enhancement (d). (e) Diffusion-weighted image shows bright high signal intensity of the lesion

7.5.5 Thyroglossal Duct Remnants

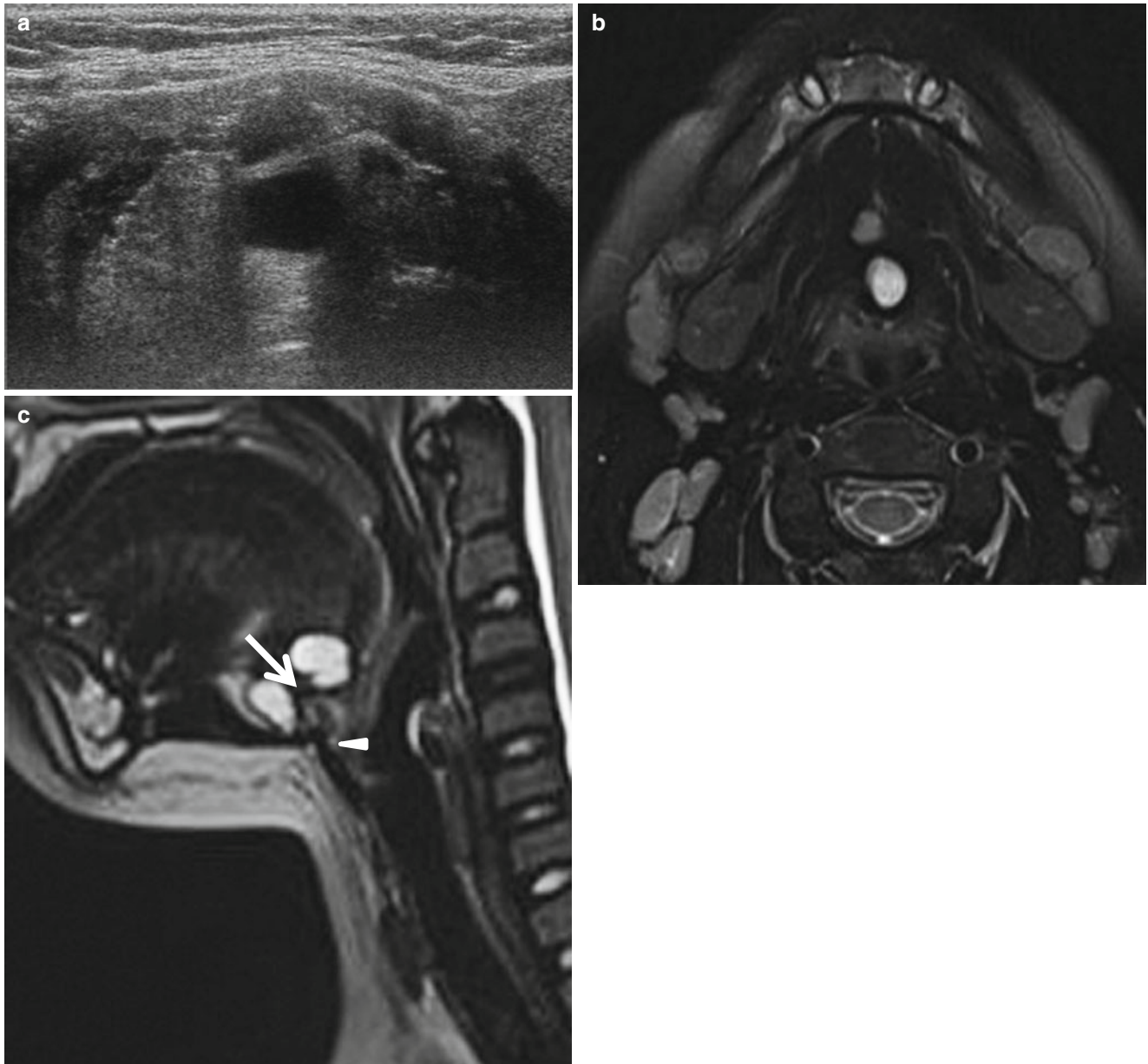


Fig. 7.7 Suprahyoid thyroglossal duct cyst in a 9-year-old boy. (a) US shows a bilocular cystic lesion in the midline aspect of the preepiglottic region. (b) Axial T2-weighted image shows a bilobed cystic mass of

high signal intensity in the midline tongue base. (c) Sagittal T2-weighted image shows a fine tract (*arrow*) between the cystic locules and the relationships between the cyst and the hyoid bone (*arrowhead*)

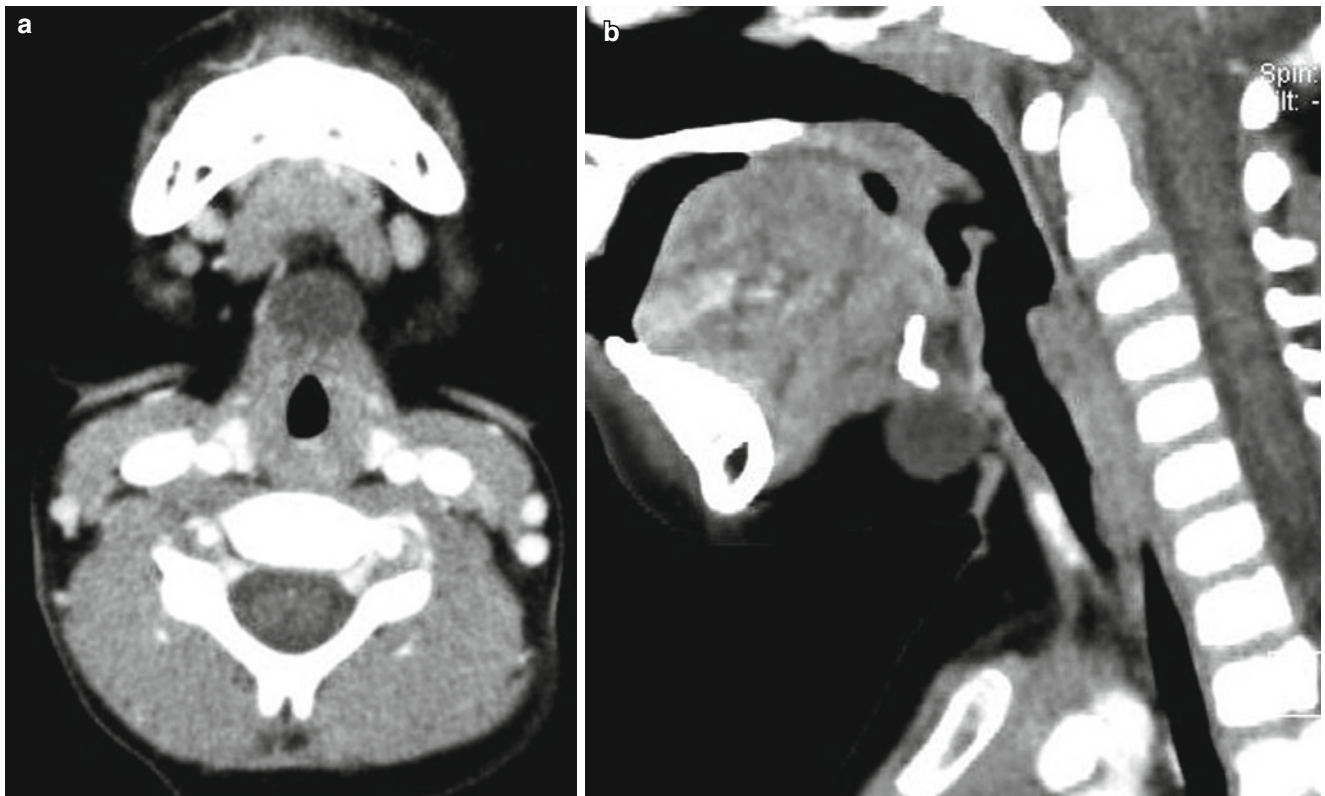


Fig. 7.8 Thyroglossal duct cyst on the level of the hyoid bone in a 3-year-old boy. (a) Contrast-enhanced axial CT scan shows a round midline cyst in the submental space. (b) Sagittal reformatted CT scan shows a well-defined unilocular, thin-walled cyst abutting the hyoid bone

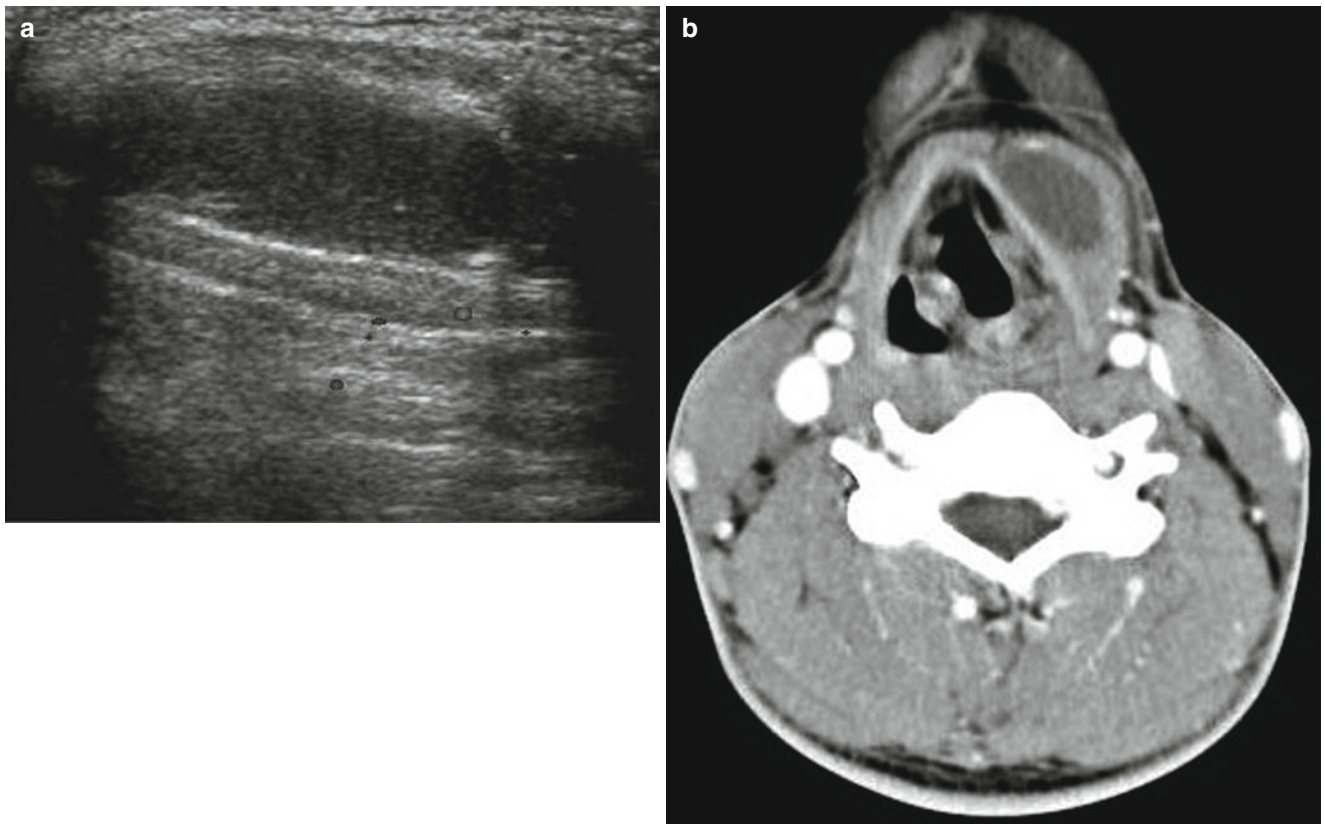


Fig. 7.9 Infrahyoid thyroglossal duct cyst in a 15-year-old boy. (a) US shows a hypoechoic cystic mass embedded in the left strap muscle. (b) Contrast-enhanced axial CT scan shows a well-defined unilocular, thin-walled cyst embedded in the left strap muscle

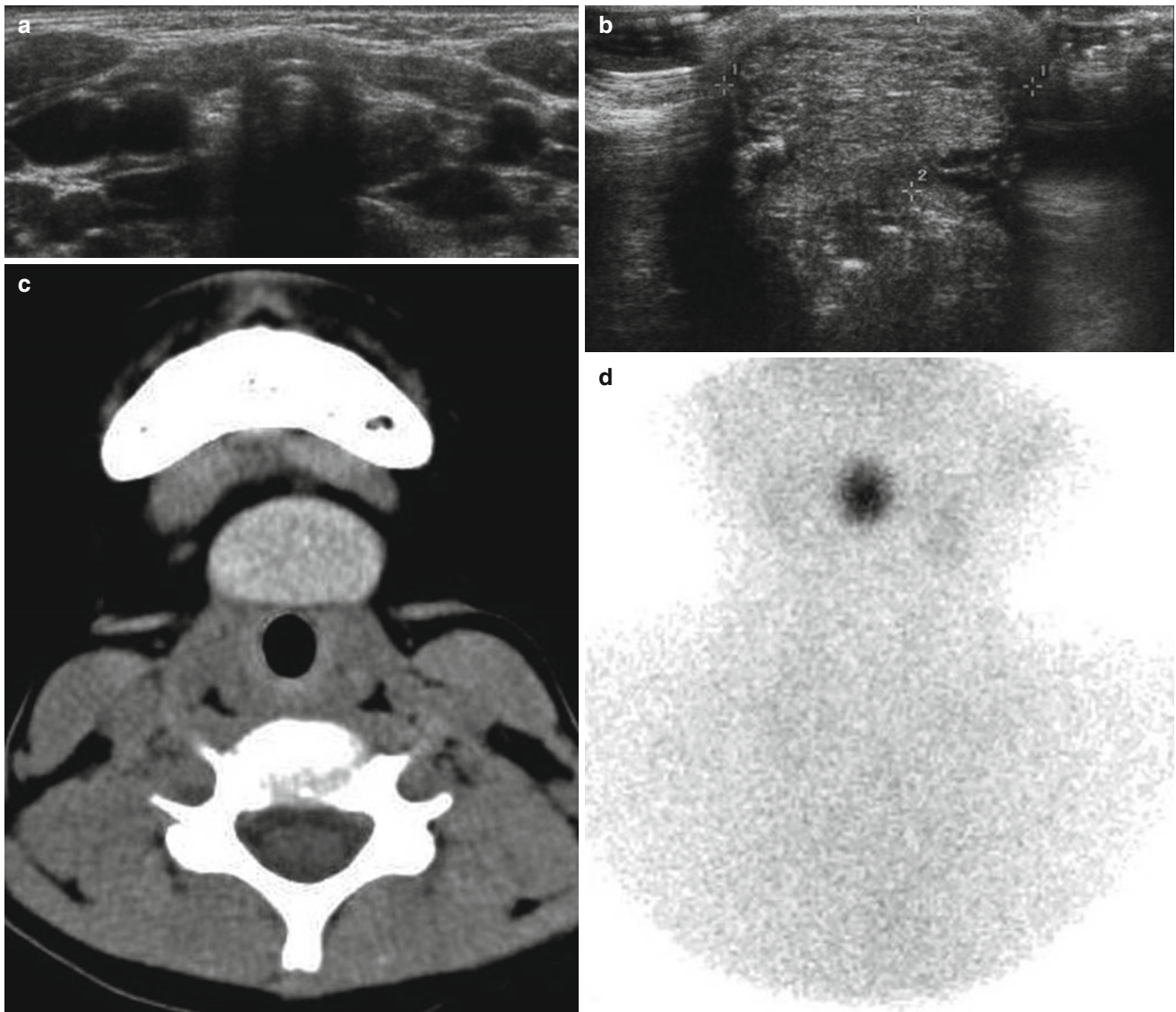


Fig. 7.10 Ectopic thyroid gland in a 7-year-old girl. (a) US shows absence of the thyroid gland at the low neck. (b) US obtained at the level of the hyoid bone shows a heterogeneous echogenic solid mass. (c) Precontrast axial CT scan shows hyperattenuated ectopic thyroid

tissue at the level of the hyoid bone. (d) Tc-99m radionuclide scan shows an ectopic lingual thyroid gland and no uptake of the radioisotope at the normal location of the thyroid gland

7.5.6 Branchial Apparatus Anomalies

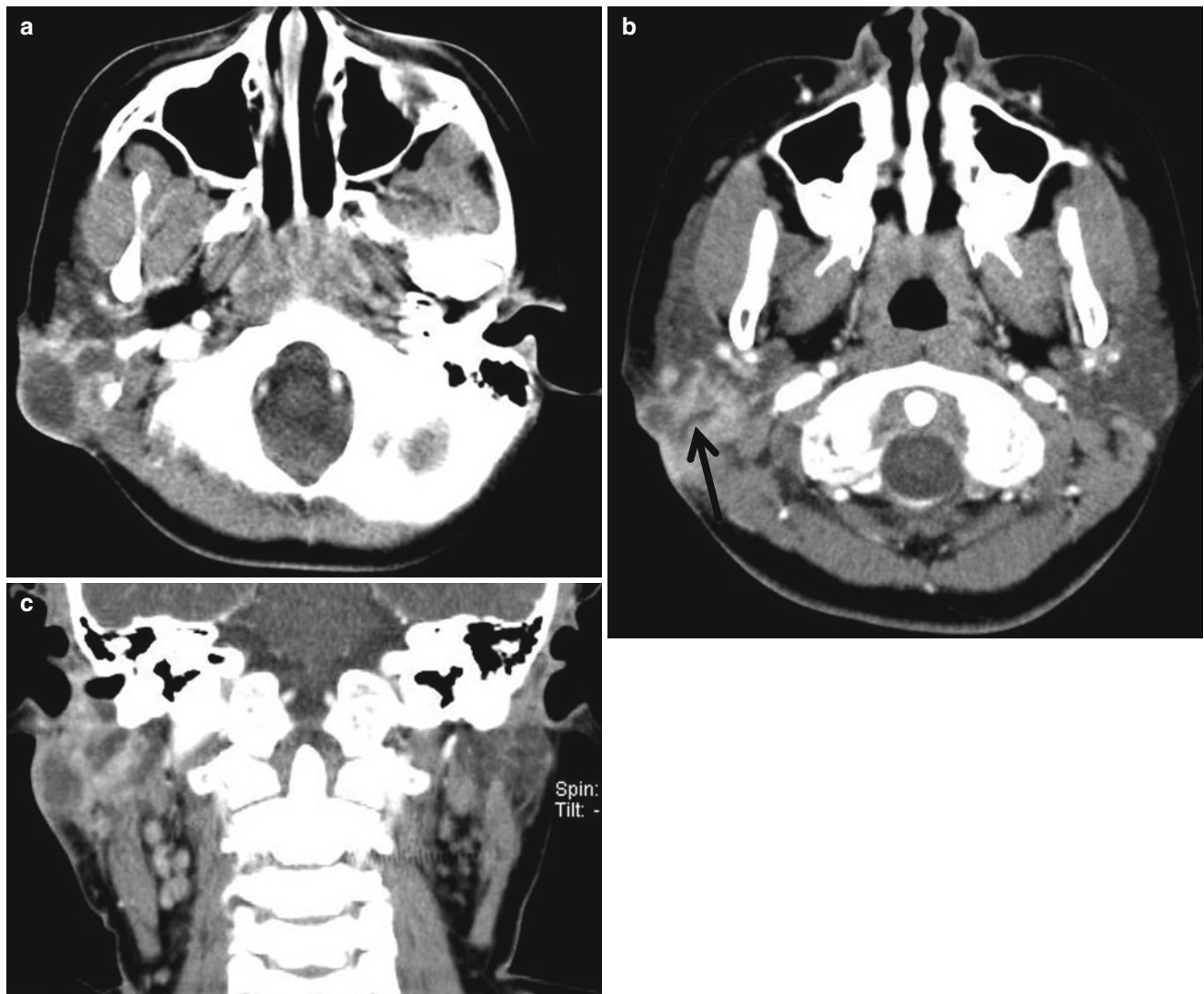


Fig. 7.11 First branchial cleft cyst in an 11-year-old girl. (a, b) Axial CT scans show a complicated, thick-walled cystic mass in the right infra-auricular soft tissue layer with a fine sinus tract (*arrow*). (c) Coronal reformatted CT scan shows the cystic mass extending just below the ear

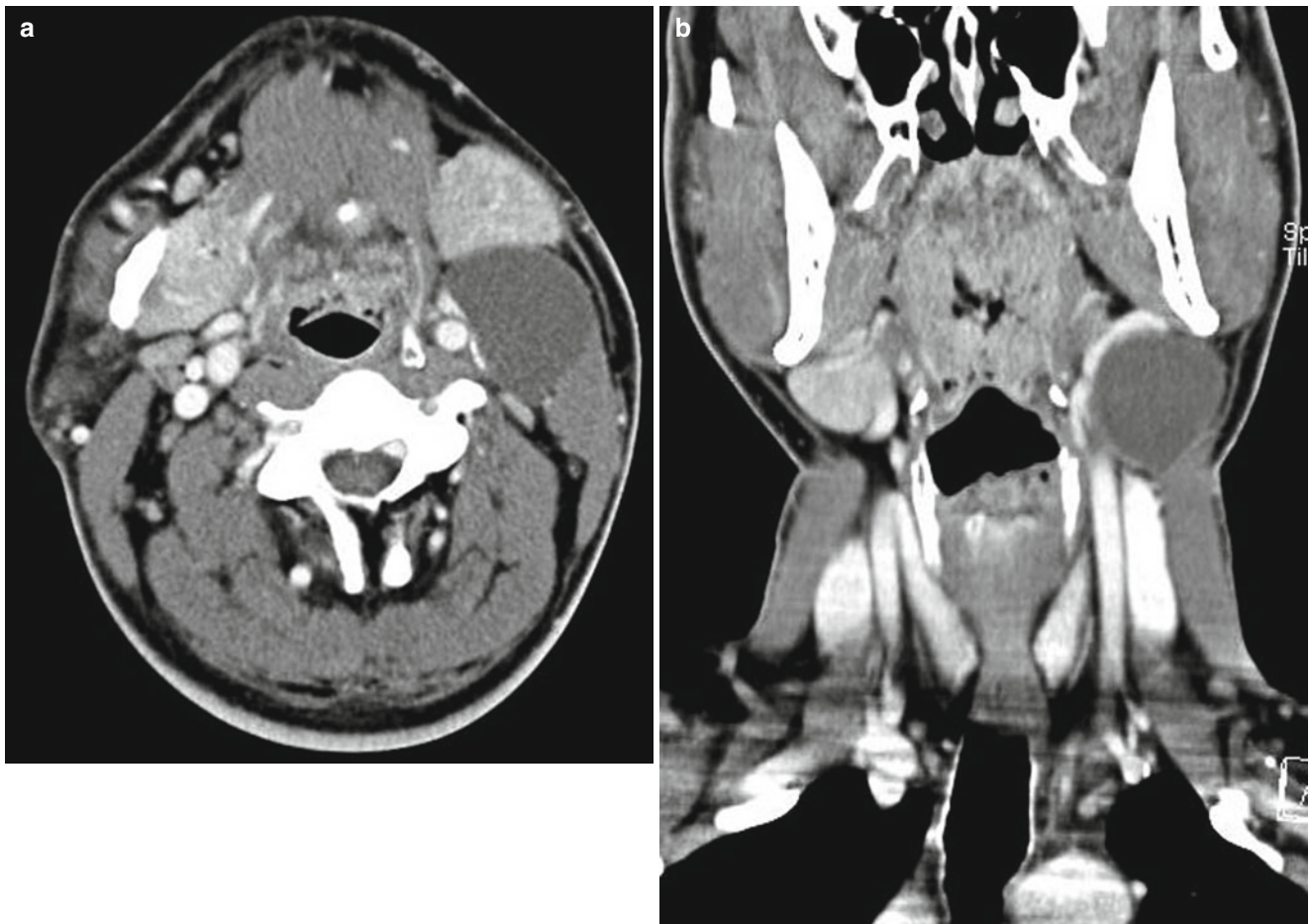


Fig. 7.12 Second branchial cleft cyst in an 18-year-old girl. (a) Axial CT scan shows a thin-walled mass with water attenuation in anteromedial to the sternocleidomastoid muscle. Note the anteriorly displaced submandibular gland, medially displaced left carotid sheath,

and posteriorly displaced sternocleidomastoid muscle. (b) Coronal reformatted CT scan shows the typical location of the elongated cyst at the angle of the mandible

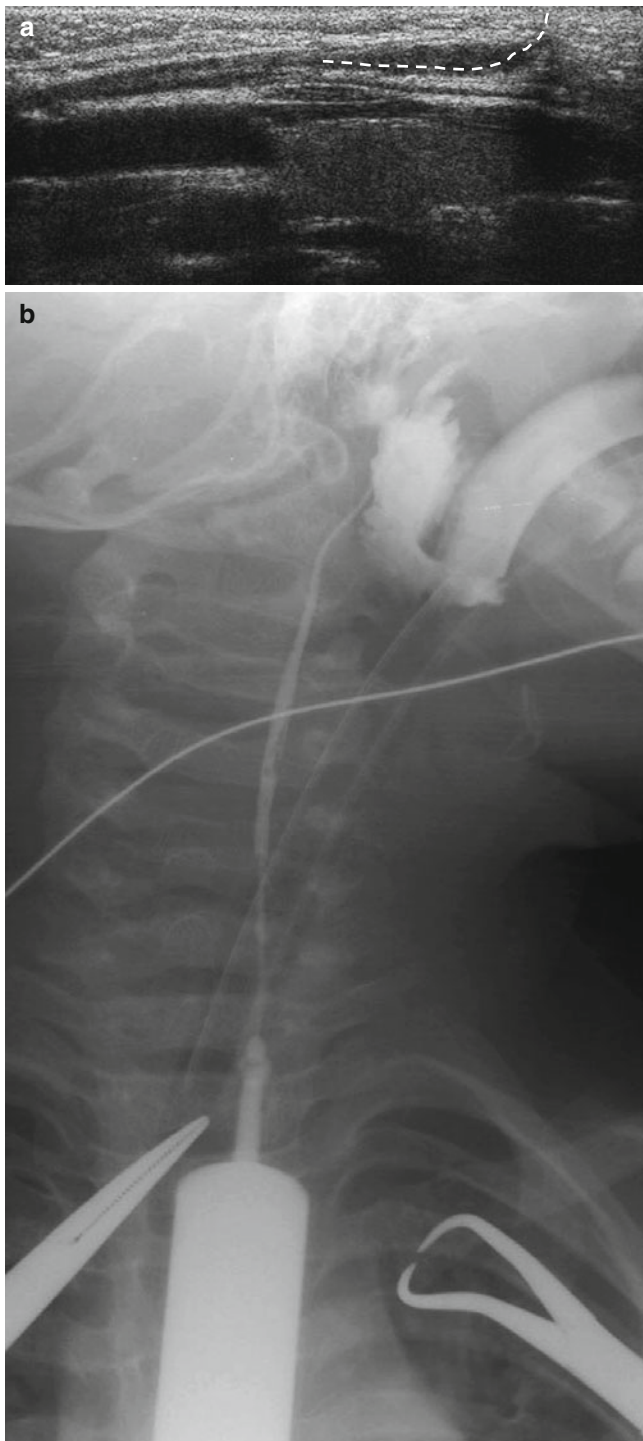


Fig. 7.13 Second branchial cleft fistula in a 2-year-old boy. **(a)** Longitudinal US of the neck shows a long, linear sinus (----) from the tiny skin pit on the anterior border of distal sternocleidomastoid muscle. US has a limited role for tracing the entire length of the sinus tract. **(b)** Operative sinogram shows the complete fistula tract extending from the skin pit in the lower neck to the right tonsillar fossa

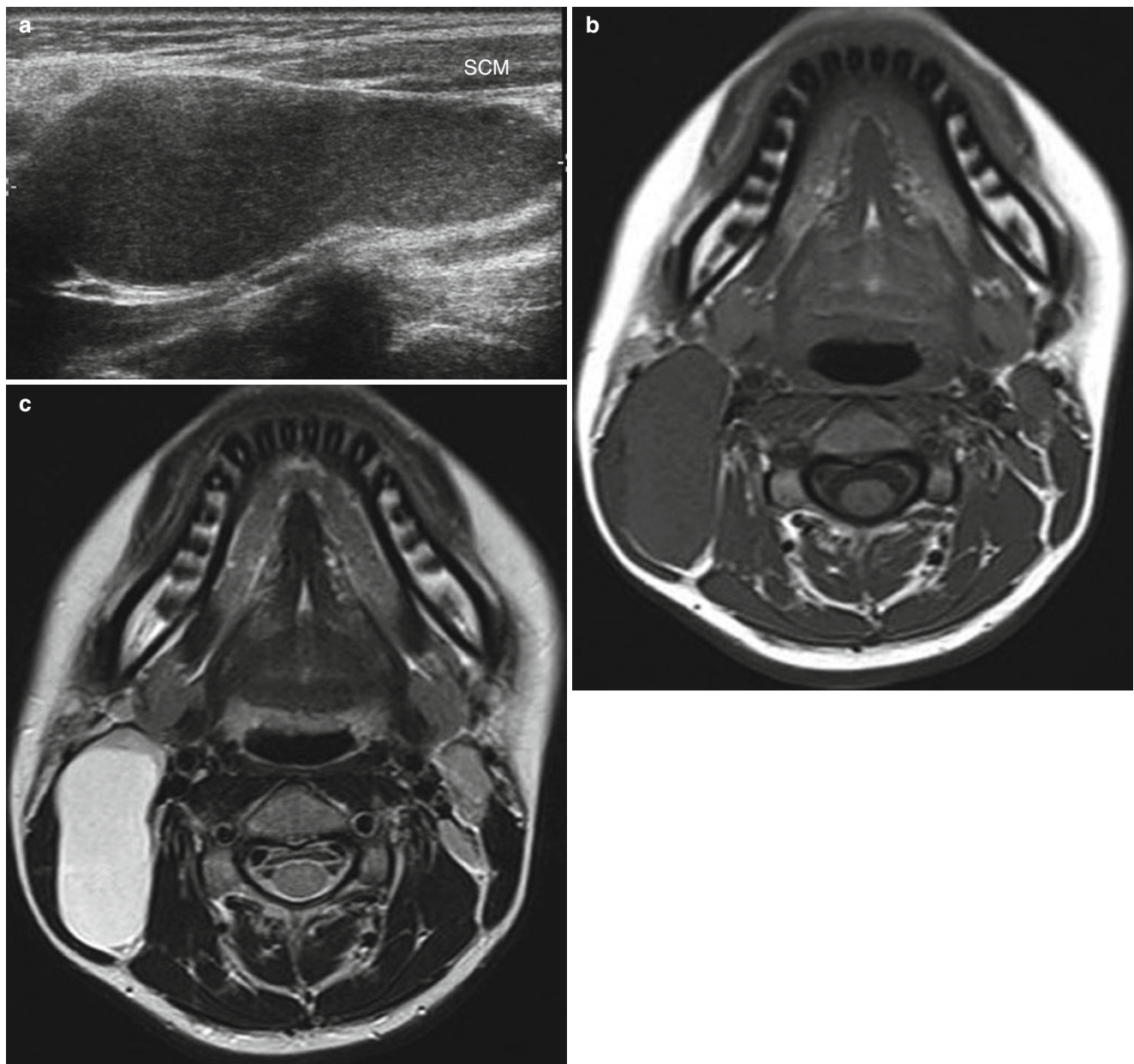


Fig. 7.14 Third branchial cleft cyst in a 16-year-old girl. (a) US shows an elongated cyst along the posterior aspect of the right sternocleidomastoid (SCM) muscle. Note the internal echogenic debridements indicating complicated or proteinaceous content. (b) Axial T1-weighted

image shows an elongated cyst of isosignal intensity. (c) Axial T2-weighted image shows the cyst of high signal intensity, posterolateral to the carotid sheath, displacing the sternocleidomastoid muscle anterolaterally

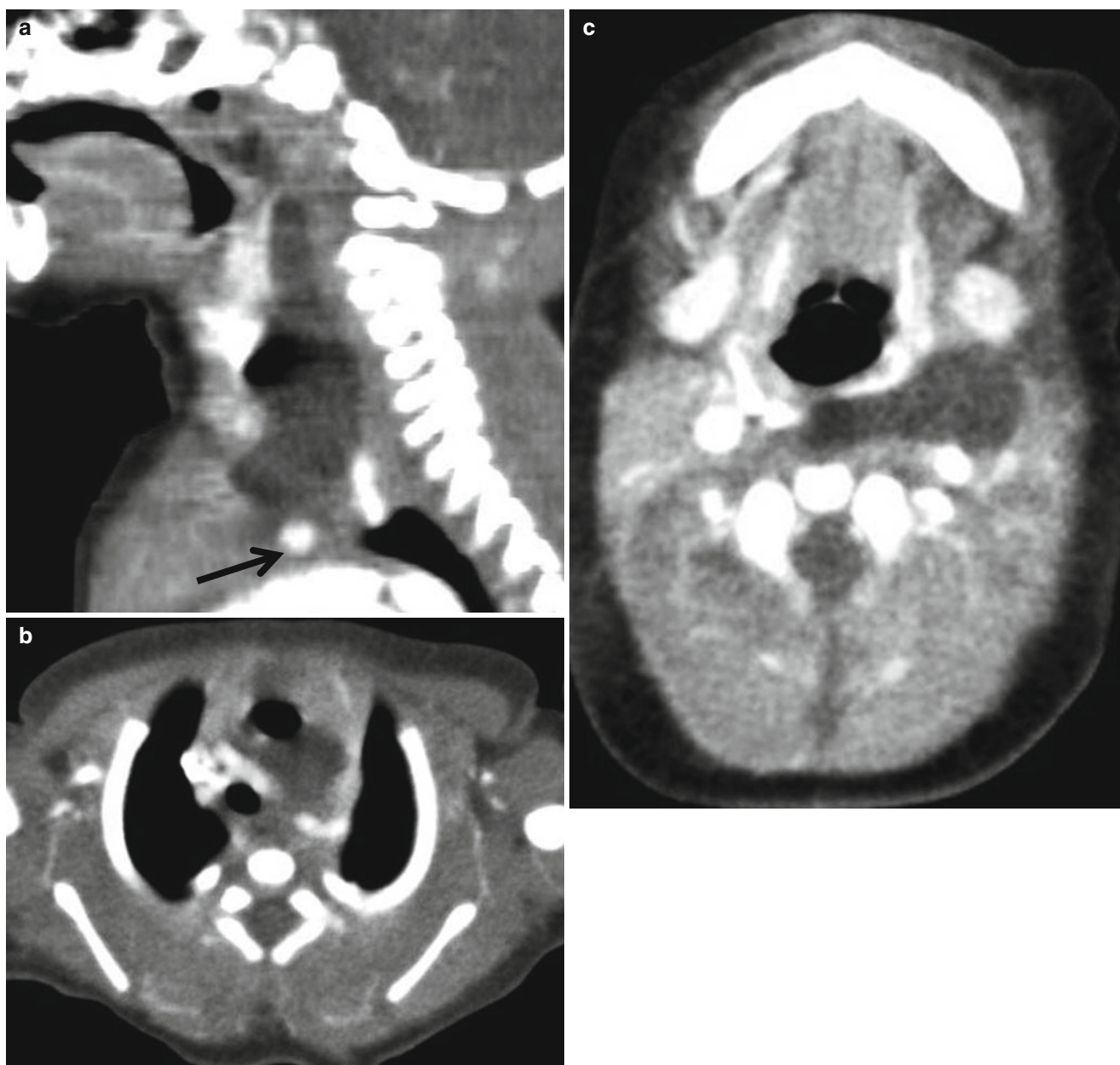


Fig. 7.15 Fourth branchial cleft cyst with a sinus in a 2-day-old neonate. **(a)** Contrast-enhanced sagittal reformatted CT scan shows a large air-containing elongated cystic mass from the hypopharynx to the level of the aortic arch (*arrow*). Note the motion artifact due to severe

respiratory difficulty. **(b, c)** Contrast-enhanced axial CT scans show that the cyst is located anterior to the aortic arch and extends to the level of the pyriform sinus. Sinogram was not performed due to severe respiratory difficulty

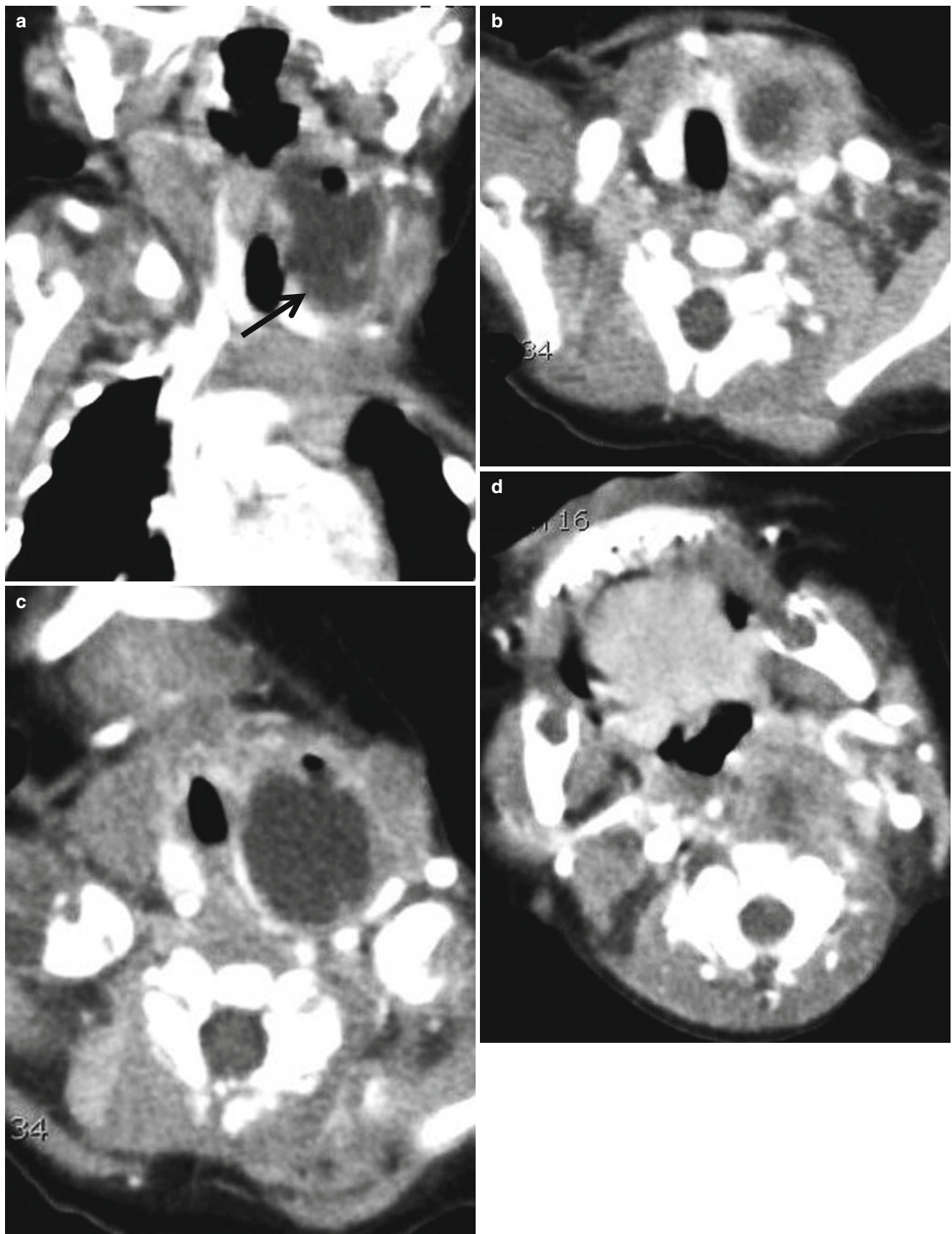


Fig. 7.16 Fourth branchial cleft cyst with a sinus in a 2-month-old infant. (a) Coronal reformatted CT scan shows an air-containing elongated cystic mass from the level of the pyriform sinus to the left low neck abutting the left thyroid gland (*arrow*). (b–d) Contrast-enhanced

axial CT scans show the cyst abutting the left thyroid gland with internal air pocket and diffuse inflammatory change in the sternocleidomastoid muscle and left hypopharynx. (e) Esophagogram shows a faint linear sinus tract from the tip of the left pyriform sinus (*arrow*)

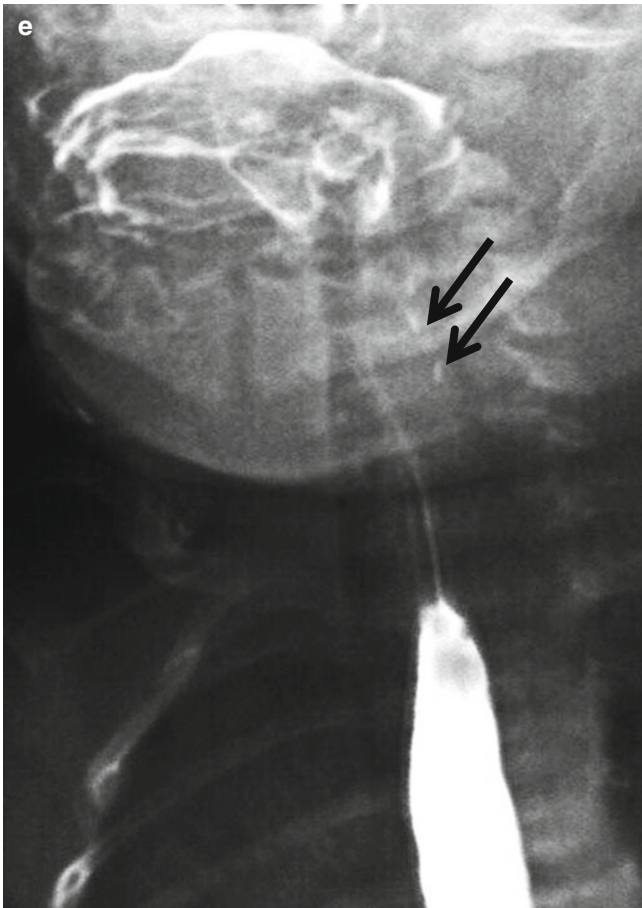


Fig. 7.16 (continued)

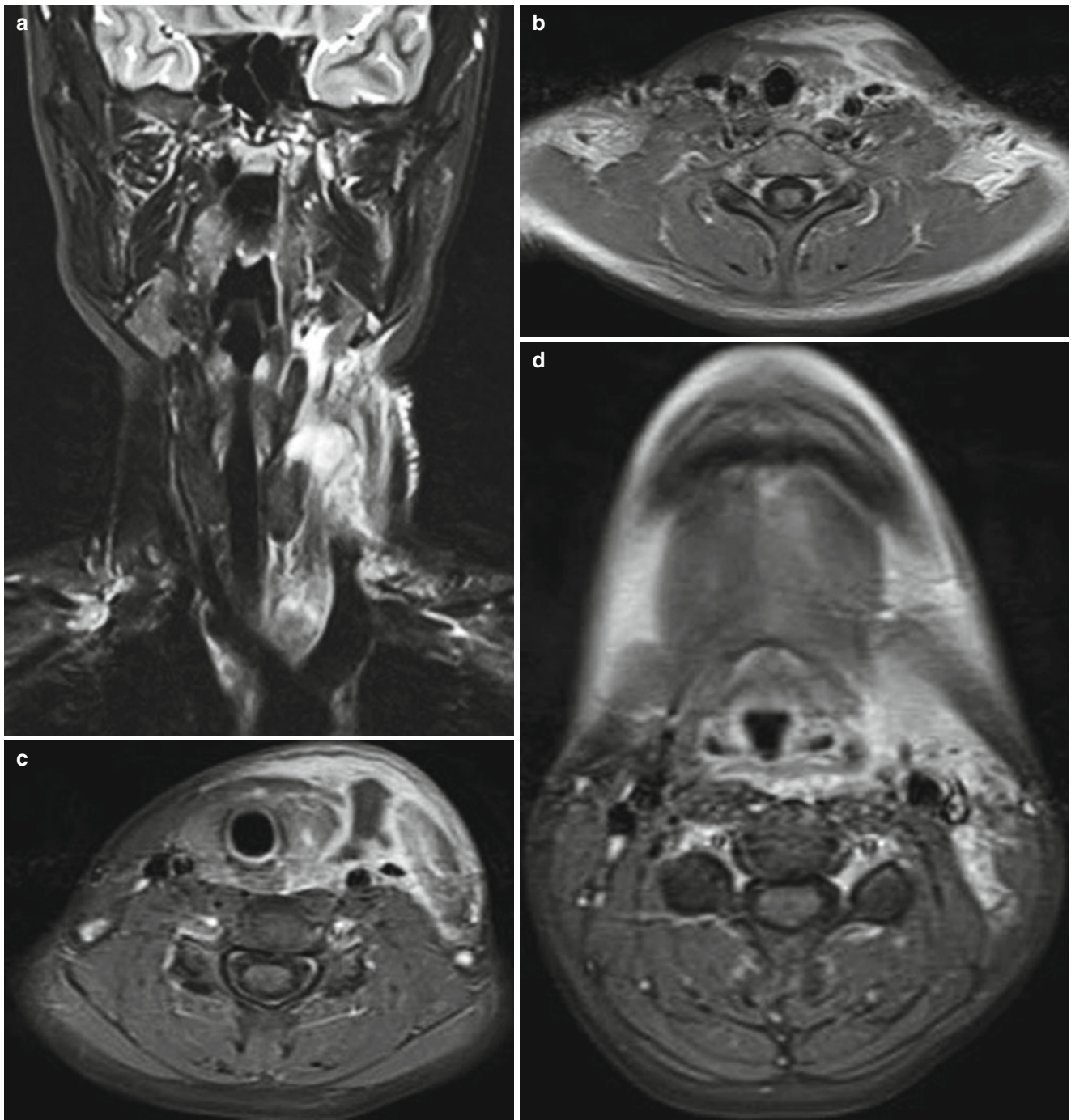


Fig. 7.17 Fourth branchial cleft sinus in a 13-year-old girl with a history of recurrent swelling on the left side of the neck. (a) Coronal T2-weighted MR image shows diffuse high signal intensity of soft tissue edema from the level of the pyriform sinus to the level of the aortic arch on the left. (b–d) Contrast-enhanced axial T1-weighted

images show swelling of the left sternocleidomastoid muscle (b), left thyroid gland with perithyroidal abscess (c), and soft tissue inflammation around the hypopharynx (d). (e) Esophagogram shows a linear sinus tract from the tip of the left pyriform sinus (arrow)

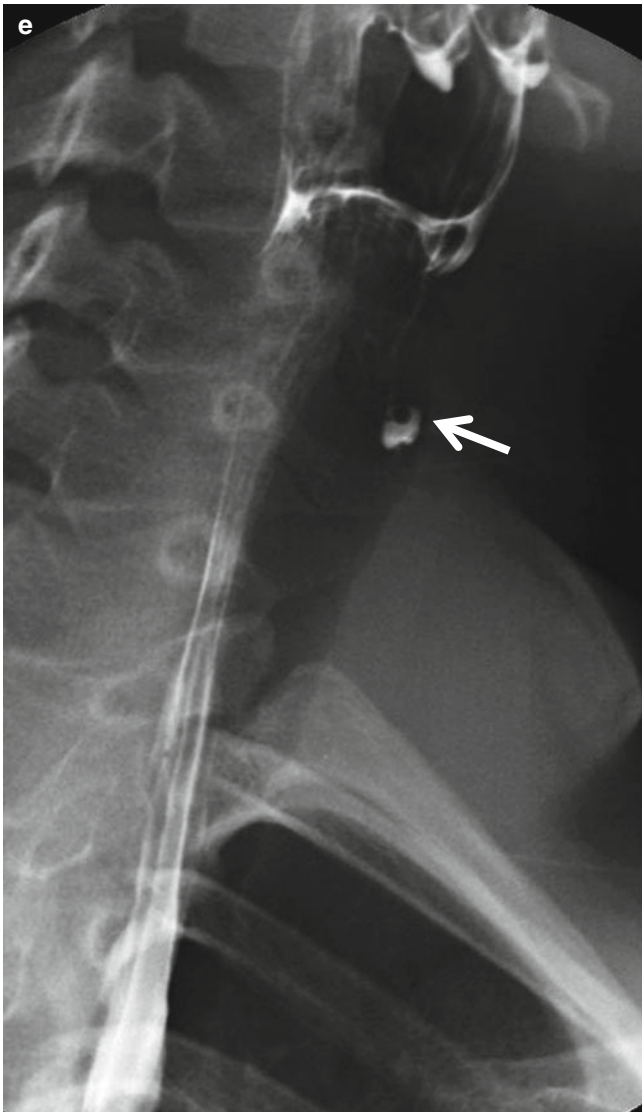


Fig. 7.17 (continued)

7.5.7 Thymic Anomalies

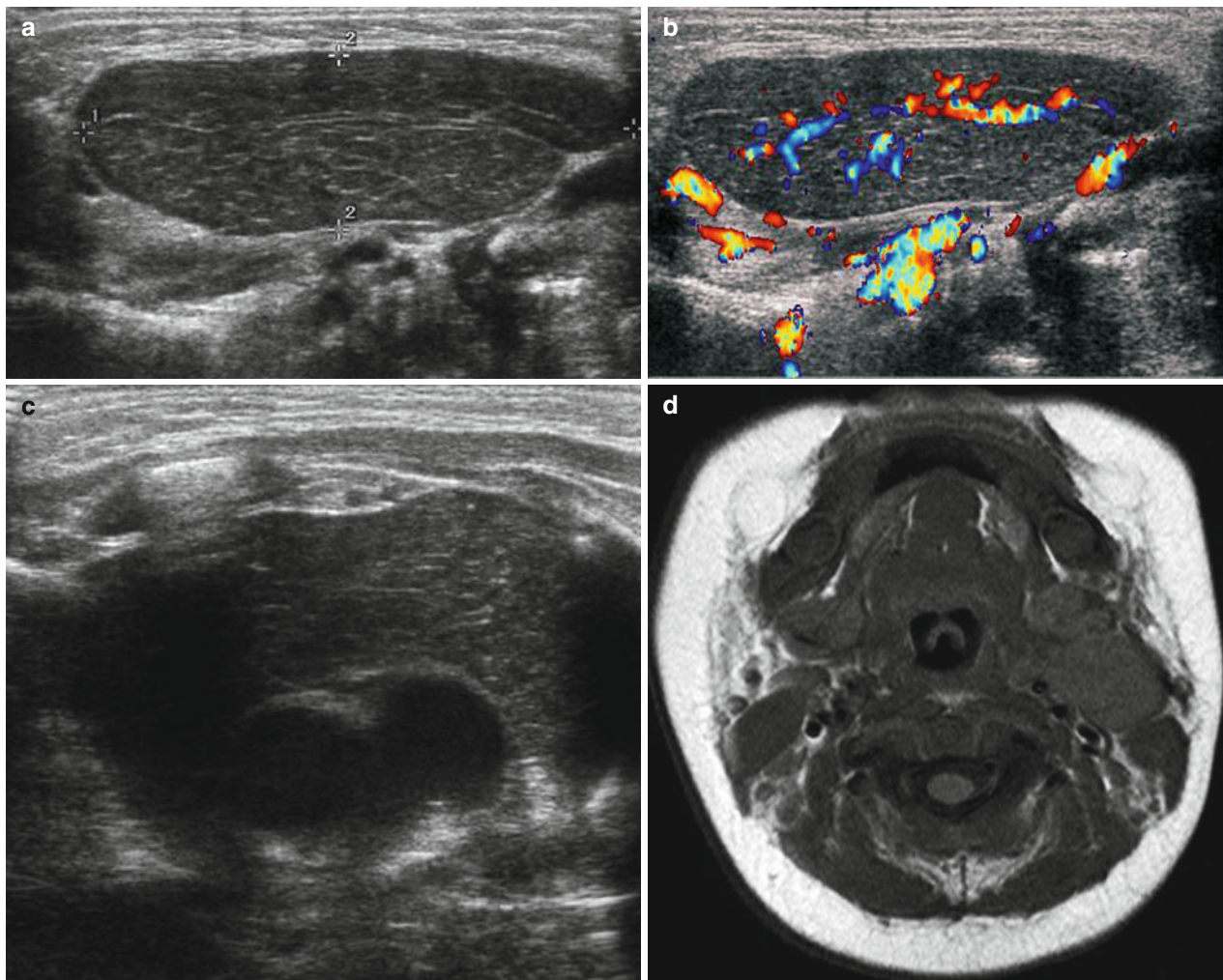


Fig. 7.18 Ectopic cervical thymus in a 12-week-old infant. (a) US shows a well-defined homogeneous, hypoechoic solid mass in the left anterior deep cervical space. (b) Color Doppler US shows minimal arterial and venous flow within the mass. (c) US also shows the same natured normal thymus in the anterior mediastinum. (d, e) Axial MR images show homogeneous isosignal intensity of the mass relative to the submandibular gland and slightly high signal intensity relative to

the muscle on both T1- (d) and T2-weighted (e) images. The mass is located posterior to the submandibular gland. (f, g) Contrast-enhanced fat-suppressed axial and coronal T1-weighted images reveal homogeneously enhancing ectopic thymus (*long arrow*), which is isointense relative to the mediastinal thymus (*arrows*). Note the different enhancements of the submandibular glands

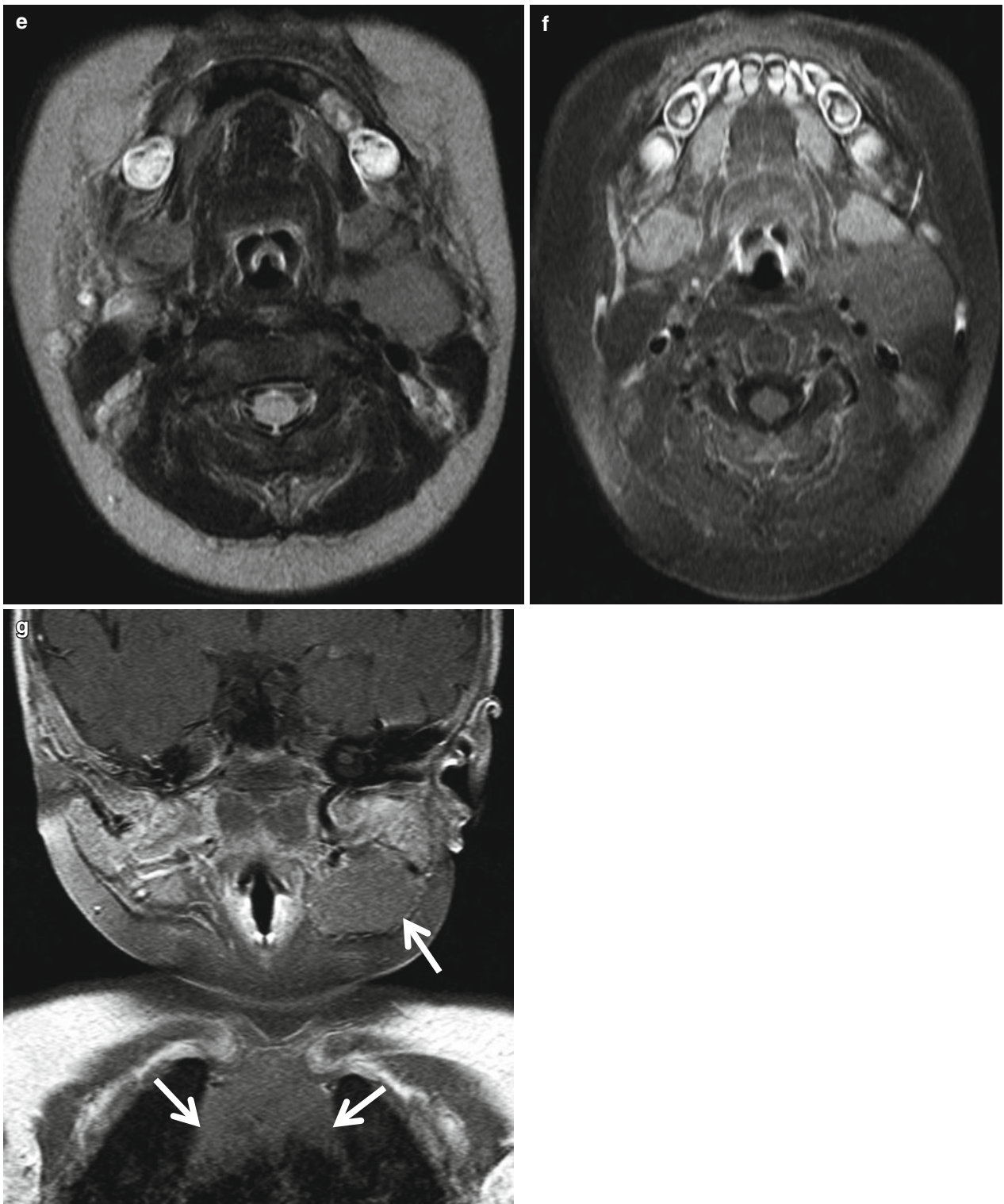


Fig. 7.18 (continued)

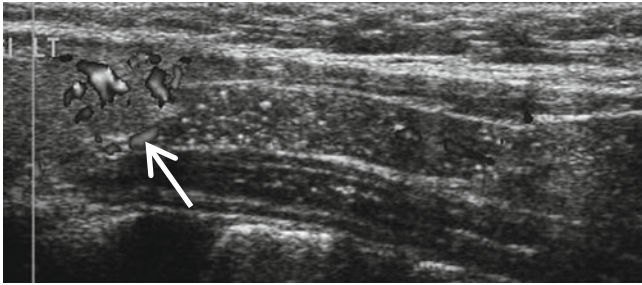


Fig. 7.19 Normal thymus with cervical extension in an 8-year-old boy. Longitudinal US scan of the left neck shows extension of the normal thymus from the anterior mediastinum to the low neck abutting the lower margin of the left thyroid gland (*arrow*). Note the “starry sky” appearance of the thymic parenchyma, which is thought to be hyper-echoic fat against the background of the remaining hypoechoic lymphoid tissue

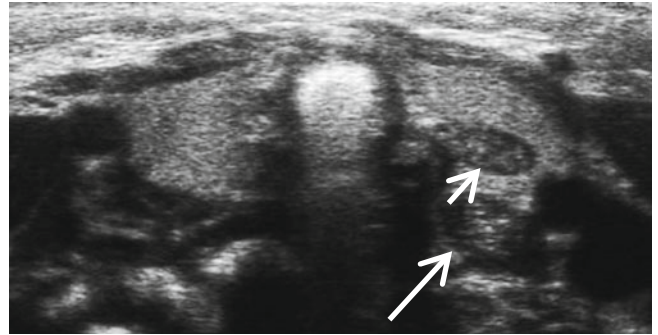


Fig. 7.20 Ectopic thymic tissue of the thyroid gland in a 4-day-old neonate. US shows a tiny low echoic solid nodule of ectopic thymus (*short arrow*), which shows the same echogenicity with the posteriorly located cervical thymus (*long arrow*) extending from the mediastinal thymus

7.5.8 Hypopharyngeal Cysts

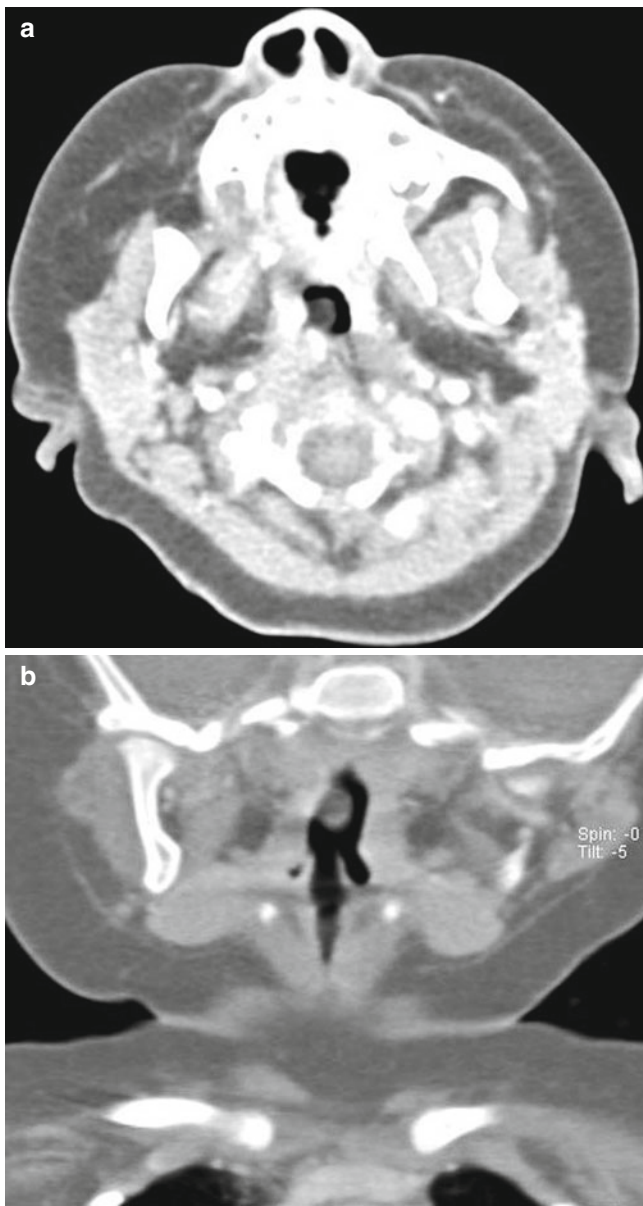


Fig. 7.21 Pharyngeal cyst in a 4-month-old infant. (**a**, **b**) CT scans of the neck show a small unilocular thin-walled cyst arising from the right lateral wall of the oropharynx

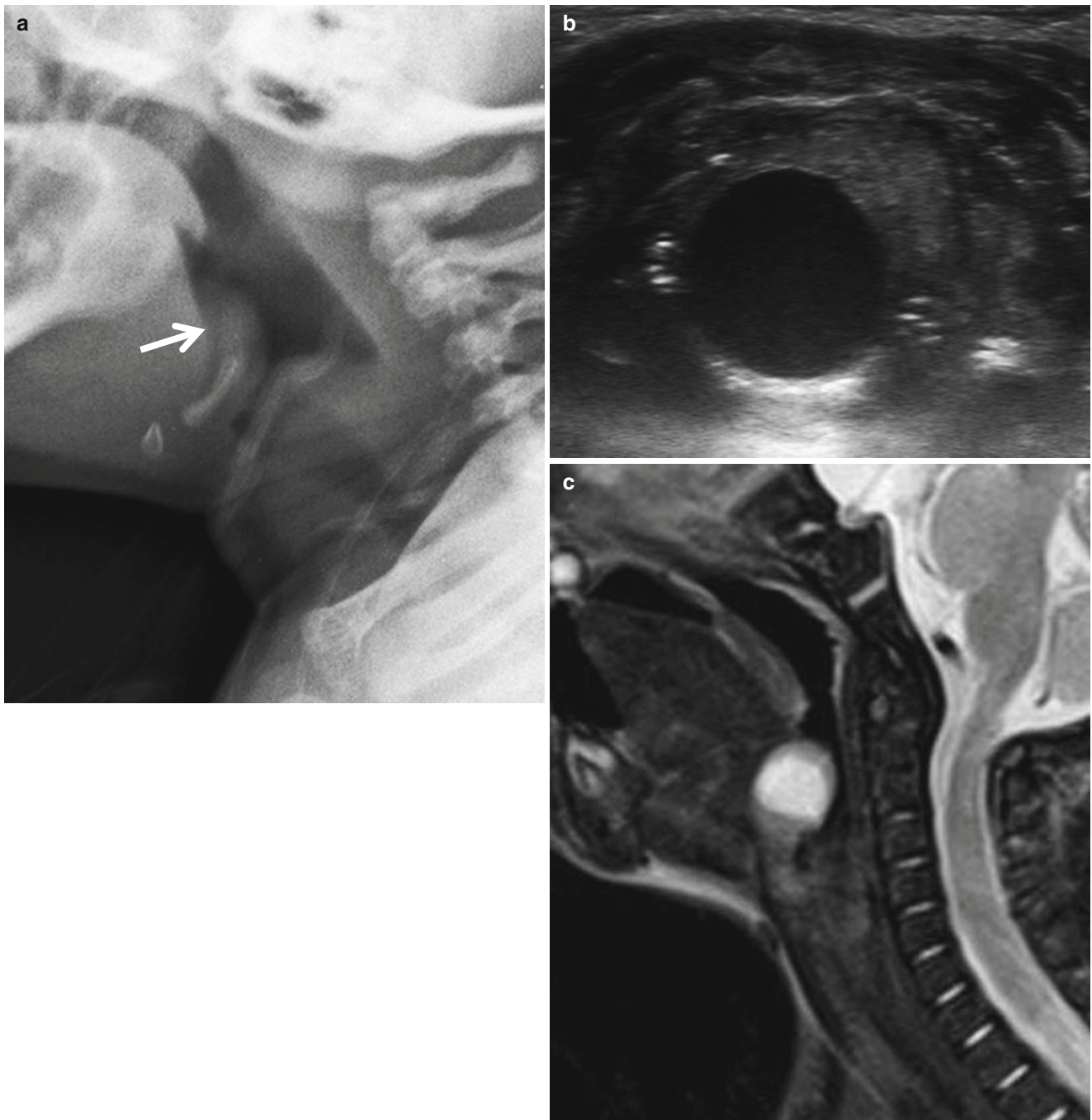


Fig. 7.22 Vallecular cyst in a 1-month-old infant. (a) Endolateral view of the neck shows a round soft tissue mass bulging into the anterior wall of the hypopharynx (*arrow*). (b) US shows a unilocular thin-walled cyst

in the preepiglottic space. (c) Sagittal T2-weighted image shows a unilocular cyst of high signal intensity arising from the vallecula



Fig. 7.23 Vallecular cyst in a 1-month-old infant. **(a)** Endolateral view of the neck shows a round soft tissue mass bulging into the anterior wall of the hypopharynx. **(b, c)** Axial and coronal reformatted CT scans

show a unilocular thin-walled cyst arising from the right lateral wall of the vallecula

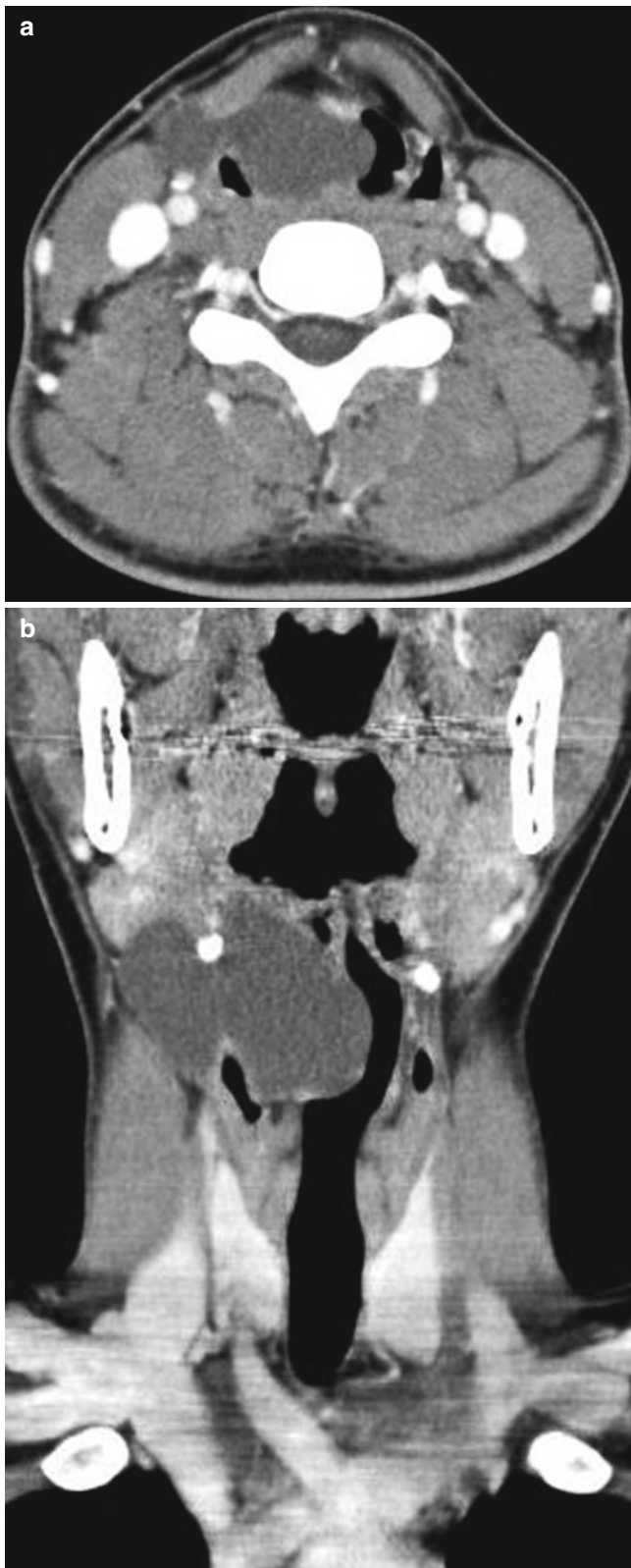


Fig. 7.24 Laryngocele in a 15-year-old boy. **(a)** Axial CT scan shows a bilobed cystic mass in the right lateral wall of the larynx. **(b)** Coronal reformatted CT scan shows a bilobed thin-walled cyst arising from the right lateral wall of the supraglottic larynx and extending into paralaryngeal soft tissue

7.5.9 Foregut Duplication Cysts

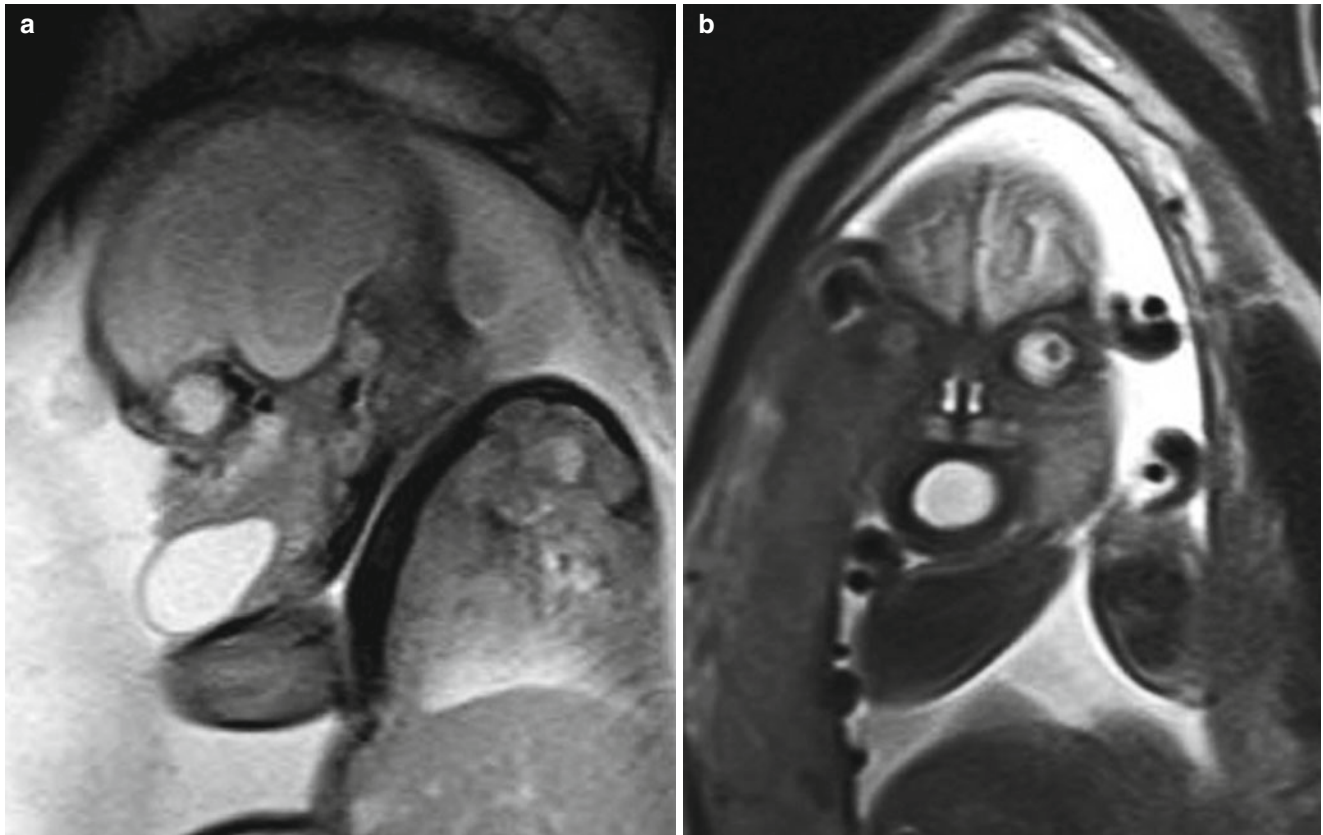


Fig. 7.25 Enteric duplication cyst in a fetus. (a) Sagittal T2-weighted MR image shows an oval-shaped cystic mass occupying the anterior two-thirds of the fetal mouth. (b) Axial and T2-weighted image shows the cystic mass in the fetal mouth

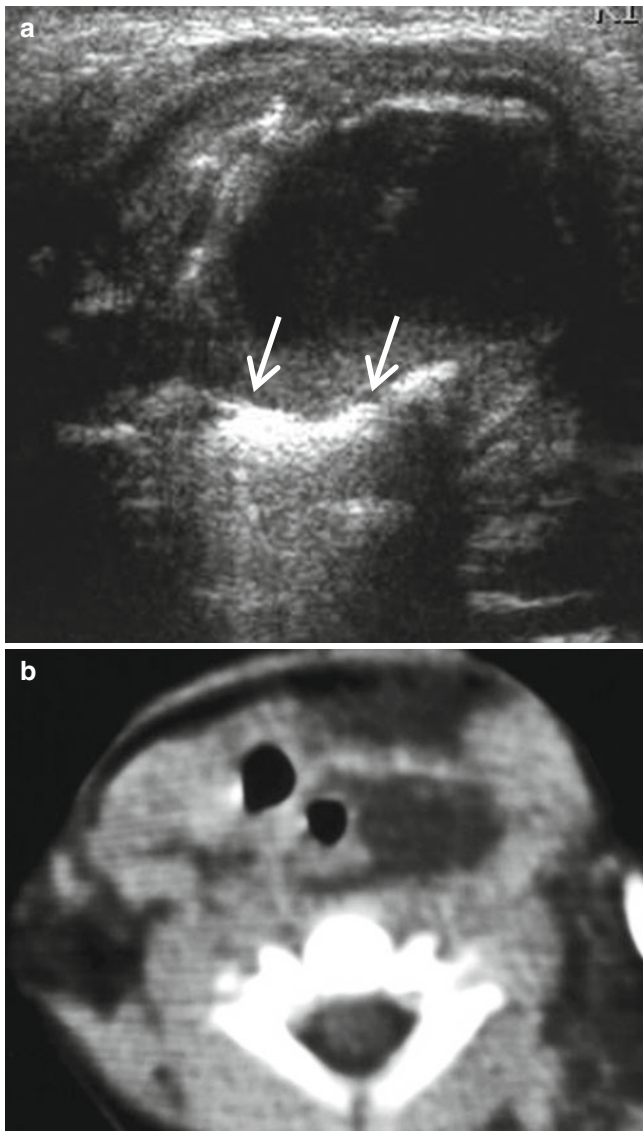


Fig. 7.26 Enteric duplication cyst in a 1-month-old infant. **(a)** US shows a thick-walled cyst in the left lateral aspect of the esophageal gas (*arrows*). **(b)** Axial CT scan shows a unilocular cyst abutting the left lateral wall of the esophagus

7.5.10 Vascular Malformations

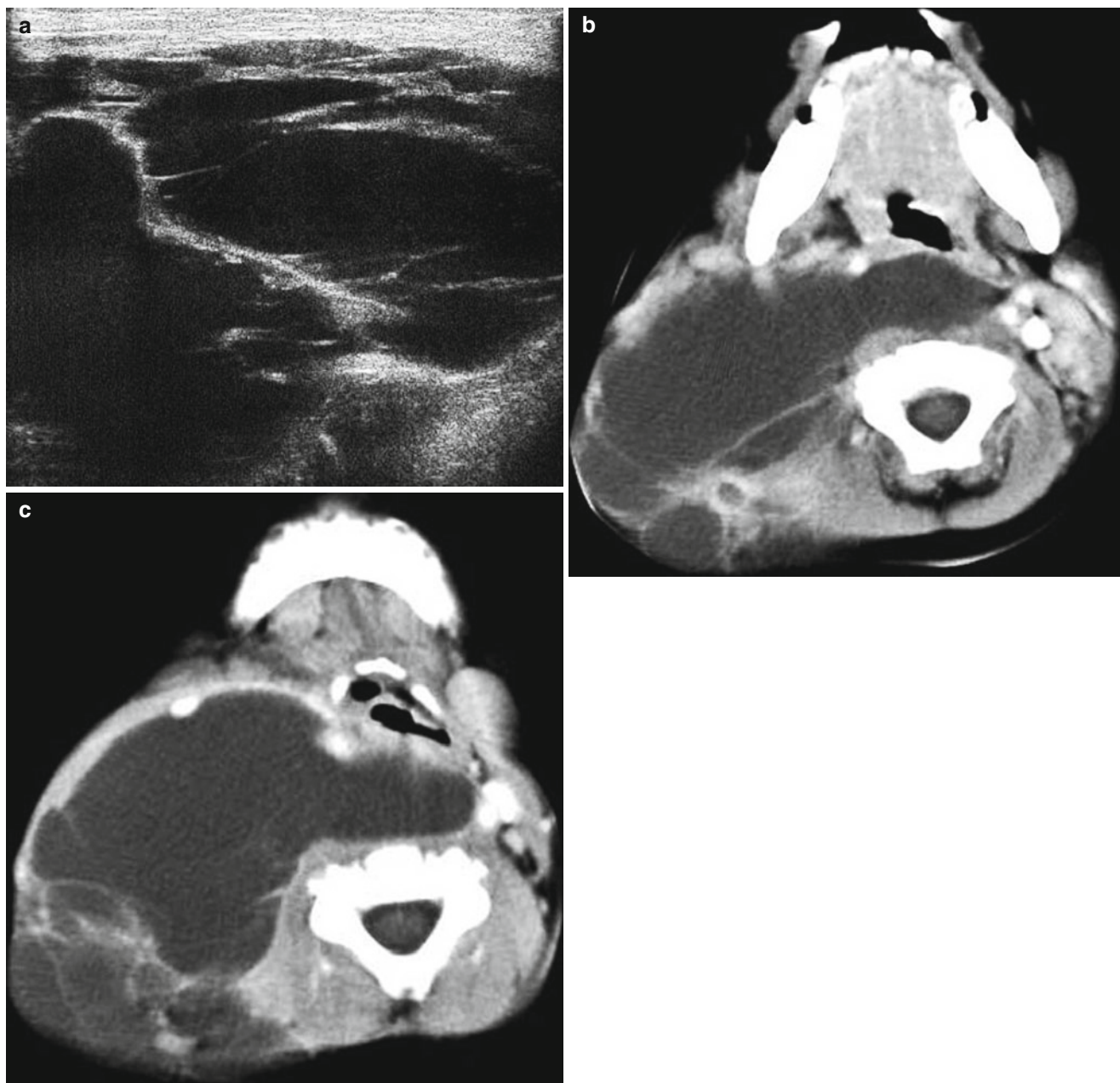


Fig. 7.27 Lymphangioma in a 1-year-old infant. (a) US shows a large, thin-walled multiseptated cystic mass. (b, c) Contrast-enhanced CT scans show a huge, multiseptated, thin-walled cystic mass in the

posterior deep cervical space insinuating into the retropharyngeal space. Note the anteriorly displaced right sternocleidomastoid muscle

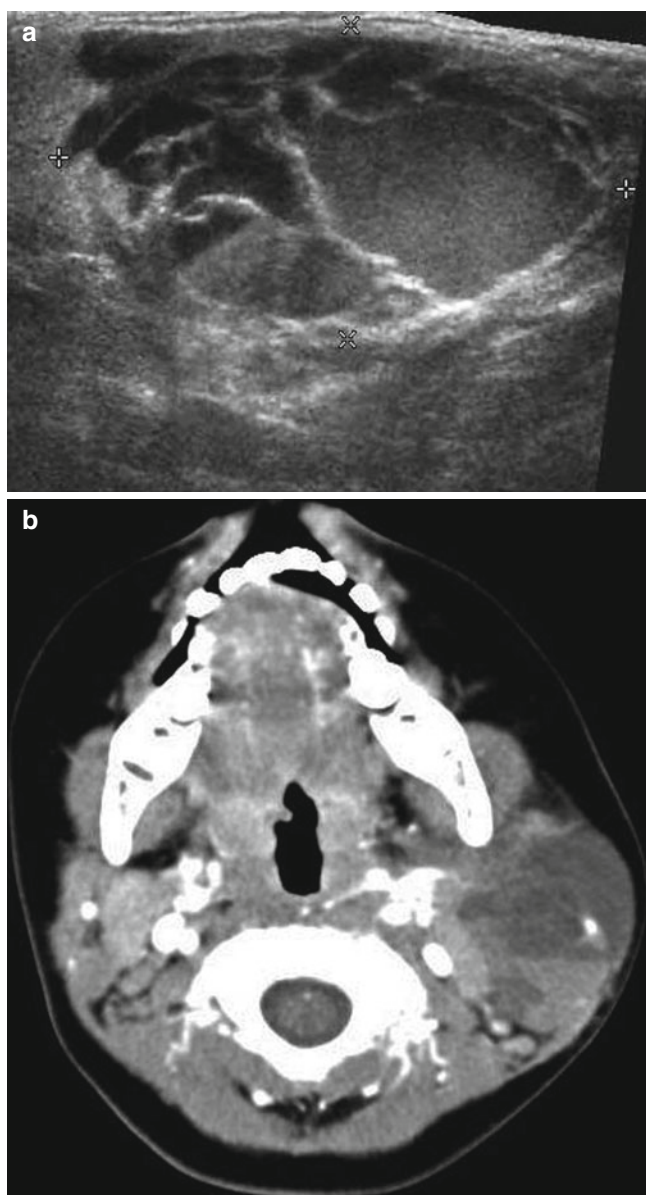


Fig. 7.28 Lymphangioma of the parotid gland in a 22-month-old boy. (a) US shows a multiseptated cystic mass with internal debris in some of the chambers. (b) Contrast-enhanced axial CT scan shows a large, thin-walled, multiseptated mass with fluid–fluid levels in the left parotid gland

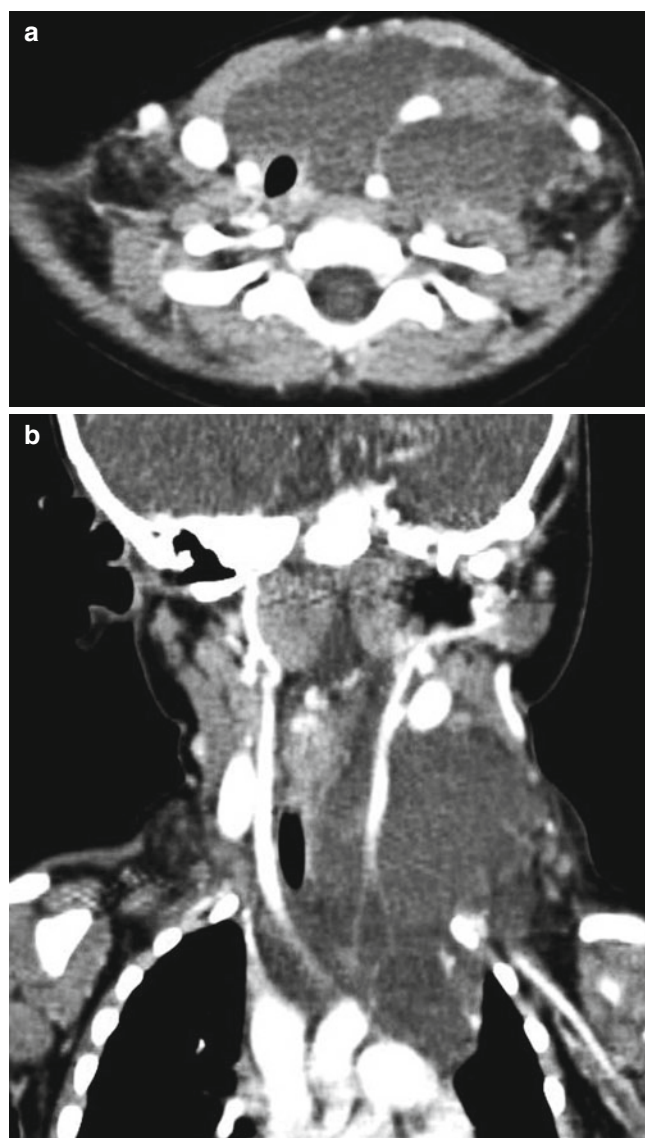


Fig. 7.29 Lymphangioma in a 10-month-old infant. (a, b) Contrast-enhanced axial and coronal CT scans show a huge, multilocular cystic mass involving the pretracheal and posterior deep cervical spaces with fluid–fluid levels and extending to the mediastinum. Note the mass insinuating around the vessels

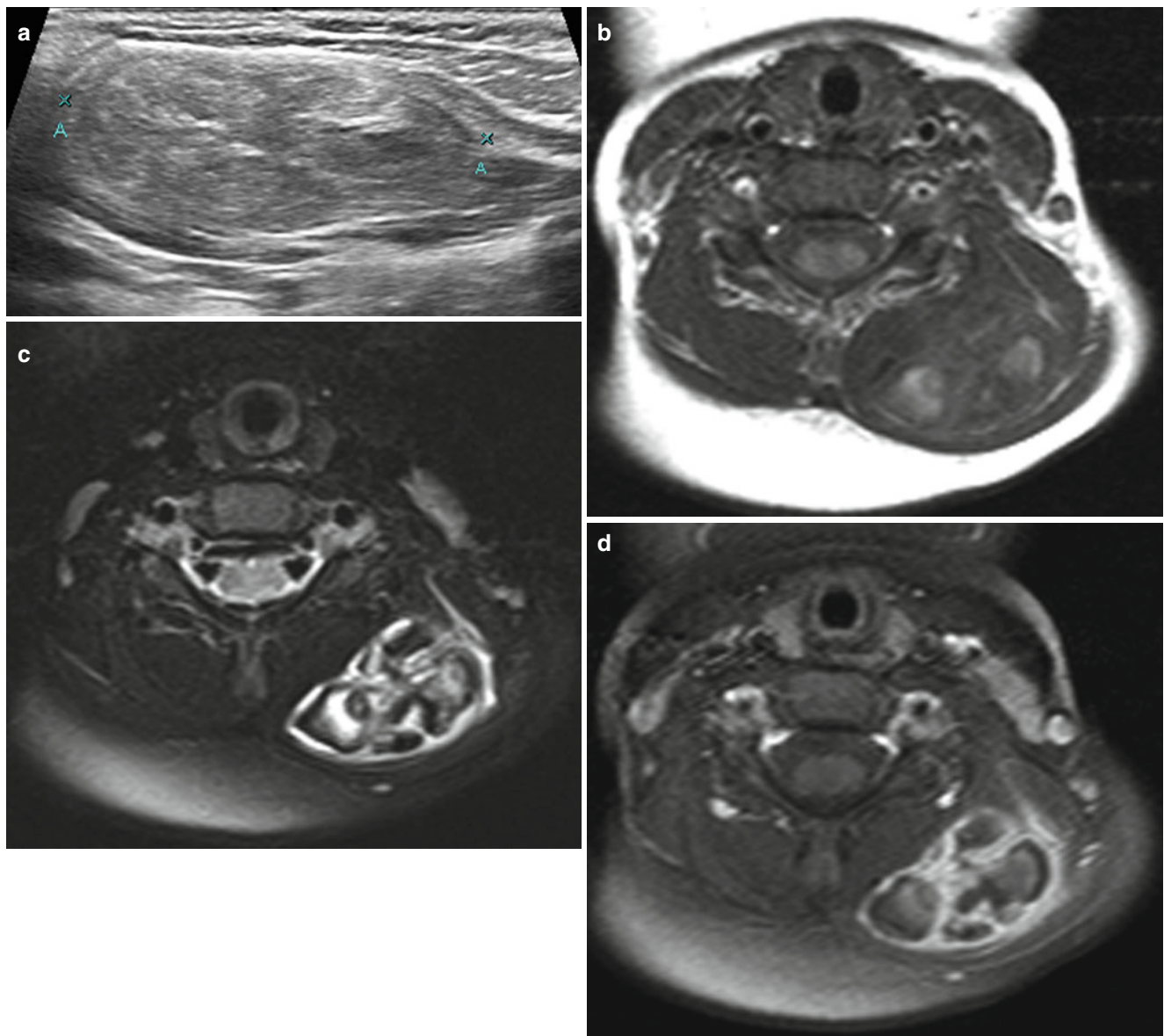


Fig. 7.30 Venous malformation in a 18-month-old girl. **(a)** US shows a heterogeneous complex mass (A) in the left posterior neck. **(b, c)** Axial T1- and fat-saturated T2-weighted images shows internal hemor-

rhage of variable signal intensities in the mass. **(d)** Contrast-enhanced fat-saturated axial T1-weighted image shows thick-walled enhancement of the septa

References

- Baker LL, Dillon WP, Hieshima GB, et al. Hemangiomas and vascular malformations of the head and neck: MR characterization. *Am J Neuroradiol*. 1993;4:307–14.
- Benson MT, Dalen K, Mancuso AA, et al. Congenital anomalies of the branchial apparatus: embryology and pathologic anatomy. *Radiographics*. 1992;12:943–60.
- Chung PS, Chung YW, Park SJ, et al. A clinicopathologic study of epiglottic and vallecular cysts. *Korean J Otorhinolaryngol*. 2004;47:157–60.
- Cigliano B, Baltogiannis N, Marco MD, et al. Cervical thymic cysts. *Pediatr Surg Int*. 2007;23:1219–25.
- Gimm O, Krause U, Wessel H, et al. Ectopic intrathyroidal thymus diagnosed as a solid thyroid lesion: case report and review of the literature. *J Pediatr Surg*. 1997;32:1241–3.
- Kieran SM, Robson CD, Nose V, et al. Foregut duplication cysts in the head and neck. Presentation, diagnosis, and management. *Arch Otolaryngol Head Neck Surg*. 2010;136:778–82.
- Koeller KK, Alamo L, Adair CF, et al. Congenital cystic masses of the neck: radiologic-pathologic correlation. *Radiographics*. 1999;19:121–46.
- Lowe LH, Booth TN, Joglar JM, et al. Midface anomalies in children. *Radiographics*. 2000;20:907–22.
- Morón FE, Morris MC, Jone JJ, et al. Lumps and bumps on the head in children: use of CT and MR imaging in solving the clinical diagnostic dilemma. *Radiographics*. 2004;24:1655–74.
- Mulliken JB, Glowacki J. Hemangiomas and vascular malformations in infants and children: a classification based on endothelial characteristics. *Plast Reconstr Surg*. 1982;69:412–22.
- Nasseri F, Eftekhari F. Clinical and radiologic review of the normal and abnormal thymus: pearls and pitfalls. *Radiographics*. 2010;30:413–28.
- Sadler TW. Head and neck. In: Sadler TW, (ed) *Langman's medical embryology*, 12th ed. Baltimore: Williams and Wilkins; 2012.
- Smirniotopoulos JG, Chiechi MV. Teratomas, dermoids, and epidermoids of the head and neck. *Radiographics*. 1995;15:1437–55.
- Som PM, Smoker WRK, Curtin HD, et al. Congenital lesions of the neck. In: Som PM, Curtin HD, editors. *Head and neck imaging*. 4th ed. St. Louis: Mosby; 2003.
- Suzuki J, Hashimoto S, Watanabe K, et al. Congenital vallecular cyst in an infant: case report and review of 52 recent cases. *J Laryngol Otol*. 2011;125:1199–203.

Hye-Kyung Yoon

Contents

8.1	Introduction	294
8.2	Imaging	294
8.3	Infections and Inflammations	294
8.3.1	Paranasal Sinusitis.....	294
8.3.2	Otitis Media and Mastoiditis.....	295
8.3.3	Retropharyngeal Abscess.....	295
8.3.4	Lymphadenitis.....	295
8.3.5	Kikuchi Disease	295
8.3.6	Kawasaki Disease.....	295
8.3.7	Infectious Mononucleosis	295
8.3.8	Tuberculosis	295
8.3.9	Sialadenitis.....	296
8.3.10	Branchial Arch Anomaly	296
8.3.11	Thyroglossal Duct Cyst.....	296
8.4	Head and Neck Trauma	296
8.4.1	Nasal Bone Fracture.....	296
8.4.2	Orbital Fracture	296
8.4.3	Temporal Bone Fracture.....	296
8.4.4	Cervical Injury	296
8.4.5	Head and Neck Foreign Body.....	297
8.5	Illustrations: Infectious and Traumatic Diseases	298
8.5.1	Fungal Paranasal Sinusitis.....	298
8.5.2	Frontal Sinusitis with Meningitis.....	300
8.5.3	Otomastoiditis with Meningitis.....	301
8.5.4	Retropharyngeal Abscess.....	302
8.5.5	Cervical Reactive Lymph Node Hyperplasia	303
8.5.6	Kikuchi Disease	304
8.5.7	Kawasaki Disease (Mucocutaneous Lymph Node Syndrome)	306
8.5.8	Infectious Mononucleosis	307
8.5.9	Tuberculous Cervical Lymphadenitis.....	308

H.-K. Yoon, M.D., Ph.D.
 Department of Radiology, Asan Medical Center,
 University of Ulsan College of Medicine,
 86, Asanbyeongwon-gil, Songa-gu, Seoul 138-736, Korea
 e-mail: hk2005.yoon@gmail.com

8.5.10	Sialadenitis	309
8.5.11	Pyriform Sinus Fistula	311
8.5.12	Second Branchial Cleft Fistula	313
8.5.13	Thyroglossal Duct Cyst.....	314
8.5.14	Mandible Condylar Fracture	315
8.5.15	Nasal Bone Fracture.....	316
8.5.16	Orbital Blowout Fracture	317
8.5.17	Temporal Bone Fracture.....	318
8.5.18	Cervical Spine Dislocation.....	319
8.5.19	Foreign Body.....	320
	References	321

8.1 Introduction

Children commonly present with a lump in the head and neck, and reactive lymph node hyperplasia is one of the most common causes of cervical lymph node enlargement. Acute lymphadenitis in association with viral illness is also common, and malignant lymphadenopathy is infrequently encountered unlike adult population. When we see patients with suppurative infection or frank abscess formation in typical locations, underlying congenital anomalies such as thyroglossal duct cyst or branchial cleft anomaly should be considered.

Traumatic injury of the head and neck is relatively common in pediatric patients. Although most of them are minor, serious injuries such as cervical fracture and/or dislocation can happen. Children have hypermobility of the spinal column, especially in the cervical spine, which can result in spinal cord injury without radiographic abnormality (SCIWORA).

8.2 Imaging

Ultrasound is the first choice of imaging modality for evaluating neck lumps (Hegde et al. 2012). It can show cystic nature of the neck mass or abscess formation in association with acute cervical lymphadenitis. CT is excellent to show the extent of diseases and anatomic relationships, but not so good at differentiating various causes of cervical lymphadenopathy unless there is associated necrosis or calcification. MRI is infrequently indicated for evaluating infectious or inflammatory diseases of the neck (Shekdar et al. 2012).

For head and cervical trauma, a stepwise approach from plain radiography to CT or MRI is needed. Cervical spine routine examinations typically include AP, lateral (neutral, flexion, extension), and open-mouth odontoid views. With the advent of CT technique, the role of plain radiographs seems to be decreasing. MRI should be

performed in patients who are suspected of having spinal cord injury.

8.3 Infections and Inflammations

8.3.1 Paranasal Sinusitis

Paranasal sinuses consist of paired air-filled cavities including maxillary, ethmoid, frontal, and sphenoid sinuses. Maxillary and ethmoid air cells are present at birth, while frontal air cells are seen between 6 and 12 years of age (Cooper and Slovis 2008). The sphenoid sinuses are absent at birth and grow to adult size between 7 and 11 years.

Traditional PNS series including Waters, Caldwell, posteroanterior, and lateral views are infrequently used for screening of the paranasal sinus inflammation. The American Academy of Pediatrics does not recommend the entire PNS series for diagnosing sinusitis in children less than 6 years old (Cooper and Slovis 2008). When indicated for an older child, it should be minimized usually to a single Waters view. Waters projection is most important and best for visualizing the maxillary sinuses. Plain films do not give sufficient information in children less than 3 years old. CT and MRI are far superior to plain radiographs in order to see inflammatory mucosal thickening and adjacent structures without overlapping.

Mucosal thickening along the sinus wall is commonly seen in asymptomatic individuals found incidentally. Air-fluid level is known to be a hallmark for acute sinus inflammation. CT and MRI play an important role in complex sinus diseases like fungal infection and in cases with possible intracranial or intraorbital extension of sinus inflammation. Serious complications of paranasal sinusitis include meningitis, epidural abscess, brain abscess, and cavernous sinus thrombosis (Fig. 8.3). Frontal osteomyelitis, which resulted from the direct extension of infection in patients with frontal sinusitis, is called “Pott puffy tumor.” Leukemia

and immunocompromised patients have an increased risk of fungal sinusitis frequently by aspergillosis and mucormycosis (Figs. 8.1 and 8.2).

8.3.2 Otitis Media and Mastoiditis

The term otitis media is derived from the inflammatory process of the middle ear cavity, which can be associated with mastoiditis. Direct extension of infection can cause meningitis, abscess, and sinus thrombosis (Fig. 8.4) (Ghosh et al. 2011). In Gradenigo syndrome, there is a triad of purulent ear discharge, pain in the 5th nerve dermatome, and ipsilateral 6th nerve palsy (Faerber et al. 2008a). Chronic otitis media can be complicated by middle ear effusion, cholesteatoma, granulation tissue, and ossicle or adjacent bone erosions.

8.3.3 Retropharyngeal Abscess

Retropharyngeal abscess is usually the result from suppurative lymphadenitis associated with head and neck infection, including tonsillitis, sinusitis, or dental infection (Cervantes et al. 2008). Although rare, it can be caused by pharyngeal perforation. On neck lateral radiography, there would be straightening of the cervical lordosis or even reversed curve (kyphosis) as well as prevertebral soft tissue thickening. However, CT scan is mandatory to see whether there is abscess formation (Fig. 8.5). Retropharyngeal abscess is the second most common after peritonsillar abscess in the head and neck region.

8.3.4 Lymphadenitis

Viral infection is very common in children and is the most common cause of enlarged cervical lymph nodes, so-called reactive hyperplasia. Infectious lymphadenitis is much more common than malignant lymphadenopathy in pediatric patients. Acute bacterial lymphadenitis is usually caused by *Staphylococcus aureus* and the streptococcus group (Cervantes et al. 2008). Imaging study is helpful when there is a suspicion of abscess formation. Enlarged lymph node is usually defined when measuring 1 cm in short axis. Lymph nodes are quite commonly encountered during performing neck ultrasound even in asymptomatic children. As long as they are elongated in shape with central hilar echogenicity and less than 1 cm in short axis, they represent reactive lymph node hyperplasia in most cases (Fig. 8.6). Whenever there is the possibility of malignant adenopathy, biopsy is needed for confirmation.

8.3.5 Kikuchi Disease

Kikuchi disease or histiocytic necrotizing lymphadenitis is a self-limiting disorder of unknown cause and characterized by painful cervical adenopathy (Han et al. 2009). It is more common in Asian children, and unlike in adult population, it has been described slightly more prevalent in boys. Cervical adenopathy has a tendency for predilection in posterior cervical location (level V). CT shows multiple, either bilateral or unilateral, cervical lymphadenopathy of clustered lymph nodes with or without internal necrosis (Figs. 8.7 and 8.8). Calcification is not a typical finding of Kikuchi disease. Radiological findings of Kikuchi disease can be similar to those of tuberculous lymphadenitis or lymphoma.

8.3.6 Kawasaki Disease

Kawasaki disease, also known as mucocutaneous lymph node syndrome, is an acute febrile vasculitis of unknown cause, which is more common in the Far East region. Cervical lymphadenopathy is one of the diagnostic criteria for Kawasaki disease. In 20–25 % of untreated patients, they can develop coronary artery aneurysm. Fever with cervical swelling is the major presenting symptom in many patients. Atypical Kawasaki disease presented as deep neck infection has been described (Roh et al. 2011), and CT may show findings of retropharyngeal fluid collection and edematous and inflammatory changes along with cervical lymphadenitis (Fig. 8.9).

8.3.7 Infectious Mononucleosis

Infectious mononucleosis is an acute infectious disease caused by Epstein-Barr (EB) virus. Cervical lymphadenopathy is quite common and can be associated with splenomegaly, pharyngitis, skin rash, or hepatomegaly. It is usually benign and self-limiting; however, rare but serious complications such as airway compression or spleen rupture can occur (Gayer et al. 2003). On CT through the neck, there are bilateral conglomerates of multiple enlarged lymph nodes, which usually show homogeneous enhancement without internal necrosis or calcification (Fig. 8.10).

8.3.8 Tuberculosis

Mycobacterium tuberculosis, *Mycobacterium bovis*, and *Mycobacterium avium-intracellulare* can cause cervical

lymphadenitis. In imaging study, there would be enlarged lymph nodes with central necrotic areas with or without calcifications. Tuberculous lymphadenitis in the neck is also known as scrofula, which is the most common extrapulmonary manifestation of tuberculous infection. Tuberculous abscess appears to be an irregular complex echogenic lesion on ultrasound rather than cystic cavity (Fig. 8.11).

8.3.9 Sialadenitis

The diagnosis of acute parotitis, usually viral in origin, is usually made on the basis of clinical findings, and thus imaging study is not routinely performed. Acute bacterial sialadenitis is not common in children. CT shows diffuse glandular enlargement with intense enhancement (Figs. 8.12 and 8.13). Chronic or recurrent sialadenitis is caused by bacterial infections, autoimmune or granulomatous diseases, or of unknown origin (Gadodia et al. 2010). Ultrasound shows diffuse enlargement of the gland with small hypoechoic areas representing dilated ducts.

8.3.10 Branchial Arch Anomaly

Branchial anomalies occur in the form of sinuses, fistulas, and cysts, which can be seen anywhere from the upper neck down to the mediastinum. The first branchial anomalies are related to the parotid gland and the external auditory canals. Anomalies of the second branchial arch are usually seen as fistulas or cysts extending from the tonsillar fossa to the skin along the anterior margin of the sternocleidomastoid muscle (Fig. 8.16).

Anomalies of the third and fourth branchial arches are encountered from time to time, and it is not so easy to differentiate them (Cervantes et al. 2008; Thomas et al. 2010). They extend from the pyriform sinus to the neck surface, above (third) or below (fourth) the level of the superior laryngeal nerve. In cases of recurrent thyroiditis or perithyroiditis, especially when left-sided, it is highly suspicious to be related to the fourth arch anomaly (Figs. 8.14 and 8.15).

8.3.11 Thyroglossal Duct Cyst

Thyroglossal duct cyst is a midline cystic mass of the neck, typically below the hyoid bone, embedded within the strap muscles. Ultrasound shows a well-demarcated cystic mass which may contain echogenic solid-appearing component when complicated. It would be more diagnostic on the basis of imaging studies when the cyst is found to be connected to the hyoid bone (Figs. 8.17 and 8.18).

8.4 Head and Neck Trauma

8.4.1 Nasal Bone Fracture

The nasal bone consists of two parallel bony plates joining at the midline (internasal suture) and articulates with ethmoid bones superiorly, maxillary bones laterally (nasomaxillary suture), and the nasal septum (inside the nose). The anterior superior part of the maxillary bone is called the frontal process of the maxilla, which is frequently injured when there is direct nasal trauma. Lateral radiography and exaggerated Waters projection may be helpful for detecting the nasal bone fracture. Nasal bone fractures can be simple, comminuted, and/or depressed. CT can show the exact location and extent of the nasal bone fractures as well as other facial bone injuries (Fig. 8.19).

8.4.2 Orbital Fracture

The orbit consists of seven bones – frontal, zygomatic, ethmoid, maxillary, sphenoid, palatine, and lacrimal bones. Orbit blowout fractures more commonly involve inferior or medial walls, which are relatively weak and easily broken by direct blows on the eye. The extraocular muscles can be entrapped through bony defects resulting in limitation of ocular muscle motion and diplopia (Figs. 8.20 and 8.21).

Orbital roof (frontal) fracture is more common in children than in adults, and it may be associated with an intracranial injury – pneumocephalus, cerebral contusion, or extraaxial hemorrhage. Plain radiography is not sufficient to show the extent and severity of the orbital fracture, and in many cases, CT is the best choice for detailed evaluation.

8.4.3 Temporal Bone Fracture

The temporal bone consists of the squamous, tympanic, petrous, and mastoid portions. The temporal bone is involved in more than 20 % of basal skull fractures. Temporal bone fractures are either longitudinal or transverse, depending on their orientation relative to the long axis of the temporal bone. Longitudinal fractures may show facial nerve palsy and ossicular disruption, resulting in conductive hearing loss, whereas transverse fractures more commonly involve sensorineural hearing loss (Figs. 8.22 and 8.23). CSF leaks are less common in transverse type.

8.4.4 Cervical Injury

Any cervical spine injury can lead to devastating results, and early recognition is often difficult. The first step for

evaluating cervical injury is plain radiographs, which should include cross-table lateral, AP, and optional open-mouth odontoid views. In low-risk patients, it is sufficient to take only plain radiographs. CT scan is reserved for high-risk patients who can get benefits in time and efficiency to prevent diagnostic delay and further injury. MRI is of benefit only for a small portion of patients who have neurological symptoms and signs.

The atlantodontoid distance on the lateral projection should be less than 4 mm, and prevertebral soft tissue thicknesses vary according to the age (Fig. 8.24).

Jefferson fracture is the classic atlas fracture due to axially directed compression force. Odontoid fractures are more common than isolated atlas fractures. Atlantoaxial rotatory subluxation is seen much more common in children than adults, presenting with pain and cock-robin neck deformity.

On AP or open-mouth odontoid view, the odontoid process is displaced toward the lateral mass of the atlas.

Spinal cord injuries without radiographic abnormality (SCIWORA) are more common in children, although true occult spinal injuries are less common than before, with the improved techniques of CT and MRI.

8.4.5 Head and Neck Foreign Body

Children are prone to penetrating injury in the head and neck region from any object like a toothbrush or a chopstick. Many objects are not radiopaque on the plain radiographs, and CT is superior to visualize the extent of tract and soft tissue injury (Fig. 8.25) (Faerber et al. 2008b; Pinto et al. 2012).

8.5 Illustrations: Infectious and Traumatic Diseases

8.5.1 Fungal Paranasal Sinusitis

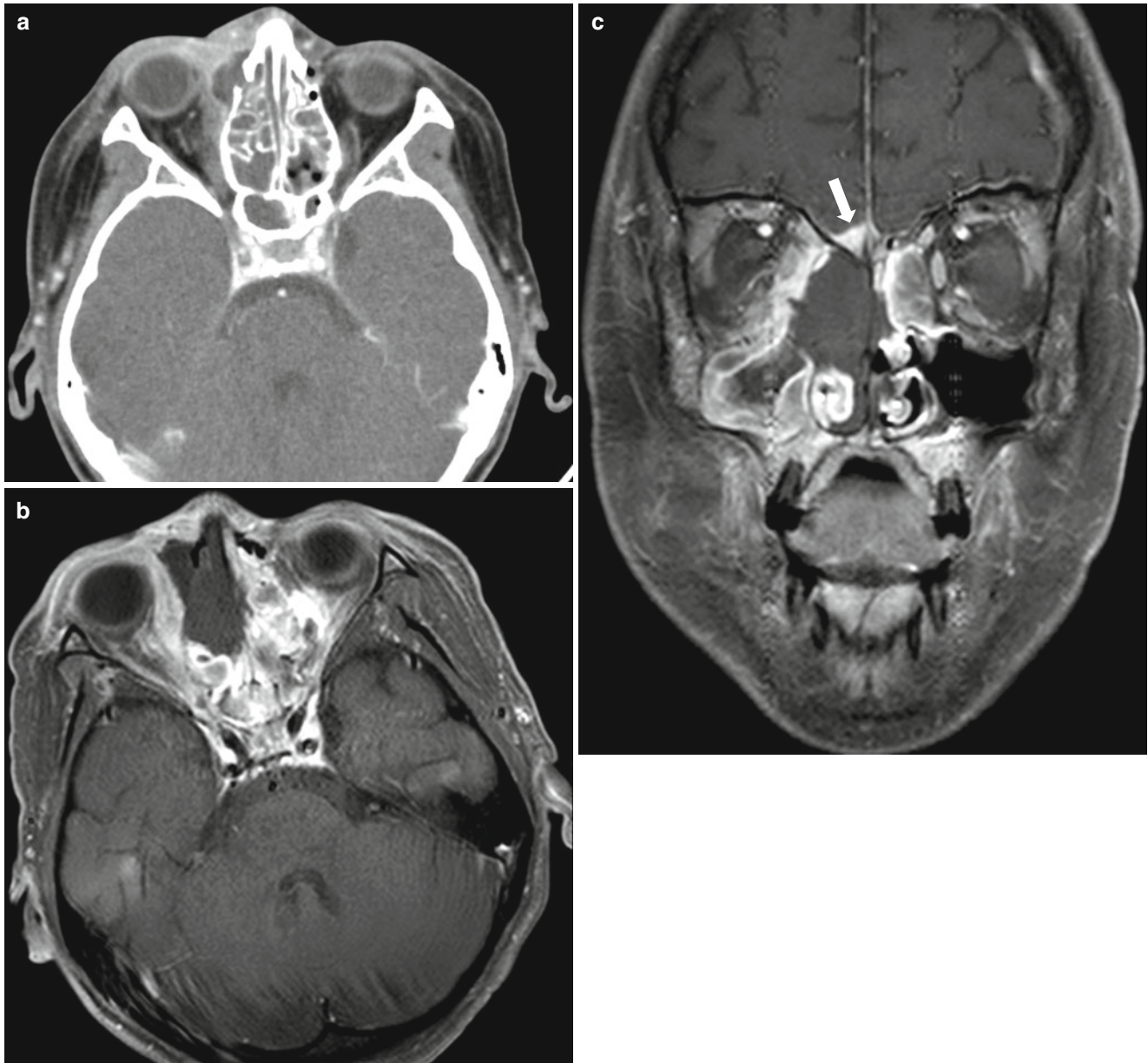


Fig. 8.1 Fungal sinusitis in leukemic patient. (a) Postcontrast CT shows sinusitis in both ethmoid and sphenoid sinuses extending to the right medial orbit with subperiosteal abscess formation. (b, c) Fat-suppressed T1-weighted axial (b) and coronal (c) images after gado-

linium administration show severe inflammatory changes in the nasal cavity and sinuses with right orbital and intracranial (*arrow*) extension. This patient was diagnosed of having acute myelocytic leukemia and invasive aspergillosis

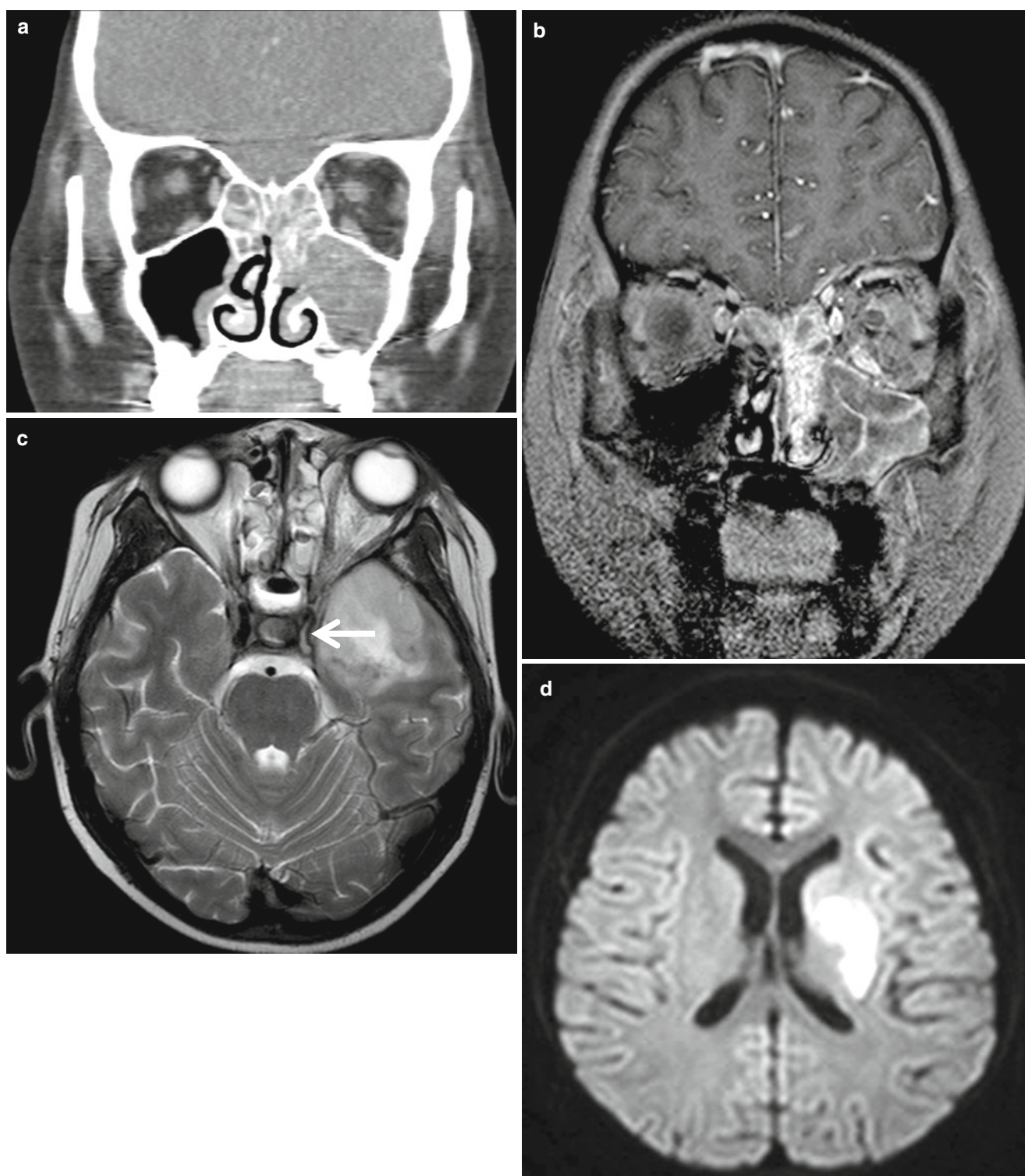


Fig. 8.2 Mucormycosis in leukemic patient. (a) Postcontrast coronal CT image shows total opacification in the left maxillary and both ethmoid sinuses. The medial wall of the left maxillary sinus is eroded, but no sinus expansion or calcification is noted. (b) Postcontrast fat-suppressed T1-weighted coronal image shows extensive sinus inflammation involving the bony structures. Meningeal enhancement is noted in

the left inferior frontal region, and left inferior rectus muscle is enhanced representing intraorbital extension. (c, d) T2-weighted axial image (c) shows brain parenchymal involvement in the left temporal lobe. Note the lack of signal void in the left internal carotid artery (arrow in c) and resultant ischemic infarction in the left basal ganglia on diffusion-weighted image (d)

8.5.2 Frontal Sinusitis with Meningitis

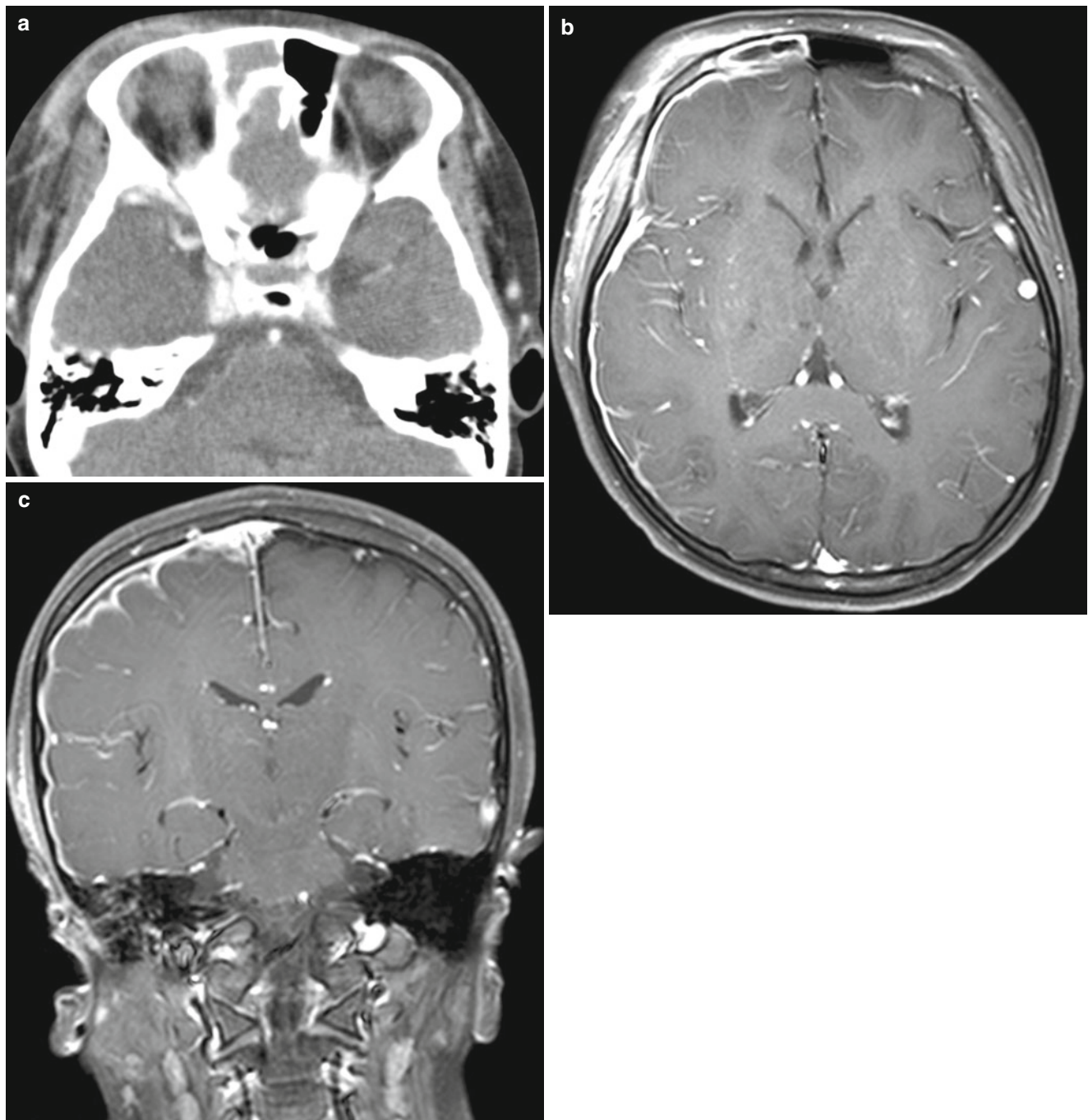


Fig. 8.3 Frontal sinusitis with meningitis in immunocompetent host. (a) Postcontrast axial scan shows right frontal sinus opacification and severe right periorbital soft tissue swelling. (b, c) Postcontrast fat-sup-

pressed T1-weighted axial (b) and coronal (c) images show right frontal sinusitis with surrounding inflammatory changes and diffuse meningeal enhancement in keeping with meningitis

8.5.3 Otomastoiditis with Meningitis

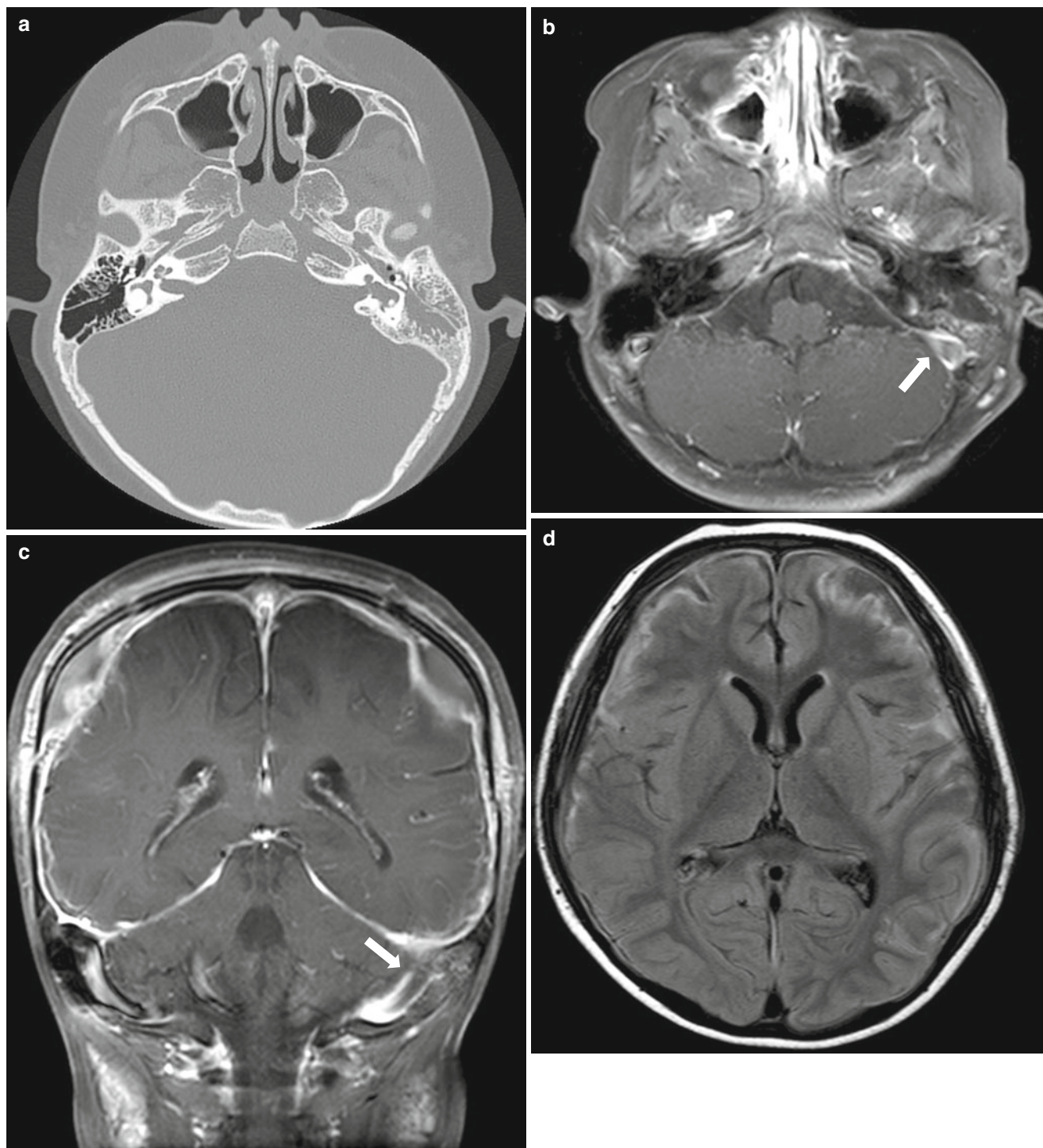


Fig. 8.4 Otomastoiditis with sinus thrombosis and recurrent pneumococcal meningitis. (a) Temporal bone CT shows abnormal soft tissue opacification in the left middle ear cavity and mastoid antrum/air cells. There is underlying congenital cochlear and vesicular dysplasia. Diffuse sclerosis is noted in the mastoid area. (b–d) MR postcontrast fat-suppressed T1-weighted axial (b) and coronal (c) images show

abnormal enhancement in the mastoid region and nonenhancing thrombosis in the left sigmoid sinus (arrows in b and c). Axial FLAIR image (d) reveals abnormal high signal intensity along the cortical gyri, extra-axial fluid collections, and diffuse meningeal enhancement, representing meningoencephalitis

8.5.4 Retropharyngeal Abscess

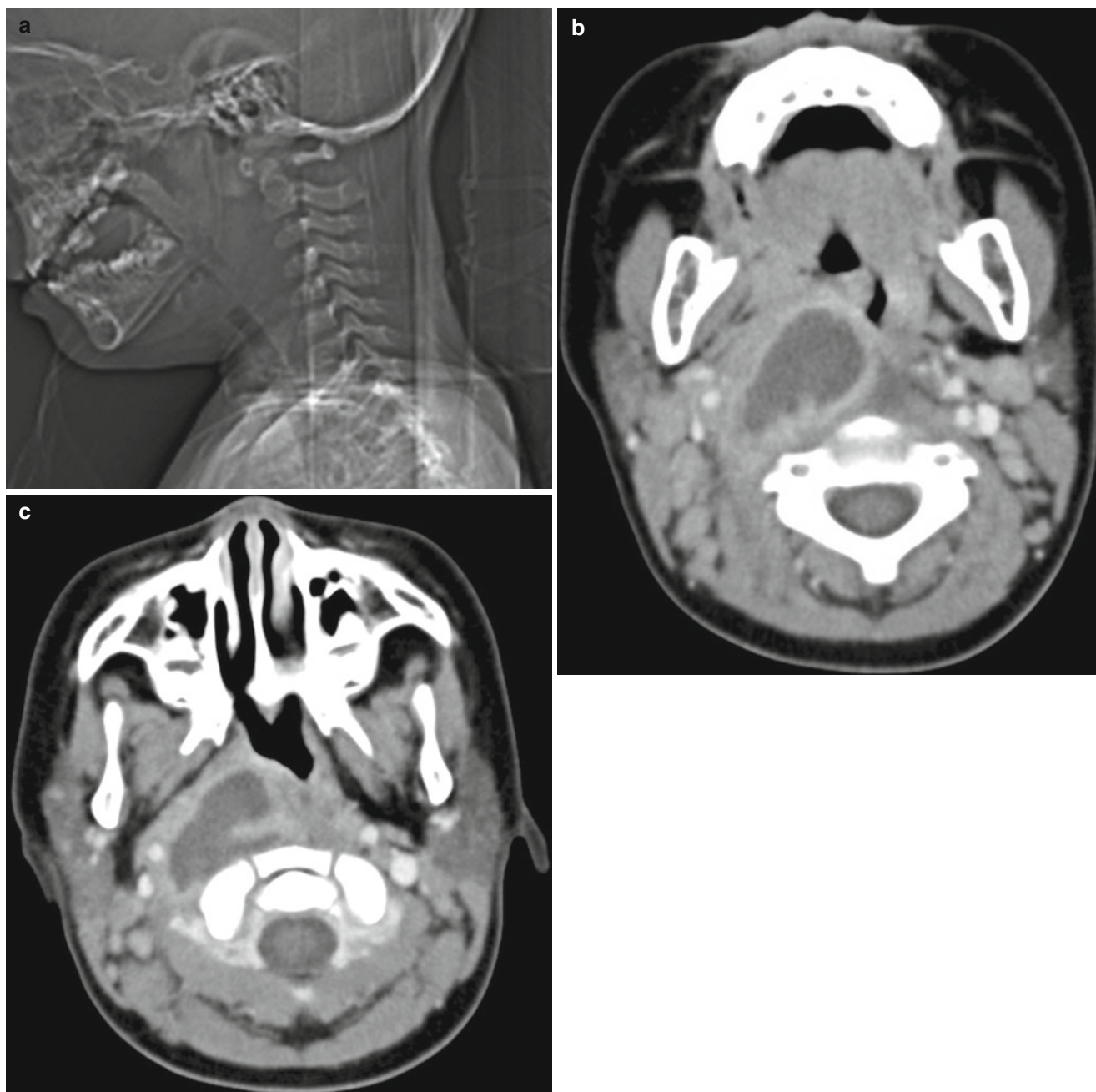


Fig. 8.5 Retropharyngeal abscess in a 3-year-old girl. (a) CT scout image shows widening of retropharyngeal prevertebral soft tissue space with oropharyngeal and hypopharyngeal airway obliteration. (b, c) Postcontrast CT scans at the mandible body level show a thick rim-

enhancing cavitary lesion in the right retropharyngeal space, which compresses the oropharyngeal airway to the opposite side. Pus was aspirated

8.5.5 Cervical Reactive Lymph Node Hyperplasia

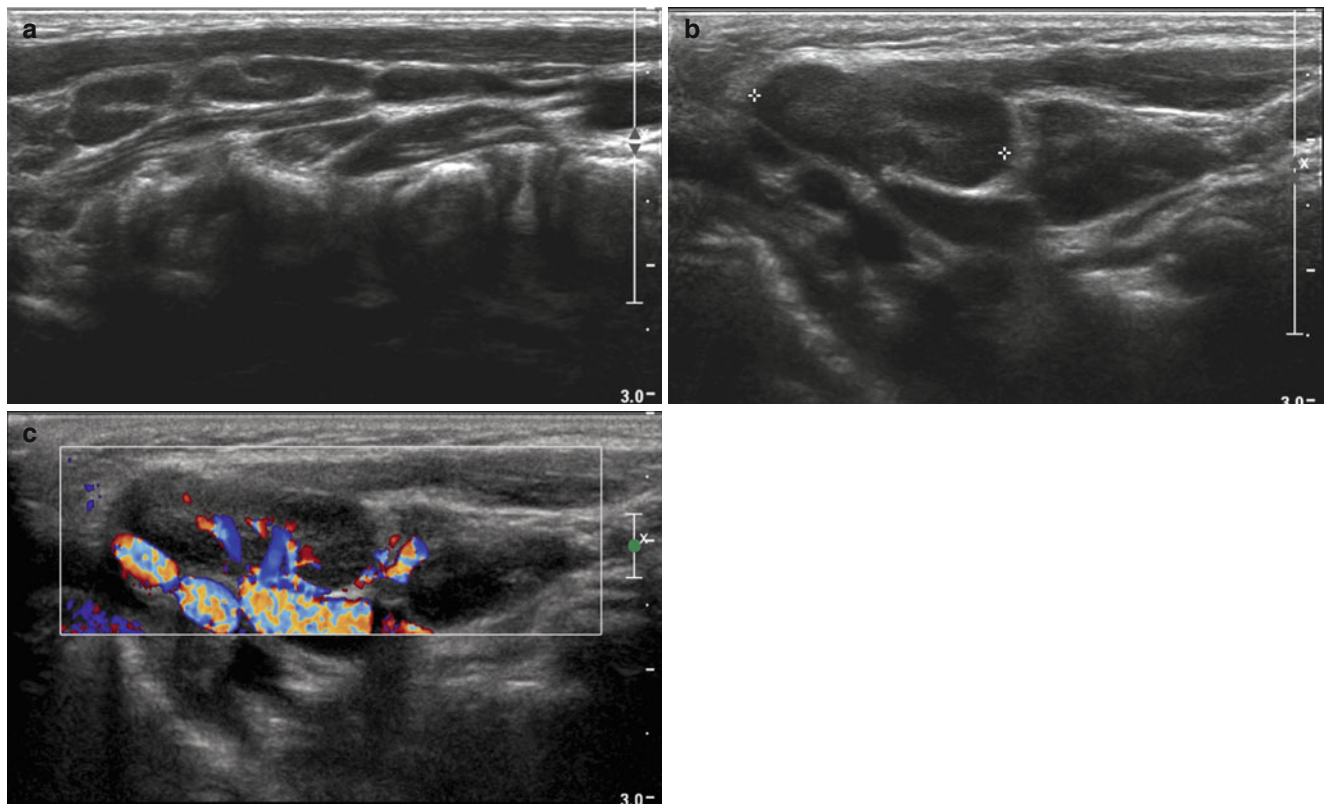


Fig. 8.6 Reactive lymph node hyperplasia in a 3-year-old boy who presented with mild fever and palpable nodules. (a, b) Ultrasound images through the right upper neck show multiple ovoid or elongated hypoechoic lesions with central linear echogenicity representing central

hilar structures, which is a characteristic finding of benign lymphadenopathy. (c) Color Doppler study reveals prominent but preserved central vascularity, which is also one of the findings of benign inflammatory lymph nodes

8.5.6 Kikuchi Disease

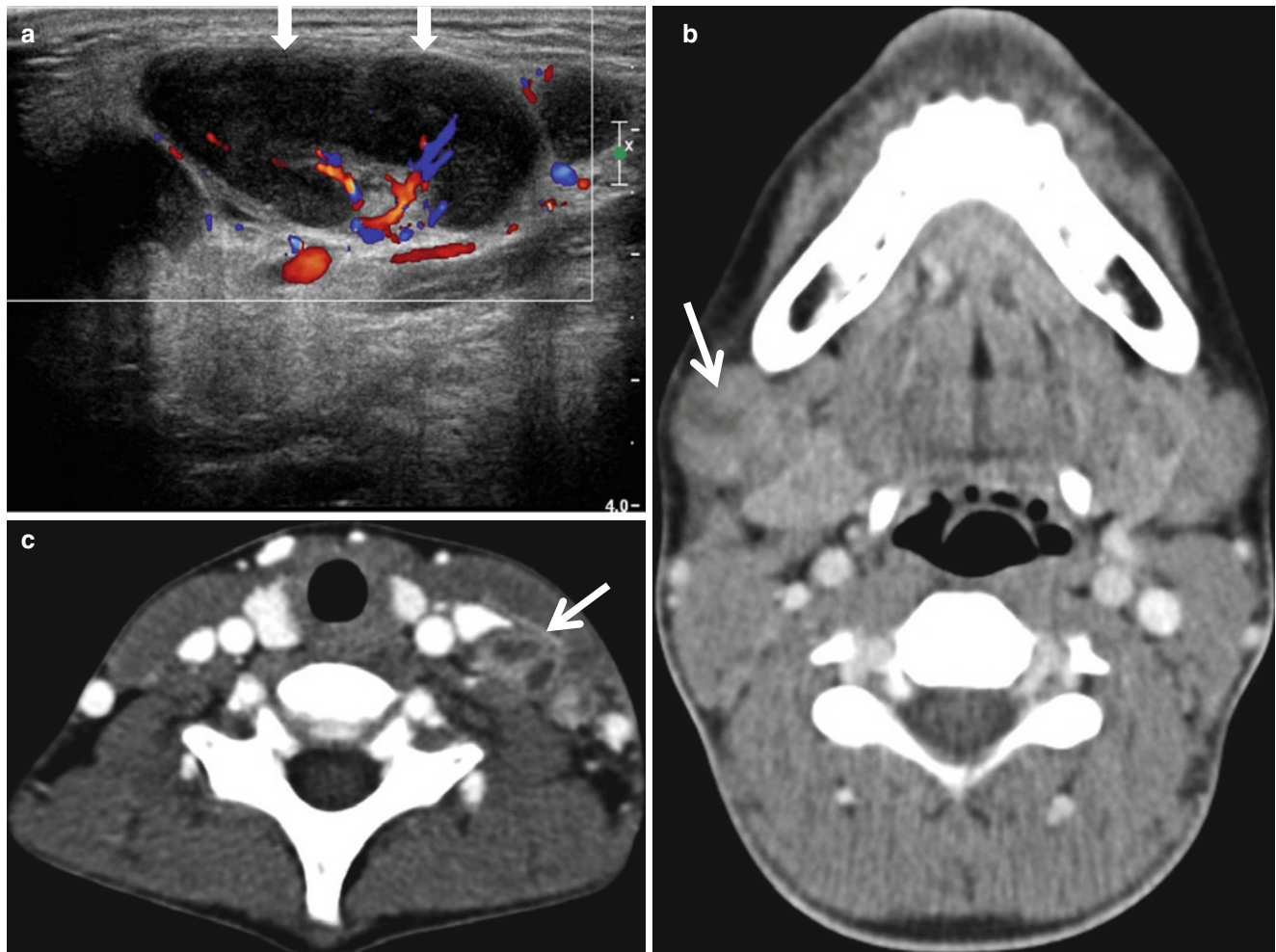


Fig. 8.7 Kikuchi disease in a 13-year-old boy. (a) Color Doppler ultrasound of the right submandibular region shows a large enlarged lymph node (arrows) with profound hypoechoogenicity and increased central vascularity. (b, c) Postcontrast CT through submandibular gland (b) and thyroid gland (c) show enlarged lymph nodes with internal low

density suggesting necrotic areas (arrows in b and c). Excisional biopsy of the cervical node revealed necrotizing lymphadenitis, consistent with Kikuchi lymphadenitis. No organism was identified on AFB and GMS staining

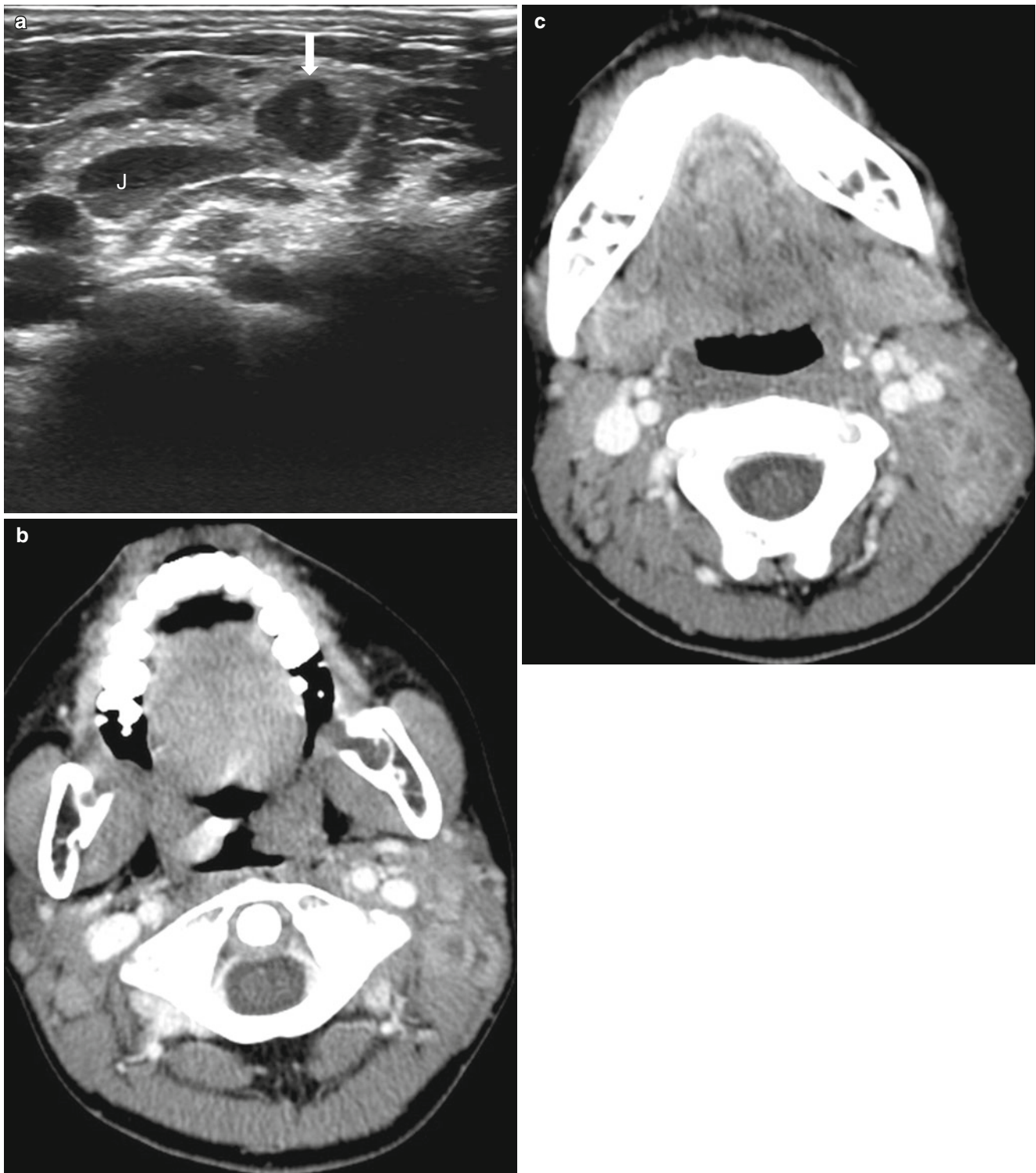


Fig. 8.8 Kikuchi disease in another 13-year-old boy. (a) Ultrasound of the left neck shows a lobulating contoured hypoechoic lesion (*arrow*) representing an enlarged lymph node just lateral to the internal jugular vein (*J*). (b, c) Postcontrast CT of the neck shows conglomerated lymph

nodes in the left posterior cervical space with rim enhancement suggesting internal necrosis. Biopsy confirmed Kikuchi disease. There is reactive lymph node hyperplasia in the right posterior neck as well

8.5.7 Kawasaki Disease (Mucocutaneous Lymph Node Syndrome)

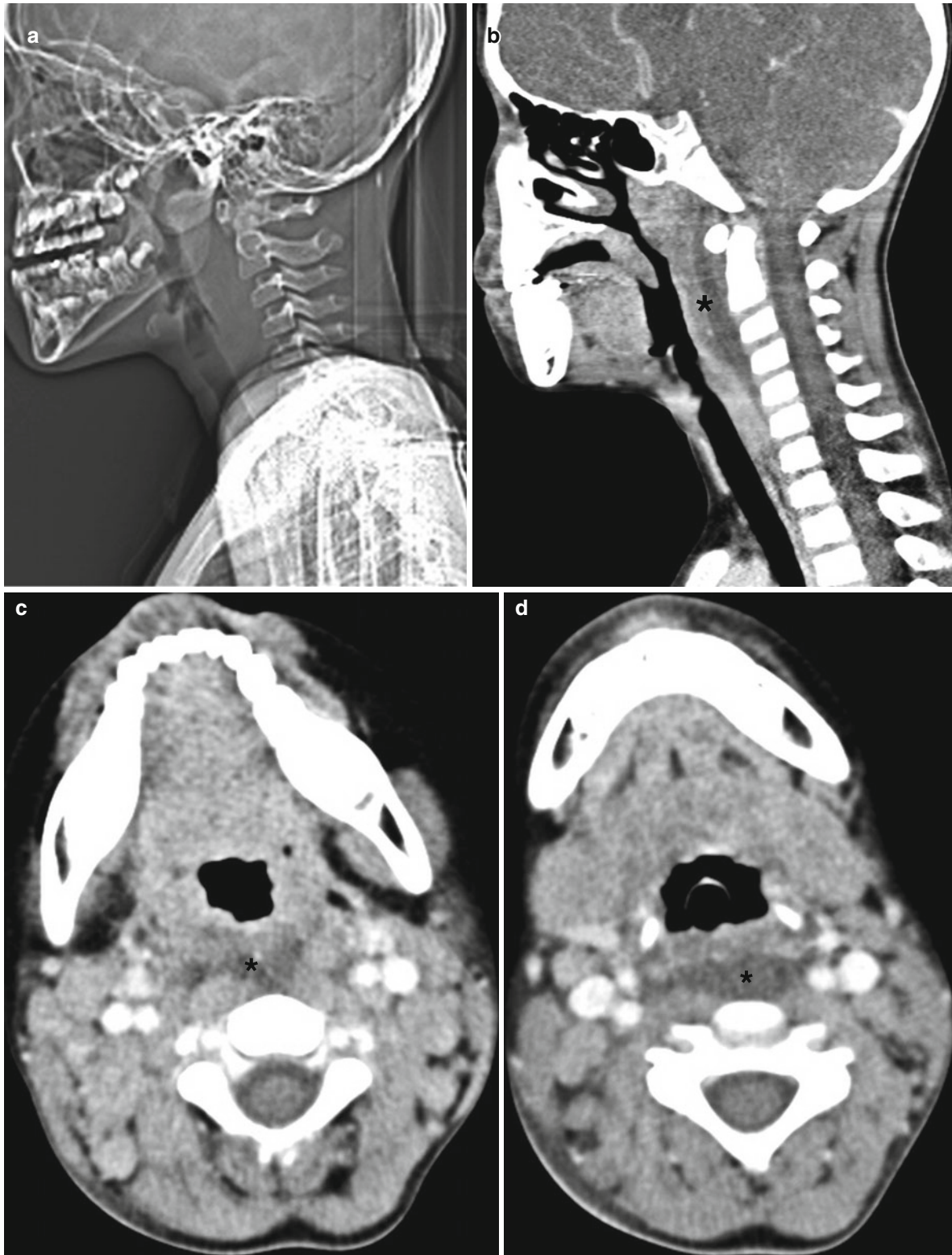


Fig. 8.9 Mucocutaneous lymph node syndrome in a 5-year-old boy. He had a history of prolonged fever, cervical adenopathy, skin rashes, strawberry tongue, and conjunctival injection, which fulfilled the diagnostic criteria for Kawasaki disease. (**a, b**) CT scout image (**a**) and sagittal reconstructed image (**b**) show retropharyngeal soft tissue space

widening with low attenuating collection (* in **b**) in the prevertebral region. (**c, d**) Axial postcontrast CT images show multiple enlarged lymph nodes along the bilateral jugular and spinal accessory chains. There is low attenuating edematous fluid collection in the retropharyngeal space (* in **c** and **d**)

8.5.8 Infectious Mononucleosis

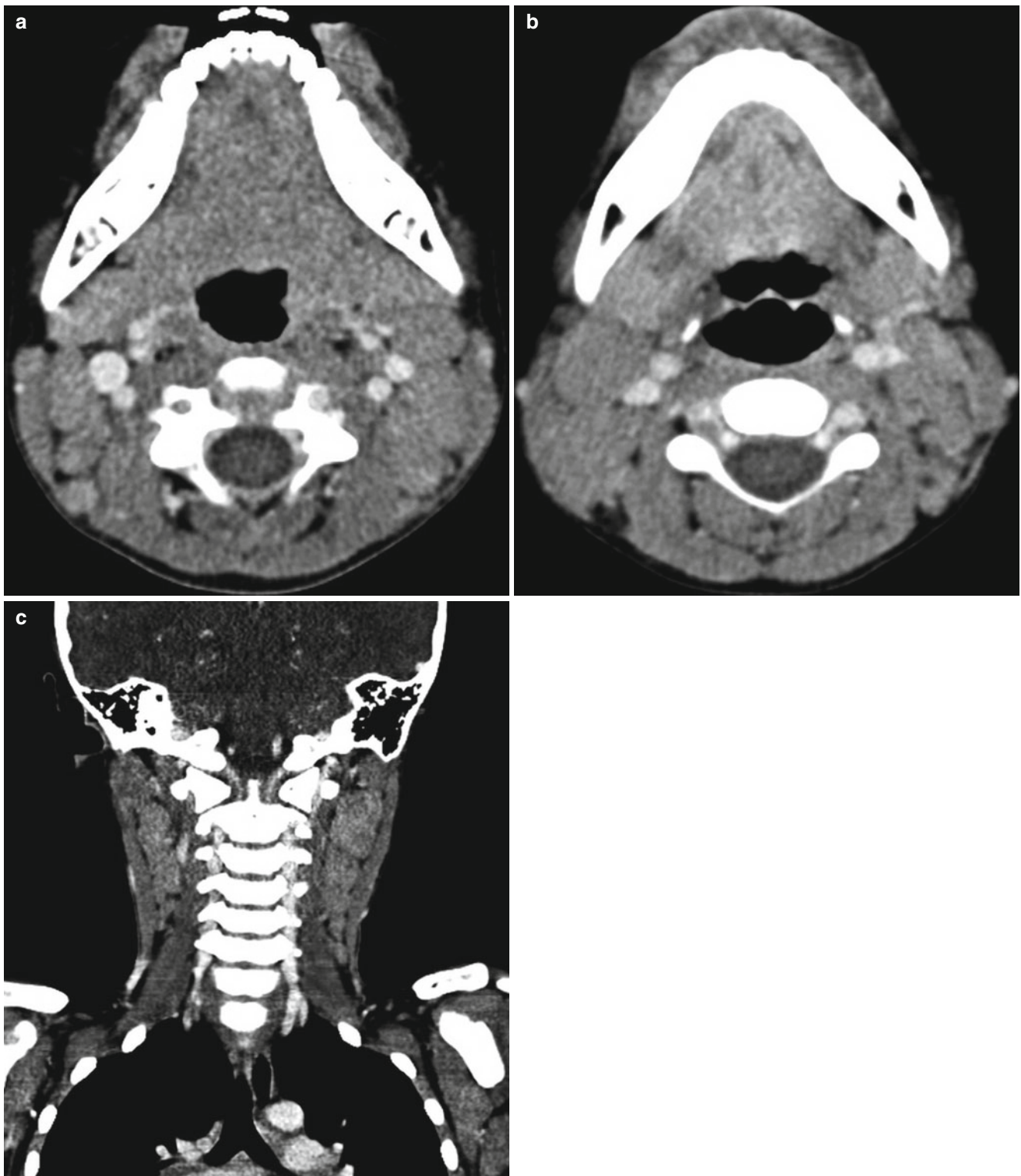


Fig. 8.10 Infectious mononucleosis in a 7-year-old boy with hepatosplenomegaly. His blood test showed atypical lymphocytosis and positive result for Epstein-Barr virus (EBV) viral capsid antigen (VCA)

IgM. (a–c) Postcontrast axial (a and b) and coronal (c) images show bilateral cervical lymphadenopathy, which is homogeneously enhanced

8.5.9 Tuberculous Cervical Lymphadenitis

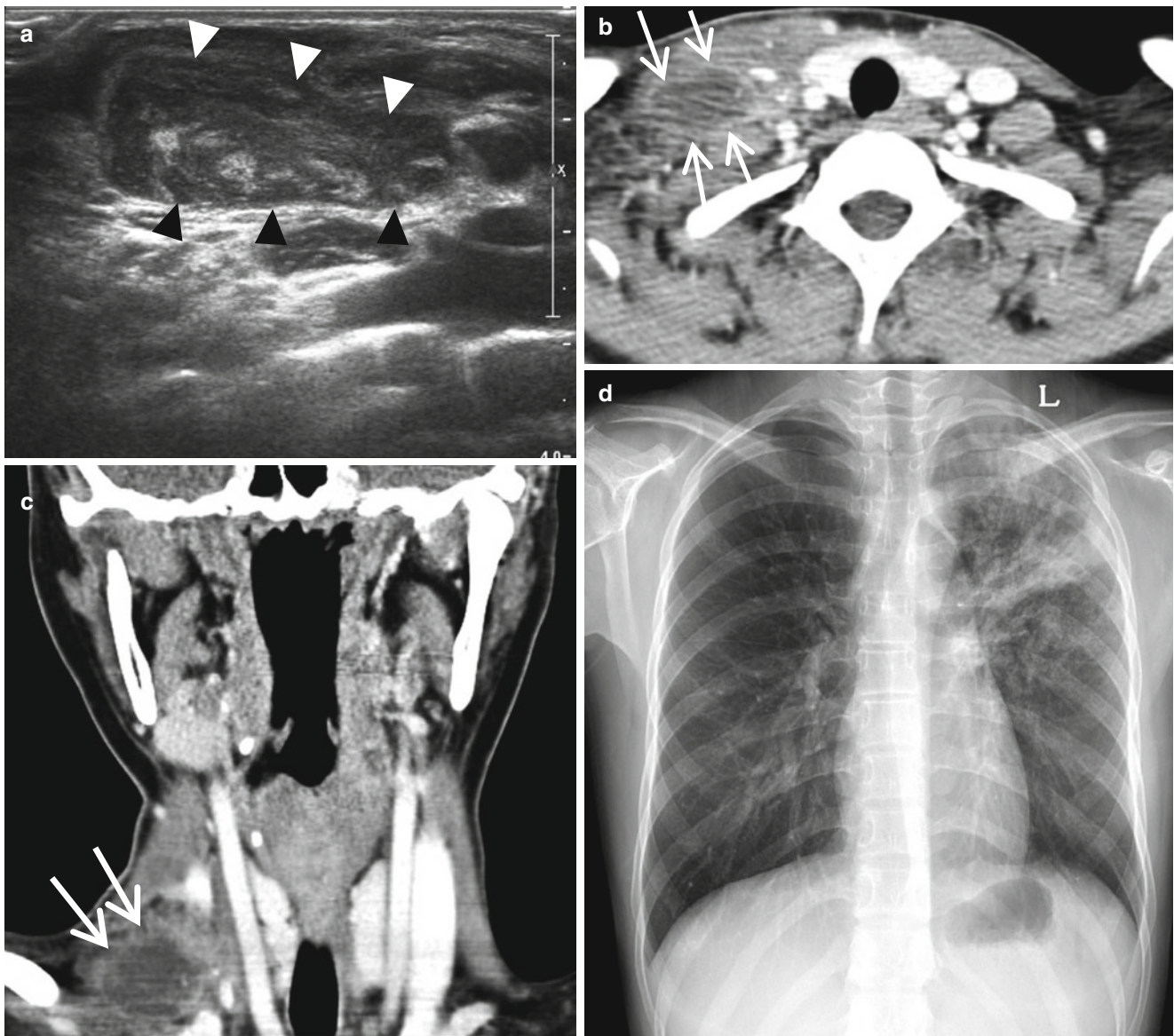


Fig. 8.11 Tuberculous cervical lymphadenitis. (a) Ultrasound shows an ill-defined hypoechoic lesion (*arrowheads*) in the right neck with internal hyperechoic foci. (b, c) Postcontrast axial (b) and coronal (c) CT images show a rim-enhancing abscess cavity (*arrows* in b and c)

in the right supraclavicular area. Ultrasound-guided aspiration revealed chronic granulomatous inflammation and positive result for *Mycobacterium tuberculosis* complex by PCR. (d) Chest PA radiograph shows active pulmonary tuberculosis in the left upper lobe

8.5.10 Sialadenitis

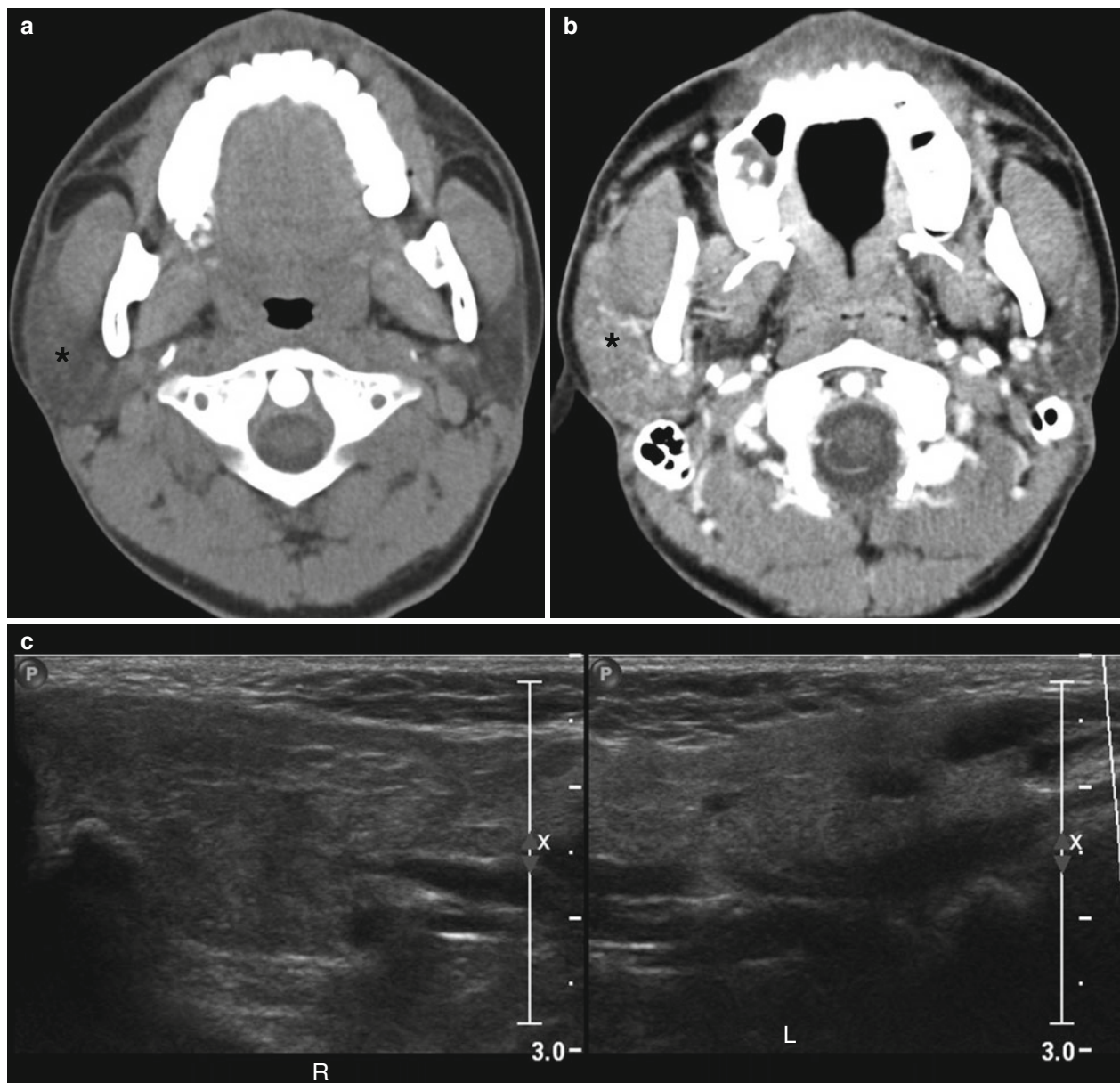


Fig. 8.12 Acute parotitis. (a, b) Precontrast (a) and postcontrast (b) CT images through the parotid gland show diffuse enlargement of the right parotid gland with increased enhancement, in keeping with sialadenitis of the right parotid gland (* in a and b). (c) Compare the enlarged right (R) parotid gland to the left side (L) on neck ultrasound

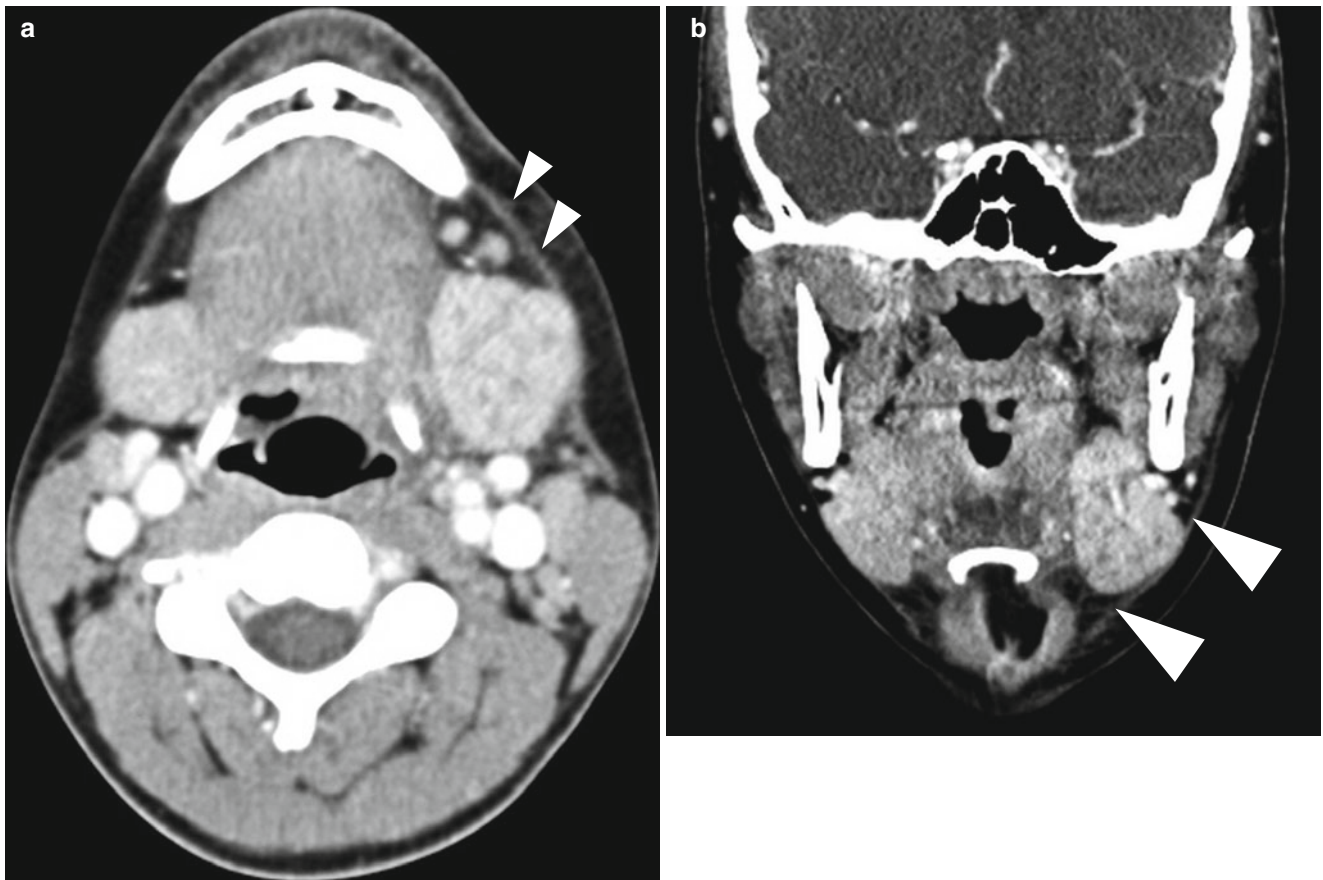


Fig. 8.13 Sialadenitis of submandibular gland. (a, b). Postcontrast axial (a) and coronal (b) images show asymmetric enlargement with prominent enhancement of the left submandibular gland. There is associated fascial thickening (*arrowheads*) with small reactive lymph nodes

8.5.11 Pyriform Sinus Fistula

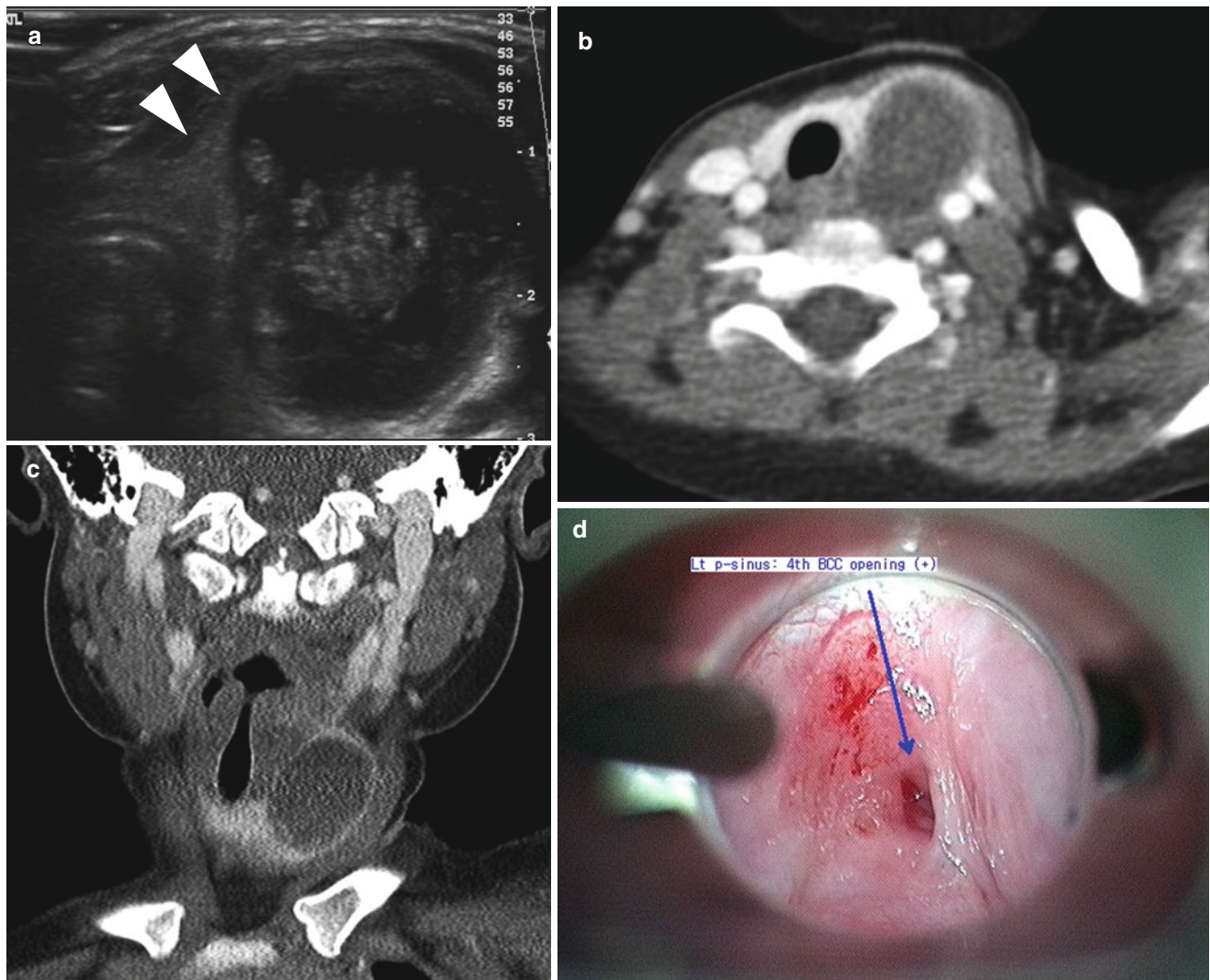


Fig. 8.14 Pyriform sinus fistula with thyroid abscess. (a) Ultrasound of the thyroid gland shows mainly cystic mass with internal debris in the left thyroid lobe. There is a beak-like appearance of the left thyroid tissue (*arrowheads*) around the cystic mass. (b, c) Postcontrast axial (b)

and coronal (c) CT images show cystic lesion with a thin smooth wall surrounded by enhancing thyroid tissue. Pus was drained by ultrasound-guided aspiration. (d) At surgery, there was an opening in the left pyriform sinus

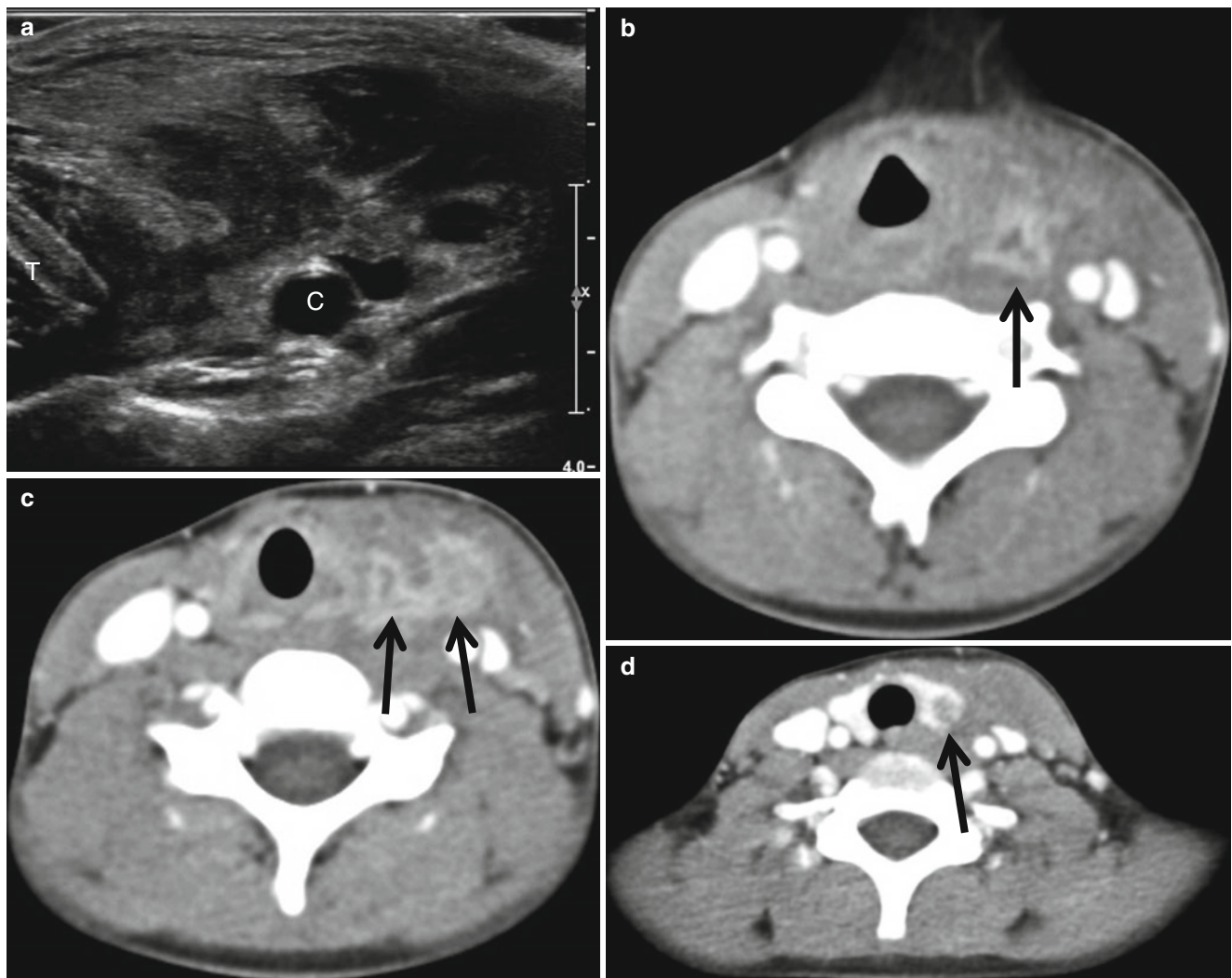


Fig. 8.15 Pyramidal sinus fistula with perithyroiditis in an 8-year-old boy. (a) Ultrasound of the left lower neck shows irregular hypoechoic area in the perithyroidal area extending to the region of pyramidal sinus in keeping with inflammation with almost abscess formation.

C common carotid artery, *T* thyroid cartilage. (b–d) Serial postcontrast axial CT images show irregular rim-enhancing lesion extending from the left pyramidal sinus (arrow in b) to lower lateral neck (arrows in c) and left thyroid gland (arrow in d)

8.5.12 Second Branchial Cleft Fistula

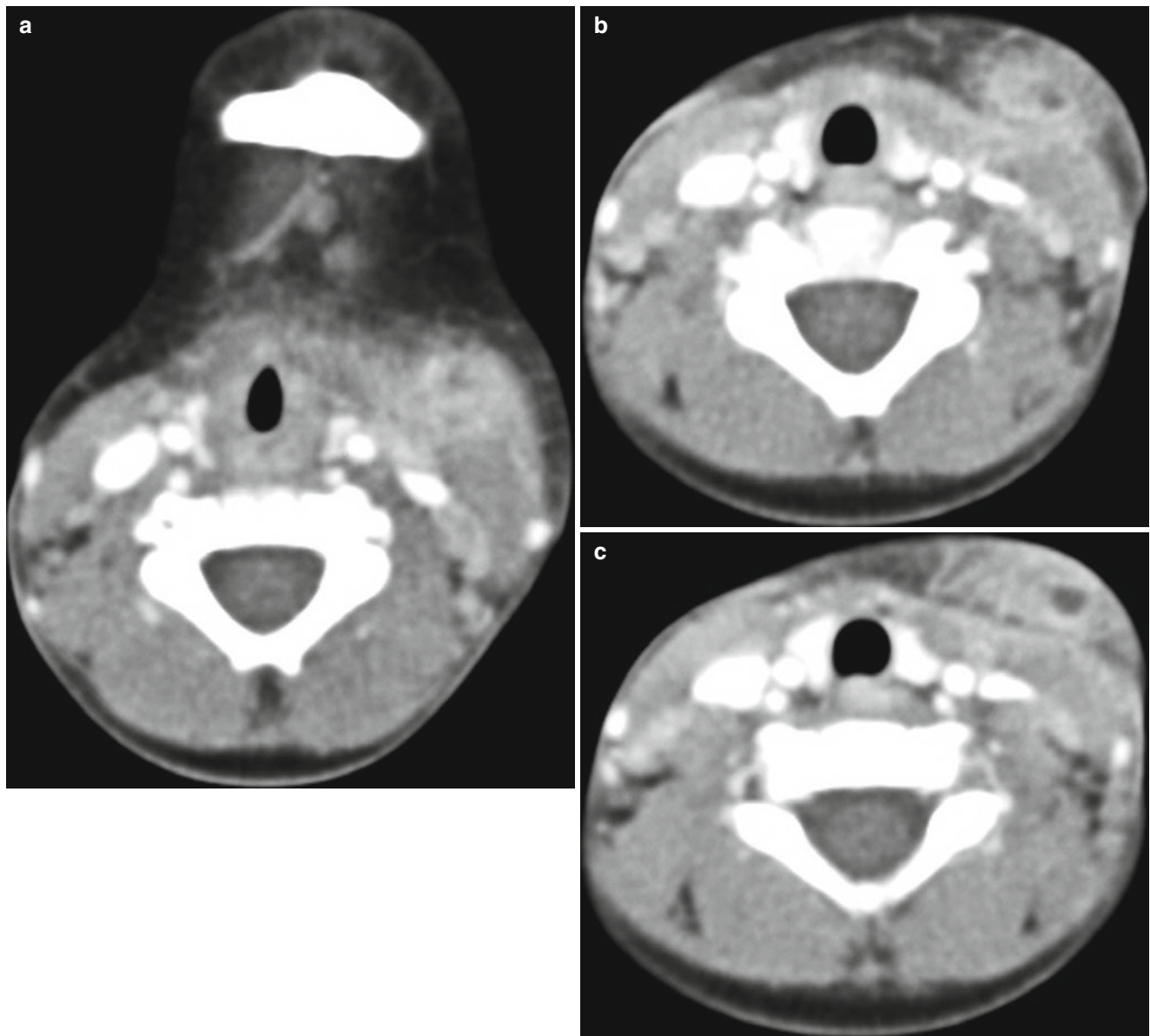


Fig. 8.16 Second branchial cleft fistula with infection in a 1.4-year-old girl. (**a–c**) Postcontrast axial CT images show rim-enhancing low attenuating lesion in the left anterior neck subcutaneous layer along the

anterior margin of the left SCM muscle. Note the perilesional infiltration with loss of tissue planes suggesting inflammation associated with small abscess

8.5.13 Thyroglossal Duct Cyst

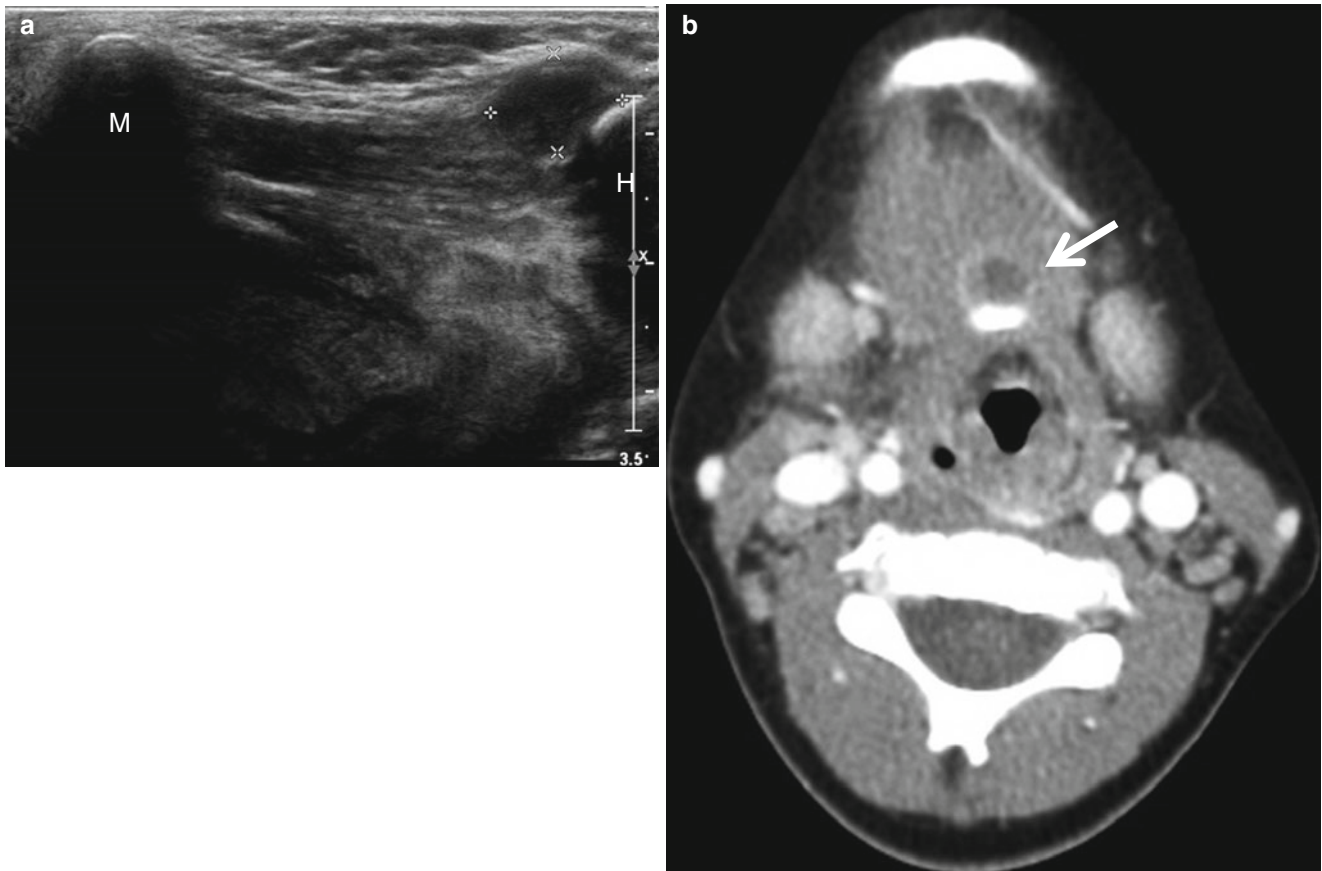


Fig. 8.17 Infected thyroglossal duct cyst. **(a)** Longitudinal ultrasound of the upper midline neck shows a small anechoic cystic lesion (marked by *cursors*) abutting the hyoid bone (*H*). *M* mandible. **(b)** Postcontrast

CT shows a small round cystic mass with rim enhancement (*arrow*) just anterior to the hyoid bone

8.5.14 Mandible Condylar Fracture

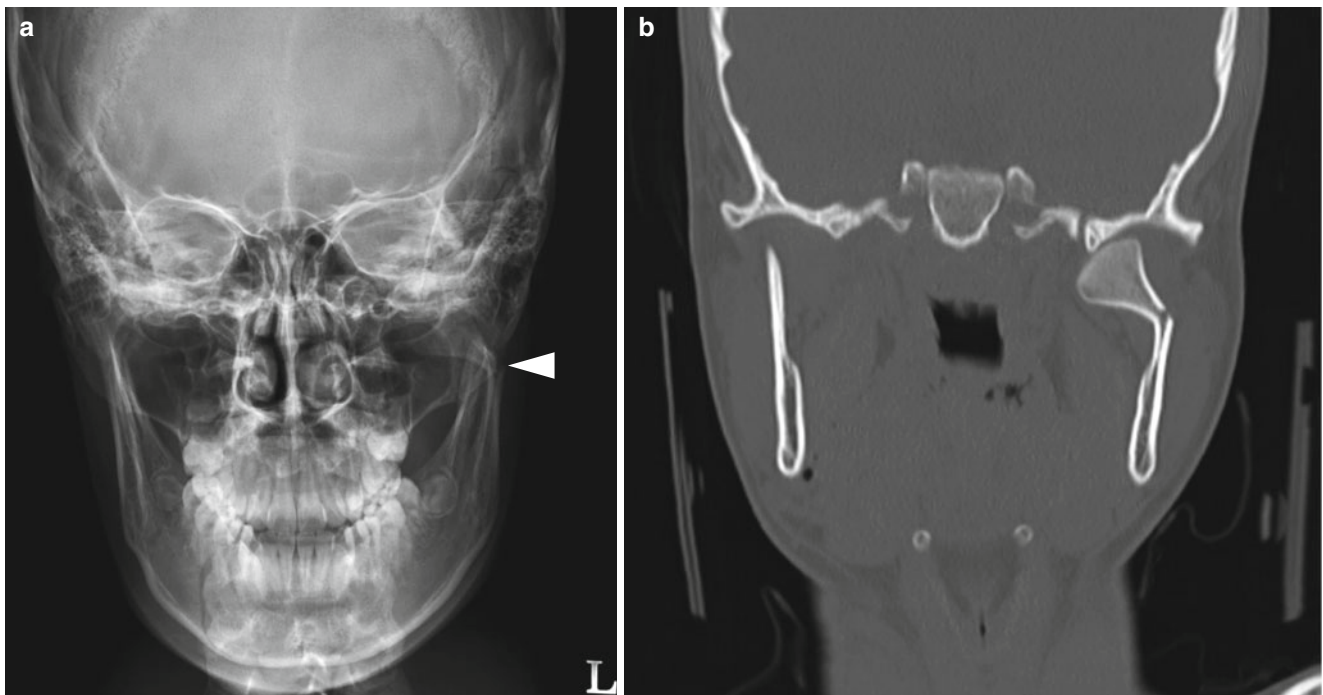


Fig. 8.18 Mandible condylar fracture. (a) Skull PA radiograph shows angulated left mandibular condyle (*arrowhead*) suggesting a fracture. (b) Coronal reformatted CT clearly shows left condylar neck fracture

with angulation with subluxed condylar head from the left temporomandibular joint

8.5.15 Nasal Bone Fracture

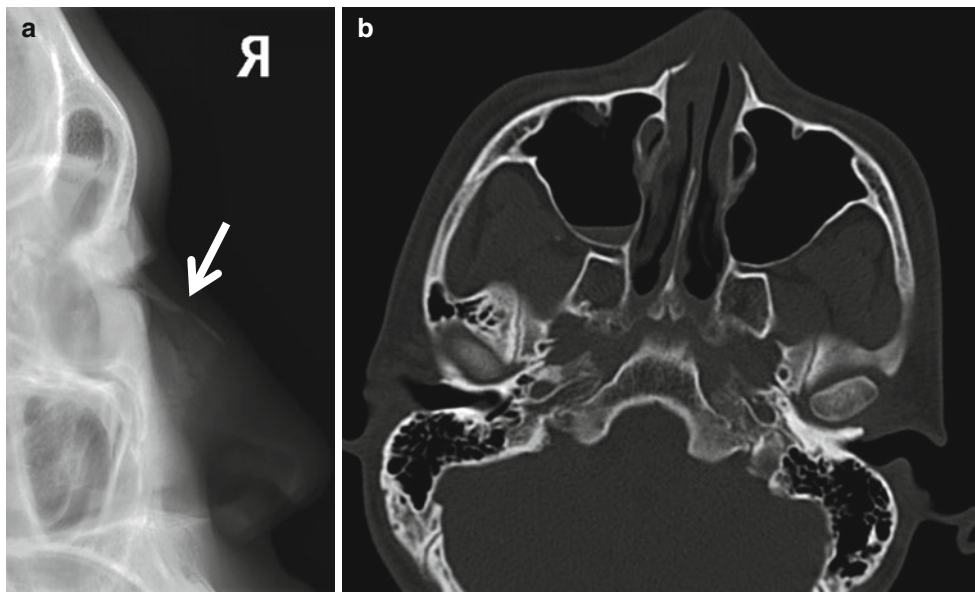


Fig. 8.19 Nasal bone fracture. **(a)** Nasal bone lateral radiograph shows focal cortical disruption in the nasal bone (*arrow*). **(b)** Facial bone CT shows right nasal bone fracture with minimally displaced bone

fragment. There is an air-fluid level in the right maxillary sinus, presumably hemosinus

8.5.16 Orbital Blowout Fracture

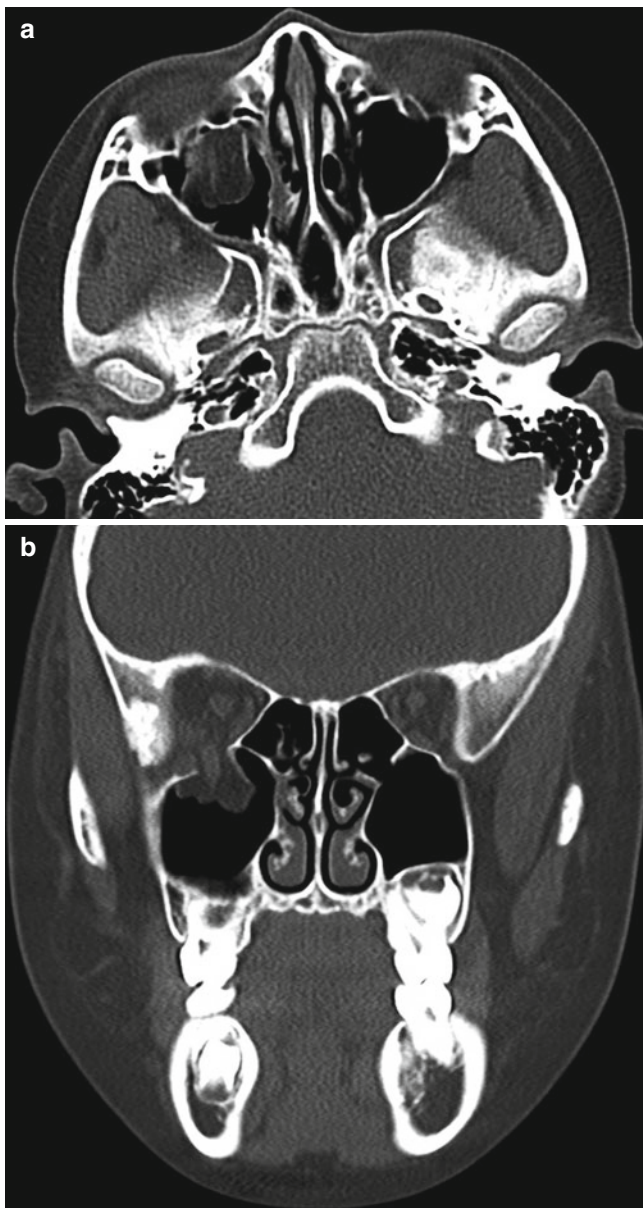


Fig. 8.20 Inferior orbital blowout fracture. (a, b) Axial (a) and coronal (b) facial bone CT show a large defect in the right orbital floor with herniation of orbital fat into the right maxillary sinus. Right inferior rectus muscle is included in the herniated content

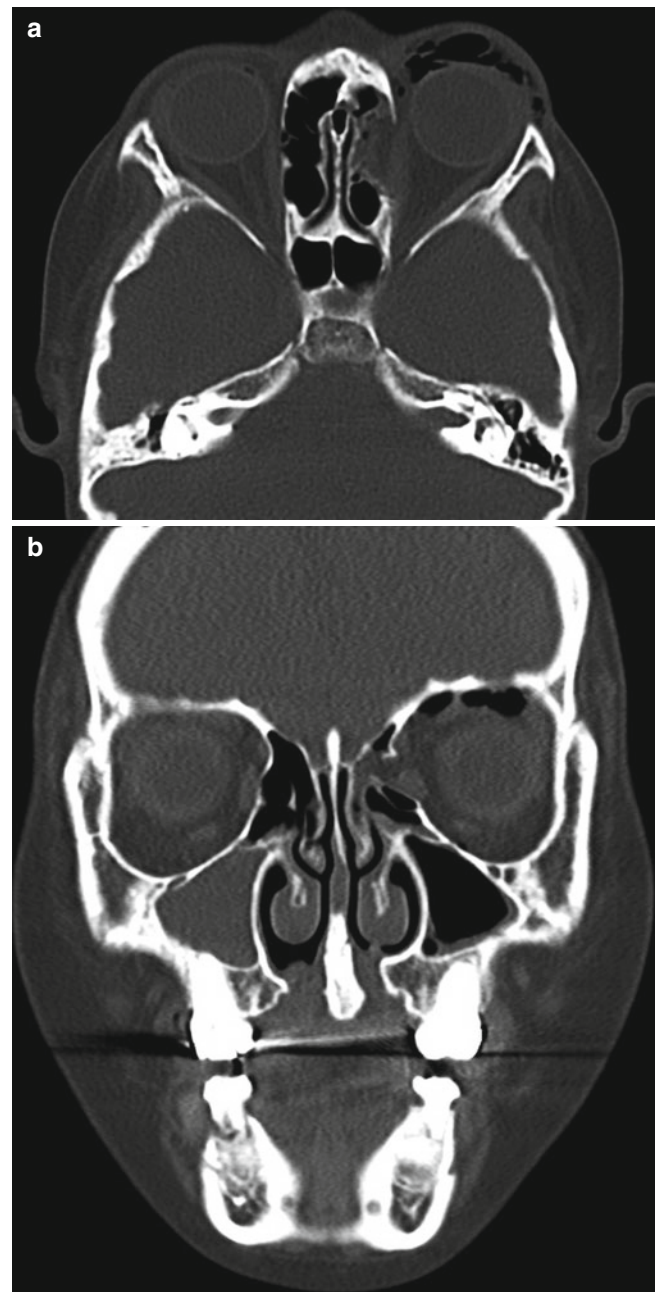


Fig. 8.21 Medial orbital blowout fracture. (a, b) Axial (a) and coronal (b) facial bone CT scans show a large defect in the medial wall of the left orbit with orbital fat herniation. There seems to be encroachment of the medial rectus muscle, which is asymmetrically thickened due to edema. Periorbital emphysema is associated. Right maxillary sinus opacification is an incidental finding

8.5.17 Temporal Bone Fracture

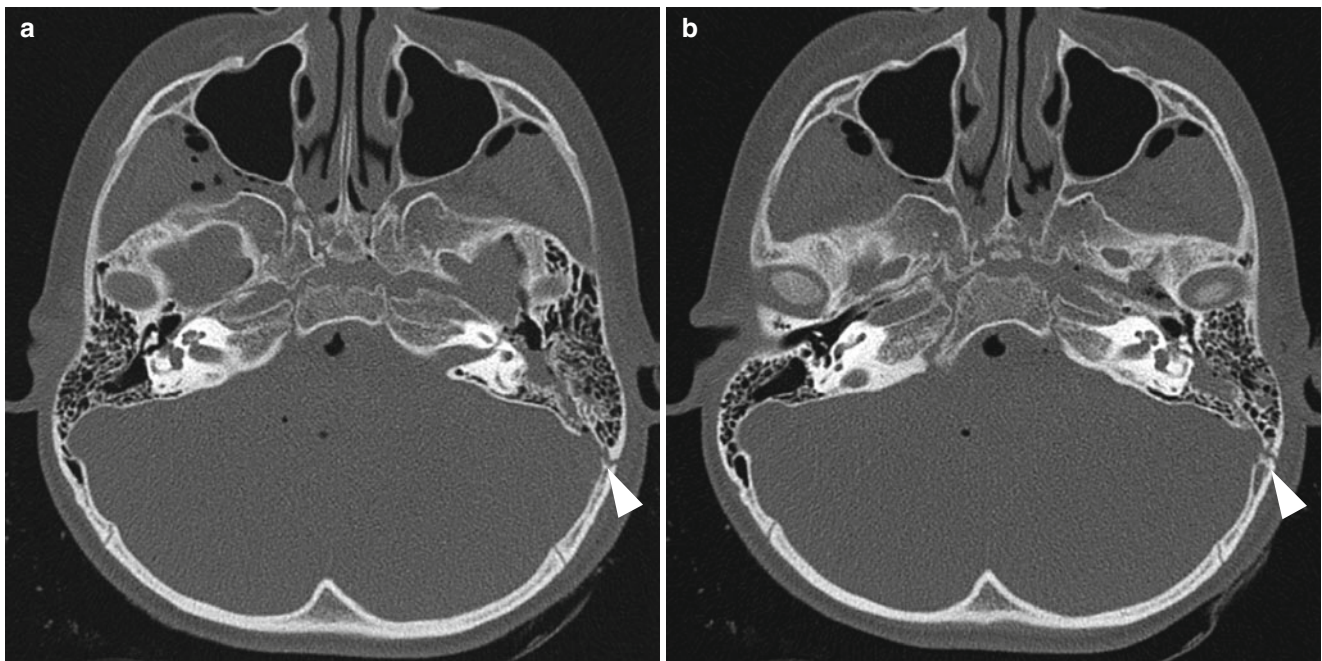


Fig. 8.22 Longitudinal temporal bone fracture with bloody otorrhea and ipsilateral facial nerve palsy. (**a, b**) Thin-section temporal bone CT scans show a longitudinal fracture through the middle ear cavity and mastoid antrum and air cells (*arrowheads* in **a** and **b**). The middle ear

ossicles appear intact. Small amount of pneumocephalus is noted in the posterior fossa. Because there was associated skull base fractures, soft tissue air densities are seen in both the infratemporal fossae

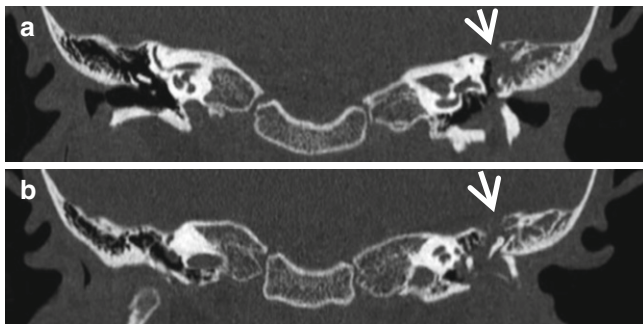


Fig. 8.23 Transverse temporal bone fracture in a 7-year-old boy. (**a, b**) Thin-section temporal bone CT with coronal reconstruction shows a cortical bone breakdown (*arrows* in **a** and **b**) through the left middle ear cavity. Note ossicular disruption

8.5.18 Cervical Spine Dislocation

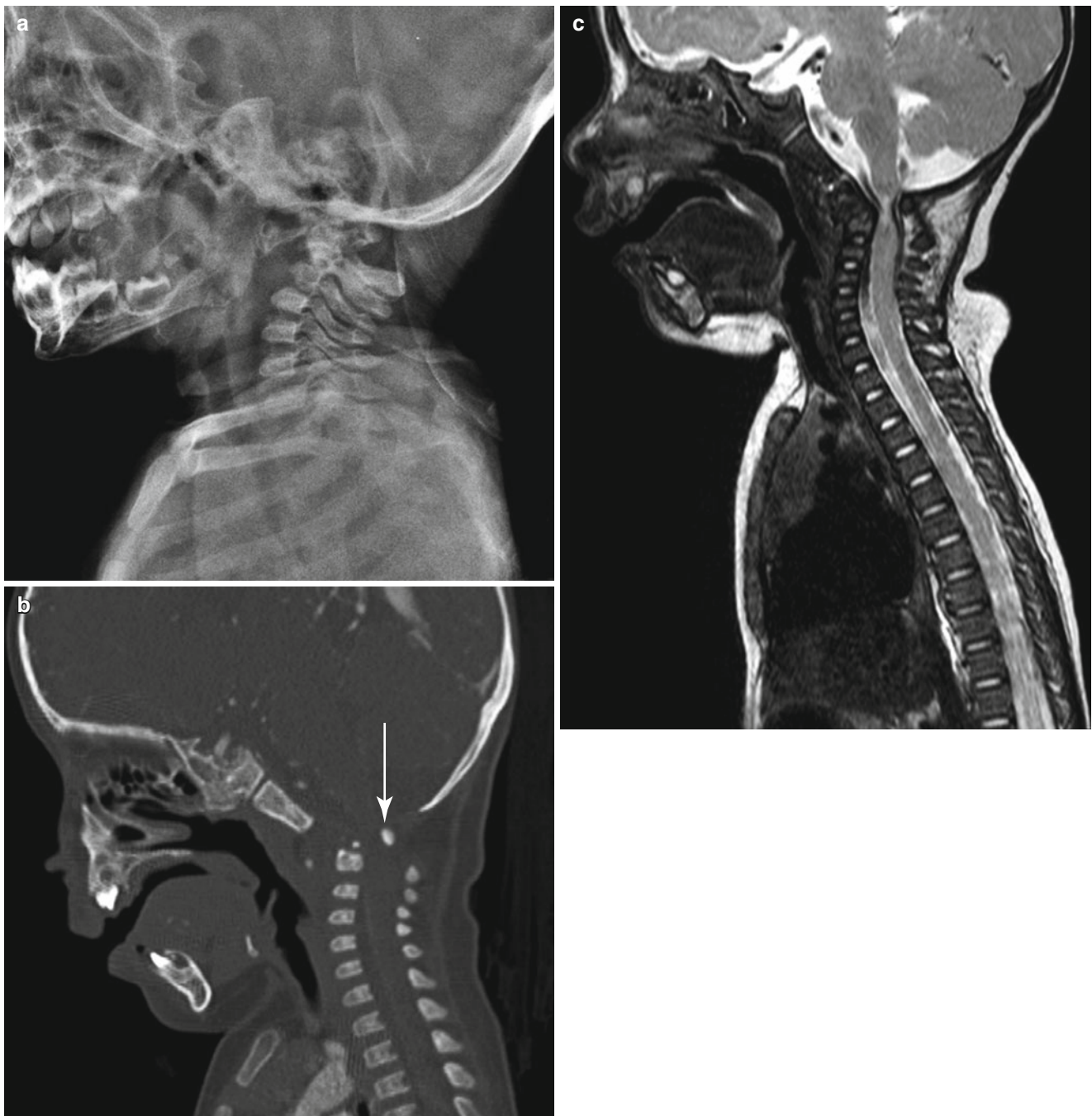


Fig. 8.24 C1–2 dislocation in a 5-month-old boy with quadriparesis. (a) Cervical spine lateral projection shows wide atlantoaxial distance. (b) Cervical spine CT with sagittal reconstruction shows anterior dislocation of C1 on C2 and severe cord compression by the posterior arch

of the atlas (*arrow*). (c) MR T2-weighted sagittal image reveals severe cord compression at C1–2 with intramedullary high signal intensity representing compressive myelopathy

8.5.19 Foreign Body

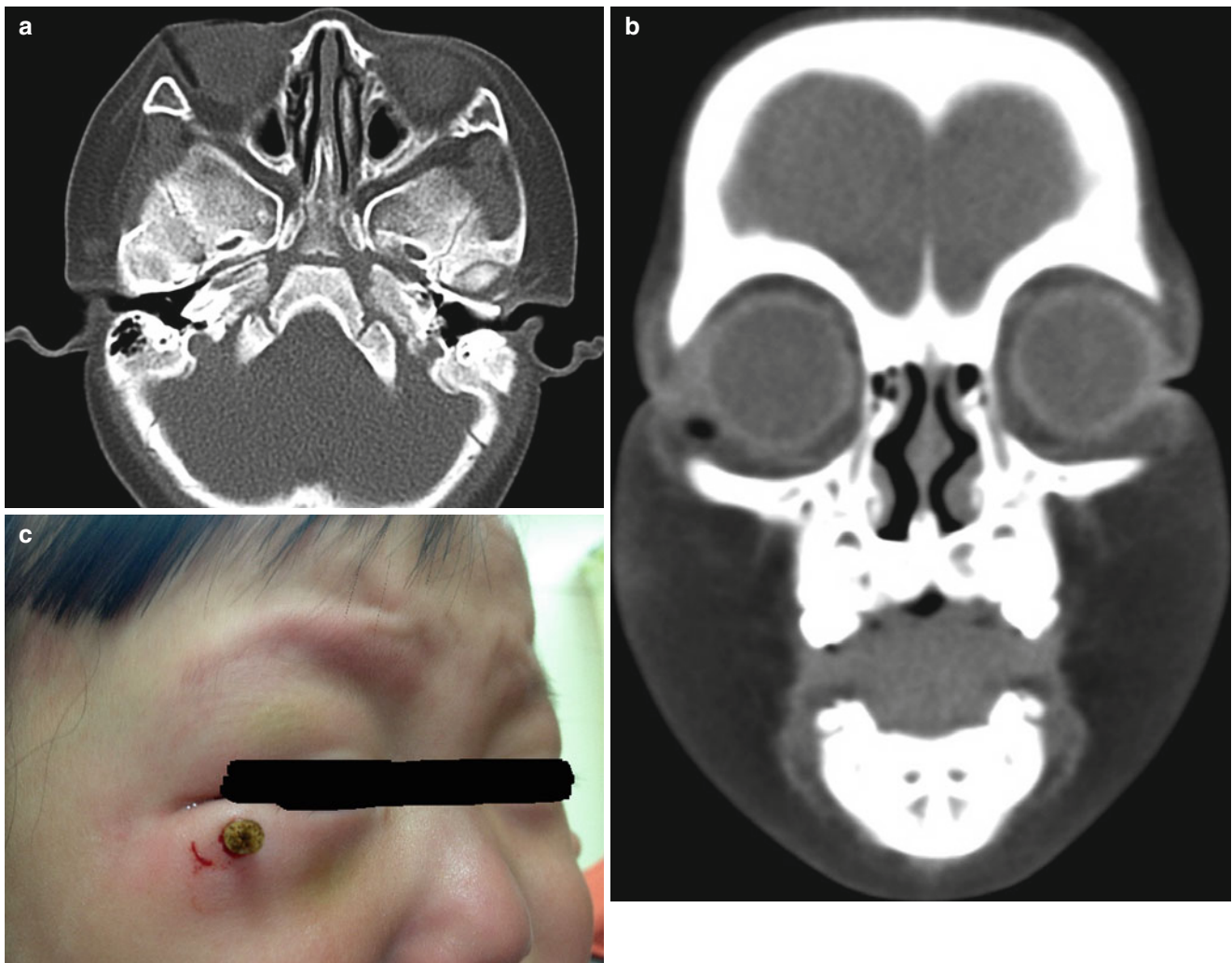


Fig. 8.25 Orbital foreign body (chopstick) in a 1-year-old girl. (a, b) Axial (a) and coronal (b) CT images show a tubular low-attenuating foreign body in the right orbit just inferolateral to the right eyeball. (c)

Gross picture of this baby girl shows broken fragment of the chopstick penetrating through the right lower eyelid. CT is the best modality for demonstrating any radiolucent or radiopaque foreign bodies

References

- Cervantes LF, Medina LS, Effmann EL. Neck and upper airway. In: Slovis TL, editor. *Caffey's pediatric diagnostic imaging*. 11th ed. Philadelphia: Mosby Elsevier; 2008.
- Cooper ML, Slovis TL. The sinuses. In: Slovis TL, editor. *Caffey's pediatric diagnostic imaging*. 11th ed. Philadelphia: Mosby Elsevier; 2008.
- Faerber EN, Booth TN, Swartz JD. Temporal bone and ear. In: Slovis TL, editor. *Caffey's pediatric diagnostic imaging*. Philadelphia: Mosby Elsevier; 2008a.
- Faerber EN, Poussaint TY, Nelson MD. The orbit. In: Slovis TL, editor. *Caffey's pediatric diagnostic imaging*. 11th ed. Philadelphia: Mosby Elsevier; 2008b.
- Gadodia A, Seith A, Sharma R, et al. MRI and MR sialography of juvenile recurrent parotitis. *Pediatr Radiol*. 2010;40:1405–10.
- Gayer G, Zandman-Goddard G, Kosych E, et al. Spontaneous rupture of the spleen detected on CT as the initial manifestation of infectious mononucleosis. *Emerg Radiol*. 2003;10:51–2.
- Ghosh PS, Ghosh D, Goldfarb J, et al. Lateral sinus thrombosis associated with mastoiditis and otitis media in children: a retrospective chart review and review of the literature. *J Child Neurol*. 2011;26:1000–4.
- Han HJ, Lim GY, Yeo DM, et al. Kikuchi's disease in children: clinical manifestations and imaging features. *J Korean Med Sci*. 2009;24:1105–9.
- Hegde AN, Mohan S, Pandya A, et al. Imaging in infections of the head and neck. *Neuroimaging Clin N Am*. 2012;22:727–54.
- Pinto A, Muzj C, Gagliardi N, et al. Role of imaging in the assessment of impacted foreign bodies in the hypopharynx and cervical esophagus. *Semin Ultrasound CT MR*. 2012;33:463–70.
- Roh K, Lee SW, Yoo J. CT analysis of retropharyngeal abnormality in Kawasaki disease. *Korean J Radiol*. 2011;12:700–7.
- Shekdar KV, Mirsky DM, Kazahaya K, et al. Magnetic resonance imaging of the pediatric neck: an overview. *Magn Reson Imaging Clin N Am*. 2012;20:573–603.
- Thomas B, Shroff M, Forte V, et al. Revisiting imaging features and the embryologic basis of third and fourth branchial anomalies. *AJNR Am J Neuroradiol*. 2010;31:755–60.

Hee Jung Lee

Contents

9.1	Introduction	324
9.2	Pathophysiology	324
9.3	Imaging	324
9.4	Spectrum of Pediatric Head and Neck Neoplasms	324
9.4.1	Benign	324
9.4.2	Malignant	326
9.4.3	Parotid Tumors	328
9.4.4	Thyroid Tumors	328
9.5	Illustrations: Neoplasms of the Head and Neck	329
9.5.1	Infantile Hemangioma	329
9.5.2	Teratoma	331
9.5.3	Nasopharyngeal Angiofibroma	333
9.5.4	Langerhans Cell Histiocytosis	336
9.5.5	Fibromatosis Colli	338
9.5.6	Lipoblastoma	339
9.5.7	Plexiform Neurofibromas	340
9.5.8	Pilomatrixoma	342
9.5.9	Lymphoma	343
9.5.10	Rhabdomyosarcoma	347
9.5.11	Chloroma	349
9.5.12	Neuroblastoma	351
9.5.13	Retinoblastoma	354
9.5.14	Pleomorphic Adenoma	355
9.5.15	Thyroid Tumors	356
	References	359

H.J. Lee, M.D., M.P.H.
 Department of Radiology, Dongsan Medical Center,
 Keimyung University School of Medicine,
 56 Dalsung Ro, Daegu 700-712, Korea
 e-mail: hjlee@dsmc.or.kr

9.1 Introduction

Classification of head and neck tumors can be variable according to anatomic sites, pathologic findings, and clinical presentations. Some tumors tend to occur preferentially in certain locations of the head and neck. For example, nasopharyngeal angiofibroma typically involves the pterygopalatine fossa. Infantile hemangioma commonly involves the orbit, parotid glands, and subglottic trachea. Pathologic findings of the tumor characterize the imaging findings of the lesions including cystic or solid in nature; the presence of calcification, fat, or bone destruction; and intratumoral vascularity. Clinical characteristics including the patient's age and the presence of associated abnormality in the other sites of the body are also important. This chapter describes the image findings of tumors and tumor-like lesions primarily occurring in the head and neck of children.

9.2 Pathophysiology

The first step for the diagnosis of head and neck neoplasm is knowledge of the anatomy and contents of each cervical compartment. The next step is the exact localization of the tumor. Some tumors tend to occur preferentially in certain locations of the head and neck. The orbit is a preferred site for hemangioma, plexiform neurofibromas, LCH, lymphoma, rhabdomyosarcoma, leukemia, and metastatic neuroblastoma. LCH and metastatic neuroblastoma have a tendency to involve the superolateral wall of the orbit, whereas rhabdomyosarcoma commonly involves the superomedial wall of the orbit. Tissue characterization of the tumor including cystic or solid in nature; the presence of calcification, fat, or bone destruction; and vascularity is crucial for differential diagnosis of the neoplasm. For example, among the above-mentioned LCH and metastatic neuroblastoma preferentially involving the superolateral wall of the orbit, a mass-associated bone destruction with spiculated periosteal reaction is more likely to be metastatic neuroblastoma rather than LCH. Clinical characteristics including the patient's age and the presence of associated abnormality in the other sites of the body are also important. Infantile hemangioma demonstrates characteristic "strawberry" appearance with rapidly proliferative phase during infancy and involutionary phases thereafter. The presence of multiple hemangiomas in the head and neck initiates neuroimaging to rule out PHACE association. Therefore, knowledge of the anatomy of the head and neck, location and tissue characterization of the tumor, and clinical characteristics are helpful in the diagnosis of pediatric head and neck neoplasm.

9.3 Imaging

Although plain radiographs have a limited role in evaluating head and neck neoplasm, radiologic diagnosis in some cases is often straightforward. For example, "floating teeth" sign of the mandible or "vertebra plana" of the cervical spine is suggestive of LCH (Meyer et al. 1955). Ultrasonography (US) is particularly useful in examining small superficial masses, differentiating cystic from solid lesions or nodal from nonnodal masses. Computed tomography (CT) and magnetic resonance (MR) imaging are used to delineate deeper lesions and are used to assess airway compression, vascular encasement, perineural spread, bone involvement, and intracranial or intraspinal extension. In cases of mainly osteolytic lesions such as LCH or metastatic neuroblastoma, CT is useful for the evaluation of intratumoral calcification, nature of the periosteal reaction associated with soft tissue mass, and defining the areas of bone destruction. Although CT allows rapid examination of the entire neck, low-dose neck CT is mandatory for minimizing radiation dose especially for the thyroid gland in children. MR imaging is useful in determining the site of tumor origin, extent of disease, and relation of tumor to adjacent anatomic structures and for follow-up after therapy. MR imaging provides excellent soft tissue contrast, and the combination of findings may aid in narrowing the differential diagnosis, such as persistent low signal intensity on T1-weighted images (T1WI) and T2-weighted images (T2WI) in some fibrotic lesions (Laor 2004). Additional diffusion-weighted imaging appears to also have a role in differentiating between malignant tumors and benign lesions. Positron emission tomography (PET) performed with fluorine 18 fluorodeoxyglucose (FDG) can be useful for grading and staging of head and neck tumors and for the detection of local tumor recurrence.

9.4 Spectrum of Pediatric Head and Neck Neoplasms

9.4.1 Benign

9.4.1.1 Infantile Hemangioma

Infantile hemangioma is the most common tumor of infancy, and more than one-half occur in the head and neck. In contrast to vascular malformation, infantile hemangioma is a true benign vascular tumor arising as a result of endothelial hyperplasia composed of capillary tuft (capillary hemangioma) (Mulliken and Glowacki 1982). The tumor undergoes cellular proliferation (cellular hemangioma) and enlargement in the first year of life (infantile hemangioma), followed

by gradual involution during early childhood. Most of the lesions are diagnosed by clinical appearance described as “strawberry marks” (strawberry hemangioma). The predilection sites are the orbit, parotid glands, chin–jawline–preauricular areas (beard distribution), and glottic or subglottic neck. Infantile hemangiomas demonstrate relatively characteristic image findings, in contrast to vascular malformations with variable image findings. Proliferating hemangiomas are well circumscribed, solid, and lobulated on US, CT, and MR imaging. US shows high-flow vascularity on color Doppler image. CT demonstrates a lobulating isoattenuated mass compared with muscle and intense enhancement. On MR, the mass is a discrete solid mass lesion of isointense to muscle on T1WI, hyperintense on T2WI, and demonstrates intense homogeneous enhancement with or without internal flow voids (Figs. 9.1 and 9.2). Involuting hemangiomas progressively shrink with increasing fibrofatty matrix, reduction in vascularity, and a relative decrease in enhancement (Baker et al. 1993).

Diffuse and segmental hemangiomas of the face may associate with PHACE(S) syndrome, which consists of posterior fossa malformations, hemangiomas, arterial anomalies related to the intracranial circulation, coarctation of the aorta or cardiac anomalies, eye abnormalities, and occasionally sternal clefting or supraumbilical raphe (a fibrous band or cleft in the midline above the umbilicus) (Frieden et al. 1996). Most infantile hemangiomas do not require surgical intervention otherwise compression to vital organs such as optic nerve or airway. The differential diagnosis includes vascular malformations and rhabdomyosarcomas. In distinction to infantile hemangiomas, vascular malformations are usually present at birth, grow commensurately with the child, and do not regress spontaneously. Rhabdomyosarcoma usually demonstrates heterogeneously enhancing mass with bone destruction or erosion.

9.4.1.2 Teratoma

Teratoma is the most common congenital tumor (tumors before 60 days of life). The head and neck are the second most common locations for teratomas among young infants, followed by sacrococcygeal region. Unlike dermoid or epidermoid cyst, teratoma is a true neoplasm arising from misplaced embryologic germ cells and composed of more than one of the three embryonic germ layers (Smirniotopoulos and Chiechi 1995). The tumor is usually a large, bulky, and heterogeneous mass that is diagnosed at prenatal US. Most craniofacial teratomas are histologically mature types and usually located in the oral cavity and pharynx (Barkovich 2005). CT and MR show variable imaging findings depending on the internal composition of the tissue from a unilocular cyst to a heterogeneous complex mass containing areas of

fat and calcification (Figs. 9.3 and 9.4). The primary differential diagnosis for a cystic neck mass in a fetus or an infant include lymphatic malformation, dermoid cyst, thyroglossal duct cyst, enteric duplication cyst, and mature cystic teratoma.

9.4.1.3 Nasopharyngeal Angiofibroma

Nasopharyngeal angiofibroma demonstrates relatively characteristic clinical and imaging appearances. The diagnosis is suspected in an adolescent male presenting with unilateral nasal obstruction and recurrent epistaxis. The tumor is a benign but highly aggressive hypervascular mass. Both CT and MR show an intensely enhancing solid mass, typically arising from the sphenopalatine foramen on lateral nasopharyngeal wall, extending into the pterygopalatine fossa. Invasion to the sphenoid via the pterygoid canal, to the orbit via the inferior orbital fissure, to the infratemporal fossa via the pterygomaxillary fissure, and to the middle cranial fossa via the foramen rotundum or vidian canal may be seen. CT is valuable in depicting bone erosion at the skull base. MR is preferred for the evaluation of tumor extension. The lesion shows low signal intensity on T1WI, heterogeneous intermediate signal intensity on T2WI, and avid enhancement with flow voids on contrast-enhanced images (Figs. 9.5 and 9.6). The differential diagnosis includes hypervascular polyps, rhabdomyosarcoma, and nasopharyngeal carcinoma (Barkovich 2005; Robson 2010).

9.4.1.4 Langerhans Cell Histiocytosis (LCH)

LCH is characterized by idiopathic proliferation of Langerhans cells in any of the sites of the reticuloendothelial system. The disease occurs among children with its peak incidence between the ages of 1 and 4, and localized and disseminated forms of the disease can occur. Head and neck manifestations of LCH occur in up to 73–82 % of cases, and the cranial vault is the most common location of osseous LCH. The radiologic appearance of LCH depends on the site of involvement and the phase of the disease. In the skull, plain radiography shows a typical lytic lesion of the skull, described as a “punched-out” or “scooped-out” lesion without reactive sclerosis or periosteal reaction, a “geographic” lesion with several conglomerated punched-out lesions, a “beveled edge” with asymmetric destruction of the inner and outer tables of the skull, and a “button sequestration” with a lytic lesion containing a residual bone fragment. Other commonly involved sites in the head and neck include the orbit, mandible, temporal bone, and cervical spine. The most typical presentation is an osteolytic lesion in the superolateral orbit with proptosis. In the mandible, the body may be nearly completely destroyed, and the teeth are left with no visible support,

and hence called floating teeth. In the cervical spine, there may be a “vertebral plana” appearance with even collapse of the vertebral body (Meyer et al. 1955). CT demonstrates an enhancing soft tissue mass with bone erosion. MR imaging shows low to intermediate signal intensity of the mass on T1WI, hyperintense on T2WI, and variable contrast-enhancement pattern, according to the phase of the disease (Figs. 9.7, 9.8, and 9.9). Both LCH and metastatic neuroblastoma involve the superolateral wall of the orbit. Neuroblastoma is suggested by a soft tissue mass with a “hair-on-end” or “spiculated” periosteal reaction. Rhabdomyosarcoma demonstrates a soft tissue mass, mainly involving the superomedial wall of the orbit with bone destruction. Lesions within the temporal bone also mimic cholesteatoma, aggressive infection, or rhabdomyosarcoma (Barkovich 2005; Robson 2010).

9.4.1.5 Fibromatosis Colli

Fibromatosis colli is a form of infantile fibromatosis involving the SCM muscle. It manifests as a firm anterior neck, more commonly on the right side, associated with torticollis in young infants. It is postulated that a cellular scar-like reaction to peripartum injury causes the pathogenesis of the lesion. The sternal or clavicular head of the muscle is usually affected. US findings are usually diagnostic, and the four types of US findings include a focal heterogeneous mass with a spindle shape, diffuse echogenic dot and lines against the hypoechoic background, diffuse hyperechogenicity along the entire muscle, and hyperechoic band in the muscle (Fig. 9.10). MR imaging demonstrates mild enlargement of the lower one-third of the SCM muscle with higher signal intensity than that of fat on T2WI. The signal intensity of the mass may vary according to the degree of fibrous and cellular tissues (Bedi et al. 1998).

9.4.1.6 Lipoblastoma

Lipoblastoma is a benign mesenchymal tumor of embryonal fat tissue, which occurs in infants and children younger than 3 years. The tumor most commonly manifests as an asymptomatic, painless, progressively growing mass. The lesion is composed of lipoblasts, capillary vessels, and myxoid and collagenous stromal tissues. Imaging findings depend on the underlying pathologic components of fat and underlying stroma (myxoid, collagenous, and capillary vessels). Fat in lipoblastoma may be seen as echogenic regions, areas of low attenuation, or areas of signal intensity identical to that of subcutaneous fatty tissue with all pulse sequences on US, CT, and MR, respectively. The myxoid areas are hypoechoic at US, low attenuation at CT, and low signal intensity on T1WI and high signal intensity on T2WI at MR (Fig. 9.11). Lipoblastomas cannot be distinguished from myxoid liposarcomas at imaging. However, liposarcomas are very rare in children younger than 3 years (Murphey et al. 2004).

9.4.1.7 Plexiform Neurofibromas

Neurofibroma is the most common neurogenic tumor seen in children and can be manifested as localized, diffuse, or plexiform types. Nearly all children with head and neck neurofibromas are diagnosed with neurofibromatosis type I, and the presence of a plexiform neurofibroma is pathognomonic for neurofibromatosis type 1. The tumor demonstrates an infiltrative growth pattern with transspatial involvement, and multiple cords and nodules of the tumor give it a “bag of worms” appearance. The predilection sites are the orbits, the skull base, or the parotid region. CT demonstrates enlarged or eroded bony orbit by the tumor with or without orbital dysplasia. MR is better at characterizing the lesion and defining the extent of the lesion. Typically, they are heterogeneous, isointense to muscle on T1WI. The tumor often demonstrates a “target” pattern of increased peripheral signal intensity and decreased central signal intensity on T2WI and variable enhancement after gadolinium administration (Suh et al. 1992) (Figs. 9.12 and 9.13).

9.4.1.8 Pilomatrixoma

Pilomatrixoma, also called as calcifying epithelioma of Malherbe, is a benign neoplasm arising from the hair matrix of cutaneous tissues. The tumor is the most common solid cutaneous tumor in young children with a mean age of 4.5 years. The lesion is commonly located on the face, neck, scalp, and in the parotid region. The mass is usually small, less than 3 cm in diameter, slow-growing, hard, tender, and confined to the subcutaneous tissue. US is the modality of diagnosis and demonstrates a well-defined, round, hyperechoic solid nodule abutting the skin with a posterior acoustic shadow. Calcification is seen in about 85 % of lesions (Beaman et al. 2007). CT and MR can be helpful in differentiating preauricular pilomatrixoma from parotid tumor by revealing a sharply margined, subcutaneous, opaque lesion that does not enhance after contrast injection or small areas of signal void that are consistent with the presence of calcifications on MR scan (Barkovich 2005; Haller et al. 1977; Robson 2010) (Fig. 9.14).

9.4.2 Malignant

9.4.2.1 Lymphoma

Lymphoma is the most common solid malignant tumor of the head and neck in children. Hodgkin lymphoma (HL) occurs primarily in early adolescence and is more common than non-Hodgkin lymphoma (NHL), which occurs throughout childhood. Affected children most commonly present with cervical lymphadenopathies. Classic HL involves contiguous lymph node groups with coexistent mediastinal lymphadenopathies in approximately 40 % of patients. NHL occurs more frequently in patients with acquired or congenital immune disorders such as AIDS and immunosuppressed transplant patients with or without EBV infection.

NHL presents as painless unilateral lymphadenopathy, and approximately 30 % of cases present with extranodal disease in the head and neck. Extranodal NHL disease involves the lymphoid tissue of the Waldeyer ring (the lymphatic tissue found in the nasopharynx, base of tongue, tonsils, and soft palate), sinonasal cavity, parotid or thyroid glands, lacrimal gland, or the jaw. NHL involving the Waldeyer ring is usually bilateral and can obliterate the airway. Burkitt lymphoma is a NHL with two distinct epidemiologic forms. The endemic African form commonly involves the oral cavity and the jaw.

US has good sensitivity and specificity for distinguishing benign, reactive lymph nodes from those infiltrated with lymphoma. The affected nodes show a round shape, absent or eccentric hilum, intranodal cystic change or marked hypoechogenicity (pseudocystic), and peripheral or distorted hypervascularity on color Doppler images. The lymphomatous node is enlarged, isoattenuating relative to muscle on CT and isointense on T1WI with heterogeneous enhancement after contrast material administration. The lesion is usually hyperintense on T2WI (Figs. 9.15, 9.16, 9.17, and 9.18). CT and MR imaging are useful for follow-up to monitor the mass and lymphomatous node regression. Whole body MRI, FDG-PET, and PET-CT are important in staging, evaluating treatment response, and monitoring for relapse of lymphoma (Figs. 9.15 and 9.16). Differential diagnosis includes leukemia, rhabdomyosarcoma, metastatic lymphadenopathies from neuroblastoma, and infectious mononucleosis. NHL involving the lacrimal gland may result in proptosis as in rhabdomyosarcoma, LCH, and metastatic neuroblastoma (Barkovich 2005; Robson 2010).

9.4.2.2 Rhabdomyosarcoma

Rhabdomyosarcoma is the most common soft tissue sarcoma and the second most common malignant tumor of the head and neck followed by lymphoma in children. The disease has two peak presentations: at 2–5 years and at 15–19 years. Rhabdomyosarcoma arises from primitive mesenchymal cells, and the most common histologic subtype is embryonal type (70–80 %) with a more favorable prognosis, followed by alveolar (10–20 %) and pleomorphic (10 %) types with an unfavorable prognosis. The predilection sites are the orbit, parameningeal, and other sites of the head and neck. Orbital rhabdomyosarcoma has the most favorable prognosis and is manifested with unilateral proptosis caused by a soft tissue mass in the superomedial aspect of the orbit. Parameningeal rhabdomyosarcoma arises from the pterygopalatine fossae, paranasal sinuses, middle ear, and mastoid process, and has the worst prognosis. Imaging finding shows a bulky soft tissue mass with variable degree of enhancement and bone destruction. The mass is isointense relative to muscle on T1WI and slightly hyperintense on T2WI, and demonstrates heterogeneous enhancement. MR imaging is the technique of choice to define the local extent of tumor and lymph node metastasis and also to assess the therapeutic

response (Fig. 9.19). The differential diagnosis for rhabdomyosarcoma depends on the location of tumor, and includes lymphoma, nasopharyngeal angiofibroma, nasopharyngeal carcinoma, LCH, and metastatic neuroblastoma (Barkovich 2005; Robson 2010; Yousem et al. 1990).

9.4.2.3 Leukemia

Leukemic infiltration usually involves cervical lymph nodes and may occasionally occur in the orbit and parotid glands. Acute myelogenous leukemia can be seen initially with orbital involvement before the diagnosis of the leukemia. Granulocytic sarcoma or chloroma is a focal mass composed of granulocytic precursors of leukemic cells. Ophthalmic manifestations in patients with leukemia are extraocular masses with or without associated osseous erosion, optic nerve, and intraocular involvement. At MR, the masses are isointense relative to the extraocular muscles on T1WI and isointense or slightly hyperintense on T2WI. Homogeneous enhancement of the enlarged orbital muscles and adjacent orbital wall may be seen after contrast enhancement. Chloromas may be bilateral, and the other cases of bilateral proptosis in children include idiopathic nongranulomatous orbital inflammation and metastatic neuroblastoma (Fig. 9.20). Idiopathic nongranulomatous orbital inflammation shows hyperintensity of the lesion on T2WI. Leukemic infiltration of the parotid gland rarely occurs. At US, the gland is diffusely enlarged with altered, variable echogenicity and increased flow. Variable attenuation and signal intensity are seen at CT and MR imaging (Barkovich 2005; Bulas et al. 1995; Robson 2010).

9.4.2.4 Retinoblastoma

Retinoblastoma is the most common intraocular tumor of childhood and arises from the neuroectodermal cells of the retinoblast. The tumor usually presents before 2 years of age. Approximately 5–10 % of cases are familial, and those with germline retinoblastoma are at high risk of associated trilateral or quadrilateral retinoblastomas (bilateral retinoblastomas+one or two midline brain tumors in the pineal or suprasellar regions). Imaging finding shows a calcified intraocular mass with variable enhancement. CT is particularly sensitive for detecting calcifications, which can be seen in approximately 95 % of retinoblastomas. MR shows variable signal intensity of the mass on both T1 and T2WI and is the best imaging modality for demonstrating retinal detachment, extraocular spread, and leptomeningeal dissemination (Fig. 9.24). More than half of the patients with retinoblastoma who present with leukocoria can also be seen with Coats' disease, toxocariasis, persistent primary hyperplastic vitreous, and retinopathy of prematurity (Kaufman et al. 1998). The findings with microphthalmia and absence of calcification in the lesions of Coats' disease, persistent primary hyperplastic vitreous, and toxocariasis would be helpful for differential diagnosis (Barkovich 2005; Castillo and Kaufmann 2003).

9.4.2.5 Neuroblastoma

Neuroblastoma is the third most common solid tumors of early childhood. This tumor is the least differentiated form of tumors that arise from primordial neural crest cells. Ganglioneuroblastoma is the intermediate form, and ganglioneuroma is the most mature. The adrenal gland is the most common site of involvement, followed by posterior mediastinum, and only 5 % of primary neuroblastomas arise in the head and neck. Cervical neuroblastoma more frequently represents metastasis from adrenal or posterior mediastinal neuroblastoma.

The tumor commonly metastasizes to the lateral orbital walls (“raccoon” eye), the skull base, and calvaria. Imaging finding shows a soft tissue mass involving the superolateral wall of the orbit with bone destruction or an extradural mass with suture widening. CT demonstrates a spiculated or “hair-on-end” periosteal reaction. MR images show a soft tissue mass that originates in the diploic space and extends beyond the inner and outer tables. The mass is isointense to muscle on both T1WI and T2WI, with avid contrast enhancement (Figs. 9.22 and 9.23).

Primary cervical neuroblastoma may be manifested as a lateral neck mass with small intratumoral calcifications. They tend to be in the parapharyngeal regions arising from the sympathetic chains, and spinal invasion is uncommon in cervical neuroblastoma (Fig. 9.21). Iodine-123 metaiodobenzylguanidine scintigraphy may help confirm the diagnosis and refine the staging of the tumor. Both LCH and metastatic neuroblastoma characteristically involve the superolateral part of the orbit. Characteristically, a spiculated or “hair-on-end” periosteal reaction may help diagnosis of neuroblastoma (Barkovich 2005; Robson 2010; Castillo and Kaufmann 2003; Yousem et al. 1990).

9.4.3 Parotid Tumors

Primary tumors of the salivary glands are rare in children, and the proportion of malignant lesions compared with

benign disease is higher in children than in adults. The common benign tumors are infantile hemangioma, lymphangioma, and pleomorphic adenoma, with the highest frequency of hemangioma. The most common nonvascular tumor is the pleomorphic adenoma that accounts for 85–90 % of all parotid tumors. Pleomorphic adenoma may be either hyperechoic or hypoechoic, and may have cystic, hypoechoic, or necrotic centers on US (Fig. 9.25).

The malignant tumors are mucoepidermoid and adenoid cystic carcinomas, lymphoma, and leukemia, with the highest frequency of mucoepidermoid carcinoma as a primary malignancy. The signal intensity and enhancement characteristics of parotid tumors are variable according to the histological type and grade. Therefore, it is difficult to distinguish benign from malignant nodules based on imaging findings. Although rare, *primary lymphoma* of the salivary glands most often involves the parotid gland and is classified as a MALToma (Barkovich 2005; Laor 2004; Robson 2010).

9.4.4 Thyroid Tumors

The most common solid solitary thyroid nodule is follicular adenoma accounting for 70 % (Fig. 9.26). Thyroid cancer is not so rare and represents about 13 % of all thyroid cancers. Three major histologic types occur in childhood: papillary (80 % of cases), follicular (15 %) (Fig. 9.27), and medullary (5 %). Risk factors for developing thyroid cancer include previous neck irradiation, multiple endocrine neoplasia (familial adenomatous polyposis and Cowden disease), and thyroiditis. US is the preferred modality for evaluating the thyroid nodules. A single lesion with mixed echogenicity is likely to represent malignant tumors, and the presence of microcalcifications is highly specific for papillary carcinoma (Fig. 9.28). Scintigraphy has an important role, because “cold” nodules have a higher frequency of malignancy. In spite of more frequent lymph node metastases in children than in adults, the prognosis of thyroid carcinoma in childhood is fairly good (Gow et al. 2003; Laurie et al. 1992).

9.5 Illustrations: Neoplasms of the Head and Neck

9.5.1 Infantile Hemangioma

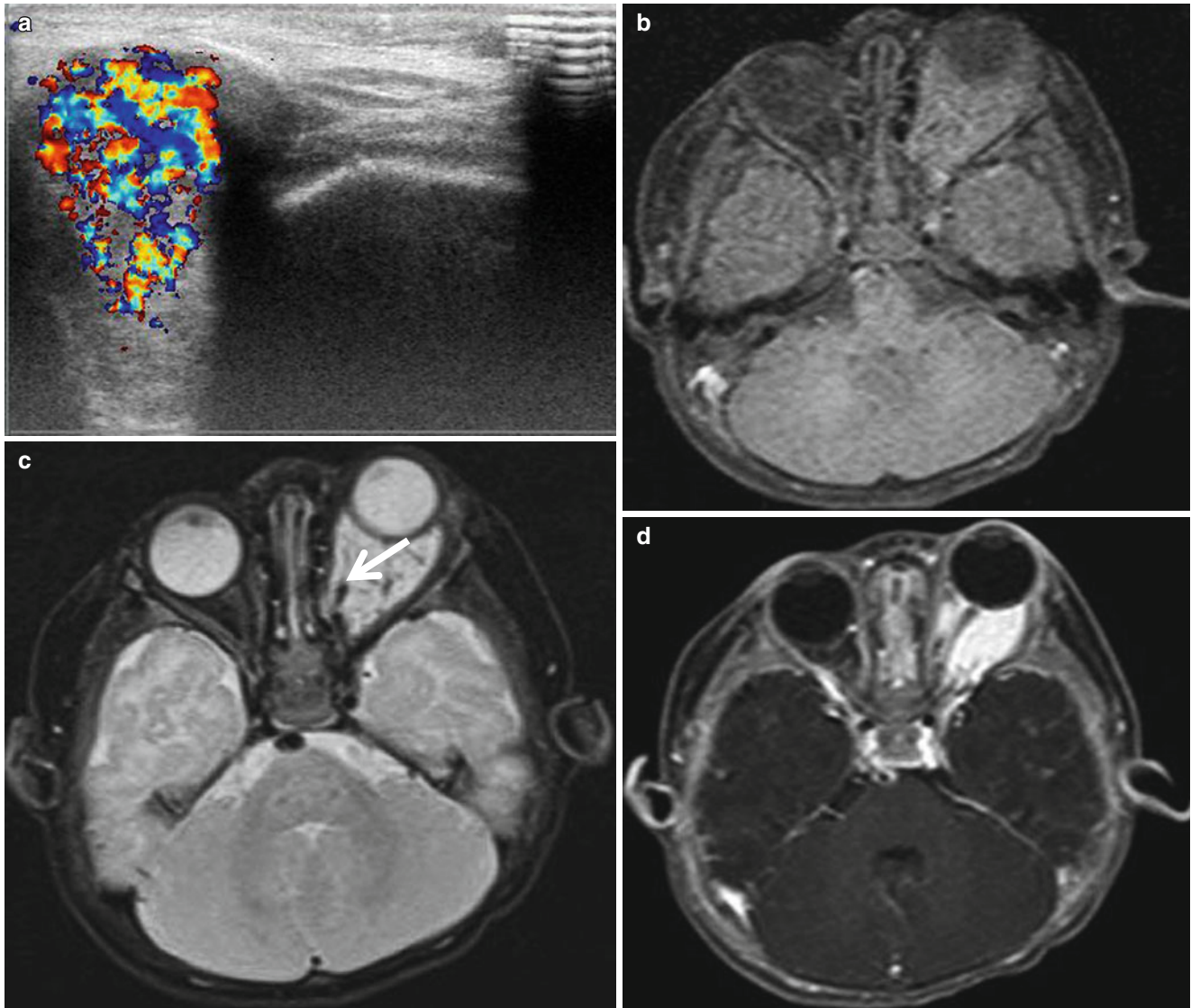


Fig. 9.1 Orbital hemangioma in a 4-month-old infant. (a) Color Doppler US shows a hypervascular solid mass in the right orbit. (b, c) Axial fat-saturated T1- and T2-weighted MR images show a soft tissue mass of homogeneous iso- and high signal intensities relative to the muscle on T1-weighted (b) and T2-weighted (c) images, respectively.

Prominent high-flow vascular flow voids (*arrow*) are seen. (d) Axial contrast-enhanced T1-weighted fat-suppressed MR image shows intense homogeneous enhancement of the mass. Note proptosis and the compressed optic nerve (*arrow*)

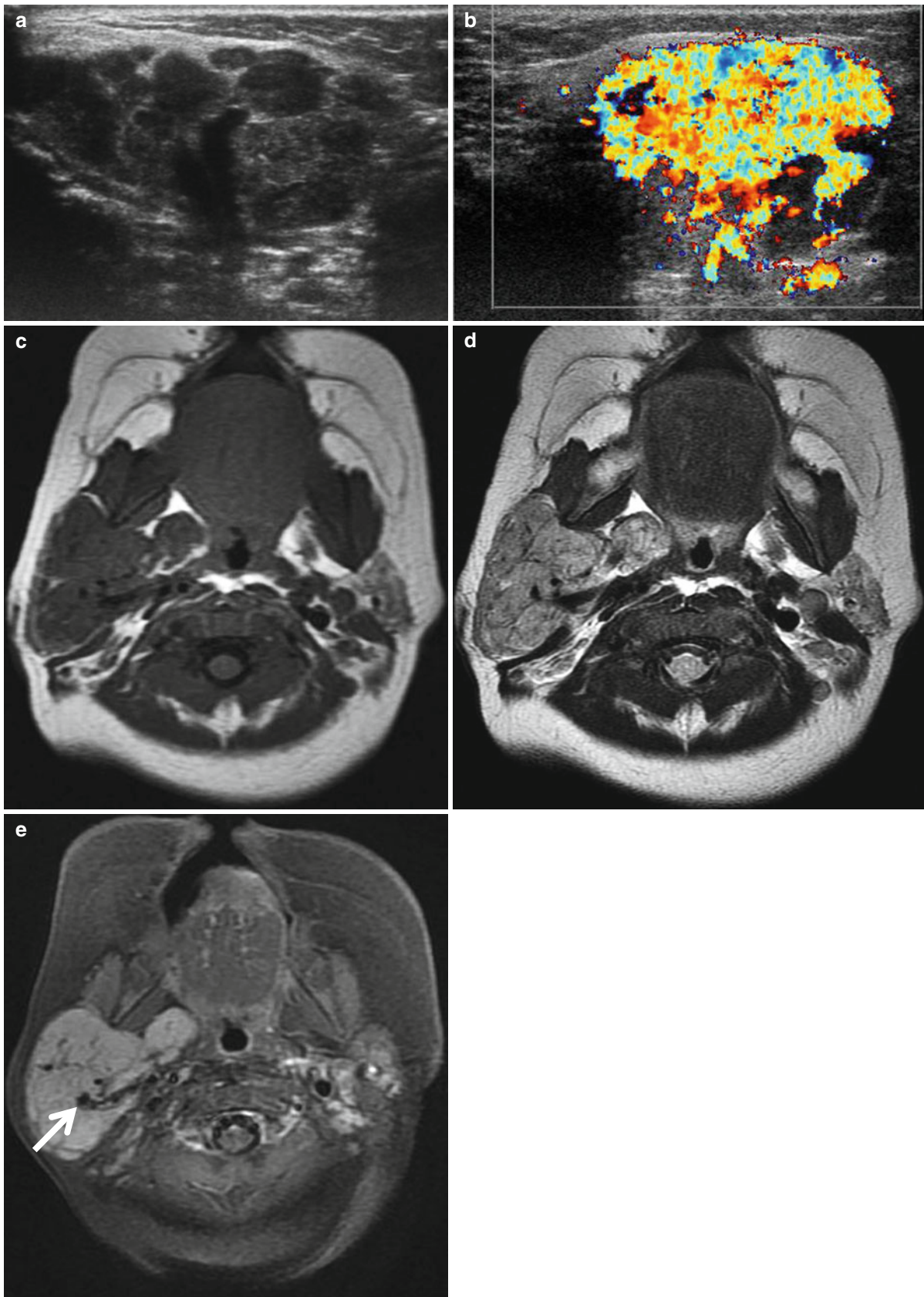


Fig. 9.2 Parotid hemangioma in a 4-month-old girl. (a, b) Gray and color Doppler US scans show a lobulating, heterogeneous solid mass with extensive hypervascularity in the right parotid gland. (c) Axial T1-weighted MR image shows a homogeneous iso-signal intensity of the mass relative to the muscle involving the entire right parotid gland.

(d) Axial T2-weighted MR image shows a slightly high signal intensity of the mass with multiple flow voids (*arrow*). (e) Axial contrast-enhanced T1-weighted fat-suppressed MR image shows intense homogeneous enhancement of the mass occupying the entire right parotid gland. Prominent high-flow vascular flow voids (*arrow*) are seen

9.5.2 Teratoma

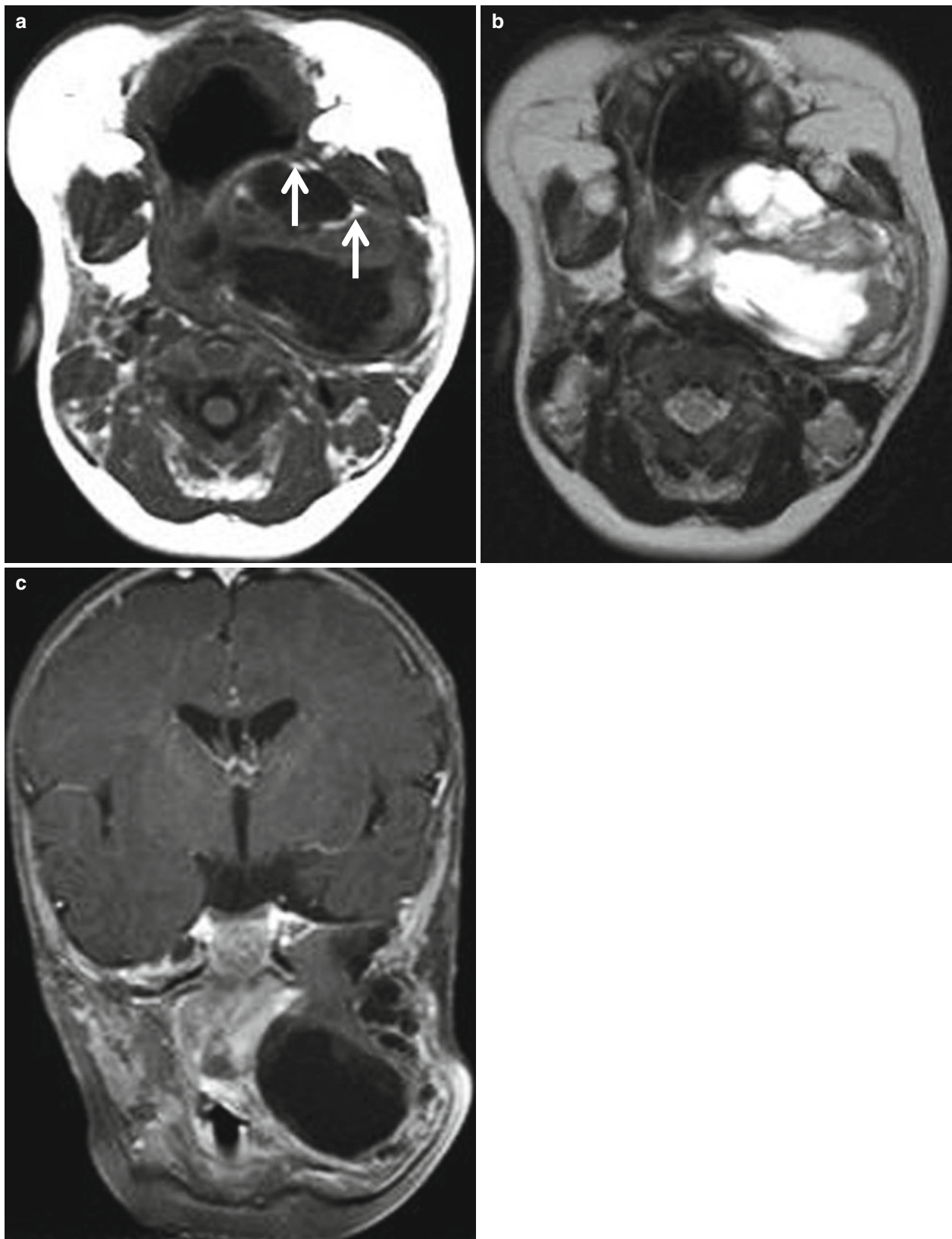


Fig. 9.3 Teratoma in a 3-month-old infant. (a) Axial T1-weighted MR image shows a large lobulating, complex mass in the left infratemporal fossa. The mass contains small foci of fatty tissues with high signal intensities (*arrows*). (b) Axial T2-weighted MR image shows peripheral solid and central cystic portions. (c) Contrast-enhanced

T1-weighted fat-suppressed coronal MR image shows the mass extending superiorly to the middle cranial fossa, medially to the parapharyngeal space, inferiorly to the submandibular space, and laterally to the parotid space. Note the severe displacement of the upper airway

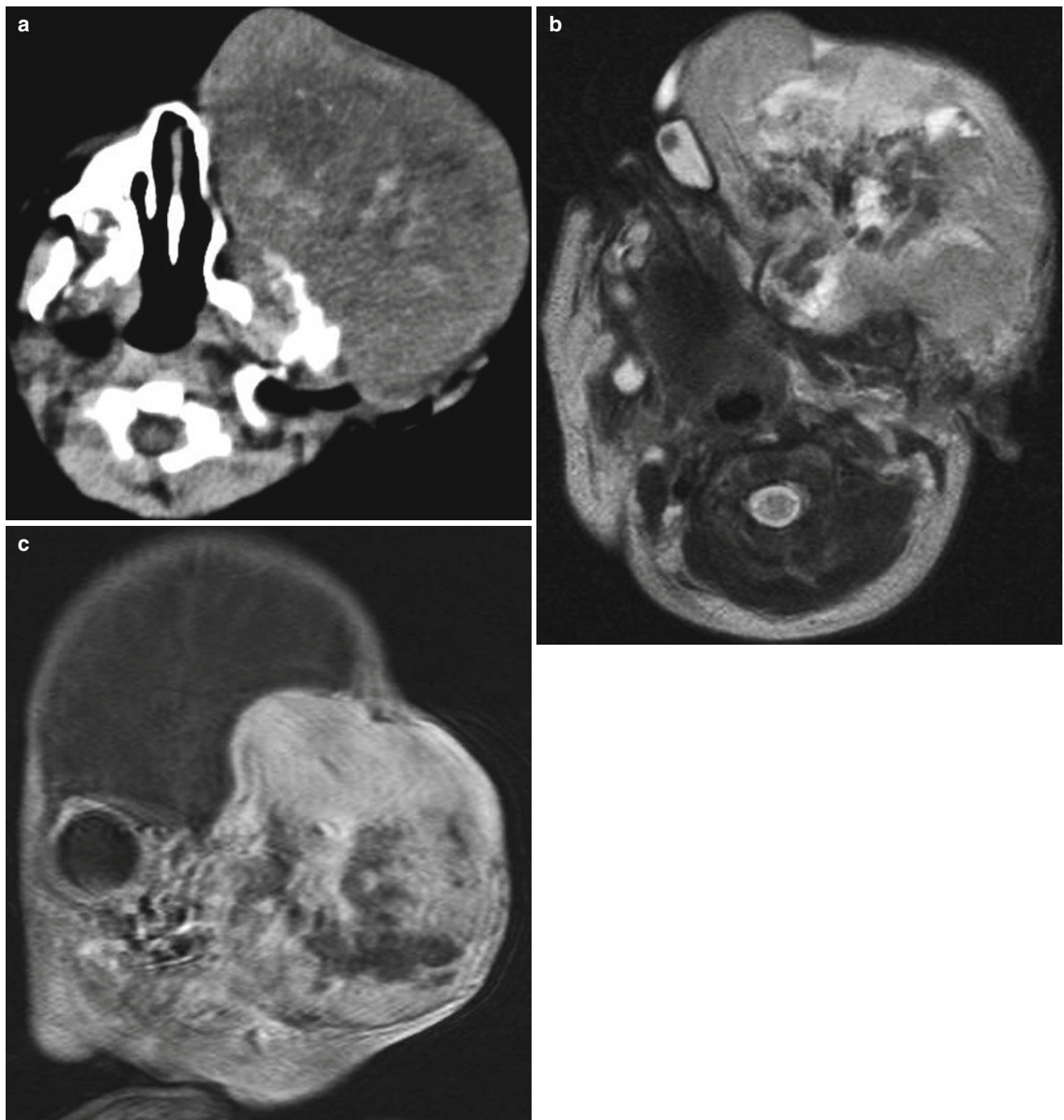


Fig. 9.4 Teratoma in a 2-day-old neonate. (a) Precontrast-enhanced CT scan shows heterogeneous attenuation of the mass with several calcific foci. Note destruction of the left frontal and temporal bones. (b) Axial T2-weighted MR image shows markedly heterogeneous high

signal intensity mass involving the entire left face and neck. Note inferomedially displaced left orbit. (c) Contrast-enhanced T1-weighted fat-suppressed coronal MR image shows intracranial extension of the tumor with heterogeneous enhancement

9.5.3 Nasopharyngeal Angiofibroma

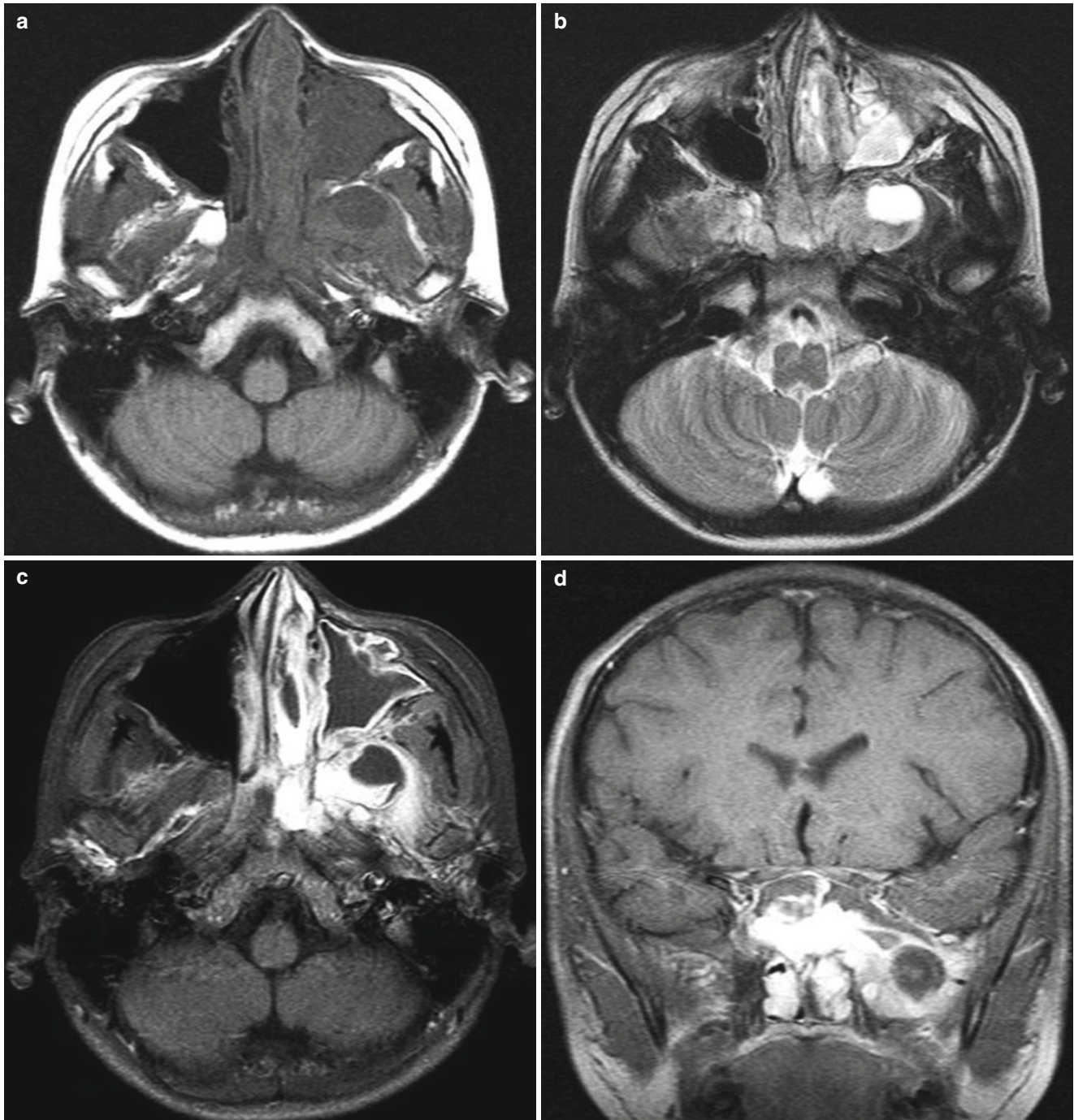


Fig. 9.5 Nasopharyngeal angiofibroma in a 10-year-old boy. (a) Axial T1-weighted MR image shows an ill-defined heterogeneous soft tissue mass of iso- to low signal intensity relative to muscle involving the left nasal cavity and nasopharynx. (b) Axial T2-weighted MR image shows heterogeneous iso- to high signal intensity of the mass with internal cystic portion. (c, d) Contrast-enhanced T1-weighted fat-suppressed axial and coronal MR images show a large, intensely enhancing tumor

obstructing the left nasal cavity and nasopharynx and extending into the pterygopalatine fossa, infratemporal fossa, and sphenoid sinus. (e) CT scan clearly demonstrates widening of the left pterygopalatine fossa (arrow) and destruction of the left pterygoid and sphenoid bones. (f) Carotid angiography with selective injection of the left external carotid artery shows arterial supply from the internal maxillary artery branches (black arrow) with an intense tumor blush

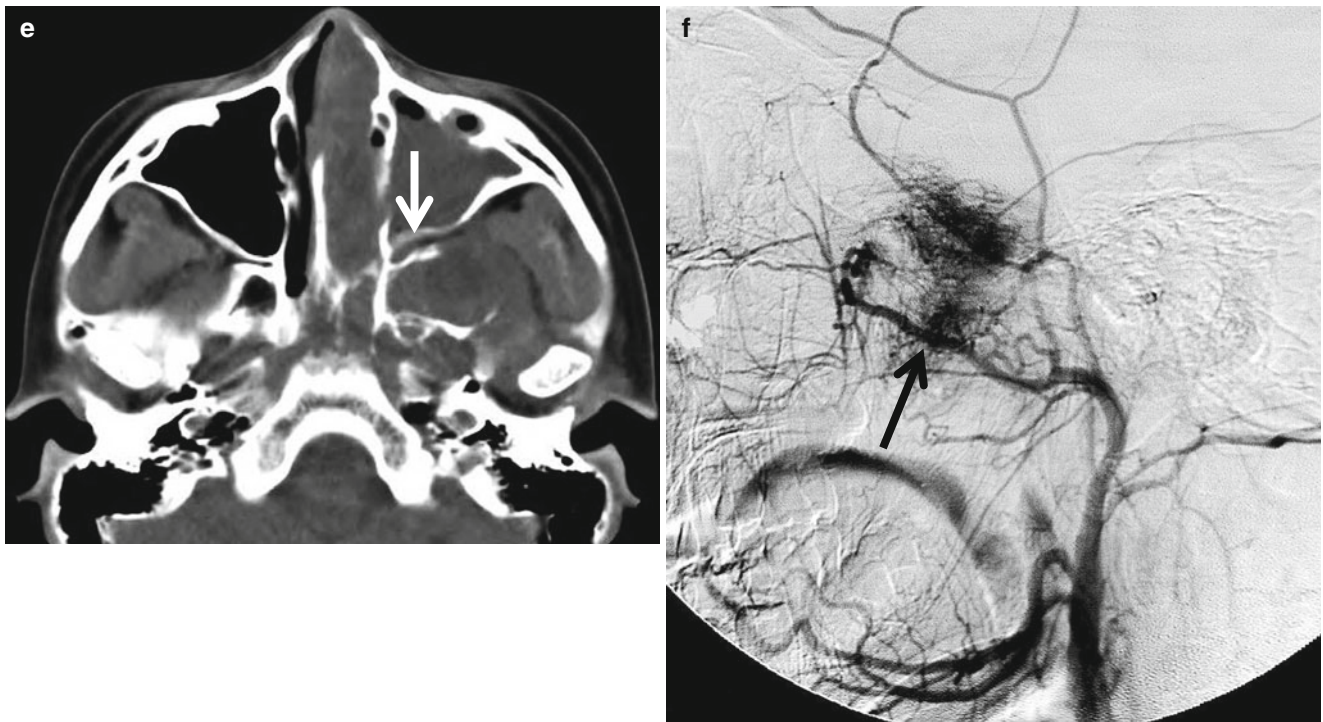


Fig.9.5 (continued)

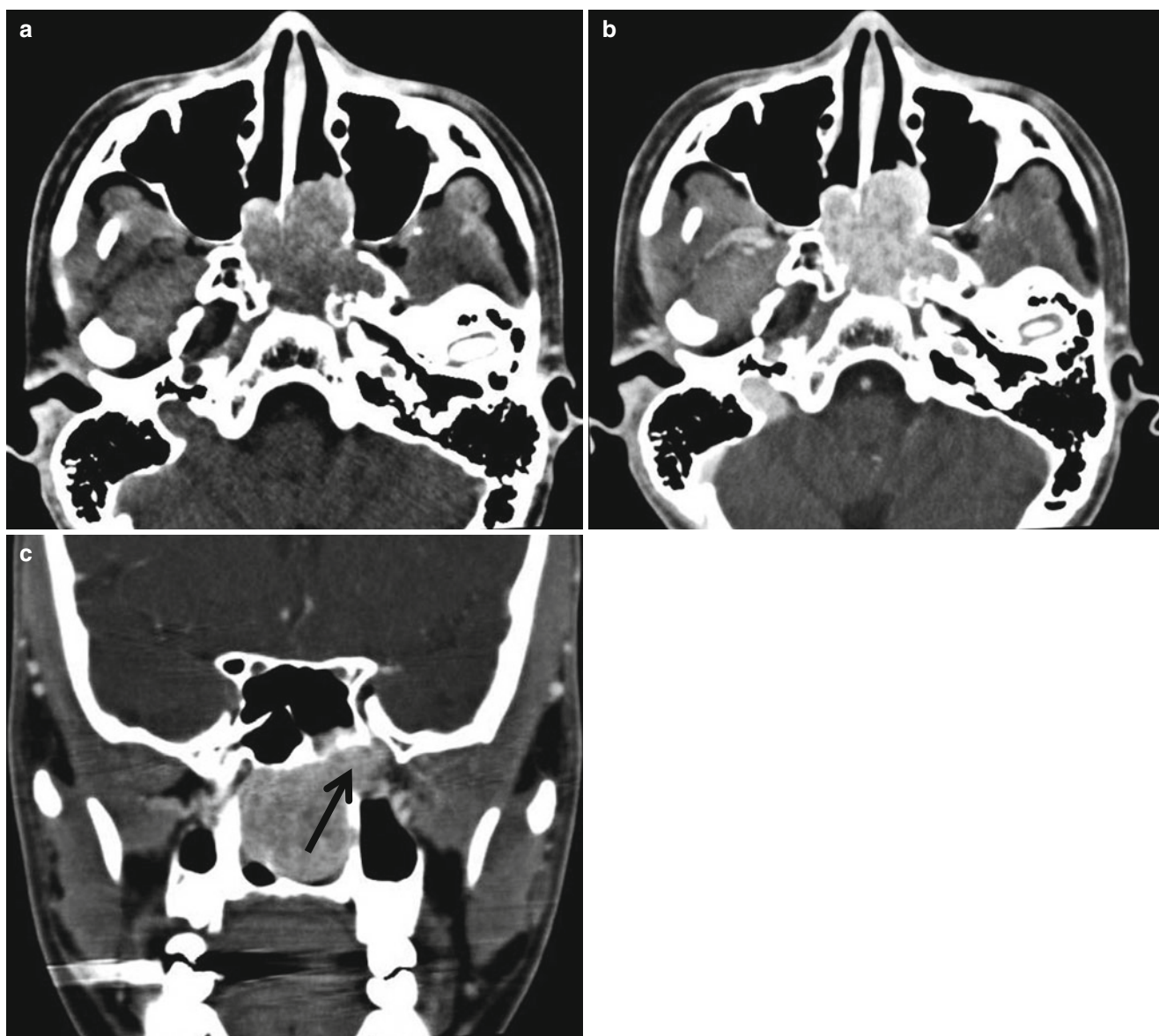


Fig. 9.6 Nasopharyngeal angiofibroma in an 18-year-old boy. (a) Nonenhanced axial CT scan shows iso- to high-attenuated soft tissue tumor obstructing the nasopharynx. (b, c) Contrast-enhanced axial and coronal reformatted CT scans show an avidly enhancing tumor

obstructing the nasopharynx extending into the left pterygopalatine fossa (*arrow*) and sphenoid sinus. Note widening of the left pterygopalatine foramen (*arrow*)

9.5.4 Langerhans Cell Histiocytosis

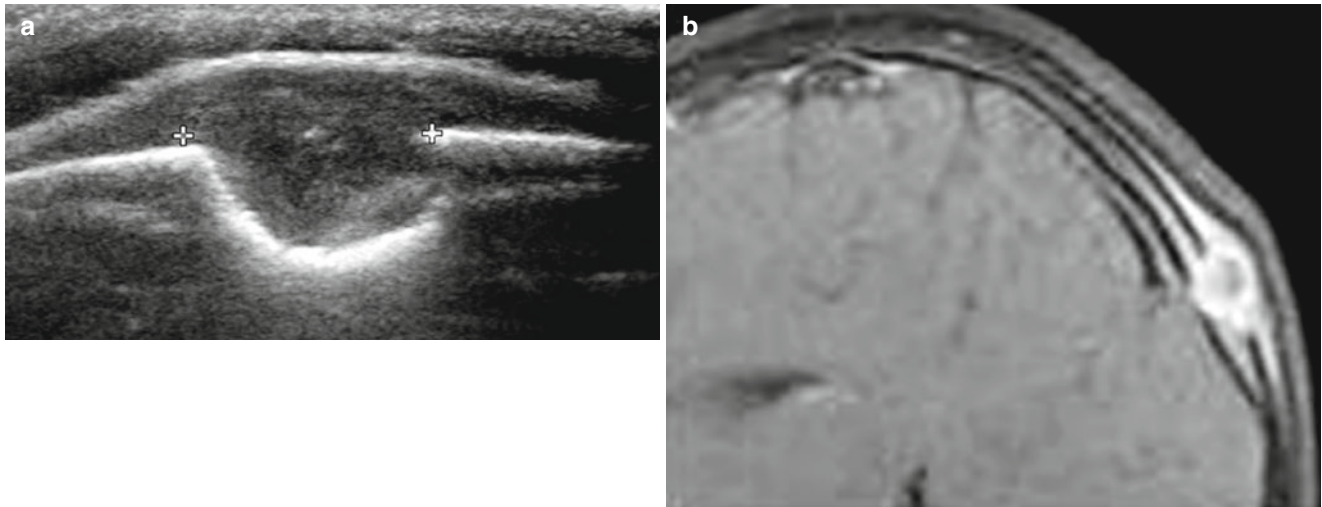


Fig. 9.7 LCH of the skull in a 2-year-old girl. (a) US shows an osteolytic lesion of a “beveled edge” with asymmetric destruction of the inner and outer tables of the skull. (b) Contrast-enhanced axial

T1-weighted fat-suppressed MR image also shows a rim-enhancing osteolytic lesion with wider destruction of the outer table of the calvarium

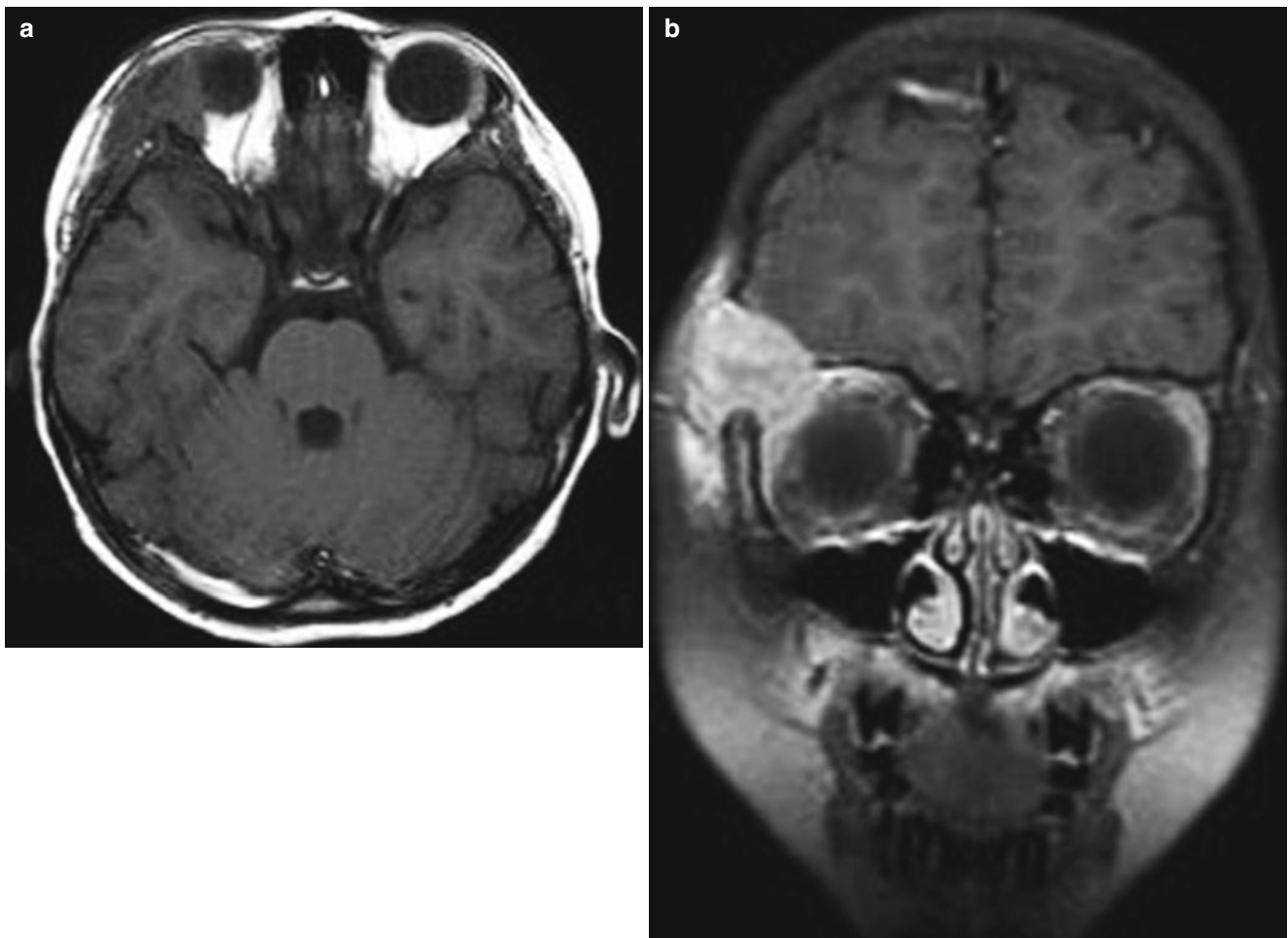


Fig. 9.8 Orbital LCH in an 8-year-old girl. (a) Axial T1-weighted MR image shows a soft tissue mass of iso-signal intensity relative to normal brain tissue in the superolateral aspect of the right orbit.

(b) Contrast-enhanced coronal T1-weighted fat-suppressed MR image shows avid enhancement of the mass extending into the epidural space and soft tissue of the frontal scalp

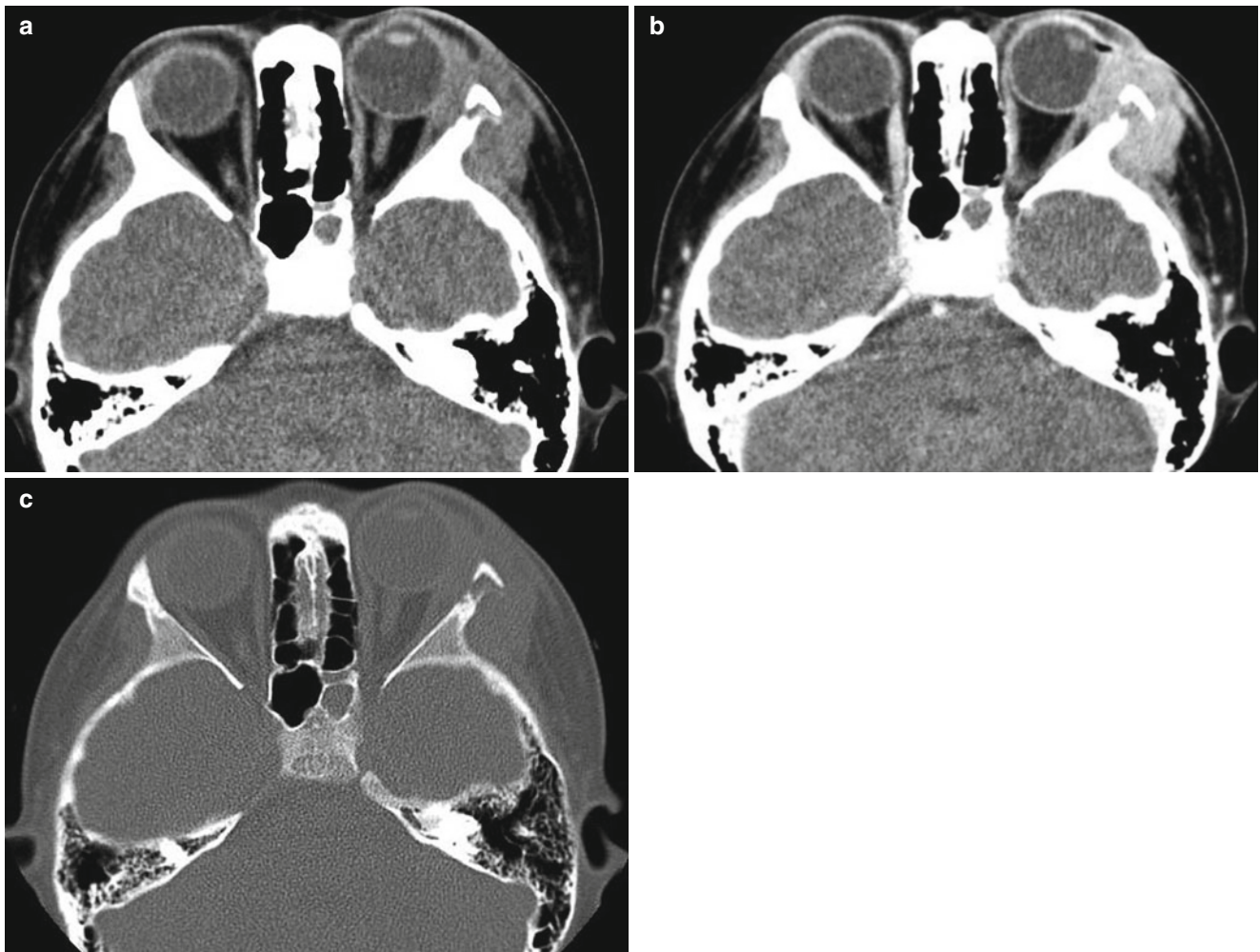


Fig. 9.9 Orbital LCH in a 7-year-old boy. (a) Nonenhanced CT shows an isoattenuated soft tissue mass in the superolateral wall of the left orbit. (b) Contrast-enhanced CT shows homogeneous enhancement of

the mass. Note proptosis of the left orbit (c) CT scan with a bone window shows destruction of superolateral wall of the left orbit

9.5.5 Fibromatosis Colli

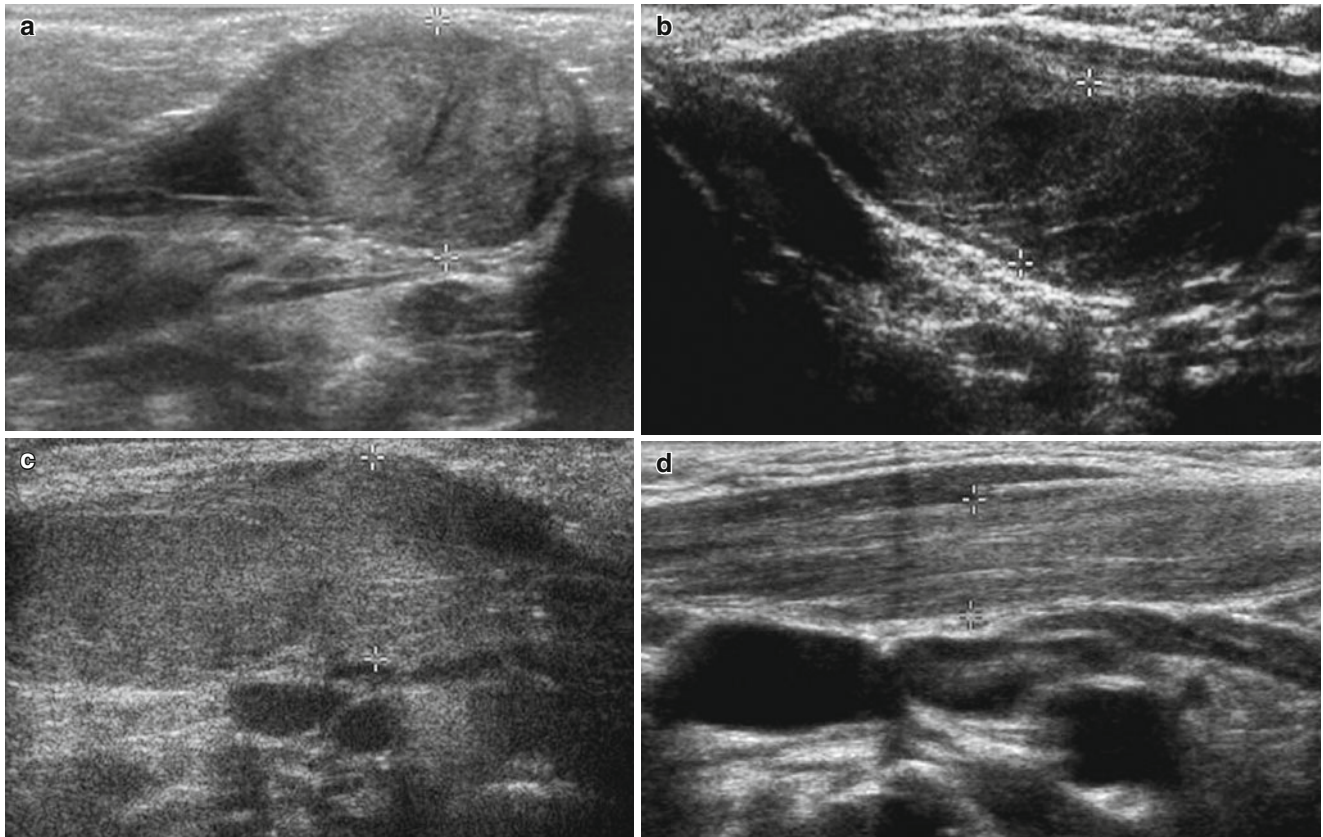


Fig. 9.10 Fibromatosis colli in infants. Various US findings of fibromatosis colli include a focal heterogeneous mass with a spindle shape (a), diffuse echogenic dot and lines against the hypoechoic background

(b), diffuse hyperechogenicity along the entire muscle (c), and hyperechoic band in the muscle (d)

9.5.6 Lipoblastoma

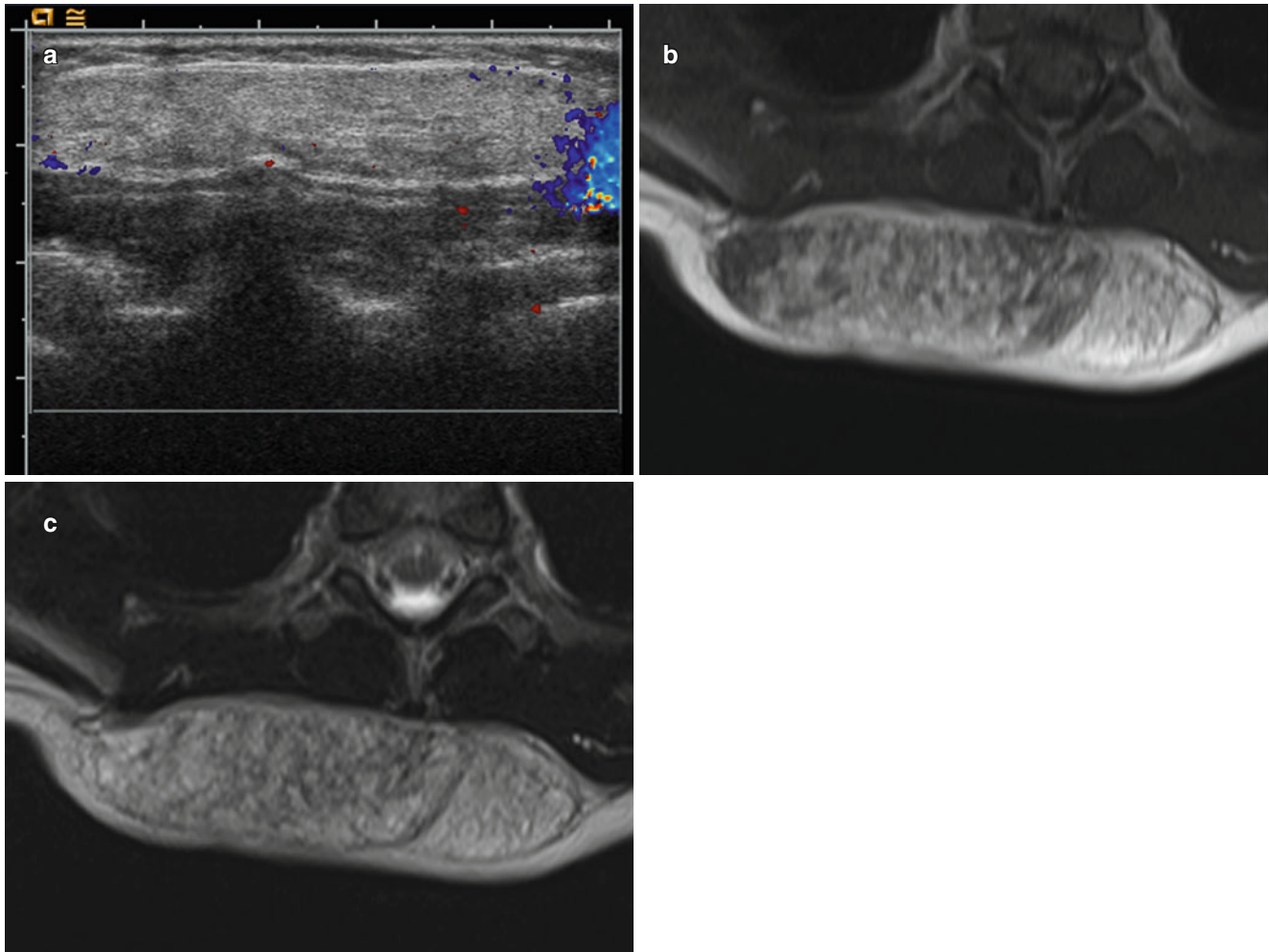


Fig. 9.11 Lipoblastoma in a 2-year-old girl. (a) Color Doppler US shows a hypovascular, echogenic solid mass in the right lower posterior neck extending to the back. (b) Axial T1-weighted image shows a well-defined mass of mixed high and iso signal intensities. (c) Axial

T2-weighted image reveals the mass of iso signal intensity to the subcutaneous fat. Multiple tiny lesions of high signal intensity in the mass suggest myxoid stroma

9.5.7 Plexiform Neurofibromas

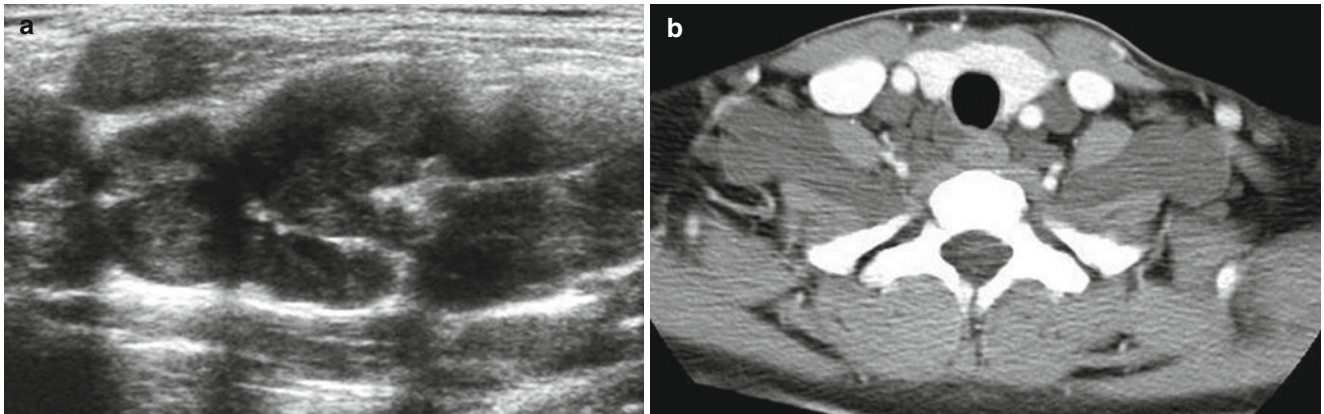


Fig. 9.12 Plexiform neurofibromatosis in an 18-year-old boy with type 1 neurofibromatosis. (a) US shows multiple nodules of neurofibromas

with a “bag of worms” appearance. (b) Contrast-enhanced CT scan shows multiple, bilateral neurofibromas along the cervical nerve roots

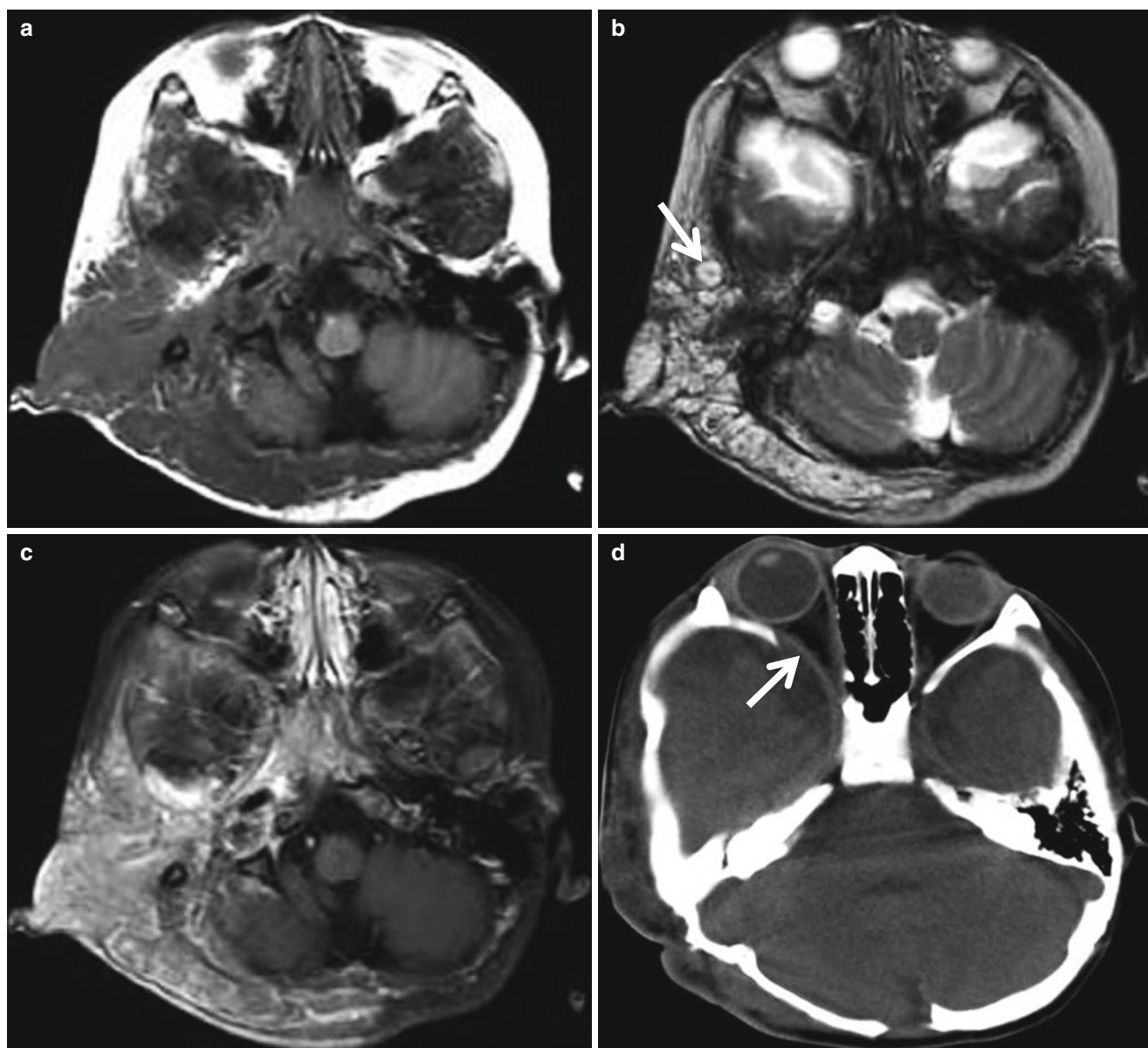


Fig. 9.13 Plexiform neurofibromatosis in a 3-year-old boy with type 1 neurofibromatosis. (a) Axial T1-weighted MR image shows an infiltrating plexiform neurofibromatosis of iso-signal intensity relative to the muscle. (b) Axial T2-weighted MR image shows heterogeneous high signal intensity of the masses with “target sign” (arrow) in some neurofibromas. (c) Contrast-enhanced T1-weighted fat-suppressed MR

image shows the tumor that extends into the retropharyngeal space, infratemporal fossa, and right parotid gland with transspatial infiltration. (d) Axial CT scan with a bone window shows bony dysplasia of the right orbit with widening of the right superior orbital fissure and proptosis

9.5.8 Pilomatrixoma

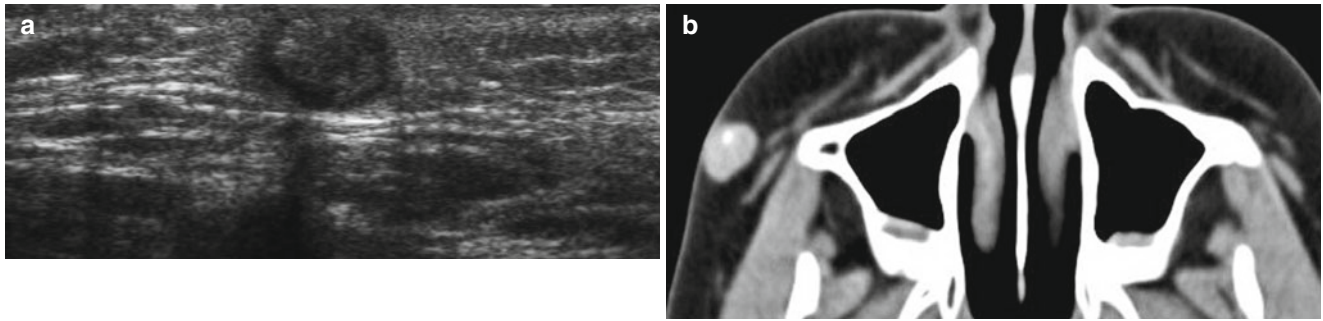


Fig. 9.14 Pilomatrixoma in a 7-year-old girl. **(a)** US shows a well-defined, round, solid nodule abutting the dermal layer of the skin with intratumoral calcifications and a posterior acoustic shadow.

(b) Noncontrast CT scan shows a small calcified dermal nodule in the right cheek

9.5.9 Lymphoma

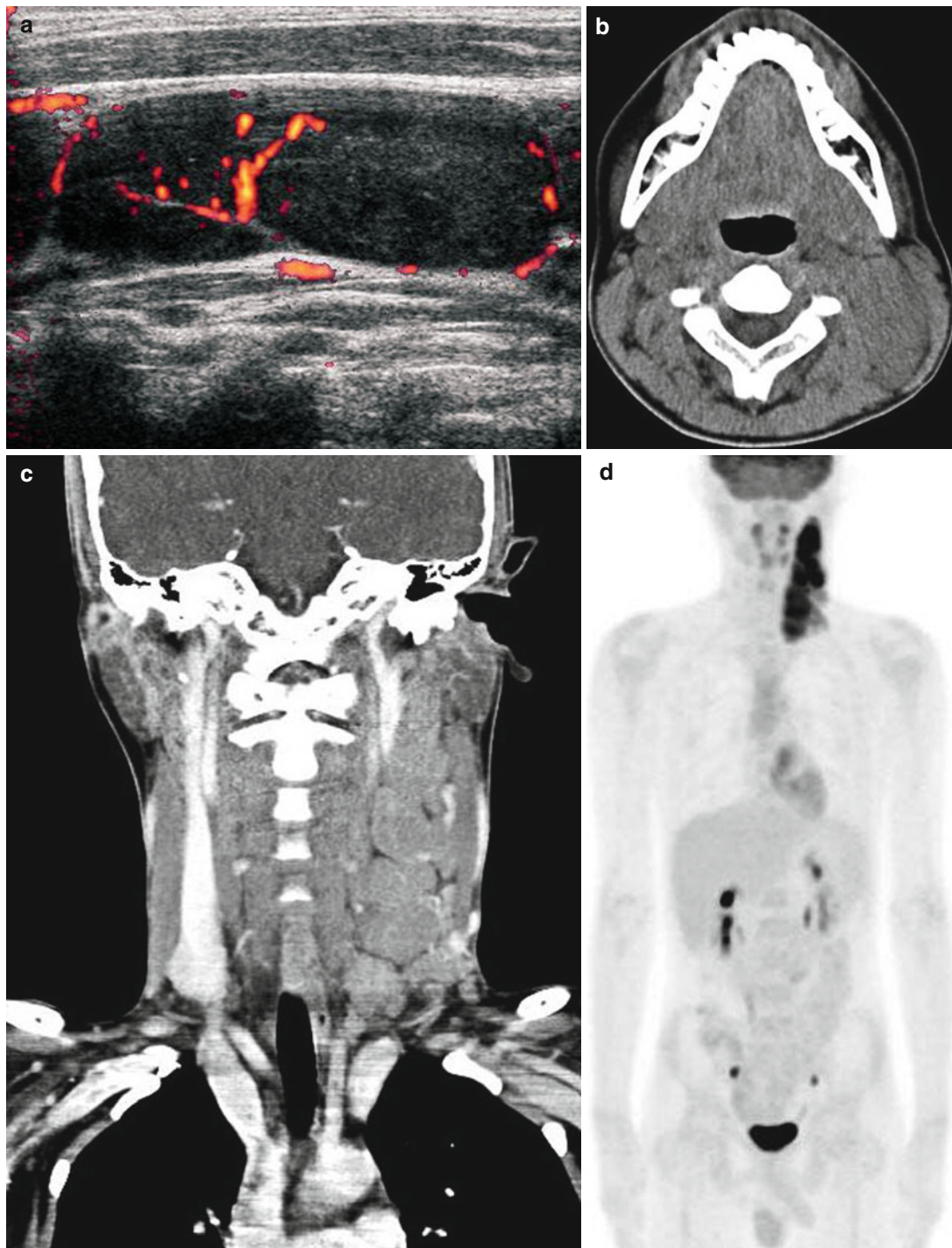


Fig. 9.15 HL in a 14-year-old boy. (a) US shows an elliptical shaped, homogeneous but large cervical lymphadenopathy with eccentrically displaced hilum and peripheral vascularity. (b) Noncontrast CT scan shows multiple large homogeneous cervical lymphadenopathies. (c) Contrast-enhanced coronal reformatted CT scan shows

homogeneously enhancing lymphadenopathies with contiguous involvement and extending to the anterior mediastinum. (d) PET CT shows intense FDG uptake along the left cervical lymph nodes contiguous to the mediastinum

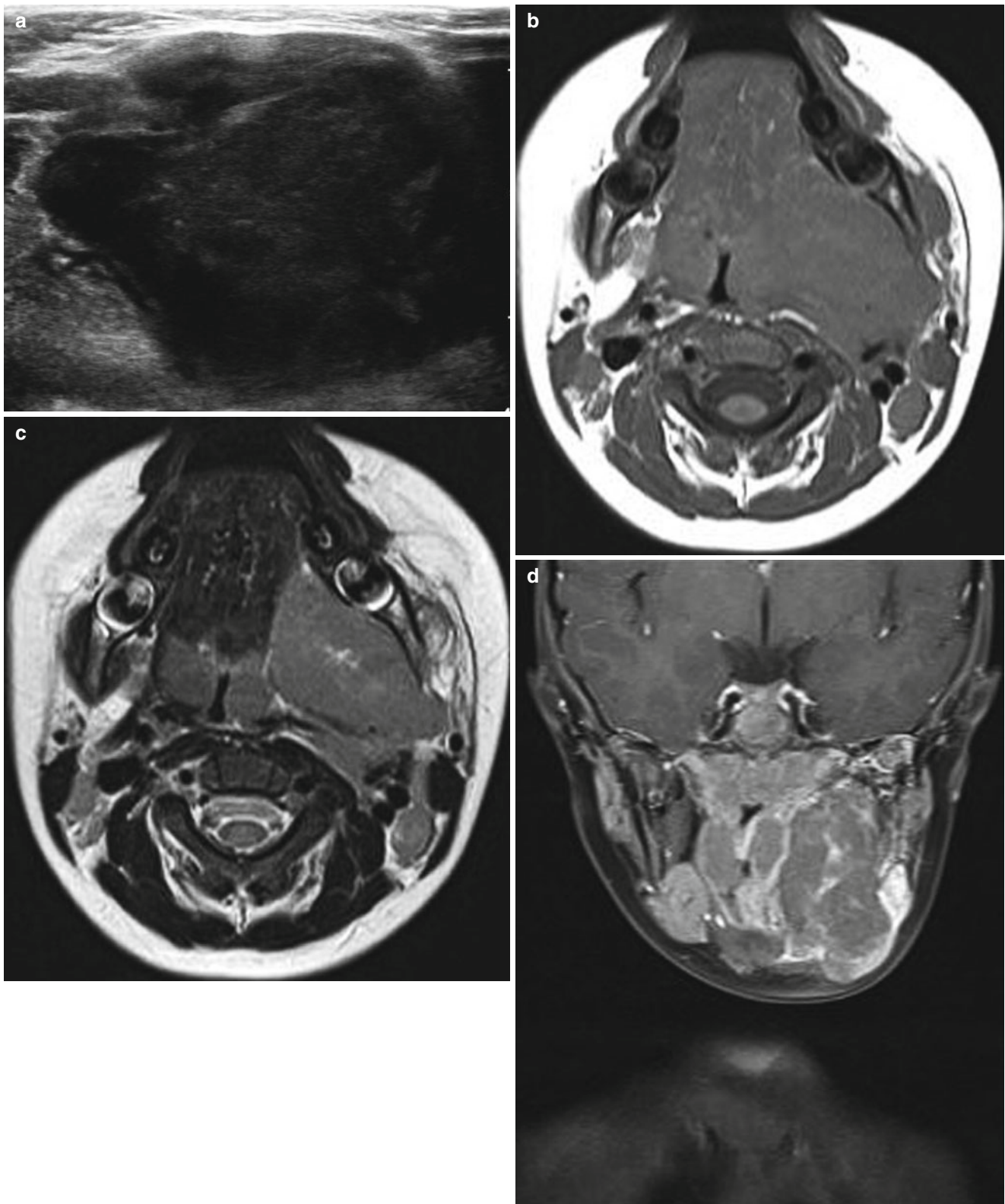


Fig. 9.16 NHL in a 3-year-old boy. (a) US shows large, very hypoechoic (“pseudocystic”) mass in the left submandibular space. (b, c) Axial T1- and T2-weighted MR images show nodular enlargement of both lingual tonsils with homogeneous iso-signal intensity, a bulky soft tissue mass in the left submandibular space, and noncontiguous cervical lymph nodes in the retropharyngeal and posterior cervical

chains. (d) Contrast-enhanced fat-suppressed coronal T1-weighted MR image shows homogeneously enhancing masses obstructing the nasopharyngeal airway. (e) PET CT shows FDT uptake involving the tumor mass of left submandibular space, both lingual tonsils, right supraclavicular lymph nodes, right proximal humerus, and multiple lymphadenopathies in the abdomen and pelvis

e

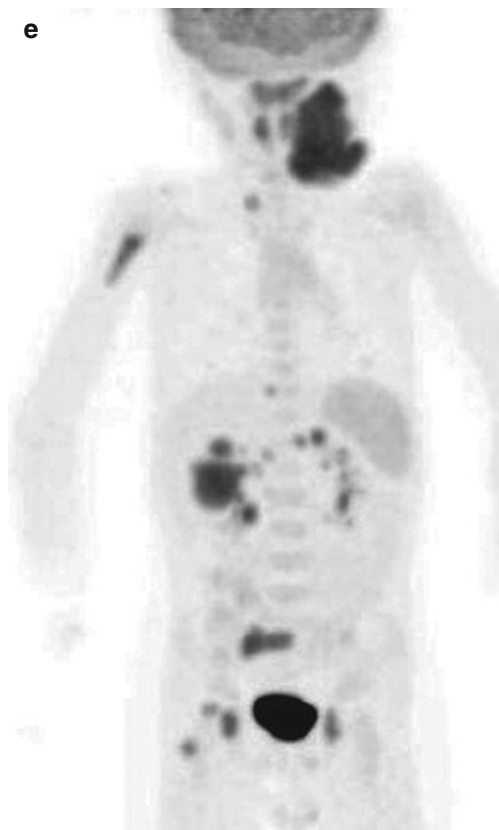


Fig. 9.16 (continued)

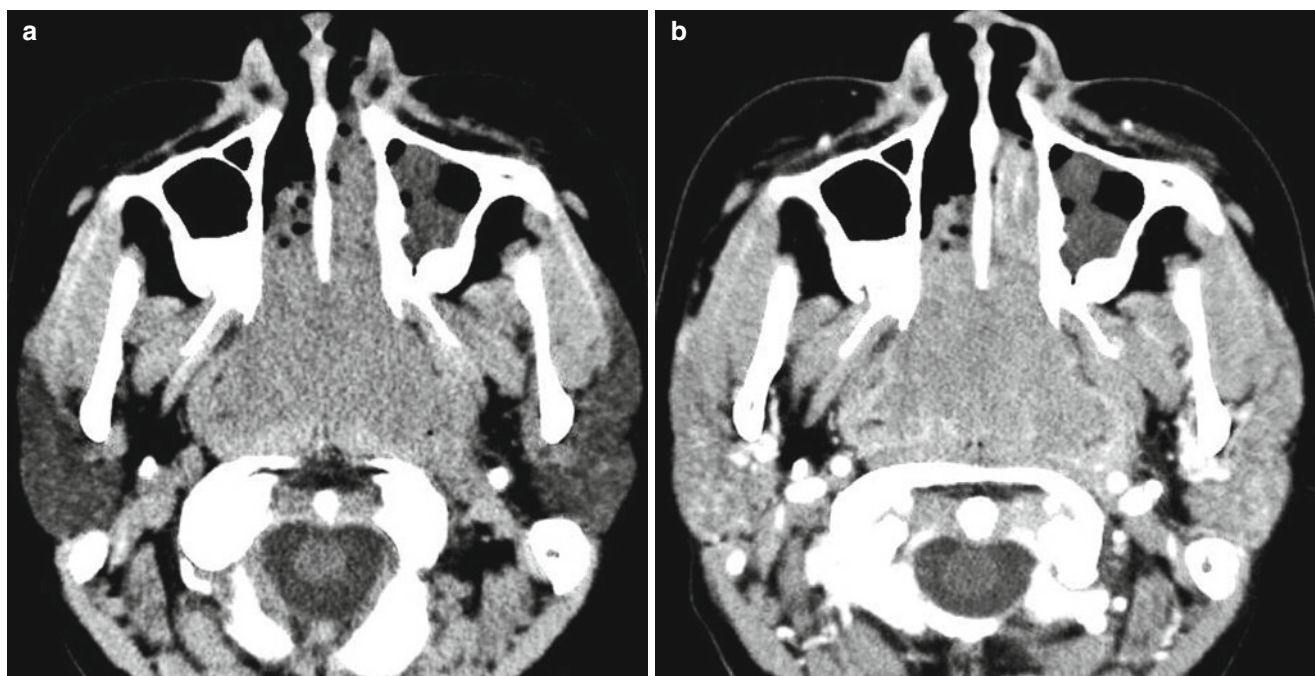


Fig. 9.17 Burkitt lymphoma in a 12-year-old boy. (a) Nonenhanced CT scan shows an isoattenuated mass relative to the muscle involving both nasal cavities and entire nasopharynx. (b) Contrast-enhanced CT shows homogeneously enhancing mass

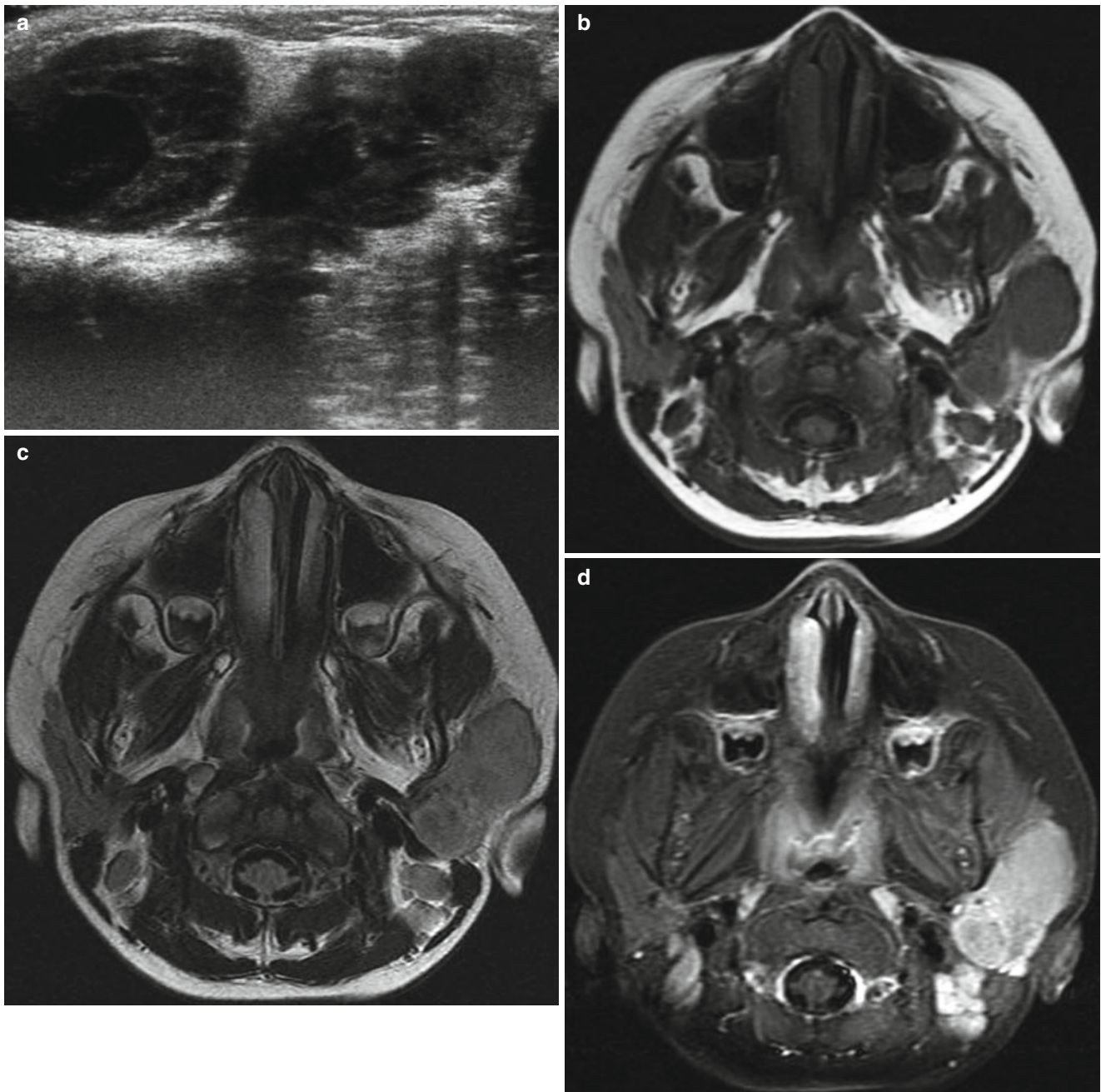


Fig. 9.18 NHL of parotid gland in a 4-year-old boy. **(a)** US shows multiple, heterogeneous, very hypoechoic (“pseudocystic”) lymphadenopathies with obliteration of normal echogenic hilum. **(b, c)** Axial T1- and T2-weighted images show solid tumor of iso-signal intensity in the

left parotid gland. **(d)** Contrast-enhanced fat-suppressed axial T1-weighted MR image shows homogeneously enhancing the tumor mass and several cervical lymph nodes in the posterior cervical chain

9.5.10 Rhabdomyosarcoma

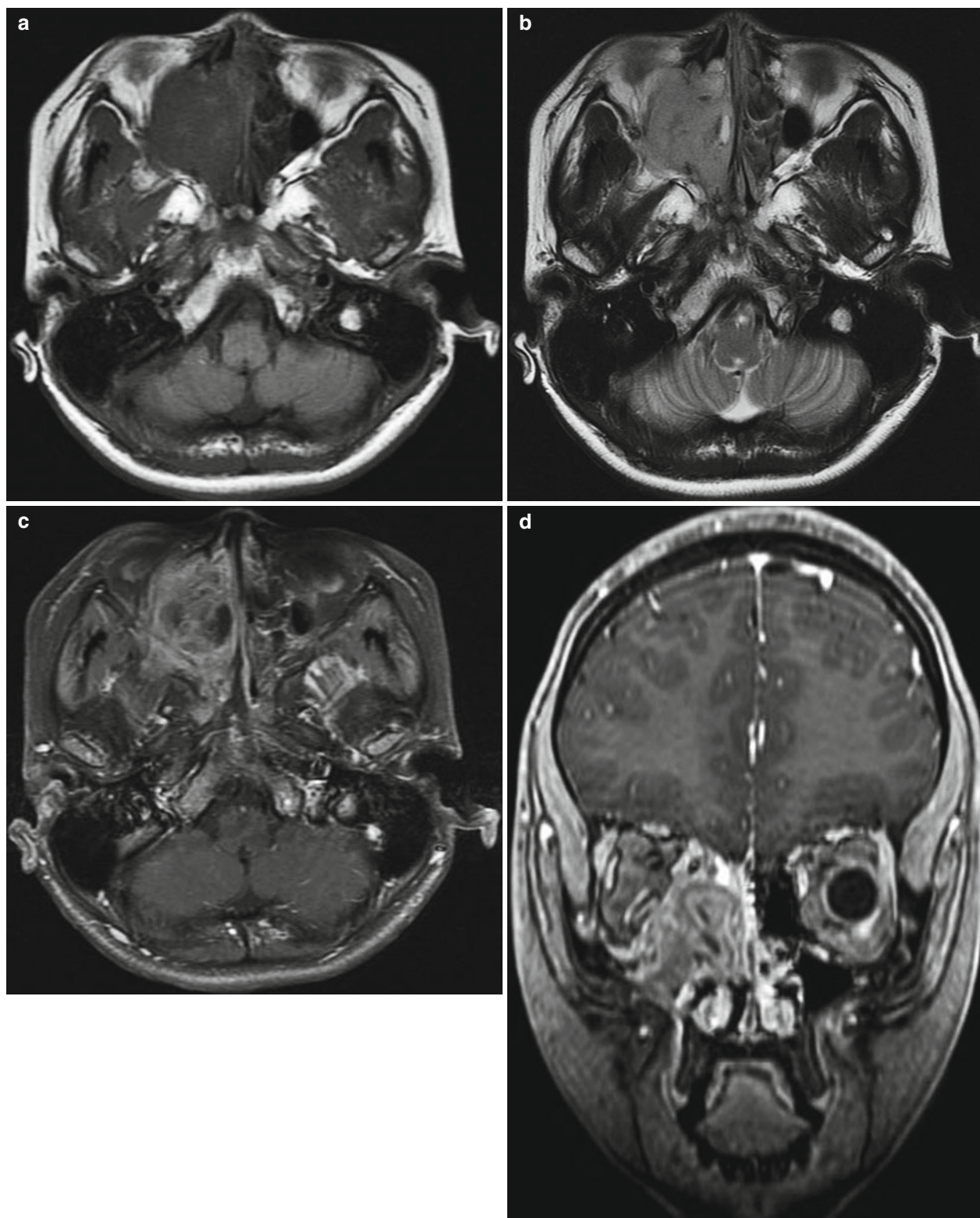


Fig. 9.19 Rhabdomyosarcoma in a 15-year-old girl. (a) Axial T1-weighted MR image shows a bulky soft tissue mass of iso-signal intensity relative to muscle in the superonasal aspect of the right orbit. (b) Axial T2-weighted MR image shows a heterogeneous slightly high signal intensity of the mass with internal necrosis and fluid-hemorrhage

levels. (c, d) Contrast-enhanced T1-weighted fat-suppressed MR images reveal heterogeneous enhancement of the mass extending into the right ethmoid and maxillary sinuses. (e) CT scan with a bone window reveals destruction of the right orbital wall and maxillary sinus

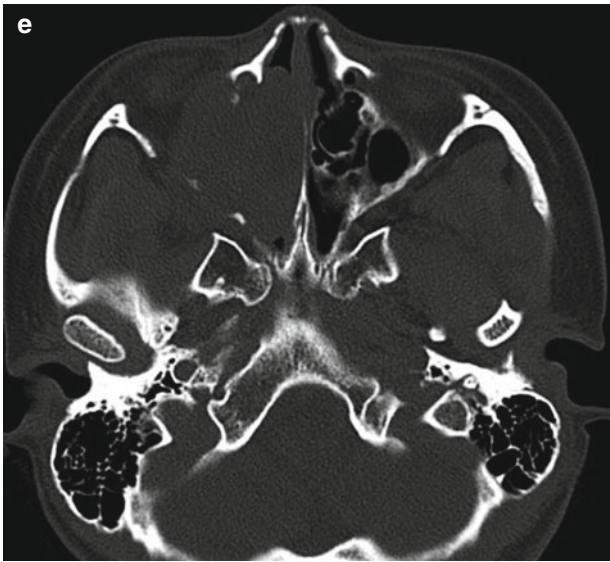


Fig. 9.19 (continued)

9.5.11 Chloroma

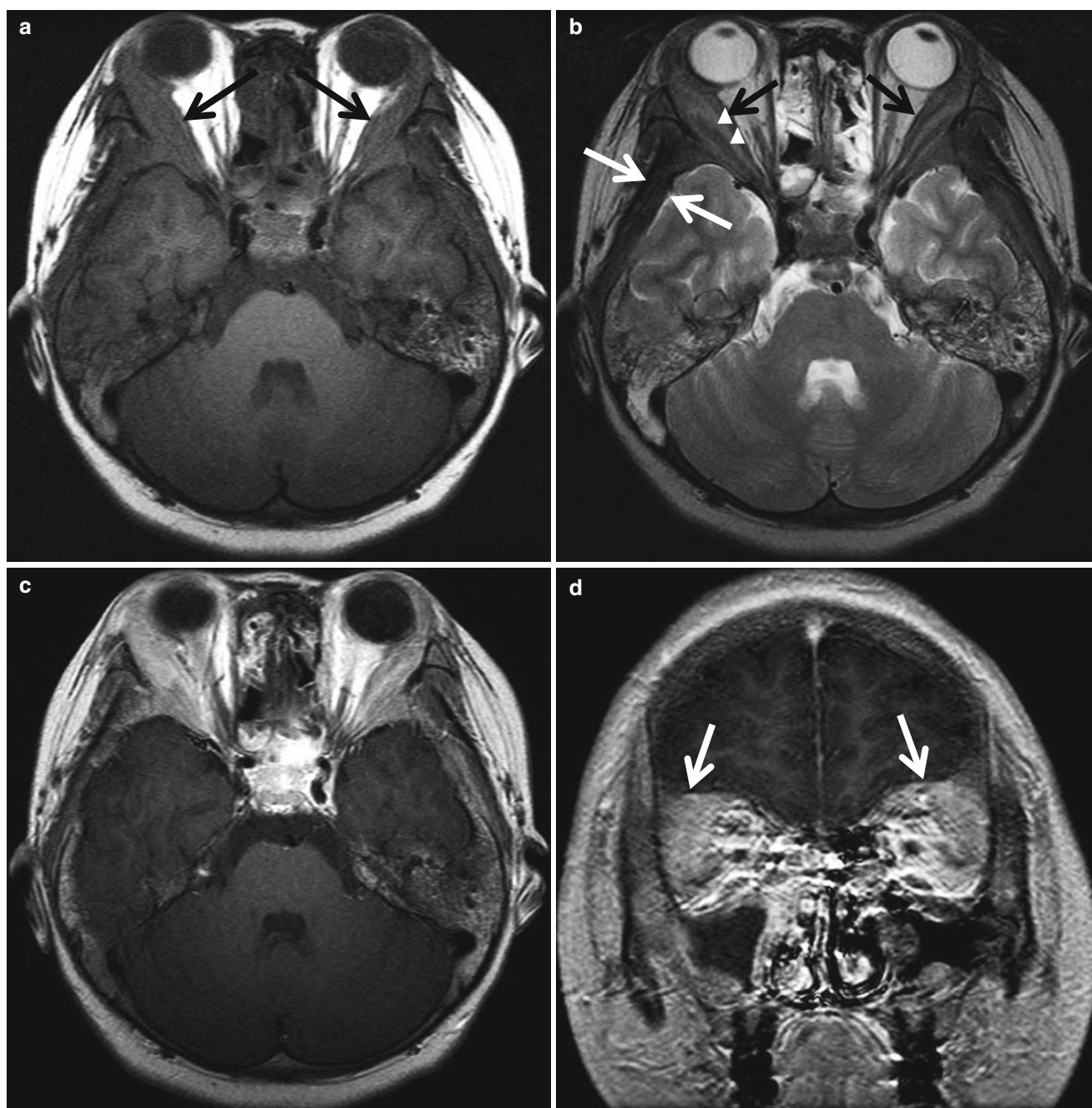


Fig. 9.20 Orbital chloromas in a 12-year-old girl with acute myelogenous leukemia. (a) Axial T1-weighted MR image shows both lateral rectus muscles (*black arrows*) diffusely thickened, with iso-signal intensity relative to muscle. (b) Axial T2-weighted image shows thickened lateral rectus muscles of iso-signal intensity (*black arrows*) and lateral orbit walls of slightly high signal intensity (*arrowheads*). Diploic spaces of both temporal bones are widened (*white arrows*). (c) Contrast-enhanced axial T1-weighted image shows homogeneously

enhancing lateral rectus muscles and bone marrow of both temporal bones. Note bilateral proptosis. (d, e) Contrast-enhanced coronal T1-weighted images show both homogeneously enhancing lacrimal glands (*arrows*) (d) and other symmetrical soft tissue masses (*arrows*) in both the frontal scalps (e). (f) CT scan with a bone window reveals permeative destruction with thick periosteal reaction (*arrows*) involving both lateral orbital walls and sphenoid and temporal bones

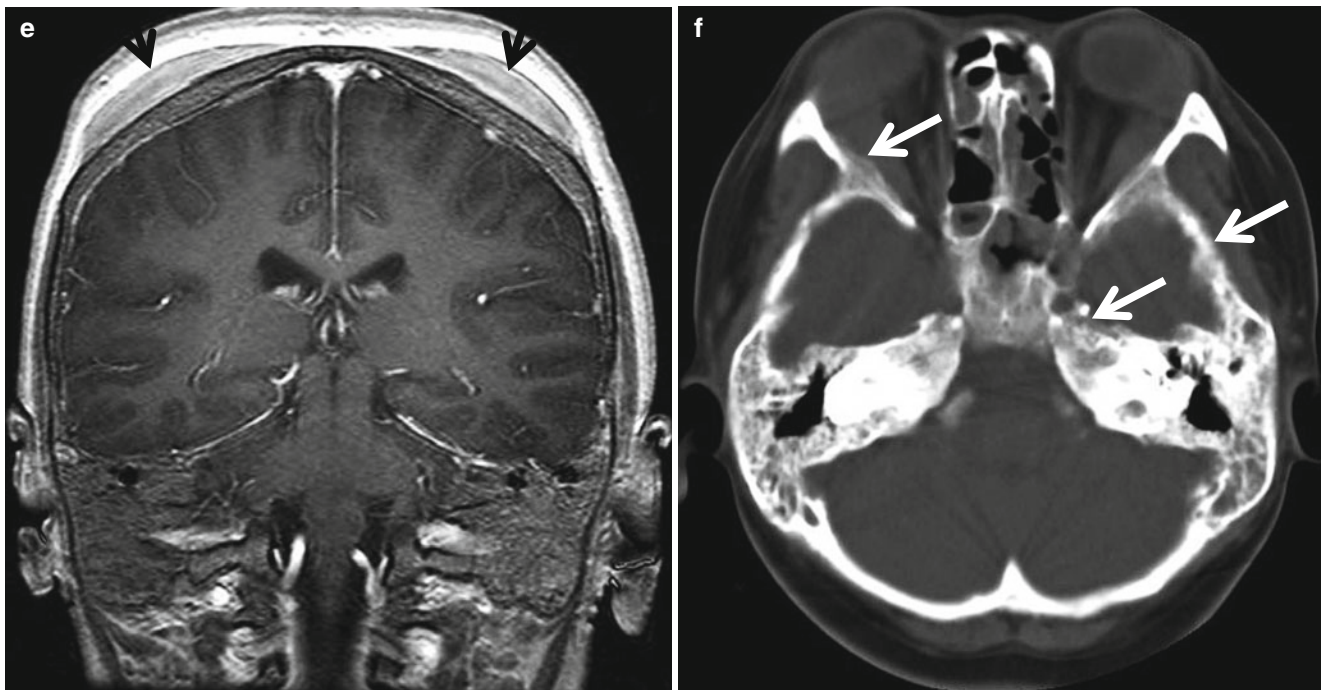


Fig. 9.20 (continued)

9.5.12 Neuroblastoma

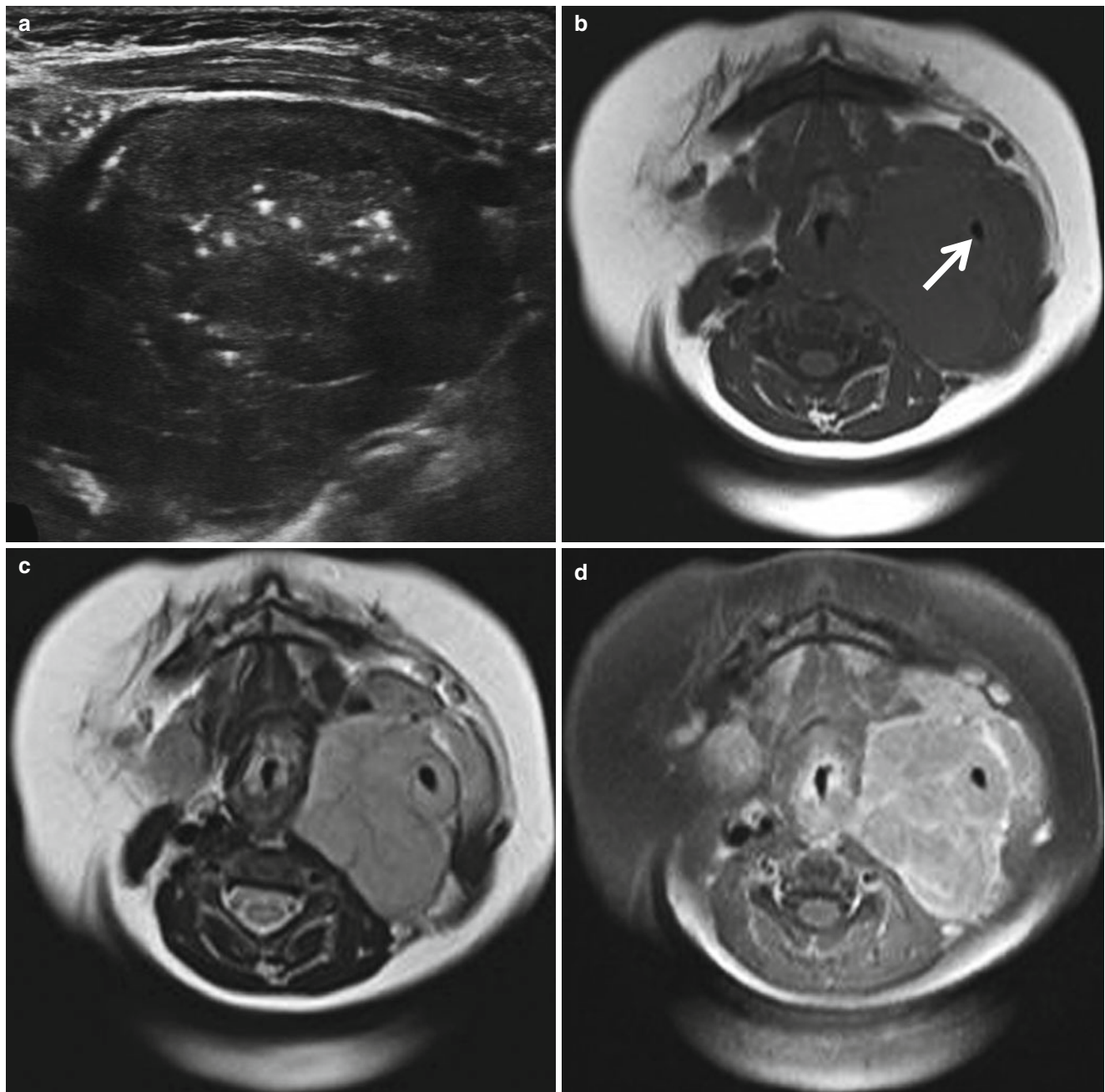


Fig. 9.21 Cervical neuroblastoma in a 5-month-old girl. **(a)** US shows a well-defined, large, solid mass with multifocal calcifications in the posterior deep cervical space. **(b)** Axial T1-weighted MR image shows a homogeneously high signal intensity of the mass relative to the mus-

cle encasing the left common carotid artery (*arrow*). **(c)** Axial T2-weighted MR image shows a slightly high signal intensity of the mass. **(d)** Axial contrast-enhanced T1-weighted fat-suppressed MR image shows homogeneous enhancement of the mass

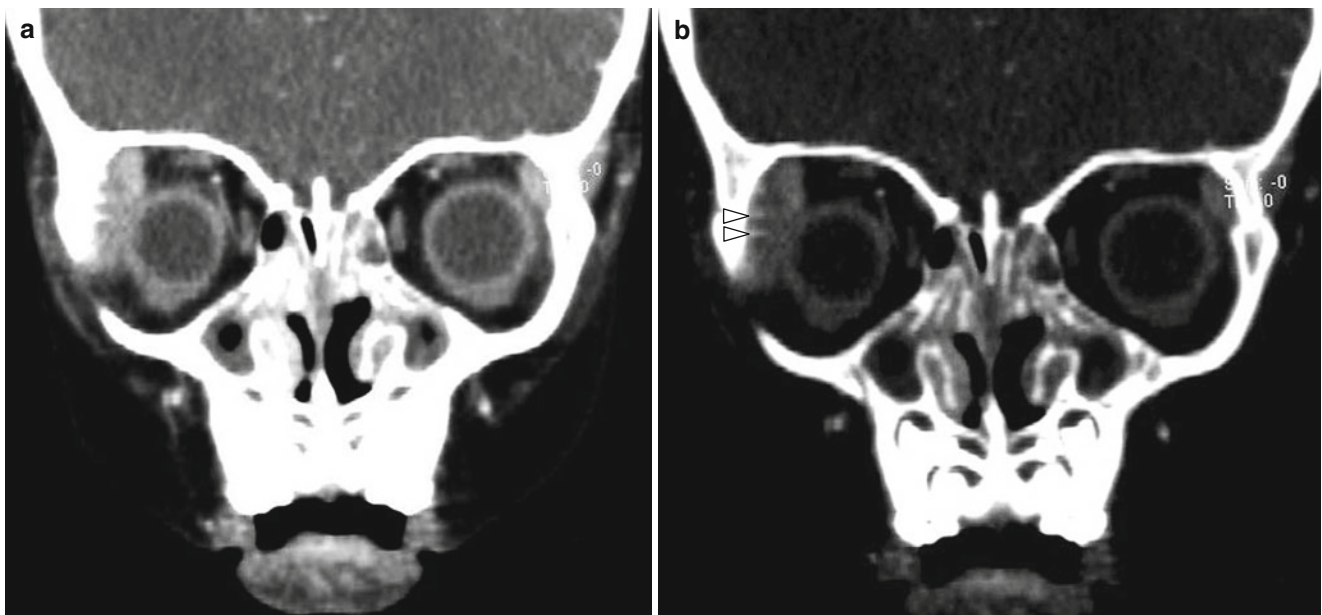


Fig. 9.22 Metastatic neuroblastoma in a 2-year-old boy. **(a)** Contrast-enhanced coronal CT scan shows a homogeneously enhancing soft tissue mass involving the superolateral wall of the right orbit. **(b)** CT scan

with a bone window reveals a spiculated (hair-on-end, sunburst pattern) (*arrowheads*) periosteal reaction of the right orbit

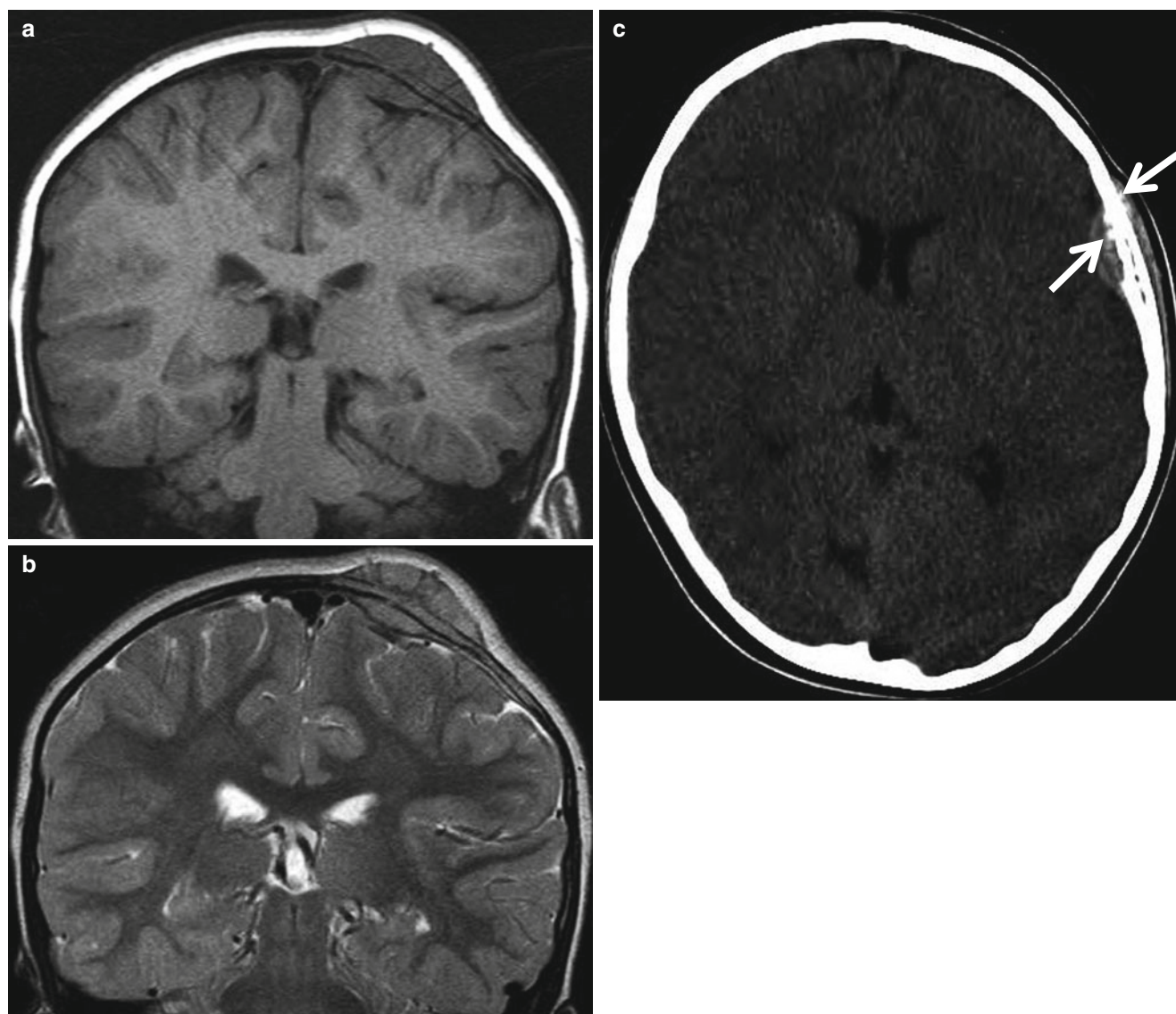


Fig. 9.23 Metastatic neuroblastoma in a 3-year-old boy. (a, b) Coronal T1- and T2-weighted MR images show a calvarial mass involving both epidural and subperiosteal spaces. The mass shows homogeneous

iso-signal intensity relative to brain tissue on both T1- and T2-weighted images. (c) CT scan with a bone window reveals a spiculated periosteal reaction (“hair-on-end”) of the cortex (*arrowhead*)

9.5.13 Retinoblastoma

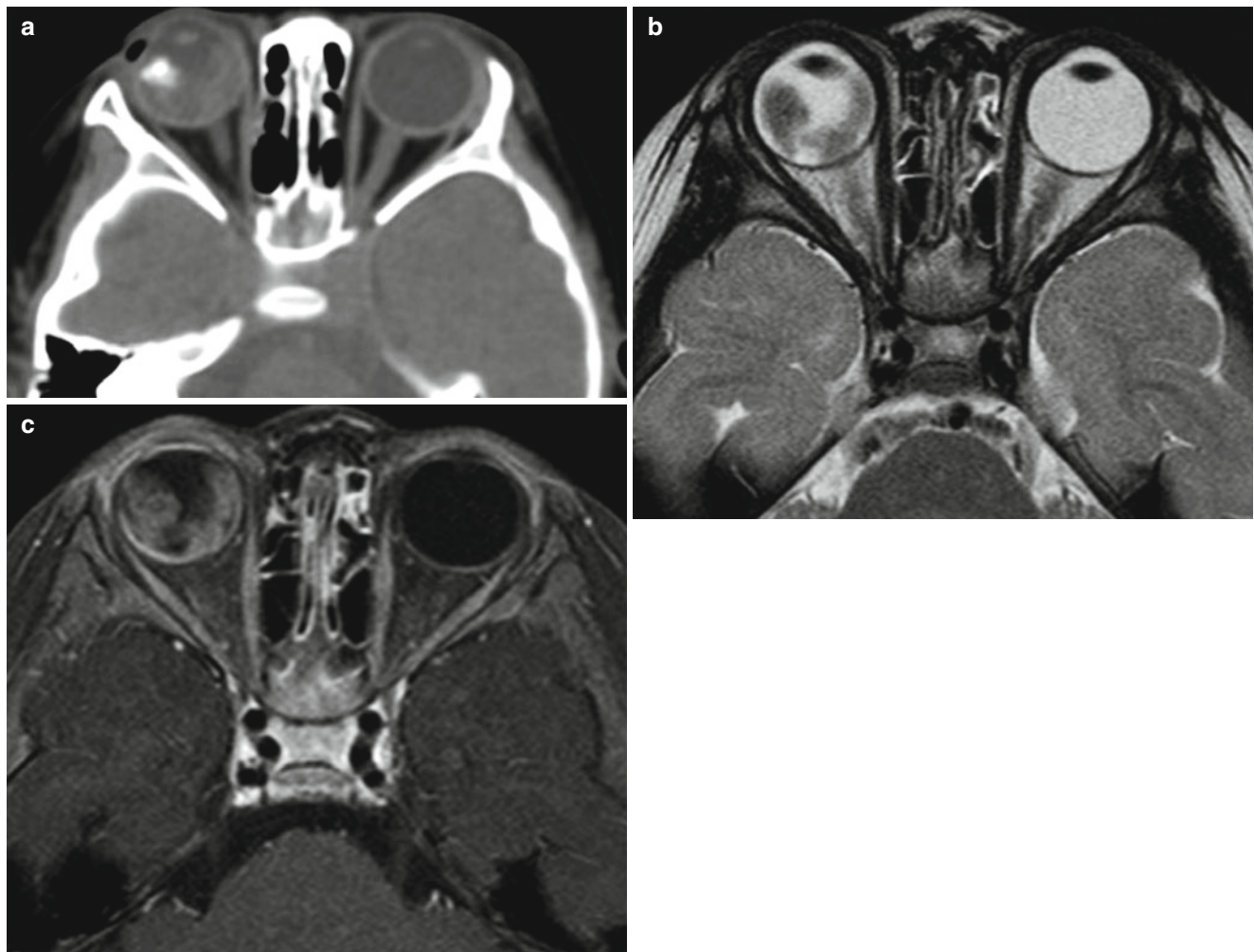


Fig. 9.24 Retinoblastoma in a 2-year-old girl. **(a)** Nonenhanced CT scan shows a densely calcified solid mass in the right globe. **(b)** Axial T2-weighted MR image shows a low signal intensity of the mass.

(c) Axial contrast-enhanced T1-weighted fat-suppressed MR image shows homogeneous enhancement of the mass with a retinal detachment

9.5.14 Pleomorphic Adenoma

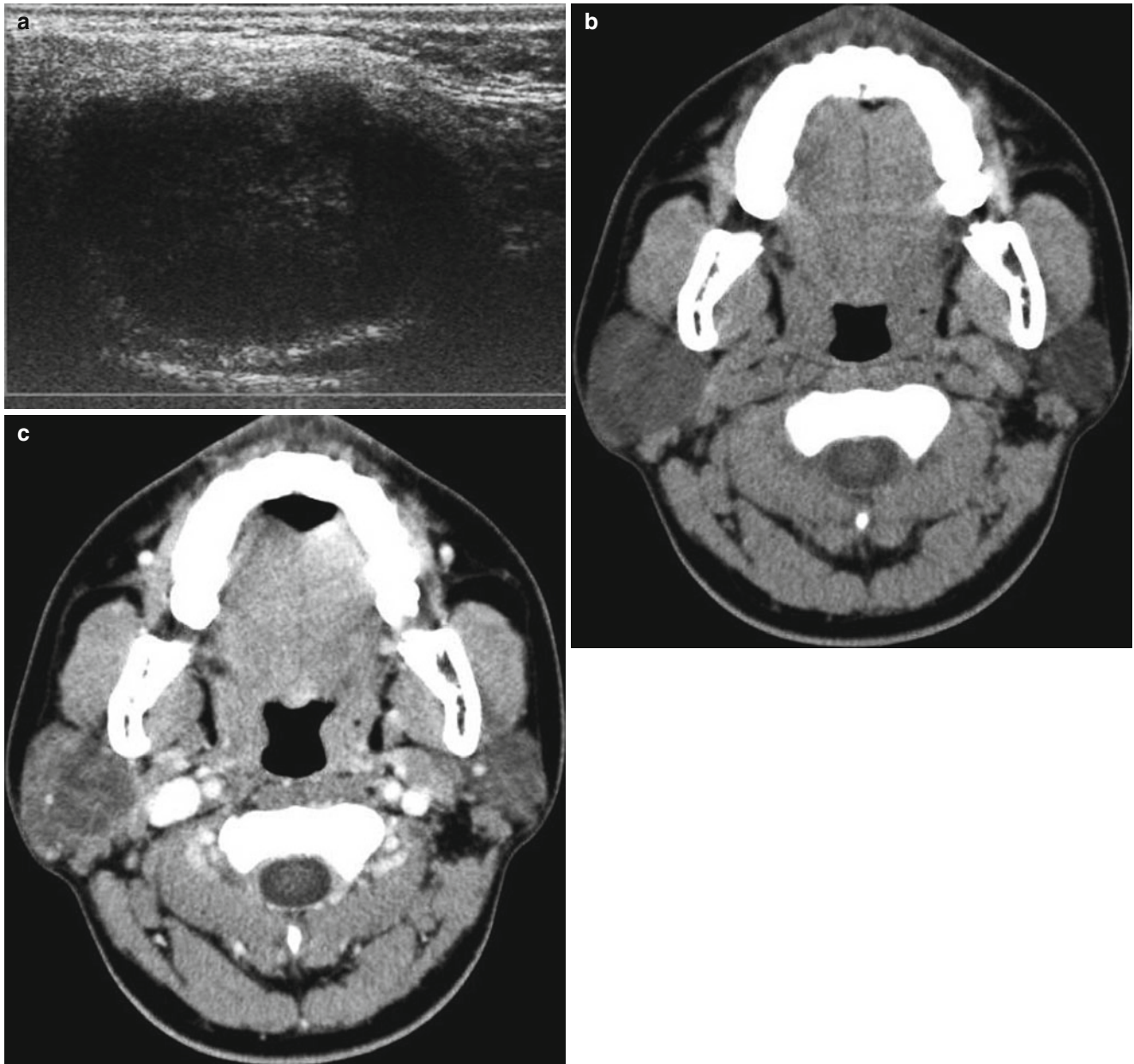


Fig. 9.25 Pleomorphic adenoma in a 13-year-old boy. (a) Color Doppler US shows a lobulating, hypoechoic, and hypovascular solid mass in the right parotid gland. (b) Nonenhanced CT scans shows an

isoattenuated mass relative to the muscles in the right parotid gland. (c) Contrast-enhanced CT shows poorly enhancing tumor

9.5.15 Thyroid Tumors

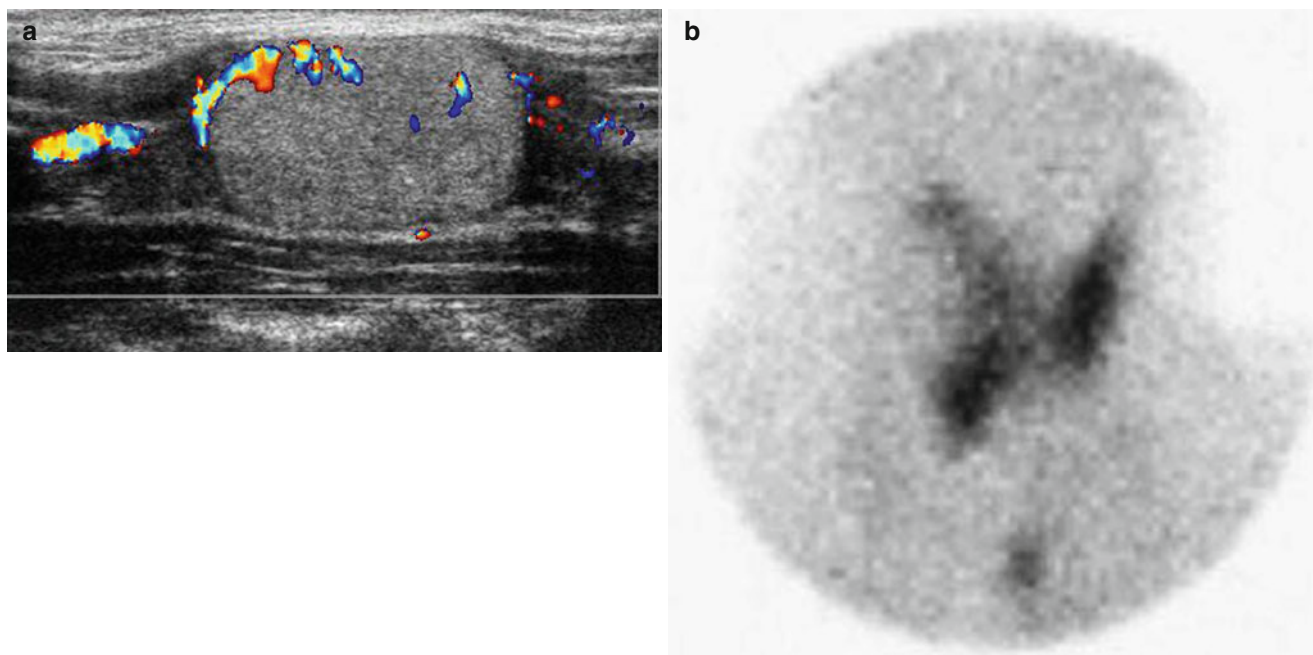


Fig. 9.26 Follicular adenoma of the thyroid gland in an 11-year-old girl. **(a)** Color Doppler US shows a well-defined hyperechoic solid mass in the right thyroid gland. The tumor is completely surrounded by a hypoechoic peripheral halo and shows no demonstrable calcification

or necrosis. Minimal vascularity in the peripheral and central portions of the mass is noted. **(b)** Radionuclide thyroid scan with Tc-99 m O₄ reveals a cold nodule in the right thyroid gland

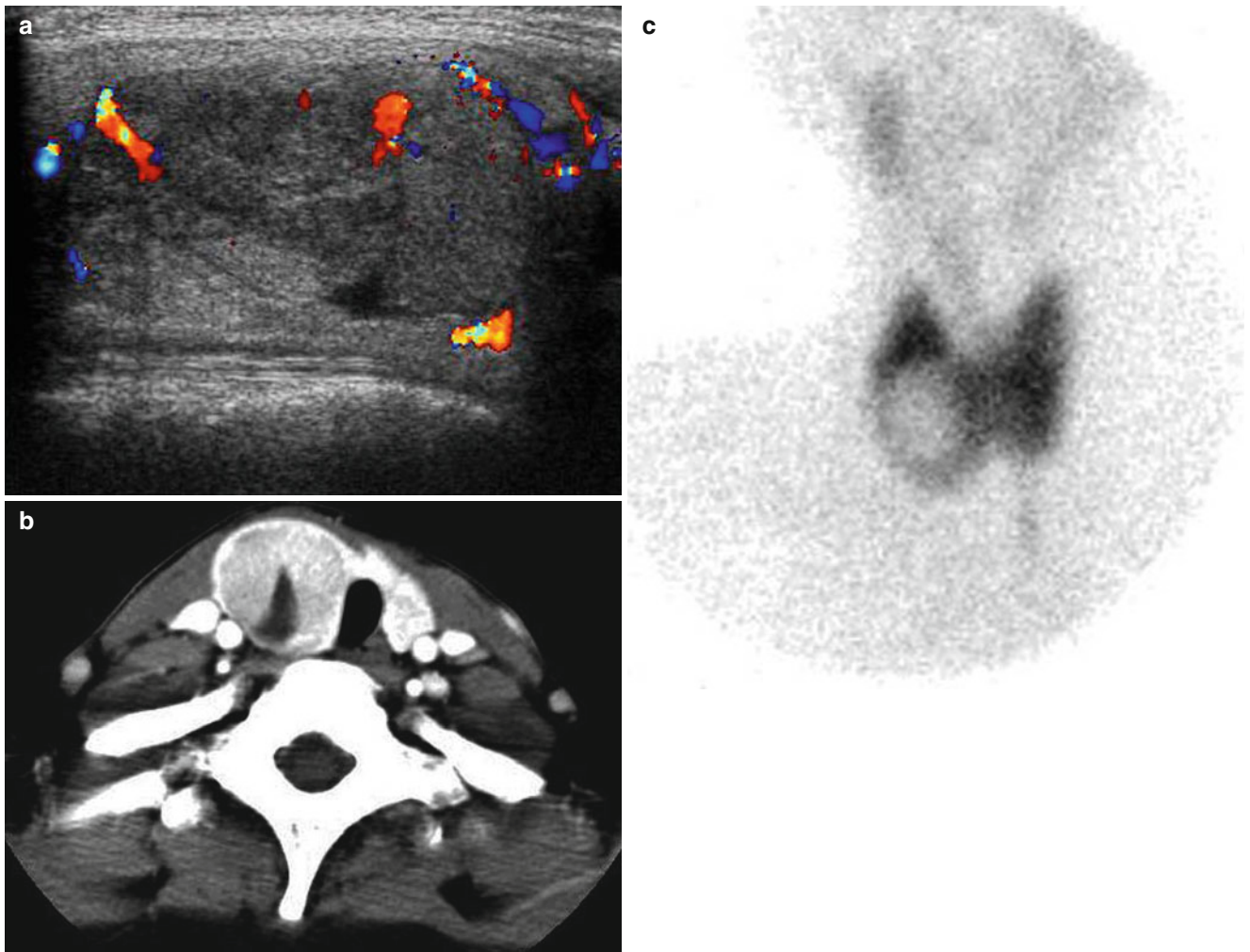


Fig. 9.27 Follicular carcinoma of the thyroid gland in a 14-year-old girl. **(a)** Color Doppler US shows a well-defined but heterogeneous solid mass in the right thyroid gland. The tumor is not completely surrounded by a hypoechoic peripheral halo and shows a focal cystic portion. No demonstrable microcalcifications are noted. Note minimal

peripheral and internal vascularity of the tumor. **(b)** Contrast-enhanced CT scan shows the avidly enhancing mass, except the cystic portion. **(c)** Radionuclide thyroid scan with Tc-99 m O4 reveals a cold nodule in the lower pole of the right thyroid gland

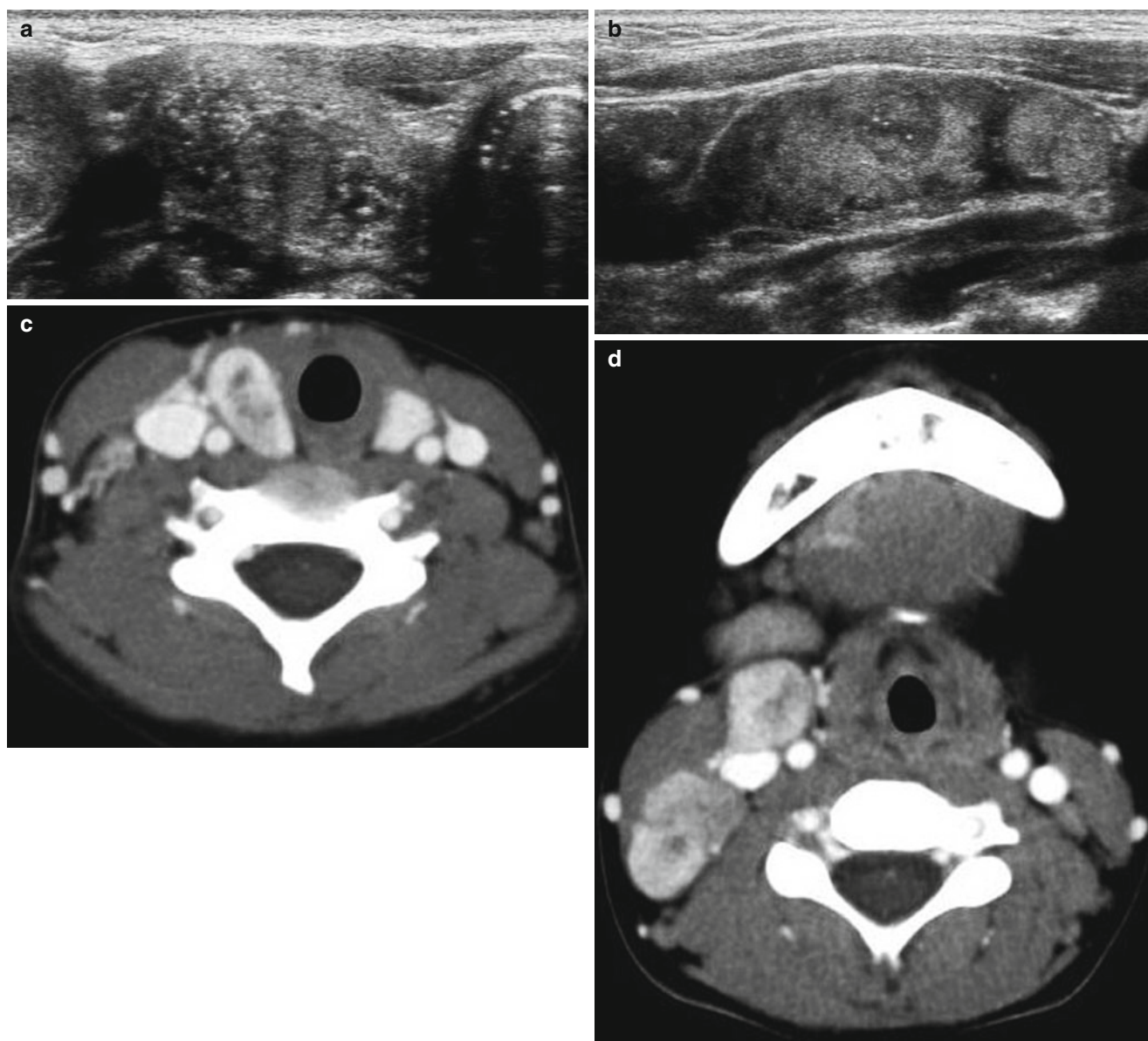


Fig. 9.28 Papillary carcinoma of the thyroid gland in an 8-year-old girl. **(a)** US shows an ill-defined heterogeneous hyperechoic solid mass in the right thyroid gland. The tumor shows numerous microcalcifications and hypervascularity on Color Doppler image. **(b)** Multiple

metastatic cervical lymphadenopathies with microcalcifications are noted. **(c, d)** Contrast-enhanced CT scans show a tumor mass in the right thyroid gland and the same natured multiple metastatic lymphadenopathies along the right cervical chains

References

- Baker LL, Dillon WP, Hieshima GB, et al. Hemangiomas and vascular malformations of the head and neck: MR characterization. *AJNR Am J Neuroradiol*. 1993;4:307–14.
- Barkovich AJ. Intracranial, orbital, and neck masses of childhood. In: Barkovich AJ, editor. *Pediatric neuroimaging*. 4th ed. Philadelphia: Lippincott Williams and Wilkins; 2005.
- Beaman FD, Kransdorf MJ, Andrews TR, et al. Superficial soft-tissue masses: analysis, diagnosis, and differential considerations. *Radiographics*. 2007;27:509–23.
- Bedi DG, John SD, Swischuk LE. Fibromatosis colli of infancy: variability of sonographic appearance. *J Clin Ultrasound*. 1998;26:345–8.
- Bulas RB, Laine FJ, Das Narla L. Bilateral orbital granulocytic sarcoma (chloroma) preceding the blast phase of acute myelogenous leukemia: CT findings. *Pediatr Radiol*. 1995;25:488–9.
- Castillo Jr BV, Kaufmann L. Pediatric tumors of the eye and orbit. *Pediatr Clin North Am*. 2003;50:149–72.
- Frieden IJ, Reese V, Cohen D. PHACE syndrome. The association of posterior fossa brain malformations, hemangiomas, arterial anomalies, coarctation of the aorta and cardiac defects, and eye abnormalities. *Arch Dermatol*. 1996;132:307–11.
- Gow KW, Lensing S, Hill DA, et al. Thyroid carcinoma presenting in childhood or after treatment of childhood malignancies: an institutional experience and review of the literature. *J Pediatr Surg*. 2003;38:1574–80.
- Haller JO, Kassner EG, Ostrowitz A, et al. Pilomatrixoma (calcifying epithelioma of Malherbe): radiographic features. *Radiology*. 1977;123:151–3.
- Kaufman LM, Mafee MF, Song CD. Retinoblastoma and simulating lesions. Role of CT, MR imaging and use of Gd-DTPA contrast enhancement. *Radiol Clin North Am*. 1998;36:1101–11.
- Laor T. MR imaging of soft tissue tumors and tumor-like lesions. *Pediatr Radiol*. 2004;34:24–37.
- Laurie AJ, Lyon SG, Lasser EC. Contrast material iodides: potential effects on radioactive iodine thyroid uptake. *J Nucl Med*. 1992;33:237–8.
- Meyer JS, Harty MP, Mahboubi S, et al. Langerhans cell histiocytosis: presentation and evolution of radiologic findings with clinical correlation. *Radiographics*. 1995;15:1135–46.
- Mulliken JB, Glowacki J. Hemangiomas and vascular malformations in infants and children: a classification based on endothelial characteristics. *Plast Reconstr Surg*. 1982;69:412–22.
- Murphey MD, Carroll JF, Flemming DJ, et al. Benign musculoskeletal lipomatous lesions. *Radiographics*. 2004;24:1433–66.
- Robson CD. Imaging of head and neck neoplasms in children. *Pediatr Radiol*. 2010;40:499–509.
- Smirniotopoulos JG, Chiechi MV. Teratomas, dermoids, and epidermoids of the head and neck. *Radiographics*. 1995;15:1437–55.
- Suh JS, Abenzo P, Galloway HR, et al. Peripheral (extracranial) nerve tumors: correlation of MR imaging and histologic findings. *Radiology*. 1992;183:341–6.
- Yousem DM, Lexa FJ, Bilaniuk LT, Zimmerman RI. Rhabdomyosarcoma in the head and neck: MR imaging evaluation. *Radiology*. 1990;177:683–6.

Hyun Woo Goo

Contents

10.1	Introduction	364
10.2	Pediatric Chest CT Imaging Techniques	364
10.3	Unilateral Pulmonary Agenesis/Aplasia	364
10.4	Unilateral Pulmonary Hypoplasia	364
10.4.1	Scimitar Syndrome.....	364
10.4.2	Horseshoe Lung	365
10.4.3	Pulmonary Vein Atresia	365
10.4.4	Congenital Diaphragmatic Hernia	365
10.5	Bronchopulmonary Foregut Malformations	365
10.5.1	Bronchogenic Cyst.....	365
10.5.2	Bronchial Atresia	365
10.5.3	Congenital Pulmonary Airway Malformation	366
10.5.4	Pulmonary Sequestration	366
10.5.5	Esophageal Bronchus/Lung	366
10.6	Congenital Lobar Hyperinflation	366
10.7	Systemic Arterial Supply to Normal Lung	367
10.8	Illustrations: CT Findings of Congenital Lung Malformations	368
10.8.1	Pulmonary Agenesis	368
10.8.2	Scimitar Syndrome.....	369
10.8.3	Horseshoe Lung	370
10.8.4	Pulmonary Vein Atresia	371
10.8.5	Congenital Diaphragmatic Hernia	372
10.8.6	Bronchogenic Cyst.....	373
10.8.7	Bronchial Atresia	374
10.8.8	Congenital Pulmonary Airway Malformation (CPAM).....	375
10.8.9	Pulmonary Sequestration	376
10.8.10	Esophageal Bronchus.....	377
10.8.11	Congenital Lobar Hyperinflation	378
10.8.12	Systemic Arterial Supply to Normal Lung	379
	References	380

H.W. Goo, M.D., Ph.D.

Department of Radiology and Research Institute of Radiology,
Asan Medical Center, University of Ulsan College of Medicine,
88, Olympic-ro 43-gil, Songpa-gu, Seoul, Korea
e-mail: hwgoo@amc.seoul.kr

10.1 Introduction

Congenital lung malformations include a spectrum of entities. They may manifest as a pure lung parenchymal abnormality, a pure vascular abnormality, or a combination of parenchymal and vascular abnormalities. In addition, two or more anomalies may occur in the same location, the so-called “hybrid” lesion, in congenital lung malformations. On the other hand, two or more separate malformations may occur in the same patient. These congenital lung malformations are more commonly seen in our clinical practice due to the widespread use of prenatal sonography. CT is exceedingly useful for the postnatal evaluation of congenital lung malformations, because the imaging modality offers unprecedented characterization of the lung, airway, and thoracic vascular abnormalities of these lesions (Daltro et al. 2004; Lee et al. 2008b; Kocaoğlu et al. 2010; Tomà et al. 2011; Watarai et al. 2012). In this chapter, the imaging features of various congenital lung malformations are described.

10.2 Pediatric Chest CT Imaging Techniques

Chest CT is increasingly used for evaluating congenital lung malformations in children. This increased clinical utility of CT is attributed to inherent merits of this imaging modality, such as excellent air–tissue contrast and short examination time (Goo et al. 2013). In addition, recent advancements of CT techniques considerably improve the image quality by allowing faster scan speed, less motion artifacts, and less image noise (Goo 2013a). It is noteworthy that pediatric chest CT can be performed under 1 mSv by using body size–adapted protocols and various radiation dose reduction techniques (Goo 2011, 2012). For instance, the combined use of low tube voltages (70 or 80 kV) and iterative reconstruction algorithms can further reduce radiation dose of pediatric chest CT. Another useful radiation dose reduction strategy in evaluating congenital lung malformations is the minimization of the scan range by confining the range to the lung lesions. Cine CT can demonstrate dynamic changes in lung parenchymal density and therefore help identify air trapping (Goo and Kim 2006). The recent introduction of the novel combined ECG and respiratory triggering can eliminate respiratory and cardiac pulsation artifacts almost completely from pediatric chest CT images of free-breathing young children. Anatomic details of congenital lung malformations provided by CT are required more for thoroscopic resection than for open resection (Nasr and Bass 2012).

10.3 Unilateral Pulmonary Agenesis/Aplasia

Pulmonary agenesis is a complete absence of the lung parenchyma, bronchi, and vascular supply. Pulmonary aplasia is distinguished from agenesis by the presence of a blind-ending rudimentary bronchus. CT shows a marked ipsilateral mediastinal shift and anterior herniation of the hyperinflated contralateral lung across midline (Fig. 10.1). CT is helpful in distinguishing agenesis/aplasia from hypoplasia or total lung atelectasis. The ipsilateral thoracic cage tends to be smaller. Unilateral pulmonary agenesis/aplasia occurs equally on either side and is often clinically inapparent. Poor clinical outcome is largely due to associated congenital anomalies.

10.4 Unilateral Pulmonary Hypoplasia

Unilateral pulmonary hypoplasia may be primary or secondary. The affected patients may present with unexplained pneumothorax or neonatal respiratory distress. In addition to a smaller volume of the affected lung, more commonly involving the right lung, CT reveals a small or atretic ipsilateral pulmonary artery. These patients have an increased risk of developing pulmonary hypertension.

10.4.1 Scimitar Syndrome

Scimitar syndrome, also known as hypogenetic lung syndrome or congenital pulmonary venolobar syndrome, is characterized by a partial anomalous pulmonary venous return in which all or part of the right pulmonary veins anomalously drain into the inferior vena cava or the right atrium via the so-called scimitar vein, right lung hypoplasia, and systemic arterial supply to the hypoplastic right lung, which can be demonstrated on CT (Fig. 10.2). Other veins, such as portal and hepatic veins, have rarely been reported as the anomalous pulmonary venous drainage sites in scimitar syndrome. Abnormal lung lobation and bilateral hyparterial bronchi in scimitar syndrome also can be depicted on CT. Associated congenital heart diseases, most commonly atrial septal defect, are seen in 25–50 % of patients with scimitar syndrome. The affected infants typically present with congestive heart failure. Symptomatic cases can be treated with surgical restoration of the pulmonary venous drainage into the left atrium and embolization of systemic artery supply.

10.4.2 Horseshoe Lung

Horseshoe lung is a rare anomaly characterized by an abnormal fusion of the posterolateral portions of both lungs through a narrow isthmus between the heart and the descending aorta (Fig. 10.3). The accurate diagnosis of horseshoe lung can be made with CT by recognizing the pulmonary arterial and bronchial supplies to the isthmic portion from the hypoplastic lung (Goo et al. 2002) (Fig. 10.3). The majority of the cases occur in conjunction with scimitar syndrome.

10.4.3 Pulmonary Vein Atresia

Pulmonary vein atresia is defined as the absence of the involved pulmonary veins. CT can not only confirm the absence of the pulmonary veins but also demonstrate smaller ipsilateral pulmonary artery and lung and pulmonary interstitial thickenings (Fig. 10.4). Patients with pulmonary vein atresia may present with recurrent infection or hemoptysis usually in infancy or childhood. Conservative management, coil embolization of systemic arterial collaterals responsible for hemoptysis, and surgical resection are considered in symptomatic cases with pulmonary vein atresia.

10.4.4 Congenital Diaphragmatic Hernia

Congenital diaphragmatic hernia commonly involves the posterolateral portion of the diaphragm, more common on the left. A various degree of pulmonary hypoplasia, especially the lower lobe, is associated with large hernia, causing respiratory distress during the neonatal period. CT can show the defect size, the herniated contents, and the volume of the ipsilateral lung (Fig. 10.5). In clinical practice, sonography is more frequently performed to evaluate congenital diaphragmatic hernia. Like congenital diaphragmatic hernia, any large congenital mass lesion results in secondary pulmonary hypoplasia.

10.5 Bronchopulmonary Foregut Malformations

Bronchopulmonary foregut malformations are resulted from defective budding, differentiation, or separation of the primitive foregut. Proposed pathogenetic mechanisms for these lesions include interrupted development of the pulmonary vasculature and in utero airway obstruction (Freedom et al. 2006). When these lesions are connected to

the gastrointestinal tract, they are called as “communicating” bronchopulmonary foregut malformations (Kim et al. 2000).

10.5.1 Bronchogenic Cyst

Bronchogenic cyst is a cyst lined by pseudostratified ciliated columnar epithelium, frequently with the smooth muscle, the mucous gland, or the cartilage, as seen in the respiratory tracts. It is the most commonly encountered cyst in the chest. Bronchogenic cyst is typically seen in the middle mediastinum, most commonly in the subcarinal location (52 %), followed by the paratracheal region (19 %) and the paraesophageal region (14 %). Bronchogenic cyst infrequently occurs in the lungs, commonly in the lower lobes. Bronchogenic cyst is seen as a round or ovoid hypodense (0–20 HU, depending on the fluid content in the cyst) cystic lesion on CT (Fig. 10.6). CT also can show not only the imaging finding of the complicated (infected or hemorrhagic) cyst, such as high CT attenuation, enhancing wall thickening, air–fluid level, or interval increase in size, but also mass effect on the adjacent structures, such as the airways, the esophagus, or the cardiovascular structures. Of note, bronchogenic cyst cannot be distinguished from other foregut duplication cysts, such as duplication cyst and enteric cyst, based on CT findings. For symptomatic patients, the cyst is managed by surgical resection or (percutaneous or transbronchial) aspiration.

10.5.2 Bronchial Atresia

Bronchial atresia is defined as atresia of a segmental or subsegmental bronchus, presumably due to cell loss or ischemia. Mucus accumulates in the patent bronchus distal to the atresia, resulting in luminal dilatation. Hyperinflation in the affected lung segment is resulted from air trapping through collateral ventilation pathways, such as interalveolar pores of Kohn and bronchoalveolar channels of Lambert. CT can demonstrate these characteristic morphological features of bronchial atresia: a mucocoele distal to the atresia with the hyperlucent but otherwise normal lung parenchyma (Fig. 10.7). In addition, collateral ventilation into bronchial atresia can be demonstrated by means of dual-energy CT technique (Goo et al. 2008, 2011; Goo 2013b). The apicoposterior segment of the left upper lobe is most commonly involved. The majority of patients with bronchial atresia are asymptomatic. Recent pathologic studies have shown that bronchial atresia is commonly associated with other congenital lung malformations, such as pulmonary

sequestration, congenital pulmonary airway malformation (CPAM), and congenital lobar hyperinflation (CLH).

10.5.3 Congenital Pulmonary Airway Malformation

CPAM, also known as congenital cystic adenomatoid malformation (CCAM), is a disorganized overgrowth of the terminal portion of the bronchiole tree instead of normal alveolar development. The lung lesion has variable degrees of bronchial communication, and CPAM receives its blood supply from the pulmonary circulation. Three types of CPAM are classically described depending on their pathologic findings: the most common type 1 lesion has at least one dominant cyst larger than 2 cm, the type 2 has multiple cysts smaller than 2 cm, and the rare type 3 is characterized by a solid-looking microcystic lesion. These pathologic types were recently extended, but their clinical impact is not substantial. CPAM is identified as a variably cystic and solid lung lesion according to the type of CPAM on CT (Shimohira et al. 2007) (Fig. 10.8). If infection is superimposed, an air-fluid level in the cystic lesion with enhancing thick wall and adjacent consolidation can be seen on CT, but associated pleural effusion is uncommonly seen or unusually small if present. CT is particularly useful for differentiating CPAM from pulmonary sequestration that is characterized by systemic arterial supply. Occasionally, CPAM and sequestration may coexist as a hybrid lesion. On the other hand, a pure cystic type of pleuropulmonary blastoma cannot be distinguished from CPAM on CT. CPAM has no lobar predilection, and multilobar involvement occurs in 5–20 % of cases. CPAM usually presents in the neonatal period (50–85 %). Surgical resection of symptomatic CPAM is indicated, but the management of asymptomatic cases remains controversial. Predictors of poor outcome include fetal hydrops, bilateral involvement (<2 %), and microcystic lesion (type 3).

10.5.4 Pulmonary Sequestration

Pulmonary sequestration is an abnormal lung tissue without connection to the tracheobronchial tree and with systemic arterial supply. There are two types of pulmonary sequestration: intralobar and extralobar types. Intralobar sequestration shows pulmonary venous drainage and shares its pleura with the adjacent lung, whereas extralobar sequestration is invested in its own pleura and shows systemic venous drainage (Fig. 10.9). Because the extralobar type has its own pleura, the lung lesion is typically shown as a nonaerated, well-circumscribed, enhancing soft tissue mass, occasionally with hypodense areas (Fig. 10.9). Pulmonary sequestration is found most commonly in the posteromedial portions of the bilateral basal lungs, with the left side more

frequently involved than the right. Extralobar sequestration may occur in or below the diaphragm. In contrast to the intralobar type, the extralobar type is frequently associated with other congenital anomalies, including diaphragmatic abnormalities and congenital heart disease, ipsilateral pulmonary hypoplasia in a large lesion, and other bronchopulmonary malformations. The extralobar type may be complicated with hemorrhagic infarction or tension hydrothorax due to torsion. However, superimposition of infection is uncommon in the extralobar type. Currently, the majority of pulmonary sequestration and CPAM are detected by prenatal sonography. Depending on the lesion size and associated congenital anomalies, the patient may have symptoms, such as respiratory distress and cyanosis. Pulmonary sequestration and/or CPAM should be suspected when recurrent lung infections occur in the same area during late childhood. On this occasion, the diagnosis of sequestration should be cautiously made, because systemic arterial collaterals may be developed in recurrent lung infections. Surgical resection is indicated in symptomatic patients with sequestration. Transcatheter arterial embolization may be used as an alternative treatment (Lee et al. 2003, 2008a). However, appropriate managements for asymptomatic lesions remain to be determined, because pulmonary sequestration often shows spontaneous regression, and the incidence of complications during follow-up is not high enough to justify elective surgery or transarterial coil embolization.

10.5.5 Esophageal Bronchus/Lung

In esophageal bronchus or lung, one of the communicating bronchopulmonary foregut malformations, a bronchus or a lung shows an abnormal connection to the esophagus. CT can be diagnostic by demonstrating this abnormal connection with persistent consolidation (Fig. 10.10). Bronchoscopy demonstrates no visualization of the involved bronchus.

10.6 Congenital Lobar Hyperinflation

A usual form of CLH, also called as congenital or infantile lobar emphysema, is progressive hyperinflation of the otherwise normal lung segment due to intrinsic or extrinsic bronchial obstruction. In a polyalveolar form, the increased number of normally expanded alveoli attributes to lung hyperinflation. As in CPAM, CLH could be identified as an opaque lung lesion on CT immediately after birth due to the retained lung fluid. On CT images performed after the retained lung fluid is cleared, CLH appears as a hyperlucent, expanded lung segment with attenuated pulmonary vascular markings (Fig. 10.11). A lobar predilection is present as follows: the left upper lobe (43 %), the right middle lobe (32 %), and the right upper lobe (20 %). CLH may occasionally

involve a segmental or subsegmental portion of the lung. Multilobar involvement of CLH is rarely seen (<1 %). CT is particularly useful for identifying multilobar involvement and mass effect on the adjacent structures. CLH usually presents in the neonatal and infantile period with respiratory distress. Surgical resection is performed for symptomatic cases.

10.7 Systemic Arterial Supply to Normal Lung

Systemic arterial supply to normal lung occurs most often in the basal segments of the left lower lobe. Normal lung and airway supplied by an anomalous systemic artery arising

from the descending thoracic aorta are an important diagnostic clue to this anomaly on CT in distinguishing it from pulmonary sequestration, with an anomalous systemic artery typically arising from the abdominal aorta (Fig. 10.12). Left-to-left shunt in the affected lung segments results in diffusely dilated systemic arteries and pulmonary veins (Fig. 10.12). CT also shows no pulmonary arterial supply to the affected lung segments (Kim et al. 2003). Patients occasionally present with recurrent bloody sputum and hemoptysis. Due to the left-to-left shunt flow through the lesion, left ventricular enlargement and congestive heart failure may develop. Surgical treatments are required in symptomatic cases with this anomaly.

10.8 Illustrations: CT Findings of Congenital Lung Malformations

10.8.1 Pulmonary Agenesis

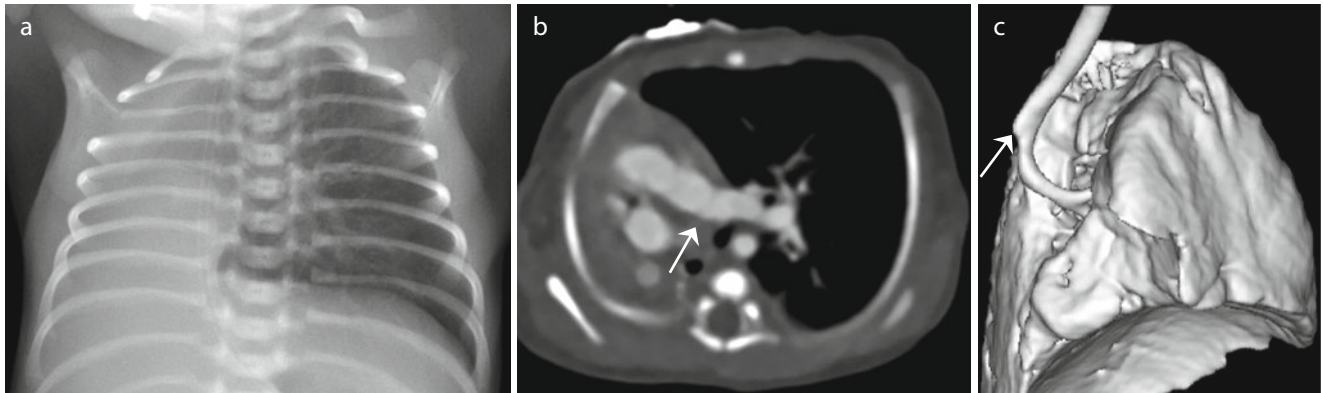


Fig. 10.1 (a–c) Right pulmonary agenesis. Plain chest radiograph shows an opacified right hemithorax with a severe mediastinal shift toward the right and the hyperinflated left lung (a). Axial CT image additionally shows the absence of the right pulmonary artery (arrow)

and the right lung (b). Right anterior oblique shaded surface display CT image reveals the absence of right main bronchus (arrow) that differentiates this anomaly from right pulmonary aplasia (c)

10.8.2 Scimitar Syndrome

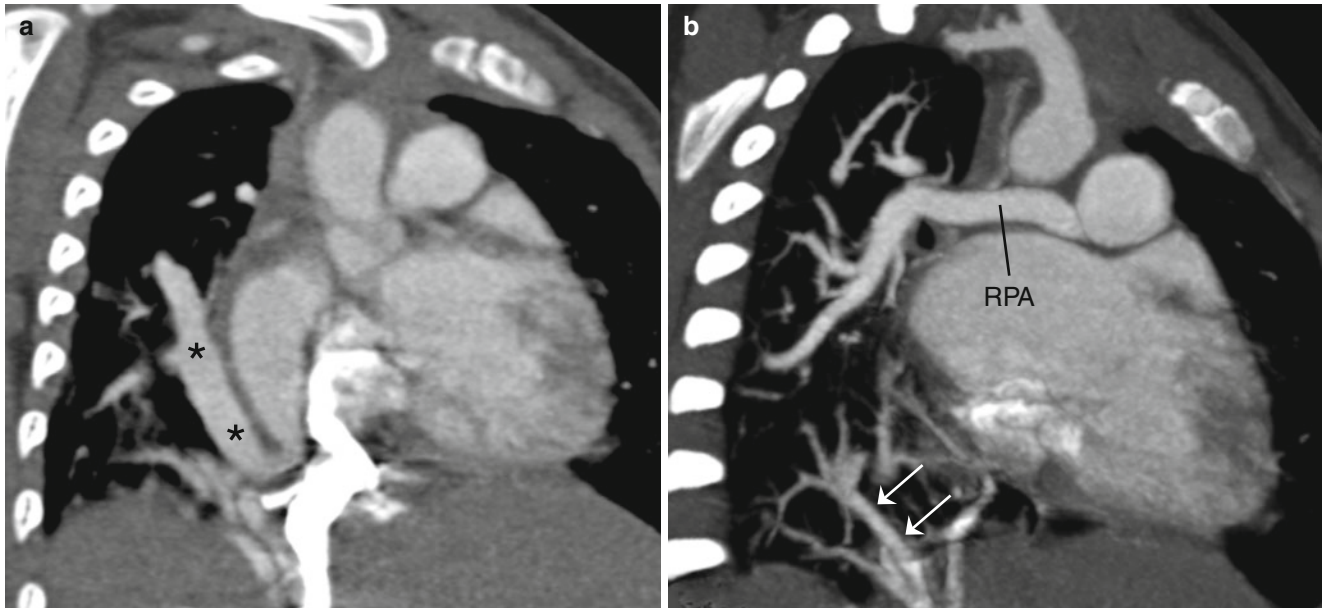


Fig. 10.2 (a, b) Scimitar syndrome. Coronal CT image demonstrates the scimitar vein (*asterisks*) anomalously draining into the right atrium–inferior vena cava junction (a). Coronal CT image shows the hypoplas-

tic right pulmonary artery (*RPA*) and systemic arterial collaterals (*arrows*) supplying the right lower lung (b)

10.8.3 Horseshoe Lung

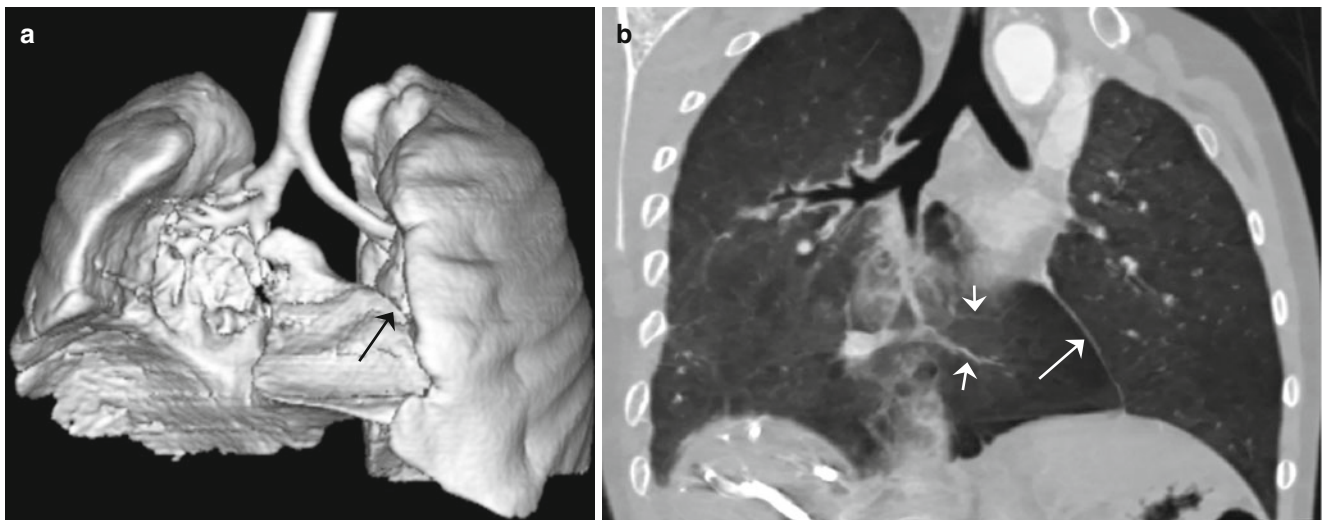


Fig. 10.3 (a, b) Horseshoe lung. Anterior shaded surface display CT image (a) and coronal minimum intensity projection CT image (b) show a fusion of both lungs and a pleural line (*long arrow*) between an

isthmus of the hypoplastic right lung and the left lung. The pulmonary vasculature (*short arrows*) in the isthmic portion is derived from the hypoplastic lung (b)

10.8.4 Pulmonary Vein Atresia

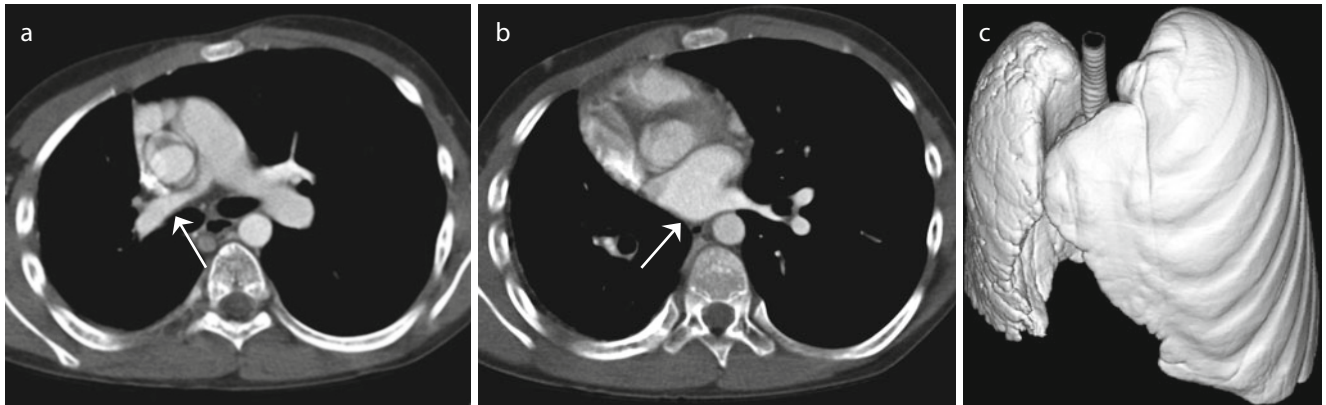


Fig. 10.4 (a–c) Right pulmonary vein atresia. Axial CT image at the pulmonary artery bifurcation level shows the hypoplastic right lung and right pulmonary artery (*arrow*) (a). Axial CT image at the left atrial level additionally reveals the absence of the right pulmonary vein

(*arrow*) (b). Anterosuperior shaded surface display CT image demonstrates numerous reticular cracks on the hypoplastic right lung surface due to transpleural collateral arteries (c)

10.8.5 Congenital Diaphragmatic Hernia

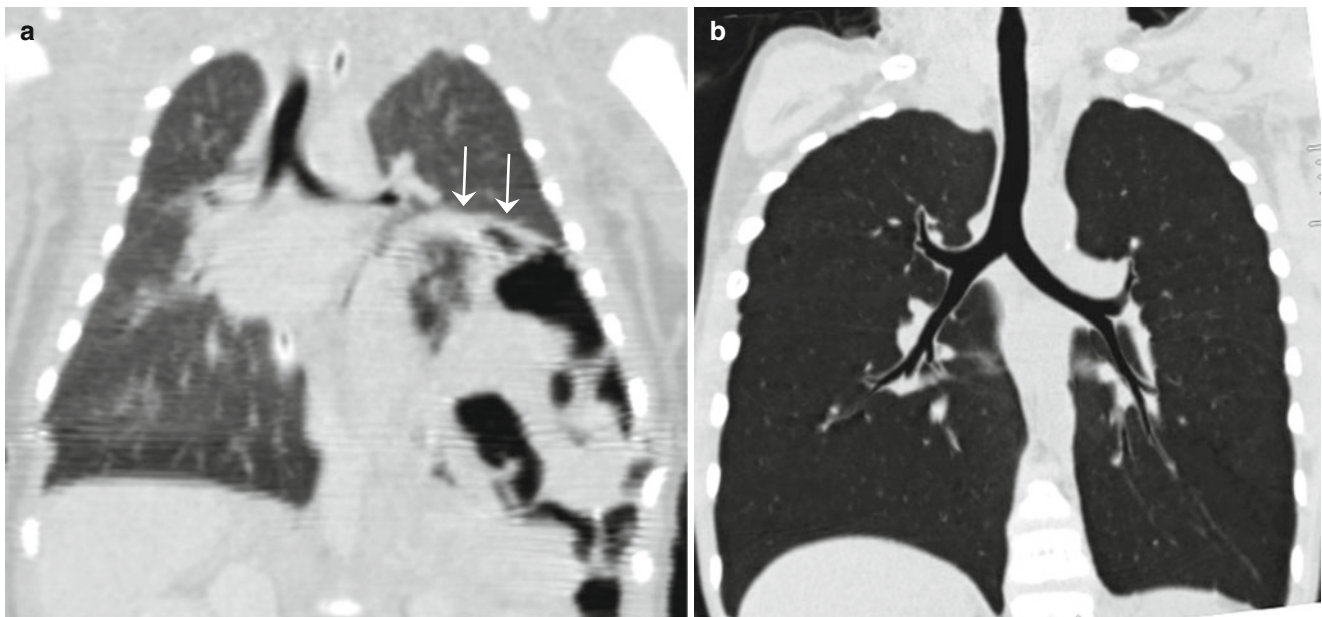


Fig. 10.5 (a, b) Congenital left diaphragmatic hernia. Coronal CT image shows the herniated abdominal contents (*arrows*) displacing the left lung upward (a). Coronal CT image 6 years after the diaphragmatic

hernia repair demonstrates almost normal size of the left bronchi and compensatory hyperinflation of the left lung (b)

10.8.6 Bronchogenic Cyst

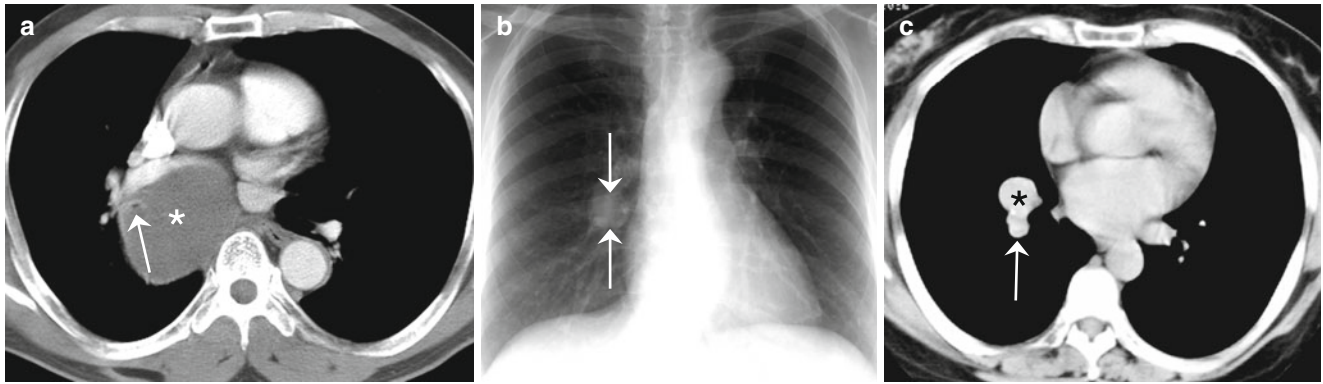


Fig. 10.6 (a–c) Bronchogenic cyst. Axial CT image shows a mediastinal cystic lesion (*asterisk*) encasing the right bronchus (*arrow*) and a mass effect on the adjacent structures (**a**). Plain chest radiograph reveals a well-circumscribed nodular lesion (*arrows*) in the medial portion of

the right lower lung (**b**). Axial CT image demonstrates a hyperdense intrapulmonary cyst (*asterisk*) in the right lower lung anterior to the descending branch (*arrow*) of the right pulmonary artery (**c**)

10.8.7 Bronchial Atresia

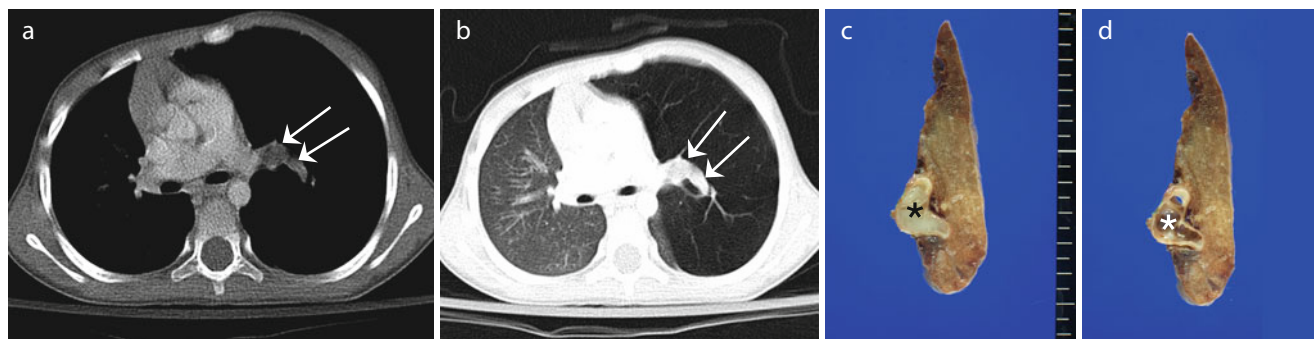


Fig. 10.7 (a–d) Bronchial atresia. Axial CT images with mediastinal (a) and lung (b) window settings show a hypodense mucocoele (arrows) in the central area of the hyperinflated left upper lobe. Photographs

show a resection specimen before (c) and after (d) the removal of mucus impacted in the dilated bronchus (asterisk)

10.8.8 Congenital Pulmonary Airway Malformation (CPAM)

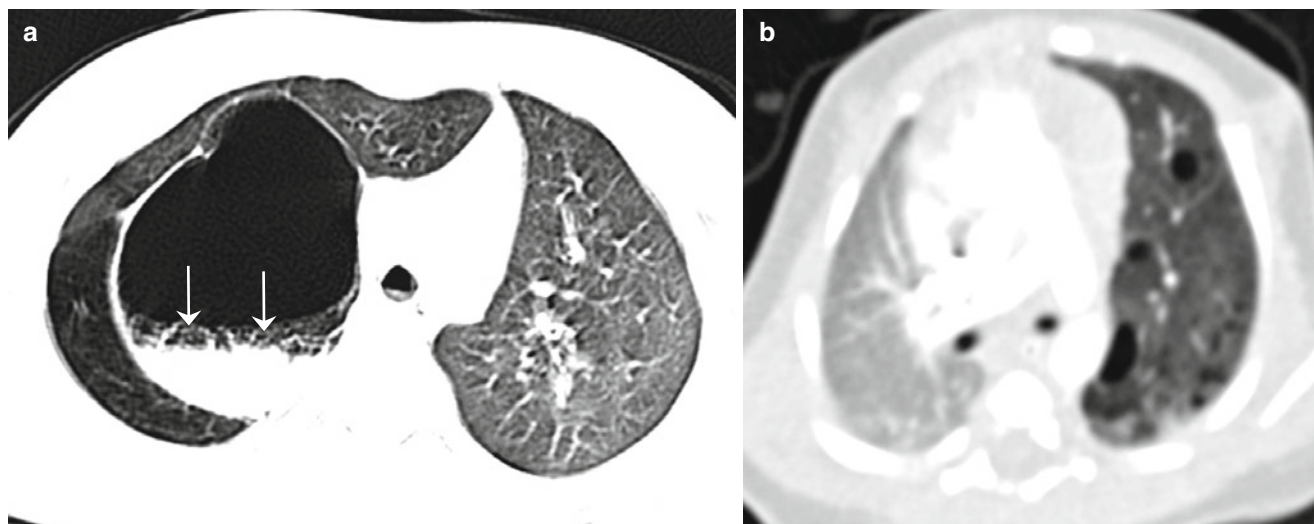


Fig. 10.8 (a, b) Congenital pulmonary airway malformation. Axial CT image shows a large thick-walled cyst with an air–fluid level (*arrows*) in the right lung that was proven as an infected congenital pulmonary

airway malformation (type 1) (a). Axial CT image reveals type 2 congenital pulmonary airway malformation with multiple small cysts in the hyperlucent left lung (b)

10.8.9 Pulmonary Sequestration

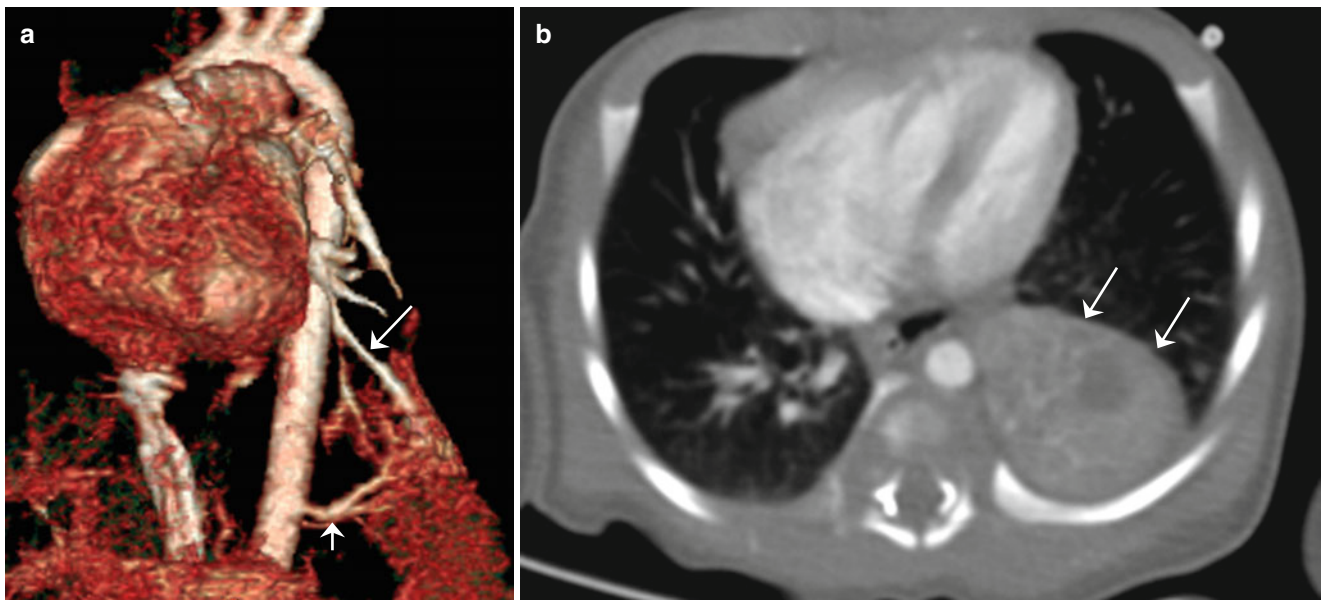


Fig. 10.9 (a, b) Pulmonary sequestration. Volume-rendered CT image shows intralobar sequestration in the left lower lobe with its feeding artery (*short arrow*) arising from the descending aorta and a draining

vein into the left lower pulmonary vein (*long arrow*) (a). Axial CT image reveals extralobar sequestration (*arrows*) with vessels and hypodense areas in the left lower lobe (b)

10.8.10 Esophageal Bronchus

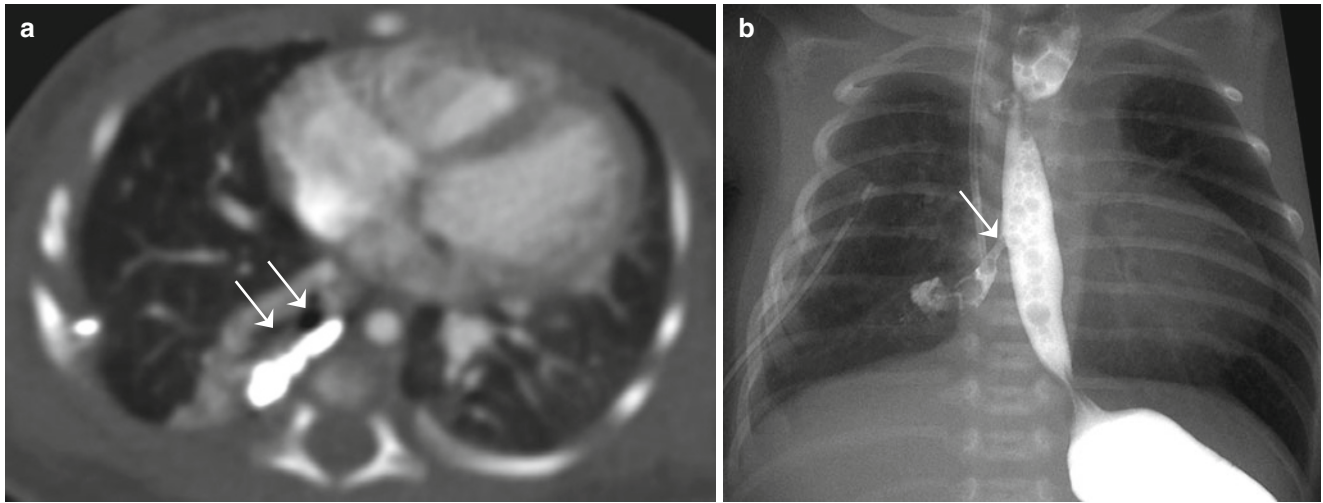


Fig. 10.10 (a, b) Esophageal bronchus. Axial CT image shows the collapsed right lower lobe with air bronchograms (*arrows*) that do not connect to the tracheobronchial tree (a). Residual thin barium is noted

in the posterior part of the lesion. Esophagography reveals an abnormal connection (*arrow*) between the right lower lobe bronchus and the esophagus (b)

10.8.11 Congenital Lobar Hyperinflation

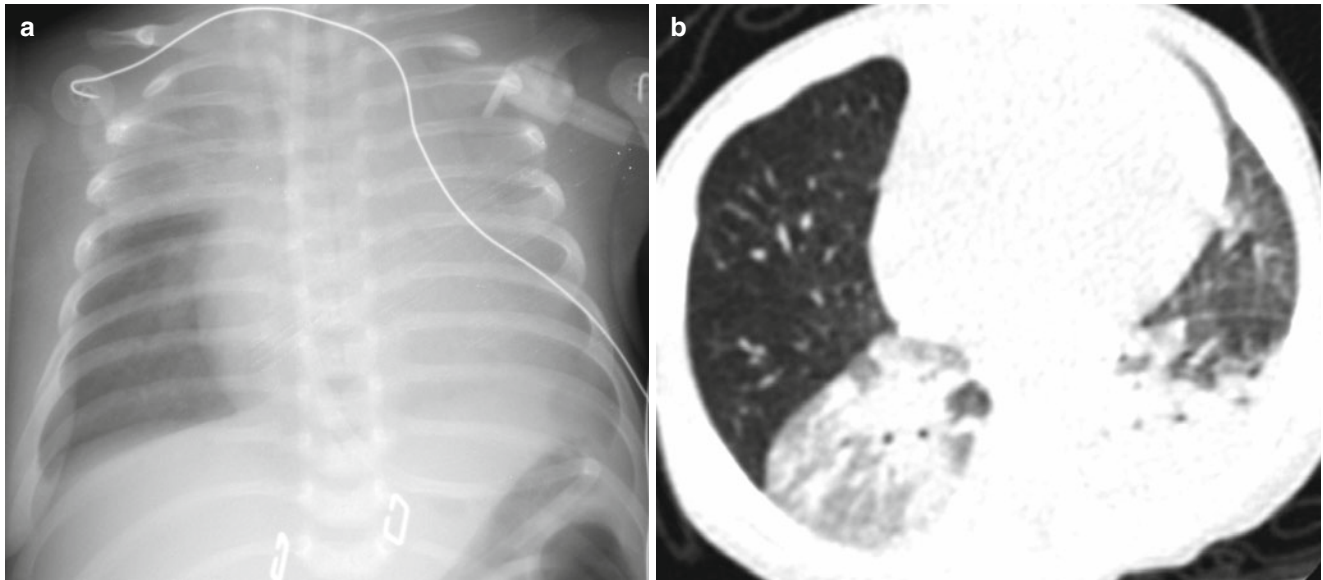


Fig. 10.11 (a, b) Congenital lobar hyperinflation. Plain chest radiograph (a) and axial CT image (b) show the hyperlucent and hyperinflated right middle lobe that was proven as congenital lobar hyperinflation

10.8.12 Systemic Arterial Supply to Normal Lung

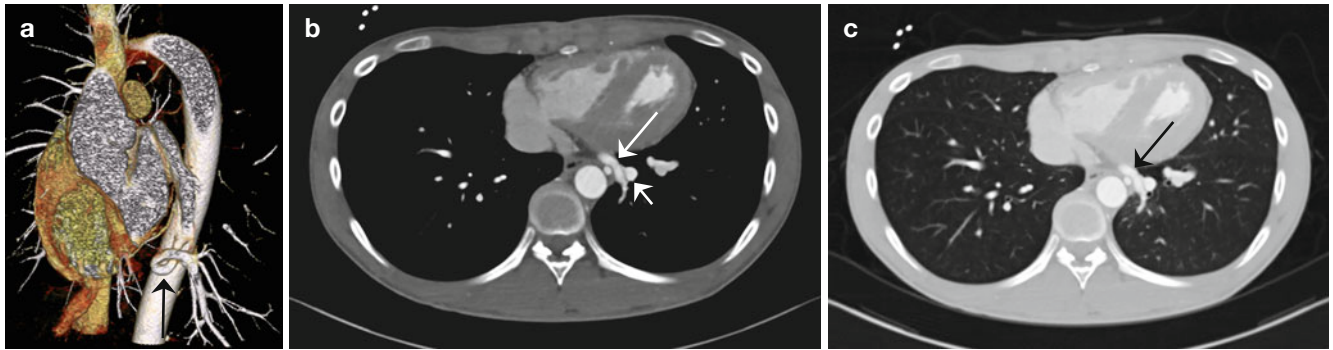


Fig. 10.12 (a–c) Systemic arterial supply to normal lung. Volume-rendered CT image shows a systemic artery (*arrow*) arising from the descending thoracic aorta and supplying the left basal lung (a). Axial CT images with mediastinal (b) and lung (c) window settings reveal a

systemic artery (*long arrow*) and a pulmonary vein branch (*short arrow*) in the normal-appearing left lower lobe, but no accompanying pulmonary artery branch

References

- Daltro P, Fricke BL, Kuroki I, et al. CT of congenital lung lesions in pediatric patients. *AJR Am J Roentgenol*. 2004;183:1497–506.
- Freedom RM, Yoo SJ, Goo HW, et al. The bronchopulmonary foregut malformation complex. *Cardiol Young*. 2006;16:229–51.
- Goo HW. Individualized volume CT dose index determined by cross-sectional area and mean density of the body to achieve uniform image noise of contrast-enhanced pediatric chest CT obtained at variable kV levels and with combined tube current modulation. *Pediatr Radiol*. 2011;41:839–47.
- Goo HW. CT radiation dose optimization and estimation: an update for radiologists. *Korean J Radiol*. 2012;13:1–11.
- Goo HW. Advanced functional thoracic imaging in children: from basic concepts to clinical applications. *Pediatr Radiol*. 2013a;43:262–8.
- Goo HW. Dual-energy lung perfusion and ventilation CT in children. *Pediatr Radiol*. 2013b;43:298–307.
- Goo HW, Kim HJ. Detection of air trapping on inspiratory and expiratory phase images obtained by 0.3-sec cine-CT in the lungs of free breathing young children. *AJR Am J Roentgenol*. 2006;187:1019–23.
- Goo HW, Kim YH, Ko JK, et al. Horseshoe lung: useful angiographic and bronchographic images using multidetector-row spiral CT in two infants. *Pediatr Radiol*. 2002;32:529–32.
- Goo HW, Chae EJ, Seo JB, et al. Xenon ventilation CT using dual-source and dual-energy technique: dynamic ventilation abnormality in a child with bronchial atresia. *Pediatr Radiol*. 2008;38:1113–6.
- Goo HW, Yang DH, Kim N, et al. Collateral ventilation to congenital hyperlucent lung lesions assessed on xenon-inhaled dynamic dual-energy CT: initial experience. *Korean J Radiol*. 2011;12:25–33.
- Goo HW, Drubach L, Lee EY. Imaging techniques. In: Coley BD, editor. *Caffey's pediatric diagnostic imaging*. 12th ed. Philadelphia: Elsevier; 2013.
- Kim CY, Goo HW, Kim HJ, et al. Communicating bronchopulmonary foregut malformation: a case report. *J Korean Radiol Soc*. 2000;43:59–61.
- Kim MJ, Goo HW, Park SI. Systemic arterial supply to the normal basal segments of the left lower lobe: case report. *J Korean Radiol Soc*. 2003;48:193–6.
- Kocaoğlu M, Frush DP, Uğurel MS, et al. Bronchopulmonary foregut malformations presenting as mass lesions in children: spectrum of imaging findings. *Diagn Interv Radiol*. 2010;16:153–61.
- Lee KH, Sung KB, Yoon HK, et al. Transcatheter arterial embolization of pulmonary sequestration in neonates: long-term follow-up results. *J Vasc Interv Radiol*. 2003;14:363–7.
- Lee BS, Kim JT, Kim EA, et al. Neonatal pulmonary sequestration: clinical experience with transumbilical arterial embolization. *Pediatr Pulmonol*. 2008a;43:404–13.
- Lee EY, Boiselle PM, Cleveland RH. Multidetector CT evaluation of congenital lung anomalies. *Radiology*. 2008b;247:632–48.
- Nasr A, Bass J. Thoracoscopic vs open resection of congenital lung lesions: a meta-analysis. *J Pediatr Surg*. 2012;47:857–61.
- Shimohira M, Hara M, Kitase M, et al. Congenital pulmonary airway malformation: CT-pathologic correlation. *J Thorac Imaging*. 2007;22:149–53.
- Tomà P, Rizzo F, Stagnaro N, et al. Multislice CT in congenital bronchopulmonary malformations in children. *Radiol Med*. 2011;116:133–51.
- Watarai F, Takahashi M, Hosoya T, et al. Congenital lung abnormalities: a pictorial review of imaging findings. *Jpn J Radiol*. 2012;30:787–97.

Young Hun Choi and In-One Kim

Contents

11.1	Introduction	382
11.2	Thymus	382
11.3	Spectrum of Diseases	382
11.3.1	Hyaline Membrane Disease	382
11.3.2	Immature Lung Syndrome	383
11.3.3	Bronchopulmonary Dysplasia (Chronic Lung Disease of Infancy)	383
11.3.4	Meconium Aspiration Syndrome	383
11.3.5	Transient Tachypnea of the Newborn	384
11.3.6	Neonatal Pneumonia	384
11.4	Air-Leak Phenomena	385
11.4.1	Pulmonary Interstitial Emphysema	385
11.4.2	Pneumomediastinum/Pneumopericardium	385
11.4.3	Pneumothorax	385
11.5	Lines, Tubes, and Catheters	386
11.6	Illustrations: Neonatal Chest Imaging	387
11.6.1	Normal Thymus	387
11.6.2	Hyaline Membrane Disease	388
11.6.3	Immature Lung Syndrome	392
11.6.4	Bronchopulmonary Dysplasia	393
11.6.5	Meconium Aspiration Syndrome	395
11.6.6	Transient Tachypnea of the Newborn	396
11.6.7	Neonatal Pneumonia	397
11.6.8	Air Leak Phenomena	403
11.6.9	Lines, Tubes and Catheters	407
	References	409

Y.H. Choi, M.D. • I.-O. Kim, M.D.
 Department of Radiology,
 Seoul National University Hospital,
 Seoul National University College of Medicine,
 101 Daehak-ro, Chongno-gu, Seoul 110-744, Korea
 e-mail: iater@snu.ac.kr

11.1 Introduction

Pulmonary disease is the most common and significant cause of morbidity in neonates. In general, the neonatal chest abnormalities can be divided into medical diseases and surgical diseases. A review of surgical lesions is provided elsewhere. This chapter reviews the common spectrum of medical diseases of the neonatal chest. The main diseases are hyaline membrane disease (HMD), meconium aspiration syndrome (MAS), transient tachypnea of the newborn (TTN), neonatal pneumonia, and bronchopulmonary dysplasia (BPD) (Ablow et al. 1977; Cleveland 1995; Strife and Crotty 2008; Cleveland and Rhein 2012).

The conventional chest radiograph remains the most frequent and important imaging tool in evaluating the newborn chest, while CT and ultrasonography have limited roles. Correlation of the findings on serial radiographs with the clinical factors is important for the correct interpretation, because understanding the neonate's prenatal and perinatal history, gestational age, and clinical condition at the time of radiography can help differentiate these diseases. Lung volume may be a useful differentiating criterion of neonatal pulmonary diseases. Classically, HMD is associated with decreased lung volume, while MAS and TTN are associated with increased lung volumes.

11.2 Thymus

When interpreting the neonatal chest radiographs, radiologists should be familiar with various configurations of the thymus. Normally, the thymus is prominent in infants; it enlarges the cardiomedastinal silhouette and may mimic cardiomegaly or mediastinal mass. The thymus involutes with increasing age and should be relatively inconspicuous by the end of the first decade. The size of the thymus can also vary with respiratory status and the patient's condition. The thymus appears small during inspiration, while it appears large during expiration. The thymus may become smaller with infection or medications, such as steroids or chemotherapeutic agents, and may rebound in size after recovery (rebound hypertrophy).

The classic radiographic appearance of a newborn's thymus is anterior superior mediastinal soft tissue that blends imperceptibly with the cardiac silhouette. If the infant is rotated, a large thymus can mimic upper lobe atelectasis (Fig. 11.1e). It may have a lateral triangular extension that looks like a sail ("sail" sign) (Fig. 11.1a). The lateral edge of the thymus is often undulating due to gentle compression by the adjacent anterior ribs ("wavy" thymic sign) (Fig. 11.1b). On the lateral view, the thymus fills the anterior superior mediastinum and has a well-defined inferior border (Nasseri and Eftekhari 2010).

If one is not sure whether a mediastinal mass or upper lobe parenchymal lesion represents the normal thymus,

ultrasound can be performed to confirm the thymus. At ultrasonography, a normal thymus has a characteristic internal architecture of homogeneous hypoechogenicity with echogenic linear or dot-like septa (Fig. 11.1f) (Han et al. 2001).

11.3 Spectrum of Diseases

11.3.1 Hyaline Membrane Disease

Hyaline membrane disease (HMD) is also called respiratory distress syndrome or surfactant deficiency disease. The pathophysiology of HMD is the result of anatomic pulmonary immaturity and the deficiency of surfactant, a lipoprotein complex produced by type II pneumocytes. The surfactant decreases surface tension and hence prevents collapse of the alveoli. The immaturity of the lung and lack of surfactant lead to a cascade of events with abnormal pulmonary compliance, atelectasis, capillary leak, and hyaline membrane formation (Stocker and Dehner 1992).

Prematurity is the most serious risk factor, and the incidence and severity of HMD are inversely proportional to gestational age. Between 60 % and 80 % of neonates born at less than 28 weeks' gestational age develop HMD, whereas only 15–30 % of those born between 32 and 36 weeks' gestational age are affected. Other risk factors include maternal diabetes, multiple birth, and Caesarean section. Secondary surfactant insufficiency may develop in birth asphyxia, sepsis, and meconium aspiration. Males are affected almost twice as often as females, and HMD is more common in whites than in blacks (Wells 2012).

The radiographic findings of HMD predictably reflect the generalized collapse that results from surfactant deficiency. Classic radiographic findings of HMD are small lung volume, symmetric diffuse fine granularities, and air bronchograms (Fig. 11.2). These radiographic findings are usually noted shortly after birth, and reach maximum severity at 12–24 h of life (Cleveland 1995; Newman 1999).

Recent advances in perinatal medicine, including strategies to delay labor, the administration of antenatal maternal glucocorticoids, and early and prevalent use of surfactant replacement therapy, have significantly decreased the incidence and severity of HMD and led to a great deal of variability in the radiographic findings of HMD (Fig. 11.3) (Dinger et al. 1997; Slama et al. 1999). Generalized underaeration of the lungs, which was described as one of the classic radiographic findings of HMD, may not be present because many initial radiographs are obtained only after the neonates have been intubated and the lungs have been artificially inflated. Furthermore, there can be variable changes in the chest radiographic findings after surfactant administration (Fig. 11.4). Asymmetric, multifocal areas of opacity may be noted and should not be mistaken for neonatal pneumonia or meconium aspiration syndrome. Localized hyperaerated

areas may mimic interstitial emphysema (Cleveland 1995). Asymmetric unilateral improvement may result in a hyperlucent lung with contralateral mediastinal shift, simulating a tension pneumothorax (Agrons et al. 2005). Proposed explanations for these asymmetric radiographic improvements following surfactant treatment are (a) maldistribution of surfactant into the right main stem bronchus, (b) insufficient amount of surfactant requiring additional applications, and (c) regional differences in aeration before surfactant treatment (Dinger et al. 1997; Slama et al. 1999).

Sudden diffuse opacification of the lungs may be seen after the initial clearing of lung opacities with surfactant treatment. The possible causes are pulmonary edema from a patent ductus arteriosus or fluid overload, hypoventilation due to decreasing ventilator support, superimposed infection, and, less commonly, diffuse pulmonary hemorrhage (Figs. 11.5 and 11.6) (Slovis and Bulas 2008).

Most premature infants that survive HMD but require continued ventilation support eventually develop bronchopulmonary dysplasia, which will be discussed in another section.

11.3.2 Immature Lung Syndrome

With advances in perinatal management, the increased survival of profoundly premature neonates of 23–26 weeks' gestational age has introduced the characteristic clinical and radiographic presentations, termed "immature lung" (Edwards et al. 1980; Cleveland 1995). These neonates have few alveoli so they cannot show large areas of atelectasis as in HMD. Unlike HMD, initial radiographs of these newborns appear normal or nearly normal, with only subtle haziness or interstitial thickening, and there is no significant air bronchogram or decreased lung volume. Nevertheless, most infants required ventilator support due to structural immaturity with alveolar paucity. Toward the end of the first week, chest radiographs show hazy diffuse opacification. Then, over several days to weeks, the radiographic pattern may evolve into a coarse, irregular pattern of BPD in most cases (Figs. 11.8 and 11.9) (Agrons et al. 2005).

11.3.3 Bronchopulmonary Dysplasia (Chronic Lung Disease of Infancy)

Initially, the term bronchopulmonary dysplasia (BPD) was introduced to describe chronic lung disease occurring in infants who survive HMD but go on to require continued ventilator support, including positive pressure ventilation and supplemental oxygen (Northway et al. 1967). Classic BPD was characterized by the necrotizing bronchiolitis and severe alveolar septal fibrosis, which led to severe heteroge-

neous morphological changes including emphysema, atelectasis, and fibrosis. Such a classic severe form of BPD is rarely seen nowadays; instead, a milder and relatively homogeneous form is more common. The new BPD is histologically characterized by oversimplified acinar morphology and minimal or mild diffuse alveolar septal fibrosis, changes more compatible with an arrest in lung development than with mechanical injury (Jobe 1999; Jobe and Bancalari 2001).

BPD can be defined as the triad of oxygen dependency, radiologic evidence of lung disease, and respiratory symptoms that persist beyond 28 days of life. Although there has been a significant reduction in the severity and mortality of BPD, the incidence is increasing, according to the improved survival rates even for very premature infants (Wells 2012).

The typical radiologic features are alternating areas of cystic lucencies and coarse band-like opacities of fibrosis and atelectasis. Overall hyperinflation of the lungs is accompanied (Figs. 11.10 and 11.11). HRCT findings include regional areas of air trapping; linear and reticular opacities representing thickened interlobular septa, subsegmental atelectasis, and fibrosis; segmental or lobar atelectasis; bronchial wall thickening; and architectural distortion (Fig. 11.10c) (Oppenheim et al. 1994; Shin et al. 2013).

Surfactant replacement therapy, antenatal steroids administration, and refined gentle assisted ventilation have changed the radiographic picture of BPD. The classic advanced BPD is less frequently seen these days. The radiographic abnormalities in BPD seen now tend to be mild, more symmetric and uniform, and the cystic lucencies are smaller (Figs. 11.11 and 11.12) (Oppenheim et al. 1994; Agrons et al. 2005; Shin et al. 2013).

Children who survive BPD show gradual improvement in chest radiographic findings during the first few years of life. However, most older children and adults with a history of BPD have residual pulmonary abnormalities identifiable on CT (Fig. 11.13) (Howling et al. 2000).

11.3.4 Meconium Aspiration Syndrome

Meconium is the material in the fetal colon throughout gestation and it is usually passed during the first 24 h after birth. Meconium aspiration syndrome (MAS) is caused by perinatal aspiration of the meconium, often associated with fetal distress in a term or near-term infant. Meconium is rarely found in the amniotic fluid prior to 34 weeks, as the passage of meconium in utero results from neural stimulation of a mature intestinal tract. Although meconium may be detected in the amniotic fluid in approximately 10–20 % of newborns, 4–5 % of neonates develop MAS, which is clinically diagnosed by the presence of meconium in the airway below the vocal cords (Cleveland and Rhein 2012).

Nowadays, the incidence of MAS continues to decline due to changing obstetric practice in post-term mothers and closer fetal monitoring (Yoder et al. 2002; Cleveland and Rhein 2012).

Aspirated meconium causes lung injury by three major mechanisms: (1) airway obstruction; (2) chemical pneumonitis; and (3) secondary surfactant deficiency. Air leak, persistent pulmonary hypertension of the newborn (PPHN), and secondary infection are frequently complicated. Long-term complications include hypoxic brain injury and bronchopulmonary dysplasia after prolonged mechanical ventilation (Wiedemann et al. 2008).

The radiographic findings in MAS vary, in part secondary to the severity of the aspiration. Typical radiographic findings include hyperinflated lungs with bilateral asymmetric rope-like parahilar opacities (Yeh et al. 1979). Air leak frequently occurs with pneumothorax in 20–40 % of the cases (Fig. 11.14). Because the severity of PPHN is the major prognostic determinant, the radiographic severity of the disease does not correlate with the clinical findings.

Treatment for MAS consists of high-frequency ventilation, exogenous surfactant, inhaled nitrous oxide, liquid ventilation, or drugs to reduce pulmonary hypertension. Meconium alters amniotic fluid and subsequently increases the risk of bacterial infection. Moreover, the opacities in MAS cannot be distinguished from those in pneumonia; thus antibiotics are usually given. MAS is the most common neonatal medical lung disease requiring extracorporeal membrane oxygenation (ECMO) therapy (Ford 2006; Slovis and Bulas 2008).

11.3.5 Transient Tachypnea of the Newborn

Transient tachypnea of the newborn (TTN), also known as retained fetal lung fluid or wet lung, is a benign transient condition caused by delayed clearance of fetal lung fluid. TTN usually occurs in near-term, term, and post-term infants who were delivered with considerable rapidity or by Caesarean section, or in hypotonic, sedated infants (Jain and Eaton 2006). Typically, the infant is well immediately after birth but becomes tachypneic over the next few hours. Despite mild to moderate signs of respiratory distress, there is usually normal oxygenation or minor hypoxemia.

On chest radiographs, mild hyperinflation of the lungs and prominent parahilar interstitial markings are seen. A small amount of pleural effusion and fluid in the fissures are frequent. The heart is normal or only minimally enlarged. They rarely develop air leaks and rapid clinical and radiologic resolutions, usually within 1 or 2 days (Figs. 11.15 and 11.16) (Kuhn et al. 1969; Wesenberg et al. 1971).

11.3.6 Neonatal Pneumonia

Neonatal pneumonia refers to infection occurring during the first 28 days of life. Neonatal pneumonia is the most common cause of neonatal sepsis, causing significant morbidity and mortality. Neonatal pneumonia can be acquired in utero (transplacentally or from infected amniotic fluid), during passage through the contaminated birth canal or just after birth. The major risk factors include prematurity, prolonged rupture of the membranes, placental infection, maternal vaginal infection, perinatal asphyxia, and aspiration. Most neonatal pneumonias are of bacterial origin and the common organisms include group B β -hemolytic streptococcus (GBS) (Fig. 11.17), *Staphylococcus aureus* (Figs. 11.18 and 11.19), and *Escherichia coli*. Other gram-negative and viral organisms are also encountered (Nissen 2007; Richardson 2012a).

Diagnosis depends on a high index of suspicion from the clinical and radiologic findings. The radiographic findings of neonatal pneumonia are not specific and blend in with other neonatal pulmonary diseases. Because neonatal pneumonias are frequently part of systemic disease, the infiltrates are usually bilateral and diffuse. Solitary lobar consolidation related to neonatal pneumonia is rare, and alternative diagnoses should be considered (Swischuk 2004; Slovis and Bulas 2008; Strife and Crotty 2008). GBS pneumonia may mimic HMD. Other organisms may produce strand-like parahilar opacities, mimicking TTN or aspiration syndromes. In some instances, there may be reticular nodular densities throughout the lungs.

11.3.6.1 Specific Organisms

11.3.6.1.1 Group B Streptococcus

Group B streptococcus infection is the most common cause of neonatal pneumonia and is acquired from in utero amnionitis or during passage through the birth canal. Both clinically and radiographically, streptococcal pneumonia may show findings similar to those of HMD (Fig. 11.17) (Ablow et al. 1977). The possibility of a complicating pneumonia should be considered when there is unexpected or unusually rapid progression of clinical and radiographic abnormalities in an infant with HMD. Identification of an effusion aids in the differentiation from HMD, because pleural effusion is more commonly associated with pneumonia (present in approximately 25 % of patients with pneumonia) and essentially never with HMD. Slightly patchier opacities and relatively large lung volume are other differentiating points (Cleveland and Rhein 2012).

11.3.6.1.2 Chlamydia Trachomatis

Chlamydia trachomatis is a relatively common pathogen in the vaginal flora. *Chlamydia pneumonia* develops between 2 weeks and 3 months of age, even though Chlamydia infection is acquired from the mother during vaginal delivery.

Pneumonia is preceded or accompanied by conjunctivitis in about 50 % of patients. The radiologic findings are diffuse interstitial opacities with hyperinflation and are severe than would be expected by the clinical findings (Fig. 11.21) (Radkowski et al. 1981).

11.3.6.1.3 *Ureaplasma Urealyticum*

An unusual clinical and imaging course has been described with *Ureaplasma urealyticum*. This has been reported to cause a mild acute course of pneumonia within 7 days of birth, but leads to the precocious onset of BPD with a poor outcome (Fig. 11.22) (Pacifico et al. 1997).

11.3.6.1.4 *Pneumonia Alba*

In congenital syphilis, *pneumonia alba* occurs. Radiographs demonstrate diffuse persistent pulmonary infiltrates (Fig. 11.23). The diagnosis can be made when other clinical and radiographic manifestations of syphilis, infection such as desquamation of the palms and soles, macular rash, hepatosplenomegaly, and osteitis are present (Halliday et al. 1986).

11.4 Air-Leak Phenomena

Air-leak phenomena include a variety of air-leak conditions: pulmonary interstitial emphysema (PIE), pneumothorax, pneumomediastinum, and lung cysts. Air leak can occur in any of the conditions that cause airway overdistention and is mostly attributed to mechanical ventilation. Premature infants are frequently mechanically ventilated and are therefore at risk for air leaks. Air leak develops from ruptured basement membranes of the alveoli and terminal bronchioles. The air moves into the perivascular and peribronchial interstitial spaces (PIE) and then dissects centripetally into the mediastinum (pneumomediastinum). When subpleural blebs formed by centrifugal migration of interstitial air rupture, free air accumulates in the pleural space, causing a pneumothorax. In rare cases, systemic air embolism occurs in intubated neonates with HMD (Agrons et al. 2005).

11.4.1 Pulmonary Interstitial Emphysema

Pulmonary interstitial emphysema can occur independently or coexist with other air-leak complications, such as pneumothorax, pneumomediastinum, and subcutaneous emphysema. Radiologically, PIE appears as tubular or cystic lucencies tracking along the bronchovascular sheaths (Boothroyd and Barson 1988). Such lucencies do not follow the predictable branching pattern of air bronchograms and may get wider in the peripheral lungs unlike air bronchograms. The involved portions of the lungs are invariably hyperinflated (Fig. 11.24).

Interstitial emphysema is usually transient, lasting for a few to several days. Rarely, PIE may persist and form a localized thin-walled cyst with mass effect mimicking other radiolucent congenital lung masses, such as congenital lobar emphysema or congenital cystic adenomatoid malformation. In such cases, CT can be helpful by demonstrating lines and dots of soft tissue attenuation within the air cysts, findings that are thought to represent bronchovascular bundles surrounded by interstitial gas (Fig. 11.24d) (Jabra et al. 1997; Donnelly et al. 2003). Sometimes, bilaterally diffuse air-filled cysts in PIE may look like the findings of developing BPD. The acuteness and time of onset are helpful differentiating features. PIE has an acute onset, whereas BPD develops gradually. PIE typically occurs during the first week of life, while cystic lucencies of BPD do not usually develop until 2 weeks of life (Richardson 2012b).

11.4.2 Pneumomediastinum/ Pneumopericardium

Pneumomediastinum is common in neonates with air leak. Chest radiographs taken in the supine position show mediastinal hyperlucency with apical masses, which represent the lobes of the thymus elevated by air (“angel wing” sign) (Fig. 11.25) and air beneath the heart (“continuous diaphragm sign”). Unusual sharp appearances of the aorta and main pulmonary artery can be noted on radiographs, due to the dissecting air around these structures. Cross-table lateral imaging can confirm the anteriorly collected air surrounding the thymus (Moseley 1960; Levin 1973).

Pneumopericardium is less common than pneumomediastinum and is usually associated with pneumomediastinum. Pericardial air surrounds the heart but is limited superiorly by the pericardial reflection. In pneumomediastinum, the elevated thymus is outlined by air and the aortic arch is seen separately from the pulmonary artery due to the air in the aortopulmonary window, while the thymus and the arch of the aorta are not outlined in the case of pneumopericardium (Slovic and Bulas 2008). Occasionally, pneumopericardium may result in cardiac tamponade. With a tension pneumopericardium, a prominent air collection surrounds the heart and the heart appears small.

11.4.3 Pneumothorax

Pneumothorax can usually be easily recognized, but several different features can be seen in neonates. Chest radiographs in infants are taken in the supine position and therefore pleural air tends to accumulate anteriorly, inferiorly and medially. Unlike in older children and adults, an apical or lateral pleural line is often not visible and lateral decubitus or cross-table

lateral views may be required to confirm small amounts of anterior pneumothorax. The diagnosis may be suggested by the difference in densities between both sides and more sharply defined borders of the mediastinum and diaphragm than normal. A deep sulcus sign may be seen, in which one costophrenic angle extends deeper than the other (Kong 2003). Anterior pneumothorax may also compress the lobe of the thymus gland, producing a bulging “pseudomass” configuration at the superior mediastinum (Figs. 11.26 and 11.27) (O’Keeffe et al. 1991). Occasionally, differentiation between medial pneumothorax and pneumomediastinum can be difficult. In such cases, decubitus imaging can be helpful by identifying the rising of air to the nondependent area, outlining the pleural surface.

Some artificial lesions can mimic pneumothorax on neonatal chest radiographs. Mild rotation of a baby on a chest radiograph can create a hyperlucent lung that stimulates pneumothorax. Prominent skin folds can extend vertically across the thorax and can be mistaken for pneumothorax (Fig. 11.29).

If the pneumothorax is small and the infant is asymptomatic, pneumothorax may be managed conservatively. Otherwise, the treatment is removal of air via a thoracoscopy tube.

11.5 Lines, Tubes, and Catheters

One of the important purposes of obtaining a chest radiograph in a neonate is to confirm the position of tubes and catheters. Early recognition of malposition is crucial for avoiding serious complications.

The ideal position of central venous catheters, including peripherally inserted central catheters (PICC), is at the junction of SVC/IVC and the right atrium (Fig. 11.31). An umbilical venous catheter (UVC) passes through the umbilical vein, the left portal vein, the ductus venosus, and the hepatic vein into the IVC, whereas an umbilical arterial cath-

eter (UAC) makes a characteristic pelvic loop by its course from the umbilicus down to the internal iliac artery before passing into the common iliac artery and aorta. The ideal tip position of UVC is at the junction of the IVC and right atrium. Malpositioned UVCs may be complicated with portal vein thrombosis and potential portal hypertension. UAC should be placed in the aorta below the ductus arteriosus and above or below the visceral arteries. The ductus arteriosus joins with the aorta at the level of the fourth thoracic vertebra and the celiac axis arises at T10–11, the inferior mesenteric artery at L1–2. Therefore, the tip should be placed between T6 and T9 for high-line positioning and at or below L3 for low-line placement (Fig. 11.30) (Cleveland and Rhein 2012).

ECMO is performed in neonates with severe, reversible respiratory failure with no response to conventional treatment. Pulmonary bypass is performed either with catheters inserted through the right internal jugular vein and common carotid artery (venoarterial) or by a dual-lumen venous catheter (veno-venous). In a venoarterial system, the venous catheter tip should be in the right atrium and the arterial catheter should course through the brachiocephalic artery and terminate at the aortic arch (Slovis and Bulas 2008).

Endotracheal tubes (ETT) should be maintained within the intrathoracic trachea between the thoracic inlet and the carina. The tip of the ETT in neonates moves inferiorly with flexion of the head and superiorly with extension of the head. Therefore, if the head is flexed upon the chest wall, the ETT tip should be slightly above the carina. If the head is quite extended, the ETT tip should be slightly below a point midway between the T1 vertebral body and the medial end of the clavicle (the level of the thoracic inlet). Complications of intubation include malposition, most often in the right main bronchus, and tracheal perforation (Cleveland and Rhein 2012).

Gastric tubes should not be positioned at the esophagogastric junction to avoid reflux and aspiration. If the tip lies high in the chest and repositioning is not possible, esophageal atresia should be considered (Fig. 11.32).

11.6 Illustrations: Neonatal Chest Imaging

11.6.1 Normal Thymus

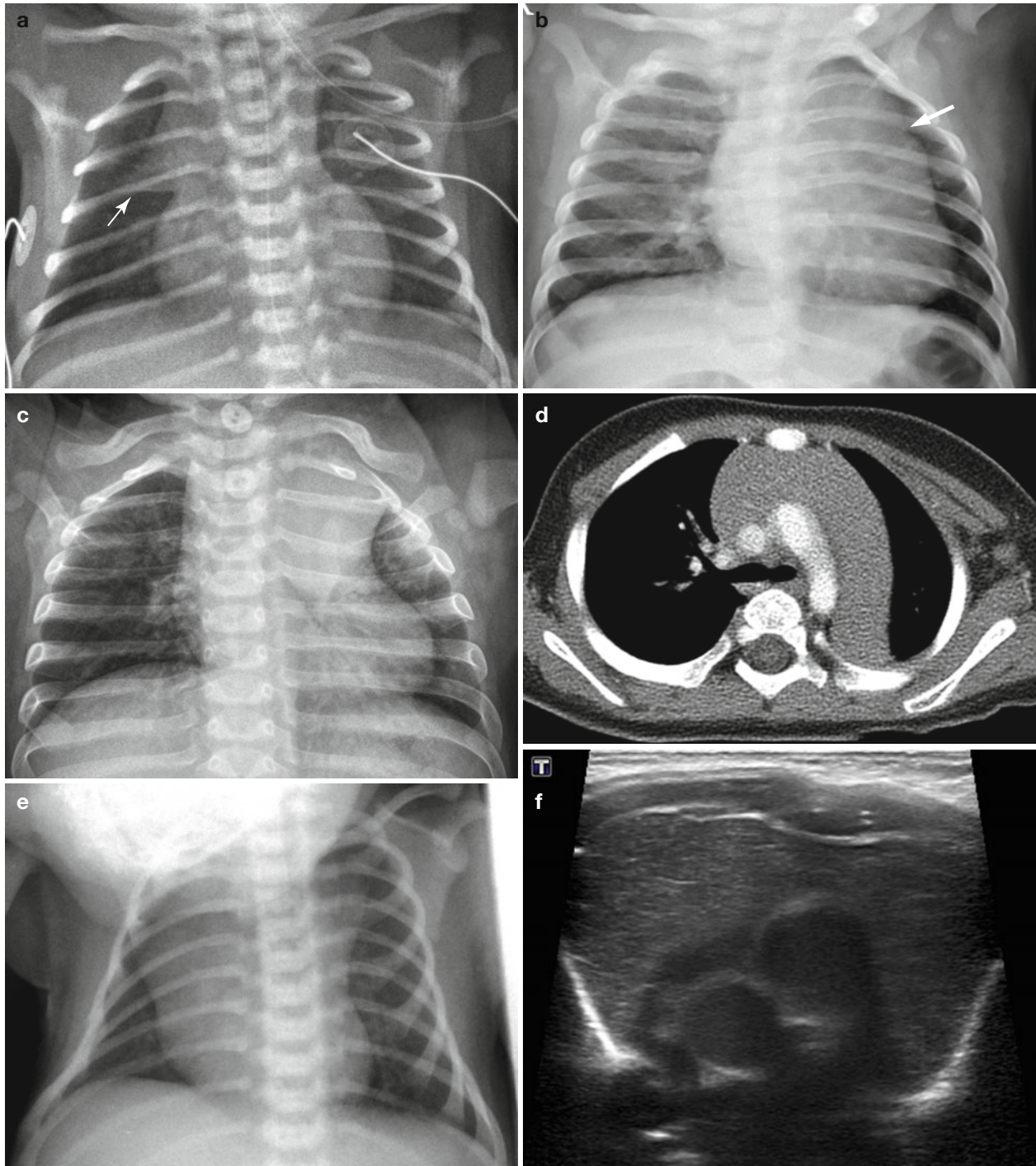


Fig. 11.1 Various appearances of a normal thymus in newborn. (a) “Sail” sign. Note triangular extension laterally that looks like a sail. (b) “Wavy thymus” sign. The *arrow* indicates the undulating margin of the thymus due to gentle compression by the adjacent anterior rib. (c, d) The prominent thymus mimics a mediastinal mass or left upper lobe parenchymal lesion. On precontrast CT, the thymus is seen as a homogeneous soft tissue structure in the anterosuperior mediastinum with

extension posteriorly and laterally along the arch of the aorta. (e, f) On this anteroposterior chest radiograph taken in a rotated position, a large thymus mimics upper lobe atelectasis. Ultrasonography was performed in order to confirm the thymus. Transverse ultrasonographic scan demonstrates linear or dot-like echogenicity within the superior mediastinal soft tissue structure, the characteristic internal pattern of the normal thymus

11.6.2 Hyaline Membrane Disease

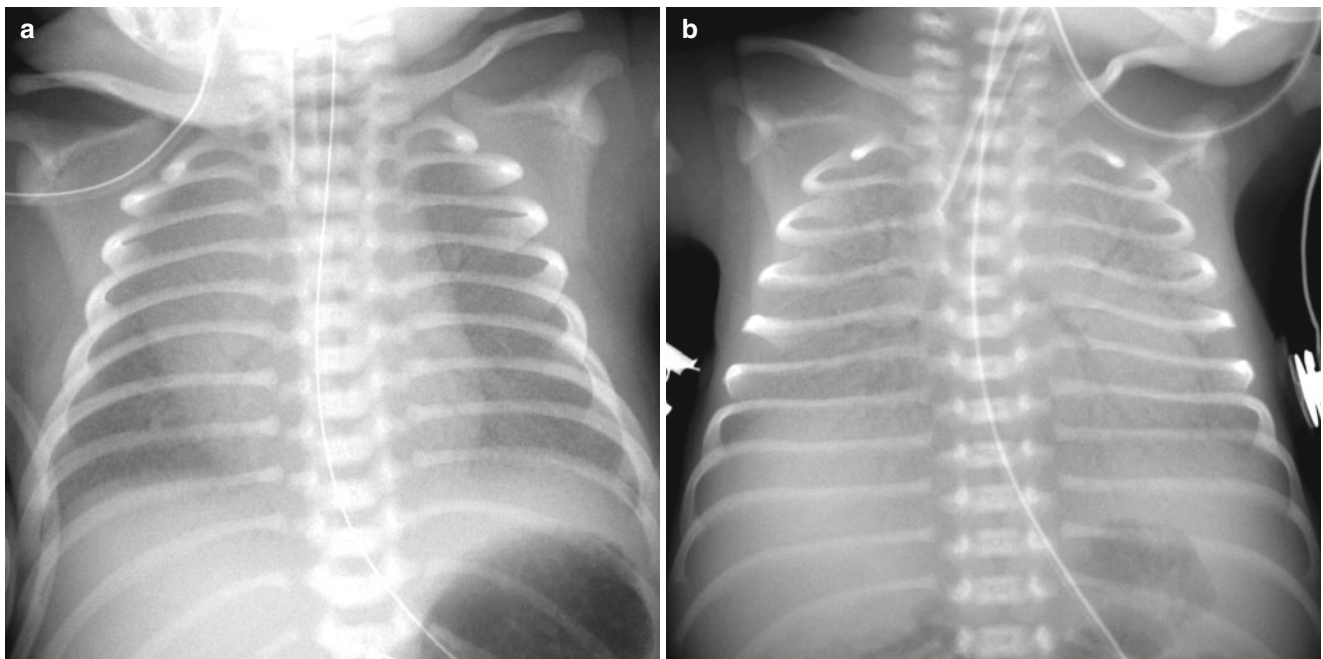


Fig. 11.2 The “classic” appearance of hyaline membrane disease. It may vary in its clinical and imaging severity. **(a)** Moderate HMD, frontal radiograph shows evenly distributed, fine granular opacification and

pulmonary hypoventilation. **(b)** Severe HMD, frontal radiograph shows white-out with air bronchograms. Note generalized underaeration of the lungs

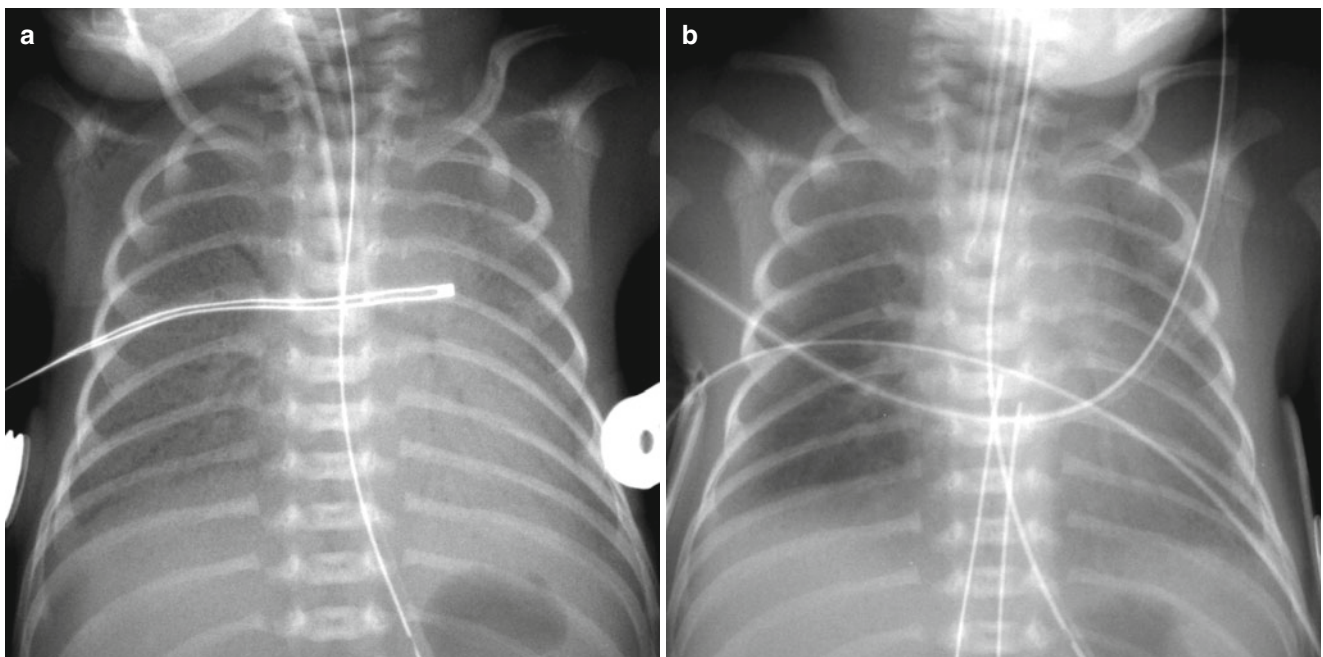


Fig. 11.3 Hyaline membrane disease in a premature neonate of 28 weeks’ gestational age. **(a)** Anteroposterior chest radiograph obtained on the first postnatal day demonstrates diffuse fine granularities, pulmonary hypoventilation, and air bronchograms. **(b)** Follow-up

infantogram obtained 2 h after surfactant treatment shows clearing of lung opacity, but haziness is still noted in the periphery and the bases of the lungs

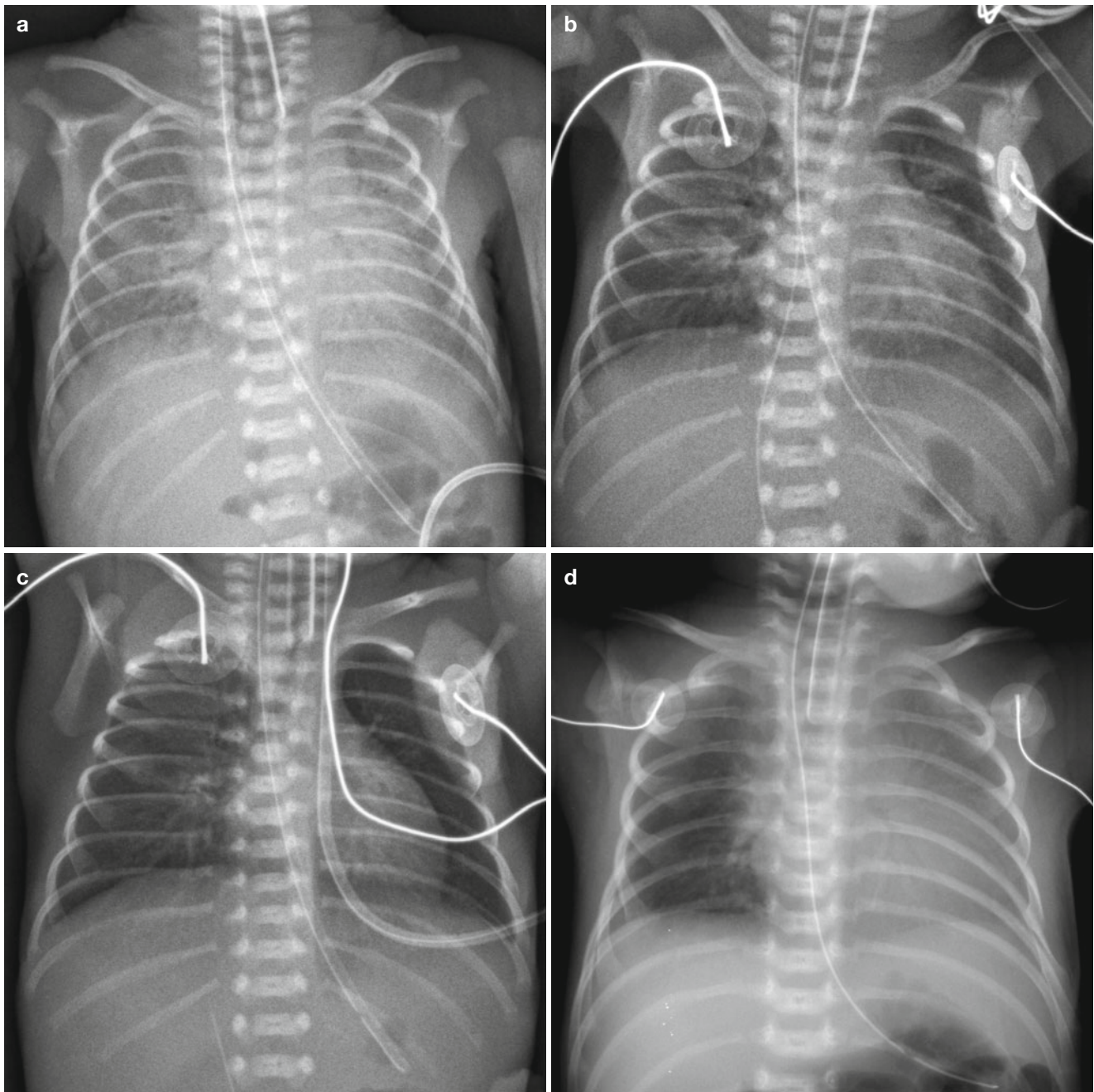


Fig. 11.4 Asymmetric surfactant effect in a newborn with hyaline membrane disease. (a) Initial chest radiograph demonstrates findings of HMD. (b) Frontal chest radiograph obtained after surfactant administration demonstrates multifocal residual parahilar opacities that mimic pneumonia or meconium aspiration syndrome. (c) Repeat chest radiograph after administration of second dose of surfactant shows clearing of

opacifications, but asymmetric diffuse faint haziness is noted only in the right lung field. (d) Asymmetric distribution of endotracheal surfactant into the right main stem bronchus in a 1-day-old preterm neonate with HMD. Frontal radiograph obtained 2 h after surfactant administration shows asymmetric clearing of HMD with the left lung more opacified

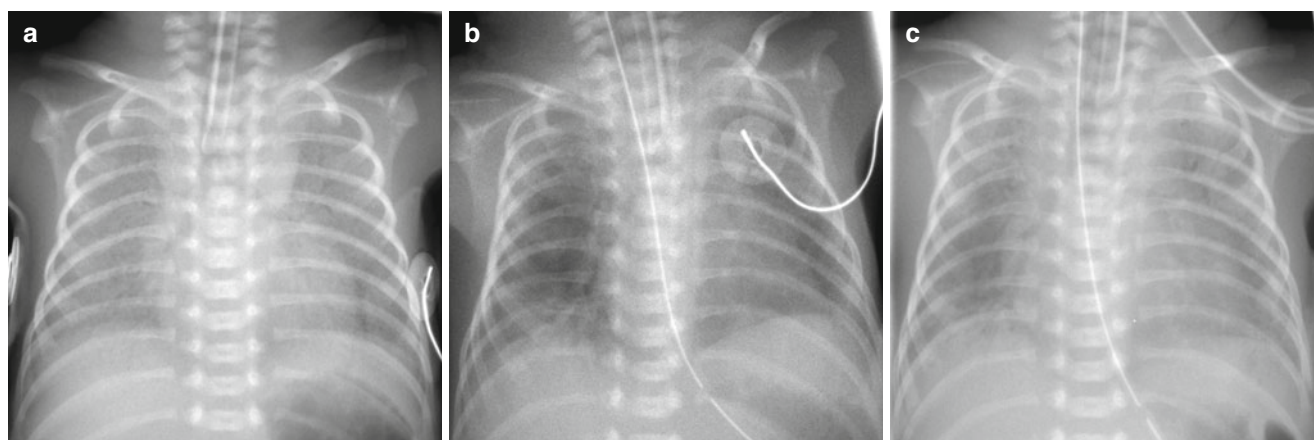


Fig. 11.5 Sudden onset of a *white-out* has several possible explanations. Pulmonary edema resulted from left-to-right shunting across a patent ductus arteriosus. (a) HMD in a 1-day-old preterm neonate. (b) On the second day of life, there is improvement with residual patchy

opacities in the periphery of the lungs. (c) On the third day of life, bilateral diffuse hazy opacification reappeared. Large PDA with left-to-right shunting was confirmed on echocardiography at that time

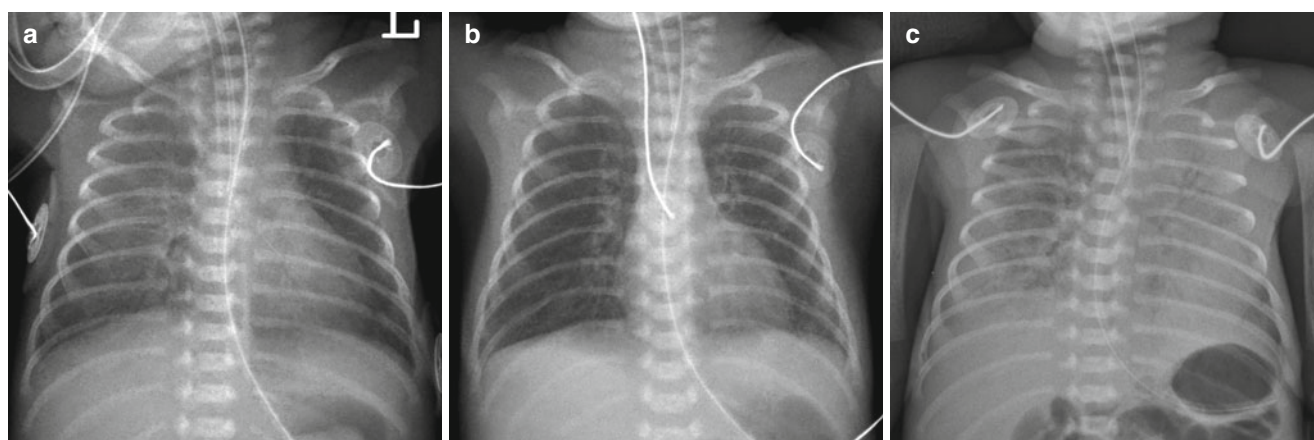


Fig. 11.6 Sudden onset of a *white-out* has several possible explanations. Pulmonary hemorrhage in a 26-week-gestational-age neonate following surfactant therapy. (a) Frontal chest radiograph obtained after one dose of surfactant shows asymmetric clearing of opacities with the left lung improved more than the right. (b) Radiograph, taken after

additional dose of surfactant shows almost clear lungs. (c) Frontal chest radiograph obtained on day 3 of life for evaluation of sudden respiratory compromise and bloody endotracheal aspirates shows diffuse heterogeneous airspace opacifications

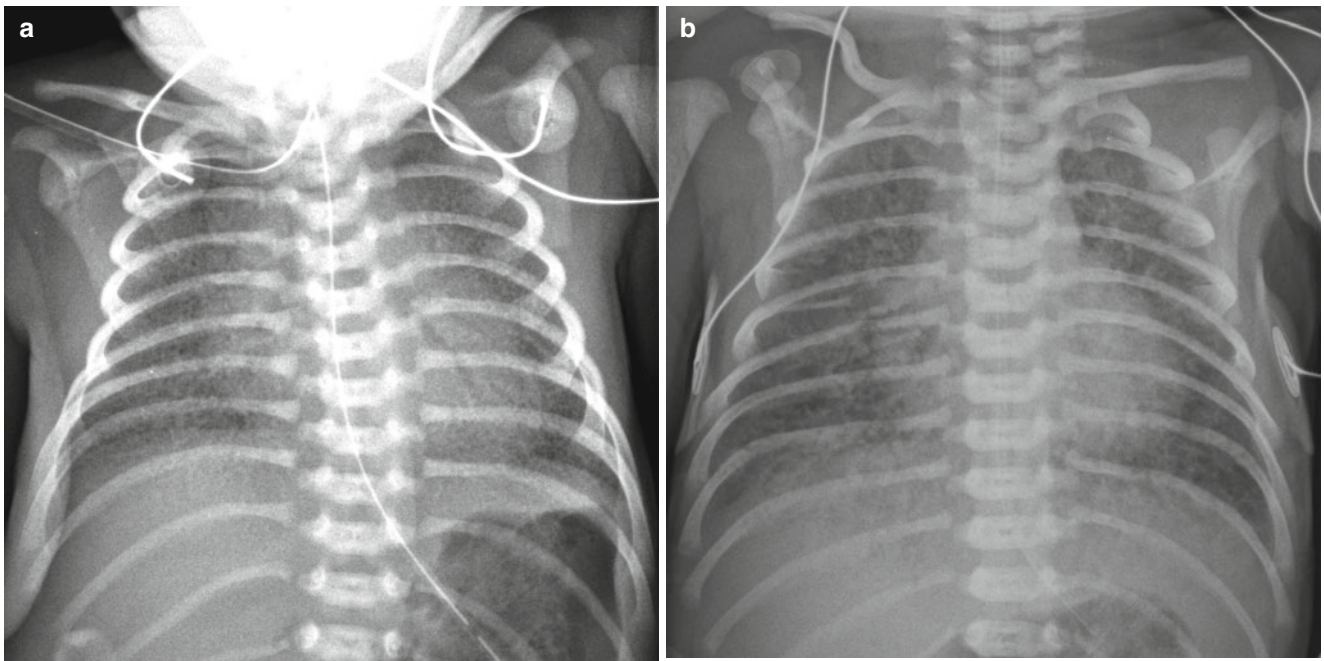


Fig. 11.7 Several diseases may mimic HMD. **(a)** Group B streptococcal pneumonia in a 34-week-gestational-age newborn. Anteroposterior radiograph shows diffuse granular opacities that look like those of typical HMD. **(b)** Total anomalous pulmonary venous return (TAPVR) in a 37-week-gestational-age neonate. Anteroposterior radiograph obtained

on the first day of life demonstrates bilateral diffuse granular opacities. The lung volume is not small, compared to that of typical HMD. TAPVR with obstruction manifests as pulmonary interstitial infiltrations without significant cardiac enlargement and can appear similar to HMD

11.6.3 Immature Lung Syndrome

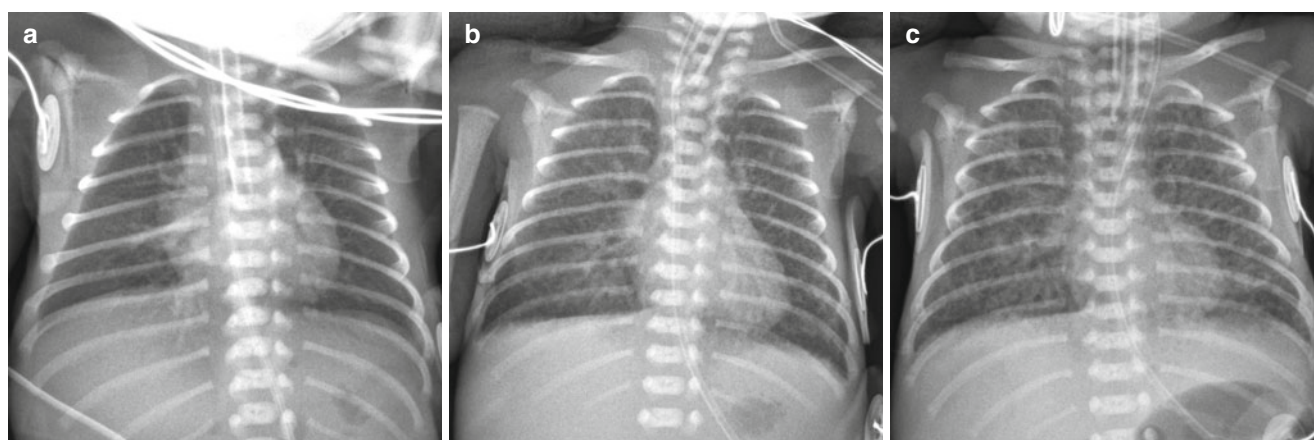


Fig. 11.8 Immature lung syndrome in a profoundly premature neonate delivered at a gestational age of 23 weeks and 6 days with a birth weight of 590 g. **(a)** Anteroposterior chest radiograph obtained on the first postnatal day shows almost clear lungs and normal lung volume. **(b)** Follow-up radiograph obtained at 9 days shows diffuse faint

haziness with interstitial thickening. **(c)** Anteroposterior radiograph obtained at 28 days shows a relatively uniform pattern of coarse interstitial opacities with generalized overaeration, which suggests progression to the recent mild form of bronchopulmonary dysplasia

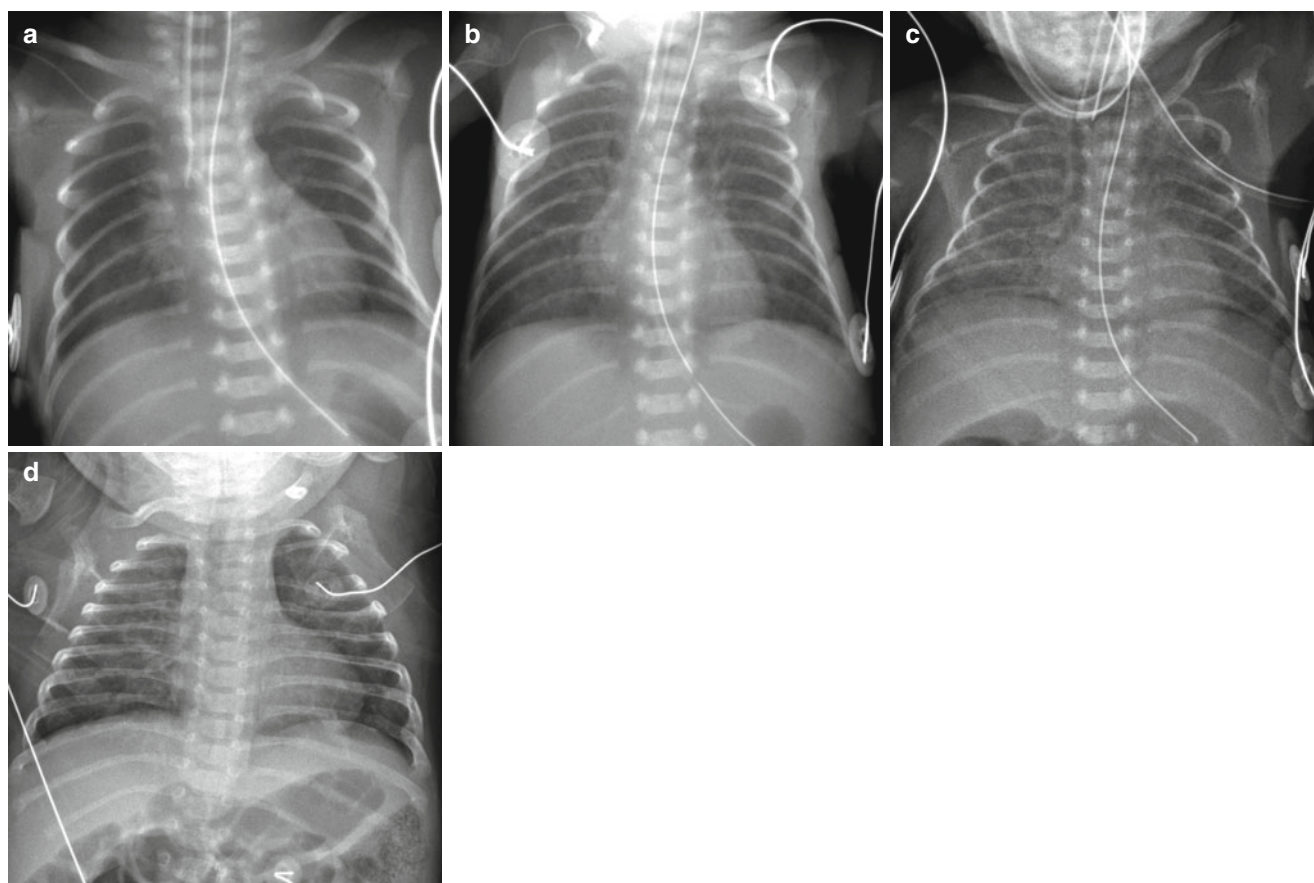


Fig. 11.9 Immature lung syndrome in a neonate born at a gestational age of 23 weeks and 4 days. **(a)** Anteroposterior radiograph obtained on the day of birth shows ill-defined central lung opacities. **(b)** At 9 days

of age, there is diffuse faint haziness. **(c, d)** Anteroposterior chest radiographs, obtained at 31 and 90 days, respectively, demonstrate slow evolution to a coarse interstitial pattern of BPD

11.6.4 Bronchopulmonary Dysplasia

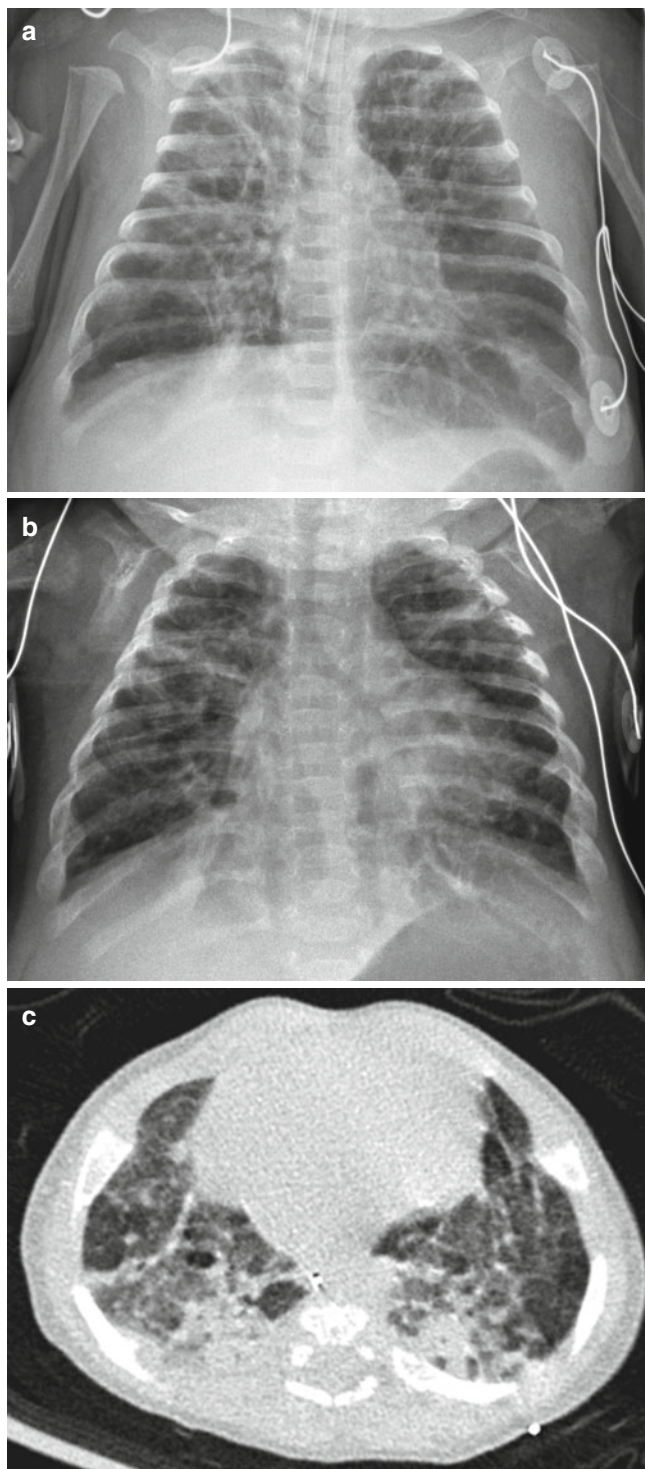


Fig. 11.10 Classic severe bronchopulmonary dysplasia (BPD). (a) Anteroposterior chest radiograph obtained in a preterm infant at 37 weeks' postmenstrual age shows hyperinflated lungs with alternating areas of lucencies and strand-like coarse opacities. (b, c) Chest radiograph (b) and CT (c) in a 4-month-old infant born at a gestational age of 27 weeks. Chest radiograph reveals diffuse coarse irregular opacities and alternating areas of hyperinflation. Axial CT scan demonstrates lucent areas of variable size, multifocal atelectasis, coarse interstitial lines of fibrosis, and architectural distortion. Bronchiectasis does not occur

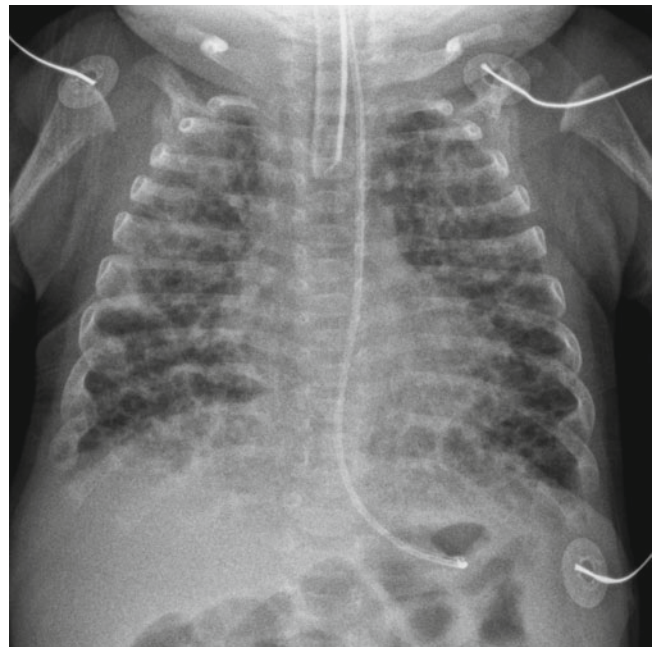


Fig. 11.11 BPD in a 10-week-old infant born at a gestational age of 31 weeks. chest radiograph shows hyperinflation and numerous small round cystic areas alternating with coarse irregular opacities. The findings are more symmetrical and uniform than those seen in Fig. 11.10

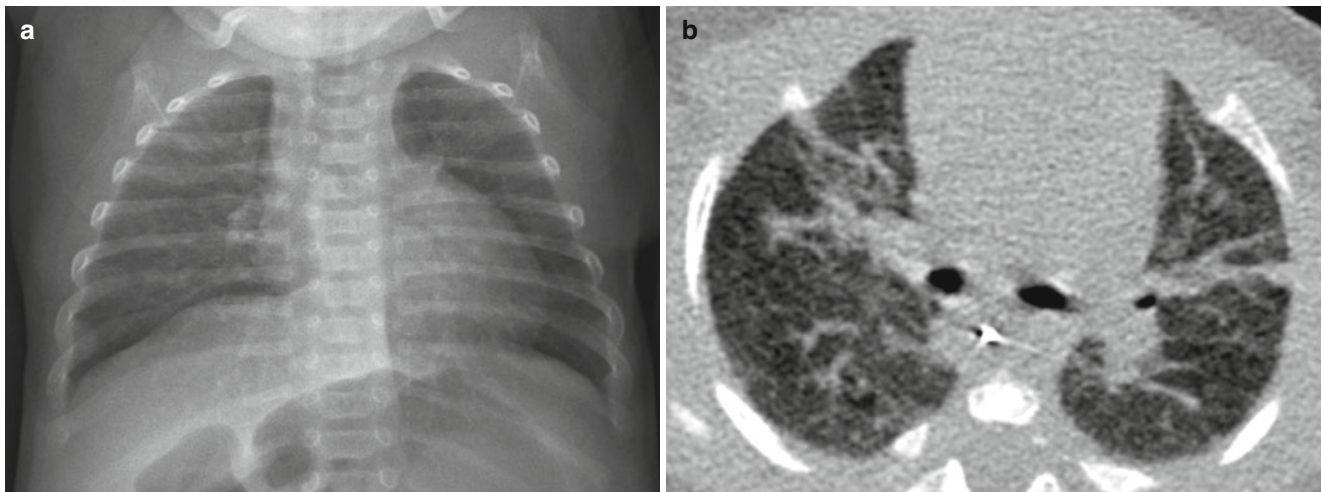


Fig. 11.12 Mild BPD in an 11-week-old infant at a gestational age of 26 weeks. (a) Chest radiograph obtained at the time of discharge shows hyperinflation and fine interstitial opacities. (b) CT performed at the same time shows multifocal linear areas of atelectasis or fibrosis

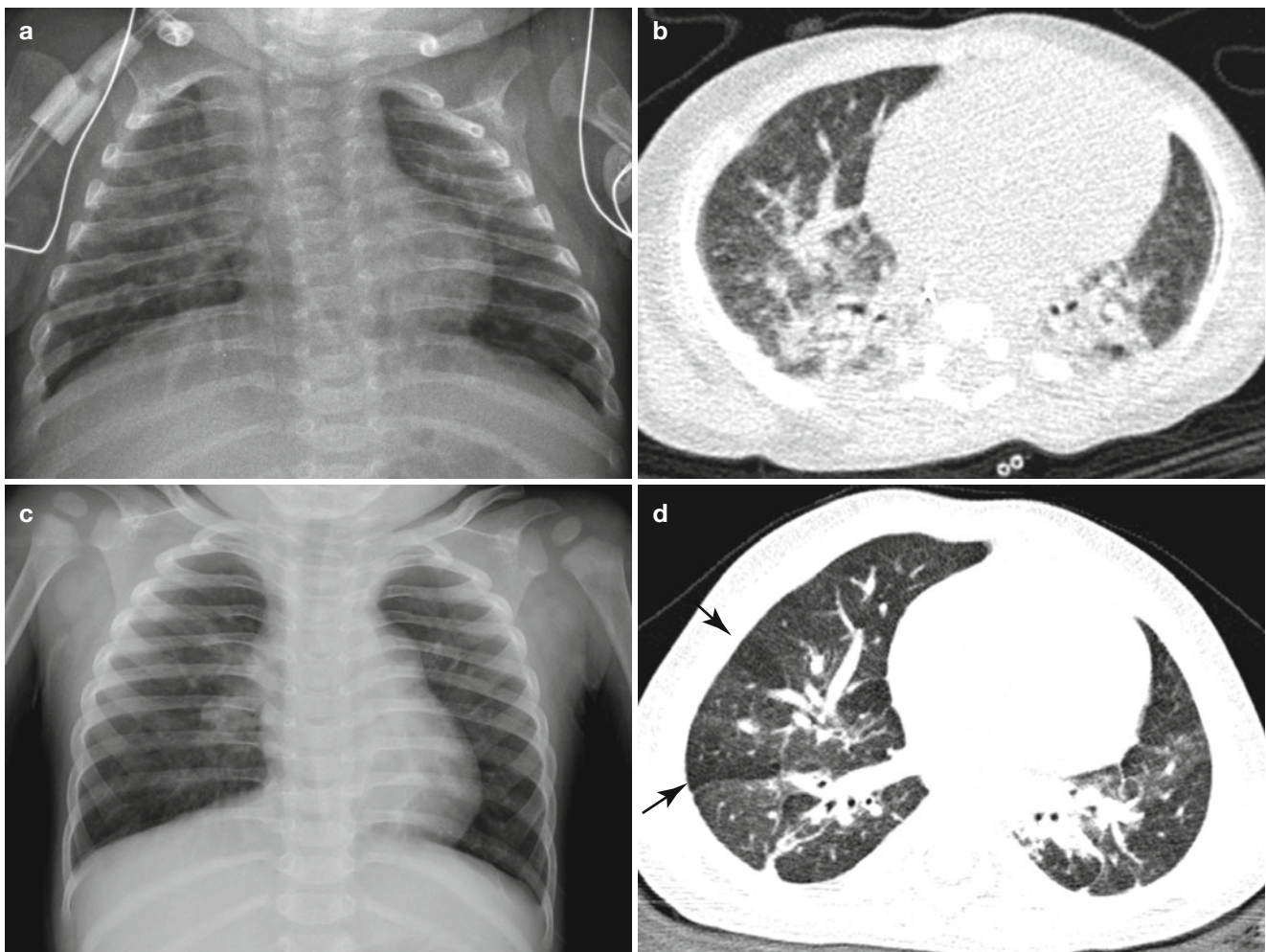


Fig. 11.13 Gradual radiologic improvement of BPD in a pre-term infant born at a gestational age of 30 weeks. (a) Frontal chest radiograph at 3 months of age shows coarse interstitial opacities and overall mild hyperinflation. (b) CT scan obtained at the same time shows multifocal atelectasis and fibrotic opacities, suggestive of BPD. (c) Follow-up chest

radiograph taken at 15 months of age reveals interval improvement of interstitial lung opacities, but there are some coarse central interstitial opacities and hyperinflation. (d) On CT image obtained at around the same time, there are improved but residual linear subpleural opacities. Multifocal areas of mosaic attenuation (*arrows*) can be seen

11.6.5 Meconium Aspiration Syndrome

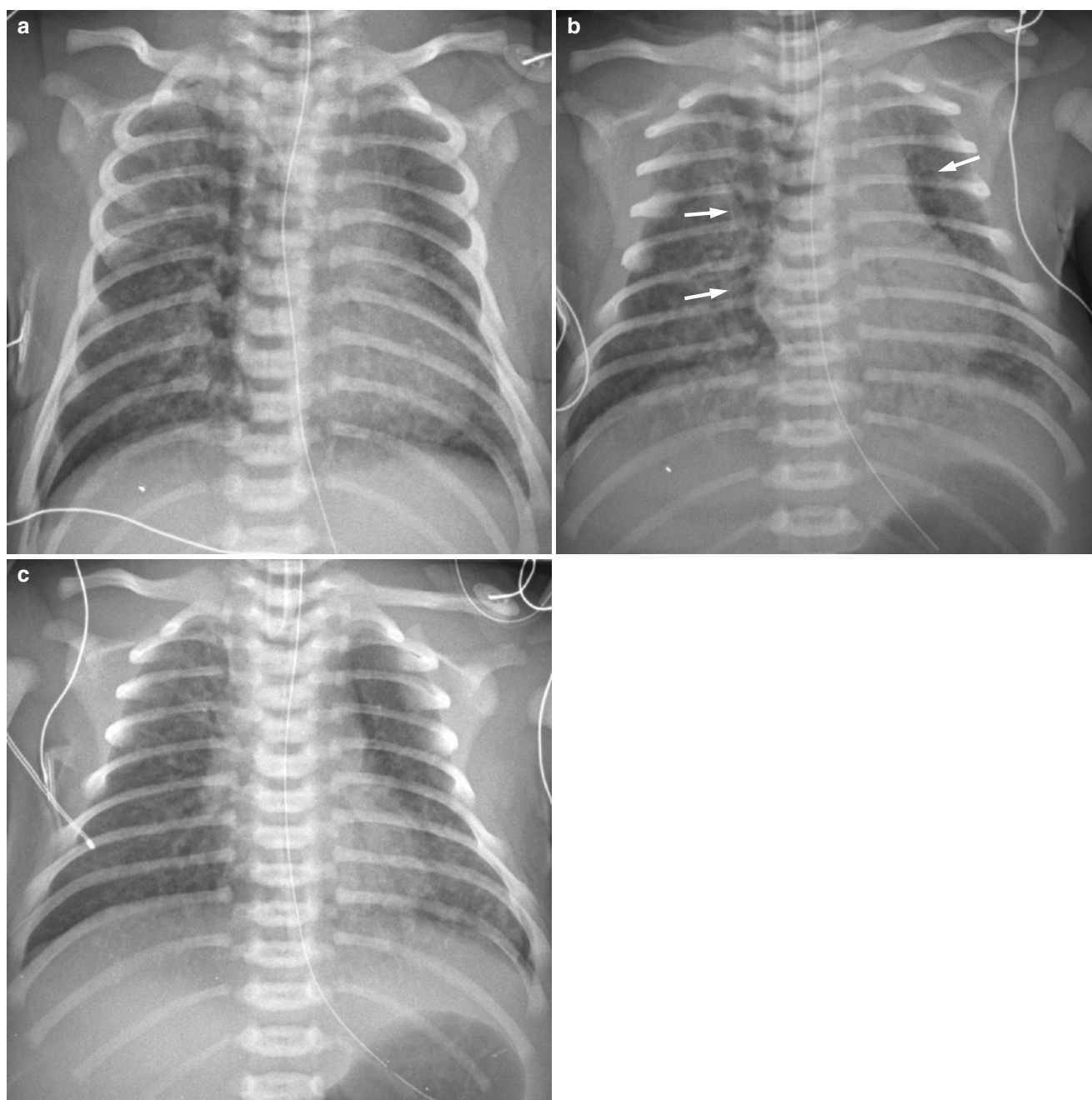


Fig. 11.14 Meconium aspiration syndrome in a 41-week-gestational-age neonate with meconium staining. (a) Anteroposterior chest radiograph demonstrates coarse opacities bilaterally. The lungs are hyperinflated.

(b) Repeat radiograph obtained 5 h later reveals pneumomediastinum (*arrows*). (c) One day later, air leak has improved, but coarse nodular opacities are still noted in both lung fields

11.6.6 Transient Tachypnea of the Newborn

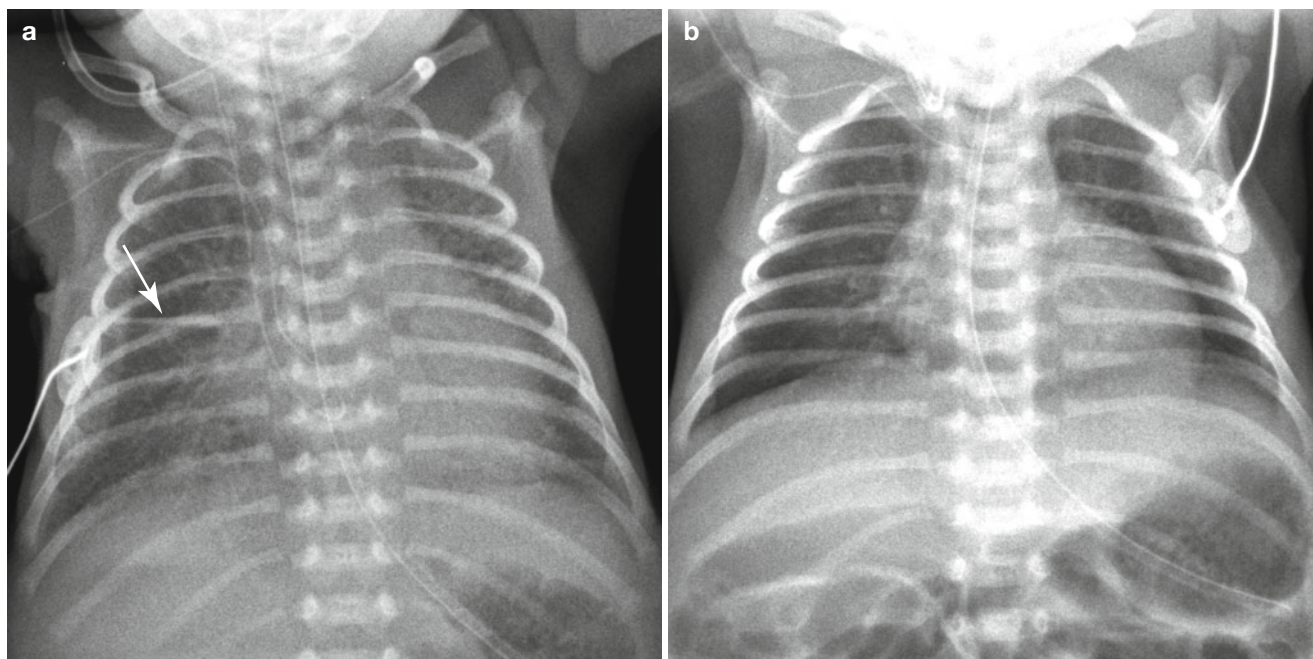


Fig. 11.15 TTN in a 34-week-gestational-age newborn, delivered due to placental abruption. (a) Initial frontal chest radiograph demonstrates cardiomegaly and bilateral parahilar strandings. A small amount of fissural fluid is seen at the right minor fissure (*arrow*). There was mild

respiratory distress, but oxygen saturation was maintained at 95 % in the room air. (b) The opacification has completely cleared on the following day

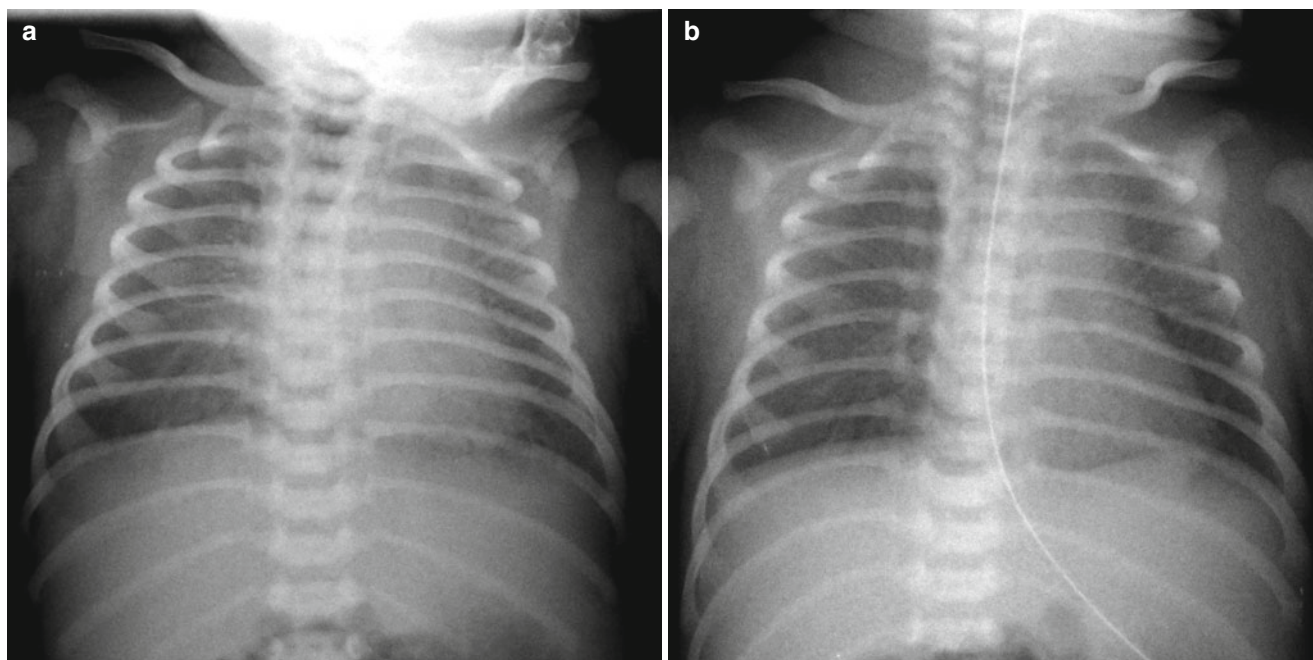


Fig. 11.16 TTN in a 40-week-gestational-age newborn. (a) Bilateral diffuse faint haziness and mild cardiomegaly are noted on a frontal radiograph obtained on the day of birth; tachypnea without cyanosis

was present at that time. (b) Such opacification has cleared on repeat radiograph obtained 1 day later. The important diagnostic clues are the patient's gestational age and rapid resolution of lung lesions

11.6.7 Neonatal Pneumonia

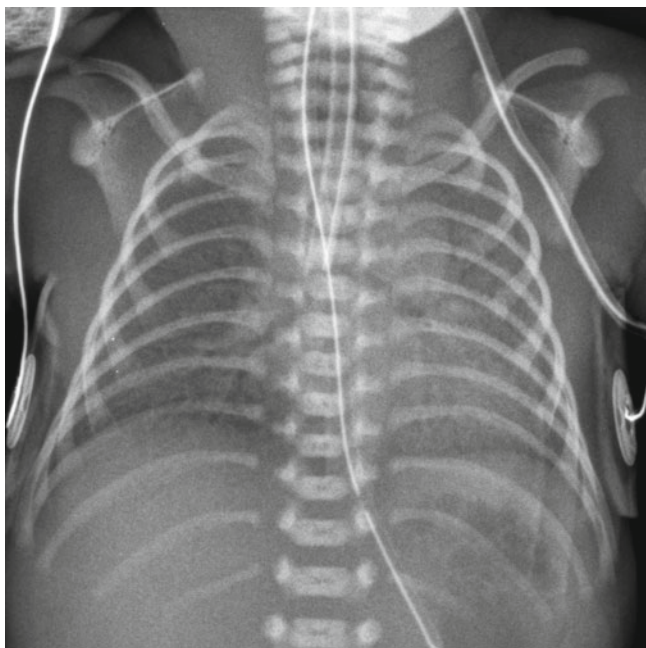


Fig. 11.17 Group B streptococcal pneumonia in a preterm neonate with a history of maternal chorioamnionitis. Anteroposterior chest radiograph reveals bilateral diffuse opacification with air bronchograms. This finding is quite similar to that of HMD

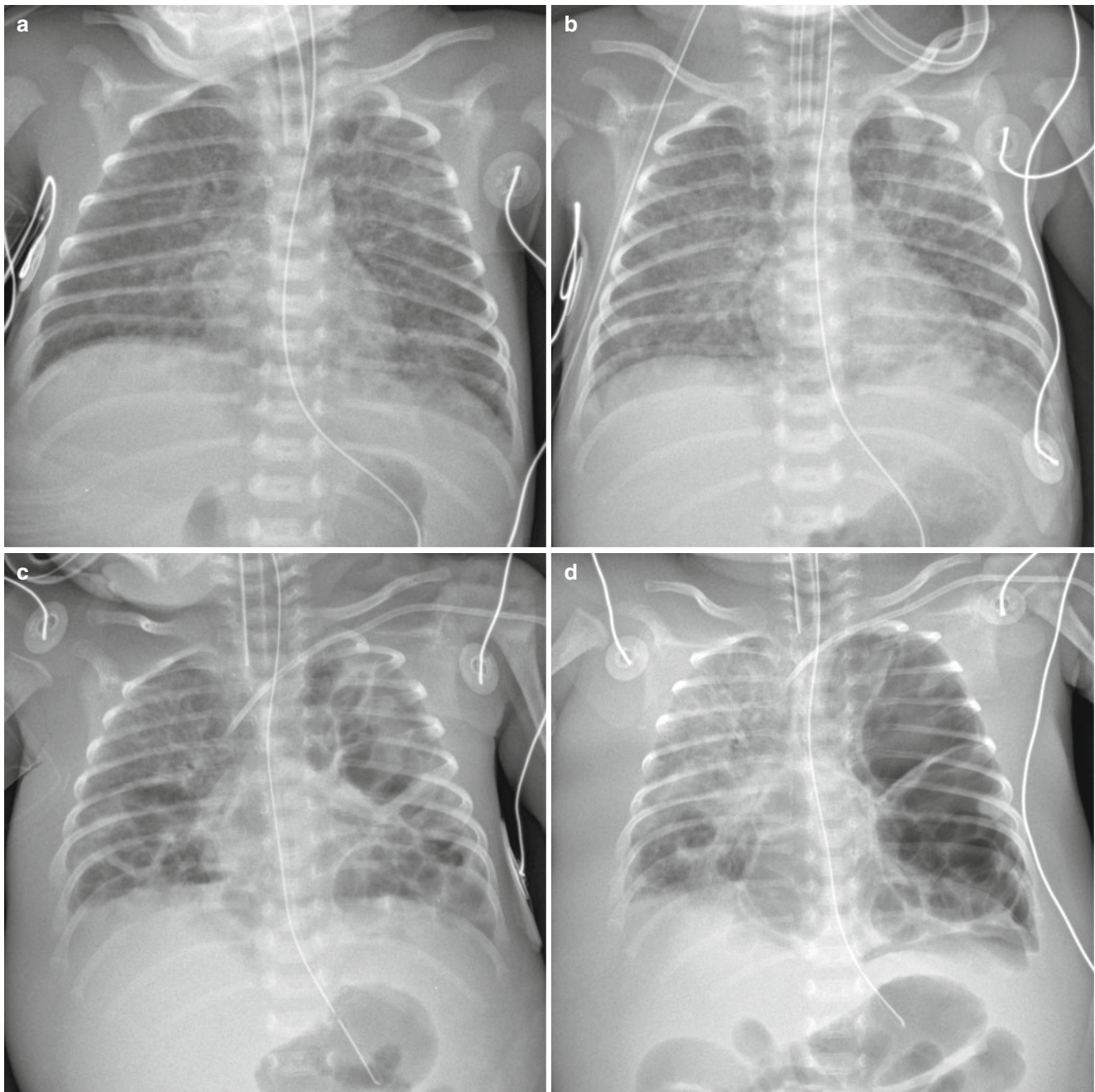


Fig. 11.18 *Staphylococcus aureus* pneumonia in a 32-week-gestational-age newborn. (a) Anteroposterior radiograph obtained at 10 days of age demonstrates diffuse uniform reticular opacities, suggestive of bronchopulmonary dysplasia. (b) Two days later, follow-up chest radiograph reveals irregular patchy infiltrates in both lungs. From that time, blood cultures were positive for methicillin-resistant *Staphylococcus*

aureus. (c) Anteroposterior radiograph obtained at 19 days of age demonstrates progression into multiple bilateral pneumatoceles. Bilateral pleural effusions and anasarca are also seen. (d) At 24 days, there is progression of the disease. Chest radiograph shows markedly enlarged pneumatoceles in left lung with mediastinal shift to the right

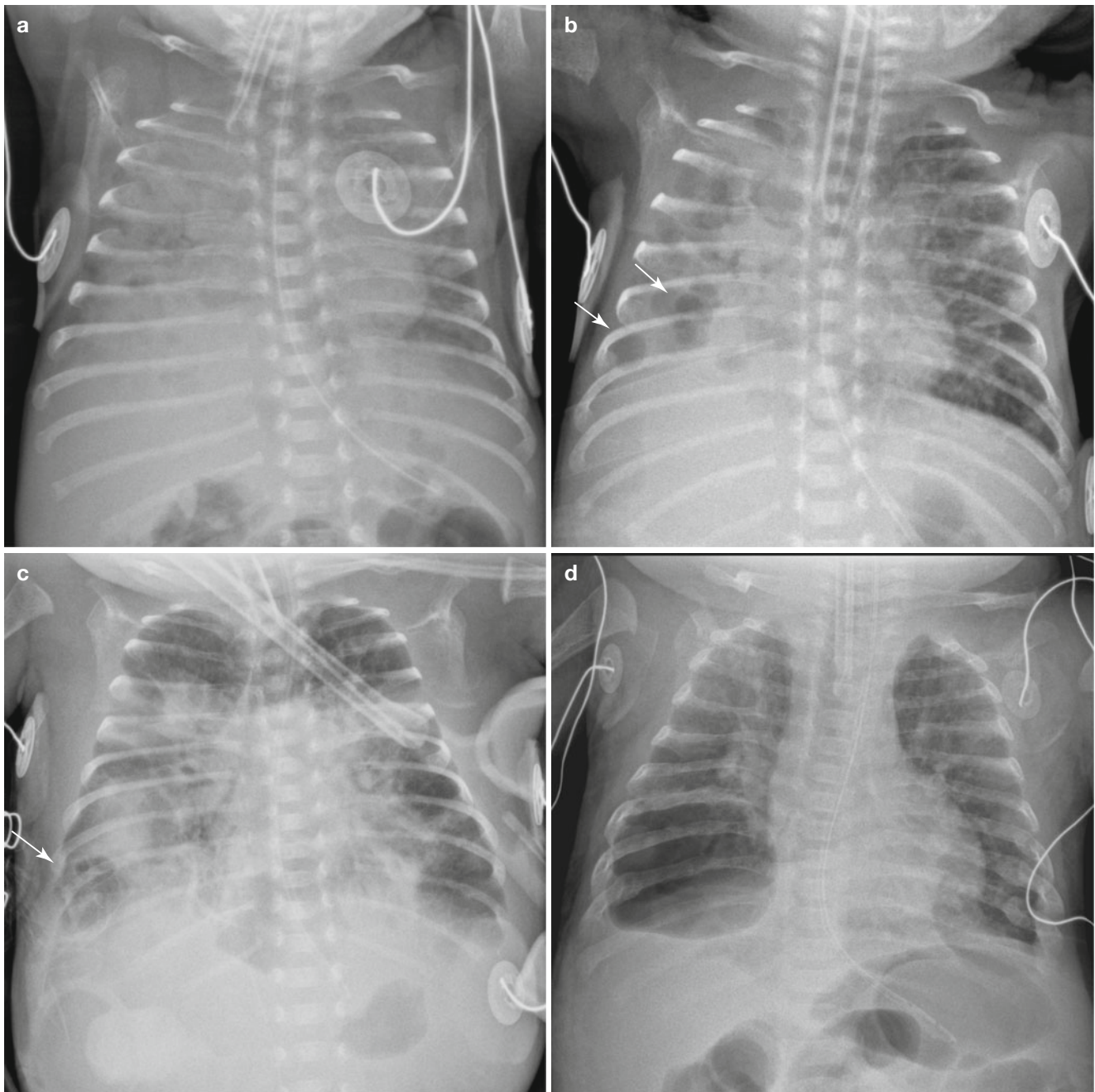


Fig. 11.19 *Staphylococcus aureus* pneumonia in a 24-week-gestational-age newborn. **(a)** Frontal radiograph obtained at 1 month of age demonstrates asymmetric bilateral opacities, typical for neonatal pneumonias other than group B pneumonia. **(b, c)** On frontal chest radiographs, performed 5 and 10 days later, respectively, there are air

cysts (arrows) within patchy consolidations. **(d)** Follow-up radiograph obtained after 3 months shows a large pneumatocele in the right lower lobe. *S. aureus* may cause severe necrotizing pneumonia with pneumatocele formation, as in this case

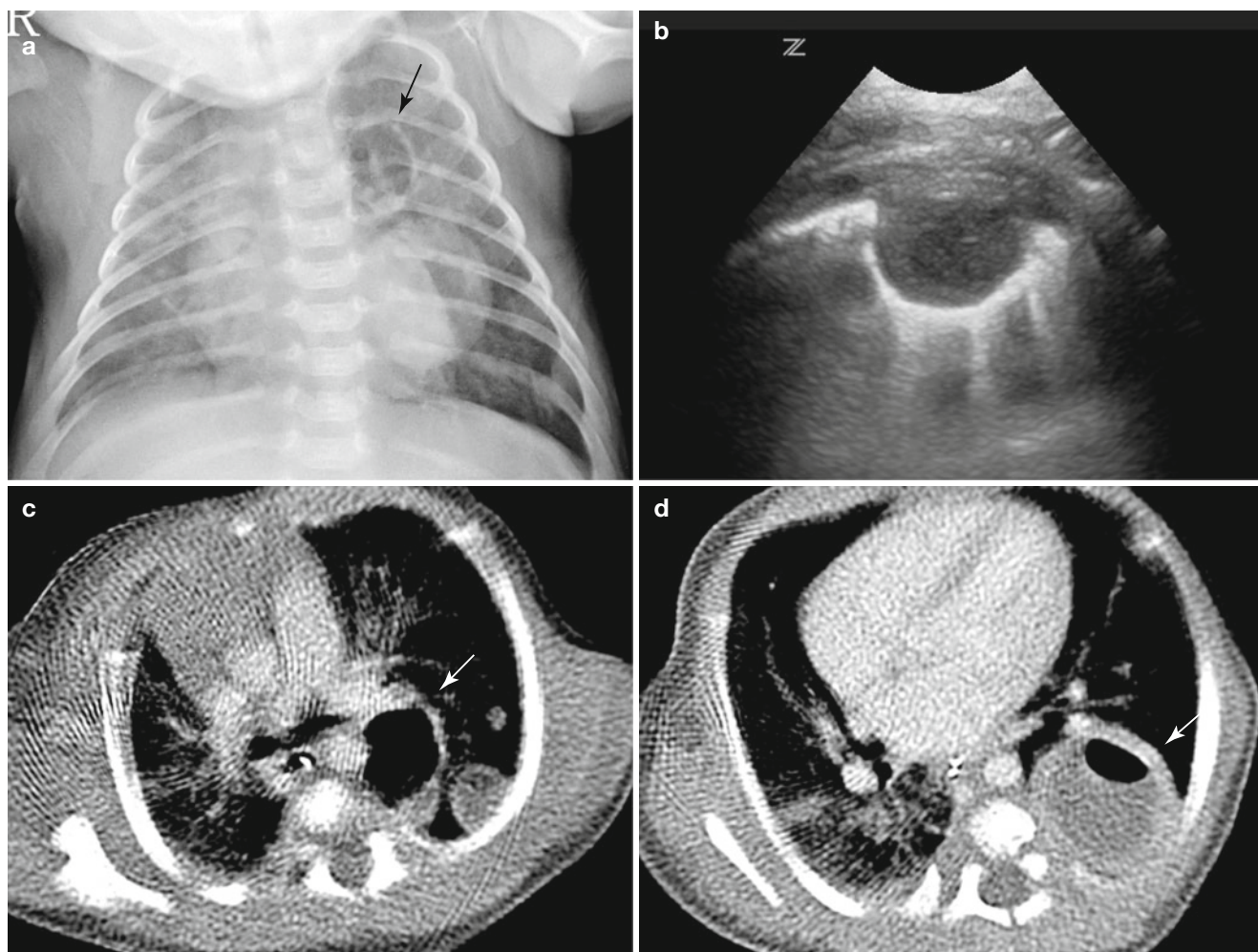


Fig. 11.20 Septic pneumonia with multiple abscesses in a 32-week-gestational-age newborn. (a) Frontal radiograph obtained at 5 weeks of age reveals a large round area of consolidation in the left lower lobe and thin-walled air cyst perihilar area (*arrow*). (b) Chest ultrasonography

reveals a round hypoechoic lesion at left lung. (c, d) Chest CT with enhancement demonstrates multiple round cavitary nodules, mainly in the left lung. Some nodules have internal airs, which suggest an airway communication (*arrows*)

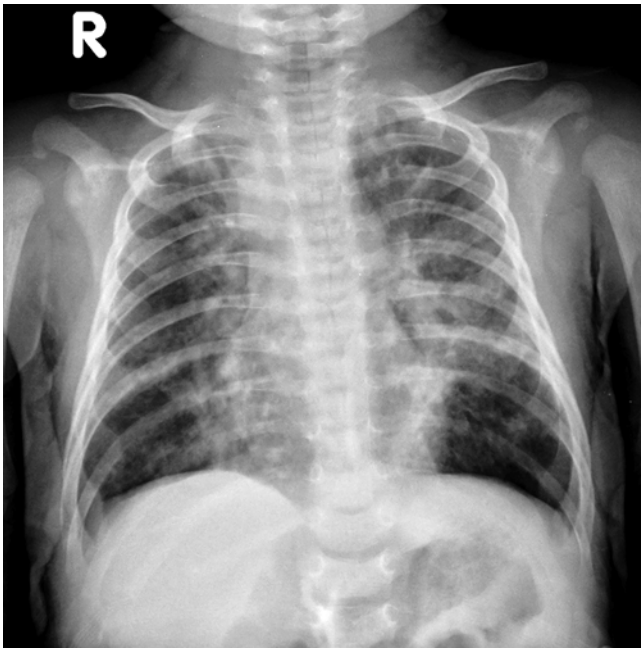


Fig. 11.21 *Chlamydia pneumonia* in a term infant. Anteroposterior chest radiograph at 6 weeks of age demonstrates bilateral diffuse interstitial infiltrates and hyperinflation. Typically, *Chlamydia pneumonia* develops between 2 weeks and 3 months of age and the imaging findings are worse than clinically anticipated

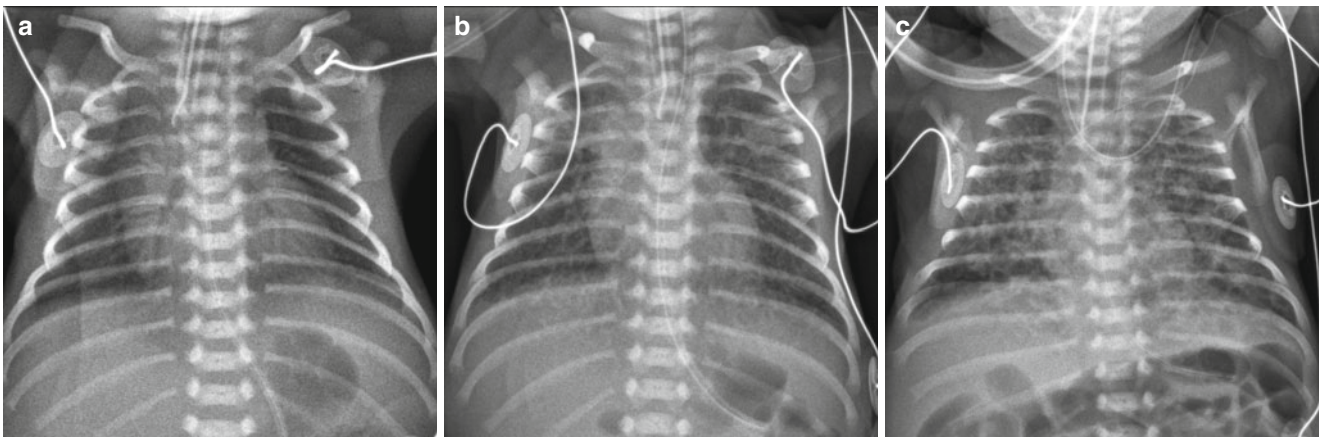


Fig. 11.22 *Ureaplasma urealyticum* pneumonia in a 26-week-gestational-age newborn. (a) On initial anteroposterior radiograph obtained on the day of birth, there is no evidence of pulmonary change. (b) Two days later, bilateral reticular opacities begin to appear. (c)

Anteroposterior chest radiograph at 1 week of age demonstrates advanced changes of BPD. *Ureaplasma urealyticum* is associated with a greater risk and earlier radiographic manifestations of BPD

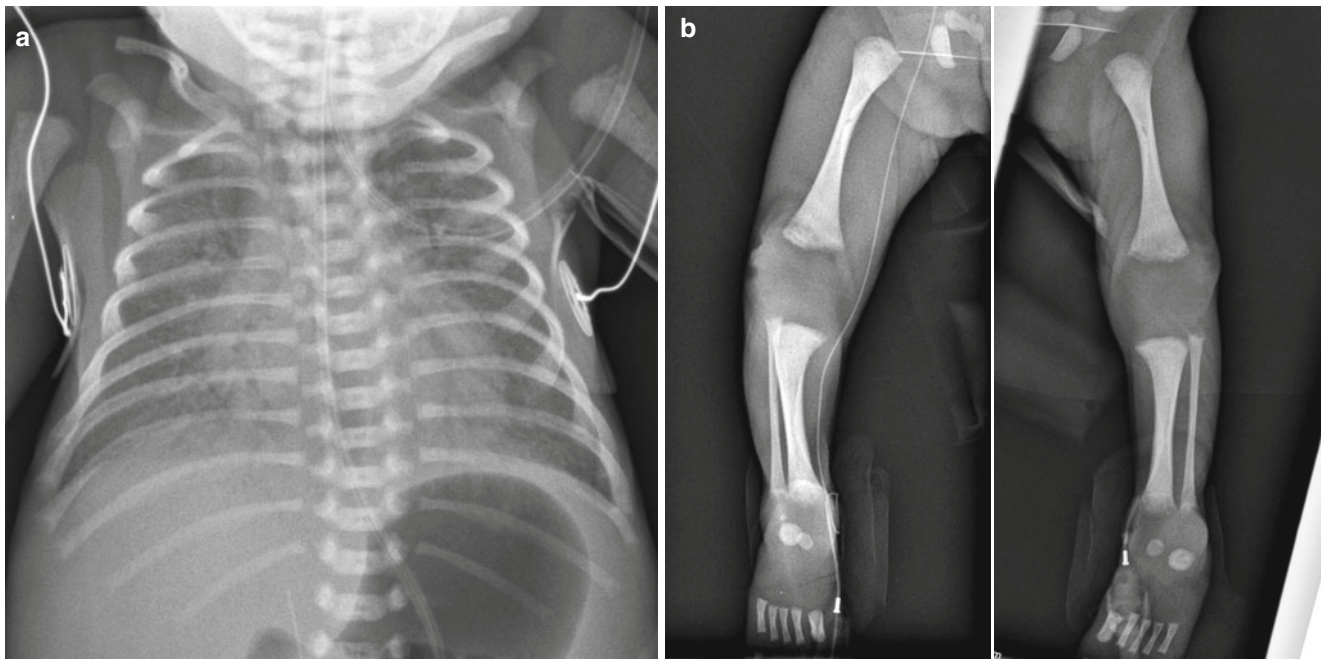


Fig. 11.23 *Pneumonia alba* in congenital syphilis in a 1-day-old pre-term neonate born at a gestational age of 32 weeks. **(a)** Anteroposterior radiograph of the chest demonstrates diffuse haziness in the lungs. Bilateral air bronchograms and mild cardiomegaly are also noted. The

neonate is not intubated, which means there was no clinically significant respiratory distress. **(b)** Radiographs of the lower extremities reveal metaphyseal lucencies and irregularities of the long bones

11.6.8 Air Leak Phenomena

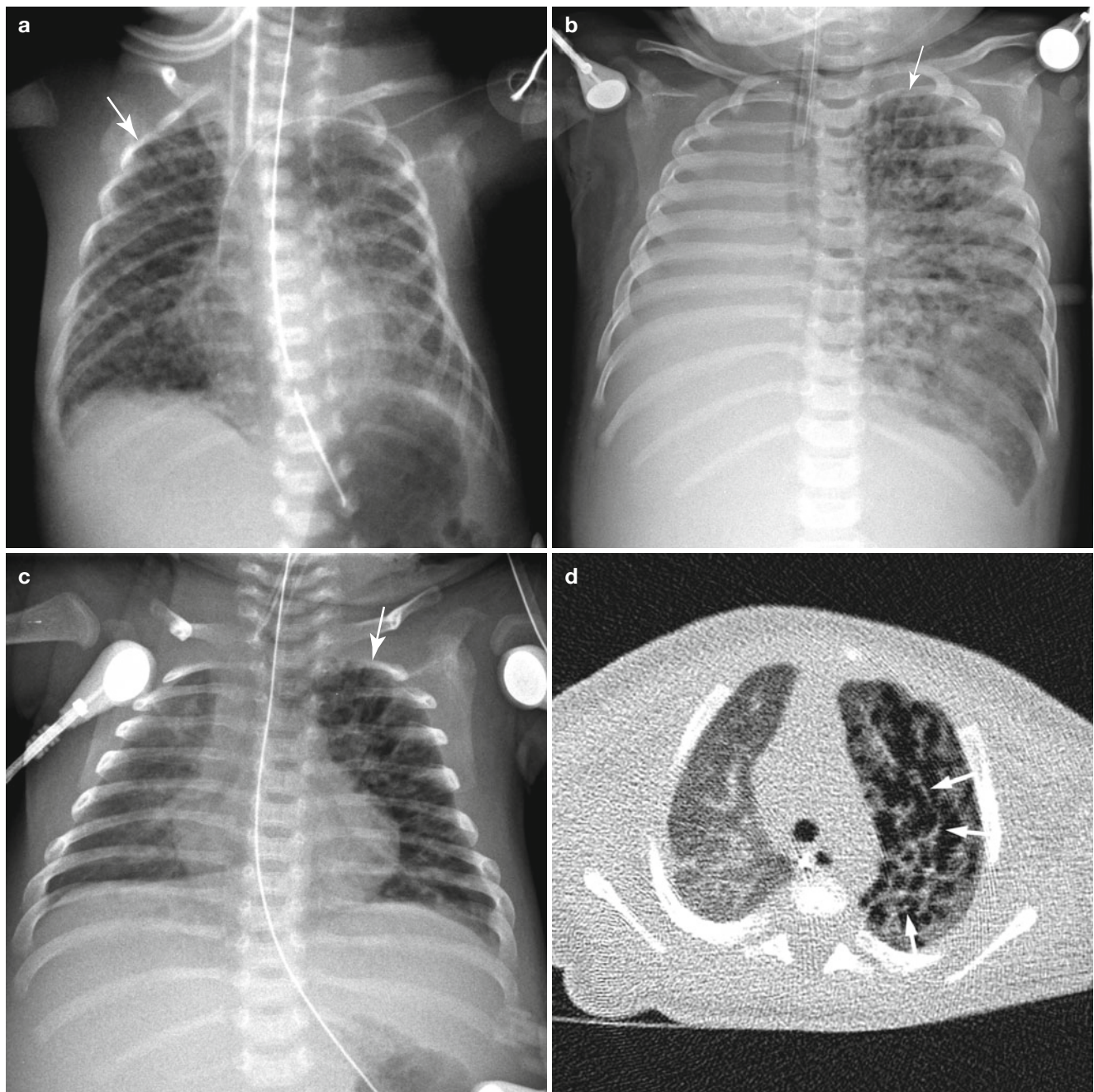


Fig. 11.24 Pulmonary interstitial emphysema (PIE) in premature infants who underwent mechanical ventilation. **(a)** Frontal radiograph shows multiple irregular tubular and small cystic lucencies within the right lung (*arrow*). Note that such lucencies are more prominent in the periphery of the lung, unlike air bronchograms. **(b)** PIE is noted in the left lung (*arrow*). There is total collapse of the right lung with shift of

the mediastinum to the right. **(c, d)** In another patient, frontal radiograph demonstrates radiating tubular and cystic lucencies in the left lung (*arrow*). Axial CT scan confirms multiple collections of interstitial gas in the left upper lobe that surround lines and dots (*arrows*) of soft tissue attenuation

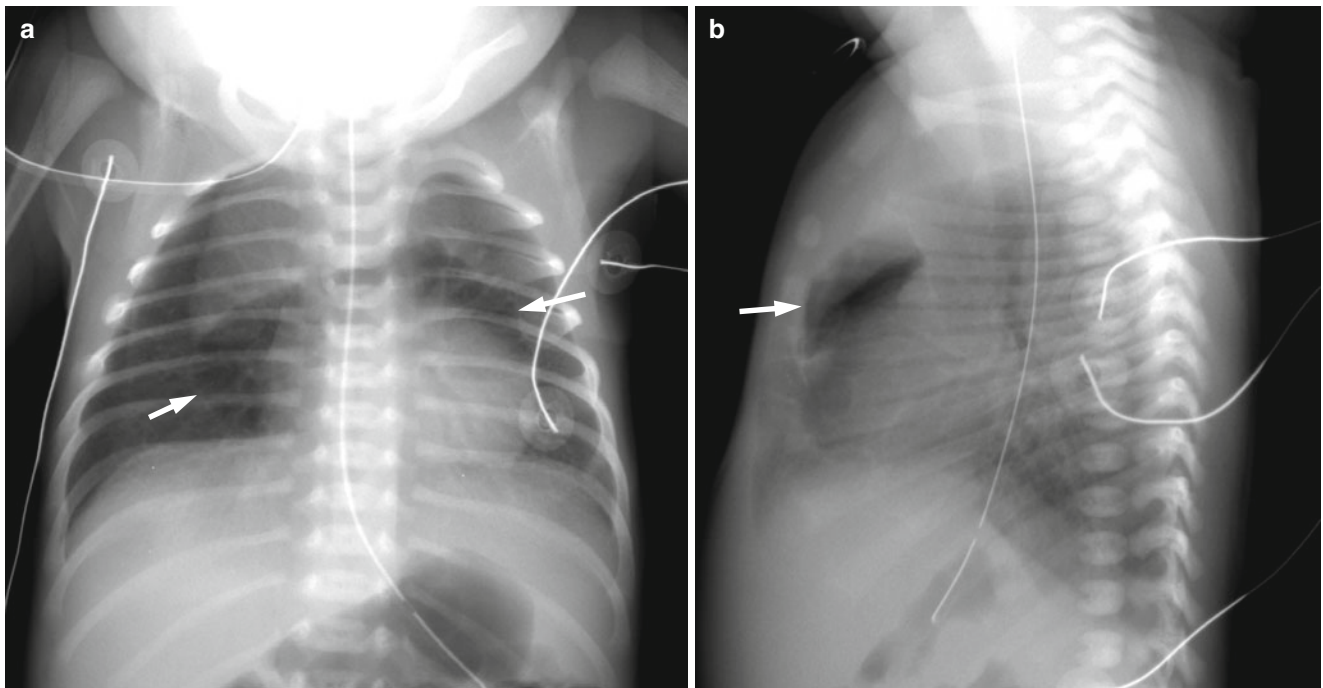


Fig. 11.25 Pneumomediastinum. Frontal and cross-table lateral chest radiographs show elevation of the thymus by a large central lucent area (mediastinal air, *arrows*)

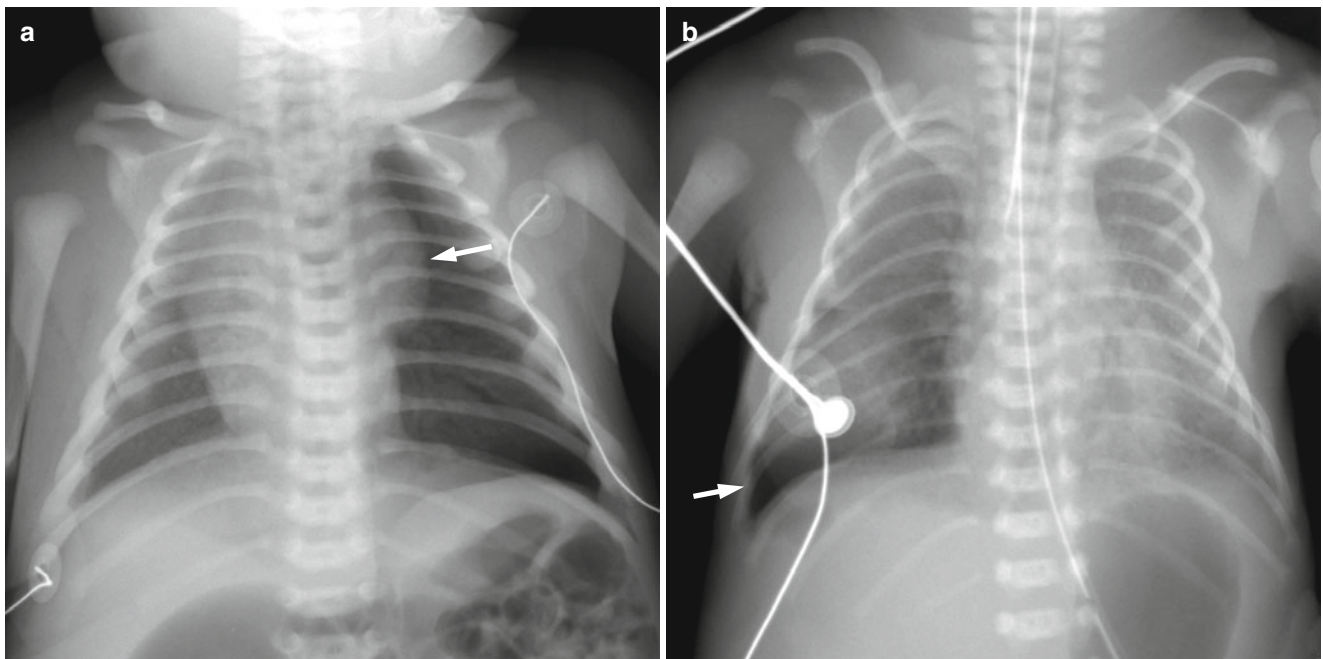


Fig. 11.26 Pneumothorax. (a) Anteroposterior chest radiograph demonstrates unilateral hyperlucency and unusually well-defined and deep costophrenic sulcus in the left hemithorax. The left lobe of the thymus is compressed by anterior pneumothorax, producing a bulging “pseudo-

mass” appearance (*arrow*). (b) Anteroposterior chest radiograph shows juxtamediastinal lucency and clear depiction of the mediastinal and diaphragmatic margins. Note a “deep sulcus” sign (*arrow*) in the right hemithorax

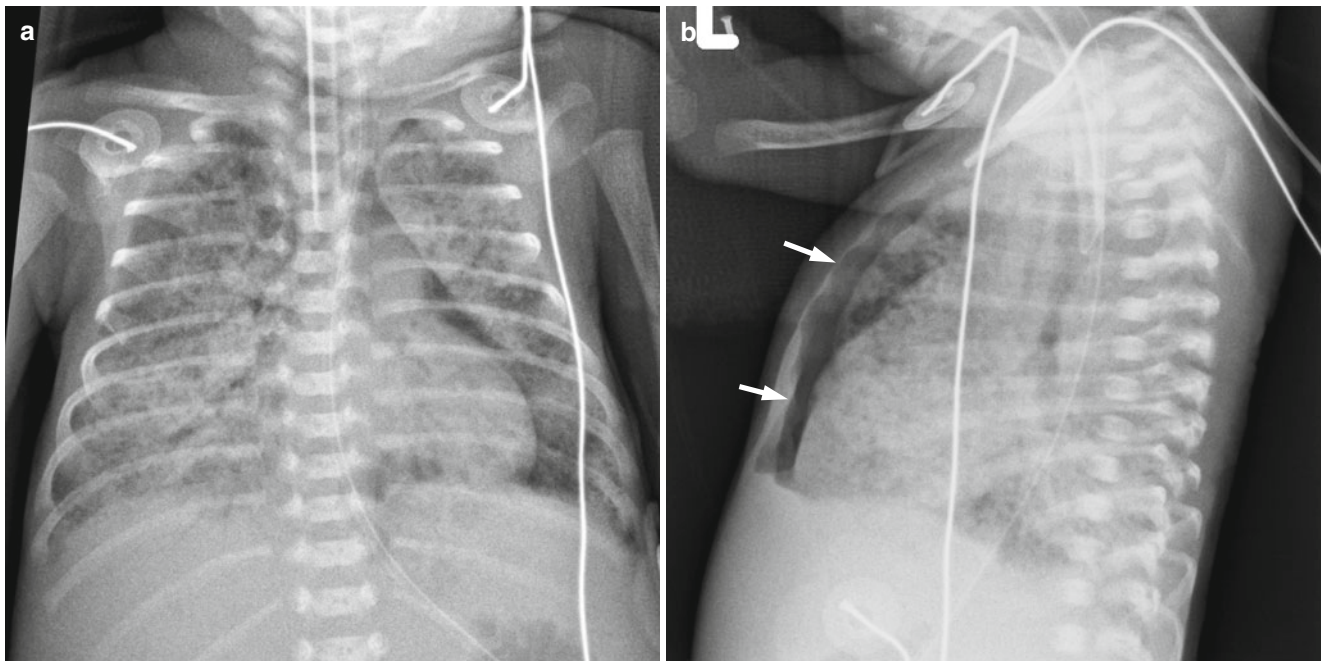


Fig. 11.27 Pulmonary interstitial emphysema (PIE) and pneumothorax. (a) Frontal radiograph demonstrates bilateral diffuse PIE with left medial pneumothorax. (b) Cross-table lateral view of the same neonate

shows air (*arrows*) in the anterior aspect of the pleural space, pushing the lung posteriorly

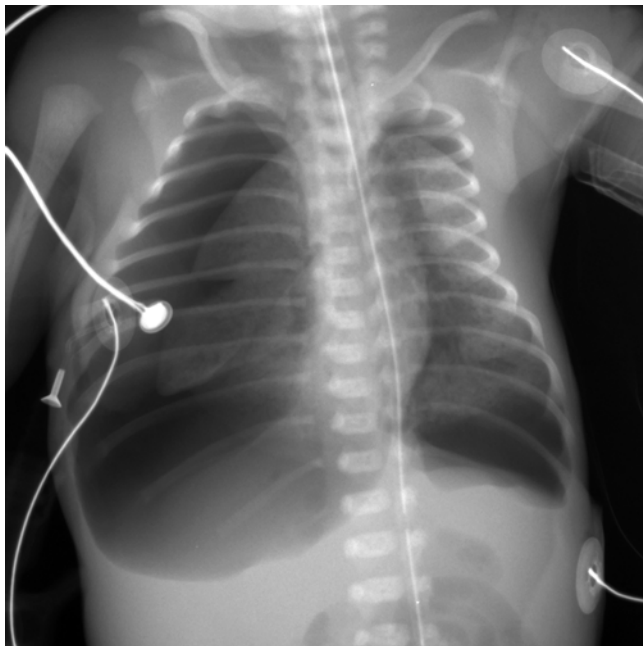


Fig. 11.28 Bilateral tension pneumothorax in a pre-term infant with hyaline membrane disease. Frontal radiograph shows large pleural air collections bilaterally. Chest cavity expansion, inversion of the diaphragms, and narrow mediastinal shadow indicate high pressure in the air-filled pleural spaces

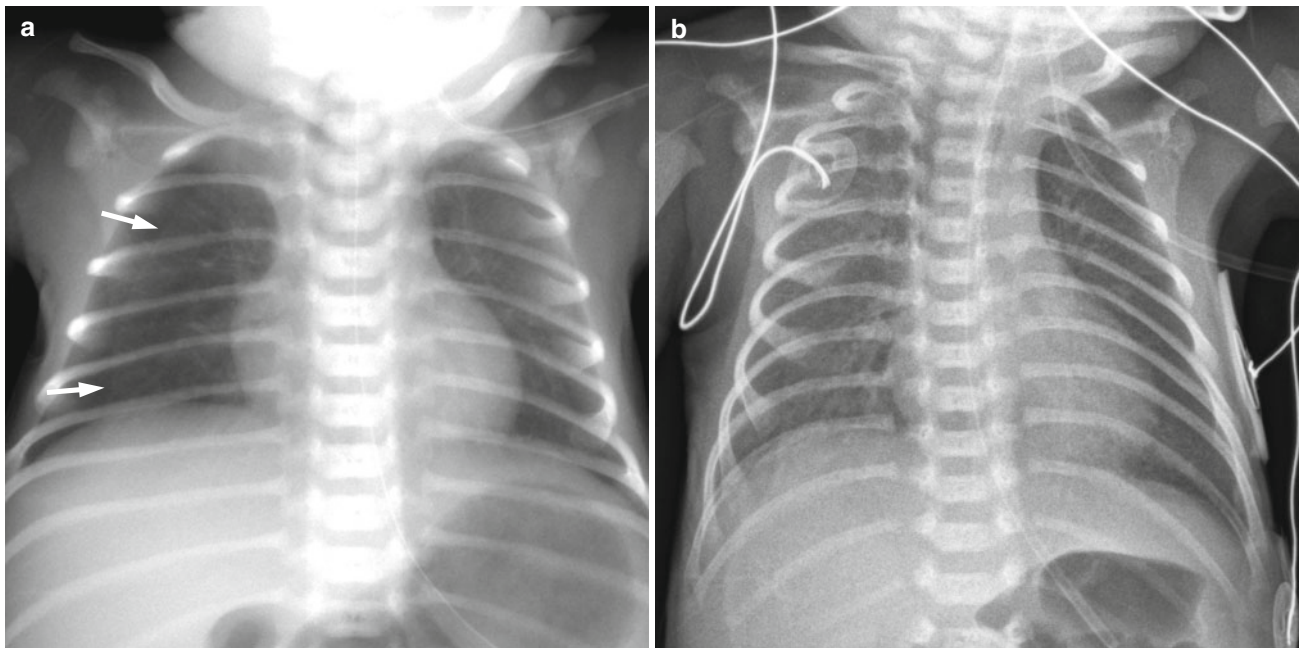


Fig. 11.29 Artifacts mimicking pneumothorax on neonatal chest radiographs. (a) Skin fold. Prominent skin fold (*arrows*) can be mistaken for pneumothorax. (b) Rotated position. Anteroposterior chest

radiograph obtained in rotated position shows apparent hyperlucency and deep costophrenic angle in left lung. Rotation of a baby on a chest radiograph can create a hyperlucent lung that mimics pneumothorax

11.6.9 Lines, Tubes and Catheters

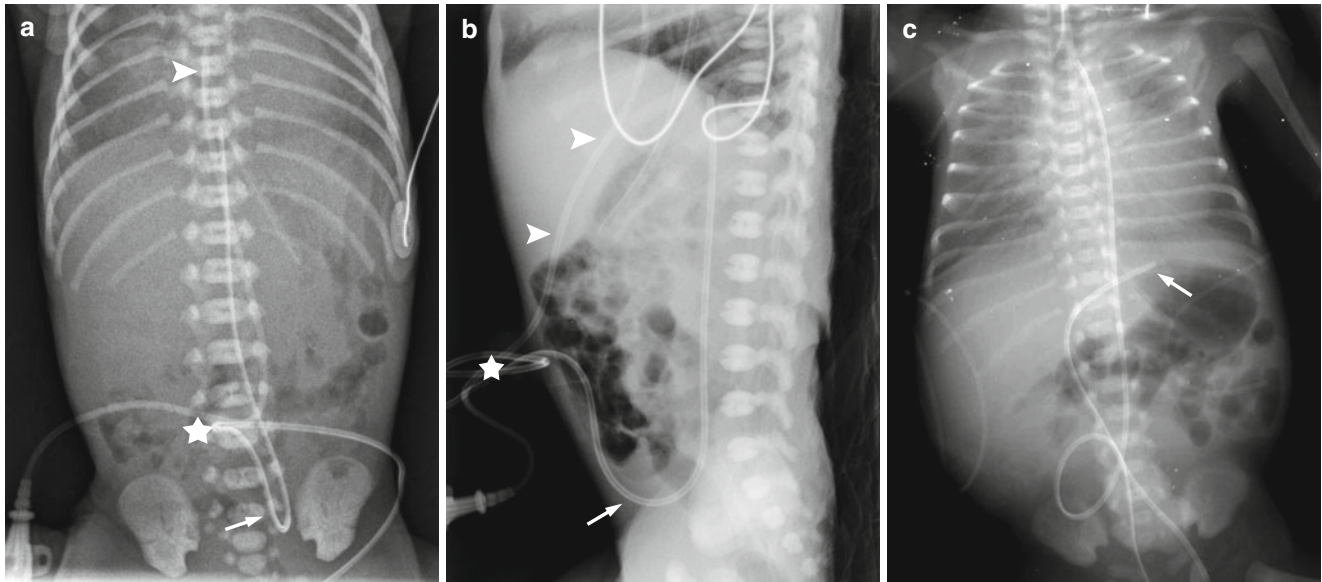


Fig. 11.30 Umbilical vessel catheterization. (a, b) Frontal (a) and cross-table lateral (b) radiographs of the abdomen show an umbilical arterial catheter (*arrow*) and umbilical venous catheter (*arrowhead*) in a neonate. The arterial catheter initially proceeds caudally via the umbilical artery, then loops cephalad into the aorta with the tip at the level of T9, whereas the venous catheter proceeds cephalad as it passes via the ductus venosus into the inferior vena cava and into the right

atrium. Note the characteristic looping (*arrow*) of the arterial catheter compared with the straight course of the venous catheter. The *asterisk* indicates the umbilicus. (c) Malposition of the umbilical catheters. The umbilical venous (*arrow*) catheter tip lies abnormally in the left portal vein. The arterial catheter is malpositioned with a tip in one of the arch vessels

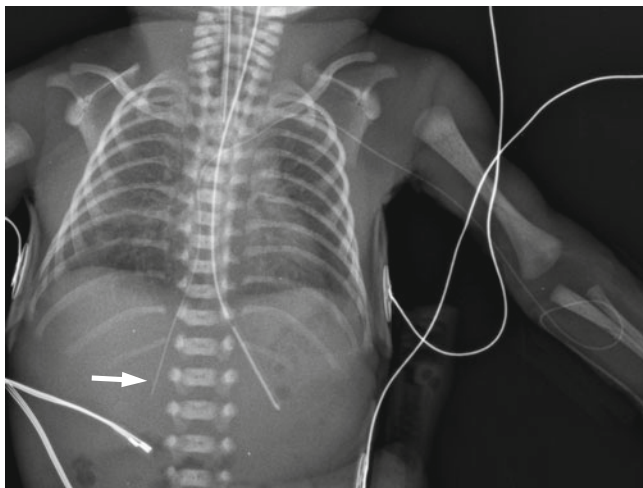


Fig. 11.31 Peripherally inserted central venous catheter (PICC). The ideal position of PICC is at the junction of SVC/IVC and the right atrium. In this neonate, PICC is too deeply inserted and the tip of PICC lies within the hepatic vein (*arrow*)

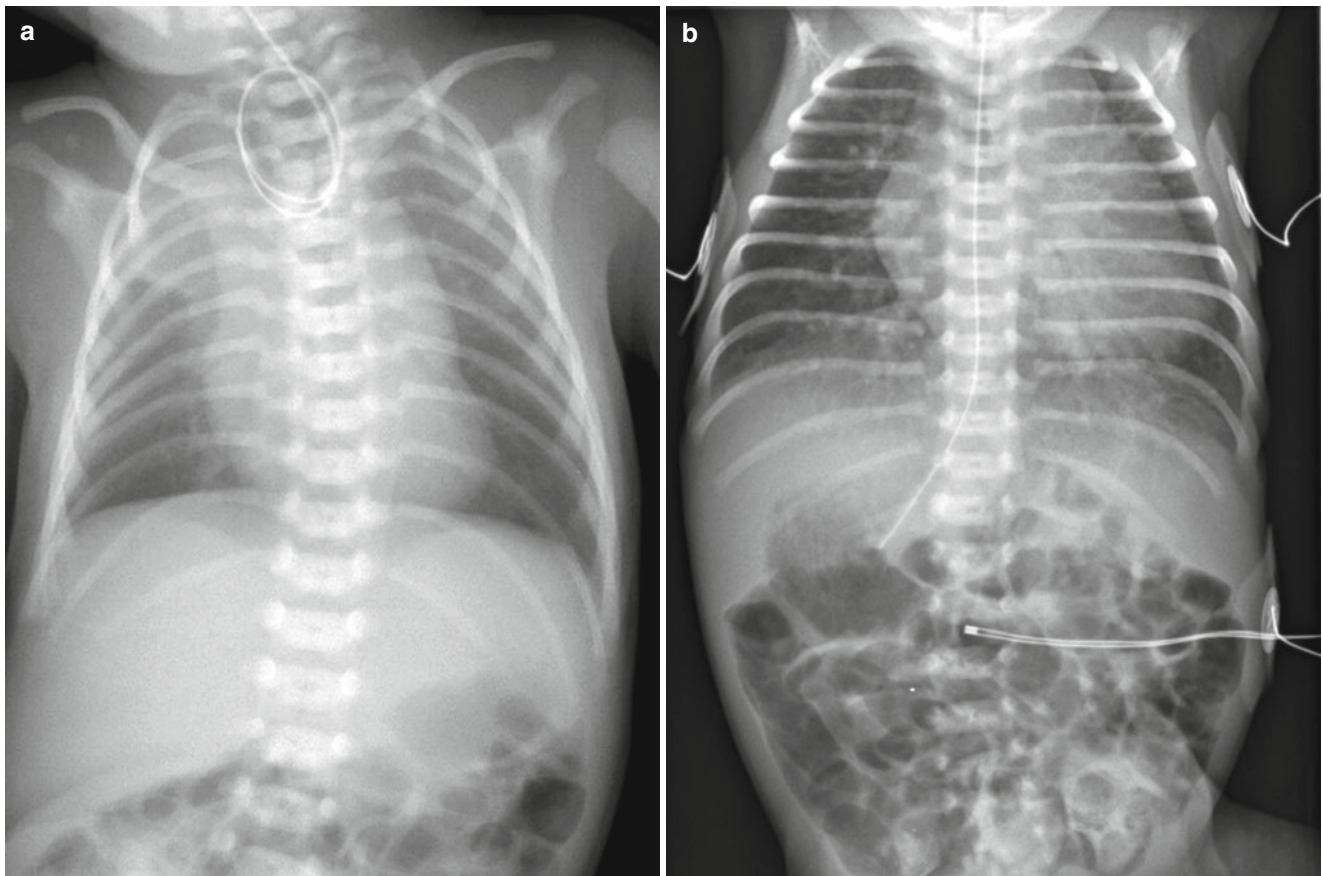


Fig. 11.32 Enteric tubes. **(a)** Esophageal atresia. Nasogastric tube lies in the upper esophageal pouch. **(b)** The tip of the gastric tube is located in the right abdomen, which suggests the left-sided stomach. Note car-

diomegaly and increased pulmonary vascularities in association with congenital heart disease

References

- Ablow RC, Gross I, Effmann EL, et al. The radiographic features of early onset Group B streptococcal neonatal sepsis. *Radiology*. 1977;124(3):771–7.
- Agrons GA, Courtney SE, Stocker JT, et al. From the archives of the AFIP: lung disease in premature neonates: radiologic-pathologic correlation. *Radiographics*. 2005;25(4):1047–73.
- Boothroyd AE, Barson AJ. Pulmonary interstitial emphysema – a radiological and pathological correlation. *Pediatr Radiol*. 1988;18(3):194–9.
- Cleveland RH. A radiologic update on medical diseases of the newborn chest. *Pediatr Radiol*. 1995;25(8):631–7.
- Cleveland RH, Rhein L. Newborn chest. Imaging in pediatric pulmonology. Boston: Springer; 2012.
- Dinger J, Schwarze R, Rupprecht E. Radiological changes after therapeutic use of surfactant in infants with respiratory distress syndrome. *Pediatr Radiol*. 1997;27(1):26–31.
- Donnelly LF, Lucaya J, Ozelame V, et al. CT findings and temporal course of persistent pulmonary interstitial emphysema in neonates: a multiinstitutional study. *AJR Am J Roentgenol*. 2003;180(4):1129–33.
- Edwards DK, Jacob J, Gluck L. The immature lung: radiographic appearance, course, and complications. *AJR Am J Roentgenol*. 1980;135(4):659–66.
- Ford JW. Neonatal ECMO: current controversies and trends. *Neonatal Netw*. 2006;25(4):229–38.
- Halliday HL, Reid MM, McClure BG. Early congenital syphilis still occurs. *Arch Dis Child*. 1986;61(4):417–8.
- Han BK, Suh YL, Yoon HK. Thymic ultrasound. I. Intrathymic anatomy in infants. *Pediatr Radiol*. 2001;31(7):474–9.
- Howling SJ, Northway Jr WH, Hansell DM, et al. Pulmonary sequelae of bronchopulmonary dysplasia survivors: high-resolution CT findings. *AJR Am J Roentgenol*. 2000;174(5):1323–6.
- Jabra AA, Fishman EK, Shehata BM, et al. Localized persistent pulmonary interstitial emphysema: CT findings with radiographic-pathologic correlation. *AJR Am J Roentgenol*. 1997;169(5):1381–4.
- Jain L, Eaton DC. Physiology of fetal lung fluid clearance and the effect of labor. *Semin Perinatol*. 2006;30(1):34–43.
- Jobe AJ. The new BPD: an arrest of lung development. *Pediatr Res*. 1999;46(6):641–3.
- Jobe AH, Bancalari E. Bronchopulmonary dysplasia. *Am J Respir Crit Care Med*. 2001;163(7):1723–9.
- Kong A. The deep sulcus sign. *Radiology*. 2003;228(2):415–6.
- Kuhn JP, Fletcher BD, DeLemos RA. Roentgen findings in transient tachypnea of the newborn. *Radiology*. 1969;92(4):751–7.
- Levin B. The continuous diaphragm sign. A newly-recognized sign of pneumomediastinum. *Clin Radiol*. 1973;24(3):337–8.
- Moseley JE. Loculated pneumomediastinum in the newborn. A thymic “spinnaker sail” sign. *Radiology*. 1960;75:788–90.
- Nasseri F, Eftekhari F. Clinical and radiologic review of the normal and abnormal thymus: pearls and pitfalls. *Radiographics*. 2010;30(2):413–28.
- Newman B. Imaging of medical disease of the newborn lung. *Radiol Clin North Am*. 1999;37(6):1049–65.
- Nissen MD. Congenital and neonatal pneumonia. *Paediatr Respir Rev*. 2007;8(3):195–203.
- Northway Jr WH, Rosan RC, Porter DY. Pulmonary disease following respirator therapy of hyaline-membrane disease. Bronchopulmonary dysplasia. *N Engl J Med*. 1967;276(7):357–68.
- O’Keeffe FN, Swischuk LE, Stansberry SD. Mediastinal pseudomass caused by compression of the thymus in neonates with anterior pneumothorax. *AJR Am J Roentgenol*. 1991;156(1):145–8.
- Oppenheim C, Mamou-Mani T, Sayegh N, et al. Bronchopulmonary dysplasia: value of CT in identifying pulmonary sequelae. *AJR Am J Roentgenol*. 1994;163(1):169–72.
- Pacifico L, Panero A, Roggini M, et al. Ureaplasma urealyticum and pulmonary outcome in a neonatal intensive care population. *Pediatr Infect Dis J*. 1997;16(6):579–86.
- Radkowski MA, Kranzler JK, Beem MO, et al. Chlamydia pneumonia in infants: radiography in 125 cases. *AJR Am J Roentgenol*. 1981;137(4):703–6.
- Richardson RR. Neonatal pneumonia. Diagnostic imaging. Pediatrics. Salt Lake City: Amirsys; 2012a.
- Richardson RR. Pulmonary interstitial emphysema. Diagnostic imaging. Pediatrics. Salt Lake City: Amirsys; 2012b.
- Shin SM, Kim WS, Cheon JE, et al. Bronchopulmonary dysplasia: new high resolution computed tomography scoring system and correlation between the high resolution computed tomography score and clinical severity. *Korean J Radiol*. 2013;14(2):350–60.
- Slama M, Andre C, Huon C, et al. Radiological analysis of hyaline membrane disease after exogenous surfactant treatment. *Pediatr Radiol*. 1999;29(1):56–60.
- Slovits TL, Bulas DI. Congenital and acquired lesions (most causing respiratory distress) of the neonatal lung and thorax. In: Slovis TL, editor. Caffey’s pediatric diagnostic imaging. Philadelphia: Mosby; 2008.
- Stocker JT, Dehner LP. Pediatric pathology. Philadelphia: Lippincott; 1992.
- Strife JL, Crotty EJ. Neonatal chest imaging. In: Lucaya J, Strife JL, editors. Pediatric chest imaging. Berlin/Heidelberg: Springer-Verlag; 2008.
- Swischuk LE. Respiratory system. In: Swischuk LE, editor. Imaging of the newborn, infant, and young child. Philadelphia: Lippincott Williams & Wilkins; 2004.
- Wells RG. Neonatal lung disease. In: Wells RG, editor. Diagnostic imaging of infants and children. New York: McGraw-Hill; 2012.
- Wesenberg RL, Graven SN, McCabe EB. Radiological findings in wet-lung disease. *Radiology*. 1971;98(1):69–74.
- Wiedemann JR, Saugstad AM, Barnes-Powell L, et al. Meconium aspiration syndrome. *Neonatal Netw*. 2008;27(2):81–7.
- Yeh TF, Harris V, Srinivasan G, et al. Roentgenographic findings in infants with meconium aspiration syndrome. *JAMA*. 1979;242(1):60–3.
- Yoder BA, Kirsch EA, Barth WH, et al. Changing obstetric practices associated with decreasing incidence of meconium aspiration syndrome. *Obstet Gynecol*. 2002;99(5 Pt 1):731–9.

Evan J. Zucker, Kushaljit S. Sodhi, Ricardo Restrepo,
and Edward Y. Lee

Contents

12.1	Introduction	412
12.2	Pathophysiology	412
12.3	Imaging	412
12.4	Spectrum of Pediatric Airway Disorders	412
12.4.1	Congenital Tracheal Stenosis	412
12.4.2	Croup.....	413
12.4.3	Bacterial Tracheitis	413
12.4.4	Epiglottitis.....	413
12.4.5	Tuberculosis	413
12.4.6	Subglottic Hemangioma.....	413
12.4.7	Recurrent Respiratory Papillomatosis.....	414
12.4.8	Carcinoid Tumor	414
12.4.9	Vascular Causes of Airway Abnormalities (Vascular Rings and Slings)	414
12.4.10	Foreign Body Aspiration.....	414
12.4.11	Traumatic Tracheobronchial Injury	415
12.4.12	Obstructive Sleep Apnea.....	415
12.4.13	Tracheobronchomalacia	415
12.5	Illustrations: Pediatric Airway Disorders	416
12.5.1	Normal Airway.....	416
12.5.2	Congenital Tracheal Stenosis	418
12.5.3	Croup.....	419
12.5.4	Bacterial Tracheitis	420
12.5.5	Epiglottitis.....	421
12.5.6	Tuberculosis	422
12.5.7	Subglottic Hemangioma.....	423
12.5.8	Recurrent Respiratory Papillomatosis.....	424
12.5.9	Carcinoid Tumor	425
12.5.10	Vascular Causes of Airway Abnormalities.....	426
12.5.11	Foreign Body Aspiration.....	428
12.5.12	Traumatic Tracheobronchial Injury	429
12.5.13	Obstructive Sleep Apnea.....	430
12.5.14	Tracheobronchomalacia	431
	References	432

E.J. Zucker, M.D.
Department of Radiology, Lucile Packard Children's Hospital,
Stanford University School of Medicine, 725 Welch Road,
Stanford, CA 94305, USA

K.S. Sodhi, M.D.
Department of Radiodiagnosis and Imaging,
Postgraduate Institute of Medical Education & Research,
Sector-12, Chandigarh 160012, India

R. Restrepo, M.D.
Department of Radiology,
Miami Children's Hospital, Miami, USA

E.Y. Lee, M.D., M.P.H. (✉)
Department of Radiology,
Boston Children's Hospital and Harvard Medical School,
300 Longwood Avenue, Boston, MA 02115, USA
e-mail: edward.lee@childrens.harvard.edu

12.1 Introduction

Airway disease is very common in the pediatric population. Prompt recognition is crucial, as many disorders are potentially life-threatening. Acutely, patients present with stridor, wheezing, and respiratory distress due to airway obstruction. Chronically, patients develop such findings as recurrent pulmonary infection or obstructive sleep apnea. While etiologies are varied, imaging plays an essential role in the diagnostic evaluation, complementing direct visualization with laryngoscopy and bronchoscopy and offering precise anatomical evaluation for preoperative assessment.

12.2 Pathophysiology

A variety of processes affect the airway, including congenital, infectious, inflammatory, traumatic, and neoplastic processes. The airway includes the nose, paranasal sinuses, pharynx (nasopharynx, oropharynx, and hypopharynx), larynx, trachea, main bronchi, peripheral bronchi, and bronchioles. Infants and young children tend to become symptomatic earlier than do their adult counterparts due to smaller airway caliber with greater collapsibility (Lee et al. 2012b). Symptoms may result from extrinsic airway compression or intrinsic airway disease.

The trachea is normally a compliant structure, allowing the intrathoracic portion to increase in diameter during inspiration and decrease during expiration. Collapse of the trachea during expiration is limited due to the supporting cartilaginous rings and contractile smooth muscle tone. However, many pathologic processes interfere with this normal physiology and can result in acute airway obstruction. In general, airway pathology may be static (independent of the respiratory cycle), dynamic (occurring only during certain portions of the respiratory cycle), or a combination of both types.

12.3 Imaging

Imaging assessment typically begins with frontal and lateral radiographs of the neck and/or chest. Inexpensive and widely available, radiographs are the first-line modality for evaluating suspected foreign body aspiration and excluding other causes of respiratory distress (Lee et al. 2012b). Proper positioning is critical, particularly for the lateral neck radiograph, which should be performed during inspiration with moderate neck extension. Rotation, flexion, or expiration may lead to spurious interpretation (Laya and Lee 2012). In children 5 years old or less, lateral deviation of the trachea is normal and should not be mistaken for pathology. This phenomenon, which tends to occur at or just above the thoracic inlet opposite the side of the aortic arch, is felt possibly due to the

relatively long tracheal length with respect to the child's short neck and rib cage (Lee et al. 2012b). Other common normal variants are anterior buckling of the trachea and widening of the retropharyngeal soft tissues during expiration and neck flexion, features that may mimic a retropharyngeal abscess (Eslamy and Newman 2009).

Ultrasound is useful for assessing neck masses, helping to distinguish cystic from solid lesions, and determine vascularity and vascular patency with Doppler techniques. Sonographic airway assessment appears promising, but is currently in investigational stages (Singh et al. 2010).

Airway fluoroscopy, sometimes in conjunction with barium swallow, is particularly useful for evaluating dynamic abnormalities such as laryngomalacia, tracheomalacia, and obstructive sleep apnea. Radiation dose-reduction techniques, such as pulsed fluoroscopy and restricting time spent using the fluoroscopic pedal, should be implemented whenever possible (Laya and Lee 2012; Lee et al. 2012b). Cine MRI utilizing fast gradient-echo sequences is an emerging modality allowing dynamic airway assessment, offering superb image contrast without ionizing radiation, but may require sedation (Donnelly 2005; Laya and Lee 2012).

Multidetector computed tomography (MDCT) with multiplanar two-dimensional (2D) and three-dimensional (3D) reformation has revolutionized evaluation of the pediatric airway. Providing exquisite anatomical detail while maintaining rapid scan times, CT often eliminates the need for sedation and intubation to achieve satisfactory imaging. Newer techniques such as paired inspiratory–expiratory MDCT, cine MDCT, and four-dimensional (4D) MDCT allow for dynamic airway assessment. The use of CT is tempered by growing concerns about the risks of radiation exposure, although research for dose reduction is ongoing (Lee et al. 2011, 2012).

12.4 Spectrum of Pediatric Airway Disorders

12.4.1 Congenital Tracheal Stenosis

Congenital tracheal stenosis is a rare anomaly in which focal or diffuse complete tracheal cartilage rings cause absent or deficient tracheal membranes, resulting in fixed tracheal narrowing. Most commonly, there is a focal stenosis involving a 2–5 cm segment of the airway. Alternatively, there may be total tracheal hypoplasia or a funnel-like stenosis with gradual tapering of the airway (Herrera et al. 2007; Lee et al. 2011, 2012b).

Initial imaging evaluation with chest radiography and fluoroscopy may demonstrate the stenosis. However, MDCT is superior and can identify the exact location and extent of narrowing, as well as assess for associated congenital anomalies, most commonly pulmonary artery sling (Lee et al. 2011,

2012b). 2D and 3D reformats and CT virtual bronchoscopy assist in preoperative planning. MRI is used primarily in evaluating other associated abnormalities such as vascular malformations.

12.4.2 Croup

Croup is a common viral airway infection characterized by diffuse laryngeal and tracheal inflammation with marked subglottic laryngeal swelling and narrowing. Parainfluenza virus 1 is the most frequent causative pathogen (Chapman et al. 2012; Cherry 2008). Imaging is not generally required, but may be obtained if more complex pathology is anticipated. Fifty percent of radiographs are normal. Classically, the AP neck radiograph demonstrates a “steeple sign” with loss of the normal shouldering edges of the subglottic airway and tapered narrowing up to the glottis. On the lateral view, the normally sharp margins of the subglottic airway are obscured (Chapman et al. 2012; Salour 2000). Advanced imaging is typically only pursued in cases of recurrent croup to exclude an underlying lesion.

12.4.3 Bacterial Tracheitis

Also known as membranous laryngotracheobronchitis, membranous croup, and exudative tracheitis, bacterial tracheitis is a rare, life-threatening infectious cause of acute airway obstruction characterized by the presence of thick, adherent tracheal membranes. Historically, *Staphylococcus aureus* was the most prevalent underlying pathogen, but now a variety of organisms are implicated. Characteristic findings on neck and chest radiography are subglottic tracheal narrowing, contour irregularity of the proximal tracheal mucosa, and tracheal membranes (classically linear). The membranes may partially or completely detach and mimic tracheal foreign bodies (Chapman et al. 2012; Sammer and Pruthi 2010). Pneumomediastinum is a rare presentation (Hedlund et al. 1998).

12.4.4 Epiglottitis

Also termed bacterial croup and supraglottitis, epiglottitis is an uncommon potentially life-threatening cause of acute airway obstruction. It is caused by a bacterial infection of the epiglottis and surrounding structures, including the aryepiglottic folds, arytenoids, and supraglottic larynx. The incidence has dropped since the advent of vaccination for *Haemophilus influenza* type b (Hib), previously the most common underlying pathogen. Lateral neck radiography demonstrates marked thickening of the epiglottis and aryepiglottic folds. The “thumbprint sign” caused by the

imprint of the swollen epiglottis on the airway is classic. Occasionally, there may be a steeple or funnel configuration of the glottic and subglottic airway on frontal neck radiography due to inflammation. Thickening of the aryepiglottic folds distinguishes epiglottitis from the normal variant known as the omega epiglottis, a uniformly thickened epiglottis with a horseshoe configuration associated with tracheomalacia (Chapman et al. 2012; John and Swischuk 1992).

12.4.5 Tuberculosis

Caused by *Mycobacterium tuberculosis*, tuberculosis (TB) is the leading infectious cause of death worldwide. Most commonly, airway symptoms result from extrinsic compression by infectious mediastinal and/or hilar lymphadenopathy, or more rarely extension of paraspinal disease. Intrinsic airway involvement is less common. Airway obstruction can occur through caseation and mucus plugging (and rarely large granuloma formation), mucosal inflammation and edema causing tracheobronchial narrowing, and bronchial fibrostenosis in the later stages (Lee et al. 2011, 2012b).

Chest radiography may demonstrate lymphadenopathy, possibly accompanied by lung parenchymal abnormalities typical of presenting TB. Extrinsic airway compression and intrinsic airway disease, characterized by tracheobronchial thickening and narrowing, are better demonstrated by MDCT with 2D and 3D reformats. CT may also demonstrate “tree-in-bud” nodular opacities in the lungs, airspace consolidation, and extrapulmonary manifestations of TB (Lee et al. 2011, 2012b). Lymph nodes with central low attenuation and rim enhancement or calcification are characteristic features (Kim et al. 1997).

12.4.6 Subglottic Hemangioma

Subglottic hemangioma is the most common benign large airway neoplasm in children. Although present at birth, the mass typically does not produce symptoms until 1–6 months of age, when rapid growth in the lesion causes increasing airway obstruction. Classically, the frontal neck radiograph demonstrates asymmetric narrowing of the subglottic airway. However, many cases of subglottic hemangioma present with symmetric subglottic airway narrowing. Additionally, asymmetric subglottic airway narrowing is not specific, and can be seen with other entities such as cysts, granulomas, and papillomas (Cooper et al. 1992). CT demonstrates a round, well-circumscribed soft tissue mass with marked contrast enhancement typically arising from the posterolateral aspect of the subglottic trachea (Lee et al. 2011, 2012b). On MRI, the lesion is T1 isointense to muscle and T2 hyperintense with avid enhancement (Nozawa et al. 1995). Ultrasound has more recently been used, characteristically demonstrating

a hypoechoic solid mass at the posterolateral aspect of the subglottic airway with intense vascularity on color Doppler (Rossler et al. 2011).

12.4.7 Recurrent Respiratory Papillomatosis

Juvenile or recurrent respiratory papillomatosis (RRP) is a rare disease, characterized by multiple laryngeal or tracheal lesions. Papilloma is the second most common benign large airway neoplasm in children, caused by human papillomavirus (HPV) types 6 and 11, acquired either in utero or during delivery via the birth canal. CT is preferred over radiographs for assessing the disease, demonstrating multiple intraluminal lesions representing papillomas, almost always involving the larynx. Lung involvement with multiple solid and/or cystic nodules is seen in 5 % of cases (Lee et al. 2011, 2012b). Rarely, lesions undergo malignant transformation. Worrisome features include rapid or significant change on follow-up imaging and increased uptake on 2-[¹⁸F]-fluoro-2-deoxy-D-glucose (F-18 FDG) positron-emission tomography (PET) (Lui et al. 1995; Szyszko et al. 2009).

12.4.8 Carcinoid Tumor

Carcinoid is the most common malignant large airway neoplasm in children. It is a neuroendocrine tumor, which can produce hormones and neuroamines, such as corticotrophin (adrenocorticotrophic hormone), gastrin, insulin, vasoactive intestinal peptide, somatostatin, bradykinin, serotonin, and histamine. The “carcinoid syndrome” with symptoms of flushing and diarrhea due to serotonin production by the tumor rarely occurs in pediatric bronchial carcinoid (Lee et al. 2011, 2012b).

Carcinoid is best evaluated on CT, characterized by a round, oval, or polypoid endobronchial nodule or mass. Contrast enhancement ranges from mild to intense. Punctate or diffuse calcification is seen in 30 % of cases. Carcinoid is most commonly found in the main stem or lobar bronchi, but 15 % of cases occur in segmental bronchi or the lung periphery. There may be hyperinflation, secondary to the “ball-valve” effect of the tumor (Lee et al. 2011, 2012b). Somatostatin receptor scintigraphy utilizing [¹¹¹In-DTPA-D-Phe1]-octreotide is useful in tumor detection and disease monitoring, as somatostatin receptors are present on most bronchial carcinoids (Moraes et al. 2003).

12.4.9 Vascular Causes of Airway Abnormalities (Vascular Rings and Slings)

Vascular rings and slings refer to mediastinal vascular anomalies that cause extrinsic compression of the large airways. The most frequently symptomatic is the double aortic

arch, in which the ascending aortic arch bifurcates into right and left aortic arches, which then join to form a common descending thoracic aorta. The aortic arches encircle the trachea and esophagus and cause extrinsic compression. In the right aortic arch with aberrant left subclavian, there is an anomalous origin of the left subclavian artery originating from the last branch of the right arch. The aberrant left subclavian artery is connected to the proximal left pulmonary artery by the left-sided ductus or remnant ligamentum arteriosum, forming a vascular ring and causing tracheal narrowing. Pulmonary artery sling is characterized by involution of the proximal left sixth arch. This results in an aberrant left pulmonary artery arising from the posterior right main pulmonary artery, coursing behind the right main bronchus and passing between the trachea and esophagus. Congenital malformation of the trachea and bronchi is also frequently seen in pediatric patients with pulmonary artery sling. The innominate artery compression syndrome is characterized by an anomalous innominate artery originating on the left side of the aortic arch and coursing obliquely from left to right, causing anterior tracheal compression (Kondrachuk et al. 2012; Lee et al. 2011).

Initial evaluation typically begins with chest radiography and barium esophagram. The laterality (or bilaterality) of the aortic arch may be identified. Classic patterns of tracheal and esophageal compression help suggest the presence of vascular ring or sling, as follows: (1) double aortic arch: anterior tracheal compression, posterior esophageal compression; (2) right arch with aberrant left subclavian: posterior esophageal compression only; (3) pulmonary sling: posterior tracheal compression, anterior esophageal compression; (4) innominate artery compression syndrome: anterior tracheal compression only. A normal esophagram generally excludes the presence of a vascular ring or sling (Hernanz-Schulman 2005). Modern MDCT and MRI provide more precise anatomical detail necessary for preoperative planning (Kondrachuk et al. 2012; Lee et al. 2012a).

12.4.10 Foreign Body Aspiration

Foreign body aspiration is a common and potentially life-threatening cause of acute respiratory distress. Children between the ages of 6 months and 3 years are most commonly affected, related to their tendency to place objects unwittingly into their mouths, their inability to adequately chew certain foods due to lack of molars, and their poorly coordinated swallowing mechanism. Foreign bodies typically lodge in the right main bronchus, which is larger than the left main bronchus and directly aligned with trachea in upright patients (Lee et al. 2011, 2012b).

Chest radiography is obtained first. Although only 10 % of airway foreign bodies are radiopaque and can be identified by radiography, other secondary signs help make the

diagnosis, including unilateral emphysema, hyperinflation, or localized air trapping on the affected side, bilateral emphysema or hyperinflation, focal airspace disease such as pneumonia and/or atelectasis, pleural effusion, subcutaneous emphysema, pneumothorax, and mediastinal shift. Air trapping can be further assessed with forced expiratory or bilateral decubitus views; however, the latter showed no clear additional diagnostic benefit in recent analysis, and the former can be technically challenging, prompting multiple repeats (Brown et al. 2012; Lee et al. 2011, 2012b).

Because radiography has only modest sensitivity and specificity for the diagnosis of foreign body (68–74 % and 45–67 %, respectively), further evaluation should include conventional bronchoscopy or CT depending on clinical concern. On CT, the foreign body may be visible as an endoluminal mass of variable attenuation depending on the composition of the aspirated material. Secondary signs include postobstructive air trapping, atelectasis, and consolidation (Lee et al. 2011, 2012b; Shin et al. 2009). Virtual bronchoscopic reconstruction methods can assist in the diagnosis and preprocedural planning.

12.4.11 Traumatic Tracheobronchial Injury

Tracheobronchial injury affects <1 % of children with penetrating or blunt thoracic trauma. Tracheal disruption typically occurs just above the carina. Bronchial injury usually occurs within 2.5 cm of the carina, most commonly involving the proximal right main bronchus. Radiographic findings may include persistent, extensive pneumothorax and/or pneumomediastinum, with air extending into the subcutaneous tissues of the neck and chest wall, despite a normally functioning chest and/or mediastinal tube. The injured bronchus may be enlarged. If completely avulsed, the “fallen lung sign” may be seen in which the affected lung collapses in a dependent position, attached to the hilum only by vascular structures. Other suspicious findings include an abnormal endotracheal tube position and anterior rib fractures. MDCT with 2D and 3D reformats is superior in precisely identifying the site of airway disruption, which is especially helpful in presurgical planning (Hammer et al. 2012; Lee et al. 2012b).

12.4.12 Obstructive Sleep Apnea

Obstructive sleep apnea (OSA) is a common disorder in which transient upper airway obstruction occurs during sleep, in spite of attempts to breathe, most often due to enlarged tonsils and adenoids. Any underlying abnormalities increasing airway resistance are risk factors, including obesity, craniofacial anomalies, congenital syndromes (Down, achondroplasia, mucopolysaccharidoses), and prior surgery. Radiography, CT, and MRI help exclude sources of extrinsic airway compression or intrinsic narrowing. Subsequently, dynamic imaging provides a more targeted assessment. Dynamic sleep fluoroscopy can help identify the precise location of airway obstruction during episodes of desaturation. More recently, cine MRI techniques have been successfully used. Compared to normal controls, patients with OSA have a greater mean change in airway diameter including the nasopharynx, oropharynx, and hypopharynx (Donnelly 2005; Donnelly et al. 2001; Laya and Lee 2012).

12.4.13 Tracheobronchomalacia

Tracheobronchomalacia (TBM) is characterized by excessive expiratory collapse of the trachea or bronchi due to softening of the airway walls, weakening of the supporting cartilage, and/or hypotonia of the supporting muscles. The diagnosis is established when there is >50 % airway collapse on expiration. Primary TBM is congenital, occurring in such settings as tracheoesophageal fistula and inborn cartilage disorders. Secondary TBM is acquired, caused by such factors as prior intubation, infection, surgery, and extrinsic compression from mediastinal vascular abnormalities (Laya and Lee 2012; Lee and Boiselle 2009; Lee et al. 2011, 2009, 2012b).

Traditionally, TBM was assessed with chest radiography and airway fluoroscopy. However, MDCT with 2D/3D reformats provides superior image quality and can precisely localize the malacia and characterize its severity and extent, including quantitative measurements. A paired inspiratory–expiratory MDCT technique is most often performed. Newer methods include cine imaging with the 64-MDCT scanner and four-dimensional imaging with the 320-MDCT scanner (Laya and Lee 2012; Lee and Boiselle 2009; Lee et al. 2011, 2009, 2012b).

12.5 Illustrations: Pediatric Airway Disorders

12.5.1 Normal Airway

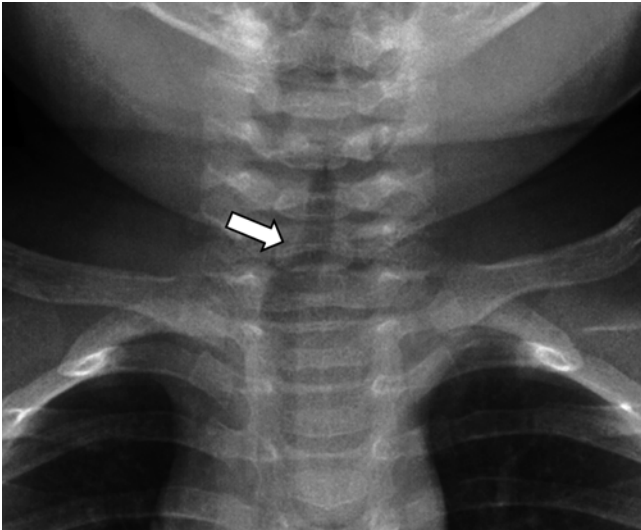


Fig. 12.1 An 18-month-old boy who underwent chest radiograph for evaluation of pneumonia in the setting of fever and elevated white blood cell count. Frontal chest radiograph demonstrates normal deviation (*arrow*) of the trachea to the right of midline at the thoracic inlet level

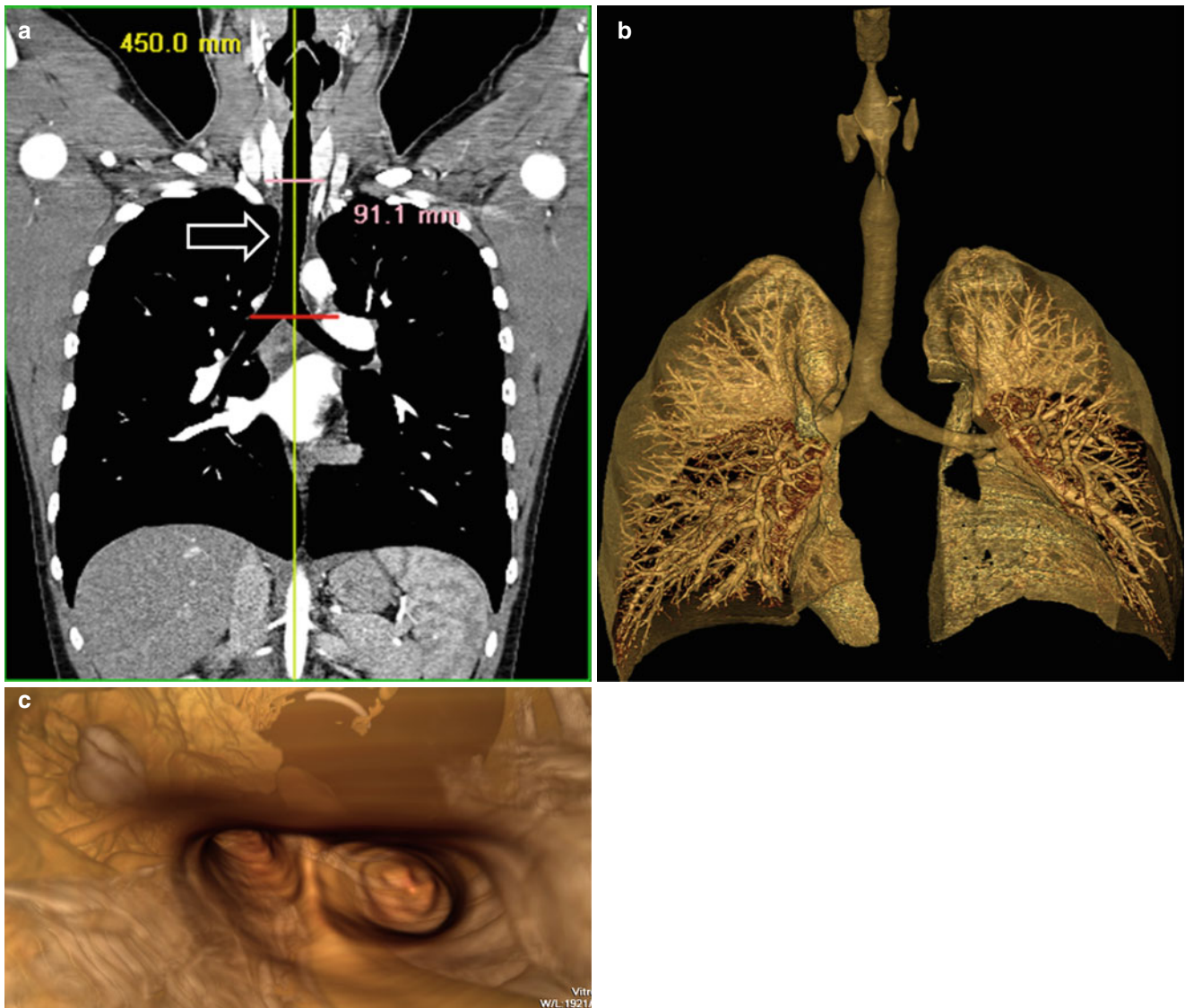


Fig. 12.2 Normal large airways of a 5-year-old girl. (a) Curved coronal reformatted CT image demonstrates a straightened view of the entire trachea (*arrow*). (b) Three-dimensional volume-rendered image of the patent large airways and lungs. (c) Three-dimensional volume-rendered

image of the internal view (i.e., virtual bronchoscopy view) of the trachea facing the carina and the main stem bronchi shows patent central airways

12.5.2 Congenital Tracheal Stenosis

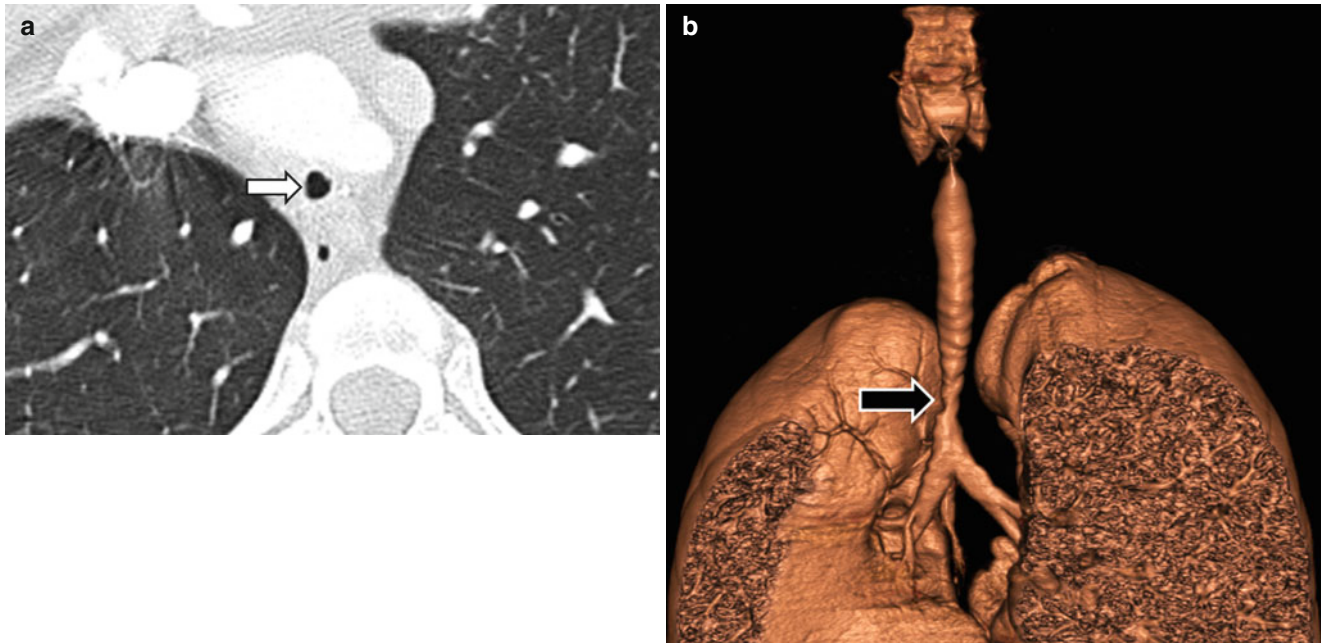


Fig. 12.3 Focal congenital tracheal stenosis in a 14-year-old girl who presented with stridor and wheezing. **(a)** Axial CT shows a narrowed trachea (*arrow*). **(b)** Three-dimensional volume-rendered image shows a high-grade short-segment tracheal stenosis (*arrow*)

12.5.3 Croup

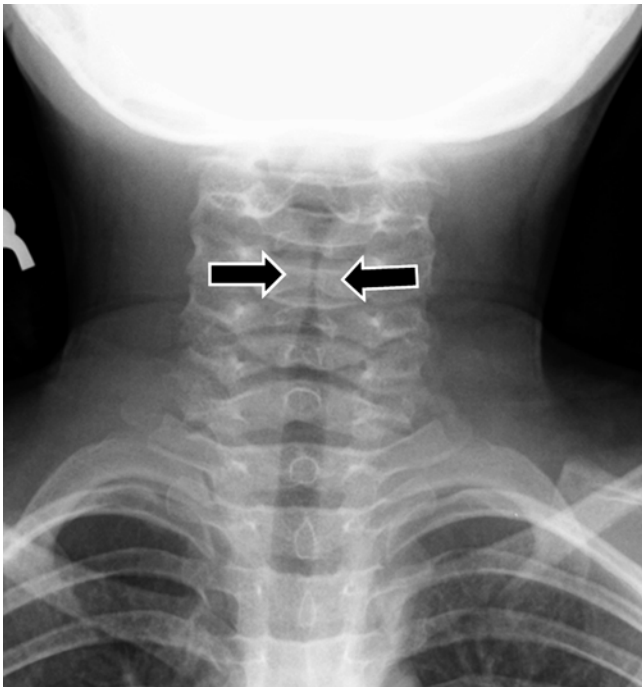


Fig. 12.4 Croup in a 2-year-old boy who presented with “barking cough.” Frontal radiograph shows symmetric subglottic narrowing (*arrows*), with loss of normal shouldering

12.5.4 Bacterial Tracheitis



Fig. 12.5 Bacterial tracheitis in a 5-year-old boy with inspiratory stridor, cough and fever. Lateral neck radiograph shows tracheal irregularity and narrowing (*arrow*) (Reprinted with permission from American Journal of Roentgenology, page W167, 2013)

12.5.5 Epiglottitis

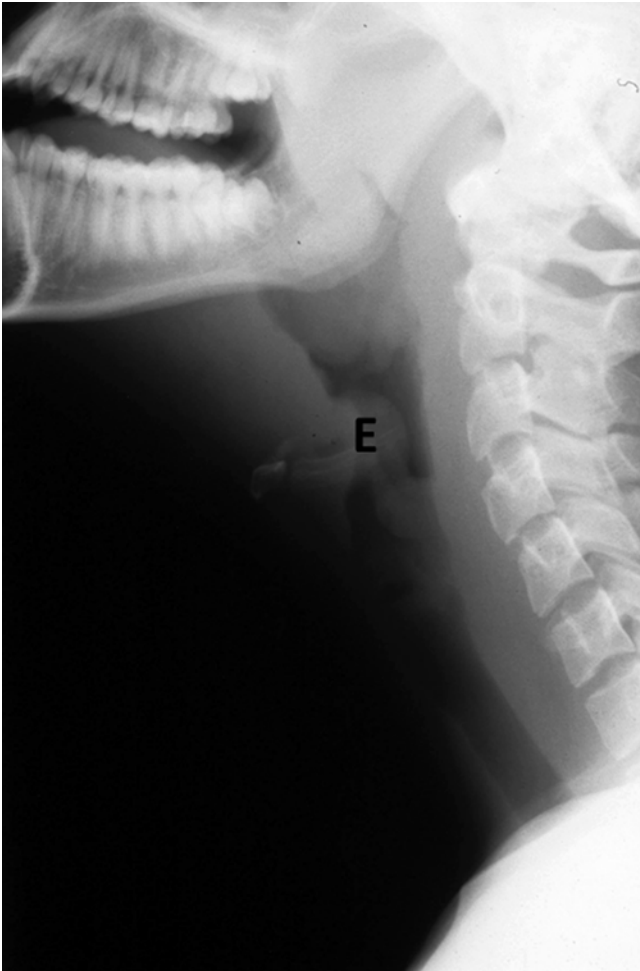


Fig. 12.6 Epiglottitis in a 6-year-old girl with fever, sore throat and drooling. Lateral radiograph shows enlarged epiglottis (*E*), which narrows upper airway (Reprinted with permission from American Journal of Roentgenology, page W168, 2013)

12.5.6 Tuberculosis

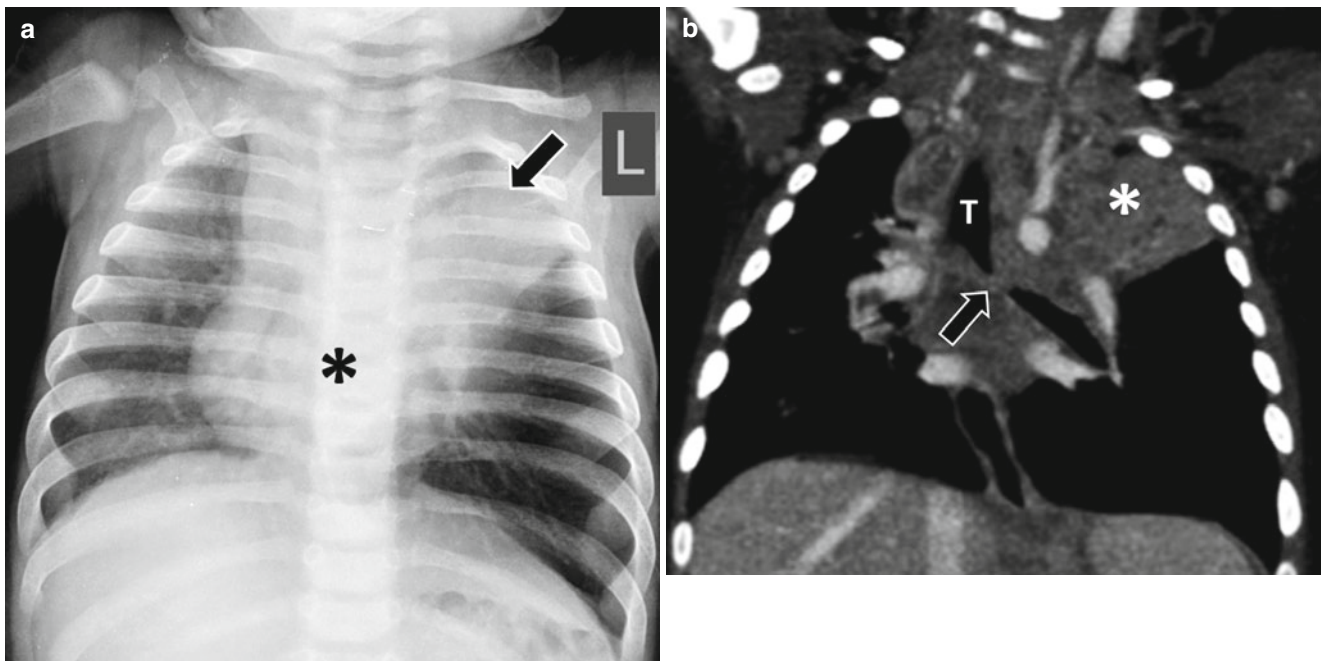


Fig. 12.7 Tuberculosis in a 6-month-old girl with a history of direct contact with active tuberculosis patient who presented with noisy breathing. **(a)** Frontal radiograph shows an opacity (*asterisk*) in the subcarinal region, likely representing an enlarged lymph node and left

upper lobe confluent atelectasis (*arrow*). **(b)** Enhanced coronal CT image shows an obstruction (*arrow*) of the left main stem bronchus. Left upper lobe confluent atelectasis (*asterisk*) is again seen. *T* trachea

12.5.7 Subglottic Hemangioma



Fig. 12.8 Subglottic hemangioma in a 2-month-old boy who presented with worsening biphasic stridor. Enhanced axial CT image shows markedly enhancing subglottic mass (*arrows*), narrowing the airway at this level

12.5.8 Recurrent Respiratory Papillomatosis

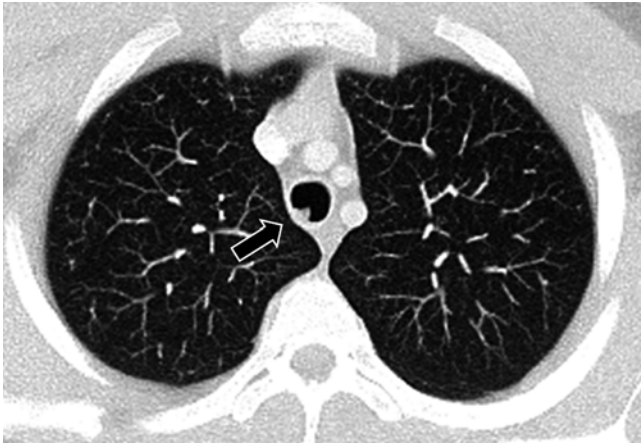


Fig. 12.9 Recurrent respiratory papillomatosis in a 17-year-old boy with known diagnosis since the age of 1.5 years. Axial CT image shows an intratracheal soft tissue lesion (*arrow*) (Case courtesy of Hedieh K. Eslamy, MD, Department of Radiology, Lucile Packard Children's Hospital, Stanford, CA)

12.5.9 Carcinoid Tumor

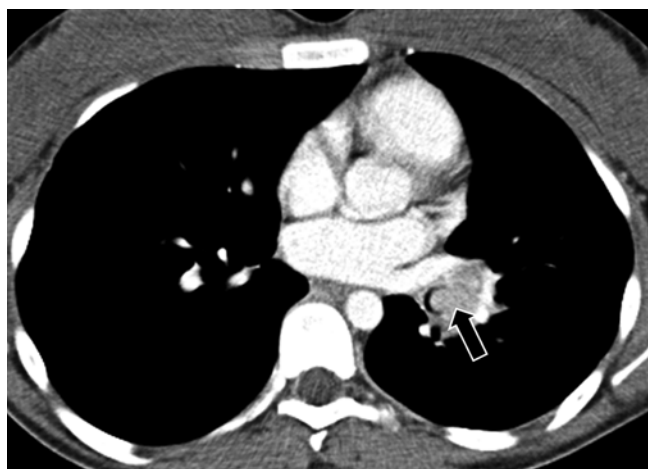


Fig. 12.10 Endobronchial carcinoid tumor in a 16-year-old girl who presented with recurrent left lower lobe pneumonia for the last 3 years. Enhanced axial CT image shows an intraluminal mass (*arrow*) involving the left lower lobe bronchus

12.5.10 Vascular Causes of Airway Abnormalities

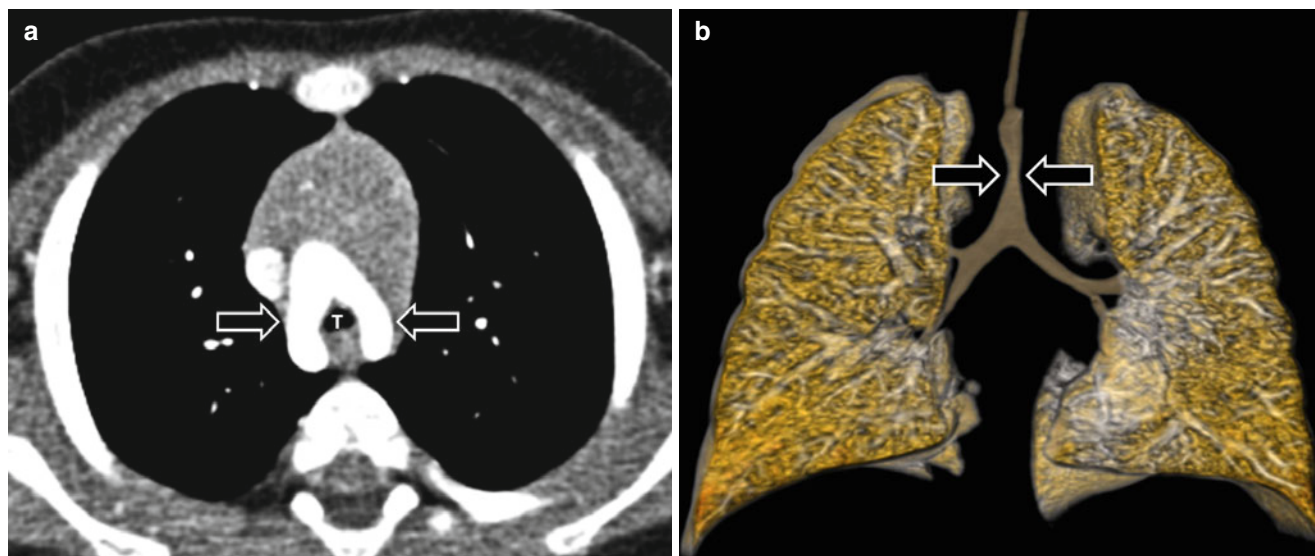


Fig. 12.11 Double aortic arch in an 8-month-old boy who presented with stridor, difficulty of feeding, and repeated apnea. **(a)** Enhanced axial CT image shows two (i.e., right and left) aortic arches (*arrows*)

surrounding a trachea (*T*). **(b)** Three-dimensional volume-rendered image of the central airways and lung shows a tracheal narrowing (*arrows*) at the level of the double aortic arch

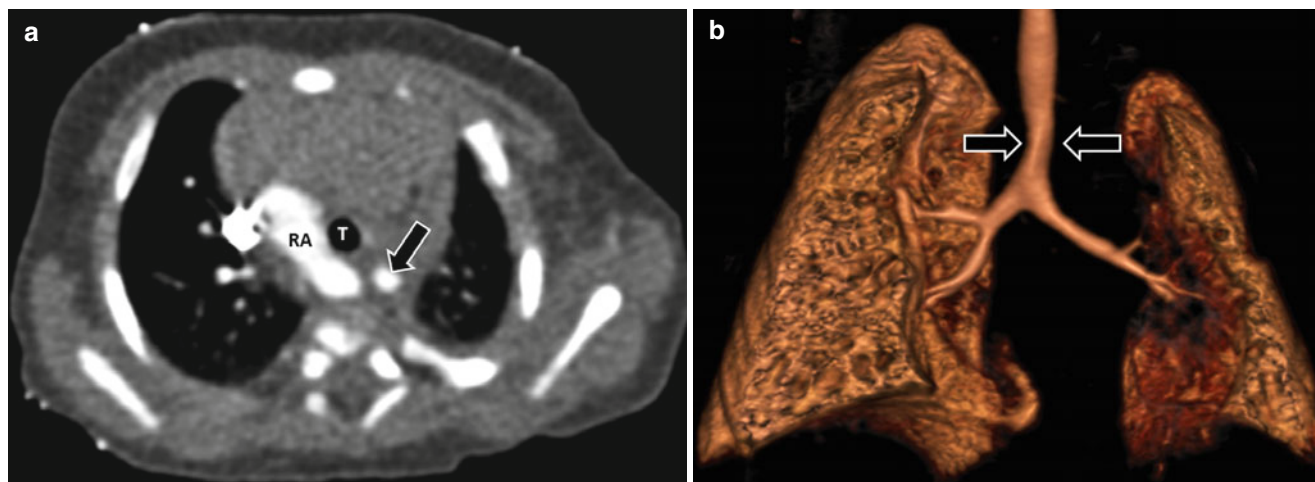


Fig. 12.12 Right aortic arch with an aberrant left subclavian artery in a 2-month-old girl who presented with respiratory distress and dysphagia. **(a)** Enhanced axial CT image shows a right aortic arch (*RA*) with an

aberrant left subclavian artery (*arrow*). *T* trachea. **(b)** Three-dimensional volume-rendered image of the central airways and lung shows a mild tracheal narrowing (*arrow*)

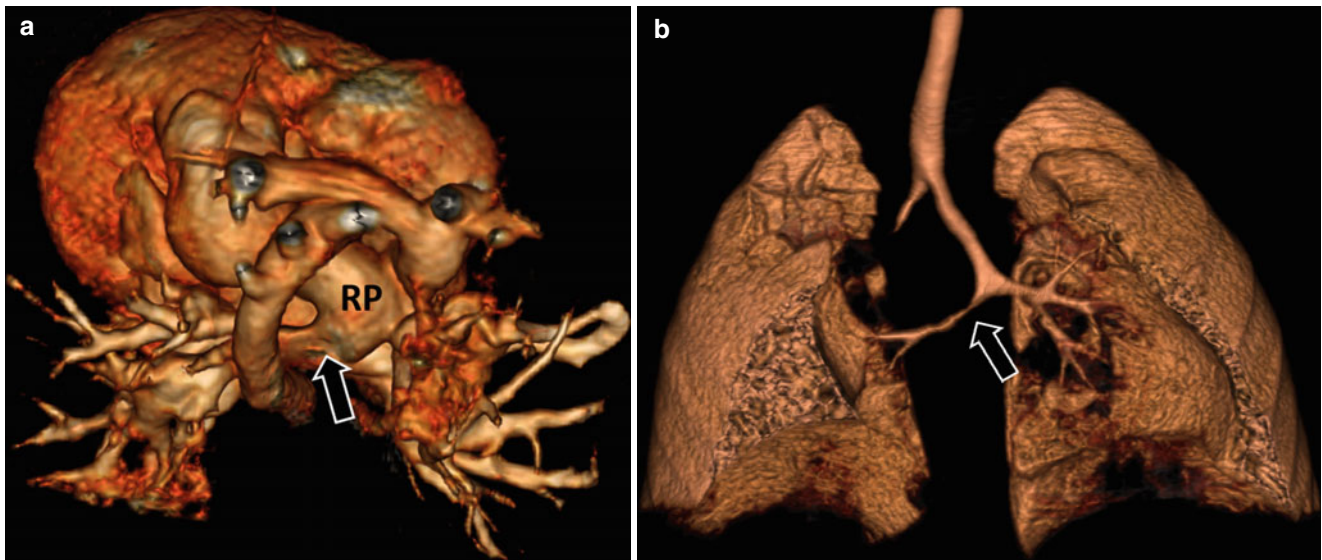


Fig. 12.13 Pulmonary artery sling in a newborn girl who presented with severe respiratory distress. **(a)** Three-dimensional volume-rendered image of the mediastinal vessels shows the left main pulmonary artery (i.e., pulmonary artery sling; *arrow*) directly arising from the right main pulmonary artery (*RP*). **(b)** Three-dimensional volume-rendered image

of the central airways and lung demonstrates multiple congenital anomalies of the central airways, including a blind-ending right upper lobe bronchus, T-shaped carina, and right main stem bronchial stenosis (*arrow*)

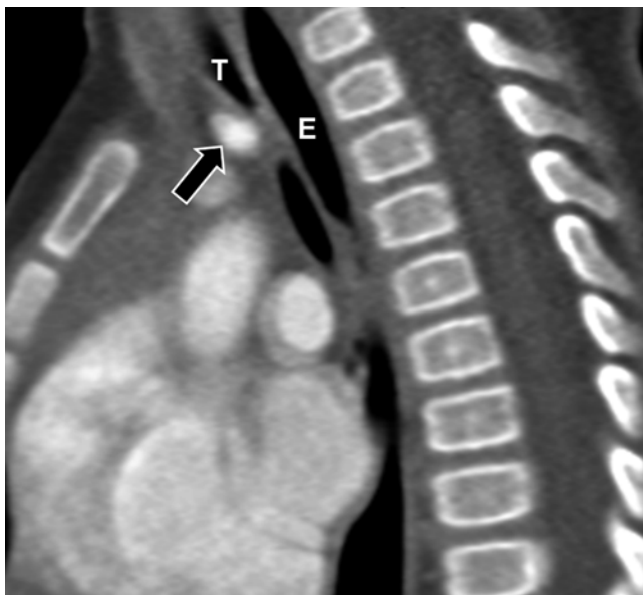


Fig. 12.14 Innominate artery compression in a 14-month-old girl who presented with recurrent cough and severe respiratory distress. Enhanced sagittal CT image shows an anterior compression of the trachea (*T*) due to innominate artery (*arrow*). *E* esophagus

12.5.11 Foreign Body Aspiration

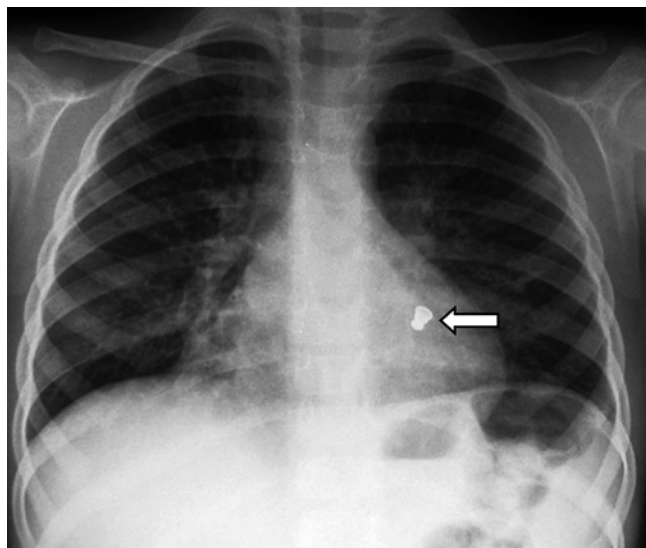


Fig. 12.15 Radiopaque foreign body in the left lower lobe bronchus in a 4-year-old boy who presented with acute onset of coughing and respiratory distress. After chest radiographs, the patient underwent bronchoscopy, which showed a metallic bottle cap lodged in the left lower lobe bronchus. Frontal chest radiograph shows a radiopaque foreign body (*arrow*) located in the left lower lobe, retrocardiac region (Reprinted with permission from *Seminars in Roentgenology*, page 183, Volume 47, No. 2, 2012)



Fig. 12.16 Foreign body in the left main stem bronchus in a 9-year-old boy who presented with acute respiratory distress. After CT, the patient underwent bronchoscopy, which showed a pen tip lodged in the left main stem bronchus. Axial CT image shows an intrabronchial opacity (*arrow*) and associated left lung collapse

12.5.12 Traumatic Tracheobronchial Injury



Fig. 12.17 Traumatic tracheal injury in a 5-year-old girl with motor vehicle accident. Axial CT image shows a focal disruption (*arrow*) of the posterolateral wall of the trachea from 6 o'clock to 8 o'clock position, with an adjacent collection of air within the mediastinum indicating tracheal rupture. Extensive pneumomediastinum is also seen. *T* trachea

12.5.13 Obstructive Sleep Apnea

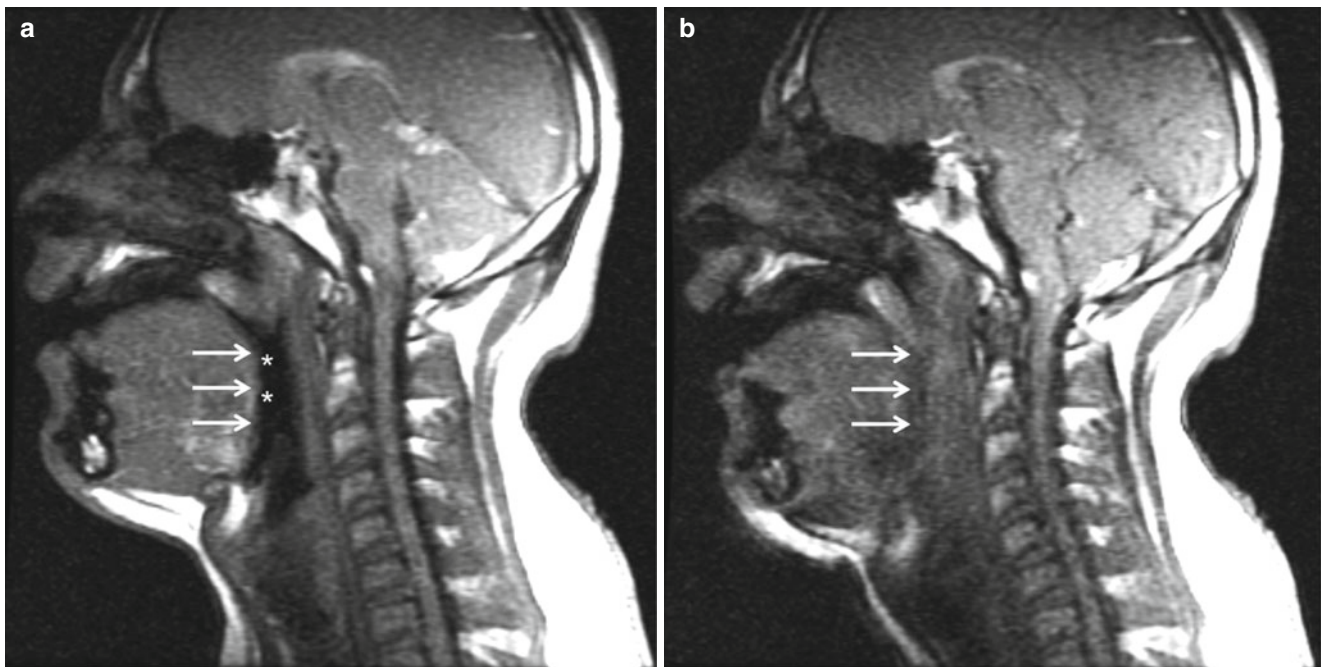


Fig. 12.18 Obstructive sleep apnea in a child with glossoptosis. (a) Sagittal cine MRI sleep study image shows the posterior edge of the tongue (*arrow*) in relation to the patent pharyngeal space (*asterisks*). (b) Sagittal cine MRI sleep study image coinciding with an episode of

oxygen desaturation shows the posterior displacement of the tongue (*arrows*) and resultant obliteration of the pharyngeal space (Reprinted with permission from *Seminars in Roentgenology*, page 155, Volume 47, No. 2, 2012. Case courtesy of Lane F. Donnelly, MD, Orlando FL)

12.5.14 Tracheobronchomalacia

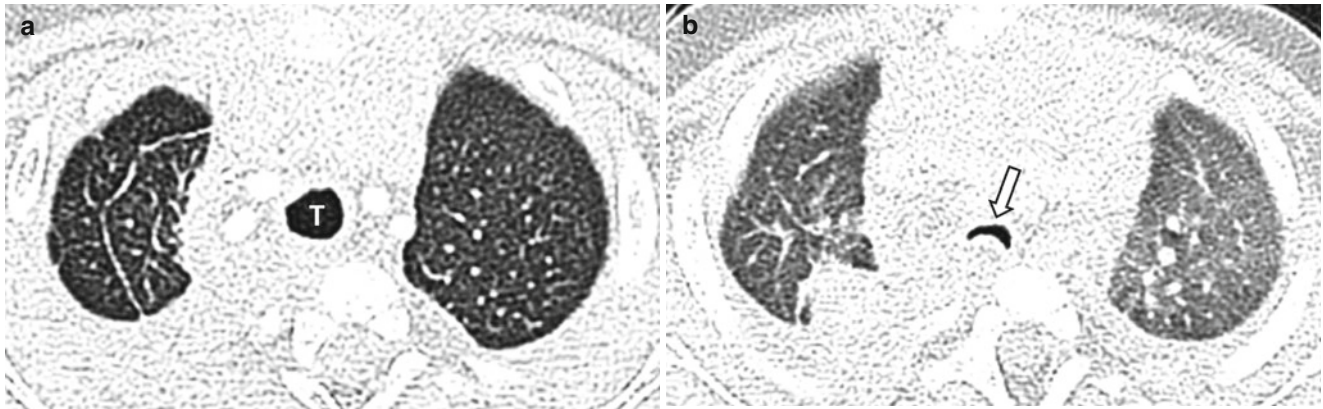


Fig. 12.19 Tracheomalacia in a 17-month-old boy with a history of prematurity who presented with recurrent severe respiratory distress and apnea. (a) Axial CT lung window image obtained at end-inspiration shows patent trachea (T). (b) Axial CT lung window image obtained at

end-expiration demonstrates a marked decrease ($>75\%$) in tracheal luminal airway caliber (arrow), consistent with CT diagnosis of tracheomalacia. Subsequently obtained bronchoscopy confirmed the diagnosis of tracheomalacia

References

- Brown JC, Chapman T, Klein EJ, et al. The utility of adding expiratory or decubitus chest radiographs to the radiographic evaluation of suspected pediatric airway foreign bodies. *Ann Emerg Med*. 2013;61:19–26.
- Chapman T, Sandstrom CK, Parnell SE. Pediatric emergencies of the upper and lower airway. *Appl Radiol*. 2012;April:10–7.
- Cherry JD. Clinical practice. Croup. *N Engl J Med*. 2008;358:384–91.
- Cooper M, Slovis TL, Madgy DN, et al. Congenital subglottic hemangioma: frequency of symmetric subglottic narrowing on frontal radiographs of the neck. *AJR Am J Roentgenol*. 1992;159:1269–71.
- Donnelly LF. Obstructive sleep apnea in pediatric patients: evaluation with cine MR sleep studies. *Radiology*. 2005;236:768–78.
- Donnelly LF, Strife JL, Myer CM. Dynamic sleep fluoroscopy in children with obstructive sleep apnea. *Appl Radiol*. 2001;December:30–4.
- Eslamy HK, Newman B. Imaging of the pediatric airway. *Paediatr Anaesth*. 2009;Suppl 1:9–23.
- Hammer MR, Dillman JR, Chong ST, et al. Imaging of pediatric thoracic trauma. *Semin Roentgenol*. 2012;47:135–46.
- Hedlund GL, Wiatrak BJ, Pranikoff T. Pneumomediastinum as an early radiographic sign in membranous croup. *AJR Am J Roentgenol*. 1998;170:55–6.
- Hernanz-Schulman M. Vascular rings: a practical approach to imaging diagnosis. *Pediatr Radiol*. 2005;35:961–79.
- Herrera P, Caldarone C, Forte V, et al. The current state of congenital tracheal stenosis. *Pediatr Surg Int*. 2007;23:1033–44.
- John SD, Swischuk LE. Stridor and upper airway obstruction in infants and children. *Radiographics*. 1992;12:625–43.
- Kim WS, Moon WK, Kim IO, et al. Pulmonary tuberculosis in children: evaluation with CT. *AJR Am J Roentgenol*. 1997;168:1005–9.
- Kondrachuk O, Yalynska T, Tammo R, et al. Multidetector computed tomography evaluation of congenital mediastinal vascular anomalies in children. *Semin Roentgenol*. 2012;47:127–34.
- Laya BF, Lee EY. Congenital causes of upper airway obstruction in pediatric patients: updated imaging techniques and review of imaging findings. *Semin Roentgenol*. 2012;47:147–58.
- Lee EY, Boisselle PM. Tracheobronchomalacia in infants and children: multidetector CT evaluation. *Radiology*. 2009;252:7–22.
- Lee EY, Litmanovich D, Boisselle PM. Multidetector CT evaluation of tracheobronchomalacia. *Radiol Clin North Am*. 2009;47:261–9.
- Lee EY, Greenberg SB, Boisselle PM. Multidetector computed tomography of pediatric large airway diseases: state-of-the-art. *Radiol Clin North Am*. 2011;49:869–93.
- Lee EY, Browne LP, Lam W. Noninvasive magnetic resonance imaging of thoracic large vessels in children. *Semin Roentgenol*. 2012a;47:45–55.
- Lee EY, Restrepo R, Dillman JR, et al. Imaging evaluation of pediatric trachea and bronchi: systematic review and updates. *Semin Roentgenol*. 2012b;47:182–96.
- Lui D, Kumar A, Aggarwal S, et al. CT findings of malignant change in recurrent respiratory papillomatosis. *J Comput Assist Tomogr*. 1995;19:804–7.
- Moraes TJ, Langer JC, Forte V, et al. Pediatric pulmonary carcinoid: a case report and review of the literature. *Pediatr Pulmonol*. 2003;35:318–22.
- Nozawa K, Aihara T, Takano H. MR imaging of a subglottic hemangioma. *Pediatr Radiol*. 1995;25:235–6.
- Rosler L, Rothoeft T, Teig N, et al. Ultrasound and colour Doppler in infantile subglottic haemangioma. *Pediatr Radiol*. 2011;41:1421–8.
- Salour M. The steeple sign. *Radiology*. 2000;216:428–9.
- Sammer M, Pruthi S. Membranous croup (exudative tracheitis or membranous laryngotracheobronchitis). *Pediatr Radiol*. 2010;40:781.
- Shin SM, Kim WS, Cheon JE, et al. CT in children with suspected residual foreign body in airway after bronchoscopy. *AJR Am J Roentgenol*. 2009;192:1744–51.
- Singh M, Chin KJ, Chan VW, et al. Use of sonography for airway assessment: an observational study. *J Ultrasound Med*. 2010;29:79–85.
- Szysko T, Gnanasegaran G, Barwick T, et al. Respiratory papillomatosis of lung and F-18 FDG PET-CT. *Clin Nucl Med*. 2009;34:521–2.

Bernard F. Laya

Contents

13.1	Introduction	434
13.2	Etiology	434
13.3	Imaging	434
13.3.1	Chest Radiograph	434
13.3.2	Ultrasound	435
13.3.3	Computed Tomography (CT) Scan	435
13.3.4	Magnetic Resonance Imaging (MRI)	435
13.4	Specific Infections	435
13.4.1	Viral Infections	435
13.4.2	Bacterial Pneumonia	436
13.4.3	Pertussis	437
13.4.4	Mycoplasma Pneumonia	437
13.4.5	Chlamydia Pneumonia	437
13.4.6	Tuberculosis	438
13.4.7	Mycotic Infections	438
13.4.8	Parasite Infections	439
13.4.9	Pulmonary Infections in the Immunocompromised Children	439
13.5	Illustrations: Infections	441
13.5.1	Respiratory Syncytial Virus (RSV) Infection	441
13.5.2	Varicella Pneumonia	442
13.5.3	SARS Infection	443
13.5.4	Influenza AH1N1 Virus Pneumonia	444
13.5.5	Postinfectious Bronchiolitis Obliterans	445
13.5.6	Swyer-James Syndrome	446
13.5.7	Bacterial Pneumonia	447
13.5.8	Parapneumonic Fluid Collection: CT Finding	448
13.5.9	Parapneumonic Fluid Collection: Ultrasound Finding	449
13.5.10	Necrotizing Pneumonia	450
13.5.11	Lung Abscess	451
13.5.12	Pneumatocele	452
13.5.13	Bronchiectasis	453
13.5.14	Pertussis	454
13.5.15	Mycoplasma Pneumonia	455
13.5.16	Chlamydia Pneumonia	456
13.5.17	Tuberculosis: Primary TB	457
13.5.18	Tuberculosis: Primary TB	458
13.5.19	Tuberculosis: Progression of Ghon Focus	459

B.F. Laya, M.D., DO
 Institute of Radiology, St. Luke's Medical Center – Global City,
 32nd Street, Bonifacio Global City, Taguig City 1634, Philippines
 e-mail: bernielaya@aol.com

13.5.20	Tuberculosis: Progression of Lymph Node Disease	460
13.5.21	Miliary TB.....	461
13.5.22	Reactivated TB.....	462
13.5.23	Aspergilloma.....	463
13.5.24	Invasive Aspergillosis.....	464
13.5.25	Histoplasmosis	465
13.5.26	Hydatid Disease	466
13.5.27	Ascariasis	467
13.5.28	Staphylococcal Abscess	468
13.5.29	Aspergillosis in the Immunocompromised	469
13.5.30	<i>Pneumocystis jiroveci</i> Infection	470
	References	471

13.1 Introduction

Lower respiratory tract infection is the most common cause of illness in children and is a significant cause of morbidity and mortality. There are also associated complications, which should be recognized in order to make correct decisions regarding interventions or management. Clinical signs and symptoms are nonspecific, especially in infants and younger children. Some children with pneumonia even present with nonrespiratory symptoms including fever, malaise, decreased appetite, irritability, weakness, chest pain, and abdominal symptoms. Physical examination is also less reliable in children than adults (Donnelly 2001). Microbiological tests are important but could be difficult to obtain especially in younger children. Various medical imaging modalities not only play an important role as an aid in diagnosis but can also help during and after therapy. Diagnosis of pneumonia calls for a combination of clinical awareness, appropriate microbiological tests, and radiological studies.

13.2 Etiology

The cause of pneumonia in a child is often difficult to identify, but the patient's age can help narrow the possible etiologies. Viral pneumonia is rare in the neonatal period because of conferred maternal antibody protection. Group B streptococcus and Gram-negative enteric bacteria are the most common pathogen in neonates (birth to 20 days), obtained through vertical transmission from the mother during birth. From age 3 weeks to 3 months, *Streptococcus pneumoniae* is the most common pathogen. Viruses are the most frequent cause of community-acquired pneumonia in infants older than 4 months and in preschool-aged children, with respiratory syncytial virus (RSV) being the most common. For school-aged children (6–16 years old), the incidence of bacterial infections from *Streptococcus* increases, although viral disease remains the most common cause (Condon 1991; Ostapchuk et al. 2004). Bacterial pneumonia can occur at

any time in preschool and school-aged children and adolescents. *Mycoplasma pneumoniae* causes 30 % of lower respiratory tract infections in school-aged children (Condon 1991; Donnelly 2001). Infectious agents causing pneumonia are not limited to viruses and bacteria, but it could also be due to *Mycobacteria*, fungi, protozoa, and parasites. Co-infection with two or more microbial agents can also occur.

13.3 Imaging

Evaluation of suspected pulmonary infection is a very common indication for an imaging study in children. The role of imaging including chest radiographs, ultrasound, computed tomography (CT), and even magnetic resonance imaging (MRI) is to detect the presence or exclusion of pneumonia, determine its location, characterize and describe the extent of pneumonia, exclude other causes of respiratory symptoms, and show complications. It is also an important tool for image-guided interventions.

13.3.1 Chest Radiograph

The cornerstone of imaging in children suspected of having pulmonary infection is the chest radiograph. The radiographic appearance reflects the pathologic process occurring in the respiratory system (Bramson et al. 2005). Frontal and lateral views are obtained when possible because hyperinflation and lymphadenopathy are more accurately evaluated on a lateral radiograph especially in younger children. Lateral decubitus views may be useful in distinguishing free flowing pleural fluid versus loculated fluid collections. Chest radiographs have inherent limitations, but despite of this, there is moderate evidence to suggest that chest radiographs are sufficiently sensitive and highly specific for the diagnosis of community-acquired pneumonia (Westra and Choy 2009).

13.3.2 Ultrasound

The use of ultrasound as an imaging tool for pulmonary infections has been increasing especially for assessment of complications. Its utility is even more important because there is no associated radiation, no sedation, no specific preparation, and the ultrasound machine can be transported to the patient's bedside. It can be used for planning thoracentesis, thoracotomy, and image-guided drainage procedures. Lower-frequency (3.5–7 MHz) sector transducers are initially used for overview through inter- and subcostal scanning, but higher-frequency (10–12.5 MHz) linear transducers are helpful for more detail in the near field.

13.3.3 Computed Tomography (CT) Scan

The development of helical and multidetector CT has revolutionized imaging evaluation of pulmonary infections. The use of intravenous contrast medium also helps optimize the assessment of pleura, mediastinum, and pulmonary parenchyma in cases of complicated pneumonia. High-resolution CT (HRCT) shows greater accuracy in characterizing diseases into interstitial, airway, and airspace processes and gives a more accurate depiction of the extent of the disease. CT has an important role when a complication is suspected, to exclude an underlying abnormality in recurrent and persistent infections, for image-guided interventions, and for the evaluation of immunocompromised children (Westra and Choy 2009). Radiation-associated risks are important to consider, and thus, a clear indication for the procedure has to be present. Low radiation dose technique with 80–120 kVp, age and thoracic thickness-adjusted low milliamperes-seconds, along with radiation dose modulation should be utilized.

13.3.4 Magnetic Resonance Imaging (MRI)

Evaluation of lung parenchyma with conventional MR imaging has limitations because of the inherent low proton density and weak MR signal as related to the low physical density of the lung. However, lung parenchymal, pleural, and lymph node inflammatory abnormalities can be visualized and characterized by MRI in children with pulmonary infections.

13.4 Specific Infections

13.4.1 Viral Infections

Peripheral airways disease or bronchiolitis are common terms ascribed to lower respiratory infection secondary to

viruses. It commonly occurs in children less than 2 years of age, typically presenting with cough, coryza, and wheezing. RSV is the most common cause, but other viral causes include rhinovirus, parainfluenza virus, human metapneumovirus, adenovirus, influenza virus, coronavirus, and human bocavirus (Eslamy and Newman 2011). Following inhalation of infected aerosols, the virus migrates to small airways and alveoli resulting to bronchoconstriction and increased mucous secretion (Aherne et al. 1970; Swischuk and Hayden 1986).

Typical chest radiographic appearances are peribronchial thickening/opacities, hyperaeration, and subsegmental atelectasis (Fig. 13.1). The peribronchial inflammation and edema manifests as increased peribronchial cuffing or thickening of the bronchial walls, which is usually asymmetric and radiates from the hila into the lung. Narrowed distal airway lumen due to bronchiolar wall edema and mucus results in hyperinflation with areas of segmental and subsegmental atelectasis (Condon 1991; Donnelly 2001). Patchy areas of airspace consolidation have also been described in viral pneumonia. CT is rarely required in the investigation of viral lower respiratory infection, but the most common CT feature is peribronchial thickening and ground-glass attenuation without consolidation (Tanaka et al. 1996).

Varicella zoster virus infection is a highly contagious but a relatively benign, self-limited disease in childhood. Varicella pneumonia is regarded as a serious manifestation in adults, but immunocompromised children are also at risk. Clinically, cough, fever, dyspnea, chest pain, and vesicular rash are generally accompanied by mild constitutional symptoms (Kim et al. 1999). Radiographs of the chest initially reveal nodular infiltrates that may progress to large segmental areas of patchy consolidation, predominantly in the bases and perihilar regions. Total clearing is virtually guaranteed, although punctate calcifications maybe evident within 2 years after acute illness (Fig. 13.2). Airspace disease associated with chicken pox in children occurs most often in the immunocompromised host (Blickman 1998).

Certain groups of viruses have been recently reported to cause severe respiratory infection leading to respiratory failure and even death. The severe acute respiratory syndrome (SARS) caused by coronavirus A (SARS-CoV) created a scare in 2003 with over 8,000 cases reported from 29 different countries. SARS presents with a prodrome of flu-like illness, followed by cough, dyspnea, and possibly acute respiratory distress. The initial radiographic manifestation is the presence of focal or diffuse interstitial opacities but rapidly progresses to bilateral areas of consolidation (Thibodeau and Viera 2004) (Fig. 13.3). Another pandemic virus is the influenza virus A H5N1 (avian influenza virus), originating from Asia and spreading over many parts of the world from 2003 to 2007. More recently, influenza virus of swine origin, designated as influenza A H1N1, was first reported in Mexico

in 2009 and has rapidly spread globally. Symptoms range from asymptomatic infection to mild upper respiratory illness, viral syndrome, diarrhea, severe pneumonia, acute respiratory distress syndrome (ARDS), and progression to multiorgan failure. Initial chest radiographs in children with a mild and self-limited clinical course are often normal, but they may demonstrate prominent peribronchial markings with hyperinflation and multifocal areas of consolidation (Lee et al. 2010) (Fig. 13.4).

13.4.1.1 Complications of Viral Pneumonia

The most common complication of viral pneumonia is a secondary bacterial infection. Viral infection can compromise the respiratory mucosa and render the host pulmonary respiratory system susceptible to develop superimposed bacterial pneumonia (Donnelly 1999).

Postinfectious bronchiolitis obliterans (constrictive bronchiolitis or obliterative bronchiolitis) is a clinical syndrome of chronic airflow obstruction associated with inflammatory changes in the small airways as response to epithelial injury associated with infections. It is particularly associated with *Adenovirus*, RSV, *Varicella*, and severe *Mycoplasma* infection. The chest x-ray findings are often nonspecific and can appear normal, but the most common abnormality is hyperaeration (Yalcin et al. 2003). On HRCT, there is a mosaic perfusion pattern (Fig. 13.5). Perfusion is diminished in areas of parenchymal attenuation due to vasoconstriction secondary to hypoxia. Inspiratory and expiratory phases of ventilation are important in HRCT to better assess air trapping in this condition (Hansell et al. 1997). Peribronchial thickening, atelectasis, bronchiectasis, and sometimes lung volume reduction can also be seen. Swyer-James is a subtype of postinfectious bronchiolitis obliterans, which is typically unilateral. It can affect one lung segment, a lobe, or the entire lung. The characteristic chest radiographic and CT findings are hyperlucency due to the pulmonary hypoperfusion, reduction of vascular and hilar markings, and volume reduction of the affected lung or lobe (Daltro et al. 2011) (Fig. 13.6).

13.4.2 Bacterial Pneumonia

Bacterial pneumonia occurs with the inhalation of the infectious agent into the airspaces. It is most commonly caused by *S. pneumoniae*, *Haemophilus influenza* type B, and *Staphylococcus aureus*. *Staphylococcus* commonly occurs in early infancy, *Haemophilus* most often between 6 and 12 months, and *S. pneumoniae* more commonly between 1 and 3 years of age. Gram-negative aerobic bacteria such as *Pseudomonas aeruginosa* and *S. aureus* are a major problem in patients with cystic fibrosis. Patients present with cough, chest pain, and high fever.

Following inhalation of the infectious agent into the airspaces, acinar exudate and edema ensues, manifesting as localized airspace consolidation with air bronchogram on chest radiographs. The typical distribution is lobar or segmental, depending on the stage of progression at the time the x-ray was obtained (Fig. 13.7a) (Condon 1991; Donnelly 1999). Round pneumonia is a spherical pneumonia, usually caused by *S. pneumoniae* (Rose and Ward 1973) (Fig. 13.7b). It is common in children less than 8 years old, maybe due to poor development of collateral pathways of ventilation (pores of Kohn and channels of Lambert). When round pneumonia is seen in children over 8 years old, other etiologies should be considered. The CT manifestations of bacterial infection are areas of consolidation with or without air bronchogram, typically with a segmental or lobar distribution and involving the lung periphery (Tanaka et al. 1996).

13.4.2.1 Parapneumonic Effusions and Empyema

Parapneumonic effusions occur most commonly in bacterial pneumonia. It represents a spectrum of inflammatory fluid collections that ranges from transudative effusion to empyema. Parapneumonic effusions complicate pneumonia in 36–56 % of cases in pediatric patients (Kurt et al. 2006), and empyema complicates an estimated 0.6 % of all childhood pneumonias (Jaffe and Balfour-Lynn 2005).

Pleural fluid can usually be detected on a frontal chest radiograph, but layering of fluid on the lateral decubitus view distinguishes a free flowing fluid from a loculated fluid.

CT scan gives a better characterization of parapneumonic effusions compared to radiographs. CT findings include enhancement and thickening of the parietal and visceral pleura, thickening of the extrapleural subcostal tissues, and increased attenuation of the extrapleural subcostal fat (Muller 1993) (Fig. 13.8). These CT characteristics do not accurately predict empyema and should not be used to distinguish between empyema and transudative effusions. In ultrasound, pleural fluid can be characterized as simple effusion, complicated effusion, or fibrothorax (pleural thickening or fibrosis) (Fig. 13.9). A simple effusion appears as a clear anechoic or cloudy hypoechoic fluid with or without swirling particles. A complicated effusion appears as a septated or multiloculated, hypoechoic fluid with fibrinous septations, with no clear demarcation between the lung and pleural components, while a fibrothorax appears as a thickened, echogenic rind of pleural plaque (Kim et al. 2000).

13.4.2.2 Lung Complications of Bacterial Pneumonia

Suppurative lung parenchyma complications represent a spectrum of abnormalities including cavitary necrosis, lung abscess, pneumatocele, bronchopleural fistula, and pulmonary gangrene.

Necrotizing pneumonia or cavitory necrosis is a complication of severe lobar pneumonia, characterized by massive necrosis and liquefaction of lung tissues resulting to multiple cavities rather than a solitary one. It is most commonly caused by *S. pneumoniae* although *Aspergillus* and *Legionella* have also been implicated in the pediatric population (Hodina et al. 2002). Evidence of cavitory necrosis complicating pneumonia is often seen on CT before or in the absence of findings in chest radiography. CT findings include lung consolidation with decreased parenchymal enhancement, loss of lung-pleura margin, and multiple thin-walled cavities lacking an enhancing border. The adjacent visceral pleura is particularly fragile and tends to rupture, causing bronchopleural fistula (Hoffer et al. 1999) (Fig. 13.10). Cavitory necrosis indicates an intense and prolonged illness, but it usually resolves without surgical intervention (Donnelly and Klosterman 1997).

Lung abscesses are thick-walled cavities containing purulent material resulting from pulmonary infection. An air-fluid level with reactive rim is a typical imaging appearance, as compared to necrotizing pneumonia where cavities occasionally have air-fluid level but without rim of enhancement (Donnelly and Klosterman 1997) (Fig. 13.11). Differentiating the two is important because abscess not responding to therapy may require drainage, whereas necrotizing pneumonia does not require invasive treatment, and intervention may even be harmful resulting in complications such as bronchopleural fistula (Hoffer et al. 1999). Pneumatoceles are thin-walled cysts without septations that develop within the lung parenchyma after an acute pneumonia (Fig. 13.12). It may represent a later or less severe stage of resolving or healing necrosis and is most often associated with *S. aureus* (Daltro et al. 2011).

Bronchiectasis is the most common long-term sequelae of lung parenchymal damage from pneumonia. It is best demonstrated on high-resolution chest CT scan, and the main diagnostic features are as follows: internal diameter of the bronchus is wider than its adjacent pulmonary artery, failure of the bronchus to taper peripherally, and visualization of bronchi in the outer 1–2 cm of the lung zones (Eslamy and Newman 2011) (Fig. 13.13).

13.4.3 Pertussis

Pertussis is a highly contagious respiratory bacterial infection caused by *Bordetella pertussis*. It infects mainly infants and young children causing symptoms that include mild fever, runny nose, and cough, which develops into a paroxysmal cough followed by whooping (whooping cough). Pneumonia is a common complication, and untreated patients may be contagious for 3 weeks or more following onset of the cough. The spread of pertussis can be prevented by immunization.

Histopathologic examination reveals an infection dominated by necrotizing bronchiolitis, intra-alveolar hemorrhage, fibrinous edema, and angiolymphatic leukocytosis (Paddock et al. 2008). Conventional radiographs reveal streaky perihilar infiltrates with most often unilateral hilar adenopathy, a pattern sometimes called the shaggy heart appearance (Blickman 1998) (Fig. 13.14).

13.4.4 Mycoplasma Pneumonia

M. pneumoniae is a common ubiquitous organism and treatable cause of community-acquired pneumonia, occurring primarily in children and young adults. It accounts for up to 30 % of all pneumonia in the general population, but the highest incidence is seen in children between 3 and 14 years of age. Of those infected, 50 % get tracheobronchitis, 30 % pneumonia, 10 % pharyngitis, and 10 % otitis media. Clinically, symptoms are less severe but more common than in true bacterial pneumonia (Blickman 1998).

The radiographic findings are nonspecific, have a broad spectrum of appearances, and may present with a pattern intermediate between the classic viral and bacterial pneumonia patterns (Hsieh et al. 2007). Some authors reported that a reticulonodular pattern or nodular opacities are typical radiographic pattern (John et al. 2001), while others stress the occurrence of confluent and patchy consolidation (Reittner et al. 2000) (Fig. 13.15). HRCT findings are thickened bronchovascular bundles, ground-glass attenuation and consolidation, centrilobular nodules, and lobular distribution (Tanaka et al. 1996; Reittner et al. 2000).

13.4.5 Chlamydia Pneumonia

Chlamydia trachomatis is an obligate intracellular parasite. Genital chlamydial infection is recognized as the world's most common sexually transmitted disease, and the high prevalence in women of childbearing age results in exposure of neonates during childbirth. Chlamydia pneumonia is a neonatal infection acquired after passage of the fetus through the cervix and vagina. The infant typically presents at 3–6 weeks of age with respiratory symptoms and occasional pulmonary hemorrhage. *C. trachomatis* should be suspected in infants who are afebrile or nontoxic and have a dry cough. These patients often have a peripheral eosinophilic pleocytosis, sometimes with concomitant conjunctivitis (Ostapchuk et al. 2004). Most chest radiographs show bilateral hyperaeration and diffuse infiltrates with a variety of radiographic patterns including interstitial, reticular nodular, atelectasis, coalescence, and bronchopneumonia (Radkowski et al. 1981) (Fig. 13.16).

13.4.6 Tuberculosis

Tuberculosis (TB) is caused by infection with the *Mycobacterium tuberculosis* complex. Once inhaled, the infected aerosolized droplet in the alveoli cascades a series of inflammatory reaction, and the bacilli also spread to nearby mediastinal lymph nodes. The alveolar site of infection (Ghon focus), the infected lymph nodes, and the associated lymphangitis form the “primary (Ranke’s) complex.” In most immunocompetent children, the infection goes into latency and the bacilli become dormant. These children usually have a reactive tuberculin skin test (TST) and/or a positive Interferon-gamma release assay (IGRA) test, but without clinical evidence of TB and generally no abnormalities on chest radiograph apart from the primary complex residual. Primary tuberculosis disease occurs if the host is unable to contain the infection, and disease progression occurs in the lungs, the lymph nodes, and adjacent structures in the thorax or could disseminate in any part of the body.

Lymphadenopathy (present in 92 %) with or without a visible Ghon focus is the radiographic hallmark of TB infection and usually involves the hilar and paratracheal regions. The Ghon focus may be too small to be radiographically visible but can also undergo caseation and calcify (Fig. 13.17). Disease progression may occur at the site of Ghon focus, within the regional lymph nodes, or following disease spread (Fig. 13.18). Parenchymal involvement in primary pulmonary TB most commonly appears as homogeneous consolidation, although it can appear patchy, linear, nodular, and mass-like. Caseation necrosis, liquefaction, or calcifications can be seen within the consolidation and can progress into extensive lung damage (Marais et al. 2004) (Fig. 13.19). Enlarged and edematous hilar, paratracheal, and subcarinal lymph nodes may cause compression of the adjacent bronchus and can lead to hyperinflation or atelectasis of the affected lung segment. Contrast-enhanced CT shows a characteristic appearance consisting of central areas of low attenuation with peripheral rim enhancement and obliteration of perinodal fat (Kim et al. 1997) (Fig. 13.20).

Pulmonary dissemination, usually seen in very young and immunocompromised patients, leads to the formation of pulmonary nodular interstitial granulomas, usually 1–2 mm in size, throughout the lungs. Chest radiographs demonstrate the usual miliary nodular pattern but CT is more sensitive for the detection of miliary TB (Kim et al. 1997) (Fig. 13.21). Adult-type disease presentation is common after primary infection in children over 10 years of age or via endogenous reactivation (postprimary TB) or reinfection. Chest radiograph shows ill-defined, fibronodular parenchymal disease and cavitation mainly involving the apical segments of the upper lobes (Perez-Velez and Marais 2012) (Fig. 13.22).

13.4.7 Mycotic Infections

13.4.7.1 Aspergillosis

Aspergillus fumigatus is a ubiquitous saprophytic mold found in many environmental sites, and infection is usually via inhalation of spores, although other routes of entry also occur. Infection can manifest as colonization of airway cavities and necrotic tissue, allergic disease, and invasive disease, which is usually acute and rapidly progressive severe disease (Foster and Alton 2003).

Airway colonization occurs in patients with underlying airway disease such as asthma and bronchiectasis. Intertwined fungal hyphae, called as mycetoma or aspergilloma, form in the pulmonary cavity or ectatic bronchi. Important underlying causes are pulmonary TB with cavitation and cystic fibrosis with bronchiectasis. Rounded soft tissue mass within a cavity forming an “air-crescent” sign is a typical appearance (Fig. 13.23). Allergic bronchopulmonary aspergillosis is characterized by mucoid impaction of the proximal bronchi presenting as fingerlike shadows involving the upper lobes on the chest radiograph. CT demonstrates the mucoid impaction of the central airways and the bronchiectasis of the segmental or subsegmental airways (Foster and Alton 2003). Invasive disease is an aggressive, rapidly disseminating and destructive disease and occurs when host defenses are impaired. It is characterized by the occlusion of large- or medium-sized arteries by plugs of hyphae causing pulmonary hemorrhage, arterial thrombosis, and infarction. Radiographic findings are nonspecific, with multiple nodules or areas of consolidation (Fig. 13.24). The typical CT finding is the halo sign due to ground-glass attenuation representing hemorrhage surrounding the pulmonary nodule or mass (Foster and Alton 2003; Eslamy and Newman 2011).

13.4.7.2 Histoplasmosis

Histoplasmosis, caused by the fungus *Histoplasma capsulatum*, is usually an asymptomatic and self-limited disease that rarely requires therapy in children other than the very young or immunocompromised. It is found in the soil of endemic areas including Central United States, Central America, and Northern South America but has also been reported in some parts of Asia (Houston 1994). After inhalation, the spores germinate within the alveoli inciting an intense tissue reaction characterized by granulomas, which may calcify. It spreads to the lymphatics and into the hilar or mediastinal lymph nodes, and systemic dissemination may occur in patients with impaired T-cell immunity (McAdams et al. 1995).

Histoplasmosis falls in one of three categories: acute, chronic pulmonary, and disseminated disease. Acute pulmonary histoplasmosis is a self-limited illness. Chronic pulmonary histoplasmosis occurs in patients with chronic lung

disease and presents similar to tuberculosis with predilection for apical and posterior segments of the lung. Disseminated histoplasmosis in children is characteristically a fulminant illness, which may or may not have pulmonary involvement. Radiologic manifestations parallel the clinical syndromes. Acute disease usually manifests as focal parenchymal consolidation with or without ipsilateral hilar adenopathy (Fig. 13.25). With healing, a nodule representing a histoplasmoma may result. Chronic histoplasmosis radiographically manifests as an upper lobe fibrocavitary disease indistinguishable from postprimary tuberculosis. Chest radiographs of patients with disseminated disease may show miliary or diffuse reticulonodular pattern that could progress to diffuse airspace opacification (McAdams et al. 1995).

13.4.8 Parasite Infections

13.4.8.1 Echinococcosis

Echinococcosis, also known as hydatid disease or hydatidosis, is a parasitic infection in humans caused by dog tapeworm, *Echinococcus granulosus*, in its larval stage. It is endemic in many sheep and cattle-raising countries throughout the world. Humans are intermediate hosts and become infected through ingestion of contaminated water or vegetables. When eggs of adult tapeworm are ingested, embryos are freed and migrate through the host's gastrointestinal mucosa and enter the portal vein and lymphatic system to various parts of the body where the embryo develops into a cyst. The wall of the cysts contains three layers: the outermost, pericyst; the middle laminated membrane layer, ectocyst; and innermost germinal layer, endocyst (Czermak et al. 2001). The lungs are the most common sites of infection in children but majority remain asymptomatic until the cyst enlarges to cause symptoms due to mass effect or due to cyst rupture (Santivanez and Garcia 2010).

Diagnosis is obtained by imaging evaluation, supported by serology. A high proportion of lung lesions are discovered incidentally on a routine x-ray, and the most prominent radiological finding is a dense, round, well-demarcated opacity that can resemble a neoplasm (Fig. 13.26a). When the growth of the cyst produces erosion in the bronchioles, air between the endocyst and pericyst can produce a "crescent or inverse crescent sign." If air continues to enter the cyst cavity, endocyst membrane can be seen floating in the most dependent part of the pericyst cavity producing the "water-lily sign" (Fig. 13.26b). CT recognizes the appearance of the cystic lesion including smaller cysts, assesses signs of cyst rupture, evaluates the surrounding structures, and helps exclude alternative differential diagnoses (Santivanez and Garcia 2010).

13.4.8.2 Ascariasis and Hookworms

Ascariasis and hookworms remain the most common intestinal nematodes in the world (Sarinas and Chitkara 1997). In the western hemisphere, parasitic pneumonia secondary to *Toxoplasma gondii* is associated with compromised hosts, particularly acquired immunodeficiency syndrome (AIDS) patients. *Strongyloides stercoralis* infestation is seen in patients receiving glucocorticoids or chemotherapy and in patients with AIDS or other causes of T-cell dysfunction (Berk and Verghese 1998). *Ascaris* infestation generally occurs through hand-to-mouth ingestion of food contaminated with parasite eggs, while hookworms are transmitted through larval penetration of the skin. Symptomatic pulmonary disease may present with fever, cough, chest pain, hemoptysis, dyspnea, and wheezing. These pulmonary symptoms could be due to Löffler's syndrome, effects of larval tissue migration, airway reactivity or bronchospasm, superimposed bacterial infection, and chronic eosinophilic pneumonia (Sarinas and Chitkara 1997). *Ascaris* and hookworm infections present with peripheral eosinophilia during larval migration phase. Chest radiographs could be normal or demonstrate nonspecific patchy pulmonary infiltrates (Fig. 13.27). CT scan could depict abnormalities better and could show ground-glass pulmonary lesions with ill-defined margins as well as nodules (Sakai et al. 2006).

13.4.9 Pulmonary Infections in the Immunocompromised Children

Causes of immunodeficiency can be divided into congenital (primary) and acquired (secondary). The range of respiratory complications encountered is broad and is influenced by both the type and degree of immunodeficiency. Chest radiographs are insensitive and may show only subtle change. HRCT detects abnormalities not visible on the plain film such as bronchial wall thickening, bronchial dilatation, and air trapping.

Various noninfectious pulmonary processes including alveolar hemorrhage, pulmonary edema, graft versus host disease, and drug reaction are also seen in the immunocompromised hosts, which can mimic pulmonary infection on imaging.

13.4.9.1 Primary Immunodeficiency

The primary or congenital immunodeficiency disorders are inherited group of disorders resulting from innate defects of the immune system. Clinical manifestations are diverse and nonspecific, which include recurrent infections, infection with opportunistic organisms, failure to thrive, skin rashes, recurrent skin sepsis, and unusual wound healing (Jeanes and Owens 2002). Primary immunodeficiency can be broadly

divided into T-cell (cellular) immune deficiency versus B cell (humoral deficiency). Humoral immunodeficiencies are the most commonly encountered type characterized by defective antibody production with increased susceptibility to pyogenic infections but able to recover from viral infections (Fig. 13.28). Examples are X-linked agammaglobulinemia, IgA deficiency, and common variable immunodeficiency. Cellular immunodeficiencies have increased susceptibility to disseminated viral and opportunistic infections. Cellular immune disorders include DiGeorge syndrome and severe combined immunodeficiency (Collingsworth 2005).

13.4.9.2 Secondary Immunodeficiency

Acquired immunodeficiencies in childhood can be caused by chemotherapy, radiation therapy, immunosuppressive therapy aimed at treating childhood malignancies, transplant rejection, rheumatologic disorders, or inflammatory or infectious diseases. It can also be due to human immunodeficiency virus (HIV) infection, malnutrition, or any state of chronic debilitation.

Bone marrow transplant requires complete eradication of the immune system. Early infectious complications are frequently caused by bacteria and fungi, most commonly Gram-negative bacteria (*Pseudomonas* and *Klebsiella*) and *Aspergillus* (Fig. 13.29). Widespread use of long-term indwelling catheters has led to an increased incidence of both staphylococcal and streptococcal pneumonia. Chest radiographs may show classic focal or lobar consolidation although atypical appearance can also be seen. Children are also at increased risk of viral infections, most importantly RSV, *Herpes simplex*, *Adenovirus*, and *Varicella*. Immunosuppressive therapy following solid organ transplantation predisposes a patient to

recurrent pulmonary infections. In these patients, viral infections can be life-threatening, but *Pneumocystis* and fungal infections (*Aspergillus* and *Candida*) can also be seen (Collingsworth 2005).

13.4.9.2.1 HIV/AIDS

Children represent 2 % of the reported cases of human immunodeficiency virus (HIV) infection. Most children are infected after vertical transmission from their mother, and majority develop acquired immunodeficiency syndrome (AIDS) early in life. There is increased susceptibility to bacterial, viral, fungal, protozoal, and opportunistic infections. Lobar or segmental consolidations are the most common patterns (Marks et al. 1996). Mycobacterial infection can be seen in AIDS patients, and the radiographic appearance mimics that seen in immunocompetent children with primary tuberculosis. *Mycobacterium avium-intracellulare* is also encountered later in the course of disease and imaging findings cannot be distinguished with other forms of mycobacterial infections (Collingsworth 2005). *Pneumocystis jiroveci* is the most common opportunistic pulmonary infection in children with AIDS, occurring in up to 50 %, and is the leading pulmonary cause of death (Jeanes and Owens 2002). Radiographic appearances are variable and include hyperinflation with diffuse bilateral interstitial or nodular infiltrates from the perihilar region to the periphery, which often progresses to widespread alveolar opacities with air bronchogram (Fig. 13.30). Cavitory nodules and cysts can be seen, with pneumothorax and/or pneumomediastinum as common complications. HRCT findings include patchy or diffuse ground-glass opacity, consolidation, cyst or cavities, centrilobular opacities, nodules, peribronchial cuffing, and interlobular septal thickening (Jeanes and Owens 2002; Collingsworth 2005).

13.5 Illustrations: Infections

13.5.1 Respiratory Syncytial Virus (RSV) Infection

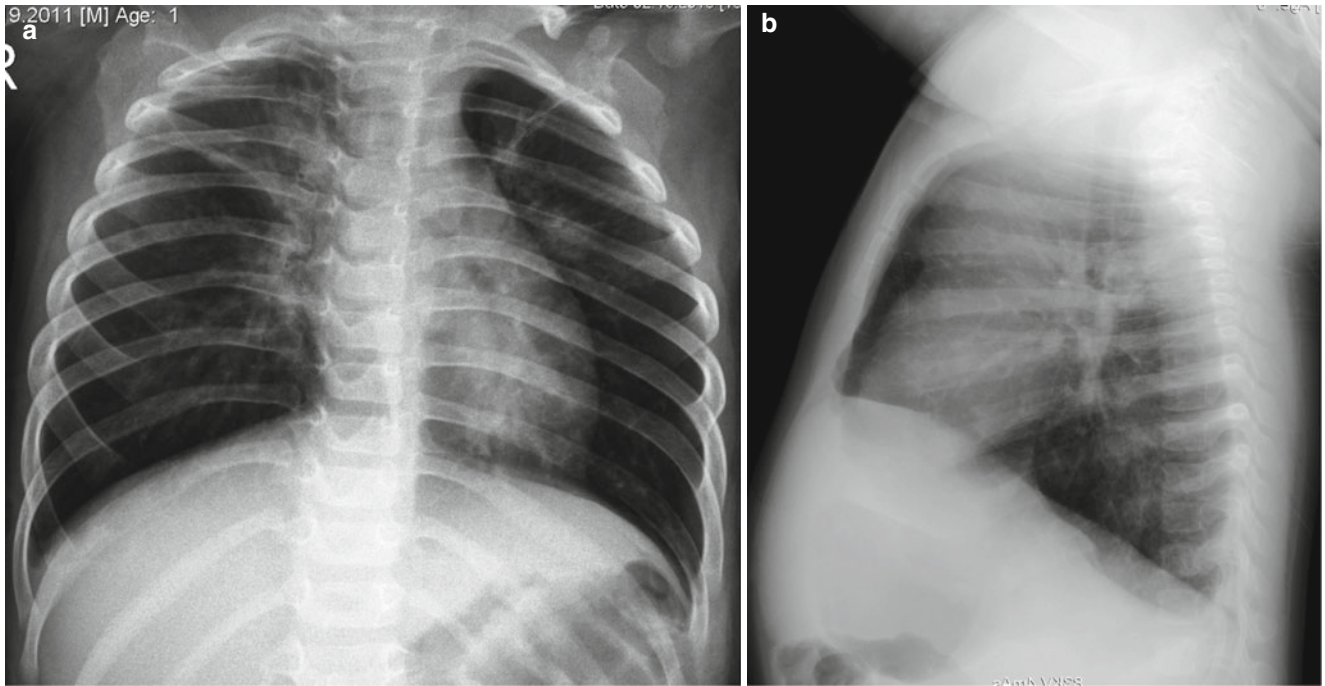


Fig. 13.1 Respiratory syncytial virus (RSV) infection in an 18-month-old boy. Frontal (**a**) radiograph demonstrates hyperaeration, perihilar peribronchial thickening, and areas of subsegmental atelectasis. Lateral view (**b**) shows depression of the diaphragm compatible with hyperaeration

13.5.2 Varicella Pneumonia

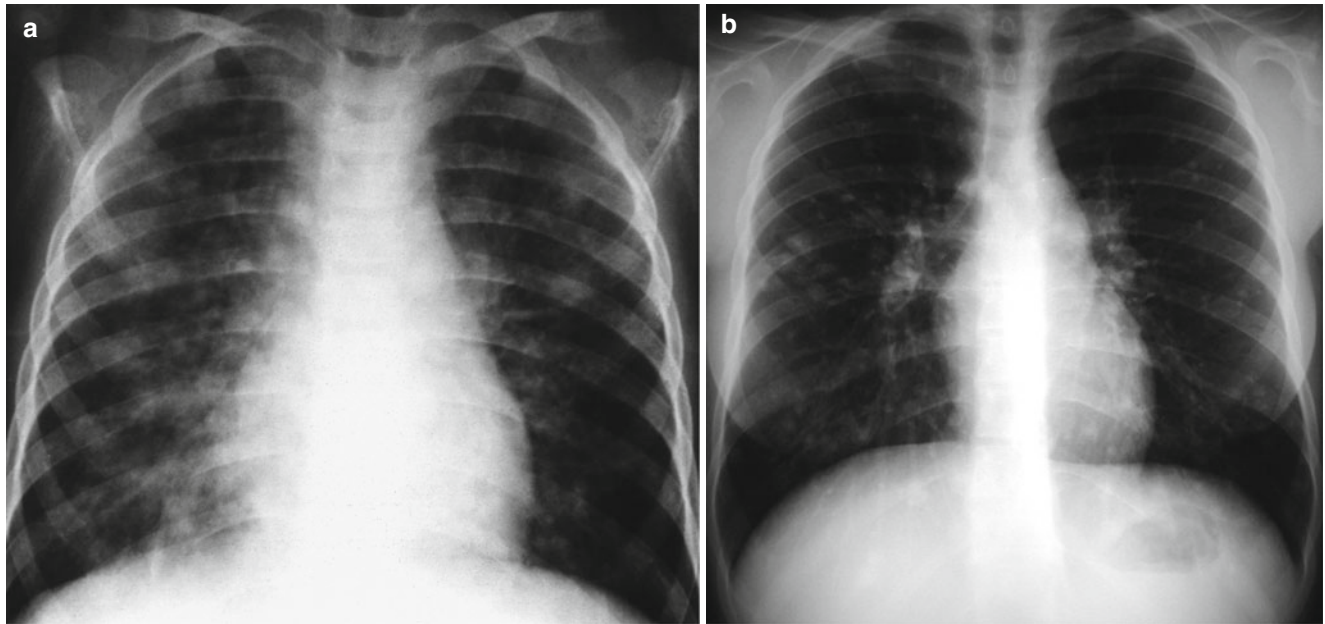


Fig. 13.2 Varicella pneumonia. Frontal chest radiograph of a 5-year-old boy showing multifocal patchy, nodular infiltrates throughout both lung fields (**a**). School requirement chest x-ray of a 15-year-old

asymptomatic girl shows multiple, small, calcified nodules in both lung fields. The patient had varicella pneumonia 3 years prior (**b**)

13.5.3 SARS Infection

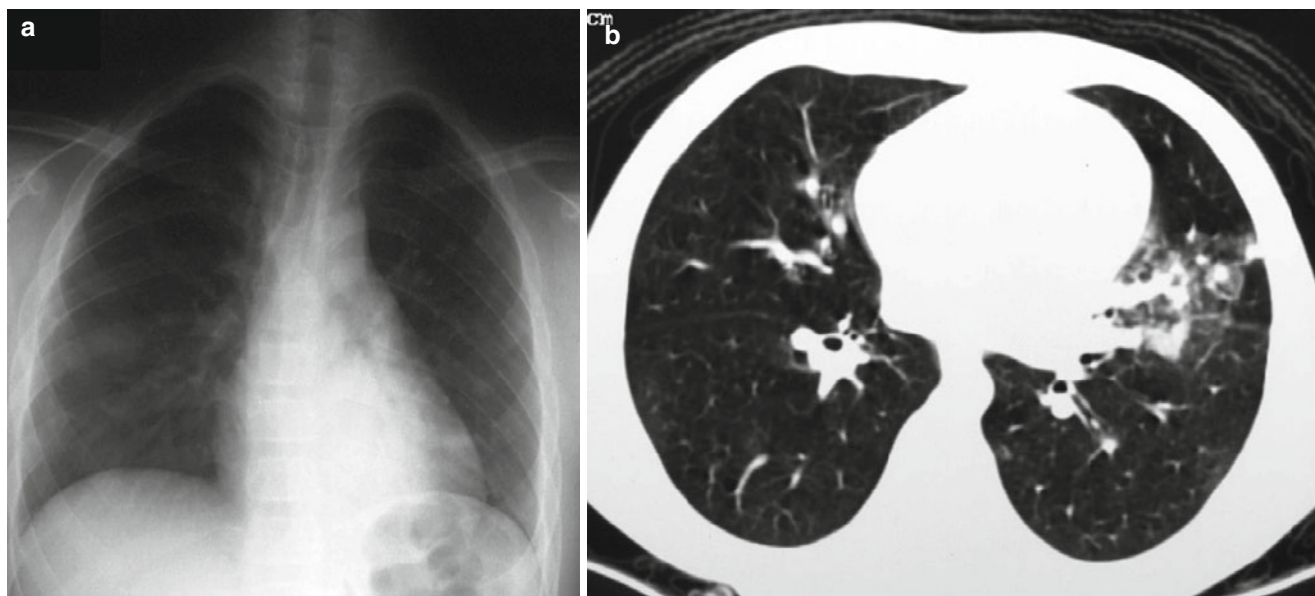


Fig. 13.3 SARS infection. Chest radiograph of a 13-year-old boy 3 days after the onset of fever shows ill-defined haziness in bilateral lower zones (**a**). An 8-year-old boy with confirmed SARS shows an

area of mixed ground-glass opacity with consolidation in the lingula on HRCT (**b**) (Cases courtesy of Winnie CW Chu, MD, from Hong Kong)

13.5.4 Influenza AH1N1 Virus Pneumonia

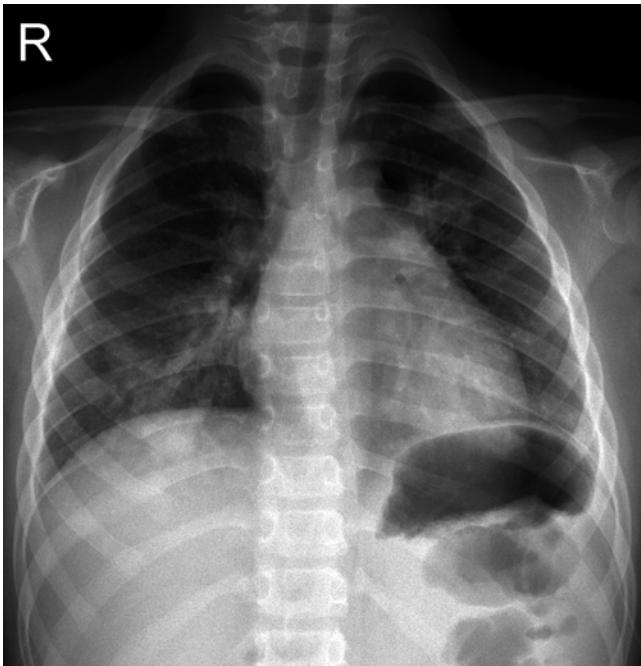


Fig. 13.4 AH1N1 virus pneumonia. Frontal chest radiograph shows generalized increase interstitial markings with multifocal patchy infiltrates (Case courtesy of Xanthe Marie Javier MD, from Philippines)

13.5.5 Postinfectious Bronchiolitis Obliterans



Fig. 13.5 Postinfectious bronchiolitis obliterans. High-resolution CT scan images in expiratory phase demonstrate the typical “mosaic perfusion” pattern

13.5.6 Swyer-James Syndrome

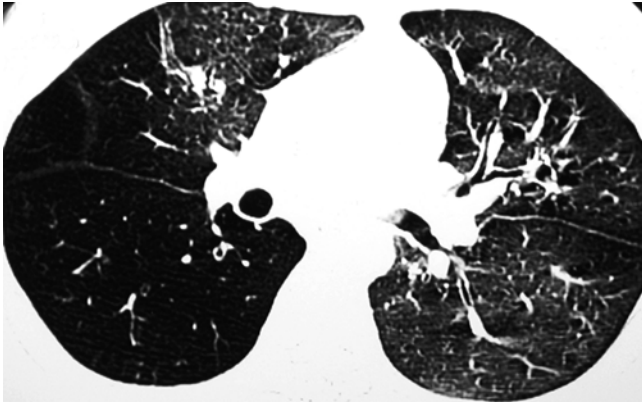


Fig. 13.6 Swyer-James syndrome in a 10-year-old girl. HRCT shows reduced attenuation and paucity of bronchovascular markings in the right lung (Case courtesy of Winnie CW Chu, MD, from Hong Kong)

13.5.7 Bacterial Pneumonia

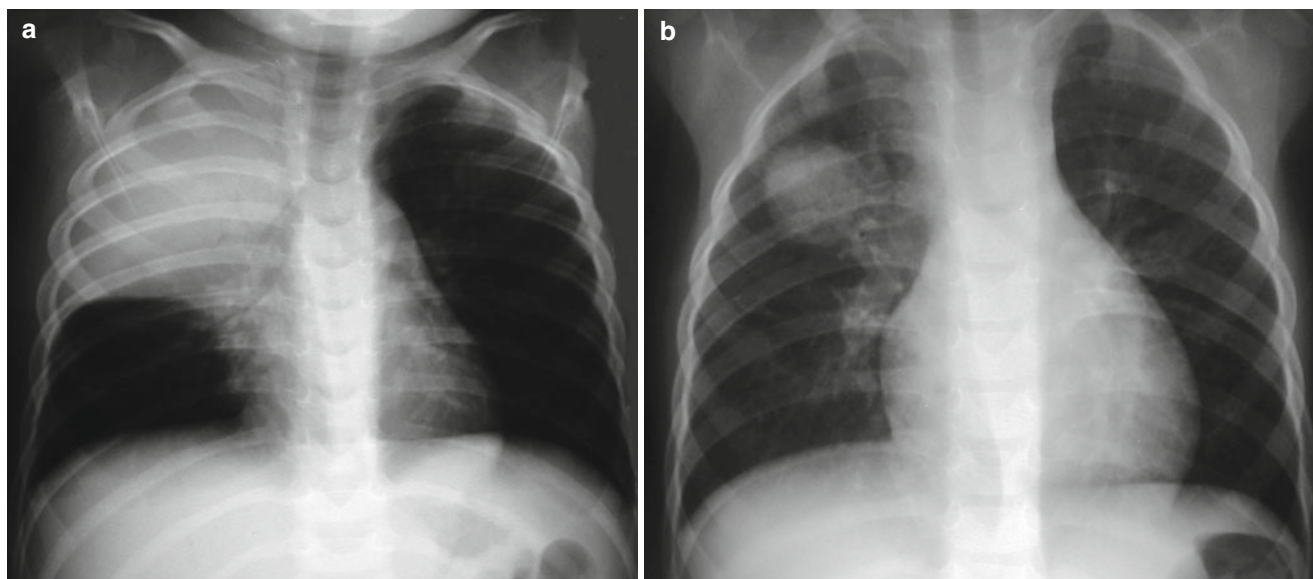


Fig. 13.7 Bacterial pneumonia. Chest radiographs of a 3-year-old girl with high fever, cough, and leukocytosis (**a**) demonstrate complete opacification of the right upper lobe. Image (**b**) shows a round, mass-like consolidation compatible with round pneumonia

13.5.8 Parapneumonic Fluid Collection: CT Finding

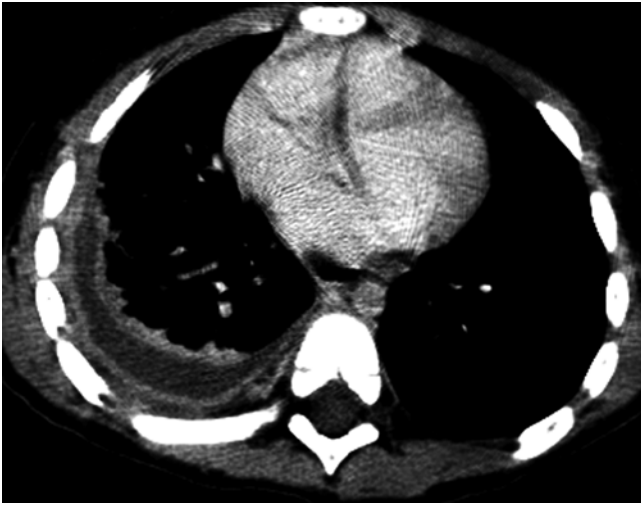


Fig. 13.8 Parapneumonic fluid collection on CT scan. Image demonstrates right-sided pleural fluid with thick enhancement of both visceral and parietal pleura

13.5.9 Parapneumonic Fluid Collection: Ultrasound Finding

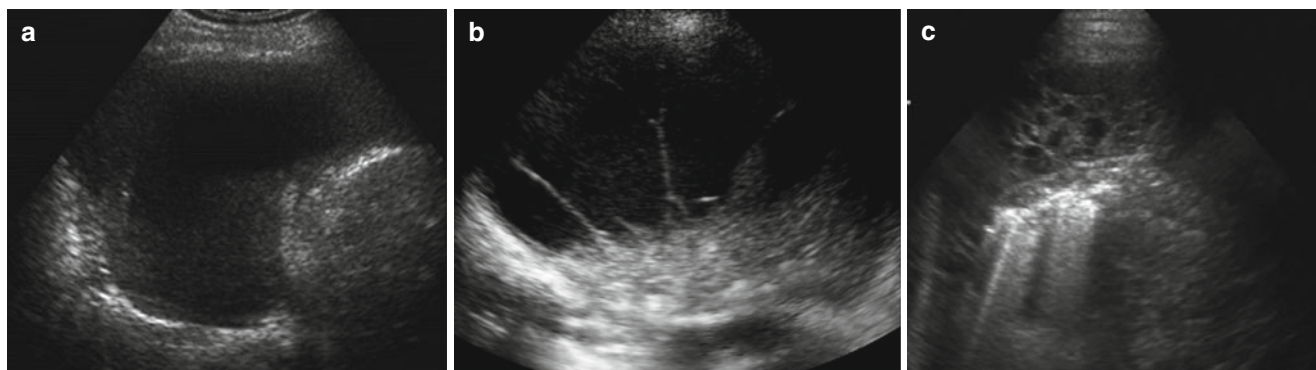


Fig. 13.9 Parapneumonic fluid collections on ultrasound. Simple effusion showing anechoic fluid without septations (**a**). Complicated fluid collection with thin septations and proteinaceous debris (**b**).

Multiloculated fluid collection with thick septations and thickened pleural lining, compatible with fibrothorax (**c**)

13.5.10 Necrotizing Pneumonia

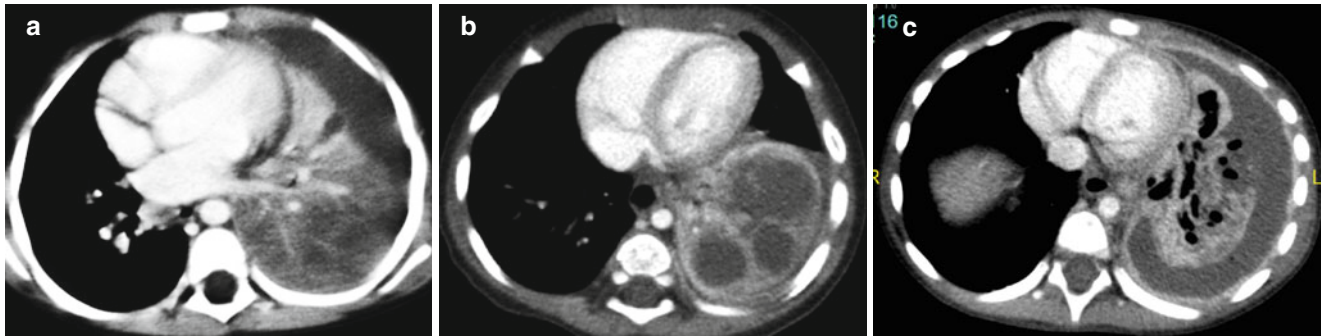


Fig. 13.10 Necrotizing pneumonia on CT. Left lower lobe consolidation showing diminished perfusion at the posterior region (**a**). Evolution of lung ischemia with development of multiple fluid-filled cavities (**b**).

Cavitary necrosis of the consolidation with bronchopleural fistula and parapneumonic fluid (**c**)

13.5.11 Lung Abscess



Fig. 13.11 Lung abscess. Chest radiograph of a 7-year-old boy with cough and high fever reveals a large abscess with air–fluid level and thick irregular border in the right mid-lung. Notice other smaller abscess inferior to the primary lesion

13.5.12 Pneumatocele



Fig. 13.12 Pneumatocele. A 6-month-old boy recovering from *Staphylococcus* pneumonia reveals thin-walled cysts in the right mid-lung field and bibasilar regions

13.5.13 Bronchiectasis



Fig. 13.13 Bronchiectasis. Axial HRCT image showing thick-walled, dilated bronchi with diameters wider than the adjacent pulmonary arteries

13.5.14 Pertussis



Fig. 13.14 Pertussis. Chest radiograph of an 18-month-old boy showing right hilar adenopathy with streaky perihilar infiltrates obscuring the cardiac shadow (shaggy heart) (Case courtesy of Marion O. Sanchez, MD, from Manila, Philippines)

13.5.15 Mycoplasma Pneumonia

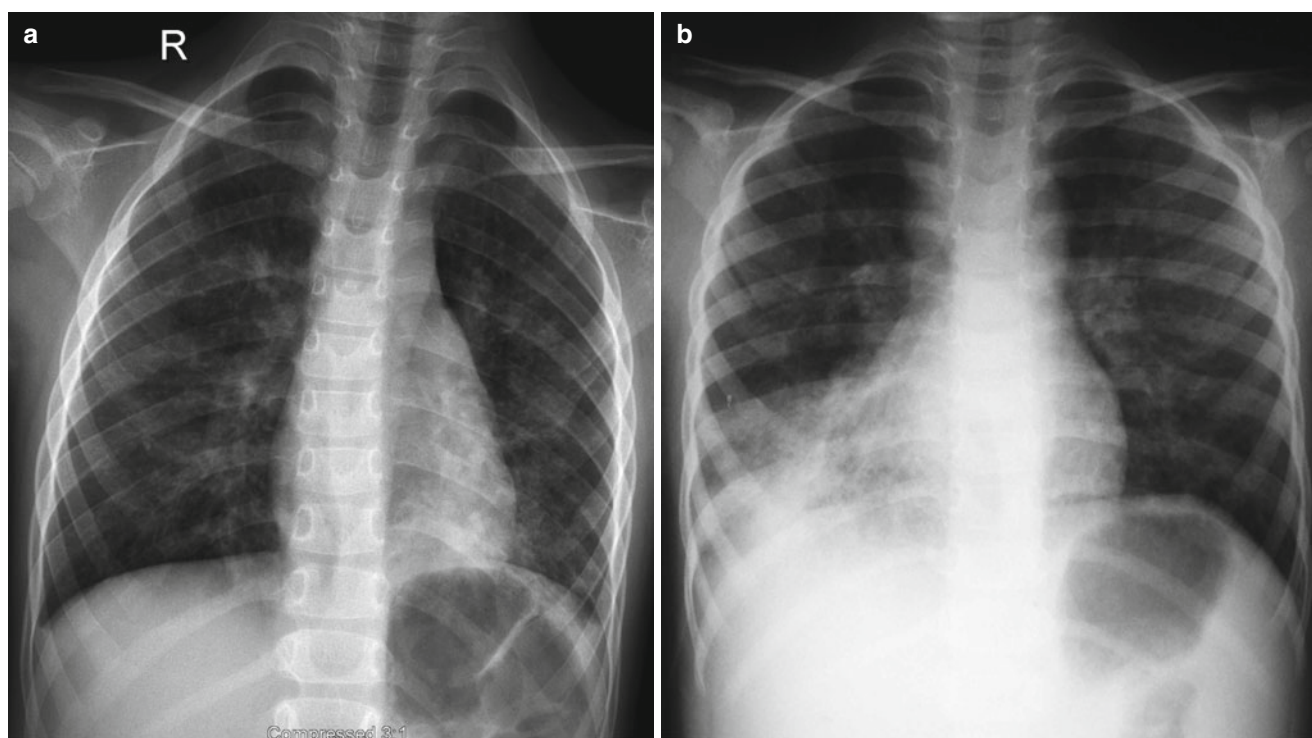


Fig. 13.15 Variable imaging pattern of *Mycoplasma pneumoniae*. Chest x-ray of a 10-year-old boy (**a**) demonstrates generalized increase interstitial marking with scattered patchy areas of opacity. Another

patient diagnosed with *Mycoplasma* infection demonstrating patchy consolidation on the right middle and lower lobes (**b**)

13.5.16 Chlamydia Pneumonia

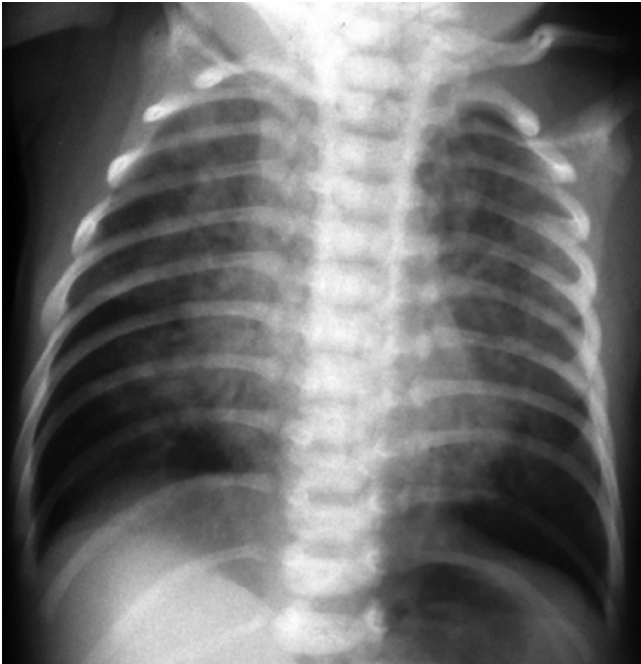


Fig. 13.16 Chlamydia pneumonia. Radiograph of an afebrile 2-week-old girl with dry cough shows bilateral hyperaeration and diffuse interstitial infiltrates, appearing coalescent on the right

13.5.17 Tuberculosis: Primary TB

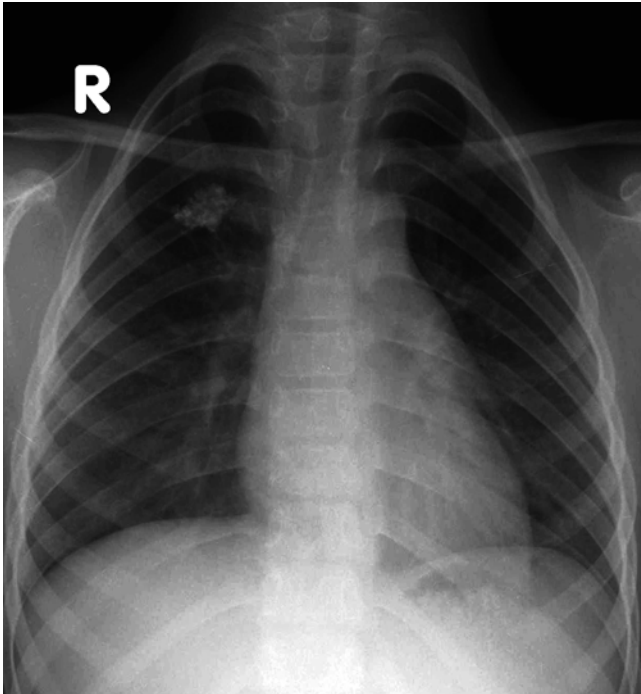


Fig. 13.17 Primary TB infection. An asymptomatic 7-year-old boy had a chest x-ray as a school requirement, which reveals a calcified granuloma on the right upper lobe. This corresponds to a calcified Ghon focus, a sign of TB infection

13.5.18 Tuberculosis: Primary TB

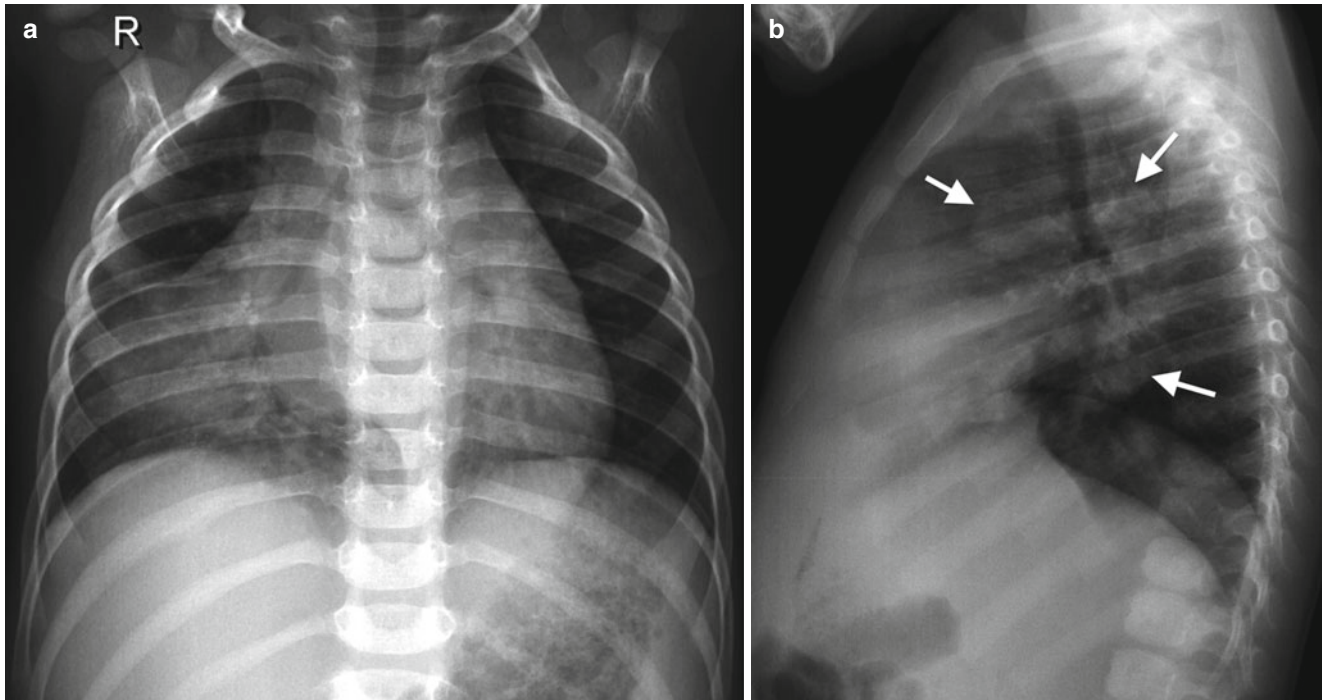


Fig. 13.18 Primary TB disease. Chest radiographs of a 2-year-old girl with chronic cough and fever showing dense right middle lobe consolidation on the frontal view (**a**) and extensive lymphadenopathy (*white arrows*) on the lateral view (**b**)

13.5.19 Tuberculosis: Progression of Ghon Focus

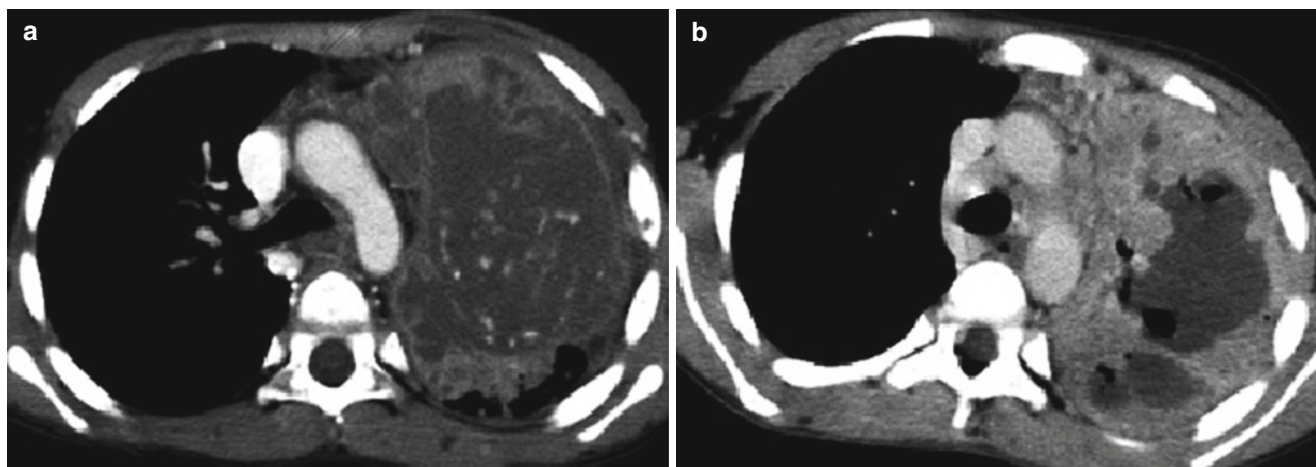


Fig. 13.19 Progression of Ghon focus. CT scan images from two different patients showing advanced progression of lung parenchymal disease from dense consolidation with ischemic changes (**a**) and cavitary necrosis with cyst formation (**b**)

13.5.20 Tuberculosis: Progression of Lymph Node Disease

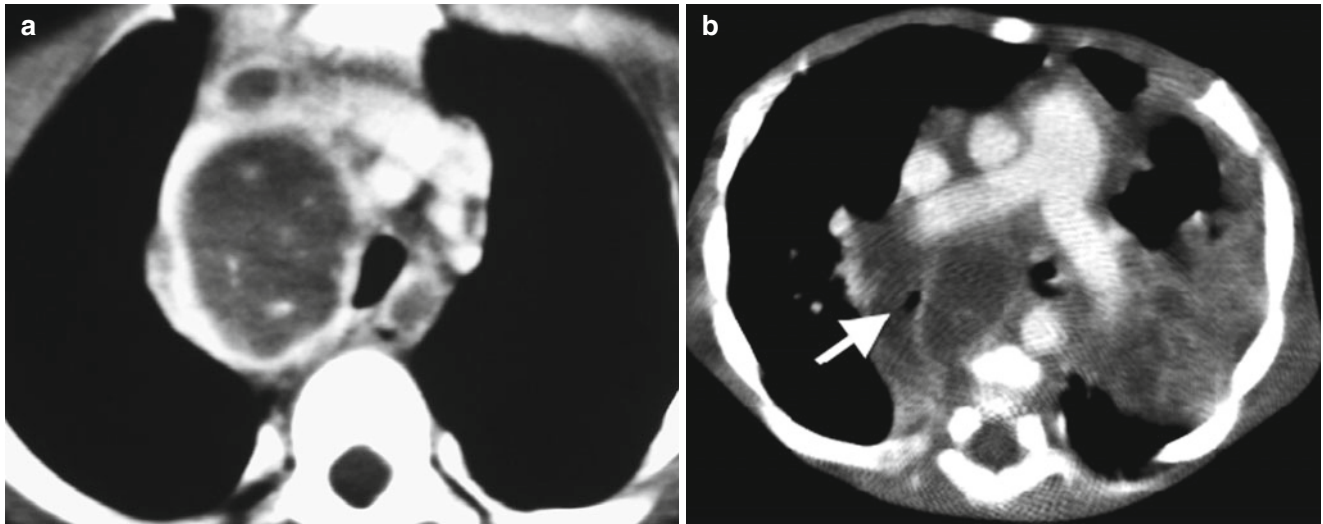


Fig. 13.20 Progression of lymph node disease. Image (a) demonstrates an enlarged right paratracheal lymph node effacing the trachea, with central hypoattenuation and peripheral contrast enhancement.

Image (b) shows extensive subcarinal lymph nodes effacing the bronchi, especially the right mainstem bronchus (*white arrow*)

13.5.21 Miliary TB

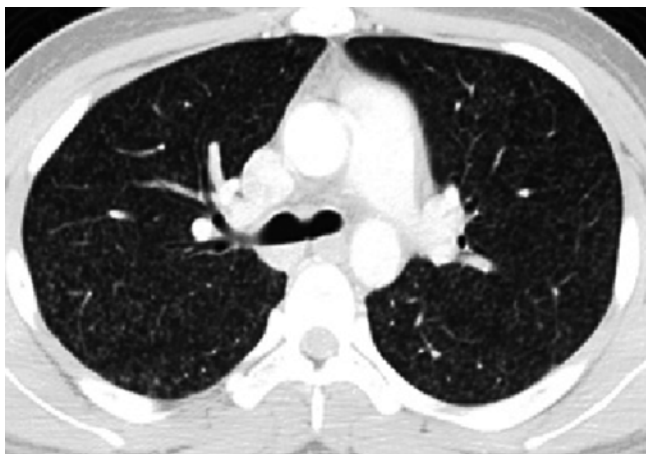


Fig. 13.21 Miliary TB. Axial CT image showing small (1–2 mm), uniform nodular densities scattered throughout both lungs compatible with disseminated TB disease

13.5.22 Reactivated TB

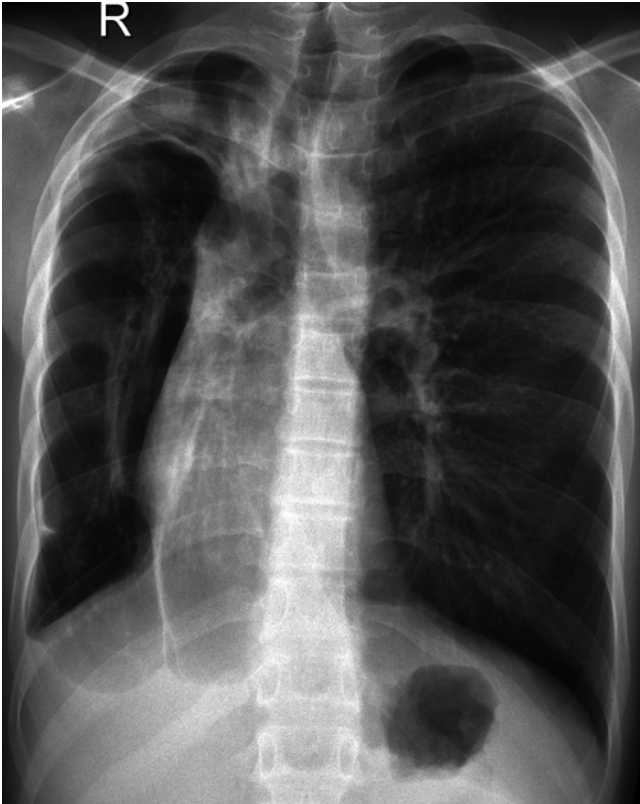


Fig. 13.22 Reactivation TB. Chest radiograph of a 13-year-old boy with chronic cough and shortness of breath showing fibrotic changes, pleural thickening, and volume loss in the right lung

13.5.23 Aspergilloma

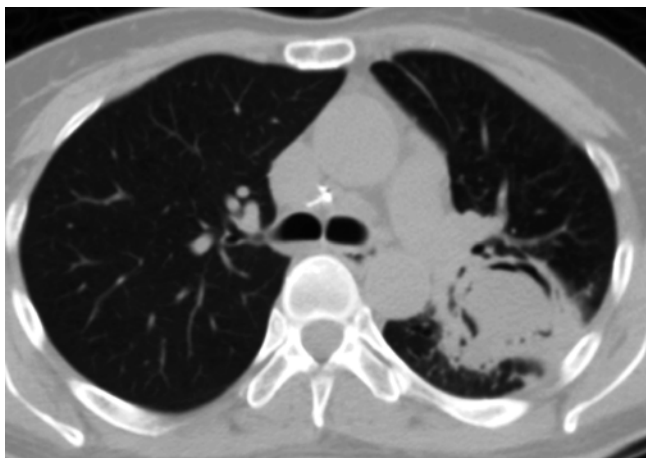


Fig. 13.23 Aspergilloma. Axial CT image of a 17-year-old girl with a soft tissue mass (aspergilloma) within a cavity in the left upper lobe, forming the “air-crescent sign”

13.5.24 Invasive Aspergillosis

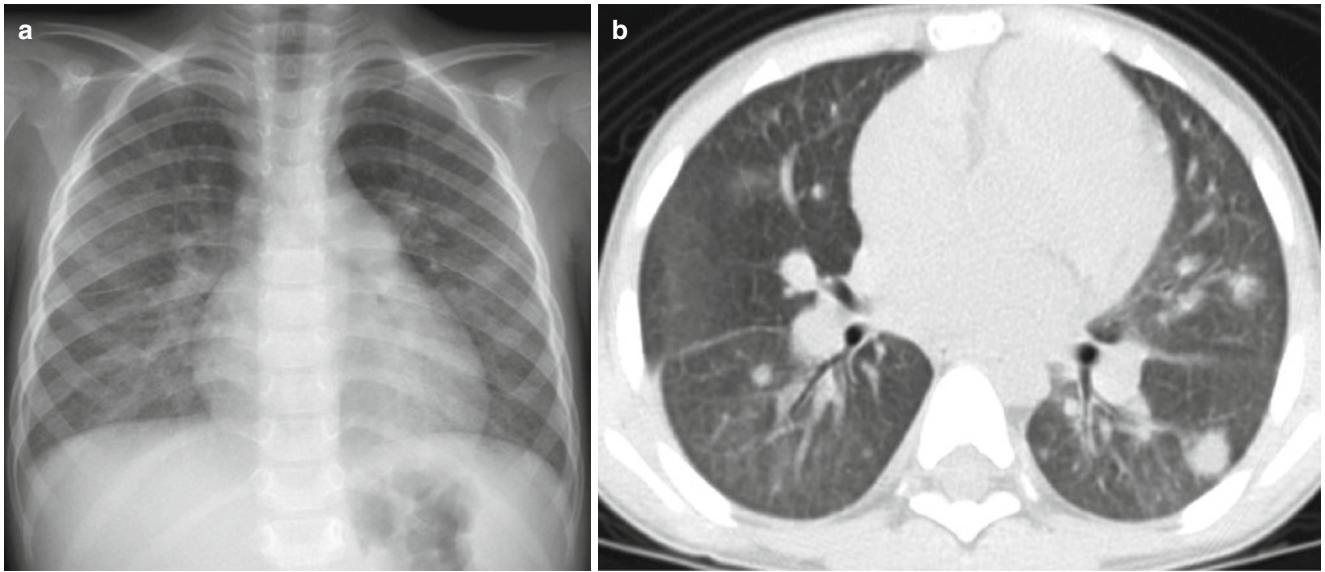


Fig. 13.24 A 5-year-old boy with confirmed invasive aspergillosis disease. Chest radiograph (a) is nonspecific but suspected nodules are seen on the left lung. Axial CT image (b) confirms the presence of non-calcified pulmonary modules in both lungs

13.5.25 Histoplasmosis

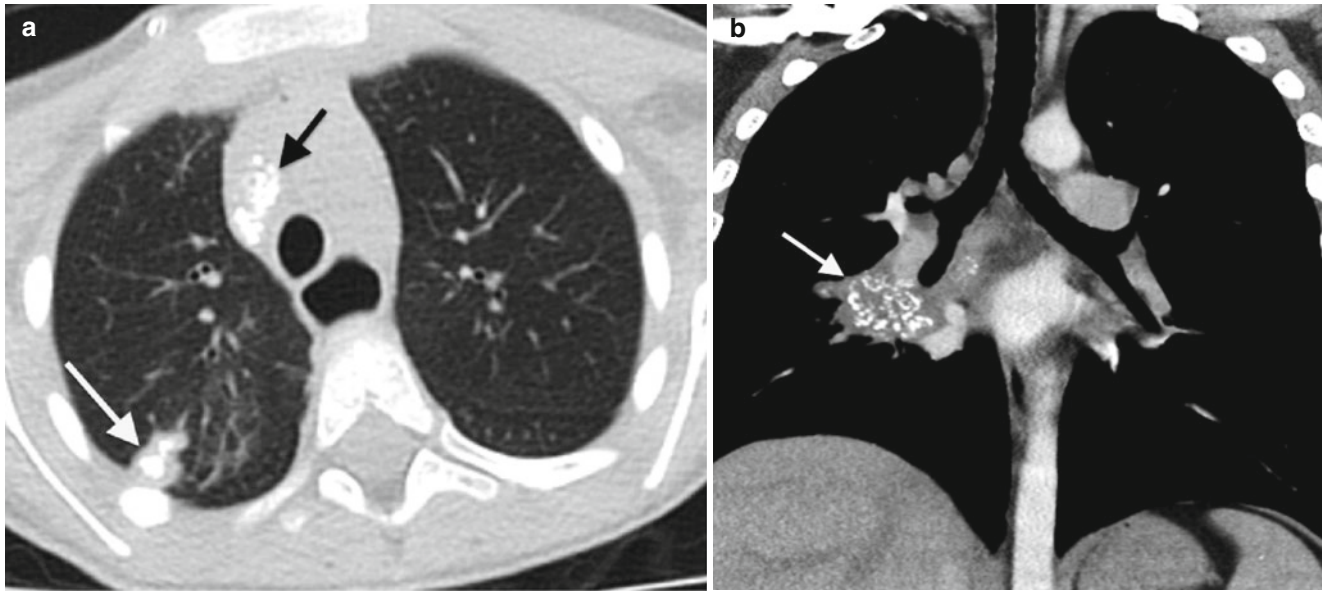


Fig. 13.25 Histoplasmosis in two different patients. Axial CT image of a 4-year-old boy (**a**) showing a calcified pulmonary nodule in the right upper lobe (*white arrow*) and calcified lymph nodes in the pretracheal region (*black arrow*). Coronal reconstructed CT image on a

7-year-old girl (**b**) shows a confluence of lymph nodes in the right infra-hilar region with calcifications (*white arrow*) (Cases courtesy of Beth Kline-Fath, MD, from Cincinnati, Ohio, USA)

13.5.26 Hydatid Disease

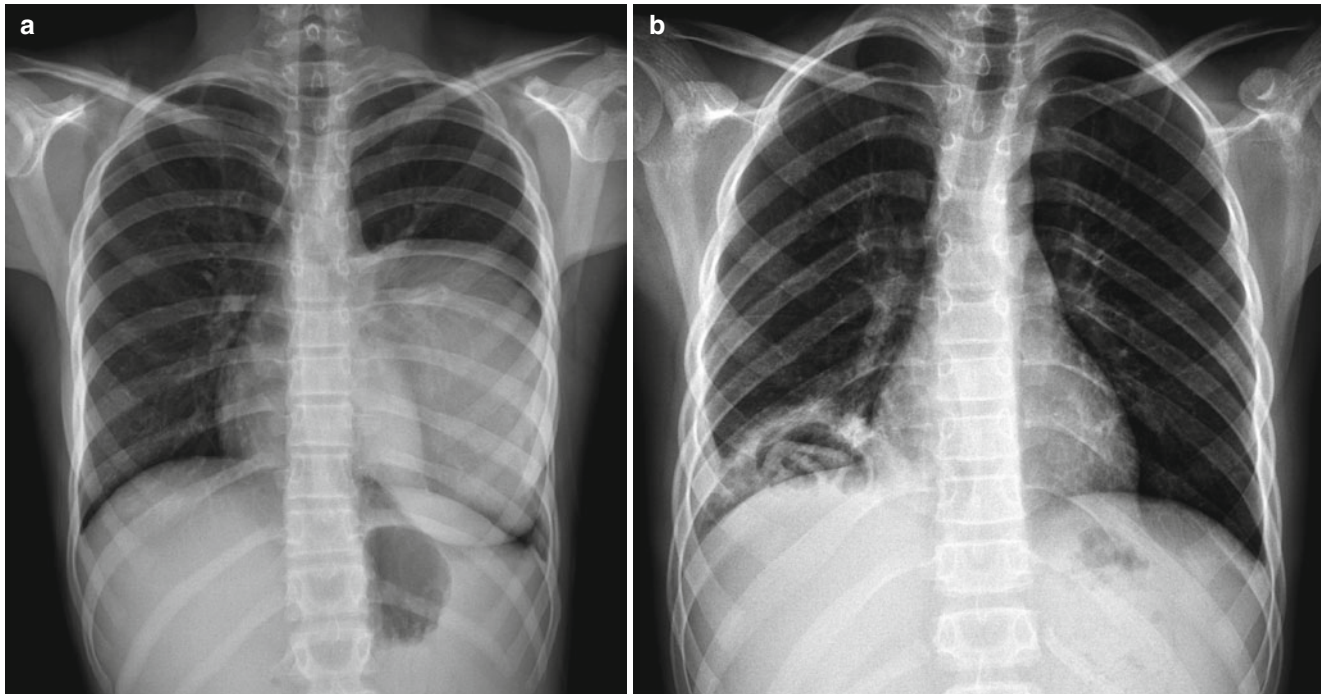


Fig. 13.26 Hydatid disease. **(a)** Radiograph of a 13-year-old girl who presented with cough and chest pain shows a mass-like opacity in the left lower lobe, later confirmed to be *Echinococcus* infection. **(b)** A 12-year-old boy with abdominal pain had a chest x-ray showing

curvilinear opacities within a cyst in the right lower lobe. This is compatible with the “water-lily” sign in hydatidosis (Cases courtesy of Ali Yikilmaz, MD, from Turkey)

13.5.27 Ascariasis

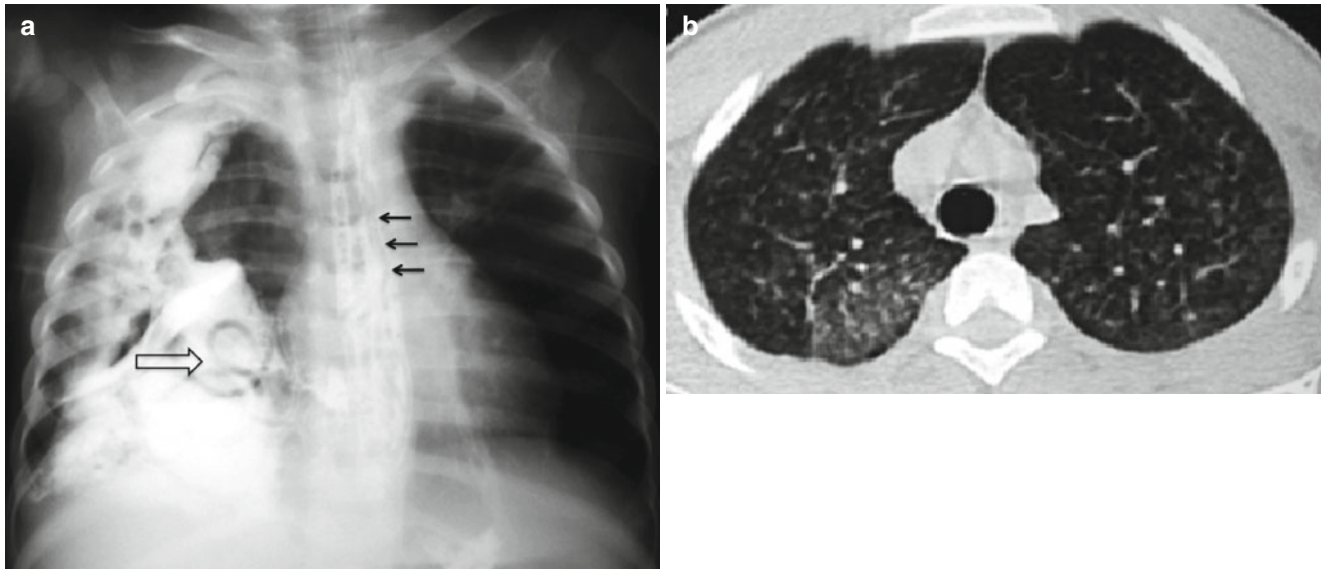


Fig. 13.27 Ascariasis. Chest radiograph following barium study (**a**) demonstrates *Ascaris* within the esophagus (*small black arrows*) as well as in the right pleural cavity (*open arrow*) indicative of esophageal

perforation. Image (**a**) is an axial CT scan image from a patient with fever, peripheral eosinophilia, and stool samples with *Ascaris* eggs (Cases courtesy of Edson Marchiori, MD, from Rio de Janeiro, Brazil)

13.5.28 Staphylococcal Abscess

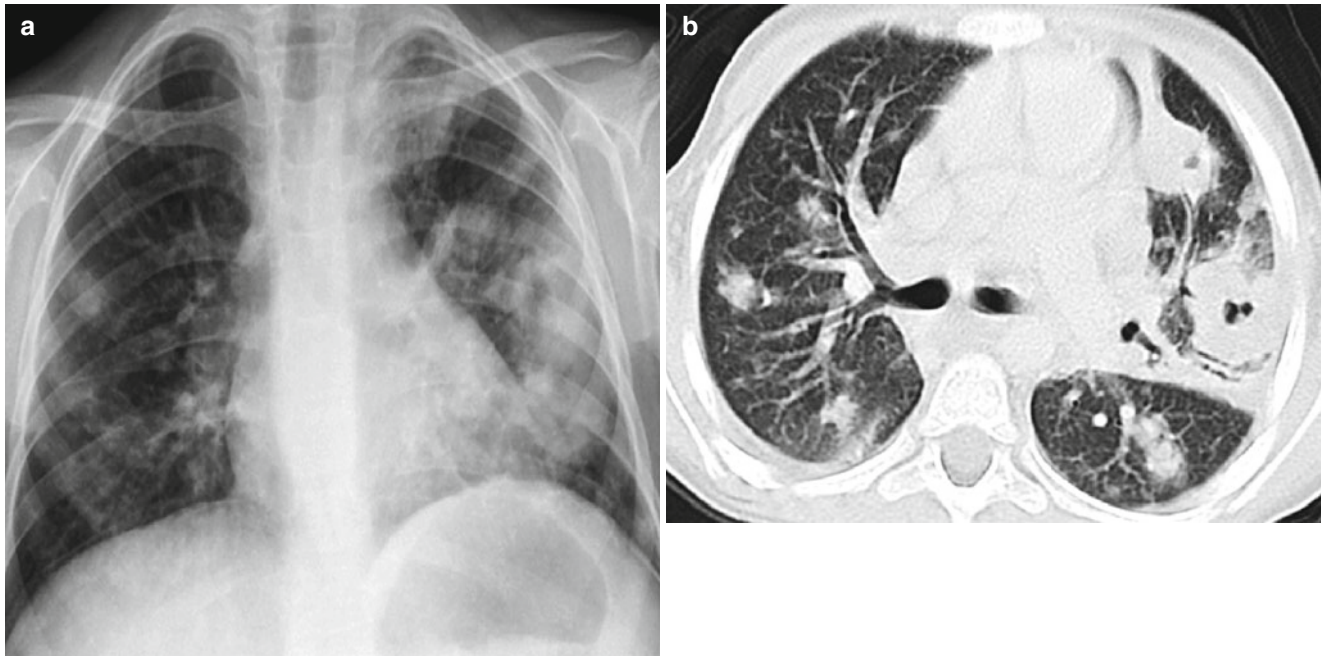


Fig. 13.28 Staphylococcal abscess. A 9-year-old boy with chronic granulomatous disease with persistent fever had a chest x-ray (a) showing multiple rounded opacities in both lung fields. Axial CT scan

(b) demonstrates multiple pulmonary nodules, some on the left has cavitation. These are proven to be multiple abscesses

13.5.29 Aspergillosis in the Immunocompromised

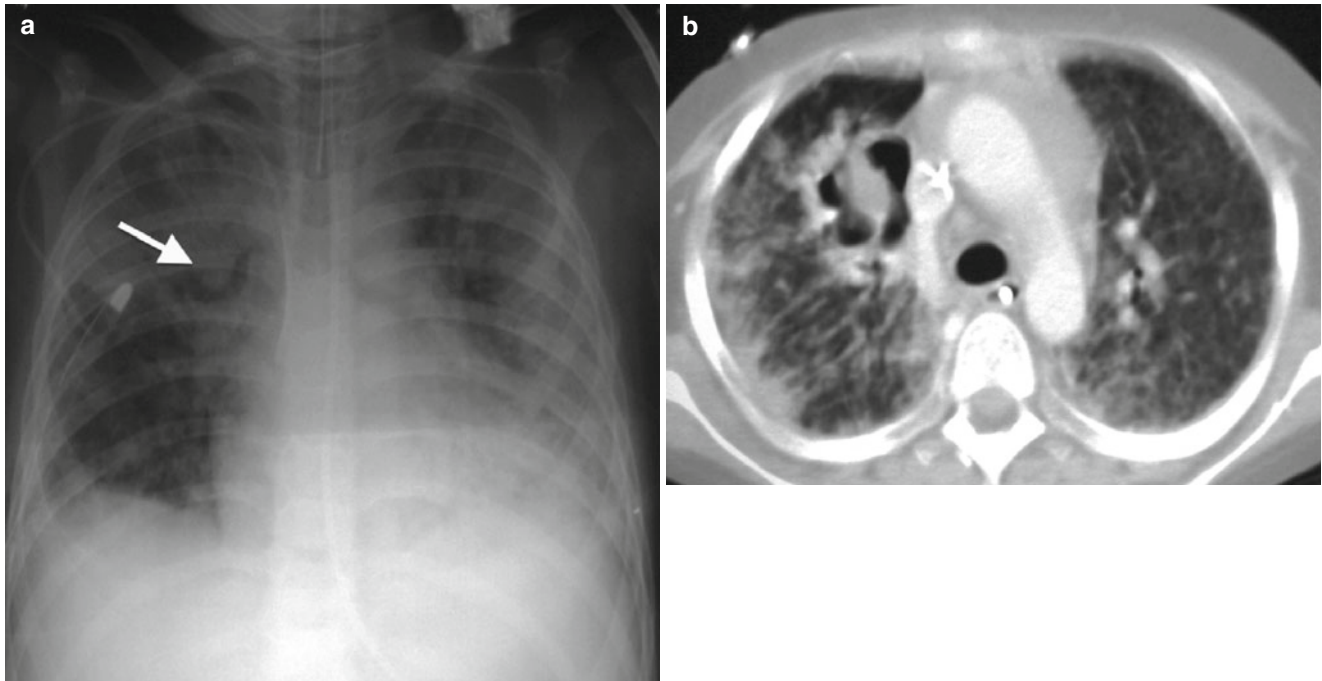


Fig. 13.29 Aspergillosis in the immunocompromised. Chest radiograph of a 3-year-old boy status post bone marrow transplant for leukemia (**a**) showing diffuse interstitial and alveolar disease with suspected

cavity in the right upper lobe (*arrow*). Axial CT image (**b**) confirms the “air-crescent sign” of aspergillosis and the diffuse interstitial/alveolar disease

13.5.30 *Pneumocystis jiroveci* Infection

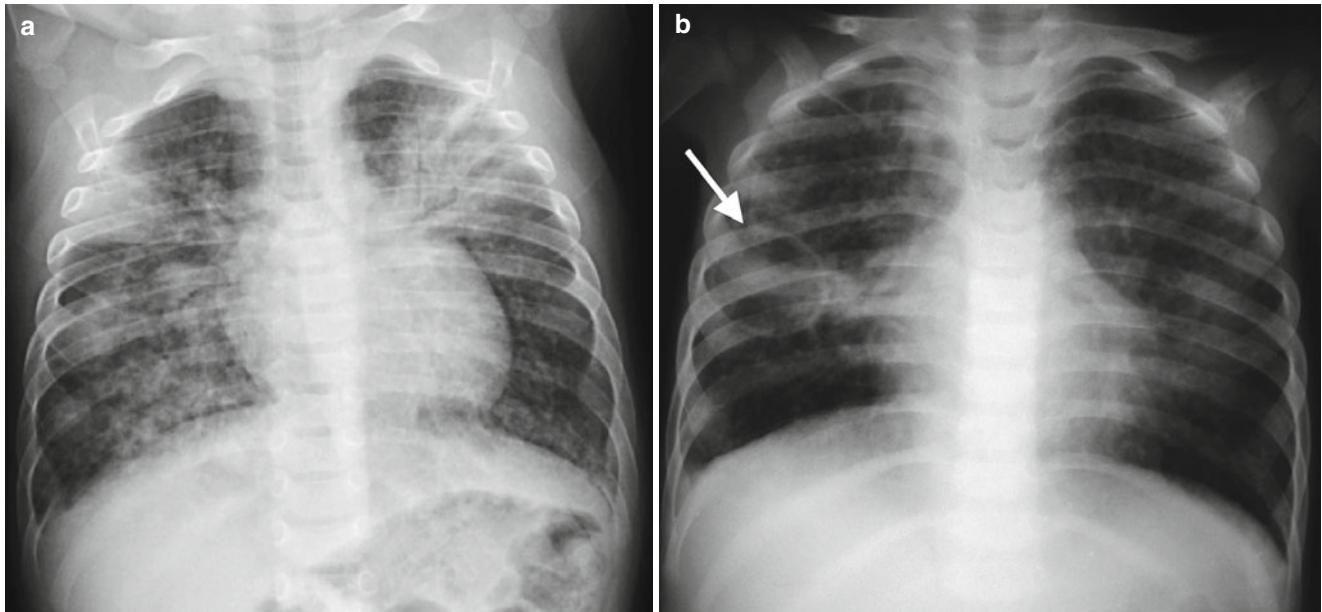


Fig. 13.30 *Pneumocystis jiroveci* infection. Radiograph of a 10-month-old boy diagnosed with severe combined immune deficiency syndrome showing diffuse reticulonodular interstitial pattern in both lungs with development of lung consolidations (**a**). Radiograph of a 14-month-old

girl with HIV infection showing diffuse, bilateral interstitial lung pattern extending from the hilum (**b**). There is a cyst noted on the peripheral right lung (*arrow*)

References

- Aherne W, Bird T, Court DS, et al. Pathological changes in virus infection of the lower respiratory tract in children. *J Clin Pathol.* 1970;23:7–18.
- Berk SL, Verghese A. Parasitic pneumonia. *Semin Respir Infect.* 1998;3(2):172–8.
- Blickman H (1998) Inflammatory lung disease, Chapter 2. In: *Pediatric radiology, the requisites*. 2ndedn. Mosby.
- Bramson RT, Griscom NT, Cleveland RH. Interpretation of chest radiographs in infants with cough and fever. *Radiology.* 2005;236:22–9.
- Collingsworth CL. Thoracic disorders in the immunocompromised. *Radiol Clin North Am.* 2005;43:435–47.
- Condon VR. Pneumonia in children. *J Thorac Imaging.* 1991;6:31–44.
- Czermak BV, Unsinn KM, Gotwald T, et al. *Echinococcus granulosus* revisited: radiologic patterns seen in pediatric and adult patients. *AJR Am J Roentgenol.* 2001;177:1051–6.
- Daltro P, Santos EN, Gasparetto TD, et al. Pulmonary infections. *Pediatr Radiol.* 2011;41 Suppl 1:S69–82. doi:[10.1007/s00247-0011-2012-8](https://doi.org/10.1007/s00247-0011-2012-8).
- Donnelly LF. Maximizing the usefulness of imaging in children with community-acquired pneumonia. *AJR Am J Roentgenol.* 1999;172:505–12.
- Donnelly LF. Practical issues concerning imaging of pulmonary infection in children. *J Thorac Imaging.* 2001;16:238–50.
- Donnelly LF, Klosterman LA. Pneumonia in children: decreased parenchymal contrast enhancement-CT sign of intense illness and impending cavitory necrosis. *Radiology.* 1997;205:817–20.
- Eslamy HK, Newman B. Pneumonia in normal and immunocompromised children: an overview and update. *Radiol Clin North Am.* 2011;49:895–920.
- Foster K, Alton H. Chronic lung infection in children. *Paediatr Respir Rev.* 2003;4:225–9.
- Hansell DM, Rubens MB, Padley SP, et al. Obliterative bronchiolitis: individual CT signs of small airways disease and functional correlation. *Radiology.* 1997;203:721–6.
- Hodina M, Hanquinet S, Snyder P, et al. Imaging of cavitory necrosis in complicated pneumonia. *Eur Radiol.* 2002;12(2):391–6. Epub 2001 Aug 28.
- Hoffer FA, Bloom DA, Colin AA, et al. Lung abscess versus necrotizing pneumonia: implications for interventional therapy. *Pediatr Radiol.* 1999;29:87–91.
- Houston S. Histoplasmosis and pulmonary involvement in the tropics. *Thorax.* 1994;49:598–601.
- Hsieh SC, Kuo YT, Chern MS, et al. Mycoplasma pneumonia: clinical and radiographic features. *Pediatr Int.* 2007;49(3):363–7.
- Jaffe A, Balfour-Lynn IM. Management of empyema in children. *Pediatr Pulmonol.* 2005;40:148–56.
- Jeanes AC, Owens CM. Chest imaging in the immunocompromised child. *Paediatr Respir Rev.* 2002;3:59–69.
- John SD, Ramanathan J, Swischuk LE. Spectrum of clinical and radiographic findings in pediatric mycoplasma pneumonia. *Radiographics.* 2001;21:121–31.
- Kim WS, Moon WK, Kim IO, et al. Pulmonary tuberculosis in children: evaluation with CT. *AJR.* 1997;168:1005–9.
- Kim JS, Ryu CW, Lee SI, et al. High resolution CT findings of varicella zoster pneumonia. *AJR Am J Roentgenol.* 1999;172:113–6.
- Kim OH, Kim WS, Kim MJ, et al. Ultrasound in the diagnosis of pediatric chest diseases. *Radiographics.* 2000;20:653–71.
- Kurt BA, Winterhalter KM, Connors RH, et al. Therapy of parapneumonic effusions in children: video-assisted thoracoscopic surgery versus conventional thoracostomy drainage. *Pediatrics.* 2006;118:547–53.
- Lee EY, McAdam A, Chaudry G, Fishman M, et al. Swine-origin influenza A (H1N1) viral infection in children: initial chest radiographic findings. *Radiology.* 2010;254(3):934–41. doi:[10.1148/radiol.09092083](https://doi.org/10.1148/radiol.09092083). Epub 2009 Dec 23.
- Marais BJ, Gie RP, Schaaf HS, Hesselink AC, et al. The natural history of childhood intrathoracic tuberculosis: a critical review of prechemotherapy literature. *Int J Tuberc Lung Dis.* 2004;8:392–402.
- Marks MJ, Haney PJ, McDermott MP, et al. Thoracic diseases in children with AIDS. *Radiographics.* 1996;16:1349–62.
- McAdams HP, Rosado-de-Christenson ML, Lesar M. Thoracic mycoses from endemic fungi: radiologic-pathologic correlation. *Radiographics.* 1995;15:255–70.
- Muller NL. Imaging of the pleura. *Radiology.* 1993;186:297–309.
- Ostapchuk M, Roberts DM, Haddy R, et al. Community acquired pneumonia in infants and children. *Am Fam Physician.* 2004;70(5):899–908.
- Paddock CD, Sanden GN, Cherry JD, et al. Pathology and pathogenesis of fatal bordetella pertussis infection in infants. *Clin Infect Dis.* 2008;47:328–38.
- Perez-Velez CM, Marais BJ. Tuberculosis in children. *N Engl J Med.* 2012;367:348–61. doi:[10.1056/NEJMr1008049](https://doi.org/10.1056/NEJMr1008049).
- Radkowski MA, Kranzler JK, Baem MO, et al. Chlamydia trachomatis in infants: radiography in 125 cases. *AJR Am J Roentgenol.* 1981;137(4):703–6.
- Reittner P, Muller NL, Heyneman L, et al. Mycoplasma pneumoniae pneumonia: radiographic and HRCT features in 28 patients. *AJR Am J Roentgenol.* 2000;174:37–41.
- Rose RE, Ward BH. Spherical pneumonias in children simulating pulmonary and mediastinal masses. *Radiology.* 1973;106:179–82.
- Sakai S, Shida Y, Takahashi N, et al. Pulmonary lesions associated with visceral larva migrans due to *Ascaris suum* and *Toxocara canis*: imaging of six cases. *AJR Am J Roentgenol.* 2006;186:1697–702.
- Santivanez S, Garcia HH. Pulmonary cystic echinococcosis. *Curr Opin Pulm Med.* 2010;16(3):257–61. doi:[10.1097/MCP.0b013e3283386282](https://doi.org/10.1097/MCP.0b013e3283386282).
- Sarinas PS, Chitkara RK. Ascariasis and hookworm. *Semin Respir Infect.* 1997;12(2):130–7.
- Swischuk LE, Hayden CK. Viral versus bacterial infections in children: is roentgenographic differentiation possible? *Pediatr Radiol.* 1986;16:278–84.
- Tanaka N, Matsumoto T, Kuramitsu T, et al. High resolution findings in community acquired pneumonia. *J Comput Assist Tomogr.* 1996;20:600–8.
- Thibodeau KP, Viera AJ. Atypical pathogens and challenges in community acquired pneumonia. *Am Fam Physician.* 2004;69(7):1699–706.
- Westra SJ, Choy G. What imaging should we perform for the diagnosis and management of pulmonary infections? *Pediatr Radiol.* 2009;39 Suppl 2:S178–83.
- Yalcin E, Dogru D, Haliloglu M, et al. Postinfectious bronchiolitis obliterans in children: clinical and radiological profile and prognostic factors. *Respiration.* 2003;70:371–5. doi:[10.1159/000072900](https://doi.org/10.1159/000072900).

Gye Yeon Lim

Contents

14.1	Introduction	474
14.2	Spectrum of Pediatric Thoracic Tumors	474
14.2.1	Lungs	474
14.2.2	Mediastinum	474
14.2.3	Chest Wall	476
14.3	Illustrations: Tumors of the Pediatric Chest	478
14.3.1	Tumors of the Lungs	478
14.3.2	Tumors of the Mediastinum	484
14.3.3	Tumors of the Chest Wall	502
	References	506

G.Y. Lim, M.D.
 Department of Radiology, The Catholic University of Korea,
 Yeouido St. Mary's Hospital,
 #62, Yeouido-dong Youngdungpo-gu, Seoul 150-010, Korea
 e-mail: shlgy@catholic.ac.kr

14.1 Introduction

Primary malignancies and benign lesions may originate in the lungs, mediastinum, and chest wall. Pulmonary tumors in children are rare; the most common lesions seen in clinical practice are metastatic disease (Meyer and Nicotra 1998). The majority of children who present with a primary or secondary pulmonary malignancy will present with nonspecific abnormalities such as cough with collapse or consolidation on the chest radiograph. The mediastinum is the most common site of chest masses in children. Mediastinal masses in pediatric patients occur in one of three mediastinal compartments (McCahon 2006; Meza et al. 1993). Chest wall tumors seen in children may arise from subcutaneous soft tissue, bony thorax, or the extrapleural region as well as in the bones of their chest wall (Franken et al. 1977). The chest wall can give rise to a wide variety of benign and malignant tumors that are primarily mesenchymal in origin. This chapter uses an anatomic approach to review the various tumors that involve the chest in children.

14.2 Spectrum of Pediatric Thoracic Tumors

14.2.1 Lungs

14.2.1.1 Inflammatory Myofibroblastic Tumor

Although primary lung tumors are relatively rare in children, the most common benign pulmonary tumor is the inflammatory myofibroblastic tumor. Inflammatory myofibroblastic tumor (also known as plasma cell granuloma, inflammatory pseudotumor, plasma cell pseudotumor, and fibrous histiocytoma) is a benign mesenchymal neoplasm characterized by plasma cells, histiocytes, and lymphocytes that rarely involves the airway in children (Kim et al. 2005). It tends to be slowly growing and locally invasive and has been thought to represent a postinflammatory reparative response to prior infections or trauma. However, there is seldom a history of trauma or of preceding infection at the site of involvement of this lesion (McCahon 2006; Kim et al. 2005). There is often a history of fever, cough, and malaise, although some patients are asymptomatic when diagnosed. This presents as a solitary, sharply margined, peripheral mass that abuts the pleura. Calcification seems to be more often a feature of inflammatory myofibroblastic tumor in young patients than in adults (Fig. 14.1). A small, non-calcified, endobronchial mass that can mimic an endobronchial adenoma is another manifestation (McHugh 2008) (Fig. 14.2). The least common appearance is that of a large, speculated mass that may show features of necrosis or cavitation. Varied enhancement of the mass is seen on CT.

14.2.1.2 Pleuropulmonary Blastoma (PPB)

PPB is a rare lung tumor occurring in children. It is recognized as being distinct from pulmonary blastoma, which is a focal lung tumor seen predominantly in adult. PPB is now considered as a true embryonic neoplasm that arises from the thoracopulmonary mesenchyme. PPB can arise in congenital cystic lung lesions. PPB is classified as follows on histological grounds: predominantly cystic (type I), cystic and solid (type II), and purely solid (type III). There is an increased tendency for malignancy from type I to type III. Type I lesions occur in infants, with types II and III being seen in slightly older children (McHugh 2008). Type I lesions are confined to the lung parenchyma or visceral pleura. Involvement of the parietal pleura, mediastinum, or diaphragm suggesting invasive overgrowth or sarcomatous elements justify a type II or III PPB (McHugh 2008). These tumors may be intrapulmonary, mediastinal, or pleural based. Small peripheral nodules are rare in children who more often have opacification of the hemithorax with a large mass and associated effusion. Ultrasonography (US) can help to distinguish the complex mass of a PPB from that of a pleural effusion. CT shows a large, predominantly low-attenuation mass with whorls of high-attenuation soft tissue (Fig. 14.3). PPB manifests as mixed cystic and solid masses in the lung periphery often adjacent to the pleura in the lower zones (Fig. 14.4). When a large, pleural-based mass is identified in a young child, PPB should be considered (Naffaa and Donnelly 2005).

14.2.1.3 Metastatic Pulmonary Tumors

Metastatic disease is the most common pulmonary malignancy in children. Among the pulmonary metastases seen in children, those from Wilms tumor (Fig. 14.5) are most common, followed by osteosarcoma (Meyer and Nicotra 1998). Other malignancies that metastasize to the lung include Ewing sarcoma, rhabdomyosarcoma, lymphoma/leukemia, hepatoblastoma, and germ cell tumors (McCahon 2006). Lesions are spread hematogenously and so are most commonly at the periphery of the lung, with greater numbers in the lower lung. Pulmonary metastases usually appear as single or multiple, round, well-defined nodules. Metastases from osteosarcoma may calcify or ossify (Fig. 14.6). Osteosarcoma and Wilms tumor metastases may rarely cavitate and when peripheral can lead to pneumothorax. Lymphangitic spread manifests as a reticular or reticulonodular pattern and occurs in lymphoma/leukemia.

14.2.2 Mediastinum

Mediastinal masses in pediatric patients occur in one of three mediastinal compartments. Chest radiography remains the initial imaging study. CT is the primary cross-sectional imaging modality used for better definition of both the

tumor location and its relationship to vital structures (Wyttenbach et al. 1998). MRI is the preferred examination for evaluating possible intraspinal extension of a posterior mediastinal mass or of suspected vascular lesions (Daldrup et al. 1998).

14.2.2.1 Anterior Mediastinum

The anterior mediastinum is the most common site of mediastinal tumors in children. Most of these tumors arise from the thymus and prevascular lymph nodes. Lymphoma, germ cell tumor, thymoma, and lymphatic malformation account for all anterior mediastinal masses (Whitten et al. 2007).

14.2.2.1.1 Lymphoma

Lymphoma is the most common anterior mediastinal mass seen in children.

Overall, non-Hodgkin's lymphoma occurs throughout childhood and is more common than Hodgkin's disease (HD) in children. HD is usually nodal, and the disease spreads in direct continuity from one nodal mass to the next (Fig. 14.7). About 85 % of patients with HD have a mediastinal mass seen at the time of their initial presentation, (Fig. 14.8) and 30 % have hilar adenopathy, which is frequently associated with direct pulmonary invasion (Williams and Alton 2003). In addition to enlarged lymph nodes or nodal conglomeration, HD may manifest as multiple pulmonary nodules and multifocal consolidations (Fig. 14.9). In contrast, non-Hodgkin's lymphoma is usually extranodal and spreads hematogenously; 50 % of these children have a mediastinal mass seen at the time of their initial presentation, and pulmonary disease may occur without adjacent adenopathy. In both types of lymphoma, pleural effusion may reflect lymphatic or venous compromise and does not necessarily indicate tumor involvement. The initial chest radiograph shows an anterior mediastinal mass with obliteration of the retrosternal clear space or mediastinal widening. The bulky anterior mediastinal mass may extend into the middle and posterior mediastinal compartments. Contrast-enhanced CT can define the extent of the disease. Lymphoma infiltrates the thymus, causing its enlargement and lobular lateral borders (Fig. 14.10). The involved thymus is frequently homogenous. Thymic involvement is almost always accompanied by involvement of mediastinal lymph nodes. Larger nodal conglomerates often become heterogeneous, with hypodense and cystic areas suggestive of necrosis (Fig. 14.11). The nodes rarely calcify before treatment, and approximately 5 % calcify after therapy. CT accurately delineates lung parenchymal involvement, pleural effusions, chest wall disease (Fig. 14.8), and complications caused by impingement on vital structures, most commonly the airway (Fig. 14.12). Rebound enlargement of the thymus often occurs following treatment. When this

occurs, the thymus is usually homogeneously enlarged without associated lymphadenopathy. Positron emission tomography (PET) is often performed in addition to CT, both at the time of the initial staging and in order to follow the treatment response (Fig. 14.9). The lymphoblastic non-Hodgkin's lymphoma is indistinguishable histologically from the lymphoblasts of acute lymphoblastic leukemia (ALL). Clinical criteria and the extent of bone marrow involvement are used for distinction between these lesions.

14.2.2.1.2 Germ Cell Tumors

Thoracic primary germ cell tumors originate from primitive germ cells that have ceased their embryologic migration in the mediastinum. The majority of these may arise in the anterior mediastinum, within or adjacent to the thymus. This group of tumors includes teratoma and malignant tumors such as seminomas, embryonal carcinomas, teratocarcinoma, and endodermal sinus (yolk sac) tumors. Most anterior mediastinal germ cell tumors are benign. On chest radiographs, most germ cell tumors usually present as a fairly large anterior mediastinal mass. The hallmarks of both benign and malignant germ cell tumors are their moderate to large size and the presence of calcification, fat, and cystic (necrotic) changes (Figs. 14.13 and 14.14). CT or MR can define the internal characteristics of the mass, depending on the tissue types present and their degree of differentiation. The presence of solid tissue within a lesion is more commonly seen in immature malignant teratomas than in mature benign tumors (Fig. 14.14). Determination of malignancy in germ cell tumors is based on their local invasion of adjacent mediastinal structures, which can be suggested on CT or MRI (Merten 1992). However, the benign or malignant nature of these tumors cannot be determined with certainty based on the imaging findings. Tumor rupture into adjacent structures such as the pleural space, pericardium, lung parenchyma, or tracheobronchial trees has been reported in some benign teratomas.

14.2.2.1.3 Thymoma

Although thymoma accounts for approximately 10 % of the anterior mediastinal masses seen in adults, it is rarely seen in children. Thymomas detected during childhood can also be associated with autoimmune disease (Merten 1992). Thymomas are classified as noninvasive or invasive thymoma. Noninvasive thymomas tend to have well-defined margins. In contrast, an invasive thymoma does extend beyond its fibrous capsule and tends to spread locally and to involve adjacent mediastinal structures and the chest wall. CT shows a lobulated, enhancing, anterior mediastinal mass, which may have thin, capsular calcification (Fig. 14.15). Cystic regions and necrosis are seen in about 30 % of these cases, particularly in larger tumors. Signs of invasion include irregular borders of mass obliteration of the mediastinal fat

planes surrounding the mediastinal vascular structures, pericardial thickening, and extension to the chest wall, pleura, or the diaphragm.

14.2.2.2 Middle Mediastinum

The middle mediastinum, also known as the vascular space, is bordered by the anterior and posterior mediastinum.

Lymph node masses account for most of the middle mediastinal masses, lymphoma being the most common (Fig. 14.16). Lymphomatous involvement of the middle mediastinum is rarely isolated and is usually accompanied by a dominant anterior mediastinal component (Fig. 14.17). Metastatic adenopathy is less common and often results from neuroblastoma, Wilms tumor, or various sarcomas, e.g., Ewing sarcoma and osteosarcoma.

14.2.2.3 Posterior Mediastinum

Neurogenic tumors are the most common cause of a posterior mediastinal mass seen in children. Neurogenic structures in the posterior mediastinum are the spinal nerves exiting through each intervertebral foramen and the thoracic sympathetic trunk. MRI is the imaging modality of choice for evaluating a posterior mediastinal mass because of the ability of MRI to accurately document it due to the presence of spinal disease (Ranganath et al. 2012).

14.2.2.3.1 Sympathetic Ganglion Tumors

About 90 % of the posterior mediastinal masses seen in children are of neurogenic origin and arise from the paravertebral sympathetic chains along the thoracic vertebral bodies. These tumors consist of three histopathologic spectrums, from malignant neuroblastoma to benign ganglioneuroma.

Neuroblastoma is the most immature and malignant form of these tumors, usually presenting in patients before the age of 5 years. The clinical presentation varies from that which is clinically silent to that which has signs of cord compression secondary to spinal canal invasion by the tumor. More specific symptoms include opsoclonus-myoclonus syndrome (ataxia with involuntary muscle and eye movements) and Horner's syndrome (ptosis, myosis, and anhydrosis) related to thoracic apical or cervical masses. Thoracic neuroblastoma is typically a less advanced malignancy than primary abdominal neuroblastoma and is associated with a better outcome. Chest radiograph findings of sympathetic ganglion tumors include a paravertebral, soft tissue mass usually vertically elongated with tapered, superior, and inferior, paravertebral margins. Calcification can be seen in 30 % of these tumors and it is sometimes associated with posterior rib or vertebral erosion or the destruction or widening of intercostal spaces (Figs. 14.18, 14.19 and 14.20). Bone metastases from neuroblastoma are also common and usually appear as lytic and permeative. Neuroblastoma tends to surround and encase blood vessels and to spread through

the neural foramina into the spinal canal. Although CT can better detect calcification and bony involvement, MR is superior for determining intraspinal extension and bone marrow involvement (Merten 1992; Ranganath et al. 2012) (Figs. 14.20 and 14.21). *Ganglioneuroblastoma* is a more mature form although it still retains a malignant character (Fig. 14.22).

Ganglioneuroma is well differentiated and benign, typically presenting in children after 10 years of age. Ganglioneuroblastoma and ganglioneuroma are difficult to differentiate from neuroblastoma because of the similar imaging characteristics seen on all imaging modalities, although they may have a more fusiform configuration than neuroblastoma. Patient age is also a diagnostic clue, although histopathologic analysis is required for a definitive diagnosis.

14.2.2.3.2 Nerve Sheath Tumors

Neurofibromas and schwannomas (neurilemmomas) are benign tumors of nerve sheath origin. In pediatric patients, these tumors most commonly arise from a preexisting plexiform neurofibroma, as seen in patients with neurofibromatosis type I. These tumors usually show decreased attenuation because of their lipid contents or cystic degeneration and have variable enhancement (Fig. 14.23).

14.2.2.4 All Compartments

14.2.2.4.1 Lymphangioma

A lymphangioma is a lymph-containing cystic or multicystic structure lined by endothelium and classified as a type of vascular malformation. This type of malformation may occur in the anterior, middle, or posterior mediastinum, in decreasing order of frequency (Ranganath et al. 2012). On US, a macrocystic lesion appears as a multiloculated or septated cystic mass, sometimes with fluid-fluid levels. US may be helpful for documenting the cystic nature of a lymphangioma but is not adequate for documenting the complete anatomic extent of mediastinal disease. These malformations show fluid-filled spaces and enhancing walls and septations on CT and MR. The presence of proteinaceous fluid or hemorrhage within these cysts can cause variable complex fluid collections (Figs. 14.24 and 14.25).

Patients with generalized lymphangiomatosis and a chylothorax associated with osteolytic lesions have a poor prognosis. Concomitant cystic lesions in the spleen are also commonly seen in this unusual patient group.

14.2.3 Chest Wall

The chest wall can give rise to a wide variety of benign and malignant tumors that are primarily mesenchymal in origin. Masses that produce rib changes are likely to be extrapleural

in location. Radiograph allows an appreciation of the location of the lesion, its extension, rib destruction, and associated intrathoracic components. Further imaging with both CT and MRI may be required in large or aggressive-looking lesions for staging. CT is better suited than MR to show metastases to the lung. Most large intrathoracic tumors that arise from the chest wall are primary and malignant. The most prevalent malignant tumors of the chest wall belong to the Ewing sarcoma, Askin tumor/peripheral primitive neuroectodermal tumor (PNET), and rhabdomyosarcoma (Ablyn et al. 1995).

14.2.3.1 Ewing Sarcoma/Peripheral Primitive Neuroectodermal Tumor (PNET)

Chest wall Ewing sarcoma and PNET, also known as Askin tumors, albeit separated histological entities, are recognized as biologically related lesions (Winer-Muram et al. 1993). These malignant tumors, seen predominantly in children and young adults, originate in the soft tissue of the chest wall, occasionally in bone, and rarely in the lung periphery. All of these tumors of the “malignant, small, round-cell type” generally manifest as peripheral chest wall masses with or without associated rib destruction, and they cannot be distinguished based on the imaging criteria alone. Ewing/PNETs are often located posteriorly in the chest and may mimic a neuroblastoma. PNET shows heterogeneous attenuation because of the hemorrhage and/or necrosis in the mass. MRI is probably superior in assessing tumor extent and local invasion. CT and MRI are complementary studies in that CT is helpful for assessing adjacent rib changes and for evaluating the lung

parenchyma for the presence of small, metastatic nodules (Winer-Muram et al. 1993) (Figs. 14.26 and 14.27).

14.2.3.2 Rhabdomyosarcoma

Rhabdomyosarcoma can arise from virtually any compartment in the chest including the lung and chest wall. The thorax is regarded as an unfavorable primary site for rhabdomyosarcoma with a tendency toward more alveolar histology, advanced disease at presentation, and tumors occurring in older children (Ablyn et al. 1995). Tumors most commonly present as large or rapidly enlarging solid masses. Irregular contrast enhancement with variable areas of low attenuation is a typical CT feature. Calcification within the mass is not a feature but destruction of adjacent ribs is occasionally seen (Fig. 14.28).

14.2.3.3 Mesenchymal Hamartoma

Mesenchymal hamartoma of the chest wall is a rare, benign, nonneoplastic lesion seen in infants and is usually present from birth. These lesions always arise in the ribs and are characterized by focal overgrowth of normal chondral and primitive mesenchymal (skeletal) elements with aneurysmal bone cyst elements. Plain radiographs show a partially calcified, extrapleural mass in the chest wall with involvement of one or more ribs. The rib deformity consists of partial or complete destruction, erosion, and enlargement. Pathognomonic features seen on CT and MR consist of a mineralized matrix and a hemorrhagic cystic component (Gwyther and Hall 1991) (Fig. 14.29). The mass may decrease in size without treatment and the patient prognosis is excellent.

14.3 Illustrations: Tumors of the Pediatric Chest

14.3.1 Tumors of the Lungs

14.3.1.1 Inflammatory Myofibroblastic Tumor

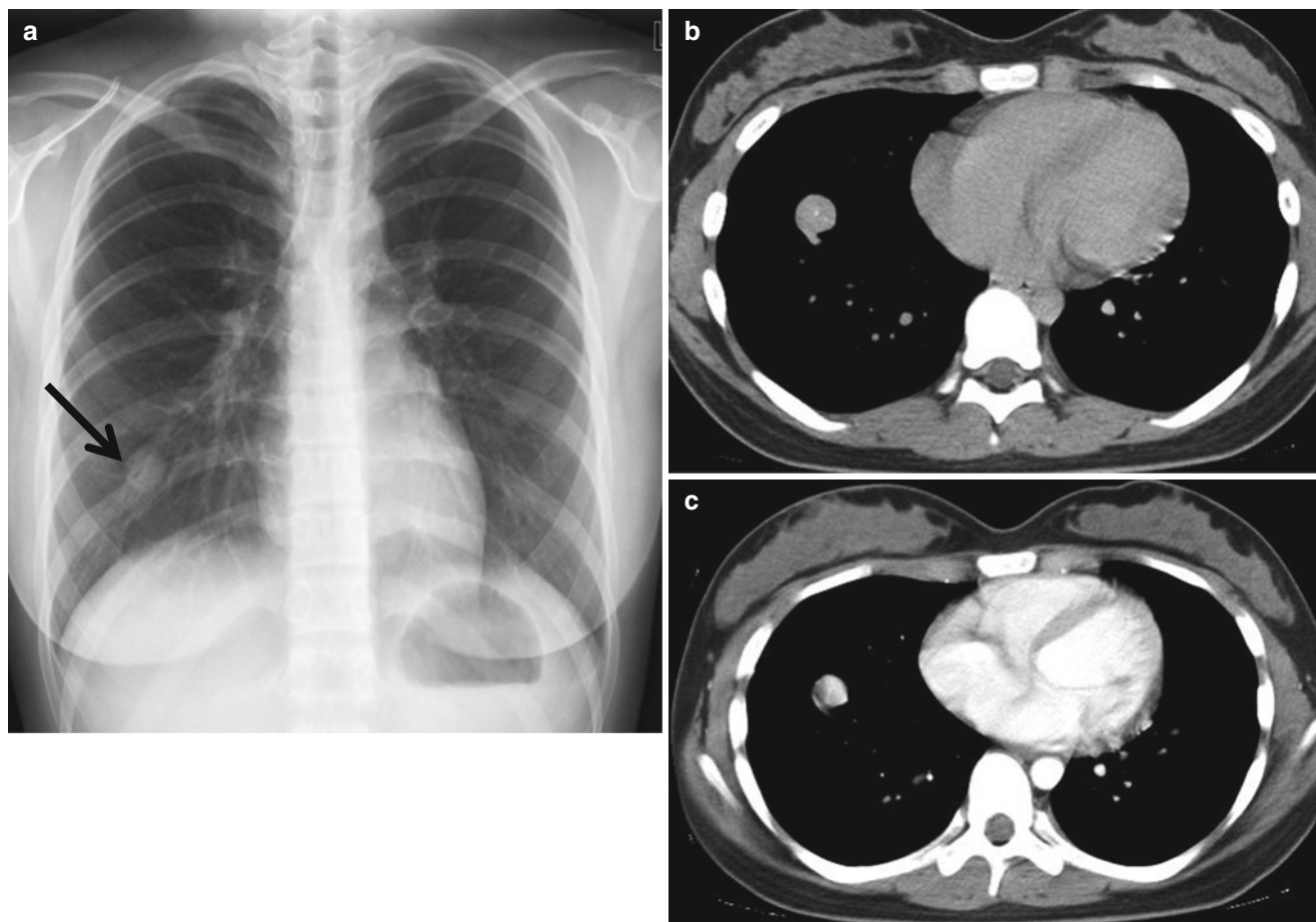


Fig. 14.1 Intraparenchymal inflammatory myofibroblastic tumor in a 16-year-old girl. (a) Plain radiograph shows a rounded, well-circumscribed opacity in the right lower lung (*arrow*). (b, c)

Nonenhanced (b) and contrast-enhanced (c) CT show a well-defined round, lung nodule containing area of calcification as well as homogeneous attenuation of enhancement

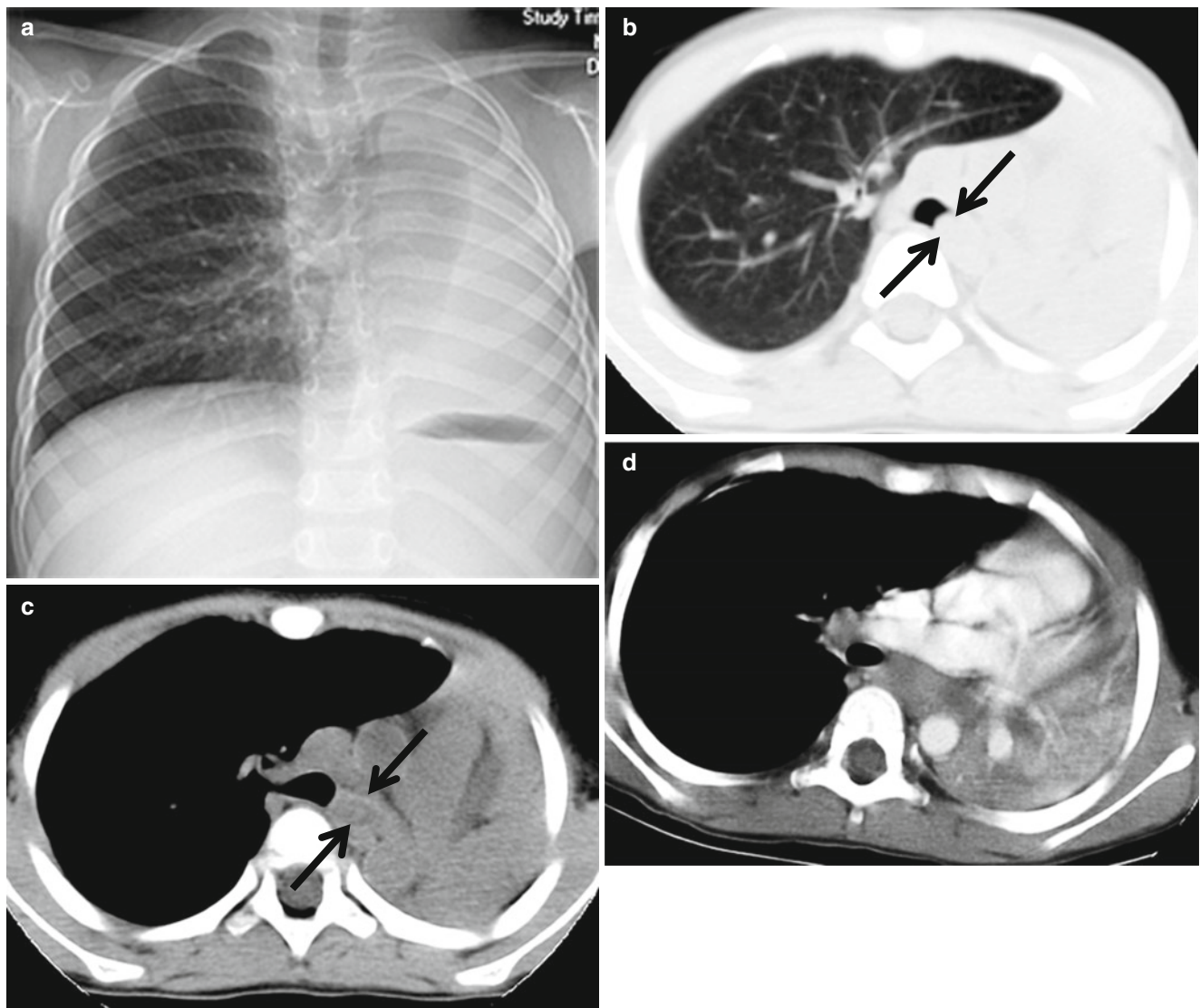
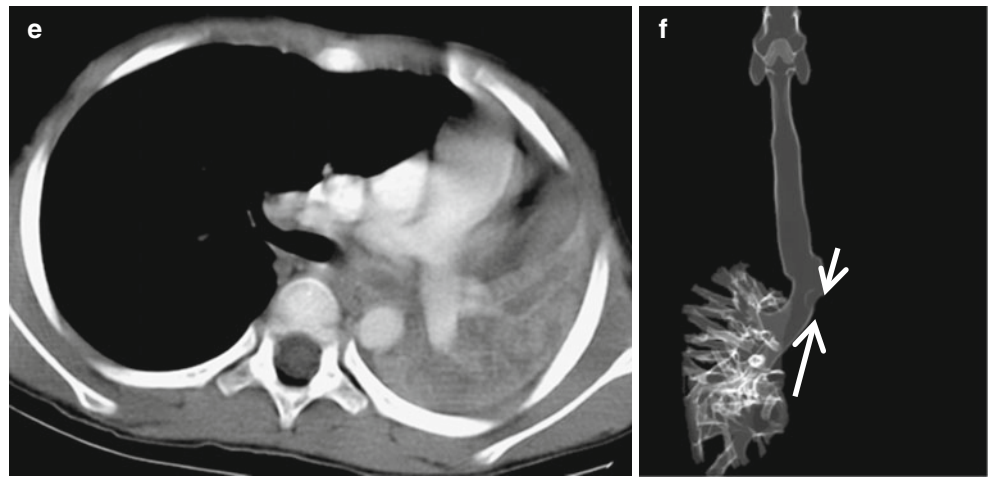


Fig. 14.2 Endobronchial inflammatory myofibroblastic tumor in a 4-year-old boy with cough and fever (Case courtesy of Hye-Kyung Yoon, MD). (a) Plain radiograph shows total opacity of the left lung with mediastinal shifting, suggesting atelectasis of the left lung. (b–e) Nonenhanced CT with lung (b) and mediastinal window (c) and

contrast-enhanced CT (d, e) show an endobronchial mass (arrows) occluding the left main bronchus with associated left lung collapse consolidation. (f) 3D volume-rendered image shows abrupt cutoff of the left main bronchus (arrows) and non-visualization of aerated left lung

Fig. 14.2 (continued)

14.3.1.2 Pleuropulmonary Blastoma

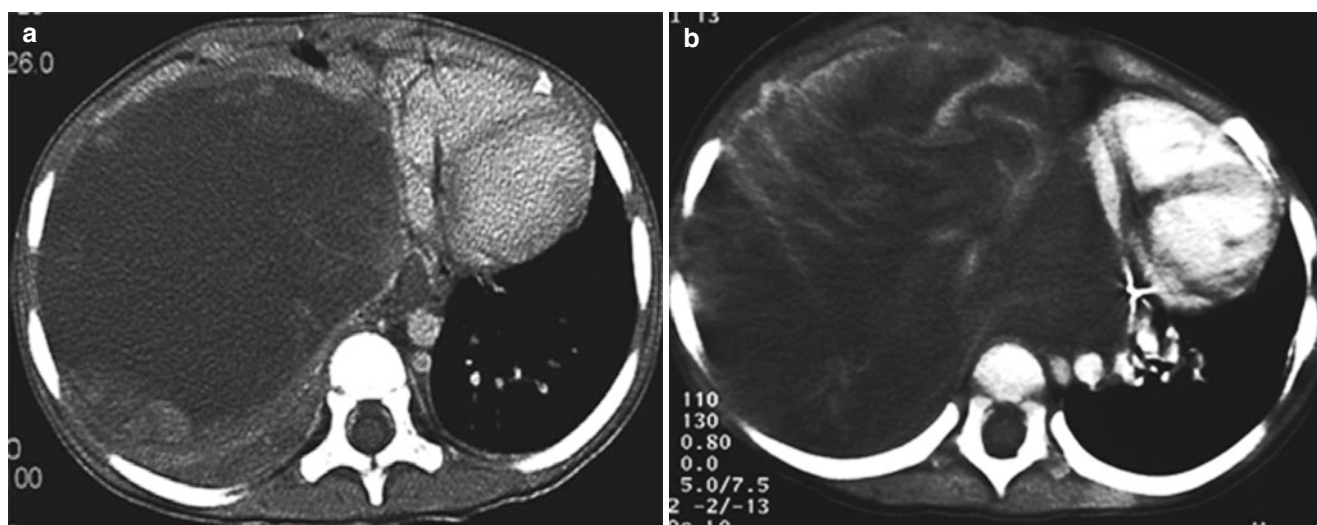


Fig. 14.3 Pleuropulmonary blastoma in a 2-year-old girl. (**a**, **b**) Nonenhanced (**a**) and contrast-enhanced (**b**) CT show a large, predominantly low-attenuation mass with whorls of high-attenuation soft tissue filling the right thorax and displacing the mediastinal contents

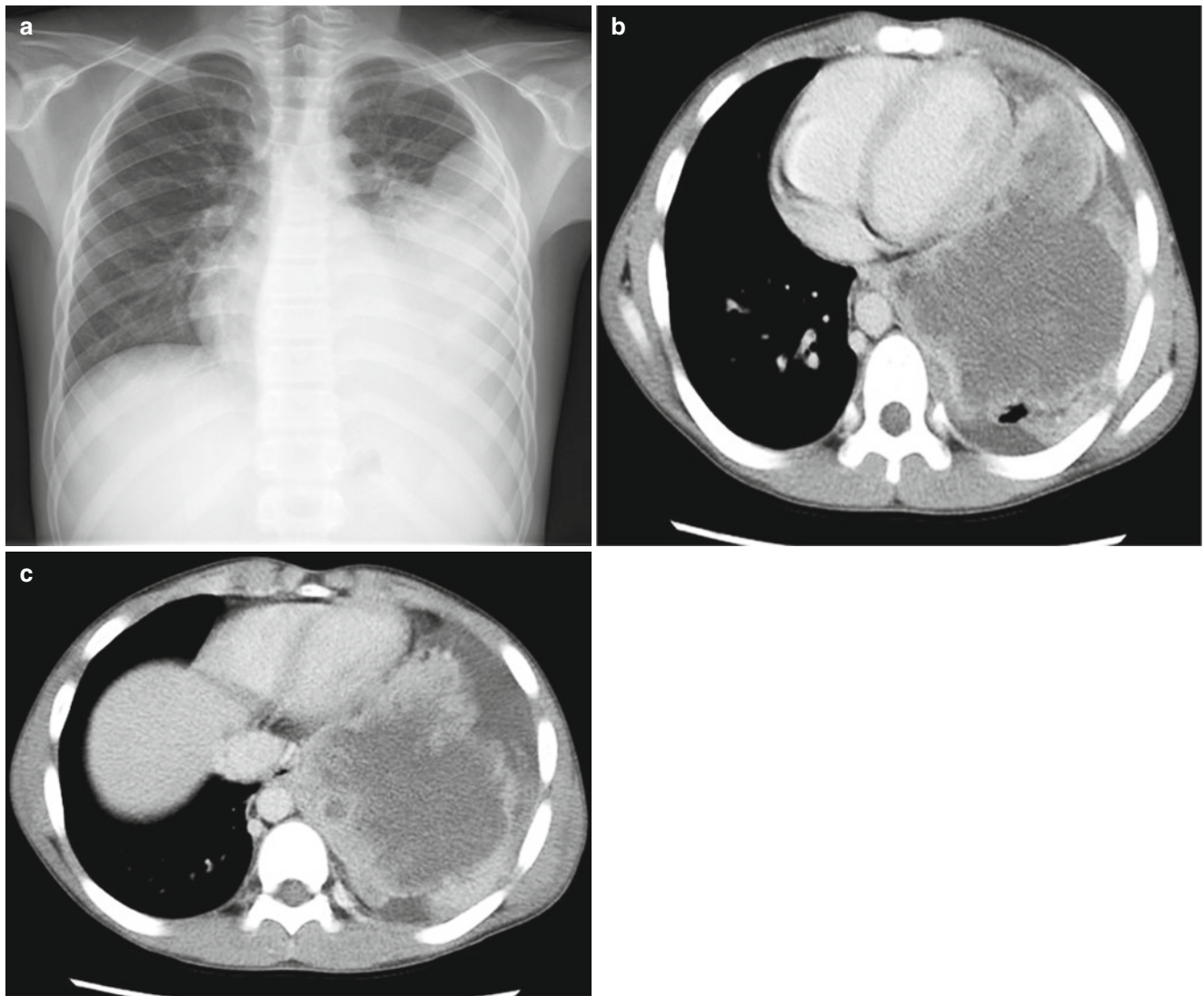


Fig. 14.4 Pleuropulmonary blastoma in a 14-year-old boy. (a) Plain radiograph shows a large opacity in the left hemithorax. (b, c) Contrast-enhanced CT shows mixed cystic and solid masses in the lung

periphery adjacent to the pleura in the mid and lower zones. The solid components of the mass lesion and internal septa show enhancement

14.3.1.3 Pulmonary Metastasis

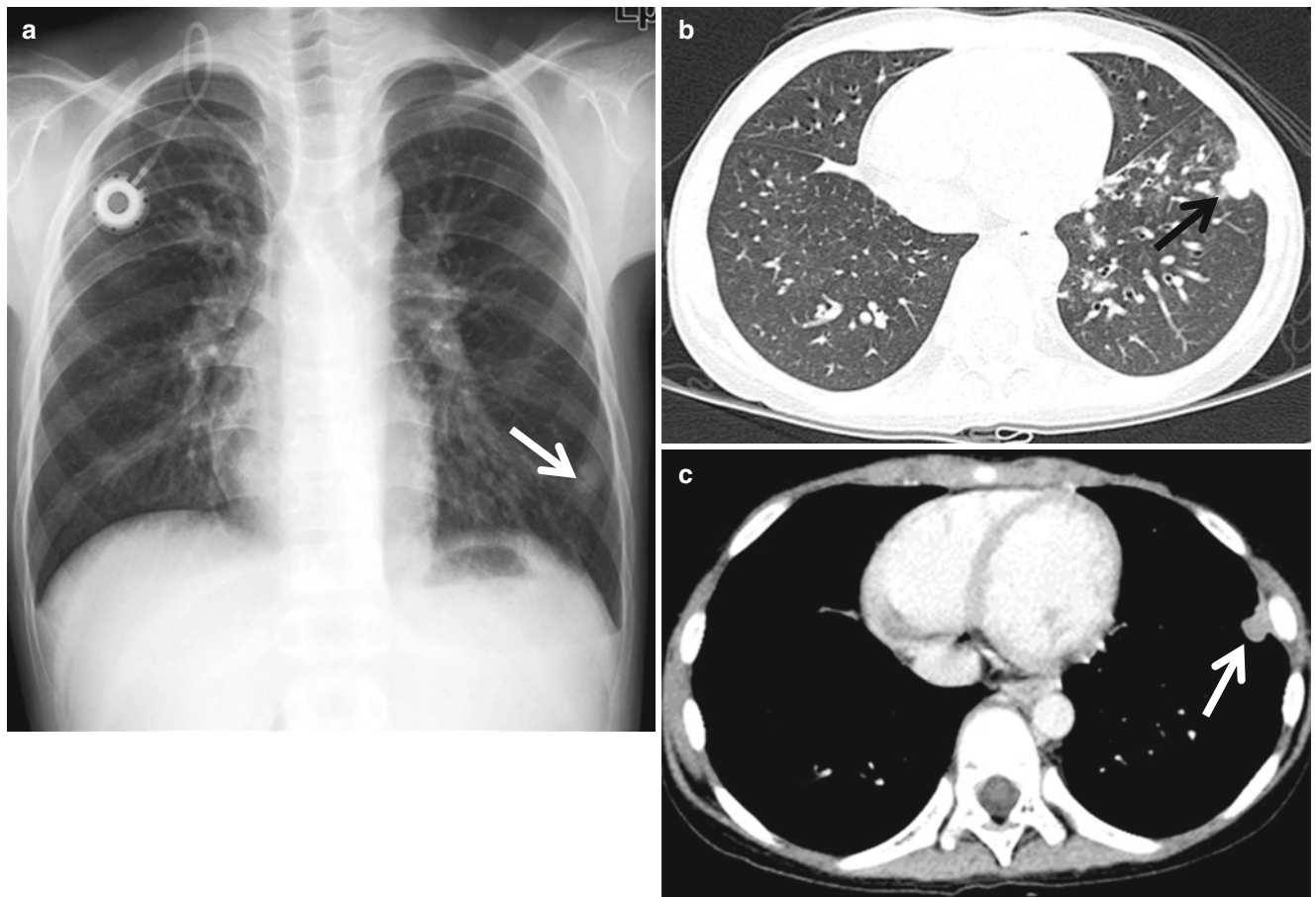


Fig. 14.5 Solitary pulmonary metastasis in a 13-year-old boy with recurrent Wilms tumor. (a) Plain radiograph shows a 15 mm nodule (arrow) in the periphery of the left lower lobe. (b, c) CT with lung

window (b) and mediastinal window (c) shows a subpleural-enhancing nodule at the left lower lobe

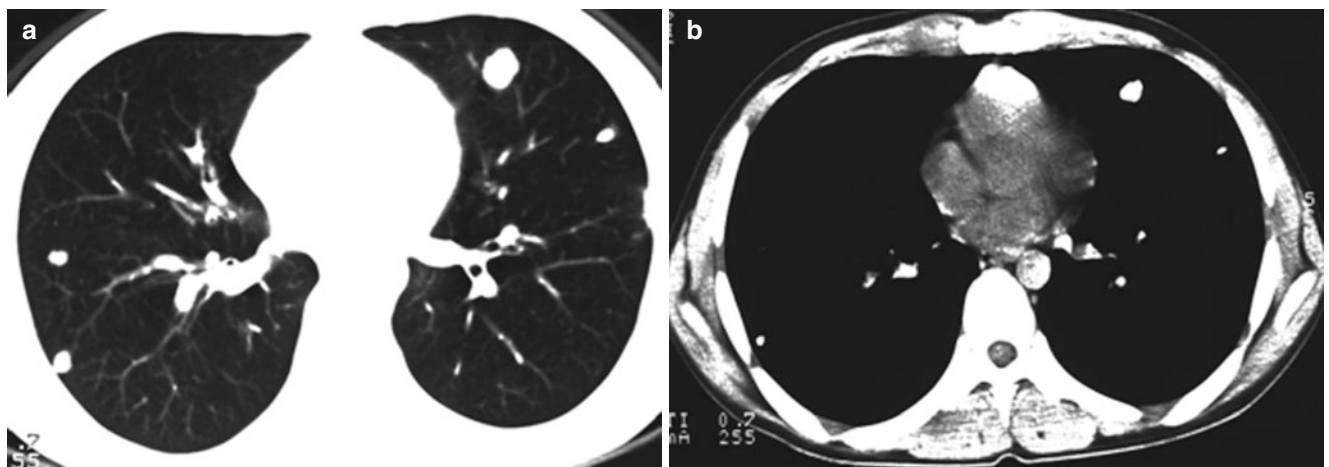


Fig. 14.6 Pulmonary metastases in a 14-year-old boy with known osteosarcoma. (a, b) Nonenhanced CT with lung (a) and mediastinal window (b) shows multiple well-defined calcified nodules, usually occurring in the peripheral areas of the lower lobes

14.3.2 Tumors of the Mediastinum

14.3.2.1 Anterior Mediastinal Tumor

14.3.2.1.1 Lymphoma

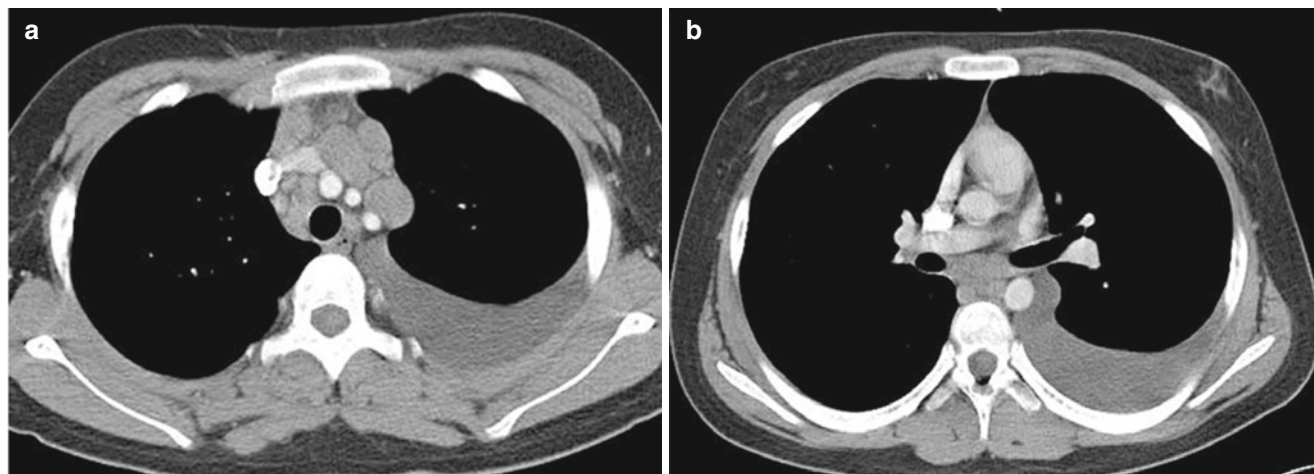


Fig. 14.7 Hodgkin's disease in a 13-year-old boy with fever and weight loss. (a, b) Contrast-enhanced CT shows discretely enlarged anterior and right paratracheal nodes, lobular anterior and middle

mediastinal lymphadenopathy, and left pleural effusion. Lymphomatous nodes appear as homogenous soft tissue attenuation with mild enhancement

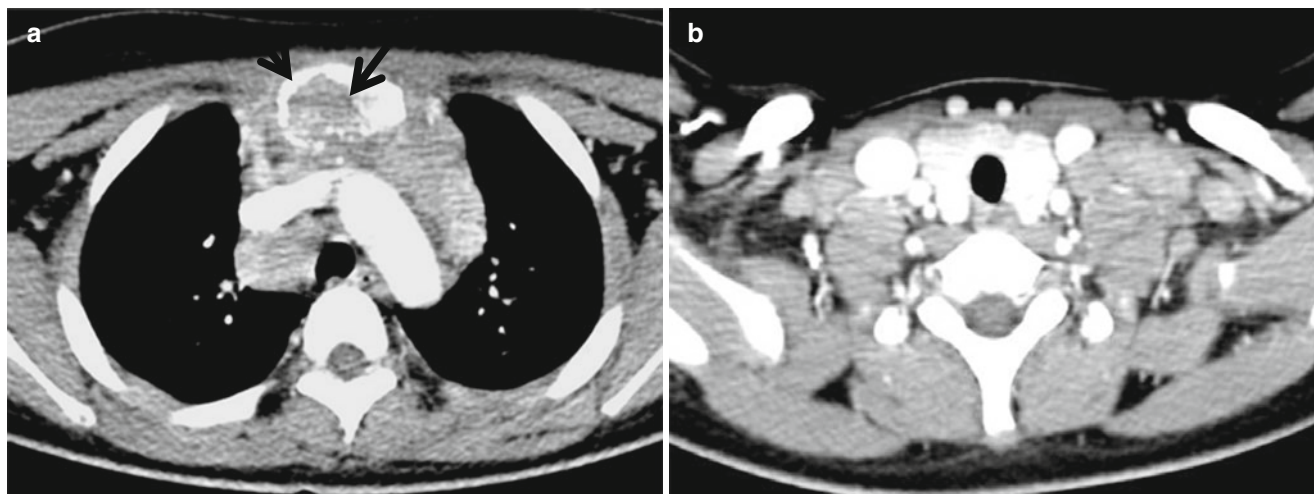


Fig. 14.8 Nodular sclerosing Hodgkin's disease in a 13-year-old girl with cervical lymphadenopathy. (a) Contrast-enhanced CT at the level of the aortic arch shows right paratracheal lymphadenopathy with a lobular anterior mediastinal mass. Invasion of anterior chest wall and

destruction of sternum (*arrows*) adjacent to the mass are noted. (b) Contrast-enhanced CT at the lower neck shows associated discretely enlarged cervical lymphadenopathy (b)

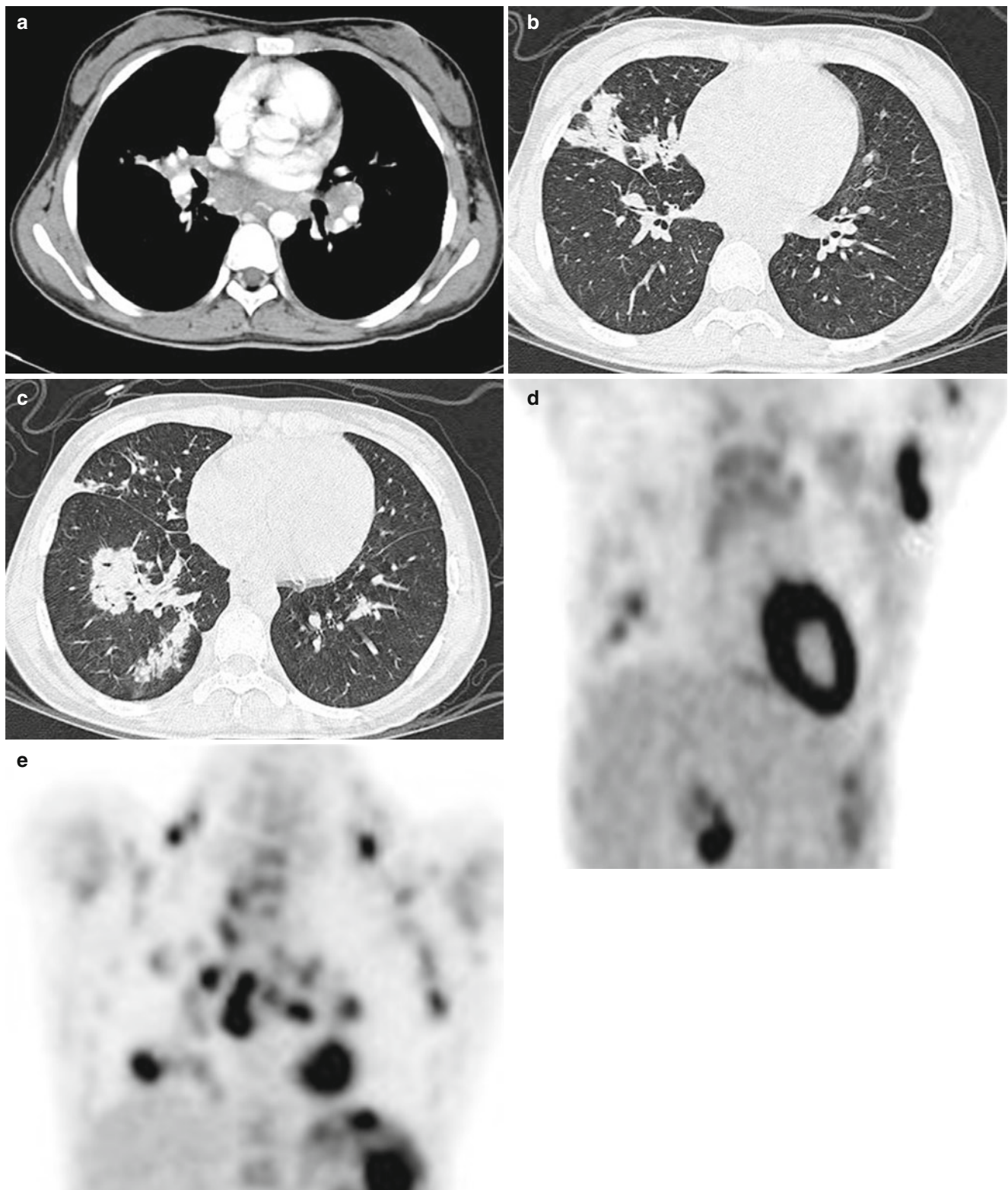


Fig. 14.9 Nodular sclerosing Hodgkin's disease in a 12-year-old girl with cervical lymphadenopathy. (a) Contrast-enhanced CT with mediastinal window shows bilateral hilar and mediastinal adenopathy with homogenous attenuation. (b, c) CT scans with lung window

show confluence and irregular margins of the pulmonary consolidations. (d, e) Coronal FDG-PET demonstrates multiple intense uptakes in the corresponding lymph nodes and lung lesions, seen on CT scans

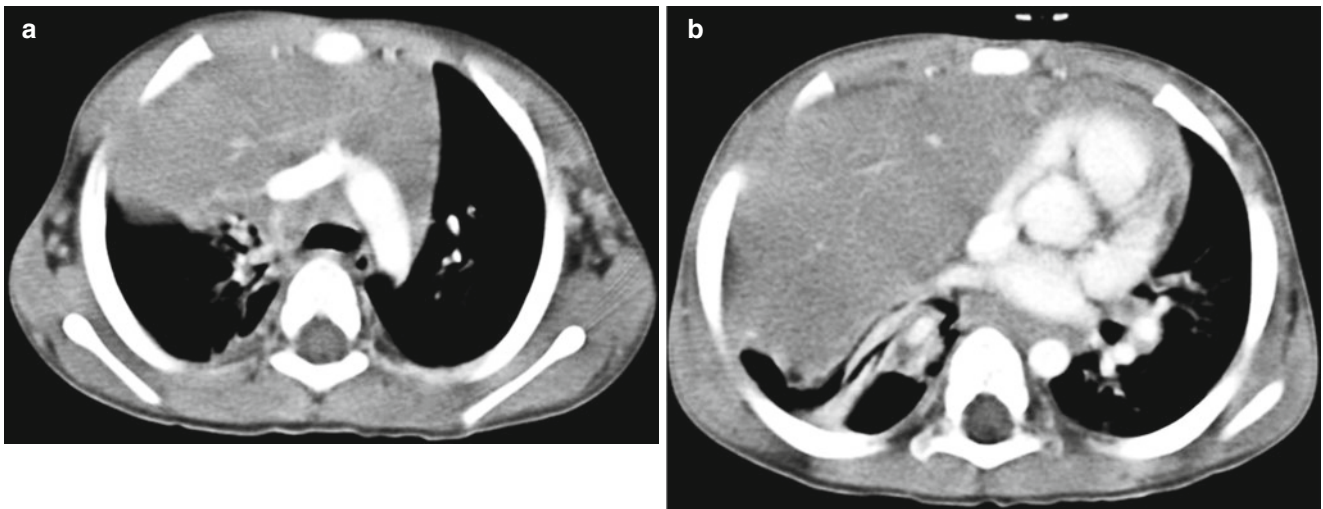


Fig. 14.10 Non-Hodgkin's lymphoma in a 2-year-old boy with productive cough. **(a, b)** Contrast-enhanced CT shows an enlarged right thymic lobe. Small linear foci of enhancement represent thymic vessels.

Note that enlarged lymph nodes are seen in the paratracheal and subcarinal regions. Note the mass effect of this mass on the adjacent mediastinal structures as well as right lower lobe atelectasis

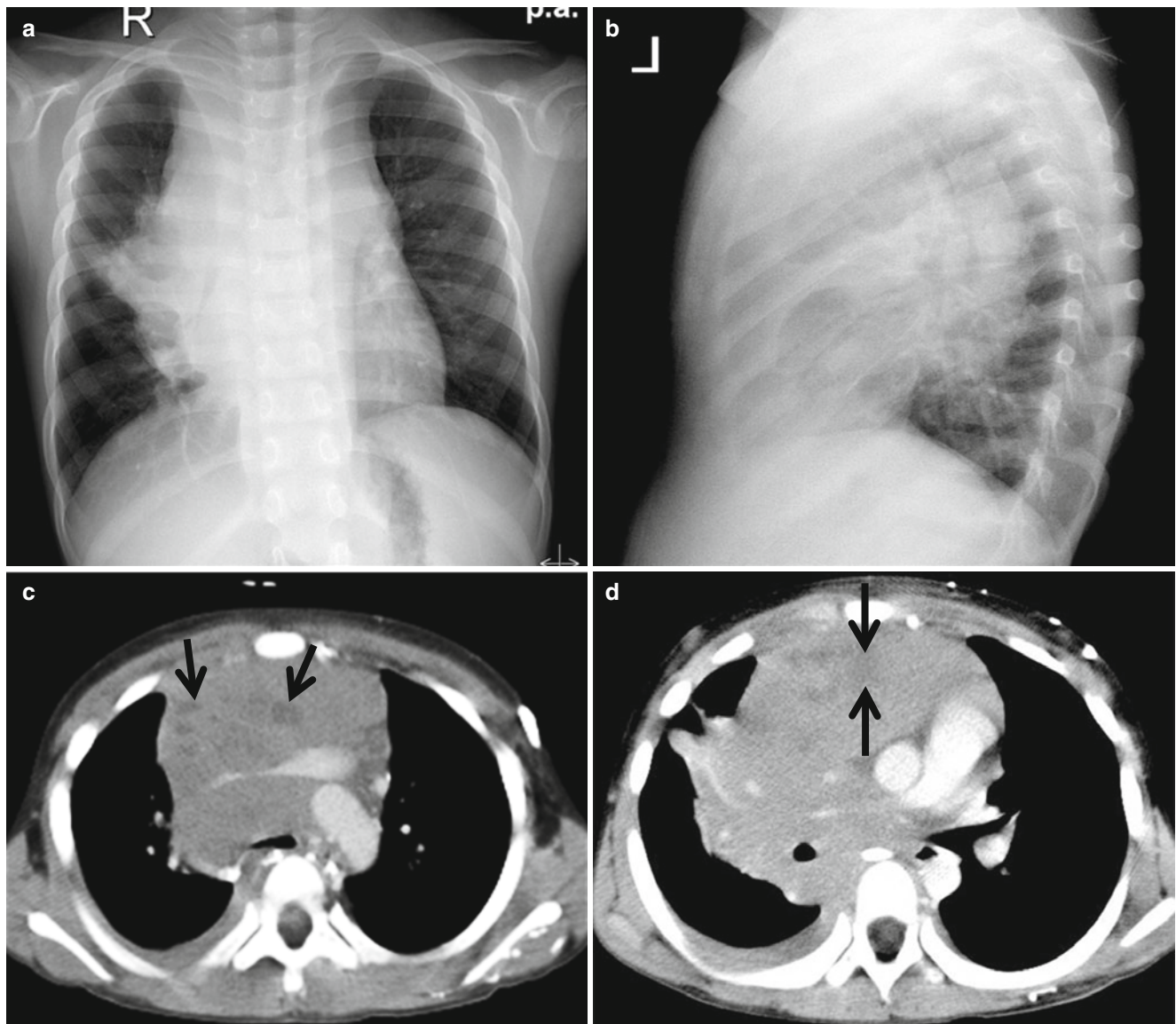


Fig. 14.11 Non-Hodgkin's lymphoma in a 7-year-old boy with dyspnea. (a) Frontal chest radiograph shows mediastinal widening. (b) Lateral chest radiograph shows that the mass is located in the anterior and middle mediastinum. (c, d) Contrast-enhanced CT shows a

lobulated mediastinal mass with the epicenter in the anterior mediastinum. This mass contains some low-attenuation areas of necrosis (arrows). Note the mass effect on the adjacent superior vena cava and enhancing pulmonary vessels. Associated right pleural effusion is noted

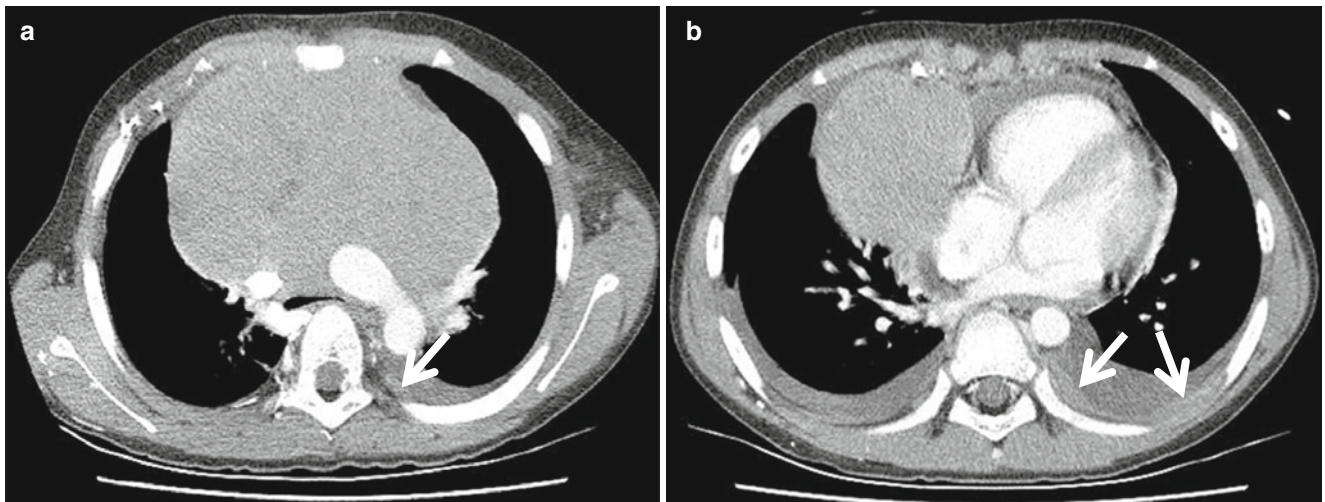


Fig. 14.12 Non-Hodgkin's lymphoma in a 10-year-old boy with mild fever. (a, b) Contrast-enhanced CT shows a large smooth, biconvex anterior mediastinal mass of uniform attenuation. The trachea and

superior vena cava are compressed and displaced, posteriorly. There are also bilateral pleural effusions with pleural masses (*arrows*) and pericardial effusion

14.3.2.1.2 Germ Cell Tumor: Teratoma

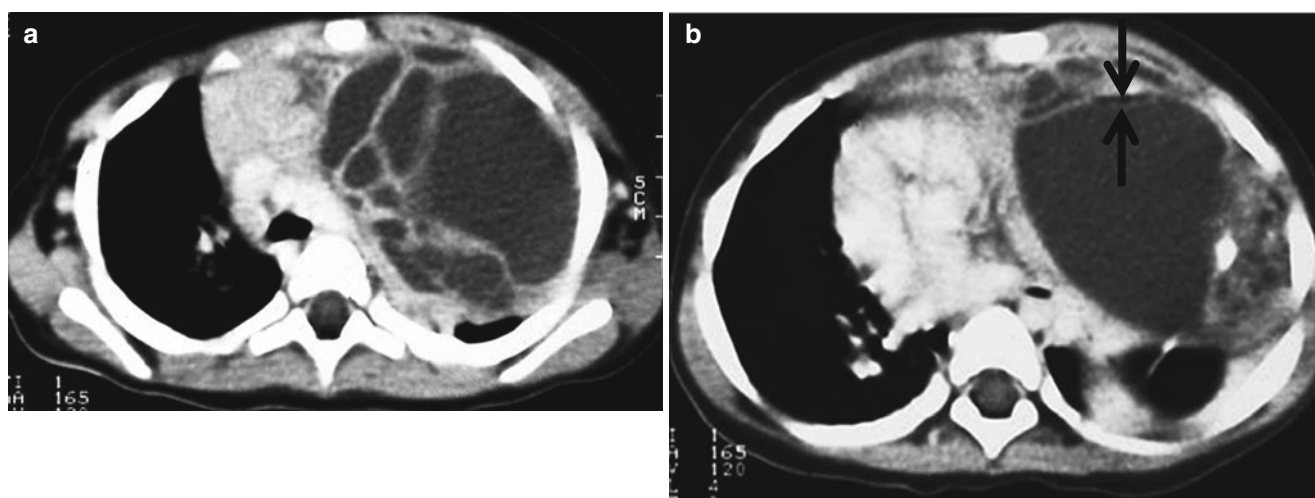


Fig. 14.13 Mature teratoma in a 13-month-old girl with respiratory distress. (a, b) Contrast-enhanced CT shows a large, complex anterior mediastinal mass containing areas of fluid, fat, (*arrows*) and calcification

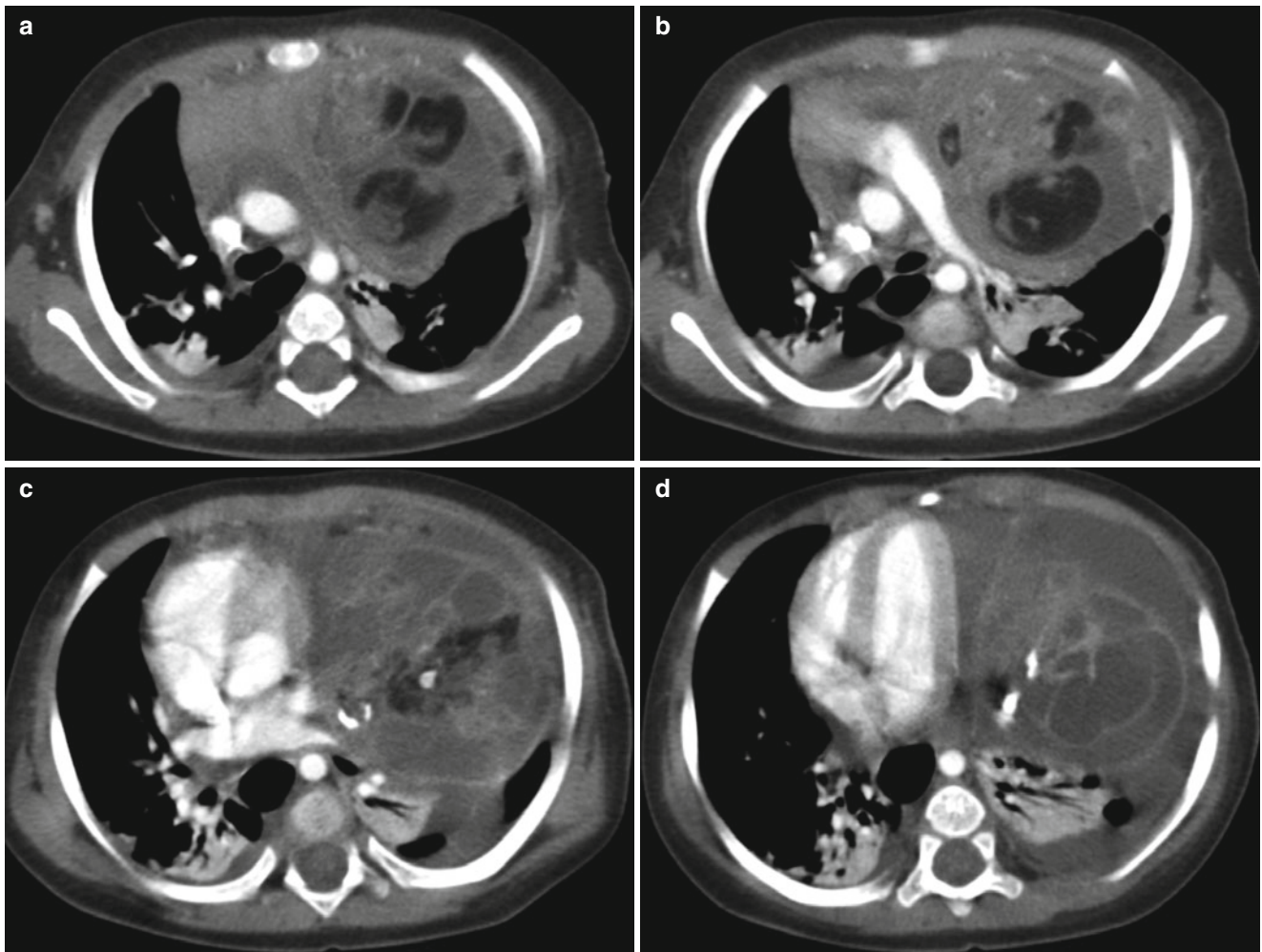


Fig. 14.14 Immature teratoma in a 2-year-old girl with respiratory distress (Case courtesy of Hye-Kyung Yoon, MD). (**a–d**) Contrast-enhanced CT shows a large, anterior mediastinal mass with

variable attenuation with dense calcifications. The mass contains solid and fatty tissues and cystic areas. This complex cystic and fatty immature teratoma displaces the mediastinum to the right

14.3.2.1.3 Thymoma

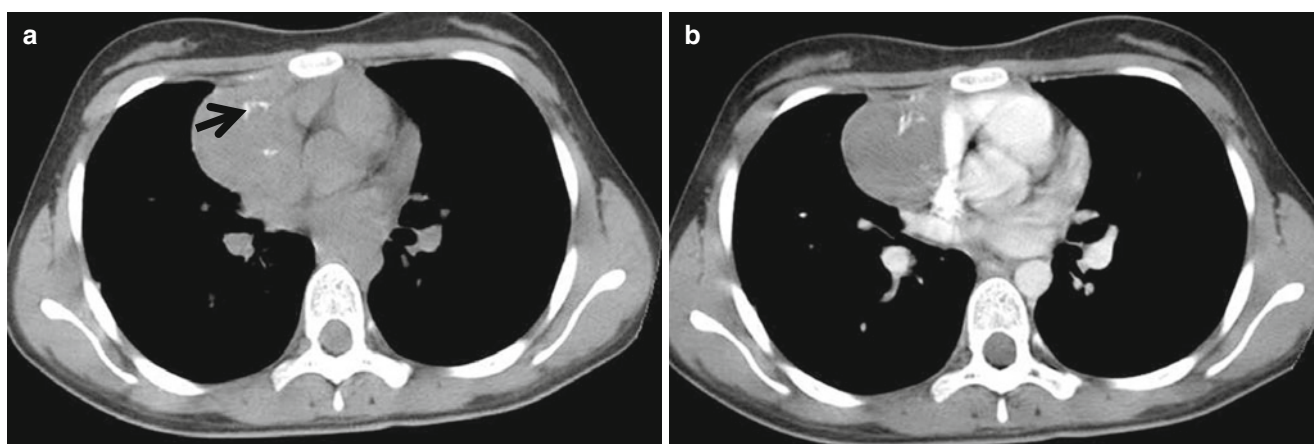


Fig. 14.15 Noninvasive thymoma in a 15-year-old girl. (a, b) Nonenhanced (a) and contrast-enhanced (b) CT show relatively homogenous right thymic mass with calcifications (*arrows*). This mass is a low-attenuating lesion with mild contrast enhancement

14.3.2.2 Middle Mediastinal Tumors

14.3.2.2.1 Lymphomatous Lymphadenopathy

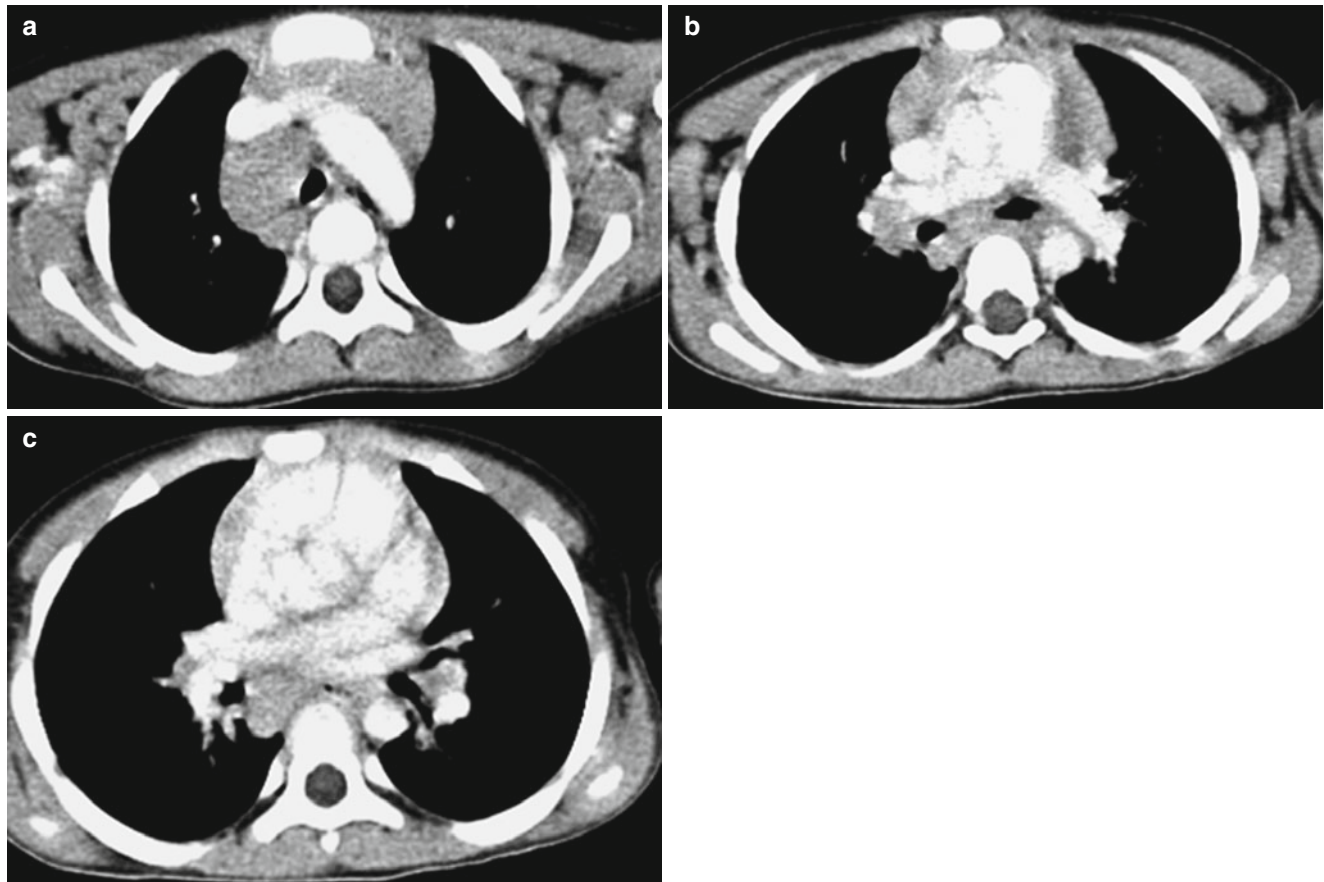


Fig. 14.16 Lymphadenopathy in the middle mediastinum in an 11-year-old boy with lymphoma. (a–c) Contrast-enhanced CT shows homogenous metastatic adenopathy in the right paratracheal, hilar, and

subcarinal regions of the middle mediastinum. Note the accompanying bilateral axillary lymphadenopathy (a)

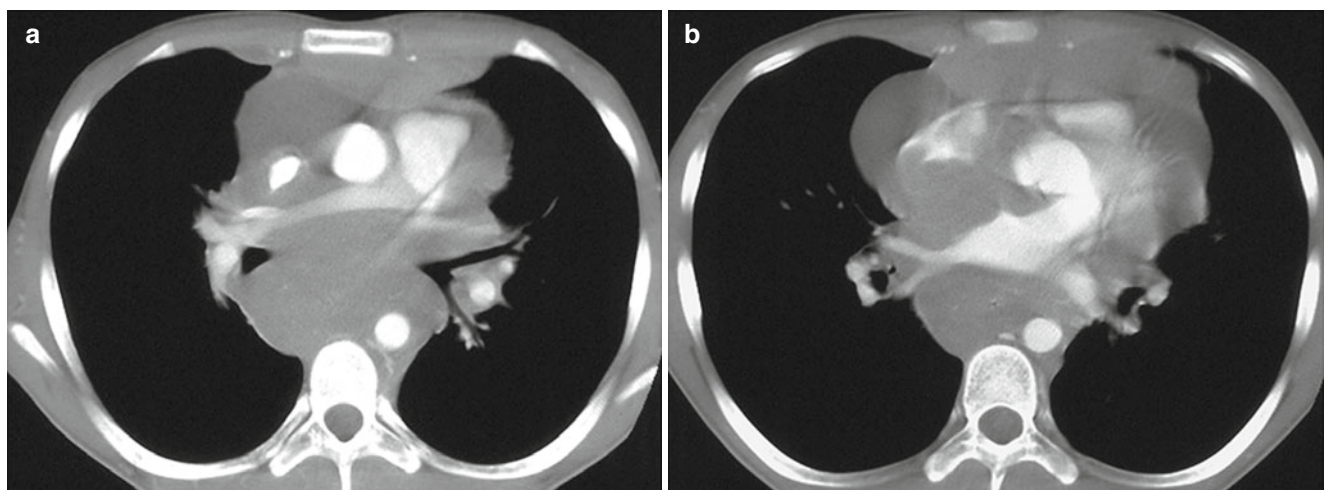


Fig. 14.17 Lymphadenopathy in a 14-year-old girl with lymphoma. (a, b) Contrast-enhanced CT shows a homogenous hypodense soft tissue mass representing conglomeration of the metastatic adenopathy in

both hilar and subcarinal regions of the middle mediastinum. This mass is accompanied by anterior mediastinal components

14.3.2.3 Posterior Mediastinal Tumors

14.3.2.3.1 Ganglion Cell Tumors

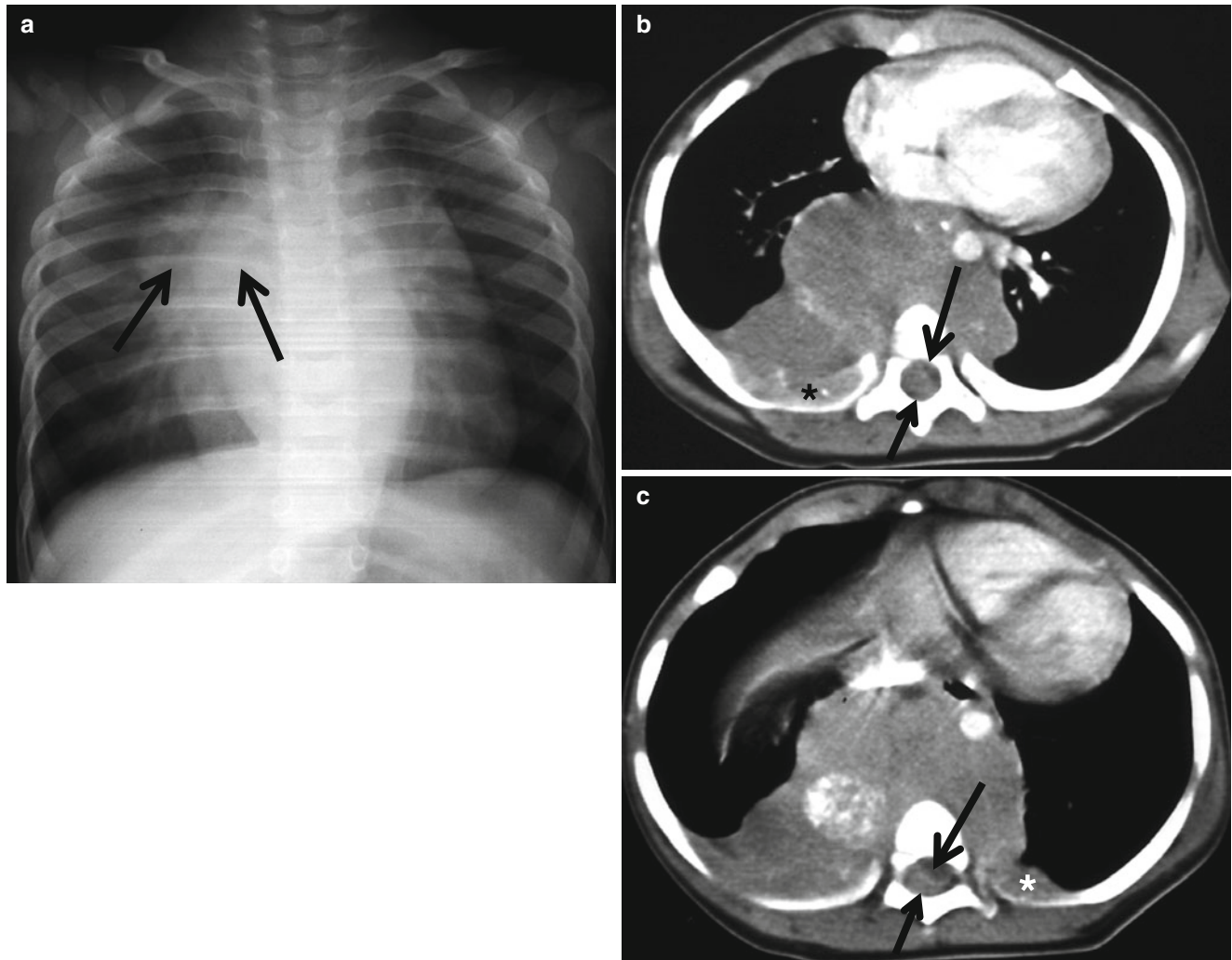


Fig. 14.18 Primary mediastinal neuroblastoma with intraspinal extension in a 12-month-old girl with irritability. **(a)** Plain radiograph shows bilateral paraspinal and posterior mediastinal masses with posterior rib erosion (*arrows*). **(b, c)** Contrast-enhanced CT shows a large soft tissue

density mass crossing the midline, encasing and displacing the enhanced descending aorta. Note the internal coarse calcification and intraspinal tumor extension (*arrows*) with adjacent rib erosion (*asterisk*)

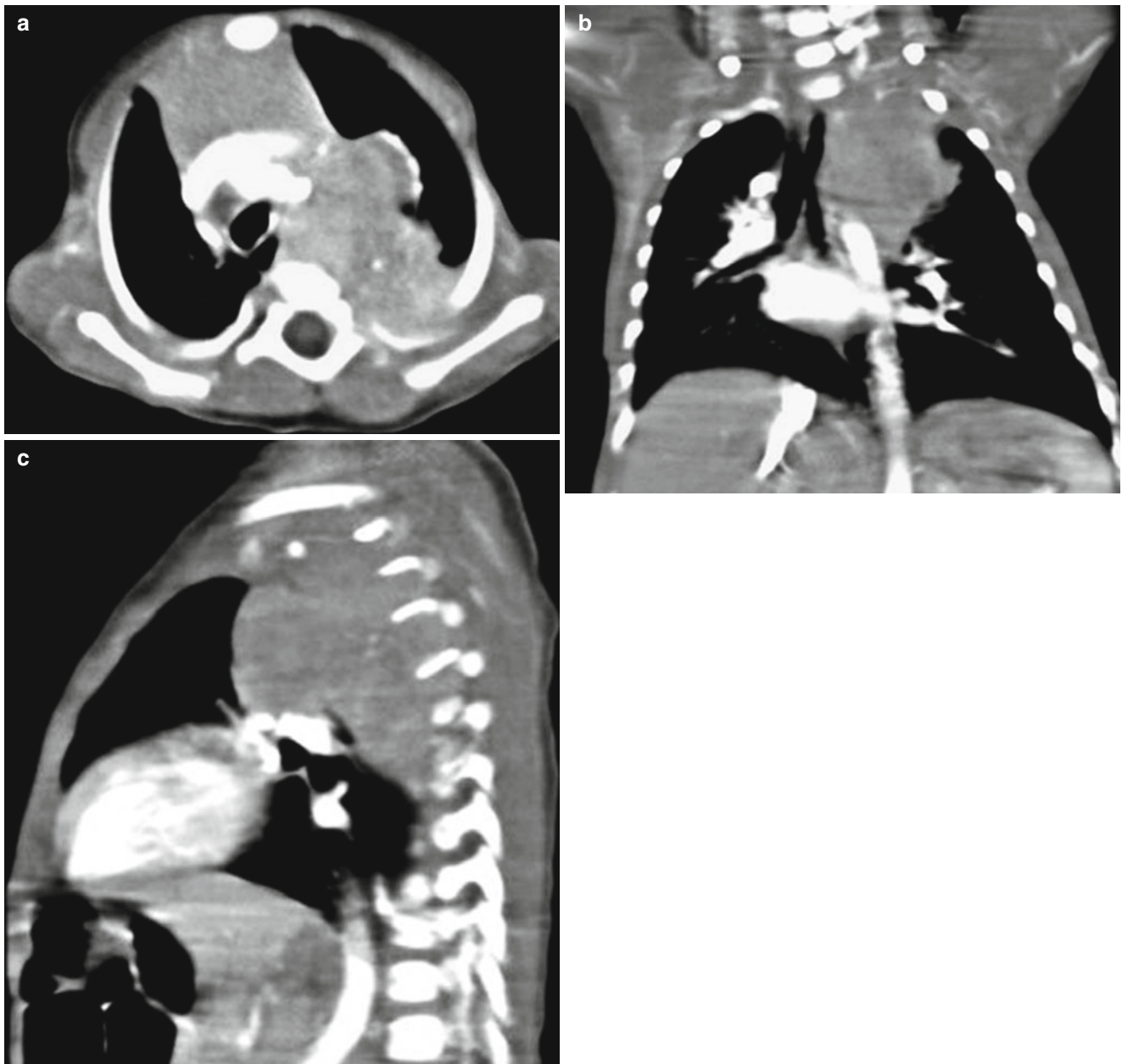


Fig. 14.19 Neuroblastoma in an infant. (a) Axial contrast-enhanced CT shows a calcified left paraspinal soft tissue mass across the midline. (b, c) Coronal and sagittal reformation CT show the craniocaudal extent and the midline extension of this posterior mediastinal mass

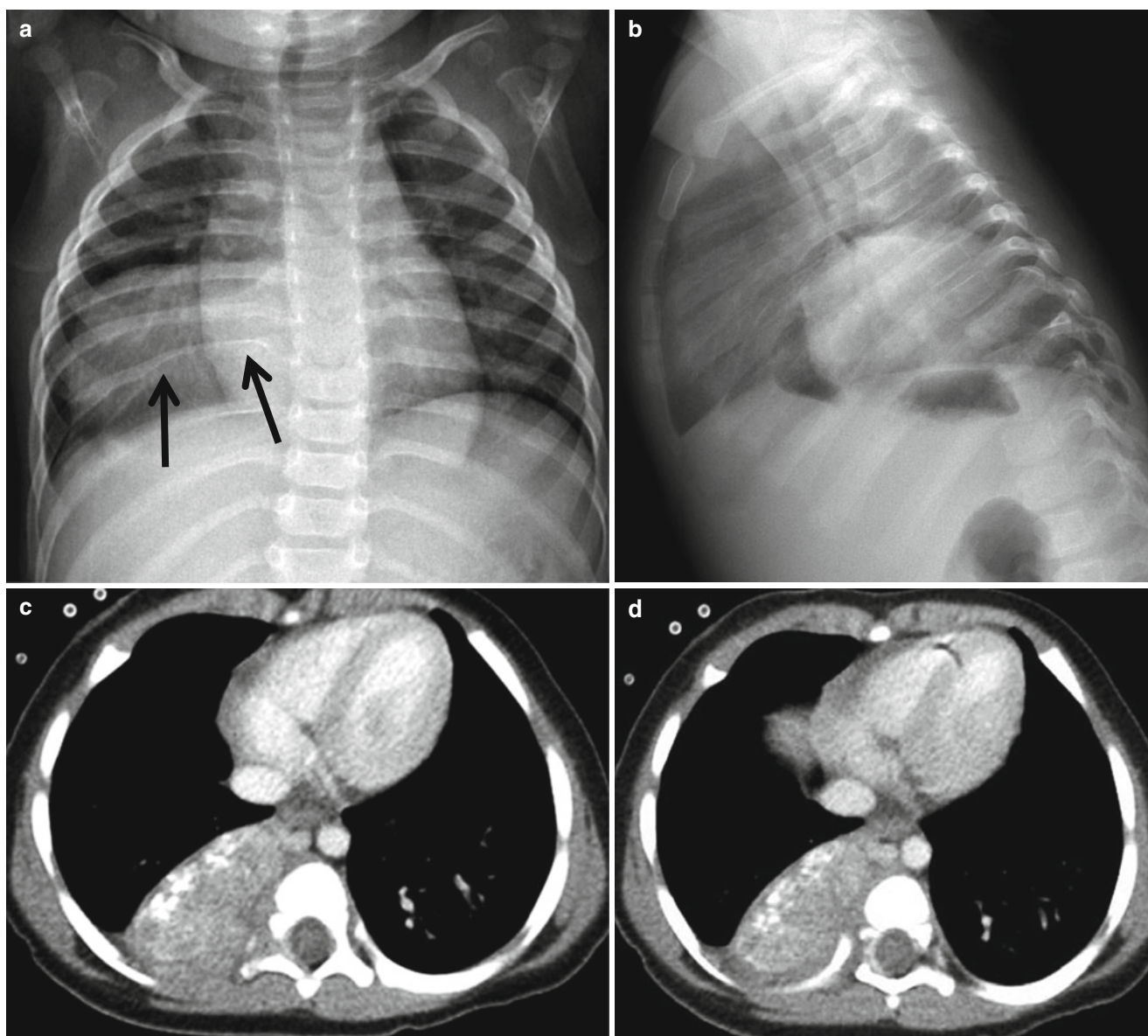


Fig. 14.20 Thoracic neuroblastoma with intraspinal extension in an 11-month-old girl with fever. (a, b) Frontal and lateral radiographs show a large opacity in the right lower zone, causing posterior rib erosion and distortion (*arrows*). (c, d) Contrast-enhanced axial CT shows a calcified

right paraspinal soft tissue mass with widening of neural foramen. (e, f) Coronal fat-suppressed enhanced T1-weighted MR images clearly show a right-sided enhancing mass lesion with intraspinal and posterior chest wall invasion

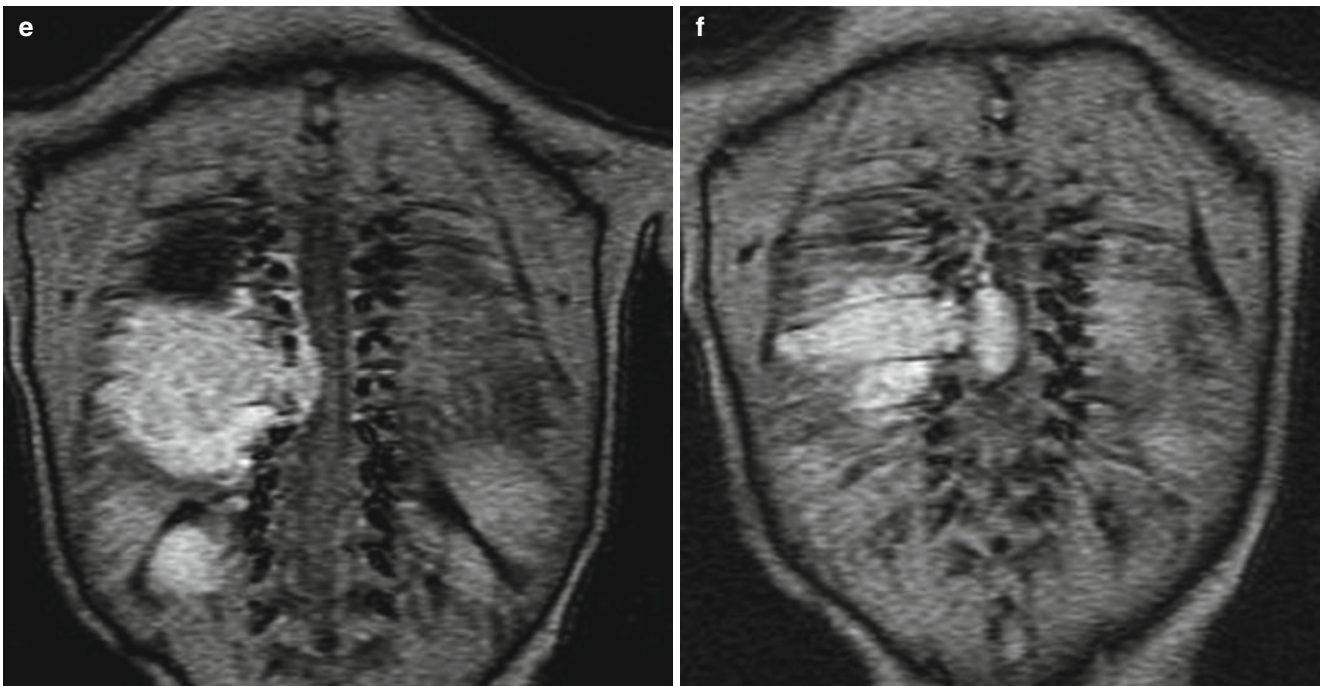


Fig. 14.20 (continued)

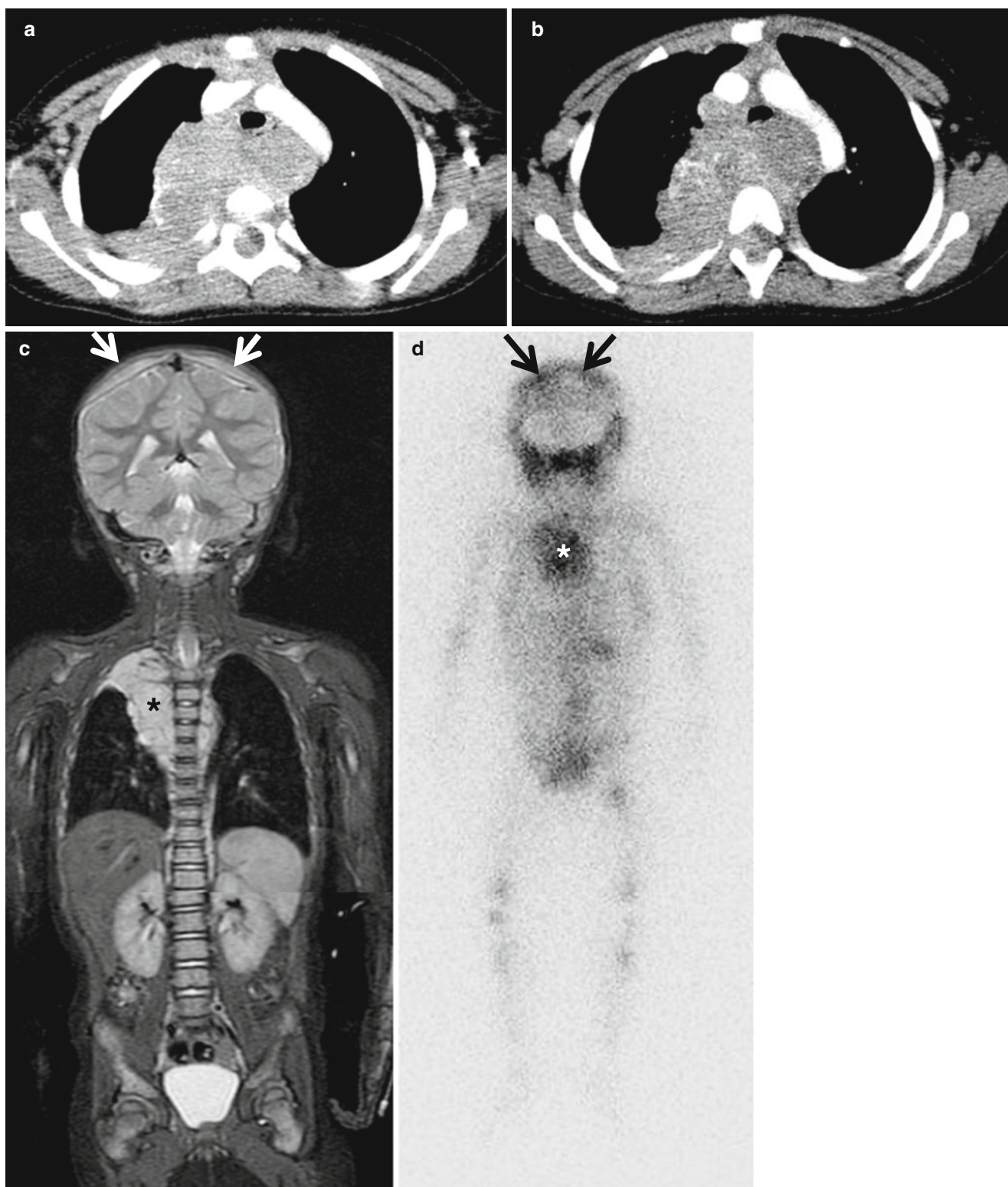


Fig. 14.21 Neuroblastoma in a 2-year-old girl. (a, b) Contrast-enhanced CT shows a large soft tissue mass crossing the midline, displacing the trachea anteriorly. Note intraspinal tumor extension. (c) Coronal STIR image of the whole-body MRI demonstrates lobulated mediastinal mass (*asterisk*). Note associated dural thickening (*arrows*)

and high signal intensities of the bone marrow, suggesting stage IV neuroblastoma. (d) Anterior views of whole-body. ¹³¹I-MIBG shows increased uptakes in the right mediastinum (*asterisk*), skull (*arrows*), and bone marrow

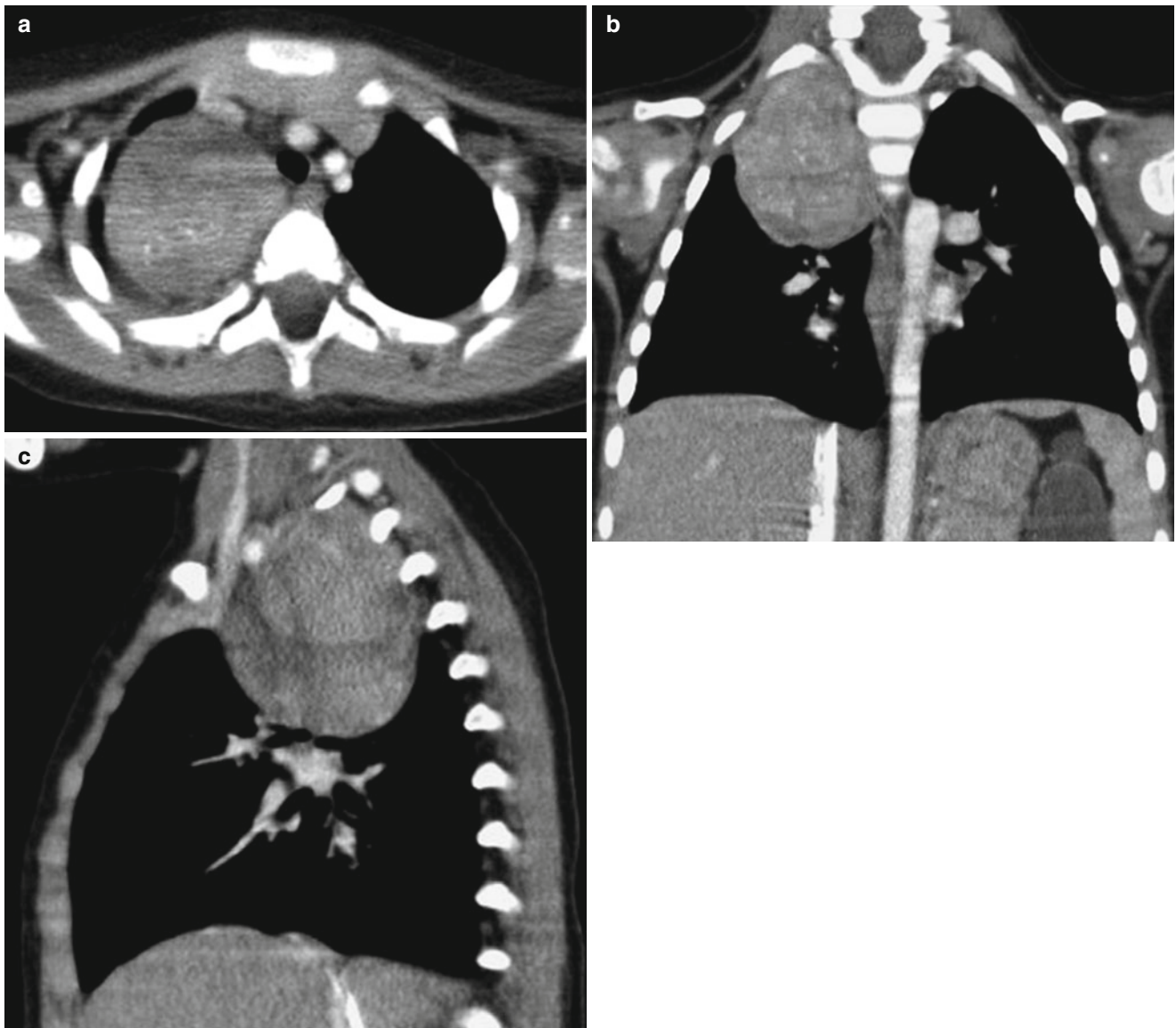


Fig. 14.22 Ganglioneuroblastoma in a 4-year-old girl with vomiting and diarrhea. **(a)** Axial contrast-enhanced CT shows a relatively well-defined enhancing paraspinal soft tissue mass with coarse

calcifications. Note the absence of intraspinal extension of this tumor. **(b, c)** Coronal and sagittal reformation CT show the craniocaudal extent of the tumor

14.3.2.3.2 Nerve Sheath Tumors: Neurofibroma

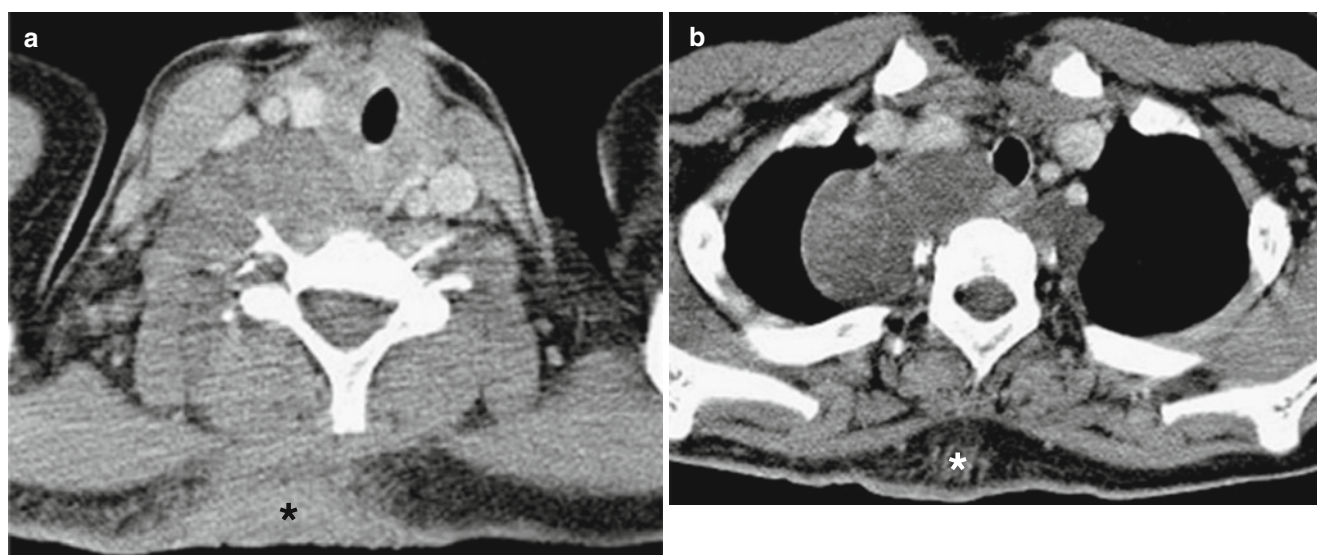


Fig. 14.23 Neurofibroma in an 11-year-old boy with known neurofibromatosis type 1. (a, b) Contrast-enhanced CT shows multiple lobulated soft tissue masses in both of the paraspinal regions and in the

patient's back region (*asterisk*). These masses appear as round or oblong posterior mediastinal masses with little enhancement because of their lipid contents or cystic degeneration

14.3.2.4 All Compartments: Lymphangioma

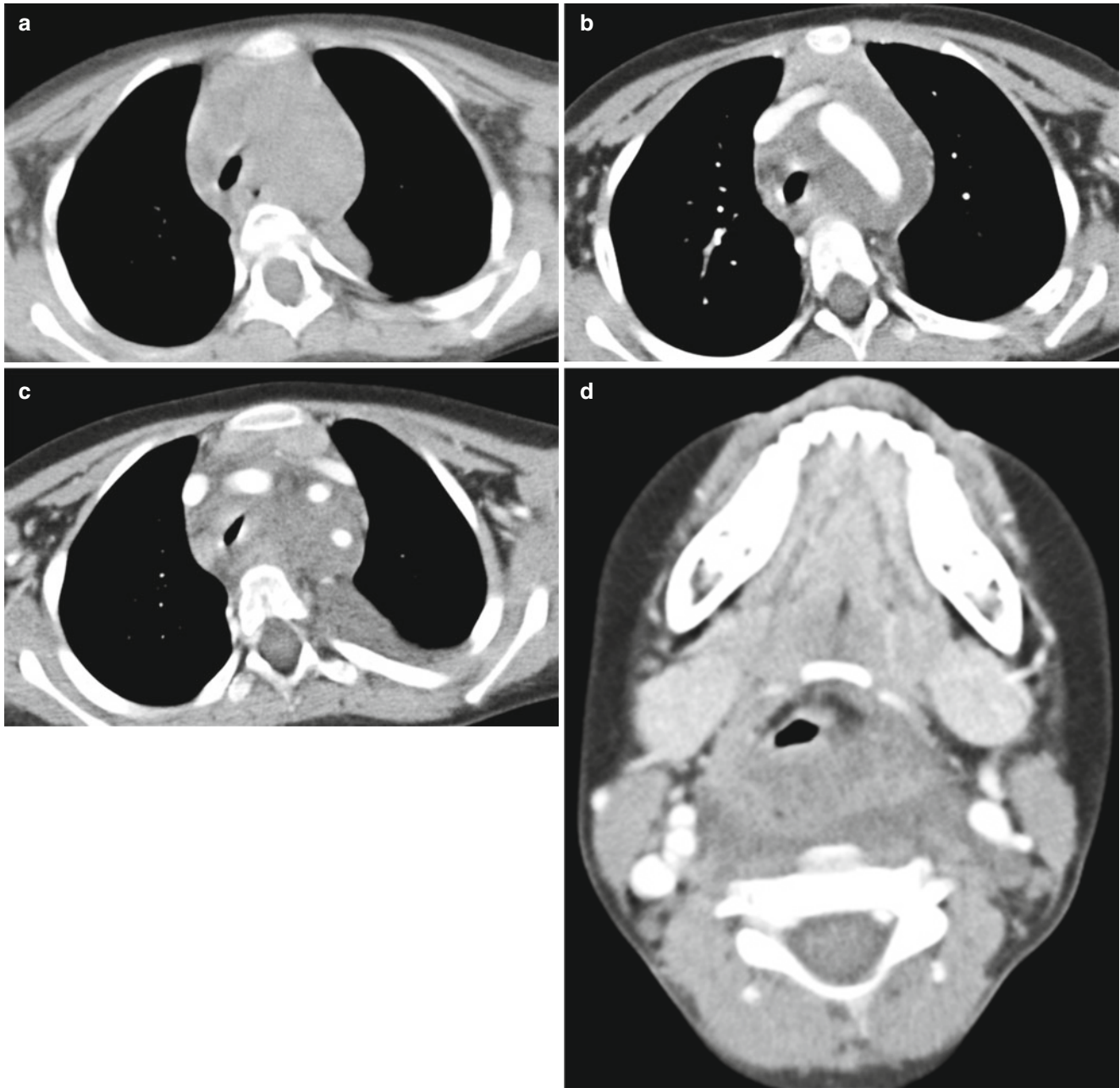


Fig. 14.24 Lymphangiomas in a 5-year-old girl with dyspnea. (a–c) Nonenhanced (a) and contrast-enhanced (b, c) CT show a large low-attenuation mass in the middle mediastinal mass encasing the thoracic

great vessels, trachea, and esophagus. The mass extends to the posterior mediastinum. (d) Note the low-attenuation mass infiltrating the retropharyngeal deep cervical spaces of the neck

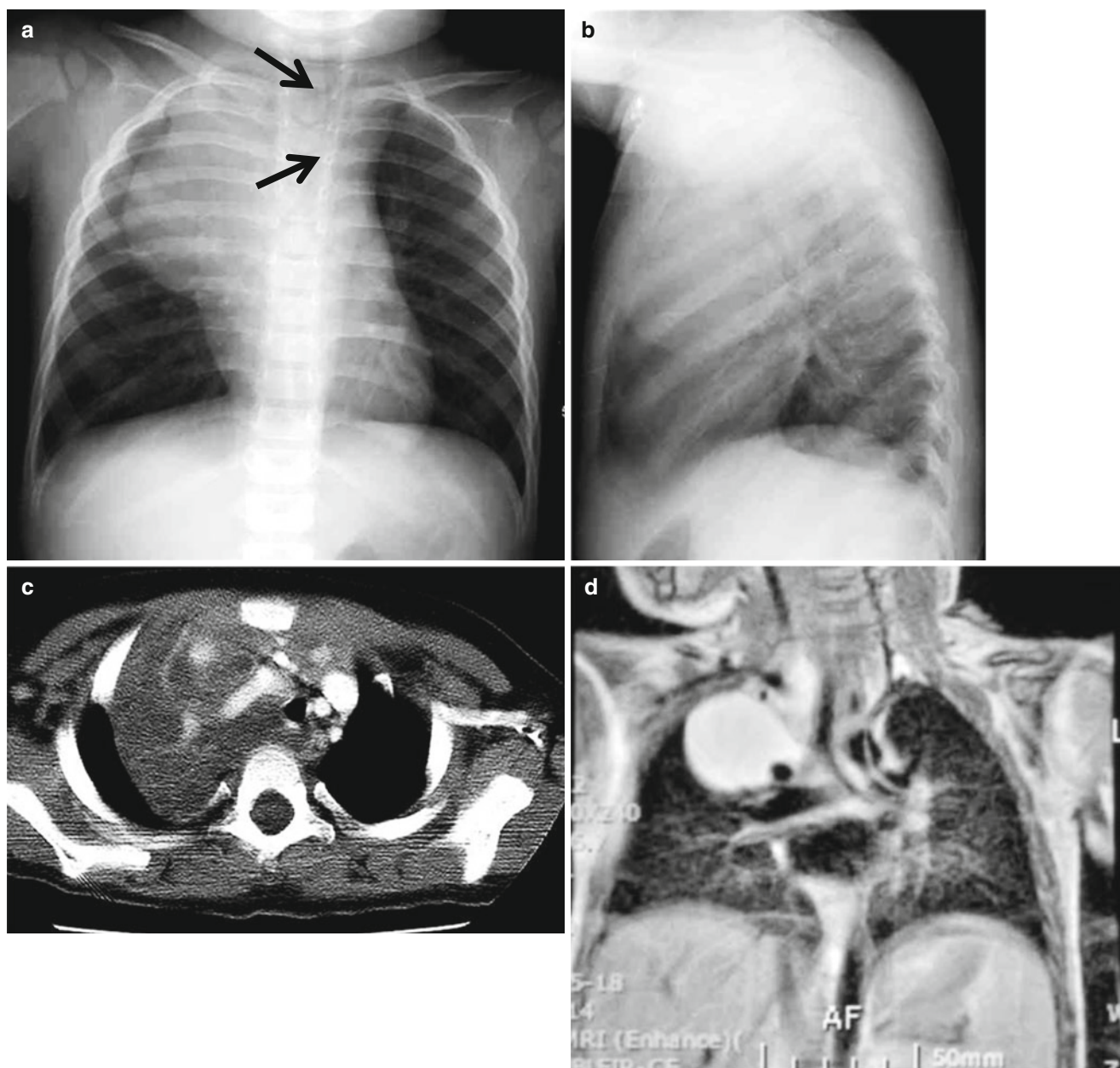


Fig. 14.25 Lymphangioma in a 15-month-old boy (Case courtesy of Hye-Kyung Yoon, MD). (**a**, **b**) Frontal and lateral radiographs show a rounded, lobulated anterior mediastinal structure with displacing the trachea to the left (*arrows*). (**c**) Contrast-enhanced CT shows a near-water

attenuation mediastinal mass with internal septation. Thymus is displaced and replaced by this mass. The lesion insinuating along the mediastinal space was confined to the mediastinum. (**d**) Coronal T2-weighted image clearly depicts the extent of this high signal intensity cystic mass

14.3.3 Tumors of the Chest Wall

14.3.3.1 Primitive Neuroectodermal Tumor (PNET)

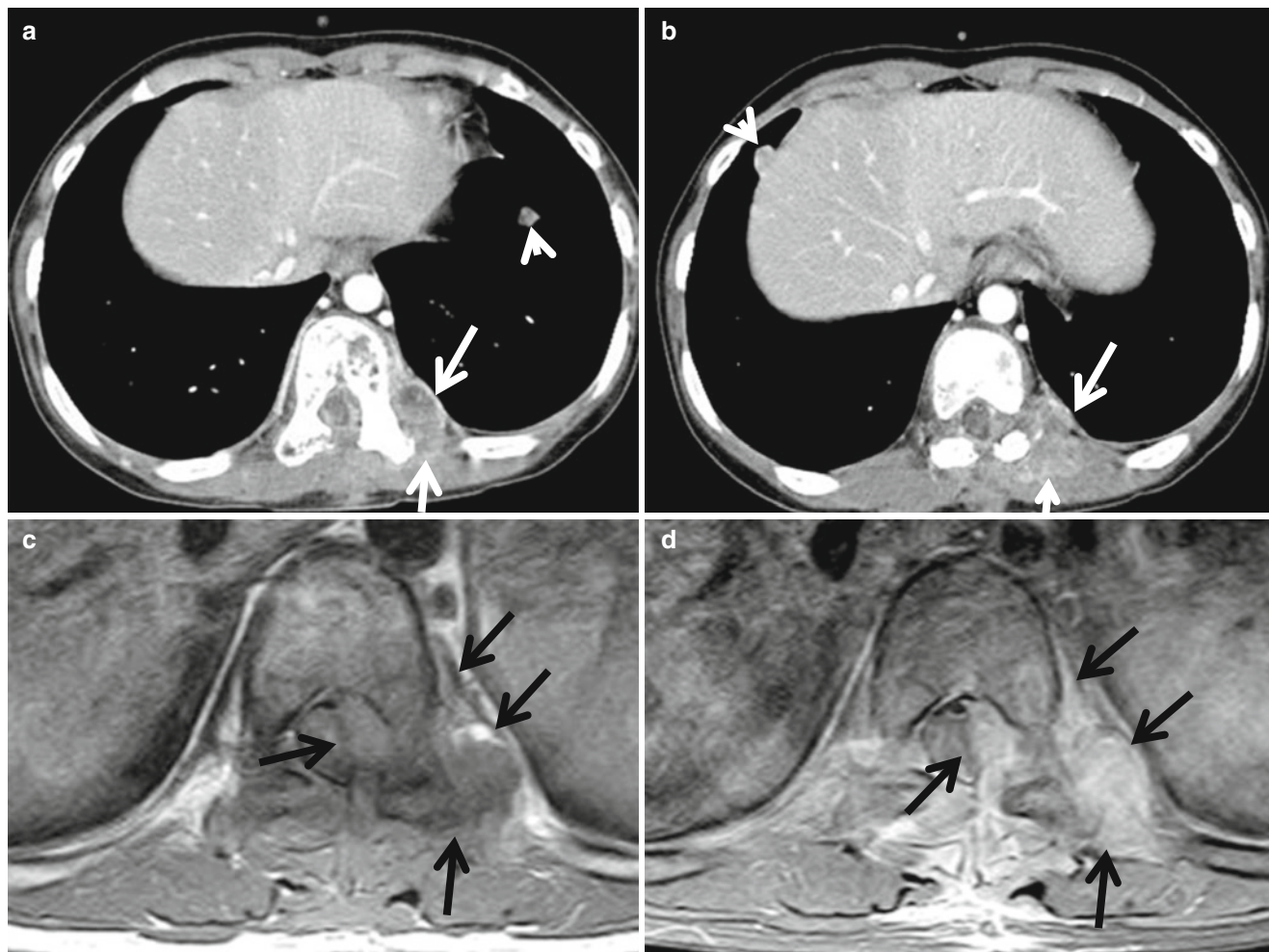


Fig. 14.26 PNET (Askin) tumor with local invasion and metastasis in a 5-year-old boy. (a, b) Contrast-enhanced CT shows a heterogeneous mass (arrows) located posteriorly in the left chest wall with extension to the back muscle and spinal canal, as well as multiple pulmonary

metastatic nodules (arrowheads). (c, d) Noncontrast (c) and contrast-enhanced T1-weighted MR (d) images clearly show the extent of a left-sided enhancing mass lesion (arrows) with intraspinal and posterior chest wall invasion

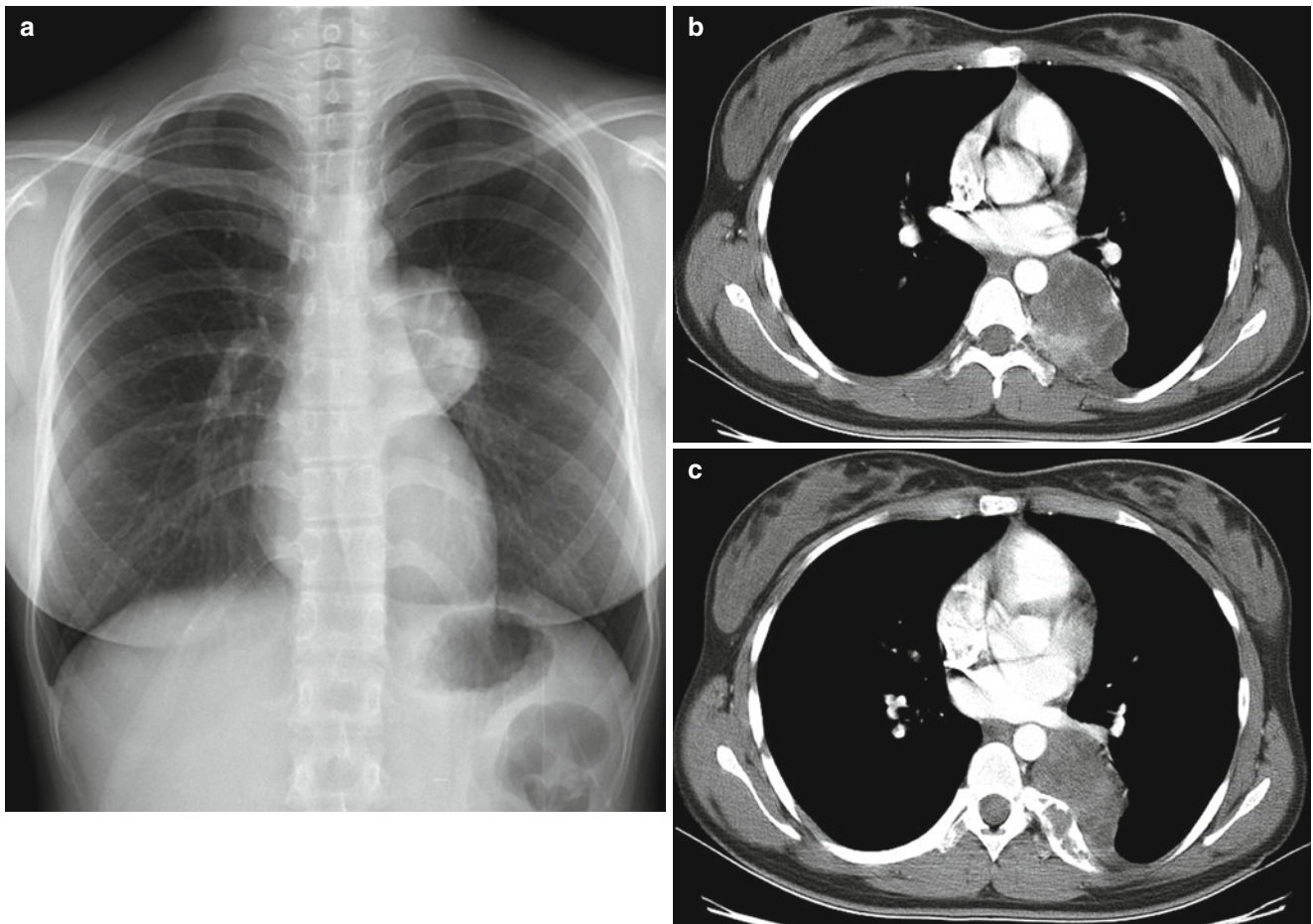


Fig. 14.27 PNET (Askin) tumor in a 15-year-old boy (Case courtesy of Hye-Kyung Yoon, MD). **(a)** Plain radiograph shows an oblong left paraspinal mass. Note lytic changes and expansion of the posterior left

rib adjacent to this mass. **(b, c)** Contrast-enhanced CT shows a heterogeneous mass located in the left paraspinal region with focal destruction of posterior portion of the rib

14.3.3.2 Rhabdomyosarcoma

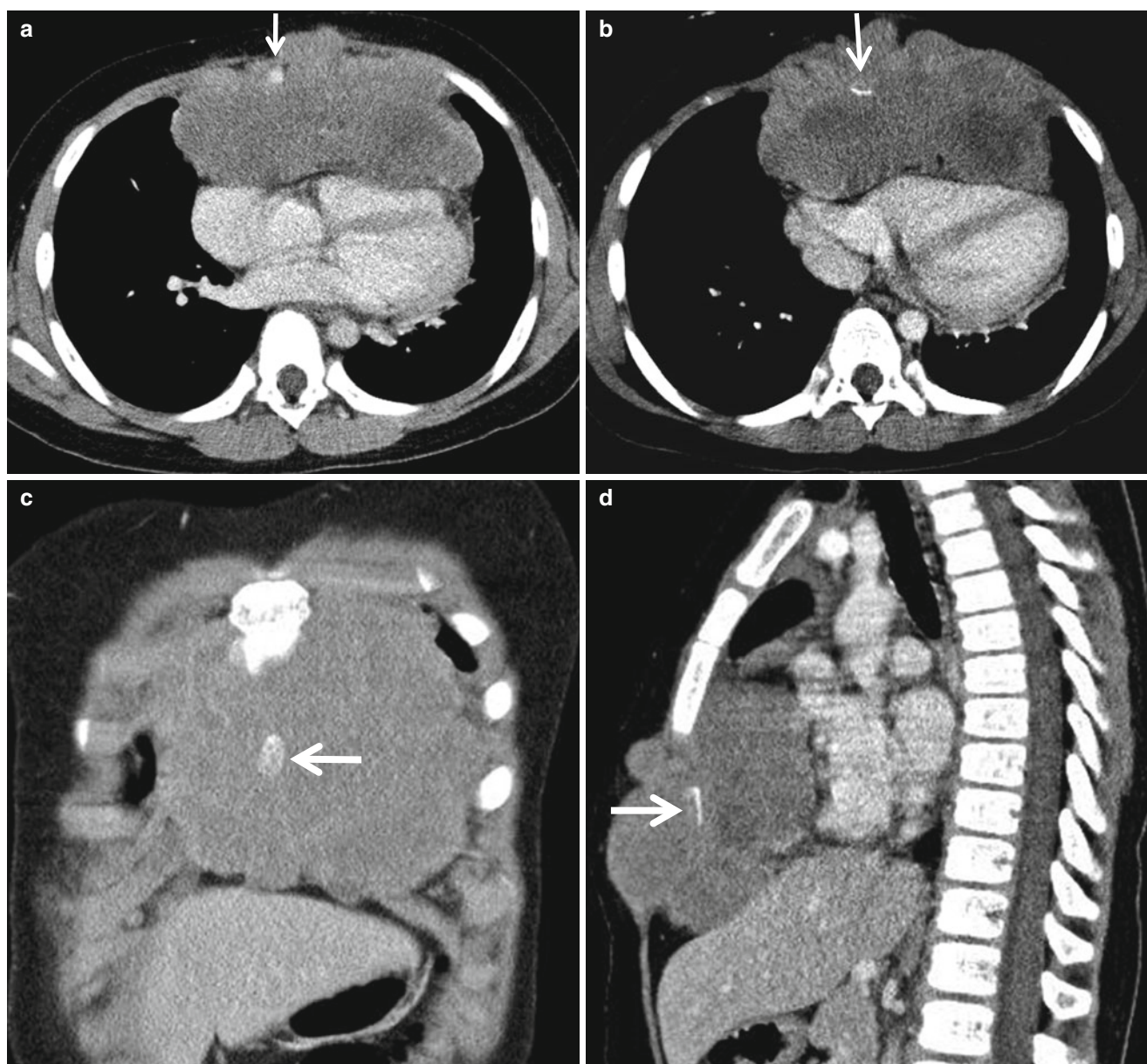


Fig. 14.28 Alveolar rhabdomyosarcoma in the anterior chest wall with sternum destruction in an 8-year-old boy presented with chest pain. (a–d) Contrast-enhanced axial (a, b), coronal (c), and sagittal (d) CT show a large lobulated anterior chest wall mass extending to the ante-

rior mediastinum and subcutaneous soft tissue. Destruction of the sternum tip (*arrow*) with an intra- and extrathoracic soft tissue mass suggests chest wall origin

14.3.3.3 Mesenchymal Hamartoma

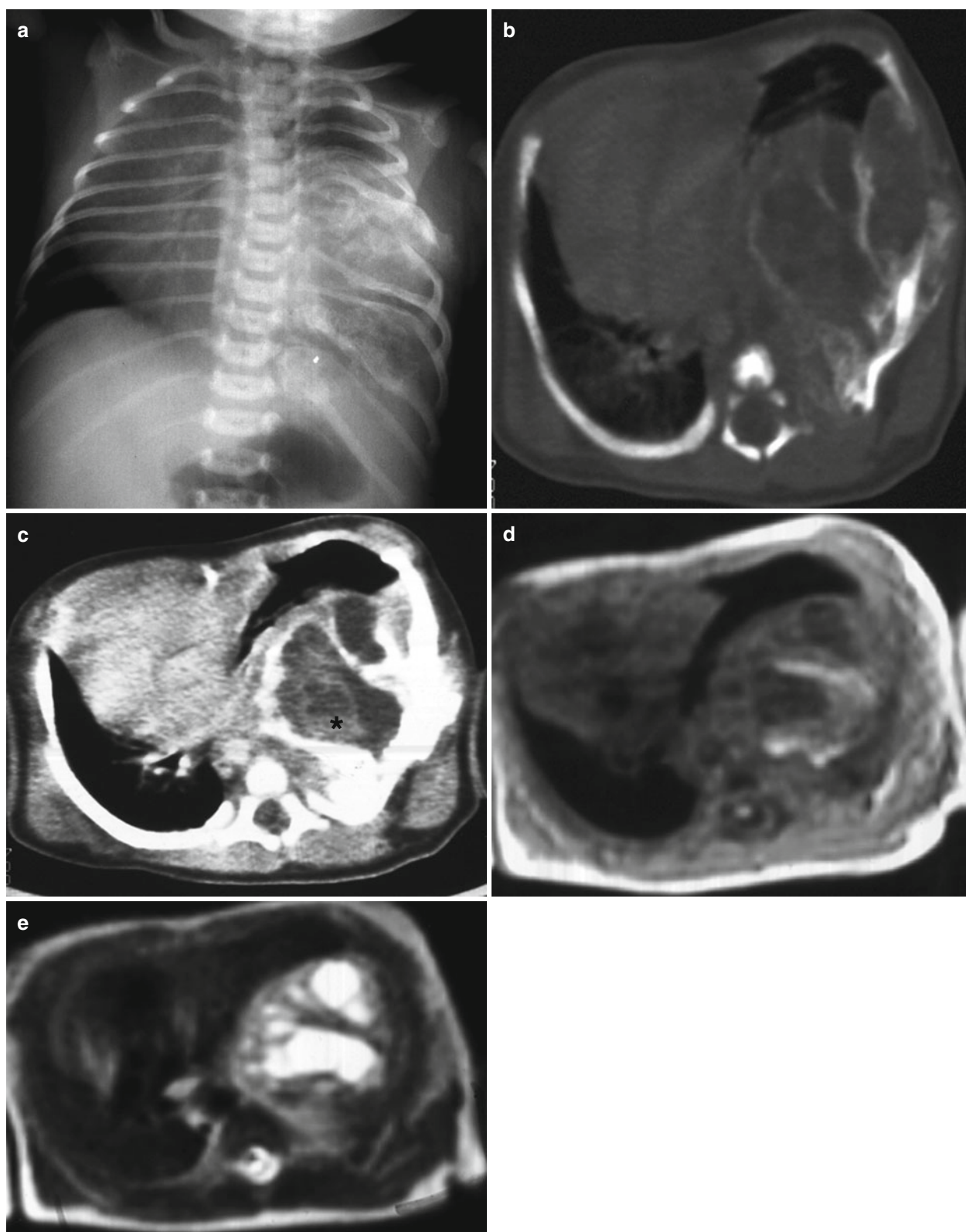


Fig. 14.29 Mesenchymal hamartoma in an infant with an intrathoracic mass found on prenatal US. (a) Plain radiograph shows a large calcified soft tissue mass with multiple rib destruction, thinning, and splaying on the left thorax. (b, c) CT with bone window (b) and contrast-enhanced CT (c) show a large lobulated, extrapleural solid and cystic mass with fluid-fluid levels (*asterisk*). Rib destruction and internal calcification

are also noted. The rib deformity appears as partial or complete destruction, erosion, and enlargement. (d, e) MR T1-weighted images (d) show iso- and low signal intensity on the solid portion and high signal intensity in the cystic portion suggesting hemorrhage, which is more prominently noted as fluid-fluid levels with different signal intensities on T2-weighted image (e)

References

- Ablin DS, Michel Azouz E, et al. Large intrathoracic tumors in children: imaging findings. *AJR Am J Roentgenol*. 1995;165:925–34.
- Daldrup HE, Link TM, Wortler K, et al. MR imaging of thoracic tumors in pediatric patients. *AJR Am J Roentgenol*. 1998;170:1639–44.
- Franken EA, Smith JA, Smith WL. Tumors of the chest wall in infants and children. *Pediatr Radiol*. 1977;6:13–8.
- Gwyther SJ, Hall CM. Mesenchymal hamartoma of the chest wall in infancy. *Clin Radiol*. 1991;43:24–5.
- Kim TS, Han J, Kim GY, et al. Pulmonary inflammatory pseudotumor (inflammatory myofibroblastic tumor): CT features with pathologic correlation. *J Comput Assist Tomogr*. 2005;29:633–9.
- McCahon E. Lung tumours in children. *Pediatr Respir Rev*. 2006;7:191–6.
- McHugh K. Chest tumours other than lymphoma. In: Lucaya J, Strife JL, editors. *Pediatric chest imaging*. 2nd revised ed. New York: Springer; 2008.
- Merten DF. Diagnostic imaging of mediastinal masses in children. *AJR Am J Roentgenol*. 1992;158:825–32.
- Meyer JS, Nicotra JJ. Tumors of the pediatric chest. *Sem Roentgenol*. 1998;33:187–98.
- Meza MP, Benson M, Slovis TL. Imaging of mediastinal masses in children. *Radiol Clin North Am*. 1993;31:583–604.
- Naffaa LN, Donnelly LF. Imaging findings in pleuropulmonary blastoma. *Pediatr Radiol*. 2005;35:387–91.
- Ranganath SH, Lee EY, Restrepo R, et al. Mediastinal masses in children. *AJR Am J Roentgenol*. 2012;198:W197–216.
- Whitten CR, Khan S, Munneke GF, et al. A diagnostic approach to mediastinal abnormalities. *Radiographics*. 2007;27:657–71.
- Williams HJ, Alton HM. Imaging of paediatric mediastinal abnormalities. *Pediatr Respir Rev*. 2003;4:55–66.
- Winer-Muram HT, Kauffman WM, Gronemeyer SA, et al. Primitive neuroectodermal tumors of the chest wall (Askin tumors): CT and MR findings. *AJR Am J Roentgenol*. 1993;161:265–8.
- Wytenbach R, Vock P, Tschappeler H. Cross-sectional imaging with CT and/or MRI of pediatric chest tumors. *Eur Radiol*. 1998;8:1040–6.

Evan J. Zucker and Edward Y. Lee

Contents

15.1	Introduction	508
15.2	Pathophysiology	508
15.3	Imaging	508
15.4	Spectrum of Pediatric Diffuse Lung Disease	509
15.4.1	Congenital Surfactant Dysfunction Disorder.....	509
15.4.2	Neuroendocrine Cell Hyperplasia of Infancy (NEHI)	509
15.4.3	Pulmonary Alveolar Proteinosis (PAP).....	509
15.4.4	Lymphangiectasia and Lymphangiomatosis	509
15.4.5	Bronchiolitis Obliterans (BO).....	510
15.4.6	Hypersensitivity Pneumonitis	510
15.4.7	Nonspecific Interstitial Pneumonia (NSIP).....	510
15.4.8	Connective Tissue and Collagen-Vascular Disease	510
15.4.9	Storage Disease.....	511
15.4.10	Cystic Fibrosis (CF).....	511
15.5	Illustrations: Pediatric Diffuse Lung Disease	512
15.5.1	Congenital Surfactant Dysfunction Disorder.....	512
15.5.2	Neuroendocrine Cell Hyperplasia.....	513
15.5.3	Pulmonary Alveolar Proteinosis	514
15.5.4	Pulmonary Lymphangiomatosis.....	515
15.5.5	Bronchiolitis Obliterans (Swyer–James–Macleod Syndrome).....	516
15.5.6	Hypersensitivity Pneumonitis	517
15.5.7	Nonspecific Interstitial Pneumonia	518
15.5.8	Systemic Sclerosis	519
15.5.9	Niemann–Pick Type B	520
15.5.10	Cystic Fibrosis	521
	References	522

E.J. Zucker, M.D.
Department of Radiology, Lucile Packard Children's Hospital,
Stanford University School of Medicine,
725 Welch Road, Stanford, CA 94305, USA

E.Y. Lee, M.D., M.P.H. (✉)
Department of Radiology, Boston Children's Hospital and Harvard
Medical School, 300 Longwood Avenue, Boston, MA 02115, USA
e-mail: edward.lee@childrens.harvard.edu

15.1 Introduction

Pediatric diffuse lung disease encompasses a broad spectrum of clinicopathological entities. The term is now preferred over Children's Interstitial Lung Disease (chILD), as the disorders often affect the alveoli, airways, blood vessels, lymphatic channels, and pleural spaces in addition to the pulmonary interstitium. The diseases are typified by a constellation of signs and symptoms commonly referred to as the "chILD syndrome." This includes (1) respiratory symptoms (cough, dyspnea, and exercise intolerance), (2) respiratory signs (resting tachypnea, adventitious sounds, retractions, clubbing, failure to thrive, and respiratory failure), (3) hypoxemia, and (4) diffuse pulmonary parenchymal abnormalities on CXR or computed tomography (CT). When more common disorders such as asthma and congenital heart disease have been excluded, >90 % of children with diffuse lung disease satisfy at least three of the above criteria. Associated morbidity and mortality rates are high, although tailored therapies are available according to the specific etiology (Guillerman 2010; Guillerman and Brody 2011; Lee et al. 2011; Lee 2013).

15.2 Pathophysiology

The pediatric diffuse lung diseases have a diverse range of pathophysiologies. In accordance with the classification system proposed by the chILD group, the disorders may be broadly classified into diseases occurring more often in infancy and diseases occurring more often in older children. The infant diseases are (1) diffuse development disorders (acinar dysplasia, congenital alveolar dysplasia, and alveolar capillary dysplasia with misalignment of pulmonary veins), (2) alveolar growth abnormalities, (3) surfactant dysfunction disorders, and (4) specific conditions of undefined etiology. Diseases in older children consist of (1) disorders of the normal host (e.g., infectious/postinfectious, hypersensitivity, and eosinophilic), (2) disorders of the immunocompromised host (e.g., opportunistic infections, post-therapeutic, and posttransplantation), (3) disorders related to systemic disease (e.g., collagen vascular disorders, storage diseases, and histiocytosis), and (4) disorders masquerading as Interstitial Lung Disease (ILD) (e.g., arterial hypertensive vasculopathy and congestive changes related to cardiac dysfunction) (Guillerman 2010; Guillerman and Brody 2011; Langston and Dishop 2004; Lee et al. 2011; Lee 2013).

The histologic patterns of pediatric diffuse lung disease differ from those seen in adult ILD, particularly for neonates and young children, carrying differing prognoses. Traditional adult pathologic entities may be seen across several chILD categories, and a given entity may present with varied pathologic patterns. For example, the nonspecific interstitial pneumonia (NSIP) pattern is seen in many chILD disorders. On

the other hand, genetic surfactant disorders can present with numerous patterns including pulmonary alveolar proteinosis (PAP), desquamative interstitial pneumonia (DIP), NSIP, and chronic pneumonitis of infancy (Guillerman 2010; Guillerman and Brody 2011; Lee et al. 2011). While knowledge is increasing, the etiology of many entities is still not entirely understood.

15.3 Imaging

The imaging assessment typically begins with chest radiographs, most commonly demonstrating hyperinflation. Chest radiographs are rarely normal in patients with diffuse lung disease but generally nonspecific. Additionally, a normal chest radiograph does not exclude diffuse lung disease (Guillerman 2010; Guillerman and Brody 2011).

HRCT is preferred for evaluation and can detect radiographically occult disease, more accurately localize and define thoracic abnormalities, and allow for more precise differential diagnosis or exact diagnosis. The radiation dose can be limited due to inherent contrast between air and lung parenchyma, the diffuse nature of disease, and the low cross-sectional attenuation of the chest in children. To minimize respiratory motion and atelectasis, sedation or general anesthesia with positive airway pressure maneuvers may be used. Alternatively, image acquisition during quiet breathing and lateral decubitus or prone positioning to reduce atelectasis and mimic inspiratory/expiratory CT is usually sufficient for diagnosis (Guillerman 2010; Guillerman and Brody 2011).

With modern CT techniques, the definition of HRCT has become blurred. In conventional HRCT as first described, noncontiguous thin (1–1.5 mm) axial sections are obtained through the lungs at specific locations or spacing increments (typically 5–20 mm) and reconstructed using a high spatial frequency algorithm. The patient is sequentially moved and stopped in the scanner at each acquisition. This method limits radiation exposure and is still generally preferred for examining known or suspected interstitial, peripheral airspace, or small airways disease. However, it is technically challenging and suffers from imaging gaps and inability to produce reformats or use intravenous (IV) contrast. With modern multidetector CT scanners, contiguous sections of the lungs in their entirety can be rapidly and simultaneously obtained as a volume, while the patient is continuously moved through the scanner. High-resolution thin-section images can be reconstructed from the volumetric data set, with similar image quality to conventional HRCT. With reformats and contiguous acquisition, this technique is superior for assessing such findings as pulmonary nodules, bronchiectasis, and mediastinal abnormalities, although at the expense of higher radiation exposure (Guillerman 2010; Guillerman and Brody 2011; Lee 2013).

15.4 Spectrum of Pediatric Diffuse Lung Disease

15.4.1 Congenital Surfactant Dysfunction Disorder

Diseases in this group are caused by genetic abnormalities resulting in surfactant dysfunction, including mutations in surfactant proteins B (SpB) and C (SpC) and the ATP-binding cassette transporter protein A3 (ABCA3). SpB and ABCA3 mutations are autosomal recessive inheritance pattern, while SpC defects are autosomal dominant. Other rare genetic disorders such as thyroid transcription factor-1 (TTF-1) abnormalities (“brain-lung-thyroid syndrome”), lysinuric protein intolerance (LPI), and granulocyte macrophage colony-stimulating factor (GM-CSF)-R α mutations also affect surfactant metabolism and are included in this category. Additional uncharacterized disorders of surfactant metabolism entities exist (Hugosson et al. 2005; Doan et al. 2008; Guillerman 2010; Guillerman and Brody 2011; Olsen et al. 2004; Lee et al. 2011).

Chest radiographs demonstrate diffuse or patchy hazy granular pulmonary opacities. HRCT is characterized by diffuse ground-glass opacity (GGO), consolidation, interlobular septal thickening, or a crazy-paving pattern. With increasing age, the ground-glass opacities decrease in extent and thin-walled parenchymal cysts develop, becoming larger and more numerous over time. Pectus excavatum is common in patients surviving past infancy, possibly due to the effects of chronic lung disease on the growing chest wall (Hugosson et al. 2005; Doan et al. 2008; Guillerman 2010; Guillerman and Brody 2011; Olsen et al. 2004; Lee et al. 2011; Lee 2013).

15.4.2 Neuroendocrine Cell Hyperplasia of Infancy (NEHI)

The etiology of NEHI remains unclear. Histopathologically, there are increased numbers of pulmonary neuroendocrine cells (PNECs) and innervated clusters of PNECs called neuroepithelial bodies in the epithelium of peripheral airways. PNECs function in oxygen sensing and fetal lung development, usually rapidly decreasing in number after the neonatal period. Some patients with NEHI demonstrate mild inflammation or fibrosis of the airways. Additionally, some cases are familial, suggesting a genetic component (Deterding 2010; Dishop 2010; Guillerman 2010; Guillerman and Brody 2011; Lee et al. 2011).

Chest radiographs demonstrate hyperinflation and variable increased perihilar opacity resembling bronchiolitis or reactive airways disease. HRCT findings are characteristic with air trapping and a mosaic attenuation pattern affecting

at least four lobes and geographic ground-glass opacities most prominent in the right middle lobe, lingula, and paramediastinal lung regions. The sensitivity and specificity of HRCT for the diagnosis is reported to be 78–83 % and 100 % when exams are interpreted by experienced pediatric thoracic radiologists (Brody et al. 2010; Deterding 2010; Dishop 2010; Guillerman 2010; Guillerman and Brody 2011; Lee et al. 2011; Young et al. 2011; Lee 2013).

15.4.3 Pulmonary Alveolar Proteinosis (PAP)

PAP is characterized by the abnormal accumulation of surfactant, a lipoproteinaceous material, within the alveoli, preventing normal gas exchange. It may be congenital due to a genetic surfactant deficiency. The acquired form occurs in older children and adults most often due an autoimmune process in which autoantibodies to granulocyte macrophage colony-stimulating factor (GM-CSF) are produced. GM-CSF normally participates in alveolar macrophage signaling, helping to clear surfactant-derived intra-alveolar lipoproteins. PAP may also be secondary to a variety of processes including leukemia, chemotherapy, toxic exposure to fumes and dusts, and other entities that impair alveolar macrophage function (Dishop 2010; Guillerman 2010; Guillerman and Brody 2011; Lee et al. 2011).

Chest radiographs demonstrate symmetric perihilar opacities extending to the peripheral portions of the lungs, generally not as consolidative and dense as would be expected for typical pneumonia. HRCT shows bilateral ground-glass opacities with smooth intra- and interlobular septal thickening in polygonal shapes, an appearance known as crazy paving. The various causes of PAP produce an indistinguishable imaging pattern (Albafouille et al. 1999; Dishop 2010; Guillerman 2010; Guillerman and Brody 2011; Lee et al. 2011; Vrielynck et al. 2008).

15.4.4 Lymphangiectasia and Lymphangiomatosis

Pulmonary lymphangiectasia is characterized by dilatation of the lymphatics draining the pulmonary interstitial and subpleural spaces. It may be congenital or acquired due to pulmonary lymphatic or venous obstruction. Pulmonary lymphangiomatosis is characterized by a proliferation of complex lymphatic channels with secondary lymphatic dilatation. Other thoracic and/or extrathoracic manifestations may be present (Deutsch et al. 2007; Guillerman 2010; Guillerman and Brody 2011; Lee et al. 2011).

Chest radiography demonstrates diffuse hazy opacification of the lungs mimicking surfactant deficiency of prematurity or genetic surfactant deficiency. Chest CT shows

diffuse, smooth thickening of the interlobular septae and peribronchovascular interstitium, patchy ground-glass opacities, and pleural effusions (often chylous). In surviving neonates or patients presenting later in infancy, less severe septal thickening and greater hyperinflation are more typical. Magnetic resonance (MR) imaging demonstrates hyperintensity of the pulmonary interstitium on T2-weighted sequences and pleural effusions. While pulmonary findings are very similar in both disorders, lymph-angiomatosis is more likely to involve extrapulmonary sites with such findings as lytic bone lesions and mediastinal soft tissue edema (Chung et al. 1999; Copley et al. 2000; Deutsch et al. 2007; Guillerman 2010; Guillerman and Brody 2011; Lee et al. 2011).

15.4.5 Bronchiolitis Obliterans (BO)

BO is characterized by a fibroblastic reparative response to injury of the small airways, resulting in occlusion of the lumen. The inciting injury is usually a respiratory viral infection (often adenovirus or influenza) with associated marked airway mucosal necrosis. Other preceding conditions include graft-versus-host disease, chronic allograft rejection in lung transplant patients, and Stevens–Johnson syndrome. Swyer–James–Macleod syndrome is a particular form of BO predominantly affecting one lung and presenting several months or years after the initial infection (Dishop 2010; Guillerman 2010; Guillerman and Brody 2011; Lee et al. 2011).

Chest radiographs are nonspecific and may be normal. The most common abnormality is hyperinflation. A hyperlucent lung on the affected side that is relatively underperfused with normal or decreased volume is characteristic of Swyer–James–Macleod syndrome. CT findings consist of air trapping accentuated on expiration, parenchymal hyperlucency, mosaic attenuation, bronchial wall thickening, bronchiectasis, and pulmonary vascular attenuation. The presence of both hyperlucency and pulmonary vascular attenuation is highly specific for moderate/severe non-transplant BO. In the Swyer–James–Macleod variant, abnormal findings are bilateral in 50 % of cases on CT even if they appear to be unilateral by radiography (Dishop 2010; Guillerman 2010; Guillerman and Brody 2011; Lee et al. 2011).

15.4.6 Hypersensitivity Pneumonitis

This ILD is characterized by pulmonary inflammation related to inhalational exposure of organic antigens usually from birds, fungi, or dusts carried by family members from the workplace. Other inciting antigens include highly reactive low molecular weight compounds found in spray paints, glues, epoxy resins, insecticides, and drugs such as

methotrexate. Pathologically, lymphocytes infiltrate the bronchioles and interstitium with giant cells and poorly developed granulomas situated around bronchioles. The disease may be acute (occurring hours after antigen exposure); subacute (due to repeated antigen exposure over weeks to months); or chronic (insidious progressive course or repeated acute episodes) (Dishop 2010; Guillerman 2010; Guillerman and Brody 2011; Lee et al. 2011).

The acute and subacute forms have similar imaging features. Although chest radiography is often normal, findings may include diffuse micronodular interstitial prominence and opacities in the mid to lower lungs, which may resemble pulmonary edema or pneumonia. HRCT demonstrates small (1–3 mm) poorly centrilobular nodules (reflecting bronchiolitis), ground-glass opacities (reflecting alveolitis), and air trapping, with relative sparing of the upper lungs. The chronic form is characterized by volume loss and fibrotic changes including irregular linear/reticular opacities, architectural distortion, and honeycombing (Dishop 2010; Guillerman 2010; Guillerman and Brody 2011; Lee et al. 2011).

15.4.7 Nonspecific Interstitial Pneumonia (NSIP)

NSIP can be idiopathic, familial, or the final common pathway of several other disorders, including autoimmune connective tissue and collagen vascular diseases, genetic surfactant disorders, and hypersensitivity pneumonitis. Histopathologically, there is a characteristic appearance with temporally and spatially uniform interstitial lymphoplasmacytic inflammation and varying degrees of fibrosis. Cellular and fibrotic subtypes have been described. Best characterized by HRCT, the typical imaging findings are ground-glass and fine linear or reticular opacities predominantly at the lung periphery. Traction bronchiectasis, volume loss (predominantly lower lobe), and honeycombing may develop over time (Brody 2005; Dishop 2010; Guillerman 2010; Guillerman and Brody 2011; Kligerman et al. 2009; Lee et al. 2011).

15.4.8 Connective Tissue and Collagen-Vascular Disease

This heterogeneous group of rheumatologic disorders is characterized by chronic inflammation and generally thought to have an autoimmune basis. Included entities are systemic lupus erythematosus (SLE), rheumatoid arthritis (RA), dermatomyositis, systemic sclerosis, Sjögren syndrome, and mixed connective tissue disease (MCTD). Most commonly, an NSIP histopathologic pattern is found. Pulmonary

lymphoid hyperplasia, organizing pneumonia (intraluminal fibrosis in the distal airways), vasculopathy, and pleuritis may also occur (Dishop 2010; Guillerman 2010; Guillerman and Brody 2011; Lee et al. 2011).

Disorders share an NSIP pattern on imaging with fine reticular or ground-glass opacities predominantly at the lung periphery and generally cannot be differentiated. Ancillary findings may suggest the diagnosis, such as a dilated esophagus in systemic sclerosis. Other findings that may be seen in juvenile systemic sclerosis include subpleural micronodules, subpleural cysts, traction bronchiectasis, and honeycombing. A subset progresses to pulmonary fibrosis with interlobular septal thickening, parenchymal bands, bronchiectasis, mediastinal lymphadenopathy, and pleural and pericardial effusions. Unlike its adult counterpart, childhood-onset SLE more commonly presents with pulmonary hemorrhage rather than ILD (Brody 2005; Dishop 2010; Guillerman 2010; Guillerman and Brody 2011; Kligerman et al. 2009; Lee et al. 2011).

15.4.9 Storage Disease

The lysosomal storage diseases are a group of genetic metabolic disorders resulting in impaired lysosomal function. In the case of Gaucher disease (most common) and Niemann–Pick disease, lipid-laden “foamy” macrophages (Gaucher cells or Niemann–Pick cells, respectively) accumulate in tissues. These lipid-laden macrophages may infiltrate the lung, causing pulmonary symptoms (Guillerman 2010; Guillerman and Brody 2011; Simpson et al. 2010).

Lung involvement in Gaucher disease is more typical of the neuronopathic type III form. Chest radiographs may show reticulonodular opacities. Potential findings on CT include ground-glass opacities, consolidation, interstitial thickening, bronchial wall thickening, thymic enlargement, and hilar and mediastinal lymphadenopathy. Pulmonary

abnormalities typically abate, but do not entirely resolve with enzyme replacement therapy. A nonspecific reticulonodular pattern with diffuse interstitial thickening is characteristic of chest radiographs and CT in Niemann–Pick disease type B. Ground-glass opacity and subcentimeter, sometimes calcified nodules, may occur. A crazy-paving pattern is seen in Niemann–Pick disease type C2. Pulmonary involvement in Niemann–Pick disease generally progresses from caudal to cranial (Guillerman 2010; Guillerman and Brody 2011).

15.4.10 Cystic Fibrosis (CF)

CF is the most common genetic cause of chronic pulmonary disease in children, resulting from autosomal recessive mutations in the cystic fibrosis transmembrane regulator (CFTR) gene. Chronic recurrent infections develop, in addition to numerous extrapulmonary manifestations such as meconium ileus in infancy. With progressive disease, there are chronic inflammatory changes leading to alteration of airway walls with epithelial erosion, partial replacement of the mucosa by granulation tissue, progressive airway dilatation resulting in bronchiectasis, and fibrotic/obliterative changes involving the small airways (Lee et al. 2011).

Chest imaging with radiographs and CT may be normal or show only mild air trapping and/or bronchiectasis early in the course of the disease. In more advanced cases, there is upper lobe predominant bronchiectasis, bronchial wall thickening, centrilobular nodular and tree-in-bud opacities, and mucus plugging with air trapping. A finger-in-glove pattern of mucoid impaction similar to allergic bronchopulmonary aspergillosis may be observed (Martinez et al. 2008). Due to chronic/recurrent infections, mediastinal and hilar lymphadenopathy are often present. Although primarily used in research settings, radiography and CT-scoring systems are available for quantifying the extent and severity of the disease (Cleveland et al. 1998; Lee et al. 2011).

15.5 Illustrations: Pediatric Diffuse Lung Disease

15.5.1 Congenital Surfactant Dysfunction Disorder

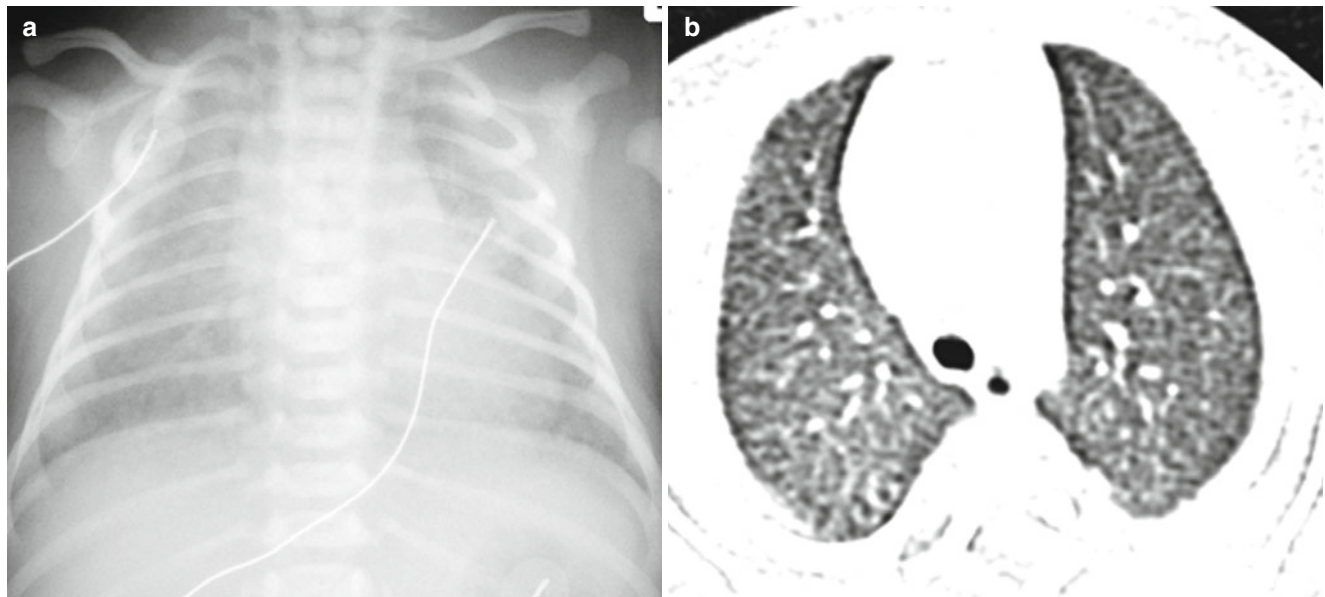


Fig. 15.1 Surfactant protein B mutation in a full-term newborn boy. (a) Frontal chest radiograph shows diffuse hazy granular opacity resembling respiratory distress syndrome of prematurity. (b) Axial lung window CT image demonstrates diffuse ground-glass pulmonary opacification

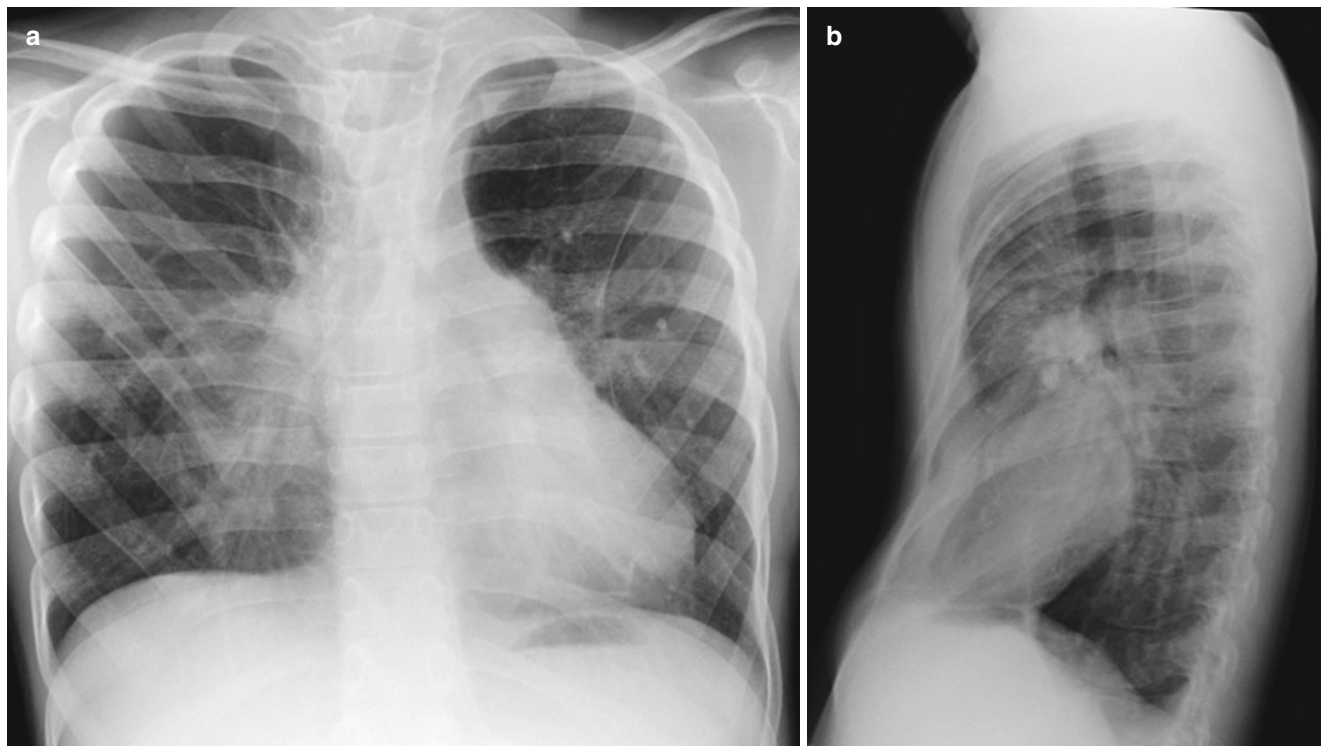


Fig. 15.2 ABCA3 mutation in a 5-year-old boy. (a) Frontal chest radiograph shows increased coarse interstitial opacities in both lungs. (b) Lateral chest radiograph demonstrates a pectus excavatum

15.5.2 Neuroendocrine Cell Hyperplasia

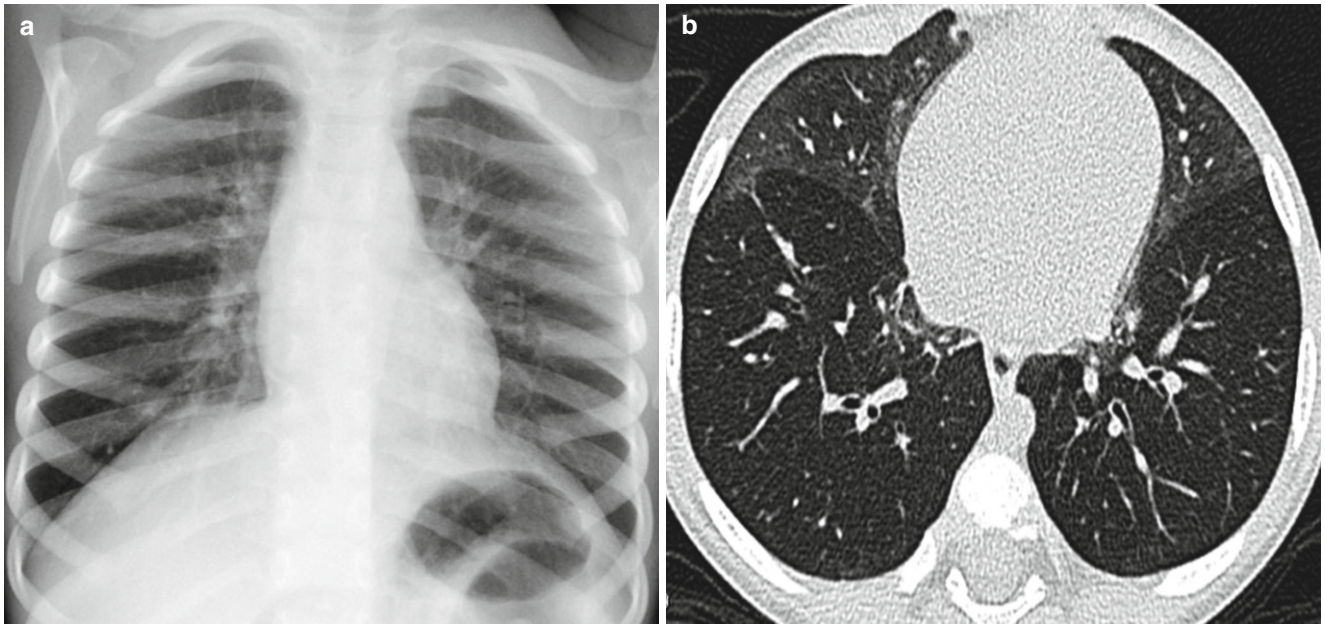


Fig. 15.3 Neuroendocrine cell hyperplasia of infancy in a 5-month-old boy who presented with persistent tachypnea, retractions, hypoxemia and crackles. **(a)** Frontal chest radiograph shows pulmonary

hyperinflation with opacities in the perihilar and paramediastinal regions. **(b)** Axial lung window CT image demonstrates geographic ground-glass opacities in the right middle lobe and lingula

15.5.3 Pulmonary Alveolar Proteinosis

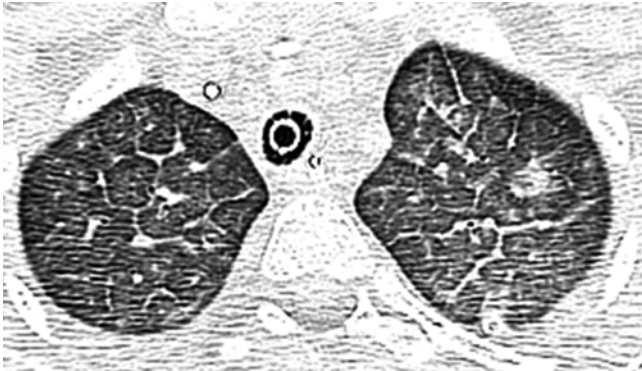


Fig. 15.4 Pulmonary alveolar proteinosis in an 8-year-old girl. Axial lung window CT image shows bilateral ground-glass opacities with smooth intra- and interlobular septal thickening in polygonal shapes, an appearance known as crazy paving

15.5.4 Pulmonary Lymphangiomatosis

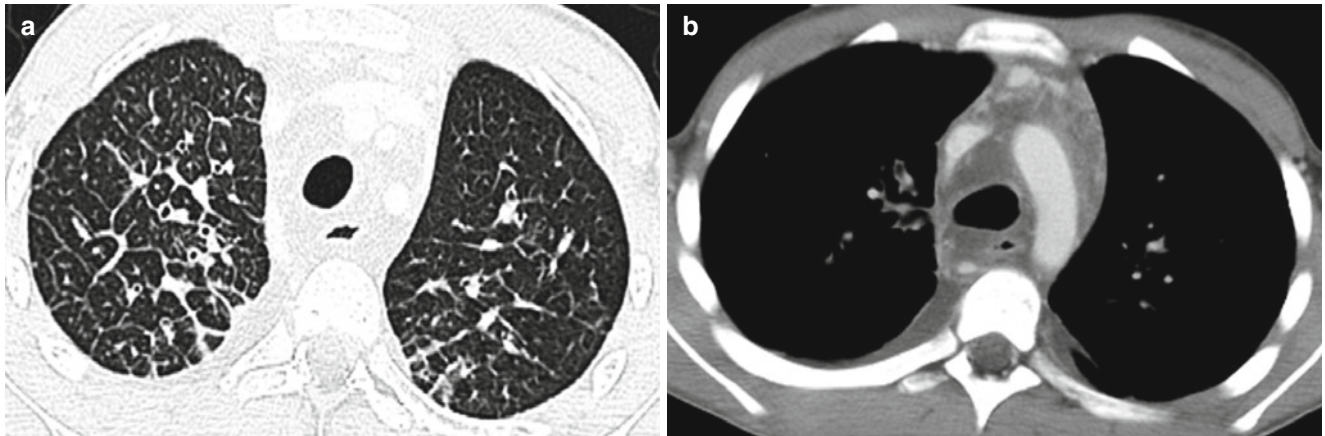


Fig. 15.5 Pulmonary lymphangiomatosis in a 5-year-old boy. **(a)** Axial lung window CT image shows interlobular septal thickening in both lungs. **(b)** Axial soft tissue window CT image demonstrates mediastinal edema and bilateral pleural effusions

15.5.5 Bronchiolitis Obliterans (Swyer–James–Macleod Syndrome)

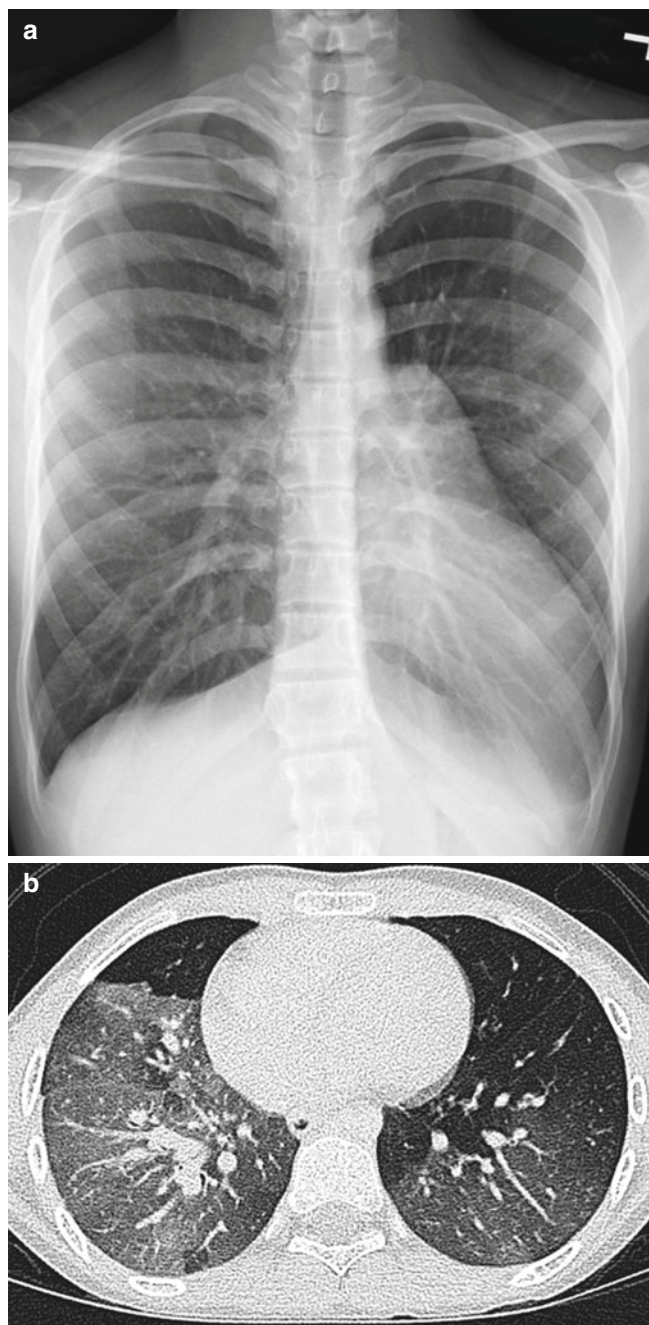


Fig. 15.6 Bronchiolitis obliterans (Swyer–James–Macleod syndrome) in a 6-year-old girl with multiple viral pneumonias. **(a)** Frontal chest radiograph shows hyperlucent left lung with decreased lung volume and underlying pulmonary vessels in comparison to the right lung. **(b)** Axial lung window CT image demonstrates accentuated hyperlucent oligemic segments of lung, worse on the left side than the right side

15.5.6 Hypersensitivity Pneumonitis

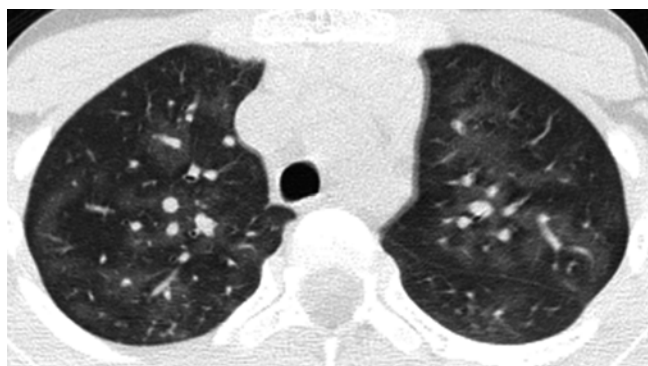


Fig. 15.7 Hypersensitivity pneumonitis in an 8-year-old boy who presented with worsening cough, fatigue, and repetitive bird exposure in his parents' farm. Axial lung window CT image shows scattered lobular areas of ground-glass attenuation in both lungs

15.5.7 Nonspecific Interstitial Pneumonia

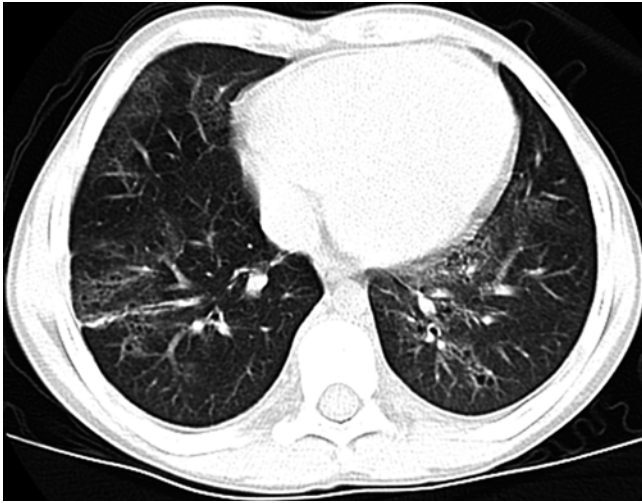


Fig. 15.8 Nonspecific interstitial pneumonia in an 11-year-old boy who presented with dry cough, shortness of breath, and fatigue. Axial lung window CT image shows a combination of ground-glass opacification and traction bronchiectasis

15.5.8 Systemic Sclerosis

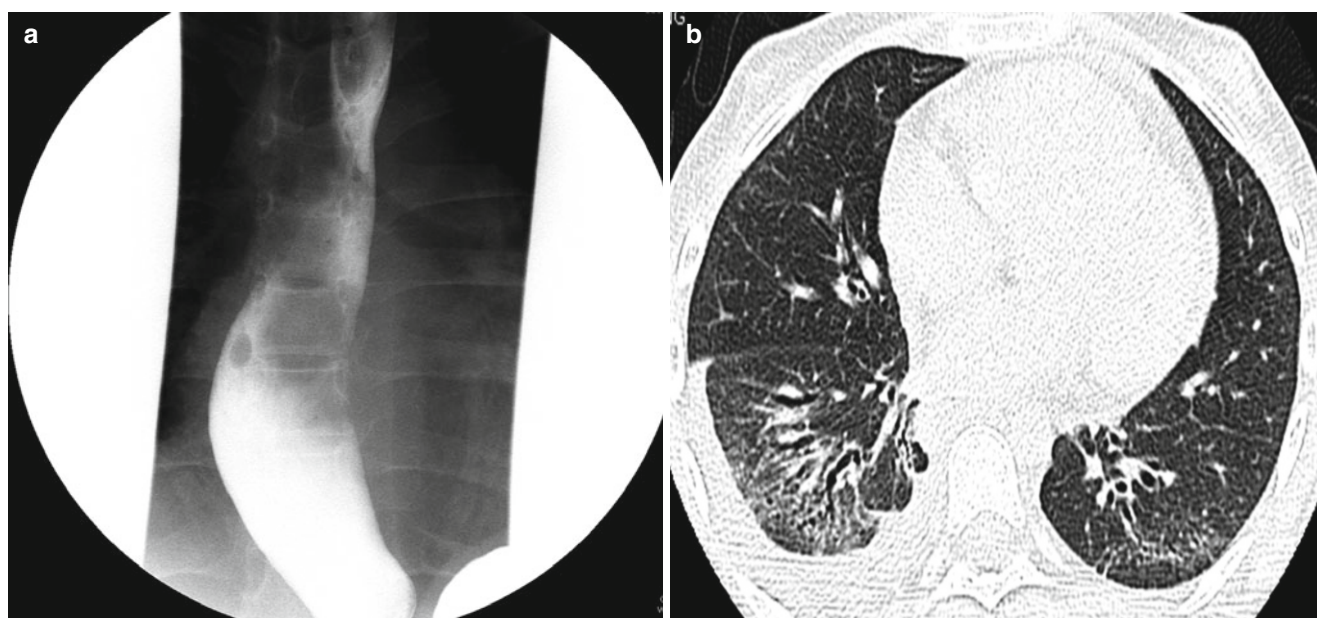


Fig. 15.9 Systemic sclerosis in a 13-year-old girl. **(a)** Frontal fluoroscopic spot image obtained during barium swallow study shows a dilated esophagus. **(b)** Axial lung window CT image demonstrates

clusters of small cysts at the lung periphery, resembling honeycombing, ground-glass opacification, and bronchiectasis

15.5.9 Niemann–Pick Type B

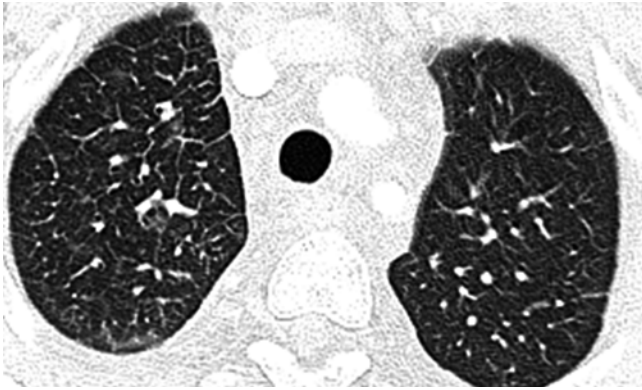


Fig. 15.10 Niemann–Pick type B in a 2-year-old girl. Axial lung window CT image demonstrates diffuse thickening of the pulmonary interstitium

15.5.10 Cystic Fibrosis

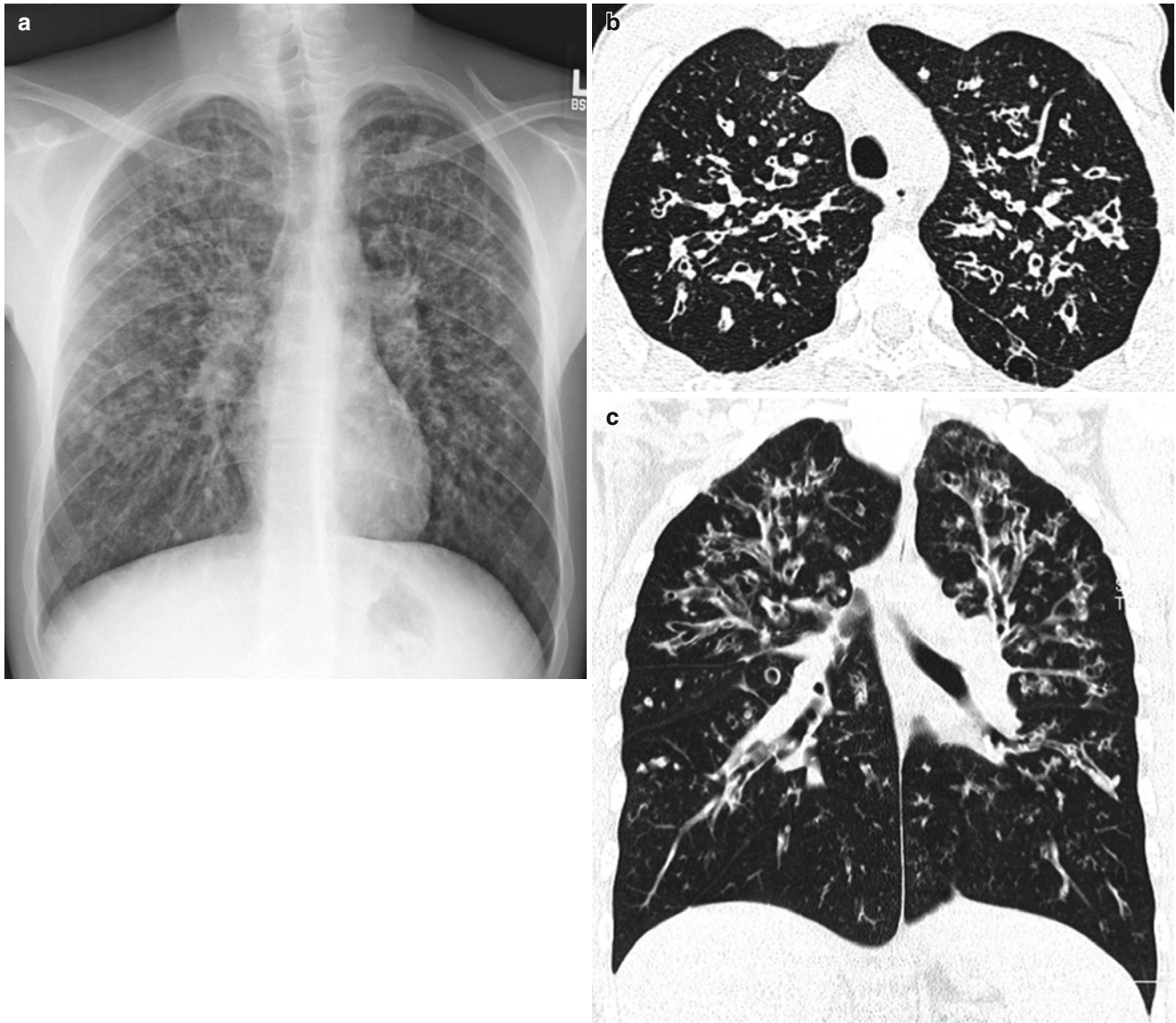


Fig. 15.11 Cystic fibrosis in a 15-year-old girl. (a) Frontal chest radiographs demonstrates diffuse bronchiectatic lung changes and areas of nodular opacities likely related to underlying mucus plugging. (b)

Axial lung window CT image shows bronchiectasis in both lungs. (c) Coronal lung window CT image demonstrates upper lobe predominant bronchiectatic changes in both lungs

References

- Albafouille V, Sayegh N, De Coudenhove S, et al. CT scan patterns of pulmonary alveolar proteinosis in children. *Pediatr Radiol*. 1999;29:147–52.
- Brody AS. Imaging considerations: interstitial lung disease in children. *Radiol Clin North Am*. 2005;43:391–403.
- Brody AS, Guillerman RP, Hay TC. Neuroendocrine cell hyperplasia of infancy: diagnosis with high-resolution CT. *AJR Am J Roentgenol*. 2010;194:238–44.
- Chung CJ, Fordham LA, Barker P, et al. Children with congenital pulmonary lymphangiectasia: after infancy. *AJR Am J Roentgenol*. 1999;173:1583–8.
- Cleveland RH, Neish AS, Zurakowski D, et al. Cystic fibrosis: predictors of accelerated decline and distribution of disease in 230 patients. *AJR Am J Roentgenol*. 1998;171:1311–5.
- Copley SJ, Coren M, Nicholson AG, et al. Diagnostic accuracy of thin-section CT and chest radiography of pediatric interstitial lung disease. *AJR Am J Roentgenol*. 2000;174:549–54.
- Deterding RR. Infants and young children with children's interstitial lung disease. *Pediatr Allergy Immunol Pulmonol*. 2010;23:25–31.
- Deutsch GH, Young LR, Deterding RR, et al. Diffuse lung disease in young children: application of a novel classification scheme. *Am J Respir Crit Care Med*. 2007;176:1120–8.
- Dishop MK. Diagnostic pathology of diffuse lung disease in children. *Pediatr Allergy Immunol Pulmonol*. 2010;23:69–85.
- Doan ML, Guillerman RP, Dishop MK, et al. Clinical, radiological, and pathological features of ABCA3 mutations in children. *Thorax*. 2008;63:366–73.
- Guillerman RP. Imaging of childhood interstitial lung disease. *Pediatr Allergy Immunol Pulmonol*. 2010;23:43–68.
- Guillerman RP, Brody AS. Contemporary perspectives on pediatric diffuse lung disease. *Radiol Clin North Am*. 2011;49:847–68.
- Hugosson CO, Salama HM, Al-Dayel F, et al. Primary alveolar capillary dysplasia (acinar dysplasia) and surfactant protein B deficiency: a clinical, radiological and pathological study. *Pediatr Radiol*. 2005;35:311–6.
- Kligerman SJ, Groshong S, Brown KK, et al. Nonspecific interstitial pneumonia: radiologic, clinical, and pathologic considerations. *Radiographics*. 2009;29:73–87.
- Langston C, Dishop MK. Infant lung biopsy: clarifying the pathologic spectrum. *Pathol Int*. 2004;54:s419–21.
- Lee EY. Interstitial lung disease in infants: new classification system, imaging technique, clinical presentation and imaging findings. *Pediatr Radiol*. 2013;43:3–13.
- Lee EY, Cleveland RH, Langston C. Interstitial lung disease in infants and children: new classification system with emphasis on clinical, imaging, and pathologic correlation. In: Cleveland RH, editor. *Imaging in pediatric pulmonology*. New York: Springer; 2011.
- Martinez S, Heyneman LE, McAdams HP, et al. Mucoid impactions: finger-in-glove sign and other CT and radiographic features. *Radiographics*. 2008;28:1369–82.
- Olsen EO, Sebire NJ, Jaffe A, et al. Chronic pneumonitis of infancy: high-resolution CT findings. *Pediatr Radiol*. 2004;34:86–8.
- Simpson Jr WL, Mendelson D, Wasserstein MP, et al. Imaging manifestations of Niemann–Pick disease type B. *AJR Am J Roentgenol*. 2010;194:W12–9.
- Vrielynck S, Mamou-Mani T, Emond S, et al. Diagnostic value of high-resolution CT in the evaluation of chronic infiltrative lung disease in children. *AJR Am J Roentgenol*. 2008;191:914–20.
- Young LR, Brody AS, Inge TH, et al. Neuroendocrine cell distribution and frequency distinguish neuroendocrine cell hyperplasia of infancy from other pulmonary disorders. *Chest*. 2011;139:1060–71.

Part IV

Cardiovascular System

Whal Lee and Eun-Ah Park

Contents

16.1	Introduction	526
16.2	Differences between CT and MRI	526
16.3	Principles of CT for Cardiovascular Imaging	526
16.3.1	Multi-detector Computed Tomography.....	526
16.3.2	Principles of EKG-Gating CT.....	526
16.3.3	Non-gating Cardiac Scan.....	527
16.3.4	Selection of kVp and mAs.....	527
16.3.5	Scan Range.....	527
16.3.6	Radiation Dose in Cardiac CT.....	527
16.3.7	Post-Processing of the CT Data Set.....	527
16.4	Principles of Cardiovascular MR Imaging	528
16.4.1	Sequences.....	528
16.4.2	EKG-Gating Cine: Segmented K-Space Filling.....	528
16.4.3	Overcoming Respiratory Motion.....	529
16.4.4	Velocity-Encoding Cine.....	529
16.4.5	T1-Weighted Image and T2-Weighted Image.....	529
16.4.6	Inversion Recovery-Delayed Enhancement Image.....	530
16.4.7	MR Angiography.....	530
16.5	Illustrations: Pediatric Cardiac Imaging I: CT and MR Techniques	531
16.5.1	Sequential Scan, Spiral Scan and Multi-detector Computed Tomography.....	531
16.5.2	Concept of EKG-Gated CTs.....	532
16.5.3	Prospective Triggered EKG-Gated CTs.....	533
16.5.4	Voluntary Motion Artifacts in EKG-Gated CTs.....	534
16.5.5	Effect of Scan Speed on Motion Artifacts.....	535
16.5.6	Cardiac Motion Artifacts in Non-gated Cardiac CTs.....	536
16.5.7	Iodine K Edge Absorption and CT X-Ray Spectrum.....	537
16.5.8	Scan Range for Cardiac CTs.....	538
16.5.9	Three-Dimensional Reconstruction.....	539
16.5.10	Examples of Pulse Sequence Diagram.....	540
16.5.11	EKG Gating and Segment K-Space Filling.....	541
16.5.12	EKG-Gated Cine.....	542
16.5.13	Different Pulse Sequences and Different Contrasts.....	543
16.5.14	Free Breathing Image Acquisition.....	544
16.5.15	Respiratory Gating Image Acquisition.....	545
16.5.16	Velocity-Encoding Cine.....	546
16.5.17	The Image of the Velocity-Encoding Cine.....	547

W. Lee, M.D., Ph.D. (✉)
Department of Radiology,
Seoul National University College of Medicine,
Seoul National University Hospital, Seoul, Korea
e-mail: whal.lee@gmail.com

E.-A. Park, M.D.
Department of Radiology,
Seoul National University Hospital, Seoul, Korea
e-mail: inameuna1@gmail.com

16.5.18	Example of T2-Weighted Image and T1-Weighted Image	548
16.5.19	Inversion Recovery Delayed Enhancement Image for Myocardium	549
16.5.20	MR Angiography	550
References		551

16.1 Introduction

Cardiac imaging in children is challenging. Invasive cardiac catheterization and angiography had been used for a long time, and echocardiography took over their important roles in the diagnosis of cardiac disorders. Computed tomography (CT) and magnetic resonance imaging (MRI) have lately been used for cardiac and vascular disease with the help of technical developments including the multi-detector CT (MDCT) and EKG-gating method (Boxt 2004; Macovski 1983; Crean 2007). The CT and MRI have stronger points over echocardiography. The sonic window is no longer a problem in CT and MRI (Fogel et al. 2006). However, CT and MRI are not real-time imaging tools, unlike echocardiography. The way to get a good image is not simple and there are many options in scanning. Knowing the basic principles of cardiac imaging with CT and MRI is essential for cardiovascular radiologists to use these updated imaging modalities (Lee 2006).

16.2 Differences between CT and MRI

Firstly, the biggest difference between CT and MRI is the use of ionizing radiation in CT. MRI uses the physical properties of the proton in a very strong magnetic field, applying strong radio frequency and rapidly flapping gradient magnetic fields to patients' bodies, but there is no radiation exposure (Lee 2006). Secondly, the usual scan is very short in CT, within several seconds, but an MRI usually takes about an hour. Thirdly, the level of sedation for imaging is also different. A CT scan can be done with light sedation, but an MRI needs deeper sedation, including general anesthesia. Fourthly, even though both imaging modalities can image anatomical structure very well, they have their own advantages on tissue evaluation. MRI has a unique property of tissue characterization and can be used for further differentiation of soft tissue mass and myocardium. On the other hand, CT can easily separate the airway and fat from other soft tissue (Taylor 2008). The air is not a good substance for MRI, even though MR can show the airways, but CT is superior to showing the air in the soft tissue, including the lung. Finally, the great difference in CT and MRI application is the functional assessment of the heart and flow quantification. MRI has a powerful tool to demonstrate cardiac motion. The cine MRI is one of the gold standards for assessing cardiac chamber volume and function nowadays. Velocity encoding cine is one of the most powerful tools for flow quantification. The MRI can assess the velocity of the blood in each pixel at

every point in time with usual 20–50 ms temporal resolution, and this information can be used to check the volume flow, time-velocity curve, or regurgitation fraction of a specific vessel (Kilner et al. 2007).

16.3 Principles of CT for Cardiovascular Imaging

16.3.1 Multi-detector Computed Tomography

The classic CT scans in a sequential mode (Fig. 16.1) (Hounsfield 1973) – that is, one single rotation scan with a fixed table position and a table feed for the next scan position and another rotation and another table feed and going on to cover the entire area of interest. The helical CT did scan with continuous table feeding and continuous gantry rotation. The scan pathway shows helical. The spiral CT is faster than the sequential single slice CT (Brink et al. 1994). In late 1990, the usual rotation time of a single slice spiral CT is 1 s.

In 1998, the first MDCT was introduced. The first generation of MDCT had four detector rows and the gantry rotation time was 0.5 s. With MDCT, the same range of the body can be scanned eight times faster. The MDCT showed rapid development and the number of detector rows increased to 8, 16, 64, 128, and 320 (Rybicki et al. 2008); the rotation time is faster up to 0.27 second. The speed of the scan of MDCT to cover some range of the body is markedly faster than single-slice CT and the breath-hold time is no longer a matter to scan the aorta.

The dual-source CT, which has two X-ray tubes and two detector sets in a single gantry, is introduced and clinically used since 2006 (Flohr et al. 2006).

16.3.2 Principles of EKG-Gating CT

EKG-gating is essential for cardiac CT because of the heart-beat. Without gating, the beating motion will be included in CT images, and therefore, most of the intracardiac structure, and other structures near the heart, will show significant artifacts. The image acquisition in the cardiac phase, such as the end-systolic phase or mid-diastolic phase in which the heart motion is the least, is the key to the EKG-gating scan (Fig. 16.2). There are two ways to perform EKG gating: One is retrospective EKG-gating reconstruction. The spiral scan continues with recording of the EKG signal, and images are retrospectively reconstructed at some cardiac phase from

the recorded EKG signal. The other is a prospective EKG-triggering scan. The sequential CT acquisition is done after noticing the R wave and there is a time delay to get to the desired cardiac phase. The table feed will be done on the next R-R period, and the next sequential CT acquisition will be done on the following R-R interval. The retrospective EKG gating reconstruction has the freedom of choosing the cardiac phase, but the radiation dose is higher due to unused data acquisition. The prospective EKG triggering needs several heartbeats to cover the whole heart. Recently developed wide detector CTs can do one-beat cardiac scans, especially in pediatric patients. The radiation dose is much lower in prospective EKG triggering methods (Fig. 16.3). The drawback of EKG-gated CT is the motion artifact from breathing or voluntary motion, especially in pediatric patients (Fig. 16.4). The breath-hold scan is recommended but not mandatory. In most small children, the free breathing EKG-gated CT can be done with acceptable breathing motion artifacts.

16.3.3 Non-gating Cardiac Scan

Even though the heart is beating, the recent fast scanners enable the cardiac scan without EKG gating (Fig. 16.5). The intracardiac structure, such as the interatrial or interventricular septum, is hard to evaluate, but the great vessels including the aorta, pulmonary arteries, central veins, or even coronary arteries can be demonstrated on a non-gating cardiac scan. Because the intracardiac structure can be usually examined by echocardiography, most of the clinical request of the cardiac CT is for evaluating large vessels rather than intracardiac structures. Non-gating cardiac scanning is one of the good options in pediatric cardiac CT. However, the cardiac motion causes an artifact that can be misunderstood as an abnormal structure; careful interpretation is needed (Fig. 16.6). One of the pitfalls is that the radiation doses of non-gating spiral scans and EKG triggered sequential scans are not so different, and the radiation dose is actually slightly lower in the EKG-triggered sequential scan because there is overscan in spiral scanning for interpolation image reconstruction. The radiation dose of the retrospective EKG gating reconstruction is always higher than that of the non-gating spiral scan or that of the EKG-triggered sequential scan.

16.3.4 Selection of kVp and mAs

The selection of kVp of contrast-enhanced CT angiography is important, especially in pediatric patients. The contrast of the iodine contrast media is much higher in lower kVp, such as 80 or 70 kVp. The reason for this finding is the K-edge of the iodine contrast. The iodine absorbs the X-ray more effectively around 33 keV, and the lower kVp setting has a relatively higher proportion of this energy level (Fig. 16.7).

The noise will be higher in lower kVp, but the increased contrast compensates for the increase in noise, and the overall contrast to the noise ratio is higher in the lower kVp in the setting of the same radiation dose. An 80 kVp or lower is highly recommended in pediatric CT angiography.

16.3.5 Scan Range

The scan range is one of the important parameters in pediatric cardiac scans. Too much of a wide scan range means a higher radiation dose. The scan range should be minimized to include all anatomical structures to be investigated. In most of the cases, the range from the slice slightly above the aortic arch to the diaphragmatic surface will be enough to cover the entire heart and great vessels. It can be more customized in the case of a follow-up examination of the arch or pulmonary arteries. In the case of an infracardiac total anomalous pulmonary venous return, the portal vein or inferior vena cava should be imaged (Fig. 16.8).

16.3.6 Radiation Dose in Cardiac CT

Using CT on a child demands great caution because of the radiation exposure. The radiation dose should be monitored and the radiologist who does the pediatric scan should keep in interest about the radiation dose in all examinations. Children are more susceptible to radiation exposure, even with lower doses of radiation. The CT radiation dose showed a wide range of difference – more than tenfold from institute to institute – in reports from the USA and Korea. The radiation dose of CT can be reduced to an insignificant level if radiologists carefully optimize the CT protocols (McCollough 2003). The key factor to reducing the radiation dose is lowering kVp while keeping minimum tube current or mAs as low as possible to obtain reasonable image noise. Optimizing the scan range and avoiding the meaningless additional phase scanning, such as a pre-contrast scan or delayed phase scan, are necessities for reducing the radiation dose. A single arterial phase is enough in most of the cases of pediatric cardiac CT. Using automatic exposure control is useful. Recently, many kinds of iterative reconstruction have been widely used, and it improves image quality by decreasing image noise without impairment of image sharpness. Therefore, the combination of iterative reconstruction and low-dose CT is highly recommended.

16.3.7 Post-Processing of the CT Data Set

Congenital heart disease often has a complex anatomy. The three-dimensional reconstruction of the CT data set has great clinical benefits (Kim et al. 2002). There are several ways to demonstrate three-dimensional structures

in a two-dimensional image display. The CT axial data sets are almost iso-voxel three-dimensional data sets with 0.3–0.5 mm in-plane pixel size and 0.4–0.6 mm z-axis resolution. Each voxel had very wide range scale of up to 2,000 HU. For demonstrating these volume data sets, the optimal window setting and the manner of display should be taken into consideration (Lotz et al. 2002). The manner of post-processing should be chosen to demonstrate the key anatomical structures or findings of the patient's disease for determining the treatment or surgical plan.

16.3.7.1 Three-Dimensional Volume Rendering

The three-dimensional volume-rendering image is a real three-dimensional image (Fig. 16.9a). The volume rendering needs the opacity-transparency function that determines which voxel will be displayed with certain degrees of transparency. The color coding according to the CT number of each voxel makes the three-dimensional images more comprehensive. With an artificial light source, the image looks like volume. This image technique is good for showing the vascular structures and airways. The opacity-transparency function can be applied multiple, and therefore the enhanced vessel and airway can be demonstrated in a different color setting. The pitfall of volume rendering is that the overlapping structure can be obscured by other structures, and stenosis of the vessel is frequently over- or underestimated.

16.3.7.2 Multiplanar Reformat

Multiplanar reformat (MPR) is not a real three-dimensional image and the information in the image is also two-dimensional. But the MPR image can be made from any plane in the volume and it is very useful for demonstrating the complex anatomy of congenital heart disease in any arbitrary plane. This technique is good for showing intracardiac structures and extracardiac great vessels, including pulmonary arteries. The classic MPR is made from the plane of single voxels, but the thick MPR is also possible by averaging the multiple layers of voxels. The curved MPR is MPR along the curved plane and good for demonstrating tortuous vessels (Fig. 16.9b). The drawback of this technique is that it is not three-dimensional information.

16.3.7.3 Maximum Intensity Projection

Maximum intensity projection is similar to thick MPR images, but the CT number of the displayed pixel is not from the average of several pixels but from the maximum CT number of the designated voxels. As the vessels usually have the highest CT number in CT angiography, this technique is very useful for demonstrating the whole length of the small vessels having a very tortuous course (Fig. 16.9c). The minimum intensity projection is also possible and good for demonstrating airways (Fig. 16.9d).

16.4 Principles of Cardiovascular MR Imaging

16.4.1 Sequences

Cardiac MR uses main strong magnetic fields, additional gradient magnetic fields, and RF pulses. The image is generated by the signal from the proton after applying gradient magnetic fields and RF pulses. The series of gradient fields and magnetic pulses are called sequences, which is a kind of software for the MR machine to make an image (Fig. 16.10). There are a number of sequences, and each sequence has a specific feature. There are also many parameters in optimizing the sequences to make better images in every different situation. To obtain a nice image, radiologists should be familiar with the characteristics of the sequences and the meaning of each parameter. The sequences can present as sequence diagrams. Although it is not necessary to understand the sequence diagram in detail as a radiologist to get a good image, having basic knowledge of the parameters in operating sequences is important for image acquisition and interpretation.

16.4.2 EKG-Gating Cine: Segmented K-Space Filling

Cine MRI is the stack of still images of each cardiac phase, with 7–30, usually 20–25 frames per heartbeat used. The sequences for cardiac cine are a balanced steady-state free precession sequence or a spoiled gradient echo sequence. The scan time is usually 8–10 s for single-slice cine image, depending on the number of segments and phase encoding steps (Fogel 2000). The single plane cine image is made from about 10 heartbeats (Fig. 16.11). The reconstruction of 20-frame still images along the cardiac cycle from 10 heartbeats needs segmented K-space filling. Each cardiac cycle is divided into 20 segments and K space information of each segment is gathered from 10 heartbeats serially. The numbers of K-space lines filled in one R-R interval vary from 9 to 20. If the number of K space filling is 13, and the phase encoding steps of each image are 130, complete filling of the K-space needs 10 heartbeats. In this particular case, the temporal resolution of the cine image is 13 times of the repetition time which is usually 3–5 ms in standard steady state free precession (SSFP) image (Fig. 16.12). In cine, the phase-encoding steps and the number of K spaces will determine the temporal resolution, the spatial resolution, and the scan time. The frame rate and heart rate are also parameters that affect the temporal resolution, spatial resolution, and the scan time (Dymarkowski 2005).

Balanced SSFP sequences provide better SNR and contrast between the blood and myocardium than spoiled gradient echo (Fig. 16.13). However, it needs a more

homogenous magnetic field and is more susceptible in field inhomogeneity. If there is any material that can cause magnetic field inhomogeneity, it would be better to use a spoiled gradient echo sequence rather than SSFP. In a very small infant, sometimes the flow artifact in SSFP is significant; in this case, the spoiled gradient is also more helpful than SSFP. The real-time cine gathers all the K space information in a single R-R interval. Although the temporal and spatial resolution is poor, the real-time cine can be used effectively in children with arrhythmias and breathing artifacts. Radial K space sampling can be used for cine imaging. Instead of using phase-encoding steps, radial K space sampling uses multiple different angles of frequency-encoding steps and back projection reconstruction like CT. There are a number of views in radial sampling, while there are a number of phase-encoding steps. Because it does not use phase encoding steps, there is no phase wrapping in small fields of view. Radial sampling is more susceptible to field inhomogeneity.

16.4.3 Overcoming Respiratory Motion

In the case where the scan time is longer than the usual breath-holding time, the respiratory motion should be considered in image acquisition. The easiest way to overcome respiratory motion is just by adding number of acquisition. The averaged image acquisition technique with free breathing allows for acquiring cine or still images with generous artifacts, which is acceptable in a clinical image reading (Fig. 16.14). The recommended number of excitation is 2 or 3 in most of the sequences. If the target organ is small, like a coronary artery, or there is a significant motion artifact after averaging, the respiratory gating or triggering is essential to obtaining an affordable image. The respiratory gating needs monitoring of the diaphragm motion; the image acquisition will take place only in a certain position of the diaphragm, which is top of the right hemi diaphragm at the end of the expiratory phase (Fig. 16.15) (Sakuma et al. 2005). The parameter for respiratory gating is the acceptance window of the diaphragm motion, which is 1.5–3 mm, depending on the target structure and patient's size (Greil et al. 2002).

16.4.4 Velocity-Encoding Cine

Velocity-encoding cine (VENC) is a unique MRI tool to assess the flow in the vessel (Kilner et al. 2007). After applying two opposite gradient magnetic fields, static protons will restore their phases, but the moving protons will show some degree of phase shift that is proportionally related to the velocity of the protons (Fig. 16.16) (Chai and Mohiaddin 2005). The phase shift map can be generated and the degree of the phase shift can be read as velocity of the proton

(Fig. 16.17). If the phase shift is over 180° or -180° , it will be read as the opposite direction of the flow. This is also a kind of phase wrapping or an aliasing artifact. To avoid aliasing, the velocity range should be determined as part of a sequence parameter. For the aorta and pulmonary artery of a child, 150 cm/s can be used for the initial velocity range. If there is aliasing with this range, the range should be increased. For the veins, 50–100 cm/s is enough. If the velocity ranges are much higher over the optimal range, the image noise increases and the value is less accurate. The number of segments in K-space filling is also adequately adjusted in the same way as the SSFP cine image. The scan time is usually longer than breath-holding time. The average technique with free breathing is preferred.

16.4.5 T1-Weighted Image and T2-Weighted Image

T1 time and T2 time are tissue-specific magnetic resonance characteristics. The proton has longitudinal magnetization and transverse magnetization. After applying radiofrequency pulses, the longitudinal magnetization is flipped to some degree and recovered by time. Some substances, such as fat, recover longitudinal magnetization quickly and some substances, such as water, recover longitudinal magnetization slowly. The time of 67 % of recovery after applying a 90° flip angle is T1 relaxation time. T1 time of fat is about 600 ms in 1.5 T and T1 time of water is about 3,000 ms in 1.5 T. The transverse magnetization is formed after applying the RF pulse. The transverse magnetization disappears with time. The time to 33 % of transverse magnetization remained is T2 decay time; T1-weighted image is designed to demonstrate the T1 effect by using short TR and long TE. T2-weighted images are designed to demonstrate the T2 effect by using a long TR and short TE. The difference of these T1 and T2 times can be used for tissue characterization in such a case of cardiac mass (Fig. 16.18). A fibroma shows low signal intensity in T1- and T2-weighted images. Pericardial cysts show high-signal intensity in T2-weighted images and lower signal intensity in T1-weighted images. One pitfall of T1-weighted images in cardiac MRI is that the effective TR is limited to R-R interval, due to the EKG gating. Therefore, the T1 effect is not as strong in lower heart rates. Another pitfall is that the signal intensity of the myocardium is not homogeneous because of the field inhomogeneity, different coil sensitivity, and cardiac motion artifacts.

T1 mapping and T2 mapping could be used to overcome the drawbacks of T1- and T2-weighted images of the cardiac scan. The mapping sequences consist of serial images acquired with different TE. Exact T1 and T2 relaxation times can be calculated by plotting each pixel in T1 recovery or T2 decay value at every single TE point (Pennell 2006).

16.4.6 Inversion Recovery-Delayed Enhancement Image

Delayed washout of contrast material from infarcted myocardium or myocardial fibrosis will cause it to appear slightly hyperintense relative to intact myocardium about 5 or 20 min after the administration of gadolinium-based contrast (Lloyd and Gupta 2005). Visualization of delayed enhancement in the infarcted myocardium can be maximized by using an inversion recovery myocardial nulling technique. With this sequence, longitudinal magnetization of the whole tissue inverts after a 180° inversion pulse, and then the image is acquired by waiting for a certain period for the recovery of the tissue's longitudinal magnetization. Each tissue has a different T1 time, according partly to their intrinsic T1 time and mainly to the concentration of the contrast material, because contrast material is a very strong T1 shortening agent. If the image acquisition is done at the time of nulling of the myocardium, the enhanced infarcted tissue and fibrosis can be demonstrated as a bright signal intensity by contrast to the dark normal myocardium. The key point of this delayed enhancement image is selecting an optimal inversion time to

null signal from the normal myocardium. The phase-sensitive inversion recovery sequence can avoid artifacts from the sub-optimal inversion time by obtaining reference images at the end of two R-R periods after the inversion pulse (Fig. 16.19). The delayed enhancement image can be used for checking myocardial fibrosis as well as myocardial infarction.

16.4.7 MR Angiography

MR angiography can be done with various techniques, but the majority of MRAs are contrast-enhanced MRAs. Injecting contrast media and getting an image at the first passing of the contrast material at the target vessel by 3D acquisition is the usual way to perform an MRA. Small vessels can be visualized in a 3D MRA. The aorta, pulmonary arteries, and pulmonary veins can also be nicely shown on an MRA (Fig. 16.20). A time-resolved MRA, in which multiple serial 3D data set is acquired can show the hemodynamics of blood flow and be useful for the evaluation of shunt lesions, anomalous pulmonary venous returns, and altered flow after fontal operations.

16.5 Illustrations: Pediatric Cardiac Imaging I: CT and MR Techniques

16.5.1 Sequential Scan, Spiral Scan and Multi-detector Computed Tomography

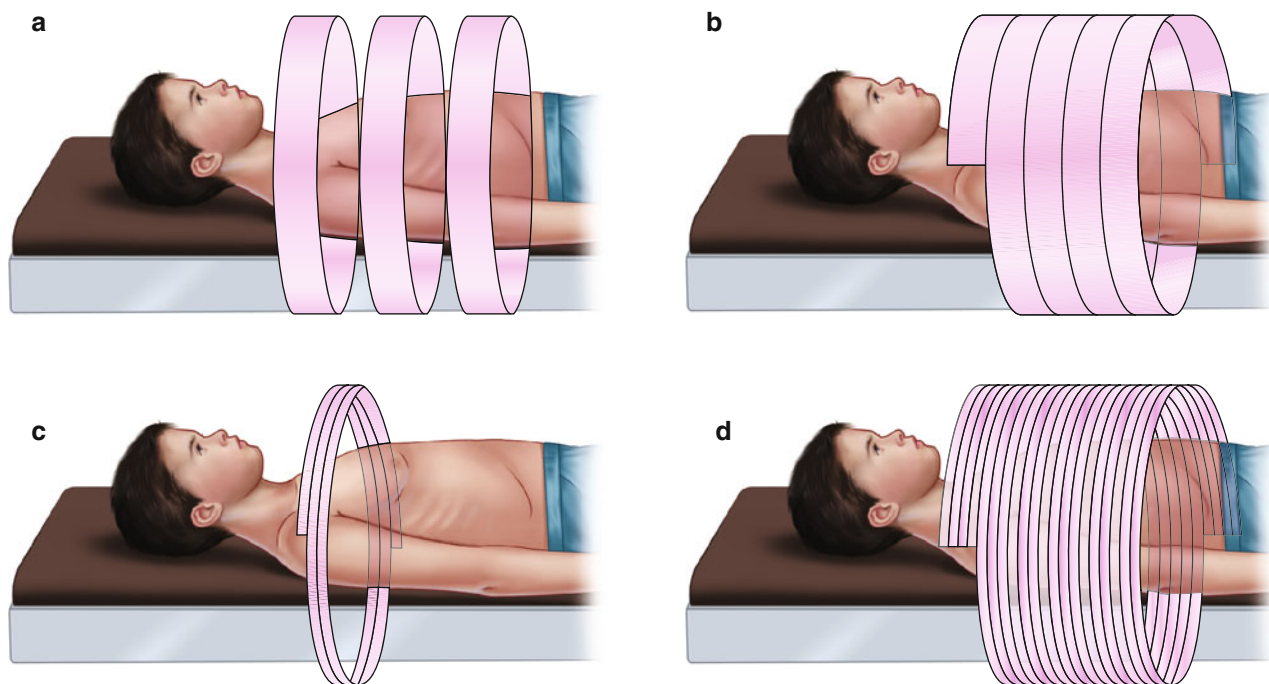


Fig. 16.1 Sequential scan, spiral scan, and multi-detector computed tomography. **(a)** The initial single-slice CT can scan only one slice by single rotation without table feed. **(b)** The helical CT can scan continuously by interpolation reconstruction, but the scan speed is not enough for an EKG-gated scan. **(c)** With single slice helical CT, when slice

thickness decreased, the scan range will be very short. **(d)** The MDCT can make 4–640 image slices by helical or sequential and the scan speed is much faster than single-slice CT. EKG gating is now possible with MDCT

16.5.2 Concept of EKG-Gated CTs

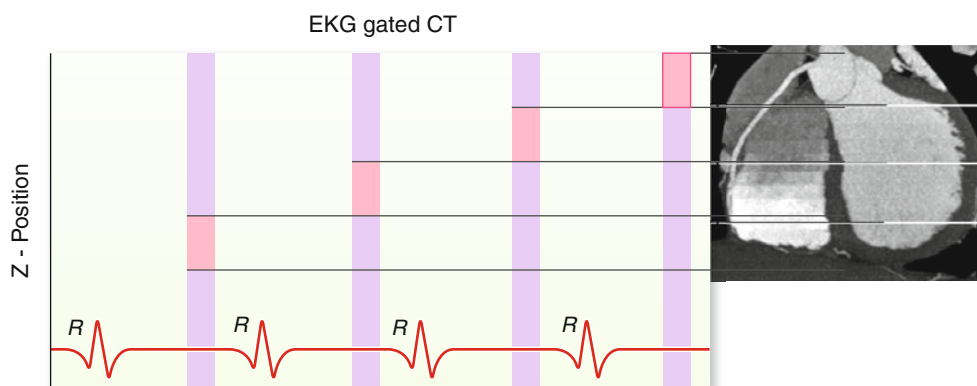


Fig. 16.2 Concept of retrospective EKG-gated CT. The heart is beating. To get the motion-free heart imaging, the imaging acquisition should be very fast; if the scan is not completed in one heartbeat, several image acquisitions in the same cardiac phase can make whole heart

image data sets with a certain cardiac phase. In EKG-gated CT, the pitch is lower than 0.5, usually 0.2, and a certain cardiac phase is used for image reconstruction although image data are acquired throughout the cardiac cycle

16.5.3 Prospective Triggered EKG-Gated CTs

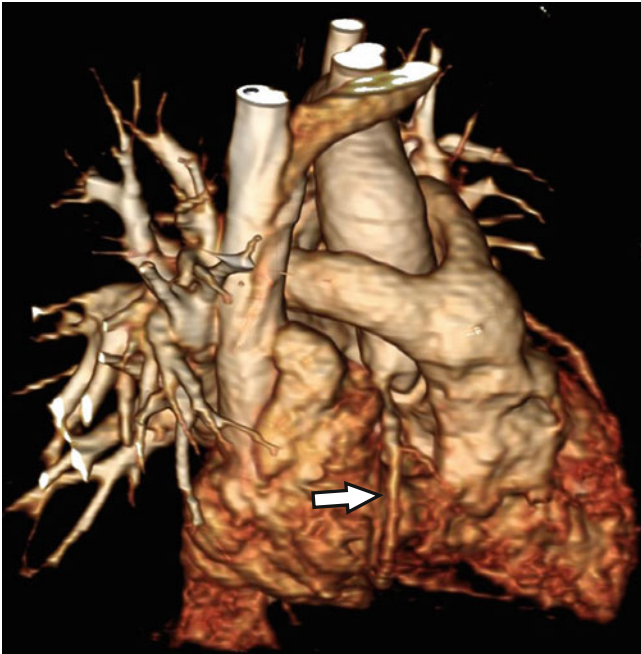


Fig. 16.3 Prospective triggered EKG-gated CT. EKG gated cardiac CT of 19-month-old 10 kg-weighted male patient with previous arterial switch operation can show the coronary arteries. The right coronary artery is nicely demonstrated (*arrow*). This is a prospective EKG triggering scan. Even though the iterative reconstruction is not used, the total radiation dose of this CT is 0.5 mSv

16.5.4 Voluntary Motion Artifacts in EKG-Gated CTs

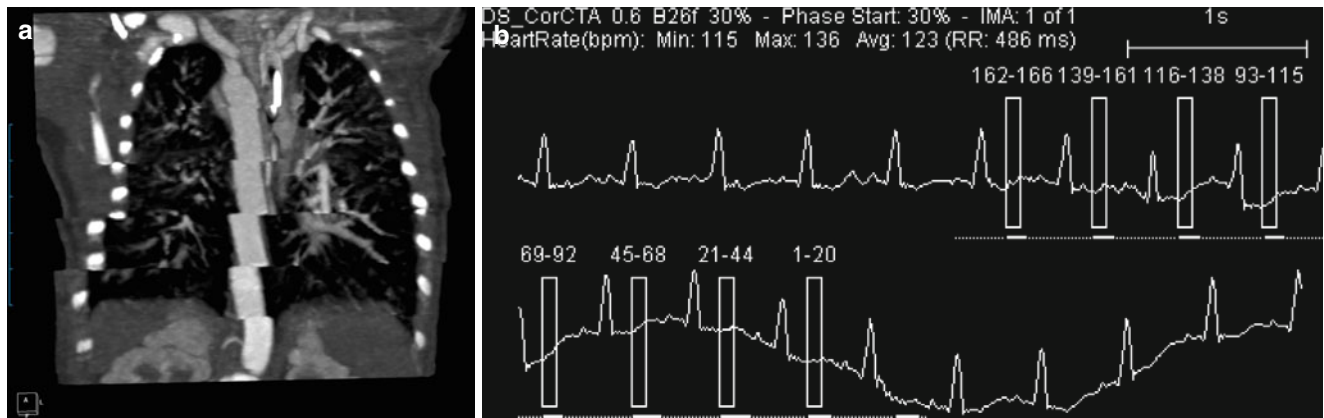


Fig. 16.4 The voluntary motion artifact in EKG-gated CT. (a) The patient was moving during the CT scan. In the EKG-gated scan, the data acquisition was done on each R-R interval and the voluntary motion resulted in the marked stair-step artifact. Note that the aorta and chest wall, as well as the pulmonary arteries' continuity, are broken. (b) The EKG information of this CT scan showed the regular heart rhythm but the baseline of the EKG is fluctuated, suggesting voluntary

motion of the patient. Each box means the data acquisition window of the R-R interval. There is a time gap for each data acquisition. The *dot* and *solid line* under the EKG strip mean the tube current modulation according to the EKG signal for reducing radiation dose by minimize radiation exposure during other phase except systolic phase which is target phase in this scan

16.5.5 Effect of Scan Speed on Motion Artifacts

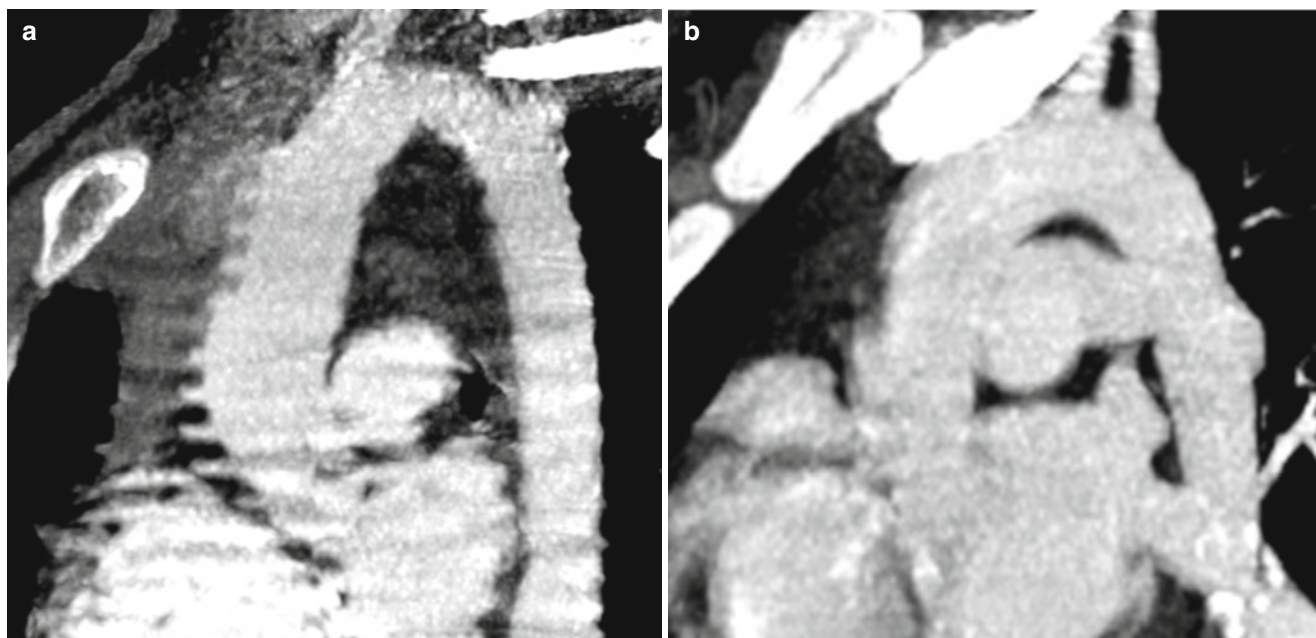


Fig. 16.5 Effect of scan speed on motion artifact. Both aorta scans are non-gated scans. Single-slice CT (**a**) scan shows more severe motion artifacts than that of a 16-channel MDCT scan (**b**). Cardiac motion artifact and respiratory motion artifact can be minimized by faster scanning

16.5.6 Cardiac Motion Artifacts in Non-gated Cardiac CTs

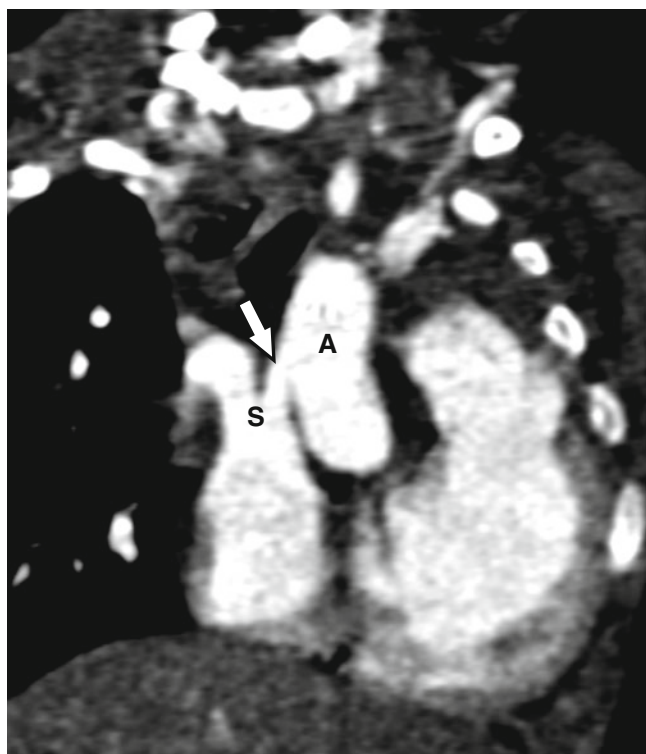


Fig. 16.6 Cardiac motion artifact in non-gated cardiac CT. The cardiac CT without gating is prone to motion artifacts. The aorta and superior vena cava seem connected, but this is a motion artifact from a heartbeat. However, the pulmonary arteries and pulmonary veins and aorta, except for the ascending aorta, can be imaged by a non-gated cardiac scan because the cardiac motions in those structures are not significant

16.5.7 Iodine K Edge Absorption and CT X-Ray Spectrum

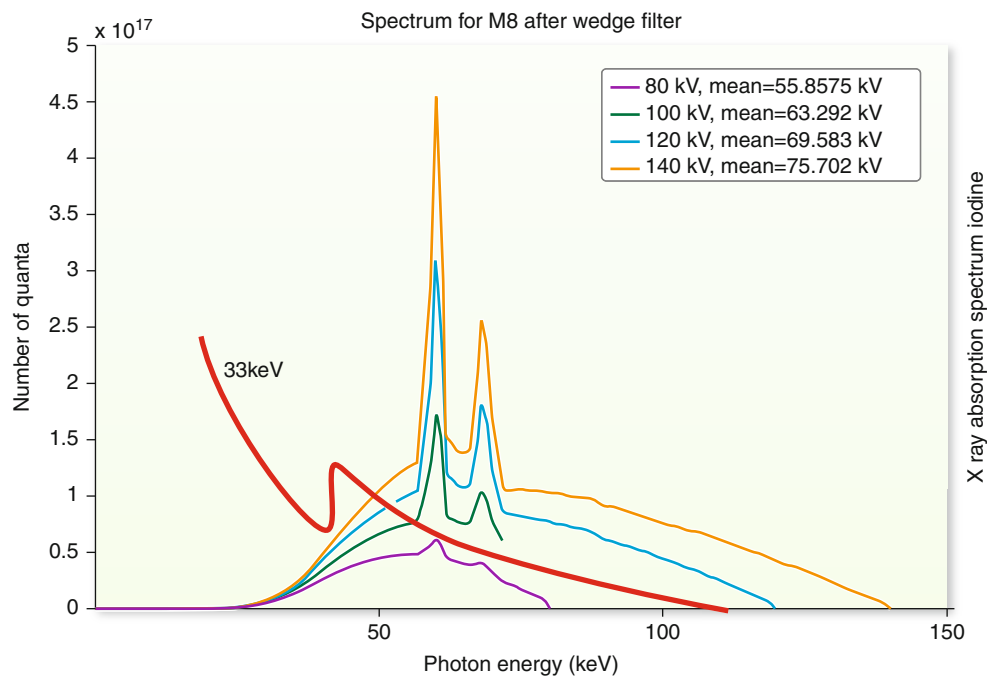


Fig. 16.7 Iodine K edge absorption and CT X-ray spectrum. Solid line indicates total X-ray absorption iodine and it has K edge absorption at 33 keV. The lower energy spectrum of 80 kVp or 100 kVp is much more

affected by this K edge absorption. The lower kVp X-ray is absorbed by iodine atoms and the CT number of iodine is higher in the CT image that was taken by a lower kVp

16.5.8 Scan Range for Cardiac CTs

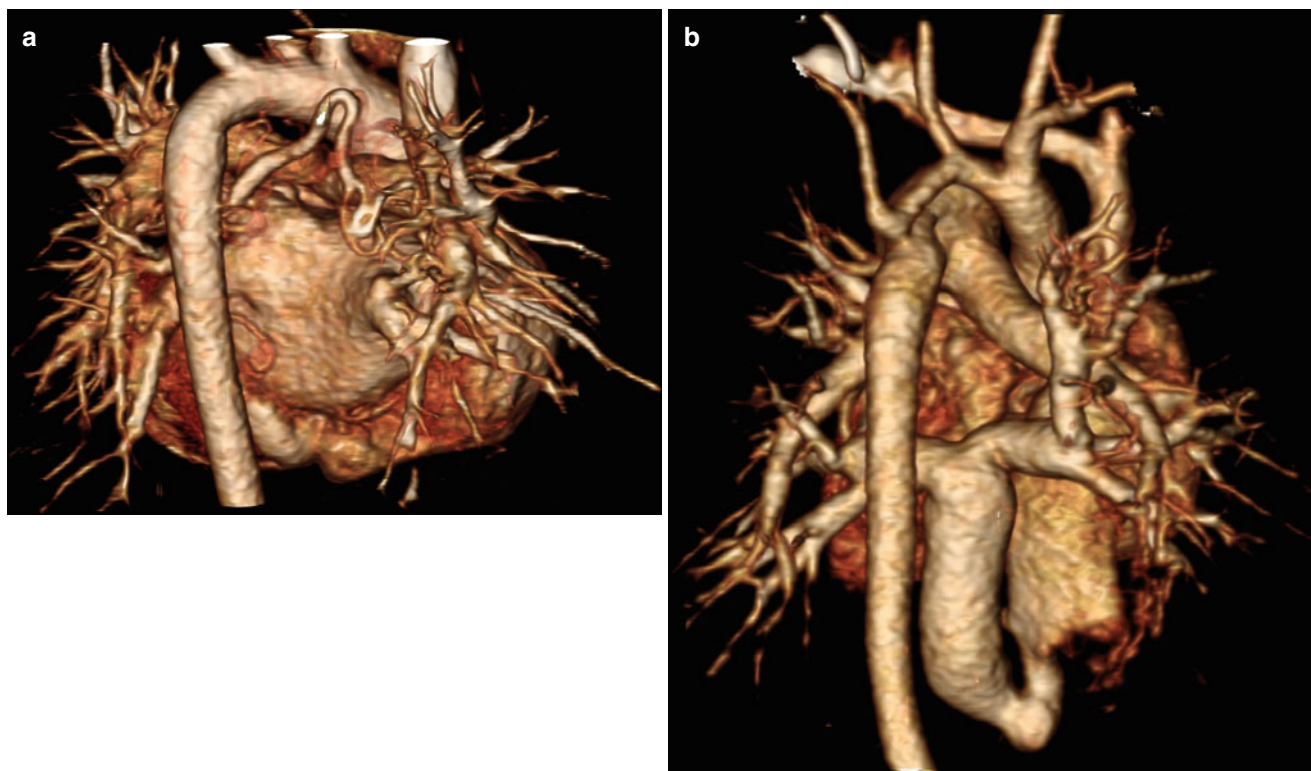


Fig. 16.8 Scan range for cardiac CT. Scan range is one of the most important parameters for radiation exposure. The scan range should be kept as short as possible. **(a)** The optimal scan range for the usual cardiac scan is from just above the aortic arch to just below the diaphragmatic surface. **(b)** This scan is intentionally done with extended scan

range. The patient had a known arch anomaly and infracardiac type total anomalous pulmonary venous return. The scan range should cover the entire aortic arch and portal vein. The scan range should be determined by radiologists based on the target structure of the CT examination, case by case

16.5.9 Three-Dimensional Reconstruction

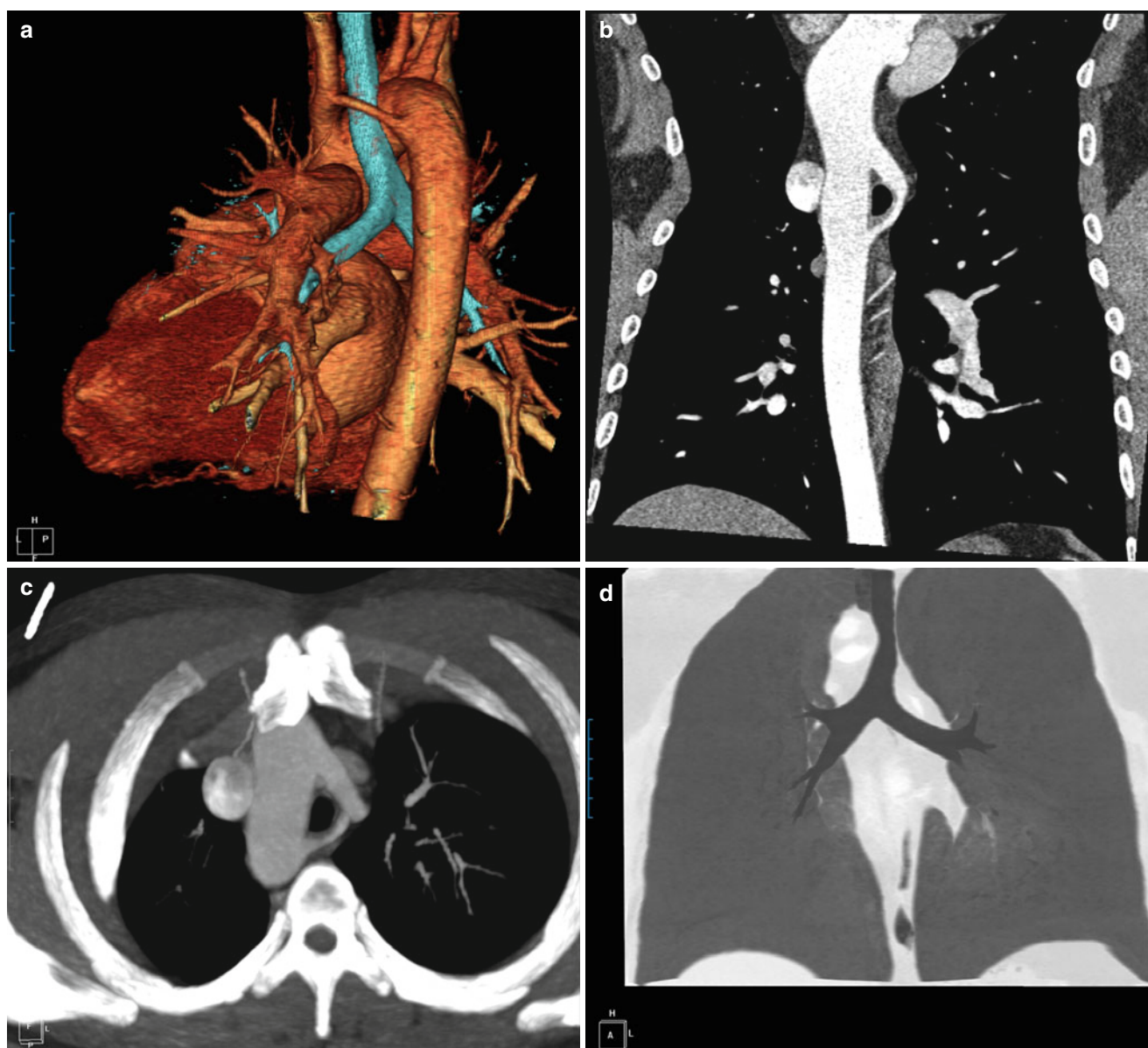


Fig. 16.9 Three-dimensional reconstruction. (a) Volume-rendering image. Volume-rendering image with color coding can demonstrate different structures with different HU at the same time. The airway is coded as *sky blue* and the contrast material is coded as *brown*. The airway and surrounding vascular structure is well demonstrated. (b) Curved multiplanar reformation. The single pixel thickness image can be generated along any arbitrary plane or even on the curved plane. This curve multiplanar reformation image is reconstructed along the central line of the aorta from the ascending aorta to the descending thoracic aorta. The double aortic arch is well demonstrated. Be careful of geometric information such as length from point to point in the image that can be distorted in curve multiplanar

reformation image. (c) Maximum intensity projection. Maximum intensity projection showed the vascular ring in the axial plane. The vascular ring cannot be displayed in a single axial slice, but maximum intensity projection demonstrates the maximum pixel value in the volume and the vascular structure and bone usually have the maximum intensities in the volume. (d) Minimum-intensity projection. In contrast to the maximum-intensity projection, it displays the pixels with minimum intensities. The air is the material of the lowest CT number. The airway and lung is a good organ to be demonstrated by minimum intensity projection. The tracheal stenosis at the level of the vascular ring of this patient is well noted on this minimum-intensity projection image

16.5.10 Examples of Pulse Sequence Diagram

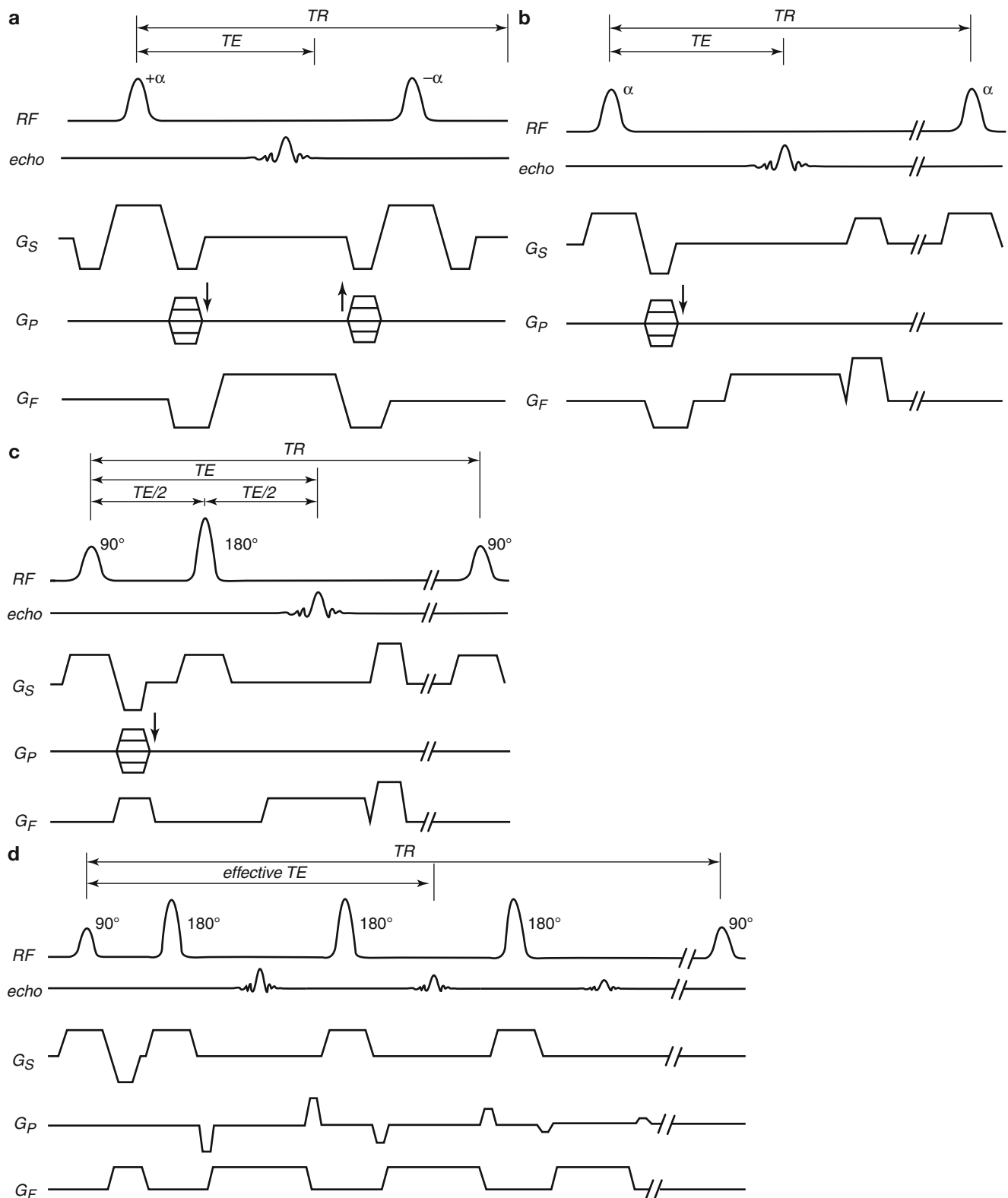


Fig. 16.10 Examples of pulse sequence diagram. Pulse diagram is the chart of the sequences of applying the RF pulse and gradient magnetic field: (a) steady-state free precession, (b) spoiled gradient echo, (c) spin echo, (d) turbo spin echo

16.5.11 EKG Gating and Segment K-Space Filling

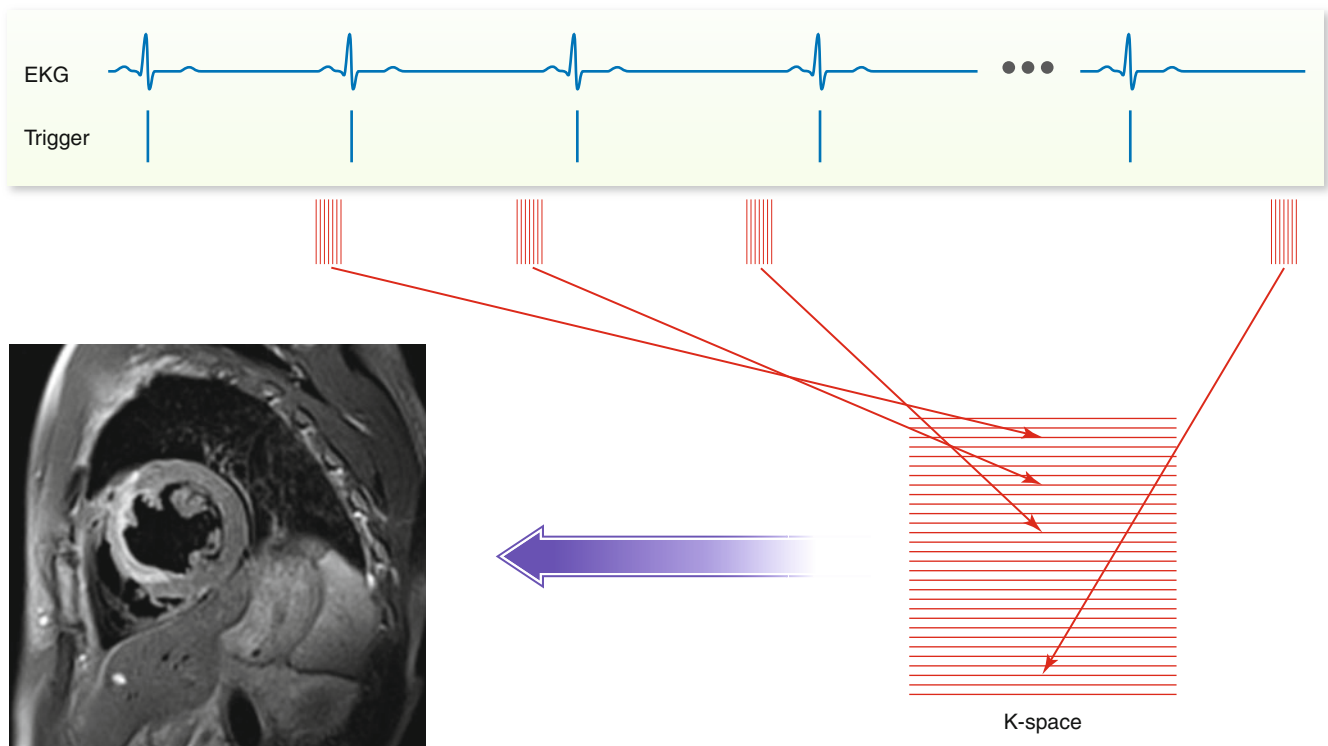


Fig. 16.11 EKG gating and segment K-space filling. The K-space of one image is filled by line-to-line but is segmented. Several lines of the K-space are filled from the information of certain cardiac phases of one R-R interval. The following information from the next R-R interval fills

the next K-space. One full-filled K space corresponds with a single MR image. The heartbeat needed to complete one K-space depends on the number of lines from each K-space as well as the total phase encoding steps

16.5.12 EKG-Gated Cine

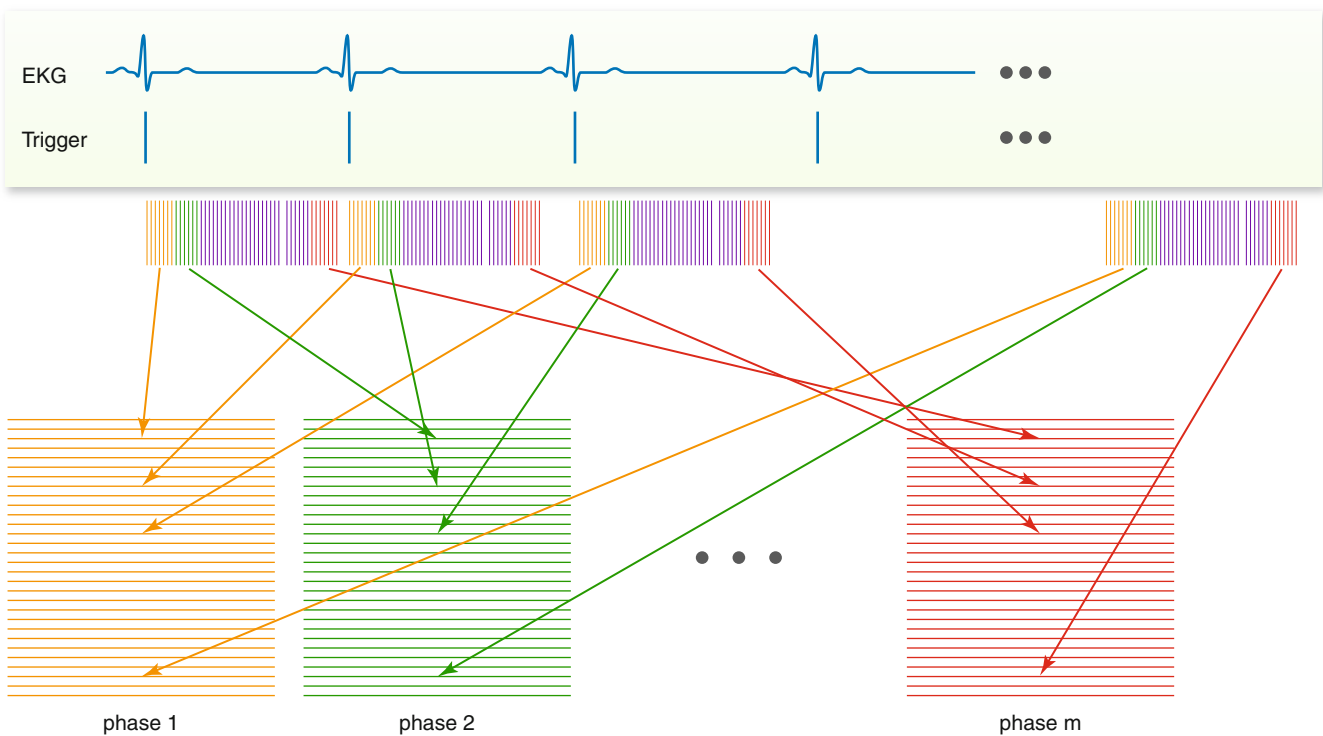


Fig. 16.12 EKG-gated cine. Cine images are serial EKG-gated images with slightly different image acquisition windows in R-R intervals. Filling multiple K-spaces for the multiple image sets of each cardiac phase for cardiac cine is performed. The number of R-R intervals to fill

all of the K-spaces is determined by the number of lines from a single R-R interval, which is called the “number of segments.” The “number of segments” also determines the number of cine images in a given heart rate

16.5.13 Different Pulse Sequences and Different Contrasts

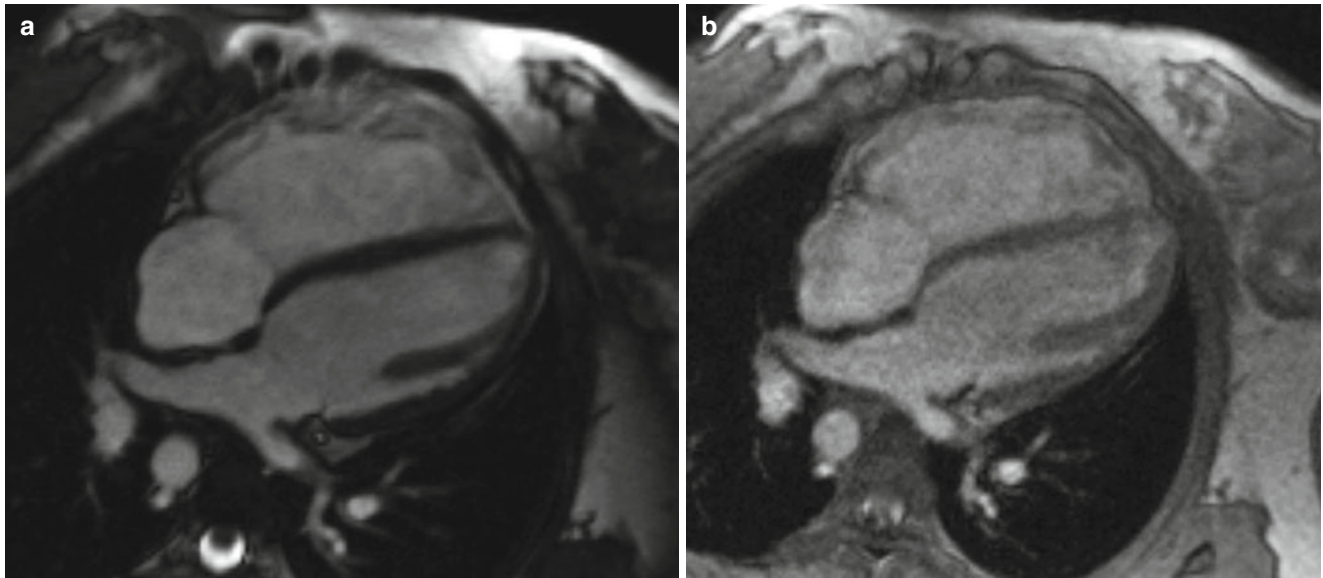


Fig. 16.13 Different pulse sequences and different contrasts. Steady-state free precession image (a) showed better contrast to noise ratio than spoiled gradient echo image (b). This difference is one of the intrinsic characteristics of the pulse sequences. The steady-state free precession

is faster and shows great contrast to noise ratio especially between myocardium and blood. However, the steady-state free precession is more susceptible to field inhomogeneity

16.5.14 Free Breathing Image Acquisition

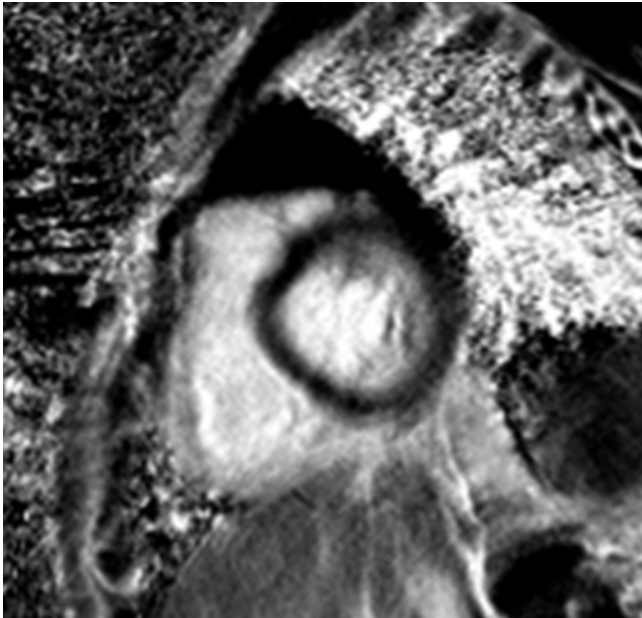


Fig. 16.14 Free breathing image acquisition. Inversion recovery image taken with free breathing and averaging of three times shows blurred but reasonably interpretable image quality. In the patient who cannot hold his breath, the free breathing acquisition is a good option that can avoid general anesthesia

16.5.15 Respiratory Gating Image Acquisition

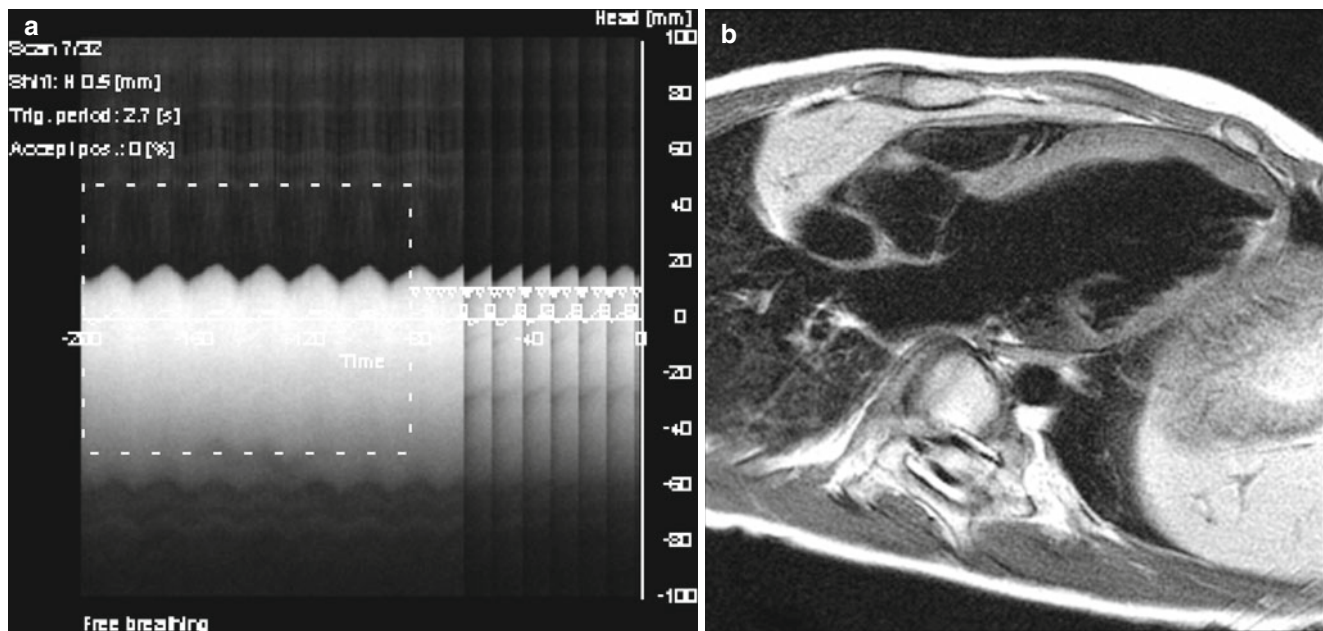


Fig. 16.15 Respiratory gating image acquisition. The respiratory gating is possible by monitoring the position of the diaphragm. (a) The interface between the black and bright is the position of the top of the diaphragm. The diaphragm's position is monitored and image acquisition is obtained only at a certain level of the diaphragm position. (b) An

example of respiratory-gated T2-weighted image shows the myocardium without motion artifact. The image quality is as good as a breath-held image and better than the image from free breathing acquisition, but the scan time is much longer than breath-holding image acquisition or free breathing average imaging acquisition

16.5.16 Velocity-Encoding Cine

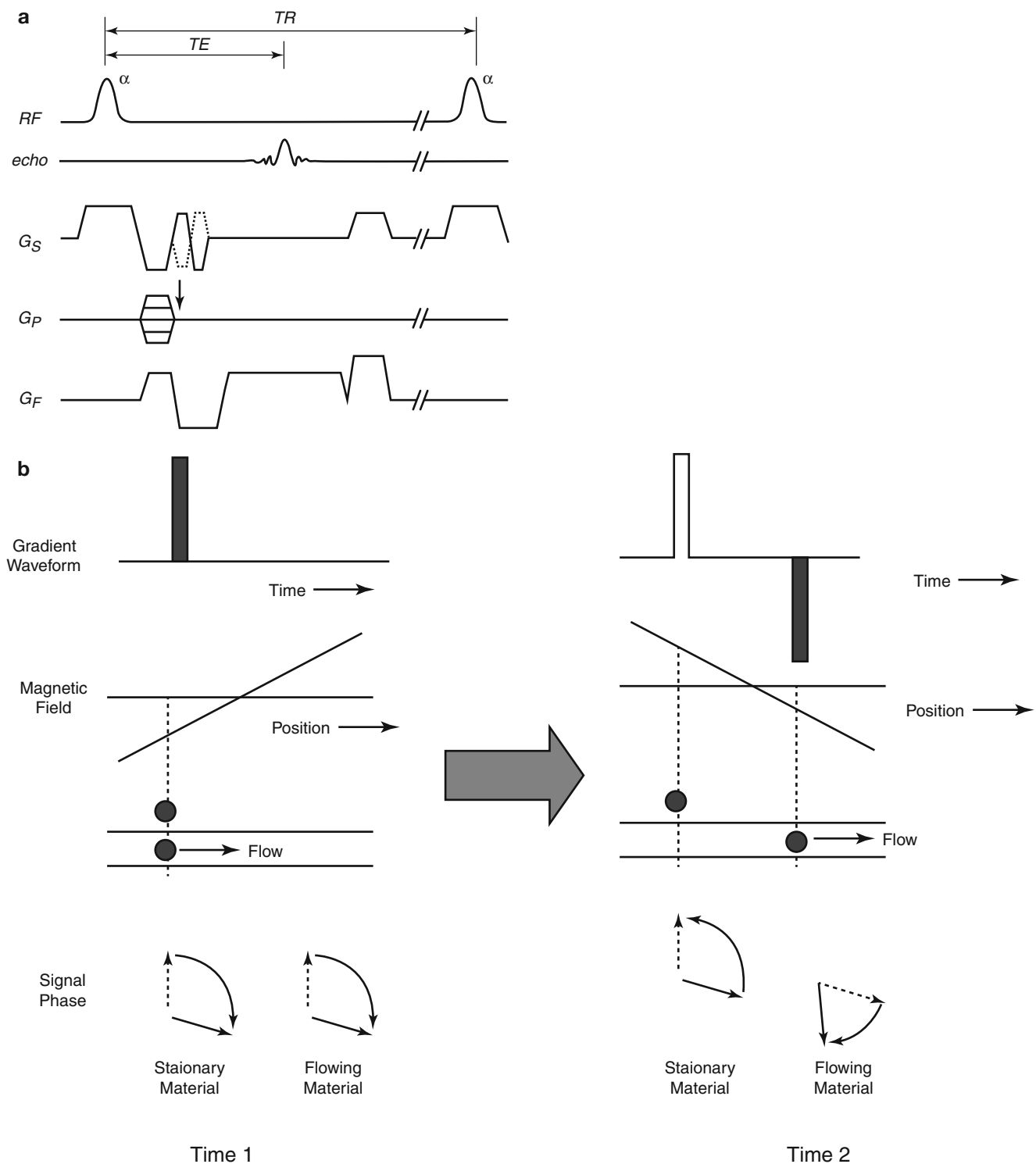


Fig. 16.16 Velocity encoding cine. **(a)** Sequence diagram of the through-plane velocity encoding cine. There is a bipolar gradient in slice selection gradient which will be applied in the opposite direction to calculate the phase difference in every image. The bipolar gradient is applied in the slice selection gradient because this is for through the plane velocity encoding cine. **(b)** Schematic drawing of the velocity encoding cine. The gradient magnetic field applied and the phase shift-

ing happened in both stationary protons and moving protons. The moving proton will experience a different strength of the magnetic field. The magnetic gradient is reversed. The phase shifting of the stationary proton will be corrected after applying the opposite magnetic gradient of the same power and the same duration. However, the moving proton's phase shift cannot be corrected and the remaining phase shift is proportionally correlated with the velocity of the moving proton

16.5.17 The Image of the Velocity-Encoding Cine

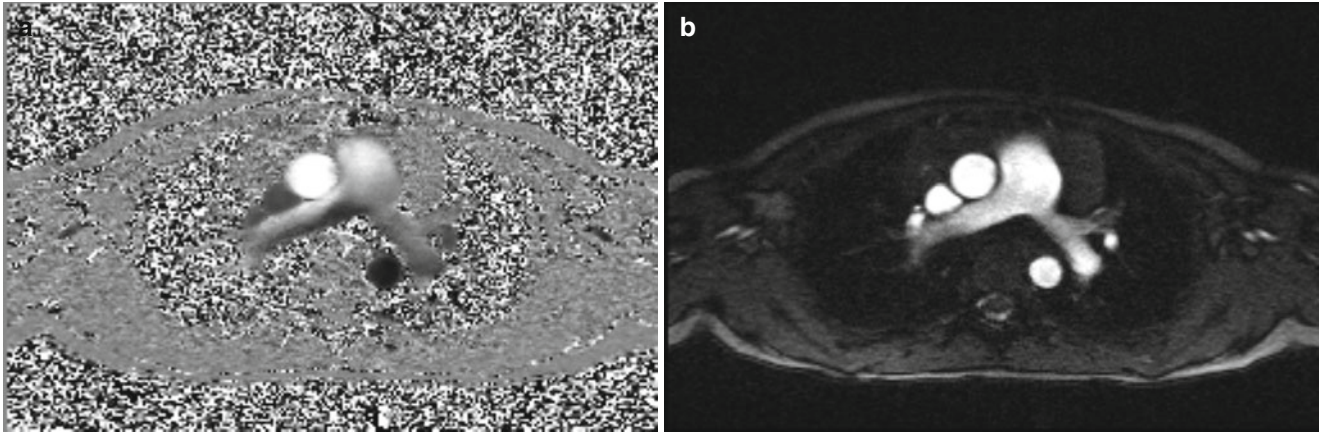


Fig. 16.17 The image of the velocity encoding cine. The phase image (a) and magnitude image (b) of the velocity encoding cine. The pixels of the phase image have information on the velocity of the each pixel. Please note that the ascending aorta and descending aorta show

differences in direction. The magnitude image is generated from the same data but the velocity information is not included. The magnitude images are usually used as an anatomical reference

16.5.18 Example of T2-Weighted Image and T1-Weighted Image

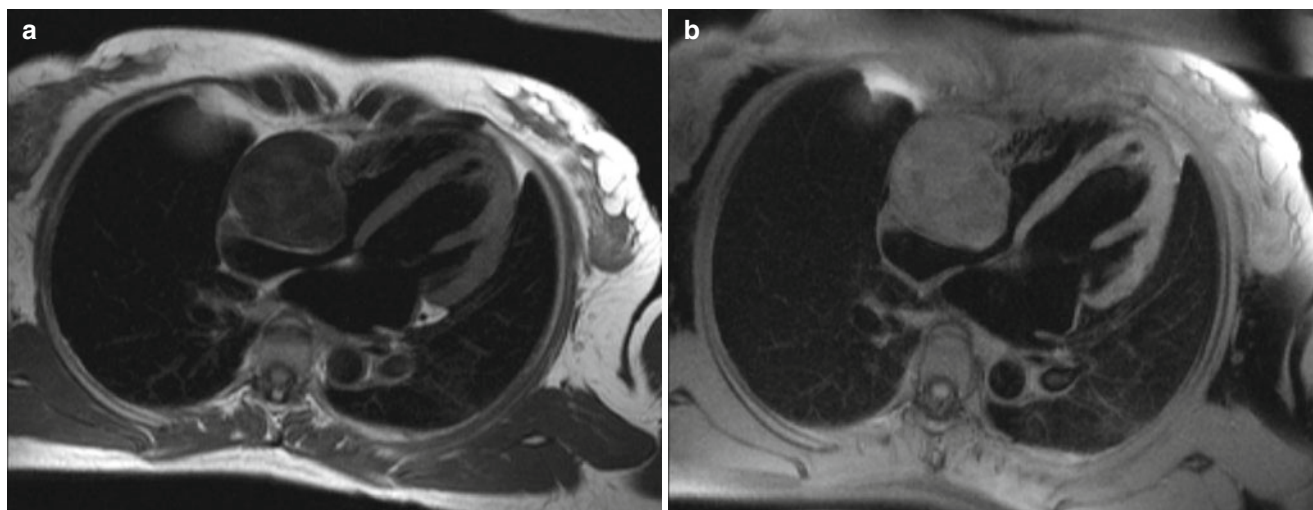


Fig. 16.18 Example of T2-weighted image and T1-weighted image. (a) The T2-weighted image shows the low-signal intensity of the mass at the right atrioventricular groove. The fat signal is bright in turbo spin echo T2-weighted image. (b) Fat-saturated T1-weighted image shows iso-signal intensity of the mass. The signal intensity of T2- and

T1-weighted image can be used for differential diagnosis of cardiac mass or other pathologies. This mass is a fibroma. The fat signal is usually bright in T1-weighted images, but in this fat-saturated image, the fat signal is well suppressed except in the left anterior chest wall area

16.5.19 Inversion Recovery Delayed Enhancement Image for Myocardium

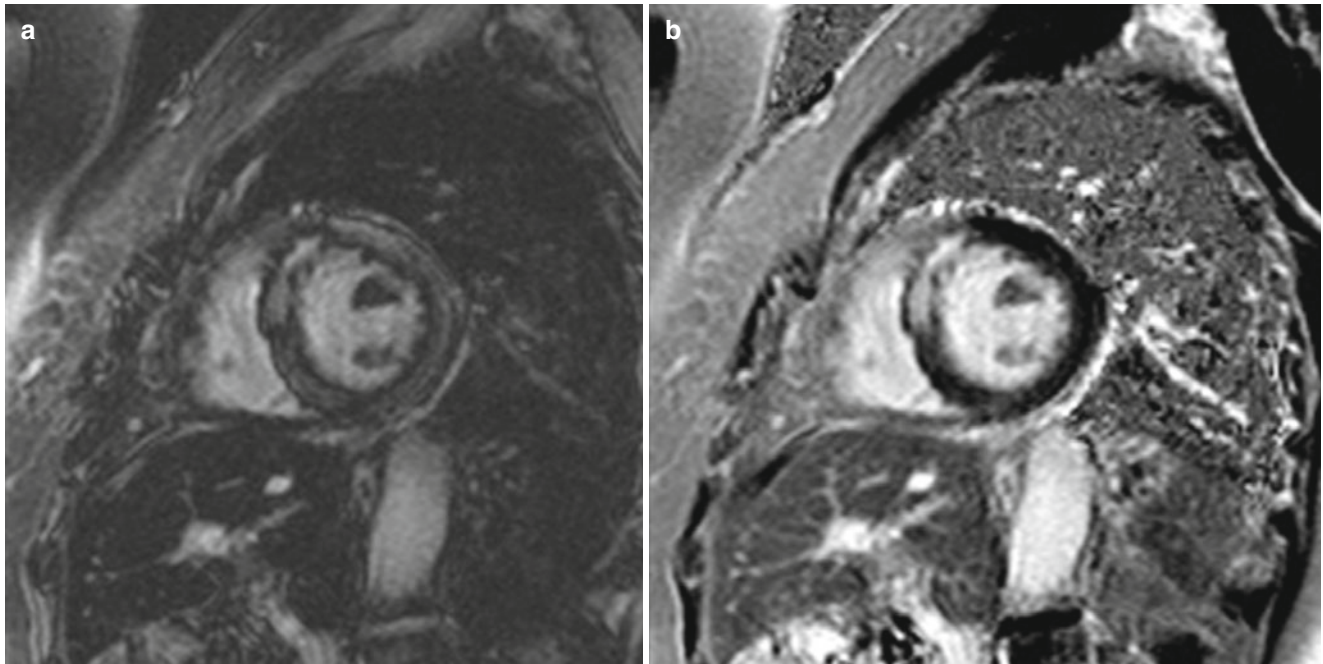


Fig. 16.19 Inversion recovery delayed enhancement image for myocardium. **(a)** The nulling point is critical to deepen the contrast between the normal myocardium and disease myocardium. **(b)** Inversion recovery curve and image acquisition time. If the image acquisition is done on suboptimal timing, the normal myocardium signal is not nulled

and the image contrast is poor. The phase-sensitive inversion recovery technique uses reference images from the end of two R-R intervals and calculate the absolute phase difference. The contrast between a normal myocardium and a diseased enhanced myocardium is constant, regardless of the image acquisition timing

16.5.20 MR Angiography



Fig. 16.20 MR angiography. The contrast-enhanced MR angiography shows residual coarctation of the aorta. The stenosis degree seems to be about 40 %. The scan time was 10 s and 0.1 mmol/kg of the gadolinium-based contrast media was used

References

- Boxt LM. Magnetic resonance and computed tomographic evaluation of congenital heart disease. *J Magn Reson Imaging*. 2004;19:827–47.
- Brink JA, Heiken JP, Wang G, et al. Helical CT: principles and technical considerations. *Radiographics*. 1994;14:887–93.
- Chai P, Mohiaddin R. How we perform cardiovascular magnetic resonance flow assessment using phase-contrast velocity mapping. *J Cardiovasc Magn Reson*. 2005;7:705–16.
- Crean A. Cardiovascular MR and CT in congenital heart disease. *Heart*. 2007;93:1637–47.
- Dymarkowski SBH. Cardiac MRI physics. Heidelberg: Springer; 2005.
- Flohr TG, McCollough CH, Bruder H, et al. First performance evaluation of a dual-source CT (DSCT) system. *Eur Radiol*. 2006;16:256–68.
- Fogel MA. Assessment of cardiac function by magnetic resonance imaging. *Pediatr Cardiol*. 2000;21:59–69.
- Fogel MA, Weinberg PM, Harris M, et al. Usefulness of magnetic resonance imaging for the diagnosis of right ventricular dysplasia in children. *Am J Cardiol*. 2006;97:1232–7.
- Greil GF, Stuber M, Botnar RM, et al. Coronary magnetic resonance angiography in adolescents and young adults with Kawasaki disease. *Circulation*. 2002;105:908–11.
- Hounsfield GN. Computerized transverse axial scanning (tomography). 1. Description of system. *Br J Radiol*. 1973;46:1016–22.
- Kilner PJ, Gatehouse PD, Firmin DN. Flow measurement by magnetic resonance: a unique asset worth optimising. *J Cardiovasc Magn Reson*. 2007;9:723–8.
- Kim YM, Yoo SJ, Kim TH, et al. Three-dimensional computed tomography in children with compression of the central airways complicating congenital heart disease. *Cardiol Young*. 2002;12:44–50.
- Lee V. Cardiovascular MRI: physical principles to practical protocols. Philadelphia: Lippincott Williams and Wilkins; 2006.
- Lloyd SG, Gupta H. Assessment of myocardial viability by cardiovascular magnetic resonance. *Echocardiography*. 2005;22:179–93.
- Lotz J, Meier C, Leppert A, et al. Cardiovascular flow measurement with phase-contrast MR imaging: basic facts and implementation. *Radiographics*. 2002;22:651–71.
- Macovski A. Medical imaging systems. Upper Saddle River: Prentice Hall; 1983.
- McCollough CH. Patient dose in cardiac computed tomography. *Herz*. 2003;28:1–6.
- Pennell D. MRI and iron-overload cardiomyopathy in thalassaemia. *Circulation*. 2006;113:f43–4.
- Rybicki FJ, Otero HJ, Steigner ML, et al. Initial evaluation of coronary images from 320-detector row computed tomography. *Int J Cardiovasc Imaging*. 2008;24:535–46.
- Sakuma H, Ichikawa Y, Suzawa N, et al. Assessment of coronary arteries with total study time of less than 30 minutes by using whole-heart coronary MR angiography. *Radiology*. 2005;237:316–21.
- Taylor AM. Cardiac imaging: MR or CT? Which to use when. *Pediatr Radiol*. 2008;38 Suppl 3:S433–8.

Hyun Woo Goo

Contents

17.1	Introduction	554
17.2	State-of-the-Art Imaging Techniques	554
17.2.1	CT	554
17.2.2	MRI	554
17.3	Preoperative Findings of Common Cardiac Defects	554
17.3.1	Atrial Septal Defect.....	554
17.3.2	Ventricular Septal Defect	555
17.3.3	Atrioventricular Septal Defect	555
17.3.4	Tetralogy of Fallot.....	555
17.3.5	Pulmonary Atresia.....	555
17.3.6	Transposition of the Great Arteries	555
17.3.7	Double Outlet Right Ventricle.....	556
17.3.8	Ebstein Anomaly	556
17.3.9	Functional Single Ventricle	556
17.4	Postoperative Findings of Common Cardiac Defects	556
17.4.1	Total Correction of Tetralogy of Fallot	556
17.4.2	Arterial Switch Operation	557
17.4.3	Rastelli Operation	557
17.4.4	Fontan Operation	557
17.5	Illustrations: CT and MRI Findings of Cardiac Defects in Congenital Heart Disease	558
17.5.1	Atrial Septal Defect.....	558
17.5.2	Ventricular Septal Defect	559
17.5.3	Tetralogy of Fallot.....	560
17.5.4	Atrioventricular Septal Defect	561
17.5.5	Pulmonary Atresia.....	562
17.5.6	Transposition of the Great Arteries	563
17.5.7	Double Outlet Right Ventricle.....	564
17.5.8	Ebstein Anomaly	565
17.5.9	Tricuspid Atresia	566
17.5.10	Hypoplastic Left Heart Syndrome	567
17.5.11	Repaired Tetralogy of Fallot	568
17.5.12	Arterial Switch Operation	569
17.5.13	Rastelli Operation	570
17.5.14	Extracardiac Conduit Fontan Operation	571
	References	572

H.W. Goo, M.D., Ph.D.

Department of Radiology and Research Institute of Radiology,
Asan Medical Center, University of Ulsan College of Medicine,
88, Olympic-ro 43-gil, Songpa-gu, Seoul, Korea
e-mail: hwgoo@amc.seoul.kr

17.1 Introduction

Recent technical developments in CT and MRI allow anatomic and functional evaluation of intracardiac structures in patients with congenital heart disease (Goo et al. 2003, 2005, 2007, 2009; Goo 2010; Goo and Yang 2010; Goo 2011a, b, c, 2012, 2013; Durongpisitkul et al. 2004; Grosse-Wortmann et al. 2008; Sena and Goo 2008; Holmes 2012). As a result, the complementary use of cardiac CT and MRI significantly improves diagnostic accuracy and confidence of congenital heart disease. Due to its wide availability and easy applicability with markedly improved image quality, cardiac CT has been increasingly used in patients with congenital heart disease even more frequently than cardiac MRI, and this trend is exceedingly prevailing in Asian countries (Tsai and Goo 2013). Echocardiography is still a primary imaging modality and particularly useful for evaluating the valves and valve apparatus. The number of diagnostic catheter angiography has markedly decreased, but this invasive imaging method is still necessary for sophisticated hemodynamic assessments, particularly for the risk assessment before Fontan operation. In this chapter, state-of-the-art CT and MRI techniques for the intracardiac assessment of congenital heart disease are briefly described. Preoperative CT and MRI findings of common cardiac defects are subsequently described and illustrated. They include atrial septal defect (ASD), ventricular septal defect (VSD), atrioventricular septal defect (AVSD), tetralogy of Fallot (TOF), pulmonary atresia, transposition of the great arteries (TGA), double outlet right ventricle (DORV), Ebstein anomaly, and functional single ventricle (FSV). Finally, typical CT and MRI findings after commonly performed cardiac surgeries, such as total correction of TOF, arterial switch operation, Rastelli operation, and Fontan operation, are then described.

17.2 State-of-the-Art Imaging Techniques

17.2.1 CT

ECG-synchronized scanning is mandatory for the accurate assessment of intracardiac structures of congenital heart disease. Retrospective ECG gating or prospective ECG triggering may be used mainly according to a child's ability to follow breathing instructions. Breath holding is usually recommended for retrospectively ECG-gated CT scanning. Radiation dose parameters including tube voltages ranging from 70 to 120 kV and tube current should be appropriately adjusted depending on a child's body habitus. To further reduce radiation dose of retrospectively ECG-gated CT scanning, ECG-controlled tube current modulation is highly beneficial. For the morphologic evaluation, one cardiac phase is

sufficient, and the end-systolic phase is generally preferred to the mid-diastolic phase at high heart rates. For the functional evaluation, a two-phase acquisition consisting of end-systolic and end-diastolic phases has a merit with respect to radiation dose reduction. To improve image quality of cardiac CT in young children by controlling breathing motion, general anesthesia, controlled ventilation, or respiratory triggering may be used if available.

17.2.2 MRI

Various imaging techniques including cine imaging, phase-contrast imaging, and navigator-gated three-dimensional (3D) non-contrast angiography are used for the anatomic and functional intracardiac assessment of congenital heart disease. MRI acquisition time has been tremendously shortened because of the combined use of multichannel body-array coil, parallel imaging, and k-t broad-use linear acquisition speed-up technique (BLAST). Further technical advancements, such as compressed sensing, may make four-dimensional (4D) evaluation of anatomy, function, and flow possible in our clinical practice in the near future. In addition, high-resolution intracardiac anatomic evaluation can be achieved by using an intravascular contrast agent.

17.3 Preoperative Findings of Common Cardiac Defects

17.3.1 Atrial Septal Defect

The interatrial septum is a result of a sequential embryological evolution of the septum primum and the septum secundum. Interatrial communication is either patent foramen ovale (PFO) or ASD. PFO, a remnant of fetal circulation, may be associated with paradoxical embolism by means of a right-to-left shunt. ASD is classified into secundum (Fig. 17.1), primum, and sinus venosus types. ASD may not be clearly distinguished from PFO on imaging. They are shown as a defect in the interatrial septum with or without shunt flow on imaging. Shunt flow through the defect tends to be more perpendicular to the interatrial septum in ASD than in PFO (Kim et al. 2008). The diagnosis of the secundum ASD without shunt flow should be carefully made on imaging because the thin fossa ovalis may not be clearly delineated on imaging and may be mistaken as the defect. The secundum defect is infrequently seen as multiple fenestrations and sometimes may rarely have atrial septal aneurysm. Echocardiography and MRI have been used to assess the technical feasibility of

transcatheter closure of ASD. The primum defect is a partial AVSD. The sinus venous defect is frequently associated with partial anomalous pulmonary venous connection (PAPVC). The interatrial septum may be entirely missing or may remain as a small strand, called as common atrium, and the condition is often seen in atrial isomerism.

17.3.2 Ventricular Septal Defect

VSD is a defect or defects in the ventricular septum consisting of the membranous and muscular parts. The size of the defect having the greatest clinical impact should be assessed on imaging. VSD is often classified into perimembranous, juxta-tricuspid and non-perimembranous, doubly committed juxta-arterial, and muscular defects. The perimembranous defect is the most common type involving the membranous part of the interventricular septum and variable extents of the adjacent muscular septum. An en face view is useful to evaluate the size and location of VSD. Septal aneurysm usually formed by the adhesion of the tricuspid valve leaflet to the rim of a perimembranous defect is responsible for a gradual reduction of shunt flow or the spontaneous closure of the defect (Fig. 17.2). Aortic regurgitation may be developed as a result of a prolapse of the aortic sinus toward the defect. In addition, a VSD may be developed by the malaligned outlet septum, the so-called malalignment defect. Anterior malalignment defect, a more common type, is seen in TOF, while the posterior type may be associated with coarctation of the aorta or interrupted aortic arch.

17.3.3 Atrioventricular Septal Defect

AVSD is a defect in the atrioventricular septum with variable involvement of the adjacent atrial and ventricular septa. The defect is divided into partial or complete form according to the absence or presence of interventricular communication in addition to primum ASD. The ventricular component of the defect involving the inlet portion accounts for the characteristic scooped appearance on an en face view (Fig. 17.4). On the other hand, AVSD may be described as balanced or unbalanced depending on whether the two ventricles are equal in size or not. Other cardiac anatomic features associated with AVSD include an unwedged aorta at the base of the ventricles, shortened left ventricular inlet, elongated left ventricular outlet responsible for the so-called gooseneck deformity, and more closely opposed papillary muscles of the left ventricle. Because of a greater shunt through the defect, patients with AVSD are more vulnerable to pulmonary vascular disease than other shunt lesions.

17.3.4 Tetralogy of Fallot

The morphologic features of TOF include subpulmonary infundibular stenosis, VSD, overriding of the aorta, and right ventricular hypertrophy (Fig. 17.3). Anterosuperior deviation of the infundibular septum is considered an anatomic substrate of TOF resulting in these features. Hypertrophy of the outlet septum and anterior muscle bundles also contributes to right ventricular outflow obstruction in TOF. With thickening and doming of the hypoplastic or dysplastic pulmonary valve, this right ventricular outflow obstruction constitutes combined pulmonary stenosis. The pulmonary annulus and pulmonary arteries are commonly hypoplastic. Any major coronary artery branches crossing the right ventricular outflow tract should be identified on imaging before total surgical correction of TOF. A right aortic arch is present in 25 % of cases.

Absent pulmonary valve syndrome is regarded as a rare variant of TOF, characterized by absent or rudimentary pulmonary valve tissue, primary pulmonary regurgitation, and aneurysmal dilatation of the central pulmonary arteries. In addition, the typical case has pulmonary annular thickening, a VSD, and absence of the ductus arteriosus. The syndrome is often associated with chromosome 22q11 deletions and DiGeorge syndrome. Patients usually present with respiratory difficulties resulting from bronchial compression by severely enlarged central pulmonary arteries.

17.3.5 Pulmonary Atresia

Pulmonary atresia with VSD shows the morphologic extreme of TOF. Anatomic details of the central pulmonary arteries and various systemic arterial sources should be evaluated on imaging for surgical planning. The presence, confluence, and size of central pulmonary artery should be accurately assessed on imaging. The systemic arterial source of pulmonary circulation includes a patent ductus arteriosus (PDA) or major aortopulmonary collateral arteries (MAPCAs) and may be single or multifocal. This systemic arterial source predisposes the pulmonary vasculature to pulmonary vascular disease if unrepaired and often shows gradual stenosis, particularly at its origin. CT is better than MRI in providing these anatomic details in pulmonary atresia prior to catheter angiography or surgery (Fig. 17.5). In pulmonary valve atresia, the pulmonary valve shows membranous obstruction.

17.3.6 Transposition of the Great Arteries

TGA is characterized by ventriculoarterial discordance, i.e., the ascending aorta arising from the morphologic right

ventricle and the pulmonary trunk arising from the morphologic left ventricle and malposition of the great arteries. In addition, the pulmonary valve shows fibrous continuity with the mitral valve in TGA. Atrioventricular connection is concordant in complete TGA and discordant in congenitally corrected TGA. The systemic and pulmonary circulations form a parallel and independent closed circuit necessitating substantial shunt flow to prevent severe cyanosis and metabolic acidosis in complete TGA, whereas congenitally corrected TGA is hemodynamically normal and often asymptomatic in the absence of associated cardiac defects. Great arteries generally show d-malposition, i.e., the ascending aorta right and anterior to the pulmonary trunk, in complete TGA, whereas they typically show l-malposition, i.e., the ascending aorta left and anterior to the pulmonary trunk, in congenitally corrected TGA. Coronary artery anatomy is exceedingly variable in TGA, which should be accurately identified before arterial switch operation with coronary artery transfer. Cardiac CT is quite useful to evaluate coronary artery anatomy and other cardiovascular morphology preoperatively in young children with TGA (Fig. 17.6).

17.3.7 Double Outlet Right Ventricle

Both the ascending aorta and the pulmonary trunk are connected to the morphologic right ventricle in DORV. When more than half of its semilunar valve is connected to a ventricle, a great artery is regarded as being connected to the ventricle: the so-called 50 % rule. DORV is a constellation of various cardiac defects hemodynamically mimicking simple VSD, TOF, and complete TGA depending on the relationship between the great arteries and the VSD and the presence or absence of right ventricular outflow tract obstruction. Therefore, DORV should be considered to be a disease complex, requiring different treatments, rather than a single entity. Both CT and MRI are useful to demonstrate these anatomic variations of DORV (Fig. 17.7).

17.3.8 Ebstein Anomaly

Ebstein anomaly is characterized by apical displacement of the septal and posterior tricuspid valve leaflets that divides the right ventricle into atrialized and functioning portions. The non-displaced anterior leaflet is usually large and redundant, and its mobility varies depending on the degree of tethering to the right ventricular free wall. According to the degree of the displacement and tethering of the tricuspid valve, the anomaly is divided into four types. Both CT and MRI may be used to calculate the volume ratio of the atrialized right ventricle to the total right ventricle having prognostic significance in Ebstein anomaly. On imaging,

the right cardiac chambers are enlarged due to tricuspid insufficiency, and a characteristic trilobed appearance, consisting of the enlarged right atrium, the atrialized right ventricle, and the functioning right ventricle, can be seen (Fig. 17.8).

17.3.9 Functional Single Ventricle

FSV is a heterogeneous group of congenital heart diseases, such as tricuspid atresia, unbalanced AVSD, and hypoplastic left heart syndrome (HLHS), in which biventricular repair is not feasible. In tricuspid atresia, the right atrium has no direct communication with the right ventricle. In the more common one of the two tricuspid atresia types, the right atrioventricular connection is absent and areolar sulcus tissue occupies the gap. In the rarer type, the tricuspid valve is present but atretic (Fig. 17.9). Unrestrictive ASD is necessary for hemodynamic stability and VSD, the so-called bulboventricular foramen, is usually present. HLHS is a spectrum of cardiac defects characterized by severe underdevelopment of the left heart-aorta complex, including the mitral valve, left ventricle, aortic valve, ascending aorta, and aortic arch. Without treatment, it is invariably fatal during the first few weeks of life. The right cardiac chambers are severely enlarged, and a rudimentary left ventricle is found in the posterior, inferior, and left portion of the heart. The dominant right ventricle provides blood flow to the aorta and coronary arteries via a patent ductus arteriosus (PDA), the so-called ductal-dependent systemic circulation (Fig. 17.10). A restrictive ASD may result in pulmonary venous congestion. Ventriculocoronary artery connections and endocardial fibroelastosis may be associated with this syndrome. The patency of the aortic arch and a PDA can be accurately evaluated on CT or MRI. In children with FSV, CT and MRI offer accurate volumetry of a marginally hypoplastic left ventricle (Grosse-Wortmann et al. 2008; Kim et al. 2013) and correct the underestimated left ventricular volume measured by echocardiography.

17.4 Postoperative Findings of Common Cardiac Defects

17.4.1 Total Correction of Tetralogy of Fallot

Currently, primary total correction at 3–6 months of age is preferred to a two-stage operation. The goals for total correction of TOF consist of VSD closure and relief of the right ventricular outflow tract obstruction. As compared with earlier transannular repair resulting in greater dyskinesia and pulmonary regurgitation, efforts to spare the pulmonary valve and to avoid a large ventriculotomy have been recently

made. Despite such improved surgical techniques, pulmonary valve replacement is necessary to improve the right ventricular function and to prevent right heart failure in a majority of patients with repaired TOF (Fig. 17.11). The right ventricular volume and function measured by MRI or CT is one of the key elements in determining optimal timing for the pulmonary valve replacement.

17.4.2 Arterial Switch Operation

Arterial switch operation is the surgical procedure of choice for complete TGA, where the aorta and the main pulmonary artery are transected above their corresponding valves and then are switched. The pulmonary trunk is brought anterior to the neo-aorta to be anastomosed with the neopulmonary artery using the so-called Lecompte maneuver. This maneuver reduces the risk of coronary artery kinking or compression after coronary artery transfer by maximizing the length of the neo-aorta (Fig. 17.12). Coronary arteries are usually excised using a button-like tissue around each artery and are then implanted into the neo-aorta. CT or MRI is used to identify postoperative complications, such as pulmonary artery stenosis, right ventricular outflow tract obstruction, supravalvular aortic stenosis, and stenosis of the reimplanted coronary arteries (Taylor et al. 2005; Ou et al. 2006). The double-switch operation performed in patients with congenitally corrected TGA is a combination of the atrial switch and arterial switch procedures.

17.4.3 Rastelli Operation

In the Rastelli procedure, a right ventricle to pulmonary artery conduit is placed and a VSD is closed (Fig. 17.13). In TGA, an intraventricular baffle from the left ventricle to the aorta via the VSD is created. The VSD may be enlarged, if necessary, during the procedure to avoid potential left ventricular outflow tract obstruction. Indications for this procedure include TGA with VSD and left ventricular outflow tract obstruction, and cardiac defects characterized by two ventricles and an overriding aorta with right ventricular outflow tract obstruction. After Rastelli operation, imaging may be performed to detect complications involving the right ventricle to pulmonary artery conduit and intraventricular baffle.

17.4.4 Fontan Operation

A staged operation usually consisting of bidirectional cavopulmonary shunt (BCS), and total cavopulmonary connection (TCPC) is performed for children with FSV. In BCS, the

systemic venous blood from the upper body is redirected to the pulmonary circulation, bypassing the right heart, by creating an end-to-side anastomosis between the superior vena cava (SVC) and the right pulmonary artery. The azygos vein is typically ligated. With bilateral SVCs, each SVC is anastomosed to its respective ipsilateral pulmonary artery. This BCS is an intermediate procedure before proceeding to a Fontan operation, typically performed between 3 and 9 months of age when pulmonary vascular resistance drops. Imaging may be used to evaluate shunt patency or to detect complications including pulmonary artery obstruction, anastomotic stenosis, pulmonary arteriovenous fistulas caused by the lack of hepatic venous blood flow to the lungs, and systemic arterial collaterals to the lungs. It should also be assessed whether the hepatic veins and the inferior vena cava (IVC) drain into the atrium with or without confluence, as this is one of important anatomic findings needed for planning the next Fontan operation. Sometimes, imaging findings can be lifesaving. Recently, coronary sinus ostial atresia with persistent left SVC could be identified on pre-BCS cardiac CT in an infant with FSV, and fatal coronary venous hypertension by ligating the persistent left SVC could be prevented in this patient by first performing coronary sinus unroofing (Kim et al. 2012).

In Fontan operation usually performed at 2–4 years of age, the systemic venous blood from the whole body bypasses the right ventricle and directly enters the pulmonary circulation. With the classic type of Fontan operation originally developed for tricuspid atresia, the anastomosis is created between the right atrium or atrial appendage and the pulmonary artery, the so-called atriopulmonary connection. However, this type of Fontan operation tends to result in gradual enlargement of the right atrium, subsequently leading to impeded pulmonary blood flow, thrombus, and arrhythmia. Therefore, Fontan operation with either the lateral tunnel or extracardiac conduit is now commonly used. In the fenestrated Fontan operation, a fenestration is created between the Fontan conduit and the right atrium and acts as a “pop-off” valve to prevent rapid volume overload to the lungs. In typical total cavopulmonary connections, SVC flow preferably goes to the right pulmonary artery and IVC flow to the left pulmonary artery, which can be assessed on MRI or CT (Fig. 17.14). However, cavopulmonary flow is variably preferential or balanced depending on the geometry of the connections. In addition, it should be noted that the lung, where hepatic venous blood flow is deficient, has a high risk of developing pulmonary arteriovenous fistulas. Imaging may be used to identify complications including stenosis and/or thrombosis in the Fontan pathway, pulmonary thromboembolism, right atrial enlargement, atrioventricular valve regurgitation, pulmonary artery stenosis, pulmonary arteriovenous fistulas, and systemic arterial collaterals to the lung.

17.5 Illustrations: CT and MRI Findings of Cardiac Defects in Congenital Heart Disease

17.5.1 Atrial Septal Defect

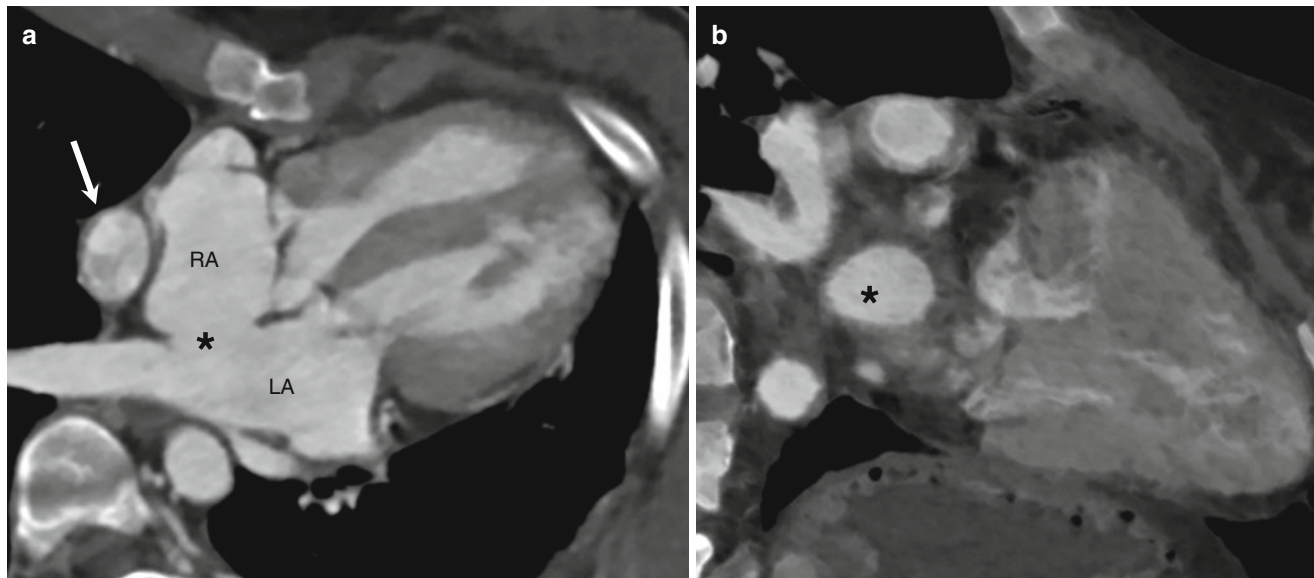


Fig. 17.1 Atrial septal defect. Four-chamber CT image shows a large secundum atrial septal defect (*asterisk*) between the right atrium (RA) and the left atrium (LA) (**a**). An extracardiac conduit (*arrow*) of Fontan

operation is noted. En face view reveals the size and shape of the atrial septal defect (*asterisk*) (**b**)

17.5.2 Ventricular Septal Defect

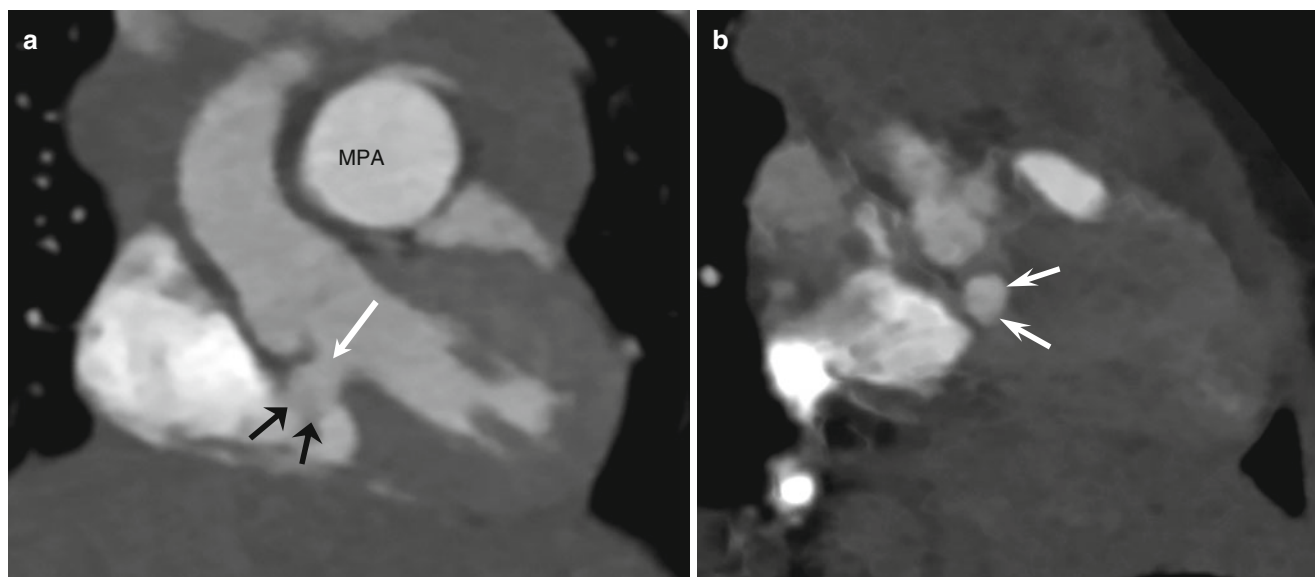


Fig. 17.2 Ventricular septal defect. Coronal CT image demonstrates a perimembranous ventricular septal defect (*long arrow*) with septal aneurysm (*short arrows*) (**a**). The dilated main pulmonary artery (*MPA*)

is noted. En face view shows the size and location of the ventricular septal defect (*arrows*) (**b**)

17.5.3 Tetralogy of Fallot

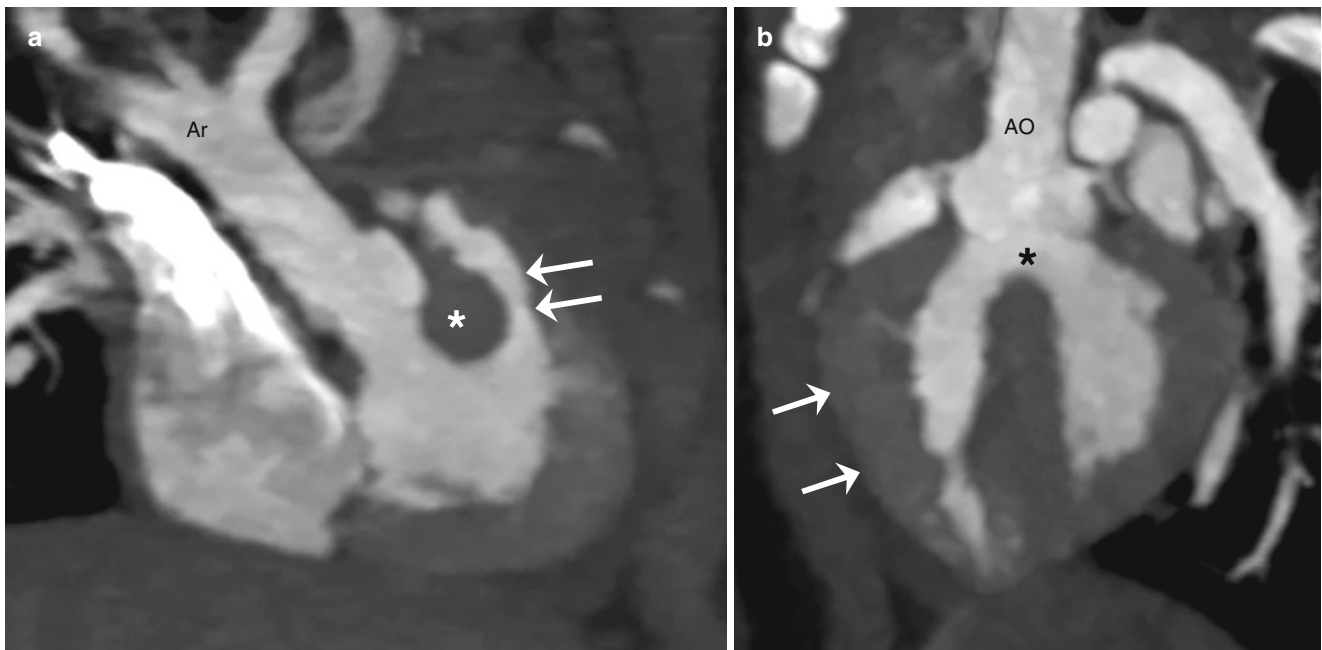


Fig. 17.3 Tetralogy of Fallot. Oblique coronal CT image shows an infundibular narrowing (*arrows*) and the stout outlet septum (*asterisk*) (**a**). The right aortic arch (*Ar*) is noted. Oblique sagittal CT image dem-

onstrates a ventricular septal defect (*asterisk*) and overriding of the aorta (*AO*) (**b**). The right ventricular hypertrophy (*arrows*) is noted

17.5.4 Atrioventricular Septal Defect

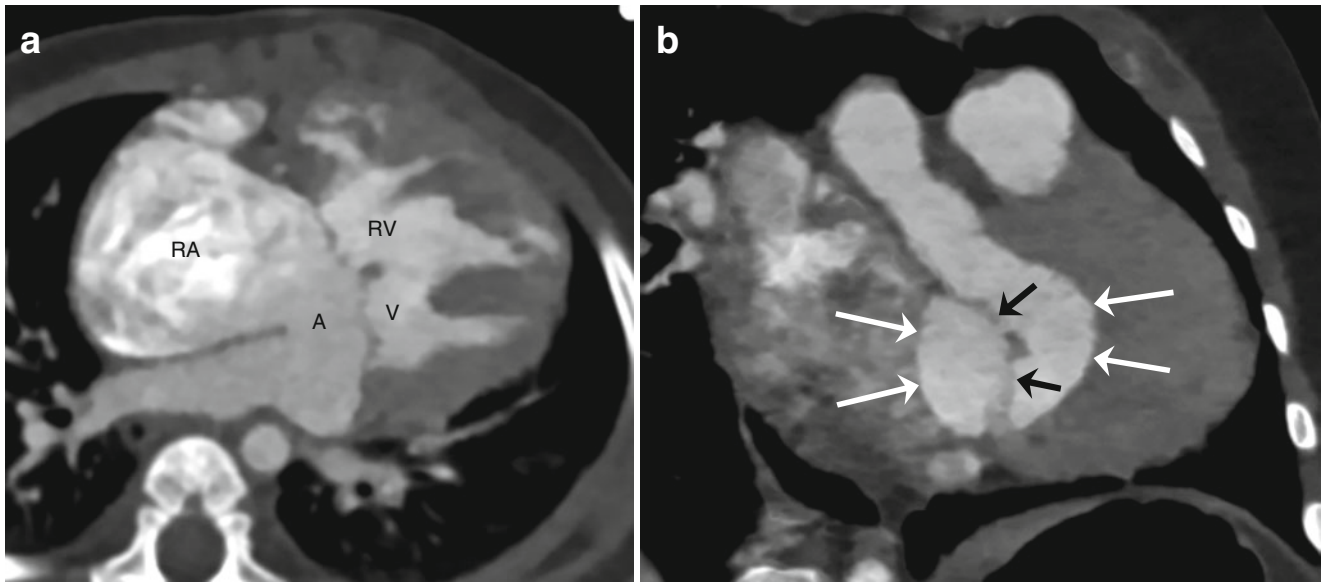


Fig. 17.4 Atrioventricular septal defect. Four-chamber CT image shows an atrioventricular septal defect consisted of a primum atrial septal defect (A) and an inlet ventricular septal defect (V) (a). The right atrium (RA)

and the right ventricle (RV) are enlarged. The right ventricular hypertrophy is also noted. En face view reveals the size and shape of the defect (long arrows) (b). The atrioventricular valve (short arrows) is noted

17.5.5 Pulmonary Atresia

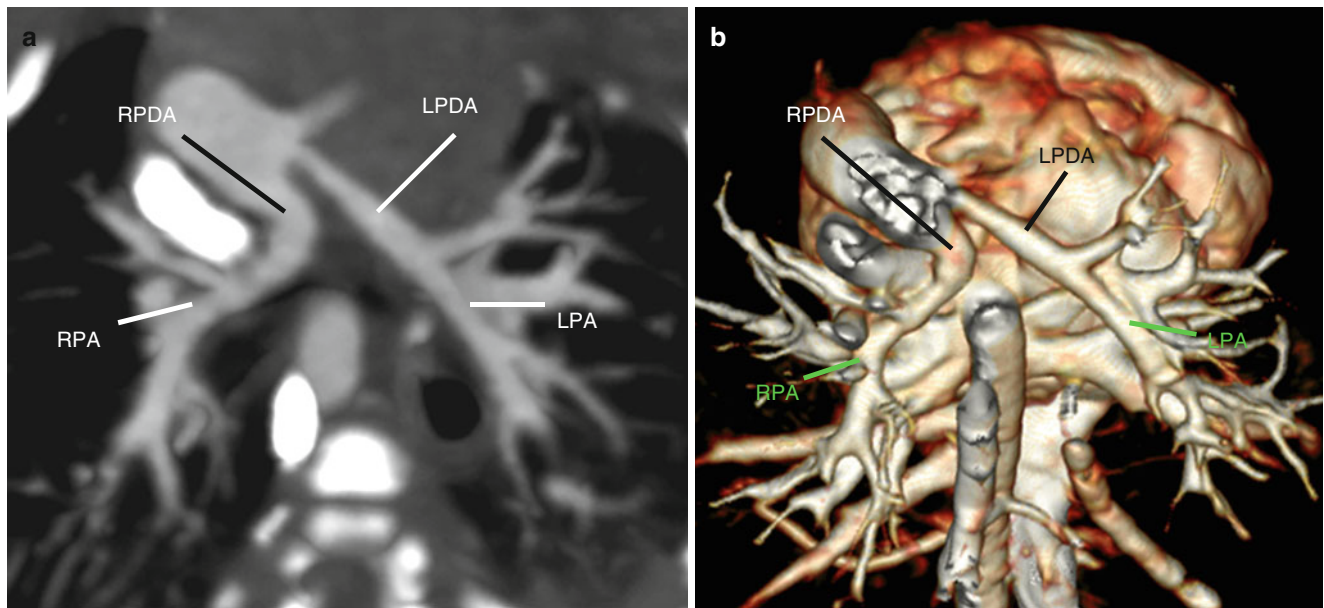


Fig. 17.5 Pulmonary atresia with non-confluent central pulmonary arteries. Oblique axial CT image (a) and volume-rendered CT image (b) demonstrate that the right (RPA) and left (LPA) pulmonary arteries

are supplied from the right (RPDA) and left (LPDA) patent ductus arteriosi, respectively

17.5.6 Transposition of the Great Arteries

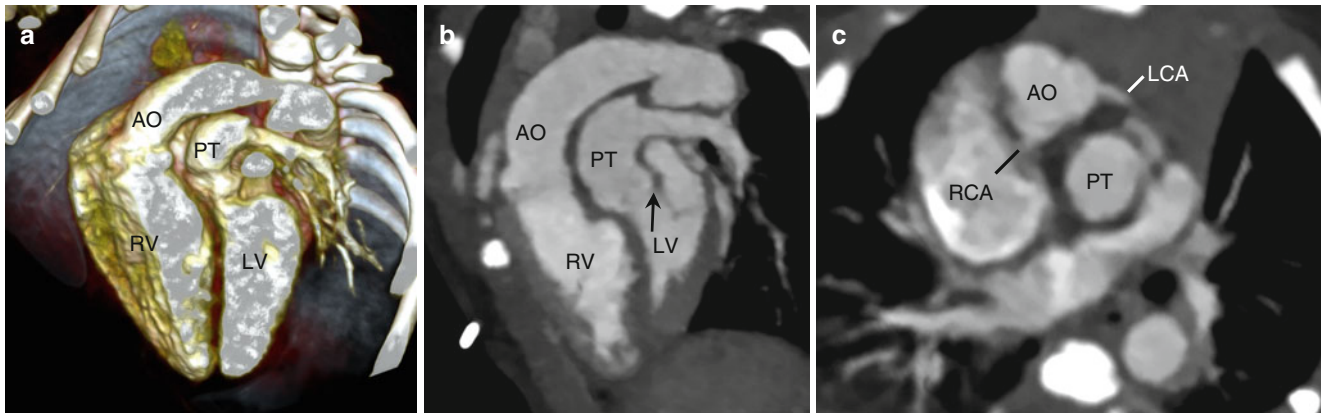


Fig. 17.6 Transposition of the great arteries. Volume-rendered CT image (**a**) and reformatted CT image (**b**) show that the ascending aorta (AO) arises from the morphologic right ventricle (RV) and the pulmonary trunk (PT) arises from the morphologic left ventricle (LV). The imaging finding is consistent with ventriculoarterial discordance. Pulmonary-mitral fibrous continuity (*arrow*) typical for transposition of

the great arteries is noted (**b**). Oblique axial CT image demonstrates the malpositioned ascending aorta right and anterior to the pulmonary trunk that refers to d-malposition of the great arteries commonly seen in complete transposition of the great arteries (**c**). The origins of the right (RCA) and left (LCA) coronary arteries are also seen

17.5.7 Double Outlet Right Ventricle

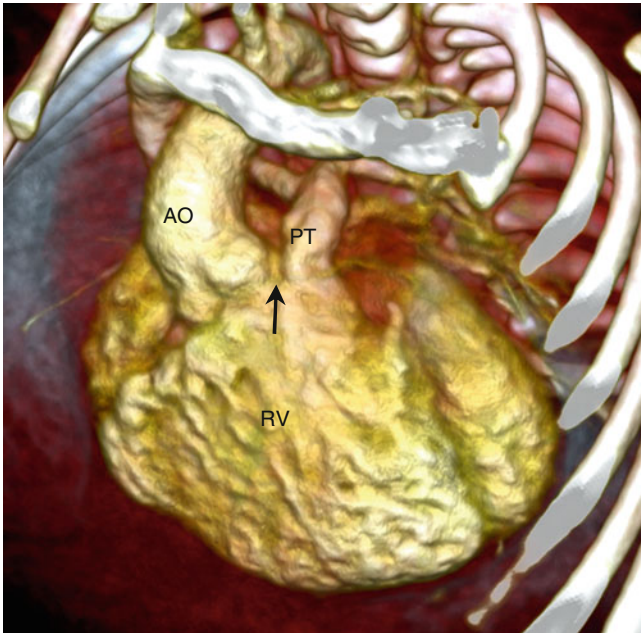


Fig. 17.7 Double outlet right ventricle. Volume-rendered CT image demonstrates that both the ascending aorta (AO) and the pulmonary trunk (PT) originate from the right ventricle (RV). Of note, the outlet septum is completely deficient (*arrow*)

17.5.8 Ebstein Anomaly

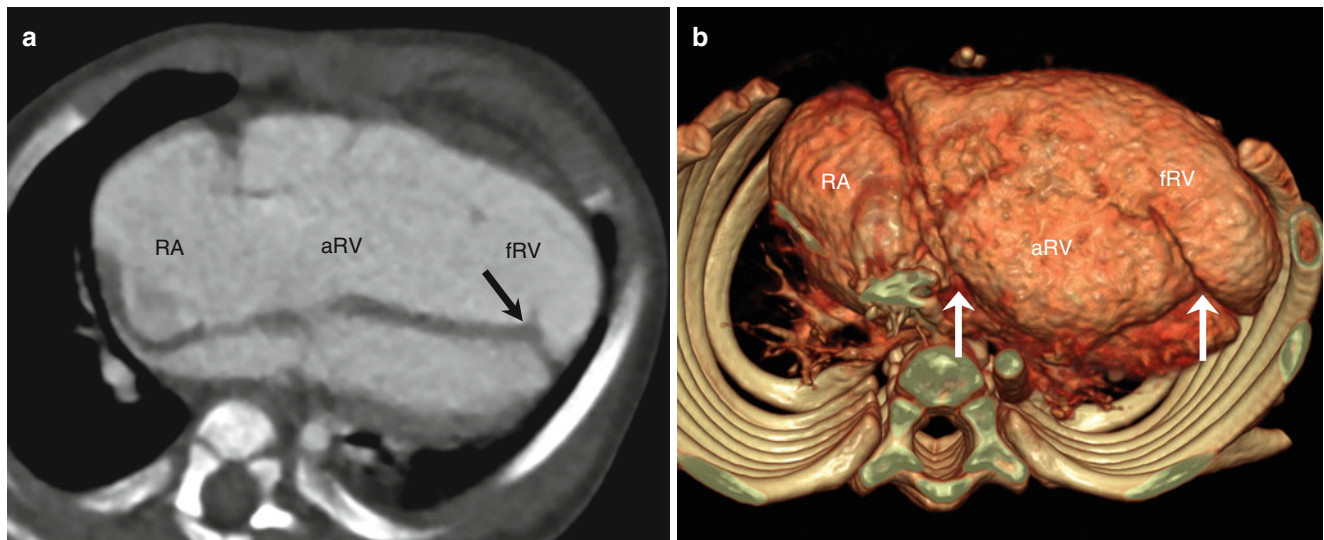


Fig. 17.8 Ebstein anomaly. Four-chamber CT image shows a diagnostic finding of the apically displaced septal attachment (*arrow*) of the tricuspid valve that divides the right ventricle into the atrialized (*aRV*) and functioning (*fRV*) portions of the right ventricle (**a**). The right

atrium (*RA*) and the right ventricle are severely dilated. Inferior volume-rendered CT image reveals a characteristic trilobed appearance (*arrows*) consisting of the enlarged right atrium, the atrialized right ventricle, and the functioning right ventricle (**b**)

17.5.9 Tricuspid Atresia

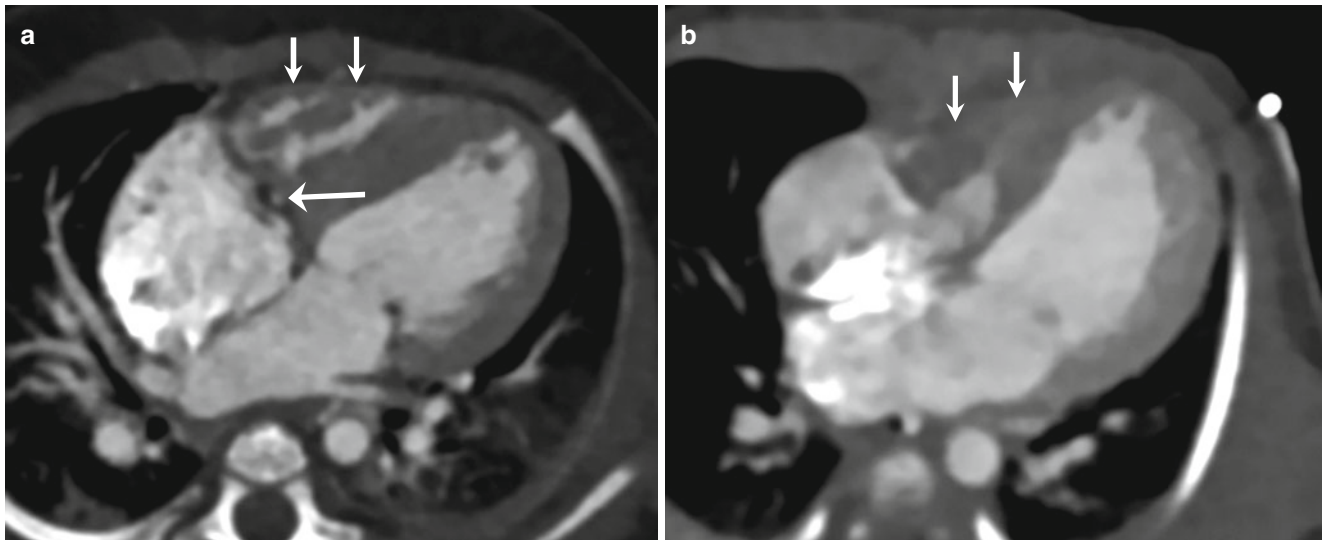


Fig. 17.9 Tricuspid atresia. Four-chamber CT image shows the absent right atrioventricular connection occupied by areolar sulcus tissue with the deeply invaginated right coronary artery (*long arrow*) (**a**). Four-

chamber CT image demonstrates the rarer type of tricuspid atresia in which the tricuspid valve is present but atretic (**b**). In both cases (**a**, **b**), the right ventricle (*short arrows*) appears severely hypoplastic

17.5.10 Hypoplastic Left Heart Syndrome

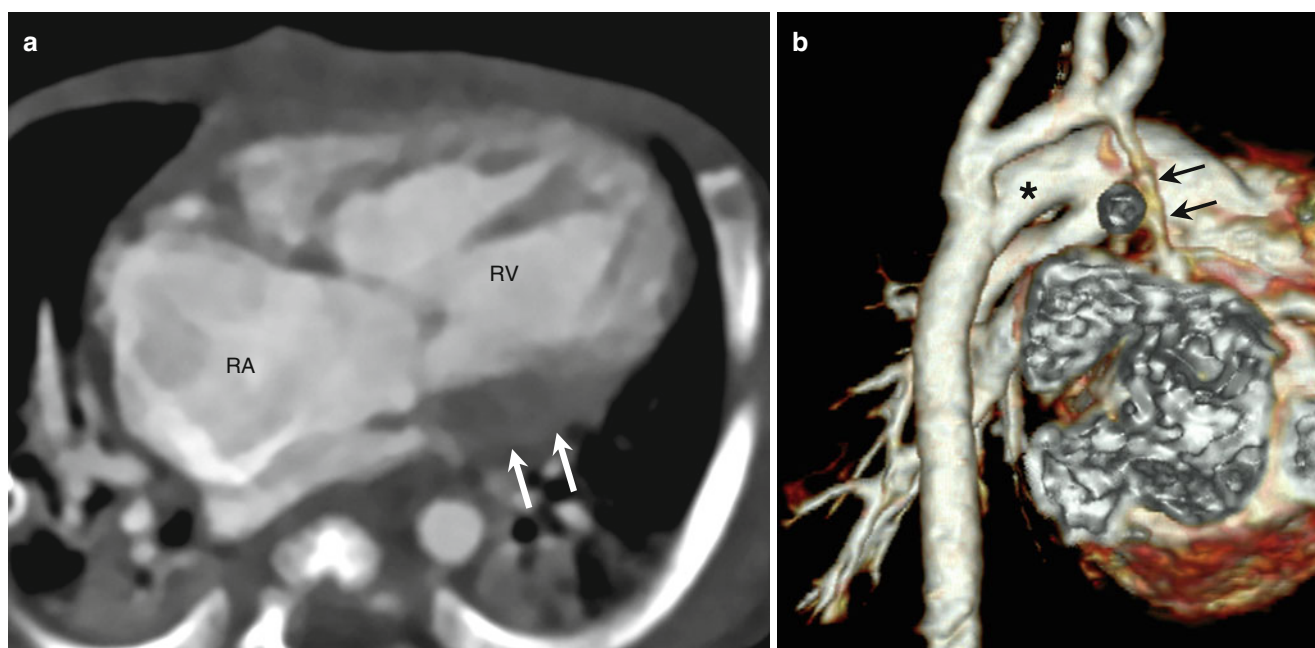


Fig. 17.10 Hypoplastic left heart syndrome. Four-chamber CT image shows a rudimentary left ventricle (*arrows*) and the markedly dilated right atrium (*RA*) and right ventricle (*RV*) (**a**). Right lateral volume-

rendered CT image reveals the hypoplastic ascending aorta (*arrows*) and a large patent ductus arteriosus (*asterisk*) (**b**)

17.5.11 Repaired Tetralogy of Fallot

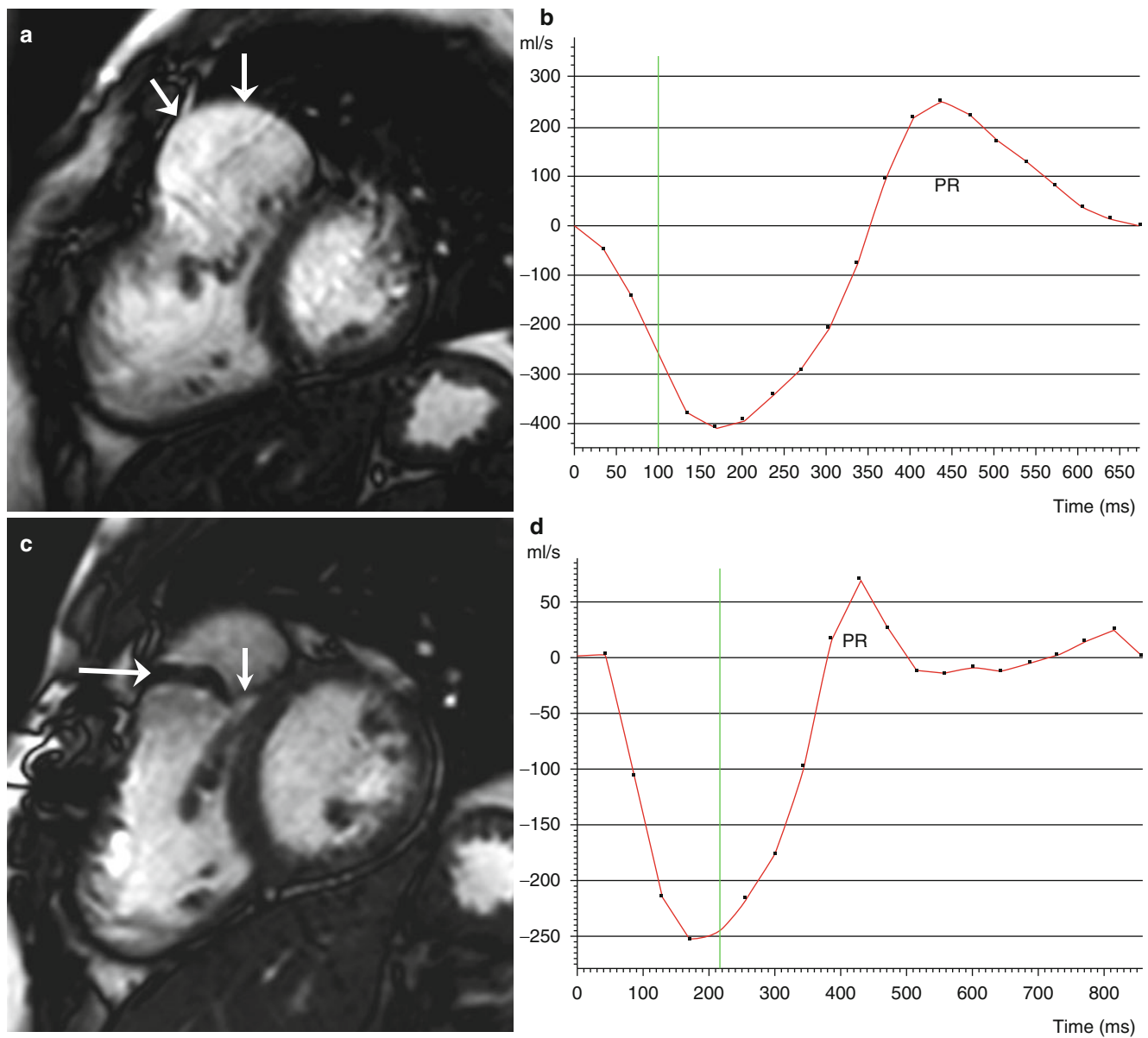


Fig. 17.11 Repaired tetralogy of Fallot. Short-axis cine MRI shows aneurysmally dilated right ventricular outflow tract (*arrows*) (**a**). The right pulmonary artery time-flow curve obtained by phase-contrast MRI demonstrates a substantial pulmonary regurgitation (*PR*) (**b**). Short-axis cine MRI after pulmonary valve replacement (*long arrow*)

reveals markedly decreased size of the right ventricle (*RV*) (**c**). A paravalvular leak (*short arrow*) is noted. The right pulmonary artery time-flow curve obtained by phase-contrast MRI demonstrates a considerable reduction of pulmonary regurgitation (*PR*) (**d**)

17.5.12 Arterial Switch Operation

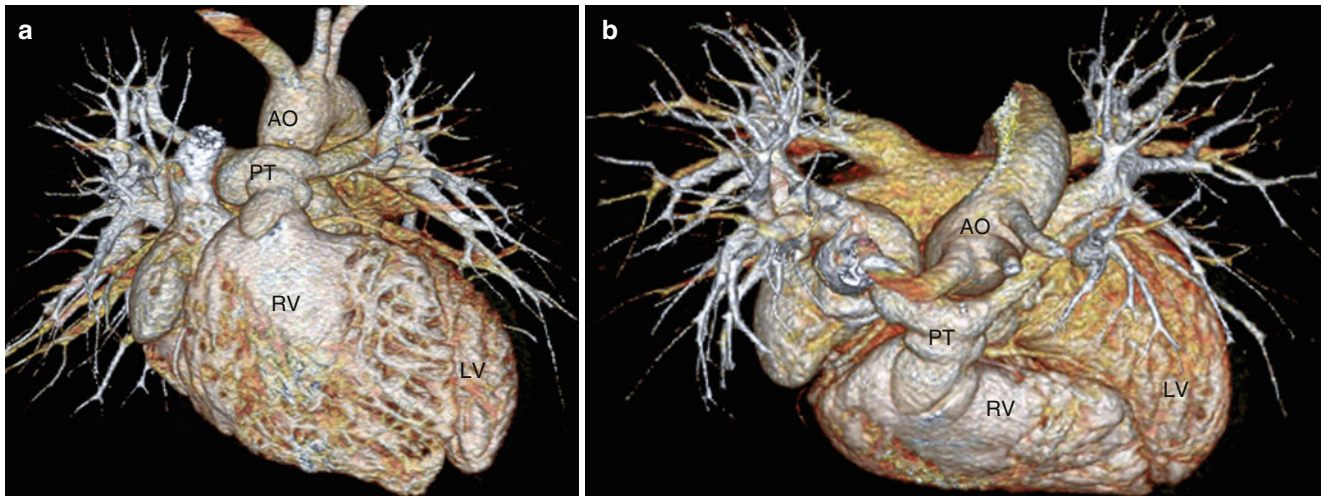


Fig. 17.12 Arterial switch operation for transposition of the great arteries. Anterior (**a**) and superior (**b**) volume-rendered CT images show that the pulmonary trunk (*PT*) and the ascending aorta (*AO*) are switched and the main pulmonary artery is identified anterior to the

aorta. As a result, the pulmonary trunk arises from the right ventricle (*RV*) and the ascending aorta arises from the left ventricle (*LV*) after arterial switch operation

17.5.13 Rastelli Operation

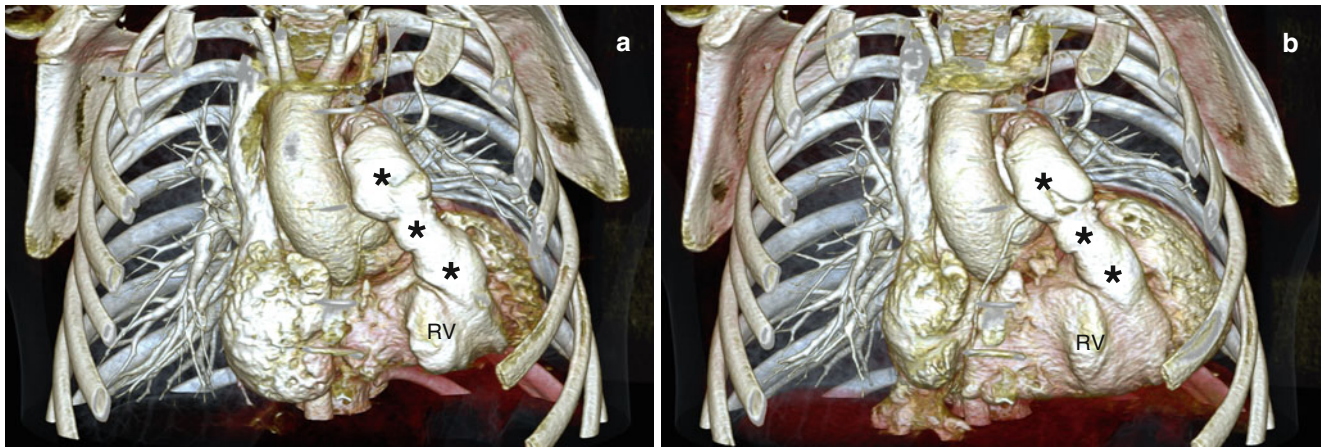


Fig. 17.13 Rastelli operation for pulmonary atresia with ventricular septal defect. Anterior volume-rendered CT images obtained at the end systole (**a**) and the end diastole (**b**) show a patent right ventricle (RV) to pulmonary artery conduit (*asterisks*) and good ventricular contraction

17.5.14 Extracardiac Conduit Fontan Operation

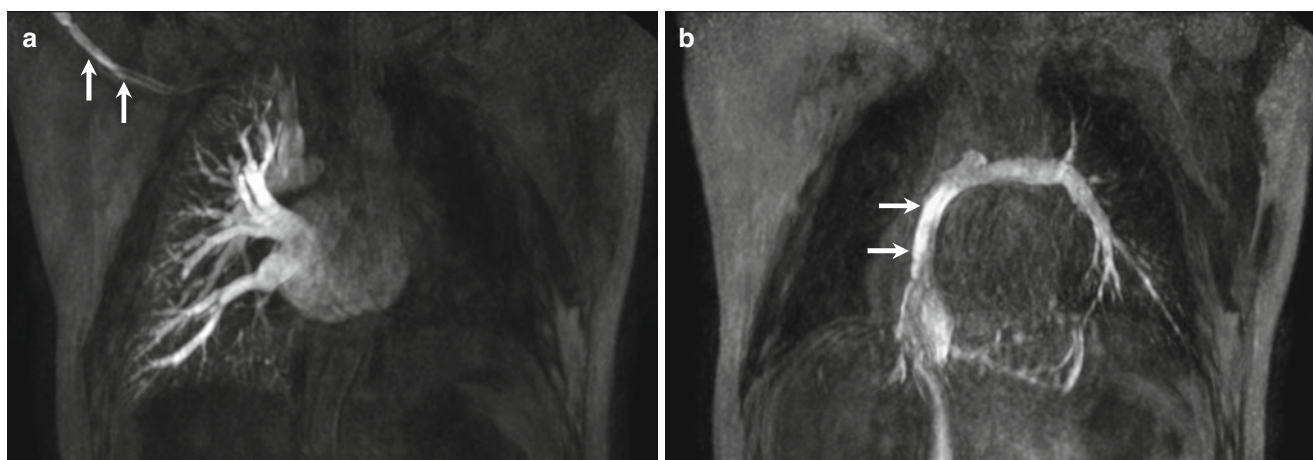


Fig. 17.14 Extracardiac conduit Fontan operation. Coronal contrast-enhanced MRA via the right arm vein shows preferential flow from the right arm vein (*arrows*) to the right lung (**a**). Coronal contrast-enhanced

MRA via the leg vein reveals preferential flow from the leg vein to the left lung (**b**). The extracardiac conduit (*arrows*) looks patent

References

- Durongpisitkul K, Tang NL, Soongswang J, et al. Predictors of successful transcatheter closure of atrial septal defect by cardiac magnetic resonance imaging. *Pediatr Cardiol*. 2004;25:124–30.
- Goo HW. State-of-the-art CT imaging techniques for congenital heart disease. *Korean J Radiol*. 2010;11:4–18.
- Goo HW. CT in pediatric heart disease. In: Saremi F, Achenbach S, Arbustini E, Narula J, editors. *Revisiting cardiac anatomy: a computed-tomography-based atlas and reference*. Oxford: Wiley-Blackwell; 2011a.
- Goo HW. Haemodynamic findings on cardiac CT in children with congenital heart disease. *Pediatr Radiol*. 2011b;41:250–61.
- Goo HW. Cardiac MDCT in children: CT technology overview and interpretation. *Radiol Clin North Am*. 2011c;49:997–1010.
- Goo HW. Pediatric congenital heart disease. In: Abramson S, editor. *Cardiac CT: the practical approach*. New York: McGraw-Hill; 2012.
- Goo HW. Current trends in cardiac CT in children. *Acta Radiol*. 2013;54:1055–62.
- Goo HW, Yang DH. Coronary artery visibility in free-breathing young children with congenital heart disease on cardiac 64-slice CT: dual-source ECG-triggered sequential scan vs. single-source non-ECG-synchronized spiral scan. *Pediatr Radiol*. 2010;40:1670–80.
- Goo HW, Park IS, Ko JK, et al. CT of congenital heart disease: normal anatomy and typical pathologic conditions. *Radiographics*. 2003;23:S147–65.
- Goo HW, Park IS, Ko JK, et al. Computed tomography for the diagnosis of congenital heart disease in pediatric and adult patients. *Int J Cardiovasc Imaging*. 2005;21:347–65.
- Goo HW, Yang DH, Park IS, et al. Time-resolved three-dimensional contrast-enhanced magnetic resonance angiography in patients who have undergone a Fontan operation or bidirectional cavopulmonary connection: initial experience. *J Magn Reson Imaging*. 2007;25:727–36.
- Goo HW, Seo DM, Yun TJ, et al. Coronary artery anomalies and clinically important anatomy in patients with congenital heart disease: multi-slice CT findings. *Pediatr Radiol*. 2009;39:265–73.
- Grosse-Wortmann L, Yun TJ, Al-Radi O, et al. Borderline hypoplasia of the left ventricle in neonates: insight for decision-making from functional assessment with magnetic resonance imaging. *J Thorac Cardiovasc Surg*. 2008;136:1429–35.
- Holmes KW. Timing of pulmonary valve replacement in tetralogy of Fallot using cardiac magnetic resonance imaging: an evolving process. *J Am Coll Cardiol*. 2012;60:1015–7.
- Kim YJ, Hur J, Choe KO, et al. Interatrial shunt detected in coronary computed tomography angiography: differential features of a patent foramen ovale and an atrial septal defect. *J Comput Assist Tomogr*. 2008;32:663–7.
- Kim C, Goo HW, Yu JJ, et al. Coronary sinus ostial atresia with persistent left superior vena cava demonstrated on cardiac CT in an infant with functional single ventricle. *Pediatr Radiol*. 2012;42:761–3.
- Kim HJ, Goo HW, Park S, et al. Left ventricle volume measured by cardiac CT in two infants with small left ventricles: a new and accurate method in determining uni- or biventricular repair. *Pediatr Radiol*. 2013;43:243–6.
- Ou P, Mousseaux E, Azarine A, et al. Detection of coronary complications after the arterial switch operation for transposition of the great arteries: first experience with multislice computed tomography in children. *J Thorac Cardiovasc Surg*. 2006;131:639–43.
- Sena L, Goo HW. Computed tomography in congenital heart disease. In: Donoghue V, editor. *Radiological imaging of the neonatal chest*. 2nd ed. Berlin: Springer; 2008.
- Taylor AM, Dymarkowski S, Hamaekers P, et al. MR coronary angiography and late-enhancement myocardial MR in children who underwent arterial switch surgery for transposition of great arteries. *Radiology*. 2005;234:542–7.
- Tsai IC, Goo HW. Cardiac CT and MRI for congenital heart disease in Asian countries: recent trends in publication based on a scientific database. *Int J Cardiovasc Imaging*. 2013;29(Suppl 1):1–5.

Yang Min Kim

Contents

18.1	Introduction	574
18.2	Pathogenesis and Pathophysiology	574
18.3	Imaging	574
18.4	Great Artery Anomalies	575
18.4.1	Coarctation of the Aorta.....	575
18.4.2	Interrupted Aortic Arch.....	575
18.4.3	Patent Ductus Arteriosus.....	576
18.4.4	Truncus Arteriosus.....	576
18.4.5	Aortopulmonary Window.....	576
18.5	Aortic Arch Anomalies and Vascular Rings	576
18.5.1	Double Aortic Arch.....	576
18.5.2	Left Aortic Arch with an Aberrant Right Subclavian Artery.....	577
18.5.3	Circumflex Left Aortic Arch.....	577
18.5.4	Right Aortic Arch with an Aberrant Left Subclavian Artery.....	577
18.5.5	Circumflex Right Aortic Arch.....	578
18.5.6	Pulmonary Artery Sling.....	578
18.5.7	Innominate Artery Compression Syndrome.....	578
18.6	Systemic Venous Anomalies	578
18.6.1	Persistent Left Superior Vena Cava.....	578
18.6.2	Retroaortic Left Brachiocephalic Vein.....	578
18.7	Pulmonary Venous Anomalies	579
18.7.1	Partial Anomalous Pulmonary Venous Return.....	579
18.7.2	Total Anomalous Pulmonary Venous Return.....	579
18.8	Illustrations: Congenital Thoracic Vascular Anomalies and Associated Airway Diseases	580
18.8.1	Coarctation of the Aorta.....	580
18.8.2	Interrupted Aortic Arch.....	583
18.8.3	Truncus Arteriosus.....	584
18.8.4	Aortopulmonary Window.....	585
18.8.5	Double Aortic Arch.....	586
18.8.6	Left Aortic Arch with Aberrant Right Subclavian Artery.....	590
18.8.7	Right Aortic Arch with Aberrant Left Subclavian Artery.....	591
18.8.8	Circumflex Right Aortic Arch.....	592
18.8.9	Pulmonary Artery Sling.....	593

Y.M. Kim, M.D., Ph.D.
Department of Radiology,
Sejong General Hospital and Heart Institute,
91-121 Sosa-dong, Sosa-gu, Bucheon, Kyunggi, Korea
e-mail: ymkimna@naver.com

18.8.10	Persistent Left Superior Vena Cava.....	594
18.8.11	Retroaortic Left Brachiocephalic Vein.....	595
18.8.12	Partial Anomalous Pulmonary Venous Return (Scimitar Syndrome).....	596
18.8.13	Total Anomalous Pulmonary Venous Return.....	598
References		600

18.1 Introduction

Congenital thoracic vascular anomalies encompass the obstruction of the normal vessels, persistence of the aberrant vessels, and anomalous connection of the thoracic aorta and its branches, thoracic systemic veins, pulmonary arteries, and pulmonary veins. A vascular ring is formed when the anomalous vessel surrounds and compresses the trachea, esophagus, or both. Although echocardiography is the primary imaging modality for evaluating congenital thoracic vascular anomalies in children, computed tomography (CT) has emerged as a useful alternative imaging modality for these conditions. By virtue of the rapid technical innovations such as superior temporal and spatial resolution and lower radiation exposure, multidetector CT (MDCT) can make a definitive and conclusive diagnosis of congenital thoracic vascular anomalies, airway compression by the anomalous vessel, and concomitant airway anomalies. Three-dimensional (3-D) CT angiography also provides straightforward and comprehensive anatomic information for selecting appropriate treatment options and for preoperative surgical planning in the patients with these anomalies. In this chapter, we describe the pathogenesis, pathophysiology, and imaging features of congenital thoracic vascular anomalies and associated airway abnormalities, and we illustrate the CT findings of these conditions.

18.2 Pathogenesis and Pathophysiology

Congenital thoracic vascular anomalies result from persistent patency of embryonic vascular segments that would normally regress, or regression of vascular segment which would normally remain patent during the development of the embryonic cardiovascular structure. Developmental malformations may cause hypoplasia or interruption of the normal vessels, persistence of anomalous vessels due to failure of regression of embryonic structures, and anomalous connections between the thoracic vasculatures. The pathogenetic mechanism of the obstructive aortic lesions is assumed to be secondary to decreased antegrade flow in the ascending aorta caused by intracardiac lesions. Depending on the severity of decrease in the aortic flow, hypoplastic left heart syndrome, aortic atresia, interruption of the aortic arch, hypoplasia of the aortic arch, or coarctation of the aorta can occur.

Vascular ring develops when anomalously persistent aortic arch derivatives encircle the central airway, esophagus, or

both. The vascular ring may be complete and sufficiently tight to cause symptoms, or it may be incomplete and loose enough such that it does not cause any symptoms. It usually causes respiratory symptoms such as wheezing, stridor, respiratory difficulty, recurrent pulmonary infection, or tracheomalacia in infants and young children, whereas it causes esophageal obstruction in older children and adults resulting in dysphagia. In addition to extrinsic compression of the central airway by the vascular ring, concomitant tracheal stenosis or tracheomalacia can also cause respiratory symptoms.

Central airway obstruction by the anomalous vessel or intrinsic airway abnormalities may complicate the natural and postoperative course of the patients with congenital cardiovascular disease. The central airway obstruction may be mistaken for a lower respiratory tract problem, as the latter is a common complication of congenital heart disease. Early detection of the central airway obstruction is important because urgent surgical intervention is often required. When surgical treatment is considered, the mechanism and severity of airway obstruction should be clearly demonstrated using 3-D CT angiography.

18.3 Imaging

As in other cardiac defects, chest radiography is the initial first-line diagnostic modality for evaluating suspected congenital thoracic vascular anomalies and associated airway disease. By careful observation of chest radiography, the sidedness or bilaterality of the aortic arch, sidedness of the descending aorta, and degree of tracheal stenosis can be determined. Furthermore it is useful for excluding other causes of respiratory problem in patients with respiratory distress. However, it is not sufficient to establish a specific diagnosis of the vascular anomaly and vascular airway compression in most of the cases.

Barium esophagography is a fast and inexpensive imaging tool for demonstrating extrinsic esophageal compression by the anomalous vessel. Pulsating nature of the esophageal indentation during fluoroscopy is suggestive of vascular esophageal compression. It is useful to establish a specific diagnosis based on the analysis of the nature and direction of esophageal indentation. Posterior esophageal indentation at the level of the aortic arch suggests the diagnosis of aortic arch anomalies such as double aortic arch, aberrant retroesophageal subclavian artery, and circumflex retroesophageal aortic arch, whereas anterior esophageal indentation at the carinal level indicates the presence of pulmonary artery sling.

Echocardiography can provide accurate anatomical and functional information in patients with congenital cardiovascular anomalies, and hence it is the mainstay of imaging from the initial evaluation up to a definite diagnosis in these patients. However, for older children and patients with congenital thoracic vascular anomalies, an accurate evaluation by echocardiography can be limited due to poor acoustic windows. Conventional angiography has been used in patients with congenital cardiovascular anomalies, and it has been regarded as the standard for establishing the diagnosis. However, its utility is markedly limited for the evaluation of extravascular structures such as the central airway and lung parenchyma.

MR imaging can provide both anatomical and functional information in patients with congenital cardiac and vascular anomalies (Weinberg 2006). MR is particularly useful in pediatric patients because it is not associated with the hazard of ionizing radiation exposure or iodinated intravenous contrast administration. However, it is not sufficient for the evaluation of airway and the lung, and anesthesia or deep sedation is required for pediatric patients due to the prolonged scan time than that in CT examination.

CT angiography with 3-D rendering provides comprehensive information about congenital thoracic vascular anomalies as well as central airway abnormalities (Lee et al. 2010). In addition, it can facilitate the understanding of the mechanism of airway obstruction by demonstrating the relationship between the offending thoracic vessels and stenotic airways. Furthermore, it is very helpful for physicians and surgeons who are not familiar with creating 3-D reconstruction images using axial CT images imaginarily.

18.4 Great Artery Anomalies

18.4.1 Coarctation of the Aorta

Coarctation of the aorta (COA) is defined as congenital focal narrowing of the aortic isthmus distal to the origin of the left subclavian artery near the insertion of the ductus arteriosus. It is a common vascular anomaly, with an incidence of 5–8 % of congenital heart disease. It may occur in isolation or in combination with other cardiac anomalies. COA is classified into preductal, juxtaductal, and postductal types, based on the relation to the ductus arteriosus. It is also classified into infantile and adult types, based on the age of presentation. In the infantile or preductal type, COA involves the isthmus portion of the aorta between the left subclavian artery and ductus (Fig. 18.1). It is usually associated with hypoplasia of the aortic arch. It manifests in infancy as heart failure. In adult type, COA typically involves the juxtaductal or slightly postductal portion (Fig. 18.2). It may be found incidentally in adults with hypertension which is a com-

mon manifestation of the COA. Pseudocoarctation is defined as an elongated and redundant descending aorta with kinking or buckling of the juxtaductal region of the aorta (Fig. 18.3). It is associated with insignificant stenosis and absence of collateral arteries and hemodynamically significant pressure gradient.

Conventional angiography and MR imaging have been used to evaluate the site and degree of aortic narrowing, extent of arch hypoplasia, presence of collateral vessels, and quantification of the collateral flow. CT angiography is now considered as a useful alternative technique to evaluate this anomaly, especially in the older children. CT imaging with 3-D rendering is particularly useful to demonstrate a short-segment aortic coarctation, which can be overlooked on axial CT images alone (Fig. 18.2) (Lee et al. 2004). CT angiography is also useful in the follow-up study for evaluating restenosis or aneurysm formation after an interventional procedure (Fig. 18.2), recurrence of coarctation of the aorta after surgical correction, and complicated central airway compression within the narrow arch after coarctoplasty (Fig. 18.1c–f).

18.4.2 Interrupted Aortic Arch

Interrupted aortic arch (IAA) is defined as discontinuity of the aortic arch between the ascending and descending aorta. IAA is an extreme form of coarctation of the aorta, and its pathogenesis is similar to that of COA. It is almost always associated with cardiovascular defects in up to 98 % of cases. The most commonly associated cardiac anomalies are ventricular septal defect (VSD) and patent ductus arteriosus (PDA). PDA is required to supply blood flow beyond the interruption to the descending thoracic aorta. It is commonly associated with conditions that decrease antegrade flow to the aortic arch, including subaortic stenosis, bicuspid aortic valve, truncus arteriosus, and aortopulmonary window. IAA is classified into three types based on the site of interruption: type A, interruption distal to the left subclavian artery; type B, interruption between the left carotid artery and the left subclavian artery (Fig. 18.4); and type C, interruption between the innominate artery and the left carotid artery. The most common form of IAA is type A (53 %), followed by type B (42 %) and type C (5 %). As the reduction in aortic flow is more severe in patients with type B or C interruption or IAA with an aberrant subclavian artery, subaortic stenosis with posterior deviation of the outlet septum is more frequently associated with these conditions (Fig. 18.4).

CT angiography is a useful complementary tool for establishing the initial diagnosis and in the follow-up study of this condition (Yang et al. 2008). Three-dimensional CT angiography with fast MDCT can demonstrate subaortic stenosis as well as posterior deviation of the infundibular septum (Fig. 18.4).

18.4.3 Patent Ductus Arteriosus

Ductus arteriosus is a prenatal vessel connecting the pulmonary artery with the isthmus portion of the aorta and/or the brachiocephalic artery. It is normally patent in fetal circulation, and it spontaneously closes within a few days after birth during transition from fetal to postnatal circulation. Patent ductus arteriosus (PDA), also termed as persistent arterial duct, results from failure of mechanisms of postnatal ductal closure. PDA is the most common left-to-right shunt lesion in newborns, and it is the third most common shunt lesion in adults. It is essential for survival of children with ductal-dependent congenital heart disease including severe COA, IAA, hypoplastic left heart syndrome, pulmonary atresia, and complete transposition of the great arteries (Fig. 18.4). Echocardiography is the imaging modality of choice for evaluating PDA. CT angiography only has a complementary role for echocardiographic examination.

18.4.4 Truncus Arteriosus

Truncus arteriosus, also termed as persistent truncus arteriosus or common arterial trunk, is an anomaly in which a common arterial vessel arising from the heart having a single truncal valve gives rise to both the aorta and pulmonary arteries. It results from an incomplete truncal septation that is responsible for separating the truncus arteriosus into the aorta and pulmonary artery. Two classification systems have been proposed based on the branching pattern of the pulmonary artery from the truncus. The Collett and Edwards classification divides the truncus arteriosus into four types: type I, the origin of both pulmonary arteries from a short pulmonary trunk; type II, branch pulmonary arteries arise in close proximity from the posterior aspect of the truncus without the main pulmonary artery (Fig. 18.5); type III, branch pulmonary arteries arise far apart from the posterolateral aspect of the truncus; and type IV, “pseudotruncus,” branch pulmonary arteries arise from the descending aorta, which is currently considered to represent pulmonary atresia with major aortopulmonary collateral artery (MAPCA). Van Praagh’s types 1 and 2 truncus arteriosus are equivalent to Collett and Edwards types I and II, respectively; type 3 represents atresia of one of the pulmonary artery branches that arise from PDA or MAPCA (Fig. 18.6); and type 4 is associated with an interrupted aortic arch.

Echocardiography is sufficient for establishing the correct diagnosis and for selecting the surgical options. MR or CT angiography only has a complementary role in demonstrating branch pulmonary arteries or the aortopulmonary collateral artery (Johnson 2010). CT angiography plays a major role in the assessment of postoperative complications, such as stenosis of the pulmonary conduit, branch pulmonary arteries, and the aortic arch, and assessment of biventricular function, pulmonary insufficiency, and neo-aortic valve function.

18.4.5 Aortopulmonary Window

Aortopulmonary window is an anomaly in which there is a communication between the pulmonary artery and the ascending aorta in the presence of two separate semilunar valves. It results from failure of fusion of the two opposing conotruncal ridges, leading to a communication between the aorta and pulmonary trunk. Aortopulmonary window may occur as an isolated lesion or it can be associated with other cardiovascular anomalies such as COA and IAA. IAA is the most commonly associated lesion, and it is almost always type A IAA. Aortopulmonary window has been classified into three types by Mori and colleagues: type I, window in the proximal aspect of the ascending aorta; type II, window in the distal part of the ascending aorta (Fig. 18.7); and type III, total type or combination of types I and II.

Diagnostic imaging can differentiate aortopulmonary window from truncus arteriosus, according to the separation of aortic and pulmonary valves. Preoperative imaging is performed using echocardiography. Postoperative complications such as pulmonary artery stenosis and aortic arch obstruction can be evaluated using CT or MR angiography.

18.5 Aortic Arch Anomalies and Vascular Rings

Aortic arch anomalies result from persistent patency of vascular segments that would normally regress, or regression of segment that would normally remain patent. Vascular rings are a group of congenital anomalies in which the trachea, esophagus, or both are surrounded and compressed by anomalous vessels. These vessels include the aortic arch and its branch vessels, pulmonary arteries, and the ductus arteriosus or ligamentum arteriosum. The hypothetical double aortic arch model proposed by Edwards can facilitate the understanding of pathogenesis and can provide an explanation for the occurrence of aortic arch anomalies and vascular rings (Edwards 1948). The illustration in Fig. 18.8 depicts the potential sites of regression in the hypothetical double aortic arch system. Table 18.1 in conjunction with Fig. 18.8 facilitates the understanding of how individual aortic arch anomalies can occur using this model.

18.5.1 Double Aortic Arch

Double aortic arch is formed by persistence of both embryonic fourth aortic arches which encircle the trachea and esophagus completely forming a vascular ring. It is the most common symptomatic vascular ring in infants and young children. It can be subdivided into double aortic arch with both arches patent and that with atretic left aortic arch. In a complete double aortic arch (Fig. 18.9), the ascending aorta bifurcates into the right and left aortic arches that cross over the ipsilateral main bronchus and join to form the descending

Table 18.1 Classification of aortic arch anomalies with corresponding site of regression and atresia

Classification	Site of regression	Atresia
1. Left aortic arch		
(a) Normal anatomy	R4, R3, Rd	
(b) Aberrant right subclavian artery	R2, Rd	
(c) Right descending aorta	R2 or R3, Ld	
(d) Isolation of right subclavian artery	R4, R2	
2. Right aortic arch		
(a) Mirror image branching	L4, Rd	
(b) Aberrant left subclavian artery	L2, Ld	
(c) Right descending aorta	L2 or L3, Rd	
(d) Isolation of left subclavian artery	L4, L2	
(e) Aberrant left innominate artery	L1, Rd	
(f) Isolation of left innominate artery	L4, L1, Rd	
3. Double aortic arch		
(a) Both arches patent		
(b) Atretic left arch	Rd	L4, L3, or L2
(c) Atretic right arch	Ld	R3

aorta. The right aortic arch is usually dominant and higher in position than the left aortic arch (Fig. 18.9). In an incomplete double aortic arch (Fig. 18.10), a portion of the left aortic arch is atretic and persists only as a fibrotic or ligamentous connection (Schlesinger et al. 2005).

Chest radiography and esophagography have been used to detect tracheal indentation or posterior esophageal indentation in the patients with double aortic arch. CT angiography is a good imaging modality for evaluating a double aortic arch, especially the incomplete type. The common carotid and subclavian arteries on each side originate separately from the respective aortic arches. Symmetrically located four brachiocephalic arteries on each side above the aortic arch on axial images are suggestive of a double aortic arch as well as other aortic arch anomalies (Figs. 18.9, 18.12, and 18.13).

18.5.2 Left Aortic Arch with an Aberrant Right Subclavian Artery

Left aortic arch with an aberrant right subclavian artery results from anomalous regression of the right fourth aortic arch between the right common carotid and right subclavian arteries. It is the most common aortic arch anomaly with an incidence of 0.5–2 %. The aberrant right subclavian artery arises from the descending aorta as a last branch and crosses the midline by following a retroesophageal course (Fig. 18.11). The aorta thus gives rise to the right carotid, the left carotid, the left subclavian, and the aberrant right subclavian arteries. Aneurysmal dilatation of the origin of

the aberrant subclavian artery from the descending aorta can occur, thus forming an aortic diverticulum of Kommerell. Right ductus arteriosus or ligamentum arteriosum with the left aortic arch, aberrant right subclavian artery, and right pulmonary artery may form a loose vascular ring. Esophageal compression by the aberrant right subclavian artery, especially with diverticulum of Kommerell, can manifest as dysphagia in approximately 10 % of adults.

CT angiography with 3-D imaging can accurately evaluate the origin, retroesophageal course of the anomalous subclavian artery, and diverticulum of Kommerell (Turkvatan et al. 2009). It can also evaluate the degree of tracheal compression caused by the vascular ring before surgical division of the ligamentum arteriosum.

18.5.3 Circumflex Left Aortic Arch

Circumflex left aortic arch, also referred to as left aortic arch with right descending aorta, is a rare anomaly in which the aortic arch passes to the left of the trachea and turns to the right behind the esophagus to become the right descending aorta (Philip et al. 2001). The right subclavian artery usually has an anomalous origin from the right descending aorta. Contrary to the aberrant right subclavian artery, the aortic arch itself, not the right subclavian artery, follows a retroesophageal course. The vascular ring is completed by the right ligamentum arteriosum that connects the right pulmonary artery and the right descending aorta with a circumflex aortic arch at the left and posterior sides. However, it is usually loose enough such that it does not cause significant tracheal compression. Esophageal compression often causes dysphagia, which is easily demonstrated by esophagography that shows the large posterior esophageal indentation caused by the retroesophageal aorta.

18.5.4 Right Aortic Arch with an Aberrant Left Subclavian Artery

Right aortic arch with an aberrant left subclavian artery is the mirror image of the left aortic arch with retroesophageal right subclavian artery with a reversed branching sequence. An aberrant left subclavian artery originates as the last branch of the right aortic arch (Fig. 18.12). The aorta gives rise to the left common carotid, the right common carotid, the right subclavian, and the aberrant retroesophageal left subclavian arteries in that order. At its origin from the descending aorta, aneurysmal dilatation can occur, thus forming an aortic diverticulum of Kommerell (Fig. 18.12). When the left-sided ductus or ligament is present, a complete vascular ring is formed with the right aortic arch, aberrant left subclavian artery, and the left pulmonary artery. This anomaly can cause dysphagia, particularly when there is an accompanying large diverticulum of Kommerell or a fibrous band of the left ligamentum arteriosum that results in the formation of a complete vascular ring.

18.5.5 Circumflex Right Aortic Arch

Circumflex right aortic arch, also referred to as right aortic arch with left descending aorta, is analogous to and is the mirror image of the left aortic arch with right descending aorta as described above. In this condition, the aortic arch passes to the right side of the trachea and turns to the left behind the esophagus to become the left descending aorta (Fig. 18.13). The left subclavian artery usually has an anomalous origin directly from the left descending aorta, and hence the left subclavian artery does not have a retroesophageal course. A vascular ring can be formed by the left ligamentum arteriosum that connects the left pulmonary artery and the left descending aorta (Fig. 18.13a), which may cause symptoms. Esophagography can demonstrate the large posterior esophageal indentation caused by the retroesophageal aorta.

18.5.6 Pulmonary Artery Sling

Pulmonary artery sling is a rare congenital anomaly caused by involution of the proximal left sixth aortic arch, in which the left pulmonary artery typically arises from the proximal right pulmonary artery and courses to the left lung between the trachea and esophagus (Fig. 18.14). A sling-like course of an anomalous left pulmonary artery around the distal trachea and carina can result in extrinsic compression of the airways. In addition to extrinsic vascular compression, intrinsic airway abnormalities such as congenital tracheal stenosis due to complete cartilaginous rings or tracheomalacia can be associated with or complicated by the underlying conditions, which can further increase the vascular airway compression. Other concomitant airway anomalies are tracheal bronchus or bridging bronchus.

CT angiography with 3-D imaging can easily demonstrate the course of the pulmonary artery sling and can provide comprehensive anatomical information about the extrinsic airway compression caused by pulmonary artery sling and congenital tracheal stenosis (Lee et al. 2010; Zhong et al. 2010). Accurate diagnosis of the pulmonary artery sling and associated airway abnormalities is required for the selection of appropriate surgical techniques including transposition of the left pulmonary artery and staged or concomitant airway surgery. Complicated tracheomalacia can be accurately diagnosed using paired inspiratory-expiratory CT.

18.5.7 Innominate Artery Compression Syndrome

Innominate artery compression syndrome can occur when the innominate artery originates from the aortic arch in the left side of the mediastinum. It crosses the path of the trachea from the left to right resulting in anterior tracheal compres-

sion. However, in most of the children, an anomalous innominate artery results in only a mild degree of tracheal compression and is rarely symptomatic. It can cause symptoms when the narrow space of superior mediastinum is crowded with vascular structures. The airway symptoms of innominate artery compression syndrome are expiratory stridor, cough, and sleep apnea.

CT can easily demonstrate the course of the innominate artery and the degree of tracheal compression on axial and reformatted CT images. Innominate artery compression is highly associated with intrinsic tracheomalacia which can cause or aggravate the respiratory symptoms. Concomitant tracheomalacia can be accurately diagnosed using paired inspiratory-expiratory CT.

18.6 Systemic Venous Anomalies

Anomalies of the systemic veins are rare, and they may occur in isolation or may be associated with cardiac disease. Common systemic venous anomalies are bilateral superior vena cava (SVC) with persistent left SVC, left SVC with mirror image venous drainage, and retroaortic left brachiocephalic vein. Understanding of these anomalies can facilitate the planning and placement of central venous catheters, cardiac pacemaker leads, hemodynamic monitoring devices, and cardioverter-defibrillator leads (Heye et al. 2007).

18.6.1 Persistent Left Superior Vena Cava

Persistent left superior vena cava results from persistence of the left anterior cardinal vein, which yields bilateral SVC or left SVC with mirror image venous drainage. The left SVC usually drains into the right atrium via the coronary sinus, which is dilated due to the overflow from the left SVC (Fig. 18.15). This congenital vascular anomaly is very rare with a reported incidence of 0.3–0.5 % in the general population and an incidence of 1.3–5 % in patients with congenital heart disease. A gateway to the coronary sinus often shows a slit-like stenosis between the left atrial appendage and the left upper pulmonary vein, which is mostly an innocent lesion that does not cause functional obstruction at this level (Fig. 18.15).

18.6.2 Retroaortic Left Brachiocephalic Vein

Retroaortic left brachiocephalic vein, also termed as low innominate vein below the aortic arch, is found in 0.5–0.6 % of patients with congenital heart disease including tetralogy of Fallot, pulmonary atresia with VSD, and truncus arteriosus. It courses posterior to the ascending aorta and underneath the aortic arch, to join the right SVC (Fig. 18.16)

(Takada et al. 1992). It does not cause hemodynamic sequelae.

18.7 Pulmonary Venous Anomalies

A common pulmonary vein arises from the dorsal mesocardium and is progressively incorporated into the posterior wall of the left atrium. According to the degree of normal incorporation into the left atrium, variable ostia and branching patterns of the pulmonary vein are formed as a normal variation. Faulty incorporation can give rise to a spectrum of pulmonary venous anomalies, including total anomalous pulmonary venous return (TAPVR), partial anomalous pulmonary venous return (PAPVR), cor triatriatum, sinus venosus defect, and pulmonary venous stenosis. Anomalous pulmonary venous return results from incomplete resorption of the common pulmonary vein and its anastomosis with the primitive venous plexus, along with persistent connections with the systemic cardinal veins. When echocardiography cannot identify all of the pulmonary veins, MR or CT angiography can be used to identify all of the pulmonary veins and to delineate the entire anomalous course (Ucar et al. 2008; Vyas et al. 2012). MR imaging can provide quantitative measurement of the shunt ratio using phase contrast imaging.

18.7.1 Partial Anomalous Pulmonary Venous Return

Partial anomalous pulmonary venous return (PAPVR) represents failure of incorporation of one or more (but not all) of the pulmonary veins into the left atrium. Anomalous pulmonary veins drain instead into the systemic veins, right atrium, or coronary sinus. The most common type of PAPVR is right upper lobe venous drainage into the SVC, which may be associated with a sinus venosus defect. The second most frequent type is the left pulmonary venous drainage into the left innominate vein, followed by anomalous drainage from the right lung into the inferior vena cava (IVC). The last condition is commonly associated with the scimitar syndrome (Fig. 18.17).

Scimitar syndrome is also known as hypogenetic lung syndrome or congenital venolobar syndrome, and in this syndrome, the right pulmonary vein anomalously drains into the IVC via the scimitar vein. The scimitar vein is a curvilinear intrapulmonary vein that resembles the Turkish sword, and it is vertically oriented near the right cardiac border. This syndrome almost exclusively involves the right lung and is associated with hypoplasia of the right lung with secondary dextroposition of the heart. It is commonly associated with more complex pulmonary developmental anomalies including bronchopulmonary sequestration, systemic arterializa-

tion of the lung, horseshoe lung, bronchogenic cyst, accessory diaphragm, and congenital diaphragmatic hernia. Horseshoe lung refers to the fusion of lower lobes across the midline to form a horseshoe shape. Chest radiographs can demonstrate the vertically oriented scimitar vein in the right lower lung and right lung hypoplasia (Fig. 18.17a) (Woodring et al. 1994). CT angiography with 3-D rendering is the most useful imaging tool for demonstrating anomalous venous drainage into the IVC, right lung hypoplasia with hypoplastic right pulmonary artery and right bronchus, anomalous systemic arterial supply, and horseshoe lung (Fig. 18.17) (Konen et al. 2003).

18.7.2 Total Anomalous Pulmonary Venous Return

Total anomalous pulmonary venous return (TAPVR) results from a failure of the connection between pulmonary veins and the left atrium, and all of the pulmonary veins drain anomalously into systemic veins, right atrium, or coronary sinus. Its pathogenesis involves a failure of normal incorporation of the common pulmonary vein into the left atrium. Depending on the site of anomalous venous drainage, TAPVR is categorized as supracardiac (type I), cardiac (type II), infracardiac (type III), or mixed (type IV). Supracardiac TAPVR is the most common type (40–50 %). The most common drainage site is the left brachiocephalic vein via the left vertical vein (Fig. 18.18), followed by the SVC and the azygous vein. In the cardiac type of TAPVR, anomalous pulmonary veins drain into the coronary sinus or right atrium. In the infracardiac type of TAPVR (Fig. 18.19), anomalous veins drain via a descending vertical vein into the portal vein, hepatic vein, or IVC. In this condition, pulmonary venous flow is commonly obstructive due to long drainage course, hepatic sinusoidal drainage, or anatomical stenosis at the level of the diaphragm or ductus venosus. However, the supracardiac or cardiac types of TAPVR usually have unobstructed pulmonary venous drainage. The diagnosis of pulmonary venous obstruction in the neonatal period is very important because the patients with pulmonary venous obstruction have worse prognosis and need urgent surgery.

Simple radiography is useful in specific conditions with TAPVR. In the supracardiac type of TAPVR draining into the brachiocephalic vein, wide superior mediastinum caused by dilated pulmonary venous pathway and the heart forms the “snowman” configuration. In the obstructive infracardiac type of TAPVR, there is a small heart and a reticular pattern of the lung field, which are suggestive of pulmonary interstitial edema. CT and MR angiography are helpful for demonstrating the infracardiac type of TAPVR, mixed type of TAPVR, and complex venous pathway. CT angiography is useful for the evaluation of the anastomotic site after repair of TAPVR.

18.8 Illustrations: Congenital Thoracic Vascular Anomalies and Associated Airway Diseases

18.8.1 Coarctation of the Aorta

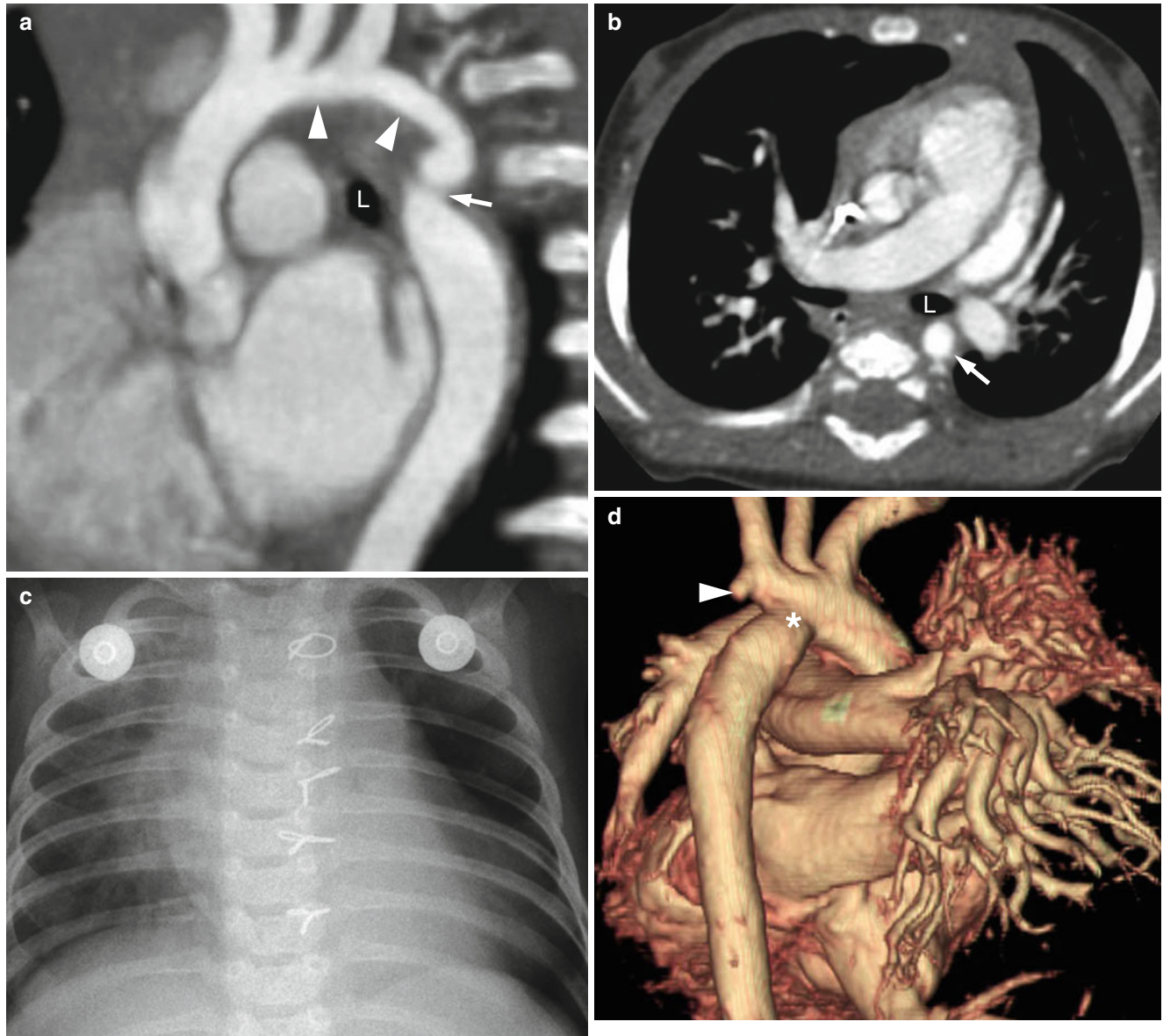


Fig. 18.1 Preductal coarctation of the aorta with aortic arch hypoplasia in a 6-week-old infant. (a, b) Initial CT images, the oblique sagittal view (a) and axial view (b) show a focal constriction (arrow) and diffuse hypoplasia of the aortic arch (arrowheads). Note the good left main bronchus (L). (c) After coarctoplasty, the infant could not be weaned from ventilation due to severe respiratory distress. Chest radiograph on the postoperative day #12 shows emphysema of the left upper lung and atelectasis of the left lower lung. (d) Follow-up CT volume-rendered image shows a wide aortic arch. The space within the aortic arch becomes narrow probably due to a some-

what anterior anastomosis of the descending aorta to the underneath of the aortic arch (*). Note the stump of the prior isthmus (arrowhead). (e) Minimal intensity projection image shows segmental occlusion of the left main bronchus (arrowheads) and resultant air trapping in the left lung. (f) Axial image shows that the left bronchus is squeezed causing obstruction in the narrow space between the ascending and descending aorta (arrow). The right pulmonary artery (RPA) is dilated to cause spatial conflict with the left main bronchus in the narrow space

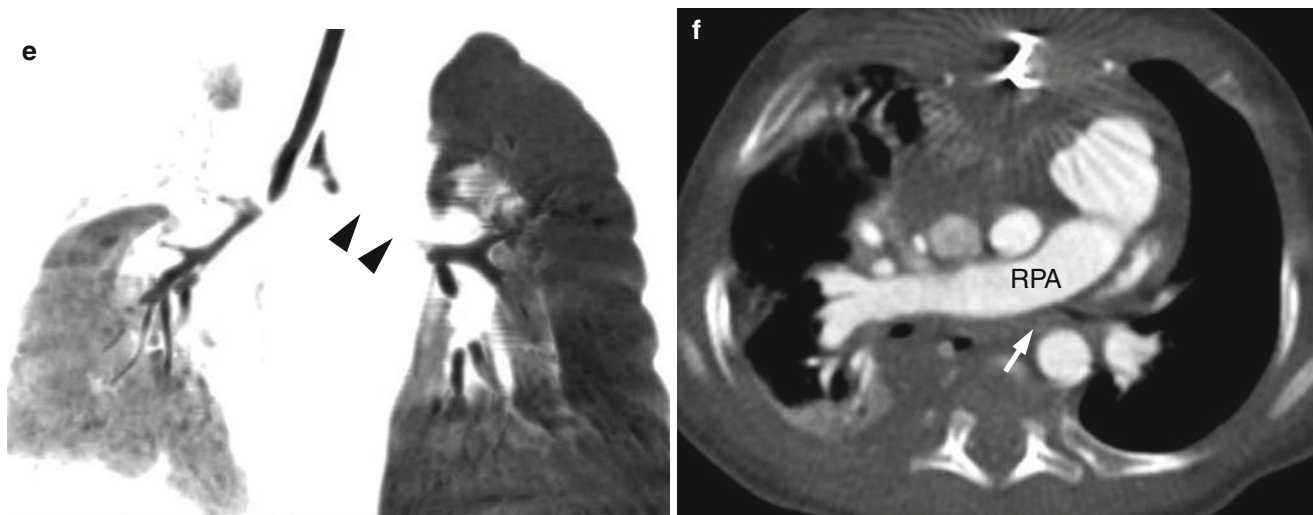


Fig. 18.1 (continued)

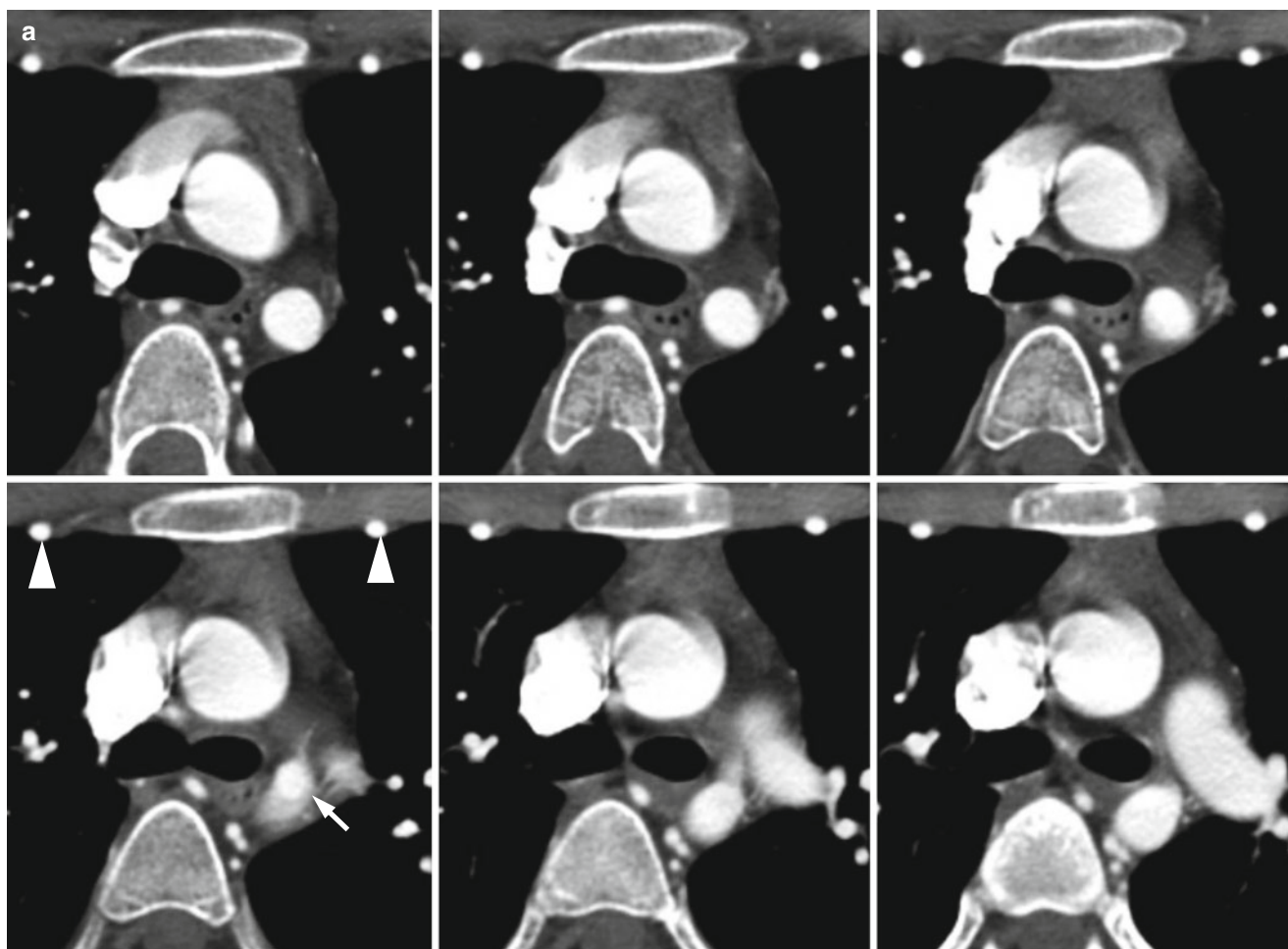


Fig. 18.2 Juxtaductal coarctation of the aorta with a posterior shelf lesion in a 15-year-old girl. (a) Consecutive axial CT images at 2.5 mm slice intervals show severe focal aortic stenosis (arrow) with subtle double contour on a slice, which was imperceptible on CT examination performed 8 years ago. Aortic lumens in the other slices are mildly hypoplastic. Note the abundant collateral vessels including dilated both internal mammary arteries (arrowheads). (b) An oblique sagittal multi-

planar reformation image well demonstrates severe short-segment coarctation of the aorta with a posterior shelf lesion (arrow) at the level of the nearly closed patent ductus arteriosus (arrowhead). (c) After deployment of a self-expandable stent, the aortic coarctation significantly improved with a mild remaining waist (arrow). Note the deformity at the proximal edge (arrowhead) caused by the excessively long stent

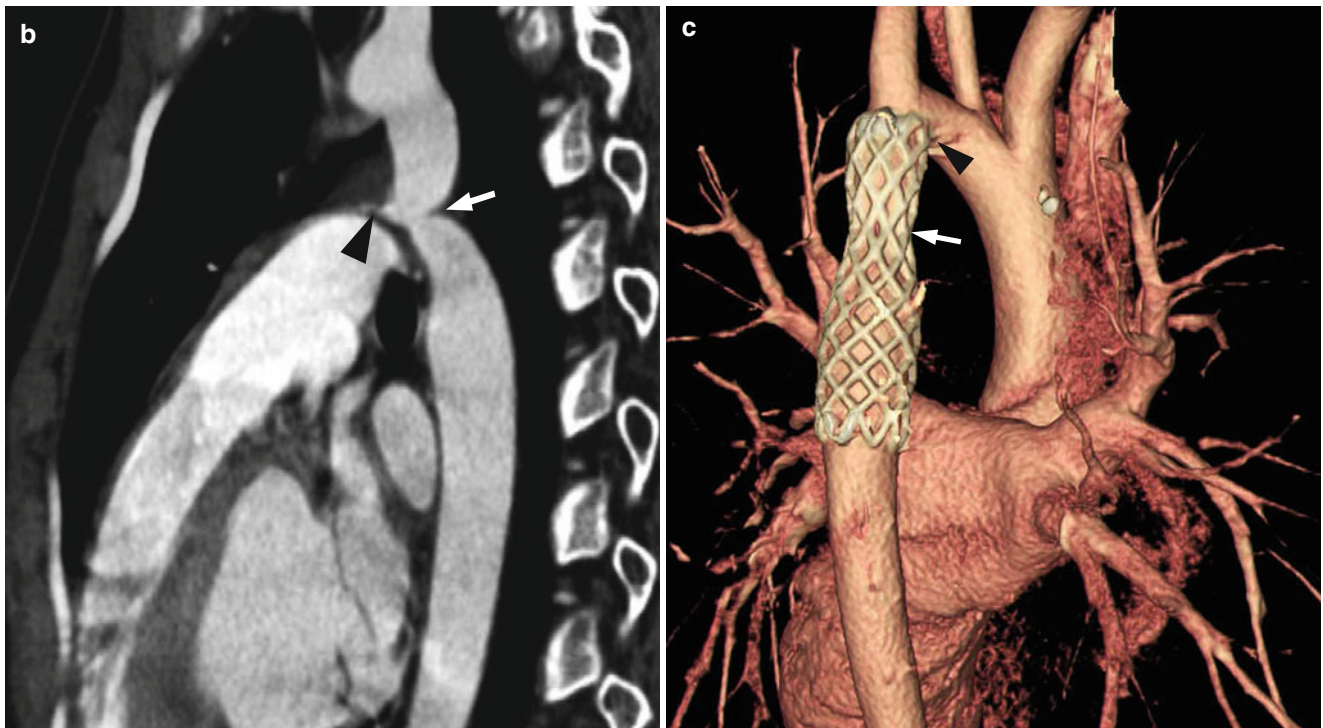


Fig. 18.2 (continued)

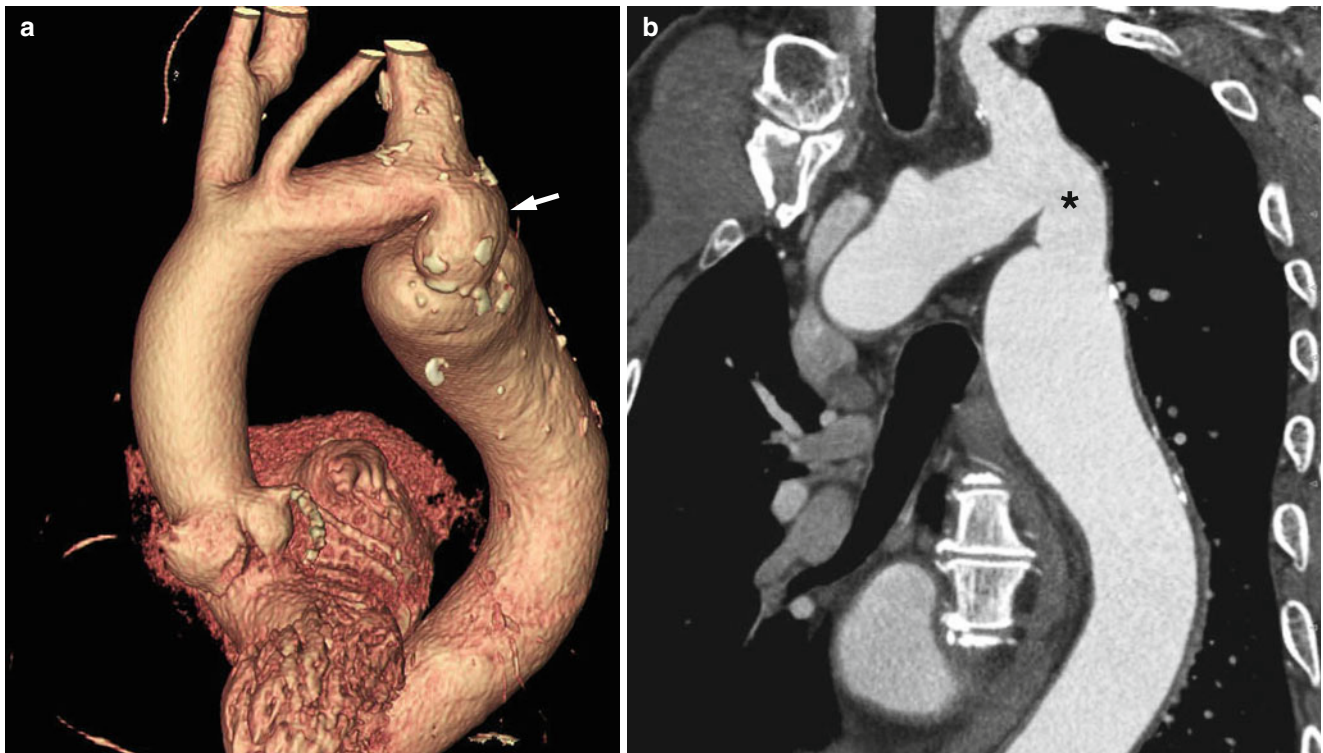


Fig. 18.3 Pseudocoarctation of the aorta in a 66-year-old man. **(a)** Volume-rendered image shows elongated and redundant aorta with kinking at the isthmic portion (*arrow*). **(b)** Curved reformation image

does not show any significant stenosis at the isthmus (*) and presence of collateral artery

18.8.2 Interrupted Aortic Arch

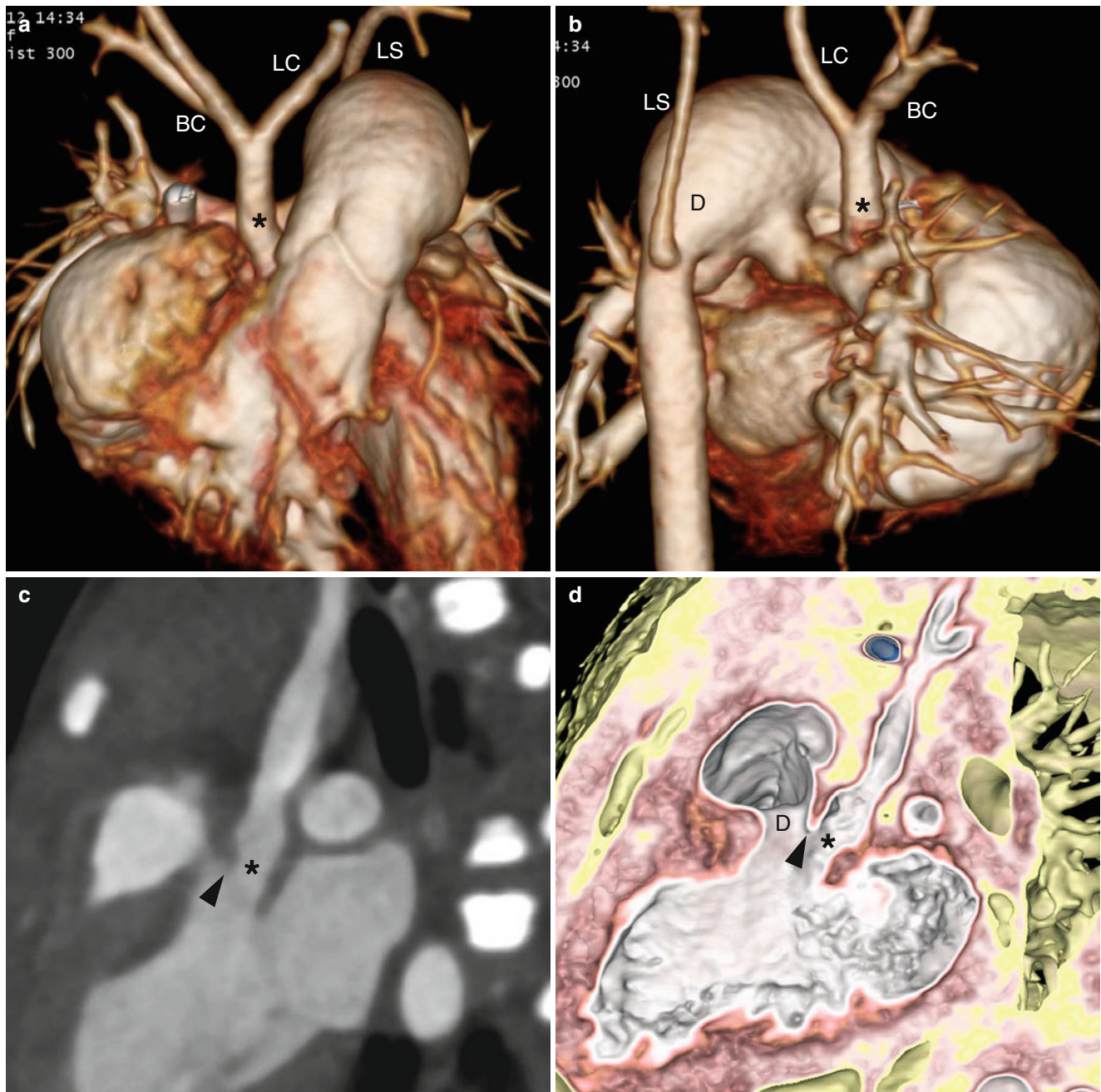


Fig. 18.4 Interrupted aortic arch type B with subaortic stenosis in a 1-month-old infant. (a, b) Volume-rendered images show long-segment interruption of the aortic arch between the left carotid artery (LC) and left subclavian artery (LS). Note the severely hypoplastic ascending aorta (*) and large patent ductus arteriosus (D). (c, d) Oblique sagittal

reformatted and volume-rendered images show posterior deviation of the infundibular septum (arrowhead), which results in subaortic stenosis (*). Also, a posterior malalignment-type ventricular septal defect is noted (D). BC right brachiocephalic artery

18.8.3 Truncus Arteriosus

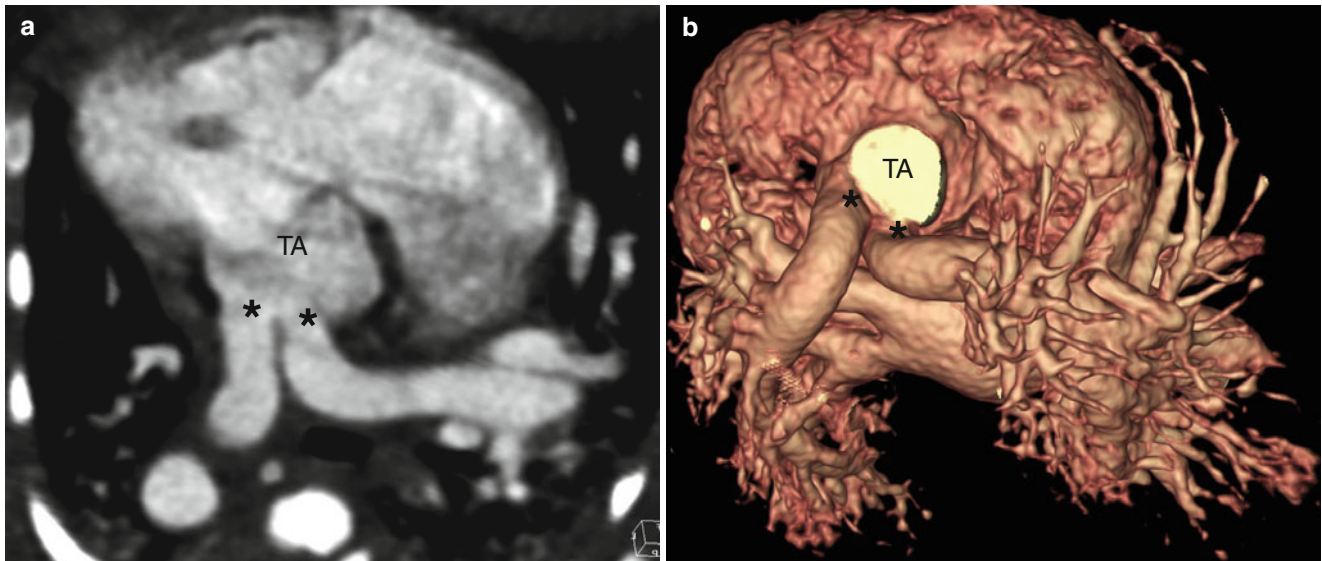


Fig. 18.5 Truncus arteriosus of Collett and Edwards type II in a 1-month-old infant. (a, b) Oblique axial reformatted image and volume-rendered images, superior view, show that both branch pulmonary

arteries (*) arise in close proximity from the posterior aspect of the truncus arteriosus (TA) without the main pulmonary artery

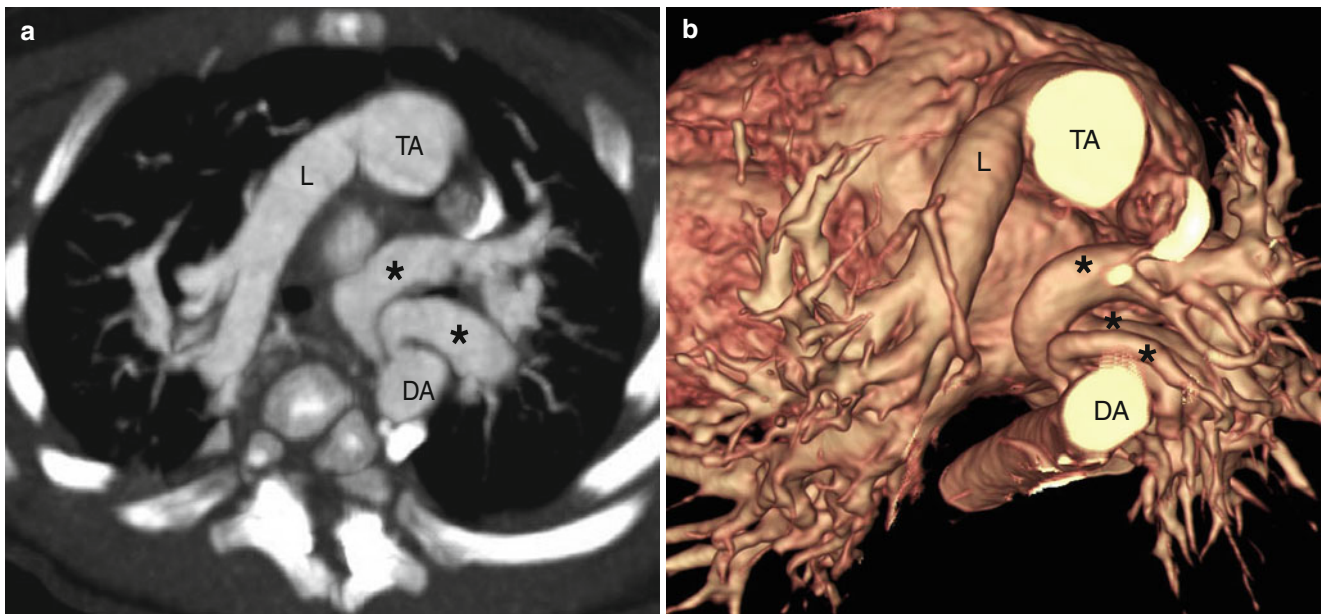


Fig. 18.6 Truncus arteriosus of Van Praagh type 3 in an 11-day-old neonate. (a, b) In the oblique axial reformatted and volume-rendered images, superior view, the left pulmonary artery (L) arises from the

truncus arteriosus (TA), while the right lung is supplied by three major aortopulmonary collateral arteries (*) arising from the descending aorta (DA)

18.8.4 Aortopulmonary Window

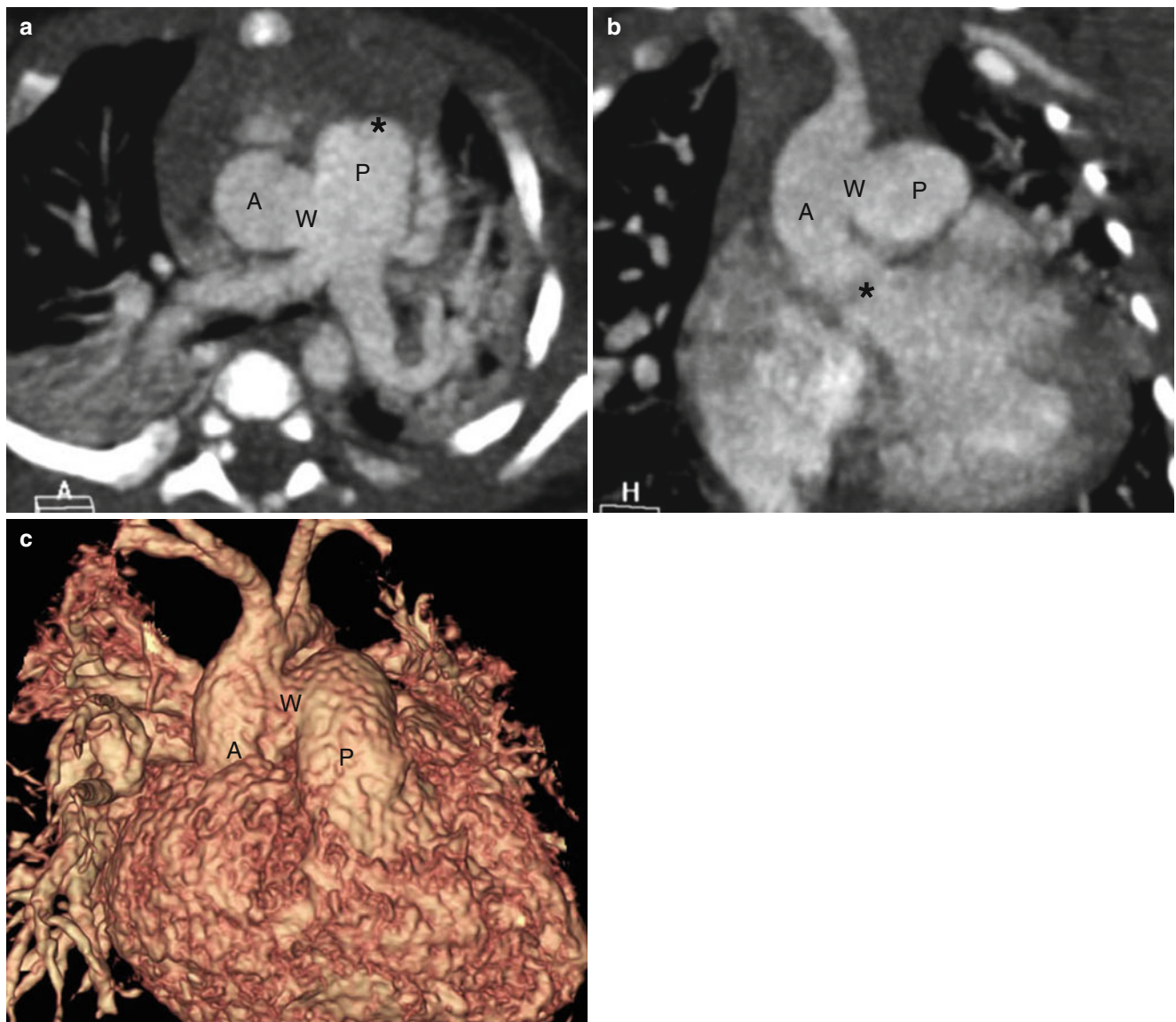


Fig. 18.7 Aortopulmonary window of type II in a 1-month-old girl. (a–c) Oblique axial (a) and coronal (b) reformatted images and volume-rendered image (c) show a communication (W) of the distal part of

the ascending aorta (A) with the main pulmonary artery (P). Two semi-lunar valves (*) are separated in the absence of a common truncus

18.8.5 Double Aortic Arch

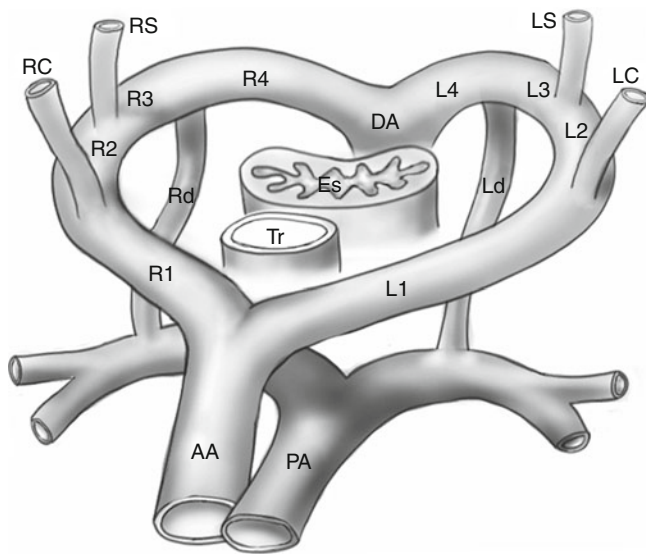


Fig. 18.8 Diagrammatic representation of Edwards' embryonic double aortic arch showing potential sites of regression in the right aortic arch (R1–R4) and in the left aortic arch (L1–L4). R1 and L1 represent the proximal segments of the right and left fourth aortic arches proximal to the common carotid arteries; R2 and L2 represent the segments of the right and left fourth aortic arches between common carotid arteries and subclavian arteries; R3 and L3 represent the segments of right and left dorsal aortic roots between the subclavian arteries and ductus arteriosus; R4 and L4 represent the right and left dorsal aortic roots; and Rd and Ld represent the right and left ductus arteriosus. Refer to Table 18.1 for the sites of regression in a specific anomaly. AA ascending aorta, PA main pulmonary artery, DA descending aorta, RC right common carotid artery, RS right subclavian artery, LC left common carotid artery, LS left subclavian artery, Tr trachea, Es esophagus

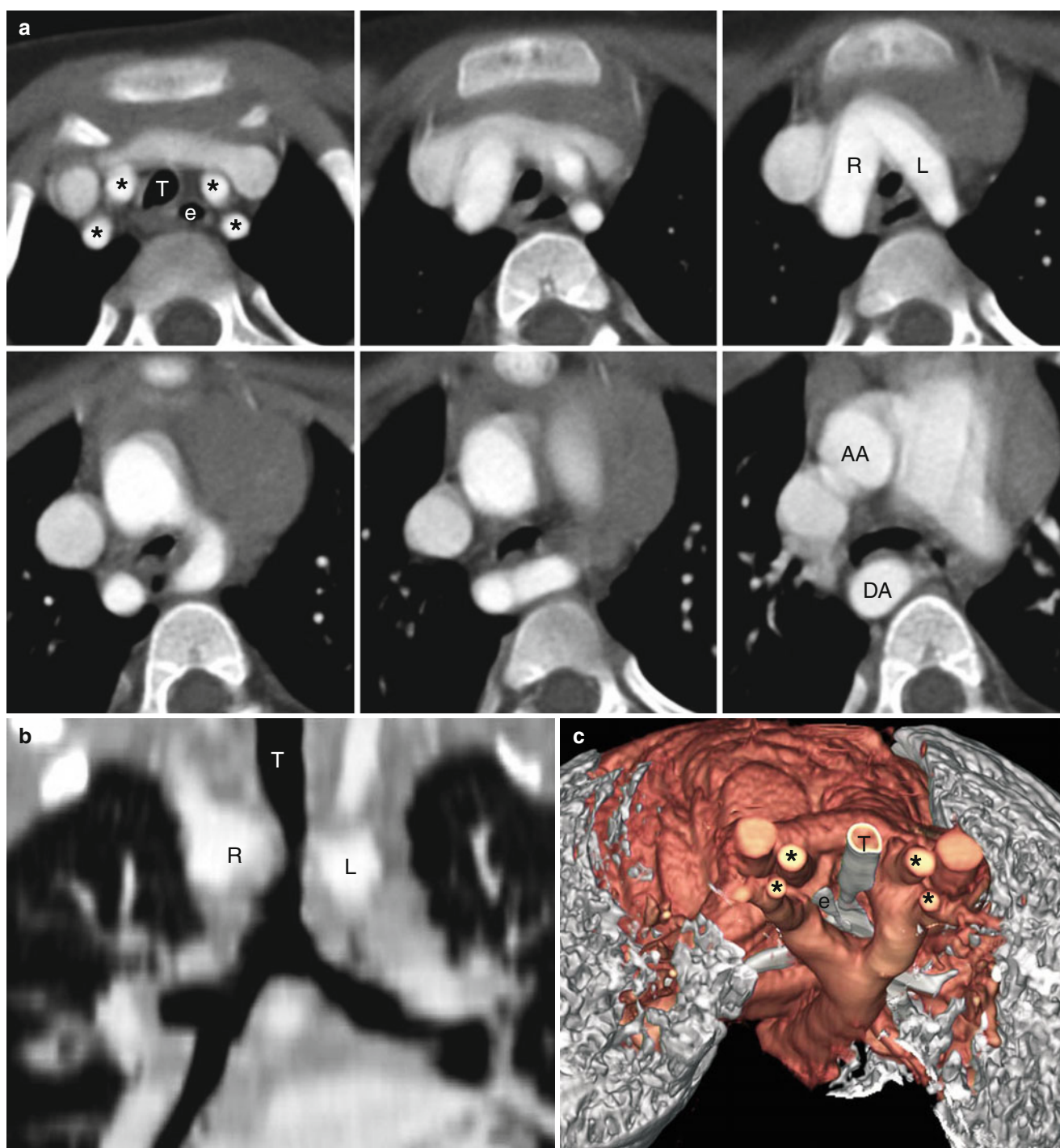


Fig. 18.9 Complete double aortic arch in a 5-year-old boy. (a) Axial CT images show a double aortic arch with both arches patent, which completely encircle the trachea (T) and the esophagus (e). (b) Coronal reformatted image shows severe focal stenosis of the trachea (T) due to compression of both arches. The right aortic arch (R) is larger in size

and higher in position than the left aortic arch (L). (c) Composite volume-rendered image, superior view, demonstrates the double aortic arch surrounding the trachea (T) and the esophagus (e) with severe tracheal stenosis at the level of the aortic arch. Note the symmetrically arranged brachiocephalic arteries on each side (*)

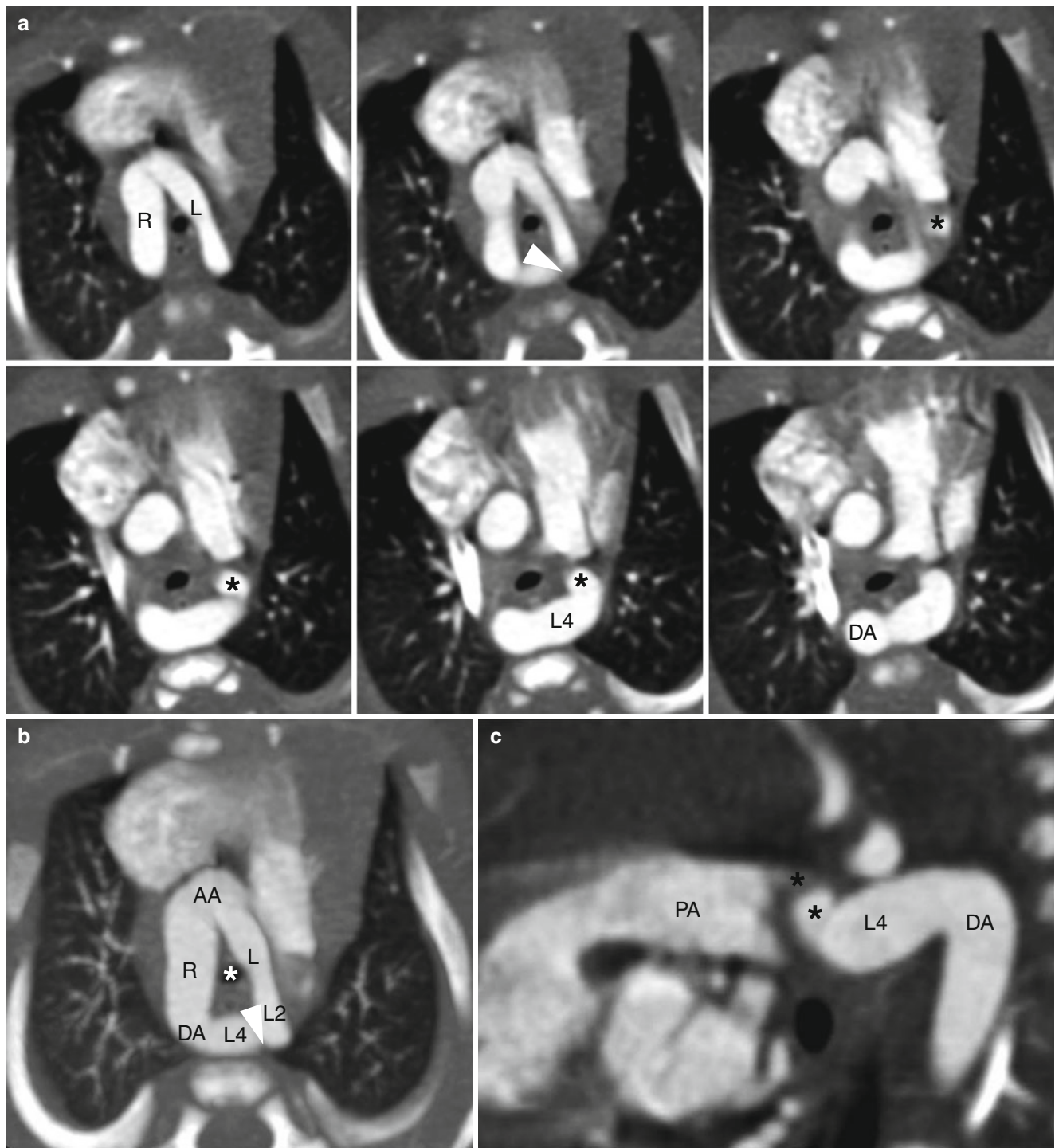


Fig. 18.10 Atretic double aortic arch in a 4-day-old boy. **(a, b)** On axial CT images **(a)** and thin-slab axial minimal intensity projection image of the aortic arch **(b)**, the right (*R*) and left (*L*) aortic arches surround the trachea and esophagus, in which a nasogastric tube is inserted. There is a small gap in the left aortic arch (*arrowheads*), which is suggestive of focal discontinuity at the L3 segment between the subclavian arteries and ductus arteriosus. **(c)** Curved reformatted image shows that the small PDA (*) is connected to the left dorsal aortic root (*L4*), and

thus a complete vascular ring is formed. **(d)** Minimal intensity projection image shows severe focal concentric tracheal stenosis (*T*) caused by the vascular ring. **(e)** Follow-up composite volume-rendered image after the division of left dorsal aorta and ductus arteriosus shows a widely excised left dorsal aortic segment at L3 and L4 (*dotted line*) and restored tracheal lumen (*T*). *AA* ascending aorta, *DA* descending aorta, *PA* pulmonary artery, L2, L3, and L4, refer to Fig. 18.13

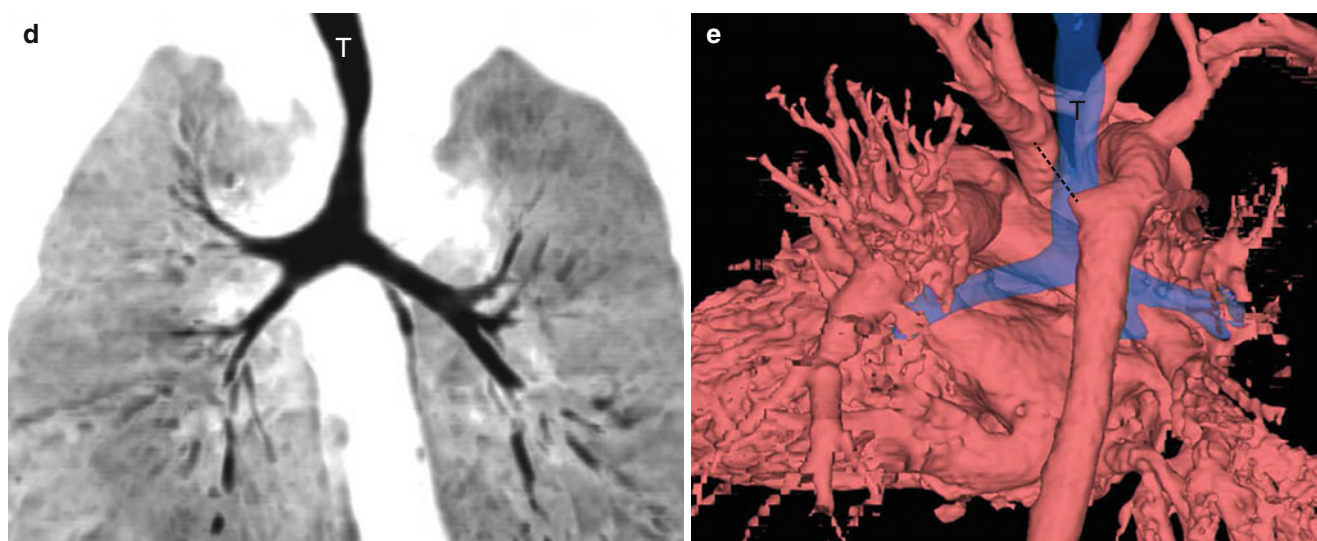


Fig. 18.10 (continued)

18.8.6 Left Aortic Arch with Aberrant Right Subclavian Artery

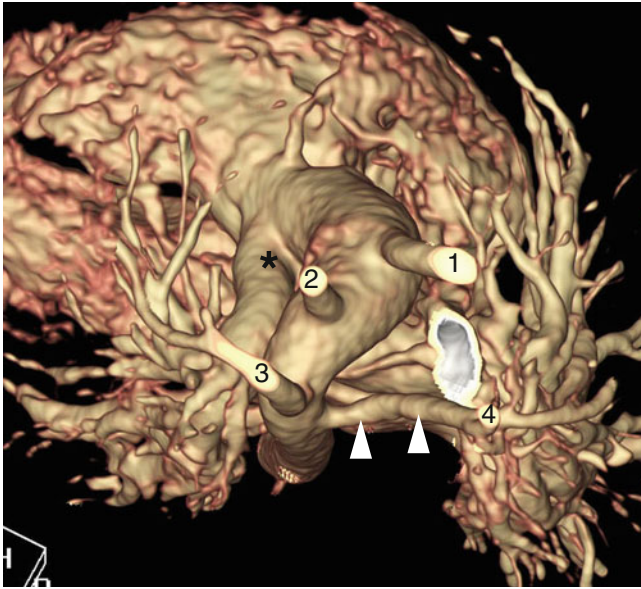


Fig. 18.11 Left aortic arch with an aberrant right subclavian artery in a 1-month-old infant with truncus arteriosus type II. Volume-rendered image, superior view, shows a left aortic arch with an aberrant retroesophageal right subclavian artery (*arrowheads*). It arises from the descending aorta as the fourth branch (4), after the right carotid artery (1), left carotid artery (2), and left subclavian artery (3). Note the left pulmonary artery (*) arising from truncus arteriosus

18.8.7 Right Aortic Arch with Aberrant Left Subclavian Artery

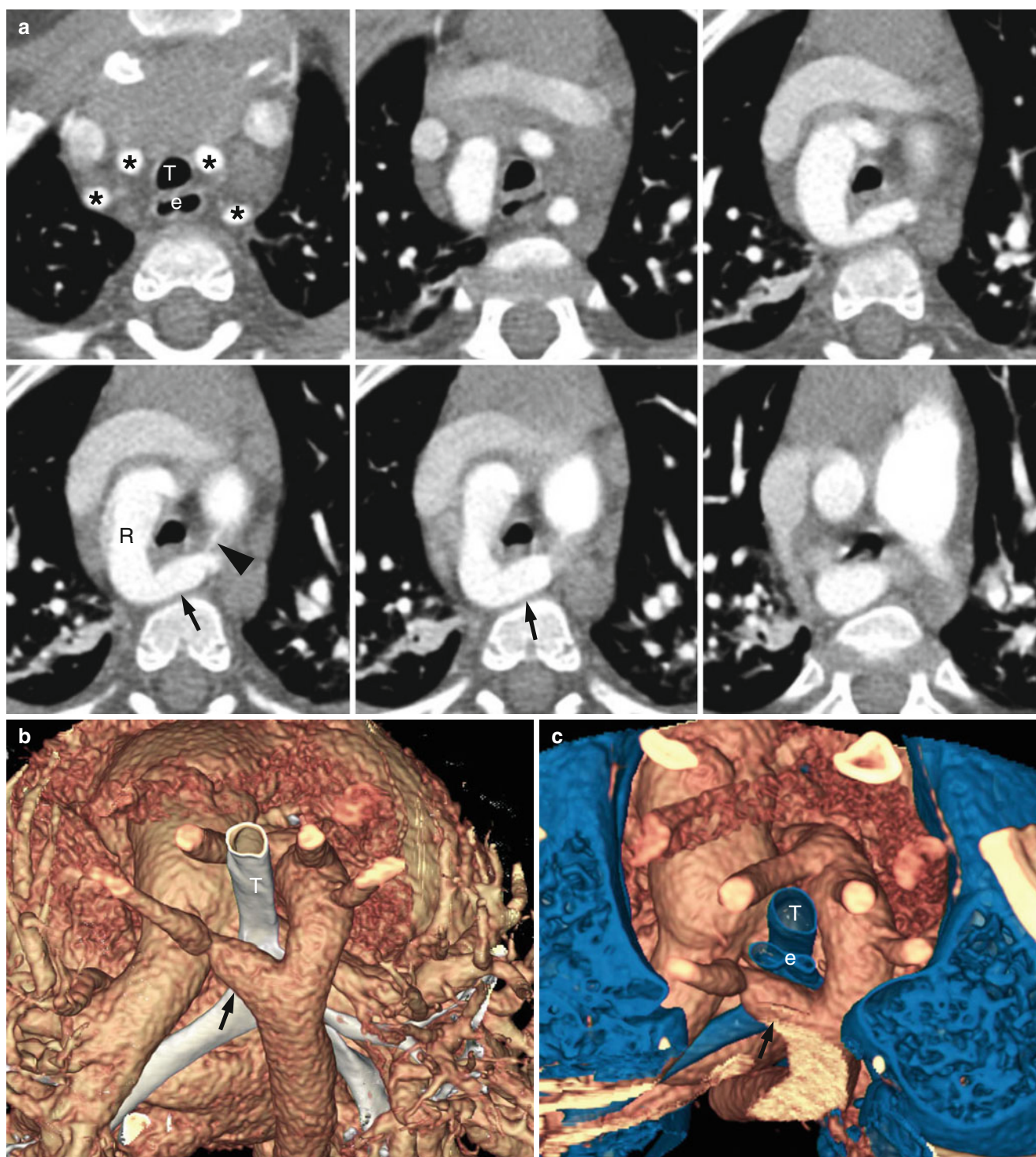


Fig. 18.12 Right aortic arch with an aberrant left subclavian artery and diverticulum of Kommerell in a 2-year-old boy. (a) Axial CT images show an aberrant left subclavian artery arising as the last branch of the right aortic arch (R). There is an aneurysmal dilatation at its origin to form a diverticulum of Kommerell (arrows), and it courses behind the esophagus to reach its normal position. A small PDA (arrowhead) connects the left subclavian artery and pulmonary artery to

form a complete vascular ring. The brachiocephalic arteries are symmetrically arranged on both sides (*). (b, c) Composite volume-rendered images clearly demonstrate the anomaly and vascular compression. The esophagus (e) as well as the trachea (T) are compressed by the aneurysm of the subclavian artery (arrow) and the vascular ring

18.8.8 Circumflex Right Aortic Arch

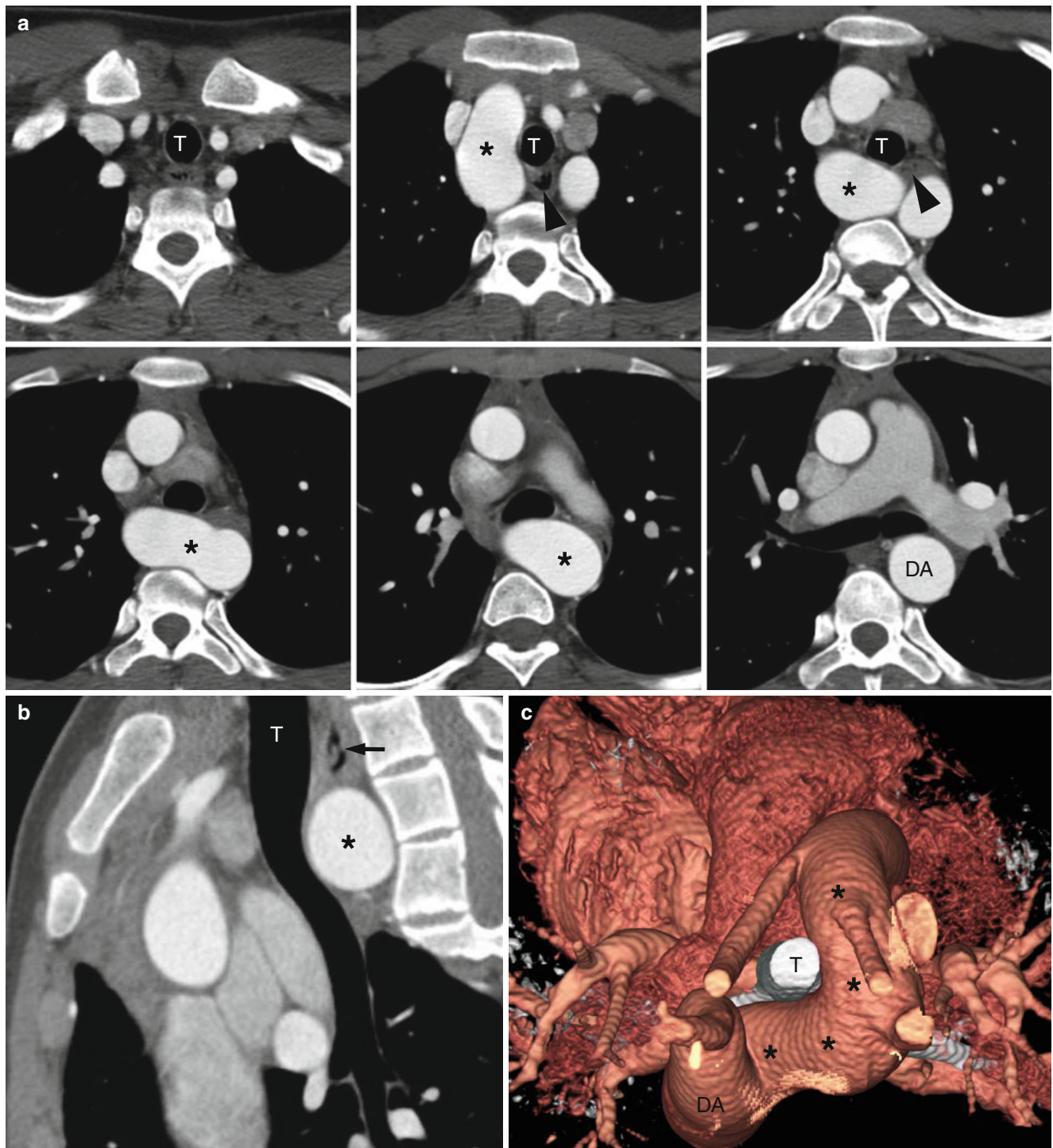


Fig. 18.13 Circumflex right aortic arch in a 16-year-old boy. (a) Axial CT images show that the circumflex right aortic arch (*) passes to the right of the trachea (T) and then courses behind the esophagus (arrowheads) to become the left descending aorta (DA). Note that the two brachiocephalic arteries are symmetrically located on both sides above the aortic arch (left upper panel). (b) Oblique sagittal reformatted image shows a large retroesophageal aortic arch (*), which pushes the

trachea anteriorly. Note the air-containing esophagus (arrow) and obliteration of its lumen at the arch level. (c) Composite volume-rendered image, superior view, also shows a circumflex right aortic arch (*) that is elongated from the right to the posterior side of the trachea (T). The anomalous left subclavian artery arises directly from the left descending aorta (DA), which does not have a retroesophageal course

18.8.9 Pulmonary Artery Sling

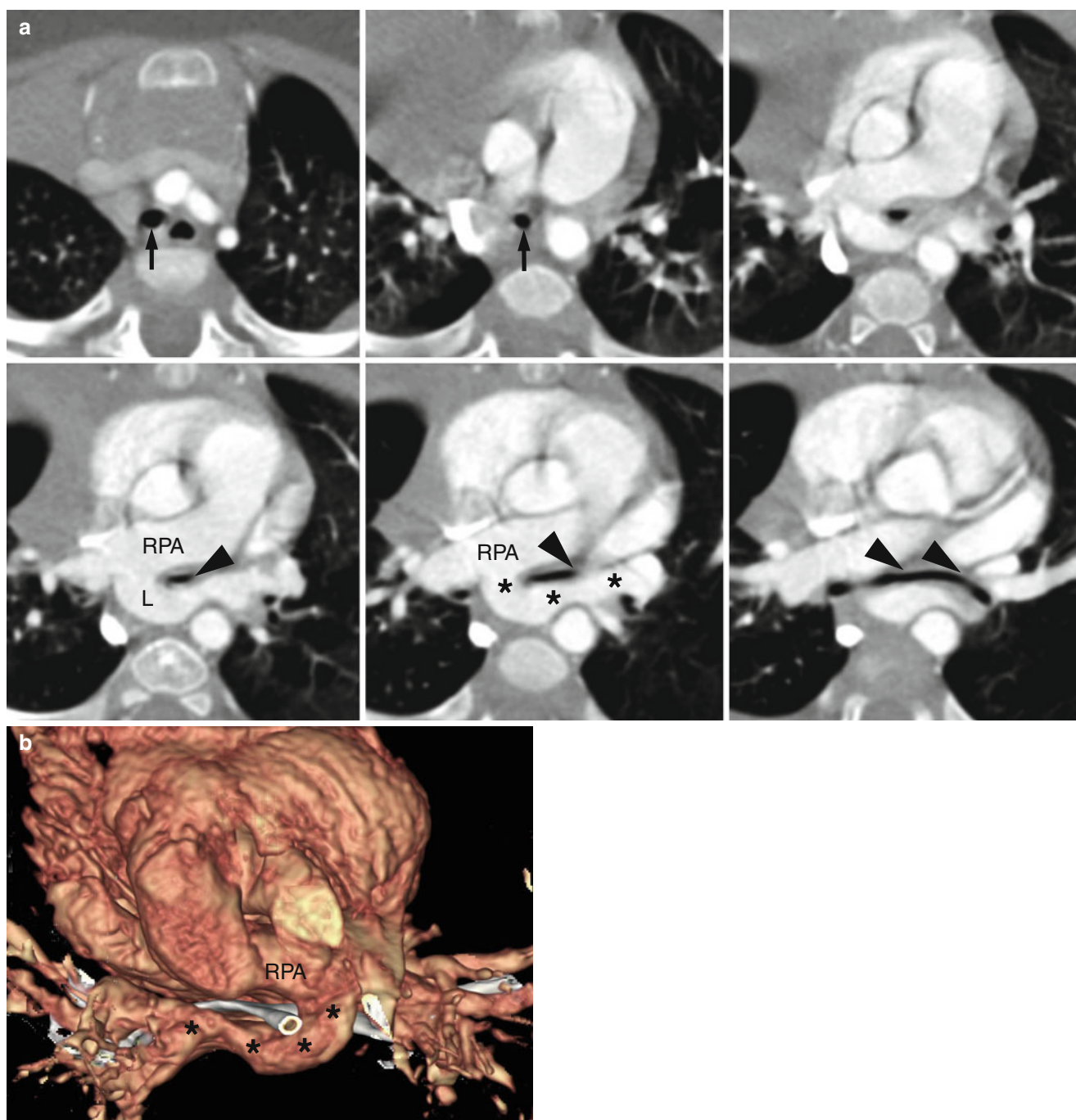


Fig. 18.14 Pulmonary artery sling in a 6-month-old boy. **(a)** Axial CT images show aberrant origin of the left pulmonary artery (*L*) from the distal portion of the right pulmonary artery (*RPA*). A sling-like course of an anomalous left pulmonary artery sandwiches the distal trachea, carina, and left bronchus (*arrowheads*) to make the airways flat. Also, a diffuse concentric stenosis of the trachea (*arrows*) far superiorly apart

from the sling is noted, which is suggestive of congenital tracheal stenosis with a complete cartilaginous ring. **(b)** Composite volume-rendered image also shows the course of the left pulmonary artery sling (*) that compresses the airway and causes concentric stenosis of the distal trachea

18.8.10 Persistent Left Superior Vena Cava

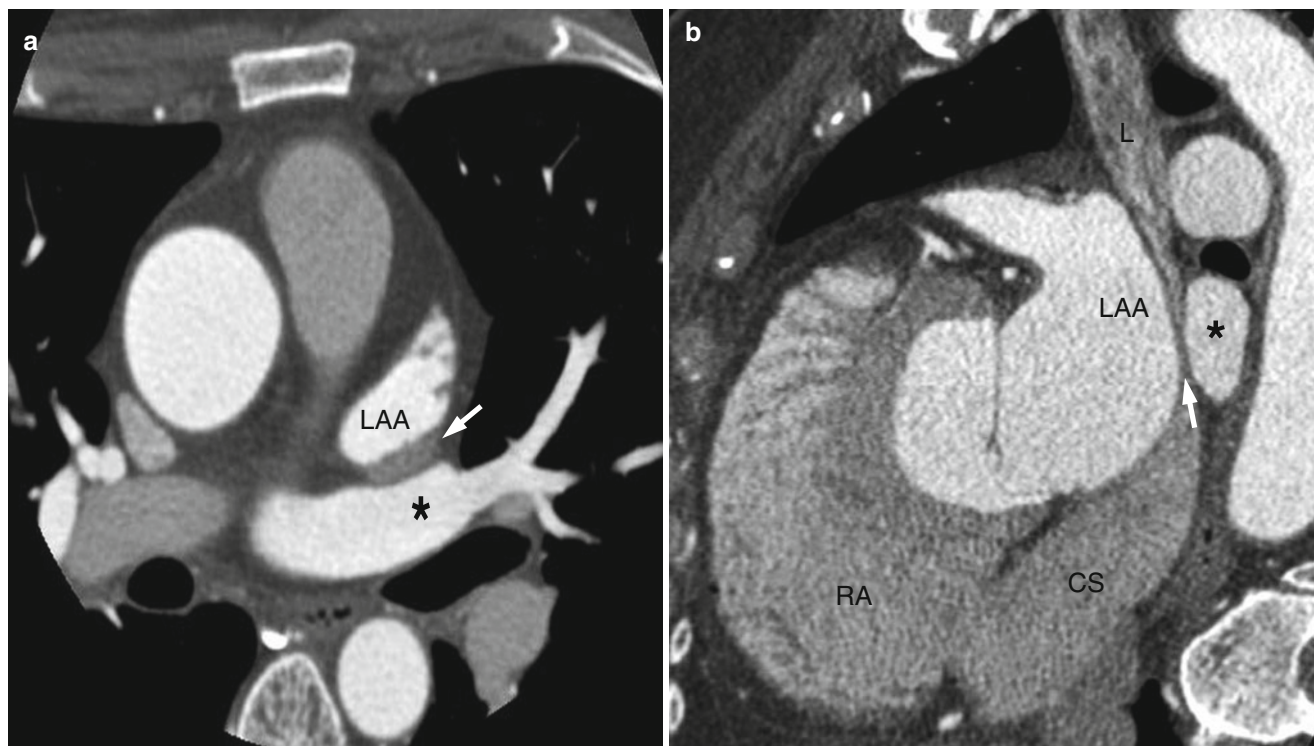


Fig. 18.15 Bilateral superior vena cava (SVC) with persistent left SVC. (a, b) Axial (a) and oblique sagittal curved MPR (b) images show a persistent left SVC (L) draining into the right atrium (RA) via the dilated coronary sinus (CS). The segment between the left atrial append-

age (LAA) and the left upper pulmonary vein (*) shows a slit-like appearance anteroposteriorly (arrow) without any hemodynamic significance

18.8.11 Retroaortic Left Brachiocephalic Vein

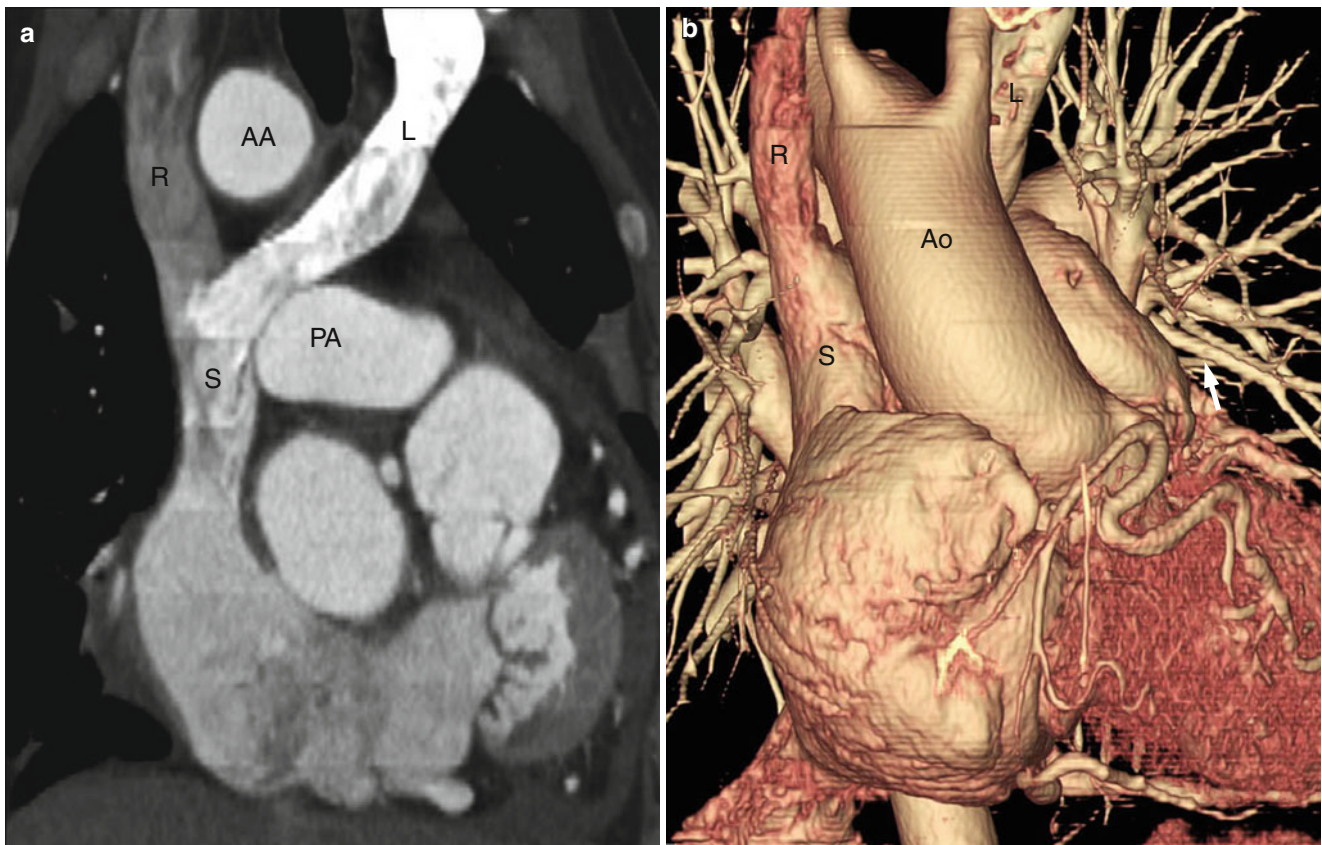


Fig. 18.16 Retroaortic left brachiocephalic vein below the aortic arch in a patient with tetralogy of Fallot. **(a, b)** Oblique coronal MPR **(a)** and volume-rendered **(b)** images show the course of a retroaortic left brachiocephalic vein (L). It passes under the aortic arch (AA), superior to

the right pulmonary artery (PA) and then posterior to the ascending aorta (Ao), and joins the right brachiocephalic vein (R) to become the SVC (S)

18.8.12 Partial Anomalous Pulmonary Venous Return (Scimitar Syndrome)

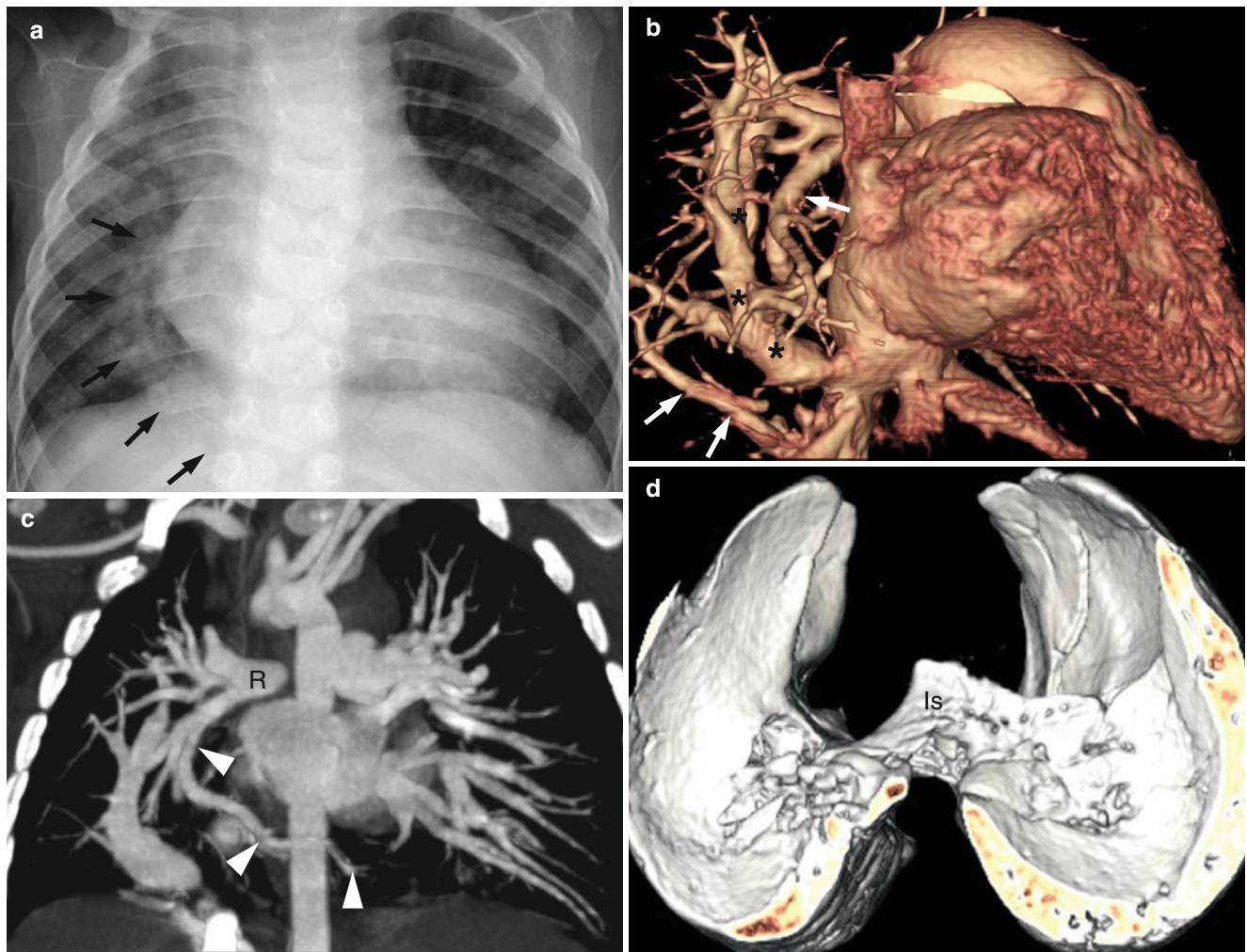


Fig. 18.17 Scimitar syndrome with partial anomalous pulmonary venous return to the IVC, systemic arterialization of the lung, and horseshoe lung in a 1-year-old boy. (a) Frontal chest radiograph shows the vertically oriented vascular shadow (*arrows*) in the hypoplastic right lung. (b) Volume-rendered image, oblique anterior view, shows three vessels in the right lower lung. The vertically oriented vessel (*) corresponds to the vertical shadow on chest angiography. It is the scimitar vein which anomalously drains the pulmonary venous flow from the

right lung into the IVC. (c) On thin-slab MIP image, a small branch (*arrowheads* in b, c) arising from the right pulmonary artery (*R*) is bridging the pulmonary artery, which crosses the midline to supply the isthmic lung tissue. (d) Volume-rendered image, inferior view, of the lung demonstrates the isthmic lung (*Is*). The horseshoe lung is formed by the isthmus that joins both lungs through a defect in the retrocardiac mediastinum. (e) Coronal MPR image shows that a systemic artery arises from the abdominal aorta to supply the right lower lung

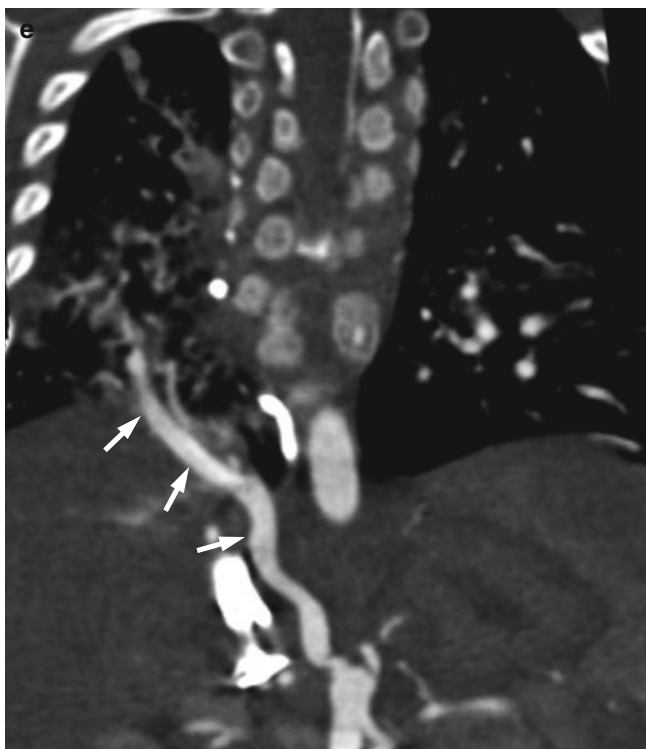


Fig. 18.17 (continued)

18.8.13 Total Anomalous Pulmonary Venous Return

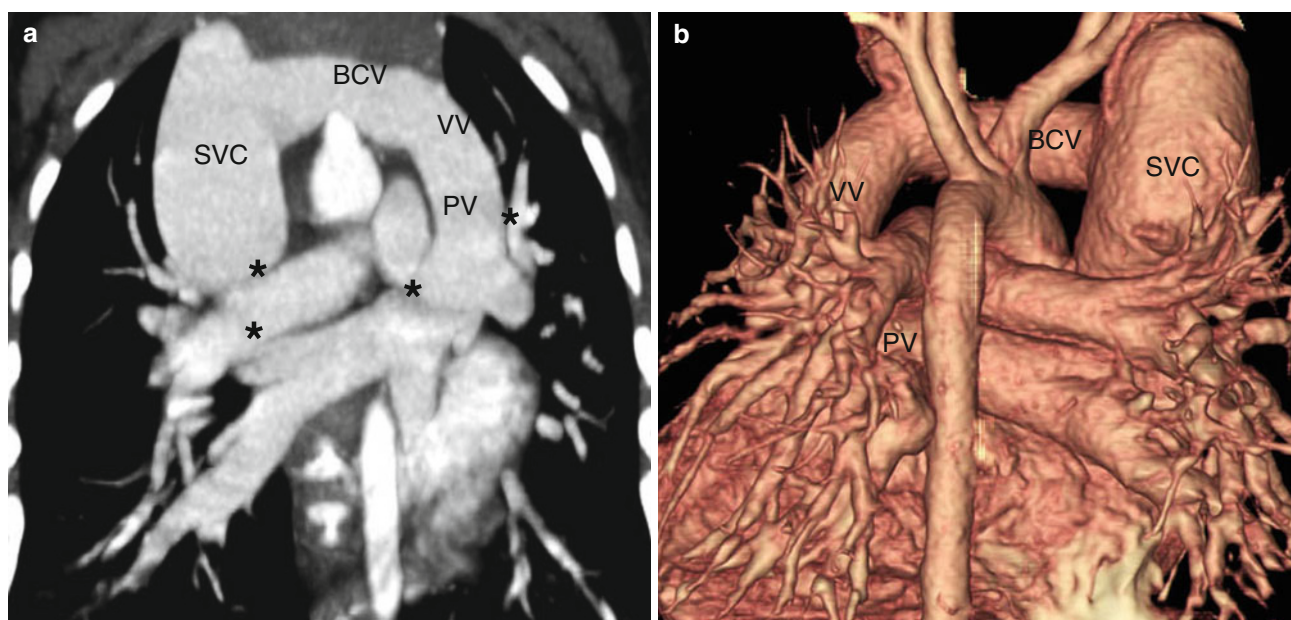


Fig. 18.18 Supracardiac type of TAPVR. (a, b) Oblique coronal MRP image and volume-rendered image, posterior view, show that the pulmonary veins merge in sequence (*). A confluent vein (PV) anomalously

drains into the left vertical vein (VV), left brachiocephalic vein (BCV), and then the SVC

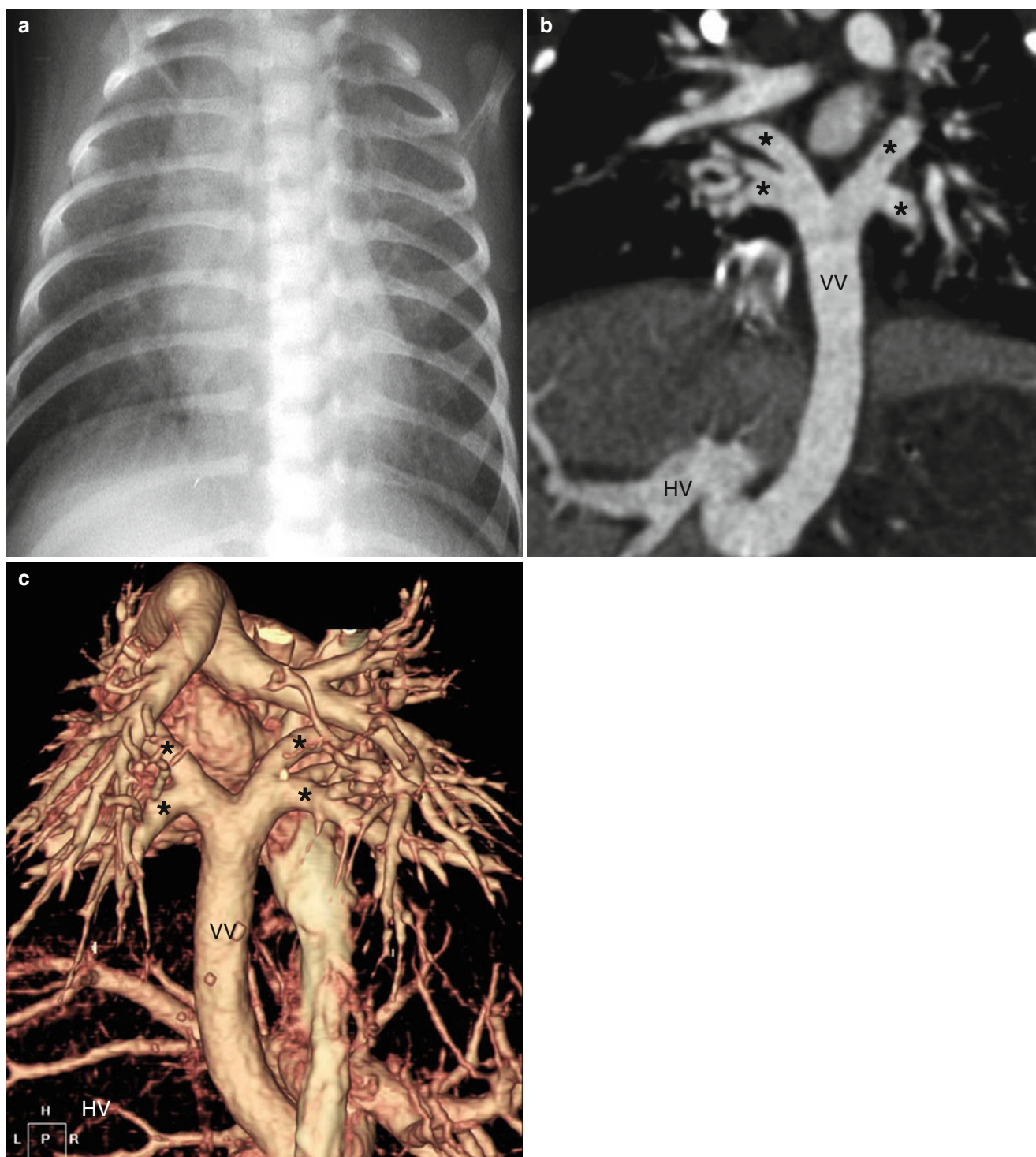


Fig. 18.19 Infracardiac type of TAPVR. (a) Frontal chest radiograph shows pulmonary interstitial edema. (b, c) MIP image, anterior view, and volume-rendered image, posterior view, show that all of the pulmo-

nary veins anomalously drain into the hepatic vein (HV) via the inferior vertical vein (VV)

References

- Edwards JE. Anomalies of the derivatives of the aortic arch system. *Med Clin North Am*. 1948;32:925–49.
- Heye T, Wengenroth M, Schipp A, et al. Persistent left superior vena cava with absent right superior vena cava: morphological CT features and clinical implications. *Int J Cardiol*. 2007;116:e103–5.
- Johnson TR. Conotruncal cardiac defects: a clinical imaging perspective. *Pediatr Cardiol*. 2010;31:430–7.
- Konen E, Raviv-Zilka L, Cohen RA, et al. Congenital pulmonary venolobar syndrome: spectrum of helical CT findings with emphasis on computerized reformatting. *Radiographics*. 2003;23:1175–84.
- Lee EY, Siegel MJ, Hildebolt CF, et al. MDCT evaluation of thoracic aortic anomalies in pediatric patients and young adults: comparison of axial, multiplanar, and 3D images. *AJR Am J Roentgenol*. 2004;182:777–84.
- Lee EY, Boisselle PM, Shamberger RC. Multidetector computed tomography and 3-dimensional imaging: preoperative evaluation of thoracic vascular and tracheobronchial anomalies and abnormalities in pediatric patients. *J Pediatr Surg*. 2010;45:811–21.
- Philip S, Chen SY, Wu MH, et al. Retroesophageal aortic arch: diagnostic and therapeutic implications of a rare vascular ring. *Int J Cardiol*. 2001;79:133–41.
- Schlesinger AE, Krishnamurthy R, Sena LM, et al. Incomplete double aortic arch with atresia of the distal left arch: distinctive imaging appearance. *AJR Am J Roentgenol*. 2005;184:1634–9.
- Takada Y, Narimatsu A, Kohno A, et al. Anomalous left brachiocephalic vein: CT findings. *J Comput Assist Tomogr*. 1992;16:893–6.
- Turkvatan A, Buyukbayraktar FG, Olcer T, et al. Multidetector computed tomographic angiography of aberrant subclavian arteries. *Vasc Med*. 2009;14:5–11.
- Ucar T, Fitoz S, Tutar E, et al. Diagnostic tools in the preoperative evaluation of children with anomalous pulmonary venous connections. *Int J Cardiovasc Imaging*. 2008;24:229–35.
- Vyas HV, Greenberg SB, Krishnamurthy R. MR imaging and CT evaluation of congenital pulmonary vein abnormalities in neonates and infants. *Radiographics*. 2012;32:87–98.
- Weinberg P. Aortic Arch Anomalies. *J Cardiovasc Magn Reson*. 2006;8:633–43.
- Woodring JH, Howard TA, Kanga JF. Congenital pulmonary venolobar syndrome revisited. *Radiographics*. 1994;14:349–69.
- Yang DH, Goo HW, Seo DM, et al. Multislice CT angiography of interrupted aortic arch. *Pediatr Radiol*. 2008;38:89–100.
- Zhong YM, Jaffe RB, Zhu M, et al. CT assessment of tracheobronchial anomaly in left pulmonary artery sling. *Pediatr Radiol*. 2010;40:1755–62.

Part V

Abdomen

Sun Wha Lee

Contents

19.1	Introduction	604
19.2	Esophagus	604
19.2.1	Esophageal Atresia and Tracheoesophageal Fistula	604
19.2.2	Laryngotracheoesophageal Clefts	604
19.2.3	Congenital Esophageal Stenosis	604
19.3	Stomach	605
19.3.1	Gastric Atresia	605
19.3.2	Gastric Volvulus	605
19.4	Small Intestine	605
19.4.1	Duodenal Atresia and Stenosis	605
19.4.2	Midgut Malrotation and Volvulus	605
19.4.3	Jejunioileal Atresia and Stenosis	606
19.4.4	Meconium Ileus	606
19.5	Colon	606
19.5.1	Anorectal Malformations	606
19.6	Illustrations: Congenital and Neonatal Gastrointestinal Diseases	608
19.6.1	Esophageal Atresia and Tracheoesophageal Fistula	608
19.6.2	Laryngoesophageal Clefts	612
19.6.3	Congenital Esophageal Stenosis	613
19.6.4	Gastric Volvulus	614
19.6.5	Duodenal Atresia and Stenosis	616
19.6.6	Midgut Malrotation and Volvulus	618
19.6.7	Jejunioileal Atresia and Stenosis	620
19.6.8	Meconium Ileus	623
19.6.9	Anorectal Malformations	624
	References	627

S.W. Lee, M.D.
Department of Radiology,
Ewha Womans University School of Medicine,
911-1 Mokdong, Yangcheon-gu, Seoul 158-710, Korea
e-mail: sonic323@ewha.ac.kr

19.1 Introduction

Congenital and neonatal gastrointestinal diseases include a wide variety of congenital anomalies. Most congenital gastrointestinal tract anomalies are detected in the newborn period, and a delay in diagnosis may cause a significant increase in the morbidity. Multiple imaging modalities including plain abdominal radiography, upper gastrointestinal (UGI) series, contrast enema, ultrasonography (US), computed tomography (CT), and magnetic resonance imaging (MRI) are required to evaluate the spectrum of these anomalies and other associated anomalies. Plain abdominal radiography is useful as the first-line study to evaluate the neonates with symptomatic congenital abnormalities. Neonates with radiographic findings of complete high gastrointestinal obstruction usually need little or no further radiologic evaluation. The UGI is the study of choice for the diagnosis of incomplete high gastrointestinal obstruction and determines the location and cause of the obstruction. Contrast enema examination provides a specific diagnosis and occasionally plays a therapeutic role when low intestinal obstruction is suspected on the basis of clinical and radiographic findings. The use of US is increasing in ill neonates and furthermore its contribution, especially in the diagnosis of midgut volvulus and other kinds of neonatal intestinal obstruction. Additionally, US has become a useful modality for the evaluation of associated genitourinary tract anomalies or abdominal mass. CT and MRI are not commonly preferred as the first-line study because of invasiveness or inconvenience. This chapter presents a variety of imaging findings of the congenital and neonatal gastrointestinal diseases, including esophageal atresia (EA) complex, laryngotracheoesophageal clefts, congenital esophageal stenosis, gastric atresia, gastric volvulus, duodenal atresia and stenosis, midgut malrotation and volvulus, jejunoileal atresia, meconium ileus, and anorectal malformations.

19.2 Esophagus

19.2.1 Esophageal Atresia and Tracheoesophageal Fistula

Esophageal atresia (EA), either alone or in combination with a tracheoesophageal fistula (TEF), is the most important congenital anomaly of the esophagus. Of the various combinations of EA and TEF, the most common is EA with TEF to the distal esophageal segment (Fig. 19.1). The cause is not clearly understood but is thought to be a developmental disorder in the formation and separation of the primitive foregut into the trachea and esophagus. Fifty percent to seventy percent of cases with EA have associated anomalies of the multiple organ systems (Benson et al.

1985). The best-known pattern is the VACTERL (vertebral, anorectal, cardiac, tracheoesophageal, renal, and limb anomalies) association.

Initial chest radiograph demonstrates a distended, air-filled, blind-ending proximal esophageal pouch and should include the abdomen to assess the presence of air in the gastrointestinal tract. In case of EA with gasless abdomen, isolated EA or EA with proximal TEF should be considered (Fig. 19.2). Injection of contrast material or air into the proximal esophageal pouch is optional, depending on the needs of the surgeon. Atelectasis and pneumonia of the right upper lobe are frequently seen. The need for additional imaging study is debatable. Three-dimensional computed tomography (CT) for preoperative localization of the aortic arch and assessment of the length of gap between the esophageal pouches has been proposed but has limitations. To investigate for the H-type fistula on esophagography, it is important to demonstrate a fistula that usually runs an upward and forward oblique course from the esophagus to the trachea (Fig. 19.3) (Berrocal et al. 1999b).

Pharyngoesophageal perforation may mimic esophageal atresia complex clinically. This acquired condition results from the inadvertent perforation of the posterior pharynx or upper esophagus by vigorous attempts at suction or difficult intubation in ill neonates. However, findings on esophagography are helpful in differential diagnosis from esophageal atresia (Fig. 19.4).

19.2.2 Laryngotracheoesophageal Clefts

The embryologic precursors of the esophagus and upper airway are divided by progressive fusion of the lateral folds separating their lumen. Incomplete fusion at the top is called the laryngoesophageal cleft, and the failure of separation extending all the way from the arytenoid to the carina is called the persistent esophagotrachea (Fig. 19.5). These anomalies are very rare developmental defects. Diagnosis is usually made by esophagography and confirmed by means of endoscopy or exploration (Bender et al. 1991).

19.2.3 Congenital Esophageal Stenosis

Congenital esophageal stenosis is rather uncommon. There are three pathologic types: cartilaginous tracheobronchial remnants, fibromuscular stenosis, and membranous diaphragm. Tracheobronchial remnants are thought to be a developmental disorder with incorporation of mesenchymal elements of the respiratory bud into the esophagus and usually involve the lower one-third of the esophagus (Diab et al. 1999). Congenital esophageal stenosis may be associated with esophageal atresia (Fig. 19.6) (Newman and Bender 1997).

Esophagography remains the standard approach for the evaluation of the site, nature, and severity of such stenosis (Fig. 19.7).

19.3 Stomach

19.3.1 Gastric Atresia

Gastric atresia is usually limited to the antrum or pyloric region and is very rare. The cause of gastric atresia is almost unknown, but the concept of localized intrauterine vascular occlusion has been suggested. Radiographic finding of complete gastric atresia is gastric distension proximal to the obstruction with absent gas in the other bowel loops, resulting in a single bubble appearance (Berrocal et al. 1999b; Rao 2006). No further radiologic evaluation is required. Gastric diaphragm itself is demonstrable with ultrasonography (US) and upper gastrointestinal (UGI) series, though there is non-specific finding on plain radiography.

19.3.2 Gastric Volvulus

Gastric volvulus is an uncommon condition in neonates and has a broad spectrum of clinical presentations. Gastric volvulus results from deficient fixation of the stomach or an abnormal position of the stomach due to a diaphragmatic abnormality (Campbell 1979; Al-Salem 2000). Gastric volvulus is usually classified as organoaxial and mesenteroaxial volvulus, according to the axis around which the stomach rotates. Organoaxial volvulus is characterized by rotation of the stomach about an axis parallel to its long axis and usually associated with a large hiatus hernia. UGI study in organoaxial volvulus shows that the lesser curvature is located inferiorly and the greater curvature superiorly and the pylorus pointed inferiorly (Fig. 19.8). Mesenteroaxial volvulus represents rotation of the stomach around its short axis, transecting the lesser and greater curvatures, and is rare, but may be a true emergency in neonates than organoaxial volvulus. Characteristic findings on UGI study of mesenteroaxial volvulus are the upside-down stomach with a beaking at the point of twist, so obstruction may occur at the pylorus or the gastroesophageal junction (Fig. 19.9) (Al-Salem 2007; Oh et al. 2008).

19.4 Small Intestine

19.4.1 Duodenal Atresia and Stenosis

Duodenal atresia and stenosis are relatively common causes of congenital gastrointestinal tract obstruction. These

anomalies result from failure of recanalization of the duodenal lumen during fetal development. The level of the obstruction almost always occurs at or just below the region of the ampulla of Vater. Associated anomalies are seen in up to 78 % of patients with duodenal atresia. The major associated chromosomal anomaly is Down syndrome. Other associated anomalies include other gastrointestinal tract atresias, renal anomalies, and congenital heart diseases (Dalla Vecchia et al. 1998).

Diagnosis of duodenal atresia is achieved mostly by radiography, which demonstrates a gas-filled dilated stomach and duodenal bulb with no distal air, known as the classic double bubble sign, but it may present as a gasless abdomen right after vomiting (Fig. 19.10) (Rao 2006). Contrast studies are usually unnecessary. In duodenal stenosis, radiograph reveals incomplete high intestinal obstruction and UGI study using small amount of barium may be useful to evaluate the location and type (intrinsic or extrinsic) of obstruction. US provides useful information in form of duodenal atresia with isolated esophageal atresia, which demonstrates the fluid-filled, dilated duodenal bulb and stomach, in the face of gasless abdomen on radiography. Duodenal web appears as an echogenic curvilinear band in the dilated proximal duodenum on US (Fig. 19.11).

19.4.2 Midgut Malrotation and Volvulus

Normally, the primitive midgut projects into the extraembryonic coelom, and then the bowel is introduced into the abdomen, and both the duodenojejunal and ileocolic segments undergo 270° counterclockwise rotation around the axis of the superior mesenteric artery. The rotation is followed in the last stage by peritoneal fixation of the bowel. Malrotation is a general term that encompasses a wide spectrum of embryologic failure of rotation and fixation of the midgut. Midgut volvulus is the most serious complication of malrotation related to narrow mesenteric attachment and is an absolute surgical and radiologic emergency in the neonates. Malrotation itself is not problematic; however, symptoms in malrotation are caused by midgut volvulus, obstruction from peritoneal (Ladd) bands, or a combination of both abnormalities (Bender et al. 1991).

Plain radiograph in midgut volvulus are entirely normal, show gastric dilation, or show dilation of multiple bowel loops (Fig. 19.12). Traditionally, the radiologic study of choice in suspected malrotation or midgut volvulus is an UGI study, which is preferred over contrast enema in neonate. The UGI findings of malrotation include the abnormally positioned duodenojejunal junction, the jejunum on the right side, and excessive redundancy of the duodenum.

Findings in midgut volvulus are the corkscrew sign (also known as the spiral sign) and duodenal obstruction with conical shape (Figs. 19.13 and 19.14) (Long et al. 1996; Berrocal et al. 1999a). However, the UGI study is relatively invasive to the neonates and also results are not always conclusive. Currently, US can be easily performed as a quick bedside screening procedure in intensive care units, particularly in the vomiting neonates, and its good diagnostic results become well known (Siegel 2010). On US evaluation, inversion of the superior mesenteric artery and superior mesenteric vein can be a reliable aid in the diagnosis of malrotation. The US features suggestive of midgut volvulus include the whirlpool sign, duodenal dilation with tapering configuration, fixed midline bowel, and dilation of the distal superior mesenteric vein (Pracros et al. 1992; Shimanuki et al. 1996; Chao et al. 2000). The whirlpool sign on color Doppler study is a valid and highly sensitive sign and represents clockwise wrapping of the gut, the mesentery, and the superior mesenteric vein around the superior mesenteric artery (Figs. 19.12 and 19.14). Three-dimensional helical CT can also exquisitely depict similar features but is an unsuitable modality in ill neonates.

19.4.3 Jejunoileal Atresia and Stenosis

Atresia and stenosis of the jejunum and ileum are the most common cause of congenital intestinal atresia and also the most frequent cause of neonatal intestinal obstruction. Jejunoileal atresia, except those that are familial, has been ascribed to an intrauterine vascular accident resulting in necrosis of the affected segment, with subsequent resorption (Dalla Vecchia et al. 1999).

Classic radiographic finding is a pattern of small bowel obstruction; a few loops with triple bubble sign suggest a high jejunal atresia, whereas distal ileal atresia usually results in more numerous uniformly dilated loops (Figs. 19.15 and 19.16). Occasionally, there are a bulbous bowel segment, meconium pseudocyst, peritoneal, intramural, and intraluminal calcifications (Figs. 19.17 and 19.18). However, it is difficult to distinguish the dilated small bowel from the colon, especially in distal ileal atresia (Berrocal et al. 1999a). Water-soluble contrast enema is advocated to exclude concomitant atresia or malrotation and to evaluate the atypical radiographic manifestations. Contrast enema in distal ileal atresia usually demonstrates a small caliber colon, indicating an unused microcolon, which can be seen with other conditions such as meconium ileus, proximal colonic atresia, and total colonic aganglionosis (Fig. 19.18) (Hernanz-Schulman 1999; Rao 2006). The size of the colon is related to the gestational age at which atresia occurs and the distance of the

atretic segment from the colon. US is not generally indicated, unless the clinical findings are atypical, perhaps suggesting an abdominal mass.

19.4.4 Meconium Ileus

Meconium ileus is a congenital low intestinal obstruction that results from impaction of thick, tenacious meconium in the distal ileum and is often the first sign of cystic fibrosis. The clinical manifestations are similar to those of ileal atresia. The classic findings on abdominal radiographs are soap bubble appearance of bowel contents, marked variation in the caliber of the distended bowel loops, and a relative lack of air-fluid levels within the dilated bowel loops. About half of cases have a complicated form associated with volvulus, small bowel atresia, perforation, and/or meconium peritonitis. Contrast enema demonstrates microcolon as well as multiple round or oval filling defects in the distal ileum and colon (Fig. 19.19). Multiple Gastrografin enemas might well be performed in the absence of any complications, as an initial method for treatment (McAlister and Kronemer 1996). On US evaluation, highly echogenic materials in the dilated bowel may be a helpful finding in distinguishing meconium ileus from ileal atresia (Siegel 2010).

19.5 Colon

19.5.1 Anorectal Malformations

Anorectal malformations comprise a wide spectrum of developmental defects involving the anorectal segment as well as the genitourinary tracts. Although several different classifications have been devised, common denominators that predominate to categorize the anorectal anomalies are the presence or absence of a normal appearing anus and puborectalis muscle. Depending on the site of blind-ending hindgut in relation to the puborectalis muscle, they are commonly subdivided into low, intermediate, and high types (Figs. 19.20 and 19.21). Approximately 50 % cases of anorectal anomalies have associated congenital anomalies, which are about twice more common in high type than low type. Currarino syndrome is an inherited disorder and includes anorectal malformation, partial agenesis of the sacrum, and a presacral mass, which may be a teratoma, anterior meningocele, or enteric cyst (Fig. 19.22) (Pfluger et al. 1996).

When physical findings do not clarify the exact nature of anomaly, it must be defined by means of radiologic

evaluation, which has been used to determine the level of the distal rectal pouch, assess the developmental state of the sphincter muscle complex, identify the fistula, and diagnose the associated anomalies. On invertography, the “M” line running through the junction of the lower third and upper two-thirds of the ischium is proved a truer equivalent of the puborectalis sling, but its diagnostic value is not sufficient in the determination of type in the newborn (Berrocal et al. 1999a). More recently, it is suggested that infracoccygeal and transperineal US are useful for the determination of the types and identification of the fistula (Figs. 19.20 and 19.21)

(Han et al. 2003; Haber et al. 2007). In low type, the distance between the distal rectal pouch and perineum is less than 15 mm on transperineal US, which is accurate in discriminating low- from intermediate- and high-type imperforate anus. However, sonographic evaluation is also subject to inaccuracies related to technical factors. Although MR imaging has proven to be the best modality of choice because of its multiplanar capability and superb anatomic detail about the sphincter muscle complex and rectal pouch, its clinical utility prior to operation is not widespread (Fig. 19.20) (Nivelstein et al. 1998).

19.6 Illustrations: Congenital and Neonatal Gastrointestinal Diseases

19.6.1 Esophageal Atresia and Tracheoesophageal Fistula

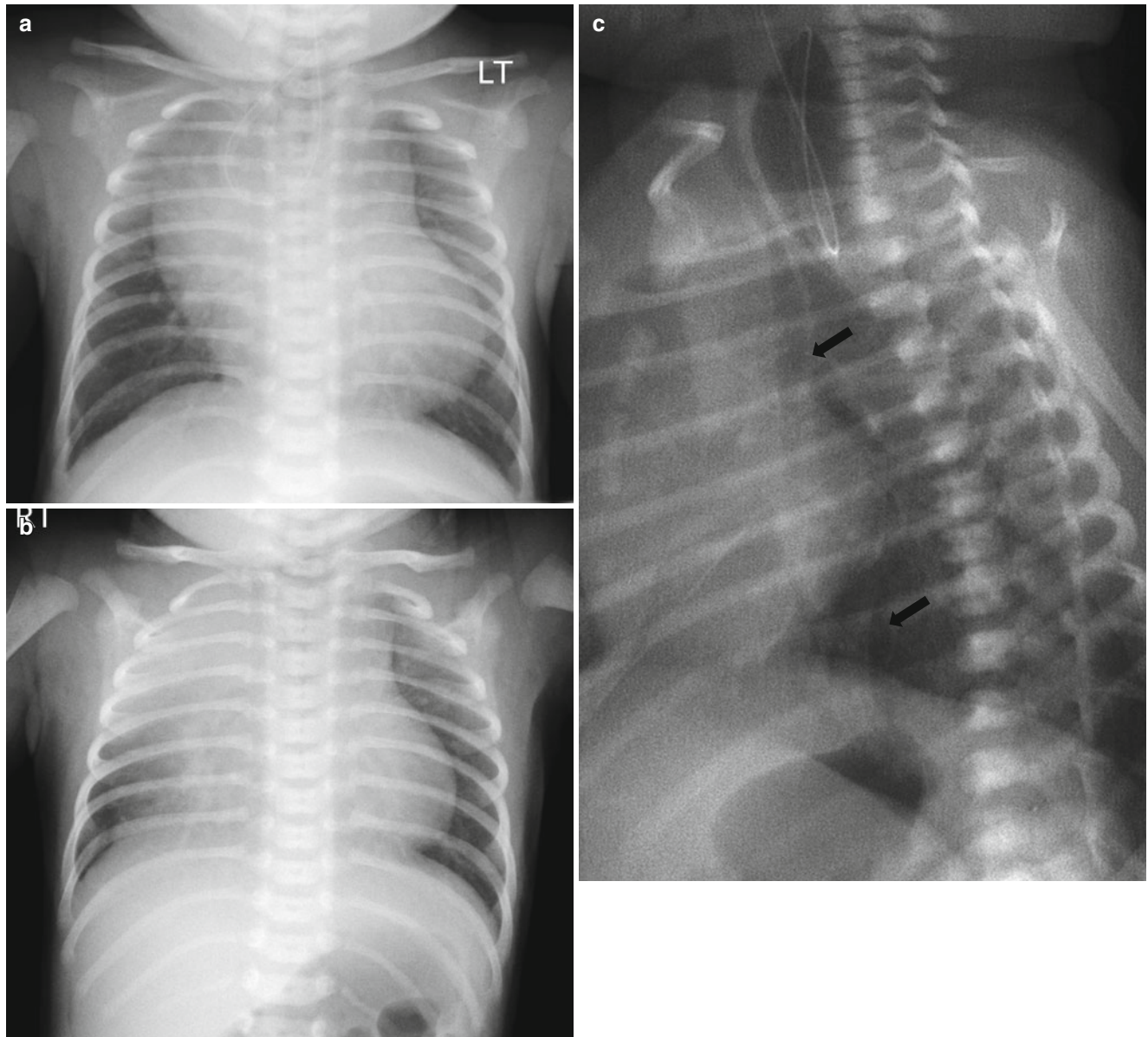


Fig. 19.1 Esophageal atresia with tracheoesophageal fistula in a neonate with excessive oral secretion. (a) Chest radiograph at 1 hour of life shows the blind-ending proximal esophageal pouch distended with air and coiled tube. (b) Chest radiograph at 1 day of life demonstrates infil-

tration of the right upper and middle lobes. The presence of gas in the stomach indicates fistulous communication between the lower esophageal segment and trachea. (c) The distal TEF and distal esophageal pouch (arrows) are briefly outlined by air on air esophagogram

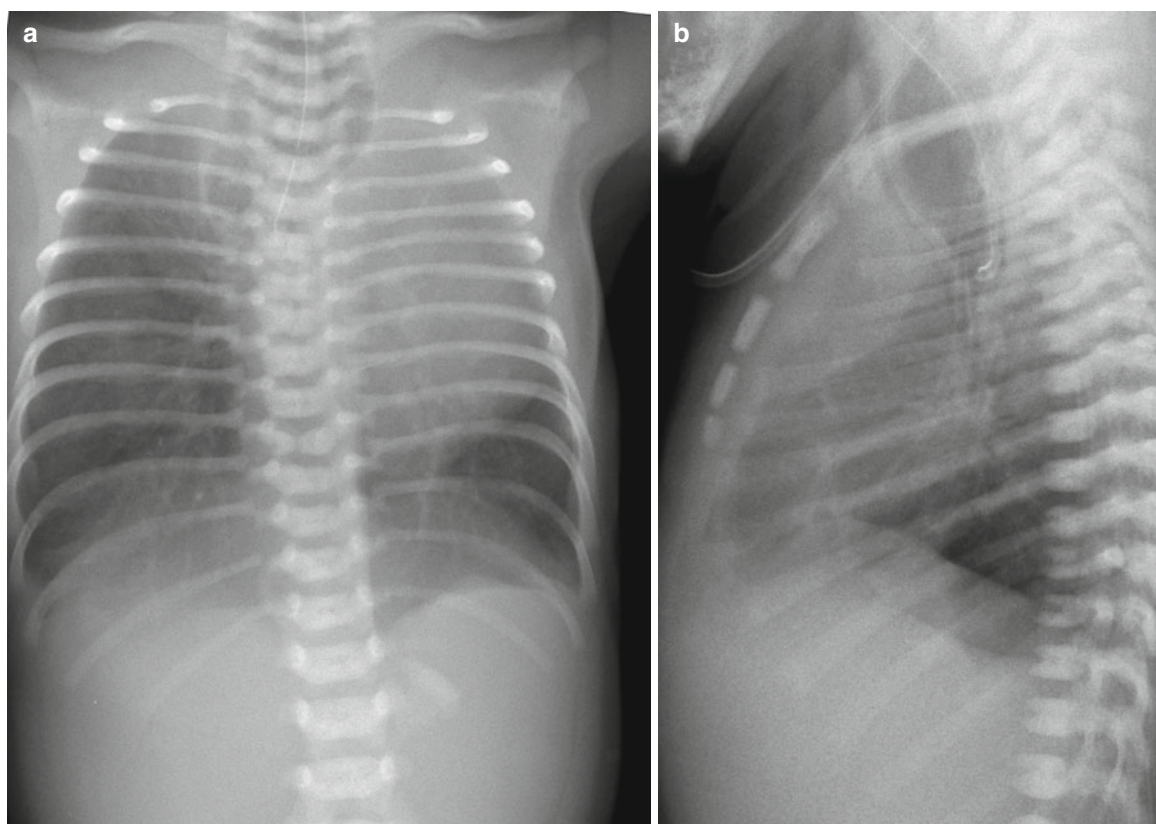


Fig. 19.2 Esophageal atresia without tracheoesophageal fistula in a 1-day-old neonate with high-type imperforate anus. **(a)** Chest radiograph shows a radiopaque tube curling in the distended proximal esophageal pouch and gasless abdomen indicating lack of a distal TEF. Note

coronal cleft in the eighth thoracic vertebra. **(b)** Lateral radiograph clearly demonstrates the distended proximal esophageal pouch with resulting anterior bowing and pressure deformity of the trachea

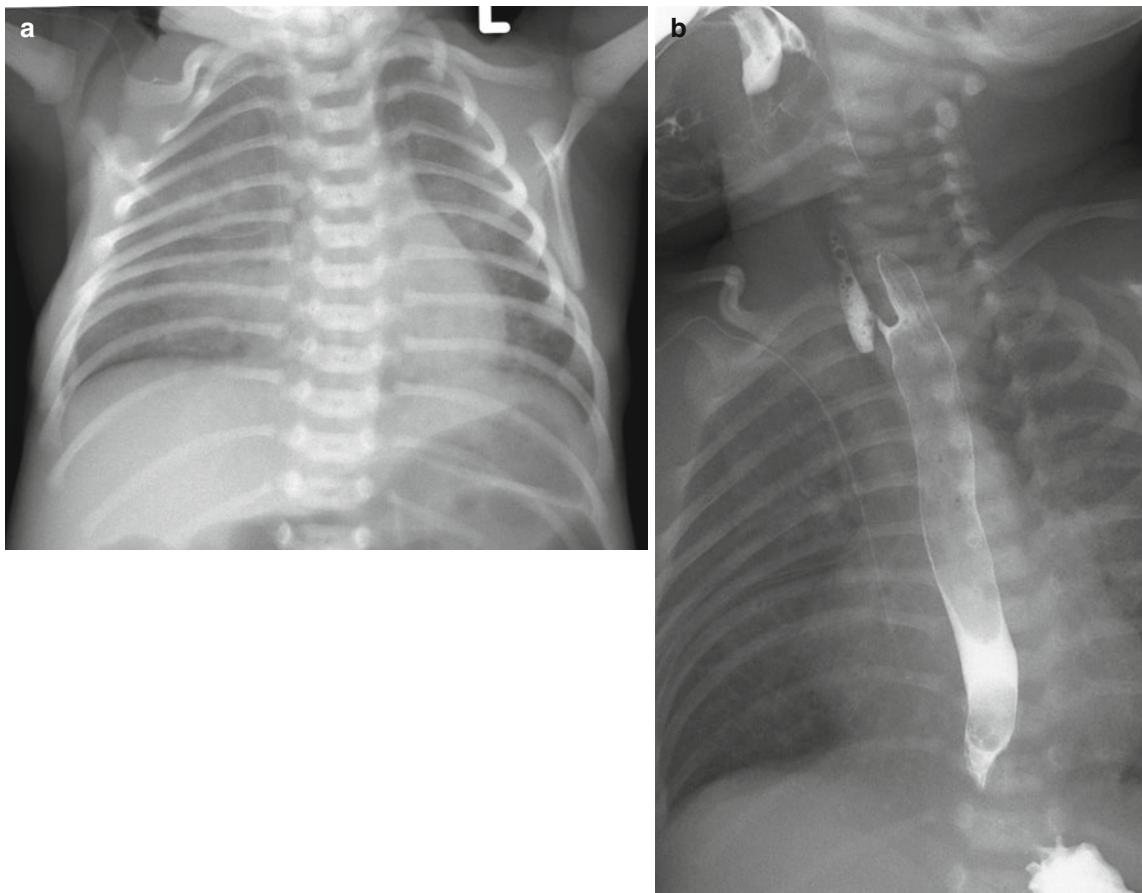


Fig. 19.3 *H-type tracheoesophageal fistula in a 12-day-old neonate.* (a) Chest radiograph shows infiltration in the right lung, which is gradually aggravated after birth. (b) Lateral view of esophagogram confirms

a fistulous tract extending from the esophagus anteriorly and cephalad toward the trachea. Note venous catheter tip at the right atrium

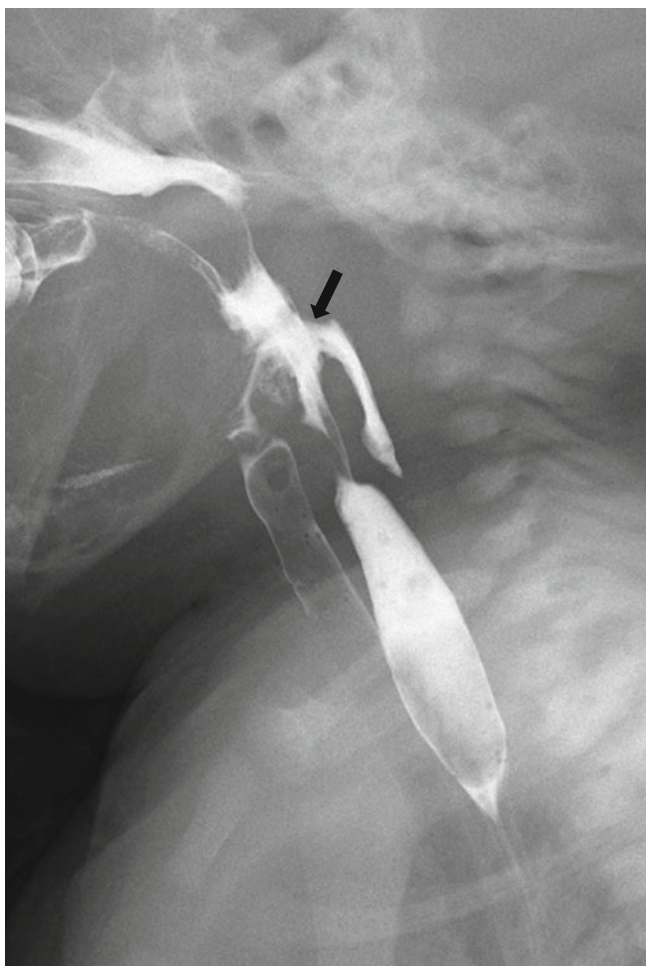


Fig. 19.4 *Pharyngoesophageal perforation in a 1-day-old neonate transferred from the outside hospital due to respiratory difficulty. The neonate was intubated after birth and underwent vigorous suctioning. Lateral view of esophagogram confirms a retroesophageal blind-ending tract from the hypopharynx, as pharyngeal pseudodiverticulum (arrow)*

19.6.2 Laryngoesophageal Clefts

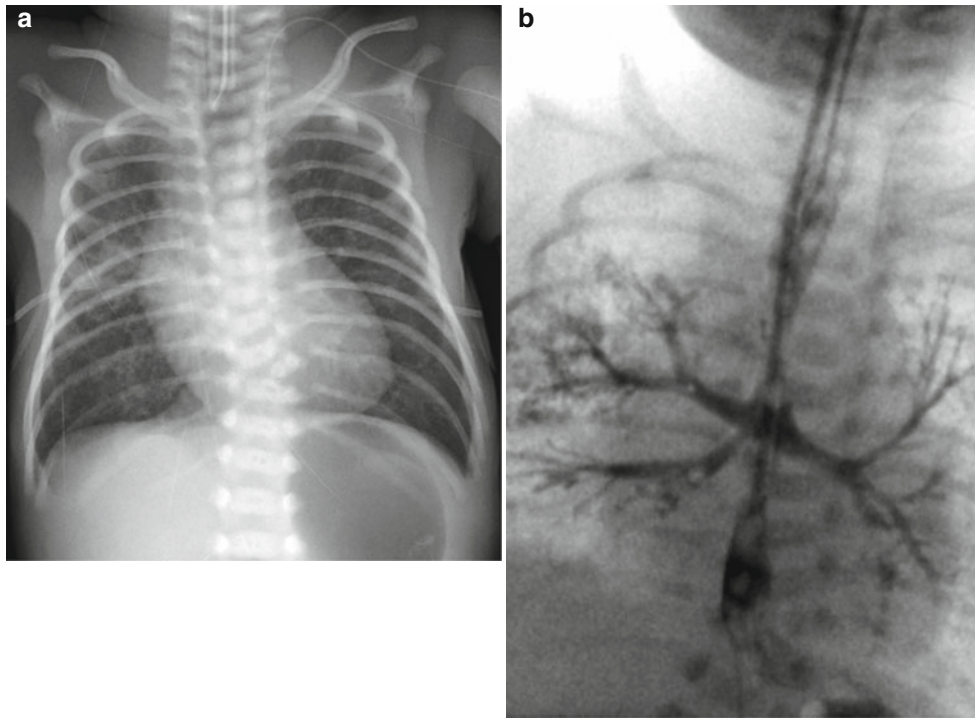


Fig. 19.5 *Persistent esophagotrachea in a premature with progressive desaturation and prenatal US diagnosis of esophageal atresia. (a)* Chest radiograph on 4 days of life demonstrates infiltrations in both lung fields and a tubular-shaped hyperlucency over the cervical and upper thoracic vertebrae. Note segmentation anomaly of the lower tho-

racic vertebrae. **(b)** Esophagogram shows a common lumen with both nasogastric and endotracheal tubes inserted. Note bronchial bifurcation from the distal one-third of a common lumen, which is distally continued to the esophagus

19.6.3 Congenital Esophageal Stenosis

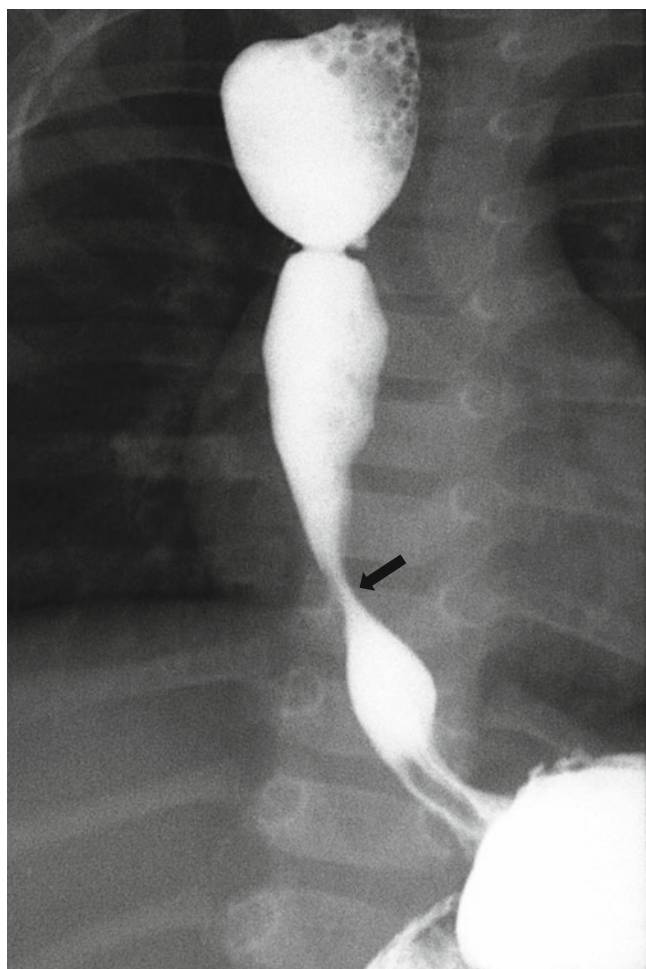


Fig. 19.6 Congenital esophageal stenosis in a 6-month-old girl with history of surgical repair of esophageal atresia. Frontal view of the esophagram demonstrates focal concentric narrowing (arrow) of the distal third of the esophagus. Note residual deformity at the proximal esophagus indicating the site of the anastomosis

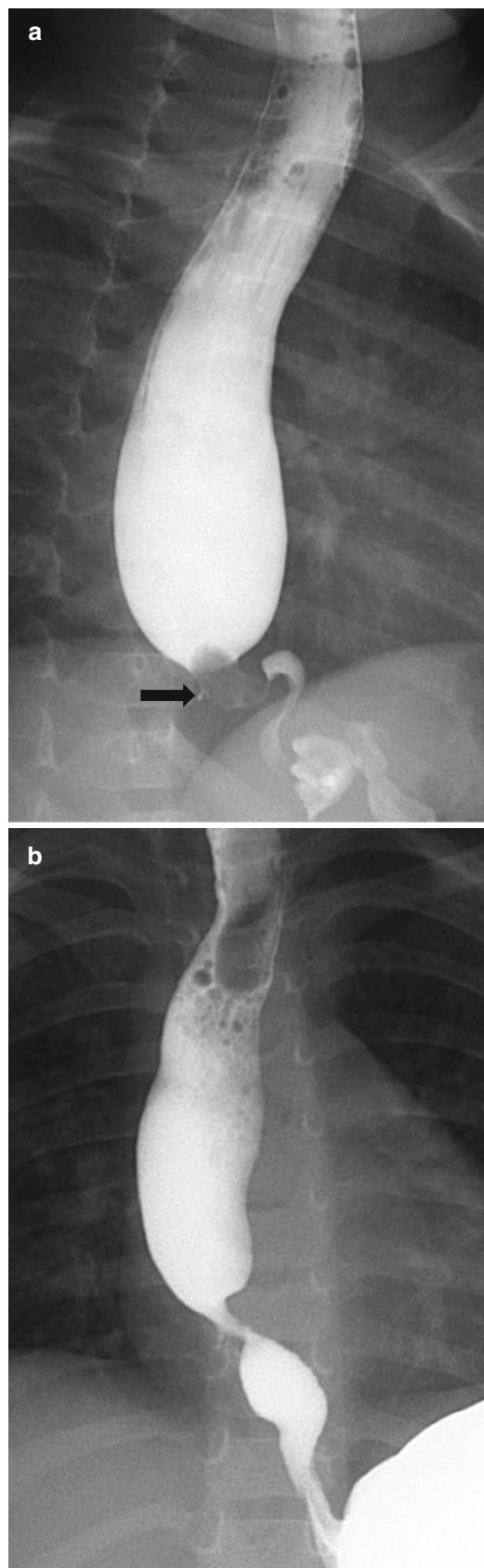


Fig. 19.7 Congenital esophageal stenosis in a 20-month-old girl with sudden onset of choking. (a) Oblique view of the esophagram demonstrates an ovoid radiolucent filling defect impacted in the distal third of the esophagus and small barium projection (arrow) along the right lateral border of the filling defect. (b) Esophagogram after endoscopic removal of a bean shows focal narrowing at the distal esophagus and clearer demonstration of barium-filled diverticulum-like structure, representing characteristic of cartilaginous tracheobronchial remnants

19.6.4 Gastric Volvulus

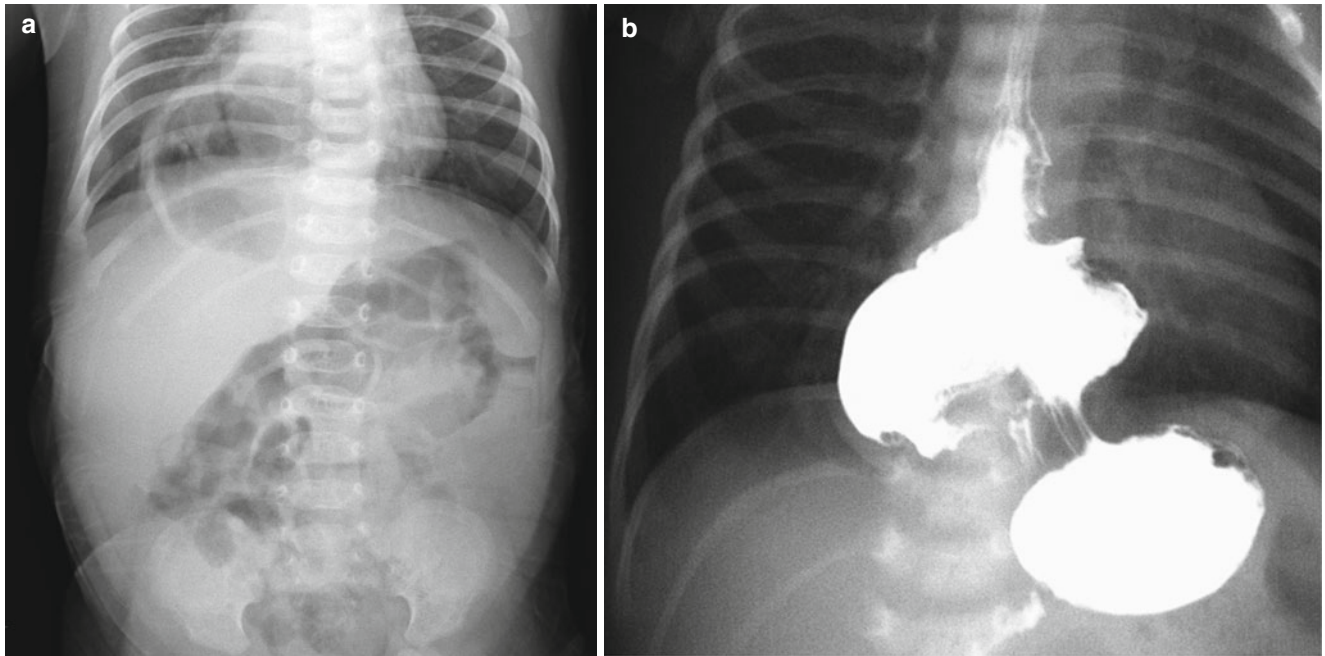


Fig. 19.8 *Organoaxial volvulus in a 12-day-old neonate with hiatal hernia. (a)* Plain radiograph shows air-filled structure with an unusual configuration in the retrocardiac and right paravertebral areas. **(b)**

Image from UGI study demonstrates partial herniation of the stomach with inferiorly pointed pylorus. The greater curvature lies to the right of and superior to the lesser curvature

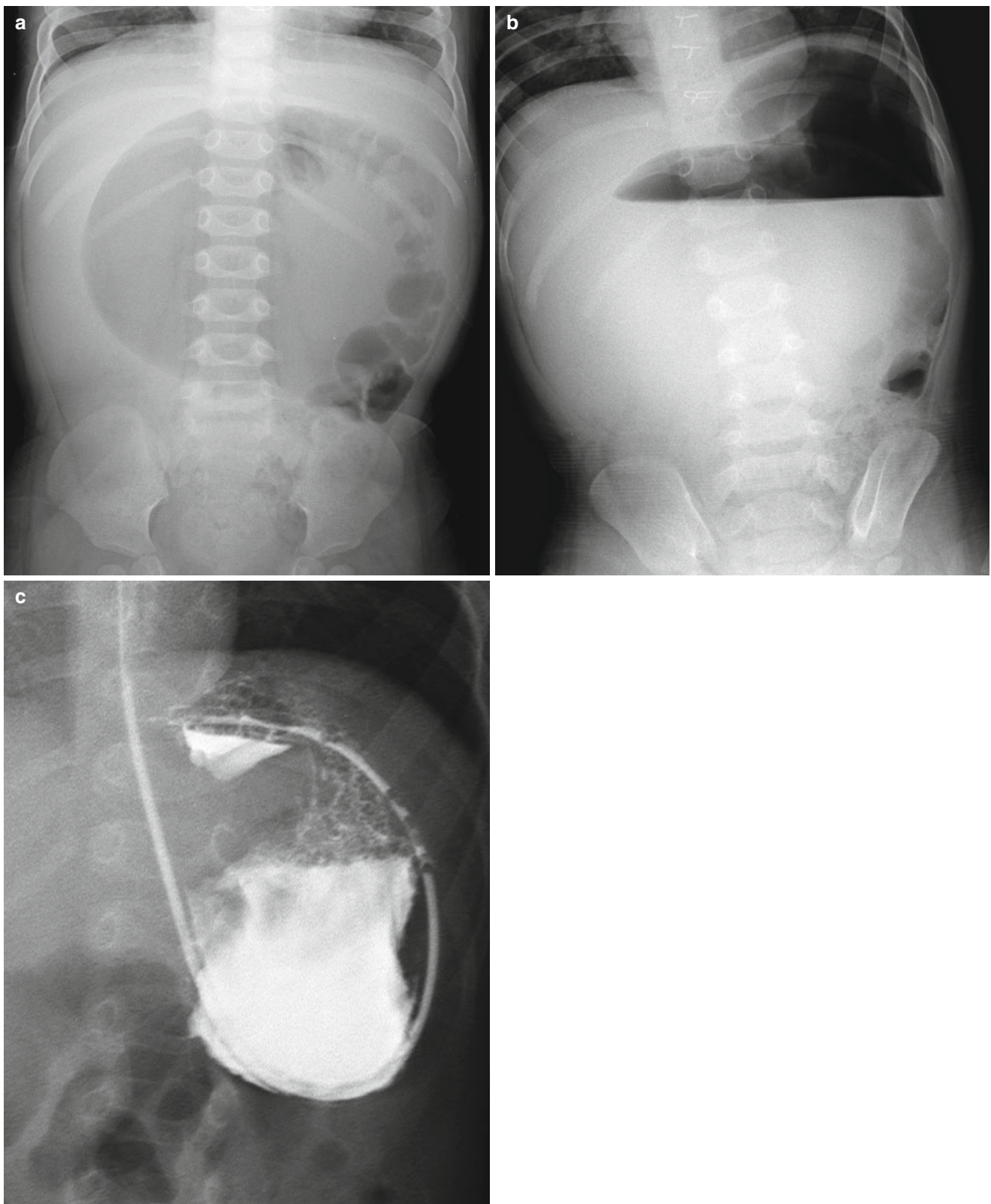


Fig. 19.9 Mesenteroaxial volvulus in a 11-month-old girl with abdominal distension and vomiting. Supine (a) and erect (b) abdominal radiographs show a marked spherical distension of the stomach with two air-fluid levels. Note sternal wirings by previous surgery for congenital heart disease. (c) Image from UGI study after gastric decompression

shows the antrum and pylorus lying above the fundus with upside-down stomach and pyloric obstruction with beaking. The lesser and greater curvatures maintain their normal relationship. Asplenia was confirmed at surgery

19.6.5 Duodenal Atresia and Stenosis

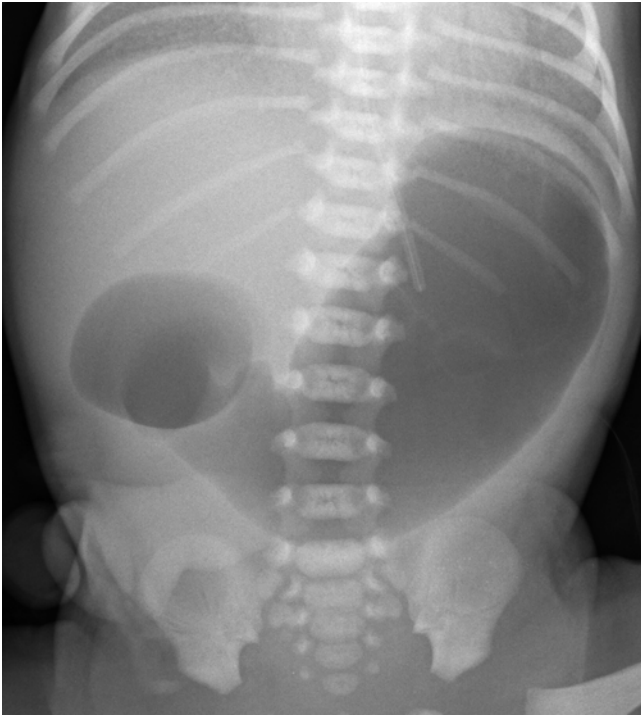


Fig. 19.10 Duodenal atresia in a 1-day-old premature presented with vomiting. Abdominal radiograph demonstrates a markedly distended stomach and duodenal bulb giving the classic double bubble sign. Note lack of gas in the rest of the intestinal tracts

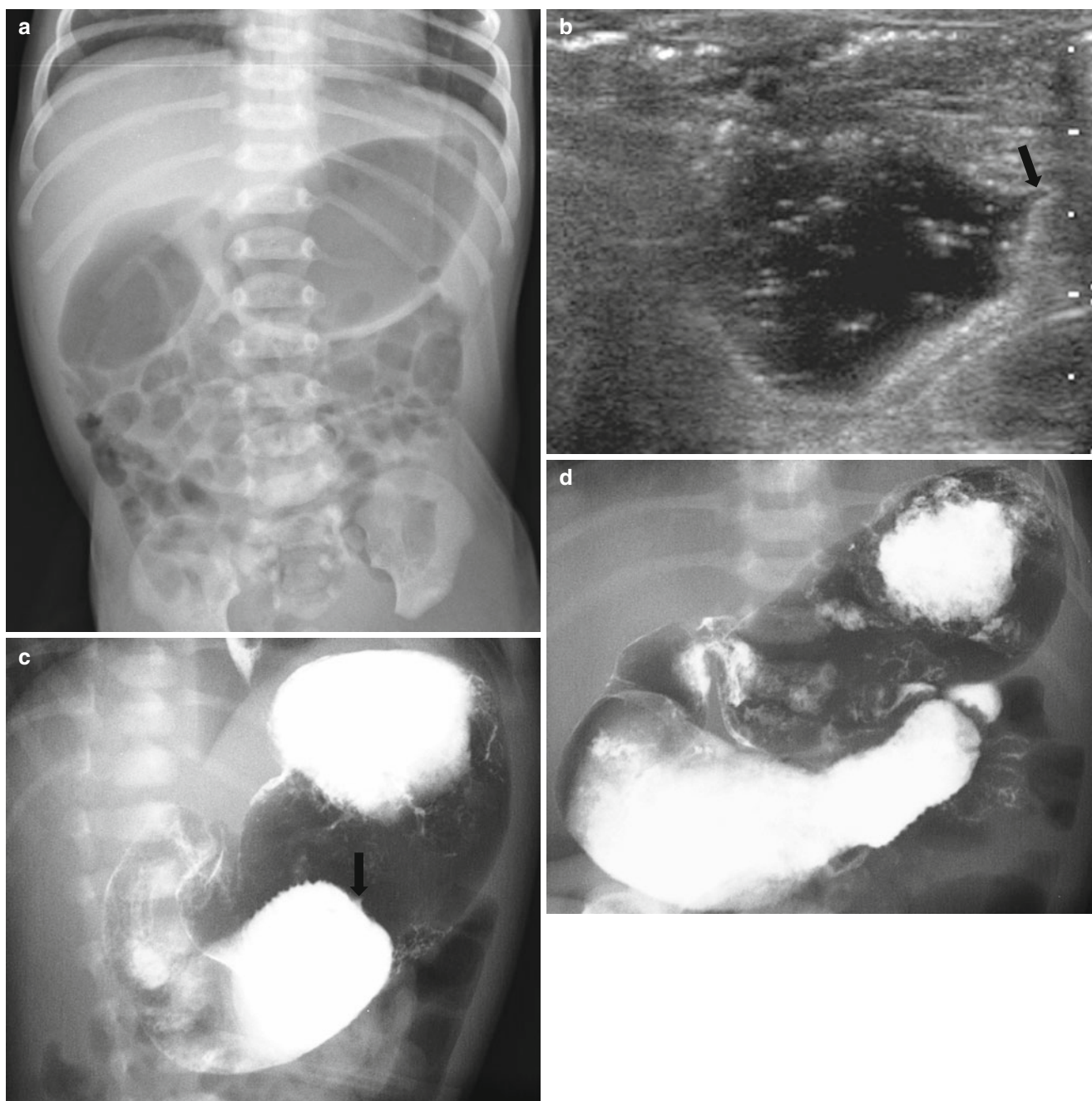


Fig. 19.11 Duodenal stenosis by web in a 4-day-old neonate with bilious vomiting. (a) Abdominal radiograph shows gaseous distension of the duodenum and nondilated scattered gas-filled bowel loops distally. (b) Transverse abdominal US shows the fluid-filled, distended duodenum with a central teat configuration in the obstructed end (arrow). (c) Images from UGI study show the barium passage halting at the third

portion of the duodenum, the bolus ending with a central teat configuration (arrow), similar to US finding. (d) Delayed image demonstrates a smooth transverse filling defect crossing the duodenal lumen and passage of barium beyond the lesion. The duodenal web with a pinpoint hole was found at surgery

19.6.6 Midgut Malrotation and Volvulus

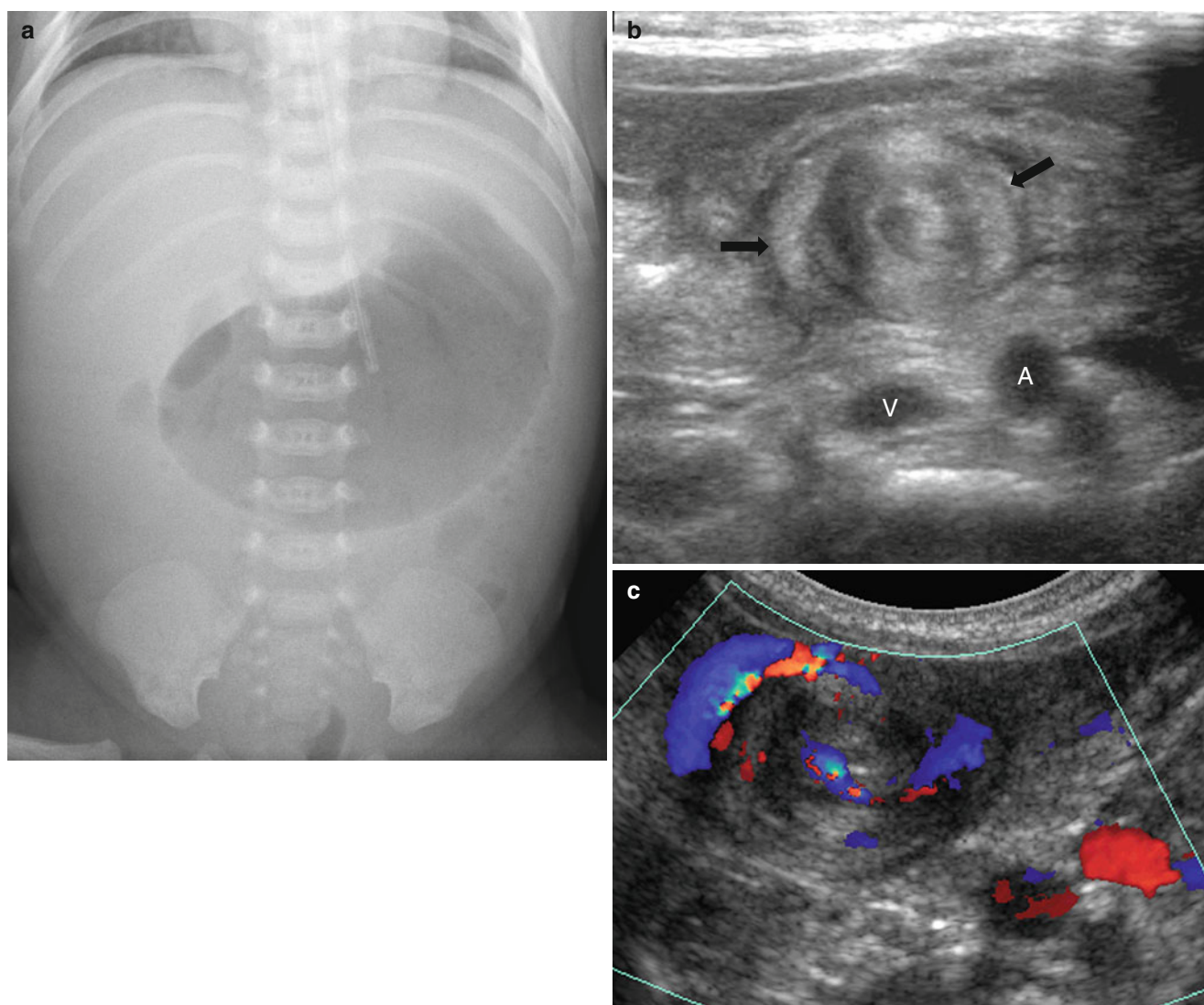


Fig. 19.12 Midgut volvulus with Ladd band in a 1-month-old boy presenting with bilious vomiting. (a) Abdominal radiograph demonstrates the distended stomach and paucity of gas in the remainder of the bowel loops. (b) Transverse US of the upper abdomen shows a whirl-like mass

(arrows) in the upper abdomen in front of the vena cava (V) and aorta (A). (c) Corresponding color Doppler study shows a clockwise whirl-pool sign with complete wrapping of the superior mesenteric vein, mesentery, and bowel loops around the superior mesenteric artery

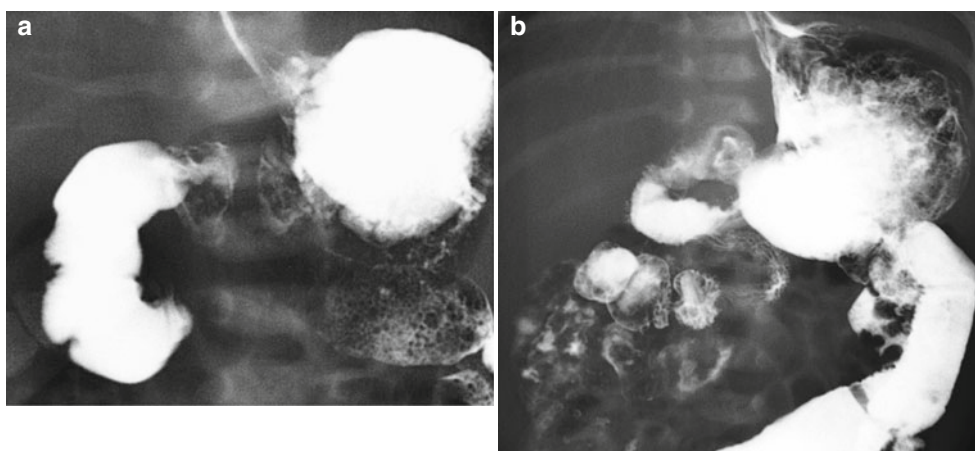


Fig. 19.13 Midgut malrotation and volvulus in a 8-day-old neonate with bilious vomiting. (a) Initial image of UGI study with compression shows dilated descending duodenum and duodenal obstruction with conical shape. (b) Delayed image of study shows the duodenum passing over the right side with a short spiraled segment distally, as well as

duodenojejunal junction being midline and low, and the proximal jejunum on the right abdomen. Note the entire colon on the left abdomen by nonrotation and barium retention related to enema study performed 2 days ago at the outside hospital

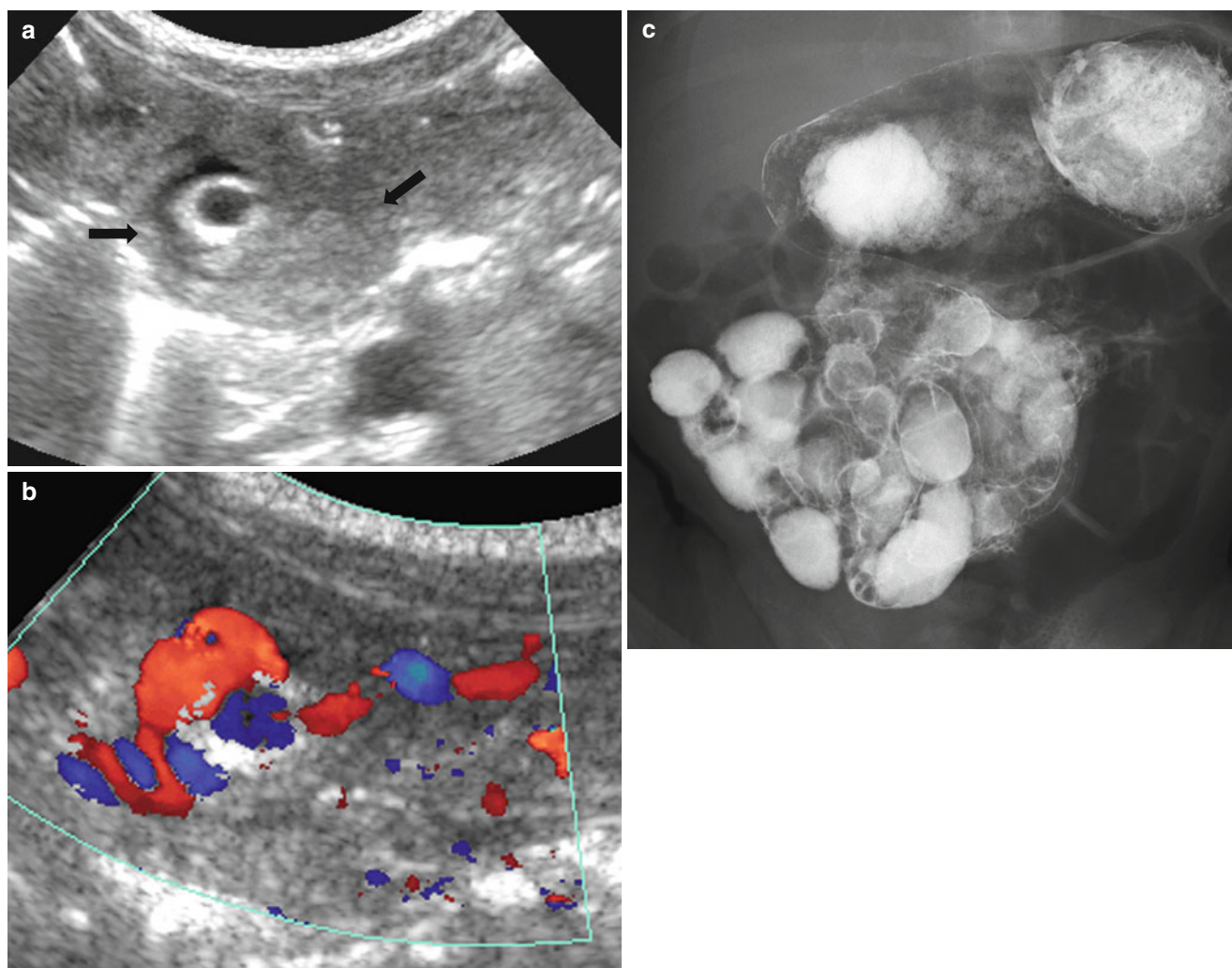


Fig. 19.14 Midgut malrotation and volvulus in a 5-day-old neonate with bloody vomiting and abdominal distension. (a) Transverse US demonstrates a poorly defined, heterogeneously hypoechoic mass lesion with an inner anechoic lesion (arrows). (b) Color Doppler study confirms a clockwise whirlpool sign. Note an inner round anechoic

lesion corresponding to the superior mesenteric artery. (c) Delayed image of UGI study shows the spiral configuration of the fourth portion of the duodenum and proximal jejunum, indicative of corkscrew sign. Note abnormal course of the duodenum and proximal jejunum

19.6.7 Jejunoileal Atresia and Stenosis

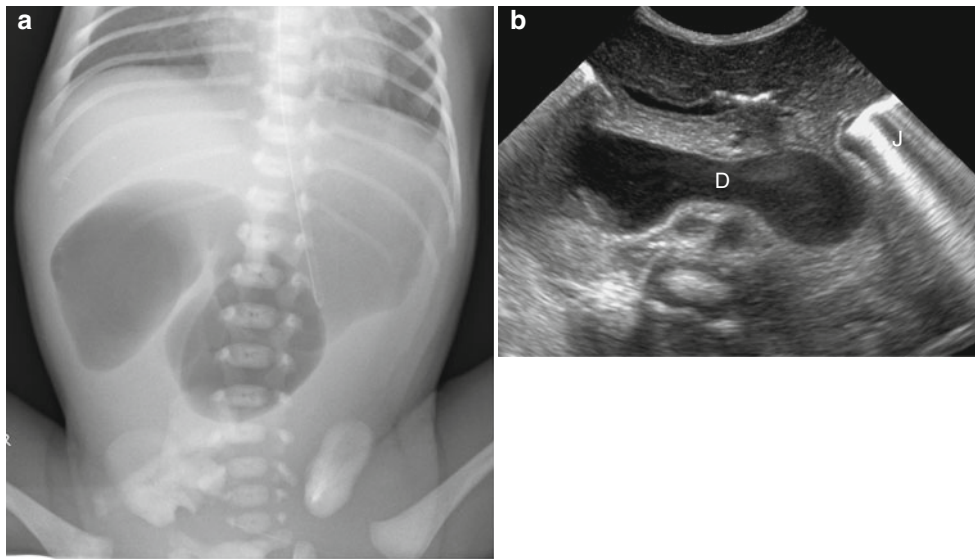


Fig. 19.15 Proximal jejunal atresia in a 1-day-old premature with pre-natal diagnosis of duodenal atresia. (a) Abdominal radiograph demonstrates gaseous distension of the stomach, duodenum, and proximal

jejunum, producing triple bubble sign. Note lack of gas in other bowel loops. (b) Transverse US shows the dilated duodenum (D) and proximal jejunum (J) with fluid and gas

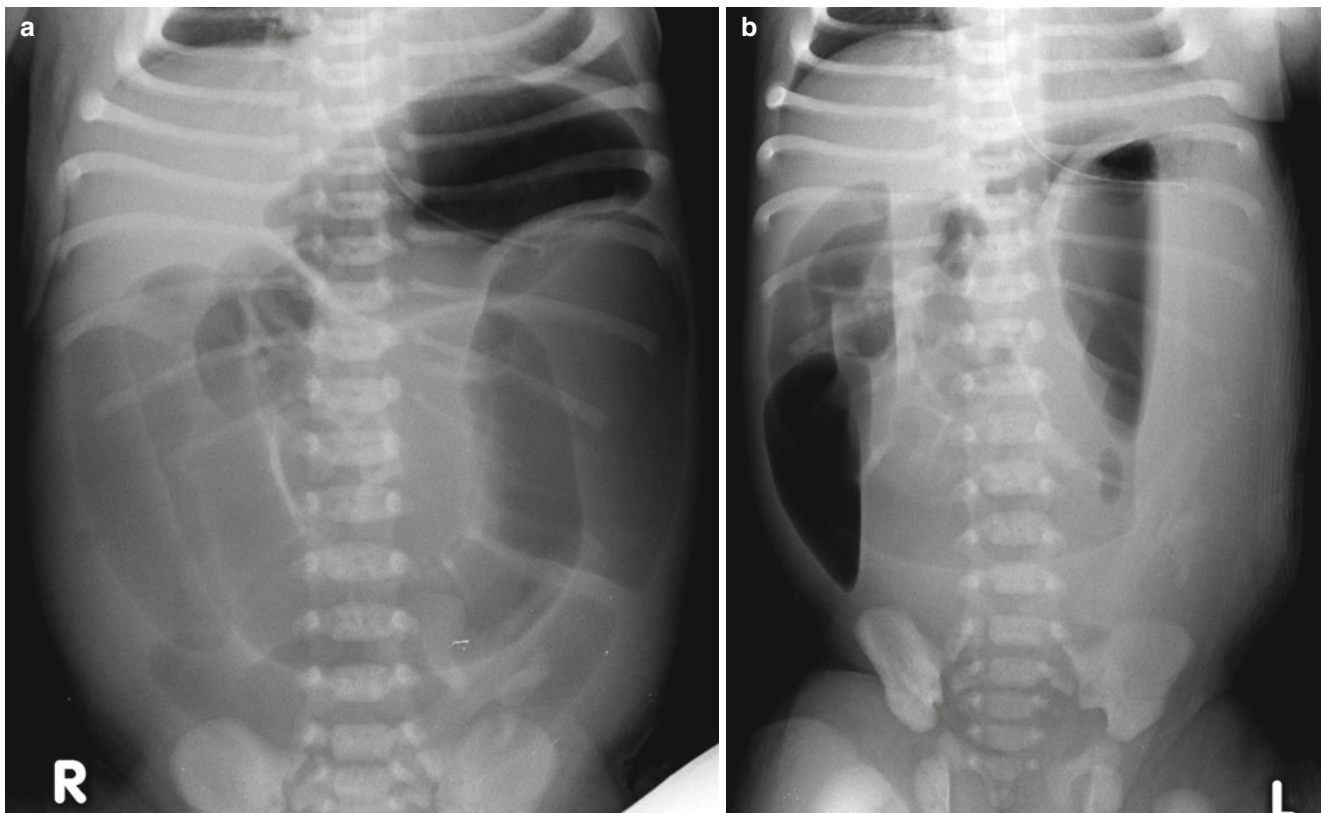


Fig. 19.16 Distal jejunal atresia in a 1-day-old neonate with prenatal US diagnosis of bowel obstruction. Abdominal radiograph in supine (a) and left lateral decubitus (b) position show several dilated small bowel

loops with multiple, different height of air-fluid levels. Note lack of gas in the colonic loops

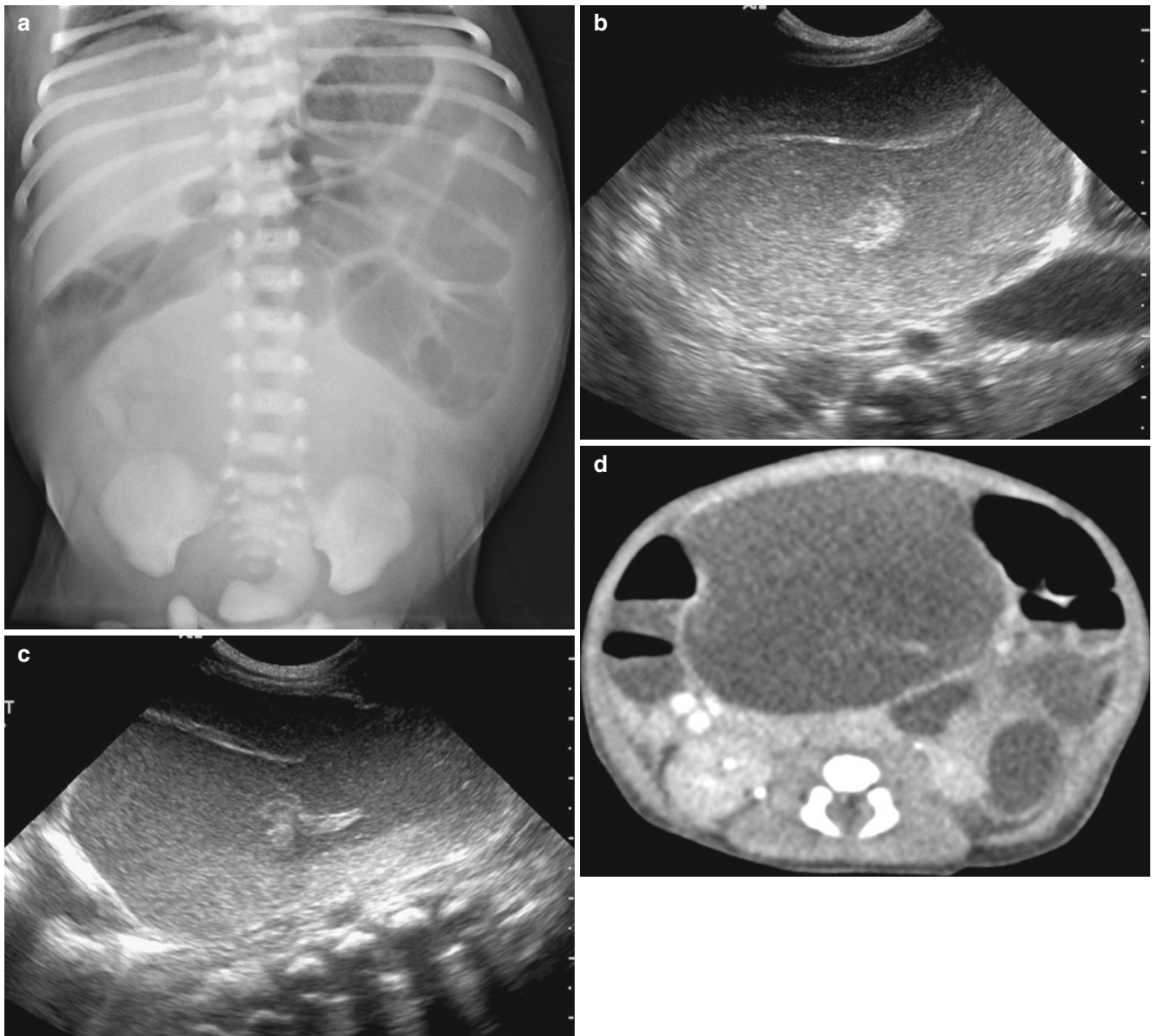


Fig. 19.17 *Jejunal atresia with meconium pseudocyst in a 1-day-old neonate with prenatal US diagnosis of abdominal mass. (a)* Abdominal radiograph demonstrates a soft tissue density mass lesion in the lower abdomen and several dilated small bowel loops. Transverse (b) and longitudinal (c) US at the midabdomen show a well-demarcated cystic

mass containing anechoic and echogenic contents and echogenic wall. (d) CT at the midabdomen confirms a large cystic mass with calcific wall. Note nodular calcifications posterolateral to the cystic mass and dilated proximal jejunum. Jejunal atresia 90 cm distal to the ligament of Treitz was found at surgery

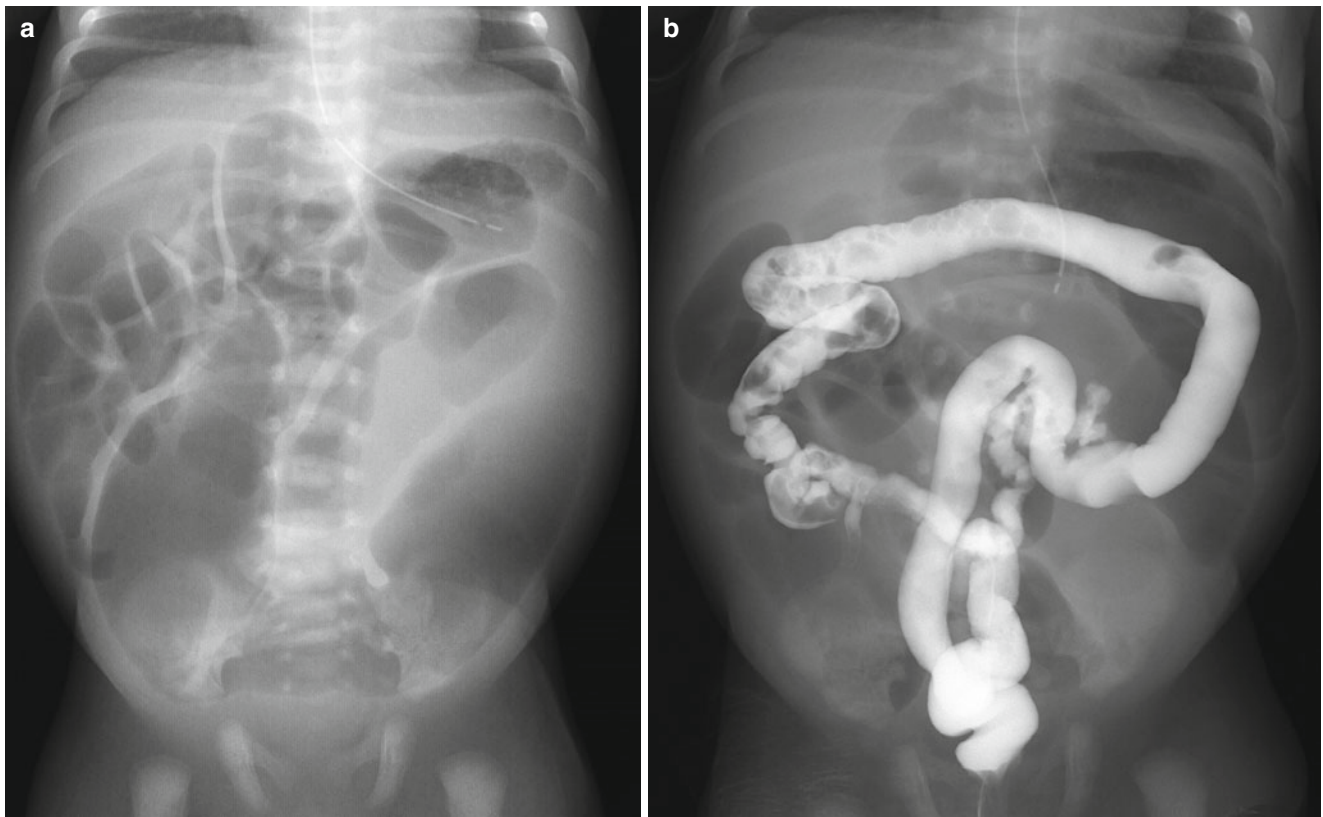


Fig. 19.18 Ileal atresia in a 7-day-old girl presenting with bilious vomiting and jaundice. **(a)** Abdominal radiograph taken 7 days after birth demonstrates dilation of the multiple small bowel loops and a bul-

bous bowel segment in the lower abdomen. **(b)** Image from contrast enema study demonstrates the small caliber colon and reflux into several relatively collapsed loops of the distal ileum

19.6.8 Meconium Ileus

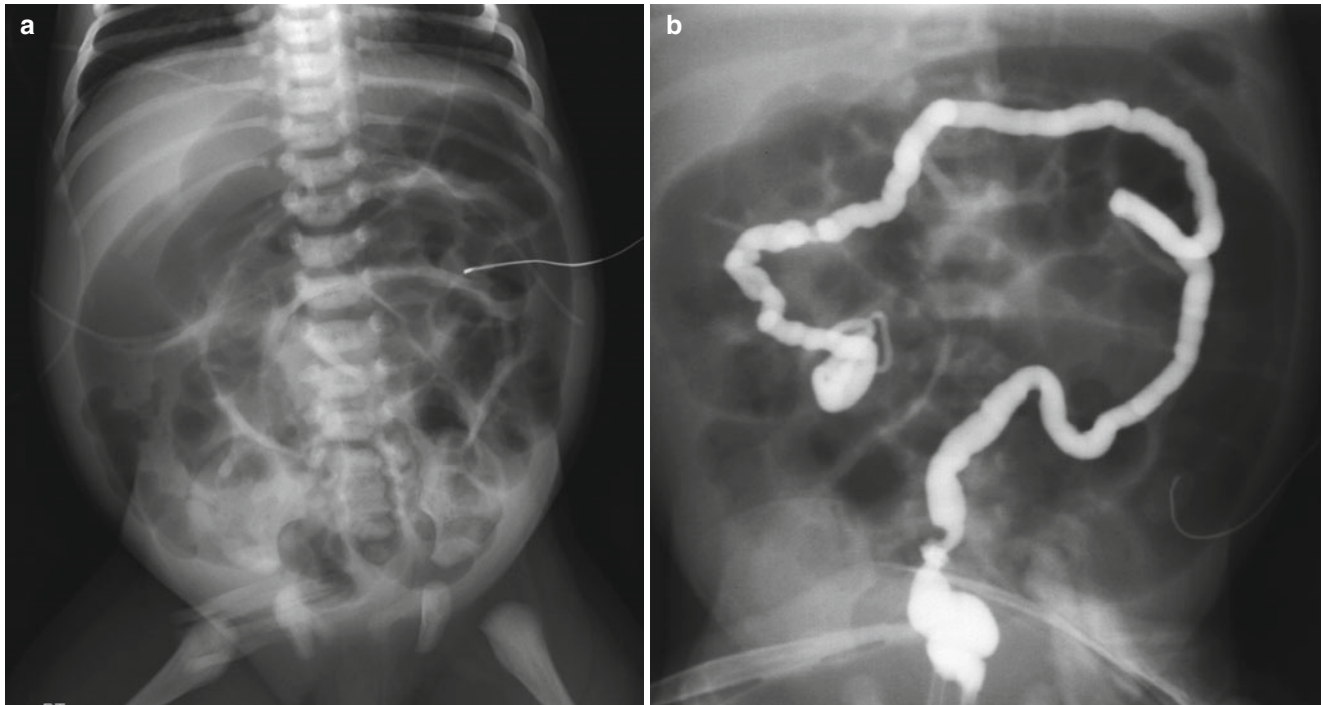


Fig. 19.19 *Meconium ileus in a 1-day-old full-term neonate with bilious vomiting and abdominal distension. (a)* Abdominal radiograph demonstrates moderately gaseous distension of the small bowel loops with mottled opacities in the bowel loops at the right lower abdomen.

(b) Image from Gastrografin enema shows an unused microcolon without reflux into the dilated ileum. Jejunotomy was performed, and there was no evidence of cystic fibrosis

19.6.9 Anorectal Malformations

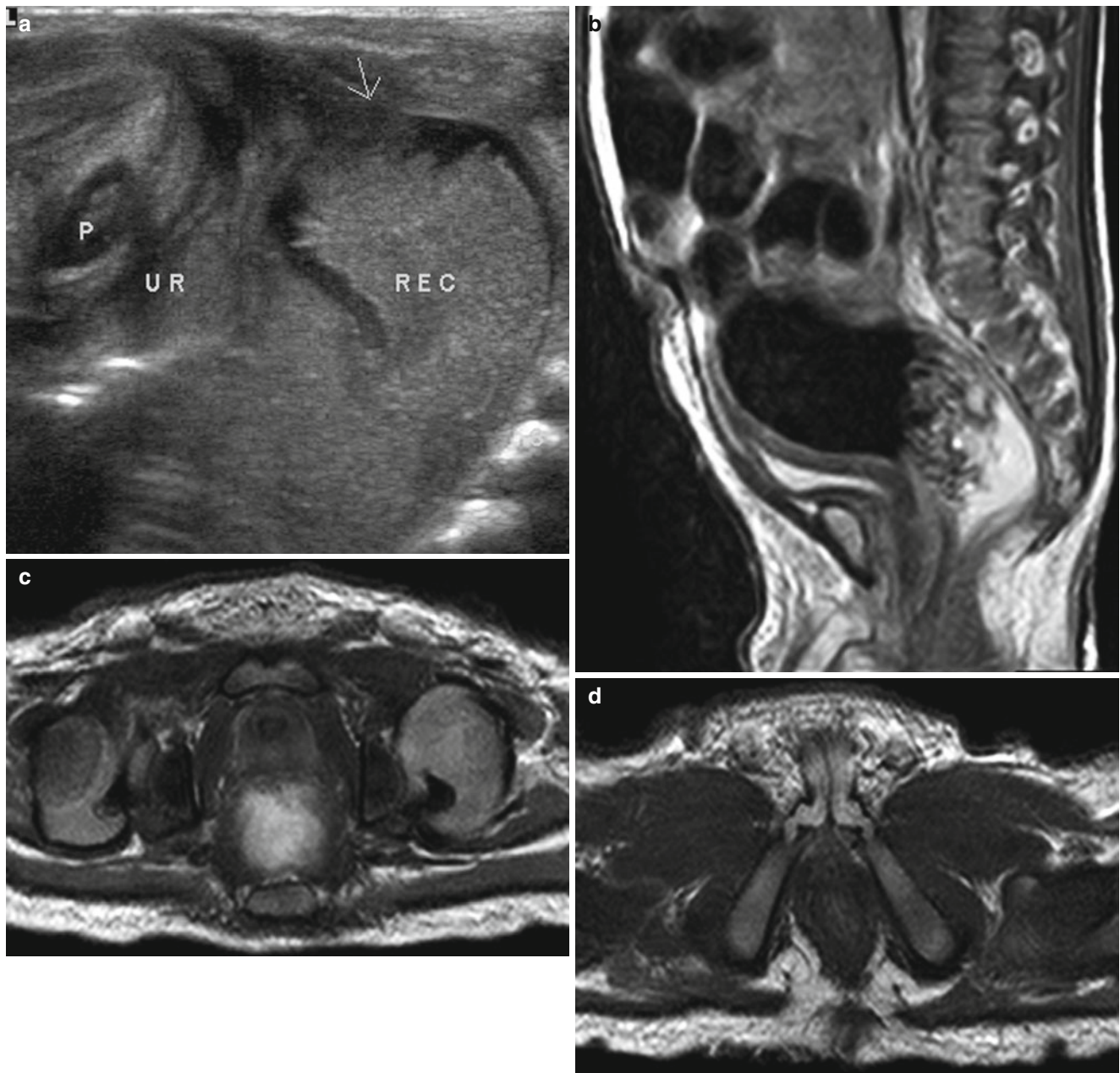


Fig. 19.20 Low-type imperforate anus with rectoperineal fistula in a 2-day-old boy. **(a)** Transperineal US demonstrates a hypoechoic linear tract (arrow) extending from the blind-ending rectal pouch (REC) into the perineum, corresponding to rectoperineal fistula. Distance between the distal rectal pouch and perineum is 10 mm. *P* symphysis pubis, *UR* urethra. **(b)** Sagittal T1-weighted MR image shows meconium-filled distal rectal pouch passing through the radiographic “M” line and

puborectalis muscle. Note a thin tract with high signal intensity extending anteriorly from the rectal pouch, indicating rectoperineal fistula. **(c)** Axial T1-weighted MR image at the level of the symphysis pubis shows good development of the puborectalis muscle. **(d)** Axial T1-weighted MR image at the level of the ischial rami shows good development of the external anal sphincter

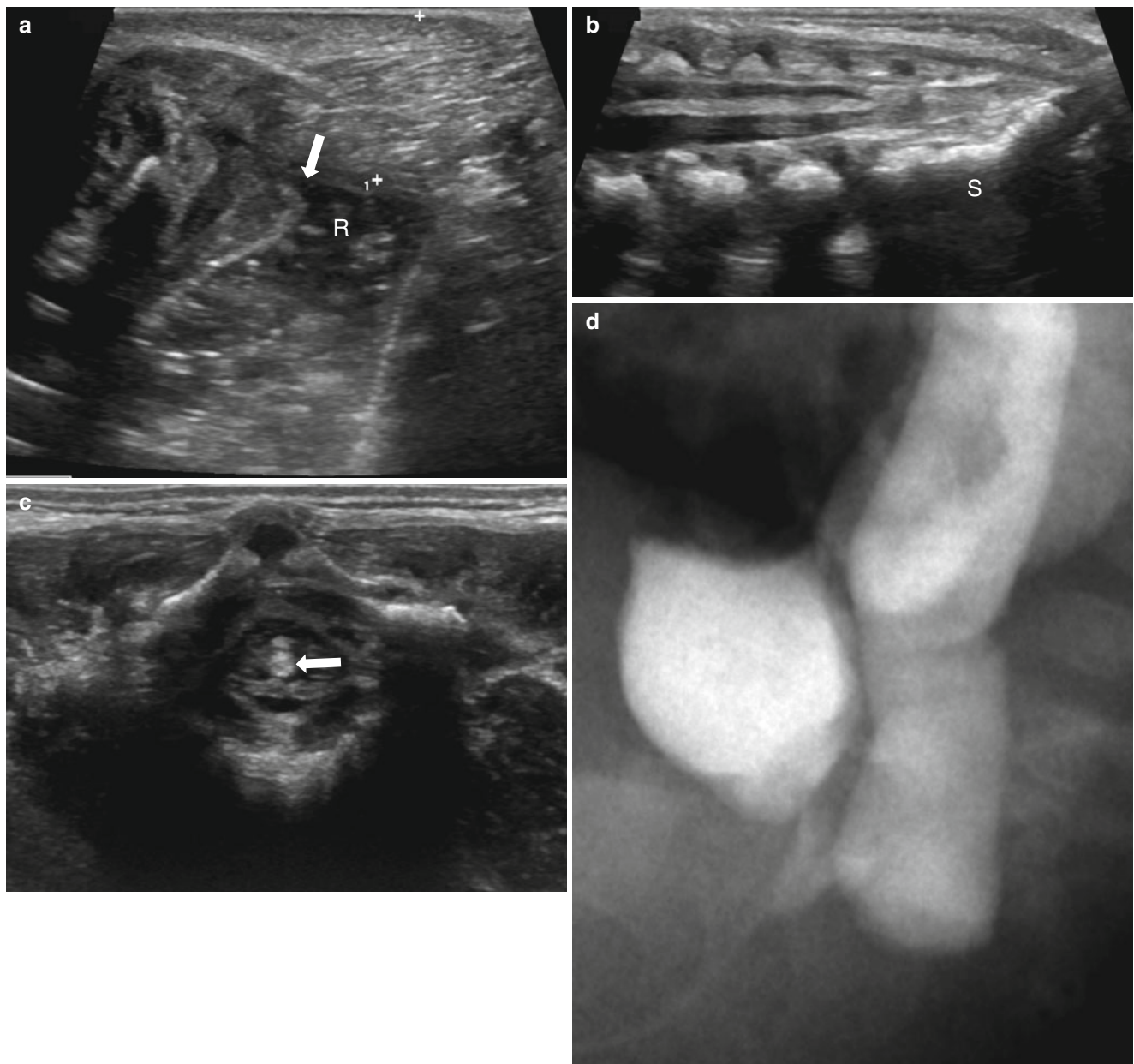


Fig. 19.21 High-type imperforate anus with a rectourethral fistula in a 2-day-old boy, associated with atrial septal defect, ventricular septal defect, and right renal agenesis. (a) Midline sagittal US demonstrates a hypoechoic tract (arrow) extending from the blind-ending rectal pouch (R) into the posterior urethra. The distance(+) between the distal rectal pouch

and perineum is 18mm. Sagittal (b) and transverse (c) US of the lumbosacral region demonstrate a thick, echogenic filum terminale (arrow), and echogenic and distorted contour of the sacral vertebral bodies (S), suggestive of fusion and segmentation anomaly. Image (d) from distal colostogram on 2 weeks of life shows a rectourethral fistula



Fig. 19.22 Currarino syndrome in a 1-day-old neonate with prenatal US diagnosis of sacral anomaly. (a) Abdominal radiograph demonstrates a scimitar sacrum with right-sided sacral bony defect and gaseous dilation of the sigmoid colon. Sagittal T1-weighted (b) and T2-weighted (c) MR images show a retrorectal, presacral mass with

heterogeneous high and low signal intensity lesions representing fatty and calcific components, which was confirmed as a mature teratoma. Note low-lying tethered cord. (d) Barium enema study demonstrates stenosis of the rectum

References

- Al-Salem AH. Intrathoracic gastric volvulus in infancy. *Pediatr Radiol*. 2000;30:842–5.
- Al-Salem AH. Acute and chronic gastric volvulus in infants and children: who should be treated surgically? *Pediatr Surg Int*. 2007;23:1095–9.
- Bender TM, Medine JL, Oh KS. Radiographic manifestations of anomalies of the gastrointestinal tract. *Radiol Clin Nor Am*. 1991;29:335–49.
- Benson JE, Olsen MM, Fletcher BD. A spectrum of bronchopulmonary anomalies associated with tracheoesophageal malformations. *Pediatr Radiol*. 1985;15:377–80.
- Berrocal T, Lamas M, Gutierrez J, et al. Congenital anomalies of the small intestine, colon, and rectum. *Radiographics*. 1999a;19:1219–36.
- Berrocal T, Torres I, Gutierrez J, et al. Congenital anomalies of the upper gastrointestinal tract. *Radiographics*. 1999b;19:855–72.
- Campbell JB. Neonatal gastric volvulus. *AJR Am J Roentgenol*. 1979;132:723–5.
- Chao HC, Kong MS, Chen JY, et al. Sonographic features related to volvulus in neonatal intestinal malrotation. *J Ultrasound Med*. 2000;19:371–6.
- Dalla Vecchia LK, Grosfeld JL, West KW, et al. Intestinal atresia and stenosis: a 25-year experience with 277 cases. *Arch Surg*. 1998;133:490–6.
- Diab N, Daher P, Ghorayeb Z, et al. Congenital esophageal stenosis. *Eur J Pediatr Surg*. 1999;9:177–81.
- Haber HP, Seitz G, Warmann SW, et al. Transperineal sonography for determination of the type of imperforate anus. *AJR Am J Roentgenol*. 2007;189:1525–9.
- Han TI, Kim IO, Kim WS. Imperforate anus: US determination of the type with infracoccygeal approach. *Radiology*. 2003;228:226–9.
- Hernanz-Schulman M. Imaging of neonatal gastrointestinal obstruction. *Radiol Clin North Am*. 1999;37:1163–86, vi–vii.
- Long FR, Kramer SS, Markowitz RI, et al. Radiographic patterns of intestinal malrotation in children. *Radiographics*. 1996;16:547–56. Discussion 556–560.
- McAlister WH, Kronemer KA. Emergency gastrointestinal radiology of the newborn. *Radiol Clin North Am*. 1996;34:819–44.
- Newman B, Bender TM. Esophageal atresia/tracheoesophageal fistula and associated congenital esophageal stenosis. *Pediatr Radiol*. 1997;27:530–4.
- Nievelstein RA, Vos A, Valk J. MR imaging of anorectal malformations and associated anomalies. *Eur Radiol*. 1998;8:573–81.
- Oh SK, Han BK, Levin TL, et al. Gastric volvulus in children: the twists and turns of an unusual entity. *Pediatr Radiol*. 2008;38:297–304.
- Pfluger T, Czekalla R, Koletzko S et al. MRI and radiographic findings in Currarino's triad. *Pediatr Radiol* 1996;26:524–7.
- Pracros JP, Sann L, Genin G, et al. Ultrasound diagnosis of midgut volvulus: the “whirlpool” sign. *Pediatr Radiol*. 1992;22:18–20.
- Rao P. Neonatal gastrointestinal imaging. *Eur J Radiol*. 2006;60:171–86.
- Shimanuki Y, Aihara T, Takano H, et al. Clockwise whirlpool sign at color Doppler US: an objective and definite sign of midgut volvulus. *Radiology*. 1996;199:261–4.
- Siegel MJ. *Pediatric sonography*. Philadelphia: Lippincott, Williams & Wilkins; 2010.

So-Young Yoo

Contents

20.1	Introduction	630
20.2	Imaging	630
20.3	Spectrum of Gastrointestinal Disorders	630
20.3.1	Hypertrophic Pyloric Stenosis	630
20.3.2	Necrotizing Enterocolitis	631
20.3.3	Intussusception	631
20.3.4	Duplication Cyst	632
20.3.5	Meckel's Diverticulum	633
20.3.6	Appendicitis	633
20.3.7	Henoch-Schönlein Purpura	634
20.3.8	Hirschsprung Disease	634
20.4	Illustrations: Non-neonatal Gastrointestinal Diseases	636
20.4.1	Hypertrophic Pyloric Stenosis	636
20.4.2	Pyloric Spasm	638
20.4.3	Necrotizing Enterocolitis	639
20.4.4	Intussusception	642
20.4.5	Duplication Cyst	646
20.4.6	Meckel's Diverticulum	649
20.4.7	Appendicitis	653
20.4.8	Henoch-Schönlein Purpura	657
20.4.9	Hirschsprung Disease	659
20.4.10	Allergic Proctocolitis	662
	References	663

S.-Y. Yoo, M.D., MPH
Department of Radiology, Samsung Medical Center,
Sungkyunkwan University School of Medicine,
50, Ilwon-dong, Kangnam-gu, Seoul 135-710, Korea
e-mail: somatom25@hanmail.net

20.1 Introduction

Although a variety of diseases, including medical and surgical conditions, can be encountered in the gastrointestinal tracts of children, the focus in this chapter will be on acute pediatric abdominal disorders in which imaging is primarily used for diagnosis. In many infants and children with suspected acute abdomen, US is the only imaging modality that may be required. The imaging examination should be tailored to look for common causes of gastrointestinal diseases based on the patient's age and presenting symptoms and signs. Abdominal radiographs are helpful primarily if small-bowel obstruction or perforation is suspected. CT is especially useful for evaluating complications of appendicitis and bowel obstruction complicated by ischemia in older children. More commonly presented medical conditions, including gastroenteritis and mesenteric lymphadenitis, which are out of the scope of this review, must be differentiated from surgical acute abdomen.

20.2 Imaging

Radiography is often the initial imaging investigation, particularly when bowel obstruction or perforation is suspected. Erect or lateral decubitus view may be needed to demonstrate free air and air-fluid levels. When compared with the neonatal period, radiography has less diagnostic accuracy for common gastrointestinal disorders such as appendicitis and intussusception. Because abdominal symptoms can be referred from thoracic pathologies that include pneumonia or pleural effusion, attention should also be paid to the covered chest when interpreting abdominal radiographs.

US plays a pivotal role in investigating pediatric abdomen with its superb advantages including no radiation hazard, no need for sedation, easy availability, and high resolution. It often allows prompt and exact diagnosis to be made in common causes of pediatric acute abdomen, such as intussusception, hypertrophic pyloric stenosis, and appendicitis, without need for further investigation. Furthermore, as a real-time exam, it allows the dynamic assessment of bowel peristalsis and compressibility as well as a focused scan where localized pain is present. To obtain diagnostic images of the gastrointestinal tract, US requires a meticulous technique including graded compression to overcome gas. The visualization of the bowel is improved by the use of a high-frequency linear transducer. To calm down an irritable infant, a feeding bottle or pacifier should be handy.

Although the use of CT has risen dramatically over the past two decades, children are particularly at risk for the adverse effects of ionizing radiation, and even low-dose radiation is involved in a small but significant increase over the lifetime risk of cancer. Therefore, CT should be reserved for the cases

in which US reveals an equivocal finding in a clinical setting of acute abdomen or is inadequately performed due to either the patient's factors, such as bowel gas and obesity, or the examiner's inexperience.

20.3 Spectrum of Gastrointestinal Disorders

20.3.1 Hypertrophic Pyloric Stenosis

Hypertrophic pyloric stenosis (HPS) is the most common cause of gastric outlet obstruction in young infancy, characterized by idiopathic hypertrophy of the circular muscle of the pylorus. The incidence varies according to regions, with a frequency of approximately 1.5–4 cases per 1,000 live births in the United States. There is a male preponderance with a ratio of 4:1 (Hernanz-Schulman 2003). Although the etiology remains unclear, a combination of hereditary and environmental factors has been implicated in its pathogenesis. Environmental factors include hypergastrinemia, abnormal innervation of myenteric plexus, cow's milk allergy, and exposure to erythromycin (Hernanz-Schulman 2003). HPS is usually presented with non-bilious, projectile vomiting in young infants between 2 weeks and 3 months of age.

Typically, the radiograph shows a gaseous distension of the stomach with paucity of distal bowel gas. The stomach may demonstrate increased peristaltic waves ("caterpillar sign") (Fig. 20.1). US has become the imaging modality of choice for the diagnosis of HPS, and it should be performed properly with high-frequency linear transducers. Examining the pylorus can be difficult if the stomach is empty. In that case, by putting the infant in a right posterior oblique position, allowing the antrum to be distended with fluid by gravity, the pylorus can be better visualized. If it is not effective, the stomach can be filled with water by bottle feeding or via nasogastric tube (Fig. 20.2). The hypertrophied pyloric muscle appears as a thick, echolucent ring (target or bull's eye appearance) with central echoes representing the convoluted, compressed mucosa on axial view (Figs. 20.1 and 20.2). US criteria varies by authors, but commonly accepted values are single pyloric muscle thickness ≥ 4 mm, and pyloric canal length ≥ 16 mm. Failure of the pyloric opening and little drainage into the duodenum can be seen in real-time as well as prominent gastric peristalsis. An overfilled stomach with a posteriorly oriented antrum can lead to a false-negative diagnosis (Blumhagen et al. 1988; Hernanz-Schulman 2003). With borderline measurement that does not meet the strict criteria for HPS, close clinical follow-up and repeat imaging is important in establishing the diagnosis. Pyloric spasm, which can mimic HPS radiologically and clinically, shows a lesser degree of thickening of the pyloric muscle (less than 3 mm) with change in the appearance of the pyloric canal,

accompanied by the intermittent drain of fluid into the duodenum (Hernanz-Schulman 2003) (Fig. 20.4). When diagnosis of IHP is not certain on US, and other anomalies are concerned, an upper gastrointestinal series (UGIS) is indicated. On UGIS, HPS typically demonstrates the elongated, narrowed pyloric canal (string sign) with a tram-track appearance due to the folding of the compressed mucosa. Shoulder sign is also noted, caused by impression of the hypertrophied muscle on the antrum or duodenal bulb (Fig. 20.3).

20.3.2 Necrotizing Enterocolitis

Necrotizing enterocolitis (NEC) is a severe intestinal inflammatory process of the gastrointestinal tract in neonates and infants associated with significant morbidity and mortality. It is one of the most common causes of surgical intervention in the premature infant. It is believed to develop secondary to a combination of multiple factors including hypoxia, infection, intensive treatment, hyperosmolar and enteric feeds, decreased gut motility, and the poor immune response of the premature infant, leading to the breakdown of the intestinal mucosal barrier followed by penetrating bacterial infection, enteric ischemia, and, finally, necrosis. Although the vast majority of cases of NEC occur in premature infants, it can also affect term babies with underlying conditions that predispose to bowel ischemia, including congenital heart disease, sepsis, or bowel obstruction. Pathologically, inflammation of the intestine begins in the mucosa and submucosa, extending transmurally (Epelman et al. 2007).

Clinical presentation is varied and often nonspecific; symptoms include abdominal distension, feeding intolerance, vomiting, bile-stained aspirates, diarrhea, and bloody stools. Neonates with severe disease may even present with shock. Mortality rate in untreated cases is high, ranging from 20–40 %; thus, early detection and prompt therapy, including bowel rest, antibiotics, and adequate hydration are essential to limit the progression and development of complications such as perforation and peritonitis (Epelman et al. 2007).

Abdominal radiography is the standard imaging modality for confirmation of suspected cases, monitoring of disease progression and surveillance for complications of NEC. In the early stages, NEC demonstrates nonspecific gaseous distension. With loss of the normal symmetric pattern of bowel gas with focal dilatation or separated bowels with a thickened wall, suspicion of NEC can be made in the appropriate clinical setting. On follow-up radiographs, fixed bowel loops with little change in the appearance of the dilated loops are a suggestive finding of NEC (Weinstein 1986). Definite diagnosis can be made with pneumatosis intestinalis, which is thought to be due to mucosal perforation secondary to ischemia with subsequent dissection of air into the bowel wall, production of intramural air by gas-forming organisms, or

both. It appears as bubbly or linear hyperlucency along the bowel wall, most commonly in the distal ileum and proximal colon. The bubbly pattern of mural gas may be difficult to differentiate from meconium mixed with air, although a bubbly stool pattern is rare within the first few weeks of life. Portal venous gas can be present, manifested as branching hyperlucencies over the liver. Portal venous gas must be differentiated from gas in the biliary tree, which is more centrally located in the larger ducts, contrary to portal venous gas, which may extend more peripherally (Fig. 20.5). In advanced NEC, pneumoperitoneum can be complicated due to bowel perforation requiring surgical intervention. In the supine position, large free intraperitoneal air appears as overall increased lucency with outlining the peritoneal cavity and the diaphragm, giving rise to the “football” sign. With intraperitoneal air, both sides of the bowel wall can be visualized (Rigler sign) as well as the falciform ligament (Fig. 20.6). A cross-table lateral view is very useful for detecting small amounts of free gas that manifest as hyperlucencies just beneath the abdominal wall or anterior to the liver (Seibert and Parvey 1977) (Fig. 20.7).

US with Doppler can be used to assess the suspected NEC for evaluation of bowel wall thickness and vascularity, presence of ascites, or free air and perfusion of superior mesenteric artery. By direct visualization of the bowel wall, including wall thickness, echogenicity, and peristalsis as well as perfusion, US is helpful not only in confirming or excluding the diagnosis of NEC but also in the early detection of ischemic or necrotic bowel before perforation occurs. Furthermore, perforation may be associated with complicated ascites, which appear as intraperitoneal fluid with low-level echoes or septations in the absence of free gas on radiography (Merritt et al. 1984; Vernacchia et al. 1985; Patel et al. 1990; Bomelburg and von Lengerke 1992; Faingold et al. 2005; Kim et al. 2005; Epelman et al. 2007). Pneumatosis intestinalis is seen as echogenic foci within the bowel wall and portal vein gas as intravenous moving echogenic foci with a spiky Doppler pattern and audible crackle (Merritt et al. 1984; Vernacchia et al. 1985). US can also detect even a small amount of free air as hyperechoic foci with shadowing either between the anterior surface of the liver and the abdominal wall or between the bowel loops (Figs. 20.7 and 20.8).

20.3.3 Intussusception

Intussusception is the most common cause of acute abdomen in early childhood. As proximal bowel (intussusceptum, entering loop) invaginates or telescopes into the more distal bowel (intussusciens, receiving loop), obstruction can develop, eventually followed by ischemia and infarction of bowel if untreated. Most intussusceptions are idiopathic,

related with lymphoid hyperplasia in the terminal ileum or mesenteric lymphadenopathy with a preceding history of viral infection. Underlying pathologic leading points including duplication cyst, Meckel's diverticulum, Henoch-Schönlein purpura, polyp, or lymphoma, although rare, are present in approximately 5 % of children, usually outside of the typical age range (3 months–3 years) of idiopathic intussusception (Fig. 20.10). Asymptomatic and transient intussusception involving only the small bowel can be seen when evaluating the abdomen for other indications, which usually require no treatment.

Clinical presentation is characterized by the clinical triad of intermittent colicky pain, palpable abdominal mass, and bloody (currant jelly) stools. Most intussusceptions are of the ileocolic type with, less commonly, ileoileal and ileoileocolic. With delayed diagnosis, it may lead to bowel necrosis and perforation.

An abdominal radiograph has low sensitivity for the detection of intussusception but is used for the detection of free peritoneal air. The presence of a crescent of air with soft tissue mass in the colon is a pathognomic radiographic finding of intussusception. More commonly, it may show a paucity of bowel gas in the right abdomen with non-visualization of air-filled cecum (Hernandez et al. 2004) (Fig. 20.9).

US has been the imaging modality of choice for diagnosing intussusception. High-frequency linear array transducers (5–12 MHz) should be used for optimal visualization of the bowel. On the transverse scan, it characteristically appears as the target or donut with the alternating concentric hypoechoic and echogenic layers, while on the longitudinal scan, a bowel-within-bowel appearance – that is, a “sandwich” or “pseudokidney” sign (Fig. 20.9). In addition, color Doppler US can be used to assess the presence of bowel ischemia. As the lack of color flow within the intussusception bowel and the presence of entrapped fluid are reported to be associated with a decreased probability of successful enema reduction, reduction should be made with more caution and gentle attempts in children with these US findings (Lim et al. 1994). The duration of symptoms is also an important factor that predicts the irreducibility (Fig. 20.11). An enema reduction by hydrostatic or air reduction under fluoroscopic or sonographic guidance has been the initial treatment of choice for symptomatic intussusception with an approximately 80–95 % success rate. Before enema reduction, all patients should have surgical consultation and be hydrated adequately with IV fluid. Contraindication of enema reduction includes peritonitis, pneumoperitoneum, and shock. Air reduction has been preferred to liquid enema because it is quick and lacks peritoneal contamination if perforation occurs. For air reduction, an adequate anal sealing is important to maintain intracolonic pressure, and the maximum pressure should be 120 mm Hg at rest. Successful reduction is defined as reflux of air into the terminal ileum and

disappearance of the soft tissue mass by intussusceptum. An edematous ileocecal valve can occasionally look like a residual intussusceptum, appearing as a soft tissue density along the medial side of the cecum with failure of air reflux into the terminal ileum (Fig. 20.12). In these circumstances, close clinical monitoring with repeat US if necessary, can help confirm complete reduction of intussusception (Peh et al. 1999). Recently, delayed repeated reduction following failure of the initial attempt has been recommended when the initial reduction moves the intussusception and the patient's condition is stable (Navarro et al. 2004). It is reported that with this approach, the success rate of reduction increases, allowing congestion and swelling to subside, facilitating the subsequent reduction attempt. During air reduction, bowel perforation can occur with a mean reported rate of 0.8 %. It may be followed by tension pneumoperitoneum, a potentially life-threatening complication that must be managed emergently by needle aspiration and prompt referral to surgery.

US-guided hydrostatic reduction, which has advantages in avoiding radiation exposure and identifying leading point and residual intussusception, is an alternative to fluoroscopic reduction and has been reported with good results. The instilled fluid and the retrograde movement of the intussusceptum are followed through the large bowel until disappearance of the intussusceptum and flow of fluid into the terminal ileum. About 10 % of intussusception is reported to recur following enema reduction. Repeat enema is both safe and effective in recurrent intussusception.

20.3.4 Duplication Cyst

Duplication cysts are uncommon congenital abnormalities that can occur anywhere in the gastrointestinal tract, most commonly in the distal ileum, followed by the esophagus, stomach, duodenum, and colon. There are several theories that explain their etiology, including persistent embryonic diverticulum, aberrant recanalization of the gut lumen, partial twinning, and hypoxic or vascular occlusive events. They are located on the mesenteric aspect of the gastrointestinal tract and share a common muscular wall and blood supply with the adjacent bowel but have a separate mucosal lining, with or without ectopic tissue, such as gastric mucosa or pancreatic tissue, which can lead to ulceration, bleeding, or transmural erosion and perforation. They are usually non-communicating with the enteric lumen.

Symptoms that include abdominal pain or distension develop with small-bowel obstruction complicated by volvulus or intussusceptions, especially when it is located in the ileum or near the ileocecal valve. On US, it typically manifests as a spherical or tubular, fluid-filled mass with the inner hyperechoic mucosa and outer hypoechoic muscle layer, which is known as a “double wall” or “gut signature” sign

(Figs. 20.13 and 20.14). The inner mucosal layer can be absent in some cases due to ulceration by gastric enzymes. Cysts appear anechoic or hypoechoic or complex secondary to hemorrhage or debris, and the shape may change with peristalsis (Kangaroo et al. 1979; Cheng et al. 2005) (Fig. 20.15). Infected duplication cysts may not show the characteristic double wall due to ulceration or erosion of the inner mucosa (Cheng et al. 2005). CT and MR imaging can be used in cases where the US findings are inconclusive. They appear as smoothly rounded, fluid-filled cysts or tubular structures with thin, slightly enhancing walls located in or adjacent to the wall of the GI tract.

Sonographic mimics of duplication cysts include torsion of an ovarian cyst (Fig. 20.16), cystic ovarian tumors, Meckel's diverticulum, mesenteric and omental cysts, and pancreatic pseudocysts (Godfrey et al. 1998).

20.3.5 Meckel's Diverticulum

Meckel's diverticulum, which occurs in 2–3 % of the population, results from the failure of involution of the omphalomesenteric duct. Occurring on the antimesenteric border of the distal ileum within 2 ft of the ileocecal valve, Meckel's diverticulum is a true diverticulum, composed of all layers of the intestinal wall, and it is lined by normal small intestinal mucosa. It frequently contains heterotopic gastric or pancreatic mucosa (Levy and Hobbs 2004).

Although it is usually asymptomatic, it becomes symptomatic with complications such as bleeding, small-bowel obstruction, and inflammation. Hemorrhage is the most frequent complication in the pediatric population, and it is almost always associated with ulceration from heterotopic gastric mucosa located within the diverticulum. Intestinal obstruction, the second most common complication, can occur in patients with Meckel's diverticulum by intussusception, obstruction from an inverted diverticulum or diverticulitis, and volvulus or internal hernia from an omphalomesenteric band or adhesion. If the typical appearance of an inverted Meckel's diverticulum is identified in the core of the intussusception, the diagnosis of Meckel's diverticulum can be made. Often, the Meckel's diverticulum cannot be identified within the intussusception on CT, and, furthermore, inverted diverticulum as a leading point can be seen as a fatty mass within the intussusceptum (Olson et al. 2009) (Fig. 20.19).

On high-resolution US, it may appear as a fluid-filled structure with the typical gut signature in the right lower quadrant and shows a connection to small-bowel loop (Fig. 20.17). Depending on the presence of complication, such as hemorrhage or inflammation, Meckel's diverticulum can be seen as a complex mass with or without small-bowel obstruction (Baldissarro et al. 2003; Thurley et al. 2009) (Fig. 20.18).

A radionuclide Meckel scan that is based on uptake of Tc-99 m pertechnetate by ectopic gastric mucosa within the omphalomesenteric duct remnant remains a useful tool for diagnosing a clinically suspected Meckel's diverticulum with a sensitivity of 85–90 % (Fig. 20.20). However, it can be falsely negative in a Meckel's diverticulum without ectopic gastric mucosa.

20.3.6 Appendicitis

Acute appendicitis is the most common condition requiring emergent abdominal surgery in childhood, with the peak at 10–19 years of age. It is caused by an obstruction of the appendix by feces or appendicolith, followed by distension, ischemia, and secondary bacterial infection with ultimate appendiceal infarction, perforation, and peritonitis if untreated.

Clinical presentation is typical with abdominal pain that is localized in the right lower quadrant in older children, accompanied with tenderness, fever, and leukocytosis. The diagnosis can often be made on the basis of a physical examination and elevated white blood cell count. However, in younger children where the condition is rare and symptoms are nonspecific, diagnostic delay is frequent with peritonitis and abscess formation more common (Sivit et al. 2001).

Abdominal radiograph, which has limited value in diagnosing appendicitis, may demonstrate ileus, often localized in the right lower quadrant, with or without visualized appendicolith but, more commonly, that appears normal or gasless due to vomiting.

US has been the primary imaging modality for diagnosing appendicitis in children with clinically equivocal findings. It also aids in the diagnosis of other conditions such as gynecologic disorders that simulate appendicitis clinically. US should be performed using linear high-frequency transducers with a graded compression technique. The inflamed appendix appears as a noncompressible, tubular, blind-ended structure with an outer wall diameter greater than 6 mm. An appendicolith, a highly echogenic focus with posterior shadowing, can be seen within the dilated appendix. Ancillary findings include periappendiceal fluid, localized ileus, increased pericecal echogenicity, and enlarged mesenteric lymph nodes (Abu-Yousef et al. 1987). Color Doppler US demonstrates increased color flow in the inflamed appendiceal wall (Quillin and Siegel 1992) (Fig. 20.21). If perforation occurs, a complex mass or localized fluid collection with fatty infiltration in the pericecal area can be seen with either a dilated or a relatively decompressed appendix (Fig. 20.22). Following abscess can be localized in the right lower quadrant or can extend deep into the pelvic cavity or subhepatic area. Pitfalls in US diagnosis of appendicitis are focal appendicitis localized at the tip or distal end, retrocecal

appendicitis (Fig. 20.24c), and perforated appendicitis. Care should be taken to examine the entire length of the appendix and not to miss distal or tip appendicitis.

CT, with its high sensitivity and specificity in diagnosing appendicitis, is useful in children with large habitus in whom evaluation with US is difficult, as well as in patients with equivocal US findings. CT also has advantages over US in evaluating perforated appendicitis and complications including abscess and peritonitis (Sivit and Applegate 2003; Strouse 2010) (Fig. 20.23). With an increasing concern for radiation hazard in children, the debate remains about primary imaging modality (CT vs. US), CT protocol, and technical factors (e.g., standard CT with or without intravenous and oral contrast, or a focused appendiceal CT with or without rectal contrast) for pediatric appendicitis. Although policies may differ depending on the institutions, CT appears to be the preferred imaging tool where trained radiologists or sonographers are not readily available. When CT is considered for children with suspected appendicitis, efforts for dose reduction should be made to minimize the radiation hazard. CT features of acute appendicitis include a distended appendix (≥ 6 mm in maximal diameter), appendiceal wall thickening with enhancement, and an appendicolith. Cecal thickening, pericecal fatty infiltration, free peritoneal fluid, mesenteric lymphadenopathy, or abscess can be associated. Alternative diagnoses mimicking appendicitis include terminal ileitis or enterocolitis of infectious or inflammatory (e.g., Crohn's disease) origin, mesenteric lymphadenitis, ureteral stone and tubo-ovarian abscess, or torsion.

20.3.7 Henoch-Schönlein Purpura

Henoch-Schönlein purpura (HSP), an acute, self-limited, small-vessel vasculitis, typically affects skin, joints, the gastrointestinal tract, and the kidneys, primarily in children. It is the most common pediatric systemic vasculitis with the peak at age at 5, and the male-to-female ratio 2:1. Although IgA appears to play a role in the immunopathogenesis of HSP, the exact causes remain unknown. Presentation is characterized by cutaneous purpura, arthritis, abdominal pain or gastrointestinal bleeding, and renal involvement. The gastrointestinal tract is commonly involved with varying degrees, from mild symptoms to complications such as intussusception, obstruction, and perforation. Proximal and mid-small bowel is commonly affected and intussusception may be present. In HSP, bowels are affected by submucosal or mural edema and hemorrhage and subsequent thrombosis of the small vessels. Gastrointestinal presentations may precede the other symptoms in 14–36 % of the patients, which makes the diagnosis difficult and may lead to unnecessary laparotomy. US, as a first-line imaging tool for acute abdominal symptoms, is important for the detection of intussusception

or bowel wall thickening, and may sometimes suggest a correct diagnosis in clinically unsuspected cases. On US, intramural hematoma appears as focal areas of wall thickening, which can be multifocal or complicated by intussusception (Connolly and O'Halpin 1994; Ozdemir et al. 1995) (Figs. 20.25 and 20.26). Renal involvement, which occurs in half the cases, can be seen as renal swelling with increased echogenicity (Fig. 20.25c). On small-bowel series, a “stack of coins” or thumbprinting appearance by intramural hemorrhage and/or edema is seen (Fig. 20.26c).

20.3.8 Hirschsprung Disease

Hirschsprung disease, also called colonic aganglionosis or congenital megacolon, results from the absence of normal ganglion cells in the intramuscular and submucosal plexuses due to the arrest of caudal migration of neural crest cells, leading to a functional obstruction. It has a male predominance with a male-to-female ratio of 4:1. Short segmental involvement of aganglionosis is the most common type, accounting for 80–90 % of the cases involving the distal sigmoid and rectum. The remaining cases include long segmental diseases such as total colonic aganglionosis (with variable involvement of the small bowel) and an ultrashort segment type limited to the internal anal sphincter. It can be associated with Down syndrome, intestinal atresia, malrotation, central hypoventilation, and neurocristopathy (Haddad syndrome) (Fig. 20.29). During the neonatal period, it can typically present with abdominal distension, vomiting, and failure to pass meconium. Sometimes presentation can be atypical, with diarrhea. Later on, it usually presents with chronic constipation with or without complications, including severe enterocolitis, perforation with peritonitis, and failure to thrive.

Abdominal radiographs show marked colonic dilatation with absent rectal gas in classic cases, or low gastrointestinal obstruction shortly after birth. Contrast enema using water-soluble contrast or barium is the imaging investigation of choice by demonstrating the transition zone, which is the junction between the distal aganglionic segment and the dilated proximal colon. Typical findings of Hirschsprung disease on contrast enema include a small, irregular rectum; reversed rectosigmoid index (R/S ratio < 1); the presence of the transition zone; and retention of contrast for over 24 h (Figs. 20.27 and 20.28). Thickening and nodularity of the colonic mucosa with cobblestone pattern also can be noted proximal to the transition zone (Fig. 20.28b). Prior to the enema, any manipulation, including digital examination or a cleansing enema should be avoided so as not to irritate the rectum. During the enema, a soft catheter without an inflating balloon should be used with the tip placed just proximal to the anus and introducing contrast in a slow and gentle

manner to prevent an obscured transition zone in a lateral position. Care should be taken not to overfill the rectum and sigmoid colon and to fill the colon only as far as the transition zone is encountered. Lateral and anteroposterior views of the rectosigmoid colon during early filling are critical. A characteristic transition zone may not always be demonstrated, but the aganglionic segment may show abnormal contractions and appear corrugated or serrated. In the neonatal period, classic findings of a contrast enema can be absent and the rectum may appear normal, making diagnosis difficult. Delayed radiographs can be helpful and, in some cases, may show a more obvious transition zone than immediate radiograph shows. Total colonic aganglionosis can also pose a diagnostic difficulty in that the colon may appear normal or somewhat shorter than normal with decreased redundancy

(the so-called “question mark colon”) on the contrast enema. In some cases, the microcolon can be seen (Fig. 20.30). The enema is also nondiagnostic in the ultrashort disease. In the suspected cases, a definite diagnosis should be made by suction or full-thickness biopsy of the rectum. Manometry can also be used in equivocal cases (O’Donovan et al. 1996; Reid et al. 2000).

Allergic proctocolitis caused by cows’ milk protein allergy can simulate Hirschsprung disease on a contrast enema by revealing irregular narrowing of the rectum with the transition zone (Fig. 20.31). With the appropriate clinical setting including eosinophilia and improvement after the elimination of cows’ milk, differentiation from Hirschsprung disease can be made, although in some cases rectal biopsy is eventually needed for confirmation (Bloom et al. 1999).

20.4 Illustrations: Non-neonatal Gastrointestinal Diseases

20.4.1 Hypertrophic Pyloric Stenosis

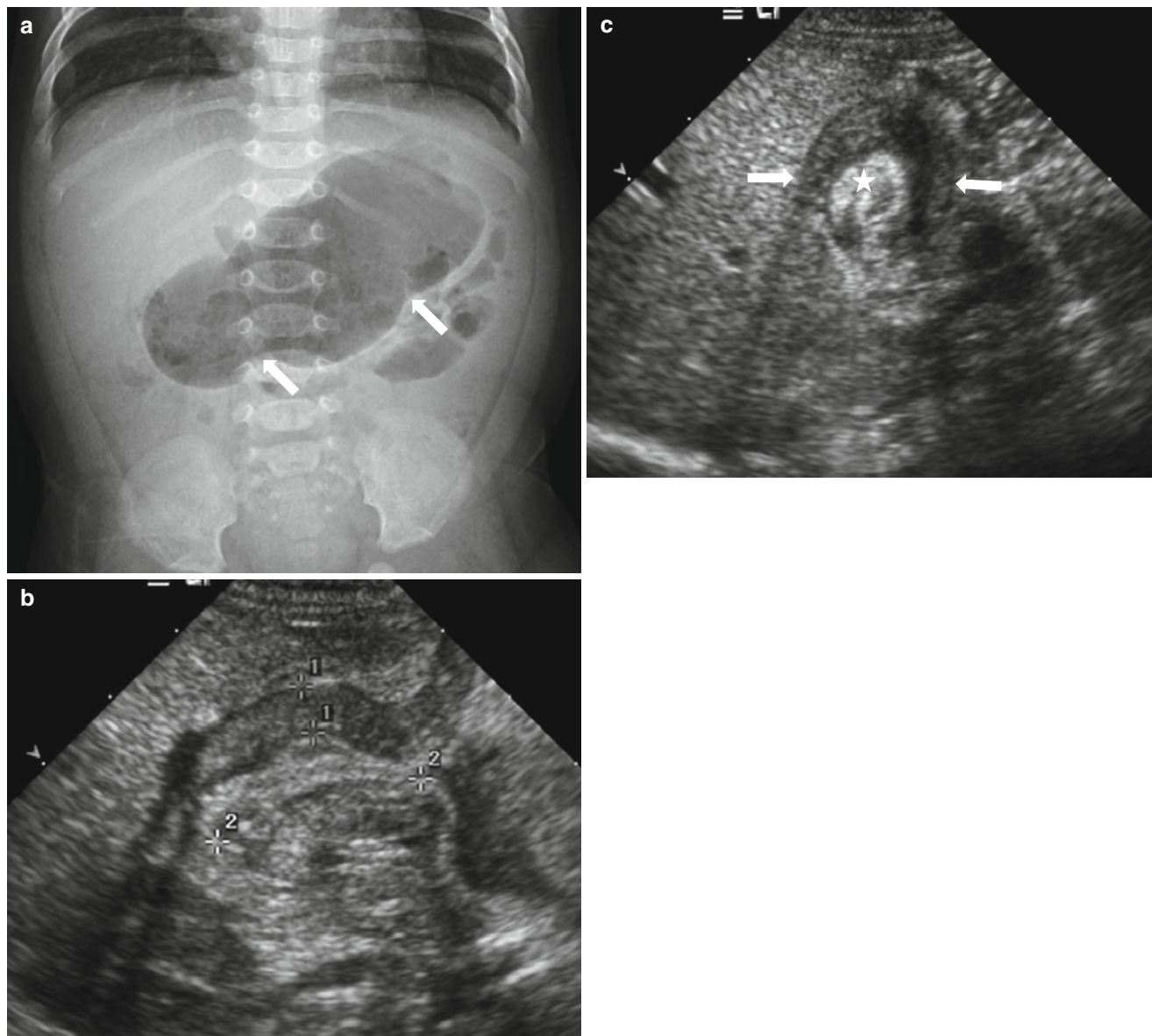


Fig. 20.1 Hypertrophic pyloric stenosis in an 8-week-old infant with vomiting. (a) Supine abdominal radiograph shows gaseous distension of the stomach with prominent peristaltic waves (arrows), called “caterpillar sign.” There is a paucity of distal bowel gas. (b, c) US images in longitudinal and transverse scan of the pylorus demonstrate

thickened elongation of the hypoechoic pyloric muscle (arrows) measured 5 mm in thickness (*cursor #1*) and 22 mm in length (*cursor #2*). Transverse scan shows a typical donut appearance of the thickened pylorus (arrows) with central increased echogenicity (asterisk) representing a crowded mucosa

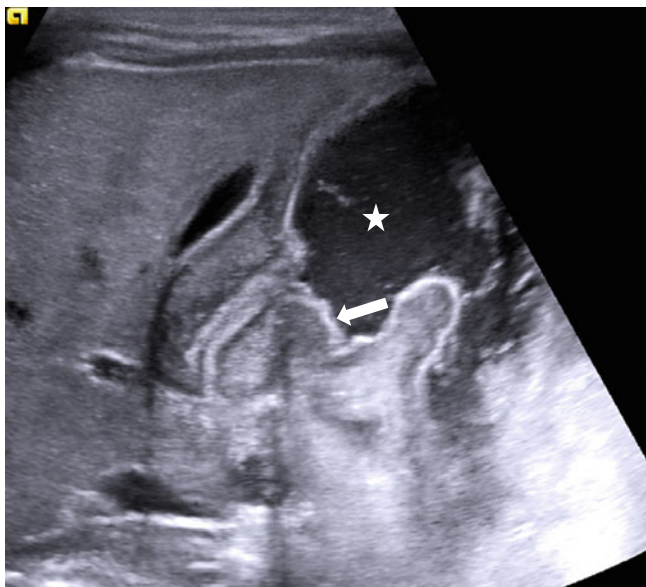


Fig. 20.2 Hypertrophic pyloric stenosis: US with fluid filling of the stomach. Longitudinal image of the pylorus after filling the stomach with fluid (*asterisk*) demonstrates fixed elongation of the pyloric canal with thickening of the muscle. Note shouldering (*arrow*) of the thickened pylorus and protrusion of the echogenic mucosa into the fluid-filled antrum

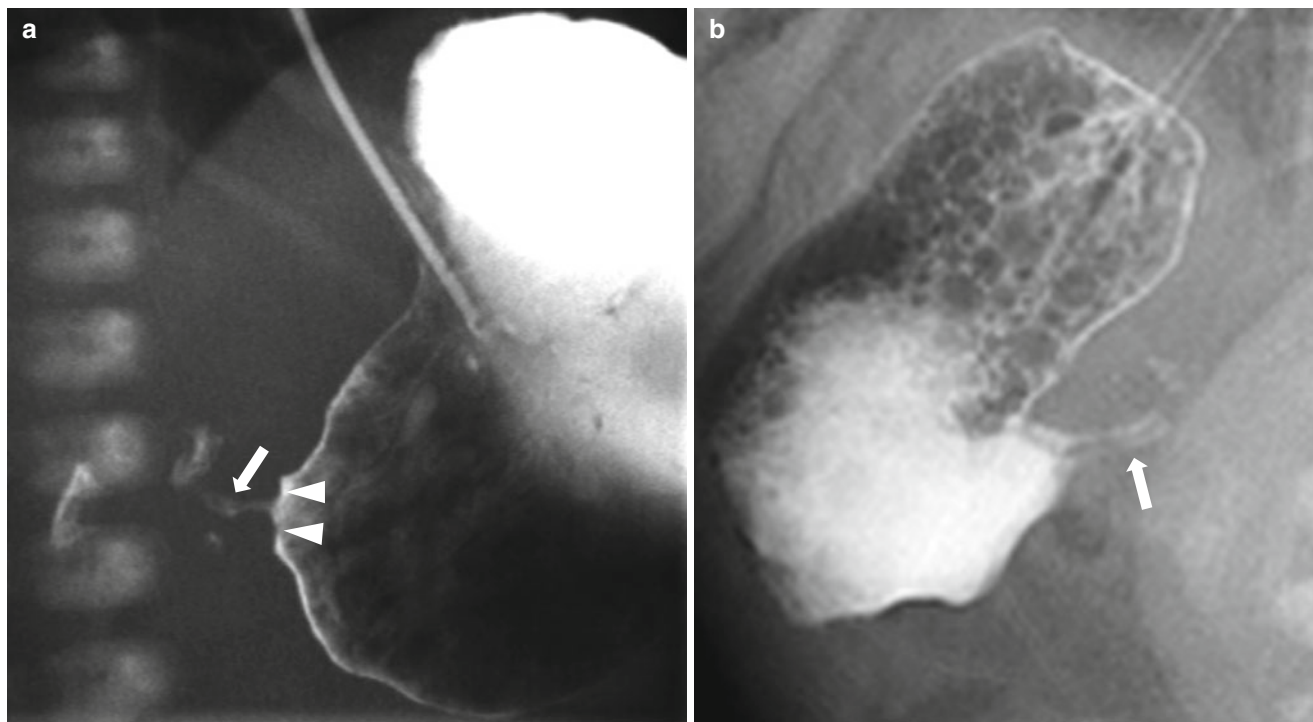


Fig. 20.3 Hypertrophic pyloric stenosis: barium study. (a) Upper GI series shows the elongated and narrowed pyloric canal (*arrows*) with impression on the antrum producing the shoulder sign (*arrowhead*). (b) In another patient, an oblique view of upper GI series shows two

parallel streaks (*arrows*) of contrast within the elongated pylorus, called a “double track” sign, representing trapped fluid between thickened folds of the pylorus

20.4.2 Pyloric Spasm

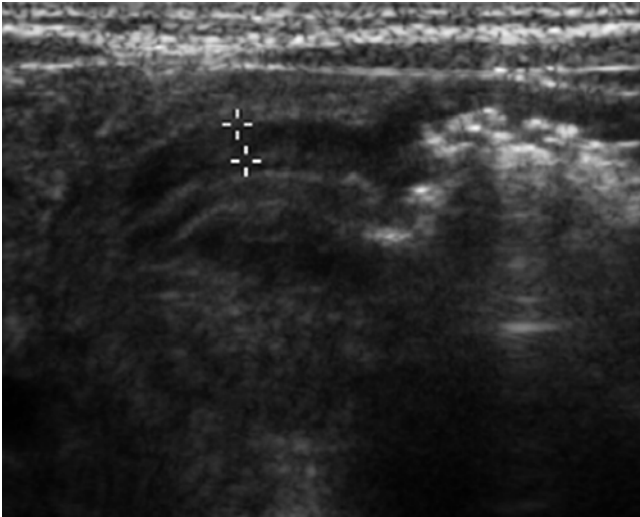


Fig. 20.4 Pyloric spasm in a 3-week-old infant with vomiting. Longitudinal US image of the pylorus shows mild thickening of the pyloric muscle, measured 2 mm in thickness (*cursor*), which does not meet the criteria for HPS. During the examination, appearance of the pyloric canal changed with the passage of fluid through the pylorus (not seen here)

20.4.3 Necrotizing Enterocolitis



Fig. 20.5 Portal vein gas and pneumatosis intestinalis in necrotizing enterocolitis. Supine radiograph in a premature baby shows portal vein gases (*arrowheads*) which appear as branching hyperlucencies within the liver. Extensive pneumatosis intestinalis seen as curvilinear or bubble-like hyperlucencies along the bowel loops is also noted in both sides of the abdomen as well as generalized distension of the bowels

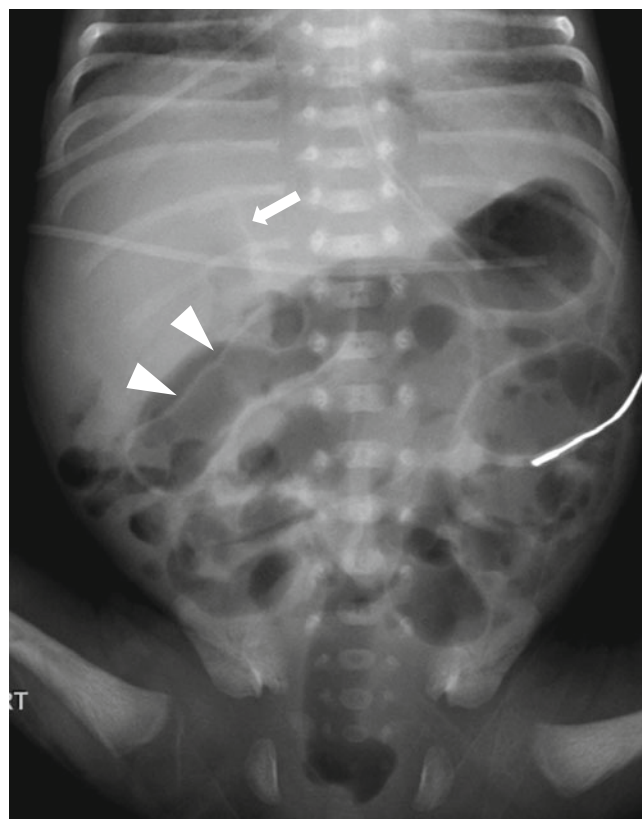


Fig. 20.6 Pneumoperitoneum in necrotizing enterocolitis. Supine radiograph in a premature baby demonstrates hyperlucency in upper abdomen with visualization of falciform ligament (*arrow*), indicating presence of intraperitoneal free air. The free air also outlines the outer wall of the bowel (*arrowheads*), which is called as Rigler sign. There is moderate diffuse enteric distension with gas

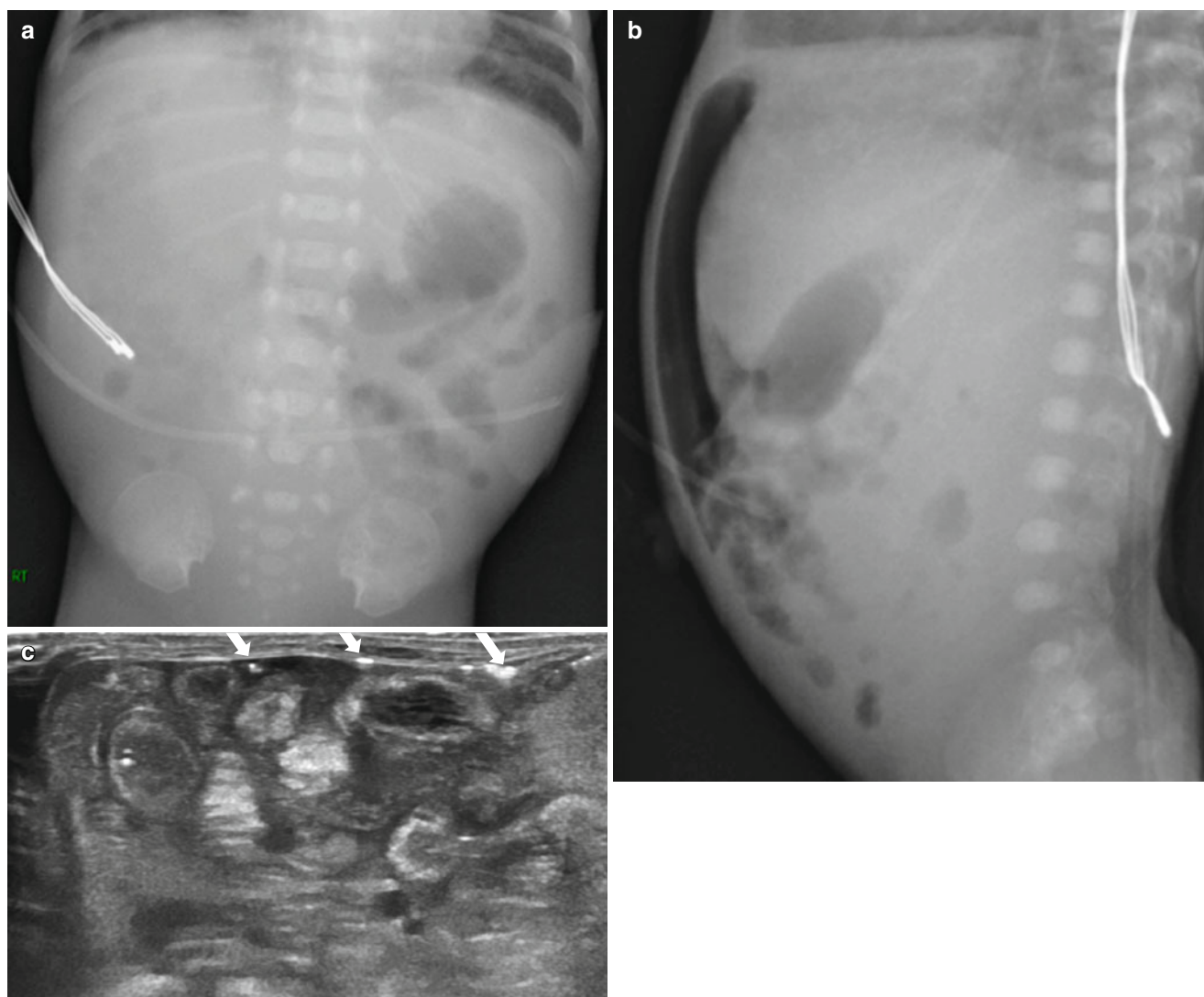


Fig. 20.7 Advanced necrotizing enterocolitis. (a) Supine radiograph shows abdominal distension and markedly asymmetric bowel gas pattern with paucity of bowel gas in right side. Hyperlucent area is noted in right upper quadrant, representing pneumoperitoneum. (b) Cross-table lateral view confirms presence of intraperitoneal free air anteriorly.

(c) US demonstrates echogenic bowel walls with complicated ascites. Free gases are seen as multifocal hyperechoic speckles (*arrows*) within the peritoneal fluid and beneath the abdominal walls. On surgery, necrosis with multiple perforations of the ileum was confirmed

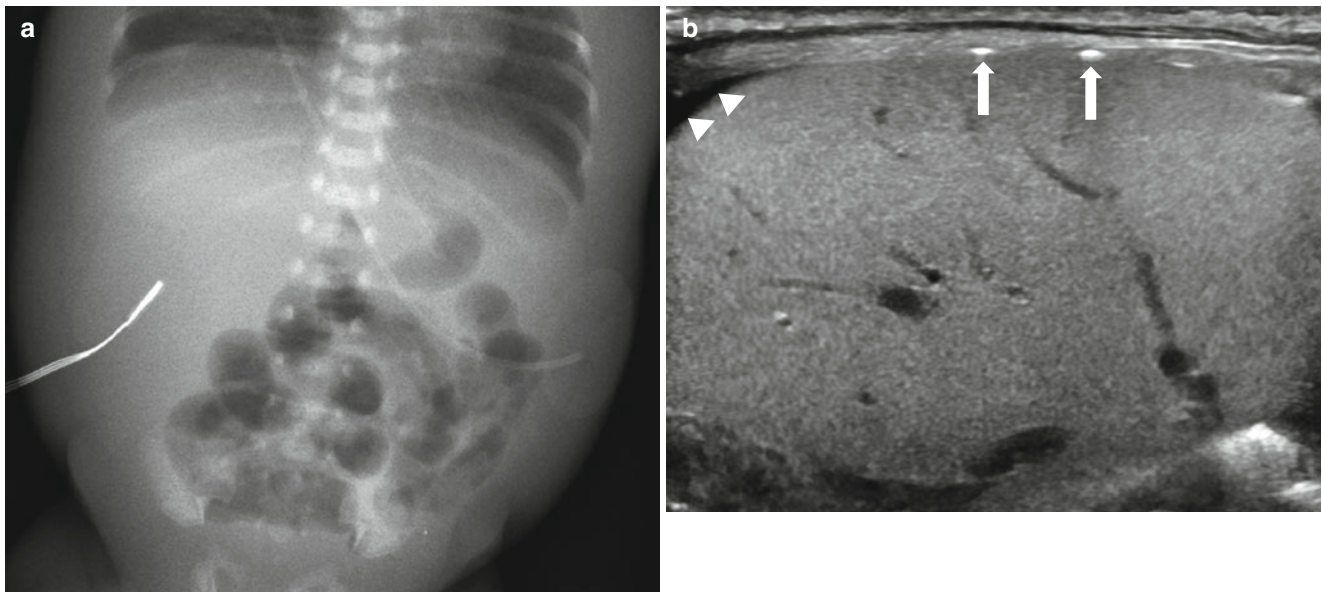


Fig. 20.8 Advanced necrotizing enterocolitis. (a) Supine radiograph in a premature baby shows gaseous dilatation of the bowel loops and marked thickening of the abdominal wall, probably due to edema. Free air is not definitely noted. (b) US demonstrates multifocal

hyperechogenicity (*arrows*) along the surface of the liver, representing free gas. Note free peritoneal fluid (*arrowheads*). Surgery confirmed perforation of terminal ileum

20.4.4 Intussusception

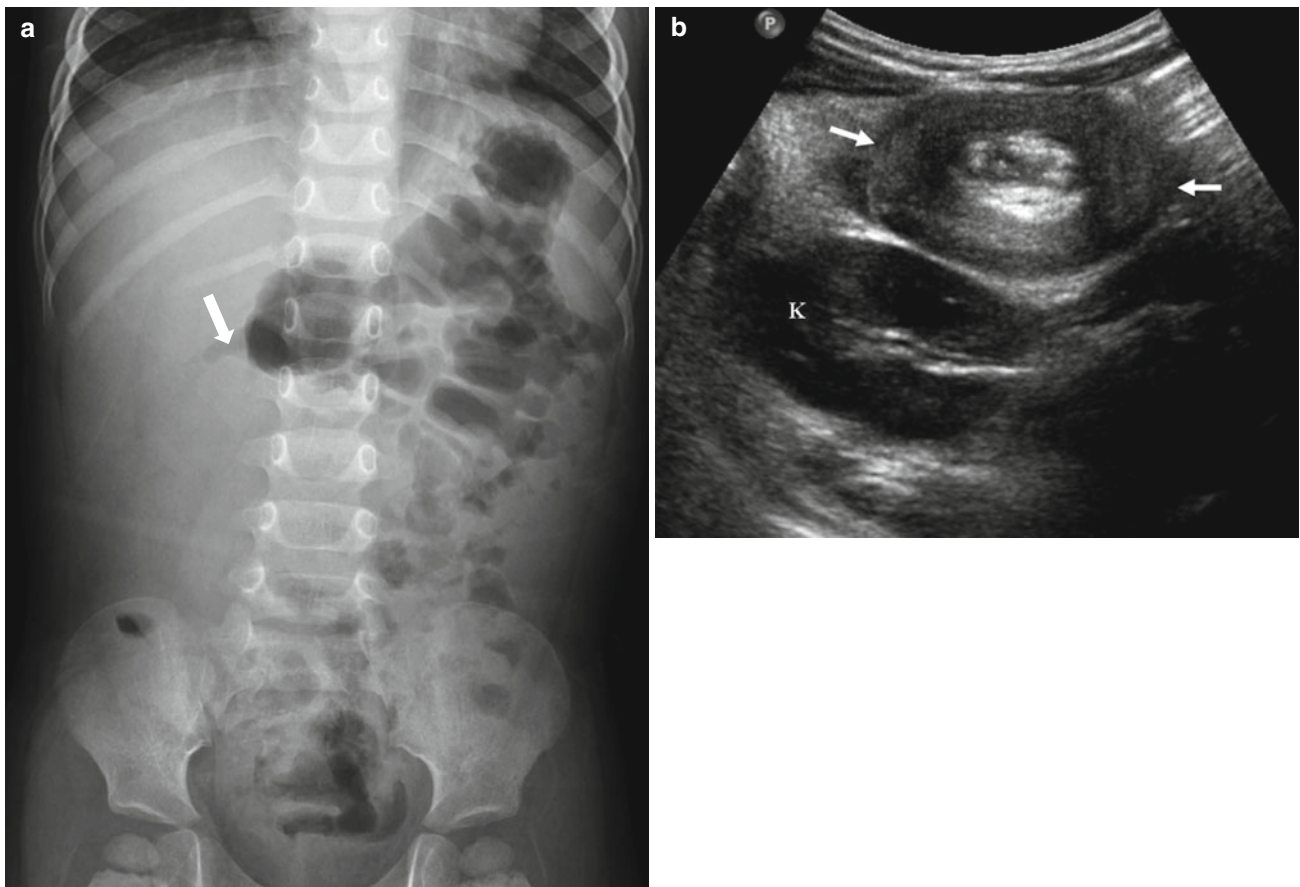


Fig. 20.9 Ileocolic intussusception in a 15-month-old boy presented with abdominal pain and bloody stool. **(a)** Abdominal radiograph shows a soft-tissue mass-like opacity (*arrows*) with relative paucity of

bowel gas in right abdomen. **(b)** US of right abdomen shows the typical appearance of intussusception (*arrows*), similar to the adjacent kidney (K), referred to as the “pseudokidney” sign

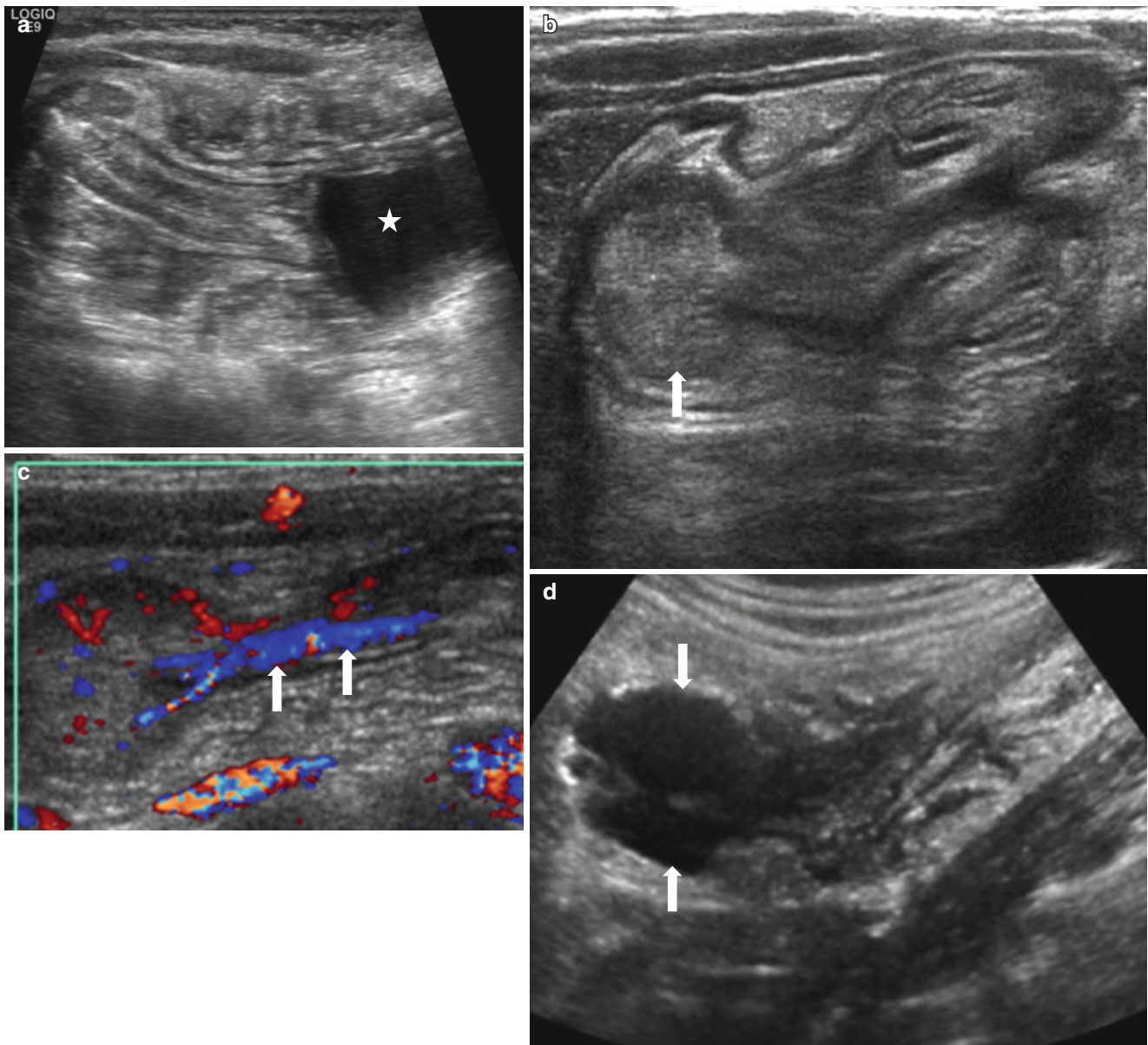


Fig. 20.10 Three different cases of intussusception with pathologic lead points. **(a)** US in a 7-month-old girl presented with cyclic irritability shows an intussusception (*arrows*) in a longitudinal axis. A cystic lesion (*asterisk*) with inner echogenic and outer hypoechoic wall is present as a lead point, which turned out to be a duplication cyst. **(b, c)** US images in a 4-year-old girl who had multiple episodes of intussusception demonstrate a polypoid lesion within the bowel leading to a short segmental ileocolic intussusception. On color Doppler image **(c)**, prominent vascular flow is noted in the polyp and the stalk (*arrows*).

Colonoscopic examination revealed a polyp in the cecum. Juvenile retention polyp was confirmed by polypectomy. **(d, e)** US **(d)** and coronal contrast-enhanced CT **(e)** images in a 12-year-old boy presented with recurrent abdominal pain show a homogenous solid mass (*arrows*) with lobulating contour leading to ileocolic intussusception. Note marked hypoechogenicity of the mass simulating cystic lesion on US. Ileocecal resection was performed and diffuse large B-cell lymphoma of terminal ileum was finally proved

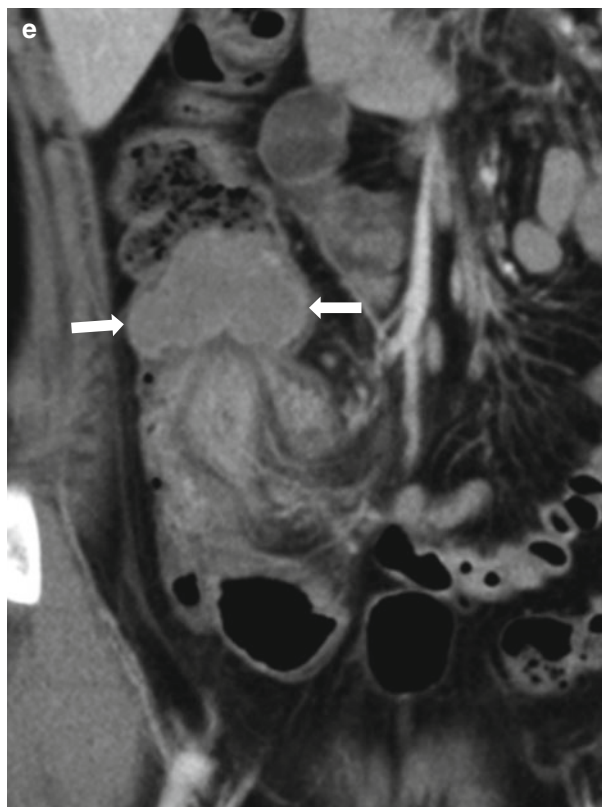


Fig. 20.10 (continued)

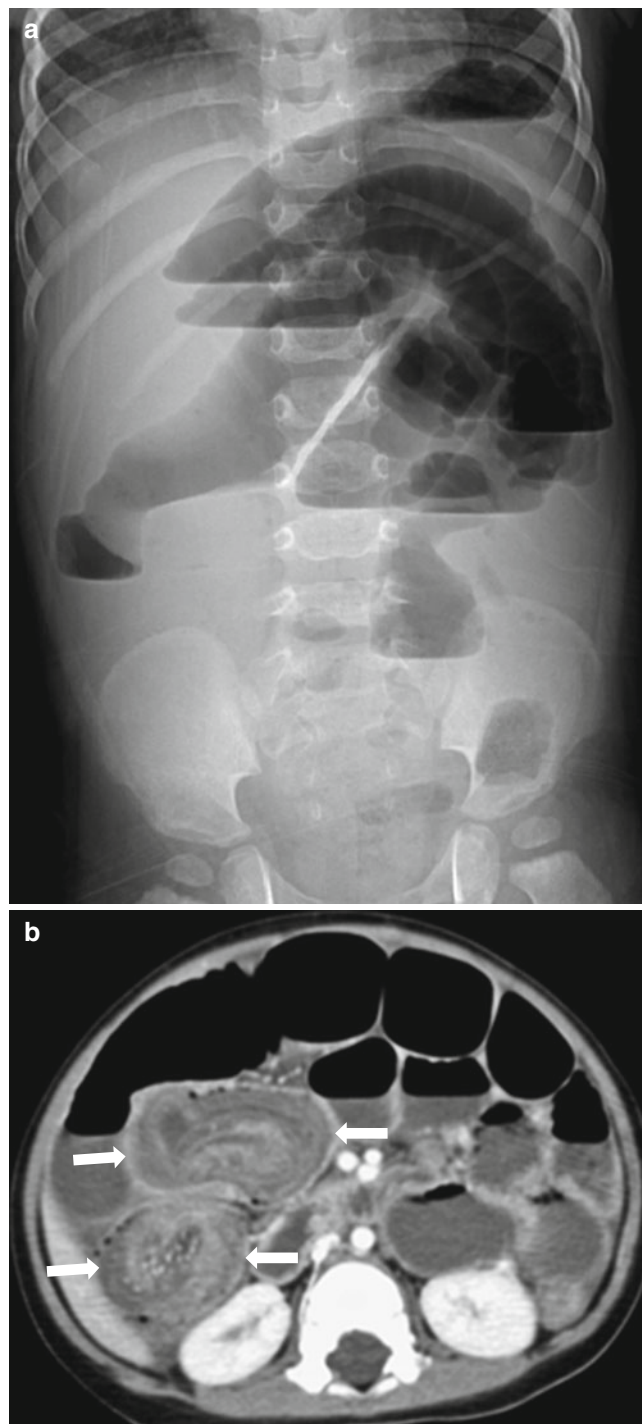


Fig. 20.11 Intussusception in a 17-month-old boy presented with a 3-day history of decreased activity. **(a)** Upright abdominal radiograph reveals marked distension of small-bowel loops with multiple air-fluid levels suggesting mechanical ileus. Pneumoperitoneum is not seen. **(b)** CT demonstrates an intussusception (*arrows*) in which the invaginated multilayered bowels show somewhat decreased enhancement of walls with entrapped fluid. Air reduction was failed and an ileoileocolic-type intussusception was confirmed, followed by surgical resection of ileoileal component due to failure of manual reduction

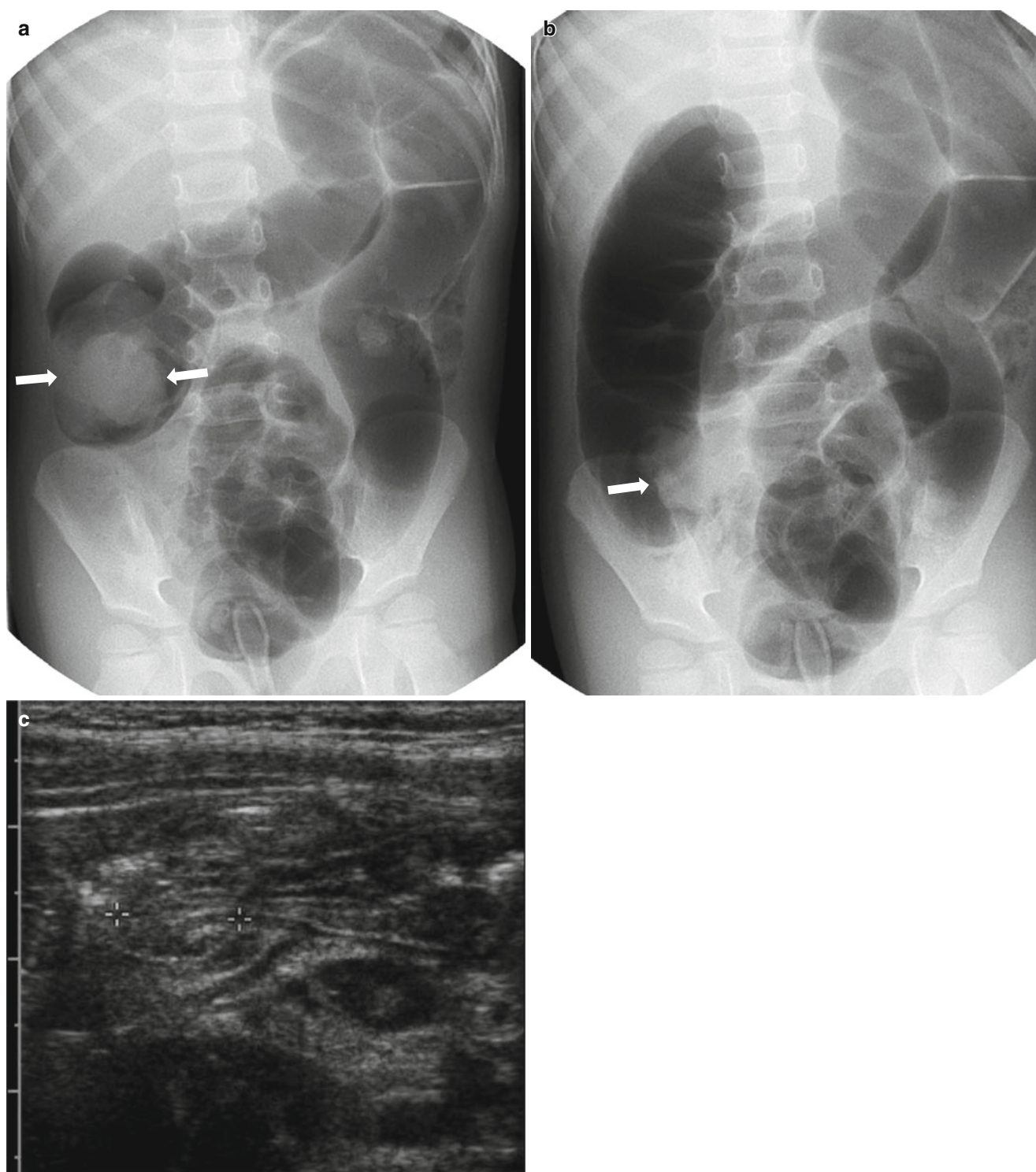


Fig. 20.12 Air reduction of intussusception: a potential pitfall. (a) Spot image taken during air reduction demonstrates an intraluminal soft tissue mass (*arrows*) in the hepatic flexure compatible with the intussusceptum. (b) Postreduction image reveals a persistent mass-like opacity (*arrows*) on the medial aspect of the cecum, in the expected

region of the ileocecal valve. This may represent an edematous ileocecal valve, a remnant intussusceptum, or a pathologic leading point. (c) Following US shortly after air reduction confirms an edematous ileocecal valve (calipers) without evidence of remnant intussusception

20.4.5 Duplication Cyst

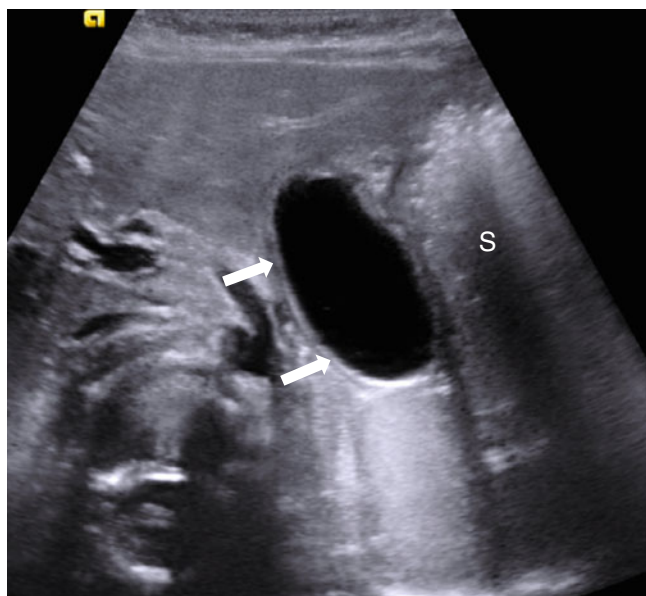


Fig. 20.13 Gastric duplication cyst in a 6-month-old infant. Transverse US image of upper mid-abdomen shows a typical duplication cyst (arrows) with “double wall” sign along the lesser curvature side of the stomach (S)

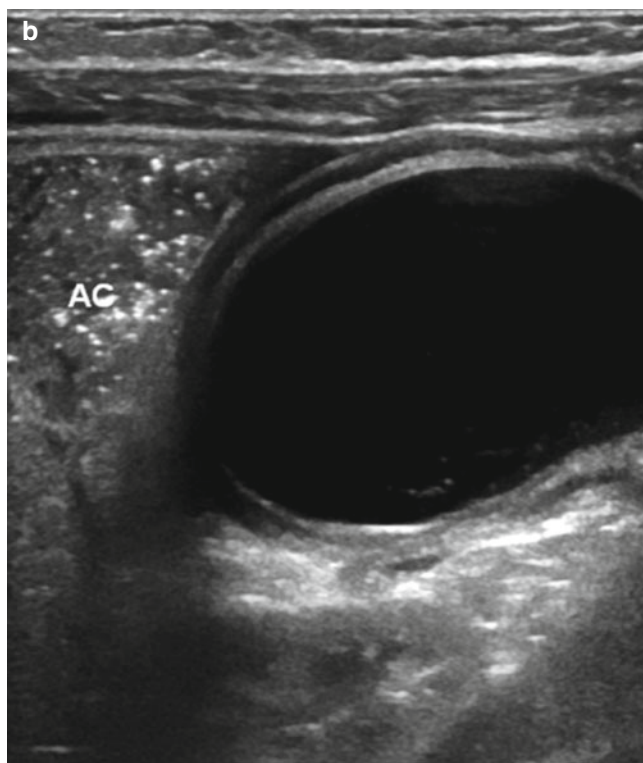
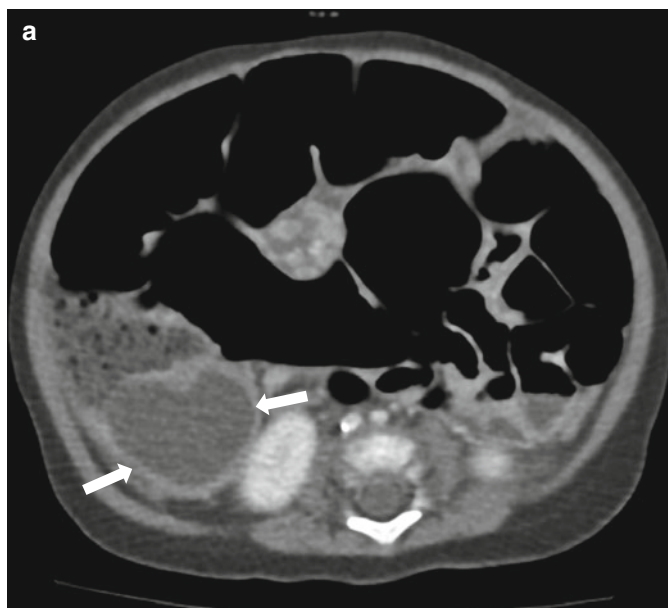


Fig. 20.14 Duplication cyst of terminal ileum presented with abdominal distension and vomiting in a 3-month-old infant. (a) Abdomen CT demonstrates diffuse gaseous dilatation of the bowel loops and a cystic mass (arrows) abutting right colon filled with feces. (b) On US, the

inner hyperechoic and outer hypoechoic wall of the cyst is well demonstrated in keeping with duplication cyst. At surgery, the duplication cyst turned out to be originating from the terminal ileum. AC ascending colon

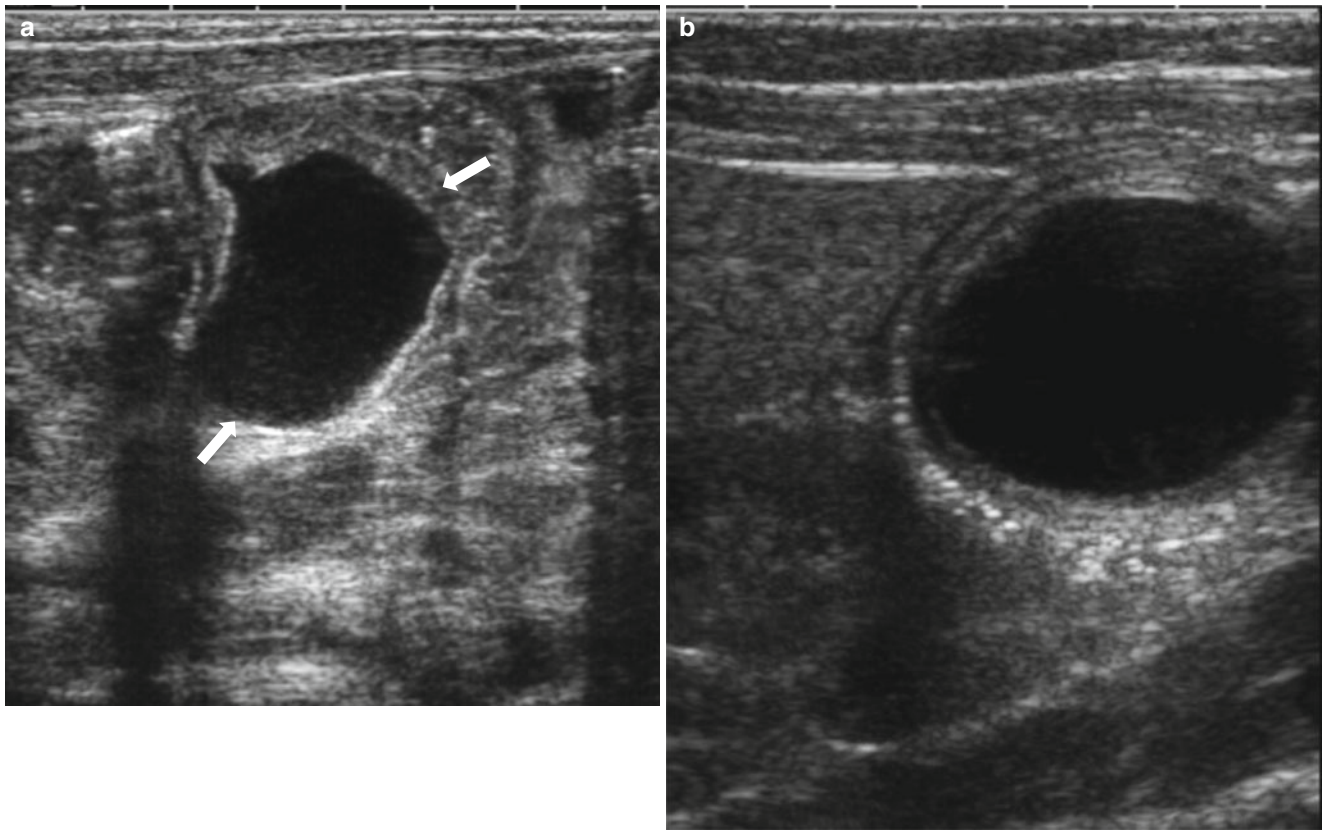


Fig. 20.15 Prenatally detected duplication cyst in a female newborn. Postnatal initial (**a**) and 2-month follow-up (**b**) US images show a duplication cyst (*arrows*) that slightly changes in its shape. Peristalsis of the

cyst was visible on real-time US. Note that the “double wall” sign is more clearly visualized on the latter US performed with a higher-frequency transducer. Prenatally, it had been suspected to be an ovarian cyst

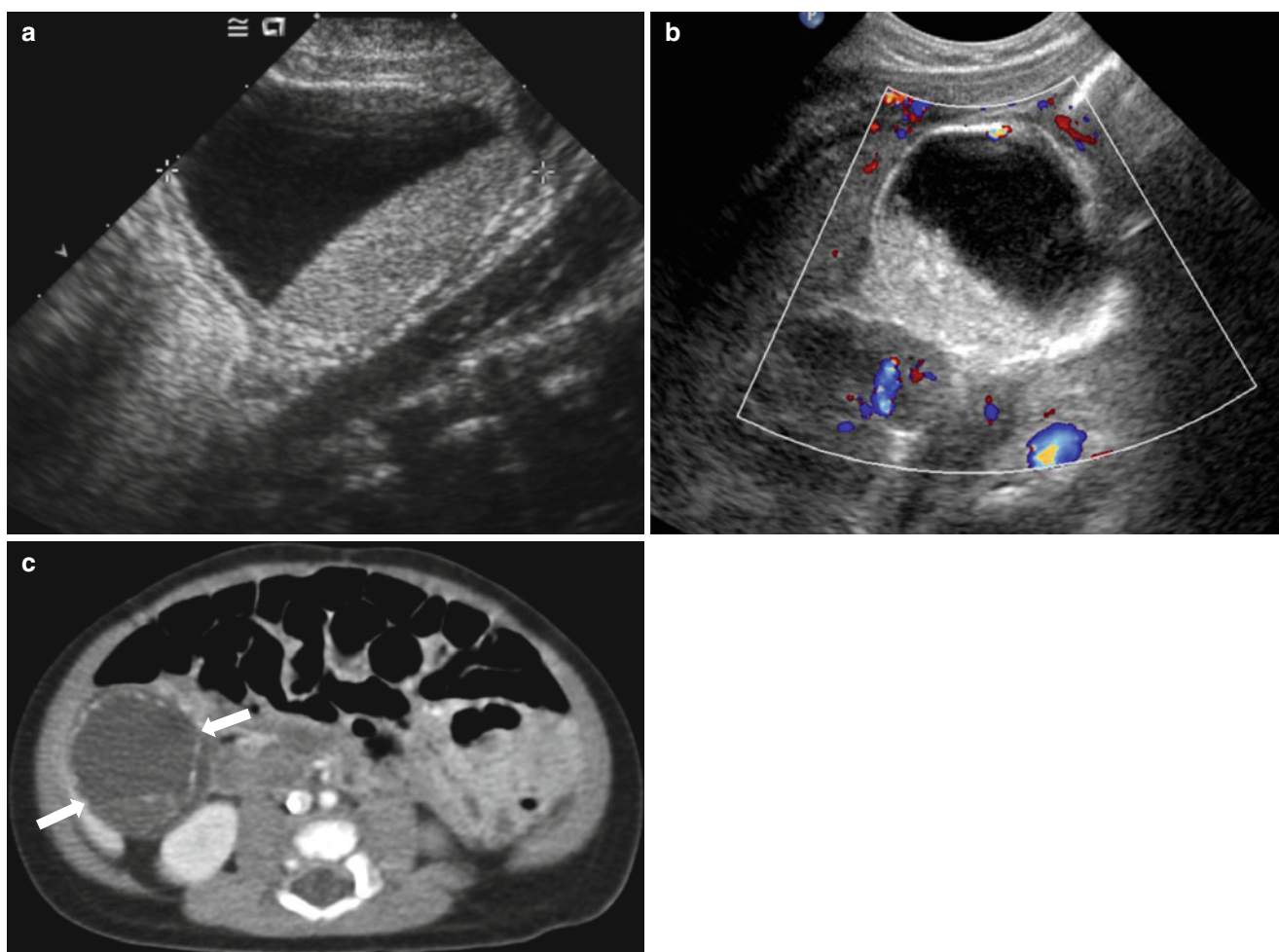


Fig. 20.16 Complicated neonatal ovarian cyst simulating a duplication cyst in a female newborn. Grayscale (a) and color Doppler (b) US images of right abdomen show a large unilocular cystic mass with internal fluid-fluid level. The wall of the cyst appears to be echogenic in inner layer and hypoechoic in outer layer, similar to

that of a duplication cyst. On CT (c), multifocal linear calcifications along the periphery of the cyst are seen, resulting in a sonographic echogenic wall. Torsion of ovarian cyst with autoamputation was surgically confirmed in this patient

20.4.6 Meckel's Diverticulum

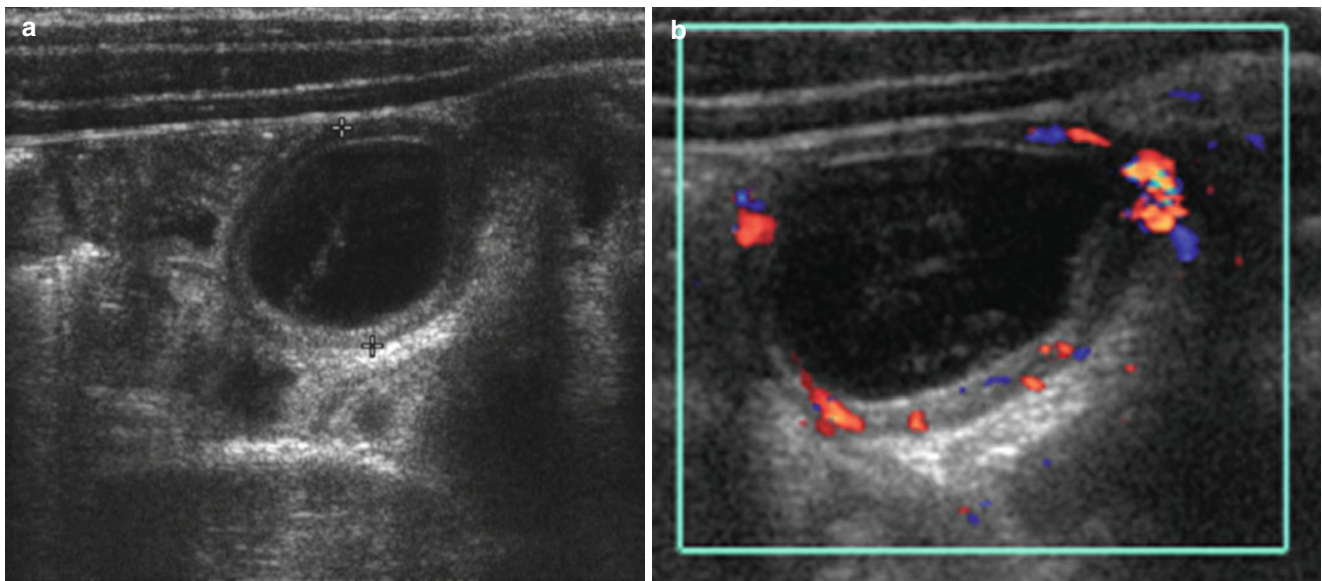


Fig. 20.17 Meckel's diverticulum in a 7-year-old boy presented with right lower quadrant pain. **(a)** Transverse US of right abdomen shows a cystic lesion (calipers) with gut signature (hyperechoic inner wall and hypoechoic outer wall). Compared with adjacent bowels that are

collapsed, it revealed loss of compressibility in real time. **(b)** Color Doppler study shows increased vascularity within the wall of the cyst, suggesting presence of inflammation. Appendix was not remarkable in this patient

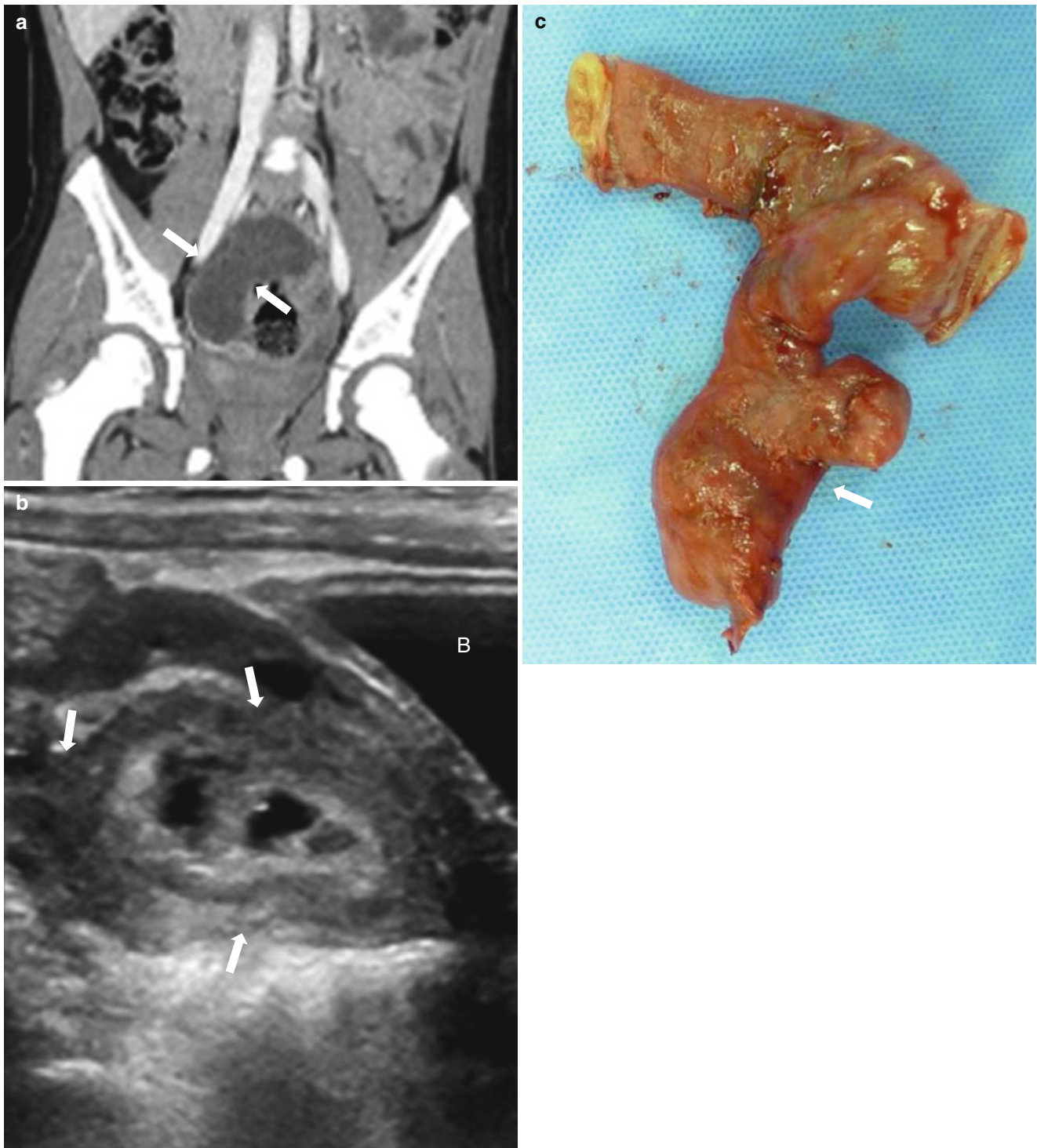


Fig. 20.18 Complicated Meckel's diverticulum in a 4-year-old girl with acute abdominal pain. (a) Coronal contrast-enhanced CT image shows a blind-end fluid-filled tubular structure (arrows) in the pelvic cavity. The wall of this structure appears to enhance partially in the lower portion. (b) Longitudinal US image better depicts the inflamed wall (arrows) of the tubular lesion as well as the presence of focal

continuity (small arrow) with the adjacent bowel. There is a small amount of peritoneal fluid. (c) At surgery, Meckel's diverticulum (arrow in c) was confirmed and segmental resection was performed as the photograph (c) shows. Pathology revealed transmural necrotizing inflammation and ulceration of Meckel diverticulum. B bladder (Courtesy of Dr. Choi YH, Seoul National University Children's Hospital)

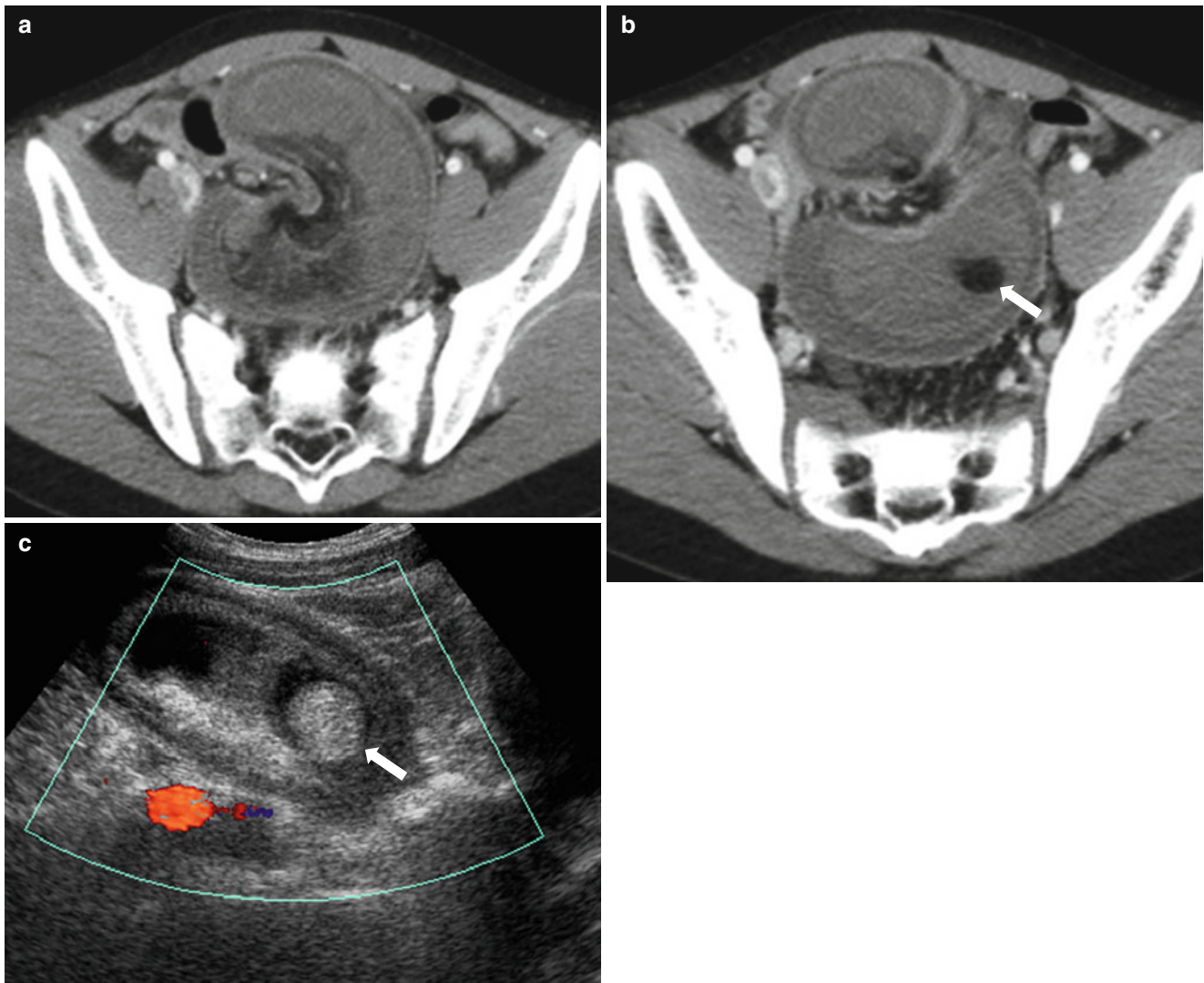


Fig. 20.19 Meckel's diverticulum complicated by intussusception in an 11-year-old boy who presented with abdominal pain developed 3 days earlier. Contrast-enhanced CT images (**a**, **b**) reveal a long segmental small-bowel intussusception of which the invaginated bowel shows fluid-filled distension and lack of enhancement of the wall as well as

entrapped fluid. There is an ovoid-shaped structure (*arrow in b*) of fat attenuation, which appears as a hyperechoic nodular lesion (*arrow in c*) on US. This represents inverted Meckel's diverticulum, which turned out to act as a lead point of this ileoileal intussusception complicated by infarct

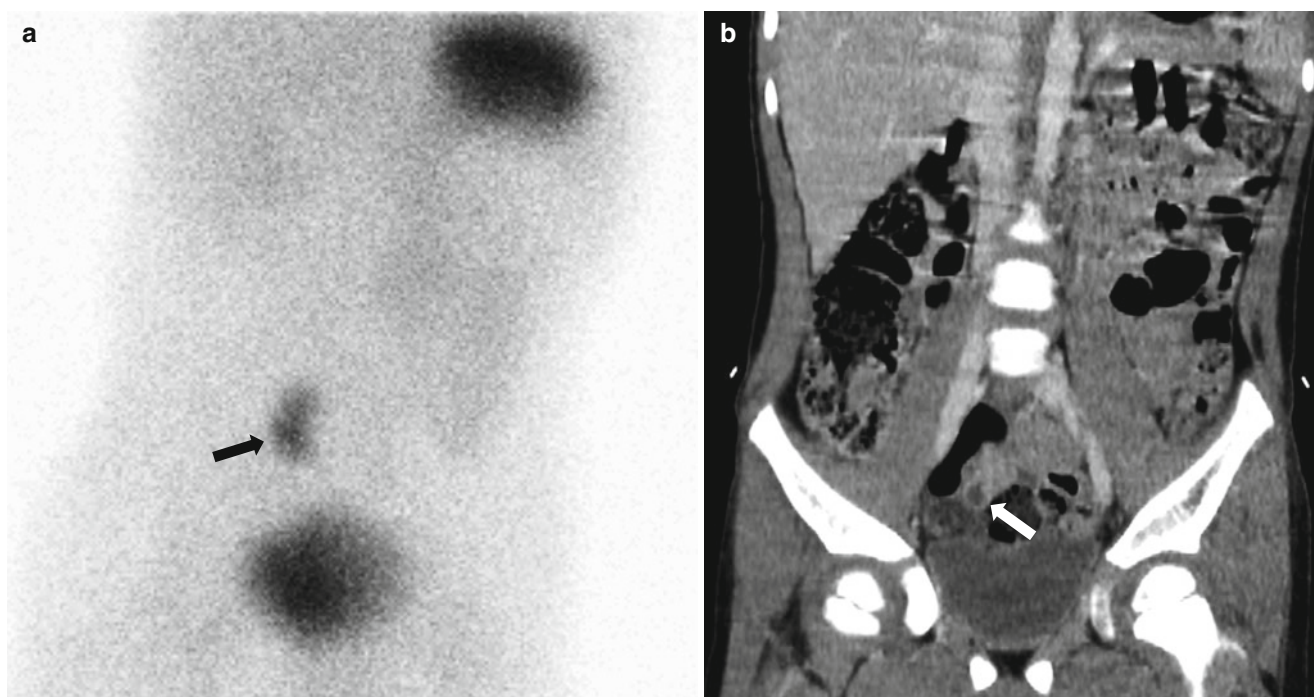


Fig. 20.20 Meckel's diverticulum in a 4-year-old boy with abdominal pain and melena. **(a)** Meckel scan obtained 30 min after Tc-99 m pertechnetate shows a focus of abnormal uptake in the right lower quadrant (*arrow*) due to ectopic gastric mucosa of Meckel's diverticulum.

Note normal activity in the stomach and bladder. **(b)** Coronal contrast-enhanced CT reveals a small cystic lesion (*arrow*) with slight degree of wall enhancement and adjacent enhancing structure in the corresponding region of Meckel's diverticulum

20.4.7 Appendicitis

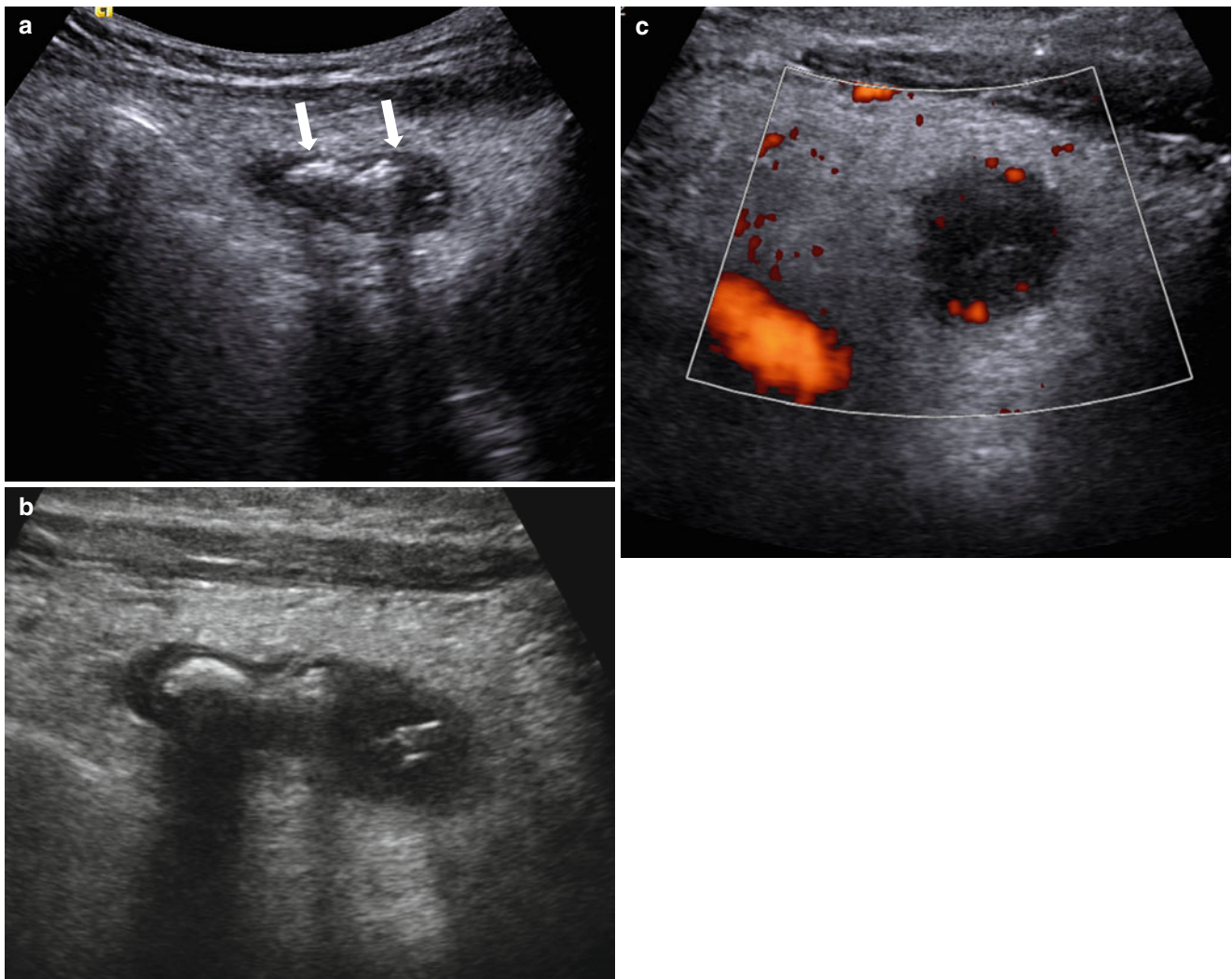


Fig. 20.21 Acute appendicitis: typical US finding in a 7-year-old girl. US images obtained with convex (**a**) and linear (**b**) transducers show a dilated appendix (*arrows*) with thickened wall and multiple appendicoliths that appear to be hyperechoic and have posterior acoustic

shadowing. Note surrounding fatty inflammation. On color Doppler study with compression (**c**), the appendix is persistently distended and increased flow is noted along the wall and the surrounding fatty tissue

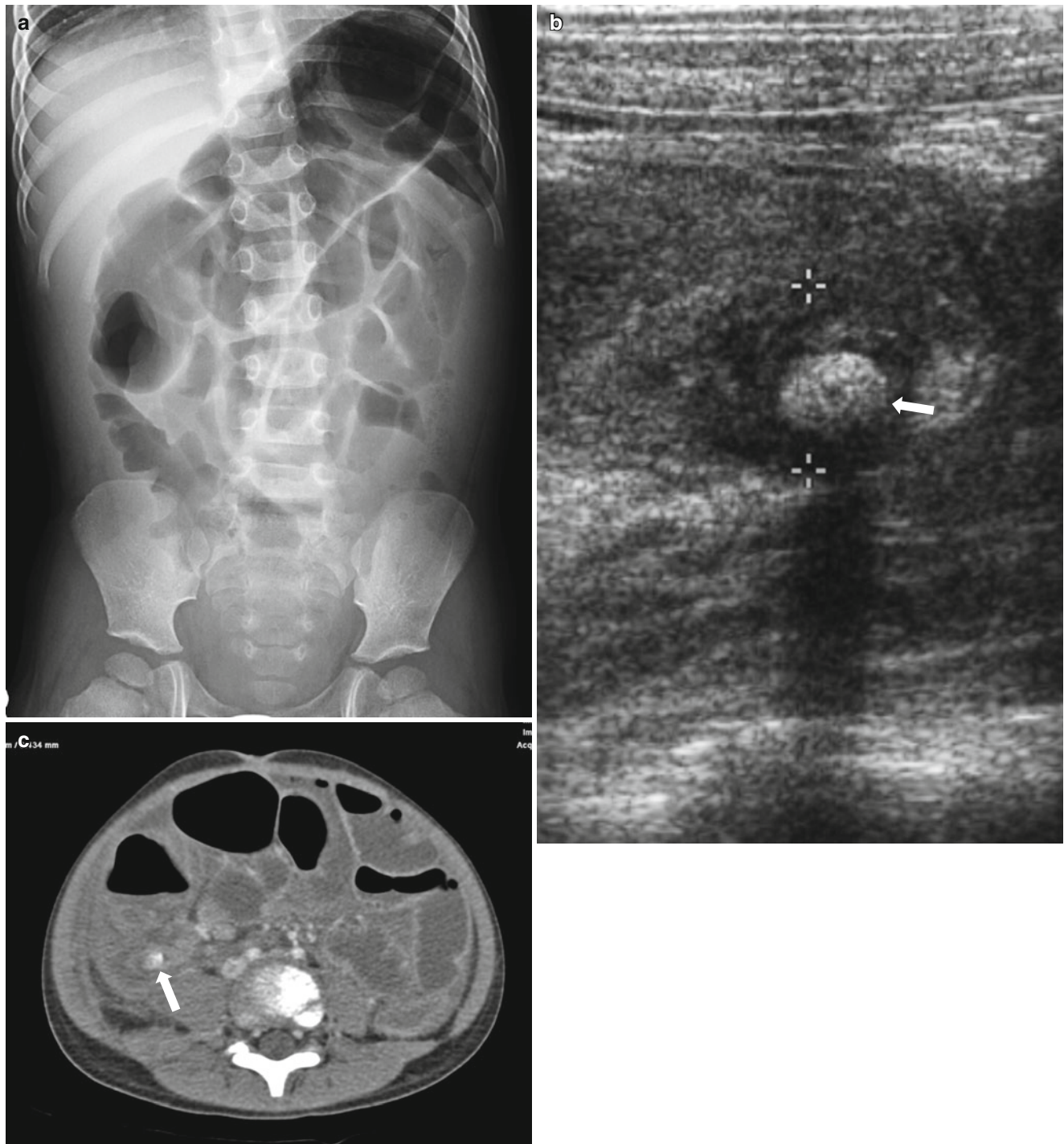


Fig. 20.22 Perforated appendicitis in a 2-year-old boy with fever and abdominal pain. (a) Supine abdominal radiograph shows ileus and suspected bowel wall thickening, especially in RLQ. Appendicolith is not definitely identified. (b) US shows an appendicolith (*arrow*) surrounded by dirty fluid collection. It was difficult to define and trace

the wall of the appendix, probably representing perforation. (c) On contrast-enhanced CT image, an appendicolith (*arrow*) is again seen in the dilated appendix. There is diffuse peritoneal enhancement with a small amount of ascites as well as fluid-filled distension of small-bowel loops, indicating peritonitis

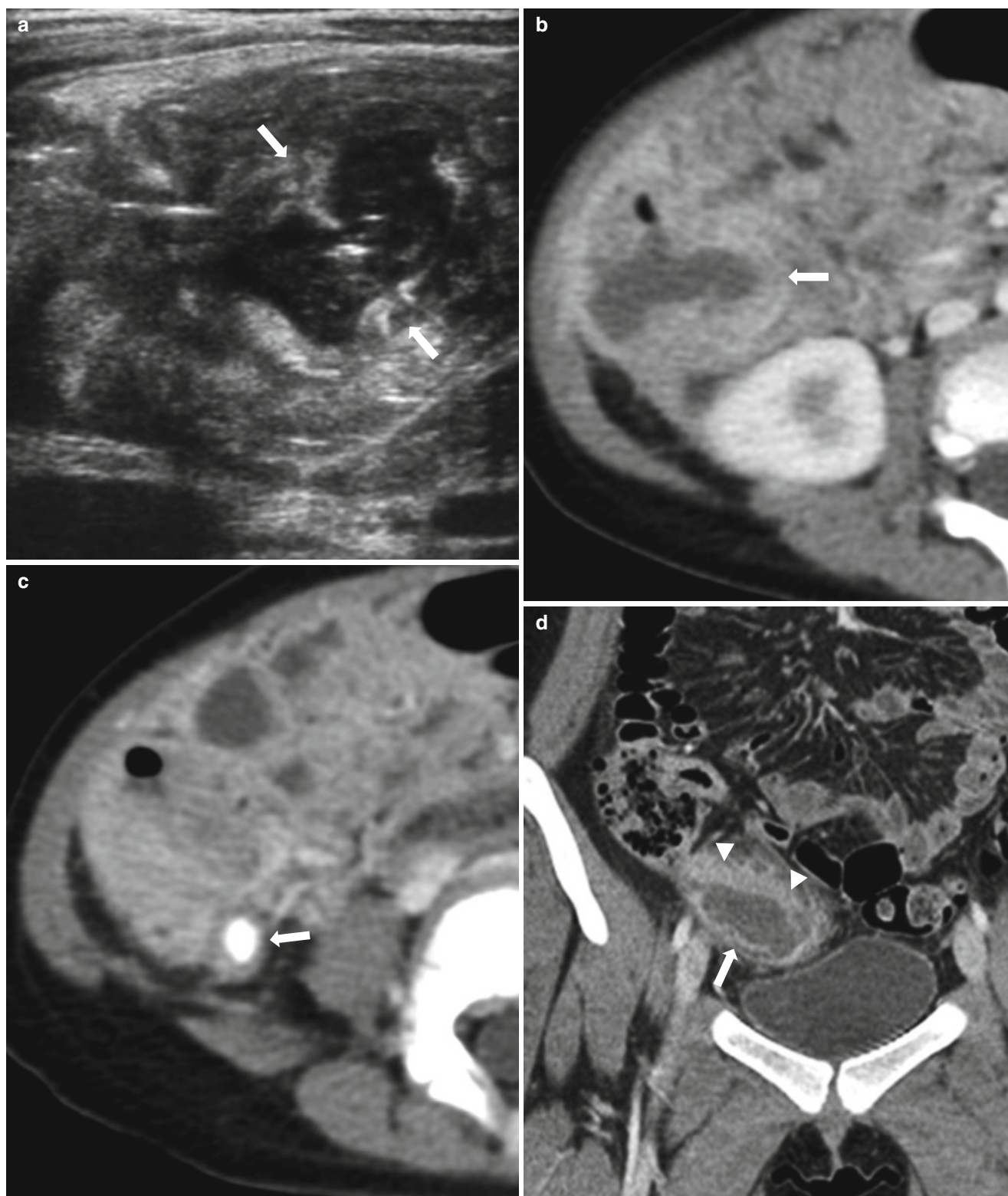


Fig. 20.23 Periappendiceal abscesses in two children. (a–c) In this 2-year-old girl, initially performed US (a) shows a cavitory lesion (arrow) surrounded by a thick wall in the right subhepatic area, suspecting abscess. Appendix was not definitely identified on US. Contrast-enhanced CT images demonstrate an abscess (arrow in b) and an appendicolith (arrow in c) within the dilated appendix with a thick

wall. Distal portion of the appendix was not traceable due to perforation. Perforated appendicitis with periappendiceal abscess located in the subhepatic area was surgically confirmed. (d) In a 12-year-old girl, coronal CT scan shows appendicitis (arrowheads) surrounded by an abscess pocket (arrow) with adjacent fatty infiltration to the pelvic cavity

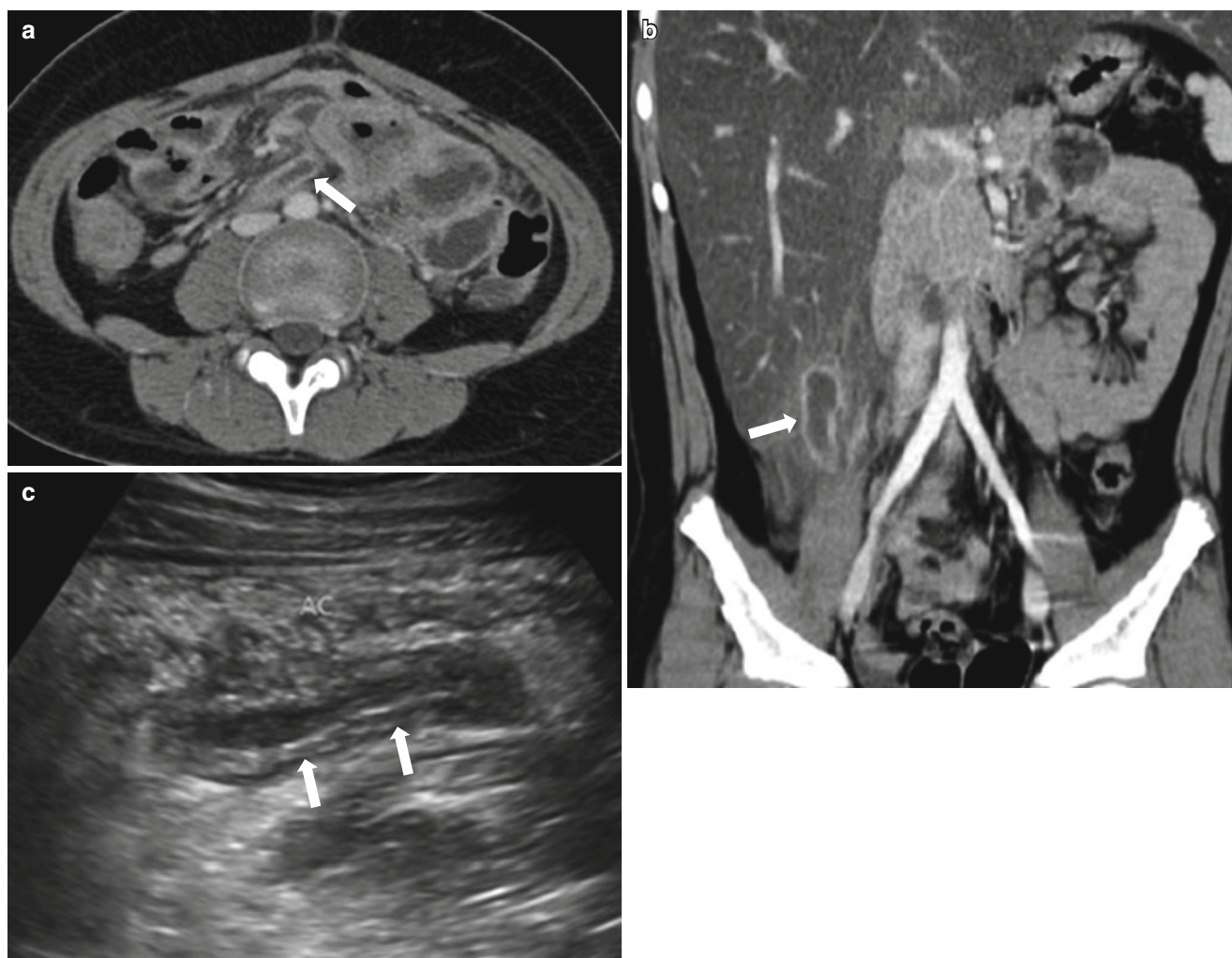


Fig. 20.24 Variable location of appendix: pitfall in diagnosing appendicitis. (a, b) CT images in two different children with acute appendicitis show anatomical variation of appendix (*arrow*), which is midline in (a) and subhepatic in (b). (c) In another 12-year-old girl who presented

with right flank pain, US, which was referred for clinical suspicion of acute pyelonephritis, shows retrocolic ascending appendix (*arrow*) which is dilated and has a thickened wall. AC ascending colon

20.4.8 Henoch-Schönlein Purpura

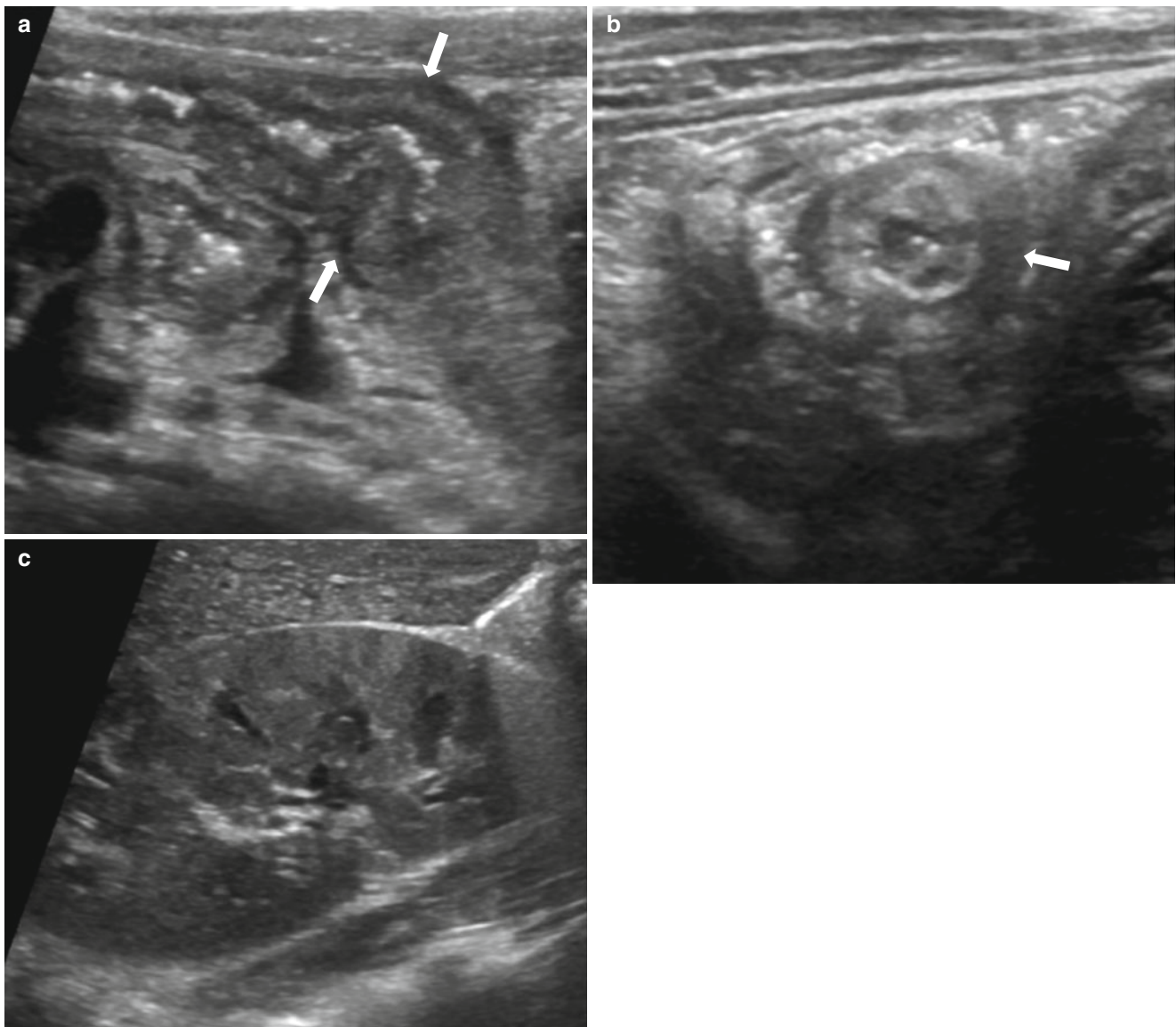


Fig. 20.25 Henoch-Schönlein purpura in a 6-year-old-boy with abdominal pain and hematochezia. US images show circumferential thickening of bowel wall (*arrows in a*) involving the ileum associated with very short segmental intussusception (*arrow in b*), which reduced

spontaneously during the examination. The kidneys in this patient showed increased parenchymal echogenicity (*c*) in keeping with renal involvement of HSP

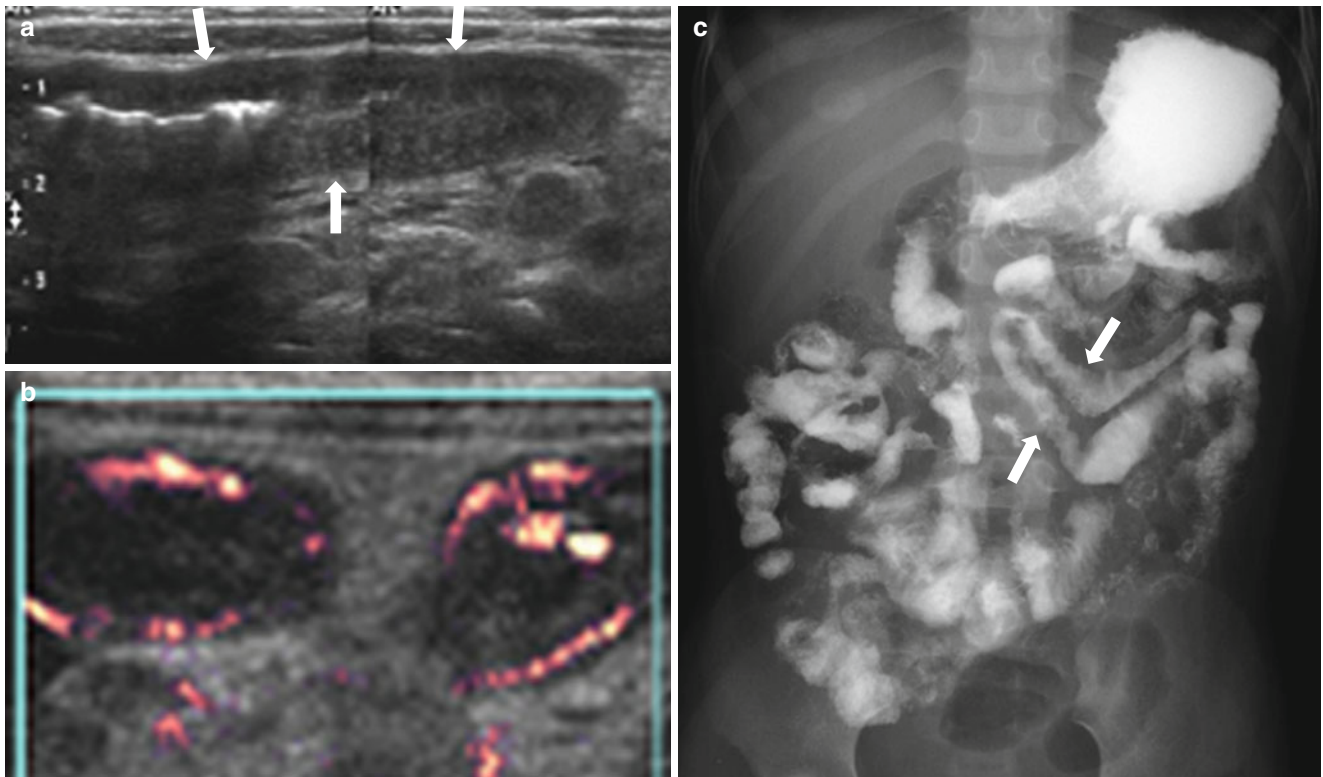


Fig. 20.26 Henoch-Schönlein purpura in a 4-year-old girl with hematemesis and abdominal pain. US images of left abdomen shows marked wall thickening of jejunal loop (*arrows* in **a**) with loss of normal bowel stratification. Increased vascularity of the thickened wall is noted

along the affected bowel on power Doppler study (**b**). Small-bowel series (**c**) demonstrates thumbprinting appearance of the proximal jejunum (*arrows*). In this patient, purpura developed 9 days after US study (Courtesy of Dr. Lee SW, Ewha Women's University Hospital)

20.4.9 Hirschsprung Disease

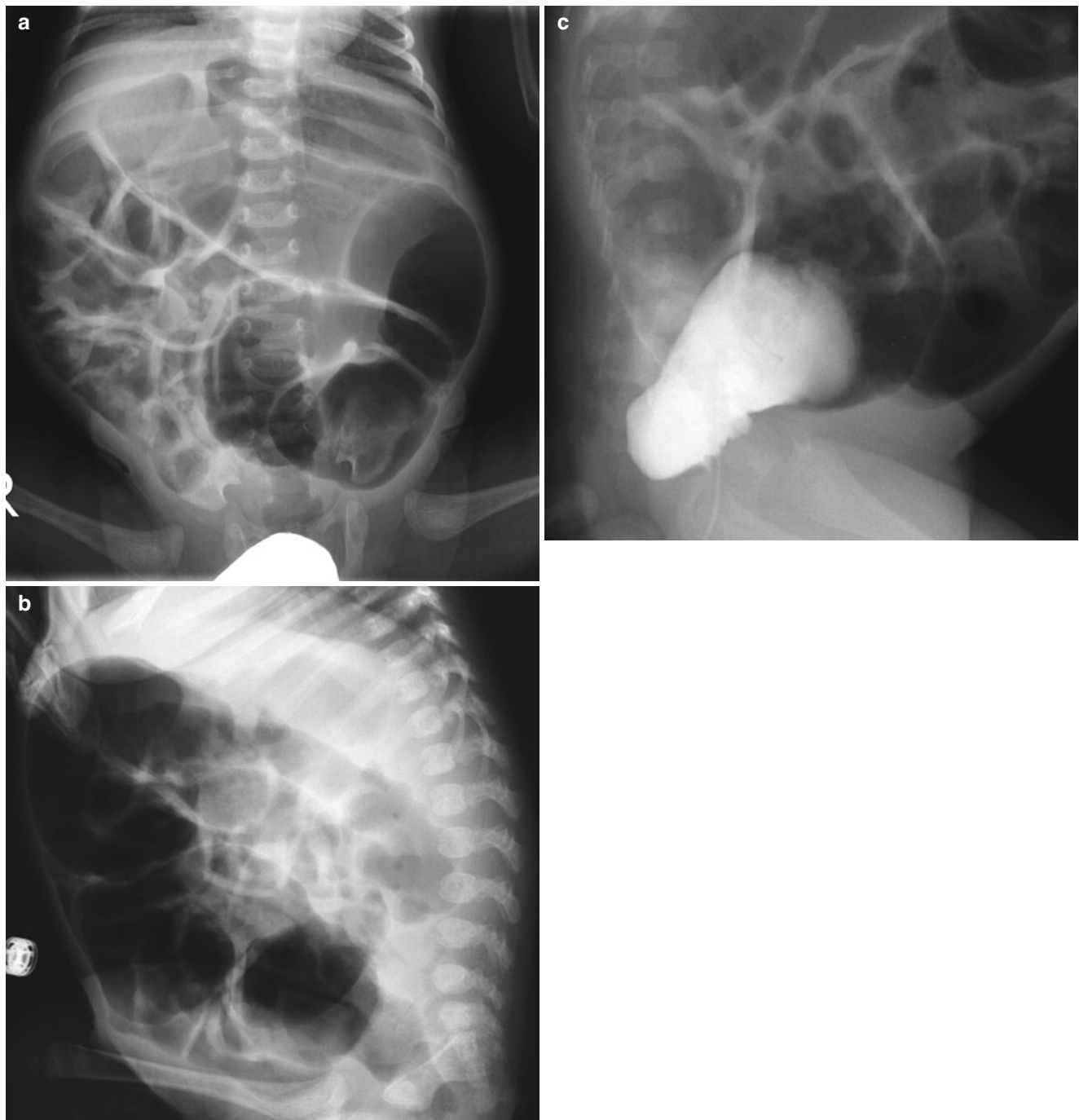


Fig. 20.27 Hirschsprung disease in a 6-week-old infant presented with abdominal distension and vomiting. (a, b) Abdominal radiographs on supine and lateral view show marked gaseous distension of colon and small bowel with relatively decreased caliber of the air-filled

rectum. (c) Lateral view of barium enema demonstrates smaller rectum than the sigmoid colon with transition zone at the rectosigmoid junction. Anterior aspect of the distal rectum shows slightly irregular contour due to contraction

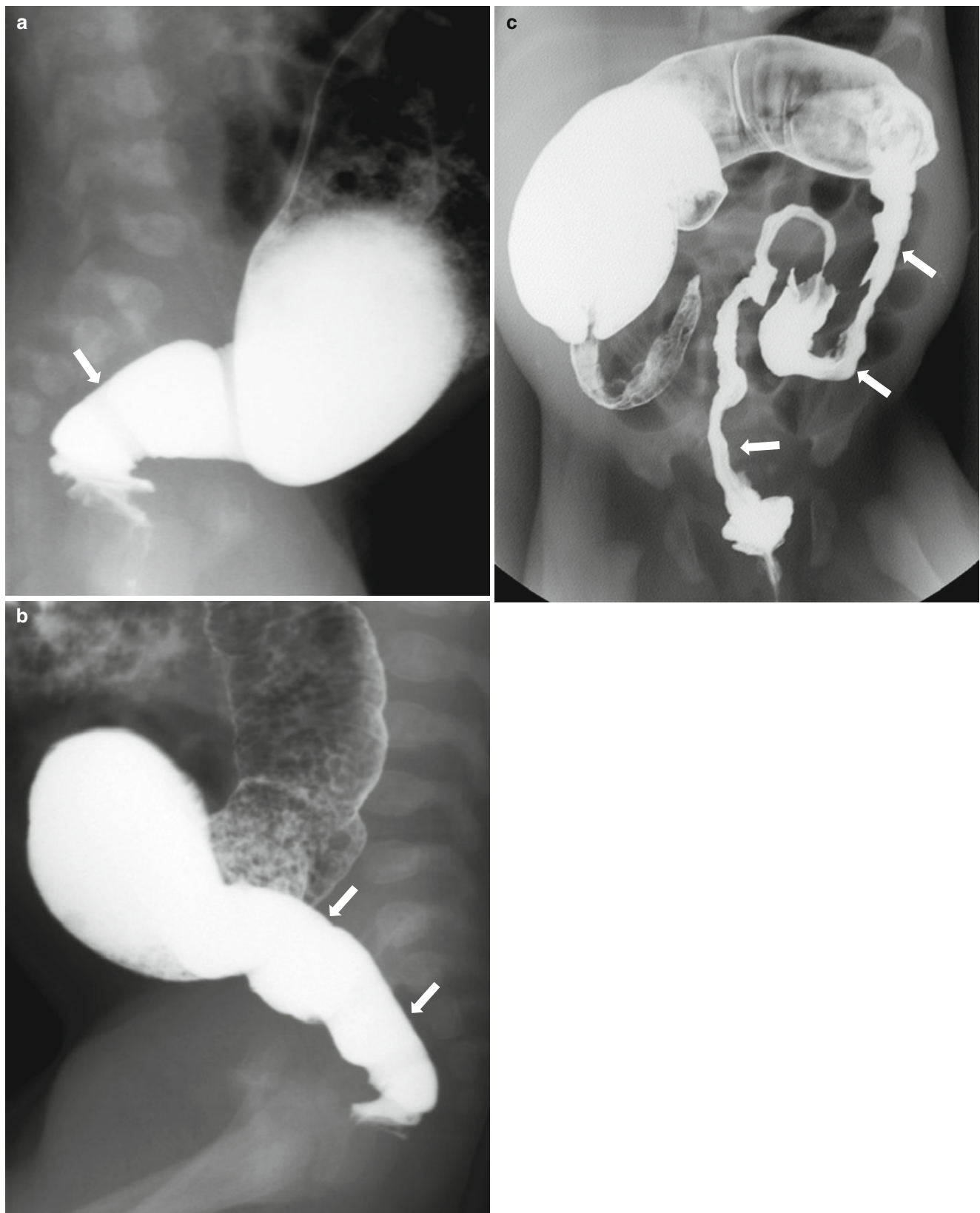


Fig. 20.28 Hirschsprung disease in three newborns with variable lengths of aganglionic segment. Barium enema images (**a–c**) obtained from three different newborns show variable length of aganglionic segment (arrows in each figure), which is of decreased caliber

compared with the colon proximal to the transition zone. Note the irregular contractions of the aganglionic segments. There is a granular appearance of the mucosa in the descending colon, representing enterocolitis in **b**

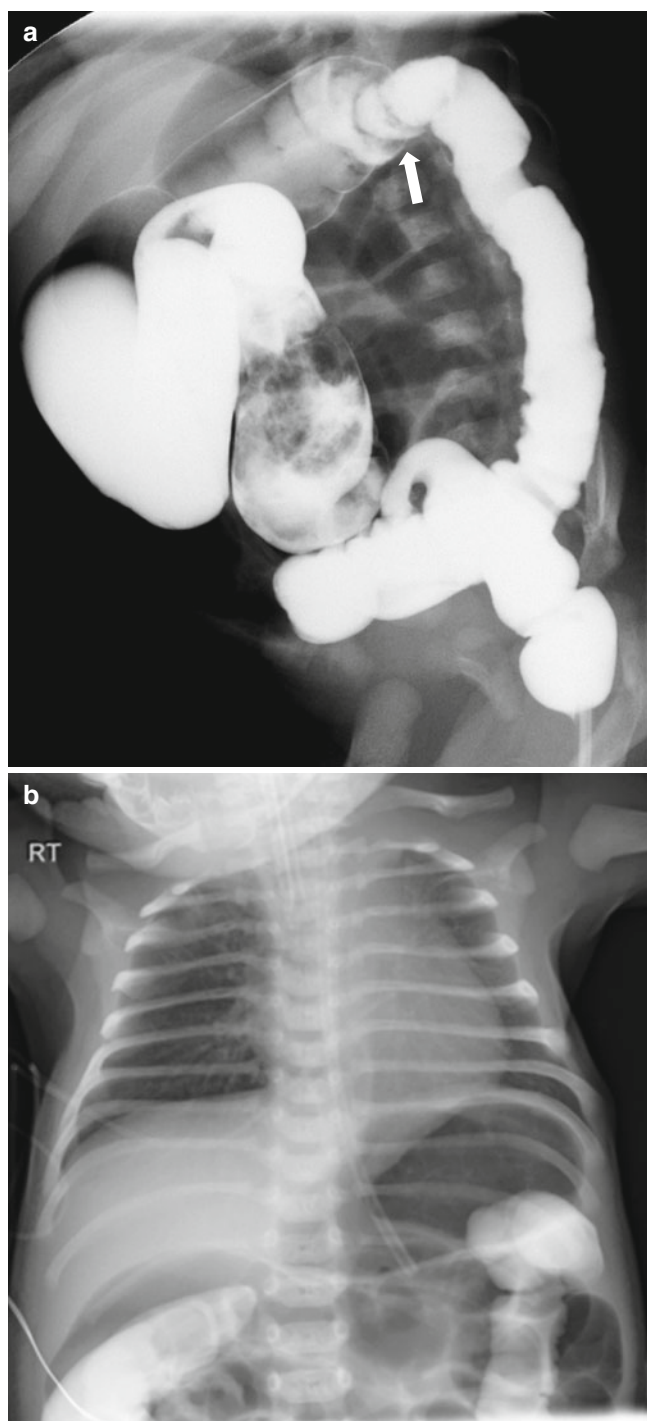


Fig. 20.29 Hirschsprung disease in a 3-day-old newborn presented with abdominal distension and apnea. (a) Oblique view of barium enema shows transition zone at the splenic flexure (arrows) and relatively decreased caliber of the long segmental aganglionic distal colon with irregular contour. (b) This baby was intubated due to central hypoventilation, and a chest radiograph several days after a barium enema shows retention of contrast in the colon as well as small-bowel dilatation. Diagnosis of Haddad syndrome was made based on biopsy confirmed aganglionosis and central hypoventilation

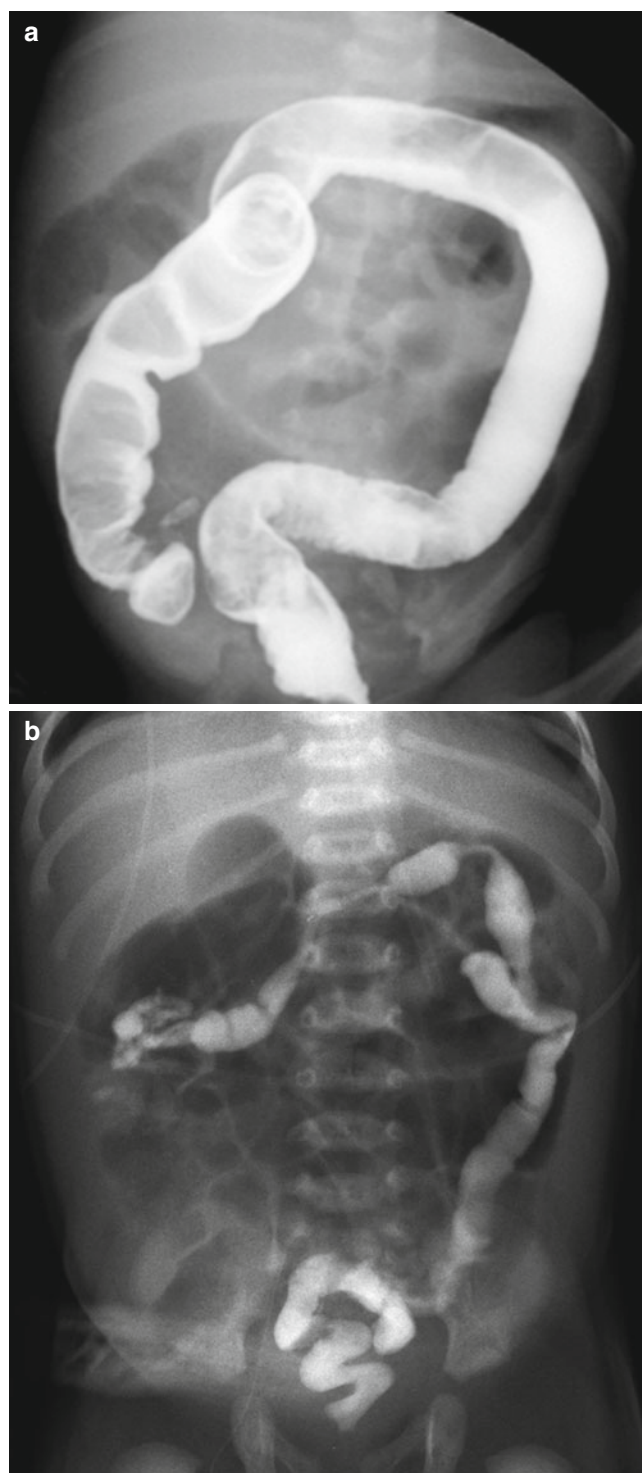


Fig. 20.30 Total colonic aganglionosis in two infants. (a) Colon study in a 3-week-old infant who presented with abdominal distension and poor oral intake with a history of failure to pass meconium shows shortened colon with decreased redundancy, assuming the question mark appearance. Transition zone is not seen. The caliber of the entire colon is slightly decreased relative to small bowels, which show gaseous distension. (b) In another 3-day-old newborn with bilious vomiting, delayed radiograph after water-soluble contrast enema shows diffusely decreased caliber of the entire colon with contrast retention. Cecum is positioned high with shortening of the ascending colon. There is gaseous distension of small-bowel loops. Pathology confirmed aganglionosis involving not only colon but also ileum

20.4.10 Allergic Proctocolitis

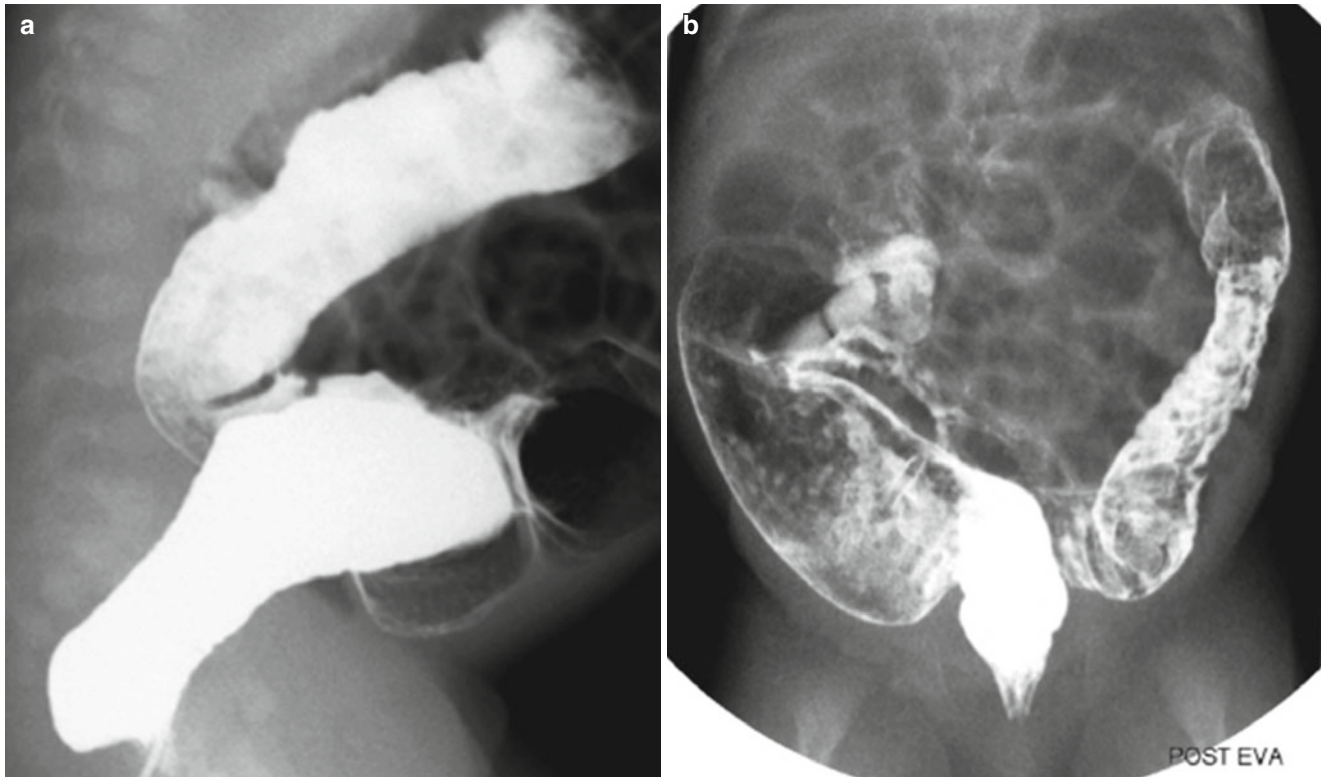


Fig. 20.31 Allergic proctocolitis in a 1-month-old infant presented with abdominal distension: a mimicker of Hirschsprung disease. **(a)** Lateral view of barium enema shows transition from relatively decreased caliber rectum to dilated sigmoid colon, mimicking Hirschsprung disease. **(b)** On delayed radiograph after evacuation,

partial evacuation of contrast is seen and multiple relative narrowing of sigmoid and descending colon due to spasm is noted with the finding of colitis. An apparent transition zone at the rectosigmoid junction is again noted. Rectal biopsy was performed and allergic proctocolitis was confirmed

References

- Abu-Yousef MM, Bleicher JJ, Maher JW, et al. High-resolution sonography of acute appendicitis. *AJR Am J Roentgenol.* 1987;149:53–8.
- Baldisserotto M, Maffazzoni DR, Dora MD. Sonographic findings of Meckel's diverticulitis in children. *AJR Am J Roentgenol.* 2003;180:425–8.
- Bloom DA, Buonomo C, Fishman SJ, et al. Allergic colitis: a mimic of Hirschsprung disease. *Pediatr Radiol.* 1999;29:37–41.
- Blumhagen JD, Maclin L, Krauter D, et al. Sonographic diagnosis of hypertrophic pyloric stenosis. *AJR Am J Roentgenol.* 1988;150:1367–70.
- Bomelburg T, von Lengerke HJ. Sonographic findings in infants with suspected necrotizing enterocolitis. *Eur J Radiol.* 1992;15:149–53.
- Cheng G, Soboleski D, Daneman A, et al. Sonographic pitfalls in the diagnosis of enteric duplication cysts. *AJR Am J Roentgenol.* 2005;184:521–5.
- Connolly B, O'Halpin D. Sonographic evaluation of the abdomen in Henoch-Schonlein purpura. *Clin Radiol.* 1994;49:320–3.
- Epelman M, Daneman A, Navarro OM, et al. Necrotizing enterocolitis: review of state-of-the-art imaging findings with pathologic correlation. *Radiographics.* 2007;27:285–305.
- Faingold R, Daneman A, Tomlinson G, et al. Necrotizing enterocolitis: assessment of bowel viability with color Doppler US. *Radiology.* 2005;235:587–94.
- Godfrey H, Abernethy L, Boothroyd A. Torsion of an ovarian cyst mimicking enteric duplication cyst on transabdominal ultrasound: two cases. *Pediatr Radiol.* 1998;28:171–3.
- Hernandez JA, Swischuk LE, Angel CA. Validity of plain films in intussusception. *Emerg Radiol.* 2004;10:323–6.
- Hernanz-Schulman M. Infantile hypertrophic pyloric stenosis. *Radiology.* 2003;227:319–31.
- Kangaroo H, Sample WF, Hansen G, et al. Ultrasonic evaluation of abdominal gastrointestinal tract duplication in children. *Radiology.* 1979;131:191–4.
- Kim WY, Kim WS, Kim IO, et al. Sonographic evaluation of neonates with early-stage necrotizing enterocolitis. *Pediatr Radiol.* 2005;35:1056–61.
- Levy AD, Hobbs CM. From the archives of the AFIP. Meckel diverticulum: radiologic features with pathologic correlation. *Radiographics.* 2004;24:565–87.
- Lim HK, Bae SH, Lee KH, et al. Assessment of reducibility of ileocolic intussusception in children: usefulness of color Doppler sonography. *Radiology.* 1994;191:781–5.
- Merritt CR, Goldsmith JP, Sharp MJ. Sonographic detection of portal venous gas in infants with necrotizing enterocolitis. *AJR Am J Roentgenol.* 1984;143:1059–62.
- Navarro OM, Daneman A, Chae A. Intussusception: the use of delayed, repeated reduction attempts and the management of intussusceptions due to pathologic lead points in pediatric patients. *AJR Am J Roentgenol.* 2004;182:1169–76.
- O'Donovan AN, Habra G, Somers S, et al. Diagnosis of Hirschsprung's disease. *AJR Am J Roentgenol.* 1996;167:517–20.
- Olson DE, Kim YW, Donnelly LF. CT findings in children with Meckel diverticulum. *Pediatr Radiol.* 2009;39:659–63. Quiz 766–657.
- Ozdemir H, Isik S, Buyan N, et al. Sonographic demonstration of intestinal involvement in Henoch-Schonlein syndrome. *Eur J Radiol.* 1995;20:32–4.
- Patel U, Leonidas JC, Furie D. Sonographic detection of necrotizing enterocolitis in infancy. *J Ultrasound Med.* 1990;9:673–5.
- Peh WC, Khong PL, Lam C, et al. Reduction of intussusception in children using sonographic guidance. *AJR Am J Roentgenol.* 1999;173:985–8.
- Quillin SP, Siegel MJ. Appendicitis in children: color Doppler sonography. *Radiology.* 1992;184:745–7.
- Reid JR, Buonomo C, Moreira C, et al. The barium enema in constipation: comparison with rectal manometry and biopsy to exclude Hirschsprung's disease after the neonatal period. *Pediatr Radiol.* 2000;30:681–4.
- Seibert JJ, Parvey LS. The telltale triangle: use of the supine cross table lateral radiograph of the abdomen in early detection of pneumoperitoneum. *Pediatr Radiol.* 1977;5:209–10.
- Sivit CJ, Applegate KE. Imaging of acute appendicitis in children. *Semin Ultrasound CT MR.* 2003;24:74–82.
- Sivit CJ, Siegel MJ, Applegate KE, et al. When appendicitis is suspected in children. *Radiographics.* 2001;21:247–62. Questionnaire 288–294.
- Strouse PJ. Pediatric appendicitis: an argument for US. *Radiology.* 2010;255:8–13.
- Thurley PD, Halliday KE, Somers JM, et al. Radiological features of Meckel's diverticulum and its complications. *Clin Radiol.* 2009;64:109–18.
- Vernacchia FS, Jeffrey RB, Laing FC, et al. Sonographic recognition of pneumatosis intestinalis. *AJR Am J Roentgenol.* 1985;145:51–2.
- Weinstein MM. The persistent loop sign in neonatal necrotizing enterocolitis: a new cause. *Pediatr Radiol.* 1986;16:71–2.

Jung-Eun Cheon

Contents

21.1	Introduction	666
21.2	Inflammatory or Infectious Disease	666
21.2.1	Crohn Disease	666
21.2.2	Ulcerative Colitis	666
21.2.3	Chronic Granulomatous Disease.....	667
21.2.4	Graft-Versus-Host Disease.....	667
21.2.5	Pseudomembranous Colitis.....	667
21.2.6	Neutropenic Colitis	667
21.2.7	Hemolytic-Uremic Syndrome	667
21.3	Neoplasm	668
21.3.1	Lymphoma	668
21.3.2	Polyps.....	668
21.3.3	Mesenteric or Omental Cyst	668
21.3.4	Desmoid Tumors and Other Mesenteric Tumors	668
21.4	Illustrations: Inflammation, Infection, and Neoplasms in the Abdomen	669
21.4.1	Crohn Disease	669
21.4.2	Crohn Disease: MR Enterography	671
21.4.3	Ulcerative Colitis	672
21.4.4	Chronic Granulomatous Disease.....	673
21.4.5	Graft-Versus-Host Disease.....	674
21.4.6	Pseudomembranous Colitis.....	675
21.4.7	Neutropenic Colitis	676
21.4.8	Hemolytic Uremic Syndrome	677
21.4.9	Burkitt Lymphoma	678
21.4.10	Peutz-Jeghers Syndrome	679
21.4.11	Cystic Lymphangioma	680
21.4.12	Inflammatory Myofibroblastic Tumor.....	681
	References	682

J.-E. Cheon, M.D.
Department of Radiology, Seoul National University Hospital,
Seoul National University College of Medicine,
101 Daehak-ro, Jongro-gu, Seoul 110-744, Korea
e-mail: cheonje@snu.ac.kr

21.1 Introduction

This chapter discusses heterogeneous groups of diseases including inflammatory, infectious, infiltrative, or tumorous conditions that involve small and large intestine, mesentery, and omentum.

21.2 Inflammatory or Infectious Disease

21.2.1 Crohn Disease

Crohn disease is a chronic, recurrent, segmental, transmural, noncaseating, granulomatous inflammatory bowel disease. The ileocolic region is the most frequently involved segment, but the disease has been described everywhere in the GI tract from the mouth to the anus. Skip lesions with asymmetric, discontinuous disease are typical. Most children with Crohn disease present with insidious onset of GI symptoms including diarrhea, abdominal pain, anorexia, abdominal mass, or perianal fistula. Associated findings may include failure to thrive with delayed puberty, fever, aphthous stomatitis, arthritis, sacroiliitis, erythema nodosum, and digital clubbing (Aideyan and Smith 1996; Fell 2012).

Radiographic evaluation of the abdomen in patients with inflammatory bowel disease may be nonspecific. Barium contrast small bowel series are frequently used to evaluate small bowel manifestations of Crohn disease. The earliest change is granularity, which probably reflects mucosal edema. More prominent mural edema results in the thickening of mucosal fold and effacement of the mucosal pattern. Typical early findings include nodular irregularity with linear and transverse ulceration. Extensive ulceration can lead to a speculated appearance and a “rose thorn” configuration, which results from deep ulcers extending into the thickened bowel wall. The intersection of multiple linear and transverse ulcers leads to a cobblestone appearance also known as pseudopolyps (Fig. 21.1a). Edema, fibrosis, and spasm lead to narrowing of the intestinal lumen that may be so profound as to be labeled the “string sign.” The mesentery becomes inflamed, thickened, and fibrotic causing separation and retraction of bowel loops (Taylor et al. 1986; Ali and Carty 2000; Antes 2001; Duigenan and Gee 2012).

Ultrasound is an excellent modality in the evaluation of patients with Crohn disease. The involved bowel segment shows a thickened wall with loss of normal alternating bands of mural hyper- and hypoechoogenicity. Surrounding hyper-echoogenicity along the involved bowel loops suggested fibrofatty proliferation in the mesentery (Fig. 21.1b). A halo of submucosal edema may give a target-like appearance to the bowel wall. The bowel wall is markedly hyperemic during exacerbation of disease (Fig. 21.1c, d). Large abscess can be identified (Ruess et al. 2000; Bremner et al. 2006; Alison et al. 2007).

CT readily identifies bowel wall thickening, mesenteric changes such as lymphadenopathy, fibrofatty proliferation, luminal narrowing and stricture formation, and phlegmon formation. Mesenteric changes include fat stranding, fibrofatty proliferation, engorged vasa recta (“comb sign”), and mesenteric lymphadenopathy (Fig. 21.1e). Major intra-abdominal complications of Crohn disease include enteroenteric fistulas, sinus tracts, and abscesses (Fig. 21.1f) (Jabra et al. 1991; Dillman et al. 2010).

MR enterography can be a useful substitute of abdomen CT or CT enterography because of no ionizing radiation. MR enterography shows similar findings seen with contrast-enhanced CT or CT enterography. MR enterography can assess peristalsis using a free-breathing cine sequence and improve visualization of penetrating disease such as ulcer, fistula, and sinus tract, particularly in the perianal region (Fig. 21.2) (Hormann 2008; Dagia et al. 2010; Casciani et al. 2011; Dillman et al. 2011; Gee et al. 2011).

21.2.2 Ulcerative Colitis

Ulcerative colitis (UC) is a chronic, idiopathic inflammatory disease that primarily involves colorectal mucosa and submucosa. The disease is characterized by mucosal inflammation, edema, and ulceration. It is accompanied by submucosal edema in the early stage and fibrosis in the later stage. Transmural disease is uncommon. The disease may be localized in the distal colon or spread to involve the entire colon and the terminal ileum, but skip areas should raise the diagnostic question of Crohn disease (North American Society for Pediatric Gastroenterology et al. 2007).

Most children with UC present with chronic diarrhea, and bloody diarrhea may appear in as many as one-third of affected patients. Many children present with non-gastrointestinal symptoms such as growth retardation, arthritis, seronegative spondyloarthropathy, uveitis, digital clubbing, stomal ulcers, and hepatic dysfunction (primary sclerosing cholangitis and autoimmune hepatitis). Patients with UC for 10 years or longer are at risk for colon cancer (Fig. 21.3) (Hugot and Bellaiche 2007; North American Society for Pediatric Gastroenterology et al. 2007).

Radiographs are nonspecific, but they may show dilatation of colon loops with loss of haustra and thumbprinting appearance of colon loops due to mucosal and submucosal edema. Barium enema shows narrowing of colorectal lumen with fine granular mucosal pattern and “collar button” ulcer due to undermining of ulcers (Fig. 21.3a). This may be accompanied by haustral thickening secondary to edema of the submucosa. The terminal ileum is secondarily affected when there is proximal colonic involvement, known as back-wash ileitis. Ultimately, the colonic wall becomes stiff, shortened, and tubular, the “lead pipe” colon secondary to fibrosis of the

submucosa. When UC is active, CT shows colonic mucosal enhancement with preservation of the smooth outer contour of the bowel. Extraluminal changes such as surrounding fat stranding and mesenteric lymphadenopathy are much less prominent than in patients with Crohn disease (Hugot and Bellaiche 2007; Duignan and Gee 2012).

21.2.3 Chronic Granulomatous Disease

Chronic granulomatous disease of childhood is a primary immunodeficiency characterized by recurrent infection, usually bacterial or fungal infection. It is caused by a defect in one of four genes encoding for NADPH oxidase; the underlying pathology is disordered phagocytosis secondary to phagocytes' inability to generate oxygen radicals. The most common GI manifestation is chronic antral gastritis. Ultrasound typically demonstrates an abnormally thickened antropyloic wall (Fig. 21.4). Chronic granulomatous disease with bowel involvement sometimes mimics Crohn disease (Ament and Ochs 1973; Marciano et al. 2004; Cannioto et al. 2009).

21.2.4 Graft-Versus-Host Disease

Graft-versus-host disease (GVHD) is a reaction of donor lymphocytes against host cells, most commonly in the skin, liver, and GI tract. Acute GVHD occurs within 3 months after transplantation through donor T-lymphocyte-mediated selective damage to epithelial cells lining recipient target organs. Patients with GI manifestations have severe diarrhea and abdominal pain. Frequent accompaniments are skin rash, liver dysfunction through involvement of the biliary epithelium, and hematologic complications.

Radiographs show multiple dilated and fluid-filled loops of small and large bowel, thickening of the bowel wall, and air-fluid level. US reveals thickening of bowel wall, sometimes with a sonolucent ring in the submucosal layer. Small bowel series show diffuse loss of mucosal pattern and mild dilatation, which have been described as "ribbon-like" bowel. CT reveals diffuse bowel abnormality from duodenum to rectum with ring-like, central bowel enhancement corresponding to thin layer of vascular granulation tissue replacing destroyed mucosa (Fig. 21.5). Similar pattern of gallbladder and urinary bladder wall enhancement, hepatomegaly with periportal low attenuation, stranding of the mesenteric fat, and ascites were also seen on CT (Mentzel et al. 2002; O'Malley and Wilson 2003).

21.2.5 Pseudomembranous Colitis

Pseudomembranous colitis is characterized by fever, diarrhea, cramping, and colonic mucositis. The condition

most commonly follows antibiotic therapy, often in debilitated or postoperative patients. Antibiotic therapy or chemotherapy alters gut flora, permitting *Clostridium difficile* overgrowth with release of toxins. The onset of diarrhea may occur 4–9 days after starting antibiotics and up to one-third present within weeks after cessation of antibiotic therapy.

Radiographs show thickened haustral folds, so-called thumbprinting appearance, most commonly in transverse colon. CT demonstrates marked colonic submucosal edema causing wall thickening and nodularity over a long colonic segment. Alternating bands of higher attenuation enteric contrast and lower attenuation thickened haustral folds make "accordion sign" (Fig. 21.6) (Ramachandran et al. 2006; Thoeni and Cello 2006).

21.2.6 Neutropenic Colitis

Neutropenic colitis, also known as typhlitis, is an inflammatory or necrotizing process that involves cecum, ascending colon, and occasionally terminal ileum, primarily seen in children with hematopoietic malignancy or in children with solid tumor who undergo high-dosage chemotherapy. Development of the disease is associated with chemotherapy-related low neutrophil count.

Radiographs are abnormal but nonspecific. US shows a massive thickening of wall of cecum and/or ascending colon that may be either hyperechoic or hypoechoic. CT show marked thickening of the affected portion of the cecum and surrounding inflammatory changes such as pericolic fat strand and thickening of fascial plane (Fig. 21.7). Intramural gas, pericolic fluid collection, or pneumoperitoneum may be seen on CT (Pear 1998; Ripolles et al. 1998; O'Malley and Wilson 2003; Hobson et al. 2005; Thoeni and Cello 2006).

21.2.7 Hemolytic-Uremic Syndrome

The hemolytic-uremic syndrome (HUS), a necrotizing vasculitis, produces acute renal insufficiency, hemolytic anemia, fever, and thrombocytopenia. The disease is probably postinfectious in etiology. Most cases are caused by a toxin from *Escherichia coli* serotype 0157:H7 found in raw or incompletely cooked beef and unpasteurized dairy products. Imaging findings consists of thickening of the involved bowel wall, more typically the colon, seen as "thumbprinting" on abdominal radiographs or contrast enema. Renal and central nervous system complications can markedly affect the course and prognosis of this disease (Fig. 21.8) (Friedland et al. 1995; Garel et al. 2004).

21.3 Neoplasm

21.3.1 Lymphoma

Burkitt lymphoma is a B-cell lymphoma with a predilection for abdominal organ, particularly the distal ileum. It is the most common lead point in children older than 4 years of age with ileocolic intussusception.

Plain radiographs may be normal and may show evidence of obstruction caused by intussusception. Ultrasound in patient with lymphoma typically reveals a mass of low or heterogeneous echogenicity. A mesenteric LN enlargement also may be seen. Lymphoma involving bowel loops is seen as marked thickening of the bowel wall. Large masses may cause aneurysmal dilatation of the bowel lumen (Fig. 21.9). Lymphoma may act as the lead point for intussusception (Chou et al. 1994; Ruess et al. 1995).

21.3.2 Polyps

Isolated juvenile polyps have been considered to be either postinflammatory or hamartomatous. They may be single or multiple, sessile, or pedunculated. There are no reported tendencies toward malignant degeneration. Juvenile polyps are typically diagnosed in children younger than 10 years, who present with painless bright red rectal bleeding. About 75–85 % of juvenile polyps occur in the rectosigmoid colon; however, they can occur anywhere in the large bowel, small bowel, or stomach. They are typically smooth and less than 2 cm in diameter.

Intestinal polyposis syndromes may be hereditary or nonhereditary. Polyposis syndrome associated with adenomatous polyps is familial adenomatous polyposis and its variant such as Gardner syndrome. Polyposis-associated hamartomatous or juvenile polyps include Peutz–Jeghers syndrome, juvenile polyposis syndrome, and Cowden syndrome. Peutz–Jeghers syndrome is an autosomal dominant hamartomatous polyposis that is characterized by hamartomatous polyps and mucocutaneous pigmentation. Most of

the hamartomatous polyps are occurred in the small bowel (Fig. 21.10). An increased incidence of adenocarcinoma in the small bowel as well as other intestinal and extraintestinal malignancies has been reported in patients with Peutz–Jeghers syndrome. Juvenile polyposis syndrome is an uncommon autosomal dominant syndrome consisting of hamartomatous polyps with malignant potential. The diagnosis can be made in a child with multiple hamartomatous colonic polyps (>5), in a child with any number of hamartomatous polyps with a positive family history of juvenile polyposis syndrome, or in a child with extracolonic hamartomatous polyps (Baldisserotto et al. 2002; Chaubal et al. 2002; Zhang et al. 2012).

21.3.3 Mesenteric or Omental Cyst

Cysts of lymphatic origin can develop in the mesentery, or less commonly, in the omentum or retroperitoneum. Mesenteric cysts most often involve the mesentery of the small bowel. The masses may be unilocular or multilocular. On sonography, the cysts are predominantly anechoic, although debris is frequently present within the fluid. Septations are readily evident on sonography. On CT, a round or multilobular fluid attenuation mass is seen (Fig. 21.11). The cyst may appear as higher signal intensity on T1-weighted image due to high-protein content (Ros et al. 1987; Ruess et al. 1995; Egozi and Ricketts 1997; Levy et al. 2006).

21.3.4 Desmoid Tumors and Other Mesenteric Tumors

Desmoid tumors may be seen in patients with Gardner syndrome (familial adenomatous polyposis, desmoid tumors, and jaw osteomas). Mesenteric neurofibroma may be seen in patients with neurofibromatosis. Rare mesenteric tumors include rhabdomyosarcoma and inflammatory myofibroblastic tumors (Fig. 21.12) (Levy et al. 2006; Kim et al. 2009).

21.4 Illustrations: Inflammation, Infection, and Neoplasms in the Abdomen

21.4.1 Crohn Disease

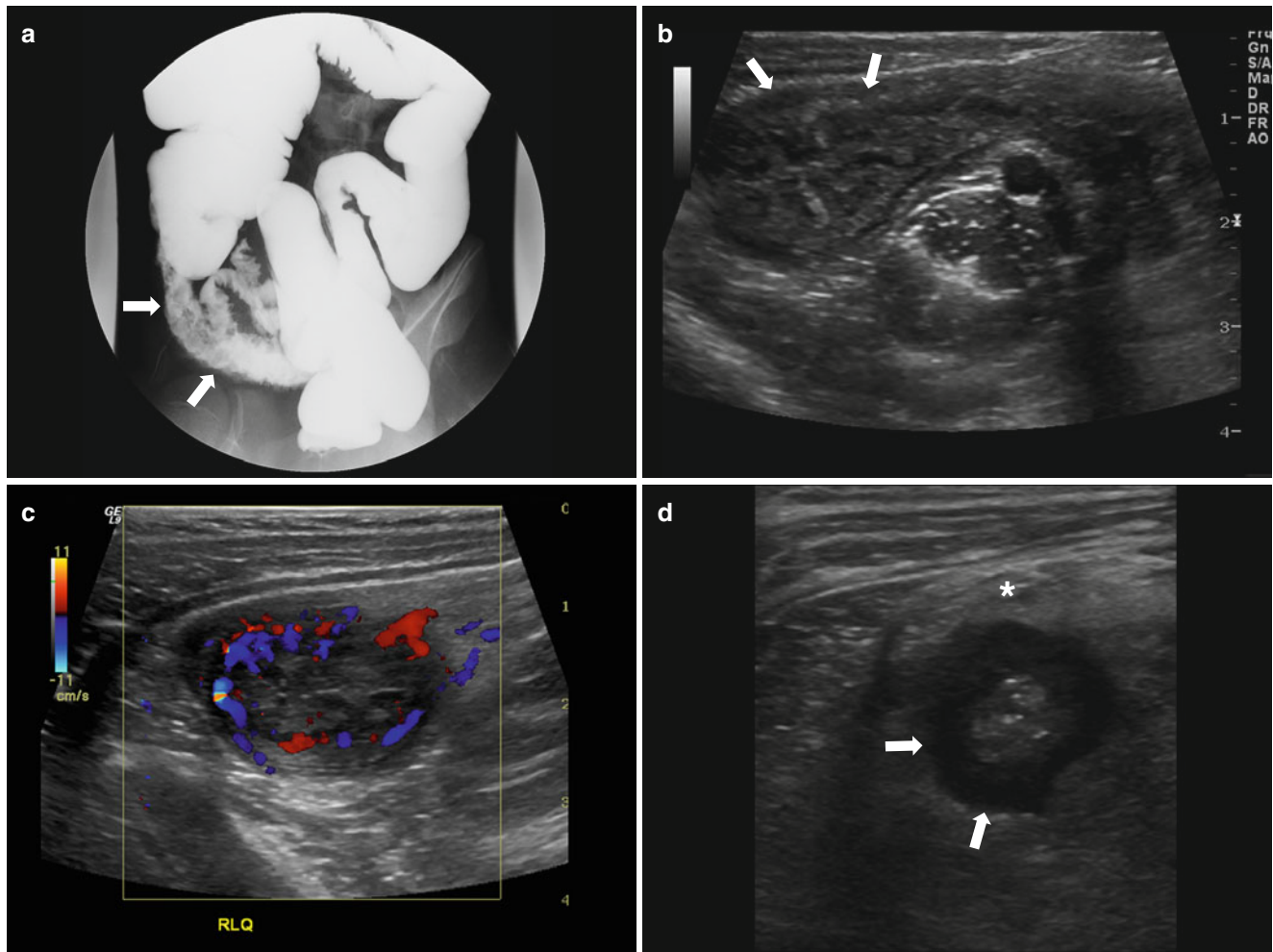


Fig. 21.1 Crohn disease. (a) Small bowel series in an 8-year-old girl with Crohn disease shows irregular loops of the distal ileum with nodular thickening of the mucosal folds and speculated borders (arrows). (b) Ultrasound of the same patient shows diffuse bowel wall thickening with submucosal low echogenicity in the distal ileum (arrows). (c) Color Doppler ultrasound shows increased vascularity of the involved distal small bowel loops. (d) Ultrasound of the same patient 6 years later shows diffuse thickening of the bowel loops with

loss of normal mucosal layering (arrows) and diffuse echogenicity (*) along the bowel loops suggesting fatty proliferation. (e) Coronal view of contrast-enhanced CT of the same patient demonstrates mucosal hyperenhancement (arrows) wall thickening and multiple mesenteric LNS in the RLQ. Note the engorged vasa recta suggesting comb sign in the LLQ (open arrow) and enhancing fistulous tract in the RLQ (arrowheads). (f) An abscess with irregular enhancing wall (arrow) is also seen in RLQ

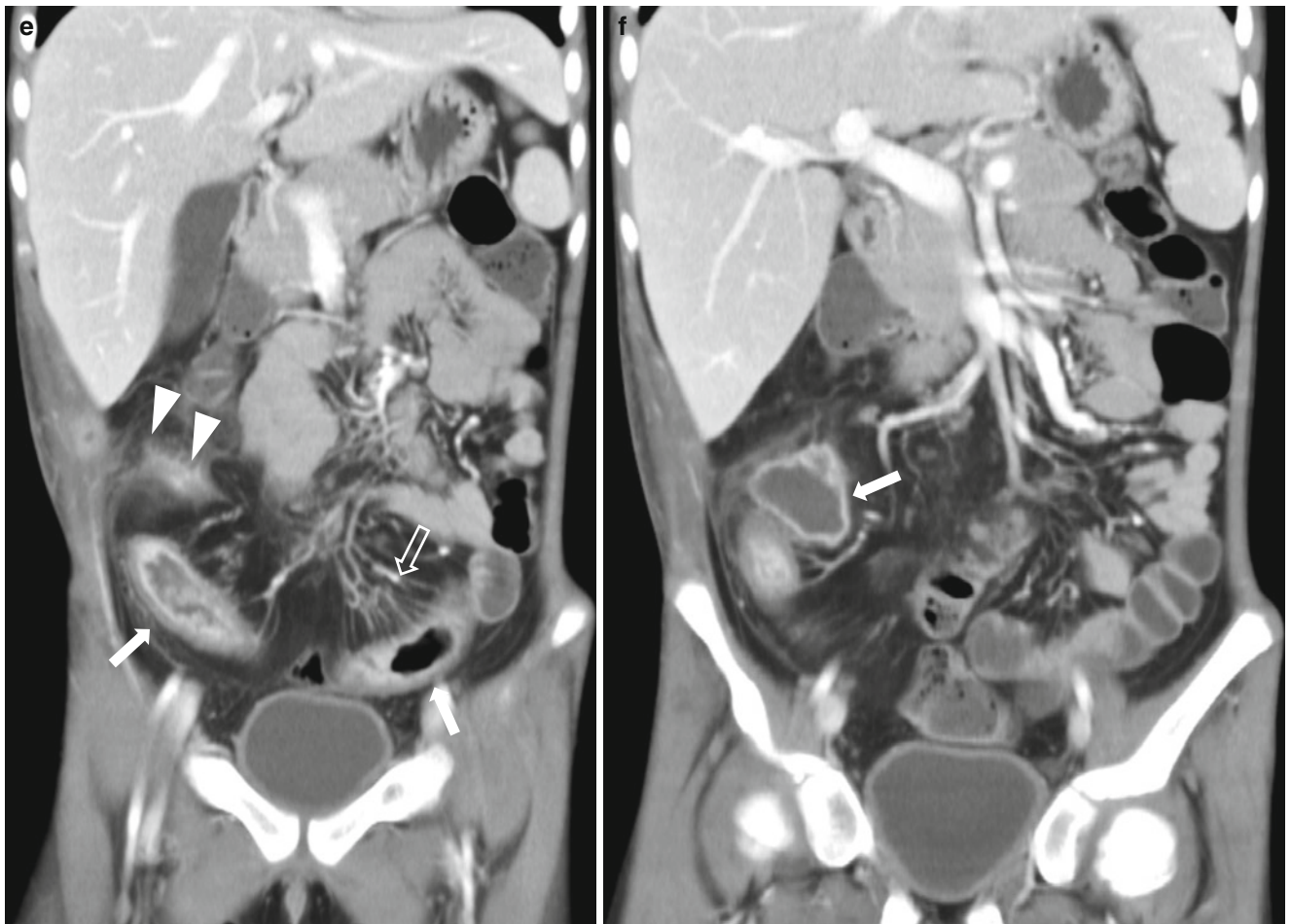


Fig. 21.1 (continued)

21.4.2 Crohn Disease: MR Enterography

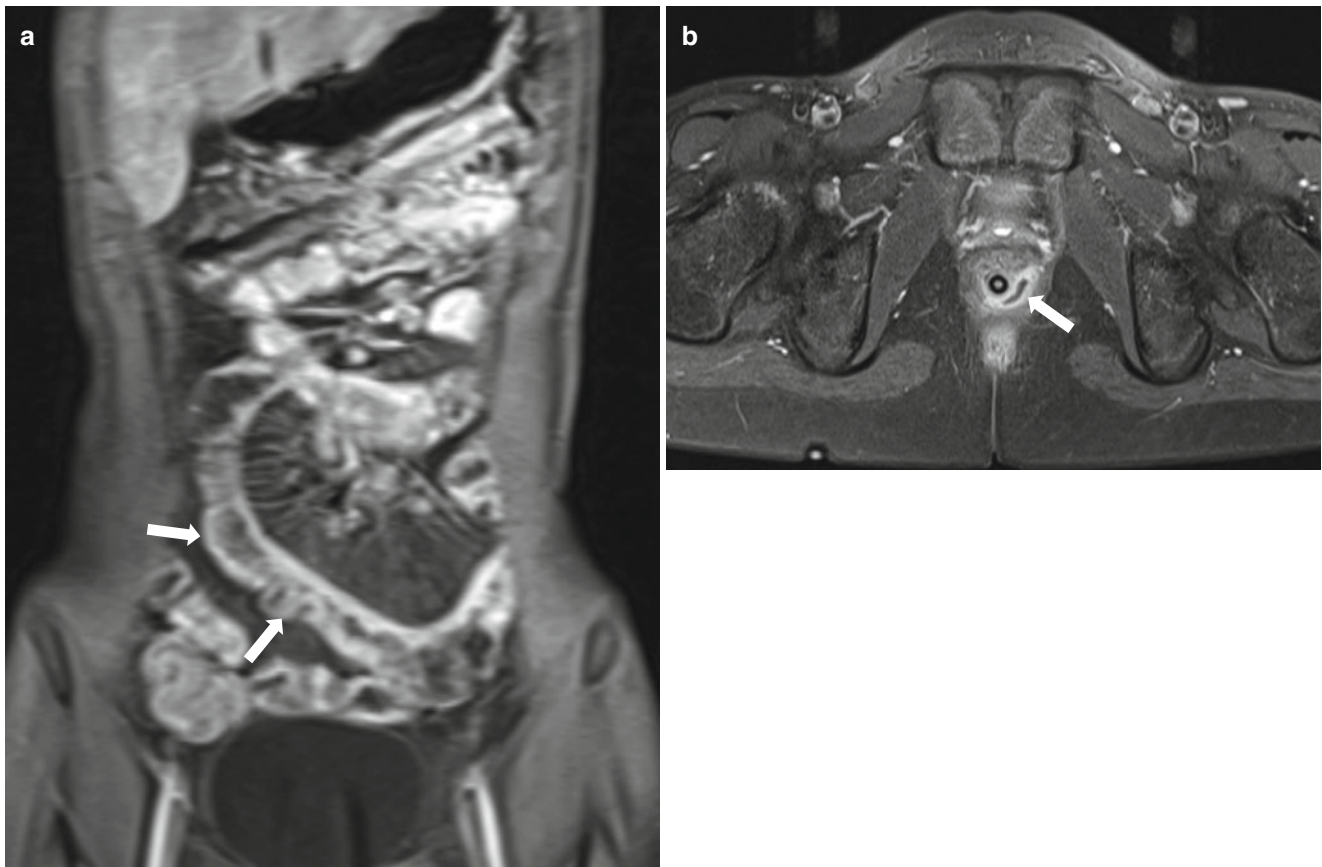


Fig. 21.2 Crohn disease: MR enterography. **(a)** Coronal view of contrast-enhanced T1-weighted image of a 19-year-old male demonstrates mucosal hyperenhancement and engorged vasa recta of the small bowel segments indicating active inflammation. Note the pseudosacculation

of the distal small bowel loops (*arrows*). **(b)** Axial view of contrast-enhanced T1-weighted image of a 10-year-old boy shows peripheral-enhancing perianal abscess from 3 to 6 o'clock direction (*arrow*)

21.4.3 Ulcerative Colitis

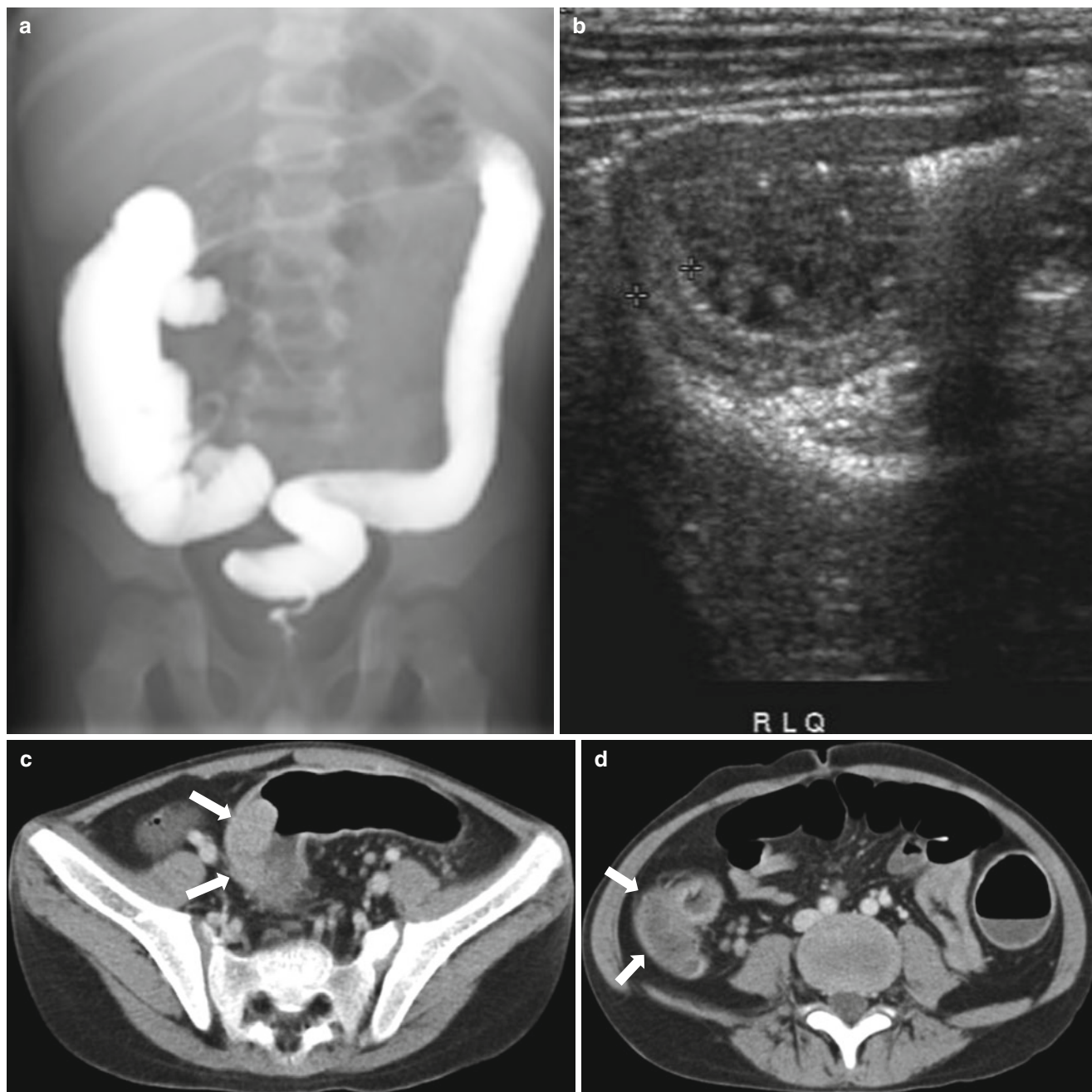


Fig. 21.3 Ulcerative colitis. (a) Barium enema of a 5-year-old boy shows loss of haustra and fine nodularities in the descending colon and transverse colon. (b) Ultrasound demonstrates diffuse bowel wall thickening in the entire colon. (c, d) Follow-up CT obtained 10 years later

shows a polypoid mass (c, arrows) in the sigmoid colon and diffuse bowel wall thickening in the ascending colon (d, arrows). Total proctocolectomy was performed and the sigmoid mass was confirmed as adenocarcinoma

21.4.4 Chronic Granulomatous Disease

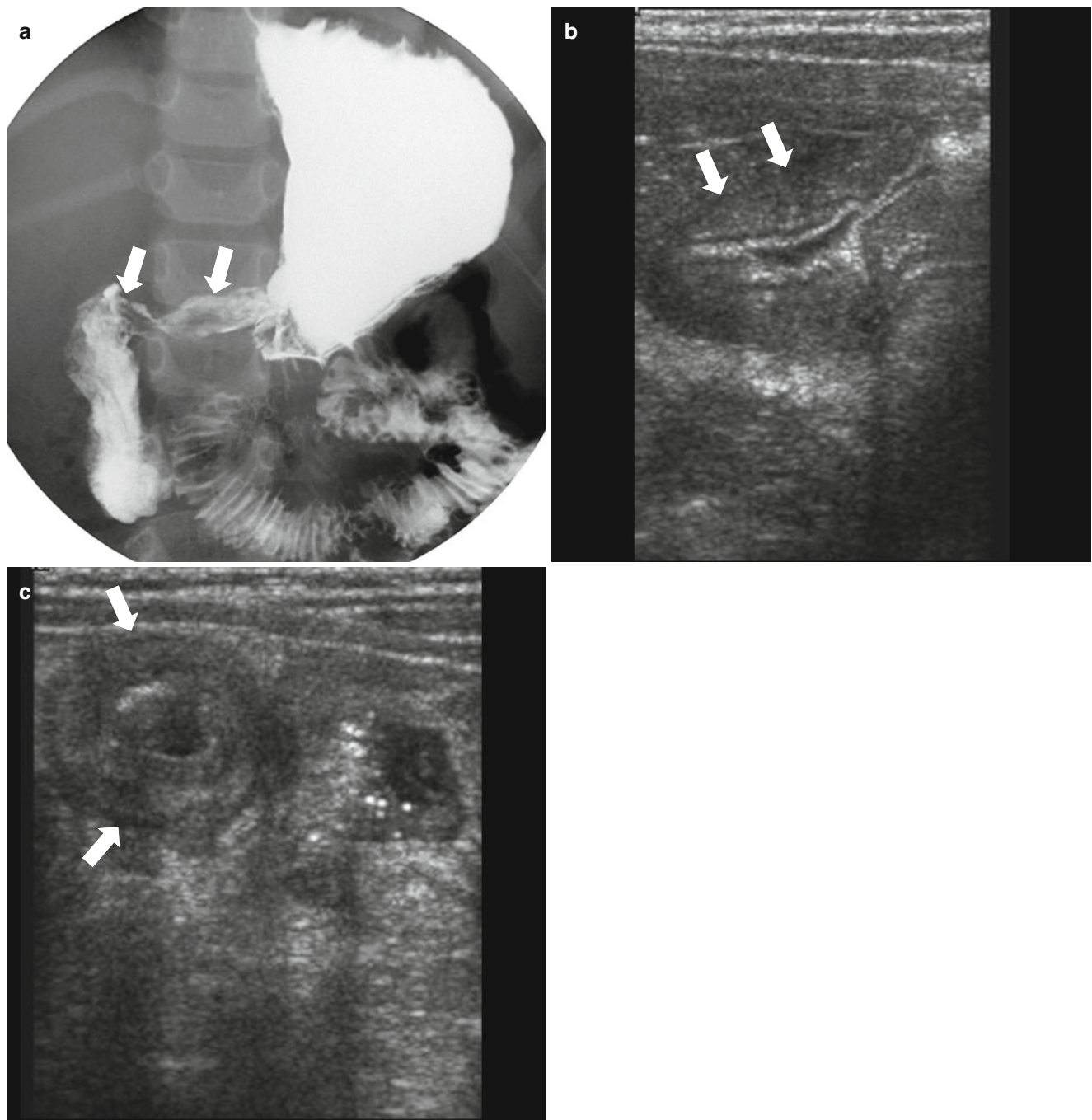


Fig. 21.4 Chronic granulomatous disease. (a) A 5-year-old boy with known chronic granulomatous disease presents with recurrent vomiting. Upper GI series demonstrates segmental narrowing of the antrum

and collapsed duodenal bulb (*arrows*). (b, c) Ultrasound images show diffuse wall thickening in the distal antrum (*arrows*, b) and duodenal bulb (*arrows*, c) suggesting chronic granulomatous disease involvement

21.4.5 Graft-Versus-Host Disease

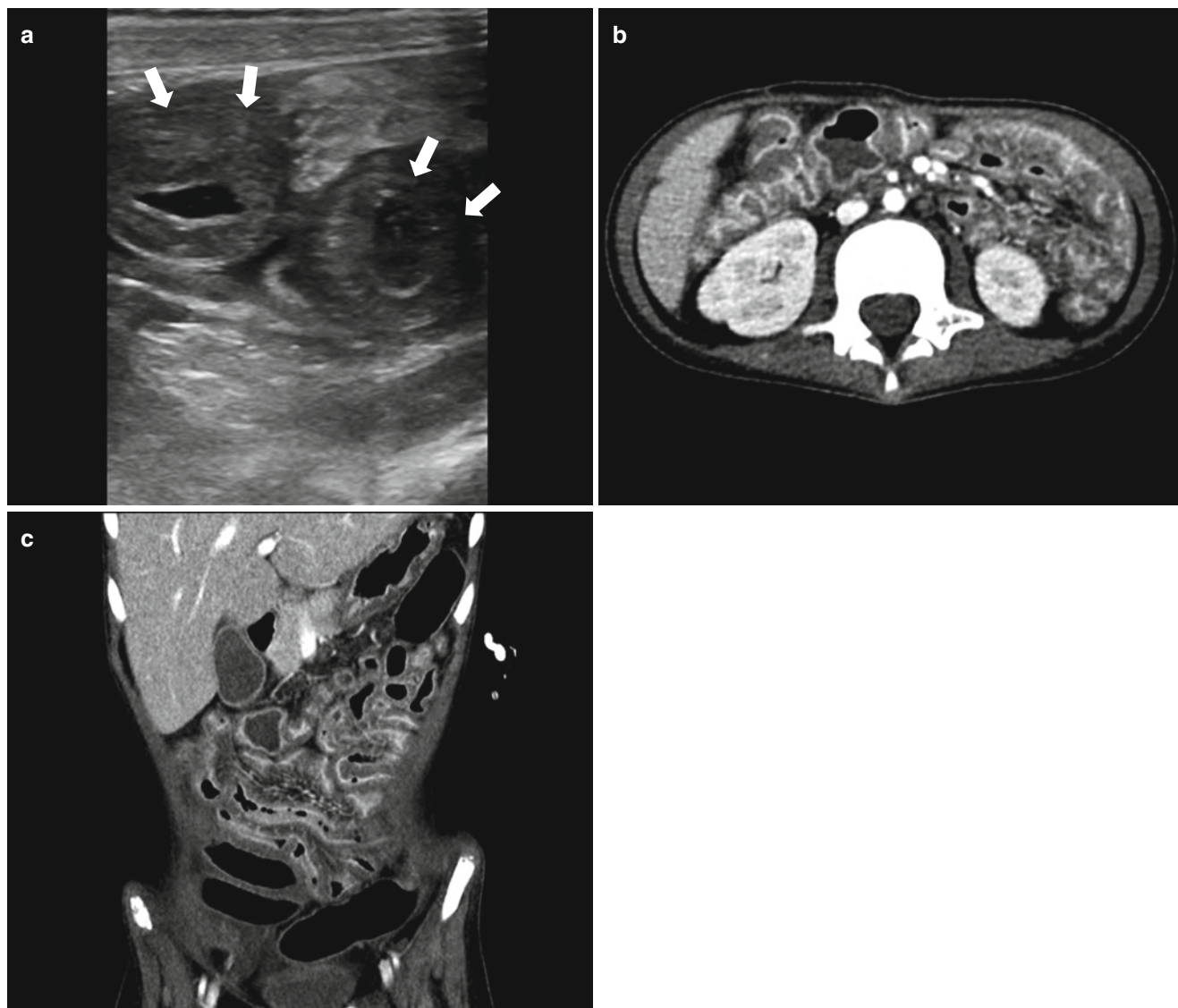


Fig. 21.5 Graft-versus-host disease. (a) Ultrasound of a 6-year-old boy with acute leukemia and recent stem cell transplantation shows diffuse bowel wall thickening in the small bowel loops with

submucosal low echogenicity in the RLQ (*arrows*). (b, c) Axial and coronal contrast-enhanced CT show thickened bowel loops and a thin layer of mucosal enhancement

21.4.6 Pseudomembranous Colitis

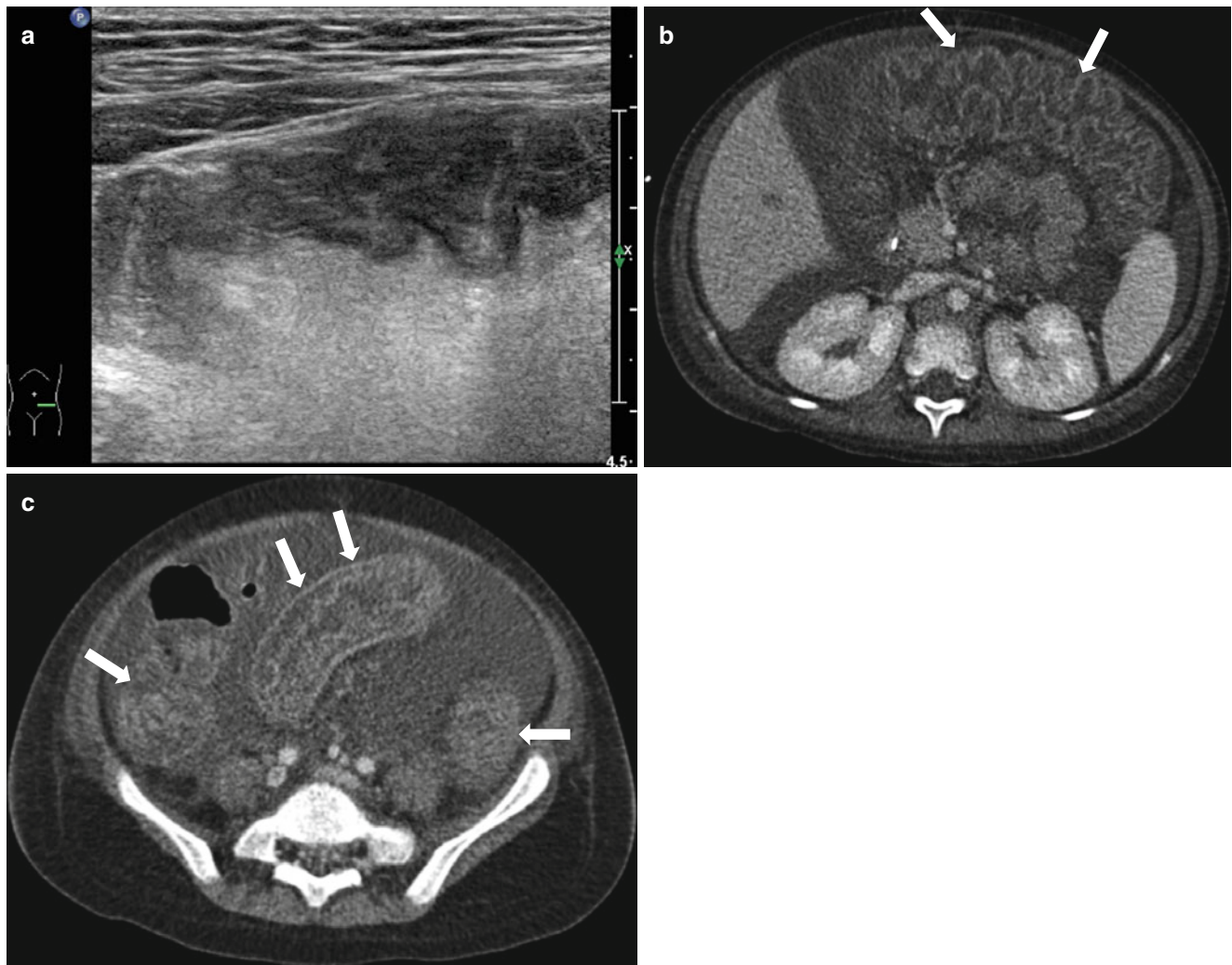


Fig. 21.6 Pseudomembranous colitis. (a) Ultrasound of a 4-year-old boy with acute leukemia shows diffuse bowel wall thickening in the LLQ. He has been treated with antibiotics since 7 days ago, and *Clostridium difficile* toxin assay was positive. (b, c) Axial images of

contrast-enhanced CT show markedly thickened haustral folds in the entire colon suggesting “accordion sign” (arrows). Moderate amount ascites are also seen on CT images

21.4.7 Neutropenic Colitis

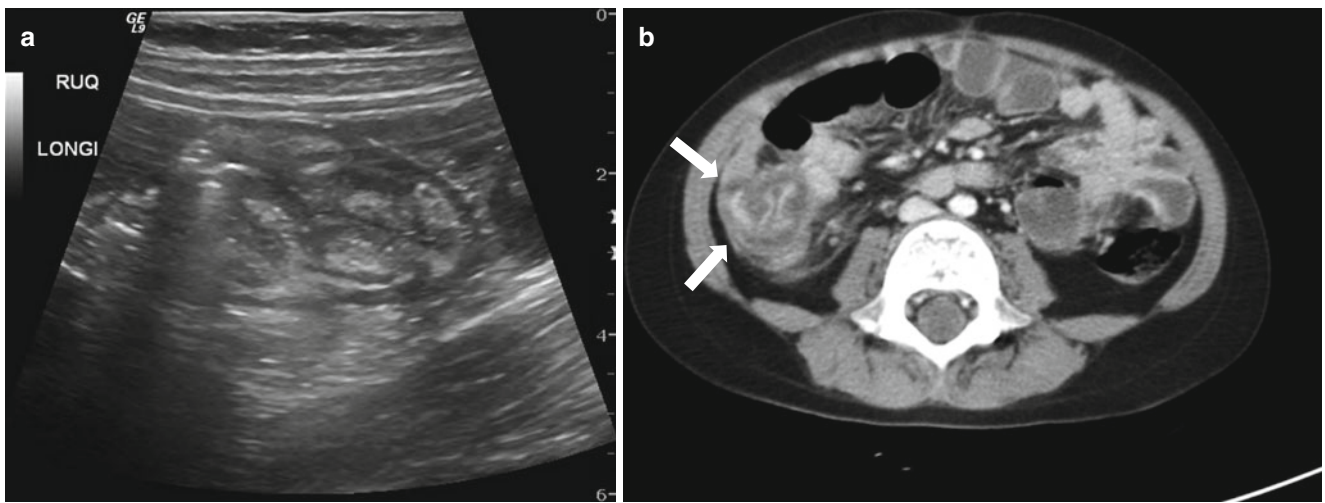


Fig. 21.7 Typhlitis in a 10-year-old with acute leukemia, status post bone marrow transplantation. **(a)** Ultrasound shows diffuse edematous thickening in the cecum and ascending colon. **(b)** Axial contrast-

enhanced CT shows circumferential wall thickening of the cecum and ascending colon with pericolic fat strands (*arrows*)

21.4.8 Hemolytic Uremic Syndrome

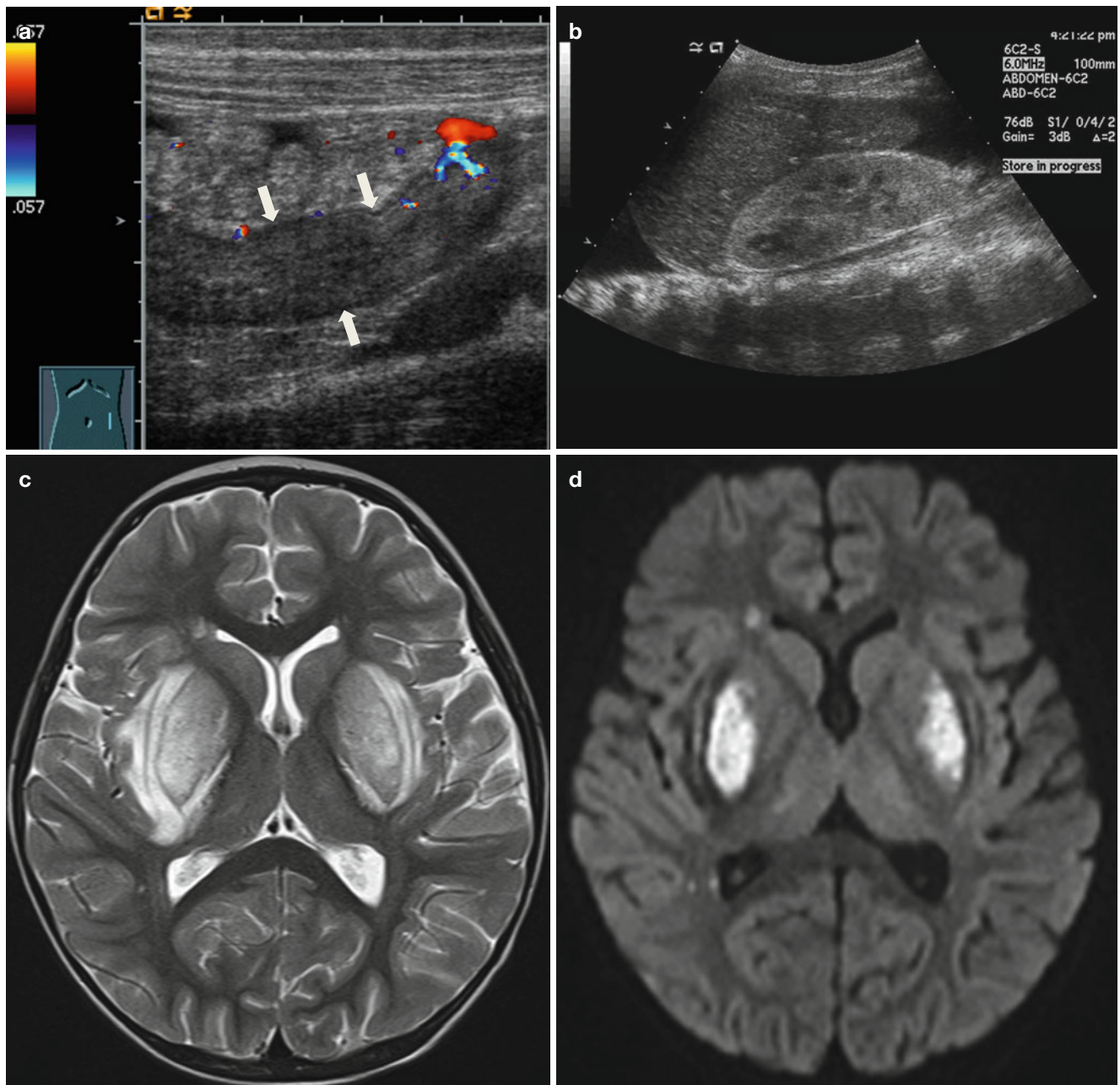


Fig. 21.8 Hemolytic-uremic syndrome. (a, b) Ultrasound of a 2-year-old girl with fever and anuria shows diffuse bowel wall thickening in the descending colon with decreased perfusion (a, arrows) and diffuse increased parenchymal echogenicity of the kidneys (b). There are mod-

erate amount of pleural effusion and ascites. (c) Axial T2-weighted image shows bilateral edematous swelling in the basal ganglia. (d) Bilateral basal ganglia lesions shows restricted diffusion

21.4.9 Burkitt Lymphoma

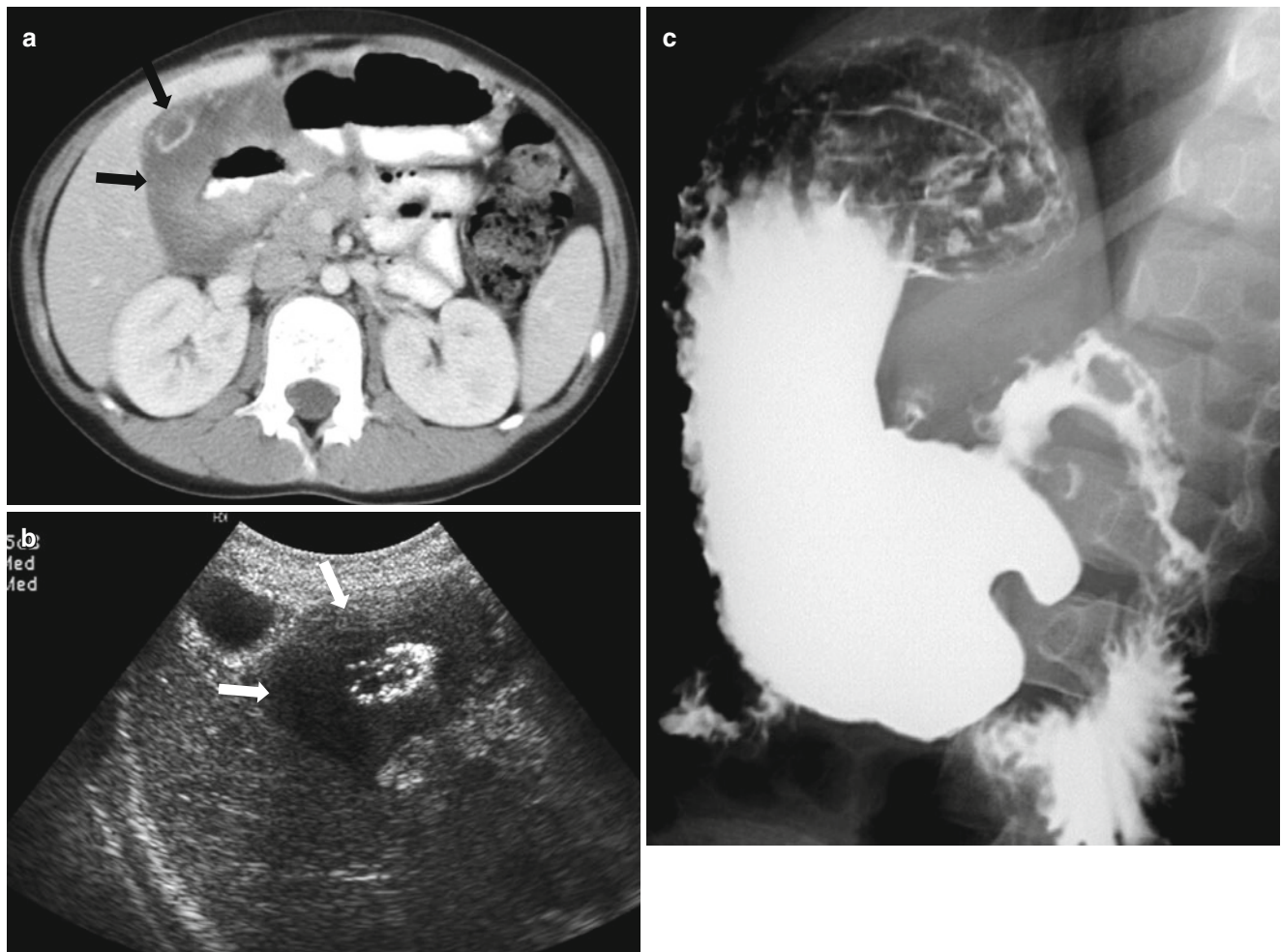


Fig. 21.9 Burkitt lymphoma with bowel involvement. (a) Contrast-enhanced CT of a 4-year-old boy presented with abdominal pain and vomiting shows hypoattenuating, diffuse wall thickening involving duodenal bulb and second portion of the duodenum (arrows). (b)

Ultrasound shows diffuse hypoechoic lesion involving duodenum (arrows). (c) Upper GI series shows irregular fold thickening involving the duodenum first and second portions

21.4.10 Peutz–Jeghers Syndrome

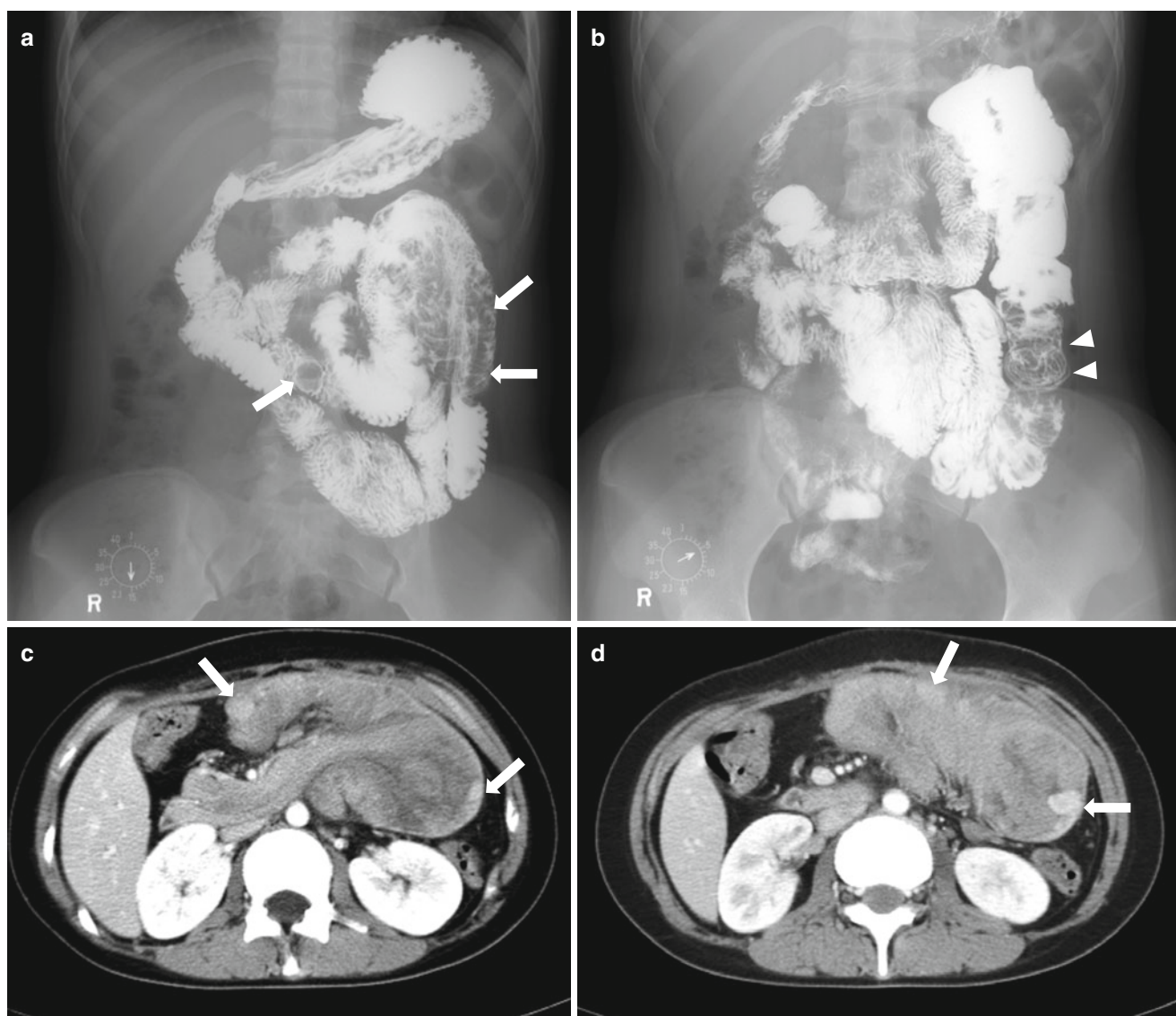


Fig. 21.10 Peutz–Jeghers syndrome. (a, b) Small bowel series show multiple polyps as filling defect in the proximal jejunum (a, arrows). Note the coil spring appearance at proximal jejunum suggesting intussusception (b, arrowheads). (c, d) Axial post-contrast CT of another

patient with Peutz–Jeghers syndrome shows a huge small bowel intussusception due to polyps. Note the enhancing polyps within the intussusceptum (arrows)

21.4.11 Cystic Lymphangioma

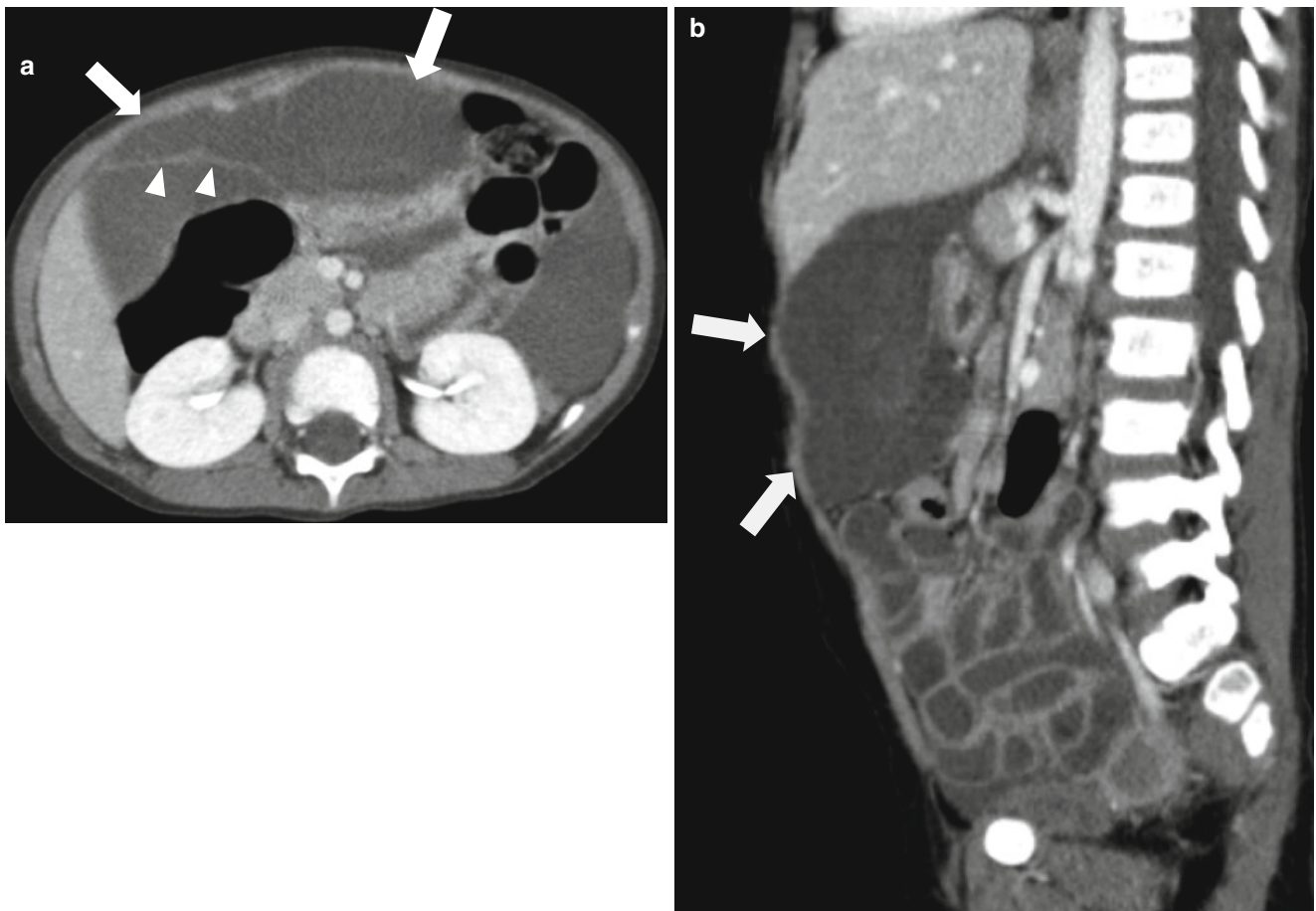


Fig. 21.11 Cystic lymphangioma in the omentum. (a, b) Axial and sagittal contrast-enhanced CT of 2-year-old boy show a huge cystic mass arising from lesser omentum (*arrows*). Fine-enhancing septa are seen within the cystic mass (*a*, *arrowheads*)

21.4.12 Inflammatory Myofibroblastic Tumor

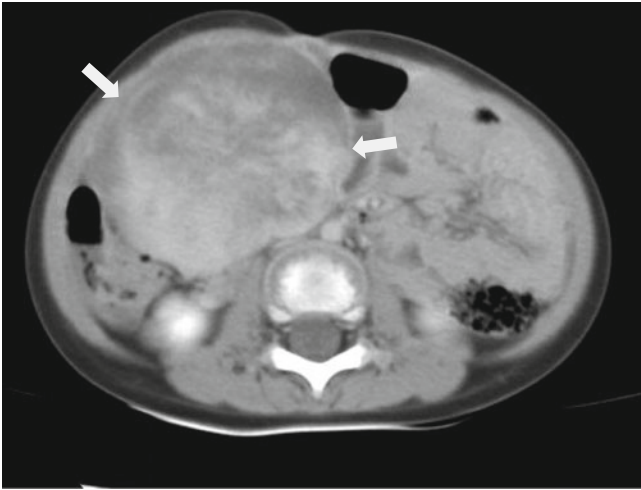


Fig. 21.12 Inflammatory myofibroblastic tumor Axial contrast-enhanced CT shows heterogeneously enhancing solid mass in the RUQ (*arrows*). Excisional biopsy reveals inflammatory myofibroblastic tumor arising from the mesentery

References

- Aideyan UO, Smith WL. Inflammatory bowel disease in children. *Radiol Clin North Am.* 1996;34:885–902.
- Ali SI, Carty HM. Paediatric Crohn's disease: a radiological review. *Eur Radiol.* 2000;10:1085–94.
- Alison M, Kheniche A, Azoulay R, et al. Ultrasonography of Crohn disease in children. *Pediatr Radiol.* 2007;37:1071–82.
- Ament ME, Ochs HD. Gastrointestinal manifestations of chronic granulomatous disease. *N Engl J Med.* 1973;288:382–7.
- Antes G. Enteroclysis in children with Crohn's disease. *Eur Radiol.* 2001;11:2341–2.
- Baldisserotto M, Spolidoro JV, Bahu Mda G. Graded compression sonography of the colon in the diagnosis of polyps in pediatric patients. *AJR Am J Roentgenol.* 2002;179:201–5.
- Bremner AR, Griffiths M, Argent JD, et al. Sonographic evaluation of inflammatory bowel disease: a prospective, blinded, comparative study. *Pediatr Radiol.* 2006;36:947–53.
- Cannito Z, Berti I, Martellosi S, et al. IBD and IBD mimicking enterocolitis in children younger than 2 years of age. *Eur J Pediatr.* 2009;168:149–55.
- Casciani E, Masselli G, Di Nardo G, et al. MR enterography versus capsule endoscopy in paediatric patients with suspected Crohn's disease. *Eur Radiol.* 2011;21:823–31.
- Chaubal N, Shah M, Dighe M, et al. Juvenile polyposis of the colon: sonographic diagnosis. *J Ultrasound Med.* 2002;21:1311–4.
- Chou CK, Chen LT, Sheu RS, et al. MRI manifestations of gastrointestinal lymphoma. *Abdom Imaging.* 1994;19:495–500.
- Dagia C, Ditchfield M, Kean M, et al. Feasibility of 3-T MRI for the evaluation of Crohn disease in children. *Pediatr Radiol.* 2010;40:1615–24.
- Dillman JR, Adler J, Zimmermann EM, et al. CT enterography of pediatric Crohn disease. *Pediatr Radiol.* 2010;40:97–105.
- Dillman JR, Ladino-Torres MF, Adler J, et al. Comparison of MR enterography and histopathology in the evaluation of pediatric Crohn disease. *Pediatr Radiol.* 2011;41:1552–8.
- Duignan S, Gee MS. Imaging of pediatric patients with inflammatory bowel disease. *AJR Am J Roentgenol.* 2012;199:907–15.
- Egozi EI, Ricketts RR. Mesenteric and omental cysts in children. *Am Surg.* 1997;63:287–90.
- Fell JM. Update of the management of inflammatory bowel disease. *Arch Dis Child.* 2012;97:78–83.
- Friedland JA, Herman TE, Siegel MJ. *Escherichia coli* O157:H7-associated hemolytic-uremic syndrome: value of colonic color Doppler sonography. *Pediatr Radiol.* 1995;25 Suppl 1:S65–67.
- Garel L, Vazquez E, Lucaya J. Clinical quiz. Bilateral thalamic infarcts in hemolytic uremic syndrome. *Pediatr Radiol.* 2004;34:92–3.
- Gee MS, Nimkin K, Hsu M, et al. Prospective evaluation of MR enterography as the primary imaging modality for pediatric Crohn disease assessment. *AJR Am J Roentgenol.* 2011;197:224–31.
- Hobson MJ, Carney DE, Molik KA, et al. Appendicitis in childhood hematologic malignancies: analysis and comparison with typhlitis. *J Pediatr Surg.* 2005;40:214–9. Discussion 219–220.
- Hormann M. MR imaging of the gastro-intestinal tract in children. *Eur J Radiol.* 2008;68:271–7.
- Hugot JP, Bellaiche M. Inflammatory bowel diseases: the paediatric gastroenterologist's perspective. *Pediatr Radiol.* 2007;37:1065–70.
- Jabra AA, Fishman EK, Taylor GA. Crohn disease in the pediatric patient: CT evaluation. *Radiology.* 1991;179:495–8.
- Kim SJ, Kim WS, Cheon JE, et al. Inflammatory myofibroblastic tumors of the abdomen as mimickers of malignancy: imaging features in nine children. *AJR Am J Roentgenol.* 2009;193:1419–24.
- Levy AD, Rimola J, Mehrotra AK, et al. From the archives of the AFIP: benign fibrous tumors and tumorlike lesions of the mesentery: radiologic-pathologic correlation. *Radiographics.* 2006;26:245–64.
- Marciano BE, Rosenzweig SD, Kleiner DE, et al. Gastrointestinal involvement in chronic granulomatous disease. *Pediatrics.* 2004;114:462–8.
- Mentzel HJ, Kentouche K, Kosmehl H, et al. US and MRI of gastrointestinal graft-versus-host disease. *Pediatr Radiol.* 2002;32:195–8.
- North American Society for Pediatric Gastroenterology H, Nutrition, Colitis Foundation of America, et al. Differentiating ulcerative colitis from Crohn disease in children and young adults: report of a working group of the North American Society for Pediatric Gastroenterology, Hepatology, and Nutrition and the Crohn's and Colitis Foundation of America. *J Pediatr Gastroenterol Nutr.* 2007;44:653–74.
- O'Malley ME, Wilson SR. US of gastrointestinal tract abnormalities with CT correlation. *Radiographics.* 2003;23:59–72.
- Pear BL. Pneumatosis intestinalis: a review. *Radiology.* 1998;207:13–9.
- Ramachandran I, Sinha R, Rodgers P. Pseudomembranous colitis revisited: spectrum of imaging findings. *Clin Radiol.* 2006;61:535–44.
- Ripolles T, Martinez-Perez MJ, Morote V, et al. Diseases that simulate acute appendicitis on ultrasound. *Br J Radiol.* 1998;71:94–8.
- Ros PR, Olmsted WW, Moser Jr RP, et al. Mesenteric and omental cysts: histologic classification with imaging correlation. *Radiology.* 1987;164:327–32.
- Ruess L, Blask AR, Bulas DI, et al. Inflammatory bowel disease in children and young adults: correlation of sonographic and clinical parameters during treatment. *AJR Am J Roentgenol.* 2000;175:79–84.
- Ruess L, Frazier AA, Sivrit CJ. CT of the mesentery, omentum, and peritoneum in children. *Radiographics.* 1995;15:89–104.
- Taylor GA, Nancarrow PA, Hernanz-Schulman M, et al. Plain abdominal radiographs in children with inflammatory bowel disease. *Pediatr Radiol.* 1986;16:206–9.
- Thoeni RF, Cello JP. CT imaging of colitis. *Radiology.* 2006;240:623–38.
- Zhang Y, Li SX, Xie LM, et al. Sonographic diagnosis of juvenile polyps in children. *Ultrasound Med Biol.* 2012;38:1529–33.

Mi-Jung Lee and Myung-Joon Kim

Contents

22.1	Liver and Biliary Disease	684
22.1.1	Anatomy and Development	684
22.1.2	Investigation of Liver and Biliary Disease.....	684
22.1.3	Imaging of Liver and Biliary Disease.....	684
22.1.4	Spectrum of Liver and Biliary Disease	684
22.2	Pancreatic Disease	687
22.2.1	Anatomy and Development	687
22.2.2	Spectrum of Pancreatic Disease.....	687
22.3	Splenic Disease	688
22.3.1	Anatomy and Development	688
22.3.2	Spectrum of Splenic Disease	688
22.4	Illustrations: Liver, Biliary Tract, Pancreas, and Spleen	689
22.4.1	Neonatal Hepatitis.....	689
22.4.2	Fungal Infection	692
22.4.3	Nonalcoholic Steatohepatitis	693
22.4.4	Glycogen Storage Disease	694
22.4.5	Biliary Atresia.....	695
22.4.6	Alagille Syndrome	696
22.4.7	Choledochal Cyst.....	697
22.4.8	Caroli Disease	698
22.4.9	Bile-Plug Syndrome.....	699
22.4.10	Spontaneous Perforation of the Bile Duct	700
22.4.11	Cholelithiasis and Cholecystitis	701
22.4.12	Hepatoblastoma.....	702
22.4.13	Hepatic Hemangioendothelioma.....	704
22.4.14	Mesenchymal Hamartoma	707
22.4.15	Focal Nodular Hyperplasia	708
22.4.16	Annular Pancreas	709
22.4.17	Acute Pancreatitis	710
22.4.18	Pancreatoblastoma	711
22.4.19	Solid and Papillary Epithelial Neoplasm	712
22.4.20	Normal Spleen	713
22.4.21	Splenomegaly.....	714
22.4.22	Splenic Hamartoma.....	716
22.4.23	Splenic Injury.....	718
	References	719

M.-J. Lee, M.D. • M.-J. Kim, M.D. (✉)
Department of Radiology, Severance Children's Hospital
and Yonsei University College of Medicine,
50 Yonsei-ro, Seodaemun-gu, Seoul 120-752, Korea
e-mail: mjkim@yuhs.ac

22.1 Liver and Biliary Disease

22.1.1 Anatomy and Development

Liver development begins during the third week of gestation, from the ventral foregut endoderm, which gives rise to the liver bud or hepatic diverticulum. The liver reaches peak relative size in the ninth week of gestation. At 12 weeks' gestation, the liver is the main site of hemopoiesis, and this function remains in the neonatal period up to 6 weeks after birth. Hepatic bud forms hepatocytes and produces bile from 13 weeks' gestation (Blickman et al. 2009).

The extrahepatic and intrahepatic biliary systems develop from the endoderm as two independent subunits, and these merge at the end of the developmental process. However, the proliferation and development of the intrahepatic biliary system continues even after birth, and the number of bile ducts per portal tract continues to increase until 15 years of age.

The arterial supply to the liver and biliary tree is variable in its origin and course due to its complex embryological development. The liver has a unique dual blood supply from the hepatic artery and portal vein.

22.1.2 Investigation of Liver and Biliary Disease

The approach to pediatric liver and biliary disease should be systematic and multidisciplinary, involving clinical chemistry, hematology, radiology, histopathology, and microbiology.

Almost two-thirds of patients with pediatric liver disease present in the neonatal period with persistent jaundice. Although physiologic jaundice is common in neonates, infants who develop severe or persistent jaundice beyond 14 or 21 days should be investigated to exclude hemolysis, sepsis, or underlying liver and biliary disease. The disease in children older than 6 months may be acute or chronic. It may be due to infection, autoimmune disease, drug-induced hepatitis, or metabolic disease, or it may be secondary to disease elsewhere. It is also essential to establish whether the jaundice is due to an increase in conjugated or unconjugated hyperbilirubinemia.

Hepatic masses in children constitute about 5 % of all intra-abdominal masses. The majority are malignant and about one-third are benign. A differential diagnosis of hepatic tumors in children can be obtained based on the age of the child, alpha-fetoprotein (AFP), and imaging characteristics.

22.1.3 Imaging of Liver and Biliary Disease

Several imaging techniques provide valuable information in the investigation and diagnosis of pediatric liver and biliary disease.

Abdominal ultrasonography (US) is commonly used as the initial test because it is noninvasive, easily available and can identify structural abnormalities of the hepatobiliary tract. It provides information on the size and consistency of the liver, biliary tract, spleen, pancreas, and kidneys; on the size of the gallbladder; and on the presence of gallstones. It may identify tumors, hemangiomas, abscesses, or cysts within the liver, and it allows targeting of lesions for liver biopsy. The gallbladder is best visualized after a 4–6 h fast. A small or absent gallbladder after fasting suggests either severe intrahepatic cholestasis or biliary atresia in the neonate. Extrahepatic bile ducts are usually identified, but intrahepatic bile ducts are rarely seen unless dilated as a result of biliary obstruction.

Computed tomography (CT) is useful but limited in children. Intravenous contrast material causes enhancement of vascular lesions and of the walls of abscesses and may be helpful in differentiating tumors from other solid masses.

Magnetic resonance imaging (MRI) is now the best way to stage or diagnose hepatic tumors and identify their vascular supply. It may provide valuable information about storage disease of heavy metals such as iron in hemochromatosis and copper in Wilson's disease. MR cholangiopancreatography (MRCP) can provide the information of both intrahepatic and extrahepatic biliary duct abnormalities.

Hepatobiliary scintigraphy uses soluble radioisotopes which are taken up well by hepatocytes despite elevated bilirubin levels. This technique can be used to demonstrate either hepatic uptake or biliary excretion. Hepatic uptake is an index of hepatic function and may be patchy in inflammatory conditions. This technique is most useful in the assessment of biliary excretion in the differential diagnosis of neonatal cholestasis. Under normal conditions, biliary excretion is completed within 4 h. Delayed excretion or no excretion after 24 h suggests severe intrahepatic cholestasis or extrahepatic biliary atresia.

22.1.4 Spectrum of Liver and Biliary Disease

22.1.4.1 Liver Disease

22.1.4.1.1 Neonatal Hepatitis

Cytomegalovirus and hepatitis B virus are the most common etiologic agents that produce chronic inflammation, fibrosis, and cirrhosis (Kelly 2008). Imaging findings with US, CT, and MRI are often normal (Figs. 22.1 and 22.2). There can be periportal edema and wall thickening of the gallbladder on US. Small-sized gallbladder can be seen in cases with severe hepatic dysfunction. Common bile duct can be seen in the pancreas head portion. MRCP is helpful in evaluating the extrahepatic bile duct and gallbladder. On hepatobiliary scintigraphy, infants with neonatal hepatitis typically have delayed uptake but appropriate excretion.

22.1.4.1.2 Fungal Infections

Fungal infections almost always occur in immune-deficient patients with hemato-oncologic malignancy or chronic disease with corticosteroid therapy. *Candida* is the most common pathogen. Imaging findings are not specific enough to differentiate fungal from viral or bacterial infection. Multiple focal lesions with variable size can be seen on US as hypoechoic lesions and on CT as low-density lesions. Bull's eye appearance, which is a hyperechoic portion in the center of a hypoechoic lesion, is a typical finding on US (Fig. 22.3) (Siegel 2011).

22.1.4.1.3 Fatty Liver Disease

Fatty liver disease can cover a severity spectrum ranging from dormant non-inflammatory fatty liver to steatohepatitis with inflammation, fibrosis, and eventually cirrhosis. Nonalcoholic fatty liver disease (NAFLD) is now the most common form of chronic liver disease in children, affecting up to 10 % of children in the United States (Tang et al. 2013). Most cases are associated with being overweight or type 2 diabetes mellitus. US or CT indicates fat density in the liver. Using MRI on opposed-phase images, focal fatty infiltration appears as a region of decreased signal intensity compared with the in-phase signal intensity (Fig. 22.4) (Boll and Merkle 2009). MRI is also helpful in grading hepatic steatosis and is a promising tool in estimating hepatic fibrosis.

Steatohepatitis is also associated with Wilson's disease, hereditary fructose intolerance, tyrosinemia, HCV hepatitis, cystic fibrosis, fatty acid oxidation defects, kwashiorkor, Reye's syndrome, respiratory chain defects, and toxic hepatopathy (ethanol and others).

22.1.4.1.4 Glycogen Storage Disease

Glycogen storage diseases are autosomal recessive disorders with different subtypes. These are characterized by the absence or deficiency of one of the enzymes responsible for producing or metabolizing glycogen. In all children in whom hepatomegaly in combination with hypoglycemia, growth retardation, and disproportional distribution of body fat is detected, the diagnosis of glycogen storage disease should be considered. The imaging findings are not specific. Increased glycogen is reflected as increased attenuation on non-enhanced hepatic CT and hyperechoic liver on US. There is an increased prevalence of hepatic adenoma and hepatocellular carcinoma (Fig. 22.5) (Boll and Merkle 2009).

22.1.4.2 Biliary Disease

22.1.4.2.1 Biliary Atresia

Biliary atresia (BA) is one of the causes of neonatal cholestasis. It presents with the progressive obliterative fibro-inflammatory changes of bile ducts. Bile duct involvement can be classified as follows: common bile duct atresia (type 1), common hepatic duct atresia (type 2), and right and left hepatic duct atresia (type 3).

Early diagnosis of BA is very important for a successful surgical outcome. Among the many imaging modalities, US plays a key role in the diagnosis of BA. In typical cases of BA, US shows normal liver echo texture, triangular cord sign, atrophic GB, non-visualization of the extrahepatic bile duct, enlarged hepatic artery, and hepatic subcapsular flows on color Doppler US (Fig. 22.6) (Lee et al. 2009), but the results of US depend on the experience of the sonographer. And in an atypical case of BA, it is not easy to make a correct diagnosis. When the diagnosis is delayed, many findings of biliary cirrhosis can be seen on US.

MRCP (Han et al. 2002; Chavhan et al. 2008) can be used, but it requires sedation or anesthesia. When the extrahepatic bile duct is visualized on MRCP, the possibility of BA can be excluded in the neonates. In these cases, the causes of neonatal cholestasis should be determined by the support of clinical and laboratory data or liver biopsy.

Contrast-enhanced CT is not used for the initial diagnosis; it is frequently used for the evaluation of various complications after surgery (Kasai portoenterostomy or liver transplantation).

In contrast to US, CT, or MRI, hepatobiliary scintigraphy requires 5 days' preparation with phenobarbital to acquire optimal results. The lack of radiotracer excretion into the bowel on 24 h' delayed scan is highly suggestive of biliary atresia. But when the liver function has deteriorated, it is difficult to differentiate biliary atresia from neonatal hepatitis.

22.1.4.2.2 Paucity of the Interlobular Bile Ducts

Bile duct paucity is present in various groups of genetic, metabolic, infectious, immunologic, or idiopathic disorders in infancy. Among the many causes of paucity of the interlobular bile ducts, Alagille syndrome has peculiar clinical features, such as abnormal face, ocular abnormality (posterior embryotoxon), butterfly vertebra, cardiovascular abnormalities, and cholestasis (Kamath et al. 2007). In addition to the clinical features, liver biopsy provides conclusive diagnosis. US does not show any specific features. MRCP can demonstrate or cannot visualize the extrahepatic bile duct in Alagille syndrome. When the extrahepatic bile duct is not seen on MRCP, it is difficult to differentiate from BA. But there is no periportal thickening or cystic lesion at the porta hepatis on MRCP of Alagille syndrome. Regardless of visualization of the extrahepatic bile duct, T2-weighted coronal images can depict the butterfly vertebra of the thoracic spine (Fig. 22.7). In nonsyndromic forms of paucity of the interlobular bile ducts, imaging studies cannot provide any specific information.

22.1.4.2.3 Choledochal Cyst

Choledochal cyst is a dilatation of the biliary tree involving the extrahepatic bile duct, intrahepatic bile duct, or both. It is a spectrum of extrahepatic and intrahepatic bile ducts malformation. Even in the fetal period, choledochal cyst can be detected on US. After birth, it can be found

Table 22.1 Todani's classification of choledochal cysts

Type 1: segmental or diffuse fusiform dilatation of the common bile duct
Type 2: diverticulum of the common bile duct
Type 3: choledochoceles
Type 4: multiple cystic dilatations of the intrahepatic and extrahepatic bile ducts
Type 5: multiple cystic dilatations of the intrahepatic bile ducts (Caroli disease)

incidentally or on abdominal US for abdominal pain or jaundice. US can detect the size of choledochal cysts, stones, or bile sludge in the gallbladder or choledochal cyst, whether the intrahepatic bile ducts are also involved or not. The type of choledochal cyst is usually divided by Todani's classification (Table 22.1) (Todani et al. 1977). Some cysts are associated with anomalous pancreaticobiliary ductal union (APBDU) and others are not. Although not all types of choledochal cysts are associated with APBDU, the focus has been on the close association with APBDU and the formation of choledochal cysts.

The most important aspect of the surgical treatment of choledochal cysts is determining the presence of intrahepatic bile duct anomalies and the relationship between the distal end of the choledochal cyst and the pancreatic duct and common channel (Takeshi et al. 2006). Therefore, the role of preoperative MRCP is to confirm the type of choledochal cyst and determine the presence of APBDU and biliary tract anomalies. Although hepatobiliary scintigraphy and CT can be used for the diagnosis, they have limitations in the demonstration of APBDU. On operative cholangiography, precise anatomy of the biliary tract and APBDU can be confirmed (Fig. 22.8).

22.1.4.2.4 Caroli Disease

Caroli disease is a congenital non-obstructive dilatation of intrahepatic bile ducts. It can present with only bile duct ectasia or be associated with hepatic fibrosis (Caroli syndrome). Diffuse, lobar, or segmental distribution of intrahepatic bile duct dilatations is seen in the liver (Fig. 22.9). A well-known diagnostic clue is the intraluminal portal vein sign (US) or central dot sign (contrast-enhanced CT) (Pariente 2005; Siegel 2011). Classic cholangiographic appearance obtained by conventional ERCP or PTC is bulbous or saccular dilatations of intrahepatic bile ducts. However, these findings can be noninvasively demonstrated by MRCP even in children. On US, CT, and MRI, sludge or calculi can be detected within the dilated bile ducts.

22.1.4.2.5 Bile-Plug Syndrome

Bile-plug syndrome is one of the causes of extrahepatic biliary obstruction in neonates and infants and associated with many etiological factors. The clinical and

laboratory findings are similar to other conditions with neonatal cholestasis. Imaging studies are important for making a correct diagnosis and guiding the treatment plan. US shows the dilated gallbladder with or without echogenic bile sludge and concentric dilatation of the common bile duct filled with echogenic bile sludge. Inspissated bile is more echogenic than bile sludge within the gallbladder. The affected common bile duct may blend with the surrounding pancreas parenchyma, causing difficulty in determining the dilated common bile duct (Gubernick et al. 2000). During conservative treatment, the bile plug may be expelled spontaneously, but if it is not, surgical irrigation should be considered.

On MRCP, the extrahepatic bile duct is diffusely dilated. A bile plug filled in the bile duct can be detected as variable-shaped, low signal-filling defects on MRCP. So MRCP is useful in evaluating the presence and extent of the bile plug. On T1-weighted image, the bile plug also has low-signal intensity, and static bile filled in the dilated common bile duct and gallbladder may have high signal intensity (Fig. 22.10).

22.1.4.2.6 Spontaneous Perforation of the Bile Duct

In neonates or infants with spontaneous perforation of the bile duct, the classic presentation is that of a previously healthy infant who develops progressive abdominal distension, irritability, and fluctuating mild jaundice (Xanthakos et al. 2003). The pathogenesis of spontaneous perforation of the bile duct is unknown, although numerous etiologies have been proposed, such as congenital weakness of the CBD, ischemia, stones, infection, distal bile duct stenosis, inspissated bile, and pancreatic reflux from anomalous pancreaticobiliary ductal union. To avoid the delayed diagnosis, this condition should be considered in the differential diagnosis of jaundice in infancy. US plays a limited role in the diagnosis of this entity. If the extrahepatic bile duct is not dilated, it is difficult to suspect this condition. The ascites and loculated fluid collection around the porta hepatis may be helpful in the diagnosis. Hepatobiliary scintigraphy confirms the diagnosis when the radioisotope is leaked from the region of the porta hepatis into the peritoneal cavity. It is the most useful imaging modality and should be used on patients suspected of having bile duct perforation (Fig. 22.11), but because of limited spatial resolution, combined anomalies of the bile duct cannot be evaluated on hepatobiliary scintigraphy. MRCP can depict the bile duct and pancreatic duct anomalies such as choledochal cyst, anomalous pancreaticobiliary ductal union, distal bile duct stenosis, and loculated fluid collection or pseudocyst formation at the porta hepatis (Lee et al. 2010).

22.1.4.2.7 Cholelithiasis and Cholecystitis

In children, development of cholelithiasis may be idiopathic or associated with obstructive biliary anomaly, total

parenteral nutrition, furosemide, hemolytic anemia, etc.. The best diagnostic tool for cholelithiasis is US. The typical US appearance is echogenic stone with posterior acoustic shadowing and its positional change (Pariente 2005; Siegel 2011). The differentiation between small, non-shadowing stones and bile sludge is sometimes difficult on US. Besides typical US findings, the sonographic Murphy sign and gallbladder wall thickening and gallbladder hydrops are suggestive of acute cholecystitis (Fig. 22.12) (Siegel 2011).

22.1.4.3 Hepatic Tumors

22.1.4.3.1 Hepatoblastoma

Hepatoblastoma is the most common primary liver tumors in young children with a peak presentation at 1–2 years of age. There is an increased risk of hepatoblastoma in Beckwith-Wiedemann syndrome, hemihypertrophy, familial adenomatosis polyposis coli, and premature or low-birth-weight infants. It is a large, well-defined, and heterogeneous liver mass in an infant. Serum AFP is typically raised in 90 % of the patients.

On US, it is a well-defined solid mass with a spoke-wheel appearance due to fibrous septa, heterogeneous echogenicity due to hemorrhage or necrosis, and typically hypervascular on Doppler US (Jha et al. 2009). CT demonstrates a large, heterogeneous, and hypoattenuating mass with heterogeneous enhancement. Calcification can be seen in 55 % of patients. On MRI, the mass shows variable signal intensity on T2-weighted images due to hemorrhage (Figs. 22.13 and 22.14).

22.1.4.3.2 Hepatic Hemangioendothelioma

Hepatic hemangioendothelioma is the most common vascular hepatic tumor seen during the first year of life. It is a heterogeneous and hypervascular mass and can be associated with cutaneous hemangioma, congestive heart failure, and consumptive coagulopathy (Kasabach-Merritt syndrome). It is usually associated with mild elevations in AFP levels (around 10,000 units), and it tends to involute spontaneously without therapy over a course of months to years.

On US, it is a complex hypoechoic or hyperechoic mass. It has a high flow on Doppler US. CT demonstrates heterogeneously hypoattenuating mass with prominent vessels. It can be solitary or multiple. An abrupt decrease in aortic caliber distal to celiac axis can be seen on CT. MRI also shows a very high-signal intensity mass on T2-weighted images with flow voids. On contrast-enhanced CT or MRI, there is a characteristic intense, nodular peripheral rim enhancement with central progression (Figs. 22.15 and 22.16) (Jha et al. 2009). During follow-up, the tumor decreases in size with increased internal calcification.

22.1.4.3.3 Mesenchymal Hamartoma

Mesenchymal hamartoma is the second most common benign hepatic tumor in children who are usually less than 2 years of

age. Imaging findings depend on the predominance of cysts or stroma (mesenchymal elements). Multiple variable-sized cysts with various amounts of stroma are seen on US or CT (Fig. 22.17) (Jha et al. 2009). Calcification or hemorrhage is not generally seen. On MRI, this tumor shows variable signal intensity on T1-weighted images depending on variable protein content.

22.1.4.3.4 Focal Nodular Hyperplasia

Focal nodular hyperplasia (FNH) is uncommon in children (5 % of benign liver tumors) and more common in girls. It may develop based on a congenital vascular malformation or due to iatrogenic hepatic vascular abnormalities.

On US, it is a non-encapsulated, solitary mass with variable echogenicity. The central scar is seen in about one-third of the cases. It is typically very similar to surrounding liver parenchyma on CT and MRI. After contrast enhancement, it shows an early and rapid enhancement in the arterial phase with a rapid washout. Retained contrast can be seen in the central scar on delayed phase which is characteristic for FNH (Fig. 22.18) (Jha et al. 2009).

22.2 Pancreatic Disease

22.2.1 Anatomy and Development

The pancreas forms from the embryonic foregut and is therefore of endodermal origin. Pancreatic development begins with the formation of ventral and dorsal buds. Each structure communicates with the foregut through a duct. The ventral pancreatic bud becomes the head and uncinate process and comes from the hepatic diverticulum. Also, differential rotation and fusion of the ventral and dorsal pancreatic buds result in the formation of the definitive pancreas.

US appearance of the normal pancreas varies widely in children (Nijs et al. 2005). It is typically isoechoic or slightly hyperechoic than the liver. It is homogeneous with variable soft-tissue attenuation on CT. Pancreatic tumors, whether benign or malignant, are rare in children.

22.2.2 Spectrum of Pancreatic Disease

22.2.2.1 Annular Pancreas

The exact etiology is unknown. Annular pancreas can cause duodenal obstruction in the neonatal period in about 50 % of patients. It is associated with other congenital anomalies in up to 70 % of infants; these include duodenal stenosis or atresia, Down syndrome, tracheoesophageal fistula, and congenital heart disease (Nijs et al. 2005).

On US, fluid-distended descending duodenum can be seen encircled by pancreatic tissue. A circumferential narrowing

of the duodenum can be identified in upper gastrointestinal series (Fig. 22.19). MRCP can demonstrate associated ductal anatomy.

22.2.2.2 Acute Pancreatitis

Acute pancreatitis is a significant cause of morbidity in children. There can be severe complications in 25 % of patients, with a 9 % recurrence and 10 % mortality rate. There are varied causes of acute pancreatitis, including idiopathic, trauma, structural anomalies, multisystem diseases, drugs and toxins, and viral infections (Darge and Anupindi 2009). Imaging features are nonspecific. US or CT may show diffuse or focal enlargement of pancreas or change in attenuation or echotexture. There may be surrounding fluid, pseudocyst formation, hemorrhage, or pancreatic duct dilatation (Fig. 22.20).

22.2.2.3 Pancreatoblastoma

Pancreatoblastoma is the most common pediatric exocrine tumor of the pancreas and occurs in young children with the mean age of 4 years. This tumor is associated with Beckwith-Wiedemann syndrome. It is usually an asymptomatic, large abdominal mass, and AFP is elevated in 25–55 % of the patients. Imaging studies typically reveal large heterogeneous masses with solid and cystic components, hyperechoic and enhancing septa, and hemorrhagic necrosis (Fig. 22.21) (Chung et al. 2006).

22.2.2.4 Solid and Papillary Epithelial Neoplasm

Solid and papillary epithelial neoplasm (SPEN) usually occurs in adolescent girls. The classic features of SPEN are a large well-encapsulated mass with varying solid and cystic components caused by hemorrhagic degeneration (Chung et al. 2006). Calcifications and enhancing solid areas may be present at the periphery of the mass (Fig. 22.22).

22.3 Splenic Disease

22.3.1 Anatomy and Development

The spleen arises from mesenchymal cells between the layers of the dorsal mesogastrium during the 5th week of gestation. The spleen's function is hematopoiesis in the fetus, with a peak at approximately 20 weeks' gestation. Accessory splenules are seen in 15 % of patients.

On US, the spleen is homogeneous, slightly more hyperechoic than the normal kidney, and isoechoic or more slightly hyperechoic than the liver. On MRI, splenic signal intensity varies with age. With contrast, splenic enhancement is initially heterogeneous due to a variable flow rate through red pulp (Fig. 22.23).

22.3.2 Spectrum of Splenic Disease

22.3.2.1 Splenomegaly

The size of the normal spleen depends on the age of the child. Its size is often measured in the longest coronal axis, averaging 6 cm at 3 months of age, 9 cm at 4 years of age, and 13 cm by 15 years of age. There are many causes of splenomegaly in children, including hemolytic anemia (Fig. 22.25), leukemia, lymphoma, portal hypertension, right heart failure, sepsis, and viral disease (Hilmes and Strouse 2007). Portal hypertension is a common cause of splenomegaly in children and is often due to extrahepatic portal vein obstruction from portal vein thrombosis (Fig. 22.24).

The role of imaging depends on the clinical presentation and the suspected diagnoses. Imaging clues to the presence of portal hypertension include heterogeneous liver, relative increase in size of the left lobe and caudate, lobular hepatic margins, and an abnormal Doppler evaluation of the portal vein including demonstration of thrombosis, reversed flow direction, or cavernous transformation (Hilmes and Strouse 2007).

22.3.2.2 Splenic Hamartoma

Hamartoma is rare, but it is the most common primary neoplasm of the spleen in children. It is a benign, well-circumscribed solid or predominantly solid tumor. On US, lesions are hypoechoic and relatively avascular, as opposed to hemangiomas. Lesions are isointense to the normal spleen on T1-weighted images and heterogeneously hypointense on T2-weighted images (Hilmes and Strouse 2007). They are usually enhanced less than normal parenchyma on CT and MRI (Fig. 22.26).

22.3.2.3 Splenic Injury

Abdominal trauma is a leading cause of death in children older than 1 year of age, and spleen is the most commonly injured intra-abdominal organ, accounting for up to 45 % of all visceral injuries (Lynn et al. 2009).

Diagnostic imaging is often critical to the early and accurate detection of splenic injury. Intravenous contrast-enhanced CT is the gold standard for evaluating blunt abdominal trauma (Fig. 22.27). Relative to CT, US is less sensitive in the diagnosis of splenic injuries. Recently, contrast-enhanced US using intravascular microbubble administration has been investigated (Oldenburg et al. 2004; Valentino et al. 2008). For homogeneous parenchymal enhancement of the spleen, the portal venous phase is optimal for detecting organ injury. Parenchymal ruptures can be associated with intraparenchymal and subcapsular hematomas, and splenic rupture is the most common injury and is easily identified by the presence of hemoperitoneum.

22.4 Illustrations: Liver, Biliary Tract, Pancreas, and Spleen

22.4.1 Neonatal Hepatitis

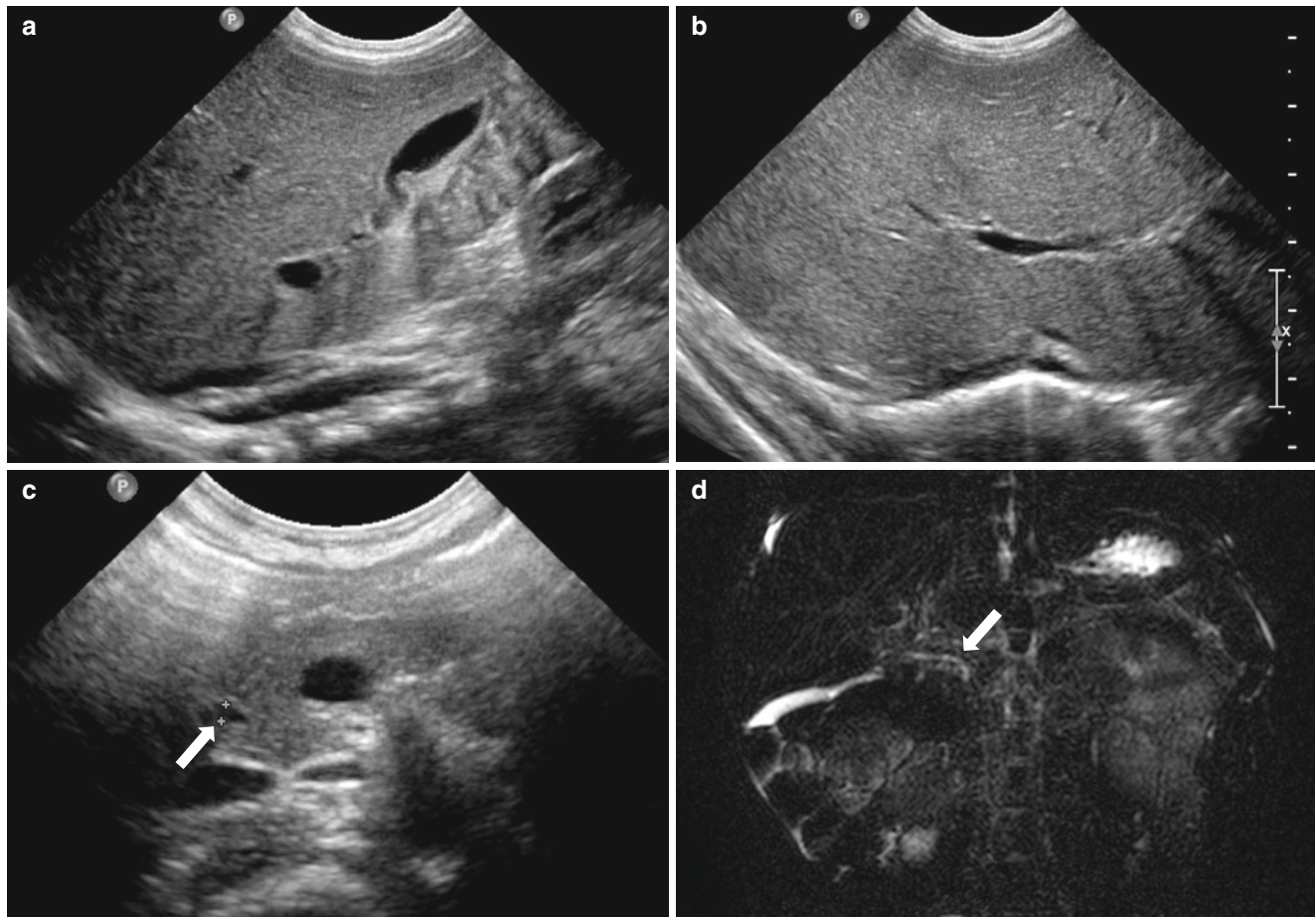


Fig. 22.1 Herpes simplex virus hepatitis in a male neonate. (a) Abdominal US shows grossly normal gallbladder. (b) Liver also shows homogenous parenchymal echogenicity without increased periportal echogenicity. (c) Common bile duct (*arrow*) is visualized on pancreas

head portion. (d) Two-dimensional T2-weighted MR cholangiopancreatography (MRCP) well demonstrates normal extrahepatic biliary duct (*arrow*)

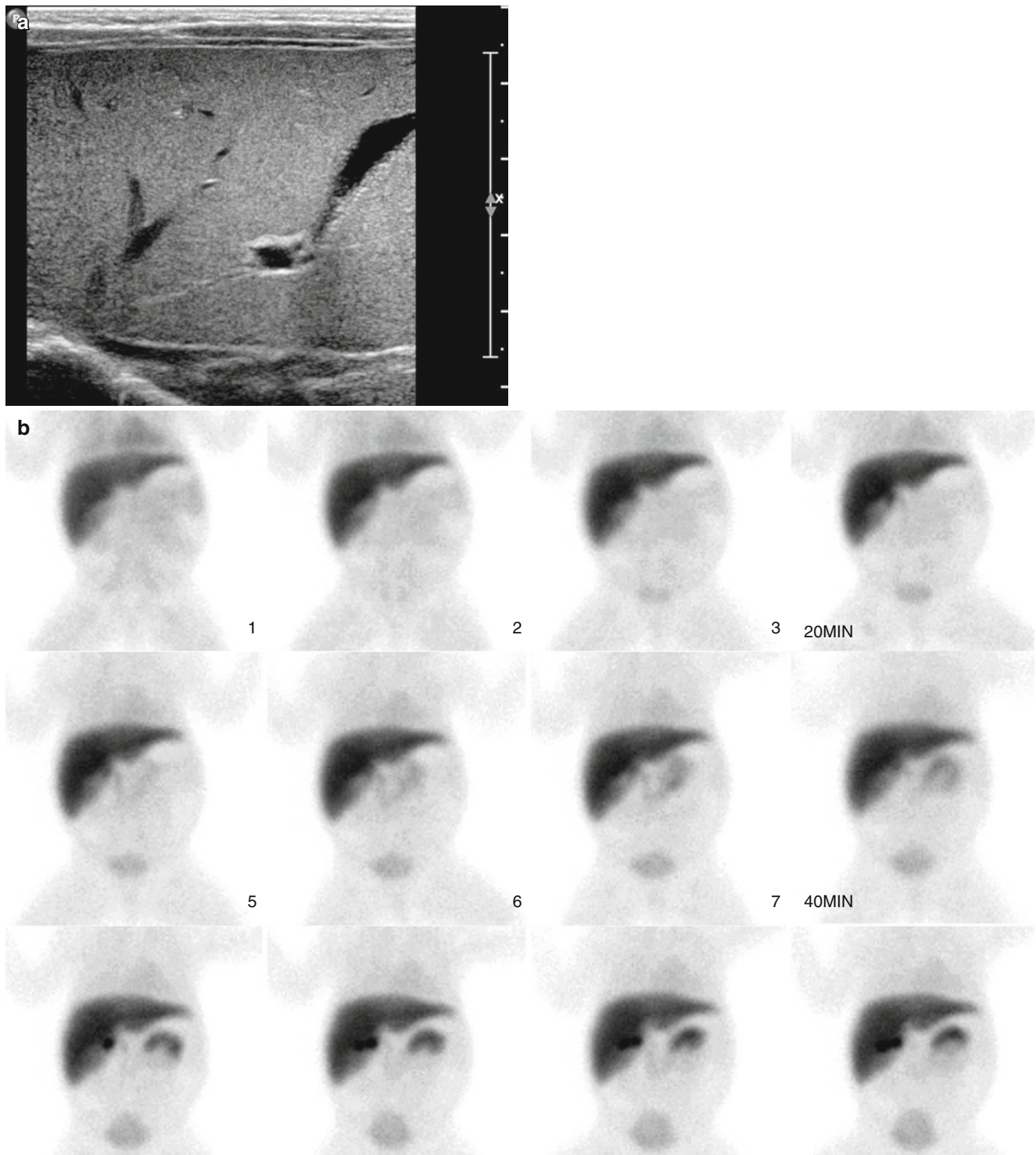


Fig. 22.2 Cytomegalovirus hepatitis in a female neonate. (a) Abdominal US shows grossly normal gallbladder without increased periportal echogenicity in liver. (b and c) Hepatobiliary scan shows good hepatic uptake with normal intra- and extrahepatic biliary transit on dynamic image (b) and normal biliary to bowel transit on 4 h delay image (c)



Fig. 22.2 (continued)

22.4.2 Fungal Infection

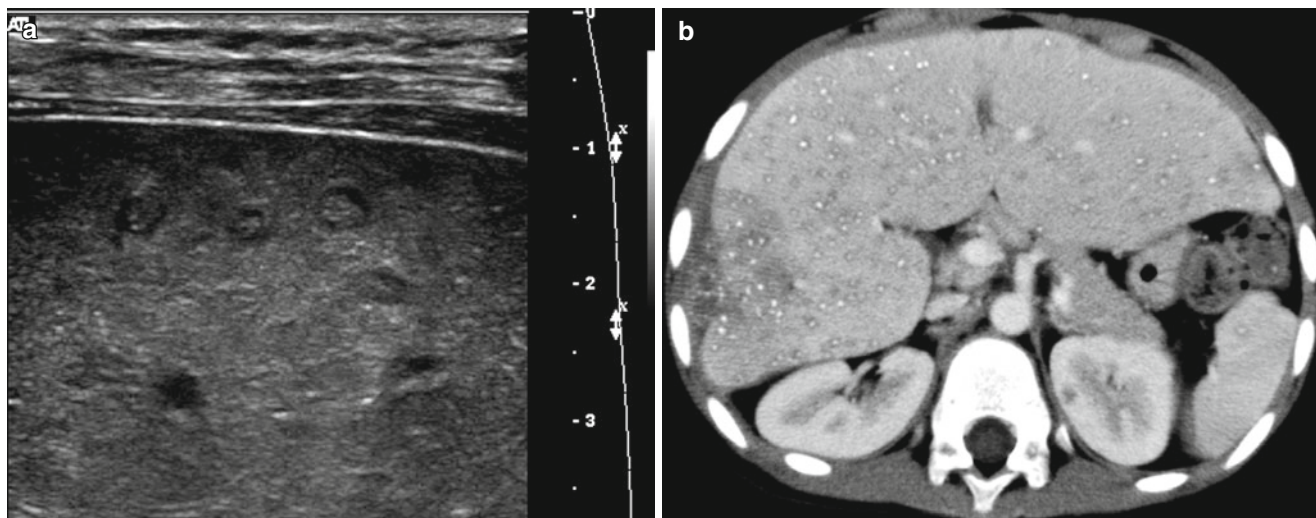


Fig. 22.3 Disseminated aspergillosis in a 6-year-old boy with aplastic anemia. **(a)** Liver US using high-frequency linear transducer shows multiple hypoechoic lesions with central hyperechoic portions (bull's

eye appearance). **(b)** Follow-up abdominal CT with contrast enhancement shows multiple low-density lesions with calcifications in liver with right perihepatic extension

22.4.3 Nonalcoholic Steatohepatitis

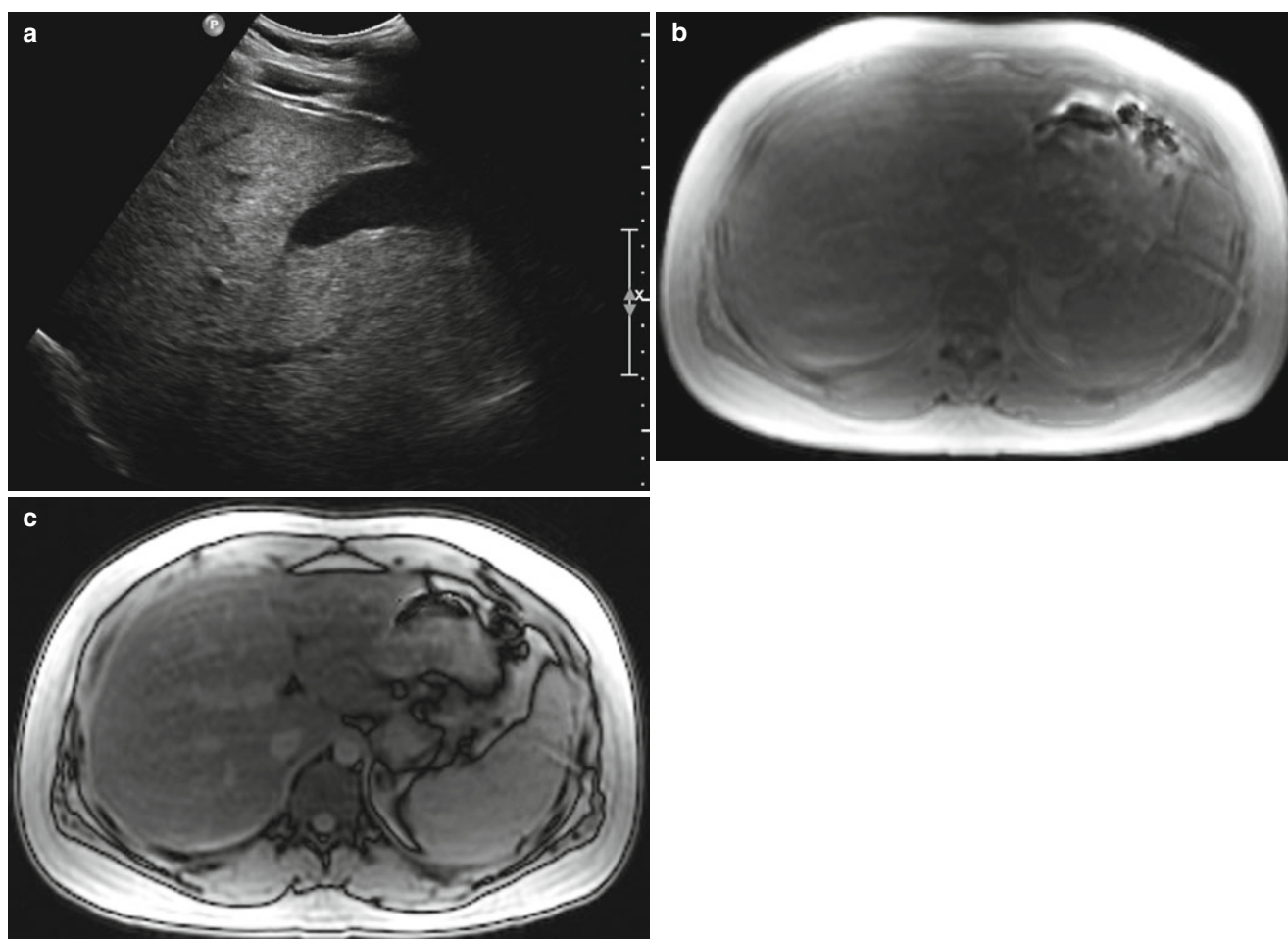


Fig. 22.4 Nonalcoholic steatohepatitis in a 14-year-old boy. (a) Abdominal US shows diffusely increased liver parenchymal echogenicity with posterior attenuation. (b and c) Axial T1-weighted gradi-

ent echo MR images show a marked decrease in the signal intensity of the liver on the opposed-phase image (c), compared with that on the in-phase image (b), suggestive of diffuse fat infiltration in liver

22.4.4 Glycogen Storage Disease

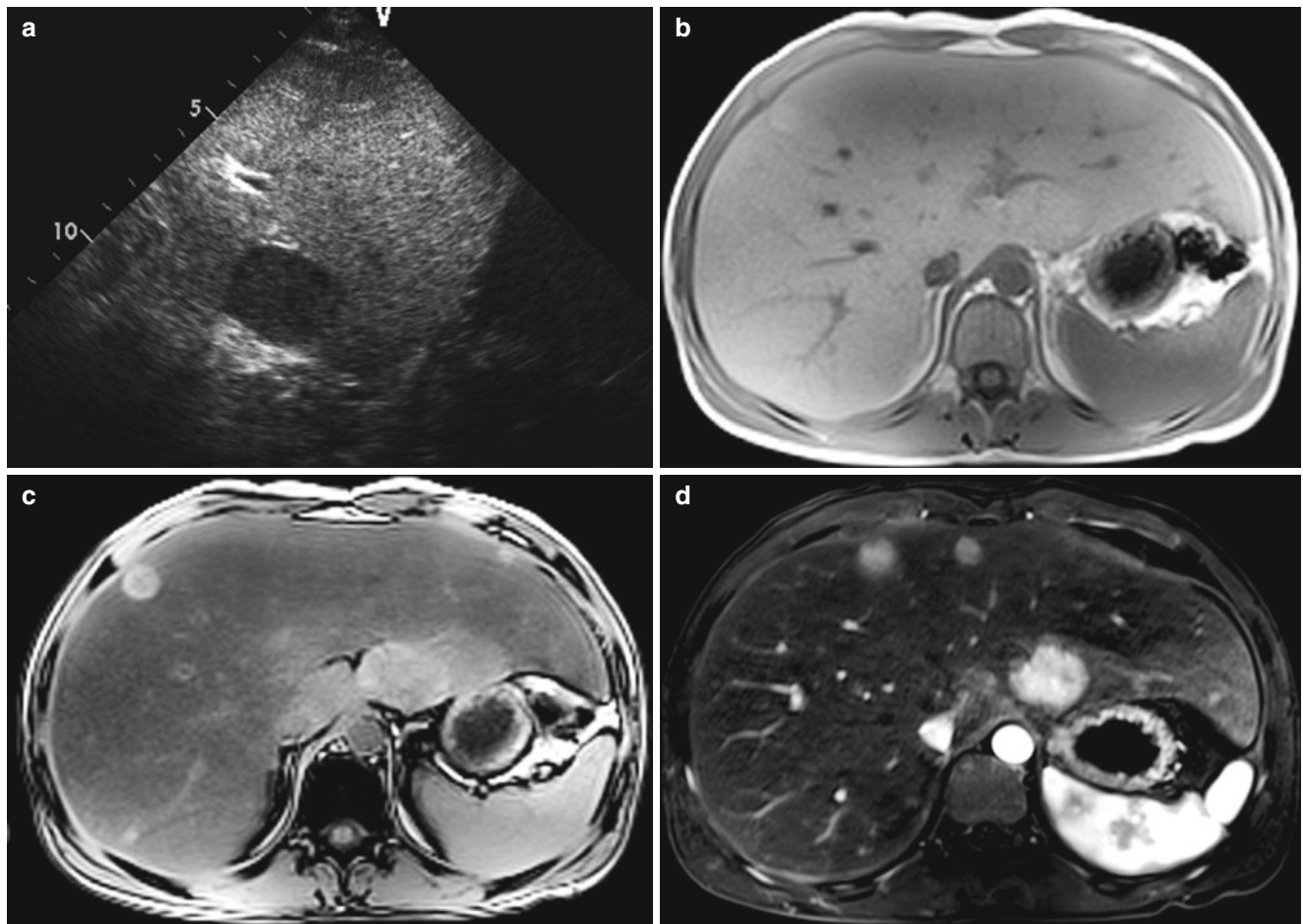


Fig. 22.5 Glycogen storage disease type I with multiple hepatic adenomas in a 19-year-old male. (a) Hypoechoic hepatic mass was incidentally found with diffusely increased liver parenchymal echogenicity during echocardiography. (b and c) Axial T1-weighted gradient echo

MR images of in-phase (b) and opposed-phase (c) show diffuse fat infiltration in liver with multiple masses. (d) T2-weighted MR image also shows multiple hepatic masses with high signal intensity

22.4.5 Biliary Atresia

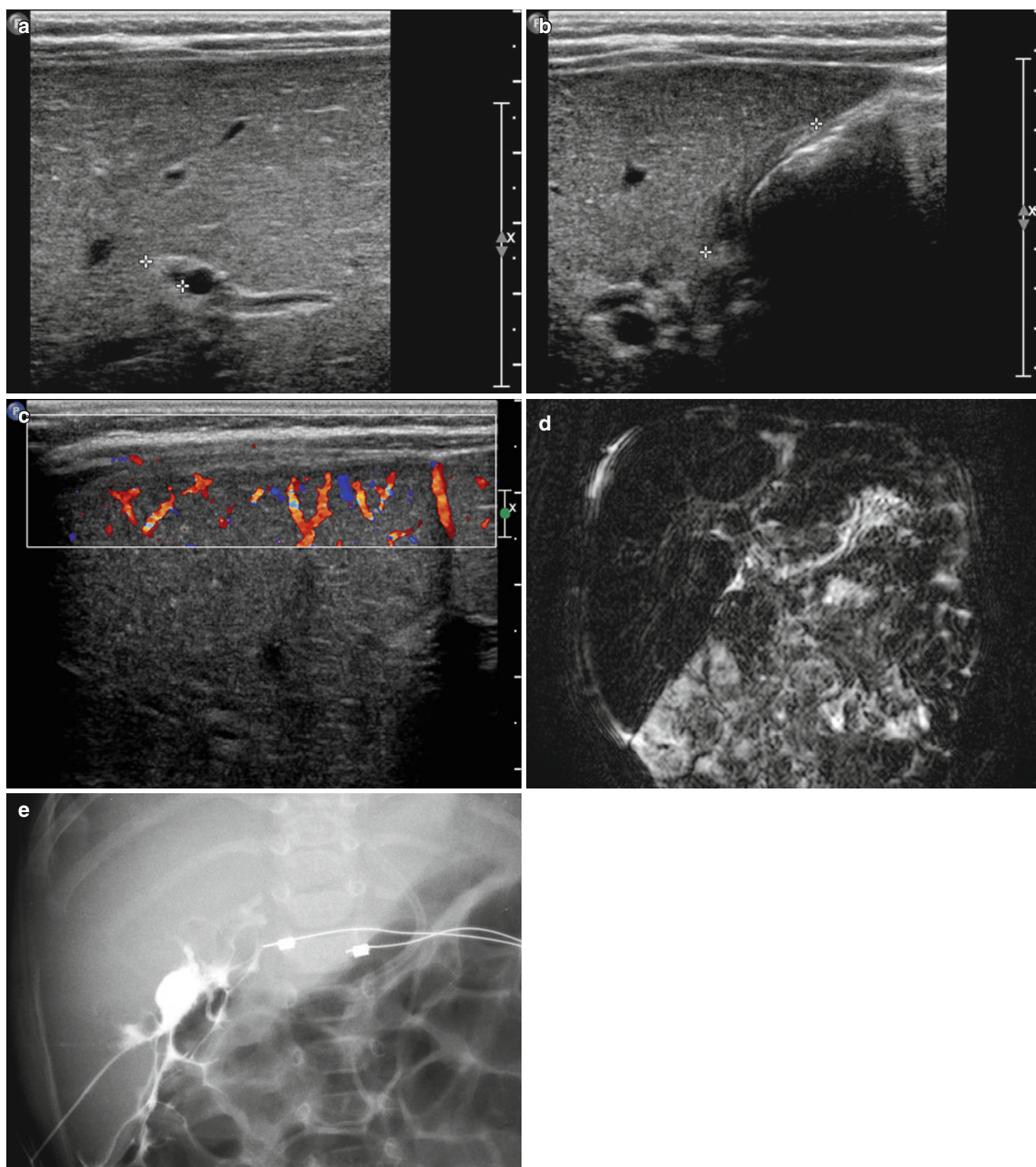


Fig. 22.6 Biliary atresia in a 3-month-old boy. (a–c) Abdominal US images show increased periportal echogenicity in liver (a), atretic gallbladder (b), and increased hepatic subcapsular flow on Doppler US (c).

(d) Two-dimensional T2-weighted MRCP does not demonstrate gallbladder and extrahepatic bile duct. (e) Intraoperative cholangiography demonstrates no opacification of intra- and extrahepatic bile ducts

22.4.6 Alagille Syndrome

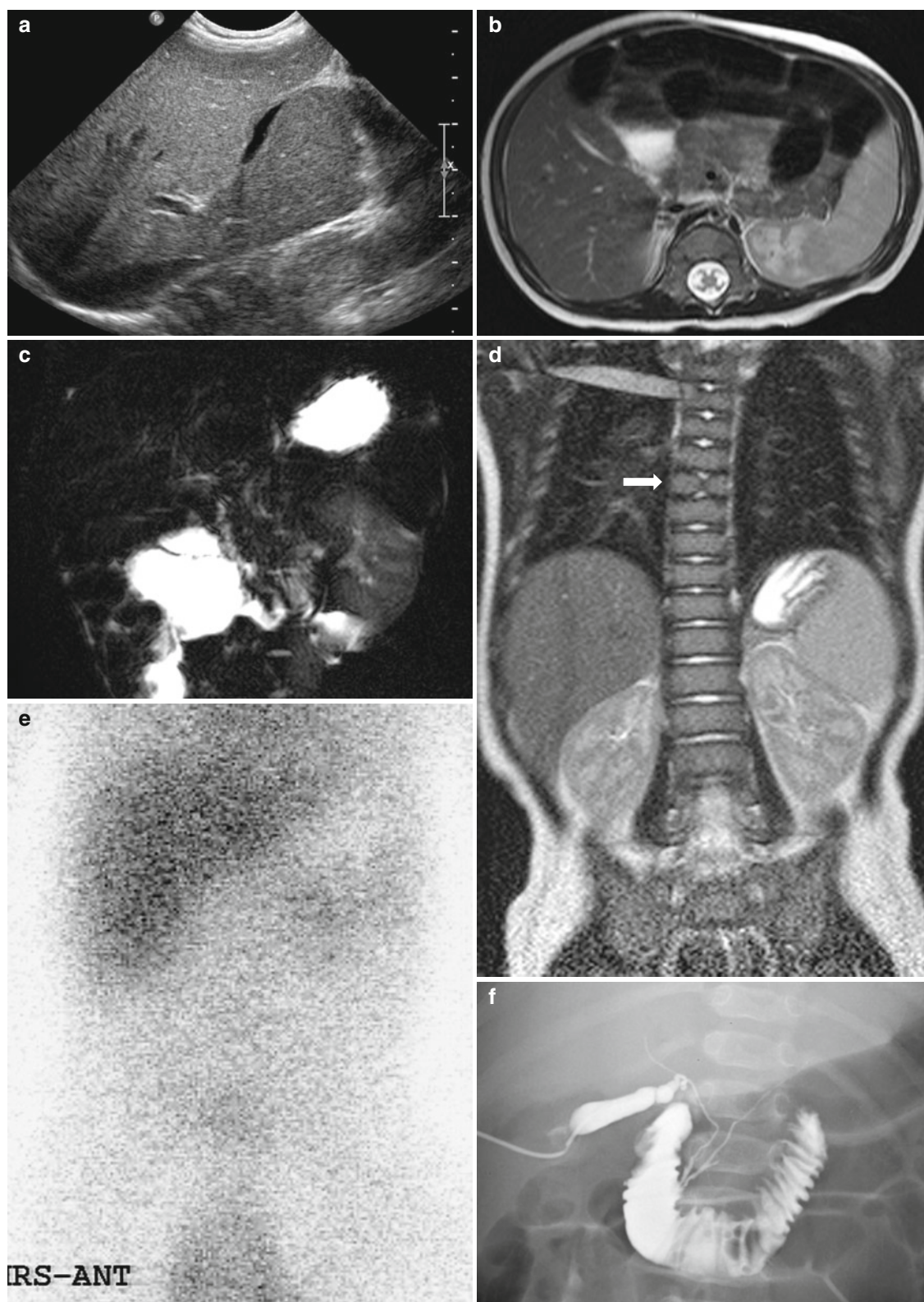


Fig. 22.7 Alagille syndrome in a 5-month-old girl. (a) Abdominal US shows collapsed gallbladder without increased periportal echogenicity. (b) T2-weighted axial MR image also shows collapsed gallbladder without increased periportal signal intensity. (c) Two-dimensional T2-weighted MRCP does not demonstrate extrahepatic bile duct. (d)

T2-weighted coronal MR image shows butterfly vertebra (*arrow*) at mid-thoracic area. (e) Hepatobiliary scan shows no biliary to bowel transit on 24 h delay image. (f) Intraoperative cholangiography demonstrates only extrahepatic bile ducts without opacification of intrahepatic bile ducts

22.4.7 Choledochal Cyst

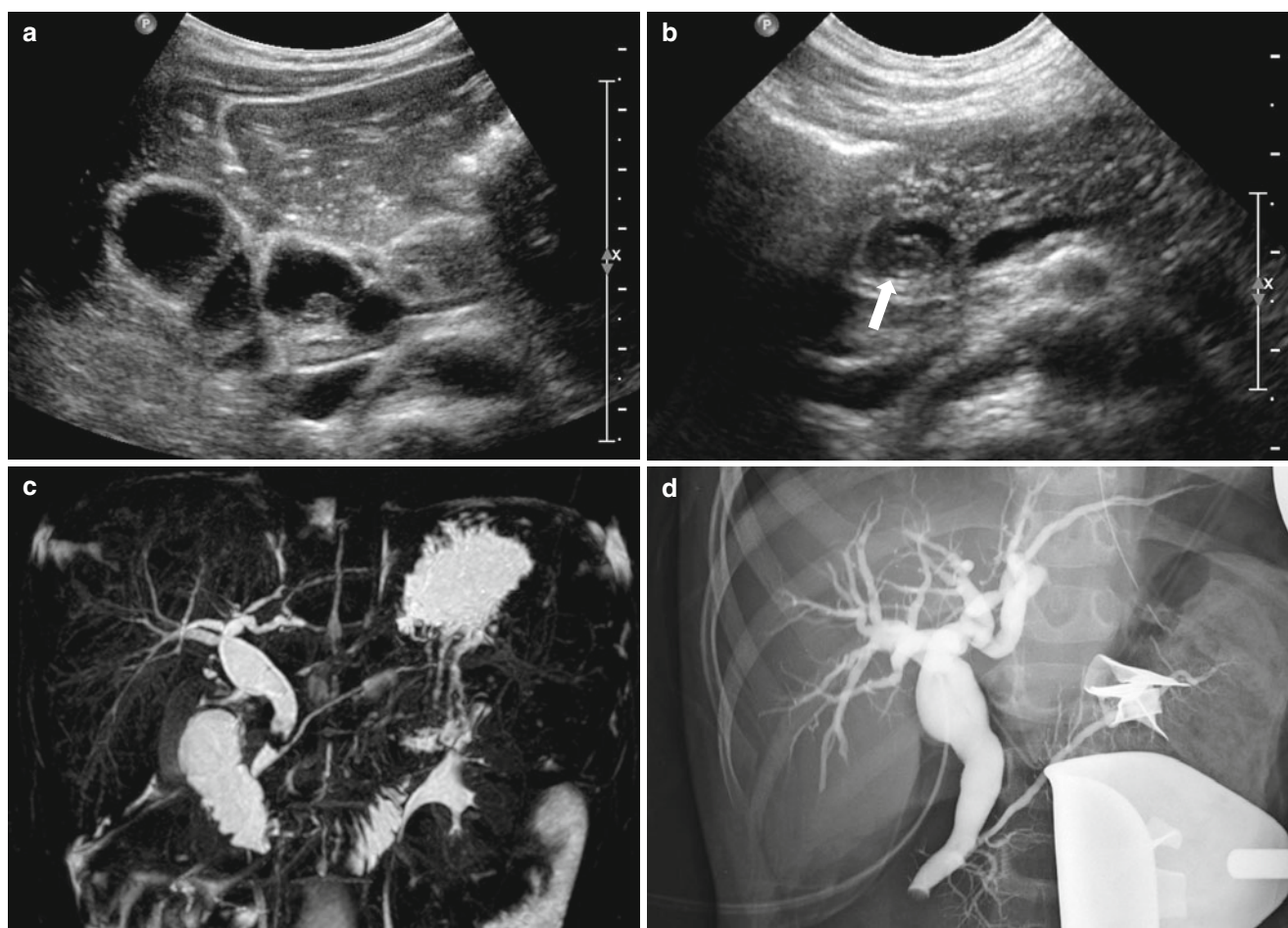


Fig. 22.8 Choledochal cyst in a 5-year-old girl. (**a** and **b**) Abdominal US images show tubular dilatation of common bile duct with internal sludge (**a**) and stone (*arrow*) in distal common bile duct in pancreas head portion (**b**). (**c**) Three-dimensional T2-weighted MRCP demon-

strates dilatation of intra- and extrahepatic bile ducts with filling defect from stone in distal common bile duct. (**d**) Intraoperative cholangiography also shows intra- and extra-hepatic bile duct dilatation suggestive of choledochal cyst

22.4.8 Caroli Disease

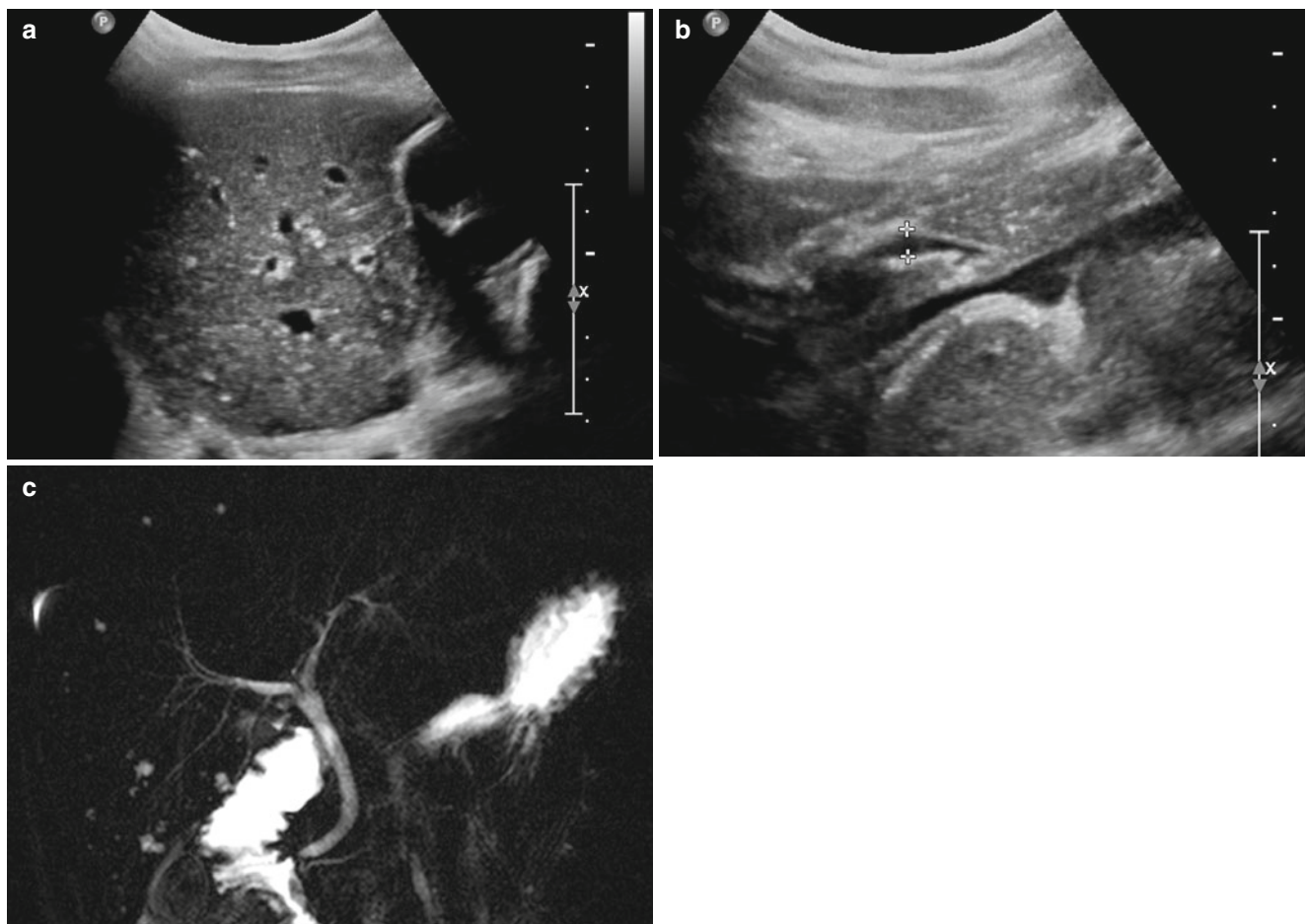


Fig. 22.9 Caroli disease in a 17-year-old girl. **(a)** Abdominal US shows multiple cystic lesions or bile duct dilatation in liver. **(b)** Diffuse and mild dilatation of common bile duct is also noted on abdominal US.

(c) Two-dimensional T2-weighted MRCP well demonstrates multiple intrahepatic cystic lesions with mild common bile duct dilatation

22.4.9 Bile-Plug Syndrome

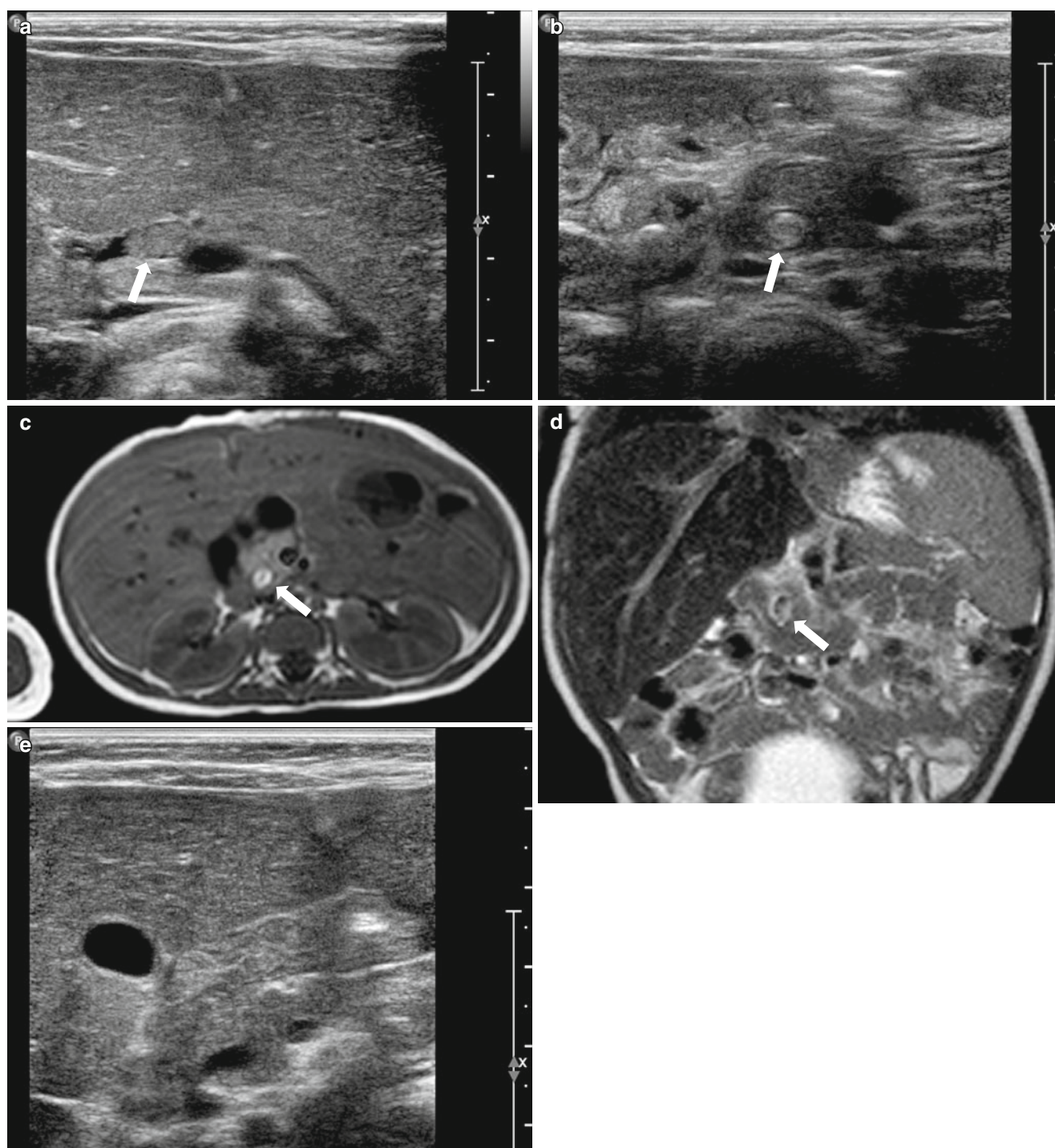


Fig. 22.10 Bile-plug syndrome in a 3-month-old girl. (a and b) Abdominal US images show compact sludge (*arrows*) in common bile duct to pancreas head portion. (c) Axial T1-weighted MR image shows high-signal intensity sludge (*arrow*) in common bile duct. (d) The

sludge (*arrow*) shows dark signal intensity on T2-weighted coronal image. (e) Follow-up abdominal US shows no remaining sludge in common bile duct

22.4.10 Spontaneous Perforation of the Bile Duct

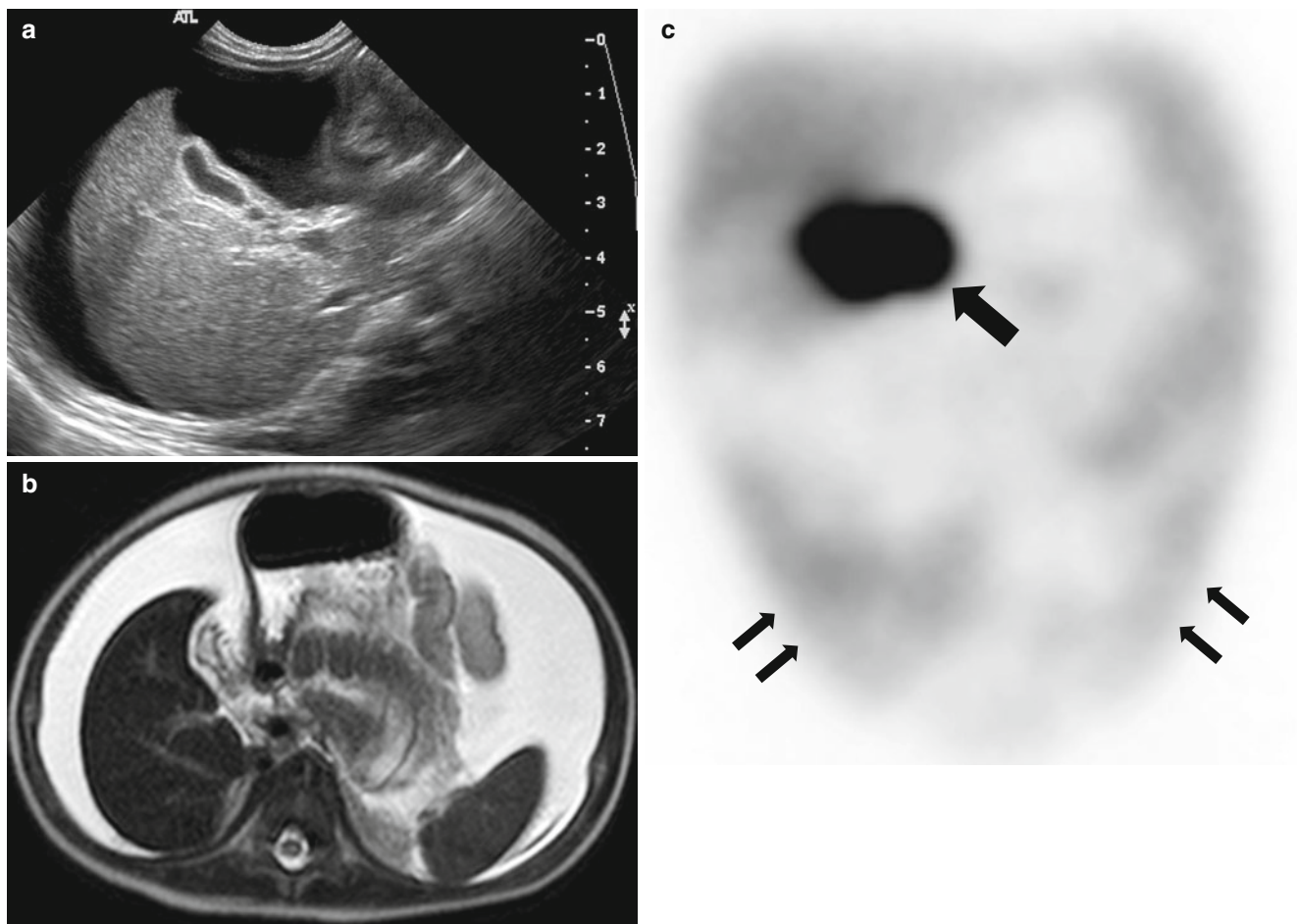


Fig. 22.11 Spontaneous perforation of the bile duct in a 4-month-old girl. (a) Abdominal US shows ascites in perihepatic area of right upper abdomen. (b) Axial T2-weighted image also shows large amount of

ascites in upper abdomen and hepatic hilar area. (c) Hepatobiliary scan shows bile leakage from hepatic hilar area (*large arrow*) preceding peritoneal soiling (*small arrows*)

22.4.11 Cholelithiasis and Cholecystitis

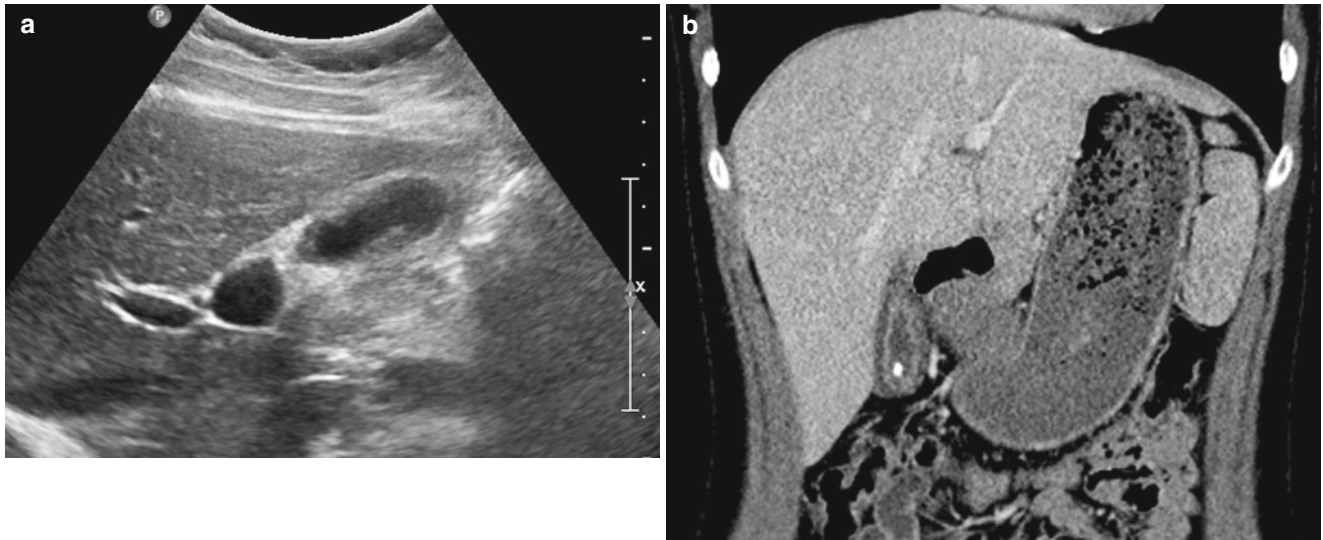


Fig. 22.12 Gallbladder stone with cholecystitis in a 10-year-old boy. (a) Abdominal US shows distended gallbladder with internal sludge and wall thickening in fundus and body area. (b) Coronal reformatted

image of contrast-enhanced abdominal CT shows gallbladder stone with diffuse wall thickening

22.4.12 Hepatoblastoma

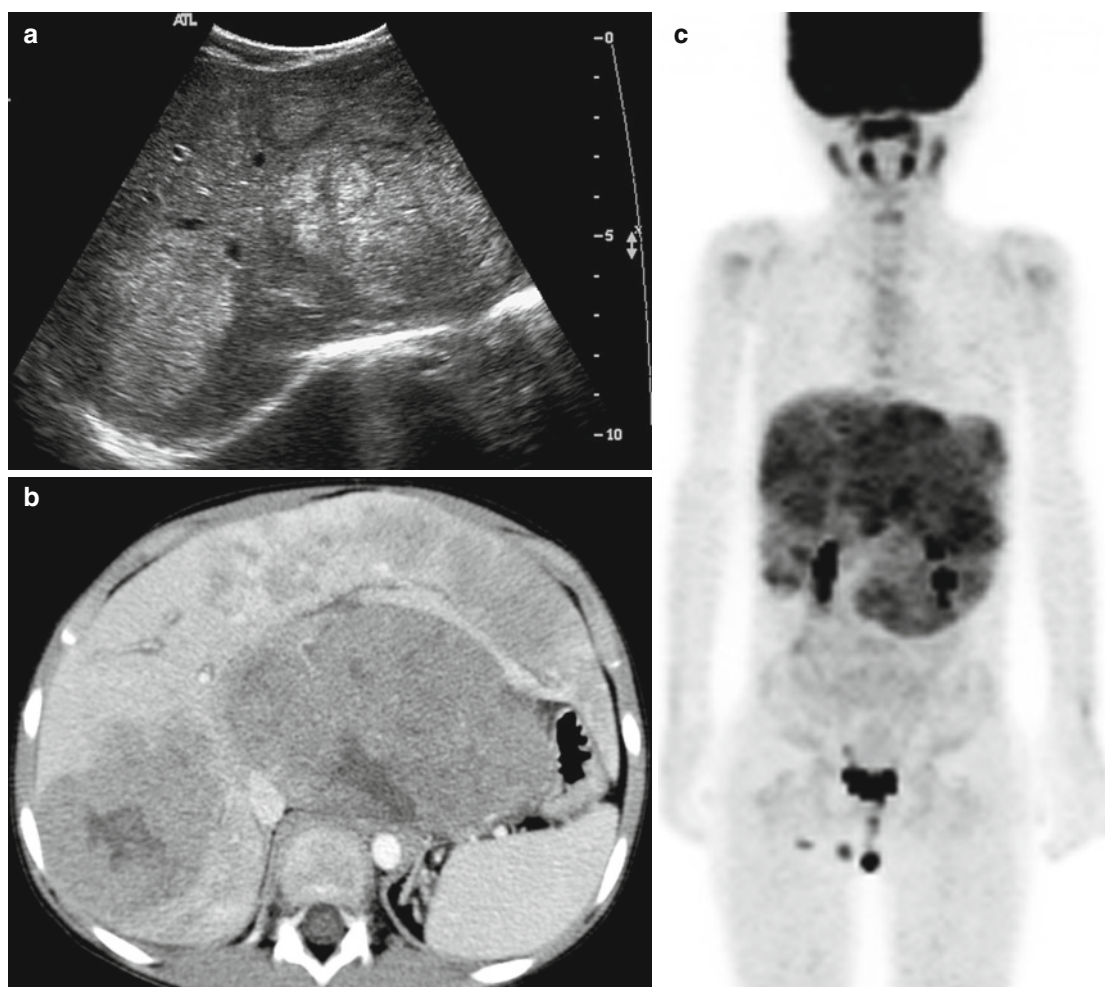


Fig. 22.13 Multiple hepatoblastomas in a 4-year-old girl. **(a)** Abdominal US shows multiple heterogeneously hyperechoic masses in liver. **(b)** Contrast-enhanced abdominal CT also shows multiple masses with some central necrosis in both lobes of liver. **(c)** 18F-fludeoxyglucose

(FDG) positron emission tomography (PET) shows heterogeneously increased FDG uptake in the hepatic masses. Initial alpha-fetoprotein (AFP) level was 721 IU/mL

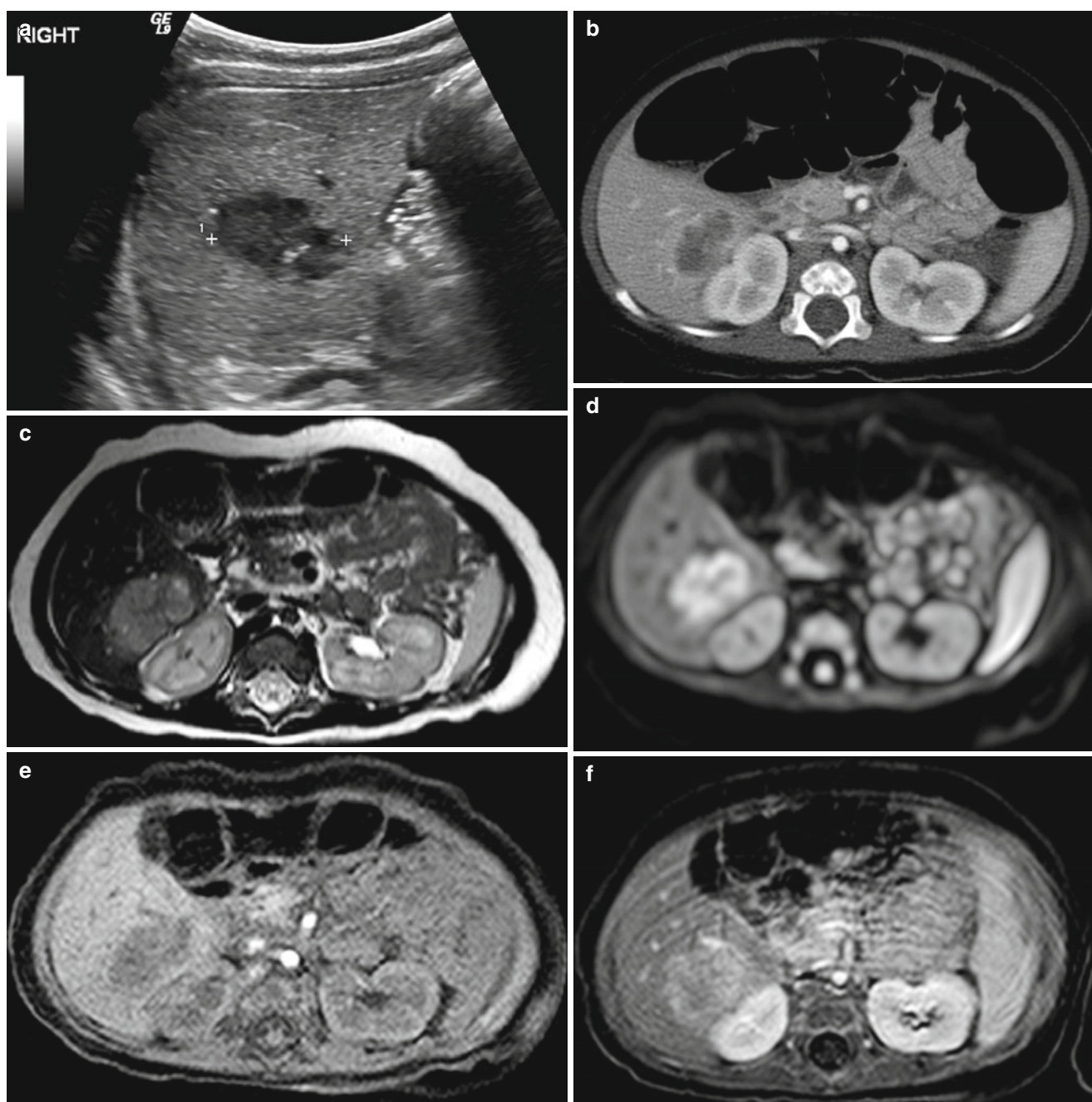


Fig. 22.14 Hepatoblastoma in a 4-month-old boy. (a) Abdomen US shows multilobulated hypoechoic mass with internal hyperechoic portion in right lobe of liver. (b) Contrast-enhanced abdominal CT shows low-density hepatic mass with peripheral enhancement. (c) T2-weighted MR image shows multilobulated mass with intermediate to high signal

intensity. (d) The mass shows diffusion restriction on diffusion-weighted image. (e) Pre-contrast T1-weighted image with fat suppression shows low-signal intensity of the mass. (f) After gadolinium enhancement, the mass shows peripheral enhancement on fat-suppressed T1-weighted image. Initial AFP level was 107 IU/mL

22.4.13 Hepatic Hemangioendothelioma

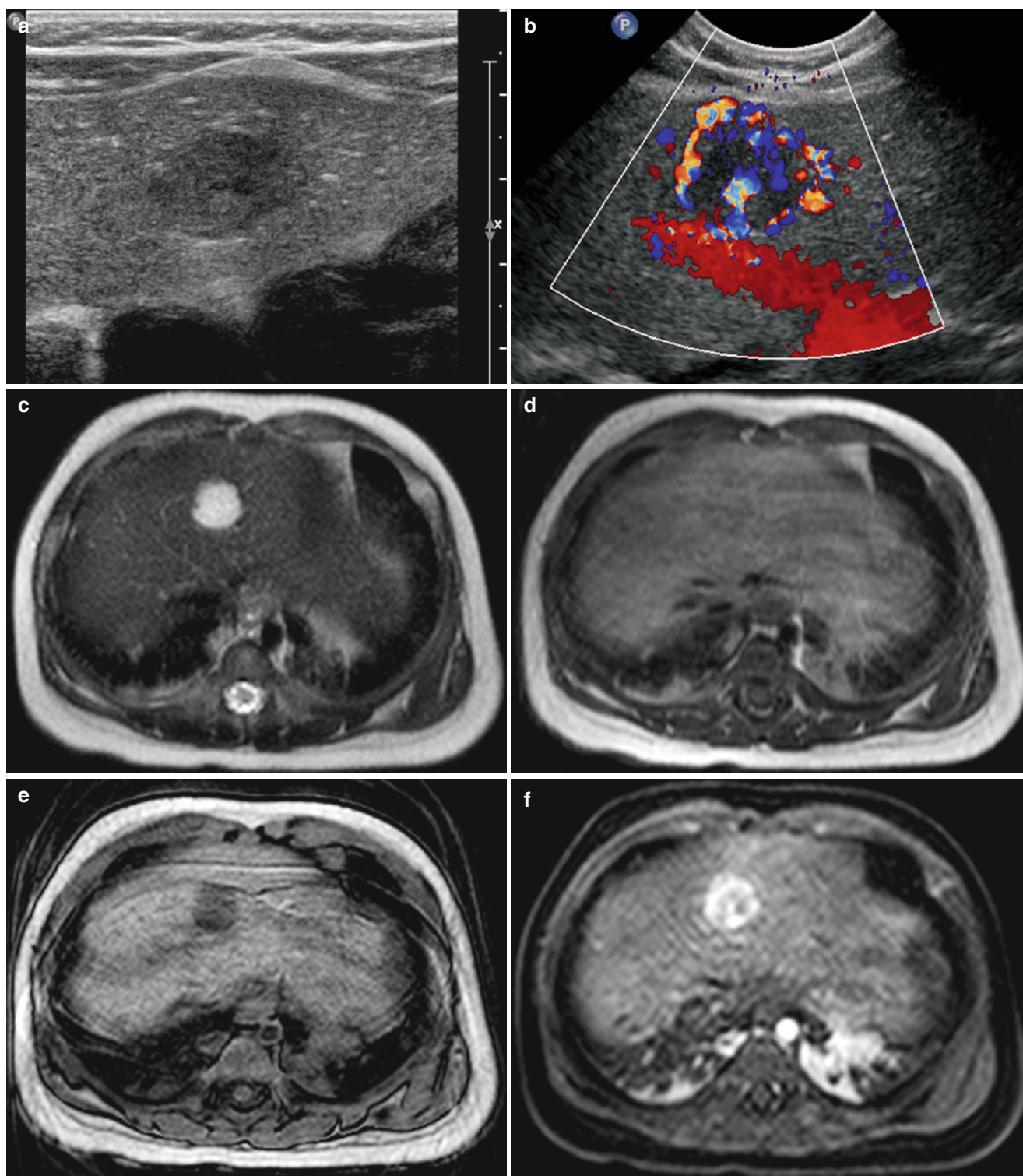


Fig. 22.15 Hepatic hemangioendothelioma in a 2-month-old girl. (a) Abdominal US shows lobulated hypoechoic mass in liver dome. (b) Color Doppler US shows marked increased vascularity in this mass. (c) T2-weighted MR image shows marked high signal intensity of this mass. (d) On T1-weighted MR image, this mass shows iso-signal intensity to surrounding liver parenchyma. (e–g) T1-weighted images with fat suppression show signal drop in this mass on pre-contrast image (e), marked peripheral enhancement on arterial phase image (f), and central progression of the enhancement on delayed image (g). Initial AFP level was 646 IU/mL.

sity to surrounding liver parenchyma. (e–g) T1-weighted images with fat suppression show signal drop in this mass on pre-contrast image (e), marked peripheral enhancement on arterial phase image (f), and central progression of the enhancement on delayed image (g). Initial AFP level was 646 IU/mL.

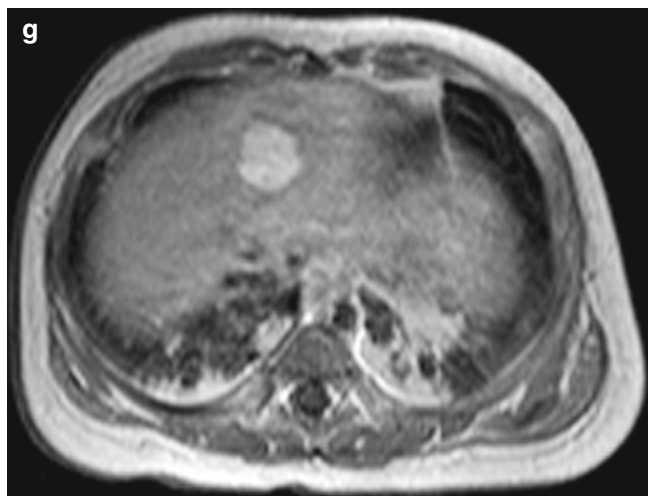


Fig. 22.15 (continued)

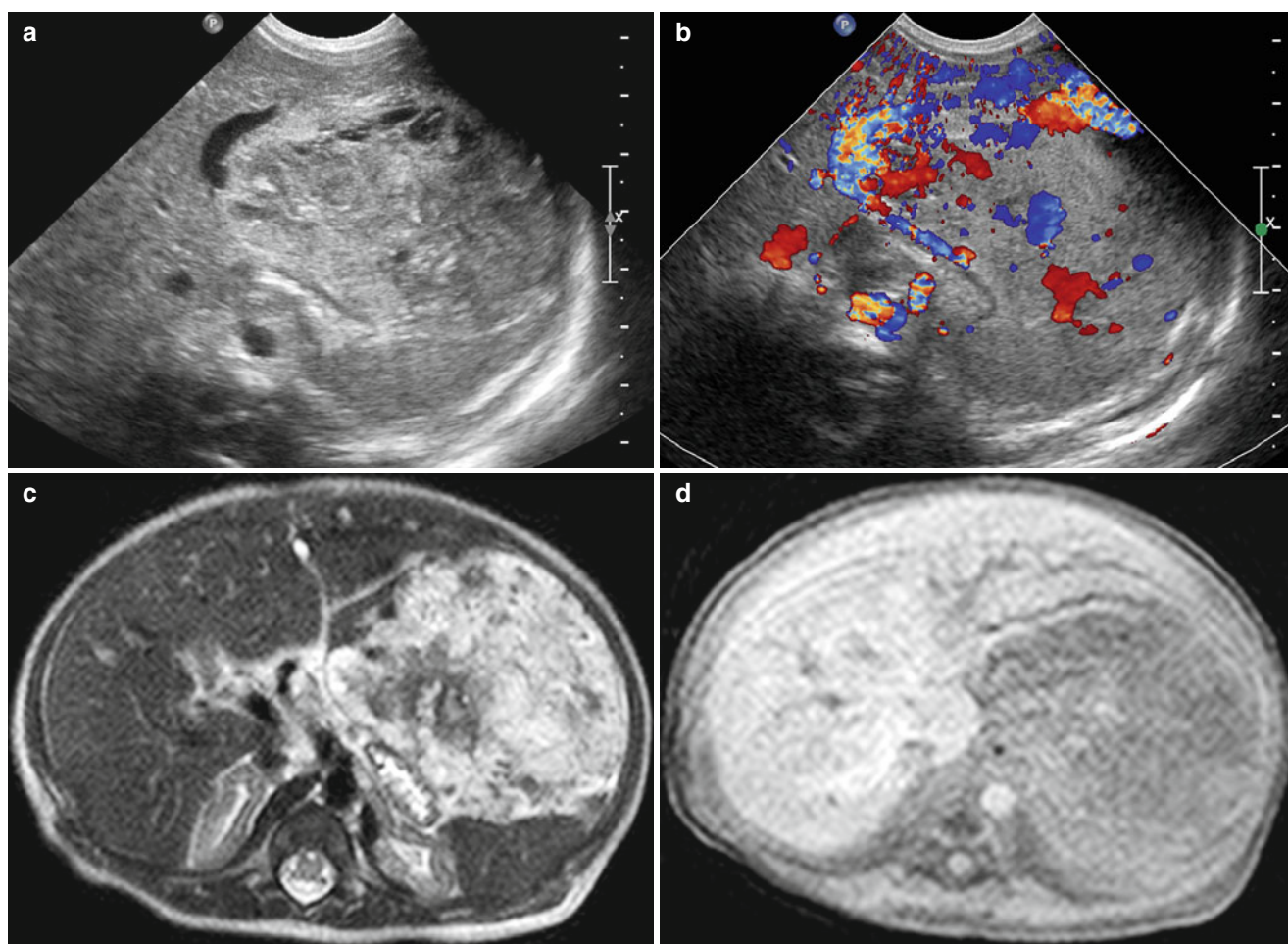


Fig. 22.16 Hepatic hemangioendothelioma in a female neonate. (a) Abdominal US shows huge, heterogeneously hyperechoic mass in left lobe of liver with surrounding engorged vessels. (b) Color Doppler US shows marked increased vascularity in this mass. (c) T2-weighted MR image shows heterogeneously high-signal intensity of this mass. (d–f) T1-weighted images with fat suppression show low-signal intensity mass with internal high signal intensity portion on pre-contrast image (d), intense, nodular peripheral enhancement on arterial phase image (e), and central progression of the enhancement on delayed image (f). Initial AFP level was 35572 IU/mL. (g) Follow-up abdominal US after 2 months shows decreased size of the hepatic mass with decreased echogenicity and increased internal hyperechoic foci suggestive of calcifications

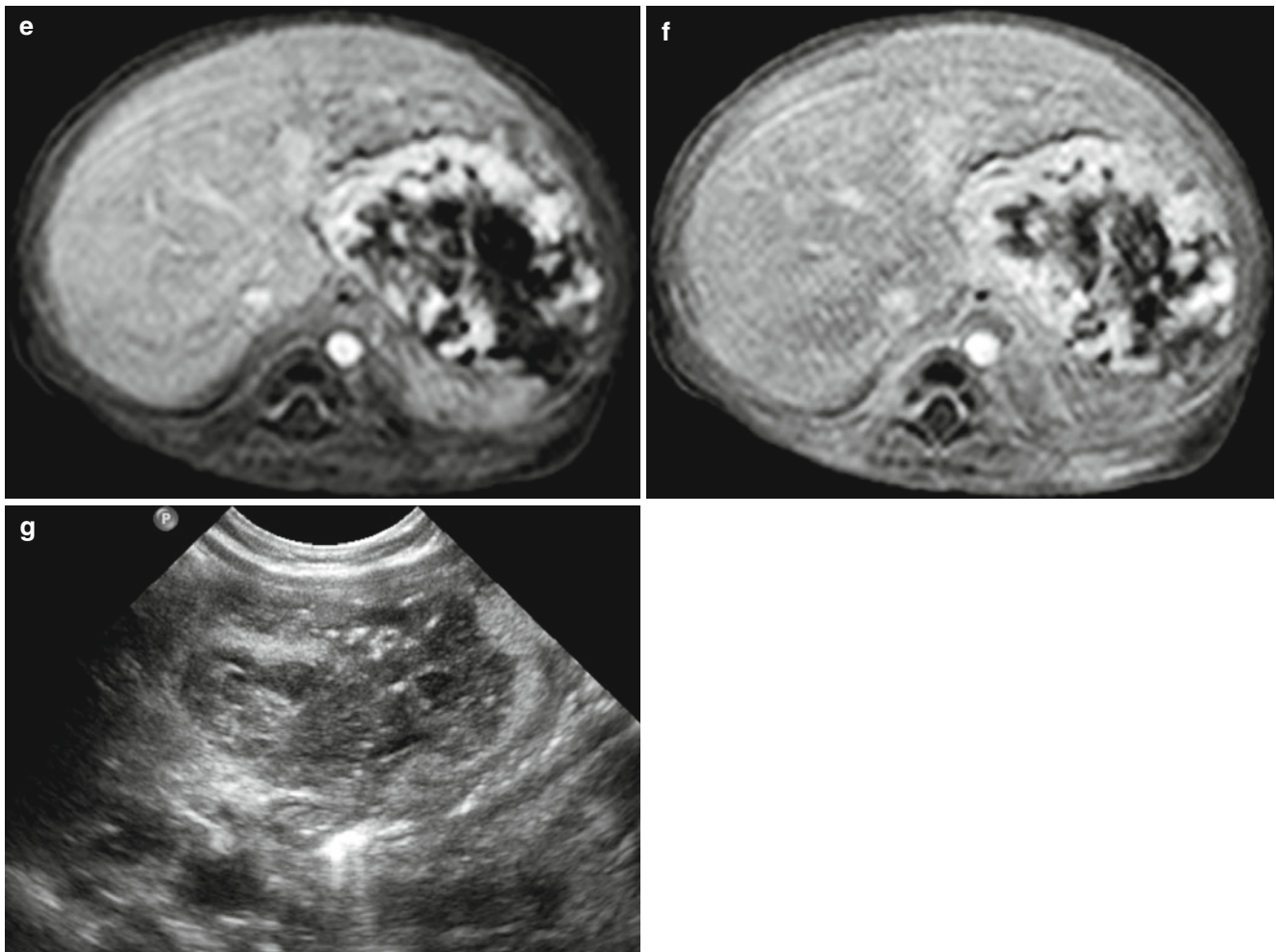


Fig. 22.16 (continued)

22.4.14 Mesenchymal Hamartoma

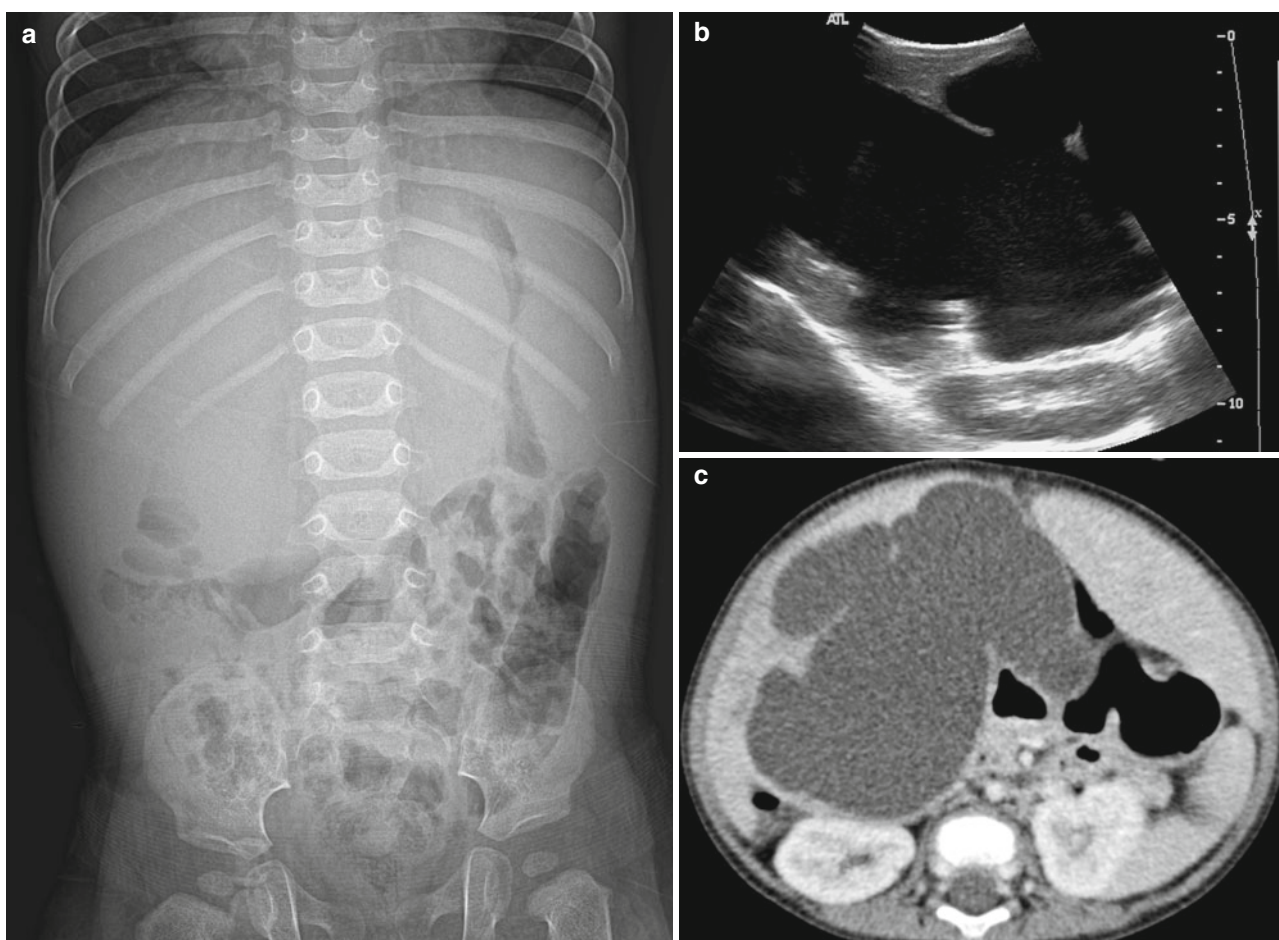


Fig. 22.17 Mesenchymal hamartoma in a 9-month-old boy. (a) Plain abdominal X-ray shows huge soft-tissue opacity in right upper abdomen. (b) Longitudinal US image of liver shows huge and

multilobulated cystic mass originated from the liver. (c) Contrast-enhanced abdominal CT also demonstrates multilobulated cystic mass from the liver

22.4.15 Focal Nodular Hyperplasia

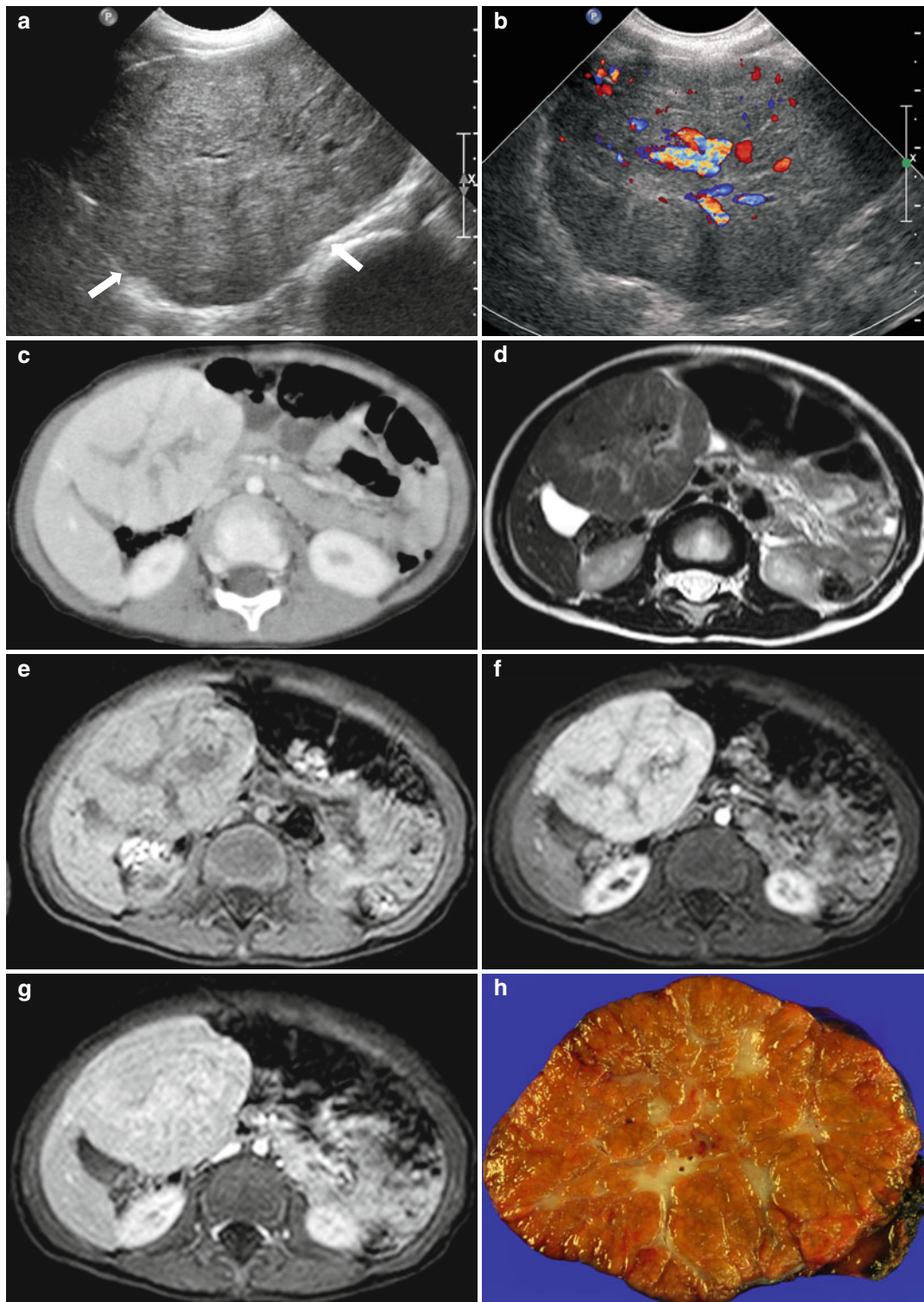


Fig. 22.18 Focal nodular hyperplasia in a 2-year-old boy. (a) Abdominal US shows exophytic isoechoic mass (*arrows*) from the liver. (b) Color Doppler US shows enlarged vessels in the center of the mass. (c) Contrast-enhanced abdominal CT demonstrates multilobulated exophytic mass with similar enhancement with surrounding liver parenchyma and central low-density portion. (d) T2-weighted MR image shows iso- to slightly high-signal intensity of this mass with cen-

tral high signal intensity portion. (e–g) T1-weighted images with fat suppression show iso-signal intensity mass with internal low-signal intensity portion on pre-contrast image (e), early and rapid enhancement on arterial phase image (f), and delayed and retained enhancement in the central scar on delayed image (g). Initial AFP level was 11 IU/mL. (h) On surgical specimen after wedge resection of the liver, multifocal whitish myxoid fibrous stellate scars are noted

22.4.16 Annular Pancreas



Fig. 22.19 Annular pancreas in a female neonate. (a) Plain abdomen shows dilated proximal duodenum (*arrow*) with normal distal small and large bowel gas. (b) Abdominal US shows duodenal second portion

(*arrow*) encircled by pancreas. (c) Upper gastrointestinal series shows circumferential narrowing of the duodenum (*arrow*)

22.4.17 Acute Pancreatitis



Fig. 22.20 Acute pancreatitis in an 11-year-old girl with juvenile rheumatoid arthritis. **(a)** Abdominal US shows diffuse enlargement of pancreas with mild surrounding infiltration. Liver shows diffusely

increased parenchymal echogenicity suggestive of fatty infiltration. **(b–d)** Contrast-enhanced abdominal CT images show diffuse pancreas swelling with peripancreatic fluid collection

22.4.18 Pancreatoblastoma

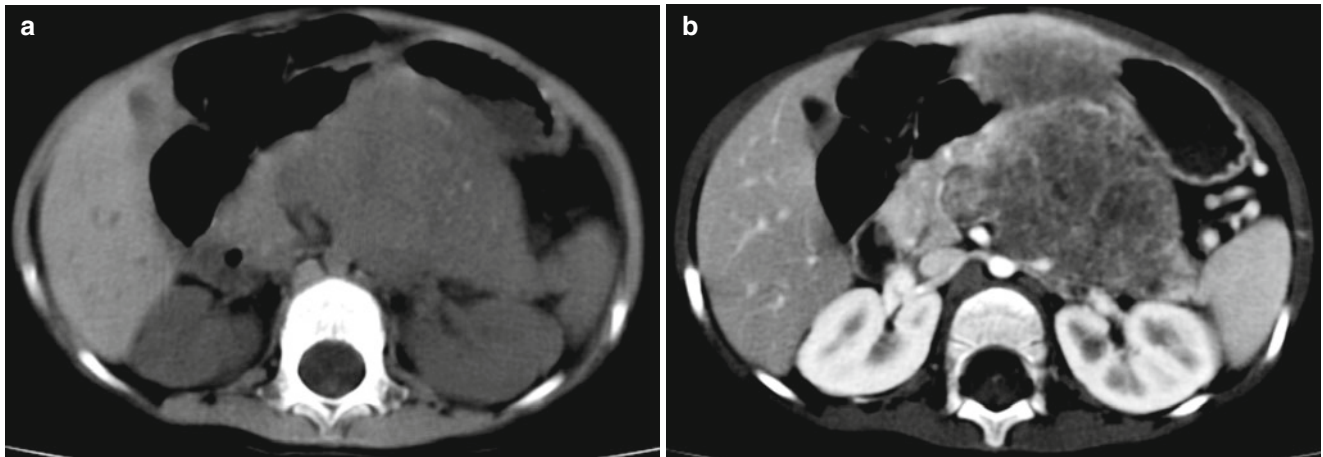


Fig. 22.21 Pancreatoblastoma in a 1-year-old girl. **(a)** Pre-contrast abdominal CT shows huge mass from pancreas body with internal tiny calcifications. **(b)** Post-contrast abdominal CT shows heterogeneous enhancement of the mass

22.4.19 Solid and Papillary Epithelial Neoplasm

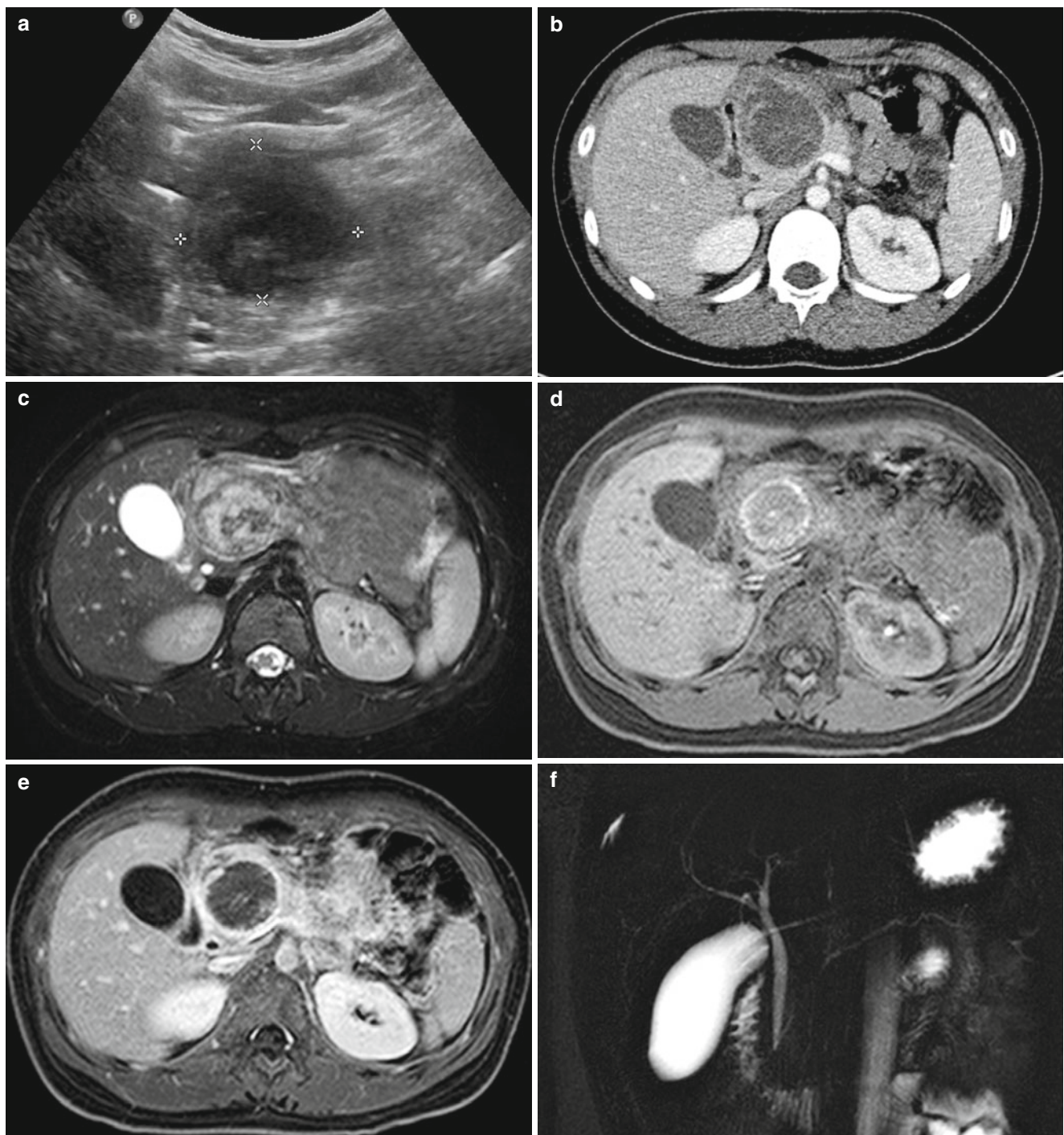


Fig. 22.22 Solid and papillary epithelial neoplasm in an 11-year-old girl. **(a)** Abdominal US shows heterogeneously hypoechoic mass in pancreas body. **(b)** Contrast-enhanced abdominal CT shows lobulated low-density mass with central hyperdense portion in pancreas body. **(c)** On T2-weighted MR image, the pancreatic mass shows heterogeneously high-signal intensity with internal dark signal intensity portion

suggestive of hemorrhage. **(d and e)** T1-weighted images with fat suppression show iso-signal intensity mass with internal high-signal intensity portion on pre-contrast image **(d)** and peripheral enhancement on post-contrast image **(e)**. **(f)** Two-dimensional T2-weighted MRCP shows intact pancreatic duct

22.4.20 Normal Spleen

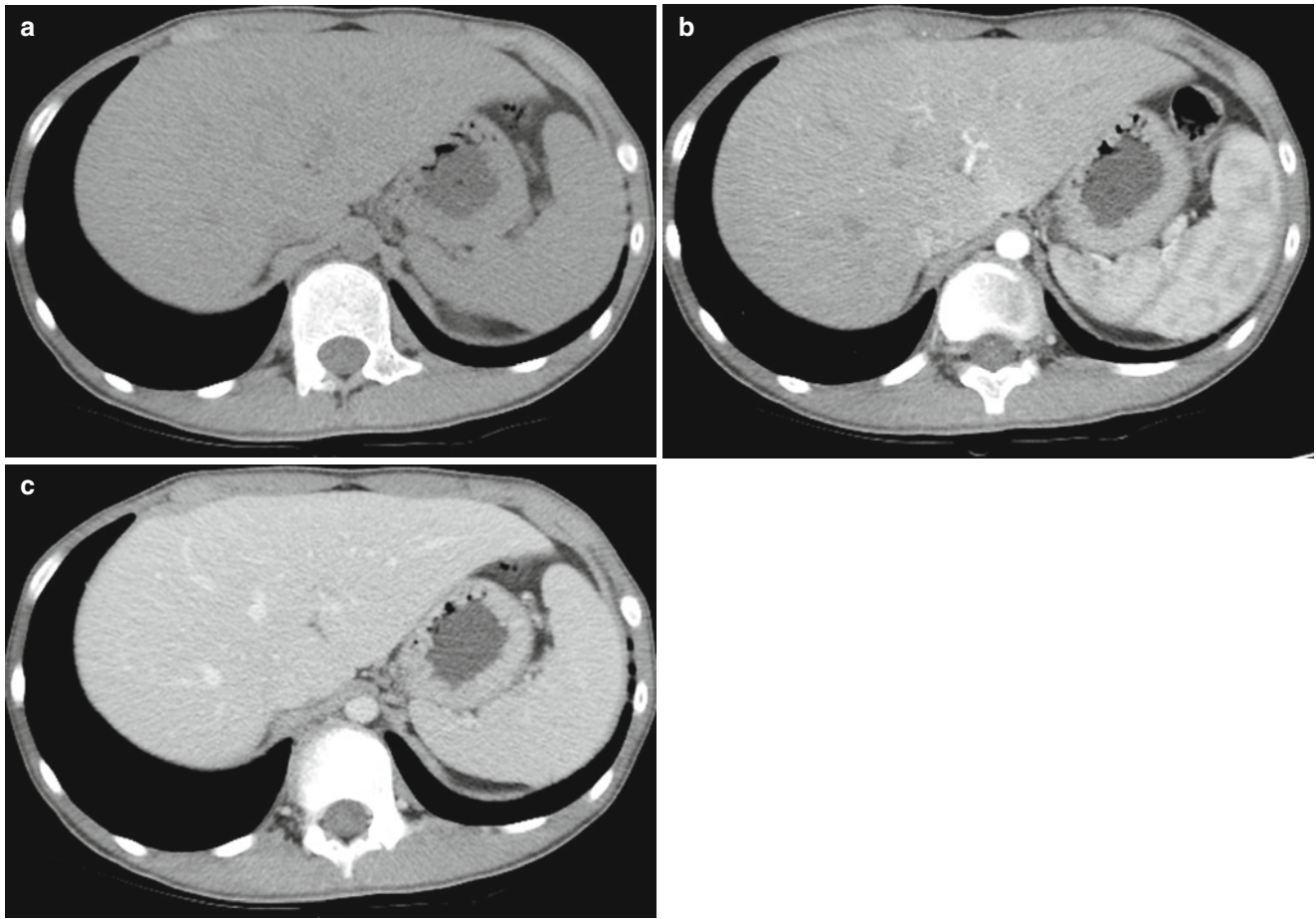


Fig. 22.23 Normal spleen in a 12-year-old boy. (a–c) On abdominal CT, normal spleen shows iso-density with liver on pre-contrast image (a), heterogeneous, zebra-striped enhancement on arterial phase (b), and homogenous enhancement on delayed phase (c)

22.4.21 Splenomegaly

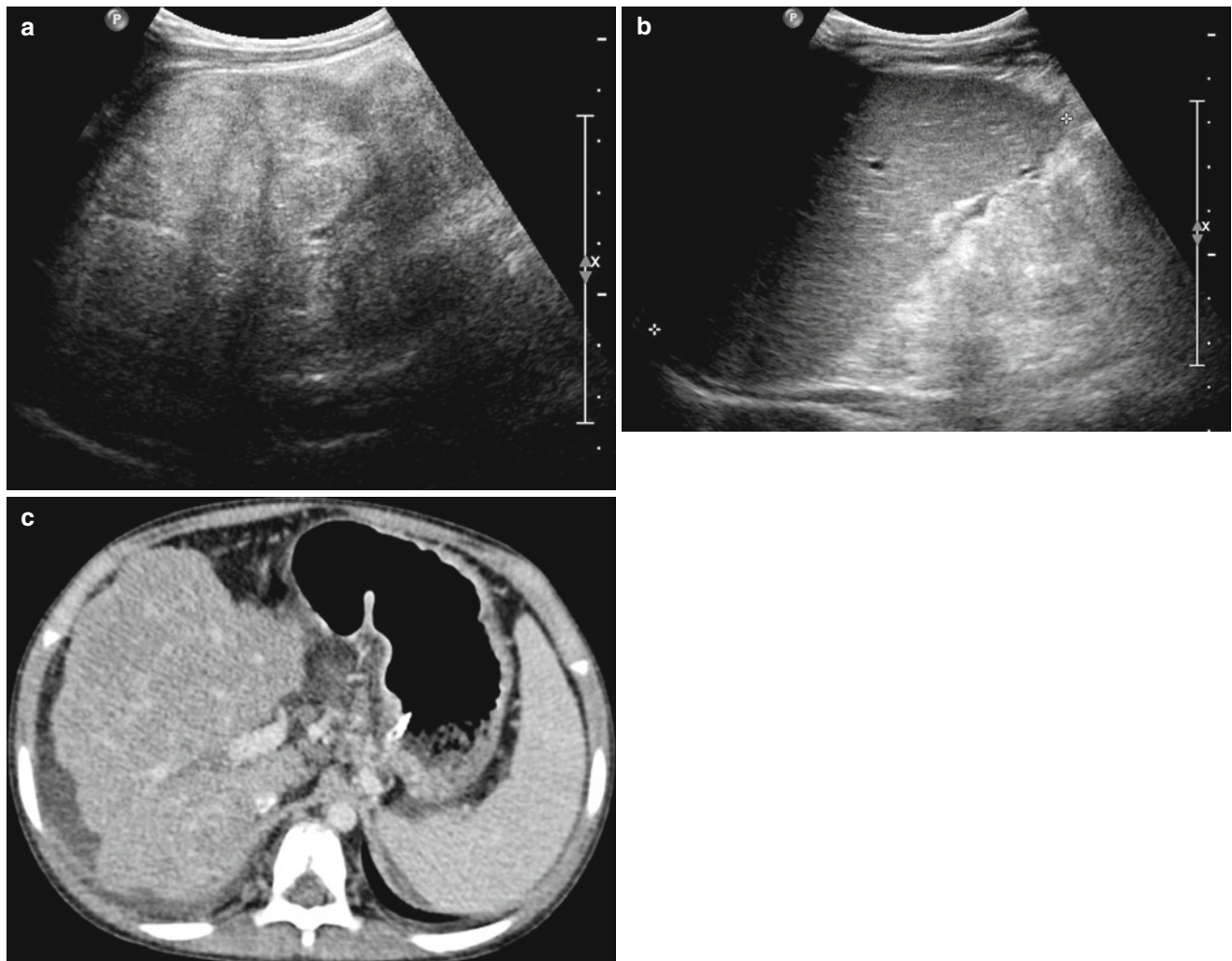


Fig. 22.24 Splenomegaly in a 3-year-old girl with liver cirrhosis and portal hypertension. (a) Abdominal US shows heterogeneous liver parenchymal echogenicity with posterior attenuation. (b) Longitudinal

US image of spleen shows splenomegaly. (c) Contrast-enhanced abdominal CT shows multinodular liver cirrhosis with splenomegaly and gastric varices

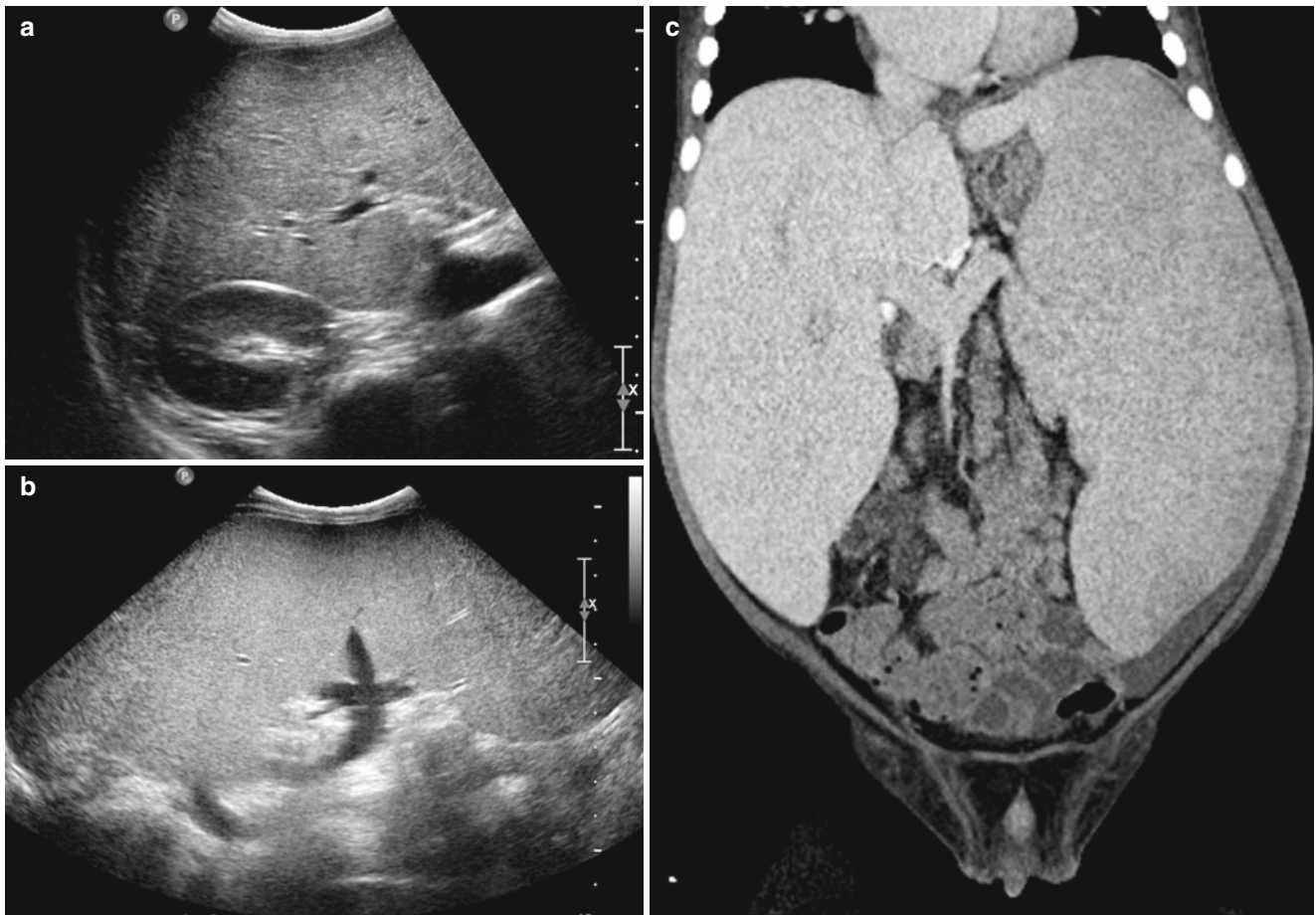


Fig. 22.25 Splenomegaly in a 3-year-old boy with hemolytic anemia. (a and b) Abdominal US images show hepatomegaly with diffusely increased parenchymal echogenicity of liver (a) and marked spleno-

megaly (b). (c) Coronal image of contrast-enhanced abdominal CT also demonstrates marked hepatosplenomegaly

22.4.22 Splenic Hamartoma

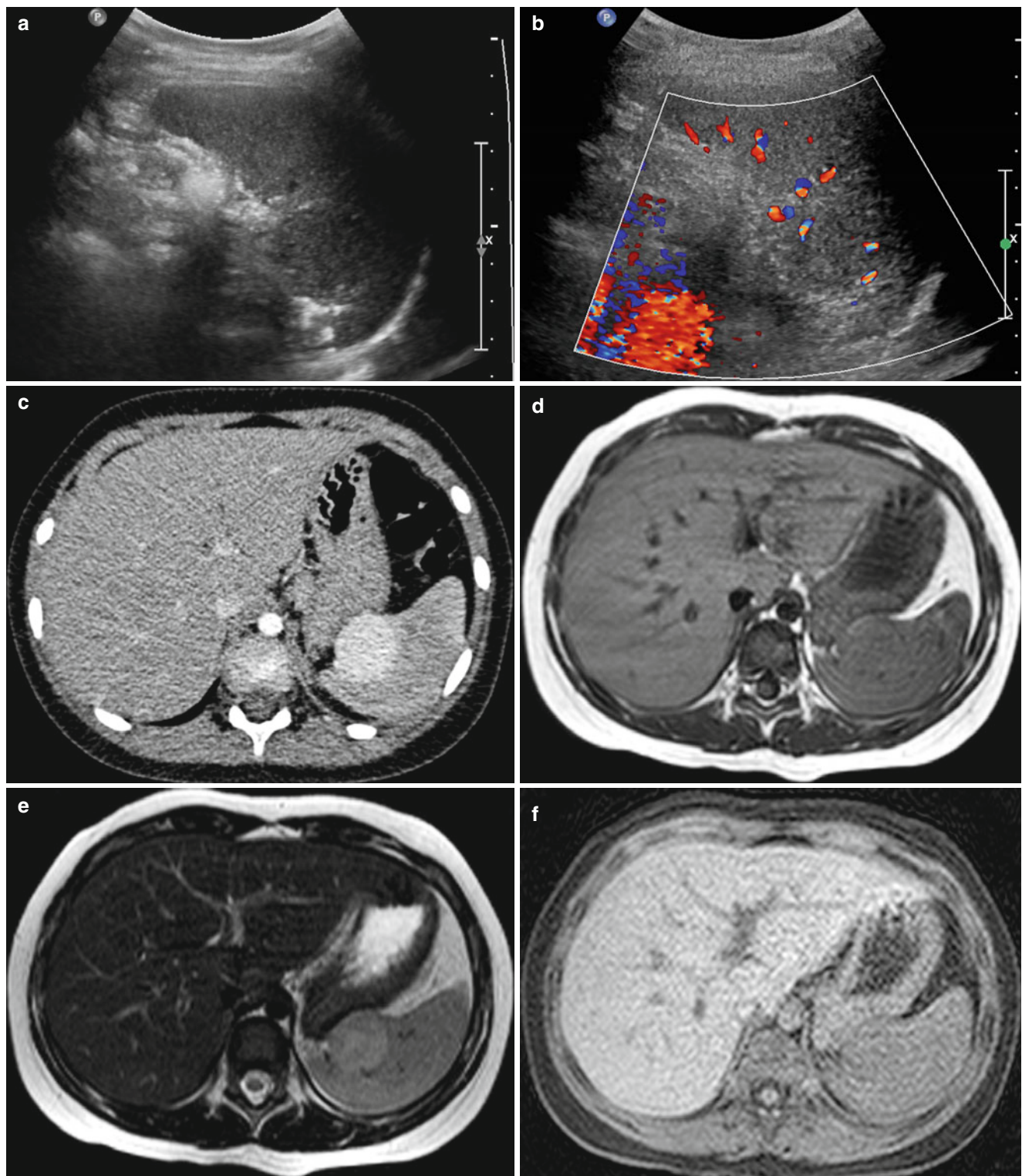


Fig. 22.26 Splenic hamartoma in a 5-year-old boy. (a) Longitudinal US image of spleen shows slightly hypoechoic and exophytic mass. (b) On color Doppler US, the mass shows slightly increased vascularity. (c) Contrast-enhanced abdominal CT shows well-homogenous enhancement of the splenic mass. (d) On T1-weighted image, the splenic mass

shows iso-signal intensity to the splenic parenchyma. (e) On T2-weighted image, the mass shows intermediate- to high-signal intensity to the splenic parenchyma. (f and g) Comparing pre- (f) and post-contrast (g) T1-weighted images with fat suppression, post-contrast image shows increased homogenous enhancement of the mass



Fig. 22.26 (continued)

22.4.23 Splenic Injury

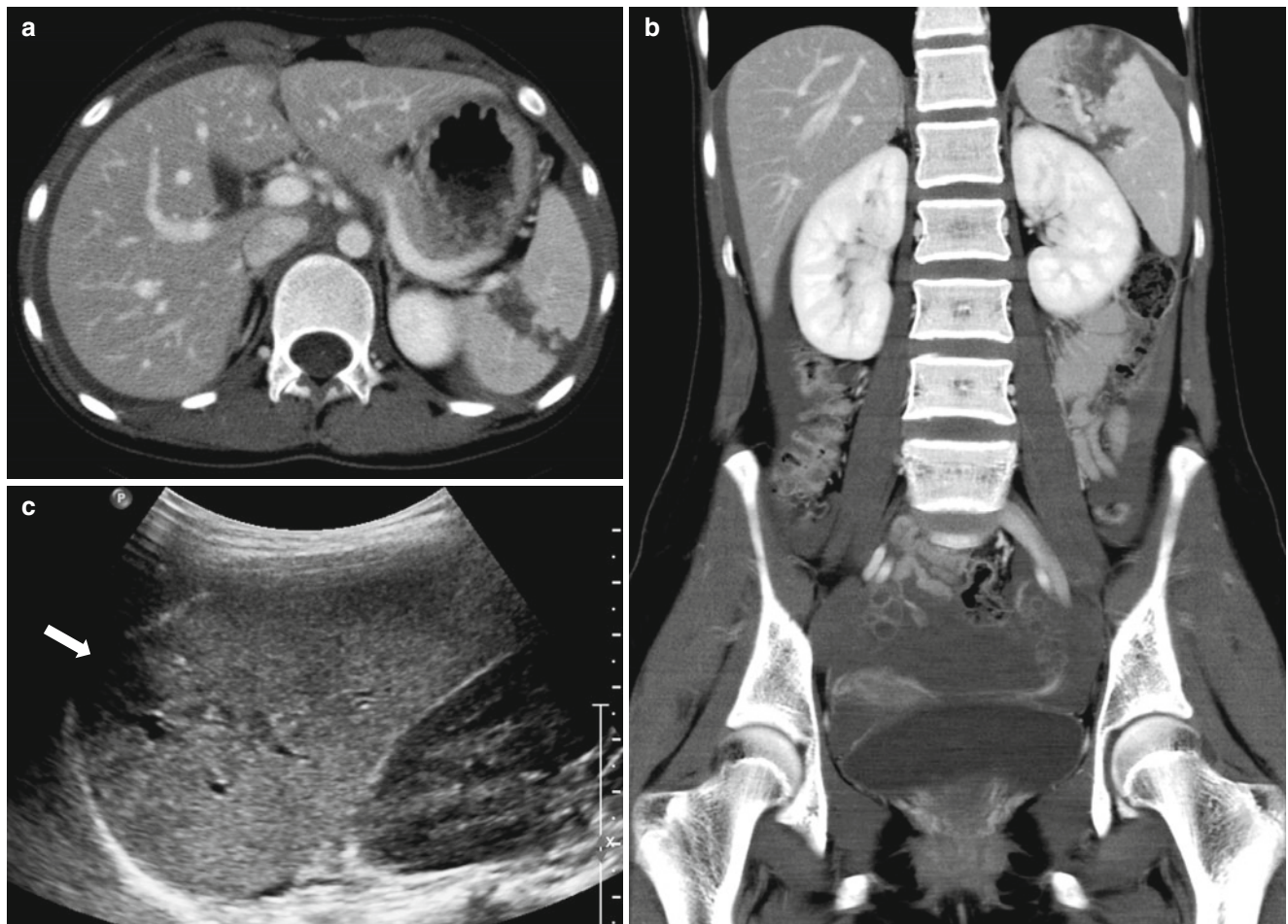


Fig. 22.27 Spleen injury in a 13-year-old girl. (**a** and **b**) Axial (**a**) and coronal (**b**) images of contrast-enhanced abdominopelvic CT show splenic fracture with hemoperitoneum. (**c**) Follow-up abdominal US shows improved but remaining splenic laceration (*arrow*)

References

- Blickman JG, Parker BR, Barnes PD. *Pediatric radiology*. Philadelphia: Mosby/Elsevier; 2009.
- Boll DT, Merkle EM. Diffuse liver disease: strategies for hepatic CT and MR imaging. *Radiographics*. 2009;29:1591–614.
- Chavhan GB, Babyn PS, Manson D, et al. Pediatric MR cholangiopancreatography: principles, technique, and clinical applications. *Radiographics*. 2008;28:1951–62.
- Chung EM, Travis MD, Conran RM. Pancreatic tumors in children: radiologic-pathologic correlation. *Radiographics*. 2006;26:1211–38.
- Darge K, Anupindi S. Pancreatitis and the role of US, MRCP and ERCP. *Pediatr Radiol*. 2009;39 Suppl 2:S153–7.
- Gubernick JA, Rosenberg HK, Ilaslan H, et al. US approach to jaundice in infants and children. *Radiographics*. 2000;20:173–95.
- Han SJ, Kim MJ, Han A, et al. Magnetic resonance cholangiography for the diagnosis of biliary atresia. *J Pediatr Surg*. 2002;37:599–604.
- Hilmes MA, Strouse PJ. The pediatric spleen. *Semin Ultrasound CT MR*. 2007;28:3–11.
- Jha P, Chawla SC, Tavri S, et al. Pediatric liver tumors – a pictorial review. *Eur Radiol*. 2009;19:209–19.
- Kamath BM, Spinner NB, Piccoli DA. Alagille syndrome. In: Suchy FJ, Sokol RJ, Balistreri WF, editors. *Liver disease in children*. Cambridge: Cambridge University Press; 2007.
- Kelly DA. *Diseases of the liver and biliary system in children*. Malden: Blackwell; 2008.
- Lee MS, Kim MJ, Lee MJ, et al. Biliary atresia: color Doppler US findings in neonates and infants. *Radiology*. 2009;252:282–9.
- Lee MJ, Kim MJ, Yoon CS. MR cholangiopancreatography findings in children with spontaneous bile duct perforation. *Pediatr Radiol*. 2010;40:687–92.
- Lynn KN, Werder GM, Callaghan RM, et al. Pediatric blunt splenic trauma: a comprehensive review. *Pediatr Radiol*. 2009;39:904–16. Quiz 1029–1030.
- Nijs E, Callahan MJ, Taylor GA. Disorders of the pediatric pancreas: imaging features. *Pediatr Radiol*. 2005;35:358–73. Quiz 457.
- Oldenburg A, Hohmann J, Skrok J, et al. Imaging of paediatric splenic injury with contrast-enhanced ultrasonography. *Pediatr Radiol*. 2004;34:351–4.
- Pariente D. The biliary tract. In: Carty H, Brunelle F, Stringer DA, editors. *Imaging children*. Edinburgh/New York: Elsevier Churchill Livingstone; 2005.
- Siegel MJ. Gallbladder and biliary tract. In: Siegel MJ, editor. *Pediatric sonography*. 3rd ed. Philadelphia: Wolters Kluwer Health/Lippincott Williams & Wilkins; 2011.
- Takeshi M, Masahiko U, Atsuyuki Y. Choledochal cyst. In: Puri P, Höllwarth M, editors. *Pediatric surgery*. 1st ed. Berlin/New York: Springer; 2006.
- Tang A, Tan J, Sun M, et al. Nonalcoholic fatty liver disease: MR imaging of liver proton density fat fraction to assess hepatic steatosis. *Radiology*. 2013;267:422–31.
- Todani T, Watanabe Y, Narusue M, et al. Congenital bile duct cysts: classification, operative procedures, and review of thirty-seven cases including cancer arising from choledochal cyst. *Am J Surg*. 1977;134:263–9.
- Valentino M, Serra C, Pavlica P, et al. Blunt abdominal trauma: diagnostic performance of contrast-enhanced US in children – initial experience. *Radiology*. 2008;246:903–9.
- Xanthakos SA, Yazigi NA, Ryckman FC, et al. Spontaneous perforation of the bile duct in infancy: a rare but important cause of irritability and abdominal distension. *J Pediatr Gastroenterol Nutr*. 2003;36:287–91.

Part VI

Genitourinary System

Mi-Jung Lee

Contents

23.1	Introduction	724
23.2	Embryology of Upper Urinary System	724
23.3	Spectrum of Congenital Anomalies of the Upper Urinary Tract	724
23.3.1	Anomalies of Kidney	724
23.3.2	Anomalies of Renal Calyces	725
23.3.3	Anomalies of Renal Pelvis and Ureter	725
23.3.4	Duplex Collecting System	726
23.4	Illustrations: Congenital Anomalies of the Upper Urinary Tract	728
23.4.1	Anomalies of Kidney: Anomalies of Form – Renal Agenesis	728
23.4.2	Anomalies of Kidney: Anomalies of Form – Renal Hypoplasia	732
23.4.3	Anomalies of Kidney: Anomalies of Rotation	734
23.4.4	Anomalies of Kidney: Anomalies of Position	735
23.4.5	Anomalies of Kidney: Anomalies of Fusion – Horseshoe Kidney	738
23.4.6	Anomalies of Kidney: Anomalies of Fusion – Crossed Fused Ectopy	739
23.4.7	Anomalies of Renal Calyces: Calyceal Diverticulum	740
23.4.8	Anomalies of Renal Calyces: Congenital Megacalycosis	743
23.4.9	Anomalies of Renal Pelvis and Ureter: Congenital Ureteropelvic Junction Obstruction	744
23.4.10	Anomalies of Renal Pelvis and Ureter: Congenital Megaureter	748
23.4.11	Anomalies of Renal Pelvis and Ureter: Ectopic Ureter	752
23.4.12	Anomalies of Renal Pelvis and Ureter: Ureterocele	754
23.4.13	Duplex Collecting System	756
	References	757

M.-J. Lee, M.D.
Department of Radiology, Severance Children's Hospital
and Yonsei University College of Medicine,
50 Yonsei-ro, Seodaemun-gu, Seoul 120-752, Korea
e-mail: mjl1213@yuhs.ac, mijung.j.lee@gmail.com

23.1 Introduction

Congenital anomalies of the upper urinary tract are common in children. These anomalies play a causative role in more than 30 % of cases of end-stage renal disease. Therefore, it is important to understand embryological process and associated multiple anomalies in this system. Ultrasonography (US) is an essential tool to evaluate congenital anomalies of the upper urinary tract in children. However, multimodality imaging including CT, MRI, intravenous urography (IVU), and radio-nuclide studies are needed to evaluate the spectrum of these diseases. This chapter presents various imaging findings of congenital anomalies of the upper urinary tract in children.

23.2 Embryology of Upper Urinary System

Normal embryological development of the kidney occurs in three stages (Fotter and Avni 2008). Pronephros is a transient rudimentary system at fourth week of gestation. Mesonephros is derived from the intermediate mesoderm and contributes to the formation of the urinary bladder and male genital system. The definitive kidney, the metanephros, is the last stage of renal development and has a dual mesoderm origin. The glomeruli and tubules arise from metanephric blastema and the excretory segments from the ureteric bud. Metanephros appears in the fifth week of gestation and migrates upward with rotation. The renal pelvis originally points ventrally, and a gradual inward and medial turning takes place. Collecting ducts of the permanent kidney develop from the ureteric bud, an outgrowth of the mesonephric duct close to its entrance to the cloaca.

23.3 Spectrum of Congenital Anomalies of the Upper Urinary Tract

23.3.1 Anomalies of Kidney

23.3.1.1 Anomalies of Form

23.3.1.1.1 Renal Agenesis

Renal agenesis is defined as congenital absence of renal parenchymal tissue and results from major disruption of metanephric development at an early stage. Causes of renal agenesis are aplasia of the Wolffian duct or absence of the ureteral bud with consecutive lack of induction of metanephrogenic tissue. Usually, there is no ipsilateral ureter and hypoplasia or anomalies of genital structures originating from the ipsilateral Wolffian and Mullerian duct. Herlyn-Werner-Wunderlich syndrome is characterized by the triad of didelphys uterus, obstructed hemivagina, and ipsilateral renal agenesis (Fig. 23.1) (Del Vescovo et al. 2012).

The majority of patients with unilateral renal agenesis are asymptomatic. Other urological abnormalities have been

reported in 40 % of unilateral cases. The contralateral kidney may be ectopic and malrotated and usually presents with compensatory hypertrophy (Fig. 23.2) (Kaneyama et al. 2004). However, if hypertrophy is not present, dysplastic or hypoplastic changes of the remaining single kidney must be considered.

The purpose of postnatal imaging is to search for ectopic kidney parenchyma, to evaluate the contralateral kidney, to assure normal renal function, and to evaluate associated abnormalities, particularly of the genital structures (Fig. 23.3), and US is used as the first step (Fig. 23.1).

23.3.1.1.2 Renal Hypoplasia

Embryologically, renal hypoplasia originates from the problems with metanephrogenic tissue differentiation. Histologically, it is defined by reduction in the number and/or size of nephrons and commonly combined with dysplastic elements. A genetic contribution to its cause is being increasingly recognized (Sanna-Cherchi et al. 2007).

Renal hypoplasia can be found unilaterally, segmental, or bilaterally (Figs. 23.4 and 23.5). Ask-Upmark kidney is a segmental manifestation of renal hypoplasia in a single system and can be due to variable causes such as regional arteritis or vesicoureteral reflux (VUR).

When disease is discovered later in childhood, various entities have to be considered for the differential diagnosis including acquired or secondary renal hypoplasia. These include renal artery stenosis, renal dysplasia, Alport syndrome, chronic glomerulonephritis, or end-stage renal disease.

23.3.1.2 Anomalies of Rotation

The fetal kidneys undergo a 90° rotation around their longitudinal axis during their ascent from the pelvis before they reach their final position by the end of the eighth week of fetal life (Wein et al. 2012).

The condition may be unilateral or bilateral. The most common type is an incomplete rotation or nonrotation (Fig. 23.6). The renal pelvis is in the anterior position or some variation between the anterior and normal medial position. Reverse rotation and hyperrotation are other major types of malrotation. In reverse rotation, the renal pelvis rotates laterally, and the renal vessels cross the kidney anteriorly to reach the hilum. In hyperrotation, the kidney rotates more than 180°, but less than 360°. The pelvis faces laterally, but the renal vessels are carried posteriorly to the kidney. Malrotation is usually discovered accidentally, during imaging of the kidney. The calyces are often distorted, even without any associated obstruction.

23.3.1.3 Anomalies of Position

Renal ectopy occurs when the kidney does not normally ascend to the retroperitoneal renal fossa (level of the second lumbar vertebra). There is a slight predilection for the left

side, and 10 % of cases are bilateral. Malrotation frequently accompanies renal ectopy.

Simple renal ectopy refers to a kidney that remains in the ipsilateral retroperitoneal space such as pelvic kidney (below the aortic bifurcation) and lumbar kidney (Fig. 23.7). Excessive cranial migration of the kidney results in a thoracic kidney, which is often detected on a routine chest radiograph as a mass (Maduekwe et al. 2011) (Fig. 23.8). Kidneys that cross the midline are referred to as crossed renal ectopy.

The diagnosis of an ectopic kidney can be made by US in most cases. The majority of patients with renal ectopy are asymptomatic. However, the ectopic kidney generally has decreased function (Fig. 23.5). The contralateral kidney may be abnormal in up to 50 % of patients, and VUR is frequently associated. Therefore, voiding cystourethrography (VCUG) is recommended. Genital anomalies, skeletal anomalies, cardiovascular lesions, and gastrointestinal abnormalities also can occur.

23.3.1.4 Anomalies of Fusion

Renal fusion occurs when a portion of one kidney is fused to the other. This occurs early in embryogenesis, before rotation is complete. Therefore malrotation is present in all cases.

23.3.1.4.1 Horseshoe Kidney

Horseshoe kidney is the most common type of renal fusion and one of the most frequent renal anomalies. It is usually characterized by fusion of the lower poles across the midline by an isthmus (Fig. 23.9). It is usually positioned low in the abdomen with the isthmus lying just below the junction of the inferior mesenteric artery and aorta. Depending on the degree of fusion, the isthmus can be composed of renal parenchyma or a fibrous band (Fotter and Avni 2008).

Ureteropelvic junction obstruction, hydronephrosis, and urolithiasis are associated. In addition, VUR should be excluded in all children with a horseshoe kidney. Patients with a horseshoe kidney appear to have an increased risk for Wilms tumor (Neville et al. 2002; Huang et al. 2004). One-third of patients with horseshoe kidney had at least one other abnormality.

23.3.1.4.2 Crossed Fused Ectopy

Crossed fused ectopy is the second most common fusion anomaly after horseshoe kidney. It usually involves abnormal movement of only one kidney across the midline with fusion of the contralateral noncrossing kidney. Therefore, the crossed ectopic kidney lies on the opposite side from the ureteral insertion of the bladder. Crossed renal ectopy is more common with fusion in 85 % than without fusion in less than 10 %. The most common form is the unilateral fused type with inferior ectopy (Fig. 23.10).

Generally, it is difficult to distinguish between crossed renal ectopy with and without fusion by US. CT and MRI are able to establish the correct diagnosis. VCUG should

be performed in all of these patients due to commonly associated VUR.

23.3.2 Anomalies of Renal Calyces

23.3.2.1 Calyceal Diverticulum

A calyceal diverticulum is an eventration of a calyx into the renal parenchyma that is filled with urine. Most of the diverticula are small and asymptomatic. While the incidence of calyceal diverticula is low, the frequency of stone formation within them is high. Up to 50 % of calyceal diverticula contain calculi or milk of calcium (Fotter and Avni 2008).

The diverticulum is usually detected by US as an isolated cystic structure. The identification of a cystic renal lesion in close proximity to the renal sinus with curvilinear, plaque-like calcification along its posterior wall is a typical finding of a stone-containing calyceal diverticulum (Stunell et al. 2010). Multiple small stones within a diverticulum become layered along its posterior wall when the patient is supine. However, the connection with the pyelocalyceal system is usually not visualized on US; it can be demonstrated on IVU or on CT (Figs. 23.11 and 23.12).

23.3.2.2 Congenital Megacalycosis

Megacalycosis is an extremely rare condition and characterized by the presence of 12–20 dilated calyces without obstruction. It seems to be related to a developmental hypoplasia of the medullary pyramids. Megacalycosis may typically also be associated with a primary megaureter, and urinary stone can occur.

An increased number of calyces with a significant disproportion between the degree of calyceal dilatation and a mildly dilated renal pelvis are the findings of this disease (Fig. 23.13). Megacalycosis must be considered in the differential diagnosis of congenital hydronephrosis, polycalycosis, and infundibular stenosis. The diagnosis is suggested by US and confirmed by diuretic renography, IVU, or MR urography. VCUG should be performed to rule out VUR (Pieretti-Vanmarcke et al. 2009).

23.3.3 Anomalies of Renal Pelvis and Ureter

23.3.3.1 Congenital Ureteropelvic Junction Obstruction

Congenital ureteropelvic junction (UPJ) obstruction is a partial or total blockage of the flow of urine that occurs where the ureter enters the kidney. It is the most common pathologic cause of antenatally detected hydronephrosis (Figs. 23.14 and 23.15).

The origin of UPJ obstruction can be multifactorial. In most cases of UPJ obstruction, the cause is intrinsic narrowing or kinking of the upper segment of the ureter. There is an

extrinsic compression in about 10 % of UPJ obstruction as an aberrant or accessory renal artery or arterial branch crossing the lower pole of the kidney and resulting in compression of the UPJ (Fig. 23.16).

Dilatation is best evaluated on an anteroposterior measurement of the renal pelvis on a transverse scan of the kidney (Fig. 23.14). However, conventional US alone does not provide information on renal function or the degree of obstruction. The best method to evaluate and to quantify obstruction is the radioisotope study (diuretic radionuclide renogram) even though this study is also limited during the first month of life due to low clearance (Ismaili and Piepsz 2013).

VCUG evaluation is also needed to exclude VUR. Once VUR is excluded, it becomes more probable that the urinary tract dilatation is secondary to obstruction. However, VUR and obstruction may coexist in the same collecting system. UPJ obstruction also can be combined with ureterovesical junction (UVJ) obstruction, urinary stone, horseshoe kidney, and urinoma. Differential diagnosis of UPJ obstruction should include multicystic dysplastic kidney, infundibular stenosis, and UVJ obstruction.

Initial renal function based upon renal scan and serial US monitoring are the findings most commonly used in determining whether or not to perform pyeloplasty. However, there are no randomized trials that provide evidence for the optimal management of congenital UPJ obstruction (Heinlen et al. 2009).

23.3.3.2 Congenital Megaureter

In children, any ureter greater than 7 mm in diameter is considered a megaureter based on measurements in fetuses greater than 30 weeks gestation and children <12 years. Primary megaureter is the second most common cause of hydronephrosis in the newborn (after UPJ obstruction), accounting for approximately 20 % of cases. The presence of a dilated ureter may correspond to primary megaureter, refluxing megaureter, nonobstructive non-refluxing megaureter, or secondary megaureter (Fotter and Avni 2008).

Primary megaureter corresponds to an obstructive dilatation of the ureter above an adynamic ureteral segment at the ureterovesical junction. The degree of associated pelvicalyceal dilatation varies. US should be performed after the first 2 days after birth, preferably at 1 week of age or later, because hydronephrosis may not be detected due to physiologic volume depletion and relative oliguria. It is important to identify the ureter's origin and insertion into the bladder to help differentiate it from bowel and from an ectopic ureter. This condition is best demonstrated on IVU or MRI.

Megaureter can be associated with VUR, which is called refluxing megaureter (Fig. 23.17). Nonobstructive non-refluxing megaureter may represent the evolution and sequelae of an antenatal dilatation of ureter (Fig. 23.18).

Secondary megaureter can occur intrinsically or extrinsically. Intrinsic causes include ureteral valves, midureteral or distal stenosis, or ureteral diverticula. Retrocaval ureter is an extrinsic secondary megaureter.

23.3.3.3 Ectopic Ureter

Ectopic ureter is diagnosed when the ureteral orifice is caudal to the normal insertion on the trigone of the bladder. Ureteral ectopy is more common with duplex kidneys. It is usually associated with poorly functioning dysplastic kidney (Fig. 23.19), and VUR into the ectopic ureter can be combined (Plaire et al. 1997).

The ectopic orifice is always found along the pathway of the developing mesonephric system. The ectopic ureter may drain into the posterior urethra (about 50 %), the seminal vesicle, or the vas deferens in boys. It drains into the urethra, the vagina, or the uterus in girls. Most girls present with a history of urinary incontinence, because their ectopic ureters terminate at sites that bypass the urethral external sphincter in two-thirds of the cases.

US is the initial diagnostic test. The ureter is often dilated down to its abnormally low position. In many cases, the ureter may be followed proximally to a dysplastic or normal upper segment moiety of a duplex system. In single-system ectopia, the kidney may be dysplastic and difficult to visualize. MRI can be helpful in suspected cases of ectopic ureters (Wang et al. 2010). VCUG should be performed to detect the presence or absence of reflux.

23.3.3.4 Ureterocele

A ureterocele is a cystic dilatation of the terminal ureter within the bladder and/or the urethra (Berrocal et al. 2002). It is more common with duplex kidneys. It can be classified as intravesical (i.e., entirely within the bladder) (Fig. 23.20) or ectopic (i.e., a portion extends beyond the bladder neck into the urethra) (Fig. 23.21). At times, differentiating between intravesical and ectopic ureteroceles may be difficult. Approximately 80 % of ureteroceles are associated with the upper pole of a duplex collecting system, and 60 % of these are ectopic (Fotter and Avni 2008), whereas intravesical ureteroceles are more common in single systems.

On US, the ureterocele appears as a well-defined cystic lesion within the bladder that is connected with the ureter, and the upper urinary tract is not necessarily obstructed or dilated (Shokeir and Nijman 2002). In duplex systems, there is about an 80 % chance that the other side will be duplex. VCUG is important to identify whether VUR is present.

23.3.4 Duplex Collecting System

Complete or partial duplication of the renal collecting system is the most common congenital anomaly of the urinary

tract. Complete duplication is thought to result from two separate ureteral buds presenting on the mesonephric duct. Complete ureteral duplication occurs in 1 out of 500 patients, most often with no complications. Abnormal duplex kidneys used to be and are still detected during the work-up of urinary tract infection or urinary dribbling in girls.

The orifice of the ureter draining the lower segment of the kidney migrates more cephalad and lateral than the ureter draining the upper part of the kidney (Weigert-Meyers rule). When both orifices open close to each other at a normal location, no complications occur. On the contrary, when they open apart from each other and away from the normal

location, complications occur: the lower pole is usually associated with VUR and the upper pole with ureteral ectopy or ureterocele with secondary obstruction. Dysplasia of the upper pole is also very common (Fig. 23.22).

US usually demonstrates the two renal poles and the hydroureteronephrosis involving one or both moieties. It displays easily intravesical ureteroceles; however, the technique cannot always demonstrate ectopic ureters. Further work-up will include VCUG and MR urography. The optimal role of MR urography can be the assessment of ectopic extravesical ureteric insertions and whenever an occult upper pole is suspected (Avni et al. 2001).

23.4 Illustrations: Congenital Anomalies of the Upper Urinary Tract

23.4.1 Anomalies of Kidney: Anomalies of Form – Renal Agenesis



Fig. 23.1 Herlyn-Werner-Wunderlich syndrome in a 15-year-old girl. (a–d) Abdominopelvic CT of axial (a and b) and coronal (c and d) images show double uterus (arrows) with distended left hemivagina

(arrowhead) due to obstruction. Left kidney is not visualized in left abdomen. (e and f) T2-weighted coronal MR images also well demonstrate uterine didelphys with left vaginal obstruction

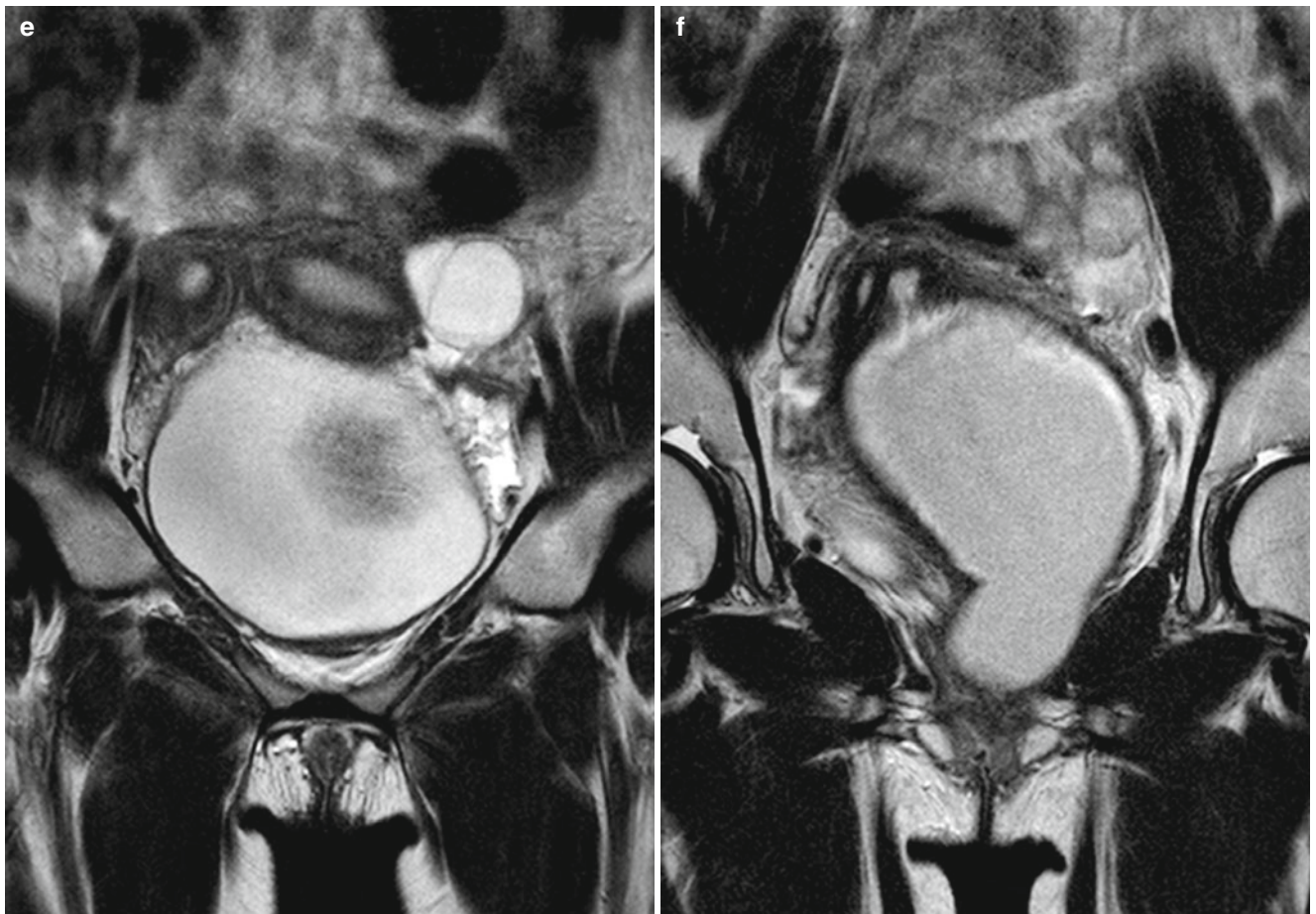


Fig. 23.1 (continued)

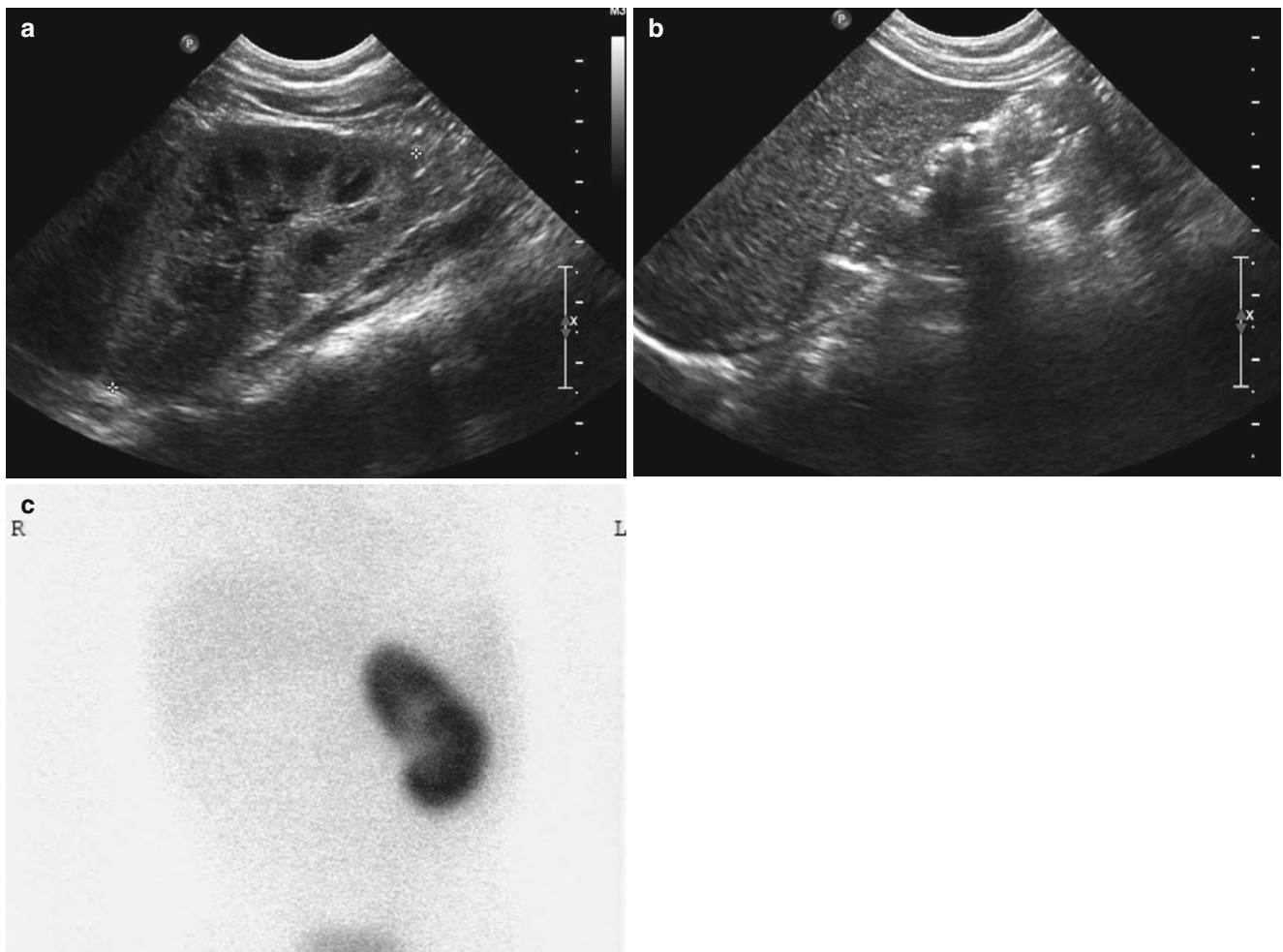


Fig. 23.2 Renal agenesis in a 3-year-old boy. (a) Abdominal US of left abdomen shows hypertrophied left kidney. (b) Right kidney is not seen in right renal fossa. (c) Tc-99 m dimercaptosuccinic acid (DMSA) scan shows grossly normal left kidney and nonvisualized right kidney

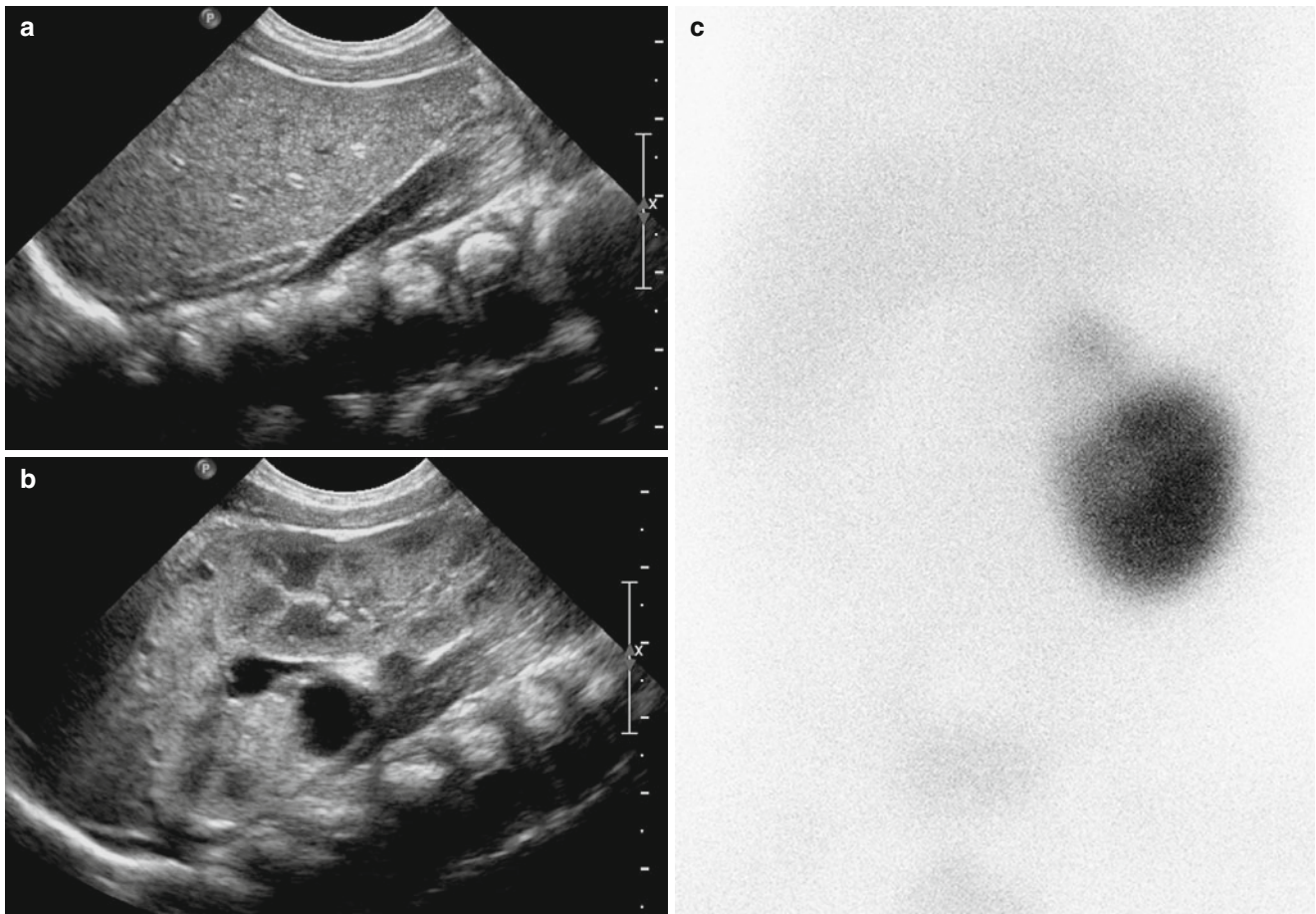


Fig. 23.3 Renal agenesis with contralateral duplex collecting system in a 3-month-old girl. (a) Right kidney is not seen in right renal fossa on abdominal US. (b) Abdominal US of left abdomen shows duplex collecting system of left kidney with multiple small cortical cysts and pel-

vic dilatation in upper pole. (c) Tc-99 m DMSA scan shows decreased uptake in the dysplastic upper pole of left kidney and nonvisualized right kidney

23.4.2 Anomalies of Kidney: Anomalies of Form – Renal Hypoplasia

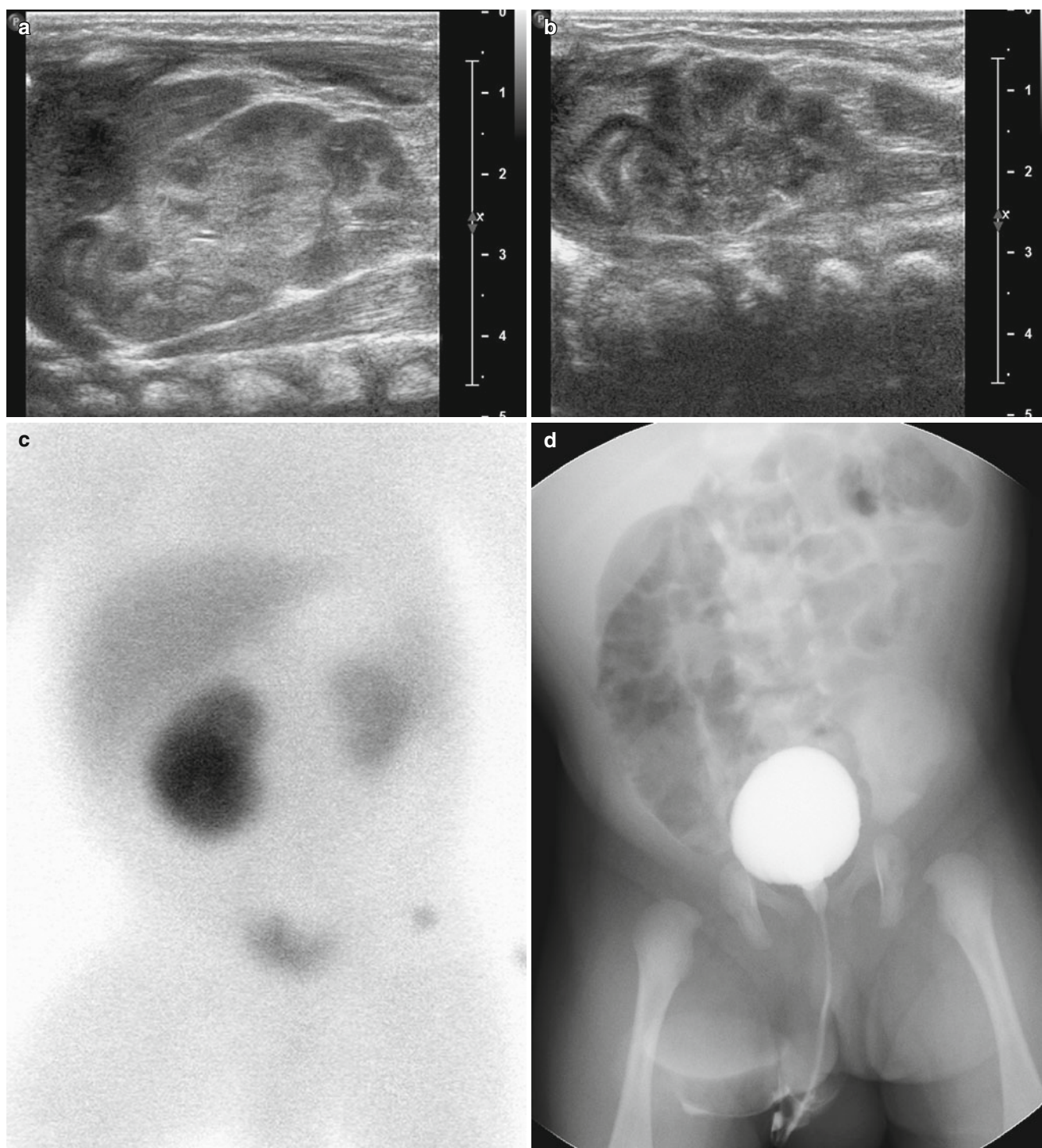


Fig. 23.4 Renal hypoplasia in a 2-month-old boy. (a and b) Abdominal US images show grossly normal right kidney (a) and relatively small left kidney (b) without other focal lesion. (c) Tc-99 m DMSA scan shows decreased uptake in the relatively small left kidney. Split renal

function was calculated to be 83 % on the right kidney and 17 % on the left kidney. (d) Voiding cystourethrography (VCUG) demonstrates no vesicoureteral reflux

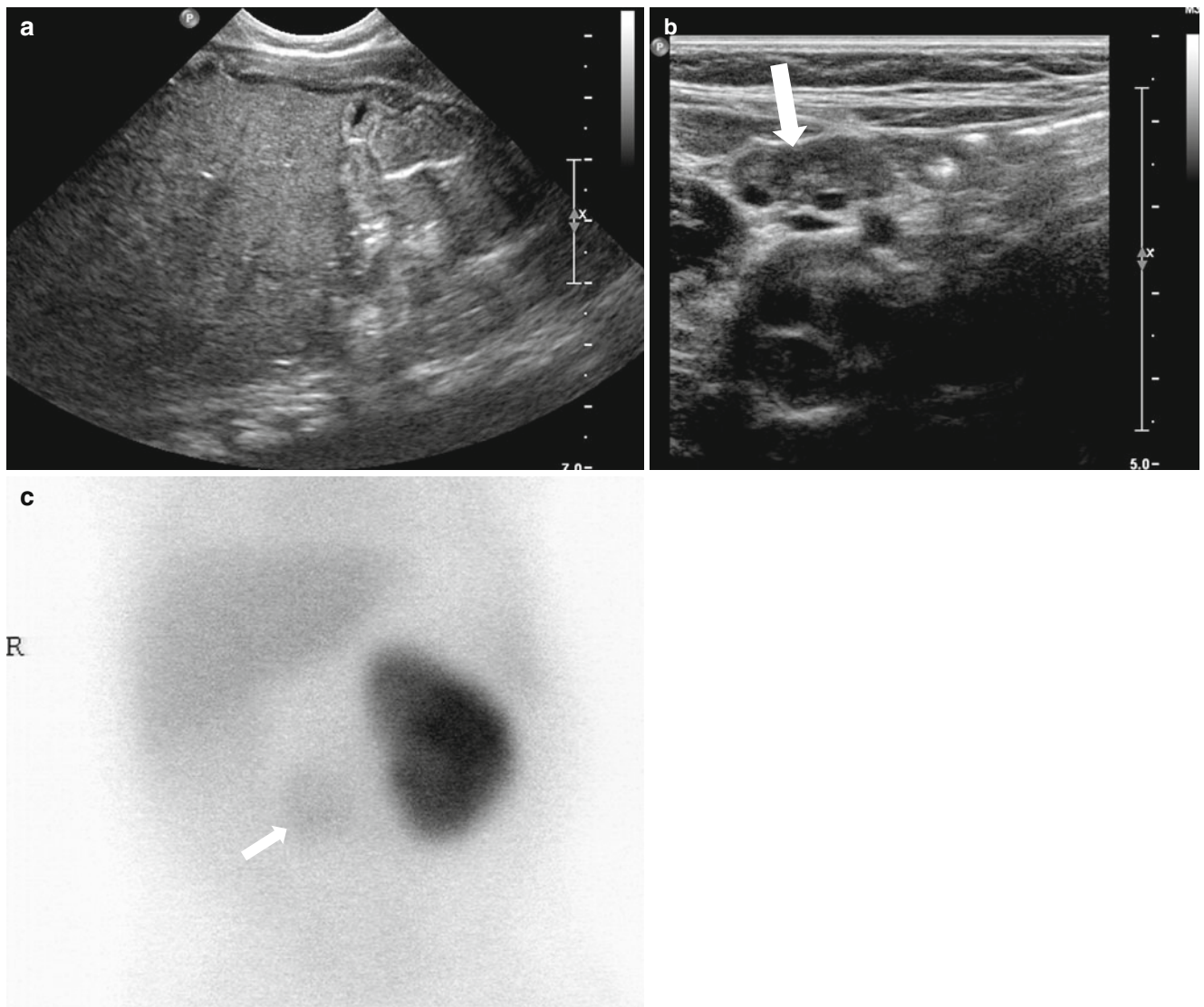


Fig. 23.5 Ectopic hypoplastic kidney in a 6-month-old boy. (a) Right kidney is not visualized in right renal fossa on abdominal US. (b) A small dysplastic kidney (arrow) with cortical cysts is noted in prevertebral area of mid abdomen on abdominal US. (c) Tc-99 m DMSA scan shows faint uptake (arrow) in the hypoplastic kidney

23.4.3 Anomalies of Kidney: Anomalies of Rotation

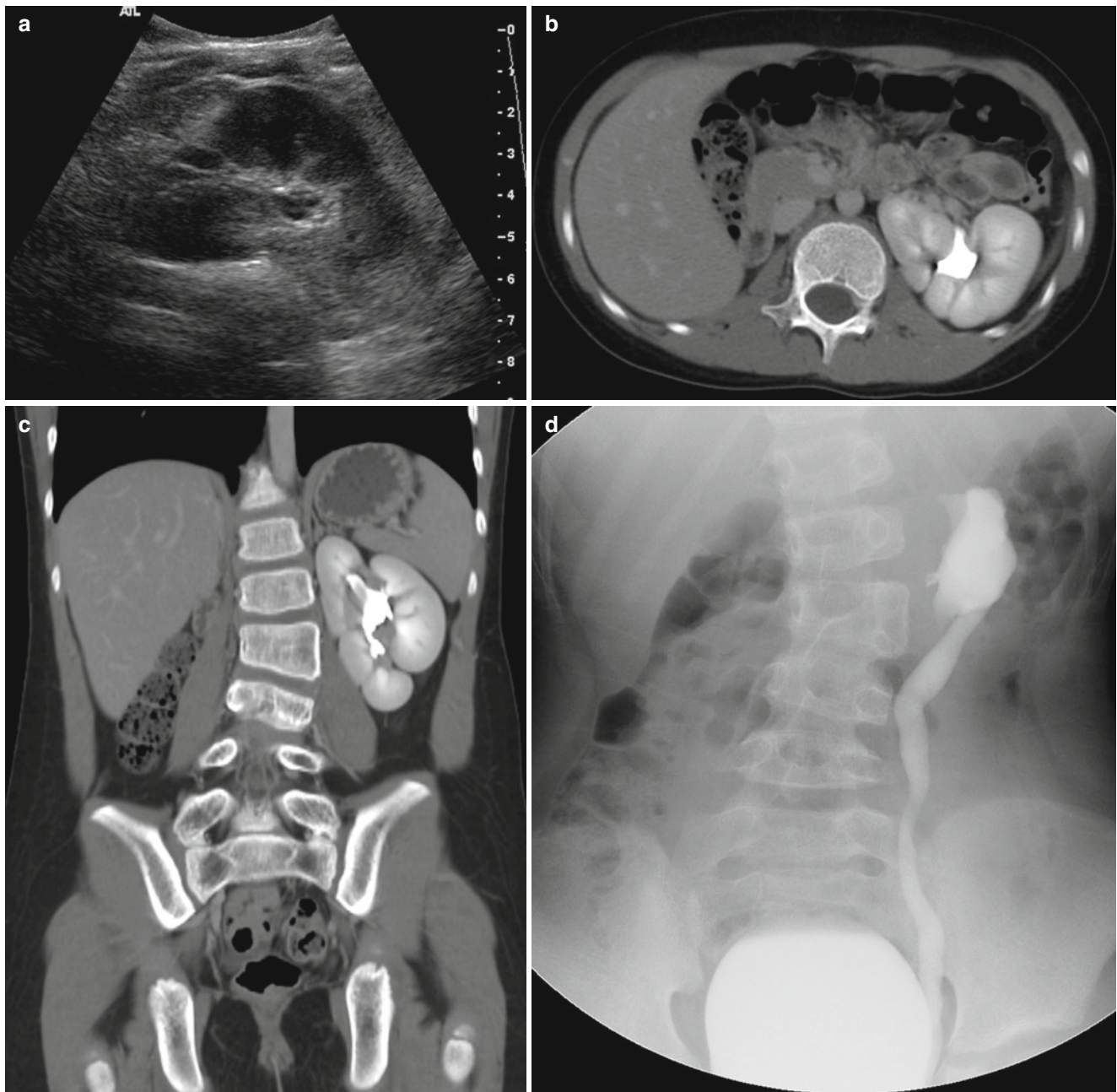


Fig. 23.6 Renal malrotation in a 9-year-old girl. (a) Left kidney shows fetal lobulation with incomplete rotation in left upper abdomen on abdominal US. (b and c) Axial (b) and coronal (c) images of abdom-

inopelvic CT also show anterior position of left renal pelvis. (d) VCUG demonstrates left vesicoureteral reflux with anterior position of renal pelvis

23.4.4 Anomalies of Kidney: Anomalies of Position

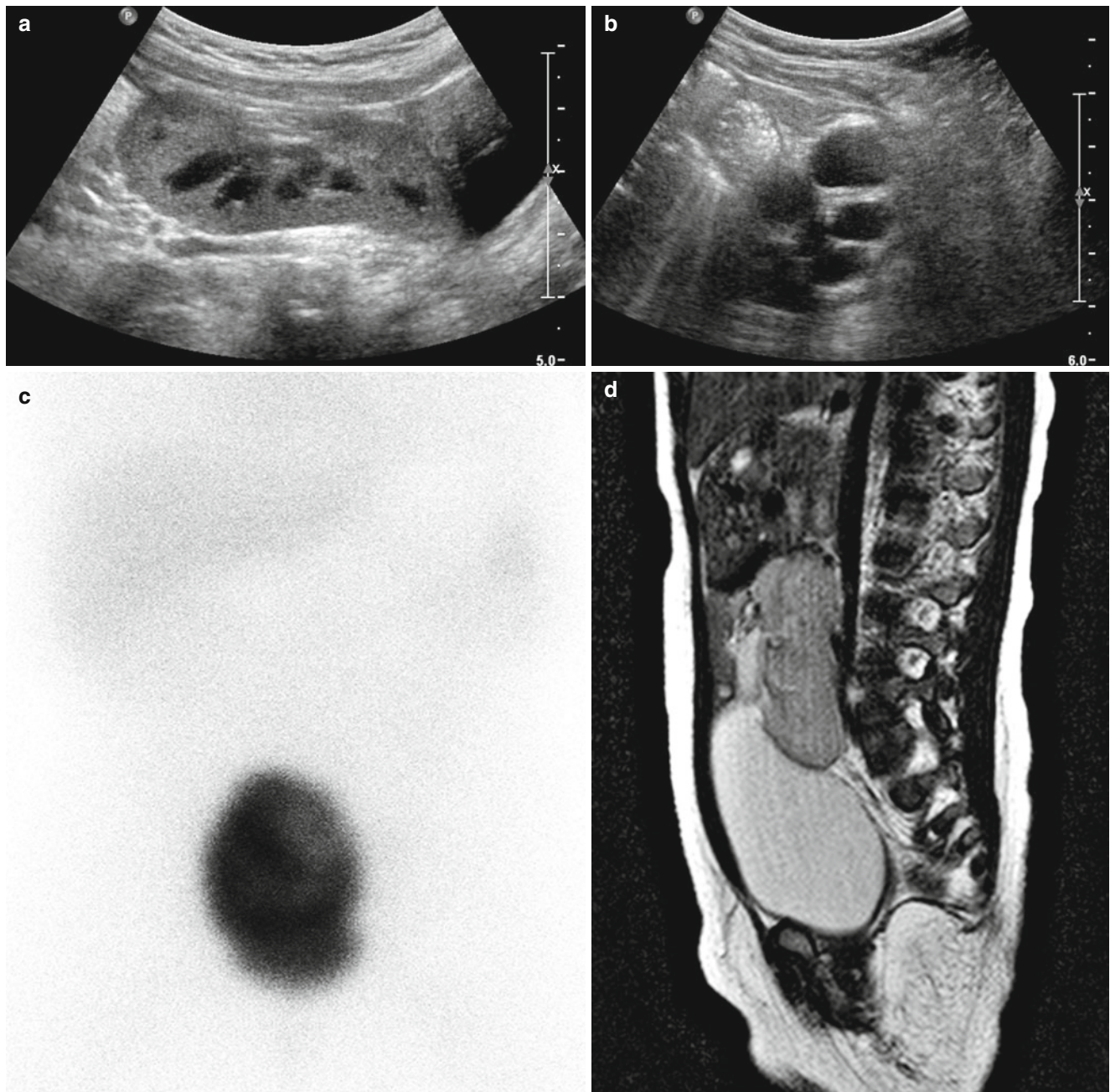


Fig. 23.7 Pelvic kidney in a 1-year-old boy. (a) Abdominal US shows hypertrophied right kidney in pelvic cavity just above urinary bladder with anterior position of renal pelvis. (b) Abdominal US of left renal fossa shows multicystic dysplastic left kidney. (c) Tc-99 m DMSA scan shows only uptake in the pelvic kidney. (d) T2-weighted sagittal MR

image shows right pelvic kidney just above urinary bladder with pelvic dilatation. (e) T2-weighted coronal MR image shows multicystic dysplastic left kidney in left renal fossa and nonvisualized right kidney in right renal fossa



Fig. 23.7 (continued)

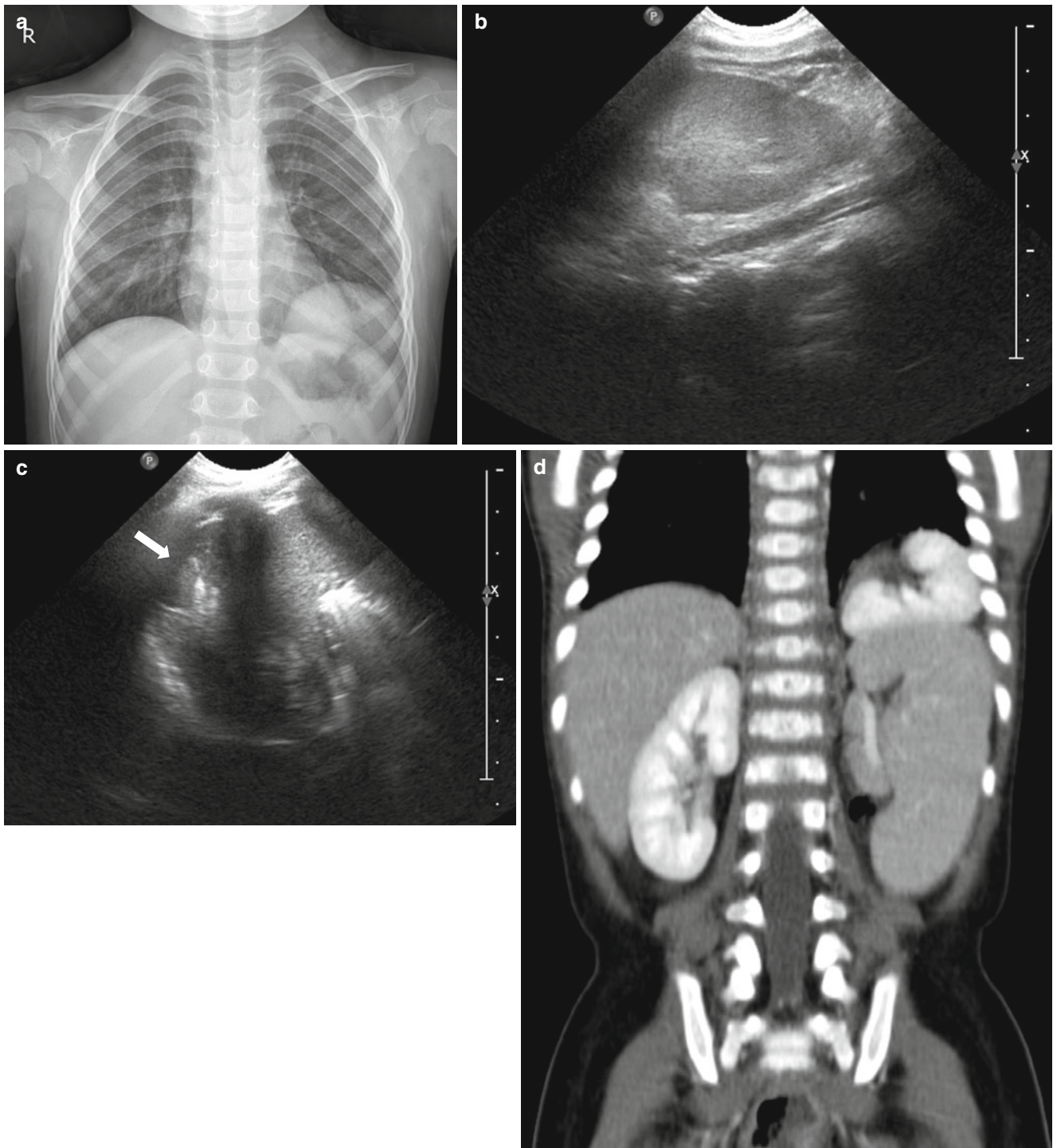


Fig. 23.8 Thoracic kidney in a 2-year-old girl. (a) Chest X-ray shows incidentally found mass lesion in left lower thorax. (b) and (c) On abdominal US, left kidney is not visualized in left renal fossa (b), and

soft tissue lesion (arrow) is defined above the spleen (c). (d) Abdominal CT shows thoracic kidney above the spleen in left lower thorax

23.4.5 Anomalies of Kidney: Anomalies of Fusion – Horseshoe Kidney

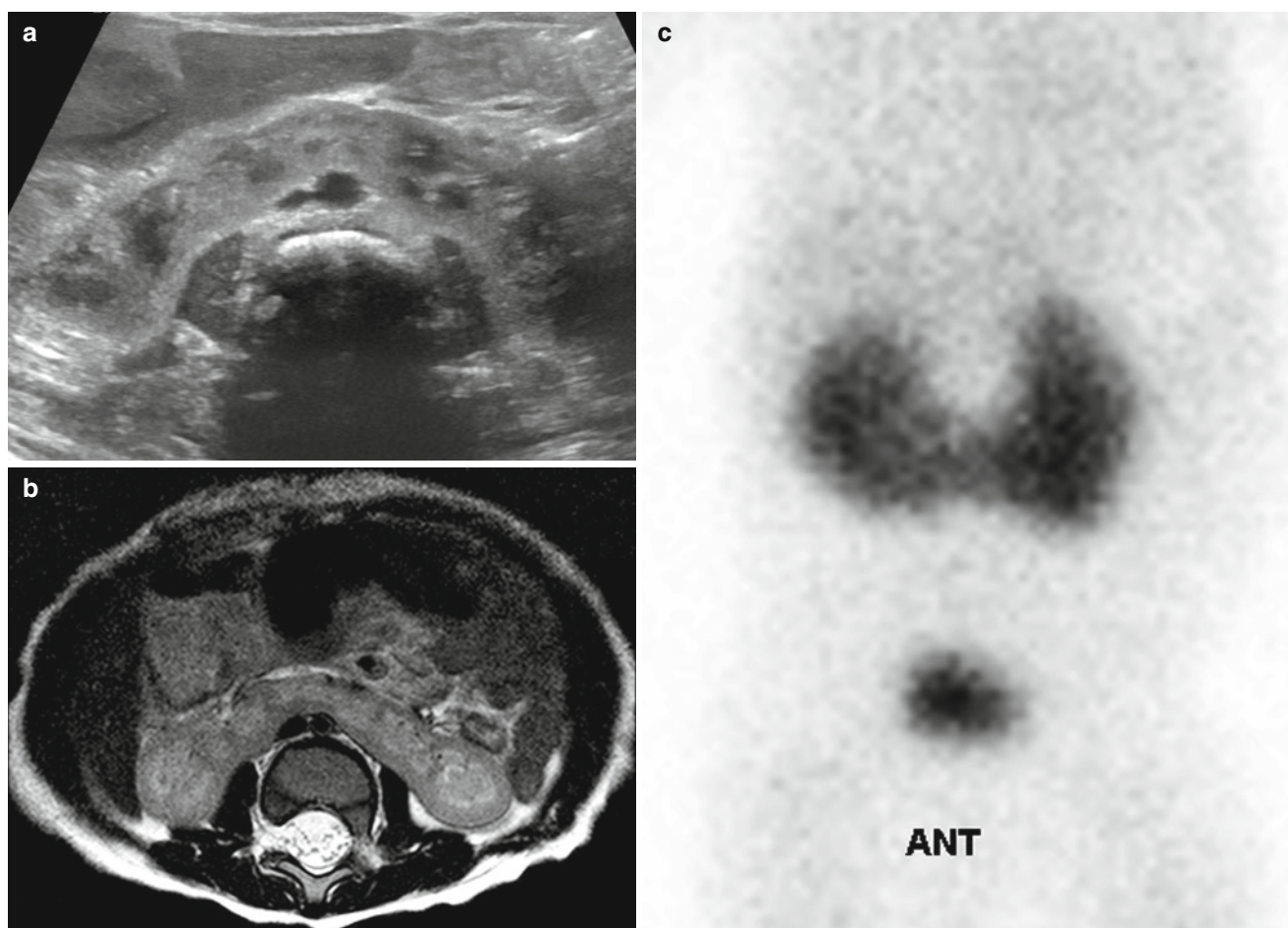


Fig. 23.9 *Horseshoe kidney in a male neonate with imperforate anus.* (a) Abdominal US of mid-transverse abdomen shows the isthmus (fused portion) of horseshoe kidney anterior to aorta and crossing mid-

line. (b) T2-weighted axial MR image shows horseshoe kidney with functional renal parenchyma at isthmus. (c) Tc-99 m DMSA scan also demonstrates functioning tissue at isthmus

23.4.6 Anomalies of Kidney: Anomalies of Fusion – Crossed Fused Ectopy

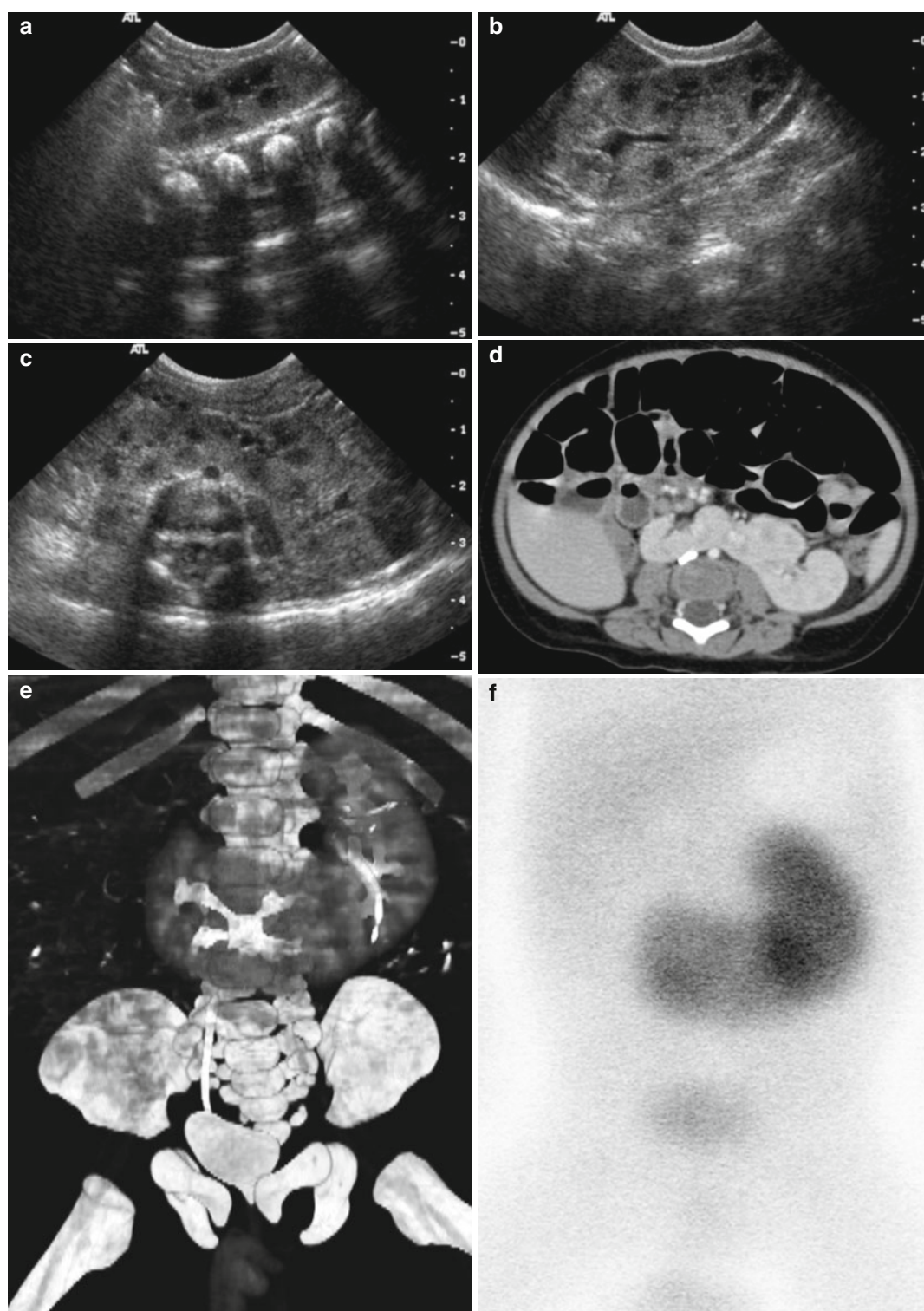


Fig. 23.10 *Crossed fused ectopy in a 5-month-old boy. (a)* Abdominal US of right renal fossa shows relatively small volume of right kidney. *(b)* US image of left abdomen shows grossly normal left kidney in left renal fossa. *(c)* Transverse US image of mid abdomen demonstrates fused portion of kidney anterior to aorta. *(d)* Contrast-enhanced CT scan of mid abdomen shows crossed ectopy of right kidney in midline

lower abdomen and noncrossing left kidney with fusion. *(e)* Three-dimensional reconstruction image of contrast-enhanced CT scan well demonstrates the unilateral fused type with inferior ectopy in this patient. *(f)* Tc-99 m DMSA scan also demonstrates crossed fused ectopy of right kidney

23.4.7 Anomalies of Renal Calyces: Calyceal Diverticulum

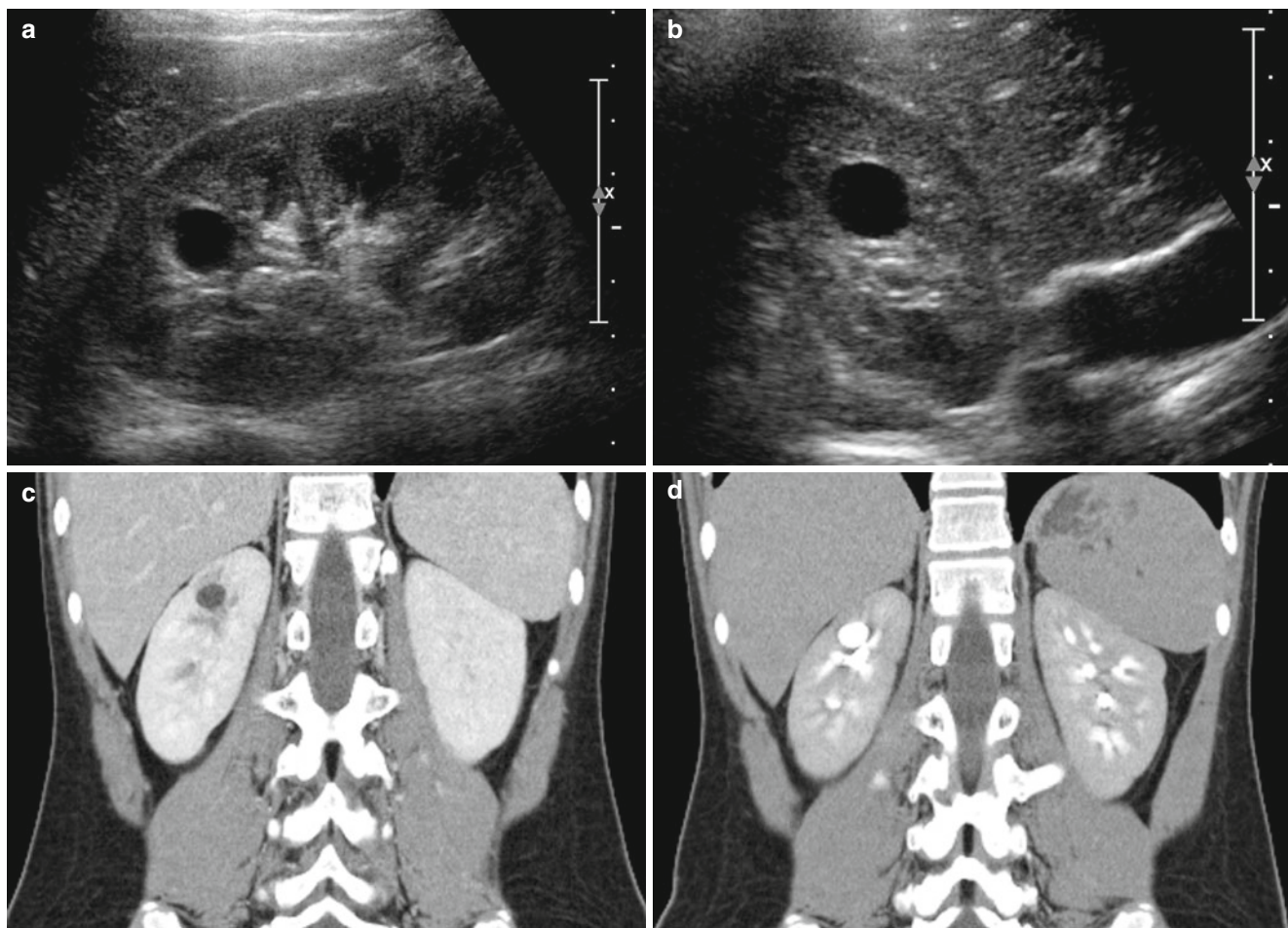


Fig. 23.11 *Calyceal diverticulum in an 11-year-old girl.* (a and b) Sagittal (a) and axial (b) images of right kidney on US show well-defined cystic lesion in the medullary portion of upper pole without visible connection with renal collecting system. (c) Contrast-enhanced

CT scan of nephrographic phase also shows cystic lesion in right kidney upper pole. (d) CT scan of excretory phase demonstrates contrast material excretion into the cystic lesion, a finding that represents a calyceal diverticulum

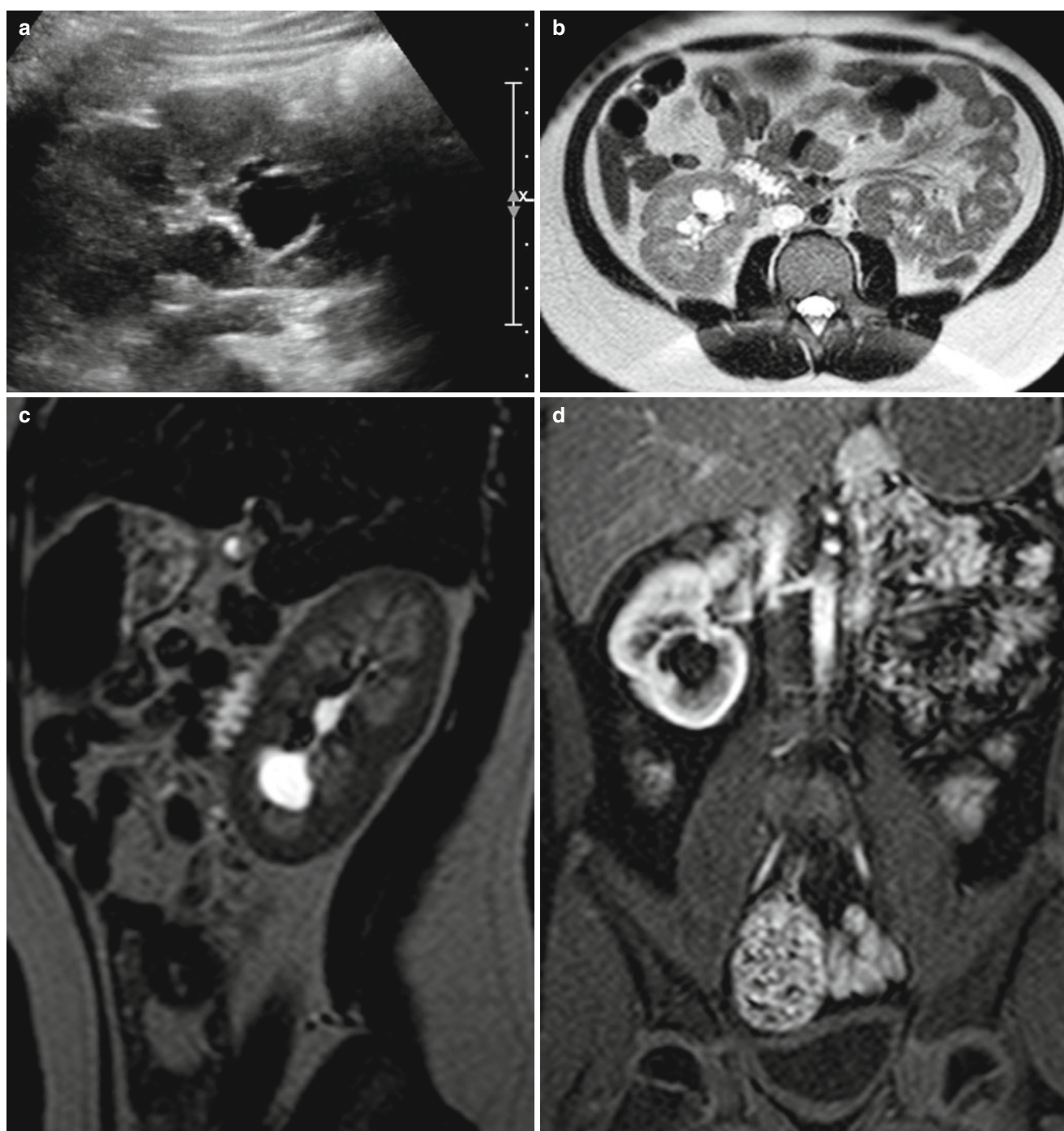


Fig. 23.12 *Calyceal diverticulum in a 10-year-old boy.* (a) Abdominal US of right kidney shows multilobulated cystic lesion in the medullary portion of lower pole. (b) T2-weighted axial MR image also shows multilobulated cystic lesion in right kidney lower pole. (c) T2-weighted sagittal MR image of right kidney demonstrates the connection between

the cystic lesion and renal pelvis. (d and e) Contrast-enhanced MR images of nephrographic phase (d) and excretory phase (e) show contrast filling in this cystic lesion. (f) Intravenous urography also demonstrates contrast excretion to the cystic lesion in right kidney lower pole suggestive of calyceal diverticulum

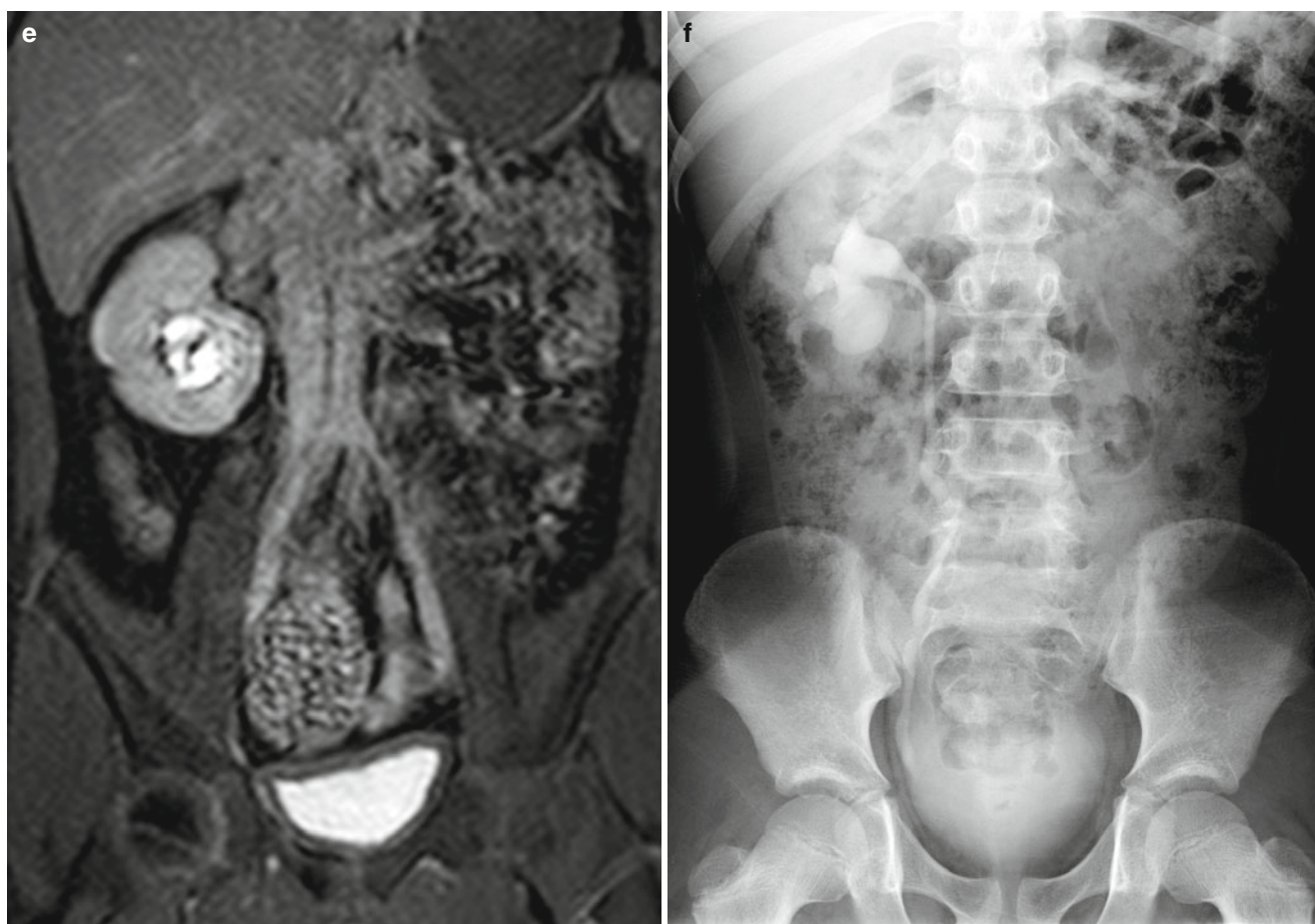


Fig. 23.12 (continued)

23.4.8 Anomalies of Renal Calyces: Congenital Megacalycosis

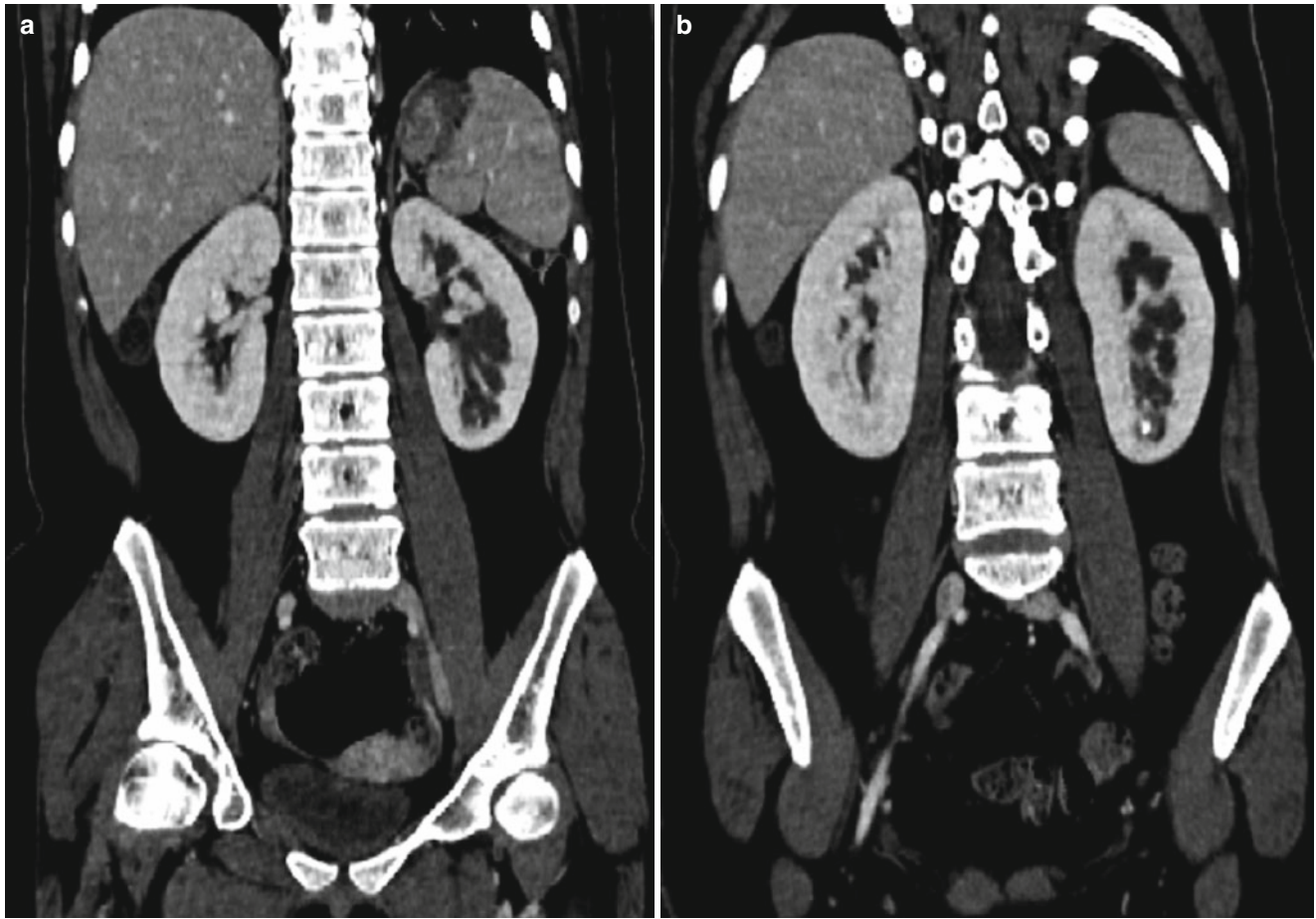


Fig. 23.13 *Congenital megacalycosis in a 15-year-old boy. (a and b) Contrast-enhanced CT scan with coronal reformat images show diffusely dilated calyces of left kidney without renal pelvic dilatation. There is a calyceal stone in left kidney lower pole (b)*

23.4.9 Anomalies of Renal Pelvis and Ureter: Congenital Ureteropelvic Junction Obstruction

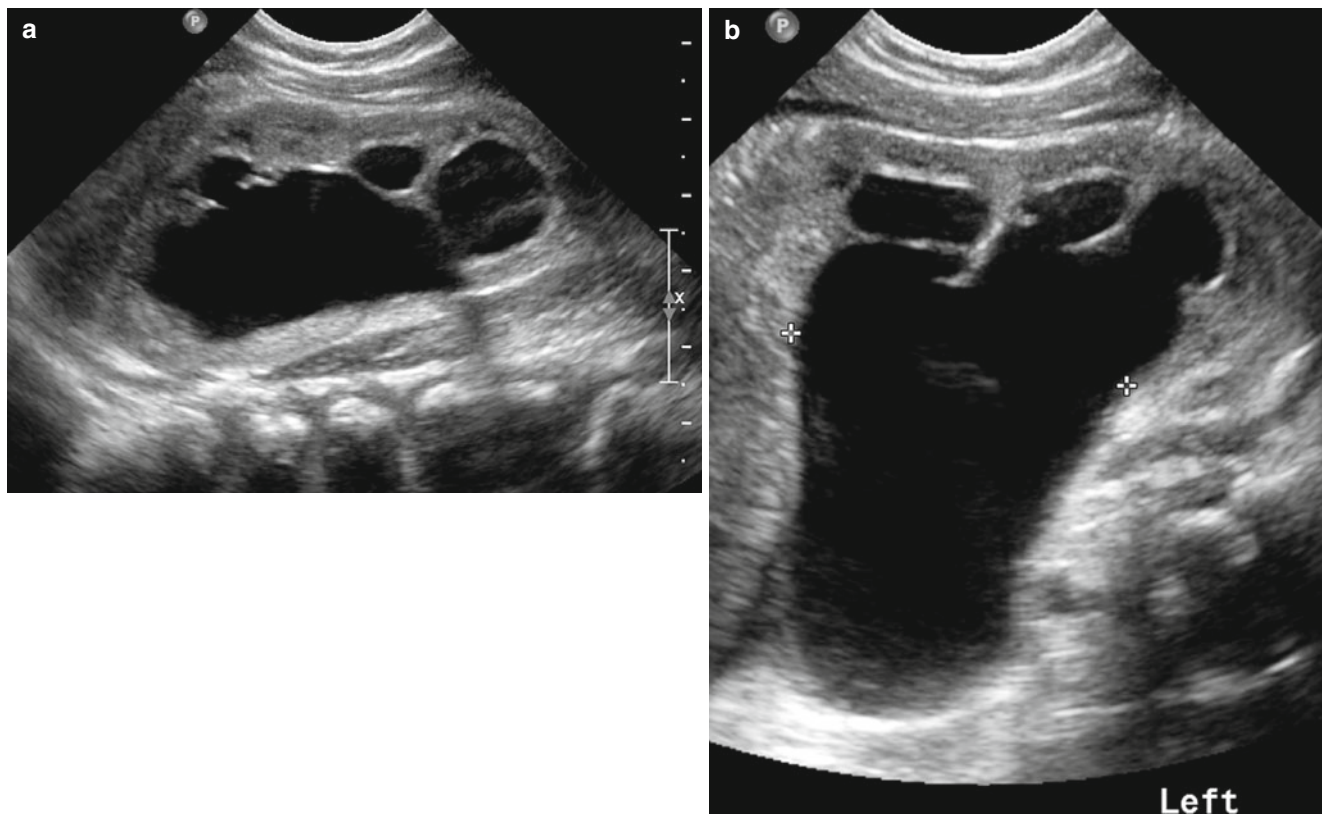


Fig. 23.14 Congenital ureteropelvic junction (UPJ) obstruction in a 2-month-old boy. (a and b) Abdominal US of left kidney with longitudinal (a) and transverse (b) images show pelvicalyceal dilatation and parenchymal thinning without ureter dilatation. (c) MAG3 diuretic

renography demonstrates delayed washout of the tracer on the left kidney suggestive of obstruction. (d) Retrograde pyelography during operation demonstrates kinking of the upper segment of ureter (arrow)

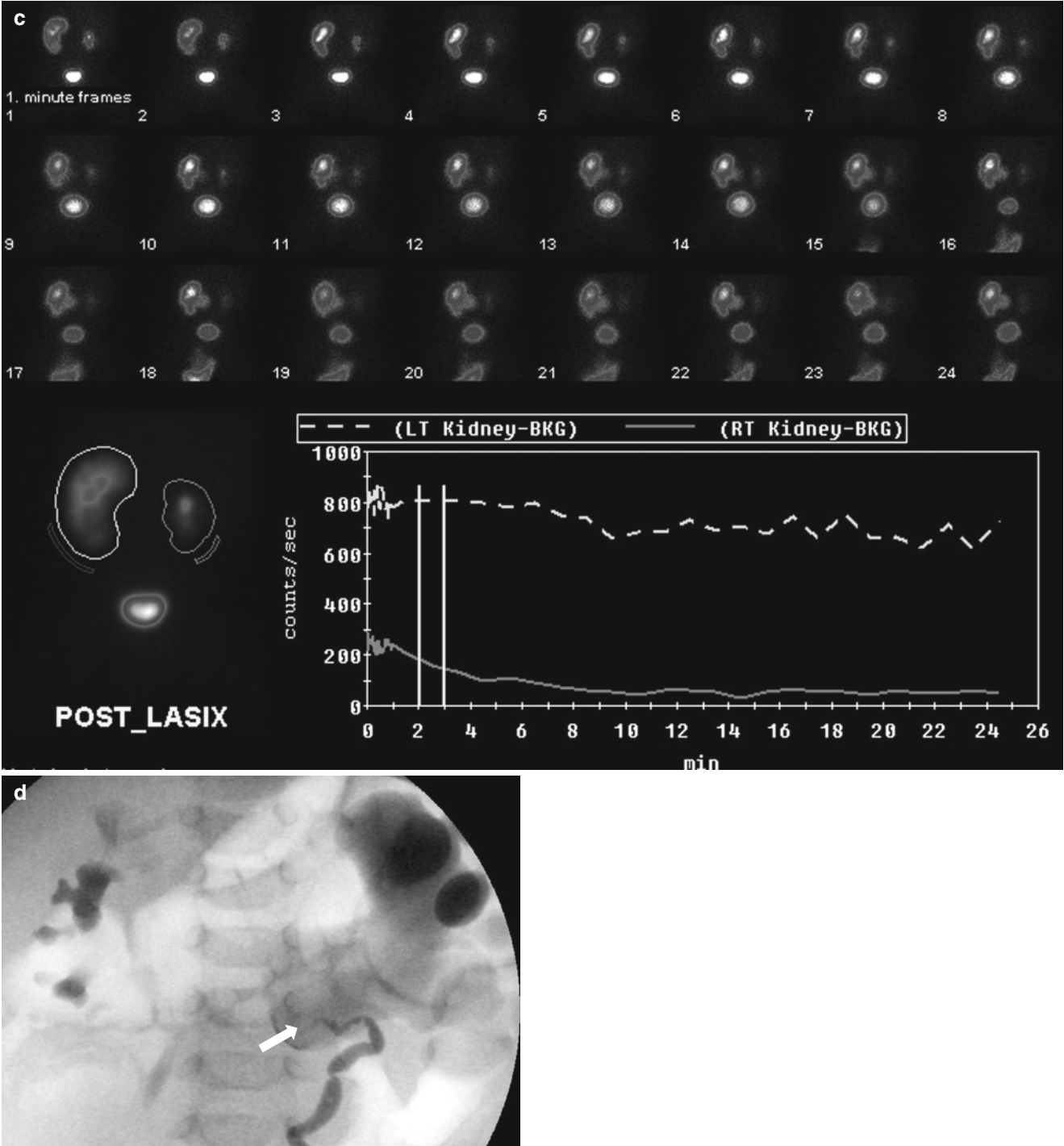


Fig. 23.14 (continued)

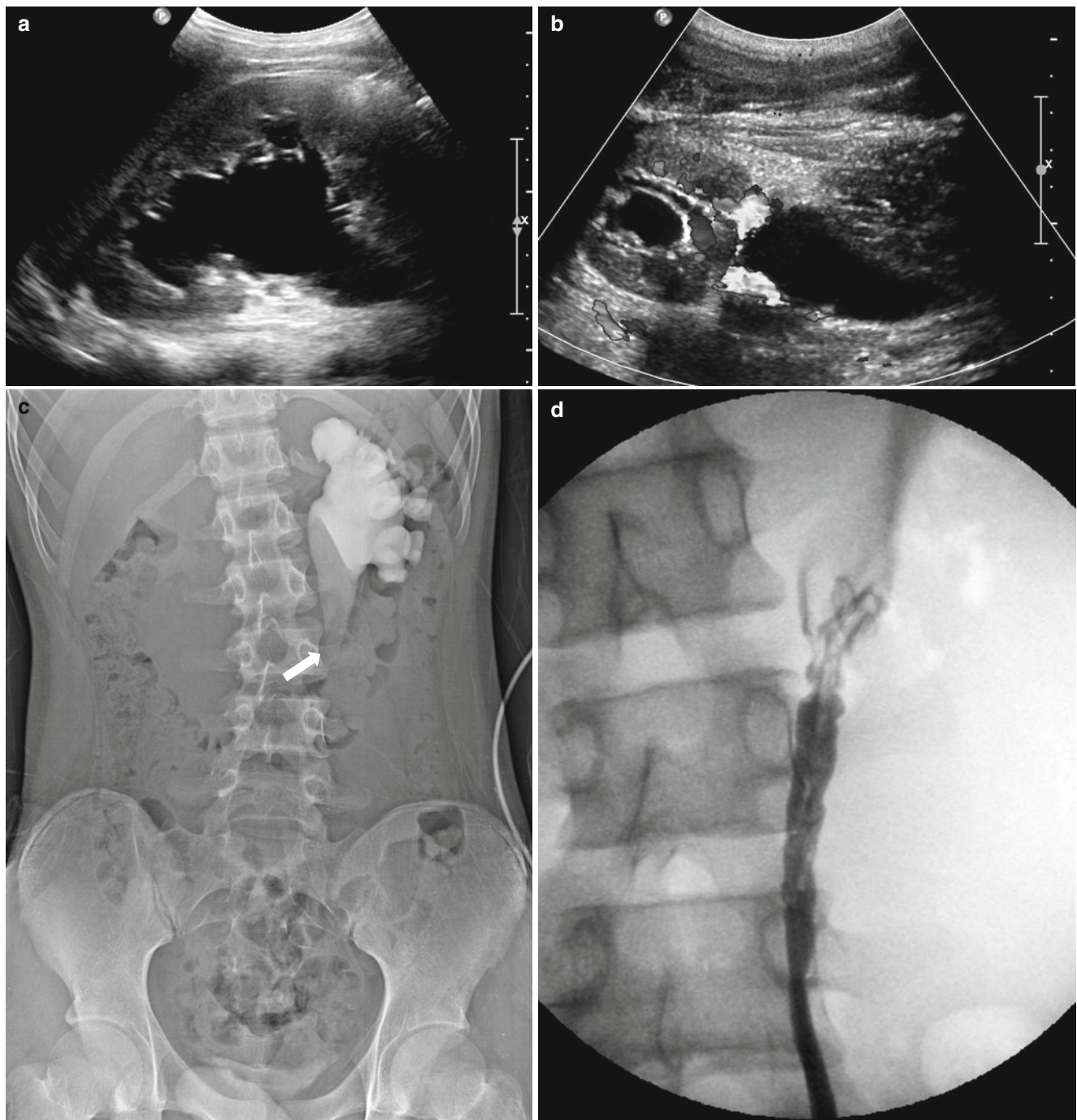


Fig. 23.15 Ureteropelvic junction obstruction due to fibroepithelial polyp in a 15-year-old boy. (a and b) Longitudinal US images of left kidney show hydronephrosis with proximal ureter dilatation (b). (c) Intravenous urography shows left hydronephrosis with delayed contrast

excretion and filling defect (arrow) in the ureteropelvic junction area. (d) Retrograde pyelography during operation also demonstrates multifocal intraluminal filling defects from the polyps in the proximal ureter

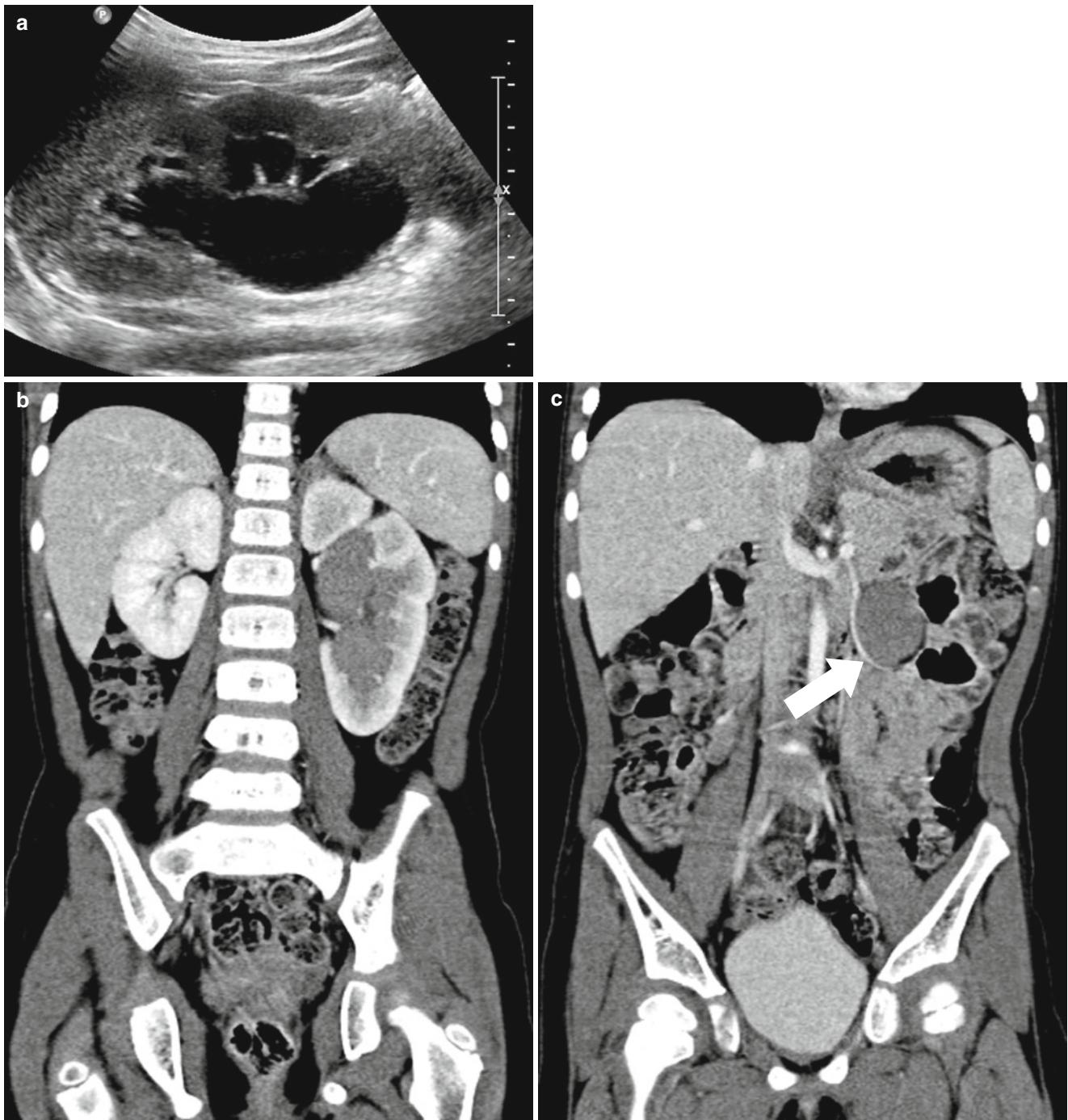


Fig. 23.16 Ureteropelvic junction obstruction due to crossing vessel in a 3-year-old girl. (a) Longitudinal US image of left kidney shows hydronephrosis without ureter dilatation. (b) Contrast-enhanced CT scan with coronal reformat image demonstrates hydronephrosis of left

kidney with diffusely decreased perfusion. (c) Coronal CT image of the left ureteropelvic junction shows accessory left renal artery (arrow) crossing the lower pole of the left kidney and resulting in compression

23.4.10 Anomalies of Renal Pelvis and Ureter: Congenital Megaureter

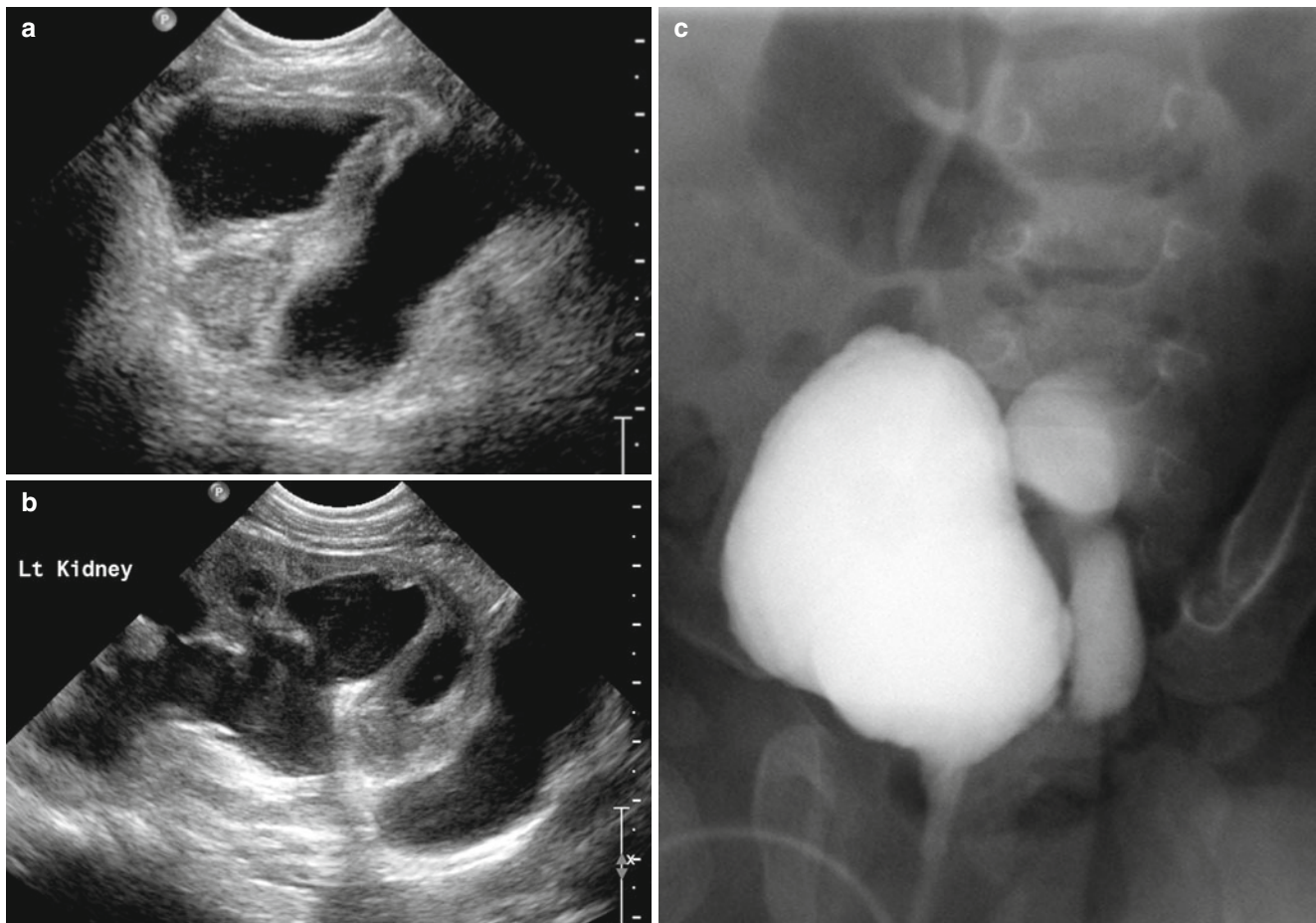


Fig. 23.17 Refluxing megaureter in a 7-month-old girl. (a) Transverse US image of urinary bladder shows markedly dilated left retrovesical ureter. (b) Longitudinal US image of left kidney shows hydronephrosis

with proximal ureter dilatation and debris in the collecting system. (c) VCUG demonstrates reflux to the left megaureter

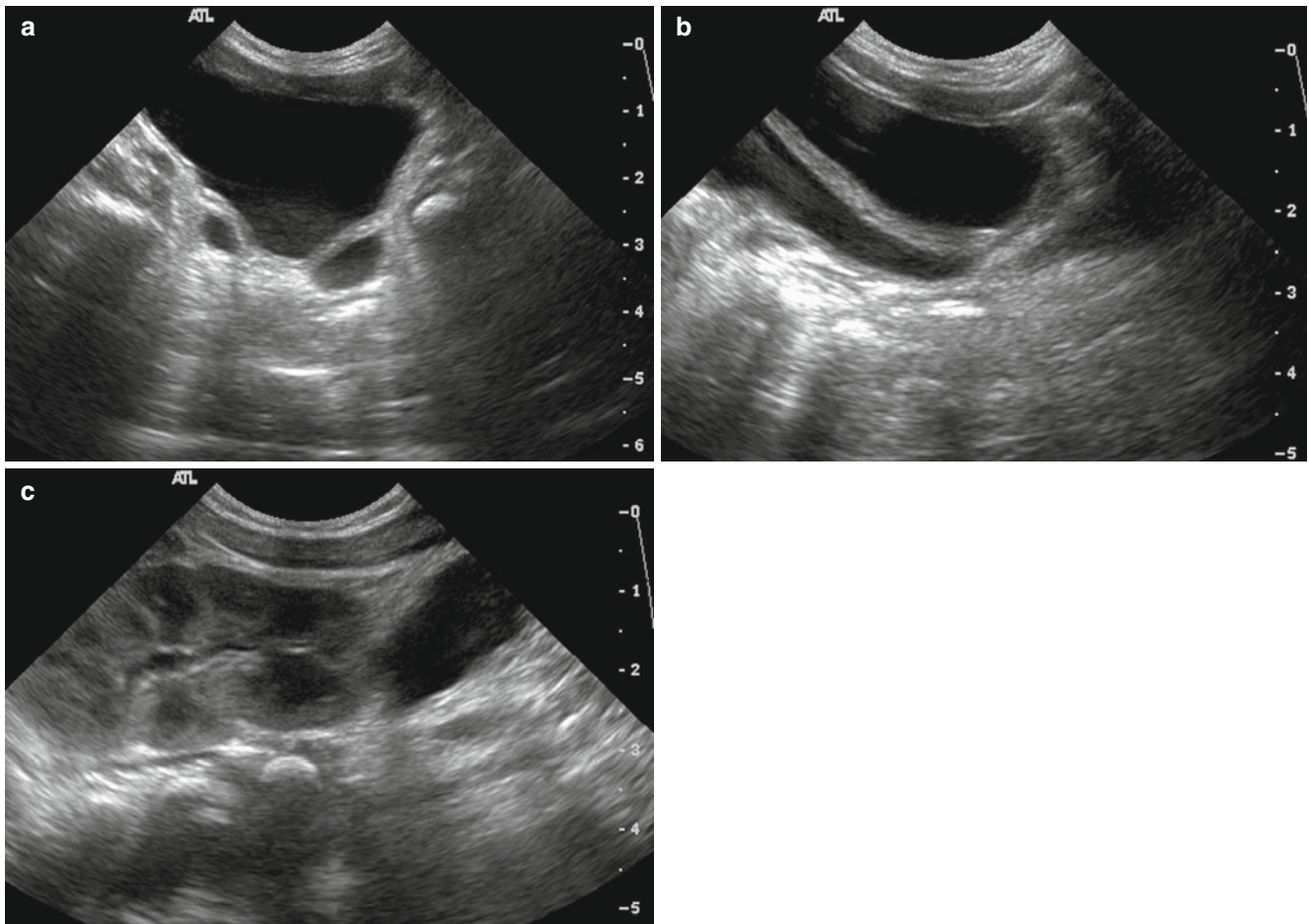


Fig. 23.18 *Non-refluxing and nonobstructive megaureter in a 3-month-old boy. (a)* Transverse US image of urinary bladder shows bilateral retrovesical ureter dilatation. *(b)* Longitudinal US image of bladder also shows diffuse dilatation of left distal ureter. *(c)* Longitudinal

US of left upper abdomen shows left proximal ureter dilatation without hydronephrosis of left kidney. *(d)* Early dynamic images of diuretic renography demonstrate nonobstructive bilateral megaureter. *(e)* VCUG demonstrates no vesicoureteral reflux

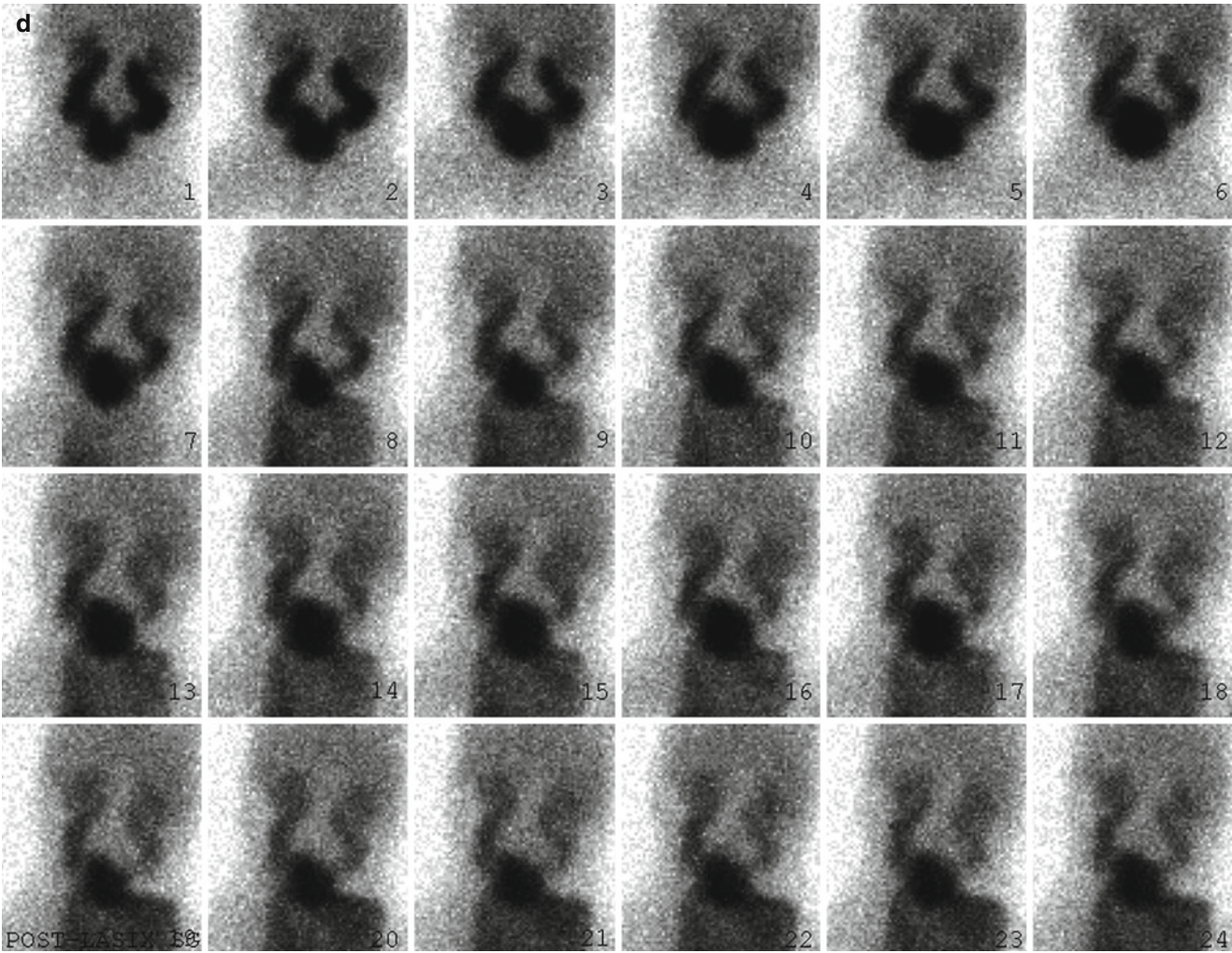


Fig. 23.18 (continued)

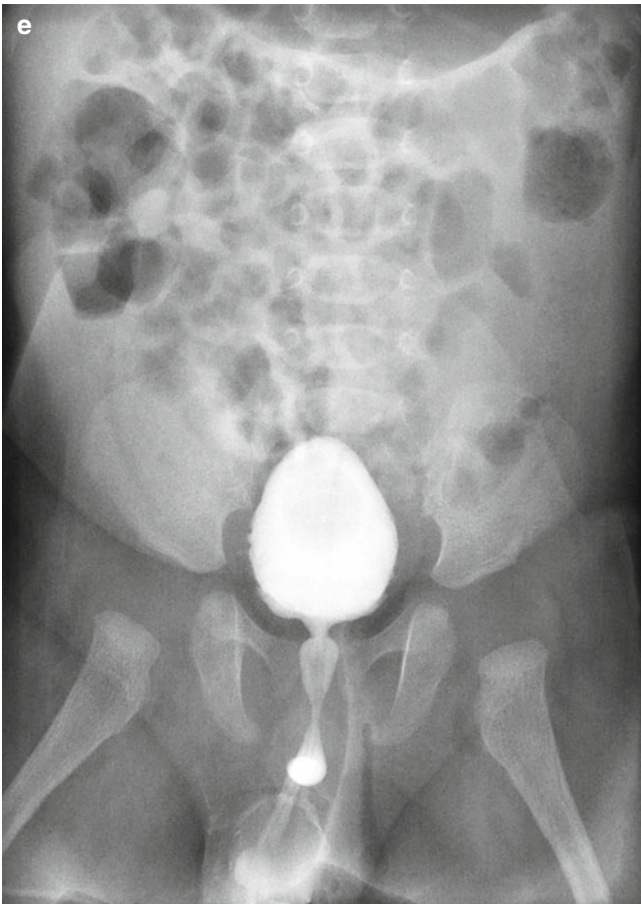


Fig. 23.18 (continued)

23.4.11 Anomalies of Renal Pelvis and Ureter: Ectopic Ureter

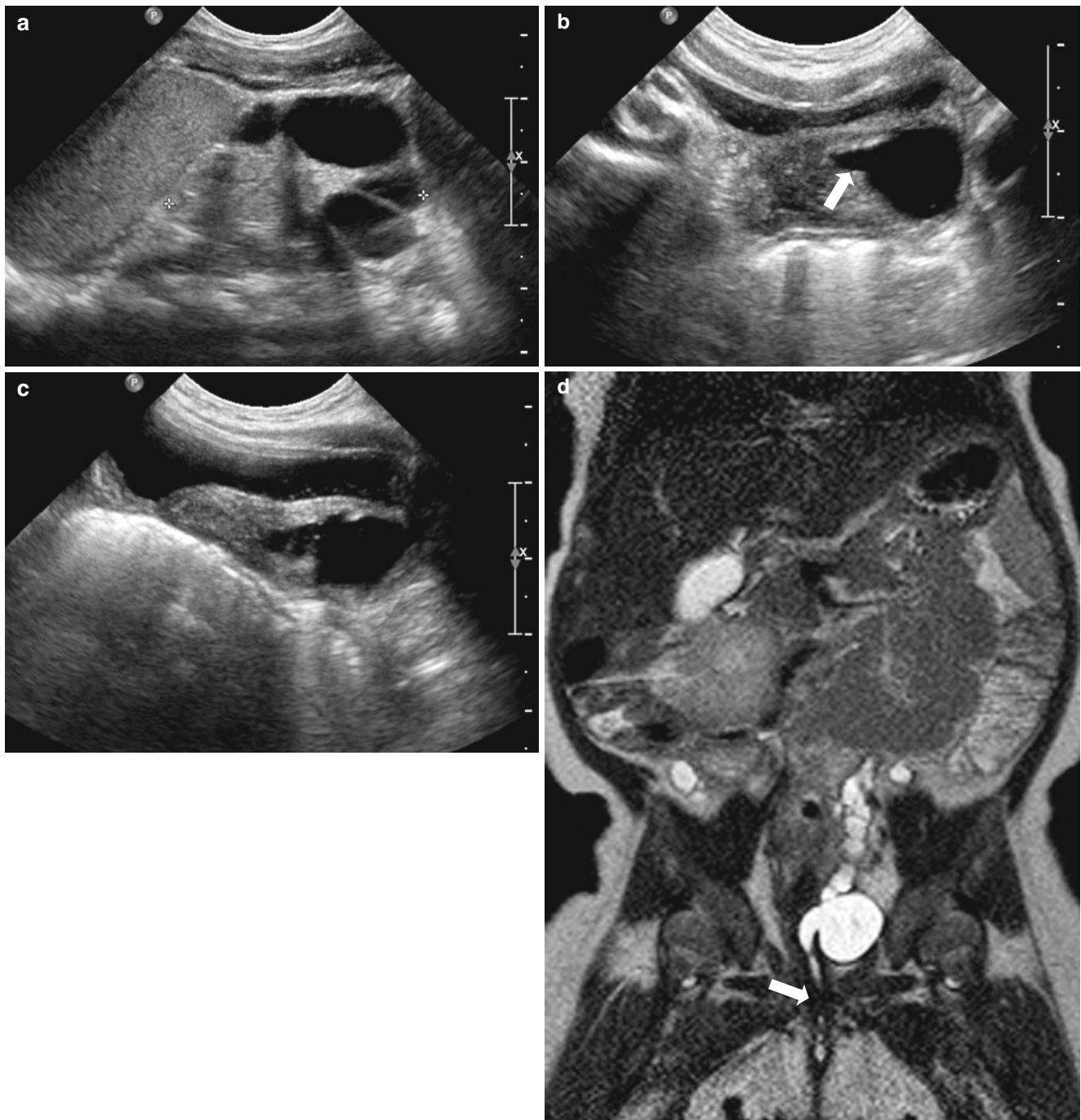


Fig. 23.19 Ectopic ureter insertion to urethra in a 2-month-old girl. (a) Longitudinal US image of left upper abdomen shows multicystic dysplastic kidney. (b) Transverse US image of urinary bladder shows dilated left distal ureter with suspicious insertion to the lower midline (arrow). (c) Longitudinal US image of urinary bladder also shows lower insertion of the left distal ureter. (d) T2-weighted coronal MR

image of abdomen and pelvis shows tortuously dilated left distal ureter with ectopic insertion to urethra (arrow). (e) T2-weighted three-dimensional MR urography also demonstrates multicystic dysplastic left kidney and dilated left ureter with ectopic insertion. (f) VCUG demonstrates no vesicoureteral reflux

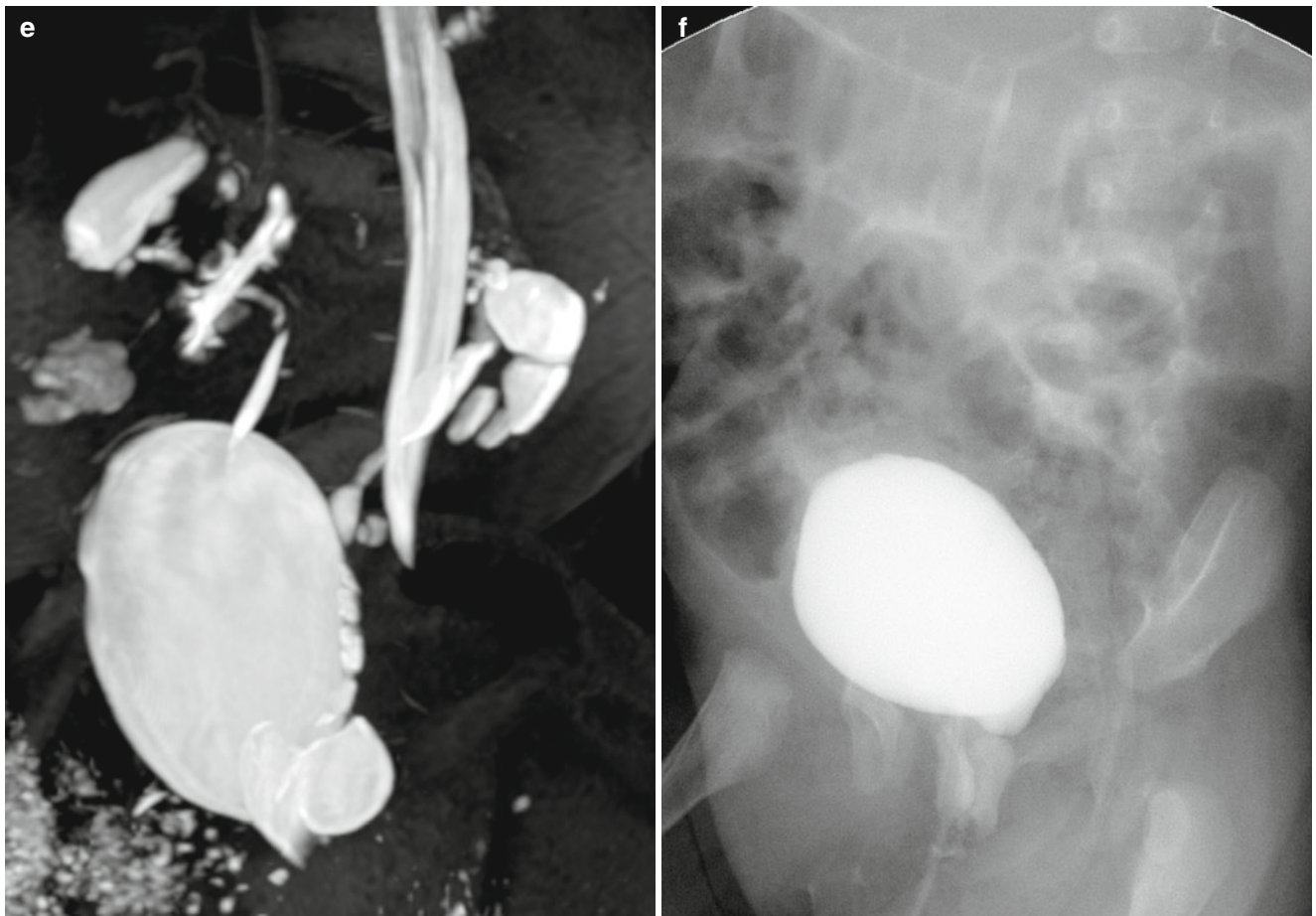


Fig. 23.19 (continued)

23.4.12 Anomalies of Renal Pelvis and Ureter: Ureterocele

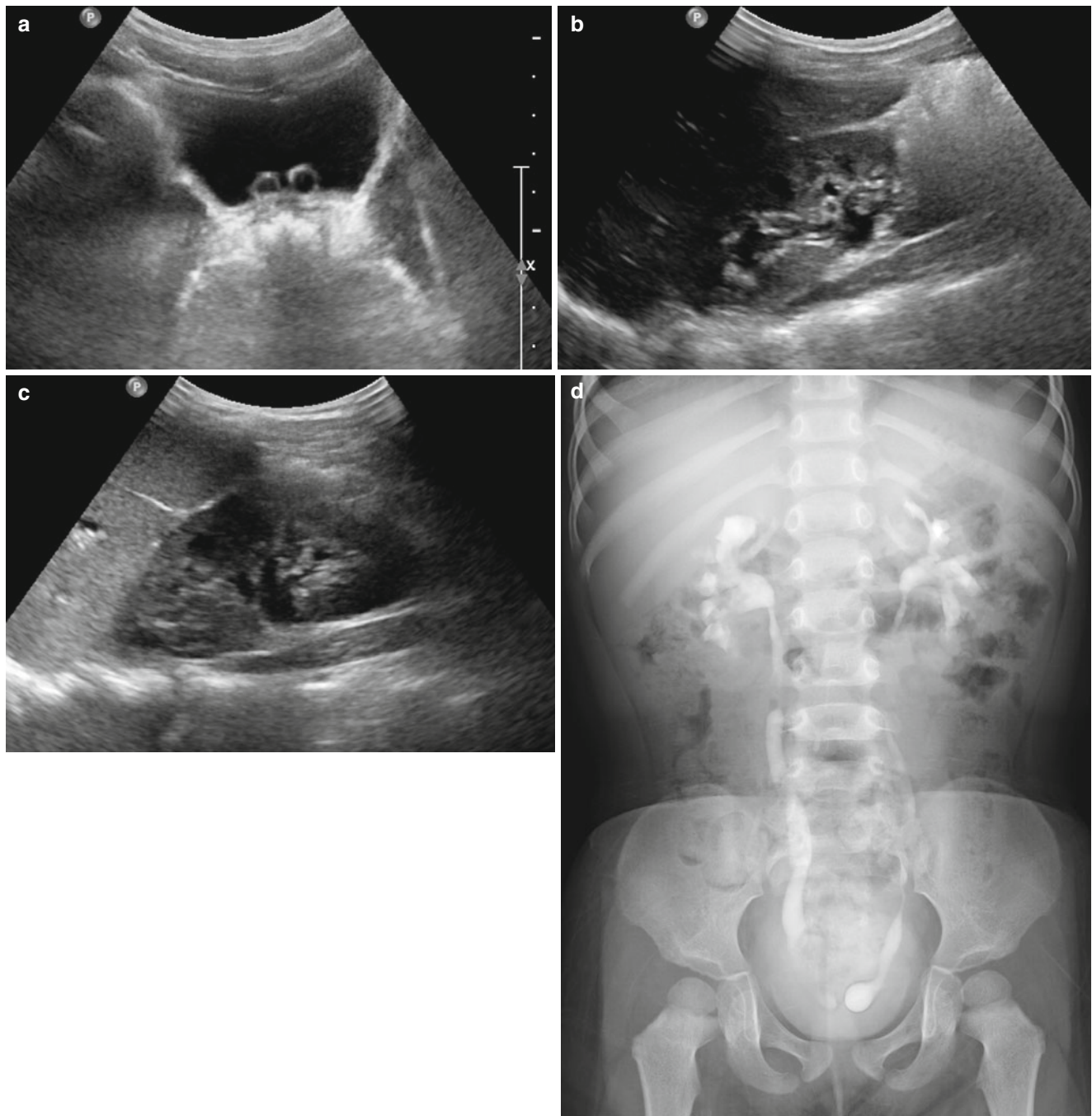


Fig. 23.20 *Bilateral intravesical ureteroceles in a 3-year-old girl. (a)* Transverse US image of urinary bladder shows bilateral intravesical ureteroceles. *(b and c)* Longitudinal US images of right *(b)* and left *(c)*

kidney show pelvic dilatation without ureter dilatation. *(d)* Intravenous urography demonstrates bilateral intravesical ureteroceles with mild hydroureteronephrosis

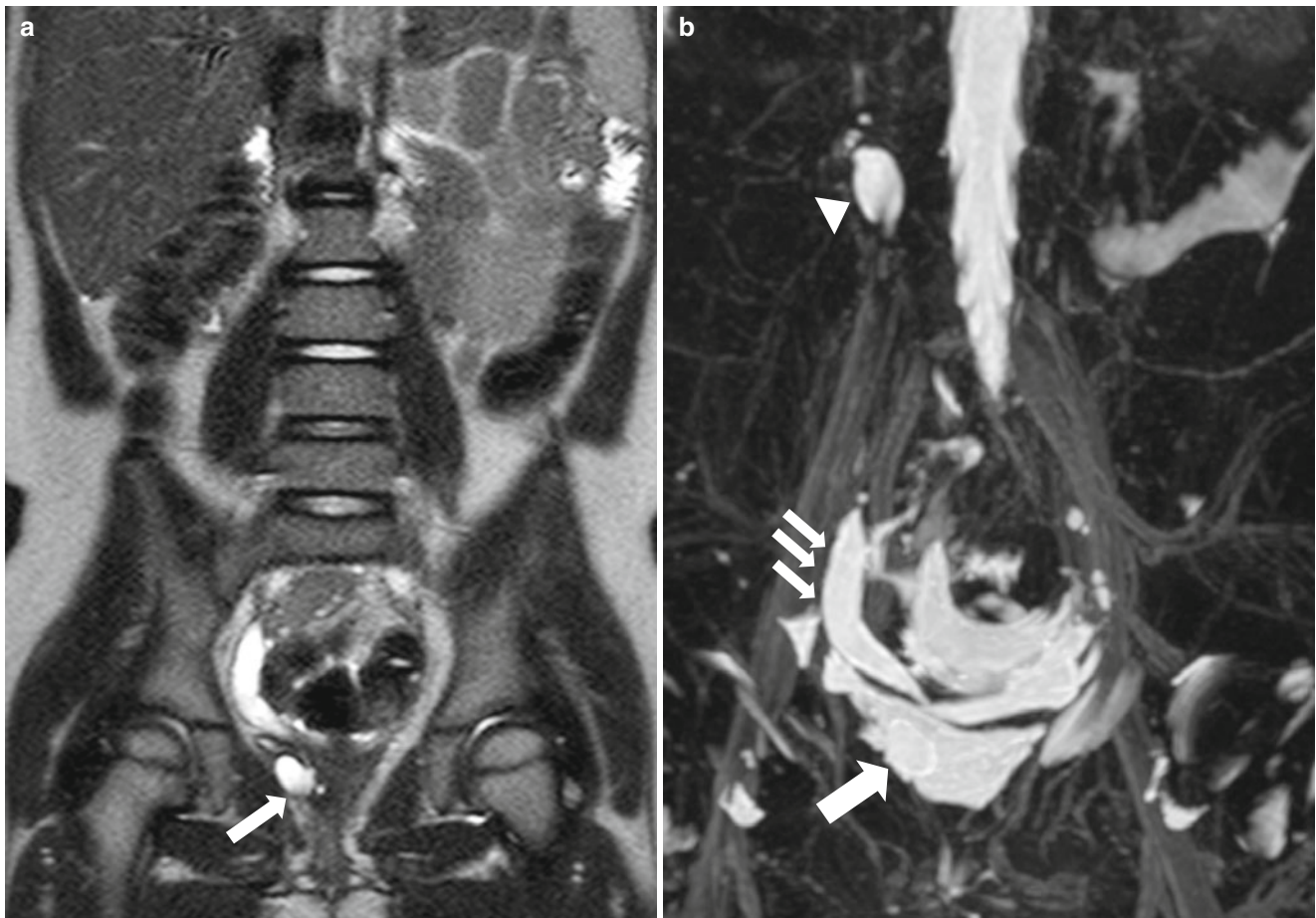


Fig. 23.21 Ectopic dysplastic kidney with ectopic ureterocele in a 5-year-old girl. (a) T2-weighted coronal MR image of abdomen and pelvis shows dilated right distal ureter with ectopic ureterocele (arrow). (b) T2-weighted three-dimensional MR urography demonstrates

multicystic dysplastic kidney (arrowhead) in right mid abdomen, dilated right distal ureter (thinner arrows), and ectopic ureterocele (thick arrow)

23.4.13 Duplex Collecting System

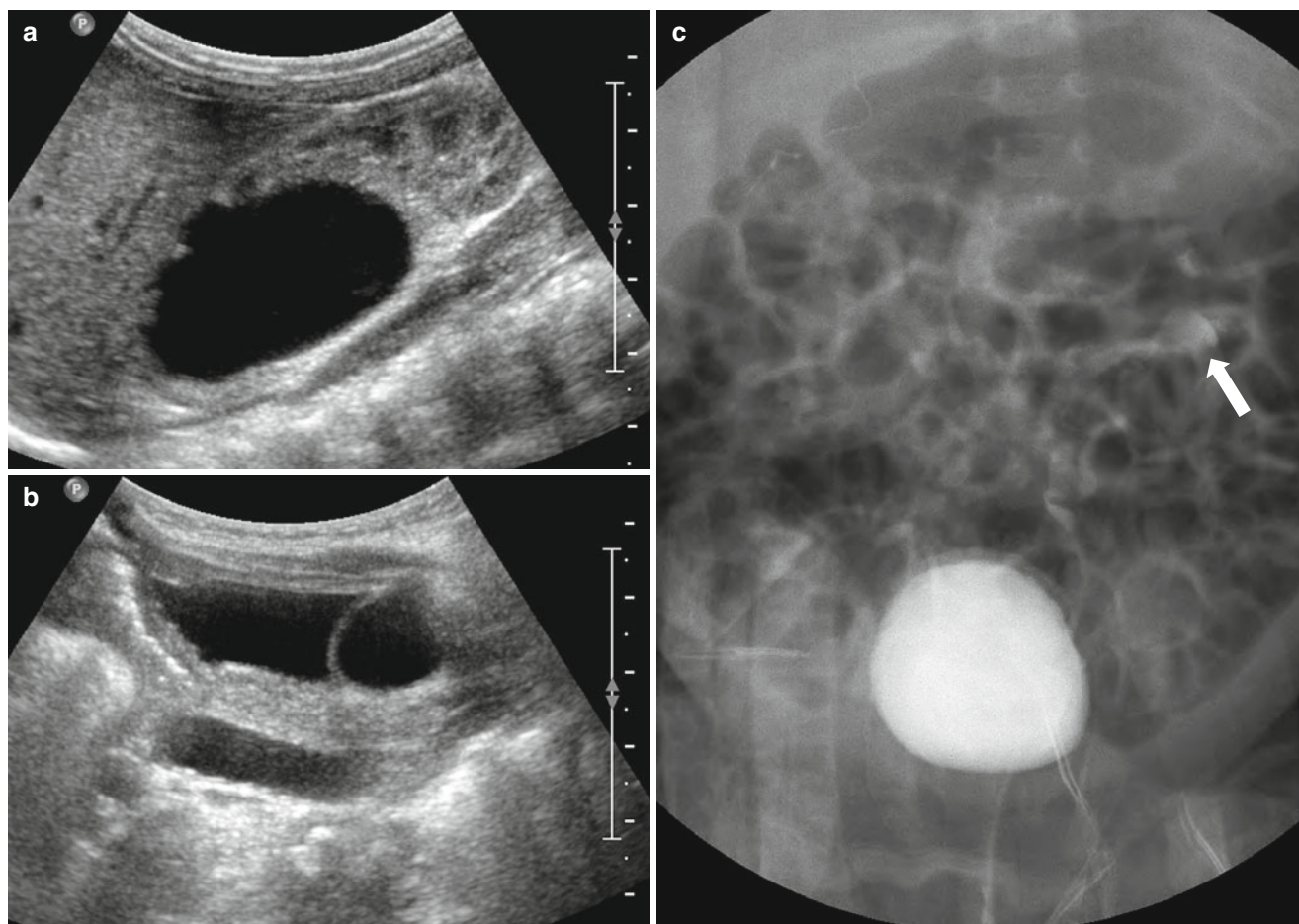


Fig. 23.22 Duplex collecting system with ureterocele and vesicoureteral reflux in a 1-month-old girl. **(a)** Longitudinal US image of left kidney shows duplex system with upper pole hydronephrosis and parenchymal thinning. **(b)** Longitudinal US image of urinary bladder

shows intravesical ureterocele with left distal ureter dilatation. **(c)** VCUG demonstrates vesicoureteral reflux to left kidney lower pole (arrow)

References

- Avni FE, Nicaise N, Hall M, et al. The role of MR imaging for the assessment of complicated duplex kidneys in children: preliminary report. *Pediatr Radiol*. 2001;31:215–23.
- Berrocal T, Lopez-Pereira P, Arjonilla A, et al. Anomalies of the distal ureter, bladder, and urethra in children: embryologic, radiologic, and pathologic features. *Radiographics*. 2002;22:1139–64.
- Del Vescovo R, Battisti S, Di Paola V, et al. Herlyn-Werner-Wunderlich syndrome: MRI findings, radiological guide (two cases and literature review), and differential diagnosis. *BMC Med Imaging*. 2012;12:4.
- Fotter R, Avni EF. *Pediatric uro radiology*. Berlin: Springer; 2008.
- Heinlen JE, Manatt CS, Bright BC, et al. Operative versus nonoperative management of ureteropelvic junction obstruction in children. *Urology*. 2009;73:521–5. Discussion 525.
- Huang EY, Mascarenhas L, Mahour GH. Wilms' tumor and horseshoe kidneys: a case report and review of the literature. *J Pediatr Surg*. 2004;39:207–12.
- Ismaili K, Piepsz A. The antenatally detected pelvi-ureteric junction stenosis: advances in renography and strategy of management. *Pediatr Radiol*. 2013;43:428–35.
- Kaneyama K, Yamataka A, Satake S, et al. Associated urologic anomalies in children with solitary kidney. *J Pediatr Surg*. 2004;39:85–7.
- Maduekwe E, Weinberg B, Samaan B, et al. Right thoracic ectopic kidney in a child with breathing difficulties—sonographic diagnosis. *J Clin Ultrasound*. 2011;39:108–10.
- Neville H, Ritchey ML, Shamberger RC, et al. The occurrence of Wilms tumor in horseshoe kidneys: a report from the National Wilms Tumor Study Group (NWTSG). *J Pediatr Surg*. 2002;37:1134–7.
- Pieretti-Vanmarcke R, Pieretti A, Pieretti RV. Megacalycosis: a rare condition. *Pediatr Nephrol*. 2009;24:1077–9.
- Plaire JC, Pope JC, Kropp BP, et al. Management of ectopic ureters: experience with the upper tract approach. *J Urol*. 1997;158:1245–7.
- Sanna-Cherchi S, Caridi G, Weng PL, et al. Genetic approaches to human renal agenesis/hypoplasia and dysplasia. *Pediatr Nephrol*. 2007;22:1675–84.
- Shokeir AA, Nijman RJ. Ureterocele: an ongoing challenge in infancy and childhood. *BJU Int*. 2002;90:777–83.
- Stunell H, McNeill G, Browne RF, et al. The imaging appearances of calyceal diverticula complicated by uroliathasis. *Br J Radiol*. 2010;83:888–94.
- Wang ZJ, Daldrup-Link H, Coakley FV, et al. Ectopic ureter associated with uterine didelphys and obstructed hemivagina: preoperative diagnosis by MRI. *Pediatr Radiol*. 2010;40:358–60.
- Wein AJ, Kavoussi LR, Campbell MF. *Campbell-Walsh urology*. Philadelphia: Elsevier Saunders; 2012.

Tae Il Han

Contents

24.1	Introduction	760
24.2	Cystic Renal Disease	760
24.2.1	Autosomal Recessive Polycystic Kidney Disease	760
24.2.2	Autosomal Dominant Polycystic Kidney Disease	760
24.2.3	Multicystic Dysplastic Kidney.....	760
24.2.4	Juvenile Nephronophthisis/Medullary Cystic Disease Complex.....	761
24.2.5	Glomerulocystic Kidney Disease.....	761
24.2.6	Multiple Malformation Syndromes with Renal Cysts	761
24.3	Renal Neoplasm	761
24.3.1	Wilms Tumor	761
24.3.2	Nephroblastomatosis.....	762
24.3.3	Clear Cell Sarcoma	762
24.3.4	Rhabdoid Tumor	762
24.3.5	Mesoblastic Nephroma	762
24.3.6	Multilocular Cystic Renal Tumor	763
24.3.7	Renal Cell Carcinoma.....	763
24.3.8	Renal Lymphoma and Leukemia	763
24.3.9	Neuroblastoma	763
24.4	Illustrations: Cystic Renal Disease and Neoplasms	765
24.4.1	Autosomal Recessive Polycystic Kidney Disease	765
24.4.2	Autosomal Dominant Polycystic Kidney Disease	767
24.4.3	Multicystic Dysplastic Kidney.....	768
24.4.4	Multiple Malformation Syndromes with Renal Cysts	770
24.4.5	Wilms Tumor	771
24.4.6	Nephroblastomatosis.....	777
24.4.7	Clear Cell Sarcoma	780
24.4.8	Rhabdoid Tumor	781
24.4.9	Mesoblastic Nephroma	784
24.4.10	Multilocular Cystic Renal Tumor	785
24.4.11	Renal Cell Carcinoma.....	786
24.4.12	Renal Lymphoma and Leukemia	787
24.4.13	Neuroblastoma	788
	References	792

T.I. Han, MD, PhD
 Department of Radiology, University of North Carolina
 School of Medicine, 101 Manning Dr., 2000 Old Clinic Bldg.
 CB#7510, Chapel Hill, NC 27599, USA
 e-mail: tae_han@med.unc.edu

24.1 Introduction

The most common abdominal masses in childhood are renal origin masses. In neonates and infants, most renal masses are usually benign. Hydronephrosis and cystic renal disease are the most common abdominal masses in the neonate.

There are many proposed classifications of cystic renal disease based on pathologic, clinical, and genetic features. Cystic renal diseases in children are subdivided into genetic and nongenetic conditions. Genetic cystic renal disease includes polycystic kidney disease (autosomal dominant, autosomal recessive), juvenile nephronophthisis, glomerulocystic kidney disease, and malformation syndromes (tuberous sclerosis, von Hippel-Lindau disease). Nongenetic cystic renal disease includes simple cyst, multicystic dysplastic kidney, medullary sponge kidney, acquired cysts, renal sinus cyst, and calyceal diverticulum (Kim and Kim 2012).

Renal tumors in children include Wilms tumor (90 %), nephroblastomatosis, clear cell sarcoma, rhabdoid tumor, mesoblastic tumor, multilocular cystic neoplasm, renal cell carcinoma, renal lymphoma, and renal leukemia (Kim 2012). While Wilms tumor is the most common abdominal malignancy in children, mesoblastic nephroma is the most common solid renal tumor in neonates and young infants. Renal cell carcinoma typically occurs in the second decade of life. The patient's age is one of the most important factors for differential diagnosis.

Ultrasonography (US) is usually the initial imaging modality for a child with a suspected abdominal mass. US is a safe, portable, and inexpensive imaging modality without radiation hazard. Computed tomography (CT) and magnetic resonance (MR) imaging are standard imaging modalities for tumor extent and metastatic disease. MR imaging is preferred for staging and follow-up in very young children because there is no radiation exposure.

24.2 Cystic Renal Disease

24.2.1 Autosomal Recessive Polycystic Kidney Disease

Autosomal recessive polycystic kidney disease (ARPKD) is characterized by cystic dilation of the renal collecting tubules and hepatic fibrosis resulting from biliary dysgenesis (dilation and proliferation of bile ductules in the portal spaces). ARPKD was previously called infantile polycystic kidney disease. ARPKD is a spectrum of severity, with the renal involvement and hepatic fibrosis varying inversely. The perinatal and neonatal forms have severe renal involvement and mild abnormalities of the liver. About half of affected newborns die during the first few days of birth because of pulmonary hypoplasia or renal insufficiency. In the juvenile form

of ARPKD, the hepatic involvement is more severe than in renal disease, and congenital hepatic fibrosis may result in portal hypertension and cirrhosis.

On US, the kidneys in the perinatal, neonatal, and infantile form of ARPKD are markedly enlarged and show diffusely increased parenchymal echogenicity, produced by multiple acoustic wall interfaces of the dilated collecting tubules (Garel 2010). The dilated tubules and numerous tiny renal cysts extending from the medulla to the renal cortex are seen with high-resolution US transducers (Figs. 24.1 and 24.2). CT and MR imaging may demonstrate enlarged kidneys with a prolonged and striated nephrogram, which is caused by stasis of contrast material in the dilated collecting tubules (Loneragan et al. 2000). In the juvenile form of ARPKD, the renal involvement consists of medullary ductal ectasia with minimal renal enlargement. US shows hypoechoic cortex and prominent echogenic pyramids (Fig. 24.3). US findings of congenital hepatic fibrosis include diffusely increased parenchymal echogenicity, biliary cysts or focal dilatations of intrahepatic bile ducts, and findings of portal hypertension (EL-Merhi and Bae 2004).

24.2.2 Autosomal Dominant Polycystic Kidney Disease

Autosomal dominant polycystic kidney disease (ADPKD) is characterized by variable-sized multiple renal cysts involving both the renal cortex and medulla. In ADPKD, the kidneys may be normal in size or enlarged. Although ADPKD is primarily a disease of adults, it has also been recognized in newborns. ADPKD was previously called adult polycystic kidney disease. Children with ADPKD present with only a few detectable renal cysts that increase with age. Renal involvement is usually symmetrical and bilateral but may be unilateral or segmental. Most children with ADPKD are asymptomatic. Symptoms first occur after age 30. ADPKD is often accompanied by hepatic cysts that increase with age. Some adult patients have an intracranial aneurysm resulting in subarachnoid hemorrhage.

US and CT demonstrate multiple cysts of variable size, depending mostly on the patient's age and gene mutation (Fig. 24.4).

24.2.3 Multicystic Dysplastic Kidney

Multicystic dysplastic kidney (MCDK) is the most common cause of abdominal mass in newborns and the most common cystic malformation of the kidney in infancy. MCDK is a severe form of nonhereditary dysplasia, which is mostly due to pelvoinfundibular atresia during renal development. It is characterized by the presence of multiple

noncommunicating renal cysts with an intervening echogenic dysplastic parenchyma. There is no functioning renal parenchyma and no central renal pelvis in the affected kidney. The less common variant of MCKD, the hydronephrotic type resulting from severe stenosis of the proximal ureter, has an identifiable renal pelvis. In contrast to true hydronephrosis, there is no renal function in the hydronephrotic MCKD. Radionuclide imaging might be used to further differentiate the hydronephrotic form of MCKD from an obstruction in a functioning kidney. MCKD is mostly unilateral but may be bilateral or segmental. Bilateral MCKD is fatal. Most cases of unilateral MCKD undergo spontaneous involution. Contralateral renal anomaly in unilateral MCKD includes ureteropelvic junction obstruction, vesicoureteral reflux, and hypoplasia. Segmental cystic dysplasia can be seen in the upper pole moiety of duplex kidneys and a portion of a horseshoe kidney.

US is the preferred initial imaging modality. US demonstrates multiple noncommunicating cysts of varying sizes with the echogenic renal parenchyma. There is no intervening normal renal parenchyma. MCKD usually gets smaller or disappears on the follow-up US studies, occasionally with no change or increase in the size of the cysts (Strife et al. 1993) (Figs. 24.5 and 24.6).

24.2.4 Juvenile Nephronophthisis/Medullary Cystic Disease Complex

Although juvenile nephronophthisis and medullary cystic disease have similar pathologies (chronic diffuse tubulointerstitial nephritis that progresses to fibrosis and terminal renal failure) and clinical features, they differ in their mode of inheritance and clinical onset. The two conditions are characterized by renal tubular atrophy and medullary cystic lesions. Impaired tubular concentration causes polyuria and polydipsia, the usual presenting symptoms. Juvenile nephronophthisis (autosomal recessive transmission) is more common and associated with extrarenal involvement (ocular, neurologic, skeletal, hepatic). Renal failure develops in the first decade in those with juvenile nephronophthisis and in the third decade in those with medullary cystic disease (autosomal dominant transmission), which is not associated with extrarenal abnormalities.

US demonstrates small echogenic kidneys with multiple small cysts at the corticomedullary junction or within the medulla (EL-Merhi and Bae 2004).

24.2.5 Glomerulocystic Kidney Disease

Glomerulocystic kidney disease is characterized by cortical glomerular cyst (cystic dilatation of Bowman space).

Most glomerulocystic kidney diseases are inherited as an autosomal dominant disease and sometimes detected in children with a family history of ADPKD. The kidneys may be normal-sized, enlarged or hypoplastic. US imaging findings are similar to polycystic kidney disease (Garel 2010). US demonstrates a normal appearance of the medulla in contrast to ARPKD.

24.2.6 Multiple Malformation Syndromes with Renal Cysts

Many syndromes can present with renal cysts. Common syndromes encountered with renal cysts are tuberous sclerosis and von Hippel-Lindau disease, which are autosomal dominant disorders.

Tuberous sclerosis complex is associated with multiple simple cortical renal cysts (20 % of patients), renal angiomyolipoma (40–80 %), and renal cell carcinoma (2 %). US demonstrates highly echogenic non-shadowing foci, representing the fatty components in angiomyolipomas (Fig. 24.7). It is difficult with US to differentiate an echogenic small renal cell carcinoma from angiomyolipomas. CT can be useful in demonstrating the presence of fat of angiomyolipoma.

24.3 Renal Neoplasm

24.3.1 Wilms Tumor

Wilms tumor is the most common renal tumor beyond the first year of life and during the first decade, whereas the mesoblastic nephroma is the most common renal tumor during the first year of life. Most cases of Wilms tumor are diagnosed between age 1 and 5, and the mean age at diagnosis is 3–4 years in children with unilateral Wilms tumor and 2–3 years in children with bilateral Wilms tumors. Clinical symptoms include a palpable abdominal mass, hypertension, abdominal pain, hematuria, and fever. Wilms tumor can occur in children with syndromes or renal anomalies, such as hemihypertrophy, Beckwith-Wiedemann syndrome, sporadic aniridia (not autosomal dominant aniridia), Drash syndrome, WAGR syndrome (Wilms tumor, aniridia, genitourinary anomalies, and mental retardation), cryptorchidism, hypospadias, and horseshoe kidney (Fig. 24.12). Bilateral tumors can arise in children with nephroblastomatosis, hemihypertrophy, sporadic aniridia, and genitourinary anomalies (Geller and Kochan 2011) (Fig. 24.11).

Wilms tumor is a malignant renal tumor arising from persistent embryonal tissue (primitive metanephric blastema) and is also called a nephroblastoma. Prognosis depends on the histologic cell type. Wilms tumors are classified into favorable (90 %) and unfavorable (10 %) histology,

depending on the presence of an anaplastic component. Wilms tumors with an anaplastic component (unfavorable histology) are associated with contiguous spread to adjacent tissues and distant metastases to the lung or liver and tend to occur in the older age group.

Wilms tumor is usually well defined by a pseudocapsule composed of compressed renal tissue; it usually expands within the renal parenchyma to displace or distort the collecting system. Wilms tumor usually contains areas of necrosis, hemorrhage, or cystic degeneration. It is a rapidly growing tumor that may extend into the renal vein, inferior vena cava, and right atrium. Metastases to the lungs and regional lymph nodes are frequent. Direct extension into the adjacent organs or the renal pelvis can occur.

US demonstrates usually a large, well-defined heterogeneously echogenic solid mass with hypoechoic lesions (hemorrhage, necrosis, or displaced calyces) (Fig. 24.9). Wilms tumor may contain hyperechoic areas of calcification and fat. Evaluation of the inferior vena cava is important for identifying tumor thrombus of Wilms tumor. CT is preferred over US for staging to evaluate tumor extent and metastases to nodes, liver, and lung. CT shows a large, well-defined mass of heterogeneous attenuation in those areas of low attenuation (necrosis or hemorrhage) and high attenuation (calcifications) (Lowe et al. 2000) (Figs. 24.8 and 24.10). The finding of a peripheral crescentic rim of renal tissue surrounding a well-defined mass is helpful in confirming the renal origin of the tumor (Fig. 24.9). Chest CT is more sensitive than chest radiograph and MR imaging in the detection of pulmonary metastatic nodules. Abdominal CT or MR imaging is the imaging modality of choice for the evaluation of patients after resection of Wilms tumor. MR imaging is an excellent modality for detecting recurrent or metastatic abdominal tumor and assessing caval patency.

24.3.2 Nephroblastomatosis

Nephroblastomatosis is characterized by nephrogenic rests within the kidney. Nephrogenic rests are foci of embryonal cells persisting beyond infancy. They may be unifocal, multifocal, or diffuse in distribution. Nephroblastomatosis has the potential of a malignant transformation into Wilms tumor. These foci are found in Beckwith-Wiedemann syndrome, hemihypertrophy, sporadic aniridia, trisomy 18, and Drash syndrome (Geller and Kochan 2011).

US demonstrates multiple hypoechoic cortical nodules or peripheral rind of hypoechoic tissue in both enlarged kidneys. Contrast-enhanced CT shows poorly enhancing cortical nodules or peripheral thick low-attenuated rind in both enlarged kidneys. MR imaging demonstrates multifocal or diffuse low-signal intensity nodules on both T1-weighted and T2-weighted images (Fig. 24.13). Nephroblastomatosis

is seen as homogeneous nodules in imaging studies, whereas Wilms tumors are usually heterogeneous (Rohrschneider et al. 1998) (Fig. 24.14).

24.3.3 Clear Cell Sarcoma

Clear cell sarcoma has been called “bone-metastasizing renal tumor of childhood.” The imaging findings and an age group of clear cell sarcoma are similar to those of Wilms tumor (Glass et al. 1991). Bone metastases associated to renal tumor in children are suggestive of clear cell sarcoma. After tissue diagnosis, bone scintigraphy or skeletal survey may be recommended for staging and for postoperative follow-up. A clear cell sarcoma is usually a solid renal mass with varying degrees of cystic necrosis, hemorrhage, and calcification (Fig. 24.15). Prognosis is poor because of its aggressive behavior, as compared with Wilms tumor, with metastases to the bones, lungs, lymph nodes, brain, liver, and soft tissue.

24.3.4 Rhabdoid Tumor

Rhabdoid tumors of the kidney are extremely aggressive malignant renal tumors of early childhood. Characteristic findings of rhabdoid tumor include early age at diagnosis and a predilection for CNS lesions. Most rhabdoid tumors occur at less than 2 years of age and are extremely rare over the age of 5. Rhabdoid tumor can occur in various organs, mainly the kidney, brain (atypical teratoid/rhabdoid tumors), and soft tissues. Rhabdoid tumor is unique among childhood renal tumors in its frequent association with primary or metastatic brain tumors. The primary brain tumors are mostly of posterior fossa origin. After pathologic diagnosis, MRI of the brain may be recommended (Fig. 24.17).

Rhabdoid tumor is usually large at presentation and frequently central in location involving the renal hilum (Han et al. 2001) (Fig. 24.18). Imaging findings of rhabdoid tumor include large subcapsular fluid collection or hematoma, lobulated surface of the tumor, and calcifications outlining tumor lobules (Fig. 24.16). Rhabdoid tumor metastasizes early to the retroperitoneal lymph nodes, lung, liver, brain, and bone.

24.3.5 Mesoblastic Nephroma

Mesoblastic nephroma is the most common solid renal tumor of infancy, usually during the first 6 months of life. Neonatal or prenatal Wilms tumor is extremely rare. Mesoblastic nephroma differs from Wilms tumor by its earlier presentation and better prognosis. It is a pathologically benign mesenchymal hamartoma but is an infiltrative mass with

ill-defined margins without capsule. Imaging findings of mesoblastic nephroma are similar to those of Wilms tumor. US demonstrates usually a large solid mass with a homogeneous or heterogeneous echotexture (Lawande 2010). CT scan demonstrates a homogeneous renal mass or a large tumor with areas of low attenuation representing hemorrhage, necrosis, or fluid collection (Fig. 24.19). CT scan at the arterial phase can demonstrate residual renal cortex trapped into the tumor resulting from the infiltrative growing. Residual contrast medium within the tumor may be seen on delayed CT scan, representing functioning nephrons trapped within the tumor. MR imaging shows low-signal intensity on T1-weighted images and high-signal intensity on T2-weighted images.

24.3.6 Multilocular Cystic Renal Tumor

Multilocular cystic renal tumor is a cystic renal tumor characterized by multiple septations. It includes two pathologically different but grossly identical tumors: cystic nephroma (CN) and cystic partially differentiated nephroblastoma (CPDN). Pathologically, CPDN has foci of blastemal cells within its septa, whereas CN does not. Grossly, multilocular cystic renal tumors have a solitary, well-circumscribed, multiseptated cystic mass without solid or nodular components. Multilocular cystic renal tumor is a benign neoplasm with a biphasic age and gender distribution, usually seen in younger boys and in women.

CN and CPDN are indistinguishable on the basis of gross pathology and imaging findings. US demonstrates a well-circumscribed multiseptated cystic renal mass (Paltiel 2007). The main differential diagnosis of the multicystic renal neoplasm includes cystic Wilms tumor. Any solid component along the septa is suspicious for cystic Wilms tumor. US is more sensitive to identify septa within the tumor than CT. MR imaging shows variable signal intensity of cyst contents and the low signal intensity capsule on all pulse sequences (Fig. 24.20).

24.3.7 Renal Cell Carcinoma

Although primary renal tumors are uncommon in the second decade of life, the incidence of renal cell carcinoma then is nearly equal to or higher than that of Wilms tumor (Geller and Kochan 2011). Renal cell carcinoma increases in incidence with age. Von Hippel-Lindau disease predisposes to the development of renal cell carcinoma, which tends to be multiple and manifest at a younger age. Imaging modalities cannot confidently distinguish renal cell carcinoma from Wilms tumor. Renal cell carcinoma in children is frequently calcified and smaller than Wilms tumor (Fig. 24.21).

24.3.8 Renal Lymphoma and Leukemia

Lymphoma of the kidney is a late manifestation of the disease and occurs more frequently in non-Hodgkin lymphoma. It usually develops secondary to hematogenous metastases or direct invasion from contiguous retroperitoneal mass. Primary renal lymphoma is extremely rare because there is no lymphoid tissue in the kidney. Renal lymphoma of the kidney is usually bilateral and homogeneous. US demonstrates multiple, homogeneously hypoechoic confluent nodules or diffuse bilateral renal enlargement or, rarely, a solitary mass. CT shows homogeneously low-attenuated multiple parenchymal nodules or diffusely enlarged kidneys with decreased contrast enhancement (Chepuri et al. 2003).

Leukemic infiltration of the kidneys may often cause diffuse renal enlargement with smooth renal contour. Imaging findings are diffuse symmetrical enlargement of kidneys, distorted calyceal architecture, and loss of corticomedullary differentiation. Focal involvement of leukemia presents as solitary or multiple masses (Hilmes et al. 2008) (Fig. 24.22).

24.3.9 Neuroblastoma

Neuroblastoma may occur in the adrenal glands (50 %) or anywhere along the sympathetic nerve chain within the neck, thorax, retroperitoneum, or pelvis. Neuroblastoma is the third most common pediatric tumor after leukemia and primary brain tumor. Neuroblastoma accounts for 10 % of all pediatric neoplasms. Neuroblastoma is mostly identified between 1 and 5 years of age, with a median age of almost 2 years. Neuroblastoma may be associated with neurofibromatosis and Hirschsprung's disease. Local invasion can occur into the liver, kidneys, and through the neural foramina into the spinal canal. Unlikely Wilms tumor, the encasement of the aorta is characteristic in neuroblastoma (Figs. 24.23 and 24.24).

Younger age, lower stage, and extra-abdominal tumor origin are the best prognostic factors. The international neuroblastoma staging system is as follows: Stage 1 (localized tumor confined to area of origin), Stage 2 (unilateral tumor), Stage 3 (tumor infiltrating across midline), and Stage 4 (dissemination of tumor). There is a special stage of disseminated neuroblastoma, stage 4S, defined as a localized primary tumor and metastatic disease confined to the liver, skin, and bone marrow (not cortical bone) in infants. Infants with stage 4S have the possibility of spontaneous regression, despite a large tumor burden, and a good prognosis. Bone metastasis is common in neuroblastomas, whereas it is very rare in Wilms tumor. Proptosis and periorbital ecchymosis are signs of metastases to the orbits.

Neuroblastoma, ganglioneuroblastoma, and ganglioneuroma represent a histologic spectrum of maturation and differentiation. Ganglioneuroma is a histologically benign,

fully differentiated counterpart of neuroblastoma. In contrast to neuroblastoma, ganglioneuroma usually occurs in older children and are found in the posterior mediastinum and retroperitoneum.

CT and MR imaging are the standard imaging modalities for tumor extent and metastatic disease (Figs. 24.25 and 24.26). MR imaging is preferred for staging and follow-up in very young children because there is no radiation exposure. US demonstrates a heterogeneous echogenic mass with hyperechoic areas (calcifications) and hypoechoic areas

(cystic, hemorrhagic, or necrotic components). Coarse, punctate, finely stippled, or curvilinear calcifications within the tumor are frequently identified with CT (Fig. 24.23). CT and MR imaging may be able to demonstrate the typical encasement and displacement of the adjacent vessels (Balassy et al. 2011) (Figs. 24.23 and 24.24). MR imaging is the best imaging modality to show intraspinal extension and to assess the bone marrow involvement. Radionuclide bone scans or ^{123}I -MIBG scans are the useful imaging modalities for identifying bone metastases.

24.4 Illustrations: Cystic Renal Disease and Neoplasms

24.4.1 Autosomal Recessive Polycystic Kidney Disease

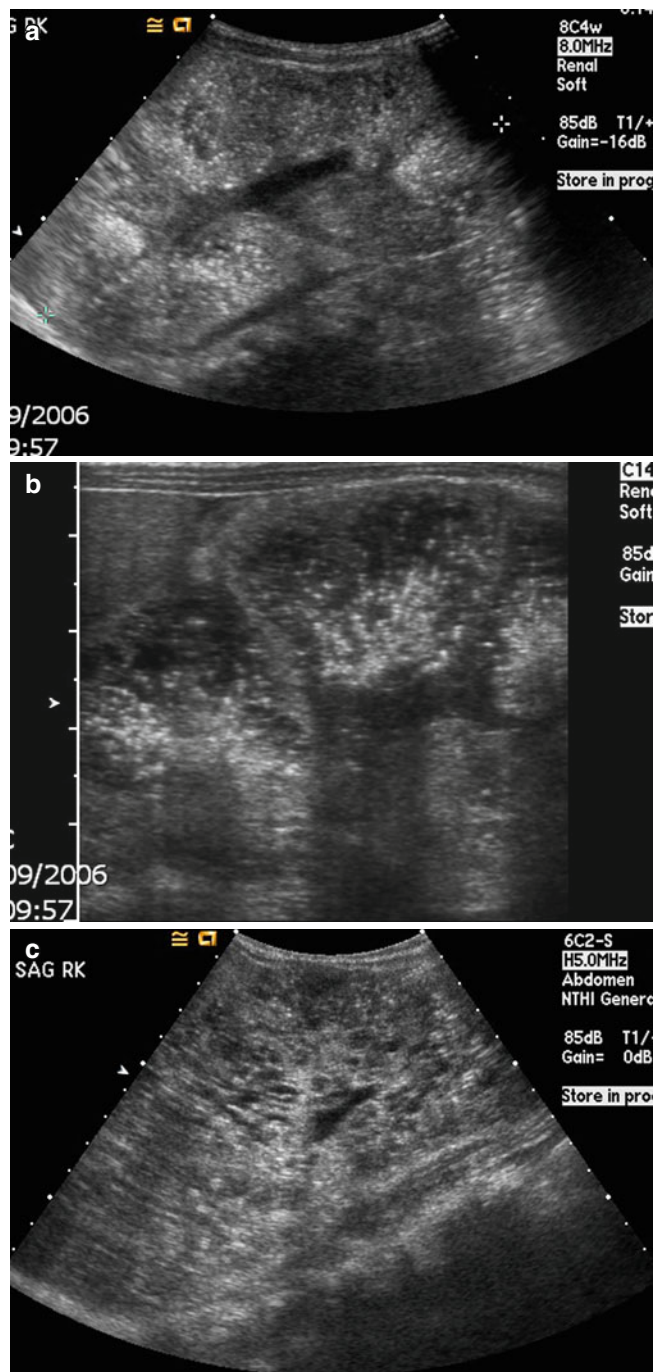


Fig. 24.1 Autosomal recessive polycystic kidney disease in a 7-day-old boy. (a) Longitudinal US shows an enlarged kidney with heterogeneously increased echogenicity. Corticomedullary differentiation is obliterated. (b) High-resolution US of the kidney shows radially oriented linear echogenicity within the renal medulla, indicating ectatic tubules. Note relative sparing of the renal cortex. (c) Follow-up US after 5 years shows multiple tiny echogenic foci and small cysts with obliteration of the corticomedullary differentiation

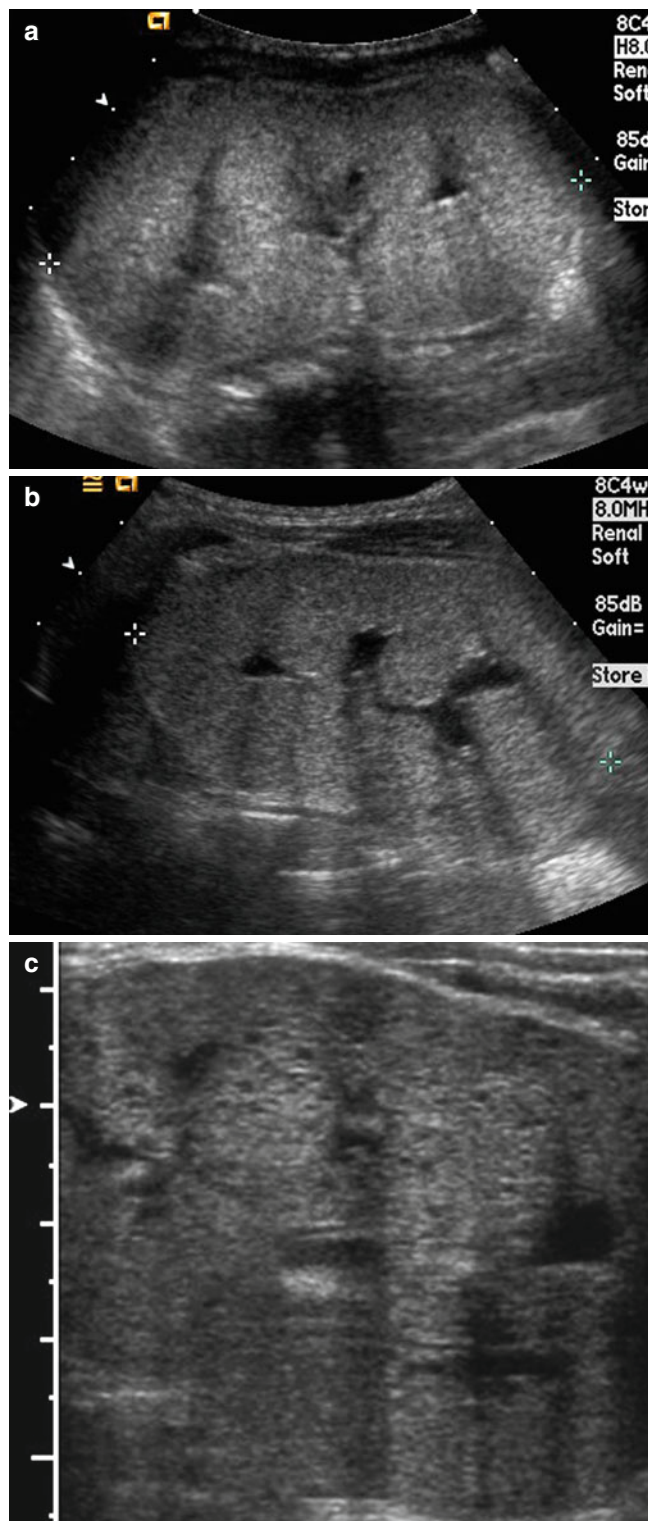


Fig. 24.2 Autosomal recessive polycystic kidney disease in a 1-day-old girl. (a and b) Longitudinal US images of right kidney (a) and left kidney (b) show diffuse echogenic foci with obliteration of the corticomedullary differentiation. (c) High-resolution US of the kidney demonstrates multiple tiny cysts within echogenic renal parenchyma

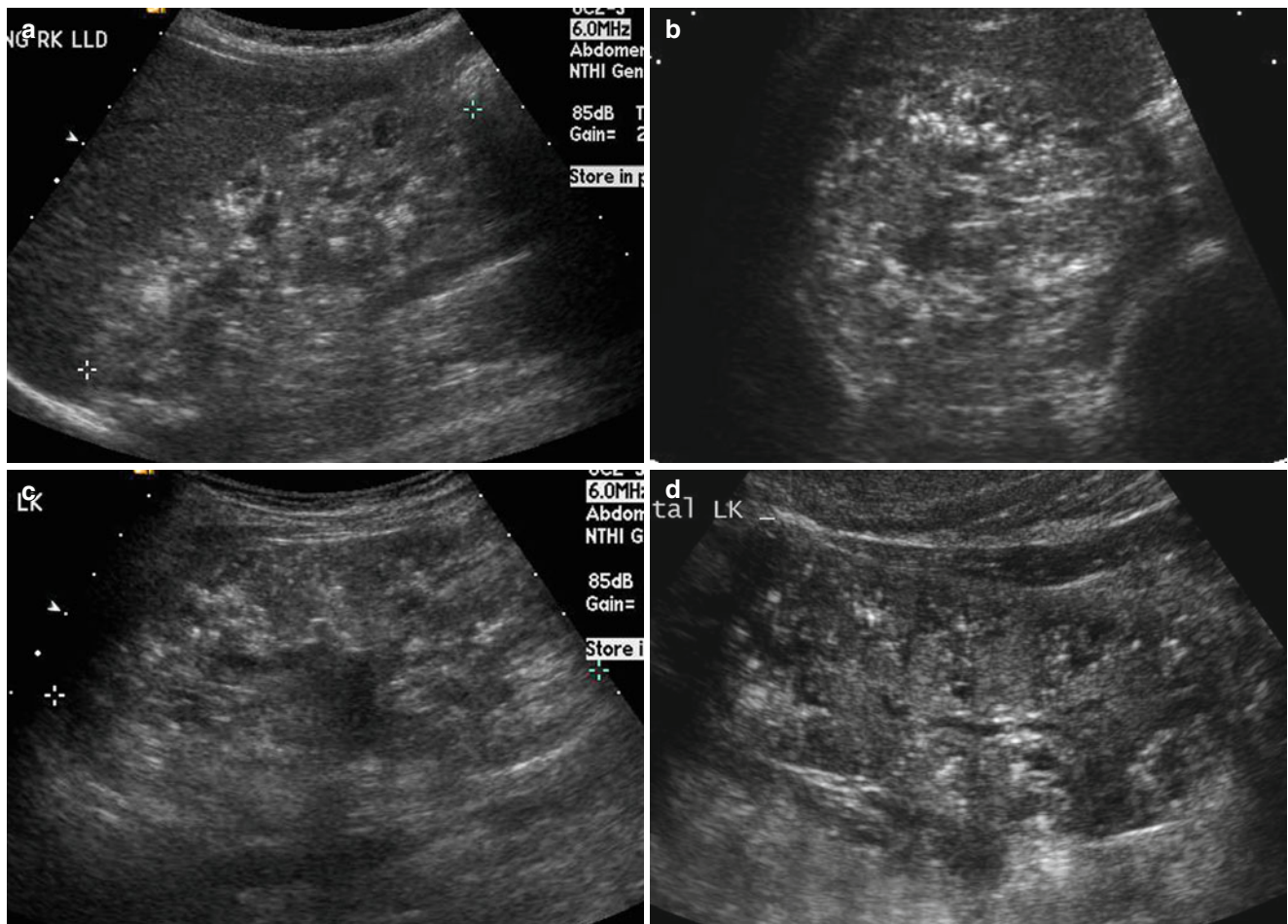


Fig. 24.3 Autosomal recessive polycystic kidney disease in a 7-year-old boy. (a and b) Longitudinal (a) and transverse (b) US images of right kidney show multiple tiny echogenic foci and small cysts with obliteration of the corticomedullary differentiation. (c) Longitudinal US of the left kidney shows numerous tiny echogenic foci and small

cysts. Note that the peripheral renal cortex is relatively spared. The renal pelvis is seen. (d) Two years later, multiple tiny echogenic foci are identified mainly within the medullary regions. The peripheral renal cortex is more spared as compared to prior US images

24.4.2 Autosomal Dominant Polycystic Kidney Disease

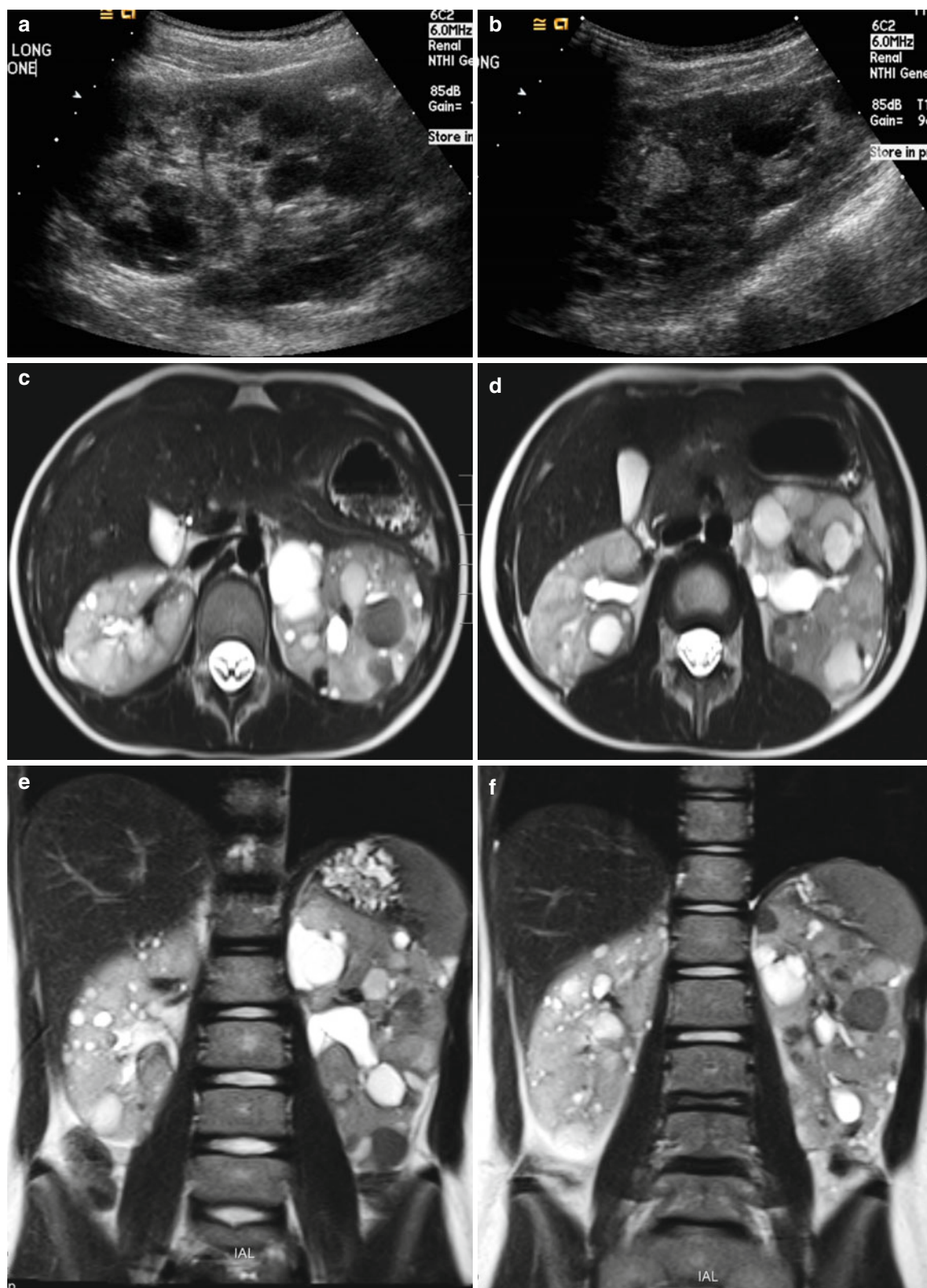


Fig. 24.4 Autosomal dominant polycystic kidney disease in a 6-year-old girl. (a and b) Longitudinal US of the left kidney demonstrates multiple, variable-sized hypoechoic cysts. Note multiple echogenic round cysts, which represent hemorrhagic cysts. (c and d) T2-weighted axial MR images demonstrate variable-sized cysts

with variable contents within the cysts. Note multiple low signal intensity cysts with fluid-fluid level, which represent hemorrhagic cysts. (e and f) T2-weighted coronal MR images show marked enlargement of both kidneys with variable-sized cysts occupying the entire kidney

24.4.3 Multicystic Dysplastic Kidney

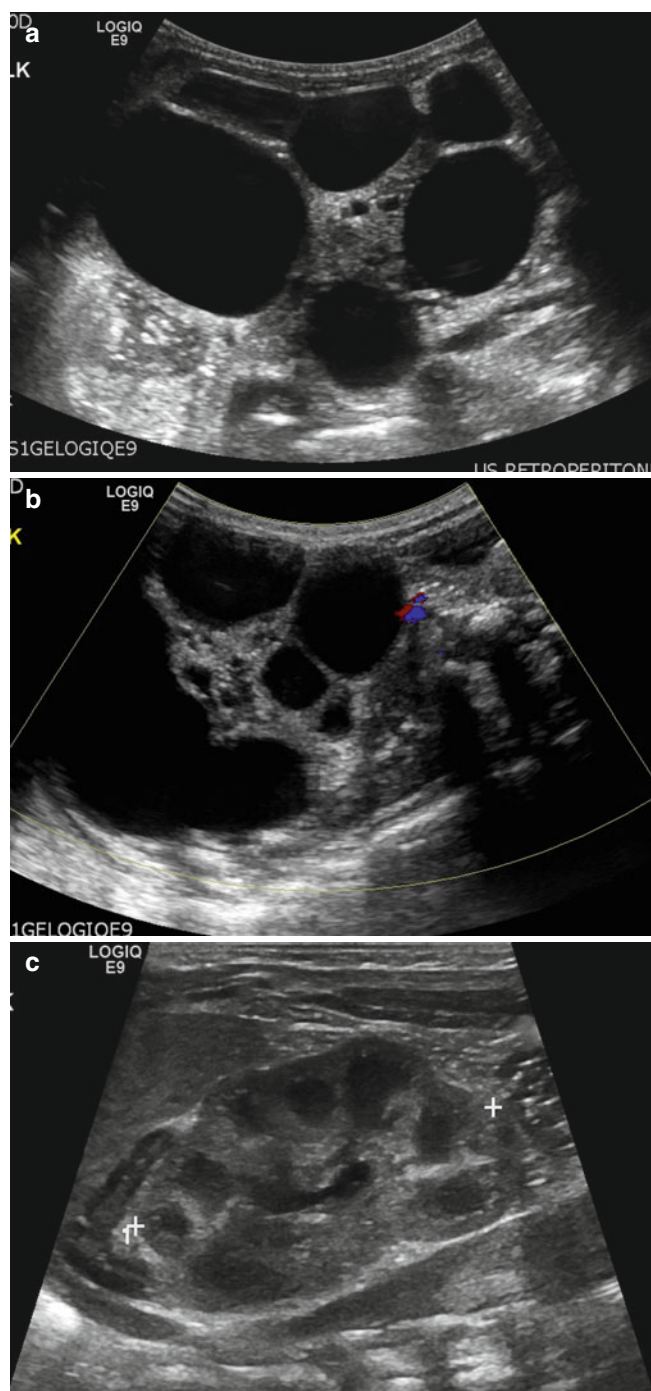


Fig. 24.5 Multicystic dysplastic kidney in a 1-day-old girl. (a) Longitudinal US of the left kidney shows multiple cysts of varying size and intervening hyperechoic area. Left kidney measures about 9.4 cm in length. Normal renal parenchyma is not demonstrated. (b) Color Doppler US of the left kidney shows no vascular structure within the intervening hyperechoic area. (c) Longitudinal US of the right kidney shows normal renal parenchyma. Right kidney measures about 4.0 cm in length

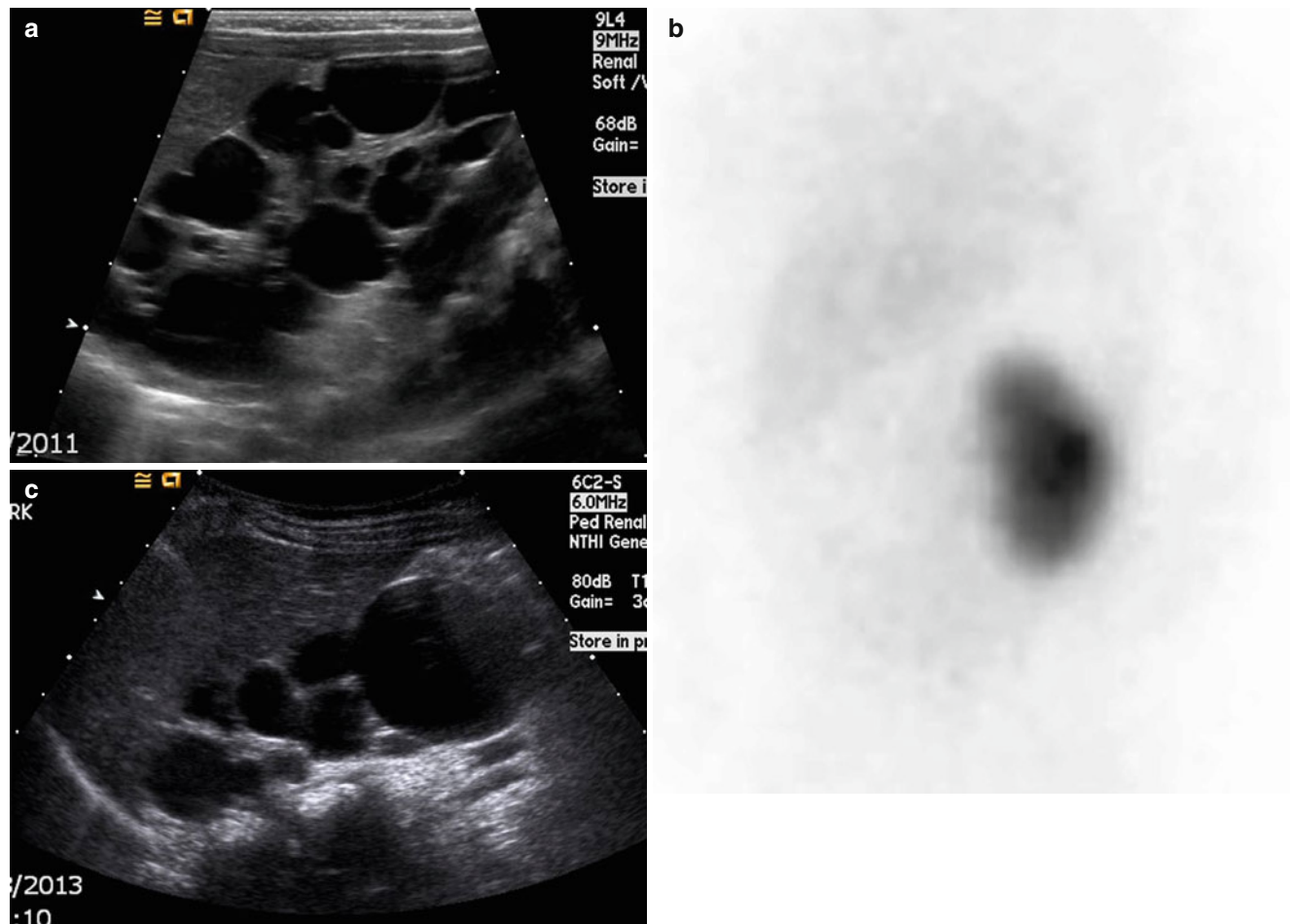


Fig. 24.6 Multicystic dysplastic kidney in a 1-month-old girl. (a) Longitudinal US of the right kidney shows multiple cysts without normal renal parenchyma. (b) An anterior view of DMSA renal

scintigraphy shows no uptake of radioisotopes in the right kidney. (c) Two years later, most of the cysts have decreased in size and number with the exception of a large cyst in the lower pole

24.4.4 Multiple Malformation Syndromes with Renal Cysts

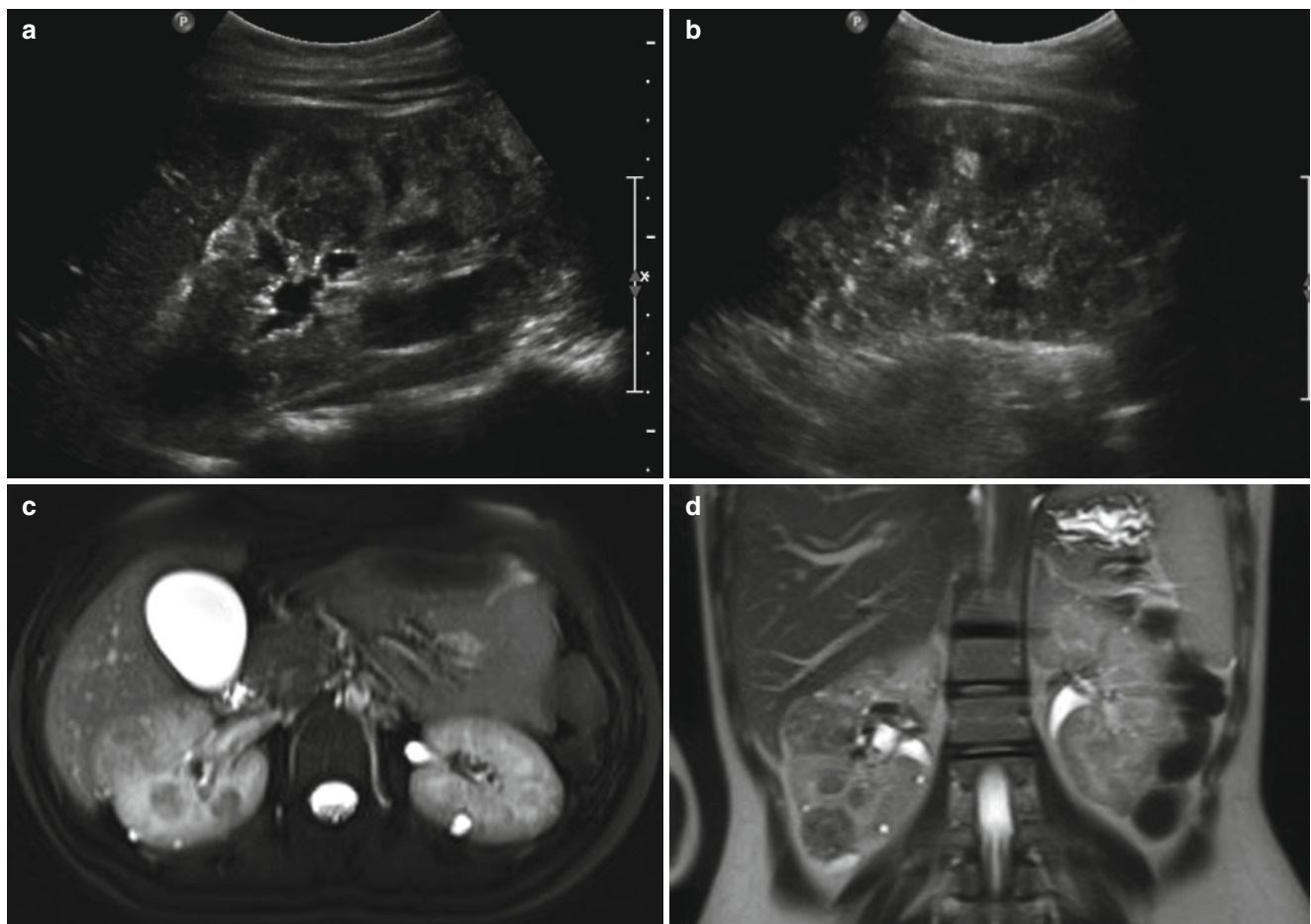


Fig. 24.7 Angiomyolipomas and renal cysts in a 17-year-old girl with tuberous sclerosis. (**a** and **b**) Longitudinal US of both kidneys shows multiple echogenic round angiomyolipomas and hypoechoic

cysts. (**c** and **d**) T2-weighted axial and coronal MR images show multiple tiny high-signal intensity renal cysts and low-signal intensity angiomyolipomas in both kidneys

24.4.5 Wilms Tumor

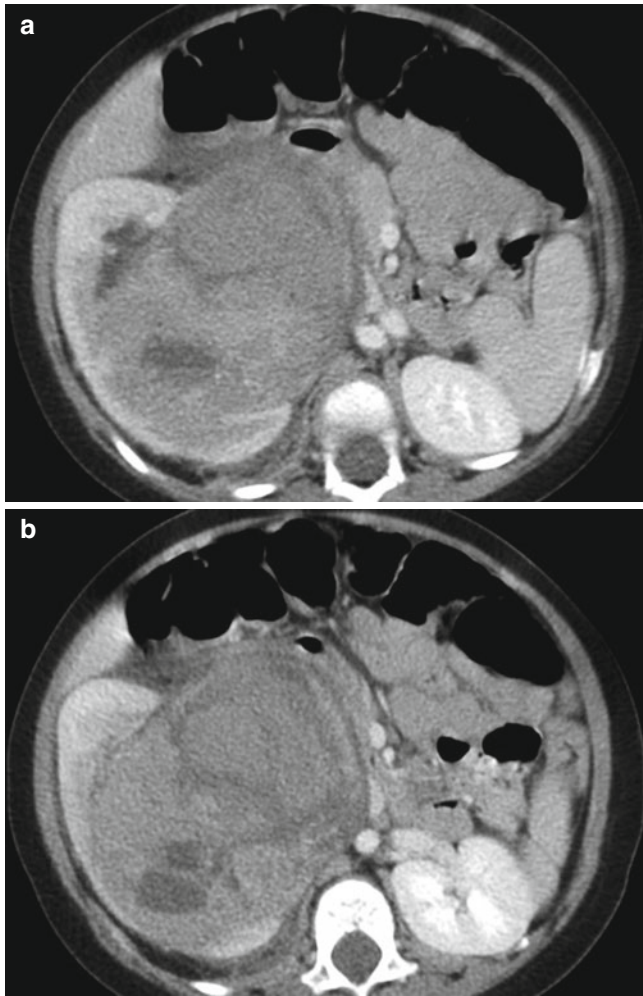


Fig. 24.8 Wilms tumor in a 1-year-old girl. (a and b) Contrast-enhanced CT scans show a heterogeneous mass arising from the renal sinus of the right kidney. The mass shows heterogeneous enhancement and irregular central necrosis and hemorrhage. The mass involves the renal sinus

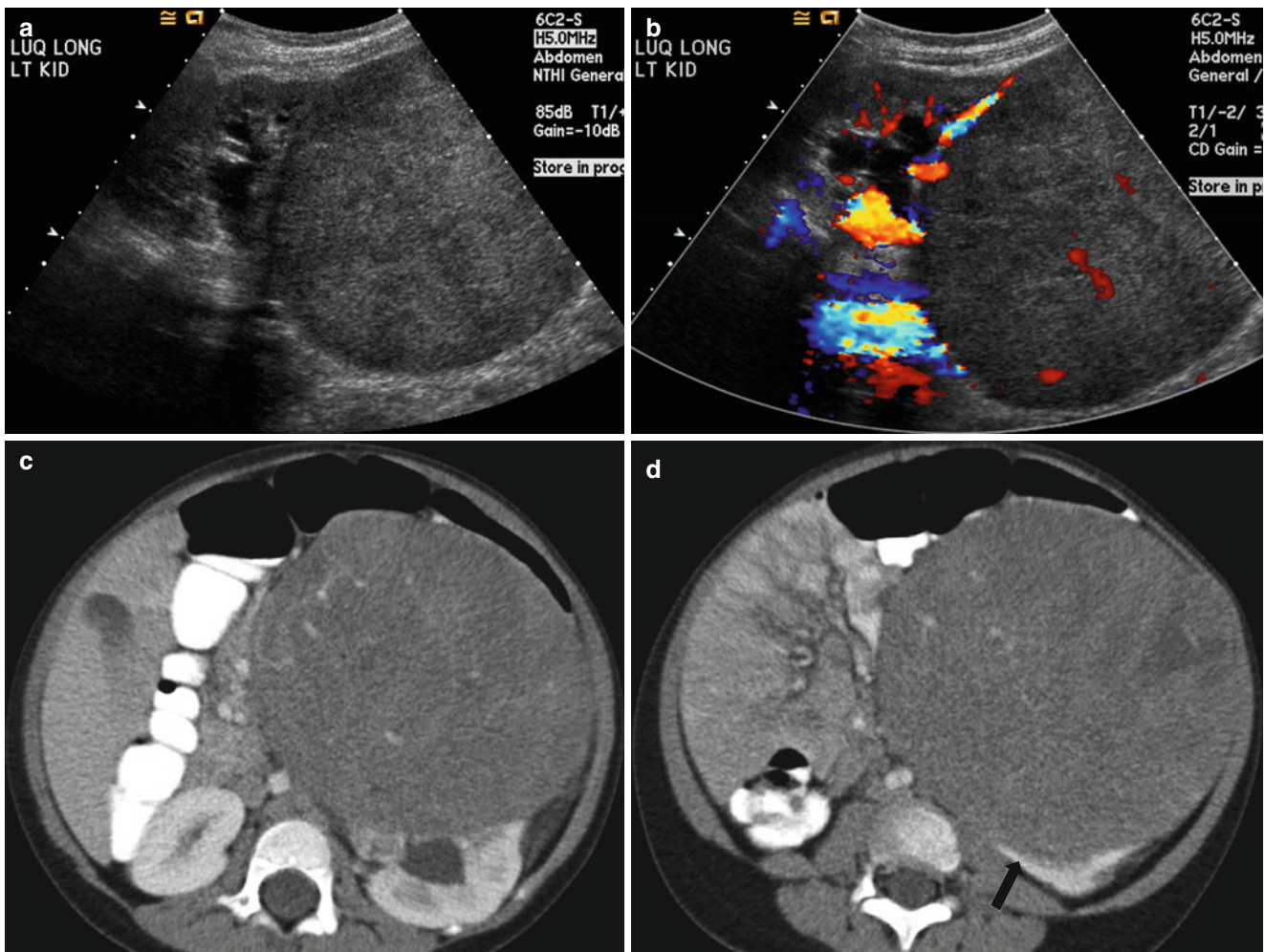


Fig. 24.9 Wilms tumor in a 3-year-old girl. (a) Longitudinal US of the left kidney shows a homogeneously echogenic mass arising from the lower pole of the kidney. Note the dilated renal pelvis of the left kidney. (b) Color Doppler US of the mass shows an intratumoral vascular structure. Note that tumor vascularity is far less than that of the normal renal

parenchyma. (c, d, and e) Contrast-enhanced CT shows a large, low-attenuated, solid mass arising from the lower pole of the left kidney. The finding of a peripheral crescentic rim (arrow) of renal tissue surrounding a well-defined mass is helpful for confirming the renal origin of the tumor

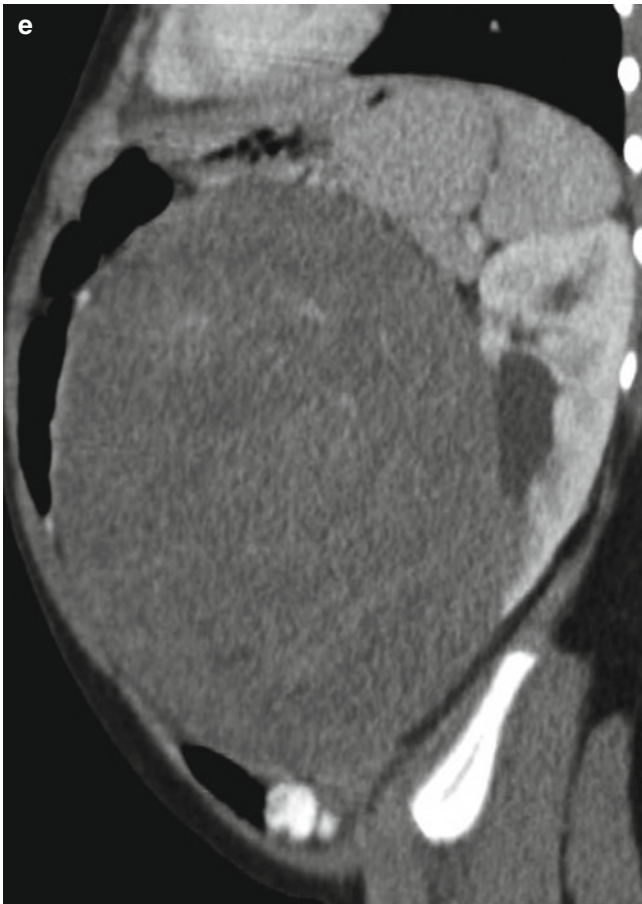


Fig. 24.9 (continued)

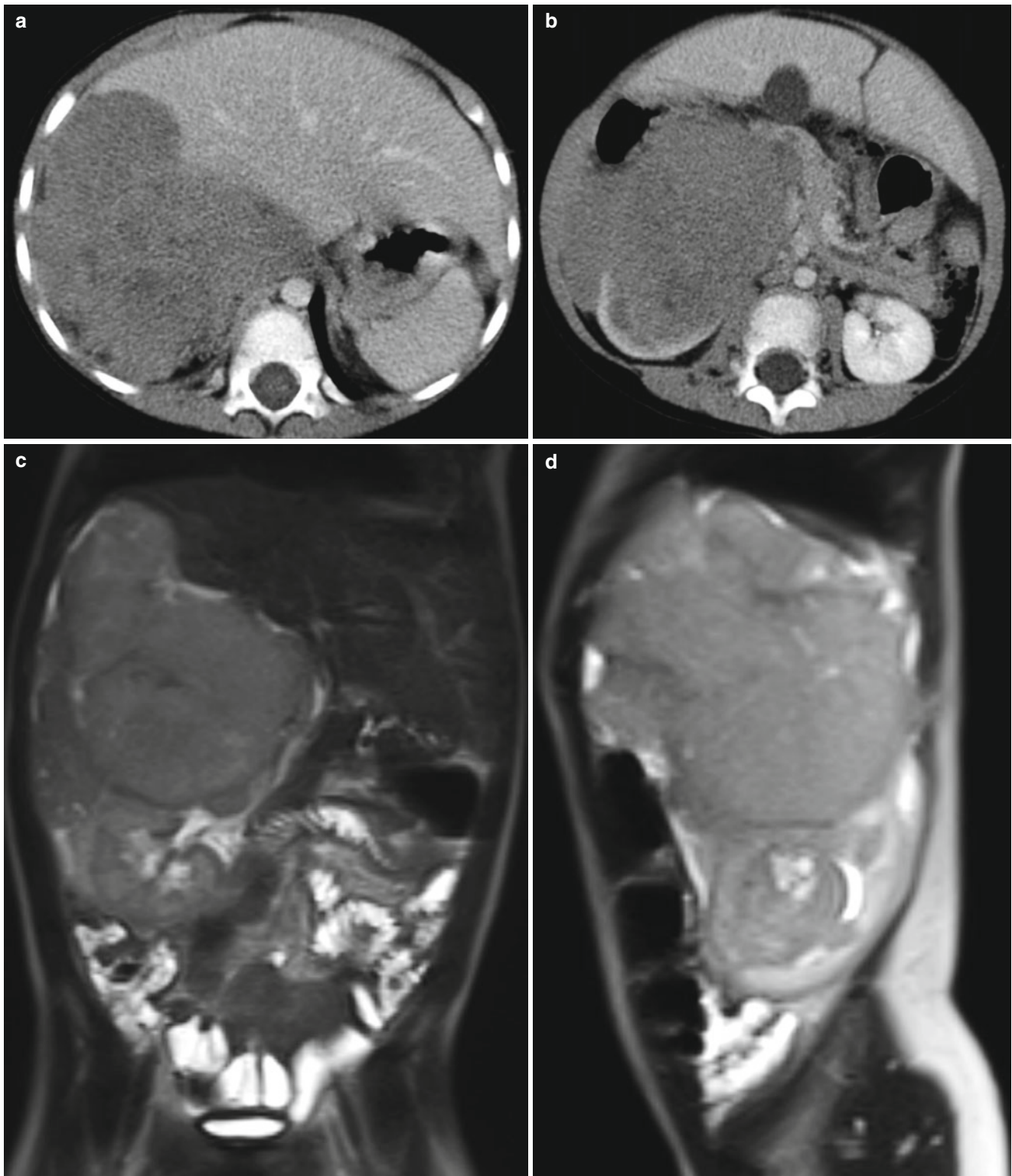


Fig. 24.10 Wilms tumor in a 2-year-old boy. (**a** and **b**) Contrast-enhanced CT scans show a large enhancing mass arising from the right kidney and extending into the right subhepatic and perirenal spaces. (**c** and **d**) T2-weighted axial MR images demonstrate a large

heterogeneous signal intensity mass arising from the right kidney. The mass extends into the right subhepatic and perirenal space suggesting tumor rupture, which is confirmed in surgery

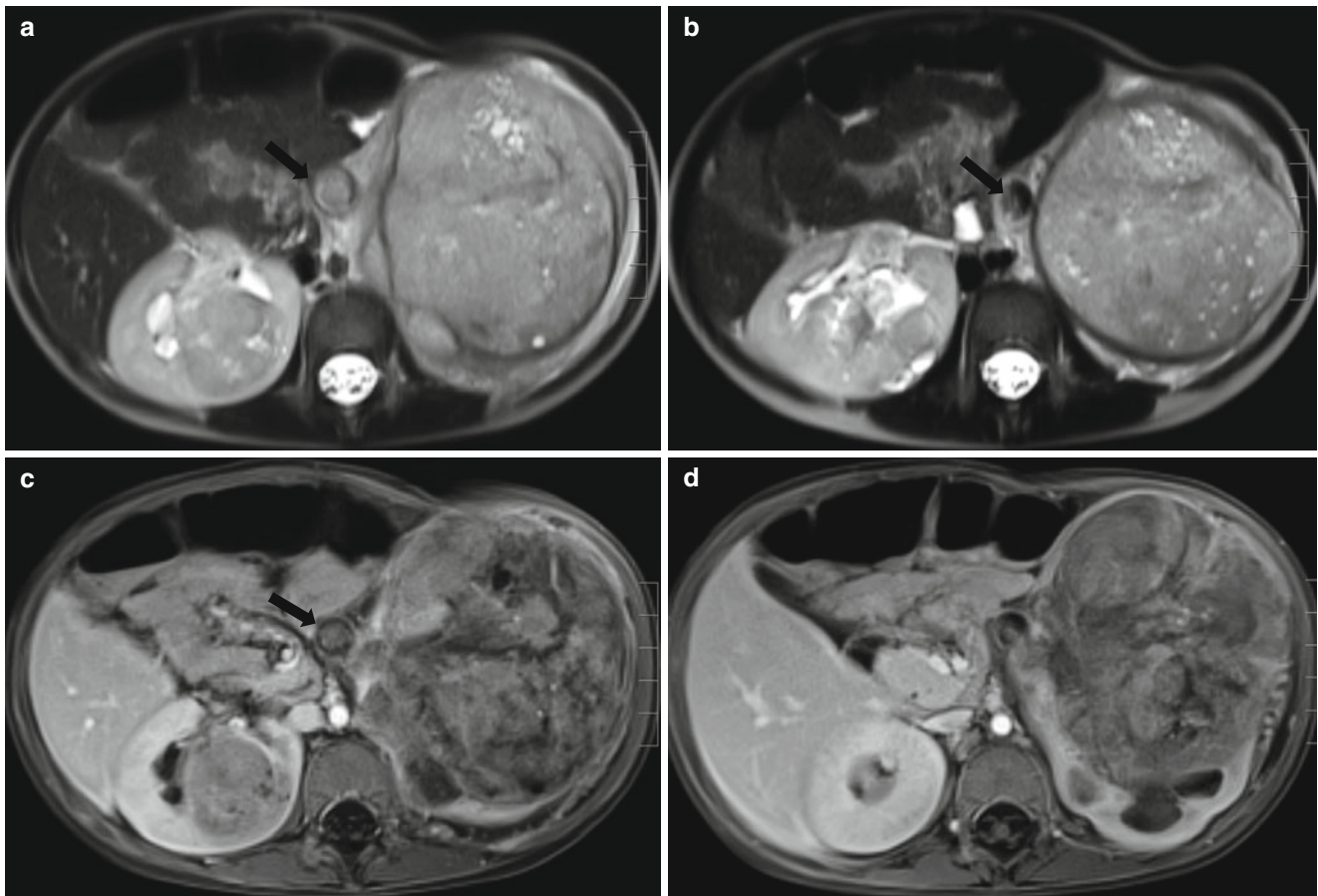


Fig. 24.11 Bilateral Wilms tumor in a 2-year-old boy with Drash syndrome. (a and b) T2-weighted axial MR images demonstrate heterogeneous signal intensity masses in both kidneys. The masses contain internal multiple tiny high-signal intensity lesions within the tumor, which represent necrotic areas. The left renal vein is distended and is

filled with tumor thrombi (arrows). (c and d) Contrast-enhanced T1-weighted axial MR images demonstrate a large, heterogeneously enhanced mass arising from the left kidney and a small homogeneously enhanced mass in the right kidney. Note tumor thrombi in the left renal vein (arrow)

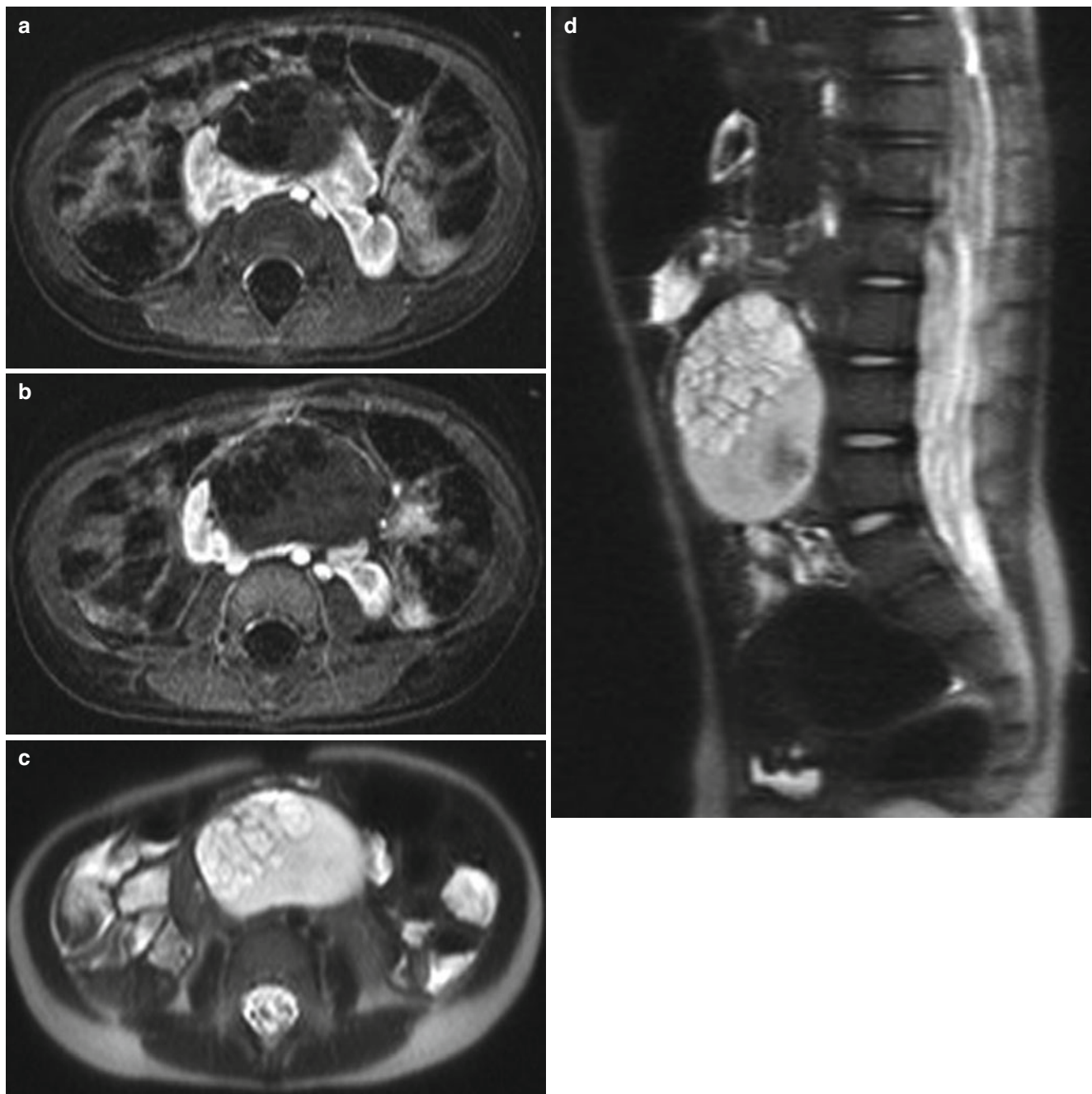


Fig. 24.12 Cystic Wilms tumor in a horseshoe kidney in a 2-year-old girl. (**a** and **b**) Contrast-enhanced T1-weighted axial MR images demonstrate a multiseptated, cystic, and partially solid mass arising from

the isthmus of the horseshoe kidney. T2-weighted axial (**c**) and sagittal (**d**) MR images demonstrate a heterogeneous large multiseptated cystic mass

24.4.6 Nephroblastomatosis

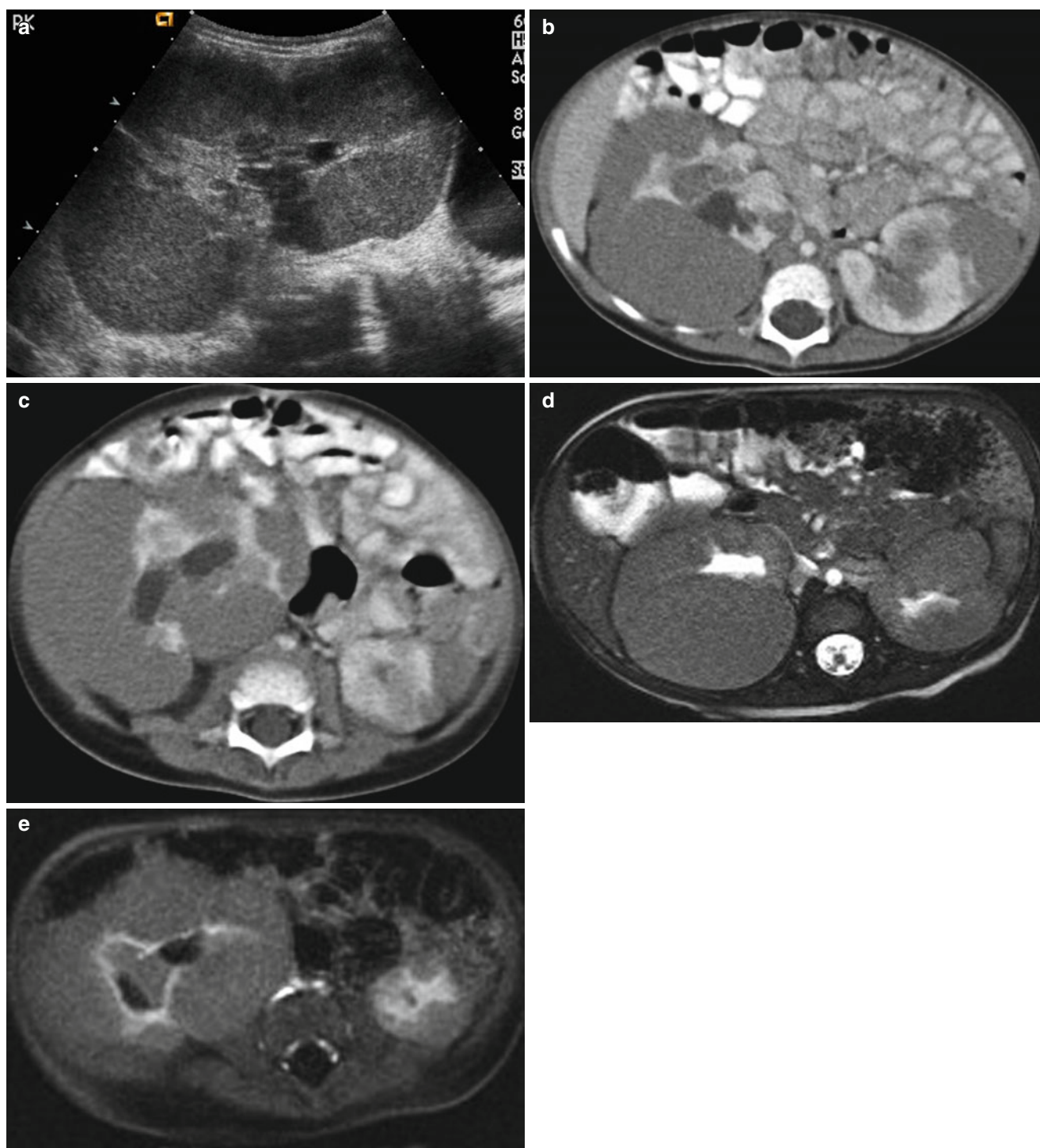


Fig. 24.13 Nephroblastomatosis in a 6-year-old girl. **(a)** Longitudinal US shows an enlarged right kidney with lobulated contour and multiple homogeneous hypoechoic cortical masses. **(b and c)** Contrast-enhanced CT scans show multiple, round, peripheral masses of low attenuation.

The right kidney is much larger than the left. **(d and e)** T2-weighted axial MR images demonstrate multiple variable-sized homogeneous masses in both kidneys

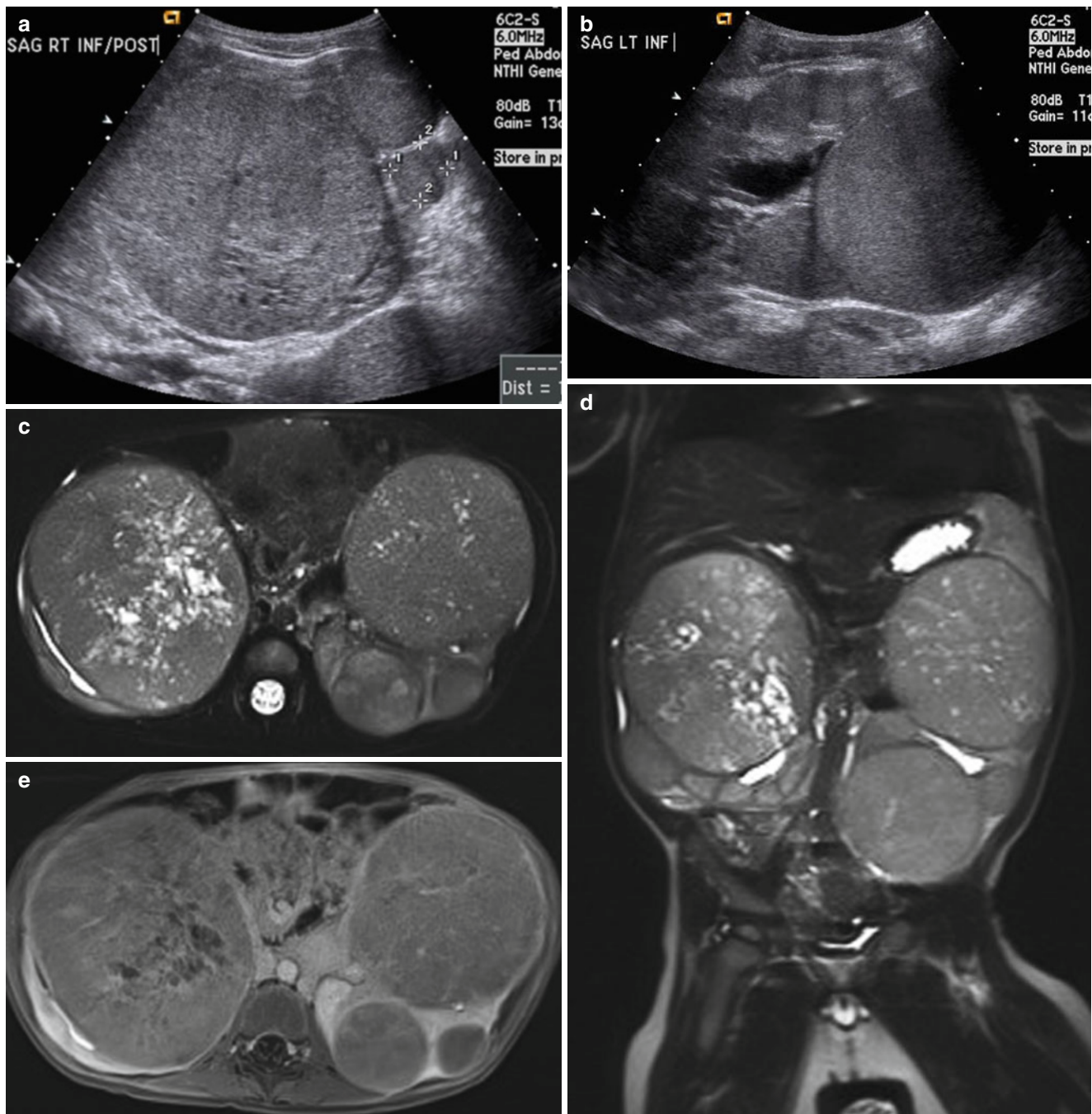


Fig. 24.14 Nephroblastomatosis and Wilms tumor in a 2-year-old boy. (a and b) Longitudinal US of the right and left kidneys shows exophytic, homogeneous echogenic masses in the lower poles of both kidneys. T2-weighted axial (c) and sagittal (d) MR images demonstrate

multiple variable-sized masses in both kidneys. There are multiple tiny high-signal intensity lesions in a large right renal mass. Contrast-enhanced T1-weighted MR images in axial (e) and coronal (f) planes show poorly enhancing masses and small cortical nodules

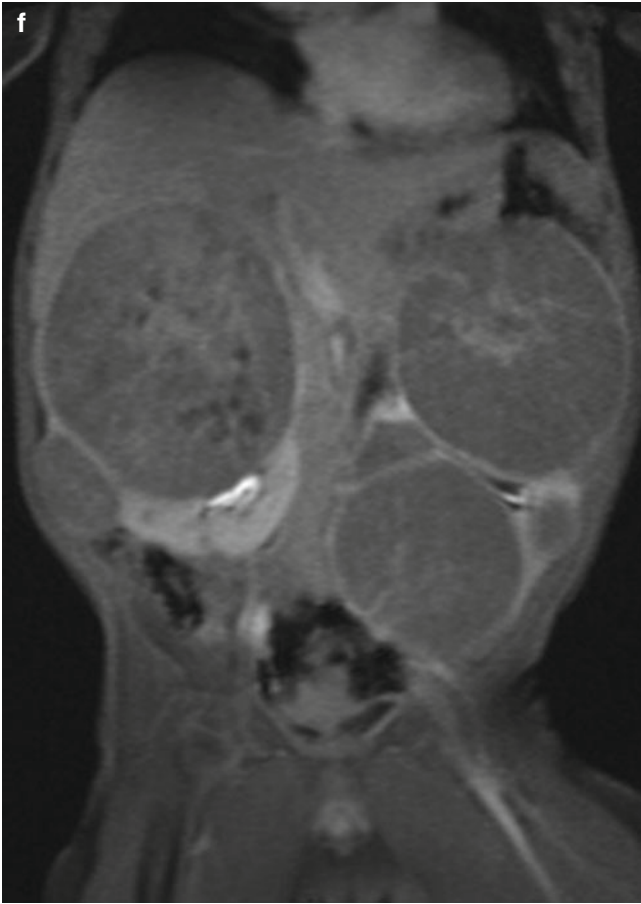


Fig. 24.14 (continued)

24.4.7 Clear Cell Sarcoma



Fig. 24.15 Clear cell sarcoma in a 16-month-old girl. (a and b) T2-weighted axial MR images show a large heterogeneous signal intensity mass arising from the left kidney. (c and d) Contrast-enhanced T1-weighted axial and coronal images show a large heterogeneously enhanced renal mass

24.4.8 Rhabdoid Tumor

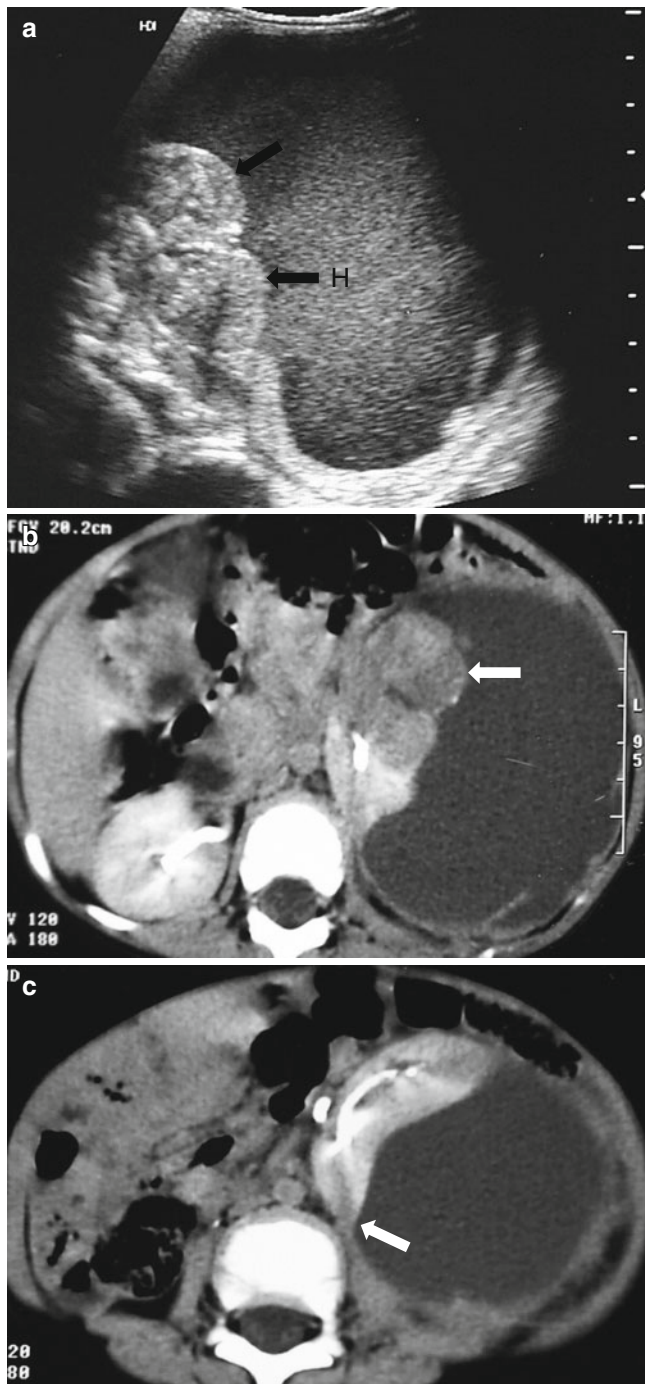


Fig. 24.16 Rhabdoid tumor of the kidney in a 6-month-old boy. (a) Longitudinal US of the left kidney shows a lobulated, heterogeneous hyperechoic mass (*black arrows*) with a large amount of subcapsular hematoma (*H*). (b) Contrast-enhanced CT scans show a poorly enhancing mass (*white arrow*) arising from the left kidney. Note also the large subcapsular hematoma, which is known to be a characteristic finding in rhabdoid tumor. (c) On the CT slice made 4 cm lower, the left kidney is displaced anteriorly by the subcapsular hematoma. Note the displaced renal pelvis and stretched renal parenchyma (*white arrow*)

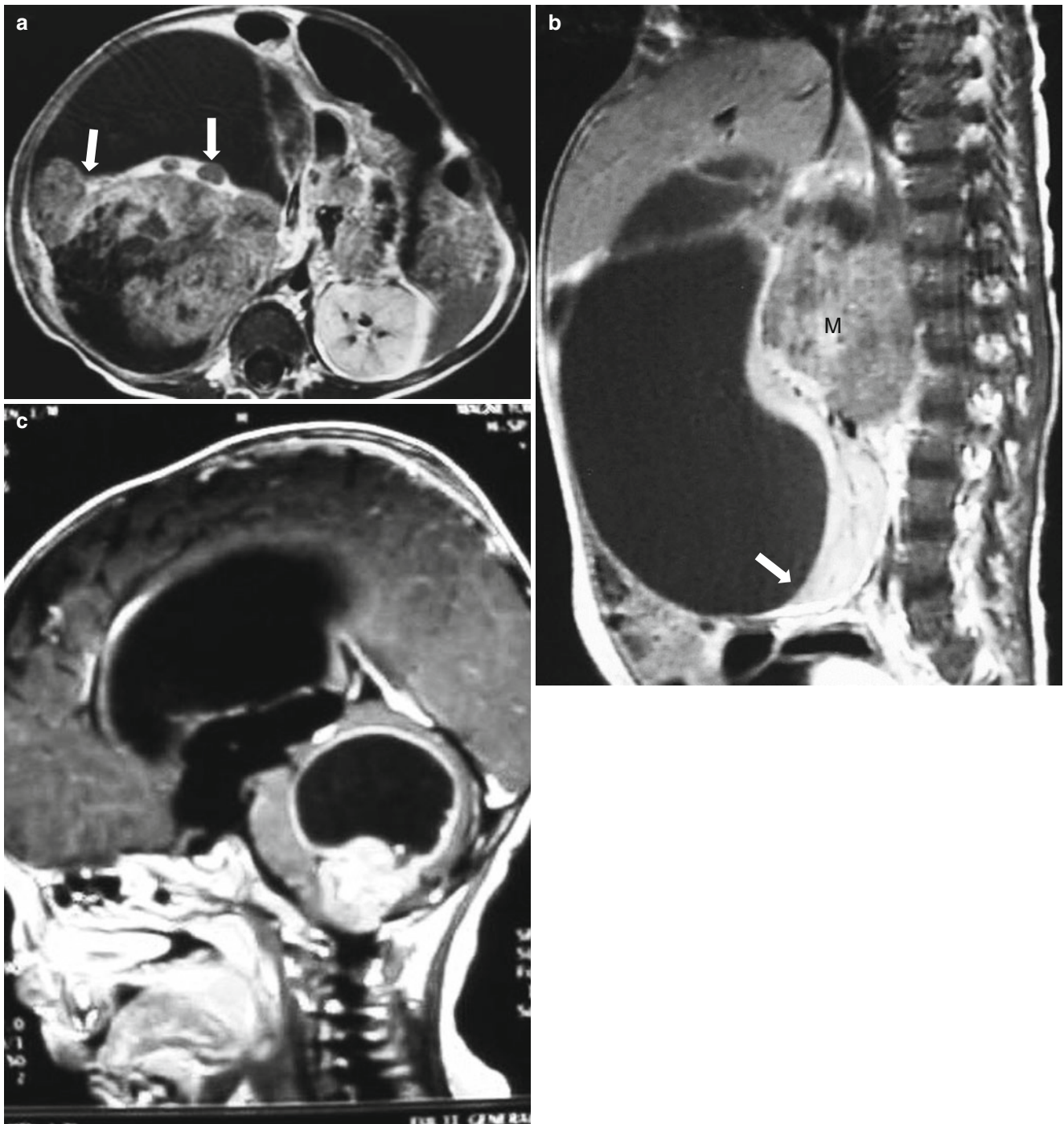


Fig. 24.17 Rhabdoid tumor of the kidney in an 8-month-old boy. (a) T1-weighted axial MR image shows a heterogeneously contrast-enhanced mass. Note the large subcapsular hematoma and stretched renal parenchyma (*white arrows*). (b) Contrast-enhanced T1-weighted sagittal MR image shows a poorly contrast-enhanced mass (*M*) arising

from the upper pole of the right kidney. Note the large subcapsular hematoma and stretched renal parenchyma (*white arrow*). (c) Contrast-enhanced T1-weighted sagittal MR image of the brain shows a midline, posterior fossa cystic mass with an intensely enhancing solid portion

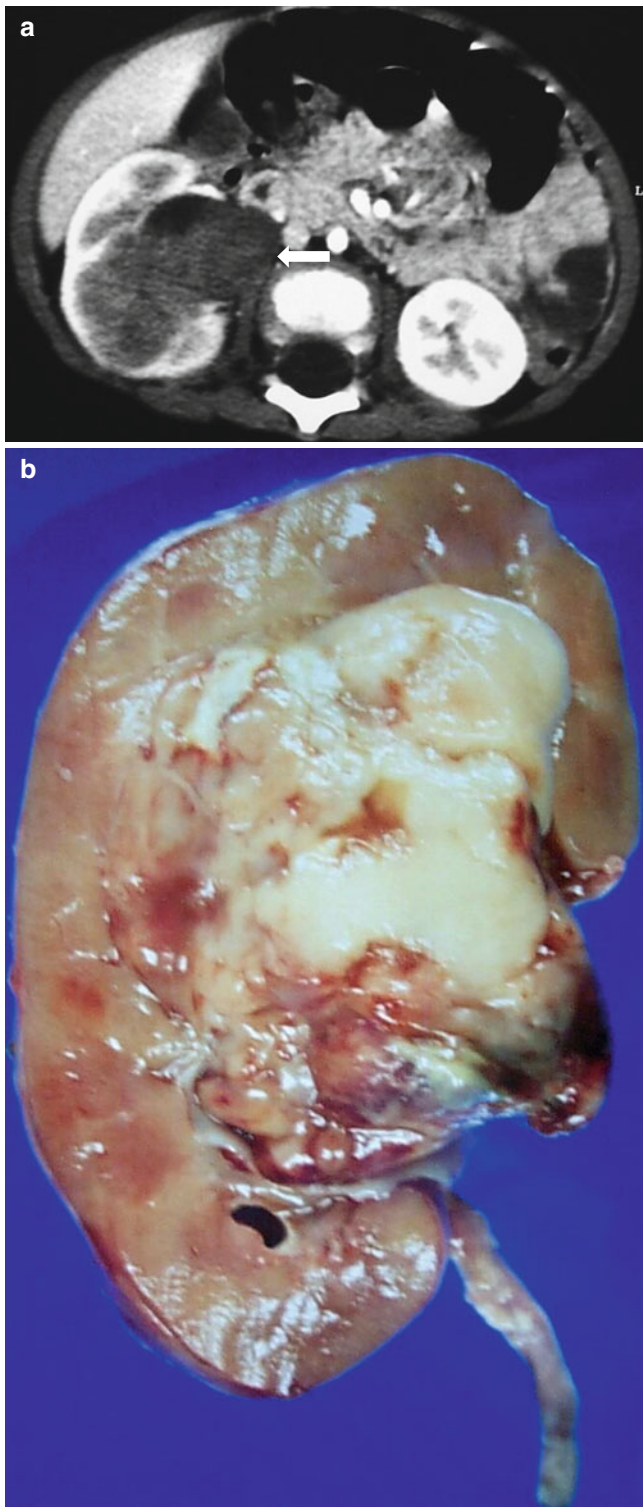


Fig. 24.18 Rhabdoid tumor of the kidney in a 12-month-old boy. (a) Contrast-enhanced CT scan shows a poorly enhancing mass occupying the renal pelvis or the right kidney, which is protruding into the renal hilum (*white arrow*). The renal pelvis is expanded by the tumor. (b) Cut surface of the gross specimen shows the mass confined in the renal sinus. Note involvement of the renal hilum

24.4.9 Mesoblastic Nephroma

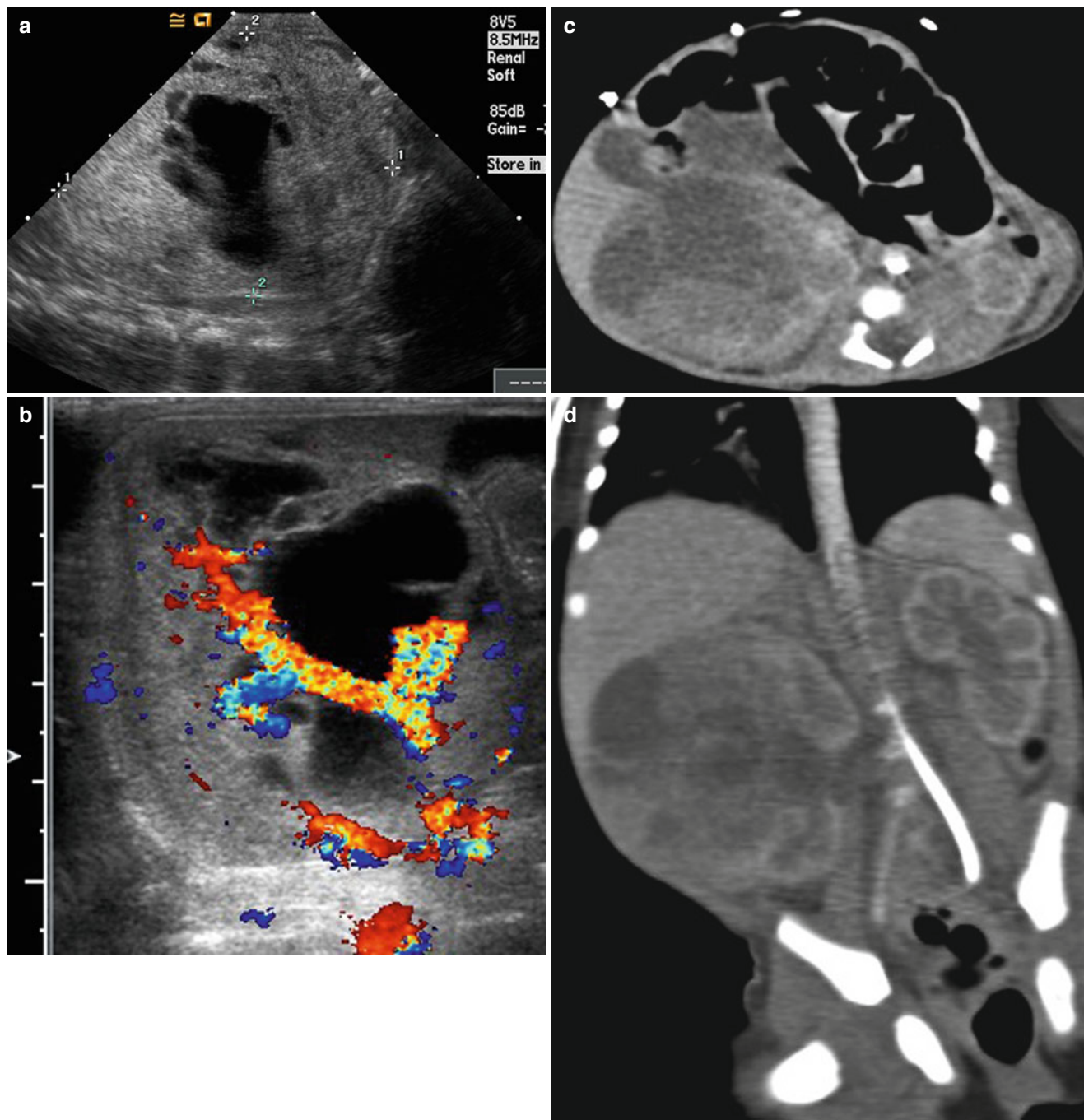


Fig. 24.19 Congenital mesoblastic nephroma in a 2-day-old girl. (a) Longitudinal US of the right kidney shows a large mixed solid and cystic tumor arising from the right kidney. (b) Color Doppler US of the right kidney shows tumor vascularity within the mass. (c and d)

Contrast-enhanced axial and coronal CT scans show a large heterogeneous mass displacing the renal parenchyma medially. The mass is poorly defined from the adjacent normal parenchyma

24.4.10 Multilocular Cystic Renal Tumor

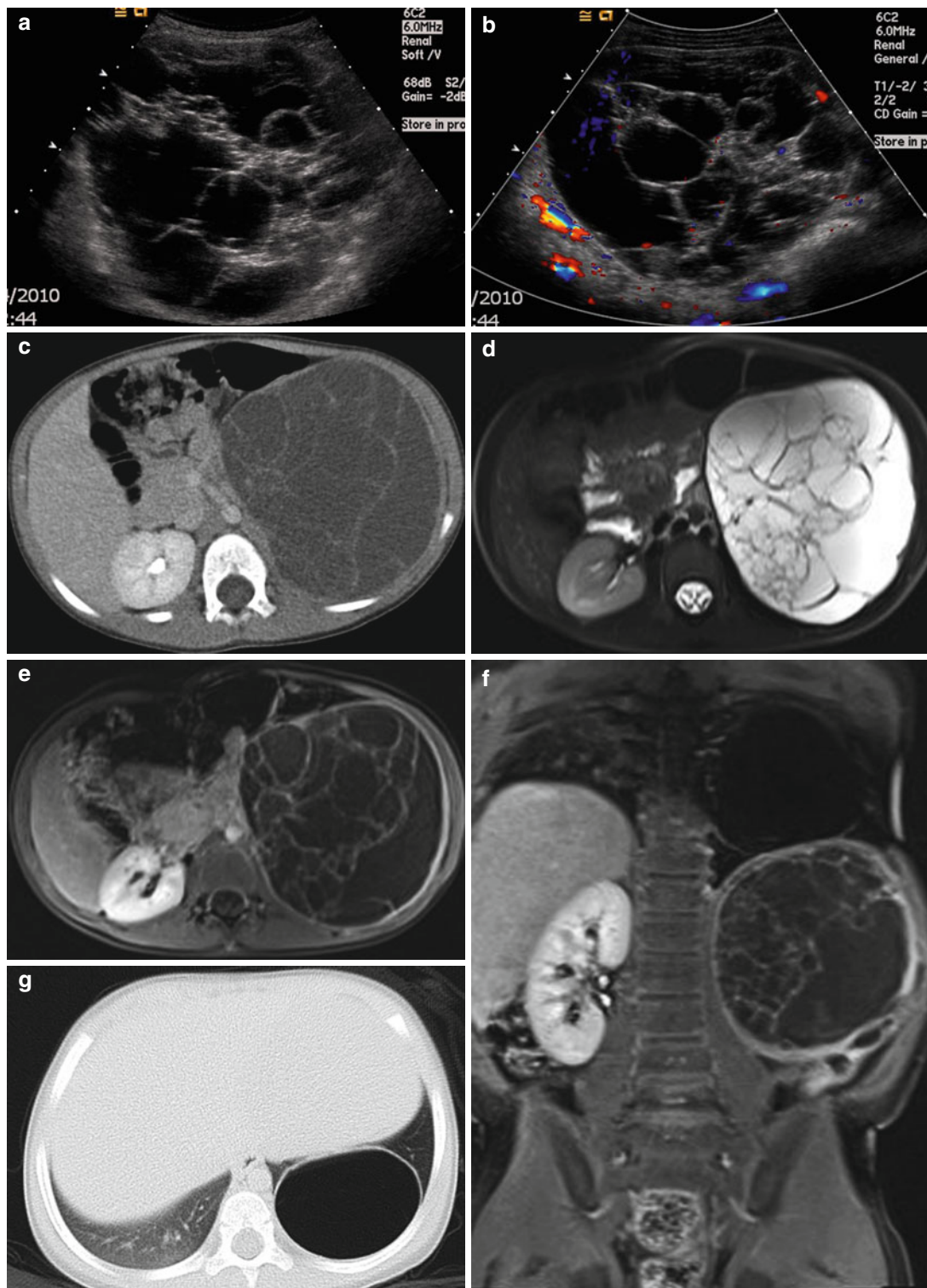


Fig. 24.20 Cystic partially differentiated nephroblastoma in a 3-year-old boy. (a) Longitudinal US of the left kidney shows a cystic mass with multiple septa. Septa appear relatively thick, presumably due to the presence of tiny cystic spaces, which are beyond the resolution ability of US. (b) Color Doppler US of the mass shows a well-circumscribed cystic mass. (c) Contrast-enhanced CT scan shows a well-defined cystic mass in the right kidney. Note numerous fine septations without solid components. T2-weighted axial (d) and contrast-enhanced T1-weighted axial (e) and

coronal (f) MR images show a multiseptated cystic mass in the left kidney. Enhancement of the septa is seen, and some of them appear to be relatively thick. A crescent of compressed renal parenchyma is seen inferior to the cystic tumor on T1-weighted coronal image. (g) Axial lung window CT image demonstrates a well-defined air-filled cystic lesion in the left lower lung, pathologically confirmed pulmonary pleuropulmonary blastoma

24.4.11 Renal Cell Carcinoma

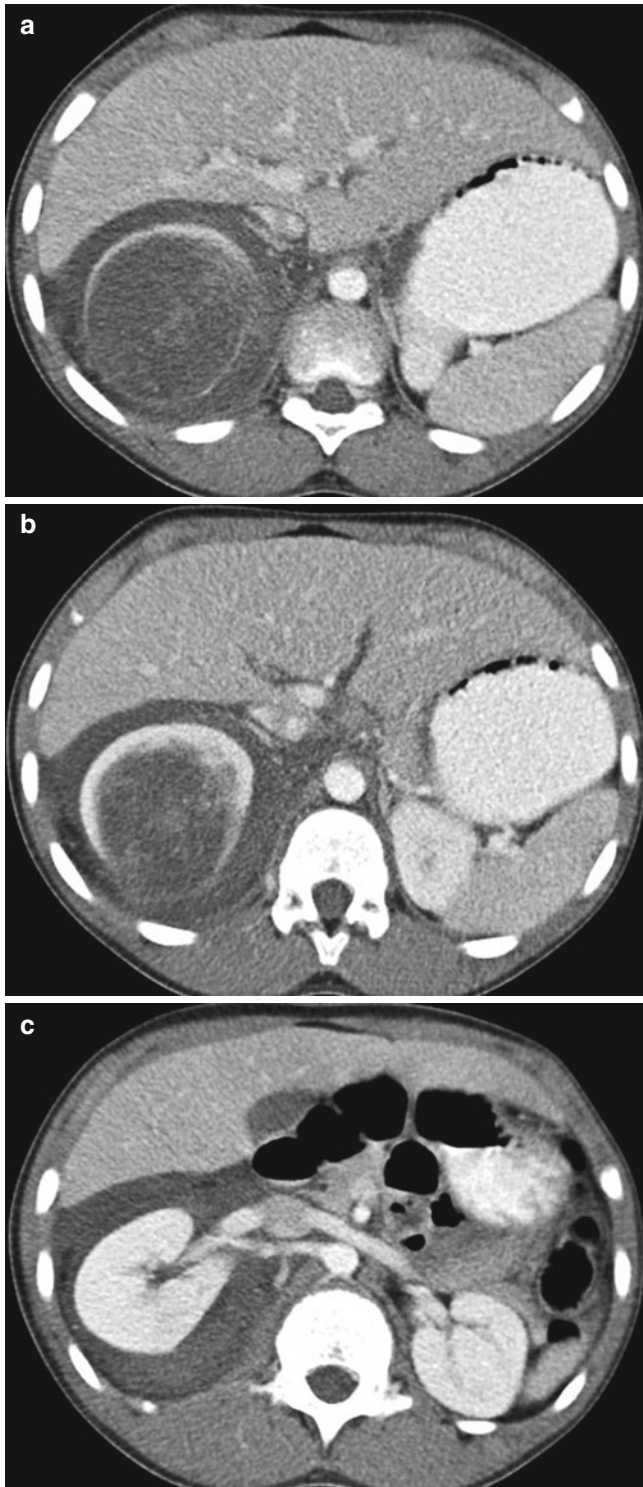


Fig. 24.21 Renal cell carcinoma in a 13-year-old boy. (a and b) Contrast-enhanced CT scans show a poorly enhancing mass arising from the right kidney. Note also the perirenal hematoma. (c) Contrast-enhanced CT scan shows the perirenal hematoma surrounding the right kidney

24.4.12 Renal Lymphoma and Leukemia

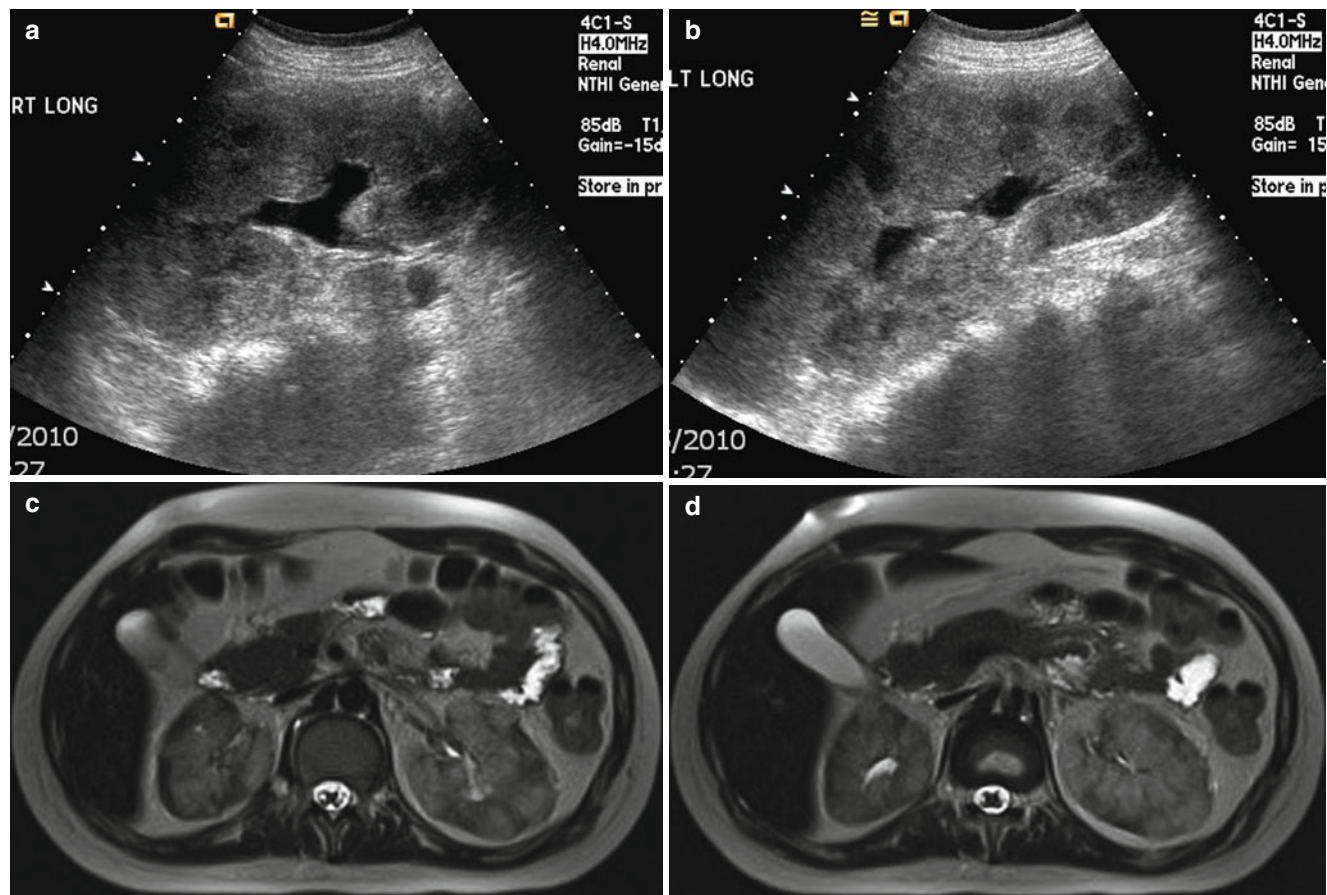


Fig. 24.22 Leukemia in a 13-year-old boy. (a and b) Longitudinal US of both kidneys shows diffusely increased echotexture of renal parenchyma and multiple hypoechoic nodules. (c and d) T2-weighted axial

MR images show diffusely increased signal intensity of the renal parenchyma and multiple cortical nodules in both kidneys

24.4.13 Neuroblastoma

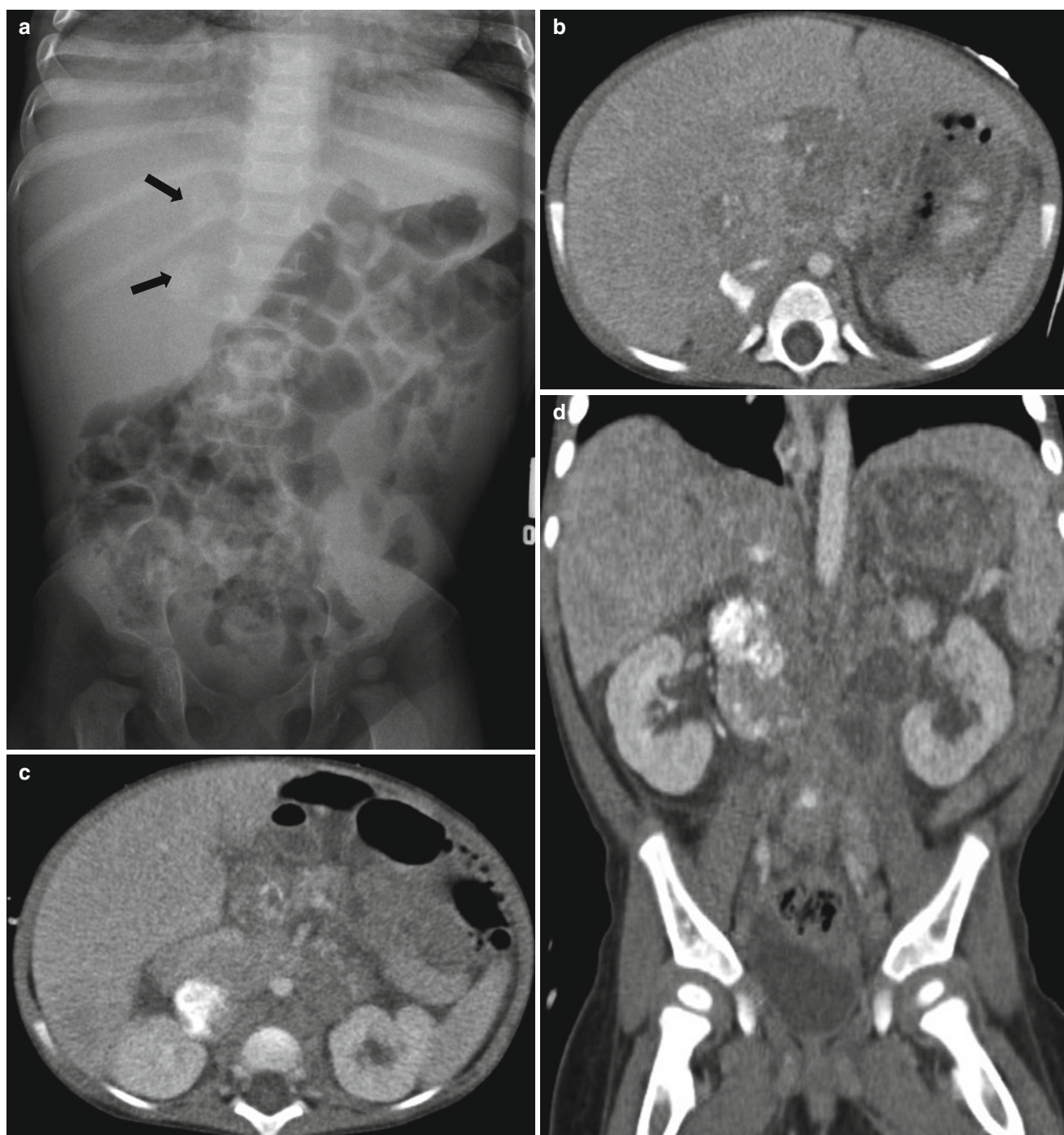


Fig. 24.23 Right adrenal neuroblastoma in a 12-month-old boy. (a) Plain radiograph of the abdomen shows subtle calcifications at right suprarenal and perirenal region (*arrows*). (b and c) Contrast-enhanced CT images in axial (b and c) and coronal (d) planes show a large

right-sided adrenal neuroblastoma that crosses to the left of the midline. The mass is hypodense with multiple calcifications that were apparent on the plain radiograph. A typical feature of neuroblastoma is the encasement of the renal arteries and aorta

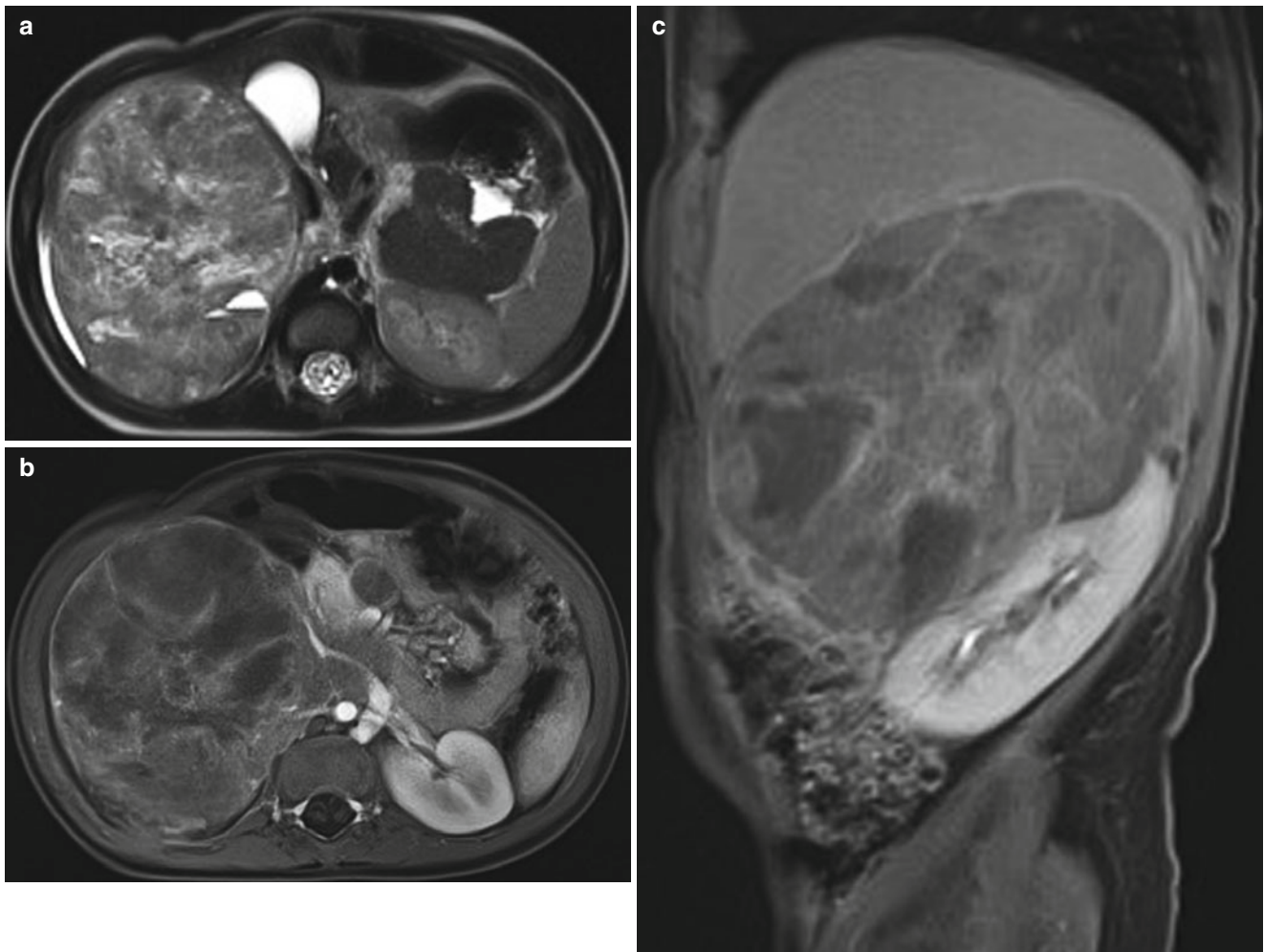


Fig. 24.24 Right adrenal neuroblastoma in a 2-year-old boy. T2-weighted axial (a) and contrast-enhanced T1-weighted axial (b) and sagittal (c) MR images show a large right-sided adrenal neuroblastoma that crosses to the left of the midline, anterior to the aorta. The mass

shows heterogeneous signal intensity on T2-weighted MR image. Sagittal image demonstrates the tumor's origin from the suprarenal region rather than the kidney

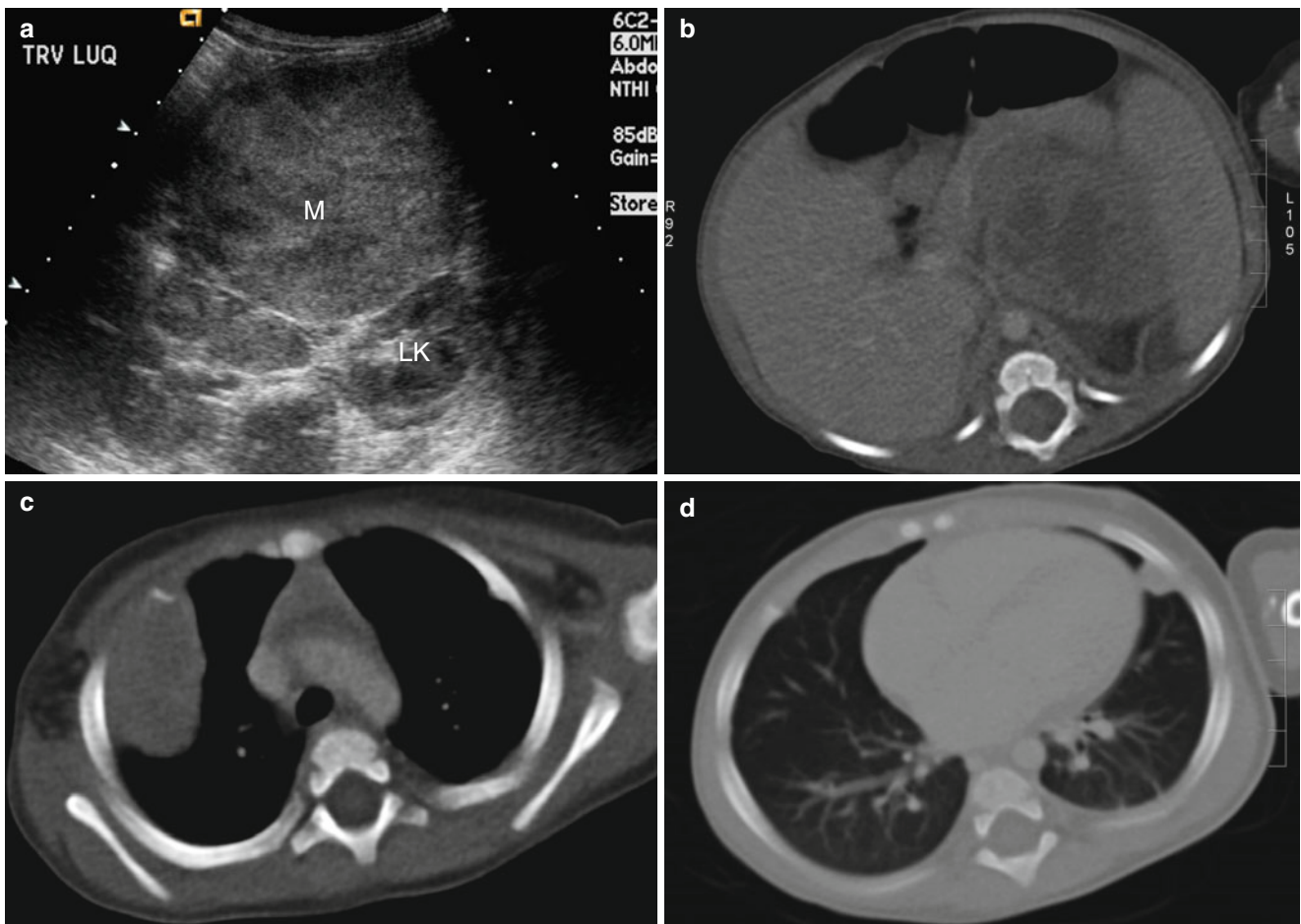


Fig. 24.25 Left adrenal neuroblastoma in a 10-month-old boy. (a) Transverse US scan of the left upper abdomen shows the presence of a large, heterogeneous, right adrenal mass (M) anterior to the left kidney (LK). (b) Axial contrast-enhanced CT image of the upper abdomen

shows the large left-sided heterogeneous neuroblastoma with the cystic component. (c) Axial contrast-enhanced CT image of the upper chest shows right anterior chest wall metastasis. (d) Axial lung window CT image shows a metastatic nodule in the left lingular segment

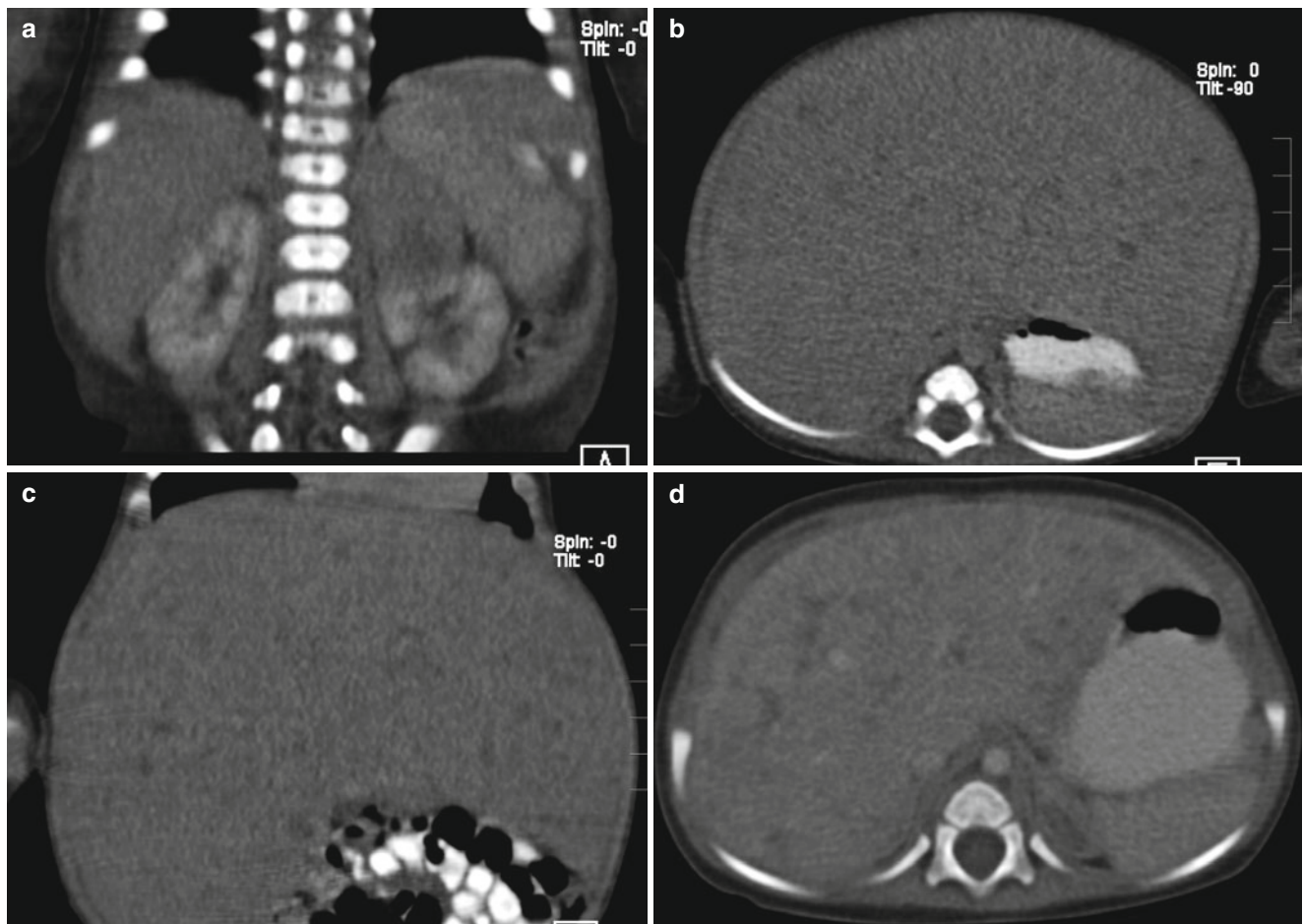


Fig. 24.26 Left adrenal neuroblastoma with multiple liver metastases in a 2-month-old boy. **(a)** Coronal contrast-enhanced CT image shows the left adrenal mass compressing the left kidney. **(b)** and **(c)** Axial and coronal CT images show a diffusely enlarged liver with multiple tiny

low-attenuation nodules. **(d)** Axial contrast-enhanced CT performed 4 months after the initial diagnosis and during chemotherapy shows interval decrease in size of liver and decrease in number of multiple metastatic nodules in the liver

References

- Balassy C, Navarro OM, Daneman A. Adrenal masses in children. *Radiol Clin North Am.* 2011;49:711–27.
- Chepuri NB, Strouse PJ, Yanik GA. CT of renal lymphoma in children. *AJR Am J Roentgenol.* 2003;180:429–31.
- EL-Merhi FM, Bae KT. Cystic renal disease. *Magn Reson Imaging Clin N Am.* 2004;12:449–67.
- Garel L. Renal cystic disease. *Ultrasound Clin.* 2010;5:15–59.
- Geller E, Kochan PS. Renal neoplasms of childhood. *Radiol Clin North Am.* 2011;49:689–709.
- Glass RBJ, Davidson AJ, Fernbach SK. Clear cell sarcoma of the kidney: CT, sonographic and pathologic correlation. *Radiology.* 1991;180:715–7.
- Han TI, Kim MJ, Yoon HK, et al. Rhabdoid tumour of the kidney: imaging findings. *Pediatr Radiol.* 2001;31:233–7.
- Hilmes MA, Dillman JR, Mody RJ, et al. Pediatric renal leukemia: spectrum of CT imaging findings. *Pediatr Radiol.* 2008;38:424–30.
- Kim WS. Pediatric renal masses. In: Kim SH, editor. *Radiology illustrated: uroradiology.* Philadelphia: Saunders; 2012. p. 339–44.
- Kim CK, Kim B. Renal cysts and cystic disease. In: Kim SH, editor. *Radiology illustrated: uroradiology.* Philadelphia: Saunders; 2012. p. 293–8.
- Lawande A. Ultrasonography in pediatric renal masses. *Ultrasound Clin.* 2010;5:433–41.
- Lonergan GJ, Rice RR, Suarez ES. Autosomal recessive polycystic kidney disease: radiologic-pathologic correlation. *Radiographics.* 2000;20:837–55.
- Lowe LH, Isuani BH, Heller RM, et al. Pediatric renal masses: Wilms' tumor and beyond. *Radiographics.* 2000;20:1585–603.
- Paltiel HJ. Sonography in pediatric renal tumors. *Ultrasound Clin.* 2007;2:89–104.
- Rohrschneider WK, Weirich A, Rieden K, et al. US, CT and MR imaging characteristics of nephroblastomatosis. *Pediatr Radiol.* 1998;28:435–43.
- Strife JL, Souza AS, Kirks DR, et al. Multicystic dysplastic kidney in children: US follow-up. *Radiology.* 1993;186:785–8.

Myung-Joon Kim

Contents

25.1	Introduction	794
25.2	Imaging for UTI	794
25.3	Spectrum of UTI	794
25.3.1	Acute Pyelonephritis	794
25.3.2	Chronic Pyelonephritis (Reflux Nephropathy)	795
25.3.3	Renal Abscess	795
25.3.4	Xanthogranulomatous Pyelonephritis (XGP)	795
25.3.5	Renal Candidiasis	795
25.3.6	Cystitis	795
25.4	Illustrations: Urinary Tract Infection	796
25.4.1	Acute Pyelonephritis	796
25.4.2	Chronic Pyelonephritis	798
25.4.3	Renal Abscess	799
25.4.4	Xanthogranulomatous Pyelonephritis	800
25.4.5	Renal Candidiasis	801
	References	802

M.-J. Kim, M.D.
 Department of Radiology, Severance Children's Hospital
 and Yonsei University College of Medicine,
 50 Yonsei-ro, Seodaemun-gu, Seoul 120-752, Korea
 e-mail: mjkim@yuhs.ac

25.1 Introduction

Urinary tract infection (UTI) is one of the most common bacterial diseases in children. Symptomatic UTI should be differentiated into upper tract infection (acute pyelonephritis, APN) representing high fever and generalized symptoms and lower tract infection (cystitis) showing voiding symptoms. If not properly treated APN, the lesions evolve the renal parenchymal necrosis, loss of nephron and renal scar. Long-term complications of UTI include reflux nephropathy, renal hypertension, and renal failure. Renal scars can be more frequently developed in following conditions: urinary tract obstruction, VUR with dilatation, bladder dysfunction, delayed treatment, and recurrent attack. The role of imaging in UTI is to detect congenital malformations, VUR, bladder dysfunction, and renal scar. There is a controversy in when and which imaging studies should be done in children with febrile UTI. However, targeted imaging approach in the evaluation of febrile UTI in children is required to avoid unnecessary invasive procedure without affecting outcomes of UTI.

25.2 Imaging for UTI

Ultrasound (US) is the primary imaging modality for the children with UTI, although the need for a use of US in case of suspected acute pyelonephritis is controversial (Paintsil 2013; Prasad and Cheng 2012; Brader et al. 2008; Rosenberg et al. 2001). The role of US is to detect underlying congenital malformation and supplementary findings suggesting acute pyelonephritis. In chronic form, US can detect renal scar (renal parenchymal thinning, calyceal dilatation, and cortical irregularities). Because of underestimating the number and extent of the renal scars, contrast-enhanced US (Darge 2010) or MRI is recommended for an accurate evaluation.

DMSA scan is the gold standard for the detection of renal involvement in UTI (O'Hara 2012; Avni et al. 2008; Prasad and Cheng 2012; Palma and Manzoni 2013; Brader et al. 2008). Focal or diffuse, decreased uptake of isotope is seen in acute pyelonephritis. Although sensitivity and specificity of DMSA scan is high, it cannot differentiate acute from chronic lesions (Avni et al. 2008).

Contrast-enhanced CT in acute pyelonephritis shows hypodense wedge-shaped area in the renal parenchyma (O'Hara 2012; Avni et al. 2008; Fernbach 2008). It is usually used in a case of renal abscess rather than in acute phase.

MRI is also an excellent tool to detect renal parenchymal infected lesion. Rather than a routine case, it can be used for the differentiation of renal abscess from tumorous condition

using diffusion-weighted image and for the evaluation of collecting system using MR urography (Renjen et al. 2012; Palma and Manzoni 2013).

Voiding cystourethrography (VCU) is an invasive and irradiating technique. So its use should be based on the age and sex of the patients even though there is a significant association between UTI and VUR. VCU should be done in an infant boy with UTI and reserved for the girls in whom US and DMSA scan show parenchymal lesions (Paintsil 2013; Prasad and Cheng 2012). Contrary to other imaging modalities, VCU shows the grade of VUR, intrarenal reflux, bladder function, and urethral anomalies. Contrast-enhanced sonocystography (Darge 2010) is an alternative in girls with UTI or follow-up case, but conventional VCU cannot be replaced by it until now.

25.3 Spectrum of UTI

25.3.1 Acute Pyelonephritis

Normal US cannot exclude acute pyelonephritis. But there are some ancillary findings suggesting acute pyelonephritis. Signs of acute pyelonephritis on US are diffuse or focal parenchymal swelling and echogenicity changes, poor corticomedullary differentiation, renal pelvic wall thickening, renal sinus hyperechogenicity, and perirenal fat hyperechogenicity (Fig. 25.1b) (O'Hara 2012; Avni et al. 2008; Fernbach 2008). The sensitivity of US in detecting acute pyelonephritis is about 50 % (Avni et al. 2008). Color or power Doppler US may increase the detection rate. But it is not easy to apply color or power Doppler US in crying children. After initiating antibiotics treatment, clinical symptoms resolve rapidly, but US findings may remain for several weeks (Avni et al. 2008). Decrease in renal volume takes about 4–5 weeks, and renal pelvic wall thickening and renal sinus hyperechogenicity remain for an even longer period. DMSA scan has high sensitivity and specificity in the detection of acute pyelonephritis (Fig. 25.1c) (Paintsil 2013; Prasad and Cheng 2012). But it has disadvantage of not differentiating acute from chronic lesions unless previous study exists.

Contrast-enhanced CT shows poorly enhancing, wedge-shaped regions extending the renal sinus to the periphery as well as diffuse or focal swelling and poor corticomedullary differentiation (Fig. 25.1d). Sometimes small abscess can be seen within the poorly enhancing renal parenchyma.

Gadolinium-enhanced MRI with T1-weighted or inversion recovery sequence shows infected renal parenchyma as low- or high-signal region, respectively.

25.3.2 Chronic Pyelonephritis (Reflux Nephropathy)

Long-term sequelae of acute pyelonephritis are permanent renal damages presenting with renal scar and chronic pyelonephritis. US shows small-sized kidney with cortical thinning, irregular renal margin, calyceal dilatation, and parenchymal echo changes (Fig. 25.2). However, US may underestimate the number and extent of renal scars. To improve the detection rate, contrast-enhanced US, CT, or MRI can be used (Darge 2010; Renjen et al. 2012).

Presently, DMSA scan is the most effective modality for the detection of renal scar and can give the information of differential renal function in each kidney.

25.3.3 Renal Abscess

In delayed or not properly treated acute pyelonephritis, renal abscess can develop (Avni et al. 2008). It can be localized in the kidney or extended into the perinephric space. On US, abscess appears as a mass with variable echogenicity depending on the necrosis (Fig. 25.3a) (O'Hara 2012; Fernbach 2008). CT and MR imaging well define the renal abscess and its extension (Fig. 25.3b).

25.3.4 Xanthogranulomatous Pyelonephritis (XGP)

XGP is an uncommon form of chronic pyelonephritis in children. Predisposing factors of XGP are urinary tract obstruction, UTI (*P. mirabilis*, *E. coli*), and altered metabolism. The most common clinical symptoms (Zugor et al. 2007) are fever and flank pain. Some children may have weight loss, malaise, and lower urinary tract symptoms. XGP can be presented with the diffuse or focal form. Preoperative diagnosis of XGP is not easy and it may be misdiagnosed as a malignant disease (Smith et al. 2010), especially in the focal form.

US demonstrates focal or diffuse enlargement of the kidney with parenchymal destruction and dilated calyces filled with echogenic debris (Fig. 25.4a, b). CT shows focal or diffuse renal enlargement, dilated collecting systems, parenchymal destructions representing low-attenuating foci with peripheral or heterogeneous enhancement, and extrarenal extension of inflammation (Fig. 25.3c). MRI is helpful to detect fat components depending on the amount of xanthoma cells and to define diffusion restriction of parenchymal and calyceal cavities. To make the diagnosis, percutaneous renal biopsy is often required. On histopathologic examination, XGP is characterized by renal parenchymal destruction, necrosis, and lipid-laden macrophages with inflammatory components. However, when a focal renal mass is associated with the history of recurrent UTI, fever, flank pain, and stone, XGP should be included in the differential diagnosis.

25.3.5 Renal Candidiasis

Renal candidiasis usually develops in immunocompromised patients or neonates requiring intensive care. US (O'Hara 2012; Fernbach 2008) can reveal diffusely increased parenchymal echogenicity resulting from fungal and inflammatory cell infiltration of the tubules and echogenic sludge or fungus balls (Fig. 25.5).

25.3.6 Cystitis

It refers to lower tract infection. On US the bladder wall is thickened evenly or irregularly. On color or power Doppler US, an increased vascularity of the bladder wall can be seen. However, bladder wall thickening (Avni et al. 2008) is not specific for cystitis; it can be noted in many other conditions (such as neurogenic bladder, bladder outlet obstruction, posterior urethral valve, drug). Echogenic debris can be seen within the urinary bladder, but it is also not specific for UTI.

25.4 Illustrations: Urinary Tract Infection

25.4.1 Acute Pyelonephritis

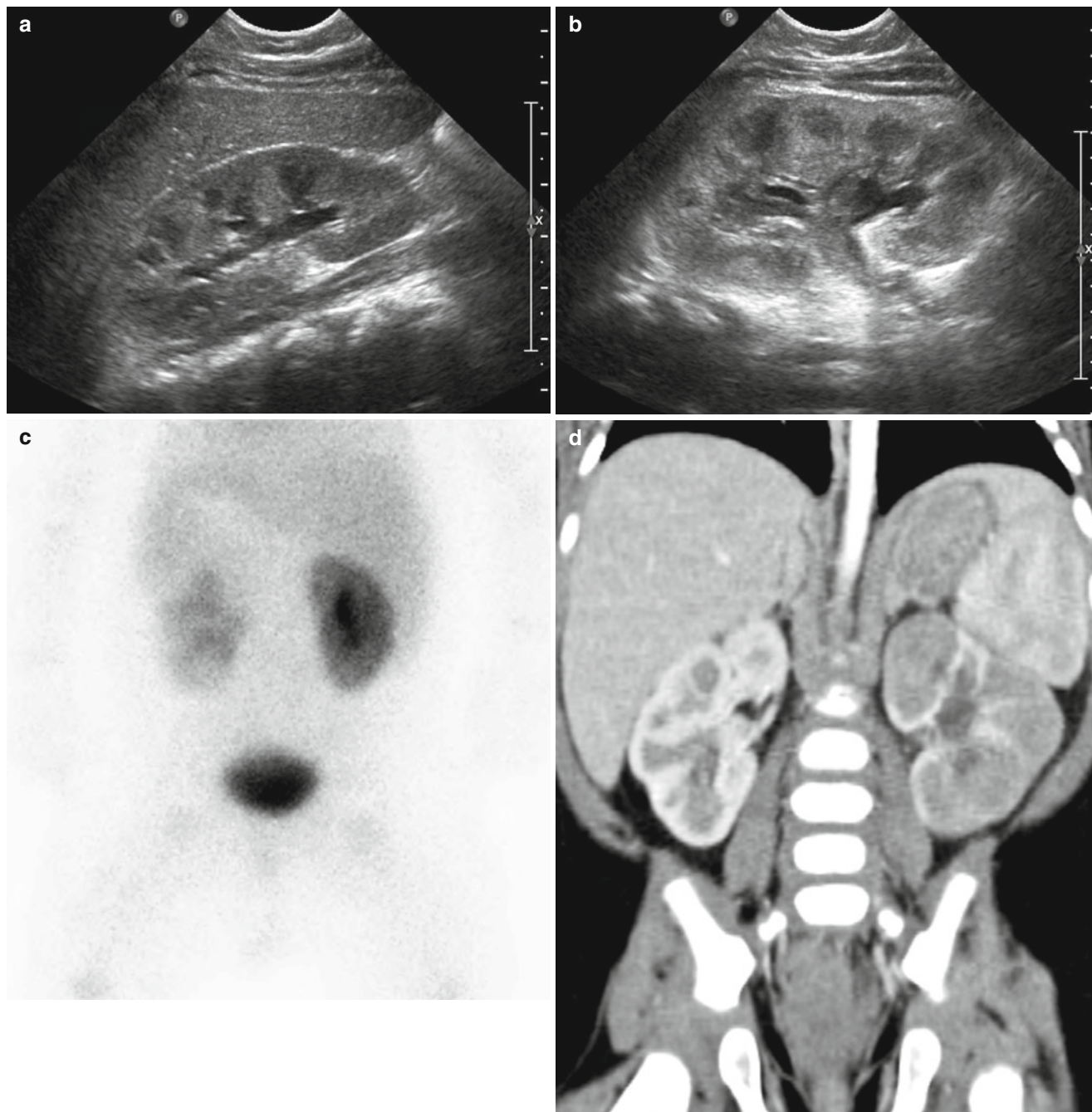


Fig. 25.1 *Acute pyelonephritis.* Sagittal US of the right kidney (**a**) shows only mild pelvic dilatation. Sagittal US of the left kidney (**b**) shows diffuse swelling with increased cortical echoes and pelvic wall thickening. DMSA scan (**c**) demonstrates multiple photopenic areas in

the left kidney. Contrast-enhanced CT (**d**) shows an enlarged left kidney with multiple, poorly enhanced regions. Voiding cystourethrography (**e**) demonstrates left-sided grade 5 VUR

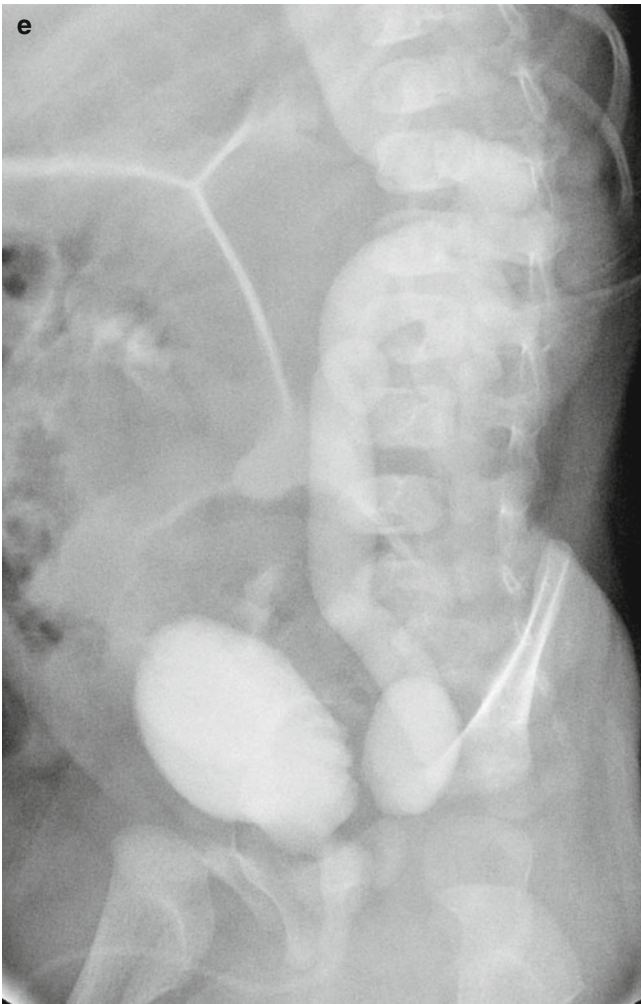


Fig. 25.1 (continued)

25.4.2 Chronic Pyelonephritis

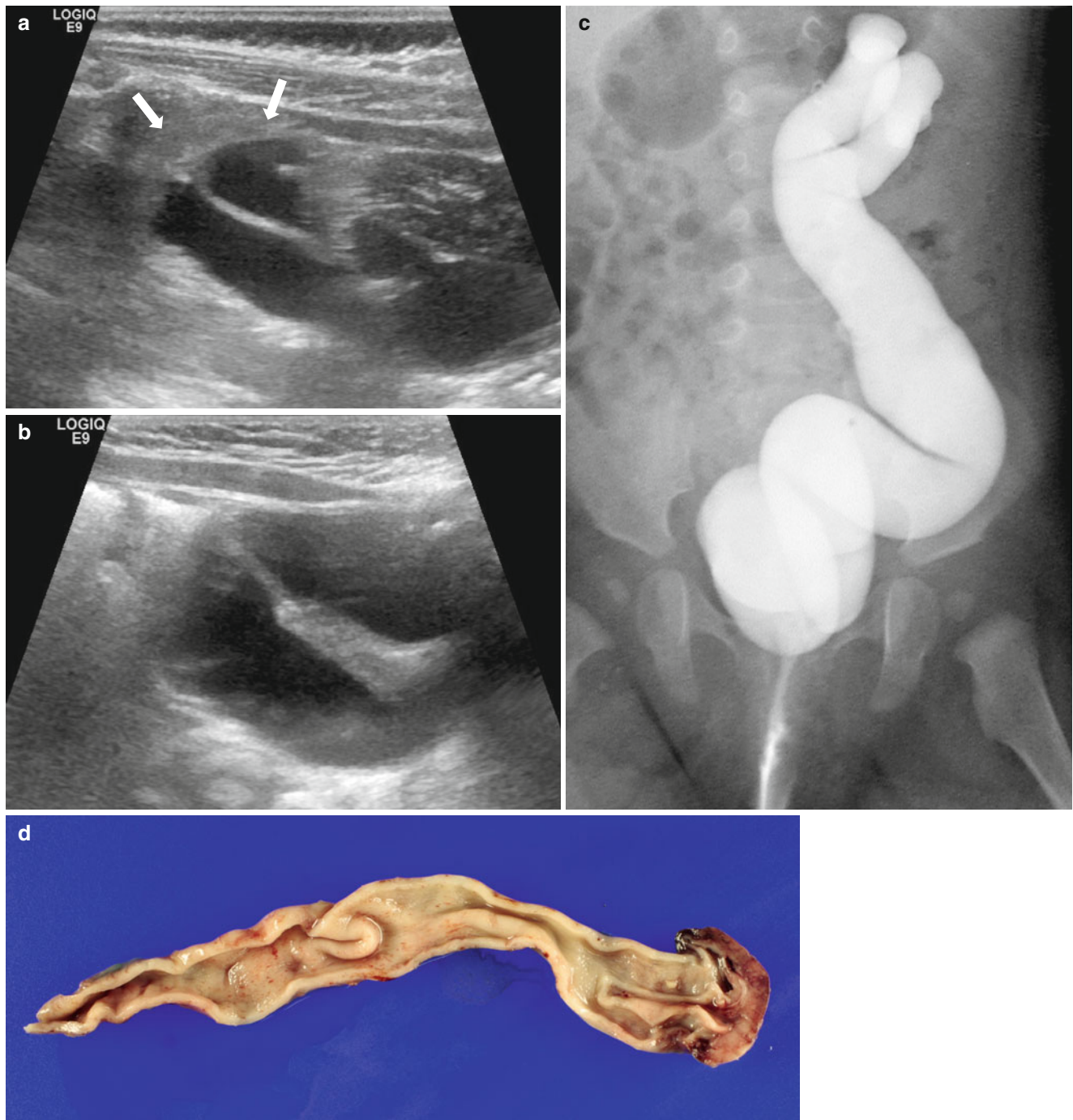


Fig. 25.2 Chronic pyelonephritis (reflux nephropathy). Sagittal US of the left kidney shows small-sized kidney (arrows) with diffusely increased parenchymal echoes and poor corticomedullary differentiation and hydronephrosis (a) and ureter dilatation (b). Voiding

cystourethrography (c) shows left-sided grade 5 VUR with megaureter. Gross specimen (d) shows a shrunken kidney without corticomedullary distinction, dilated ureter, and bifid renal pelvis

25.4.3 Renal Abscess

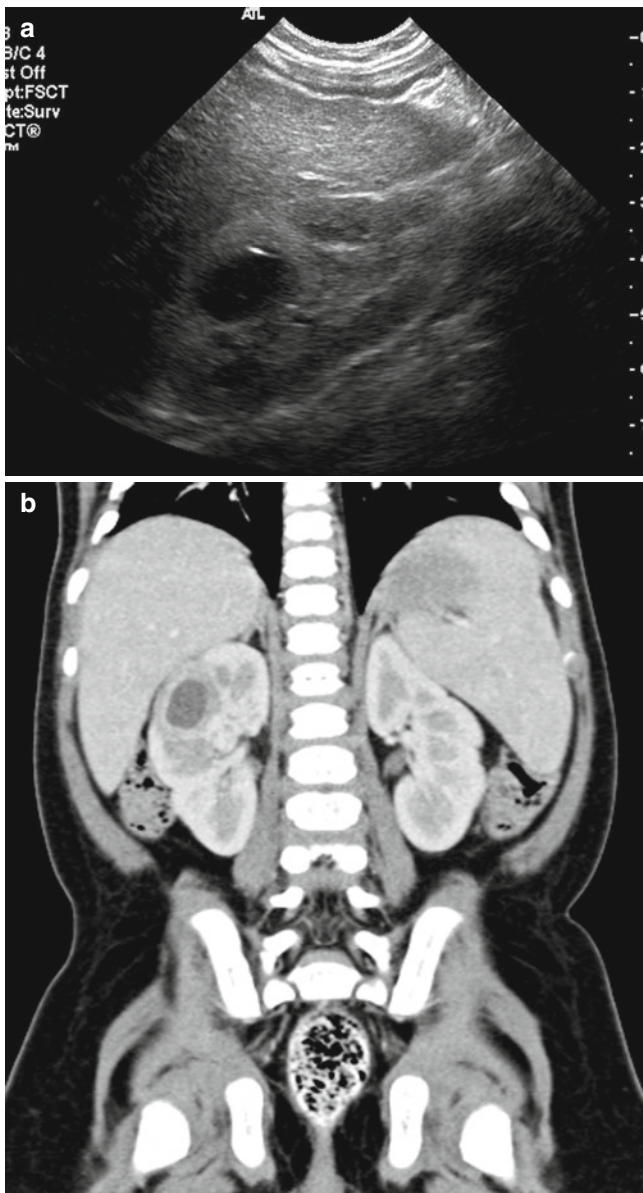


Fig. 25.3 *Renal abscess.* Sagittal US of the right kidney (**a**) shows round hypoechoic abscess surrounded by hyperechoic, inflammatory parenchyma. Corresponding contrast-enhanced CT (**b**) demonstrates the abscess formation with wall enhancement

25.4.4 Xanthogranulomatous Pyelonephritis

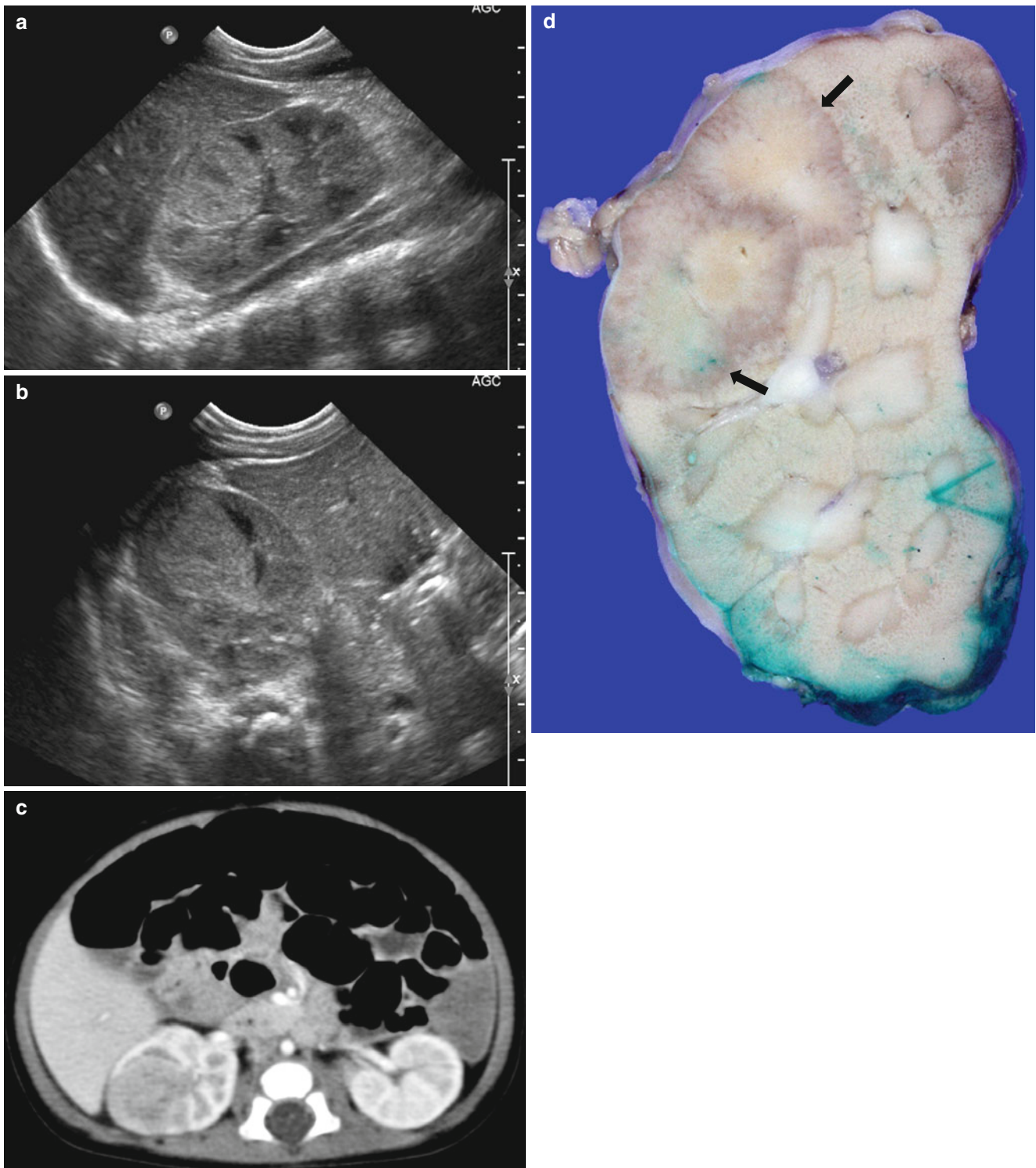


Fig. 25.4 *Xanthogranulomatous pyelonephritis.* Sagittal (a) and transverse (b) US of the right kidney show round, hyperechoic mass-like lesion containing hypoechoic portions. Contrast-enhanced CT (c) shows poorly enhancing mass-like lesion in the right kidney. Gross

specimen (d) shows a relatively well-demarcated, mass-like lesion (arrows) with scattered yellowish tint in the upper and mid portion of the kidney

25.4.5 Renal Candidiasis

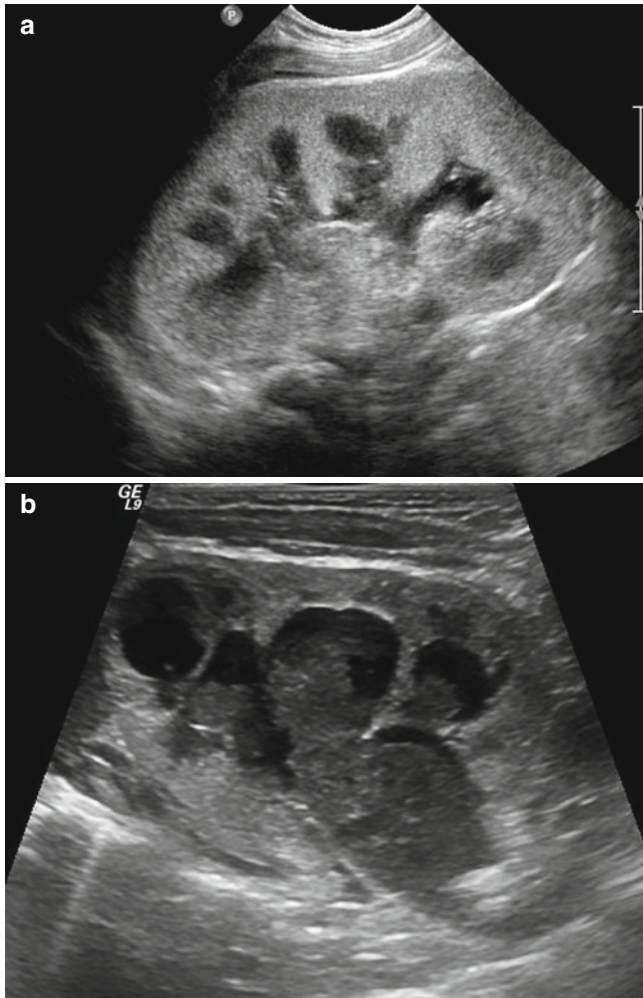


Fig. 25.5 *Renal candidiasis*. Diffuse hyperechoic pattern (**a**); US showing highly echogenic cortex of the right kidney. Sludge pattern (**b**); US of the right kidney in another patient shows multiple, echogenic sludge balls with hydronephrosis

References

- Avni FE, Hall M, Cassart M, et al. Urinary tract infection. In: Fotter R, editor. *Pediatric uroradiology*. 2nd ed. Berlin/Heidelberg: Springer-Verlag; 2008.
- Brader P, Riccabona M, Schwartz T, et al. Value of comprehensive renal ultrasound in children with acute urinary tract infection for assessment of renal involvement: comparison with DMSA scintigraphy and final diagnosis. *Eur Radiol*. 2008;18:2981–9.
- Darge K. Voiding urosonography with US contrast agent for the diagnosis of vesicoureteric reflux in children: an update. *Pediatr Radiol*. 2010;40:956–62.
- Fernbach SK. Infections. In: Slovis TL, editor. *Caffey's pediatric diagnostic imaging*. 11th ed. Philadelphia: Mosby Elsevier; 2008.
- O'Hara SM. Approach to the pediatric genitourinary tract. In: Donnelly LF, editor. *Diagnostic imaging pediatrics*. 2nd ed. Salt Lake City: Amirsys; 2012.
- Paintsil E. Updates on recent guidelines for the management of urinary tract infections in children: the shifting paradigm. *Curr Opin Pediatr*. 2013;25:88–94.
- Palma DD, Manzoni G. Different imaging strategies in febrile urinary tract infection in childhood. What, when, why? *Pediatr Radiol*. 2013;43:436–43.
- Prasad MM, Cheng EY. Radiographic evaluation of children with febrile urinary tract infection: bottom-up, top-down, or none of the above? *Adv Urol*. 2012. doi:[10.1155/2012/716739](https://doi.org/10.1155/2012/716739).
- Renjen P, Bellah R, Hellinger JC, et al. Advances in urologic imaging in children. *Radiol Clin North Am*. 2012;50:207–18.
- Rosenberg HK, Ilaslan H, Finkelstein MS. Work-up of urinary tract infection in infants and children. *Ultrasound Q*. 2001;17:87–102.
- Smith EA, Styn N, Wan J, et al. Xanthogranulomatous pyelonephritis: an uncommon pediatric renal mass. *Pediatr Radiol*. 2010;40:1421–5.
- Zugor V, Schott GE, Labanaris AP. Xanthogranulomatous pyelonephritis in childhood: a critical analysis of 10 cases and of the literature. *Urology*. 2007;70:157–60.

Su-Mi Shin

Contents

26.1	Introduction	804
26.2	Development of the Urinary Bladder and Urethra	804
26.3	Spectrum of Bladder and Urethra Disease	804
26.3.1	Urachal Anomalies	804
26.3.2	Congenital Anomalies of the Bladder	804
26.3.3	Cystitis	805
26.3.4	Neoplasms of the Bladder	805
26.3.5	Neurogenic Bladder	806
26.3.6	Bladder Stone	806
26.3.7	Anomalies of the Urethra	806
26.3.8	Prostatic Utricle	807
26.4	Illustrations: Bladder and Urethra Disease	808
26.4.1	Urachal Anomalies	808
26.4.2	Bladder Exstrophy	811
26.4.3	Prune-Belly Syndrome	812
26.4.4	Bladder Diverticula	813
26.4.5	Megacystis	815
26.4.6	Cystis	816
26.4.7	Neoplasms of the Bladder	819
26.4.8	Neurogenic Bladder	822
26.4.9	Bladder Stone	823
26.4.10	Posterior Urethral Valves	824
26.4.11	Urethral Polyps	826
26.4.12	Urethral Duplication	827
26.4.13	Urethral Strictures	828
26.4.14	Urethral Fistula	829
26.4.15	Megalourethra, Anterior Urethral Diverticula, and Anterior Urethral Valve	830
26.4.16	Prostatic Utricle	833
	References	834

S.-M. Shin, M. D.
Department of Radiology, SMG-SNU Boramae Medical Center,
20, Boramae-Ro 5-Gil, Dongjak-Gu, Seoul 156-707, Korea
e-mail: susemi513@hanmail.net, susemi513@gmail.com

26.1 Introduction

Abnormalities of the lower urinary tract may be of congenital, inflammatory, neoplastic, and neurogenic origin. In infants or children with suspected underlying urologic structural abnormalities, screening ultrasonography (US) is the choice of initial diagnostic study. Voiding cystourethrography (VCUG) is performed to evaluate the presence of vesicoureteral reflux (VUR) and to assess the anatomy of bladder and urethra. Voiding dysfunction and enuresis are also common indications. Computed tomography (CT) and magnetic resonance (MR) imaging are unsuitable for general screening but provide anatomic detail and added diagnostic specificity (Berrocal et al. 2002).

26.2 Development of the Urinary Bladder and Urethra

The urinary bladder and urethra are derived from the primitive urogenital sinus (a ventral part of the cloaca) and adjacent splanchnic mesenchyme. The cloaca, the terminal portion of the hindgut, is divided into the dorsal primitive rectum and ventral primitive urogenital sinus by the growth of the urorectal septum. The urogenital sinus gives rise to the urinary bladder, which is cranially continuous with allantois (later urachus) and caudally with the urethra. During division of the cloaca, the caudal portions of the mesonephric ducts are incorporated into the wall of the urinary bladder, thus forming the trigone of the bladder. The ureters and mesonephric ducts with time obtain the separate entrances into the urinary bladder.

In the male, the pelvic part of the urogenital sinus gives rise to the prostatic and membranous part of the urethra. The penile urethra is partly formed by the closure of urethral folds, while its most distal portion is formed by an inward penetration of ectodermal cells on the tip of the glans (Saraga-Babic and Sapunar 1994).

26.3 Spectrum of Bladder and Urethra Disease

26.3.1 Urachal Anomalies

The urachus is a normal embryonic structure that connects between the bladder dome and the umbilicus. It is normally obliterated during the fourth or fifth month of gestation, remaining as a fibrous band. Incomplete obliteration of the urachal lumen results in four major types of abnormalities: patent urachus, urachal sinus, urachal diverticulum, and urachal cyst. The *patent urachus* is an open channel from the bladder to the umbilicus through which urine can leak. The

urachal sinus is a persistence of the urachus at its umbilical end. The *urachal diverticulum* is persistence of the urachus at its bladder end. The *urachal cyst* is persistence of the intermediary segment with a fibrous attachment to the bladder wall and umbilicus (Siegel 2002).

Leakage of urine at the umbilicus suggests the presence of a patent urachus. The diagnosis is confirmed by catheterization of the bladder through the umbilicus (Fig. 26.1) or by VCUG in the lateral projection. Infected urachal cyst demonstrates mixed echogenicity at US and thick-walled cystic or mixed attenuation at CT in the midline lower abdominal wall (Figs. 26.2 and 26.3) (Bates 2008; Yu et al. 2001).

26.3.2 Congenital Anomalies of the Bladder

26.3.2.1 Bladder Exstrophy

Bladder exstrophy is the result of incomplete closure of the midline lower abdominal wall in utero. Failure of migration of mesenchymal cells between ectoderm and cloaca early in fetal life leads to bladder exstrophy. It is often referred to as the *exstrophy-epispadias complex*. In classic exstrophy, the bladder is exposed on the anterior abdominal wall. There is associated epispadias, wide separation of the symphysis pubis, and outward rotation of the acetabula and lower limbs. The hips may be dislocated (Fig. 26.4) (Mourtzinis and Borer 2004).

26.3.2.2 Prune-Belly Syndrome

Prune-belly syndrome (Eagle-Barrett syndrome) always occurs in boys and is characterized by the triad of absence or deficiency of the abdominal wall musculature, urinary tract dilatation, and cryptorchidism. The pathogenesis of prune-belly syndrome is controversial, but the two main theories currently suggested are high-grade urethral obstruction early in utero and a primary mesodermal defect. The abdominal wall looks wrinkled with bulging of the flanks, which is a characteristic appearance resulting from muscular deficiency (Bloom and Slovis 2008; Siegel 2002; Volmar et al. 2003).

There appear to be two groups of patients. The first group has an obstructing lesion of the urethra (urethral atresia or posterior urethral valves) that leads to death soon after birth. The second group presents with a functional abnormality of bladder emptying but no urethral obstruction and usually survives the neonatal period, developing chronic urinary tract disease. At US, dilated and tortuous ureters with bilateral hydronephrosis are common findings, and kidneys usually show varying degrees of dysplasia and, sometimes, cystic changes. VCUG is used to demonstrate a distended bladder with an irregular contour and bilateral VUR (Fig. 26.5) (Berrocal et al. 2002).

26.3.2.3 Bladder Duplication

Bladder duplication is a rare anomaly that consists of two distinct bladder chambers, each drained by a separate urethra. The septa may divide the bladder in the sagittal or transverse planes (Richman and Taylor 1982; Siegel 2002).

26.3.2.4 Bladder Diverticula

Bladder diverticulum is an outpouching of the bladder mucosa through fibers of the detrusor muscle. Bladder diverticula may be primary (congenital) or secondary (acquired). Paraureteral or Hutch diverticulum, which is a common type of primary diverticulum, is located laterally and cephalad to the ureteral orifice and is associated with significant VUR. Primary diverticula occur in association with cutis laxa, Menkes syndrome, Williams syndrome, and Ehlers–Danlos syndrome. Secondary bladder diverticula are the result of chronically increased intravesical pressure with hypertrophy of the bladder musculature and may be seen in patients with posterior urethral valve (PUV) or neurogenic bladders. Diverticula are easy to diagnose at VCUG during voiding (Figs. 26.6 and 26.7) (Bates 2008; Evangelidis et al. 2005; Nasrallah and McMahon 1999). In infants and young children, the incompletely full bladder may transiently herniate through the internal inguinal ring producing so-called bladder ears (Fig. 26.6). This is a normal finding and disappears with increased bladder distension and should not be confused with a diverticulum (Bates 2008).

26.3.2.5 Megacystis

Megacystis is a descriptive term for a large, smooth-walled bladder. *Congenital megacystis* is characterized by a huge bladder in the absence of obstruction, reflux, or other pathology (Fig. 26.8). *Megacystis-megaureter syndrome* refers to a large bladder, dilated ureteral orifices, and dilated refluxing ureters. During micturition, large volumes of urine flow back into the ureters from the bladder. This urine flows back into the bladder between cycles of micturition, eventually producing an atonic, thin-walled, dilated bladder (Nasrallah and McMahon 1999; Siegel 2002). *Megacystis-microcolon-intestinal hypoperistalsis (MMIH) syndrome* is an uncommon functional obstruction of the bladder and intestine. It is an autosomal recessive disorder and occurs almost exclusively in girls. This syndrome is characterized by a dilated bladder, hydronephrosis, hydronephrosis, microcolon, and dilated small bowel. The entire gastrointestinal tract is hypoperistaltic (Siegel 2002).

26.3.3 Cystitis

Cystitis is usually bacterial or viral in origin, but other causes include fungal infection, drug therapy (particularly cyclophosphamide), and indwelling catheters. Patients present

with dysuria, frequency, and hematuria. Hemorrhagic cystitis is one of the most common causes of gross hematuria in children. It is a self-limited disease that generally subsides in a few days to 2 or 3 weeks without sequelae. Cyclophosphamide cystitis is a sterile inflammatory reaction of the bladder mucosa occurring primarily in oncologic patients undergoing preparative therapy for bone marrow transplantation. The common sonographic findings of cystitis are diffuse bladder wall thickening (>3 mm), echogenic debris, and a fluid–fluid level in the bladder lumen. Occasionally, cystitis produces focal wall thickening, which is difficult to differentiate from tumor based on imaging findings; therefore, cystoscopy and biopsy may be necessary for diagnosis (Figs. 26.9 and 26.10) (Allen and Alexander 2005; McCarville et al. 2000; Siegel 2002).

Cystitis cystica or cystitis glandularis are benign proliferative lesions of the mucosa that are usually localized to the trigone and ureteral orifices. The etiology is unknown, but may be the sequelae of recurrent or chronic infection. US shows a localized, broad-based, irregular, isoechoic or hyperechoic soft tissue mass, often mimicking a bladder neoplasm (Fig. 26.11) (Siegel 2002).

26.3.4 Neoplasms of the Bladder

26.3.4.1 Malignant Neoplasm of Bladder

Bladder tumors in children are rare and more often malignant than benign. Embryonal rhabdomyosarcoma is the most common neoplasm of the lower urinary tract in childhood. Bladder rhabdomyosarcoma usually manifests in the first 2 or 3 years of life and typically involves the submucosal region of the trigone; less often, it originates in the dome of the bladder. The tumor is locally invasive and frequently extends toward the bladder outlet, causing urethral obstruction (Fig. 26.12). Affected children usually present with urinary retention or painless gross hematuria.

On intravenous urography (IVU) and VCUG, bladder rhabdomyosarcoma shows a large and often lobulated filling defect in the posteroinferior aspect of the bladder. Sonographically, it usually appears as a polypoid mass projecting into the anechoic bladder lumen and less commonly as irregular bladder wall thickening (Fig. 26.13). Diffuse bladder wall thickening by rhabdomyosarcoma can be confused with cystitis, although the thickening is usually uniform in cystitis, whereas it is irregular in tumor infiltration. Whereas the initial diagnosis is often made with US, CT and MRI are required for evaluating extent of disease and presence of metastases.

Transitional cell carcinoma and leiomyosarcomas are rare in children and may also manifest as an intraluminal polypoid mass or as wall thickening (Argons et al. 1997; Bates 2008; Siegel 2002).

26.3.4.2 Benign Neoplasm of the Bladder

Benign bladder tumors include neurofibroma, hemangioma, pheochromocytoma, transitional cell papilloma, nephrogenic adenoma, and leiomyoma. Neurofibromas of the bladder may occur as part of systemic neurofibromatosis or as an isolated lesion. Neurofibromatosis can produce marked focal thickening of the bladder wall or diffuse thickening with a lobulated, irregular wall (Fig. 26.14). Other benign tumors present as focal wall thickening or as an echogenic soft tissue mass projecting into the bladder lumen (Bates 2008; Siegel 2002).

26.3.5 Neurogenic Bladder

Normally, all parts of the lower urinary tract (i.e., the detrusor, internal, and external sphincters) function together to allow storage and evacuation of urine. A neurogenic bladder results when these components fail to act as a coordinated unit (Siegel 2002). The neurogenic bladder in childhood is most often congenital due to spinal dysraphism or sacral agenesis. Acquired causes are cerebral palsy and traumatic injury to the spine (Bauer 2008). The lower motor neuron lesions result in smooth, large-capacity, thin-walled bladders. Lesions above the sacral reflex produce a trabeculated, small, thick-walled bladder (Figs. 26.15, 26.16, and 26.17) (Siegel 2002).

26.3.6 Bladder Stone

Bladder stones usually relate to intravesical foreign body, infection with urea-splitting organisms (usually *Proteus* species), bladder augmentation, exstrophy of the bladder, hypercalciuria, and stasis of urine (Lebowitz and Vargas 1987). Bladder stones are usually round homogenous radiopaque on plain radiographs and sometimes reach a very large size. On sonography, they are echogenic foci with sharp acoustic shadowing and shift to the dependent portion of the bladder with changes in patient position (Fig. 26.18).

26.3.7 Anomalies of the Urethra

26.3.7.1 Posterior Urethral Valves

Posterior urethral valves (PUV) are the most common cause of urethral obstruction in boys. Pathologically, urethral valves are obstructing folds of the urethral tissue. Three types of valves have been described, although the existence of type II and type III valves is controversial. Type I valves, the most common, are folds that attach below the verumontanum, usually at the level of the membranous urethra. Type II valves are mucosal folds that arise above the verumonta-

num. Type III valve is a diaphragm with a central aperture that arises distal to the verumontanum (Casale 1999).

The diagnosis is typically made on VCUG and demonstrates an abrupt transition from a dilated posterior urethra to a small, bulbous urethra at the level of the valves (Fig. 26.19). Bladder wall trabeculation or muscular hypertrophy is commonly seen. PUV is associated with vesicoureteral reflux, bilateral hydronephrosis, renal dysplasia, urinary ascites, and subcapsular or perirenal urinomas in newborns (Figs. 26.20 and 26.21) (Cremin 1986; Macpherson et al. 1986).

26.3.7.2 Urethral Polyps

Congenital urethral polyps are a rare cause of urethral obstruction. Histologically, these polyps are fibroconnective tissue core covered by transitional cell epithelium. They arise near the verumontanum and often attach to it by a stalk. Pedunculated polyps can prolapse into the bladder, obstructing the bladder neck or the urethra. Symptoms are nonspecific and include intermittent urethral obstruction, urinary retention, enuresis, hematuria, and infection (Caro et al. 1986; Siegel 2002).

VCUG remains the imaging gold standard in males. Before voiding, the tip of the polyp is frequently located at the level of bladder neck, causing a small rounded filling defect. In the voiding phase, the polyp moves downward into the distal posterior urethra. At the end of voiding, the polyp is displaced backward to the level of bladder neck by the contraction of the external urethral sphincter. US may demonstrate a pedunculated mass with medium-level echogenicity at the bladder base and indirect signs of bladder outlet obstruction such as hydronephrosis and large bladder with or without bladder wall hypertrophy (Fig. 26.22) (Bates 2008).

26.3.7.3 Urethral Duplication

Urethral duplication is a rare congenital anomaly. Considering the many different anatomic variants, there is probably no common embryologic pathway to explain all the various form of duplication. Sagittal plane duplication is most common with ventral and dorsal urethra. Usually, the ventral urethra is the most functional and contains the urethral sphincter and verumontanum. According to the location of the accessory urethral opening on the dorsal or ventral aspect of the penis, urethral duplications are divided into epispadic (the most common type) and hypospadic types, respectively. VCUG is adequate if both urethral channels can be clearly identified (Fig. 26.23). Retrograde urethrography (RGU) may be necessary for hypoplastic channels not visualized on VCUG. Cystoscopy may be performed to confirm the radiographic findings and to ensure which urethra contains the sphincteric mechanism and normal verumontanum (Bates 2008; Salle et al. 2000).

26.3.7.4 Urethral Strictures

Urethral strictures are relatively uncommon and usually secondary to iatrogenic or external trauma (iatrogenic instrumentation, catheterization, or straddle injury) (Figs. 26.24 and 26.25). Strictures often occur at the penoscrotal junction, an area that is vulnerable to internal trauma. The diagnosis is readily established by VCUG when the bladder can be catheterized. Compression of the distal penis during voiding or RGU results in distension of the normal urethra and a better delineation of the true extent of the stricture (Bates 2008; Gallentine and Morey 2002).

26.3.7.5 Urethral Fistula

Boys with high imperforate anus frequently have a connection from the rectum to the lower urinary tract, usually at the level of the prostatic urethra (Fig. 26.26), although more distal and proximal communications occasionally occur. The fistula is well demonstrated with VCUG (Berrocal et al. 2002).

26.3.7.6 Megalourethra, Anterior Urethral Diverticula, and Anterior Urethral Valve

Megalourethra is a rare congenital disorder characterized by abnormal dilatation of the penile urethra without any evident obstruction. The *scaphoid* type is due to poor development of the corpus spongiosum, whereas in the more severe *fusiform* type, the corpora cavernosa are also affected. In the milder form, which involves only the urethra and corpus spongiosum, the urethra dilates in a scaphoid (boat-shaped) fashion during voiding because the dorsal aspect is supported by the intact corpora cavernosa. Fusiform megalourethra is characterized by a long, dilated, floppy urethra that results from a congenital deficiency of the corpora cavernosa. The condition is usually associated with other congenital anomalies such as lower urinary tract duplication, prune-belly syndrome,

and urethral fistula. VCUG allows visualization of the dilated urethra (Berrocal et al. 2002; Wakhlu et al. 1996).

Anterior urethral diverticulum is a saccular outpouching of the ventral aspect of the anterior urethra into the corpus spongiosum, usually near the penoscrotal junction. *Anterior urethral valve* is a semilunar fold very much like the anterior lip of urethral diverticulum. VCUG is an important diagnostic tool for the differential diagnosis between anterior urethral valve and urethral diverticulum. There may be dilatation of the anterior urethra proximal to a valve, which mimics a diverticulum. However, in the case of anterior urethral valve, the proximal end of the urethral dilatation forms an obtuse angle with the ventral floor of the urethra. Conversely, the proximal lip of a urethral diverticulum forms an acute angle with the ventral floor of the urethra (Figs. 26.27, 26.28, and 26.29) (Karnak et al. 1997).

26.3.8 Prostatic Utricle

Prostatic utricle is a blind-ending pouch located on the verumontanum of the prostatic urethra that represents a remnant of the müllerian duct system. In males, the müllerian ducts regress under the influence of müllerian-inhibiting factor produced by the fetal testis, leaving the prostatic utricle as a vestige. Because regression of the utricle is androgen mediated, utricular cysts are found with increased frequency in boys with failure of normal fusion of the urogenital folds resulting in hypospadias. Sonography shows a midline cyst with or without internal echoes, posterior and caudal to the bladder base. An opacified prostatic utricle is usually well demonstrated at lateral VCUG, appearing as a posterior urethral diverticulum (Figs. 26.30 and 26.31) (Berrocal et al. 2002; Lopatina et al. 2004).

26.4 Illustrations: Bladder and Urethra Disease

26.4.1 Urachal Anomalies

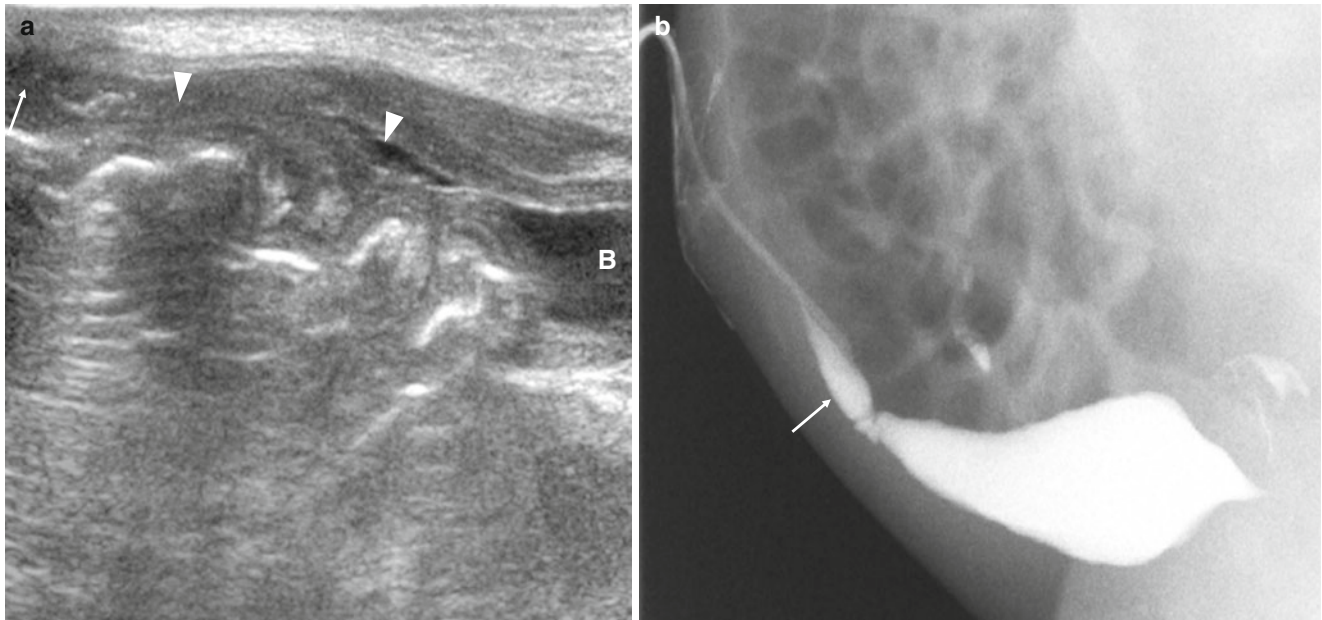


Fig. 26.1 Patent urachus in a 1-month-old neonate with urine leakage from umbilicus. **(a)** Longitudinal US shows a urine-filled patent urachus (*arrowheads*) extending from the dome of bladder (*B*) to the umbi-

licus (*arrow*). **(b)** Lateral view during a fistulography through the opening of umbilicus shows a fistulous tract (*arrow*) leading from the umbilicus to the dome of bladder

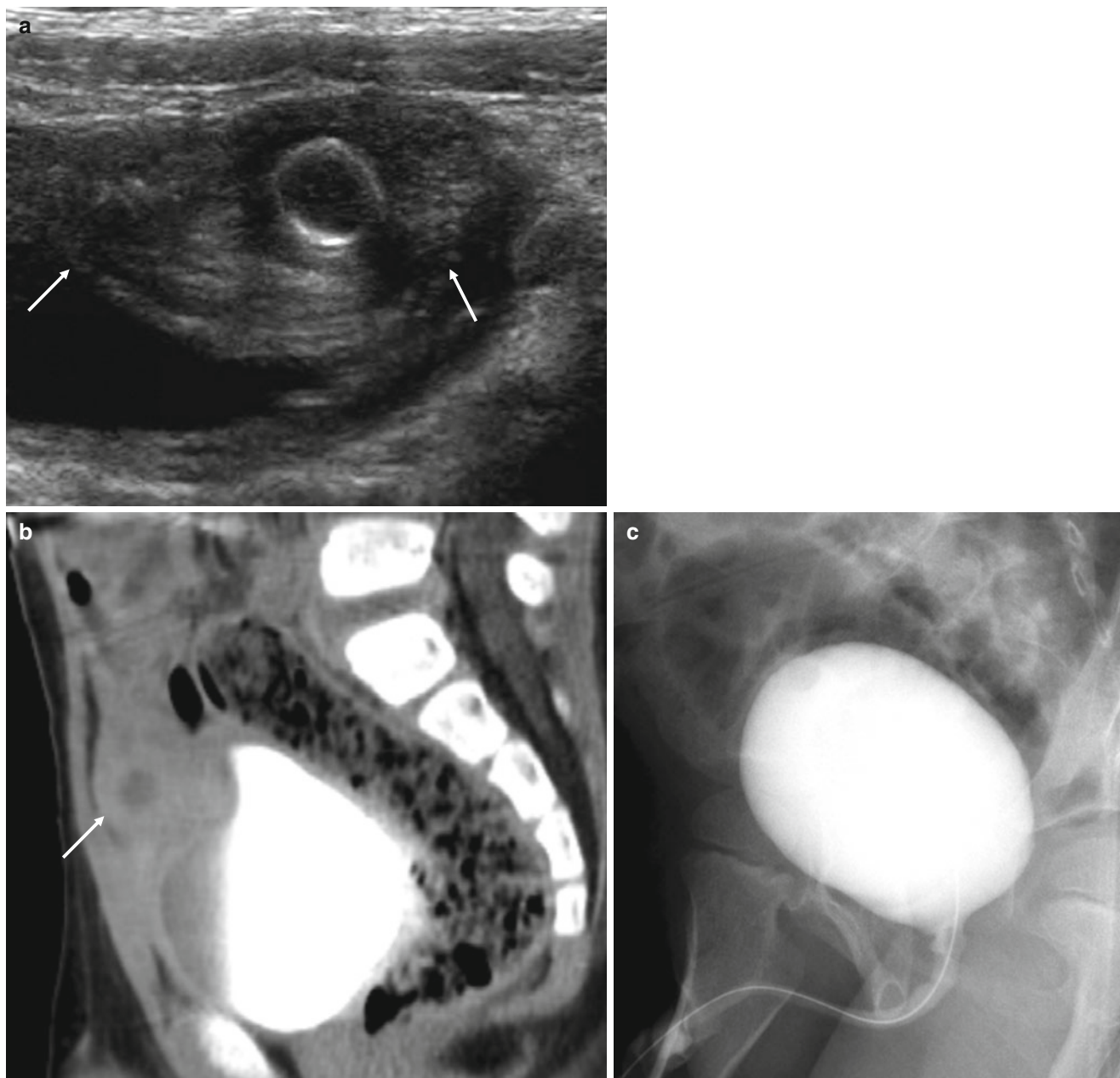


Fig. 26.2 Infected urachal cyst in a 3-year-old male. (a) Transverse US shows a complex cystic lesion (*arrows*) lying along the course of the urachus between the bladder and the umbilicus. The lesion demonstrates an internal cystic lesion with thicker outer wall. (b) Sagittal

contrast-enhanced CT scan shows a peripheral enhancing, thick-walled cystic lesion (*arrow*) with perilesional infiltration at the bladder dome area. (c) Lateral view during a VCUG shows no evidence of urachal diverticulum

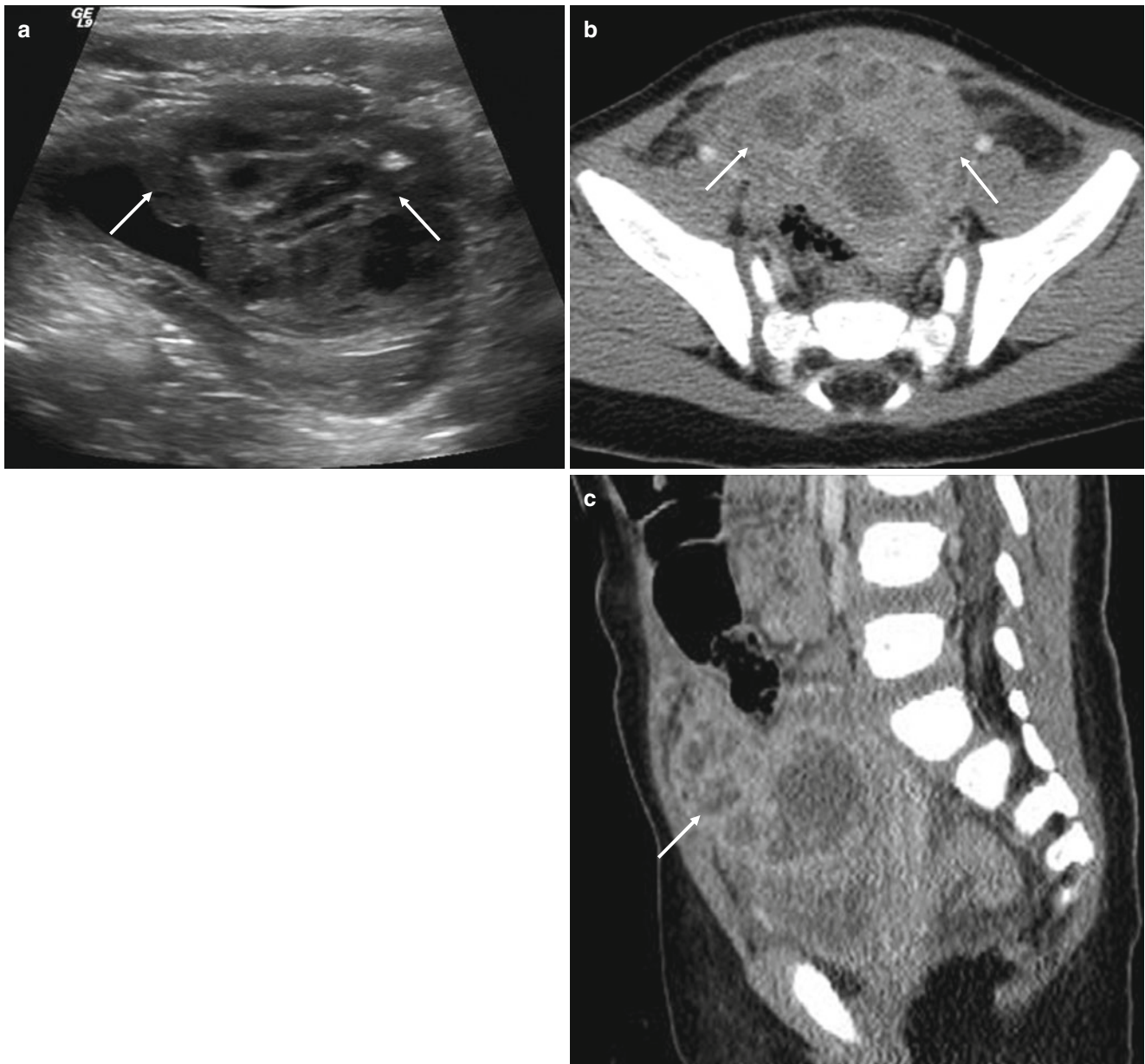


Fig. 26.3 Urachal abscess due to infected urachal cyst in a 1-year-old male. (a) Transverse midline US shows a large complex echoic mass (arrows) at the bladder dome area. (b, c) Axial (a) and sagittal (b) con-

trast-enhanced CT scans demonstrate enhancing thick-walled mass with low-density center consistent with abscess (arrows)

26.4.2 Bladder Exstrophy

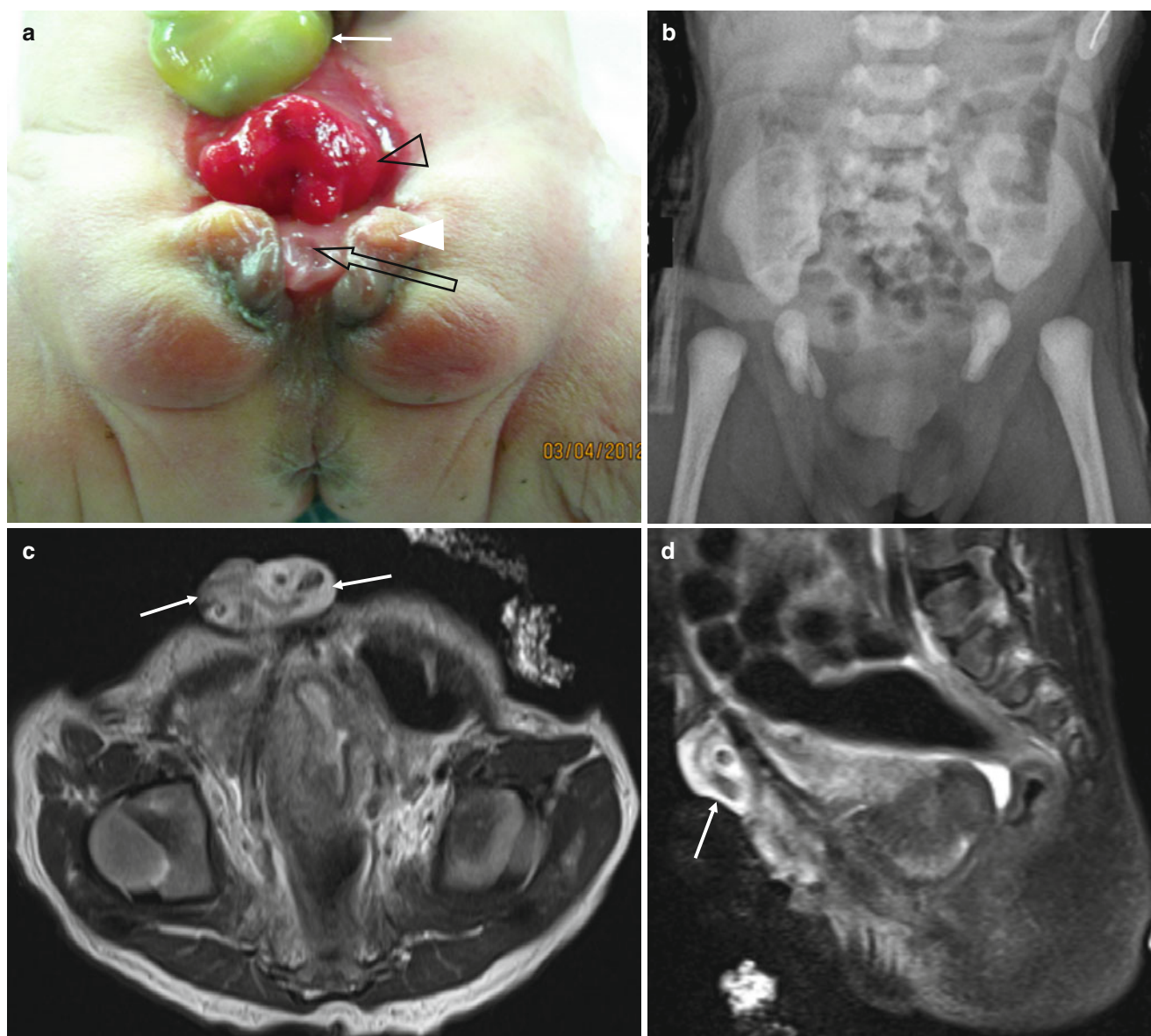


Fig. 26.4 Bladder exstrophy in a 2-day-old female infant. (a) Photograph shows the exposed bladder mucosa (*open arrowhead*) below the umbilical cord stump (*white arrow*). Also, note the exposed urethra (*open arrow*) and wide separation of labia (*white arrowhead*). (b) Anteroposterior supine radiograph shows wide separation of the

symphysis pubis with outward rotation of the pelvic bone. The hips are dislocated. (c, d) Axial (c) and sagittal (d) T2-weighted MR images show a soft tissue outpouching (exposed bladder, *arrows*) below the umbilical cord stump. No bladder is noted in the pelvic cavity

26.4.3 Prune-Belly Syndrome

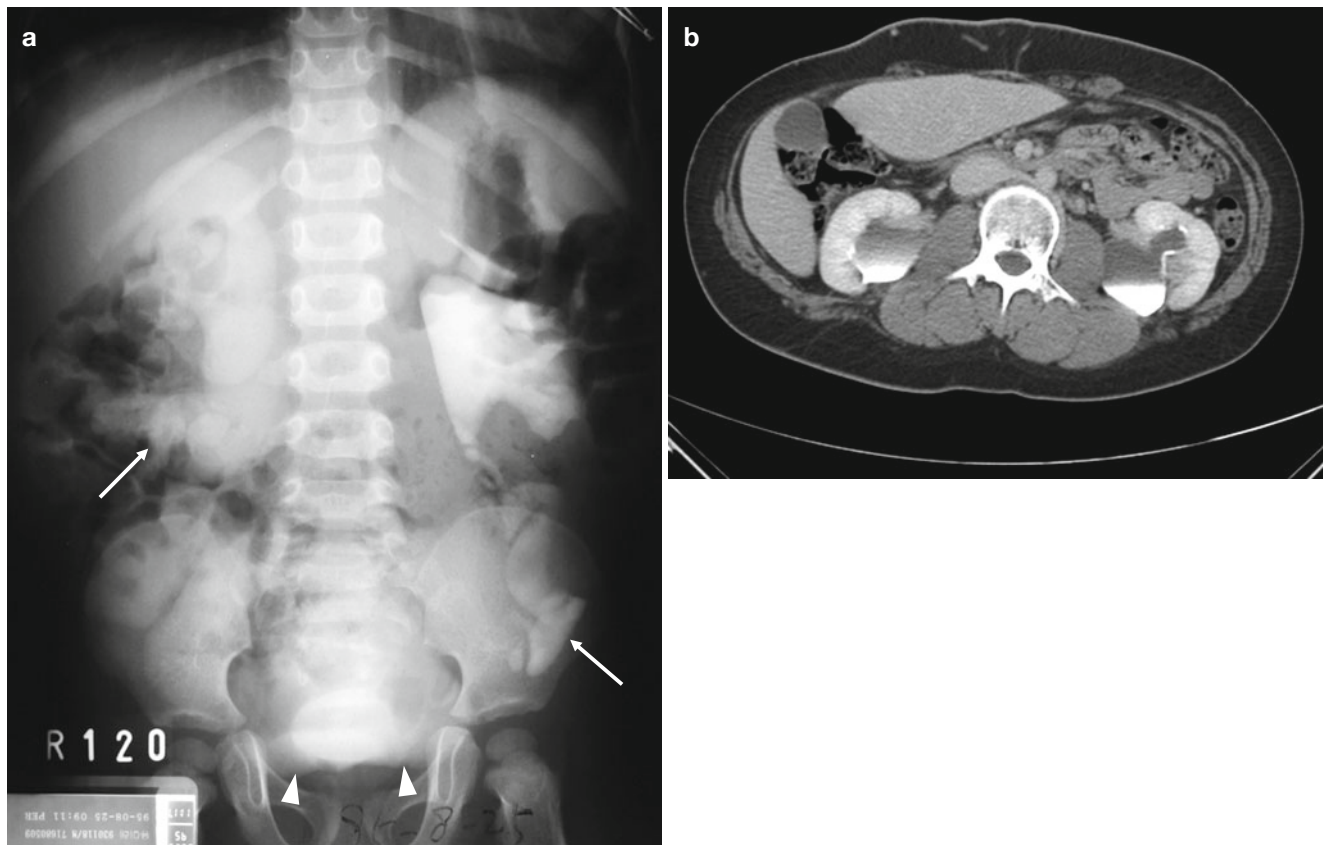


Fig. 26.5 Prune-belly syndrome in a 2-year-old male. **(a)** A 120-min intravenous urography (IVU) shows a huge bladder (*arrowheads*) and bilateral hydronephroureterosis with severe tortuous dilated ureters

(*arrows*). **(b)** Fourteen years later, follow-up axial contrast-enhanced CT scans demonstrate absent or deficient abdominal musculature, hydronephrosis, and renal dysplasia with small kidneys

26.4.4 Bladder Diverticula

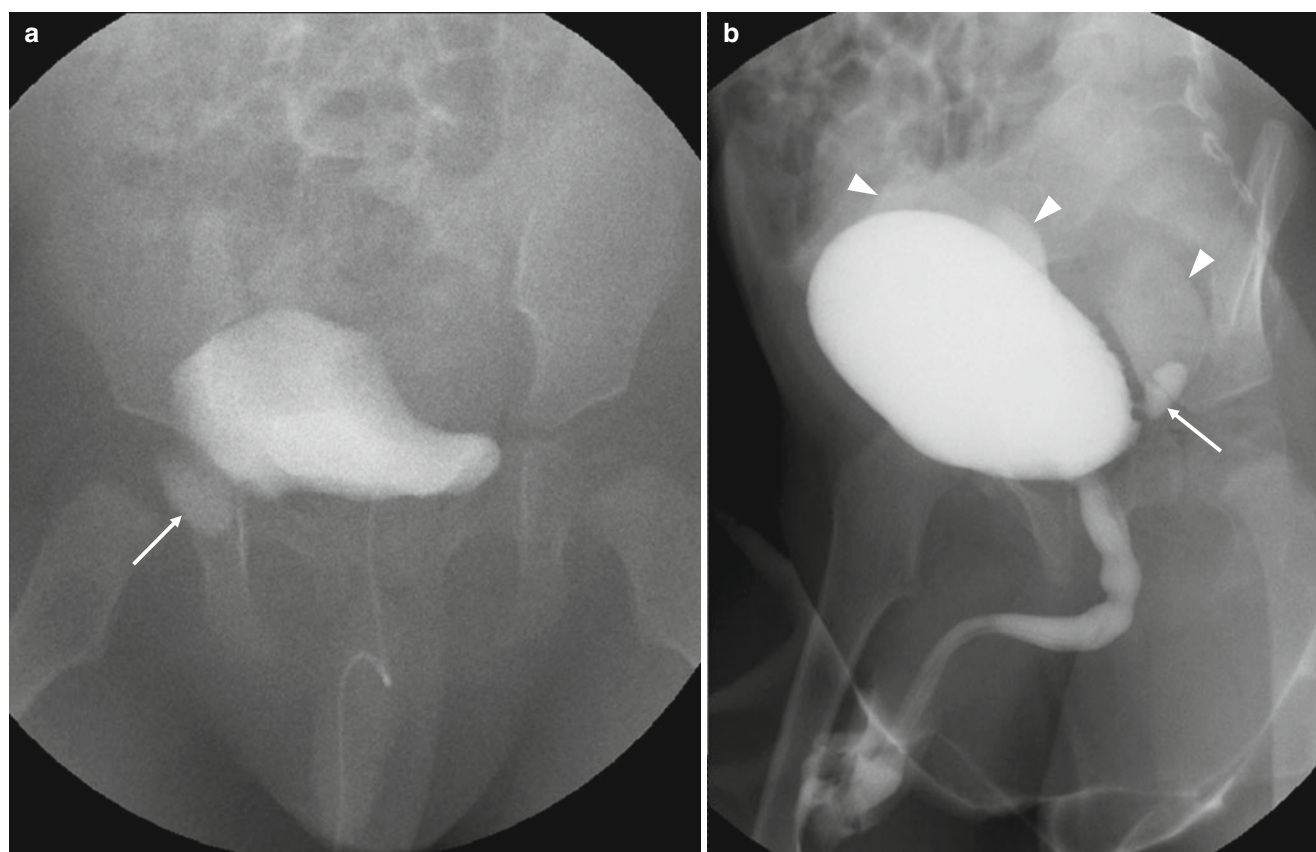


Fig. 26.6 Hutch diverticulum and bladder ear in a 6-month-old male. (a) VCUG shows a transient lateral herniation (*arrow*) of the bladder (“bladder ears”). (b) Right lateral oblique view during VCUG shows a

small left-sided paraureteral bladder diverticulum (*arrow*) (“Hutch diverticulum”). Bilateral vesicoureteral reflux with severe tortuous ureters (*arrowheads*) is also seen

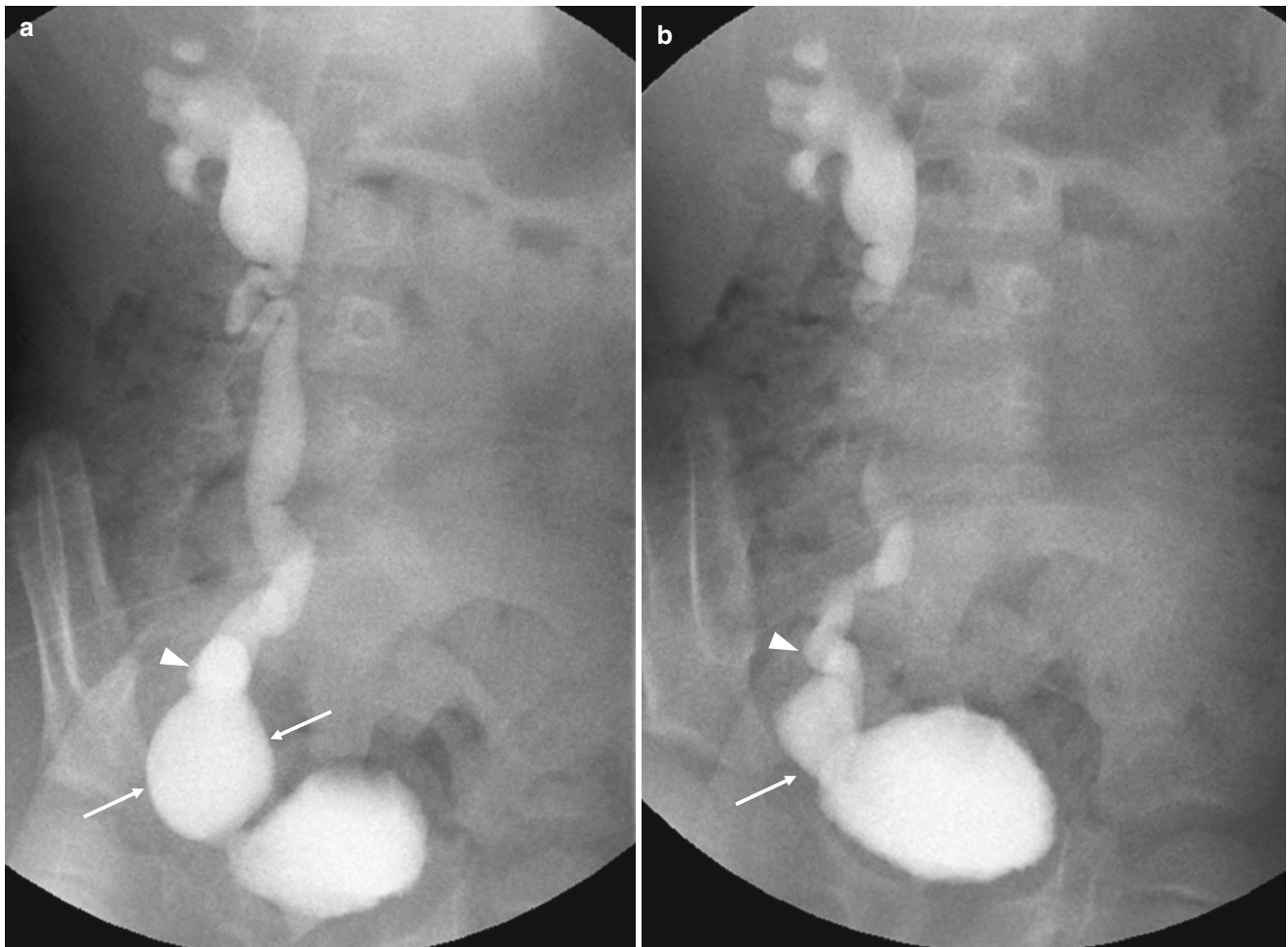


Fig. 26.7 Bladder diverticulum in a 3-year-old male. (**a**, **b**) Oblique (**a**) and anterior (**b**) images during VCUG show the ureter (*arrowhead*) inserting directly into the bladder diverticulum (*arrows*). This type of

lesion prevents normal maturation of the ureterovesical junction and requires surgery to correct the reflux

26.4.5 Megacystis

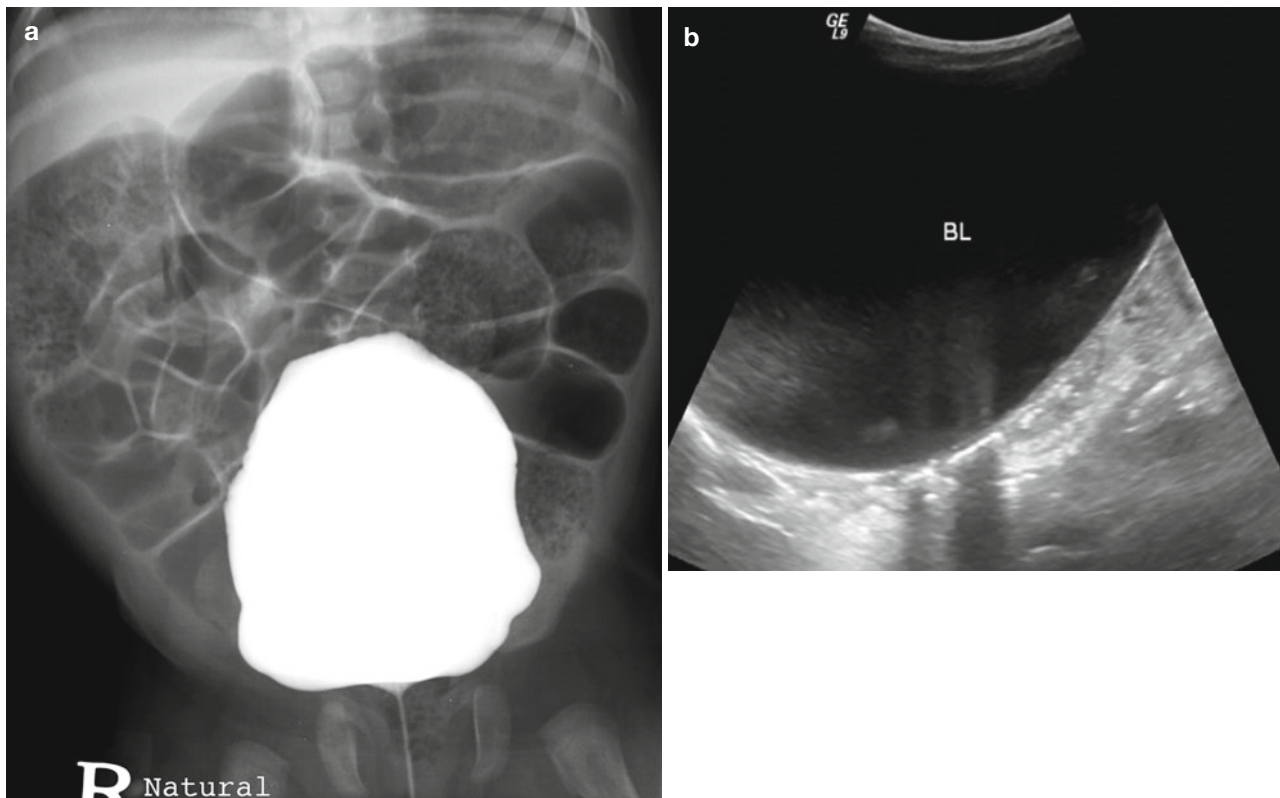


Fig. 26.8 Megacystis in a 29-month-old female. (a) Anterior image during VCUG shows a large urinary bladder. (b) Six years later, follow-up longitudinal US shows persistent large urinary bladder (BL)

26.4.6 Cystitis

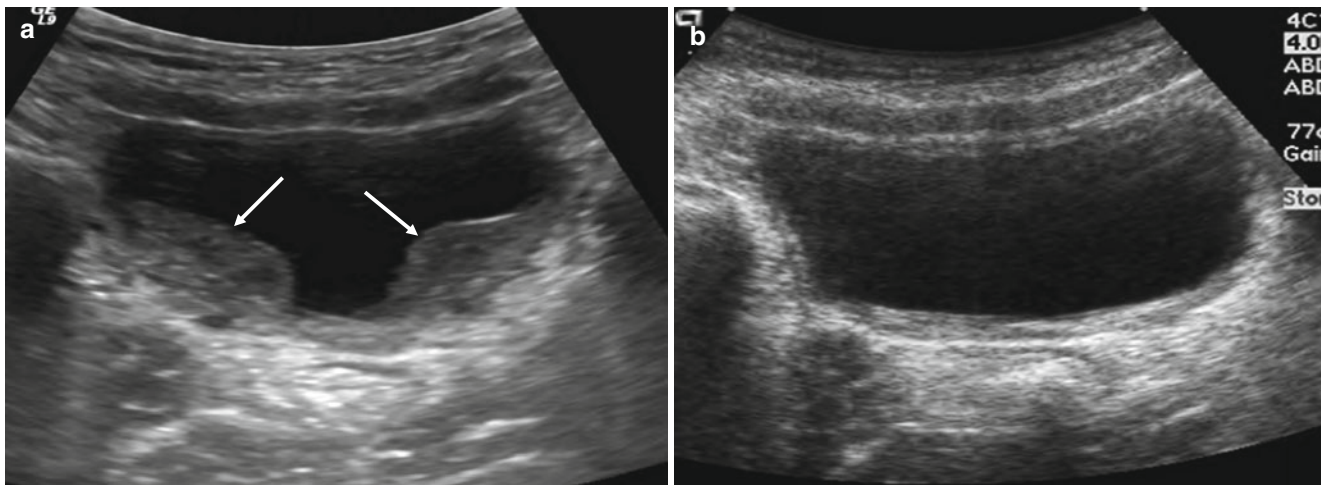


Fig. 26.9 Hemorrhagic cystitis in an 11-year-old male. (a) Transverse US shows focal thickenings of the posterior wall of the bladder (arrows). (b) Three weeks later, follow-up transverse US demonstrates a marked decreased wall thickening of the bladder

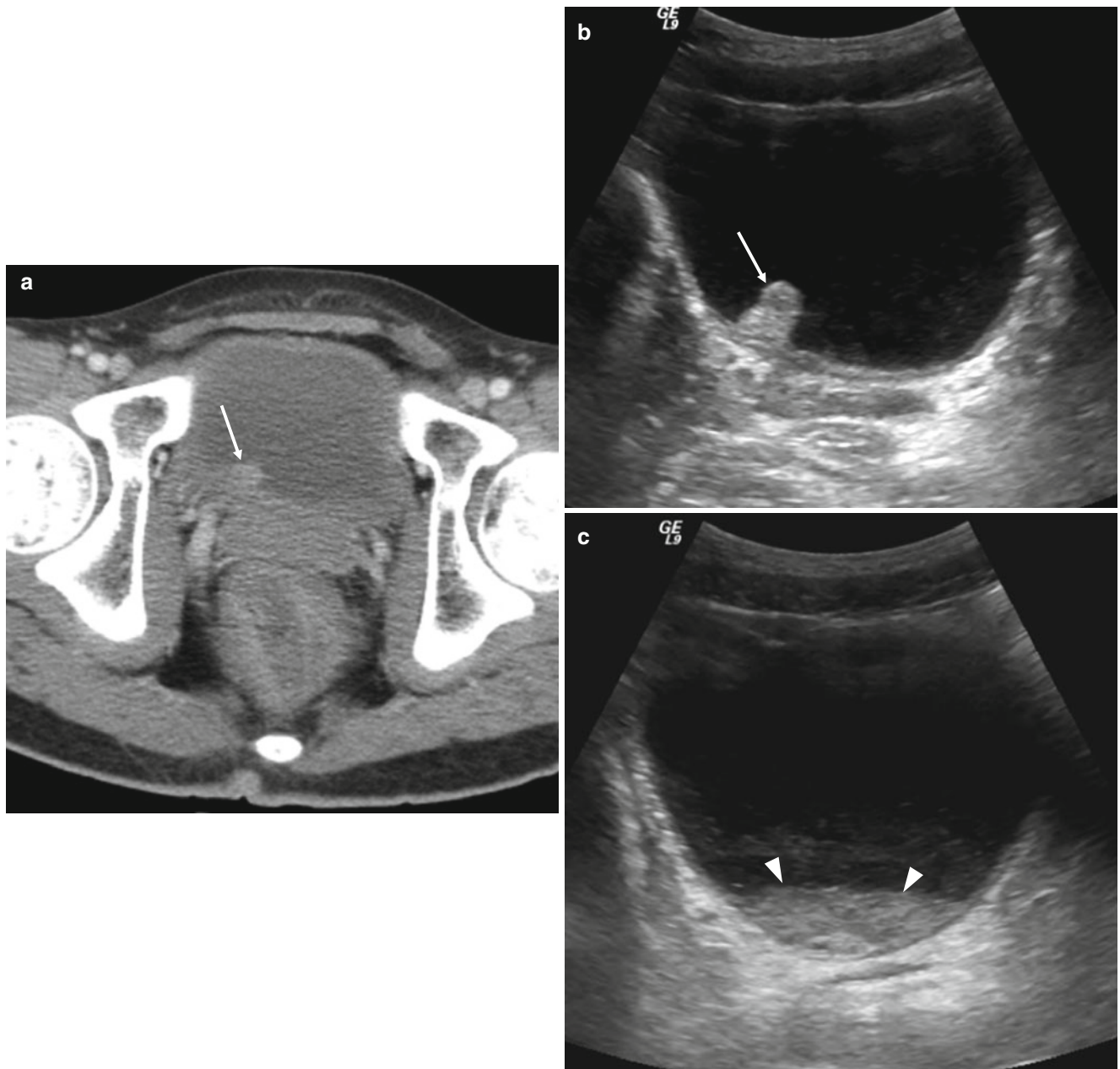


Fig. 26.10 Cyclophosphamide-induced hemorrhagic cystitis in a 14-year-old male who received allogeneic-peripheral stem cell transplantation (PBSCT) for aplastic anemia. **(a)** Axial contrast-enhanced CT shows focal protruding lesion (*arrow*) in the posterior wall of the

bladder. **(b, c)** Transverse US images demonstrate a bilobed echogenic lesion (*arrow* in **b**) at the right ureterovesical junction level and an echogenic debris with fluid–fluid level (*arrowheads* in **c**) in the bladder base

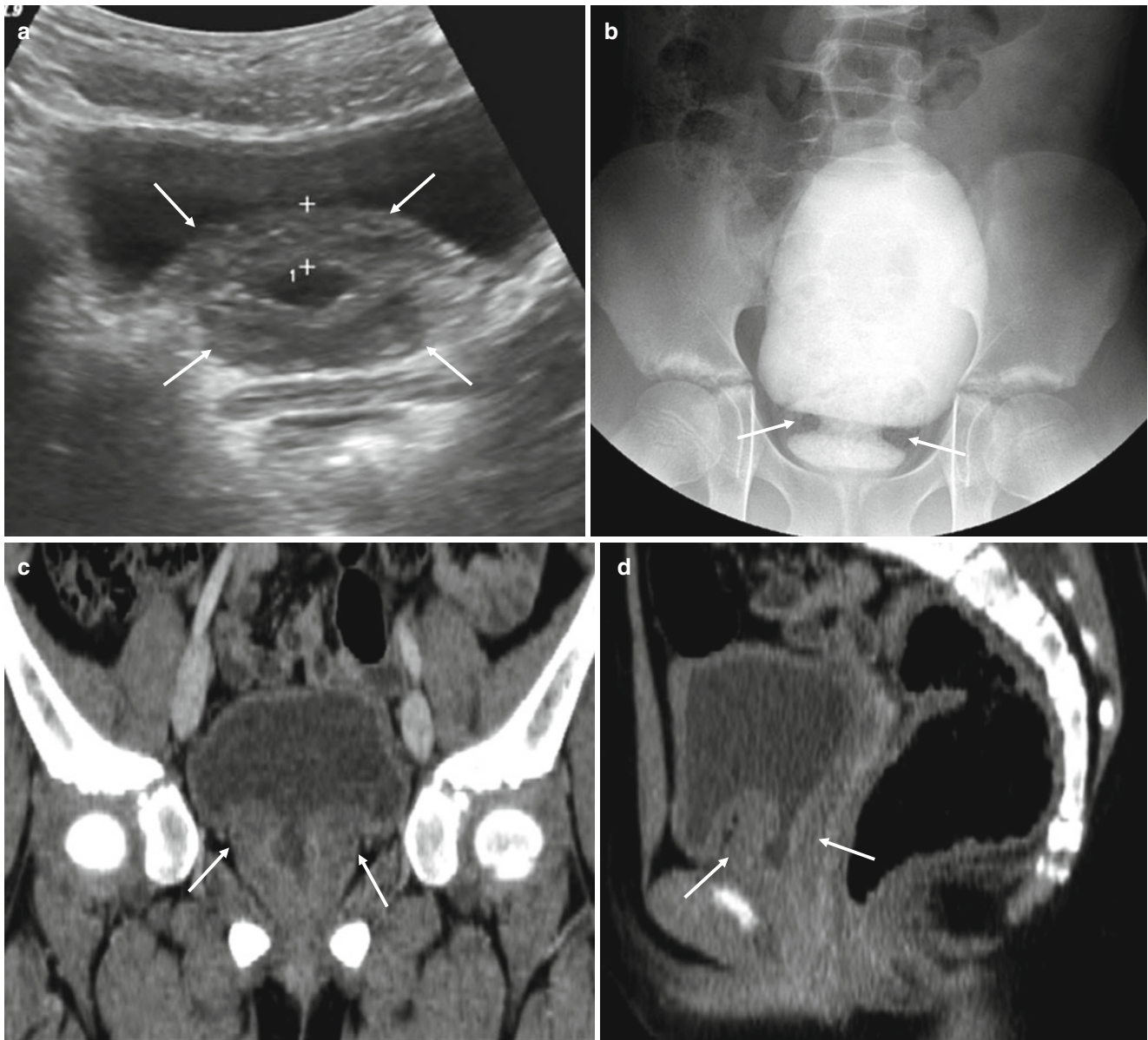


Fig. 26.11 Cystitis cystica in an 11-year-old female. (a–d) Transverse US (a), VCUG (b), and contrast-enhanced CT images (c, d) show diffuse concentric wall thickening (arrows) at the bladder outlet. Bladder

outlet is seen as a dumbbell shape with true bladder neck and false bladder neck on VCUG. Cystoscopic biopsy revealed cystitis cystica

26.4.7 Neoplasms of the Bladder

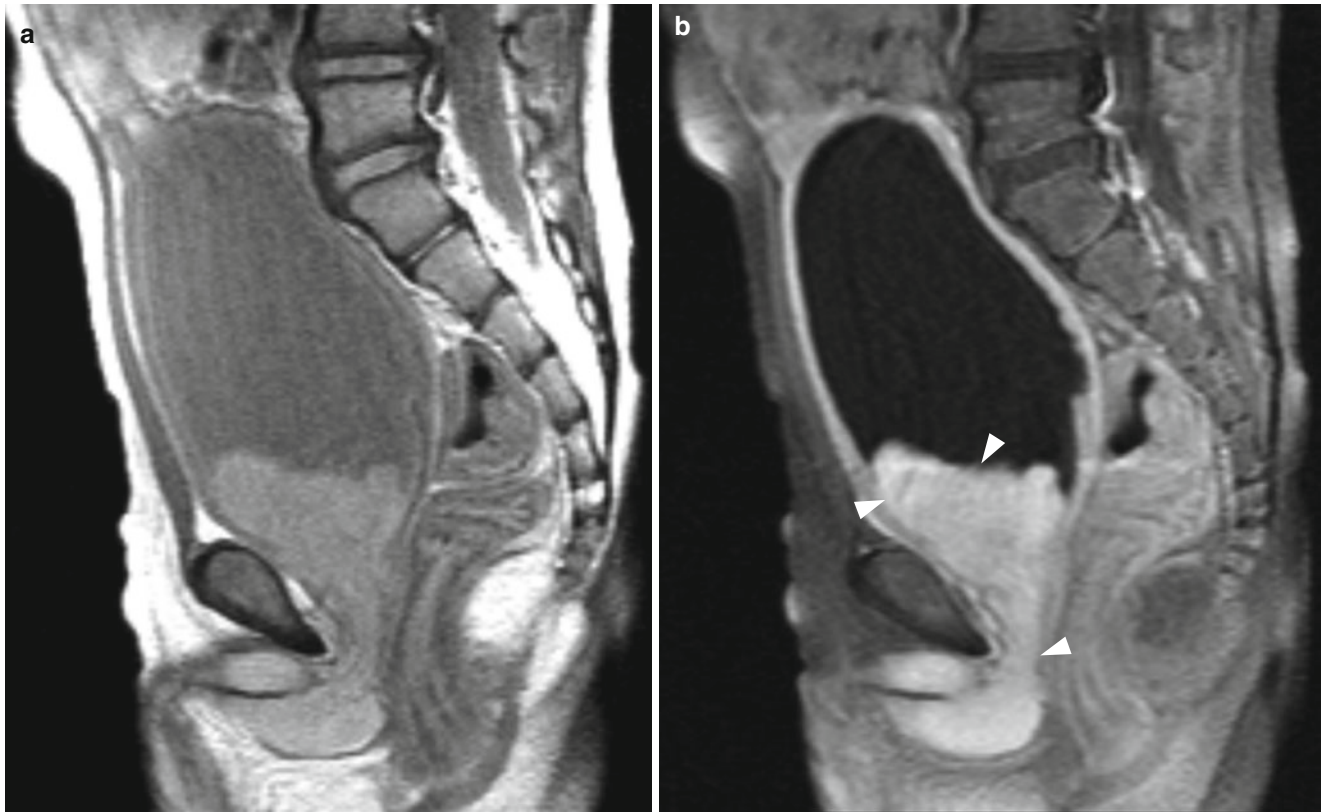


Fig. 26.12 Embryonal rhabdomyosarcoma in a 3-year-old male. (**a**, **b**) Sagittal T2-weighted (**a**) and contrast-enhanced T1-weighted (**b**) MR images show a lobulated mass (*arrowheads*) extending from the bladder base to the prostatic urethra



Fig. 26.13 Embryonal rhabdomyosarcoma in an 18-month-old male. (a) Bladder image from VCUG shows a lobulated filling defect (*black arrows*) in the bladder base. (b) Transverse US shows a solid intravesical mass (*arrowheads*) in the bladder base. (c, d) Sagittal contrast-

enhanced CT (c) and T1-weighted MR (d) images show a large, heterogenous enhancing, polypoid mass (*arrows*) extending from the bladder base to the prostatic urethra and prostate

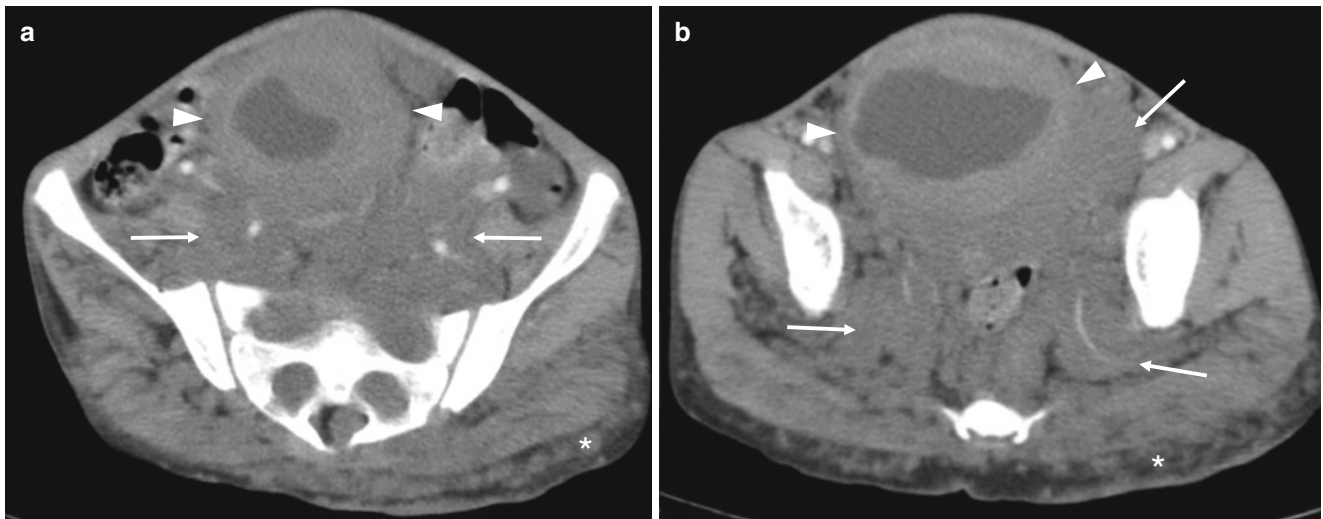


Fig. 26.14 Neurofibromatosis with direct involvement of the bladder in a 7-year-old female. (**a, b**) Axial contrast-enhanced CT scans show large peritoneal masses (*arrows*) with widening of sacral neural foramina and extending to the pelvis outlet through the sciatic notch. Also

note multiple nodular masses (*asterisks*) extending to the subcutaneous layer of buttock. Bladder is displaced anteriorly and has diffuse wall thickening (*arrowheads*)

26.4.8 Neurogenic Bladder

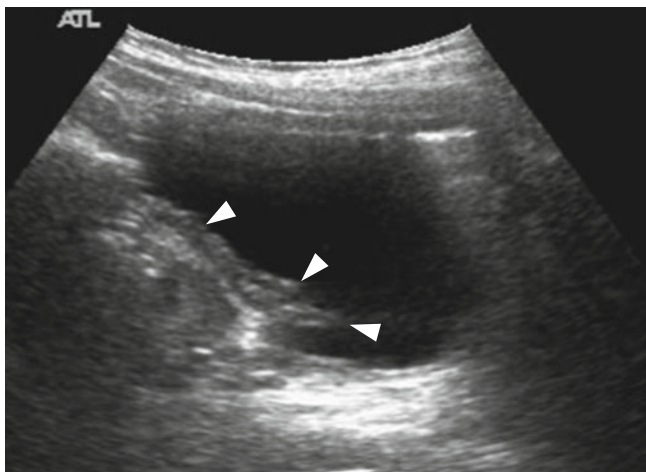


Fig. 26.15 Neurogenic bladder in a 12-year-old female. Transverse US shows a trabeculated bladder wall thickening (*arrowheads*)

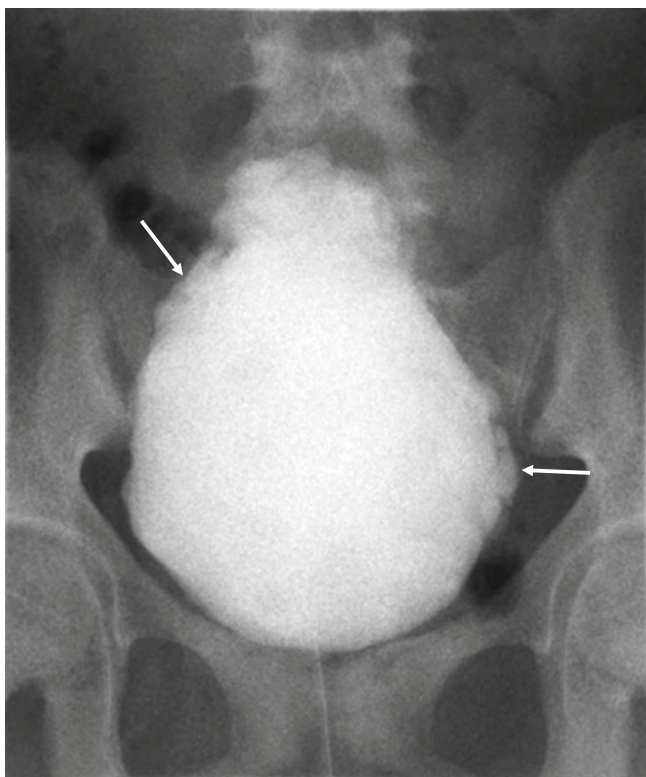


Fig. 26.16 Neurogenic bladder in a 15-year-old female. Anterior image during VCUG shows a trabeculated bladder with multiple small diverticula (*arrows*)

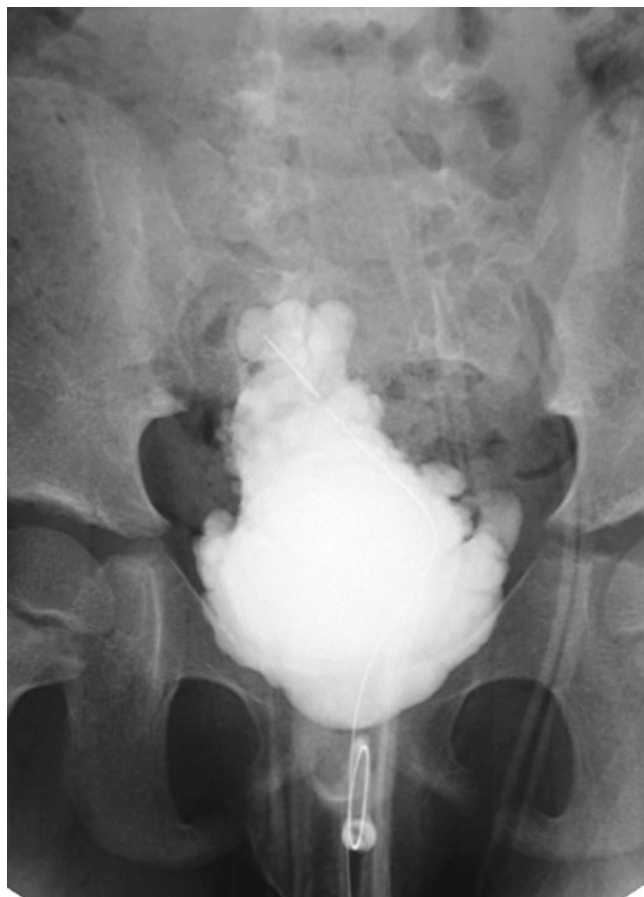


Fig. 26.17 Neurogenic bladder in a 6-year-old male who underwent surgery for meningomyelocele. Anterior image during VCUG reveals a typical "Christmas tree" appearance of the bladder with marked increased trabeculation

26.4.9 Bladder Stone

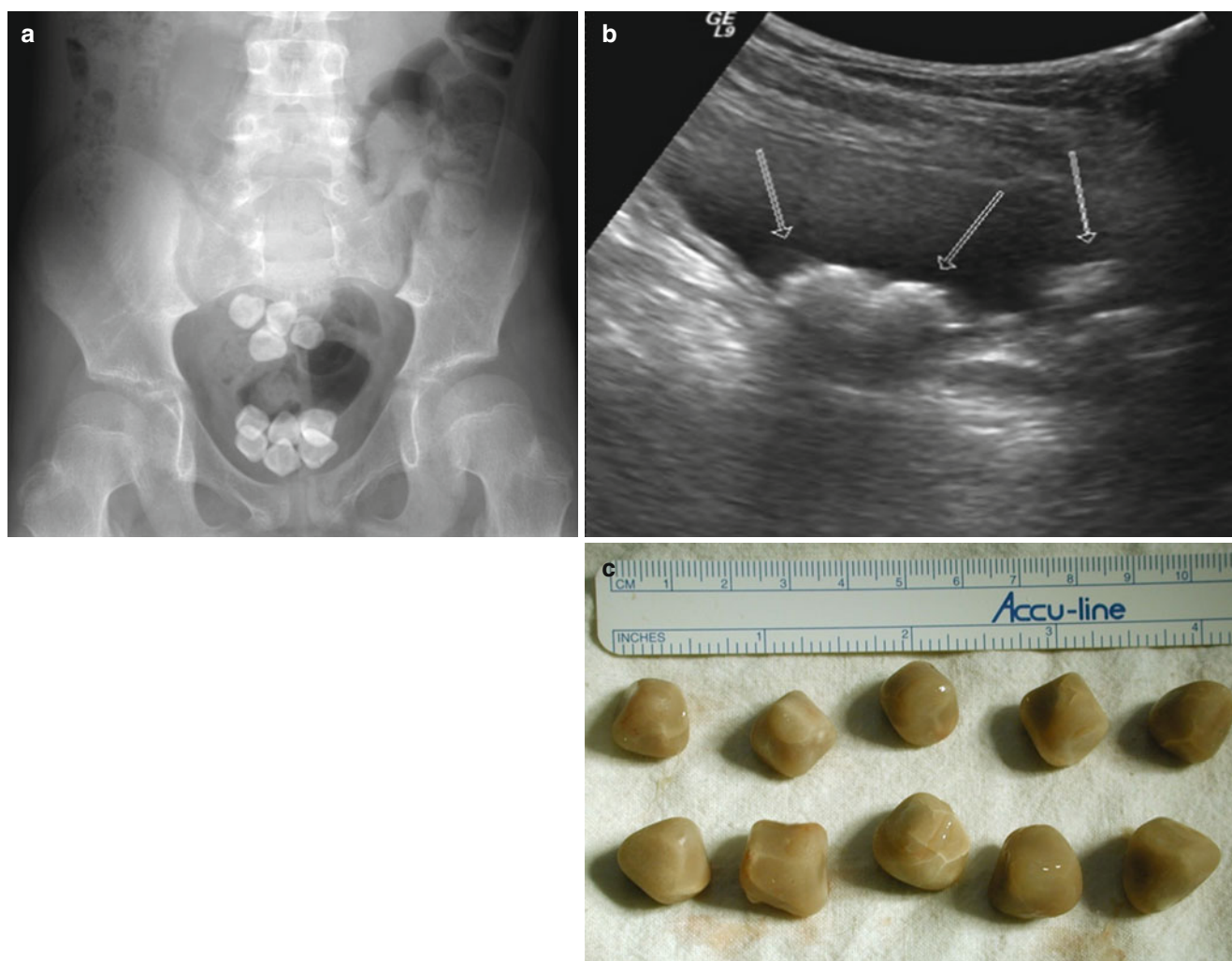


Fig. 26.18 Multiple bladder stones in a 12-year-old female who underwent bladder augmentation for the neurogenic bladder. (a) Plain radiograph shows multiple radiopaque stones in the pelvic cavity. Note bony defect of the sacrum associated with surgery for meningomyelo-

cele. (b) Transverse US image shows echogenic foci (*arrows*) with acoustic shadowing in bladder base. (c) Photograph shows the removed bladder stones

26.4.10 Posterior Urethral Valves



Fig. 26.19 Posterior urethral valve in a 3-year-old male. Oblique image during VCUG shows elongation and dilatation of posterior urethra (*asterisk*) with abrupt transition at the level of valves (*arrow*)

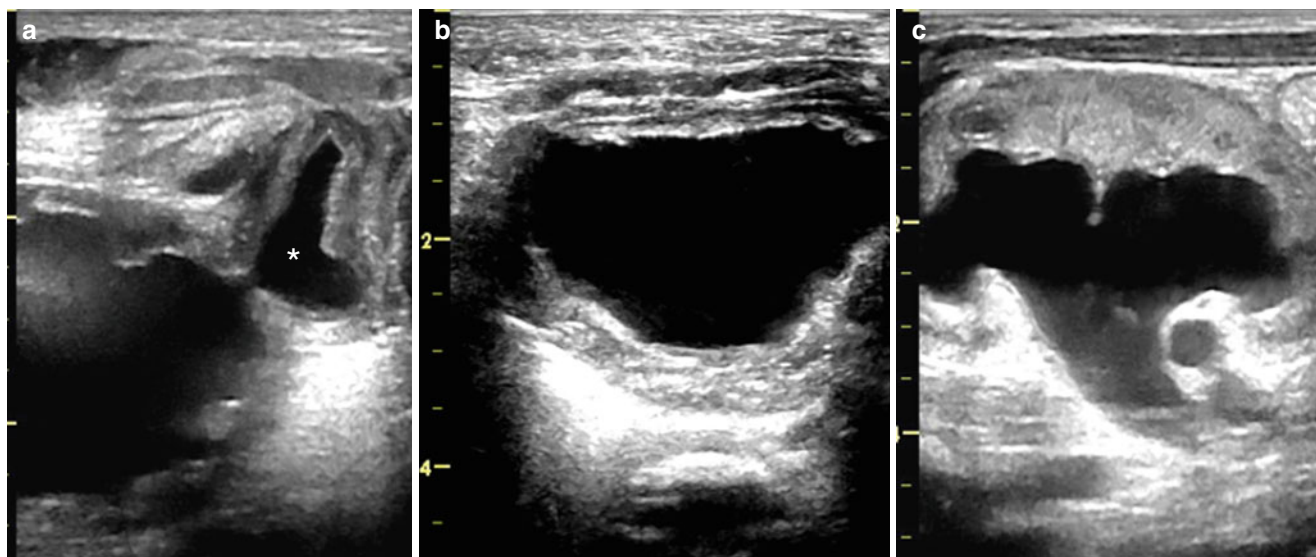


Fig. 26.20 Posterior urethral valve in a 4-day-old male. (a) Longitudinal US shows dilated posterior urethra (*asterisk*). (b) Longitudinal US shows an echogenic kidney with poor corticomedullary differentiation and hydronephrosis. (c) Transverse US demonstrates a diffuse trabeculated bladder.

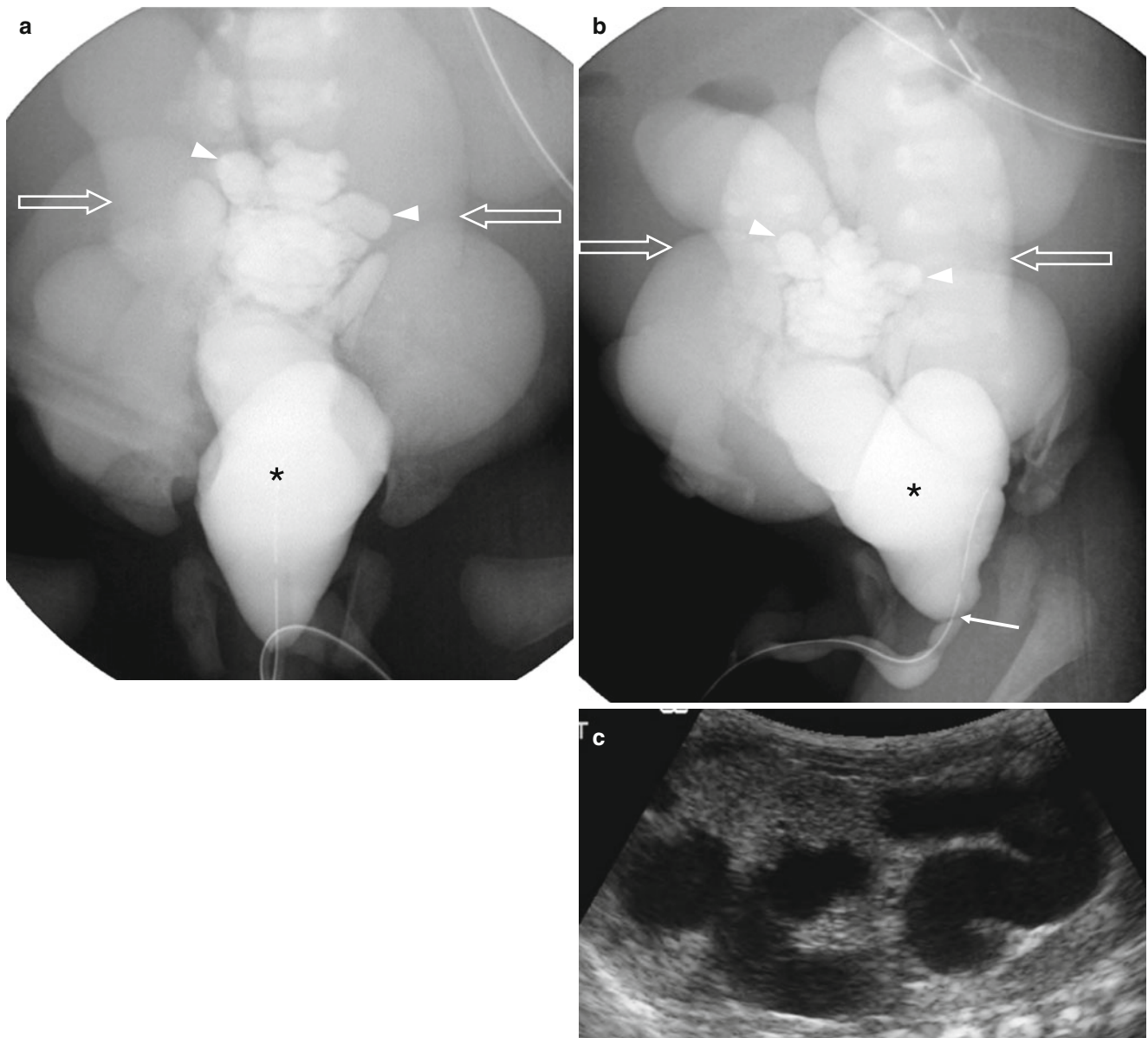


Fig. 26.21 Posterior urethral valve in a 1-day-old male. (**a**, **b**) Anterior (**a**) and oblique (**b**) images during VCUG show a marked dilatation and elongation of posterior urethra (*asterisk*) with abrupt transition at the level of valves (*arrow*) to narrow anterior urethra. Also note a coarse

trabeculated bladder (*arrowheads*) with small capacity and severe bilateral vesicoureteral reflux (*open arrows*). (**c**) Longitudinal US image shows an echogenic left kidney with absent corticomedullary differentiation and hydronephrosis

26.4.11 Urethral Polyps

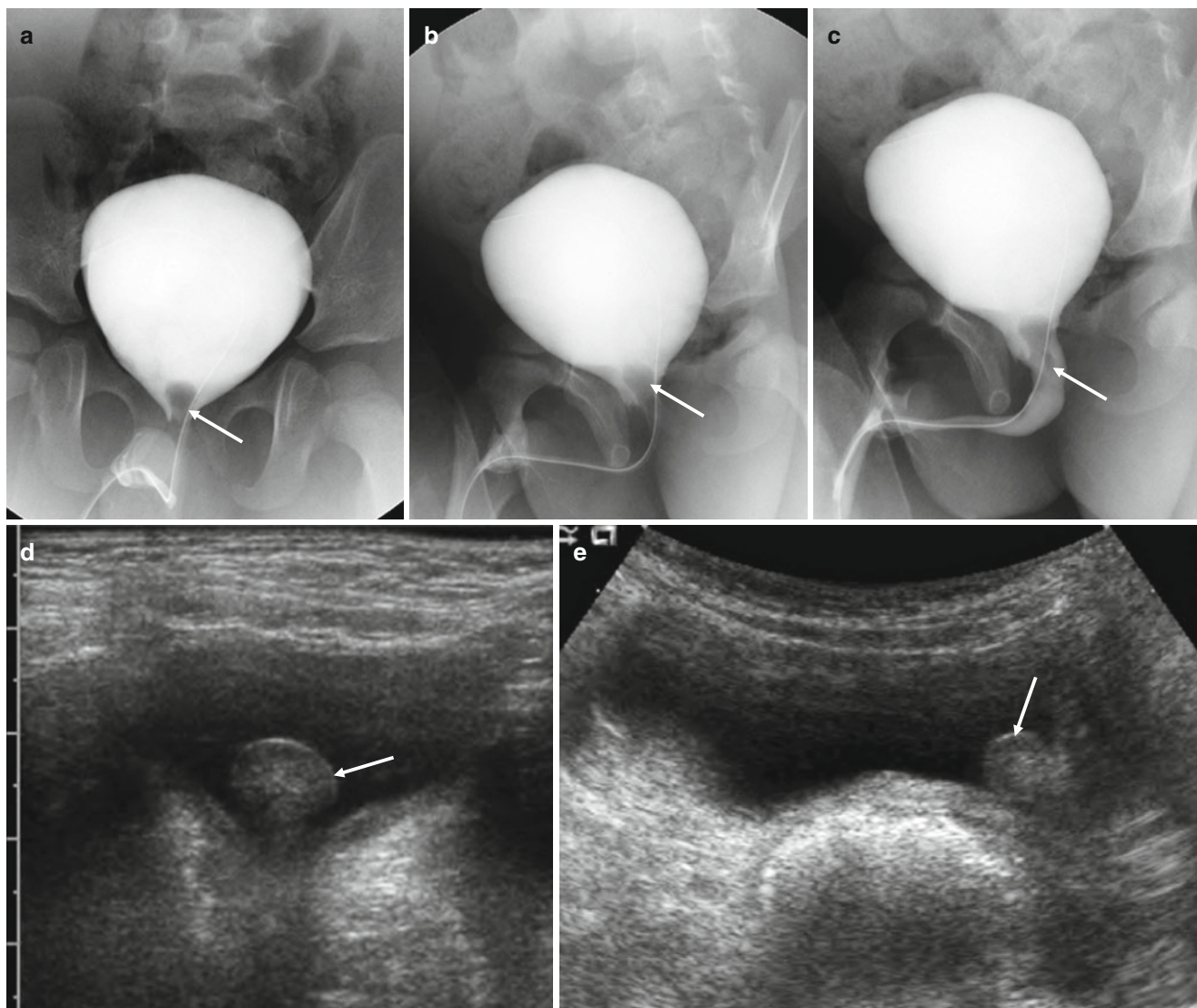


Fig. 26.22 Urethral polyp in a 2-year-old male. (a, b) Anterior (a) and oblique (b) images during VCUG show a pedunculated filling defect (arrows) at the level of bladder neck. (c) With voiding, the polyp moves into the urethra and the stalk (arrow) is better appreciated with the

attachment to the posterior urethra. (d, e) Transverse (d) and longitudinal (e) US images show a pedunculated mass (arrows) with medium-level echogenicity at the bladder base

26.4.12 Urethral Duplication

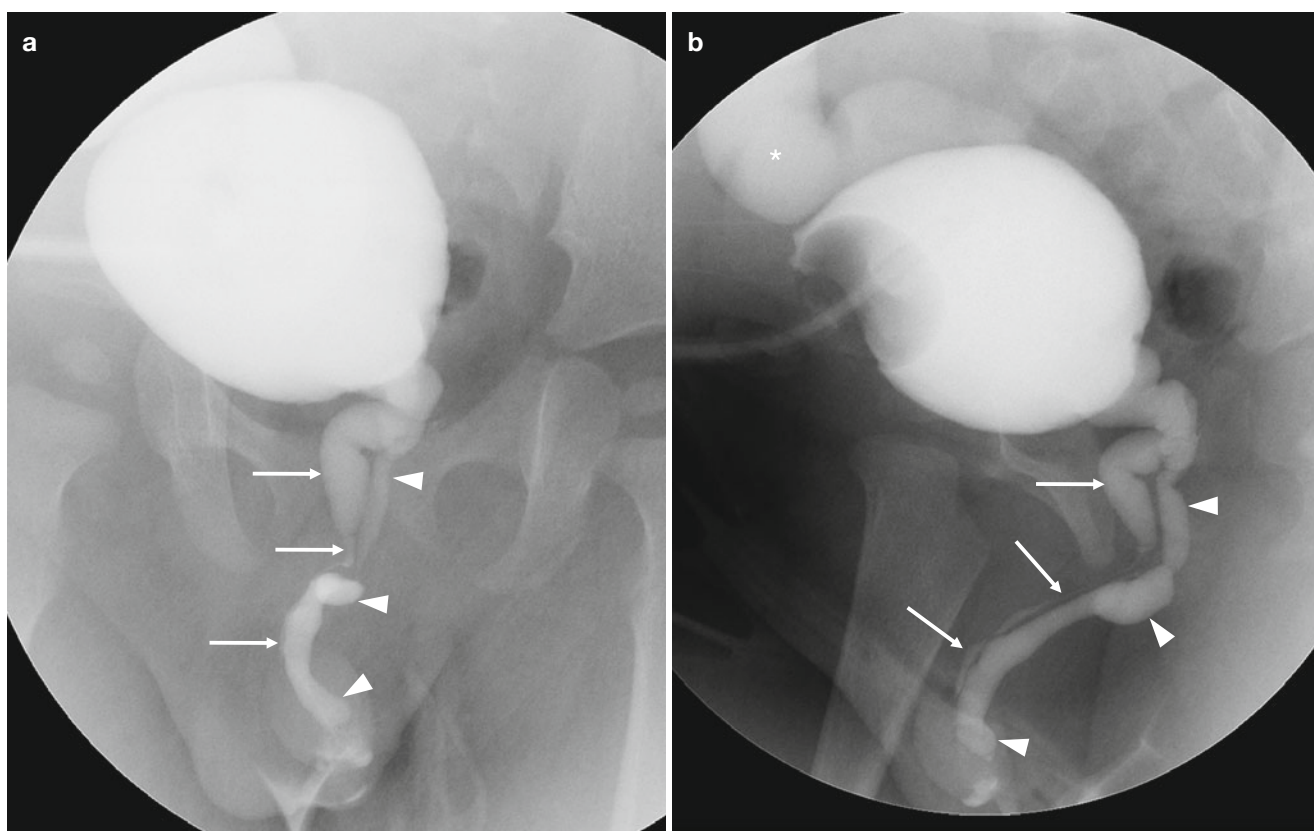


Fig. 26.23 Urethral duplication in an 11-month-old male. (**a**, **b**) Anterior (**a**) and oblique (**b**) images during VCUG through vesicosotomy show a duplication of the urethra originating from the prostatic urethra. The dorsal urethra (*arrows*, pseudo-urethra) has a dilated proximal portion and a stenotic distal portion, and the ventral urethra

(*arrowheads*, true functioning urethra) unusually ends in the hypospadiac position (this is a rare case that the functioning ventral urethra ends in a hypospadiac location). Severe vesicoureteral reflux (*asterisk*) is also seen

26.4.13 Urethral Strictures

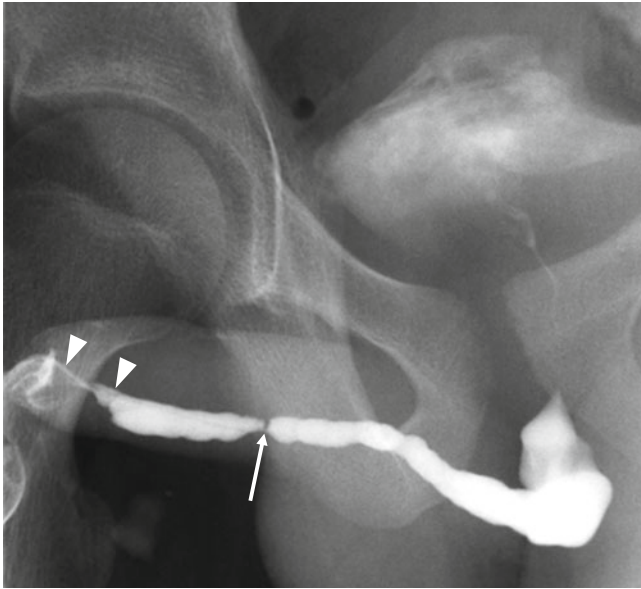


Fig. 26.24 Urethral strictures in a 12-year-old male who received urethral injury during catheterization 5 months earlier. RGU shows a tight stricture in the midportion of the pendulous urethra (*arrow*) and a segmental severe narrowing in the distal end of pendulous urethra (*arrowheads*)

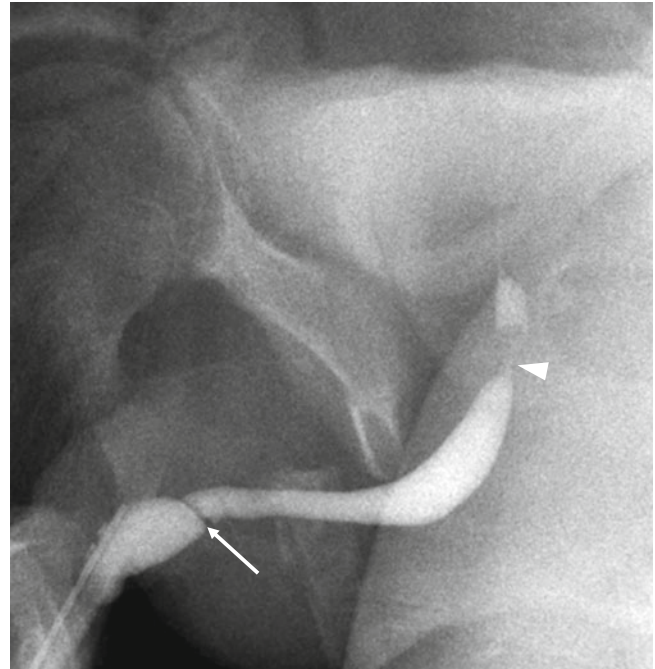


Fig. 26.25 Urethral strictures in an 11-year-old male who underwent surgery for the penoscrotal hypospadias and the polyp of verumontanum. RGU shows a short tight stricture in the midportion of the pendulous urethra (*arrow*, operation site of hypospadias) and another stenosis at the operation site of verumontanum (*arrowhead*)

26.4.14 Urethral Fistula

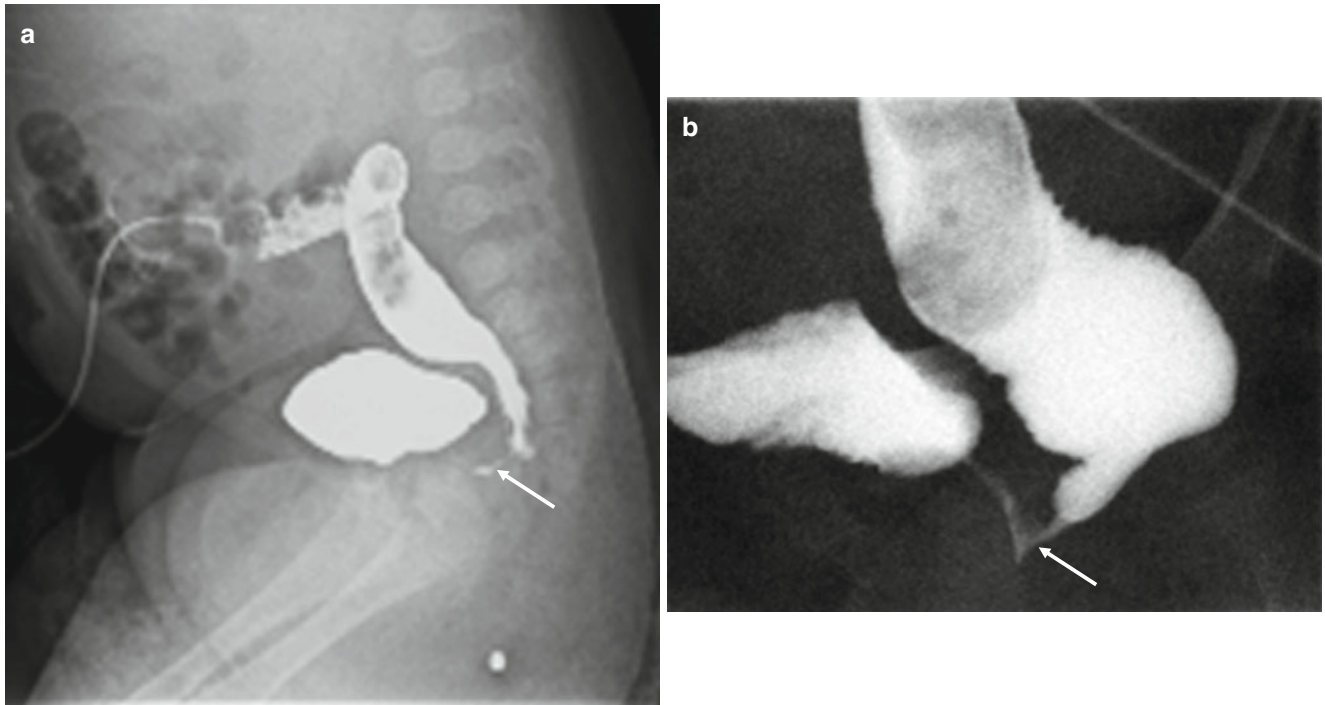


Fig. 26.26 Recto-urethral fistula in a 2-month-old male with high type of imperforate anus. (**a, b**) Lateral (**a**) and magnitude (**b**) images during loopogram through colostomy show an imperforate anus with recto-prostatic urethral fistula (*arrow*)

26.4.15 Megalourethra, Anterior Urethral Diverticula, and Anterior Urethral Valve

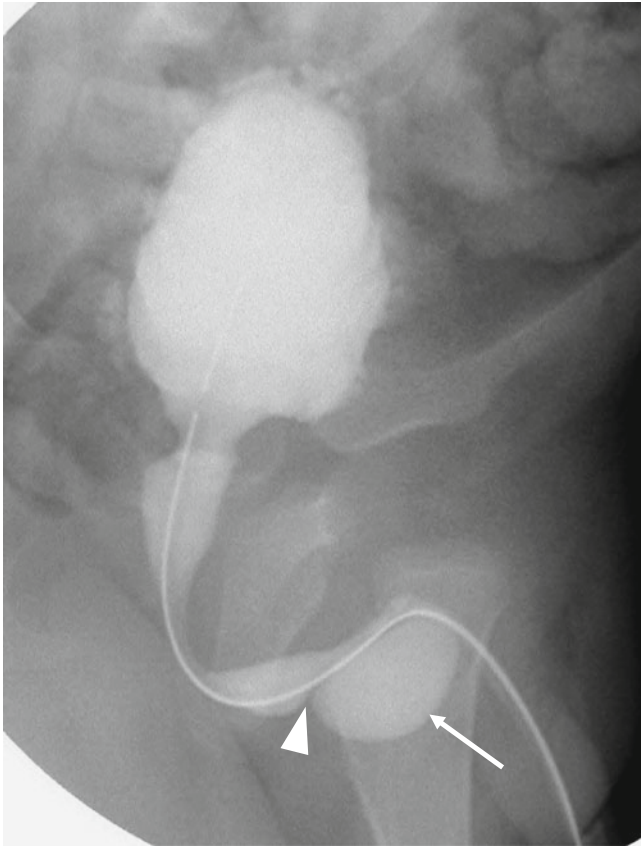


Fig. 26.27 Anterior urethral diverticulum in a 1-year-old male. Oblique image during VCUG shows a saccular outpouching (*arrow*) of the ventral surface of the penile urethra, usually near the penoscrotal junction. Acute angle is formed at the junction of the posterior lip with the urethra (*arrowhead*). Also note severe wall thickening of the bladder with pseudo-diverticula formation

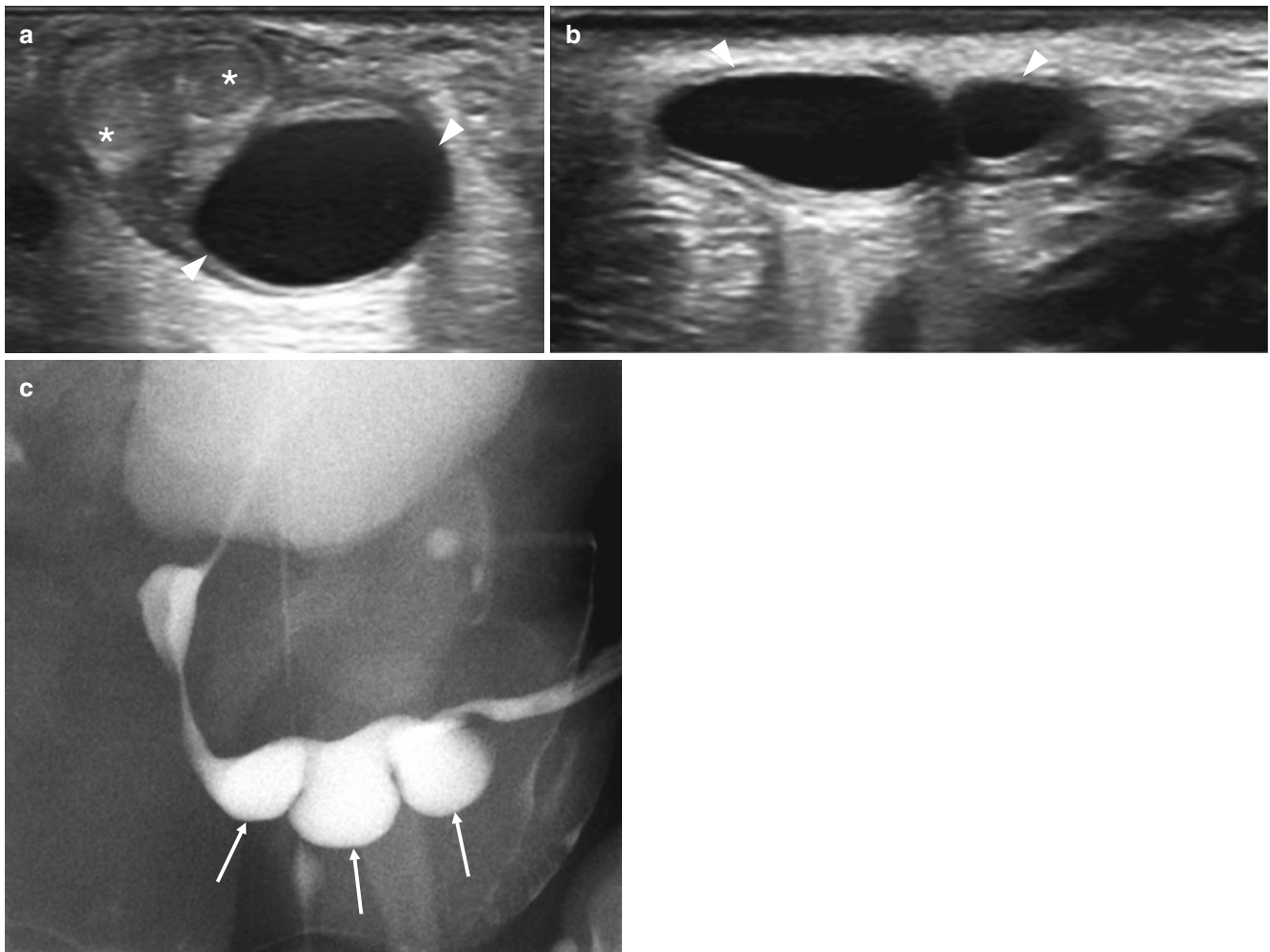


Fig. 26.28 Anterior urethral diverticulum in a 1-month-old male. (a, b) Transverse (a) and longitudinal (b) US images show an elongated shape, thick-walled cystic lesions (*arrowheads*) at the level of proximal

anterior urethra. *Asterisks*: corpus cavernosum. (c) Oblique image during VCUG shows a multi-saccular outpouching (*arrows*) of the ventral surface of the anterior urethra

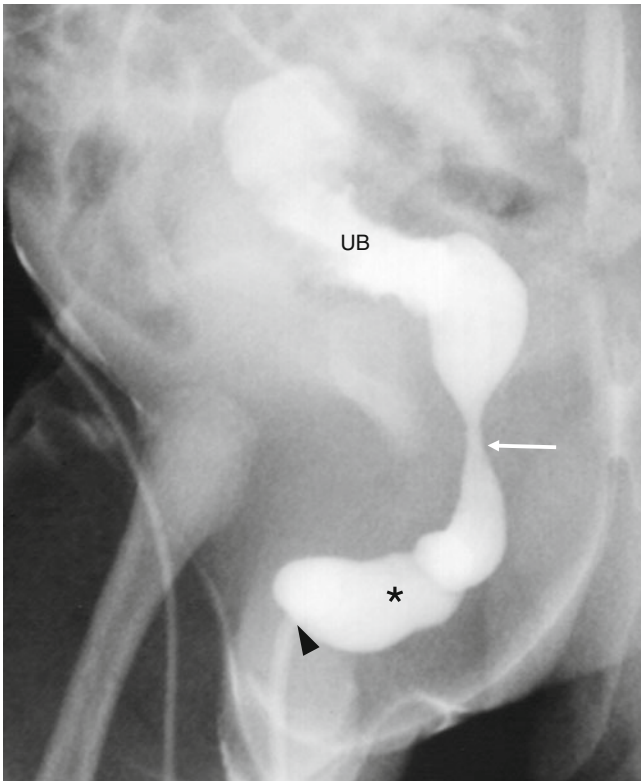


Fig. 26.29 Anterior urethral valve in a 13-day-old male. Oblique image during VCUG shows a focal saccular dilatation (*asterisk*) of the anterior urethra, proximal to the valve (*arrowhead*). The dorsal wasting (*arrow*) at the urogenital diaphragm is normal. *UB* urinary bladder

26.4.16 Prostatic Utricle

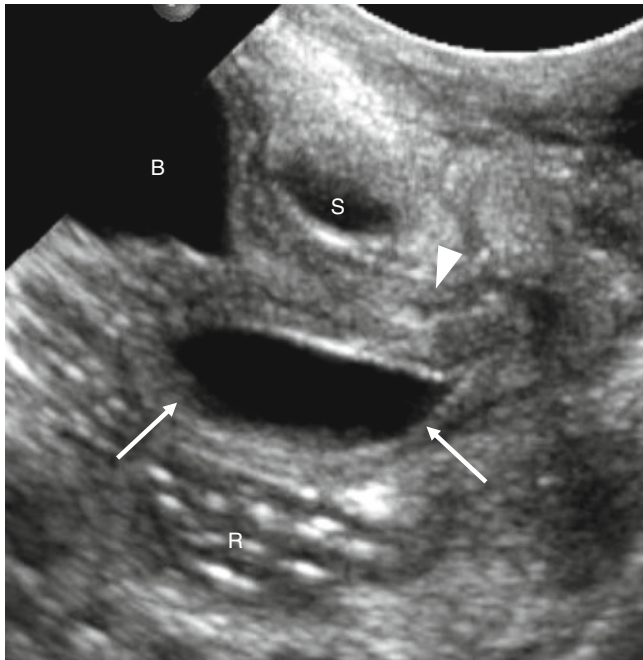


Fig. 26.30 Utricle in a 2-day-old male with hypospadias. Longitudinal US image shows a teardrop-shaped midline cyst (*arrows*) near the posterior urethra (*arrowhead*), posterior and caudal to the bladder (*B*). *S* symphysis pubis, *R* rectum

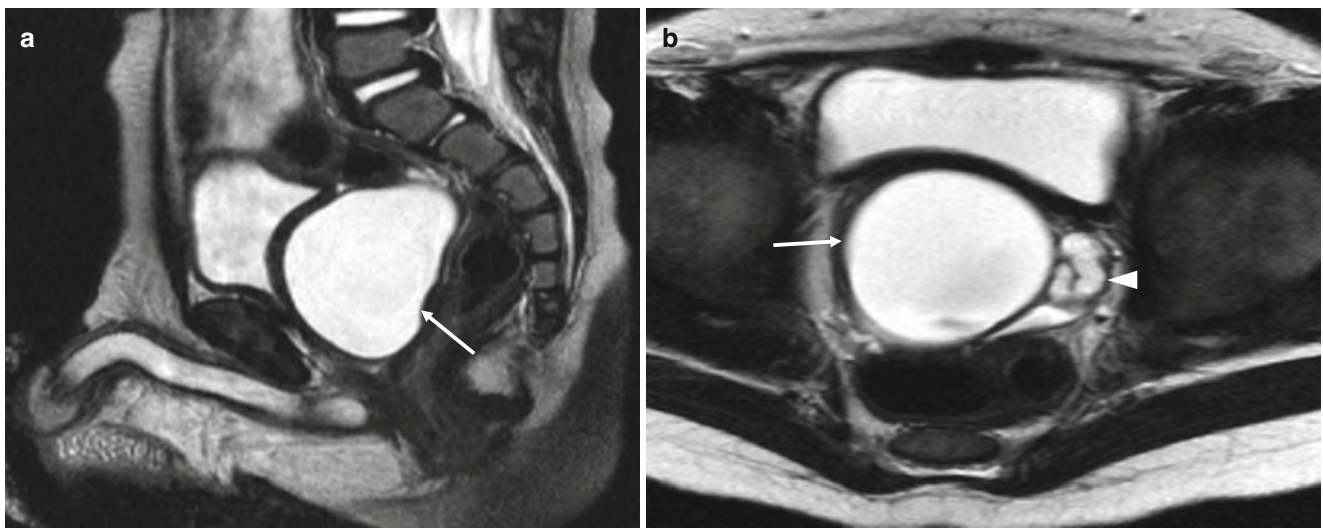


Fig. 26.31 Utricle in a 2-year-old male. (**a**, **b**) Sagittal (**a**) and axial (**b**) T2-weighted MR images show a midline cystic mass (*arrows*) in the rectovesical pouch. The dilated seminal vesicles (*arrowhead*) are displaced due to utricle cyst

References

- Agrons GA, Wagner BJ, Lonergan GJ, et al. From the archives of the AFIP. Genitourinary rhabdomyosarcoma in children: radiologic-pathologic correlation. *Radiographics*. 1997;17:919–37.
- Allen CW, Alexander SI. Adenovirus associated haematuria. *Arch Dis Child*. 2005;90:305–6.
- Bates DG. The bladder and urethra. In: Slovis TL, editor. *Caffey's pediatric diagnostic imaging*. 11th ed. Philadelphia: Mosby Elsevier; 2008.
- Bauer SB. Neurogenic bladder: etiology and assessment. *Pediatr Nephrol*. 2008;23:541–51.
- Berrocal T, López-Pereira P, Arjonilla A, et al. Anomalies of the distal ureter, bladder, and urethra in children: embryologic, radiologic, and pathologic features. *Radiographics*. 2002;22:1139–64.
- Bloom DA, Slovis TL. The dilated urinary tract. In: Slovis TL, editor. *Caffey's pediatric diagnostic imaging*. 11th ed. Philadelphia: Mosby Elsevier; 2008.
- Caro PA, Rosenberg HK, Snyder 3rd HM. Congenital urethral polyp. *AJR Am J Roentgenol*. 1986;147:1041–2.
- Casale AJ. Posterior urethral valves and other obstructions of the urethra. In: Gonzales ET, Bauer SB, editors. *Pediatric urology practice*. Philadelphia: Lippincott Williams & Wilkins; 1999.
- Cremin BJ. A review of the ultrasonic appearances of posterior urethral valve and ureteroceles. *Pediatr Radiol*. 1986;16:357–64.
- Evangelidis A, Castle EP, Ostlie DJ, et al. Surgical management of primary bladder diverticula in children. *Pediatr Surg*. 2005;40:701–3.
- Gallentine ML, Morey AF. Imaging of the male urethra for stricture disease. *Urol Clin North Am*. 2002;29:361–72.
- Karnak I, Senocak ME, Büyükpamukçu N, et al. Rare congenital abnormalities of the anterior urethra. *Pediatr Surg Int*. 1997;12:407–9.
- Lebowitz RL, Vargas B. Stones in the urinary bladder in children and young adults. *AJR Am J Roentgenol*. 1987;148:491–5.
- Lopatina OA, Berry TT, Spottswood SE. Giant prostatic utricle (utriculus masculinus): diagnostic imaging and surgical implications. *Pediatr Radiol*. 2004;34:156–9.
- Macpherson RI, Leithiser RE, Gordon L, et al. Posterior urethral valves: an update and review. *Radiographics*. 1986;6:753–91.
- McCarville MB, Hoffer FA, Gingrich JR, et al. Imaging findings of hemorrhagic cystitis in pediatric oncology patients. *Pediatr Radiol*. 2000;30:131–8.
- Mourtzinos A, Borer JG. Current management of bladder exstrophy. *Curr Urol Rep*. 2004;5:137–41.
- Nasrallah PF, McMahon DR. Anatomic abnormalities of the bladder. In: Gonzales ET, Bauer SB, editors. *Pediatric urology practice*. Philadelphia: Lippincott Williams & Wilkins; 1999.
- Richman TS, Taylor KJ. Sonographic demonstration of bladder duplication. *AJR Am J Roentgenol*. 1982;139:604–5.
- Salle JL, Sibai H, Rosenstein D, et al. Urethral duplication in the male: review of 16 cases. *J Urol*. 2000;163:1936–40.
- Saraga-Babic M, Sapunar D (1994) Atlas of human embryology. Chronolab AG. <http://www.embryo.chronolab.com/ureters.htm>. Accessed 6 June 2013.
- Siegel MJ. Urinary tract. In: Siegel MJ, editor. *Pediatric sonography*. 3rd ed. Philadelphia: Lippincott Williams & Wilkins; 2002.
- Volmar KE, Nguyen TC, Holcroft CJ, et al. Phimosis as a cause of the prune belly syndrome: comparison to a more common pattern of proximal penile urethra obstruction. *Virchows Arch*. 2003;442:169–72.
- Wakhlu AK, Wakhlu A, Tandon RK, et al. Congenital megalourethra. *J Pediatr Surg*. 1996;31:441–3.
- Yu JS, Kim KW, Lee HJ, et al. Urachal remnant diseases: spectrum of CT and US findings. *Radiographics*. 2001;21:451–61.

Yong-Woo Kim

Contents

27.1	Introduction	836
27.2	Imaging	836
27.2.1	Uterus and Ovary	836
27.2.2	Testis	836
27.3	Spectrum of Pediatric Uterus, Ovary, and Testis Diseases	836
27.3.1	Uterus and Ovary	836
27.3.2	Testis	841
27.4	Illustrations: Pediatric Uterus, Ovary, and Testis Diseases	846
27.4.1	Hydrometrocolpos.....	846
27.4.2	Vaginorectal Fistula	847
27.4.3	Precocious Puberty.....	848
27.4.4	Congenital Anomalies of Uterus and Vagina.....	849
27.4.5	Tuboovarian Abscess	853
27.4.6	Ovarian Torsion.....	854
27.4.7	Hernia of Uterus and Ovary	855
27.4.8	Ovarian Cyst	857
27.4.9	Ovarian Tumor: Germ Cell Tumor	858
27.4.10	Ovarian Tumor: Sex Cord-Stromal Tumor	863
27.4.11	Ovarian Tumor: Epithelial Tumor.....	864
27.4.12	Ovarian Tumor: Secondary Neoplasm.....	866
27.4.13	Cryptorchidism (Undescended Testis).....	867
27.4.14	Transverse Testicular Ectopia	868
27.4.15	Inguinoscrotal Hernia.....	869
27.4.16	Hydrocele.....	871
27.4.17	Varicocele.....	873
27.4.18	Epididymo-orchitis	874
27.4.19	Testicular Torsion.....	875
27.4.20	Torsion of the Testicular Appendages.....	877
27.4.21	Scrotal Trauma.....	878
27.4.22	Testicular Microlithiasis.....	879
27.4.23	Testicular Tumor: Germ Cell Tumor.....	880
27.4.24	Testicular Tumor: Secondary Tumor	882
	References	883

Y.-W. Kim, M.D.
Department of Radiology, Pusan National University
Children's Hospital, Pusan National University,
College of Medicine, Beomeo-ri, Mulgeum-eup, Yangsan,
Gyeongnam 626-770, Korea
e-mail: kyw47914@gmail.com

27.1 Introduction

The pain and/or mass is the most common clinical indication for imaging the pediatric pelvis. Other indications are abnormalities of sexual development, including ambiguous genitalia, precocious puberty, vaginal bleeding, and amenorrhea. The evaluation of the pediatric pelvis requires the knowledge of the developmental changes occurring in the various stages of pediatric life. The imaging evaluation of testis, uterus, and ovary diseases, including US, CT, and MRI, is essential for accurate diagnosis. To be familiar with imaging findings of uterus, ovary, and testis diseases is helpful for diagnosis and preoperative evaluation.

27.2 Imaging

27.2.1 Uterus and Ovary

US is the primary modality for the evaluation of the pediatric gynecologic organs, often enabling a definitive diagnosis. Transabdominal US needs a distention of bladder to displace gas-filled bowel loops out of the pelvis and to allow easier visualization of the ovaries and uterus. Adequate bladder filling usually can be achieved by oral intake of fluid. Because neonates and young children are difficult to control bladder and tend to void at lower volumes, they require proper timing and a flexible US schedule. A 7.5- or 5.0-MHz transducer is usually used for the neonate and toddler, a 5.0 MHz for the prepubertal child, and a 5.0 or 3.5 MHz for the adolescent (Garel et al. 2001; Siegel 2002a).

Doppler imaging is useful to identify vascular structures and provides information about flow characteristics, which help characterize gynecologic tumors and diagnose adnexal torsion (Quillin and Siegel 1994).

CT is useful for tumor staging. CT is also sensitive in the evaluation of masses with calcification and/or fat. MRI has an important role in evaluating complex urogenital anomalies because of its excellent soft tissue contrast and multiplanar capability.

27.2.2 Testis

For imaging of the scrotum, US is usually the first-line imaging modality. Major indications include evaluation of a scrotal mass or pain, scrotal inflammation, scrotal fluid collection, varicocele, and impalpable testis. With the advanced color Doppler US, US became the most useful tool in the evaluation of scrotal diseases. On US, the normal testis has a homogeneous echo texture of medium echogenicity. The mediastinum testis is seen as a hyperechoic line extending caudally from the testicular hilum. The tunica albuginea is

usually not seen on US. The epididymis is seen as an elongated structure that surrounds the testis. The head, body, and tail of the epididymis vary in size, shape, and echogenicity. The echogenicity of the epididymis is similar to or lower than that of the testis (Woodward et al. 2002; Dogra et al. 2003; Aso et al. 2005).

MRI can be used as a problem-solving modality. It is indicated when US is equivocal or suboptimal or when there is a discrepancy between the clinical and US findings. On MRI, the normal testis is seen as a sharply demarcated oval structure with homogeneous signal intensity. It presents intermediate signal intensity on T1-weighted images and high signal intensity on T2-weighted images. The tunica albuginea is seen as a thin stripe of low signal intensity on both T1- and T2-weighted images. The mediastinum testis appears as a characteristic low-intensity stripe on T2-weighted images. The signal intensity of the epididymis is similar to that of the testis on T1-weighted images and much lower than that of the testis on T2-weighted images (Woodward et al. 2002; Kim et al. 2007).

Other imaging modalities including CT, radioisotope scintigraphy, and angiography are used rather infrequently. Because of limited spatial resolution and risk of radiation damage to the testis, CT is not commonly used for imaging of the scrotum. However, it is useful in localization of undescended abdominal testis and is most commonly used for staging of testicular cancer. Radioisotope scan can be used for the differential diagnosis of acute scrotum (Hricak et al. 1995).

27.3 Spectrum of Pediatric Uterus, Ovary, and Testis Diseases

27.3.1 Uterus and Ovary

27.3.1.1 Hydro(metro)colpos

Hydro(metro)colpos is defined as a dilated uterus and vagina. The causes of the obstruction range from vaginal atresia to imperforate hymen to a vaginal diaphragm. Infantile hydro(metro)colpos often presents as an abdominal mass by excessive accumulation of vaginal or uterine secretions resulting from the influence of maternal hormone. Most cases of hydro(metro)colpos caused by imperforate hymen are not discovered until menarche and then present with amenorrhea with cyclic lower abdominal pain or an abdominal mass (Siegel 2002a; Garel et al. 2001).

US reveals a tubular fluid-filled midline mass representing the dilated vagina with or without internal echoes from the accumulated secretions (Fig. 27.1a). Transperineal US may be helpful for accurate evaluation of the level and extent of vaginal obstruction (Siegel 2002a). A contrast-enhanced CT and MRI scan of the abdomen and pelvis demonstrate

significant hematocolpos that is causing marked distention of the cervix and vagina (Junqueira et al. 2009) (Fig. 27.1).

27.3.1.2 Rectovaginal Fistula

Rectovaginal fistula is an abnormal connection between the rectum and the vagina. Gas or stool may leak from the bowel into the vagina. Some rectovaginal fistulas can be closed on their own. Most will need a surgery for repair. The most common causes of a rectovaginal fistula are Crohn's disease; complications following surgery to the perineum (area between vagina and rectum), vagina, rectum, or anus; radiation treatment or cancer in the pelvic area; and perianal infection. The usual symptoms are passing stool or gas via the vagina, foul-smelling vaginal discharge, and recurrent vaginal infections (Teresa and Jaime 2010).

Transperineal US reveals hypoechoic fistula tract with or without air and fecal materials. Fistulography with contrast demonstrates contrast-filling fistula tract between vagina and rectum (Fig. 27.2).

27.3.1.3 Precocious Puberty

Precocious puberty is defined as the development of secondary sex characteristics (including menarche) before 8 years in girls and 9 years in boys. Precocious puberty is classified into two types: (1) central, or true, precocious puberty and (2) peripheral, or pseudo-, precocious puberty (Chung et al. 2012).

Central precocious puberty (true precocious puberty) is gonadotropin-dependent and always isosexual. This entity is idiopathic (approximately 85–90 %) or related to a central nervous system (CNS) lesion. Central precocious is usually idiopathic in girls, whereas the vast majority of cases in boys are due to an intracranial lesion. Brain MRI is essential to evaluate CNS conditions leading to central precocious puberty, such as tuber cinereum hamartoma or increased intracranial pressure (Fig. 27.3). US shows the augmentation of uterine and ovarian volumes with adult pear configuration and a midline endometrial echo (Siegel 2002a; Chung et al. 2012).

Peripheral precocious puberty (pseudoprecocious puberty) is gonadotropin-independent and may be isosexual or heterosexual. It is caused by an excess in circulating estrogen, the sources of which may be the ovaries, adrenal gland, or exogenous (Fig. 27.4). Autonomous ovarian follicular cysts are the most frequent cause of peripheral precocious puberty. Bone age is often normal. Serum assays show a high estradiol level, low levels of follicle stimulating hormone and luteinizing hormone, and no response to stimulation with luteinizing hormone–releasing hormone. US demonstrates a stimulated uterus and a unilateral follicular ovarian cyst with characteristic “daughter cyst sign” in girls and testicular mass or unilateral diffuse enlargement in boys (Chung et al. 2012; Garel et al. 2001).

27.3.1.4 Congenital Anomalies of Uterus and Vagina

The uterus, fallopian tubes, and upper two-thirds of the vagina are formed by fusion of the two Müllerian ducts by 6 weeks of gestational age (Fig. 27.5). Incomplete fusion of the distal segment of the Müllerian ducts results in various degrees of bifidity of the uterus or vagina, or both. Partial fusion of only the caudal ends of the Müllerian ducts results in a *bicornuate uterus* (Fig. 27.6). Complete nonfusion results in a *uterine didelphys* (Fig. 27.7), in which unilateral vaginal obstruction can be associated with ipsilateral renal anomaly such as agenesis or severe dysplasia. The US findings of uterine didelphys and bicornuate uterus are two widely divergent horns, a deep concave fundal cleft, and two separate endometrial cavities. The distinguishing point of two diseases is that a uterine didelphys has two separate uterine horns and cervixes and a bicornuate uterus has one cervix and one vagina (Siegel 2002a).

Failed development of unilateral Müllerian duct results in a unicornuate uterus, and the affected horn may be absent or hypoplastic. If a rudimentary horn is present, it may or may not contain endometrium, and it may or may not communicate with the developed uterine cavity (Fig. 27.8). Failed or arrested development of both Müllerian ducts results in absence or hypoplasia of the uterus, *uterine agenesis or hypoplasia*. Mayer–Rokitansky–Küster–Hauser syndrome or Müllerian agenesis is characterized by an absent or rudimentary uterus with vaginal atresia and normal ovaries (Fig. 27.9). Renal anomaly such as agenesis or ectopia is frequently associated with skeletal or spinal anomaly in the patients with this syndrome (Siegel 2002a; Junqueira et al. 2009).

The diagnosis of Müllerian duct anomalies can be made by various imaging modalities. MRI is the best choice in the diagnosis of Müllerian duct anomalies, because the presence or absence of functional endometrium in the uterus and cervix can be determined on T2-weighted images. On cross-sectional imaging, hypoplastic uterus has a small length (less than 5 cm), reduced intercornual distance (less than 2 cm), and poor zonal differentiation (Junqueira et al. 2009).

27.3.1.5 Tubo-ovarian Abscess

Pelvic inflammatory disease occurs commonly in sexually active adolescents. It is recognized on the basis of clinical criteria (pelvic pain, fever, cervical motion, and adnexal tenderness) and laboratory criteria (*Chlamydia trachomatis* in 45 % of cases). The inflammatory process begins in the cervix, ascending to the endometrium, to the fallopian tubes, and, rarely, to the ovaries, parametrium, and peritoneal cavity (Siegel 2002a; Surratt and Siegel 1991).

US is useful only for detecting complications such as hydrosalpinx, pyosalpinx, tubo-ovarian abscess, and cul-de-sac abscess. Pyosalpinx appears as a hypoechoic tubular

mass with internal debris, whereas tubo-ovarian abscess is seen as a complex mass with debris, septations, and irregular thick walls (Siegel 2002a). At CT, a tubo-ovarian abscess often appears as a soft tissue mass with central areas of lower attenuation and thick enhancing walls (Fig. 27.10). Occasionally, air or an air–fluid level may be seen. Thickening of adjacent bowel and mesentery can also be seen (Surratt and Siegel 1991).

27.3.1.6 Ovarian Torsion

The ovarian torsion is a twisting of the ovary on its ligamentous supports containing vessels for ovarian blood supply. It may involve only the ovary, but more often accompanies torsion of the fallopian tube. Ovarian torsion is a rare problem within the pediatric population and about 15 % of ovarian torsion occurs in children. Torsion occurs more frequently in adolescents and young women. For premenarchal patients, adnexal torsion occurs mostly in neonates. Torsion occurs frequently (60 %) on the right side presumably because the sigmoid colon leaves limited space for adnexal movement. Ovarian torsion presents as acute abdominal pain in children. Symptoms of ovarian torsion can be confusing, simulating gastroenteritis, appendicitis, intussusceptions, or any other acute abdominal disorder in a girl. In children, torsion of the normal ovary is due to the excessive mobility of the ovary and relatively long fallopian tube. Ovarian torsion occurs more commonly in patients with predisposing lesions such as an ovarian cyst or an ovarian mass (teratoma) (Siegel 2002a; Matthew and Bobby 2012).

On US, the involved ovary appears markedly enlarged with multiple enlarged follicles at the periphery, or as a complex cystic mass. Other findings include a dilated fallopian tube, cul-de-sac fluid, and underlying pathology such as a cyst or tumor. Color Doppler US can be helpful in the diagnosis of torsion by demonstrating the absence of flow in the ovary. Teratoma undergoes torsion in 30 % of cases and is bilateral in 10 % of pediatric and adolescent cases (Siegel 2002a). CT or MRI is more objective and helpful, especially in detecting hemorrhagic component when presentation is subacute. The torsion knot is also occasionally demonstrable on CT or MRI (Fig. 27.11). Common CT and MRI features of adnexal torsion include fallopian tube thickening, smooth wall thickening of the twisted adnexal cystic mass, ascites, and uterine deviation to the twisted side (Rha et al. 2002).

27.3.1.7 Hernia of Uterus and Ovary

An inguinal mass is a common finding in infancy. In female infants, the most common causes of inguinal mass are intestinal inguinal hernia and inguinal hernia containing ovary. During the third month of fetal life, the peritoneum outlining the abdominal wall protrudes into the internal ring to form an outpouching, which is known as the processus vaginalis in males and the canal of Nuck in females. The canal of Nuck

follows the round ligament that extends from the ovary to the labia. The canal closes within 1 year after birth. The small intestine, bladder, omentum, testes, ovary, fallopian tube, and uterus have all been described within the inguinal canal hernia (Jedrzejewski et al. 2008). In females, the hernia often presents as a nontender, small, firm groin mass. In females, nonreducible ovaries are found at approximately 4–37 % inguinal hernias at the time of surgery, of which 2–33 % are twisted and sometimes infarcted (Jedrzejewski et al. 2008; Rasalkar et al. 2010).

Ultrasound is an excellent modality for evaluating structural abnormalities of the groin. The well-defined ovoid mass with peripheral cysts and a hypoechoic mass containing a hyperechoic region are the key US findings, suggesting that the ovary and the endometrium of the uterus passed through the inguinal canal (Fig. 27.12) (Jedrzejewski et al. 2008). Concurrent use of color Doppler depicts the vascularity (Fig. 27.13) and can reveal early vascular compromise.

27.3.1.8 Ovarian Tumors

Ovarian masses in children consist of functional cyst in approximately 60 % and neoplasm in 40 % of cases. About two-thirds of ovarian tumors are benign, and one-third of ovarian neoplasms are malignant. The ovarian tumors are classified of their origin as germ cell tumors (60–90 %), sex cord-stromal tumors (10–13 %), epithelial tumors (5–11 %), and miscellaneous tumors. Teratomas and cystadenomas are the most common benign ovarian tumors in children, with teratomas occurring more commonly than cystadenomas (Garel et al. 2001; Shah et al. 2011).

US is the initial study of choice for screening of pelvic masses due to its widespread availability and ease of use. Although it is often difficult to distinguish benign versus malignant ovarian tumors, US features suggesting malignancy include papillary projections, calcification, fluid in the cul-de-sac, tumors larger than 10 cm in largest diameter, lesions with irregular walls, and thickened irregular septa (Timmerman et al. 2008; Siegel 2002a).

The CT findings indicating malignancy are same with US. However, the mass may be better visualized in larger patients on CT. Ascites, hepatic metastases, lymphadenopathy, and omental, mesenteric, or peritoneal implants suggest intra-abdominal spread. Extensive omental implants may occur, referred to as omental caking (Shah et al. 2011). CT is the initial study of choice for staging, as it allows for visualization of spread into the chest, abdomen, and pelvis. MRI is superior to CT in some cases when evaluating the invasion of pelvic side wall and adjacent organs (Siegel 2002a).

Ovarian Cyst

Ovarian cysts may be classified as physiologic, functional, or neoplastic. When a normal mature follicle fails to involute and continues to enlarge secondary to hormonal imbalance,

a functional or retention cyst results. These cysts may develop from preovulatory follicles (follicular cysts) or from postovulatory follicles (corpus luteum cysts) and usually range from 4 to 10 cm in size. It is important to recognize that normal physiologic follicles are less than 3 cm in diameter. Retention cysts are usually asymptomatic and detected incidentally on sonograms, but corpus luteum cysts tend to be more symptomatic. Follicular and corpus luteum retention cysts cannot be differentiated with imaging studies. Serial sonography is essential, since the majority of functional cysts demonstrate cyclic changes or regress spontaneously (Surratt and Siegel 1991; Siegel 2002a).

On US, a nonhemorrhagic functional cyst is a classically anechoic, thin-walled, unilocular mass with posterior acoustic enhancement (Fig. 27.14). Hemorrhagic cysts have a wide spectrum of sonographic findings, reflecting the age of the blood. Most hemorrhagic ovarian cysts (85 %) are seen as complex masses and contain septations, low-level echoes, a fluid–debris level, or clotted blood. The remaining cysts are homogeneous and usually hyperechoic to uterus. More than 90 % of lesions have increased sound transmission reflecting its underlying cystic nature. The cysts are avascular on color Doppler imaging (Siegel 2002a).

Germ Cell Tumors

Germ cell tumors constitute the most common type of ovarian neoplasms and usually affect postpubertal females. The most common presenting symptom of these tumors is abdominal pain, followed by abdominal distention and a palpable mass. The histological subtypes of germ cell tumors according to the World Health Organization (WHO) include teratoma (mature, immature, and mixed), dysgerminoma, endodermal sinus tumor (yolk sac tumors), embryonal carcinoma, polyembryoma, and ovarian nongestational choriocarcinoma (Epelman et al. 2011).

Teratomas

Teratomas are the most common germ cell tumor and more common in adolescence than in childhood. Of the teratomas, about 90 % are benign and 10 % are malignant. Though typically asymptomatic, two-thirds of patients may present with an abdominal or pelvic mass, the remainder with pain secondary to torsion, hemorrhage, or rupture. Teratomas are usually unilateral, but bilateral in 10–25 % of cases (Fig. 27.15), and undergo torsion in up to 30 % of cases (Surratt and Siegel 1991; Garel et al. 2001).

Mature cystic teratomas or dermoid cysts typically contain mature tissues of ectodermal (skin, brain), mesodermal (muscle, fat, bone, cartilage), and endodermal (mucinous or ciliated epithelium) origin. Cystic teratoma is the most common tumor, accounting for two-thirds of pediatric ovarian tumors and more than 90 % of all benign ovarian neoplasms (Surratt and Siegel 1991; Outwater et al. 2001). Immature

teratomas typically affect a younger age group and have a worse prognosis. The level of malignancy is determined by the proportion and degree of neuroectodermal tissue differentiation (Epelman et al. 2011). Immature teratomas are usually larger (14–25 cm) and show a predominantly solid appearance with scattered foci of fat and calcifications (Fig. 27.16).

The US findings of teratomas are variable depending on the contents of the lesion, such as sebum, serous fluid, teeth, bone, hair, and fat. Teratomas are often complex, ranging from purely cystic to completely solid with echogenic calcifications and/or fat, mural nodules, floating debris, fluid levels, or any combination of the aforementioned components (Fig. 27.17). Mural nodules, the so-called Rokitansky nodule, are seen in up to 70 % of postpubertal females and 40 % of prepubertal females (Siegel 2002a). Acoustic shadowing on US occurs in up to 50 % of teratomas and it is secondary to calcification or a matted mixture of sebum and hair (Surratt and Siegel 1991).

On CT, ovarian teratomas show a variable mixture of internal fat, fluid, and calcification. Mural nodules (*dermoid plugs*), fat–fluid levels, and floating debris may also be seen (Surratt and Siegel 1991). CT is usually adequate to characterize ovarian masses and define tumor extension. Teratomas rarely rupture into the peritoneal cavity, bladder, small bowel, rectum, sigmoid colon, vagina, or through the abdominal wall. Multiple small peritoneal implants and variable ascites may simulate carcinomatosis or tuberculous peritonitis (Epelman et al. 2011; Shah et al. 2011). Imaging findings of immature teratomas are usually larger (>7.5 cm) and demonstrate prominent areas of soft tissue, scattered foci of fat, and fewer calcifications. Specifically, the suggestive findings of malignancy are central necrosis within a solid mass, thickened irregular septa, and papillary projections (Epelman et al. 2011).

MRI reveals a heterogeneous lesion of variable signal intensity. Serous fluid is of low intensity on T1-weighted and bright on T2-weighted sequences, whereas intralesional fat is of high signal intensity on T1-weighted and T2-weighted sequences. Fat-suppressed sequences are useful to distinguish between intratumoral nonsuppressing hyperintense blood products and suppressing fat. Calcified structures, such as bone and teeth, as well as hair, demonstrate low T1 and T2 signal intensity. Contrast-enhanced image shows variable enhancement of the solid portions and the cyst walls (Fig. 27.18) (Surratt and Siegel 1991). Other findings such as fat–fluid levels, floating debris, dependent layering, calcifications, and rounded mural nodules (Fig. 27.15) may also be seen well (Shah et al. 2011; Epelman et al. 2011).

Ovarian Dysgerminoma

Dysgerminoma is the least differentiated type of germ cell tumor and is equivalent to seminoma in males. Dysgerminoma

is rare in the pediatric population, but it is the most common malignant ovarian germ cell tumor. This tumor is either pure or combined with other elements and mainly affects adolescent and young girls. The median age of presentation is 16 years, and tumor markers include lactate dehydrogenase and β -HCG (Shah et al. 2011; Epelman et al. 2011).

Because it has a nonspecific imaging appearance, it is difficult to differentiate from other ovarian masses. With imaging, ovarian dysgerminomas show a solid, lobulated mass (Fig. 27.19). Enhancement of fibrovascular septa is also present after contrast administration (Shah et al. 2011). It is not uncommon to see fine stippled calcifications or small cysts within the tumor, due to the result of necrosis and hemorrhage. Bilateral involvement occurs in approximately 10–15 % of cases. Dysgerminoma is the only ovarian malignancy that spreads via the lymphatic system (pelvic and retroperitoneal LNs) and is highly radiosensitive (Epelman et al. 2011).

Endodermal Sinus Tumors (Yolk Sac Tumors)

Ovarian endodermal sinus tumor, also known as yolk sac tumor, shows selective differentiation toward yolk sac and vitelline structures (Siegel 2002a). These tumors are rare in the pediatric population, but they are the second most common malignant germ cell tumor (20 %) after dysgerminoma. The average age at presentation is between 18 and 19 years, and they are typically large at the time of diagnosis. Patients have an elevated AFP in 75 % of tumors and AFP can be a useful marker for evaluation of tumor recurrence. Cross-sectional imaging with US, CT, and MR shows a large, complex pelvic mass that extends into the abdomen and contains both solid and cystic components (Fig. 27.20). The cystic areas are composed of epithelial-lined cysts produced by tumor or of coexisting mature teratomas (Jung et al. 2002). Extension into peritoneum and adjacent structures, including the spinal canal, is not uncommon (Shah et al. 2011). These tumors grow rapidly and have a poor prognosis.

Malignant Mixed Germ Cell Tumor

Malignant mixed germ cell tumor is composed of more than one of the malignant germ cell tumors mentioned above, comprising 8 % of all malignant germ cell tumors of the ovary (Brammer et al. 1990). The imaging appearance varies according to individual constituents of tumor. They are usually complex, predominantly solid masses with varying amounts of cystic components (Fig. 27.21).

Sex Cord-Stromal Tumors

Sex cord-stromal neoplasms originate from nongerminative tissue and arise from sex-cord-derived cells (granulosa cells in the normal ovary, Sertoli cells in ovarian tumors) and ovarian stromal cells (fibroblasts, theca cells, and Leydig cells). The most common tumors are granulosa cell

(75 %) and Sertoli–Leydig cell tumors (15 %) (Siegel 1997). The most common presenting symptom is abdominal pain with or without an associated abdominal mass (Epelman et al. 2011). Sex cord-stromal neoplasms are usually hormonally active and are classically associated with either isosexual precocious puberty (juvenile granulosa cell tumor) or virilization and hirsutism (Sertoli–Leydig cell tumors) (Siegel 2002a). Sex cord-stromal tumors metastasize by lymphogenous spread to regional or distant lymph nodes and/or hematogenous dissemination to the lungs and liver (Shah et al. 2011).

Fibroma–Thecoma

Fibromas, thecomas, or fibrothecomas are forms of a spectrum of benign tumors arising from the stromal components of the ovaries. These tumors are infrequent and are even more unusual in the pediatric population. Fibromas are the most common of the sex cord-stromal tumor and rarely seen in patients younger than 40 years of age and are classically associated with Meigs syndrome, ascites and right-side pleural effusion, which resolve following tumor resection (Outwater et al. 1998). Their US and MRI appearances are variable and depend on the amount of fibrous tissue. US reveals a homogeneous hypoechoic mass with posterior acoustic shadowing. These tumors typically have a low signal on T1- and T2-weighted images (Fig. 27.22). Additionally, the delayed, weak enhancement in dynamic contrast exams is seen due to a preponderance of fibrous tissue in tumors. With CT, these tumors manifest as a homogeneous solid tumor with a variable degree of delayed enhancement. Calcifications may be present (Jung et al. 2002). As these neoplasms increase in size, myxoid or cystic degeneration can occur, causing a heterogeneous appearance and less contrast enhancement. Ascites has been reported in 30–82 % of these patients (Outwater et al. 1998; Epelman et al. 2011).

Epithelial Tumors

Epithelial neoplasms of the ovary, including cystadenomas and cystadenocarcinoma, represent about 10–17 % of all ovarian tumors in children and are extremely uncommon in premenarchal girls (Shah et al. 2011). Most epithelial neoplasms are serous, followed by other miscellaneous epithelial tumors, mucinous tumors, endometrioid tumors, and clear cell tumors, in order of frequency. Each of these tumors is further classified as benign, borderline, or malignant, according to the histological characteristics and clinical behavior of the tumor (Epelman et al. 2011). Cystadenomas are the most common histological types in the pediatric age group, with serous types being more common than mucinous types. Presenting symptoms include nonspecific abdominal pain or a painless abdominal mass (Morowitz et al. 2003).

Serous cystadenomas appear as unilocular or multilocular cystic masses with homogeneous cystic components and thin septa and wall but without papillary projections. On MRI, these tumors show a variable appearance, but are typically large cystic pelvic or abdominal masses ranging from 4 to 20 cm in size. The contrast-enhanced image shows enhancement of the thin septa and cyst wall (Fig. 27.23) (Shah et al. 2011).

Mucinous cystadenomas rarely occur in the pediatric population, occurring more frequently in postpubertal females. Mucinous cystadenomas have the potential to be malignant mucinous cystadenocarcinomas and may metastasize through peritoneal/omental seeding. On US, CT, and MRI, they typically present as large, multiloculated cystic masses with thin septations and locules that contain fluids of different CT attenuations or MR signal intensities. The locules in these tumors are typically small and numerous (Fig. 27.24) (Jung et al. 2002; Shah et al. 2011).

Cystadenocarcinoma is exceedingly rare in the pediatric population. It presents as an asymptomatic pelvic or abdominal mass or with findings related to metastatic disease. Imaging findings, suggesting malignant tumors, include a thick, irregular wall, thick septa, papillary projections, and a large soft tissue component with necrosis (Fig. 27.25). Ancillary findings that increase diagnostic confidence for malignancy are pelvic organ invasion and implants (peritoneal, omental, mesenteric) (Jung et al. 2002).

Secondary Ovarian Neoplasms

Secondary neoplasms include leukemia and lymphoma. Metastatic spread to the ovary is rare in children, and it usually occurs hematogenously. It is most commonly associated with mucinous adenocarcinoma of the colon, followed by Burkitt lymphoma, alveolar rhabdomyosarcoma, Wilms tumor, neuroblastoma, and retinoblastoma, in order of frequency. Bilateral involvement is encountered in as many as 56 % of these patients (McCarville et al. 2001). Large or bilateral ovarian masses should raise suspicion of an underlying malignancy elsewhere that has metastasized to the ovary (Shah et al. 2011). Imaging findings are unilaterally or bilaterally enlarged, variably enhancing solid lesions with small peripheral follicles (Fig. 27.26).

27.3.2 Testis

27.3.2.1 Processus Vaginalis–Related Disorders Cryptorchidism (Undescended Testis)

Cryptorchidism or undescended testis refers to the condition in which the testis is not located at its normal position within the scrotum. The testes originate within the retroperitoneum and migrate downward through the internal inguinal ring, inguinal canal, and external inguinal ring to the scrotum.

Cryptorchidism is caused by complete or partial failure of the intra-abdominal testes to descend into the scrotal sac. The undescended testis may be located anywhere along the normal course of testicular descent, from the level of the inferior pole of the kidney to the upper scrotum (Dogra et al. 2003). The most common location is in the inguinal canal (72 %), followed by prescrotal (20 %) and abdominal (8 %) locations (Dogra et al. 2003). In 80 % of patients, the testis is palpable in the inguinal canal and there is no need for an imaging evaluation. In 20 % of patients with cryptorchidism, the testis is nonpalpable and the imaging evaluation is needed to identify whether a viable testis is present (Siegel 2002a; Vijayaraghavan 2011).

US is useful only for identifying testes in the inguinal canal or the prescrotal region just beyond the external inguinal ring (Fig. 27.27). The undescended testis is usually smaller and isoechoic or hypoechoic relative to the normal testis (Fig. 27.28) (Aso et al. 2005). When the testis is located in the abdomen, shadowing from bowel gas impairs its visualization at US. MRI can be performed for evaluation of suspected abdominal testes. Since abdominal testes are prone to malignant degeneration (risk ratio of 2.5 to 8) (Dogra et al. 2003), laparoscopic surgery may be required in these cases.

Transverse Testicular Ectopia

Transverse testicular ectopia (TTE) is a rare congenital anomaly in which both testes migrate toward the same hemiscrotum. In most cases, the correct diagnosis is not made preoperatively, because TTE is clinically misdiagnosed as an undescended testis on the contralateral side or as a symptomatic inguinal hernia or as a testis tumor on the side to which the ectopic testis has migrated (Cho et al. 2007). US and MRI can detect the two testes with each spermatic cord at the same side and so provide useful information about any associated anomalies (Fig. 27.29).

Inguinoscrotal Hernia

Inguinoscrotal hernia is defined as the passage of intestinal loops and/or omentum into the scrotum, through an incomplete obliterated processus vaginalis. It is most common in preterm neonates, especially at 32 weeks gestation (Aso et al. 2005). The hernia is more frequently located on the right side, since the right processus vaginalis closes after the left (Siegel 2002b). The hernia most commonly contains bowel and omentum. Rare contents include other abdominal organs, such as Meckel diverticulum, urinary bladder, and others (Dogra et al. 2003).

US examination is indicated in patients with inconclusive physical findings, in patients with acute scrotum, and to investigate contralateral involvement. At grayscale US, the scrotum is partially occupied by one or more round structures containing air bubbles or fluid (Fig. 27.30). The diagnosis of hernia is achieved by visualization of air

bubble movement and/or intestinal peristalsis during the real-time examination (Dogra et al. 2003). The herniated omentum is seen as a highly echogenic structure. US examination should include both inguinal canals, since a clinically inapparent contralateral hernia can be found in 88 % of cases. Inguinal rings larger than 4 mm are an indication for prophylactic herniorrhaphy (Aso et al. 2005). Color or power Doppler US may be used to investigate vascularity within the omentum as well as intestinal and testicular perfusion (Fig. 27.31). Urgent surgery is indicated when the imaging study shows an akinetic dilated bowel loop (*a sign of strangulation*) or impaired testicular perfusion (Garriga et al. 2009).

Hydrocele (Scrotal Versus Cord)

Hydrocele is an abnormally large collection of fluid between the visceral and parietal layers of the tunica vaginalis and/or along the spermatic cord. It is the most common cause of painless scrotal swelling in children (Aso et al. 2005). The normal scrotum contains 1–2 mL of serous fluid in the potential tunica vaginalis cavity, and it should not be mistaken for hydrocele. Nearly all hydroceles are congenital in neonates and infants. Congenital hydroceles are associated with a patent processus vaginalis that allows entry of peritoneal fluid into the scrotal sac (Martin et al. 1996). Most congenital hydroceles (80 %) resolve spontaneously before the age of 2 years. In older children and adolescents, hydroceles are usually acquired and are the result of an inflammatory process, testicular torsion, trauma, or a tumor (Aso et al. 2005; Dogra et al. 2003).

At US, congenital hydrocele appears as an anechoic fluid collection surrounding the anterolateral aspects of the testis and sometimes extending to the inguinal canal (Fig. 27.32b). It may occasionally manifest as a fluid collection with low-level swirling echoes, secondary to protein aggregation or deposition of cholesterol crystals (Gooding et al. 1997).

Hydrocele of the spermatic cord is a rare anomaly that results from an aberration in the closure of the processus vaginalis. It is a loculated fluid collection along the spermatic cord, separate from the testis and the epididymis and located above them (Martin et al. 1996). There are three types of spermatic cord hydrocele: communicating, funicular, and encysted (Fig. 27.33) (Garriga et al. 2009).

A *communicating hydrocele* is associated with complete patency of the processus vaginalis. At US, it appears as a fluid collection that extends from the pelvis through the deep inguinal ring to the scrotum (Figs. 27.32a and 27.33b).

A *funicular hydrocele* is a result of abnormal obliteration of the deep inguinal ring, with constriction just above the testis. At US, it resembles a peritoneal diverticulum, appearing as a fluid collection that communicates with the peritoneum at the deep inguinal ring and that does not surround the testicle (Fig. 27.33c) (Martin et al. 1996).

An *encysted hydrocele* is enclosed between two constrictions at the deep inguinal ring, just above the testis. It does not communicate with the peritoneum. An encysted hydrocele may be located anywhere along the spermatic cord (Martin et al. 1996). Its size and shape do not change with increased peritoneal pressure. At US, an ovoid or round mass is seen along the spermatic cord and the internal echogenicity varies depending on the contents (Figs. 27.33d and 27.34) (Garriga et al. 2009).

27.3.2.2 Varicocele

Varicocele is an abnormal dilatation of veins in the pampiniform plexus of the spermatic cord and is usually caused by incompetent valves in the internal spermatic vein. It is relatively common and most cases are idiopathic. Varicocele is found mainly in adolescents and young adults (Aso et al. 2005; Chen and John 2006). Varicocele is more frequent on the left side for the following reasons: (a) The left testicular vein is longer; (b) the left testicular vein enters the left renal vein at a right angle; (c) the left testicular artery in some men arches over the left renal vein, thereby compressing it; and (d) the descending colon distended with feces may compress the left testicular vein (Mehta and Dogra 1998; Dogra et al. 2003).

At US, the varicocele appears as multiple, anechoic, tortuous tubular structures along the spermatic cord. The dilated veins have varying sizes larger than 2 mm in diameter that are usually best visualized superior and/or lateral to the testis. On color Doppler images, venous flow is better demonstrated during the Valsalva maneuver or erect position (Fig. 27.35) (Dogra et al. 2003). Varicocele may affect testicular growth; hence, testicular volumes should be systematically measured and asymmetries assessed with US (Aso et al. 2005).

27.3.2.3 Acute Scrotum

The *acute scrotum* refers to a clinical picture of sudden-onset scrotal pain, redness, and swelling; it is most commonly caused by acute epididymo-orchitis, torsion of the testicular appendages, or testicular torsion. Since scrotal involvement is usually unilateral, we begin the examination on the asymptomatic side to have a basis for comparison. Color Doppler imaging should always be added to the grayscale US study for evaluation of intratesticular vessels of low flow velocity. Comparable transverse Doppler scans of both testes are essential to study testicular perfusion discrepancies. The Doppler US findings are inconclusive, and nuclear medicine or MRI can assist in the diagnosis and management decision (Siegel 2002b; Aso et al. 2005).

Epididymo-orchitis

Epididymo-orchitis is a common cause of acute scrotum in children and usually results from descending infection, such

as urinary tract infection. The infection usually originates in the bladder or prostate gland, spreads through the vas deferens and the lymphatics to the epididymis, and finally reaches the testis, causing epididymo-orchitis. Isolated orchitis is very rare. The clinical manifestation ranges from mild tenderness to a severe febrile process. There are two peaks of prevalence: under 2 years of age and over 6 years of age. Most cases of epididymo-orchitis occur in boys over 6 years of age. The predisposing causes to epididymitis are imperforate anus, ureteral ectopia to the seminal vesicle, bladder exstrophy, neurogenic bladder, posterior urethral valves, and dysfunctional voiding, particularly seen in patients under 2 years of age (Aso et al. 2005).

Clinically, scrotal pain associated with epididymitis is usually relieved when the testes are elevated over the symphysis pubis (*the Prehn sign*). In adolescents, most cases are secondary to sexually transmitted organisms such as *Chlamydia trachomatis* and *Neisseria gonorrhoeae*. In prepubertal boys, the disease is most frequently caused by *Escherichia coli*. Complications of acute epididymitis include chronic pain, infarction, abscess, gangrene, infertility, atrophy, and pyocele (Siegel 2002b; Dogra et al. 2003; Chen and John 2006).

On US, the epididymal head is the most affected region, and reactive hydrocele and wall thickening are frequently present. The epididymis is focally or diffusely enlarged, and depending on the time of evolution, decreased, increased, or heterogeneous echogenicity are usually observed. On color Doppler imaging, the inflammation produces increased blood flow within the epididymis, testis, or both (Fig. 27.36) (Dogra et al. 2003).

Testicular Torsion

Testicular torsion occurred by twisting of the spermatic cord. In testicular torsion, venous obstruction occurs first, followed by obstruction of arterial flow and ultimately by testicular ischemia. The extent of testicular ischemia will depend on the degree of twisting (180° – 720°) and the duration of the torsion (Chen and John 2006). The testicular salvage rate depends on the degree of torsion and the duration of ischemia. A nearly 100 % salvage rate exists within the first 6 h after the onset of symptoms; a 70 % rate, within 6–12 h; and a 20 % rate, within 12–24 h (Siegel 2002b). Two types of testicular torsion have been described: intravaginal and extravaginal, the former being more common. Sonography, particularly color Doppler sonography, is the imaging method of choice to evaluate patients with acute scrotal pain (Siegel 2002b).

Intravaginal torsion occurs within the tunica vaginalis. A predisposing factor is the “bell clapper” deformity, in which the tunica vaginalis inserts high on the spermatic cord, preventing fixation of the testis to scrotum and allowing the testis to rotate freely on its vascular pedicle. It can occur at any

age but is more common in adolescents. Patients present with sudden onset of scrotal or lower abdominal pain, often accompanied by nausea, vomiting, and low-grade fever. Clinical findings include a tender testis with a transverse lie and a swollen, erythematous hemiscrotum (Aso et al. 2005). US findings vary with the duration and degree of rotation of the spermatic cord. The reduced or absent vascular perfusion in the affected testis in conjunction with readily detectable flow in the contralateral testis is diagnostic of acute torsion on color Doppler image (Fig. 27.37) (Dogra et al. 2003). In late torsion, color Doppler imaging typically shows marked hyperemia of the scrotal wall and paratesticular soft tissue with absent testicular flow (*rim sign*) (Fig. 27.37) (Siegel 2002b).

Extravaginal torsion is seen mainly in newborns and occurs prenatally in most cases. Torsion occurs outside the tunica vaginalis when the testes and gubernacula are not fixed and are free to rotate. The testis is typically infarcted and necrotic at birth and the hemiscrotum is swollen and discolored. US findings vary and include an enlarged heterogeneous testis, ipsilateral hydrocele, skin thickening, and no color Doppler flow signal in the testis or spermatic cord (Fig. 27.38) (Aso et al. 2005).

A definitive diagnosis of complete testicular torsion is made when blood flow is visualized on the normal side but is absent on the affected side. Incomplete torsion refers to cord twisting of less than 360° , in which some arterial flow persists in the affected testis (20 %). Meticulous comparison of the two testes by using transverse views is necessary in these cases (Siegel 2002b). Normal echogenicity with mild testicular enlargement is a good sign of viability, whereas marked enlargement, heterogeneous echotexture, and scrotal wall hypervascularity are signs of testicular infarction and necrosis (Fig. 27.38) (Siegel 2002b).

Torsion of the Testicular Appendages

The testicular appendages are remnants of the embryonic mesonephric and paramesonephric ducts and consist of vascularized connective tissue. The appendages are sessile structures, which predispose them to torsion. Torsion of the appendix testis or appendix epididymis is the most common cause of acute scrotal pain in prepubertal boys, with an incidence of 26–70 %. The peak incidence occurs between 6 and 12 years and it is more frequent on the left side (Siegel 2002b; Monga et al. 1999).

Affected patients typically present with gradual or sudden intense pain, usually localized in the upper pole of the testis. In approximately one-third of patients, a small, firm paratesticular nodule with bluish skin discoloration (“*blue-dot sign*”) is palpated in the upper scrotum. This finding is a pathognomonic, and US examination is not necessarily required for the diagnosis when it is present (Aso et al. 2005; Siegel 2002b).

The role of US examination is to exclude testicular torsion and acute epididymo-orchitis. At US, the twisted appendage is seen as a round extratesticular mass with high or mixed echogenicity depending on the evolution time. Associated findings include an enlarged epididymal head, reactive hydrocele, and thickening of scrotal skin. On color Doppler US, increased peripheral flow may be seen around the twisted testicular appendage, and there is no Doppler signal in the twisted appendage (Fig. 27.39); the epididymis and scrotal tunics are hypervascularized. Within days, the torsed appendix may atrophy and calcify, and then become detached, leaving a scrotal calcification, known as a scrotolith (Fig. 27.40) (Siegel 2002b; Chen and John 2006).

27.3.2.4 Scrotal Trauma

Scrotal trauma is not uncommon and typically results from a child abuse, motor vehicle accident or straddle injury, athletic injuries, or falls (Aso et al. 2005). The peak age range is from 10 to 30 years, and approximately 50 % of injuries are from athletic activity. Since swelling and pain limit physical examination, US is an ideal examination tool. Trauma can result in contusion, hematoma, fracture, or rupture of testis. Testicular hematoma produces a heterogeneously enlarged testis with focal areas of increased or decreased parenchymal echogenicity depending on the age of the hematoma. Color Doppler US shows a normally perfused testis except for focal areas of absent vascularity in the area of the hematoma (Siegel 2002b).

Testicular rupture results from disruption of the tunica albuginea and leads to extrusion of testicular contents into the scrotal sac. It is rare and surgical emergency, and more than 80 % of ruptured testes can be saved if surgery is performed within 72 h after injury (Dogra et al. 2003). US findings of testicular rupture include an interruption of the tunica albuginea, a heterogeneous testis with irregular poorly defined borders, scrotal wall thickening, and a large hematocele (Fig. 27.41). Color and power Doppler US are helpful to demonstrate disruption in the normal capsular blood flow of the tunica vasculosa (Siegel 2002b). Heterogeneous intratesticular lesions are made by hemorrhage or infarction. Direct visualization of a fracture line is rare and seen in only 17 % of cases (Dogra et al. 2003). MRI increases the diagnostic confidence and is useful in preoperative work-up of testicular rupture.

27.3.2.5 Testicular Microlithiasis

Testicular microlithiasis is a condition in which calcifications form in the lumen of the seminiferous tubules. It is an uncommon condition usually discovered incidentally at US examinations performed for unrelated reasons. The etiology is unknown. Testicular microlithiasis can be associated with several conditions, such as cryptorchidism, alveolar microlithiasis, congenital urethroperineal fistula,

Klinefelter syndrome, and germ cell neoplasm. The cryptorchidism is the most common (50 %) associated condition (Aso et al. 2005). Testicular microlithiasis is considered to be a premalignant condition. Thus, annual US follow-up is recommended for at least several years after diagnosis (Ganem et al. 1999).

The typical US appearance is characteristic and multiple nonshadowing echogenic foci measuring 2–3 mm and randomly scattered throughout the testicular parenchyma (Fig. 27.42) (Siegel 2002b). The presence of five or more foci on any single view in one testis is abnormal. The calcifications tend to be uniform in size and are distributed in a diffuse pattern (Fig. 27.43) or in peripheral clusters (Fig. 27.42) (Backus et al. 1994).

27.3.2.6 Tumors

Testicular tumors account for approximately 1 % of all pediatric solid tumors. They have two peaks of prevalence, before 3 years of age and in the postpubertal period, and usually manifest as a painless scrotal mass (Shah et al. 2011). But in approximately 10 % of patients, testicular tumor is associated with pain due to hemorrhage or infarction, mimicking torsion or epididymitis. Testicular tumors are divided into two groups: germ cell tumors and non-germ cell tumors (Aso et al. 2005).

US is the initial modality of choice to image scrotal masses. The principal role of US examination in the testicular masses is to confirm the presence of a lesion, determine its site of origin, and characterize its contents. Grayscale US is nearly 100 % sensitive for detection of testicular tumors, whereas the accuracy of US in distinguishing between intratesticular and extratesticular masses is 90–100 % (Siegel 2002b). This distinction is important because the majority of extratesticular masses are benign and intratesticular masses are more likely to be malignant (Dogra et al. 2003). Color Doppler and power Doppler US demonstrate increased vascularity in the majority of malignant tumors and help to better define testicular involvement (Shah et al. 2011).

CT is helpful for staging. MRI may be used for staging and as a problem-solving technique in some cases. The sensitivity in differentiating between intratesticular and extratesticular lesion is nearly 100 % (Siegel 2002b).

Germ Cell Tumors

Germ cell tumors represent 70–90 % of childhood testicular neoplasms. These tumors are classified on a pathologic basis into seminomatous, which are rare in the pediatric population, and nonseminomatous subtypes. Nonseminomatous germ cell tumors are further subdivided into yolk sac tumors, teratoma/teratocarcinoma, embryonal, and choriocarcinoma varieties.

Yolk sac tumor (endodermal sinus tumor) is the most common (80–90 %) germ cell tumor in childhood and mostly

occurs before the age of 2 years (Siegel 2002b). Clinically, patients present with asymptomatic testicular enlargement and an elevated serum α -fetoprotein (AFP) level in more than 90 % of cases. The marker is also useful in follow-up to check for regression or recurrence of tumor or presence of metastasis (Shah et al. 2011). The US findings are nonspecific, usually showing a solid mass replacing the entire testis (Fig. 27.44). The presence of hypoechoic areas within the tumor, which indicates areas of necrosis, is a frequent finding.

Teratoma is the second most common germ cell tumor and is classified as mature or immature. Testicular teratoma typically occurs in boys younger than 4 years and is usually benign (Siegel 2002b). The sonographic appearance depends on the components of the three germinal layers. Teratoma may appear as a cystic lesion with peripheral solid components (Fig. 27.45) or a complex mass with cystic components, calcifications, and echogenic intratumor fat. These tumors are usually benign in prepubertal children, so tissue-sparing surgery may be possible. However, they are often malignant in adolescents and require orchiectomy (Shah et al. 2011).

Testicular epidermoid cyst is the most common benign testicular tumor with no malignant potential in prepubertal boys. This relatively uncommon benign tumor is of germ cell origin, but contains only ectodermal tissue (Arellano et al. 2011). The cyst contains cheesy material and may resemble a solid tumor at US. The US appearance of epidermoid cyst varies with the maturation, compactness, and quantity of keratin within the cyst. Four US patterns have been described: (a) a target appearance – an echogenic center surrounded by halo, (b) a sharply defined mass with a rim of calcification, (c) a solid mass with a hyperechoic rim, and (d) the classic appearance of an “onion-ring” pattern with concentric alternating rings of hyperechoic and hypoechoic layers (Fig. 27.46). This onion-ring pattern is considered characteristic of an epidermoid cyst and corresponds to its natural evolution (Kim et al. 2007). The presence of well-delineated borders and avascularity at color Doppler US favors the diagnosis (Fig. 27.46). The combination of an onion-ring configuration, negative tumor-marker status, and avascularity

in the lesion helps to differentiate testicular epidermoid cyst from other germ cell tumors (Arellano et al. 2011). MRI can assist in identification in inconclusive cases. A similar onion-ring appearance with alternating bands of high and low T2 signal intensity can be revealed at MRI. On contrast-enhanced images, they are seen as sharply demarcated, hypointense, nonenhancing lesions. Since they have no malignant potential, conservative surgery is recommended in all cases (Kim et al. 2007).

Non-Germ Cell Tumors

Non-germ cell tumors, which are less frequent than germ cell tumors, can develop from the gonadal stroma (Leydig cell tumor), sex cord cells (Sertoli cell tumor), or sex cord cells plus stroma (gonadoblastoma).

Secondary Testicular Tumors

Secondary testicular tumors are caused by leukemia, lymphoma, and metastasis from solid tumors. These tumors represent less than 10 % of all testicular tumors (Shah et al. 2011). Secondary involvement is more common in patients with acute lymphoblastic leukemia and non-Hodgkin B-cell lymphoma. Testicular tumor involvement can occur at the time of initial diagnosis or after bone marrow remission. The testis can act as a sanctuary site for tumor cells, because the blood–testis barrier may prevent high levels of chemotherapeutic drugs. Clinically, patients present with painless, usually bilateral, testicular enlargement. At US, there are two types of involvement in both leukemia and lymphoma. The diffuse type is more common than the focal type. Typical US appearance by leukemic or lymphomatous infiltration is enlarged, homogeneous, hypoechoic testis, but focal hypoechoic masses may also occur (Fig. 27.47) (Siegel 2002b). Tumor involvement is usually bilateral, but it can be unilateral or asymmetric. Increased blood flow is seen on color Doppler images, simulating an inflammatory lesion (Fig. 27.47) (Mazzu et al. 1995). Both leukemia and lymphoma have distinctive low signal intensity on T2-weighted MR image that differs from most tumors, which are T2 high signal intensity (Boechat 1996).

27.4 Illustrations: Pediatric Uterus, Ovary, and Testis Diseases

27.4.1 Hydrometrocolpos

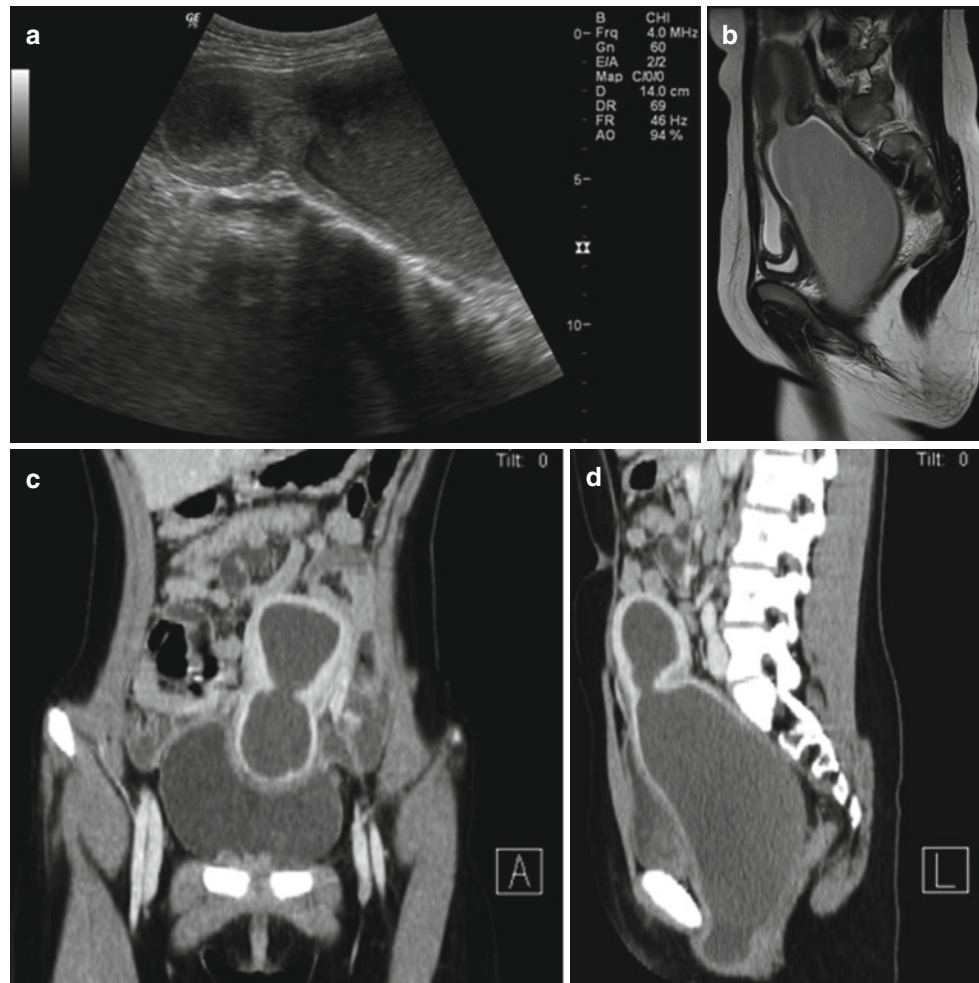


Fig. 27.1 Hydrometrocolpos in a 12-year-old girl with amenorrhea. (a) Longitudinal US shows a dilated, echogenic fluid-filled vagina and uterus. (b) T2-weighted sagittal MR image shows markedly dilated

vagina and endometrial cavity with hemorrhage of intermediate signal intensity. (c, d) Contrast-enhanced coronal and sagittal CT scans show cystic dilatation of the vagina and uterus due to vaginal obstruction

27.4.2 Vaginorectal Fistula

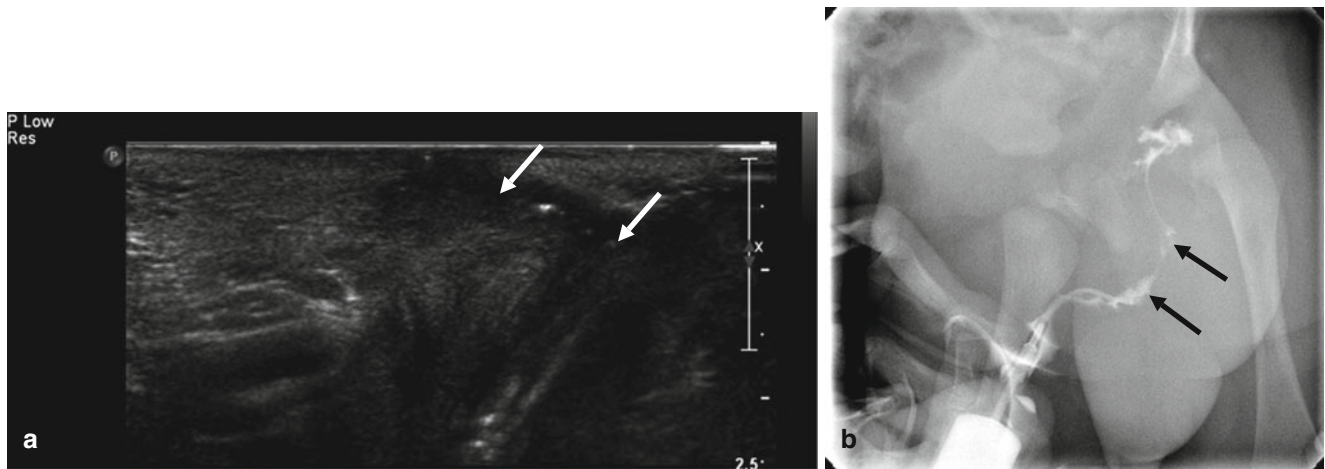


Fig. 27.2 Vaginorectal fistula in an infant with swelling and pus from labia. (a) Perineal US shows hypoechoic fistula tract with some hyperechoic air, connecting with rectum. (b) Fistulography shows contrast-filled, fistula tract from labia to rectum

27.4.3 Precocious Puberty

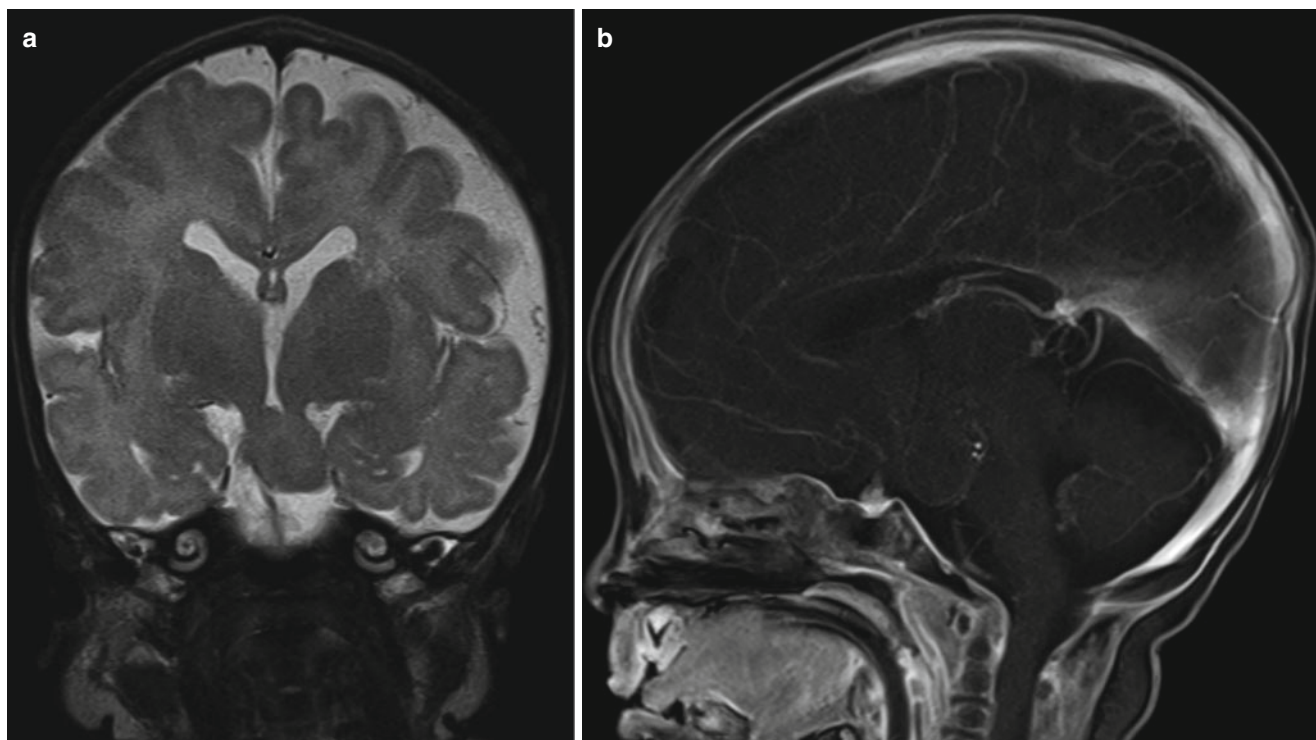


Fig. 27.3 Central precocious puberty in 5-year-old girl with vaginal bleeding. (a) T2-weighted coronal MR image shows focal mass at tuber cinereum. (b) Contrast-enhanced sagittal T1-weighted MR image shows no contrast enhancement of mass in tuber cinereum

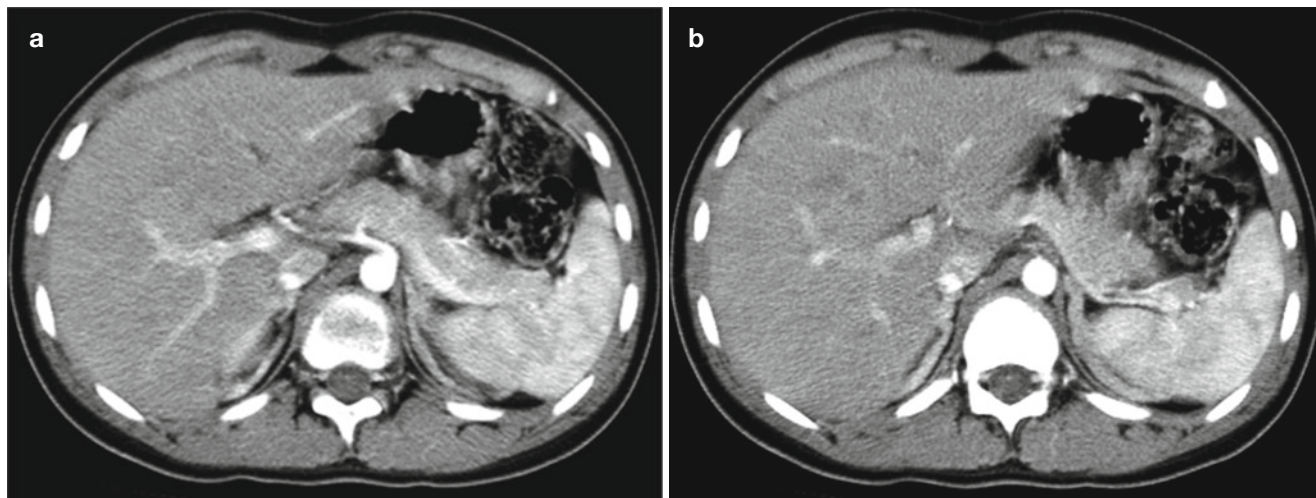


Fig. 27.4 Peripheral precocious puberty in 15-year-old girl with massive vaginal bleeding. (a) and (b) Contrast-enhanced axial CT scans show diffuse enlarged both adrenal glands, suggesting adrenal hyperplasia

27.4.4 Congenital Anomalies of Uterus and Vagina

Müllerian development

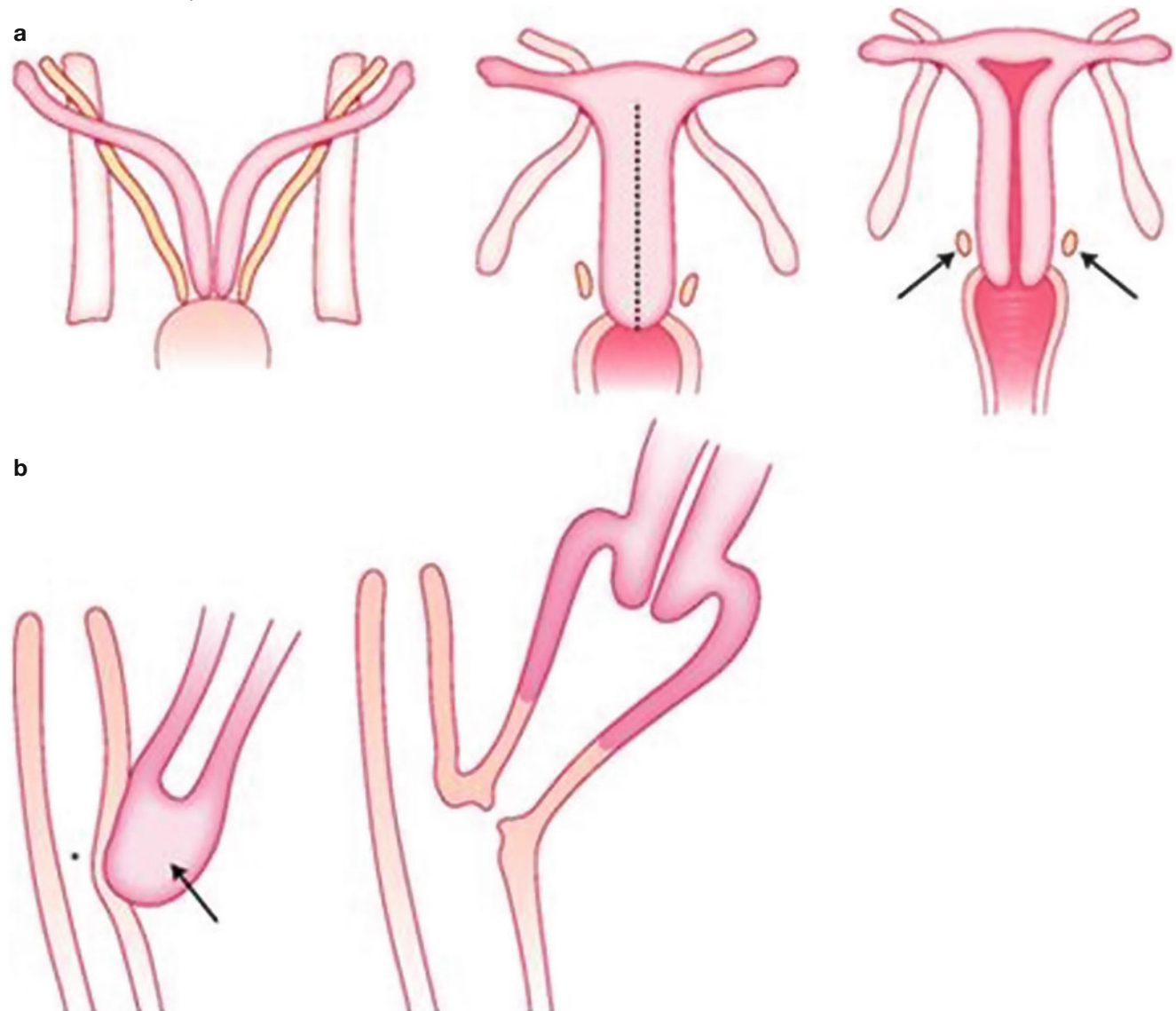


Fig. 27.5 Schematic drawing of müllerian development. (a) Both müllerian ducts (arrows) fuse on the midline to form the uterus. The proximal part of the duct gives rise to the fallopian tube. The Wolffian ducts (arrows) regress and the distal remnant of the Wolffian duct forms the

Gartner duct. (b) This diagrams shows that the uterovaginal canal (arrow) reaches the urogenital sinus (asterisk). The vagina is formed by both the müllerian ducts and the urogenital sinus (From *Radiology illustrated Gynecologic imaging*)

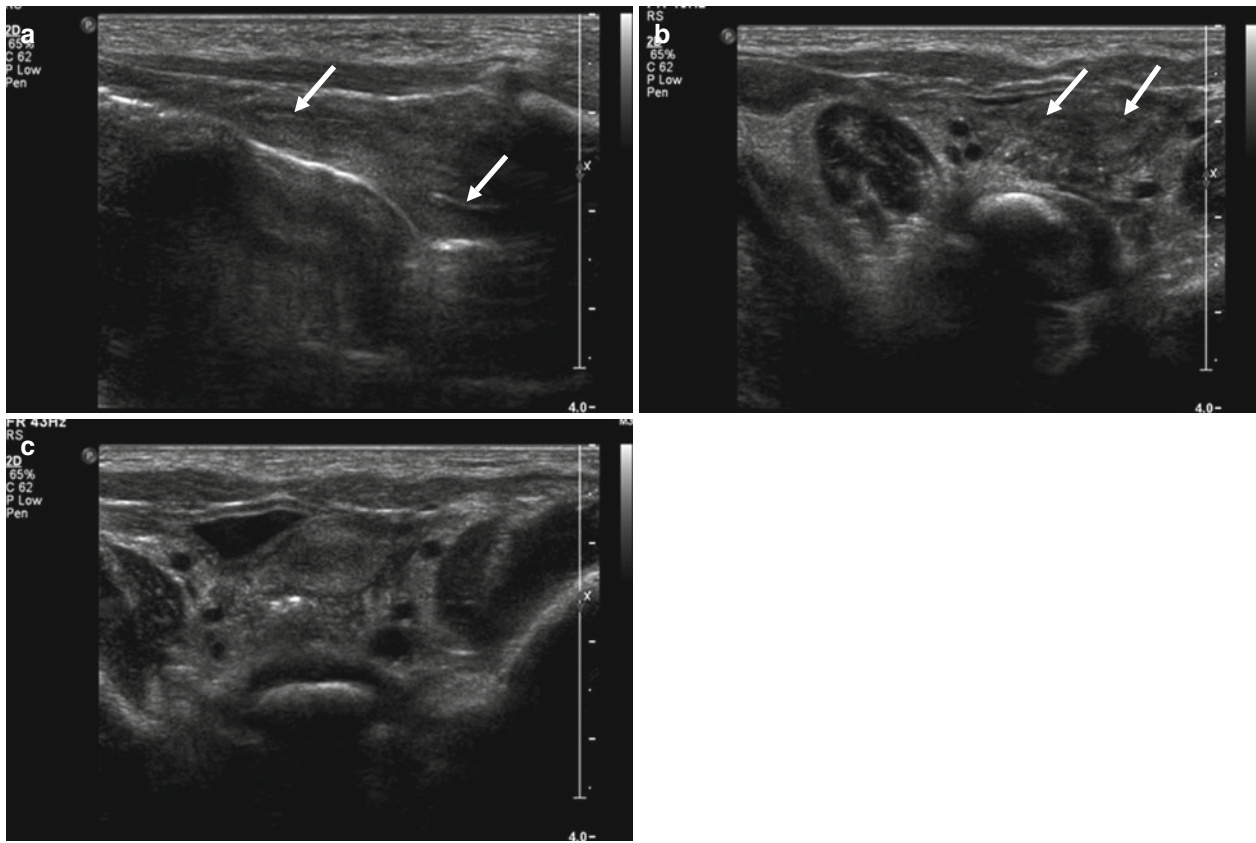


Fig. 27.6 US of a bicornuate uterus in a 2-month-old girl. (a) Oblique sagittal US shows two endometrial cavities in two horns. (b, c) Sequential axial US shows divergence of the uterine horns and a single uterine cervix

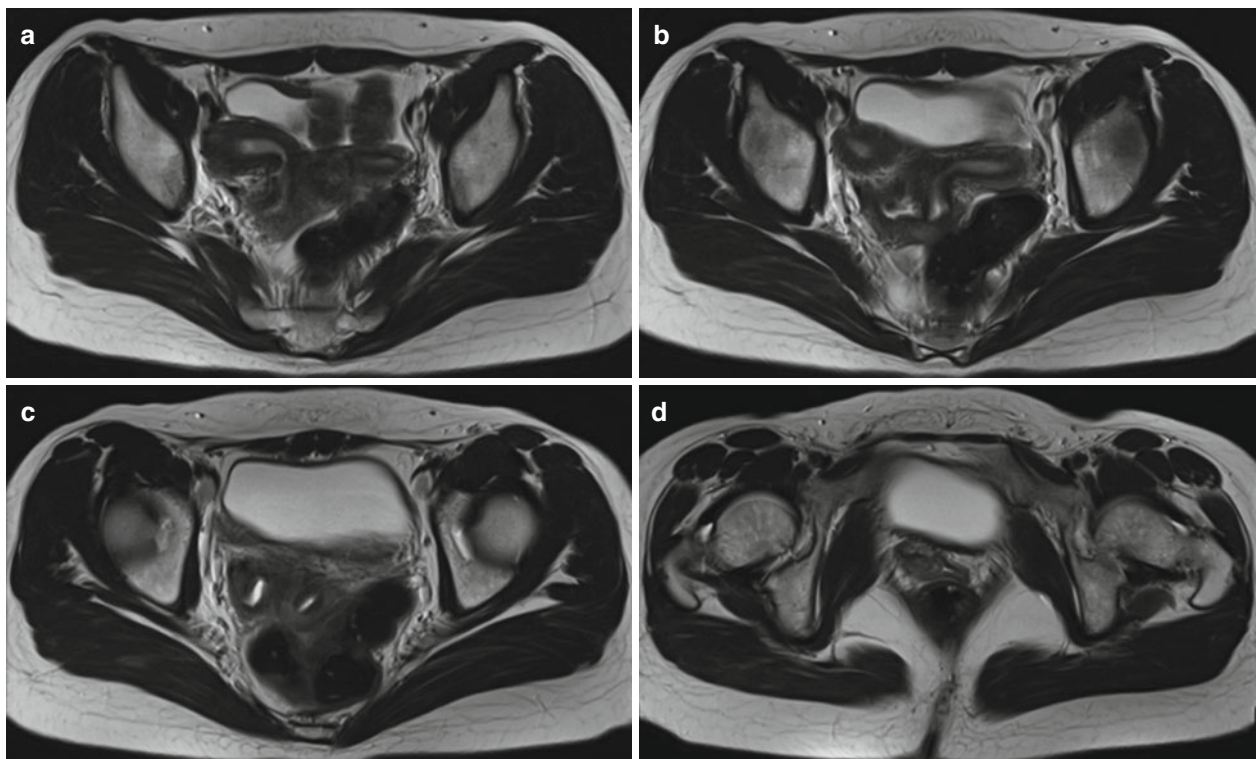


Fig. 27.7 Uterine didelphys in a 15-year-old girl. T2-weighted axial MR images of pelvis show two uterine horns (a, b), two cervixes (c), two separate vaginal lumens (d)

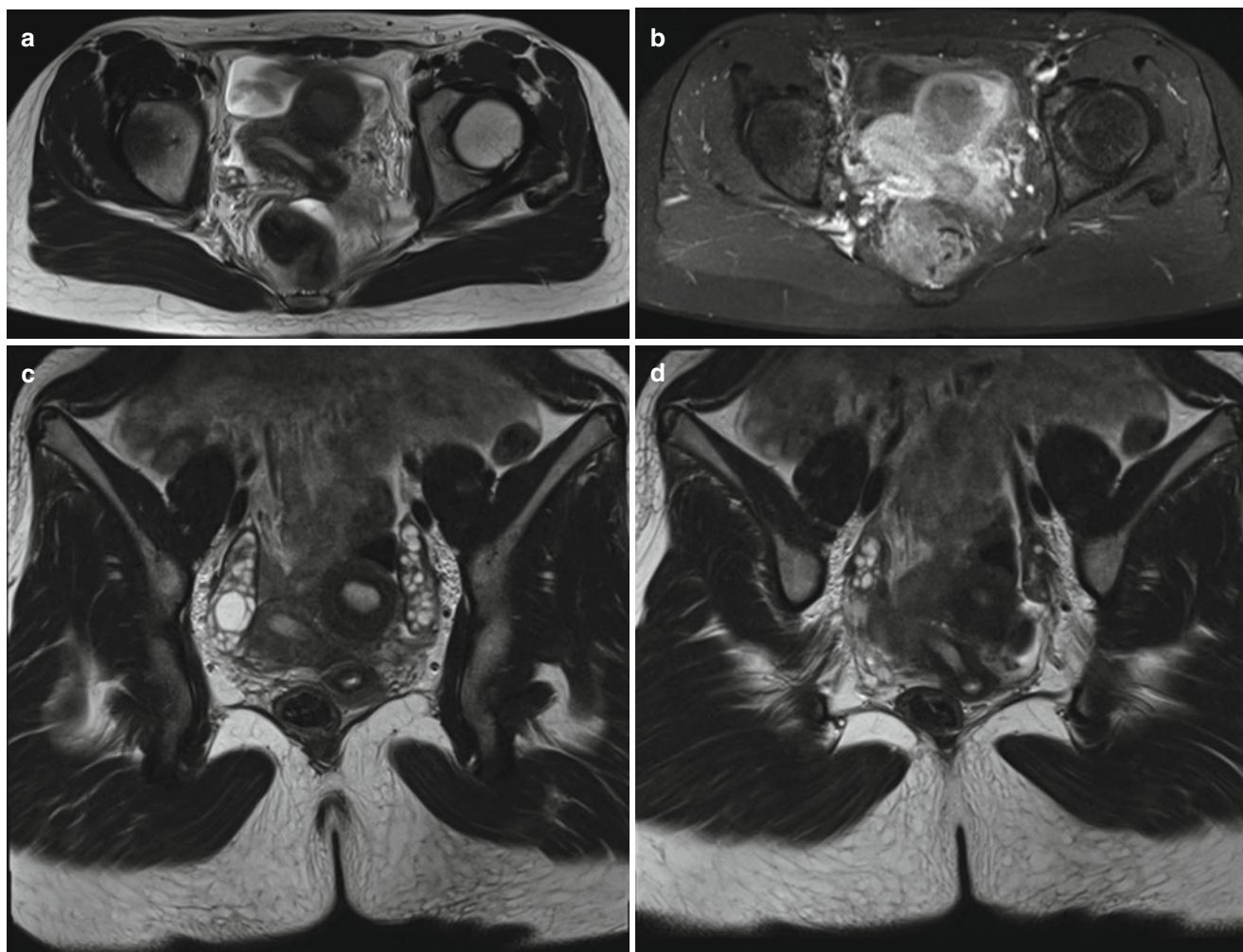


Fig. 27.8 Unicornuate uterus with noncommunicating rudimentary horn in a 14-year-old girl. (a, c, d) T2-weighted MR images show unicornuate uterus and separated rudimentary horn containing endometrial

cavity not communicating to opposite horn. (b) Contrast-enhanced T1WI shows enhancing endometrium in unicornuate uterus and rudimentary horn

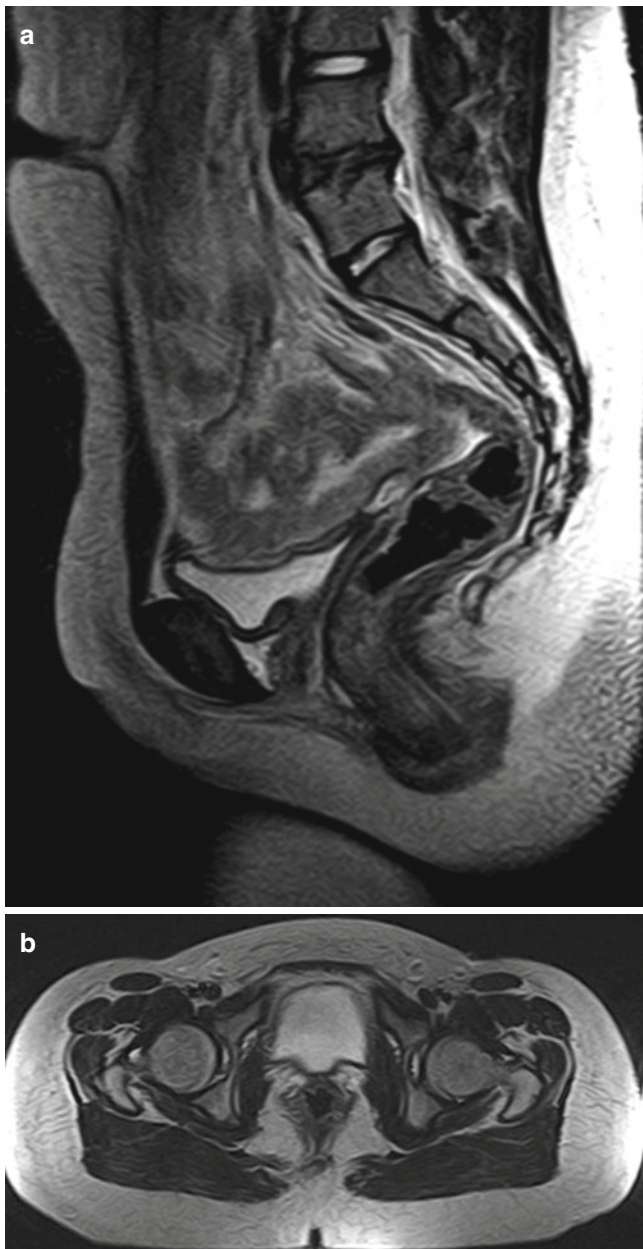


Fig. 27.9 Aplasia of the entire segments of uterus and vagina (Mayer-Rokitansky-Küster-Hauser syndrome) in a 14-year-old patient. **(a)** Midsagittal T2-weighted MR image reveals no vagina and uterus. **(b)** Axial T2WI at the level of the femur head shows no vagina between the bladder and the rectum

27.4.5 Tuboovarian Abscess

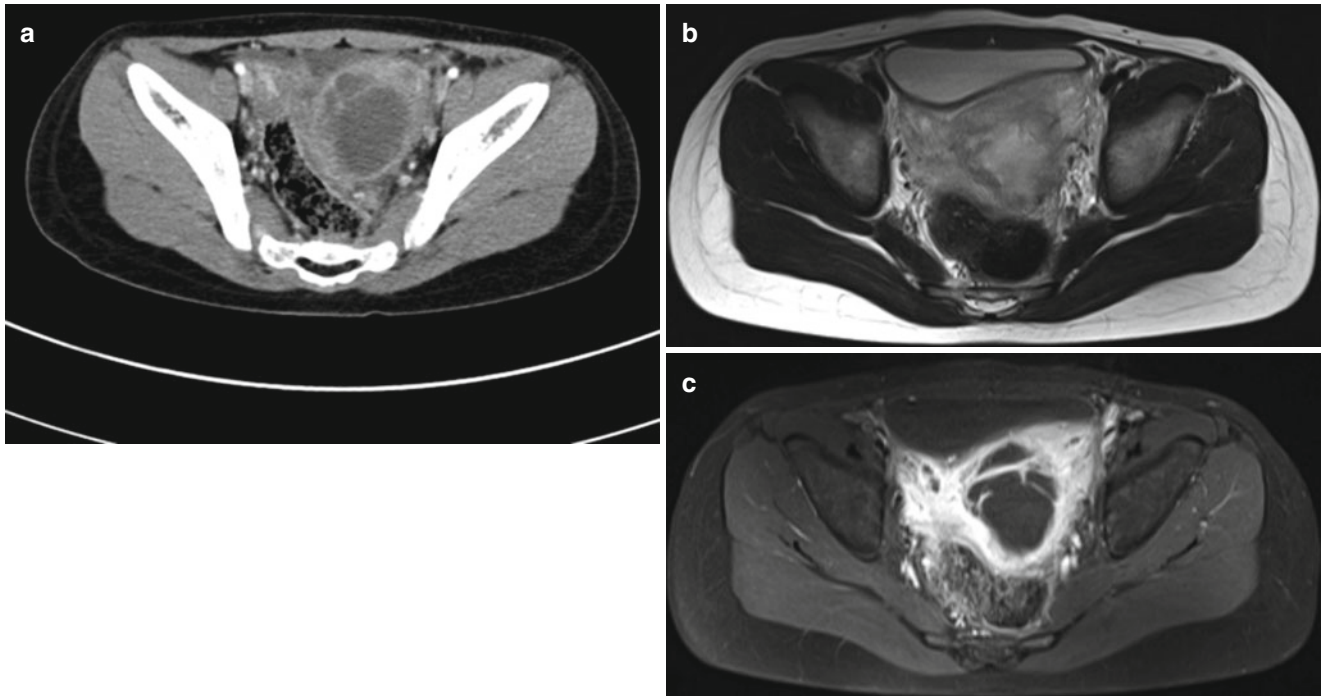


Fig. 27.10 Left tubo-ovarian abscess in an 11-year-old girl. (a) Contrast-enhanced CT scan shows a large cystic mass in left adnexa. This mass has thick wall and septa, and has poor demarcation from the adjacent organs, suggesting adhesion with the uterus and rectosigmoid

colon. (b) Axial T2WI shows a thick-walled, septate, cystic lesion in the left adnexa containing heterogeneous high signal intensity. (c) Contrast-enhanced T1WI reveals strong enhancement of the wall and septa of the lesion with infiltration of adjacent organs

27.4.6 Ovarian Torsion

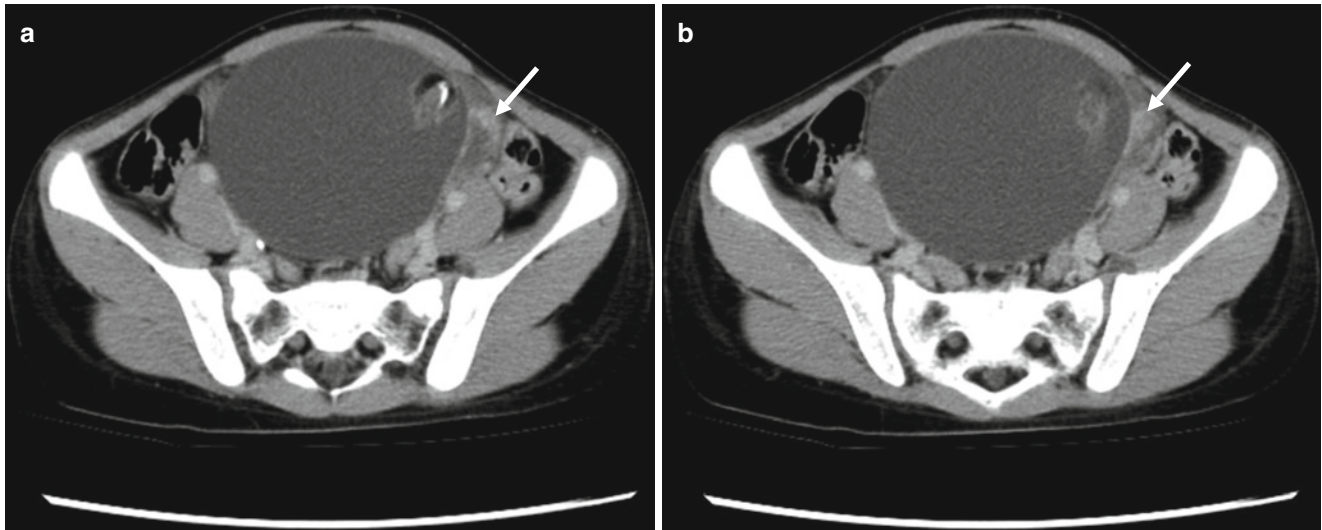


Fig. 27.11 Torsion of cystic mature teratoma in a 9-year-old girl. (a, b) Contrast-enhanced CT scans show cystic mass with fat and calcification and conglomerated vascular structure connecting the mass to the

left uterine conus, which represents vascular congestion of the twisted pedicle (*arrow*). At surgery, there was 360-degree torsion and oophorectomy was performed

27.4.7 Hernia of Uterus and Ovary

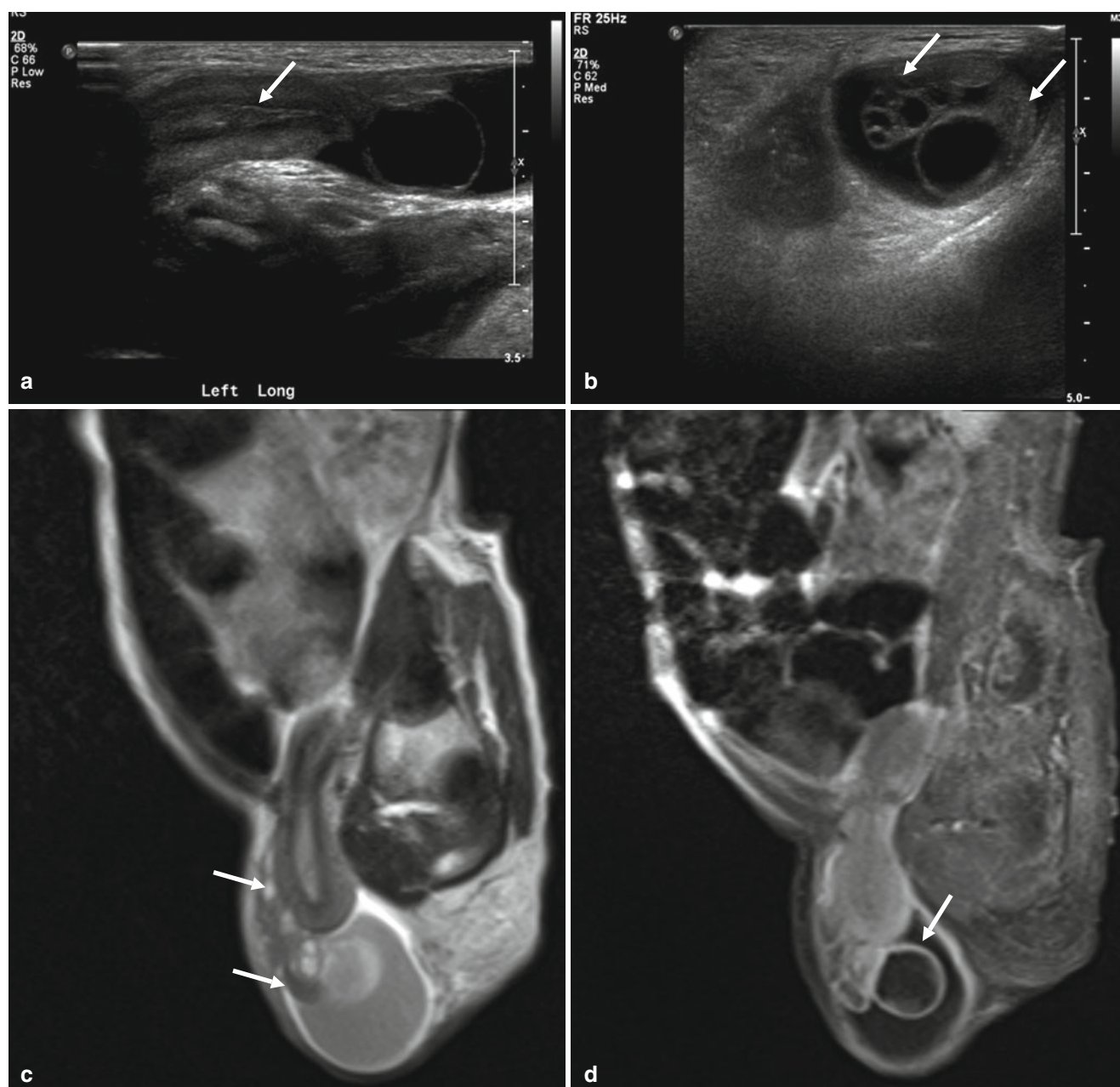


Fig. 27.12 Herniation of ovary and uterus in a 3-month-old girl. Longitudinal (a) and transverse (b) US images of left inguinal canal show a herniated uterus and two ovaries (arrows) with small cyst and

multiple follicles. Sagittal T2WI (c) and contrast-enhanced T1WI (d) demonstrate a herniation of uterus and two ovaries (arrows in c) with multiple follicles and small follicular cyst (arrow in d)

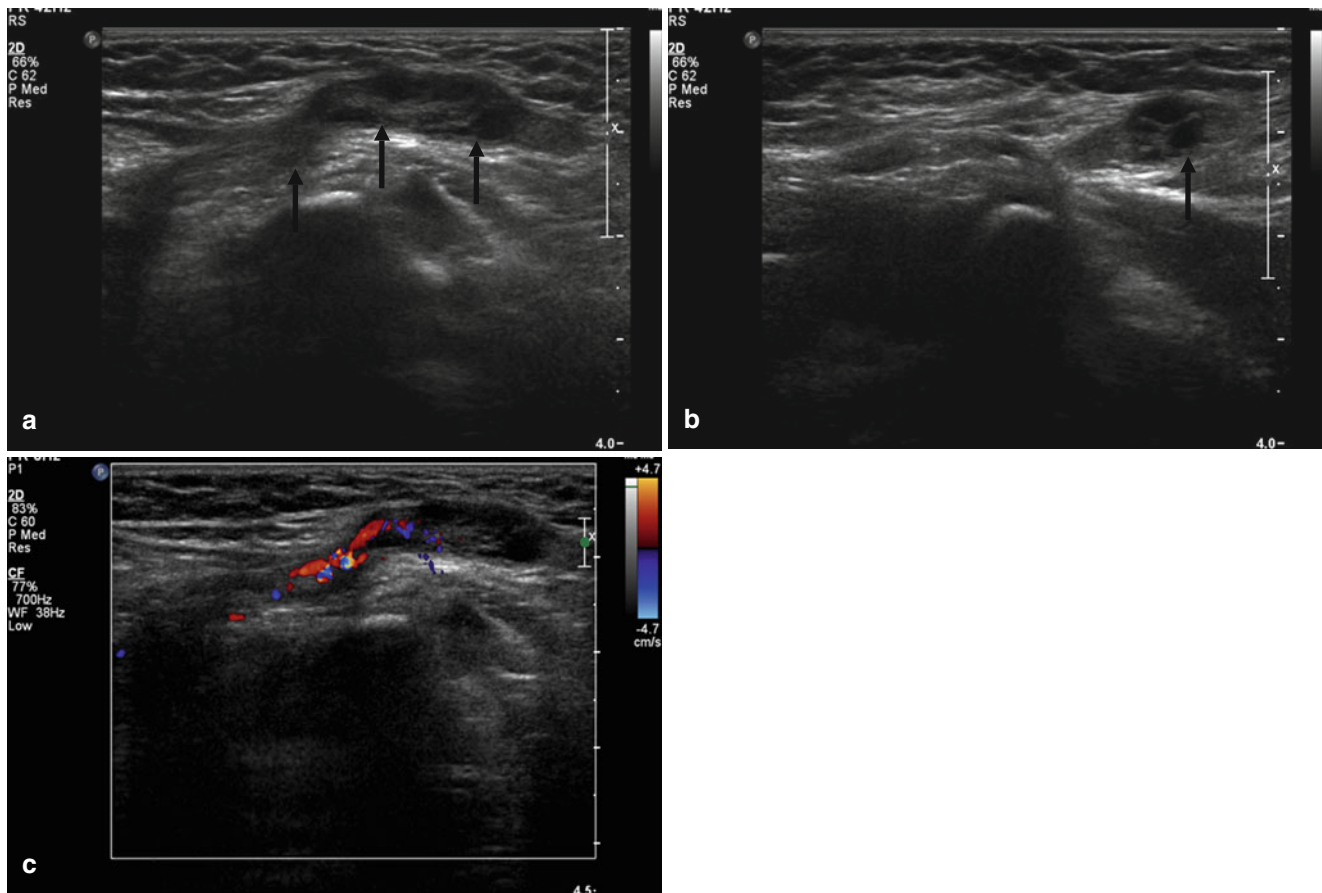


Fig. 27.13 Ovary herniation into the inguinal canal in a 1-year-old girl. Longitudinal (a) and transverse (b) US images of the left inguinal canal show a herniation of ovary with peripheral small follicles. Color Doppler (c) US demonstrates flow signals in the pedicle of the ovary.

27.4.8 Ovarian Cyst

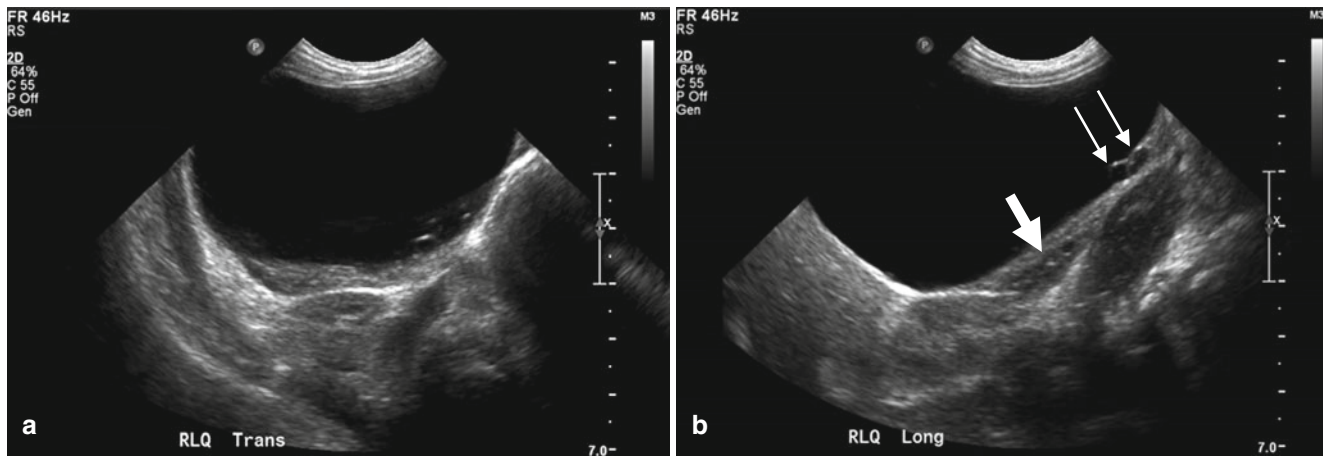


Fig. 27.14 Large ovarian cyst in a 3-month-old girl. (a) Transverse US of right lower abdomen shows a large cystic mass with imperceptible wall inferior to the kidney. The maximal diameter was about 7 cm.

(b) Longitudinal US shows multiple daughter cysts (arrows) and ovarian tissue (thick arrow) in the peripheral portion of a large cyst of the left ovary

27.4.9 Ovarian Tumor: Germ Cell Tumor

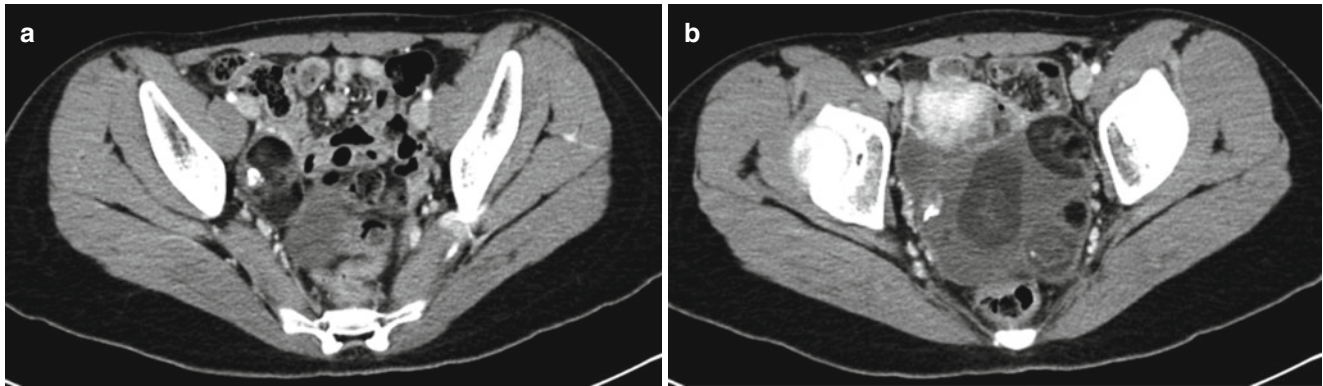


Fig. 27.15 Bilateral ovarian teratomas in a 15-year-old girl. (a) Axial contrast-enhanced CT scan shows a right ovarian mass containing fat and mural nodule with calcification. (b) Axial contrast-enhanced CT

scan shows a left ovarian cystic mass containing fat, calcification, serous fluid, and mural nodule

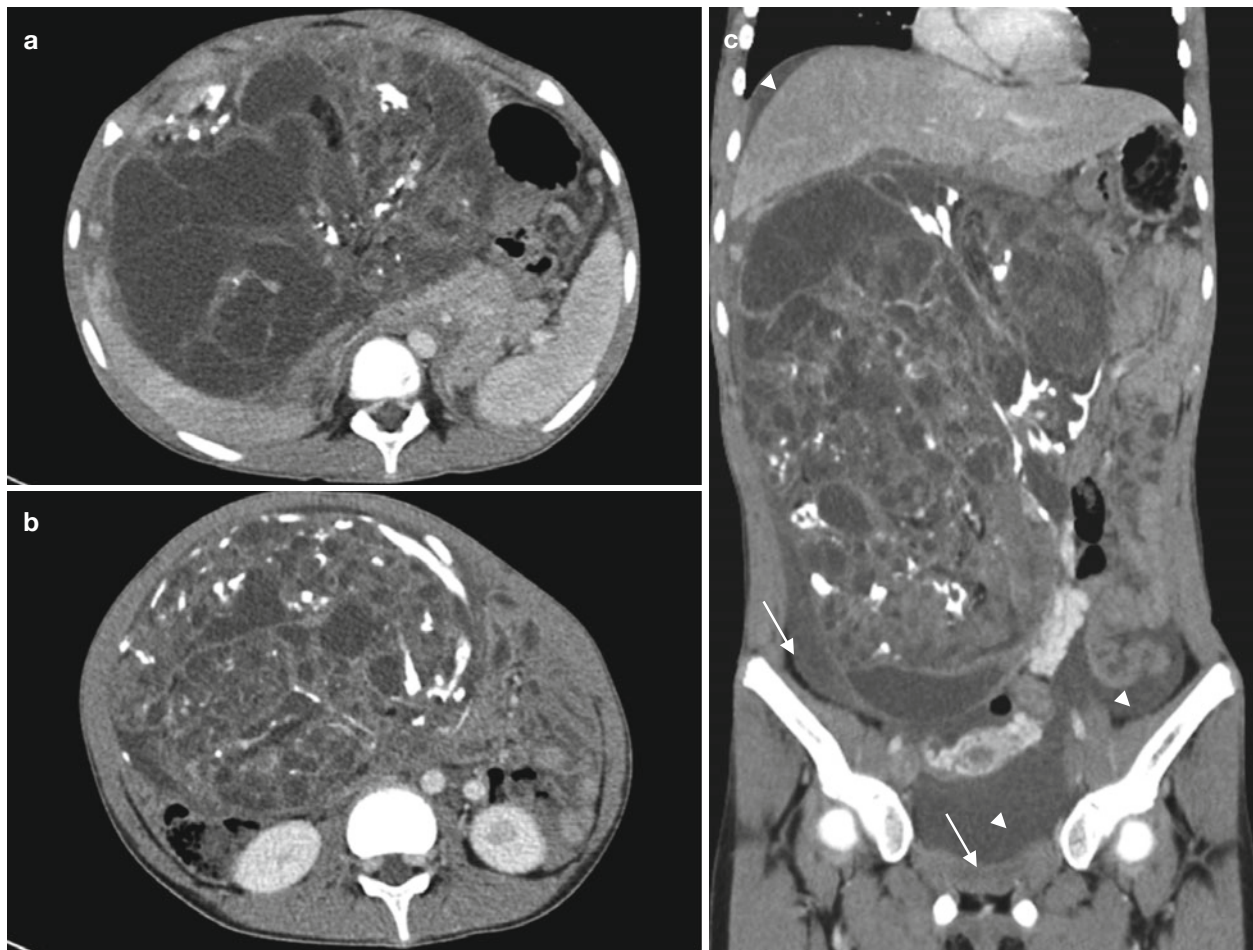


Fig. 27.16 Ruptured immature teratoma in a 13-year-old girl. (a, b) Contrast-enhanced CT scans show a huge, predominantly solid mass containing fat and calcifications filling the abdomen and pelvic cavity.

(c) Coronal CT scan shows ascites (*arrowheads*), and peritoneal thickening with enhancement (*arrows*) suggest tumor seeding. Laparotomy revealed ruptured immature teratoma with peritoneal seeding

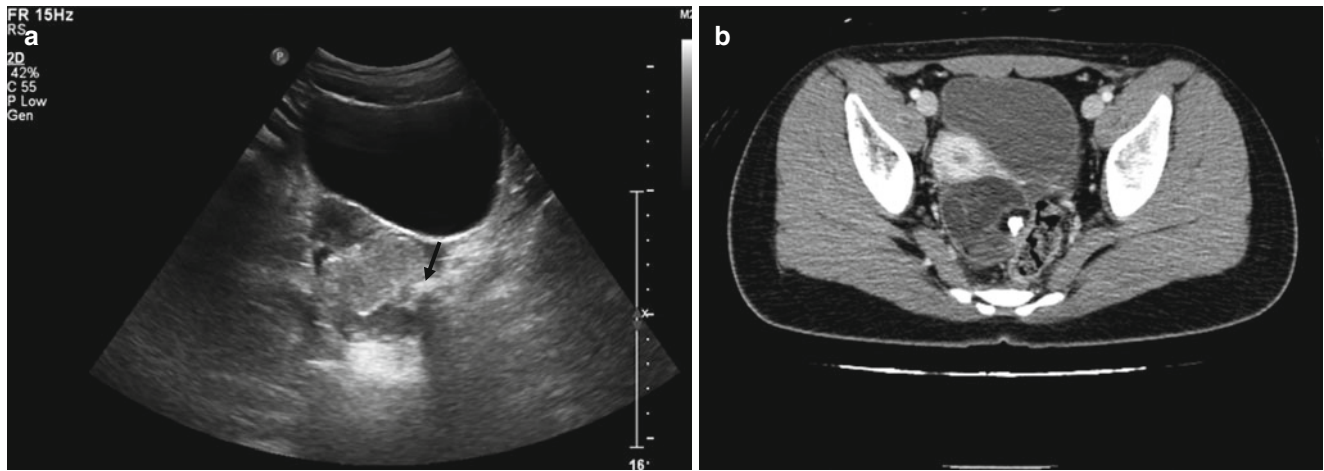


Fig. 27.17 Ovarian teratoma in a 13-year-old girl. (a) Transverse US of the pelvic cavity shows a echogenic mass containing hyperechoic nodule with posterior shadowing (*arrow*) suggesting calcification. (b)

Contrast-enhanced CT demonstrates fat and calcification in the cystic mass. At pathologic examination, ovarian teratoma containing fat, hair, sebaceous tissue, and calcification was confirmed

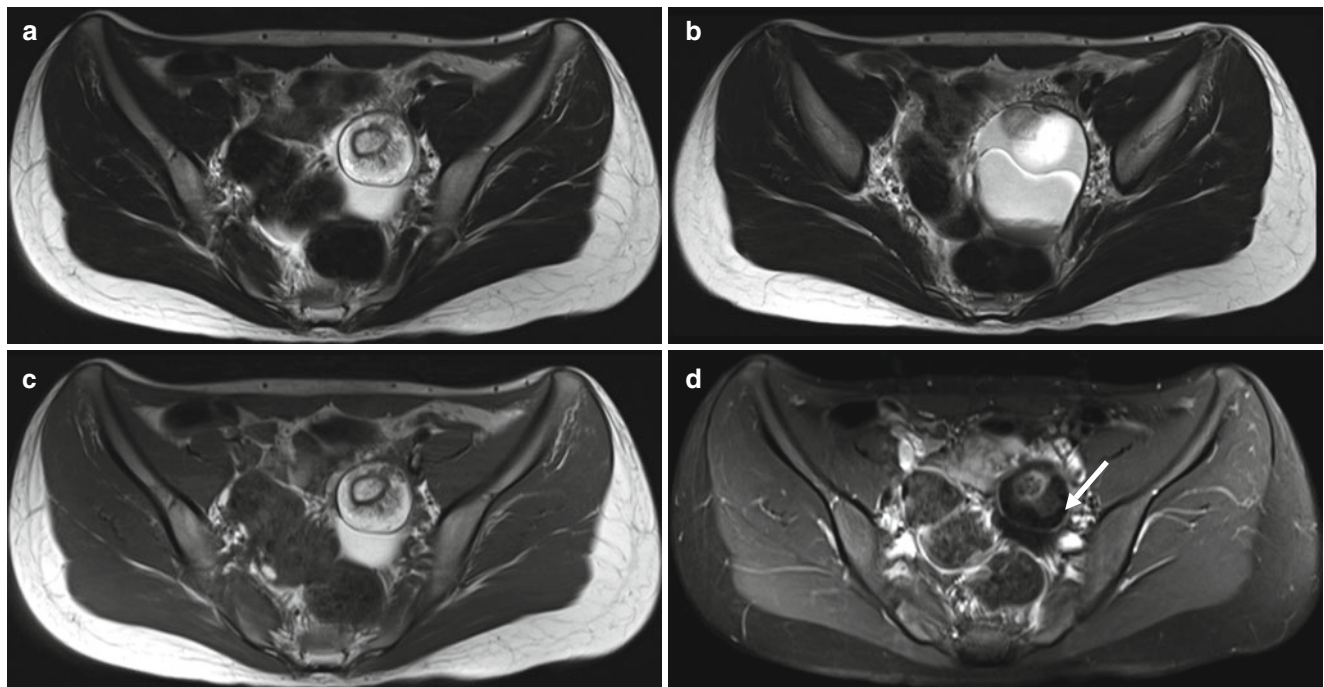


Fig. 27.18 Mature cystic teratoma in a 16-year-old girl. Axial T2-weighted (a, b) and T1-weighted (c) MR images show left ovarian cystic mass containing fat, calcification, and mural nodule.

Contrast-enhanced, fat-suppressed, T1-weighted (d) image demonstrates strong suppression of the signal of fat (*arrow*)

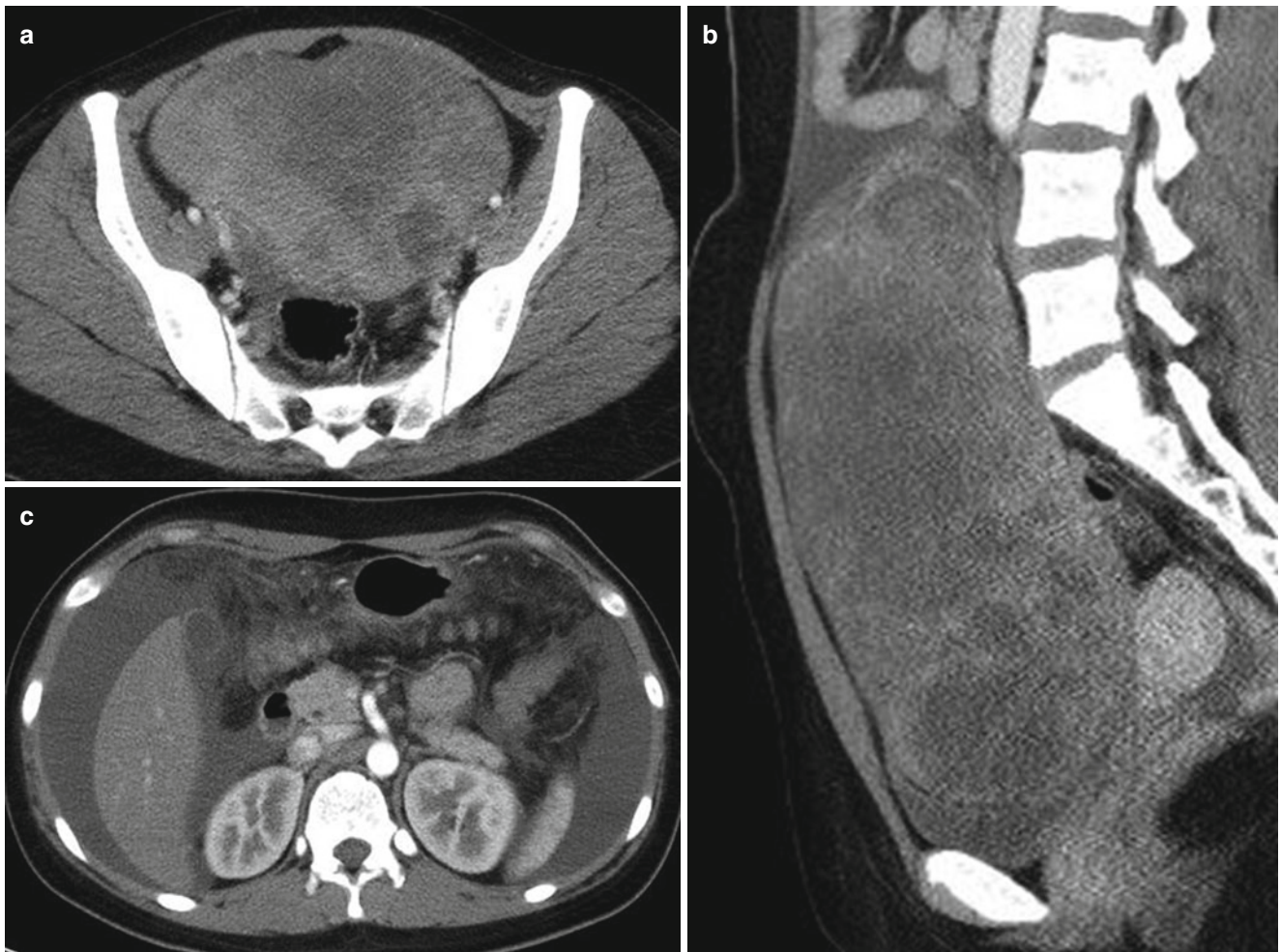


Fig. 27.19 Dysgerminoma of left ovary in a 15-year-old girl. (a, b) Contrast-enhanced axial and sagittal CT scans show a large solid enhancing mass in pelvic cavity. The mass has multifocal low-attenuation areas. (c) Contrast-enhanced axial CT scan of upper abdomen demonstrates large amount of ascites and ill-defined increased attenuation of omentum, suggesting peritoneal seeding

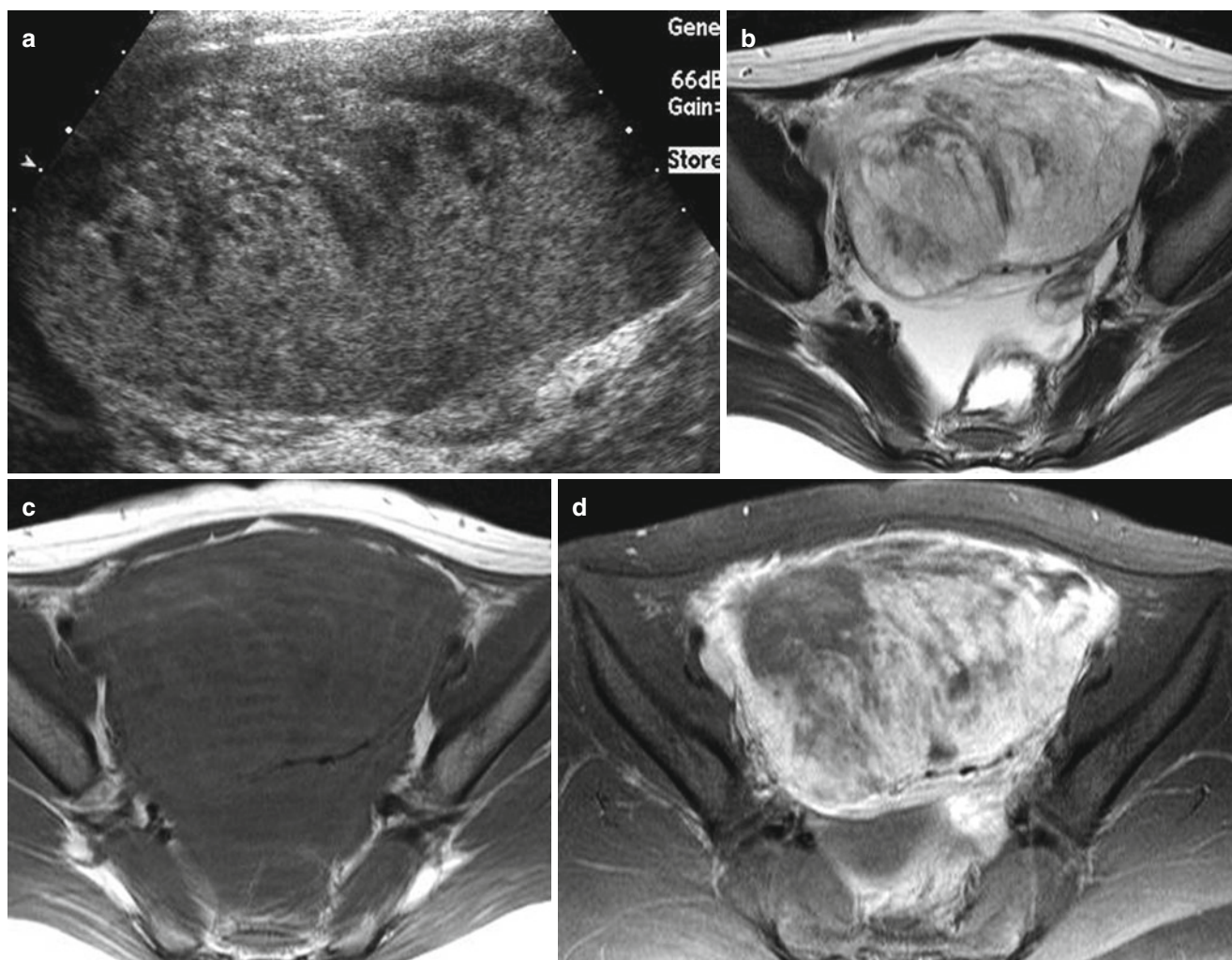


Fig. 27.20 Endodermal sinus tumor of right ovary in a 13-year-old girl. **(a)** Axial US scan of pelvis demonstrates solid mass with hypoechoic necrotic area. **(b)** T2-weighted axial MR image shows a large mass with heterogeneous signal intensity and small ascites in the

pelvic cavity. **(c)** On T1-weighted axial MR image, this mass shows areas of high signal intensity due to hemorrhage. **(d)** On contrast-enhanced, fat-suppressed, T1-weighted axial MR image, this mass shows heterogeneous enhancement and irregular necrotic areas

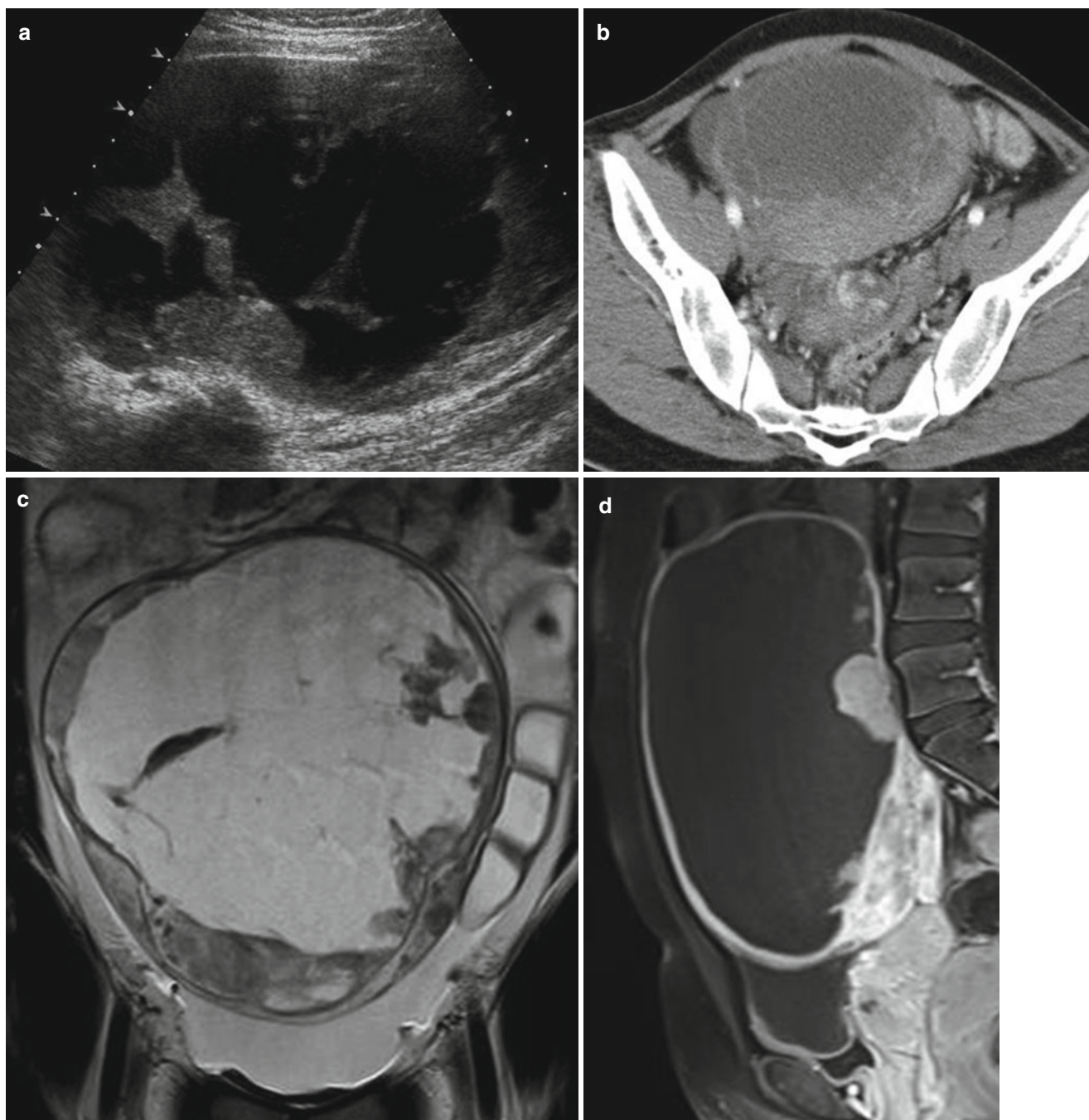


Fig. 27.21 Mixed germ cell tumor composed of dysgerminoma and endodermal sinus tumor in a 16-year-old girl. **(a)** Axial US scan of pelvis shows large cystic mass with septa and some solid portions. **(b)** Contrast-enhanced axial CT scan shows a large mass with enhancing septa and solid portions. **(c)** T2-weighted coronal MR image shows a

huge, lobulated mass in the lower abdomen and pelvic cavity. This mass is mainly cystic and has some solid portions. **(d)** Contrast-enhanced, fat-suppressed, T1-weighted, sagittal MR image demonstrates huge cystic mass with enhancing thick wall and solid portions. The serum AFP was increased (3,000 ng/mm³)

27.4.10 Ovarian Tumor: Sex Cord-Stromal Tumor

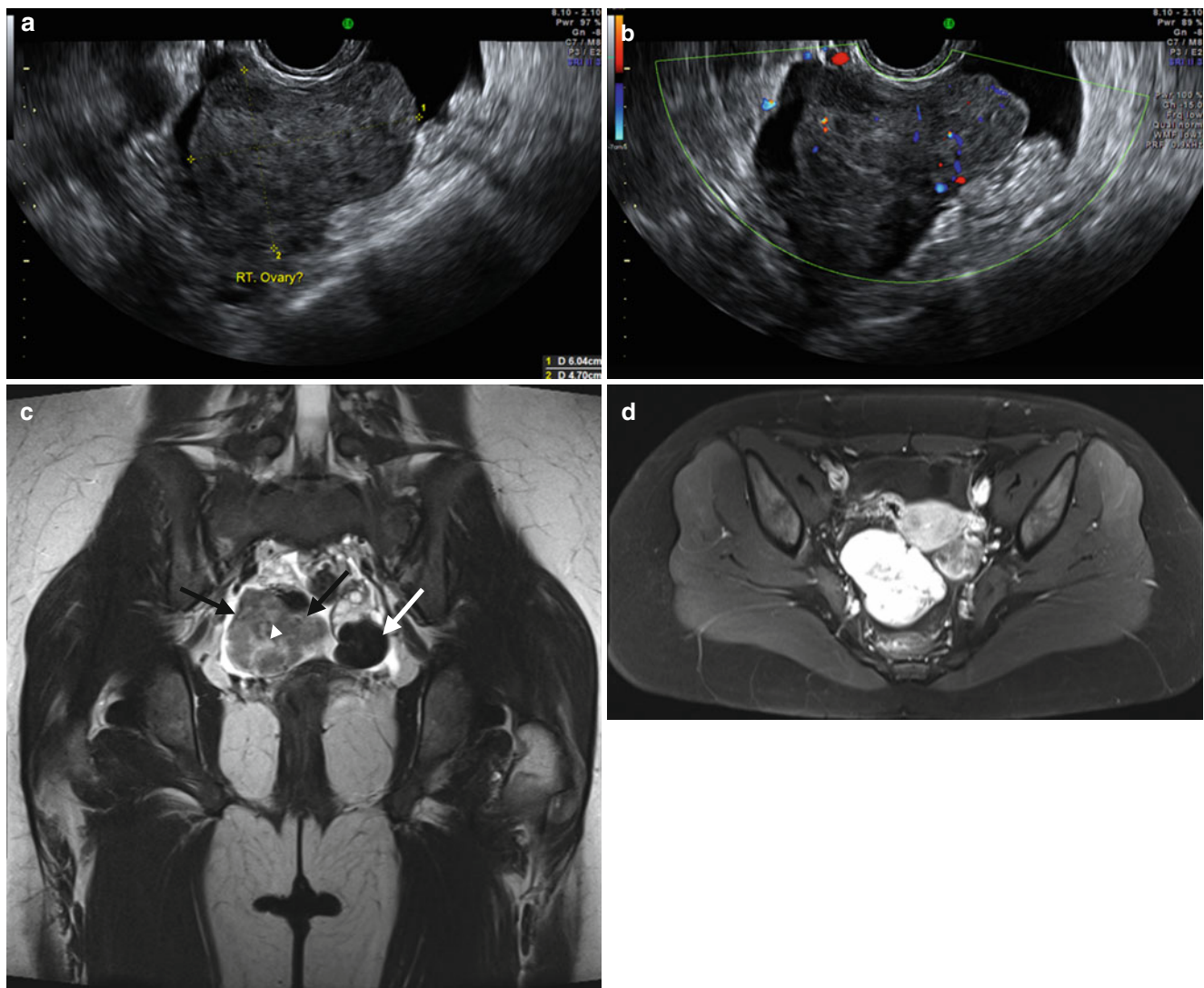


Fig. 27.22 Bilateral ovarian fibromas appearing as a predominantly solid mass in a 14-year-old girl. (a, b) Endorectal US scans of pelvis show a solid mass without increased color flow in right adnexa. Coronal T2-weighted (c) MR image shows a heterogenous low-intense, solid mass (dark arrows) containing central, high-intensity, necrotic foci

(arrowhead) in right ovary and round, hypointense, solid nodule (white arrow) in inferior portion of left ovary. The signal intensity of the mass is very low, which is a characteristic finding of a fibrous tumor. There is small ascites in pelvis. (d) Axial contrast-enhanced T1WI demonstrates strong enhancement of ovarian solid masses

27.4.11 Ovarian Tumor: Epithelial Tumor

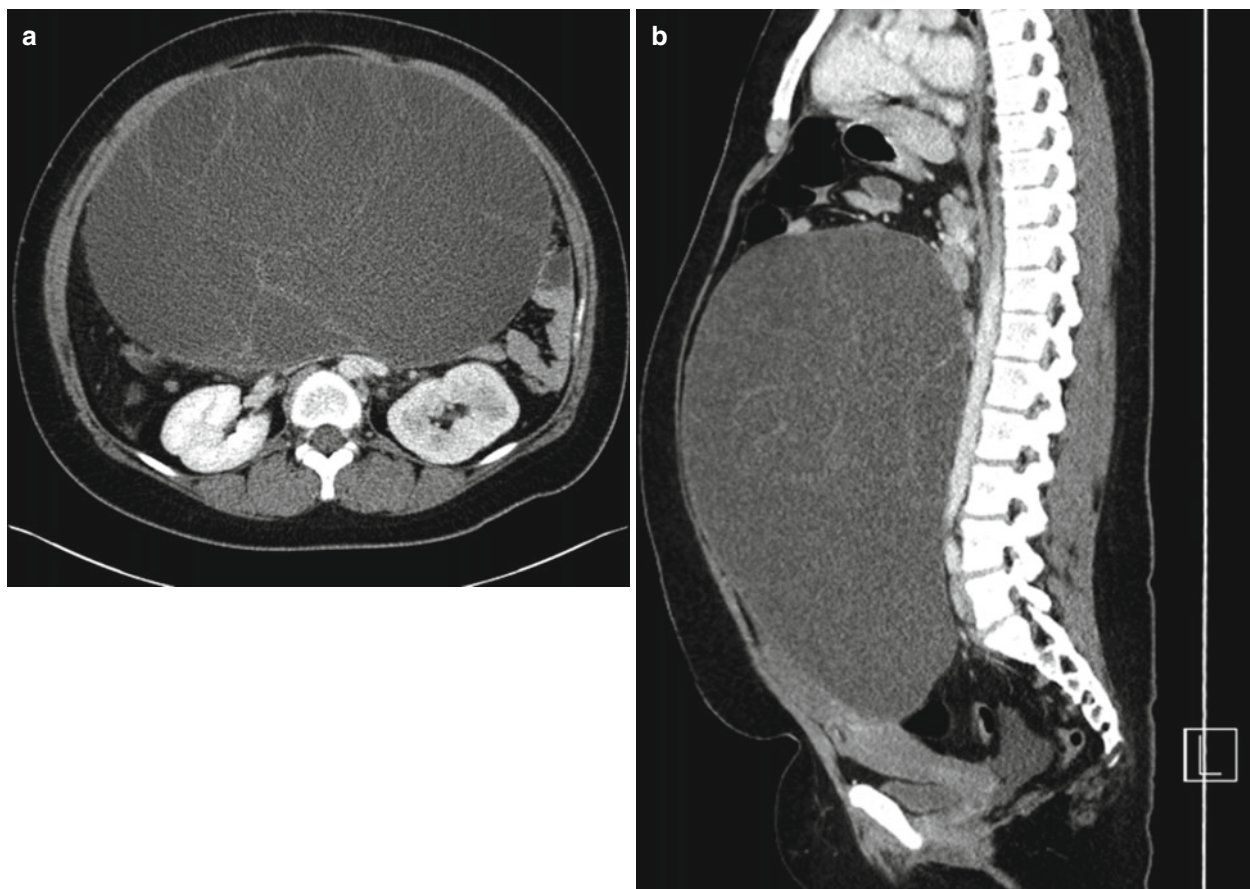


Fig. 27.23 Serous cystadenoma in a 16-year-old girl. Contrast-enhanced axial (a) and sagittal (b) CT scans show multiseptated, huge cystic mass displacing the uterus anteriorly. Note that the locules of the mass have similar attenuation

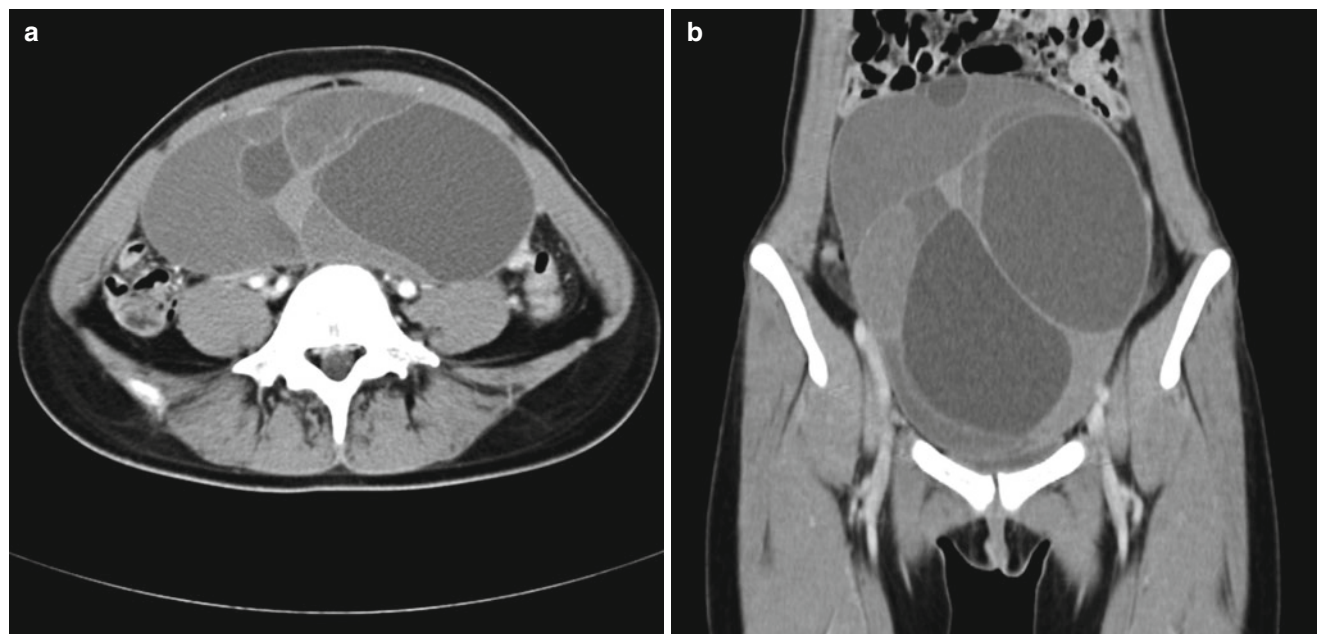


Fig. 27.24 Mucinous cystadenoma in a 18-year-old girl. Contrast-enhanced axial (a) and coronal (b) CT scans show multiseptated, huge cystic mass in abdomino-pelvic cavity. Note that the locules of the mass have different attenuations

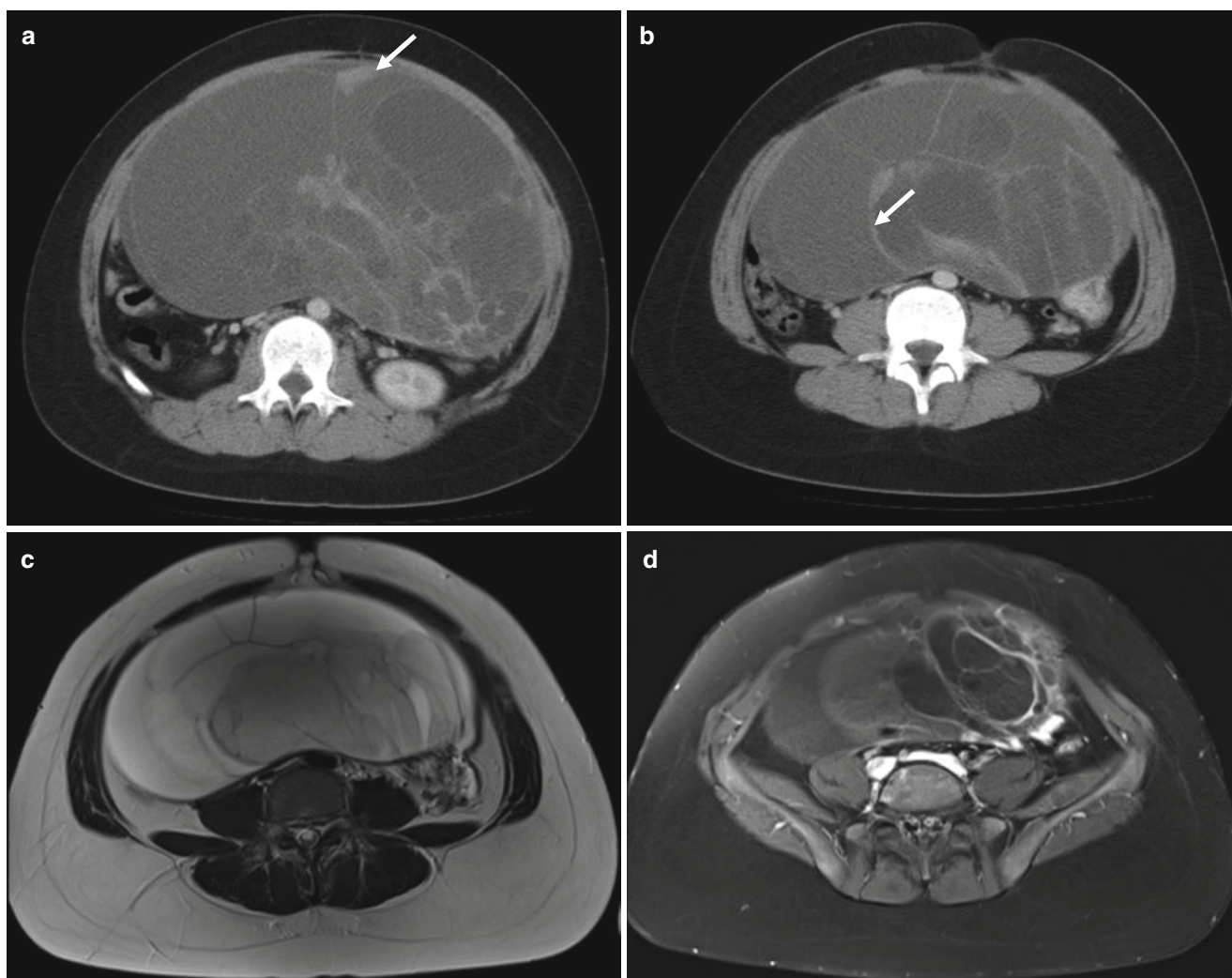


Fig. 27.25 Mucinous tumor of borderline malignancy in a 16-year-old girl. **(a, b)** Contrast-enhanced CT scans show a large cystic mass with thick septa and nodular solid components (*arrows*). Note that the peripheral wall of the mass is thin and even. **(c)** T2-weighted axial MR

image shows a large multilocular cystic mass with multiple septa in left ovary. **(d)** Contrast-enhanced, fat-suppressed, T1-weighted axial image reveals prominent enhancement of the wall and septa of the mass. Note that some of the septa are thick and subtle enhancing solid component

27.4.12 Ovarian Tumor: Secondary Neoplasm

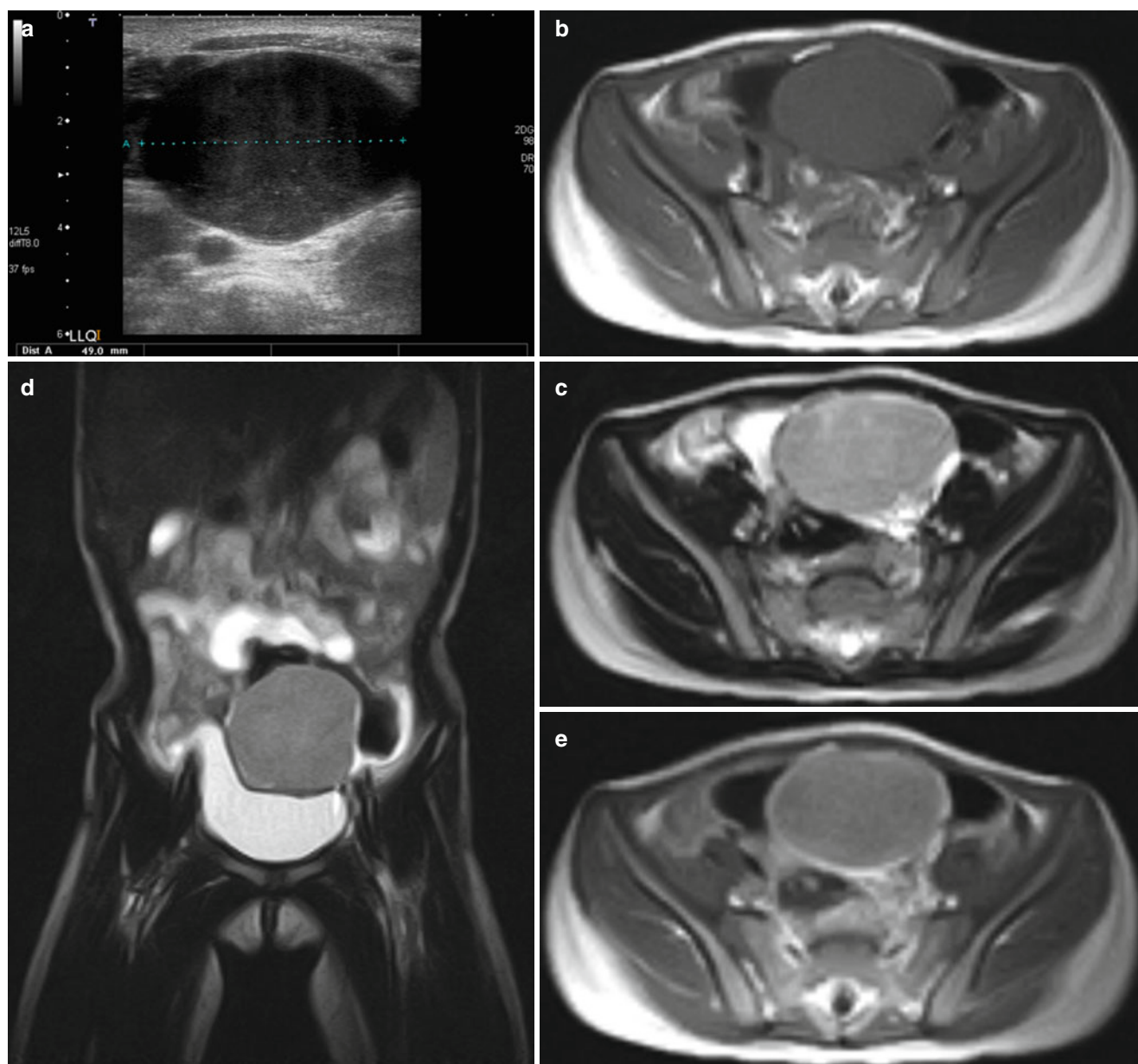


Fig. 27.26 Ovarian lymphoma in a 8-year-old girl. (a) Transverse US image shows homogenous hypoechoic mass in left adnexa. Axial T1WI (b), axial and coronal T2WIs (c, d) show homogeneous solid mass of

relatively low signal intensity. (e) Axial contrast-enhanced T1-weighted MR image demonstrates homogenous and relatively strong enhancement of mass

27.4.13 Cryptorchidism (Undescended Testis)

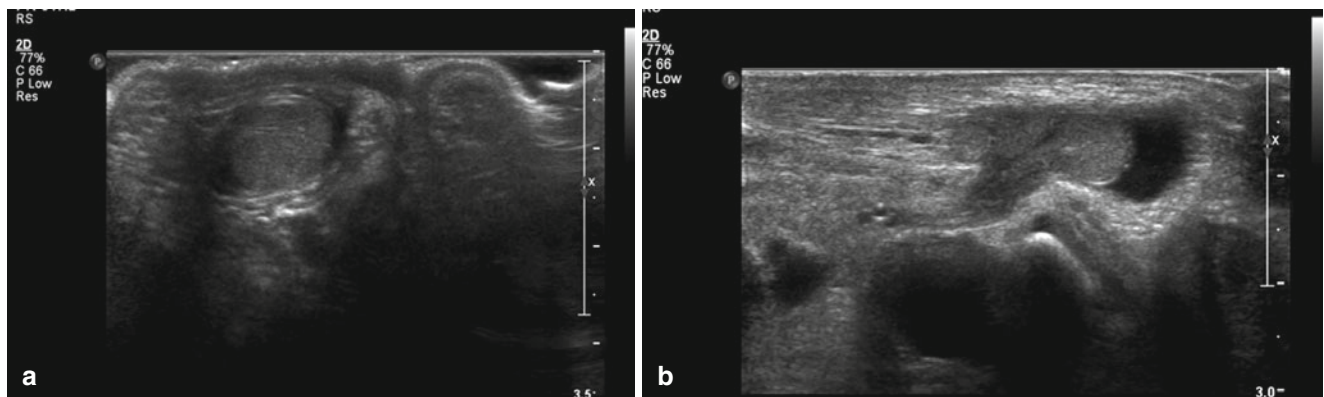


Fig. 27.27 Left undescended testis in a 1-year-old boy. (a) Axial US scan of scrotum shows empty left scrotal sac without testis. (b) Sagittal US image of left inguinal region shows relatively small, undescended testis with peripheral fluid

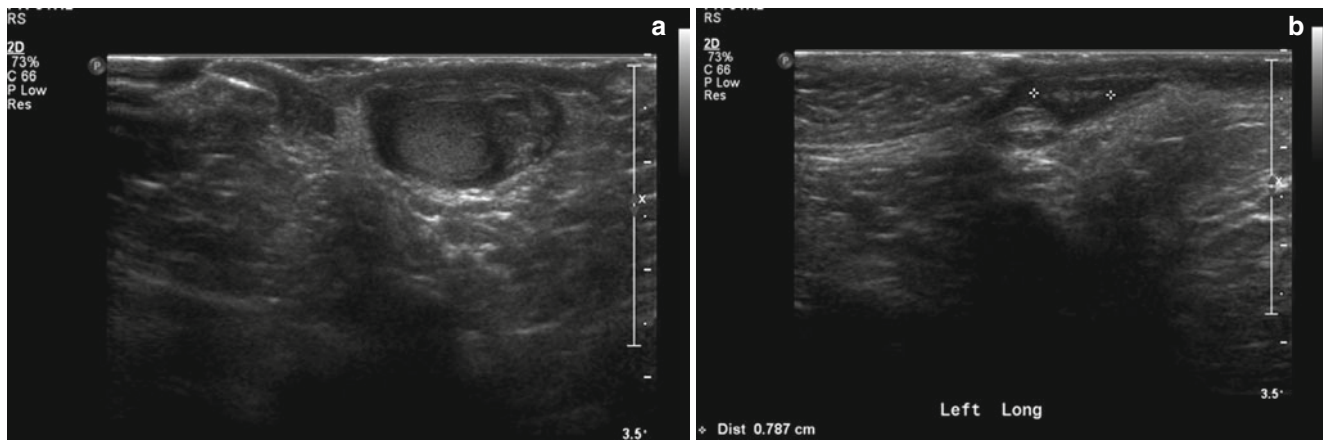


Fig. 27.28 Right undescended testis in a 10-month-old boy. (a) Axial US scan of scrotum shows empty right scrotal sac without testis. (b) Sagittal US image of right inguinal region shows small, atrophied, hypoechoic undescended testis

27.4.14 Transverse Testicular Ectopia

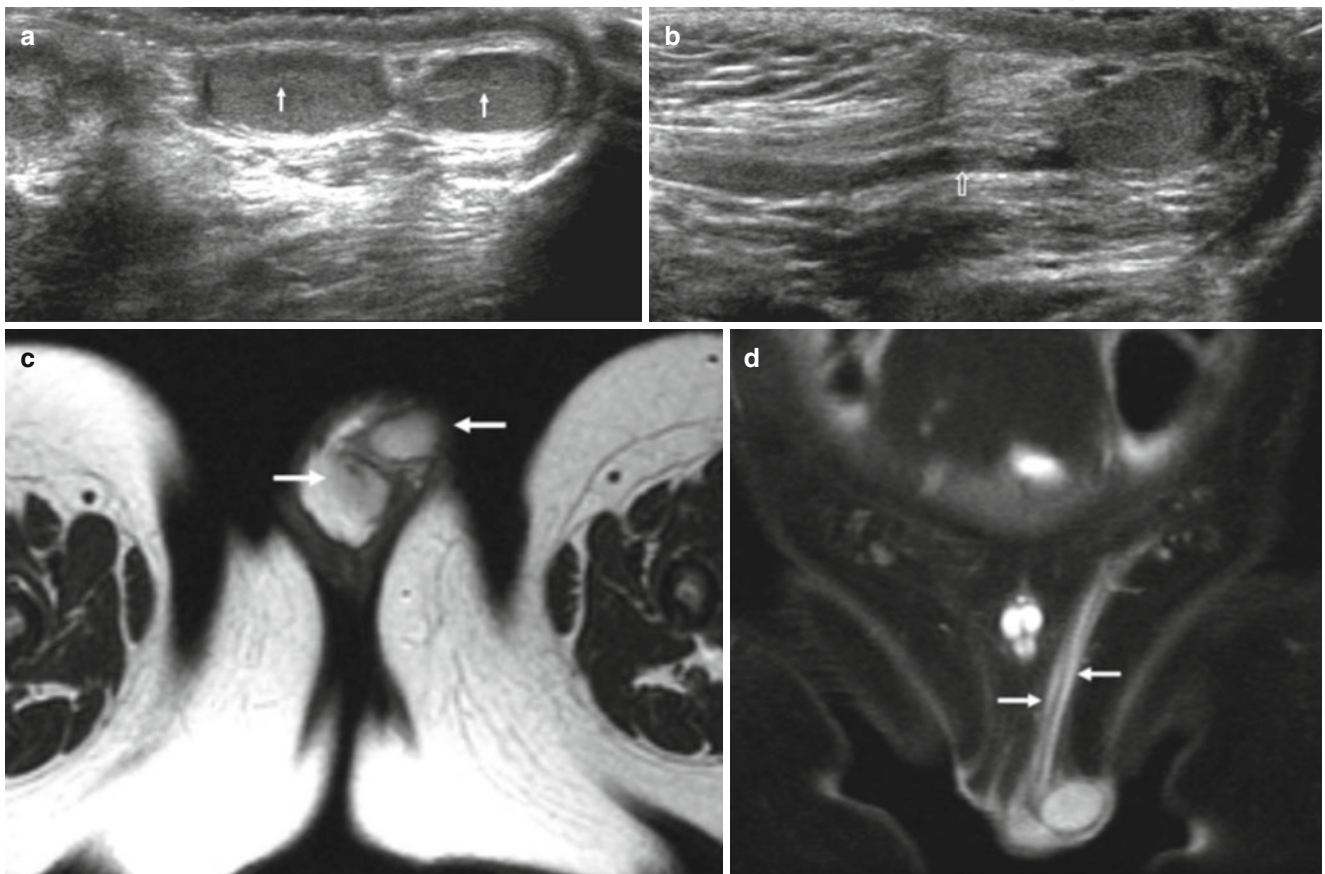


Fig. 27.29 Left transverse testicular ectopia presenting as right undescended testis in a 10-month-old boy. **(a)** Longitudinal US scan of left scrotum shows two testes in left hemiscrotum with empty right hemiscrotum. The mediastinum testis (*arrows*) is identified as an echogenic band. **(b)** Longitudinal US scan of left suprascrotal area reveals a testis

and its own spermatic cord (*open arrow*) extending to the left inguinal canal. **(c)** T2-weighted axial MR image shows hyperintense two testes (*arrows*) in left scrotum. **(d)** Gadolinium-enhanced T1-weighted coronal image shows that each testis has its own spermatic cord (*arrows*) extending to the left inguinal canal (From Hye-Sun Cho et al. 2007)

27.4.15 Inguinoscrotal Hernia

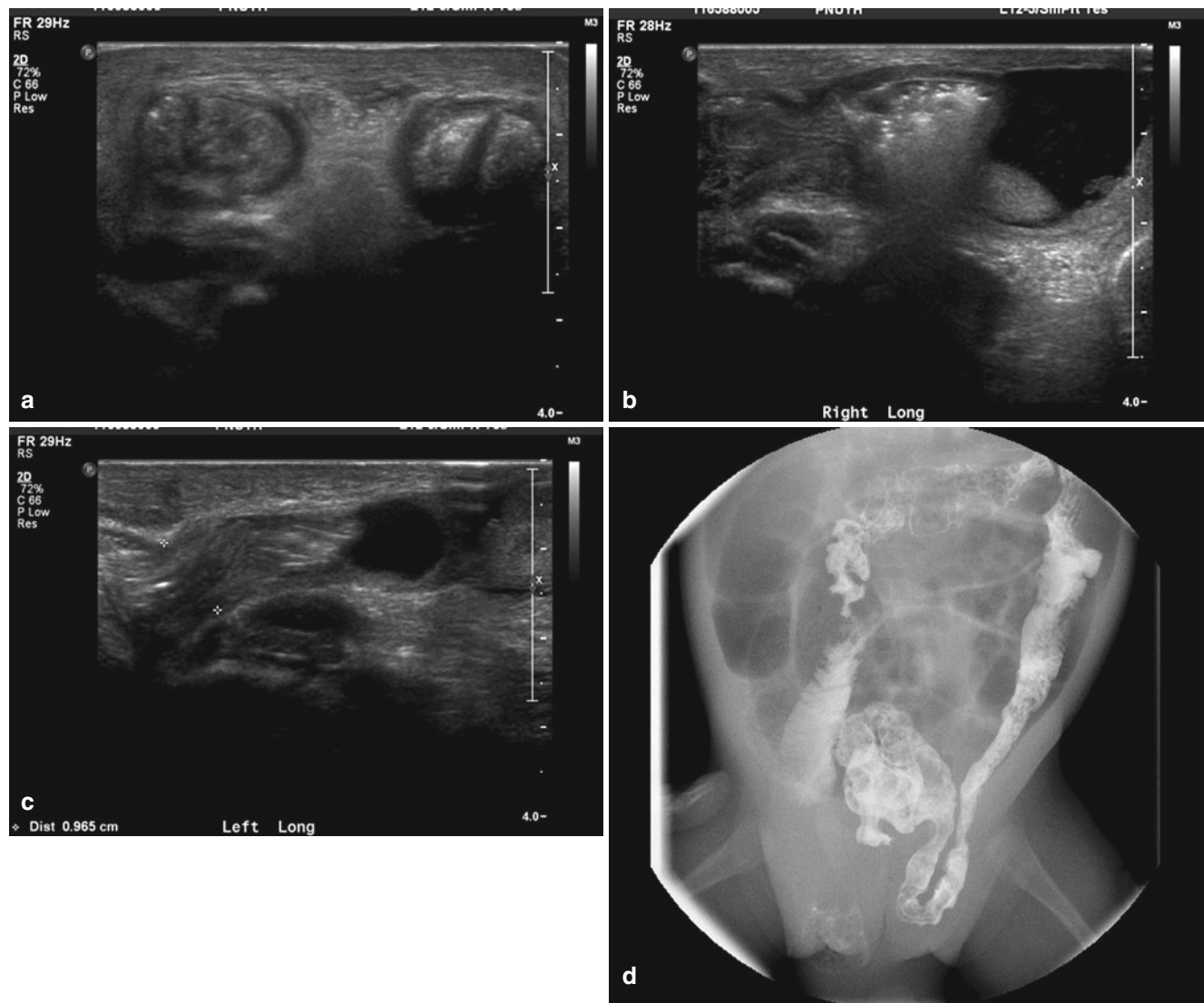


Fig. 27.30 Bilateral inguinoscrotal hernia in a 1-year-old boy with scrotal swelling. Axial US scan of scrotum (a) and longitudinal US of both inguinal regions (b, c) show herniation of bowel loop with hyperchoic air and echogenic omentum with peripheral fluid into scrotum.

Barium enema (d) demonstrates a herniation of sigmoid colon into left scrotum and a loop of terminal ileum into right scrotum, and associated small bowel ileus

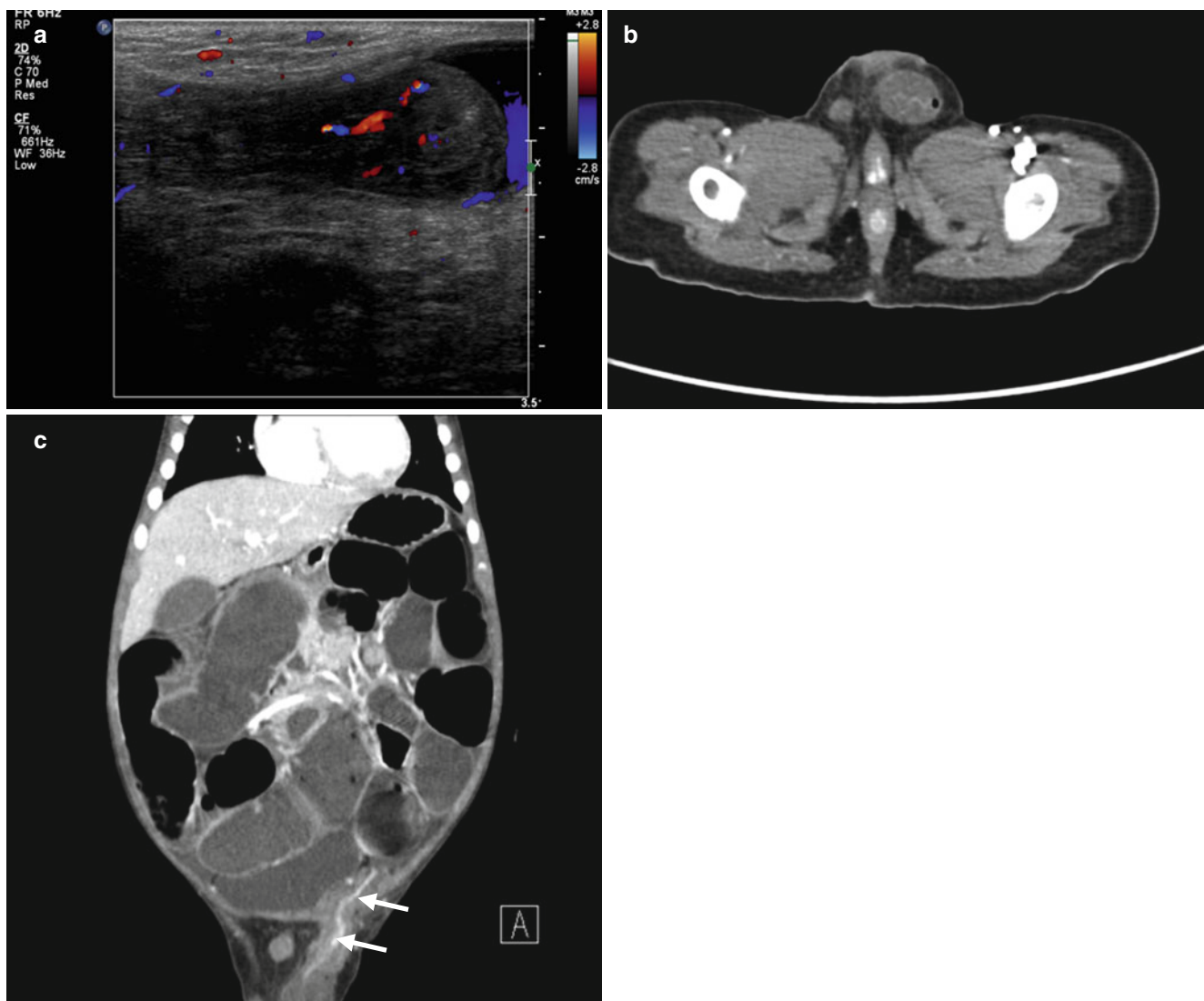


Fig. 27.31 Left inguinoscrotal hernia in a 2-year-old boy with scrotal swelling. (a) Longitudinal color Doppler US scan shows a herniation of intestinal loop and echogenic omentum into scrotum, and blood flow

signal in both bowel loop and omentum. Axial (b) and coronal (c) CT scans demonstrate herniation of small bowel loop and its supplying vessel (*arrows*), and associated small bowel ileus

27.4.16 Hydrocele

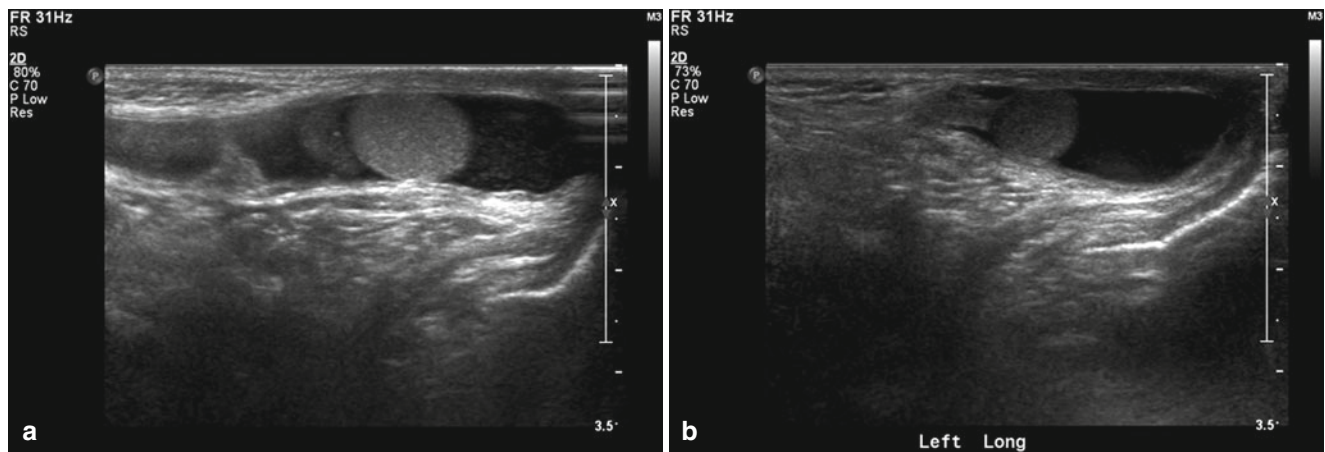


Fig. 27.32 Bilateral hydrocele in a 2-year-old boy. (a) US scan of right scrotum shows a fluid collection surrounding the testis and communicating with peritoneum, suggesting patent processus vaginalis. (b) US

scan of left scrotum demonstrates a fluid collection surrounding the testis and not communicating with peritoneum

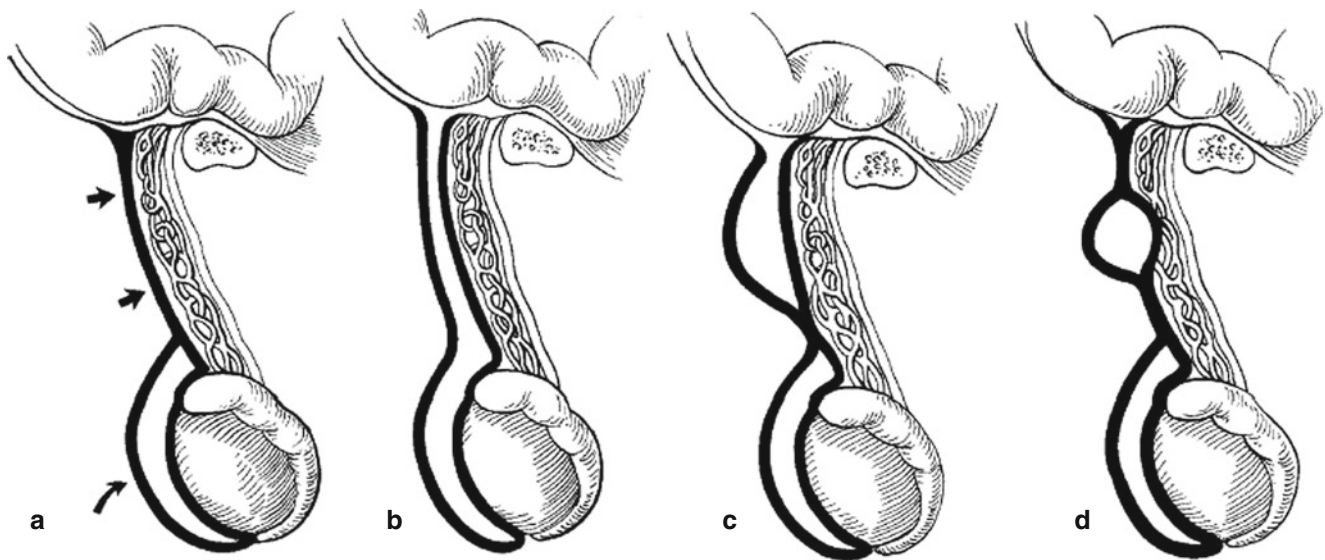


Fig. 27.33 (a) Normal closure of the processus vaginalis. Straight arrows indicate the funicular process; curved arrow is the tunica vaginalis. (b) Communicating hydrocele. There is complete patency of the processus vaginalis, (c) Funicular hydrocele of the spermatic cord. The

diverticulum communicates with the peritoneum only. (d) Encysted hydrocele of the spermatic cord. This enclosed collection does not communicate with the peritoneum or tunica vaginalis. (From Martin et al. 1996)

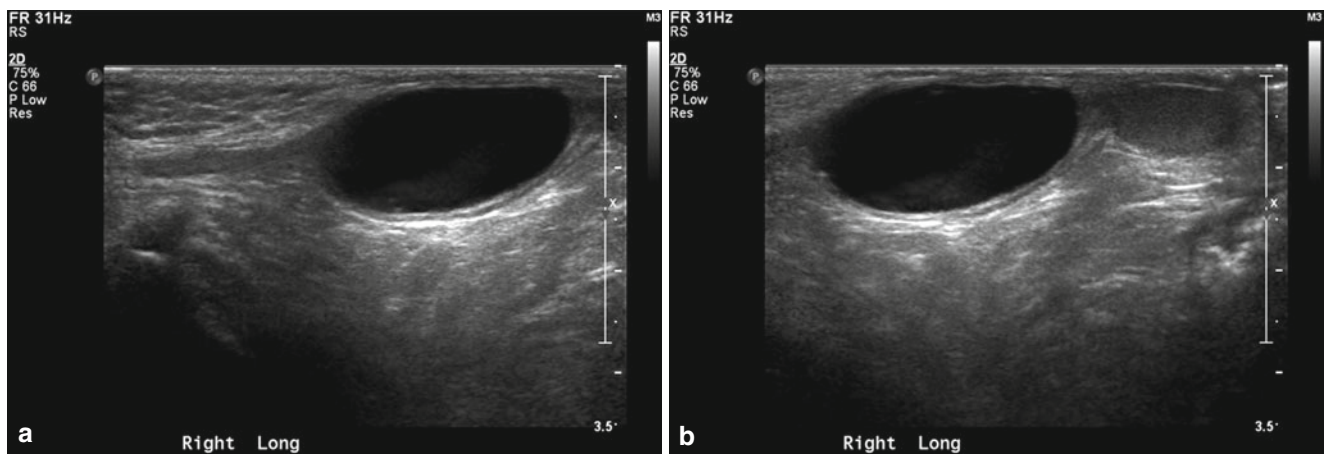


Fig. 27.34 Spermatic cord hydrocele (encysted hydrocele) in a 1-year-old boy. Longitudinal US images of inguinal region (**a**) and scrotum (**b**) show ovoid cystic lesion proximal to the testis. This focal fluid collec-

tion in spermatic cord does not communicate with the peritoneum or the scrotum

27.4.17 Varicocele

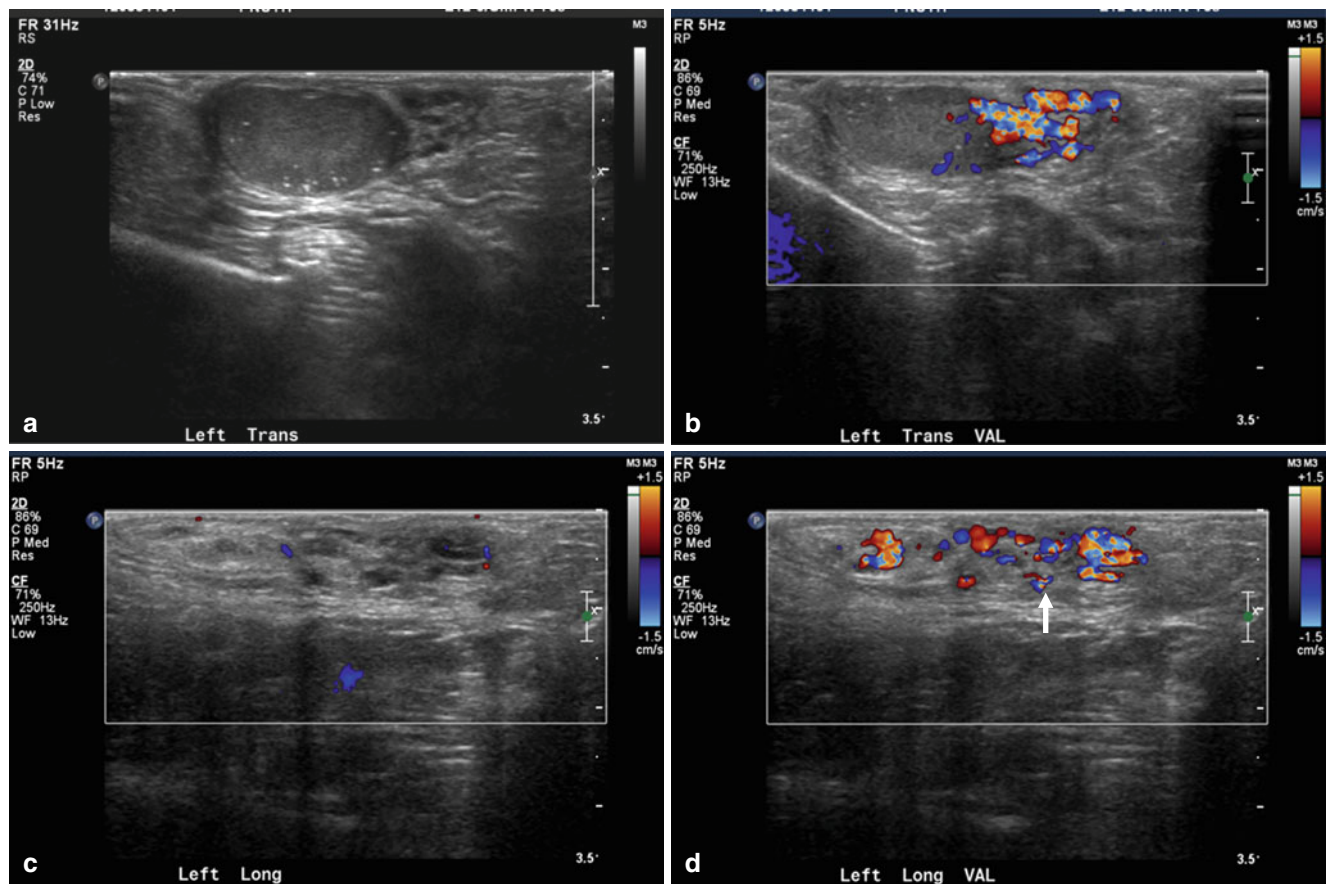


Fig. 27.35 Left varicocele in a 13-year-old boy. (a) Axial US scan of the left hemiscrotum shows multiple anechoic structures along the epididymis and tiny hyperechoic dots in peripheral of testis, representing microlithiasis. (b) Color Doppler image shows increased color flow in

the anechoic structures. (c, d) Color Doppler images of spermatic cord in the suprascrotal region demonstrate increased color flow in the anechoic structures during the Valsalva maneuver (arrow in d)

27.4.18 Epididymo-orchitis

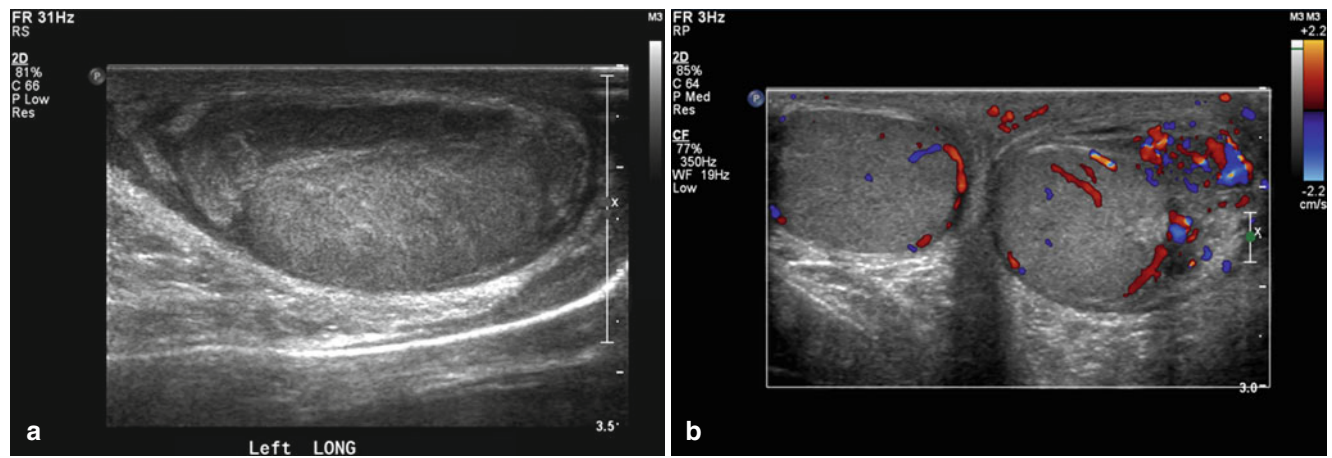


Fig. 27.36 Left epididymo-orchitis in a 12-year-old boy. (a) Longitudinal US of left scrotum shows a diffusely enlarged epididymis and heterogenous increased echogenicity of left testis with diffuse scro-

tal swelling. (b) Axial color Doppler image demonstrates diffuse thickening of left scrotal wall and increased color flow signal in epididymis and testis

27.4.19 Testicular Torsion

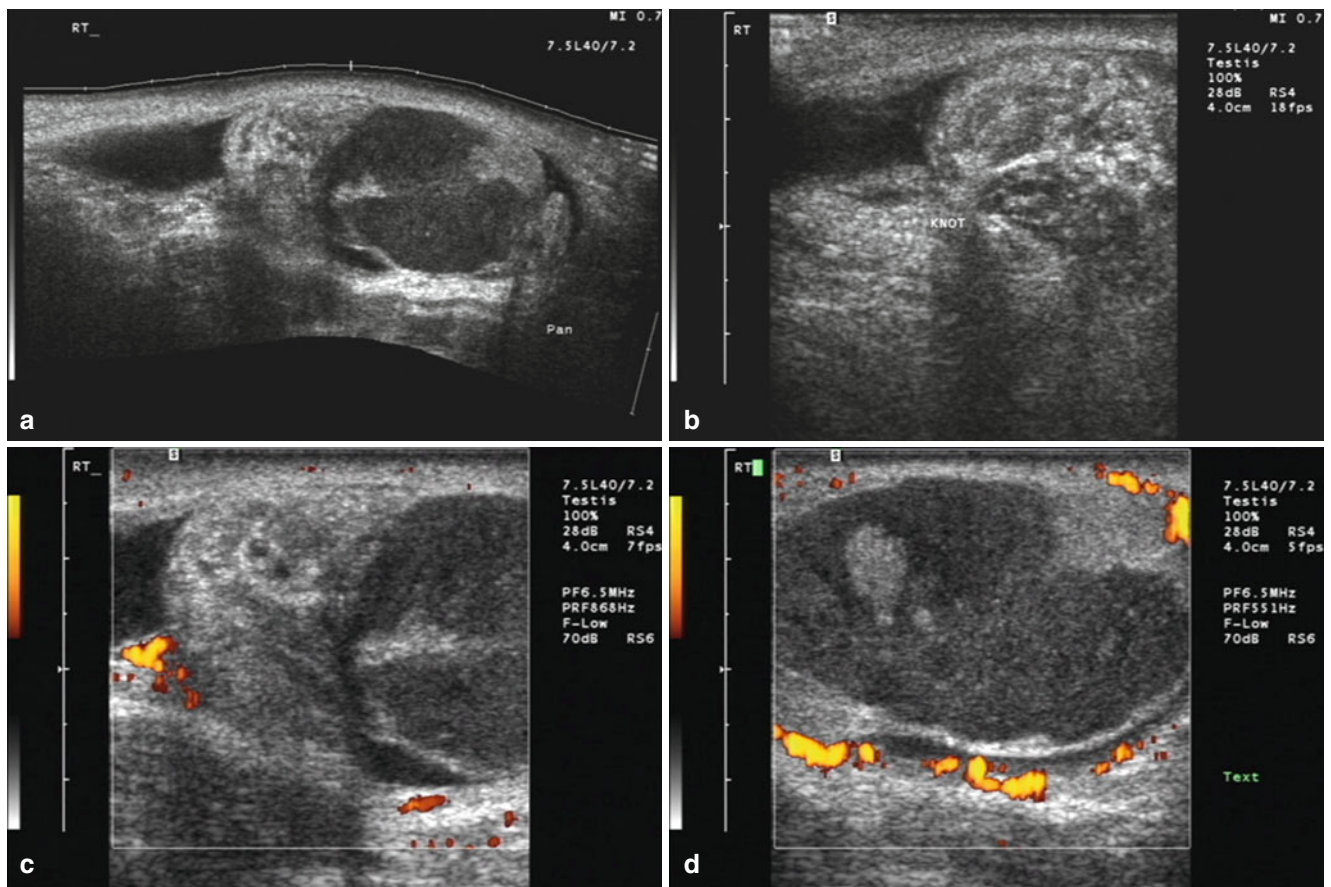


Fig. 27.37 Testicular torsion in a 10-year-old boy. Panorama view (a) and oblique (b) US scans of right scrotum show twisting of epididymis and testis, and heterogeneously hypoechoic testis with small fluid col-

lection. Color Doppler images (c, d) reveal no color flow in testis but increased color flow in the scrotal wall (Courtesy by Prof. Seong-Kuk Yoon, Dong-A university Hospital, Busan)

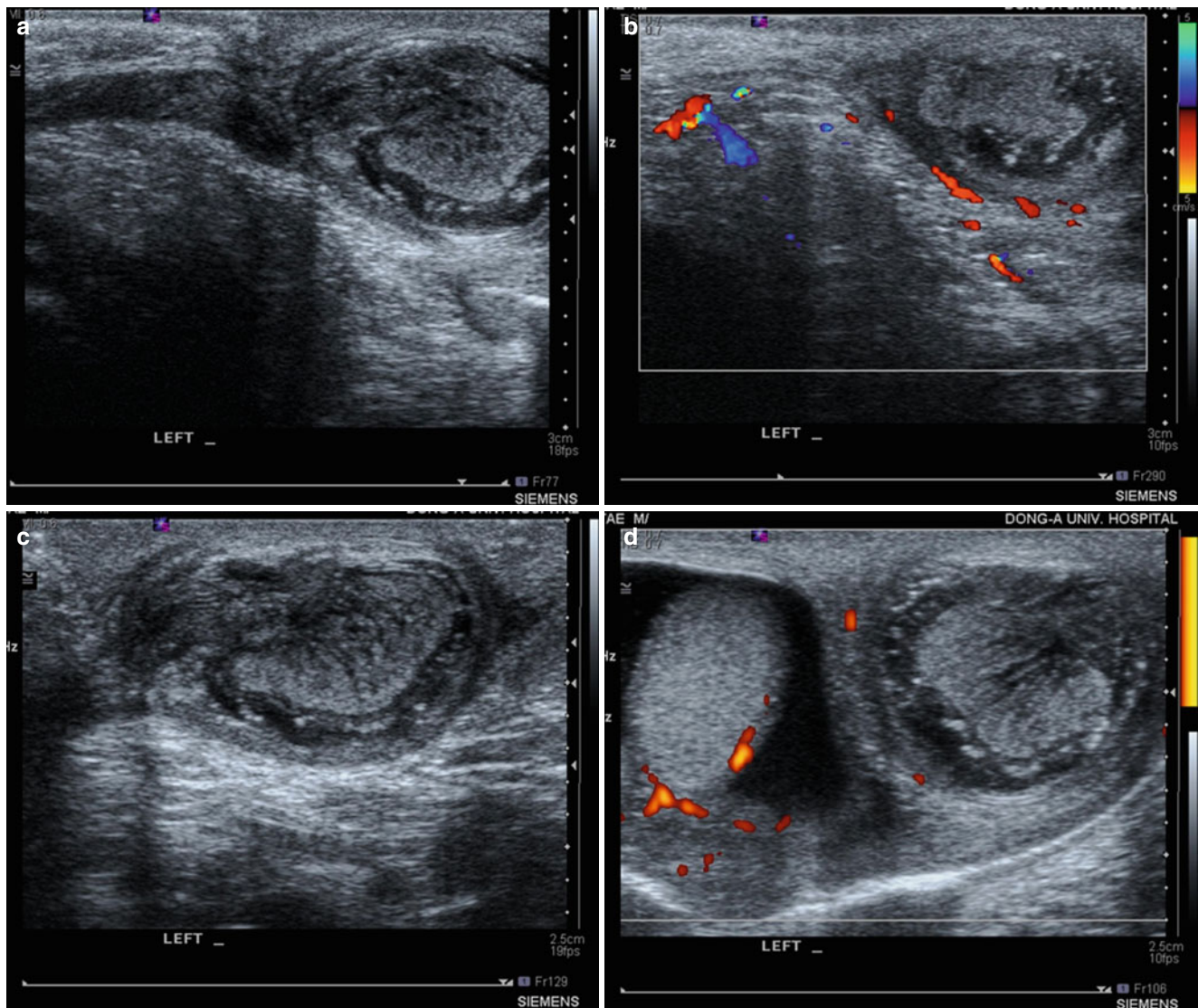


Fig. 27.38 Extravaginal testis torsion of the left testis in an infant. Longitudinal (a) and transverse (c) US scans of left scrotum show heterogeneously enlarged testis and torsion knot in spermatic cord, representing outside the tunica vaginalis. Color Doppler images (b, d) reveal

an enlarged, heterogenous echogenic left testis. The blood flow is not detected in testis (Courtesy by Prof. Seong-Kuk Yoon, Dong-A university Hospital, Busan)

27.4.20 Torsion of the Testicular Appendages

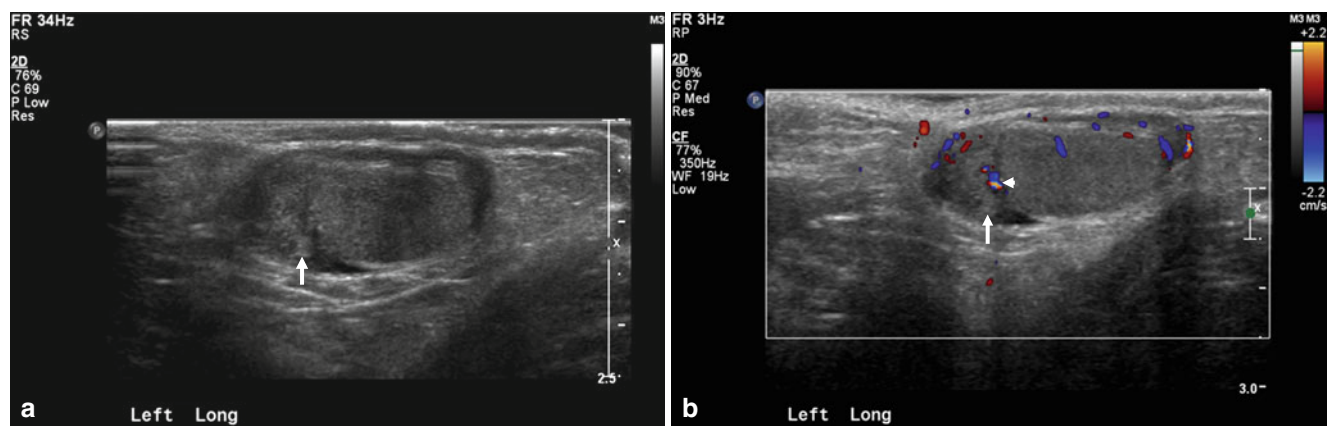


Fig. 27.39 Appendix testis torsion in an 8 year-old boy with scrotal pain. Longitudinal US scan (a) of left hemiscrotum shows a echogenic mass (arrow) between testis and epididymal head. The mass represents a twisted appendix testis. Color Doppler image (b) reveals that the

twisted appendage is avascular (arrow) and increased peripheral flow around twisted appendage (arrow head). Mild reactive hypervascularity is seen at the epididymal head and scrotal tunics

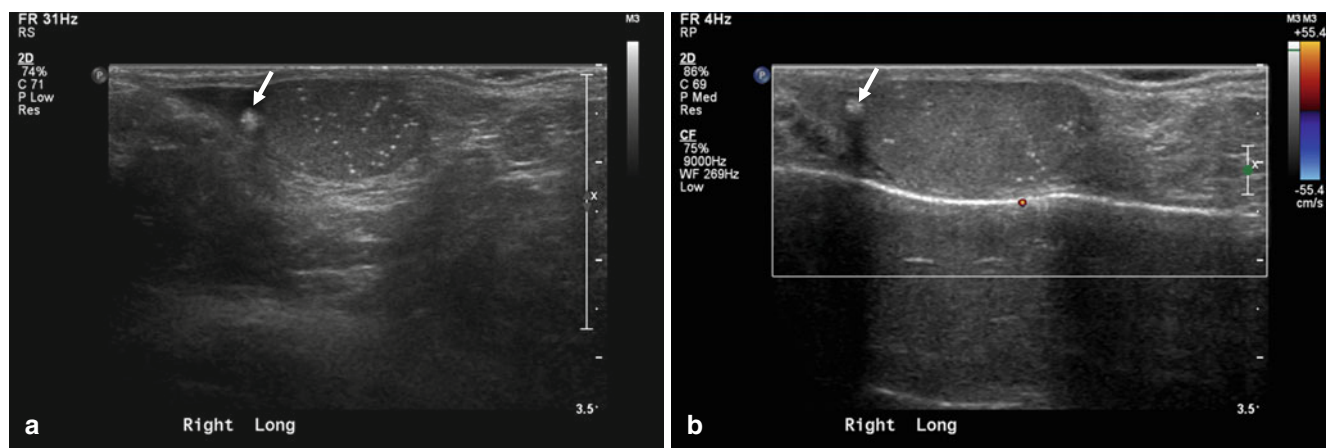


Fig. 27.40 Scrotolith after torsion of testicular appendages in a 13-year-old boy. Longitudinal US scans (a, b) of left testis show focal hyperechoic nodule with posterior shadowing at suprastesticular area.

The testis has underlying microlithiasis. This patient has past history of scrotal pain, suggesting appendage torsion

27.4.21 Scrotal Trauma

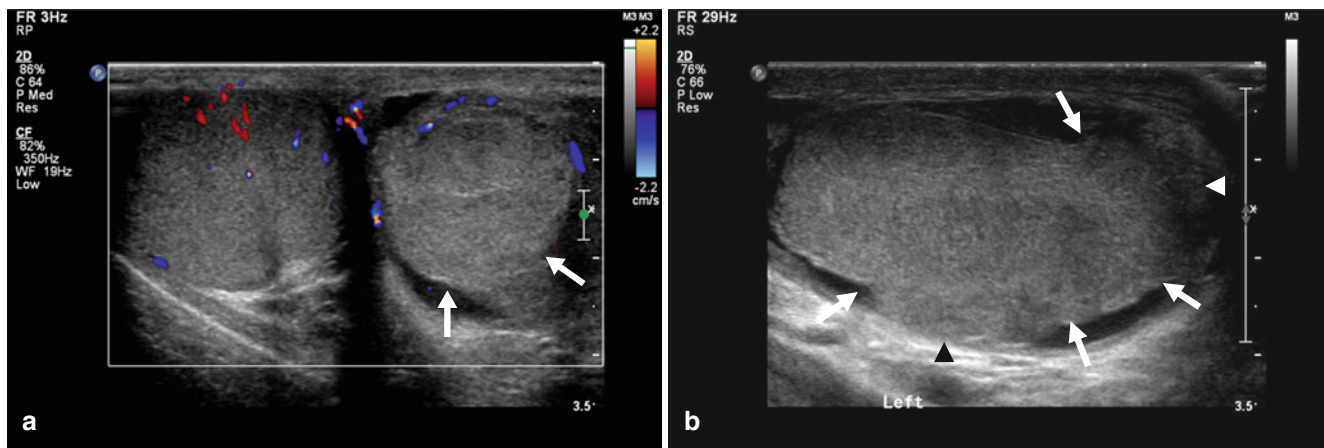


Fig. 27.41 Testicular rupture in a 12-year-old boy with scrotal trauma. Color Doppler image (a) shows slightly decreased echogenicity and decreased color flow in left testis. Longitudinal US (b) demonstrates

heterogeneous echogenic mass (*arrowheads*) across the defect in the tunica albuginea (*arrows*) in the inferior and posterior aspect of left testis

27.4.22 Testicular Microlithiasis

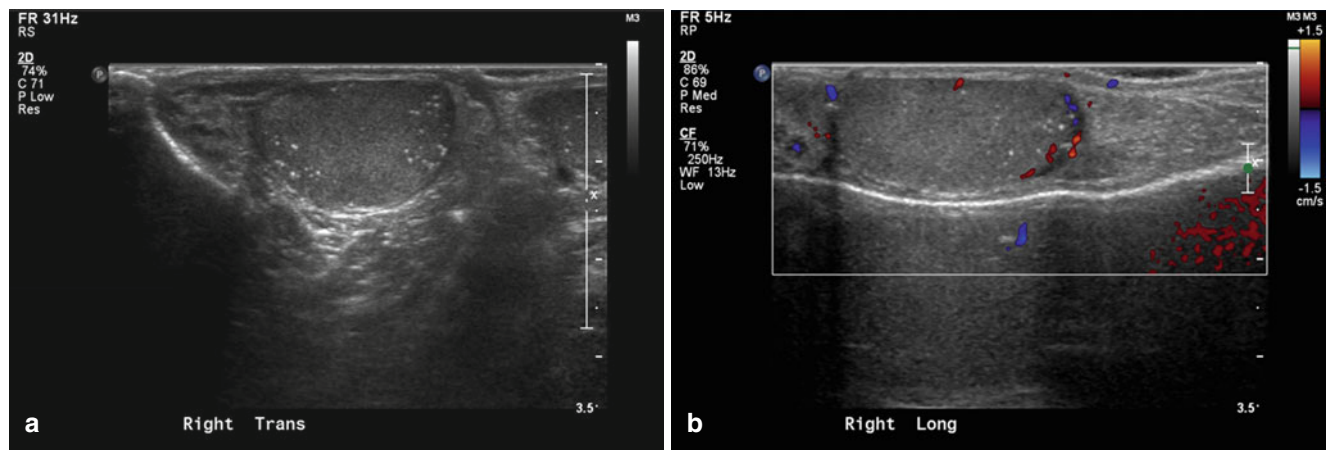


Fig. 27.42 Testicular microlithiasis in a 13-year-old boy. Transverse (a) US and longitudinal color Doppler (b) images of the scrotum demonstrate multiple echogenic foci scattered in the periphery of both testes

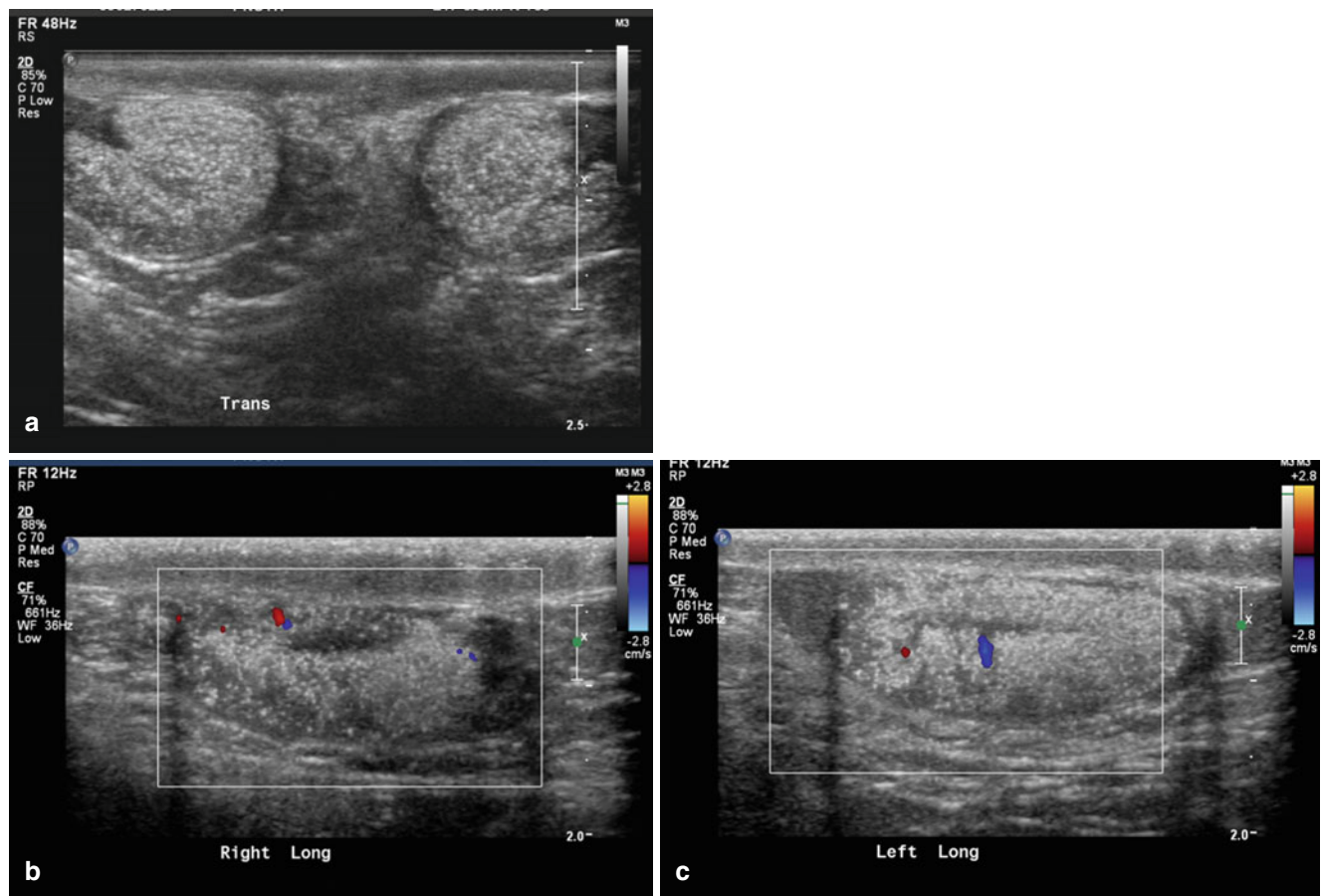


Fig. 27.43 Testicular microlithiasis in a 10-year-old boy. Transverse (a) US of the scrotum demonstrates multiple echogenic foci scattered throughout both testes. Longitudinal color Doppler (b, c) images of

both testis show normal color flow in both testis. These lesions were discovered at scrotal US performed for unrelated reasons

27.4.23 Testicular Tumor: Germ Cell Tumor

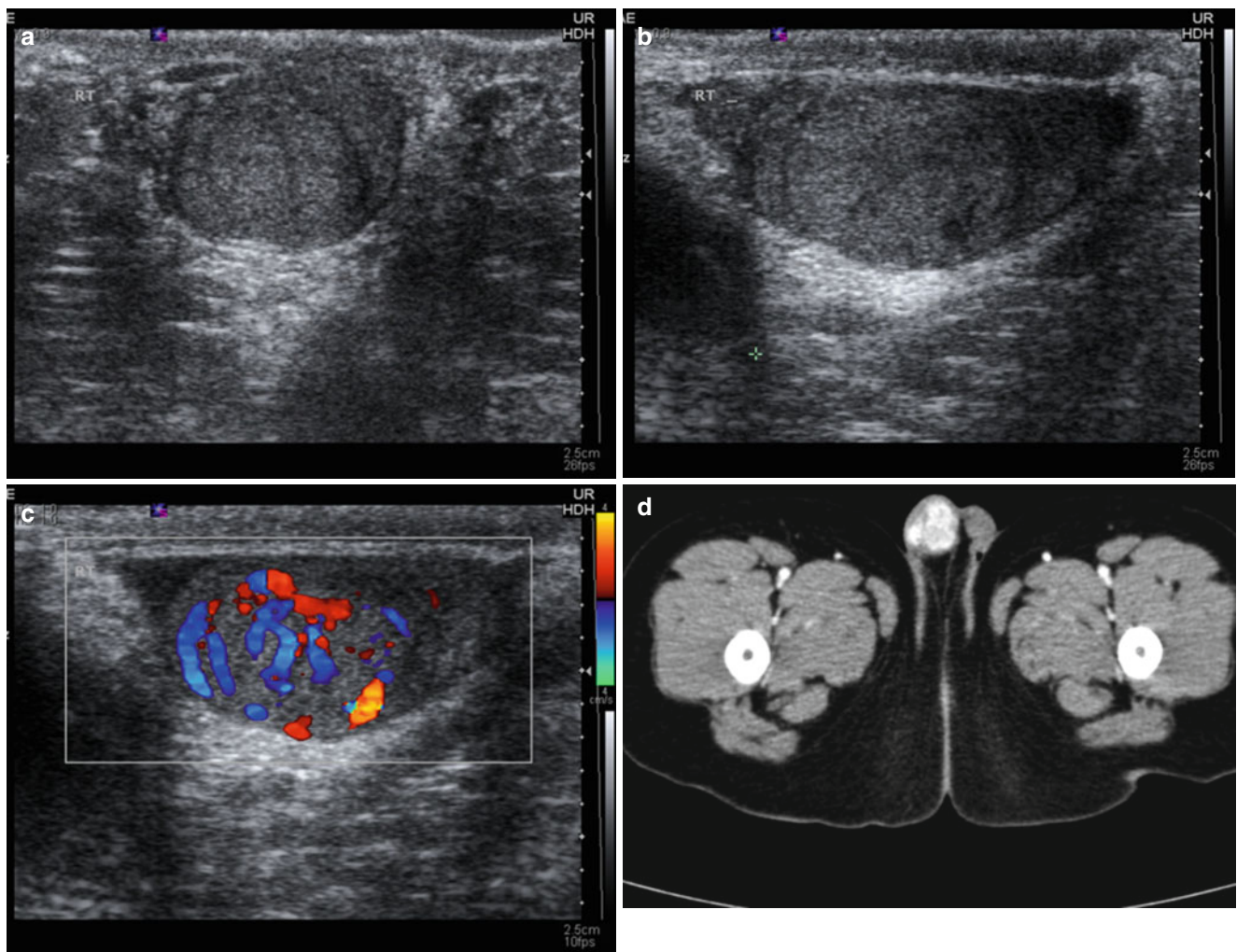


Fig. 27.44 Yolk sac tumor in a 2-year-old boy with scrotal mass. Transverse (a) and longitudinal (b) US scan of the right hemiscrotum show a solid tumor replacing testis. Color Doppler US (c) image shows

increased color flow within the mass. Contrast-enhanced CT (d) reveals well-enhancing mass in right testis and no retroperitoneal LN enlargement, representing metastasis

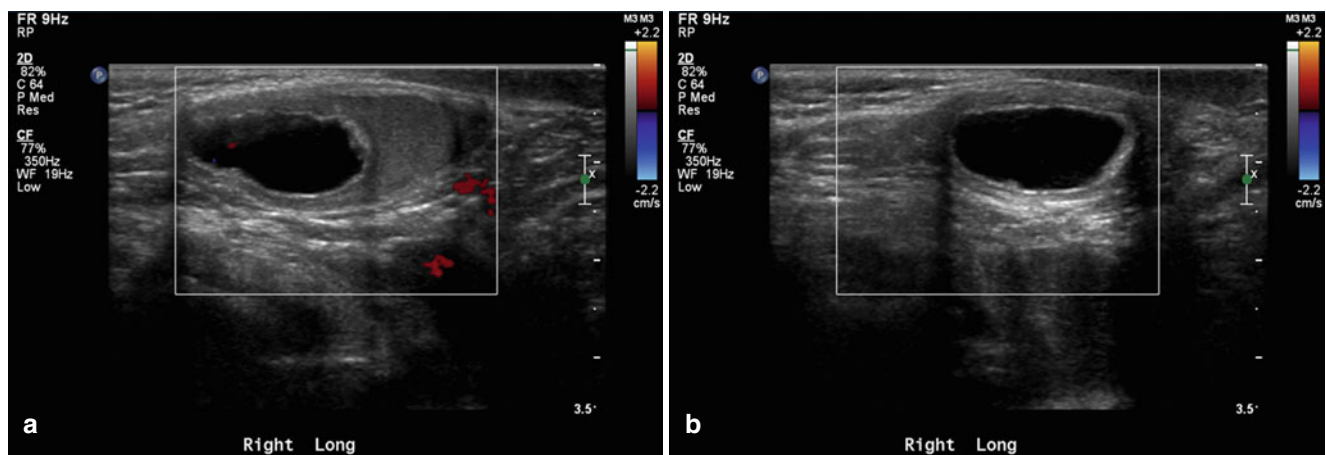


Fig. 27.45 Mature cystic teratoma in a 2-year-old boy with painless mass. Longitudinal (a) and transverse (b) US scans show a cystic mass with echogenic borders and with peripheral solid components. A rim of normal testis is also seen

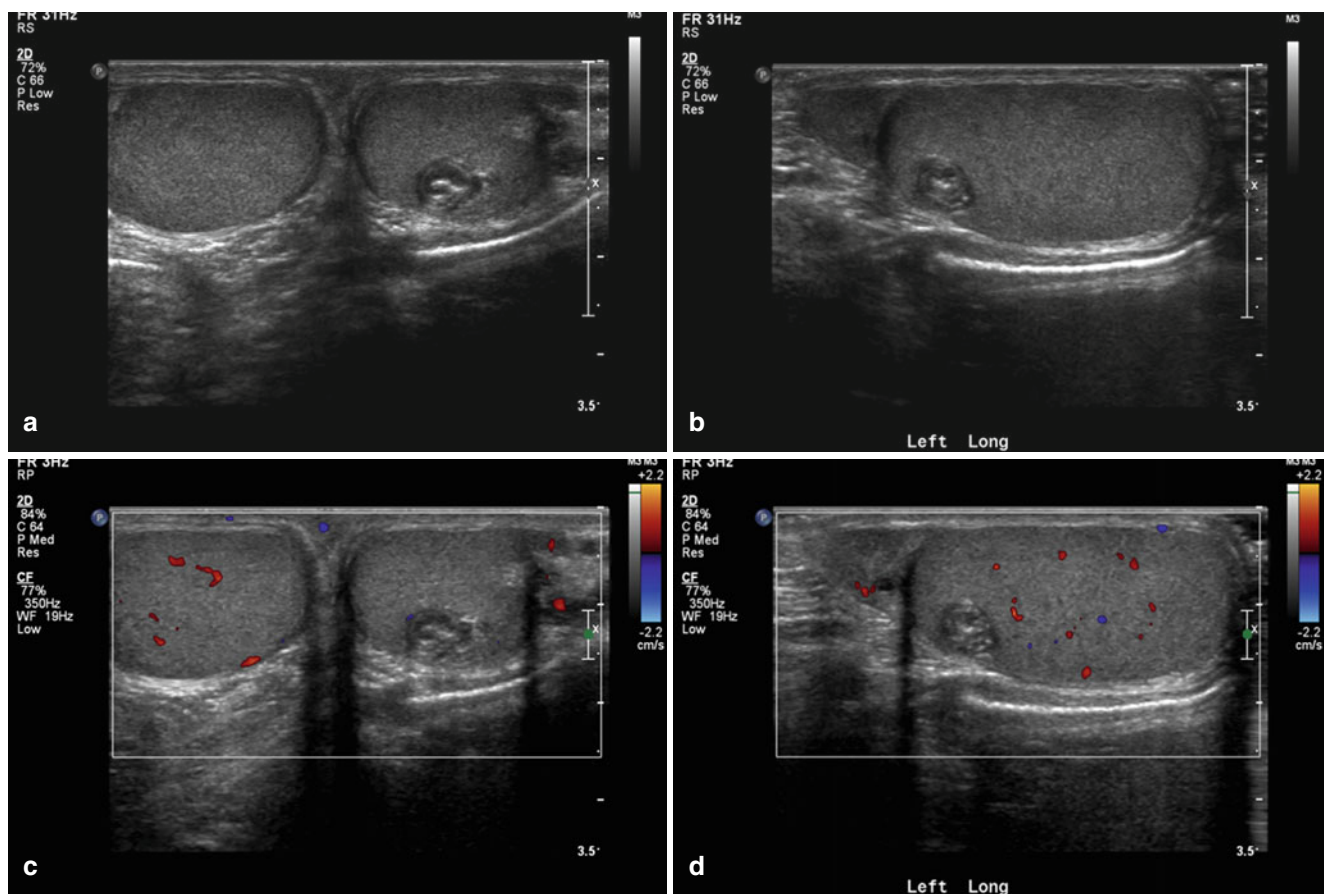


Fig. 27.46 Testicular epidermoid cyst in an 11-year-old boy. Transverse (a) and longitudinal (b) US scans of the left testis show small, well-circumscribed, round mass. The mass is primarily cystic and shows posterior sonic enhancement and internal alternating hyper-

echoic and hypoechoic layers, representing (onion-ring pattern). Transverse (c) and longitudinal (d) color Doppler images reveal well-delineated borders and avascularity of mass

27.4.24 Testicular Tumor: Secondary Tumor

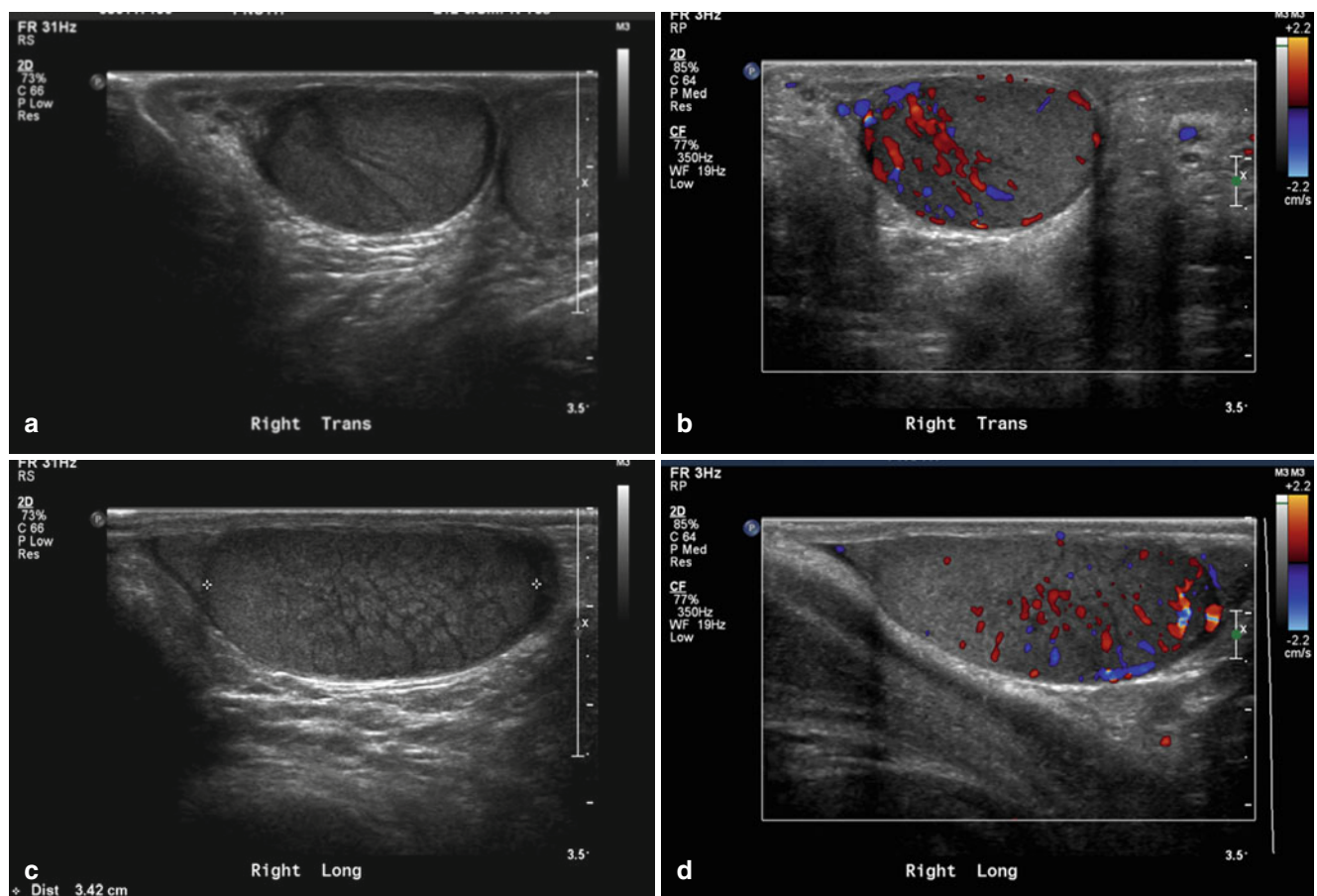


Fig. 27.47 Histologically proved focal leukemic involvement of right testis in a 13-year-old boy with ALL. Transverse (a) and longitudinal (c) US scans of the right testis show focal hypoechoic area with reticu-

lar septa at lower pole. Transverse (b) and longitudinal (d) color Doppler images demonstrate increased color flow in the hypoechoic area of right testis

References

- Arellano CM, Kozakewich HP, Diamond D, et al. Testicular epidermoid cysts in children: sonographic characteristics with pathological correlation. *Pediatr Radiol*. 2011;41(6):683–9.
- Aso C, Enríquez G, Fité M, et al. Gray-scale and color Doppler sonography of scrotal disorders in children: an update. *Radiographics*. 2005;25(5):1197–214.
- Backus ML, Mack LA, Middleton WD, et al. Testicular microlithiasis: imaging appearances and pathologic correlation. *Radiology*. 1994;192(3):781–5.
- Boechat MI. MR imaging of the pediatric pelvis. *Magn Reson Imaging Clin N Am*. 1996;4(4):679–96.
- Brammer 3rd HM, Buck JL, Hayes WS, et al. From the archives of the AFIP. Malignant germ cell tumors of the ovary: radiologic-pathologic correlation. *Radiographics*. 1990;10(4):715–24.
- Chung EM, Biko DM, Schroeder JW, et al. From the radiologic pathology archives: precocious puberty: radiologic-pathologic correlation. *Radiographics*. 2012;32(7):2071–99.
- deBeche-Adams TH, Bohl JL. Rectovaginal fistulas. *Clin Colon Rectal Surg*. 2010;23(2):99–103.
- Dogra VS, Gottlieb RH, Oka M, et al. Sonography of the scrotum. *Radiology*. 2003;227(1):18–36.
- Epelman M, Chikwava KR, Chauvin N, et al. Imaging of pediatric ovarian neoplasms. *Pediatr Radiol*. 2011;41(9):1085–99.
- Ganem JP, Workman KR, Shaban SF. Testicular microlithiasis is associated with testicular pathology. *Urology*. 1999;53:209–13.
- Garel L, Dubois J, Grignon A, et al. US of the pediatric female pelvis: a clinical perspective. *Radiographics*. 2001;21(6):1393–407.
- Garriga V, Serrano A, Marin A, et al. US of the tunica vaginalis testis: anatomic relationships and pathologic conditions. *Radiographics*. 2009;29(7):2017–32.
- Gooding GA, Leonhardt WC, Marshall G, et al. Cholesterol crystals in hydroceles: sonographic detection and possible significance. *AJR Am J Roentgenol*. 1997;169:527–9.
- Hricak H, Kim B, Hamm B. Imaging techniques, anatomy, artifacts, and bioeffects. In: Hricak H, Hamm B, Kim B, editors. *Imaging of the scrotum*. New York: Raven Press; 1995.
- Hye-Sun Cho, Yong Woo Kim, Seok Jin Choi, et al. Transverse testicular ectopia diagnosed by US and MR imaging: a case report. *J Korean Radiol Soc*. 2007;56:73–6.
- Jedrzejewski G, Stankiewicz A, Wiecek AP. Uterus and ovary hernia of the canal of Nuck. *Pediatr Radiol*. 2008;38(11):1257–8.
- Jung SE, Lee JM, Rha SE, et al. CT and MR imaging of ovarian tumors with emphasis on differential diagnosis. *Radiographics*. 2002;22:1305–25.
- Junqueira BL, Allen LM, Spitzer RF, et al. Müllerian duct anomalies and mimics in children and adolescents: correlative intraoperative assessment with clinical imaging. *Radiographics*. 2009;29(4):1085–103.
- Kim W, Rosen MA, Langer JE, et al. US-MR imaging correlation in pathologic conditions of the scrotum. *Radiographics*. 2007;27(5):1239–53.
- Martin LC, Share JC, Peters C, et al. Hydrocele of the spermatic cord: embryology and ultrasonographic appearance. *Pediatr Radiol*. 1996;26(8):528–30.
- Mazzu D, Jeffrey Jr RB, Ralls PW. Lymphoma and leukemia involving the testicles: findings on gray-scale and color Doppler sonography. *AJR Am J Roentgenol*. 1995;164:645–7.
- McCarville MB, Hill DA, Miller BE, et al. Secondary ovarian neoplasms in children: imaging features with histopathologic correlation. *Pediatr Radiol*. 2001;31(5):358–64.
- Mehta AL, Dogra VS. Intratesticular varicocele. *J Clin Ultrasound*. 1998;26:49–51.
- Monga M, Scarpero HM, Ortenberg J. Metachronous bilateral torsion of the testicular appendices. *Int J Urol*. 1999;6:589–91.
- Morowitz M, Huff D, von Allmen D. Epithelial ovarian tumors in children: a retrospective analysis. *J Pediatr Surg*. 2003;38:331–5.
- Outwater EK, Wagner BJ, Mannion C, et al. Sex cord-stromal and steroid cell tumors of the ovary. *Radiographics*. 1998;18(6):1523–46.
- Outwater EK, Siegelman ES, Hunt JL. Ovarian teratomas: tumor types and imaging characteristics. *Radiographics*. 2001;21(2):475–90.
- Phebe Chen, John S. Ultrasound of the acute scrotum. *Appl Radiol*. 2006;35:8–17.
- Quillin SP, Siegel MJ. Transabdominal color Doppler ultrasonography of the painful adolescent ovary. *J Ultrasound Med*. 1994;13(7):549–55.
- Rasalkar DD, Paunipagar BK, Chu WCW. Ovarian inguinal hernia complicated by ovarian torsion. *J Hong Kong Col Radiol*. 2010;13:86–7.
- Rha SE, Byun JY, Jung SE, et al. CT and MR imaging features of adnexal torsion. *Radiographics*. 2002;22(2):283–94.
- Ryan MF, Desai BK. Ovarian torsion in a 5-year old: a case report and review. *Case Rep Emerg Med*. 2012;2012:1–3. doi:10.1155/2012/679121.
- Shah RU, Lawrence C, Fickenscher KA, et al. Imaging of pediatric pelvic neoplasms. *Radiol Clin North Am*. 2011;49(4):729–48.
- Siegel MJ. Pelvic tumors in childhood. *Radiol Clin North Am*. 1997;35(6):1455–75.
- Siegel MJ. Female pelvis. In: Siegel MJ, editor. *Pediatric sonography*. 3rd ed. Philadelphia: Lippincott Williams & Wilkins; 2002a.
- Siegel MJ. Male genital tract. In: Siegel MJ, editor. *Pediatric sonography*. 3rd ed. Philadelphia: Lippincott Williams & Wilkins; 2002b.
- Surratt JT, Siegel MJ. Imaging of pediatric ovarian masses. *Radiographics*. 1991;11(4):533–48.
- Timmerman D, Testa AC, Bourne T, et al. Simple ultrasound-based rules for the diagnosis of ovarian cancer. *Ultrasound Obstet Gynecol*. 2008;31:681–90.
- Vijayaraghavan SB. Sonographic localization of nonpalpable testis: tracking the cord technique. *Indian J Radiol Imaging*. 2011;21(2):134–41.
- Woodward PJ, Sohaey R, O'Donoghue MJ, et al. From the archives of the AFIP: tumors and tumorlike lesions of the testis: radiologic-pathologic correlation. *Radiographics*. 2002;22(1):189–216.

Part VII

Musculoskeletal System

Jung-Eun Cheon

Contents

28.1	Introduction	888
28.2	Radiological Assessment	888
28.3	Common Radiographic Features of Specific Genetic Skeletal Disorders	888
28.3.1	Achondroplasia Group	888
28.3.2	Type II Collagenopathy	889
28.3.3	Metatropic Dysplasia Group	889
28.3.4	Short Rib-Polydactyly Group	889
28.3.5	Multiple Epiphyseal Dysplasia and Pseudoachondroplasia Group	890
28.3.6	Metaphyseal Chondrodysplasia Group	890
28.3.7	Dysplasia with Prominent Membranous Bone Involvement.....	890
28.3.8	Dysostosis Multiplex Group	891
28.3.9	Dysplasia with Decreased Bone Density	891
28.3.10	Dysplasia with Increased Bone Density	891
28.4	Illustrations: Genetic Skeletal Disorders	892
28.4.1	Radiographic Assessment of Disproportional Skeletal Growth	892
28.4.2	Achondroplasia	893
28.4.3	Spondyloepiphyseal Dysplasia Congenita.....	897
28.4.4	Kniest Dysplasia	898
28.4.5	Metatropic Dysplasia	899
28.4.6	Short Rib Polydactyly	901
28.4.7	Asphyxiating Thoracic Dysplasia	902
28.4.8	Pseudoachondroplasia.....	903
28.4.9	Multiple Epiphyseal Dysplasia	904
28.4.10	Metaphyseal Chondrodysplasia	905
28.4.11	Shwachman-Diamond Syndrome	906
28.4.12	Cleidocranial Dysplasia	907
28.4.13	Mucopolysaccharidosis: Morquio's Disease.....	908
28.4.14	Osteogenesis Imperfecta: Newborn	909
28.4.15	Osteopetrosis	910
	References	911

J.-E. Cheon, M.D.

Department of Radiology, Seoul National University Hospital,
 Seoul National University College of Medicine,
 101 Daehak-ro, Chongno-gu, Seoul 110-744, Korea
 e-mail: cheonje@snu.ac.kr

28.1 Introduction

Genetic skeletal disorders comprise two broad categories, including skeletal dysplasia and dysostosis. Skeletal dysplasias refer to a heterogeneous group of conditions in which there is a widespread disturbance of bone and cartilage growth, beginning during the early stages of fetal development and evolving throughout life, while dysostoses comprise conditions that occur as a result of embryonic morphogenic defects in the first 6 weeks of fetal life resulting in defective bone formation. Skeletal dysplasia occurs as a result of defects in structural proteins, metabolic processes, or growth plate regulation; the phenotypes in this group of conditions continue to evolve throughout life. In other words, previously apparently unaffected bones and joints may subsequently demonstrate abnormality. On the contrary, the malformations caused by dysostosis do not spread to involve previously normal bones and joints, i.e., the phenotypes are static throughout life. The latest International Nosology and Classification of Genetic Skeletal Disorders provides an overview of recognized diagnostic entities and groups them by clinical and radiographic features and molecular pathogenesis. In the 2010 revision, 456 conditions were included and placed in 40 groups defined by molecular, biochemical, and/or radiographic criteria (Ikegawa 2006; Warman et al. 2011).

28.2 Radiological Assessment

When faced with a request for the radiological investigation of a child with a suspected genetic skeletal disorder, the radiologist should recommend performing a series of radiographs known collectively as a skeletal survey. Routine skeletal survey includes skull (AP and lateral view), thoracolumbar spine (AP and lateral), chest, pelvis, upper and lower limb, and hand radiographs. After obtaining the radiographs, systematic assessment will be helpful to make a specific diagnosis.

First, a disproportional skeletal growth should be assessed at the radiographs. A quick look at the spine will readily help decide if there is platyspondyly leading to short-trunked disproportion (Fig. 28.1a). Similarly, looking at the extremities may help in defining rhizomelia, mesomelia, and acromelia (Fig. 28.1b). And then, anatomic localization should be performed. Abnormal development of epiphyses, metaphyses, and diaphyses has given rise to the original nomenclature using those site names. An overall look at the radiological survey will suggest epiphyseal dysplasias by the presence of very small (delayed ossification) and/or irregularly ossified epiphyses. If the metaphyses are widened, flared, and/or irregular, the diagnosis of a form of metaphyseal dysplasia is established. Diaphyseal dysplasia is present when there is diaphyseal widening and/or cortical thickening or marrow

space expansion or restriction. Every bony structure should be looked at in an effort to combine the clinical and radiographic assessment. Pathognomonic findings help to narrow the group of differential diagnosis leading to a specific entity (Markowitz and Zackai 2001; Mortier 2001; Vanhoenacker et al. 2001; Offiah and Hall 2003; Nishimura 2010; Alanay and Lachman 2011).

28.3 Common Radiographic Features of Specific Genetic Skeletal Disorders

28.3.1 Achondroplasia Group

Achondroplasia group includes three specific entities: thanatophoric dysplasia, achondroplasia, and hypochondroplasia. They all have the same chromosomal locus (4p16.3). The gene/protein abnormality in all of them is a different mutation or group of mutations in fibroblast growth factor receptor 3 (FGFR-3). FGFR-3 acts on growth plate chondrocytes to regulate linear growth. FGFR is expressed in all pre-bone cartilage, and its function is to slow down or inhibit endochondral ossification (Lemyre et al. 1999).

28.3.1.1 Thanatophoric Dysplasia

Thanatophoric dysplasia is the most common lethal form of dwarfism. The radiographic features of thanatophoric dysplasia include markedly flattened vertebral bodies; small, flared iliac bones and flat acetabulum; short extremities with flaring and irregularity of the metaphyses; and proportionately large skull. Pronounced flattening of the vertebral bodies, with more constriction of their midportions and wide intervertebral disc spaces, is evident. The appearance of each vertebra on frontal radiographs resembles an inverted U or an H. The bowed femora resemble telephone receivers (Langer et al. 1969).

28.3.1.2 Achondroplasia

Achondroplasia is the most common form of dwarfism. The abnormality seen in the bone of patients with achondroplasia is failure of endochondral ossification. Intramembranous and periosteal ossifications are undisturbed. Prenatal diagnosis by amniocentesis or chorionic villi sampling detects FGFR-3 point mutation (Azouz et al. 1998; Carter et al. 2007).

Radiographic findings of the pelvis include squared iliac bones with small sacrosclastic notches and flat acetabular angles. Shortening of the tubular bones, especially the proximal ones, and metaphyseal flaring are seen (Fig. 28.2). In infancy, ice cream scoop shape of the proximal femur may be seen (Fig. 28.2). A V-shaped configuration of the distal femoral growth plate (chevron deformity) may be seen (Fig. 28.3). Shortening of the tubular bones in the

hand and feet is evident. There is a separation between the middle and the ring finger, which has been described as trident hand (Fig. 28.2d). Skull radiograph shows a large cranium and a small foramen magnum (Fig. 28.4). Growth failure occurs at the neurocentral synchondrosis. The vertebral bodies are flattened and appear bullet shaped in infancy and early childhood. The interpedicular distances of the lower lumbar vertebrae, which normally increase proceeding distally, remain the same at all levels or decrease in the lower lumbar region. In the lateral projection of the spine, the pedicles are short, the backs of the vertebral bodies are often concave (scalloping), and the spinal canal is small (Fig. 28.3) (Kornak and Mundlos 2003; Offiah and Hall 2003).

28.3.2 Type II Collagenopathy

Type II collagenopathies are a heterogeneous group of disorders, all of which show some relationship to each other not only molecularly but also clinically and radiographically. They have in common involvement of the spine and epiphyseal ossification delay or dysplasia (Spranger et al. 1994).

28.3.2.1 Spondyloepiphyseal Dysplasia Congenita

Spondyloepiphyseal dysplasia congenita (SEDC) results in obvious short-trunked dwarfism and short limbs with abnormal epiphyses. Inheritance is by autosomal dominant transmission, but most cases are sporadic. SEDC is caused by mutation in the COL2A1 locus on chromosome 12, which encodes the type II collagen $\alpha 1$ chain. This results in abnormal type II collagen. Radiographic findings include a decreased height of the vertebral bodies and, in infancy, pear-shaped or oval vertebral bodies. Hypoplasia of the odontoid process may be associated with atlantoaxial dislocation. Typical appearance in the pelvis includes a marked delay in ossification of the pubic bones and proximal portion of the femora. Normally modeled, but shortened, long bones demonstrate significant ossification delay and hypoplastic or dysplastic appearance of the epiphyses (Fig. 28.5) (Spranger and Langer 1970).

28.3.2.2 Kniest Dysplasia

Kniest dysplasia is a rare, severe form of chondrodysplasia characterized by dwarfism, progressive joint stiffness and contractures, retinal detachment, cleft palate, midface hypoplasia, and hearing loss. Kniest dysplasia is an autosomal dominant disorder. The dysplasia is the result of mutations of COL2A1, which leads to defective type II collagen.

Radiographic findings include short bowed tubular bones with exaggerated metaphyseal flare, dumbbell femurs,

and generalized ossification delay; epiphyses becoming dysplastic and then later even megaepiphyses; and irregular calcification in growth plate area. Platyspondyly with end plate irregularity is apparent, and coronal cleft of the vertebral bodies is seen in infancy (Fig. 28.6) (Dwek 2005; Yazici et al. 2010).

28.3.3 Metatropic Dysplasia Group

28.3.3.1 Metatropic Dysplasia

Metatropic dysplasia is discoverable in the newborn with a relatively long trunk and markedly short limbs. Over time, the limbs become more disproportionately short, and the trunk assumes a moderate to severe kyphoscoliosis, producing a short-trunked and short-limbed type of dwarfism. The changing nature of the clinical presentation led to the name *metatropic*, meaning a changing or variable course. The spine demonstrates dense wafer vertebral bodies in infancy and platyspondyly with kyphoscoliosis in affected children and young adults. The halberd (hunting ax)-shaped proximal femurs and trumpet-shaped metaphyses are seen in the affected newborns. The short tubular bones of the hand and feet show a dumbbell pattern (Fig. 28.7) (Kannu et al. 2007).

28.3.4 Short Rib-Polydactyly Group

The short rib dysplasia with or without polydactyly group of disorders is a rather diverse group. The group consists of short rib polydactyly disorders, asphyxiating thoracic dysplasia, and chondroectodermal dysplasia (Ellis-van Creveld syndrome) (Fig. 28.8) (Yang et al. 1987).

28.3.4.1 Asphyxiating Thoracic Dysplasia

Asphyxiating thoracic dysplasia is a disorder with a mixed prognosis. Many affected patients die in the perinatal period from respiratory complications. Survivors may die from renal complications later in life. The characteristic radiographic features are a narrow thorax and short, horizontally oriented ribs with wide, irregular costochondral junctions. The clavicles may have a high, handlebar appearance. The acetabular roofs are flat, with downward spike-like projections, the so-called triradiate or trident acetabulum. Long tubular bones show generalized shortening, precocious proximal femoral epiphysis ossification, and cone-shaped epiphysis in hands (Fig. 28.9). Asphyxiating thoracic dysplasia has many radiographic and histologic features that are similar to those of chondroectodermal dysplasia, a possible allelic disease (Yang et al. 1987; Vanhoenacker et al. 2004).

28.3.5 Multiple Epiphyseal Dysplasia and Pseudoachondroplasia Group

28.3.5.1 Pseudoachondroplasia

Pseudoachondroplasia is characterized by short-limbed dwarfism in which both the epiphyses and the metaphyses are involved. Pseudoachondroplasia is usually transmitted as an autosomal dominant. Most cases are the results of spontaneous mutations. There has been a genetic linkage of pseudoachondroplasia to the pericentromeric region of chromosome 19. This region encodes for cartilage oligomeric matrix protein (COMP), which is a large extracellular matrix protein expressed in cartilage, ligament, and tendon tissue. COMP plays a role in calcium binding within cartilage.

The appearance of newborns with pseudoachondroplasia is normal, and the rhizomelic shortening becomes noticeable from 2 years of age. The skull and facies in pseudoachondroplasia are normal. Spinal radiographs reveal oval or biconvex vertebrae, with central tongue-like protrusion. The interpedicular distance in the lumbar spine is normal in pseudoachondroplasia. The long bones are short and broad, with flaring of the metaphyses. Ossification of the epiphyses is delayed. When the epiphyses do ossify, they appear irregular and fragmented. The pelvis has normal sacrosciatic notches. The acetabula are shallow but not horizontal (Fig. 28.10) (Susic et al. 1997; Lachman et al. 2005).

28.3.5.2 Multiple Epiphyseal Dysplasia

Multiple epiphyseal dysplasia (MED) is a genetically heterogeneous group of diseases characterized by variable degrees of epiphyseal abnormalities, a delay in the appearance of the epiphyses, and irregular, symmetric epiphyseal formation, primarily involving the hip and knee joints. To date, mutations in six different genes have been shown to cause MED; the genes encoding cartilage oligomeric matrix protein (COMP), matrilin-3 (MATN3), and the alpha 1–3 chains of type IX collagen (COL9A1, COL9A2, COL9A3) have all been shown to result in autosomal dominant MED, and a specific mutation in the diastrophic dysplasia sulfate transporter (DTDST) has been shown to be associated with an autosomal recessive form of MED (Lachman et al. 2005).

The principal finding on radiographs is a delay in the appearance of the ossification centers. When the epiphyseal ossifications do appear, they are small, fragmented, mottled, and flattened.

The proximal femur is most often affected. The findings on hip radiographs may be easily confused with those of bilateral Legg-Calve-Perthes disease. Clues to the diagnosis are the presence of symmetric involvement in MED versus the metachronous findings in LCP disease. MED is distinguished from SED by the absence of severe vertebral changes (Fig. 28.11) (Unger et al. 2008).

28.3.6 Metaphyseal Chondrodysplasia Group

Metaphyseal chondrodysplasia denotes a group of bone dysplasia characterized by failure of normal mineralization of the zone of provisional calcification, leading to widened physes and enlarged knobby metaphysis. Because the longitudinal growth of the bone is affected, affected patients are short, and angular deformities may occur. In all types of this dysplasia, the epiphyses are spared.

28.3.6.1 Metaphyseal Chondrodysplasia, Schmid Type

The Schmid type is the most common form of metaphyseal chondrodysplasia. Inheritance is autosomal dominant. Mutations present on chromosome 6 affect the C-terminal non-helical domain of type X collagen (COL10A1) in Schmid's metaphyseal chondrodysplasia.

Radiographs show splaying, irregularity, and cupping of the metaphyses. The proximal femoral metaphysis is particularly irregular and splayed, and there is medial beaking. A triangular bone fragment may be present on the inferior aspect of the femoral neck. Angular deformities, particularly genu varum, are common after the child has been walking (Fig. 28.12) (Spranger 1977; Lachman et al. 1988).

28.3.6.2 Shwachman-Diamond Syndrome

This is a rare autosomal recessive disorder, also known as metaphyseal chondrodysplasia with pancreatic insufficiency and cyclic neutropenia, which entails helpful diagnostic clinical clues of malabsorption and recurrent infection. Radiological findings include metaphyseal changes especially knee and/or hip, anterior rib irregularity, and lipomatosis of the pancreas (Fig. 28.13) (Berrocal et al. 1995; Makitie et al. 2004; Nishimura et al. 2007).

28.3.7 Dysplasia with Prominent Membranous Bone Involvement

28.3.7.1 Cleidocranial Dysplasia

Cleidocranial dysplasia is a disorder in which the bones formed by intramembranous ossification (primarily the clavicles, cranium, and pelvis) are abnormal. It is inherited as an autosomal dominant trait. The characteristic finding in the cleidocranial dysplasia is hypoplasia or the absence of clavicles. Skull radiographs show multiple wormian bones and persistently open anterior fontanelle. The pelvis shows bilateral involvement. Pelvis radiographs show delay in ossification of the pubic bones, a wide symphysis pubis, and high narrow iliac wings (Fig. 28.14) (Gupta et al. 1992; Markowitz and Zackai 2001).

28.3.8 Dysostosis Multiplex Group

28.3.8.1 Mucopolysaccharidoses

Mucopolysaccharidoses (MPS) constitute a heterogeneous group of lysosomal storage disease. The intracellular degradation of micromolecular compounds by lysosomal enzyme is abnormal in this group of disease, leading to intracellular accumulation of semidegraded compounds. The overall incidence of MPS is 1 in 25,000 live births. The MPS are subdivided based on their enzyme deficiency and the type of substance that accumulates. The most common of the MPS are Morquio's syndrome (MPS types IVA and IVB) and Hurler syndrome (MPS type IH). Dysostosis multiplex is the constellation of bone dysplasia features seen variably in MPS, mucopolipidosis, and multiple other storage diseases that produce a skeletal dysplasia.

All MPS lead to abnormally short stature. Radiographic changes are also seen in the skull, leading to abnormal facies. Hurler syndrome as the stereotypical example of MPS demonstrates enlarged, thick calvaria, with J-shaped sella. The clavicles are broad, especially medially. The scapulae are short and stubby. The ribs are oar shaped and broader anteriorly than posteriorly. The vertebral bodies are ovoid when immature. Thoracolumbar gibbus (sharply angled kyphosis) with anterior and inferior beaked vertebral bodies inferiorly pointed small ilia, steep acetabular roof, and coxa valga. Long bones often have thickened cortices and wide diaphyses. The second through fifth metacarpal are pointed at their proximal ends, and the phalanges are bullet shaped (Fig. 28.15) (Levin et al. 1997; Markowitz and Zackai 2001; Rasalkar et al. 2011).

28.3.9 Dysplasia with Decreased Bone Density

28.3.9.1 Osteogenesis Imperfecta

Osteogenesis imperfecta (OI) is a group of clinically heterogeneous genetic disorders caused by type I collagen abnormalities characterized by increased bone fragility resulting in frequent fractures with malunion and bowing. The affected genes COLA1 and COLA2 are found on chromosomes 17q and 7q, respectively. OIs show variable phenotypes. Original

types I–IV are based on clinical and radiological manifestation and inheritance. Types V–IX are proposed due to mutations outside type I collagen genes and/or different phenotypes and inheritance. OI type II is almost the most common lethal skeletal dysplasia, severity of OI (mild-→severe) type I<IV<VI<VII<III<II.

The best diagnostic clue of early diagnosis of OI type II is numerous in utero or perinatal fractures of short, poorly mineralized bones. Radiographic findings of other types of OI include kyphoscoliosis, biconcave or flattened vertebral bodies (platyspondyly), compression fractures, coxa vara, protrusio acetabuli, diaphyseal overtubulation (thin, gracile), thin cortex, and bowing (Fig. 28.16). It is difficult to type OI radiographically. OI type V shows hyperplastic callus formation, radioulnar interosseous membrane calcification, or radial head dislocation. Radiograph after biphosphate therapy demonstrates “zebra” sign: sclerotic metaphyseal bands paralleling growth plates and the number of bands is equal to the number of treatments (Dutton 1987; Lachman et al. 1992; Paterson et al. 1993; Sillence 1994).

28.3.10 Dysplasia with Increased Bone Density

28.3.10.1 Osteopetrosis

Osteopetrosis or marble bone disease is a rare bone dysplasia characterized by failure of osteoclast to resorb bone with both of the autosomal dominant and autosomal recessive subtypes. Several gene mutations have been found to be responsible for osteoclast dysfunction. In patients with osteopetrosis, acidification function of osteoclast, which is required to dissolve bone matrix, is defective, and calcified chondroid and primitive bone persist, leading to osteosclerosis and increased brittleness of the bones. Radiographically, the hallmark of osteopetrosis is increased density within the medullary portion of the bone with relative sparing of the cortices. The classic “bone-within-bone” appearance, particularly in the pelvis, or the “sandwich vertebra” appearance characterized by dense end plate sclerosis can be seen on radiographs (Fig. 28.17) (Ihde et al. 2011).

28.4 Illustrations: Genetic Skeletal Disorders

28.4.1 Radiographic Assessment of Disproportional Skeletal Growth

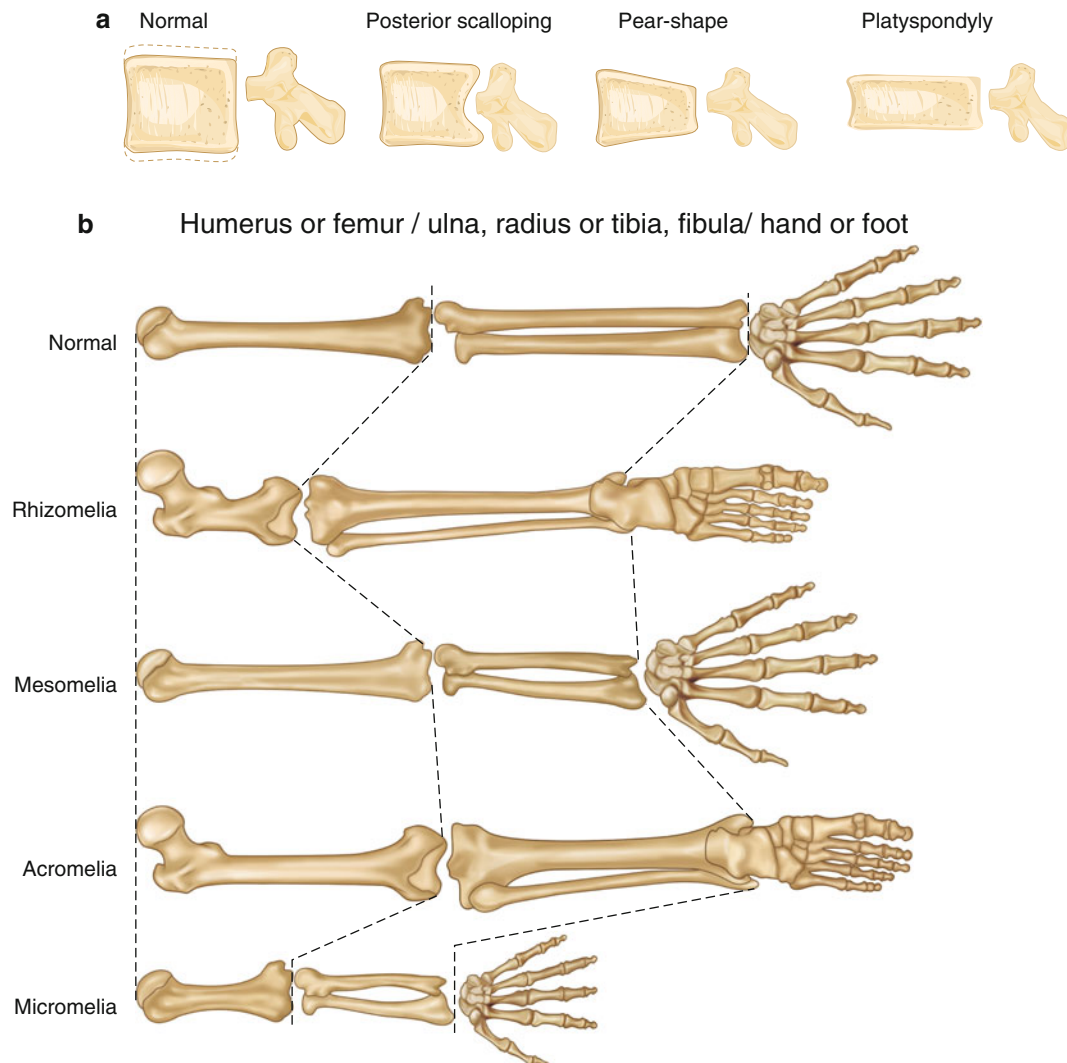


Fig. 28.1 Radiographic assessment of disproportional skeletal growth. (a) Spine. (b) Extremities

28.4.2 Achondroplasia

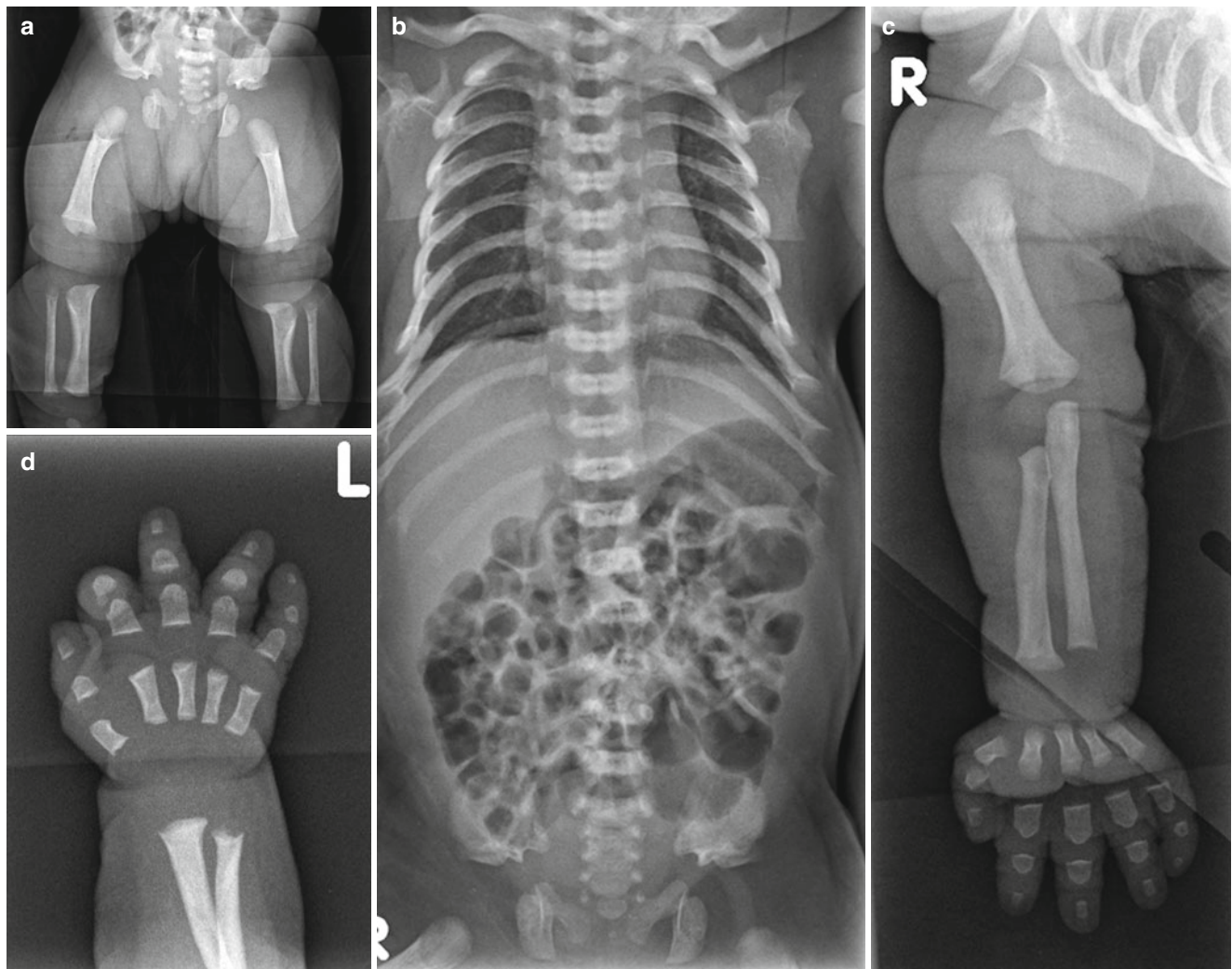


Fig. 28.2 *Achondroplasia: newborn.* (a) Anteroposterior view of the pelvis and lower extremities shows horizontal acetabula, square iliac bones, and short sacrosciatic notches. Note the oval transradiancy of proximal femora and sloping metaphyses showing ice cream scoop appearance. (b) Anteroposterior view of the spine shows slightly flat

vertebral bodies and increased height of the intervertebral space. The interpediculate distance decreases from the upper to the lower lumbar spine. (c) Rhizomelic shortening is evident in the upper extremity. (d) Hand radiograph demonstrates wide separation of the third and fourth phalanges suggesting a trident hand

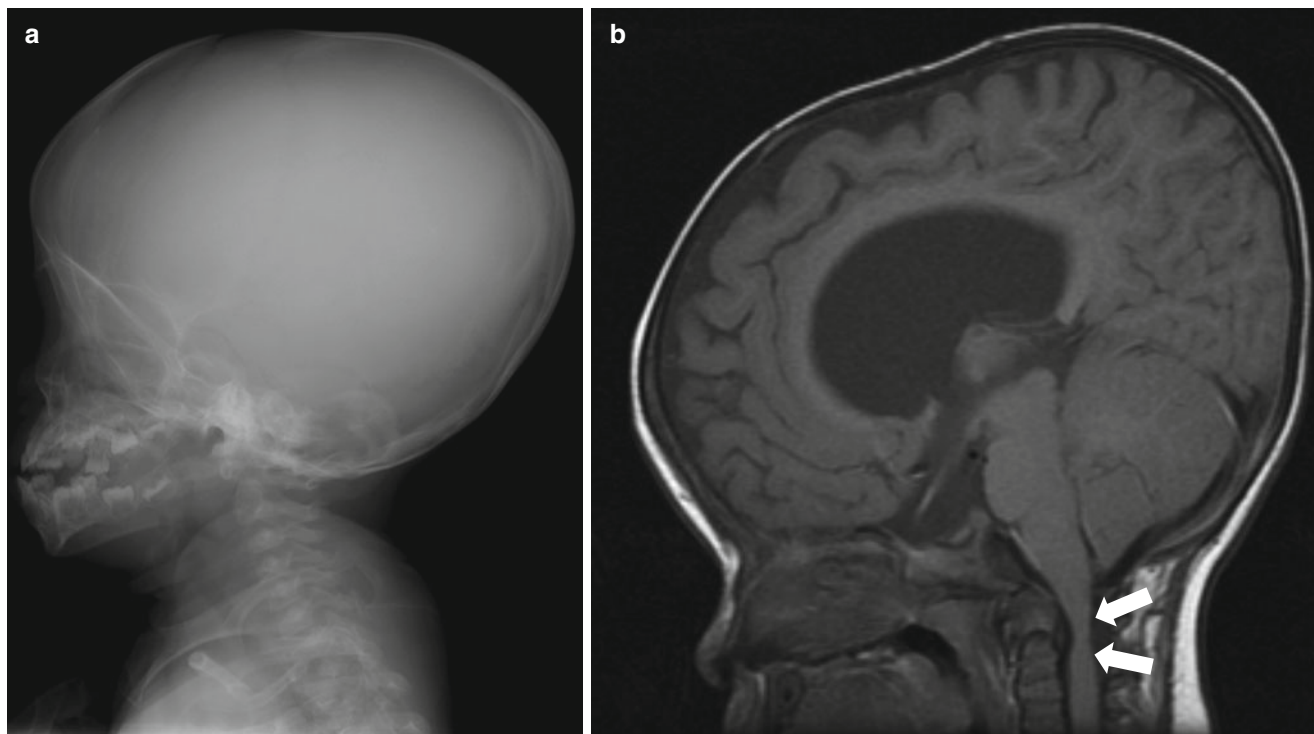
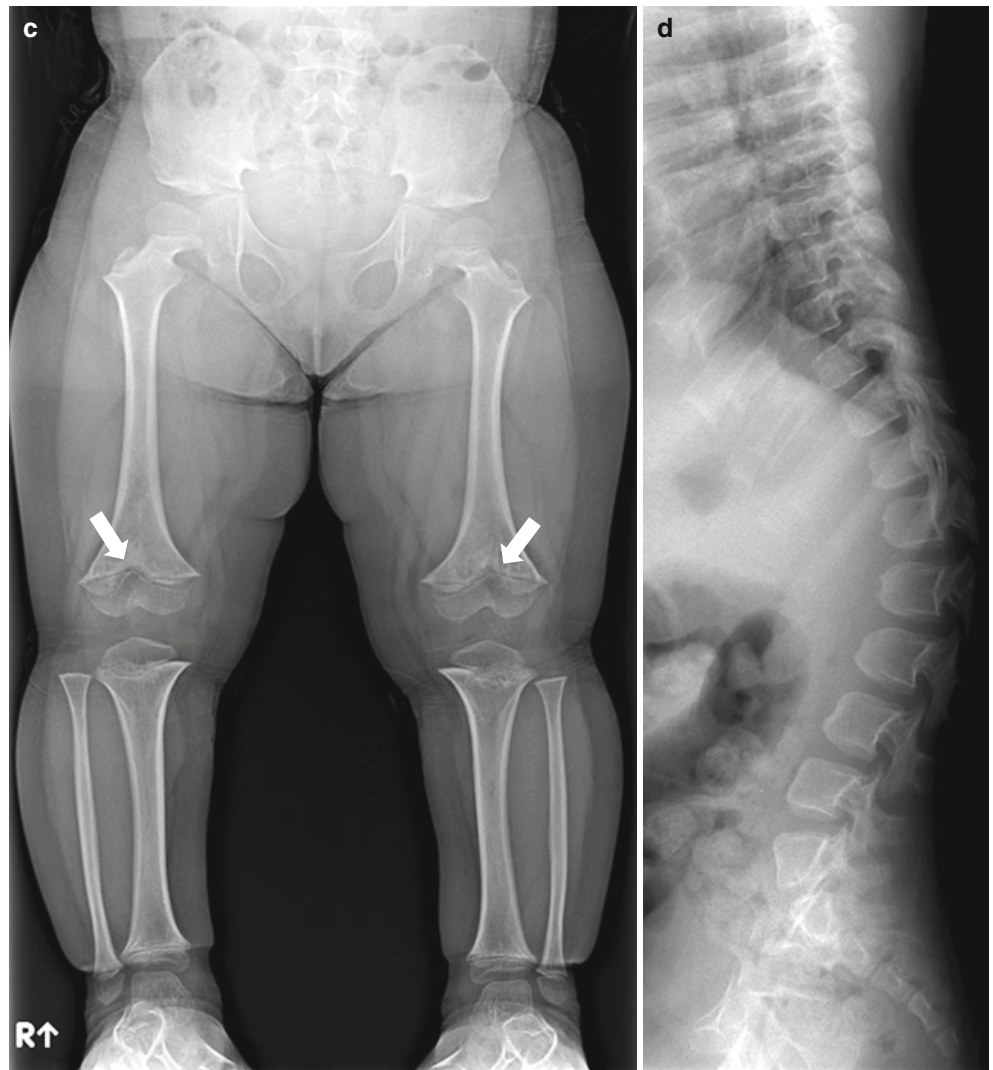


Fig. 28.3 *Achondroplasia: older child.* (a) Skull lateral view of a 3-year-old boy shows macrocephaly and narrow skull base with J-shaped sella. Note the frontal bowing and midface hypoplasia. (b) Sagittal T1-weighted image of the same patient demonstrates hydrocephalus and narrow foramen magnum (arrows). (c) Lower extremity radiograph of a

6-year-old boy shows short tubular bones and mild metaphyseal flaring with V-shaped distal femoral growth plate (arrow). (d) Lateral view of the spine in a 4-year-old boy shows variable degrees of anterior wedging of the vertebral bodies, causing gibbus. The posterior aspect of the vertebral bodies is concave, and the pedicles are short

Fig. 28.3 (continued)

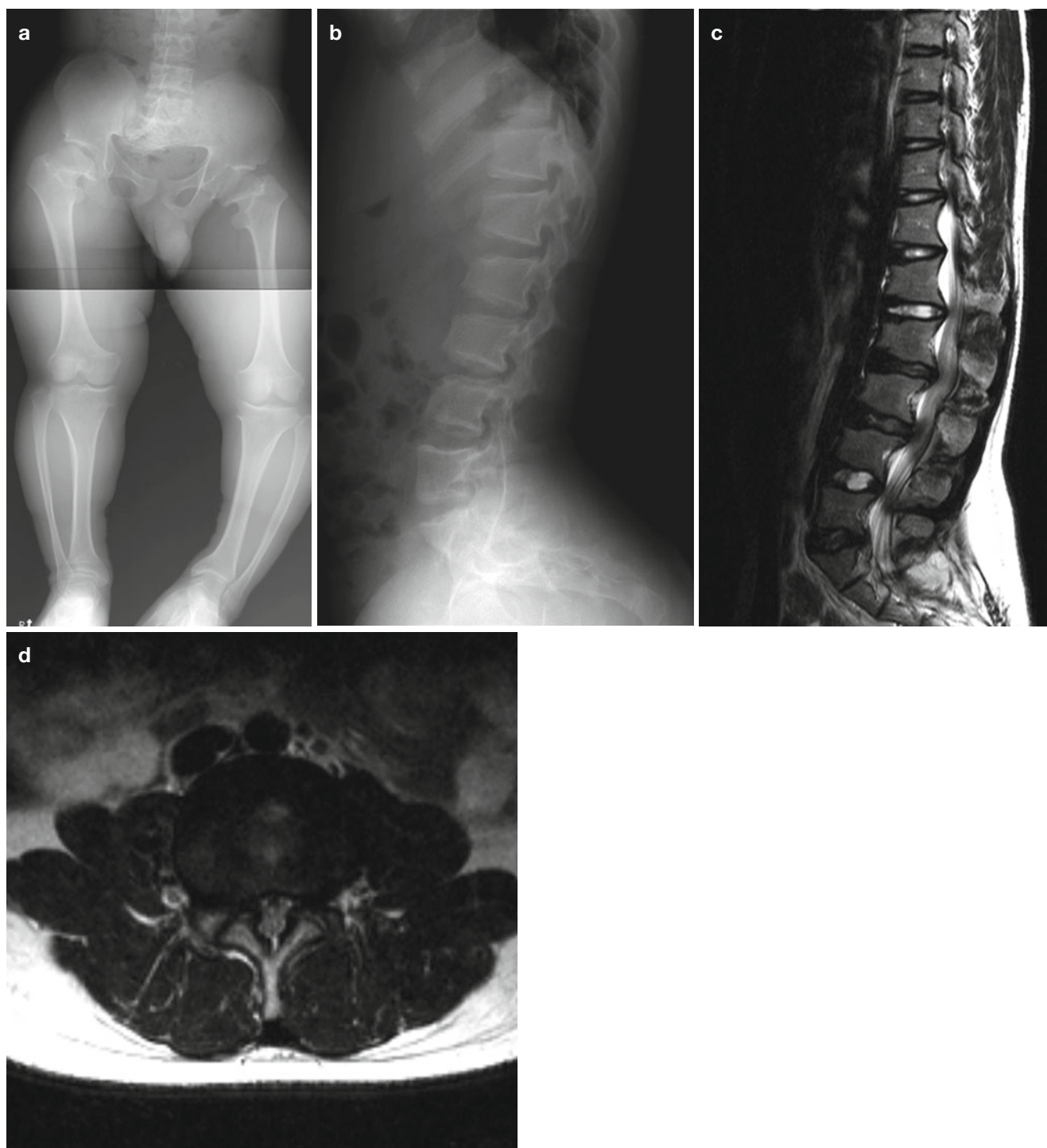


Fig. 28.4 *Achondroplasia: adolescent.* (a) Pelvis and lower extremity radiograph of a 17-year-old boy shows typical champagne glass-type pelvic inlet with squared iliac wing and horizontal acetabular roof. Short and thick tubular bones, short femoral neck, and left genu varum deformities are seen in the lower extremities. (b) The lateral view of thoracolumbar

spine in a 13-year-old girl shows posterior scalloping of the vertebral bodies and narrow spinal canal. There is increased angulation at the lumbosacral junction. (c–d) T2-weighted sagittal (c) and axial images (d) of the same patient show diffuse narrowing of the spinal canal at the level of lumbar spine and posterior scalloping of the vertebrae

28.4.3 Spondyloepiphyseal Dysplasia Congenita

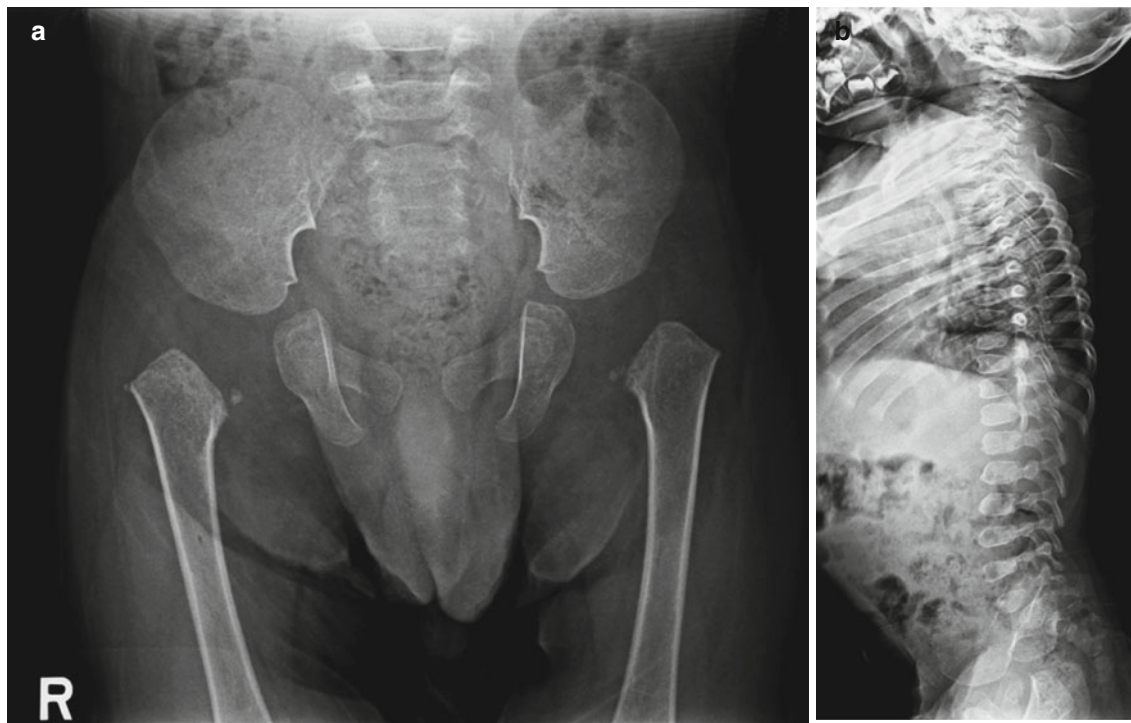


Fig. 28.5 *Spondyloepiphyseal dysplasia congenita*. (a) Anteroposterior view of pelvis in a 20-month-old boy shows short pubic rami and small femoral secondary ossification center. (b) Lateral view shows flat

vertebral bodies. The thoracolumbar vertebral bodies show dorsal wedging giving them a “pear-shaped” appearance

28.4.4 Kniest Dysplasia

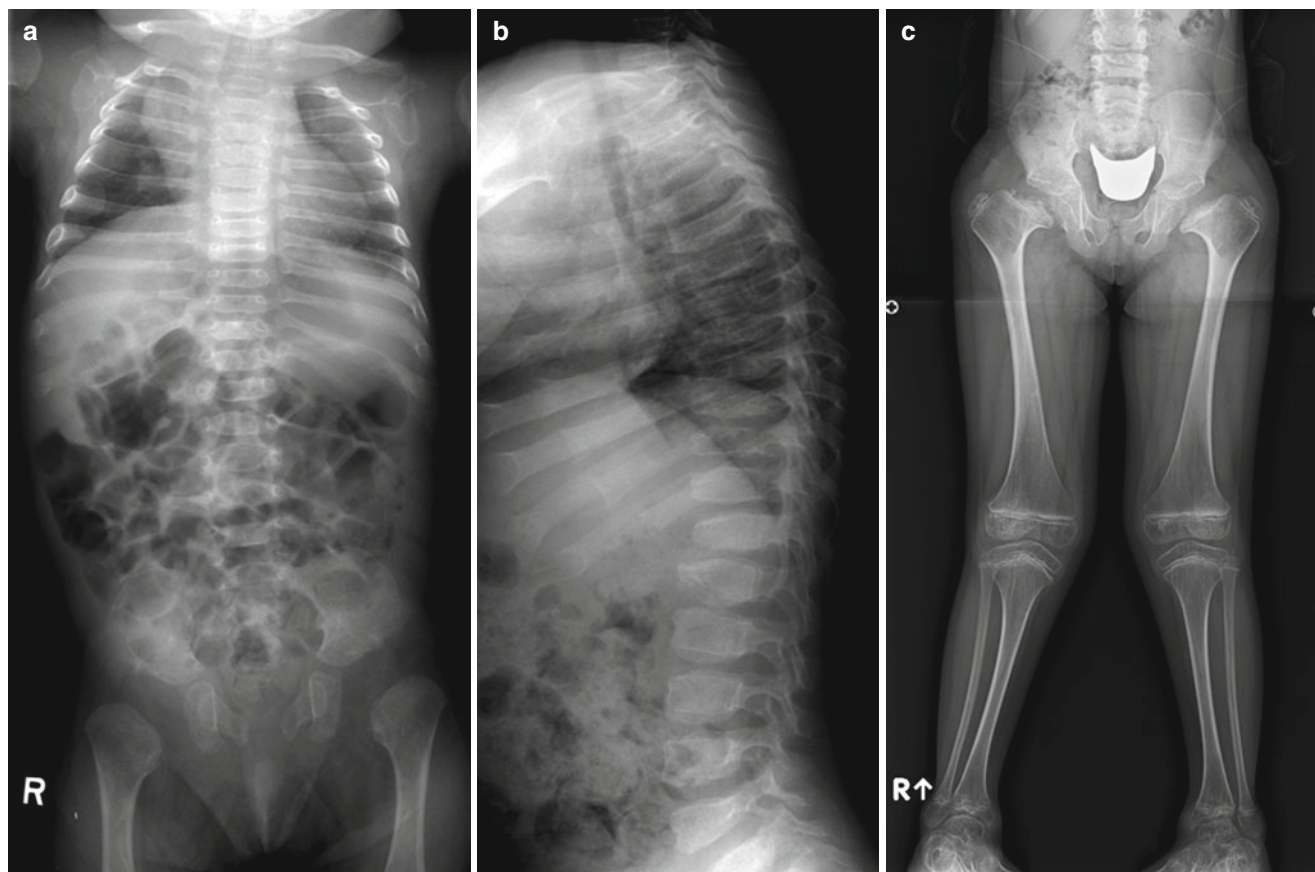


Fig. 28.6 *Kniest dysplasia*. (a–b) Spine radiographs of an 8-month-old girl show flat vertebrae with anterior wedging. The ilia are short and proximal epiphyses are not ossified. (c) Anteroposterior view of a

7-year-old girl shows broad and short femoral neck and delayed femoral head ossification. The epiphyses at the knee are large, and the growth plate of the tibiae has an inverted V shape

28.4.5 Metatropic Dysplasia

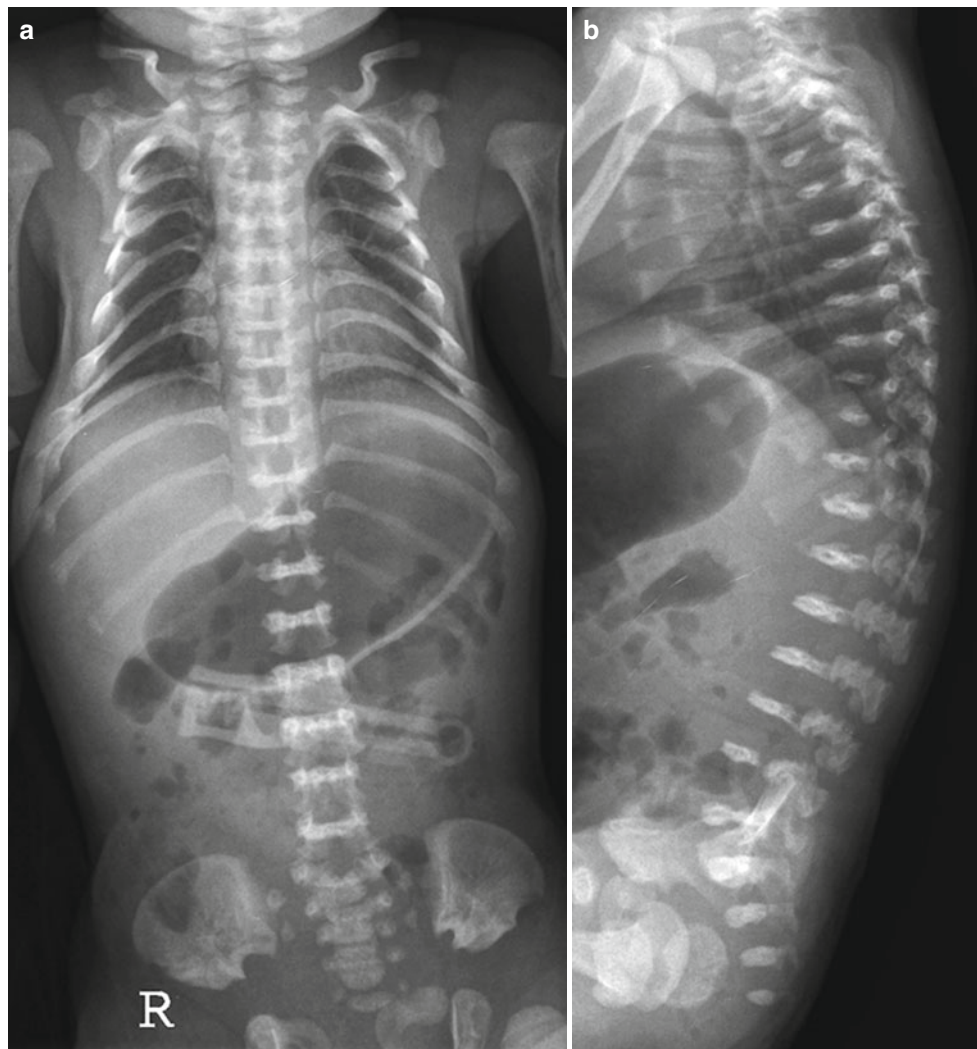


Fig. 28.7 *Metatropic dysplasia*. (a–b) Newborn. Anteroposterior and lateral views of thoracolumbar spine show marked platyspondyly giving “wafer-thin vertebra”. (c) Four years. Lateral view of thoracolumbar spine shows exaggerated thoracolumbar kyphosis and platyspondyly. (d) The iliac wings are crescent shaped, the lower portions of the ilia

are hypoplastic, and sacrosciatic notches are narrow. The acetabular roofs are broad and horizontal and the pubic and ischial bones, short and thick. The tubular bones are short and flared at both ends giving “dumbbell-shaped” femora

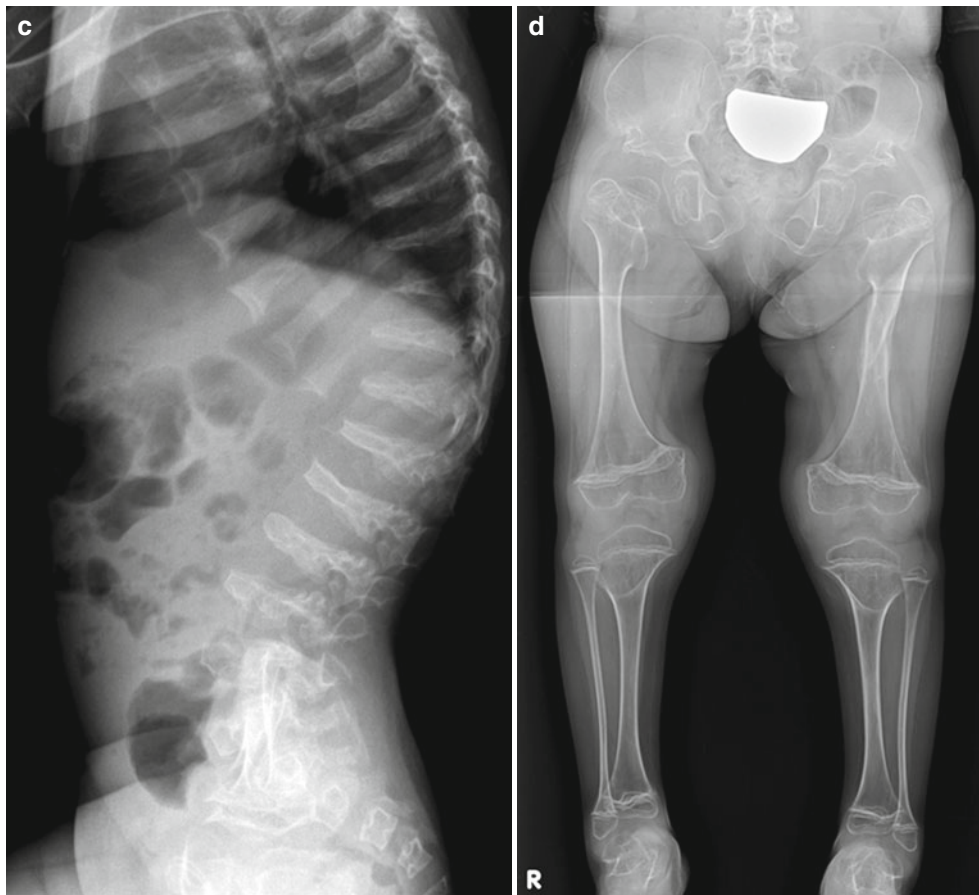


Fig. 28.7 (continued)

28.4.6 Short Rib Polydactyly

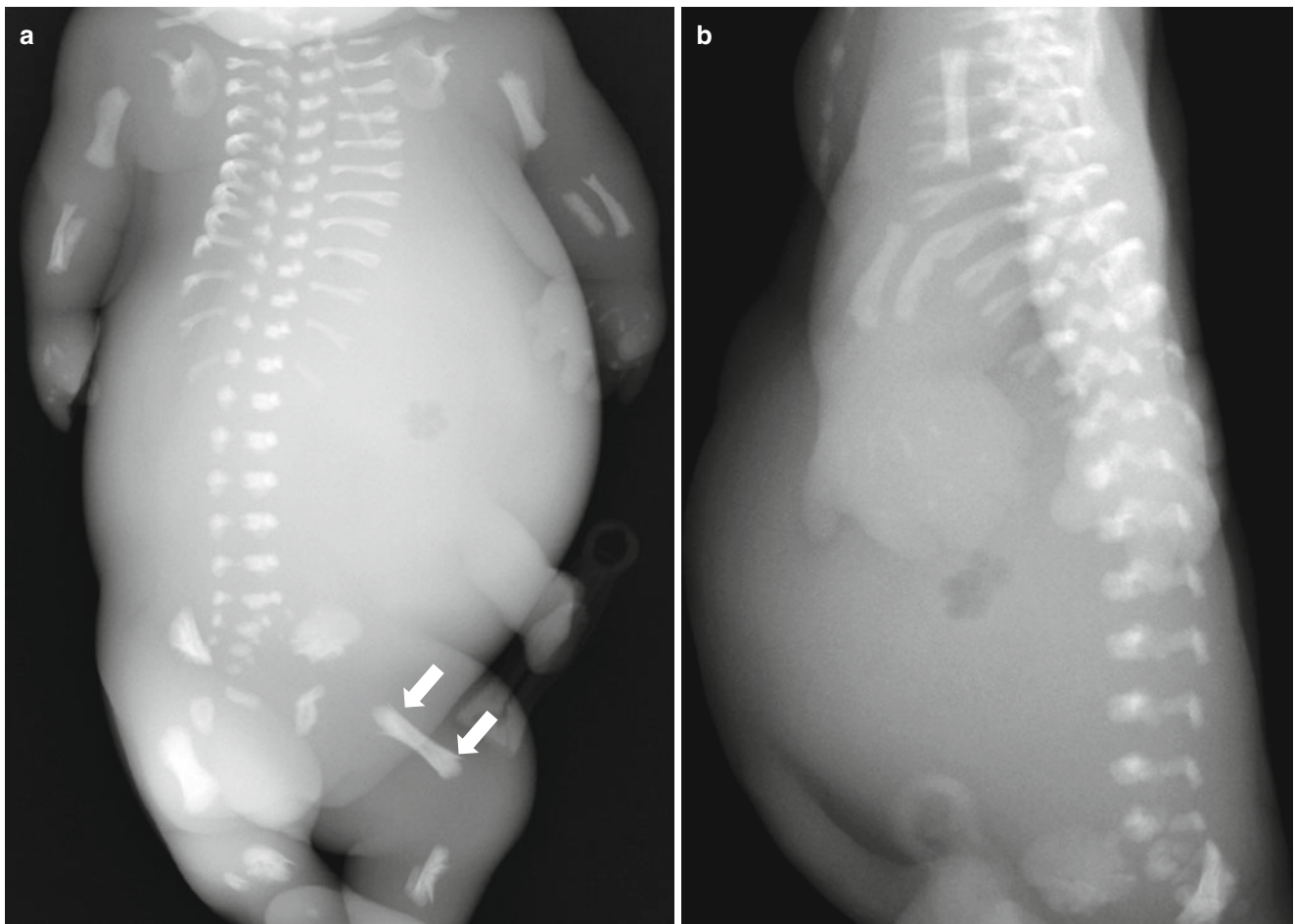


Fig. 28.8 *Short rib polydactyly.* (a) Stillbirth. Anteroposterior view of the chest and abdomen shows horizontally oriented, severely shortened ribs with restricted thoracic cage and protruded abdomen. The long

tubular bones are shortened with spurs of bone extending longitudinally, giving a “banana peel” appearance (*arrows*). (b) Lateral view of the spine shows small vertebral bodies with irregular end plates

28.4.7 Asphyxiating Thoracic Dysplasia

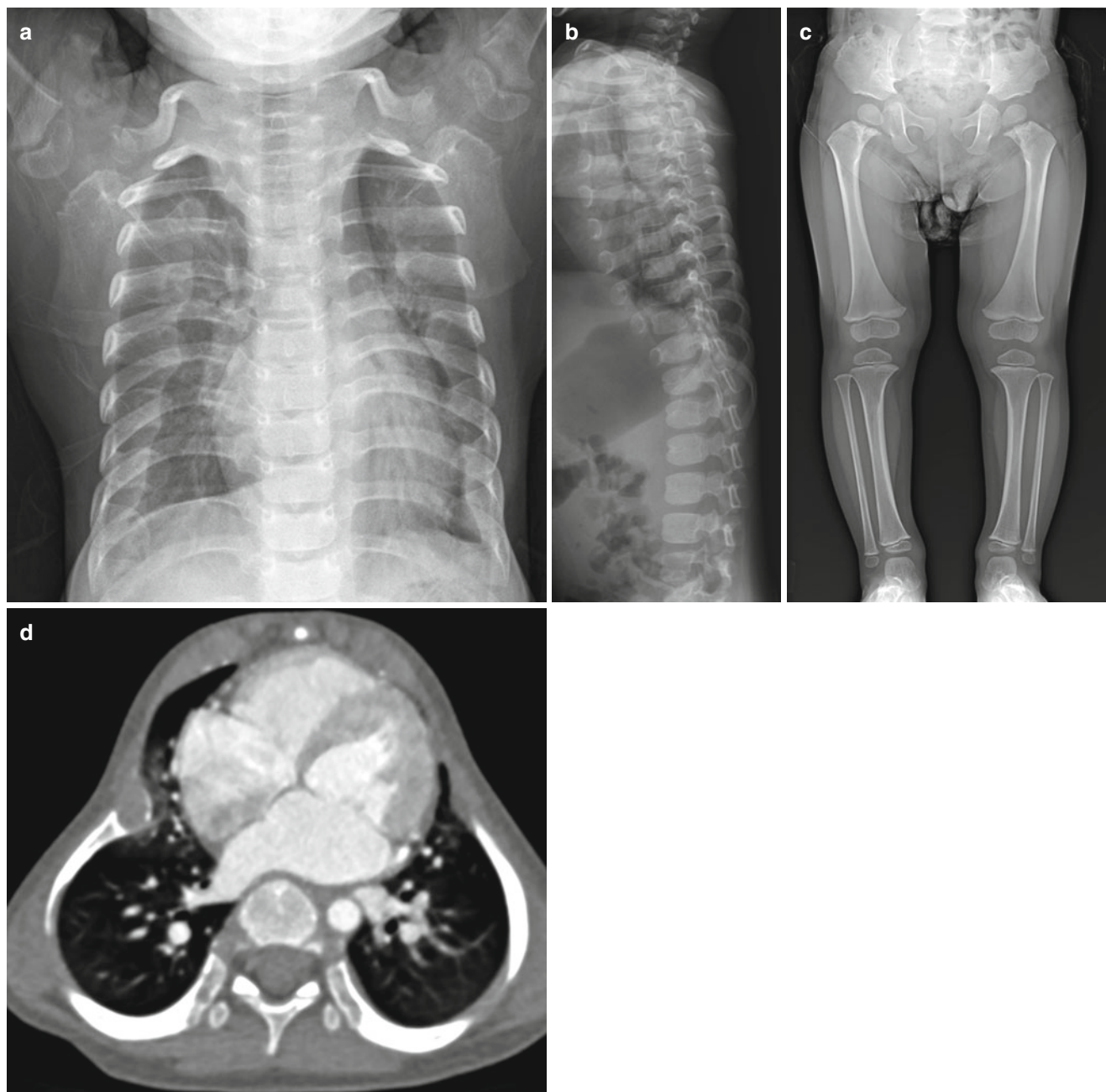


Fig. 28.9 *Asphyxiating thoracic dysplasia.* (a–b) 1 year. Anteroposterior view of chest and spine lateral view show moderately short ribs with irregular costochondral junctions, narrow thorax, and handle bar

appearance of the clavicles. (c) The iliac bones are short in cephalocaudal dimension. There are metaphyseal irregularities in the tubular bones. (d) Chest CT demonstrates deformed thoracic cage with small lung volume

28.4.8 Pseudoachondroplasia

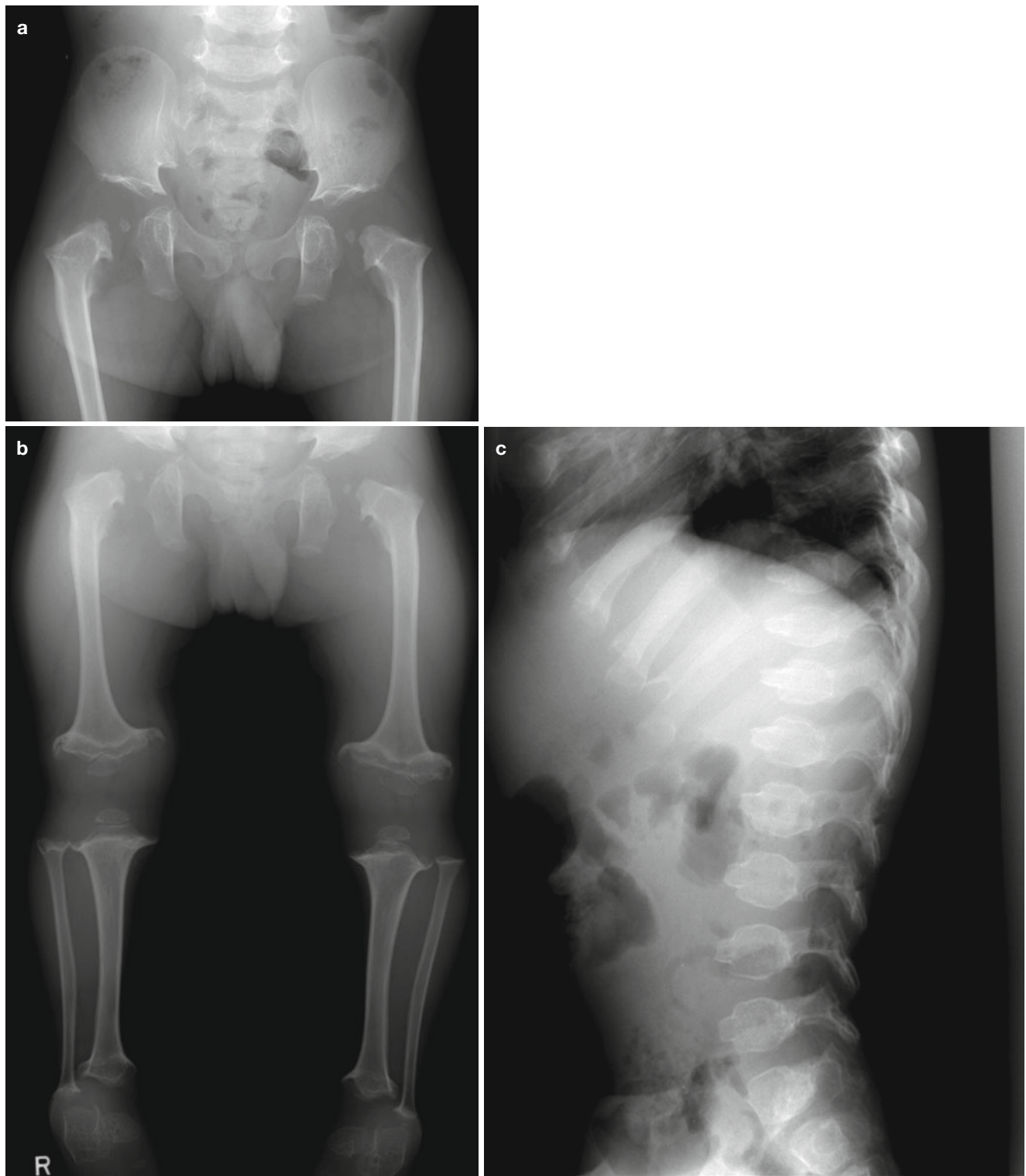


Fig. 28.10 *Pseudoachondroplasia*. (a) Anteroposterior view of pelvis shows deep acetabula, long femoral neck, and small femoral head ossification center. (b) The tubular bones are severely shortened with wide,

irregular metaphyses. (c) Lateral view of the thoracolumbar spine shows an anterior protrusion of the central aspects of the vertebral bodies and a biconvex configuration of the upper and lower vertebral plates

28.4.9 Multiple Epiphyseal Dysplasia

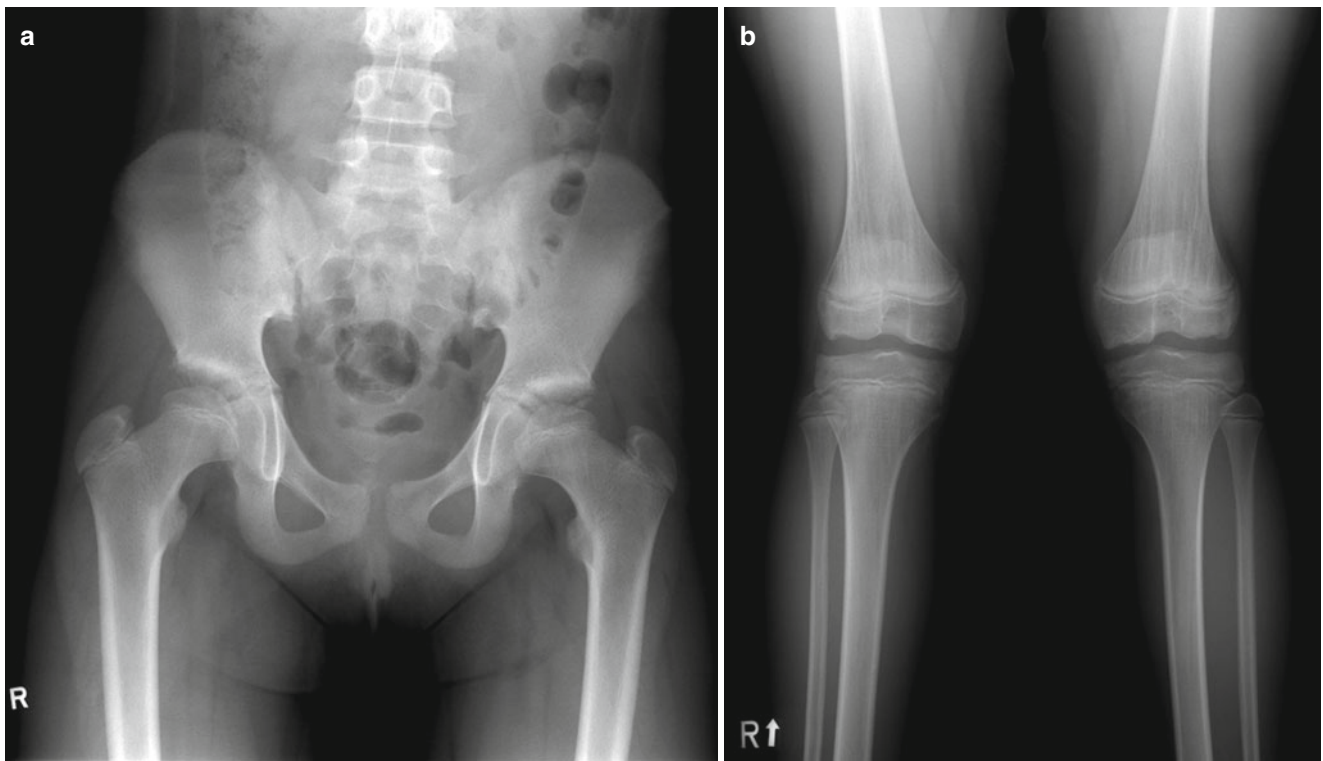


Fig. 28.11 *Multiple epiphyseal dysplasia.* (a–b) Anteroposterior views show small proximal femoral head ossification and flattened and irregular distal femoral epiphysis

28.4.10 Metaphyseal Chondrodysplasia

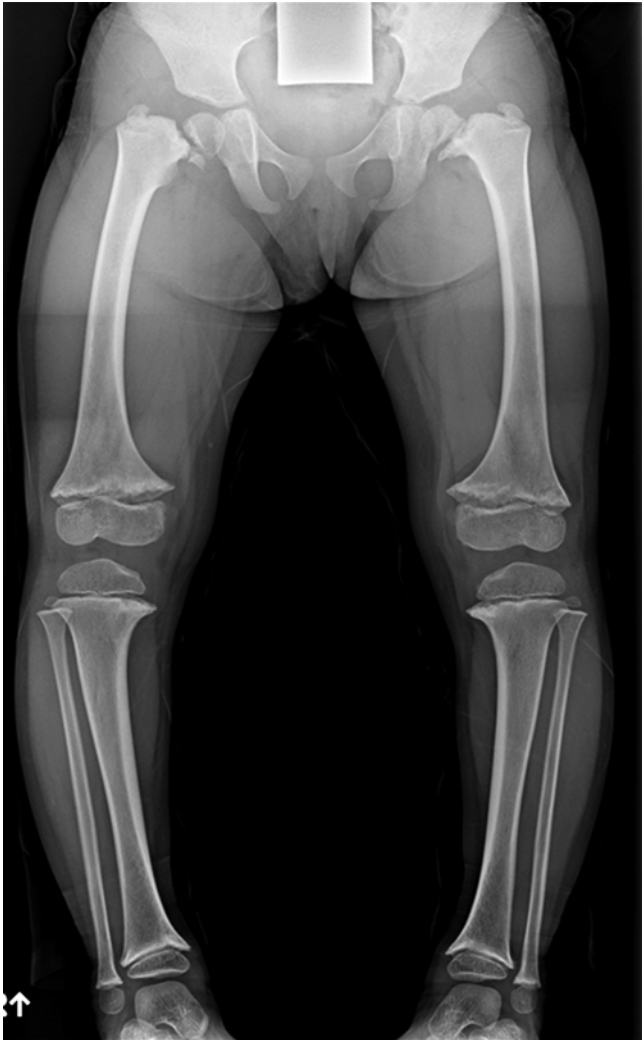


Fig. 28.12 *Metaphyseal chondrodysplasia*. A 3-year-old girl. The femoral necks are short and in various positions. The physeal plates are wide and irregular

28.4.11 Shwachman-Diamond Syndrome

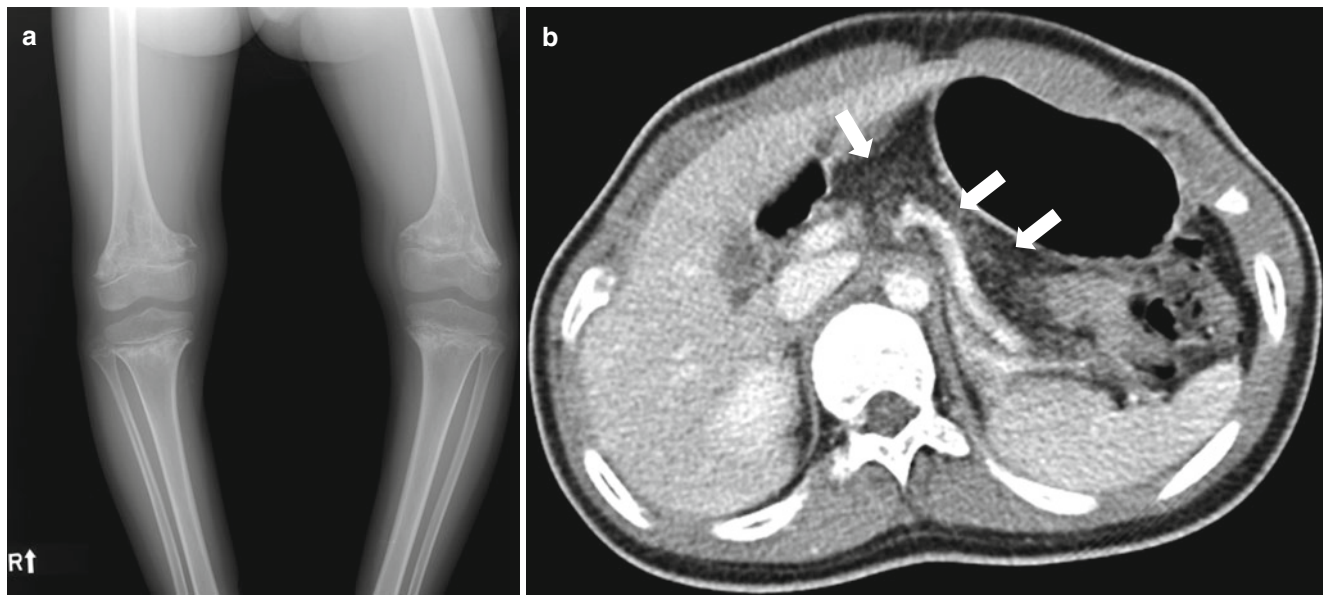


Fig. 28.13 *Shwachman-Diamond syndrome.* (a) Metaphyseal ossification is markedly irregular with splaying and fraying of the metaphyses. (b) Abdomen CT demonstrates pancreatic lipomatosis (arrows)

28.4.12 Cleidocranial Dysplasia

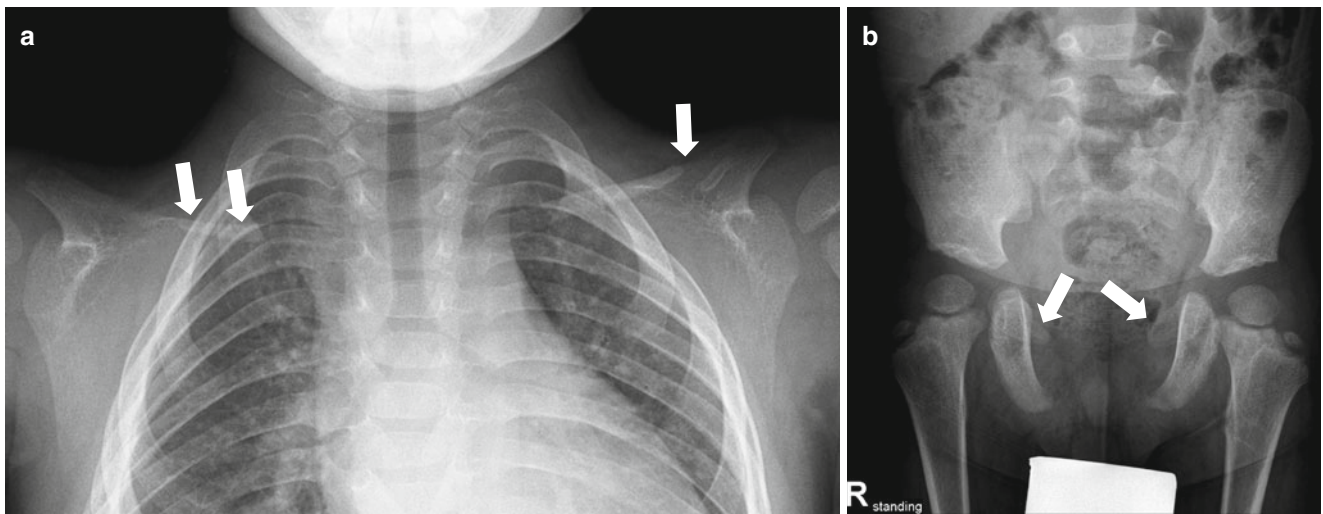


Fig. 28.14 *Cleidocranial dysplasia*. (a) Bilateral hypoplastic clavicles (*arrows*) are noted on chest radiograph. (b) Anteroposterior view of pelvis shows narrow iliac wing, short pubic ramus (*arrows*) with wide symphysis pubis. Coxa valga with rounded capital femoral epiphysis

28.4.13 Mucopolysaccharidosis: Morquio's Disease



Fig. 28.15 *Mucopolysaccharidosis: Morquio's disease.* (a) 5-year-old boy. The lower portions of the ilia are hypoplastic, and acetabular fossae are shallow, and the iliac wings are flared. The flattened femoral epiphyses and wide metaphyses are seen. (b) There are broad, short,

and undermodeled metacarpals and phalanges. Note the proximally pointed second to fifth metacarpals and narrow carpal bone angle. (c) The vertebral bodies have an oval shape with central anterior bony protrusion

28.4.14 Osteogenesis Imperfecta: Newborn

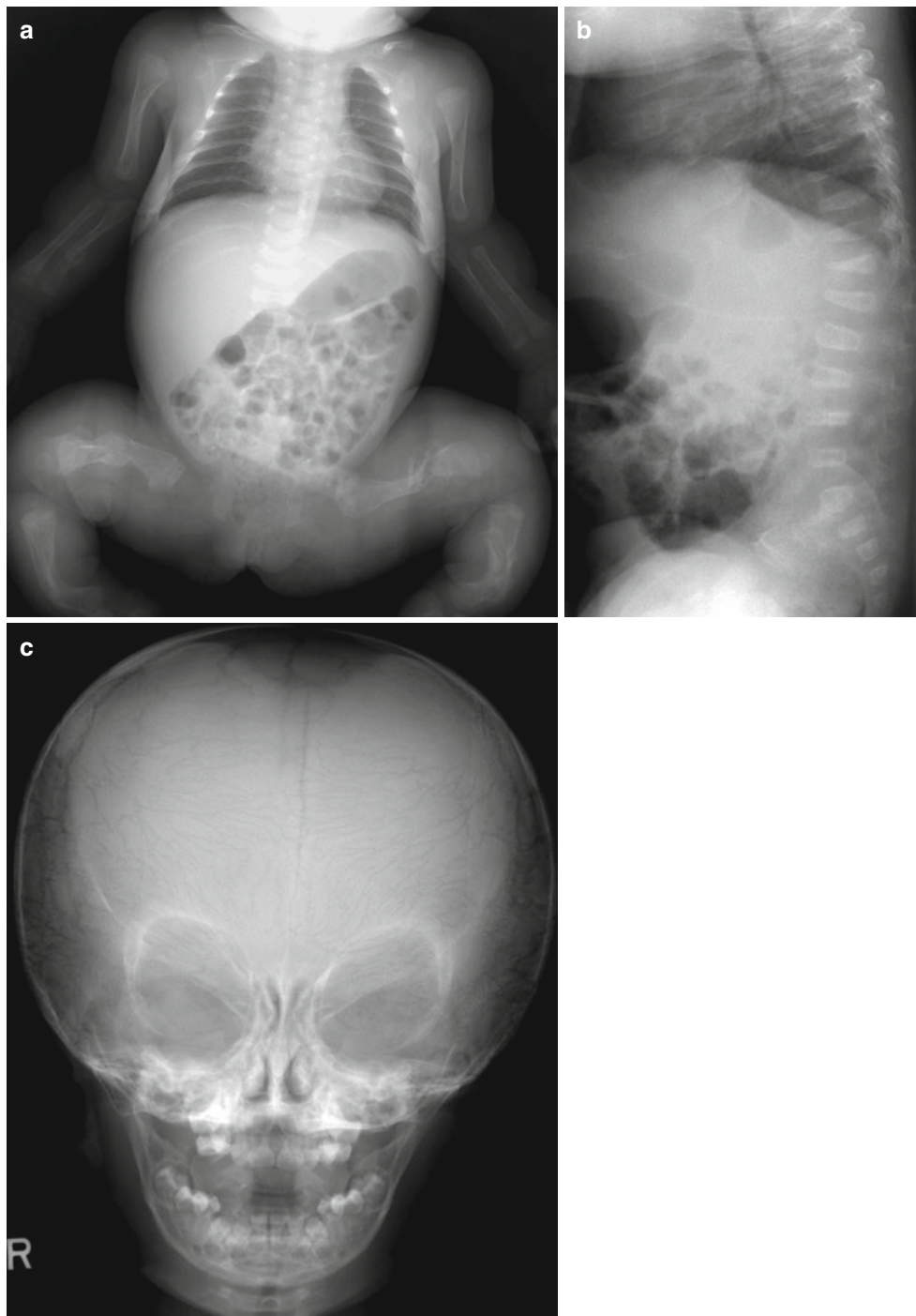


Fig. 28.16 *Osteogenesis imperfecta: newborn.* (a–b) Anteroposterior radiograph and spine lateral radiograph show multiple fractures in the long tubular bones and flat vertebral bodies. There is a generalized

decrease of bone densities. (c) Skull anteroposterior view shows prominent wormian bone formation

28.4.15 Osteopetrosis

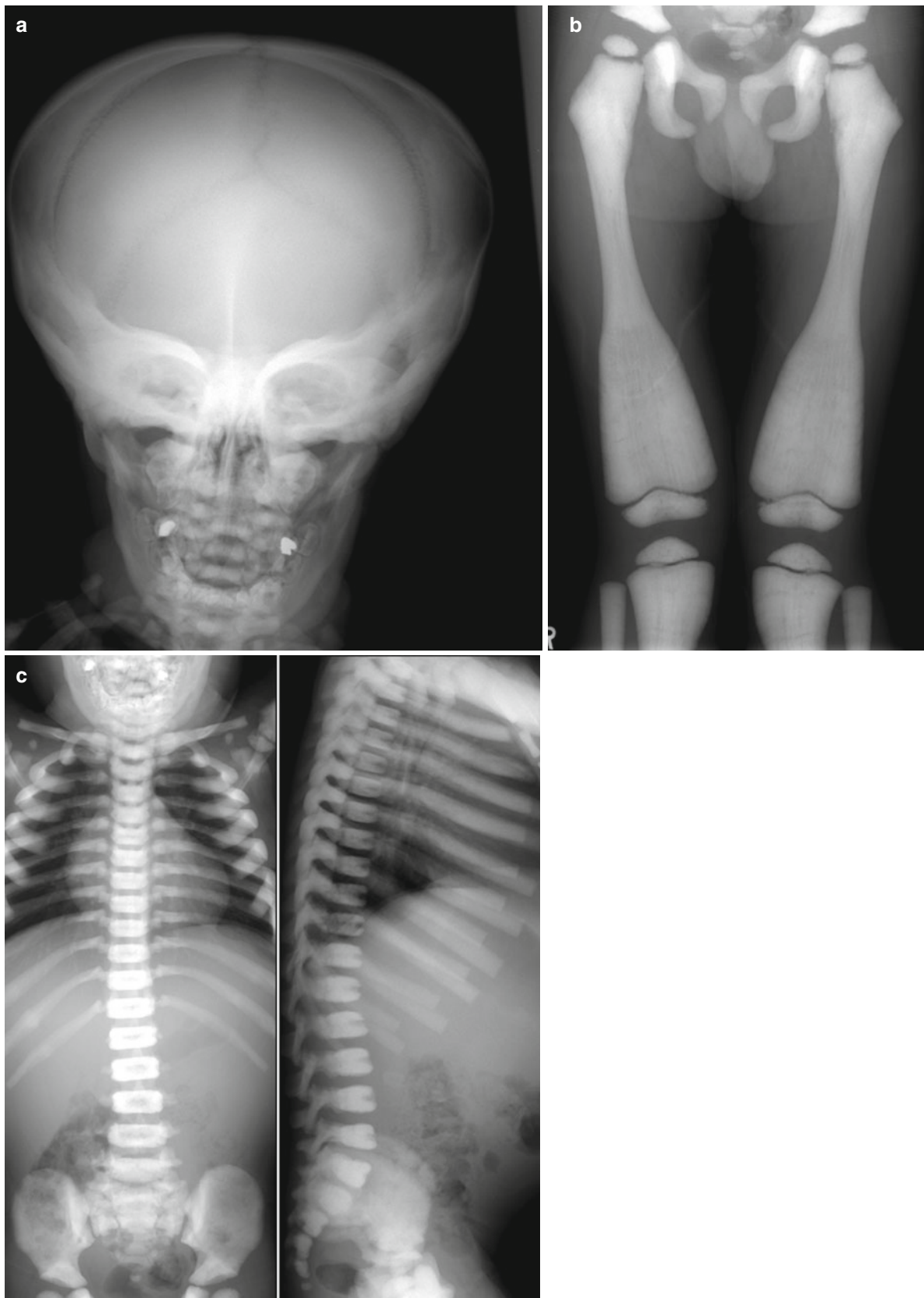


Fig. 28.17 *Osteopetrosis*. (a–c) Radiographs show overall increased density of the osseous structures due to the accumulation of immature bone. Note the undermodeling of tubular bones. Lateral spine radiograph shows the characteristic sandwich vertebra appearance

References

- Alanay Y, Lachman RS. A review of the principles of radiological assessment of skeletal dysplasias. *J Clin Res Pediatr Endocrinol*. 2011;3:163–78.
- Azouz EM, Teebi AS, Eydoux P, et al. Bone dysplasias: an introduction. *Can Assoc Radiol J*. 1998;49:105–9.
- Berrocal T, Simon MJ, al-Assir I, et al. Shwachman-Diamond syndrome: clinical, radiological and sonographic findings. *Pediatr Radiol*. 1995;25:356–9.
- Carter EM, Davis JG, Raggio CL. Advances in understanding etiology of achondroplasia and review of management. *Curr Opin Pediatr*. 2007;19:32–7.
- Dutton RV. A practical radiologic approach to skeletal dysplasias in infancy. *Radiol Clin North Am*. 1987;25:1211–33.
- Dwek JR. Kniest dysplasia: MR correlation of histologic and radiographic peculiarities. *Pediatr Radiol*. 2005;35:191–3.
- Gupta SK, Sharma OP, Malhotra S, et al. Cleido-cranial dysostosis—skeletal abnormalities. *Australas Radiol*. 1992;36:238–42.
- Ilde LL, Forrester DM, Gottsegen CJ, et al. Sclerosing bone dysplasias: review and differentiation from other causes of osteosclerosis. *Radiographics*. 2011;31:1865–82.
- Ikegawa S. Genetic analysis of skeletal dysplasia: recent advances and perspectives in the post-genome-sequence era. *J Hum Genet*. 2006;51:581–6.
- Kannu P, Aftimos S, Mayne V, et al. Metatropic dysplasia: clinical and radiographic findings in 11 patients demonstrating long-term natural history. *Am J Med Genet A*. 2007;143A:2512–22.
- Kornak U, Mundlos S. Genetic disorders of the skeleton: a developmental approach. *Am J Hum Genet*. 2003;73:447–74.
- Lachman RS, Rimoin DL, Spranger J. Metaphyseal chondrodysplasia, Schmid type. Clinical and radiographic delineation with a review of the literature. *Pediatr Radiol*. 1988;18:93–102.
- Lachman RS, Tiller GE, Graham Jr JM, et al. Collagen, genes and the skeletal dysplasias on the edge of a new era: a review and update. *Eur J Radiol*. 1992;14:1–10.
- Lachman RS, Krakow D, Cohn DH, et al. MED, COMP, multilayered and NEIN: an overview of multiple epiphyseal dysplasia. *Pediatr Radiol*. 2005;35:116–23.
- Langer Jr LO, Spranger JW, Greinacher I, et al. Thanatophoric dwarfism. A condition confused with achondroplasia in the neonate, with brief comments on achondrogenesis and homozygous achondroplasia. *Radiology*. 1969;92:285–94 passim.
- Lemyre E, Azouz EM, Teebi AS, et al. Bone dysplasia series. Achondroplasia, hypochondroplasia and thanatophoric dysplasia: review and update. *Can Assoc Radiol J*. 1999;50:185–97.
- Levin TL, Berdon WE, Lachman RS, et al. Lumbar gibbus in storage diseases and bone dysplasias. *Pediatr Radiol*. 1997;27:289–94.
- Makitie O, Ellis L, Durie PR, et al. Skeletal phenotype in patients with Shwachman-Diamond syndrome and mutations in SBDS. *Clin Genet*. 2004;65:101–12.
- Markowitz RI, Zackai E. A pragmatic approach to the radiologic diagnosis of pediatric syndromes and skeletal dysplasias. *Radiol Clin North Am*. 2001;39:791–802, xi.
- Mortier GR. The diagnosis of skeletal dysplasias: a multidisciplinary approach. *Eur J Radiol*. 2001;40:161–7.
- Nishimura G. Genetic basis for skeletal disease. Radiological approach for genetic skeletal disorders. *Clin Calcium*. 2010;20:1175–81.
- Nishimura G, Nakashima E, Hirose Y, et al. The Shwachman-Bodian-Diamond syndrome gene mutations cause a neonatal form of spondylometaphyseal dysplasia (SMD) resembling SMD Sedaghatian type. *J Med Genet*. 2007;44:e73.
- Offiah AC, Hall CM. Radiological diagnosis of the constitutional disorders of bone. As easy as A, B, C? *Pediatr Radiol*. 2003;33:153–61.
- Paterson CR, Burns J, McAllion SJ. Osteogenesis imperfecta: the distinction from child abuse and the recognition of a variant form. *Am J Med Genet*. 1993;45:187–92.
- Rasalkar DD, Chu WC, Hui J, et al. Pictorial review of mucopolysaccharidosis with emphasis on MRI features of brain and spine. *Br J Radiol*. 2011;84:469–77.
- Sillence DO. Craniocervical abnormalities in osteogenesis imperfecta: genetic and molecular correlation. *Pediatr Radiol*. 1994;24:427–30.
- Spranger JW. Metaphyseal chondrodysplasia. *Postgrad Med J*. 1977;53:480–7.
- Spranger JW, Langer Jr LO. Spondyloepiphyseal dysplasia congenita. *Radiology*. 1970;94:313–22.
- Spranger J, Winterpacht A, Zabel B. The type II collagenopathies: a spectrum of chondrodysplasias. *Eur J Pediatr*. 1994;153:56–65.
- Susic S, McGrory J, Ahier J, et al. Multiple epiphyseal dysplasia and pseudoachondroplasia due to novel mutations in the calmodulin-like repeats of cartilage oligomeric matrix protein. *Clin Genet*. 1997;51:219–24.
- Unger S, Bonafe L, Superti-Furga A. Multiple epiphyseal dysplasia: clinical and radiographic features, differential diagnosis and molecular basis. *Best Pract Res Clin Rheumatol*. 2008;22:19–32.
- Vanhoenacker FM, Van Hul W, Gielen J, et al. Congenital skeletal abnormalities: an introduction to the radiological semiology. *Eur J Radiol*. 2001;40:168–83.
- Vanhoenacker FM, Van de Perre S, de Jongh K, et al. Asphyxiating thoracic dysplasia. *JBR-BTR*. 2004;87:50.
- Warman ML, Cormier-Daire V, Hall C, et al. Nosology and classification of genetic skeletal disorders: 2010 revision. *Am J Med Genet A*. 2011;155A:943–68.
- Yang SS, Langer Jr LO, Cacciarelli A, et al. Three conditions in neonatal asphyxiating thoracic dysplasia (Jeune) and short rib-polydactyly syndrome spectrum: a clinicopathologic study. *Am J Med Genet Suppl*. 1987;3:191–207.
- Yazici Z, Kline-Fath BM, Laor T, et al. Fetal MR imaging of Kniest dysplasia. *Pediatr Radiol*. 2010;40:348–52.

Choon-Sik Yoon and Sungjun Kim

Contents

29.1	Introduction	914
29.2	Nonneoplastic Disorders	914
29.2.1	Calcification	914
29.2.2	Ossification	914
29.2.3	Localized Vascular Lesion	914
29.2.4	Generalized Vascular Lesion	915
29.2.5	Miscellaneous	915
29.3	Neoplastic Disorders	915
29.3.1	Benign Neoplasm	915
29.3.2	Malignant Neoplasm	917
29.4	Illustrations: Soft Tissue Diseases	919
29.4.1	Myositis Ossificans Progressiva	919
29.4.2	Infantile Hemangioma	921
29.4.3	Venous Malformation	924
29.4.4	Lymphatic Malformation	925
29.4.5	Arteriovenous Malformation	926
29.4.6	Klippel-Trenaunay Syndrome	928
29.4.7	Compartment Syndrome	930
29.4.8	Fibromatosis Colli	932
29.4.9	Desmoid Type Fibromatosis	933
29.4.10	Nodular Fasciitis	934
29.4.11	Plexiform Neurofibroma	935
29.4.12	Schwannoma	936
29.4.13	Lipoblastoma	937
29.4.14	Lipoma	938
29.4.15	Pilomatricoma	939
29.4.16	Granuloma Annulare	940
29.4.17	Rhabdomyosarcoma	941
29.4.18	Synovial Sarcoma	943
29.4.19	Infantile Fibrosarcoma	944
29.4.20	Sclerosing Epithelioid Fibrosarcoma	945
29.4.21	Alveolar Cell Soft Part Sarcoma	946
29.4.22	Angiosarcoma	947
29.4.23	Burkitt Lymphoma	948
	References	949

C.-S. Yoon, M.D., Ph.D. (✉) • S. Kim, M.D., Ph.D.
 Department of Radiology, Gangnam Severance Hospital,
 Yonsei University, 211 Eonju-ro, Gangnam-Gu,
 Seoul 135-720, South Korea
 e-mail: yoons58@yuhs.ac; agn70@yuhs.ac

29.1 Introduction

No clear definition of “soft tissue” is present, but its broad definition includes skin, fibrous tissue, fat, voluntary muscles, and neurovascular structures. In this chapter, a number of disorders involving soft tissue in pediatric patients and their imaging findings are included. Inflammation and infection of soft tissue would be excluded in this chapter because they will be separately detailed in the other chapters. Categorization of disorders can provide a meaningful, practical diagnostic approach when they are appropriately performed. However, any categorization of the diverse soft tissue disorders is arbitrary. The summary of the soft tissue disorders is briefly covered according to the classical categorization of nonneoplastic and neoplastic disorders, and presentation of illustrative images will follow. Radiography and cross-sectional imaging findings will be described.

29.2 Nonneoplastic Disorders

29.2.1 Calcification

Calcification, that is, soft tissue deposition of calcium, is generally classified into three types: metastatic calcification, calcinosis, and dystrophic calcification (Resnick 2002). Metastatic calcification is related to the metabolic disease associated with calcium and phosphorus metabolism such as hyperparathyroidism, hypoparathyroidism, renal osteodystrophy, milk alkali syndrome, vitamin D intoxication, and sarcoidosis. Dystrophic calcification means calcium deposition at the devitalized or damaged tissue. Most of dystrophic calcification can be categorized into localized and widespread types as follows: localized calcification due to tissue damage or inflammation caused by skin ulcer, granuloma, or mass-like lesions such as epidermal cyst and widespread calcification associated with generalized inflammation or connective tissue diseases such as dermatomyositis, scleroderma, and systemic lupus erythematosus. Calcinosis means idiopathic soft tissue calcification without associated known metabolic abnormality and tissue damage (Resnick 2002; Emery 2008).

29.2.2 Ossification

Osteoma cutis is a terminology used for primary or secondary new bone formation at the skin. It is manifested as a subdermal small subcentimetric nodule or nodules. Primary lesions can be associated with Albright’s osteodystrophy and pseudohypoparathyroidism. Secondary lesions can be associated with neoplasm or inflammation (Emery 2008).

Fibrodysplasia (myositis) ossificans progressiva is a rare soft tissue disorder which shows the characteristic feature of initial soft tissue inflammation and subsequent proliferative fibrous tissue resulting in bone formation. It can occur at any part of the body. Generally, it becomes evident in the first decade of life, and radiographic mineralization also occurs during the first decade. Radiographically, ossification of thoracic and abdominal walls, which may show bridging and pseudoarticulation leading to ankylosis and contracture, is commonly seen. Bridging ossification of vertebral column is commonly observed resembling the finding of juvenile chronic arthritis or Klippel-Feil syndrome. This kind of ossification progresses from axial to appendicular skeleton in proximal to distal manner. Hand and foot abnormalities such as microdactyly, hallux valgus, and ankylosis of interphalangeal joints are commonly associated (Emery 2008) (Fig. 29.1).

29.2.3 Localized Vascular Lesion

According to the classification system of the International Society for the Study of Vascular Anomalies, vascular anomalies are classified into either vascular tumor or vascular malformation based on cellular turnover, histological features, natural history, and physical phenotypes. Vascular tumors including infantile hemangioma, congenital hemangioma, and Kaposiform hemangioendothelioma demonstrate cellular proliferation and hyperplasia which are the characteristics of neoplasm histologically. Infantile hemangioma, which is the most common vascular tumor, regresses spontaneously over time. In contrast, vascular malformations do not show neoplastic features, whereas they show dysplastic vascular channels and exhibit normal endothelial turnover. Vascular malformations grow proportional to the growth of children without regression. Vascular malformation is subclassified into low-flow malformation and high-flow malformation according to the flow dynamics. Low-flow vascular malformations are classified into venous, lymphatic, capillary, mixed (capillary-venous and capillary-lymphatic-venous) according to the morphologically dominant vascular channel. High-flow vascular malformation is generally arteriovenous malformation (Flors et al. 2011).

Infantile hemangioma occurs in the first few weeks of life in a strawberry-like mass lesion. The lesion rapidly grows but involutes as grayish dark red mass by the age of 7–10 years. In proliferation phase, MR imaging features show well-defined lobulated mass with flow voids on spin echo images. On gadolinium-enhanced T1-weighted images, the lesion shows early homogeneous enhancement. In involution phase, MR imaging shows high signal intensity on T1-weighted sequence reflecting fat replacement of the lesion, and enhancement of the lesion decreases (Flors et al. 2011) (Figs. 29.2 and 29.3).

Low-flow vascular malformation generally occurs in childhood or early adulthood. MR imaging of venous and lymphatic malformations demonstrates lobulated mass which infiltrates through the tissue planes. On gadolinium-enhanced T1-weighted sequence, venous malformation shows gradual diffuse enhancement on delayed images (Fig. 29.4). Gadolinium-enhanced T1-weighted images in macrocystic lymphatic malformation show rim and septal enhancement, but microcystic lesion shows no significant or slight diffuse enhancement (Fig. 29.5). Capillary malformation is commonly superficially located, and MR imaging reveals just nonspecific skin-thickness lesion (Flors et al. 2011).

High-flow vascular malformation also occurs in childhood or early adulthood. MR images of high-flow vascular malformation commonly show no well-defined mass. Enlarged feeding arteries and veins with nidus are depicted, and early enhancement is observed on gadolinium-enhanced sequence (Flors et al. 2011) (Fig. 29.6).

29.2.4 Generalized Vascular Lesion

Klippel-Trenaunay syndrome is characterized by the triad of capillary hemangiomas, varicose veins, and hemihypertrophy. Hypertrophy involves all layers of soft tissue as well as osseous structures in monomelic distribution (Fig. 29.7). The major radiographic differential diagnoses are Maffucci's syndrome, neurofibromatosis, and macrodystrophia lipomatosa. Maffucci's syndrome can be discerned by its peculiar bone abnormality of enchondromatosis. Macrodystrophia lipomatosa differs from Klippel-Trenaunay syndrome in that it only involves the digit. Vascular malformation with various vascular channels with hypertrophy is seen on cross-sectional images (Lohrmann et al. 2007; Emery 2008; Stein-Wexler 2009).

Proteus syndrome is a sporadic congenital disorder that produces multifocal overgrowth of tissue. Its clinical feature is characterized by overgrowth of the long bones, asymmetric macrocephaly, striking vertebral anomalies, hyperostosis, partial gigantism of hands or feet, limb asymmetry, connective tissue nevi, lipomas, and vascular malformations. Radiographically, progressive skeletal abnormalities such as macrodactyly, scoliosis, asymmetric overgrowth, and limb-length discrepancy are the most frequent and striking findings. Soft tissue abnormalities such as fatty, muscular, and vascular malformations follow (Jamis-Dow et al. 2004).

29.2.5 Miscellaneous

Macrodystrophia lipomatosa is a congenital nonhereditary disorder which shows localized limb enlargement particularly

restricted to digit. It can affect both upper and lower extremities, and enlargement of the digits typically follows the distribution of the corresponding nerves. The nerves are infiltrated with the fibroadipose tissue. Although differentiation with neurofibromatosis is not easy clinically, MR imaging that can differentiate between neurofibroma and fibroadipose tissue infiltration is helpful (Emery 2008).

Compartment syndrome is the disease where muscular compartment pressure increases causing venous congestion resulting in necrosis of the muscles and nerves if not being decompressed by fasciotomy. Currently, the most common presentation of compartment syndrome in children is following a fracture (Flynn et al. 2011). Historically, compartment syndrome has been diagnosed on the basis of clinical finding and use of pressure measurement for the compartment. MR imaging is only indicated when the clinical diagnosis is inconclusive or when identifying the involved muscle compartment needs to be assessed for operation plan. The MR imaging findings are associated with diffuse hemorrhage and edematous swelling in the muscles of the affected compartments (Shelly et al. 2009) (Fig. 29.8).

29.3 Neoplastic Disorders

Attempting to make a specific diagnosis only with the use of imaging tools appears to be futile in many clinical situations. However, imaging tools of ultrasonography (US) and MR imaging can narrow the differential diagnosis when applied with clinical information such as the duration of tumor presence, growth pattern and time, overlying skin change, and associated focal and systemic symptoms. US is useful for small and superficial lesions as a first-line modality. However, for large and/or deep lesions, MR imaging is the tool of choice. In this section, clinical and/or imaging characteristics of pediatric soft tissue tumors will be briefly discussed based on their features which will help the readers differentiate from each other.

29.3.1 Benign Neoplasm

29.3.1.1 Fibromatosis Colli

Fibromatosis colli specifically occurs at the sternocleidomastoid muscle. It demonstrates scar-like fibroblast proliferation, and it is thought to be associated with pre- or perinatal muscle injury. The mass becomes clinically evident at 2–8 weeks after birth causing torticollis in up to 30 % of cases. The mass usually involutes over time (4–8 months) spontaneously. The diagnosis is readily made with US, and further imaging modality such as MR imaging is rarely used. On US, the mass appears as focal fusiform or diffuse enlargement of the sternocleidomastoid muscle (Laffan et al. 2009) (Fig. 29.9).

29.3.1.2 Infantile Myofibromatosis

Infantile myofibroma or myofibromatosis is the most common benign tumor in infancy. They can be found at any age, but it has been reported to occur under the age of 2 years in around 88 % of cases. The lesions are known to regress spontaneously. Histologically, myofibroma/myofibromatosis appears as nodules with two distinct components: one characterized by bundles of myofibroblasts arranged in fascicles and the other characterized by less-differentiated cells usually arranged around hemangiopericytoma-like vessels. When myofibromatosis involves visceral organ, it is reported to show high mortality rate, as high as 75 %. When being superficially located being visualized at the skin, the lesion appears as a firm reddish-purple nodule. US and MR imaging show frequent central necrosis. It can show calcification. However, echotexture on US and signal on MR imaging are nonspecific in many cases (Laffan et al. 2009; Navarro 2011).

29.3.1.3 Nodular Fasciitis

Nodular fasciitis is a benign proliferation of fibroblastic/myofibroblastic fascicles due to uncertain etiology. It is more commonly seen in young adults in the third or fourth decades, but it may occur in children. Particularly, the cranial form almost exclusively occurs to children under the age of 2 years. They often grow fast with pain generation misleading the clinicians, who are unfamiliar to this disease category, to consider it as a malignancy or infection. Treatment includes local excision. MR imaging appearance is known to be nonspecific, but the most common histological type of “myxoid-type” lesion shows signal which is slightly hyperintense to that of muscle on T1-weighted images and hyperintense on T2-weighted images. After administration of a gadolinium contrast agent, homogeneous enhancement is observed (Laffan et al. 2009; Navarro 2011) (Fig. 29.11).

29.3.1.4 Neurogenic Tumor

As for neurogenic tumor, two nerve sheath origin tumors of neurofibroma and schwannoma are generally considered. In children, neurofibroma is the most common tumor originated from peripheral nerves. Schwannoma, which is more common in young adults, is less common in children. In surgeon’s perspective, neurofibroma is known to be not easily separated from the adjacent nerve often mandating sacrifice of the nerve, whereas schwannoma is readily separated from the nerve from which the tumor originated (Fig. 29.13). Neurofibromas are categorized into the following three types: a localized form, a diffuse form, and a plexiform. Localized form and diffuse form usually manifest as a solitary lesion, whereas plexiform can manifest as a generalized lesion with multiplicity. Plexiform neurofibroma is one of the hallmarks of neurofibromatosis type 1. US finding is nonspecific. MR imaging of localized neurofibroma sometimes demonstrates typical “target sign” and “fascicular

signs,” and the signs are considered to be quite specific imaging finding that can differentiate neurogenic tumors from the other soft tissue tumors. Plexiform neurofibroma shows different imaging findings according to the layer where it locates: deep versus superficial. Deep plexiform neurofibroma, which locates deep to the subcutaneous tissue, appears as multinodular/fascicular masses, which is sometimes described as a “bag-of-worms appearance.” Each nodule/fascicle sometimes shows target sign (Fig. 29.12). Superficial plexiform neurofibroma shows diffuse infiltrative morphology along the skin surface and/or subcutaneous tissue lacking target sign. Hence, superficial plexiform neurofibromas are sometimes mistaken for venous malformations (Laffan et al. 2009).

29.3.1.5 Lipoblastoma

Lipoblastoma is an uncommon benign adipocytic tumor of infant and early childhood. It accounts for approximately 30 % of adipocytic tumors in children. It is usually diagnosed within the first 3 years of life and only rarely seen over the age of 8 years. The treatment of choice is wide surgical excision with variedly reported recurrence rate ranging 9–25 %. On US, lipoblastoma more often appears as relatively homogeneous hyperechoic mass, albeit it can be hypo- or isoechoic as compared with adjacent muscles. On MR imaging, the features can be varied according to the nonfat stromal contents but are often well-lobulated masses with high signal intensity on T1- and T2-weighted images reflecting high-fat content (Fig. 29.14). Liposarcoma is hardly differentiated from lipoblastoma, but liposarcoma is extremely rare in children (Navarro et al. 2009; Navarro 2011).

29.3.1.6 Lipoma

In pediatric patients, lipoma accounts for around 66 % of adipocytic tumor. However, lipoma comprises only 4 % of all soft tissue tumors in children unlike in adults. Imaging findings of lipoma in children are not different from those of adults (Navarro et al. 2009) (Fig. 29.15).

29.3.1.7 Pilomatricoma

Pilomatricoma is a benign subcutaneous tumor that arises from hair matrix and is most commonly found in children and young adults. These lesions are most commonly located in the head and neck (68 % of cases) with 29 % involving the trunk and 17 % on the extremities. Pilomatricomas are superficially situated and typically present as subcutaneous or dermal nodules. On MR imaging, pilomatricomas typically have a homogeneous intermediate signal intensity on T1W images and heterogeneous intermediate signal intensity on T2W images and are considered to be covered with a connective tissue capsule, which enhances after gadolinium administration. However, lesion centers do not enhance prominently, with the exception of septal enhancement.

Peritumoral edema or inflammation can also be identified. On US, calcium deposition is commonly visualized, and incidence of calcification on pathologic studies has been reported as 69–85 % of cases (Fig. 29.16). When being calcified, differential diagnoses are a calcified lymph node, ossifying hematoma, and hemangioma with phlebolith (Lim et al. 2007; Laffan et al. 2009).

29.3.1.8 Granuloma Annulare

Granuloma annulare is an idiopathic skin disease which is a nonneoplastic self-limited condition. It may be divided into four or more types, and the subcutaneous type can mimic soft tissue tumor; hence it is covered in this section. It generally occurs in pediatric and young adult patients, but it is usually seen between the ages of 2 and 5 years. It presents as a rapidly growing, nontender subcutaneous mass showing a predilection for the pretibial and scalp region. On US, the image is depicted as an ill-defined hypoechoic mass showing close relation to the adjacent muscle fascia. On MR imaging, it also shows ill-defined margin showing extension to the superficial fascia of the adjacent muscle but not crossing it (Navarro 2011) (Fig. 29.17).

29.3.2 Malignant Neoplasm

29.3.2.1 Rhabdomyosarcoma

Rhabdomyosarcoma, which accounts for two-thirds of all sarcomas in children, is the most common soft tissue sarcoma of pediatric patients. It can occur anywhere in the body, even in the parts where striated muscle is lacking, though being thought to arise from primitive mesenchymal cell committed to develop into striated muscle. Rhabdomyosarcomas are classified into embryonal, alveolar, and pleomorphic types. The pleomorphic type almost exclusively occurs in adults, so will not be discussed further. The embryonal type is the most common accounting for around 80 % and is generally found in the head and neck and in the genitourinary tract. The alveolar type, which accounts for 20 % of childhood rhabdomyosarcoma, has a poorer prognosis and generally occurs at the extremities. US and MR imaging findings are known to be nonspecific (McDowell 2003; Laffan et al. 2009; Navarro 2011) (Figs. 29.18 and 29.19).

29.3.2.2 Synovial Sarcoma

Synovial sarcoma is the second common pediatric soft tissue sarcoma, second only to rhabdomyosarcoma. It is more common in young adults than in pediatric patients. Only 30 % of the lesions are seen in patients less than 20 years of age. The name of this neoplasm can mislead clinicians to think it originates from synovial tissue; hence, it occurs in the joints or other synovial lining organs such as tendons and bursae. However, it occurs in the joints in only 6–10 % of

cases though it is most often found in a juxta-articular location. US feature is nonspecific. MR imaging findings are also nonspecific in general. However, when a radiologist encounters a juxta-articular soft tissue mass showing heterogeneous signal, with avid gadolinium contrast enhancement and with fluid levels on MR imaging, synovial sarcoma should be listed as one of the most important differential diagnoses (Laffan et al. 2009) (Fig. 29.20).

29.3.2.3 Infantile Fibrosarcoma

Both infantile- and adult-type fibrosarcoma can occur in children. However, infantile type, also known as congenital fibrosarcoma, is exceedingly more common than adult type accounting for around 12 % of soft tissue malignancies in infants. Adult-type fibrosarcoma occurs in far later age, most commonly between 10 and 15 years of age. Infantile type shows more favorable prognosis (5-year survival rate of 80 %) than does adult type (5-year survival rate of 60 %). Gross morphology of infantile fibrosarcoma can be confused with infantile hemangioma clinically because they accompany changes of skin color. However, less homogeneous contrast enhancement and lack of flow-related signal void of infantile fibrosarcoma on MR imaging help the differential diagnosis (Laffan et al. 2009; Navarro 2011) (Fig. 29.21).

29.3.2.4 Miscellaneous

Except for the aforementioned malignant tumors which show relatively prominent predilection for pediatric age, the following tumors possibly occur in children, but are relatively rare soft tissue malignant neoplasm in childhood: dermatofibrosarcoma protuberans, alveolar soft part sarcoma, angiosarcoma, Ewing/primitive neuroectodermal tumor, granulocytic sarcoma, and lymphoma. Clinical features and imaging findings of them are briefly discussed below.

Dermatofibrosarcoma protuberans is most commonly seen in middle-age adults, but has also been reported in children. It most commonly occurs on the trunk or proximal extremity. It originates in the dermis and extends into the deeper soft tissue. Overlying skin change can occur due to its superficial location leading to misconception as vascular malformation or hemangioma. Imaging finding is nonspecific except for its superficial location as compared with the other soft tissue tumors (Laffan et al. 2009).

Alveolar soft part sarcoma rarely occurs in pediatric patients accounting for around 5 % of pediatric nonrhabdomyosarcoma soft tissue sarcomas. It slowly grows and is named as such for the presence of eosinophilic cell nests that contain cytoplasmic granules resembling histological morphology of respiratory alveoli. Due to its prominent vascularity, the tumor may sometimes be pulsatile at physical examination. On MR imaging, signal void can be seen in and periphery of the mass associated with serpiginous high-flow vessels and scattered calcification. Avid enhancement is seen

with a gadolinium contrast agent (Suh et al. 2000; Laffan et al. 2009) (Fig. 29.23).

Angiosarcoma in pediatric patients is extremely rare. It has varied anatomic distribution but usually has predilection for liver and deep soft tissue in the trunk, pelvis, head and neck, and mediastinum. Imaging findings are nonspecific (Ayadi and Khabir 2010) (Fig. 29.24).

Ewing tumor and primitive neuroectodermal tumor are commonly discussed together because they are considered to be in the same line at the different stages of neuroectodermal tumor differentiation as recent molecular genetic studies having shown that both entities have the same characteristics that make them indistinguishable from each other. This entity is more commonly seen in skeleton, but the extraskel-etal form has also been commonly described in detail. It is, however, seldom seen in children of Asian or African descent. Imaging feature is nonspecific (Laffan et al. 2009).

Granulocytic sarcoma is a lump of primitive granulocytic precursors and occurs in approximately 5 % of cases of acute myelogenous leukemia. On MR imaging, T2-weighted images of the mass can reportedly show signal intensity which is isointense to muscle (Stein-Wexler 2009).

Primary extranodal soft tissue lymphoma is rare, accounting for only up to 2 % of all soft tissue tumors. Primary extranodal soft tissue lymphoma with later disseminated disease has a poor prognosis as compared with primary nodal or skeletal lymphoma. On MR imaging, lymphoma shows variable morphology form as a superficial nodular mass though as a deeper diffuse, infiltrative mass. It frequently infiltrates multiple muscle groups and may involve adjacent bone (Fig. 29.25). Lymphoma should be considered in the differential diagnosis of all soft tissue masses in the immune-compromised patients (Laffan et al. 2009; Chun et al. 2010).

29.4 Illustrations: Soft Tissue Diseases

29.4.1 Myositis Ossificans Progressiva

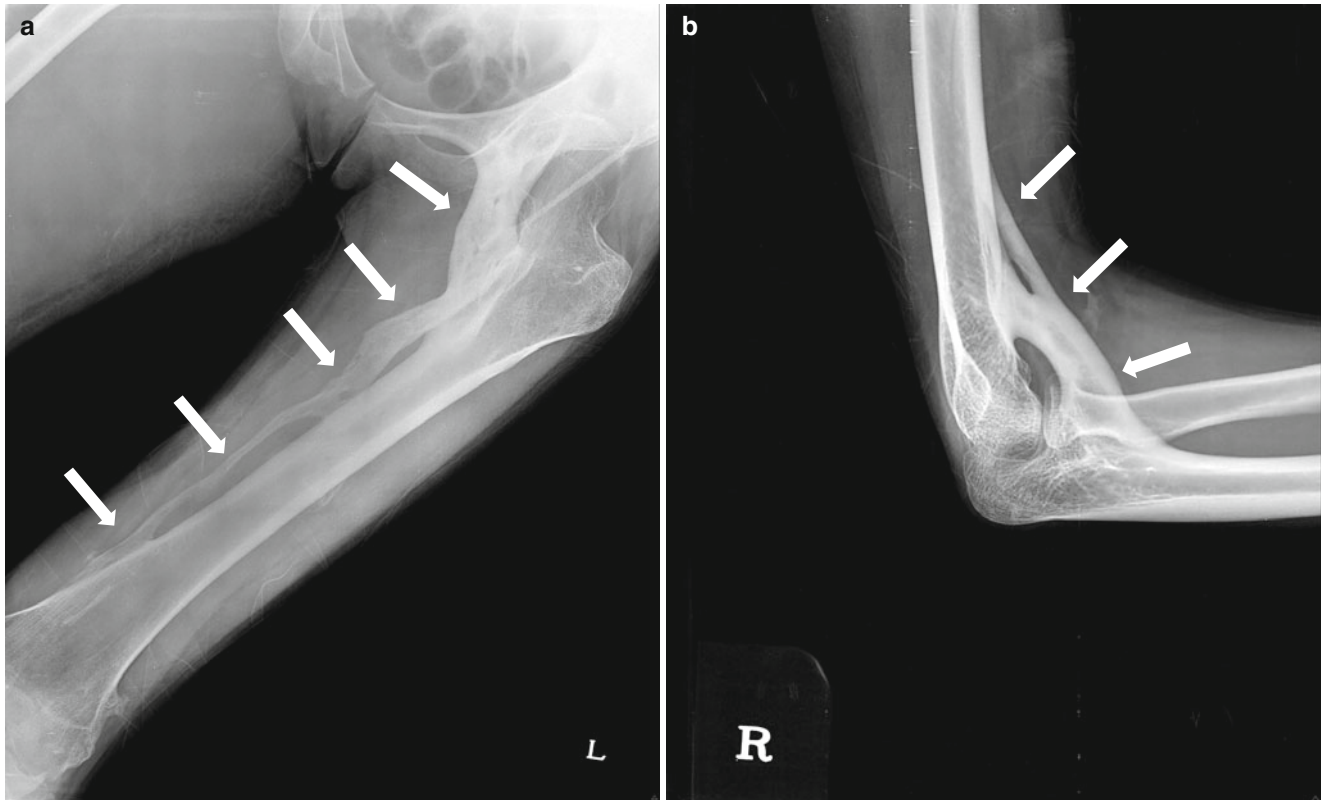


Fig. 29.1 Radiographs and MR images of an 18-year-old girl who sustained myositis ossificans progressiva. She presented with edema of the right leg. **(a)** A radiograph of the left femur shows dense bridging ossification (*arrows*) in medial aspect of thigh. **(b)** Lateral radiograph of the elbow shows bony bridge (*arrows*) between the ventral aspect of humerus and ulna. **(c)** An anteroposterior (AP) radiograph of a foot shows dense soft tissue ossification resulting in the appearance of exostoses from the metatarsal bone of great toe with mild hallux valgus (*arrows*). Ankylosis of interphalangeal joint of great toe is also observed

(*arrowheads*). **(d)** Lateral radiograph of the neck shows ankylosis of vertebral bodies and facet joints mimicking morphology of ankylosing spondylitis or Klippel-Feil syndrome (*arrowheads*). Note the bridging ossification bar (*arrows*) of the posterior neck portion presumably located at the nuchal ligament. **(e)** Axial T1-weighted MR image shows isointense signal intensity of the swollen muscles (*arrows*). **(f)** Axial T2-weighted fat-suppressed MR image shows hyperintense signal intensity of the swollen muscles at the medial and posterior compartments (*arrows*)



Fig. 29.1 (continued)

29.4.2 Infantile Hemangioma

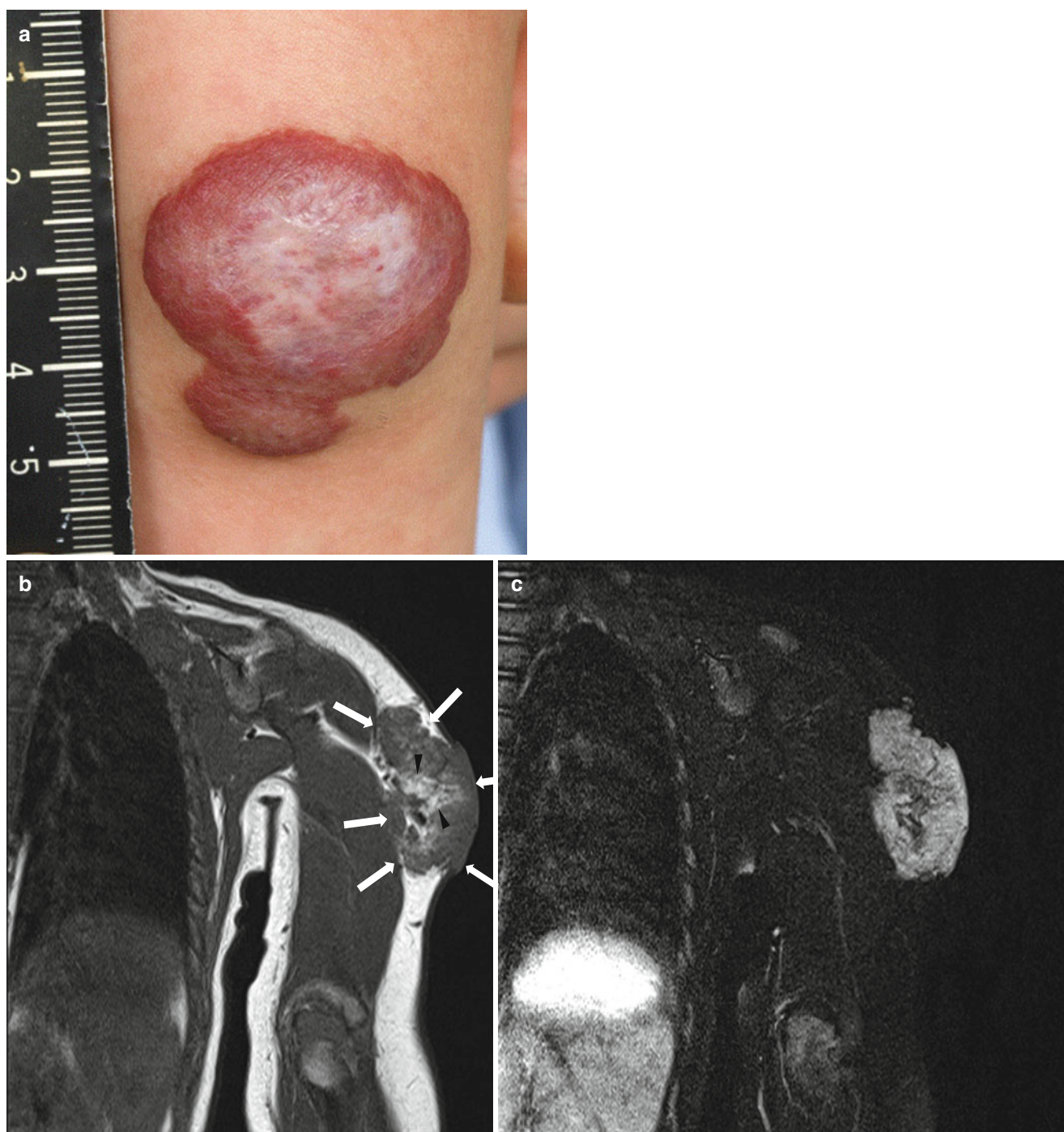


Fig. 29.2 Gross photograph and MR images of an 11-month-old girl with infantile hemangioma at the left arm. **(a)** Gross photograph shows a superficially located strawberry-like lump. **(b)** Coronal T1-weighted MR image shows well-defined isointense soft tissue mass (*arrows*) relative to muscle in subcutaneous through cutaneous layer of the Lt. arm. Intralesional high signal intensity portions (*arrowheads*) suggest

inhibitions of fat component. **(c)** Coronal fat-suppressed T2-weighted MR image shows hyperintense lobulated soft tissue mass. **(d)** Coronal gadolinium-enhanced fat-suppressed T1-weighted MR image shows diffuse enhancement of the mass. Aforementioned intralesional fat component is not enhanced (Courtesy of In-One Kim and Young-Hun Choi of Seoul National University Hospital)

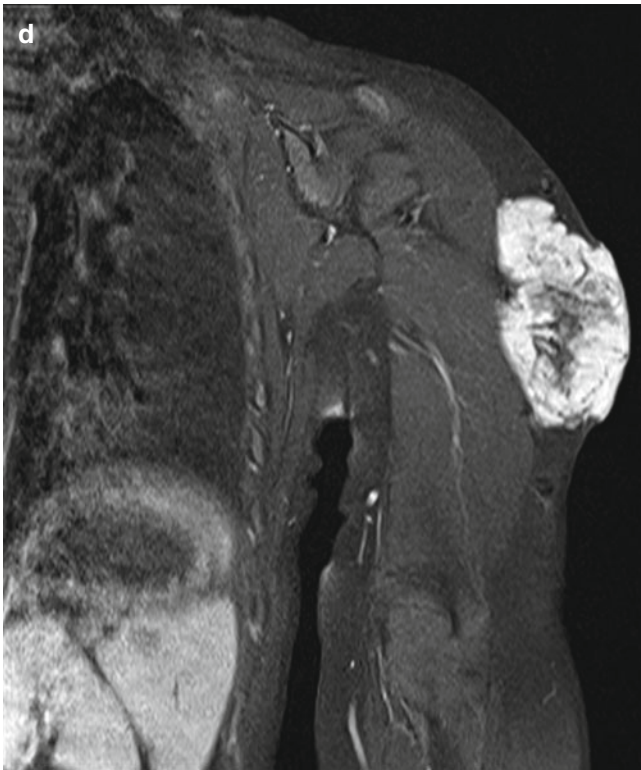


Fig. 29.2 (continued)

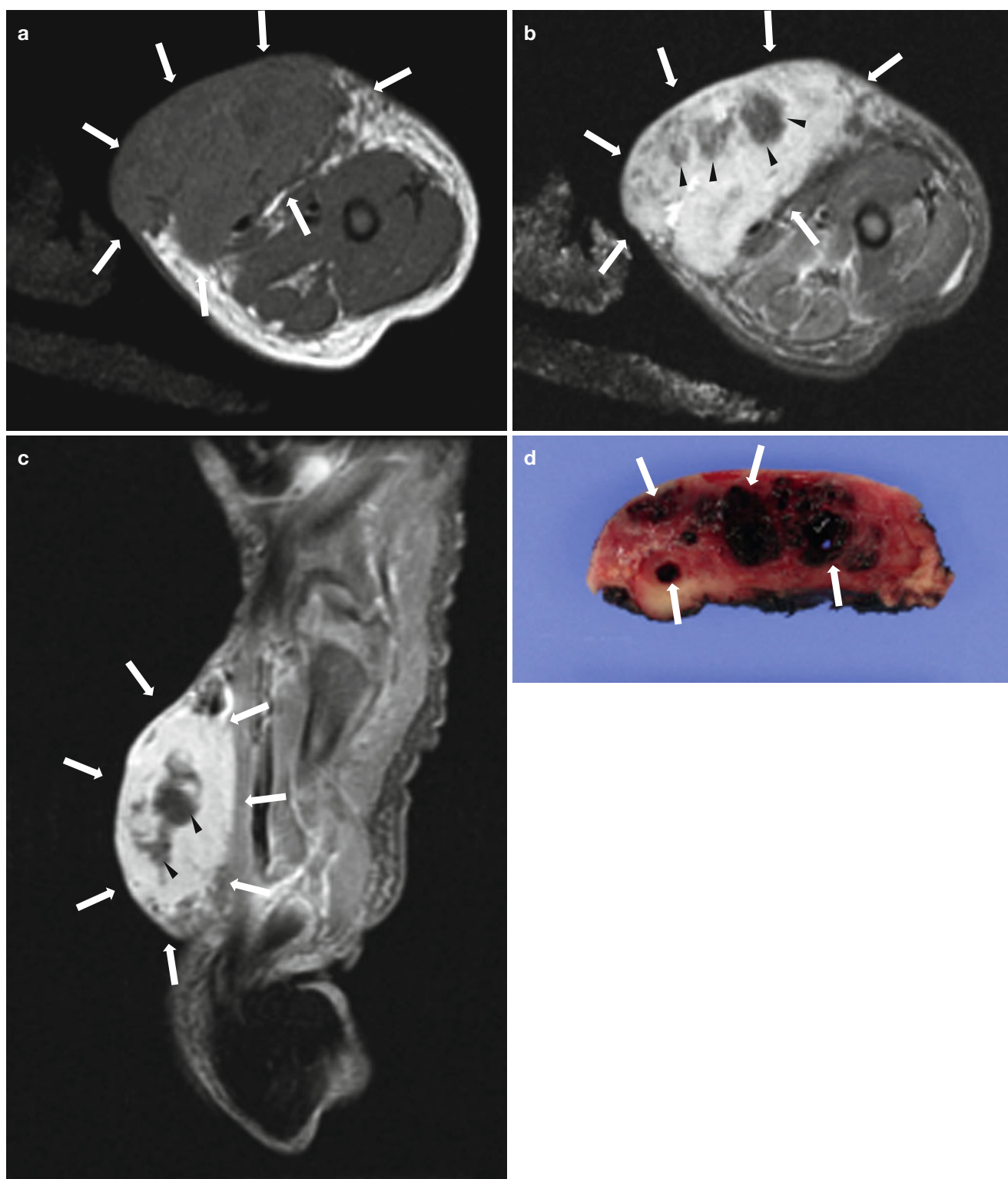


Fig. 29.3 MR images and gross photograph of a 4-day-old girl with infantile hemangioma at the left thigh. (a) Axial T1-weighted MR image shows a lobulated soft tissue mass (*arrows*) with isointense signal intensity relative to muscle confined to subcutaneous soft tissue of thigh. (b) Axial fat-suppressed T2-weighted MR image shows hyperintense lobulated soft tissue mass (*arrows*). Intralesional hypointense foci (*arrowheads*) reflect thrombi. (c) Sagittal gadolinium-enhanced fat-

suppressed T1-weighted MR image shows diffuse enhancement of the mass (*arrows*). Nonenhanced foci (*arrowhead*) also reflect the presence of thrombi. (d) Photograph of the cut surface of the excised specimen shows multiple hemorrhagic cystic spaces (*arrows*) with/without thrombi (Courtesy of In-One Kim and Young-Hun Choi of Seoul National University Hospital)

29.4.3 Venous Malformation

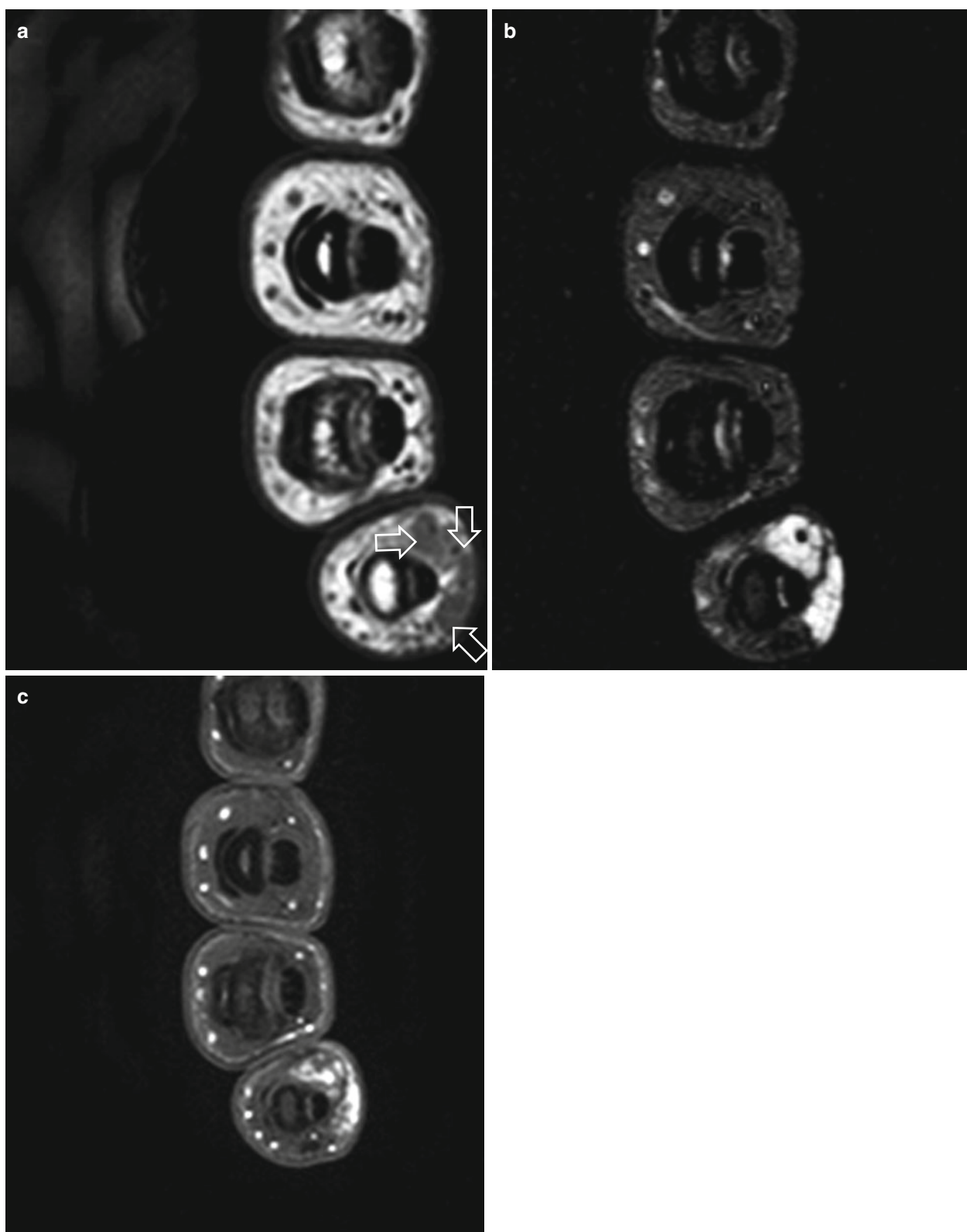


Fig. 29.4 MR images of an 18-year-old girl with venous malformation in the fifth finger. **(a)** Axial T1-weighted MR image shows well-defined soft tissue mass (*arrows*) which shows hypointense signal in volar aspect of fifth finger. **(b)** Axial fat-suppressed T2-weighted MR image of the

mass shows a lobulated contour with multilocular appearance due to venous space that shows hyperintense signal separated by thin hypointense septa (*arrowheads*). **(c)** Axial gadolinium-enhanced fat-suppressed T1-weighted MR image of the mass shows patch enhancement

29.4.4 Lymphatic Malformation

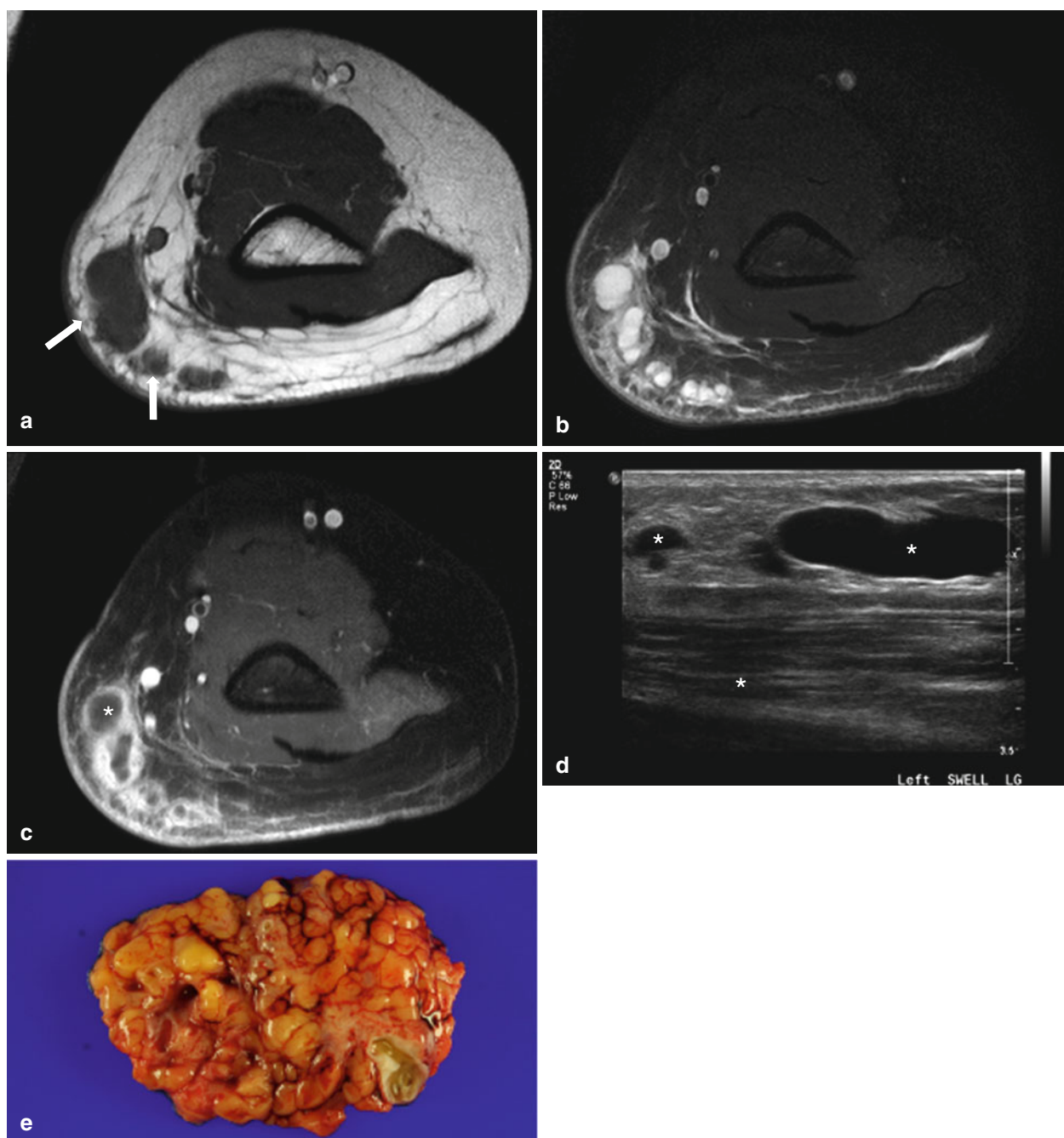


Fig. 29.5 MR images and gross photograph of a 13-year-old boy with lymphatic malformation at the left upper arm. **(a)** Axial T1-weighted MR image shows multiloculated subcutaneous mass (*arrows*) that is predominantly isointense relative to muscle, with some hyperintense subcutaneous fat interspersed within the lesion. **(b)** Axial fat-suppressed T2-weighted MR image shows the mass with multilocular cystic portions that show fluid signal. **(c)** Axial gadolinium-enhanced

fat-suppressed T1-weighted MR image shows enhancement of surrounding connective tissue. No enhancement in central portion of cysts (*). Lack of enhancement of the lymph-filled space helps differentiate lymphatic malformation from venous malformation. **(d)** US shows multicystic fluid-filled mass (*) in subcutaneous fatty layer of upper arm. **(e)** Gross photograph of completely excised specimen shows a multilobulated surface

29.4.5 Arteriovenous Malformation

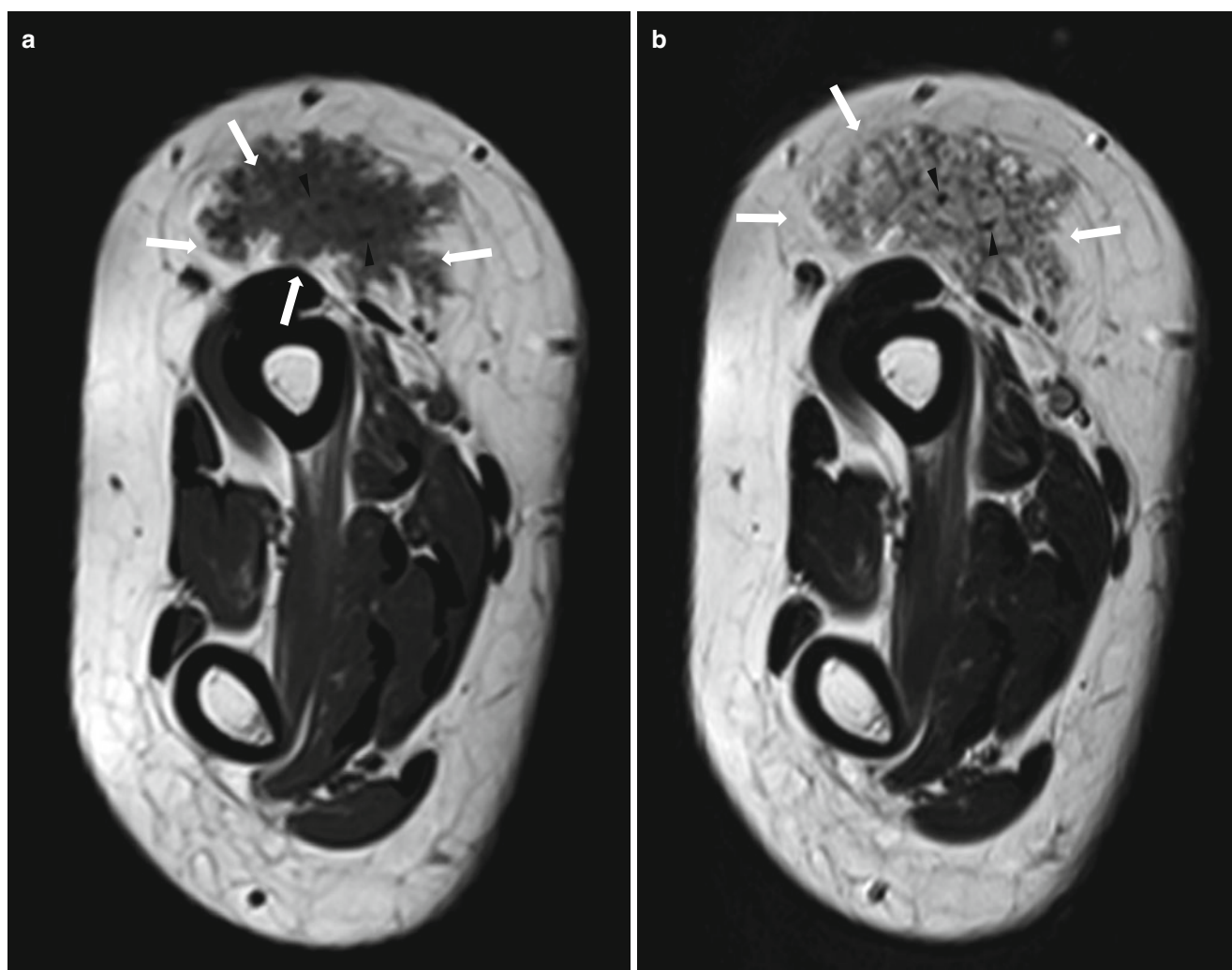


Fig. 29.6 MR images of a 17-year-old female patient with arteriovenous malformation. (a) Axial T1-weighted MR image shows isointense tangled mass (arrows) in subcutaneous layer of distal forearm. (b) Axial T2-weighted MR image shows the mass (arrows) with slightly hyperintense signal intensity relative to muscle. (c) Axial T2-weighted fat-suppressed MR image shows the mass (arrows) with bright signal intensity. (d) Axial gadolinium-enhanced fat-suppressed T1-weighted

MR image shows heterogeneous enhancement of the mass (arrows). Note multiple signal void foci (arrowheads of a, b, c, and d) representing the high-flow vessels that are characteristic of this vascular malformation (e, f). Coronal gadolinium-enhanced fat-suppressed T1-weighted MR images show the supplying radial arterial branch (e, arrow) and engorged draining vein (f, arrow).

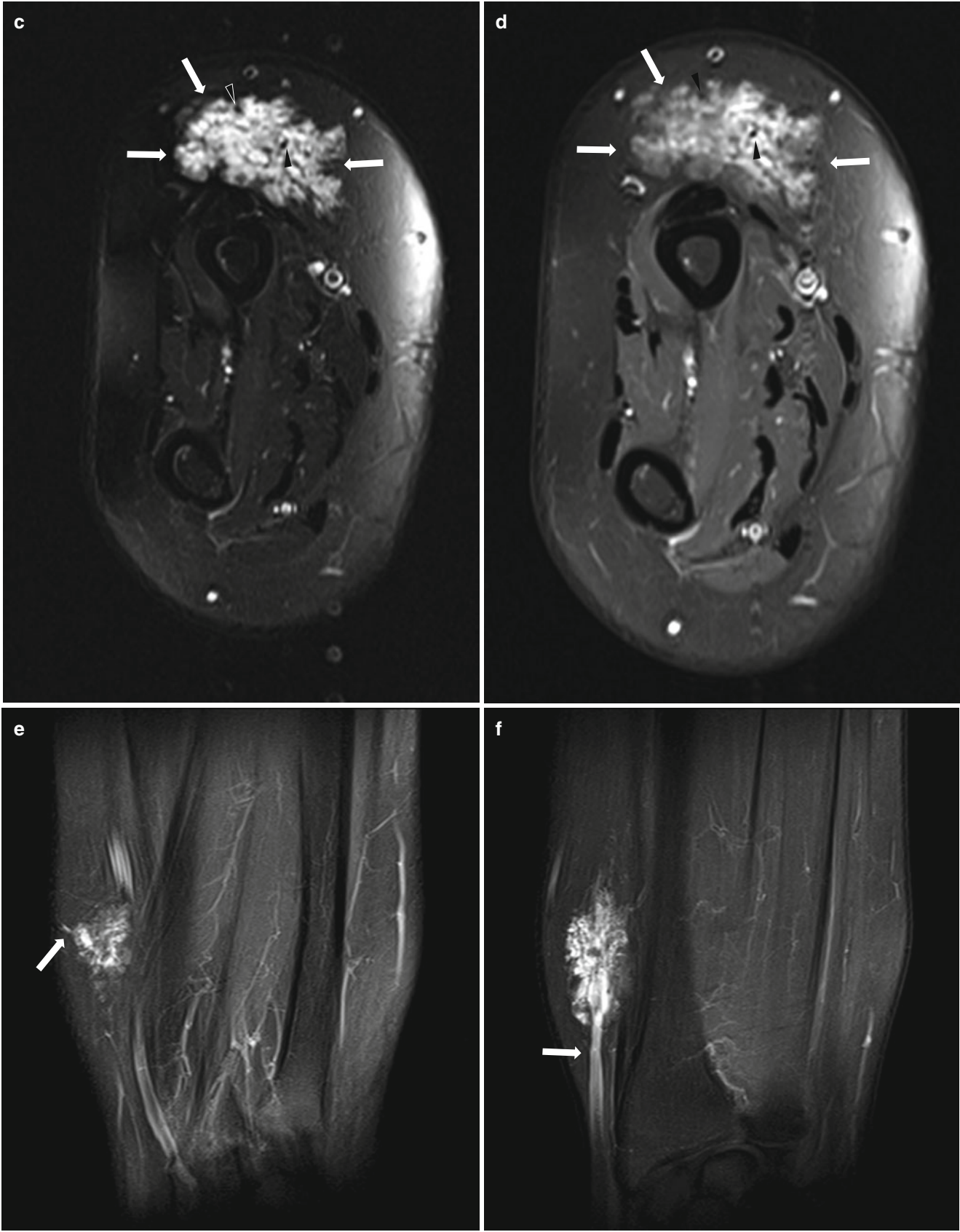


Fig. 29.6 (continued)

29.4.6 Klippel-Trenaunay Syndrome

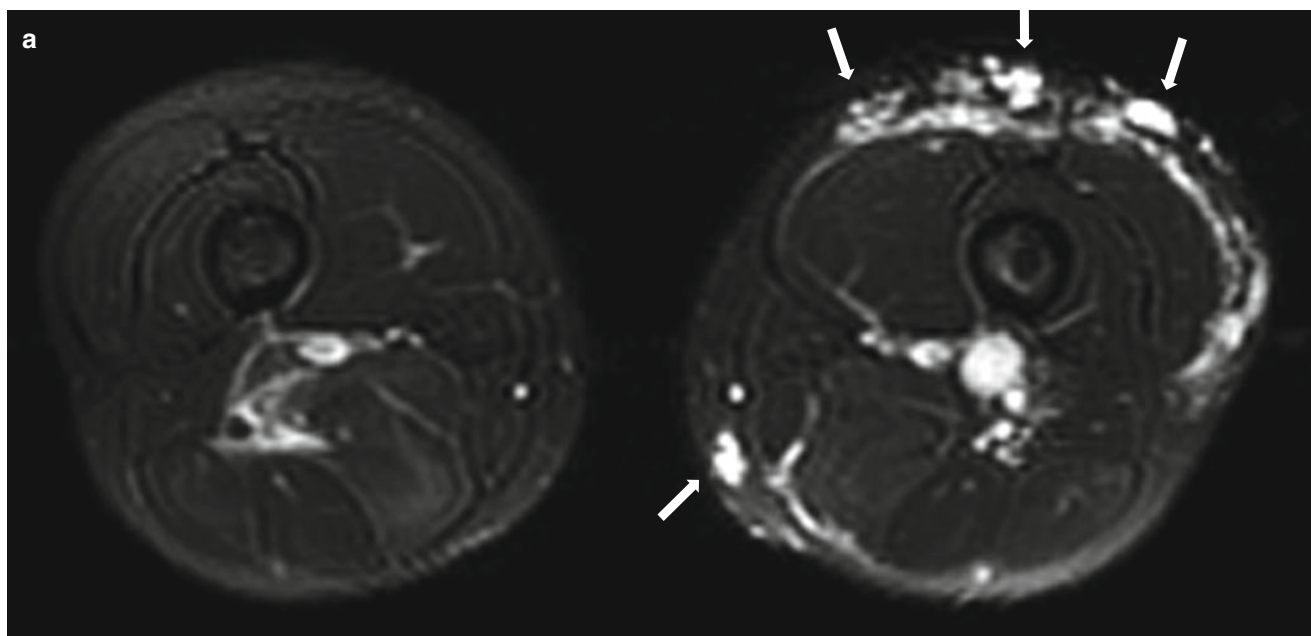


Fig. 29.7 MR images of a 19-year-old male patient who presented with asymmetric hypertrophy of the left thigh and is diagnosed as having Klippel-Trenaunay syndrome. **(a)** Axial fat-suppressed T2-weighted MR image shows asymmetric surface vein dilatation and vascular mal-

formation (*arrows*) of the left thigh. Axial fat-suppressed T2-weighted MR image of upper **(b)**, mid **(c)**, and lower **(d)** level of the left thigh shows dilated vascular structures with vascular malformation involving subcutaneous and inter-/intramuscular area

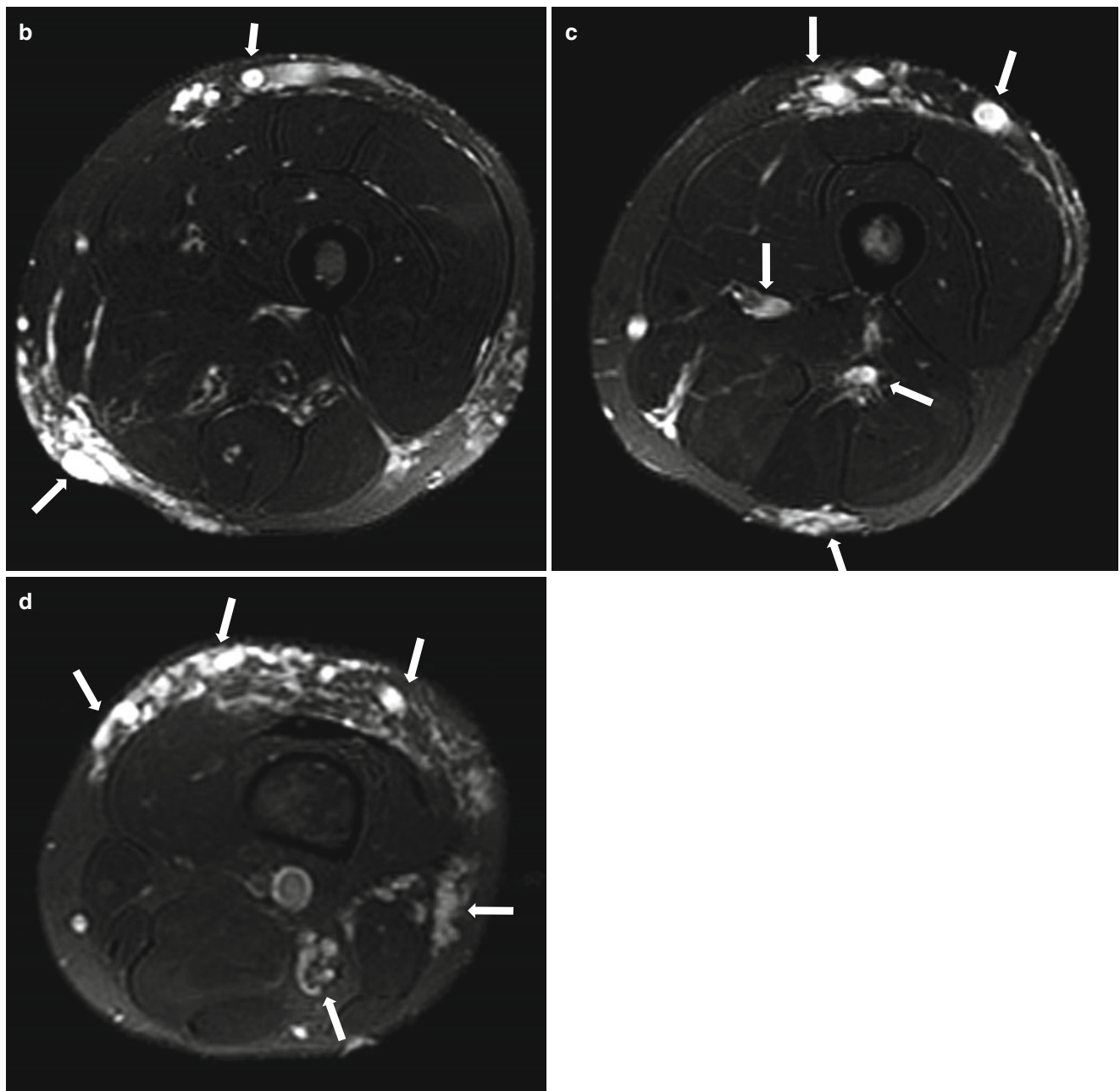


Fig. 29.7 (continued)

29.4.7 Compartment Syndrome

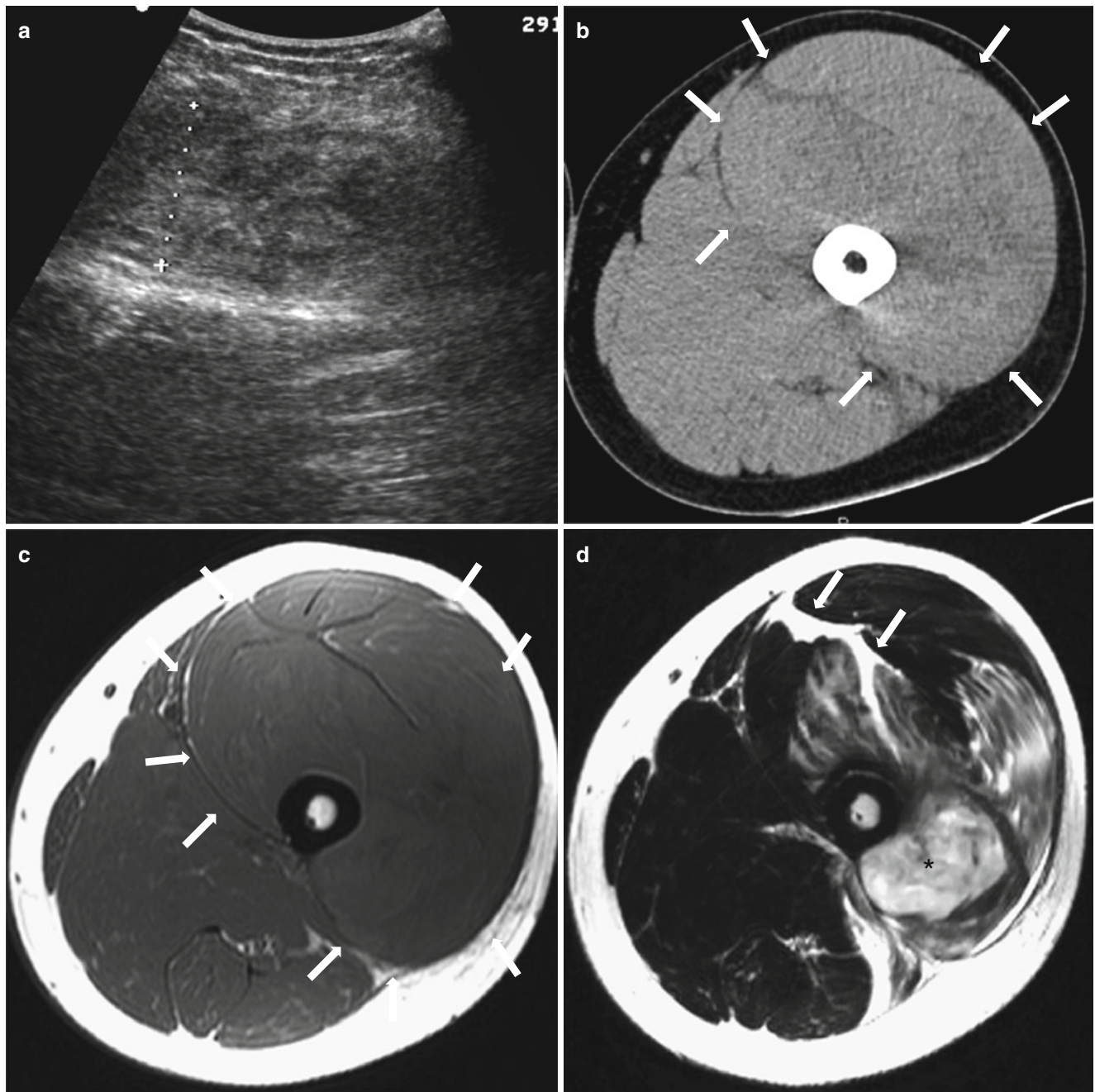


Fig. 29.8 Acute anterior compartment syndrome of the left thigh in an 18-year-old patient with swelling and pain after twisting injury. (a) US of left thigh shows diffuse swelling of vastus muscles with heterogeneous echo. (b) Precontrast CT scan also shows diffuse swelling of vastus muscles (arrows). (c) Axial T1-weighted MR image shows swelling of the entire anterior compartment muscles (arrows). (d) Axial T2-weighted MR image can reveal areas of muscle edema and a pre-

sumable hematoma (*) within vastus muscles with hemorrhagic fluid (arrows) along the intermuscular fascial planes. (e) Vastus intermedius and lateralis muscles show mild, patchy enhancement (arrowheads) on axial gadolinium-enhanced T1-weighted image. Note nonenhanced muscle area (*) which was mentioned above as a hematoma. (f) Follow-up US after 2 months shows improved muscle edema with linear calcifications (arrows)

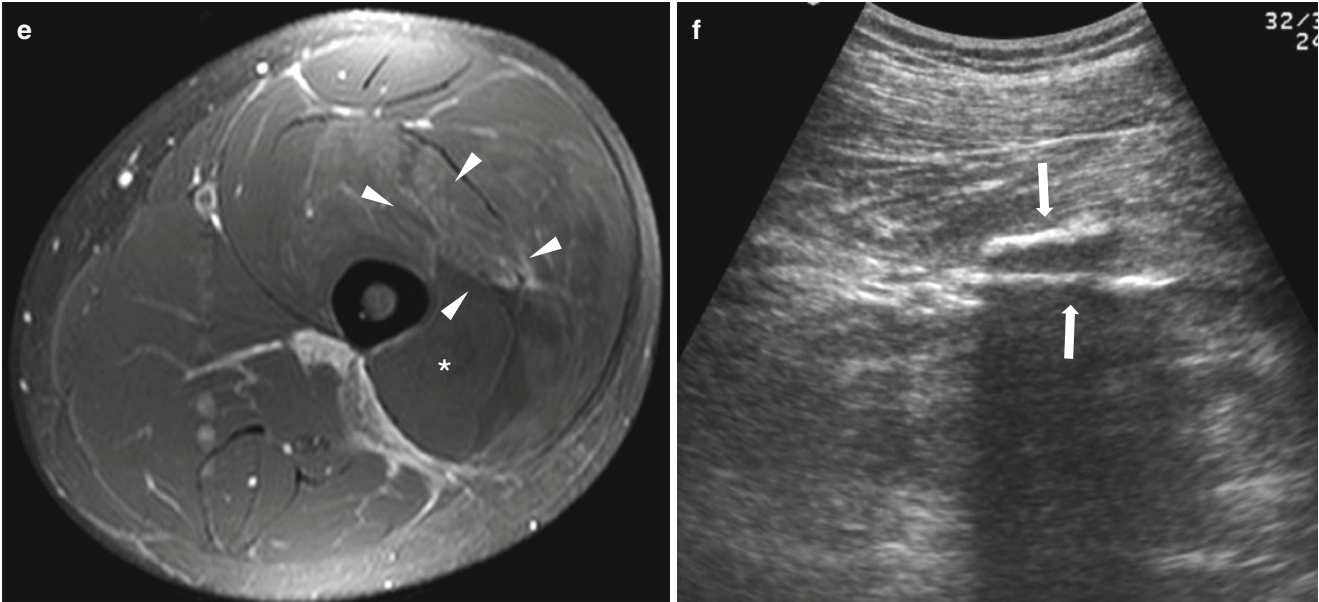


Fig. 29.8 (continued)

29.4.8 Fibromatosis Colli

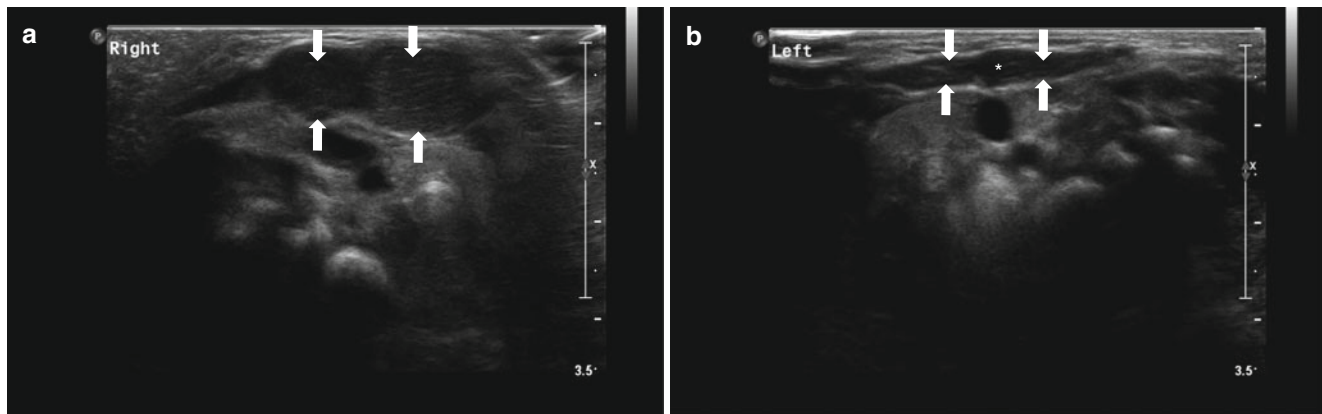


Fig. 29.9 US images of an 18-day-old boy who presented with fibromatosis colli. **(a)** Longitudinal oblique US image of the anterolateral neck shows nodular thickening of the sternocleidomastoid muscle

(arrowheads). **(b)** Longitudinal oblique US image of the contralateral sternocleidomastoid muscle shows normal shape (*arrows*)

29.4.9 Desmoid Type Fibromatosis

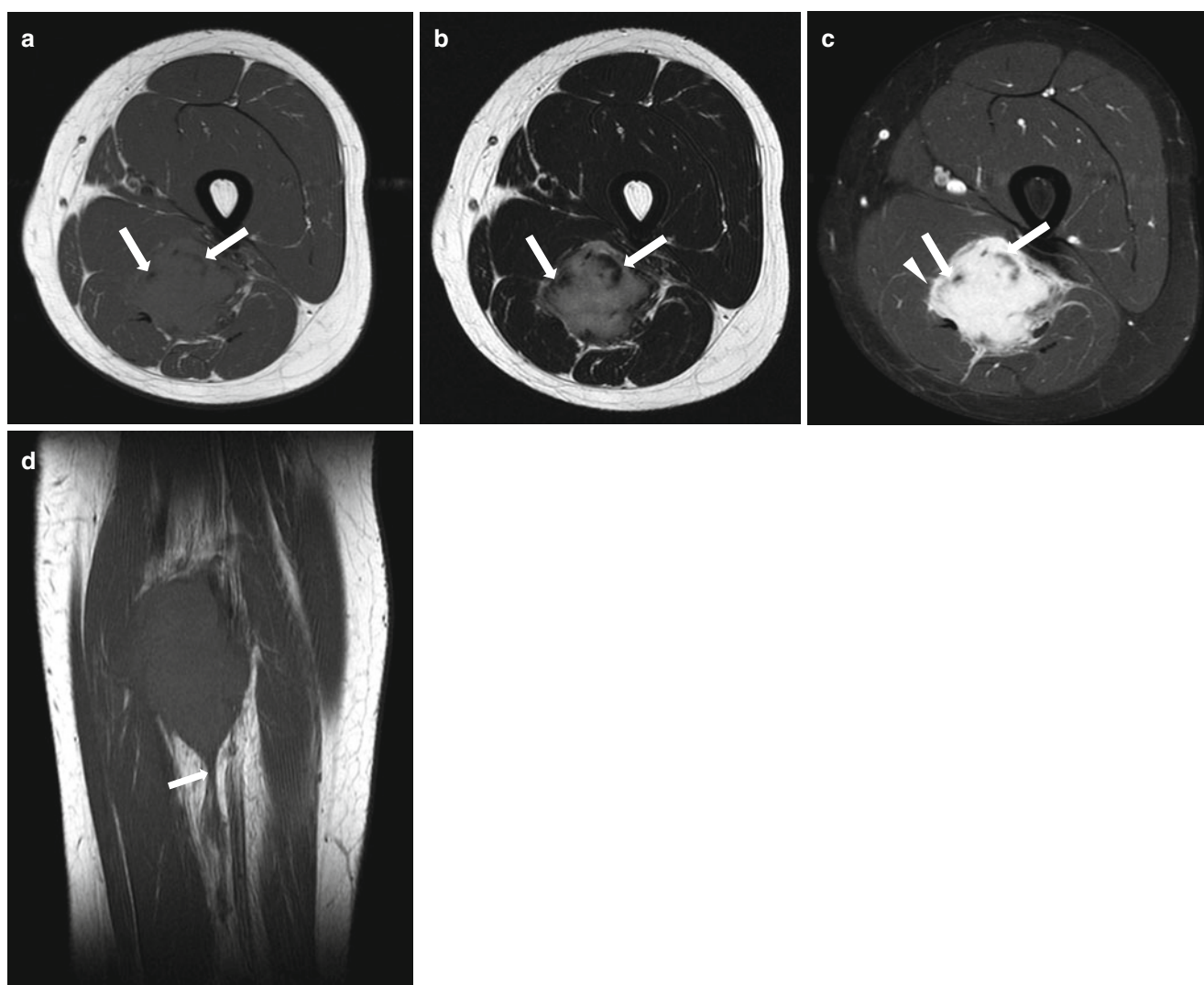


Fig. 29.10 MR images of a 12-year-old boy who sustained desmoid-type fibromatosis in the thigh. Three MR images at the same level (**a**, **b**, **c**) show a mass with lobulating border in posterior compartment of thigh. Axial T1-weighted (**a**) and axial T2-weighted (**b**) MR images show low signal intensity foci (*arrow*), which are more prominent on T2-weighted image. (**c**) Axial gadolinium-enhanced fat-suppressed

T1-weighted MR image shows intense enhancement of the mass with infiltrative margins (*arrowhead*). The low signal foci seen on T1- and T2-weighted images are not enhanced partly (*arrow*), which suggest that the region is composed of collagen fibers. (**d**) Coronal T1-weighted MR image shows linear inferior extension of the mass along the fascia, which is called fascial tail sign (*arrow*)

29.4.10 Nodular Fasciitis

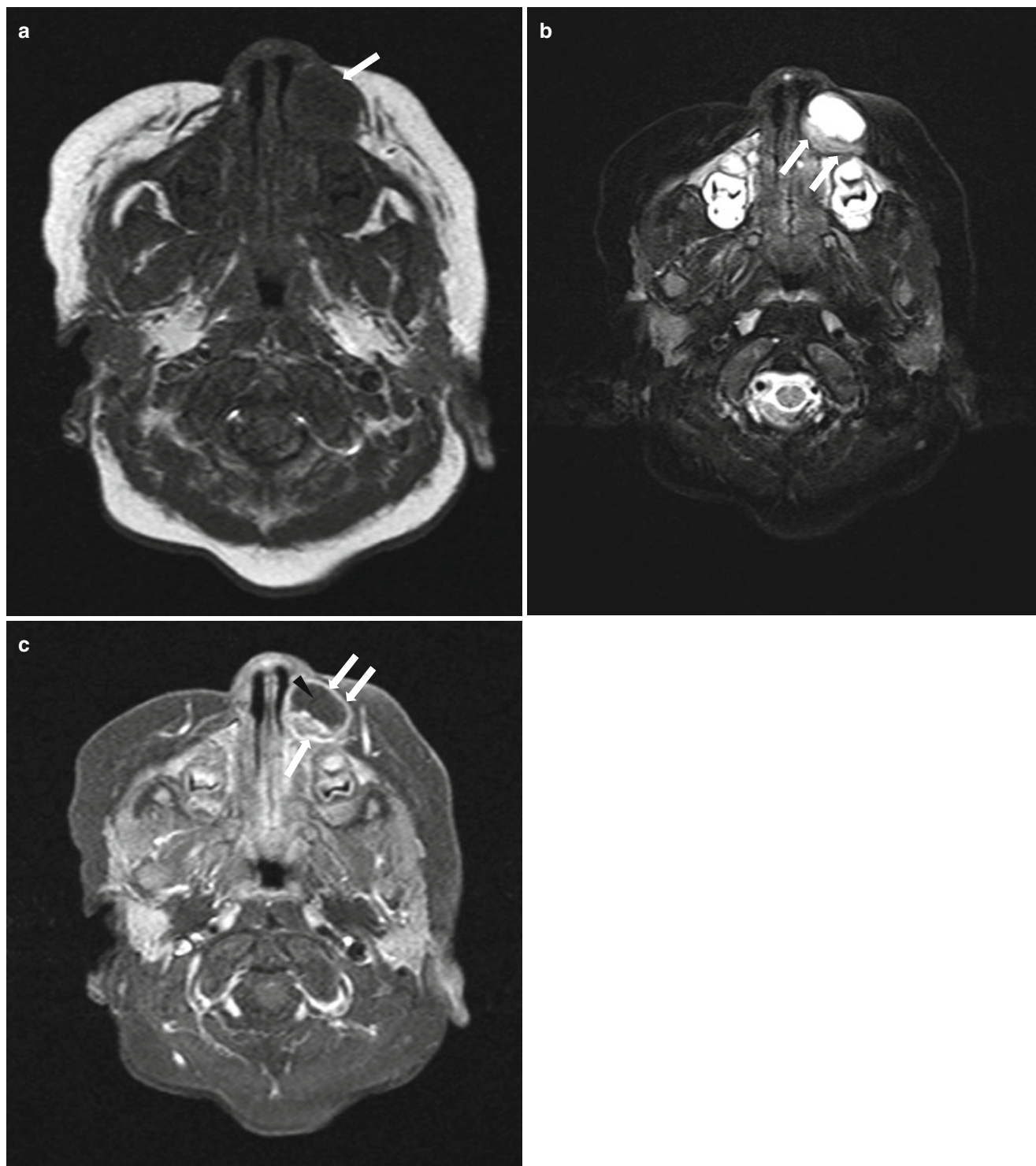


Fig. 29.11 Nodular fasciitis in the face of a 9-month-old boy. (a) Axial T1-weighted MR image shows a mass in the left nasal ala (*arrow*). (b) Axial fat-suppressed T2-weighted MR image also shows a well-circumscribed lesion. Central portion of the lesion shows bright signal intensity (*arrowhead*). Periphery of the mass shows lower but high signal intensity as compared with the inner portion (*arrows*). (c) Axial

gadolinium-enhanced fat-suppressed T1-weighted MR image shows peripheral rim-like enhancement (*arrows*), and the central portion which shows bright signal on fat-suppressed T2-weighted image is not enhanced suggesting possibility of necrosis (*arrowhead*) (Courtesy of In-One Kim and Young-Hun Choi of Seoul National University Hospital)

29.4.11 Plexiform Neurofibroma



Fig. 29.12 Plexiform neurofibroma in the knee of a 15-year-old boy. (a) Axial T1-weighted MR image shows lobulated masses which show iso/slightly high signal intensity compared to muscle in popliteal fossa (arrows). (b) Axial T2-weighted MR image shows lobulated hyperintense mass with target sign (arrowheads), which is typical of this entity. The target sign is associated with a central zone of low signal intensity

(fibrovascular zone) surrounded by a peripheral zone with high signal intensity (myxoid zone). Coronal (c) and sagittal (d) short-tau inversion recovery MR images show lobulating mass also with target sign (arrowheads) and clustered multifascicular appearance, known as morphology of “bag of worms”

29.4.12 Schwannoma

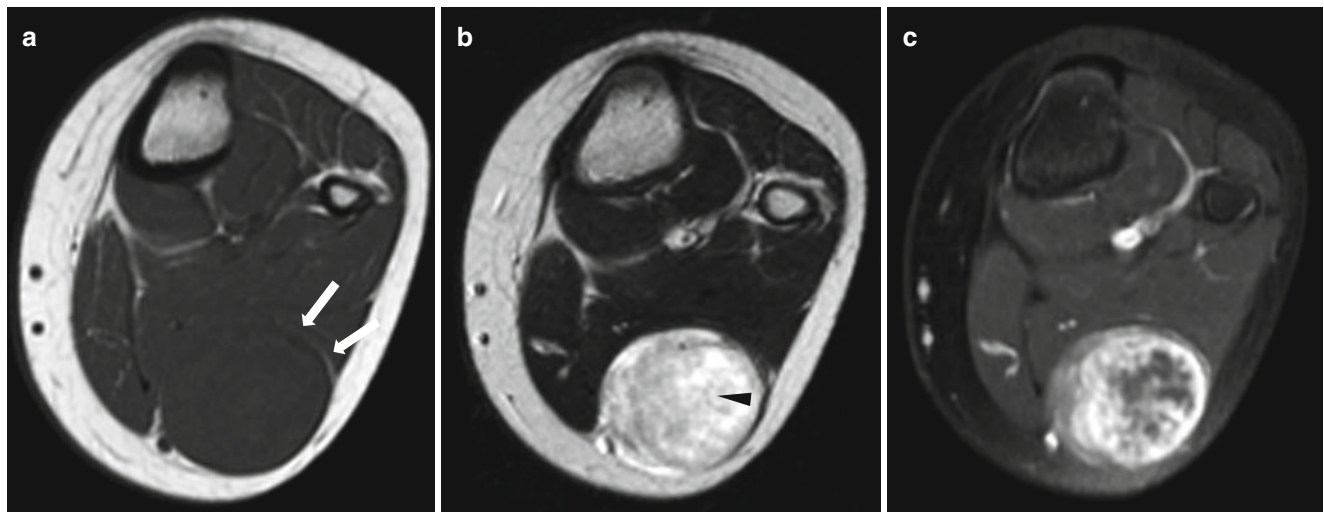


Fig. 29.13 Schwannoma in the arm of a 7-year-old girl. **(a)** Axial T1-weighted MR image shows a round mass showing isointense signal relative to muscle. Note a surrounding thin fat rim (*arrows*) which is known as split-fat sign. **(b)** Axial T2-weighted MR image shows well-defined mass with heterogeneous high signal intensity greater than that

of fat. Multiple ring-like structures (*arrowhead*) are seen throughout the lesion, which is known as fascicular sign commonly seen in nerve sheath tumors. **(c)** Axial gadolinium-enhanced fat-suppressed T1-weighted MR image shows heterogeneous enhancement of this mass

29.4.13 Lipoblastoma



Fig. 29.14 Lipoblastoma in lower leg of a 2-year-old girl who presented with an enlarging mass. **(a)** Radiograph shows fat-contained bulging soft tissue mass density (*arrows*). **(b)** Axial T1-weighted MR image shows a relatively well-defined lobulating mass (*arrows*) involving the musculature in anterior compartment of the lower leg. Most portion of the mass shows high signal intensity suggesting fat component though thick connective tissue septae (*arrowheads*) are visualized.

(c) Axial fat-suppressed T2-weighted MR image shows low signal intensity suggesting signal deprivation from the fat component though portion with high signal suggesting the presence of nonfat component is seen (*arrowheads*). **(d)** Coronal gadolinium-enhanced fat-suppressed T1-weighted MR image shows heterogeneous enhancement of the lesion

29.4.14 Lipoma

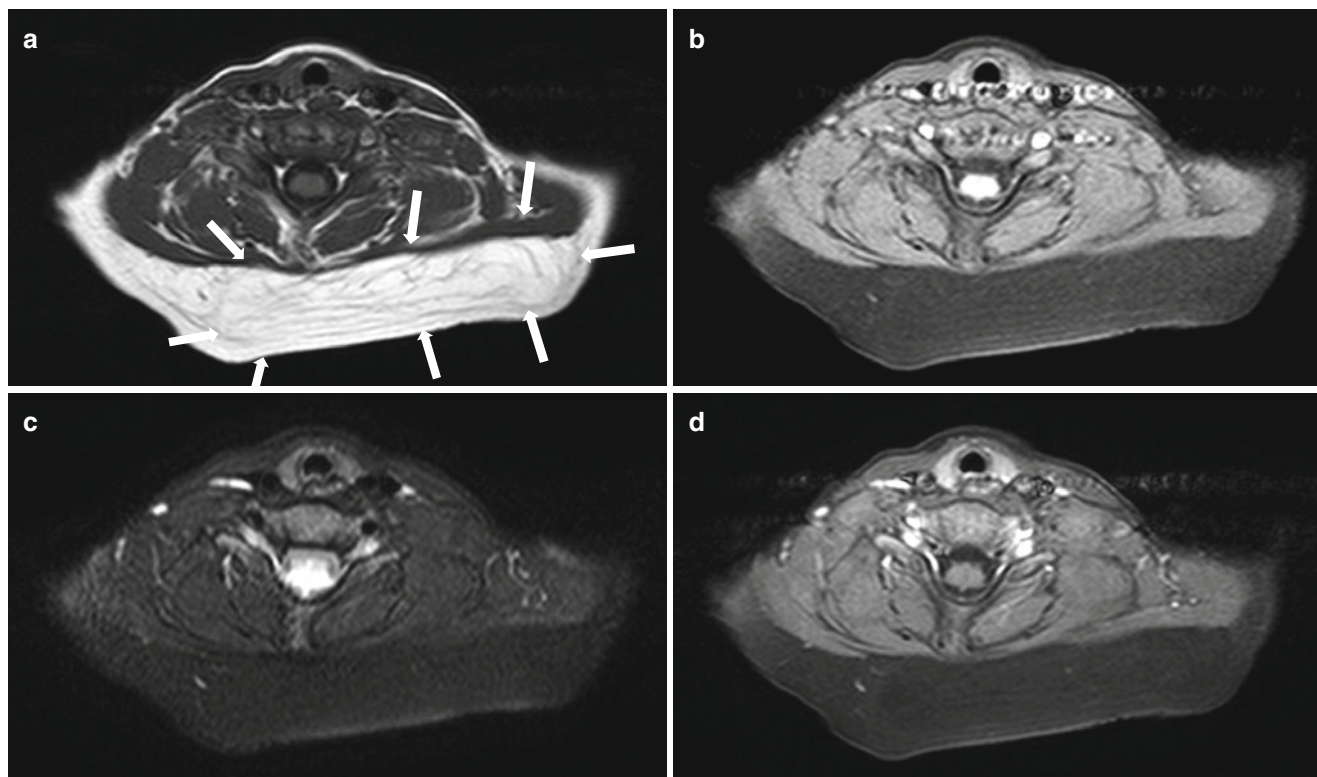


Fig. 29.15 Lipoma in posterior neck of a 3-year-old boy. (a) Axial T1-weighted MR image shows relatively well-capsulated mass with fat signal intensity (*arrows*) involving entire subcutaneous fat layer of posterior neck. (b, c, d) This mass is indistinguishable from the surround-

ing subcutaneous fat tissue on axial fat-suppressed T1-weighted MR image (b), axial fat-suppressed T2-weighted MR image (c), and axial gadolinium-enhanced fat-suppressed T1-weighted MR image (d). Enhancement of this mass is not seen

29.4.15 Pilomatricoma

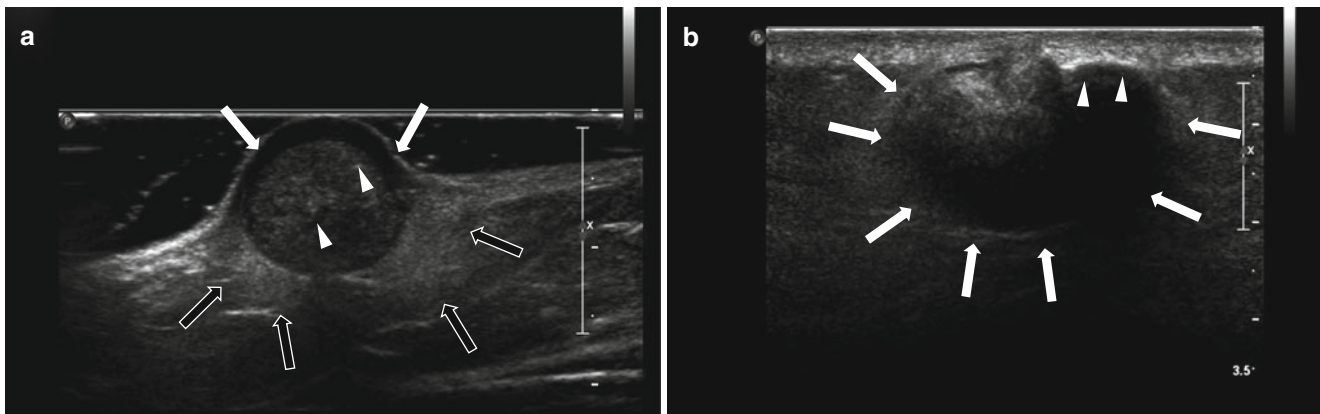


Fig. 29.16 US findings of pilomatricoma. **(a)** Pilomatricoma in the arm of a 13-day-old boy. US image shows well-defined, slightly hyperechoic mass relative to muscle in the arm. The lesion has a hypoechoic rim (*white arrows*), tiny echogenic spots (*arrowheads*), and peritumoral

hyperechogenicity (*black arrows*). **(b)** Pilomatricoma in the posterior neck of a 14-day-old girl. US image shows mass (*arrows*) with dense calcification (*arrowheads*) with posterior acoustic shadowing

29.4.16 Granuloma Annulare

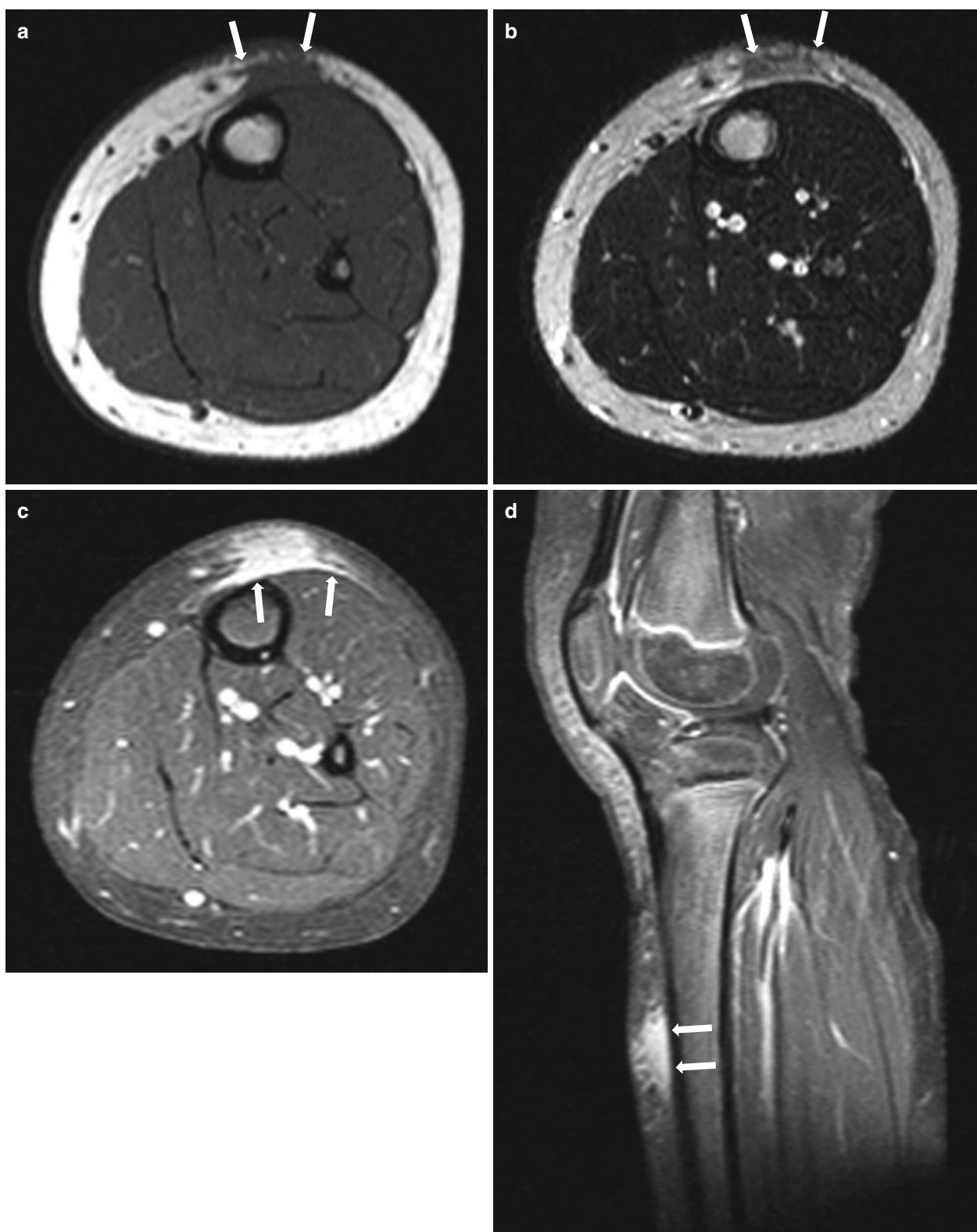


Fig. 29.17 Granuloma annulare in the lower leg of a 4-day-old boy. (a) Axial T1-weighted MR image shows ill-defined isointense mass (arrows) relative to muscle in subcutaneous layer of anterior lower leg. (b) On axial T2-weighted MR image, the mass shows heterogeneous signal intensity (arrows). (c, d) Axial (c) and sagittal (d) gadolinium-

enhanced fat-suppressed T1-weighted MR images show intense enhancement of mass abutting but not involving the underlying musculature and tibia (arrows) (Courtesy of In-One Kim and Young-Hun Choi of Seoul National University Hospital)

29.4.17 Rhabdomyosarcoma

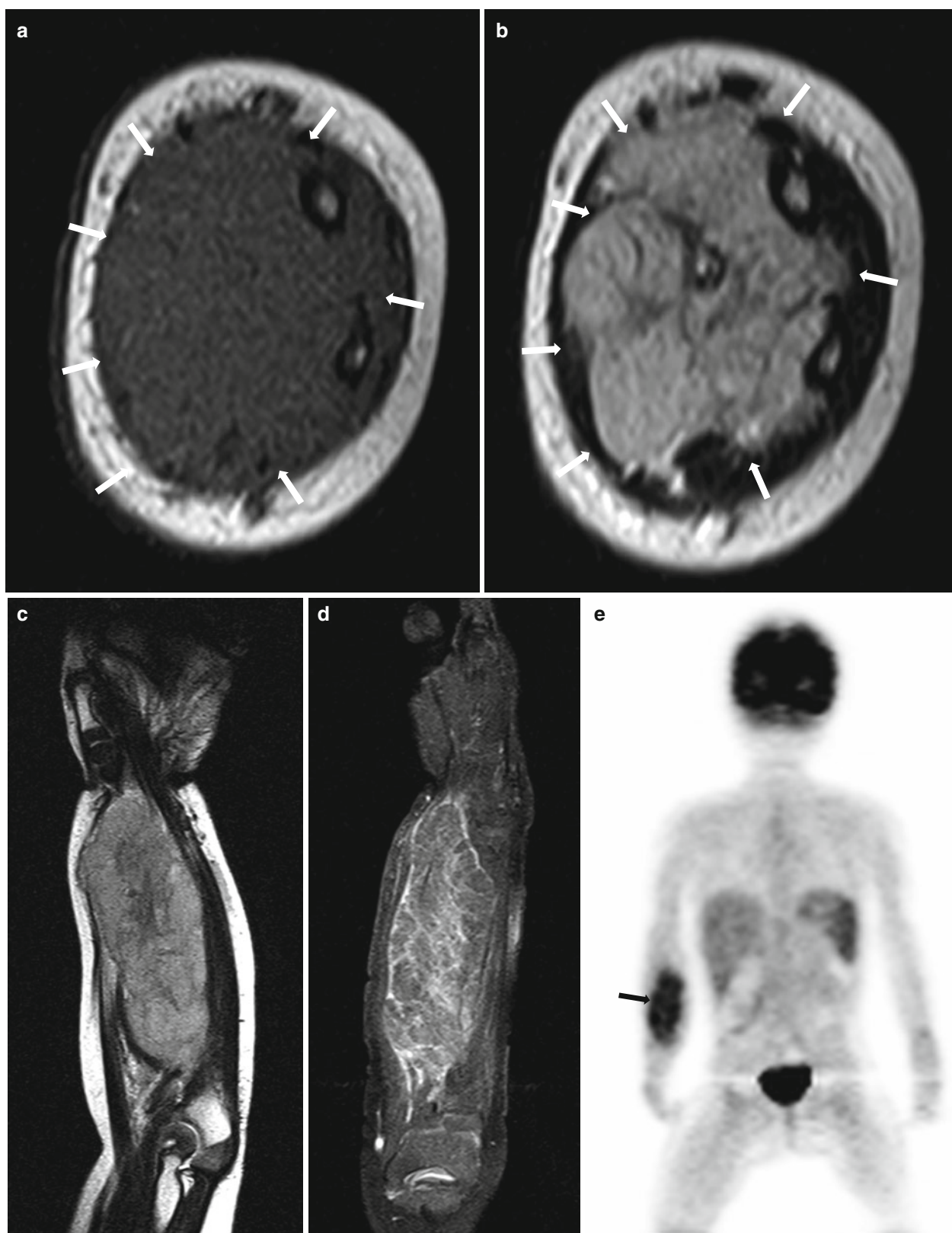


Fig. 29.18 Rhabdomyosarcoma in the arm of a 1-year-old boy. (a) Axial T1-weighted MR image shows a mass (*arrows*) with isointense signal intensity compared to muscle. (b) Axial T2-weighted MR image of the mass (*arrows*) shows heterogeneous hyperintense signal compared to muscle. (c) Coronal T2-weighted MR image shows elongated

mass with heterogeneously high signal intensity. (d) Sagittal gadolinium-enhanced fat-suppressed T1-weighted MR image shows heterogeneous enhancement. (e) 18F-fluorodeoxyglucose (FDG) positron-emission tomography-computed tomography (PET-CT) image shows high FDG uptake of the mass (*arrow*)

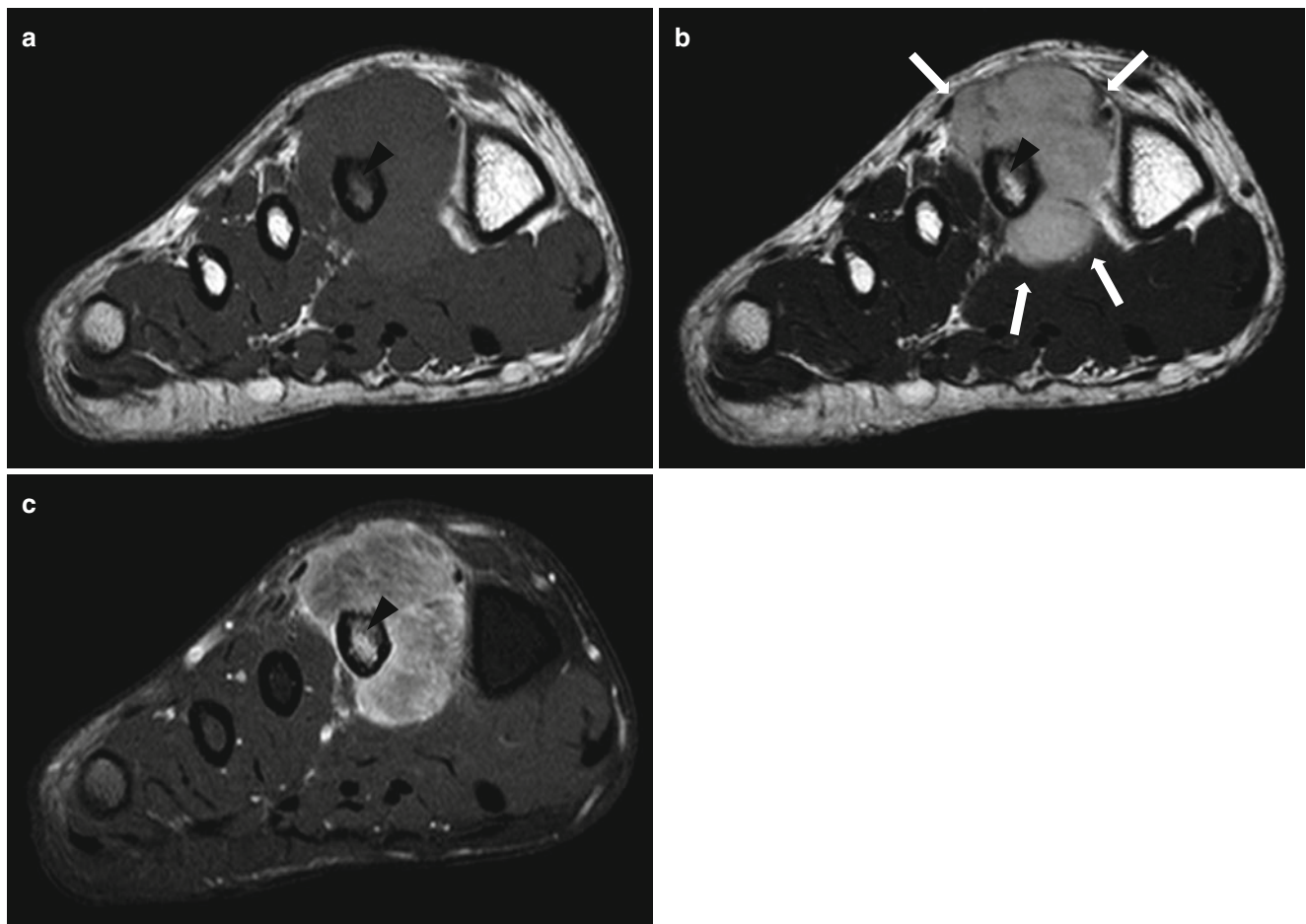


Fig. 29.19 Alveolar rhabdomyosarcoma in foot of a 13-year-old boy. (a) Axial T1-weighted MR image shows a mass with isointense signal intensity compared to muscle. (b) Axial T2-weighted MR image of the mass shows a lobulated border of the mass (*arrows*) showing heterogeneously high signal intensity compared to muscle. (c) Axial gadolin-

ium-enhanced fat-suppressed T1-weighted MR image shows heterogeneous enhancement. Marrow signal change of the second metatarsal bone on all images (*arrowheads* in **a**, **b**, and **c**) suggests the tumor invasion

29.4.18 Synovial Sarcoma

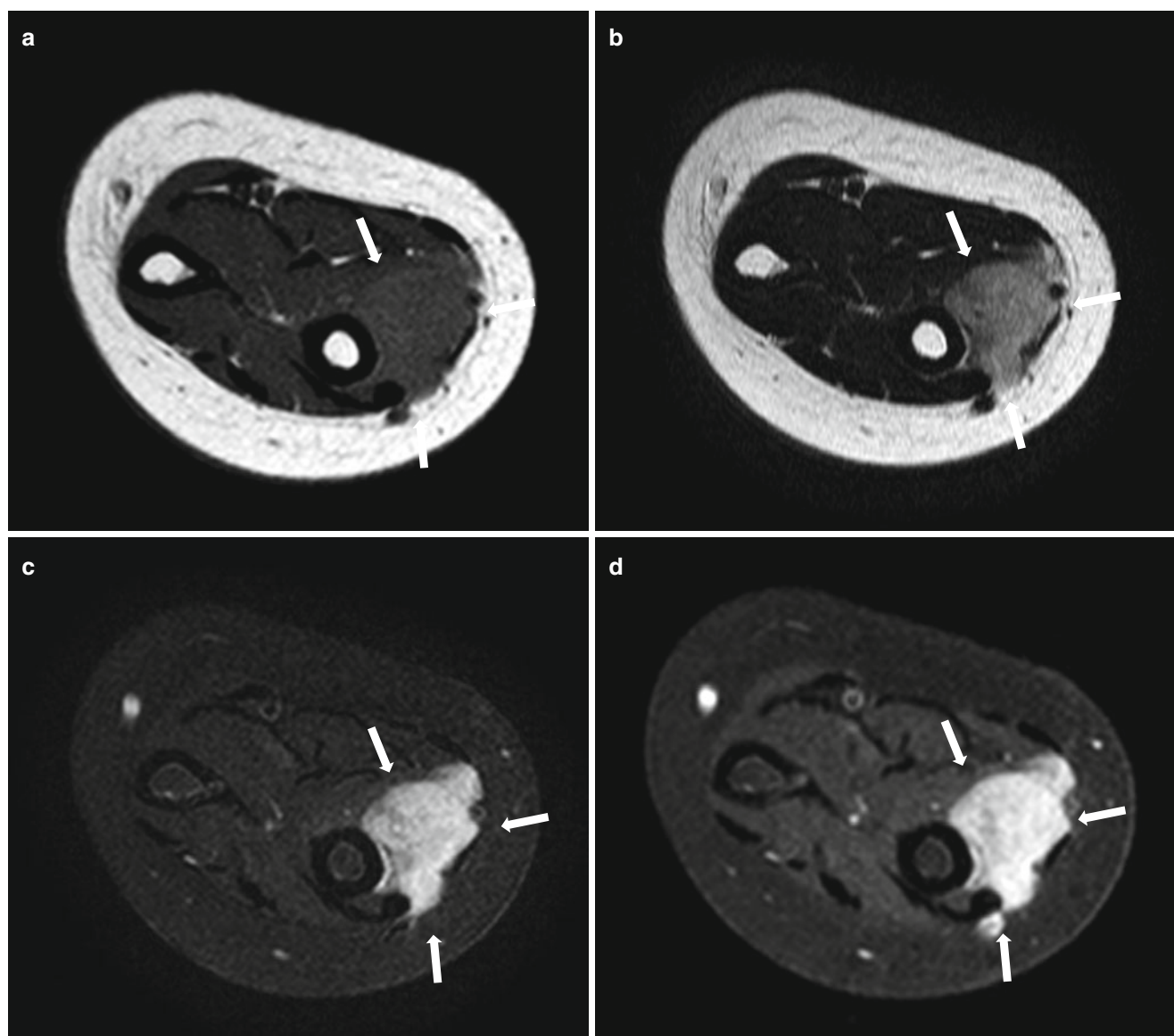


Fig. 29.20 Synovial sarcoma in arm of a 10-year-old girl. (a) Axial T1-weighted MR image shows a mass (*arrows*) with isointense signal relative to muscle. (b) Axial T2-weighted MR image shows the lobulated border of the mass (*arrows*) with heterogeneously high signal

intensity. (c) Axial fat-suppressed T2-weighted MR image of the mass (*arrows*) shows bright signal intensity. (d) Axial gadolinium-enhanced fat-suppressed T1-weighted MR image shows diffuse heterogeneous enhancement of the mass (*arrows*)

29.4.19 Infantile Fibrosarcoma

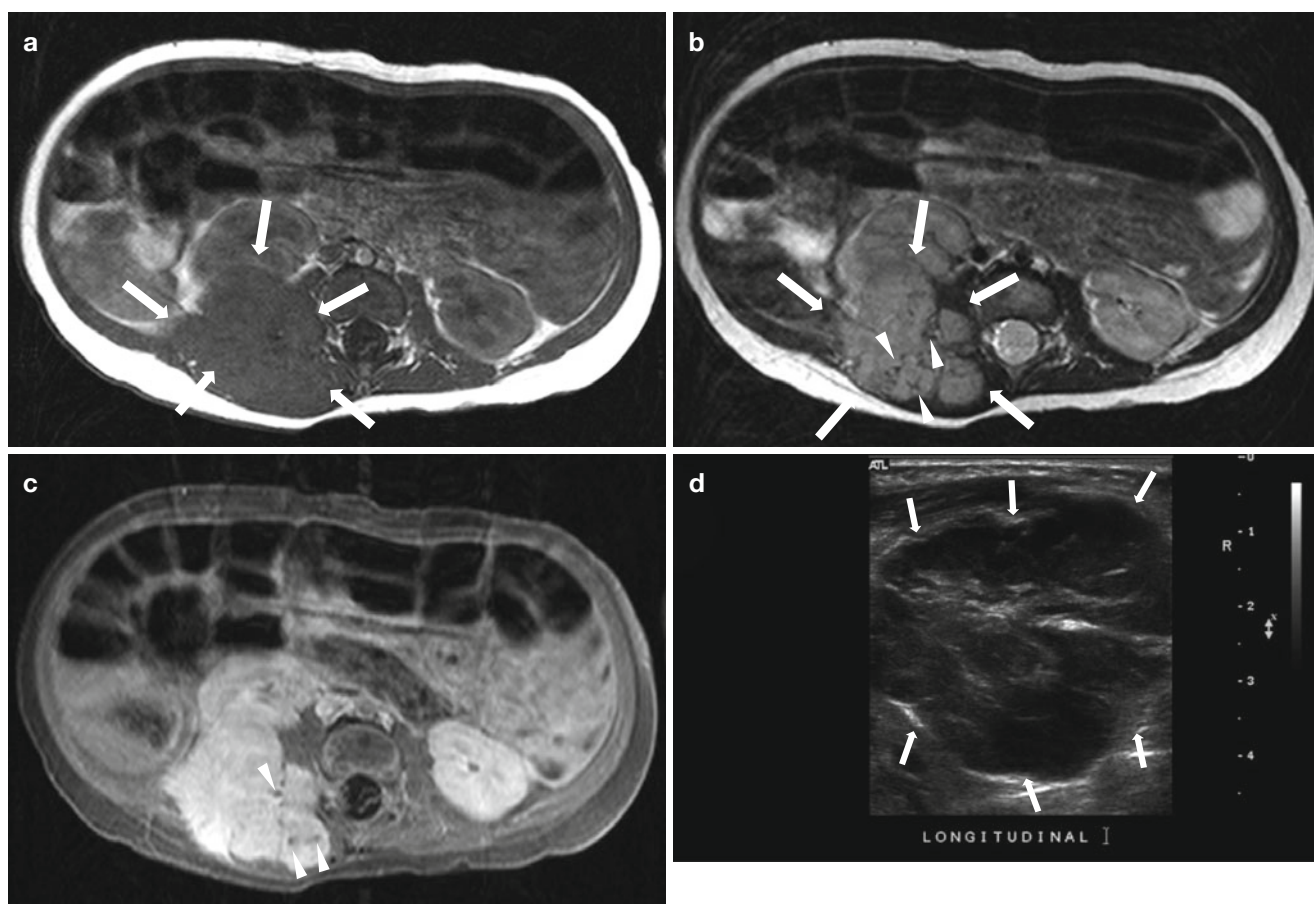


Fig. 29.21 MR images and US of a 2-month-old boy with infantile fibrosarcoma. **(a)** Axial T1-weighted MR image of the abdomen reveals a mass (*arrows*) showing isointense signal relative to the unaffected muscles. **(b)** Axial T2-weighted MR image shows well-defined lobulated mass (*arrows*) involving the right paravertebral muscles and retroperitoneal space. This mass shows diffuse inhomogeneously hyperintense signal with scattered area of low-signal foci (*arrowheads*).

(c) Axial gadolinium-enhanced fat-suppressed T1-weighted MR image shows diffuse enhancement of the mass. The low-signal foci seen on T2-weighted image are not enhanced partly (*arrowheads*), which presumably suggest that the region is composed of collagen fibers. **(d)** US shows lobulated contour of the mass (*arrows*) with mainly heterogeneously hypoechoic echogenicity.

29.4.20 Sclerosing Epithelioid Fibrosarcoma

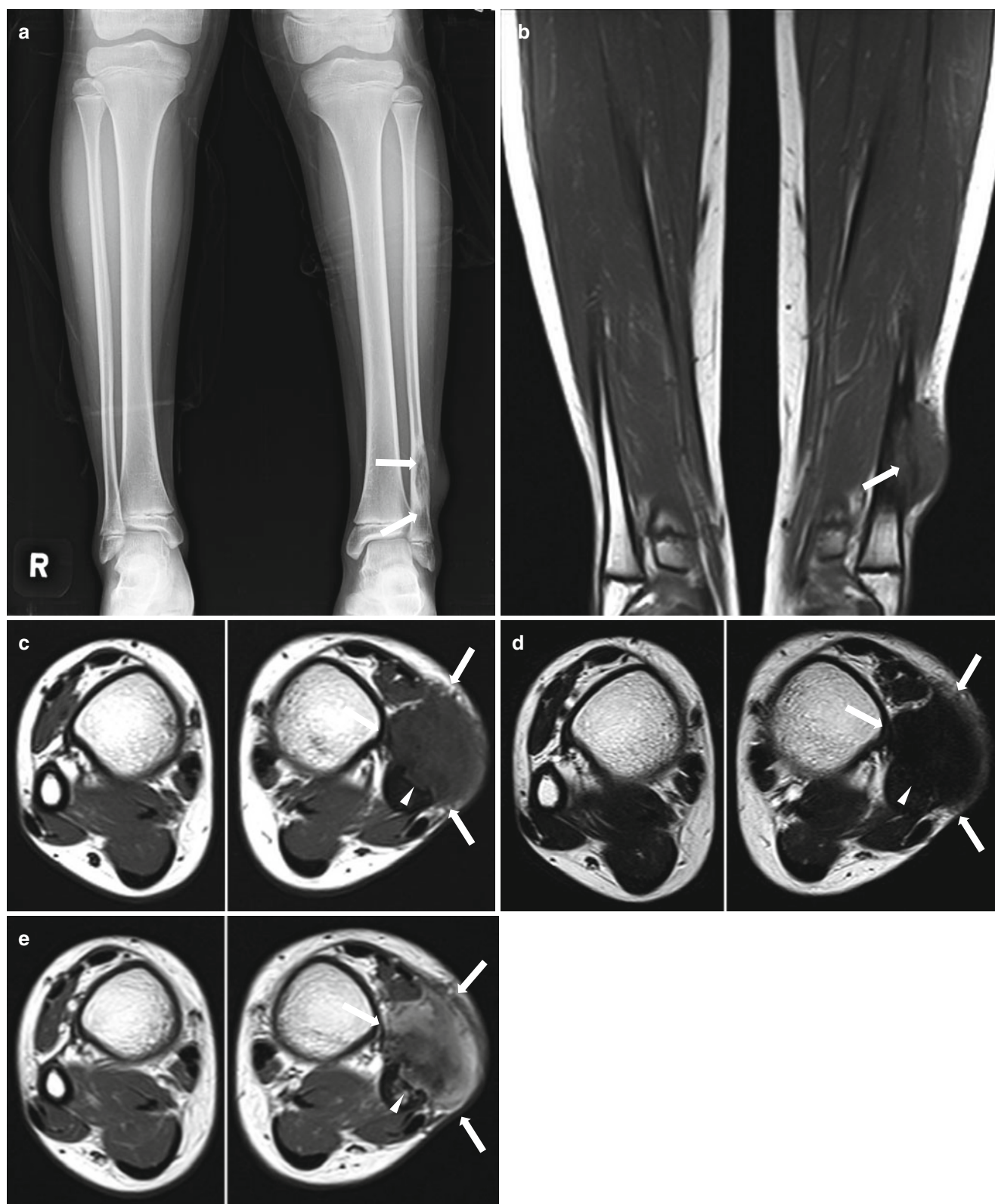


Fig. 29.22 Sclerosing epithelioid fibrosarcoma in lower leg of a 10-year-old boy. (a) Radiography of the lower leg reveals a soft tissue mass density and an osteolytic lesion of the adjacent distal fibular meta-diaphysis (arrows). (b) Coronal T1-weighted MR image shows invasion of fibula by the mass (arrow). (c, d, e) Well-defined soft tissue

mass (arrows) is seen on axial T1-weighted (c), axial T2-weighted (d), and axial gadolinium-enhanced T1-weighted (e) MR images with invasion of adjacent fibula (arrowheads). It shows dark signal intensity on T2WI (d) and shows heterogeneous enhancement after gadolinium enhancement (e)

29.4.21 Alveolar Cell Soft Part Sarcoma

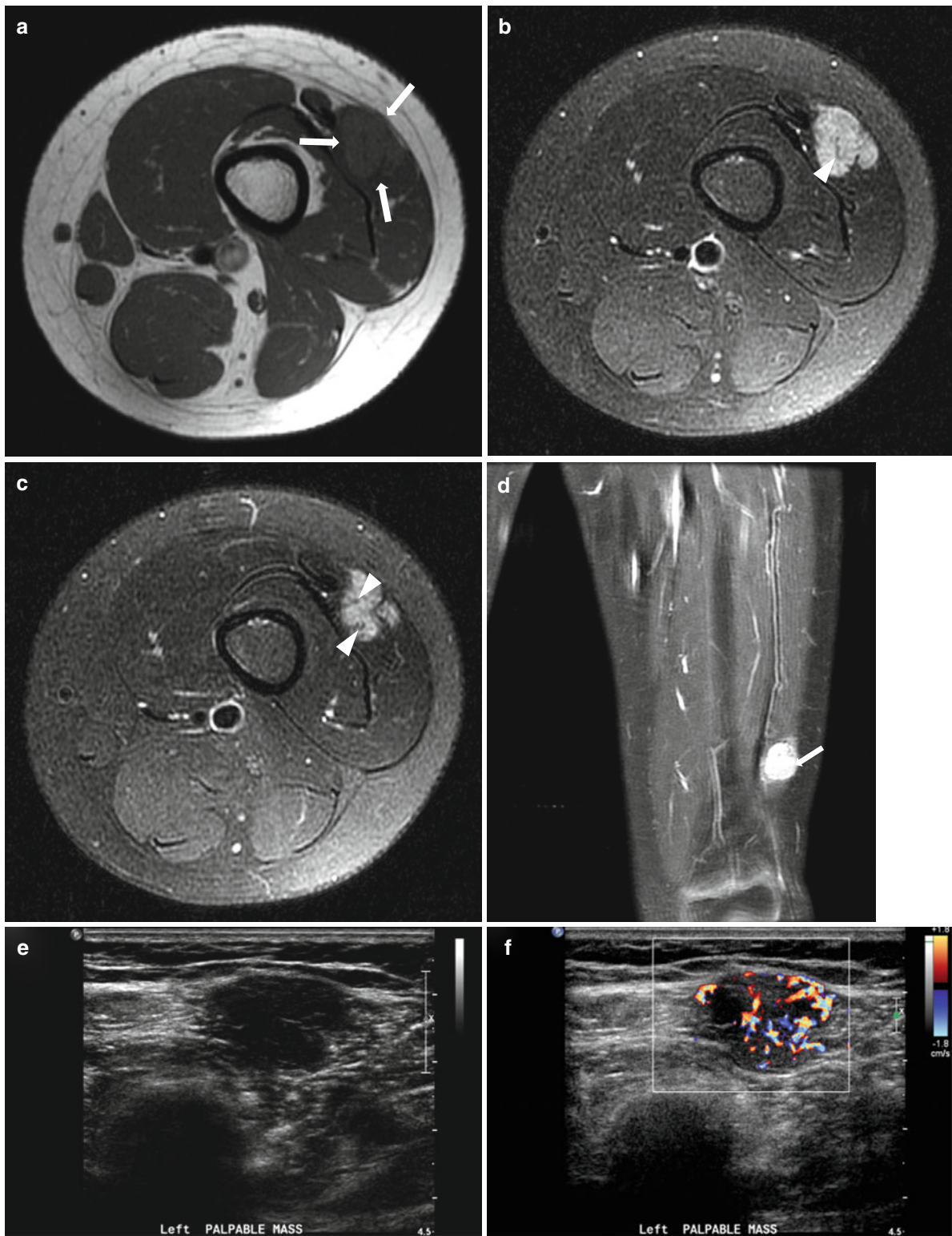


Fig. 29.23 Alveolar cell soft part sarcoma in thigh of a 10-year-old girl. (a) Axial T1-weighted MR image shows a mass in vastus lateralis muscle showing mildly hyperintense signal compared to muscle (arrows). (b, c) Axial fat-suppressed T2-weighted MR images show a well-defined mass with hyperintense signal intensity. Low signal spots,

presumably flow-related voids (arrowheads), are evident. (d) Coronal gadolinium-enhanced fat-suppressed T1-weighted MR image shows avid enhancement of the mass. (e) US image shows hypoechoic mass with lobulated border. (f) Color Doppler US image shows high vascularity of the mass

29.4.22 Angiosarcoma

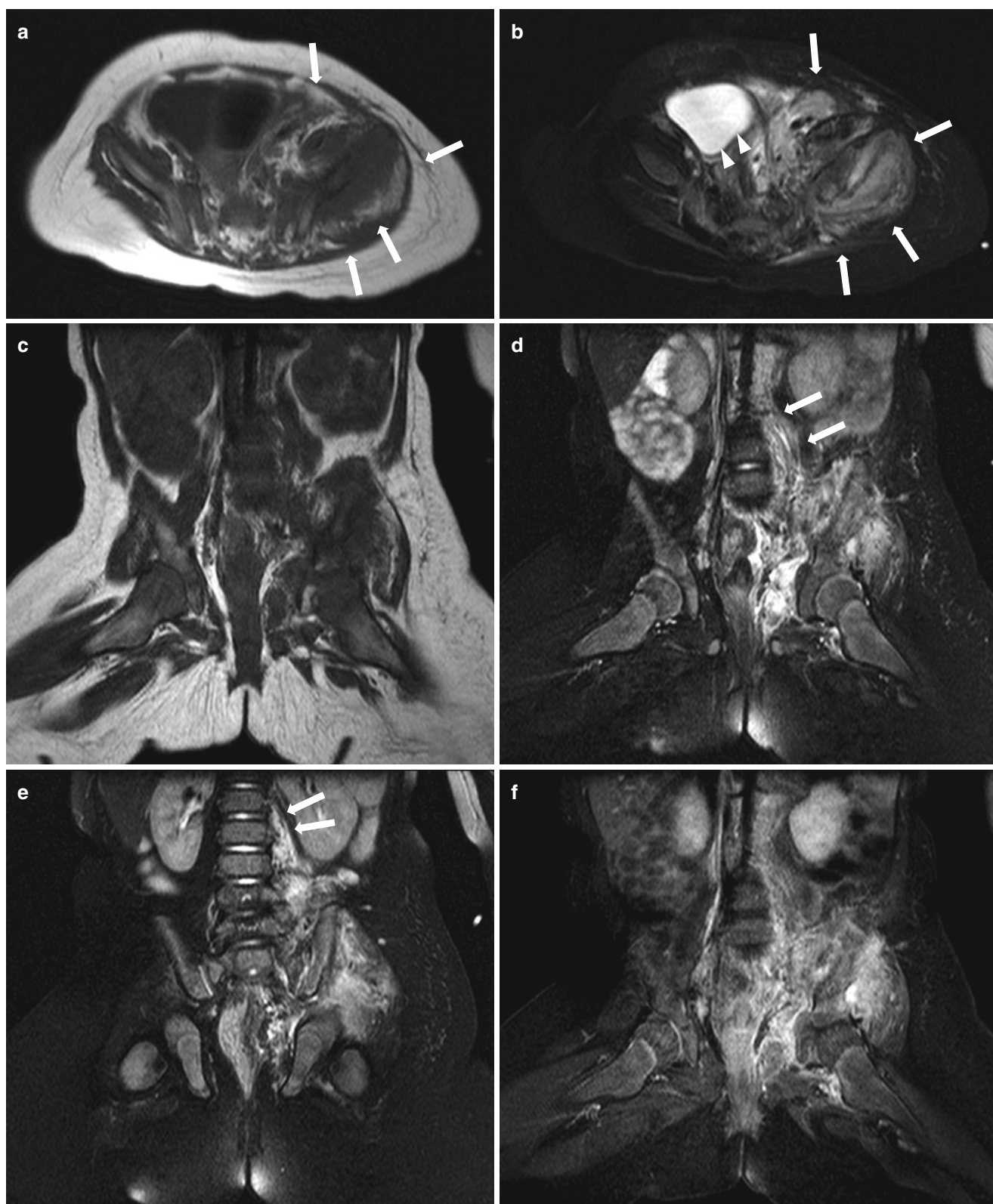


Fig. 29.24 Angiosarcoma in pelvis of a 5-month-old boy. (a) Axial T1-weighted MR image shows isointense soft tissue mass (*arrows*) relative to muscle involving Lt. pelvis with iliac bone destruction. (b) Axial fat-suppressed T2-weighted MR image shows the ill-defined infiltrative mass (*arrows*) with heterogeneous high signal intensity. Urinary bladder is compressed by the mass (*arrowheads*). (c, d, e)

Coronal T1-weighted MR image (c) and coronal fat-suppressed T2-weighted MR image (d, e) show ill-defined infiltrative soft tissue mass in pelvic cavity and extending psoas muscle (d, *arrows*) and paravertebral muscles (e, *arrows*). (f) Coronal gadolinium-enhanced T1-weighted MR image shows heterogeneous enhancement of the mass

29.4.23 Burkitt Lymphoma

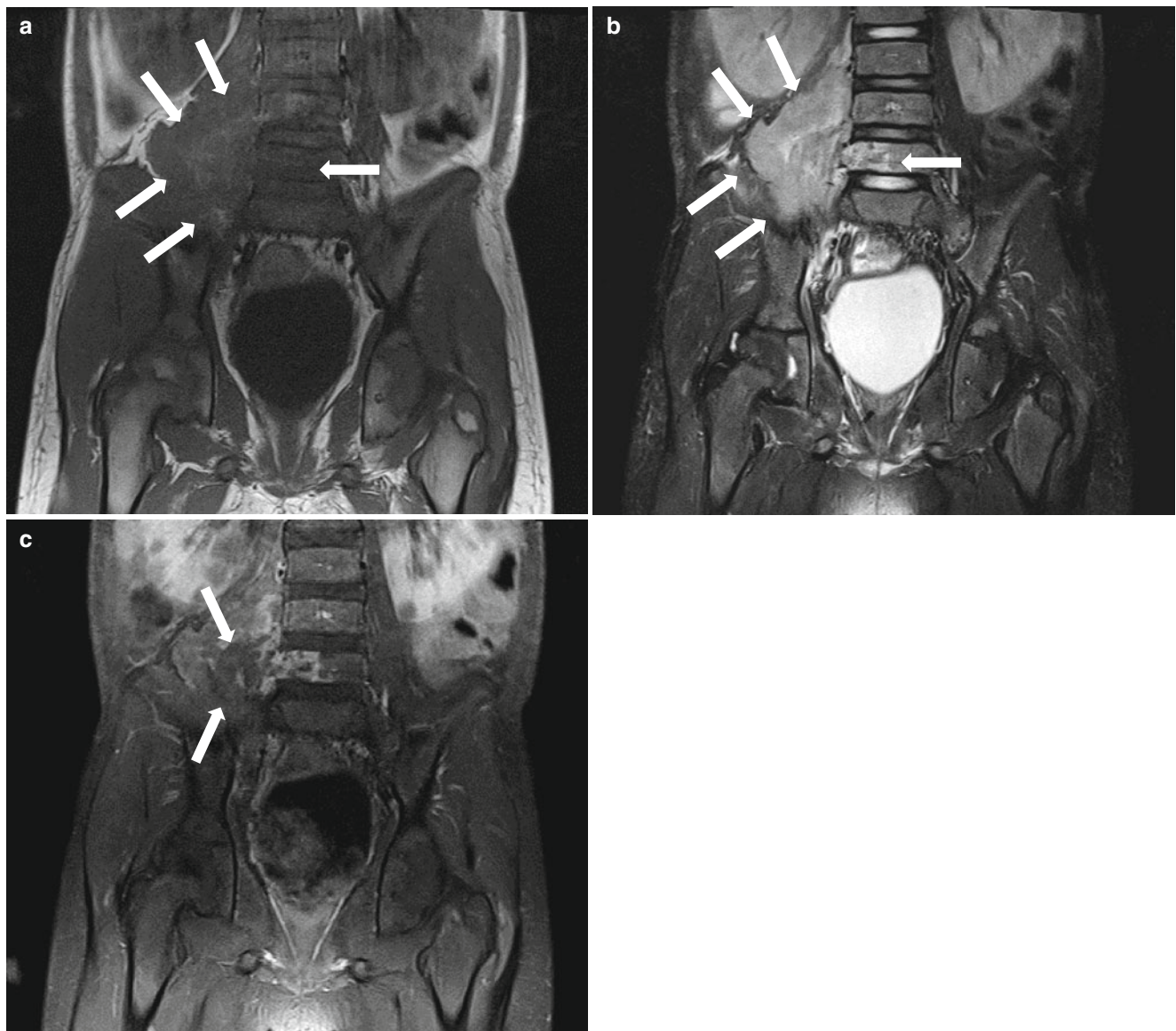


Fig. 29.25 Burkitt lymphoma in a 7-year-old boy. (a) Coronal T1-weighted MR image shows a mass (*arrows*) with heterogeneously hyper- and isointense signal to muscle. (b) Coronal fat-suppressed T2-weighted MR image shows lobulated mass (*arrows*) with heteroge-

neous high signal intensity involving Rt. psoas muscle and L5 vertebral body. (c) Coronal gadolinium-enhanced T1-weighted MR image shows heterogeneously weak enhancement of the mass with presumable central necrotic portion (*arrows*)

References

- Ayadi L, Khabir A. Pediatric angiosarcoma of soft tissue: a rare clinicopathologic entity. *Arch Pathol Lab Med*. 2010;134:481–5.
- Chun CW, Jee WH, Park HJ, et al. MRI features of skeletal muscle lymphoma. *AJR Am J Roentgenol*. 2010;195:1355–60.
- Emery K. The soft tissues. In: Slovis TL, Caffey J, editors. *Caffey's pediatric diagnostic imaging*. 11th ed. Philadelphia: Mosby/Elsevier; 2008.
- Flors L, Leiva-Salinas C, Maged IM, et al. MR imaging of soft-tissue vascular malformations: diagnosis, classification, and therapy follow-up. *Radiographics*. 2011;31:1321–40.
- Flynn JM, Bashyal RK, Yeager-McKeever M, et al. Acute traumatic compartment syndrome of the leg in children: diagnosis and outcome. *J Bone Joint Surg Am*. 2011;93:937–41.
- Jamis-Dow CA, Turner J, Biesecker LG, et al. Radiologic manifestations of Proteus syndrome. *Radiographics*. 2004;24:1051–68.
- Laffan EE, Ngan BY, Navarro OM. Pediatric soft-tissue tumors and pseudotumors: MR imaging features with pathologic correlation: part 2. Tumors of fibroblastic/myofibroblastic, so-called fibrohistiocytic, muscular, lymphomatous, neurogenic, hair matrix, and uncertain origin. *Radiographics*. 2009;29:e36.
- Lim HW, Im SA, Lim GY, et al. Pilomatricomas in children: imaging characteristics with pathologic correlation. *Pediatr Radiol*. 2007;37:549–55.
- Lohrmann C, Bartholoma JP, Foeldi E, et al. Magnetic resonance lymphangiography in Klippel-Trenaunay syndrome. *Br J Radiol*. 2007;80:e188–92.
- McDowell HP. Update on childhood rhabdomyosarcoma. *Arch Dis Child*. 2003;88:354–7.
- Navarro OM. Soft tissue masses in children. *Radiol Clin North Am*. 2011;49:1235–1259, vi–vii.
- Navarro OM, Laffan EE, Ngan BY. Pediatric soft-tissue tumors and pseudo-tumors: MR imaging features with pathologic correlation: part 1. Imaging approach, pseudotumors, vascular lesions, and adipocytic tumors. *Radiographics*. 2009;29:887–906.
- Resnick D. Soft tissue disorders. In: Resnick D, editor. *Diagnosis of bone and joint disorders*. 4th ed. Philadelphia: Saunders; 2002.
- Shelly MJ, Hodnett PA, MacMahon PJ, et al. MR imaging of muscle injury. *Magn Reson Imaging Clin N Am*. 2009;17:757–773, vii.
- Stein-Wexler R. MR imaging of soft tissue masses in children. *Magn Reson Imaging Clin N Am*. 2009;17:489–507, vi.
- Suh JS, Cho J, Lee SH, et al. Alveolar soft part sarcoma: MR and angiographic findings. *Skeletal Radiol*. 2000;29:680–9.

Tae Yeon Jeon and So-Young Yoo

Contents

30.1	Introduction	952
30.2	Imaging	952
30.3	Spectrum of Skeletal Trauma	952
30.3.1	Incomplete Fracture	952
30.3.2	Toddler's Fracture	952
30.3.3	Physeal Injury	953
30.3.4	Elbow Fracture	953
30.3.5	Apophyseal Injury	953
30.3.6	Stress Fracture	954
30.3.7	Nonaccidental Injury (Child Abuse)	954
30.3.8	Normal Anatomy and Variants Mimicking Trauma	955
30.4	Illustrations: Pediatric Skeletal Trauma	956
30.4.1	Incomplete Fracture	956
30.4.2	Toddler's Fracture	957
30.4.3	Physeal Injury	959
30.4.4	Elbow Fracture	962
30.4.5	Apophyseal Injury	964
30.4.6	Nonaccidental Injury (Child Abuse)	966
30.4.7	Normal Anatomy and Variants Mimicking Trauma	967
	References	968

T.Y. Jeon, M.D. (✉) • S.-Y. Yoo, M.D.
 Department of Radiology, Samsung Medical Center,
 Sungkyunkwan University School of Medicine,
 50, Ilwon-dong, Kangnam-gu, Seoul 135-710, Korea
 e-mail: hathor97.jeon@samsung.com; somatom25@hanmail.net

30.1 Introduction

Pediatric bone affords unique fracture patterns that are different from those of adult bone. The growing bone develops from a relatively porous and elastic type of biomechanical material to the more rigid bone of an adult. The unique anatomic features of pediatric bone are the presence of thick periosteum and physis.

The thicker and stronger periosteum in children makes fractures heal more rapidly with greater remodeling than in adults. Periosteal new bone formation can be expected to be radiographically present 7–10 days after injury. Children tend to heal completely, and delayed union or nonunion rarely occurs.

The ligaments and tendons are stronger than the physis, and they are more resistant to stress or torsional force, resulting in physeal fractures in the setting of trauma. Physeal and epiphyseal injuries can lead to significant growth disturbance.

30.2 Imaging

Plain radiography is the first-line imaging modality and very few patients require imaging beyond radiography. It is important to note that when imaging skeletal trauma, radiographs should be obtained with at least two orthogonal views. Comparative views are often necessary to determine whether radiographs are abnormal (Ducou Le Pointe and Sirinelli 2005).

Ultrasound (US) is particularly valuable in the infants or young children with radiolucent cartilaginous epiphyseal injuries which are not visible by radiography. US usually can establish the epiphyseal separation injury of the shoulder or elbow in newborns, as a result of birth trauma. US can identify hemarthrosis, subperiosteal hematoma, cortical fracture, and musculo-ligamentous injuries. It is also indicated for detection of retained foreign bodies in the extremities (Oestreich 1991).

CT plays a role in cases of complex injuries (comminuted fracture, fractures involving epiphysis) or pelvic fracture to define the extent of fracture and its relationship to the joint surface, the size of fracture segments, and the presence of intra-articular loose bodies. CT is also useful to demonstrate bone bridge formation and consequent deformities following physeal injuries (Brown et al. 2004; Lemburg et al. 2010).

MRI allows for excellent evaluation of cartilage, bone marrow, ligaments, tendons, and surrounding soft tissues. Cartilage-specific sequences (such as 3D volume SPGR) are helpful to demonstrate unossified epiphyseal and metaphyseal injuries as well as bone bridge formation after physeal injuries (Ecklund and Jaramillo 2002; Jaramillo and Laor 2008). Radiographically occult fractures or stress fractures are often best imaged with MRI, representing a fracture line within the edematous marrow.

30.3 Spectrum of Skeletal Trauma

30.3.1 Incomplete Fracture

In young infants and children, incomplete fractures are common due to the increased elasticity of the bones. Incomplete fractures do not involve the entire width of the bone, with a portion of cortex remaining intact. They are often quite subtle, and comparative views are mandatory in some cases.

30.3.1.1 Buckle or Torus Fracture

This fracture results from a compression failure of bone that typically occurs at the junction of the metaphysis and diaphysis (Fig. 30.1). The more cortical diaphyseal bone may be pushed into the more porous metaphyseal bone (Fig. 30.2). It is commonly seen in the wrist, resulting from a fall on the outstretched hand. Caution should be paid not to miss a slight cortical irregularity at the distal ends of the long bones (Hernandez et al. 2003). As buckle fractures heal, a zone of sclerosis develops along the fracture line.

30.3.1.2 Greenstick Fracture

This fracture results from a bending or an angulation force, and the cortical break occurs on the convex side, while the concave side undergoes plastic deformation with a cortical discontinuity, similar to bending of a green twig (Fig. 30.3). This type of fracture usually involves the mid-diaphysis, and common sites are radius, ulna, fibula, and clavicle. The greenstick fracture may be the strong risk factor for repeat fracture, occurring in 84~100 % of forearm refractures (Schwarz et al. 1996; Park et al. 2007).

30.3.1.3 Plastic Bending Fracture

This is a bowing fracture of a long bone subjected to a longitudinal compression or angulation force and can be considered the precursor of the classic greenstick fractures. They occur most often in the forearm and fibula, associated with fracture or dislocation of the adjacent bone, for example, bowing of the ulna associated with radial head dislocation. Plastic bending fracture usually produces no periosteal new bone formation and significant callus formation, and the bone may be permanently deformed. If it occurs in a child younger than 4 years or less than 20°, the angulation could correct with growth (Mabrey and Fitch 1989).

30.3.2 Toddler's Fracture

In young children less than 6 years of age, torsion of the foot may produce a spiral, nondisplaced fracture of the distal tibia due to the relatively strong periosteum compared to the elastic bone (Fig. 30.4). It occurs after low-energy trauma and manifests as limping or refusal to walk without witnessed traumatic episodes. Less commonly it involves proximal

tibia, fibula, tarsal, or metatarsal bones. The initial radiograph may be inconspicuous and often even normal. When a fracture is suspected but not visualized on routine view, oblique view may be helpful since this fracture is sometimes seen only on a single view. A technetium bone scan and MRI may reveal increased uptake or low-signal linear fracture. Repeat radiographs 1–2 weeks after injury usually demonstrate periosteal new bone formation or sclerosis (Tenenbein et al. 1990; Halsey et al. 2001) (Fig. 30.5).

30.3.3 Physeal Injury

Physeal injury is relatively common in children representing 15 % of all fractures. It is usually classified by the Salter-Harris classification (Salter and Harris 1963), which is listed by the location of the fracture (Fig. 30.6).

In the type I injury, the epiphysis is separated completely from the metaphysis and the surrounding bone is not involved (Fig. 30.7). This can be easily missed and malalignment between epiphysis and metaphysis can be a clue with asymmetrical widening of the physis compared with the contralateral side. Slipped capital femoral epiphysis, which is epiphysiolysis of the proximal femoral epiphyseal ossification center, is a kind of type I injury (Fig. 30.8). In the type II injury, the most common Salter-Harris fracture pattern, the injury courses through the physis and extends to the metaphysis; the epiphysis is not involved in the injury (Fig. 30.9). A type III fracture is intra-articular and traverses the epiphysis and physis. A type IV fracture is also intra-articular and involves the epiphysis as well as metaphysis. The fracture line courses through the physis. It occurs most often in the lateral condyle of the distal humerus and the distal tibia. A type V fracture is a crush injury to the physis, resulting from compressive force (Ogden 1981). Although this injury is uncommon, it has a high risk of growth disturbance. The higher the grades of injuries, the greater likelihood that the physis will be damaged, which can result in complications such as premature closure of the physis, causing limb shortening or angular growth deformity (Czitrom et al. 1981). MRI demonstrates premature closure of the physis earlier and provides valuable prognostic information regarding size and location of the physeal bridging (Borsa et al. 1996; Ecklund and Jaramillo 2002) (Fig. 30.10).

30.3.4 Elbow Fracture

Fractures around the elbow are among the most common fractures in children, but elbow fractures often are difficult to detect because of the complex developmental anatomy of the elbow. Understanding the normal ossification centers of the elbow is essential to avoid overlooking elbow injuries (Fig. 30.11a). Furthermore, attention to soft tissue findings

(positive fat pad signs) and normal osseous alignment (anterior humeral and radiocapitellar lines) (Fig. 30.11b) can help to identify subtle fractures. Imaging evaluation should always begin with conventional elbow radiography that includes anteroposterior and lateral views. Oblique views and comparison views of the opposite limb may also be helpful.

Hyperextension or valgus stress usually resulting from falling on the outstretched arm is the most common cause of elbow fractures. The supracondylar fractures are the most common elbow fractures in children under 8 years of age, followed by lateral condyle fracture and medial epicondyle fracture (Lins et al. 1999; Carson et al. 2006). The majority of supracondylar fractures result from extension injuries, and they can be identified with the use of the anterior humeral line (Fig. 30.12a,b). Lateral condyle fractures are considered to be Salter-Harris type IV fractures, as the fracture line crosses the metaphysis, physis, and epiphysis (Fig. 30.12c, d). Medial epicondyle fractures (the so-called Little League elbow) are avulsion injuries caused by traction from the ulnar collateral ligament or the forearm flexor muscles that arise from the medial epicondyle (Fig. 30.12e). Approximately half of these fractures are associated with elbow dislocations (Carlioz and Abols 1984). Elbow fractures have high rate of complications such as neurovascular injury and angulation deformity (Campbell et al. 1995).

30.3.5 Apophyseal Injury

Apophyseal injuries typically occur in active adolescents between the ages of 8 and 15 years as the apophysis is the weakest point of the musculotendinous osseous complex. There are three types of apophyseal injuries: (1) acute avulsion fracture caused by sudden, unbalanced muscle contraction; (2) chronic nonunion avulsion fracture; and (3) apophysitis caused by overuse from repetitive microtrauma (Micheli 1987).

Avulsion fractures of the pelvic apophyses are common, and they are usually caused by sudden contraction of the hamstrings, adductor magnus, iliopsoas, and hip flexors in athletes participating in sports (Figs. 30.13 and 30.14). The ischial tuberosity which is the attachment site of hamstring muscle group is the most common site (Jaimes et al. 2012).

Apophysitis may be associated with bony protuberance which can be misinterpreted as neoplastic or infectious process. It is a kind of stress fracture of the apophysis, analogous to a nondisplaced Salter-Harris type I injury. Apophysitis commonly affects the tibial tuberosity (Osgood-Schlatter disease), the medial epicondyle (Little League elbow), the calcaneal apophysis (Sever's disease), the bottom of the patella (Sinding-Larsen-Johansson syndrome), and the base of the fifth metatarsal bone (Iselin's disease).

Although not usually required, CT is helpful in the diagnosis if radiographic findings of avulsion injury are equivocal or if the injury is not in the acute phase. MRI often shows extensive soft tissue and bone marrow edema that may be misinterpreted as an aggressive lesion. Recognition of characteristic imaging features and familiarity with musculotendinous anatomy will aid in accurate diagnosis of avulsion injuries.

Most of patients with apophyseal injuries respond well to nonsurgical management with no long-term functional limitations. Surgical treatment is only considered when significant fracture displacement occurs (Kocher and Tucker 2006).

30.3.6 Stress Fracture

Stress fractures are divided into fatigue fractures and insufficiency fractures. Fatigue fractures occur when normal bone is injured by abnormal burden, while insufficiency fractures occur when abnormal bone is subject to normal burden. Pediatric stress fractures usually refer to fatigue fractures, resulting from chronic and repetitive workload. These injuries are more common in female athletes than men. The common sites of stress fractures in children include the tibia, fibula, metatarsals, cuboid, calcaneus, and femur.

They should be considered in a child with pain on weight bearing without radiographic evidence of fracture in the acute setting. Follow-up examinations may be useful to demonstrate periosteal reaction or sclerosis, which confirm the diagnosis (Gaeta et al. 2005). Although radionuclide scans can be helpful in evaluating the pain, MRI is currently considered the best diagnostic modality for stress fracture, with its high sensitivity and specificity (Jaramillo and Shapiro 1998). Marrow edema appears as a zone of low signal intensity on T1-weighted and high signal intensity on STIR and T2-weighted MR images, while fracture line is depicted as linear low signal intensity on T1- and T2-weighted MR images. After contrast administration, the marrow edema enhances, which makes the fracture line more conspicuous (Jaimes et al. 2012).

30.3.7 Nonaccidental Injury (Child Abuse)

Skeletal injuries are well-known manifestations of nonaccidental injuries. About half of skeletal injuries in children younger than 1 year of age are attributable to physical abuse. Recognition of abuse-related injuries is very important to protect the abused children, as well as their siblings.

In cases of suspected child abuse, conventional radiography is the primary screening examination. International guidelines for the skeletal survey have been revised collaboratively by the American College of

Table 30.1 Standard skeletal surveys for known or suspected non-accidental injury (ACR-SPR practice guideline for skeletal surveys in children, revised 2011)

Appendicular skeleton
Humeri (AP)
Forearms (AP)
Hands (PA)
Femurs (AP)
Lower legs (AP)
Feet (AP)
Axial skeleton
Thorax (AP, lateral, right, and left obliques), to include ribs, thoracic, and upper lumbar spine
Pelvis (AP), to include the midlumbar spine
Lumbosacral spine (lateral)
Cervical spine (lateral)
Skull (frontal and lateral)

Radiology (ACR) and the Society for Pediatric Radiology (SPR) (American College of Radiology and Society for Pediatric Radiology 2011) (Table 30.1). Skeletal survey should consist of a complete depiction of each anatomic region with separate radiographic exposure. Each extremity should be obtained in at least the frontal projection. Axial skeleton should be imaged in two projections. Additional views as needed may include the Towne view of the skull and lateral projections of the appendicular skeleton. In cases of equivocal findings, repeat skeletal survey (approximately 14 days after initial examination) has shown to increase sensitivity and specificity (Kleinman et al. 1996). Bone scintigraphy is indicated as a supplemental study when the skeletal survey is negative in cases of suspected child abuse (Conway et al. 1993).

The skeletal survey should determine a level of specificity based on the nature, location, and chronicity of injury; however, no fracture in itself is pathognomic for child abuse. Fractures with high specificity of child abuse include rib fractures (especially posterior), classic metaphyseal lesions, scapular fractures, spinous process fractures, and sternal fractures. The classic metaphyseal lesions (Fig. 30.15a) are also known as corner or bucket-handle fractures, commonly caused by shearing force in manual assaults. Rib fractures are highly specific findings of abuse in cases of traumatic brain lesion, and they usually result from severe squeezing and shaking of the chest (Fig. 30.15b). Fractures with moderate specificity comprise multiple fractures, fractures of different ages, epiphyseal separations, vertebral body fractures and subluxations, digital fractures in nonambulatory children (Fig. 30.15c), and complex skull fractures. Common skeletal injuries with low specificity for child abuse consist of clavicular fractures (Fig. 30.15b), long bone shaft fractures, linear skull fractures, and subperiosteal new bone formation (Kleinman 1998; van Rijn and Sieswerda-Hoogendoorn 2012).

Metabolic bone disease such as rickets, skeletal dysplasia, osteogenesis imperfecta, and osteomyelitis can mimic child abuse. Thus, they should be excluded as a predisposing cause of multiple fractures.

30.3.8 Normal Anatomy and Variants Mimicking Trauma

Awareness of the normal developmental changes and variants in children is important, in order not to make errors in the interpretation of pediatric imaging. Irregularities of mineralization and secondary ossification centers are often confused with fracture. The ischiopubic synchondrosis can normally appear as asymmetric and bulky lesion, mimicking healing

fracture (Fig. 30.16). Irregularity of distal femoral epiphysis is commonly observed on radiographs in children and is frequently bilateral, but not always symmetrical (Fig. 30.17). Normal physiologic periosteal new bone formation is most pronounced between 1 and 4 months, and most frequently involves femur, tibia, and humerus. Classic metaphyseal lesions which are seen in child abuse should be differentiated from normal metaphyseal variants including beaking or fragmentation (Kellenberger 2009; Keats and Anderson 2012).

Although most anatomic variants are asymptomatic, some variants such as os trigonum and os naviculare may be indeed clinically significant, causing pain (Lawson 1994). Thus, correlation with the radiographic findings and the clinical context is vital, and symptomatic variants can be further evaluated by bone scintigraphy or MRI.

30.4 Illustrations: Pediatric Skeletal Trauma

30.4.1 Incomplete Fracture



Fig. 30.1 Buckle fracture of the right distal radius in a 7-year-old girl with falling on outstretched hand. Right wrist radiograph shows a typical buckle fracture with outward buckling of the cortex (arrow)



Fig. 30.3 Greenstick fracture in a 4-year-old girl who fell off a bike. Lateral radiograph shows greenstick fracture on the convex side of the radius (arrow) and buckle fracture on the concave side of ulna (arrowhead)

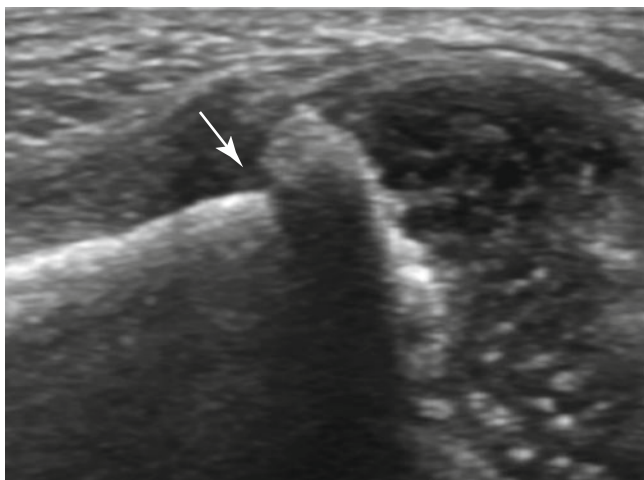


Fig. 30.2 Buckle fracture in a newborn boy who presented with irritability. Ultrasonography of the right humerus shows buckle fracture at the junction of metaphyseal and diaphyseal bone (arrow). The more porous metaphyseal bone fails in compression

30.4.2 Toddler's Fracture

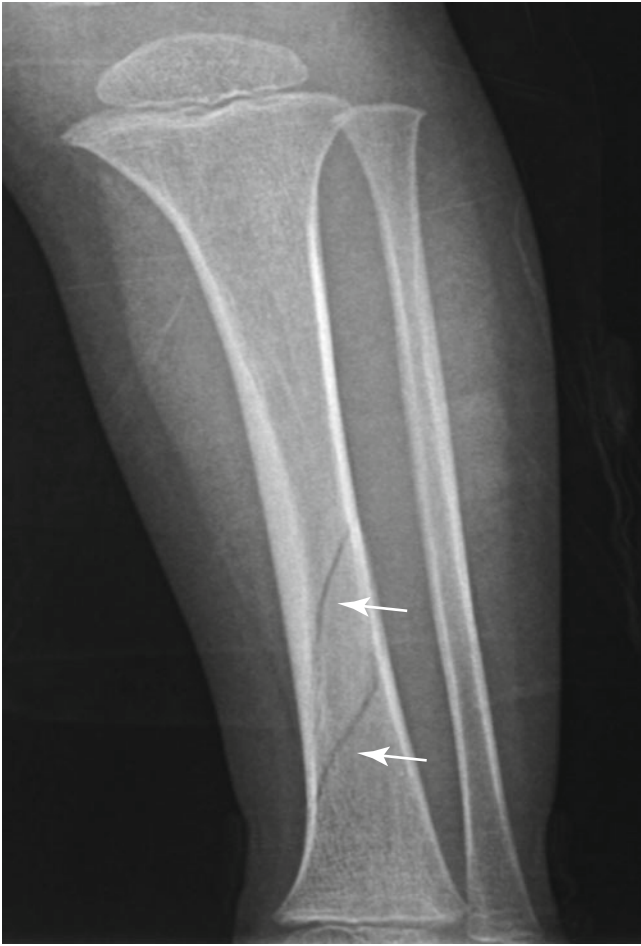


Fig. 30.4 *Toddler's fracture in a 3-year-old boy.* Radiograph of the left lower leg shows spiral, nondisplaced fractures (*arrows*) through the distal tibia

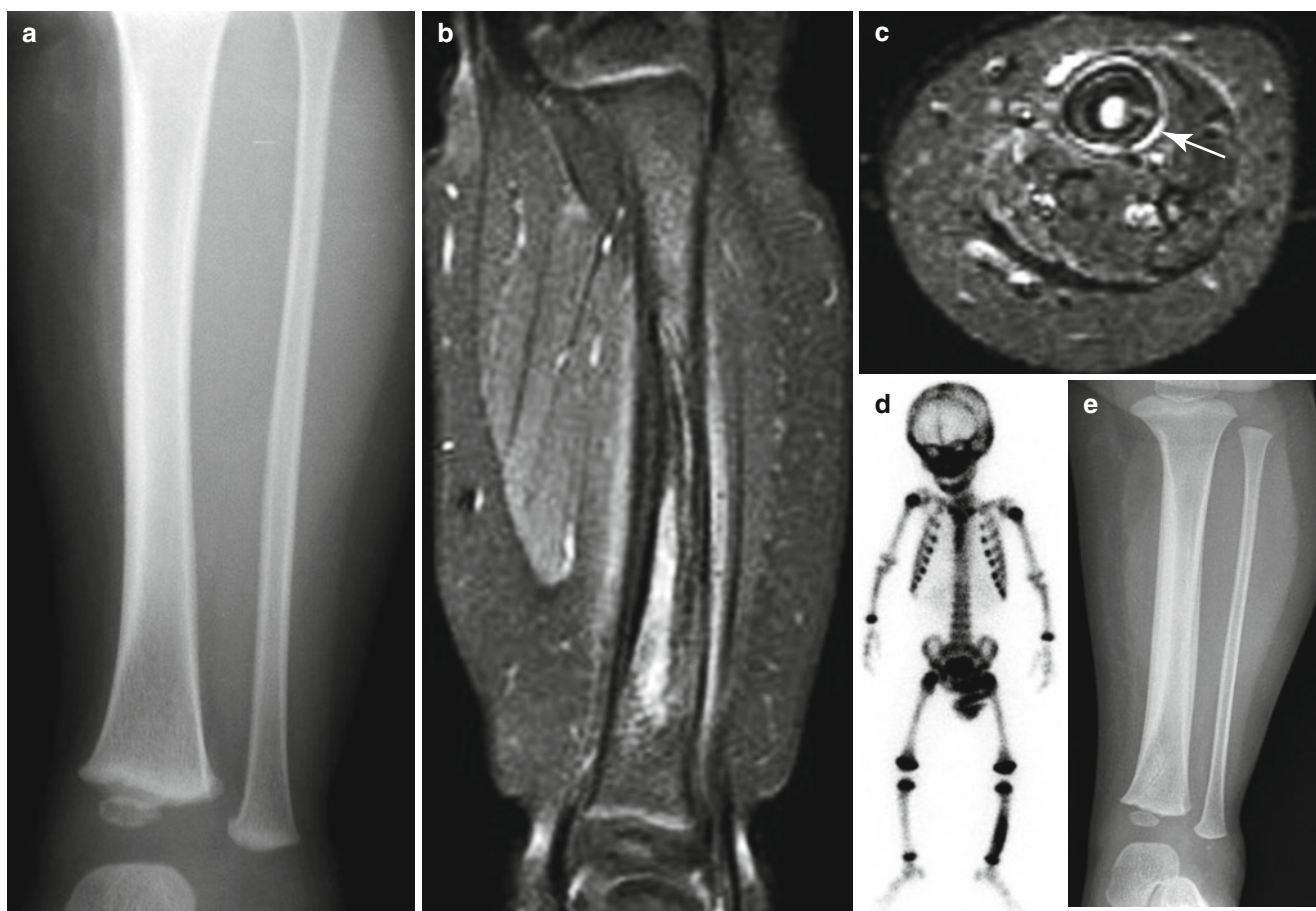


Fig. 30.5 Toddler's fracture in a 2-year-old boy presented with limping gait. (a) Initial radiograph of left lower leg shows no bony abnormalities. (b, c) Fat-suppressed contrast-enhanced T1-weighted sagittal (b) and axial (c) MR images show fracture line (arrow in c) with surrounding marrow edema and periosteal reaction. (d) Bone scan shows increased uptake in the left tibia shaft. (e) Follow-up radiograph after 2 weeks reveals cortical thickening with periosteal reaction of the tibia (Courtesy of Dr. Lee HJ, Keimyung University School of Medicine)

rounding marrow edema and periosteal reaction. (d) Bone scan shows increased uptake in the left tibia shaft. (e) Follow-up radiograph after 2 weeks reveals cortical thickening with periosteal reaction of the tibia (Courtesy of Dr. Lee HJ, Keimyung University School of Medicine)

30.4.3 Physeal Injury

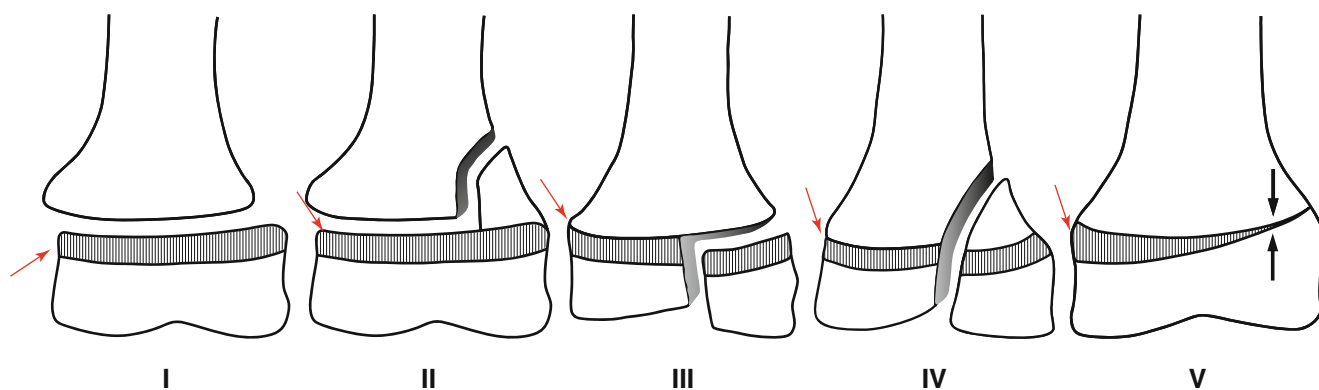


Fig. 30.6 Illustrations of the Salter-Harris classification of physeal injuries (see text)

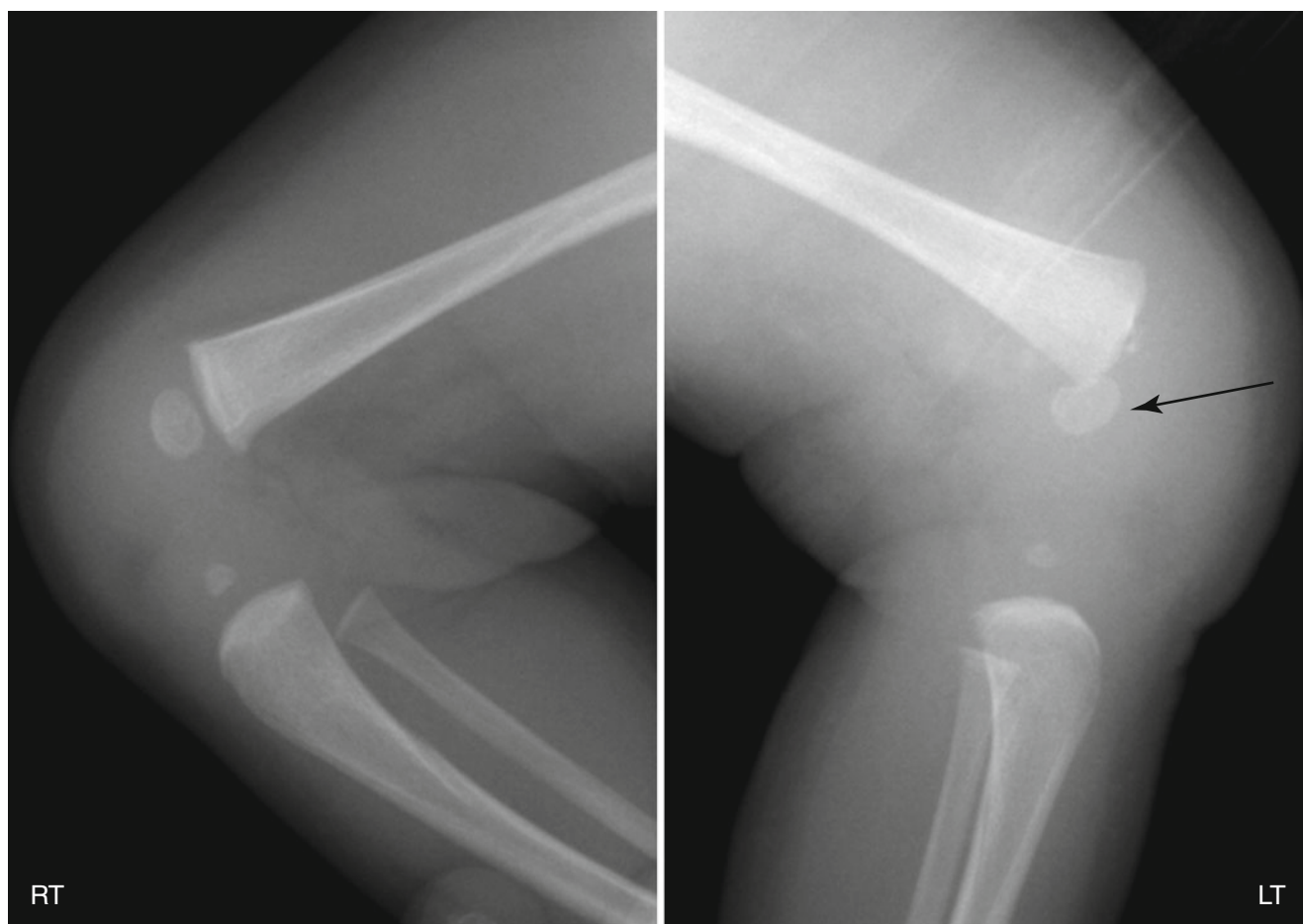


Fig. 30.7 *Salter-Harris type I fracture in a newborn baby.* Lateral radiographs of the knee show a complete posterior slip of epiphysis of the left distal femur (arrow) due to a fracture through the physis (Courtesy of Dr. Kim IO, Seoul National University Children's Hospital)

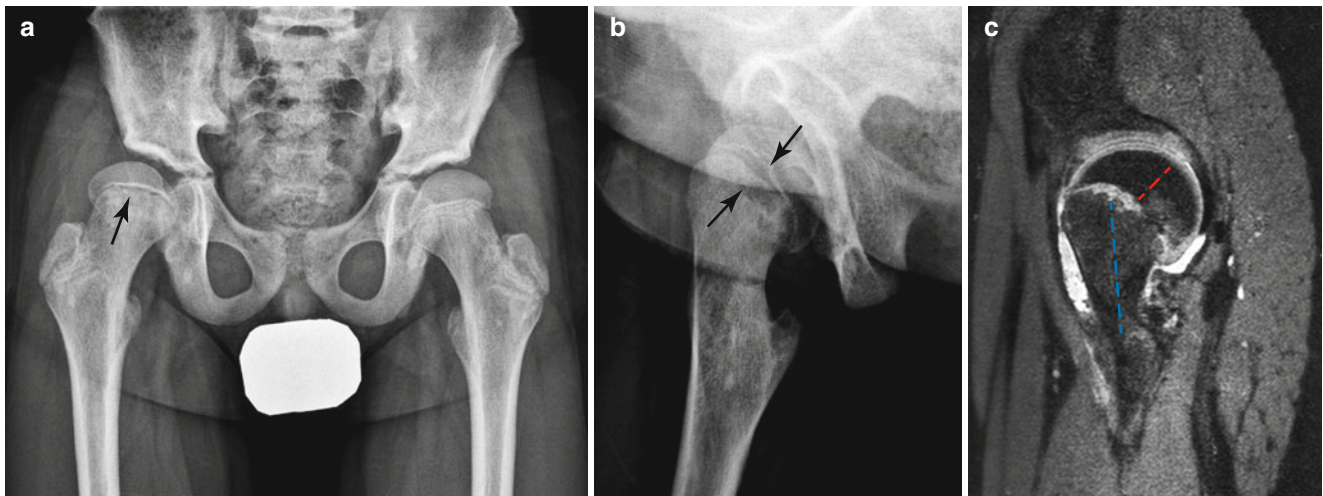


Fig. 30.8 Slipped capital femoral epiphysis, which is an example of Salter-Harris type 1 fracture, in a 12-year-old boy with hip pain. (a, b) Anteroposterior with neutral position and oblique radiographs show asymmetric widening of the physis of the right proximal femur (arrows). (c) 3D VISTA sagittal MR image depicts posterior rotation of the femoral epiphysis (red dotted line) relative to the metaphysis (blue dotted line), indicating retroversion at the epiphyseal-metaphyseal junction

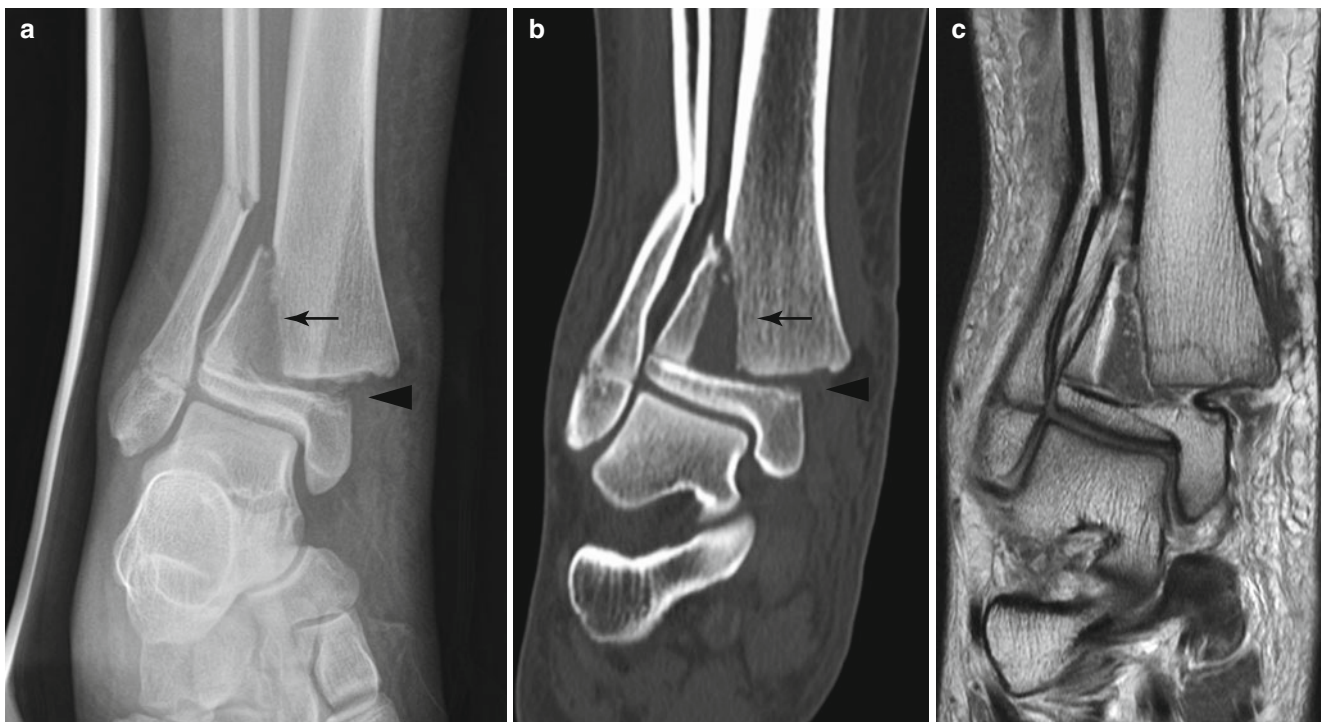


Fig. 30.9 Salter-Harris type 2 fracture in an 11-year-old girl who had sustained a fall from height and injured her right ankle. (a, b) Anteroposterior radiograph and coronal CT image of the right ankle show a displaced metaphyseal fracture (arrow) and an extension into the physis (arrowhead) with a fibular shaft fracture by an abduction injury. (c) Proton density coronal MR image also demonstrates Salter-Harris type 2 fracture involving right ankle with soft tissue swelling and effusion

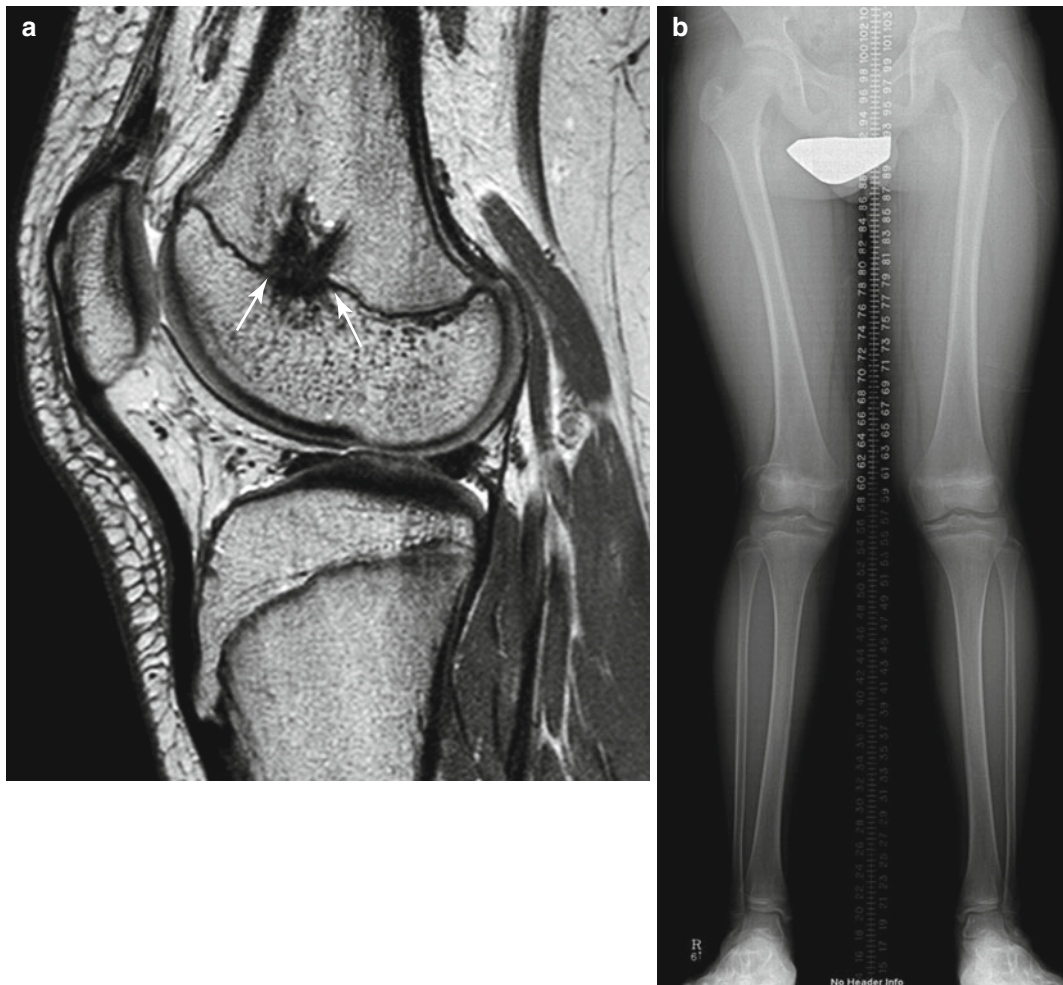


Fig. 30.10 Premature physal closure in a 13-year-old boy after Salter-Harris type 2 fracture. **(a)** Sagittal proton density MR image shows a bony bridge (arrows) along the central, lateral aspect of the

right distal femoral physis. **(b)** Anteroposterior radiograph of lower extremities shows a right valgus deformity with limb shortening

30.4.4 Elbow Fracture

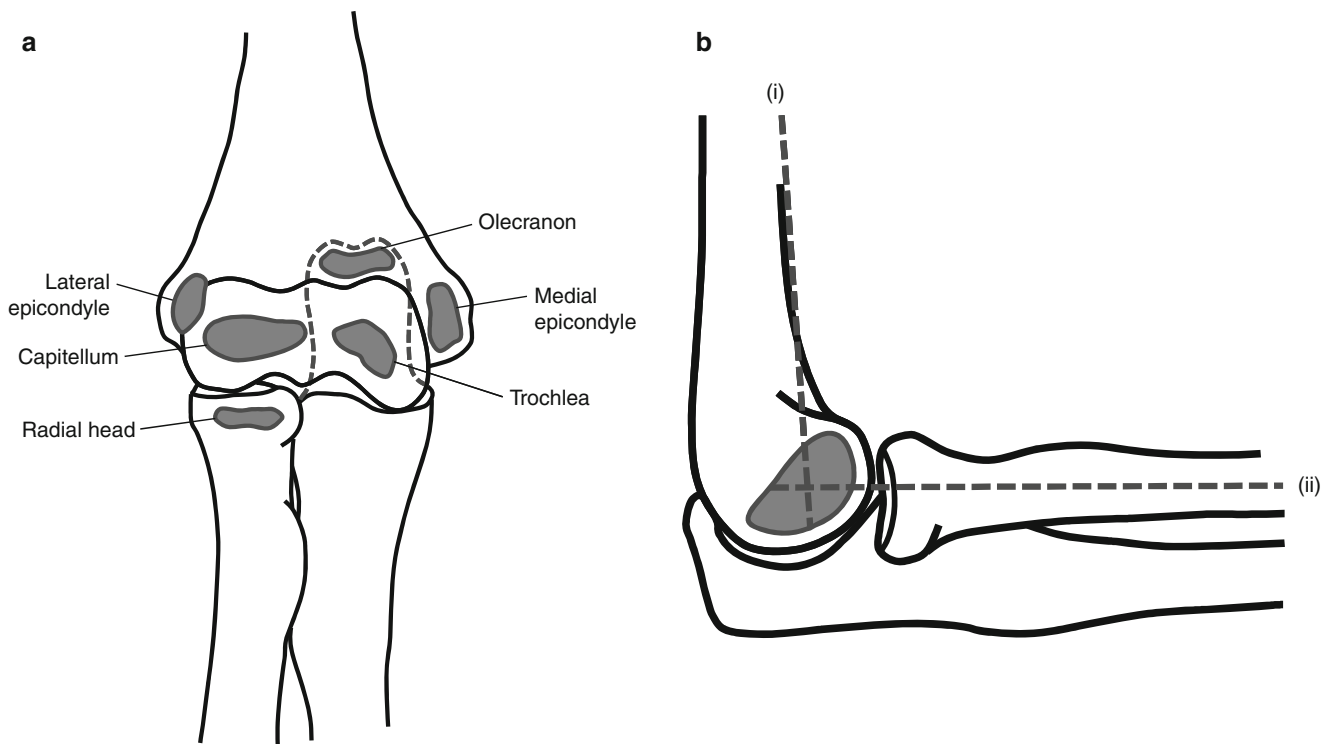


Fig. 30.11 Illustrations of the secondary ossification centers and normal osseous alignment of the elbow. **(a)** This order of the appearance of ossification center is specified in the mnemonic C-R-I-T-O-E (Capitellum, Radial head, Internal or medial epicondyle, Trochlea, Olecranon, External or lateral epicondyle). These appear at 2, 4, 6, 8,

10, and 12 years of age, respectively, and disappear 2 years later. **(b)** Anterior humeral line (i) on the lateral view along the anterior surface of the humerus should pass through the middle third of the capitellum. Radiocapitellar line (ii) drawn through the center of the radial neck should cross the center of the capitellum



Fig. 30.12 Elbow fractures. (a) Typical supracondylar fracture with posterior angulation of distal humeral fragment (*arrow*). (b) More subtle supracondylar fracture with posterior buckle (*arrow*). The anterior humeral line (*dotted line*) passes through the anterior third of the capitellum (C). Notice positive fat pad sign (*arrowheads*). (c) Displaced lateral condyle fracture. Anteroposterior view shows an obvious lateral

condyle fracture with lateral displacement of the fragment (*arrow*). (d) More subtle, nondisplaced lateral condyle fracture (*arrowheads*). The fracture line extends through the metaphysis of the lateral distal humerus just above the ossification center of the capitellum. (e) Avulsion fracture of the medial epicondyle (*arrow*) with marked unilateral soft tissue swelling along the medial elbow. C capitellum

30.4.5 Apophyseal Injury

Fig. 30.13 Common sites of pelvic avulsion fractures. ASIS anterior superior iliac spine, AIIS anterior inferior iliac spine

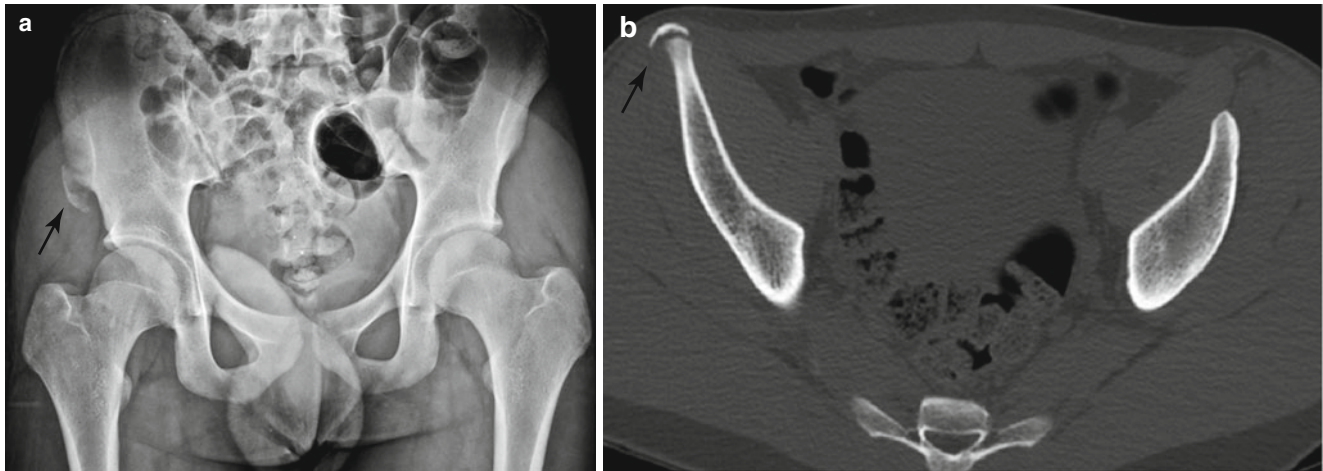
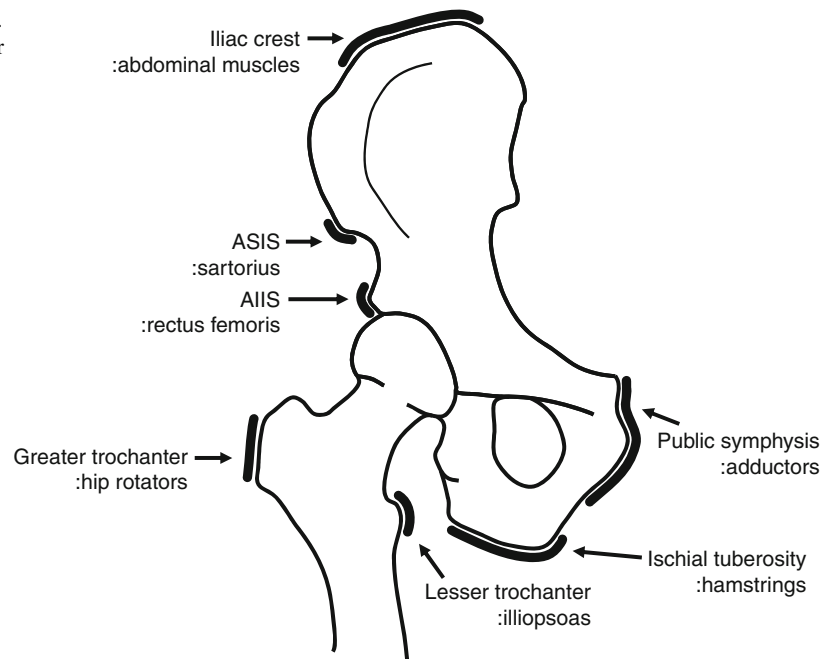


Fig. 30.14 Acute and chronic avulsion fracture of the pelvis. (a, b) Acute avulsion fracture of the anterior superior iliac spine (ASIS). Anteroposterior radiograph and axial CT scan of the pelvis show a curved, sharply margined bony fragment at the ASIS (arrows).

(c, d) Acute avulsion fracture of the anterior inferior iliac spine (arrows). (e–g) Chronic nonunion avulsion fracture. Anteroposterior radiograph and CT scans show a smoothly margined bony fragment of the right ischial tuberosity (arrows)



Fig. 30.14 (continued)

30.4.6 Nonaccidental Injury (Child Abuse)

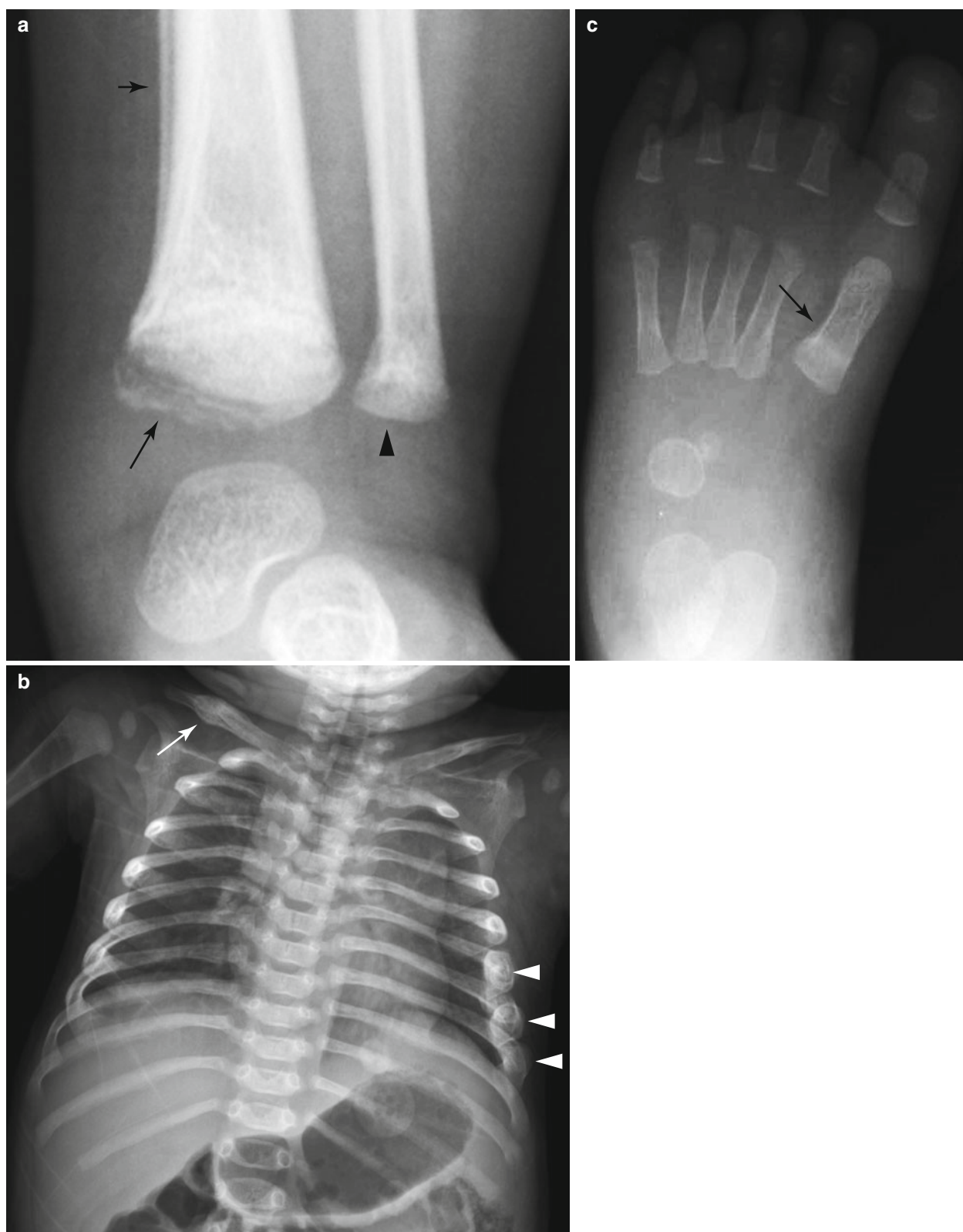


Fig. 30.15 *Skeletal findings of child abuse.* (a) Classic metaphyseal lesion in an abused 7-month-old boy. Anteroposterior radiograph of the ankle shows a rim of bone (*long arrow*) separated from the tibial shaft by the lucent metaphyseal fracture. There is subtle periosteal bone along the medial tibial shaft (*short arrow*). Classic metaphyseal lesion of the distal fibula is also faintly seen (*arrowhead*). (b) Multiple rib

fractures in an abused 4-month-old boy. Anteroposterior radiograph of the chest shows multiple healing rib fractures with callus formation on the left, lateral (*arrowheads*), and right clavicular fracture (*arrow*). This patient also has buckle fracture (c, *arrow*) of the base of the first metatarsal bone

30.4.7 Normal Anatomy and Variants Mimicking Trauma

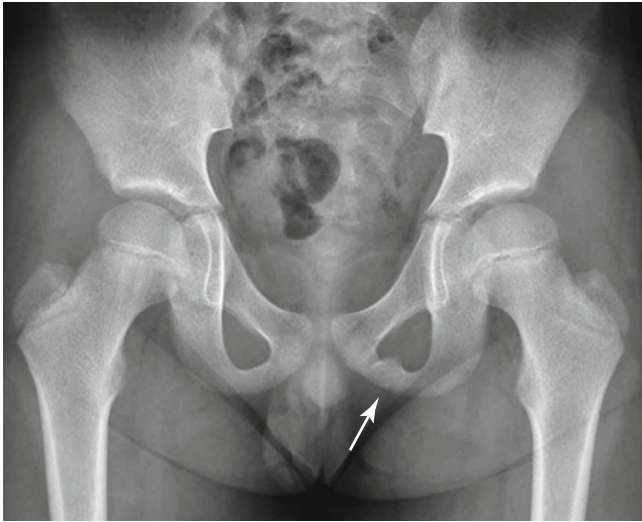


Fig. 30.16 *Asymmetric ischiopubic synchondrosis in an 8 year-old boy.* Anteroposterior pelvis radiograph shows asymmetrical bulging lesion (*arrow*), mimicking healing fracture with callus formation at the left ischiopubic junction

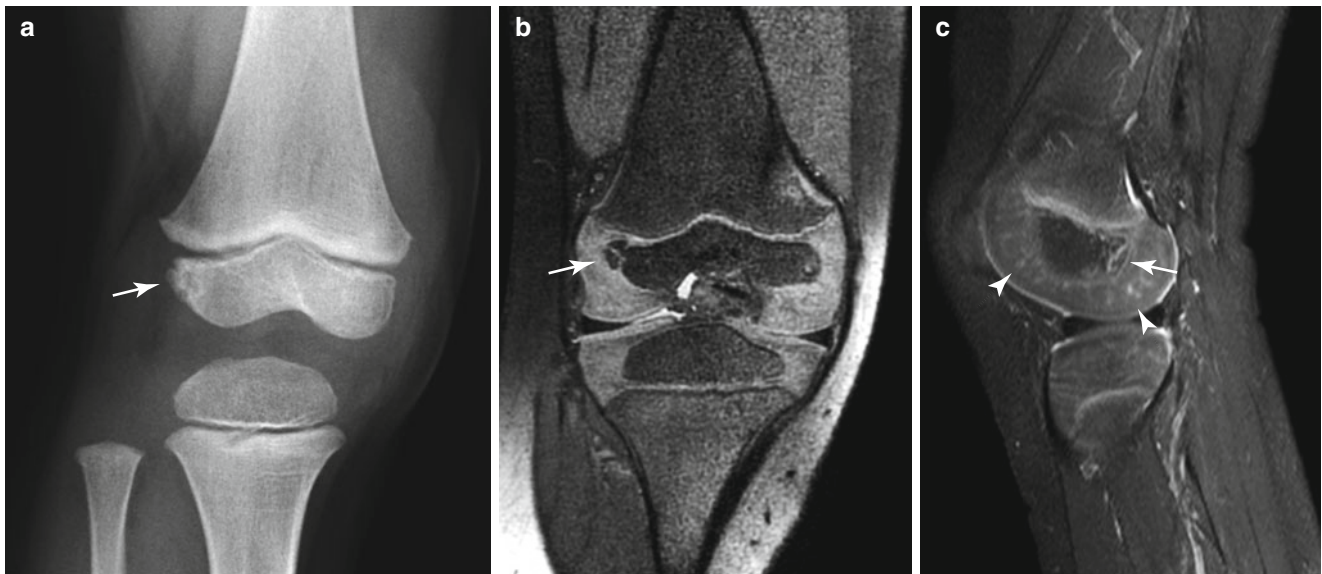


Fig. 30.17 *Irregularity of distal femoral epiphysis* (a) Anteroposterior radiograph of the right knee shows a marginal irregularity (*arrow*) at the lateral epiphysis of the distal femur. (b, c) Coronal proton density fat-suppression VISTA image (b) and sagittal contrast-enhanced T1-weighted image (c) show cortical irregularity and fragmentation

(*arrow*) at the distal epiphysis of lateral femoral condyle, posteriorly, but shows no marrow edema in the epiphysis. This appearance is considered normal. Note that normal vascular canals of epiphyseal cartilage aligned in a spoke-wheel pattern (*thin arrows*)

References

- American College of Radiology and Society for Pediatric Radiology (2011) ACR-SPR practice guideline for skeletal surveys in children, revised. American College of Radiology Res. 54.
- Borsa JJ, Peterson HA, Ehman RL. MR imaging of physeal bars. *Radiology*. 1996;199:683–7.
- Brown SD, Kasser JR, Zurakowski D, et al. Analysis of 51 tibial triplane fractures using CT with multiplanar reconstruction. *AJR Am J Roentgenol*. 2004;183:1489–95.
- Campbell CC, Waters PM, Emans JB, et al. Neurovascular injury and displacement in type III supracondylar humerus fractures. *J Pediatr Orthop*. 1995;15:47–52.
- Carloz H, Abols Y. Posterior dislocation of the elbow in children. *J Pediatr Orthop*. 1984;4:8–12.
- Carson S, Woolridge DP, Colletti J, et al. Pediatric upper extremity injuries. *Pediatr Clin North Am*. 2006;53:41–67, v.
- Conway JJ, Collins M, Tanz RR, et al. The role of bone scintigraphy in detecting child abuse. *Semin Nucl Med*. 1993;23:321–33.
- Czitrom AA, Salter RB, Willis RB. Fractures involving the distal epiphyseal plate of the femur. *Int Orthop*. 1981;4:269–77.
- Ducou Le Pointe H, Sirinelli D. Limb emergencies in children. *J Radiol*. 2005;86:251–2.
- Ecklund K, Jaramillo D. Patterns of premature physeal arrest: MR imaging of 111 children. *AJR Am J Roentgenol*. 2002;178:967–72.
- Gaeta M, Minutoli F, Scribano E, et al. CT and MR imaging findings in athletes with early tibial stress injuries: comparison with bone scintigraphy findings and emphasis on cortical abnormalities. *Radiology*. 2005;235:553–61.
- Halsey MF, Finzel KC, Carrion WV, et al. Toddler's fracture: presumptive diagnosis and treatment. *J Pediatr Orthop*. 2001;21:152–6.
- Hernandez JA, Swischuk LE, Yngve DA, et al. The angled buckle fracture in pediatrics: a frequently missed fracture. *Emerg Radiol*. 2003;10:71–5.
- Jaimes C, Jimenez M, Shabshin N, et al. Taking the stress out of evaluating stress injuries in children. *Radiographics*. 2012;32:537–55.
- Jaramillo D, Laor T. Pediatric musculoskeletal MRI: basic principles to optimize success. *Pediatr Radiol*. 2008;38:379–91.
- Jaramillo D, Shapiro F. Musculoskeletal trauma in children. *Magn Reson Imaging Clin N Am*. 1998;6:521–36.
- Keats TE, Anderson MW (2012) Atlas of normal roentgen variants that may simulate disease. 9th edn. Elsevier Saunders. Philadelphia.
- Kellenberger CJ. Pitfalls in paediatric musculoskeletal imaging. *Pediatr Radiol*. 2009;39 Suppl 3:372–81.
- Kleinman PK. Diagnostic imaging of child abuse. St. Louis: Mosby; 1998.
- Kleinman PK, Nimkin K, Spevak MR, et al. Follow-up skeletal surveys in suspected child abuse. *AJR Am J Roentgenol*. 1996;167:893–6.
- Kocher MS, Tucker R. Pediatric athlete hip disorders. *Clin Sports Med*. 2006;25:241–53, viii.
- Lawson JP. International Skeletal Society lecture in honor of Howard D. Dorfman. Clinically significant radiologic anatomic variants of the skeleton. *AJR Am J Roentgenol*. 1994;163:249–55.
- Lemburg SP, Lilienthal E, Heyer CM. Growth plate fractures of the distal tibia: is CT imaging necessary? *Arch Orthop Trauma Surg*. 2010;130:1411–7.
- Lins RE, Simovitch RW, Waters PM. Pediatric elbow trauma. *Orthop Clin North Am*. 1999;30:119–32.
- Mabrey JD, Fitch RD. Plastic deformation in pediatric fractures: mechanism and treatment. *J Pediatr Orthop*. 1989;9:310–4.
- Micheli LJ. The traction apophysitis. *Clin Sports Med*. 1987;6:389–404.
- Oestreich AE. Imaging of the skeleton and soft tissue in children. *Curr Opin Radiol*. 1991;3:889–94.
- Ogden JA. Injury to the growth mechanisms of the immature skeleton. *Skeletal Radiol*. 1981;6:237–53.
- Park HW, Yang IH, Joo SY, et al. Refractures of the upper extremity in children. *Yonsei Med J*. 2007;48:255–60.
- Salter RB, Harris WR. Injuries involving the epiphyseal plate. *J Bone Joint Surg Am*. 1963;45:587–622.
- Schwarz N, Pienaar S, Schwarz AF, et al. Refracture of the forearm in children. *J Bone Joint Surg Br*. 1996;78:740–4.
- Tenenbein M, Reed MH, Black GB. The toddler's fracture revisited. *Am J Emerg Med*. 1990;8:208–11.
- van Rijn RR, Sieswerda-Hoogendoorn T. Educational paper: imaging child abuse: the bare bones. *Eur J Pediatr*. 2012;171:215–24.

Hee Kyung Kim

Contents

31.1	Introduction	970
31.2	Infectious Disorder of the Bone and Joint	970
31.2.1	Pyogenic Osteomyelitis.....	970
31.2.2	Septic Arthritis	970
31.2.3	Tuberculous Arthritis.....	971
31.2.4	Congenital Syphilis	971
31.3	Infectious Disorders of the Soft Tissue	971
31.3.1	Pyomyositis.....	971
31.4	Noninfectious Inflammatory Diseases of the Bones and Joints	971
31.4.1	Inflammatory Arthritis.....	971
31.4.2	Other Noninfectious Inflammatory Joint Diseases	972
31.4.3	Miscellaneous Disorder of the Joint.....	973
31.5	Noninfectious Inflammatory Diseases of the Soft Tissue	974
31.5.1	Dermatomyositis	974
31.5.2	Eosinophilic Fasciitis	974
31.6	Illustrations: Infection and Inflammation of the Musculoskeletal System	975
31.6.1	Infectious Disorder of the Bone and Joint; Acute Osteomyelitis.....	975
31.6.2	Infectious Disorder of the Bone and Joint; Septic Arthritis.....	980
31.6.3	Infectious Disorder of the Bone and Joint; Tuberculous Arthritis	982
31.6.4	Infectious Disorder of the Bone and Joint; Congenital Syphilis.....	983
31.6.5	Infectious Disorders of the Soft Tissue; Pyomyositis	984
31.6.6	Noninfectious Inflammatory Diseases of the Bones and Joints; Juvenile Idiopathic Arthritis.....	985
31.6.7	Noninfectious Inflammatory Diseases of the Bones and Joints; Juvenile Spondyloarthropathies	988
31.6.8	Noninfectious Inflammatory Diseases of the Bones and Joints; Chronic Recurrent Multifocal Osteomyelitis	989
31.6.9	Other Noninfectious Inflammatory Joint diseases; Hemophilic Arthropathy	991
31.6.10	Other Noninfectious Inflammatory Joint Diseases; Neuropathic Arthritis	992
31.6.11	Miscellaneous Disorder of the Joint; Pigmented Villonodular Synovitis	994
31.6.12	Miscellaneous Disorder of the Joint; Synovial Osteochondromatosis.....	996
31.6.13	Miscellaneous Disorder of the Joint; Lipoma Arborescens	997
31.6.14	Miscellaneous Disorder of the Joint; Childhood Malignancies Presenting with Arthritis.....	998
31.6.15	Miscellaneous Disorder of the Joint; Synovial Vascular Malformation	1001
31.6.16	Noninfectious Inflammatory Diseases of the Soft Tissue; Dermatomyositis	1002
31.6.17	Noninfectious Inflammatory Diseases of the Soft Tissue; Eosinophilic Fasciitis	1004
	References	1005

H.K. Kim, M.D.
Department of Radiology, Cincinnati Children's Hospital
Medical Center, 3333 Burnet Avenue, Cincinnati, OH 45229, USA
e-mail: hee.kim@cchmc.org

31.1 Introduction

This chapter will describe various infectious and inflammatory disorders of the musculoskeletal system in children. Familiarity with characteristic imaging findings of infectious and inflammatory disorders will enable a more confident and accurate differential diagnosis. Some infectious musculoskeletal disorders, including pyogenic osteomyelitis and septic arthritis, are acute processes for which early diagnosis and prompt treatment are critical, while others, such as tuberculous arthritis, are more insidious. Inflammatory arthritis and chronic recurrent multifocal osteomyelitis are sterile inflammatory disorders with multiple joint and bone involvement. Other types of inflammatory arthritis may be associated with underlying disease, such as hemophilic arthropathy and neuropathic arthritis. Miscellaneous joint disorders, including pigmented villonodular synovitis, synovial osteochondromatosis, lipoma arborescens, leukemic arthritis, and synovial vascular malformation, are rare in children but can present with joint pain mimicking inflammatory arthritis. Imaging plays an important role in evaluation of all of these disorders. Plain radiographs are the first step in initial evaluation. Ultrasound exam is useful for evaluation of joint effusion and soft tissue abnormalities. MR imaging offers superior tissue contrast and often requires sedation.

31.2 Infectious Disorder of the Bone and Joint

31.2.1 Pyogenic Osteomyelitis

31.2.1.1 Acute Osteomyelitis

Osteomyelitis is an infection of the bone and bone marrow. There are three routes of spread of infection: hematogenous, direct implantation, and contiguity. In hematogenous spread of infection, the metaphysis of the long bones are primarily affected.

Imaging evaluation can be performed with plain radiographs as first step. In early osteomyelitis, soft tissue swelling may be seen, but periosteal reaction and bone destruction are usually not appreciated until at least 7–10 days after disease onset (Fig. 31.1). Bone scintigraphy (bone scan) is useful in initial assessment and localization of the infectious/inflammatory process in osteomyelitis because it has high sensitivity (82 %). Increased uptake within the involved bone at all three phases (angiographic, blood pool, and 2 h delayed bone phases) is suggestive of osteomyelitis (Fig. 31.1). In acute osteomyelitis, MR imaging demonstrates an ill-defined area of low T1 and high T2 bone marrow signal reflecting edema. Intramedullary exudates and a poorly demarcated area of soft tissue swelling are also observed (Fig. 31.1). Post-contrast T1-weighted imaging (WI) is the best sequence on which to detect an abscess, which is demonstrated by localized fluid signal

with rim enhancement (Fig. 31.1). A poor demarcation between abnormal and normal bone marrow is an excellent predictor of acute osteomyelitis and can differentiate it from chronic osteomyelitis or neoplasm of the bone. Ultrasound is adequate to evaluate periosteal fluid collection or abscess; periosteal elevation by an anechoic zone of more than 2 mm is a characteristic sign of subperiosteal abscess (Fig. 31.2) and requires prompt surgical drainage (Howard et al. 1993).

31.2.1.2 Brodie's Abscess

Brodie's abscess is seen in subacute osteomyelitis as a radio-lucent area with well-circumscribed sclerosis (Fig. 31.3).

31.2.1.3 Sclerosing Osteomyelitis and Sequestration

Dense cortical thickening is a finding of chronic osteomyelitis that may be seen months or years after infection and is known as Garré sclerosing osteomyelitis (Fig. 31.4). Cortical extension of infection results in an area of sequestration of a vascular bone surrounded by pus and thickened bone, called a sequestrum (Fig. 31.5).

31.2.2 Septic Arthritis

Septic arthritis is one of the disease entities that require urgent surgical intervention to avoid devastating destructive joint changes. In infants and children less than 18 months of age, the metaphyses and epiphyses of the long bones are cosupplied by a transphyseal vessel. The transphyseal vessels allow the spread of infection into the epiphysis and joints in these young children.

When there is clinical suspicion of septic arthritis, initial imaging evaluation is focused on the presence of joint effusion, not definitive diagnosis of septic arthritis. The absence of joint effusion is an important finding that can exclude septic arthritis with high accuracy (100 % negative predictive value) (Hopkins et al. 1995). Presence of a significant joint effusion with synovial thickening is a sign of underlying inflammation, which can be seen in noninfectious (sterile) inflammatory synovial disease as well as septic arthritis (Fig. 31.6) (Hopkins et al. 1995).

On plain radiographs, joint effusions of the knee, ankle, and elbow (Fig. 31.6) can be detected. However, plain radiographs are limited in the evaluation of joint effusions of the hip, shoulder, and sacroiliac joints, which are better evaluated with ultrasound, CT, or MR imaging. Differentiation of septic arthritis from noninfectious inflammatory arthritis is difficult on any imaging modality. On ultrasound exam, neither the size nor echogenicity of joint effusion enables correlation with sterility of joint effusion (Jaramillo et al. 1995). On MR exam, the presence of bone marrow edema in septic arthritis of the hip was shown to be useful in the differentiation of transient synovitis in one study (Lee et al.

1999). However, bone marrow edema is seen in osteomyelitis as well as in reactive changes in noninfectious conditions, and therefore differentiation of those entities is difficult.

Soft tissue or intraosseous abscess formation, cartilage and bone erosion, and destructive changes (Fig. 31.7) are seen as secondary changes related to septic arthritis.

If joint effusion is detected in a patient with clinical suspicion of septic arthritis, prompt diagnostic aspiration of the effusion should be performed to exclude septic arthritis (Kan et al. 2010).

31.2.3 Tuberculous Arthritis

Tuberculous (TB) arthritis usually results from hematogenous spread of *Mycobacterium tuberculosis*; musculoskeletal involvement is found in approximately 1–3 % of all TB infections and is more common in children. Diagnosis of TB arthritis can be delayed due to its insidious onset and indolent disease course. Plain radiographs demonstrate joint effusion in 3–4 weeks after disease onset. Later manifestations include joint space narrowing, erosion, and destruction. Phemister's triad of periarticular osteoporosis, gradual joint space narrowing, and osseous erosion is the classic finding of TB arthritis. Unlike pyogenic arthritis, which has rapid joint space destruction, joint space is relatively preserved in many patients with TB arthritis. Bone erosion resulting from the proliferation of granulation tissue occurs over a longer time course (Fig. 31.8). MR imaging demonstrates joint effusion with occasional rice bodies, synovitis, tenosynovitis, and cortical erosions. However, these findings are not specific for TB arthritis. Based on imaging alone, differentiation TB arthritis from inflammatory or pyogenic arthritis is still difficult. In TB arthritis, extra-articular abscess formation and bone erosions with rim enhancement are more common than noninfectious inflammatory arthritis (Choi et al. 2009). Lack of bone marrow edema and an abscess with thin, smooth margins may be useful to differentiate TB arthritis from pyogenic arthritis. In pyogenic arthritis, bone marrow edema is more commonly seen, and an abscess has more irregular and relatively thick walls (Burk et al. 1988). Another sign that is more suggestive of TB arthritis is a tram track appearance resulting from a linear fluid signal from the joint space with rim enhancement (Fig. 31.9) (Parmar et al. 2004). However, due to overlap between imaging findings of TB arthritis, noninfectious inflammatory arthritis, and pyogenic arthritis, it is important to pursue cultures of synovial fluid and synovium (Erdem et al. 2005).

31.2.4 Congenital Syphilis

Congenital syphilis is a transplacental infection due to *Treponema pallidum* that occurs during the second to third

trimesters of gestation. Plain radiographs in infants with congenital syphilis demonstrate multiple bone involvement with metaphyseal lucent bands and periosteal new formation of the diaphysis (Fig. 31.10). These findings reflect stress responses and can be seen in other disseminated infections. A focal area of destructive changes in the medial aspect of the proximal tibial metaphysis with preservation of a few millimeters of recently formed metaphysis (Laval-Jeantet collar) is called “Wimberger's sign” (Fig. 31.10). Wimberger's sign is strongly suggestive of congenital syphilis, and diagnosis is made in conjunction with serologic testing.

31.3 Infectious Disorders of the Soft Tissue

31.3.1 Pyomyositis

Pyomyositis is a bacterial infection of the skeletal muscle that mainly affects children between 2 and 5 years. It is more common in tropical areas; however, the incidence is increasing in temperate areas. Pyomyositis is characterized by abscess within the muscles, often following minor trauma. MR imaging shows localized fluid signal with peripheral rim enhancement within the muscle suggesting abscess and can be associated with cellulitis, myositis, and fasciitis (Fig. 31.11) (Gordon et al. 1995).

31.4 Noninfectious Inflammatory Diseases of the Bones and Joints

31.4.1 Inflammatory Arthritis

31.4.1.1 Juvenile Idiopathic Arthritis

Juvenile idiopathic arthritis (JIA) is the most common inflammatory arthritis. It is diagnosed in children under age 16 years who have more than 6 weeks of symptom duration. JIA is classified into seven categories based on the number and types of the involved joints and combined symptoms (Petty et al. 2004). Oligo- or pauci-articular arthritis, with less than five joints involved, is the most common type and accounts for 50–60 % of JIA. It is subclassified based on duration and extension of disease: persistent type (<6 months of duration) versus extended type (>6 months of duration) (Weiss and Ilowite 2007). Systemic and polyarticular arthritis types have more than five joints involved. The systemic type accounts for 10–20 % of JIA and is typically seen in children younger than 5 years. Systemic arthritis is associated with systemic symptoms including spiking fevers, lymphadenopathy, rash, hepatosplenomegaly, and serositis (Weiss and Ilowite 2007). Polyarticular arthritis is subclassified by the presence of rheumatoid factor (RF) into RF positive type, which is less common and similar to adult onset rheumatoid arthritis, and RF negative type, which is

more common. The remaining types of JIA include psoriatic arthritis (2–15 %), enthesitis-related arthritis (1–7 %), and undifferentiated arthritis. Juvenile ankylosing spondylitis and inflammatory bowel disease-related arthropathy are subtypes of enthesitis-related arthritis (Weiss and Ilowite 2007).

The etiology of JIA is an immune response cascade initiated by infection in an immunologically susceptible individual. The primary pathology is synovial inflammation and hypertrophy resulting from cross-reaction of the antigen–antibody to the synovial membrane. The disease is progressive and results in cartilage or bone erosion with eventual joint deformities observed in approximately one-third of affected patients.

Imaging findings on plain radiographs depend on disease stage. In early stages, soft tissue swelling, periarticular osteopenia, joint effusion, and periosteal reaction are seen. Persistent hyperemia results in accelerated skeletal maturation and squaring of the carpal bones. In more advanced stages, joint space narrowing, erosions, and ultimately ankylosis are observed (Fig. 31.12). The knee joint (Fig. 31.13) is most commonly involved, followed by ankle, wrist, hand, shoulder, cervical spine (Fig. 31.14), temporomandibular joint (Fig. 31.15), and sacroiliac joint.

MR imaging with intravenous gadolinium injection is better than plain MR imaging in the evaluation of cartilage erosion and synovial hypertrophy and can demonstrate the most characteristic findings of JIA, which are synovial hypertrophy and joint effusion. In the knee joint, synovial thickening more than 3 mm is considered abnormal. The thickened synovium has variable signal intensities on T1- and T2-WI (Gyls-Morin et al. 2001). Chronic inflammation and fragmentation of synovium results in rice bodies in the joint spaces (Fig. 31.13). Hypoplastic menisci from mass effect of the adjacent thickened synovium, popliteal cysts, lymphadenopathy, and tenosynovitis can also be seen in JIA.

31.4.1.2 Juvenile Spondyloarthropathies

Juvenile spondyloarthropathies is a group of disorders that includes juvenile ankylosing spondylitis, reactive arthritis (Reiter's syndrome), juvenile psoriatic arthritis, and arthritis associated with inflammatory bowel disease. These diseases occur under the age of 16 years and have the common imaging findings of sacroiliitis and enthesitis. The other joint involvement and findings are similar to JIA. Bilateral and asymmetric sacroiliitis with erosions, reactive sclerosis (particularly on the iliac side), pseudo-widening, and indistinct margin are best evaluated on MR imaging with intravenous contrast (Fig. 31.16).

31.4.1.3 Chronic Recurrent Multifocal Osteomyelitis

Chronic recurrent multifocal osteomyelitis (CRMO) is a sterile inflammatory bone disorder. It has recently been considered a hereditary disorder or another manifestation of an associated autoimmune disorder. CRMO primarily affects children from 4 to 14 years with female predominance. The clinical presentation of CRMO is prolonged (over several years), with recurrent and multifocal pain, swelling, and occasional fever. It is often misdiagnosed or simply treated with anti-inflammatory medicines. The metaphyses of the long bones are most commonly involved, followed by the clavicles and spine, and bilateral involvement is common (Fig. 31.17). Bone scan can be used as an initial exam to detect multifocal bone involvement (Fig. 31.18). Plain radiographs demonstrate mixed sclerotic and lytic lesions within the metaphyses of the long bones (Fig. 31.17). On MR images, bone marrow edema is visualized in the active disease state, but in contrast to subacute or chronic osteomyelitis, abscess formation is not observed (Fig. 31.18). In the reparative state, destructed bones demonstrate healing with sclerosis, remodeling, and normalization, which occur within 2 years after disease onset. Subsequent exacerbations with a repetitive cycle of active and reparative states result in progressive hyperostosis and sclerosis of the metaphysis (Fig. 31.18). Diagnosis of CRMO is primarily made by exclusion of other infectious, inflammatory etiologies or neoplasms, and biopsy with histological confirmation is often required (Iyer et al. 2011). SAPHO (synovitis, acne, pustulosis, hyperostosis, and osteitis) is a term used to unify idiopathic inflammatory and infectious disorders of bone and skin.

31.4.2 Other Noninfectious Inflammatory Joint Diseases

31.4.2.1 Transient Synovitis

Transient synovitis is an inflammatory synovitis affecting the hip joint that is self-limited in nature. This entity is described in the chapter on hip joint disorders.

31.4.2.2 Hemophilic Arthropathy

Hemophilia is an X-linked autosomal recessive blood coagulation disorder resulting from a lack of coagulation factor VIII or IX. Hemophilic arthropathy is related to repeated intra-articular hemorrhage (hemarthrosis) occurring spontaneously or due to minor trauma. Hemarthrosis accounts for most bleeding events (85 %) in hemophilia and begins in the first and second decades of life. The knee, elbow, ankle, hip, and shoulder joints are most commonly involved. Recurrent

hemarthrosis and hyperemia lead to synovitis, overgrowth of the epiphysis, and eventual degeneration of the joints. Imaging findings are dependent on the disease state and can be graded using the Arnold-Hilgartner staging on plain radiograph: Stage 0, normal; 1, joint effusion and soft tissue swelling; 2, periarticular osteopenia and overgrowth of the epiphysis; 3, bone erosion and widening of the notch of the distal humerus and femur; 4, joint space narrowing (Fig. 31.19); and 5, joint contracture and deformity (Arnold and Hilgartner 1977; Luck et al. 2004).

MR imaging is very useful to detect early changes such as hemarthrosis (blood clot in the joint, fluid–fluid level) and cartilage erosion. Hemosiderin deposition results in characteristic low T1 and low T2 signal within the thickened synovium, which can be best seen on gradient echo sequences (Fig. 31.19) (Kerr 2003; Doria 2010). In advanced stages, degenerative changes including subchondral cysts, cartilage thinning, or erosions can be seen (Fig. 31.19).

31.4.2.3 Neuropathic Arthritis

Neuropathic arthritis is a joint destructive disorder secondary to repetitive trauma over long time period. This is frequently seen in patients with neurosensory loss such as with myelomeningocele or syringomyelia. Plain radiographs demonstrate progressive fracture and dislocation of the joint (Fig. 31.20). MR findings of neuropathic joint include fragmentation of the cartilage and bones, synovial thickening, effusion, and ligament and menisci injuries. Lack of inflammation in the periarticular space in the neuropathic joint and an underlying history of neuropathy can be helpful to differentiate it from pyogenic arthritis.

31.4.3 Miscellaneous Disorder of the Joint

31.4.3.1 Pigmented Villonodular Synovitis

Pigmented villonodular synovitis (PVNS) is an idiopathic proliferative disorder of the synovium. It is relatively rare in children and has a benign course in most cases. The knee is most frequently involved (80 %) followed by the hip, ankle, shoulder, and elbow joints. PVNS has two types: diffuse PVNS is more common and involves the entire synovium of the affected joint, and localized PVNS is less common and can mimic a fibrous neoplasm. Giant cell tumor and benign giant cell synovioma are other names for localized PVNS. Microscopically, the affected synovium has villonodular proliferation with hemosiderin deposition. Plain radiographs show soft tissue swelling with or without degenerative arthritis (Fig. 31.21). The larger joints (knees and shoulders) are preserved from degenerative changes, but tight joints such as the hip can have degenerative changes with joint space

narrowing later (Dorwart et al. 1984; Goldman and DiCarlo 1988). MR imaging has a characteristic appearance with low T1 and low T2 signal lesions; diffuse PVNS has diffuse linear or frond-like proliferation of the synovium (Fig. 31.21), and localized PVNS has a localized mass (Fig. 31.22). Gradient echo sequences are useful to differentiate PVNS from other fibrous lesions (synovial hypertrophy with fibrosis in JIA or fibrous tumor). On gradient echo sequences, hemosiderin deposition causes blooming from susceptible artifact (Llauger et al. 1999). PVNS is treated by surgical resection, but the local recurrence rate is relatively high at up to 50 %.

31.4.3.2 Synovial Osteochondromatosis

Synovial osteochondromatosis is an idiopathic synovial proliferative disease with the formation of intrasynovial chondro-osseous bodies. It is relatively rare in children and has a benign nature with single-joint involvement. Three phases of the disease process have been described: *active phase* with chondral proliferation in the synovium without intra-articular loose bodies, *transitional phase* with both intrasynovial chondral proliferation and formation of intra-articular loose bodies, and *quiescent phase* with ceasing of chondral proliferation in the synovium. The degree of ossification determines the imaging findings on plain radiographs and MR images. Ossification of the loose bodies occurs in 70 % cases and is termed *synovial osteochondromatosis*. *Synovial chondromatosis*, which contains purely unmineralized cartilage, accounts for the remaining 30 %. In case of synovial osteochondromatosis, plain radiographs (Fig. 31.23) or CT scans (Fig. 31.23) demonstrate multiple even-sized calcified nodules over the joint. MR imaging demonstrates multiple even-sized intra-articular loose bodies with cartilage signal (isointense T1 and high T2 signal intensity). Areas of dark T1 and T2 signal within the individual loose bodies are seen in cases of ossification and are more conspicuous on gradient echo sequences due to blooming. With maturation of bone cortex in the loose bodies, mature fatty marrow signal (high T1 and high T2 signal) can be detected on MR.

31.4.3.3 Lipoma Arborescens

Lipoma arborescens is a benign fatty proliferative disease of the synovium that is rare in children. The knee is the most commonly affected joint. Plain radiographs demonstrate joint effusion. MR findings are characteristic with frond-like synovial proliferation with persistent fat signal on all sequences (Fig. 31.24) (Martin et al. 1998; Vilanova et al. 2003). While lipoma arborescens is commonly associated with degenerative joint disease in adults, it can occur in a younger population without underlying disease.

31.4.3.4 Childhood Malignancies Presenting with Arthritis

Some childhood malignancies can present with arthritis clinically mimicking inflammatory arthritis, including metastatic neuroblastoma (Fig. 31.25), lymphoma, leukemia (Fig. 31.26), and primary bone tumors. Leukemic arthritis is more common in children and is seen in 12–65 % of pediatric leukemia. It typically presents with transient joint pain with a predilection for large joints such as knees and shoulders. Leukemic infiltration of the synovium, hemorrhage, and metaphyseal periostitis cause joint pain and can be seen in the absence of hematologic abnormality in 5 % of patients. Radiologic findings include joint effusion, periostitis, lytic or sclerotic bone lesions, and metaphyseal lucent bands, although plain radiograph findings are often normal. MR imaging demonstrates diffuse abnormal bone marrow with low T1 and high T2 signal intensities (Fig. 31.26) (Cohen et al. 1984).

31.4.3.5 Synovial Vascular Malformation

Vascular malformation involvement of the intra-articular space is rare, but typically presents in children and young adults. It is classified by the type of vasculature: capillary, venous, arterial, lymphatic, and mixed components. Intra-articular synovial involvement results in recurrent hemarthrosis and can be misdiagnosed as hemophilic arthropathy. Delayed diagnosis can lead to poor clinical outcome with progressive arthropathy. Plain radiographs can demonstrate soft tissue mass, phlebolith, maturation of the epiphysis, arthropathy, and leg-length discrepancy. MR findings of vascular malformation depend on the vascular component; venous type has homogeneous enhancement (Fig. 31.27), while lymphatic type has peripheral enhancement on post-contrast images (Fig. 31.27). Arteriovenous malformations have flow voids on T2-weighted images due to the high flow nature of the vessel (Legiehn and Heran 2006).

31.5 Noninfectious Inflammatory Diseases of the Soft Tissue

31.5.1 Dermatomyositis

Juvenile dermatomyositis (JDM) is the most common type of inflammatory myopathy and typically occurs in children between 5 and 14 years of age. It is characterized by insidious onset of bilateral symmetric muscle weakness and violaceous skin rash. Skin rash and three of the following four criteria are necessary for diagnosis of JDM: proximal muscle weakness, elevated muscle enzymes, findings of inflammatory myopathy on electromyography (EMG), and/or inflammatory myositis on muscle biopsy. MR imaging shows symmetric muscle and perimuscular edema on water-sensitive sequences (T2-weighted image with fat suppression or short inversion recovery (STIR) sequences) (Fig. 31.28). Soft tissue calcification is seen in 30–70 % of patients and occurs at areas exposed to trauma (elbows, knees, and buttocks) (Fig. 31.29). MR imaging is useful to evaluate muscle edema/inflammation as well as to localize muscle biopsy. Reticulated high T2 signal changes in subcutaneous fat are associated with a more aggressive and chronic course of the disease process (Johnson et al. 2006; Ladd et al. 2011).

31.5.2 Eosinophilic Fasciitis

Eosinophilic fasciitis is a rare disease entity of diffuse fasciitis associated with serum eosinophilia. It presents with significant extremity swelling followed by skin indurations. MR imaging demonstrates high T2 signal within the fascia and fascial thickening with adjacent muscle edema and fascial enhancement on post-contrast T1-weighted images (Fig. 31.30) (Moulton et al. 2005). MR imaging is also useful to reassess patients after treatment.

31.6 Illustrations: Infection and Inflammation of the Musculoskeletal System

31.6.1 Infectious Disorder of the Bone and Joint; Acute Osteomyelitis



Fig. 31.1 A 10-year-old boy with acute osteomyelitis. (a) Plain radiograph of the right femur demonstrates no bony abnormalities. (b) Bone scan 2 h delayed image demonstrates increased uptake in the proximal diaphysis of the right femur (arrows). (c) Sagittal T2-weighted MR image demonstrates bone marrow edema (*) with poor interface

between normal and abnormal marrow as well as soft tissue swelling (arrowheads). (d) Post-contrast axial T1-WI demonstrates contrast enhancement of the bone marrow (*) and soft tissue (small white arrows). Soft tissue abscess with rim enhancement and internal fluid is seen (black arrow)

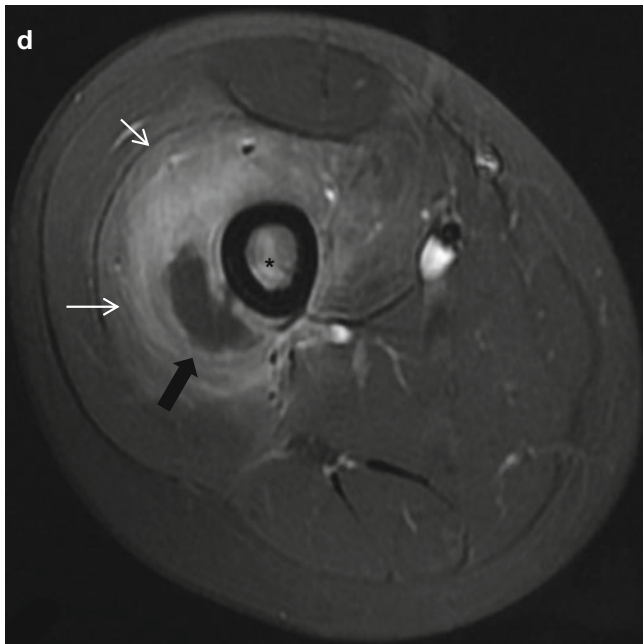


Fig. 31.1 (continued)

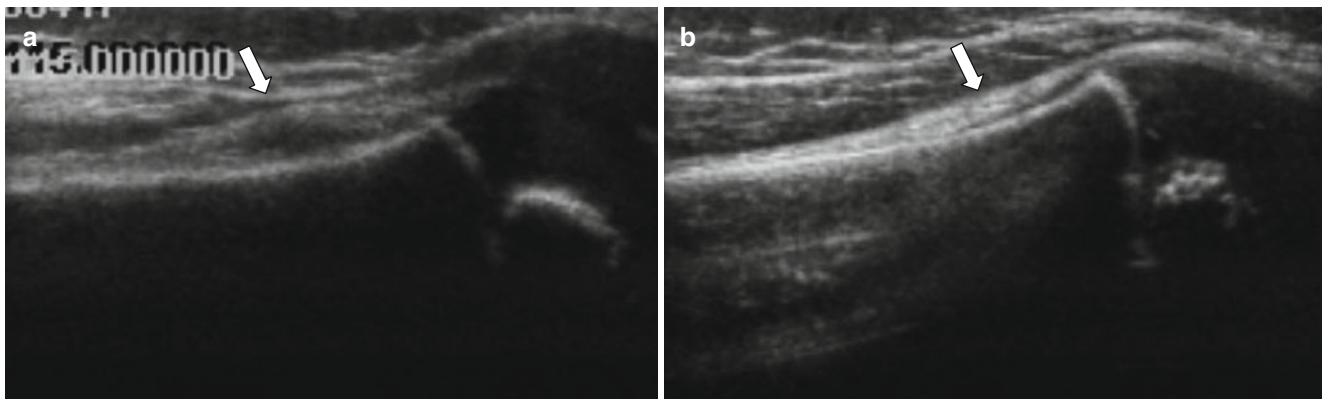


Fig. 31.2 A 5-year-old girl with subperiosteal abscess. (a) Ultrasound exam of the right femur demonstrates periosteal lifting with subperiosteal fluid (arrow). (b) Exam of the contralateral side demonstrates normal appearance of the periosteum (arrow)



Fig. 31.3 A 12-year-old girl with *Brodie's abscess*. (a) Plain radiograph of the left femur demonstrates a single well-circumscribed osteolytic lesion with sclerosis (arrows). (b, c) Coronal T2-WI with fat

suppression (b) and post-contrast sagittal T1-WI with fat suppression (c) demonstrate an area of fluid signal (*) with enhancing rim (black arrows). Subperiosteal abscess is seen (white arrow)



Fig. 31.4 A 3-month-old boy with sclerosing osteomyelitis. *Subacute-chronic phase*: 2 months after disease onset. **(a)** Plain radiographs of the right tibia-fibula demonstrate cortical thickening, periosteal new bone formation (*small black arrows*), and intramedullary mixed sclerotic and osteolytic changes. Pathologic fracture is identified. *Acute*

phase: immediately (6 days) after disease onset. **(b)** Plain radiograph demonstrates soft tissue swelling (*arrowheads*). **(c)** Post-contrast T1-WI MR image demonstrates soft tissue swelling, bone marrow enhancement, and subperiosteal abscess formation (*arrow*)



Fig. 31.5 A 16-year-old boy with *sequestrum of the lumbar spine*. CT scan of the lumbar spine demonstrates sequestrum (*arrow*) surrounded by soft tissue. Right transverse process and posterior element of the spine show cortical thickening and sclerosis (*small black arrows*)

31.6.2 Infectious Disorder of the Bone and Joint; Septic Arthritis

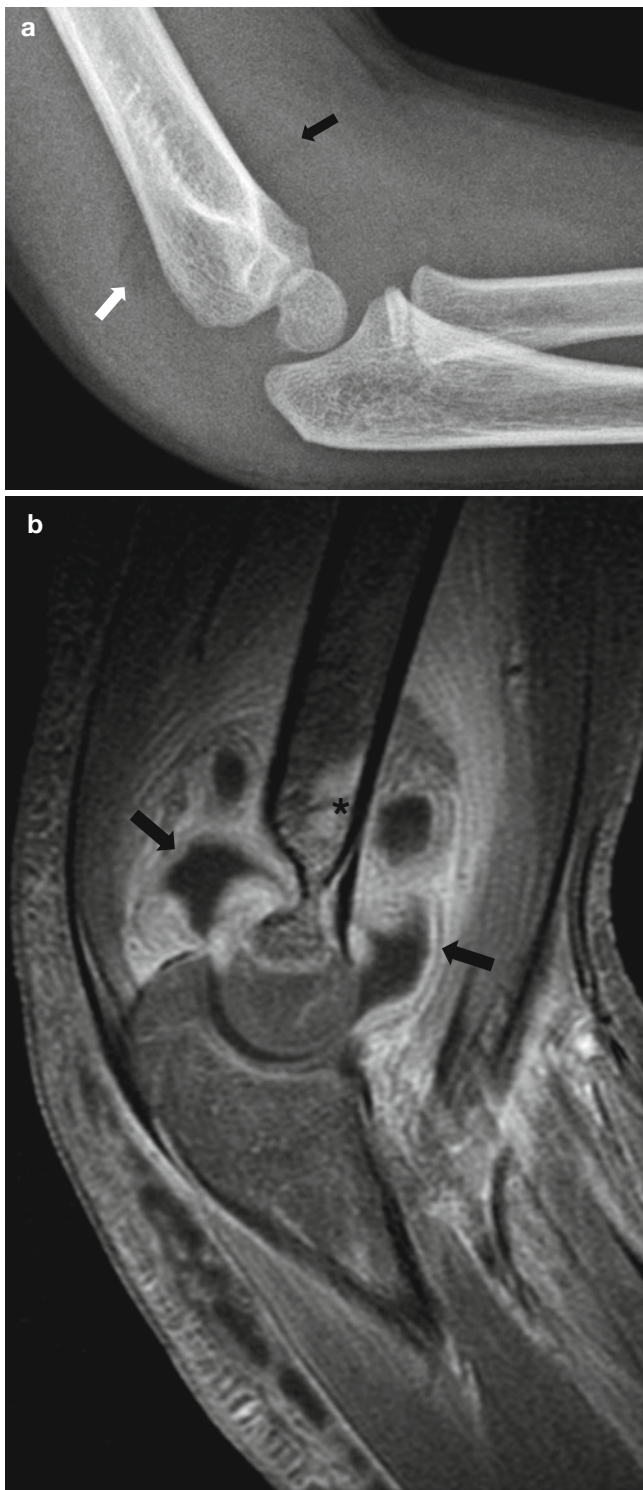


Fig. 31.6 A 3-year-old girl with septic arthritis. (a) Plain radiograph of the elbow demonstrates a large joint effusion with shifting of the anterior (*black arrow*) and posterior (*white arrow*) fat pads. (b) Post-contrast sagittal T1-WI with fat suppression demonstrates abundant enhancing synovium (*black arrows*), soft tissue swelling, and bone marrow edema (*)

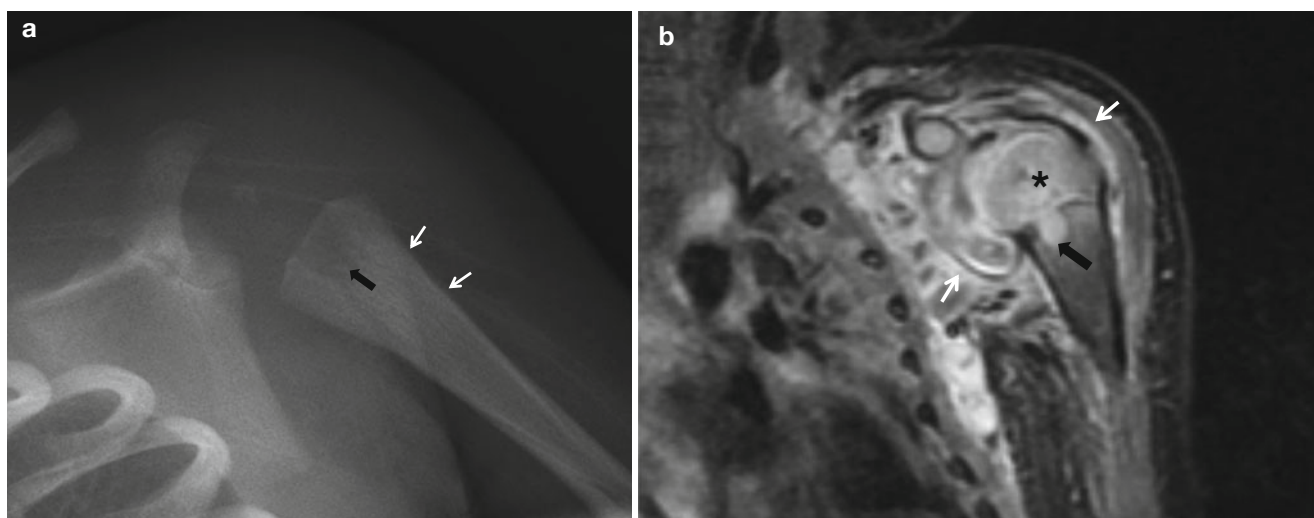


Fig. 31.7 A 3-week-old girl with septic arthritis. (a) Plain radiograph of the left shoulder demonstrates periosteal reaction (*small white arrows*) and destructive change (*black arrow*) of the left proximal humerus. (b) Post-contrast coronal T1-WI with fat suppression demon-

strates synovial enhancement (*small white arrows*) and intraosseous abscess formation (*black arrow*). Bone marrow edema and enhancement of the epiphysis of the humerus suggesting osteomyelitis is seen (*)

31.6.3 Infectious Disorder of the Bone and Joint; Tuberculous Arthritis

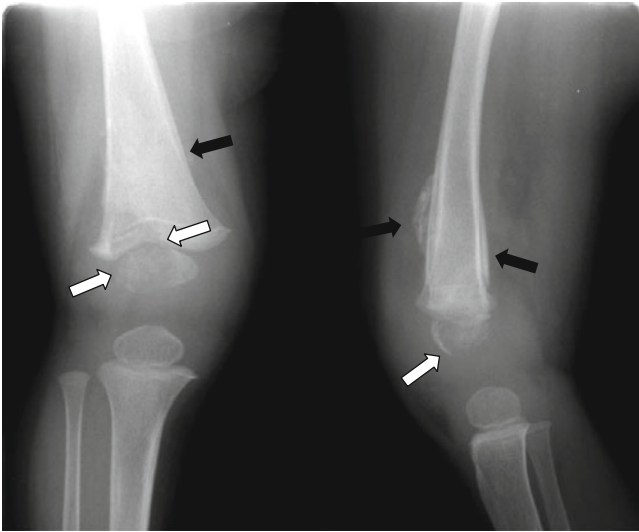


Fig. 31.8 A 2-year-old girl with tuberculosis. Plain radiograph of the right distal femur demonstrates bone destruction (*white arrows*) and periosteal reaction (*black arrows*) (Courtesy of JE Cheon M.D., Seoul, Korea)

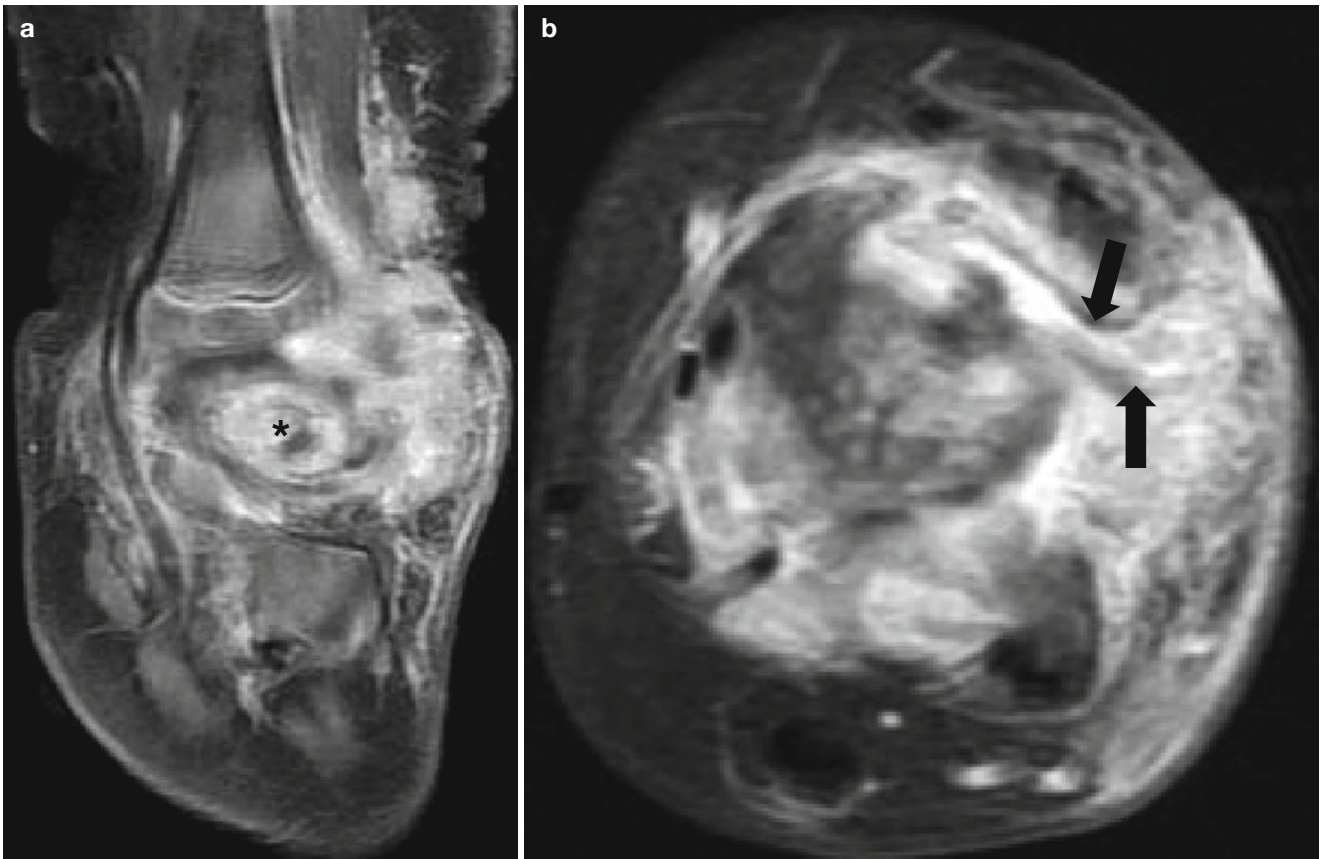


Fig. 31.9 A 2-year-old girl with tuberculosis arthritis of the ankle. (a) Post-contrast sagittal T1-WI with fat suppression demonstrates intraosseous abscess formation and bone erosion (*) and synovitis.

(b) Post-contrast axial T1-WI with fat suppression demonstrates dermal sinus track with tram track appearance (*arrows*) (Courtesy of JE Cheon M.D., Seoul, Korea)

31.6.4 Infectious Disorder of the Bone and Joint; Congenital Syphilis

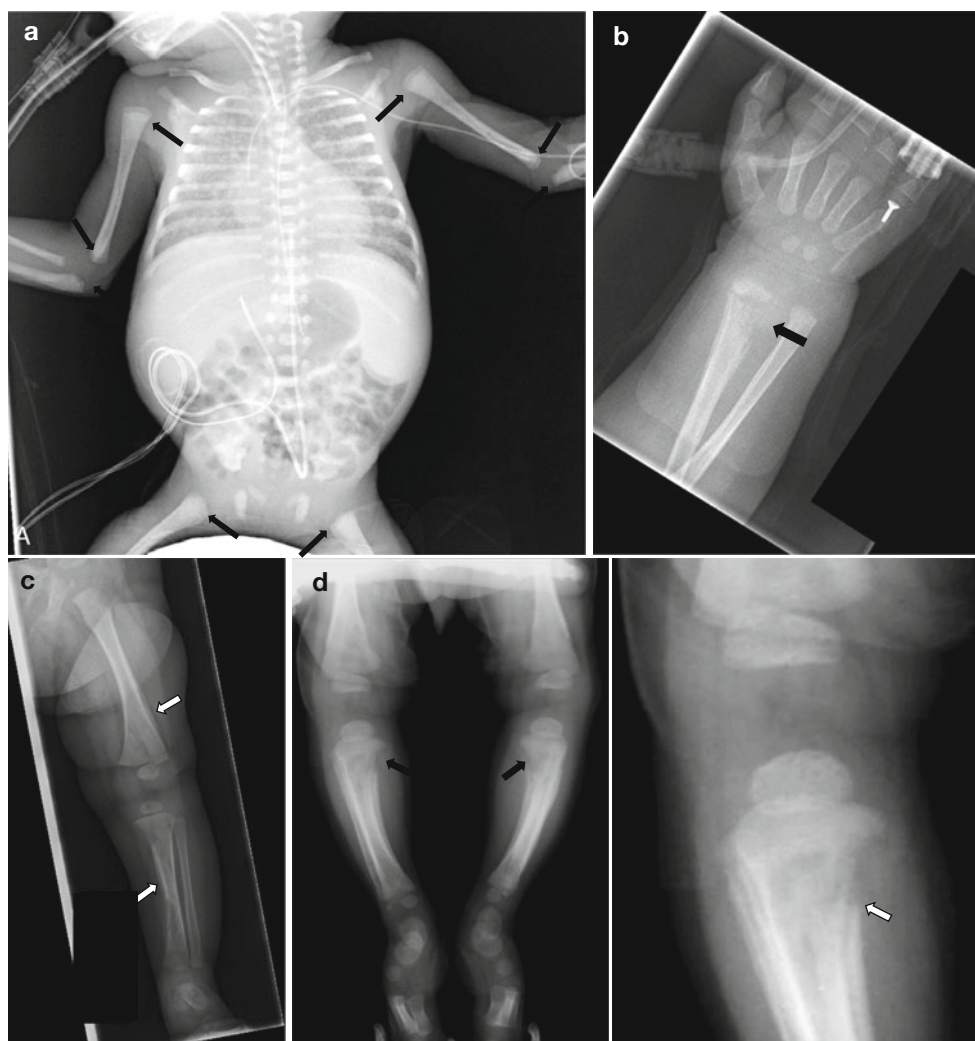


Fig. 31.10 *Congenital syphilis.* (a) Infantogram of a newborn baby demonstrates multifocal metaphyseal lucent bands (arrows). (b, c) A 2-month-old boy with congenital syphilis. Radiographs of the wrist (b) and lower leg (c) demonstrate metaphyseal lucencies (black arrow) and multiple areas of periosteal new bone formation (white arrows).

(d) Another 2-month-old boy with congenital syphilis. Lower extremity and cone-down view of the right knee show Wimberger's sign bilaterally (black arrows). Characteristic Laval-Jeantet collar, representing spared newly formed metaphysis, is seen (white arrow)

31.6.5 Infectious Disorders of the Soft Tissue; Pyomyositis

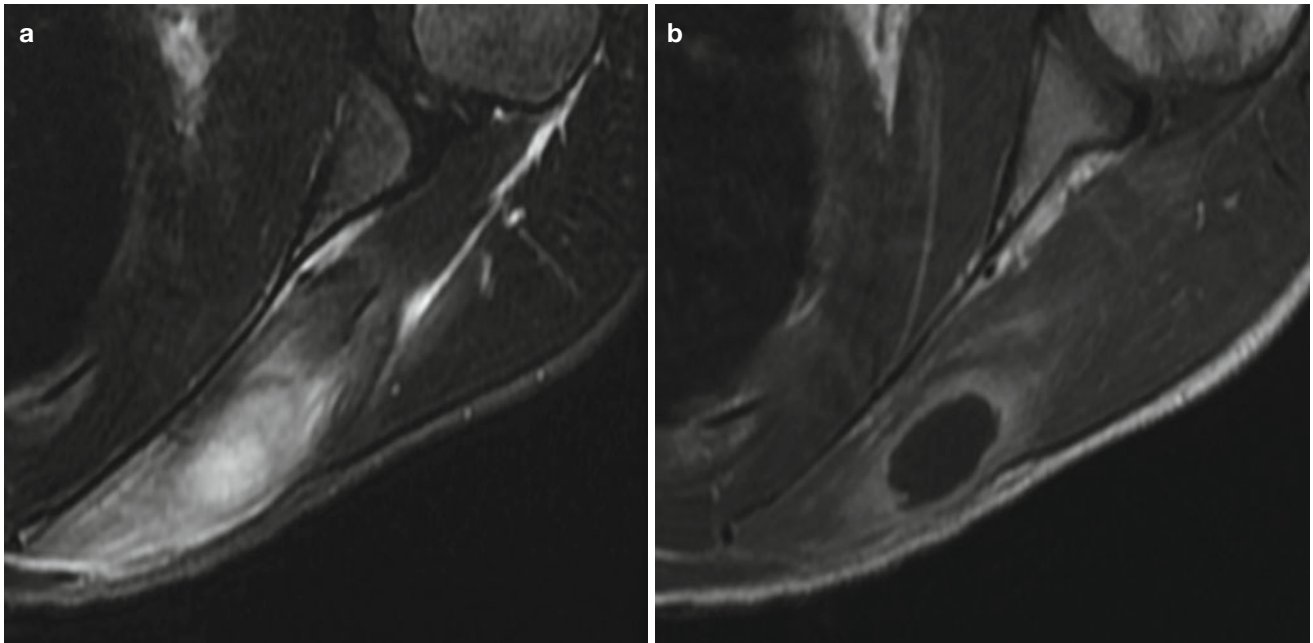


Fig. 31.11 A 11-year-old boy with *pyomyositis of the shoulder*. (a) Axial T2-WI with fat suppression and (b) Post-contrast axial T1-WI with fat suppression demonstrate well-circumscribed fluid collection with rim enhancement

31.6.6 Noninfectious Inflammatory Diseases of the Bones and Joints; Juvenile Idiopathic Arthritis

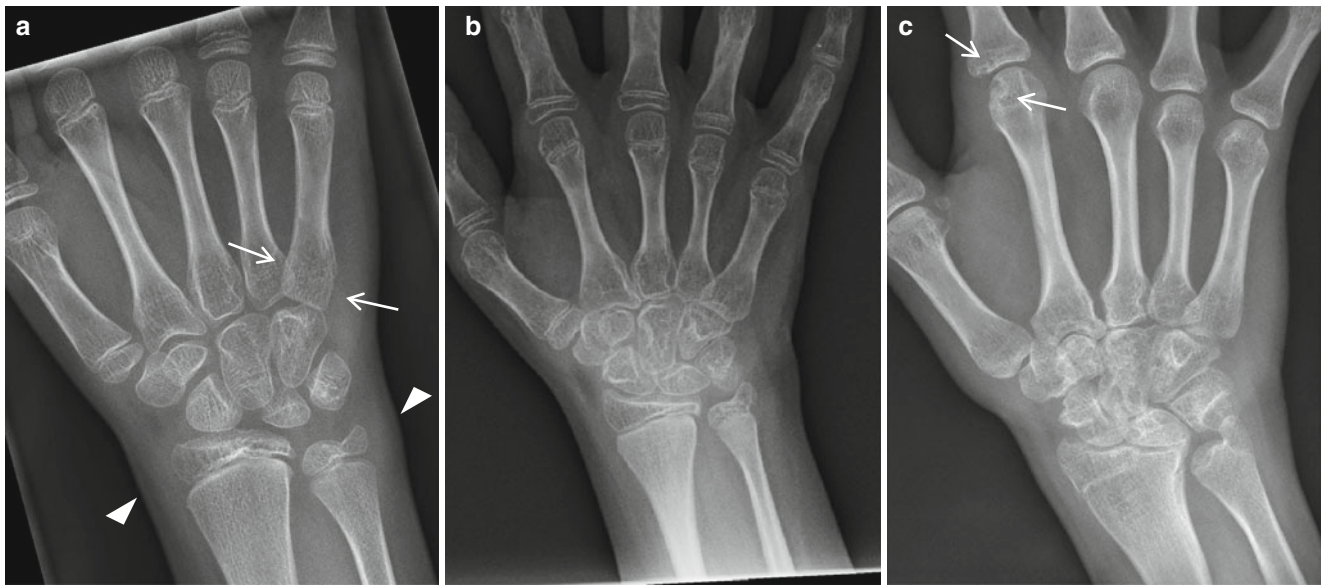


Fig. 31.12 Juvenile idiopathic arthritis in different stages in different patients. (a) A 9-year-old girl with JIA. Wrist radiograph demonstrates periarticular osteopenia (white arrows) and soft tissue swelling (arrowheads). (b) An 11-year-old girl with JIA. Wrist radiograph demonstrates

squaring of carpal bones with intercarpal joint space narrowing. (c) A 15-year-old girl with JIA. Wrist radiograph demonstrates loss of joint space in the intercarpal joints due to destruction of the cartilage, proximal migration of the scaphoid and lunate bones, and erosions (white arrows)

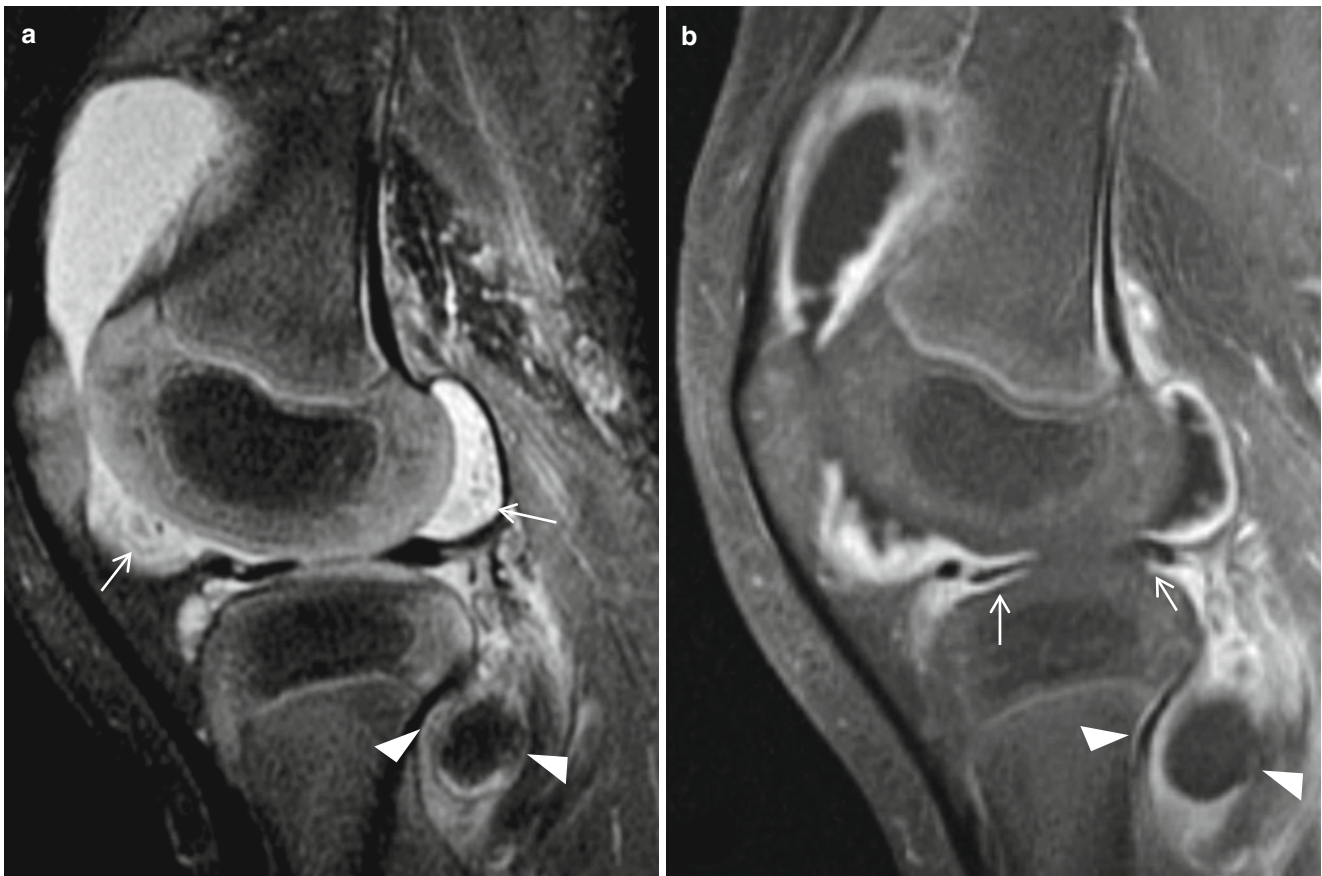


Fig. 31.13 A 3-year-old girl with JIA. (a) Sagittal T2-WI with fat suppression demonstrates a large joint effusion with high T2 signal synovium, which was not differentiated from adjacent fluid. Hypointense rice bodies (arrows) and popliteal cyst (arrowheads) are

seen. (b) Post-contrast sagittal T1-WI with fat suppression image demonstrates diffuse synovial enhancement and popliteal cyst (arrowheads). Anterior and posterior horn of the meniscus is hypoplastic (arrows)

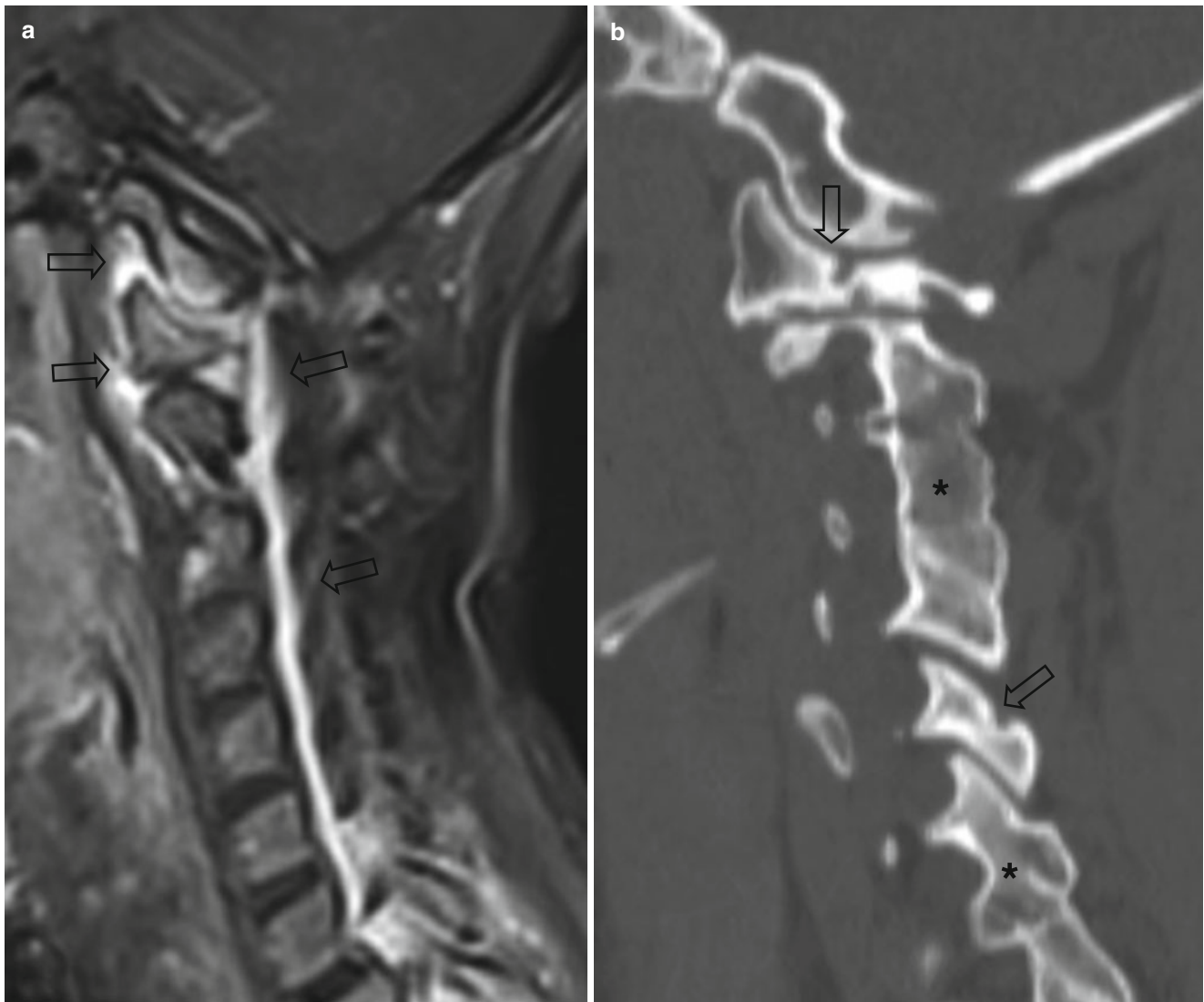


Fig. 31.14 *JIA of the cervical spine.* (a) A 15-year-old girl with JIA. Post-contrast sagittal T1-WI with fat suppression of the cervical spine demonstrates synovial enhancement and soft tissue swelling (arrows).

(b) A 16-year-old girl with JIA. Cervical spine CT scan demonstrates bone erosion (arrows) and multilevel fusion of the posterior elements (*) (Courtesy of AC Merrow, M.D., Cincinnati, Ohio, USA)

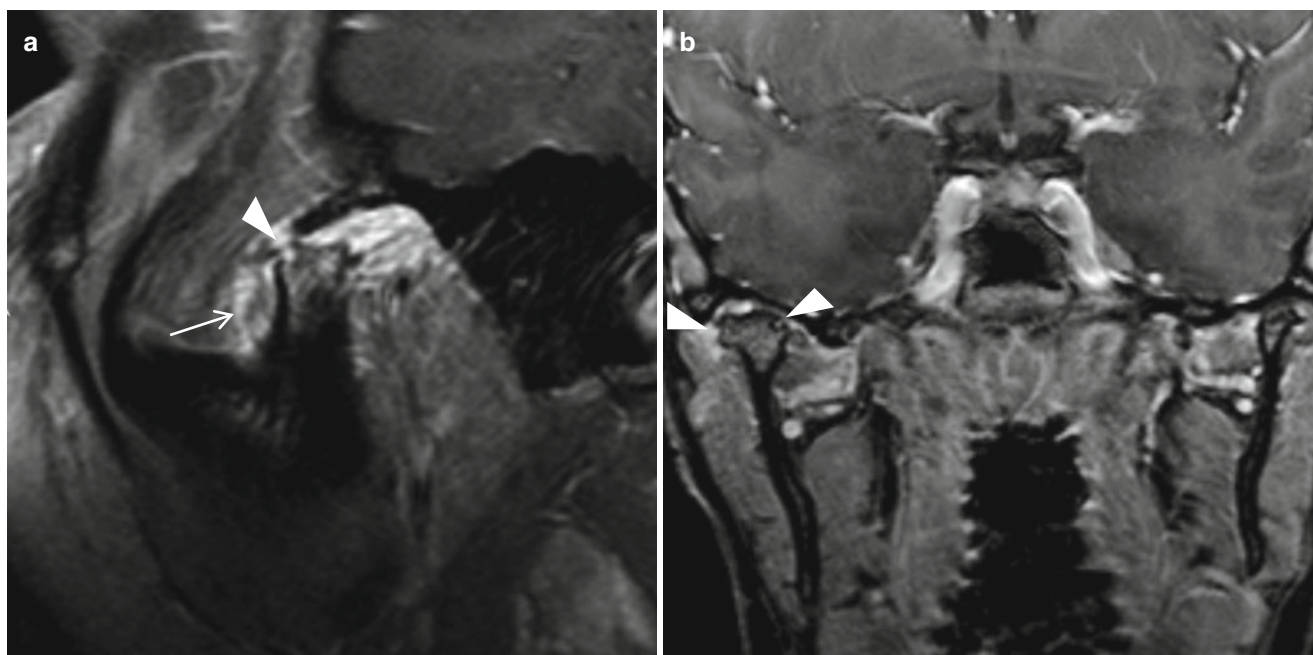


Fig. 31.15 A 17-year-old girl with JIA of the temporomandibular joint. **(a)** Post-contrast sagittal T1-WI with fat suppression with the patient open mouth demonstrates dislocation of the mandibular condyle, synovial enhancement (*arrow*), and flattening and shortening of the

mandibular condyle with erosion (*arrowhead*). **(b)** Coronal post-contrast T1-WI with fat suppression with the patient closed mouth demonstrates both mandibular condyles are within the joints. Hypertrophy of the right mandibular condyle with flattening and erosion (*arrowhead*) is seen

31.6.7 Noninfectious Inflammatory Diseases of the Bones and Joints; Juvenile Spondyloarthropathies

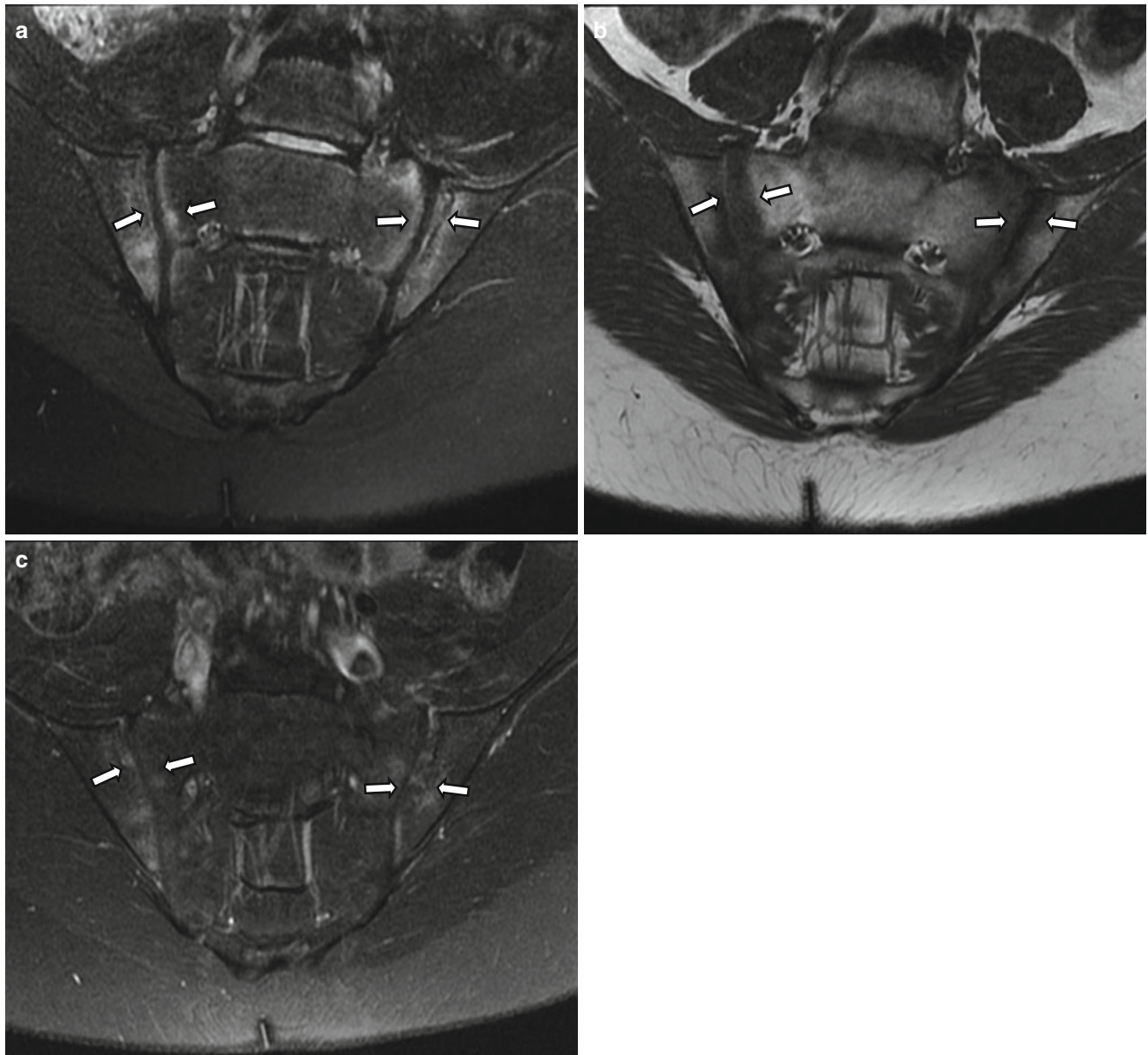


Fig. 31.16 A 14-year-old HLA B27-positive boy with ankylosing spondylitis. Oblique coronal T2-WI with fat suppression (**a**), T1-WI (**b**), and post-contrast T1-WI with fat suppression (**c**) demonstrate bilateral bone marrow edema (*arrows*) within the sacroiliac joint

31.6.8 Noninfectious Inflammatory Diseases of the Bones and Joints; Chronic Recurrent Multifocal Osteomyelitis

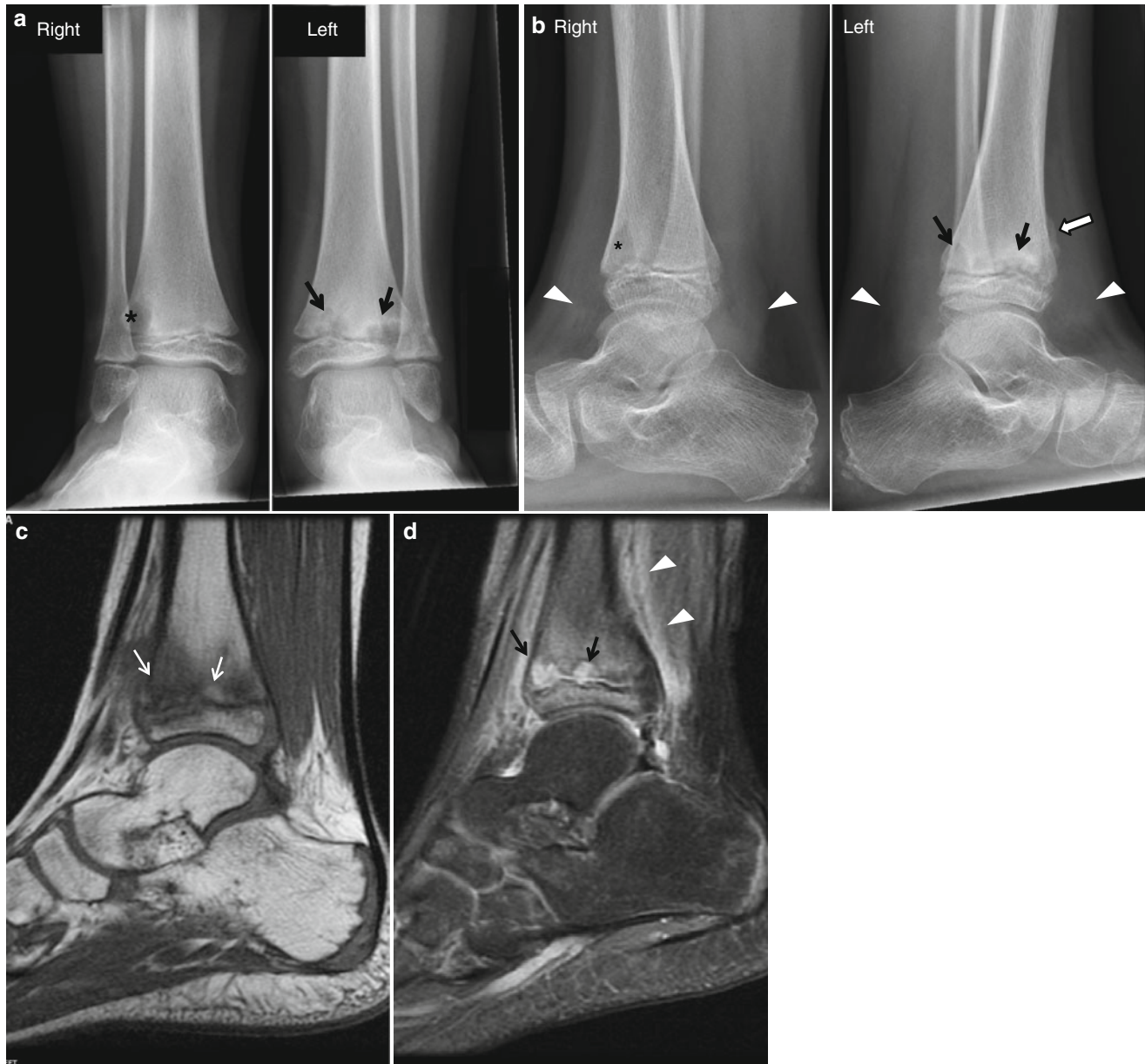


Fig. 31.17 A 14-year-old boy with chronic recurrent multifocal osteomyelitis (CRMO). (a) Frontal radiographs of the ankles demonstrate an osteolytic lesion (*) on the right and metaphyseal sclerosis and lucencies (arrows) on the left. (b) Lateral radiographs demonstrate deep soft tissue swelling (arrowheads), an osteolytic lesion (*), metaphyseal

sclerosis and lucencies (arrows), and periosteal reaction (white arrow). (c, d) Sagittal T1-WI (c) and T2-WI with fat suppression (d) of the left ankle demonstrate a well-circumscribed area of low T1 and high T2 signal of the metaphysis (arrows) and soft tissue swelling (arrowheads)

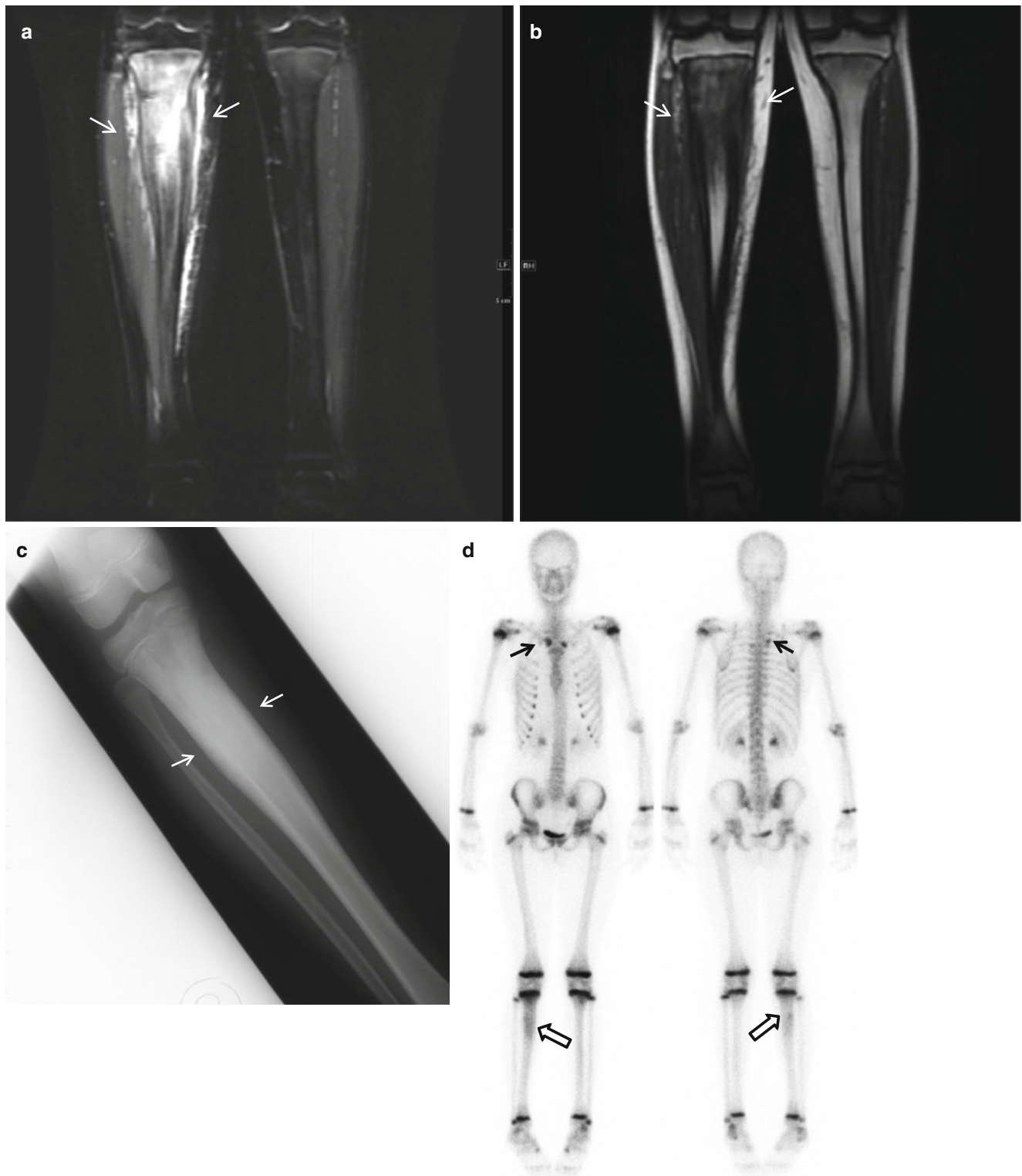


Fig. 31.18 A 12-year-old girl with CRMO. (a, b) Coronal T2-WI with fat suppression (a) and T1-WI (b) demonstrate bone marrow edema with soft tissue swelling (arrows) of the right proximal tibial metaphysis, diaphysis, and metadiaphysis. (c) Follow-up radiograph 2 years after disease onset demonstrates diffuse sclerotic change and cortical

thickening of the proximal tibial metadiaphysis and diaphysis (arrows). (d) Bone scan performed after the patient presented with recurrent pain in the right tibia and new onset right clavicle pain demonstrates increased uptake in the right clavicle (small black arrows) and right proximal tibia (white arrows)

31.6.9 Other Noninfectious Inflammatory Joint diseases; Hemophilic Arthropathy



Fig. 31.19 A 17-year-old boy with *hemophilic arthropathy*. (a) Frontal and lateral radiographs of the elbow demonstrate hypertrophy of the radial head (*arrows*), joint space narrowing, subchondral sclerosis, and cystic changes. (b, c) Sagittal T2-WI with fat suppression

(b) and gradient echo sequence images (c) demonstrate linear dark signal along the synovium (*arrows*) suggesting hemosiderin deposition, subchondral cyst (*arrowhead*), and joint space narrowing

31.6.10 Other Noninfectious Inflammatory Joint Diseases; Neuropathic Arthritis

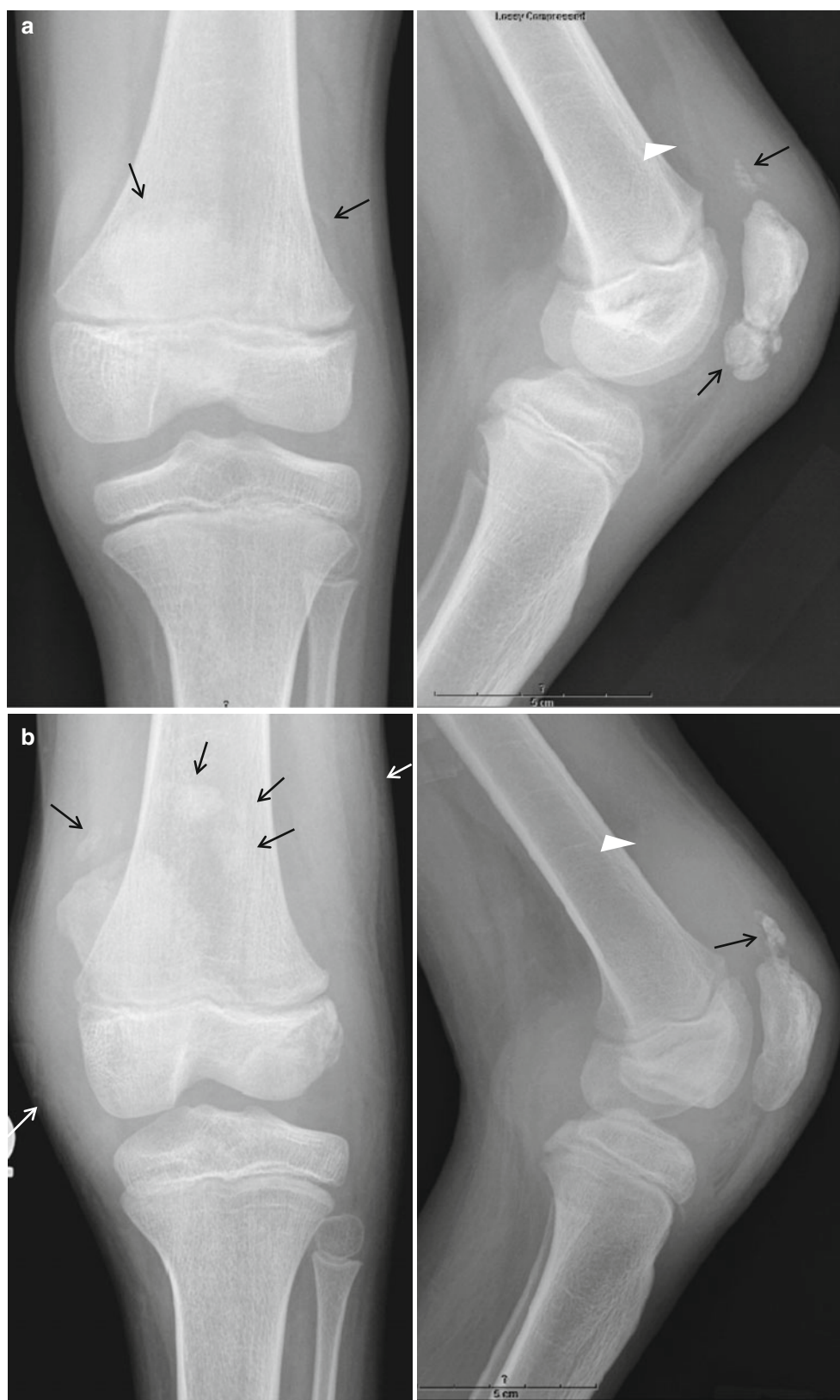


Fig. 31.20 A 6-year-old boy with myelomeningocele and neuropathic joint. (a) Initial radiographs of the knee joint demonstrate fragmentation of the patella (arrows) and a large joint effusion (arrowhead). (b) Follow-up radiographs 8 months later demonstrate soft tissue swelling (white arrows), progressive fracture of the patella (arrows), and a large

joint effusion (arrowhead). (c) Follow-up radiographs 12 months later demonstrate more soft tissue swelling and progressive fragmentation of the patella and a new finding of a lateral femoral condyle fracture. Several bone fragments are embedded in the soft tissue (arrows)

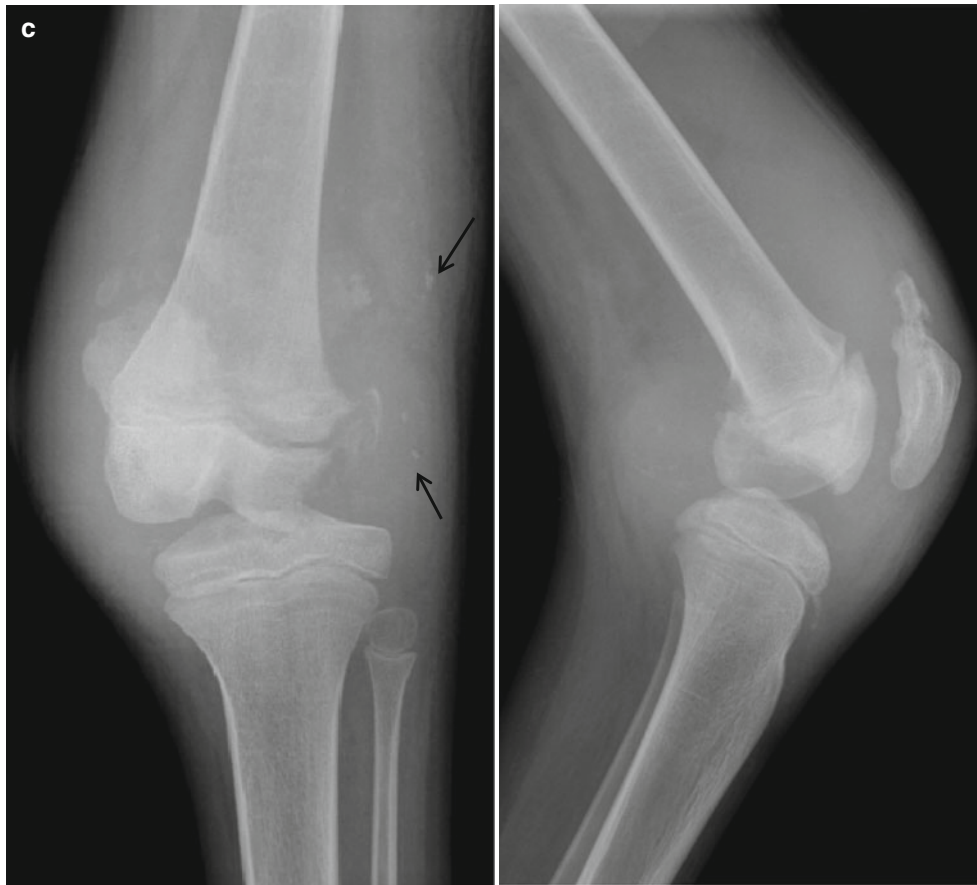


Fig. 31.20 (continued)

31.6.11 Miscellaneous Disorder of the Joint; Pigmented Villonodular Synovitis

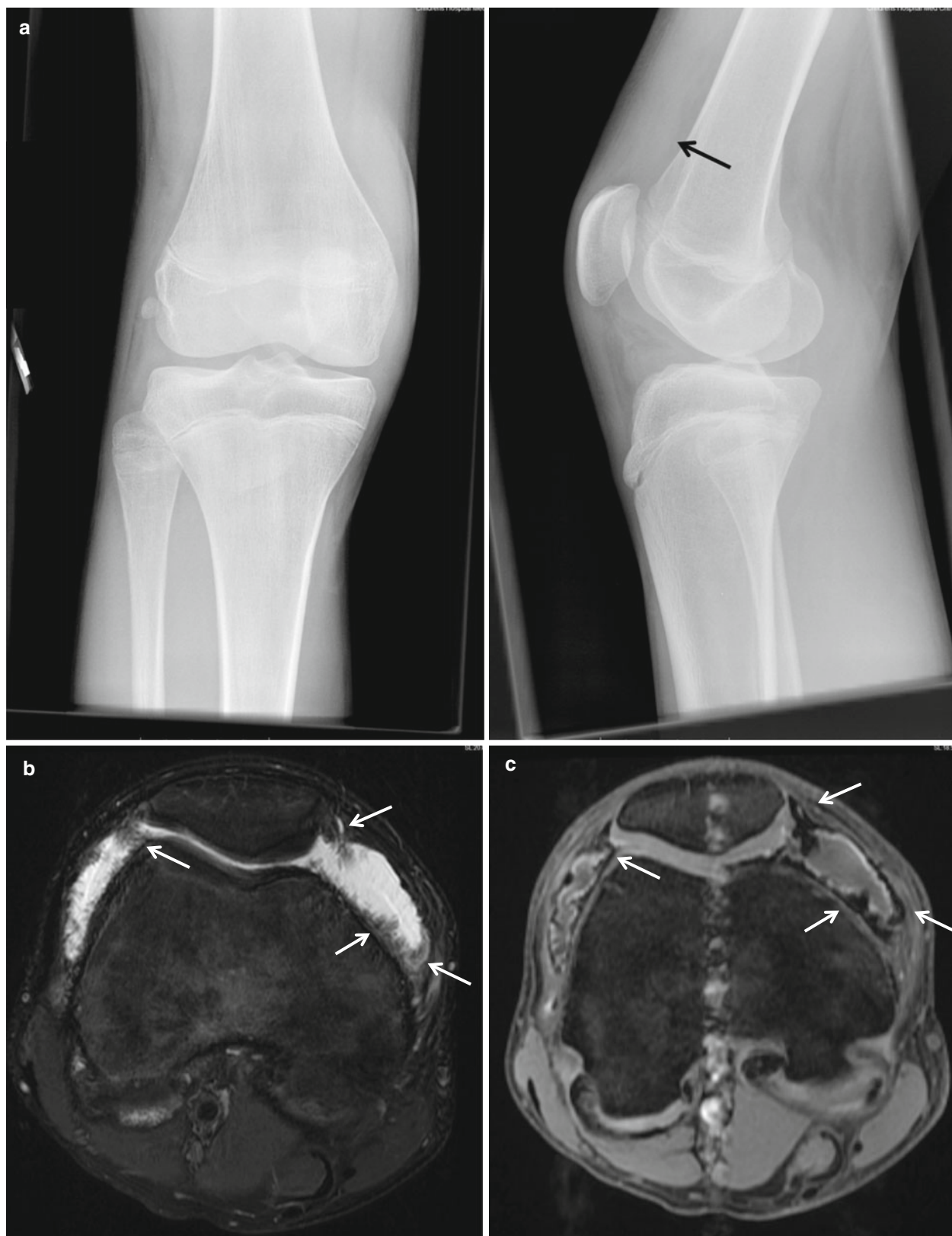


Fig. 31.21 A 13-year-old boy with diffuse pigmented villonodular synovitis (PVNS). (a) Plain radiograph demonstrates joint effusion (arrow). There is no bone erosion or calcification. (b, c) Axial T2-WI with fat suppression (b) and gradient echo sequence (c) demonstrate

frond-like proliferation of the synovium with dark signal from hemosiderin deposition, which was more prominent on gradient echo image due to blooming artifact (arrows)

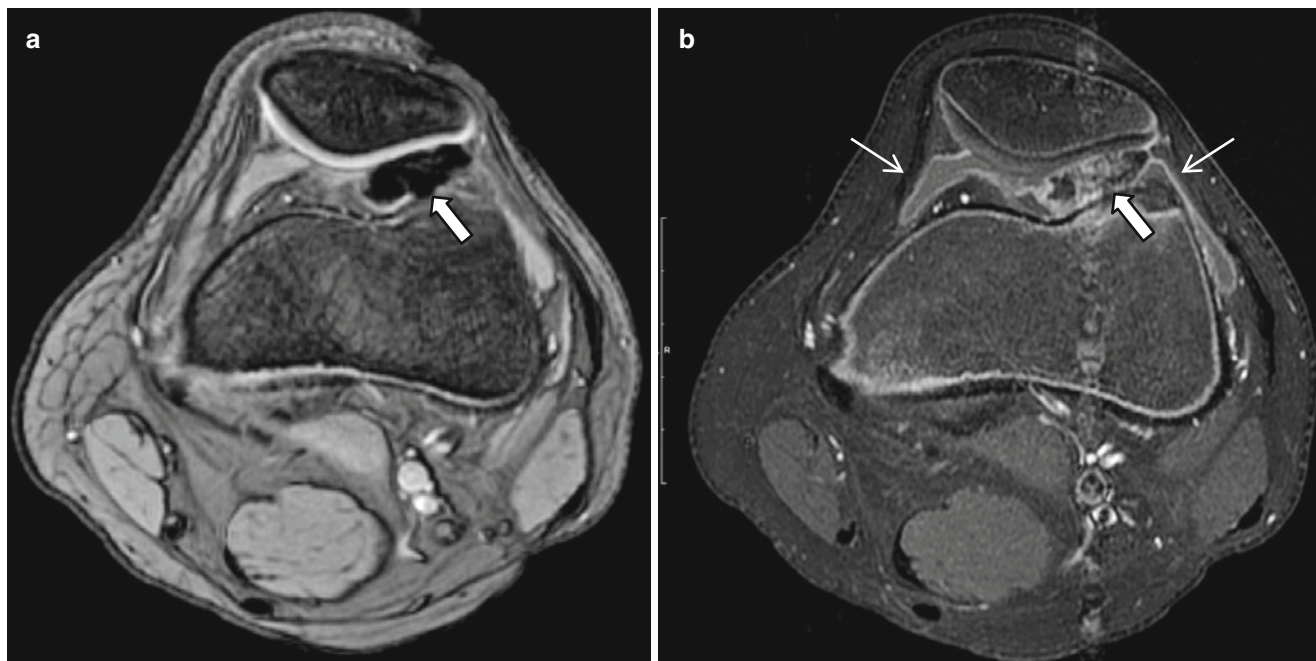


Fig. 31.22 A 15-year-old boy with localized PVNS. (a, b) Axial gradient echo sequence (a) and post-contrast axial T1-WI with fat suppression (b) demonstrate a single ovoid-shaped dark signal mass (arrows)

with synovial enhancement (small white arrows) (Reprinted by permission from HK Kim; *Pediatric Radiology*. 2011;41:495–511)

31.6.12 Miscellaneous Disorder of the Joint; Synovial Osteochondromatosis



Fig. 31.23 A 15-year-old girl with synovial osteochondromatosis. (a) Plain radiograph of the shoulder demonstrates multiple calcific bodies in the right glenohumeral joint (black arrow). (b) Sagittal T2-WI demonstrates multiple dark signal even-sized intra-articular loose bodies

suggesting ossified bodies. (c) Post-contrast axial T1-WI with fat suppression image demonstrates diffuse synovitis (arrows). (d) CT scan demonstrates even-sized calcified nodules (arrows) (Reprinted by permission from HK Kim; *Pediatric Radiology*. 2011;41:495–511)

31.6.13 Miscellaneous Disorder of the Joint; Lipoma Arborescens

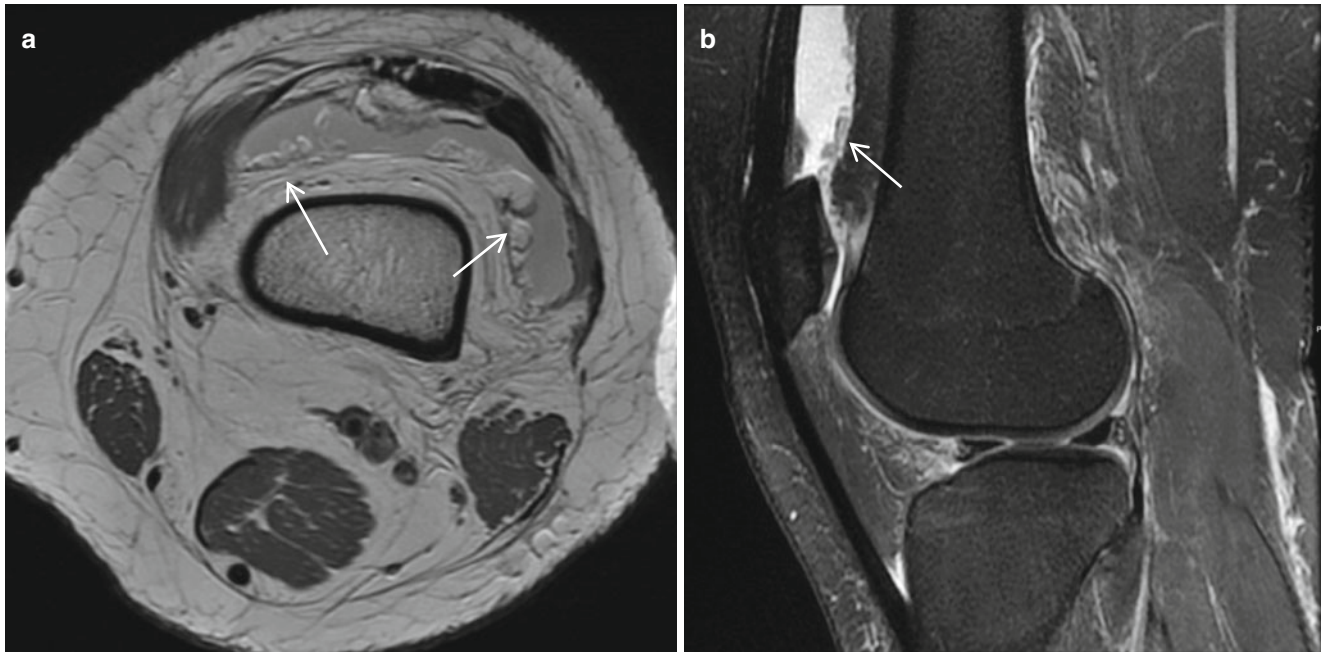


Fig. 31.24 A 16-year-old girl with *lipoma arborescens*. (a) Axial intermediate sequence image demonstrates frond-like fatty proliferation of the synovium (arrows). (b) Sagittal T2-WI with fat suppression demonstrates low signal intensity from fat suppression (arrow)

31.6.14 Miscellaneous Disorder of the Joint; Childhood Malignancies Presenting with Arthritis

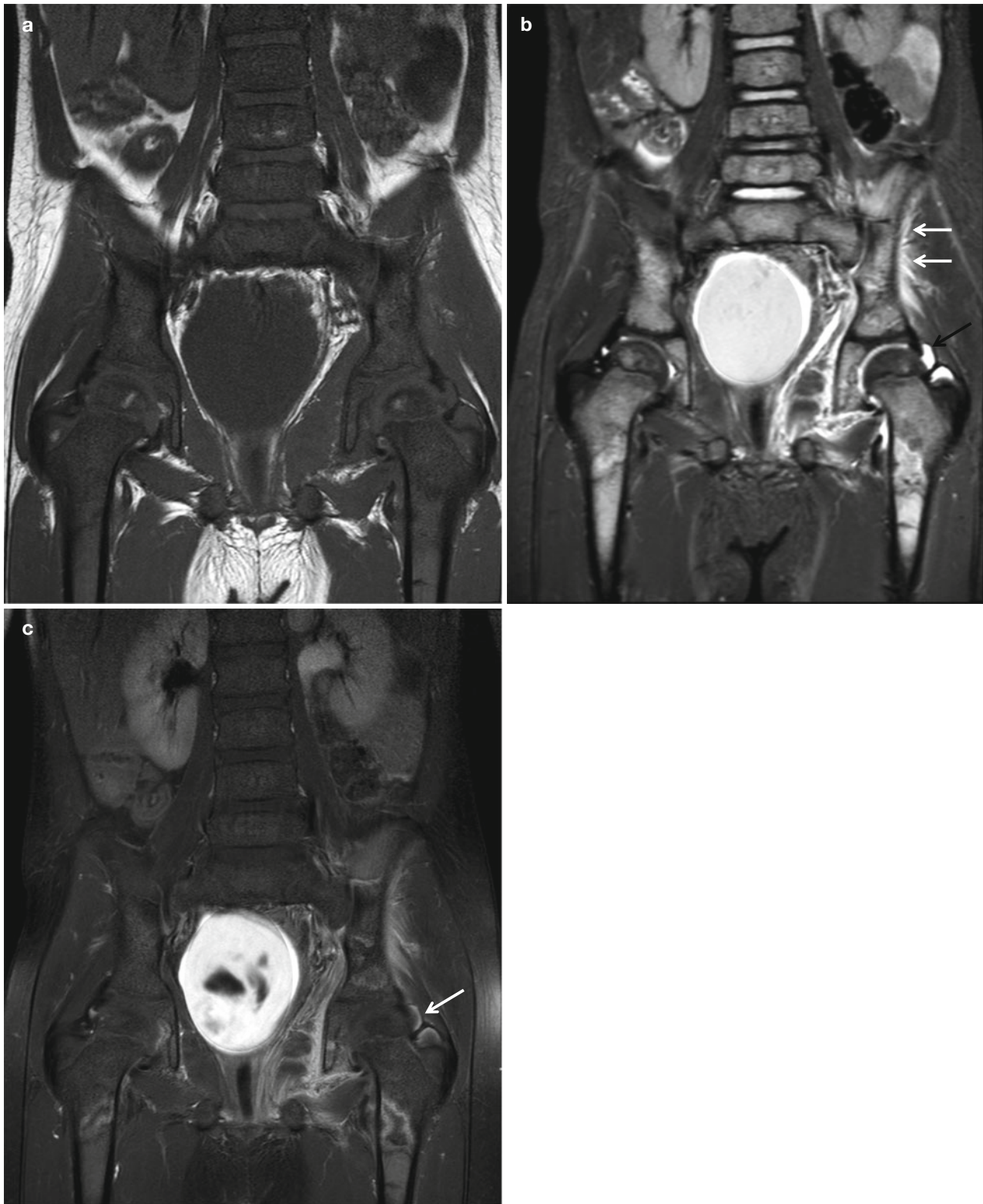


Fig. 31.25 A 4-year-old boy with left hip pain from metastatic neuroblastoma. (a, b) Coronal T1-WI (a) and T2-WI with fat suppression (b) demonstrate abnormal low T1 and high T2 marrow signal of the all imaged spines and pelvic bones. Left hip joint effusion (black arrow) and periostitis (white arrows) are seen. (c) Post-contrast coronal T1-WI

with fat suppression demonstrates synovial enhancement of the left hip (arrow). (d) Metaiodobenzylguanidine (MIBG) scan demonstrates multiple sites of increased skeletal uptake suggesting bone metastasis. Metastatic neuroblastoma was confirmed by bone marrow biopsy and microscopic examination

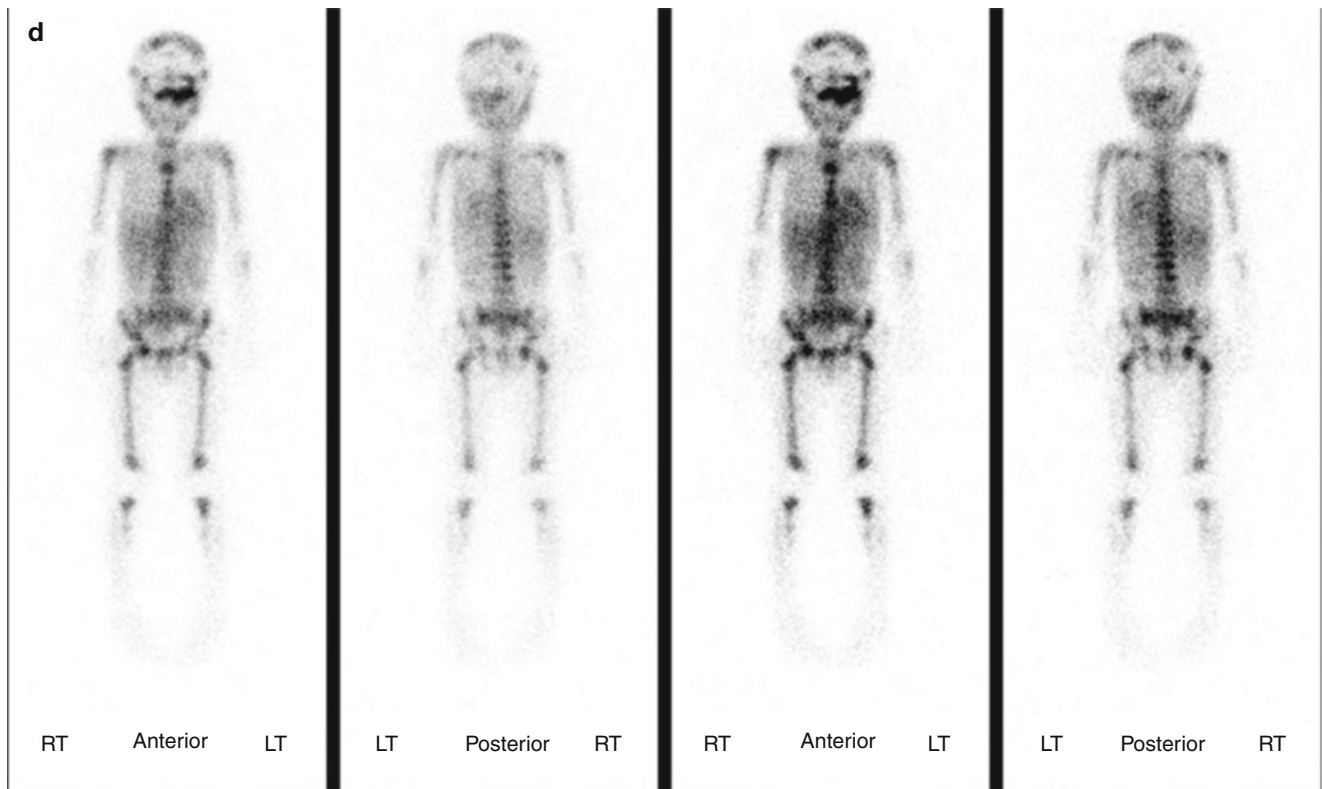


Fig. 31.25 (continued)

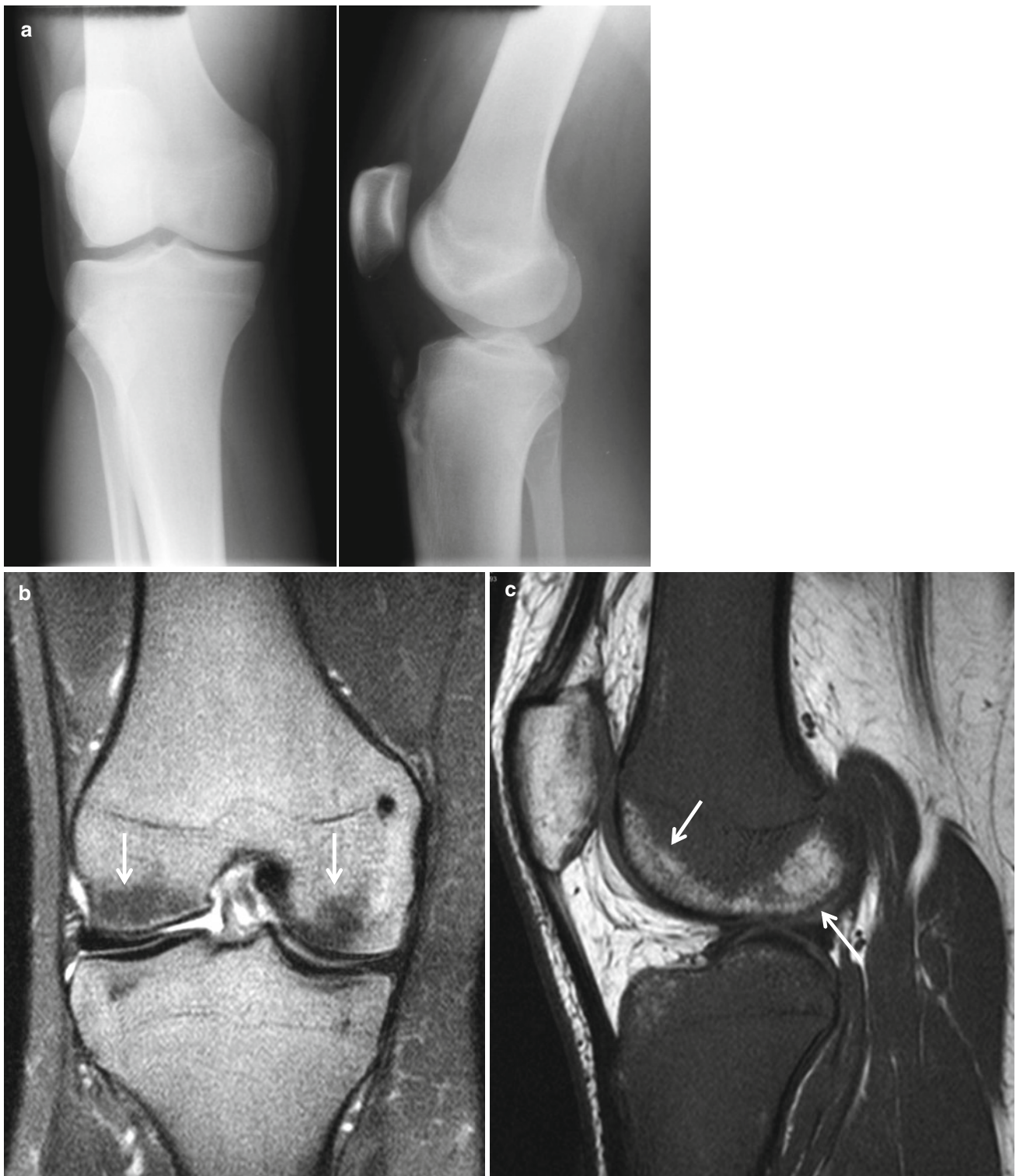


Fig. 31.26 A 17-year-old boy presented with left knee pain from chronic myeloid leukemia. (a) Plain radiographs of the knee demonstrate no bony abnormalities. (b, c) Coronal T2-WI with fat suppression (b) and sagittal intermediate signal intensity images (c) demonstrate

diffuse abnormal bone marrow signal sparing the patella and a very small portion of the femoral condyles (arrows). Bone marrow biopsy and microscopic examination confirmed chronic myeloid leukemia

31.6.15 Miscellaneous Disorder of the Joint; Synovial Vascular Malformation



Fig. 31.27 A 6-year-old boy with intra-articular venolymphatic malformation. (a) Sagittal T2-WI with fat suppression demonstrates intra-articular high T2 signal mass (white arrows) with dark signal foci suggesting phleboliths (small black arrows). (b) Post-contrast axial

T1-WI with fat suppression demonstrates heterogeneous enhancement suggesting a venous component and peripheral rim-like enhancement suggesting lymphatic components (small black arrows)

31.6.16 Noninfectious Inflammatory Diseases of the Soft Tissue; Dermatomyositis

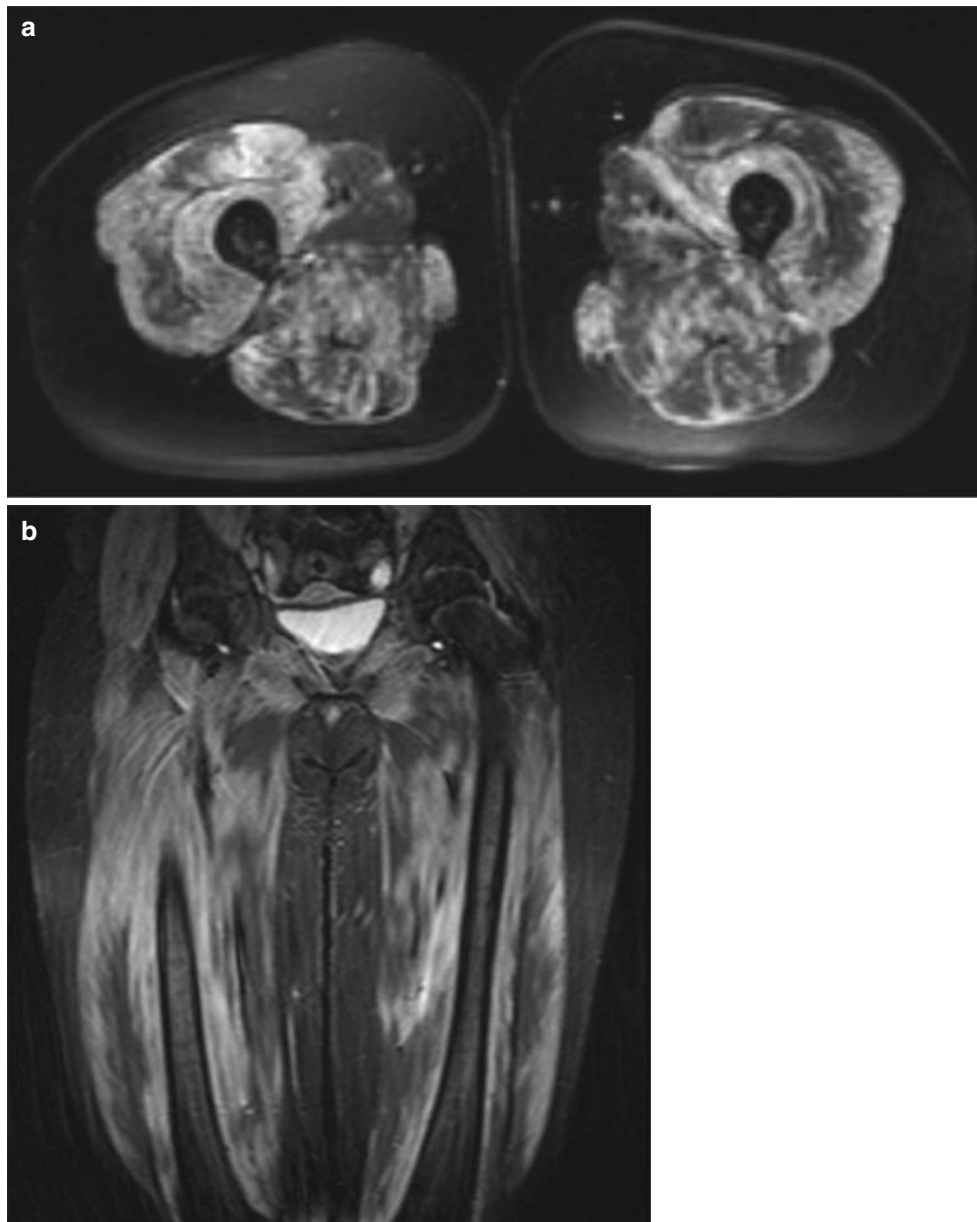


Fig. 31.28 An 11-year-old girl with *dermatomyositis*. (a, b) Axial (a) and coronal T2-WI with fat suppression images (b) of the thighs demonstrate bilateral muscle edema suggesting myositis

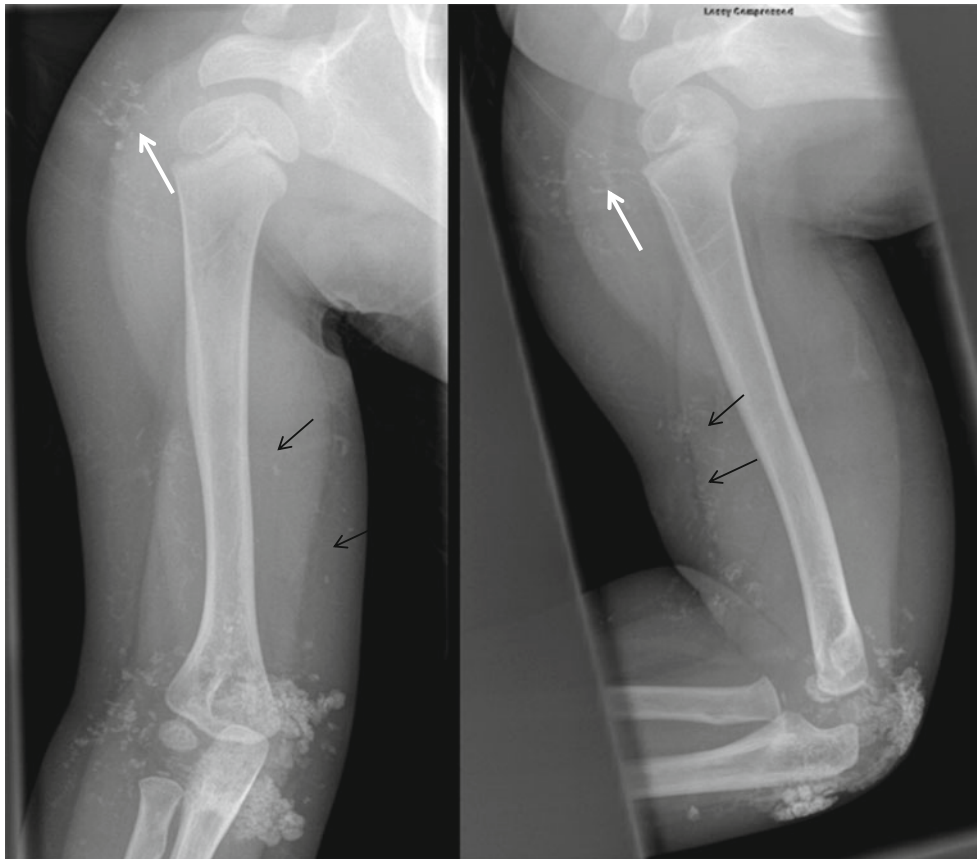


Fig. 31.29 A 3-year-old girl with dermatomyositis. A 3-year-old girl with dermatomyositis with extensive soft tissue calcifications of the shoulder (arrow) and elbow. Other more faint calcifications are seen around the mid portion of the upper arm (small black arrows)

31.6.17 Noninfectious Inflammatory Diseases of the Soft Tissue; Eosinophilic Fasciitis

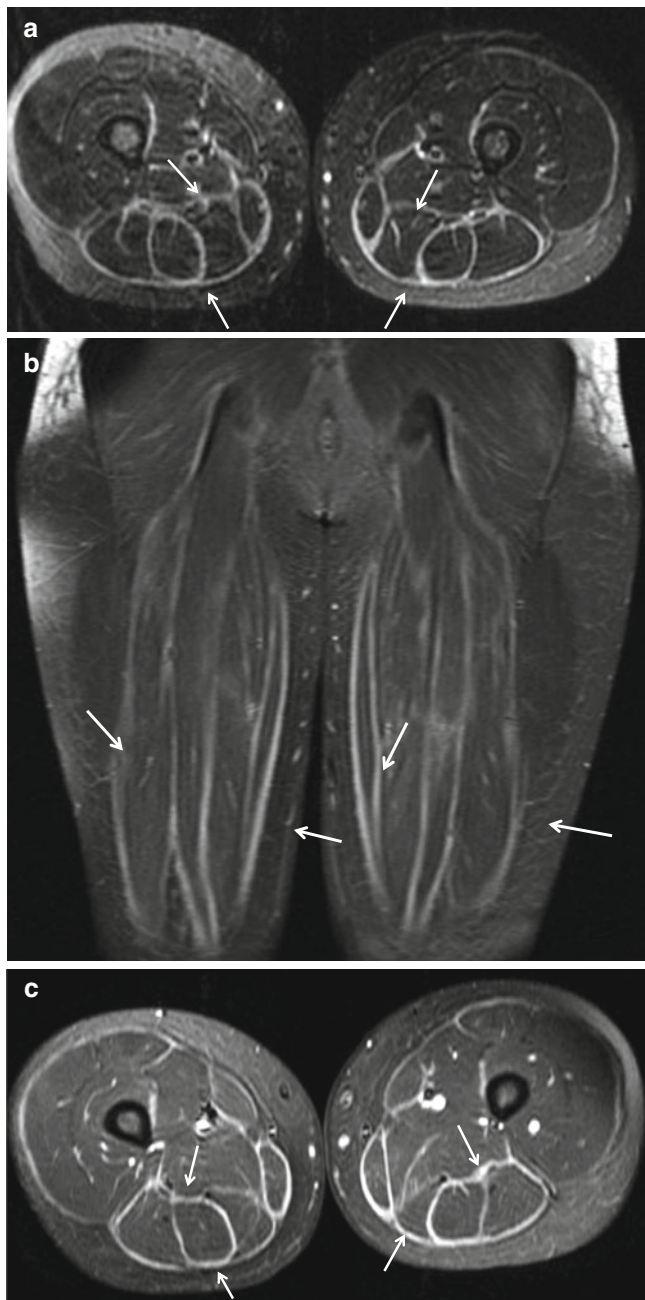


Fig. 31.30 A 15-year-old boy with *eosinophilic fasciitis*. (**a**, **b**) Axial (**a**) and coronal T2-WI with fat suppression (**b**) demonstrate diffuse bilateral high T2 signal along the fascial planes of the muscles (*arrows*). (**c**) Post-contrast axial T1-WI with fat suppression demonstrates thick enhancement of the fascia (*arrows*). No muscle edema is seen

References

- Arnold WD, Hilgartner MW. Hemophilic arthropathy. Current concepts of pathogenesis and management. *J Bone Joint Surg Am*. 1977; 59:287–305.
- Burk Jr DL, Dalinka MK, Kanal E, et al. Meniscal and ganglion cysts of the knee: MR evaluation. *AJR Am J Roentgenol*. 1988;150:331–6.
- Choi JA, Koh SH, Hong SH, et al. Rheumatoid arthritis and tuberculous arthritis: differentiating MRI features. *AJR Am J Roentgenol*. 2009; 193:1347–53.
- Cohen MD, Klatte EC, Baehner R, et al. Magnetic resonance imaging of bone marrow disease in children. *Radiology*. 1984;151:715–8.
- Doria AS. State-of-the-art imaging techniques for the evaluation of haemophilic arthropathy: present and future. *Haemophilia*. 2010;16 Suppl 5:107–14.
- Dorwart RH, Genant HK, Johnston WH, et al. Pigmented villonodular synovitis of synovial joints: clinical, pathologic, and radiologic features. *AJR Am J Roentgenol*. 1984;143:877–85.
- Erdem H, Baylan O, Simsek I, et al. Delayed diagnosis of tuberculous arthritis. *Jpn J Infect Dis*. 2005;58:373–5.
- Goldman AB, DiCarlo EF. Pigmented villonodular synovitis. Diagnosis and differential diagnosis. *Radiol Clin North Am*. 1988;26: 1327–47.
- Gordon BA, Martinez S, Collins AJ. Pyomyositis: characteristics at CT and MR imaging. *Radiology*. 1995;197:279–86.
- Gylys-Morin VM, Graham TB, Blebea JS, et al. Knee in early juvenile rheumatoid arthritis: MR imaging findings. *Radiology*. 2001;220: 696–706.
- Hopkins KL, Li KC, Bergman G. Gadolinium-DTPA-enhanced magnetic resonance imaging of musculoskeletal infectious processes. *Skeletal Radiol*. 1995;24:325–30.
- Howard CB, Einhorn M, Dagan R, et al. Ultrasound in diagnosis and management of acute haematogenous osteomyelitis in children. *J Bone Joint Surg Br*. 1993;75:79–82.
- Iyer RS, Thapa MM, Chew FS. Chronic recurrent multifocal osteomyelitis: review. *AJR Am J Roentgenol*. 2011;196:S87–91.
- Jaramillo D, Treves ST, Kasser JR, et al. Osteomyelitis and septic arthritis in children: appropriate use of imaging to guide treatment. *AJR Am J Roentgenol*. 1995;165:399–403.
- Johnson K, Davis PJ, Foster JK, et al. Imaging of muscle disorders in children. *Pediatr Radiol*. 2006;36:1005–18.
- Kan JH, Young RS, Yu C, et al. Clinical impact of gadolinium in the MRI diagnosis of musculoskeletal infection in children. *Pediatr Radiol*. 2010;40:1197–205.
- Kerr R. Imaging of musculoskeletal complications of hemophilia. *Semin Musculoskelet Radiol*. 2003;7:127–36.
- Ladd PE, Emery KH, Salisbury SR, et al. Juvenile dermatomyositis: correlation of MRI at presentation with clinical outcome. *AJR Am J Roentgenol*. 2011;197:W153–8.
- Lee SK, Suh KJ, Kim YW, et al. Septic arthritis versus transient synovitis at MR imaging: preliminary assessment with signal intensity alterations in bone marrow. *Radiology*. 1999;211: 459–65.
- Legiehn GM, Heran MK. Classification, diagnosis, and interventional radiologic management of vascular malformations. *Orthop Clin North Am*. 2006;37:435–74, vii–viii.
- Laugier J, Palmer J, Roson N, et al. Pigmented villonodular synovitis and giant cell tumors of the tendon sheath: radiologic and pathologic features. *AJR Am J Roentgenol*. 1999;172:1087–91.
- Luck Jr JV, Silva M, Rodriguez-Merchan EC, et al. Hemophilic arthropathy. *J Am Acad Orthop Surg*. 2004;12:234–45.
- Martin S, Hernandez L, Romero J, et al. Diagnostic imaging of lipoma arborescens. *Skeletal Radiol*. 1998;27:325–9.
- Moulton SJ, Kransdorf MJ, Ginsburg WW, et al. Eosinophilic fasciitis: spectrum of MRI findings. *AJR Am J Roentgenol*. 2005;184: 975–8.
- Parmar H, Shah J, Patkar D, et al. Tuberculous arthritis of the appendicular skeleton: MR imaging appearances. *Eur J Radiol*. 2004;52: 300–9.
- Petty RE, Southwood TR, Manners P, et al. International League of Associations for Rheumatology classification of juvenile idiopathic arthritis: second revision, Edmonton, 2001. *J Rheumatol*. 2004;31: 390–2.
- Vilanova JC, Barcelo J, Villalon M, et al. MR imaging of lipoma arborescens and the associated lesions. *Skeletal Radiol*. 2003; 32:504–9.
- Weiss JE, Ilowite NT. Juvenile idiopathic arthritis. *Rheum Dis Clin North Am*. 2007;33:441–70, vi.

Hye-Kyung Yoon

Contents

32.1	Introduction	1008
32.2	Imaging	1008
32.3	Common Pediatric Benign Bone Tumors	1008
32.3.1	Exostosis (Osteochondroma)	1008
32.3.2	Enchondroma	1008
32.3.3	Osteoid Osteoma	1008
32.3.4	Chondroblastoma	1008
32.3.5	Giant Cell Tumor	1009
32.3.6	Bone Cysts	1009
32.3.7	Fibrous Cortical Defect (Non-ossifying Fibroma)	1009
32.3.8	Fibrous Dysplasia	1009
32.3.9	Osteofibrous Dysplasia	1009
32.3.10	Langerhans Cell Histiocytosis	1009
32.4	Common Pediatric Malignant Bone Tumors	1010
32.4.1	Osteosarcoma	1010
32.4.2	Ewing's Sarcoma	1010
32.4.3	Lymphoma/Leukemia/Metastasis	1010
32.5	Illustrations: Pediatric Bone Tumors	1011
32.5.1	Osteochondroma	1011
32.5.2	Enchondroma	1014
32.5.3	Osteoid Osteoma	1015
32.5.4	Chondroblastoma	1016
32.5.5	Giant Cell Tumor	1017
32.5.6	Simple Bone Cyst	1018
32.5.7	Aneurysmal Bone Cyst	1020
32.5.8	Non-ossifying Fibroma	1021
32.5.9	Fibrous Dysplasia	1022
32.5.10	Osteofibrous Dysplasia	1024
32.5.11	Langerhans Cell Histiocytosis	1025
32.5.12	Conventional Osteosarcoma	1028
32.5.13	Juxtacortical Osteosarcoma	1031
32.5.14	Ewing Sarcoma	1033
32.5.15	Primary and Secondary Lymphoma	1034
32.5.16	Metastatic Neuroblastoma	1036
	References	1037

H.-K. Yoon, M.D., Ph.D.
 Department of Radiology, Asan Medical Center,
 University of Ulsan College of Medicine,
 86 Asanbyeongwon-gil, Songa-gu, Seoul 138-736, Korea
 e-mail: hk2005.yoon@gmail.com

32.1 Introduction

The incidence of bone tumors is more likely age dependent. Osteosarcoma is the most common malignant tumors, followed by Ewing's sarcoma. There is a preferred location within the bone, e.g., epiphysis, metaphysis, and diaphysis. The differential diagnosis can be narrowed down by considering the following: (1) patient's age, (2) involved skeleton, (3) the location within the specific bone, (4) central or eccentric, (5) single or multiple, and (6) aggressiveness on imaging.

32.2 Imaging

Regardless of the location of bone tumors, the initial imaging modality should be plain radiography. Radiographs are useful for confirming the presence of bone tumor and its location in order to get closer to the diagnosis and guide for selection of further imaging modality. Typical benign tumors are well demarcated, with narrow transition zone and sclerotic rim, expansile rather than infiltrating, showing benign-type periosteal reaction (Kaste et al. 2008). Malignant tumors show aggressive imaging features including poorly defined margins, permeative or moth-eaten pattern of bone destruction, wide transition zone with less sclerosis, and malignant-type periosteal reactions (e.g., onion skin and hair on end). On CT and MRI, there may be associated soft tissue mass which favors malignant tumors. Although some benign bone tumors are easily identified on plain radiography and do not need further imaging study, most bone tumors require further study for more correct diagnosis or as a guidance of interventional procedure. Ultrasound, CT, MRI, bone scintigraphy, and PET scanning can aid the diagnosis depending on what the tumor nature is (Walter et al. 2011). MRI is the most preferred imaging modality for detailed evaluation of the malignant bone tumor.

32.3 Common Pediatric Benign Bone Tumors

32.3.1 Exostosis (Osteochondroma)

Osteochondroma is one of the most common pediatric bone tumors and thought to be a developmental defect rather than a true tumor. They are usually asymptomatic; however, symptomatic presentations are not uncommon which are caused by irritation of adjacent tissues. A bursa may develop due to associated inflammation. Malignant transformation is worrisome, but fortunately it is exceedingly rare unless it is inherited cases.

It commonly involves the long bone metaphyses and about one-third of cases are found around the knee joint, either sessile or pedunculated. Continuity of cortex and

medullary cavity from the mother bone is a hallmark of osteochondroma. MRI is superior to CT for demonstrating the cartilaginous cap which is a hyperintense crescent usually less than 5 mm (upper normal limit of 10 mm) (Figs. 32.1 and 32.2).

Osteochondromas can occur in oncology patients who received radiation therapy with latent periods varying from 3 to 16 years.

Epiphyseal manifestation of the osteochondroma is known as *dysplasia epiphysealis hemimelica* (Trevor's disease), more common in boys. The lower extremity is usually affected unilaterally (Azouz et al. 1985) (Fig. 32.3). MRI is helpful for defining epiphyseal abnormality which is predominantly cartilaginous.

32.3.2 Enchondroma

Enchondroma is a benign cartilaginous tumor which can occur in the pediatric population. It usually involves the small tubular bones of the hands and feet in the metaphysis or metadiaphysis (Bierry et al. 2012). On radiography and CT, punctuate or the so-called "chondroid" calcifications can be appreciated, and on MRI, signal intensity follows cartilage on all sequences, revealing predominantly high signal on T2-weighted images (Fig. 32.4). Ollier disease is characterized by multiple enchondromatosis which is basically a mesodermal dysplasia. Maffucci syndrome is enchondromatosis accompanied by vascular malformations (Fig. 32.5).

32.3.3 Osteoid Osteoma

Osteoid osteomas are relatively common in teenagers and young adults with slightly more male prevalence (Iyer et al. 2012). This is usually less than 1.5 cm in lengths and night pain is the presenting symptom. Radiologically, calcified nidus appears as a central sclerotic area surrounded by radiolucent rim which is associated with cortical thickening and periosteal new bone formation. MRI can clearly show bone marrow edema and surrounding soft tissue changes (Fig. 32.6). Differential diagnosis may include Brodie's abscess, stress fracture, and/or osteomyelitis.

32.3.4 Chondroblastoma

Chondroblastoma is common in the second decade of life, involving the epiphyses of long bones. Almost half of lesions occur prior to physeal closure. It can have a component of aneurysmal bone cyst. Radiography shows an eccentric well-defined radiolucent lesion with sclerotic margins in an epiphysis or apophysis. Calcified chondroid matrix is seen in about one-third (Fig. 32.7).

32.3.5 Giant Cell Tumor

Giant cell tumor is rarely seen before skeletal maturation, rarely in the first decade of life. It is more common in the distal femur and proximal tibia. In pediatric patients before skeletal maturity, it usually occurs in the metaphysis abutting the physis (Hoeffel et al. 1996). It appears as a geographic osteolytic lesion in the long bones without calcified or ossified matrix (Fig. 32.8). In about 15 %, there can be associated component of aneurysmal bone cyst (Kaste et al. 2008).

32.3.6 Bone Cysts

Simple bone cyst, or unicameral cyst, is commonly found incidentally and asymptomatic unless complicated by pathologic fracture (Fig. 32.10). Cysts migrate into the diaphysis as the bones grow. Unicameral cysts are occasionally seen in the calcanei almost always located near the neck of the calcaneus (Fig. 32.9).

Aneurysmal bone cyst (ABC) is either primary or secondary, and most of them are thought to be reactive and secondary. Radiography shows an expansile “soap-bubble” lesion with thin smooth bony walls. CT and MRI can demonstrate fluid–fluid levels due to degraded blood products, which are characteristic of the lesion (Fig. 32.11). Secondary ABC components with fluid–fluid levels can be identified in various benign bone lesions like fibrous dysplasia, chondroblastoma, GCT, non-ossifying fibroma, and simple bone cyst.

32.3.7 Fibrous Cortical Defect (Non-ossifying Fibroma)

Fibrous cortical defect (FCD) and non-ossifying fibroma (NOF) are considered histologically identical and arbitrarily divided by size of 2 cm. FCDs are essentially a normal variant, detected incidentally. Radiography is usually sufficient to diagnose them and biopsy is not indicated. They are most common in the metaphyses of the long bones of the lower extremity and more commonly posterior (Fig. 32.12). FCD and cortical desmoids are histologically similar. FCDs appear as small, well-defined, and cortex-based lesions. Metaphyseal FCDs and NOFs are migrated into the diaphysis with skeletal growth.

32.3.8 Fibrous Dysplasia

Fibrous dysplasia can be monostotic or polyostotic and the majority involves only one skeletal part (monostotic). Polyostotic form is often syndromic such as the McCune-Albright syndrome (precocious puberty, cutaneous café-au-lait lesions, and unilateral polyostotic fibrous dysplasia) (Fig. 32.14).

Fibrous dysplasia in the long bones causes endosteal scalloping and bone expansion, the so-called “shepherd’s crook” deformity and “ground-glass” matrix. There is no periosteal reaction unless fractured. MRI reveals similar signal intensity to muscle on T1-weighted images and variable signal on T2-weighted images depending on the component although hyperintense in most cases (Fig. 32.13).

32.3.9 Osteofibrous Dysplasia

Osteofibrous dysplasia or ossifying fibroma is a proliferation of the fibro-osseous tissue. It is an eccentric, lucent, multi-loculated lesion involving the anterior cortex of the tibia. There is associated cortical thickening and anterior bowing (Fig. 32.15). Eccentric cortical location is the differential point from fibrous dysplasia in medullary location. Radiological as well as pathologic differentiation between osteofibrous dysplasia and adamantinoma is difficult.

32.3.10 Langerhans Cell Histiocytosis

Langerhans cell originates from CD34+ cells of the bone marrow, and the traditional term of “histiocytosis X” is no longer used. Infection was once known as one of the causes, but now it is accepted to be the neoplastic process. Traditionally, patients with Langerhans cell histiocytosis (LCH) were divided into three categories depending on the involved system: only bone involved in eosinophilic granuloma; cranial lesions, diabetes insipidus, and exophthalmos in Hand-Schuller-Christian disease; and the disseminated form in Letterer-Siwe disease in infants and younger children. Nowadays, a revised classification is used including restricted (monostotic and polyostotic) form or extensive (visceral organ involvement) form (Kilborn et al. 2003). It is also accepted that LCH is a spectrum of disease rather than distinguishable entities.

The skull is most frequently involved, followed by the femur, mandible, pelvis, ribs, and spine (Fig. 32.16). LCH is the most common cause of the vertebra plana in children (Fig. 32.18). Long bone lesions occur in the metaphysis or diaphysis.

Most LCH bone lesions are well defined (“punched out”) and purely osteolytic with endosteal scalloping (Fig. 32.18). Sometimes it can be permeative and aggressive with periosteal new bone formation which may be either single layered or multilayered. Skull lesions show beveled edges. On MRI, there is extensive bone marrow and soft tissue edema representing associated inflammatory reaction which, in turn, produces an aggressive appearance simulating malignancy (Jeh et al. 2012) (Fig. 32.17). Soft tissue mass is associated in about 30 % of lesions. Multiple bony lesions are suggestive of LCH. Skeletal survey and, more recently, whole-body

MRI are used for initial workup and disease follow-ups (Steinborn et al. 2008).

Localized LCH to the skeletal system carries a favorable prognosis, and there have been some cases of showing spontaneous regression. Children with multiple lesions or associated systemic disease are managed more aggressively with steroids and chemotherapeutic agents (Ghanem et al. 2003).

32.4 Common Pediatric Malignant Bone Tumors

32.4.1 Osteosarcoma

Osteosarcoma is the most common pediatric malignant bone tumor, and the peak age is 15–25 years. There are histological variants in osteosarcoma including telangiectatic, parosteal, and periosteal subtypes. Osteosarcoma can occur secondarily to previous radiation therapy and can arise in patients with enchondromatosis, exostoses, and fibrous dysplasia. The long bones are affected in about 70 % and it usually arises from the medullary cavity of the long bone metaphyses (Kaste 2011).

Radiography is essential for the diagnosis of the malignant bone tumors. There is a large osteolytic mass mixed with sclerosis involving the long bone metaphyses (Fig. 32.19). The cortices are destroyed rather than expanded, showing “sunburst” periosteal reaction and Codman triangles (Fig. 32.20). Conventional osteosarcomas can be purely lytic without periosteal reaction.

MRI is the modality of choice next to the radiography to see the extent of marrow disease and surrounding soft tissue involvement as well as for surgical decision (Figs. 32.19 and 32.20). Marrow involvement is clearly seen on T1-weighted images as a well-defined hypointense area. It is important to detect skip areas of metastases (Fig. 32.21). On T2-weighted images, the signal intensity depends on the degree of bone matrix formation, either hyperintense or hypointense. Fat-suppression images can show the lesions more conspicuously. Contrast-enhanced fat-suppressed T1-weighted images are useful for evaluating relationship between the tumor and the major vessels and in detecting joint involvement and intratumoral necrosis.

Lung metastasis is common and can be calcified. It may produce pneumothorax, hemothorax, or malignant pleural effusion. Initial staging workup should include chest CT for screening of lung metastasis (Meyer et al. 2008) (Fig. 32.21).

Telangiectatic variant osteosarcoma shows lytic bony lesions rather than sclerotic lesions with or without bony expansion and little periosteal reactions. It can mimic aneurysmal bone cyst especially on MRI having fluid–fluid levels.

Parosteal osteosarcoma is considered to be of low histological grade, while periosteal osteosarcoma probably is classified as an intermediate-grade osteosarcoma (Figs. 32.22 and 32.23). More superficial parosteal osteosarcoma grows outwardly, usually involving the posterior aspect of the distal femur. Dense ossification is characteristic on CT and MRI: the differential diagnosis can include myositis ossificans.

32.4.2 Ewing's Sarcoma

Ewing's sarcoma is the second most common malignant bone tumors in children and young adults ranging from 10 to 25 years of age (Wootton-Gorges 2009). Ewing family including Ewing's sarcoma and primitive neuroectodermal tumor can involve both bone and soft tissue. They are highly aggressive small round cell tumors, and the majority of the cases carry a EWS-FLI 1 fusion sequence. Ewing's sarcoma involves flat bones and tubular bones (metaphysis and diaphysis) almost equally.

Radiographically, lamellated “onion-skin”-type periosteal reaction is known as a characteristic finding of Ewing's sarcoma along with a permeative bony lesion. Extensive marrow involvement is seen on MRI and these tumors can make permeative growth without significant cortical bone loss (Fig. 32.24).

Lung metastasis is not uncommon even in the initial diagnosis, and chest CT is necessary for tumor staging (Meyer et al. 2008).

32.4.3 Lymphoma/Leukemia/Metastasis

Primary lymphoma of the skeletal system is rare (Fig. 32.25). It most commonly occurs in the lower extremities (Mengiardi et al. 2005). The findings on the plain radiography are subtle, either sclerotic or osteolytic. MRI can reveal extensive marrow involvement (Fig. 32.26) and disproportionally large soft tissue masses as compared to the extent of cortical destruction.

In leukemic patients, there would be widespread bone marrow abnormality on MRI even though a focal destructive bony lesion can mimic a primary bone malignancy in some cases. Granulocytic sarcoma or chloroma usually involves the soft tissue rather than the bone.

Neuroblastoma is the most common source of metastatic bone disease which is usually seen as metaphyseal osteolytic lesions (Fig. 32.27). MIBG scan is more useful than conventional technetium-99 m MDP bone scintigraphy for evaluating skeletal involvement. Whole-body MRI and 18F-FDG PET/CT would be also useful for detecting diffuse skeletal tumor involvement (Papaioannou and McHugh 2005).

32.5 Illustrations: Pediatric Bone Tumors

32.5.1 Osteochondroma

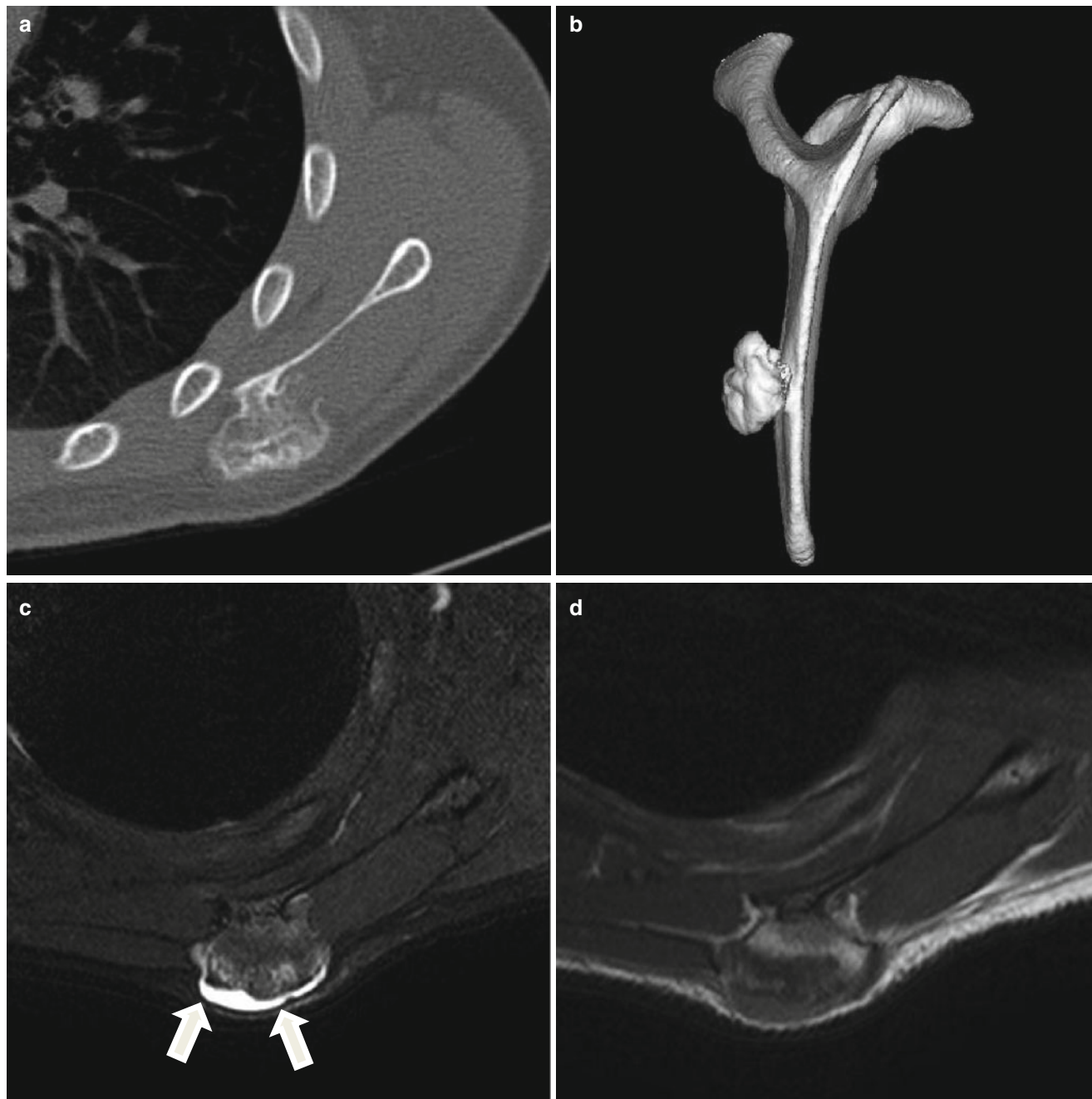


Fig. 32.1 Osteochondroma in the left scapula. (a) Axial CT image shows a protruding bone-forming mass arising from the left inferomedial scapula of which the medullary cavity is continuous with the mass. (b) 3D reconstruction image of the scapula clearly demonstrates

mushroom-shaped osteochondroma arising from the scapula. (c, d) Axial STIR (c, short-tau inversion recovery) and T1-weighted (d) images show scapular osteochondroma with hyperintense cartilaginous cap (arrows in c)

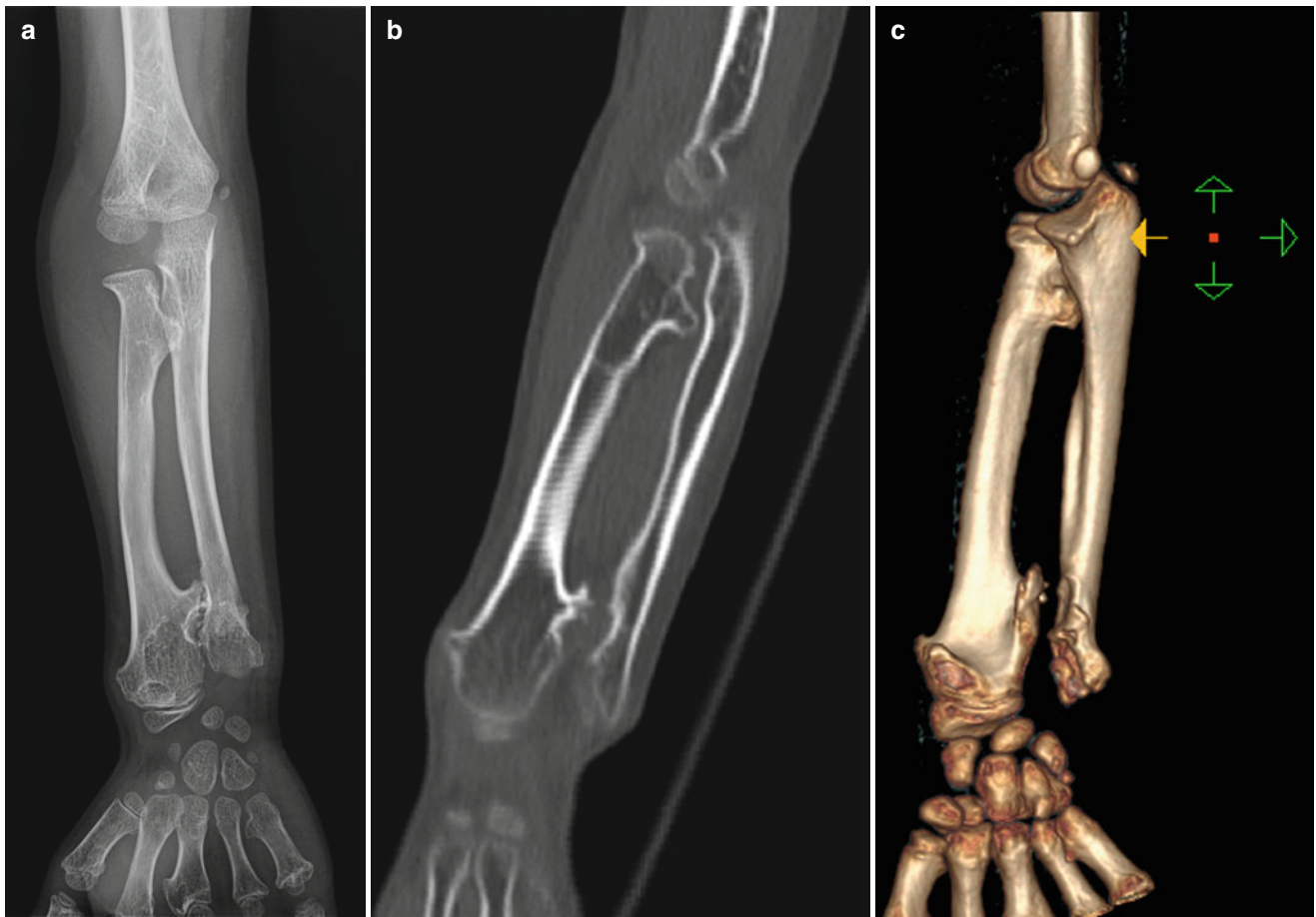


Fig. 32.2 Osteochondromatosis in an 8-year-old boy. (a–c) Forearm radiography (a), coronal CT image (b), and 3D reconstruction image (c) show multiple sessile osteochondromas involving the radius and

ulna. The ulna is short and the radiocarpal joint is slanted, resulting in the so-called Madelung deformity

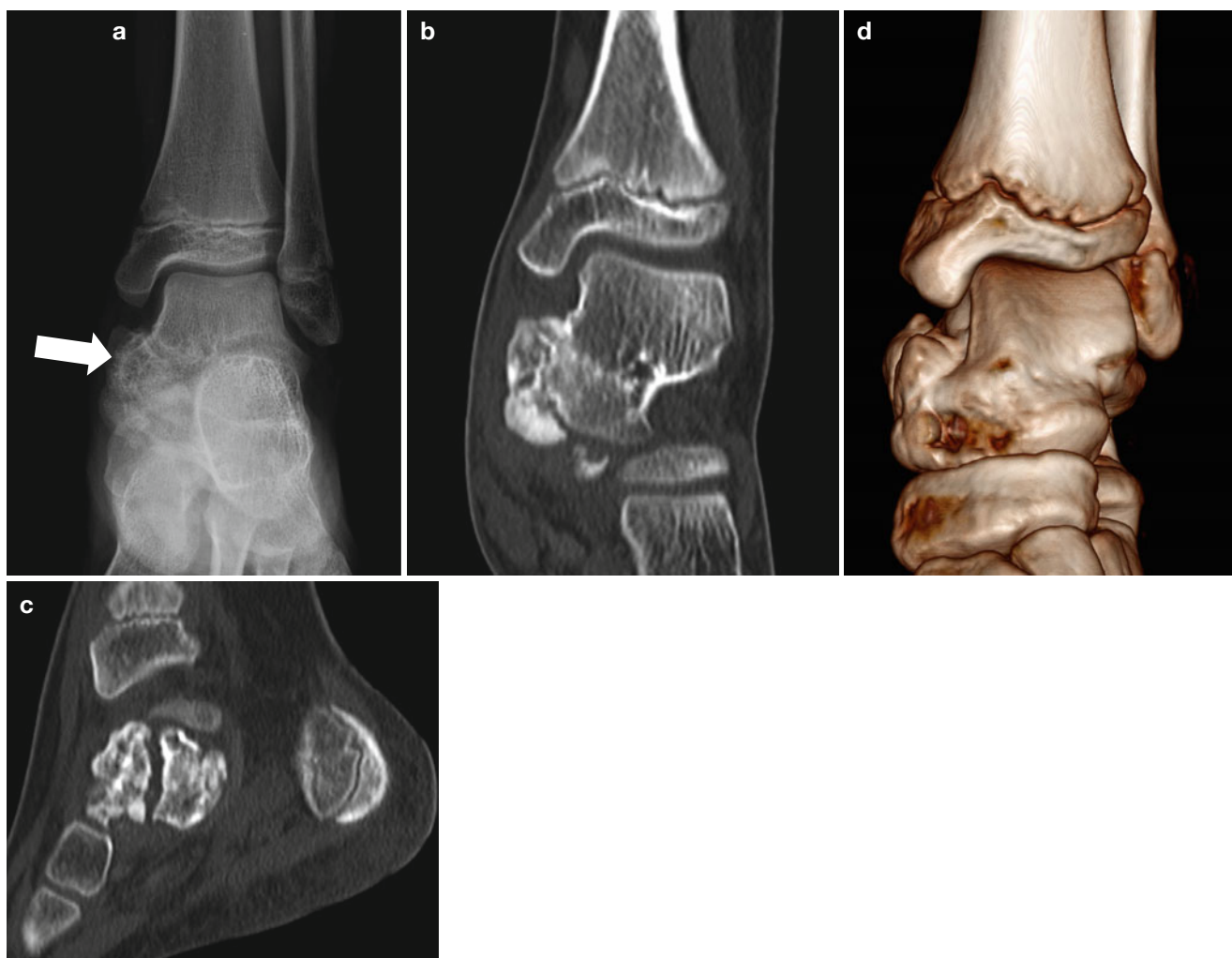


Fig. 32.3 *Epiphyseal dysplasia hemimelica (Trevor's disease)* in a 9-year-old girl. **(a)** Left ankle AP radiograph shows a protruding bony lesion with bubbly appearance (*arrow*) in the medial aspect of the left talus. **(b–d)** Coronal **(b)** and sagittal **(c)** CT images show a lobulating

contoured bony protuberance arising from the talus of which the cortex and medullary cavity are continuous with the mother bone. 3D reconstructed image **(d)** well visualizes a protruding bony mass in the medial talus

32.5.2 Enchondroma

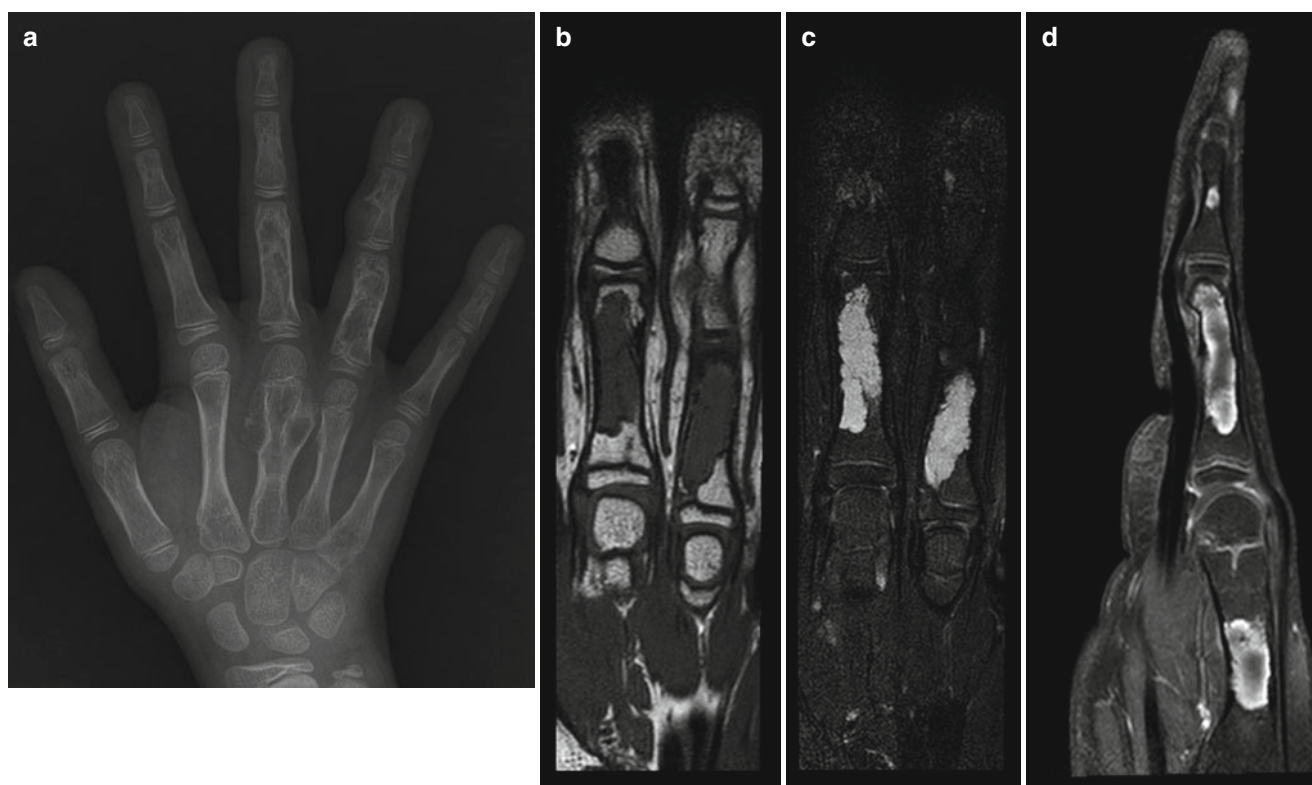


Fig. 32.4 *Enchondromas in an 11-year-old boy.* (a) Left-hand radiography shows relatively well-demarcated osteolytic lesions involving the short tubular bones of the hand with coarse trabeculations within the lesions. (b–d) MR T1-weighted coronal (b), STIR coronal (c), and postcontrast T1-weighted sagittal (d) images reveal well-demarcated

and intensely enhancing bony lesions involving the phalangeal bones. Note dark signal intensity sclerotic rims around the lesions with narrow transition zones. Bright signal intensity on T2-weighted and STIR images is in keeping with the chondroid matrix



Fig. 32.5 *Maffucci syndrome.* Both hand AP radiographs show multiple bizarre osteolytic bony lesions involving metacarpals and phalangeal bones which are consistent with enchondromatosis. There are also

multiple soft tissue masses with internal rounded calcifications representing phleboliths. Maffucci syndrome is consisting of enchondromatosis and hemangiomas or vascular malformations

32.5.3 Osteoid Osteoma



Fig. 32.6 *Osteoid osteoma in a 3-year-old boy. (a)* Small round osteolytic lesion is seen in the left distal femur metadiaphysis with adjacent cortical thickening (*arrow*). **(b)** CT shows a round radiolucent lesion with central dense spot representing calcified nidus. There is associated

thick periosteal reaction and bone sclerosis. **(c)** Contrast-enhanced MR reveals enhancement along the periphery of the bony lesion with surrounding soft tissue enhancement

32.5.4 Chondroblastoma

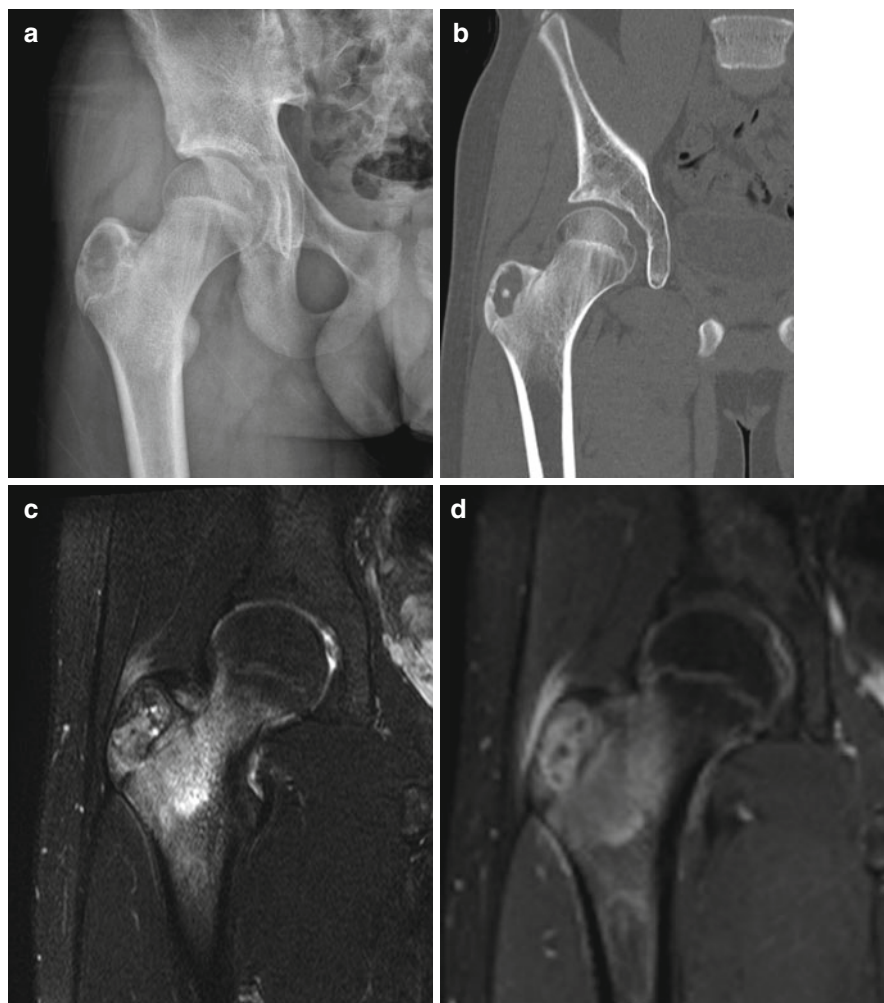


Fig. 32.7 Chondroblastoma in a 15-year-old boy. (a, b) Plain radiography (a) and CT (b) show a well-demarcated osteolytic lesion in the right femur greater trochanter. Note the lesion involving the apophysis (analog to the epiphysis) and there is no cortical bone disruption. (c, d) MR fat-suppressed T2-weighted image (c) and postcontrast

T1-weighted (d) coronal images show hyperintense and well-enhancing lesion in the greater trochanter with dark signal foci within the mass representing calcifications. Hyperintense marrow edema is seen in the femoral neck

32.5.5 Giant Cell Tumor



Fig. 32.8 Giant cell tumor in a 22-year-old female patient. (a) Right-knee AP radiograph shows a well-demarcated expansile osteolytic bony lesion with internal septa involving the proximal tibial epiphysis and metaphysis. The physes are completely closed in this patient. (b–d) MR T1-weighted (b) image reveals well-circumscribed hypointense bony

lesion in the right proximal tibia with sclerotic rim and narrow transition. The lesion is of heterogeneous high signal intensity on fat-suppressed proton-density image (c) and is well enhanced after administration of gadolinium (d)

32.5.6 Simple Bone Cyst

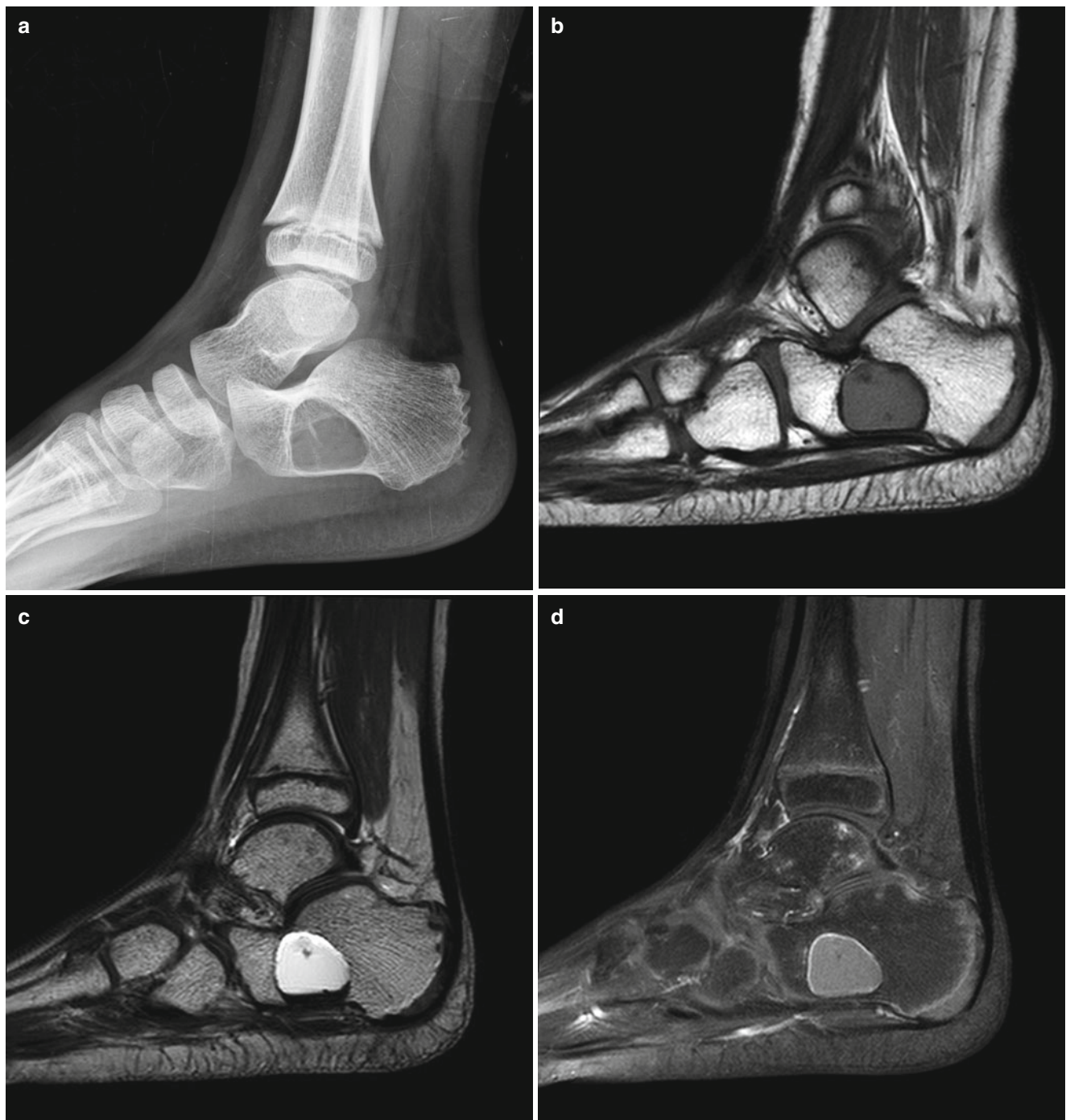


Fig. 32.9 Simple bone cyst of the calcaneus. (a) Lateral ankle radiograph shows a sharply marginated cystic lesion in the calcaneal neck portion which is surrounded by sclerotic rim. (b–d) MR T1-weighted image (b) reveals a well-demarcated hypointense bone cyst in the cal-

caneus without enhancement on fat-suppressed T1-weighted image (d). Note the bright high signal intensity representing cystic nature of the lesion on fast spin-echo T2-weighted image (c)



Fig. 32.10 *Simple bone cyst with pathologic fracture.* (a) There is a well-demarcated cystic lesion in the left humerus proximal diaphysis with cortical disruption and angulations representing associated pathologic fracture. (b–d) MR T1-weighted images before (b) and after (d) contrast administrations show a well-circumscribed intramedullary cystic

lesion without solid-enhancing area. On T2-weighted axial image (c), there is a hemorrhage-fluid level which is due to an associated fracture. Periosteal new bone formation is noted with surrounding soft tissue enhancement suggesting reactive changes

32.5.7 Aneurysmal Bone Cyst

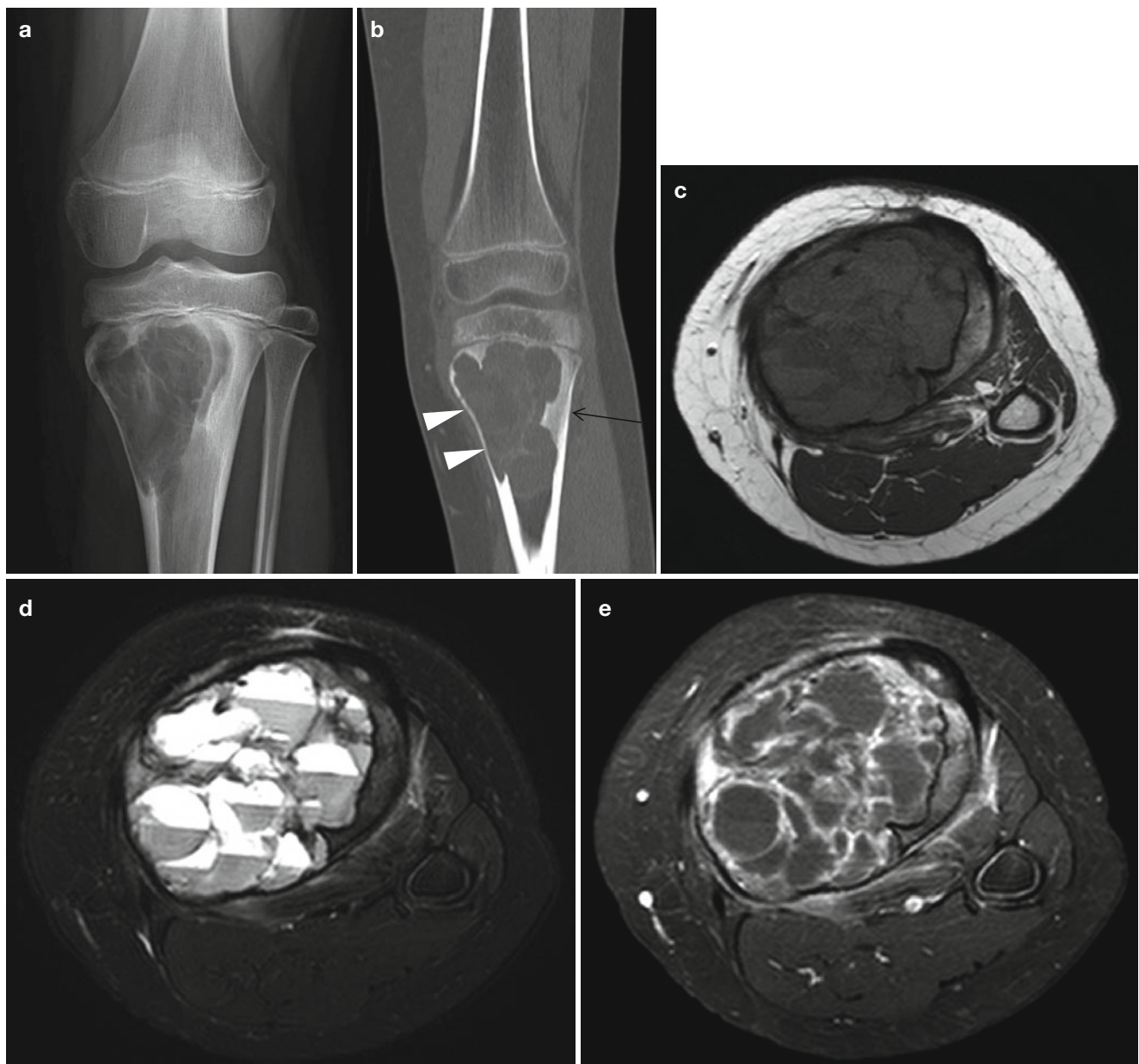


Fig. 32.11 Aneurysmal bone cyst in a 14-year-old girl. (a) Left-knee AP radiograph shows a well-demarcated cystic lesion with suspicious intervening septations in the left proximal tibia abutting the physis. (b) Coronal CT scan reveals intramedullary cystic lesion with lobulating contour and internal fine septations. Endosteal scalloping is clearly seen

along the medial cortex (*arrowheads*) as seen on the plain radiograph. There is also associated sclerosis laterally (*arrow*). (c–e) T1-weighted (c) and T2 SPAIR (d) axial images show multiseptated cystic mass with hemorrhage levels, characteristic of the aneurysmal bone cyst. Contrast-enhanced axial image (e) depicts only septal and cyst wall enhancement

32.5.8 Non-ossifying Fibroma

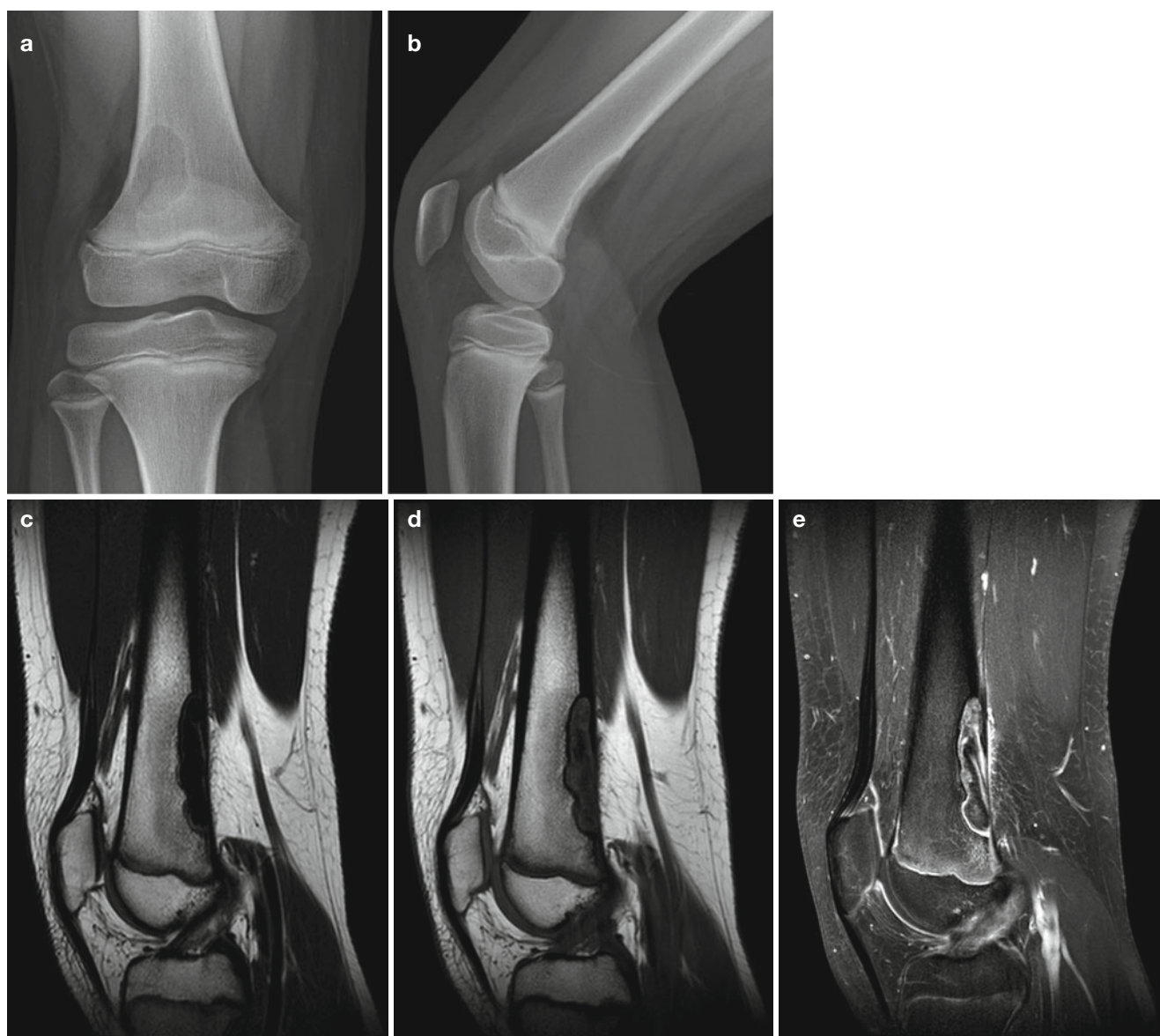


Fig. 32.12 *Non-ossifying fibroma in a 12-year-old boy.* (a, b) Right-knee AP (a) and lateral (b) radiographs show a well-circumscribed and elongated radiolucent bony lesion in the right distal femur which is eccentrically located at the posterior cortex. (c–e) The lesion appears

hypointense on MR T2-weighted sagittal image (c) and isointense with hypointense center on T1-weighted image (d). Postcontrast fat-suppressed T1-weighted image (e) reveals heterogeneous and mostly peripheral enhancement of the lesion

32.5.9 Fibrous Dysplasia

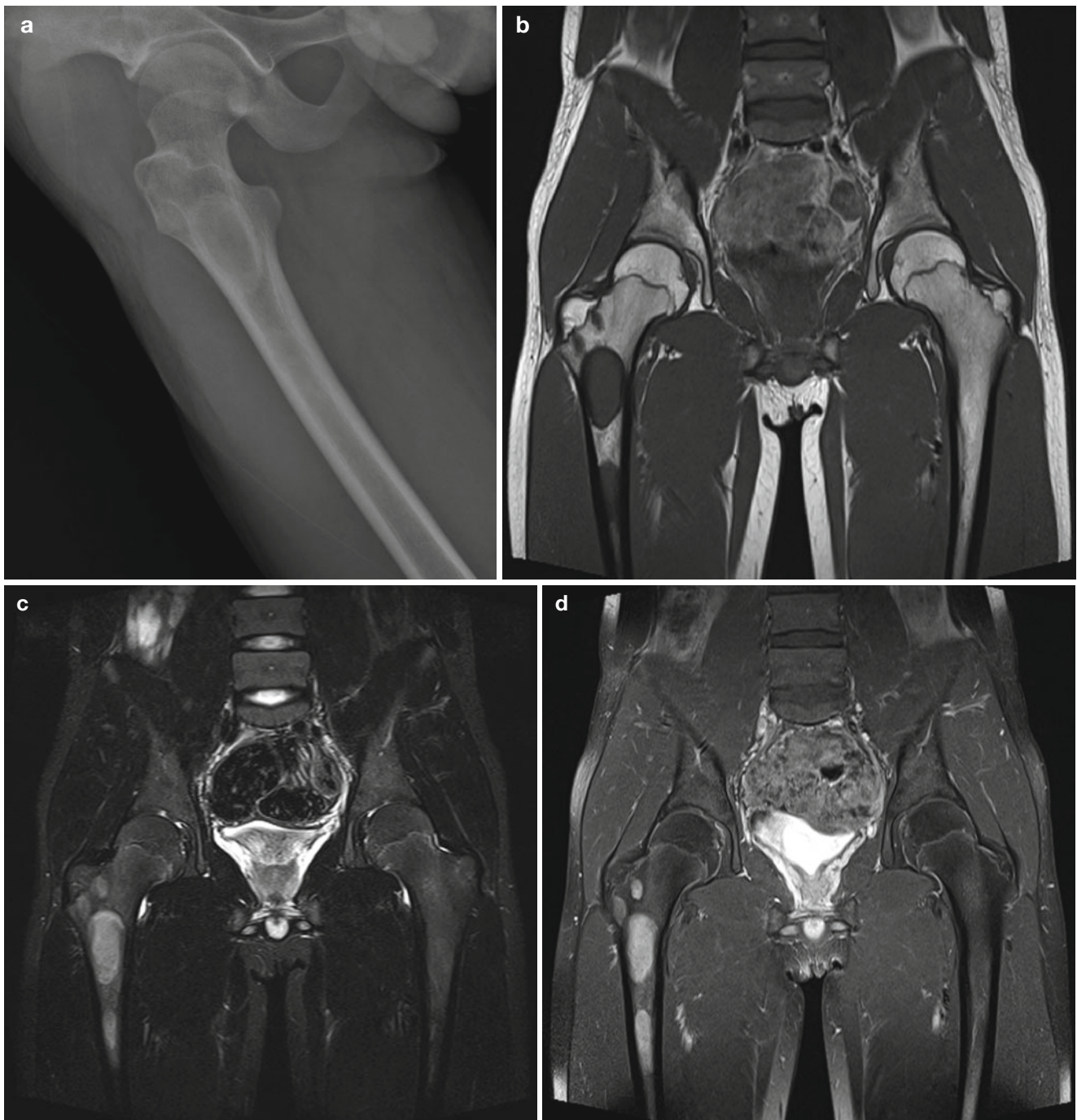


Fig. 32.13 *Fibrous dysplasia.* (a) A well-demarcated ovoid bony lesion is noted in the right proximal femur with a ground-glass matrix, highly suggestive of fibrous dysplasia. (b–d) MR T1-weighted image (b) shows sharply margined hypointense lesions (at least four in this

scan) in the right proximal femur with sclerotic rims. The lesions are hyperintense on T2-weighted image (c) and intense and homogeneously enhanced after gadolinium administration (d)

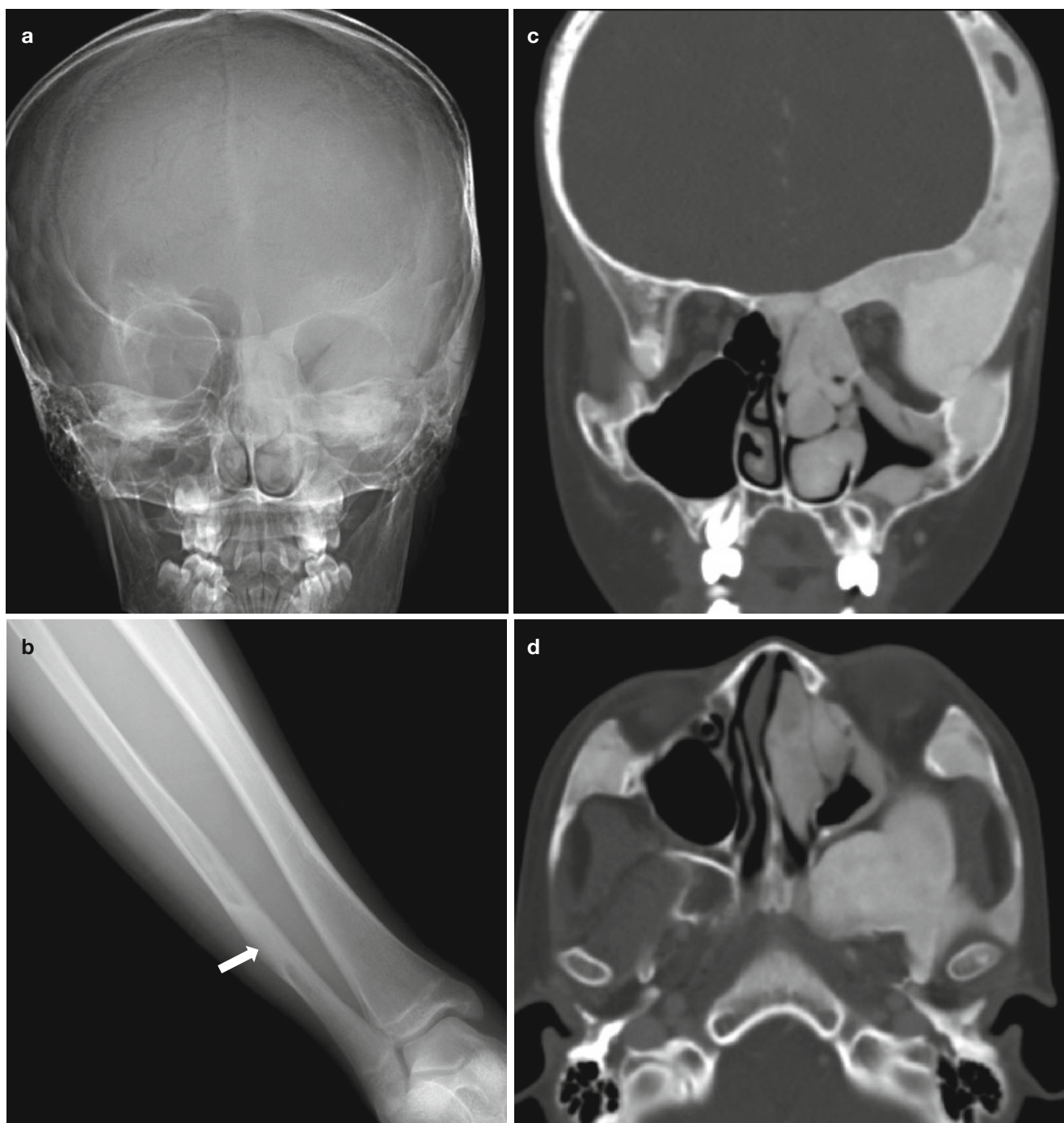


Fig. 32.14 *McCune-Albright syndrome with fibrous dysplasia.* (a) Left bony orbit, ethmoid sinus, and maxilla are diffusely sclerotic, which is a consistent finding with fibrous dysplasia. (b) Small radiopaque lesion (arrow) is seen in the right distal fibula with a ground-glass matrix

representing another focus of fibrous dysplasia. (c–d) Coronal (c) and axial (d) CT scan are excellent to show the extent of the lesion with narrowing of the foramen and fissures

32.5.10 Osteofibrous Dysplasia



Fig. 32.15 *Osteofibrous dysplasia in a 4-year-old boy.* (a) An expansile bony lesion with mixed sclerosis and lucency is seen in the midshaft of the ulna. There is an associated radiolucent line representing pathologic fracture. (b) Coronal CT shows similar findings to that on the plain radiography. The lesion has a ground-glass matrix and surround-

ing sclerosis. (c, d) T1-weighted (c) and fat-suppressed T2-weighted (d) sagittal images show T1 low-signal and T2 high-signal lesion in the ulna with internal dark signal foci. Radiological findings are quite similar to those of fibrous dysplasia, and central location within the medullary cavity is somewhat unusual for osteofibrous dysplasia

32.5.11 Langerhans Cell Histiocytosis

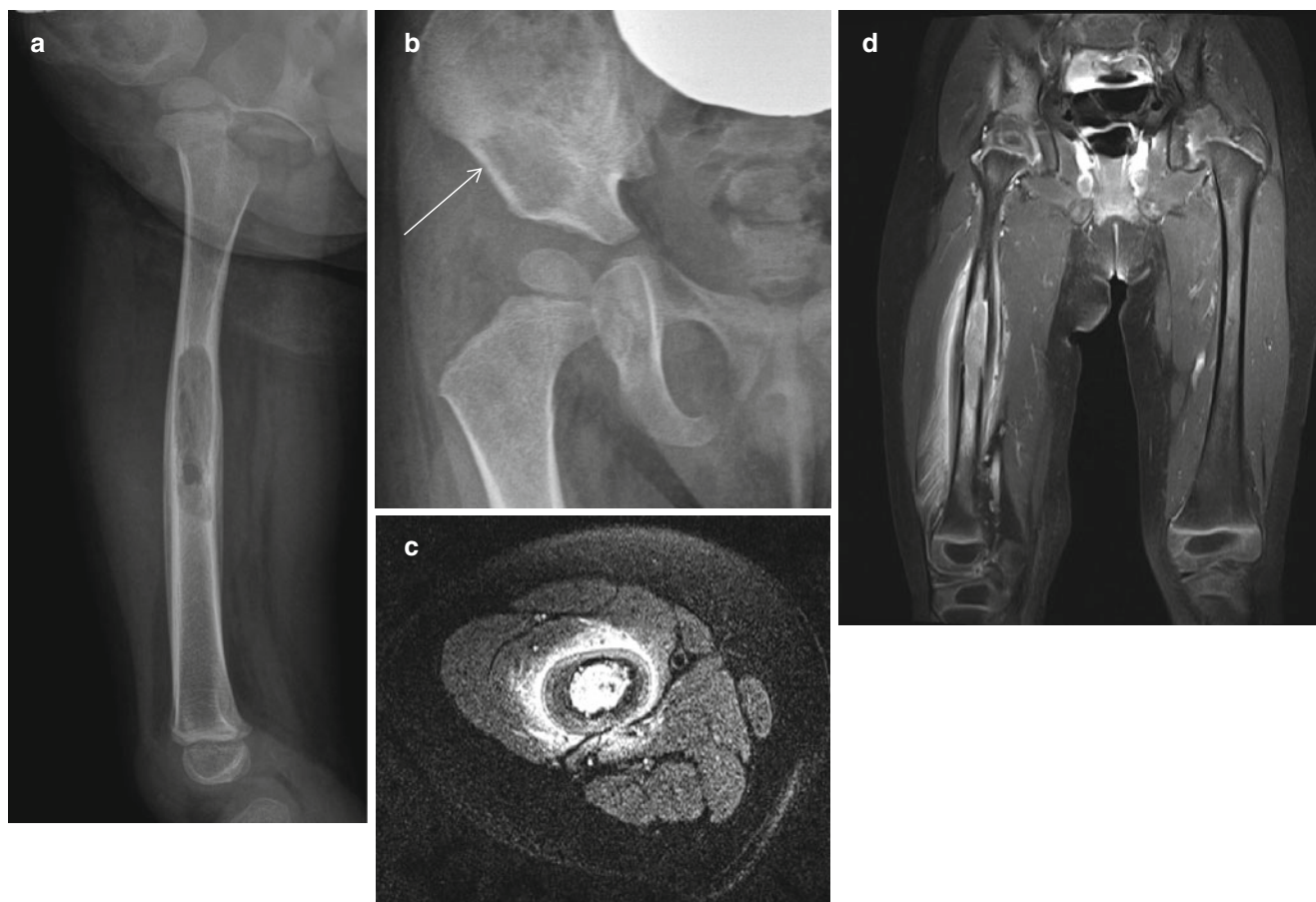


Fig. 32.16 *Langerhans cell histiocytosis.* (a, b) Plain radiographs show well-demarcated osteolytic lesions involving the midshaft of the right femur and right acetabulum (arrow). Note the solid-type periosteal new bone formation in the right femur. (c, d) Axial T2 SPAIR

image (c) shows hyperintense bony lesion with periosteal reaction and surrounding soft tissue changes. Bone and soft tissue lesions are well enhanced after administration of gadolinium (d). There is an enhancing bone and soft tissue lesion in the right acetabulum as well

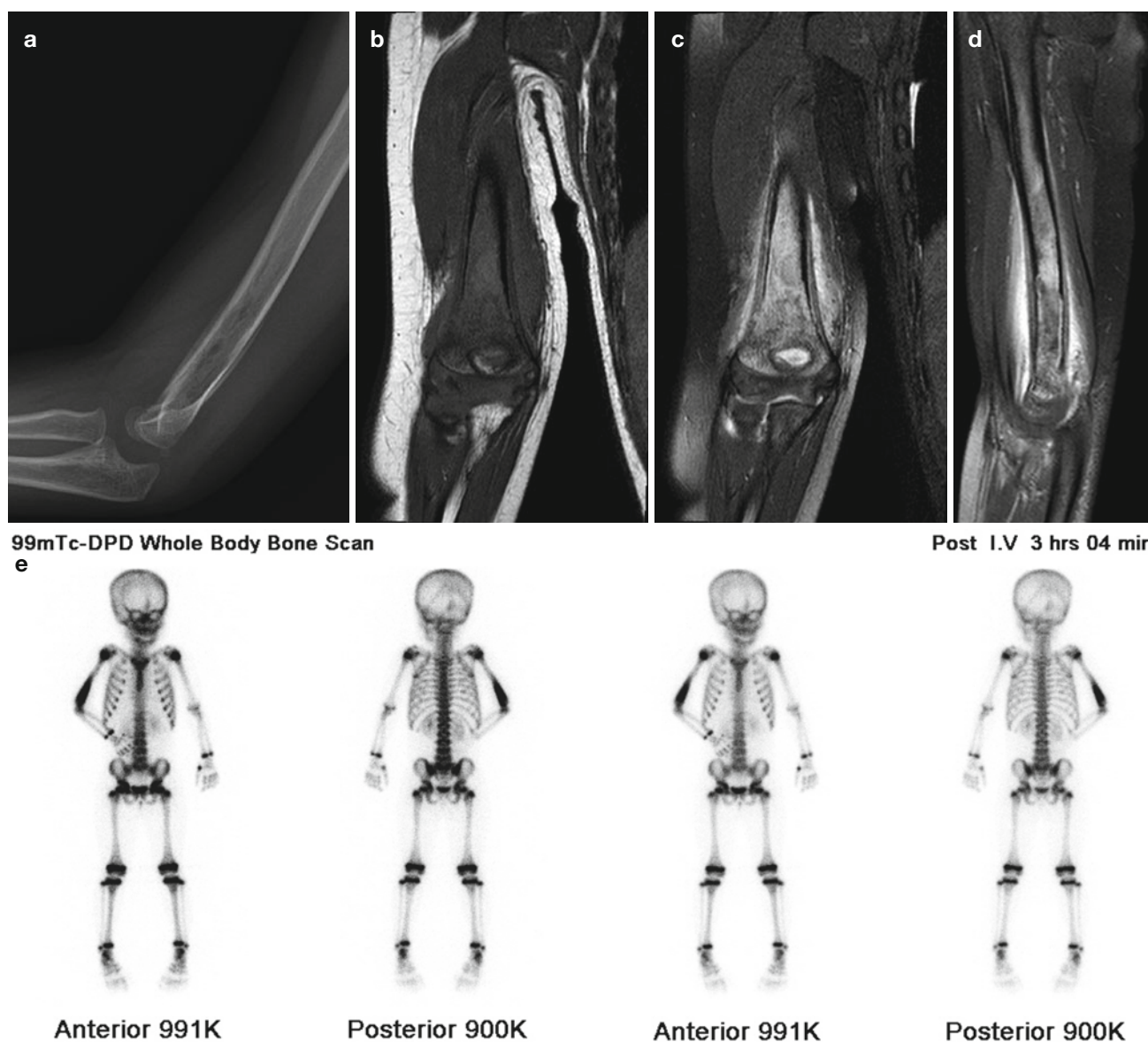


Fig. 32.17 *Langerhans cell histiocytosis in a 3-year-old boy.* (a) Humerus lateral radiograph shows an ill-defined radiolucent bony lesion with a moth-eaten or permeative appearance involving the meta-diaphyses with lamellated periosteal reaction. (b–d) MR T1-weighted image (b) shows abnormal marrow replaced by low signal intensity in the distal humerus metadiaphysis which is a hyperintense bony lesion on fat-suppressed T2-weighted image (c). Bone and surrounding soft

tissue is well enhanced after administration of gadolinium. Note periosteal reaction along the distal humerus. (e) Bone scintigraphy shows intense uptake in the right distal humerus which mimicked malignancy. In an early phase of LCH, it is often not easy to differentiate it from acute osteomyelitis or malignant tumor clinically as well as radiologically

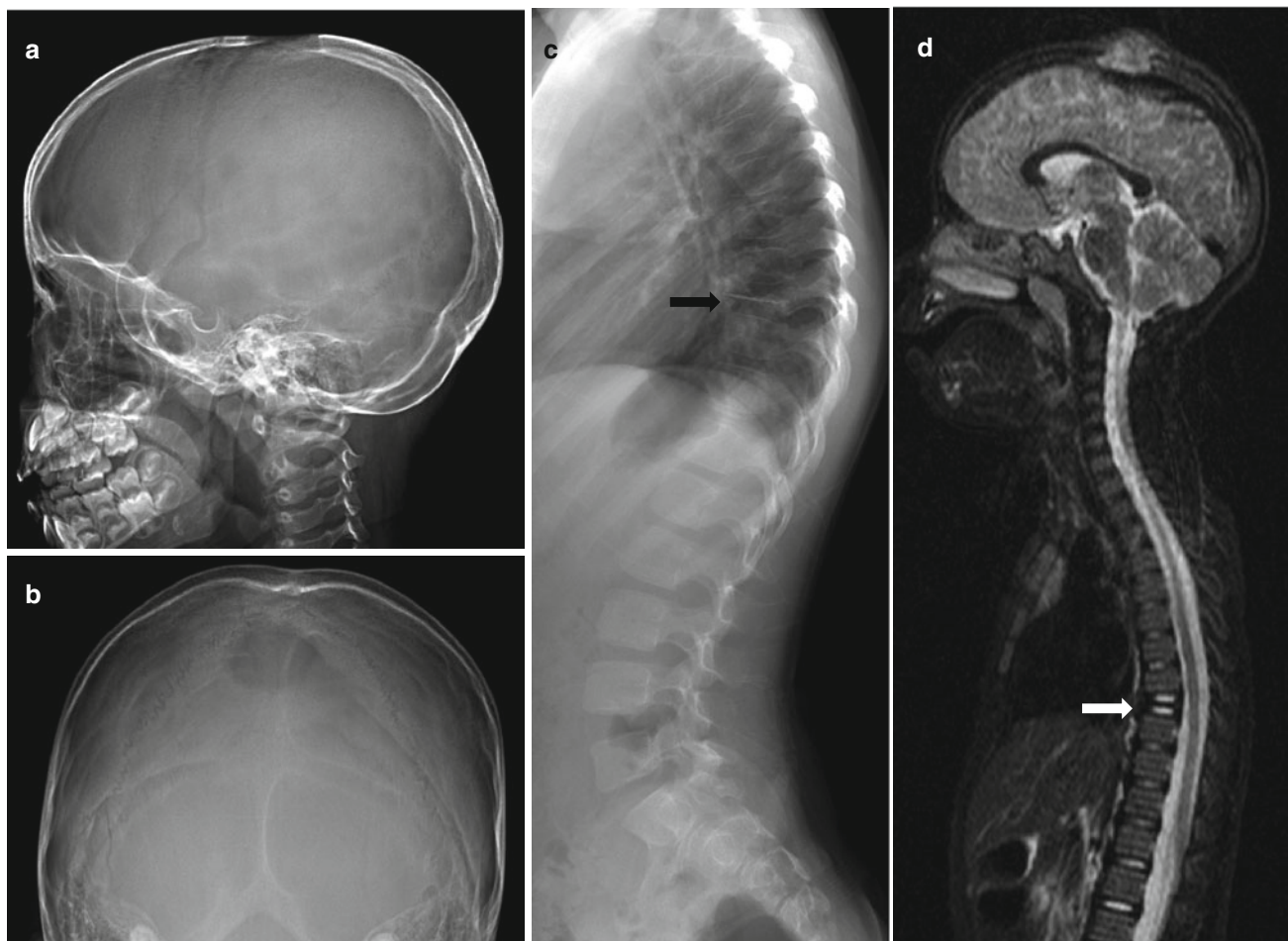


Fig. 32.18 *Langerhans cell histiocytosis, polyostotic.* (a, b) Skull lateral and Townes projections show a well-circumscribed, clearly marginated osteolytic lesion in the vertex. (c) Whole-spine lateral radiograph shows complete collapse of the ninth thoracic vertebral

body, the so-called vertebra plana (arrow). (d) Whole-body MRI STIR sagittal image reveals bulky mass at the vertex and T9 vertebra plana (arrow)

32.5.12 Conventional Osteosarcoma

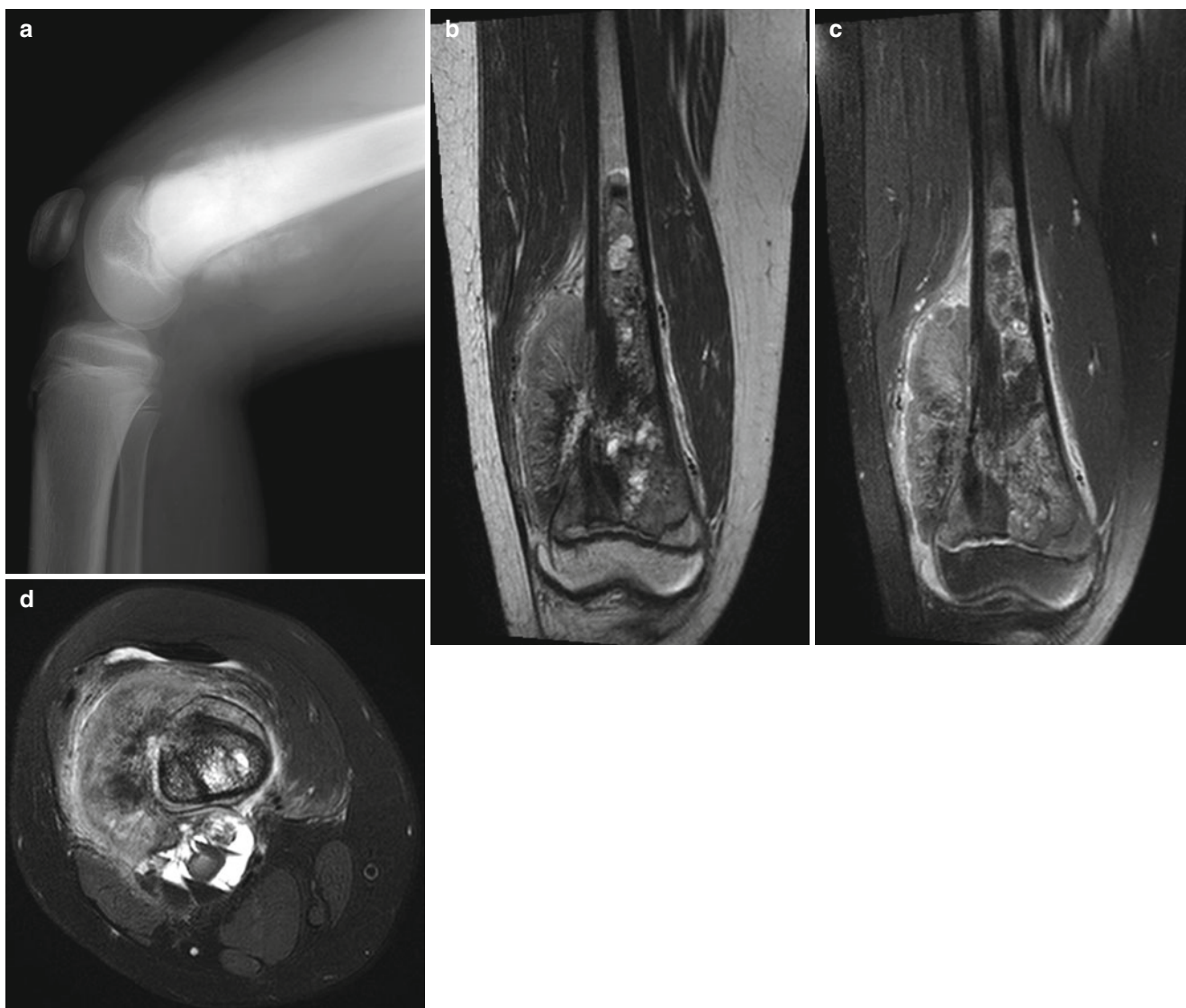


Fig. 32.19 *Classic osteosarcoma in a 16-year-old girl.* (a) Ill-defined osteosclerotic bony lesion is seen in the right distal femur metadiaphysis. There is an associated malignant-type periosteal reaction, and the transition between tumor and normal marrow is wide. (b–d) MR T2-weighted coronal (b), postcontrast fat-suppressed T1-weighted coronal (c), and axial T2 SPAIR (d) images show a large heterogeneous

intra- and extraosseous mass with cortical destruction in the right distal femur. Periosteal elevation with subperiosteal tumor growth is well demonstrated on axial scan, (d) and there are also cystic changes with dark signal hemorrhage levels posteriorly. The tumor abuts the physis; however, the epiphysis is mostly spared

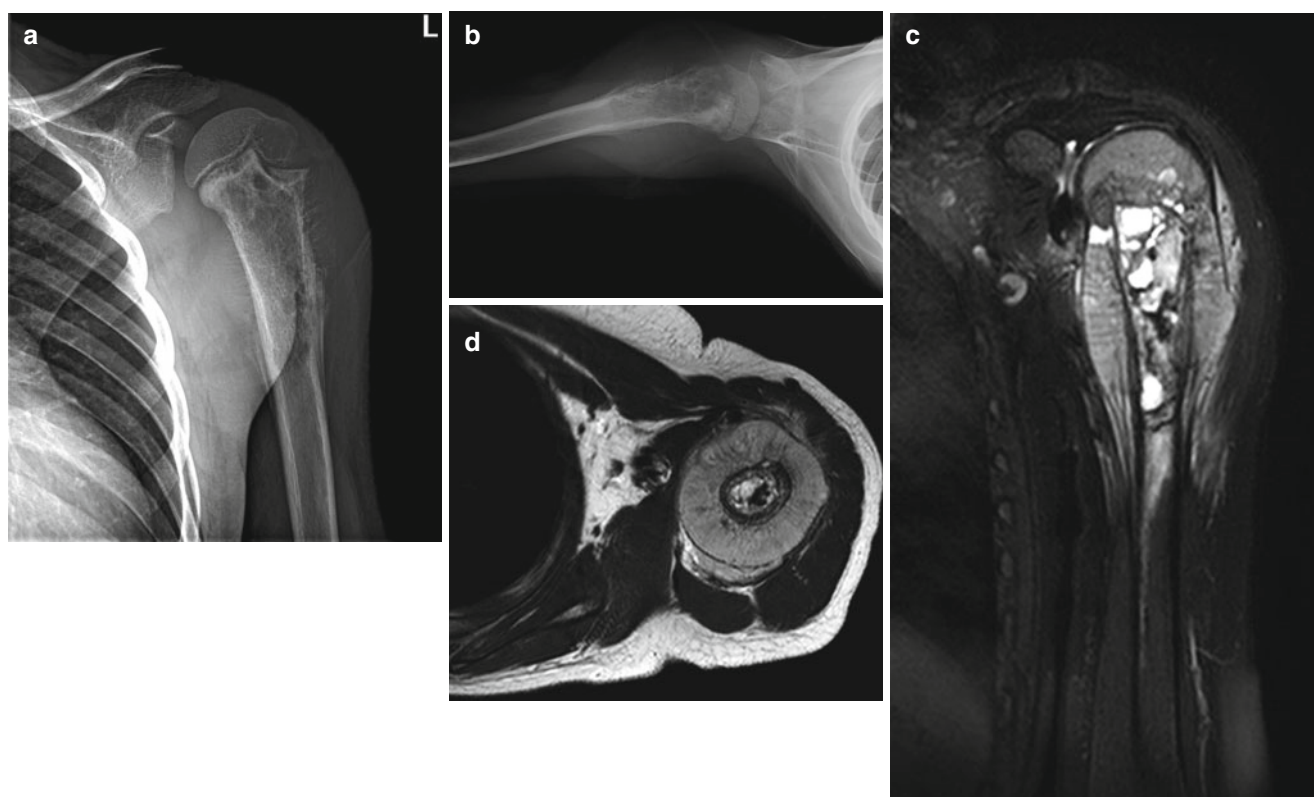


Fig. 32.20 *Osteosarcoma in a 10-year-old boy.* (a, b) Left humerus radiographs show ill-defined osteolytic lesion in the left humerus meta-diaphysis with relative lack of blastic activity in this case. There is malignant periosteal reaction of a “hair-on-end” appearance and a “Codman triangle.” (c, d) T2 SPAIR coronal (c) and axial (d) images

clearly define the tumor extent in both longitudinal and axial directions. The periosteum is elevated by the infiltrating tumor mass. Radiating low signal intensities representing “hairs on end” are well demonstrated on axial T2-weighted image (d)

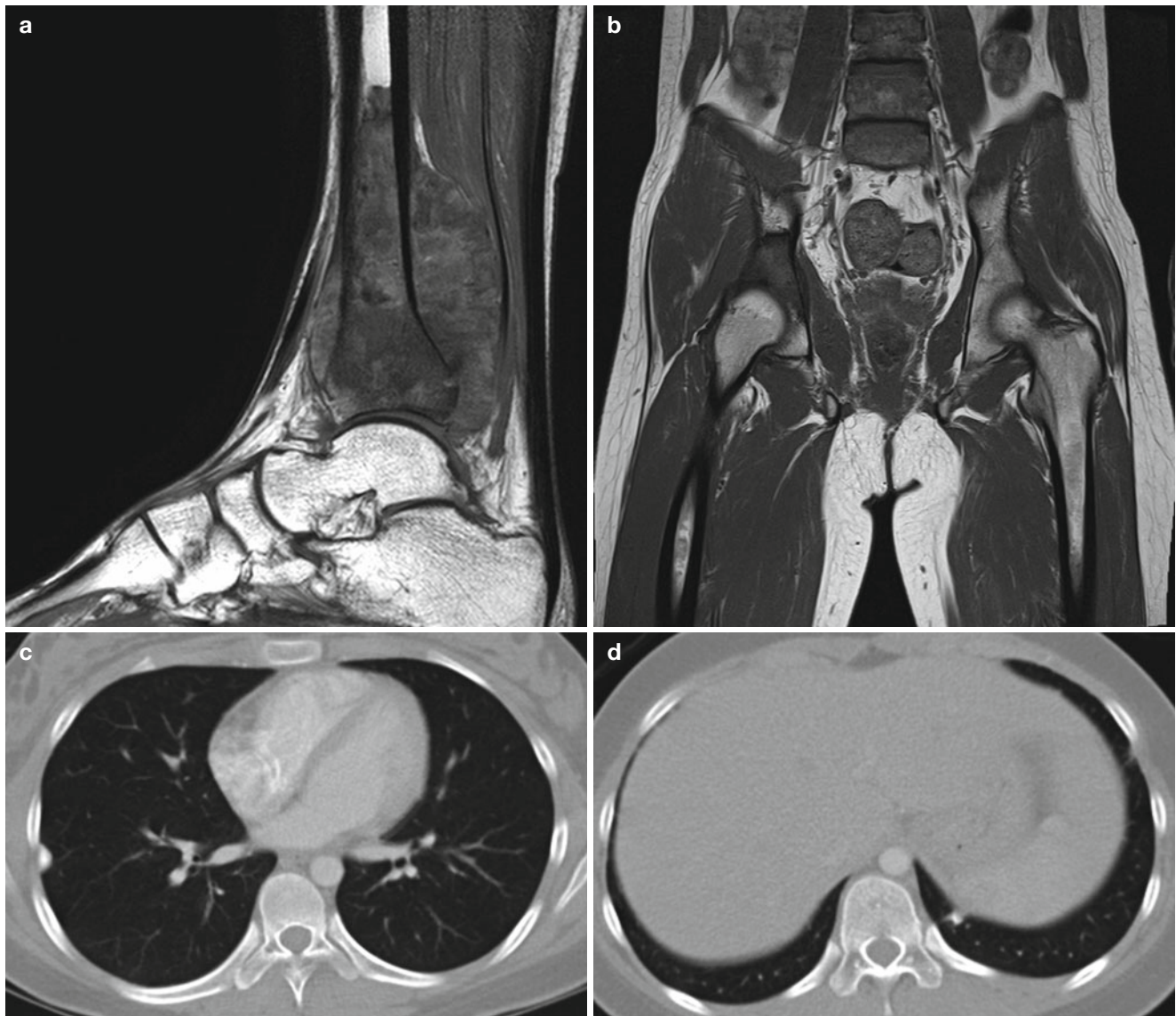


Fig. 32.21 *Osteosarcoma with pelvis and lung metastasis.* (a) Intraosseous and extraosseous tumor representing osteosarcoma in the left distal tibia on T1-weighted sagittal image. (b) Low signal intensity bony lesion is seen in the right acetabulum on precontrast T1-weighted

image in keeping with pelvic bone metastasis. (c, d) Lung CT shows calcified metastatic nodules in the right lower lobe subpleural region and left lung base abutting the left hemidiaphragm

32.5.13 Juxtacortical Osteosarcoma

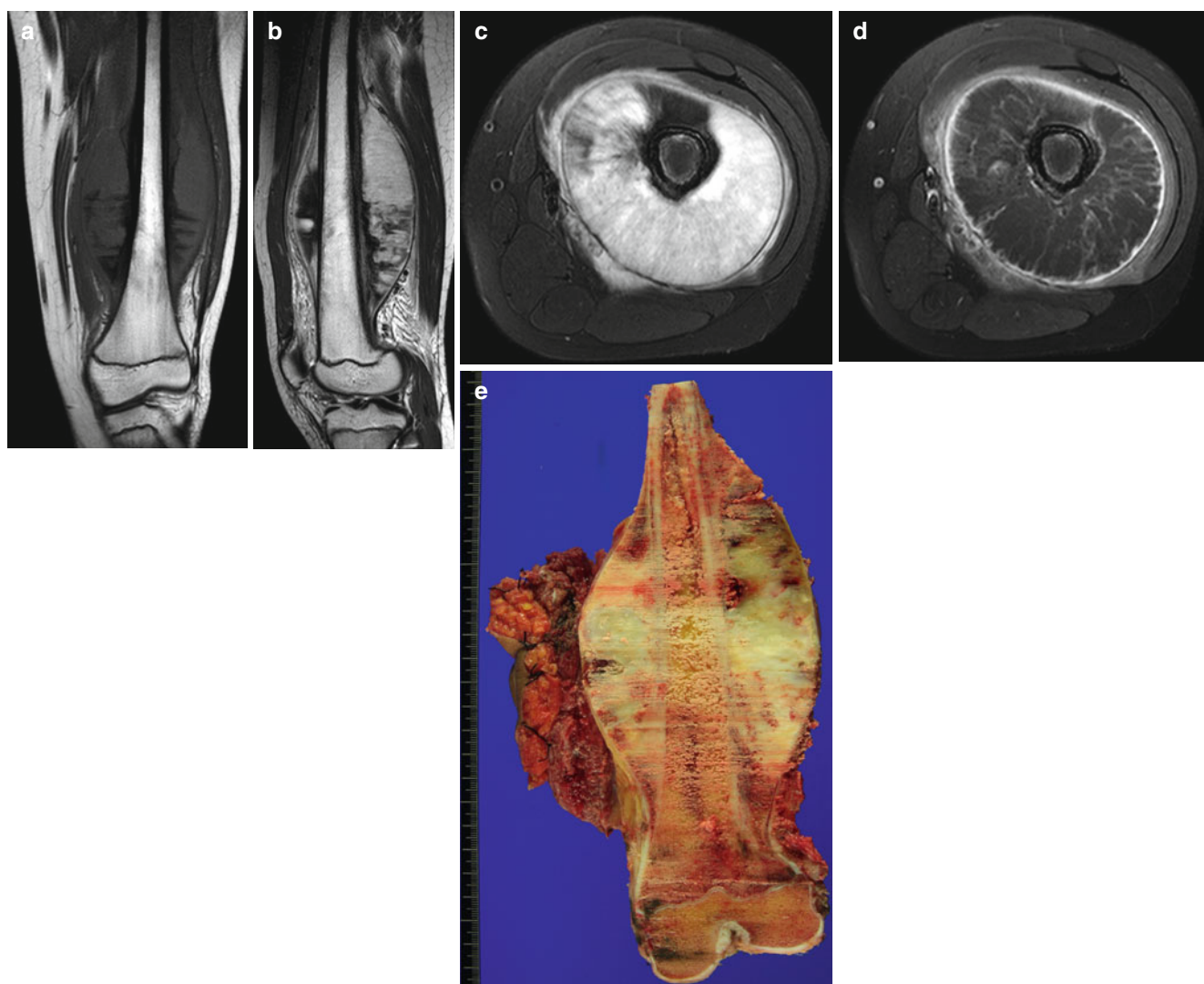


Fig. 32.22 *Periosteal osteosarcoma in a 10-year-old girl. (a–d)* MR T1-weighted coronal (a), T2-weighted sagittal (b), fat-suppressed T2-weighted axial (c), and gadolinium-enhanced fat-suppressed T1-weighted axial (d) images show a bulky periosteal mass with spar-

ing of the medullary cavity. The pathologic examination revealed the chondroblastic-type osteosarcoma with no marrow involvement (e, gross specimen)

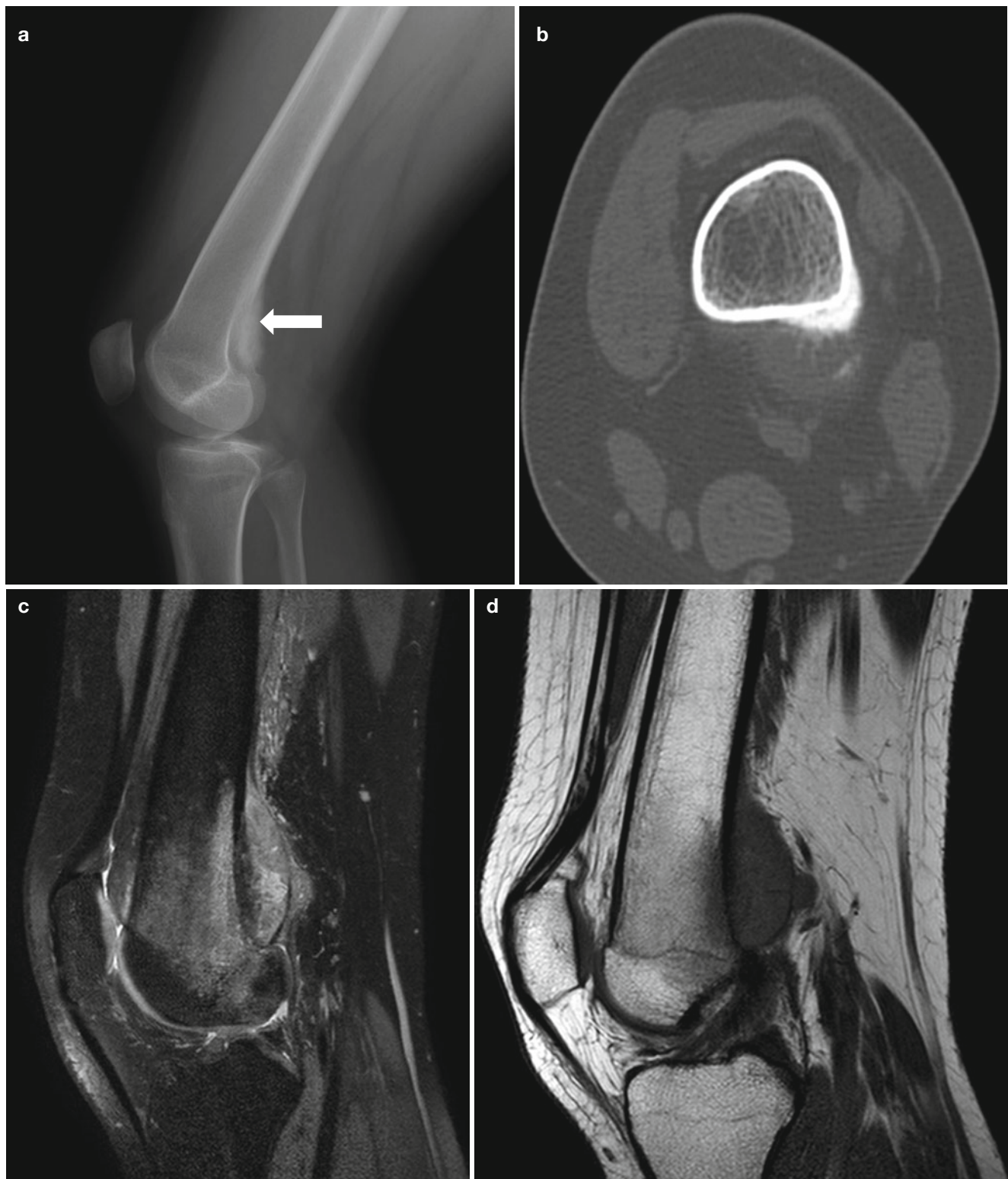


Fig. 32.23 Presumed juxtacortical or periosteal osteosarcoma in a 15-year-old girl. (a) Densely ossified lesion is seen along the posterior cortex of the left distal femur (arrow). (b) Axial CT scan shows a juxtacortical soft tissue mass with ossifications along the posterolateral cortex of distal femur. (c, d) Fat-suppressed proton-density VISTA

sagittal (c) and T1-weighted sagittal (d) images show the soft tissue mass in the left distal femur as seen on plain radiography and CT. There is some marrow signal change and pathologic examination confirmed marrow involvement

32.5.14 Ewing Sarcoma

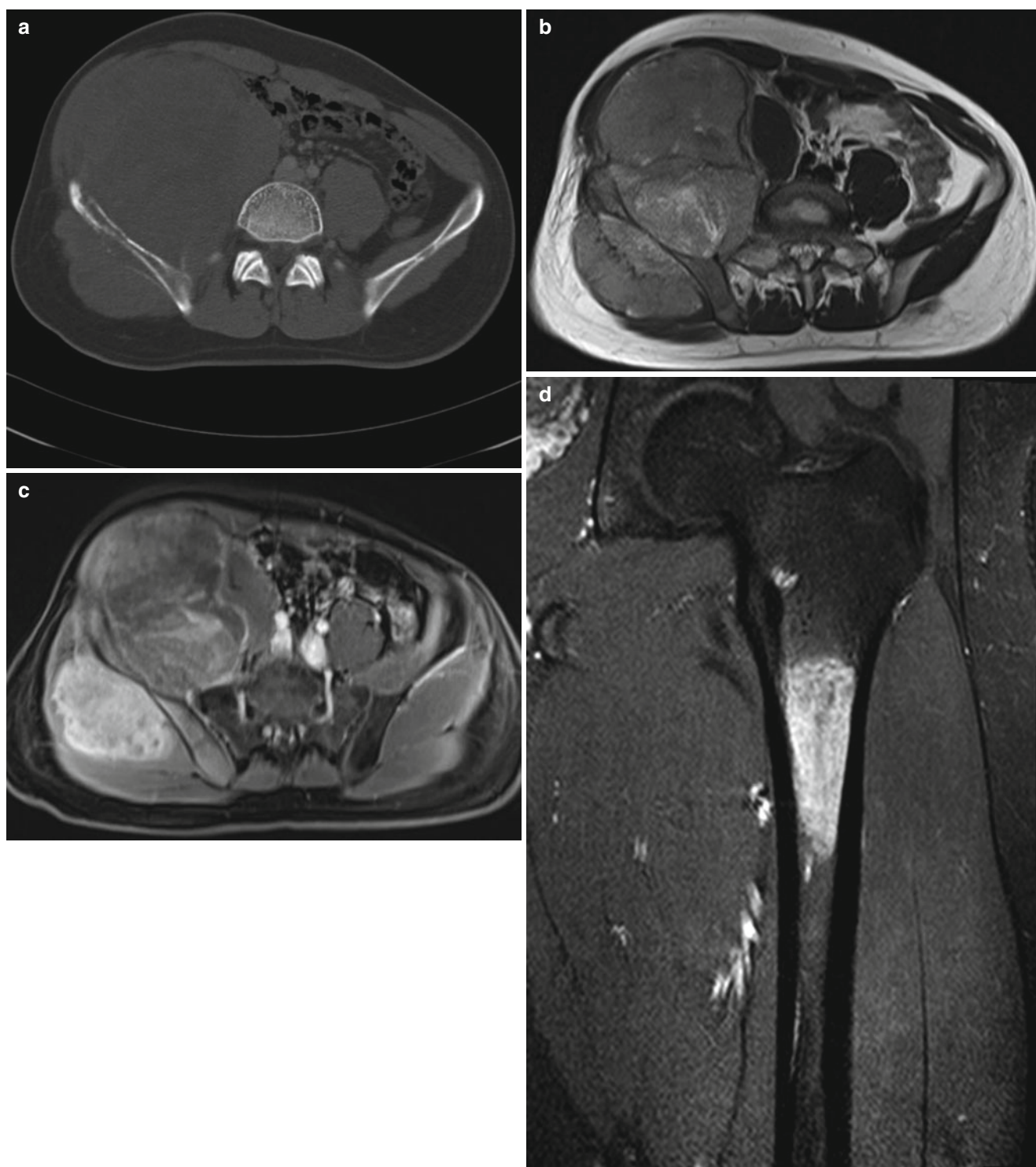


Fig. 32.24 Ewing's sarcoma involving flat bone with bone metastasis. (a) Pelvis CT through the lower abdomen shows a huge soft tissue mass in the right lower quadrant with permeative bone destruction of the right ilium. There is asymmetric bulging of right gluteus muscle as compared to the opposite side with periosteal elevation (*arrowheads*). (b, c) T2-weighted (b) and postcontrast fat-suppressed T1-weighted (c)

images show a huge heterogeneously enhancing mass with abnormal marrow signal intensity involving the entire right ilium. The cortical lining is somewhat preserved relative to the mass size which is a characteristic finding of the so-called small round cell tumors. (d) Postcontrast T1-weighted image of the left femur shows metastatic bony lesion

32.5.15 Primary and Secondary Lymphoma

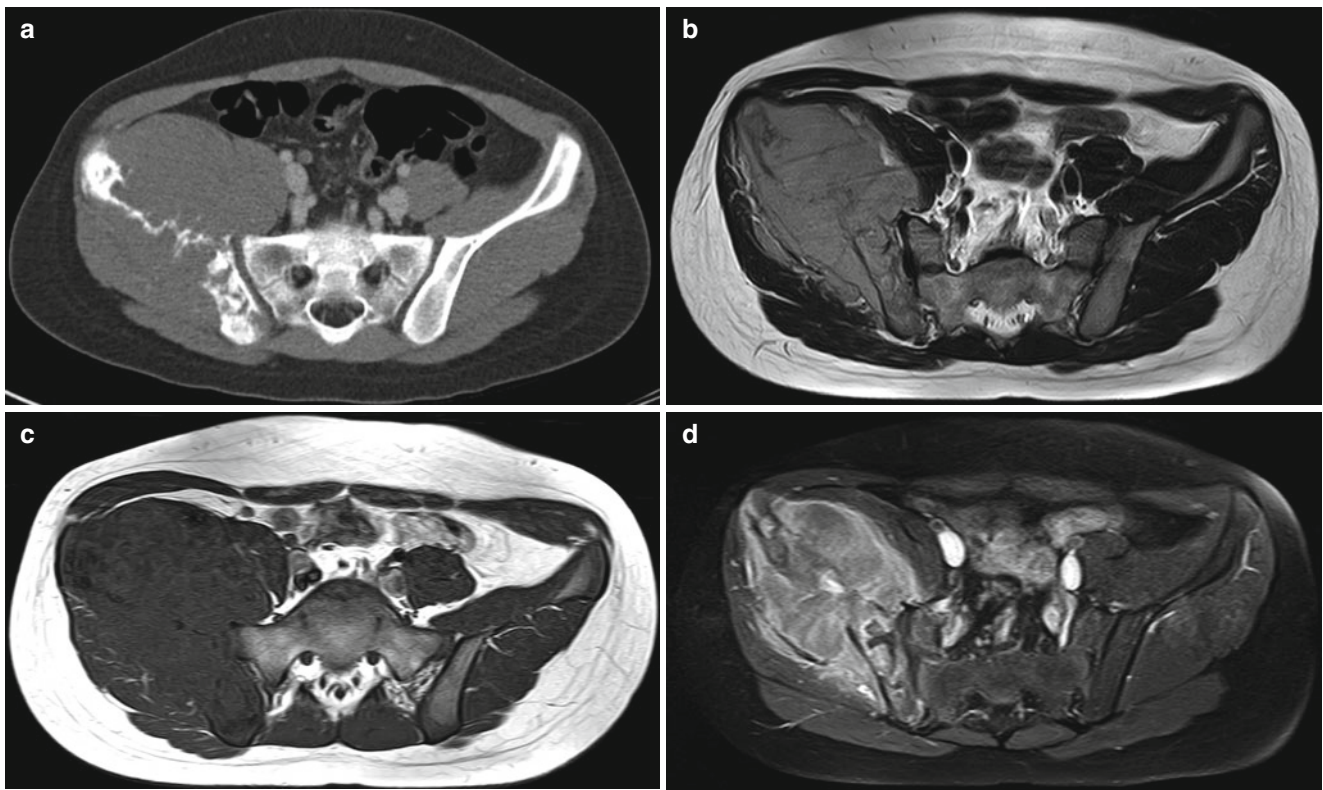


Fig. 32.25 *Primary lymphoma of ilium.* (a) CT shows a large soft tissue mass destroying the right ilium. (b–d) T2-weighted axial (b), T1-weighted axial (c), and postcontrast fat-suppressed axial (d) images

show rather homogeneous soft tissue mass with cortical bone disruption of the right ilium

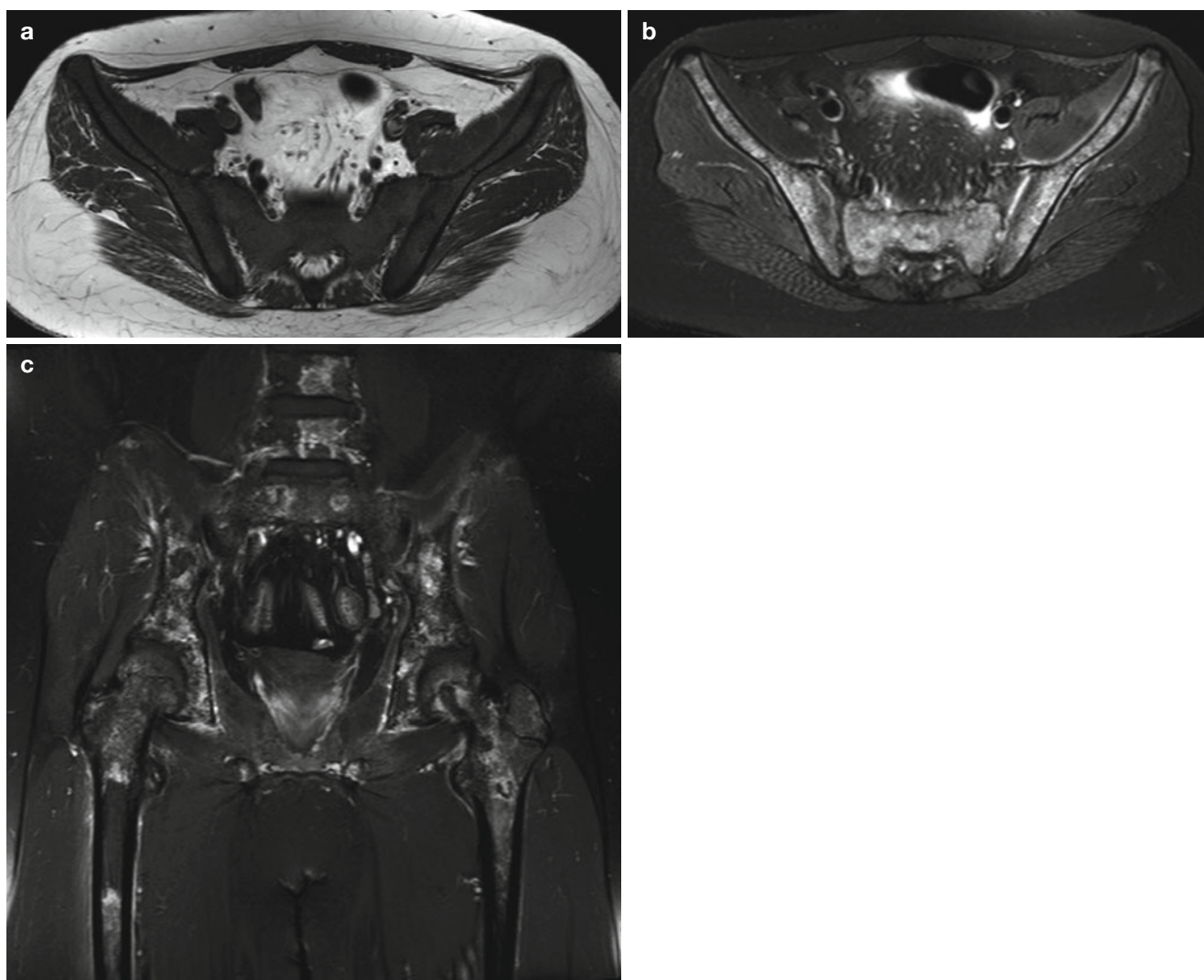


Fig. 32.26 *Plasmablastic lymphoma.* (a–c) T1-weighted axial (a), T2 STIR axial (b), and postcontrast fat-suppressed coronal (c) images show diffusely abnormal bone marrow with heterogeneous enhancement in the lower lumbar spine, sacrum, pelvic bones, and both proximal

femurs, raising a suspicion of hematologic malignancy. Bone marrow biopsy confirmed the diagnosis of plasmablastic lymphoma, a highly aggressive variant of diffuse large B cell lymphoma

32.5.16 Metastatic Neuroblastoma

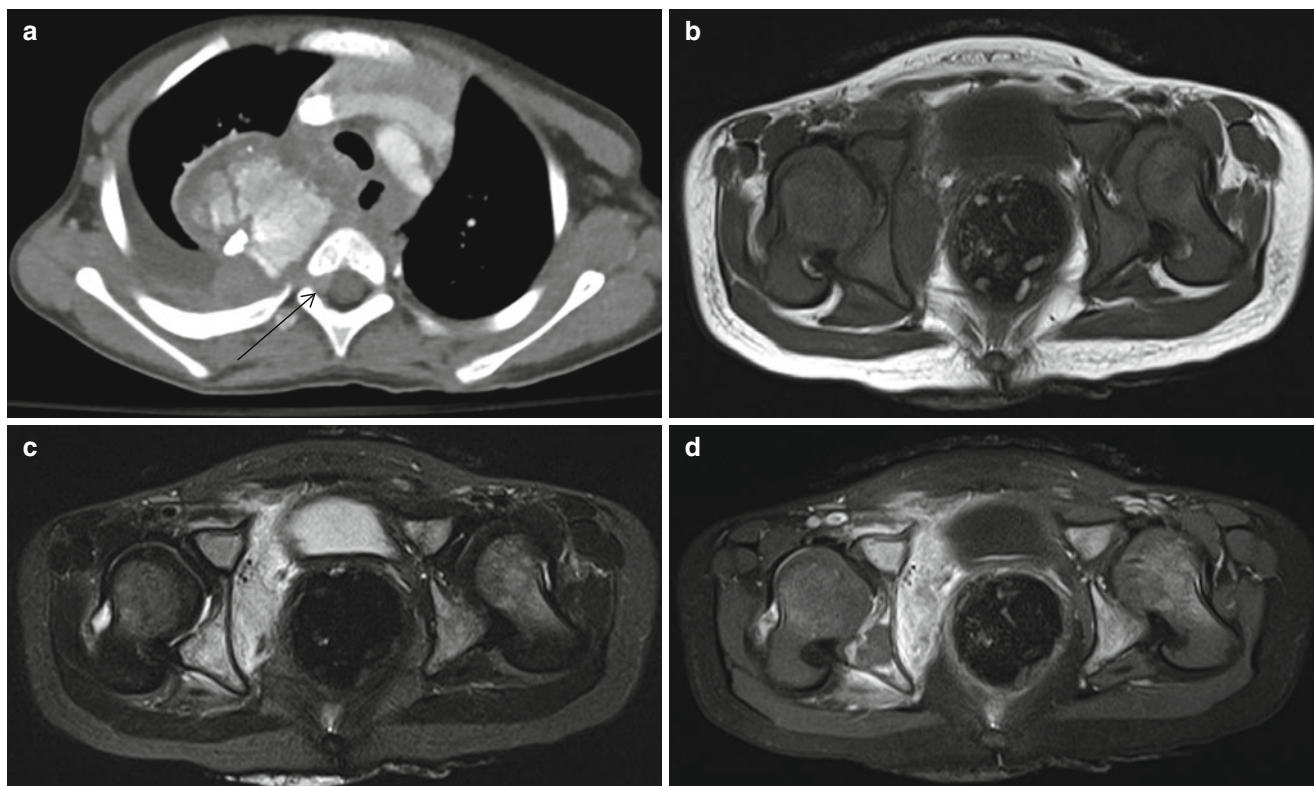


Fig. 32.27 *Mediastinal neuroblastoma with bone metastasis.* (a) Chest CT shows a large calcified mass in the posterior mediastinum extending through the right side neural foramen of the thoracic spine (arrow). Right pleural effusion is associated. (b–d) T1-weighted axial (b), T2 STIR axial (c), and postcontrast fat-suppressed T1 axial (d)

images show the right ischial bone lesion with ill-defined soft tissue mass formation medially. The bone marrow of the pelvic bones and both proximal femurs are diffusely abnormal, suggesting diffuse bone marrow involvement by neuroblastoma. The cortical lining of the right ischium is relatively preserved

References

- Azouz EM, Slomic AM, Marton D, et al. The variable manifestations of dysplasia epiphysealis hemimelica. *Pediatr Radiol*. 1985;15:44–9.
- Bierry G, Kerr DA, Nielsen GP, et al. Enchondromas in children: imaging appearance with pathological correlation. *Skeletal Radiol*. 2012;41:1223–9.
- Ghanem I, Tolo VT, D'Ambra P, et al. Langerhans cell histiocytosis of bone in children and adolescents. *J Pediatr Orthop*. 2003;23:124–30.
- Hoeffel JC, Galloy MA, Grignon Y, et al. Giant cell tumor of bone in children and adolescents. *Rev Rhum Engl Ed*. 1996;63:618–23.
- Iyer RS, Chapman T, Chew FS. Pediatric bone imaging: diagnostic imaging of osteoid osteoma. *AJR Am J Roentgenol*. 2012;198:1039–52.
- Jeh SK, Jee WH, Hong SJ, et al. Extracranial skeletal Langerhans cell histiocytosis: MR imaging features according to the radiologic evolutionary phases. *Clin Imaging*. 2012;36:466–71.
- Kaste SC. Imaging pediatric bone sarcomas. *Radiol Clin North Am*. 2011;49:749–65, vi–vii.
- Kaste SC, Strouse PJ, Fletche rBD, et al. Benign and malignant bone tumors. In: Slovis TL, editor. *Caffey's pediatric diagnostic imaging*. 11th ed. Philadelphia: Mosby Elsevier; 2008.
- Kilborn TN, Teh J, Goodman TR. Paediatric manifestations of Langerhans cell histiocytosis: a review of the clinical and radiological findings. *Clin Radiol*. 2003;58:269–78.
- Mengiardi B, Honegger H, Hodler J, et al. Primary lymphoma of bone: MRI and CT characteristics during and after successful treatment. *AJR Am J Roentgenol*. 2005;184:185–92.
- Meyer JS, Nadel HR, Marina N, et al. Imaging guidelines for children with Ewing sarcoma and osteosarcoma: a report from the Children's Oncology Group Bone Tumor Committee. *Pediatr Blood Cancer*. 2008;51:163–70.
- Papaioannou G, McHugh K. Neuroblastoma in childhood: review and radiological findings. *Cancer Imaging*. 2005;5:116–27.
- Steinborn M, Wortler K, Nathrath M, et al. Whole-body MRI in children with Langerhans cell histiocytosis for the evaluation of the skeletal system. *Rofo*. 2008;180:646–53.
- Walter F, Federman N, Apichairuk W, et al. 18F-fluorodeoxyglucose uptake of bone and soft tissue sarcomas in pediatric patients. *Pediatr Hematol Oncol*. 2011;28:579–87.
- Wootton-Gorges SL. MR imaging of primary bone tumors and tumor-like conditions in children. *Magn Reson Imaging Clin N Am*. 2009;17:469–87, vi.

Jung-Eun Cheon

Contents

33.1	Introduction	1040
33.2	Congenital and Developmental Disorders	1040
33.2.1	Proximal Femoral Focal Deficiency	1040
33.2.2	Developmental Coxa Vara.....	1040
33.2.3	Developmental Dysplasia of the Hip	1040
33.3	Acquired Disorders	1041
33.3.1	Legg-Calvé-Perthes Disease	1041
33.3.2	Slipped Capital Femoral Epiphysis.....	1042
33.3.3	Septic Arthritis	1042
33.3.4	Juvenile Idiopathic Arthritis.....	1042
33.3.5	Idiopathic Chondrolysis	1043
33.3.6	Osteoid Osteoma.....	1043
33.4	Illustrations: Pediatric Hip Disorders	1044
33.4.1	Proximal Femoral Focal Deficiency	1044
33.4.2	Developmental Coxa Vara.....	1045
33.4.3	Hip Ultrasonography: Coronal View.....	1046
33.4.4	Hip Ultrasonography: Transverse View	1047
33.4.5	Developmental Dysplasia of the Hip: Ultrasonographic Findings	1048
33.4.6	Developmental Dysplasia of the Hip: Radiographic Findings.....	1049
33.4.7	Developmental Dysplasia of the Hip: Postoperative Imaging Findings	1050
33.4.8	Legg-Calve-Perthes Disease: Initial Stage.....	1051
33.4.9	Legg-Calve-Perthes Disease: Evolution of Radiographic Abnormalities	1052
33.4.10	Legg-Calve-Perthes Disease: MRI Findings.....	1053
33.4.11	Legg-Calve-Perthes Disease: Metaphyseal Changes	1054
33.4.12	Slipped Capital Femoral Epiphysis: Radiographic Findings	1055
33.4.13	Slipped Capital Femoral Epiphysis: MRI Findings	1056
33.4.14	Slipped Capital Femoral Epiphysis: Avascular Necrosis as a Complication	1057
33.4.15	Ultrasonography for Joint Effusion.....	1058
33.4.16	Neonatal Septic Arthritis of the Hip.....	1059
33.4.17	Idiopathic Chondrolysis	1060
33.4.18	Osteoid Osteoma.....	1061
	References.....	1062

J.-E. Cheon, M.D.
 Department of Radiology, Seoul National University Hospital,
 Seoul National University College of Medicine,
 101 Daehak-ro Chongno-gu, Seoul 110-744, Korea
 e-mail: cheonje@snu.ac.kr

33.1 Introduction

Pediatric hip disorders encompass a wide range of pediatric hip problems including congenital and developmental disorders and acquired disorders. Typically, the history, onset of symptoms, and age of the patient help the diagnosis with a physical examination and imaging studies.

33.2 Congenital and Developmental Disorders

33.2.1 Proximal Femoral Focal Deficiency

Proximal femoral focal deficiency (PFFD) encompasses a spectrum from mild shortening and hypoplasia of the femur to severe deficiency of the femur and dysplasia of the acetabulum. PFFD is unilateral in approximately 90 % of cases. PFFD is associated with other ipsilateral deformities including fibular hemimelia, shortening of the tibia, deformity of the foot, and deficiency of the lateral ray of the foot (Anton et al. 1999; Maldjian et al. 2007; Biko et al. 2012) (Fig. 33.1).

33.2.2 Developmental Coxa Vara

Coxa vara is defined as an abnormally small femoral neck-shaft angle. Coxa vara has been classified into three broad categories: congenital, developmental, or acquired secondary to other conditions (Weinstein et al. 1984). Congenital coxa vara is characterized by a primary cartilaginous defect in the femoral neck. This can be a congenital short femur or part of a PFFD. Acquired coxa vara can be caused by a number of conditions including trauma, infection, slipped capital femoral epiphysis, and Legg-Calvé-Perthes disease. Developmental or infantile coxa vara can be secondary to abnormal proliferation of cartilage cells in the medial physis, which results in greater growth laterally (Dillon et al. 2005). Characteristic radiographic findings of developmental coxa vara include a decreased femoral neck-shaft angle, a wide and irregular vertically aligned physis, and a triangular metaphyseal bony fragment that is medial and inferior to the physis (Pavlov et al. 1980; Beals 1998) (Fig. 33.2).

33.2.3 Developmental Dysplasia of the Hip

Developmental dysplasia of the hip (DDH) encompasses a range of abnormalities of the femoral head–acetabular relationship and development. Normal acetabular development requires

appropriate positioning of the femoral head within the acetabulum. DDH can occur before or after birth and adaptive changes between femoral head and acetabulum can be developed during or beyond neonatal period. The acetabular dysplasia seen in DDH has several causes. Approximately 98 % of DDH occurs during the last month of gestation and may be secondary to mechanical or physiologic causes. Mechanical causes include oligohydramnios and breech presentation. Intra-uterine fetal constraint can cause other congenital musculoskeletal deformities including clubfoot, torticollis associated with fibromatosis colli, and skull molding. Maternal hormones and genetics contribute to hip joint laxity. DDH is much more common in girls (9:1 girls vs. boys) and is more common when a parent of sibling has had DDH. The prevalence of DDH varies from 1 in 100 births in clinically screened population to 8 in 100 births in sonographically screened population. Teratologic hip dysplasia, which is seen in approximately 2 % of individual with DDH, occurs during weeks 12–18 of gestational period with underlying neuromuscular disorders, myelomeningocele, arthrogryposis, or caudal regression syndrome (Dezateux and Rosendahl 2007; Bracken and Ditchfield 2012).

33.2.3.1 Ultrasonography

Ultrasonography (US) has replaced the routine use of plain radiographs in the initial diagnosis and subsequent follow-up of uncomplicated, nonteratologic DDH. US can be performed with the infant in either the supine or the lateral position and includes a coronal midacetabular image at rest (Fig. 33.3) and a transverse flexion view with stress (Fig. 33.4). The coronal view may be performed with the hip flexed or in the neutral position. The appearances of the following structures are described: the position of the femoral head, the bony acetabular slope, the superior lateral margin, and the labrum. Measurements including α and β angles and femoral head coverage are optional. During the transverse view with the hip in 90° flexion, stress is applied by pushing the femur posteriorly, in an attempt to provoke dislocation (analogous to the Barlow maneuver). A reverse stress maneuver (pulling and abducting the femur, analogous to the Ortolani maneuver) can be used to assess reduction of a dislocated hip. The hips were classified morphologically as normal ($\alpha \geq 60^\circ$), immature ($50^\circ \leq \alpha < 60^\circ$), mildly dysplastic ($43^\circ \leq \alpha < 50^\circ$), or severely dysplastic ($\alpha < 43^\circ$) (Fig. 33.5) (Morin et al. 1985; Harcke 1994; Rosendahl and Toma 2007; American Institute of Ultrasound in and American College of 2009; Bracken and Ditchfield 2012; Koenig et al. 2012).

33.2.3.2 Radiography

In the older infant and child, plain radiographs are useful for the assessment and follow-up of treatment. Several classic

lines are helpful in evaluating the immature hip (Fig. 33.6). Hilgenreiner's line is a line through the triradiate cartilages. Perkin's line, drawn at the lateral margin of the acetabulum, is perpendicular to Hilgenreiner's line. Shenton line should form a smooth continuous arc from the obturator foramen to the medial aspect of the femoral neck. In a normal hip, the medial beak of the proximal femoral metaphysis lies in the lower, inner quadrant produced by the junction of Hilgenreiner's and Perkin's lines. The acetabular index, which is an angle formed by the junction of Hilgenreiner's line and a line drawn along the acetabular surface, should normally measure less than 30°. The classic radiographic features of late-diagnosed DDH include an increased acetabular index, disruption of the Shenton line, and delayed appearance of the femoral secondary ossification center (Fig. 33.6b) (Donaldson and Feinstein 1997; Dezateux and Rosendahl 2007)

33.2.3.3 MRI

MRI is valuable in imaging patients with failed reduction or complicated DDH. MRI accurately demonstrates the many causes of failed reduction including invagination of the labrum or joint capsule, indentation of the iliopsoas tendon, fibro-fatty pulvinar, and hypertrophy of the ligamentum teres. MRI after surgical reduction of DDH requires neither sedation nor additional restraints because all infants are placed in a spica abduction cast and the imaging time is kept to a minimum. Previous MRI literature supports the notion that excessive abduction impairs blood flow to the femoral epiphysis and may lead to ischemia. In patients in whom there is a question of AVN secondary to ischemia during treatment-related abduction, the evaluation of the femoral head perfusion can be achieved with contrast-enhanced perfusion imaging. Enhancement pattern after gadolinium administration was rated as either asymmetric or focally or globally decreased enhancement. The hips, which showed a global decrease in perfusion, were ten times more likely to develop AVN (Fig. 33.7) (Dillon et al. 2005; Dwek 2009; Tiderius et al. 2009; Desai et al. 2011).

33.3 Acquired Disorders

33.3.1 Legg-Calvé-Perthes Disease

Legg-Calvé-Perthes disease (LCP) is a condition in which an avascular event affects the capital femoral epiphysis. After avascular event, growth of the ossific nucleus stops and the bone becomes dense. The dense bone is subsequently resorbed and replaced by new bone, and as this occurs the mechanical properties of the femoral head are altered such

Table 33.1 Waldenström's classification of the stages of Legg-Calvé-Perthes disease

Stage	Radiographic findings
Initial (increased density stage)	Increased density of femoral head, with or without subchondral fracture; radiolucencies appear in the metaphysis
Fragmentation stage	Varying pattern of lucency appear in epiphysis; the femoral head may be flattened and widen; metaphyseal changes resolve
Reossification stage	New bone appears in femoral head which gradually reossifies
Residual (healed) stage	Femoral head is fully reossified and remodels to maturity

that the head tends to flatten and enlarge. Once the new bone is in place, the head slowly remodels until skeletal maturation is achieved. Most patients are boys between the age of 5 and 8 years. Almost 90 % of LCP is unilateral. There is bilateral involvement, but it is rarely synchronous. The age at presentation is the most significant prognostic indicator. Children who are older than age 8 are more likely to develop a disability. The goal of treatment in LCP is to limit the late onset of degenerative joint disease. Therapy is aimed at maintaining congruence between the developing femoral epiphysis and the acetabulum, thereby limiting stress on the femoral head, preventing lateral extrusion of the femoral epiphysis, and allowing for normal epiphyseal shaping (Wenger et al. 1991; Kim 2010; Dimeglio and Canavese 2011).

33.3.1.1 Radiography

Early radiographs may be unremarkable. With time the femoral head may develop increased density. A crescentic subchondral lucency reflecting a subchondral fracture may develop. Radiographically, the subchondral fracture is best visualized on a frog lateral projection of the hip (Fig. 33.8). The condition may progress with increased sclerosis. There is subsequent fragmentation within a small flattened femoral head. Focal radiolucencies may develop adjacent to the physis involving both the epiphysis and the metaphysis. Over time, there is remodeling and reossification of the femoral head. The femoral head tends to become flattened (coxa plana) and enlarged (coxa magna), and the femoral neck becomes broad (Fig. 33.9). Four radiographic stages of modified Waldenström's classification – initial, fragmentation, reossification, and residual – are commonly summarized in Table 33.1. The lateral pillar classification system modified by Harring and coworkers is based on radiographic changes in the lateral portion of the femoral head when it enters the fragmentation stage, as seen on the anteroposterior view

Table 33.2 Lateral pillar classification system

Group	Lateral pillar radiographic findings ^a
A	No density change No loss of height
B	Some density changes Height ≥ 50 % Central pillar collapse
B/C	Thin lateral pillar Borderline height
C	Height < 50 %

^aAnteroposterior radiographs

(Table 33.2). It has been reported to have greater interobserver reliability and to be a better predictor of the final outcome (Herring et al. 1992, 2004; Kim 2010).

33.3.1.2 MRI

MRI is useful in cases of suspected LCP when radiographs are unrevealing, because it is highly sensitive for the detection of early ischemia. Signal intensity alterations of the femoral head that indicate marrow edema are early signs of LCP. MRI can demonstrate the presence and extent of infarction of the femoral head and enhancement of lateral column of the femoral head, suggesting recanalization that is associated with good prognosis (Fig. 33.10). Transphyseal enhancement or transphyseal bone bridging on MR images has been considered as one of the bad prognostic factors. Extension of physeal cartilage into the metaphysis reflects the same process responsible for the radiographic findings of metaphyseal radiolucencies (Fig. 33.11) (Sebag et al. 1997; Song et al. 2000; Dwek 2009; Jaramillo 2009; de Sanctis 2011).

33.3.2 Slipped Capital Femoral Epiphysis

Slipped capital femoral epiphysis (SCFE) is defined as the displacement of the femoral head relative to the femoral neck and shaft. SCFE is more common in boys than in girls (2.5:1), and affected children are frequently obese. In approximately one-third of patients, there is bilateral (but not typically simultaneous or symmetric) involvement of the hips. SCFE is most commonly idiopathic; however, it also has been noted in conjunction with renal osteodystrophy and endocrinopathies, including hypothyroidism and hypopituitarism. There is a history of trauma in approximately 50 % of patients. The earliest radiographic sign is widening and irregularity of the physis with rarefaction in its juxtaepiphyseal portion. In the normal hip, a line drawn tangential to the superior femoral neck (Klein line) on the AP view intersects a small portion of the lateral capital epiphysis; while typical

posterior displacement of the capital epiphysis has occurred, this line does not intersect the capital femoral epiphysis. With chronic slip, sclerosis may be seen in the medial femoral neck with bone remodeling (buttressing) (Fig. 33.12). CT and MR may also be used to make the diagnosis of SCFE. Diffuse or globular physeal widening is the earliest evidence of SCFE on MRI (Fig. 33.13). Due to complete loss of osseous continuity, SCFE is associated with high incidence of avascular necrosis as a complication (Fig. 33.14) (Dwek 2009; Tins et al. 2009; Jarrett et al. 2013).

33.3.3 Septic Arthritis

Early diagnosis of septic arthritis is crucial because any delay in the initiation of appropriate treatment can result in a poor outcome such as destruction of the femoral head, degenerative arthritis, or permanent deformity. The most common diagnostic dilemma is that septic arthritis cannot be confidently differentiated from transient synovitis, the most common disease entity in pediatric patients with an irritable hip, on the basis of clinical, laboratory, and radiographic findings (Lee et al. 1999).

Although US is highly accurate in the detection of hip effusion, differentiation of septic arthritis from transient synovitis or other arthritides cannot be achieved with US. Therefore, joint fluid aspiration is essential for early diagnosis of septic arthritis (Fig. 33.15) (Zawin et al. 1993; Robben et al. 1999).

MRI may play an important role in noninvasive differentiation of septic arthritis from transient synovitis in the pediatric patient with an irritable hip. Signal intensity alterations in the bone marrow of the affected hip joint and contrast enhancement of the soft tissues are useful in the differentiation of septic arthritis from transient synovitis. In transient synovitis, contralateral (asymptomatic) joint effusions are more common than septic arthritis, and bone marrow signal intensity alteration is usually absent in transient synovitis (Fig. 33.16) (Lee et al. 1999; Dowen et al. 2006; Yang et al. 2006; Kwack et al. 2007).

33.3.4 Juvenile Idiopathic Arthritis

Juvenile idiopathic arthritis (JIA) is a heterogeneous group of disorders. JIA is defined as a chronic arthritis that persists for a minimum of six consecutive weeks in one or more joints, commencing before the age of 16 years and after active exclusion of other causes. Hip involvement is frequent and is associated with significant morbidity and functional problem.

Contrast-enhanced MRI is the most sensitive imaging modality available to determine whether arthritis is present, but it rarely helps in establishing a specific diagnosis. MRI can be helpful, however, in clarifying the differential diagnosis such as pelvic osteomyelitis or para-articular osteoid osteoma. MRI also can reveal hemosiderin deposition and hemarthrosis suggestive of bleeding disorders, pigmented villonodular synovitis, and synovial vascular malformation. The synovial intima lacks a tight junction or basement membrane and thus allows rapid diffusion of gadolinium compounds into the joint fluid. Therefore, images must be obtained immediately after intravenous injection of contrast materials to display only synovial enhancement caused by active pannus (Argyropoulou et al. 2002; Malattia et al. 2010).

33.3.5 Idiopathic Chondrolysis

Idiopathic chondrolysis of the hip is an uncommon pediatric disorder that occurs during adolescence. It is characterized by pain and limp, with a rapid loss of articular cartilage of the femoral head and acetabulum, resulting in narrowing of the joint space and progressive stiffness in the joint. Conventional radiographic hallmarks include a concentrically narrowed joint space <3 mm without the osteophyte formation typical of osteoarthritis, accompanied by

osteopenia. Other findings include protrusio acetabuli, subchondral cysts, widening of the femoral head and neck, and premature physal closure. A geographic pattern of bone marrow edema centered within the proximal femoral epiphysis accompanied by ipsilateral ill-defined adjacent acetabular bone marrow edema, mild synovial hypertrophy, and little or no joint fluid is a characteristic early MRI finding of idiopathic chondrolysis (Fig. 33.17) (Rowe and Ho 1996; Johnson et al. 2003; Laor and Crawford 2009).

33.3.6 Osteoid Osteoma

Intra-articular osteoid osteoma, which occurs within or near a joint, is considered a separate clinical entity. The most commonly involved joint is the hip. Intra-articular osteoid osteoma is rare, and its clinical manifestations may be puzzling. Imaging findings of intra-articular osteoid osteoma differ from those of intracortical osteoid osteoma. With intra-articular osteoid osteoma, reactive cortical thickening is minimal or absent, a finding believed to be due to a lack of cambium, the inner layer of the periosteum. At CT, the nidus is well defined and round or oval with low attenuation. An area of high attenuation may be seen centrally, a finding that represents mineralized osteoid (Fig. 33.18) (Ebrahim et al. 2001; Gaeta et al. 2004; Szendroi et al. 2004).

33.4 Illustrations: Pediatric Hip Disorders

33.4.1 Proximal Femoral Focal Deficiency

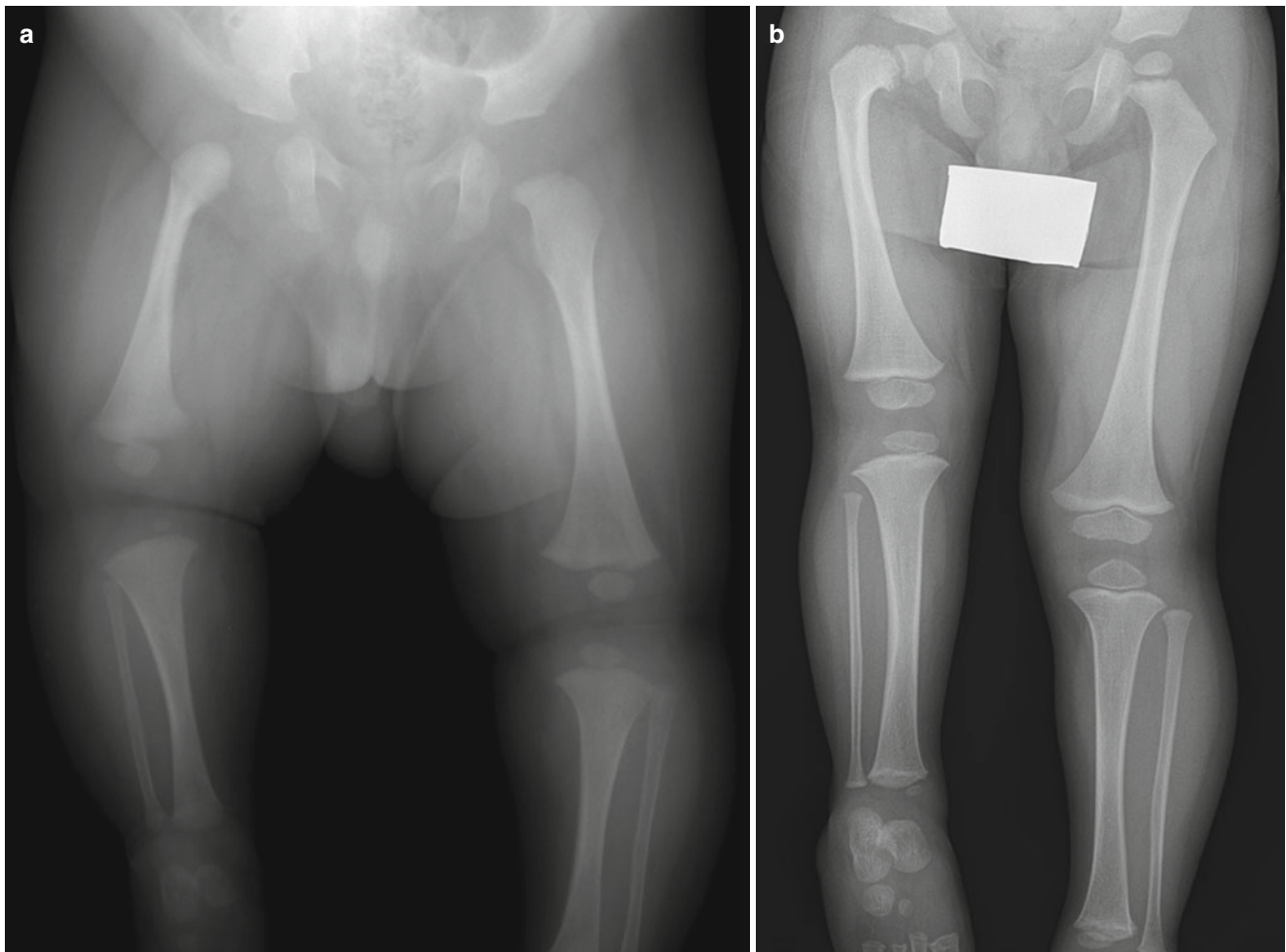


Fig. 33.1 Proximal femoral focal deficiency. (a) Anteroposterior radiograph of a 4-month-old infant with a short right femur shows hypoplastic right femur. Right acetabulum is relatively normal. (b)

Follow-up radiograph obtained 3 years later shows a short right femur with coxa vara deformity. Note the hypoplastic right proximal femoral epiphysis and flattened right proximal tibia epiphysis

33.4.2 Developmental Coxa Vara

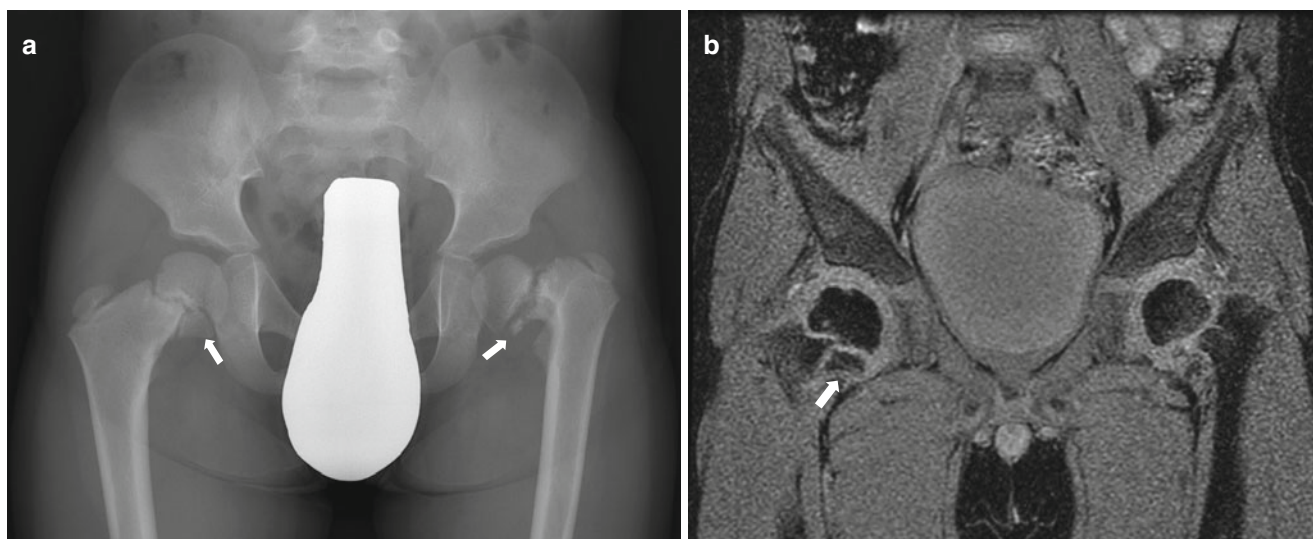


Fig. 33.2 Bilateral coxa vara. **(a)** Proximal femoral growth plates are vertically tilted. Slight fragmentation (*arrows*) is seen at the medial aspect of each proximal femoral growth plate. Note the wide left

proximal femoral growth plate. **(b)** Coronal GRE image shows vertically tilted proximal femoral growth plate and bony fragment at medial aspect of the proximal femoral metaphysis (*arrow*)

33.4.3 Hip Ultrasonography: Coronal View

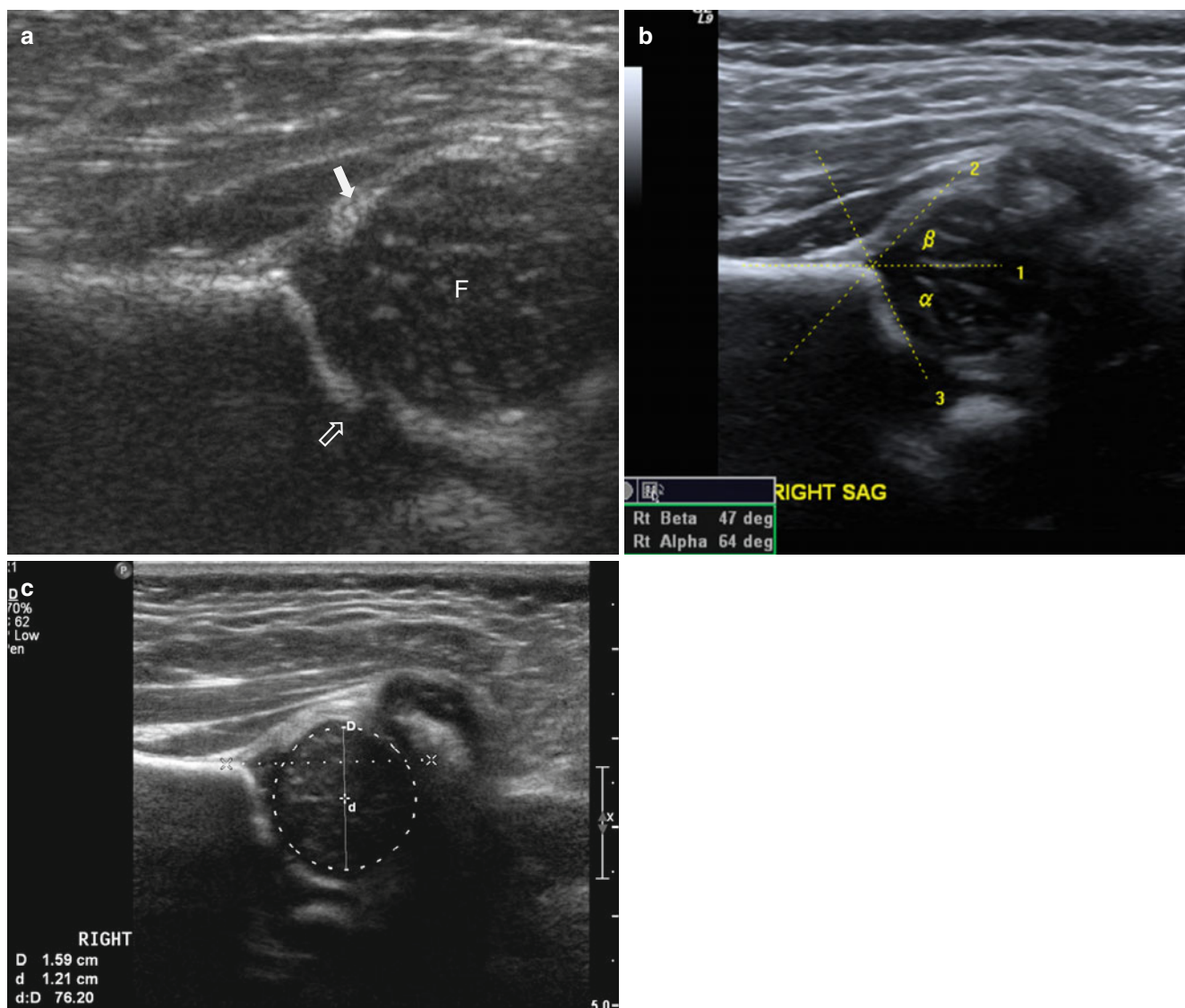


Fig. 33.3 Normal hip ultrasonography: coronal view. (a) Coronal view of hip joint in the standard plane shows low echoic femoral head (F) resting against the bony acetabulum. Note the fibrocartilaginous tip of labrum (arrow) and junction of bony ilium and triradiate cartilage (open arrow). (b) Normal hip ultrasonogram with alpha and beta angles used in measurement. Alpha angles above 60° are normal. (c) Normal

hip ultrasonogram with femoral head coverage index measurement. Coronal view of ultrasound demonstrates use of manufacturer processing to draw a horizontal line along the iliac bone and then outline the cartilaginous femoral head to measure percent coverage of the femoral head. Better than 50 % coverage is normal

33.4.4 Hip Ultrasonography: Transverse View

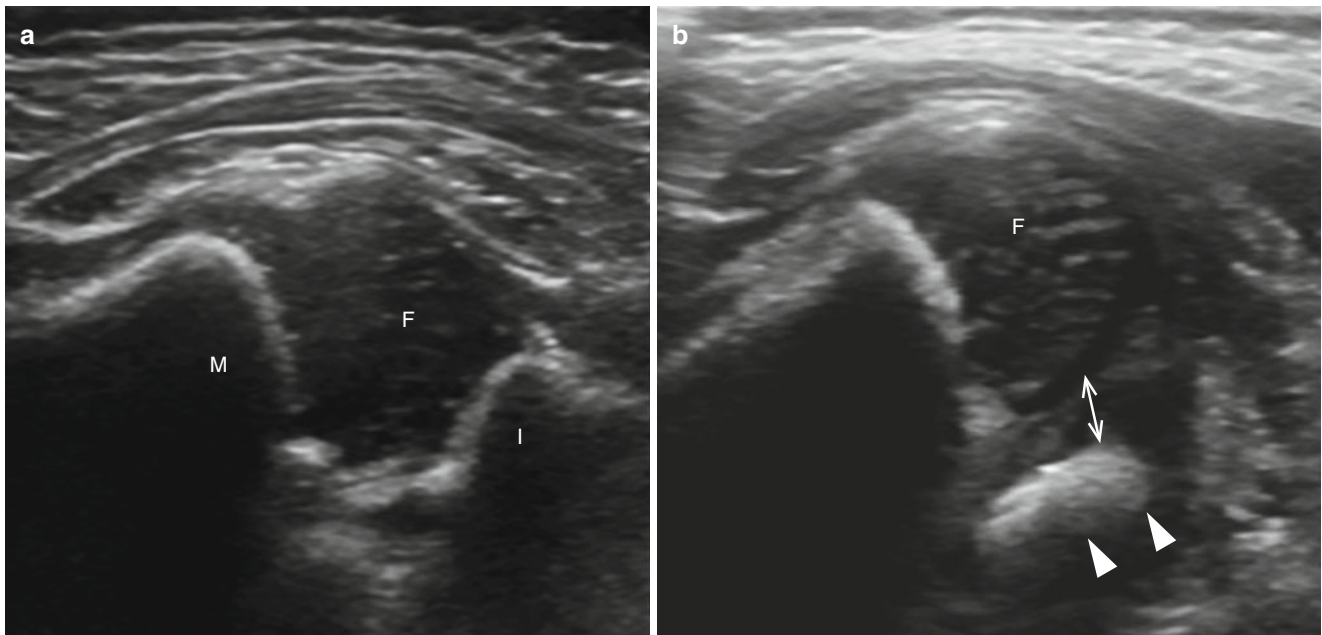


Fig. 33.4 Transverse view of the hip ultrasonography. **(a)** Normal transverse sonogram of the hip with the 90° hip joint flexion shows low echoic femoral head (*F*) between metaphysis (*M*) and ischium (*I*). **(b)** Instability of the hip in a newborn baby. With instability and

displacement, the femoral head moves laterally and posteriorly. The laterally displaced femoral head (*F*) has no contact with the ischium (*arrowheads*) with the widening of space between femoral head and ischium (*arrows*)

33.4.5 Developmental Dysplasia of the Hip: Ultrasonographic Findings

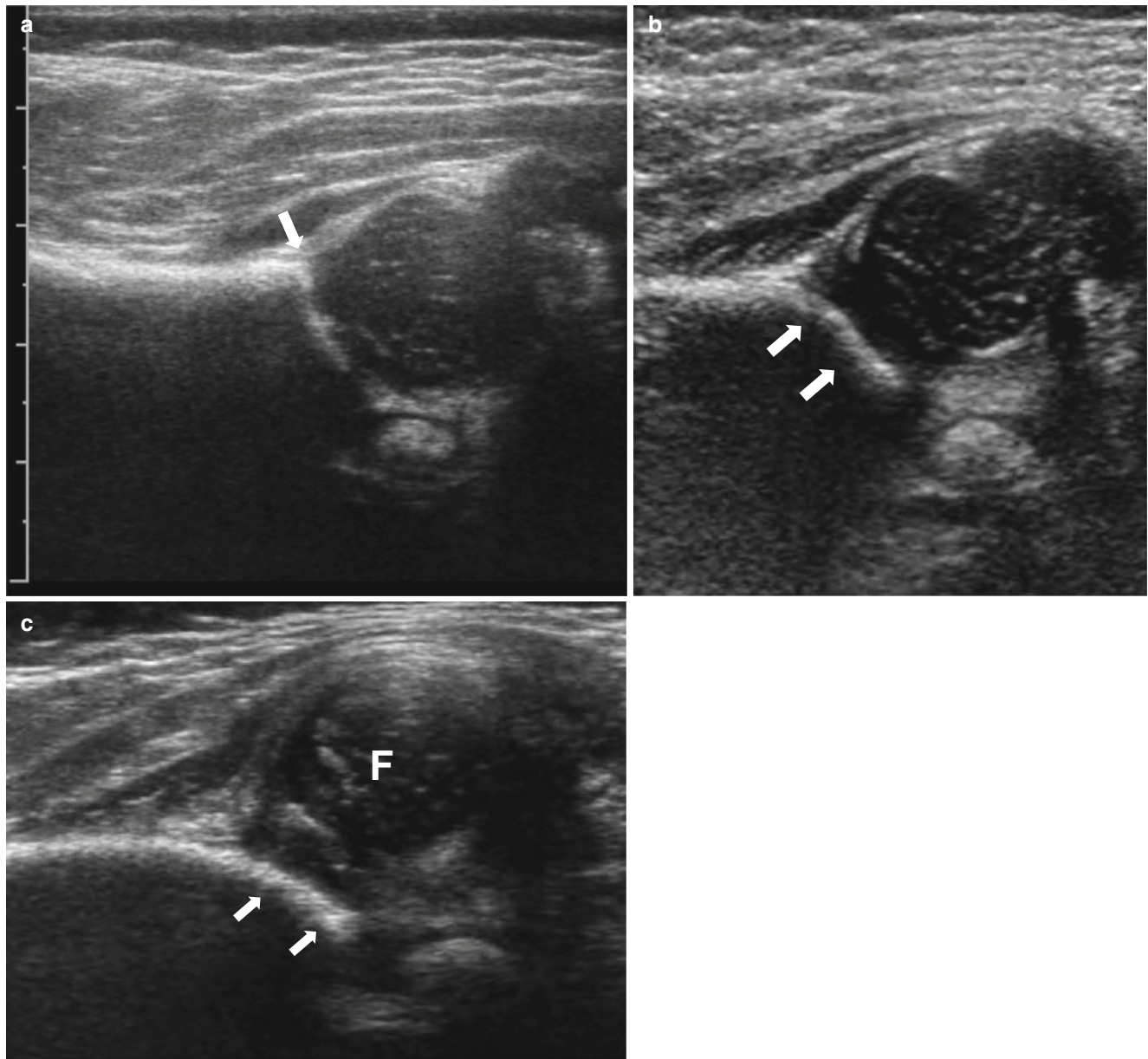


Fig. 33.5 Ultrasonographic spectrum of developmental dysplasia of the hip. (a) Normal hip. The superior acetabular rim is angular (*arrow*). (b) Lateral edge of the bony acetabulum shows rounded appearance

(*arrows*) suggesting bony acetabular dysplasia. (c) Coronal view of ultrasound shows complete superior and lateral dislocation of the left femoral head from the shallow acetabulum (*arrow*)

33.4.6 Developmental Dysplasia of the Hip: Radiographic Findings

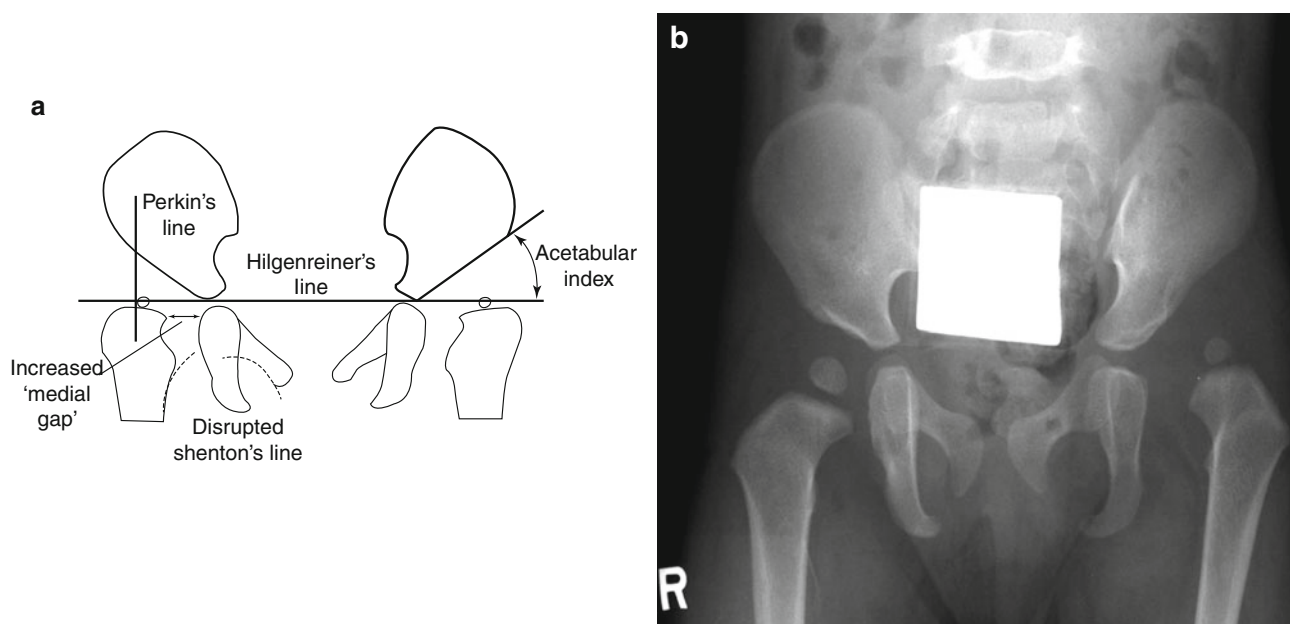


Fig. 33.6 Radiographic findings of developmental dysplasia of the hip. (a) Radiographic measurement used in evaluating developmental dysplasia of the hip. Hilgenreiner's line is drawn through the triradiate cartilage. Perkin's line is drawn perpendicular to Hilgenreiner's line at the margin of the bony acetabulum. Shenton line curves along the femoral metaphysis and connects smoothly to the inner margin of the pubis.

Medial gap is measured to quantify proximal and lateral displacement of the hip. The acetabular index is the angle between the lines drawn along the margin of the acetabulum. (b) Anteroposterior radiograph shows relatively small left femoral head ossification center, slightly steep left acetabular roof, and rounded left superior acetabular rim compared to the normal right side

33.4.7 Developmental Dysplasia of the Hip: Postoperative Imaging Findings

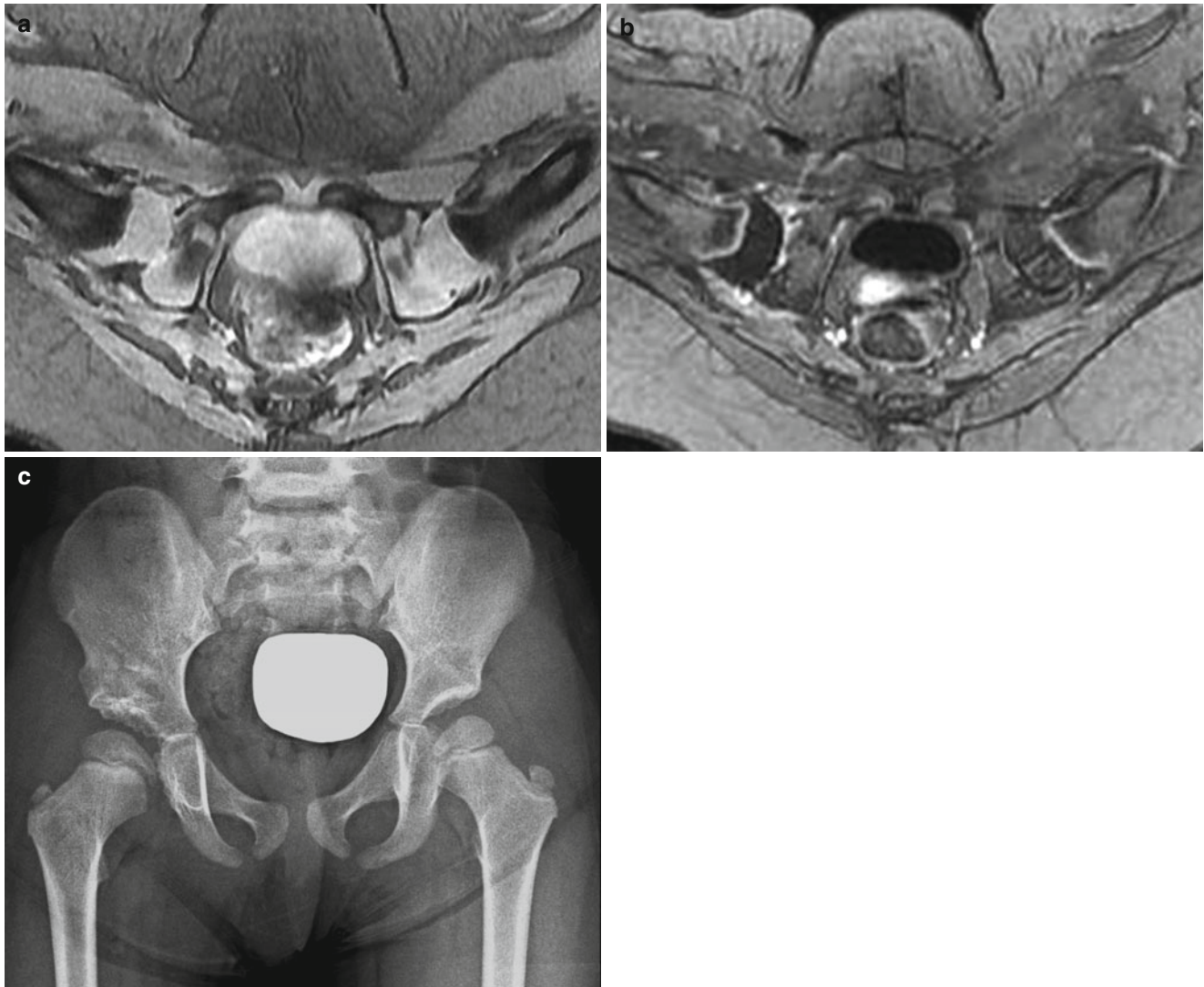


Fig. 33.7 Postoperative imaging for developmental dysplasia of the hip. (a) Axial GRE image of a 4-month-old girl with right DDH shows well-contained right femoral head. (b) Contrast-enhanced axial image shows global decrease of femoral head perfusion which suggests

ischemia damage of the right femoral head. (c) Follow-up radiograph shows deformed femoral epiphysis and widening of the proximal femoral metaphysis, suggesting ischemic damage of the femoral head

33.4.8 Legg-Calve-Perthes Disease: Initial Stage

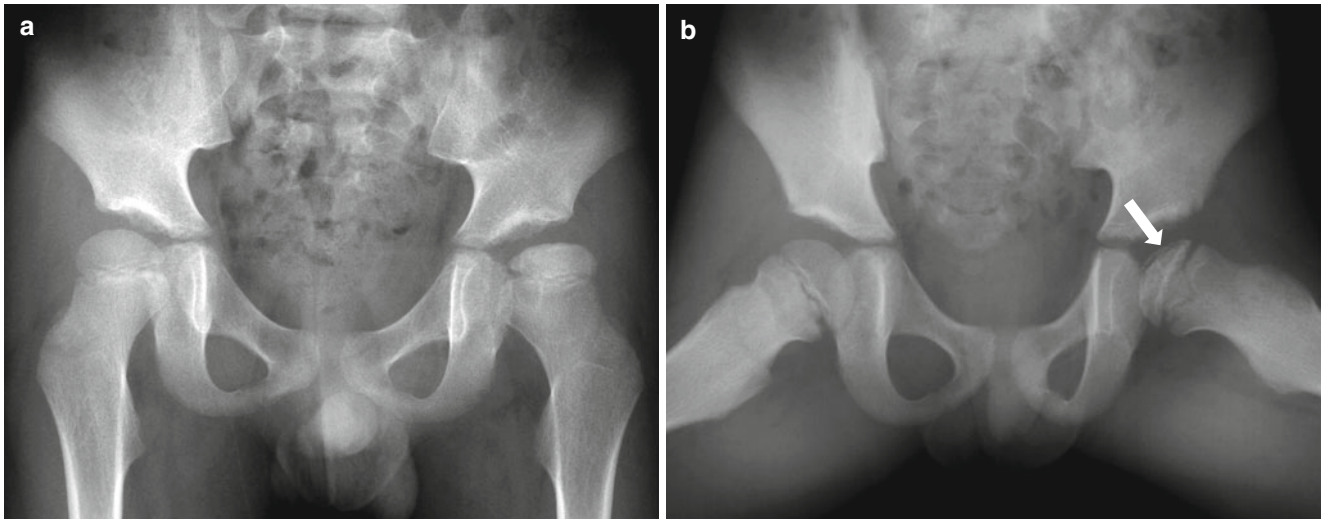


Fig. 33.8 Initial stage of LCP disease. (a) Anteroposterior radiograph in a 5-year-old boy with a left-sided limp shows a dense sclerosis in the left femoral head. (b) Frog-leg lateral view shows subchondral radiolucency (*arrow*) with sclerosis in the left femoral head

33.4.9 Legg-Calve-Perthes Disease: Evolution of Radiographic Abnormalities

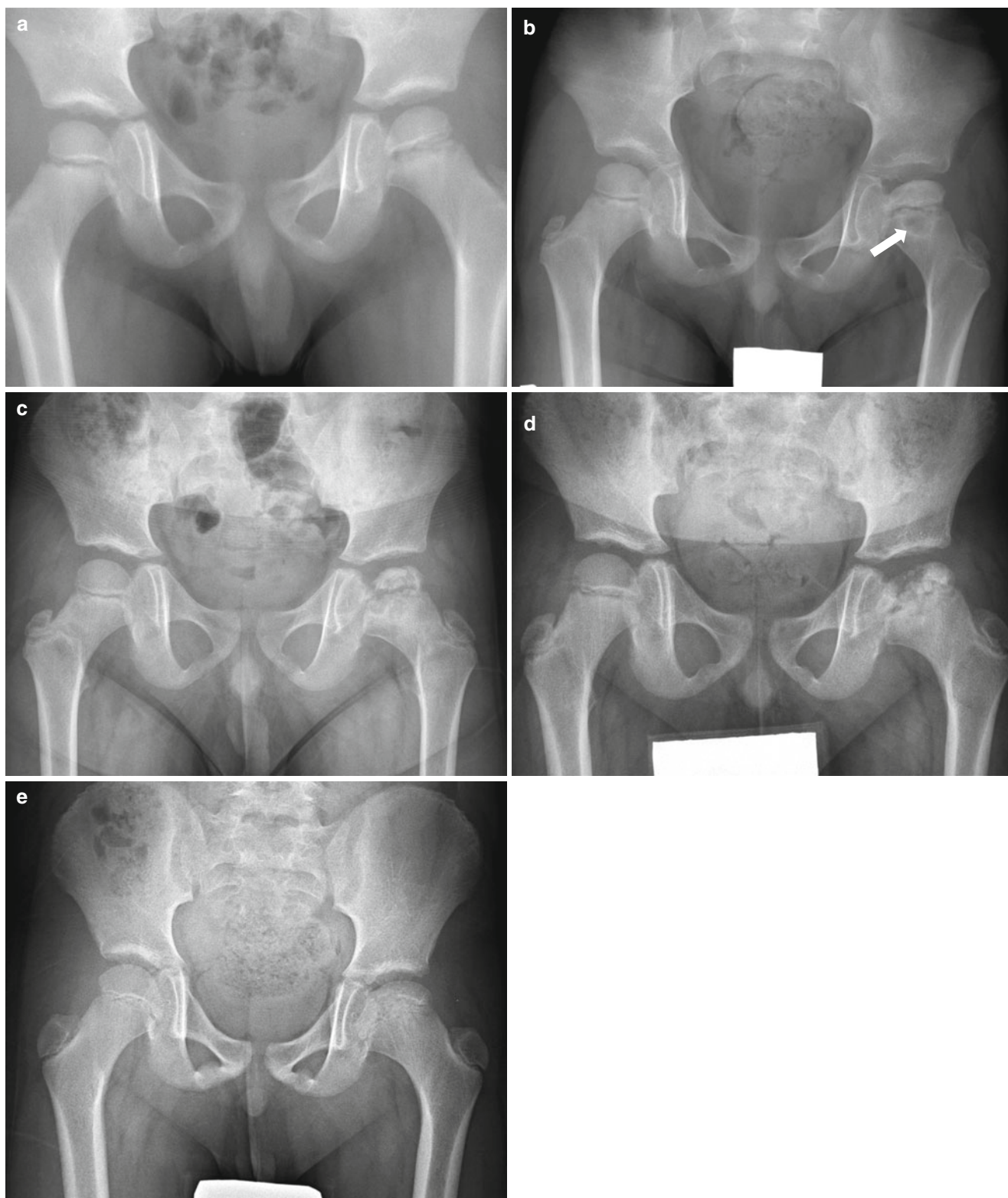


Fig. 33.9 Evolution of radiographic abnormalities in LCP disease. (a) Initial radiograph in a 6-year-old boy with left limping gait shows no specific abnormality. (b) Anteroposterior radiograph obtained 6 months later shows increased sclerosis and slight asphericity of the left femoral head. Note the radiolucent area with sclerotic rim (arrow) in the left

proximal femur. (c) Anteroposterior radiograph at the age of 7 shows progressed bone resorption with vertical fissuring in the left femoral head. (d) Follow-up radiograph shows reossification of the left proximal femoral epiphysis. (e) Anteroposterior radiograph at the age of 9 shows wide and flat left femoral head with progressed remodeling

33.4.10 Legg-Calve-Perthes Disease: MRI Findings

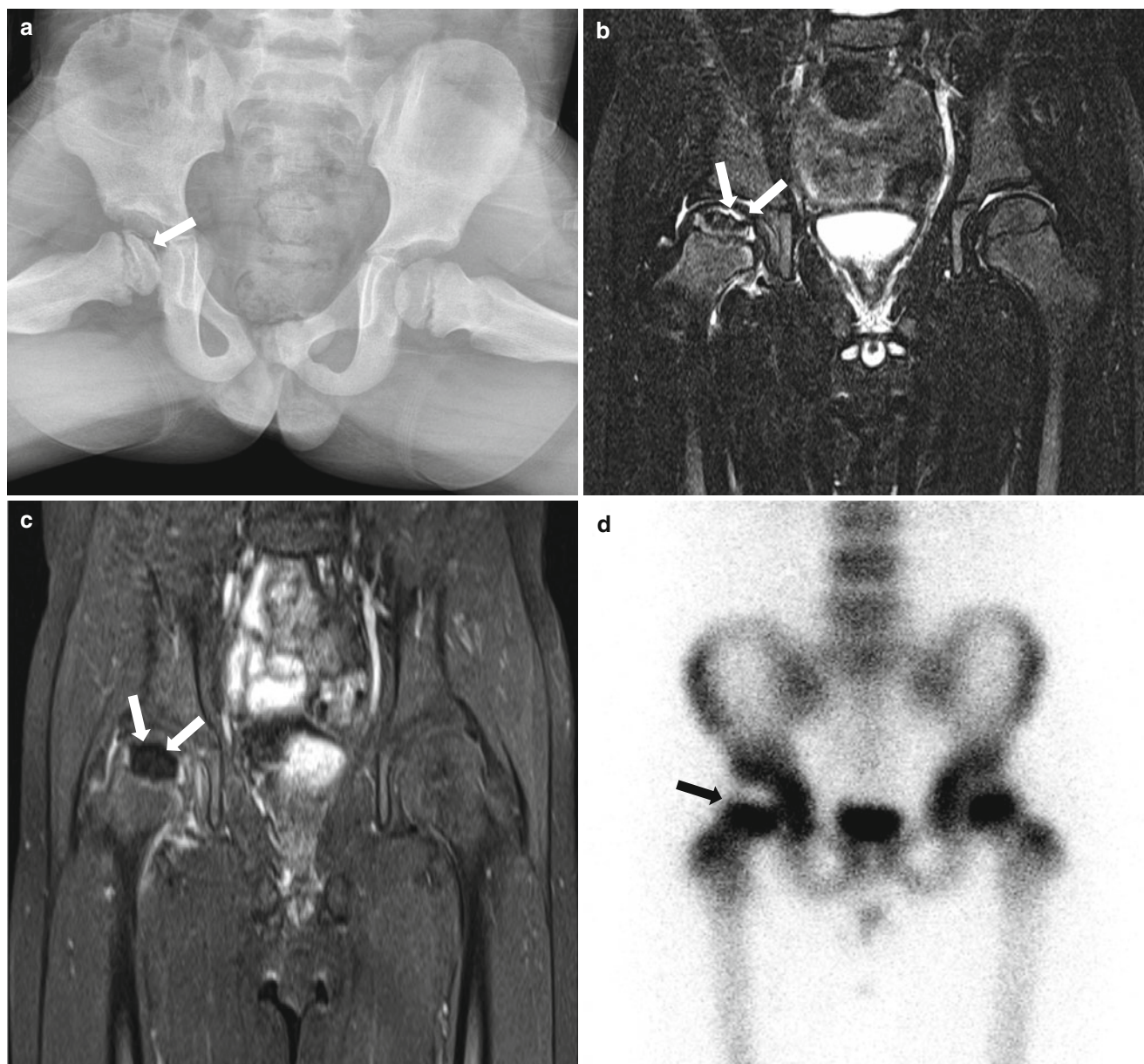


Fig. 33.10 MRI appearance of an early-stage LCP disease. (a) Frog-leg lateral view of a 7-year-old boy shows collapsed femoral head with sclerosis in the right hip joint. Note the subchondral radiolucency (arrow). (b) Coronal T2-weighted MR image shows heterogeneous signal intensity of the right proximal femoral epiphysis with crescent

shape subchondral high signal intensity in the right femoral head (arrows). (c) Contrast-enhanced T1-weighted image demonstrates geographic nonenhancing area, suggesting avascular area (arrows). (d) Bone scan shows photon defect in the right femoral head (arrow)

33.4.11 Legg-Calve-Perthes Disease: Metaphyseal Changes

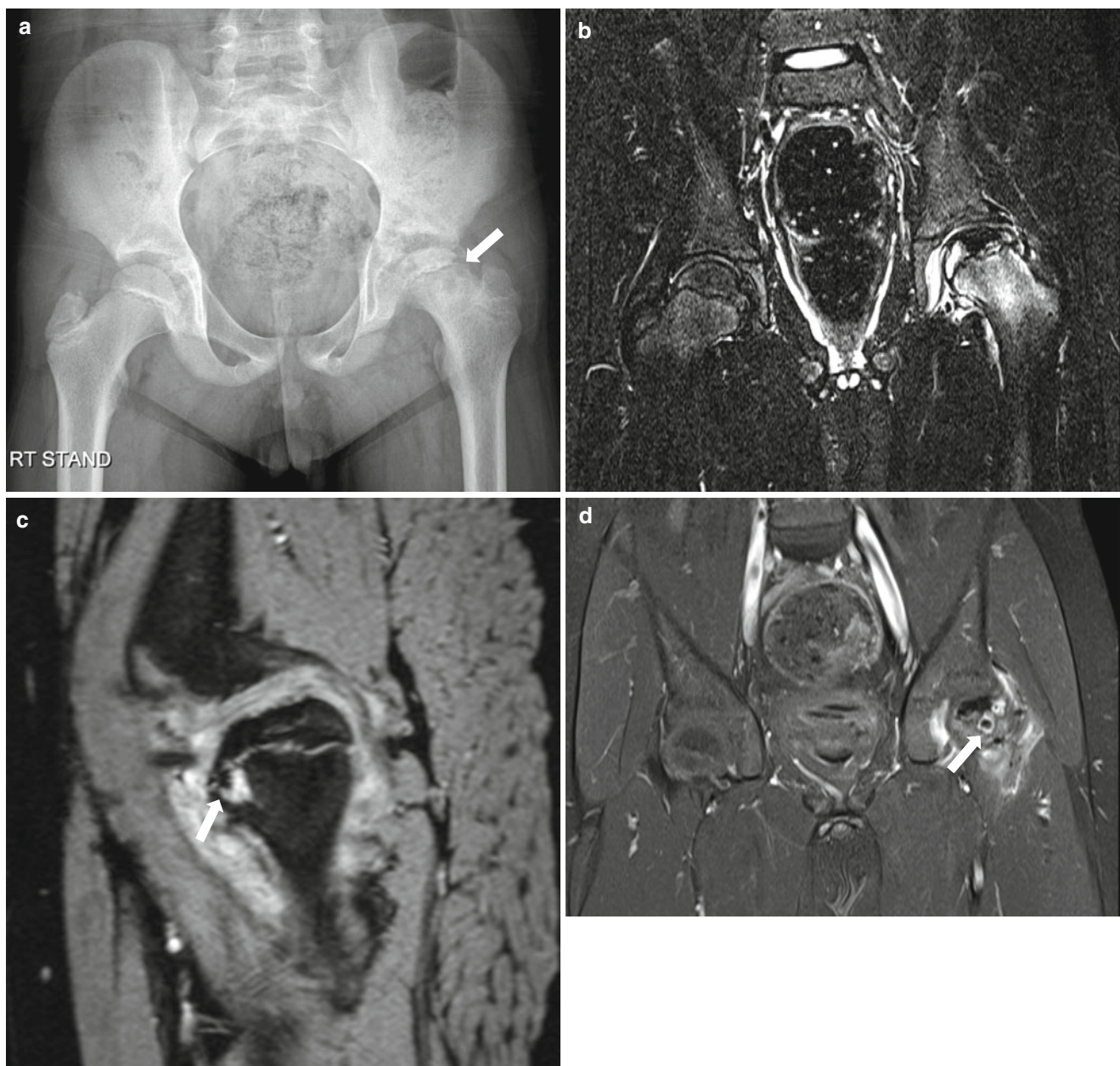


Fig. 33.11 LCP disease with metaphyseal changes. (a) Anteroposterior radiograph of a 9-year-old boy shows irregular sclerotic and lytic lesion in the left femoral head and associated radiolucency in the left proximal femoral metaphysis (*arrow*). (b) Coronal T2-weighted MR image shows heterogeneous signal intensity of the left proximal femoral epiphysis with diffuse increased signal intensity in the left proximal

femoral metaphysis suggesting bone marrow edema. (c) Sagittal GRE image demonstrates a focal high signal intensity lesion attached to growth plate (*arrow*) which reflects the radiolucent area on radiograph. (d) The metaphyseal lesion shows ring enhancement (*arrow*) on contrast-enhanced T1-weighted image. There is decreased contrast enhancement in the left proximal femoral epiphysis

33.4.12 Slipped Capital Femoral Epiphysis: Radiographic Findings

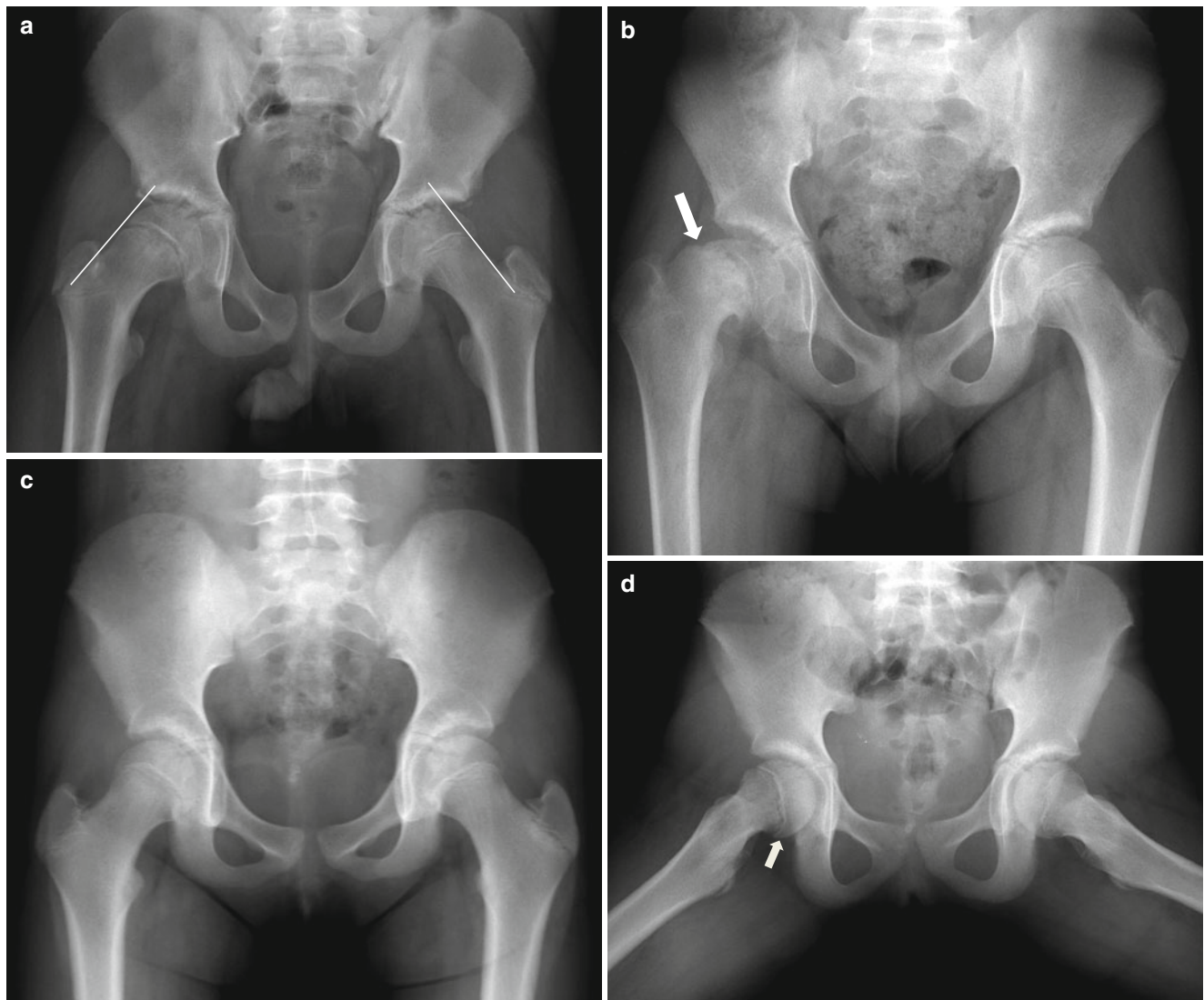


Fig. 33.12 Radiographic appearance of slipped capital femoral epiphysis. (a) Appearance of acute SCFE. Anteroposterior radiograph in an 11-year-old boy with acute-onset right hip pain shows an abnormally widened proximal femoral growth plate. Klein line, a line drawn along the lateral border of the femoral neck, would not intersect the femoral head. Normally, a small portion of the left femoral head should be lying lateral to the Klein line. (b) Anteroposterior radiograph in a 12-year-old boy with many months of right thigh discomfort shows slipped femoral

epiphysis and ill-defined sclerosis in the right proximal metaphysis with bending of the femoral neck. Note the bony hump (*arrow*) in the superior portion of the femoral neck, suggesting remodeling of the femoral neck. (c, d) It is essential to obtain frog-leg lateral radiography of the hip whenever anteroposterior radiographic findings are subtle (c). In an 11-year-old boy with clinically suspected slipped capital femoral epiphysis, frog-leg lateral radiograph shows asymmetric widening of the growth plate and mild posterior slipping of the femoral head (*arrow*, d)

33.4.13 Slipped Capital Femoral Epiphysis: MRI Findings

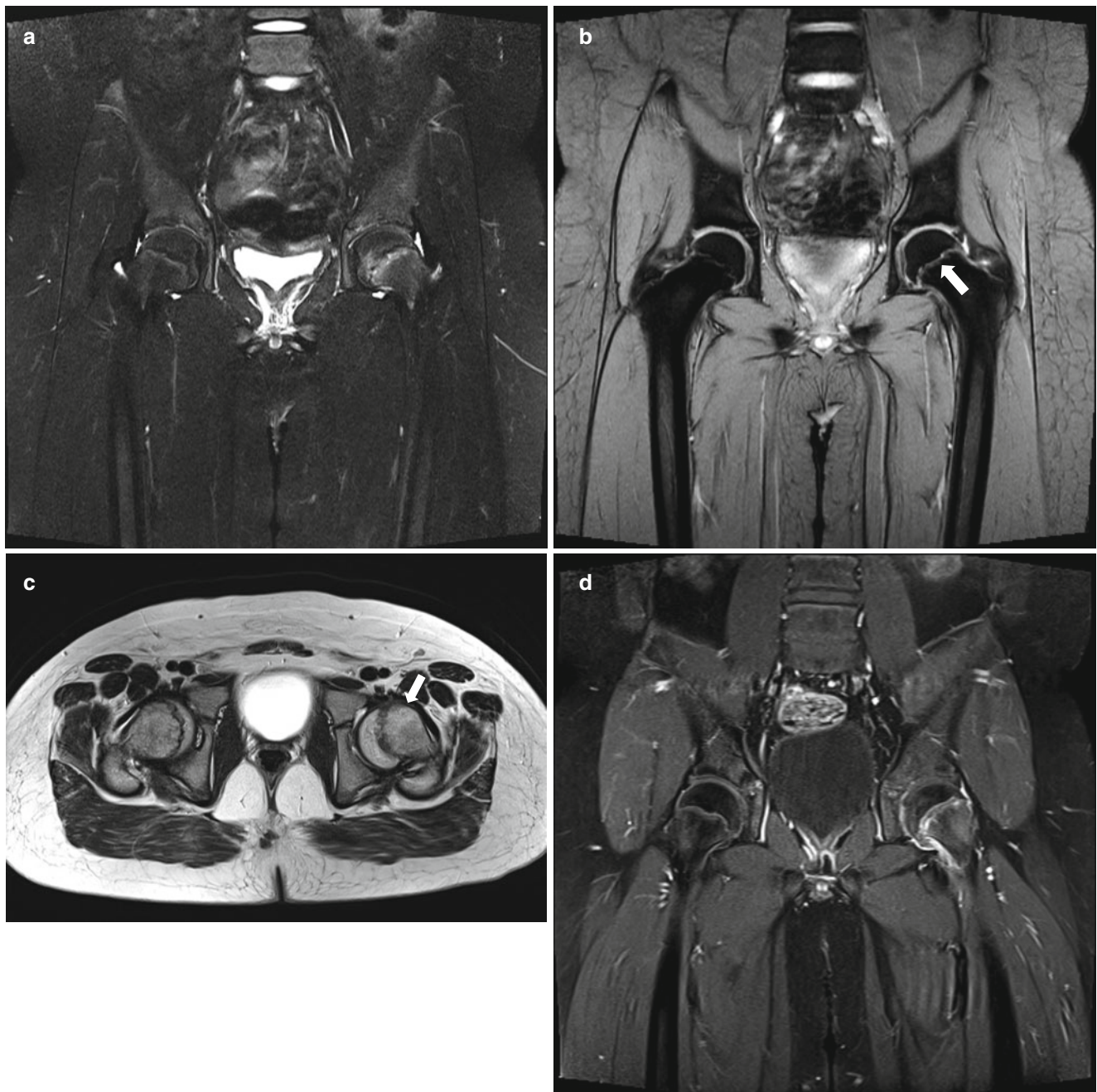


Fig. 33.13 MRI appearance of slipped capital femoral epiphysis. (a) Coronal T2-weighted image demonstrates asymmetric widening of the left proximal femoral growth plate with mild metaphyseal and epiphyseal bone marrow edema. (b) Coronal gradient echo image clearly demonstrates asymmetric widening of the left proximal femoral

growth plate (*arrow*) (c) Axial T2-weighted image shows posteriorly rotated left proximal femoral epiphysis and widening of the proximal femoral growth plate. Note the anterior metaphyseal bump in the left proximal femur (*arrow*) (d) On contrast-enhanced T1-weighted image, left femoral head perfusion is preserved

33.4.14 Slipped Capital Femoral Epiphysis: Avascular Necrosis as a Complication

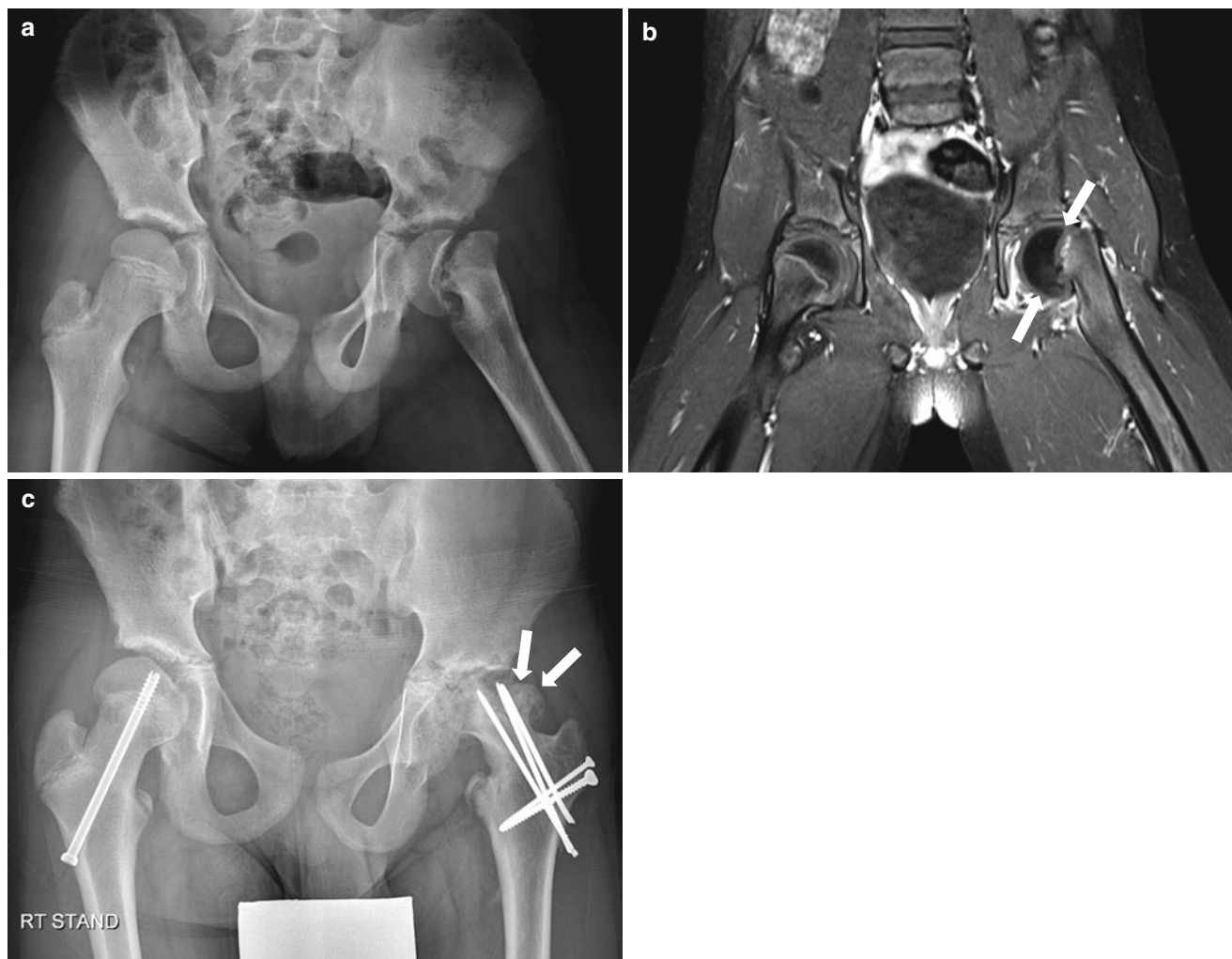


Fig. 33.14 Avascular necrosis of the femoral head in a 13-year-old boy with severe slipped capital femoral epiphysis. (a) Anteroposterior radiograph shows severe displacement of the femoral capital epiphysis and widening of the proximal femoral growth plate. (b) Contrast-enhanced T1-weighted image demonstrates slipped femoral epiphysis

and diffuse decreased femoral head perfusion (*arrow*). (c) Follow-up radiograph after reduction of the left slipped femoral capital epiphysis and prophylactic screw fixation of the right hip shows avascular necrosis of the left femoral head (*arrows*)

33.4.15 Ultrasonography for Joint Effusion

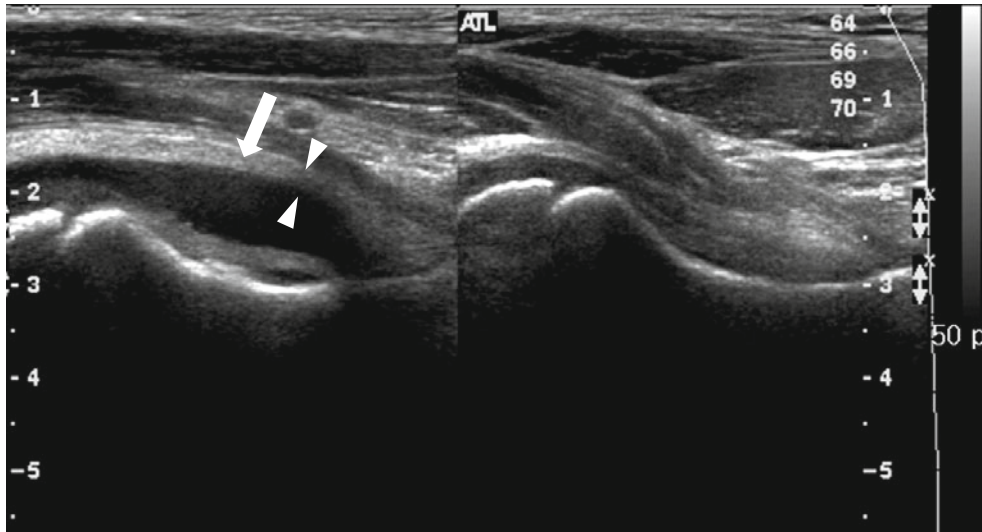


Fig. 33.15 Ultrasonography for joint effusion. Longitudinal view of hip ultrasound (*left*) shows a widened anechoic joint space with a convex anterior margin (*arrow*). Note the synovial thickening along the

femoral neck (*arrowheads*). Longitudinal view of hip ultrasound of a normal hip (*right*) for comparison shows a concave anterior margin along the anterior femoral neck

33.4.16 Neonatal Septic Arthritis of the Hip

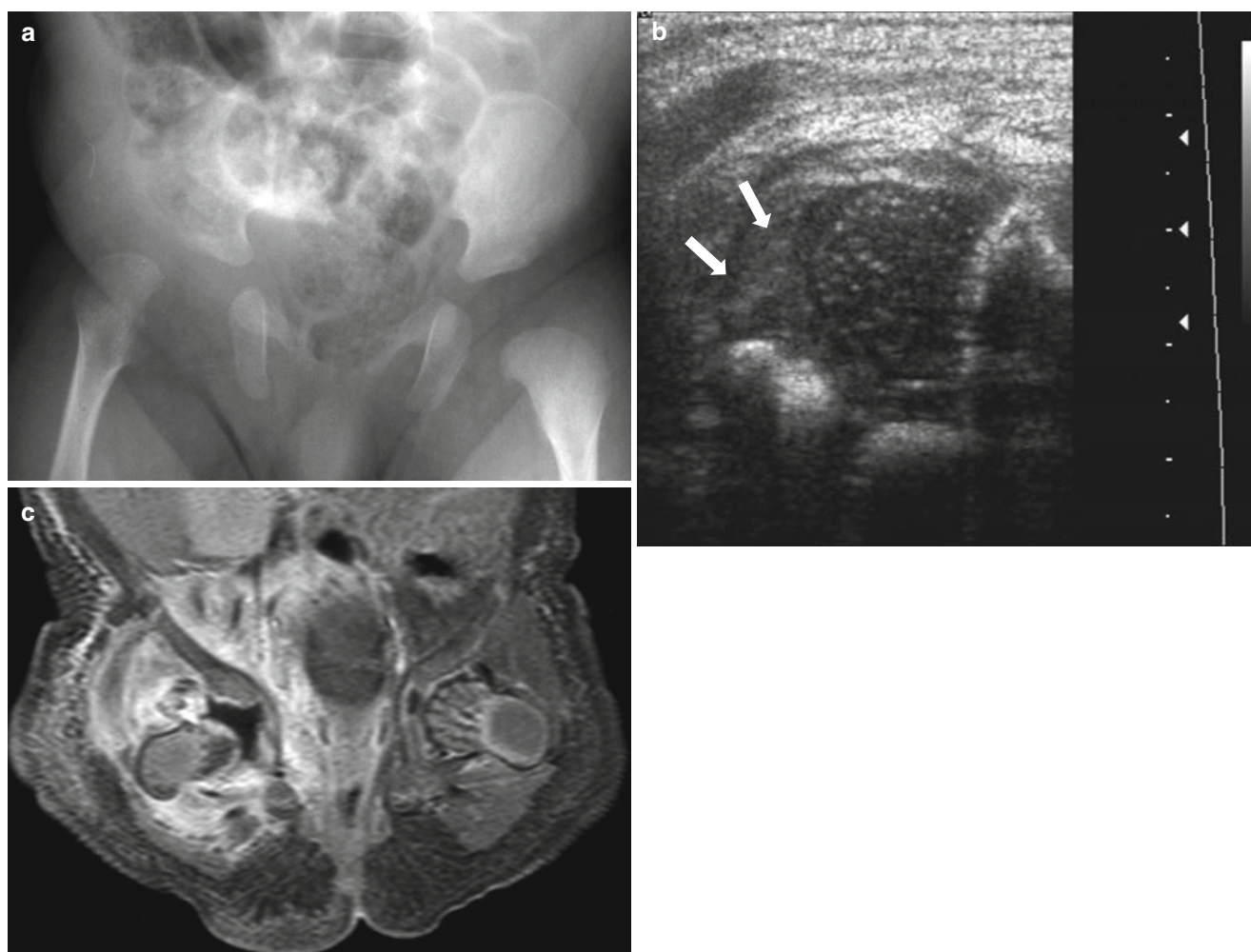


Fig. 33.16 Neonatal septic arthritis of the hip. (a) Anteroposterior radiograph of a neonate with painful swelling of the right proximal thigh shows superolateral displacement of the proximal femur. (b) Transverse view of right hip ultrasonogram shows ill-defined heterogeneous

echogenicity (*arrows*) in the right hip joint. (c) Contrast-enhanced T1-weighted image shows dislocated right hip joint with moderate amount of joint effusion in the right hip. Note the diffuse soft tissue swelling and enhancement in the right buttock and right iliopsoas muscles

33.4.17 Idiopathic Chondrolysis

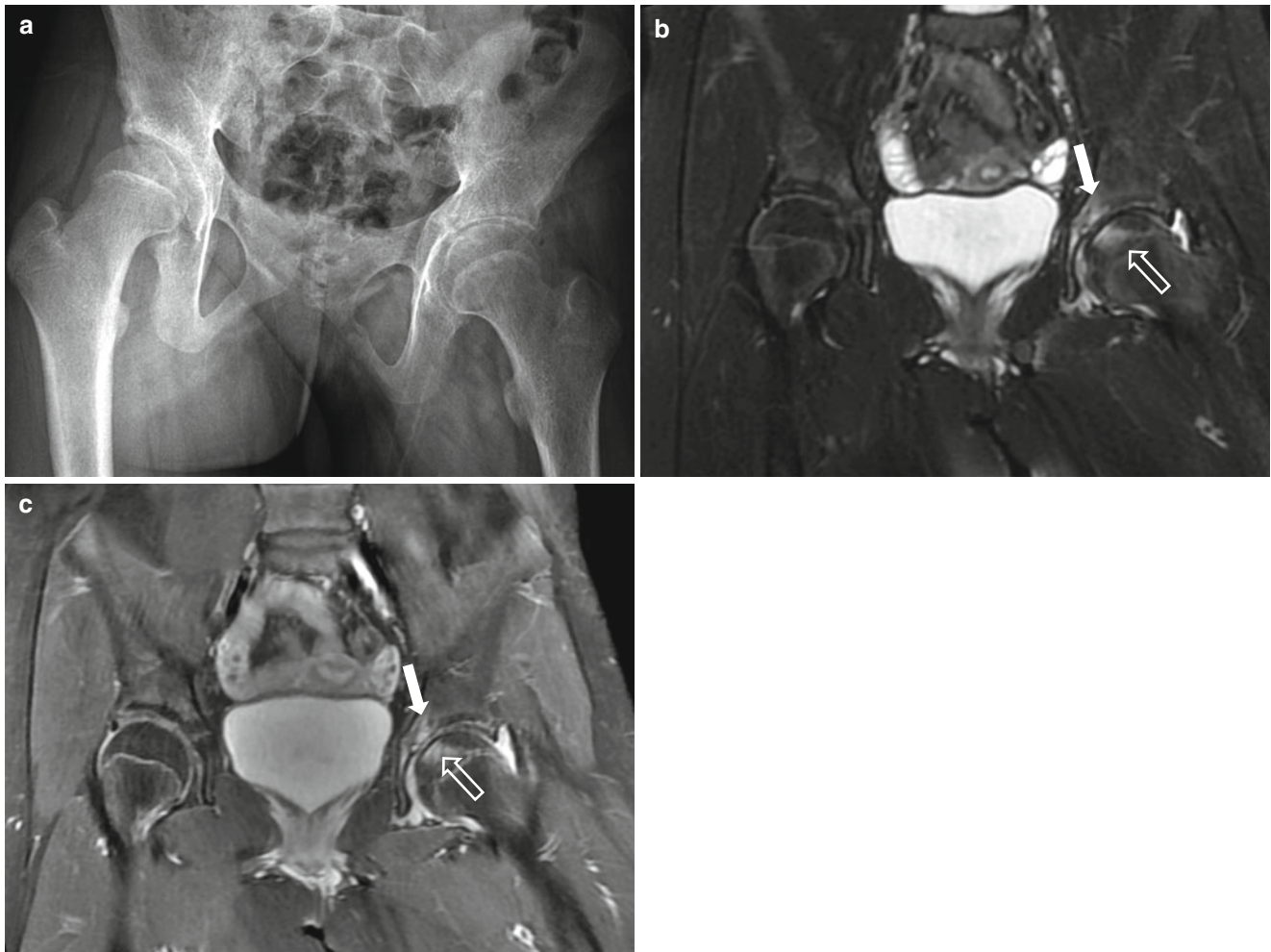


Fig. 33.17 Idiopathic chondrolysis. (a) A 14-year-old girl with left hip joint pain. Anteroposterior radiograph demonstrates diffuse narrowing of the left hip joint with suspected marginal sclerosis in the left acetabulum. (b, c) Coronal T2-weighted image and contrast-enhanced

T1-weighted image show patchy bone marrow edema with enhancement involving left acetabulum (*arrow*) and left femoral epiphysis (*open arrow*)

33.4.18 Osteoid Osteoma

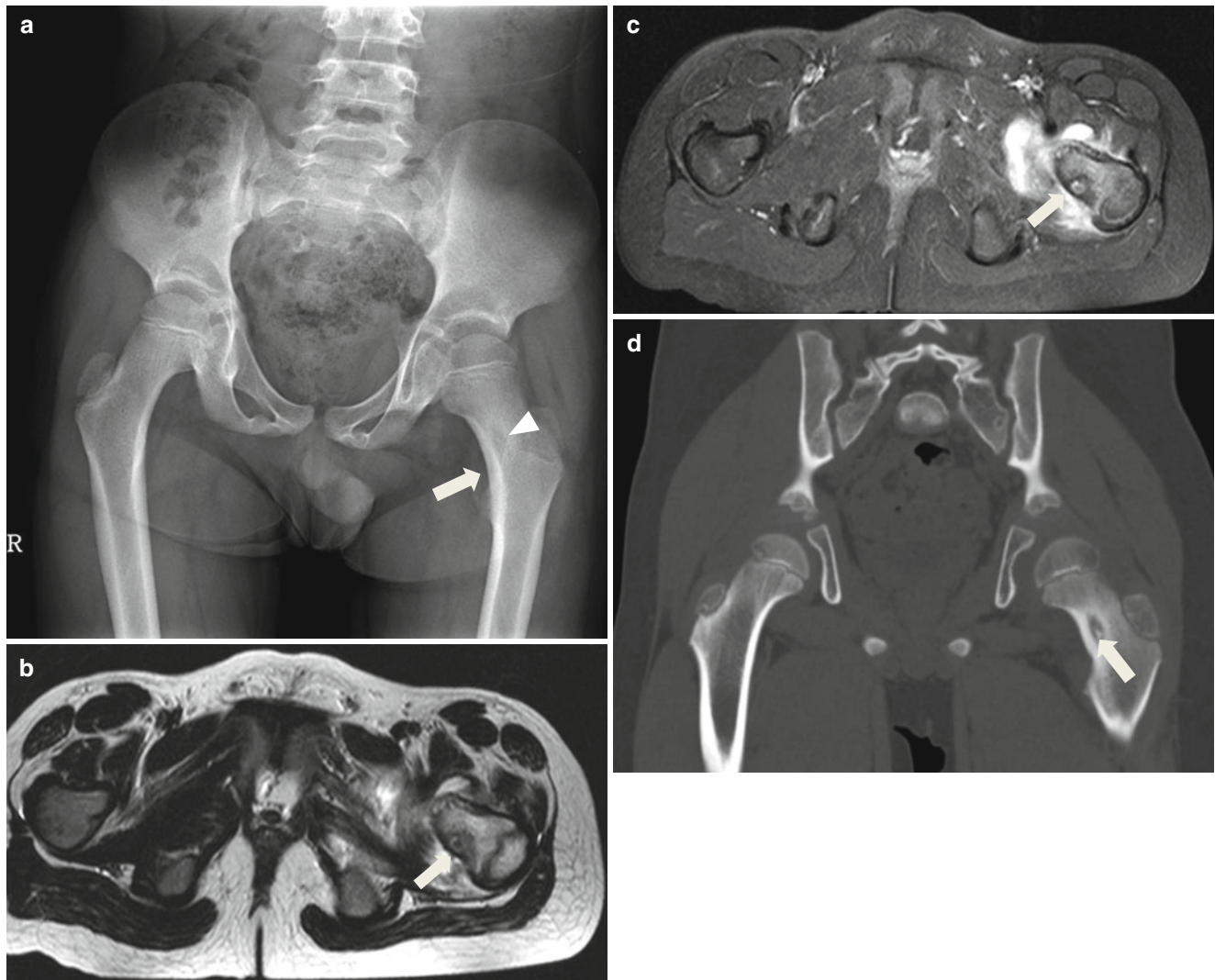


Fig. 33.18 Osteoid osteoma. (a) Anteroposterior radiograph shows localized thickening of the cortex in the left proximal femur (arrows), and ill-defined osteolytic area in the left proximal femur (arrowheads). (b) Axial T2-weighted image shows a cortical-based lesion (arrow) within the femoral neck with surrounding muscle and bone marrow edema. (c) Contrast-enhanced T1-weighted image shows peripherally

enhancing nidus (arrow) in the left femoral neck with surrounding bone marrow edema. Note the surrounding synovial tissue and muscles enhancement. (d) Noncontrast CT in the same patients shows a tiny sclerotic focus (arrow) within the radiolucent nidus along the femoral neck and surrounding sclerosis

References

- American Institute of Ultrasound in M, American College of R. AIUM practice guideline for the performance of an ultrasound examination for detection and assessment of developmental dysplasia of the hip. *J Ultrasound Med*. 2009;28:114–9.
- Anton CG, Applegate KE, Kuivila TE, et al. Proximal femoral focal deficiency (PFFD): more than an abnormal hip. *Semin Musculoskelet Radiol*. 1999;3:215–26.
- Argyropoulou MI, Fanis SL, Xenakis T, et al. The role of MRI in the evaluation of hip joint disease in clinical subtypes of juvenile idiopathic arthritis. *Br J Radiol*. 2002;75:229–33.
- Beals RK. Coxa vara in childhood: evaluation and management. *J Am Acad Orthop Surg*. 1998;6:93–9.
- Biko DM, Davidson R, Pena A, et al. Proximal focal femoral deficiency: evaluation by MR imaging. *Pediatr Radiol*. 2012;42:50–6.
- Bracken J, Ditchfield M. Ultrasonography in developmental dysplasia of the hip: what have we learned? *Pediatr Radiol*. 2012;42:1418–31.
- de Sanctis N. Magnetic resonance imaging in Legg-Calve-Perthes disease: review of literature. *J Pediatr Orthop*. 2011;31:S163–7.
- Desai AA, Martus JE, Schoenecker J, et al. Spica MRI after closed reduction for developmental dysplasia of the hip. *Pediatr Radiol*. 2011;41:525–9.
- Dezateux C, Rosendahl K. Developmental dysplasia of the hip. *Lancet*. 2007;369:1541–52.
- Dillon JE, Connolly SA, Connolly LP, et al. MR imaging of congenital/developmental and acquired disorders of the pediatric hip and pelvis. *Magn Reson Imaging Clin N Am*. 2005;13:783–97.
- Dimeglio A, Canavese F. Imaging in Legg-Calve-Perthes disease. *Orthop Clin North Am*. 2011;42:297–302, v.
- Donaldson JS, Feinstein KA. Imaging of developmental dysplasia of the hip. *Pediatr Clin North Am*. 1997;44:591–614.
- Downen DJ, Khan AL, Henman PD. Magnetic resonance imaging in suspected septic arthritis can avoid unnecessary surgery. *Arch Dis Child*. 2006;91:1032.
- Dwek JR. The hip: MR imaging of uniquely pediatric disorders. *Magn Reson Imaging Clin N Am*. 2009;17:509–20, vi.
- Ebrahim FS, Jacobson JA, Lin J, et al. Intraarticular osteoid osteoma: sonographic findings in three patients with radiographic, CT, and MR imaging correlation. *AJR Am J Roentgenol*. 2001;177:1391–5.
- Gaeta M, Minutoli F, Pandolfo I, et al. Magnetic resonance imaging findings of osteoid osteoma of the proximal femur. *Eur Radiol*. 2004;14:1582–9.
- Harcke HT. Screening newborns for developmental dysplasia of the hip: the role of sonography. *AJR Am J Roentgenol*. 1994;162:395–7.
- Herring JA, Neustadt JB, Williams JJ, et al. The lateral pillar classification of Legg-Calve-Perthes disease. *J Pediatr Orthop*. 1992;12:143–50.
- Herring JA, Kim HT, Browne R. Legg-Calve-Perthes disease. Part I: classification of radiographs with use of the modified lateral pillar and Stulberg classifications. *J Bone Joint Surg Am*. 2004;86-A:2103–20.
- Jaramillo D. What is the optimal imaging of osteonecrosis, Perthes, and bone infarcts? *Pediatr Radiol*. 2009;39 Suppl 2:S216–9.
- Jarrett DY, Matheney T, Kleinman PK. Imaging SCFE: diagnosis, treatment and complications. *Pediatr Radiol*. 2013;43 Suppl 1:S71–82.
- Johnson K, Haigh SF, Ehtisham S, et al. Childhood idiopathic chondrolysis of the hip: MRI features. *Pediatr Radiol*. 2003;33:194–9.
- Kim HK. Legg-Calve-Perthes disease. *J Am Acad Orthop Surg*. 2010;18:676–86.
- Koenig JK, Pring ME, Dwek JR. MR evaluation of femoral neck version and tibial torsion. *Pediatr Radiol*. 2012;42:113–5.
- Kwack KS, Cho JH, Lee JH, et al. Septic arthritis versus transient synovitis of the hip: gadolinium-enhanced MRI finding of decreased perfusion at the femoral epiphysis. *AJR Am J Roentgenol*. 2007;189:437–45.
- Laor T, Crawford AH. Idiopathic chondrolysis of the hip in children: early MRI findings. *AJR Am J Roentgenol*. 2009;192:526–31.
- Lee SK, Suh KJ, Kim YW, et al. Septic arthritis versus transient synovitis at MR imaging: preliminary assessment with signal intensity alterations in bone marrow. *Radiology*. 1999;211:459–65.
- Malattia C, Damasio MB, Basso C, et al. Dynamic contrast-enhanced magnetic resonance imaging in the assessment of disease activity in patients with juvenile idiopathic arthritis. *Rheumatology (Oxford)*. 2010;49:178–85.
- Maldjian C, Patel TY, Klein RM, et al. Efficacy of MRI in classifying proximal focal femoral deficiency. *Skeletal Radiol*. 2007;36:215–20.
- Morin C, Harcke HT, MacEwen GD. The infant hip: real-time US assessment of acetabular development. *Radiology*. 1985;157:673–7.
- Pavlov H, Goldman AB, Freiburger RH. Infantile coxa vara. *Radiology*. 1980;135:631–40.
- Robben SG, Lequin MH, Diepstraten AF, et al. Anterior joint capsule of the normal hip and in children with transient synovitis: US study with anatomic and histologic correlation. *Radiology*. 1999;210:499–507.
- Rosendahl K, Toma P. Ultrasound in the diagnosis of developmental dysplasia of the hip in newborns. The European approach. A review of methods, accuracy and clinical validity. *Eur Radiol*. 2007;17:1960–7.
- Rowe LJ, Ho EK. Idiopathic chondrolysis of the hip. *Skeletal Radiol*. 1996;25:178–82.
- Sebag G, Ducou Le Pointe H, Klein I, et al. Dynamic gadolinium-enhanced subtraction MR imaging—a simple technique for the early diagnosis of Legg-Calve-Perthes disease: preliminary results. *Pediatr Radiol*. 1997;27:216–20.
- Song HR, Dhar S, Na JB, et al. Classification of metaphyseal change with magnetic resonance imaging in Legg-Calve-Perthes disease. *J Pediatr Orthop*. 2000;20:557–61.
- Szendroi M, Kollo K, Antal I, et al. Intraarticular osteoid osteoma: clinical features, imaging results, and comparison with extraarticular localization. *J Rheumatol*. 2004;31:957–64.
- Tiderius C, Jaramillo D, Connolly S, et al. Post-closed reduction perfusion magnetic resonance imaging as a predictor of avascular necrosis in developmental hip dysplasia: a preliminary report. *J Pediatr Orthop*. 2009;29:14–20.
- Tins B, Cassar-Pullicino V, McCall I. The role of pre-treatment MRI in established cases of slipped capital femoral epiphysis. *Eur J Radiol*. 2009;70:570–8.
- Weinstein JN, Kuo KN, Millar EA. Congenital coxa vara. A retrospective review. *J Pediatr Orthop*. 1984;4:70–7.
- Wenger DR, Ward WT, Herring JA. Legg-Calve-Perthes disease. *J Bone Joint Surg Am*. 1991;73:778–88.
- Yang WJ, Im SA, Lim GY, et al. MR imaging of transient synovitis: differentiation from septic arthritis. *Pediatr Radiol*. 2006;36:1154–8.
- Zawin JK, Hoffer FA, Rand FF, et al. Joint effusion in children with an irritable hip: US diagnosis and aspiration. *Radiology*. 1993;187:459–63.

Hong Eo

Contents

34.1	Introduction	1064
34.2	Spectrum of Disease	1064
34.2.1	Infantile Cortical Hyperostosis (Caffey's Disease).....	1064
34.2.2	Periosteal New Bone Formation.....	1064
34.2.3	Bone Infarction.....	1064
34.2.4	Osteochondrosis	1064
34.2.5	Metabolic and Endocrinologic Disease.....	1065
34.2.6	Vitamin-Related Bone Disease	1066
34.2.7	Congenital Foot Deformities.....	1067
34.2.8	Tarsal Coalition	1067
34.3	Illustrations: Miscellaneous Musculoskeletal Disease	1068
34.3.1	Infantile Cortical Hyperostosis (Caffey's Disease).....	1068
34.3.2	Periosteal New Bone Formation.....	1069
34.3.3	Bone Infarction.....	1070
34.3.4	Kohler Disease	1071
34.3.5	Freiberg Disease	1072
34.3.6	Sever Disease	1073
34.3.7	Idiopathic Juvenile Osteoporosis	1074
34.3.8	Hypothyroidism.....	1075
34.3.9	Hypopituitarism and Growth Hormone Deficiency	1076
34.3.10	Hyperparathyroidism.....	1077
34.3.11	Pseudohypoparathyroidism	1078
34.3.12	Rickets.....	1079
34.3.13	Club Foot.....	1080
34.3.14	Vertical Talus.....	1081
34.3.15	Metatarsus Varus	1082
34.3.16	Talocalcaneal Coalition	1083
	References	1084

H. Eo, M.D.
Department of Radiology, Samsung Medical Center,
#50, Ilwon-Dong, KangNam-Gu, Seoul 135-710, South Korea
e-mail: rtombow@gmail.com

34.1 Introduction

In this chapter, miscellaneous musculoskeletal diseases, which are not discussed, will be dealt with. Periosteal new bone formation including Caffey's disease, bone infarction, osteochondrosis, metabolic bone disease such as hyperparathyroidism, vitamin-related bone disease, and congenital foot deformity are included. These diseases are not common, but good prognosis is based on exact diagnosis including radiologic finding.

34.2 Spectrum of Disease

34.2.1 Infantile Cortical Hyperostosis (Caffey's Disease)

Infantile cortical hyperostosis originally was described in 1945 by Caffey and Silverman (Caffey and Silverman 1945). Etiology is still unknown, most cases are sporadic, and there is no predilection for race, sex, or geographic location. However, reports of familial occurrence have been documented (Borochowitz et al. 1991). Most cases usually present in the first few months of life, with acute inflammation of soft tissue, including irritability, pain, and swelling, elevated sedimentation rate (ESR), and onset after the age of 6 months probably does not occur; it can be Caffey's dysplasia. Caffey's disease is considered a benign, self-limiting disease, resolving over months, with rarely persistent or recurrent findings (Swischuk 2004b).

In most usual cases, there is asymmetric subperiosteal/cortical new bone formation. Mandible, clavicles, ribs, and long bones are most commonly involved (Fig. 34.1). The involvement of the vertebrae and small bones of the hands and feet has not been shown. Mandibular involvement is pathognomonic of Caffey's disease, but does not occur in all cases. Long bone lytic lesions are rare. Involvement of the flat bones and bones of the face and calvarium is much less common. Calvarial involvement shows lytic defects, while facial involvement presents with swelling over the cheeks. The patient with the extension of the orbit can present with proptosis, ptosis, or glaucoma. Scapular involvement, often isolated, is not unusual and may present as pseudoparalysis of the extremity (Caffey 1957).

34.2.2 Periosteal New Bone Formation

Whenever the periosteum is irritated, periosteal new bone formation is seen. After intramedullary blood, pus, or tumor extends through the cortex to elevate and irritate the periosteum, this occurs (Swischuk 2004c).

In patients with malignancy, rapid periosteal elevation such as single or multiple thin layers of bone is formed. At the point where the abnormal periosteum joins the normal cortex, a triangle often occurs. This is referred to as "Codman's triangle" (Fig. 34.2c). With benign problems such as osteomyelitis, this same triangle is sometimes seen. And another periosteal new bone formation associated with vertical spiculations of bone assures a malignant bone tumor.

Markedly separated, or "ballooned," periosteal new bone is usually seen in patients with marked subperiosteal bleeding in scurvy, the battered child syndrome (Fig. 34.2d), hemophilia, and neurogenic patients.

Periosteal new bone formation along the long bones is normal at around 2–3 months of infants, especially in immature infants (Fig. 34.2a). It results from exuberant normal bone growth.

34.2.3 Bone Infarction

Osteonecrosis is the death of cellular elements of bone marrow by ischemia. Osteonecrosis of epiphysis is referred as avascular necrosis, and ischemic injury of metaphyseal and diaphyseal is called as a bone infarction. Generally, bone infarction in childhood is seen with sickle cell disease and Gaucher's disease, secondarily with medications such as steroids and with vasculitis, radiation therapy, trauma, or joint effusion (Swischuk 2004a).

Destructive, radiolucent changes usually occur in the metaphyses but in more severe cases can extend into the diaphysis. In any case, differentiation from osteomyelitis often is difficult and requires complete clinical and radiologic correlation. Sclerosis is seen with healing (Swischuk 2004a). MRI frequently shows a nonspecific pattern of low signal intensity on T1-weighted images and high signal intensity on T2-weighted images (Fig. 34.3). In other words, this is the bone marrow edema pattern. After contrast injection, non-enhanced areas are visible within the lesion, the extent of which could depend on the chronicity of the lesion (Saini and Saifuddin 2004). The presence of soft tissue abscess can be the important finding indicative of infection.

Bone scan also has been used in the differentiation of infarction from osteomyelitis. In the early stage, bone scan shows decreased flow and uptake of isotope in the infarcted bone. But generally, hot or positive bone scan could be shown in active or healing osteomyelitis (Swischuk 2004a).

34.2.4 Osteochondrosis

Osteochondrosis involves various bones in the body and is largely a problem of older children with immature skeleton. Most commonly, the bones involved include the

tarsal navicular (Kohler's disease) and the femoral capital epiphysis (Legg-Calve-Perthes disease). The latter, however, is more common but previously described. Kohler disease is presented between 2 and 8 years of age, and boys are three to five times more likely to be affected (Tsirikos et al. 2003). It is suspected in patients most commonly with midfoot pain and focal tenderness over the navicular bone on examination (Tsirikos et al. 2003). Freiberg disease, which is not commonly seen in children, is commonly shown by disordered ossification of the second metatarsal head. So it has a painful condition of the forefoot occurring most often in adolescent girls who play ballet or dance (Air and Rietveld 2010). Sever disease is a common cause of heel pain in young athletes. It is caused by repeated tensile forces on the calcaneal apophysis by the Achilles tendon (Atanda et al. 2011).

In Kohler disease, fragmentation, sclerosis, and flattening of the navicular bone are the characteristics (Fig. 34.4), and if swelling is seen over the area, the diagnosis is assured (Borges et al. 1995). This latter point is important because normal fragmentation of this bone also occurs. Freiberg disease is demonstrated with sclerosis and varying degrees of flattening of second metatarsal head in plain radiography (Fig. 34.5). Bilateral involvement occurs in less than 10 % of patients (Carmont et al. 2009). In Sever disease, the calcaneus appears sclerotic and fragmented in plain radiography (Fig. 34.6). But, it is normally appearing and symptom is important in diagnosis.

34.2.5 Metabolic and Endocrinologic Disease

34.2.5.1 Idiopathic Juvenile Osteoporosis

Idiopathic juvenile osteoporosis is of unknown etiology, uncommon, and self-limited disease of adolescence with profound osteoporosis. Skeletal pain is common, especially in the spine. The serum calcium, phosphorus, and alkaline phosphatase levels are normal (Smith 1995).

Radiographs show universal collapse of the vertebral bodies (Fig. 34.7) and often metaphyseal fractures of long bones. The different diagnoses include Cushing's syndrome, osteogenesis imperfecta, leukemia, and metastatic disease. In osteogenesis imperfecta, the width of the bones may be abnormally thin and most fractures occur in the diaphysis (Juhl et al. 1998). But, in idiopathic juvenile osteoporosis, width of the long bones is normal, although the cortex is thin and metaphyseal fractures are common.

34.2.5.2 Hypothyroidism

The most common form of hypothyroidism in the childhood is congenital hypothyroidism, known as cretinism, resulting from the absence or underdevelopment of the thyroid gland. Cretinism also can be seen in the infants of mothers who ingest excessive iodide or antithyroid medication during

pregnancy and in a few infants who are unable to convert inorganic iodine into active hormone (States 2001).

Infants with cretinism tend to present with prolonged gestation, large size at birth, prominent fontanelles, respiratory distress, hypothermia, hypoactivity, poor feeding, delayed stooling, abdominal distension, peripheral cyanosis, and edema.

In juvenile hypothyroidism, acquired thyroid deficiency after birth, the findings usually are less severe than in cretinism.

Typical radiologic finding of cretinism is delayed bone age (Fig. 34.8). The ossification centers often are malformed and irregular in shape. In addition, the bones of these infants may be more dense than usual. This is of unexplained etiology, but hypercalcemia can be seen in some of these patients. In childhood, certain epiphyses, especially the head of femur, show a tendency to ossify from numerous small irregular centers rather than from a single one as normal. So, the femoral head develops a flattened shape.

The radiography shows unduly wide sutures, overly dense bones, and large fontanelles of skull as the evidence of delayed ossification. In addition, excessive wormian bone formation is common, and there is delay in development of the mastoid and paranasal sinus air cavities. In older infants and children, the sella turcica can enlarge in a symmetrical rounded fashion, which is caused by rebound hypertrophy of the anterior portion of the pituitary gland. After treatment, it can regress. This rounded sella often is referred to as a "cherry" sella. With the combination with other calvarial findings, this can be highly suggestive of hypothyroidism.

34.2.5.3 Hyperthyroidism

When the mother suffers from hyperthyroidism at the time of delivery or has undergone surgical or medial thyroidectomy for the disease during gestation, hyperthyroidism can be seen in the neonate. Baby with hyperthyroidism demonstrates hyperactivity, restlessness, increased hunger, weight loss, increased pulse rate, cardiac failure, and other features of typical hyperthyroidism such as myopathy and exophthalmos (Riggs et al. 1972).

The radiologic findings consist of accelerated bone maturation and premature closure of the cranial sutures. In addition, brachydactyly can result from the premature epiphyseal fusion. Thyroid acropachy, which reveals the periosteal new bone formation of metacarpals and phalanges, is rare in children.

34.2.5.4 Hypopituitarism and Growth Hormone Deficiency

Hypopituitarism is partial or complete insufficiency of pituitary hormone secretion. The most common pituitary hormone deficiency is growth hormone deficiency. Congenital hypopituitarism is uncommon and results from central

nervous system tumors and malformations, septo-optic dysplasia, pituitary hypoplasia or aplasia, and empty sella syndrome (Argyropoulou et al. 1992). Acquired causes include cranial irradiation, infection, infiltrative disease, trauma, and hypoxic insult.

In growth hormone deficiency, skeletal manifestation is delayed skeletal growth and maturation. Radiography reveals a delay in the appearance and growth of ossification centers (Fig. 34.9). The only finding of the skull is a small pituitary fossa. Suprasellar calcification may suggest a craniopharyngioma.

34.2.5.5 Hyperparathyroidism

Parathyroid hormone (PTH) decreases tubular absorption of phosphorus in kidney, resulting in increased urinary phosphorus excretion and reduced serum phosphorus levels. Another action on the kidney is increasing the active form of vitamin D, which stimulates calcium and phosphorus absorption from the gastrointestinal tract. And PTH increases bone resorption. So, the levels of calcium and phosphorus are increased in blood (Ruda et al. 2005).

Primary hyperparathyroidism is rare in childhood and extremely rare in the newborn infant. Infants with primary hyperparathyroidism usually are very ill, and the condition is often fatal (Kollars et al. 2005). In other instances, secondary hyperparathyroidism develops in infants delivered of hypoparathyroid mothers and also of mothers with renal insufficiency. This probably represents secondarily in older infants and children with renal disease and long-term furosemide therapy, leading to renal rickets or renal osteodystrophy.

In primary hyperparathyroidism, radiographic findings consist of profound demineralization of the skeleton, marked subperiosteal bone resorption, and, in infants after the neonatal period, metastatic soft tissue calcification.

In secondary hyperparathyroidism, there is characteristic sub- and endosteal bone resorption along the middle phalanges of the hand, upper inner metaphyseal edges of the tibiae, distal radius and ulna, and both the inner and the outer aspects of the femoral neck (Figs. 34.10 and 34.11). In addition, there is also bone resorption at other sites such as the flat bones ribs and lateral ends of the clavicles. Brown tumors are uncommon.

34.2.5.6 Hypoparathyroidism and Pseudohypoparathyroidism

Neonatal hypoparathyroidism is uncommon and often familial. Clinically, these infants often present with tetany (Whyte and Weldon 1981). Pseudohypoparathyroidism is a congenital disorder, which is due to failure of the normal response to parathyroid hormone. It also is rare in infancy, and as with hypoparathyroidism, the presenting problem usually is that of tetany. In both, hypocalcemia and hyperphosphatemia are present.

In hypoparathyroidism, skeletal finding in the majority of these patients usually is normal. With pseudohypoparathyroidism, however, shortening of the fourth and fifth or even third metacarpal is commonly presented and becomes more pronounced as the patient grows older (Fig. 34.12). In addition, calcification in the basal ganglia can be seen in these patients.

34.2.6 Vitamin-Related Bone Disease

34.2.6.1 Hypervitaminosis

Excess intake of vitamins A and D can result in toxicity from errors in dosage as the child grows. With hypervitaminosis D, metastatic calcification in the media of the blood vessels, kidneys, heart, gastric wall, falx cerebri, tentorium, and adrenal glands may be seen. Hypervitaminosis A is seen most frequently in young infants as a result of errors in dosage, too. Clinical manifestations include anorexia, poor weight gain, pruritus, hepatomegaly, splenomegaly, and pain and swelling over the long bones (James et al. 1982; Miller and Hayon 1985).

With hypervitaminosis D, radiologic findings usually consist of increased density of the bones, very dense zones of provisional calcification, and calcification of structures such as the falx, kidneys, and various soft tissues. In some cases, excessive periosteal new bone deposition may be seen, but periosteal new bone deposition is the hallmark of chronic vitamin A intoxication. The most commonly involved bones demonstrating periosteal new bone deposition are the tibiae, ulnae, and fourth and fifth metatarsals.

34.2.6.2 Rickets (Vitamin D Deficiency)

Vitamin D deficiency rickets does not develop for 3 months or so after birth because enough vitamin D is transferred from the mother to the infant. Congenital rickets is uncommon in the developed country but occurs if there is decreased vitamin D intake or synthesis in the mother. In the postnatal period, inadequate vitamin D intake results in dietary deficiency rickets (Harrison and Harrison 1975). Neonatal rickets is uncommon but occurs in premature infants of very low birth weight. In premature infants, the requirements of calcium phosphate and vitamin D are greater than those of infants born at term. Neonatal rickets may be presented in infants who have necrotizing enteritis or respiratory distress syndrome.

In the active stage, coarse demineralization of the bones, loss of cortical distinction, cupping, fraying and irregularity of the metaphyseal region, loss of definition of the epiphyses, widening of the physes, and, in severe cases, pathologic epiphyseal–metaphyseal fractures occur (Swischuk and Hayden 1979). These changes are more obvious in regions of active growth such as, in order of decreasing frequency, the costochondral junctions of middle ribs, both ends of I femur,

proximal humerus, both ends of the tibia, and the distal radius and ulna (Figs. 34.13 and 34.14). With healing, the zones of provisional calcification become more definite and white, periosteal new bone is deposited around the diaphysis, and cupping of the metaphyses becomes more clearly apparent. When rickets have completely healed, only the deformities from bowing or fracture remain as evidence of the disease.

34.2.6.3 Scurvy

Scurvy is caused by vitamin C deficiency. The clinical manifestations are irritability, digestive disturbance, loss of appetite, and tenderness and swelling, particularly of the lower extremities. Swelling of the gums is also characteristic. Because vitamin C is necessary for normal osteoblastic activity, the organic matrix of bone cannot be laid down without it. The serum alkaline phosphatase level is usually low (Resnick 2002).

The radiologic diagnosis of scurvy is based on the finding in the long bones, especially at their distal end such as knee. Typical findings consist of white lines of Frankel, the scurvy zone, Pelkan spurs, and Wimberger's ring sign. "White lines of Frankel" is preservation of the zones of provisional calcification underlying the osteoporotic demineralization of the bones. Beneath this white line is a radiolucent line or the scurvy zone. Pathologic fractures, most commonly corner metaphyseal fractures, occur through this area. In their healing phase, these are termed "Pelkan spurs." Wimberger's ring sign is termed as the epiphyses ringed by a fine white line. Subperiosteal bleeding and bleeding elsewhere in the body are existing. After the subperiosteal bleeds heal, large cloaks of ballooned periosteal new bone form around the bones (Resnick 2002).

34.2.7 Congenital Foot Deformities

Clubfoot, known as talipes equinovarus, is the most common foot deformity in the neonate. It may be seen as an isolated

finding caused by intrauterine abnormalities including severe oligohydramnios, a constriction in the uterus, or the amniotic band syndrome or in association with underlying neurologic or neuromuscular disease. Vertical talus, known as talipes equinovarus, is a much less common deformity and can be considered the opposite of the common clubfoot. In metatarsus varus, the forefoot primarily is deformed (Harty 2001).

The three principal components of clubfoot are adduction (varus deformity) of the forefoot, equinus deformity of the foot at the ankle (plantar flexion), and inversion of the foot (Fig. 34.15). In vertical talus, the foot is elevated with vertical talus, and there is a marked flatfoot deformity (Fig. 34.16). In metatarsus varus, there is marked varus deviation of the metatarsals and toes, but talocalcaneal relationships remain relatively normal (Fig. 34.17).

34.2.8 Tarsal Coalition

Congenital fusion of tarsal bones is commonly referred to as "tarsal coalition." Fusion most commonly occurs between the talus and calcaneus or between the calcaneus and navicular. But, symptomatic talonavicular fusion also can occur. Often, tarsal coalitions can lead to unusual rigidity and congenital spastic flatfoot (Patel 2009).

In talocalcaneal coalition, a so-called C sign can be visualized in lateral view (Fig. 34.18). A "C sign" is formed by the medial outline of the talar dome and a bony bridge between the talar dome and the sustentaculum tali. Calcaneonavicular coalition can be seen on conventional radiographs of the foot. In calcaneonavicular coalition, the anterior process of the calcaneus becomes elongated, resulting in the so-called anteater nose sign. Other findings consist of medial wedging of the navicular bone, and the abnormality is usually clearly seen on oblique views. Computed tomography (CT) is best for the demonstration of these conditions, but they also can be seen on plain films where deformed tarsal bones provide clues for the diagnosis. So, CT studies must be carefully used.

34.3 Illustrations: Miscellaneous Musculoskeletal Disease

34.3.1 Infantile Cortical Hyperostosis (Caffey's Disease)

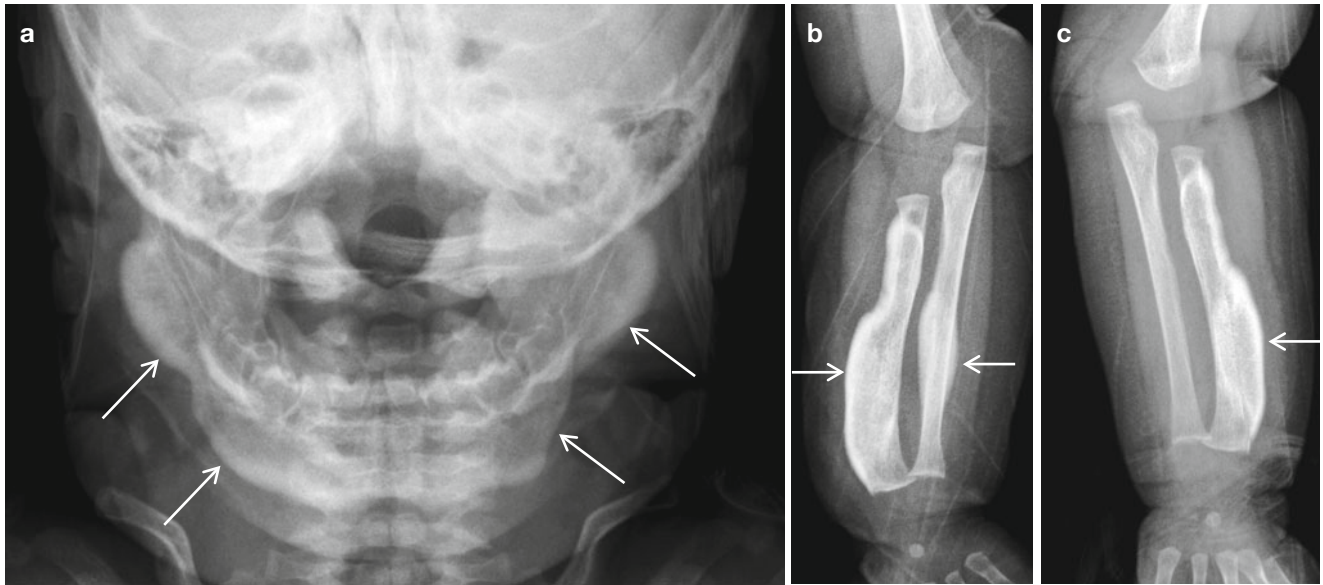


Fig. 34.1 A 2-month-old girl presented with the swelling of bilateral forearm. (a) Typical periosteal new bone formation (*arrows*) of mandible. (b, c) Periosteal new bone formation (*arrows*) of radius and ulna

34.3.2 Periosteal New Bone Formation



Fig. 34.2 Periosteal new bone formation. (a) Normal infant. (b) Single layer of periosteal new bone formation (*arrow*). This case is associated with incomplete fracture. (c) Typical Codman's triangle in the malig-

nant bone tumor. This patient had an osteosarcoma. (d) Extensive periosteal new bone formation in the battered child syndrome

34.3.3 Bone Infarction

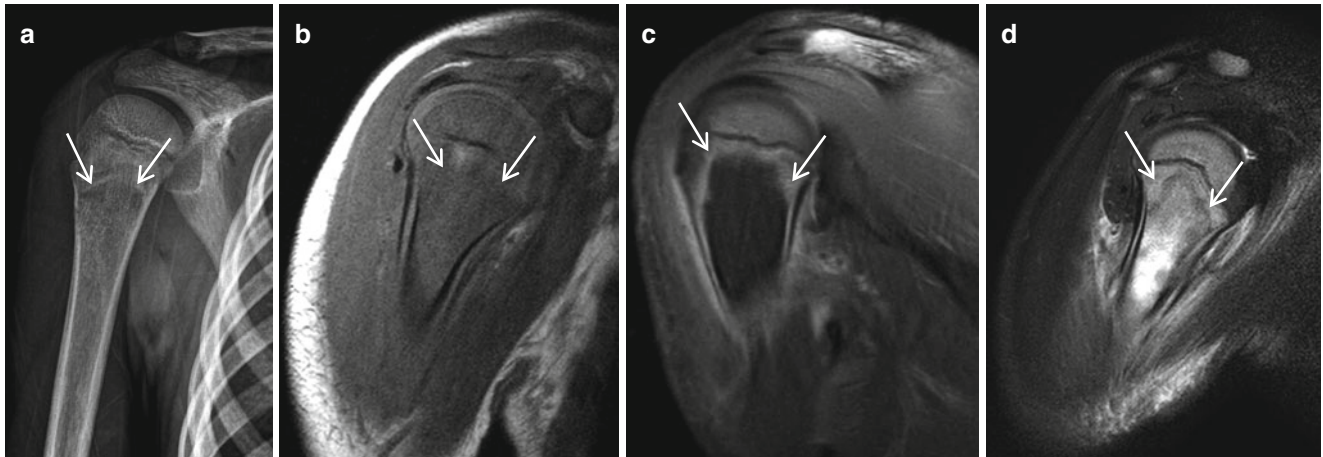


Fig. 34.3 A 6-year-old boy presented with the pain of right humerus. He had chemotherapy due to leukemia. **(a)** Osteolytic lesion (*arrows*) in humerus. **(b)** Low-signal-intensity lesion in the T1-weighted MR

image. **(c)** Nonenhancing lesion (*arrows*) in T1-weighted MR image with the enhancement of gadolinium. **(d)** High-signal-intensity lesion (*arrows*) in the T2-weighted MR image

34.3.4 Kohler Disease

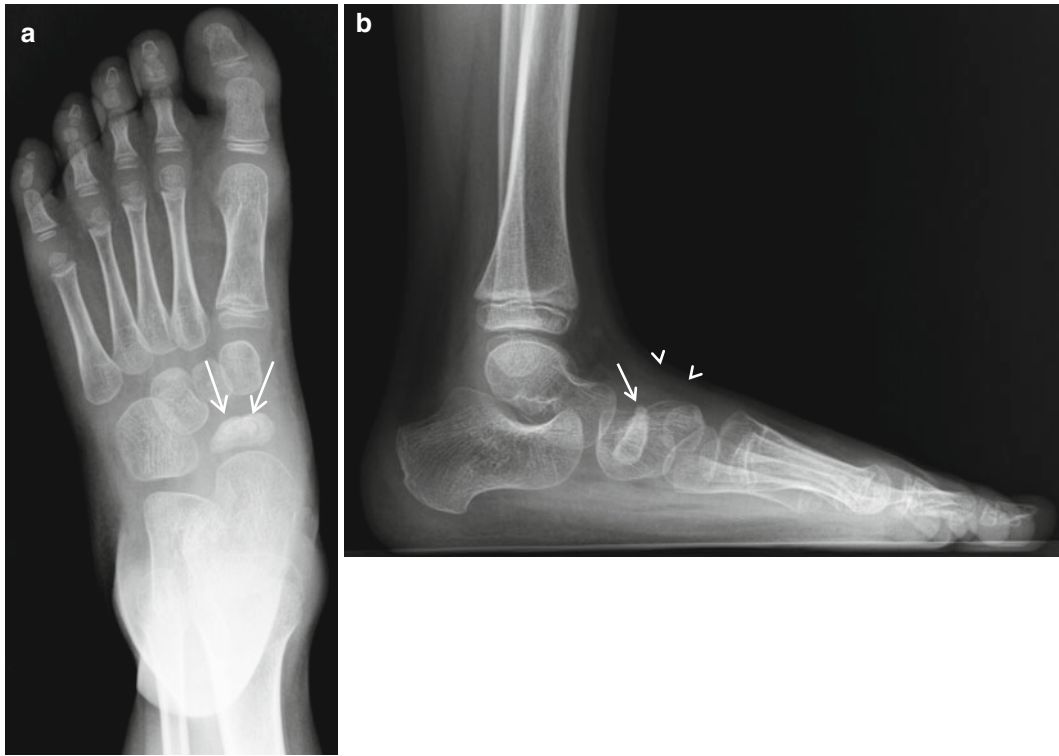


Fig. 34.4 A 6-year-old boy presented with foot pain. (**a, b**) Irregularity and sclerosis of the navicular bone (*arrows*) with soft tissue swelling (*arrowheads*)

34.3.5 Freiberg Disease



Fig. 34.5 A 13-year-old girl presented with foot pain. Note the flattening and sclerosis of secondary metatarsal bone (*arrow*)

34.3.6 Sever Disease



Fig. 34.6 An 11-year-old boy presented with heel pain, demonstrating the sclerosis and fragmentation of calcaneus (*arrows*)

34.3.7 Idiopathic Juvenile Osteoporosis



Fig. 34.7 A 13-year-old boy presented with the back pain. Note the biconcave appearance of vertebral bodies with diffusely decreased bone density

34.3.8 Hypothyroidism

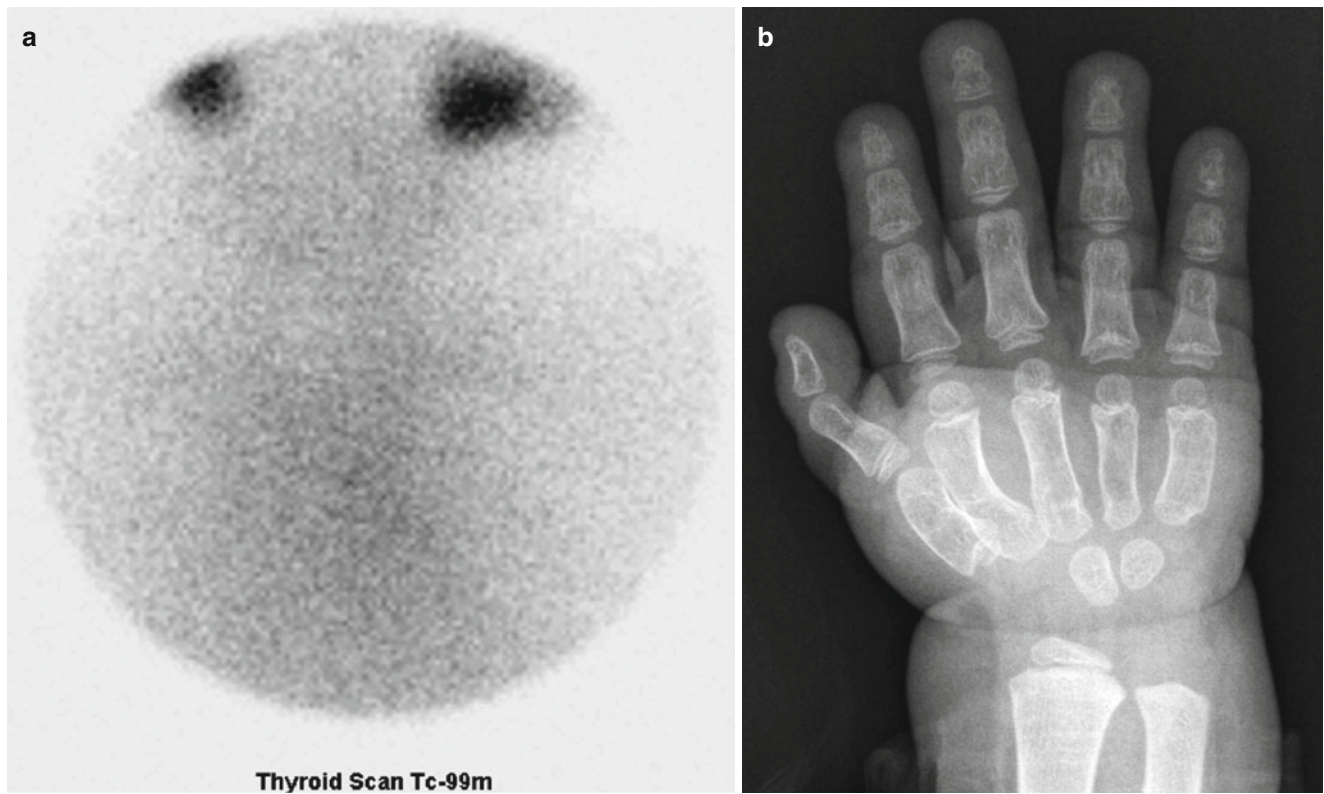


Fig. 34.8 A 4-year-old girl presented with developmental delay. (a) No definite uptake of thyroid gland on the thyroid scan. (b) Note the delay of bone age

34.3.9 Hypopituitarism and Growth Hormone Deficiency

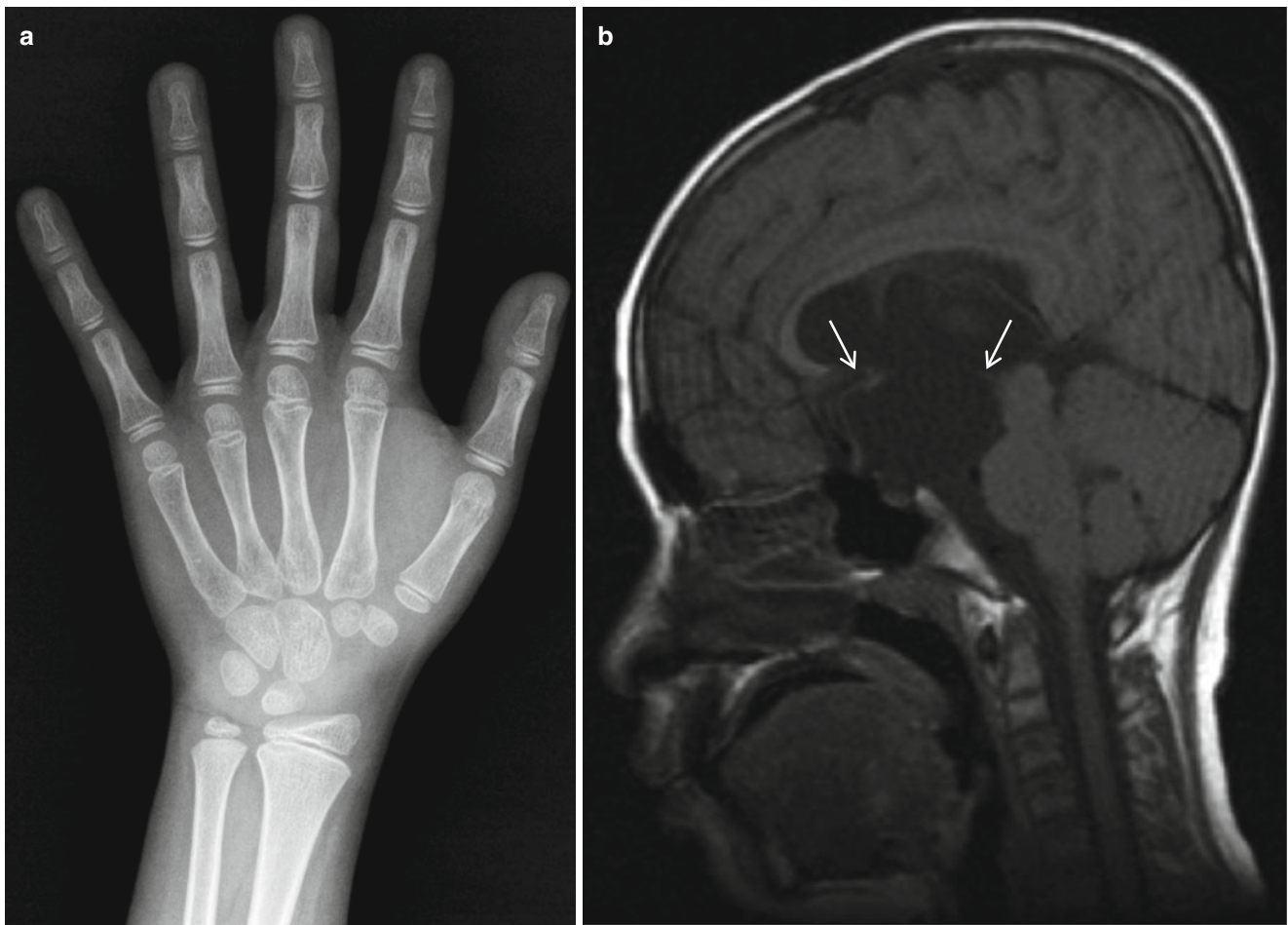


Fig. 34.9 A 12-year-old boy presented with suprasellar arachnoid cyst. **(a)** Note the delay of bone age. **(b)** Suprasellar arachnoid cyst (*arrows*) is demonstrated

34.3.10 Hyperparathyroidism

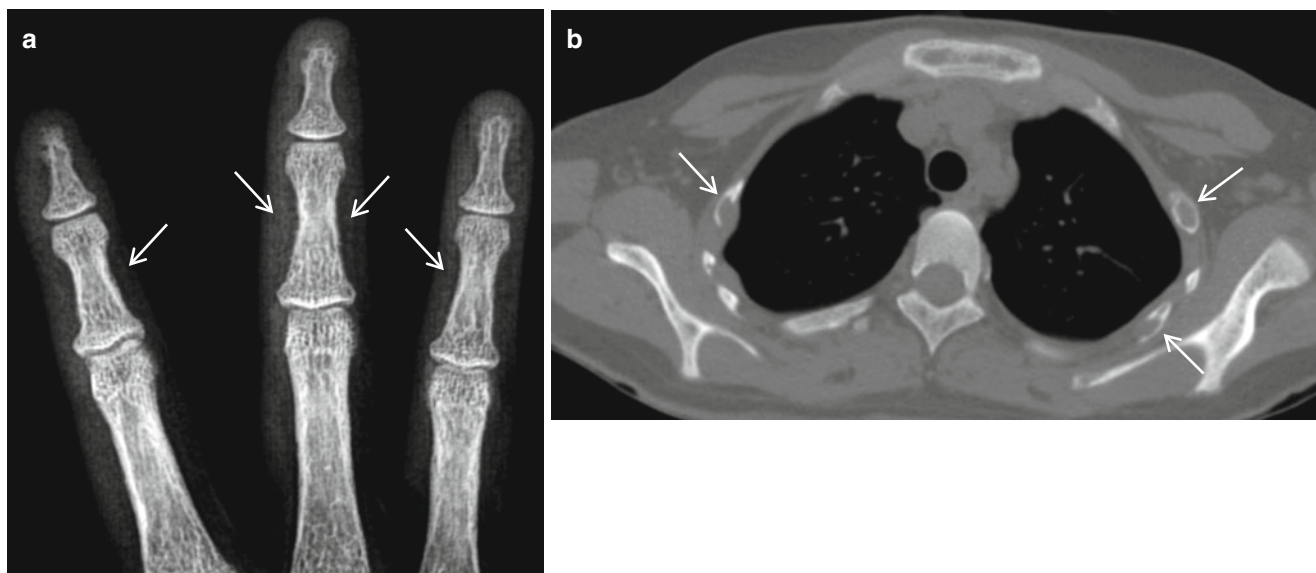


Fig. 34.10 A 16-year-old girl presented with multiple bone masses. (a) Typical subperiosteal bone resorption (*arrows*) of the middle phalanges. (b) Multiple osteolytic masses (*arrows*) in ribs, which are the pathologically proven brown tumor

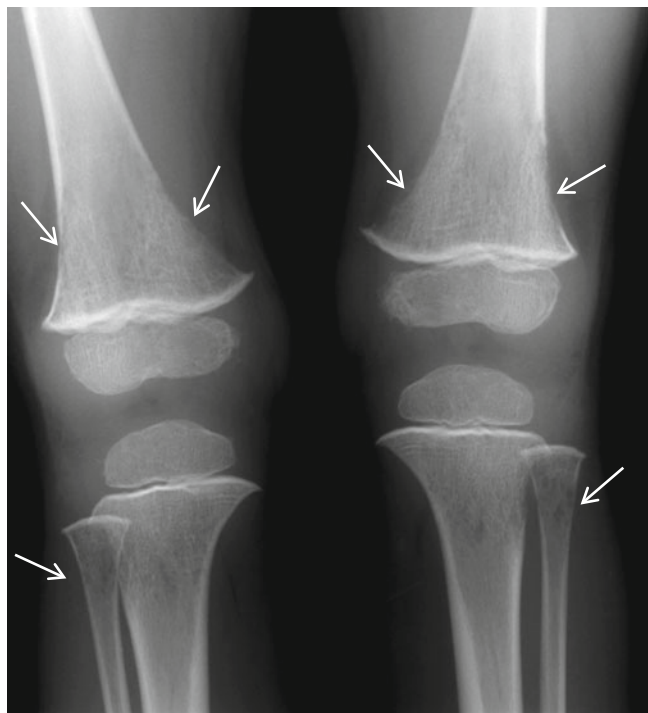


Fig. 34.11 A 2-year-old boy presented with knee pain. Note the subperiosteal resorption (*arrows*) around the bilateral knees

34.3.11 Pseudohypoparathyroidism



Fig. 34.12 A 4-year-old girl presented with the short length of finger. Characteristic shortening of the fourth and fifth metatarsal bones with slightly ballooned bones

34.3.12 Rickets



Fig. 34.13 A 9-month-old girl presented with food allergy. Note the typical widening and flaring of the metaphysis in the distal radius and ulna



Fig. 34.14 A 3-year-old boy presented with genu varum. Typical bowing of knee and widening and flaring of metaphysis were demonstrated

34.3.13 Club Foot

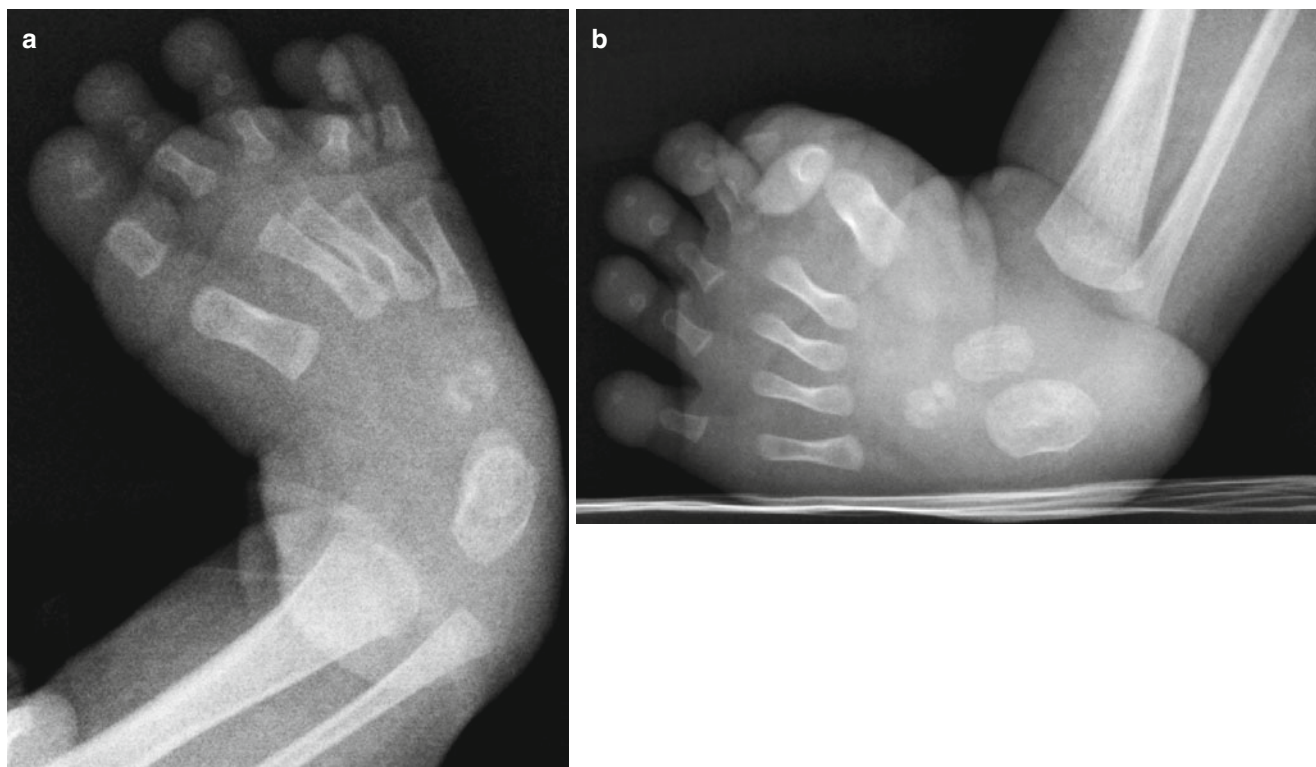


Fig. 34.15 A newborn infant presented with foot deformity. **(a)** Note the forefoot varus and decreased angle between talus and calcaneus. **(b)** Typical inversion of the foot with parallel angle of talus and calcaneus

34.3.14 Vertical Talus

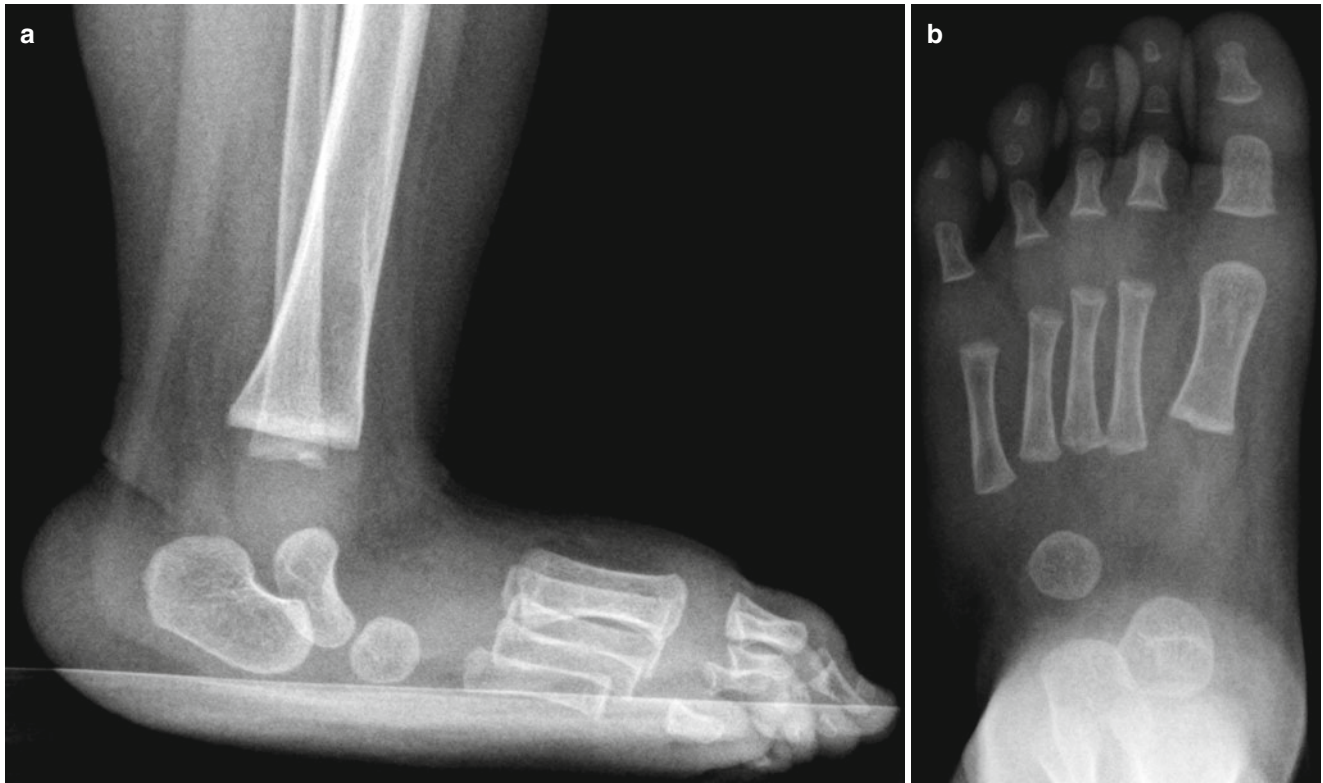


Fig. 34.16 An 8-month-old boy presented with foot deformity. (a) The vertical talus with marked flatfoot deformity. (b) Normal angle between the talus and the calcaneus

34.3.15 Metatarsus Varus



Fig. 34.17 A 5-day-old boy presented with foot deformity. Note the varus deformity of forefoot, but slight increase of angle between the talus and the calcaneus. Compare the club foot (Fig. 34.15)

34.3.16 Talocalcaneal Coalition

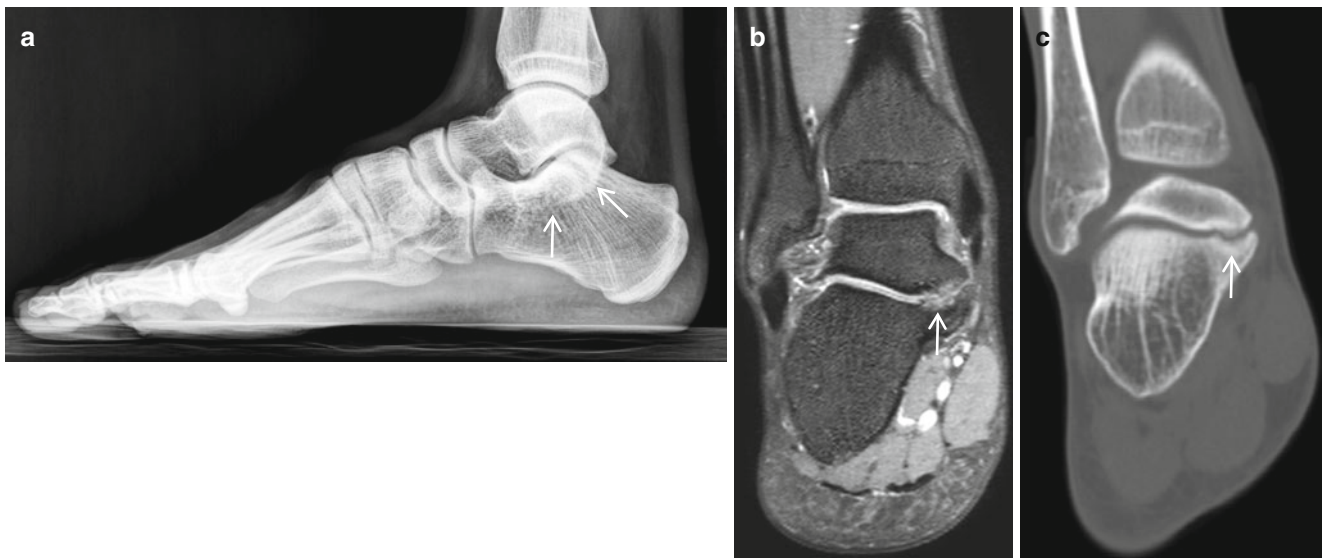


Fig. 34.18 A 17-year-old boy presented with foot pain. (a) Characteristic “C sign” (*arrows*). (b) Irregularity and narrowing of talocalcaneal joint (*arrow*). (c) Irregularity and narrowing of talocalcaneal joint (*arrow*) with subchondral cyst and bone edema

References

- Air ME, Rietveld AB. Freiberg's disease as a rare cause of limited and painful relieve in dancers. *J Dance Med Sci*. 2010;14:32–6.
- Argyropoulou M, Perignon F, Brauner R, et al. Magnetic resonance imaging in the diagnosis of growth hormone deficiency. *J Pediatr*. 1992;120:886–91.
- Atanda Jr A, Shah SA, O'Brien K. Osteochondrosis: common causes of pain in growing bones. *Am Fam Physician*. 2011;83:285–91.
- Borges JL, Guille JT, Bowen JR. Kohler's bone disease of the tarsal navicular. *J Pediatr Orthop*. 1995;15:596–8.
- Borochowitz Z, Gozal D, Misselevitch I, et al. Familial Caffey's disease and late recurrence in a child. *Clin Genet*. 1991;40:329–35.
- Caffey J. Infantile cortical hyperostosis; a review of the clinical and radiographic features. *Proc R Soc Med*. 1957;50:347–54.
- Caffey J, Silverman M. Infantile cortical hyperostosis: preliminary report on a new syndrome. *AJR*. 1945;54:16.
- Carmont MR, Rees RJ, Blundell CM. Current concepts review: Freiberg's disease. *Foot Ankle Int*. 2009;30:167–76.
- Harrison HE, Harrison HC. Rickets then and now. *J Pediatr*. 1975;87:1144–51.
- Harty MP. Imaging of pediatric foot disorders. *Radiol Clin North Am*. 2001;39:733–48.
- James MB, Leonard JC, Fraser Jr JJ, et al. Hypervitaminosis A: a case report. *Pediatrics*. 1982;69:112–5.
- Juhl JH, Crummy AB, Kuhlman JE. Idiopathic juvenile osteoporosis. In: Paul and Juhl's essentials of radiologic image. Philadelphia: Lippincott Williams & Wilkins; 1998.
- Kollars J, Zarroug AE, van Heerden J, et al. Primary hyperparathyroidism in pediatric patients. *Pediatrics*. 2005;115:974–80.
- Miller JH, Hayon II. Bone scintigraphy in hypervitaminosis A. *AJR Am J Roentgenol*. 1985;144:767–8.
- Patel CV. The foot and ankle: MR imaging of uniquely pediatric disorders. *Magn Reson Imaging Clin N Am*. 2009;17:539–47. vii.
- Resnick D. Hypervitaminosis and hypovitaminosis. In: Resnick D, editor. *Diagnosis of bone and joint disorder*. 4th ed. Philadelphia: WB Saunders; 2002.
- Riggs Jr W, Wilroy Jr RS, Etteldorf JN. Neonatal hyperthyroidism with accelerated skeletal maturation, craniosynostosis, and brachydactyly. *Radiology*. 1972;105:621–5.
- Ruda JM, Hollenbeak CS, Stack Jr BC. A systematic review of the diagnosis and treatment of primary hyperparathyroidism from 1995 to 2003. *Otolaryngol Head Neck Surg*. 2005;132:359–72.
- Saini A, Saifuddin A. MRI of osteonecrosis. *Clin Radiol*. 2004;59:1079–93.
- Smith R. Idiopathic juvenile osteoporosis: experience of twenty-one patients. *Br J Rheumatol*. 1995;34:68–77.
- States LJ. Imaging of metabolic bone disease and marrow disorders in children. *Radiol Clin North Am*. 2001;39:749–72.
- Swischuk LE. Bone infarction. In: *Imaging of the newborn, infant, and young child*. 5th ed. Philadelphia: Lippincott Williams & Wilkins; 2004a.
- Swischuk LE. Infantile cortical hyperostosis (Caffey's disease). In: *Imaging of the newborn, infant, and young child*. 5th ed. Philadelphia: Lippincott Williams & Wilkins; 2004b.
- Swischuk LE. Periosteal new bone formation. In: *Imaging of the newborn, infant, and young child*. 5th ed. Philadelphia: Lippincott Williams & Wilkins; 2004c.
- Swischuk LE, Hayden Jr CK. Rickets: a roentgenographic scheme for diagnosis. *Pediatr Radiol*. 1979;8:203–8.
- Tsirikos AI, Riddle EC, Kruse R. Bilateral Kohler's disease in identical twins. *Clin Orthop Relat Res*. 2003;409:195–8.
- Whyte MP, Weldon VV. Idiopathic hypoparathyroidism presenting with seizures during infancy: X-linked recessive inheritance in a large Missouri kindred. *J Pediatr*. 1981;99:608–11.

Index

A

ABC. *See* Aneurysmal bone cyst (ABC)
Abscess capsules, 77
Absence of septum pellucidum, 216
Achondroplasia, 888–889
Acquired immunodeficiency syndrome (AIDS), 440
Acromelia, 888
Acute avulsion fracture, 953
Acute disseminated encephalomyelitis (ADEM), 78
Acute osteomyelitis, 970
Acute parotitis, 296
Acute pyelonephritis, 790
Acute scrotum, 842
Acute transverse myelitis (ATM), 79
Agyria-pachygyria, 5
AH1N1, 435
AH5N1, 435
Air-leak, 385–386
Airway, 526
Airway disease, 412
Alagille syndrome, 685
Alexander disease (AD), 49
Allergic proctocolitis, 635
Alveolar soft part sarcoma, 917
Anaplastic astrocytomas, 107
Anaplastic oligodendrogliomas, 109
Aneurysmal bone cyst (ABC), 113, 1009
Angiosarcoma, 918
Annular pancreas, 687–688
Anomalies of rotation, 724
Anomalous pancreaticobiliary ductal union (APBDU), 682
Anorectal malformations, 606
Anterior fontanelles, 210
Anterior humeral, 953
Anterior urethral diverticula, 807
Anterior urethral valve, 807
Aortic arch anomalies, 576
Aortopulmonary window, 576
Apophyseal injury, 953–954
Apophysitis, 953
Appendicitis, 633–634
Arachnoid cyst, 108
Arterial infarct, 159
Arterial switch operation, 557
Arteriovenous malformation, 161–162
Ascariasis, 439
Askin tumor, 477
Aspergillosis, 438
Asphyxia, 156
Asphyxiating thoracic dysplasia, 889
Astroblastoma, 109
Astrocytomas, 107–109, 112

Atlanto-axial dislocation, 161
Atlanto-occipital dislocation, 161
Atrial septal defect, 554–555
Atrioventricular septal defect, 555
Atypical teratoid/rhabdoid tumors (ATRT), 107, 110, 112
Autosomal recessive polycystic kidney disease (ARPKD), 760
Avulsion fracture, 953

B

Bacterial cerebritis/abscess, 78
Bacterial infections/pneumonia, 434, 436–437
Bacterial tracheitis, 413
Balanced SSFP, 528
Band heterotopia, 6
Barium esophagography, 574
Basal cell nevus syndrome, 107
Basal ganglia germinomas, 110
Battered child syndrome, 1064
Beckwith-Wiedmann syndrome, 761
Bell clapper deformity, 843
Benign bone tumors, 1008
Bicornuate uterus, 837
Bile plug syndrome, 686
Biliary atresia, 685
Birth trauma, 159–160
Bladder, 804
 diverticula, 805
 duplication, 805
 ears, 805
 exstrophy, 804
 rhabdomyosarcoma, 805
 stones, 806
Blue-dot sign, 843
Bone infarction, 1064
Brain
 abscess, 78
 tumors, 106
Brain stem tumors, 108
Branchial arch anomaly, 296
Branchial cleft cyst, 260
Brodie's abscess, 970
Bronchial atresia, 365–366
Bronchiectasis, 437
Bronchiolitis obliterans (BO), 510
 Swyer–James–Macleod syndrome, 510
Bronchogenic cyst, 365
Bronchopulmonary dysplasia. *See* chronic lung disease of infancy
Bronchopulmonary foregut malformations, 365–366
Buckle or torus fracture, 952
Bundle of probst, 6

C

- Caffey's disease, 1064
- Calcaneonavicular coalition, 1067
- Calcar avis, 211
- Calcification, 914
- Callosal dysgenesis, 6, 215
- Calyceal diverticulum, 725
- Canal of Nuck, 838
- Canavan disease (CD), 49
- Candidiasis, 77
- Capillary hemangioma, 324
- Caput succedaneum, 159
- Carcinoid tumor, 414
 - carcinoid syndrome, 414
- Caroli disease, 686
- Caudothalamic groove, 210, 211
- Cavernous hemangiomas, 261
- Cavernous malformations, 162
- Central precocious puberty. *See* True precocious puberty
- Central venous catheters, 386
- Cephalhematoma, 159
- Cephalocele, 5
- Cerebellar ataxia, 78
- Cerebellar hemorrhage, 157
- Cerebellar infarction, 214
- Cerebral hemispheric tumors, 108
- Cerebral infarction, 214
- Cervical neuroblastoma, 328
- Cervical spine injury, 296
- Cervical thymus, 260
- Cervicomedullary kink, 5
- CF. *See* Cystic fibrosis (CF)
- Chest radiography, 574
- Chiari II malformations, 5, 216
- Chiari malformations, 215
- Child abuse, 954
- Childhood malignancies presenting with arthritis, 974
- Children's interstitial lung disease (chILD), 508
- Chlamydia pneumonia, 437
- Chloroma, 327
- Choanal atresia, 259
- Cholecystitis, 686–687
- Choledochal Cyst, 685–686
- Cholelithiasis, 686–687
- Chondroblastoma, 1008
- Chondroectodermal dysplasia, 889
- Choriocarcinoma, 110
- Choroid plexus, 211
 - hemorrhages, 212
 - tumors, 111, 112
 - various patterns, 211, 226
- Chronic, 953
- Chronic granulomatous disease, 667
 - bowel involvement, 667
- Chronic lung disease of infancy, 383
- Chronic pyelonephritis, 795
- Chronic recurrent multifocal osteomyelitis (CRMO), 972
- Circumflex left aortic arch, 577
- Circumflex right aortic arch, 578
- Classic metaphyseal lesions, 954, 955
- Clear cell sarcoma, 762
- Cleidocranial dysplasia, 890
- Closed-lip type, 216
- Closed type, 216
- Clubfoot, 1067
- Coarctation of the aorta (COA), 575
- Codman's triangle, 1064
- Colonic aganglionosis, 634
- Communicating hydrocele, 842
- Compartment syndrome, 915
- Complete form of double aortic arch, 576
- Congenital diaphragmatic hernia, 365
- Congenital brain malformations, 215
- Congenital brain tumors, 112
- Congenital esophageal stenosis, 604
- Congenital lobar hyperinflation, 366–367
- Congenital malformations, 215–217
- Congenital pulmonary airway malformation, 366
- Congenital surfactant dysfunction disorder
 - ATP-binding cassette transporter protein A3 (ABCA3), 509
 - Brain-lung-thyroid syndrome, 509
 - Surfactant proteins B (SpB), 509
 - Surfactant proteins C (SpC), 509
- Congenital syphilis, 971
- Congenital thoracic vascular anomaly, 574
- Congenital tracheal stenosis, 412–413
- Connective tissue and collagen-vascular disease, 510–511
- Constrictive bronchiolitis, 436
- Contrast enema, 606
- Contrast media, 530
- Contusion, 161
- Conventional angiography, 575
- Corpus callosum
 - agenesis, 215, 243
 - partial agenesis, 215, 244
- Corpus luteum cysts, 839
- Cortical desmoid, 1009
- Cortical vein signs, 212
- Coxa vara, 1040, 1044, 1045
- Cranial sonography, 210, 211, 213, 214
 - characteristics, 216
- Craniopharyngioma, 110–111
- Crenitism, 1065
- Crohn disease, 666
- Crossed fused ectopy, 725
- Croup, 413
 - steep sign, 413
- Cryptococcosis, 77
- Cryptorchidism, 841
- CSF dissemination of tumors, 113
- CT angiography, 575
- CT scan, 106
- Currarino syndrome, 606
- Cystic fibrosis (CF), 511, 606
- Cystic hygroma, 261
- Cystic nephroma (CN), 763
- Cystic partially differentiated nephroblastoma (CPDN), 763
- Cystic renal disease, 760–761
- Cystitis, 795, 805
- Cysts, 113
- Cytomegalovirus (CMV), 76

D

- Dandy-Walker complex, 6, 215
- Dandy-Walker malformation, 215
- Delayed enhancement, 530
- de Morsier syndrome. *See* Septo-optic dysplasia
- Dermatofibrosarcoma protuberans, 917
- Dermatomyositis, 974
- Dermoid and epidermoid tumors, 108
- Dermoid cyst, 259

Dermoid plugs, 839
 Developmental hip dysplasia (DDH), 1040–1041
 MRI Legg-Calve-Perthes disease, 1040, 1041
 Perkin's lines, Hilgenreiner's line, Shenton line, 1041
 ultrasonography, 1040, 1046, 1047
 Developmental venous anomalies (DVAs), 162
 Diencephalic syndrome, 110
 Diencephalon, 4
 Diffuse brain swelling, 160
 Diffuse excessive high signal intensity (DEHSI), 157
 Diffusion-weighted imaging (DWI), 106
 Dorsal induction, 4
 Double aortic arch, 576–577
 Double bubble sign, 605
 Double cortex, 6
 Double outlet right ventricle, 556
 Double wall sign, 632
 Drash syndrome, 761
 Duodenal atresia, 605
 Duodenal web, 605
 Duplex collecting system, 726–727
 Duplication cyst, 632–633
 Dural arteriovenous fistula, 163
 Dysembryoplastic neuroepithelial tumors, 109
 Dysostosis, 888
 Dysplasia epiphysealis hemimelica, 1008

E

Ebstein anomaly, 556
 Echinococcosis, 439
 Echocardiography, 575
 Echogenic pseudolesions, 211
 ECMO therapy. *See* Extracorporeal membrane oxygenation (ECMO) therapy
 Ectopic thyroid gland, 259
 Ectopic ureter(s), 726, 727
 EDH. *See* Epidural hemorrhage (EDH)
 Effusions, parapneumonic, 436
 EKG-gating method, 526
 Elbow fracture, 953
 Empyema, 436
 Encephaloceles, 5, 215
 Encephalomalacia, 214
 Enchondroma, 1008
 Encysted hydrocele, 842
 Endodermal sinus tumors, 840
 Endotracheal tubes (ETT), 386
 Enteric duplication cyst, 261
 Enterovirus, 78
 Eosinophilic fasciitis, 974
 Eosinophilic granuloma, 1009
 Ependymomas, 107, 112–113
 Epidermoid cyst, 259
 Epididymo-orchitis, 842–843
 Epidural hemorrhage (EDH), 160, 212
 Epiglottic cyst, 260
 Epiglottitis
 omega epiglottis, 413
 thumbprint sign, 413
 Epithelial tumors, 840–841
 Esophageal atresia (EA), 604
 Esophageal bronchus/lung, 366
 Ewing's sarcoma, 477, 1010
 Ewing tumor, 918
 Extracorporeal membrane oxygenation (ECMO) therapy, 384, 386

Extradural tumors, 113
 Extradural tumors, 113
 Extraparenchymal tumors, 108
 Extravaginal torsion, 843

F

Fatigue fractures, 954
 Fatty liver disease, 681
 FCD. *See* Fibrous cortical defect (FCD)
 Fibroblast growth factor receptor 3 (FGFR-3), 888
 Fibrodysplasia (myositis) ossificans progressiva, 914
 Fibroma, 529
 Fibroma-thecoma, 840
 Fibromatosis colli, 326, 915
 Fibrous cortical defect (FCD), 1009
 Fibrous dysplasia, 1009
 Filar cyst, 217
 Finger-in-glove, 511
 First pass, 530
 Fixed rotatory C1–C2 subluxation, 161
 Flip angle, 529
 Focal nodular hyperplasia, 687
 Follicular adenoma, 328
 Follicular cysts, 839
 Fontan operation, 557
 Foregut duplication cysts, 261
 Foreign body aspiration, 414–415
 Freiberg disease, 1065
 Functional single ventricle (FSV), 556
 Funicular hydrocele, 842

G

Gangliocytomas, 109
 Gangliomas, 109
 Ganglioneuroblastoma, 476, 763
 Ganglioneuroma, 476, 763
 Gastric atresia, 605
 Gastric tube, 386
 Gastric volvulus, 605
 Gaucher disease, 511
 Germ cell tumors, 110, 111, 475, 839, 844
 Germinal matrix, 4
 Germinal matrix hemorrhage (GMH), 157, 211–213
 grade 1, 212
 grade 2, 212
 grade 3, 212
 grade 4, 212
 Germinomas, 110, 111
 Giant cell tumor, 1009
 Glioblastomas, 107
 Globoid cell leukodystrophy. *See* Krabbe disease
 Glomerulocystic kidney disease, 761
 Glycogen storage disease, 685
 GMH/IVH, 212
 Gonadoblastoma, 846
 Gorlin syndrome. *See* Basal cell nevus syndrome
 Grade(s), 157
 Gradenigo syndrome, 295
 Graft-vs-host disease (GVHD), 667
 Granulocytic sarcoma, 113, 918
 Granuloma annulare, 917
 Granulosa cell, 840
 Greenstick fracture, 952
 Growth hormone deficiency, 1066
 Guillain-Barré syndrome (GBS), 79

H

Haddad syndrome, 634
Haemophilus influenza, 436
 Hand-foot-and-mouth disease (HFMD), 78
 Hand-Schuller-Christian disease, 1009
 Head and neck, 294
 Head and neck tumors, 324
 Head trauma, 160
 Helical, 526
 Hemangioendothelioma, 687
 Hemangioma, 328
 Hemihypertrophy, 761
 Hemimegalencephaly, 216
 Hemimegalencephaly accompanies band heterotopias, 216
 Hemolytic-uremic syndrome (HUS), 667
 Hemophilic arthropathy, 972–973
 Hemorrhage, 161
 Hemorrhagic cystitis, 805
 Hemorrhagic venous infarctions, 213
 Henoch-Schönlein purpura (HSP), 632, 634
 Hepatoblastoma, 687
 Herpes encephalitis, 77–78
 Heterotopia, 6
 HIE. *See* Hypoxic-ischemic brain injury (HIE)
 High-flow vascular malformation, 915
 High-resolution CT (HRCT), 508
 Hirschsprung disease, 634–635
 Histoplasmosis, 438–439
 HIV. *See* Acquired immunodeficiency syndrome (AIDS)
 Hodgkin's disease, 477
 Holopresencephaly, 216
 Holoprosencephaly, 5
 alobar type, 215
 lobar type, 216
 semilobar type, 216
 Hookworms, 439
 Horseshoe kidney, 725, 726
 Horseshoe lung, 365, 579
 HPS. *See* Hypertrophic pyloric stenosis (HPS)
 HSP. *See* Henoch-Schönlein purpura (HSP)
 H-type fistula, 604
 Hutch diverticulum, 805
 Hyaline membrane disease (HMD). *See* Respiratory distress syndrome; Surfactant deficiency disease
 Hydranencephaly, 216
 Hydrocele of the spermatic cord, 842
 Hydrocephalus, 216
 Hydro(metro)colpos, 836
 Hyperparathyroidism, 1066
 Hypersensitive pneumonitis, 510
 Hyperthyroidism, 1065
 Hypertrophic pyloric stenosis (HPS), 630–631
 Hypervitaminosis, 1066
 Hypoparathyroidism, 1066
 Hypopituitarism, 1065–1066
 Hypothalamic hamartoma, 111
 Hypothalamic/optic astrocytomas, 110
 Hypothyroidism, 1065
 Hypoxic-ischemic brain injury (HIE)
 childhood stroke, 159
 clinical significance and treatment, 158–159
 HIE in term infants, 158
 imaging, 156
 injury in preterm infants, 157–158
 pathophysiology, 156
 patterns of brain injury, 156–157

Hypoxic-ischemic encephalopathy, 212–214
 diffuse, 214
 focal or multifocal, 214

I

Idiopathic chondrolysis, 1043, 1060
 Idiopathic juvenile osteoporosis, 1065
 Imaging, 106, 574–575
 Immature lung, 383
 Immature teratomas, 839
 Immunodeficiency
 primary (congenital), 439–440
 secondary (acquired), 440
 Imperforate hymen, 836
 Incomplete form of double aortic arch, 577
 Incomplete fracture, 952
 Infantile cortical hyperostosis, 1064
 Infantile fibrosarcoma, 917
 Infantile hemangioma, 324, 914
 Infantile myofibroma or myofibromatosis, 916
 Infarcted myocardium, 530
 Infarction
 border zone/watershed, 214, 239
 Infectious disease, 214–215
 Infectious mononucleosis, 295
 Inflammatory myofibroblastic tumors, 474, 668
 mesentery, 668
 Infratentorial tumors, 106–108
 Inguinoscrotal hernia, 841–842
 Innominate artery compression syndrome, 414, 578
 Insufficiency fractures, 954
 Interrupted aortic arch (IAA), 575
 Intracranial hemorrhage, 211–213
 Intradural-extramedullary (IDEM) tumors, 113
 Intramedullary tumors, 112
 Intravaginal torsion, 843
 Intraventricular hemorrhage, 211, 212
 Intussusception, 631–632
 Inversion recovery, 530
 Inverted Meckel's diverticulum, 633
 Iodine contrast media, 527
 Ionizing radiation, 526
 Ischiopubic synchondrosis, 955
 Iselin's disease, 953
 Iterative reconstruction, 527
 IVH, 212

J

Jejunoileal atresia, 606
 Joubert syndrome, 7
 Juvenile idiopathic arthritis (JIA), 971–972, 1042–1043
 Juvenile nephronophthisis, 761
 Juvenile pilocytic astrocytomas, 107
 Juvenile polyposis syndrome, 668
 Juvenile spondyloarthropathies, 972

K

Kasabach-Merritt syndrome, 687
 Kawasaki disease, 295
 K-edge, 527
 Kikuchi disease, 295
 Klippel-Trenaunay syndrome, 915
 Kniest dysplasia, 889

Kohler disease, 1065
Krabbe disease, 47

L

Langerhans cell histiocytosis (LCH), 113, 325–326, 1009
Laryngeal cyst, 260
Laryngoesophageal cleft, 604
Laryngotracheoesophageal cleft, 604
Lateral condyle fractures, 953
LCH. *See* Langerhans cell histiocytosis (LCH)
Left aortic arch with aberrant right subclavian artery, 577
Legg-Calve-Perthes disease
 lateral pillar classification system, 1041, 1042
 radiographic stages, 1041
Leigh disease, 48
Lenticulostriate vasculopathy, 214
Leptomeningeal cyst, 160
Letterer-Siwe disease, 1009
Leukemia, 113, 327
Lipoblastoma, 326, 916
Lipoma, 108, 916
Lipoma arborescens, 973
Lissencephaly, 5, 216
Little Leaguer's elbow, 953
Lobar holoprosencephaly, 216
Longitudinal magnetization, 529
Low-flow vascular malformation, 915
Low innominate vein below the aortic arch, 578
Lung abscesses, 437
Lymphadenitis, 295
Lymphangiectasia and lymphangiomatosis, 509–510
Lymphangioma, 328, 476
Lymphatic malformation, 261
Lymphoma, 113, 326–327, 475, 668, 1010
 bowel involvement, 668
Lymphomatous involvement of the middle mediastinum, 476
Lysosomal storage disease, 511
Lysosome, 47

M

Macro dystrophia lipomatosa, 915
Maffucci syndrome, 1008
Magnetic field, 528
Malignant bone tumors, 1010
Malignant germ cell tumors, 111
Malignant mixed germ cell tumor, 840
Mastoid fontanelle, 210, 211
Mastoiditis, 295
Mature cystic teratomas/dermoid cysts, 839
Maximum intensity projection, 528
Mayer-Rokitansky-Küster-Hauser syndrome, 837
McCune-Albright syndrome, 1009
Meckel's diverticulum, 632, 633
Meconium aspiration syndrome, 383–384
Meconium ileus, 606
Medial epicondyle fractures, 953
Medullary cystic disease complex, 761
Medullary sponge kidney, 760
Medulloblastoma, 107
Megacalycosis, 725
Megacystis, 805
Megacystis-megaureter syndrome, 805
Megacystis-microcolon-intestinal hypoperistalsis (MMIH) syndrome, 805

Megalencephalic leukoencephalopathy with subcortical cysts (MLC), 49
Megalourethra, 807
Megaureter, 726
Meigs syndrome, 840
Meningiomas, 111–113
Meningitis, 214
Meningocele, 5
Menkes disease, 49–50
Mesencephalon, 4
Mesenchymal hamartoma, 477, 687
Mesenteric cyst, 668
Mesenteroaxial volvulus, 605
Mesoblastic nephroma, 762–763
Mesomelia, 888
Metachromatic leukodystrophy, 47
Metanephros, 724
Metaphyseal chondrodysplasia, Schmid type, 890
Metastatic neuroblastoma, 328
Metastatic pulmonary tumors, 474
Metatarsus varus, 1067
Metatropic dysplasia, 889
Metencephalon, 4
Microcolon, 606
Midbrain tumors, 108
Midgut malrotation, 605–606
Mild-to-moderate hypoperfusion, 157
Minimum intensity projection, 528
Mitochondrial encephalopathy, lactic acidosis, and stroke-like episodes (MELAS), 48
Mixed germ cell tumors, 110
Moyamoya syndrome, 163
MPS. *See* Mucopolysaccharidosis (MPS)
MR angiography, 530
MR cholangiopancreatography (MRCP), 684
MRCP. *See* MR cholangiopancreatography (MRCP)
MR enterography, 666
 inflammatory bowel disease, 666
MR image, 575
MR imaging, 106
MR spectroscopy, 106
Mucinous cystadenomas, 841
Mucopolysaccharidosis (MPS), 47, 891
Müllerian agenesis, 837
Multicystic dysplastic kidney (MCDK), 760–761
Multi-detector CT (MDCT), 526
Multifocal leukoencephalopathy, 78
Multilocular cystic renal tumor, 763
Multiplanar reformat (MPR), 528
Multiple epiphyseal dysplasia (MED), 890
Multiple sclerosis (MS), 79
Mycoplasma pneumonia, 437
Myelencephalon, 4
Myelination, 4
Myelomeningocele, 5
Myocardial fibrosis, 530
Myxopapillary ependymoma, 112

N

Nasal bone fracture, 296
Nasolacrimal duct cyst, 258
Nasopharyngeal angiofibroma, 325
Necrotizing enterocolitis (NEC), 631
Necrotizing pneumonia, 437
Neonatal hepatitis, 684

Neonatal meningitis, 77
 Neonatal pneumonia, 384
 congenital syphilis, 385
 C. trachomatis, 384–385
 group B *streptococcus*, 384
 P. alba, 385
 U. urealyticum, 385
 Neoplasms
 bladder, 805
 brain, 106
 spine, 112–113
 Neoplastic disorders, 915
 Nephroblastomatosis, 762
 Neurenteric cysts, 113
 Neuroblastoma, 476, 763–764, 1010
 Neurocutaneous syndromes, 215
 Neuroendocrine cell hyperplasia of infancy (NEHI), 509
 pulmonary neuroendocrine cells, 509
 Neurofibroma(s), 113, 326, 476, 916
 bladder, 806
 Neurofibromatosis type 1 (NF1), 7, 326
 Neurofibromatosis type 2 (NF2), 108
 Neurogenic bladder, 806
 Neurogenic tumors, 113
 Neuromyelitis optica (NMO), 79
 Neuronal formation, 4
 Neuronal migration, 4
 Neuropathic arthritis, 973
 Neurosonography, 210–252
 Neurulation, 4
 Neutropenic colitis, 667
 Nidus, 161
 Niemann–Pick disease, 511
 Nodular fasciitis, 916
 NOF. *See* Non-ossifying fibroma (NOF)
 Non-accidental injury, 954
 child abuse, 161
 Noncavitary injury, 157
 Non-gating cardiac scan, 527
 Non-germ cell tumors, 846
 Non-Hodgkin's lymphoma, 475
 Nonlissencephalic cortical dysplasia, 6
 Non-ossifying fibroma (NOF), 1009
 Nonspecific interstitial pneumonia (NSIP), 510
 Normal variants and pitfalls, 210, 211
 Number of segment, 529

O

Obliterative bronchiolitis, 436
 Obstructive sleep apnea, 415
 Oligodendrogliomas, 109
 Ollier disease, 1008
 Omental cyst, 668
 Onion-ring pattern, 845
 Opacity-transparency function, 528
 Orbit blowout fractures, 296
 Organoaxial volvulus, 605
 Osgood–Schlatter disease, 953
 Os naviculare, 955
 Ossification, 914
 Ossifying fibroma, 1009
 Osteochondroma, 1008
 Osteochondrosis, 1064–1065
 Osteofibrous dysplasia, 1009

Osteogenesis imperfecta (OI), 891
 Osteoid osteoma, 1008, 1043, 1061
 Osteonecrosis, 1064
 Osteopetrosis, 891
 Osteosarcoma, 1010
 Os trigonum, 955
 Ovarian cysts, 838
 Ovarian dysgerminoma, 839–840

P

Pancreatitis, 688
 Pancreatoblastoma, 688
 Papillary carcinoma, 328
 Paranasal sinusitis, 294–295
 Paraspinal neurogenic tumors, 113
 Parosteal osteosarcoma, 1010
 Partial anomalous pulmonary venous return (PAPVR), 579
 Partial hypoxia, 157
 Patent ductus arteriosus (PDA), 576
 Patent processus vaginalis, 842
 Patent urachus, 804
 Pathogenesis, 574
 Pathophysiology, 106, 574
 Paucity of the interlobular bile ducts, 685
 Pediatric chest CT imaging techniques, 364
 Pediatric diffuse lung disease, 508
 Pediatric trauma, 159
 Pelizaeus–Merzbacher disease, 49
 Pelvic inflammatory disease, 837
 Pelvic kidney, 725
 Perforation of the bile duct, 686
 Perfusion MR imaging, 106
 Pericardial cysts, 529
 Periosteal new bone formation, 1064
 Peripherally inserted central catheters (PICC), 386
 Peripheral neurofibromatosis, 7
 Peripheral precocious puberty. *See* Pseudoprecocious puberty
 Peripheral primitive neuroectodermal tumor, 477
 Periventricular echogenic halos, 211, 213
 Periventricular leukomalacia, 157, 211, 213
 Peroxisomes, 47
 Persistent esophagotrachea, 604
 Persistent left superior vena, 587
 Pertussis, 437
 Peutz–Jeghers syndrome, 668
 PHACE(S) syndrome, 325
 Pharyngoesophageal perforation, 604
 Phase shift map, 529
 Physeal injury, 953
 Physiologic periosteal new bone formation, 955
 Pial AVFs, 162
 PICC. *See* Peripherally inserted central catheters (PICC)
 Pigmented villonodular synovitis (PVNS), 973, 994
 Pilomatricoma, 916–917
 Pilomatrixoma, 326
 Pilomyxoid astrocytoma, 110
 Pineal parenchymal tumors, 111
 Pineal region tumors, 111
 Pineoblastomas, 111
 Pineocytomas, 111
 Plastic bending fracture, 952
 Platypondyly, 888
 Pleomorphic adenoma, 328
 Pleuropulmonary blastoma (PPB), 474

- Plexiform neurofibroma, 326
 PNET. *See* Primitive neuroectodermal tumors (PNET)
 Pneumatocoles, 437
 Pneumatosis intestinalis, 631
Pneumocystis jirovecii, 440
 Pneumomediastinum, 385
 angel wing sign, 385
 continuous diaphragm sign, 385
 Pneumonia
 etiology, 434
 imaging, 434
 Pneumopericardium, 385
 Pneumoperitoneum, 631
 Pneumothorax, 385–386
 Polymicrogyria, 6, 215, 216
 Pontine gliomas, 108
 Positive fat pad signs, 953
 Posterior fontanelle, 210
 Posterior urethral valves (PUV), 806
 Postinfectious Bronchiolitis obliterans. *See* Constrictive bronchiolitis;
 Obliterative bronchiolitis
 Postnatal trauma in infants and young children, 160–161
 Pott puffy tumor, 294
 Precocious puberty, 837
 Prehn sign, 843
 Primary tumors, 328
 Primitive neuroectodermal tumors (PNET), 109–110, 112, 113.
 See also Askin tumor
 Processus vaginalis, 841
 Profound asphyxia, 158
 Profound injury, 157
 Prominent calcar avis, 211
 Prosencephalon, 4
 Prospective EKG-triggering, 527
 Prostatic utricle, 807
 Proteus syndrome, 915
 Proximal femoral focal deficiency, 1040, 1044
 Prune-belly syndrome, 804
 Pseudoachondroplasia, 890
 Pseudohypoparathyroidism, 1066
 Pseudokidney sign, 632
 Pseudomembranous colitis, 667
Pseudomonas aeruginosa, 436
 Pseudoprecocious puberty, 837
 Pulmonary alveolar proteinosis (PAP), 509
 Pulmonary artery sling, 578
 Pulmonary atresia, 555
 Pulmonary infection. *See* Pneumonia
 Pulmonary interstitial emphysema, 385
 Pulmonary sequestration, 366
 Pulmonary vein atresia, 365
 PUV. *See* Posterior urethral valves (PUV)
 Pyomyositis, 971
 Pyriform aperture stenosis, 259
- R**
 Radial glial fibers, 4
 Radial sampling, 529
 Radiation dose, 527
 Radiation exposure, 526, 527
 Radiocapitellar lines, 953
 Rasmussen encephalitis, 79
 Rastelli operation, 557
 Rectosigmoid index, 634
 Rectovaginal fistula, 837
 Recurrent respiratory papillomatosis, 414
 human papillomavirus, 414
 Reference planes, 210
 Renal abscess, 795
 Renal agenesis, 724
 Renal candidiasis, 795
 Renal cell carcinoma, 763
 Renal ectopy, 724, 725
 Renal hypoplasia, 724
 Renal lymphoma and leukemia, 763
 Renal scars, 794
 Resistive index (RI), 214
 Respiratory distress syndrome, 382
 Respiratory gating, 529
 Retained fetal lung fluid, 384
 Retinoblastoma, 327
 Retroaortic left brachiocephalic vein, 578–579
 Retropharyngeal abscess, 295
 Retrospective EKG-gating reconstruction, 526, 527
 Reye syndrome, 78–79
 Rhabdoid tumors, 762
 Rhabdomyosarcoma, 327, 477, 917
 Rhizomelia, 888
 Rhombencephalon, 4
 Rickets, 1066–1067
 Right aortic arch with aberrant left subclavian artery, 577
 Rokitansky nodule, 839
 RSV, 435
- S**
 Salivary glands, 328
 Salter-Harris classification, 953
 Scan range, 527
 Schizencephaly, 6, 216
 Schwannomas, 108, 113, 476, 916
 Scimitar syndrome, 364, 579
 Sclerosing osteomyelitis and sequestration, 970
 Scrotal trauma, 844
 Scrotolith, 844
 Scurvy, 1067
 SDH, 160, 161
 Secondary ovarian neoplasms, 841
 Secondary testicular tumors, 845
 Segmented K-space filling, 528–529
 Sellar and juxtasellar tumors, 110–111
 Septic arthritis, 970–971, 1042
 Septo-optic dysplasia, 5, 216
 Sequences, 528
 Sequential, 526
 Serous cystadenomas, 841
 Sertoli-Leydig cell tumors, 840
 Sever disease, 1065
 Severe acute respiratory syndrome (SARS), 435
 Severe hypoperfusion, 157
 Sever's disease, 953
 Sex cord-stromal tumors, 840
 Shearing injury, 160
 Short rib-polydactyly, 889
 Shwachman-diamond syndrome, 890
 Simple bone cyst, 1009
 Sinding-Larsen-Johansson syndrome, 953
 Single bubble appearance, 605
 Skeletal dysplasia, 888

Skull fracture, 160, 161
 Slipped capital femoral epiphysis (SCFE), 1040
 MRI, 1042
 radiography, 1042
 Slipped capital femoral epiphysix, 953
 Soap bubble appearance, 606
 Soft tissue lymphoma, 918
 Solid and papillary epithelial neoplasm, 688
 Spinal cord injury, 160
 Spinal dysraphism, 217
 Spinal injury in young children, 160–161
 Spinal sonography, 217
 Spiral CT, 526
 Splenic hamartoma, 688
 Splenic injury, 688
 Splenomegaly, 688
S. pneumoniae, 436
 Spondyloepiphyseal dysplasia congenital (SEDC), 889
 Sporadic aniridia, 761
Staphylococcus aureus, 436
 Steatohepatitis, 685
 Stenosis, 605, 606
 Storage disease, 511
 Stress fracture, 954
 Subacute sclerosing panencephalitis (SSPE), 78
 Subarachnoid hemorrhages, 212
 Subdural empyema, 214
 Subdural hemorrhage, 212
 Subependymal giant cell astrocytoma, 109
 Subgaleal hemorrhage, 159–160
 Subglottic hemangioma, 413–414
 Supracondylar fractures, 953
 Supratentorial ependymoma, 109
 Surfactant deficiency disease, 382
 Swyer-James, 436
 Synovial osteochondromatosis, 973
 Synovial sarcoma, 917
 Synovial vascular malformation, 974
 Systemic arterial supply to normal lung, 367

T

Talocalcaneal coalition, 1067
 TAPVR. *See* Total anomalous pulmonary venous return (TAPVR)
 Tarsal coalition, 1067
 Tectal gliomas, 108
 T1 effect, 529
 Telencephalon, 4
 Temporal bone fracture, 296
 Teratoma, 110–112, 325, 475, 839–840, 845
 Testicular epidermoid cyst, 845
 Testicular hematoma, 844
 Testicular microlithiasis, 844
 Testicular rupture, 844
 Testicular torsion, 843
 Testicular tumors, 844
 Tethered cord, 217
 Tetralogy of Fallot, 555
 Thanatophoric dysplasia, 888
 Thick MPR, 528
 Thoracic kidney, 739
 Three-dimensional reconstruction, 527
 Thymoma, 475–476
 Thymus, 382
 sail sign, 382
 wavy thymic sign, 382

Thyroglossal duct cyst (TGDC), 259, 296
 Thyroiditis, 296
 Thyroid tumors, 328
 Time-resolved MRA, 530
 Tissue characterization, 526
 T1 mapping, 529
 T2 mapping, 529
 Toddler's fracture, 952–953
 Torsion of the testicular appendages, 843–844
 Torticollis, 326
 Total anomalous pulmonary venous return (TAPVR), 527, 579
 Total colonic aganglionosis, 635
 Total correction of tetralogy of fallot, 556–557
 Toxoplasmosis, 76–77
 Tracheobronchial remnants, 604
 Tracheobronchomalacia, 415
 Tracheoesophageal fistula (TEF), 604
 Transient synovitis, 972, 1042
 Transient tachypnea of the newborn. *See* Retained fetal lung fluid;
 Wet lung
 Transposition of the great arteries, 555–556
 Transverse magnetization, 529
 Transverse testicular ectopia (TTE), 841
 Traumatic tracheobronchial injury, 415
 fallen lung sign, 415
 Trevor's disease. *See* Dysplasia epiphysealis hemimelica
 Triple bubble sign, 606
 True precocious puberty, 837
 Truncus arteriosus, 576
 T1 time, 529
 T2 time, 529
 Tuber cinereum hamartoma, 837
 Tuberculosis, 413, 438
 tree-in-bud, 413
 Tuberculous (TB) arthritis, 971
 Tuberculous lymphadenitis, 296
 Tuberculous meningitis, 77
 Tuberos sclerososis, 215, 761
 Tubo-ovarian abscess, 837–838
 T1-weighted image, 529
 T2-weighted image, 529
 Type II collagenopathy, 889
 Typhlitis, 667

U

UAC. *See* Umbilical arterial catheter (UAC)
 Ulcerative colitis, 666–667
 Umbilical arterial catheter (UAC), 386
 Umbilical venous catheter (UVC), 386
 Undescended testis. *See* Cryptorchidism
 Unicornuate uterus, 837
 Unified theory, 5
 Unilateral pulmonary agenesis/aplasia, 364
 Unilateral pulmonary hypoplasia, 364–365
 Upper cervical injuries, 161
 Urachal anomalies, 804
 Urachal cyst, 804
 Urachal diverticulum, 804
 Urachal sinus, 804
 Ureterocele, 726, 727
 Ureteropelvic junction obstruction, 725
 Urethra, 804
 Urethral duplication, 806
 Urethral fistula, 807
 Urethral polyps, 806

Urethral strictures, 807
Urinary tract infection (UTI), 794
Uterine agenesis or hypoplasia, 837
Uterine didelphys, 837
UVC. *See* Umbilical venous catheter (UVC)

V

Vaginal atresia, 836
Vaginal diaphragm, 836
Vallecular cyst, 260
Variants and pitfalls, 211
Varicella pneumonia, 435
Varicellar zoster encephalitis, 78
Varicocele, 842
Vascular malformation, 261, 914
Vascular ring and sling
 double aortic arch, 414
 innominate artery compression syndrome, 414
 pulmonary artery sling, 414
 right aortic arch with aberrant left subclavian artery, 414
Vascular tumor, 914
Vein of Galen malformations, 162, 215
 choroidal type, 162
 embolizations, 162
 mural type, 162
Velocity-encoding cine (VENC), 529
Venous infarct, 159
Venous malformation, 261
Venous sinus thrombus, 159
Ventral induction, 4
Ventricular septal defect, 555
Ventriculus terminalis, 217
Vertebral, anorectal, cardiac, tracheoesophageal, renal, and limb anomalies (VACTERL) association, 604

Vertical talus, 1067
Viral infections, 435–436
Vitamin D deficiency, 1066
Volume rendering, 528
Volvulus, 605–606
Von Hippel-Lindau disease, 761
VUR, 794
VZV-associated stroke, 78

W

WAGR syndrome, 761
Watershed injury, 158
Wavy thymic sign, 382
Wet lung, 384
Whirlpool sign, 606
White matter injury, 157
Wilms tumor, 761–762
Wilson's disease, 50

X

X-Adrenoleukodystrophy, 47–48
Xanthogranulomatous pyelonephritis (XGP), 795

Y

Yolk sac tumors, 110, 844. *See also* Endodermal sinus tumors

Z

Zellweger syndrome, 48